8th ECCOMAS Thematic Conference on Smart Structures and Materials

6th International Conference on Smart Materials and Nanotechnology in Engineering

SMART 2017

5 – 8 June 2017, Madrid, Spain

Alfredo Güemes, Ayech Benjeddou, José Rodellar and Jinsong Leng (Eds)



8th Conference on
Smart Structures and Materials
SMART 2017

6th International Conference on
Smart Materials and Nanotechnology
in Engineering
SMN2017

5 – 8 June 2017
Madrid, Spain

A publication of:

International Center for Numerical Methods in Engineering (CIMNE)
Barcelona, Spain



Printed by: Artes Gráficas Torres S.L., Huelva 9, 08940 Cornellà de Llobregat, Spain

ISBN: 978-84-946909-3-8

TABLE OF CONTENTS

Welcome 7

Sponsors 9

SUMMARY.....11

Contents 13

Plenary Lecture 30

Papers 77

Authors Index 1927

Welcome

On behalf of the European Community on Computational Methods in Applied Sciences (ECCOMAS) we are pleased to welcome you to Madrid for the 8th ECCOMAS Thematic Conference on Smart Structures and Materials (SMART2017), held at the Department of Aeronautics, Polytechnic University of Madrid, Spain. Previous editions have been the very successful conferences in Poland (Jadwisin 2003, and Gdansk 2007), Portugal (Lisboa 2005, Porto 2009, Azores 2015), Germany (Saarbrücken 2011) and Italy (Torino 2013).

The meeting is held together with the 6th International Conference on Smart Materials and Nanotechnology in Engineering. Past Conference venues for this meeting were Weihai (China), Shenzhen (China), Gold Coast (Australia) and Vancouver (Canada). By merging both meetings a synergistic effect has been achieved, receiving over 250 contributions from all over the world; delegates are coming from 36 different countries, five continents are represented at the Conference.

The aim of this Conference has been to gather the smart technologies community, providing a forum for the discussion of the current state of the art in the field and generating inspiration for future ideas on a multidisciplinary level. Smart structures and materials encompass sensing, actuation and control capabilities to be combined from a systems approach, on a macro, meso, micro or even nano scale, and have triggered a variety of new research areas with impacts in the wider field of engineering and science. We hope that the different works presented at this conference provide an insight to the state of the art for smart technologies today and that the discussions might point directions for future research and collaboration among this community.

Altogether, more than 220 original contributions are presented, including 7 plenary lectures and 4 keynote lectures, reflecting the current state of the art in research and advances in the field of smart structures and materials. The proceedings of SMART2017, which include the full papers, will be made available to all participants, and also they will be included at the conference website http://congress.cimne.com/smart2017 /.

We would like to take this opportunity to express our sincere appreciation to the authors and participants for their contributions, to the mini- symposia organizers and to all members of the organizing and scientific committees involved in the preparation of this conference. Also a special note of appreciation to Ms. Laia Aranda, for her valuable contribution in all aspects related to the secretariat and preparation of the conference. The organizing committee is also grateful to the Polytechnic University of Madrid for hosting the conference and for all the logistic support provided. We acknowledge the sponsorship of the following Institutions and companies: AERNNOVA (Spain), CNRS, UTC-Sorbonne Universities, ROBERVAL and SUPMECA (France), CRC/TR39 PT-PIESA Project (Germany), Carinthian Tech Research AG (Austria), FIDAMC (Spain).

Wishing you a fruitful Conference and a pleasant stay in Madrid,

A. Güemes (Spain), A. Benjeddou (France), J. Rodellar (Spain), J. Leng (China)
Conference Chairmen

Sponsors

The conference organizers acknowledge the support towards the organization of the Conference to the following organizations:

CTR Carinthian Tech Research AG

CRC/TR 39 PT-PIESA

SUPMECA

UTC

CNRS

FIDAMC

SUMMARY

PLENARY LECTURE..... 30

PAPERS 77

Adaptive Structures & Damping of Vibrations 77

Advanced Finite Element Models for Smart Structures Analysis 176

Applications of Smart Technologies to Wind Turbines..... 237

Constitutive Modeling and Computation of Ferroelectric, Ferromagnetic and Multiferroic Materials 302

CRC/TR 39 PT-PIESA Project..... 348

Design, Development and Applications of Smart Materials and Structures 400

Embedded Smart Materials Technology..... 538

Energy Harvesting, Power and Storage 618

Identification, Control and Structural Health Monitoring of Civil 698

Magnetorheological Composites: Materials and Applications 851

Morphing Structures 917

Multifunctional Structures with Integrated Piezoelectric Elements 1042

Nano-Reinforcement toward Strong and Smart Materials..... 1172

Non-linear Modeling of Smart Materials and Structures..... 1255

Poster Session 1359

SAW Sensors, Actuators, Filters and their Applications 1409

Smart Materials Capable of Recoverable Inelastic Strain 1465

Smart Micro-Mechatronic Systems..... 1590

Smart Periodic Structures for Vibration Control..... 1632

Soft Active Materials and Mechanics..... 1744

Structural Health Monitoring 1750

Authors Index 1927

CONTENTS

PLENARY LECTURE

Convergence of Technologies in Manufacturing, Mechanics and Materials 32
K.P. Chong

Experimental Method and Constitutive Model of Electromagnetic Thin Films and Laminates under Multi-Field Loading 33
D.N. Fang

Guided Acoustic Wavefields for Damage Detection/Characterization and Novel Transducer Designs 34
M. Ruzzene

Highlights and Challenges in Damage Assessment of Composite Structures 35
W. Ostachowicz, P. Malinowski and T. Wandowski

Mitigating Vehicle Shock Loads in Occupant Protection Systems using High Speed Magnetorheological Flows 50
N.M. Wereley

Multidisciplinary Approach for a Commercial Transport Aircraft Rudder with Morphing Characteristics 51
M.A. Castillo Acero

Smart behaviour of CNT Modified Adhesive Films for Carbon Fiber Composite Repair 66
A. Ureña, C. García-Nieto, X.F. Sánchez-Romate, J. Rams and M. Sánchez

PAPERS

Adaptive Structures & Damping of Vibrations

Active Washer for Smart Mechanical Linkage 77
C. Belly, A. Guignabert, R. Riquer, G. Chevallier, P. Butaud, G. Matten and N. Peyret

Adaptable Pneumatic Shock-Absorber 86
R. Faraj, C. Graczykowski, K. Hinc, J. Holnicki-Szulc, L. Knap and J. Seńko

Decentralized Damping of Vibrations in 2D Frame Structures Using Controllable Nodes 94
B. Poplawski, G. Mikułowski, A. Mróz and Ł. Jankowski

Exploring Targeted Energy Transfer for Vibration Damping in Nonlinear Piezoelectric Shunts 104
K. Dekemele, R. De Keyser and M. Loccufier

Fault Detection and Fault Tolerant Control of Vehicle Semi-Active Suspension System with Magnetorheological Dampers 115
Y. Peng, M. Yu, X. Xu, X. Du and J. Fu

Impact of Magnetorheological Semi-Active Stabilizer Bar on Vehicle Rollover 129
X. X. Bai, S. X. Xu and L. J. Qian

Mitigation of Dynamic Response in Frame Structures by Means of Smart Joints 138
R. Faraj, B. Popławski, G. Suwała, Ł. Jankowski and J. Holnicki-Szulc

Prestress Accumulation- Release (PAR) for Damping of Free Vibrations in Frame Structures. Experimental Study of a Lab-Scale Demonstrator with Piezo-Actuated Semi-Active Nodes 145
A. Mróz, J. Holnicki-Szulc and K. Sekuła

Theoretical and Experimental Investigation of High-Speed Bearings with an Adaptive and Non-Linear Structure 157
G. Zywica and P. Baginski

Vibration Mitigation of Frame Structures based on Semi-Active Piezo Joints 166
G. Mikułowski, G. Suwała, L. Knap and J. Holnicki-Szulc

Advanced Finite Element Models for Smart Structures Analysis

A Multilayered Plate Elements Accounting Node-Dependent Kinematics for Static Analysis of Piezoelectric Structures 176
E. Carrera, G.M. Kulikov and S. Valvano

Analysis of Primal and Dual Variables in Structural Shape Control by Piezoelectric Patches using Solid Shell Finite Elements 188
F. Kpeky, F. Abed-Meraim and E.L. Daya

Finite Element Analysis of Laminated Piezoelectric Shells Via Sampling Surfaces Formulation 200
S.V. Plotnikova, G.M. Kulikov, E. Carrera, A.A. Mamontov and S.A. Mamontov

Node-Dependent Kinematic One-dimensional FEM Models for the Analysis of Beams with Piezo-patches 207
E. Carrera, M. Cinefra, G. Li and E. Zappino

Prescription of Voltage versus Intensity in Thermoelectric Cells for different Pulse Shapes and Thermoelement Geometries. 219
J.L. Pérez-Aparicio, P. Moreno-Navarro and R. Palma

Strong and Weak Sampling Surfaces Formulations for Three-Dimensional Stress Analysis of Piezoelectric Plates 231
G. M. Kulikov

Applications of Smart Technologies to Wind Turbines

Dynamic Structural Design Modification and Field Verification for a Small-Sized Vertical Axis Wind Turbine 237
J.-H. Yi, W. Kim, T. H. Han and S. Yim

Structural Damage Detection for Hybrid Offshore Wind and Tidal Current Turbine 247
W. Kim, J.H. Yi and J.S. Park

Structural Design and Experimental Investigations of a Shape-adaptive Slat for Wind Energy Rotor Blades 255
O. Huxdorf, J. Riemenschneider, P. Lorsch and M. Radestock

Structural Design Optimization of a Morphing Trailing Edge Flap for Wind Turbine Blades 267
T. Barlas, Y.-H. Lin and H. Madsen

Structural Health Monitoring and Repair of the Blades for Small Wind Turbines 278
N. Constantin and S. Sorohan

Torque and Pitch Control for a Floating Offshore Wind Turbine 290
J. Rodellar, C. Tutivén, Y. Vidal and L. Acho

Unmeasured Strain Estimation on Bottom-Fixed Offshore Structures by Multimetric Data Fusion and Kalman Filtering with Data Buffer 291
R. P. Palanisamy, S.-H. Sim, W. Kim, J.-H. Yi and W. M. Jeong

Constitutive Modeling and Computation of Ferroelectric, Ferromagnetic and Multiferroic Materials

A Boundary Element Formulation for Microstructural Modelling of Multilayer Actuator Layers 302
M. Biglar, F. Stachowicz, T. Trzepieciński and M. Gromada

A Cohesive Zone Model for Damage in Multiferroic Composites under Magnetoelectromechanical Loading 314
A. Schlosser and A. Ricoeur

Consistent Thermodynamics Framework and Numerical Simulations for Elasticity and Plasticity Coupled with Thermo-Electro-Magnetic Fields 315
A. Ibrahimbegovic, P. Moreno-Navarro and J.L. Perez-Aparicio

Modeling Performance of Particulate Magnetoelectric Composites and Devices 327
E. J. Barbero and T. I. Muchenik

Mutual Thermo-Electro-Mechanical Coupling Effects in Ferroic Materials including Temperature Dependent Material Parameters and Phase Transition 328
M. Wingen and A. Ricoeur

Nonlinear Numerical Simulation of Magnetoelectric and Damage Behaviour in Multiferroic Composites 336
A. Avakian and A. Ricoeur

CRC/TR 39 PT-PIESA Project

Aluminum Die Castings with the Property of active Vibration Damping - Process Technology and Functional Verification -. 348
D. Himmler, M. Schwankl, C. Pohle, C. Körner, S. Kimme and W. Drossel

Effect of the Integration of Piezoceramic Composites into Structural Components on their Poling Condition and Polarizability 349
K. Hohlfeld, S. Eßlinger, A. Eydam, A. Winkler, S. Gebhardt, T. Weber, M. Gude, N. Modler, G. Gerlach, G. Suchaneck, A. Michaelis, A. Schönecker, A. Schönecker and P. Neumeister

Experimental and Numerical Study on Inherent Sensory Characteristics of Piezoceramic Micro Parts during Joining by Forming in Metal Sheets ... 359
W.-G. Drossel, A. Schubert, M. Putz, H-J. Koriath, V. Wittstock, S. Peter, S. Hensel, B. Müller, A. Pierer and M. Schmidt

Integration of Piezoceramic Composites in Aluminium Die Casting Structures and their Functional Characterization 370
S. Rhein, J. Wedler, S. Stein, C. Körner, M. Schmidt, A. Michaelis and S. Gebhardt

Investigations on Laser Assisted Wire Bonding by Means of Droplet Joining of Novel Thermoplastic Compatible Piezoceramic Modules 371
S. Stein, T. Weber, A. Winkler, M. Schmidt and M. Gude

Non-destructive Characterization of Fibre Reinforced Thermoplastic Components with embedded Piezoceramic Modules 383
A. Winkler, M. Wüst, S. Rupitsch and N. Modler

Piezoceramics in Sheet-Metal Compounds for Icing Detection 493
W.-G. Drossel, M. Nestler, T. Mäder and J. Schönherr

Design, Development and Applications of Smart Materials and Structures

Adaptive Cntrol for Boinspired Micro Air Vehicle 400
J. Crespo-Moreno, M. A. Barcala-Montejano, A. A. Rodríguez-Sevillano, J. F. Alonso-Alarcón, R. Bardera-Mora, D. Shportenko and A. Romero-García

Ballistic Impact Response of a New Smart Structure Material Designed by Fibre Metal Laminates 412
X.. Xie and SJ. Wu

Biomimetic Micro Air Vehicle Controlled by Wing-Grids 413
Á. A. Rodríguez-Sevillano, M. A. Barcala-Montejano, R. Bardera-Mora, M. León-Calero, J. García-Ramírez and J. de Nova-Trigueros

Coupled Piezoelectric Transducer Array Optimization through Simulation Techniques For guided Wave Testing of Cylindrical Structures 424
X. Niu, H.P. Chen and H. Marques

Damage Indexes Robustness for Structural Health Monitoring of a Stiffened Smart Composite Plate 436
N. Mechbal and M. Rebillat

Detection and Localisation of Water Intrusion in Glass Fibre Reinforced Composite using THz Spectroscopy 445
M. Mieloszyk, K. Majewska and W. Ostachowicz

Gain-Scheduling H∞ Control of a Smart Beam with Parameter Varying 453
C. Onat, M. Sahin and Y. Yaman

Hydrogen Permeation of DLC-Coated Stainless Steels 464
M. Tamura

Lateral-Torsional Buckling of Pultruded Fiber Reinforced Polymer Cantilever Angle Beams 471
J. Thumrongvut

Modeling of Dissipative Dielectric Elastomers affected by Viscoelasticity and Current Leakage 480
C.C. Foo, J. Liu and Z.Q. Zhang

Optimal Active Twist Comparative Design and Testing of Helicopter Rotor Blades with C and D-Spars 490
E. Barkanov, A. Kovalov, P. Wierach and J. Riemenschneider

Simple Auxetic Tubular Structures 502
X. Ren, J. Shen, H. Tian and Y.M. Xie

Smart Cellulose-Hydrogel Composites for 4D Printing 511
M. Mulakkal, R. Trask and A. Seddon

Structural Optimization of a Five-Unit Single-Branch Truss-Z Modular Structure 525
M. Zawidzki, Ł. Jankowski and J. Szklarski

Theoretical and Experimental Study on Silicone Pneumatic Artificial Muscles 536
R. Soleymani and H. Khajehsaeid

Vibration Control of Smart Composite Beam 537
B. Kuider, S. Zuaoui, B. Frouk Benallel and N. Mohammed

Embedded Smart Materials Technology

A Fused Filament Fabrication Procedure for Smart Components with Embedded Electronics 538
G. Nisi Gaterol, M. Eugeni, S. Atek and P. Gaudenzi

Cast Metal with Intelligence - From Passive to Intelligent Cast Components 550
R. Carlsson, L. Elmquist and C. Johansson

Detection and Localisation of Fibre Optics Embedded into Glass Fibre Reinforced Composite Samples using Infrared Thermography 561
K. Majewska, M. Mieloszyk and W. Ostachowicz

Experimental Study of Non-Uniform Strains in Composites with Embedded Fiber Bragg Grating 571
A. Anoshkin, V. Matveenko, I Shardakov, N Kosheleva, E Spaskova, A Voronkov, G. Shipunov, V. Zuiko and D. Lobanov

Fibre Optic Sensor Embedding in Metals using Low Cost TIG Welding and High Precision Laser Brazing 577
T. Grandal, S. Fraga, G. Castro, E. Vazquez, J. A. Vazquez and A. Zornoza

Implementation of FBG Optical Sensors within a Laser-Assisted Fiber Placement Process for On-Line Monitoring of High Temperature Thermoplastic Materials Consolidation 583
D. Saenz-Castillo, F. Rodriguez-Lence and A. Güemes

Laminates with Integrated Piezoelectric Transducers: Influence of the Transducers Location along the Thickness-axis on the Structural Performance 594
X. Chen, Y. Meyer, R. Lachat and M. Ouisse

Registration of Technological Strain in Polymer Composite Samples using Embedded Fiber - Optic Strain Sensors 606
V.P. Matveenko, N.A. Kosheleva, I.N. Shardakov and A.A. Voronkov

Energy Harvesting, Power and Storage

An Asymptotically Correct Beam Type Piezoelectric Energy Harvester Model 618
S. Banerjee and S. Roy

Development of Li1.4Al0.4Ti1.6(PO4)3 Solid Electrolyte-Based Power Composites: Characterisation of Electrical Properties and Mechanical Properties 619
G. Liao, S. Geier, T. Mahrholz, P. Wierach and M. Wiedemann

Experimental Validation of a Porous Piezoelectric Energy Harvester 630
G. Martinez-Ayuso, H.H. Khodaparast, Y. Zhang, C.R. Bowen, M.I. Friswell, A.D. Shaw, H. Madinei and J.I. Roscow

Flywheel Proof Mass Transducer for Energy Harvesting Applications 642
A. Kras and P. Gardonio

Investigation of Interfacial Conditions for Li1.4Al0.4Ti1.6(PO4)3 Solid Electrolyte-based Multifunctional Energy Storage Devices 654
G. Liao, S. Geier, T. Mahrholz, P. Wierach and M. Wiedemann

Phase-Field Study of Stress-Induced Polarization Switching for Vibration Energy Harvesting 666
D. Wang, R. Melnik and L. Wang

Preliminary Investigation of the Energy Harvesting System Intended for use on an ORC Microturbine 674
T. Z. Kaczmarczyk, G. Żywica, E. Ihnatowicz, M. Lubieniecki and J. Roemer

Vibration Energy Harvesting with Electromagnetic and Piezoelectric Seismic Transducers: Experimental Results 686
L. Dal Bo and P. Gardonio

Identification, Control and Structural Health Monitoring of Civil

A Machine Learning Methodology for Structural Damage Classification in Structural Health Monitoring 698
F. Pozo, Diego A. Tibaduiza, M. Anaya and J. Vitola

Advanced Vibration Control of Large Structures with Distributed Multi-actuator System and Partial State Information 709
F. Palacios-Quiñonero, J. Rubió-Massegú, J.M. Rossell and J. Rodellar

Application of Advanced Technologies in Construction of Concrete Dams using Wireless Temperature Measuring and Monitoring Systems 721
J. Majrouhi Sardroud

Continuous Dynamic Monitoring of a Stone-Masonry Tower using a few Accelerometers: From Automated OMA to Damage Assessment 731
A. Cabboi, C. Gentile and A. Saisi

Continuous Dynamic Monitoring of large Civil structures: Different Perspectives of Application 732
A. Cunha, E. Caetano, C. Moutinho and F. Magalhães

Damage Evaluation based on the Flexibility Matrix 745
B. Olmos, J. Jara and G. Martinez

Damage Identification in Vibrating Rods under uncertain Elastically Restrained End Conditions 754
M. Dilena, M. Fedele Dell'Oste and A. Morassi

Designing a Smart TMD for a Composite Steel-Concrete Slender Slab 764
J.M. Soria, I.M. Díaz, J.H. García-Palacios, G. Marinas and E. Pereira

Dynamic Properties Evolution of Medium-Length RC Bridges 776
J. Jara, U. Galván, G. Martínez and B. Olmos

Energy Capacity Influence on Modal Parameters of Prestressed Concrete Box Girders 785
O. S. Luna Vera, C. W. Kim and Y. Oshima

Estimating the Tensile Force in Ancient Metallic Tie-Rods from Vibration Measurements 796
C. Gentile and A. Ruccolo

Experimental Dynamic Characterization of the Morelia Cathedral using Operational Modal Analysis 797
G. Martínez, J.. Jara, B.. Olmos and L. Mejía

Proposal and Comparison of Different Optimal Tuning Criteria for TMDs 809
A. Magdaleno, J. Fernandez, J.M. Garcia-Teran, M. Cacho-Perez and A. Lorenzana

Static and Dynamic analysis of Masonry tower of Allahabad University, India 821
A. Kumar and K. Pallav

Taking into Account the Uncertainty in the TMD Design for the Vibration Serviceability of a Footbridge 831
Javier F. Jiménez-Alonso and Andrés Sáez

Vibration Control of a Dining Hall: MIMO and SISO Design 839
E. Pereira, W. Xidong, C. Alén, J. H. García-Palacios and I. M. Díaz

Vibration Control of a Dining Hall: Structure Modelling 850
J. H. García-Palacios, J. M. Soria, X. Wang, I. M. Díaz and E. Pereira

Magnetorheological Composites: Materials and Applications

A Soft Electromagnetically Controlled Robotic Gripper to Manipulate Delicate Food Products 851
Y. Choi, Ch. Hartzell and N. Wereley

Aggregation Kinetics of Carbonyl Iron Particles under Magnetic Fields: Influence of Particle-Wall Interactions and Confinement 852
K. Shahrivar, E. Carreón-González, R. Agís and J. de Vicente

Characterization of Carbon Black-Filled Natural Rubber and Silicone Magnetorheological Elastomers under Pure Shear Loading 860
S. Yarra, G. Pekcan, M. Behrooz and F. Gordaninejad

Compressive Properties of Adaptive Magnetorheological Impact Foams 871
N. Wereley and Y. Choi

Development and Optimization of a Novel Magnetorheological Fluid Brake with No Zero-Field Viscous Torque for Automotive Applications 872
H. Shamieh and R. Sedaghati

Finite Element Method Simulations in Magnetorheology 883
J. Morillas and J. de Vicente

Impact Responses of a Magnetorheological Energy Absorber 892
X. X. Bai, S. Shen, F. L. Cai and S. Yang

Inverse Modelling of Magnetorheological Elastomer Isolator with Recurrent Neural Network and Genetic Algorithms for Real-time Control 893
G. Liao, J. Fu, J. Lai, J. Bai and M. Yu

Monitoring Sedimentation of Magnetorheological Fluids using a Vertical Axis Inductance Monitoring System with a Low Aspect Ratio Sensing Coil 904
M. Wen, J. Chambers, S. Sherman, N. Wereley and M. Yu

Preparation of Magnetorheological Fluids 905
H. Cheng, M. Wang, Ch. Liu, H. Shu and N.M. Wereley

Sound Transmission Loss of Sandwich Panels Partially Treated with MR Fluid and Viscoelastic Core Layer 906
M. Hemmatian and R. Sedaghati

Time-Dependent Viscoelastic Properties of Magnetorheological Paste with Cement as Carrier 916
Y. Li and W. Li

Morphing Structures

3D Design of a Large-Displacement Droop-Nose Wing Device 917
S. Vasista and H.P. Monner

A Multistable Helical Structure Enabled by Automated Fibre Placement 929
R. Telford and P.M. Weaver

A Spanwise Morphing Flap Featuring Multistability 931
Q. Ai and P. Weaver

Behavior Characterization of Machine Knit SMA 943
L. Zhuang, J. Luntz, D. Brei, S. Ahlquist and P. Alexander

Closed-Loop Control of the Smart Spring - An Analytical Solution 957
F. Nitzsche and M. Arras

Compliance and Instability in Morphing Structures 969
A.F. Arrieta, F. Runkel, G. Molinari and P. Ermanni

Design and Fabrication of a Shape Memory-Based Bio-Inspired Morphing Wing 971
P. Leal, H. Stroud and D. Hartl

Design and Manufacturing of a Morphing Trailing Edge using a 3D-Printed Piezoelectric Polymer 984
A. Moosavian, M. H. Malakooti, J. Lin, H. A. Sodano and D. J. Inman

Development of a Morphing Wing in a Micro Air Vehicle 993
M.A. Barcala-Montejano, Á.A. Rodríguez-Sevillano, R. Bardera-Mora, J. García-Ramírez, M. León-Calero and J. de Nova-Trigueros

Effect of Shape Memory Alloy Actuator Partial Transformation on the Performance of Morphing Wind Turbine Airfoils 1005
T. Machairas, A. Karakalas, A. Kontogiannis, A. Solomou, V. Riziotis and D. Saravanos

Morphing Winglets based on Compliant Structures 1018
C. Wang, H. Khodaparast, M. Friswell and A. Shaw

Numerical Investigation of Damping of Torsional Beam Vibrations by Viscous Bimoments 1030
D. Hoffmeyer and J. Høgsberg

Multifunctional Structures with Integrated Piezoelectric Elements

Benchmark Exact Free Vibration Solutions for Multilayered Piezoelectric Composite Plates 1042
F. Moleiro, C.M. Mota Soares, C.A. Mota Soares, A.L. Araujo and J.N. Reddy

Determination of Passive RL-Circuit Parameters for Damping Vibrations on the Basis of the Solution of the Problem on Natural Vibrations of Electroelastic Bodies 1054
V. Matveenko, D. Oshmarin, N. Sevodina, N. Iurlova and M. Iurlov

Dynamic Control of Deformable Mirrors for Adaptive Optics 1064
K. Wang, D. Alaluf, B. Mokrani and A. Preumont

Effect of Adhesive Layer Properties on the Energy Harvesting Performance of a Plate with Topologically Optimized Networks of Piezoelectric Patches 1077
J.Q. Velasquez and M.A. Trindade

Extension to Piezoelectric Plates of the Ritz - Sublaminate Generalized Unified Formulation Approach 1089
M. D'Ottavio, L. Dozio, R. Vescovini and O. Polit

Finite Element Techniques for the Characterization of Effective Properties of Transverse Piezoelectric Macro-Fibre Composites 1101
M.A. Trindade and A. Benjeddou

Modeling of Dynamic Processes in the Systems with Piezoelectric Elements and External Electric Circuits on the Basis of Equivalent Electric Circuits 1113
V.P. Matveenko, D.. Oshmarin, N.V. Sevodina, N.A. Iurlova and M.A. Iurlov

Passive Multimodal Damping of Vibrations in Structures with Piezoelectric Elements and External Electric Circuits 1125
V. Matveenko, D. Oshmarin, N. Sevodina, N. Iurlova and M. Iurlov

Some Homogenization Models of Nanosized Piezoelectric Composite Materials of Types Ceramics - Pores and Ceramics - Ceramics with Surface Effects 1137
A. Nasedkin

Vibration Suppression of Plates by Optimally Placed and Calibrated Piezoelectric RL Shunt Damping 1148
J. Toftekær, J. Høgsberg, A. Benjeddou and S. Krenk

Vibroacoustic Analysis of Laminated Sandwich Panels with Viscoelastic Core and Piezoelectric Patches 1160
A. Araujo, J. Belinha, A. Ferreira and C. Mota Soares

Nano-Reinforcement toward Strong and Smart Materials

A Nanocomposite-inspired Smart Sensing Coating for Acousto-ultrasonics-based Structural Health Monitoring: Modeling, Validation and Application 1172
Y Liao, M Liu, H Xu, L.M. Zhou and Z Su

Application of Carbon Nanotubes-Based Hierarchical Hybrids in Damage Sensing of Structural Composite Materials 1183
D. He, W. Li, B. Fan and J. Bai

Crack Propagation Monitoring on Bonded Joints with Novel Carbon Nanotube doped Adhesive Films 1184
X.F. Sánchez-Romate, C. Sbarufatti, M. Sánchez, A. Bernasconi, D. Scaccabarozzi, A. Güemes and A. Ureña

Graphene Based Conducting Architectures to Make Quantum Resistive Sensors (QRS) for Health Monitoring 1192
J. F. Feller and M. Castro

Improving Dielectric Properties of Polymeric Matrix Composites by the Thermal Treatment 1202
B. Fan, F. Bedoui, D. He and J. Bai

Investigation of Composition- and Ion-Depending Actuation Mechanism of CNT-Architectures 1203
S. Geier, T. Mahrholz, P. Wierach and M. Sinapius

Manufacture and Characterization of Transparent Conductor Polymer Coatings Doped with Graphitic Nanofillers 1215
S.G. Prolongo, N. Rolston, B. Watson, A. Printz and R. Dauskardt

Nanocomposites Spray Quantum Resisitve Sensors (Sqrs) for the Structural Health Monitoring of Composite Wind Blade 1224
A. Lemartinel, M. Castro, J. De Luca and J.F. Feller

Preparation, Characterization and Analyses of Albumin Nanoparticles loaded with Aluminum Chloride Phthalocyanine (AlClPc) 1233
T. Lopes, A. Tedesco and A. Ponton

Ultrasensitive, Stretchable Strain Sensors Based on Fragmented Carbon Nanotube Papers 1244
G. Lubineau, J. Zhou, H. Yu, X. Xu, F. Han and Y. Xin

Non-linear Modeling of Smart Materials and Structures

A Mixed Finite Element Formulation for Modeling the Viscoelastic Response of Electroactive Polymers at Finite Deformation 1255
D. Bishara and M. Jabareen

Constitutive Modeling of Hysteresis in Nitinol and Steel Strands through Data-Driven Strategies 1265
P. Brewick, S. Masri, W. Lacarbonara and B. Carboni

Description of Damage and Healing of a Self-Healing Anisotropic Material 1276
S. Specht, J. Bluhm and J. Schröder

Finite Element Analysis of Piezolaminated Structures with Both Geometric and Electroelastic Material Nonlinearities 1284
S.Q. Zhang, S.Y. Zhang, M. Chen and J. Bai

Linear Response of a Planar FGM Beam with Non-Linear Variation of the Mechanical Properties 1285
G. Balduzzi, M. Aminbaghai and J. Füssl

New Mixed Finite Elements for the Discretization of Piezoelectric Structures and Macro-Fibre Composites 1295
A. Pechstein and A. Humer

Non-Linear Analysis of a Pre-Stressed Piezoelectric Multi-Layer Plate 1307
F. Toth, M. Dorfmeister, M. Schneider, U. Schmid and M. Kaltenbacher

Nonlinear Electro-Elasticity for Piezoelectric Materials and Structures using a Multiplicative Decomposition of the Deformation Gradient 1316
A. Humer, E. Staudigl and M. Krommer

Nonlinear Modelling of Dielectric Elastomer Single Layer Plates using a Multiplicative Decomposition of the Deformation Gradient to Account for Electrostriction 1328
E. Staudigl, M. Krommer and Yu. Vetyukov

Non-Linear Switching Kinetics of Ferroelectric Mono-Domain Single Crystals 1340
V. Boddu, F. Endres and P. Steinmann

Numerical Study of Interaction of Nonlinear Guided Waves with Breathing Damage in Isotropic Material 1347
S. Gschossmann and M. Schagerl

Stress-Free Actuation Response Field Dependent Nonlinearity Handling for Piezoelectric Smart Structures: a Critical Review 1358
A. Benjeddou

Poster Session

Damage Identification Method for Three-Dimensional Truss Structures Based on Substructuring Approach and Varx Modelling 1359
U. Ugalde, J. Anduaga, O. Salgado and A. Iturrospe

IC Debonding Failure Detection in RC Beams Strengthened with FRP using Impedance Sensors and a Hierarchical Clustering Methodology 1369
R. Perera, E. Sevillano, A. Ruiz and L. Torres

Monitoring of an External Prestressing used as a Strengthening Technique in a Historical Masonry Steeple 1378
M. LLorens, R. Senis, B. Moreno and S. Pavon

Seismic Monitoring of the Civic Tower in Rieti equipped with a Non-Conventional TMD 1388
E.M. Tronci, M. De Angelis, D. Pietrosanti and G. Cordisco

Signal-Based Bending Stress Monitoring using Guided Waves in Hollow Cylinders 1390
J. Quiroga, L. Mujica, R. Villamizar, M. Ruiz and J. Camacho

Synthesis and Characterization of Bismaleimide Based Thermosetting Polymeric System with Two-Way Reversible Shape Memory Behavior 1398
Q. Zhang, Y. Liu and J. Leng

Thermal and Mechanical Properties of Self-Healing Epoxy/Graphene Nanocomposites 1399
I. Aguirre de Cárcer, M.G. Prolongo, C. Salom and S.G. Prolongo

SAW Sensors, Actuators, Filters and their Applications

Computational and Experimental Analysis of Surface Acoustic Wave Propagation on Piezoelectric GaAs Layer 1409
C. Maruccio, M. Scigliuzzo, S. Rizzato, G. Quaranta and G. Maruccio

Finite Element Simulation of Lithium Niobate Based Surface Acoustic Wave Delay Lines for Pressure and Temperature Sensing 1421
H. Chambon, P. Nicolay, G. Bruckner and A. Benjeddou

SAW Delay Lines as Wireless Sensors for Industrial Applications 1433
G. Bruckner, J. Bardong, A. Binder and P. Nicolay

Simulation of the Properties and Behaviour of an Implantable Passive and Wireless Surface Acoustic Wave Rfid Tag, for Structural Health Monitoring Applications 1444
P. Nicolay, H. Chambon and G. Bruckner

Wireless Passive Resonant SAW Sensors for Monitoring Temperature, Strain, Torque and Pressure 1453
V. Kalinin

Smart Materials Capable of Recoverable Inelastic Strain

A Finite Strain Constitutive Model Considering Transformation Induced Plasticity for Shape Memory Alloys under Cyclic Loading 1465
Th. Baxevanis, L. Xu and D. Lagoudas

Domain Interfaces and Fatigue Failure of NiTi Polycrystalline Strips 1478
S Zhang and Y.J. He

Effect of Loading Rate on Mechanical Behavior of NiTiNOL Plate - An Experimental and Computational Study 1490
F. Mutlu, G. Ozerim and G. Anlas

Evolution of Martensitic Transformation in Loaded NiTi Components: Comparison of Synchrotron XRD Tomography Data with FEM Simulations 1491
P. Sedlak, M. Frost, L. Heller, L. Kaderavek and P. Sittner

Finite-Element Analysis of Hydrogen Effect on Deflected Orthodontic NiTi Wire 1502
W. Elkhal Letaief, A. Fathallah, T. Hassine and F. Gamaoun

Hybrid Shape-Memory-Alloy-Textile Actuator Integrated Compression Garment 1511
J. Kennedy, N. Castaneda, A. Kontsos and A. Fontecchio

Induction Heating of Shape Memory Alloy Components Using Liquid Metal Energy Circuits for High Bandwidth Distributed Actuation. 1524
B. Bielefeldt, J. Mingear and D. Hartl

In-Situ Laser-Ultrasonic Characterization of Austenite-Martensite Transformation 1538
P. Stoklasová, P. Sedlák, H. Seiner, M. Janovská, T. Grabec, K. Zoubková, M. Ševčík, J. Zídek and M. Landa

Long Storage Effects on Ni-Ti Specimens: A Laboratory Testing Campaign 1547
S. Casciati, F. Casciati and L. Faravelli

Macroscopic Martensitic Transformation Front in NiTi Shape Memory Alloys: Experimental Observations and Numerical Reconstruction 1548
M. Frost, P. Sedlák, P. Sedmák and P. Šittner

Morphing Wing I - Finite Element Modelling of a NiTi SMA Wire 1559
W.L.H. Wan A Hamid, L. Iannucci and P. Robinson

Non-Uniform Transformation Behaviour of NiTi in a Discrete Condition due to the Functionally Graded Design 1560
B.S. Shariat and R. Bakhtiari

Numerical Simulation of a Self-Healing Bolted T-stub using Iron-based Shape Memory Alloy 1561
Ch. Cisse, W. Zaki and T. Ben Zineb

Self-Heating Method for Fatigue Limit Determination on NiTi Alloys after Hydrogen Embrittlement 1572
M. Rokbani, L. Saint-Sulpice, S. Arbab Chirani and T. Bouraoui

Shape Memory Alloy Foams: 3D Topology Reconstitution and Numerical Analysis of Superelastic Behaviour 1581
S. Zhu, C. Bouby, A. Cherouat and T. Ben Zineb

Size Effects in a Shape Memory Alloy Rod caused by Inhomogeneity of Temperature and Stress Fields Studied through Solving of A 1d Connected Thermal and Mechanical Problem 1582
A.E. Volkov, A.S. Kukhareva, N.A. Volkova and Y.V. Malkova

Smart Micro-Mechatronic Systems

Dexterous Robotic In-Hand Manipulation of Micro-Objects: From Trajectories Planning to Experimental Validation 1590
J.A. Seon, R. Dahmouche, B. Brazey and M. Gauthier

Hybrid Force-Position Control of the Robotic Hand Prosthesis Promain-I 1597
A. Rubiano Fonseca, J.L. Ramirez and L. Gallimard

Remote Optical Powering using Fiber Optics in Micro-Mechatronic Systems 1598
J.D. López-Cardona, C. Vázquez, D.S. Montero, P.J. Pinzón, A. Tapetado and P. Contreras

Shape Memory Alloy (SMA) Based Actuation Mechanism for a Soft Robotic Hand Prosthesis 1609
J.L. Ramirez, A. Rubiano and O. Polit

Shape Memory Alloy Element Design and Characterization for an Optically Driven Quadristable Actuator 1610
H. Al Hajjar, S. Venegas Bayona, S. Chandgadkar, X. Liu, E. Dore and F. Lamarque

Structuring and Describing Requirements in a Flexible Mesh for Development of Smart Interdisciplinary Systems 1622
I. Graessler and J. Hentze

Smart Periodic Structures for Vibration Control

A Method for an Optimal Design of Periodic Structures 1632
G. Cazzulani, E. Belloni, E. Riva, J. Marconi and F. Braghin

Design of a Smart Periodic Beam with Coupling between Local Resonances and Bragg Band Gaps 1643
E. Belloni, G. Cazzulani, M. Cenedese and F. Braghin

Energy Flow Characteristics of Periodically Distributed Piezoelectric Shunting Circuits 1656
Y. Fan, O. Bareille, M. Ichchou, L. Li and J.-P. Laine

Inertia Multiplication in Phononic Crystals for Low Frequency Bandgaps 1657
T. Delpero, G. HannemaBa, B. Van Damme, S. Schoenwald, A. Zemp and A. Bergamini

Merging Mechanical and Electromechnical Locally Resonant Bandgaps in Metamaterials 1669
C. Erturk, M. Ruzzene and A. Erturk

Non-reciprocal Elastic Wave Propagation in Time-Space Periodic Structures 1677
K. Yi, M. Collet and S. Karkar

Smart Panel with Switching and Sweeping Piezoelectric Patch Vibration Absorbers 1689
L. Dal Bo, D. Casagrande and P. Gardonio

Ultrasonic Wave Propagation in Periodic Ceramic Micro-Scaffolds fabricated by Robocasting 1702
H. Seiner, A. Kruisova, P. Sedlak, M. Landa, P. Miranzo, B. Roman-Manso and M. Belmonte

Vibration Damping in Periodic 1D-Structures by R-Shunted Piezoelectric Elements 1710
J. Høgsberg

Wave Finite Element Method for Electromechanical Periodic Waveguides 1721
B. Lossouarn, M. Aucejo and J.-F. Deü

Wave Propagation Control in 1D Hybrid Phononic Crystal using Miniaturized Programmable Floating Virtual Inductances 1731
E. Flores Parra, A. Bergamini, L. Kamm, P. Zbinden and P. Ermanni

Soft Active Materials and Mechanics

Deformation Mechanics of Carbon-Fiber Reinforced Shape-Memory-Polymer Composites 1744
X. Lan, L. Liu, Y. Liu and J. Leng

Active Deformable Composite Structures: Opportunities and Challenges 1745
J. Leng and Y. Liu

Mechanoluminescence-Based Active Sensing for Structural Health Monitoring and Failure Prevention 1746
Y. He, Y. Liu and J. Leng

Numerical and Experimental Studies on Broadband Piezoelectric Energy Harvester induced by Magnets 1747
Q. Lu, Y. Liu and J. Leng

Softening of Particle Filled Dielectric Elastomer under the Actions of Force and Voltage 1748
Y. Liu, L. Liu and J. Leng

Thermodynamics and Instability of Dielectric Elastomer 1749
L. Liu, Y. Liu and J. Leng

Structural Health Monitoring

Defect Detection combining Multi-Frequency Ultrasonic Guided Waves and Topological Derivative 1750
A, Martínez, J.A. Güemes, J.M. Perales and J.M. Vega

Delamination Monitoring in Electrically Conductive Composites 1760
M. Quaresimin, S.K. Nothdurfter, M. Zappalorto, F. Panozzo, A. Rullo and N. De Rossi

Evaluation of the Probability of Failure using Bayesian Theorem for Real-time Condition Monitoring 1766
A. Iwasaki

Guided Wave Time-reversal Imaging of Macro-features in Anisotropic Composites with Sparse Distributed Measurement Locations 1775
A. Eremin, E. Glushkov, N. Glushkova and R. Lammering

Health and Usage Monitoring of INTA Unmanned Aircrafts for Surveillance and Flying Target 1783
M. Frovel, R. Atienza and F. Terroba

Impact Detection and Identification in Sensorized Structures by Neural Network Processing of Dynamic Transient Histories 1792
V. Ramírez and D. Garijo

Investigation of the Electromechanical Impedance Changes related to the State of the Investigated Structures 1804
P. Fiborek, P. Malinowski, P. Kudela, T. Wandowski and W. Ostachowicz

Modelling the Correlation between the Damage State and the Electrical Resistance Change in Symmetric Laminates 1813
M. Zappalorto, M. Quaresimin, F. Panozzo, P. A. Carraro and N. De Rossi

Multi-Level Damage Detection Strategy for Composite Structures 1820
Z. Sharif Khodaei and M.H. Aliabadi

Non-Destructive Evaluation of Delamination in Composite Material Based on Vibrational Approach 1821
G. Serovaev, A. Shestakov and D. Oshmarin

On The Determination of Material Degradation in Composites by use of Non-Linear Wave Propagation Analysis 1831
N. Vu Ngoc, N. Rauter and R. Lammering

Scattering Analysis of Lamb Waves at Subsurface Cracks in Isotropic Plates 1843
C. Humer, C. Kralovec and M. Schagerl

Sensor Integration and Data Explotation of Structural Health Monitoring Network Integrated on a Unmananned Aerial Vehicle (UAV) 1854
A. Fernandez-Lopez, M. Frovel, A. Lozano-Martin, P. Fernandez-Diaz-Maroto, I. Gonzalez-Requena, J.M. Pintado, M.A. Torre, F. Terroba and A. Guemes

Sensor Optimization for Impact Detection - A Bayesian Approach 1855
V. Mallardo, Z. Sharif Khodaei and M.H. Aliabadi

Sparsity Constrained Extended Kalman Filter Concept for Damage Localization and Identification in Mechanical Structures 1866
D. Ginsberg, C.- P. Fritzen and O. Loffeld

Structural Damage Localization through an Innovative Hybrid Ensemble Approach 1878
G. Moreno-Beltrán, J. Camacho-Navarro, M. Ruiz, R. Villamizar and L. Mujica

Structural Health Monitoring (SHM) of Structures by Electromechanical Impedance (EMI) Technique using Nonlinear Material Model of Piezoelectric Medium 1890
N. Mallik and S. Singh

Structural Health Monitoring By Combining Machine Learning And Data Assimilation Techniques 1900
E. Lopez, G. Quaranta, E. Abisset-Chavanne and F. Chinesta

Wave Based Characterization of Low-Velocity Impacts on Composite Plate Structures Using Piezoelectric Sensors 1912
T. C. Theodosiou, C. S. Rekatsinas and D. A. Saravanos

Wind turbine fault detection through singular spectrum analysis 1926
F. Pozo, Y. Vidal and L. Acho

PLENARY LECTURE

8th ECCOMAS Thematic Conference on Smart Structures and Materials
SMART 2017
June 5 – 8, 2017
Madrid, Spain

Convergence of Technologies in Manufacturing, Mechanics and Materials

K.P. Chong

Dept. of Mechanical & Aerospace Engineering
George Washington University
Washington, DC, USA
e-mail: kchong@gwu.edu, web page: http://www.gwu.edu/

ABSTRACT

An overview on converging technologies that are the primary drivers of the 4th Industrial Revolution will be presented, followed by the new developments in advanced manufacturing, nano-, bio-, information-technologies and cognitive sciences. Convergence of these transformative technologies will be discussed.

Emphases are on advanced manufacturing, nano mechanics/materials, smart materials, multi-scale problems and simulation methods.

8th ECCOMAS Thematic Conference on Smart Structures and Materials
SMART 2017
June 5-8, 2017
Madrid, Spain

Experimental Method and Constitutive Model of Electromagnetic Thin Films and Laminates under Multi-Field Loading

D.N. Fang

Beijing Institute of Technology, Beijing, China

Peking University, Beijing, China

e-mail: fangdn@pku.edu.cn, web page: http://www.bit.edu.cn/

ABSTRACT

Ferroelectrics, ferromagnetic, magnetoelectric thin films and composite laminates, have been widely used in modern industries, owing to their excellent coupling properties and quick responses. Their deformation behaviors under mechanical loading are affected considerably by an external electric or magnetic field. To provide a deep understanding of the intrinsic coupling properties, a novel electro-magneto-mechanical multi-field nanoindentation apparatus and a novel multi-field bulge-test instrument were designed and constructed. Characterization methods were also established for deformation of electromagnetic thin-films and laminates. The experimental results reveal the size-dependency of various mechanical properties in the electromagnetic materials, ranging from the Young's modulus, to the hardness. Notably, these properties can be well controlled by applying external electric/magnetic fields. Furthermore, a new size-dependent nonlinear constitutive model is developed for the magnetoelectric composite laminates to account for the coupling mechanisms under multi-field loading. The results are meaningful for the design and quality assessment of the electromagnetic functional devices.

8th ECCOMAS Thematic Conference on Smart Structures and Materials
SMART 2017
June 5 – 8, 2017
Madrid, Spain

Guided Acoustic Wavefields for Damage Detection/Characterization and Novel Transducer Designs

M. Ruzzene

D. Guggenheim School of Aerospace Engineering
G.W. Woodruff School of Mechanical Engineering
Georgia Institute of Technology Atlanta, GA 30332
e-mail: ruzzene@gatech.edu, web page: http://www.ruzzene.gatech.edu/

ABSTRACT

The application of wave-based inspection methods for the analysis of the state of health of structural components has received significant attention in recent years. The propagation and GUW, together with the application of Scanning Laser Vibrometry for full wavefield measurement enables the introduction of novel damage detection techniques which are based on the application of filtering techniques in the frequency/wavenumber space. Goal of these techniques is to separate the contribution of damage from the overall response of the structure, thus highlighting its presence and location.

This presentation will provide an overview of techniques developed for the analysis of guided wavefield, and their application for damage detection, structural characterization, and for the design of novel transducers for Structural Health Monitoring. These transducers feature patterns that enable wave steering through the selection of the excitation frequency, and the measurement of multiple strain components for surface acoustic wave-based sensing of strain.

VIII ECCOMAS Thematic Conference on Smart Structures and Materials
SMART 2017
A. Güemes, A. Benjeddou , J. Rodellar and Jinsong Leng (Eds)

HIGHLIGHTS AND CHALLENGES IN DAMAGE ASSESSMENT OF COMPOSITE STRUCTURES

WIESŁAW OSTACHOWICZ[*,†], PAWEŁ MALINOWSKI[*], TOMASZ WANDOWSKI[*]

[*] Institute of Fluid Flow Machinery, Polish Academy of Sciences
Fiszera 14 St, 80-231Gdansk, Poland
e-mail: wieslaw@imp.gda.pl, https://www.imp.gda.pl/en/o4/z1/

† Warsaw University of Technology, Faculty of Automotive and Construction Machinery,
Narbutta 84 St, 02-524 Warsaw, Poland

Key words: Damage assessment, Composite structures, Bonded joints, Delaminations

Abstract. The paper presents multidisciplinary methods and techniques oriented towards damage identification and assessment in composite structures reinforced by carbon and glass fibres. A simulated damage in the form of teflon insert as well as real damage in the form of delamination were investigated. The paper reports applications of electromechanical impedance EMI and guided wave propagation methods. Presented methods are also suitable for performance of bonded joints assessment. Particularly the investigations concern contaminated bonds caused by both manufacturing (e.g. release agent) and in–service contaminations (e.g. de–icer). Techniques for detection of weak bonds are presented together with signal processing approaches.

1 INTRODUCTION

Nowadays aerospace structures are made more and more often out of various composite materials like glass/carbon fiber reinforced polymers (GFRPs, CFRPs) or glass laminate aluminum reinforced epoxy (GLARE). Due to this fact the up-to-date NDT techniques should handle with the wide range of these materials and potential defect types that could initiate and grow in such materials. Beside of typical damage like matrix cracking and delamination cause by impact [1],[2] attention should be focused on such a problems like for example the surface quality, the performance of structural bonds or moisture content. The process of adhesive bonding for aerospace structures nowadays is present at the manufacturing process as well as in service in the form of composite repair patches.
Nowadays composite structures need to be assessed using conventional NDT, extended NDT (ENDT) or SHM techniques in order to maximize the safety of exploitation of such structures what is very important in the case of aerospace structures. Still very popular methods are ultrasound testing (UT) method, Eddy current method or X-ray based methods. However, many other structural assessment methods have been developed. The examples are the

methods based on electromechanical impedance (EMI) or guided wave propagation (GW). Both techniques can be used in SHM when piezoelectric transducers are utilized for generation and sensing purposes. In the case of guided wave propagation this method could be used also utilized as NDT technique when non-contact measurements are conducted using laser scanning vibrometer whereas the guided wave excitation is realized using piezoelectric transducer.

Moreover external factors need to be considered is real SHM solutions. External factors have influence on measurement results for such methods like electromechanical impedance or guided wave propagation. Sensitivity of both method to temperature changes are reported in literature [3],[4]. Changing temperature causes changes in the measurements characteristics for the electromechanical impedance method. Temperature change is manifested as horizontal shift of frequency peaks [5],[6]. EMI method is also influenced by changing the load of investigated structure [6],[7]. In the case of guided wave based method, the velocity of guided wave propagation depends on material properties that on the other hand depends on temperature. As consequence velocity of guided wave propagation changes according to the temperature change. These features need to be taken into account in the SHM. Signal processing algorithm for compensation of temperature influence need to be utilized.

This paper is divided into two major sections. Firstly, the electromechanical impedance method and results are presented. Secondly, the guided wave propagation method based on laser vibrometry together with results are presented.

2 EMI METHOD

EMI method is based on measurements of electrical parameters of a piezoelectric transducer coupled with the investigated structure. Due to electromechanical coupling of piezoelectric transducer and the host structure, mechanical resonances of structure can be observed in electrical characteristics of piezoelectric transducer. Probably the first published record about the method was made by Liang et al. who proposed an one-dimensional equation [8].

In the EMI method electrical parameters like impedance, admittance, their real parts (respectively resistance and conductance) and their imaginary parts (reactance and susceptance) can be registered and analyzed. According to literature, imaginary part of electrical parameters is used for monitoring of bonding layer between transducer and structure or diagnosis of the transducer itself [9], while the real part of electrical parameters is utilized for monitoring of the structure. Reactance was utilized as a parameter that allows to detect transducer debonding, while the resistance was used for assessment of the structure [10]. However, also both the resistance and susceptance were used to detect sensor faults in other research [11].

2.1 Assessment of adhesive bonding by EMI

Samples that comprise of two adhesively bonded subsamples were investigated. The material used for subsamples manufacturing was Hexcel M21E with $[0, 0, 45, -45]_s$ layup. Each subsample had a planar size of 100 mm x 100 mm. These subsamples were bonded together with FM 300-2 adhesive film. Two cases of pre-bond modifications were investigated. The modified samples were compared against reference samples. The investigations included: 3 reference samples, 9 samples with pre-bond thermal treatment, 9 samples with pre-bond

contamination with de-icing fluid. The thermal treatment was performed by exposure of the samples to elevated temperatures before bonding. Three samples were prepared for each temperature: 220, 260, 280˚C. TD1, TD2 and TD3 sample symbols were assigned, respectively. The pre-bond contamination was prepared by dip coating of the plates in a water solution of the de-icer with three concentrations. After drying the potassium formiate, which is present in the de-icing fluid, forms a thin layer on the CFRP. The potassium (K) content measured with XPS was taken as a measure of contamination. The contamination resulted in three samples contaminated at 6.4 at.% of K (DI1 samples) and six samples contaminated at 10.9-12.0 at.% of K (DI2 samples).
The conductance spectra were measured for the samples in 3-5 MHz ran and the RMS index was calculated. The results are presented as a mean value for each level of modification. In order to make the comparison the mean RMS values were presented as a percent change in relation to the mean RMS value calculated for the reference samples. Figure 1 depicts the result for all the cases. An increasing value of RMS is observed. The samples treated at 220˚C differ for the reference by less than 20%, while samples treated at 280˚C have the largest value, exceeding 50 %. In the results for contamination with the de-icing fluid (DI) one can notice similar behaviour. The lover level of delamination (DI1 - 6.4 at.% of K) differ by lee than 20% from the reference case. The higher amount of contamination (DI2) results in an RMS value increase by more than 20%.

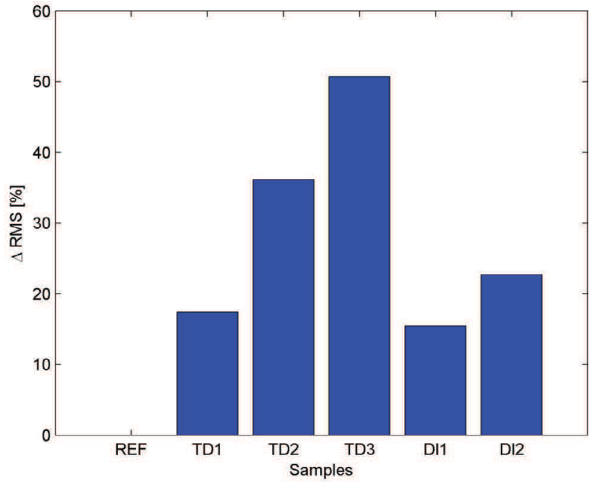

Figure 1. Relative RMS results for the samples with pre-bond thermal treatment (TD) and the samples with pre-bond de-icer contamination (DI)

2.2 Delamination detection by EMI

The EMI was also investigated for damage detection purposes. The investigated object was a 500 mm x 500 mm x 3 mm plate made of glass fibre reinforced polymer (GFRP sample) . The sample was made of 8 plies of biaxial fabric. In order to simulate damage a square (10 mm x 10 mm) teflon tape was inserted between the second and the third layer. The teflon was located in the right lower corner 120 mm away from the closest two edges. A network of four sensors were bonded to the sample surface. One sensor (P1) was bonded at the location of the

teflon insert The three remaining sensors (P1, P2, P3) were located symmetrically at the remaining three corners of the plate. We investigated the change of RMS value and the location of conductance maximum. The change was caused by bonding of the sensors and the state of the sample in the vicinity of the sensors. One can notice that after bonding the RMS value (energy) dropped for all cases (Figure 2). The drop is virtually uniform for the sensors P2-P4 bonded to the healthy part of the sample. However, there is a significant difference for P1 sensor that was bonded at the location of simulated delamination. In terms of frequency change one can notice that the frequency increases for P2 and P4 and decreases for P1 and P3 (Figure 3). However in terms of absolute values the change for P1 is the lowest, slightly lower than for the P4 sensor. The sensors located at the location of artificially made damage was clearly distinguish form the remaining cases. Teflon detection was successful.

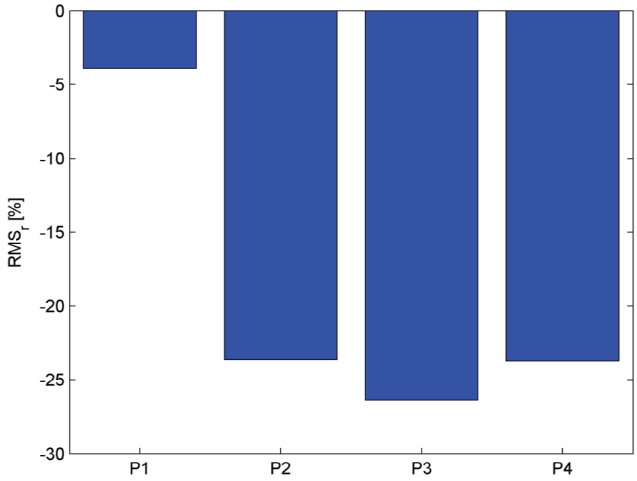

Figure 2. Relative conductance RMS change after bonding sensors (P1-P4) to the investigated GFRP sample

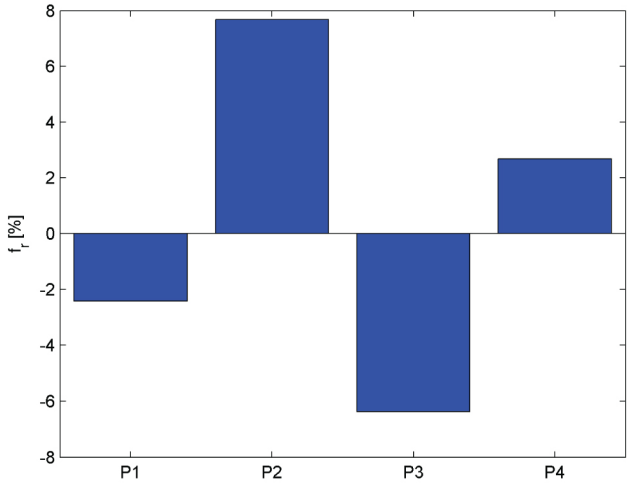

Figure 3. Relative change of conductance maximum peak frequency after bonding sensors (P1-P4) to the investigated GFRP sample

3 GUIDED WAVE PROPAGATION METHOD

This section is related to guided wave propagation method which can be utilized in the purpose of damage detection and localization. This method is based on the fact that any kind of discontinuities in structural element are the source of change in guided wave propagation. In the approach presented in this paper full wavefield method was utilized. The guided waves were excited using piezoelectric transducer (Noliac NCE51 piezoelectric disc with diameter 10 mm and thickness 0.5 mm) while the guided wave sensing process was conducted using Polytec Scanning Laser Doppler Vibrometer SLDV.

3.1 Simulated delaminations in GFRP samples

In the first step measurements were conducted for Glass Plastic Reinforced Polymer (GFRP) panel with dimensions 500 mm x 500 mm and thickness ~1.5 mm. Panel consists of twelve layers of VV192T/202 IMP503 prepregs with orientations: $[0/90/0/90/0/90]_S$. In this panel four circular teflon inserts, each with diameter 20 mm, were embedded between layers of lamina in order to simulate delaminations (Figure 4). Teflon inserts were located at different depth what can be noticed in the Figure 5.

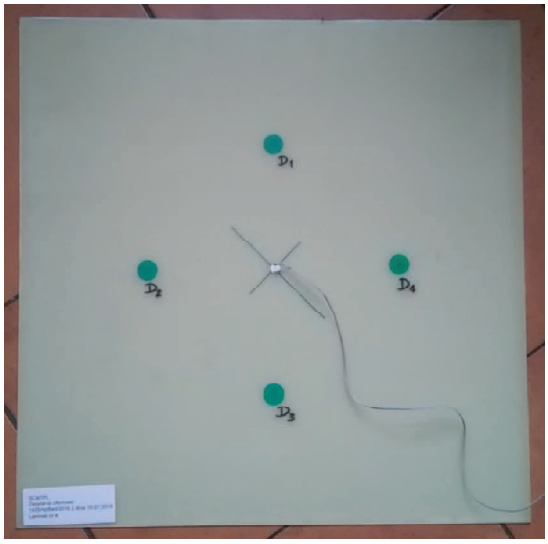

Figure 4. View of GFRP sample no. 1

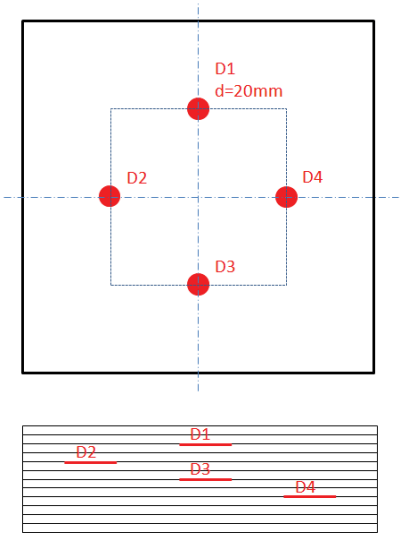

Figure 5. Teflon insert locations in the GFRP sample no. 1

In the Figure 6 results of full wavefield measurements in the form of frames chosen from animation of guided wave propagation were presented. Measurements were taken for excitation frequency 200 kHz. Analyzing results in Figure 6a) propagation of symmetric and antisymmetric fundamental modes S0 and A0 could be noticed. In the Figure 6b) interactions of S0 mode with teflon inserts could be noticed – mode S0 is converted to A0' mode. The amplitude of A0' mode (as result of mode conversion) depends on the depth at which teflon insert was inserted. Amplitude of A0' mode is largest in the case of teflon insert denoted as D1 that is located below second layer counting from top of the panel where the measurements were performed.

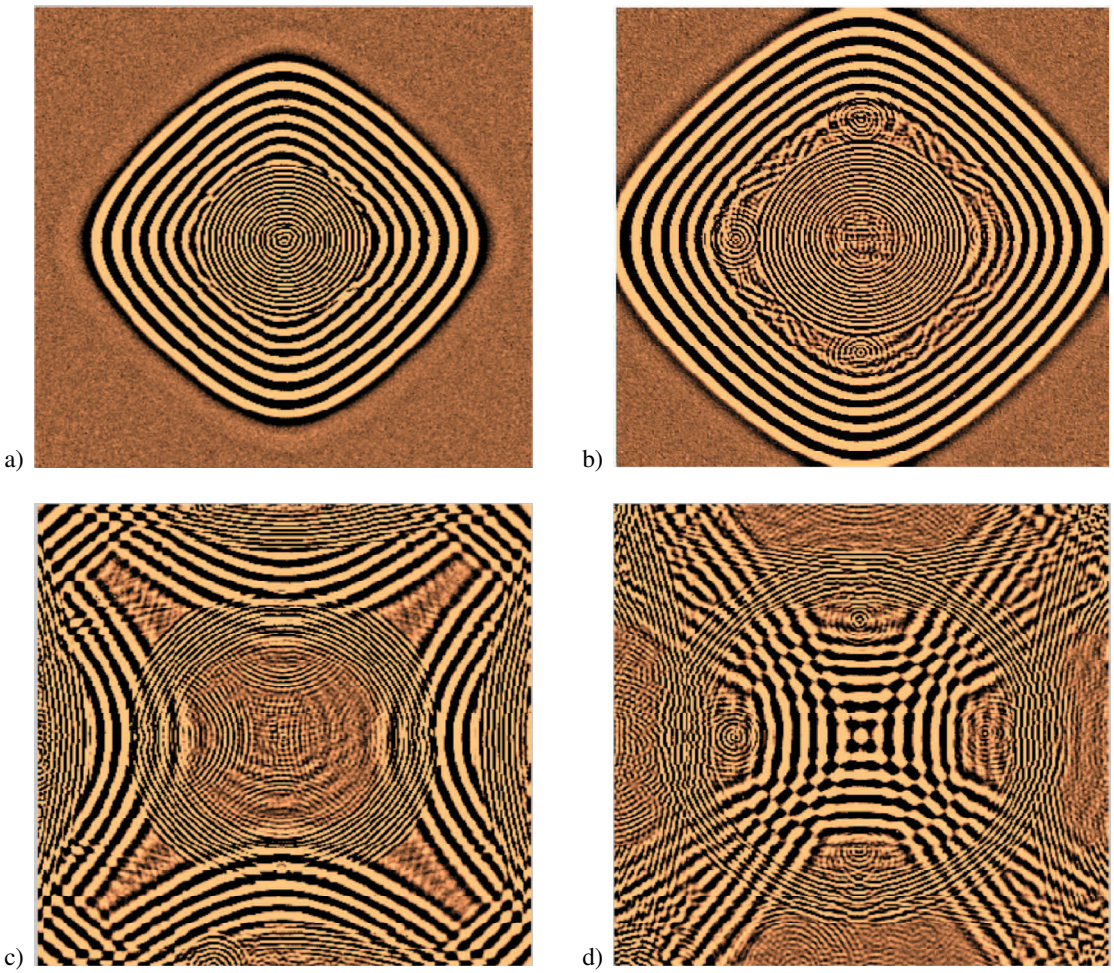

Figure 6. Selected frames from animation of guided wave propagation in GFRP sample no.1: a-d) subsequent frames

Amplitude of A0'mode is smallest amplitude for the teflon insert denoted as D4 which is located eight layers from the top (deepest). What is interesting, mode conversion phenomenon is clearly visible for the case of teflon insert denoted as D3, which is placed symmetrically in respect to the panel thickness. According to the literature mode conversion phenomenon occurs only for the discontinuities placed non-symmetrically in respect to the thickness of composite laminate. This fact was proved by the numerical simulations which results were published in [12]. Numerical result for carbon fibre reinforced polymer CFRP showed that there is no mode conversion in the case of symmetrically placed delamination (simulated by node separation in the spectral elements). In the case of experimental results for CFRP panel presented in the paper [12] mode conversion occurred for symmetrically as well non-symmetrically placed delamination (simulated by teflon insert). These experimental result for CFRP panel agree with results for GFRP panel presented here. According to the paper [13] the existence of discontinuity destroys the symmetry of the wave, resulting in mode conversion. It means that location of delamination never is perfectly symmetrical in the

relation to the panel thickness. This is obvious for real structures where it is hard to achieve ideal symmetry.
In the Figure 6c) S0 to A0 mode conversion phenomenon could be noticed as a consequence of S0 interaction with panel boundaries. In the Figure 6d) reflections of A0 mode from teflon inserts could be noticed. After carefully analysis of results presented in Figure 6c) and Figure 6d) additional local S0/A0' mode conversion could be noticed in the point located at the bottom panel edge. There was very small notch at panel surface just on the edge which caused mode conversion phenomenon.
In the next step signal processing algorithm was utilized in order to visualize the simulated delamination locations. The simply and widely used full wavefield signal processing is calculation of Weighted Root Mean Square (WRMS) for the time domain signals at discrete time interval. As consequence energy distribution related to propagation of wave and its interaction with discontinuities in the structure is obtained. In the WRMS algorithm weight factor is utilized which decreases the importance of the time samples at the beginning when excitation is applied (large wave amplitudes) and increases the importance of the samples closer to the end of signal where waves amplitudes are small due to damping. The Weighted Root Mean Square (WRMS) can be calculated using formula:

$$WRMS = \sqrt{\frac{1}{N}\sum_{k=1}^{N} w_k s^2} \tag{1}$$

where the weighting factor w_k is defined as follows:

$$w_k = k^m, \quad m \geq 0 \tag{2}$$

In the Figure 7 WRMS energy maps for guided wave propagation in the GFRP panel with four circular teflon inserts (Figure 4 and Figure 5) were presented. Both WRMS energy maps were constructed for the excitation frequency 200 kHz.

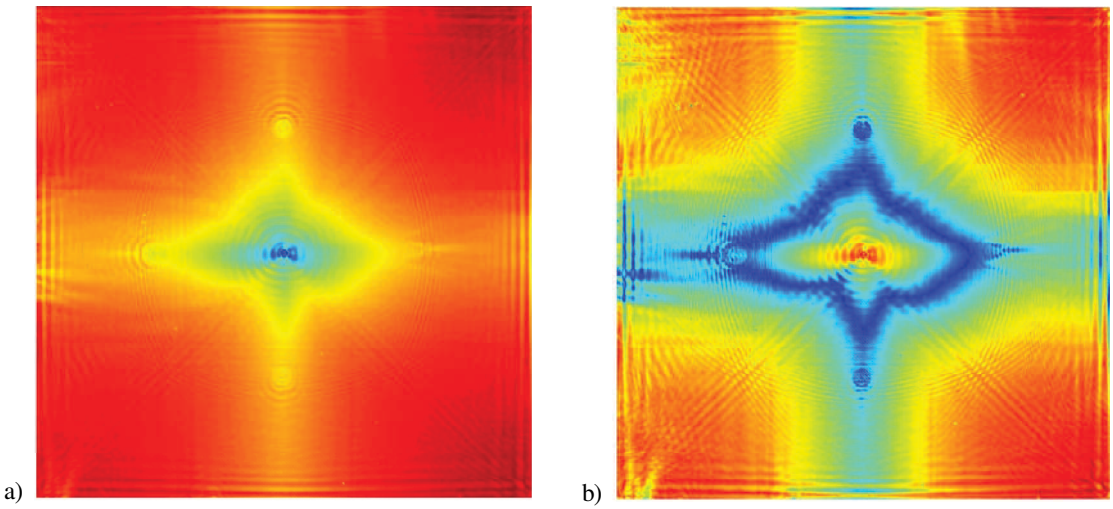

a) b)

Figure 7. WRMS guided wave energy maps for: a) m=0.1, b) m=0.65; GFRP sample no. 1

Energy map in the Figure 7a) was constructed for parameter *m* equal to 0.1. Locations of four circular teflon inserts can be easily noticed analyzing of guided wave energy concentrations near the defects. Moreover, strong energy concentration along angles 0° and 90° could be noticed. This is caused by orientation of glass fabric reinforcement in the panel.
Energy map presented in the Figure 7b) was constructed for parameter *m* equalto 0.65. In this case change of energy distribution due to teflon inserts as well as orientation of glass fabric reinforcement is much more visible.
Analogus measurements and signal processing were performed for second GFRP sample. This sample was manufactures using the same material like sample no. 1 and using the same number of layers and its orientations. In this sample planar locations of teflon inserts were changed (Figure 9). Now the inserts are not located at directions 0° and 90° along which strong energy concetration occurs. In the Figure 9 selected frame presenting propagation of S0 and A0 modes in this sample was showed. Measurements were taken for excitation frequency 200 kHz. In this case S0/A0' mode conversion phenomenon in the regions were teflon inserts were located can be also noticed. However, amplitudes of A0' mode generated in the consequence of S0 mode conversion are lower than in the case of previous sample. In this case amplitudes of A0' mode also depends on the deept were the insert was located.

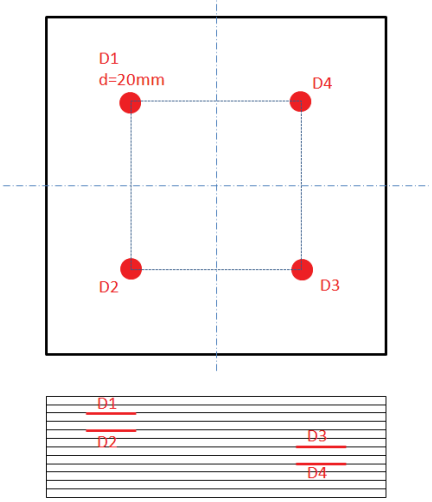

Figure 8. Teflon insert locations in the GFRP sample no. 2

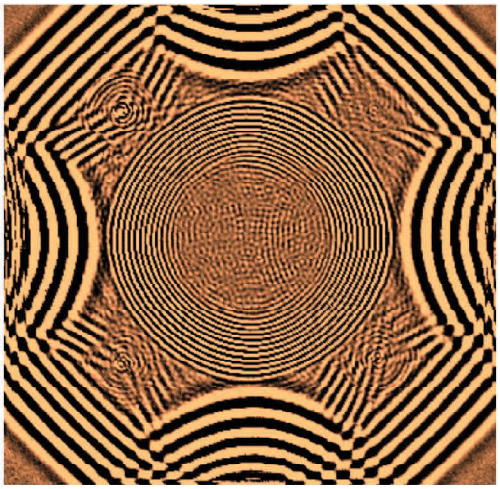

Figure 9. Selected frame from animation of guided wave propagation in GFRP sample no. 2

In the next step WRMS energy maps for coeeficient *m* equal to 0.1 and 0.65 were constructed – see Figure 10a) and Figure 10b) respectively. In the case of *m*=0.1 changes of energy distribution caused by teflon inserts are amost invisible (Figure 10a)). Locations of teflon inserts denoted D1-D3 could be noticed in the case of WRMS energy map constructed for *m*=0.65. Location of insert D4 is almost invisible – it is the deepest insert in the panel.

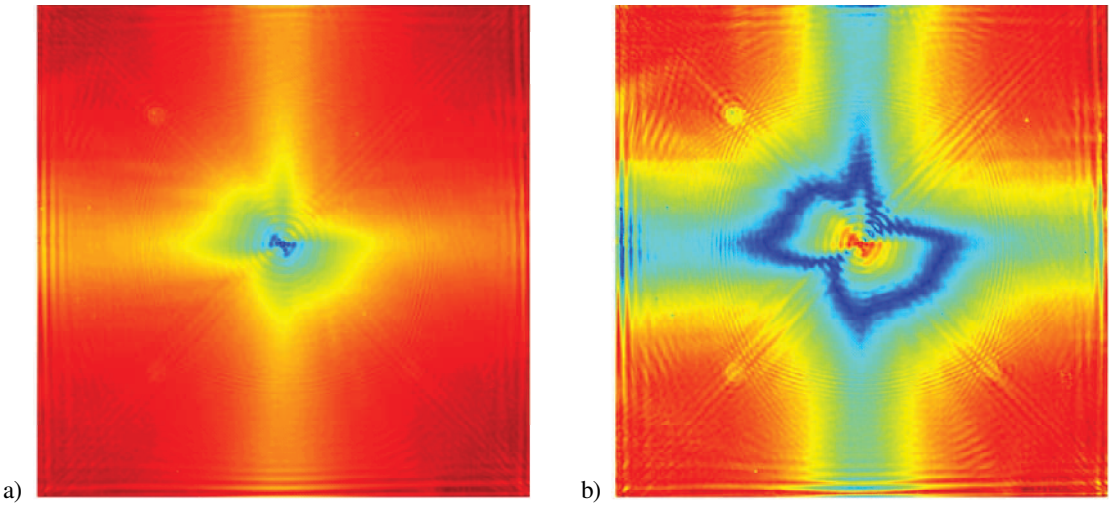

Figure 10. WRMS guided wave energy maps for: a) m=0.1, b) m=0.65; GFRP sample no. 2

In the further research third GFRP sample was utilized (Figure 11). This sample was manufactures using the same material like sample no. 1 and no. 2 using the same number of layers and the same orientations. In this case influence of different shapes of teflon on the guided wave propagation was investigated. All teflon inserts were located at the same depth (Figure 12).

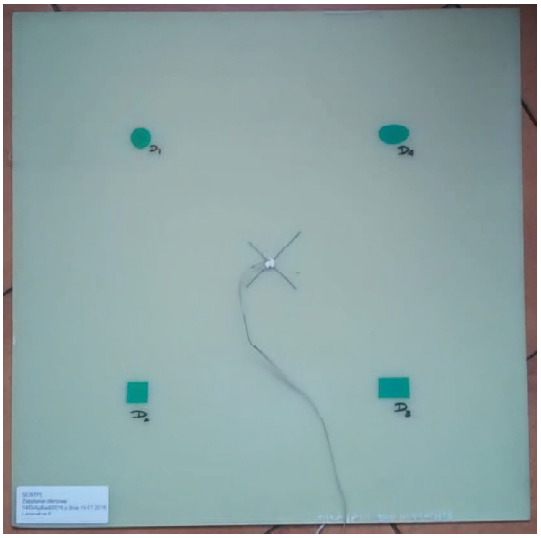

Figure 11. View of GFRP sample no.3

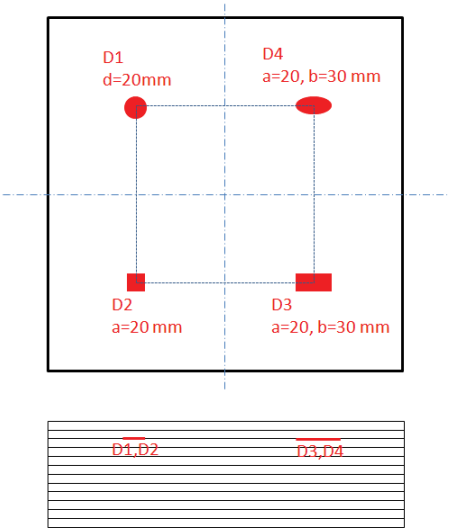

Figure 12. Teflon insert locations in the GFRP sample no. 3

In the Figure 13 selected frame presenting propagation of S0 and A0 modes for excitation frequency 200 kHz in the GFRP sample no. 3 was showed. This frame was selected because it clearly shows interactions of S0 mode with teflon inserts with different shapes. Due to interaction of S0 mode with teflon inserts, phenomenon of S0/A0' mode conversions is observed. In the Figure 14 magnifications of wavefield around teflon inserts were presented.

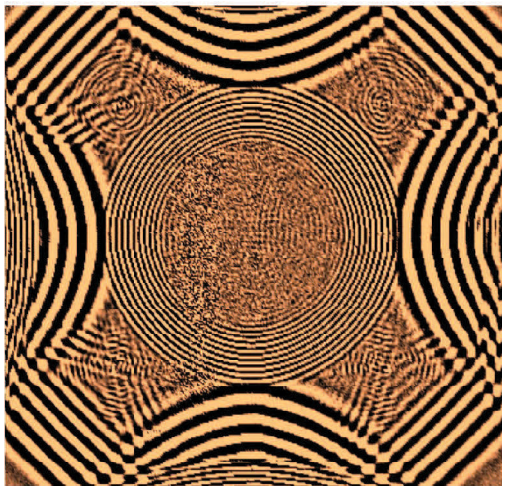

Figure 13. Selected frame from animation of guided wave propagation in GFRP sample no. 3

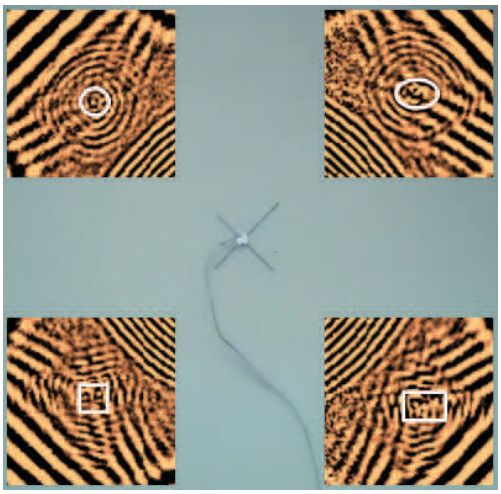

Figure 14. Wavefield around the teflon inserts capturing – S0/A0' mode conversion - GFRP sample no. 3

Analyzing wavefield around each teflon insert it can be observed that wavefront of new A0' mode depends on the shape of teflon insert. In the case of circular and elliptical insert wavefront has circular and elliptical shape. In the case of square and rectangular we could notice that wavefront is formed on the edges of teflon insert. Moreover, entrapment of A0' mode in the region of teflon insert is also observed. Similar effects were observed in [12], [14].

a) b)

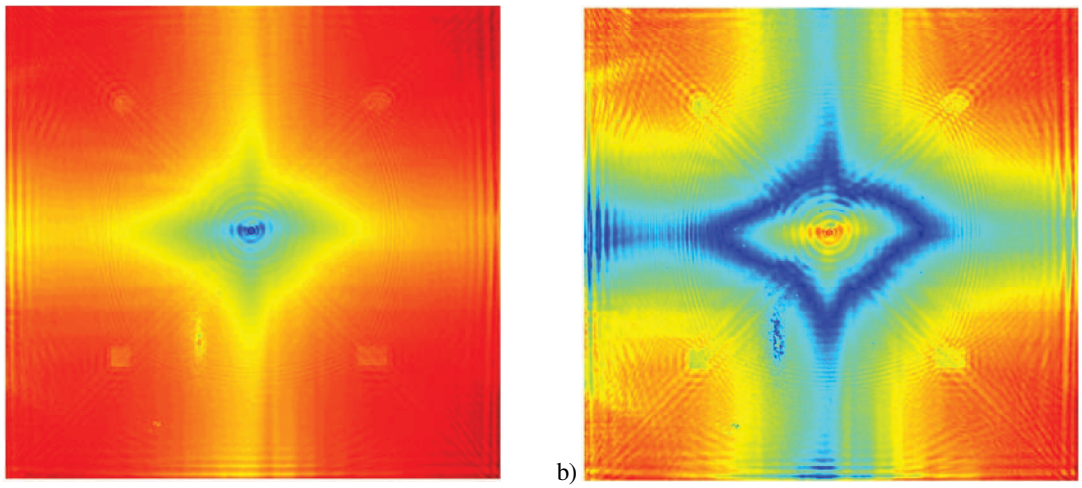

Figure 15. WRMS guided wave energy maps for: a) m=0.1, b) m=0.65; GFRP sample no. 3

In the next step WRMS energy maps for GFRP sample no. 3 and coefficient m equal 0.1 and 0.65 were constructed – see Figure 15a) and Figure 15b) respectively. Energy map presented in Figure 15a) indicates clearly the shapes of all embedded in panel teflon inserts.

Utilization of higher values of *m* coefficient (0.65) allows to improve slightly the contrast between referential regions of sample and regions with teflon inserts. It should be underlined that in this case teflon inserts were located out of the directions of glass fabric reinforcements oriented at angles 0° and 90°.

3.2 Delamination in CFRP L-shape sample

In previous section authors investigated GFRP samples with teflon inserts simulating delaminations. The aim of research was to investigate the interactions of guided wave modes with discontinuities with different shapes and locations (planar as well as in the thickness).
In this sections results of investigation of guided wave interaction with true delamination in CFRP panel were presented. Panel were made out of 16 layers of CFRP pre–pregs GG204P IMP503 42 with following orientations $[0/90/0/90/0/90/0/90]_S$. Total thickness of panel was ~3.5 mm. From rectangular panel, smaller rectangular section was cut-off using water jet, creating L-shape panel. During water jet cutting process large delamination was created in the corner. In this delamination two layers of prepreg, counting from the top of panel were separated from the rest part of the panel. Total thickness of two layer was ~0.4 mm.
In the Figure 16 selected frames taken from animation of guided wave propagation in L-shape CFRP panel with delamination were presented. Guided waves were excited using piezoelectric transducer located at the middle of the bottom edge of panel. In this case excitation frequency was equal 200 kHz. Measurement were taken at the top surface using laser vibrometer.

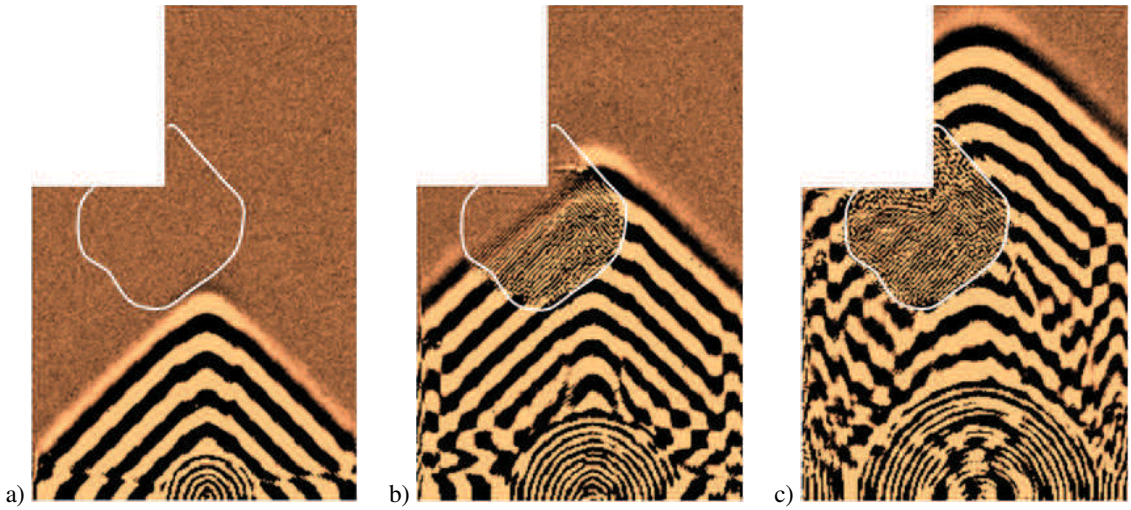

Figure 16. Selected frames from animation of guided wave propagation in L-shape CFRP sample with delamination

Analyzing frame presented in Figure 16a) propagation of S0 and A0 modes can be observed. Both modes could be simple distinguished. Mode S0 propagate with higher velocity than A0 mode and has larger wavelength. In the frame presented Figure 16b) interaction of S0 mode with delamination could be observed. Approximated shape of delamination located in the corner is marked by white curve. In the delaminated region propagation of two wave modes

can be observed: mode with length comparable to S0 and mode with much smaller wavelength than S0 and also slightly smaller than A0 – called here A0'. The second mode results from mode conversion phenomenon. In the Figure 16c) propagation of mode with smaller wavelength than A0 could be observed. Moreover, phenomenon of entrapment of A0' mode in the delaminated region of panel is clearly visible.

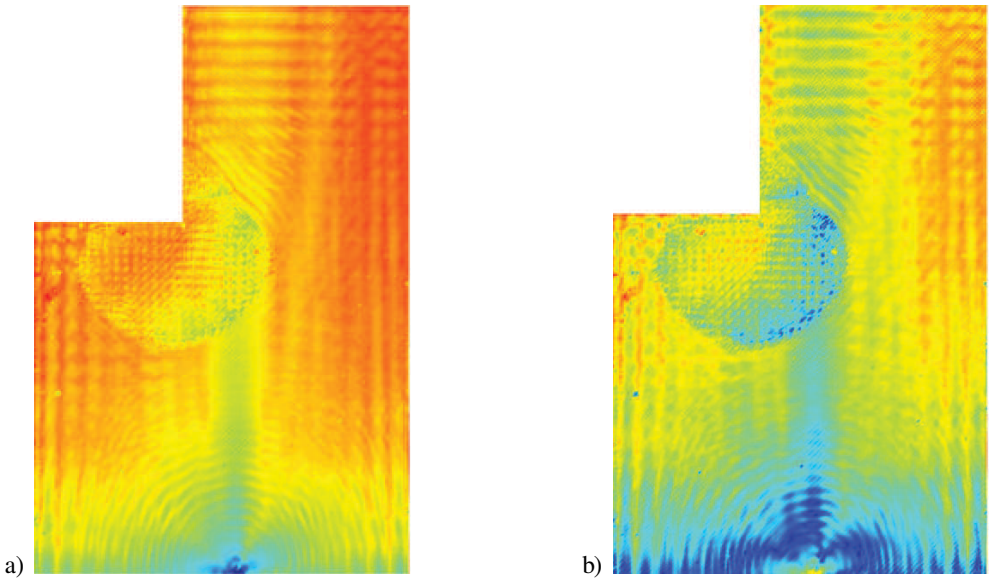

Figure 17. WRMS guided wave energy maps for: a) m=0.1, b) m=0.65; L-shape CFRP sample with delamination (measurements at top surface)

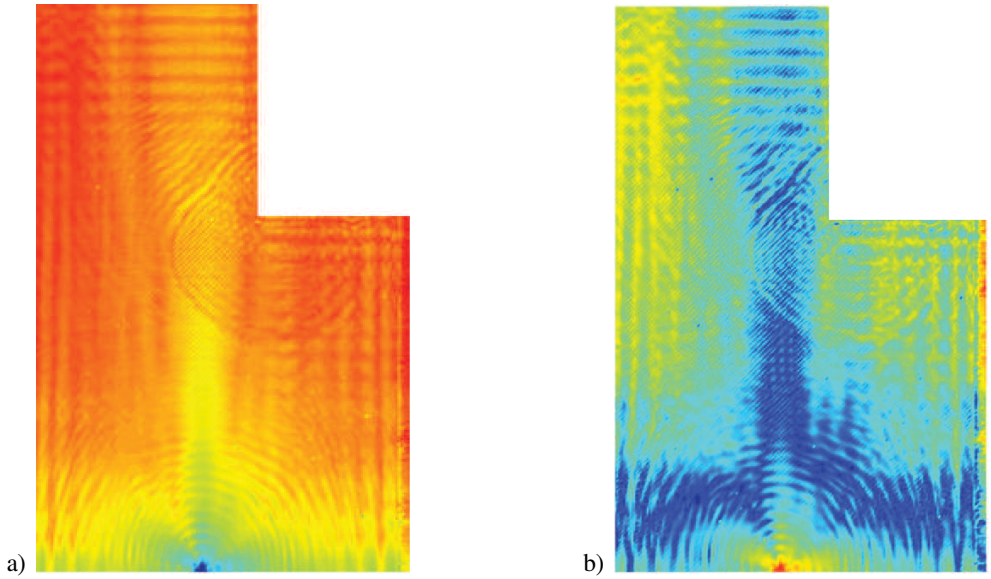

Figure 18. WRMS guided wave energy maps for: a) m=0.1, b) m=0.65; L-shape CFRP sample with delamination (measurements at bottom surface)

Next step was related to construction of WRMS energy map for propagating elastic waves.
In the Figure 17a) and Figure 17b) WRMS energy maps constructed respectively for the coefficient values 0.1 and 0.65 were presented. In both cases analyzing WRMS energy maps, delaminated region could be easily distinguished.
In next step measurements were taken at the bottom surface of panel. At this side of the panel thickness of material in the delaminated zone is equal ~3.1 (14 layers of prepregs). In the Figure 18a) and Figure 18b) WRMS energy maps for guided wave propagation were constructed for the *m* coefficient equal respectively to 0.1 and 0.65. Delaminated region could be distinguished in both presented cases in Figure 18. However, the contrast of energy distribution in delaminated and referential region is not so high like in previous case (measurements on the top surface).
Results presented in this section shows that proposed damage localization approach based on WRMS energy maps works properly not only in the case of artificially simulated defect using teflon insert but also in the case of real delamination.

4 CONCLUSIONS

It was shown that the EMI method indicates some sensitivity to the modification of adhesive bonds of CFRP samples. There is an increase in RMS index as the modification severity is higher so the bond quality level determination could be possible. This was observed both for thermally treated samples and contaminated with de-icing fluid.
It was shown that the EMI method is sensitive to a delamination simulated by a teflon insert. The change of RMS value clearly indicates which of the sensors is located on 'damaged' material. The change of the RMS is the lowest for this case. This suggest that delamination causes that only two layers of GFRP interacts with the sensor allowing it to vibrate more freely than in the remaining cases where the sensors is bonded to a 8-layer thick part of the plate.
Moreover, damage localisation algorithm based on WRMS energy maps was verified for the case of simulated delaminations (using teflon inserts) as well as in the case of true delamination. Utilization of teflon insert allowed to investigate influence of simulated damage location (planar and in the thickness) and its shape on guided wave mode interactions with it. Attention was focused on the phenomenon of S0/A0' mode conversion due to interaction of elastic wave with teflon inserts. Results showed that amplitude of A0' mode created as result of S0 mode conversion depends on the depth where the teflon insert is located. Mode conversion phenomenon occurs even for the case of teflon layer placed symmetrically in the respect to panel thickness. Radiated wave field for A0' mode is strictly related to the shape of teflon inserts. Moreover, entrapment effect for A0' mode was noticed. This effect was observed in the regions where teflon inserts were located. Utilisation of interactions of A0 and S0 mode with teflon inserts allow to localise the planar location of insert and to identify its shape. In this case WRMS energy maps were utilized.
In the next step sample with true delamination was investigated. In this case mode conversion phenomenon was also observed. Application of WRMS energy map based damage localisation algorithm allow to localise the location of delamination and identify its approximated shape.

ACKNOWLEDGEMENTS

Authors would like to gratefully acknowledge financial support given by National Science Centre, Poland by the decision no. DEC-2013/11/D/ST8/03355.
Authors would like to gratefully acknowledge financial support under grant agreement no. UMO-2014/13/D/ST8/03167 in the frame of SONATA project entitled: "Investigation of elastic wave mode conversion phenomenon in thin-walled structures with discontinuities".
The research was funded by the Polish National Science Centre under grant agreement no DEC-2013/10/A/ST8/00071 in the frame of MAESTRO project entitled: Excitation and control of mechanical waves in nonlinear media.
Part of this research has received funding from the European Union's Horizon 2020 research and innovation programme under grant agreement No 636494 (project entitled: "Quality assurance concepts for adhesive bonding of aircraft composite structures by advanced NDT - ComBoNDT").

REFERENCES

[1] Tian, Z., Yu, L. and Leckey, C. Delamination detection and quantification on laminated composite structures with Lamb waves and wavenumber analysis. *Journal of Intelligent Material Systems and Structures* (2015) 26(13): 1723-1738.
[2] Ren, Y., Qiu, L. Yuan, S. and Su, Z.: A diagnostic imaging approach for online characterization of multi-impact in aircraft composite structures based on a scanning spatial-wavenumber filter of guided wave. *Mechanical Systems and Signal Processing* (2017) 90: 44-63.
[3] Grisso, B.L. and Inman, D.J. Temperature corrected sensor diagnostics for impedance-based SHM. *Journal of Sound and Vibration* (2010) 329, 2323–2336.
[4] Baptista, F.G., Budoya, D.E., Almeida, V.A. and Ulson, J.A. An experimental study on the effect of temperature on piezoelectric sensors for impedance-based Structural Health Monitoring. *Sensors* (2014) 14, 1208-1227.
[5] Lim, H.J., Kim, M.K., Sohn, H. and Park, C.Y. Impedance based damage detection under varying temperature and loading conditions. *NDT&E International* (2011) 44:740–750.
[6] Annamdas, V.G.M., Yang, Y. and Soh, C.K. Influence of loading on the electromechanical admittance of piezoceramic transducers. *Smart Materials and Structures* (2007) 16.
[7] Benmeddour, F., Grondel, S., Assaad, J. and Moulin, E. Experimental study of the A_0 and S_0 Lamb waves interaction with symmetrical notches. *Ultrasonics* (2009) 49(2): 202-205.
[8] Liang, C, Sun, F.P., Rogers, C.A. Coupled electro-mechanical analysis of adaptive material system—determination of the actuator power consumption and system energy transfer. *J. Intell. Mater. Syst. Struct.* (1994) 5: 12-20.
[9] Park, G., Farrar, C.R., Lanza di Scalea, F. and Coccia, S. Performance Assessment and Validation of Piezoelectric Active-Sensors in Structural Health Monitoring. *Smart Mater. Struct.* (2006) 15(6): 1673–1683.
[10] Giurgiutiu, V. *Structural Health Monitoring with piezoelectric wafer active sensors*. Elsevier, Academic Press (2008).
[11] Buethe, I., Moix–Bonet, M., Wierach, P. and Fritzen, C.-P. Check of Piezoelectric Transducers Using the Electro–Mechanical Impedance. *Proc. 7th European Workshop on Structural Health Monitoring* (2014), Nantes, France.
[12] Wandowski, T., Kudela, P., Malinowski, P. and Ostachowicz, W. Defect induced guided waves mode conversion. *Proc. SPIE 9805, Health Monitoring of Structural and Biological Systems 2016*, 98050O (2016), doi:10.1117/12.2218233

[13] Jin, J., Quek, S.T. and Wang, Q. Wave boundary element to study Lamb wave propagation in plates. Journal of Sound and Vibration (2005) 288: 195–213.
[14] Tian, Z., Leckey, C., Yu, L., Seebo, J.P. Impact induced delamination detection and quantification with guided wavefield analysis. *Proc. SPIE 9435*, (2015); doi:10.1117/12.2083358

8th ECCOMAS Thematic Conference on Smart Structures and Materials
SMART 2017
June 5 – 8, 2017
Madrid, Spain

Mitigating Vehicle Shock Loads in Occupant Protection Systems using High Speed Magnetorheological Flows

N.M. Wereley

University of Maryland
College Park, MD 20742 Maryland, USA
e-mail: wereley@umd.edu, web page: http://www.umd.edu

ABSTRACT

Controlling dissipation of energy in vehicle systems, especially with the goal of protecting occupants from potentially injurious shock, crash or blast loads, is a critical issue as the cumulative impact of these load spectra on chronic health and acute injury are becoming better understood. Energy is dissipated utilizing a stroking element, such as a hydraulic damper or energy absorber. However, it is difficult to anticipate precisely what range of occupant mass an occupant protection system might be expected to protect, or what shock spectra the system might encounter.

Therefore, adaptation of stroking load is required to enable a system to have sufficient adjustability or control of energy dissipation across a wide range of anticipated disturbances, as well as robustness. The goals of this research are threefold: (1) to develop field magnetorheological (MR) fluids that suitable for these applications, (2) to develop magneto-rheological energy absorbers (MREAs) that enable adaptation of stroking load to minimize lumbar loads in the human spine and to minimize the potential for injury, and (3) to use adaptive seat suspension technology to protect occupants from a wide range of shock spectra, as well as to accommodate variable occupant mass.

VIII ECCOMAS Thematic Conference on Smart Structures and Materials
SMART 2017
A. Güemes, A. Benjeddou , J. Rodellar and Jinsong Leng (Eds)

KEYNOTE

MULTIDISCIPLINARY APPROACH FOR A COMMERCIAL TRANSPORT AIRCRAFT RUDDER WITH MORPHING CHARACTERISTICS.

MIGUEL Á. CASTILLO ACERO *

* VP Technology Development Aernnova,
Av. Manoteras, 20. 5th Floor, Madrid, 28050, Spain
e-mail: miguelangel.castillo@aernnova.com, www.aernnova.com

Key words: airframe, structures, additive manufacturing, multidisciplinarity, rudder, morphing, lateral, directional, aircraft, stability, control.

Abstract. The history of aviation is linked to the research and development of different physical and mathematical scientific fields. In our historic aviation records good examples can be found of studies and implementations. These cover not only new unconventional and disruptive aircraft configurations, but also the research and introduction of new materials and processes to make the airframe lighter and stronger. Also there have been continuous developments are available in the prediction of the aerodynamic loads that size an airplane to be safe, stable, controllable, and with adequate flying qualities.

Today there is a growing social demand to minimize environmental impact in all industrial sectors. Our aviation industry is also under this scrutiny. This is the reason why new requirements are emerging as eco- sustainability, in addition to compliance with the safety and certification requirements together with the challenges of being global economical competitive in an increasingly demanding world. In this line, it is remarkable to state that aircraft fuel consumption, and thus emissions of carbon dioxide, is directly linked by three key aircraft parameters, Breguet formula related: weight, drag and specific consumption of the power plant. The development of technology innovations in these three drivers must continue and this has to be approached from a multidisciplinary perspective.

This keynote focuses on summarizing the influence of the improvements in different aeronautics disciplines enabled by novel materials and additive manufacturing process, based on the introduction of a non conventional morphing curved rudder in a transport aircraft configured with under the wing podded engines. In particular, the morphed structure manufacturing and assembly aspects are detailed.

1 INTRODUCTION

The opportunity to consider an unconventional rudder arises from the observation of nature: birds can fly and manoeuvre modifying the curve of the trailing edge of the wings. Our commercial aircraft control surfaces are flat and rotate around its hinge line with a deflection angle in a simpler manner. There is an opportunity to improve, imitating nature, and make these control surfaces to be controlled by acting on their mean curve. The research on additive manufactured materials together with new actuators, enable new airfoils controlled deformation. The nature provides inspirational designs that are currently challenging conventional design principles as is the case of the configuration included in figure 1.



Figure 1: Biomimicry inspired airfoil structure [1]

The morphing research of a non conventional lifting or control surface requires a multidisciplinary approach. The search for airworthy and efficient morphing systems requires the concurrency of different disciplines. In consequence, the morphing system configuration is the result of the best compromise solution of different optimizations among the different perspectives: aerodynamics, materials, manufacturing processes and structures, power requirements, weight and flight mechanics, handling qualities and control. The figure 2 is representative of this compromise solution process.

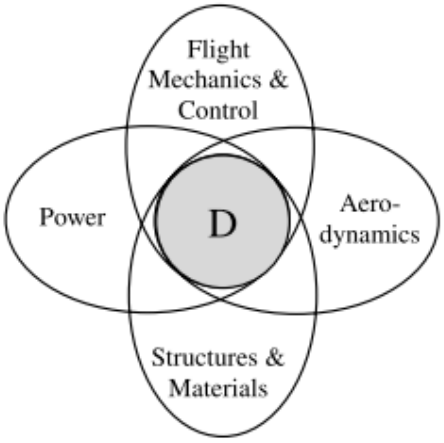

Figure 2: Disciplines involved in airframe morphing [2]

As an example of this highly multidisciplinary environment, to develop a morphing system, the figure 3 sketches an aerodynamic load alleviation system based on airfoil morphing controlled deformations.

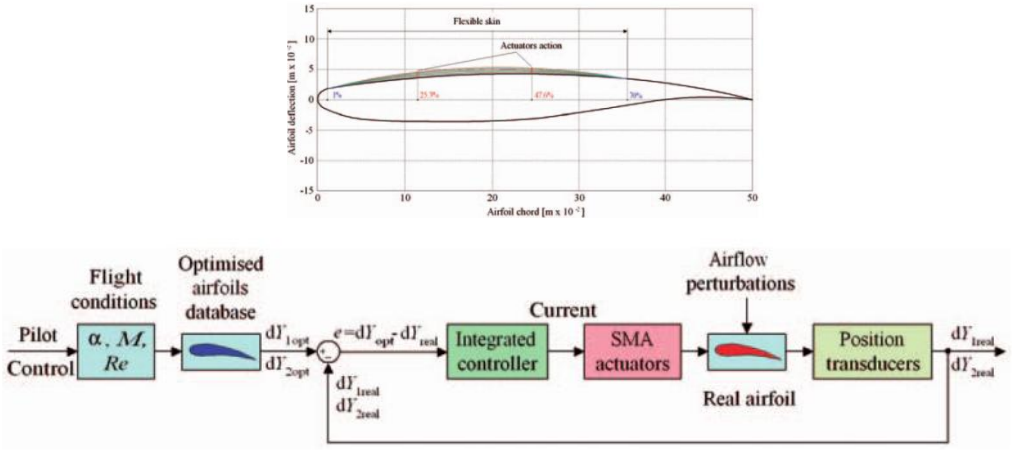

Figure 3: Load alleviation system based in morphing [3]

The adaptive trailing edge morphing design targets to be innovative, providing multi-disciplinary solution in order to create a structure able to withstand aeroelastic and aerodynamic loads. The design pretends to optimize aerodynamic efficiency by increasing the rolling moment, whilst reducing the drag and mass to the safe minimum, figure 4, [4].

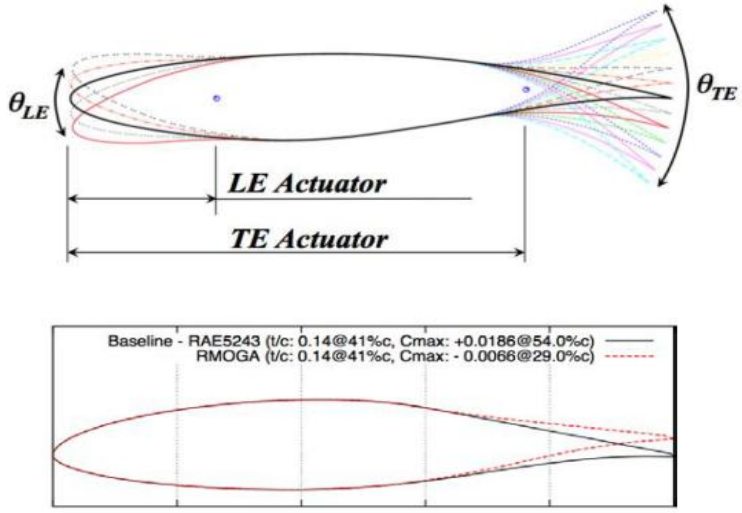

Figure 4: Morphing airfoil aerodynamic optimization [4]

The tendency of morphing technology will be essential to increase aircraft versatility and could be applied for commercial aircrafts. The flow control literature includes good advances in the adaptive lifting surfaces morphing domain. This is another good source of examples of the benefit on the multidisciplinary research with the purpose for flow control [5].

The modern transport aircraft fin is mainly sized by static loading stiffness and strength requirements. There are two static load cases that size most of the vertical empennage, fix and movable control rudder surface, the lateral gust during approach and landing, and the

engine out during take-off. The later load case is even more critical than the lateral gust due to the trend to increase engine thrust for higher capacities on twin engines under the wing configurations. This platform is the preferred choice for big transport commercial aircraft due to its higher fuel efficiency and the reduction of maintenance costs in relation to four engined one. The focus of this study aims to increase rudder aerodynamic efficiency based on a morphing solution and, in consequence, enable its size reduction, not only because of the potential weight and drag reductions, but also because there are operational benefits on static and dynamic stability which can be achieved, which is the main goal of this research.

The airfoil morphing has been analysed to delay the boundary layer transition from laminar to turbulent has been previously analysed with SMA actuators, [6]. The aerodynamic improvement assessment of non-conventional curved rudder has proved to bring potential increment of 15% on lateral force when deflected [7]. The aerodynamic pressure distribution for morphed rudder is smoother than the resulting for a conventional one.

The new unconventional rudder can curve chord-wise, while maintaining straight lines span-wise. The new rudder deflection angle is measured as the one that forms the line connecting the hinge line with the aft trailing edge point. Therefore the only difference between the new and the conventional rudder for a given deflection angle, is that the unconventional one presents a curvature that is the base of the aerodynamic improvement. The development of an airworthy structural solution for such a rudder is the objective of previous works [7], [8], see figure 5 below.

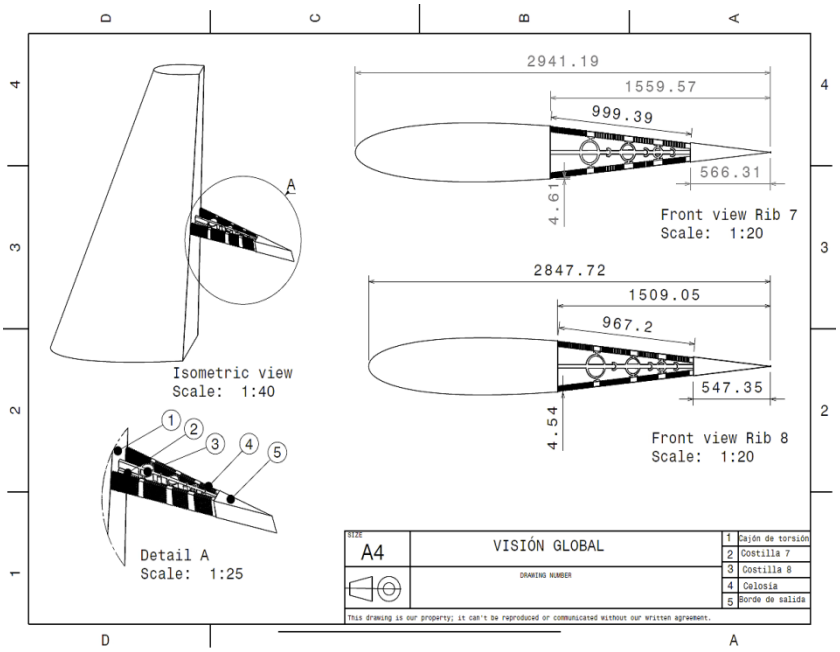

Figure 5: Morphing rudder structural architecture

There are expected difficulties in manufacturing and assembling a morphing rudder fully compliant with airworthiness requirements. The selection of the actuators is critical. They have to provide enough force and displacement at low weight and within space allocation constraints in the torsion box trailing edge volume. The selection of the actuator is coupled with the orthotropic stiffness of the morphing panels also weight constrained. The actuator power has to be selected to curve the rudder and so deform adequately he panel chord-wise. The manufacturing of these highly orthotropic panels by a certifiable aerospace, either standard or innovative, method is a challenge. The final integration of the solution must comply with functional, weight and performance requirements, therefore the assembly of the complex resultant mechanism must be very accurate and easy maintenance serviceable.

Studies that partially cover the airworthiness requirements of a morphing rudder, from static stability point of view, are required prior to flight clearance of the flight demonstrators. There is a need to study the lateral directional static stability of a transport aircraft in which the rudder has been reconfigured to provide a constant 15% more lateral load during deployment. The aircraft is under 1g stationary load cruise condition. The study of shape-morphing adaptive control surface of an airfoil has provided a significant number of research in compliant mechanisms for aircraft [9]–[11], wind energy [12], [13] and other UAVs, Unmanned Aerial Vehicles [14], [15].

The literature include recent developments on morphing tailless configuration aircraft flight control from different perspectives, as aeroelastic improvements [16]–[18]; the use of distributed shape-change effectors arrays in a flight control system [19]. Again, the study of new UAV configurations, has resulted on a relevant number of publications on lateral stability analysis and control [20].

The Aerodynamic studies based on CFD Open Foam, the flight Mechanics and control studies are performed on Static stability engine-out condition, at critical take off speed, aircraft velocity 85 m/s, air density at sea level, dry air 1.237 kg/m3. The lateral- directional aerodynamic coefficients were derived based on aircraft data and Matlab code. The Dynamic Stability was studied on lateral directional equations on the frequency domain, cruise condition. Power studies are based on the actuation selection which is driven by the morphing mechanism and also on the overall system weight, in comparison with the conventional rudder. These studies have been reported in previous author papers, [7]-[8].

2 STRUCTURAL DESIGN APPROACH

The Morphed Rudder design relies on a riblets. These riblets are articulated, figure 6. The number of riblets is a compromised solution between the achievement of smooth air contour, smoother as more discrete number of riblets, and the weight associated to a bigger number of them. The data and parameters considered in the conceptual design are selected in the initial stages of the design process.

$$d_0, \theta_0, k_1, k_2, n_{ribs}, d_{herr}, d_{tail}$$

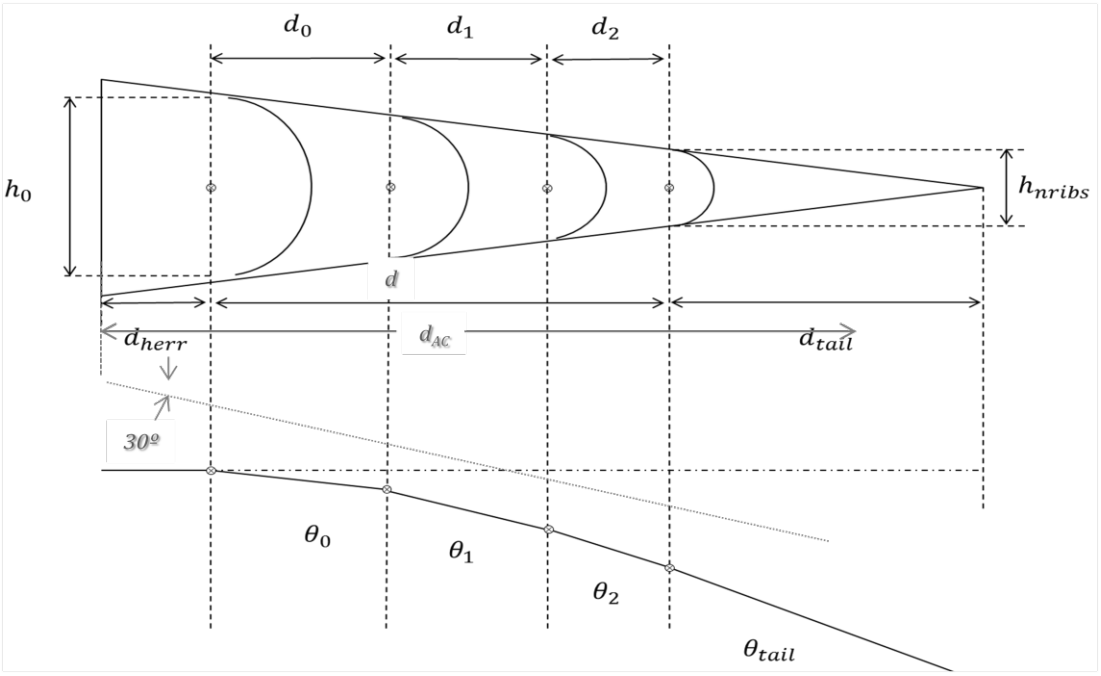

Figure 6 Morphing Rudder internal riblets geometry

The Morphed Rudder Structural analysis based on riblets geometries and rotation laws. Different approached can be considered. The mathematical models of such a geometries enable the computation in search of an optimum design.

$$\theta_{i+1} = k_1\theta_i \;\rightarrow\; \theta_i = (k_1)^i\theta_0$$
$$d_{i+1} = k_2\, d_i \;\rightarrow\; d_i = (k_2)^i d_0$$

The mathematical links between the parameters, have to be considered in order to further advance on the optimum solution.

$$d_{AC} = d_{herr} + d_{tail} + \sum_0^{n_{ribs}} d_i \rightarrow\; d_{AC} = d_{herr} + d_{tail} + d_0\frac{{k_2}^{n_{ribs}}-1}{k_2-1}$$

$$d_{AC}\sin 30 = d_{herr}\sin 0 + d_{tail}\sin\theta_{tail} + \sum_0^{n_{ribs}} d_i\sin\theta_i \rightarrow \frac{d_{AC}}{2} = d_{tail}\sin\theta_{n_{ribs}+1} + \sum_0^{n_{ribs}} (k_2)^i d_0\sin\left((k_1)^i\theta_0\right)$$

It has been studied morphable skin structures and many alternatives to the classic concept of rigid skin panel. The development of these structures is an important knowledge based on suitable deformable systems. For example, the “Double-C” shape-skeleton panels, figure 7. These skin panels consists of a substructure called skeleton formed by a series of stringers and additional geometry features in between which acts as a spring. As result of that the skin

acquires flexible superficial properties in the morphing direction and rigid properties in the perpendicular one.

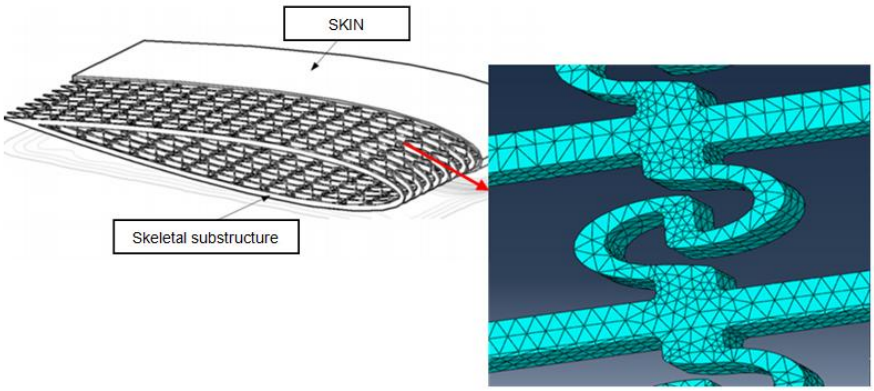

Figure 7: Double C shape skeleton panels

Structural integrity analysis is also implemented by means of Abaqus FEM, figure 8, to show a very preliminary test applying the concept of morphing mechanism.

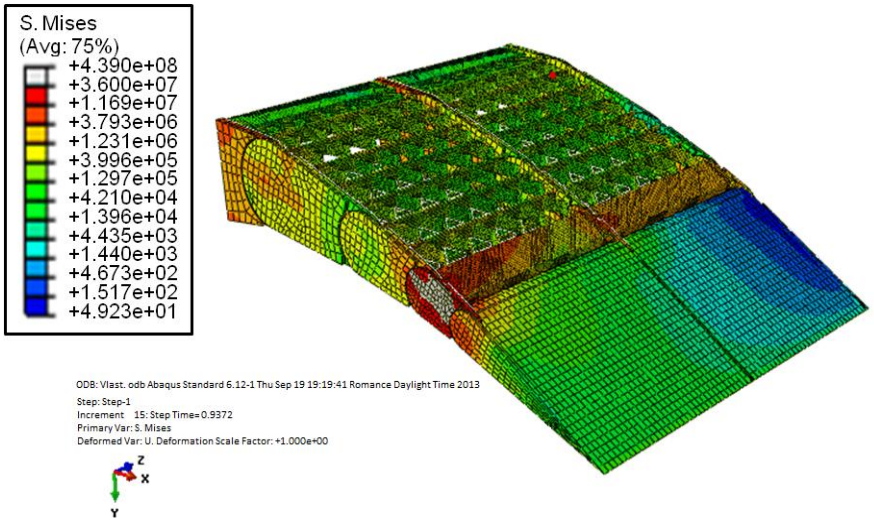

Figure 8: Abaqus static mechanical testing for internal structure design

The design of morphing skin structures has been carried out further with emphasis in the design of the various skin lattice structures, figure 9. Numerical characterisation of the geometric unit-cell and optimisation is developed focusing on the mechanical behaviour of these morphing skins. Numerical simulations using Finite Element Method through Abaqus commercial program were performed for the best selection of the unit-cell configuration. Behind the development of the design concept, a lot of work has been realized regarding optimization and characterization of the structures, through FEM analysis figure 10.

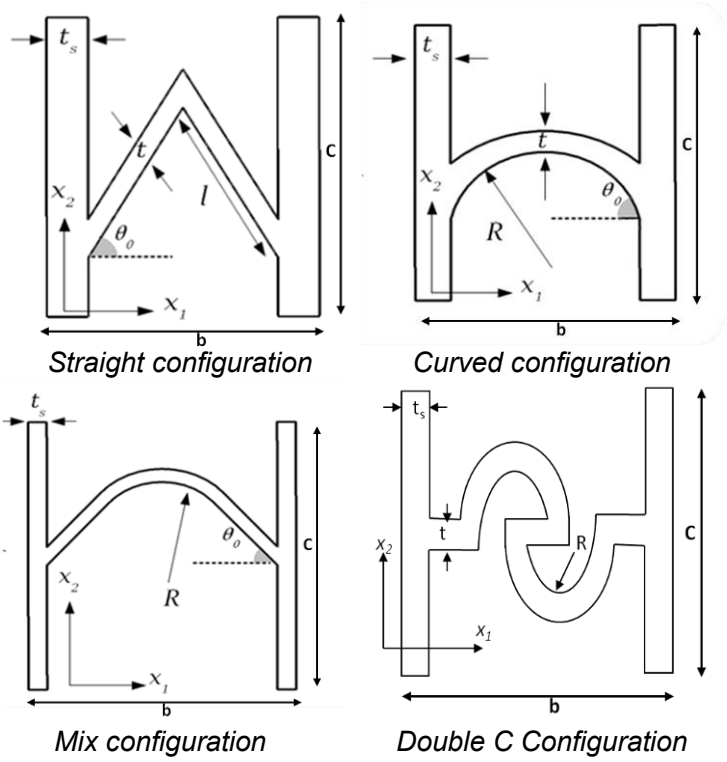

Figure 9: Unit cell of studied skin lattice structures

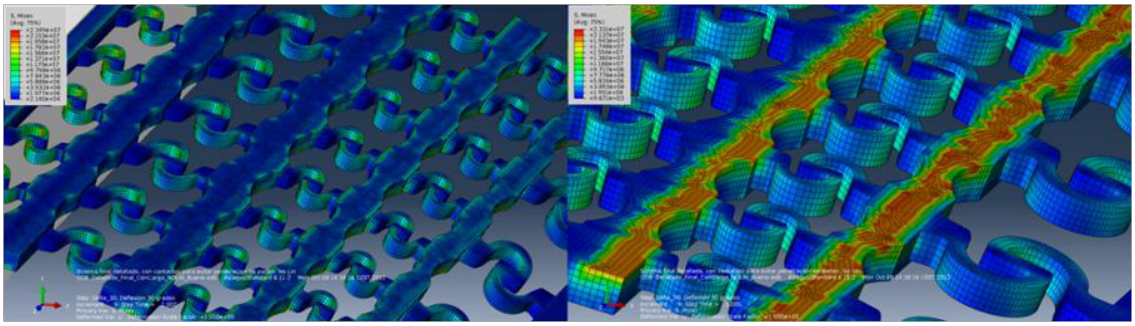

Figure 10: Double C shape skeleton panel Abaqus FEM analysis.

3 MATERIALS AND PROCESSES

Aernnova has carried out extensive research to select a suitable material candidate for the deformable skin skeleton design. The research leads to SLS (Selective Laser Sintering) technique; a technique which is very suited for morphing geometries such as the unit-cells presented as skeleton skin. The PA12 polyamide material is selected for this process due to its good ductile and toughness properties. In addition, the material is light weight and cheap, which favors the decrease of weight penalties, a crucial part in the implementation of a morphing device. However, the material is damaged due to its hygroscopic nature and

humidity impoverishes its material properties, making it brittle. Tests have been performed by saturating the manufactured pieces of PA12 in water particles and then performing static tests to analyze it's tensile and fracture effects. Variations of PA12 materials with incorporated hard particles are also looked into for property enhancements and compensation for the moisture drawback. Materials investigated included GFN containing glass beads, HST containing ceramic fibers and PA12 base material. For humidity study, specimens are created for each component and these are submerged in water at a constant temperature of 90ºC in order to accelerate the water saturation process. Specimens are also kept at a dry constant temperature of 90ºC for dry condition testing, figure 11Figure 11. The process is carried out for the different types of PA12 materials specimen which are later used for the mechanical testing.

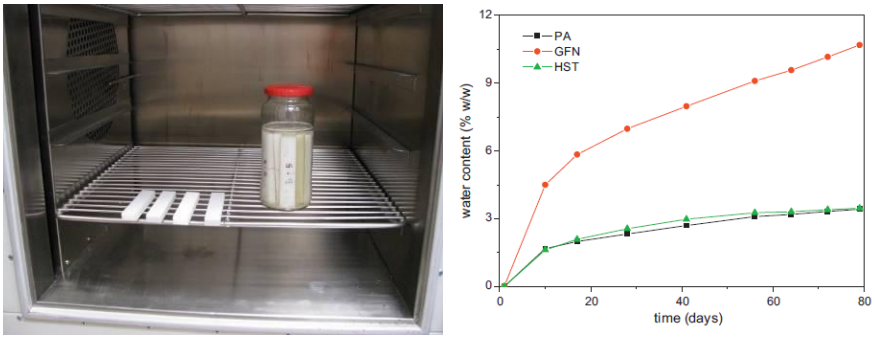

Figure 11: Drying and Water saturation process

Various mechanical tests are performed to investigate the behaviour of these types of PA12 materials after the water saturation and drying process. The experimental testing and characterisation are carried out following standard norms of test justification involving static tensile, compression, fracture and fatigue testing. Mechanical properties from the experimental testing showed interesting results. The yield strength Improves under dry conditions and no toughness alteration for altered PA12 with spheres and fibre compounds. Materials presented impoverished toughness and tensile properties. This is especially affected the toughness properties of the base PA12 material, figure 12.

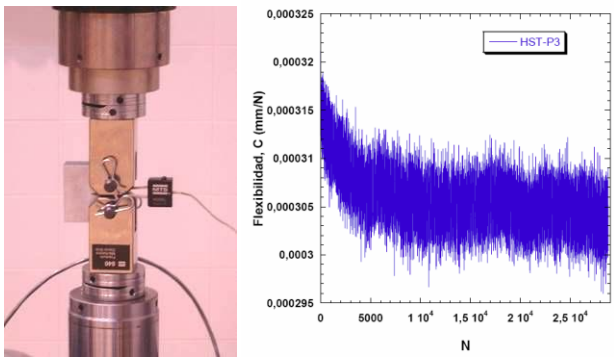

Figure 12: Fatigue testing and cyclic loading application

4 FLUID- STRUCTURES INTERATION

The structural implementation of the solution has to be checked from local deformations at deflection of the surface exposed to the air flow. The airfoil pressure distributions and skins internal loading can create local deformations that are translated into deviations of the actual airfoil in relation to the theoretical one, figure 13.

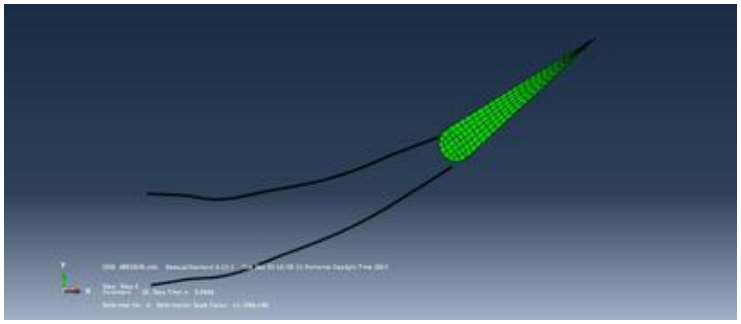

Figure 13 Local deformations study of the morphing structural concept

The aeroelastics analysis is pending and it is relevant given the change in the vortex-frequency due to the rudder morphing [7], and the weight and stiffness effect of the new design in relation to the conventional one.

5 MANUFACTURING AND ASSEMBLY

The EU FP7 SARISTU project has given essential experience on morphing structures from the manufacturing and assembly point of view. Starting by preliminary dummy demonstrator, then the ATED 2-bay demonstrator, figure 14, experience is obtained from these phases which achieved an important milestone. This leads to the improved manufacturing and assembly process of the final 5-bay demonstrator of ATED.

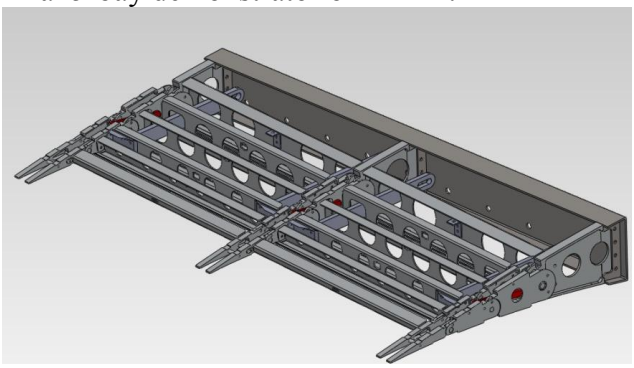

Figure 14 Internal Structure display

The manufacturing process was performed successfully by selecting the optimal materials for the further machining and bending processes. The internal structure of the ATED is a skeletal structure which is crucial for the correct transmission of movement from the actuator and structural integrity as load support. Holes are also included in the design phase in the components of the internal structure for the accommodation of cable routing, sensor

installation and furthermore reducing the overall weight of the structure. The manufactured components included the following features:

- Segmented ribs, carrying rotational movement for the structural morphing.
- Spar-x that supports the metallic skin sections of the morphing skin.
- Rear spar which carries the actuators and also structurally supports de whole ATED.

The actuator chain and bars were manufactured to control the morphing movement in the ATED by transforming the produced rotations into displacement of the actuation bar. The actuator chain was mounted at the base of the ATED rear spar and the actuation bar was fitted through the spar-x and connected to the actuation chain, figure 15.

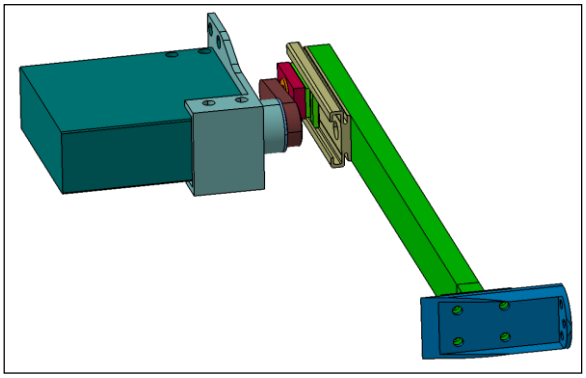

Figure 15: Actuator chain DMU

The Dead Box (DB) skin is an interface between the Wing Box and the Trailing Edge structure. It is made of an upper and lower skin panel as shown in figure 16. The union position at the ATED is located at the rear spar flange, 1st spar-x flange and the rib flange (1st section only).

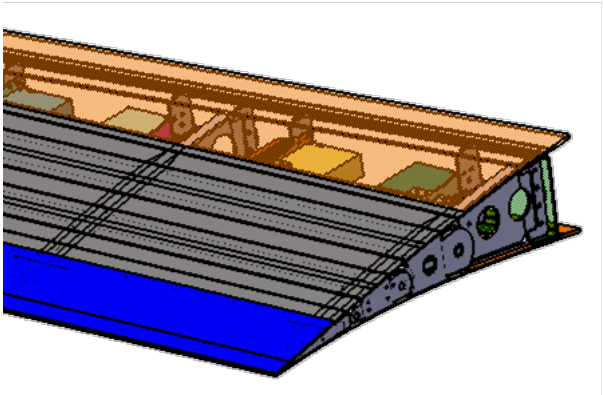

Figure 16: Skins connecting ATED and torsion box

The morphing skins are located in the upper and lower surfaces of the trailing edge. The 2-bay demonstrator offered important acquired experience to be implemented for the manufacture and assembly of the ATED 5-Bay Demonstrator, figure 17.



Figure 17: Internal structure of 5 Bay Demonstrator

A proof of concept of the morphing skin was manufactured by the already mentioned SLS additive manufacturing process, as a physical demonstrator, it can be observed in figure 18.

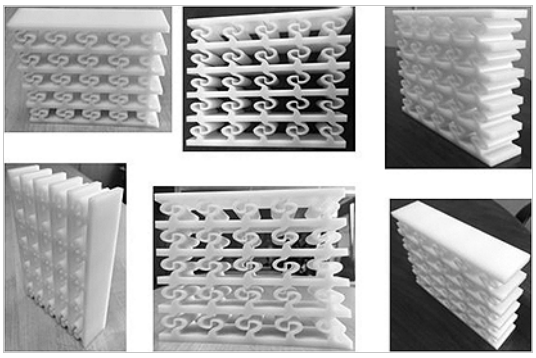

Figure 18: SLS manufactured Double C configuration PA12 material.

6 CONCLUSIONS AND CHALLENGES FOR FUTURE STUDIES

From previous author studies, the new morphed rudder presents the following enhancements:

- 15% potential improvement in aerodynamic lift, [7]
- Higher frequency of the vortices detachment, [7]
- It is enabled by new highly orthotropic panels produced by additive manufacturing, [8]
- The new panels show secondary module from a certain level of deflection, [21]
- Static stability, increased yawing moment available 8% at engine out, in consequence decrease in the minimum speed lateral control 4%, [22]

- Studies on dynamic stability free control commands result in a decrease of the yaw amplitudes on Dutch Roll frequencies [23]
- For fixed controls, the yaw divergence is predicted to appear sooner, [23].

This paper presents additional manufacturing and assembly experience on similar morphing structures on EU FP7 SARISTU project. These developments have brought to a current technological maturity close to TRL 3 for a morphing rudder at an aircraft system level.

The most relevant remaining challenges for future studies are listed below:

- Selection of actuators, structural sizing and complete weight impact assessment.
- Wind tunnel tests to verify aerodynamics morphing effects without and with NLF, HLFC system
- Stability analysis of more load cases to complete studies of flying qualities.
- Keep on investigating methods to optimizing the highly orthotropic panels geometric configuration.
- Miniaturization of geometric cells and step into three dimensions features
- New additive manufacturing features and use of different raw materials.
- Complete test campaign of the highly orthotropic 3D printed panels
- Complete rudder static, fatigue and Damage tolerance tests.
- Ground vibration test , FEM correlation and Aeroelastic studies and assessment.

REFERENCES

[1] Elzey D. M.; A. Y. N. Sofla and Wadley H. N. G. (2003). "A bio-inspired, high-authority actuator for shape morphing structures." Proceedings, de SPIE, vol. 5053, pp. 92–100.

[2] Vasista S.; Tong L. and Wong K. C. (2012). "Realization of Morphing Wings: A Multidisciplinary Challenge," Journal of Aircraft, vol. 49 (January), pp. 11–28.

[3] Grigorie T. L.; Popov A. V.; Botez R. M.; Mamou M. and Mebarki Y. (2011). "On-off and proportional-integral controller for a morphing wing. Part 1: Actuation mechanism and control design," in Proceedings of the Institution of Mechanical Engineers, Part G: Journal of Aerospace Engineering, 2011, vol. 226 (Jul), pp. 131–145.

[4] Lee D. S.; Gonzalez L. F.; Periaux J. and Onate E. (2012). "Robust Aerodynamic Design Optimisation of Morphing Aerofoil / Wing using Distributed MOGA," 28TH International Congress of the Aeronautical Sciences, ICAS 2012, vol. 25, pp. 13–24.

[5] Stanewsky E. (2001). "Adaptive wing and flow control technology," Progress in Aerospace Sciences, vol. 37, pp. 583–667.

[6] Barbarino M. (2014). "Airframe noise reduction technologies applied to high-lift devices," en las actas, proceedings, de "3AF / CEAS Conference Greener Aviation: Clean Sky breakthroughs and worldwide status", 12- 14 March 2014, Brussels, Belgium.

[7] M. A. Castillo-Acero, C. Cuerno-Rejado, and M. A. Gomez-Tierno, "Aerodynamic Modelling for a Morphing Rudder," in RAeS Applied Aerodynamics Conference 2014, Bristol, UK, 2014.

[8] M. A. Castillo-Acero, M. A. Gomez-Tierno, and C. Cuerno-Rejado, "Morphing Structure for a Rudder," in 4th Aircraft Structural Design Conference, RAeS, Belfast, UK, 2014.

[9] Pecora R.; Amoroso F. and Magnifico M. (2013). "Design and Experimental Validation of a Morphing Wing Flap Device" proceedings, "6th ECCOMAS Conference on Smart Structures and Materials. SMART2013", 24-26 Junio 2013, Politecnico di Torino, Italia.

[10] Sofla A. Y. N.; Meguid S. A.; Tan K. T. and Yeo, W. K. (2010). "Shape morphing of aircraft wing: Status and challenges," Materialds and Design, vol. 31 (Mar), pp. 1284–1292.

[11] Osborn R. F.; Kota S.; Hetrick J. A.; Geister D. E.; Tilmann C. P. and Joo J. (2004). "Active Flow Control Using High-Frequency Compliant Structures," Journal of Aircraft, vol. 41 (Mayo), pp. 603–609.

[12] Puterbaugh M. and Beyene A. (2011). "Parametric dependence of a morphing wind turbine blade on material elasticity," Energy, vol. 36 (Jan), pp. 466–474.

[13] Lachenal X.; Daynes, S. and Weaver P.M. (2013). "Review of morphing concepts and materials for wind turbine blade applications," Wind Energy, vol. 16 (Feb), pp. 283–307.

[14] Gamboa P.; Vale J.; Lau F. J. P. and Suleman A. (2009). "Optimization of a Morphing Wing Based on Coupled Aerodynamic and Structural Constraints," AIAA Journal, vol. 47 (Sept), pp. 2087–2104.

[15] Cadogan D. (2004). "Morphing Inflatable Wing Development for Compact Package Unmanned Aerial Vehicles," proceedings, 45th AIAA/ ASME/ ASCE/ AHS/ ASC Structures, Structural Dynamics and Materials Conference, 19-22 April 2004, Palm Springs, USA.

[16] Yang J.; Nangia R.N.; Cooper J.E.; Simpson J. A. e Ibp F. (2014). "Optimisation of Morphing Wings for Improved Environmental Performance Dept of Aerospace Engineering , University of Bristol , BS81TH , UK," proceedings, de "3AF / CEAS Conference Greener Aviation: Clean Sky breakthroughs and worldwide status", 12- 14 March 2014, Brussels, Belgium.

[17] Simpson J.; Anguita-Delgado L.; Nilsson B.; Vaccaro V. and Kawiecki G. (2005). "Review of the European Research Project 'Active Aeroelastic Aircraft Structures (3As)," proceedings, "European Conference Aerospace Science (EUCASS)" 4-7 Jul 2005, Moscú, Rusia.

[18] Courchesne S.; Popov A. V. and Botez R.M. (2012). "New aeroelastic studies for a morphing wing," INCAS bulletin ISSN 2066- 8201. Vol. 4, Issue 2/2012, pp.19- 28.

[19] Thomas F. O.; Corke T. C.; Iqbal M.; Kozlov A. and Schatzman D. (2009). "Optimization of Dielectric Barrier Discharge Plasma Actuators for Active Aerodynamic Flow Control," AIAA Journal, vol. 47 (Sept), pp. 2169–2178.

[20] Kamuran T. and Jafarov E. M. (2006). "Lateral Dynamic Modeling of Hezarfen Unmanned Aerial Vehicle (UAV) and H_∞ Loop Shaping Robust Control System Design," Proceedings, "10th WSEAS International Conference on SYSTEMS", Vouliagmeni, Atenas, Grecia, 10-12 Jul 2016, pp. 369–374.

[21] Castillo Acero M. A., Cuerno C. and Gómez Tierno M. A, "Highly Orthotropic Panels Structural Stability, Farrar and Bloch Waves Theory," in *3rd Int. Conference on Buckling and Postbuckling Behaviour of Composite Laminated Shell Structures*, Oct 2015, Braunscweig, Germany.

[22] Castillo Acero M. A., Cuerno C. and Gómez Tierno M. A. "Morphed vertical tailplane assessment for certification requirements," in *5th CEAS Air & Space Conference 7-11 Sept 2015 Delft University of Technology (The Netherlands)*, 2015.

[23] Castillo Acero M. A. (2016). "Studies to configure a non-conventional rudder on a commercial transport aircraft: aerodynamics, structures and lateral- directional static and dynamic stability." Proceedings 6th EASN International Conference, Porto, 18th October 16, Portugal.

VIII ECCOMAS Thematic Conference on Smart Structures and Materials
SMART 2017
A. Güemes, A. Benjeddou , J. Rodellar and Jinsong Leng (Eds)

SMART BEHAVIOUR OF CNT MODIFIED ADHESIVE FILMS FOR CARBON FIBER COMPOSITE REPAIR

A. UREÑA, C. GARCÍA-NIETO, X.F. SÁNCHEZ-ROMATE, J. RAMS, M. SÁNCHEZ

Materials Science and Engineering Area
Universidad Rey Juan Carlos (URJC)
Calle Tulipán, s/n, 28933 Móstoles, Madrid, Spain
e-mail: alejandro.urena@urjc.es, www.urjc.es

Key words: Adhesive, repair, composite, SHM, CNT

Abstract. Epoxy adhesives films were doped by spraying an aqueous dispersion of carbon nanotubes. Sensing capability of carbon fiber reinforced composite coupons with bonded patch repairs was evaluated; several single lap shear and Mode-I fracture energy tests were conducted and their electrical responses were characterized. It was observed that electrical resistance increases with mechanical strain due to tunnelling effect on CNT percolating networks and increases of electrical resistance associated to crack propagations could be also detected.

Once the smart behaviour if the adhesive joints was identified by means of mechanical tests in normalized adhesive joined specimens, panels (400 x 400mm) with square co-bonded patches, made using the same curing cycle based on the repaired material one, were prepared using CNT doped adhesive films. These panels were mechanical tested to determine the effect of the doping treatment on the mechanical behaviour of the repairs, at the same time that electric measurements were carried out to identified local failures during testing. Obtained results showed that structural film adhesives could be surface doped with CNT providing sensing capabilities to be used in structural health monitoring of adhesive repairs in composite structures.

1 INTRODUCTION

Composite primary structures repairing is a priority issue in the aerospace industry. When a composite structure suffers an in-service damage, if it is weakened due to fibers breakage or delaminations, it is necessary to make a structural repairing. This kind of repairs, unlike cosmetic or temporary ones, consist on a substitution of damaged fibers and plies in order to restore the original mechanical performance. One of the possible solutions is to apply composite patches by using adhesives [1-2]. However, in order to ensure the quality of these repairs, it is necessary to develop novel inspection techniques, especially non-destructive tests (NDT), such as ultrasounds (C-Scan), vibrothermography or shearograpgy. They are able to detect damage onset in this type of repairs in composite structures [3-4].

An alternative to NDT is providing to the adhesive joint a multifunctional behaviour. The present work aims to analyze the monitoring capability of bonded joints by using adhesive films previously doped with carbon nanotubes (CNT). In previous works, it has been proved that CNT networks are able to properly detect strain and discontinuities (failures) by means of electrical resistance change measurements [5-6].

There are many research in which this CNT network was created by dispersing CNT on a paste adhesive (generally an epoxy based one) using the conventional dispersing techniques (such as three roll mill calendering or toroidal stirring). However, in this work, CNTs were applied directly over the adhesive surface by spraying an aqueous CNT solution [7]. Previously to sensing characterization, a study of the mechanical properties on standardized Mode-I and Single Lap Shear (SLS) specimens has been carried out. Once the multifunctional behaviour of these joints was identified, panels with a composite repair patch were manufactured, using the proposed adhesive. Mechanical testing of these panels has showed the Structural Health Monitoring (SHM) capabilities of CNT doped adhesive joints.

2. EXPERIMENTAL PROCEDURE

2.1 Materials

Adhesive was a FM300, supplied by Cytec. It is an epoxy based adhesive film with a wide-open knit tricot carrier. For the present study, the FM300K was used, with a surface weight of 244 g/m^2, nominal thickness of 0.2 mm, being considered the one with the highest performance within FM300 series. More specifically, it has a shear strength allowable of 36.8 MPa at 24 ºC and 20.4 MPa at 150 ºC.

CNT doping was carried out by spraying an aqueous CNT dispersion over the adhesive surface, using an airbrush. Pressure was set to 0.1 MPa at 40 cm distance. Multiwall CNTs were supplied by Nanocyl, with the commercial name of NC3152, with an average diameter of 9.5 nm and a length up to 1 μm. They have a 90 % C purity and are amino-functionalized. To stabilize the CNT dispersion, a surfactant called sodium dodecyl sulphate (SDS) was used at 1.0 wt. % content. 0.1 wt. % CNT dispersion was achieved by means of ultrasonication, using a horn sonicator of 400 W power and 24 Hz frequency. Sonication was done during 20 min at an irradiation acoustic time of 0.5 s and horn amplitude of 80 %. After sonication process, a centrifugation stage was done at 5000 rpm during 10 min.

CFRP substrates were manufactured by intermediated modulus unidirectional tape prepegs (IMA/M21E). Carbon fiber and prepeg surface weight are 194 ± 5 g/m^2 and 294 ± 9 g/m^2. Resin weight fraction is 34 % and laminate density is 1.58 g/cm^3. Several 500 x 500 mm panels were manufactured at a $[0]_n$ layer sequence with different thickness depending on tests requirements in order to manufacture the normalized coupons for Mode-I and SLS tests. Curing was done in autoclave with a vacuum bag using a double ramp temperature curing cycle. Maximum curing temperature and pressure were 180 ºC and 0.9 MPa respectively, during 8 h.

2.2 Mechanical tests

SLS joints were tested using the AITM 1-0019 standard. Adhesive joints were manufactured by co-bonding. Total thickness of each substrate was 2.024 mm, corresponding to a $[0]_{11}$ layer sequence. Mechanical testing was done at room temperature at a test rate of 0.5 mm/min.

Electrical monitoring of SLS specimens was carried out as shown in Figure 1a. Two electrodes made of copper wire with silver ink were attached to the center of the overlapping area, at 7.5 mm and 12.5 mm distance from the edge in the main load and the transversal direction, respectively. Monitoring was carried out, thus, in the transversal direction of the adhesive joints. Electrical acquisition was carried out by using a digital multimeter Agilent 34410A.

Moreover, Mode-I energy fracture (GIC) tests were conducted in order to determine the strength of the adhesive joints as a function of crack length. These tests were carried out according to AITM 1-0053 standard. The electrical response of the adhesive joints were measure during the mechanical testing. In this case, the total thickness of each substrate was 1.472 mm, corresponding to a $[0]_8$ layer sequence.

Electrical monitoring of Mode-I specimens was done as shown in Figure 1b. Two electrodes made of copper wire with silver ink were attached at 60 mm distance of the load application point. Thus, monitoring was carried out in the transversal direction, like in the SLS specimens.

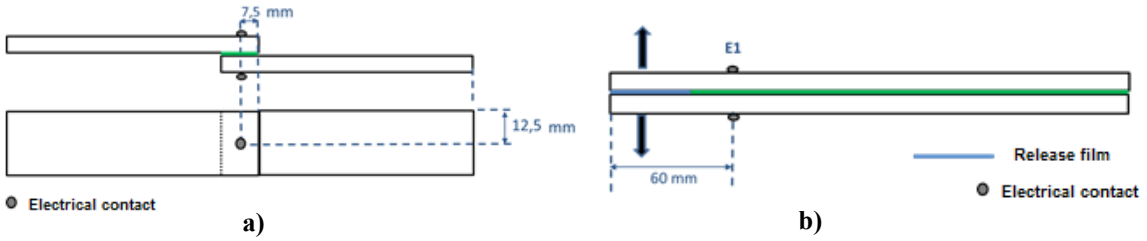

Figure 1: Configurations of electrical contact for sensorization during: a) SLS test; and b) GIC test.

2.3 Panel repair tests

A 400 x 400 mm composite panel was defined with an applied repair. This repair was a composite patch scarf (repair path with a constant slope). The material of the pristine panel was the same as used previously, IMA/M21E. Layer sequence was $(45/-45/90/0/90/-45/45/90/0/90/-45/45/90/0/45/-45)_s$ with a total thickness of 5.888 mm.

The patch repair was manufactured by using the same prepeg. This repair was done over 16 plies with a total thickness of 2.944 mm, being the ply of the base of the cone repair oriented at -45º. The rest of the plies were oriented following a similar stacking sequence than the original laminate. An outer 45º ply was placed over the entire repair. Figure 2 shows a schematic of the

patch repair. Adhesive film was the FM300K with the same cure cycle than previously described.

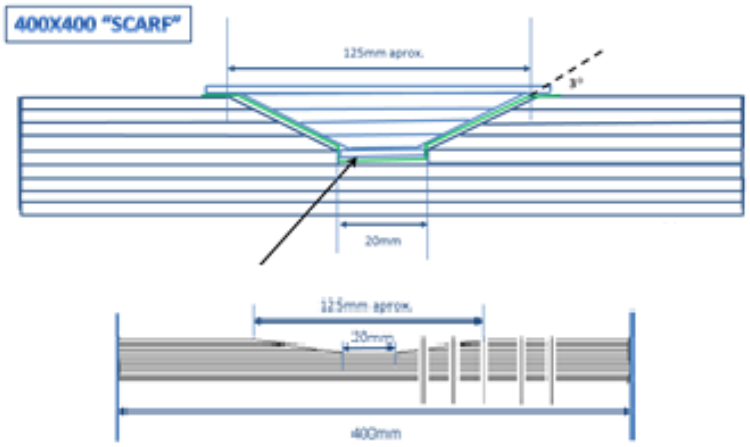

Figure 2: Schematics of the patch repair in a 400 x 400 mm composite panel

Once manufactured, the panel was subjected to mechanical testing in order to prove sensing capabilities of CNT doped adhesive film. The aim was to compare the electrical response of the adhesive with the measurements obtained with conventional strain gauges. This would allow comparing the different technologies (strain gauges, electrical sensing and acoustics), giving a more detailed understanding of the mechanical performance of the panel.

A shear test was carried out in the panel. Six rectangular rosettes RY81-6-350 with 350 Ω and eight strain gauges LY41-6-350 with linear geometry and 350 Ω were placed in the panel. The disposition is shown in Figure 4, where the outer and the inner (Side A and B, respectively) surface of the panel is represented. The outer corresponds to the composite patch repair side. In addition, the corners were cut according to the required tooling for the mechanical tests.

In combination with rosettes and strain gauges, an electrical sensing scheme was defined. This electrical network (blue circles) was composed by five channels (E1 to E5) and it is shown in Figure 3. E1 and E3 were placed in the load axis at 10 mm from the corner of the patch. E2 was placed at 20 mm from the center of the repair. E4 and E5 channels were placed near the right and left corners of the patch at 10 mm.

Figure 4 shows an image of the mechanical test in a tensile testing machine with a 500 kN load cell at a test rate of 0.5 mm/min. Test would end by collapsing of composite panel or by reaching the maximum allowable of the testing machine.

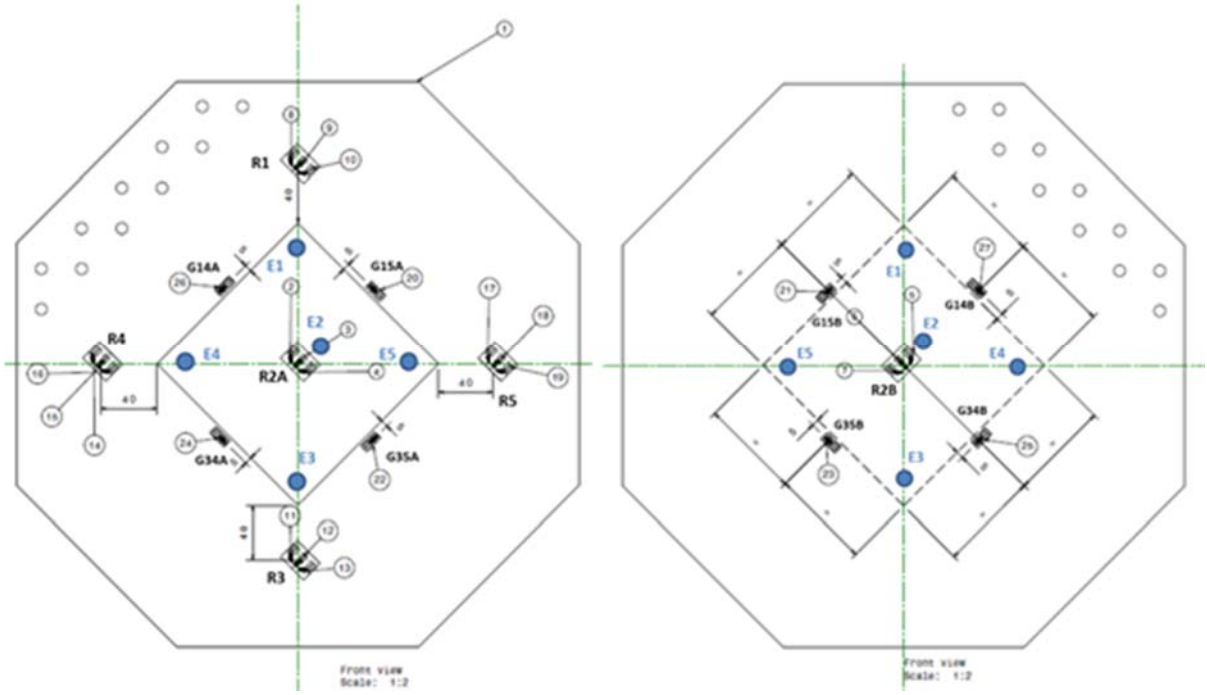

a) b)

Figure 3. Schemes of the extensometry and electric sensorization of a repaired composite panel: a) front face; b) back face.

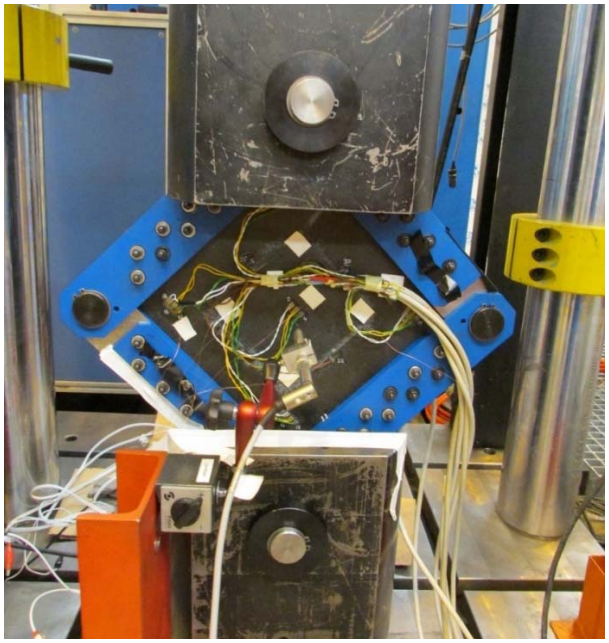

Figure 4. Experimental arrangement of the shear test of the repaired composite panel

2.4 Non-destructive testing

Previously to mechanical testing, composite repaired panel was inspected by ultrasounds. The results did not show neither discontinuities higher than 36 mm^2 nor volumetric porosity. Therefore, from the inspection point of view, the repair was considered valid. After mechanical testing, ultrasonic inspection was carried out again and the discontinuities and defects were characterized, allowing correlating the electrical response with the NDT results.

3 RESULTS AND DISCUSSION

The electrical monitoring of SLS joints could lead to different behaviours on the electrical response, defined as Type I and II, which are shown in Figure 5. Both of them presents an initial constant trend, associated to a minimum strain threshold from which the system is able to detect electrical changes. After that, an increase of the electrical resistance is observed, corresponding to higher strain levels. This tendency could be linear or exponential depending on the prevalence of contact and tunnelling effect between adjacent CNTs, respectively. Instabilities may be due to crack initiation as well as local failures (i.e. microcavities, local disbonds). Finally, a sudden increase of the electrical resistance is observed, corresponding to the final failure of the joint.

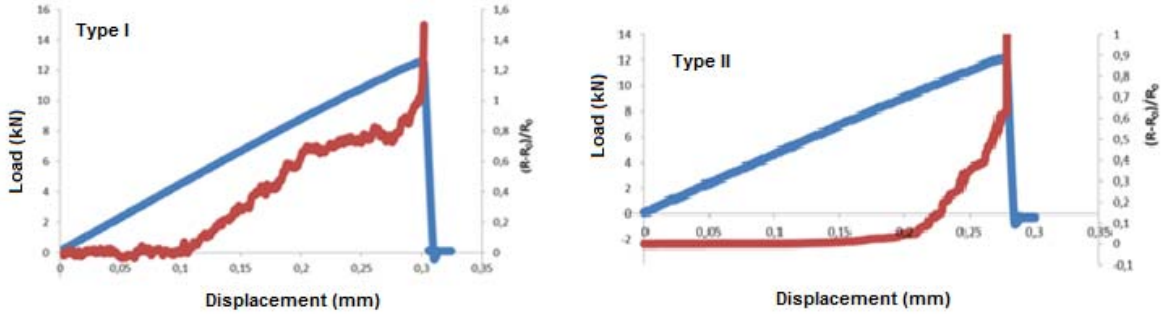

Figure 5. Single lap shear test curves. Mechanical response (blue curve). Electrical response (red curve).

On the other hand, electromechanical curves of Mode-I test specimens allow correlating the electrical response of the joint with the crack propagation. Figure 6 shows an example of these curves. An initial stage with a slight increase of the electrical resistance is observed just before crack initiation and due to adhesive deformation. When crack initiation took place, a sharp rise of the electrical resistance is noticed due to breakage of conductive pathways. From this point, a steady increase of the electrical resistance as well as sudden rises are observed. This is due to the combination of two effects, the adhesive deformation and the breakage of electrical pathways along the joint. Sudden drops can be also associated to the presence of microcavities as commented before on SLS tests. The test was ended once crack length was 60 mm from the initial pre-crack, correlated to a piano hinge displacement of 26 mm. For that reasons, a sudden change of the electrical resistance is not observed at the end of the test because Mode-I specimen was not totally broken.

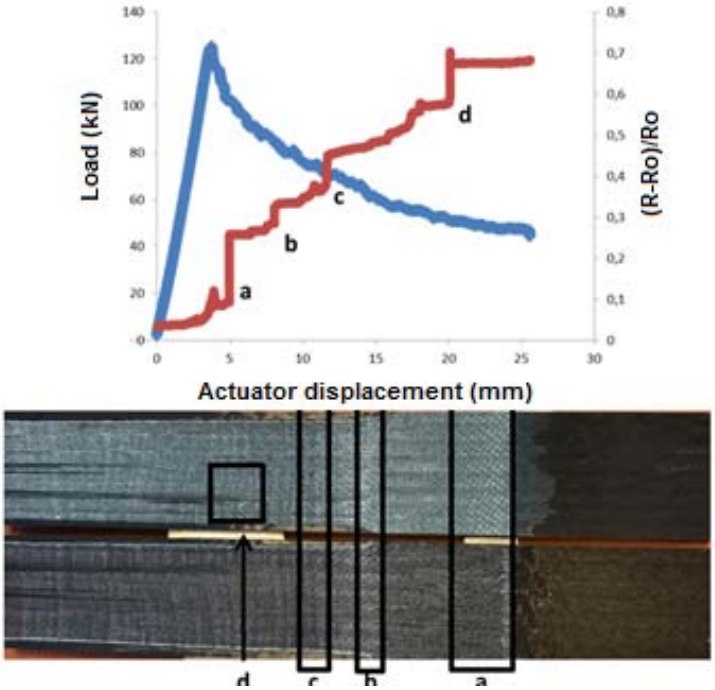

Figure 6. GIC test curves. Mechanical response (blue curve). Electrical response (red curve). Correlation with failure mode.

The analysis of the fractured surfaces of Mode-I specimens, once they were totally open, shows a clear correlation between changes on failure modes and the sudden changes observed in the electrical resistance during crack propagation. Although the mechanical curve does not present the typical behaviour of an unstable crack growing (called *stick-slip* behaviour), the fractured surface and the electrical response clearly show this unstable behaviour. Figure 6 correlates the sudden changes of the electrical resistance (a, b, c and d points) with the different failure modes. Thus, at points a and c, a change from type D, that is, interface failure between the uncured substrate and the adhesive film, to type E failure, that is, interface failure between the cured substrate and the adhesive film, is observed whereas at points b and d the change in the failure mode is the opposite.

Regarding to the repaired panel, the NDT inspection after the test showed the presence of two disbond areas (Figure 7):

- **Disbond area *A*:** it was detected in the upper region of the patch repair. It was not possible to determine if the bottom echo came from the interface between the substrate and the adhesive film (adhesive failure) or inside the adhesive (cohesive failure). Damage extent was similar to an equilateral triangle of 10 mm.

- **Disbond area *B*:** it was detected in the lower region of the patch repair with dimensions of 61 x 10 mm^2, approximately. Similarly to disbond area *A*, it was not possible to determine if the failure was located in the interface between substrate and adhesive film or inside the adhesive



Figure 7. Ultrasonic inspection of repaired panel after shear testing.

The results obtained by the sound level meter during the mechanical test are shown in Figure 8. The environmental sound was between 69 and 71 dB. By taking into account this reference, several sounds at different magnitude were detected. The first one of them was detected at 283 kN with a magnitude of 79 dB. Then, the second one was detected at 297 kN, reaching a value of 80 dB. After 330 kN, several sounds were recorded with higher intensities: at 332 kN, a sound with a magnitude of 87 dB was detected; at 337 kN, the acoustic emission reached a value of 90 dB; and at 344 kN, the highest acoustic emission was detected, with a value of 111 dB. From this point until the end of the test (430 kN), no more anomalous sounds were recorded.

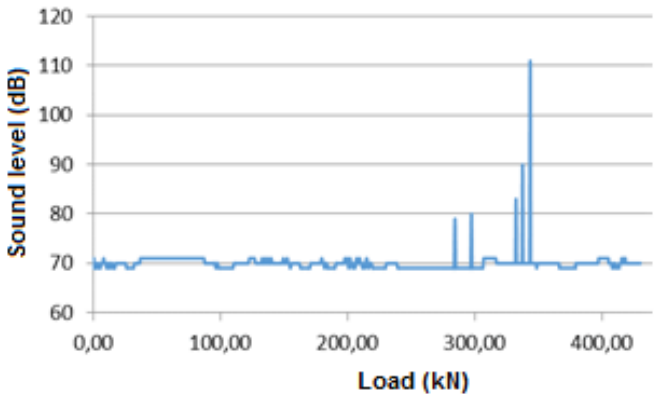

Figure 8. Detected sounds during mechanical testing of repaired panel

Finally, a correlation between inspection, acoustic emission and strain gauges and electrical sensing was established. The results of sensing and strain gauges for loads of 332 kN and 367 kN do not show variations that could be correlated to disbonds.

The analysis at 337 kN showed that the most significant variation on the strain gauge and sensing curves took place at the E1 channel. Figure 9 shows the electrical response of the E1 channel and the strain gauge response of the nearest rosette, R1 from 0 to 430 kN. At 337 kN, a sudden change on the electrical curve, R1_c was observed. In addition, a disbond were also observed in the area *A*. Therefore, it can be concluded that the disbond took place at 337 kN.

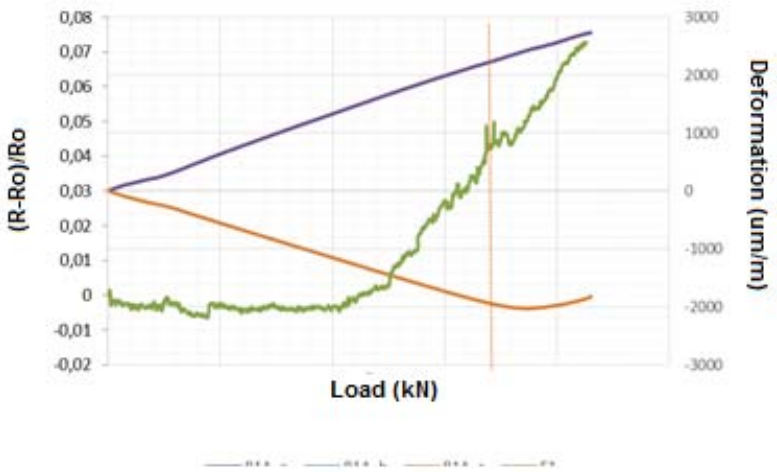

Figure 9. Correlation between extensometric measurements and electrical sensorization for emitted sound at 337 kN

On the other hand, the most significant changes on the sensing and strain gauge curve at 344 kN took place in the E3 and E5 channels. Figure 10 shows the strain gauge response of the nearest rosettes, G35A and G35B in combination with the electrical response. At 344 kN, a noticeable change on G35A and G35B curves was observed. As a disbond was detected during the inspection phase, it can be concluded that it took place at 344 kN.

A complete analysis of electromechanical curves of E1 and E3 channels allows to distinguish two regions:

a) The region (I) under 220 kN in which the normalized resistance presents a slight decrease up to minimum values of 0.25 and 1 %, respectively. This decrease of the electrical resistance has been already explained in previous studies [8-9], being associated to local compressions through thickness during the test leading to the formation of new electrical pathways. By taking into account the panel geometry in the upper region of the patch repair, the compression effect takes place in the initial stage of the mechanical test, until a strain threshold is reached.

b) The second region (II) takes place from 220 kN until the end of the test. It is characterized by a progressive increase of the electrical resistance with strain. The results are similar to those observed for the normalized SLS coupons. As commented before, higher deformations leads to lower conductivities as the distance between adjacent particles is increased.

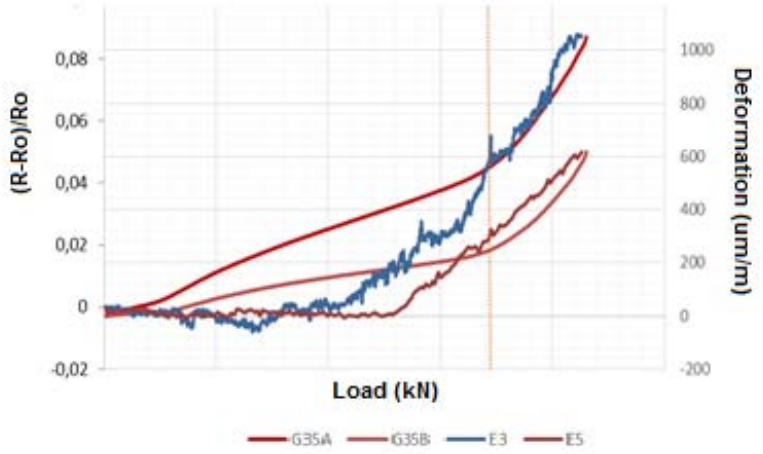

Figure 10. Correlation between extensometric measurements and electrical sensorization for emitted sound at 344 kN

Moreover, the detected disturbances on E1 and E3 channels could be explained by assuming that, once disbond takes place suddenly, the contact surfaces can be touching again. This would explain the rises and drops of the electrical resistance.

4. CONCLUSIONS

- Surface doped adhesive films with 0.1 wt. % CNT are able to evaluate the mechanical integrity of CFRP co-bonded joints.
- SLS tests prove the potential of the proposed adhesives to monitor properly the deformation with applied force. Moreover, the final failure is clearly detected by electrical sensing.
- Mode-I tests prove the ability of CNT doped adhesive to monitor crack propagation. It allows to distinguish between different failure modes and mechanical behaviors.
- A composite structural repair done with this adhesive film can be monitored during deformation. The sensitivity of CNT networks allows to detect disbonds that are efficiently detected with other inspection techniques

ACKNOWLEDGEMENTS

The author would like to acknowledge the *Comunidad de Madrid Government* [Program MULTIMAT-CHALLENGE S2013/MIT-2862] and the *Ministerio de Economía y Competitividad* of the Spanish Government [Project MAT2016-78825-C2-1-R] for their financial support.

REFERENCES

[1] K.B. Katnam a,n, L.F.M.DaSilva b, T.M.Young. "Bonded repair of composite aircraft structures: A review of scientific challenges and opportunities." Composites Part A: Applied Science and Manufacturing. 43, 1587-1598, 2012.

[2] C.H. Wang, A.J. Gunnion. ".Optimum shapes of scarf repairs". Composites Part A: Applied Science and Manufacturing. 40, 1407–1418, 2009.

[3] L. Pieczonka, W.J. Staszewski, T. Uhl, S. Pavlopoulou, C. Soutis. "Nondestructive testing of composite patch repairs". 11th European Conference on Non-Destructive Testing (ECNDT 2014), October 6-10, 2014, Prague, Czech Republic.

[4] M. Genest M. Martinez, N. Mrad G. Renaud,A. Fahr: Pulsed thermography for non-destructive evaluation and damage growth monitoring of bonded repairs. Composite Structures. 88, 112–120, 2009.

[5] J. Rams J, M. Sánchez A. Ureña, A Jiménez-Suárez, M. Campo A Güemes. "Use of carbon nanotubes for strain and damage sensing of epoxy-based composites". International Journal of Smart and Nano Materials, 3, 152–161 (2012)

[6] R. Moriche, M Sánchez, S.G. Prolongo, A. Jiménez-Suárez, A. Ureña. "Structural health monitoring in multiscale composite materials: Nanoreinforced epoxy matrices and coated fabrics". 8th European Workshop on Structural Health Monitoring, EWSHM 2016, vol. 3 (2016).

[7] A. Ureña, M. Sánchez, J. Rams, C. García-Nieto. "Adhesivo tipo film, dispositivo y método para evaluar la integridad estructural de uniones pegadas". Patent N. ES2574443. Expedition date: 10/03/2017.

[8] D. Zhang, L. Ye, D. Wang, Y. Tang, S. Mustapha, Y. Chen. "Assessment of transverse impact damage in GF/EP laminates of conductive nanoparticles using electrical resistivity tomography." Composites Part A: Applied Science and Manufacturing, vol. 43, 1587-1598, 2012.

[9] R. Moriche. "Desarrollo de sensores estructurales de resinas epoxi basados en nanopartículas de grafeno." Doctoral Thesis. Universidad Rey Juan Carlos, 2015.

VIII ECCOMAS Thematic Conference on Smart Structures and Materials
SMART 2017
A. Güemes, A. Benjeddou , J. Rodellar and Jinsong Leng (Eds)

ACTIVE WASHER FOR SMART MECHANICAL LINKAGE

CHRISTIAN BELLY*, ADRIEN GUIGNABERT, AURELIEN RIQUER, GAËL CHEVALLIER†, PAULINE BUTAUD, GAËL MATTEN AND NICOLAS PEYRET∞

* Cedrat Technologies
59 Chemin du Vieux Chêne 38246 Meylan Cedex, France
e-mail: {christian.belly}{adrien.guignabert}{aurelien.riquer}@cedrat-tec.com, web page: http://www.cedrat-technologies.com

† FEMTO-ST Institute, Applied Mechanics Dpt.
Université de Bourgogne Franche-Comté 25000 Besançon, France
e-mail: {gael.chevallier}{pauline.butaud}{gael.matten}@femto-st.fr

∞ Laboratoire QUARTZ - SUPMECA – EA7393
3 rue Fernand Hainaut 93407 Saint-Ouen Cedex – France
e-mail: nicolas.peyret@supmeca.fr

Key words: Piezo actuator, smart structures, active washer,

Abstract. Bolted connection is the most common way to assemble mechanism. It is widely used in transport domains, such as aerospace, rail, aircrafts… Ensuring that the minimum torque value is always present in the assembly is one of the main maintenance tasks for those components. A possible way to carry out those actions is to implement active component in the bolted assembly. A solution is proposed in this document. Construction, potentialities, performances (based on lap-joint demonstrator) and limitations are identified and confronted to other techniques.

1 INTRODUCTION

Control of the tightening tension in critical bolted connections (rotor - blade or undercarriage - hub - wheel links, gearbox, motor group ...) is a niche market but is a real need for maintenance, which essentially consists in ensuring that the minimum torque value is always present in the assembly. Without this maintenance, carried out at regular intervals, the risks are significant for structures (fatigue, corrosion and crack occurrence). For example, maintenance operations for torque verification on a helicopter requires up to sixty hours every 1000 flight hours (400 concerned linkages). Moreover, several theoretical works have been performed in order to improve the vibration damping by semi-active control of the tightening load [1][2][3].

Uncertainties and dynamic problems of bolted joints are widely treated in the literature [4]. Farther than detecting and monitoring the screw tension [5], the present paper proposes to counteract the preload loose using active components placed either under screw head or nut. This active washer component allows targeting several techniques, such as:

- Keeping constant preload within bolted assembly and make it stable through time,
- Act on linkage damping of mechanical linkage due to dry friction and/or as a complement to damping elastomer,

- Low frequencies protocol for structural decoupling.

The paper is composed of four parts. Firstly, for helping the reader to identify awaited benefits, the interest of actively controlled bolted assembly tension is shown. Secondly, a configurations trade-off is detailed, allowing catching advantages and intrinsic limitations of several concepts. Thirdly, experimental results are given on a single active washer and also on a lab user case, in order to compare with uncontrolled behaviour. Different techniques as described previously are considered in this experimental part. Finally, application fields and potentialities are pointed out introducing real user cases.

2 ABOUT THE INTEREST TO CONTROL BOLT TENSION

From Festjens H. [7] work, it has been shown that both the natural frequency and the damping ratio depends on the clamping torque and the vibration amplitude, see Figure 1. According to vibration amplitudes, the natural frequency is decreasing whereas the damping increases up to a maximum reached near the total sliding threshold and decreases after this limit. The clamping torque allows to tune these evolutions making the threshold shifting.

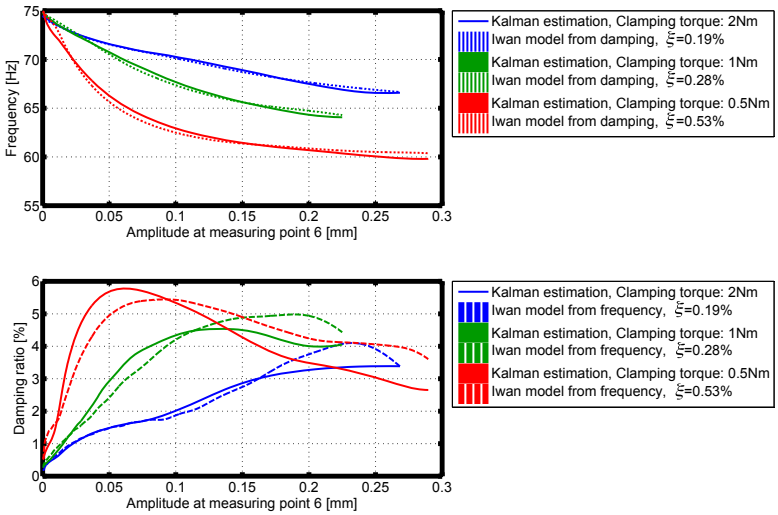

Figure 1: Natural frequency and Damping ratio according to several clamping torque and vibration amplitudes [7]

This result brings out the opportunity to adapt the value of the natural frequencies and the amplitude of the damping. In order to get interesting vibration control performances, our goal is to tune the natural frequency in order to prevent resonances. This idea is inspired from the work of Guyomar et al. [8] on the continuous switching of a piezoelectric device. Here the switching can occur between two extreme tightening torques in order to modify the resonance frequency continuously, see [3] for more explanations.

3 CONFIGURATIONS OF ACTIVE WASHER

The proposed technique is to integrate piezo active material in the bolted assembly. This

leads to a few control strategies. Firstly, as long as the tension in the bolt is able to be monitored, compensation can be performed using the actuator. In that case, correct correlation in stiffness and stroke of the active component has to be found. Secondly, a strategy consisting in creating discontinuity in boundary condition can be implemented, using the actuator close to its border between free and hard stop conditions. Thirdly, impact on displacement transfer function can be established in order to get experimental determination of behaviour.

Stiffness adaptation

The stiffness adaptation consists in making efficient adaptation between stiffness of the bolt assembly and the stiffness and stroke of the active component. Figure 2 is presenting the link between the behaviour coming from bolt stiffness (two cases: soft and stiff bolts) and the behaviour coming from the actuator (two cases: strong and long stroke actuators).

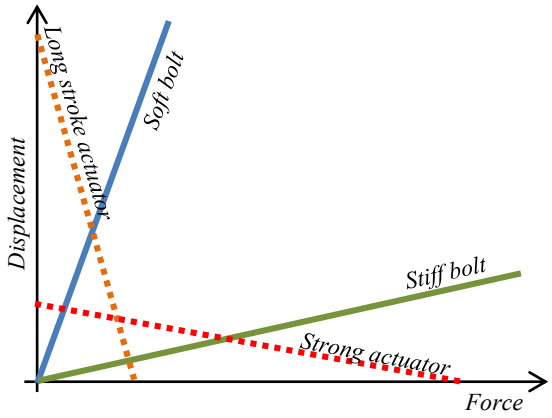

Figure 2: Force/displacement relation between bolt and actuator

Main limitation is coming from bolt, which is typically long, so elastic (see Figure 3). A M4 screw, admitting 20mm free length admits a 130N/µm stiffness. As a comparison, 10mm piezo stack made from rings (diam 8mm) admits typically a 130N/µm stiffness for 12µm free stroke. Therefore, useful stroke and force is intrinsically halved. Additionally, part of displacement is lost in contact stiffness's. Therefore, true contribution of actuator is limited. It can be also noticed that, increasing stroke using longer piezo stack requires also to increase length of bolt. So benefits is not linear.

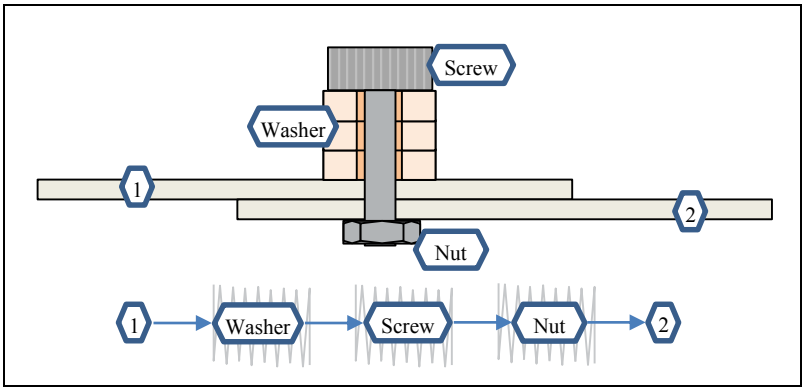

Figure 3: Bolted assembly and force path

Another contributor to small stiffness is potential soft material (visco-elastic) between the two layers of lap-joint. This additional layer can allow target damping characteristics. The axial stiffness is strongly lowered, making necessary to be able to perform longer stroke.

Actuator selection

Possibility to reach longer stroke, able to adapt to mechanism uncertainties and local parasitic stiffness's appears to be interesting. In that case, because of limits in volume, especially length) and costs, it is necessary to consider amplification. Proposed solution consists in mechanical amplification is the frame of APA® (Amplified Piezo Actuators).

Amplified Piezo Actuators APA® have already been considered in damping strategies [6]. Those kind of actuators offer larger strokes than direct actuators by amplifying displacement due to its shape. The flattest the actuator is, the more amplified the displacement is. In return, stiffness of the actuator is reduced. Typically, mechanical amplification being ruled by a factor α, stiffness is divided by $2\alpha^2$.



Figure 4: APA95-PTW-MD actuator, from [6]

The actuator (Figure 4) can generate up to 8.5kN of blocked force for 100µm free stroke. The support with additional viscoelastic material is able to improve the mechanical parameters of actuator, with changes the stiffness and damping characteristics. Application targeted by this application is machining and cancellation of chatter. Its relatively large size (approx. 100x100x100mm^3) makes it not relevant for targeted application.

Available volume is roughly a few centimetre square. This size makes eligible use of standard 5x5x20mm^3 piezoelectric stack within elliptical shape. Standard APA40SM actuator, creating 200N blocked force and 50µm free stroke is chosen. In lap-joint configuration, structural strength is performed using standard bolt linkage. Parallel active bolt are then used to adapt overall damping behaviour. The proposed design is integrating a central stiffener, non-linear, which is creating possible discontinuity in contact of internal surfaces of actuator (see Figure 5). Typically, when force going through actuator is rather low, actuator stiffness is taken in consideration. As a contrary, when force applied is high, either by external preload or by actuator self-force, the actuator stiffness is short-circuited, leading to a standard nut behaviour. Discontinuity between both states is considered as possibly beneficial for damping issues. In further part of the document, this component is called active washer.

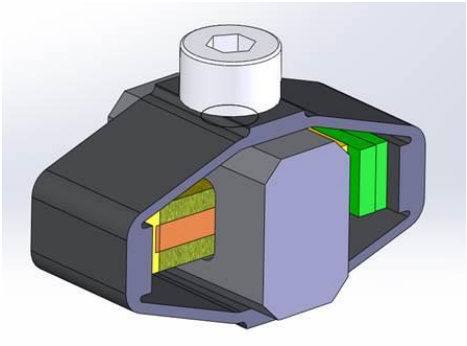

Figure 5: CAD view of active washer/nut.

4 ACTIVE WASHER PROTOTYPE AND APPLICATION IN LAP-JOINT

4.1 Active washer performance

Experimental trials of the proposed prototypes (see Figure 6) has been carried out. Aim of the characterization is to determine the possibility to place actuators is such a position that its own stiffness changes with input voltage.

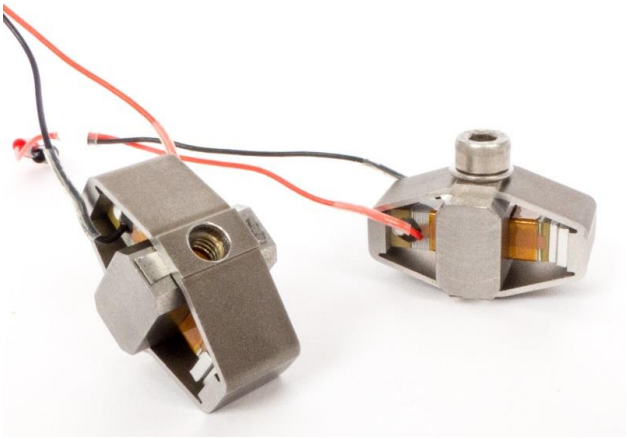

Figure 6 : Two active washer prototypes

Comparison between standard actuator and central ring configuration is presented in Figure 7. Actuator is powered using National Instruments board, driven by Signal Express software and associated with linear amplifier LA75 from Cedrat Technologies. Polytec laser is used, with 8µm/V gain in measurement. Generation and Acquisition are done simultaneously, with 10Hz sine 8.5Vpp signal. This corresponds to 170Vpp piezo actuator voltage. Applied voltage is within the range [-20:+150V]. Overall pattern is showing a hysteresis loop, classical in piezoelectric actuator response. Discontinuity coming from central ring is visible on the slope.

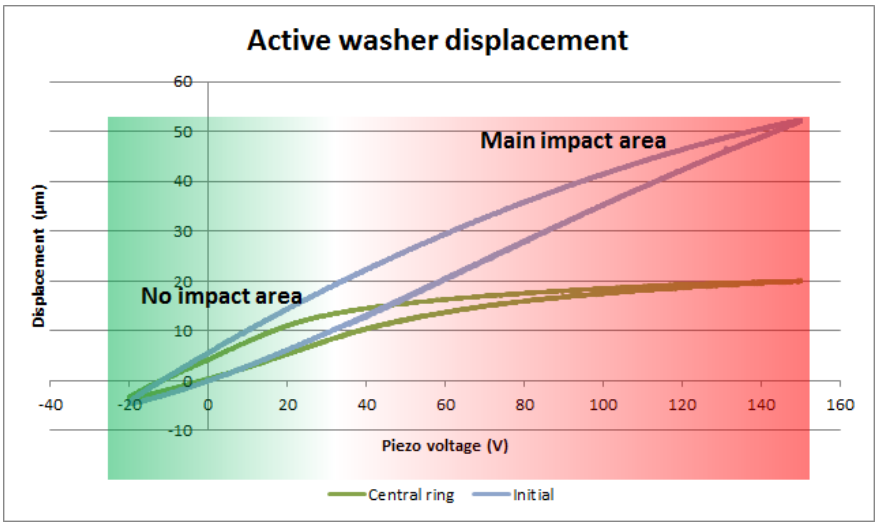

Figure 7 : Behaviour difference in standard condition or with internal stiffener

On the previous figure, displacement remains almost unchanged for input voltage from -20V to 20V, above this voltage, slope of the displacement curves changes. This is result of change in stiffness placed in parallel to the piezo actuator. This stiffness is a combination of contact stiffness and ring part stiffness. Numerical values are visible on Figure 8.

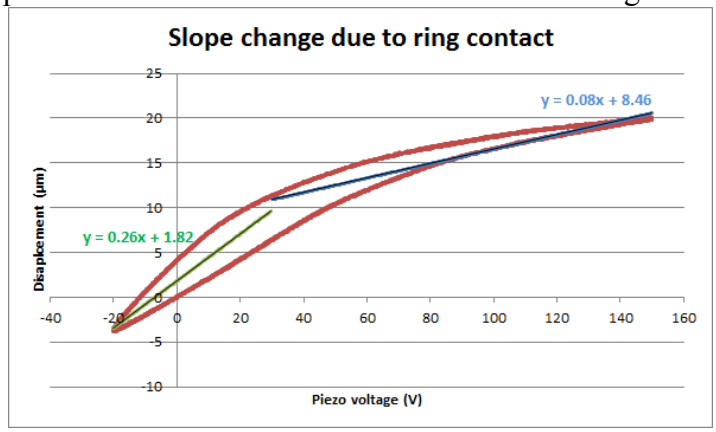

Figure 8 : Slope change in displacement

Standard stiffness of actuator is 3.7N/µm. This corresponds to blocked force (i.e. 194N is APA40SM) divided by free displacement 52µm. The slope in free displacement is 0.30µm/V. On active washer, initial slope is close to standard one, with 0.26µm/V. High voltage slope is smaller (0.08µm/V). This value allows to estimate equivalent stiffness of the actuator to be close to 14.1N/µm, revealing a 3 or 4 times increase in stiffness. Such kind of stiffness evolution will create a 1.7 to 2 factor in normal mode frequency, giving potential adaptation of modal landscape of structure. Integration onto standard user case lap-joint is presented in further part.

4.2 Integration on Lap-joint and experimental benefits.

The prototypes have been integrated in a lap-joint constituted with two plates linked by three

screws, see Figure 9. The central screw is a passive one strongly tightened in order to ensure the reliability of the structure. The external screws are less tightened in order to provide damping. The smart washers are integrated in these joints. In order to evaluate their efficiency, the lap joint has been tested in a vibration set-up constituted with a clamp, a shaker and a 3D laser vibrometer.

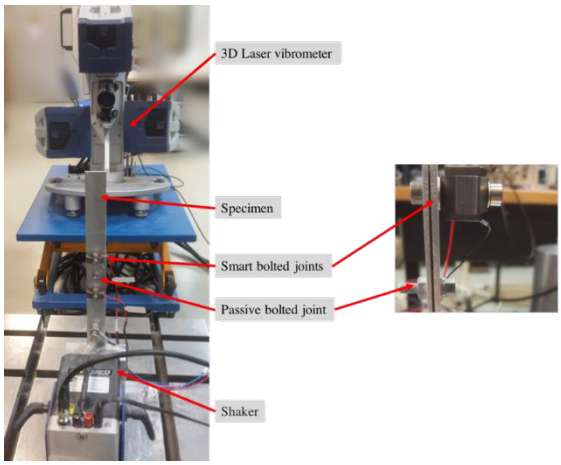

Figure 9: Vibration setup

The lap-joint is excited in the [0-2000] Hz frequency range with the shaker driven by a random signal. The signal is measured all over the surface of the setup in three directions thanks to the Polytec 3D Vibrometer. Then, we integrate the velocity over the surface in order to get a single scalar measure according to the frequency. This measured is weighted by the excitation level to build the Frequency Response Function, see Figure 10. This FRF exhibits several resonance frequencies. To evaluate the effect of the active washer, we build the FRF for three different voltages applied to the piezo actuators from -20V to + 145V. -20V corresponds to a 16cNm tightening torque whereas +145V corresponds to a 11cNm. From a vibration point of view, this means that the resonance frequencies are lower when the voltage is high and greater when the voltage is low. Obviously, the frequency shift depends on the Eigen mode we observe. The second Eigen mode is the most energetically coupled and the frequency shift is equal to 5%. These first results allow to expect an interesting vibration mitigation. Further investigations will focus on the control law that allows to maximize the efficiency.

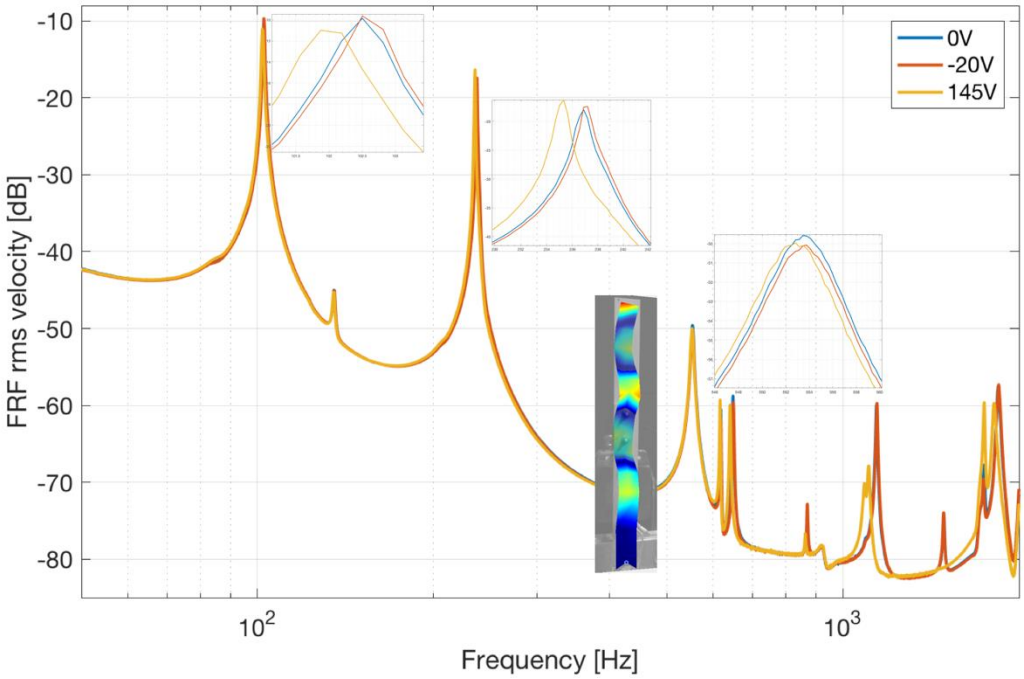

Figure 10: Frequency Response Functions according to several voltages.

5 IDENTIFIED LIMITS AND FUTURE WORK

To achieve the goal of this work, several technical developments are still in progress. The most important technical limit to overcome is to get the highest tightening load variation as possible. To improve the prototype, one has to manage the kinematic amplification thanks to an optimized design of the actuator. Secondly, we have to find the optimal placement for the active bolted connections. To get it, the setup has to be simulated numerically in order to compute the placement that allows to get the best energy coupling.

ACKNOWLEDGEMENTS

This work has been performed in the frame of French FUI CLIMA project. Authors want to thank ASTech, Minalogic, Micro-Techniques and PNB Supporting clusters, from Région Ile-de France, Auvergne-Rhones-Alpes and Bourgogne-Franche-Comté.

REFERENCES

[1] Karim, Y., & Blanzé, C. (2014). Vibration reduction of a structure by design and control of a bolted joint. Computers & Structures, 138, 73-85.

[2] Gaul, L., Hurlebaus, S., Wirnitzer, J., & Albrecht, H. (2008). Enhanced damping of lightweight structures by semi-active joints. Acta Mechanica, 195(1-4), 249-261.

[3] Bouaziz H., Peyret N., Abbes, M.S., Chevallier, G., Haddar, (2016) M. Vibration reduction by control of the tightening load. International Journal of Applied Mechanics, 8(6)

[4] Ibrahim, R. A., and C. L. Pettit. "Uncertainties and dynamic problems of bolted joints and other

fasteners." Journal of sound and Vibration 279.3 (2005): 857-936.

[5] Caccese, Vincent, Richard Mewer, and Senthil S. Vel. "Detection of bolt load loss in hybrid composite/metal bolted connections." Engineering Structures 26.7 (2004): 895-906.

[6] Kras A., Bourgain F., Claeyssen F. (2014). Amplified Piezo Actuator APA® with Viscoelastic Material for Machine Tool Semi-Active Damping System. Journal of Machine Engineering, Vol. 14, No. 3

[7] Festjens, H. (2014). Contribution à la caractérisation et à la modélisation du comportement dynamique des structures assemblées (Doctoral dissertation, Châtenay-Malabry, Ecole centrale de Paris).

[8] Richard, C., Guyomar, D., Audigier, D., & Bassaler, H. (2000, April). Enhanced semi-passive damping using continuous switching of a piezoelectric device on an inductor. In SPIE's 7th Annual International Symposium on Smart Structures and Materials (pp. 288-299). International Society for Optics and Photonics.

VIII ECCOMAS Thematic Conference on Smart Structures and Materials
SMART 2017
A. Güemes, A. Benjeddou , J. Rodellar and Jinsong Leng (Eds)

ADAPTABLE PNEUMATIC SHOCK-ABSORBER

Rami Faraj[*], Cezary Graczykowski[*], Krzysztof Hinc[*], Jan Holnicki-Szulc[*], Lech Knap[**], Jarosław Seńko[**]

* Institute of Fundamental Technological Research Polish Academy of Sciences, Warsaw, Poland
e-mail: rfaraj@ippt.pan.pl, cgraczyk@ippt.pan.pl, holnicki@ippt.pan.pl

** Warsaw University of Technology, Faculty of Automotive and Construction Machinery Engineering, Poland
e-mail: lknap@pw.edu.pl, jsenko@pw.edu.pl

Key words: Adaptable, Semi-passive, Impact Absorption, Pneumatic Shock-absorber.

Abstract. Pneumatic dampers are still an attractive subject of research in both modelling and experimental testing. Progress in the field of sensors and actuators allows to construct more and more efficient absorbers and dampers based on active or semi-active control algorithms. However, passive and semi-passive solutions are also developed because of their lower costs and simplicity. This paper presents adaptable pneumatic shock-absorber that allows to obtain optimal impact absorption and energy dissipation by a single reconfiguration performed at the beginning of the process. The absorber is composed of two cylinders including at least one narrow rectangular slot and adequate number of outflow vents precisely shaped for certain impact scenarios. During operation of the device the air is released through overlapping slots and selected vents, which provides constant value of the generated force. As a result, the shock-absorber works as a passive device but provides minimal value of the reaction force in similar manner as semi-active system equipped with fully controllable mechanical valve. The paper presents the results of numerical simulations of adaptable shock-absorber operation and attempts of demonstrator construction aimed at conducting experimental verification of the concept.

1 INTRODUCTION

In the last decade a rapid growth of various technical solutions aimed at protecting of structures against external vibrations or impacts is observed. High technology solutions are composed of physical, cybernetic layers and physical interfaces between these layers. All system components must cooperate with each other in order to effectively protect the structure. The physical layer is responsible for processing signals from physical environment through the cybernetic layer to some sort of intelligence in the form of a computer program [1]. The computer program is usually a numerical model of physical layer of the system and is used to calculate controlling signals able to interfere the physical layer through interfaces. All system components including sensors, numerical model of physical processes and actuator based interfaces are crucial for system operation. In the case of the cyber physical systems (CPS)

dedicated to protect structures against vibrations and impact, so-called semi-active or active dampers as energy absorbers are used. Those absorbers can change their properties adequately to control signals from cybernetic layer. There are many papers which describe recent investigations of such absorbers with the use of standard or smart materials both from theoretical point of view [2-3] and experimental validation [4-5]. Although most mechanical systems are becoming increasingly dependent on these devices, all of them require at least small amount of additional energy to work or to process controlling signals [6]. Undoubted advantage of such systems is possibility of changing their characteristics [7-8] which allows to adapt shock-absorbers to identified load conditions [9]. On the other hand, for specific applications, such as flying high altitude objects, some disadvantages of these systems can be noticed e.g. additional mass of electronic components, actuators and sources of energy, sensitivity to external signals disturbing control system. For such applications purely mechanical and lightweight absorbers are still more attractive alternative, for instance aluminium honeycomb sandwich structures [10] which were used in Apollo 11 space mission. Similar passive solutions are used for impact absorption in helicopter seats [11], where dissipation of energy by plastic deformations can be obtained at different load levels ensuring relatively effective shock absorption in case of different occupant weight and excitation [12].

In the paper we present the results of numerical investigations of the SOFT-DROP pneumatic absorber which in semi-passive version has minimal number of electronic components and no smart materials inside. Atmospheric air is used as working medium. Such a device is a semi-passive absorber and its simple design allows for easy adjustment of its properties just before the impact that has to be identified. Moreover, a simple purely passive version of the shock-absorber can be designed. In this case, selection of optimal valve shape and air compression distance is an optimal design activity instead of single system reconfiguration.

2 SEMI-PASSIVE IMPACT ABSORPTION

In the Institute of Fundamental Technological Research Polish Academy of Sciences diverse shock-absorbers for reliable mitigation of the impact during touchdown of light weight objects were investigated. Main requirement in such systems design is simple construction and small self-weight. One of most prospective solution meeting these requirements is the SOFT-DROP device – pneumatic semi-passive shock-absorber [13] which allows to adapt its characteristic to identified impact conditions.

General concept

The SOFT-DROP device is a single chamber pneumatic shock absorber composed of two cylinders, the outer cylinder with the slot and inner cylinder with the vent of variable shape. Operation of the device includes phase of air compression and phase of gas deflation. During the first phase, air is compressed to the pressure determined by the relative position of outer cylinder's slot and inner cylinder's vent. In the second phase air is released through overlapping slot and vent. Optimal air compression and deflation for identified impact conditions are obtained by selection of initial cylinder's relative position and shape of the vent, which are determined by solution of the inverse problem of the shock-absorber dynamics. It means that

control actions are required only at the very beginning of the shock-absorption process. After reconfiguration, the SOFT-DROP works as an passive device but the result is the same as in case of real-time control ensuring minimal value of the absorber's reaction force.

Significant advantage of presented device is the fact of using air under the atmospheric pressure as an operational gas inside the shock-absorber. This eliminates the problem of gas leakages and the requirement of precise sealing of the device. On the other hand, the use of non-pressurized gas causes that solution is dedicated for absorption of low energy impacts, which slightly limits its applicability.

In Fig. 1. scheme of the SOFT-DROP system and photos of its first demonstrator are presented. Depicted preliminary version of the shock-absorber does not allow for adaptation of the system to the actual loading by the change of the vent shape since it serves for initial laboratory tests aimed at basic verification of device operation and the feature of maintaining constant value of generated force under specific load conditions. In further stage of research, the construction of the demonstrator will be altered in order to achieve semi-passive system adaptable to actual load conditions.

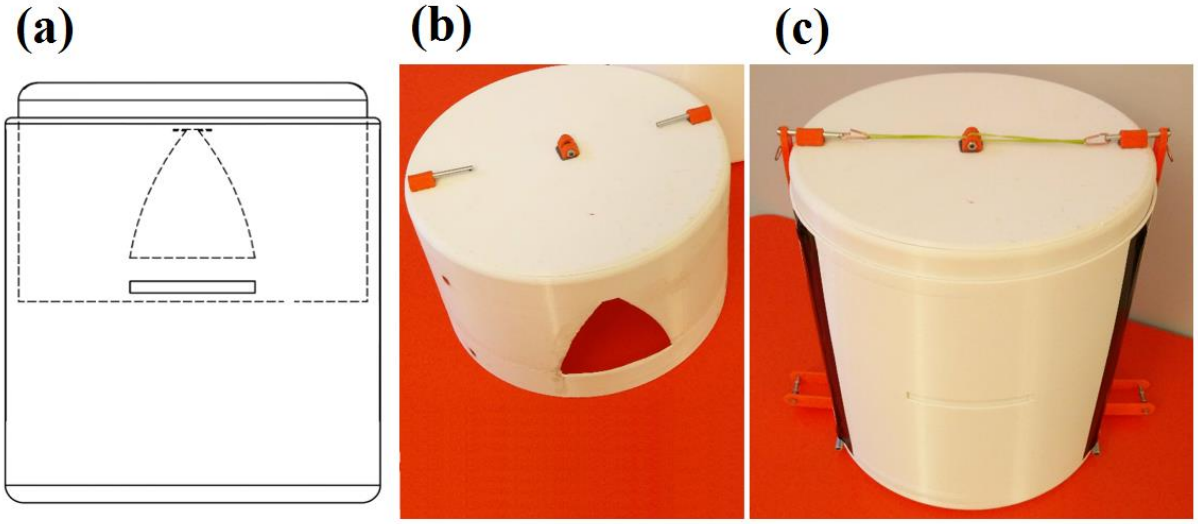

Figure 1: Construction of the SOFT-DROP system : (a) 2D scheme of the shock-absorber construction, (b) top cylinder made in 3D printing technology, (c) assembled demonstrator od SOFT-DROP device

From the concept to the practice

Quantitative analyses of the system operation, which will be thoroughly discussed in the next section, resulted in simplification of general concept of described above concept of the SOFT-DROP device. The preliminary tests indicated that initial relative position of cylinders, which determines pressure after compression phase and strongly influences system operation for various loading conditions. In contrast, the lack of vent shape change only slightly changes assumed optimal efficiency of the system. As a result, a satisfactory operation of the device for various impact conditions can be provided exclusively by changing the relative distance between cylinders of the shock-absorber. Therefore, the final concept of the SOFT-DROP assumes initial design of the shock-absorber for the highest predicted values of the impacting object's mass and initial velocity, and then adjustment of the relative position of cylinders

(further called compression distance) for various load conditions. Such design concept seems to be relatively simple, thus feasible to be realized in practical engineering application.

3 NUMERICAL ANALYSES

3.1 Optimal operation of the device

In the reference to the proposed approach to the SOFT-DROP shock-absorber design and operation, the corresponding numerical analysis based on the selected case study was performed. The assumed values of the most important design parameters for exemplary shock-absorber amortizing the mass under the impact conditions are shown in Table 1.

Table 1: Design parameters of the SOFT-DROP shock-absrober

Operating pressure [atm]	Operating gas	Diameter [m]	Stroke [m]	Suspended mass [kg]	Initial velocity of the mass [m/s]
1	air	0.15	0.0725	5	2.5

The numerical model of the SOFT-DROP system was developed according to previous literature studies [14]. The following assumptions were applied during simulation of the touchdown process:

- Cylinders non-deformable;
- No uncontrollable leaks of the operational gas;
- No friction in the system;
- Idealized condition of the contact with the ground (one degree of freedom model)

The inverse problem of the shock-absorber dynamics was solved in order to determine the required release of gas from the absorber and next the corresponding required effective outflow area. The computation reveled that initial relative position of cylinders has to be equal 0.0256 [m] and the outflow area resulting from overlapping of the slot and the outflow vent has to decrease gradually in terms of relative cylinders' displacement (Fig. 2).

The reaction forces generated by the SOFT-DROP device as a function of time and in function of top cylinder displacement are presented in Fig. 3. In the first phase of the SOFT-DROP system operation the response is the same as pneumatic spring but then the release of gas through properly shaped outflow vent enables maintaining constant value of the generated force until 95% of the stroke is achieved. At the end of the stroke the overpressure has to be reduced by instant release of the remaining volume of gas. In numerical simulation it was assumed that final release of gas occurs during last 5% of the total stroke and that area of the outflow vent is exactly the same as at the beginning of the deflation phase.

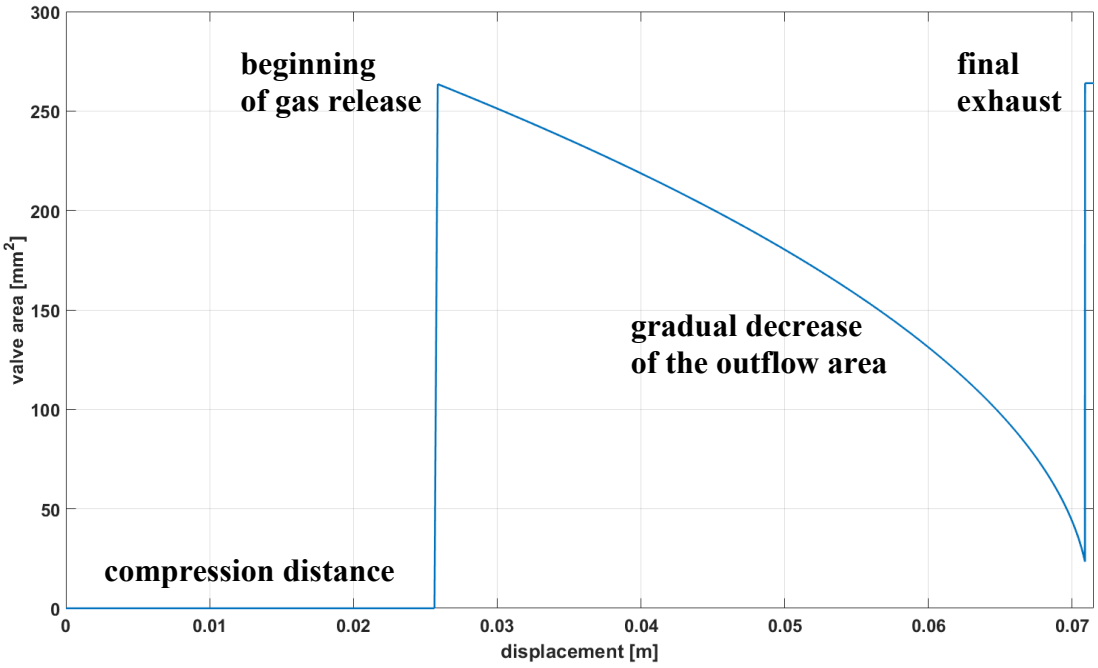

Figure 2: Effective area of the absorber vent as the function of top cylinder displacement

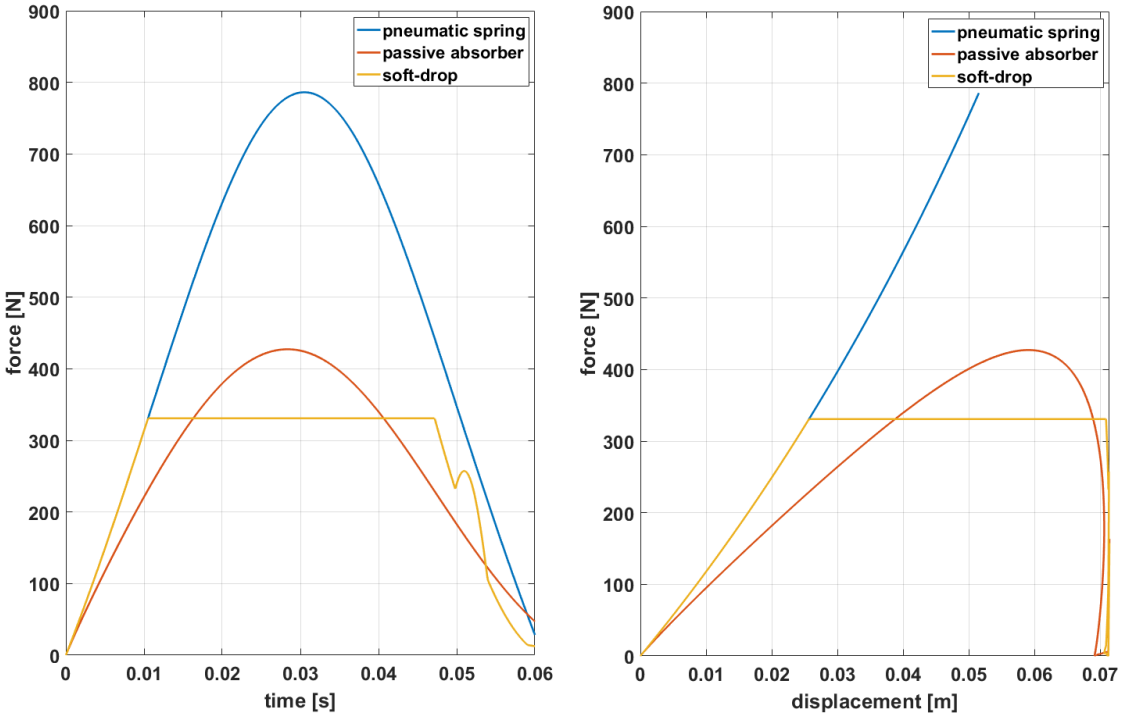

Figure 3: Reaction force in function of time and displacement for pneumatic spring, passive pneumatic absorber and SOFT-DROP device

3.2 Adaptation capabilities of the proposed solution

Fig. 4. presents the influence of changes in amortized mass and its initial velocity for the operation of the proposed semi-passive SOFT-DROP device and the conventional fully passive absorber with a vent of a constant area. In case of semi-passive SOFT-DROP device the initial adaptation procedure involves small changes of initial relative position of cylinders (compression distance), while the shape of the vent remains the same for all impact conditions. The effect of such simplification of the general concept of SOFT-DROP device causes that operation of the shock-absorber is not optimal since generated force is not maintained constant and entire stroke of the absorber is not utilized. Nevertheless, the obtained mechanical characteristics of the shock absorber clearly resembles the optimal response and it is still satisfactory since it is much better than for conventional passive device.

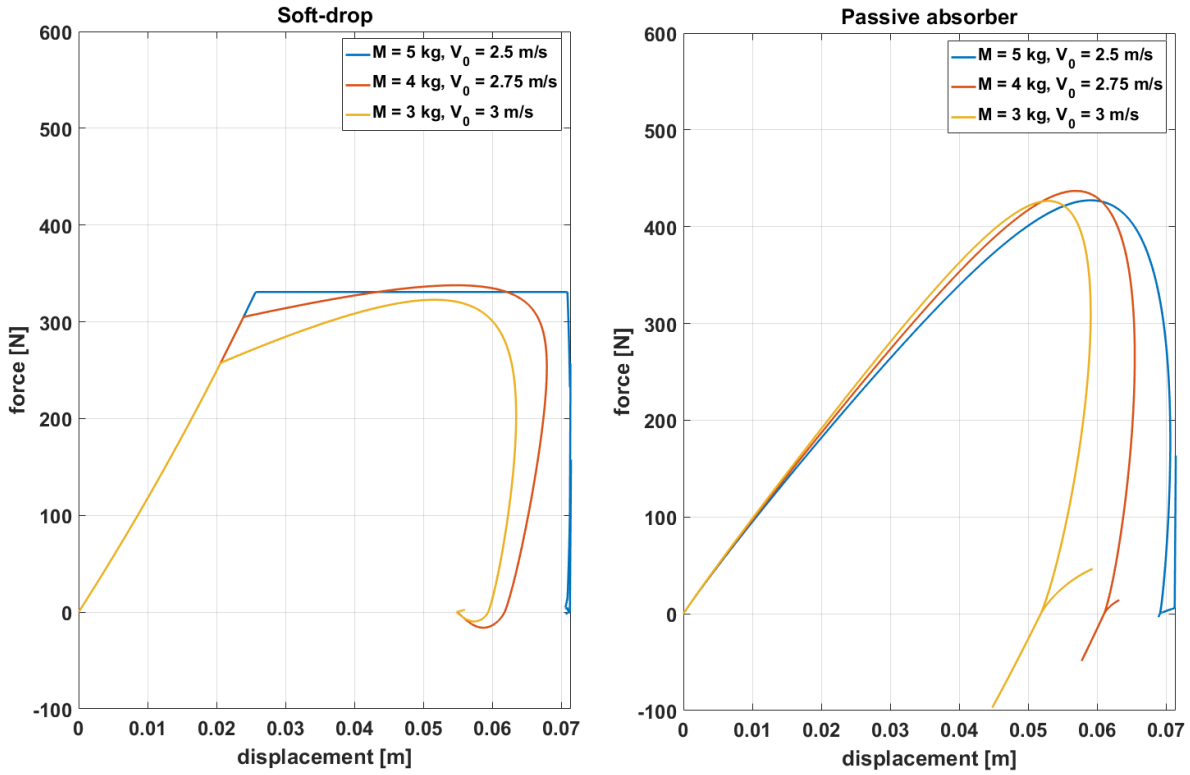

Figure 2: Reaction force as a function of displacement for SOFT-DROP device and passive absorber with constant vent area subjected to various load conditions

4 CONCLUSIONS

In this paper SOFT-DROP device – a semi-passive, adaptable solution for shock-absorption was proposed and its operation for different impact conditions was discussed. Implementation of general concept of the SOFT-DROP which includes control of gas compression distance and proper shaping of the outflow vent ensures optimal impact absorption and energy dissipation. Nevertheless, more practical approach based exclusively on changing

the compression distance was proved to provide suboptimal shock absorption. The most important advantages of the shock-absorber were highlighted by the comparison with typical pneumatic shock-absorber.

ACKNOWLEDGMENT

The scientific work was funded from the budget for education in the years 2015–2019 as a research project within the program under the name 'Diamond Grant'.
Support of the National Science Centre, Poland, granted through the projects Ad-DAMP (DEC-014/15/B/ST8/04363) and AIA (DEC-2012/05/B/ST8/02971), is gratefully acknowledged.

REFERENCES

[1] Marwedel, P., Embedded system design: Embedded systems foundations of cyber-physical systems, *Springer Science & Business Media*, 2010.

[2] Lee J.H., Kim K.J., "Modeling of nonlinear complex stiffness of dual-chamber pneumatic spring for precision vibration isolations", *Journal of Sound and Vibration*, **301**, pp. 909-926, 2007.

[3] Powers B. E., Wereley N. M., Choi Y., Analysis of impact loads in a magnetorheological energy absorber using a Bingham plastic model with refined minor loss factors accounting for, turbulent transition, *Meccanica*, 51(12):3043–3054, **2016**.

[4] Mikułowski G., Wiszowaty R., "Pneumatic Adaptive Absorber: Mathematical Modelling with Experimental Verification", *Mathematical Problems in Engineering*, Vol. **2016**, pp. 7074206-1-14, 2016.

[5] Mikułowski G., Holnicki-Szulc J., Adaptive landing gear concept - feedback control validation, *Smart Materials and Structures*, Vol. **16**, No. 6, pp.2146-2158, 2007.

[6] Holnicki-Szulc J., Graczykowski C., Mikułowski G., Mróz A., Pawłowski P., Wiszowaty R., Adaptive Impact Absorption - the Concept and Potential Applications, *International Journal of Protective Structures*, Vol. **6**, No.2, pp.357-377, 2015.

[7] Makowski M., Knap L., Reduction of wheel force variations with magnetorheological devices, *Journal of Vibration and Control*, Vol. **20**(10) pp. 1552–1564, 2014.

[8] Weber F., Semi-active vibration absorber based on real time controlled MR damper, *Journal of Mechanical Systems and Signal Processing*, Vol. **46**(2), pp-272-288, 2014.

[9] Faraj R., Holnicki-Szulc J., Knap L., Seńko J., Adaptive inertial shock-absorber, *Smart Materials and Structures*, Vol. **25**, pp. 035031-1-9, 2016.

[10] Pickett A. K., Lamb A. J. Chaudoye F., Materials characterization and crash modeling of composite aluminum honeycomb sandwich material, *International Journal of Crashworthiness*, **14**(1): 1–15, 2009.

[11] Desjardins, S. P., The Evolution of Energy Absorption Systems for Crashworthy

Helicopter Seats, *Journal of American Helicopter Society*, Vol. **51**, (2), pp. 150-163, 2006.

[12] Murugan M., Tabiei A., Hiemenz G., System Level Crash Sled Simulations for Evaluating Helicopter Adaptive Seat Damper, *International Journal of Innovative Research in Science, Engineering and Technology*, **5**(3): 2779-2790, 2016.

[13] Faraj. R, Graczykowski C., Holnicki-Szulc J., patent pending P.419285, Absorber pneumatyczny o adaptowalnej charakterystyce odpowiedzi, wypełniony powietrzem atmosferycznym, zwłaszcza do łagodzenia przyziemienia zrzucanych ładunków.

[14] Graczykowski C., "Mathematical models and numerical methods for the simulation of adaptive inflatable structures for impact absorption", *Computers and Structures*, Vol. **174**, pp.3-20, 2016.

VIII ECCOMAS Thematic Conference on Smart Structures and Materials
SMART 2017
A. Güemes, A. Benjeddou, J. Rodellar and J. Leng (Eds)

DECENTRALIZED DAMPING OF VIBRATIONS IN 2D FRAME STRUCTURES USING CONTROLLABLE NODES

B. Poplawski[a*], G. Mikułowski[a], A. Mróz[b] and Ł. Jankowski[a]

[a] Institute of Fundamental Technological Research, Polish Academy of Sciences
Pawińskiego 5B, 02-106 Warsaw, Poland
e-mail: bpop@ippt.pan.pl, gmikulow@ippt.pan.pl, ljank@ippt.pan.pl

[b] ADAPTRONICA Sp. z o.o.
Szpitalna 32, 05-092 Łomianki, Poland
e-mail: amroz@adaptronica.pl

Key words: Vibration damping, Smart structures, Semi-active control, PAR strategy, Decentralized damping strategy

Abstract. Extensive research efforts have been recently devoted to semi-active structural control [1, 2] with its paradigms of smart self-adaptivity and low consumption of energy, which is used for local adaptation rather than to generate external control forces. Considered application areas include adaptive landing gears, seismic isolation systems, vehicle-track/span systems, power train electro-mechanical systems, damping of flexible space structures, vehicle crashworthiness, arctic engineering, wind turbines, etc. A part of the research concerns semi-active management of strain energy for damping of structural vibrations. Early works considered truss structures with stiffness-switched bars [3]. They later evolved into either standalone one degree of freedom stiffness-switched dampers and isolators [4] or investigations in triggering modal energy transfer to highly-damped high-order modes, see, e.g., [5, 6]. The latter researches seem all to study the fundamental vibration mode of a cantilever beam with two detachable layers and differ mainly in the actuator technologies; the main idea is to employ actuators for a quick release of the vibration-related strain energy. This research extends the problem to general 2D frames. Controllable truss-frame nodes are incorporated into the structure. Thanks to their controllable ability to transmit moments, they allow for a quick transition between truss and frame modes. We propose a new, decentralized, closed-loop control strategy based on local energy measures. Vibration damping is more effective than in the previously studied control scheme based on a global energy measure, especially for higher vibration modes. Mitigation of vibrations will be presented in representative numerical examples, including a comparison to the global energy-based control strategy. Finally, results of experimental study, conducted on a structure analogous to the one from numerical simulations, will be demonstrated.

1 INTRODUCTION

Semi-active control techniques, utilized in damping of structural vibrations, proved to be very effective in numerous applications. Research areas of semi active systems are extensive and contain such fields as earthquakes protection [7], mitigation of vehicles suspension vibrations [8], adaptive landing gears [9], widely understood shock and vibration protection [10] or space structures vibrations damping [5]. The advantages of semi-active systems, compared to passive or active methodologies, can be treated as an explanation for the growing number of scientists conducting research in this area.

Passive vibration damping systems are used in engineering for many years because of their simplicity of operation. They passively produce reaction forces, in response to excited movement of the structure, which cause vibrations to decay. Their advantage is the passivity, which determines the aforementioned plainness of design and application. Passive damping systems can be optimized for a specific structure in a relatively easy way. They do not require any sensors, controllers or external power supply. The basic flaw of passive systems arises from their inability of adjustment to different excitation conditions. This is often the reason why these methods of vibrations damping cannot be effectively applied in demanding applications.

Active control systems are the subject of research in not much less extent than passive systems. Their popularity is associated with the great efficiency of vibrations damping, with which they are identified. Most often they consist of large hydraulic actuators attached to crucial structural elements, system of sensors and a controller, which, thanks to appropriate control algorithm, can cause satisfactory energy absorption [11]. They are very effective, but a significant shortcoming, which is the possible instability of the structure associated with high control forces, or in case of power failure, can make them dangerous in applications where high reliability is required. Another drawback is high energy demand resulting from the use of servomotors.

Semi-active vibration damping systems can be located between passive and active ones. They can achieve comparable efficacy to active systems while avoiding their disadvantages. Their energy consumption is very low because of negligible control forces introduced to the system. This also eliminates the susceptibility to instabilities related with high control loads. Well-designed semi-active system has a comparable trustworthiness to passive solutions, which is frequently essential. Combination of the advantages of both, passive and active damping systems results in very good performance in terms of reliability as well as damping effectiveness.

The fundamental idea, which is the genesis of semi-active control, is the structural adaptivity [12]. These control systems do not introduce external forces to the structure. They are modifying its structural properties, such as local stiffness, moment of inertia or local structural topology. Thanks to these techniques, controlled structure is adapting to existing conditions in a way such that its vibrations damping capabilities are significantly enhanced. Nevertheless theoretical difficulty in derivation of optimal control laws is a disadvantage. Topology reconfiguration makes it very difficult to apply the theory of optimal control for these systems.

Semi-active control algorithms can be implemented as continuous control techniques, i.e. making use of pneumatic systems [13] for smooth adjustments of the structure, or as a bang-bang type of control [3, 14]. On/off strategies are based on structural reconfiguration, which involve reformulation of selected structural constraints. One of the concepts for vibrations

suppression in frame or truss structures is to excite high-frequency local vibrations by short-term reduction of local stiffness. A part of the strain energy of the structure, accumulated in the low-frequency vibration modes, is transmitted into high-frequency modes. Energy of these vibrations is generally dissipated very effectively by means of standard material damping mechanism. This leads to quick attenuation of vibration amplitudes. The described damping technique is called prestress-accumulation release (PAR) strategy [15].

Almost all preceding researches investigate the same basic example of the first, fundamental vibration mode of a cantilevered beam [5, 6, 15, 16]. This contribution focuses on 2D frame structure, which is a much more complex system. Selected beam is equipped with blockable hinges at its end nodes. These semi-active nodes can change their state between frame-like mode and truss-like mode (coupled/uncoupled rotational degrees of freedom between neighboring beams). Exemplary frame with described nodes is presented in Figure 1.

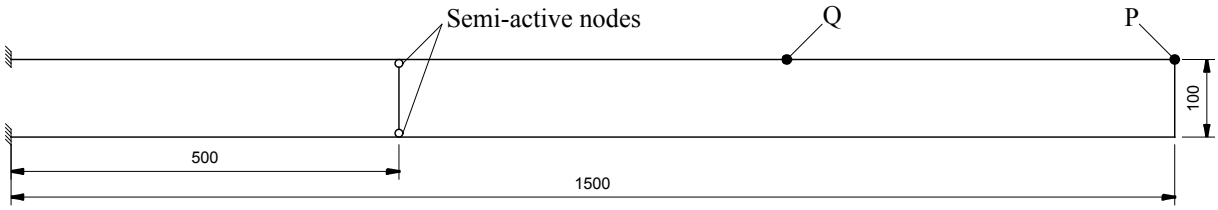

Figure 1: Considered 2D frame structure equipped with semi-active nodes (dimensions in [mm])

Technique of vibrations mitigation presented here, utilizes the PAR concept. Strain energy accumulated in the beam equipped with semi-active nodes is released into its high-frequency local vibrations in the moment of uncoupling rotational degrees of freedom. In this contribution we propose a closed-loop decentralized control strategy, which is based on local strain energy measures. The advantage of this approach over global energy measures, presented in recent paper [17], can be noticed both in vibrations mitigation efficiency and in implementation complexity in real structures.

2 MODEL OF THE SEMI-ACTIVE NODE

There are two main approaches to formulation of the mathematical model of controllable nodes considered herein:

1. *Dry friction modeling.* This model is the most consistent with reality among any others and has been successfully used in earlier researches [14, 18]. Physical realization of nodes with the ability to switch from truss to frame mode of operation is done by varying the normal force between frictional surfaces of the node, which is clamping them together. The actual moment transfer mechanism in this case is based on dry friction, so this model is best suited to reality. However, the resulting mathematical model is nonlinear, which makes it difficult to use with optimal control theory.

2. *Switching between different models.* In this approach mathematical model of the structure is switched between different implementations during the simulation. The system remains linear in-between the switchings and models the ideal truss-frame nodes with zero or

infinite moment-bearing ability. This technique involves changes in the effective number of DOFs of the structure, which, as in case of the dry friction model, provoke theoretical difficulties in view of optimal control theory.

Theoretical difficulties associated with both described solutions, led to the emergence of the third concept proposed in [17]. Finite element model of semi-active node is build as a hinge with two unaggregated rotational DOFs with rotational damper, which can couple them at any time and block relative rotations. In truss-like mode of the node, damping coefficient of the damper is set to zero, so these DOFs remain uncoupled and moment is not transmitted between neighboring beams. Switching to frame-like mode is performed by changing damping coefficient to a large value, which effectively couples DOFs and blocks the reciprocal movement. In this state the semi-active node imitates the behavior of frame node. Damping coefficient of the semi-active nodes needs to be properly chosen in order to ensure good agreement with purely frame model. Such definition of the model determines its application only to transient analyses.

Equation of motion of the system without any external excitation forces reads:

$$M\ddot{x}(t) + \left(C + \sum_{i=1}^{N} \gamma_i(t) C_i \right) \dot{x}(t) + Kx(t) = 0, \quad x(t_0) = x_0, \quad \dot{x}(t_0) = 0 \tag{1}$$

where M is the mass matrix, K stands for the stiffness matrix, C is the damping matrix of the structure in the truss-like state with all hinges unblocked. Control function $\gamma_i \in [0, \gamma_{max}]$ can be interpreted as damping coefficient in the ith semi-active node. C_i represents rotational DOFs coupling matrix, which for two and three coupled DOFs are:

$$L_i^T \begin{bmatrix} 1 & -1 \\ -1 & 1 \end{bmatrix} L_i, \qquad L_i^T \begin{bmatrix} 1 & -0.5 & -0.5 \\ -0.5 & 1 & -0.5 \\ -0.5 & -0.5 & 1 \end{bmatrix} L_i \tag{2}$$

where L_i is the transformation matrix from global coordinate system to local coordinate system of the element.

3 CONTROL ALGORITHM

The objective function F to be minimized in the global optimum control problem, can be defined as the integral of the total energy of the construction:

$$F = \int_{t_0}^{t_f} \left(\frac{1}{2} \dot{x}^T(t) M \dot{x}(t) + \frac{1}{2} x^T(t) K x(t) \right) dt \tag{3}$$

for the system defined by the differential equation of motion (1), with constraint defined by boundary values of control functions γ_i.

Reformulation of the problem, utilizing state-space approach, allows for the employment of the Pontryagin minimum principle [19]. It leads to the conclusion that globally optimal control functions $\gamma_i^{opt}(t)$ are of the bang-bang type:

$$\gamma_i^{opt}(t) = \begin{cases} 0 & \text{if } w(t) < 0 \\ \gamma_{max} & \text{if } w(t) > 0 \end{cases} \tag{4}$$

where $w(t)$ is called the switching function. It depends on the displacement vector $x(t)$ and a co-state vector $u(t)$ which satisfies the co-state equation that is the original equation of motion of the system with negative structural damping and a pseudo load vector. Negative structural damping in the co-state equation excludes the possibility of its integration forward in time. This is the reason why it cannot be used for the computation of optimal control (4) in real time. Nevertheless, control strategy (4) is of great relevance, as it shows that optimal control strategy has a bang-bang nature.

Structural energy dissipation occurs by excitation of high-frequency local oscillations in beams equipped with semi-active nodes. Strain energy of the beam, which is related to bending, is transmitted into its quickly damped, higher modes of vibrations when controllable nodes are simultaneously switched to truss-like state. After sufficient part of the energy is dissipated, nodes can be switched to frame-like state, thereby allowing once again for strain energy accumulation. This approach allows to consider such beam as an independent dissipative device. Control loop needs to be fed back with strain energy of the controlled beam signal, which can be easily measured locally using strain gauges. Most of this energy could be released into high-frequency local vibrations.

Theoretical difficulties associated with derivation of the formal optimal control strategy, resulted in creation of heuristic control algorithm described by the following steps:

1. Beam stays in the frame-like state until its strain energy reaches maximum.
2. At the moment of maximum energy semi-active nodes switch to the truss-like state.
3. After time t_0 or when elastic energy falls below the threshold, semi-active nodes switch back to the initial, frame-like state.
4. Repeat from step 1.

Above control algorithm is presented clearly in Figure 2.

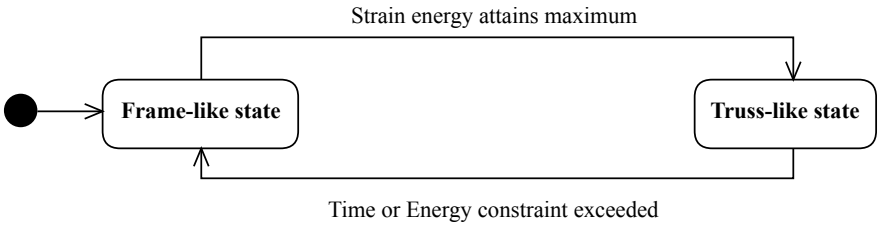

Figure 2: Heuristic control algorithm

Time t_0 should be established as some very small value, so the global stiffness of the structure would be not compromised. It could be set to one period of the bending vibrations (S-type) of the controlled beam.

4 NUMERICAL EXAMPLE

Structure considered in this contribution is presented in Figure 1. It is a 2D frame built of steel beams with 5x5 [mm] cross-section. The left end nodes are fixed and the middlemost

vertical beam is equipped with the semi-active nodes which makes it a dissipative device. This model was presented earlier with global energy measure control algorithm [17]. Herein results obtained with this algorithm are compared to local energy measure control strategy. Three different cases are considered, where each of the first three vibration modes of the structure is set as the initial displacement condition.

The time course of vertical displacement of point P (marked in Figure 1) for the first vibration mode is presented in Figure 3. Frame model, without any semi-active nodes, is used as a reference case, where only material damping is included. Two semi-active control strategies: with global energy measure (SAGEM) and with local energy measure (SALEM), are compared to optimal passive damping. Optimal passive damping was found by inserting rotational dampers in place of semi-active nodes and adjusting their damping coefficient to provide the best oscillations mitigation performance. Vertical black line indicates the moment of the first control action described in previous paragraph and shown in Figure 2.

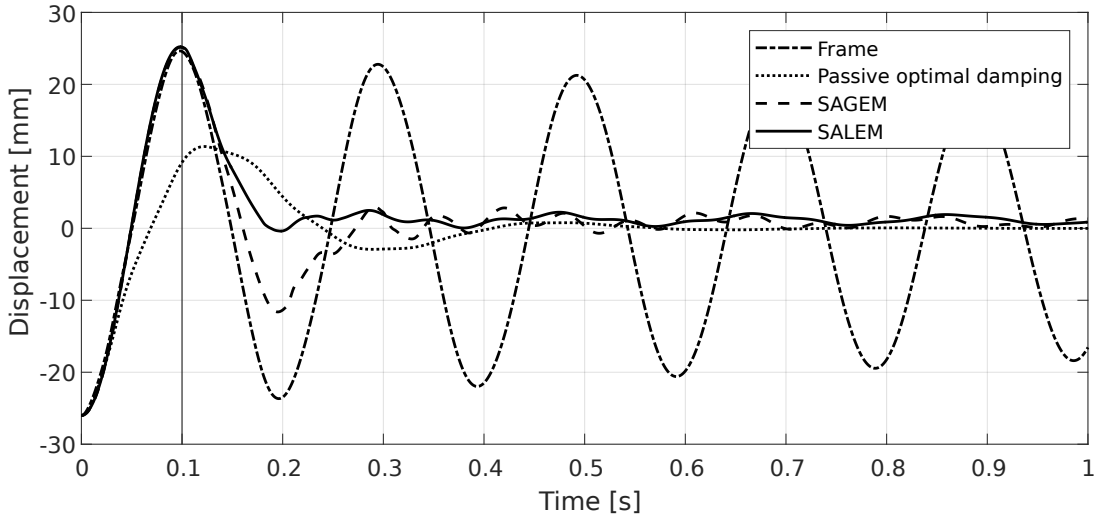

Figure 3: Vertical displacement of point P for the first mode shape

Local energy measure control strategy (solid line) is characterized by excellent vibrations mitigation capabilities. Despite the delay in the start of the control action, in comparison to the passive strategy, oscillations are damped after just 0.2 [s] and a quarter of a vibrations cycle. After that time only residual displacements remain. It is certainly the best result of all three considered options. This demonstrates the effectiveness of the semi-active control strategy based on local energy measure.

For the case of second mode shape, global energy measure control strategy does not perform satisfactorily. It does not mitigate vibrations, but introduced disorder causes a change in structure's dynamic response resulting in fading of the 2nd mode and the 1st mode appearing after a couple of vibration cycles. This procedure can bring oscillations suppression, because 1st mode is efficiently damped using this control scheme, however the duration of the control action may be unacceptable. Control strategy based on local energy measurement is much more efficient.

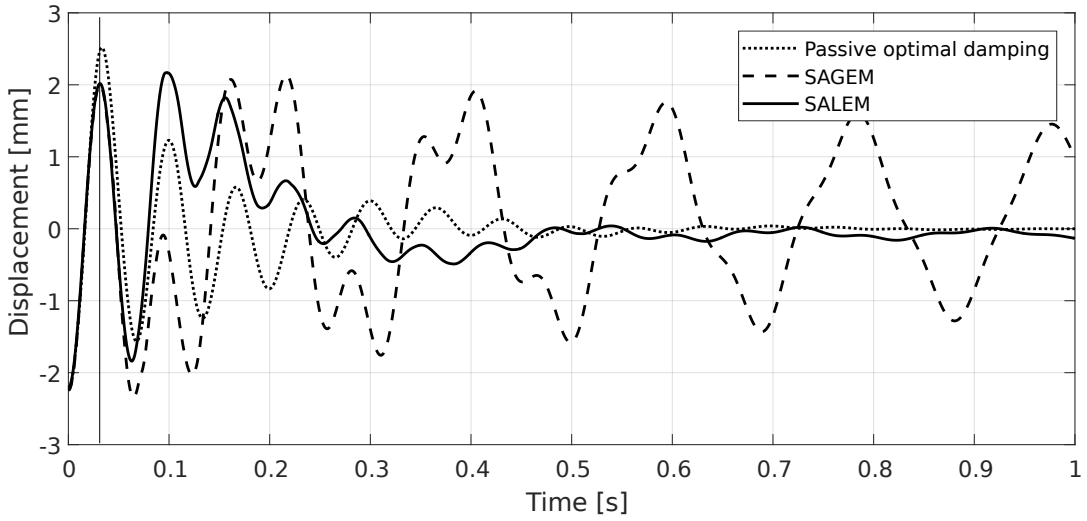

Figure 4: Vertical displacement of point P for the second mode shape

Oscillations damping rate is comparable with the passive optimal case. This is a significant qualitative change over the SAGEM control.

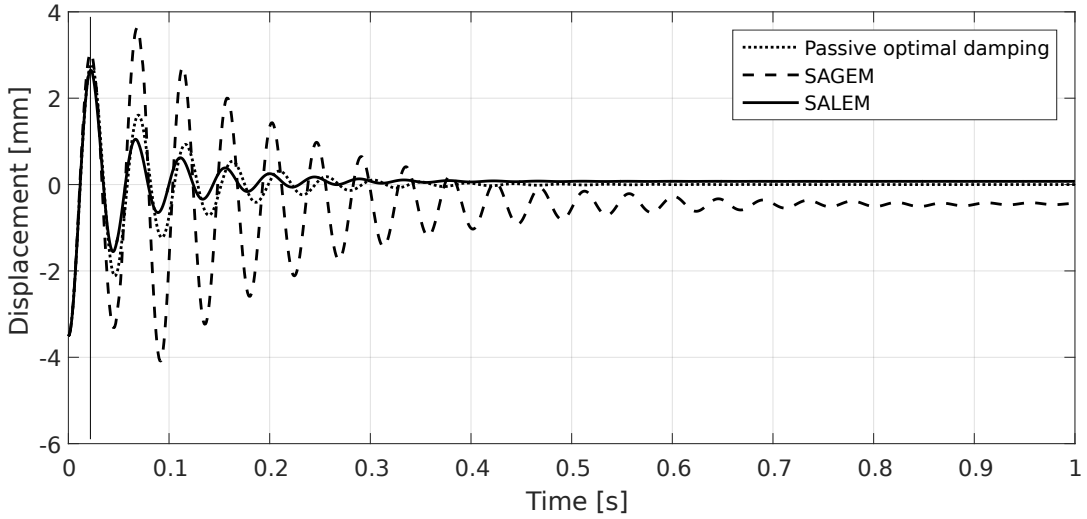

Figure 5: Vertical displacement of point Q for the third mode shape

Superiority of the SALEM control strategy over SAGEM and optimally adjusted passive dampers is seen for the third mode shape. Time courses of vertical displacement for this mode shape are presented in Figure 5. Performance of the SAGEM control is poor, this algorithm should not be used in this case. SALEM control, in opposition to SAGEM, performs very well. Oscillations are damped even quicker than in optimal passive case. This result is achieved by changing the way of energy dissipation, which was described in paragraph 3.

5 PRELIMINARY EXPERIMENTAL RESULTS

A laboratory stand was build in order to verify the results obtained in numerical analyses. Tested frame structure is visualized in Figure 6. It is geometrically similar to the one considered in the numerical example. The frame is build in a modular manner, which allows for its simple expansion with additional segments.

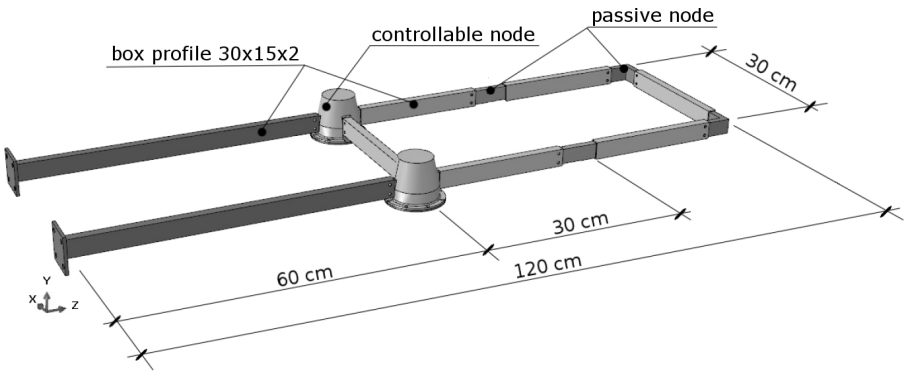

Figure 6: Frame structure used in experiment

Initial displacement conditions were set as a small in-plane displacement of the tip which excited mainly the first two global vibration modes. Comparison of the tip displacement between uncontrolled and controlled structure is presented in Figure 7. The displacements were not obtained by direct measurements, but on the way of double integration of the accelerations by the data acquisition system.

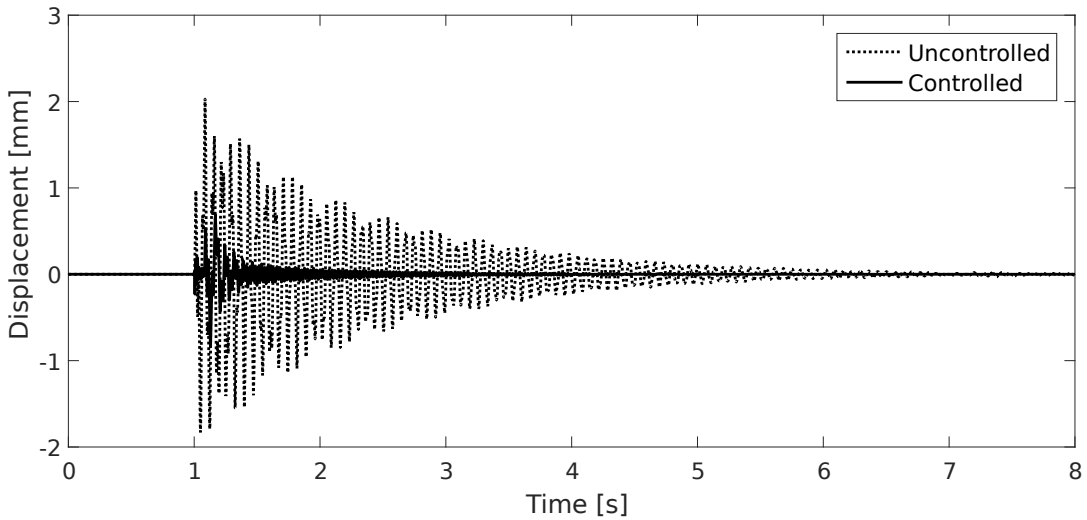

Figure 7: Comparison of tip displacements

It is easily noticeable that utilization of the control system results in significant attenuation of oscillations. Excited oscillations are damped after a couple of vibration cycles.

6 CONCLUSIONS

A semi-active decentralized control technique based on structural reconfiguration was proposed in this contribution. Numerical results obtained for exemplary frame structure are very promising and a preliminary experiment confirms the effectiveness of the developed control strategy.

ACKNOWLEDGMENTS

We gratefully acknowledge the financial support of the National Science Centre, Poland, granted through the project Ad-DAMP (DEC-2014/15/B/ST8/04363).

REFERENCES

[1] Hurlebaus, S. and Gaul, L. Smart structure dynamics. *Mech Syst Signal Pr*, Vol. **20**, pp. 255–281, (2006).

[2] Spencer Jr, B. and Nagarajaiah, S. State of the Art of Structural Control, *J Struct Eng–ASCE*, Vol. **129**, pp. 845–856, (2003).

[3] Onoda, J., Endo, T., Tamaoki, H. and Watanabe, N. Vibration suppresion by variable-stiffness members. *AIAA Journal*, Vol. **29**, pp. 977–983, (1990).

[4] Ledezma Ramirez, D.F., Ferguson, N.S. and Brennan, M.J. Shock isolation using an isolator with switchable stiffness. *J Sound Vib*, Vol. **330**, pp. 868–882, (2011).

[5] Mróz, A., Holnicki-Szulc, J. and Biczyk, J. Prestress accumulation-release technique for damping of impact-born vibrations: Application to self-deployable structures. *Math Probl Eng*, article id 720236, (2015).

[6] Bajkowski, J.M., Dyniewicz, B. and Bajer, C.I. Semi-active damping strategy for beams system with pneumatically controlled granular structure. *Mech Syst Signal Pr*, Vol. **70–71**, pp. 387–396, (2016).

[7] Symans, M.D. and Constantinou, C. Semi-active control systems for seismic protection of structures: a state-of-the-art review. *Engineering Structures*, Vol. **21**, Issue 6, pp. 469–487, (1999).

[8] Shen, Y., Golnaraghi, F. and Heppler, R. Semi-active vibration control schemes for suspension systems using magnetorheological dampers. *Journal of Vibration and Control*, Vol. **12**, Issue 1, pp. 3–24, (2006).

[9] Mikułowski, G. and Jankowski, Ł. Adaptive landing gear: optimum control strategy and potential for improvement. *Shock Vib*, Vol. **16**, pp. 175–194, (2009).

[10] Jankowski, Ł., Graczykowski, C., Pawłowski, P., Mikułowski, G., Ostrowski, M., Poplawski, B., Faraj, R., Suwała, G. and Holnicki-Szulc, J. Adaptive self-protection against shock and vibration. *Advances in Science and Technology*, Vol. **101**, pp. 133-142, (2017).

[11] Yamamoto, M., Aizawa, S., Higashino, M. and Toyama, K. Practical applications of active mass dampers with hydraulic actuator. *Earthquake Engng. Struct. Dyn.*, Vol. **30**, pp. 1697–1717, (2001).

[12] Holnicki-Szulc, J., Pawłowski, P. and Wikło, M. High-performance impact absorbing materials – the concept, design tools and applications. *Smart Materials and Structures*, Vol. **12**, pp. 461–467, (2003).

[13] Graczykowski, C. Mathematical models and numerical methods for the simulation of adaptive inflatable structures for impact absorption. *Computers & Structures*, Vol. **174**, pp. 3–20, (2016).

[14] Gaul, L. and Nitsche, R. Friction control for vibration suppression. *Mechanical Systems and Signal Processing*, Vol. **14**, pp. 139-150, (2000).

[15] Mróz, A., Orłowska, A. and Holnicki-Szulc, J. Semi-active damping of vibrations. Prestress Accumulation-Release strategy development. *Shock and Vibration*, Vol. **17**, pp. 123–136, (2010).

[16] Dyniewicz, B., Bajkowski, J.M. and Bajer, C.I. Semi-active control of a sandwich beam partially filled with magnetorheological elastomer. *Mech Syst Signal Pr*, Vol. **60-61**, pp. 695–705, (2015).

[17] Poplawski, B., Graczykowski, C. and Jankowski, Ł. Controllable truss-frame nodes in semi-active damping of vibrations. *Advances in Science and Technology*, Vol. **101**, pp. 89–94, (2017).

[18] Gaul, L., Lenz, J. and Sachau, D. Active damping of space structures by contact pressure control in joints. *Mechanics of Structures and Machines*, Vol. **26**, pp. 81–100, (1998).

[19] Kirk, D.E. *Optimal control theory: an introduction (republication)*, Dover Publications, (2004).

VIII ECCOMAS Thematic Conference on Smart Structures and Materials
SMART 2017
A. Güemes, A. Benjeddou, J. Rodellar and J. Leng (Eds)

EXPLORING TARGETED ENERGY TRANSFER FOR VIBRATION DAMPING IN NONLINEAR PIEZOELECTRIC SHUNTS

KEVIN DEKEMELE*, ROBIN DE KEYSER* AND MIA LOCCUFIER*

*Department of Electrical Energy, Metals, Mechanical construction and Systems (EEMMECS)
Ghent University
Technologiepark 914, Tech Lane Ghent Science Park, B-9052 Zwijnaarde, Belgium
e-mail: kevin.dekemele@ugent.be

Key words: Passive vibration control, Target energy transfer, Piezoelectric shunt, Nonlinear shunt

Abstract. Recently, shunted piezoelectric (PE) patches have been heavily investigated as passive dynamic vibration absorbers (DVAs) to reduce vibrations in mechanical structures. These piezoelectric patches serve as an alternative to mechanical DVAs, which require physical space both for the DVA itself and its stroke, while a piezoelectric DVA only requires space for an electronic circuit. Typically, the patch is shunted with a resistor and an inductor. As attaching the patch and the shunt on a mechanical structure is equivalent to mechanically attaching a spring, mass and damper, mechanical DVA tuning rules are applied to dimensionalize the circuit. This equivalence between mechanical and piezoelectric DVAs is utilized in the paper to apply the advances of the more mature mechanical DVA research field. The effect of nonlinear stiffness in mechanical DVAs has been thoroughly investigated. A typical nonlinear phenomenon is called targeted energy transfer (TET), where the vibration energy is suddenly transferred from the structure to the DVA. In this paper, a nonlinear shunt is proposed, equivalent to a nonlinear mechanical DVA. Then, by applying the nonlinear mechanical DVAs tuning rules, the TET phenomenon is also found in PE patch with a nonlinear shunt.

1 INTRODUCTION

Excessive vibration in mechanical structures can lead to material fatigue or even structural failure. These vibrations can also have an effect on humans, they can experience discomfort, noise pollutions or develop health problems. In *passive vibration absorption*, excessive vibrations in a *main system* are mitigated by adding several passive absorbing elements. As opposed to *active absorption*, passive absorption requires no power source and no sensor, making it an elegant and robust solution to vibration reduction in engineering structures. The elastic structure of fig.1a represents the main structure to be protected such as a building, a metal structure, a turbine vane, an airplane wing, car bodywork, ... A passive element is a correctly dimensioned structure, locally added to the main system, that absorbs and/or counter-acts vibrations of

the main system. It is often called a *dynamic vibration absorber* (DVA). The most commonly used DVA is the mechanical type, where a correctly tuned mass-spring-damper system is added to the main structure, see fig.1b. More recently, the DVA of the piezoelectric (PE) type has been given a lot of attention in research. It was first proposed by Hagood and Von Flotow in 1991 [1], where a piezoelectric patch, attached on a beam, was shunted with a resistance and an inductance, as shown in fig.1c. The deformation of this patch induces a voltage in the shunt, caused by the direct piezoelectric effect, causing a charge flow in the shunt. The electric energy is then dissipated in the shunt. While the mechanical DVA both needs space for the mass-spring-damper and its stroke, the PE DVA only needs space for its shunt and does not vibrate itself. In this sense the PE DVA is a *solid state* vibration absorber. Many different type of shunt circuits have been proposed, an overview can be found in [2]. This paper focusses on the piezoelectric DVA, more specifically, on nonlinear shunts, as an analogy for the nonlinear mechanical DVA's.

The main structure is assumed to be linear, and can be decomposed into *linear normal modes* (LNM). Information of the LNM is then used to tune a linear vibration absorber. One of the first, and still very popular tuning method was proposed by Den Hartog [3], where a single vibration mode is damped with an analytic frequency response function optimization. These linear, single mode absorbing DVAs are still used intensively today in both research and industry. Adding a PE DVA with a resistor-inductor (RL) circuit is equivalent to adding a spring-mass-damper, with the inductor being the mass, the resistor being the damper and the an material capacitance being the spring. This was first shown in [4], where the Den Hartog tuning was applied to obtain RL values.

However, these linear DVAs have a few downsides. When properties of the main structure or DVA change (eigenfrequencies, modeshape, ..), for example by age, heavy or sustained loads or by structural modifications, the performance of the DVA might deteriorate seriously. This deterioration is called *detuning* of the absorber. Another downside is the inability to absorb more than one mode with a single DVA. To tackle these downsides, nonlinear vibration absorbers have been proposed, having a nonlinearizable stiffness. In [5] it was shown that DVA with cubic or non-smooth stiffness is more robust against detuning and that a single DVA can absorb multiple eigenmodes.

When the DVA is nonlinear, the main system is still assumed to be linear, while the compound system (main structure + DVA) is now nonlinear. The dynamics of the nonlinear compound system are analysed with so called *nonlinear normal modes* (NNM), a nonlinear extension of LNM. A NNM can be defined as a (nonnecessarily synchronous) periodic motion of the conservative system [7]. The most important differences between LNM and NNM for this paper, is that NNM can differ both in frequency and modeshape, depending on the energy in the structure, and that NNMs can suddenly appear or disappear above a certain energy level, so-called mode bifurcations. A LNM will always have the same frequency and mode shape for every energy level of the compound system and they do not appear or disappear depending on this energy level. NNMs have been around since the 1960s as a theoretical curiosity but recently got more attention in nonlinear vibration absorption [6] and nonlinear structural dynamics [7]. Many numerical and analytic methods [5, 8] have been developed to obtain NNM. As every class of nonlinear systems requires a different analysis method, the numeric toolbox NI2D [9] is used to investigate the system and generate the NNM.

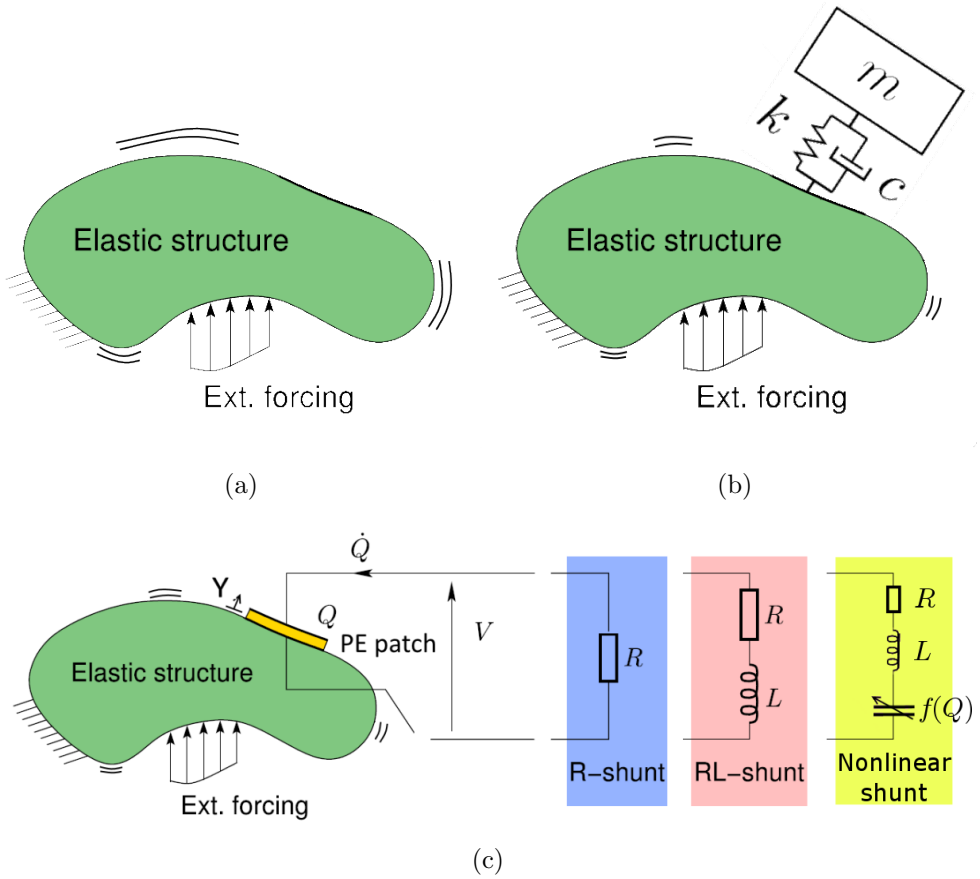

Figure 1: (a) A mechanical elastic structure can experience excessive vibration under forcing or initial conditions. (b) A mechanical DVA, consisting of a mass-spring-damper system can be tuned to mitigate the vibration. (c) A piezoelectric DVA, shunted by an R, RL or the proposed nonlinear circuit. The reduction of vibrations in (b) and (c) is shown here as smaller 'movement' lines. Figures are adapted from [12]

The mechanism of vibration absorption for the considered nonlinear DVAs is called *targeted energy transfer* (TET). It is defined as a sudden, irreversible transfer of vibration energy from the main structure to the DVA [5]. An important property of TET is that this mechanism only occurs when the initial or forcing energy in the main structure is above a certain threshold. This threshold was analytically expressed in [10] where it was shown that a NNM mode bifurcation is responsible for this threshold.

In electric circuits, nonlinearities are often undesirable and avoided, but deliberate nonlinearities have been introduced in for instance variable capacitors (called varicaps) in AM/FM radio tuners, while more recently, in the context of piezoelectric shunts, so-called *synthetic impedances* have been developed, allowing to generate any desired electrical impedance [11]. For now these synthetic impedances have been used to synthesize linear impedances, but can be extended to

nonlinear ones, as the voltage/current relation is programmed in a DSP.
The main contribution of this paper is that TET is possible in a shunted piezoelectric patch if special nonlinear electrical components are added. As an RL shunt is equivalent to adding a linear mechanical DVA, this equivalence is to allow for TET. In section 2, the dynamic model of the effect of the PE patch and shunt (with a nonlinear component) on the main system is constructed. By adding a nonlinear capacitor in series with the inductance and resistor the mechanical-electrical equivalence is extended so that this capacitor is a nonlinear spring connecting the inductance mass with the ground. This nonlinear capacitor is designed to ensure TET in the shunt. In the past, this type of nonlinear, grounded mechanical vibration absorber has been given some attention [6] but most research on TET was investigated ungrounded nonlinear absorbers[5, 10, 13]. In the 3rd section, the NNMs of the compound system are derived, and it is shown that when the shunt contains a 'cubic capacitor', TET indeed does occur if energy in the main system is high enough. In the 4th section, simulations are performed and show the typical properties of TET; as the energy threshold and increased robustness against detuning.

2 SYSTEM ANALYSIS

A continuous mechanical main system is considered with a displacement $\mathbf{Y}(\mathbf{x}, t)$, at point $\mathbf{x}$ of the structure at time t. The piezoelectric patch has a charge Q flowing through the shunt and has a voltage V over its electrodes. The main system is assumed to be linear, and either by a mode reduction of the analytic expression [14] , or with a FEM formulation [12], can be decomposed in a discrete number of modes:

$$\mathbf{Y}(\mathbf{x}, t) = \sum_{i=1}^{N} \mathbf{\Phi}_i(\mathbf{x}) q_i(t) \tag{1}$$

with $\mathbf{\Phi}_i(\mathbf{x})$ the i-th mode shape and $q_i(t)$ the i-th modal coordinate. The main structure, subjected to both the external forces and piezoelectric force, fig.1c, can be formulated as:

$$\ddot{q}_i + 2\zeta_i\omega_i\dot{q}_i + \omega_i^2 q_i - \underbrace{\chi_i V}_{\text{PE force}} = \underbrace{F_{i,ext}}_{\text{External force}} \quad , \quad i \in [1, N] \tag{2}$$

with ω_i the eigenfrequency of the mode, ζ_i the modal damping and χ_i the modal electromechanical coupling factor (MEMCF)[14].

$$C_p V - Q + \sum_{i=1}^{N} \chi_i q_i = 0 \tag{3}$$

with C_p the equivalent electrical capacitance of the piezoelectric patch. To simplify the analysis, no external forcing is assumed and motion of the mechanical structure is assumed to be dominated by a single mode j, simplifying (2) and (3) to:

$$\begin{aligned} \ddot{q}_j + 2\zeta_j\omega_j\dot{q}_j + \omega_j^2 q_j - \chi_j V &= 0 \\ C_p V - Q + \chi_j q_j &= 0 \end{aligned} \tag{4}$$

The proposed shunt contains a resistor R, inductor L and in series, a general electrical component that produced a voltage $V_Z = f(Q)$:

$$V = -L\ddot{Q} - R\dot{Q} - f(Q) \tag{5}$$

This allows (4) and (5) to be rewritten as:

$$\begin{aligned} \ddot{q}_j + 2\zeta_j\omega_j\dot{q}_j + \omega_j^2 q_j + \frac{\chi_j^2}{C_p}(q_j - \frac{Q}{\chi_j}) = 0 \\ \chi_j^2 L\frac{\ddot{Q}}{\chi_j} + \chi_j^2 R\frac{\dot{Q}}{\chi_j} + \chi_j f(Q) + \frac{\chi_j^2}{C_p}(\frac{Q}{\chi_j} - q_j) = 0 \end{aligned} \tag{6}$$

or by introducing the variable $\mathcal{Q} = \frac{Q}{\chi_j}$, a charge with unit m:

$$\begin{aligned} \ddot{q}_j + 2\zeta_j\omega_j\dot{q}_j + \omega_j^2 q_j + \frac{\chi_j^2}{C_p}(q_j - \mathcal{Q}) = 0 \\ \chi_j^2 L\ddot{\mathcal{Q}} + \chi_j^2 R\dot{\mathcal{Q}} + \chi_j f(\mathcal{Q}) + \frac{\chi_j^2}{C_p}(\mathcal{Q} - q_j) = 0 \end{aligned} \tag{7}$$

which can be interpreted as a two degree of freedom mechanical system, see fig.2. It is as if the modal system is connected with the 'inductance' mass $\chi_j^2 L$ through the linear spring $\frac{\chi_j^2}{C_p}$. The 'inductance' mass itself is also grounded, like the modal system, through a damper, $\chi_j^2 R$. The general impedance $f(\mathcal{Q})$ can be seen as some kind of stiffness connecting the inductance mass to the ground. For instance, if $f(\mathcal{Q}) = \frac{\mathcal{Q}}{C_{lin}}$, actually a linear capacitor, then it is as if a linear spring connects the inductance mass to the ground.

The impedance $f(\mathcal{Q})$ will be designed in order to ensure targeted energy transfer. If $V_z = f(\mathcal{Q}) = \frac{\mathcal{Q}^3}{C_{cub}}$, TET occurs when the system energy is above a threshold coinciding with a NNM mode bifurcation.

3 NONLINEAR NORMAL MODES

Nonlinear normal modes are possibly synchronous periodic solutions of the conservative system. System (7) still has damping, so by setting $R = 0$ and $\zeta_j = 0$ the underlying conservative system reads:

$$\begin{aligned} \ddot{q}_j + \omega_j^2 q_j + \frac{\chi_j^2}{C_p}(q_j - \mathcal{Q}) = 0 \\ \chi_j^2 L\ddot{\mathcal{Q}} + \frac{\chi_j^4\mathcal{Q}^3}{C_{cub}} + \frac{\chi_j^2}{C_p}(\mathcal{Q} - q_j) = 0 \end{aligned} \tag{8}$$

To construct these nonlinear normal modes, it is assumed that steady state motion of (8) is a synchronous, single frequency vibration:

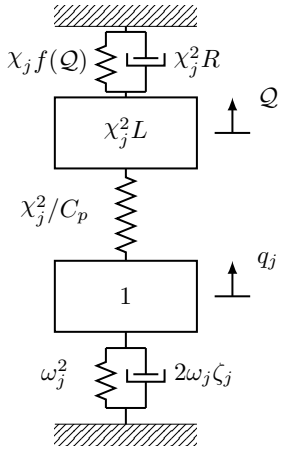

Figure 2: The mechanical equivalent of the structure/patch system

$$\begin{aligned} q_j &= A cos(\omega t) \\ \mathcal{Q} &= B cos(\omega t) \end{aligned} \tag{9}$$

of which both, A, B and ω are unknown. When replacing (9) in a linear system with n-degree of freedom, n solutions for ω will be found, the eigenfrequencies, and for each ω, eigenvectors or mode shape, which fixes the ratio between A and B. Both the frequencies and eigenvectors will not change depending on the magnitude A or B. In nonlinear system, the 'eigenfrequencies' and the mode shapes depend on the magnitude of A and B.

Replacing (9) in (8) yields the following solutions for A and B:

$$B = \pm \sqrt{\frac{4C_{cub}}{3\chi_j^4} \frac{\chi_j^2 L(\omega_j^2 - \omega^2 + \frac{\chi_j^2}{C_p}) - \frac{\chi_j^2}{C_p}(\omega_j^2 - \omega^2)}{\omega_j^2 - \omega^2 + \frac{\chi_j^2}{C_p}}} \tag{10}$$

$$A = \frac{\frac{\chi_j^2}{C_p} B}{\omega_j^2 - \omega^2 + \frac{\chi_j^2}{C_p}} \tag{11}$$

The potential energy in the conservative system is:

$$E = \frac{1}{2}\omega_j^2 A^2 + \frac{\chi_j^2}{2C_p}(A - B)^2 + \frac{\chi_j^4}{4C_{cub}} B^4 \tag{12}$$

which is the total energy as when the assumed motion (9) is maximal, the speed is zero. In NNMs, it is custom to graphically plot the so-called *frequency-energy plot* (FEP), which reveals

the relation (12) and the frequency. Using the numerical values for the nonlinear shunt on tab.1, the FEP is plotted on fig.3 using the toolbox NI2D.

The FEP clearly shows a change of eigenfrequency as the energy increases. In linear systems, the FEP would just consist of horizontal lines. There are 2 main curves, called branches. The first, the $S11+$ branch, is the in-phase nonlinear mode of the system while the second, $S11-$, is the out of phase motion. Both of these branches start horizontally at the linearised frequencies, that is the eigenfrequencies of (8) if it is linearised. As the energy increases, the upper branch $S11-$ bifurcates for $log(E) = -0.817$ into 3 solutions. The branch $S11-$ bifurcates again for $log(E) = -0.174$. It is this last bifurcation and the associated energy that are linked with TET [5, 10, 15]. If the initial energy is just above this $log(E) = -0.174$, the energy in the main system will be transferred to the absorber, where it will be dissipated if there is damping present. Just below this energy level, the energy stays in the main system, and is only slowly mitigated. It is assumed that initially, only the main system has an initial speed. This is called the *impulsive excitation*. The initial (kinetic) energy in the system is then:

$$E = \frac{1}{2}\dot{q}_j^2 = \frac{1}{2}\omega_j^2 A^2 > 10^{-0.174} \Rightarrow \dot{q}_j > 1.15 m/s \tag{13}$$

which yields the required initial speed to trigger TET. In the next section, simulations are performed to show this sudden change in behaviour as the initial speed changes and a nonlinear shunt is compared to a linear one.

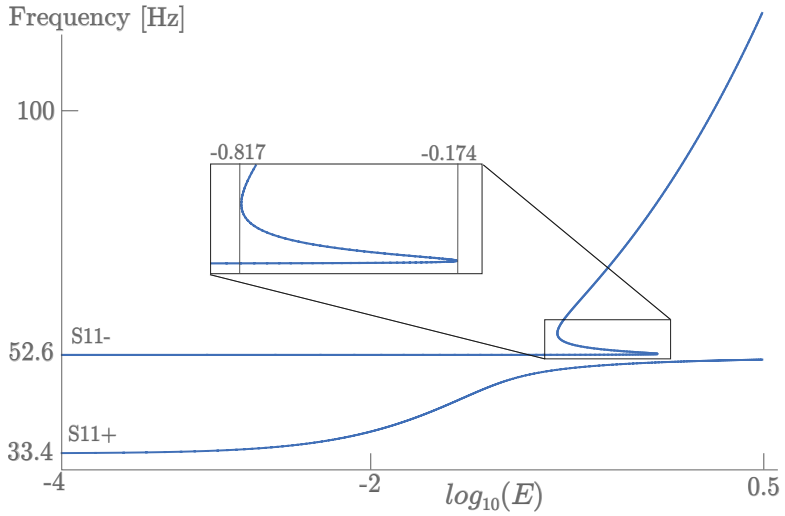

Figure 3: The nonlinear normal modes of system (8), visualised with the frequency-energy plot

4 Simulations

In [14] a cantilever beam was fitted with a piezoelectric patch. The mechanical and piezoelectric parameters from this setup are used to simulate both a nonlinear and linear shunt. The tuning of the linear shunt was performed in [14] see tab.1 for numerical values, with only a

Table 1: Numerical values of mechanical system and shunt. The values for the linear shunt are taken from a mechanical setup from [14]

Quantity	Linear	Nonlinear
ω_j $[\frac{rad}{s}]$	324.5	324.5
χ_j $[\frac{C}{m}]$	0.0045	0.0045
C_p $[F]$	$9.16 \cdot 10^{-9}$	$9.16 \cdot 10^{-9}$
R $[\Omega]$	$58.62 \cdot 10^{3}$	$58.62 \cdot 10^{3}$
L $[H]$	1060	2400
C_{cub} $[\frac{C^3}{V}]$	—	$9.16 \cdot 10^{-18}$

resistor and inductor in the shunt circuit. For the nonlinear shunt, the values used to draw the NMM are used.
First, the designed nonlinear shunt is simulated for several initial $\dot{q}_j(0)$, see fig.4. In the previous section, is was determined that $\dot{q}_j(0)$ should be above 1.15 m/s for TET to happen. When the initial speed is below the critical value (here $\dot{q}_j(0) = 0.8$ m/s), the main system vibrations, fig.4a, mitigate very slowly, and the absorber charge, fig.4b, is low compared to the other initial speeds. If the main system is excited with $\dot{q}_j(0) = 1.15$ m/s, the vibrations are reduced very fast, and the absorber charge is persistently larger than before. If the initial speed is then further increased (here $\dot{q}_j(0) = 1.5$ m/s, the vibration reduction is slower, yet still significantly faster than when the initial speed was below 1.15 m/s.

The fact that this vibration absorber don't work below, optimally on, and suboptimally above the energy threshold was already discussed in [5].

Next, the main system's vibration reduction is compared when using the nonlinear shunt and a tuned linear shunt, tuned in [14], on fig.5. First, the main system is excited with the optimal initial speed for the nonlinear shunt, fig.5a. Here, the linear absorber is better than the nonlinear one in the beginning. After 0.29 s however, the linear and nonlinear shunts have reduced the main system vibration to somewhat the same level. A correctly tuned linear absorber is always faster than a correctly tuned absorber of the kind on fig.2 [5, 16]. One of the advantages of the nonlinear shunt is that it is more robust. If the main system is detuned, by reducing eigenfrequency ω_j three times by 0.9, so $\omega_j = 290$, 260 and 232 rad/s, it is observed that linear shunt's performance deteriorates a lot faster than the nonlinear shunt, fig.5a, fig.5b and fig.5c.

5 Conclusion

In this paper, it is shown that the targeted energy transfer (TET) phenomenon, normally associated with mechanical dynamic vibration absorbers (DVA), also occurs in piezoelectric DVAs for a carefully designed shunt. By assuming a single vibration mode in the main system, the electrical charge in the shunt is equivalent to a mechanical displacement. In this mechanical-electrical equivalence, an RL shunt is then seen as a mass spring damper system, attached on the main structure. If a nonlinear electrical element is added in the shunt, the shunt is equivalent to a nonlinear mechanical DVA so the tuning rules to achieve TET in mechanical DVA can be applied to the nonlinear shunt. Some simulations were performed to show the initial energy

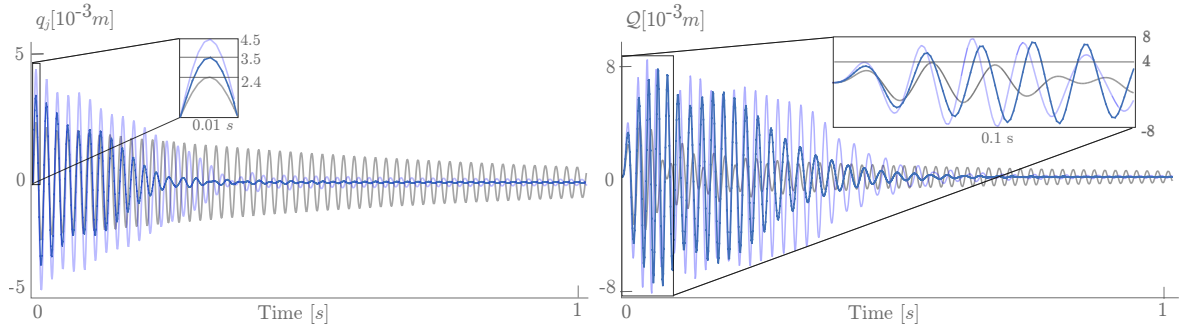

(a) (b)

Figure 4: The main systems displacement q_j (a) and charge in the nonlinear shunt$\mathcal{Q}$ (b) for initial main system's speed $\dot{q}_j = 0.8\ m/s$ (grey), $\dot{q}_j = 1.15\ m/s$ (dark blue) and $\dot{q}_j = 1.5\ m/s$ (light blue)

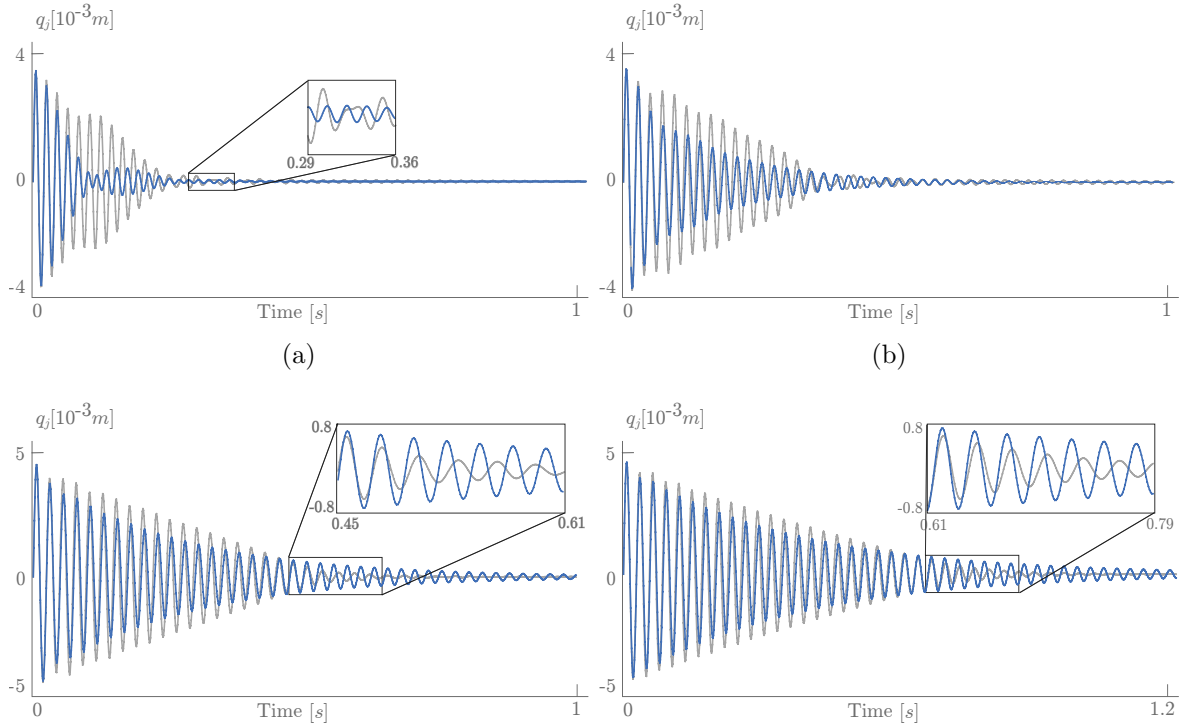

(a) (b)

(c) (d)

Figure 5: The main systems displacement q_j for initial speed $\dot{q}_j = 1.15$ both when using a linear shunt (blue) and nonlinear shunt (grey) (a), for a detuned eigenfrequency $\omega_j = 290\ rad/s$ (b), $\omega_j = 260\ rad/s$ (c) and $\omega_j = 232\ rad/s$ (d)

dependence on the performance of TET. The nonlinear shunt was also compared to a linearly tuned shunt. While a perfectly tuned linear shunt mitigate vibrations faster than the nonlinear shunt, the nonlinear shunt is a lot more robust if there is detuning.

Acknowledgements

The results presented in this paper were partly obtained using the NI2D software developed by the Space Structures and Systems Laboratory (S3L), University of Lige.

REFERENCES

[1] Hagood, N.W. and Von Flotow, A. Damping of structural vibrations with piezoelectric materials and passive electrical networks. *Journal of Sound and Vibration* (1991) **146**:243-268

[2] Mao, Q. and Pietrzko, S. *Control of Noise and Structural Vibration: A MATLAB-Based Approach*, Springer (2013).

[3] Den Hartog, J.P. *Mechanical vibrations*, McGraw Hill, (1940).

[4] Neubauer, M., Oleskiewicz, R., Popp, K. and Kryzynski, T. Optimization of damping and absorbing performance of shunted piezo elements utilizing negative capacitance. *Journal of Sound and Vibration* (2006) **298**:84-107

[5] Vakakis, A.F., Gendelman, O.V., Bergman, L.A., Mcfarland, D.M., Kerschen, G. and Lee, Y.S. *Nonlinear Targeted Energy Transfer in Mechanical and Structural Systems*, Springer, (2008).

[6] Kerschen, G., Vakakis, A.F., Lee, Y.S., Mcfarland, D.M., Kowtko, J.J. and Bergman, L. A. Energy Transfers in a System of Two Coupled Oscillators with Essential Nonlinearity: 1:1 Resonance Manifold and Transient Bridging Orbits. *Nonlinear Dynamics* (2005) **42**:283-303.

[7] Kerschen, G., Peeters, M., Golinval, J.-C. and Vakakis, A.F. Nonlinear normal modes, Part I: A useful framework for the structural dynamicist. *Mechanical Systems and Signal Processing* (2009) **23**:170-194.

[8] Peeters, M., Vigui, R., Kerschen, G. and Golinval, J.-C. Nonlinear normal modes, Part II: Toward a practical computation using numerical continuation techniques *Mechanical Systems and Signal Processing* (2009) **23**:195-216.

[9] NOLISYS. `http://www.nolisys.com/`, 25/02/2017

[10] Petit, F., Loccufier, M. and Aeyels, D. The energy thresholds of nonlinear vibration absorbers. *Nonlinear Dynamics* (2013) **74**:755-767

[11] Nečsek, J., Vclavk, J. and Marton, P. Digital synthetic impedance for application in vibration damping. *Review Of Scientific Instruments* (2016) **87**:024704

[12] Thomas, O., De, J.-F. and Ducarne, J. Vibrations of an elastic structure with shunted piezoelectric patches: efficient finite element formulation and electromechanical coupling coefficients. *Int. J. Num. Meth. Engng.* (2009) **80**:235-268.

[13] Lee, Y.S., Kerschen, G., Vakakis, A.F., Panagopoulos, P., Bergman, L. A., Mcfarland, D.M. Complicated dynamics of a linear oscillator with a light, essentially nonlinear attachment. *Physica D* (2005) **204**:41-69.

[14] Thomas, O., Ducarne, J. and De J.-F. Performance of piezoelectric shunts for vibration reduction. *Smart Materials and Structures* (2012) **21**:015008.

[15] Kerschen, G., Lee, Y. S., Vakakis, A. F., McFarland, D. M., and Bergman, L. A. Irreversible passive energy transfer in coupled oscillators with essential nonlinearity. *SIAM Journal on Applied Mathematics* (2005) **66**:648-679.

[16] Petit, F., Loccufier, M., and Aeyels, D. Feasibility of nonlinear absorbers for transient vibration reduction. *Proceedings of ISMA 2010: international conference on noise and vibration engineering*(2010):12191233

VIII ECCOMAS Thematic Conference on Smart Structures and Materials
SMART 2017
A. Güemes, A. Benjeddou , J. Rodellar and Jinsong Leng (Eds)

Fault detection and fault tolerant control of vehicle semi-active suspension system with magnetorheological dampers

Youxiang Peng†, Miao Yu *, Xiaoying Xu† , Xiumei Du† and Jie Fu †

* Key Lab for Optoelectronic Technology and Systems, Ministry of Education, College of Optoelectronic Engineering, Chongqing University, Chongqing 400044, China
e-mail: yumiao @cqu.edu.cn

Abstract

In engineering application， the sensor or actuator fault will lead to seriously damage to mechanical systems. The research of sensor or actuator fault diagnosis and fault-tolerant control is very important to improve the safety and reliability of the system. The paper investigates the fault diagnosis and fault-tolerant methods of vehicle suspension system with Magnetorheological (MR) damper (actuator). First of all, the quarter-vehicle suspension system model is established. Then, an unknown input observer (UIO) is employed to detect the actuator fault in the vehicle MR suspension system. Next, the correlation coefficient method is used to isolate the fault of actuator fault in the system. Lastly, the skyhook fault-tolerant controller is designed for control compensation. The simulation results under sine excitation, random excitation and pump excitation show that the perfomance of the proposed fault-tolerent controller always outweight that of without fault-tolerant when actuator occurs fault.

Key words: Vehicle semi-active suspension, Unknown input observer (UIO), Fault tolerant control, Magnetorheological (MR) dampers

1 INTRODUCTION

Due to the fast response speed, low energy consumption and simple structure, the magneto-rheological (MR) semi-active suspension has attracted more attention in engineering fields. The control algorithm of the semi-active suspension is the key to guarantee the reliable and stable system. The skyhook control [1, 2], the fuzzy control [3,4], optimal control [5], H-infinite control [6] have been proved to be effectiveness to improve suspension performance. These above-mentioned algorithms are assumed the actuators or sensors to be fault-free operation. However, when actuator or sensor occurs fault, the system performance will be reduced or failed because of no corresponding detection and fault-tolerence methods.

To solve the problem, researchers studied fault-tolerant control. Fault-tolerant control is mainly divided into three aspects, fault diagnosis、isolation and fault-tolerant control. For the the fault diagnosis of vehicle MR semi-active suspension system, there are whole order Luenberger observer [7], the Kalman filter[8], the unknown input observer (UIO) group [9]

in the existing literature. Luenberger observer has the simple structure but poor robustness to disturbance. Kalman filter is generally used in state estimation under white noise disturbance. when the road input pulse disturbance is met, it will influence the reliability of state estimation. Due to good robustness and the decoupling ability between the state estimation error and disturbance, the UIO has been used widely [10]. The road excitation such as impulse, random is time-varing and also very difficult to be measured for the operating vehicle system. Therefore, UIO is suitable for vehicle MR vehicle suspension fault diagnosis.

For the problem of fault isolation, it is usually used mathematical method to solve the malfunction coefficient, but the method is too complex to achieve [8, 11]. Ref. [12] put forward a way to calculate the correlation coefficient between the residual and the fault characteristic signal, then according to the correlation coefficient to isolate fault. The mehtod can isolate sensor or actuator failures effectively, and also has the characteristic of simply structure and easy to be implemented.

In respect of fault-tolerant control, the study of the vehicle suspension system is relatively poor, it mainly include H-infinite control, sliding mode control and LQG control, etc. Ref. [13] designed H-infinity fault-tolerenc controller to reduce the impact of actuator fault in vehicle semi-active suspension. LQG controller was used to deal with the actuator gain failure in semi-active suspension system [14]. The sliding mode control was employed to compensate the actuator fault in the magneto-rheological suspension system [8].

Based on the above analysis, this paper employs UIO to identify the actator fault detection of MR vehicle suspension system. Then, by calculating the correlation coefficient between the residual and the fault characteristic signal, the fault is isolated, the fault is isolated. Finally, skyhook fault-tolerant control strategy with little complexity is desinged to compensate fault, and maintain a certain control performance.

2 MAGNETO-RHEOLOGICAL SUSPENSION'S FAULT MODELING

2.1 The Model of Quarter Suspension System

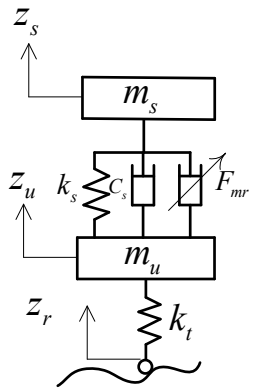

Figure 1: The quarter vehicle semi-active suspension model

The quarter vehicle dynamic model is shown in Figure 1. Based on Newton's motion law, the dynamic equation is shown as：

$$\begin{cases} m_s\ddot{z}_s = -k_s\left(z_s - z_u\right) - c_s\left(\dot{z}_s - \dot{z}_u\right) - F_{mr} \\ m_u\ddot{z}_u = k_s\left(z_s - z_u\right) + c_s\left(\dot{z}_s - \dot{z}_u\right) - k_t\left(z_u - z_r\right) + F_{mr} \end{cases} \tag{1}$$

where m_s is sprung mass, m_u is unsprung mass, $\ddot{z}_s, \dot{z}_s, z_s$ are sprung acceleration, velocity, displacement, respectively, $\ddot{z}_u, \dot{z}_u, z_u$ are unsprung acceleration, velocity, displacement, respectively, z_r is the displacement of road input , k_s is uspension stiffness, c_s is damping coefficient, k_t is tire stiffness, F_{mr} is the output force of MR damper.

The state equation can be formulated as:

$$\begin{cases} \dot{x}(t) = Ax(t) + Bu(t) + Ed(t) \\ y(t) = Cx(t) + Du(t) \end{cases} \tag{2}$$

where $x(t) = \left[z_s - z_u, \dot{z}_s, z_s, \dot{z}_u\right]$ are the state variables, $d(t) = z_r$ is the road input, $u(t) = F_{mr}$ is the control input, $y(t) = \left[\ddot{z}_s, z_u, \dot{z}_s\right]$ is the output vector, and

$$A = \begin{bmatrix} 0 & 1 & 0 & -1 \\ -(ks/ms) & -(cs/ms) & 0 & cs/ms \\ 0 & 1 & 0 & 0 \\ (kt+ks)/mu & cs/mu & -kt/mu & -cs/mu \end{bmatrix},\ B = \begin{bmatrix} 0 \\ -1/ms \\ 0 \\ 1/mu \end{bmatrix},\ E = \begin{bmatrix} 0 \\ 0 \\ 0 \\ kt/mu \end{bmatrix},$$

$$C = \begin{bmatrix} -(ks/ms) & -(cs/ms) & 0 & cs/ms \\ -1 & 0 & 1 & 0 \\ 0 & 1 & 0 & 0 \end{bmatrix}$$

Due to the unknown $u(t)$, output euqation can be rewritten as:

$$\bar{y}(t) = y(t) - Du(t) = Cx(t) \tag{3}$$

Then the state equation can be reformulated as:

$$\begin{cases} \dot{x}(t) = Ax(t) + Bu(t) + Ed(t) \\ \bar{y}(t) = Cx(t) \end{cases} \tag{4}$$

2.2 Actuator Fault Model

There are gain change, stuck and constant deviation fault in MR suspension system. The actuator gain fault occurs easily, so it is considered only in this paper. When the actuator has gain fault, the output $u_f(t)$ can be written as：

$$u_f(t) = u(t) - \delta u(t) \tag{5}$$

where δ is fault gain coefficient, $\delta \in [0,1]$, $u(t)$ is actuator control output force under normal condition.

It can be seen from the features of gain change fault：

When $\delta = 1$， the actuator has completely gain damage

When $\delta = 0$， the actuator is trouble-free

When $0 < \delta < 1$， the actuator has part gain damage

3 FAULT DIAGNOSE AND ISOLATION

The paper uses the UIO to dectect the actuator fault and correlation coefficient method to isolate the fault.The block diagram of fault diagnose and isolation system can be seen in Figure 2.

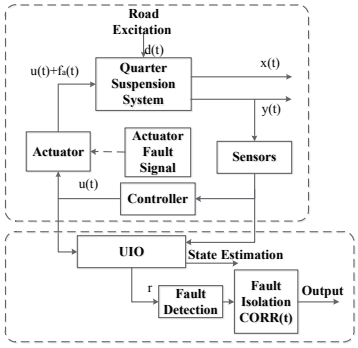

Figure 2: Block diagram of fault diagnose and isolation system.

3.1 UIO

UIO equation is

$$\begin{cases} \dot{z}(t) = Fz(t) + TBu(t) + Ky(t) \\ \hat{x}(t) = z(t) + Hy(t) \end{cases} \tag{6}$$

Where $\hat{x} \in R^n$ is the estimate state vector， $z \in R^n$ is the state of UIO, F, T, K, H are the design matrixes in order to get the unknown input decoupling and meet other design requirem ents.

Remark1: By the linear transformation of the equation of state, the state vector is divided into two parts in UIO, one is measured directly, the other is estimated by disturbance decoupling observer. So it can be decoupled from the UIO's state estimation error.

Sutracts Equation (4) from Equation (6), the estimation error $e(t)$ and output error $r(t)$ can be obtained as follows:

$$e(t) = x(t) - \hat{x}(t) \tag{7}$$

$$r(t) = y(t) - \hat{y}(t) = Ce(t) \tag{8}$$

For $e(t)$ meets the following equation：

$$\dot{e}(t)=(A-HCA-K_1C)e(t)-\left[F-(A-HCA-K_1C)\right]z(t)-\left[K_2-(A-HCA-K_1C)H\right]y(t)$$
$$-\left[T-(I-HC)\right]Bu(t)-(HC-I)Ed(t) \tag{9}$$

where

$$K=K_1+K_2 \tag{10}$$

If make the following equation is established:

$$\begin{cases}(HC-I)E=0\\ T=I-HC\\ F=A-HCA-K_1C\\ K_2=FH\end{cases} \tag{11}$$

Then,the state estimation error is

$$\dot{e}(t)=Fe(t) \tag{12}$$

If all the eigenvalues of F are stability, $e(t)$ will gradually close to zero, namely $\hat{x}\to x$. The system residual $r(t)$ is 0. So $r(t)$ can be assumed to be the judgment of system state.

Before given the necessary and sufficient condition of UIO, there are two lemmas：

Lemma 1 Equation (11) can be solved and only if

$$rank(CE)=rank(E) \tag{13}$$

And its special solution for：

$$H^*=E\left[(CE)^T(CE)\right]^{-1}(CE)^T \tag{14}$$

Lemma 2 Make the $C_1=(C;CA)$,the matrix of (C_1,A) detection can be equivalent to the (C,A) can be detected.

Theorem 1 The necessary and sufficient condition that Equation (6) is the observer of system (4) is：

$$rank(CE)=rank(E)$$
$$(C,A_1) \text{ can be detected}$$

where

$$A_1=A-E\left[(CE)^T(CE)\right]^{-1}(CE)^TCA \tag{15}$$

3.2 Actuator Fault Detection and Isolation

By combining state residual error Equation (6) and (7), the steady state solution in the system residual error can be obtained:

$$r_{sa} = \lim_{t\to\infty} \int_0^t Ce^{(A_1 - K_1 C)(t-\sigma)} TBf_a(\sigma) d\sigma \tag{16}$$

In order to detect actuators fault, the following equation is required:

$$CTB \neq 0 \tag{17}$$

When actuator has fault, the steady-state solution r_{sa} of residual $r(t)$ and fault actuator corresponding eigenvector $v = CTB$ in Equation (16) is in the same direction, which means that their angle is 0. Then, the correlation coefficient $\mathrm{CORR}(\mathrm{t})$ between r_{sa} of residual $r(t)$ and fault actuator eigenvector $v = CTB$ satisfies

$$\mathrm{CORR}(\mathrm{t}) = \frac{\left| r(t)^T v \right|}{\left\| r(t) \right\|_2 \left\| v \right\|_2} \tag{18}$$

$\mathrm{CORR}(\mathrm{t})$ reflects the angle between steady-state solution r_{sa} of residual $r(t)$ and fault actuator eigenvector $v = CTB$. It can be seen that the greater the correlation coefficient value, the smaller the angle. $\mathrm{CORR}(\mathrm{t}) = 1$ means that fault vector v is fault position, and then the fault can be isolated.

3.3 Simulation Results and Analysis

Simulation is carried out in this section to verify performance of diagnose and isolation of designed UIO and correlation coefficient method for actuator fault in MR suspension system. The suspension parameters are shown in Table 1.

Table 1: The quarter vehicle MR suspension parameters

Parameters	Values
Suspension stiffness k_s	$2\times10^4 \ \ N/m$
Tire stiffness k_t	$1.81\times10^5 \ \ N/m$
Damping coefficient c_s	500 $N\cdot s/m$
Sprung mass m_s	350 kg
Unsprung mass m_u	50 kg

The pole assignment method is used to design UIO. That all the eigenvalues of the matrix $A - HCA - K_1 C$ have negative real parts can guarantee that state error equation (9) is asymptotically stable. Then the UIO's feedback gain matrix K_1 can be solved：

$$K_1 = \begin{bmatrix} -0.63515 & -23.71257 & 0.09263 \\ 1 & 0 & 52 \\ -0.24742 & 14.00035 & 0.64654 \\ 17.79471 & -959.93327 & 63.99244 \end{bmatrix}$$

It is assumed that the actuator gain faults occur, and the fault coefficient is $\delta = 0.8$ and $\delta = 0.3$, respectively. Based on UIO and correlation coefficient method, the diagnose results are shown in Table 2 and Figure 2-5.

Table 2: Actuator fault mode and isolation result

Fault	Fault parts	Fault situation	$\mathrm{CORR}(t)$
Fault 1	Actuator	Gain coefficient $\delta = 0.8$ in 15 seconds	0.9415
Fault 2	Actuator	Gain coefficient $\delta = 0.3$ in 12 seconds	0.9441

It can be seen from Table 2, Figure 3 and 4:

(1)The actuator is non-fault in 15 s, so the residual value is always zero.

(2)The actuator occur gain fault at 15s, the residual value is no longer zero. Meanwhile, the $\mathrm{CORR}(t)$ is close to 1, which means the actuator occurs fault.

For the case of $\delta = 0.3$ in Figure 5 and 6, same conclusions can be drawn, which are not reanalysed for readability and repeatability.

Therefore, UIO and correlation coefficient method can diagnose and isolate fault of actuator effectively.

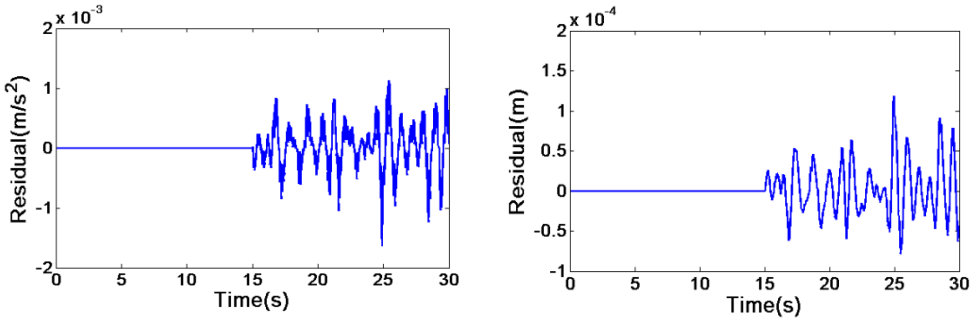

(a) (b)

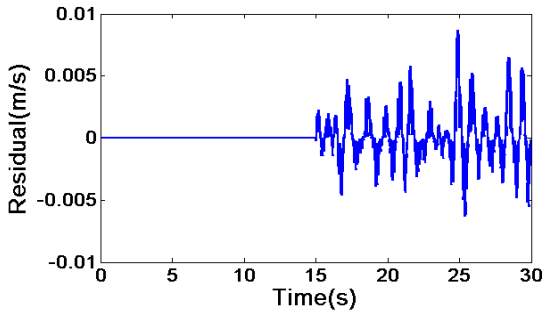

(c)

Figure 3: The system residual of Fault 1: (a) The residual of $\ddot{z}_s$; (b) The residual of z_u ;(c) The residual of $\dot{z}_s$

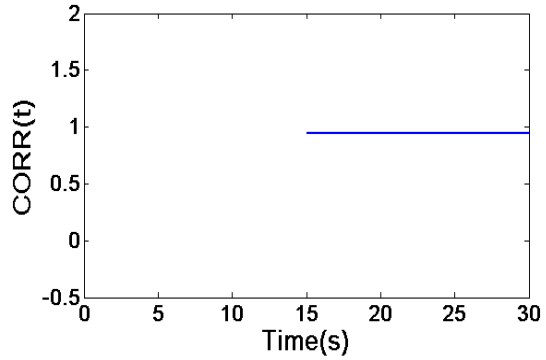

Figure 4: The correlation coefficient of Fault 1

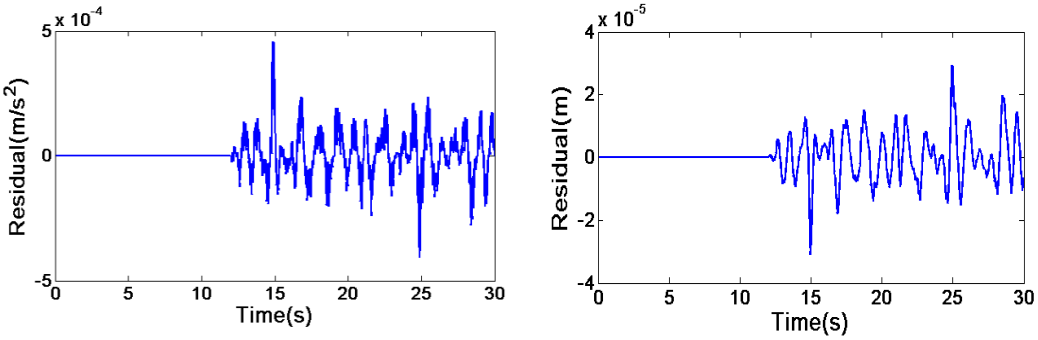

(a) (b)

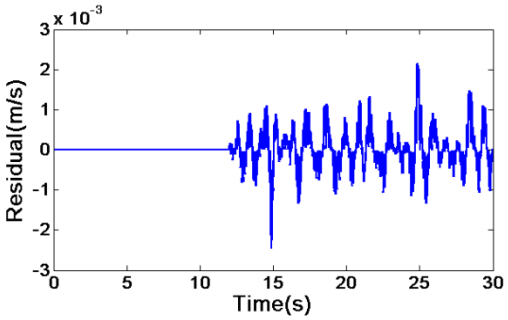

(c)

Figure 5: The system residual of Fault 2: (a) The residual of $\ddot{z}_s$;(b) The residual of z_u ;(c) The residual of $\dot{z}_s$

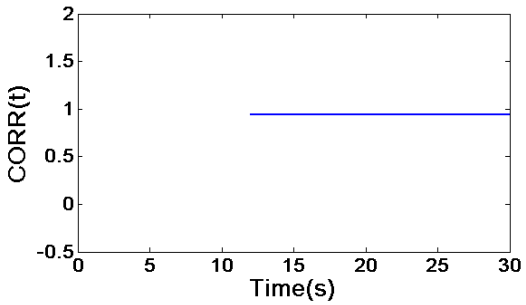

Figure 6: The correlation coefficient of Fault 2

4 SKYHOOK FAULT-TOLERANT CONTROLLER DESIGN

The performance of MR damper is relevent to the mechanical structure and magnetic fields generated by coil. When piston channel is partial of blockage or coil is aging in MR damper, the output force will be abnormal.The block diagram of skyhook fault-tolerant system is shown in Figure 7.

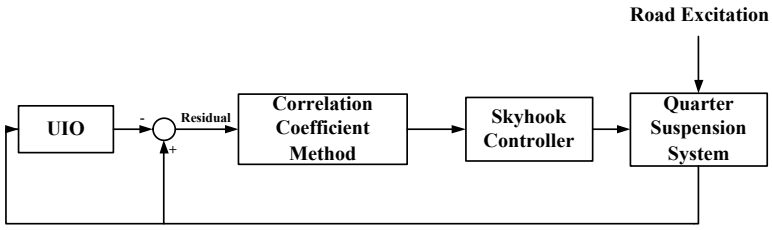

Figure 7: Block diagram of skyhook fault-tolerant system.

Consider actuator fault

$$F_a(t) = \delta u(t) \tag{19}$$

$$F_d(t) = u(t) - F_a(t) = (1-\delta)u(t) \tag{20}$$

where δ is gain coefficient, $F_d(t)$ is the actual output force under fault, $F_a(t)$ is fault, $u(t)$ is expected output force, and $F_a(t) \le u(t)$.

And

$$u(t) = \begin{cases} F_{\max} & \dot{z}_s(\dot{z}_s - \dot{z}_u) \ge 0 \text{ and } \left|C_{sky}\dot{z}_s\right| \ge \left|F_{\max}\right| \\ C_{sky}\dot{z}_s & \dot{z}_s(\dot{z}_s - \dot{z}_u) \ge 0 \text{ and } \left|C_{sky}\dot{z}_s\right| < \left|F_{\max}\right| \\ 0 & \dot{z}_s(\dot{z}_s - \dot{z}_u) < 0 \end{cases}$$

where F_{sat} is the maximum output force of MR damper, C_{sky} is the coeficent of skyhook controller.

For the actuator gain fault, the fault-tolerant control strategy is designed as follows:

$$u_{FT}(t)=\begin{cases} F_{\max}, & \dfrac{F_d(t)}{1-\delta}\geq F_{\max} \\ \dfrac{F_d(t)}{1-\delta}, & \dfrac{F_d(t)}{1-\delta}<F_{\max} \end{cases} \tag{21}$$

where $u_{FT}(t)$ is the output of fault-tolerance controller.

5 SIMULATION AND ANALYSIS OF FAULT-TOLERENCE CONTROL

The vibration suppresion performance of MR suspension with desinged skyhook fault tolerence control algorith is simulated under $\delta=0.8$ and sine excitation, random excitation and impulse excitation, respectivley.

5.1 Sine Excitation

The sine excitation is set as amplitude of 0.01m and 1Hz frequency. Based on the designed skyhook fault tolerenc controller, spring mass acceleration responses with passive controller, non-fault tolerence and fault-tolerence controller under sine excitation are given in Figure 6. The decreacement is listed in Table 3.

It can be seen from Figure 8 and Table 3, the spring mass acceleration decreacement with fault tolerant control algorithm is more than non-fault tolerence, and the attenuation rate is 36.33% and 21.3%, respectively.

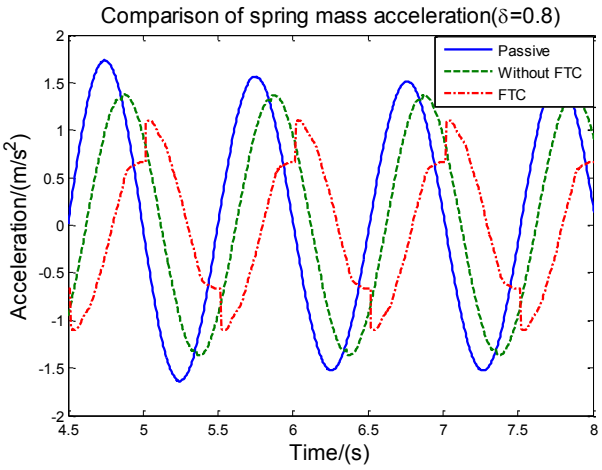

Figure 8: Spring mass acceleration response under sine excitation

Table 3: Sprung acceleration amplitude

Control mode	Passive	Fault mode	Fault-tolerant mode
The acceleration amplitude	1.734	1.364	1.104
Attenuation rate	-	21.3%	36.33%

5.2 Random Excitation

Random road is common appearance in vehicle operation, which is considered to verify the performance of the designed fault tolerance controller in this section. The random excitation

is generated by B level road with white noise which is shown in Figure 9. The speed is 40 Km/h.

The accerleration response of MR suspension system under random input is shown in Figure 10. Comparison of sprung acceleration root mean square (RMS) under fault-tolerance controller and non-fault controller is shown in Table 4. The RMS value of sprung acceleration under the fault tolerance controller is smaller than that under the non-fault tolerance controller and passive controller, and the value is reduced by41.84% while the non-fault tolerance controller controller only achieves 25.16%.

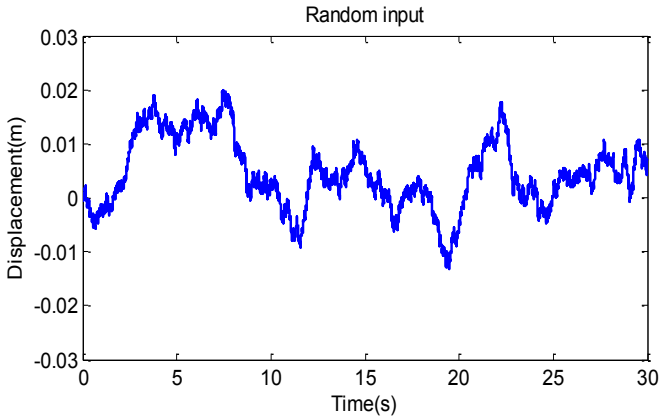

Figure 9: Random input in time domain

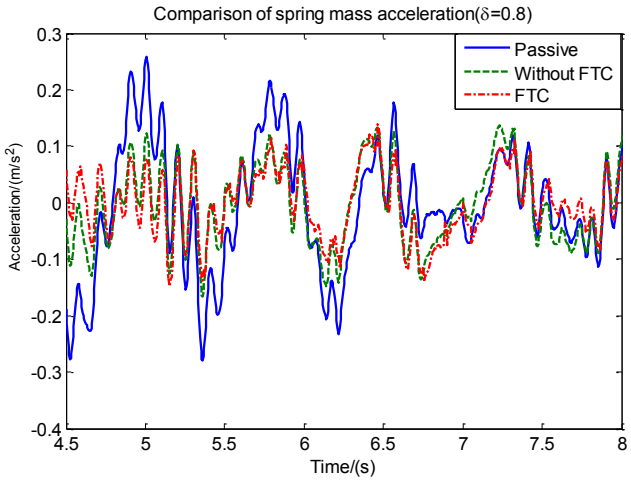

Figure 10: Spring mass acceleration response under random excitation

Table 4: Comparison of Sprung acceleration RMS under different controllers

Control mode	Passive	Fault mode	Fault-tolerant mode

The acceleration amplitude	0.3585	0.2683	0.2085
Attenuation rate	-	25.16%	41.84%

5.3 Pulse Excitation

When the velicle with acutator gain fault operates on the impulse road, which is shown in Figure 11, the acceleration response with faul tolerance controller is shown in Figure 12. And the Comparison of sprung acceleration maximum peak is shown in Table 5. Compared with the values of non-fault tolerance controller and passive, the maximu peak acceleration is reduced by 70.59%. So the fault tolerant control algorithm improves the performance of the system fault case.

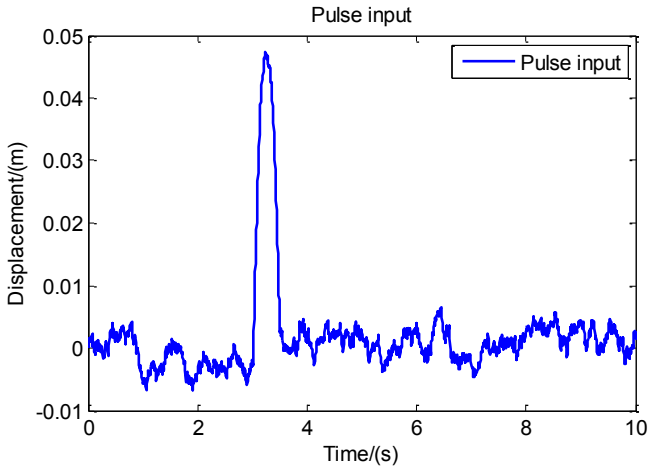

Figure 11: Pulse input in time domain

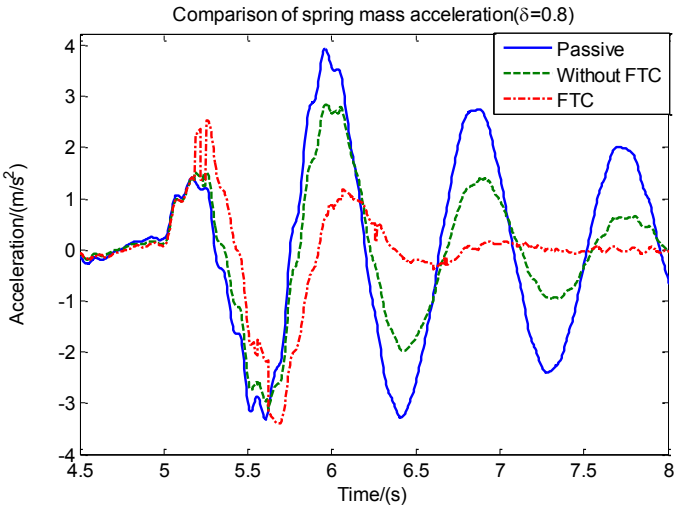

Figure 12: Spring mass acceleration response under pulse excitation

Table 5: Comparison of sprung acceleration maximum peak

Control mode	Passive	Fault mode	Fault-tolerant mode
The acceleration amplitude	3.927	2.82	1.155

Attenuation rate	-	28.19%	70.59%

In a word, it is also more effective for actuator fault with fault tolerance controller than non-fault tolerance controller and passive controller.

6 CONCLUSIONS

The paper employs UIO and correlation coefficient mothed to diagnose and isolate fault, and skyhook fault tolerence controller to suppress the vibration of vehilcle MR suspension system with actuator gain fault. According to the relationship between the residual signal and fault vector produced by UIO, the correlation coefficient is obtained to diagnose and isolate the actuator fault. Then, the skyhook fault-tolerant controller is designed to compensate the gain fault. The simulation results show that the designed fault diagnosis scheme can effectively detect and isolate actuator gain fault, and the proposed skyhook fault-tolerent controller can attenuate the maximum peak of the sprung mass acceleration by 59.04% in comparison with non-fault tolerance.

REFERENCES

[1] Bakar S A A, Jamaluddin H, Rahman R A, et al. Vehicle ride performance with semi-active suspension system using modified skyhook algorithm and current generator model. International Journal of Vehicle Autonomous Systems. 2008, 6(3): 197-221.

[2] Sulaiman S, Mohd. Samin P, Jamaludd H, et al. Groundhook control of semi-active suspension for heavy vehicle. Journal of Sound & Vibration. 2012, 172(3): 391-411.

[3] Ali S F, Ramaswamy A. Optimal fuzzy logic control for MDOF structural systems using evolutionary algorithms. Engineering Applications of Artificial Intelligence. 2009, 22(3): 407-419.

[4] Yu M, Liao C R, Chen W M, et al. Study on MR Semiactive Suspension System and its Road Testing. Journal of Intelligent Material Systems & Structures. 2006, 17: 801-806.

[5] Jahromi A F, Zabihollah A. Linear Quadratic Regulator and Fuzzy controller application in full-car model of suspension system with Magnetorheological shock absorber. 2010.

[6] Du H, Sze K Y, Lam J. Semi-active H-infinity control of vehicle suspension with magneto-rheological dampers. Journal of Sound & Vibration. 2005, 283(3): 981-996.

[7] Yang L Q,Chen W W. Vehicle Hydraulic Active Suspension Fault Diagnosis and Isolation Based on Residual Error Information. China Mechanical Engineering. 2012, 23(14): 1746-1752.

[8] Dong X, Guan Z, Yu M. Adaptive sliding mode fault tolerant control for semi-active suspension using magnetorheological dampers. Journal of Intelligent Material Systems & Structures. 2015, 22(22): 1653-1660

[9] Yetendje A, Seron M, Dona J D. Diagnosis and actuator fault tolerant control in vehicle active suspension. 2007.

[10] Chen J, Patton R J. Robust Model-Based Fault Diagnosis for Dynamic Systems. Kluwer Academic Publishers, 1999.

[11] Rezaei H, Khosrowjerdi M J, Saadat A. SMO-based fault tolerant control design for three phase induction motors// IECON 2012 -, Conference on IEEE Industrial Electronics Society. IEEE, 2012:2494-2499.

[12] Yang W. Fault tolerant flight control systems. Northwestern polytechnical university press, 2007.

[13] Gao Z G, Chen W W, Wang H B, etc. Fault-tolerant Control of Vehicle Semi-active Suspension Based on Fault Compensation. Automotive Engineering 2016 (6) : 705-715.

[14] Yang L Q, Chen W W, Zhang R Y, etc. Fault-tolerant Control and Experiment on Vehicle Semi-active Suspension System Based on Control Law Reconfiguration. Transactions of the Chinese Society for Agricultural Machinery. 2013 (10) : 1-9.

VIII ECCOMAS Thematic Conference on Smart Structures and Materials
SMART 2017
A. Güemes, A. Benjeddou , J. Rodellar and Jinsong Leng (Eds)

IMPACT OF MAGNETORHEOLOGICAL SEMI-ACTIVE STABILIZER BAR ON VEHICLE ROLLOVER

XIAN-XU BAI, SHI-XU XU AND SHENG SHEN

Laboratory for Adaptive Structures and Intelligent Systems (LASIS)
Department of Vehicle Engineering
Hefei University of Technology
230009 Hefei, People's Republic of China
E-mail: bai@hfut.edu.cn

Key words: Stabilizer Bar, Magnetorheological Damper, Rollover, Semi-active Control, Piece-Wise Control.

Abstract. The goal of this paper is to simultaneously improve the safety (anti-roll performance) and ride comfort of vehicles during fast cornering or over road irregularities via our previously proposed magnetorheological (MR) semi-active stabilizer bar. The MR stabilizer bar featuring a rotary MR damper provides small torsional torque at low speed to improve ride comfort, while large torsional torque to enhance the safety at high speed cornering. To further verify the feasibility and effectiveness of the proposed MR stabilizer bar, the mathematical model of the dynamic system is established, and the passive-on control performance of a specific full vehicle is studied via a commercial dynamics simulation software ADAMS. In addition, the piece-wise control algorithm using lateral acceleration information for the MR stabilizer bar is carried out.

1 INTRODUCTION

Traffic accidents due to vehicle rollover lead to huge losses to the society and economy [1-3]. Passive stabilizer bars can effectively improve the vehicle roll safety, but cannot provide decent ride comfort, as compared to active and semi-active stabilizer bar systems [2-7]. Sampson et al from University of Cambridge [2-4] investigated a semi-active anti-roll system equipped with two actuators with high-roll-stiffness and low-roll-stiffness properties for heavy vehicles. During high speed cornering, a high-roll-stiffness is provided for the vehicle, while low-roll-stiffness when at low speed cornering. Such damping settings would improve stability of heavy vehicles and require low power supply, and it is shown that this system will increase the limit of the lateral acceleration up to 12.5%. Ohta et al from Aisin Seiki and Toyota [5-6] used a DC motor to realize an active stabilizer bar. The semi-active stabilizer bar systems have a comparable controllable performance of the active systems but simpler structures and control systems, as compared to the active ones. However, both the existing active and semi-active anti-roll systems still need further investigation and optimization, because of too big installation space and too much high cost.

Magnetorheological (MR) fluids are a smart material that changes rheological properties under applied magnetic fields [8-11]. MR fluids exhibit Newtonian-like behavior when no

magnetic field applied. The rheological properties expressed as yield stress increases monotonously with the increase of the magnetic field intensity. Because of the rapid response and large controllable damping of MR fluids, MR actuators and their semi-active control systems attracted a lot of attentions [12-18]. The MR technology is widely investigated in vehicular suspensions [13,14], seat suspensions [15], mounting systems [16,17], and military equipment field [18]. In this paper, the vehicle roll model equipped with a MR stabilizer bar is established. In order to discuss certain types of vehicle roll motions in different driving scenarios and in different torques of the MR stabilizer bar, passive-on control and piece-wise control are carried out based on the semi-active stabilizer bar proposed in previous work [19] and compared with conventional stabilizer bar.

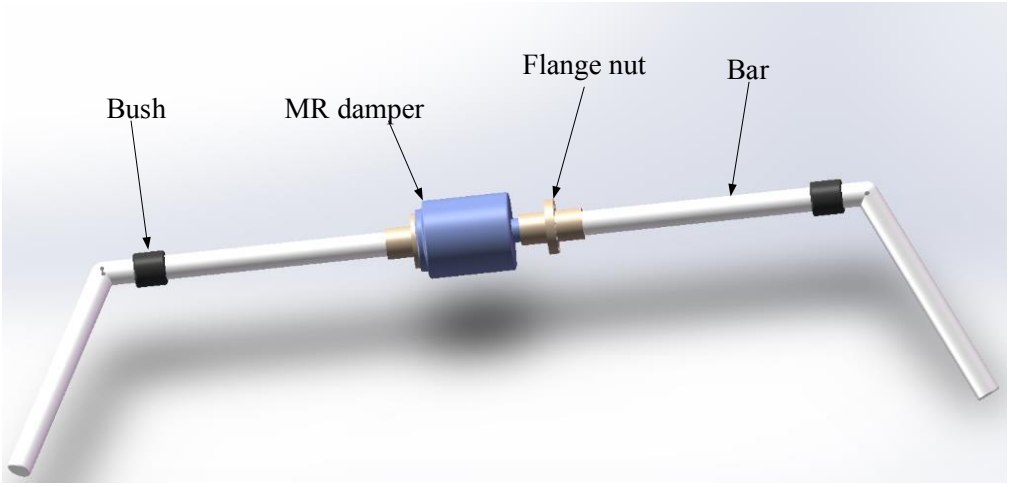

Figure 1: The configuration of the MR stabilizer bar.

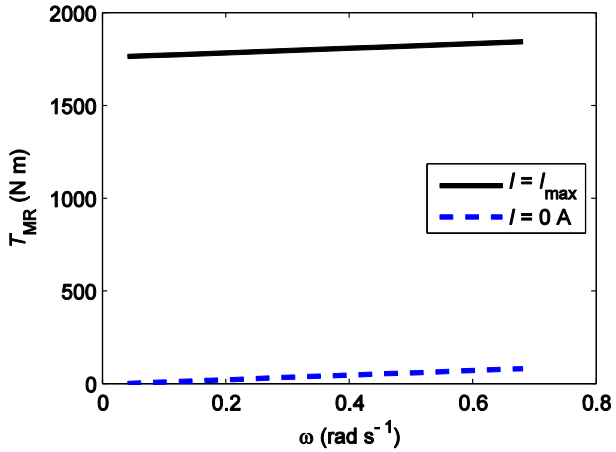

Figure 2: The controllable torque range of the MR rotary damper.

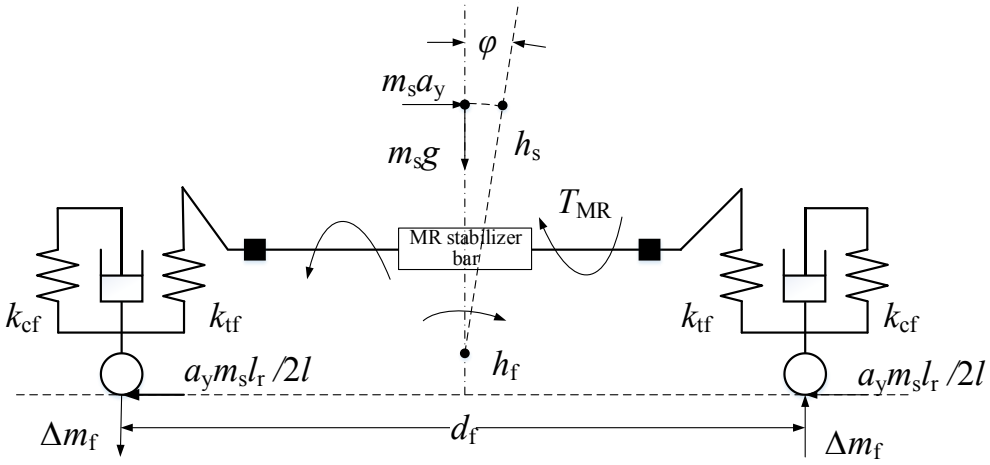

Figure 3: Vehicle roll model equipped with the MR stabilizer bar.

2 ROLL MODEL EQUIPPED WITH A MR STABILIZER BAR

2.1 MR stabilizer bar

Figure 1 shows the configuration of the MR stabilizer bar [19]. Its overall appearance is U-shaped, and the bar is mainly composed of a MR rotary damper, right and left bars, flange nuts and bushes. The MR rotary damper is installed between the right and left bars of stabilizer bar. The body case of the MR damper and the rotor axle are installed with the right and left bars using the flange nuts. The bars are installed with vehicle body or frame through the bushes. The longitudinal section ends of the U shape in stabilizer bar are connected to suspension guide arms (not shown in the figure).

The output torque range of the employed MR rotary damper in Figure 1 is presented in Figure 2. Before the magnetic saturation, the torque increases with the magnetic field intensity induced by the excitation coils with applied current. As shown in Figure 2, the controllable torque increases with rotating speed, and the maximal torque T_{MR} is around 1800 Nm.

2.2 Roll model

Based on the roll model equipped with conventional stabilizer bar [20,21], the roll model equipped with MR semi-active stabilizer bar is shown in Figure 3. Assuming that the vehicle itself and driving road conditions are ideal, so the roll angle only depends on the speed and turning radius. Based on the roll center, the vehicle's sprung mass roll torque equilibrium is

$$\begin{cases} (k_{\mathrm{f}}+k_{\mathrm{r}})\varphi_0 + T_{\mathrm{MRf}} + T_{\mathrm{MRr}} = a_{\mathrm{y}} m_{\mathrm{s}} h_{\mathrm{s}} + m_{\mathrm{s}} g h_{\mathrm{s}} \varphi_0 \pi/180 \\ k_{\mathrm{f}}\varphi_0 = 2(k_{\mathrm{cf}}+k_{\mathrm{tf}})\varphi_0 \\ T_{\mathrm{MRr}} = \frac{1-\alpha}{\alpha} T_{\mathrm{MRf}} \end{cases} \tag{1}$$

where φ_0 is the roll angle between the installation of stabilizer bar and vehicle body or frame; k_{f} and k_{r} are the roll angle stiffnesses of front and rear suspensions; a_{y} is lateral acceleration

of vehicle body; h_s is the distance of roll center and center of mass; k_{cf} and k_{tf} are the roll angle stiffnesses of spring and stabilizer bar; T_{MRf} and T_{MRr} are the torques of the front and rear MR stabilizer bars; and α is the ratio of the front roll angle stiffness to full vehicle roll angle stiffness.

According to Equation (1), the lateral acceleration of vehicle body can be expressed as

$$a_y = \frac{T_{MRf}+\alpha\varphi_0(k_f+k_r-m_s h_s g\pi/180)}{\alpha m_s h_s} \tag{2}$$

Based on the center of mass, vehicle's unsprung mass equilibrium equation is

$$\begin{cases} k_f\varphi_0 + T_{MRf} = \Delta m_f d_f - a_y m_s l_r h_f/l \\ k_r\varphi_0 + T_{MRr} = \Delta m_r d_r - a_y m_s l_f h_r/l \end{cases} \tag{3}$$

where l_f and l_r are the distance of full load mass center to front and rear axles respectively; l is wheelbase; h_f and h_r are the height of the front and rear roll center respectively; Δm_f and Δm_r are the vertical force difference of the front and rear axles between the left and right wheels; d_f and d_r are the front and rear wheel tracks respectively. Δm_f in Equation (3) is

$$\Delta m_f = (k_f\varphi_0 + T_{MRf} + a_y m_s l_r h_f/l)/d_f \tag{4}$$

Under a vertical force, pneumatic tires will vertically deform. The stiffness characteristics of tires usually use the applied load and deformation to express, and it is approximately a linear relationship between load applied and deformation. Therefore, in the most basic driving dynamics model, tires will often be simplified as a linear spring with constant stiffness. The wheels under the vertical force component induced the body roll angle is

$$\Delta\varphi = \arctan\frac{2\Delta m_f}{K_z d_f} \tag{5}$$

where K_z is the vertical stiffness of wheels.

According to Equations (2) and (5), and within the working range of the stabilizer bar, the relationship between roll angle φ and lateral acceleration a_y can be expressed as

$$\varphi = \frac{a_y\alpha m_s h_s - T_{MRf}}{\alpha(k_f+k_r-m_s h_s g\pi/180)} + \arctan\frac{2\Delta m_f}{K_z d_f} \tag{6}$$

Table 1: Piece-wise control algorithm.

a_y (m s^{-2})	f (mm)	T_{MR} (M)
< 0.5	< 4	0.7
0.5 – 1.5	4 – 12	1
1.5 – 3	12 – 24	1.5
≥ 3	≥ 24	2

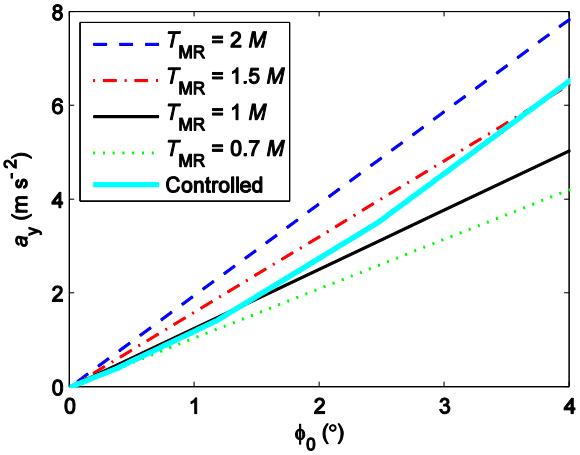

Figure 4: Relationship between roll angle and lateral acceleration with different T_{MR}.

2.4 Control algorithm of the MR stabilizer bar

As shown in the Table 1 and Figure 4, the passive-on control of MR stabilizer bar sets maximal T_{MR} equals to 0.7M, 1M, 1.5M, and 2M. M is the torque of conventional stabilizer bar and is proportional to vertical movement relative displacement f of the longitudinal section ends of the U shape in stabilizer bar [19]. The piece-wise control algorithm is proposed based on lateral acceleration a_y and/or relative displacement f. The relationship between roll angle and lateral acceleration under different maximal MR rotary damper torque T_{MR} and under piece-wise control is shown in Figure 4. In passive-on control mode, the bearable lateral acceleration of the vehicle equipped with the MR stabilizer bar increasing significantly up to 2.80 m s^{-2} as compared to the conventional one, and the body roll angle increased by 0.02° slightly because of the influence of tire deformation. It indicates that large T_{MR} can improve the vehicle's roll safety.

3 ADAMS/CAR MODELLING AND SIMULATION

3.1 Comparison of ADAMS model and mathematical model

In order to verify the consistency of the established full vehicle model and the mathematical model, full vehicle simulation analysis is conducted to investigate the relationship between the roll angle and lateral acceleration. As shown in Figure 5, in the scope of the stabilizer bar of vehicles are in steady state, the ADAMS model and mathematical model agree well with each other. Exceed the scope of the stabilizer bar, vehicle will have a tendency to instability and the roll angle will increase rapidly with the increase of lateral acceleration.

3.2 Full vehicle simulation

3.2.1 Single lane change

Steering wheel angle and lateral acceleration, and roll angle of the single lane change

simulation are shown in Figures 6(a) and 6(b), respectively. In the simulation, at speed of 56 km/h and the steering wheel first turns left with 270°, then turns right with 540° and turns left with 270° later within 2 s. The maximal roll angles decrease with the increase of T_{MR}, as shown in Figure 7(b). According to the rollover test requirement to input steering wheel angle, the maximal roll angles are all beyond the working scope of the stabilizer bar, when T_{MR} is 0.7M, 1M, 1.5M, and 2M, the roll angles are 14.5°, 10.28°, 7.93°, and 7.17°, respectively. The stabilizer bar under piece-wise control can generate smaller a_{y} and φ than the T_{MR} equals to 1M and 0.7M in the first half process. Moreover, when T_{MR} is 0.7M, lateral acceleration and its fluctuation are much larger than others, the vehicle is in a critical state of risk of rollover.

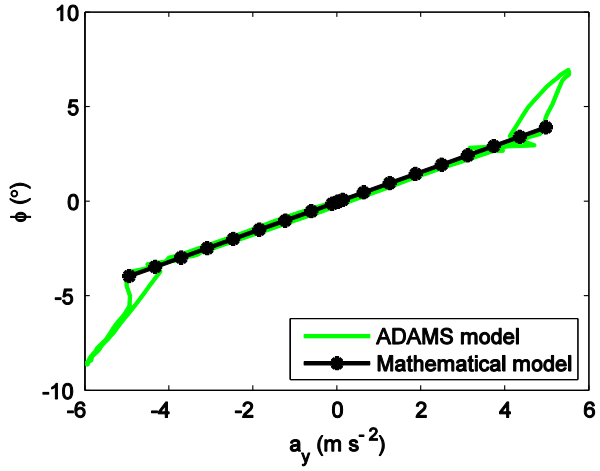

Figure 5: Comparison of ADAMS model and mathematical model.

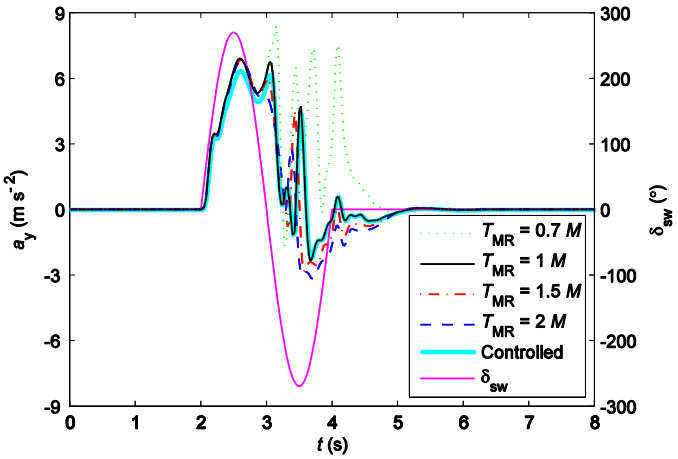

(a)

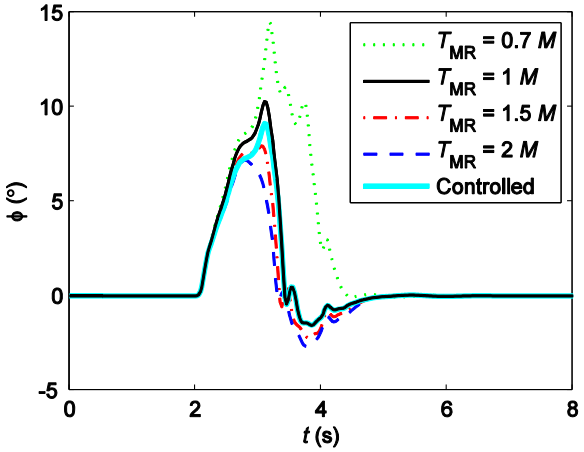

(b)

Figure 6: Simulation results in the single lane change scenario: (a) steering wheel angle and lateral acceleration and (b) roll angle.

3.2.2 Road pulse input

In the simulation, a road pulse input block (i.e., a triangular convex block) is set on one side of the ground vehicle. Lateral acceleration and roll angle of road pulse input simulation are shown in Figures 7(a) and 7(b), respectively. Two peaks of lateral acceleration and roll angle are caused by the front and rear wheels when running through the road pulse input block. When T_{MR} is $0.7M$, the peak of lateral acceleration is the minimal, 2.61 m s^{-2}, and when T_{MR} is $2M$, it reaches to a maximal value of 3.15 m s^{-2}. When T_{MR} is $0.7M$, $1M$, $1.5M$, and $2M$, the roll angles generated by front wheels are 0.63°, 0.65°, 0.67°, and 0.69° respectively. The roll angle decreases with the decrease of T_{MR}. The stabilizer bar under piece-wise control performs better than the T_{MR} equals to $1M$ in a_{y}, and similar to the T_{MR} equals to $1M$ (*i.e.*, better than $1.5M$ and $2M$) in φ.

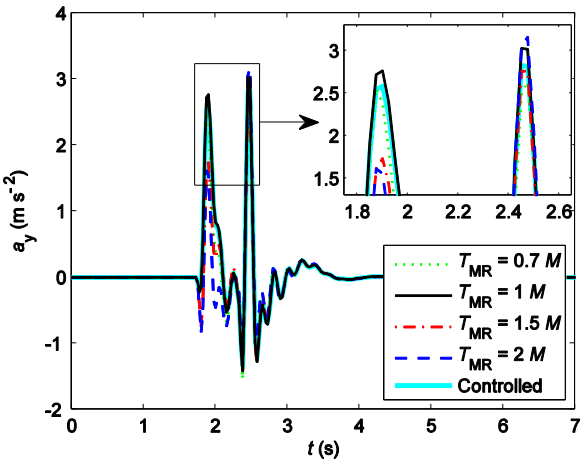

(a)

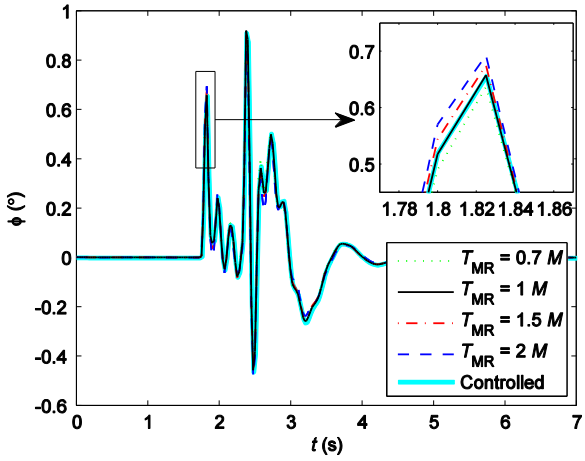

(b)

Figure 7: Simulation results in the road pulse input scenario: (a) lateral acceleration and (b) roll angle.

4 CONCLUSIONS

Simulations for scenarios of single lane change and road pulse input based on ADAMS/Car full vehicle model were carried out to investigate the vehicle dynamics performance when applying controllable torques of the MR stabilizer bar. In detail, with the increase of the torque of the MR stabilizer bar, the roll angle of the vehicle decreases and the bearable lateral acceleration increases, i.e., better safety. When at road pulse, the vehicle equipped with MR stabilizer bar with smaller torsional torque generates smaller lateral acceleration, i.e., better ride comfort. When using piece-wise control, the MR stabilizer bar performs better than the conventional stabilizer bar.

ACKNOWLEDGEMENTS

The authors wish to acknowledge the Key Research and Development Project of Anhui Province (Grant No. 1704E1002211), the Equipment Pre-Research Foundation of China during the 13th Five-Year Plan Period (Grant No. 6140240040101), and the Fundamental Research Funds for the Central Universities (Grant No. JZ2017HGTB0202), for their support of this research.

REFERENCES

[1] Jarossi, L., Matteson, A., and Woodrooffe, J. Trucks involved in fatal accidents fact book 2006. *The University of Michigan Transportation Research Institute* (2008), No. UMTRI-2008-42.

[2] Sampson, D.J.M. Active roll control of articulated heavy vehicles. *University of Cambridge* (2000).

[3] Stone, E.J. Semi-active anti-roll bars for heavy vehicles. *University of Cambridge* (2004).

[4] Stone, E.J. and Cebon, D. Control of semi-active anti-roll systems on heavy vehicles. *Vehicle System Dynamics* (2010) **48**(10): 1215-1243.

[5] Ohta, Y., Kato, H., Yamada, D., Sato, K., Fukino, T., Nobuyama, E., and Buma, S. Development of an electric active stabilizer system based on robust design. *SAE Technical Paper* (2006), No. 2006-01-0758.
[6] Suzuki, S., Buma, S., Urababa, S., Nishihara, A., and Taneda, A. Development of electric active stabilizer suspension system. *SAE Technical Paper* (2006), No. 2006-01-1537.
[7] BeijingWest Industries (BWI) Co. Ltd. http://www.bwigroup.com/product/asbs-active-stabilizer-bar-systems/
[8] Yu, M. Study on control system of automobile magnetorheological semi-active suspension. *Chongqing University* (2003). (In Chinese)
[9] Li, W.H., Chen, G., and Yeo, S.H. Viscoelastic properties of MR fluids. *Smart Materials and Structures* (1999) **8**(4): 460.
[10] Claracq, J., Sarrazin, J., and Montfort, J.P. Viscoelastic properties of magnetorheological fluids. *Rheologica Acta* (2004) **43**(1): 38-49.
[11] Chen, P., Qian, L.J., Bai, X.X., and Choi, S.B. Velocity-dependent characteristics of magnetorheological fluids in squeeze mode considering the hydrodynamic and the magnetic field interactions. *Journal of Rheology* (2017) **61**(3): 378-389.
[12] Bai, X.X. and Wereley, N.M. A fail-safe magnetorheological energy absorber for shock and vibration isolation. *Journal of Applied Physics* (2014) **15**(17): B535 (3pp).
[13] Dutta, S. and Choi, S.B. A nonlinear kinematic and dynamic modeling of Macpherson suspension systems with a magneto-rheological damper. *Smart Materials and Structures* (2016), Vol. 25, No. 3, Article no. 035003.
[14] Bai, X.X., Hu, W., and Wereley, N.M. Magnetorheological damper utilizing an inner bypass for ground vehicle suspensions. *IEEE Transactions on Magnetics* (2013) **49**(7): 3422-3425.
[15] Bai, X.X., Jiang, P., and Qian, L.J. Integrated semi-active seat suspension for both longitudinal and vertical vibration isolation. *Journal of Intelligent Material Systems and Structures* (2016), doi: 1045389X16666179. (Published online first)
[16] Choi, Y.T. and Wereley, N.M. Self-powered magnetorheological dampers. *Journal of Vibration and Acoustics* (2009) **131**(4): 044501.
[17] Chen, P., Bai, X.X., Qian, L.J., and Choi, S.B. A magneto-rheological fluid mount featuring squeeze mode: analysis and testing. *Smart Materials and Structures* (2016) **25**(5): 055002 (13pp).
[18] Hiemenz, G.J., Hu, W., and Wereley, N.M. Semi-active magnetorheological helicopter crew seat suspension for vibration isolation. *Journal of Aircraft* (2008) **45**(3): 945-953.
[19] Bai, X.X., Xu, S.X., and Shen, S. Magnetorheological stabilizer bar for ground vehicles. *Industrial and Commercial Applications of Smart Structures Technologies 2017, Proceedings of SPIE*, Vol. 10166.
[20] Gosselin-Brisson, S., Bouazara, M., and Richard, M. J. Design of an active anti-roll bar for off-road vehicles. *Shock and Vibration* (2009) **16**(2): 155-174.
[21] Zulkarnain, N., Imaduddin, F., Zamzuri, H., and Mazlan, S.A. Application of an active anti-roll bar system for enhancing vehicle ride and handling. *Humanities, Science and Engineering (CHUSER), 2012 IEEE Colloquium on, IEEE* (2012), 260-265.

VIII ECCOMAS Thematic Conference on Smart Structures and Materials
SMART 2017
A. Güemes, A. Benjeddou , J. Rodellar and Jinsong Leng (Eds)

MITIGATION OF DYNAMIC RESPONSE IN FRAME STRUCTURES BY MEANS OF SMART JOINTS

Rami Faraj, Błażej Popławski, Grzegorz Suwała, Łukasz Jankowski, Jan Holnicki-Szulc

Institute of Fundamental Technological Research, Polish Academy of Sciences
Pawinskiego 5B, 02-106 Warsaw, Poland.
e-mail: rfaraj@ippt.pan.pl, bpop@ippt.pan.pl, gsuwala@ippt.pan.pl, ljank@ippt.pan.pl, holnicki@ippt.pan.pl

Key words: Vibration Damping, Structure Response, Smart Structure, Structural Control.

Abstract. This paper discusses passive and semi-active techniques of structural control by means of smart joints, and then it proposes a specific smart joints system for frame structures and tests its capability in mitigation of free vibrations. Basically, the proposed solution modifies frame beams by addition of truss-type hinges, and its effectiveness relies on the softening effect that occurs in compression due to geometric nonlinearities and which triggers the highly-damped high-frequency response modes of the structure. First, the finite element (FE) model of the specific frame structure with geometrical nonlinearities is derived, and the proposed passive joints are described and incorporated into the model. Then, their principle of operation and effectiveness is examined numerically for the first two natural modes of vibrations with various initial displacement amplitudes. An objective function is proposed to assess joints placement, based on the efficiency in mitigation of the excited vibrations.

1. INTRODUCTION

Mitigation of structure response is still an important and current research topic. Most papers are focused on vibration damping problems, both free [1-5] and forced [6, 15]. Nevertheless, absorption of impact loads is also the subject of an ongoing research [1,7]. Vibration damping techniques are generally divided into three groups: passive, active and semi-active. Passive solutions, which are the simplest and the most reliable, usually incorporate frictional, viscous or pneumatic dampers. For some applications, mainly in civil engineering, systems of tuned-mass-dampers (TMD) [16] and tuned-inerter-dampers (TID) [8] are applied. Also combination of both systems, TMD and inerters, are analyzed [9]. Another passive technique for suppression of structural vibrations relies on the introduction of initial stresses in the structure [10], which influence its natural frequencies and amplitudes. Active vibration suppression is often considered in the context of counteracting the effects of earthquakes or strong winds, which can be very dangerous for high-rise buildings [11]. Common practice in such cases is to use large hydraulic actuators for which the application of an appropriate control algorithm can lead to satisfactory results of energy absorption [12]. The best possible solution is often associated with active control and significant control forces, despite potential dangers appearing in case of the control system failure. In recent years a growing interest in semi-active

vibration damping techniques can be noticed. Semi-active approach combines the advantages of passive and active systems. Well designed, they can be very reliable, even in case of power failure, and as efficient as active systems. They have been used in seismic tremors protection for many years [13] as a more trustworthy alternative to active strategies. They can also be applied to mitigate vibrations of vehicles suspension [14], frames and trusses [1-4] and other engineering structures.

The solution proposed here is based on the use of specific joints, selectively activated for identified excitation conditions in order to improve vibration damping effect. An important advantage of the proposed joints is that the mechanism of free vibration damping is purely passive. After activation of the joints, energy is dissipated passively but as soon as vibrations are suppressed, joints are deactivated and the structure turns again into its basic frame configuration.

2. DAMPING OF FRAME FREE VIBRATIONS WITH SMART JOINTS

The discussed novel technique of free vibration damping was developed in the Institute of Fundamental Technological Research, Polish Academy of Sciences, and it is discussed here using an exemplary case study. The main advantage of such solution is its passive operation and the ability of adaptation to the excitation conditions. Moreover, dissipation in the excited structure, both in case of activated and blocked joints, is realized by the mechanism of structural material damping without additional dampers. The proposed smart joints in the activated mode do not transfer any moment between the neighboring elements. In the inactive mode, they do not modify the typical frame connection between the frame elements.

The subject of analysis is the frame structure presented in Fig. 1. The structure is equipped with proposed joints that enable modification of the effective global stiffness of the structure. In case of free vibrations, joints are activated and additional rotational degrees of freedom are added to the nodes, which turn in this way into hinges (no transmission of moments). The effect is the nonlinearly decreasing effective bending stiffness in the involved part of the frame and excitation of higher modes which are efficiently mitigated by structural material damping. An important issue to be considered during the placement of the smart joints is not to change the structure into a mechanism. Moreover, the temporary effect of weakening of the structure should be taken into account, too.

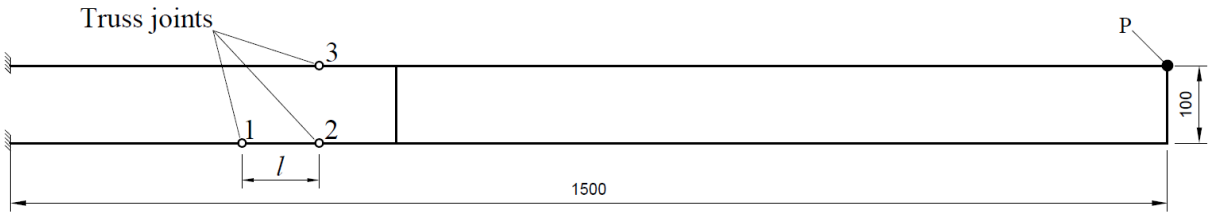

Figure 1. Scheme of the analyzed structure (dimensions in [mm])

The effectiveness of free vibration damping in frame structures is assessed by means of the assumed goal function, which in the present case study was defined as the time integral of the global potential structural energy:

$$I = \int_{t=0}^{t=1s} \left(\frac{1}{2} \boldsymbol{x}^{\mathrm{T}} \boldsymbol{K} \boldsymbol{x} \right) dt \tag{1}$$

Additionally, other quality indices or constraints can also be considered. For instance, an important factor is the amplitude of displacements of the point in the structure with the highest vibration amplitude. Optimal values of the selected goal function (1) not always go together with the mentioned criterion.

3. NUMERICAL ANALYSES

The free vibration dynamics of the frame structure presented in the previous section is described by the typical equation of motion:

$$\boldsymbol{M}\ddot{\boldsymbol{x}} + \boldsymbol{C}\dot{\boldsymbol{x}} + \boldsymbol{K}\boldsymbol{x} = \boldsymbol{0} \tag{2}$$

The structure was divided into 128 beam finite elements of the same length. The smart joints were modeled by uncoupling the rotational degrees of freedom between the neighboring elements. The damping matrix $\boldsymbol{C}$ was composed of the coefficients described by the Rayleigh model of damping. Because of the geometric nonlinearity introduced by the smart joints, nonlinear analyses were performed for all simulations. The differential equations of motion were integrated using the Newmark method combined with the iterative Newton scheme for update of the stiffness matrix.

A number of numerical analyses was performed to examine the effectiveness of the proposed solution (in terms of the assumed goal function) and to find the optimal placement of the smart joints in the structure. Placement of the joints was considered only in the left section of the frame because of the longitudinal deformations that occur in this area and which are needed to achieve a better vibration damping by implementation of proposed joints system. Simulations included initial displacements corresponding to the first and the second mode of structural vibrations, each of three different amplitudes (small, medium and large). Tab. 1 compares the values of the goal function for the structure without the smart joints and the structure with selectively placed joints.

Table1. Goal function values [$\cdot 10^{-3}$] for the original frame structure and the structure enhanced with the proposed smart joints: (1) original frame structure, (2) best joints placement, (3) worst joints placement

No of mode	**Small initial displacement**			**Medium initial displacement**			**Large initial displacement**		
	1	**2**	**3**	**1**	**2**	**1**	**1**	**2**	**3**
1	1.3	0.35	1.2	8.2	2.6	7.8	49.6	30.8	48.2
2	1.5	0.71	1.2	11.4	8.4	10.4	428.8	412.3	512.4

Optimization of joints placement in the structure in relation to the goal function was defined as a search for the optimal position of the first joint and the distance to the second joint (length l of the truss element). In Fig. 2. and Fig. 3., the values of the goal function normalized

with respect to the value obtained for the original structure without any joints are presented. The graphs shown in Fig. 2. present maps of the normalized goal function for different amplitudes of the initial displacement conditions in the case of the first vibration mode. The optimal position and length of the truss rod can be specified based on these maps. The advantageous effect of the smart joints related to the introduced geometrical nonlinearity in the structure is easily seen. Effectiveness of the solution decreases with the increase of the initial displacements amplitude but even then the values of the goal function are considerably lower than the values obtained for the original structure.

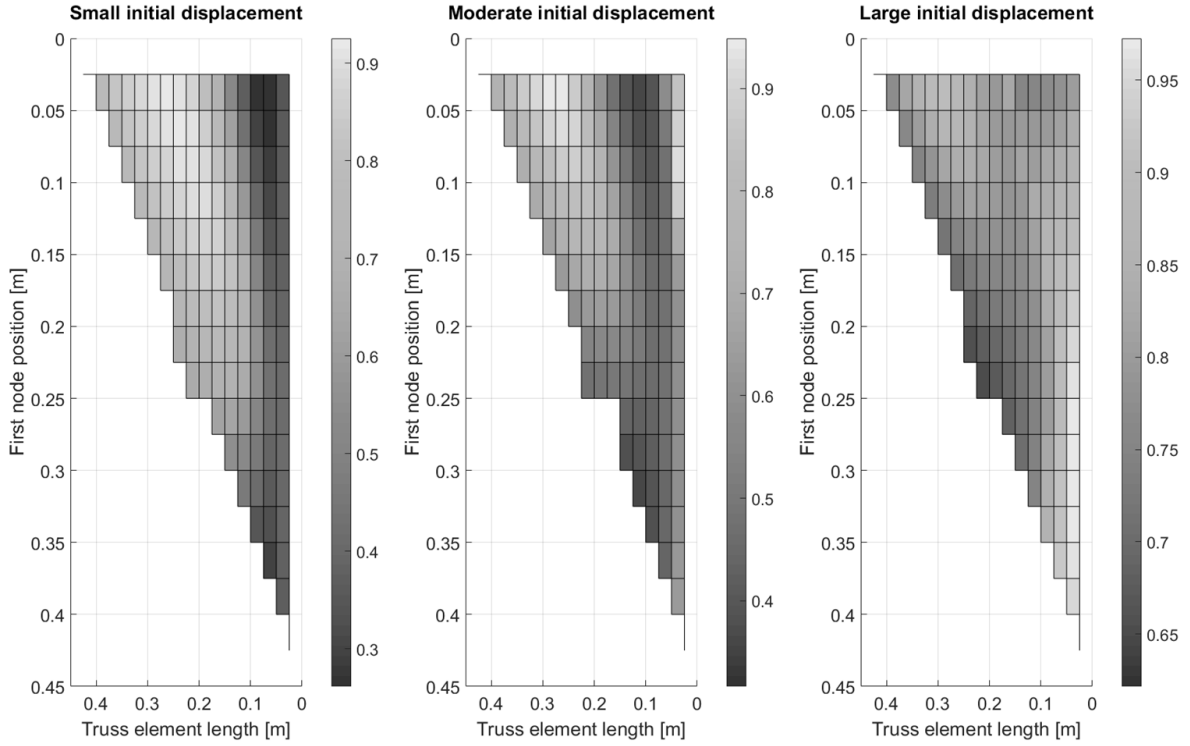

Figure 2. Values of the goal function depending on the position of the first joint and on the length of the truss element for different initial displacements of the entire structure (mode 1)

For small and moderate initial displacement of the structure, the smart joints should be placed in short distance to the fixed end or in the proximity of the vertical beam. For a large initial displacement, the first joint should be placed near the middle of the left section of the structure and the second joint in the proximity of the vertical beam.

Analogous graphs for the case of second mode excitation (initial displacement) were shown in Fig. 3. The effectiveness of the smart joints for the second mode of structural vibration is lower than for the first mode. However, for small and moderate initial amplitudes of the free vibrations, the proposed solution is definitely advantageous. The values of the goal function suggest that the beginning of the truss rod (the first joint) should be placed near the fixed end of the structure for all analyzed initial conditions.

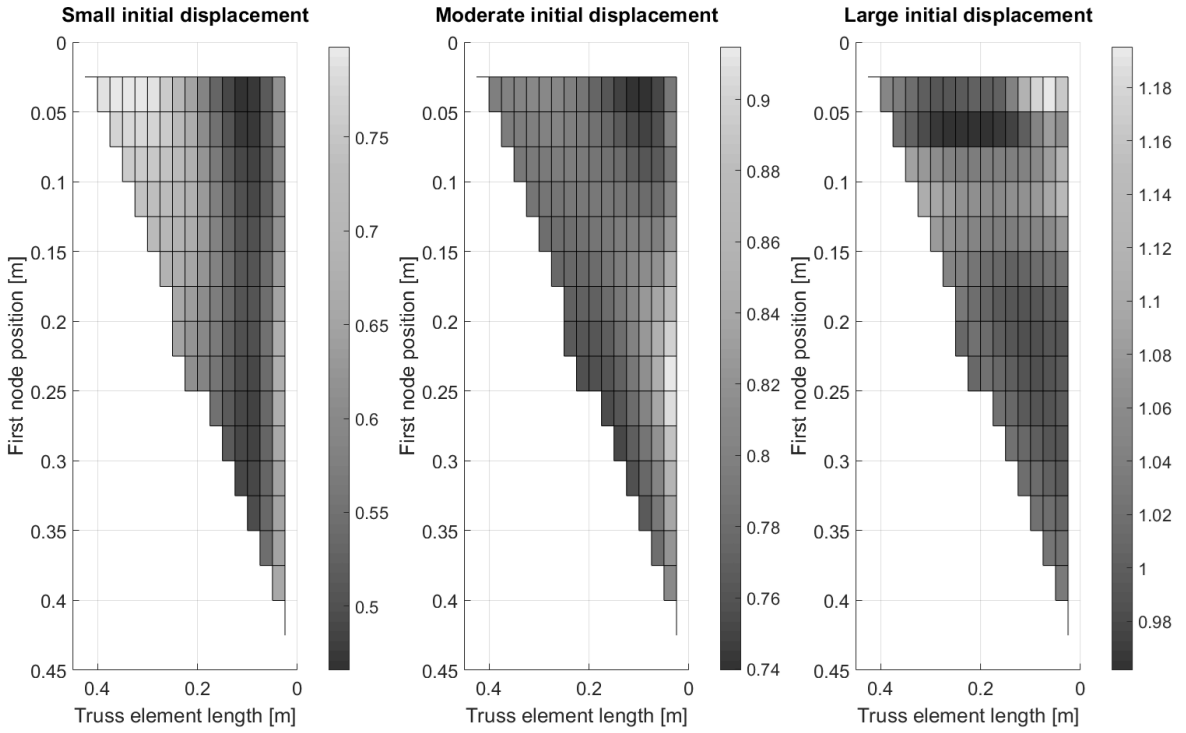

Figure 3. Values of the goal function depending on the position of the first joint and on the length of the truss element for different initial displacements of the entire structure (mode 2)

In Fig. 4, the time history of the vertical displacement of point P is shown (small initial displacement, mode 1). Despite the fact that the use of the smart joints is efficient in terms of the goal function (integral of the global potential energy) also for the worst placement of the smart joints, for the worst placement the vibration of point P is less damped than in original construction.

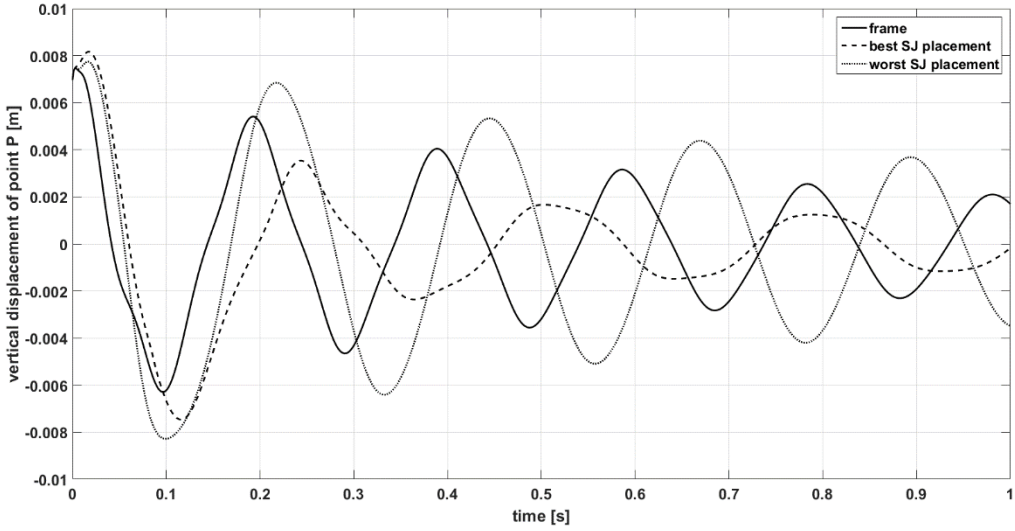

Figure 4. Vertical displacement of point P for small initial displacement of the structure (mode 1)

According to the numerical analyses, an adaptable scheme of smart joints usage can be proposed by activation of selected joints according to the identified load conditions. It allows to achieve an adaptable, passively operating system with enhanced damping capabilities. After suppression of vibrations, the smart joints should be deactivated so that the structure retrieves its original stiffness.

4. CONCLUSIONS

In this contribution, smart joints were proposed as a passive-like solution for free vibration damping. Nonlinear FEM analyses were conducted in a selected case study to present the potential of the proposed technical solution. Search of optimal placement of joints was performed based on the assumed goal function and an additional quality index was evaluated. Proposed solution ensures improvement of global damping capabilities of frame structure for variety of the initial structure displacement conditions. The advantageous effect is more significant for modes of structural vibration in which large longitudinal displacements appear. System of smart joints presented in the paper can be used in structures which are not subjected to the static lateral loads.

REFERENCES

[1] A. Mróz, J. Holnicki-Szulc and J. Biczyk, Prestress accumulation–release technique for damping of impact-born vibrations: Application to self-deployable structures, *Math Probl. Eng.*, article id 720236, (2015).
[2] B. Popławski, C. Graczykowski and Ł. Jankowski, "Controllable truss-frame nodes in semi-active damping of vibrations", *Advances in Science and Technology*, Vol. **101**, pp. 89–94, (2017).
[3] A.A. Ferri and B.S. Heck, "Analytical investigation of damping enhancement using active and passive structural joints", *Journal of Guidance, Control, and Dynamics*, Vol. **15**, pp. 1258–1264, (1992).
[4] J. Onoda and K. Minesugi, "Semiactive vibration suppression of truss structures by Coulomb friction", Journal of Spacecraft and Rockets, Vol. **31**, pp. 67–74, (1994).
[5] Pisarski D., Bajer C.I., Dyniewicz B. and Bajkowski J.M. Vibration control in smart coupled beams subjected to pulse excitations. *Journal of Sound and Vibration* (2016) **380**:37-50.
[6] Michajłow M., Jankowski Ł., Szolc T. and Konowrocki R. Semi-active reduction of vibrations in the mechanical system driven by an electric motor, *Optimal Control Applications & Methods* (2017).
[7] R. Faraj, J. Holnicki-Szulc, L. Knap, J. Seńko, Adaptive inertial shock-absorber, *Smart Mater. Struct.* **25** (2016) 035031.
[8] Lazar I F, Neild S A and Wagg D J, Using an inerter based device for structural *vibration suppression Earthq. Eng. Struct. Dyn.* **43** 1129–47 (2014).
[9] Brzeski, P., Perlikowski, P., Effects of play and inerter nonlinearities on the performance of tuned mass damper*, Nonlinear Dyn*, pp. 1-15 (2016).

[10] Suwała G., Knap L., Holnicki-Szulc J., Prestressing for Reduction of Local Vibrations in a Rotorcraft, *Eng. Trans.*,Vol.**64**, No.3, pp.367-380, (2016).
[11] Kobori, T., Takahashi, M., Nasu, T., Niwa, N. and Ogasawara, K., Seismic response controlled structure with Active Variable Stiffness system, *Earthquake Engng. Struct. Dyn.*, **22**: 925–941, (1993).
[12] Yamamoto, M., Aizawa, S., Higashino, M. and Toyama, K., Practical applications of active mass dampers with hydraulic actuator, *Earthquake Engng. Struct. Dyn.*, **30**: 1697–1717, (2001).
[13] Michael D. Symans, Michael C. Constantinou, Semi-active control systems for seismic protection of structures: a state-of-the-art review, *Engineering Structures*, Vol **21**, Issue 6, pp 469-487, (1999).
[14] Y. Shen, F. Golnaraghi, R.Heppler, Semi-active Vibration Control Schemes for Suspension Systems Using Magnetorheological Dampers, *Journal of Vibration and Control,* Vol **12**, Issue 1, pp. 3 – 24.
[15] Onoda, J., Minesugi, K., Semiactive vibration suppression by variable-damping members, *AIAA Journal* **34**, 355-361 (1996).
[16] M. Setareh, R. D. Hanson, Tuned Mass Dampers to Control Floor Vibration from Humans, *Journal of Structural Engineering*, Vol. **118** (1992).

VIII ECCOMAS Thematic Conference on Smart Structures and Materials
SMART 2017
A. Güemes, A. Benjeddou, J. Rodellar and J. Leng (Eds)

PRESTRESS ACCUMULATION-RELEASE (PAR) FOR DAMPING OF FREE VIBRATIONS IN FRAME STRUCTURES. EXPERIMENTAL STUDY OF A LAB-SCALE DEMONSTRATOR WITH PIEZO-ACTUATED SEMI-ACTIVE NODES.

ARKADIUSZ MRÓZ*†, JAN HOLNICKI-SZULC† AND KRZYSZTOF SEKUŁA*

*Adaptronica Sp. z o. o.
ul. Szpitalna 32, 05-092 Łomianki, Poland
e-mail: amroz@adaptronica.pl, ksekula@adaptronica.pl, web page: http://www.adaptronica.pl

† Institute of Fundamental Technological Research, Polish Academy of Sciences (IPPT)
Department of Intelligent Technologies
ul. Pawińskiego 5B, 02-106 Warsaw, Poland
e-mail: holnicki@ippt.pan.pl - Web page: http://www.ippt.pan.pl

Key words: Adaptive Structures, On-Off Control, Variable Stiffness Joint

Abstract. This paper presents results of experimental tests of a demonstrator structure equipped with variable stiffness nodes for suppression of free vibrations. So called Prestress Accumulation-Release (PAR) strategy for on-off control of these nodes is utilized. The obtained system is semi-active. The core of the controllable nodes are linear piezo-actuators.

1 INTRODUCTION

So called Prestress Accumulation-Release strategy, which allows for conversion of portions of strain energy of a vibrating structure into kinetic energy of local, well damped, higher frequency vibrations, has been discussed in preceding publications. In particular in [1] and [2] this approach has been numerically applied to layered and frame structures respectively. The effectiveness of this semi-active technique appears to be extremely high, typically suppressing over 90 % of the fundamental mode of vibrations after only few free oscillation periods. Therefore an attempt has been made to build a demonstrator and verify the theoretical effectiveness in a series of lab tests. First a concept of an active structural joint has been elaborated and presented in [3]. A chosen literature overview is also given in [3] pointing at other concepts for semi-active suppression of structural vibrations. In addition the attention is drawn to [4], in which a linear active element is presented capable of controlling the axial force transferred via a truss member. The goal of present work, which is a continuation of [3], is to present in detail the manufactured active joint as well as to present results of tests, in which two active joints were built into a

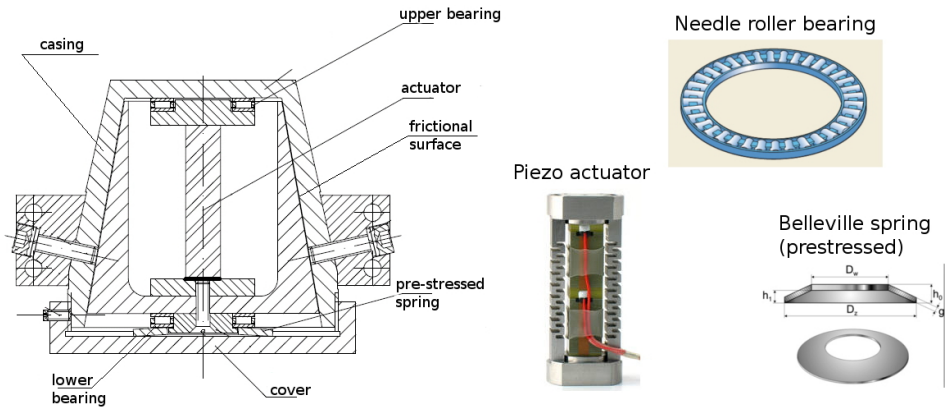

Figure 1: Adaptive node cross-section with its internal components.

demonstrator frame structure and utilized in accordance with PAR strategy to mitigate free vibrations.

2 PAR NODE CONCEPT AND REALIZATION

The active device suitable for demonstration of the PAR strategy should allow to transfer possibly big moment in its "stiff" or "frame" state and reduce its stiffness as close to zero as possible in its "truss" state. Furthermore the active device should sustain its maximum stiffness in passive operation which makes it fail safe.
Major features of the adaptive node are shown on the cross-section depicted in Figure 1. The core of the adaptive node is Cedrat prestressed piezo-actuator PPA 40L which allows for high force generation (order of 3000 N at small weight and dimensions, and at very small stroke (order of 40 μm). The inner conical surface is in contact with the outer conical surface, thus producing the frictional resistance to applied moment depending on the contact normal force between the adjacent surfaces. The conical fit assembly is described in detail in [5]. The normal force in turn depends on the net force produced by the actuator and the prestressed disc spring. Thus the maximum moment transferred by the connection may take any value between the rated maximum, corresponding to 150 V applied to piezo stacks and the minimum corresponding to no voltage applied. In practice the minimum value is never zero because of imperfectly matched spring force, imprecision in actuator nest manufacturing and bearing imperfections. More details about the PAR node concept can be found in [3].

3 STATIC MODEL

A simplified mathematical model of the adaptive node has been elaborated allowing for analysis of static forces acting within a node in both passive and active operation. The main goal for this model was adequate choice of the node body stiffness, pre-stressed spring stiffness and the estimation of the spring initial displacement. Moreover the model allows for verification of the effective actuator force and the maximum moment transferred without slip.
A simple physical model, which has been elaborated is based on the adaptive node layout shown in Figure 1 and comprises all meaningful elements in terms of static response, i.e.:

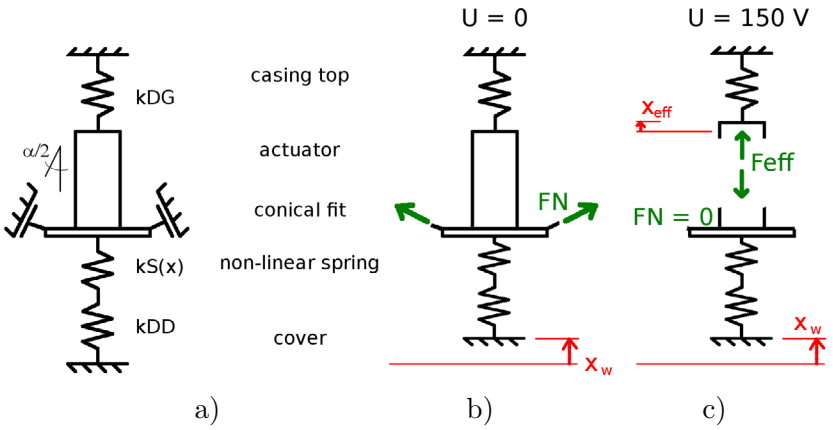

Figure 2: Physical model of the adaptive node: a) main components, b) passive state, c) active state.

- two springs in series, one modelling the cover deflection (kDD) and one modelling the non-linear Belleville spring ($kS(x)$),
- a force representing interaction between the inner part of the node and the casing,
- an actuator force as a function of applied voltage,
- a linear spring connected in parallel with the actuator and modelling stiffness of the upper part of casing (kDG),
- all springs are connected on one side with rigid base, modelling the stiff part of the casing.

Assumed physical model of the adaptive node is shown in Figure 2a).

3.1 Passive operation

In passive operation no voltage is applied to the piezoelectric stacks. It was assumed that the compressive force generated with the pre-stressed spring is entirely transferred to the casing through the conical surfaces and hence the force in the actuator is practically zero (cf. Fig. 2 b)). This is possible provided precise machining of the actuator nest. Pre-stressing of the spring is obtained with applying to it displacement x_w by means of a fine threaded cover. The force F_N normal to the conical fit is given with equation:

$$F_N = \frac{F_A}{\sin(\alpha/2) + \mu\cos(\alpha/2)}, \tag{1}$$

where μ is the friction coefficient and α is the cone angle. F_A is the axial compressive force in the node obtained by equating spring forces in serial connection:

$$F_A = \frac{kS\,kDD}{kS + kDD} \cdot x_w, \tag{2}$$

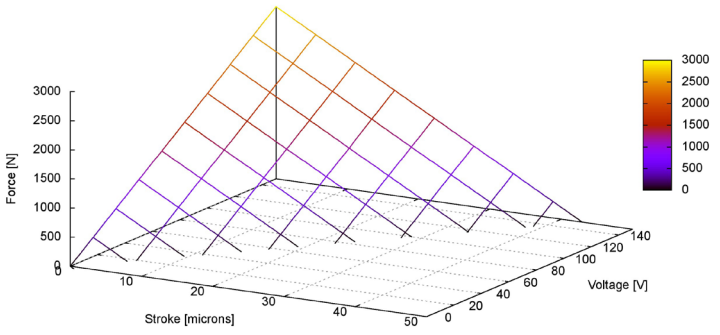

Figure 3: Characteristic of Cedrat Technologies actuator type PPA40L.

where kS is the Belleville spring stiffness linearised in vicinity of the pre-stress deflection. In fact, the Belleville springs have strong non-linear characteristic, therefore the axial compression force is obtained iteratively from the equation:

$$Fs(x1) = kDD \cdot (x_w - x1), \tag{3}$$

where $x1$ is the deflection of the disc spring. The maximum moment M_f which may be transferred via the connection is obtained from the slip condition for frictional conical surfaces with middle diameter dm:

$$|M_f| - \mu\, 0,5\, dm\, F_N \leq 0. \tag{4}$$

3.2 Active operation

In active state voltage is applied to the piezoelectric stacks and the resulting effective force in the actuator is equal to:

$$F_{act} = -\frac{u}{u_{max}} \cdot FB + \frac{V}{V_{max}} \cdot FB. \tag{5}$$

Characteristic calculated according to equation (5) for a chosen actuator is shown in Fig. 3.
It can be seen that the maximum blocking force FB is actually obtained at maximum applied voltage V_{max} only if the actuator is fully blocked, i.e. stroke u equals zero. Otherwise the actuator force is decreased by amount proportional to the stroke. We assume that the adaptive node design is optimal if the actuator at its nominal voltage is able to cancel out the axial force generated by the pre-stressed spring thus reducing the friction force between the conical surfaces to zero. Such situation is shown in Fig. 2 c). The design objective is therefore to maximize the moment bearing capability of the adaptive node in passive mode on one hand while providing enough actuation force to reduce, preferably to zero, the transferred moment in active mode – on the other hand. The effective force (and stroke) in the actuator depends on the stiffness of the casing top. The effective force and stroke corresponding to the steel casing top $\phi 55\, mm$ and thickness between $2\, mm$ and $5\, mm$ is shown in Figure 4. For example at casing thickness equal to 5mm the maximum effective force equals $3643\, N$ which is 88% of the nominal blocking force.

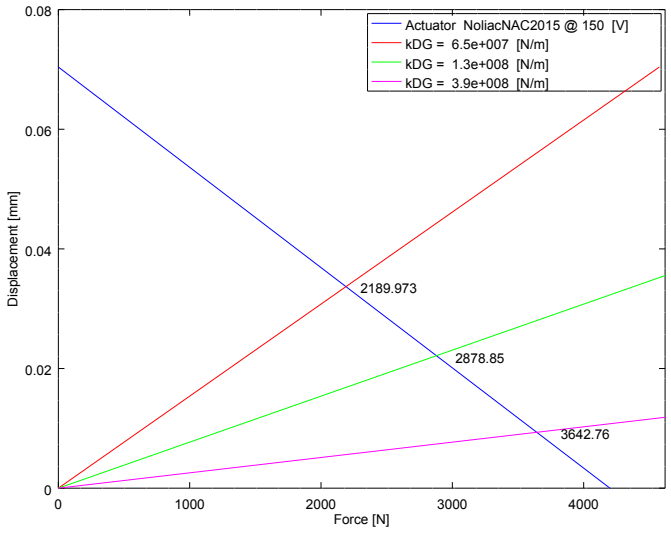

Figure 4: Values of maximum effective force in a chosen actuator at various stiffness of the casing top.

The pre-stressed disc spring dimensions and its initial displacement should allow sufficient pressure in the frictional surfaces, while not exceeding the actuator effective force. Various configurations have been analysed, finally converging to commercially available disc spring of the characteristic shown in Figure 5. Shown operating point corresponds to $0,8\,mm$ initial displacement and the maximum moment in static operation equal to ca $47\,Nm$.

4 DEMONSTRATOR STAND

A simple demonstrator has been built to verify the effectiveness of adaptive nodes in mitigation of free vibrations. The demonstrator structure comprises a cantilever steel frame equipped with two adaptive nodes as shown in Fig. 6. The main elements of the assembled experimental stand are (numbers in accordance with Fig. 7):

1. frame structure,
2. semi-active PAR nodes equipped with Cedrat Technologies PPA40L actuators,
3. two channel, controllable voltage amplifier for piezo stacks actuation Cedrat LA75B-2,
4. control and data acquisition measurement card National Instruments USB-6211,
5. laser vibrometer OFV-505 (5a) with controller (5b),
6. work station with LabView software for data acquisition and control.

During the tests the vibration velocity of the top end of the structure is recorded with laser vibrometer. The same control signal is applied to the piezoelectric stacks of both actuators in accordance with the PAR control strategy. In addition longitudinal vibrations were measured with two accelerometers placed in vicinity of adaptive nodes. Three types of tests have been carried out:

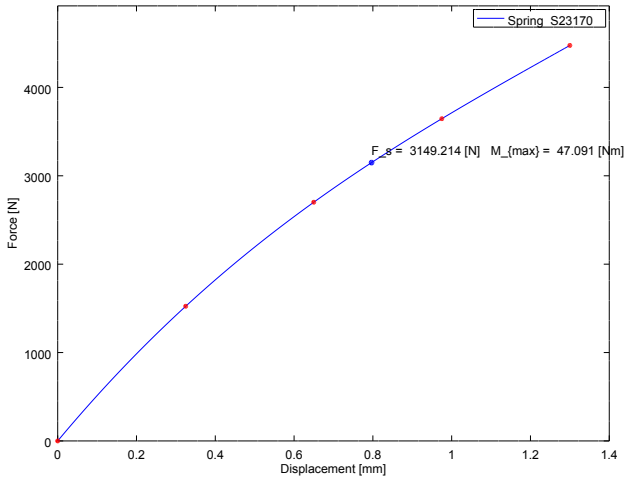

Figure 5: Characteristic of the used spring with the operating point at $0,8\,mm$.

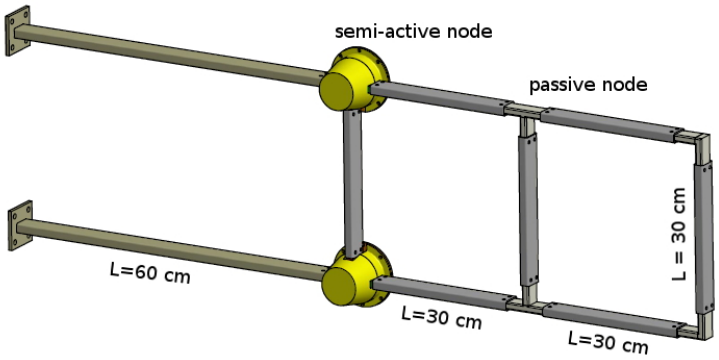

Figure 6: Cantilever beam with two adaptive nodes.

- free vibrations with adaptive nodes in passive state (max. stiffness),
- free vibrations with adaptive nodes in active state (min. stiffness),
- free vibrations with adaptive nodes controlled in accordance with PAR strategy.

The goal of first two tests was to compare the frequency response of acceleration in order to estimate shift in the eigen frequency between the passive and active state of operation. A considerable shift in in-plane bending eigen frequency would be a good indicator that the change of operation mode of adaptive nodes indeed contributes to the overall stiffness of the structure and thus some mitigation effect might be expected.

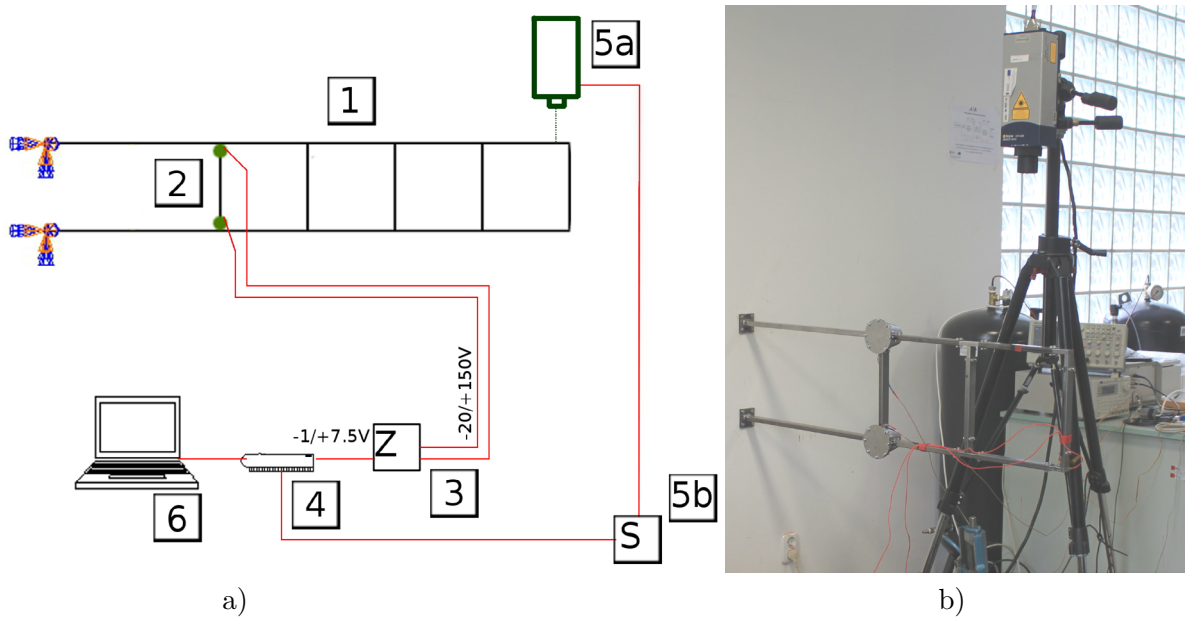

a) b)

Figure 7: Experimental stand: a) Schematic representation, b) General view.

5 RESULTS OF EXPERIMENTS

5.1 Node characteristic

Both adaptive nodes have been tested for their individual characteristic. For this purpose the outer conical surface have been fixed, while a known, increasing force have been applied on a known geometric eccentricity to the inner conical surface until the slip. The maximum moment in the connection corresponding to the beginning of slip is calculated for various actuator control voltage, giving the individual characteristic shown in Fig. 8. The actually obtained maximum moments between 55 and 59 Nm are underestimated by the static model, which may be attributed to the difficulty in accurate regulation of the initial displacement of disc springs. Satisfactory compliance is obtained if the value of $0,95\,mm$ is used instead of $0,80\,mm$. Further it can be observed that the actual moment transferred is not zero at maximum actuation voltage. Some friction still exists on the frictional surfaces even at maximum applied actuator effective force probably because insufficient precision in machining of the actuator nest. Nevertheless obtained variation in moment bearing capability between ca. 6 and 56 Nm provides fairly large range for modification of local stiffness if the adaptive node is used as a structural element. Relative to its mass and dimensions the adaptive node prototype seems to be an efficient variable stiffness device, compared for example to magneto-rheologic fluid based devices.

5.2 Eigen frequency shift

In the first two series of tests of the demonstrator structure adaptive nodes worked either in passive (frame) mode and active (truss) mode. In both cases an initial displacement has been applied to the cantilever end initiating the free in-plane vibrations. The first out-of-plane eigen mode have been sufficiently separated, so that the vertical initial displacement initiates

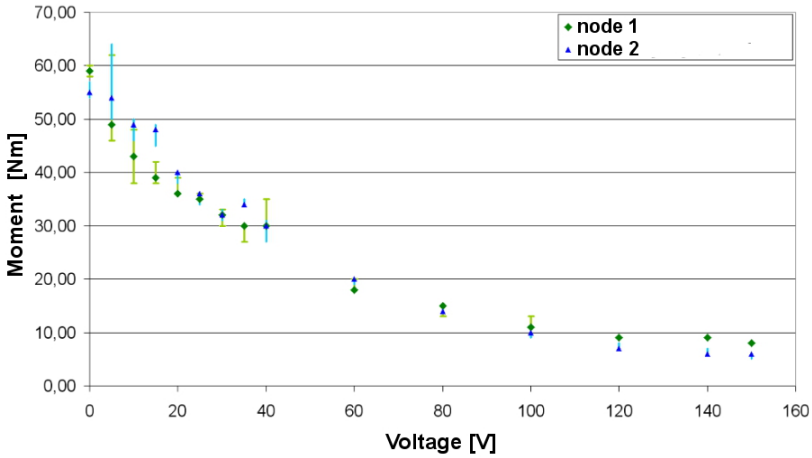

Figure 8: Moment characteristic of two adaptive nodes.

mostly the in-plane vibrations. The frequency response based on the cantilever tip acceleration (differentiated vibrometer velocity signal) is compared in Fig. 9. It can be seen that the first in-plane eigen mode in the truss operation is shifted left by 26 % and accompanied by generally higher damping while the second in-plane eigen mode stays practically unchanged (cf. Table 1). The higher damping is due to some friction corresponding to the remaining moment in truss mode operation.

Table 1: Eigen frequencies of the demonstrator structure in frame (ω_f) and truss(ω_t) modes.

Mode shape No	Description	$\omega_f\,[Hz]$	$\omega_t\,[Hz]$	Difference [%]
1	1st in-plane bending	14.1	10.4	26.2
2	2nd in-plane bending	38.5	38.1	0.9

5.3 Vibration mitigation

In the third series of tests adaptive nodes have been controlled in accordance with the PAR strategy. Upon detection of maximum cantilever deflection adaptive nodes have been switched to the active state for a short period of time, after which the passive state has been restored. As result the structural stiffness have been reduced locally for a very short period of time, sufficient to introduce high frequency, well damped longitudinal vibrations. Each time such operation is repeated, a part of the mechanical energy is transferred to the higher frequency vibrations and effectively damped with material damping.
As can be seen in the typical time series shown in Fig. 10 the vibration amplitude of the fundamental mode is almost completely damped out. The remaining vibrations correspond to the second in-plane bending eigen mode and could possibly by reduced if more adaptive nodes were used and placed in positions optimal for the second eigen mode mitigation. The reference tests

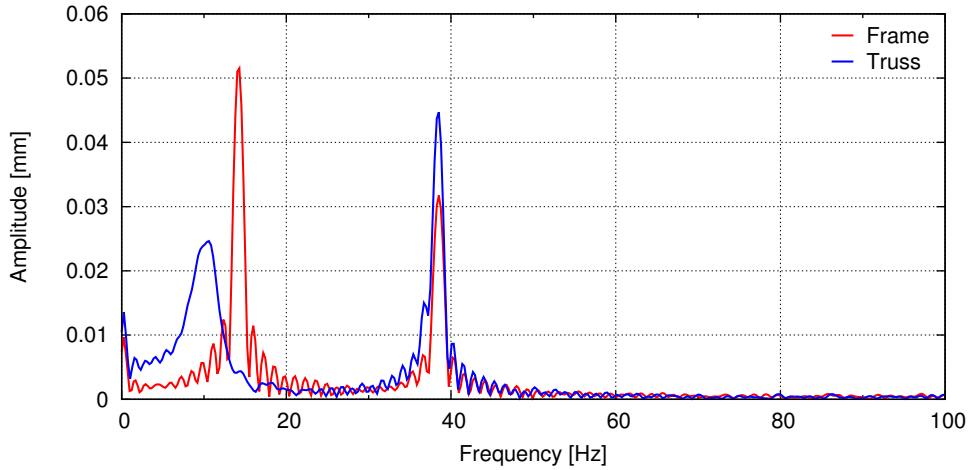

Figure 9: Difference in free vibration frequency response between structure with adaptive nodes in passive operation (frame mode) and in active operation (truss mode).

correspond to the passive operation where no control signal is applied and the adaptive nodes work at their maximum stiffness.

The control procedure has been activated upon first detection of threshold displacement ($+0,1\,mm$ in this case) and deactivated half a second later. During this time period the on-off PAR control algorithm produced the control signal as shown in Fig. 11. In fact, no further advantage is taken of a longer time duration of the control activation. This is due to the fact that after initial half a second the remaining vibration amplitudes do not generate moments in adaptive nodes which exceed the minimum moment transferred through the connection. As result there is no difference between the active and passive mode and no further mitigation occurs, except the "normal" damping in the passive operation.

For each recorded displacement time series the successive amplitude values were compared with the initial amplitude value (equal ca. $1,0\,mm$). In particular, the ratio of the amplitude after 3rd, 6th and 10th oscillation periods to the initial amplitude are listed in Table 2 both for the reference case and for six controlled tests. Over 97 % of the amplitude have been mitigated after 10 oscillation periods with adaptive nodes as compared to ca. 35 % for the reference case.

As shown in Fig. 11 the time duration t_i of a single rectangle impulse signal is very short, equal

Table 2: Comparison of vertical displacement amplitudes after 3, 6 and 10 oscillation periods.

No of oscillation cycles	Relative amplitude %						
	w/o control	with control, Test No					
	REF	1	2	3	4	5	6
3	88,6	84,1	33,8	49,9	33,5	78,6	34,5
6	76,0	7,4	8,2	5,5	8,9	15,0	11,7
10	64,4	2,1	3,8	1,3	2,3	2,1	2,9

to $5\,ms$ in this case. Different values of t_i were tested to investigate its influence on the overall

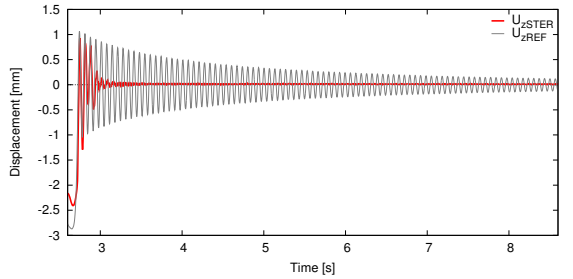

a)

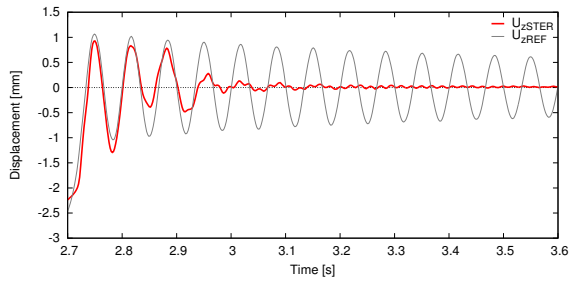

b)

Figure 10: Typical vertical displacements of the cantilever tip: a) full time history, b) zoomed time window.

response. In general time t_i should be long enough to fully switch the adaptive node to the truss mode, taking into account the dynamics of the actuator and accompanying electronics, but on the other hand it should be short so as to not weaken the structure for excessive amount of time. Furthermore too long duration of a single truss mode results in general in frictional dissipation instead of releasing of prestress resulting in longitudinal vibrations which is the main feature of the PAR strategy. In an extreme case the overall damping of the structure permanently operating in truss mode should be much smaller than overall damping of the structure subjected to the actuation in accordance with PAR strategy. This is confirmed with the tests performed for varying duration of a single truss mode t_i between $2\,ms$ and $30\,ms$, as shown in Table 3. The optimum time duration used in subsequent tests was $5\,ms$.

In the optimal situation the truss mode is actually initiated in the adaptive node at the time

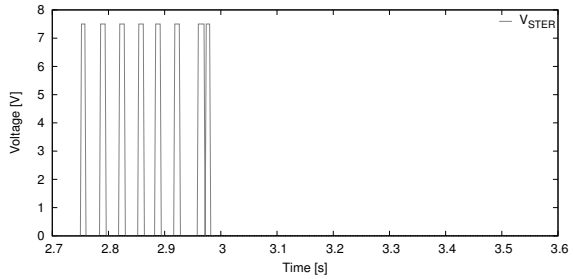

Figure 11: Typical control signal applied to the piezostack controller.

Table 3: Comparison of vertical displacement amplitudes after 5 oscillation periods relative to the initial amplitude, for different t_i.

	Truss mode duration t_i [ms]								
	2	3	4	5	6	8	10	20	30
Relative amplitude %	89	88	40	17	22	18	17	36	78

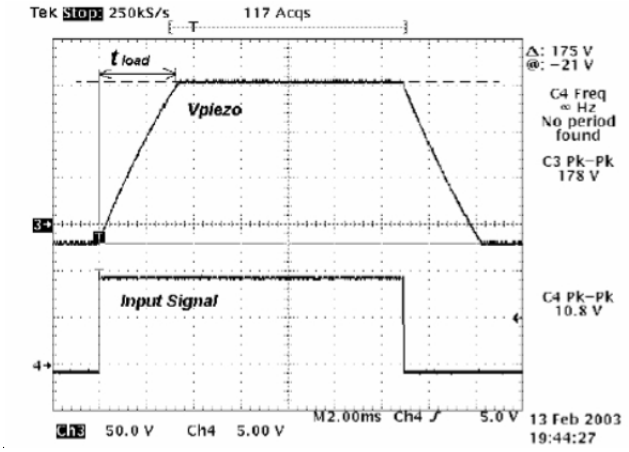

Figure 12: Step response of Cedrat LA-75B voltage amplifier according to the manufacturer.

instant of zero velocity, which corresponds to maximum deflection and maximum strain in the adjacent members. In practice two factors were identified which introduce the offset to the optimum time:

1. the voltage amplifier which drive the piezo-actuators introduces the time constant so that rectangular signal set is actually applied as trapezoid signal to the piezo stacks (cf. Figs. 12 and 13),

2. in order to filter out false triggers on the velocity signal, a short moving averaging has been done before detection of the zero velocity.

Due to above reasons some effort is needed before a good truss mode initiation time is obtained based on the filtered velocity signal. In this proof-of-concept work simple trial-and-error method was sufficient to tune the system performance and the further work requires better tools to properly find the switching time and also a better, impulse voltage amplifier could be used for this on-off control algorithm.

6 CONCLUSIONS AND POSSIBLE APPLICATIONS

- A piezo-based active structural joint with variable moment bearing capability has been designed, built and used as active element in a demonstrator frame structure as a core of semi-active free vibration suppression system.

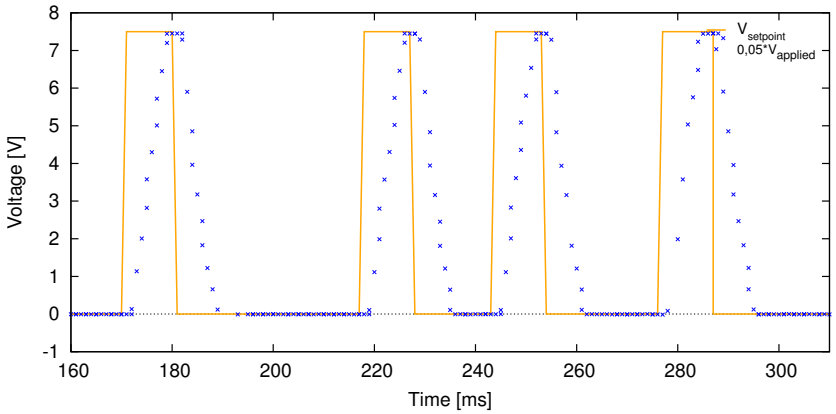

Figure 13: Set control signal versus voltage actually applied to piezo stacks.

- It was demonstrated in a series of experimental tests that utilizing PAR control strategy in such a system allows for very efficient mitigation of fundamental mode of vibrations, typically suppressing 95 % of the displacement amplitude after 10 oscillation cycles.
- The system may be redesigned, given a specific application, in particular it may be downscaled to mitigate microvibrations of a light-weight structures. Among possible applications are mitigation of vibrations of satellites, stabilisation of sensitive equipment and other situations where excessive vibration affects the performance of equipment or generates undesired noise.

ACKNOWLEDGEMENT

Financial support of the National Science Centre, Poland, granted through the project AdDAMP (DEC-2014/15/B/ST8/04363) is gratefully acknowledged.

REFERENCES

[1] A. Mroz, A. Orlowska, and J. Holnicki-Szulc. Semi-active damping of vibrations. prestress accumulation-release strategy development. *Shock and Vibration*, 17(2):123–136, 2010.

[2] A. Mróz, J. Holnicki-Szulc, and J. Biczyk. Prestress accumulation-release for damping of impact borne vibrations. numerical analysis of simple frame fructures. In *Proc. of the 6th World Conference on Structural Control and Monitoring*. Barcelona, Spain, 15-17 July 2014.

[3] A. Mróz and J. Holnicki-Szulc. Mechanical energy management for semi-active damping of impact borne vibrations. In *Proc. of the 7th ECCOMAS Thematic Conference on Smart Structures and Materials*. Ponta Delgada, Azores, Portugal, 3-6 June 2015.

[4] Junjiro Onoda, Takao Endot, Hidehiko Tamaoki, and Naoyuki Watanabe. Vibration suppression by variable-stiffness members. *AIAA journal*, 29(6):977–983, 1991.

[5] Adrian Creitaru and Niculae Grigore. Tribological considerations regarding the functional domain determination of the conical fit assembly. *Machine Design*, 3(3):199–204, 2011.

VIII ECCOMAS Thematic Conference on Smart Structures and Materials
SMART 2017
A. Güemes, A. Benjeddou , J. Rodellar and Jinsong Leng (Eds)

THEORETICAL AND EXPERIMENTAL INVESTIGATION OF HIGH-SPEED BEARINGS WITH AN ADAPTIVE AND NON-LINEAR STRUCTURE

GRZEGORZ ŻYWICA[*], PAWEŁ BAGIŃSKI[†]

Department of Turbine Dynamics and Diagnostics
Institute of Fluid Folw Machinery, Polish Academy of Sciences
Fiszera 14, 80-231 Gdansk, Poland
e-mail: [*]gzywica@imp.gda.pl, [†]pbaginski@imp.gda.pl, www.imp.gda.pl

Key words: Foil Bearings, High-Speed Bearings, Adaptive Structures, Non-Linear Geometries

Abstract. This article presents the results of computational simulation and experimental research performed on gas foil bearings, with the special attention paid to the properties of a flexible set of foils, as one of the decisive factors contributing to a proper functioning of the bearings. The issues such as the nonlinear nature of the foil bearing's supporting structure and significant changes in its stiffness depending on the load and deformation were discussed in detail. The article also fully explains the mechanism of dissipation of energy that can come from the vibration of the rotating system and from external loads as well. It was demonstrated that thanks to the phenomena occurring in its flexible components, the foil bearing can and does adapts itself to varying operational conditions over a large range of speeds and loads. The conclusions that were drawn on the basis of theoretical analyses were successfully verified with the results from the experimental research. It was shown that vibrations of the rotor supported by well-designed foil bearings can remain at very low levels, even at very high speeds.

1 INTRODUCTION

As scientists and engineers continue to make improvements to modern machinery, many of the new microturbines and turbocompressors are now smaller, more compact, and are equipped with more advanced bearing systems. They are designed to withstand extreme conditions covering very high rotational speeds (over 100,000 rpm) and high temperatures (above 200 °C) as well. Rolling bearings are extensively used under such conditions where fluid-film slide bearings simply would not work. Therefore, it is necessary to develop new, unconventional bearing systems [1-3]. One of such solutions is a gas foil bearing in which additional components (made of very thin sheet metals) are mounted between the journal and the bush (Fig. 1) so as to improve stiffness and damping properties [4]. A set of thin foils demonstrates superior vibration damping properties which vastly improves dynamic properties of a rotating system with such bearings, especially at high rotational speeds [5]. Depending on configuration and materials used, foil bearings can be divided into several generations, which can offer different load capacities [6].

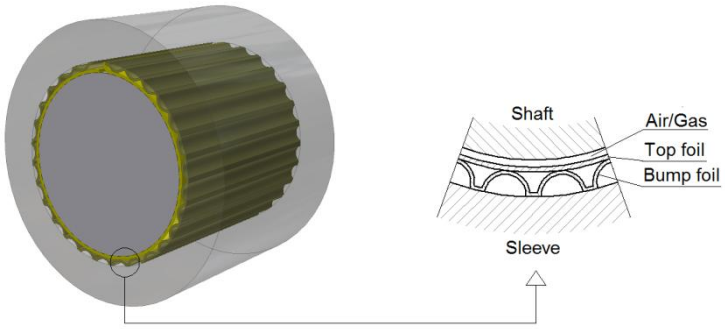

Figure 1: Isometric view of a foil bearing and its basic parts

Because a set of foils comprises the components of a relatively high flexibility, its geometry varies according to the rotational speed, temperature and load [7]. In other words, the bearing tailors itself to the actual operating conditions of a rotating system. In addition to the excellent damping of rotor vibration and high resistance to external loads, a flexible support makes it possible to obtain an optimal thickness of the lubricating gap along the entire perimeter of the bearing. It may, therefore, be concluded that the foil bearing's capacity for adjustment is unique among bearings, making it a great candidate for operation under very harsh conditions, like high temperature, speed, etc. Thanks to the use of properly profiled bump and top foils, foil bearings are characterised by very high durability and long service life [4,8]. Because foil bearings do not require an external lubrication, it is possible to reduce the weight of a machine, which is particularly attractive in aviation [9]. As all gas bearings, foil bearings also have certain drawbacks, chief among them being their low load capacity and unstable operation at low speeds [4]. Therefore, further research is underway to improve characteristics of foil bearings, so as to fully develop their potential and innovative abilities and thus contribute to a wider application to different types of machinery.

Foil bearings studies described in literature concern both experimental and numerical analyses as well as modelling issues. Given that at lower rotational speeds of foil bearings the friction is present between the journal and the top foil, much attention is paid to tribological issues. A foil bearing with an improperly selected pair of friction materials can become damaged after a short time of usage. Therefore, research on the friction torque and the load capacity of a foil bearing, under different conditions as well as taking into account materials selection, is very important [10]. For most effective results, advanced plastics or ceramic-metal composites are used, depending on temperature levels [4,10-13]. The wear of the top foil and journal surfaces leads to a local increase of temperature, which disturbs the stable operation of a bearing, even at high rotational speeds. This phenomenon is known in the literature as the thermal instability of foil bearings [14]. A rapid rise in journal temperature causes an increase in bearing preload which usually leads to a higher moment of friction and, consequently, the rotor needs to be stopped.

As a foil bearing is considered very difficult to model, numerical models are often used only at the initial design stage. Sometimes they may be also applied to analyse the phenomena that are extremely difficult or even impossible to measure at a real bearing. Such models need to take account of several complex phenomena, such as nonlinear mechanical deformations of thin foils, contact phenomena, heat transfer, thermal deformations, flow phenomena occurring

in the lubricating gap, and last but not least, fluid-structure interaction. Due to the difficulties in developing reliable numerical models, it can be observed that in some cases the differences between the experiment and simulation results can be as high as 500% [9].

Despite these difficulties, attempts are being taken to create models capable of reflecting mechanical and thermal phenomena occurring in foil bearings. Currently, works on the numerical models of foil bearings are being carried out in many research centres all over the world [5,7,14-17]. Such works have also been undertaken at the IMP PAN in Gdańsk. The following part of this article discusses the selected foil bearings properties, which are very important for their researching and modelling. These properties result from the nonlinear nature of such bearings and they provide the capability of adjusting the geometry to the actual operating conditions.

2 NONLINEAR MODEL OF THE FOIL BEARING STRUCTURE

The analysis of foil bearings requires taking into account the nonlinear properties of the structural supporting layer, which arise from its geometry and the supporting conditions. This part of the article discusses the modelling process of the foil bearing structure using the finite element method. There has been developed a three-dimensional numerical model striving to represent the actual system as faithfully as possible. The model takes into consideration the geometry of the system and the contact phenomena between all mating surfaces. Since in a first generation foil bearing the structural supporting layer consists of elastic damping elements that are evenly spaced along the perimeter (on which the top foil rests), only a part of the set of foils was implemented in the model for the purposes of preliminary analyses. The rationale behind this approach is the fact that in a large majority of modern foil bearings, this layer comprises several sets of short bump foils properly spaced along the circumference, supporting the top foil. So the properties of the entire set of foils are affected by the characteristics of individual bump foils. Figure 2 shows the zoomed-in fragment of the structural supporting layer and its location on the bush.

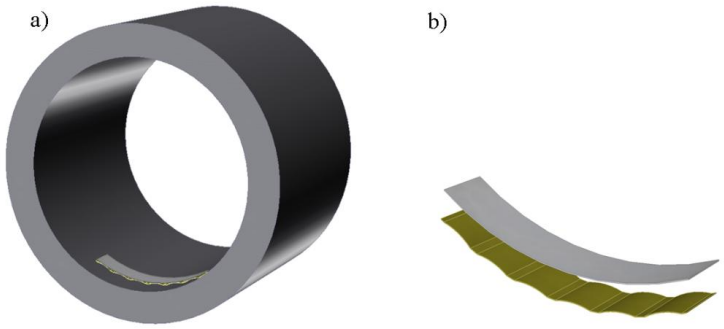

Figure 2: The analysed fragment of the foil bearing (a – location on the bush, b – zoomed-in fragment of the top and bump foils

Computational simulations were carried out using the model in which the bush curvature was neglected. This approach is quite common in the literature [18,19]. The dimensions of the top and bump foils, adopted for the analysis, are demonstrated in Fig. 3. It was assumed that

both foils are made of steel with the following characteristics: $\rho = 7800$ kg/m^3, $E = 2.1 \cdot 10^{11}$ Pa, $\nu = 0.3$.

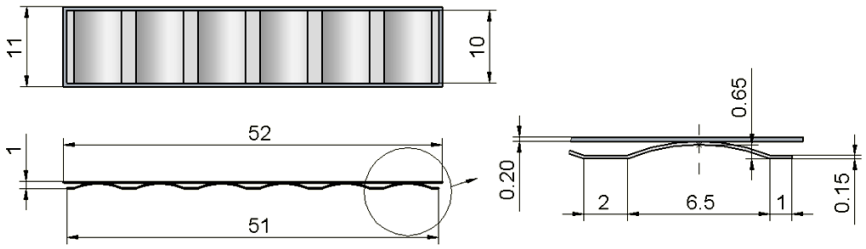

Figure 3: Dimensions of the analysed fragment of the foil bearing

In order to conduct the analysis in question the following boundary conditions were incorporated into the model: (1) constraints corresponding to all outer edge nodes of the top foil are symmetric; (2) the bush surface on which the bump foil rests is infinitely rigid; (3) the displacements of one of the ends of the bump foil were made impossible by taking away all degrees of freedom (i.e. a rigid connection with the bush); (4) contact was modelled between the upper surface of the bump foil and the lower surface of the top foil as well as between the lower surface of the top foil and the bush; (5) the coefficient of friction was set to 0.1.

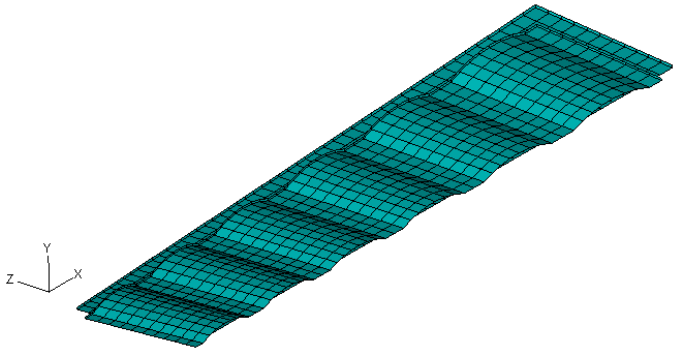

Figure 4: FEM model of the foil set

Figure 4 presents the discrete representation of the foil set geometry (i.e. a FEM model), obtained as a result of the optimisation of a finite element mesh. The three-dimensional hexahedral elements of the type C3D8R were employed for the creation of the model [20]. This model was also subjected to an experimental verification, the results of which confirmed its high usefulness in predicting the properties of the structural supporting layer of a foil bearing [21]. It was used for the simulation analysis that investigates the impact of various parameters on the properties of the structural supporting layer of a foil bearing, including such parameters as the foil thickness, the number of bumps and their geometry, the coefficient of friction and properties of the construction material. Such analysis, done at the design stage of a new foil bearing, allows for its optimisation to be carried out in order to direct that design toward having desired features without performing many experimental tests.

Let us now take a closer look at the foil bearing structure and its geometric nonlinearity that has a very large impact on both static and dynamic properties of a rotating system equipped with such a bearing. It turns out that the stiffness of the tested bearing structure can vary greatly depending on the applied load level (Fig. 5). In the case at hand, the foil set was subjected to a gradually increasing pressure (from 0 Mpa to 1.0 Mpa) acting on the top foil. The displacement curve of the foil set is almost linear at low loads, but above the value of 0.35 MPa, its character changes. A similar tendency can be observed after the load increased to 0.65 MPa.

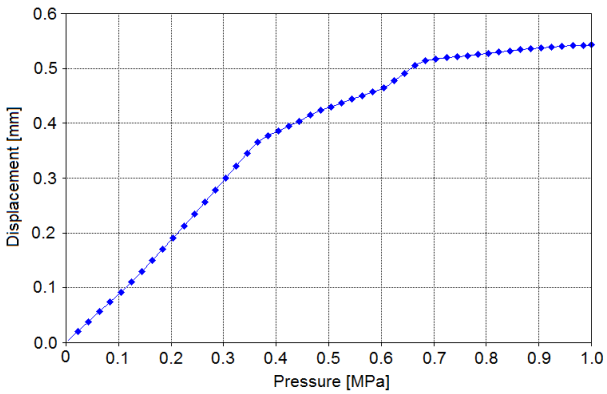

Figure 5: Displacement of the top foil vs. load

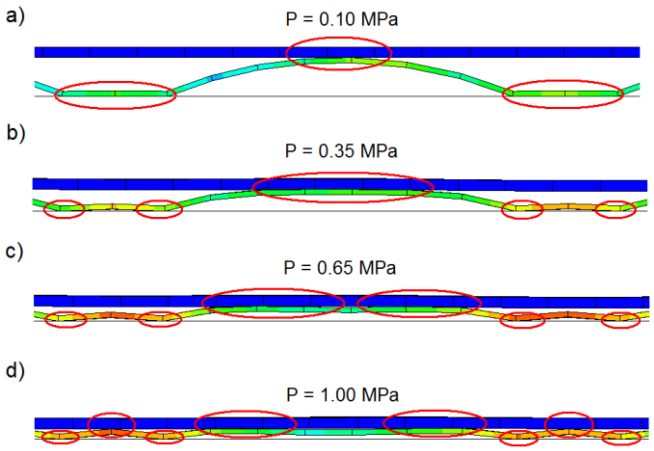

Figure 6: The occurrence of additional contact points between the top and the bump foils, according to the load

A thorough analysis of the displacements of the foil set helped to clarify this anomaly. It turned out that the displacements depend not only on the load level but also on the way the top foil is supported (Fig. 6). As the load increases, the top foil gets more support points—the more the higher the load. This highly progressive nature of the structural supporting layer of the foil bearing is very beneficial because the displacements of the journal decrease along with the increase in the bearing load. This has a good effect on the accuracy of the shaft alignment and helps in reducing the rotor vibration level even at high operating loads. It can be even said that, owing to the geometry of the bump foil, the support is able to adapt itself to

the load it is subjected to. An adaptation of the bearing itself to the actual operating conditions of the rotor was also observed during experimental studies, as discussed in the next part of this article.

3 CHARACTERISTICS OF FOIL BEARINGS DURING OPERATION

Experimental investigations were conducted using a test rig that is well-suited for testing foil bearings (Fig. 7). The rotor equipped with two foil bearings was driven by an electrospindle that offers the maximum speed of 24,000 rpm, which can be easily regulated. Bearing supports that can be split into parts facilitate the assembly of bearings. All the components of the test rig are attached to a steel plate that rests on vibroisolators. The mass of the entire test rig is approximately 130 kg. The measurement system allows for the measurement of the rotational speed, relative vibrations of the rotor, absolute vibrations of the bearing supports and temperature distributions inside bearings.

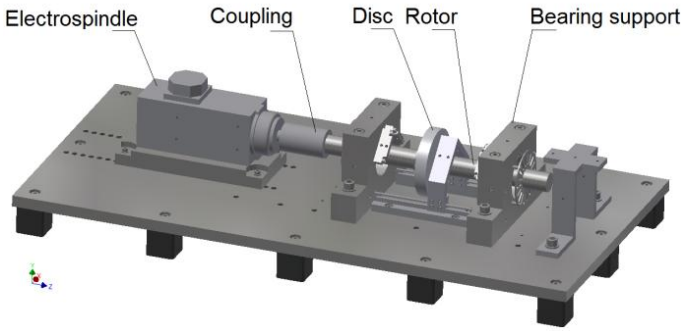

Figure 7: Scheme of the test rig for testing the dynamic performance of the rotor with foil bearings

The research was conducted for the foil bearing with a bump foil consisting of several segments. Three separately mounted bump foils were placed along the circumference of the bearing sleeve, each of them consisted of 4 segments, obtained by a transversal cut of the foil. The geometry of the tested foil bearing was described in previous publications [4]. The final shape of a bump foil is achieved by a two-step process. During the first stage, bumps are formed on a flat foil (Fig. 3). Next, the final curvature of a bump foil is obtained, having a radius almost equal to a radius of the hole in the bearing sleeve (Fig. 2b). The nominal diameter of the tested foil bearing is 34 mm. In order to assemble a bearing system, a journal must be pushed into pre-assembled bearing, and such an arrangement demonstrates no radial clearance. After a gradual wearing-in of a bearing, when the mated foils fit smoothly, a certain radial clearance is obtained – a pre-requisite for a smooth operation of a bearing. It depends on many factors such as ambient temperature, way the wearing-in of a bearing proceeds, load, thickness of the top foil coating, etc.

The investigations show that both dynamical and thermal characteristics of the tested foil bearings changed during their operation. It was most noticeable during the run-up and run-down of the rotor. Very interesting results were obtained for new bearings in which the wearing-in of the top foil coating took place within the initial several dozens of seconds of their operation. The graph presenting the temperatures measured in one of the new bearings at four measuring points located inside this bearing is shown in Fig. 8. The bearing journal was

gradually accelerated to a speed of 15,000 rpm and reached it after 50 seconds. The speed was maintained for 180 seconds—up to the 230th second of the measurement—and then was decreased to a speed of 12,000 rpm. In the initial period of the experiment, the temperature of the top foil increased sharply to 65 °C, reaching it at the maximum speed. Subsequently, the foil temperature decreased just as fast as it had increased before, and after the 150th second, it did not exceed a value of 35 °C until the very end of the measurement. The highest and the lowest temperatures were measured respectively at the lower and upper part of the bearing (i.e. at the angle positions of 200° and 20°, respectively—see Fig. 8b). The lowest measured temperature was close to the ambient temperature.

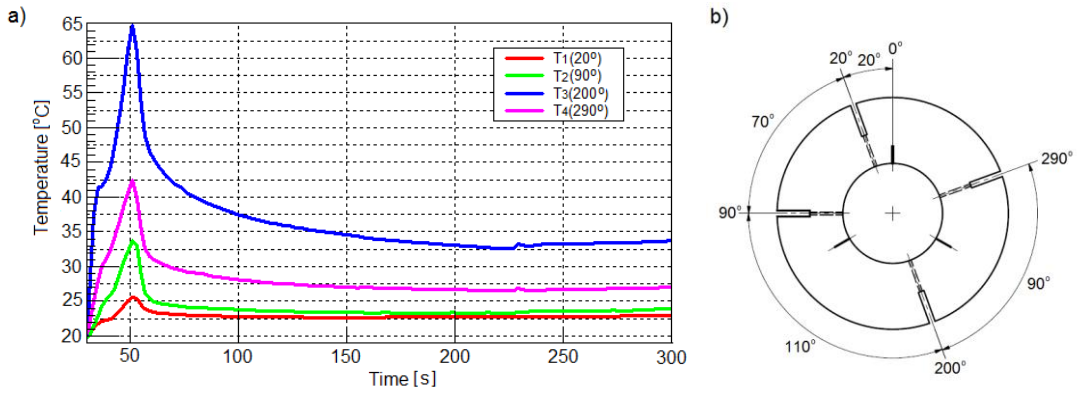

Figure 8: Temperature of the top foil measured during the wearing-in process vs. time (a) and the placement of the measuring points inside a foil bearing (b)

The registered temperature distribution resulted from the type of the bearing load. The biggest load - gravitational forces, were acting at the bottom of the bearing. It has been noted that the increase of temperature was accompanied with a high friction torque, which made rotor start-up more difficult. Subsequently, after wearing-in of the bearing, friction decreased significantly so that speed control of the electrospindle by frequency converter did not pose a problem.

During the experimental study, vibration measurements were also carried out. The results of these measurements reveal that in the mixed friction area, before the creation of a gaseous lubricating film, the relative vibrations of the bearing journals had high amplitudes (up to 0.4 mm). After reaching a speed of 20,000 rpm, the vibration amplitude of the two bearings decreased sharply and then remained at a very low level, i.e. around 0.04 mm. Such a low vibration level means that the system has a very good dynamic performance after the creation of a lubricating film.

It can be noticed that when increasing the speed of the rotor, the foil bearing constantly adjusts itself to the actual operating conditions. When a bearing operates at low rotational speeds, a gaseous supporting layer does not yet exist and the occurring vibrations are very low, as a result of excellent damping properties of thin foils. When increasing the speed the vibrations of the system also increase, until a stable lubricating film forms itself. The highest vibration levels occur within a narrow speed range when the process of forming a lubricating film is interrupted and there is a surface contact between the top foil and the journal. This is the most dangerous speed range, during which a very rapid wear of the bearing components

may take place. Therefore, this range of speeds should be exceeded as quickly as possible. At higher speeds, a gaseous lubricating film stabilises itself and the flexible foil set adapts its geometry to the new conditions. Under this operating conditions, the gaseous supporting layer usually has a thickness from several to over a dozen micrometers, which means that it is very rigid and has poor damping properties. A set of properly profiled foils fulfils the role of a damper, so that the rotor can rotate with extremely high speeds and the vibration level is very low.

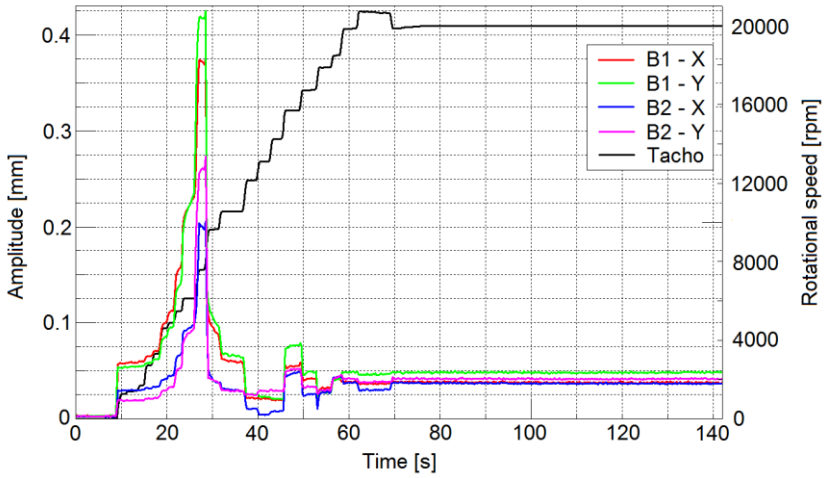

Figure 9: The relative vibration of the bearing journals during the rotor run-up up to a speed of 20,000 rpm vs. time (B1 – bearing no. 1, B2 – bearing no. 2, X and Y – the horizontal and vertical direction, respectively)

4 CONCLUSIONS

The article discusses selected issues related to the modelling and experimental investigation of gas foil bearings. Bearings of this type exhibit unusual properties that are unheard of in other bearing types. The structural supporting layer of the bearing has a progressive stiffness, which means that its deformations decrease progressively as the load increases. The main advantage of a foil bearing, as regards the operational reliability, lies in the ability to adapt its geometry to the load conditions. This ability has been verified experimentally, as the vibrations of bearing journals are very low at high rotational speeds. Although there was a sharp increase in the bearing temperature and the vibration amplitude during the run-up, it was only observed within a very narrow speed range and the system exhibited very good dynamic performance. For this reason, foil bearings are increasingly being used as components of innovative fluid-flow machinery with high-speed and lightly loaded rotors.

ACKNOWLEDGMENT

The investigation was financed by National Science Centre in Poland, under the research project no. 2016/21/D/ST8/01711 entitled “Examination and modelling of anti-vibration processes occurring in high-speed bearings with variable geometry”.

REFERENCES

[1] DellaCorte, C. Oil-Free Shaft support system rotordynamics: past, present and future challenges and opportunities. *Mechanical Systems and Signal Processing* (2012) 29: 67–76.

[2] Kiciński, J. and Żywica, G. *Steam microturbines in distributed cogeneration*. Springer (2014).

[3] Bruckner, R. J. An assessment of gas foil bearing scalability and the potential benefits to civilian turbofan engines. *Proceedings of ASME Turbo Expo 2010*, Glasgow (UK).

[4] Żywica, G., Bagiński P. and Banaszek S. Experimental studies on foil bearing with a sliding coating made of synthetic material. *Journal of Tribology* (2016) 138(1): 011301.

[5] Kiciński J. and Żywica, G. The numerical analysis of the steam microturbine rotor supported on foil bearings. *Advances in Vibration Engineering* (2012) 11(2):113-119.

[6] Nalepa, K., Pietkiewicz, P. and Żywica, G. Development of the foil bearing technology. *Technical Sciences* (2009) 12:229-240.

[7] Żywica, G., Kiciński J. and Bagiński, P. The static and dynamic numerical analysis of the foil bearing structure. *Journal of Vibration Engineering & Technologies* (2016) 4(3):213-220.

[8] Howard, S. A. Rotordynamics and design methods of an oil-free turbocharger. *Tribology Transactions* (1999) 42(1):174-179.

[9] Agrawal, G.L. Foil air/gas bearing technology - an overview. *ASME Paper* No. 97-GT-347, (1997).

[10] Heshmat, H., Hryniewicz, P. Walton II, J. F. et al. Low-friction wear-resistant coatings for high-temperature foil bearings. *Tribology International* (2005) 38:1059-1075.

[11] DellaCorte, Ch. A new foil air bearing test rig for use to 700 °C and 70,000 rpm, *NASA Technical Report* No. TM-107405, Washington (1997).

[12] Gupta, S., Filimonova, D., Zaitsevb, V., et al. Study of tribofilms formed during dry sliding of Ta2AlC/Ag or Cr2AlC/Ag composites against Ni-based superalloys and Al2O3. *Wear* (2009) 267:1490-1500.

[13] Fanning, Ch.E. and Blanchet, T.A. High-temperature evaluation of solid lubricant coatings in a foil thrust bearing. *Wear* (2008) 265:1076-1086.

[14] Radil, K. and Zeszotek, M. An experimental investigation into the temperature profile of a compliant foil air bearing. *Tribology Transactions* (2004) 47(4):470-479

[15] Gad, A.M. and Kaneko, S. A new structural stiffness model for bump-type foil bearings: application to generation II gas lubricated foil thrust bearing. *ASME Journal of Tribology* (2014) 136(4):041701-13

[16] Aksoy, S. and Aksit, M.F. A Fully coupled 3D thermo-elastohydrodynamics model for a bump-type compliant foil journal bearing. *Tribology International* (2015) 82:110-122

[17] Feng, K., Hu, J., Liu, W. et al. Structural characterization of a novel gas foil bearing with nested compression springs: analytical modeling and experimental measurement. *ASME Journal of Engineering for Gas Turbines and Power* (2015) 138(1):012504-11

[18] Lez, S., Arghir, M. and Frene, J. Static and dynamic characterization of a bump-type foil bearing structure. *ASME Journal of Tribology* (2007) 129:75-83.

[19] Ku R., Heshmat H. Compliant foil bearing structural stiffness analysis: part I - theoretical model including strip and variable bump foil geometry. *ASME Journal of Tribology* (1992) 114:394-400.

[20] ABAQUS Inc: *ABAQUS Analysis User's Manual.* 2016

[21] Kiciński, J., Żywica, G., Rządkowski, R., Drewczyński, M. Numerical modelling of the structural layer of foil bearing. *Acta Mechanica et Automatica* (2008) 2(1):45-50.

VIIIECCOMAS Thematic Conference on Smart Structures and Materials
SMART 2017
A. Güemes, A. Benjeddou , J. Rodellar and JinsongLeng (Eds)

ADAPTIVE TECHNIQUES FOR SUPPRESION OF FORCED VIBRATIONS

Grzegorz Mikułowski*, Grzegorz Suwała*, Lech Knap, Jan Holnicki-Szulc*,**

* Institute of Fundamental Technological ResearchPolishAcademy of Sciences, Warsaw, Poland
e-mail: gmikulow@ippt.pan.pl, gsuwala@ippt.pan.pl, holnicki@ippt.pan.pl

**WarsawUniversity of Technology, Faculty of Automotive and Construction Machinery Engineering, Warsaw, Poland
e-mail: l.knap@pw.edu.pl

Key words: Adaptive structures, forced vibrations, avoiding resonance, structural fuses.

Abstract. Adaptive structures, equipped with so-called structural fuses (based on fast responding piezo-devices), able to connect/disconnect instantly selected structural interface, allows effective protection against resonance induction via externally forced vibrations. The presented case study demonstrates haw forced vibrations with modifiable frequencies can be smoothly received, if structural fuses are properly activated/deactivated when the external excitation approaches the structural eigen frequencies.

1 INTRODUCTION

During last two decades a rapid growth of various solutions aimed at absorbing impact energy or protecting structures against external sources of vibrations is observed. Those systems usually constitute an entire spectrum between the extremes of passive and active systems.

In passive solutions, optimum design for crashworthiness is equivalent to maximization of absorption capacity in predetermined impact scenarios only [1], while for other load conditions (different mass, velocity or direction, etc.) structural response can be suboptimal [2]. The most often scenario considered in optimization corresponds usually to the most dangerous load, which is infrequent in practice. As a result, a passively optimized structure responds suboptimally for most of its operational lifetime. This is especially clear in the case of landing gears, which are designed for the most demanding touchdown, but whose everyday usage involves much smaller vertical velocities and loads [3].

The opposite extreme are active absorption systems, which comprise actuators to generate external forces. Active strategies are theoretically very effective and (at least for linear systems) well-researched [4]. But those solutions have important disadvantages, especially in impact absorption, which include application of large external control forces, the correspondingly high energy consumption, as well as their susceptibility to instabilities in case of power loss, control delays or actuator failure.

Adaptive systems, located in-between the extremes of passive and active systems, are based on semi-active control strategies [5].The same as active systems, adaptive systems areoften designed to cope with various types of loading but they act in different way. The absorbers, or the actuators, are not used to generate external forces but are generally used to change properties of the structure in predetermined relation to identified loading scenario. In this way adaptive systems only need energy for recognizing type of external loadand supplying adapters with controlling signals. The ability to quickly identify and determine type of external load as well as the absorber design and properties are very important for the efficiency of adaptive systems.There are many papers which describe recent investigations of impact identification methods and various types of absorbers, which are usually based on the use of so-called smart materials. For example, the group of pneumatic/hydraulic flow control shock-absorbers with actively controlled piezo-valves determines the first class of AIA (Adaptive Impact Absorption)requiring real time feed-back control of piezo-actuators[6], [7]. The other class of absorbers [8] requires precise in time switching between two active interfaces of adaptive inerter (so-called SPINMAN), causing switching of the spin of rotating inertial cylinders for conversion of linear impact energy into rotation of the inerter.

Other problem related to performance of adaptive structures and stabilization of their dynamic response is identification (usually in real time) of dynamic excitation. It is especially a challenging issue for the impact loads, when in few milliseconds not only the kinetic energy of the impact, but also the impact velocity has to be determined [9].

As it is mentioned above, the strategy of controlling absorbers is also crucial one and have direct impact on efficacy of adaptive systems. In this paper we discuss the problems related to algorithm, methods and techniques which can be used for supressing forced vibrations of the adaptive structure shown in Fig. 1. For example, concentrating on satellite aerospace engineering, the following requirements are crucial: a) necessity of artificial vibration damping system due to flexibility of the structure and its low natural damping, b) necessity of low weight of the proposed damping system, c) necessity of high reliability (simplicity) of the proposed system, d) preference of fluid-less techniques because of leakage danger. Therefore, semi-active (or even smart-passive) AIA damping systems will be preferable for aero-applications, where phyro-activated deployment on the orbit (typically applicable technique) causes problems for sensitive instrumentation.

Our previous investigations [10], [11] have shown that many problems with suppression of forced vibrations can be resolved by introducing the concept of pre-designed pre-stressing techniques. Feasibility study for control of eigen vibrations in flexible truss structures of parabolic mirrors on the orbit, by means of inducing self-stresses has been already performed [12]. It has been demonstrated that ca 15% reduction of local vibration amplitude is available via proper pre-stressing of the structure. This techniques, so-called PAR (Prestress Accumulation-Release), used in adaptive system for damping of impact born vibrations is extremely effective.

Finally, in this paper we discuss and analyze the case study of the flexible structure shown in Fig. 1, exposed to excited vibrations and equipped with PAR absorbers in the form of

switchable joints [11]. We introduce the new concept of suppressing local vibrations via proper in-time control of these absorbers. Also the results of numerical simulations, as well as the results of experimental investigations, are presented and discussed.

2 BASIC FORMULAS

The general form of equations of motion can be expressed as follows:

$$M\ddot{x} + C\dot{x} + Kx = F \tag{1}$$

where M, $C$and$K$are symmetric $n \times n$mass, damping and stiffness matrices, respectively, $\ddot{x}$, $\dot{x}$, $x$denote n-dimensional column vectors of space variables (accelerations, velocities and displacements, respectively), while the vector Fdenotes external forces acting on the system. Neglecting damping effect and external forces, the above equation takes the following form:

$$M\ddot{x} + Kx = 0 \tag{2}$$

which describes free vibration of an undamped system. The general solution of equation (2) can be expressed as follows:

$$x = \phi e^{j\omega t} \tag{3}$$

where$\phi$is an n-dimensional vector called a mode shape,ω denotes the frequency of vibration and t denotes time. Substitution of the above relation to the equation (2) leads to:

$$(K - \omega^2 M)\phi = 0. \tag{4}$$

We are interested in non-trivial solutions satisfying the following formula:

$$det(K - \omega^2 M) = 0 \tag{5}$$

which is known as the characteristic equation. The roots of equation (5) are known as the eigenvalues while their square roots are referred to as the natural frequencies of the system. Each distinct eigenvalue $\omega_i^2, i = 1,2, \dots, n$ has a corresponding mode shapeϕ_i, which satisfies equation:

$$M^{-1}K\phi_i = \omega_i^2\phi_i. \tag{6}$$

The mode shapes are often used to pair corresponding natural frequencies, obtained from numerical and experimental modal analysis. In this paper the MAC (Modal Assurance Criterion) coefficient has been used as a measure of correlation between two eigenmodes of vibration:

$$MAC = \frac{|\phi_{EM}^T \phi_{NA}|^2}{(\phi_{EM}^T \phi_{NA})(\phi_{NA}^T \phi_{NA})} \tag{7}$$

where ϕ_{NA},ϕ_{EM}-are mode shapes of vibration obtained from numerical and experimental modal analysis, respectively.

3 NUMERICAL MODEL OF FLEXIBLE STRUCTURE

A numerical model (Fig. 1) of flexible structure mockup has been elaborated taking advantage of Abaqus program. The finite element model has been assembled from 350 beam elements, two connector elements (revolute joint) and six point masses, added in nodes corresponding to the structural joint locations.The housing of semi-active joints has been modeled in a

simplified manner using beam elements, whereas a connector element has been used to model bending stiffness of the active end of the joints, i.e. the ends connected by a transverse element. Those ends can operate in two states, referred to in this paper as a framemode (transferring the bending moment), anda truss mode (not moment-bearing).The boundary conditions have been defined by fixing two supporting points on the left hand side of the structure.

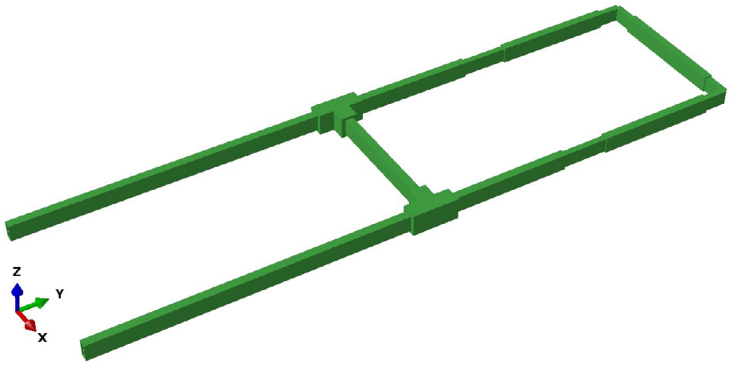

Figure 1: Numerical model of the experimental setup.

In order to identify the properties of the semi-active joints, the model updating procedure has been conducted in two steps. In the first step, the housing stiffness of the joint has been identified, whereas in the second stage, thebendingstiffness of the active endhas been investigated.The updating procedure has been based on the results obtained from the experimental modal analysis, however, only those natural frequencies for which the mode shapes remained in the XY plane of the structure have been taken into account (neither the torsional forms nor the flexure forms in the ZY plane have been included in the process of identification).Moreover, it has been assumed that the semi-active jointsare identicalandhave the same stiffness parameters. For the purpose of the first step, thesemi-active nodesduring the experiment have been switched to truss modeto minimizethe influence of the bendingstiffness of the active end on the natural frequencies. Then, the optimization problem has been formulated in which equivalent stiffness of the housing joint is found by minimizing the differences between the appropriate natural frequencies.Good agreement between the numerical and experimental results has been achieved as shown in Table1. Figure 2 shows the first four natural frequencies and mode shapes determined from the updated model.

Table 1: Comparison of experimental and numerical natural frequencies obtained in the first step.

Mode	Measured frequency [Hz]	Computed frequency [Hz]	MAC value
1	11.3	11.30	0.98
2	39.4	39.44	0.99
3	121.7	119.30	0.90
4	152.8	162.40	0.80

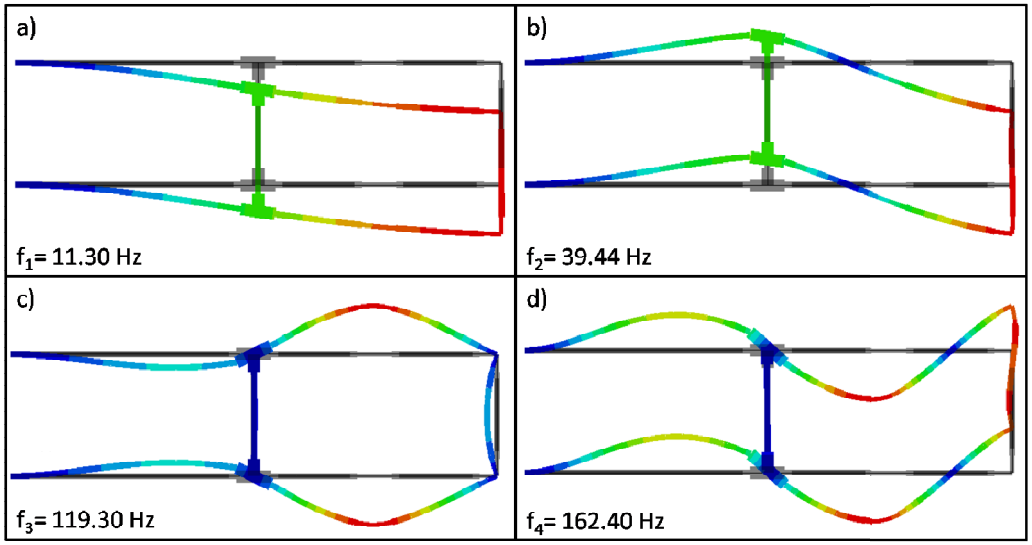

Figure 2: First four mode shapes of numerical model.

In the second step, the semi-active nodes have been switched to frame mode in order to perform identification of bending stiffness of the active end. The change of the operating state of nodes increases the rigidity of the structure, which is reflected in the natural frequencies as shown in Table 2. It has been observed that the all first fournatural frequency have increased by 28%,1.6%, 5%, 2.3% respectively, but the forms of vibrations have remained similar in its nature.

Table 2: Comparison of experimental and numerical natural frequencies obtained in the second step.

Mode	Measured frequency [Hz]	Computed frequency [Hz]	MAC value
1	14.5	14.47	0.99
2	40.1	40.7	0.99
3	125.3	126.67	0.91
4	166.3	177.98	0.89

4 EXPERIMENTAL INVESTIGATION

The experimental verification of the investigated concept was conducted in a laboratory environment. The objective was to propose for tests a slender structure with a low level of natural material damping in order to increase its susceptibility to mechanical excitations. The chosen mechanical structure was a steel frame mounted in a cantilever configuration, as depicted in Fig. 3. The frame was structured as two segments of the dimensions of 300 mm x 600 mm, which gave the total span of the structure equal to 1200 mm. The individual elements were designed as steel profiles 15 mm x 30 mm in a cross-section. The frame connections have been made by passive joints positioned in points P8 and P16 and semi-active joints positioned in points P4 and P12 (see in Fig. 3). The complete structure was mounted on a stiff support in points P1 and P9.

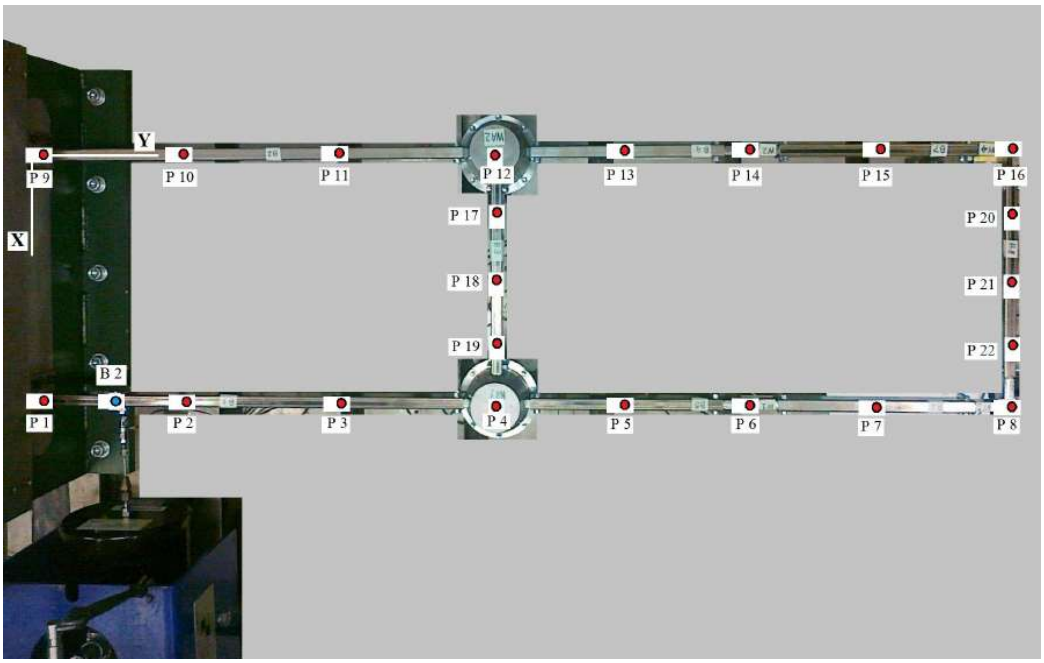

Figure 3: Experimental setup.

The semi-active joints were designed with three connecting ends, two of which were passive, elastic and the third one was semi-active, allowed to obtain an elasto-ideally plastic characteristic in angular movement in OXY plane (Figure 4). The semi-active joints were designed as dry friction devices with operating surfaces controlled with a piezoelectric actuator. The general mechanical response of the frame was modified in the domain of structural stiffness in the OXY plane. The semi-active joints were operated in two modes: frame and truss. In the case of the frame mode, the semi-active ending behaved in accordance with an elastic constitutive law. When the semi-active joints were operated in the truss mode, the joints did transmit 20 times lower torque in comparison to the another mode.

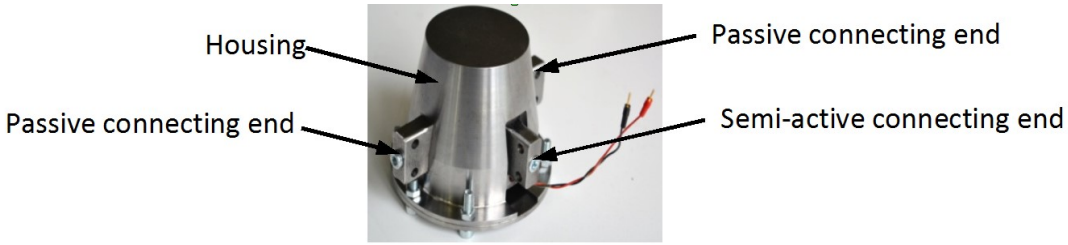

Figure 4: Experimental setup.

The frame was instrumented with a set of vibration type accelerometers positioned in points depicted as P1 – P22 (Fig. 3). The excitation of the frame was carried out by a modal shaker and a modal hammer.

The objectives of the experimental tests conducted on the frame were: a) to characterize the object in the domain of the frequency response and b) to reveal the controllability of the system. The frame was tested in accordance with two routines: operational modal analysis and frequency response function. The operational modal analysis was conducted in order to characterize the dynamical response of the structure and the FRF analysis was conducted in order to define the control space of the object and to characterize the semi-active control strategy.

Assuming danger of externally forced critical harmonic excitation (eg. close to the first eigen-frequency 14.5 Hz), reduction of the vibration amplitude for the monitored frame by deactivation of the semi-active joints and transition between frame and truss modes has been analyzed. The moment of deactivation of the joints were chosen on the basis of online FFT analysis, and the increasing of the amplitude. The control strategy adopted for the demonstration task was based on on-line monitoring of the dominant frequency of the excited vibration. Figure 3 depicts a comparison between the frequencyresponses of the frame in frame and truss modes. The transition in values of the eigen frequencies in dependence on the mode of operation are reflected in the position of the peaks on the plot.

The result of the control program execution for the 1st eigen mode is depicted in Fig. 6 and for the 2nd eigen mode in Fig. 7. The control strategy was to switch the semi-active joints operation from the truss to the frame mode at the moment dependent on the frequency response of the structure.

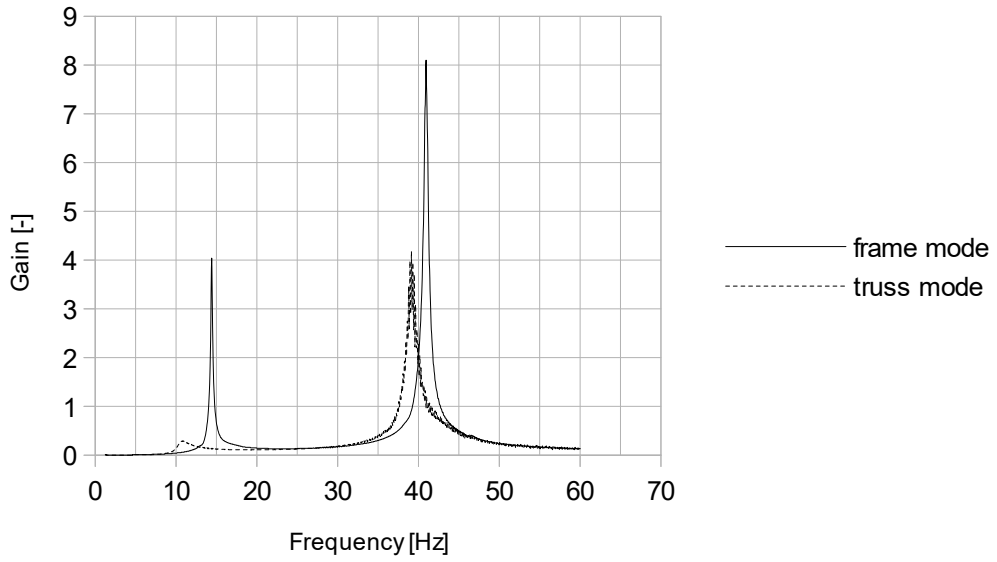

Figure 5: Frequency response of the frame for the 1st and 2ndeigen mode (measurement point P16).

The presented results reveal that the proposed semi-active control approach allows to reduce the amplitudes of the structure vibration of the resonance transition phase effectively. The gain attenuation magnitudes are presented in Table 3.

Table 3: Gain attenuations as a result of the control implementation.

	1st eigen frequency	2nd eigen frequency
Gain attenuation	23.76	4.02

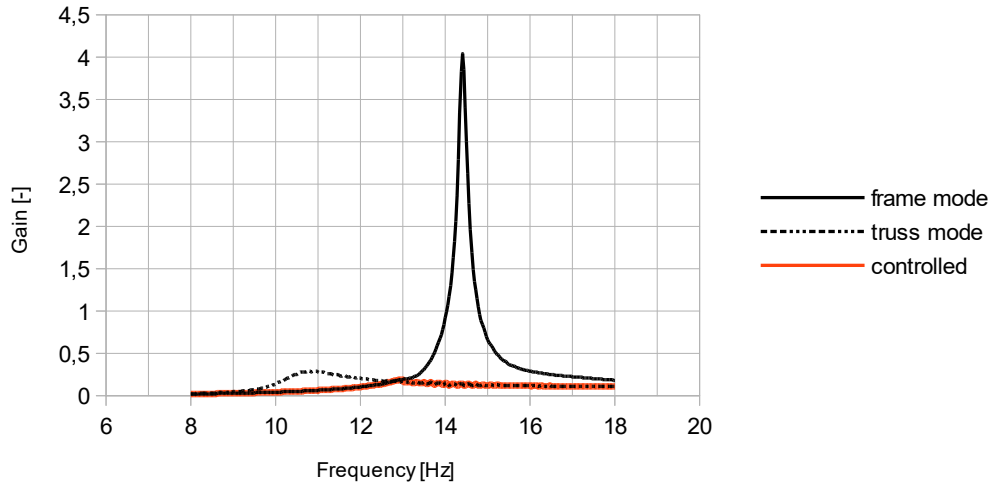

Figure 6: Frequency response of the controlled frame for the 1st eigen mode (measurement point P16).

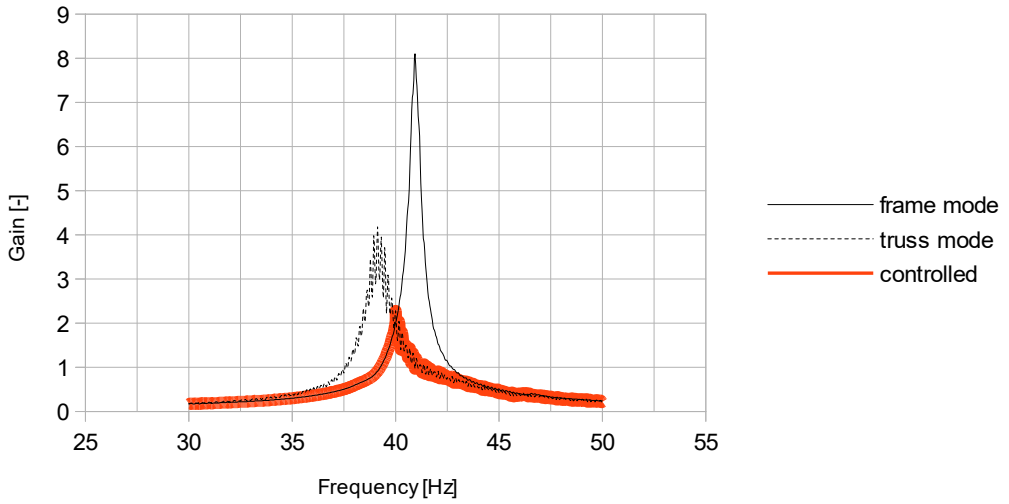

Figure 7: Frequency response of the controlled frame for 2nd eigen mode (measurement point P16).

5 CONCLUSIONS

The case study demonstrated in this paper is motivated by the following, practical situation. Externally forced harmonic excitation (with frequency over 45 Hz) transmitted to the flexible frame structure (eg. satellite on the orbit) can be dangerous if slowing down and passing with decreasing frequencies through the second structural eigen frequency (40,1 Hz) and the first one (14,5 Hz). Our proposed switching off the adaptive joint allows us to pass safely the critical frequencies. The analyzed case study shows that the corresponding small shifting of the structural eigen-frequencies (between the frame-like and the truss-like structures) gives us as the result dramatic improvement in gain attenuations (4 times in the case of second mode and over 23-times in the case of the second mode.

It can be also demonstrated, that properly tuned initial stresses induced in the structure via initial distortions (incompatibilities) forced in one location can effectively reduce vibration amplitudes in other, selected location. However, the side effect of such operation can be increase of vibration amplitudes in other location on the structure. One can say, that prestressing technique can be effective in local isolation of structural vibration amplitudes, caused by some critical, external excitation. Important advantage of the proposed technique, especially for aeronautic and aerospace applications, is a new option for reducing unwanted vibrations, without increasing the structural mass.

The magnitude of modification of the dynamic, structural response depends on overall structural stiffness and sensitivity of defined objective function for admissible structural modifications in selected localizations. The above results motivate authors for further, more methodological studies on control of structural dynamic response, based on modifiable prestressing technique, what will be published in a separate paper. The challenges to be overcome require including material damping effect, what will make the computational task more heavy, but also will lead to more realistic results. Also, the problem of prestress optimization (location for generation of prestress distortions and their magnitude) and technologies for prestress inducing (preferable in a modifiable manner) are open questions.

ACKNOWLEDGMENT

Financial support from the Polish research project AIA (Adaptive Impact Absorption), founded by NCN (National Science Council) No. 2012/05/B/ST8/02971, is gratefully acknowledged.

REFERENCES

[1] H. Fang, K Solanki, M.F Horstemeyer. Numerical simulations of multiple vehicle crashes and multidisciplinary crashworthiness optimization. *Int J Crashworthines*,10 (2005) 161-172.

[2] W.J. Witteman, R.F.C. Kriens. The necessity of an adaptive vehicle structure to optimize deceleration pulses for different crash velocities. *17th Int Technical Conf on the Enhanced Safety of Vehicles (ESV)*, 2001, paper no. 320.

[3] G. Mikułowski, Ł. Jankowski. Adaptive Landing Gear: optimum control strategy and potential for improvement, *Shock Vib*16 (2009), 175-194.

[4] A. Preumont, Vibration Control of Active Structures: An Introduction, third ed., *Springer Science+Business Media*, 2011.

[5] B. Basu et al., A European Association for the Control of Structures joint perspective. Recent studies in civil structural control across Europe, *Struct Control Hlth*21 (2014), 1414-1436.

[6] G. Mikulowski, R. Wiszowaty, J. Holnicki-Szulc.Characterization of a piezoelectric valve for an adaptive pneumatic shock absorber, *Smart Materials and Structures*, vol. 22, no. 12, 2013, pp. 125011-1-12

[7] C. Graczykowski, J. Holnicki-Szulc. Protecting offshore wind turbines against ship impacts by means of Adaptive Inflatable Structures, *Shock and Vibration*, vol. 16, no. 4,2009, pp. 335-353 , pdf, doi: 10.3233/SAV-2009-0473

[8] R.Faraj, J. Holnicki-Szulc, L. Knap, J. Seńko.Adaptive inertial shock-absorber, *Smart Materials and Structures*, 25(3):035031. 2016.

[9] K. Sekula , C. Graczykowski , J. Holnicki-Szulc. On-line impact load identification, *Shock and Vibration*, vol. 20, no. 1, 2013, pp. 123-141

[10] A. Mroz, A. Orlowska, J. Holnicki-Szulc. Semi-active damping of vibrations. Prestress Accumulation-Release strategy development, *Shock and Vibration*, vol. 17, no. 2, 2010, pp. 123-136 , pdf, doi: 10.3233/SAV-2010-0502

[11] A. Mróz, J. Holnicki-Szulc, J. Biczyk, Prestress Accumulation-Release Technique for Damping of Impact-Born Vibrations: Application to Self-Deployable Structures, *Mathematical Problems in Engineering*, 2015:720236.

[12] J. Holnicki-Szulc, R.T.Haftka, Vibration Mode Shape Control by Prestressing, *AIAA Journal*, vol. 30, No. 7, 1991.

[13] G.Suwala, L.Knap, J. Holnicki-Szulc.Prestressing for damping of local vibrations, *Eng. Trans.*,vol. 64, No. 3, pp 367–380, 2016.

VIII ECCOMAS Thematic Conference on Smart Structures and Materials
SMART 2017
A. Güemes, A. Benjeddou, J. Rodellar and J. Leng (Eds)

A MULTILAYERED PLATE ELEMENTS ACCOUNTING NODE-DEPENDENT KINEMATICS FOR STATIC ANALYSIS OF PIEZOELECTRIC STRUCTURES

E. CARRERA[†], G.M. KULIKOV[*] AND S. VALVANO[†]

[†]Department of Mechanical and Aerospace Engineering, Politecnico di Torino
Corso Duca degli Abbruzzi 24, 10129, Turin, Italy
stefano.valvano, erasmo.carrera {@polito.it}, www.mul2.com

[*] Department of Applied Mathematics and Mechanics, Tambov State Technical University
Sovetskaya Street 106, 392000 Tambov, Russia
kulikov@apmath.tstu.ru

Key words: Node-Dependent Kinematics, Piezoelectric materials, Multifield problems, Plate, Unified Formulation

Abstract. The present work deals with the static analysis of multilayered plates embedding piezoelectric layers as actuators and sensors. Finite Elements (FE) with equivalent-single-layer and layer-wise capabilities are employed to ensure an accurate description of the mechanical and electric fields in the layers. A new class of finite elements for the analysis of composite and piezoelectric multilayered plates is proposed. By making use of node-dependent plate theory assumptions, the new finite element allows for the simultaneous analysis of different subregions of the problem domain with different kinematics and accuracy, in a global/local sense. The structural theory of the plate element is a property of the FE node in this present approach, and the continuity between two adjacent elements is ensured by adopting the same kinematics at the interface nodes. The main advantage of the present variable-kinematics element and related global/local approach is that no ad-hoc techniques and mathematical artifices are required to mix the fields coming from two different and kinematically incompatible adjacent elements, because the plate structural theory varies within the finite element itself. It is possible to reduce the computational costs by assuming refined theories only in those zones/nodes of the structural domain where the resulting strain and stress states present a complex distribution. At the same time, computationally cheaper, low-order models can be used in the remaining parts of the plate where a localized detailed analysis is not necessary. With node-dependent kinematics it is possible to keep the order of the expansion of the state variables and models along the main reference plane of the plate structure as a parameter of the model. The electrical potential assumption for the layered actuators and sensors has been extended, from a layer-wise (LW) modeling, to an equivalent-single-layer (ESL) description, in the same way the displacements assumptions on the composite layers are described by a ESL and LW models. Some results from the static analysis of plates under electro-mechanical loads will be provided, in order to show the efficiency of models presented.

1 INTRODUCTION

Plate structures have a predominant role in a variety of engineering applications. Nevertheless, the use of new materials, such as composites layered materials and/or piezoelectric layers, leads to increasingly complex structural designs that require careful and detailed analysis. The analysis of layered composite structures is complicated in practice. In some cases, structures may contain regions where three-dimensional (3D) stress fields occur. To accurately capture these localized 3D stress states, solid models or higher-order theories are necessary. However, the high computational costs represent the drawback of refined plate theories or three-dimensional analyses. Analytical solution for general smart structural problems is a very tough task, and they exist, only, for very few specialized and idealized cases. Meanwhile, the finite element method has become the most widely used technique to model various physical processes, including piezoelectricity. The introduction of piezoelectric material into a passive structure naturally leads to a multilayered component, and it has been recognized that classical models are not suitable for an accurate design of such structures, see for example the review article of Noor and Burton [1]. The fundamentals of the modeling of piezoelectric materials have been given in many contributions, in particular in the pioneering works of Mindlin [2], EerNisse [3], Tiersten and Mindlin [4], and in the monograph of Tiersten [5]. The embedding of piezoelectric layers into plates and shells sharpens the requirements of an accurate modeling of the resulting adaptive structure due to the localized electro-mechanical coupling, see e.g. the review of Saravanos and Heyliger [6]. Some of the latest contributions to the Finite Elements (FEs) analysis of piezoelectric shells that are based on exact geometry solid-shell element was developed by Kulikov et al. [7, 8], and a piezoelectric solid-shell element with a mixed variational formulation and a geometrically nonlinear theory was developed by Klinkel et al. [9]. Although the enormous improvements and formulations of higher-order plate structural theories, considerable work has been recently directed towards the implementation of innovative solutions for improving the analysis efficiency for complex geometries and assemblies, possibly in a global/local scenario. In this manner, the limited computational resources can be distributed in an optimal manner to study in detail only those parts of the structure that require an accurate analysis. In general, two main approaches are available to deal with a global/local analysis: (1) refining the mesh or the FE shape functions in correspondence with the critical domain; (2) formulating multi-model methods, in which different subregions of the structure are analysed with different mathematical models. The first mentioned approaches can be addressed as single-theory or single-model methods. Differently, in the case of multi-theory methods, in which different subregions of the structure are analysed with different structural theories with kinematically incompatible elements, the compatibility of displacements and equilibrium of stresses at the interface between dissimilar elements have to be achieved. A wide variety of multiple model methods have been reported in the literature. In general, multi-theory methods can be divided into sequential or multistep methods, and simultaneous methods. In a sequential multi-model, the global region is analysed with an adequate model with a cheap computational cost to determine the displacement or force boundary conditions for a subsequent analysis at the local level. The local region can be modeled with a more refined theory, or it can be modeled with 3-D finite elements, see [10, 11]. The simultaneous multi-model methods are characterized by the analysis of the entire structural domain, where different subregions are modeled with different mathematical models and/or distinctly different

levels of domain discretization, in a unique step. A well-known method to couple incompatible kinematics in multi-model methods, is the use of Lagrange multipliers, which serve as additional equations to enforce compatibility between adjacent subregions. In the three-field formulation by Brezzi and Marini [12], an additional grid at the interface is introduced. The unknowns are represented independently in each sub-domain and at the interface, where the matching is provided by suitable Lagrange multipliers. Ben Dhia *et al.* [13, 14] proposed the Arlequin method to couple different numerical models by means of a minimization procedure. This method was adopted by Biscani *et al.* [15] for the mechanical analysis of plates and by Biscani *et al.* [16] for the electro-mechanical analysis of plates.
In the present work, the hierarchical characteristics of Unified Formulation (UF) by Carrera are used to develop a new simultaneous multiple-model method for 2D elements with node-dependent kinematics. This node-variable capability given by UF enables one to vary the kinematic assumptions within the same finite plate element. The expansion order of the plate element is, in fact, a property of the FE node in the present approach. Therefore, between finite elements, the continuity is ensured by adopting the same expansion order in the nodes at the element interface. This method has shown its potentiality in the mechanical analysis of plate structure, see [17]. Here the node-dependent variable kinematics is extended to the electro-mechanical analysis of multilayered plate structure. In this manner, global/local models can be formulated without the use of any mathematical artifice. As a consequence, computational costs can be reduced assuming refined models only in those zones with a quasi-three-dimensional stress field, whereas computationally cheap, low-order kinematic assumptions are used in the remaining parts of the plate structure.

2 REFINED AND HIERARCHICAL THEORIES FOR PLATES

This work proposes a class of new finite elements which allows employing different kinematic assumptions in different subregions of the problem domain. To highlight the capabilities of the novel formulation, a four-node plate elements with node-dependent kinematics is shown in Figure 1. The element proposed in this example makes use of a second-order ESL refined theory at node 1 and 8. On the other hand, a fourth-order ESL refined theory are employed at node 6 and 7, respectively. Therefore, a first-order layer-wise theory is used at node 3 and 4. Finally, a second-order layer-wise plate theory is assumed at node 2 and 5. As it will be clear later in this paper, thanks to the hierarchical capabilities of UF by Carrera, the choice of the nodal plate theory is arbitrary and variable-kinematics plate elements will be used to implement multi-model methods for global-local analysis. Before discussing the present formulation, a brief overview of classical and higher-order plate theories is given below or the sake of completeness. Plates are bi-dimensional structures in which one dimension (in general the thickness in the z direction) is negligible with respect to the other two dimensions.

Higher Order Theories written in Unified Formulation framework. According to Unified Formulation by Carrera [18], refined models can be formulated in a straightforward manner by assuming an expansion of each of the primary variables by arbitrary functions in the thickness direction. Thus, each variable can be treated independently from the others, according to the required accuracy. This procedure becomes extremely useful when multifield problems are in-

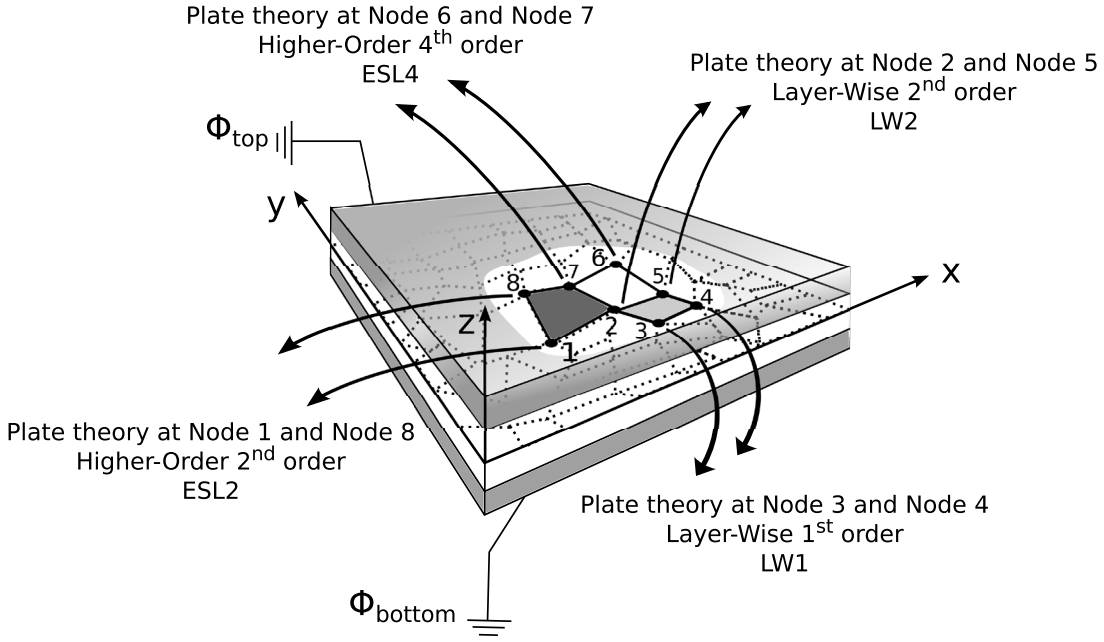

Figure 1: Node-dependent kinematic finite element example for a piezoelectric plate.

vestigated such as thermoelastic and piezoelectric applications [19, 20]. In a displacement-based formulation, UF states, in fact, that the three-dimensional displacement field and the electric potential are the combination of through-the-thickness functions weighted by the generalized unknown variables:

$$\begin{aligned} u(x,y,z) &= F_0(z)\,u_0(x,y) + F_1(z)\,u_1(x,y) + ... + F_N(z)\,u_N(x,y) \\ v(x,y,z) &= F_0(z)\,v_0(x,y) + F_1(z)\,v_1(x,y) + ... + F_N(z)\,v_N(x,y) \\ w(x,y,z) &= F_0(z)\,w_0(x,y) + F_1(z)\,w_1(x,y) + ... + F_N(z)\,w_N(x,y) \\ \Phi(x,y,z) &= F_0(z)\,\Phi_0(x,y) + F_1(z)\,\Phi_1(x,y) + ... + F_N(z)\,\Phi_N(x,y) \end{aligned} \tag{1}$$

Similarly, in a compact form one has:

$$\begin{aligned} \boldsymbol{u}(x,y,z) &= F_s(z)\boldsymbol{u}_s(x,y) \qquad s = 0,1,...,N \\ \Phi(x,y,z) &= F_s(z)\Phi_s(x,y) \qquad s = 0,1,...,N \end{aligned} \tag{2}$$

where $\boldsymbol{u}(x,y,z)$ is the three-dimensional displacement vector, and $\Phi(x,y,z)$ is the electric potential; F_s are the thickness functions depending only on z; $\boldsymbol{u}_s$ is the generalized displacement vector of the variables; s is a sum index; and N is the number of terms of the theory expansion. Depending on the choice of the thickness functions, F_s, and the number of terms in the plate kinematics, N, various theories can be implemented.
For example, higher-order theories can be expressed by making use of Taylor-like expansions of the generalized unknowns along the thickness. In the case of generic expansions of N terms, HOT displacement field and the electric potential can be expressed as in equation 3.

$$
\begin{aligned}
u(x,y,z) &= u_0(x,y) + z\,u_1(x,y) + ... + z^N\,u_N(x,y) \\
v(x,y,z) &= v_0(x,y) + z\,v_1(x,y) + ... + z^N\,v_N(x,y) \\
w(x,y,z) &= w_0(x,y) + z\,w_1(x,y) + ... + z^N\,w_N(x,y) \\
\Phi(x,y,z) &= \Phi_0(x,y) + z\,\Phi_1(x,y) + ... + z^N\,\Phi_N(x,y)
\end{aligned}
\tag{3}
$$

The classical models, CLT and FSDT kinematics, are particular cases of the full linear expansion, obtained from equation 3 imposing $N = 1$. For more details see [18].
The limitations, due to expressing the unknown variables in function of the midplane position of the plate, can be overcome in several ways. A possible solution can be found employing the Legendre polynomials. They permit to express the unknown variables in function of the top and bottom position of a part of the plate thickness. In the case of Legendre-like polynomial expansion models, the displacements and the electric potential are defined as follows:

$$
\begin{aligned}
\boldsymbol{u} &= F_0\,\boldsymbol{u}_0 + F_1\,\boldsymbol{u}_1 + F_r\,\boldsymbol{u}_r = F_s\,\boldsymbol{u}_s, \qquad s = 0,1,r\ , \quad r = 2,...,N \\
\Phi &= F_0\,\Phi_0 + F_1\,\Phi_1 + F_r\,\Phi_r = F_s\,\Phi_s, \qquad s = 0,1,r\ , \quad r = 2,...,N
\end{aligned}
\tag{4}
$$

$$
F_0 = \frac{P_0 + P_1}{2}, \quad F_1 = \frac{P_0 - P_1}{2}, \quad F_r = P_r - P_{r-2}. \tag{5}
$$

in which $P_j = P_j(\zeta)$ is the Legendre polynomial of j-order defined in the ζ-domain: $-1 \leq \zeta \leq 1$. $P_0 = 1$, $P_1 = \zeta$, $P_2 = (3\zeta^2 - 1)/2$, $P_3 = (5\zeta^3 - 3\zeta)/2$, $P_4 = (35\zeta^4 - 30\zeta^2 + 3)/8$.
For the Layer-Wise (LW) models, the Legendre polynomials and the relative top and bottom position are defined for each layer k. For the Equivalent Single Layer model, the Legendre polynomials and the relative top and bottom position are defined for the whole multilayer.

3 FINITE ELEMENTS WITH NODE-DEPENDENT KINEMATICS

Thanks to UF by Carrera, FEM arrays of classical to higher-order plate theories can be formulated in a straightforward and unified manner by employing a recursive index notation. By utilizing an FEM approximation, the generalized displacements of equation2 can be expressed as a linear combination of the shape functions to have

$$
\begin{aligned}
\boldsymbol{u}_s(x,y) &= N_j(x,y)\boldsymbol{u}_{s_j} \qquad j = 1,...,(\text{nodes per element}) \\
\boldsymbol{\Phi}_s(x,y) &= N_j(x,y)\boldsymbol{\Phi}_{s_j} \qquad j = 1,...,(\text{nodes per element})
\end{aligned}
\tag{6}
$$

where $\boldsymbol{u}_{s_j}$ is the vector of the generalized displacements nodal unknowns, $\boldsymbol{\Phi}_{s_j}$ is the vector of the generalized electric potential nodal unknowns and N_j can be the usual Lagrange shape functions. j denotes a summation on the element nodes. Since the principle of virtual displacements in used in this paper to obtain the elemental FE matrices, it is useful to introduce the finite element approximation of the virtual variation of the generalized displacement vector $\delta\boldsymbol{u}_\tau$, and the virtual variation of the generalized electric potential $\delta\boldsymbol{\Phi}_\tau$,

$$
\begin{aligned}
\delta\boldsymbol{u}_\tau(x,y) &= N_i(x,y)\delta\boldsymbol{u}_{\tau_i} \qquad i = 1,...,(\text{nodes per element}) \\
\delta\boldsymbol{\Phi}_\tau(x,y) &= N_i(x,y)\delta\boldsymbol{\Phi}_{\tau_i} \qquad i = 1,...,(\text{nodes per element})
\end{aligned}
\tag{7}
$$

In equation 7, δ denotes the virtual variation, whereas indexes τ and i are used instead of s and j, respectively, for the sake of convenience.
In this work, and according to equations 2, 6 and 7, the thickness functions F_s and F_τ, which determine the plate theory order, are independent variables and may change for each node within the plate element. Namely, the three-dimensional displacement field, the electric potential and their related virtual variations can be expressed to address FE node-dependent plate kinematics as follows:

$$\begin{aligned}
\boldsymbol{u}(x,y,z) &= F_s^j(z) N_j(x,y) \boldsymbol{u}_{s_j} \qquad s=0,1,...,N^j \quad j=1,...,\text{(nodes per element)} \\
\Phi(x,y,z) &= F_s^j(z) N_j(x,y) \boldsymbol{\Phi}_{s_j} \qquad s=0,1,...,N^j \quad j=1,...,\text{(nodes per element)} \\
\delta\boldsymbol{u}(x,y,z) &= F_\tau^i(z) N_i(x,y) \delta\boldsymbol{u}_{\tau_i} \quad \tau=0,1,...,N^i \quad i=1,...,\text{(nodes per element)} \\
\delta\Phi(x,y,z) &= F_\tau^i(z) N_i(x,y) \delta\boldsymbol{\Phi}_{\tau_i} \quad \tau=0,1,...,N^i \quad i=1,...,\text{(nodes per element)}
\end{aligned} \tag{8}$$

where the subscripts τ, s, i, and j denote summation. Superscripts i and j denote node dependency, such that for example F_τ^i is the thickness expanding function and N^i is the number of expansion terms at node i, respectively.

For the sake of clarity, the displacement field of a variable kinematic plate element as discussed in Figure 1 is described in detail hereafter. For example, taking into account the description of the displacement field of the darkest element, the global displacement field of the element is approximated as follows:

- Node 1 Plate Theory = HOT with $N^1 = 2$ Eq. (3)
- Node 2 Plate Theory = LW with $N^2 = 2$ Eq. (4)
- Node 7 Plate Theory = HOT with $N^7 = 4$ Eq. (3)
- Node 8 Plate Theory = HOT with $N^8 = 2$ Eq. (3)

In a CUF-based FE framework and according to equation 8, it is easy to verify that the displacements at a generic point belonging to the plate element can be expressed as given in equation 9. In this equation, only the displacement component along x-axis is given for simplicity reasons:

$$\begin{aligned}
u(x,y,z) = &\left(u_{0_1} + z\,u_{1_1} + z^2\,u_{2_1}\right) N_1(x,y) + \left[\left(\frac{1+\zeta_k}{2}\right) u_{0_2} + \left(\frac{1-\zeta_k}{2}\right) u_{1_2} + \right. \\
&\left. + \left(\frac{3\zeta_k^2-1}{2} - 1\right) u_{2_2}\right] N_2(x,y) + \left(u_{0_7} + z\,u_{1_7} + z^2\,u_{2_7} + z^3\,u_{3_7} + z^4\,u_{4_7}\right) N_7(x,y) + \\
&+ \left(u_{0_8} + z\,u_{1_8} + z^2\,u_{2_8}\right) N_8(x,y)
\end{aligned} \tag{9}$$

It is intended that, due to node-variable expansion theory order, the assembling procedure of each finite element increases in complexity with respect to classical mono-theory finite elements. In the present FE approach, in fact, it is clear that both rectangular and square arrays are handled and opportunely assembled for obtaining the final elemental matrices.
Therefore, to overcome the numerical problems related to the shear locking, it is possible to use many computational procedures, such as reduced integration, selective integration [21], and the mixed interpolation of tensorial components (MITC) [22]. In this paper, a MITC technique is used to overcome the shear locking phenomenon, for more details see [20].

3.1 FUNDAMENTAL NUCLEUS OF THE STIFFNESS MATRIX

Given UF and FE approximation, the governing equations for the static response analysis of the multi-layer plate structure can be obtained by using the principle of virtual displacements, which states:

$$\int_{\Omega_k}\int_{A_k} \left\{ \delta\boldsymbol{\epsilon}_k^T \boldsymbol{\sigma}_k - \delta\boldsymbol{\mathcal{E}}_k^T \boldsymbol{\mathcal{D}}_k \right\} d\Omega_k dz_k = \delta L_e \tag{10}$$

where the term on the left-hand side represents the virtual variation of the strain energy; Ω and A are the integration domains in the plane and the thickness direction, respectively; $\boldsymbol{\epsilon}$ and $\boldsymbol{\sigma}$ are the vector of the strain and stress components; $\boldsymbol{\mathcal{E}}$ and $\boldsymbol{\mathcal{D}}$ are the vector of the electric field and electric displacements components; and δL_e is the virtual variation of the external loadings; k represents the nth layer, and T means the vector transposition. The constitutive equations are the following:

$$\begin{aligned} \boldsymbol{\sigma}_k &= \boldsymbol{C}_k \boldsymbol{\epsilon}_k - \boldsymbol{e}_k \boldsymbol{\mathcal{E}}_k \\ \boldsymbol{\mathcal{D}}_k &= \boldsymbol{e}_k \boldsymbol{\epsilon}_k + \boldsymbol{\varepsilon}_k \boldsymbol{\mathcal{E}}_k \end{aligned} \tag{11}$$

where $\boldsymbol{C}$ is the vector of the material stiffness coefficients, $\boldsymbol{e}$ is the vector of the piezoelectric stiffness coefficients, and $\boldsymbol{\varepsilon}$ is the vector of the permittivity coefficients. The mechanical strains $\boldsymbol{\epsilon}$ and the electric field $\boldsymbol{\mathcal{E}}$ are related to the mechanical displacements $\boldsymbol{u}$ and the electric potential Φ via the geometrical relations as follows:

$$\begin{aligned} \boldsymbol{\epsilon} &= \boldsymbol{D}_g \boldsymbol{u} \\ \boldsymbol{\mathcal{E}} &= -\boldsymbol{D}_{eg} \Phi \end{aligned} \tag{12}$$

where $\boldsymbol{D}_g$ and $\boldsymbol{D}_{eg}$ are the vectors containing the differential operators defined as follows:

$$\boldsymbol{D}_g = \begin{bmatrix} \dfrac{\partial}{\partial_x} & 0 & 0 \\ 0 & \dfrac{\partial}{\partial_y} & 0 \\ \dfrac{\partial}{\partial_y} & \dfrac{\partial}{\partial_x} & 0 \\ \dfrac{\partial}{\partial_z} & 0 & \dfrac{\partial}{\partial_x} \\ 0 & \dfrac{\partial}{\partial_z} & \dfrac{\partial}{\partial_y} \\ 0 & 0 & \dfrac{\partial}{\partial_z} \end{bmatrix} \qquad \boldsymbol{D}_e g = \begin{bmatrix} \dfrac{\partial}{\partial_x} \\ \dfrac{\partial}{\partial_y} \\ \dfrac{\partial}{\partial_z} \end{bmatrix} \tag{13}$$

By substituting the constitutive equations 11 for composite elastic materials, the linear geometrical relations 12 as well as equation 8 into equation 10, the linear algebraic system in the form of governing equations is obtained in the following matrix expression:

$$\begin{aligned} \delta \boldsymbol{u}_{\tau i}^k &: \boldsymbol{K}_{uu}^{k\tau sij} \boldsymbol{u}_{sj}^k + \boldsymbol{K}_{u\Phi}^{k\tau sij} \Phi_{sj}^k = \boldsymbol{P}_{u_{\tau i}}^k \\ \delta \boldsymbol{\Phi}_{\tau i}^k &: \boldsymbol{K}_{\Phi u}^{k\tau sij} \boldsymbol{u}_{sj}^k + \boldsymbol{K}_{\Phi\Phi}^{k\tau sij} \Phi_{sj}^k = \boldsymbol{P}_{\Phi_{\tau i}}^k \end{aligned} \tag{14}$$

In compact form:

$$\delta \boldsymbol{u}^k_{\tau i} \, : \, \boldsymbol{K}^{k\tau sij} \, \boldsymbol{u}^k_{sj} \, = \, \boldsymbol{P}^k_{\tau i} \tag{15}$$

where

$$\boldsymbol{K}^{k\tau sij} = \begin{bmatrix} \boldsymbol{K}_{uu} & \boldsymbol{K}_{u\Phi} \\ \boldsymbol{K}_{\Phi u} & \boldsymbol{K}_{\Phi\Phi} \end{bmatrix}^{k\tau sij} \tag{16}$$

where $\boldsymbol{K}^{k\tau sij}$ is a 4×4 matrix, called fundamental nucleus of the electro-mechanical stiffness matrix, and its explicit expression is given in [23]. The mechanical part $\boldsymbol{K}^{k\tau sij}_{uu}$ is a 3×3 matrix, the coupling matrices $\boldsymbol{K}^{k\tau sij}_{u\Phi}$, $\boldsymbol{K}^{k\tau sij}_{\Phi u}$ have dimension 3×1 and 1×3 respectively, and the electrical part $\boldsymbol{K}^{k\tau sij}_{\Phi\Phi}$ is a 1×1 matrix. The nucleus is the basic element from which the stiffness matrix of the whole structure is computed. The fundamental nucleus is expanded on the indexes τ and s to obtain the stiffness matrix of each layer k. Then, the matrixes of each layer are assembled at the multi-layer level depending on the approach considered. $\boldsymbol{P}^k_{\tau i}$ is a 3×1 matrix, called fundamental nucleus of the external load.

4 NUMERICAL RESULTS

To assess this new finite element, a four-layer cross-ply square plate with a cross-ply Gr/Ep composite core [0°/90°] and PZT-4 piezoelectric external skins, simply-supported boundary condition is considered. The static analysis of the plate structure is evaluated in sensor configuration. For the sensor case, a bi-sinusoidal transverse normal pressure is applied to the top surface of the plate:

$$p\,(x, y, z_{top}) = p^o_z \, sin(m\pi x/a) sin(n\pi y/b) \tag{17}$$

with amplitude $p^o_z = 1$ and wave numbers $m = 1$, $n = 1$. The potential at top and bottom position is imposed $\Phi_t = \Phi_b = 0$. The square plate has the following geometrical data: $a = b = 4.0$, and $h_{tot} = 1.0$. In respect to the total thickness, a single piezoelectric skin is thick $h_p = 0.1 h_{tot}$, while the single core layer is thick $h_c = 0.4 h_{tot}$. The material properties of the plate are given in Table 1. The results are evaluated in the plate center.

In order to compare the results with other solutions present in literature [16], the mid-plane domain of the plane structure was subdivided into two zones along the axes x and y, as shown in figure 2, and multi-theory models *Case A* and *Case B* are depicted on the FE discretization of a quarter of the plate. Some results of the transverse mechanical displacement w, transverse normal stress σ_{zz}, electric potential Φ, and tranvserse electric displacement $\mathcal{D}_z$ evaluated along the plate thickness in the center plate, are given in figure 3, Results are compared with the exact $3D$ solutions provided by Heyliger [24]. Figures 4(a) and 4(b) show the three-dimensional distributions of the transverse shear stress σ_{xz} of the variable kinematic multi-model *Case A* and *Case B* configuration. The results show the enhanced global/local capabilities of the *Case A* model, which is able to predict correctly the stress state in the center zone where the loading is bigger.

5 CONCLUSIONS

A new methodology for global/local analysis of composite plate structure under electro-mechanical loadings has been introduced in this work. This approach makes use of advanced finite plate elements with node-dependent kinematics. The finite element arrays of the generic

Table 1: Material data for multilayered plate.

Mechanical Properties									
	$E_{11}\,[GPa]$	$E_{22}\,[GPa]$	$E_{33}\,[GPa]$	$\nu_{12}\,[-]$	$\nu_{13}\,[-]$	$\nu_{23}\,[-]$	$G_{12}\,[GPa]$	$G_{13}\,[GPa]$	$G_{23}\,[GPa]$
Gr/EP	132.38	10.756	10.756	0.24	0.24	0.49	5.6537	5.6537	3.606
$PZT-4$	81.3	81.3	64.5	0.329	0.432	0.432	30.6	25.6	25.6
Electrical Properties									
	$e_{15}\,[C/m^2]$	$e_{24}\,[C/m^2]$	$e_{31}\,[C/m^2]$	$e_{32}\,[C/m^2]$	$e_{33}\,[C/m^2]$	$\tilde{\varepsilon}_{11}/\varepsilon_0\,[-]$	$\tilde{\varepsilon}_{22}/\varepsilon_0\,[-]$	$\tilde{\varepsilon}_{33}/\varepsilon_0\,[-]$	$\varepsilon_0\,[C/Vm]$
Gr/EP	0	0	0	0	0	3.5	3.0	3.0	$8.85*10^{-12}$
$PZT-4$	12.72	12.72	-5.20	-5.20	15.08	1475	1475	1300	$8.85*10^{-12}$

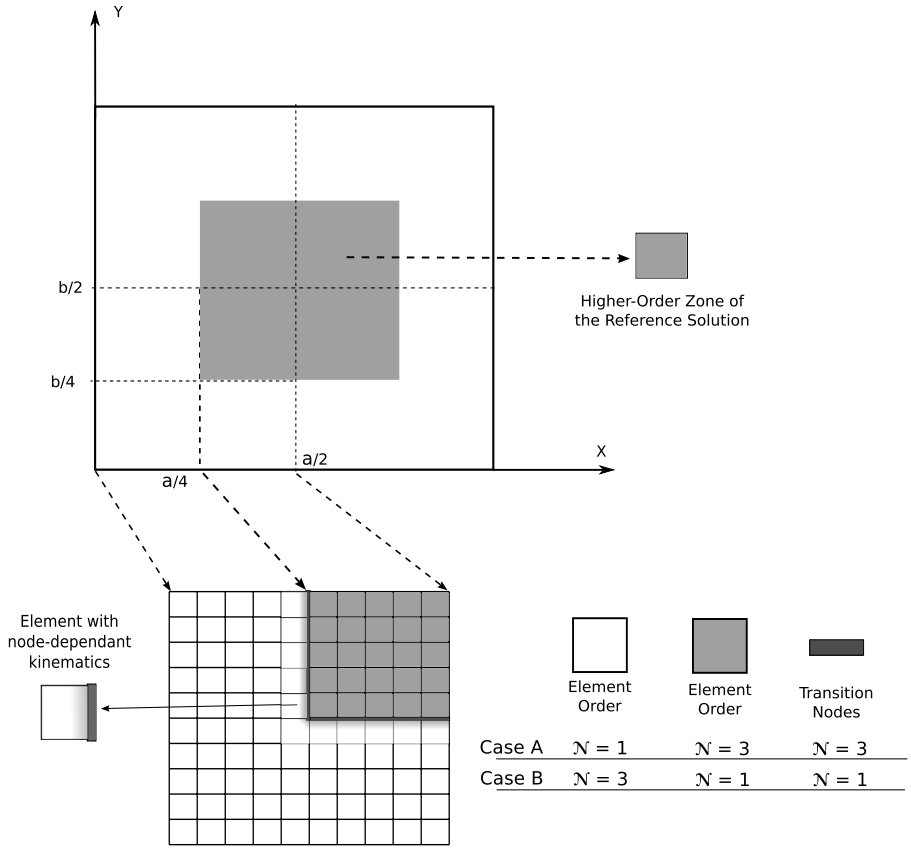

Figure 2: Mesh zones of the composite plate with piezoelectric skins and graphical representation of the multi-theory models, based on layer-wise models.

plate element are formulated in terms of fundamental nuclei, which are invariants of the theory approximation order. In this manner, the plate theory can vary within the same finite elements

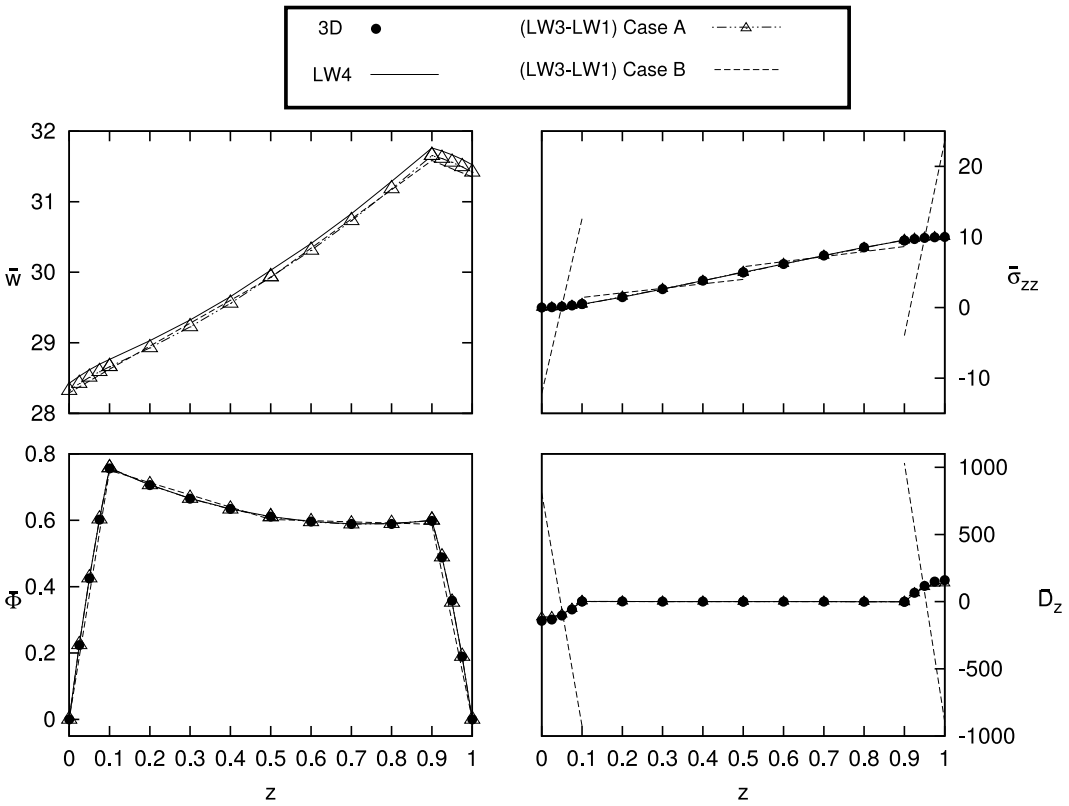

Figure 3: Transverse mechanical displacement w, transverse normal stress σ_{zz}, electric potential Φ, and tranvserse electric displacement $\mathcal{D}_z$ evaluated in the center plate.

with no difficulties. Thus, given a finite element model, the theory approximation accuracy can be enriched locally in a very straightforward manner by enforcing the same kinematics at the interface nodes between kinematically incompatible plate elements. The resulting global/local approach is very efficient because it does not employ any mathematical artifice to enforce the displacement/stress continuity, such as those methods based on Lagrange multipliers or overlapping regions. The proposed methodology has shown good potentiality in the analysis of composite plate embedding piezoelectric skins.

REFERENCES

[1] A K Noor and W S Burton. Assessment of computational models for multi-layered composite shells. *Applied Mechanics Review*, 43:67–97, 1990.

[2] R D Mindlin. Forced thickness-shear and flexural vibrations of piezoelectric crystal plates. *Journal of Applied Physics*, 23:83–91, 1952.

[3] E P EerNisse. Variational method for electroelastic vibration analysis. *IEEE Transaction on Sonics and Ultrasonics*, 14(4):153–213, 1967.

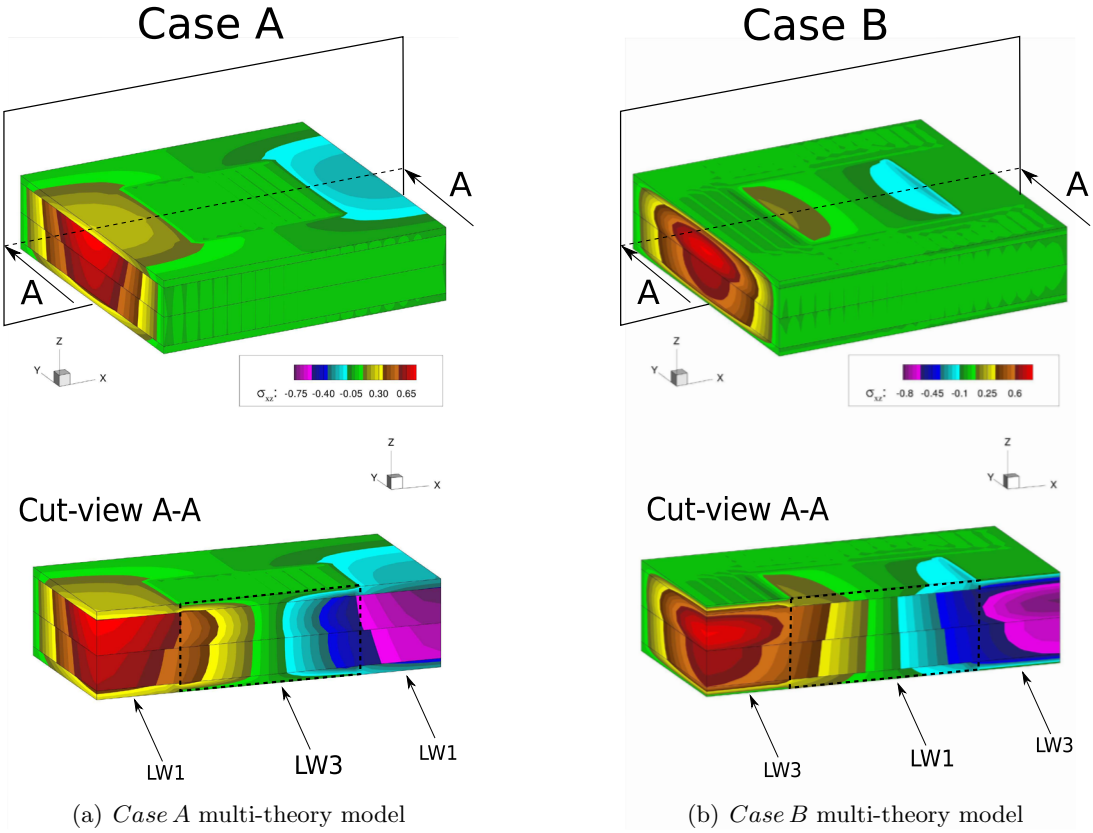

(a) *Case A* multi-theory model

(b) *Case B* multi-theory model

Figure 4: Composite four-layered plate. Transverse shear stress σ_{xz}. Multi-model theories.

[4] H F Tiersten and R D Mindlin. Forced vibrations of piezoelectric crystal plates. *Quarterly of Applied Mathematics*, 20(2):107–126, 1962.

[5] H F Tiersten. Linear piezoelectric plate vibrations. *New York Plenum Press*, 1969.

[6] D A Saravanos and P R Heyliger. Mechanics and computational models for laminated piezoelectric beams, plates and shells. *Applied Mechanics Review*, 52(10):305–324, 1999.

[7] G M Kulikov and S V Plotnikova. Exact geometry piezoelectric solid-shell element based on the 7-parameter model. *Mechanics of Advanced Materials and Structures*, 18:133–146, 2011.

[8] G M Kulikov and S V Plotnikova. A new approach to three-dimensional exact solutions for functionally graded piezoelectric laminated plates. *Composite Structures*, 106:33–46, 2013.

[9] S Klinkel and W Wagner. A piezoelectric solid shell element based on a mixed variational formulation for geometrically linear and nonlinear applications. *Computers & Structures*, 86:38–46, 2008.

[10] D M Thompson and O H Jr Griffin. 2-D to 3-D Global/Local Finite Element Analysis of Cross-Ply Composite Laminates. *Journal of Reinforced Plastics and Composites*, 9:492–502, 1990.

[11] K M Mao and C T Sun. A Refined Global-Local Finite Element Analysis Method. *International Journal for Numerical Methods in Engineering*, 32:29–43, 1991.

[12] F Brezzi and L D Marini. The three-field formulation for elasticity problems. *GAMM Mitteilungen*, 28:124–153, 2005.

[13] H Ben Dhia. Multiscale mechanical problems: the Arlequin method. *Comptes Rendus de lAcademie des Sciences Series IIB Mechanics Physics Astronomy*, 326(12):899–904, 1998.

[14] H Ben Dhia. Further insights by theoretical investigations of the multiscale Arlequin method. *International Journal for Multiscale Computational Engineering*, 6(3):215–232, 2008.

[15] F Biscani, G Giunta, S Belouettar, E Carrera, and H Hu. Variable kinematic plate elements coupled via Arlequin method. *International Journal for Numerical Methods in Engineering*, 91:1264–1290, 2012.

[16] F Biscani, P Nali, S Belouettar, and E Carrera. Coupling of hierarchical piezoelectric plate finite elements via Arlequin method. *Journal of Intelligent Material Systems and Structures*, 23(7):749–764, 2012.

[17] E Carrera, A Pagani, and S Valvano. Multilayered plate elements accounting for refined theories and node-dependent kinematics. *Composites Part B*, 2017. doi:10.1016/j.compositesb.2017.01.022

[18] E Carrera, M Cinefra, and E Petrolo M. abd Zappino. *Finite Element Analysis of Structures through Unified Formulation*. John Wiley & Sons, 2014.

[19] M Cinefra, S Valvano, and E Carrera. Heat conduction and Thermal Stress Analysis of laminated composites by a variable kinematic MITC9 shell element. *Curved and Layered Structures*, 1:301–320, 2015.

[20] M Cinefra, S Valvano, and E Carrera. A layer-wise MITC9 finite element for the free-vibration analysis of plates with piezo-patches. *International Journal of Smart and Nano Materials*, 6(2):85–104, 2015.

[21] T J R Hughes, M Cohen, and M Horaun. Reduced and selective integration techniques in the finite element methods. *Nuclear Engineering and Design*, 46:203–222, 1978.

[22] K J Bathe and E Dvorkin. A formulation of general shell elements - the use of mixed interpolation of tensorial components. *International Journal for Numerical Methods in Engineering*, 22:697–722, 1986.

[23] M Cinefra, E Carrera, and S Valvano. Variable Kinematic Shell Elements for the Analysis of Electro-Mechanical Problems. *Mechanics of Advanced Materials and Structures*, 22(1-2):77–106, 2015.

[24] P Heyliger. Static behavior of laminated elastic/piezo-electric plates. *AIAA Journal*, 32(12):2481–2484, 1994.

VIII ECCOMAS Thematic Conference on Smart Structures and Materials
SMART 2017
A. Güemes, A. Benjeddou , J. Rodellar and Jinsong Leng (Eds)

ANALYSIS OF PRIMAL AND DUAL VARIABLES IN STRUCTURAL SHAPE CONTROL BY PIEZOELECTRIC PATCHES USING SOLID–SHELL FINITE ELEMENTS

F. KPEKY[*,‡], F. ABED-MERAIM[†,‡] AND E.M. DAYA[*,‡]

[*] Laboratoire d'Étude des Microstructures et de Mécanique des Matériaux (LEM3)
Université de Lorraine
Ile du Saulcy, 57045 Metz, France
e-mail: fessal.kpeky@univ-lorraine.fr, el-mostafa.daya@univ-lorraine.fr / www.lem3.fr

[†] Laboratoire d'Étude des Microstructures et de Mécanique des Matériaux (LEM3)
Arts et Métiers ParisTech
4 rue Augustin Fresnel, 57078 Metz, France
e-mail: farid.abed-meraim@ensam.eu / www.lem3.fr

[‡] Laboratory of Excellence on Design of Alloy Metals for low-mAss Structures (DAMAS)

Key words: Piezoelectric effect, Smart Structures, Finite elements, Solid–shell, Shape control.

Abstract. This paper presents an assessment of the performances of new piezoelectric solid–shell finite elements. Compared to conventional solid and shell elements, the solid–shell concept reveals to be very attractive, due to a number of well-established advantages and computational capabilities. This paper focuses on two element formulations, denoted SHB15E and SHB20E, which represent a quadratic prismatic solid–shell element and its hexahedral counterpart, respectively. The current analysis consists in an evaluation of primal and dual variables during the process of shape control of structures. The interest in this solid–shell approach is shown through a set of selective and representative plate and shell benchmark problems. The results obtained by the proposed formulations are compared with those given by state-of-the-art piezoelectric elements available in ABAQUS.

1 INTRODUCTION

Smart materials and structures are nowadays increasingly used in several areas of engineering. They can be found in automotive, aeronautics, aerospace, etc., where they are used for shape and vibration control [1-3], or in auscultation of civil infrastructures. They also have medical applications, such as pacemakers, civil engineering usage, where they serve to monitor the state of health of civil infrastructures [4-6], among many other fields. Piezoelectric materials, which represent a particular class of smart materials, have the ability

to generate an electrical potential when subjected to mechanical loading. They also have the ability to deform under application of electrical potential. These properties provide them interest in several engineering domains, where they are generally used as very thin transducers, or as sensors and actuators.

The prediction of the behavior of such materials therefore becomes important for their proper implementation. One of the least costly ways to do this is via numerical modeling, and most commonly through the finite element method. Since the early works of Allik and Hughes [7], several tools have been proposed in the literature to model piezoelectric structures. A large variety of 2D and 3D piezoelectric finite elements have actually been developed [8-10]. Examples of these are the Classical Laminate Plate Theory (CLPT) models, the Carrera Unified Formulation (CUF) models [11], among many others. Despite the availability of all of these models in the literature, worth noting is the lack of finite elements capable of low-cost modeling of structures combining thin and thick layers. Although, recently, authors such as Kulikov and Plotnikova [12, 13], as well as Nestorović et al. [14, 15], are stepping up to the proposal of solid–shell FE, the only alternative in commercial software packages like ABAQUS still remains the use of solid elements with refined meshes. To overcome these limitations, we have developed a family of piezoelectric finite elements using the solid–shell technology based on the works of Abed-Meraim et al. [16, 17]. These recently developed FE consist of hexahedral and prismatic solid–shell elements, using an in-plane reduced-integration scheme and a special direction designated as the “thickness”.

The main objective of this work is to assess the performance of the proposed elements through the calculation of primal and dual variables. To this end, the paper is organized as follows. Section 2 presents the coupled electromechanical constitutive equations as well as the discretized problem to be solved by the finite element method. Section 3 briefly outlines the formulation of the piezoelectric solid–shell elements. A set of selective and representative benchmark tests are conducted in Section 4, in order to assess the performance of the proposed piezoelectric solid–shell elements, for validation purposes. This paper is closed by Section 5, which summarizes the main contributions along with some concluding remarks.

2 CONSTITUTIVE EQUATIONS AND DISCRETIZATION OF THE PROBLEM

2.1 Electromechanical constitutive equations

Piezoelectric materials have the capability of generating electricity when subjected to mechanical loading (sensors). Conversely, they also have the ability to deform under electrical charging (actuators). These properties are described by the following coupled electromechanical equations:

$$\begin{cases} \boldsymbol{\sigma} = \mathbf{C} \cdot \boldsymbol{\varepsilon} - \mathbf{e}^{T} \cdot \boldsymbol{E} \\ \boldsymbol{D} = \mathbf{e} \cdot \boldsymbol{\varepsilon} + \boldsymbol{\kappa} \cdot \boldsymbol{E} \end{cases} \tag{1}$$

where $\boldsymbol{\sigma}$ and $\boldsymbol{\varepsilon}$ represent, respectively, the vector form of the stress and strain tensors; $\boldsymbol{D}$ and $\boldsymbol{E}$ denote the electric displacement and electric field vector, respectively; while $\mathbf{C}$, $\mathbf{e}$ and $\boldsymbol{\kappa}$ stand for the elastic, piezoelectric and dielectric permittivity matrix, respectively.

The discretized forms $\{\boldsymbol{\varepsilon}\}$ and $\{\boldsymbol{E}\}$ for the strain tensor and the electric field vector are related, respectively, to the discretized displacement $\{\boldsymbol{u}\}$ and to the discretized electric potential $\{\boldsymbol{\phi}\}$, using the discrete gradient operators $\left[\mathbf{B}^{u}\right]$ and $\left[\mathbf{B}^{\phi}\right]$, as follows:

$$\begin{cases} \{\boldsymbol{\varepsilon}\} = \left[\mathbf{B}^{u}\right]\{\boldsymbol{u}\} \\ \{\boldsymbol{E}\} = -\left[\mathbf{B}^{\phi}\right]\{\boldsymbol{\phi}\} \end{cases} \tag{2}$$

In the current contribution, the discrete gradient operators $\left[\mathbf{B}^{u}\right]$ and $\left[\mathbf{B}^{\phi}\right]$ are obtained by finite element discretization for each of the proposed piezoelectric solid–shell formulations SHB15E and SHB20E, as will be shown in Section 3 (see [18, 19] for more details).

2.2 Discretized problem

The variational principle pertaining to piezoelectric materials, which provides the governing equations for the associated boundary value problem, is described by the Hamilton principle [7]. In this weak form of equations of motion, the Lagrangian and the virtual work are appropriately adapted to include the electrical contributions, in addition to the more classical mechanical fields

$$\begin{aligned} &-\int_V \rho\ddot{\boldsymbol{u}}\cdot\delta\boldsymbol{u}\,dv - \int_V \boldsymbol{\sigma}\cdot\delta\boldsymbol{\varepsilon}\,dv + \int_V \boldsymbol{f}_v\cdot\delta\boldsymbol{u}\,dv + \int_S \boldsymbol{f}_s\cdot\delta\boldsymbol{u}\,ds + \boldsymbol{f}_p\cdot\delta\boldsymbol{u} \\ &= -\int_V \boldsymbol{D}\cdot\delta\boldsymbol{E}\,dv + \int_V \boldsymbol{q}_v\cdot\delta\boldsymbol{\phi}\,dv + \int_S \boldsymbol{q}_s\cdot\delta\boldsymbol{\phi}\,ds + \boldsymbol{q}_p\cdot\delta\boldsymbol{\phi} \end{aligned} \tag{3}$$

where ρ is the material density; $\boldsymbol{q}_v$, $\boldsymbol{q}_s$ and $\boldsymbol{q}_p$ denote volume, surface and point charge, respectively; while $\boldsymbol{f}_v$, $\boldsymbol{f}_s$ and $\boldsymbol{f}_p$ represent volume, surface and point force, respectively.

The finite element discretization of the boundary value problem governed by Eq. (3) generally leads to the following system of discretized equations:

$$\begin{cases} \left[\mathbf{M}^{uu}\right]\{\ddot{\boldsymbol{U}}\} + \left[\mathbf{K}^{uu}\right]\{\boldsymbol{U}\} + \left[\mathbf{K}^{u\phi}\right]\{\boldsymbol{\phi}\} = \{\boldsymbol{F}\} \\ \left[\mathbf{K}^{\phi u}\right]\{\boldsymbol{U}\} + \left[\mathbf{K}^{\phi\phi}\right]\{\boldsymbol{\phi}\} = \{\boldsymbol{Q}\} \end{cases} \tag{4}$$

where all matrices and vectors involved in Eq. (4) are explicitly defined in Table 1.

Table 1: Explicit forms for the vectors and matrices resulting from electromechanical coupling

$\left[\mathbf{M}^{uu}\right] = \int_V \left[\boldsymbol{N}^u\right]^T \rho \left[\boldsymbol{N}^u\right] dv$	Mass matrix
$\left[\mathbf{K}^{uu}\right] = \int_V \left[\mathbf{B}^u\right]^T [\mathbf{C}] \left[\mathbf{B}^u\right] dv$	Stiffness matrix
$\left[\mathbf{K}^{\phi\phi}\right] = -\int_V \left[\mathbf{B}^\phi\right]^T [\boldsymbol{\kappa}] \left[\mathbf{B}^\phi\right] dv$	Dielectric matrix
$\left[\mathbf{K}^{u\phi}\right] = \int_V \left[\mathbf{B}^u\right]^T [\mathbf{e}]^T \left[\mathbf{B}^\phi\right] dv;\ \left[\mathbf{K}^{\phi u}\right] = \left[\mathbf{K}^{u\phi}\right]^T$	Piezoelectric coupling matrix
$\{\boldsymbol{F}\} = \int_V \left[\boldsymbol{N}^u\right]^T \{\boldsymbol{f}_v\} dv + \int_S \left[\boldsymbol{N}^u\right]^T \{\boldsymbol{f}_s\} ds + \boldsymbol{f}_p$	Force vector
$\{\boldsymbol{Q}\} = -\int_V \left[\boldsymbol{N}^\phi\right]^T \{\boldsymbol{q}_v\} dv - \int_S \left[\boldsymbol{N}^\phi\right]^T \{\boldsymbol{q}_s\} ds - \boldsymbol{q}_p$	Electrical charge vector

3 PIEZOELECTRIC SOLID–SHELL FINITE ELEMENT FORMULATIONS

The proposed quadratic piezoelectric solid–shell finite elements SHB15E and SHB20E are extensions of the quadratic prismatic and hexahedral solid–shell elements SHB15 and SHB20, which were developed in [16], based on purely mechanical modeling. The starting point for these piezoelectric extensions is the addition of one piezoelectric degree of freedom to each node of their mechanical finite element counterparts. The outline of these formulations is given in the following sections.

3.1 Kinematics and interpolation

The piezoelectric solid–shell elements SHB15E and SHB20E denote a fifteen-node prismatic element and a twenty-node one, respectively. These elements have at each of their nodes three displacement degrees of freedom as well as one electric degree of freedom. Similar to their mechanical counterparts SHB15 and SHB20, a special direction is chosen, designated as the "*thickness*", normal to the mean plane of these elements. Also, an in-plane reduced-integration rule is adopted, with $3 \times n_{\text{int}}$ integration points for the SHB15E element and $4 \times n_{\text{int}}$ for the SHB20E (see, e.g., Fig. 1, in the particular case of $n_{\text{int}} = 5$).

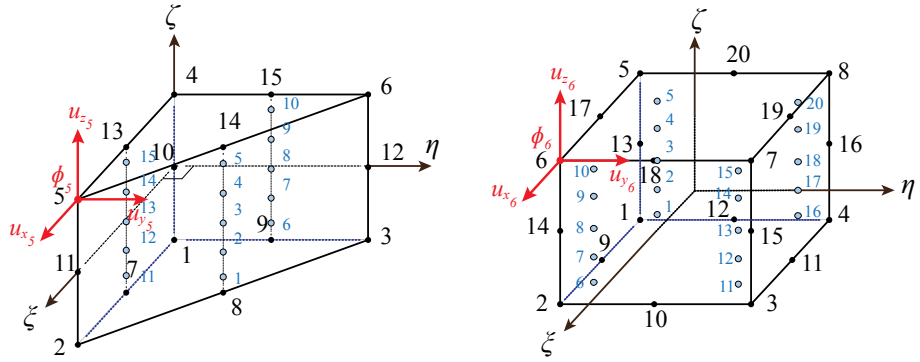

Figure 1: Schematic representation for the reference geometry of the SHB15E and SHB20E elements as well as for the location of their integration points in the case when the number of through-thickness integration points is $n_{\text{int}} = 5$

For the SHB15E and SHB20E elements, the spatial coordinates x_i are related to the nodal coordinates x_{iI} using quadratic shape functions, as follows:

$$x_i = x_{iI} N_I(\xi, \eta, \zeta) \tag{5}$$

where i represents the spatial directions and ranges from 1 to 3; while I stands for the node number, which ranges from 1 to 15, for the SHB15E element, and from 1 to 20 for the SHB20E. Likewise, the displacement field u_i and potential field ϕ are related to the nodal displacements u_{iI} and nodal potentials ϕ_I, respectively, using the shape functions

$$\begin{cases} u_i = u_{iI} N^u{}_I(\xi, \eta, \zeta) \\ \phi = \phi_I N^\phi{}_I(\xi, \eta, \zeta) \end{cases} \tag{6}$$

Note that in Eqs. (5) and (6) above, the convention of implied summation over the repeated index I has been adopted.

3.2 Discrete gradient operators

For both elements SHB15E and SHB20E, the corresponding discrete gradient operators $\left[\mathbf{B}^u\right]$ and $\left[\mathbf{B}^\phi\right]$ can be derived in the following compact form:

$$\mathbf{B}^u = \begin{bmatrix} \boldsymbol{b}_1^T + h_{\alpha,1}\boldsymbol{\gamma}_\alpha^T & \mathbf{0} & \mathbf{0} \\ \mathbf{0} & \boldsymbol{b}_2^T + h_{\alpha,2}\boldsymbol{\gamma}_\alpha^T & \mathbf{0} \\ \mathbf{0} & \mathbf{0} & \boldsymbol{b}_3^T + h_{\alpha,3}\boldsymbol{\gamma}_\alpha^T \\ \boldsymbol{b}_2^T + h_{\alpha,2}\boldsymbol{\gamma}_\alpha^T & \boldsymbol{b}_1^T + h_{\alpha,1}\boldsymbol{\gamma}_\alpha^T & \mathbf{0} \\ \boldsymbol{b}_3^T + h_{\alpha,3}\boldsymbol{\gamma}_\alpha^T & \mathbf{0} & \boldsymbol{b}_1^T + h_{\alpha,1}\boldsymbol{\gamma}_\alpha^T \\ \mathbf{0} & \boldsymbol{b}_3^T + h_{\alpha,3}\boldsymbol{\gamma}_\alpha^T & \boldsymbol{b}_2^T + h_{\alpha,2}\boldsymbol{\gamma}_\alpha^T \end{bmatrix} \quad ; \quad \mathbf{B}^\phi = \begin{bmatrix} \boldsymbol{b}_1^T + h_{\alpha,1}\boldsymbol{\gamma}_\alpha^T \\ \boldsymbol{b}_2^T + h_{\alpha,2}\boldsymbol{\gamma}_\alpha^T \\ \boldsymbol{b}_3^T + h_{\alpha,3}\boldsymbol{\gamma}_\alpha^T \end{bmatrix} \tag{7}$$

where the expressions of $\boldsymbol{b}_j^T$, $h_{\alpha,j}$ and $\boldsymbol{\gamma}_\alpha^T$ can be found in reference [16], along with additional details on their derivation. Note again that, in Eq. (7) and in what follows, the convention of implied summation over the repeated index α is adopted, with α ranging from 1 to 11, for the SHB15E element, and from 1 to 16 for the SHB20E.

Similar to the purely mechanics-based solid–shell elements SHB15 and SHB20 (see, e.g., [16]), the benchmark tests performed with the piezoelectric solid–shell counterparts SHB15E and SHB20E did not reveal any particular locking and, accordingly, no specific enhanced assumed strain techniques have been applied to these quadratic solid–shell elements.

4 NUMERICAL TESTS AND DISCUSSIONS

In this Section, a set of representative plate and shell benchmark tests is conducted to evaluate the performance of the proposed piezoelectric solid–shell finite elements.

4.1 Shape control of square plate with piezoelectric patch models

One important advantage taken from the piezoelectric behavior is in the application to the shape control of structures. In order to show the interest of solid–shell finite elements in this type of modeling, we consider a square aluminum plate of 200×200 mm^2 with a thickness of 8 mm. This plate is covered on both sides with a pair of localized PZT-5H patches, as shown in Fig. 2. Each patch has dimensions of 80×80 mm^2 with a thickness of 1 mm. The material parameters are reported in Table 2. With regard to loading conditions, the plate is subjected to a uniformly distributed load of 100 N.m^{-2} over its entire surface. A constant voltage is then supplied incrementally to the PZT-5H actuators, which are polarized in opposite directions, until the plate is flattened. Fig. 3 shows the magnitude of deflection of the composite plate under different applied input voltages. The results provided by the solid–shell elements SHB15E and SHB20E are reported in Tables 3 and 4, where they are compared with the results given by the ABAQUS solid elements C3D15E and C3D20E. On the whole, it appears that fewer overall degrees of freedom (dof) are required for the proposed piezoelectric solid–shell elements to achieve convergence, as compared to ABAQUS elements.

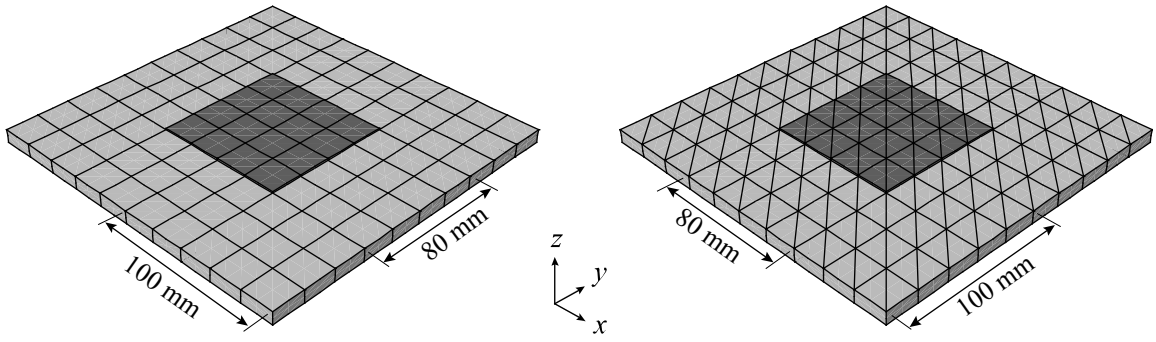

Figure 2: Schematic representation of the square plate with piezoelectric patches meshed with SHB15E and SHB20E elements

Table 2: Material properties used for all simulations

PZT-5H	$C_{11} = C_{22} = 127.2$ GPa ; $C_{33} = 117.4$ GPa $C_{12} = 80.21$ GPa ; $C_{13} = C_{23} = 84.67$ GPa $C_{44} = C_{55} = C_{66} = 22.99$ GPa $e_{15} = e_{24} = 17.03$ C/m^2 $e_{31} = e_{32} = -6.62$ C/m^2 ; $e_{33} = 23.24$ C/m^2 $\kappa_{11} = \kappa_{22} = 1.509 \times 10^{-8}$ F/m ; $\kappa_{33} = 1.269 \times 10^{-8}$ F/m
Aluminum	E = 70.3 GPa ; $\nu = 0.345$

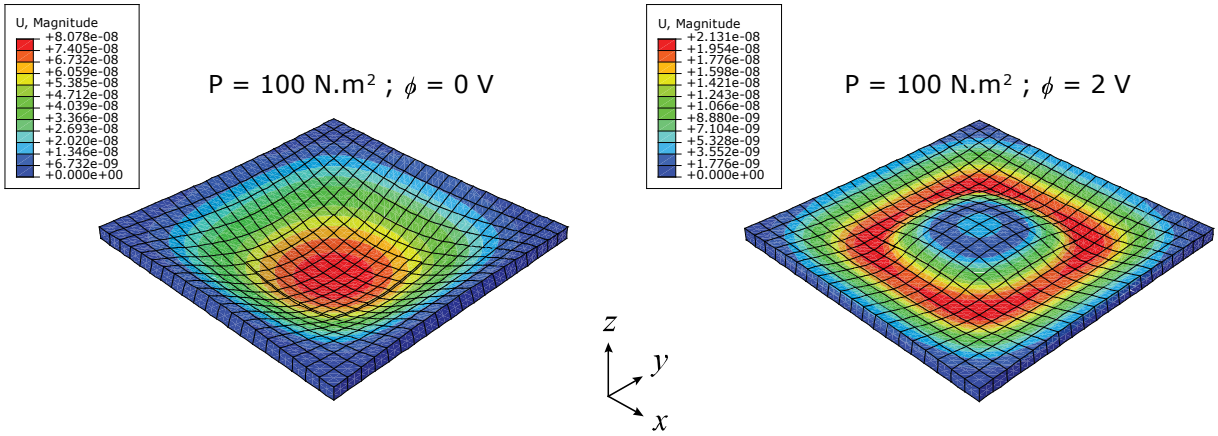

Figure 3: Shape of the plate for two different applied voltages

Table 3: Primal and dual variables for the plate shape control test (P=100N.m^2; ϕ=0V)

	C3D15E (20×20×3)×2	**SHB15E** (10×10×3)×2	**C3D20E** (20×20×3)	**SHB20E** (10×10×3)
Primal variables				
$U_z^{\max}$ (m)	8.111×10^{-8}	8.047×10^{-8}	8.078×10^{-8}	8.183×10^{-8}
Dual variables				
$\varepsilon_{zz}^{\min}$	-9.965×10^{-8}	-1.100×10^{-7}	-9.920×10^{-8}	-1.001×10^{-7}
$\varepsilon_{zz}^{\max}$	1.556×10^{-7}	1.780×10^{-7}	1.546×10^{-7}	1.832×10^{-7}
σ_{xx}^{mn} (Pa)	-6.554×10^{3}	-6.133×10^{3}	-6.233×10^{3}	-6.752×10^{3}
$\sigma_{xx}^{\max}$ (Pa)	8.100×10^{3}	7.780×10^{3}	7.892×10^{3}	7.653×10^{3}
$E_z^{\min}$ (V.m^{-1})	-9.229×10^{1}	-9.323×10^{1}	-9.240×10^{1}	-9.297×10^{1}
$E_z^{\max}$ (V.m^{-1})	9.229×10^{1}	9.323×10^{1}	9.240×10^{1}	9.292×10^{2}
$D_z^{\min}$ (C.m^{-2})	-2.961×10^{-6}	-3.094×10^{-6}	-2.950×10^{-6}	-3.026×10^{-6}
$D_z^{\max}$ (C.m^{-2})	4.782×10^{-6}	4.713×10^{-6}	4.757×10^{-6}	4.782×10^{-6}

Table 4: Primal and dual variables for the plate shape control test (P=100N.m^2; ϕ=2V)

	C3D15E (20×20×3)×2	**SHB15E** (10×10×3)×2	**C3D20E** (20×20×3)	**SHB20E** (10×10×3)
Primal variables				
$U_z^{\max}$ (m)	2.182×10^{-8}	2.220×10^{-8}	2.130×10^{-8}	2.177×10^{-8}
Dual variables				
$\varepsilon_{zz}^{\min}$	-8.962×10^{-7}	-8.987×10^{-7}	-8.749×10^{-7}	-8.954×10^{-7}
$\varepsilon_{zz}^{\max}$	9.076×10^{-7}	9.292×10^{-7}	8.971×10^{-7}	8.889×10^{-7}
σ_{xx}^{mn} (Pa)	-7.381×10^{4}	-7.488×10^{4}	-6.905×10^{4}	-7.325×10^{-4}
$\sigma_{xx}^{\max}$ (Pa)	7.039×10^{4}	6.838×10^{4}	6.827×10^{4}	7.005×10^{-4}
$E_z^{\min}$ (V.m^{-1})	-2.315×10^{3}	-2.259×10^{3}	-2.289×10^{3}	-2.122×10^{3}
$E_z^{\max}$ (V.m^{-1})	2.284×10^{3}	2.274×10^{3}	2.277×10^{3}	2.181×10^{3}
$D_z^{\min}$ (C.m^{-2})	-4.656×10^{-5}	-4.576×10^{-5}	-4.220×10^{-5}	-4.397×10^{-5}
$D_z^{\max}$ (C.m^{-2})	4.712×10^{-5}	4.677×10^{-5}	4.206×10^{-5}	4.242×10^{-5}

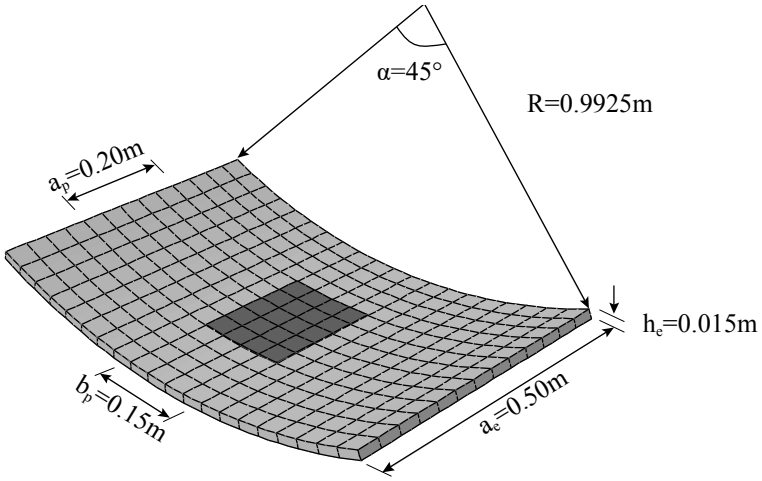

Figure 4: Schematic representation of the curved shell with piezoelectric patch meshed with C3D20E

4.2 Curved shell with piezoelectric patches

This benchmark test is inspired by the tests performed by Koconis et al. [20, 21], who proposed models for the shape control of shell structures. Here, we consider a simply supported curved shell, on top of which is bonded a localized PZT-5H patch with a thickness of 1 mm, as shown in Fig. 4. All other geometric parameters are also indicated in this figure. A constant voltage $\phi = 10$ V is then applied to the PZT-5H actuator, which is polarized in the thickness. Similar to the preview test, the results provided by the solid–shell elements SHB15E and SHB20E are compared with those given by the ABAQUS solid elements C3D15E and C3D20E. A convergence study is conducted on different variable fields in order to identify the minimum number of degrees of freedom required to achieve convergence for all variables. In Figs. 5–7, are presented the convergence curves and field maps for the tip displacement, the strain, and the electric flux, respectively. From this convergence analysis, it appears that fewer degrees of freedom are required for the proposed solid–shell finite elements to achieve convergence, as compared to ABAQUS elements. More specifically, less dof are required for the computation of primal variables, as compared to the computation of dual variables. Indeed, about 10,000 dof reveal sufficient to evaluate the displacement with an error margin smaller than 5%, whereas 10 times more dof are needed to obtain deformations and electric flux within the same margin of error.

This test also allows us to emphasize some additional advantages of the solid–shell concept, compared to standard finite elements, especially in situations where the geometry is curved.

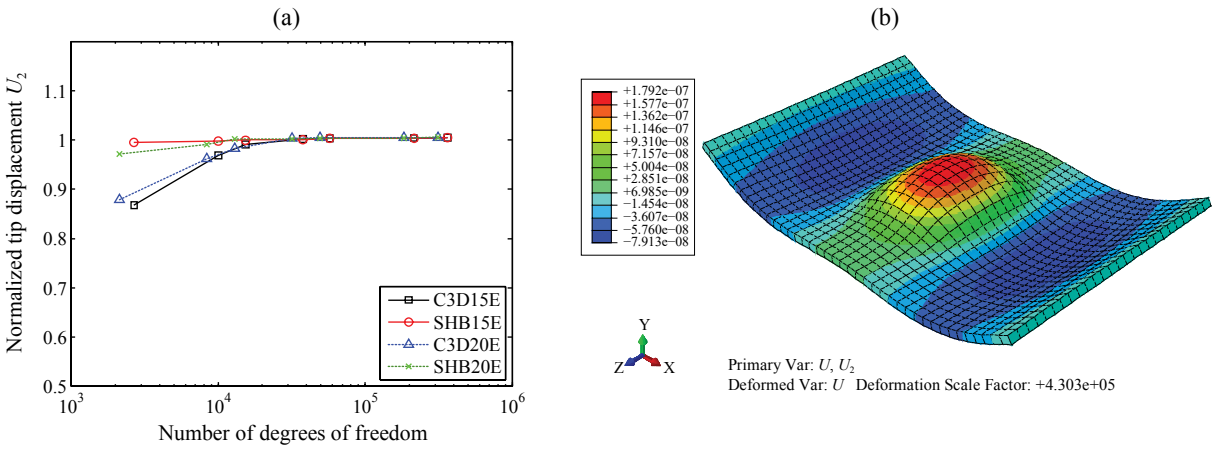

Figure 5: (a) Convergence curves and (b) Field map of displacement U_2 for the actuated curved shell

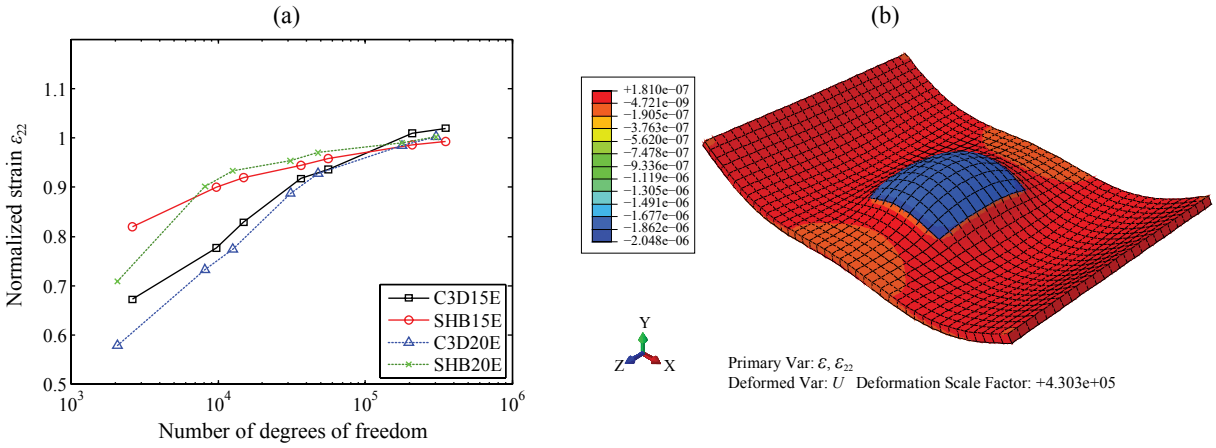

Figure 6: (a) Convergence curves and (b) Field map of strain ε_{22} for the actuated curved shell

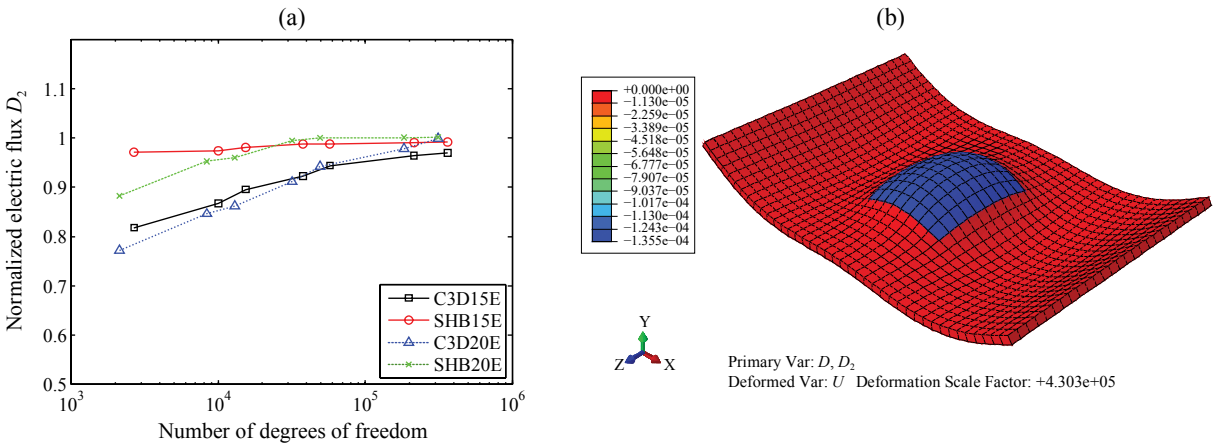

Figure 7: (a) Convergence curves and (b) Field map of electric flux D_2 for the actuated curved shell

5 CONCLUSIONS

In this paper, a performance assessment of recently proposed piezoelectric solid–shell finite elements has been presented. The analysis consists in an evaluation of primal and dual variables under electromechanical loading conditions. These investigations are conducted in the context of shape control of structures. A set of selective and representative benchmark tests has been performed on plate and shell structures, on which piezoelectric patches are bonded. The obtained simulation results have been compared to their counterparts given by state-of-the-art finite elements available in ABAQUS. In all of the benchmark tests investigated, the proposed quadratic solid–shell elements have shown better performance, as compared to their ABAQUS counterparts, while systematically necessitating much less degrees of freedom for similar accuracy. It has also been revealed that particular attention should be paid to the modeling of electromechanical coupling in order to improve the efficient computation of dual variables.

REFERENCES

[1] Belouettar, S., Azrar, L., Daya, E.M., Laptev, V. and Potier-Ferry, M. Active control of nonlinear vibration of sandwich piezoelectric beams: A simplified approach. *Computers and Structures* (2008) **86**:386-397.

[2] Nguyen, Q. and Tong, L. Voltage and evolutionary piezoelectric actuator design optimisation for static shape control of smart plate structures. *Materials & Design* (2007) **28**:387-399.

[3] Olsen, H.F. Electronic control of noise, vibration and reverberation. *Journal of the Acoustical Society of America* (1956) **28**:972-976.

[4] Duan, W.H., Wang, Q. and Quek, S.T. Applications of Piezoelectric Materials in Structural Health Monitoring and Repair: Selected Research Examples. *Materials* (2010) **3**:5169-5194.

[5] Park, G., Cudney, H. and Inman, D. Impedance-based health monitoring of civil structural components. *Journal of Infrastructure Systems* (2000) **6**:153-160.

[6] An, Y.K., Kim, M.K. and Sohn, H. Piezoelectric transducers for assessing and monitoring civil infrastructures. *Sensor Technologies for Civil Infrastructures* (2014) **55**:86-120.

[7] Allik, H. and Hughes, T.J.R. Finite element method for piezoelectric vibration. *International Journal for Numerical Methods in Engineering* (1970) **2**:151-157.

[8] Mindlin, R.D. Forced Thickness-Shear and Flexural Vibrations of Piezoelectric Crystal Plates. *Journal of Applied Physics* (1952) **23**:83-88.

[9] Plagianakos, T.S. and Papadopoulos, E.G. Higher-order 2-D/3-D layerwise mechanics and finite elements for composite and sandwich composite plates with piezoelectric layers. *Aerospace Science and Technology* (2015) **40**:150-163.

[10] Shiyekar, S.M. and Kant, T. Higher order shear deformation effects on analysis of laminates with piezoelectric fibre reinforced composite actuators. *Composite Structures* (2011) **93**:3252-3261.
[11] Robaldo, A., Carrera, E. and Benjeddou, A. A unified formulation for finite element analysis of piezoelectric adaptive plates. *Computers & Structures* (2006) **84**:1494-1505.
[12] Kulikov, G.M. and Plotnikova, S.V. Geometrically exact four-node piezoelectric solid-shell element. *Mechanics of Advanced Materials and Structures* (2008) **15**:199-207.
[13] Kulikov, G.M. and Plotnikova, S.V. The Use of 9-Parameter Shell Theory for Development of Exact Geometry 12-Node Quadrilateral Piezoelectric Laminated Solid-Shell Elements. *Mechanics of Advanced Materials and Structures* (2014) **22**:490-502.
[14] Nestorović, T., Marinković, D., Chandrashekar, G., Marinković, Z. and Trajkov, M. Implementation of a user defined piezoelectric shell element for analysis of active structures. *Finite Elements in Analysis and Design* (2012) **52**:11-12.
[15] Nestorović, T., Marinković, D., Shabadi, S. and Trajkov, M. User defined finite element for modeling and analysis of active piezoelectric shell structures. *Meccanica* (2014) **49**:1763-1774.
[16] Abed-Meraim, F., Trinh, V.D. and Combescure, A. New quadratic solid–shell elements and their evaluation on linear benchmark problems. *Computing* (2013) **95**:373-394.
[17] Abed-Meraim, F. and Combescure, A. An improved assumed strain solid-shell element formulation with physical stabilization for geometric non-linear applications and elastic-plastic stability analysis. *International Journal for Numerical Methods in Engineering* (2009) **80**:1640-1686.
[18] Kpeky, F., Abed-Meraim, F., Boudaoud, H. and Daya, E.M. Linear and quadratic solid–shell finite elements SHB8PSE and SHB20E for the modeling of piezoelectric sandwich structures. *Mechanics of Advanced Materials and Structures* (2017) http://dx.doi.org/10.1080/15376494.15372017.11285466.
[19] Kpeky, F., Abed-Meraim, F. and Daya, E.M. New linear and quadratic piezoelectric solid-shell finite elements. *Applied Mathematics and Computation,* in press (2017).
[20] Koconis, D.B., Kollár, L.P. and Springer, G.S. Shape control of composite plates and shells with embedded actuators. II. Desired shape specified. *Journal of Composite Materials* (1994) **28**:262-285.
[21] Koconis, D.B., Kollár, L.P. and Springer, G.S. Shape control of composite plates and shells with embedded actuators. I. Voltages specified. *Journal of Composite Materials* (1994) **28**:415-458.

FINITE ELEMENT ANALYSIS OF LAMINATED PIEZOELECTRIC SHELLS VIA SAMPLING SURFACES FORMULATION

S. V. PLOTNIKOVA[*], G. M. KULIKOV[*], E. CARRERA[†], A. A. MAMONTOV[*] AND S. A. MAMONTOV[*]

[*] Laboratory of Intelligent Materials and Structures
Tambov State Technical University, Sovetskaya, 106, Tambov 392000, Russia
plotnikovasvetlana62@gmail.com

[†] Department of Mechanical and Aerospace Engineering
Politecnico di Torino, Corso Duca degli Abbruzzi 24, 10129, Turin, Italy
erasmo.carrera@polito.it

Key words: Piezoelectricity, Hybrid-Mixed Solid-Shell Element, Layered Piezoelectric Shell, Sampling Surfaces Method.

Abstract. A hybrid-mixed ANS four-node piezoelectric shell element by using the sampling surfaces (SaS) technique is developed. The SaS formulation is based on choosing inside the nth layer I_n SaS located at Chebyshev polynomial nodes in order to introduce the displacements and electric potentials of these surfaces as basic shell unknowns. The interfaces and outer surfaces are also included into a set of SaS. Such choice of unknowns with the consequent use of Lagrange polynomials of degree $I_n - 1$ in the thickness direction for displacements, strains, electric potential and electric field allows the presentation of the laminated piezoelectric shell formulation in a very compact form. To implement the efficient analytical integration throughout the element, the enhanced ANS method is employed. The proposed hybrid-mixed four-node piezoelectric shell element is based on the Hu-Washizu variational equation and exhibits a superior performance in the case of coarse meshes. It could be useful for the 3D stress analysis of thick and thin doubly-curved layered piezoelectric shells since the SaS formulation gives the possibility to obtain numerical solutions with a prescribed accuracy, which asymptotically approach the exact solutions of elasticity as the number of SaS tends to infinity.

1 HU-WASHIZU VARIATIONAL SAS FORMULATION

Consider a laminated shell of the thickness *h*. Let the middle surface Ω be described by orthogonal curvilinear coordinates θ_1 and θ_2, which are referred to the lines of principal curvatures of its surface. The coordinate θ_3 is oriented along the unit vector normal to the middle surface. According to the SaS concept, we choose inside the *n*th layer I_n SaS $\Omega^{(n)1}, \Omega^{(n)2},..., \Omega^{(n)I_n}$ located at Chebyshev polynomial nodes and interfaces $\Omega^{[n-1]}$ and $\Omega^{[n]}$

(see Figure 1), where the index $n = 1,2,...,N$ identifies the belonging of any quantity to the *n*th layer; *N* is the number of layers.

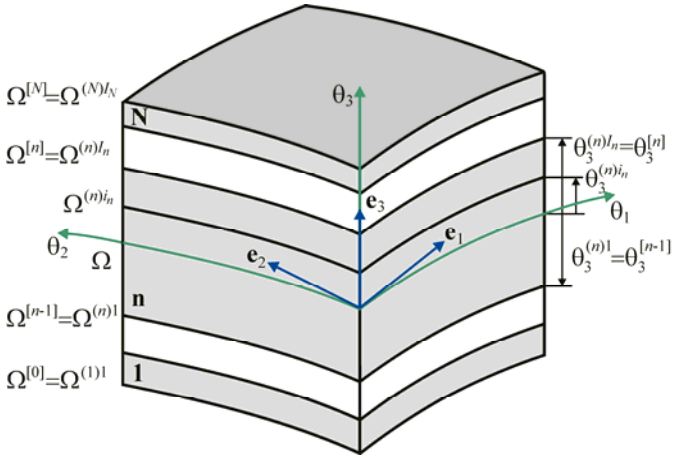

Figure 1: Geometry of the layered piezoelectric shell

The through- thickness SaS approximations [1] can be written as

$$[u_i^{(n)}\ \varepsilon_{ij}^{(n)}\ \sigma_{ij}^{(n)}\ \varphi^{(n)}\ E_i^{(n)}] = \sum_{i_n} L^{(n)i_n}[u_i^{(n)i_n}\ \varepsilon_{ij}^{(n)i_n}\ \sigma_{ij}^{(n)i_n}\ \varphi^{(n)i_n}\ E_i^{(n)i_n}], \tag{1}$$

where $u_i^{(n)}, \varepsilon_{ij}^{(n)}, \sigma_{ij}^{(n)}, \varphi^{(n)}, E_i^{(n)}$ are the displacements, strains, stresses, electric potential and electric field of the *n*th layer; $u_i^{(n)i_n}, \varepsilon_{ij}^{(n)i_n}, \sigma_{ij}^{(n)i_n}, \varphi^{(n)i_n}, E_i^{(n)i_n}$ are the displacements, strains, stresses, electric potential and electric field of SaS of the *n*th layer $\Omega^{(n)i_n}$; $L^{(n)i_n}(\theta_3)$ are the Lagrange basis polynomials of degree $I_n - 1$ related to the *n*th layer:

$$L^{(n)i_n} = \prod_{j_n \neq i_n} \frac{\theta_3 - \theta_3^{(n)j_n}}{\theta_3^{(n)i_n} - \theta_3^{(n)j_n}} \quad (i_n, j_n = 1,2,...,I_n), \tag{2}$$

where the indices i_n, j_n identify the belonging of any quantity to the SaS of the *n*th layer.

The proposed hybrid-mixed piezoelectric solid-shell element is based on the Hu-Washizu variational equation of electroelasticity in which displacements, strains and stresses are utilized as independent variables [2]:

$$\delta \iint_{\Omega} \sum_{n} \int_{\theta_3^{[n-1]}}^{\theta_3^{[n]}} \left[\frac{1}{2} \eta_{ij}^{(n)} C_{ijkl}^{(n)} \eta_{kl}^{(n)} - E_k^{(n)} e_{kij}^{(n)} \eta_{ij}^{(n)} - \frac{1}{2} E_i^{(n)} \in_{ij}^{(n)} E_j^{(n)} - \sigma_{ij}^{(n)} (\eta_{ij}^{(n)} - \varepsilon_{ij}^{(n)}) \right] dV = \delta W, \tag{3}$$

where $dV = A_1 A_2 (1 + k_1\theta_3)(1 + k_2\theta_3) d\theta_1 d\theta_2 d\theta_3$ is the infinitesimal volume element; A_1, A_2 and k_1, k_2 are the coefficients of the first fundamental form and principal curvatures of the middle surface; $\theta_3^{[n-1]}$ and $\theta_3^{[n]}$ are the transverse coordinates of interfaces; $\varepsilon_{ij}^{(n)}$ and $\eta_{ij}^{(n)}$ are the displacement-dependent and displacement-independent strains; $C_{ijkl}^{(n)}$, $e_{kij}^{(n)}$ and $\in_{ij}^{(n)}$ are the

elastic, piezoelectric and dielectric constants; W is the work done by external electromechanical loads. Here, the summation on repeated Latin indices is implied.

Following the SaS technique (1), we introduce the next assumption of the hybrid-mixed solid-shell element formulation. Assume that the displacement-independent strains are distributed through the thickness of the nth layer as follows:

$$\eta_{ij}^{(n)} = \sum_{i_n} L^{(n)i_n} \eta_{ij}^{(n)i_n}, \tag{4}$$

where $\eta_{ij}^{(n)i_n}$ are the displacement-independent strains of SaS of the nth layer.

2 FINITE ELEMENT FORMULATION

The finite element formulation is based on a simple interpolation of the shell via exact geometry four-node piezoelectric solid-shell elements

$$u_i^{(n)i_n} = \sum_r N_r u_{ir}^{(n)i_n}, \quad \varphi^{(n)i_n} = \sum_r N_r \varphi_r^{(n)i_n}, \tag{5}$$

where $N_r(\xi_1, \xi_2)$ are the bilinear shape functions of the element; $u_{ir}^{(n)i_n}$ and $\varphi_r^{(n)i_n}$ are the displacements and electric potentials of SaS $\Omega^{(n)i_n}$ at element nodes; ξ_1, ξ_2 are the normalized curvilinear coordinates θ_1, θ_2; the nodal index r runs from 1 to 4. The term "exact geometry" reflects the fact that the parametrization of the middle surface is known a priori and, therefore, the coefficients of the first and second fundamental forms are taken exactly at element nodes.

To implement the efficient analytical integration throughout the element, the enhanced ANS method is employed:

$$\varepsilon_{ij}^{(n)i_n} = \sum_r N_r \varepsilon_{ijr}^{(n)i_n}, \quad E_i^{(n)i_n} = \sum_r N_r E_{ir}^{(n)i_n}, \tag{6}$$

where $\varepsilon_{ijr}^{(n)i_n}$ and $E_{ir}^{(n)i_n}$ are the displacement-dependent strains and electric field of SaS of the nth layer at element nodes. The main idea of such approach can be traced back to the ANS method developed by many scientists for the isoparametric finite element formulation. In contrast with above formulation, we treat the term "ANS" in a broader sense. In the proposed exact geometry four-node solid-shell element formulation, all components of the displacement-dependent strain tensor and electric field vector are assumed to vary bilinearly throughout the biunit square in (ξ_1, ξ_2)-space.

To overcome shear and membrane locking and have no spurious zero energy modes, the robust strain and stress interpolations [3] are utilized:

$$\left[\eta_{11}^{(n)i_n} \ \eta_{22}^{(n)i_n} \ \eta_{33}^{(n)i_n} \ \eta_{12}^{(n)i_n} \ \eta_{13}^{(n)i_n} \ \eta_{23}^{(n)i_n}\right]^{\mathrm{T}} = \mathbf{P}\,\boldsymbol{\Psi}^{(n)i_n}, \quad \boldsymbol{\Psi}^{(n)i_n} = \left[\Psi_1^{(n)i_n} \ \Psi_2^{(n)i_n} \ \ldots \ \Psi_{12}^{(n)i_n}\right]^{\mathrm{T}}, \tag{7}$$

$$\left[\sigma_{11}^{(n)i_n} \ \sigma_{22}^{(n)i_n} \ \sigma_{33}^{(n)i_n} \ \sigma_{12}^{(n)i_n} \ \sigma_{13}^{(n)i_n} \ \sigma_{23}^{(n)i_n}\right]^{\mathrm{T}} = \mathbf{P}\boldsymbol{\Xi}^{(n)i_n}, \quad \boldsymbol{\Xi}^{(n)i_n} = \left[\Xi_1^{(n)i_n} \ \Xi_2^{(n)i_n} \ \ldots \ \Xi_{12}^{(n)i_n}\right]^{\mathrm{T}}, \tag{8}$$

$$\mathbf{P}=\begin{bmatrix} 1 & 0 & 0 & 0 & 0 & 0 & \xi_2 & 0 & 0 & 0 & 0 & 0 \\ 0 & 1 & 0 & 0 & 0 & 0 & 0 & \xi_1 & 0 & 0 & 0 & 0 \\ 0 & 0 & 1 & 0 & 0 & 0 & 0 & 0 & \xi_1 & \xi_2 & 0 & 0 \\ 0 & 0 & 0 & 1 & 0 & 0 & 0 & 0 & 0 & 0 & 0 & 0 \\ 0 & 0 & 0 & 0 & 1 & 0 & 0 & 0 & 0 & 0 & \xi_2 & 0 \\ 0 & 0 & 0 & 0 & 0 & 1 & 0 & 0 & 0 & 0 & 0 & \xi_1 \end{bmatrix}$$

that provides a correct rank of the element stiffness matrix.

Substituting first the through-thickness SaS approximations (1), (4) and then the finite element interpolations (5)-(8) into the Hu-Washizu variational equation (3), we arrive at the element equilibrium equations. Eliminating the column matrices $\mathbf{\Psi}^{(n)i_n}$ and $\mathbf{\Xi}^{(n)i_n}$ on the element level, the following system of linear equations are obtained:

$$\begin{bmatrix} \mathbf{K}_{uu} & \mathbf{K}_{u\varphi} \\ \mathbf{K}_{\varphi u} & \mathbf{K}_{\varphi\varphi} \end{bmatrix} \begin{bmatrix} \mathbf{U} \\ \mathbf{\Phi} \end{bmatrix} = \begin{bmatrix} \mathbf{F}_p \\ \mathbf{F}_q \end{bmatrix}, \tag{9}$$

where $\mathbf{K}_{uu}, \mathbf{K}_{u\varphi}, \mathbf{K}_{\varphi u}=(\mathbf{K}_{u\varphi})^{\mathrm{T}}, \mathbf{K}_{\varphi\varphi}$ are the element stiffness matrices; $\mathbf{U}$ and $\mathbf{\Phi}$ are the element displacement and electric potential vectors of order $12N_{\mathrm{SaS}}$ and $4N_{\mathrm{SaS}}$; $\mathbf{F}_p$ and $\mathbf{F}_q$ are the element-wise mechanical and electric surface vectors; $N_{\mathrm{SaS}}=\sum_n I_n - N + 1$ is the total number of SaS.

It is worth noting that the element stiffness matrices are evaluated without the expensive numerical matrix inversion that is impossible in available isoparametric hybrid-mixed finite element formulations.

3 NUMERICAL EXAMPLE

Consider a simply supported symmetric three-layer cylindrical shell with equal ply thicknesses under the imposed transverse deformation on the top surface

$$u_3^+ = u_0 \sin\frac{\pi\theta_1}{L}\cos 2\theta_2, \tag{10}$$

where L is the length of the shell and $u_0 = 10^{-8}\,\mathrm{m}$. The both outer layers are composed of the PZT-4 with the material properties given in [1, 4]. The middle layer is made of the fictitious material with the elastic constants exactly half of the PZT-4 and the piezoelectric and dielectric constants exactly double those of the PZT-4. The bottom and top surfaces are assumed to be electrically grounded. To compare the results with the exact solution of Heyliger [4], we take $L = R^+ = 0.01\mathrm{m}$, where R^+ is the radius of the top cylindrical surface.

Due to symmetry of the problem, only one octant of the shell ($L/2 \le \theta_1 \le L$, $0 \le \theta_2 \le \pi/2$) is modeled by a fine uniform mesh 48×96. To analyze the results, we introduce the following scaled variables:

$$\overline{u}_1 = 10^{11}\times u_1(L,\,0,\,z), \quad \overline{u}_3 = 10^{11}\times u_3(L/2,\,0,\,z),$$

$$\overline{\sigma}_{13} = 10^{-3} \times \sigma_{13}(L,\, 0,\, z), \quad \overline{\sigma}_{23} = 10^{-3} \times \sigma_{23}(L/2,\, \pi/4,\, z), \tag{11}$$
$$\overline{\varphi} = \varphi(L/2,\, 0,\, z), \quad \overline{D}_3 = 10^{6} \times D_3(L/2,\, 0,\, z), \quad z = \theta_3 / h.$$

Figure 2 displays the distributions of displacements, transverse shear stresses, electric potential and electric displacement in the thickness direction for different values of the slenderness ratio $S = R^{+}/h$ taking five SaS for each layer. A comparison with the exact SaS solution [1] and Heyliger's exact 3D solution [4] is also presented. These results demonstrate convincingly the high potential of the proposed hybrid-mixed SaS solid-shell element formulation. This is due to the fact that the boundary conditions on the bottom and top surfaces for transverse shear stresses and the continuity conditions at interfaces for transverse shear stresses and electric displacement are satisfied with a high accuracy.

Consider next the same symmetric three-layer cylindrical shell subjected to electric loading on the top surface whereas the bottom surface is electrically grounded:

$$\varphi^{-} = 0, \quad \varphi^{+} = \varphi_0 \sin\frac{\pi\theta_1}{L}\cos 2\theta_2, \tag{12}$$

where $\varphi_0 = 10\,\mathrm{V}$. The bottom and top surfaces of the plate are assumed to be traction free. The obtained results are compared with the exact SaS solution [1]. Figure 3 shows the through-thickness distributions of displacements, transverse shear stresses, electric potential and electric displacement (11) in the thickness direction for different slenderness ratios *S* by choosing five SaS for each layer. It is seen that the boundary conditions on the bottom and top surfaces and continuity conditions at interfaces for transverse shear stresses and electric displacement are satisfied again correctly.

ACKNOWLEDGEMENTS

This work was supported by the Russian Ministry of Education and Science (Grant No. 9.1148.2017/ПЧ and Grant No. 9.4914.2017/ВУ).

REFERENCES

[1] Kulikov, G.M. and Plotnikova, S.V. A sampling surfaces method and its application to three-dimensional exact solutions for piezoelectric laminated shells. *Int. J. Solids Struct.* (2013) **50**:1930-1943.

[2] Kulikov, G.M. and Plotnikova, S.V. The use of 9-parameter shell theory for development of exact geometry 12-node quadrilateral piezoelectric laminated solid-shell elements. *Mech. Advanced Mater. Struct.* (2015) **22**:490-502.

[3] Kulikov, G.M. and Plotnikova, S.V. Non-linear exact geometry 12-node solid-shell element with three translational degrees of freedom per node. *Int. J. Numer. Methods Eng.* (2011) **88**:1363-1389.

[4] Heyliger, P. A note on the static behavior of simply-supported laminated piezoelectric cylinders. *Int. J. Solids Struct.* (1997) **34**:3781-3794.

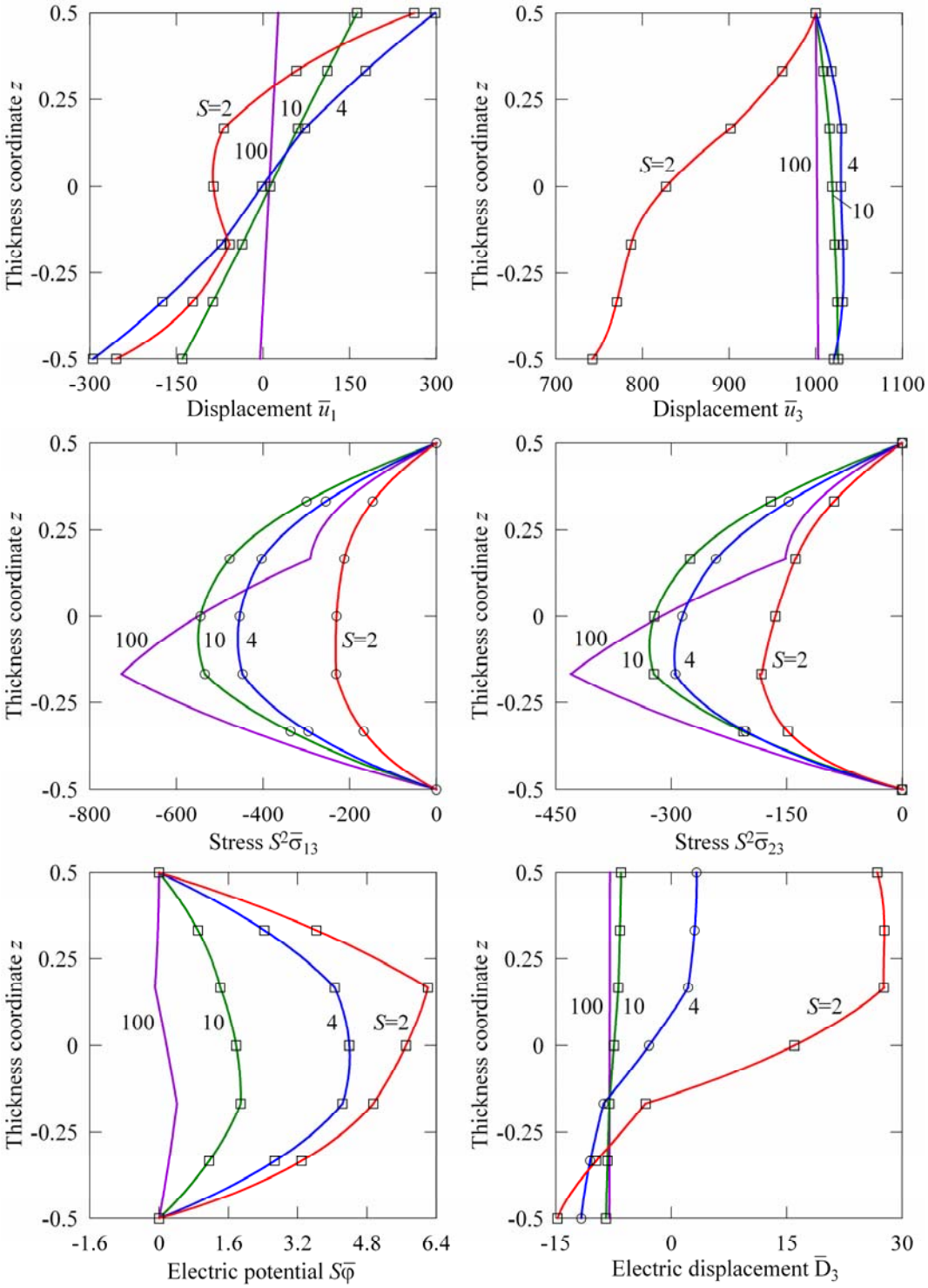

Figure 2: Through-thickness distributions of displacements, transverse shear stresses, electric potential and electric displacement for a three-layer cylindrical shell subjected to mechanical loading for $I_1 = I_2 = I_3 = 5$: exact geometry SaS solid-shell element (─), exact SaS solution [1] (○) and Heyliger's exact 3D solution [4] (□)

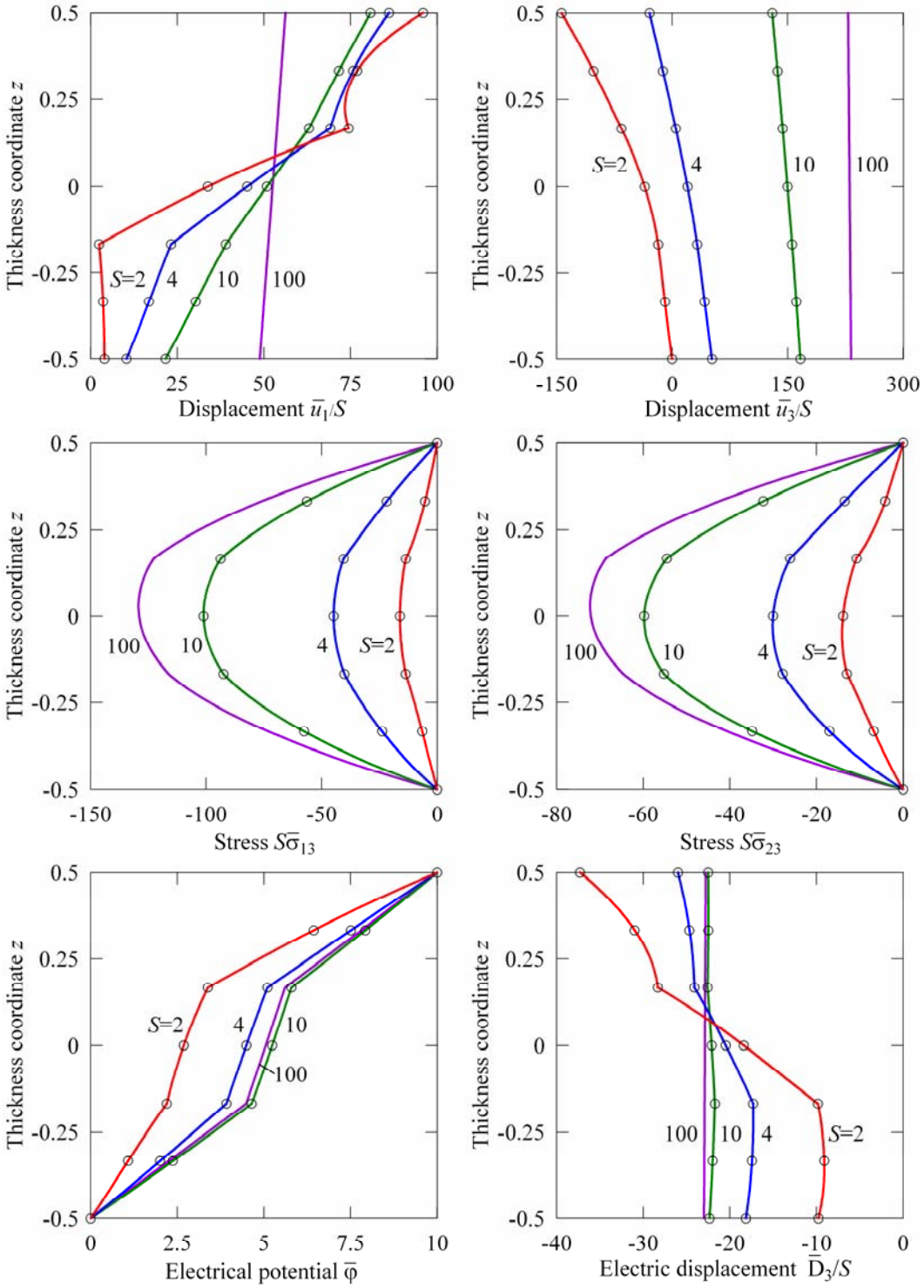

Figure 3: Through-thickness distributions of displacements, transverse shear stresses, electric potential and electric displacement for a three-layer cylindrical shell subjected to electric loading for $I_1 = I_2 = I_3 = 5$: exact geometry SaS solid-shell element (—) and exact SaS solution [1] (○)

VIII ECCOMAS Thematic Conference on Smart Structures and Materials
SMART 2017
A. Güemes, A. Benjeddou, J. Rodellar and J. Leng (Eds)

NODE-DEPENDENT KINEMATIC ONE-DIMENSIONAL FEM MODELS FOR THE ANALYSIS OF BEAMS WITH PIEZO-PATCHES

ENRICO ZAPPINO*, GUOHONG LI* AND ERASMO CARRERA*

*Department of Mechanical and Aerospace Engineering
Politecnico di Torino
Corso Duca degli Abruzzi 24, 10129, Torino, Italy
e-mail: erasmo.carrera@polito.it, web page: http://www.mul2.com

Key words: Beam element, Carrera Unified Formulation, Piezo-patch, Node-dependent kinematics

Abstract. This paper presents a new class of advanced FEM beam models with node-dependent kinematics for the analysis of beam structures with piezo-patches. ESL (Equivalent Single-layer) models and LW (Layer-wise) models each have both advantages and disadvantages considering accuracy and computational resources consumed. Refined beam elements with different kinematic descriptions from node to node are proposed to integrate ESL and LW models to reach an optimal balance between accuracy and numerical solution costs. Taking advantage of the LW kinematics defined on the cross-sections of the beam elements, local piezo-patches can be modeled without special coupling methods. The models proposed are obtained by adopting Carrera Unified Formulation (CUF), which separates the displacement field into functions defined on the cross-section of a beam and nodal shape functions depending on the axial coordinates in the context of FEM. This feature permits the definition of different kinematics on each node and the interpolation of them over the element axial domain, leading to advanced beam models with a kinematic transition. Governing equations for beam models with node-dependent kinematics accounting for electromechanical effects are derived from the Principle of Virtual Displacement (PVD). LW kinematics are used to approximate the local area with piezo-patches, and ESL models are adopted in the region with low stress gradient. The effectiveness of the proposed approach is validated by comparing the obtained results with solutions taken from literature and 3D FEM modeling.

1 INTRODUCTION

Piezoelectric materials feature a reversible process that an electrical field causes straining (direct effect) while stresses cause an electric potential (reverse effect). Such an effect has prompted the development of various "smart structures". Piezoelectric components are usually bonded to the surface or embedded into the structures to act as actuators or sensors. The

segmented distribution of piezoelectric patches will lead to local effects that need to be specially considered which raises the requirement for effective modeling approaches.

Crawley and De Luis (1987), Crawley and Anderson (1990) developed analytical models for both surface-bonded and embedded piezoelectric actuators in one-dimensional structures. Researchers also proposed various 2D models such as models based on the Classical Lamination Theory (CLT) by Lee (1990) and Wang and Rogers (1991), First-Order Shear Deformation Theory (FSDT) models by Huang and Wu (1996) and Jonnalagadda et al. (1994), as well as Higher-Order Theory (HOT) solutions by Mitchell and Reddy (1995). Vidoli and Batra (2000) used a generalization of the Hellinger-Prange-Reissner principle to derive constitutive relations and equilibrium equations for anisotropic 1D and 2D models for piezoelectric bodies.

Carrera (Carrera, 2002) proposed Unified Formulation (CUF) as a new methodology to construct refined 1D and 2D models. CUF introduces thickness functions $F_\tau(z)$ to 2D theories and $F_\tau(x,z)$ to 1D models. These functions enrich the displacement field in the through-the-thickness domain of 2D models and over the cross-section of 1D models, which can employ either series expansion or interpolation polynomials. In the framework of CUF, various theories based on both Equivalent Single Layer (ESL) and Layer-wise (LW) models can be depicted(Cinefra et al., 2015b; Cinefra and Valvano, 2016). The introduction of *fundamental nuclei* (FNs) allows the governing equations to be derived in a compact manner (Carrera et al., 2016, 2017). Based on CUF, Carrera and Fagiano (2007), Carrera et al. (2010), and Carrera and Robaldo (2010) proposed advanced plate elements with *a priori* continuous transverse electromechanical variables by applying Reissner Mixed Variational Theorem (RMVT). Cinefra et al. (2015a) adopted an axiomatic/asymptotic technique to detect the "best" plate model to capture the static response of piezoelectric plates, in which the models are constructed by employing the Principle of Virtual Displacements (PVD). Miglioretti et al. (2014) and Zappino et al. (2016) adopted refined electromechanical beam FEM models with variable kinematics in the analysis of structures with piezoelectric components, which are based on PVD.

In this work, as an innovative methodology to construct advanced FEM models, node-dependent kinematics based on CUF, is proposed, and refined one-dimensional elements for the analysis of structures with piezo-patches are presented. Variable LW/ESL kinematics from node to node are implemented in the proposed method. The capabilities of such an approach are demonstrated with a cantilever beam structure with a surface bonded piezo-patch.

2 ONE-DIMENSIONAL ELECTROMECHANICAL MODEL

2.1 Preliminaries

Considering the coupling between electronic and mechanical field, by treating the electronic potential ϕ as a primary variable, a generalized displacement vector $\boldsymbol{q}$ can be adopted:

$$\boldsymbol{q} = \{u_x, u_y, u_z, \phi\}^T \tag{1}$$

The electric field vector $\boldsymbol{E}$ is:

$$\boldsymbol{E} = \{E_x, E_y, E_z\} = \{\partial_x, \partial_y, \partial_z\}\phi \tag{2}$$

Accordingly, the generalized strain vector, $\bar{\boldsymbol{\varepsilon}}$, can be written as:

$$\bar{\boldsymbol{\varepsilon}} = \{\varepsilon_{xx}, \varepsilon_{yy}, \varepsilon_{zz}, \varepsilon_{yz}, \varepsilon_{xz}, \varepsilon_{xy}, E_x, E_y, E_z\}^T = \boldsymbol{D}\boldsymbol{q} \tag{3}$$

where the matrix of differential operator $\boldsymbol{D}$ is:

$$\boldsymbol{D} = \begin{bmatrix} \frac{\partial}{\partial x} & 0 & 0 & 0 \\ 0 & \frac{\partial}{\partial y} & 0 & 0 \\ 0 & 0 & \frac{\partial}{\partial z} & 0 \\ 0 & \frac{\partial}{\partial z} & \frac{\partial}{\partial y} & 0 \\ \frac{\partial}{\partial z} & 0 & \frac{\partial}{\partial x} & 0 \\ \frac{\partial}{\partial y} & \frac{\partial}{\partial x} & 0 & 0 \\ 0 & 0 & 0 & \frac{\partial}{\partial x} \\ 0 & 0 & 0 & \frac{\partial}{\partial y} \\ 0 & 0 & 0 & \frac{\partial}{\partial z} \end{bmatrix} \tag{4}$$

The electromechanical constitutive equations (*e-form*) in the case of the principle of virtual displacement (PVD) can be expressed as follows:

$$\begin{aligned} \boldsymbol{\sigma} &= \boldsymbol{C}\boldsymbol{\varepsilon} - \boldsymbol{e}^T\boldsymbol{E} \\ \boldsymbol{D}_e &= \boldsymbol{e}\boldsymbol{\varepsilon} + \boldsymbol{\chi}^T\boldsymbol{E} \end{aligned} \tag{5}$$

in which $\boldsymbol{D}_e$ is the electric displacement vector $\{D_x, D_y, D_z\}^T$, and $\boldsymbol{\sigma}$ is the mechanical stress vector, $\boldsymbol{C}$ the matrix of mechanical material coefficients. In this paper, the piezoelectric components used are polarized in the z direction, thus the explicit form of the dielectric permittivity matrix $\boldsymbol{\chi}$ becomes:

$$\boldsymbol{\chi} = \begin{bmatrix} \tilde{\chi}_{11} & \tilde{\chi}_{12} & 0 \\ \tilde{\chi}_{21} & \tilde{\chi}_{22} & 0 \\ 0 & 0 & \tilde{\chi}_{33} \end{bmatrix} \tag{6}$$

and the piezoelectric stiffness coefficients $\boldsymbol{e}$ will be as follows:

$$\boldsymbol{e} = \begin{bmatrix} 0 & 0 & 0 & \tilde{e}_{14} & \tilde{e}_{15} & 0 \\ 0 & 0 & 0 & \tilde{e}_{24} & \tilde{e}_{25} & 0 \\ \tilde{e}_{31} & \tilde{e}_{32} & \tilde{e}_{33} & 0 & 0 & \tilde{e}_{36} \end{bmatrix} \tag{7}$$

The generalized stress vector can be arranged as:

$$\bar{\boldsymbol{\sigma}} = \{\sigma_{xx}, \sigma_{yy}, \sigma_{zz}, \sigma_{yz}, \sigma_{xz}, \sigma_{xy}, D_x, D_y, D_z\}^T \tag{8}$$

Thus the constitutive equation can be written as:

$$\begin{Bmatrix} \sigma_{xx} \\ \sigma_{yy} \\ \sigma_{zz} \\ \sigma_{xz} \\ \sigma_{yz} \\ \sigma_{xy} \\ D_x \\ D_y \\ D_z \end{Bmatrix} = \begin{bmatrix} \tilde{C}_{11} & \tilde{C}_{12} & \tilde{C}_{13} & 0 & 0 & \tilde{C}_{16} & 0 & 0 & -\tilde{e}_{31} \\ \tilde{C}_{21} & \tilde{C}_{22} & \tilde{C}_{23} & 0 & 0 & \tilde{C}_{26} & 0 & 0 & -\tilde{e}_{32} \\ \tilde{C}_{31} & \tilde{C}_{32} & \tilde{C}_{33} & 0 & 0 & \tilde{C}_{36} & 0 & 0 & -\tilde{e}_{33} \\ 0 & 0 & 0 & \tilde{C}_{44} & \tilde{C}_{45} & 0 & -\tilde{e}_{14} & -\tilde{e}_{24} & 0 \\ 0 & 0 & 0 & \tilde{C}_{54} & \tilde{C}_{55} & 0 & -\tilde{e}_{15} & -\tilde{e}_{25} & 0 \\ \tilde{C}_{61} & \tilde{C}_{62} & \tilde{C}_{63} & 0 & 0 & \tilde{C}_{66} & 0 & 0 & -\tilde{e}_{36} \\ 0 & 0 & 0 & \tilde{e}_{14} & \tilde{e}_{15} & 0 & \tilde{\chi}_{11} & \tilde{\chi}_{12} & 0 \\ 0 & 0 & 0 & \tilde{e}_{24} & \tilde{e}_{25} & 0 & \tilde{\chi}_{21} & \tilde{\chi}_{22} & 0 \\ \tilde{e}_{31} & \tilde{e}_{32} & \tilde{e}_{33} & 0 & 0 & \tilde{e}_{36} & 0 & 0 & \tilde{\chi}_{33} \end{bmatrix} \begin{Bmatrix} \varepsilon_{xx} \\ \varepsilon_{yy} \\ \varepsilon_{zz} \\ \varepsilon_{xz} \\ \varepsilon_{yz} \\ \varepsilon_{xy} \\ E_x \\ E_y \\ E_z \end{Bmatrix} \tag{9}$$

which can be expressed in a more compact form:

$$\bar{\boldsymbol{\sigma}} = \tilde{\boldsymbol{H}}\bar{\boldsymbol{\varepsilon}} \tag{10}$$

2.2 CUF-based beam elements with node-dependent kinematics

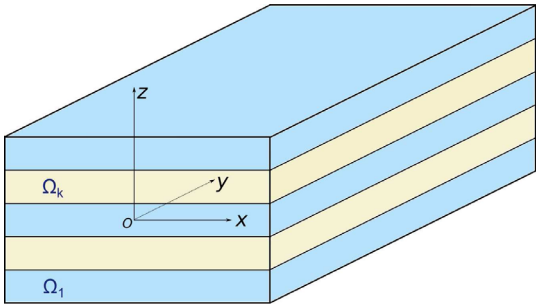

Figure 1: Geometry and reference system of a laminated beam model.

This section presents the refined one-dimensional models for electromechanical analysis. For a slender layered structure, the reference coordinate system is as shown in fig. 1. According to CUF, beam models can be refined by further expanding a generic function $F_\tau(x,z)$ defined on the cross-section, leading to the following expression:

$$\boldsymbol{q} = F_\tau(x,z)\boldsymbol{q}_\tau(y) \qquad \tau = 1,\cdots,M. \tag{11}$$

in which M represents the number of expansion terms, and $\boldsymbol{q}_\tau(y)$ is a vector defined along the axis of the beam. To define the cross-section functions $F_\tau(x,z)$, various theories can be employed. Two-parameter Lagrange interpolation polynomials over nine points will lead to expansions denoted as "LE9", and the explicit form of the expansions is:

$$\begin{aligned} F_\tau =& \frac{1}{4}(r^2+rr_\tau)(s^2+ss_\tau) && \tau = 1,3,5,7 \\ F_\tau =& \frac{1}{2}s_\tau^2(s^2+ss_\tau)(1-r^2)+\frac{1}{2}r_\tau^2(r^2+rr_\tau)(1-s^2) && \tau = 2,4,6,8 \\ F_\tau =& (1-r^2)(1-s^2) && \tau = 9 \end{aligned} \tag{12}$$

Taylor series expansions can also be incorporated, and the corresponding advanced models can be denoted as "TEn", where n indicates the highest order of the polynomials adopted. For more details, the reader is referred to Carrera et al. (2014). The Taylor-like expansions apply to ESL models, and Lagrange-type expansions suit LW framework.

When such models are applied to construct beam models, Lagrangian shape functions $N_i(y)$ will be used to approximate the vector of axial unknowns $\boldsymbol{q}_\tau(y)$:

$$\boldsymbol{q} = N_i(y)F_\tau(x,z)\boldsymbol{q}_{i\tau}(y) \qquad \tau = 1,\cdots,M; \quad i = 1,\cdots,N_n. \tag{13}$$

If F_τ depends on node i, a beam element with node-dependent kinematics can be constructed, whose displacement functions can be described as:

$$\boldsymbol{q} = N_i(y)F_\tau^i(x,z)\boldsymbol{q}_{i\tau}(y) \qquad \tau = 1,\cdots,M; \quad i = 1,\cdots,N_n. \tag{14}$$

In fig. 2 a beam element with four nodes formulated with node-dependent kinematics is shown. With the help of the Lagrangian shape functions, individually defined nodal kinematics can be interpolated over the axial domain of a beam element, obtaining elements with variable LW/ESL cross-section kinematics from node to node.

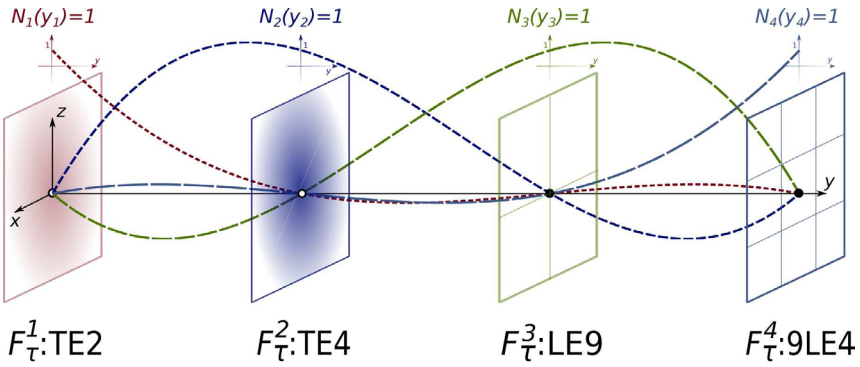

Figure 2: A B4 element with node-dependent kinematics.

2.3 Electromechanical governing equations for refined beam elements

The stiffness of the beam elements, as well as the external load vector, can be derived by applying the Principle of Virtual Displacement (PVD). By substituting the constitutive equations, the following expression can be attained:

$$\delta L_{int} = \int_V \delta \bar{\boldsymbol{\varepsilon}}^T \bar{\boldsymbol{\sigma}} dV = \delta L_{ext} \tag{15}$$

If the geometrical relations and shape functions are substituted into the above expression, one can obtain:

$$\delta L_{int} = \delta \boldsymbol{q}_{i\tau} \int_V N_i \boldsymbol{I} F_\tau^i \boldsymbol{D}^T \tilde{H} \boldsymbol{D} F_s^j \boldsymbol{I} N_j dV \boldsymbol{q}_{sj} = \delta L_{ext} \tag{16}$$

in which $\boldsymbol{I}$ is a 4×4 identity matrix. In a more compact form, the above expression can be written as:

$$\delta L_{int} = \delta \boldsymbol{q}_{\tau i}^T \boldsymbol{K}_{ij\tau s} \boldsymbol{q}_{sj} \tag{17}$$

where $\boldsymbol{K}_{ij\tau s}$ is the stiffness matrix, which as also known as *fundamental nucleus*, whose explicit expression is:

$$\boldsymbol{K}_{ij\tau s} = \int_V N_i \boldsymbol{I} F_\tau^i \boldsymbol{D}^T \tilde{H} \boldsymbol{D} F_s^j \boldsymbol{I} N_j dV \tag{18}$$

The external work due to the concentrated load $\boldsymbol{P}$ can be expressed as:

$$\delta L_{ext} = \boldsymbol{P} \delta \boldsymbol{q}^T \tag{19}$$

By substituting the FEM displacement functions, the external work can be written as:

$$\delta L_{ext} = F_{\tau}^{i} N_i \boldsymbol{P} \delta \boldsymbol{q}_{\tau i}^{T} \tag{20}$$

2.4 Modeling of piezo-patches with node-dependent kinematics

The modeling of the piezo-patches with CUF-based node-dependent kinematics has been illustrated in fig. 3. Taking advantage of the framework of LW models and Lagrange expansions, different integration domains can be separately defined then connected by the expansions defined at the domain interfaces.

In this example, the cross-sectional nodes belong to the piezoelectric zone have an extra degree of freedom for electric potential except for the mechanical ones. Thus the FNs of electromechanical stiffness are 4×4, while for those nodes only lie in the mechanical zone the mechanical FNs of the stiffness have the shape of 3×3. At the same time, the nodes located at the interface (between the piezoelectric patch and the mechanical structure) possesses four degrees of freedom, but only the mechanical ones will be considered for the integration to obtain the stiffness. On the other hand, in the region without the piezoelectric patch, variable nodal ESL(TE)/LW(LE) kinematics can be adopted to reduce the total computational expenses.

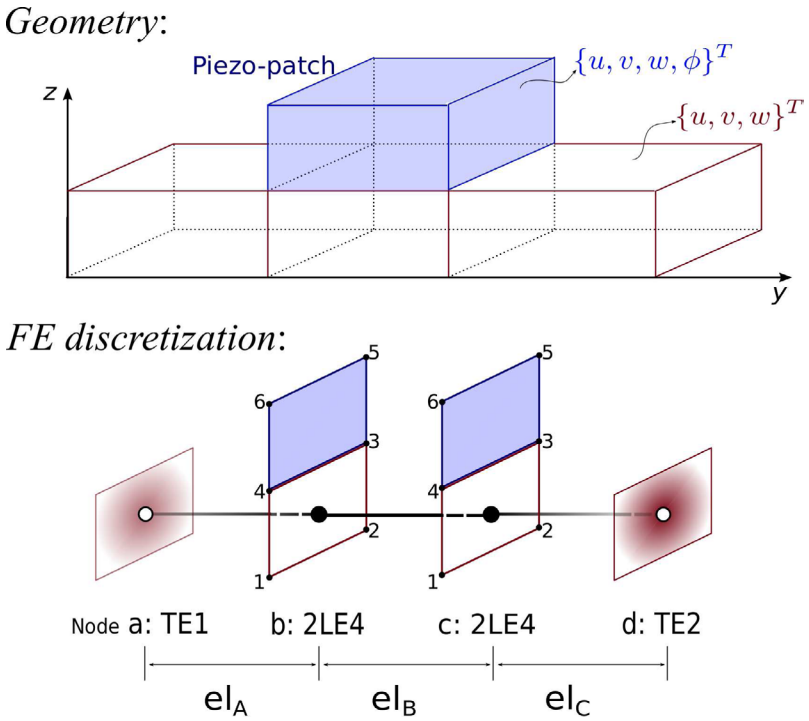

Figure 3: FEM modeling of piezoelectric patches with node-dependent kinematics.

3 NUMERICAL RESULTS

A slender aluminum beam actuated by a PZT piezoelectric patch is considered in this section as a numerical assessment case, of which the reference solution is provided by Biscani et al.

(2012). The geometry feature of the structure is shown in fig. 4, which has width $a = 0.01$m and length $b = 0.1$m. The thickness of the aluminum beam and the piezo-patch are 0.002m and 0.001m, respectively. The square piezo-patch made of PZT-4 (refer to table 1 for the material properties) is bonded to the top surface of the aluminum beam on the clamped end, which takes up the whole width range. In this assessment case, the piezo-patch acts as an actuator, and an electric potential of 1 V is defined on its top surface and 0 V on the bottom.

The FEM discretization scheme of the structure has been illustrated in fig. 4. The slender structure is divided into three zones along the axial direction y, and in the zones contain and neighboring the piezo-patch, $2 \times m$ uniformly distributed B4 elements are assigned, while in the rest 80% of the structure another m B4 elements are employed. Thus $3 \times m$ refined B4 elements will be adopted to capture the response of the structure. Except for mono-models with only LE expansions, TE kinematics will also be used in the less-critical region, which will lead to a reduction of the computational costs.

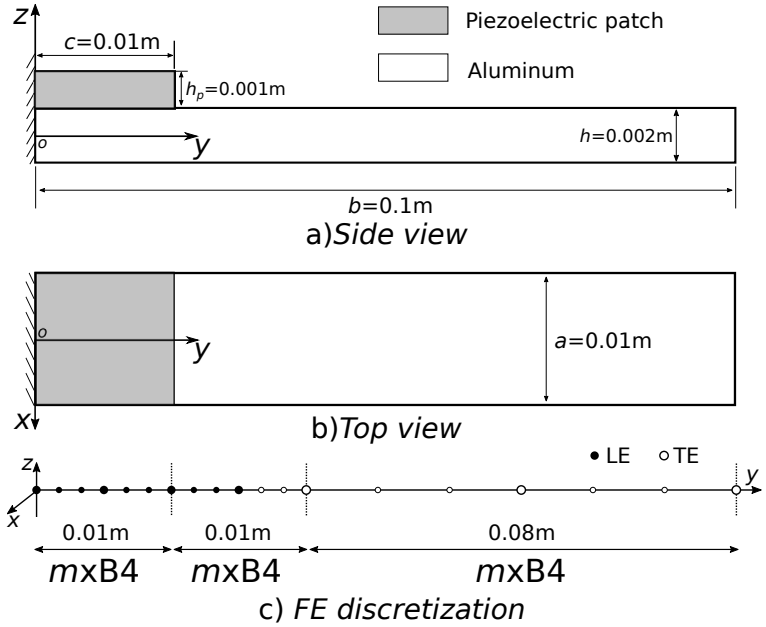

Figure 4: Geometrical feature and FEM discretization of a slender beam with piezo-patch.

Table 1: Material properties of PZT-4

E_1,E_2 [GPa]	E_3 [GPa]	G_{12} [GPa]	G_{13},G_{23} [GPa]	ν_{12}	ν_{13}, ν_{23}	e_{31},e_{32} [C/m^2]	e_{33} [C/m^2]	e_{15},e_{24} [C/m^2]	χ_{11},χ_{22}	χ_{33}
81.3	64.5	30.6	25.6	0.329	0.432	-5.2	15.8	12.72	$1475\chi_0$	$1300\chi_0$

Vacuum permittivity: $\chi_0 = 8.85 \times 10^{-12}$ F/m

The refined beam models adopted in this work and their results have been summarized in table 2. The convergence process with the refinement of beam mesh and the cross-sectional kinematics can be observed from the results in the table. Note that the nodal kinematics denoted in table 2 refers to the expansion functions defined on the cross-section that contains the piezo-patch, in which the piezoelectric and mechanical domain employ the same kinematics. For example, 4LE9 refers to a model uses 2LE9 in the piezoelectric cross section and another 2LE9 in the mechanical one, 2×1 $(x \times z)$ sub-domains for each. Accordingly, 16LE9 represents 4×2 $(x \times z)$ sub-domains for each cross-section. A FEM model with 24 B4 elements (73 nodes) employing uniform cross-sectional kinematics 16LE9 can guarantee the numerical convergence. Results provided by a 3D ABAQUS model are also listed for comparison, which consists of piezoelectric brick elements (C3D20RE) with the mesh of $20 \times 20 \times 10$ $(x \times y \times z)$ for the piezo-patch, and $20 \times 200 \times 10$ 3D quadratic elements with reduced integration (C3D20R) for the substrate beam. CUF-based refined models lead to results in high agreement with the ABAQUS solution as well as those by Biscani et al. (2012).

TE kinematics is applied to the region on the free end of the beam, leading to models 16LE9$^{\times 25}$-TE2$^{\times 48}$ and 16LE9$^{\times 49}$-TE2$^{\times 24}$, where the superscripts indicate the number of nodes on which the corresponding nodal kinematics are adopted. Such models with variable LW(LE)/ESL(TE) kinematics can reduce the total degrees of freedom.

From table 2 it can be observed that the refined beam models have comparable accuracy with the 3D model consists of much more refined mesh. Node-dependent kinematic beam model with variable LW(LE)/ESL(TE) capabilities 16LE9$^{\times 49}$-TE2$^{\times 24}$ can lead to results with the same accuracy level but few computational costs comparatively. Meanwhile, 16LE9$^{\times 49}$-TE2$^{\times 24}$ is more computationally economic but gives less accurate results.

Table 2: Displacement and stress evaluation on the cantilever beam with a piezo-patch.

Mesh	Kinematics	$-u_z^{\sharp}[10^{-8}\text{m}]$	$-u_z^{\diamondsuit}[10^{-8}\text{m}]$	$-\sigma_{yy}^{\dagger}$[KPa]	$-\sigma_{yz}^{\divideontimes}$[KPa]	DOFs
12×B4	4LE9	2.482	5.192	5.878	0.5149	2250
12×B4	16LE9	2.444	5.109	5.131	0.6692	12852
24×B4	16LE9	2.452	5.125	5.009	0.6612	25164
24×B4	16LE9$^{\times 25}$-TE2$^{\times 48}$	2.656	5.592	5.028	0.2979	14346
24×B4	16LE9$^{\times 49}$-TE2$^{\times 24}$	2.452	5.125	5.009	0.6612	19908
ABAQUS-3D		2.451	5.125	5.087	0.6381	196281
Biscani-2D(LD3)		2.309	4.871	–	–	–

$\sharp$ At $(x = 0, y = b/2, z = 0)$; $\diamondsuit$ at $(x = 0, y = b, z = 0)$;
$\dagger$ at $(x = 0, y = c/2, z = -h/2)$; $\divideontimes$ at $(x = a/2, y = c/2, z = 0)$.

The variation of deflection w and σ_{yy} along the axial direction is as plotted in fig. 5. For the deflection w, both 16LE9$^{\times 25}$-TE2$^{\times 48}$ and 16LE9$^{\times 49}$-TE2$^{\times 24}$ show continuous and smooth variation, but when y goes beyond the range of the refined zone, the solution provided by 16LE9$^{\times 25}$-TE2$^{\times 48}$ is comparatively inaccurate. For σ_{yy} distribution along the axis, it can be observed that when the number of nodes employing LE kinematics on the clamped end increases

from 25 to 49, a more smooth variation can be achieved and comparable accuracy with the uniform LE model can be reached.

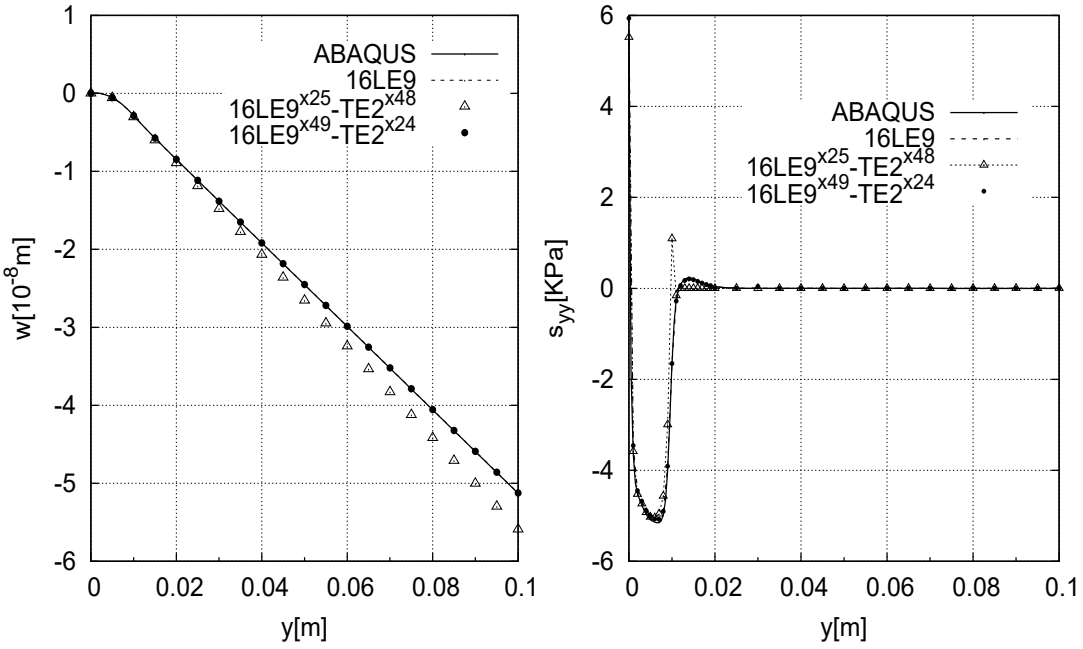

(a) w, $(0, y, 0)$ (b) σ_{yy}, $(0, y, -\frac{h}{2})$

Figure 5: Variation of w and σ_{yy} along the axis of the beam with a piezo-patch.

The contour plot of σ_{yz} on cross-section $y = c/2$ obtained with the mono-model 16LE9 is as shown in fig. 6, and its change over the thickness on the edge $(a/2, c/2, z)$ as well as $(x, c/2, 0)$ is as illustrated in fig. 7. The comparison with ABAQUS solution demonstrates that the adopted refined beam model constructed with node-dependent kinematics 16LE9$^{\times 49}$-TE2$^{\times 24}$ can provide results with satisfactory accuracy. For 16LE9$^{\times 25}$-TE2$^{\times 48}$, even if refined models are adopted in the patched range, a poor stress estimation in this region is still found because of the unfavorable transition between the peripheral zone and the refined area.

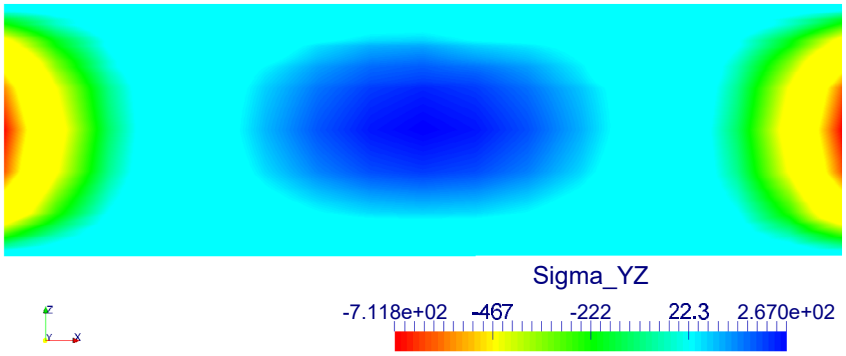

Figure 6: Contour plot of σ_{yz} on cross-section $y = c/2$ of the beam with a piezo-patch.

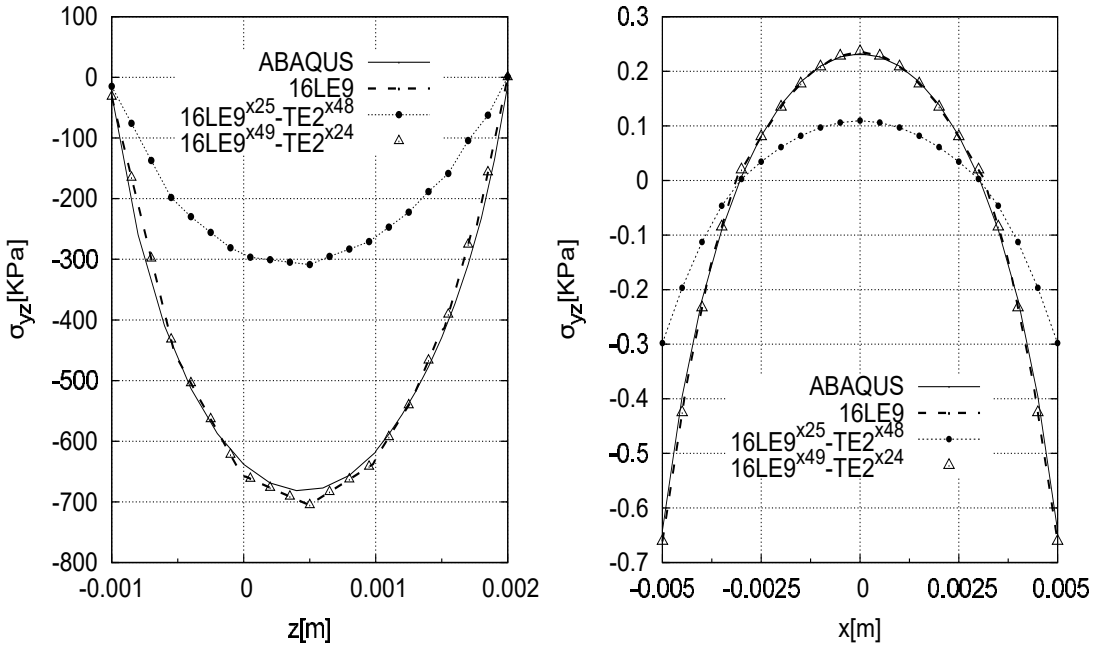

(a) σ_{yz}, $(\frac{a}{2}, \frac{c}{2}, z)$ (b) σ_{yz}, $(x, \frac{c}{2}, 0)$

Figure 7: Variation of σ_{yz} on cross-section $y = c/2$ of the beam with a piezo-patch.

4 CONCLUSIONS

Based on Carrera Unified Formulation (CUF), node-dependent kinematic one-dimensional models are proposed, with which advanced beam elements accounting for piezo-patches with variable LW/ESL nodal description can be formulated. The proposed beam elements are assessed through the static analysis of a structure with a surface-bonded piezo-patch. The following conclusions can be drawn:

- Taking advantage of the individually defined cross-sectional kinematics on each node,

patches attached to the substrate structure can be considered in the framework of one-dimensional modeling while keeping the compactness of the formulation in a unified manner.

- In the proposed models, the coupled electromechanical model is only used in the domain of the piezoelectric patch, while pure mechanical constitutive relations are applied to the substrate structure, which is realized with the help of LW models adopting Lagrange expansions.

- Node-dependent kinematic beam models with variable LW/ESL capabilities can reduce the computational costs without loosing numerical accuracy for the studied structure imposed to extension actuation.

As a versatile approach, CUF-based node-dependent kinematics can be adopted in building numerically efficient FEM models for the analysis of structures with segmented piezoelectric components.

References

Biscani, F., Nali, P., Belouettar, S., and Carrera, E. (2012). Coupling of hierarchical piezoelectric plate finite elements via arlequin method. *Journal of Intelligent Material Systems and Structures*, 23(7):749–764.

Carrera, E. (2002). Theories and finite elements for multilayered, anisotropic, composite plates and shells. *Archives of Computational Methods in Engineering*, 9(2):87–140.

Carrera, E., Büttner, A., and Nali, P. (2010). Mixed elements for the analysis of anisotropic multilayered piezoelectric plates. *Journal of Intelligent Material Systems and Structures*, 21(7):701–717.

Carrera, E., Cinefra, M., and Li, G. (2017). Refined finite element solutions for anisotropic laminated plates. *Composite Structures*, pages –.

Carrera, E., Cinefra, M., Li, G., and Kulikov, G. (2016). MITC9 shell finite elements with miscellaneous through-the-thickness functions for the analysis of laminated structures. *Composite Structures*, 154:360–373.

Carrera, E., Cinefra, M., Petrolo, M., and Zappino, E. (2014). *Finite element analysis of structures through Unified Formulation*. John Wiley & Sons.

Carrera, E. and Fagiano, C. (2007). Mixed piezoelectric plate elements with continuous transverse electric displacements. *Journal of Mechanics of Materials and Structures*, 2(3):421–438.

Carrera, E. and Robaldo, A. (2010). Hierarchic finite elements based on a unified formulation for the static analysis of shear actuated multilayered piezoelectric plates. *Multidiscipline Modeling in Materials and Structures*, 6(1):45–77.

Cinefra, M., Lamberti, A., Zenkour, A. M., and Carrera, E. (2015a). Axiomatic/asymptotic technique applied to refined theories for piezoelectric plates. *Mechanics of advanced materials and structures*, 22(1-2):107–124.

Cinefra, M. and Valvano, S. (2016). A variable kinematic doubly-curved MITC9 shell element for the analysis of laminated composites. *Mechanics of Advanced Materials and Structures*, 23(11):1312–1325.

Cinefra, M., Valvano, S., and Carrera, E. (2015b). Heat conduction and thermal stress analysis of laminated composites by a variable kinematic MITC9 shell element. *Curved and Layered Structures*, 2(1).

Crawley, E. F. and Anderson, E. H. (1990). Detailed models of piezoceramic actuation of beams. *Journal of Intelligent Material Systems and Structures*, 1(1):4–25.

Crawley, E. F. and De Luis, J. (1987). Use of piezoelectric actuators as elements of intelligent structures. *AIAA journal*, 25(10):1373–1385.

Huang, J. H. and Wu, T.-L. (1996). Analysis of hybrid multilayered piezoelectric plates. *International Journal of Engineering Science*, 34(2):171–181.

Jonnalagadda, K., Blandford, G., and Tauchert, T. (1994). Piezothermoelastic composite plate analysis using first-order shear deformation theory. *Computers & structures*, 51(1):79–89.

Lee, C. (1990). Theory of laminated piezoelectric plates for the design of distributed sensors/actuators. part i: Governing equations and reciprocal relationships. *The Journal of the Acoustical Society of America*, 87(3):1144–1158.

Miglioretti, F., Carrera, E., and Petrolo, M. (2014). Variable kinematic beam elements for electro-mechanical analysis. *Smart Structures and Systems*, 13(4):517–546.

Mitchell, J. and Reddy, J. (1995). A refined hybrid plate theory for composite laminates with piezoelectric laminae. *International Journal of Solids and Structures*, 32(16):2345–2367.

Vidoli, S. and Batra, R. (2000). Derivation of plate and rod equations for a piezoelectric body from a mixed three-dimensional variational principle. In *Advances in Continuum Mechanics and Thermodynamics of Material Behavior*, pages 23–50. Springer.

Wang, B.-T. and Rogers, C. A. (1991). Laminate plate theory for spatially distributed induced strain actuators. *Journal of Composite Materials*, 25(4):433–452.

Zappino, E., Carrera, E., Rowe, S., Mangeot, C., and Marques, H. (2016). Numerical analyses of piezoceramic actuators for high temperature applications. *Composite Structures*, 151:36–46.

VIII ECCOMAS Thematic Conference on Smart Structures and Materials
SMART 2017
A. Güemes, A. Benjeddou, J. Rodellar and J. Leng (Eds)

PRESCRIPTION OF VOLTAGE VERSUS INTENSITY IN THERMOELECTRIC CELLS FOR DIFFERENT PULSE SHAPES AND THERMOELEMENT GEOMETRIES.

J.L. PÉREZ-APARICIO*, PABLO MORENO-NAVARRO†, ROBERTO PALMA‡

*Mecánica de Medios Continuos, Universitat Politècnica de València
Camino de Vera s/n, 46011 Valencia, Spain
e-mail: jopeap@mes.upv.es

† Laboratoire de Mécanique Roberval, Université de Technologie de Compiègne
Centre de Recherches Royallieu, 60200 Compiègne, France
e-mail: pablo.moreno-navarro@utc.fr

‡ Department of Mechanical Engineering and Construction, Universitat Jaume I
Avda. Sos Baynat, s/n, 12071 Castellón, Spain
email: rpalma@uji.es

Key words: Thermoelectrics, Peltier Cells, Finite Elements, Multiphysics, Electric Boundary Conditions

Abstract. Peltier cells working as heat pumps can be fed with electric intensity or with voltage, provoking the application of one of them (prescribed magnitude) irregular distributions of the other (induced magnitude). The duality of prescriptions is found both in practical applications and in analytical and numerical simulations. During steady state both prescriptions are equivalent, but under a transient situation the differences can be substantial. These differences are more complicated if realistic material properties which depend on temperature are considered, instead of the simplifying constant-temperature properties. In this work, analytical, semi-analytical and numerical studies of a Bi_2Te_3 thermocouple are performed, identifying the electric and thermal dynamic terms which are differently activated during the pulse. The thermally induced stresses in some of the situations can be above the admissible, then a complete understanding of the real outcomes is a must.

1 INTRODUCTION

The electric feeding of Peltier cells working as heat pumps in the laboratory or the industry is most often carried out with a voltage drop (voltage sources), although in some cases current (intensity) sources are also connected. The prescription of voltage V to maximize overcooling during steady state, V_{op}, s should be the most straightforward in numerical models (for instance

with the Finite Elements Method, FE), [1], [2] since this potential is the electric degree-of-freedom. But most often electric intensity is prescribed as a boundary condition in the analytical ones [3], [4] or even with the FE itself—with mixed methods or special techniques. The situation is even more complicated in simulations for pulsed (dynamic) Peltier cells, when the electric input is increased for a short period of time to briefly boost the cooling: overcooling followed by an overheating.

Since it is difficult to find closed-form solutions in the analytical developments of coupled problems, often the simplified assumption of constant material properties (CP) is considered. This implies that these properties are not function of the basic variables (most often the temperature T), which is not true in thermoelectric materials (TM) even in the normal functioning range. The same simplification is sometimes assumed when commercial FE codes, which are not easy to modify, are applied even to complicated geometries, under dynamics, non-linearities etc.

As will be shown in this work, if CP is considered the differences between both prescriptions can be significant during the transient produced by the pulse although not during steady state, for any TE geometry. If the more physical and realistic variation of properties (VP) with T is included in the model, the differences in transient are not negligible, and in some cases significant.

For a Peltier working as a heat pump, the optimal voltage to maximize cooling during steady state is quite independent of the TE geometry and only depends on the *Seebeck* coefficient and the temperature of the hot face T_h, prescribed in this work to 50 °C. However, the optimal intensity requires more complicated expressions, especially when the thermoelement (TE) is not a parallelepiped of constant cross-section. The temperature will be operated in the absolute *Kelvin* scale although in the results it will be expressed in °C.

Extensive comparisons of V, T and electric flux j_x evolutions are obtained with a special FE element developed in previous publications, see [5]; this FE is based on the research code `FEAP` [6] and the comparisons are for three different pulse shapes: step, ramp and sinusoidal. The results are explained identifying terms of fast and slow dynamics from semi-analytical and simplified formulae. Finally, and taking advantage of the full coupling of the numerical model, the induced thermal stresses are given, highlighting the differences obtained with the two prescriptions.

2 OPTIMAL VOLTAGE AND INTENSITY IN STEADY-STATE

Analytical and semi-analytical expressions to explain trends in electrical, thermal and mechanical transient distributions are developed in this section.

The optimal intensity I_{op} to maximize overcooling (to reach the minimum T in the cold face, T_{css}) under CP and for the standard parallelepiped TE geometry, is given in the classical reference [7]; for a linear TE variation, appears in [8] among other references:

$$I_{op} = \alpha\ \gamma\ T_{css}\ \phi \qquad \begin{cases} \phi = \dfrac{A}{l} & \text{Constant cross-section} \\ \phi = \left[\dfrac{1}{d_1} \ln \dfrac{A(l)}{A(0)}\right]^{-1} & \text{Linear cross-section} \end{cases} \tag{1}$$

where in the top equation A is the constant cross-sectional area of the TE in a plane perpendicular to the electric flux, l the TE length, α the coupling *Seebeck* coefficient and γ the electric conductivity; in the bottom equation d_1 is the TE slope and $A(0)$, $A(l)$ the areas of the TE ends.

Note that I_{op} is a function of only material properties and the prescribed T_h (see Eq. (10) for the expression of T_{css}), and also of the TE geometry, represented by the form factor ϕ. Other closed-form and semi-analytical expressions can be found in [8] for more general geometries.

From these results, the voltage drop (between the TE ends, ΔV) produced by a prescribed I_{op} during steady state is first studied; in turn this voltage drop is also the voltage difference ΔV_{op} which if prescribed would maximize overcooling, and the equivalence holds for any geometry. In reality, the electric field is gauged to zero on the hot face: $V_h = 0$; therefore the voltage drops can be substituted by their corresponding value.

Again from [7], the simplified one-dimensional (1D) balance of heat power under CP is:

$$Q = \alpha\ I\ T_c - \kappa\ \phi\ (T_h - T_c) \mp \frac{1}{2\ \gamma\ \phi}\ I^2 \tag{2}$$

where κ is the thermal conductivity and T_c the variable cold face temperature. The minus sign in the fraction corresponds to the TE end close to the cold face, Q_c, and the plus sign to the hot face, Q_h.

Establishing the balance of electric and thermal energies $I_{op}V_{op} = Q_h - Q_c$ and from the two equations, it is immediate to find the optimal potential between faces during steady state:

$$V_{op} = \alpha\ T_h \tag{3}$$

which only depends on the coupling property and T_h, that is, it is independent of the TE geometry—that was not the case for I_{op} in Eq. (1). This equation shows the well known fact that the sign of the voltage drop V is equal to that of α.

While these solutions are more or less straightforward under CP, it is impossible or very difficult to find closed-form solutions under VP: it is then necessary in the latter to use approximations and specific information from the FE numerical method.

3 ANALYTICAL STUDIES

Although the FE model can produce all results which are needed in this work with high accuracy, to understand the outcome of Section 4 it is necessary to gain some insight into the analytical formulation. The electric flux transport equation for thermoelectricity is from basic works, for instance [7]:

$$\boldsymbol{j} = -\gamma\ \nabla V - \alpha\gamma\ \nabla T \tag{4}$$

where $\boldsymbol{j}$ is the electric flux. The first term of the right hand side represents electric conduction (*Ohm*'s law) and the second the coupling *Seebeck*. From Eq. (4), it can be understood that for an uncoupled material the prescription of $\boldsymbol{j}$ is completely equivalent to that of V. For a coupled TM during steady state, ∇V and ∇T do not change and the equivalence holds, but during the transient state the two gradients do change with time. Then, the prescription of $\boldsymbol{j}$ or V is not equivalent due to the coupled and different nature of electric and thermal dynamics. If the material properties depend on T (as usually is the case for TM), this equivalence does not hold anymore since even *Ohm*'s law will be influenced by the thermal field trough $\gamma(T)$.

3.1 Voltage under CP with prescribed intensity

The first objective is to calculate the voltage drop along the TE under CP prescribing I—the calculation prescribing V is trivial. Integrating the one-dimensional (1D) version of Eq. (4) for a TE with constant A:

$$V = -\frac{x\ j_x}{\gamma} - \alpha\ T + C \tag{5}$$

where C is an integration constant and $j_x = I/A(x)$; x is the 1D coordinate along the TE length, with $x = 0$ defining the cold face and $x = l$ the hot face. Since the dynamics of electricity are very fast, this equation is assumed valid for both steady and transient state. The much slower thermal dynamics include the temporal variation of T and for VP also of α, γ and κ.

In standard Peltier cells the TE's are connected electrically in series and thermally in parallel with an alumina encasement and copper electric connectors both with a high κ; therefore, the T of the two TE ends can be consider very similar to those of the cold and hot faces. Then, Eq. (5) can be particularized for both TE ends and the voltage drop in the TE is:

$$V \equiv V_c - V_h = -\alpha\ T_c + \frac{l\ j_x}{\gamma} + \alpha\ T_h \tag{6}$$

When the TE is driven by prescription of electric flux or equivalently of electric intensity, at any instant of a pulse with gain $P(t)$ the increment between $V(t)$ and the V_{ss} at steady state is:

$$\left.\begin{aligned} V(t) &= \alpha\ \left[T_h - T_c(t)\right] + P(t)\ \frac{I_{op}}{\gamma\ \phi} \\ V_{ss} &= \alpha\ \left[T_h - T_{css}\right] + \frac{I_{op}}{\gamma\ \phi} \end{aligned}\right\} \Rightarrow V(t) - V_{ss} = \underbrace{\alpha\ \left[T_{css} - T_c(t)\right]}_{\texttt{S}} + \underbrace{\left[P(t) - 1\right]\ \frac{I_{op}}{\gamma\ \phi}}_{\texttt{F}} \tag{7}$$

It is interesting to note that inserting Eq. (1) into the left bottom expression $V_{ss} \equiv V_{op} = \alpha\ T_h$ is obtained as in Eq. (3), proving that there is no difference in prescribing voltage or intensity during steady state if the 1D model holds. Also, P can be function of time for a general pulse; only for the particular case of a step pulse this gain P is a piece-wise constant. Finally, in Eq. (7) the form factor ϕ has been recovered; even if the integration of Eq. (6) is more complicated when the area is not constant, the resulting Eq. (7) is exactly the same. In the right hand side of the this resulting expression, the two terms have a clear meaning:

- `S` "Slow" dynamics which depend on thermal field, in particular that of the cold face. During overcooling, $T_c(t) < T_{css}$ and V increases through the pulse (vice-versa during overheating).
- `F` "Fast" dynamics which depend on the electric field, in particular the pulse gain $P(t)$.

The differences between both dynamics are of one or two orders of magnitude if the pulse application is sudden, for instance for the step pulse in Figure 2 left. If the pulse is "smooth", for instance the one in Figure 1 right, the differences are smaller although they still exist.

If now Eq. (1) is substituted but into the resulting Eq. (7) right, an alternative expression is:

$$V(t) - V_{op} = \alpha\ \left[P(t)\ T_{css} - T_c(t)\right] \tag{8}$$

where it can be observed that for steady state, $P = 1$ and $T_c(t) = T_{css}$ automatically gives $V(t) = V_{op}$. In Eq. (8) `F` and `S` are also represented by the two right terms.

Only for comparison purposes in this subsection, when the TM is driven by prescription of voltage drop Eq. (3), directly $V(t) = P(t)\ V_{op}$ and therefore from Eq. (3):

$$V(t) - V_{op} = \alpha\ \left[P(t) - 1\right]\ T_h \tag{9}$$

which only contains `F`, proportional to the pulse. The expression of T_{css} was given in [9] as:

$$T_{css} = \frac{-1 + \sqrt{1 + 2\ T_h\ Z}}{Z} \tag{10}$$

where the figure of merit is $Z = \alpha^2\gamma/\kappa$. From this equation, it can be demonstrated that always $T_h > T_{css}$: if the contrary occurs an implication is $(\alpha^2\gamma\ T_{css})^2 < 0$, an impossible inequality. It can also be demonstrated that most often $T_h > T_c(t)$, then comparing Eqs. (8) and (9) it can be established that V prescribing I_{op} will always be lower than prescribing V_{op}, as can be seen in the top first and third of Figures 3 and 4 at the pulse maximum. Another difference between both prescriptions is the `S` term of Eq. (7) which modifies the voltage during the pulse, see the small variation of the third top plot of Figures 3.

3.2 Intensity under CP with prescribed voltage

In this subsection the electric intensity which crosses the TE during pulse is studied, under CP and prescribing V_{op}. If j_x from Eq. (6) is solved:

$$j_x = \frac{\gamma}{l}\ \Big[\alpha\ (T_c - T_h) + V_c - V_h\Big] \tag{11}$$

The next step is to calculate the difference between intensities during steady state and at a generic instant of the transient when the voltage is pulsed with $P(t)$:

$$\left.\begin{aligned} I_{op} &= \phi\ \Big[\alpha\gamma\ \big(T_{css} - T_h\big) + \gamma\ V_{op}\Big] \\ I(t) &= \phi\ \Big[\alpha\gamma\ \big(T_c(t) - T_h\big) + \gamma\ P(t)\ V_{op}\Big] \end{aligned}\right\} \Rightarrow$$
$$I(t) - I_{op} = \phi\ \Big[\underbrace{\alpha\gamma\ \big(T_c(t) - T_{css}\big)}_{\texttt{S}} + \underbrace{\big(P(t) - 1\big)\ \gamma\ V_{op}}_{\texttt{F}}\Big] \tag{12}$$

Again if Eq. (3) is inserted in the first equation, Eq. (1) is recovered, proving that both prescriptions give the same results under steady state if the 1D model holds. Both types of dynamics appear in the right hand side of the last equation. If now Eq. (3) is inserted into this last equation an equivalent expression can be written:

$$I(t) - I_{op} = \alpha\gamma\ \phi\ \Big\{T_c(t) - T_{css} + \big[P(t) - 1\big]\ T_h\Big\} \tag{13}$$

Only for comparison purposes in this subsection, when the TE is driven by prescription of I_{op}, directly from Eq. (1):

$$I(t) - I_{op} = \alpha\gamma\ \phi\ \big[P(t) - 1\big]\ T_{css} \tag{14}$$

Since the form factor ϕ is generic, this equation is valid for any TE geometry. Again considering $T_h > T_{css}$, $T_h > T_c(t)$ and that $T_c(t)$ is of the same order as T_{css}, comparing the last two equations it can be established that the $I(t)$ prescribing voltage is higher than prescribing intensity, as can be appreciated in the first Figures 3, 4, top row.

By conservation of electric charge I is always constant, but j_x will be constant only for a uniform cross-section; for an area variation along x this j_x is inversely proportional to $A(x)$, and a small transversal component appears in the lateral sides.

The analytical results developed in the previous two subsections perfectly agree with those of FE under CP (FECP) for voltage and electric flux. A parametric study has been performed for constant or variable section, several l and pulses of several shapes.

As an example, in Figure 1 left the particular case of a ramp pulse prescribing voltage under the CP hypothesis is plotted; the ordinate electric flux is the increment from the steady state I_{op}/A to the temporal value. The right figure for a sinusoidal voltage-driven pulse of the same maximum gain and duration, is also generated with FE but under the VP hypothesis (FEVP) and the agreement is also very good except when the gain is maximum. The reason for this discrepancy is that for this short TE the voltage distribution is more complicated at these instants than the quadratic assumed in the next subsection.

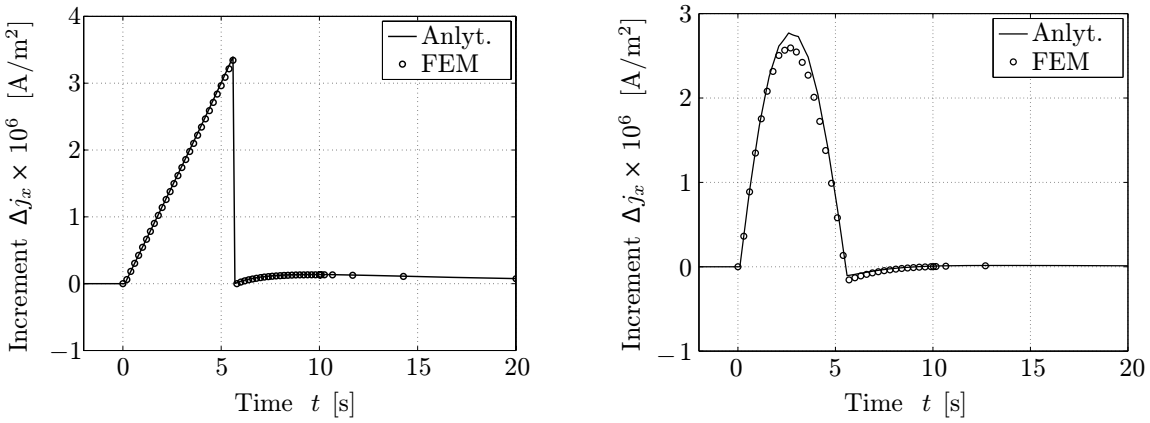

Figure 1: Increment of electric flux for constant cross-section thermoelement of length 3×10^{-3} m, voltage-prescribed pulse gain 2.5, duration 5.5 s. Ramp pulse and constant properties (left), sinusoidal pulse and variable properties (right). Analytical results from Eqs. (12), (15); Finite Element results from [9].

3.3 Electric magnitudes under VP

This subsection follows the same steps as the two previous ones, but the direct integration of the basic transport equation is not possible anymore due to the T-dependency of the material properties in the kernel. V cannot be isolated, but the Eq. (5) under prescribed voltage becomes:

$$l\ j_x = -\int_0^l \gamma(T)\ \frac{\mathrm{d}V}{\mathrm{d}x}\ \mathrm{d}x - \int_0^l \alpha(T)\ \gamma(T)\ \frac{\mathrm{d}T}{\mathrm{d}x}\ \mathrm{d}x \tag{15}$$

While the second integral depends only on the thermal field with `S`, the first couples both the electric and thermal fields and therefore influences the two dynamics: the separation is not possible anymore. This coupling did not appear under CP, Eqs. (7) and (12).

The second integral can be a function of only T changing the integration limits to $T(0) \approx T_c$ and $T(l) \approx T_h$. The VP can with good precision be expressed as quadratic polynomials, [10]:

$$\alpha(T) = \alpha_0 + \alpha_1\ T + \alpha_2\ T^2\ ; \qquad \gamma(T) = \gamma_0 + \gamma_1\ T + \gamma_2\ T^2 \tag{16}$$

and by direct integration:

$$\int_{T_c}^{T_h} \alpha(T)\ \gamma(T)\ \mathrm{d}T = \sum_{i=0}^{2}\sum_{j=0}^{2} \frac{\alpha_i\ \gamma_j}{1+i+j}\ \left(T_h^{1+i+j} - T_c^{1+i+j}\right) \tag{17}$$

The first integral cannot be expressed in terms of only V, since γ depends on T and it is not possible to -a priori- calculate $V(x)$ or a relationship between it and $T(x)$. For an approximated solution, the numerical Simpson (exact for polynomials up to the quadratic order) rule is applied:

$$\int_0^l \gamma(T)\ \frac{\mathrm{d}V}{\mathrm{d}x}\mathrm{d}x\ \approx \frac{l}{6}\ \left[\gamma(T)\ \frac{\mathrm{d}V}{\mathrm{d}x}\bigg|_{x=0} + 4\gamma(T)\ \frac{\mathrm{d}V}{\mathrm{d}x}\bigg|_{x=l/2} + \gamma(T)\ \frac{\mathrm{d}V}{\mathrm{d}x}\bigg|_{x=l}\right] \tag{18}$$

where an approximation of some values must be found with a FE run: T_c (at $x = 0$, also used for Eq. (17)) and T_m, V_m at $x = l/2$. A quadratic polynomial $V(x) = V_0 + V_1\ x + V_2\ x^2$ is adjusted from the known V_c, V_h and the obtained V_m with coefficients:

$$V_0 = V_c\ ; \qquad V_1 = \frac{-V_h + 4V_m - 3V_c}{l}\ ; \qquad V_2 = \frac{2V_h - 4V_m + 2V_c}{l^2} \tag{19}$$

With this polynomial, the derivatives of $V(x)$ are easily evaluated at the three integration points of Eq. (18). The electric conductivities at these points can also be calculated with Eq. (16) with the known T_h and the obtained T_c, T_m.

To give an idea of the voltage variations during the pulse, Figure 2 left shows the FE-calculated $V(t)$ for a TE under a step pulse of voltage prescription. At the start of the pulse V_m suddenly jumps due to `F` from Eq. (18), and its value is the average between V_c and V_h as a result of the linearity of $V(x)$ during steady state. But when the pulse progresses, the T-increase forces an approximately quadratic V-decrease. At the pulse removal, again due to `F` the voltage reduces the same amount which was increased at the start and V_m slowly returns again to the average value. Eq. (18) can now be rewritten as:

$$\int_0^l \gamma(T)\ \frac{\mathrm{d}V}{\mathrm{d}x}\mathrm{d}x\ \approx\ \frac{l}{6}\ \Big[\gamma(T_c)\ V_1 + 4\ \gamma(T_m)\ (V_1 + V_2\ l) +\ \gamma(T_h)\ (V_1 + 2\ V_2\ l)\Big] \tag{20}$$

Unlike the formulae of the previous two sections, these semi-analytical results are not directly useful since they need data from the numerical FE method, but the expressions will help differentiating slow and fast dynamics, a difficult task only with the numerical results.

To make the interpretation of Eq. (20) more difficult, T_c decreases fast during the first part of the pulse (due to *Peltier*) and increases slowly after, while T_m growths exponentially from

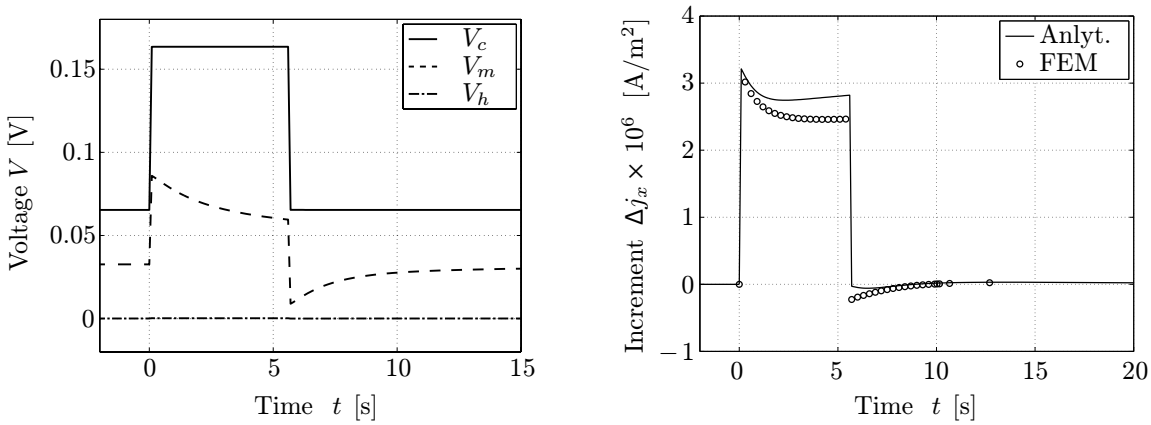

Figure 2: Voltage at bottom V_c, middle V_m and top V_h of a thermoelement (left). Electric flux increment from steady state (right, analytical Eq. (15)). For both, Finite Element results under variable properties; thermoelement length $3{\times}10^{-3}$ m, pulse gain 2.5, duration 5.5 s under prescribed voltage pulse.

the beginning (both increments due to *Joule*); V_m in Figure 2 left follows a contrary tendency to that of T_m.

The previous tendencies influence the temporal evolution of the electric flux increment, right figure. Comparisons of the semi-analytical flux from Eqs. (17), (20) with those of FEVP (considered "exact") are very good for a high $l = 7{\times}10^{-3}$ m and reasonable for short one $l = 3{\times}10^{-3}$ m during the transient (Figures 1, 2 right). The reason is that the quadratic approximation of $\mathrm{d}V/\mathrm{d}x$ is accurate enough for the long TE's but not for short ones, since the non-linearity of j_x during the pulse is much more pronounced in the latter. During steady state, the comparisons for all l are almost perfect.

The following equations relate the induced magnitude, right before the pulse application (steady state, 0^-) and right after the pulse application (beginning of transient state, 0^+) to study `F`. It is assumed that the T distribution does not change much in this very short time period. Although the results are valid for any pulse shape, the conclusions that will be described are more conclusive for a pulse with a sudden introduction of the gain (e.g. the constant-P step) to separate both dynamics.

From the two expressions inside the brace of Eqs. (7) and (12), assuming $T(0^+) \approx T_{css}$:

$$\frac{V(0^+)}{V(0^-)} = 1 + (P-1)\,\frac{T_{css}}{T_h}\,; \qquad \frac{j_x(0^+)}{j_x(0^-)} = 1 + (P-1)\,\frac{T_h}{T_{css}} \tag{21}$$

If the ratios of the two left sides are calculated with FECP and FEVP, they exactly coincide, demonstrating that `F` is the same for both material hypothesis at the pulse start. Consequently, it is `S` which causes the distribution differences between both prescriptions, fact which will be discussed in the following section. In turn, the equality between numerical (left hand side) and semi-analytical (right hand side) of both equations is almost perfect, meaning: i) the previous statement on dynamics is reinforced, ii) the analytical models are accurate within the assumed hypothesis.

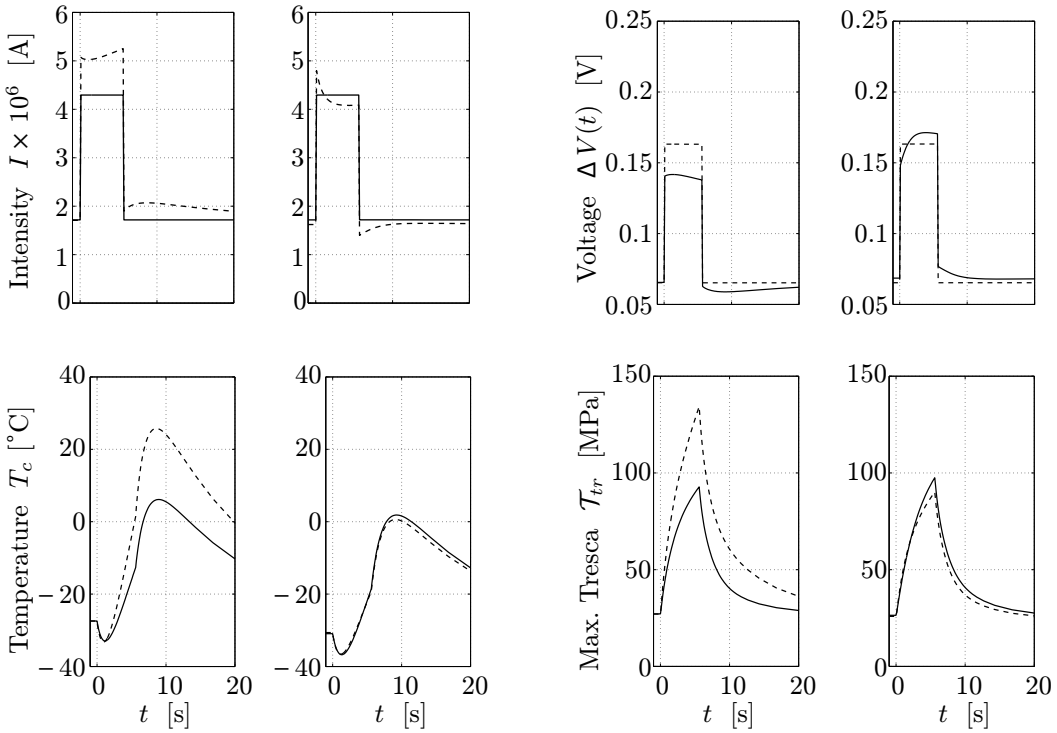

Figure 3: Temporal variations for a thermoelement of length $3{\times}10^{-3}$ m and step pulse of gain 2.5, duration 5.5 s. Finite element results, left column of each vertical pair with constant, right column with variable properties. Continuous lines for prescribed intensity, dashed for prescribed voltage.

4 TRANSIENT DISTRIBUTIONS

In the following figures, transient distributions of several electric intensity and voltage, temperature and the thermally induced Tresca stresses for the shortest TE length (the most challenging one) are presented. The studied pulses are the common step (Figure 3) and the not so common sinusoidal (Figure 4). Both pulses are prescribed starting with the steady-state value defined by either V_{op} (dashed line) or I_{op} (solid line), then applying a gain $P = 2.5$. The first and third columns are for FECP, the other two for FEVP.

The V and I distributions abruptly change at the pulse application due to `F`, and due to the coupling, the T distribution also changes. The T evolution during the transient state causes variations in the material properties of Eq. (16) when VP is considered, directly provoking additional and variable `S` from Eq. (20). Although this `S` under CP is very small compared with the `F`, under VP reaches the same order of magnitude sometime during the pulse.

It can be appreciated that under CP, the induced magnitude is always strictly above or below the prescribed: as was demonstrated in Sections 3.1, 3.2 under CP the electric energy is much higher when V is prescribed than when I is. This increase is evident in the higher intensity of the top first plot. For this reason, in the bottom first plot T during overheating is much higher with the first prescription.

Under VP the induced distribution can cross the prescribed one, and due to the additional S—responsible for the non-linearities of the induced distributions—the energy is very similar for both prescriptions. Consequently, in the bottom second figure the two T are also very similar. In spite of the strong difference in the T evolutions of the bottom first plot, the maximum T_c achieved is very similar; this is due to the limit in overcooling which a pulsed TE can achieve, no matter the amount of extra electric energy introduced, see [9].

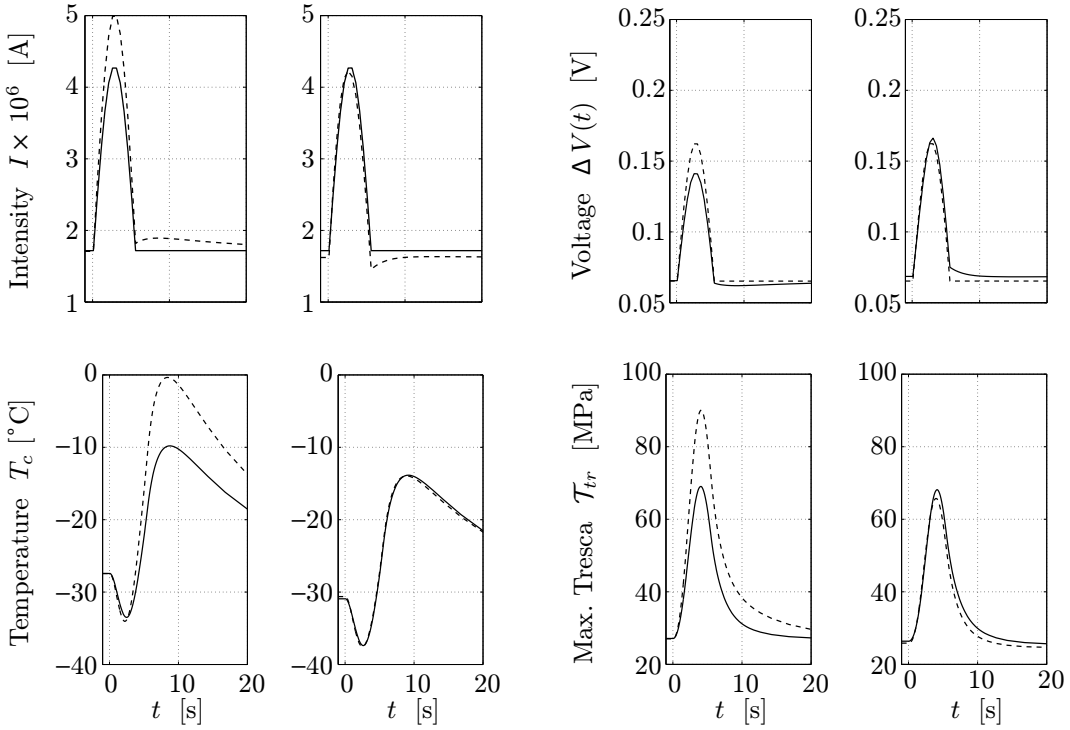

Figure 4: Temporal variations for a thermoelement of length 3×10^{-3} m and sinusoidal pulse of maximum gain 2.5, duration 5.5 s. Finite element results, left column of each pair with constant, right column with variable properties. Continuous lines for prescribed intensity, dashed for prescribed voltage.

As in Figure 2, the induced increment of magnitudes at the pulse introduction is equal to the decrement at pulse removal; this equality explains why I or V can be above or below each other at the removal.

For the non-constant, sinusoidal pulse of Figure 4, F is of the same order as S since the gain increases slowly; in this situation, it is not possible to clearly differentiate both dynamics.

Starting from the uniform initial temperature $T_0 = 20$ °C, the variation of T is a consequence of the coupling with the electric flow crossing the TE: up to a limit, the higher P the lower T_c (usually negative) but the maximum T also is higher, located near the TE middle and shifted towards to the hot face. In turn, the induced thermal stresses will be proportional to $T(x) - T_0$ and from Eq. (20) their maximums approximately to $T_m - T_0$ since the central point has a higher numerical weight than the others. In reality the thermal difference tends to produce free

strains, but in locations close to mechanical restrictions, stresses will appear. These restrictions can be due to boundary or repetition conditions or to the joint between two materials with different expansion coefficients (viz. [9]). Since the problem is completely 3D, all stress tensor components, including the shears, will be relevant.

Applying the classical failure criterion of Tresca and its equivalent stress $\mathcal{T}_{tr} = |\mathcal{T}_{I} - \mathcal{T}_{III}|$ (roman number subindices mean principal directions), the maximum $\mathcal{T}_{tr}$ occurs at the end of the pulse due the largest T increase from the *Joule* effect. The maximum stresses are located in the intersection of solder and thermocouple, near the heat sink and also in the hot spot by the TE middle. In the third and fourth bottom plots of Figure 3 it is evident that the $\mathcal{T}_{tr}$ distributions follow those of the temperature; for CP, the maximum equivalent stress (at any point of the TE) reaches a very dangerous 135 Mpa under CP and a worrying 98 Mpa under VP.

5 CONCLUSIONS

A complete study on differences between prescribing voltage or intensity in thermoelectrics has been developed. Several pulse shapes (with the same gains and durations) and thermoelement geometries have been considered, as well as material properties depending or not depending on temperature. The main conclusions are:

- In thermoelectric materials, prescribing one electric variable implies that the complementary electric variable depends not only on the prescribed magnitude as usual, but also on temperature.

- This dependency between electric and temperature creates two separated behaviors on the transient pulsed regime: fast (for electric field) and slow dynamics (for thermal field).

- Under constant material properties, it is possible to obtain closed-form expressions to describe the differences between both prescriptions. However, under variable properties further knowledge on voltage and temperature distributions is required.

- Fast dynamics are not influenced by temperature dependent properties; thus, in the case of a step pulse both dynamics can easily be discriminated at a glance in contrast to other smoother time-dependent pulse shapes. The maximum pulse gain is the critical factor in fast dynamics.

- Slow dynamics under constant material properties are not as important as under variable properties, since in the latter additional slow dynamics appear. The pulse duration is the critical factor in this type of dynamics.

- Under variable properties, dynamics are strongly influenced by the properties' dependency on temperature; for the present thermoelectric material, the particular properties help keeping the results of both prescriptions very close. Nevertheless, in other materials noticeable differences which would require specific studies could appear.

REFERENCES

[1] Huang, B.J. and Chin, C.J. and Duang, C.L. A design method of thermoelectric cooler. *Int. J. of Refrigeration* (2000) **23**:208–218.

[2] Lin, S. and Ma, M. and Wang, J. and Yu, J. Experiment investigation of a two-stage thermoelectric cooler under current pulse operation. *Applied Energy* (2016) **180**:628–636.

[3] Liu, D. and Zhao, F.Y. and Yang, H. and Tang, G.F. Theoretical and experimental investigations of thermoelectric heating system with multiple ventilation channels. *Applied Energy* (2015) **159**:458–468.

[4] Ma, M. and Yu, J. Experimental study on transient cooling characteristics of a realistic thermoelectric module under a current pulse operation. *Energy Conversion & Management* (2016) **126**:210–216.

[5] Pérez–Aparicio, J.L. and Palma, R. and Taylor, R.L. Multiphysics and thermodynamic formulations for equilibrium and non-equilibrium interactions: non-linear finite elements applied to multi-coupled active materials. *Archives of Computational Methods in Engineering* (2016) **23**:535–583.

[6] Taylor, R.L. *FEAP A Finite Element Analysis Program: User Manual, http://www.ce.berkeley.edu/feap*. University of California, Berkeley, (2010).

[7] Rowe, D.M. *CRC Handbook of Thermoelectrics*. CRC Press, (1995).

[8] Pérez-Aparicio, J.L. and Moreno-Navarro, P. and Gómez-Hernández, J.J. Combined pulse and geometry optimization for pulsed thermoelectrics using multicoupled finite elements. *Energy* (2017) **Submitted**.

[9] Pérez-Aparicio, J.L. and Palma, R. and Moreno-Navarro, P. Elasto-thermoelectric nonlinear, fully coupled, and dynamic finite element analysis of pulsed thermoelectrics. *Applied Thermal Engineering* (2016) **107**:398–409.

[10] Pérez–Aparicio, J.L. and Palma, R. and Taylor, R.L. Finite Element Analysis and Material Sensitivity of Peltier Thermoelectric Cells Coolers. *Int. J. of Heat & Mass Transfer* (2012) **55**:1363-1374.

STRONG AND WEAK SAMPLING SURFACES FORMULATIONS FOR THREE-DIMENSIONAL STRESS ANALYSIS OF PIEZOELECTRIC PLATES

GENNADY M. KULIKOV

Laboratory of Intelligent Materials and Structures
Tambov State Technical University,
Sovetskaya, 106, Tambov 392000, Russia
e-mail: gmkulikov@mail.ru

Key words: Piezoelectricity, 3D Stress Analysis, Layered Piezoelectric Plate, Sampling Surfaces Method.

Abstract. This paper focuses on implementation of the sampling surfaces (SaS) method [1] for the three-dimensional (3D) stress analysis of layered piezoelectric plates. The SaS formulation is based on choosing inside the layers the arbitrary number of not equally spaced SaS parallel to the middle surface in order to introduce the displacements and electric potentials of these surfaces as basic plate unknowns. Such choice of unknowns permits the presentation of the proposed piezoelectric plate formulation in a very compact form. The SaS are located inside each layer at Chebyshev polynomial nodes that improves the convergence of the SaS method significantly. Therefore, the SaS formulation can be applied efficiently to analytical solutions for layered piezoelectric plates, which asymptotically approach the 3D exact solutions of electroelasticity as the number of SaS tends to infinity. The strong SaS formulation is based on integrating the equilibrium equations of piezoelectricity, whereas the weak SaS formulation is based on a variational approach proposed earlier by the author [2].

1 VARIATIONAL SAS FORMULATION

Consider a layered piezoelectric plate of the thickness h. Let the middle surface Ω be described by Cartesian coordinates x_1 and x_2. The coordinate x_3 is oriented in the thickness direction. According to the SaS concept, we choose inside the nth layer I_n SaS $\Omega^{(n)1}$, $\Omega^{(n)2}$,..., $\Omega^{(n)I_n}$ parallel to the middle surface. The transverse coordinates of SaS of the nth layer located at Chebyshev polynomial nodes are written as

$$x_3^{(n)i_n} = \frac{1}{2}(x_3^{[n-1]} + x_3^{[n]}) - \frac{1}{2}h_n \cos\left(\pi \frac{2i_n - 1}{2I_n}\right), \tag{1}$$

where $x_3^{[n-1]}$ and $x_3^{[n]}$ are the transverse coordinates of interfaces $\Omega^{[n-1]}$ and $\Omega^{[n]}$; $h_n = x_3^{[n]} - x_3^{[n-1]}$ is the thickness of the nth layer; the index $n = 1,2,...,N$ identifies the belonging of any quantity to the nth layer, where N is the number of layers; the index $i_n = 1,2,...,I_n$ identifies the belonging of any quantity to the SaS of the nth layer.

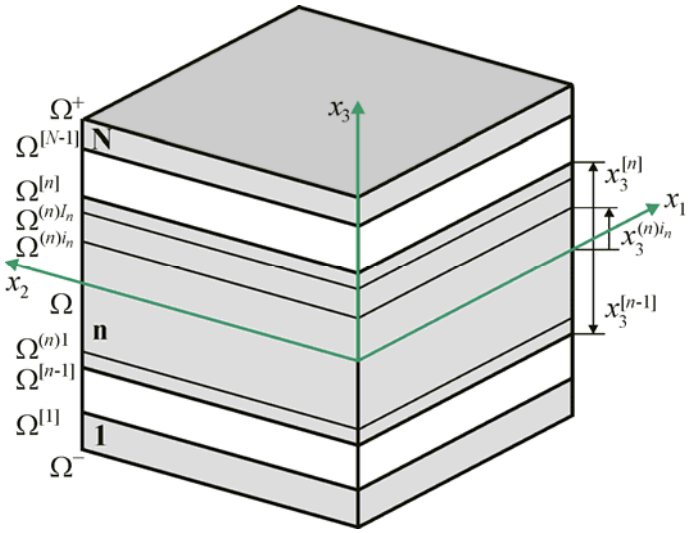

Figure 1: Geometry of the layered piezoelectric plate

The through-the-thickness SaS approximations can be expressed as

$$[u_i^{(n)}, \varepsilon_{ij}^{(n)}, \sigma_{ij}^{(n)}, \varphi^{(n)}, E_i^{(n)}, D_i^{(n)}] = \sum_{i_n} L^{(n)i_n} [u_i^{(n)i_n}, \varepsilon_{ij}^{(n)i_n}, \sigma_{ij}^{(n)i_n}, \varphi^{(n)i_n}, E_i^{(n)i_n}, D_i^{(n)i_n}], \quad (2)$$

where $u_i^{(n)}, \varepsilon_{ij}^{(n)}, \sigma_{ij}^{(n)}, \varphi^{(n)}, E_i^{(n)}, D_i^{(n)}$ are the displacements, strains, stresses, electric potential, electric field and electric displacements of the nth layer; $u_i^{(n)i_n}, \varepsilon_{ij}^{(n)i_n}, \sigma_{ij}^{(n)i_n}, \varphi^{(n)i_n}, E_i^{(n)i_n}, D_i^{(n)i_n}$ are the displacements, strains, stresses, electric potential, electric field and electric displacements of SaS of the nth layer $\Omega^{(n)i_n}$; $L^{(n)i_n}(x_3)$ are the Lagrange basis polynomials of degree $I_n - 1$ corresponding to the nth layer:

$$L^{(n)i_n} = \prod_{j_n \neq i_n} \frac{x_3 - x_3^{(n)j_n}}{x_3^{(n)i_n} - x_3^{(n)j_n}} \quad (i_n, j_n = 1, 2, ..., I_n). \quad (3)$$

The variational SaS formulation for the laminated piezoelectric plate is based on a variational equation

$$\delta \iiint_{\Omega} \sum_{n} \int_{x_3^{[n-1]}}^{x_3^{[n]}} \frac{1}{2} \left(\sigma_{ij}^{(n)} \varepsilon_{ij}^{(n)} - D_i^{(n)} E_i^{(n)} \right) dx_1 dx_2 dx_3 = \delta W, \quad (4)$$

where W is the work done by external electromechanical loads. Here, the summation on repeated Latin indices is implied.

2 STRONG SAS FORMULATION

For simplicity, we consider the case of linear piezoelectric materials given by

$$\sigma_{ij}^{(n)} = C_{ijkl}^{(n)} \varepsilon_{kl}^{(n)} - e_{kij}^{(n)} E_k^{(n)}, \quad D_i^{(n)} = e_{ikl}^{(n)} \varepsilon_{kl}^{(n)} + \in_{ik}^{(n)} E_k^{(n)}, \quad (5)$$

where $C_{ijkl}^{(n)}$, $e_{kij}^{(n)}$ and $\in_{ik}^{(n)}$ are the elastic, piezoelectric and dielectric constants of the *n*th layer.

The equilibrium equations and charge equation of electrostatics in the absence of body forces and free charges can be written as

$$\sigma_{ij,j}^{(n)} = 0, \tag{6}$$

$$D_{i,i}^{(n)} = 0, \tag{7}$$

where the symbol $(\ldots)_{,i}$ stands for the partial derivatives with respect to coordinates x_i.

The boundary conditions on bottom and top surfaces are defined as

$$u_i^{(1)}(-h/2) = w_i^- \text{ or } \sigma_{i3}^{(1)}(-h/2) = p_i^-, \quad \varphi^{(1)}(-h/2) = \Phi^- \text{ or } D_3^{(1)}(-h/2) = Q^-, \tag{8}$$

$$u_i^{(N)}(h/2) = w_i^+ \text{ or } \sigma_{i3}^{(N)}(h/2) = p_i^+, \quad \varphi^{(N)}(h/2) = \Phi^+ \text{ or } D_3^{(N)}(h/2) = Q^+, \tag{9}$$

where w_i^-, p_i^-, Φ^-, Q^- and w_i^+, p_i^+, Φ^+, Q^+ are the prescribed displacements, surface tractions, electric potentials and electric charges at the bottom and top surfaces.

The continuity conditions at interfaces are

$$\begin{aligned} &u_i^{(m)}(x_3^{[m]}) = u_i^{(m+1)}(x_3^{[m]}), \quad \sigma_{i3}^{(m)}(x_3^{[m]}) = \sigma_{i3}^{(m+1)}(x_3^{[m]}), \\ &\varphi^{(m)}(x_3^{[m]}) = \varphi^{(m+1)}(x_3^{[m]}), \quad D_3^{(m)}(x_3^{[m]}) = D_3^{(m+1)}(x_3^{[m]}), \end{aligned} \tag{10}$$

where the index $m = 1, 2, \ldots, N-1$ identifies the belonging of any quantity to the interface $\Omega^{[m]}$.

Satisfying the equilibrium equations and charge equation (6) and (7) at inner points $x_3^{(n)m_n}$ inside the layers, the following differential equations are obtained:

$$\sigma_{i1,1}^{(n)m_n} + \sigma_{i2,2}^{(n)m_n} + \sum_{i_n} M^{(n)i_n}(x_3^{(n)m_n})\sigma_{i3}^{(n)i_n} = 0, \tag{11}$$

$$D_{1,1}^{(n)m_n} + D_{2,2}^{(n)m_n} + \sum_{i_n} M^{(n)i_n}(x_3^{(n)m_n})D_3^{(n)i_n} = 0, \tag{12}$$

where $M^{(n)i_n} = L_{,3}^{(n)i_n}$ are the derivatives of the Lagrange basis polynomials whose values at SaS $\Omega^{(n)m_n}$ are evaluated in papers [1, 2] and $m_n = 2, 3, \ldots, I_n - 1$.

Next, we satisfy the boundary conditions

$$\begin{aligned} &\sum_{i_1} L^{(1)i_1}(-h/2)u_i^{(1)i_1} = w_i^- \text{ or } \sum_{i_1} L^{(1)i_1}(-h/2)\sigma_{i3}^{(1)i_1} = p_i^-, \\ &\sum_{i_1} L^{(1)i_1}(-h/2)\varphi^{(1)i_1} = \Phi^- \text{ or } \sum_{i_1} L^{(1)i_1}(-h/2)D_3^{(1)i_1} = Q^-, \end{aligned} \tag{13}$$

$$\begin{aligned} &\sum_{i_N} L^{(N)i_N}(h/2)u_i^{(N)i_N} = w_i^+ \text{ or } \sum_{i_N} L^{(N)i_N}(h/2)\sigma_{i3}^{(N)i_N} = p_i^+, \\ &\sum_{i_N} L^{(N)i_N}(h/2)\varphi^{(1)i_N} = \Phi^+ \text{ or } \sum_{i_N} L^{(N)i_N}(h/2)D_3^{(N)i_N} = Q^+ \end{aligned} \tag{14}$$

and the continuity conditions that result in

$$\sum_{i_m} L^{(m)i_m}(x_3^{[m]})u_i^{(m)i_m} = \sum_{i_{m+1}} L^{(m+1)i_{m+1}}(x_3^{[m]})u_i^{(m+1)i_{m+1}},$$
$$\sum_{i_m} L^{(m)i_m}(x_3^{[m]})\sigma_{i3}^{(m)i_m} = \sum_{i_{m+1}} L^{(m+1)i_{m+1}}(x_3^{[m]})\sigma_{i3}^{(m+1)i_{m+1}},$$
$$\sum_{i_m} L^{(m)i_m}(x_3^{[m]})\varphi^{(m)i_m} = \sum_{i_{m+1}} L^{(m+1)i_{m+1}}(x_3^{[m]})\varphi^{(m+1)i_{m+1}},$$
$$\sum_{i_m} L^{(m)i_m}(x_3^{[m]})D_3^{(m)i_m} = \sum_{i_{m+1}} L^{(m+1)i_{m+1}}(x_3^{[m]})D_3^{(m+1)i_{m+1}}. \qquad (15)$$

Thus, the proposed strong SaS formulation deals with $4(I_1 + I_2 + ... + I_N)$ governing equations (11)-(15) for finding the same number of SaS displacements $u_i^{(n)i_n}$ and SaS electric potentials $\varphi^{(n)i_n}$. These differential and algebraic equations have to be solved to describe the response of the layered piezoelectric plate.

3 NUMERICAL EXAMPLE

Consider a symmetric three-layer piezoelectric square plate with the stacking sequence [0/90/0] and thicknesses $h_1 = h_2 = h_3 = h/3$ composed of PVDF whose material properties are given in [2, 3]. The plate is subjected to the sinusoidally distributed transverse load defined as

$$p_3^- = 0, \quad p_3^+ = p_0 \sin\frac{\pi x_1}{a}\sin\frac{\pi x_2}{b}.$$

The bottom and top surfaces are assumed to be electrically grounded. To compare the results derived with the exact solution of Heyliger [3], we accept $h = 0.01\,\mathrm{m}$ and $p_0 = 3\,\mathrm{Pa}$.

Figure 2 shows the through-thickness distributions of transverse shear stresses, electric potential and electric displacement for different values of the slenderness ratio a/h taking seven SaS for each layer. These results demonstrate convincingly the high potential of the strong SaS formulation because the boundary conditions on bottom and top surfaces for the transverse stresses and the continuity conditions at interfaces for the transverse stresses and electric displacement are satisfied exactly. Note that in a variational SaS formulation [2] the boundary conditions on outer surfaces and the continuity conditions at interfaces are satisfied approximately.

Consider next the same symmetric three-layer square plate subjected to electric loading

$$\Phi^- = 0, \quad \Phi^+ = \Phi_0 \sin\frac{\pi x_1}{a}\sin\frac{\pi x_2}{b}.$$

The bottom and top surfaces of the plate are assumed to be traction free. The obtained results are compared with Heyliger's exact solution [3] in the case of choosing $h = 0.01\,\mathrm{m}$ and $\Phi_0 = 200\,\mathrm{V}$. Figure 3 displays the distributions of transverse shear stresses, electric potential and electric displacement in the thickness direction for different slenderness ratios employing again seven SaS for each layer.

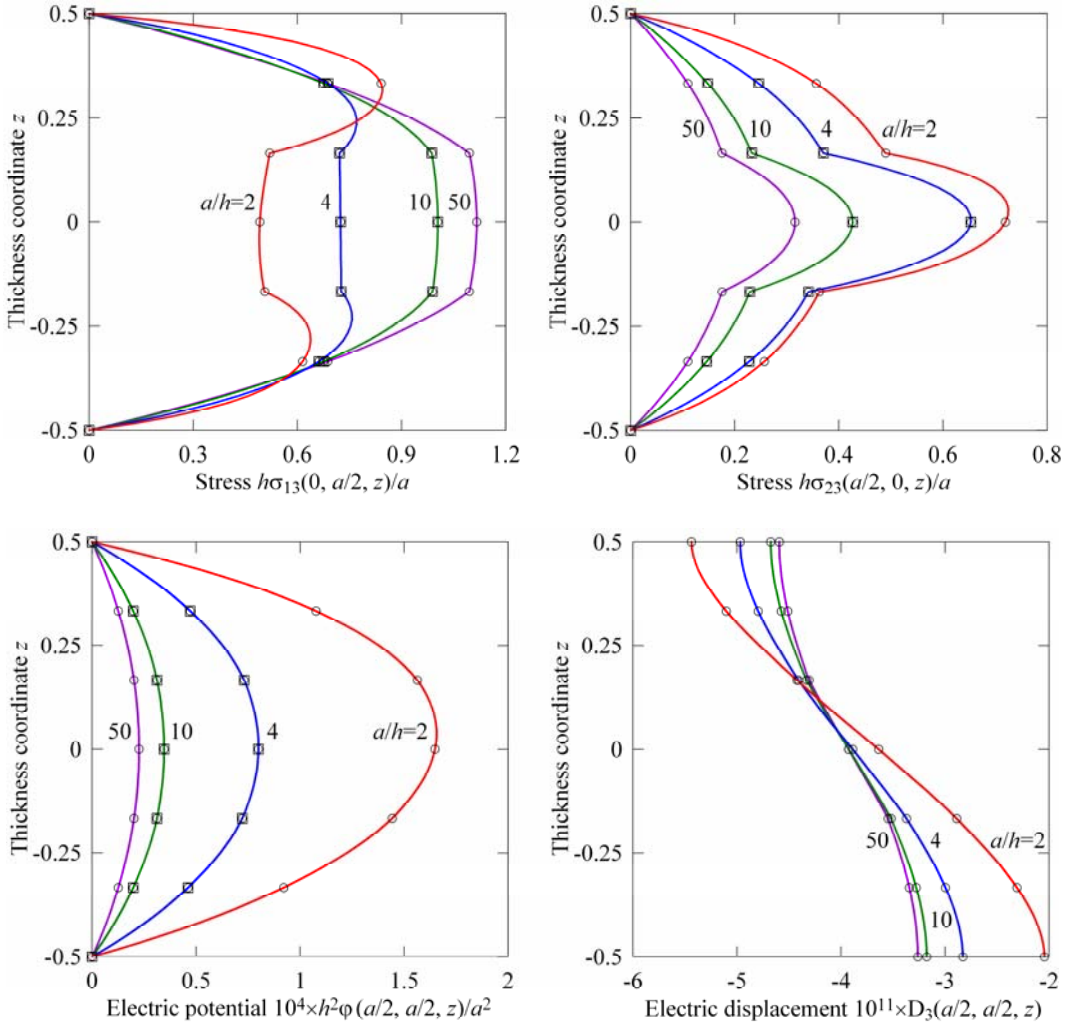

Figure 2: Through-thickness distributions of transverse shear stresses, electric potential and electric displacement for a three-layer plate subjected to mechanical loading for $I_1 = I_2 = I_3 = 7$: strong SaS formulation (—), variational SaS formulation [2] (○) and Heyliger's solution [3] (□), where $z = x_3 / h$

ACKNOWLEDGEMENTS

This work was supported by the Russian Ministry of Education and Science (Grant No. 9.1148.2017/ПЧ and Grant No. 9.4914.2017/ВУ).

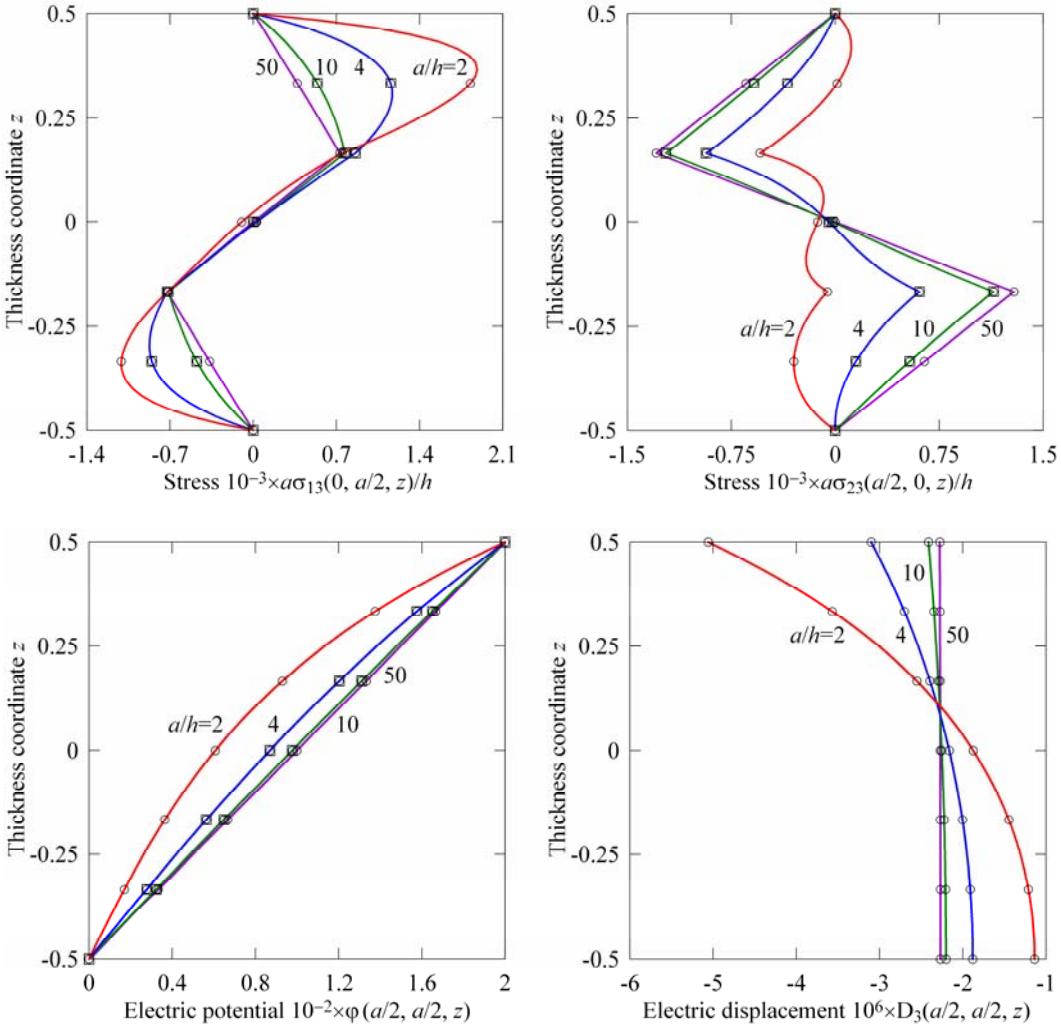

Figure 3: Through-thickness distributions of transverse shear stresses, electric potential and electric displacement for a three-layer plate subjected to electric loading for $I_1 = I_2 = I_3 = 7$: strong SaS formulation (—), variational SaS formulation [2] (○) and Heyliger's solution [3] (□), where $z = x_3 / h$

REFERENCES

[1] Kulikov, G.M. and Plotnikova, S.V. Exact 3D stress analysis of laminated composite plates by sampling surfaces method. *Composite Struct*. (2012) **94**:3654-3663.

[2] Kulikov, G.M. and Plotnikova, S.V. Three-dimensional exact analysis of piezoelectric laminated plates via a sampling surfaces method. *Int. J. Solids Struct.* (2013) **50**:1916-1929.

[3] Heyliger, P. Exact solutions for simply supported laminated piezoelectric plates. *J. Applied Mech*. (1997) **64**:299-306.

VIII ECCOMAS Thematic Conference on Smart Structures and Materials
SMART 2017
A. Güemes, A. Benjeddou , J. Rodellar and Jinsong Leng (Eds)

DYNAMIC CHARCTERISTICS ANALYSIS AND DESIGN MODIFICATION FOR A SMALL-SIZED VERTICAL AXIS WIND TURBINE

JIN-HAK YI*, WONSUL KIM*, TAEK HEE HAN* AND SUNGYUL YIM†

* Coastal and Environmental Engineering Division
Korea Institute of Ocean Science and Technology (KIOST), Republic of Korea
e-mail: yijh@kiost.ac.kr, w.kim@kiost.ac.kr, taekheehan@kiost.ac.kr

† AnytekSys Ltd., Seoul, Republic of Korea
e-mail: yimsungyul@gmail.com

Key words: Vertical Axis Wind Turbine, Dynamic Characteristics Analysis, Dynamic Design Modification, Stochastic Subspace Identification, Resonance

Abstract. The dynamic characteristics including natural frequencies and rotor excitation frequencies are evaluated for a 10 kW vertical axis wind turbine for investigating the root cause of excessive vibration of a structure near 30RPM of rotor speed. Acceleration responses are measured at 12 distributed locations from ambient vibration tests during non-operational and operational conditions. The natural frequencies for the lowest two vibration modes, i.e. f_1 and f_2, are estimated from both conditions and excitation frequencies such as 1P, 2P, 4P frequencies, are also identified according to the rotor rotational speed using the responses under operational conditions (i.e. power generation condition). It is verified that the excessive vibration is due to the resonance between the 4P excitation and the 1st vibration modes. To mitigate the resonance issue, dynamic design modification is carried out to increase the stiffness and the 1st natural frequency by filling concrete inside the steel tower. It is found that the 1st natural frequency could be maximally increased up to about 20.4% by filling inside the steel tower with concrete to 7 m by numerical simulation. After the concrete filling, the acceleration responses are measured again and it is observed that the 1st natural frequency is increased as amount of 21.3% by concrete filling and the increasing rate of 21.3% is very close to the one obtained from the numerical simulation, i.e. 20.4%

1 INTRODUCTION

Although interests on renewable energy development such as wind power and photovoltaic have not greatly increased due to the relatively low oil price and stable domestic power supply environment over the past few years, research activities and investment in renewable energy is still necessary for the reduction of carbon emissions that have been strengthened since the COP21[1].

Among many renewable energy resources, wind power is more economically and technically feasible than other ones. In the case of onshore wind power, it is well known that

the cost of energy (COE) has already reached a level of grid parity [2], which means that the COE of onshore wind power is similar to the cost of generating electricity by the conventional fossil fuel. Many wind farms have already been built and are being operated in Korea, and as of 2015, the total installed capacity is reported as 804 MW. In recent years, attention has been paid to the construction of offshore wind farms to solve the difficulty of securing sites for onshore wind farms and to use better wind resources. A commercial wind turbine of several MW class is being widely used for the construction of such a large wind farm, and the small- and medium-sized wind turbines that are targeted in this study are turbines of a scale necessary for energy-independent island projects and urban wind power systems [3].

Small- and medium-sized wind turbines ranging from several kW to tens of kW have been developed for various types of turbines such as lifting or drag type, horizontal-axis or vertical-axis type, 2-bladed, 3-bladed or 4-bladed type. Researches on the overall structural dynamic characteristics evaluation and monitoring of individual turbines are very limited [4]. In this study, dynamic characteristics such as natural frequencies and modal damping ratios of a 10 kW two-bladed lifting-type vertical-axis wind turbine are analyzed. Through this experimental study, the root cause of excessive vibration occurring when the rotor rotational speed is close to 30RPM is investigated. Through field measurement of the wind turbine structure, it is confirmed that the root cause of excessive vibration is the resonance between the 4P excitation mode, which is equivalent to 4 times of the rotor rotation speed, and the first vibration mode. In order to widen the admissible rotor rotational speed without resonance, the concrete filling inside the steel tower is applied. The effect of concrete filling on the natural frequency is investigated by additional field measurement. This study can be helpful for the design of small and medium size wind turbine towers considering the future operating conditions or to examine the resonance of the whole system.

2 STOCHASTIC SUBSPACE IDENTIFICATION

In this study, the stochastic subspace identification (SSI) is applied to estimate the dynamic characteristics of a structure. SSI is formulated based on a block Hankel matrix with a correlation matrix of response data and it can be classified as SSI-BR (Balanced Realization) and SSI-CVA (Canonical Variate Analysis) according to the method of constructing the Hankel matrix [5-8]. In this study, the SSI-CVA method is applied to obtain more stable results [8]. Since many literatures about SSI method are available, the fundamental ideas are briefly summarized in this paper. First, the SSI-CVA method constructs a block-Hankel matrix by using the cross-correlation matrix from the stochastic discrete state equation (see equation (1)) considering the external load as a Gaussian random normal distribution load.

$$\begin{aligned} \mathbf{z}(k+1) &= \mathbf{A}\mathbf{z}(k) + \mathbf{w}(k) \\ \mathbf{y}(k) &= \mathbf{C}\mathbf{z}(k) + \mathbf{v}(k) \end{aligned} \tag{1}$$

$$\mathbf{R}(k) = E\left[\mathbf{y}(k+m)\mathbf{y}(m)^T\right] = \mathbf{C}\mathbf{A}^{k-1}E\left[\mathbf{z}(m+1)\mathbf{y}(m)^T\right] = \mathbf{C}\mathbf{A}^{k-1}\mathbf{G} \tag{2}$$

where $\mathbf{A}$ and $\mathbf{C}$ are the system matrix and the observation matrix, respectively, and $\mathbf{z}(k)$ and $\mathbf{y}(k)$ are a state vector and an observation vector, respectively. $\mathbf{w}(k)$ and $\mathbf{v}(k)$ are a random normal distribution load vector and a noise vector for the observation vector, respectively, and they have no correlation with each other. A block-Hankel matrix with the cross-correlation

matrix can be constructed as follows and it can be decomposed into a observability matrix, $\mathbf{O}_{n_1}$, and an extended controllability matrix, $\mathbf{C}_{n_2}^{ext}$, as in the last in Eq. (3) .

$$\begin{aligned}\mathbf{H}_{n_1,n_2}^{SSI} &= \begin{bmatrix} \mathbf{R}_1 & \cdots & \mathbf{R}_{n_2} \\ \vdots & \ddots & \vdots \\ \mathbf{R}_{n_1} & \cdots & \mathbf{R}_{n_1+n_2-1} \end{bmatrix} = \begin{bmatrix} \mathbf{CG} & \cdots & \mathbf{CA}^{n_2-1}\mathbf{G} \\ \vdots & \ddots & \vdots \\ \mathbf{CA}^{n_1-1}\mathbf{G} & \cdots & \mathbf{CA}^{n_1+n_2-1}\mathbf{G} \end{bmatrix} \\ &= \begin{bmatrix} \mathbf{C} \\ \vdots \\ \mathbf{CA}^{n_1-1} \end{bmatrix} \begin{bmatrix} \mathbf{G} & \cdots & \mathbf{A}^{n_2-1}\mathbf{G} \end{bmatrix} = \mathbf{O}_{n_1}\mathbf{C}_{n_2}^{ext}\end{aligned} \tag{3}$$

SSI-CVA can be formulated by multiplying the weighting matrices ($\mathbf{W}_1$ and $\mathbf{W}_2$) before and after the block Hankel matrix as in Eq. (4a) and then singular value decomposition (SVD) is performed. Then a unitary matrix ($\mathbf{U}_1$) and a singular value matrix ($\mathbf{\Sigma}$) are obtained as shown in Eq. (4a). Finally, the controllability matrix can be obtained using the weighting matrix, unitary matrix and singular value matrix as in (4d) [7].

$$\mathbf{W}_1\mathbf{H}_{n_1,n_2}^{SSI}\mathbf{W}_2 = \begin{bmatrix}\mathbf{U}_1 & \mathbf{U}_2\end{bmatrix}\begin{bmatrix}\mathbf{\Sigma}_1 & \mathbf{0} \\ \mathbf{0} & \mathbf{\Sigma}_2\end{bmatrix}\begin{bmatrix}\mathbf{V}_1^T \\ \mathbf{V}_2^T\end{bmatrix} \approx \mathbf{U}_1\mathbf{\Sigma}_1\mathbf{V}_1^T \Leftrightarrow \mathbf{W}_1\mathbf{O}_{n_1}\mathbf{C}_{n_2}^{ext}\mathbf{W}_2 \tag{4a}$$

$$\mathbf{W}_1 = (\mathbf{L}^+)^{-1},\ \mathbf{W}_2 = (\mathbf{L}^-)^{-1} \tag{4b}$$

$$\mathbf{R}^+ = \begin{bmatrix} \mathbf{R}_0 & \cdots & \mathbf{R}_{n_1-1}^T \\ \vdots & \ddots & \vdots \\ \mathbf{R}_{n_1-1} & \cdots & \mathbf{R}_0 \end{bmatrix} = \mathbf{L}^+\mathbf{L}^{+T},\ \mathbf{R}^- = \begin{bmatrix} \mathbf{R}_0 & \cdots & \mathbf{R}_{n_2-1}^T \\ \vdots & \ddots & \vdots \\ \mathbf{R}_{n_2-1} & \cdots & \mathbf{R}_0 \end{bmatrix} = \mathbf{L}^-\mathbf{L}^{-T} \tag{4c}$$

$$\therefore \mathbf{O}_{n_1} = \mathbf{W}_1^{-1}\mathbf{U}_1\mathbf{\Sigma}_1^{1/2} \tag{4d}$$

The system matrix ($\mathbf{A}$) can be calculated from the matrices $\mathbf{O}_{n_1-1}^{\uparrow}$ and $\mathbf{O}_{n_1-1}$ obtained by subtracting one block below and one block from the observability matrix, as shown in equation (5).

$$\mathbf{O}_{n_1-1}^{\uparrow} = \mathbf{O}_{n_1-1}\mathbf{A} \tag{5}$$

where, $\mathbf{O}_{n_1-1}^{\uparrow} \equiv \begin{bmatrix} \mathbf{CA} \\ \mathbf{CA}^2 \\ \vdots \\ \mathbf{CA}^{n_1-1} \end{bmatrix}$, $\mathbf{O}_{n_1-1} \equiv \begin{bmatrix} \mathbf{C} \\ \mathbf{CA} \\ \vdots \\ \mathbf{CA}^{n_1-2} \end{bmatrix}$

The eigenvalue (λ_k), the natural frequency (ω_k), the mode damping ratio (ζ_k) and the actual mode vector (ϕ_k) for the k-th mode of the continuous state equation can be obtained as

shown in the following equations (6) and (7) using the system matrix.

$$\mathbf{A\Psi} = \mathbf{M\Psi} \ (\mathbf{M} = diag(\mu_1, \cdots, \mu_N), \ \mathbf{\Psi} = [\boldsymbol{\psi}_1, \cdots, \boldsymbol{\psi}_N] \tag{6}$$

$$\lambda_k = \frac{1}{\Delta t}\ln(\mu_k), \ \zeta_k = -\mathrm{Re}(\lambda_k)/|\lambda_k|, \ \omega_k = -\mathrm{Im}(\lambda_k)/\sqrt{1-\zeta_k^2}, \ \boldsymbol{\varphi}_k = \mathbf{C}\boldsymbol{\psi}_k \tag{7}$$

3 EVALUATION OF DYNAMIC CHARACTERISTICS OF A WIND TURBINE STRUCTURE BEFORE DYNAMIC MODIFICATION

3.1 Overview of Wind Turbine and Field Measurement

The 10-kW vertical axis wind turbine used in this study is a two-bladed lifting-type turbine as shown in Fig. 1, and the tower height from the foundation to the rotor is 10 m. The distance between the center axes of the two blades is 6.0 m, and the height of the blades is 7.0 m. The diameter and thickness of the steel towers are 800 mm and 25 mm, respectively.

For the field measurements, three accelerometers are installed at 4 m, 7 m, 10 m, and 12 m from the foundation, respectively, to measure the acceleration response under two different conditions, i.e. (1) the condition that the rotor is not rotating because the wind speed is low and (2) the condition that the rotor rotates close to 30RPM due to the good wind speed condition.



Figure 1: Target wind turbine

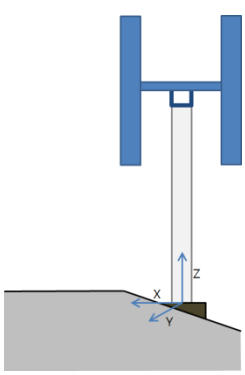

(a) Definition of Axis

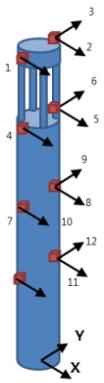

(b) Sensor No.

Figure 2: Installed Sensors

3.2 Dynamic Characteristics Analysis of a Wind Turbine Structure in the Frequency Domain

In order to analyze the root cause of excessive vibration near 30RPM, first, the main dynamic characteristics of the wind turbine structure are evaluated by using the power spectrum in the frequency domain. Fig. 3 shows the time history data and spectrum of acceleration during non-operational (Fig. 3a) and operational (Fig. 3b). The excitation frequencies and natural frequencies can be analyzed from the power spectral density functions.

Fig. 3(a) shows the measurement result when the rotor is not rotated. From these results, it can be seen that the natural frequencies of the structure can be analyzed, and the natural frequencies of the first and second modes are 2.1 Hz and 5.2 Hz, respectively. Meanwhile, the excitation frequencies can also be analyzed from Fig. 3(b) from the measurement data during power generation, that is, while the turbine is rotating. It is found that periodic excitation components such as 1P, 2P, and 4P occur in this case of a two-bladed turbine, compared with the case where a periodic component of 1P, 3P, and 6P occurs in a three-bladed horizontal axis wind turbine [9]. In particular, when the rotational speed of rotor is 27-29RPM, in other words, the 4P excitation frequency is 1.80 ~ 1.93Hz, its frequency is very close to the first natural frequency of the structure, i.e. 2.1Hz. Hence, it can be concluded that the resonance can occur and excessive vibration can be observed due to the resonance.

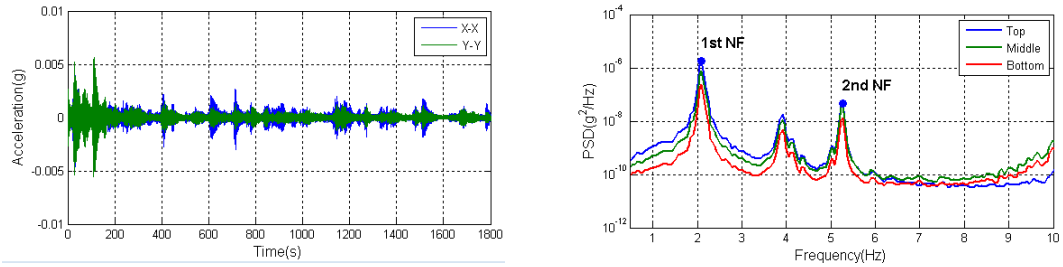

(a) Ambient vibration tests during non-operational condition

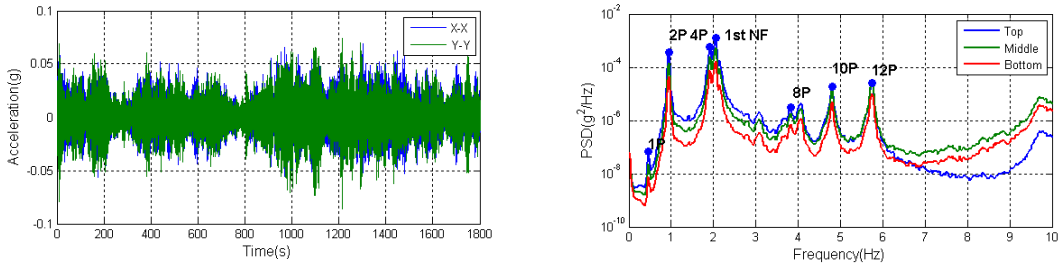

(b) Ambient vibration tests during operational condition

Figure 3: Acceleration time histories and their power spectral density functions

3.3 Analysis of Dynamic Characteristics of Wind Turbine Structures by SSI-CVA

In the previous research, the LS-FDD method [10] based on LSM (least square method) and frequency domain decomposition (FDD) method [11] have been used to analyze the modal characteristics of this wind turbine [12][13]. In this study, SSI-CVA method, which can estimate the natural frequencies more accurately, is used to analyze the dynamic characteristics of the structure, although the computation time is relatively long. Fig. 4 shows the stabilization chart obtained from the SSI-CVA method based on the acceleration response during non-operating condition, and it is found that two stable modes can be identified near 2.1Hz and 5.3Hz. The solid line indicates the first singular values in FDD method.

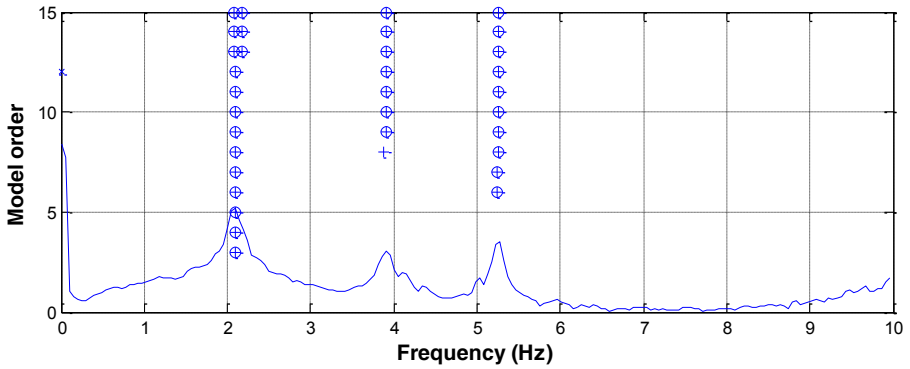

Figure 4: Stabilization chart with singular values from frequency domain decomposition

Table 1 shows the comparison between the natural frequencies obtained from the LS-FDD method and SSI-CVA. The mean of the first natural frequency is 2.101Hz, which is very close to the 2.099Hz from LS-FDD method. On the other hand, the dispersion coefficient is 0.360%, which is 0.045% smaller than 0.405% of the LS-FDD method.

	LS-FDD(Yi et al. 2017)		SSI-CVA (present)	
	f_1	f_2	f_1	f_2
1st Test	2.086	5.290	2.092	5.274
2nd Test	2.096	5.294	2.095	5.280
3rd Test	2.108	5.302	2.111	5.287
4th Test	2.105	5.296	2.103	5.282
5th Test	2.101	5.300	2.103	5.283
Average	**2.099**	**5.296**	**2.101**	**5.281**
COV(%)	**0.405**	**0.090**	**0.360**	**0.090**

* COV denotes the coefficient of variation.

4. EVALUATION OF DYNAMIC CHARACTERISTICS OF WIND TURBINE STRUCTURES AFTER DYNAMIC DESIGN MODIFICATION

4.1 Dynamic Design Modification of Wind Turbine Structure

From the first field measurement, it has been concluded that the excessive vibration is caused by the resonance between the 4P excitation and the 1st natural vibration modes. Therefore, it is necessary to increase the admissible maximum rotor rotational speed in order to raise the power output and to reduce the vibration. Various methods can be applied for this purpose. In this study, the concrete is filled inside the existing steel tower to increase the stiffness and natural frequency as well. However, when the filling height is too high, the effect of increasing the mass is greater than the effect of increasing the stiffness. Therefore, the optimal filling height needs to be determined first through numerical analysis.

The numerical modal analysis of the wind turbine structure is performed using a commercial structural analysis program, i.e. LUSAS. For the modeling, tower, flange,

stiffener and upper disk are modeled as 4 node shell elements, and the turbine support member on the tower is modeled using 2 node beam element. In this study, the blades and generators are considered as concentrated mass at the mass center of the rotor-nacelle-assembly in the upper part of the tower, and the bottom part of the tower is considered as a complete fixed support condition without detailed modeling of the foundation. The actual stiffness can be taken into account by using modal updating, but this study does not include it because the previous studies reveal that the rate of increase or decrease of the natural frequency due to the stiffness change is not significantly affected by the initial model [14].

Fig. 5 shows the increase rate of the first natural frequency according to concrete filling height. It can be found that the natural frequency is increased up to 20.4% when the concrete filling height is 7 m, and the natural frequency decreases when the filling height is higher than this. Therefore, it is planned to fill up the concrete in the actual wind turbine tower up to 7 m height based on the numerical analysis results.

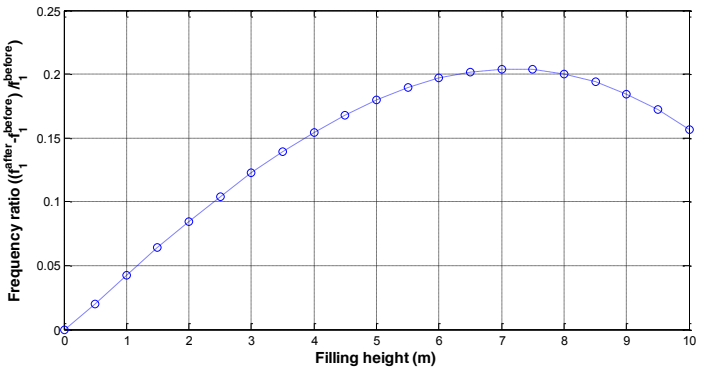

Figure 5: Frequency increasing ratio with concrete filling inside the steel tower

4.2 Evaluation of Dynamic Characteristics after Dynamic Design Modification of Wind Turbine Structure

Based on the results of the numerical analysis, the concrete is filled up to 7 m height inside the steel tower of the wind turbine, and the field measurement is carried out again about two months later considering the curing time. The accelerometers are installed at the same position as in the field measurement. The experiment is conducted under only non-operating condition due to the low wind speed. Fig. 6 shows that two stable modes are extracted around 2.5 Hz and 5.3 Hz in the stabilization chart obtained by SSI-CVA with measurement data. Table 2 shows the comparison of natural frequencies before and after concrete filling. In the first mode, it can be seen that the natural frequency has increased by more than 20% from the existing 2.1 Hz to 2.5 Hz while there is not significant increase in the second mode. It is because that the sensitivity of the tower stiffness on the 2nd natural frequency is much lower than that for the 1st mode. In addition, the increase rate of the first mode (i.e. 21.3%) is very close to the numerical result, i.e. 20.4%. Although the numerical analysis model is not updated using the experimentally obtained natural frequency, it can be indirectly understood that it is a sufficient level of numerical analysis model to see the change rate according to the change of stiffness.

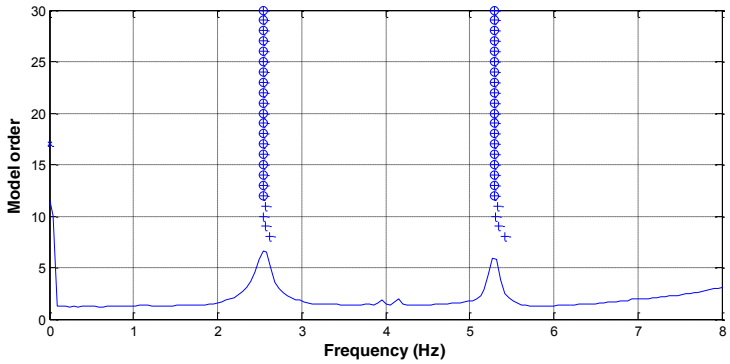

Figure 6: Stabilization chart and singular values from frequency domain decomposition

Table 2: Natural frequencies before and after filling

	Natural frequencies (Hz)		Increasing ratio (%)
	Before concrete filling	After concrete filling	
1st mode	2.101	2.550	21.3
2nd mode	5.281	5.293	0.2

5. CONCLUSION

The purpose of this study is to investigate the root cause of excessive vibration and to mitigate the cause of excessive vibration for the 10kW small vertical wind turbine structure with excessive vibration near 30RPM. In order to estimate the dynamic characteristics of the structure, field measurements are carried out and the following conclusions are derived.

(1) Unlike a typical horizontal axis three-bladed wind turbine, it is confirmed that the periodic components such as 1P, 2P, and 4P occur in the case of the two- bladed vertical axis wind turbine. Especially, when the rotor speed is about 27-29RPM at the time of field measurement, the corresponding 4P excitation frequency is 1.80-1.93Hz which is slightly smaller than the first natural frequency of the structure, i.e. 2.1Hz. Hence, it is confirmed that excessive vibration occurs due to resonance between 4P excitation and the 1st vibration modes.

(2) By analyzing the natural frequency of the structure by applying the SSI-CVA method, it is possible to obtain a more consistent natural frequency than that of the LS-FDD method. But the differences are very small and negligible.

(3) In order to increase the power output and mitigate the excessive vibration, concrete is filled in the steel tower to increase the first natural frequency of the existing wind turbine structure. Numerical result shows that natural frequency can be increased by 20.4% when concrete is filled up to 7 m height.

(4) It is confirmed that the natural frequency of the first mode increased from 2.1Hz to 2.54Hz by conducting the field measurement after filling the concrete. Based on this result, the admissible maximum rotational speed for avoiding resonance can be increased from 30RPM to 36RPM, about up to 20 % in this case.

In the case of the target small-sized two-bladed vertical-axis wind turbine, excessive

vibration occurred due to the resonance with the first vibration mode where the rotational speed of the rotor is near 30RPM. In order to mitigate this vibration, the dynamic design is modified by concrete filling. And its effect is confirmed by field measurements. In this case, when resonance occurs in the rotor rotation speed range smaller than the design RPM, dynamic design modification through design change of the stiffness or mass of the structure is effective, but additional introduction of the enhanced control algorithm such as control widh speed exclusion zone algorithm [15] for avoiding resonance is necessary in the future.

ACKNOWLEDGMENT

This research is a part of the project titled "Development of active-controlled tidal stream generation technology" funded by the Ministry of Oceans and Fisheries, Korea (20110171) and KIOST R&D Program (project No. PE99521).

REFERENCES

[1] Jang, Y.-C., Bang, K.-Y., Lee, K.-Y., Kim, K.-N. Analysis of energy security by the diversity indices: A case study of South Korea, *Journal of Energy Engineering* (2014) **23**(2): 93-101. (in Korean)

[2] US Energy Information Administration, *Levelized cost and levelized avoided cost of new generation resources in the annual energy outlook 2016*. AEO2016 Levelized Costs.

[3] Jeong, M.-S., Moon, C.-J., Chang, Y.-H., Park, T.-S., Kim, Y.-G., Son, C.-G. A Study on Wind Turbine Power Generation Predictions Applies to Energy Independence Island, *Proceedings of the Korean Institute of Illuminating and Electrical Installation Engineers*. (2015) 92-92. (in Korean)

[4] Kim, S., Nam, Y.S., and Eun, S. Vibration Characteristics of the Tower Structure of a 750 kW Wind Turbine Generator. *Transactions of the Korean Society for Noise and Vibration Engineering* (2005) **15**(2): 219-224. (in Korean)

[5] Overschee V.P. and De Moor, B., (1996), *Subspace Identification for Linear Systems*, Kluwer Academic Publisher.

[6] Peeters, B. and De Roeck, G. (1999) Reference-Based Stochastic Subspace Identification for Output-Only Modal Analysis, *Mechanical Systems and Signal Processing* (1999) **13**(6): 855-878.

[7] Hermans, L. and Van Der Auweraer, H. Modal Testing and Analysis of Structures under Operational Conditions: Industrial Applications, *Mechanical Systems and Signal Processing* (1999) **13**(2): 193-216.

[8] Yi, J.-H. and Yun, C.-B. Comparative study on modal identification methods using output-only information. *Structural Engineering and Mechanics* (2004) **17**(3-4): 445-466.

[9] Osgood, R.M., 2001, *Dynamic Characterization Testing of Wind Turbines*, NREL/TP-500-30070.

[10] Yi, J-H, Park, J.-S., Han, S.-H., and Lee K.-S. Modal identification of a jacket-type offshore structure using dynamic tilt responses and investigation of tidal effects on modal properties. *Engineering Structures* (2013) **49**: 767-781.

[11] Brinker, R., Zhang, L. and Andersen, P. Modal Identification from Ambient Response Using Frequency Domain Decomposition, *Proceedings of 16th International Modal*

Analysis Conference, San Antonio, Texas, USA, (2000) 625-630.
[12] Yi, J-H, Kim, W, Han, T.H., Yim, S. Dynamic response measurements and analysis on a 10 kW class vertical axis wind turbine. *Proceedings of Korean Society of Coastal Disaster Prevention* (2016) 107-113. (in Korean)
[13] Yi, J-H, Kim, W, Han, T.H., Yim, S. Dynamic response measurements and analysis on a 10 kW class vertical axis wind turbine. *Transactions of the Korean Society for Noise and Vibration Engineering* (2007) **27**(1): 107-113. (in Korean)
[14] Lee, J.J., Lee, J.W., Yi, J.H., Yun, C.B., Jung, H.Y. (2005) Neural networks-based damage detection for bridges considering errors in baseline finite element models. *Journal of Sound and Vibration* (2005) **280**: 555-578.
[15] Licari, J., Ekanayake, J., Jenkins, N., Investigation of a speed exclusion zone to prevent tower resonance in variable-speed wind turbines, *IEEE Transactions on Sustainable Energy* (2003) **4**(4): 977-984.

VIII ECCOMAS Thematic Conference on Smart Structures and Materials
SMART 2017
A. Güemes, A. Benjeddou , J. Rodellar and Jinsong Leng (Eds)

STRUCTURAL DAMAGE DETECTION FOR HYBRID OFFSHORE WIND AND TIDAL CURRENT TURBINE

WONSUL KIM [*], JIN-HAK. YI [†] AND JIN-SOON PARK [†]

[*] Coastal Development Research Center
Korea Institute of Ocean Science & Technology (KIOST)
787 Haean-ro(st.), Sangnok-gu, Ansan-si, Gyeonggi-do,Korea
e-mail: w.kim@kiost.ac.kr, www.kiost.ac.kr

[†] Coastal Development Research Center
Korea Institute of Ocean Science & Technology (KIOST)
787 Haean-ro(st.), Sangnok-gu, Ansan-si, Gyeonggi-do,Korea
e-mail: yijh@kiost.ac.kr, jpark@kiost.ac.kr, www.kiost.ac.kr

Key words: Hybrid Offshore Wind and Tidal Current Turbine, Structural Health Monitoring, Damage Detection, Frequency Domain Decomposition, Coherence Function.

Abstract. Among various renewable energies, wind power has more commercially competitiveness and has been developed very fast for several decades. Further, recently to efficiently utilize ocean resources, there is rising interest on the integrated exploitations of an offshore wind and tidal current energy. Such the hybrid offshore wind and tidal current turbine (HOWTCT) plays an important role in supporting the energy-generating components (blades, hub and nacelle) and resisting wind and wave loads. The purpose of present study is to develop a SHM system and damage detection for the supporting structure of HOWTCT through indoor experiments. Accelerometers at four height levels were installed from the ground to the top. The coherence function between two sets of the measured acceleration responses was employed, and then the averaged integrations of coherence (AIC) function with the frequency were used to identify the damage detection. As a result, it was found that the damage detection for the foundation damage with the operations of wind turbine, tidal turbine and wind and tidal turbines was accurately predicted by the AIC function.

1 INTRODUCTION

Since the Kyoto Protocol took effect in 1997, there is lots of interest in the world on global warming and climate change resulting from the excessive use of fossil fuel. Subsequently, in 2015 COP21, known as the 2015 Paris Climate Conference, announces to reduce greenhouse gas emissions to limit the global temperature. Renewable energies have been emerged from the perspectives of securing energy supply and addressing the challenges of climate change, greenhouse gas emission reduction. Among those renewable energies, wind power has more commercially competitiveness and has been developed very fast for several decades [1-2]. Many countries have been started to accelerate deploying not only onshore wind power, but also offshore wind power. As a result, the contribution of wind power to the world total generation capacity is expected to reach 8% by 2018 [3-5]. Wind turbines of the same

capacity have been developed to be bigger and bigger to obtain a large amount of power at low wind speed. To support a bigger wind turbine, a new tower design which is a hybrid-tower design featuring of a concrete and a steel part has been also developed. Further, recently to efficiently utilize ocean resources, the integrated exploitations of offshore wind and ocean energy such as tidal current energy have been carried out by a couple of researches [6-7]. Such the hybrid offshore wind and tidal current turbine (HOWTCT) plays an important role in supporting the energy-generating components (blades, hub and nacelle) and resisting wind and wave loads. In addition, recently the structural health monitoring (SHM) technology has been receiving considerable interest in the field of wind power generation. Implementation of such an SHM system not only provides an efficient health indicator for early damage detection, but also assists in understanding the dynamic behaviors of a wind turbine system or tidal current turbine system under normal operational conditions. However, with the increasing size of the wind turbine for harvesting more energy, the studies about SHM system for the tower structure supporting HOWTCT are still not sufficient. Therefore, it is necessary to develop the SHM system for the supporting structure to secure the structural safety, as well as, to obtain sustainably the electronic power from the HOWTCT tower structure.

The purpose of present study is to develop SHM system and damage detection technology for the supporting structure of the HOWTCT using conceptual HOWTCT model. Coherence function was employed to propose an appropriate damage detection technique for the tower structure supporting HOWTCT. The averaged integration of the correlation function along the frequency points over the measuring range was used as damage indicator for damage identification.

2 INDOOR EXPERIMENTS AND DAMAGE DETECTION

2.1 Experimental model

Figure 1 shows the schematic design of HOWTCT model used in the indoor experiment and sensor arrangements. Measuring sensors which are accelerometers, strain gauges and tilt meters were installed on the HOWTCT model as shown in Figure 1.

Particularly, the accelerometers were distributed from the ground to the top of the HOWTCT model in X- and Y-direction. To simulate the ideal damage, the HOWTCT model was divided into two sections connected by bolts. The vibration was generated by the rotors with two blades for the tidal current turbine and with four blades for the wind turbine. Table 1 lists the damage scenarios of the HOWTCT model. Four different damage states were considered as shown in Table 1. Healthy state (HS) represents the original state of the HOWTCT model. Foundation damage state (FDS) represents the damage of the base. Tower damage state (TDS) represents the damage of the tower flange. Multi damage state (MDS) represents the damage of the base and tower flange simultaneously. The damage was simulated at the base and the tower flange by loosening three bolts for the base and two bolts for the tower flange. In each damage case, it was considered for three types of operations which one is case of the operation of the wind turbine only, second is case of the operation of the tidal turbine, and last is the case of operation of the wind and tidal turbines simultaneously as shown in Table 1. Furthermore, the rotor speeds for the wind and tidal current turbines were fixed to 300 rpm for the wind turbine and 600 rpm for the tidal turbine, respectively. The sampling frequency was 300 Hz. The measuring time was 60 minute.

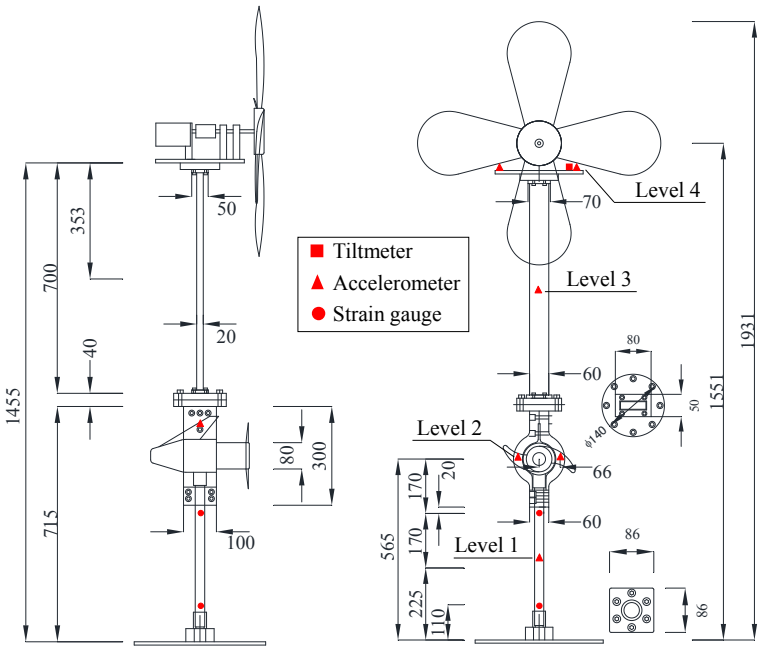

Figure 1: Schematic design of HOWTCT model for damage detection and measuring sensor arrangements

Table 1: Damage scenario and operating condition

Damage Scenario	Operating condition
Healthy state (HS)	Only wind turbine
	Only tidal turbine
	Wind + tidal turbine
Foundation damage state (FDS)	Only wind turbine
	Only tidal turbine
	Wind + tidal turbine
Tower damage state (TDS)	Only wind turbine
	Only tidal turbine
	Wind + tidal turbine
Multi (Foundation & tower) damage state (MDS)	Only wind turbine
	Only tidal turbine
	Wind + tidal turbine

2.1 A correlation criterion for damage detection

In this study, correlation criterion for correlating measured frequency responses from multiple sensors which is one of a response-based method was employed for structural damage detection for the tower structure supporting HOWTCT. The coherence at a specific frequency is modal assurance criterion. The coherence function is a scalar quantity indicating the causal relationship between measured frequency responses at different locations as follows [8]:

$$\mathrm{Coh}_{ij}(f)=\frac{\left|G_{ij}(f)\right|^2}{G_i(f)G_j(f)} \tag{1}$$

where, $G_i(f)$ and $G_j(f)$ are the power spectral density at height levels i and j, respectively. $G_{ij}(f)$ is cross power spectral density between height levels i and j. $\mathrm{Coh}_{ij}(f)$ is a real-valued function of frequency between zero and unity. In this study, the acceleration data was divided into six segments corresponding to 10 minute, and then six coherence functions can be obtained. In calculating the coherence function, the reference point for the acceleration response was set at height level 3 where the largest value of acceleration response was occurred. Figure 2 shows an example of the coherence function at height levels 3 and 1 for different damage states with the operation of the wind turbine. Furthermore, it is likewise calculated in a manner corresponding to the modal assurance criterion. The averaged integration of coherence (AIC) function over the actual response values at each frequency can be defined as:

$$\mathrm{AIC}_{\mathrm{ij}}=\frac{1}{\mathrm{N}}\sum_{n=1}^{N}Coh_{ij}(f_n) \tag{2}$$

The AIC_{12} is a real constant between zero and unity to indicate the change of structural responses at height levels i and j. Hence, this can be used as damage indicators for damage identification.

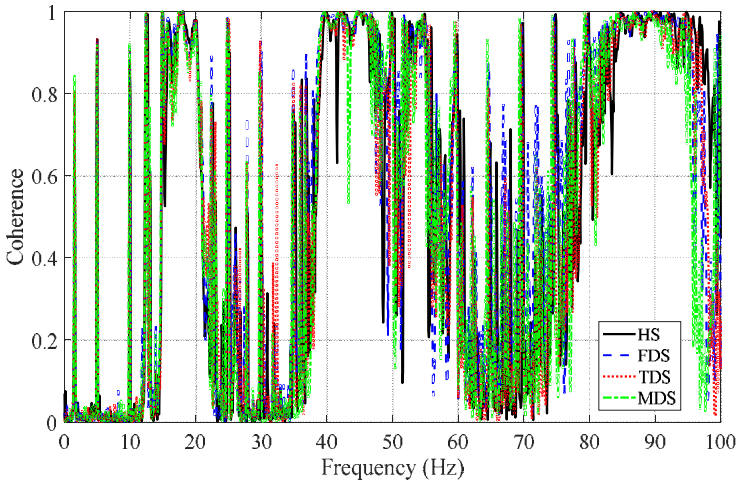

Figure 2: Example of correlation fucntion at levels 3 and 1 for different damage states with operation of wind turbine

3 RESULTS AND REMARKS

The damage identification (AIC) results for different damage states and operation conditions are presented in Figures 3~5. In Figures 3~5, the dashed lines represent upper and lower limits of the AIC for the healthy state, and these can be obtained by three standard deviations of coherence which lies within 99.7% probability by assuming normal distribution. From Figure 3, AIC results for different damage states with the operation of the wind turbine

showed similar distribution, but AIC values were depended on the damage states and height levels. The AIC_{31} and AIC_{32} for damage states seems to have lower correlation with damage states, expect the FDS for height levels 3 and 1 and the TDS for height levels 3 and 2, respectively. On the other hand, the AIC_{34} for the damage states entirely exhibited high correlation compared with that of the HS. It implies that the damage detection is accurately predicted by the correlation criterion. Another notable observation was that if the excitation response on the hybrid offshore wind and tidal current turbine structure is small, the AIC is sensitive to damage states.

From Figure 4, AIC results for the HS with the operation of the tidal turbine depended on height levels. AIC_{31}, AIC_{32} and AIC_{34} for the FDS and MDS were slightly smaller than those of the HS. It implies that the damage detection is accurately predicted for the FDS and MDS.

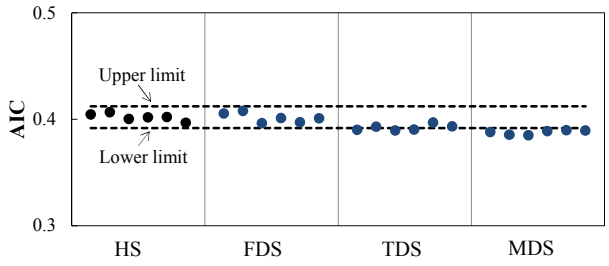

(a) Levels 3 and 1

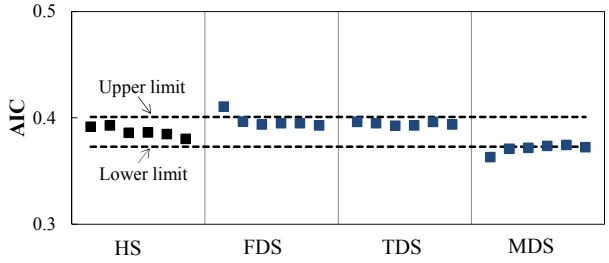

(b) Levels 3 and 2

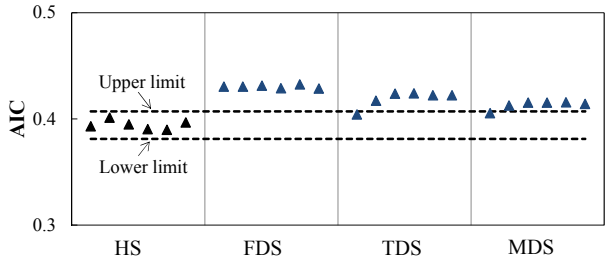

(c) Levels 3 and 4

Figure 3: Damage identification (AIC) results for different damage states with operation of wind turbine

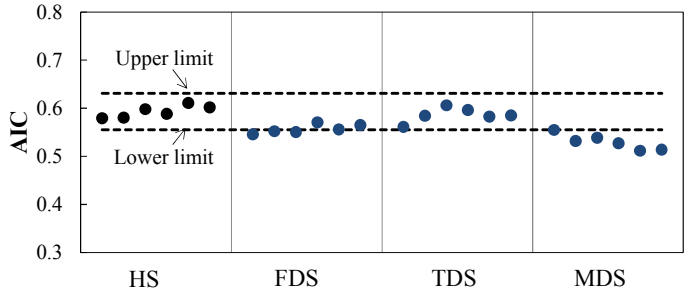

(a) Levels 3 and 1

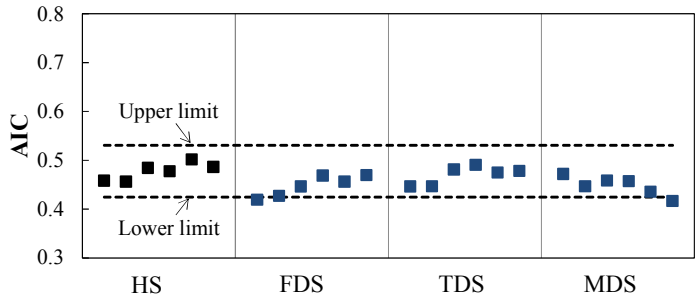

(b) Levels 3 and 2

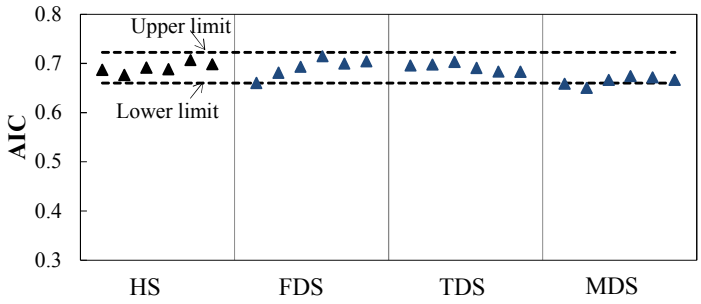

(c) Levels 3 and 4

Figure 4: Damage identification (AIC) results for different damage states with operation of tidal turbine

On the other hand, it should be noted that AIC_{31}, AIC_{32} and AIC_{34} for the TDS were almost same with those of the HS, i.e., the damage detection for the TDS could not be predicted in the operation of the tidal turbine.

From Figure 5, AIC results for the HS with the operation of the wind and tidal turbine also depended on height levels as shown in Figure 4. Notable observation was that the damage detection (AIC_{31}, AIC_{32} and AIC_{34}) for the FDS were predicted accurately. On the other hand, the damage detection (AIC_{31}, AIC_{32} and AIC_{34}) for the TDS and MDS could not be clearly predicted. Therefore, it is required to examine the effect of damage state and operating condition on the AIC by using coherence function.

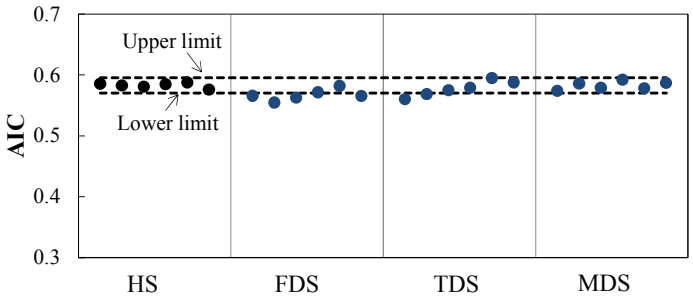

(a) Levels 3 and 1

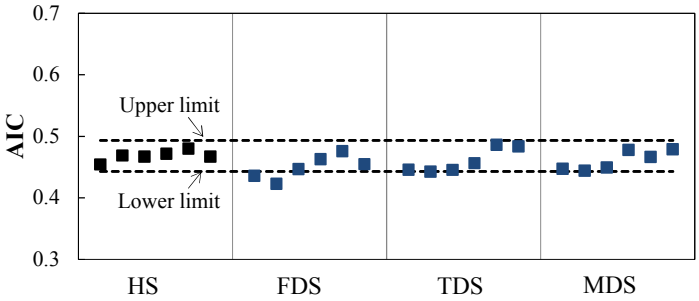

(b) Levels 3 and 2

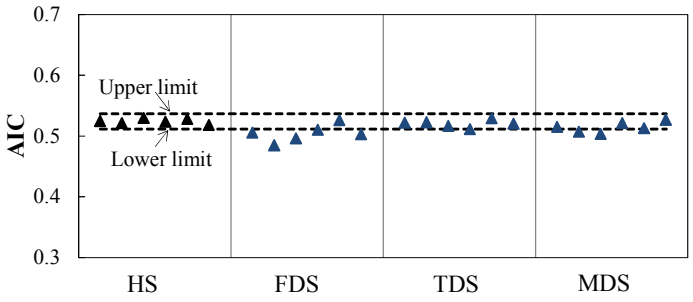

(c) Levels 3 and 4

Figure 5: Damage identification (AIC) results for different damage states with operation of wind and tidal turbine

4 CONCLUSIONS

The purpose of the present study is to investigate the damage detection for the supporting structure of a hybrid offshore wind and tidal current turbine through the indoor experiments. In this study, correlation technique between two sets of the acceleration responses was employed to propose an appropriate damage detection technique with various damage locations. The averaged integration of the coherence function with frequency was used as damage indicator for damage identification. This study shows the possibility of devising health monitoring and damage assessments using the correlation criteria. More detailed study is required to develop the approaches that can accurately recognize and assess the structural

damage states of the hybrid offshore wind and tidal current turbine structure.

ACKNOWLEDGEMENTS

This research was financially supported by the Ministry of Land, Infrastructure and Transport (MOLIT) of the Korean government (code 12 Technology Innovation E09) and by the Korea Institute of Ocean Science and Technology (PE99521).

REFERENCES

[1] Mohammad, S. N., Das N.K. and Roy S. A review of the state of the art of generators and power electronics for wind conversion systems, 3rd international conference on the developments in renewable energy technology(ICDRET) (2014): 29-31

[2] Tchakoua, P., Wamkeue, R., Ouhrouche, M., Slaoui-Hasnaoui, F., Tameghe, T.A. and Ekemb, G. Wind turbine condition monitoring: State-of-the-art review, new trends, and future challenges, Energies (2014) 7: 2595-2630.

[3] Fried, L., Sawyer, S., Shukla, S. and Qiao, L. Global Wind Report 2012-Annual Market Update, Global Wind Energy Council (GWEC): Brussels, Belgium, 2013.

[4] Zhang, P. *Small Wind World Report 2012,* World Wind Energy Association (WWEA): Bonn, Germany, 2012.

[5] Renewables 2012: *Global Status Report,* REN21: Paris, France, 2012.

[6] Veigas, M., Carballo, R. and Iglesias, G. Wave and offshore wind energy on an island, Energy Sustain Dev (2014) **22**: 57-65.

[7] Fan, Y., Mu, A. and Ma, T. Modeling and control of a hybrid wind-tidal turbine with hydraulic accumulator, Energy (2016) **112**: 188-199.

[8] Allemang, R.J. and Brown, D.J. A correlation coefficient for modal vector analysis, 1st International Modal Analysis Conference (1982): 110-116.

VIII ECCOMAS Thematic Conference on Smart Structures and Materials
SMART 2017
A. Güemes, A. Benjeddou, J. Rodellar and J. Leng (Eds)

STRUCTURAL DESIGN AND EXPERIMENTAL INVESTIGATIONS OF A SHAPE-ADAPTIVE SLAT FOR WIND ENERGY ROTOR BLADES

OLIVER HUXDORF*, JOHANNES RIEMENSCHNEIDER†, PAUL LORSCH‡ AND MARTIN RADESTOCK§

German Aerospace Center (DLR)
Institute of Composite Structures and Adaptive Systems
Lilienthalplatz 7, 38108 Braunschweig, Germany
e-mail: *oliver.huxdorf@dlr.de, †johannes.riemenschneider@dlr.de, ‡paul.lorsch@dlr.de, §martin.radestock@dlr.de

Key words: Wind Energy, Morphing, Adaptive Systems, Slat, Rotor Blade

Abstract. The trend towards larger rotor blades is still continuing, since the generated electrical power is proportional to the square of the blade length. However increasing rotor blade length will also increase the blades weight by the radius cube. Consequently mass induced loads such as centrifugal loads also increase. In addition larger blades lead to increased dynamic blade loads induced by vertical wind gradients and turbulent inflow conditions. A morphing slat that allows a dynamic gap variation between the slat's trailing edge and the main profile offers a great opportunity to reduce such fatigue loads. In order to show the proof of concept of such a shape-adaptive slat, a wind tunnel experiment was designed and executed. This paper presents the development of the shape-adaptive slat in wind tunnel scale. In order to ensure the fatigue behaviour a parameter study for the slat's design is done. The objective is to avoid a concentrated local strain maximum in the case of the deformed slat. As a next step, six slat segments are manufactured to investigate the deformation behaviour and to validate the simulations in a static experiment. The same segments are used to perform long-term fatigue investigations with dynamic slat deformations. Based on the experimental results a heat treated steel is selected to manufacture the final wind tunnel slat.

1 INTRODUCTION

The trend towards larger wind energy rotor blades is still continuing, since the generated electrical power is proportional to the square of the blade length. On the negative side larger wind energy rotor blades lead to increasingly and therefore critical dynamic blade loads at the blade root. These loads are induced by turbulent inflow conditions, vertical flow speed gradients due to the surface boundary layer and increased blade weights by radial length cubed in combination with changing blade orientations relative to the gravity. Consequently further blade up-scaling is limited by increased dynamic blade loads.

Recently investigations to the reduction of blade root loads by passive technologies such as bend twist coupling are done in [1, 2]. Another approach with more potential than passive methods and the possibility of direct lift control are active technologies. An overview of such technologies, their potentials and issues is given in [3]. Several investigations to camber variation with flexible trailing edges and conventional trailing edge flaps are done by the Danish Technical University (DTU) [4, 5, 6], Sandia National Laboratories (SNL) [7], Technical University Berlin [8] and Sandia National Laboratories together with FlexSys Inc. [9].

An alternative approach to camber variation is the use of shape-adaptive slats for wind energy rotor blades. This technology also offers the opportunity of direct lift control. The use of non-deformable rigid movable slats' is a well-known technology in aircraft applications. Existing patents for non-deformable wind energy rotor blade slats are proposed in [10, 11, 12]. Recent investigations with a fixed non-deformable auxiliary leading edge slat at a zero twist quasi-two-dimensional profile of type DU 97-W-300, which is described in [13], are done in [14]. Further investigations of [15] with a rigid retrofitted leading edge slat at the inner part of the 10 MW reference turbine RWT10, from the Danish LightRotor project, show the potential of leading edge slats' at wind energy turbines, especially the effect of an increased energy yield. The general effects of a non-deformable slat can be summarized with a delay in stall and an increased range of angles of attack in which the airfoil is working efficient. In contrast to a non-deformable slat a shape-adaptive slat also offers the opportunity of direct lift control.

In order to show the proof of concept this paper presents the development of a shape-adaptive slat with the possibility of a camber angle variation for wind tunnel investigations. Such a slat enables a changing gap size between the slat's trailing edge and the main profile. In case of a known incoming short-term inflow fluctuation as well as different flow speeds at various azimuth blade positions the slat's shape can be switched with the objective to control the aerodynamic forces and therefore to reduce dynamic blade root loads. This leads to an improved fatigue behaviour of the blade root and allows the design of larger and lighter blades. A short overview of the development procedure of this shape-adaptive slat is presented in [16]. A more detailed description of the development procedure is presented now in this paper.

2 GEOMETRY

As a first step to develop the shape-adaptive slat for wind tunnel investigations the non-deformed aerodynamic profile is defined in [17] in an optimization process. The starting point is the DU 91-W2-250 profile, which is shown in figure 1. Detailed information to this profile is given in [13]. The outcome of this study are two different aerodynamic profiles which are also shown in figure 1. The first one is characterized by a superimposed large cambering slat in front of the unmodified DU 91-W2-250 profile. The second profile is described by a modified main profile with a low cambering slat in front of them. The low cambering slat and the corresponding main profile are completely integrated in the original DU 91-W2-250 profile. Hence the second slat version is called "the integrated slat". Furthermore [17] compares the superimposed as well as the integrated profile in terms of lift and efficiency. Due to the better efficiency, the integrated slat is selected to develop the shape-adaptive slat for wind tunnel investigations.

The given geometry of the slat and the main profile is presented in figure 1. As shown the slat's suction side and the whole rear part of the main profile are identical with the original

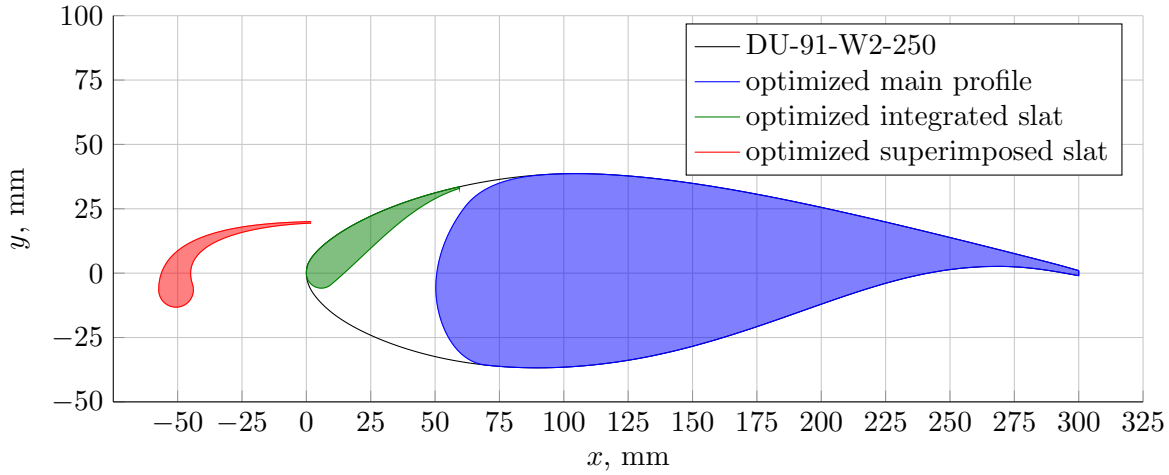

Figure 1: Integrated slat in red with the corresponding main profile in blue compared with the original DU 91-W2-250 profile in black. The geometry is presented in wind tunnel scale. The figure is based on data of [17].

DU 91-W2-250 profile. The main profile has a chord c_{main} of 250 mm and a maximum thickness t_{main} of 75 mm. The slat has a chord c_{slat} of 69 mm and a maximum thickness t_{slat} of 13.4 mm. In case of a non-deformed slat the shortest distance between the main profile and the trailing edge of the slat denoted as g is 6.4 mm. The experimental aerodynamic investigations were executed in a wind tunnel from the University of Oldenburg. The measuring section of this wind tunnel has a width of 805 mm. Hence the main profile of the wind tunnel model has a span s_{main} of 805 mm. In order to prevent friction between the side surfaces of the slat and the wind tunnel walls the slat has a span s_{slat} of 803 mm.

3 REQUIREMENTS

As a next step the essential slat deformation requirements are defined. As a main requirement it has to be possible to close the gap completely. In order to be able to reduce dynamic blade loads the second essential requirement is a shape variation frequency f of 5 Hz for the full amplitude. As a secondary requirement an additional gap enlargement beyond the non-deformed gap size should be possible.

4 CONCEPT DESCRIPTION

In order to design the shape-adaptive slat in wind tunnel scale, different structural concepts are investigated. Among others a concept with slat integrated pressurized cells as in [18] and [19], shape integrated piezoceramic actuators as used in [20] and the use of a kinematic chain as described in [21] are investigated and discussed. Each of these concepts has a significant disadvantage for the given requirements. The most promising and therefore the finally selected concept uses a kinematic mechanism as shown in figure 2. In order to ensure a continuous slat deformation as well as to minimize flow disturbances induced by the kinematics itself four span-wise positions are defined to deform the slat's compliant middle section as well as to fix

the slat's leading edge at the main profile (compare figure 2(a)). As shown in figure 2(b) the intermediate regions of these four positions allow an air flow between the pressure side of the slat and the main profile. The kinematics consists of a connecting rod (blue) and a shaft (brown). A stepping motor (not shown) is used to drive the shaft and therefore to deform the middle section of the slat. As a result the gap will be closed or opened.

In order to improve the fatigue behaviour, to reduce the necessary deformation forces and to reduce the resultant strain in case of a deformation the slat is designed as a hollow profile. Further fatigue improvements are realized with a slotted pressure side of the slat.

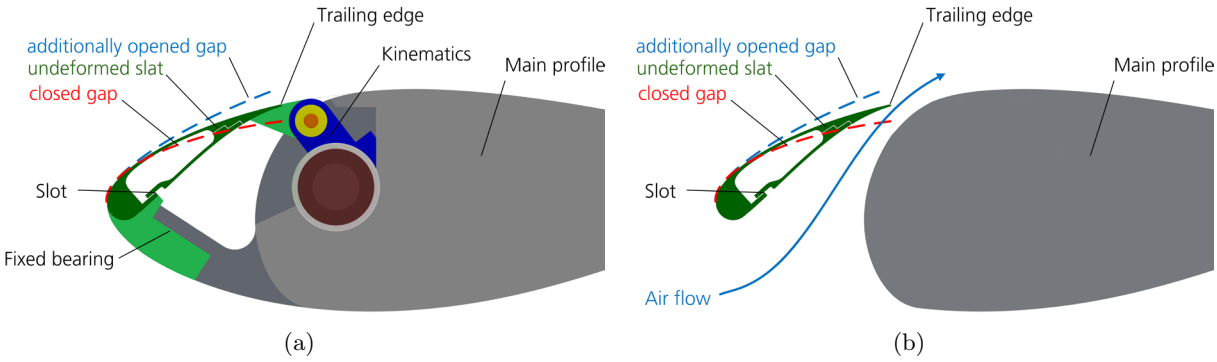

Figure 2: Working principle of the shape-adaptive slat with sketched deformed slat shapes. (a) Structural concept in the span-wise plane of the actuation stations. (b) Structural concept at the span-wise planes away from the actuation stations.

The presented concept of a shape-adaptive slat is developed for use on a scaled wind tunnel model. Future investigation deals with the up-scaling of the selected concept.

5 DESIGN PROCESS

This section presents the detailed design process of the slat. In a first step the slat's inner contour is optimized in a parameter study to minimize the resultant strains in case of a deformed slat and therefore to improve the fatigue behaviour. As a next step six identical slat segments are manufactured to investigate the deformation behaviour of the slat and to validate the generated FE models. Afterwards these segments are used for fatigue investigations. This section will be closed with a short description of the final wind tunnel model.

5.1 Parameter study for fatigue improvements

The objective of this study is to minimize the resultant maximum strain in case of a deformed slat and therefore to improve the fatigue behaviour as well as to ensure the fatigue strength during the whole wind tunnel measurements. This is achieved with a parameter study of the inner contour of the slats' suction side. The general objective is to spread a resultant possibly concentrated local strain maximum to the whole compliant middle section of the slat. In contrast to the soft requirement of an additional gap enlargement the possibility of a completely closed gap is a hard requirement. Consequently this load case is used for the following numerical investigations.

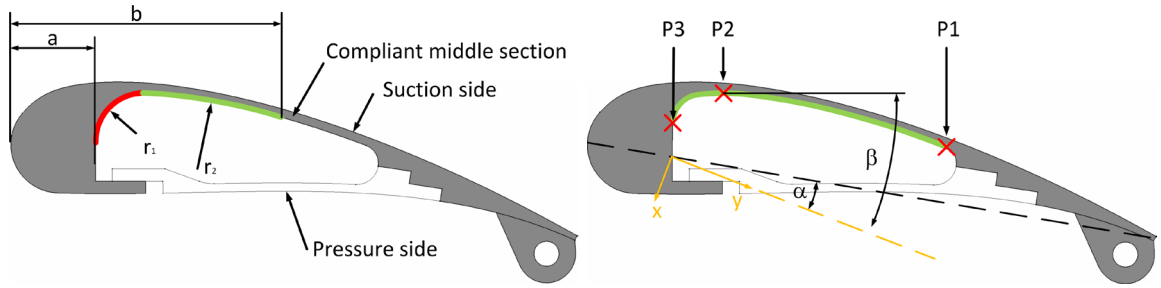

(a) (b)

Figure 3: Sketch of two different approaches to describe the inner contour of the slat's pressure side. (a) Two tangential radii as contour description. (b) Polynomial function as contour description.

In order to describe the slats inner contour two different approaches are used. The first approach uses two tangential radii to describe the inner contour and is shown in figure 3(a). In order to get a definite contour description the following boundary conditions are defined. Both radius r_1 and radius r_2 merge tangentially to each other and to the slats' front as well as rear part. The starting point of radius r_1 is defined with parameter a. The end point of radius r_2 is defined with parameter b. The contour variation is achieved with various values for the parameters a, b and r_2. Parameter r_1 is defined as a result of the remaining three parameters and the associated boundary conditions.

As a second approach the inner contour is described with different polynomial functions of orders 5 to 12 and various corresponding coefficients c_i. A sketch of the approach is shown in figure 3(b). A definite polynomial contour is achieved with the following boundary conditions. First, the polynomial function is only considered between the x coordinates of point $P1$ and point $P3$. The polynomial function is tangential to the slat's front part in point $P3$ as well as to the rear part in point $P1$. In order to achieve a contour variation the coordinates x and y of Point $P2$ and the slope β in the same point are used as parameters. In order to generate full definite polynomials only six functional coefficients with $c_i \neq 0$ are used. For functions with orders higher or equal than 6 the four even leading coefficients as well as the linear and the absolute coefficients are used. In case of order 5 each coefficient is used to define the function. The polynomial functions of order 10 are identified as best contour description. This function type is used for the detailed parameter study.

In order to perform the parameter study a combination of different tools is used. The base is built with a parametric CAD - model in Catia. The parameter variations are realized with Matlab. For each parameter combination the CAD - model is updated by Matlab. The resultant slat's inner contour of each combination is exported to a parametric FE - model in Ansys. The numerical calculations are done with a two-dimensional FE - model of the slats' structure in plane of one actuation station (compare sketched plane

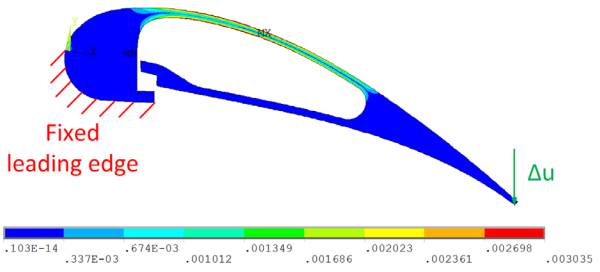

Figure 4: Resultant numerical strain distribution in case of a completely closed gap.

in figure 2(a)). The used FE - model is shown in figure 4. In order to simulate the expected loads the slats' leading edge is defined as fixed. The middle section deforms in consequence of the attached displacement Δu.

The best performing configuration in terms of minimized strains is achieved with a polynomial function of order 10. The resultant strain distribution is shown in figure 4. The maximum strain ε is approximately 0.3 %. Based on this result and to ensure the fatigue strength of the wind tunnel model during the whole wind tunnel measurements a heat treated steel of type 30CrNiMo8 is used as the material for the wind tunnel model of the slat. This results in a mechanical stress σ of 630 N/mm^2. Of course there is the potential for further strain reductions, for example with other contour descriptions, but due to the limited time this has to be explored outside of this project. Additional strain reductions could be reached with thinner slat skins, but the combination of the slats dimensions with milling as the manufacturing process leads to a minimum skin thickness t_{skin} of 1 mm. Otherwise the risk of vibrations during the manufacturing process and therefore increased manufacturing inaccuracies is to high.

As shown in figure 4, the pressure side of the slat's skin is slotted. In case of a closed gap the pressure side's skin raises from the front part of the slat. This effect is also shown in figure 4. In case of an additional gap enlargement the pressure side's skin shores at the slat's front part.

5.2 Manufacturing

Based on the results above a pre version of the slat is designed. In a next step this design is used to manufacture six identical slat segments with a span s of 40 mm. One slat segment is shown as an example in figure 5. As can be seen the force application point (connection with kinematics) is located in an extension of the slats' trailing edge. The slats' bearing is realized with two bolts putted in an extension at the slats' leading edge. The bolts are not shown.

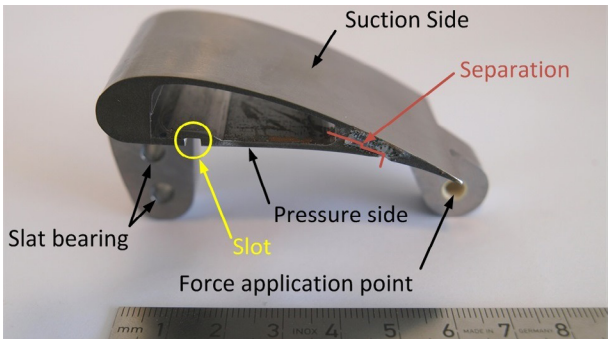

Figure 5: Manufactured slat segment.

In order to manufacture the slat segments the slats' suction and pressure sides are manufactured separately in a CNC milling process. Afterwards both sides are glued together. The same manufacturing process is used for the final wind tunnel model of the slat.

5.3 Static investigations

As next step one slat segment is used for static investigations. The objective is to determine the real slat's deformation behaviour, the resultant strain distribution, the necessary deformation forces to close the gap completely and to validate the generated numerical tools. The used experimental setup is shown in figure 6(a).

Two bolts are used to fix the slat's leading edge at a massive block. Another bolt is used to fix different gravity forces at the force application point. An optical measuring system called GOM ARAMIS^{TM}[22] is used to detect the deformation behaviour and the strain distribution

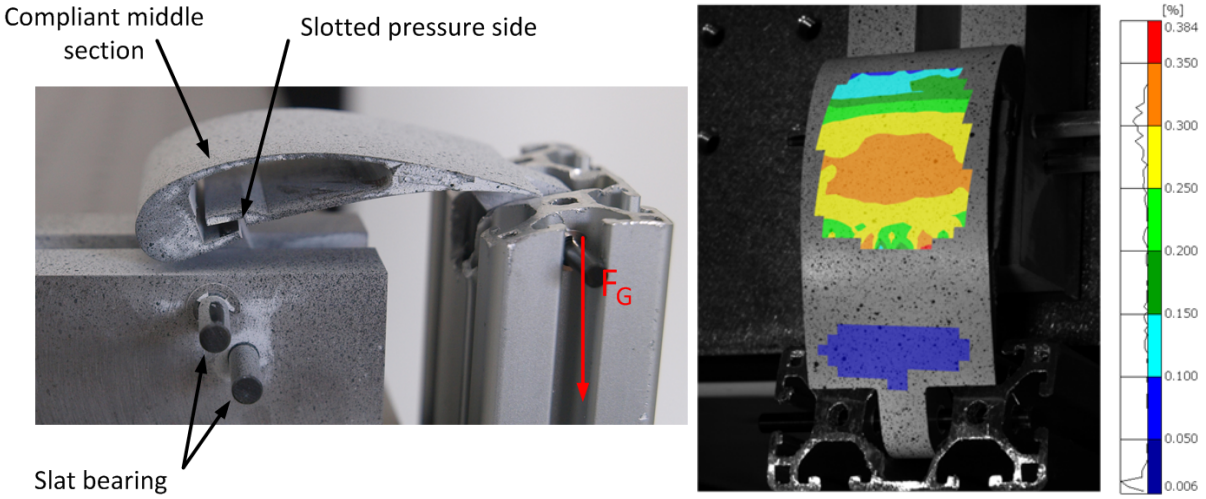

(a) (b)

Figure 6: Experimental setup to validate the resultant simulated strain distribution (left) with the resultant experimental strain distribution in the case of a fully closed gap (right).

for different load steps. As shown in figure 6(b) only the compliant middle section and the rear slat shortly before the trailing edge are measured, because of light reflections and system restrictions.

The determined shifting curve of the slat's trailing edge is sketched in figure 8. As can be seen the resultant shifting curve is not identical to the direction of the shortest gap between the slat's trailing edge and the surface of the main profile. In order to close the gap completely a displacement at the force application point u_{close} of approximately 9 mm is required. The corresponding force F_{close} is 120 N. The resultant maximum strain ε_{close} is 0.34 %. It follows a deviation of 12 % compared to the numerical results of figure 4, which is in an acceptable range. The resultant mechanical stress σ_{close} is 714 N/mm^2. The permitted maximum fatigue strength without a stress offset is figured out from the Smith diagram (diagram TB 3-1 in [23]) in figure 7 and is approximately 610 N/mm^2. Therefore the existing maximum mechanical stress is higher than the permitted fatigue strength without a stress offset. This means the fatigue strength for a dynamic shape variation with an amplitude of $u_{close} \approx 9$ mm is not allowed. The resultant maximum permitted stress for an additional gap

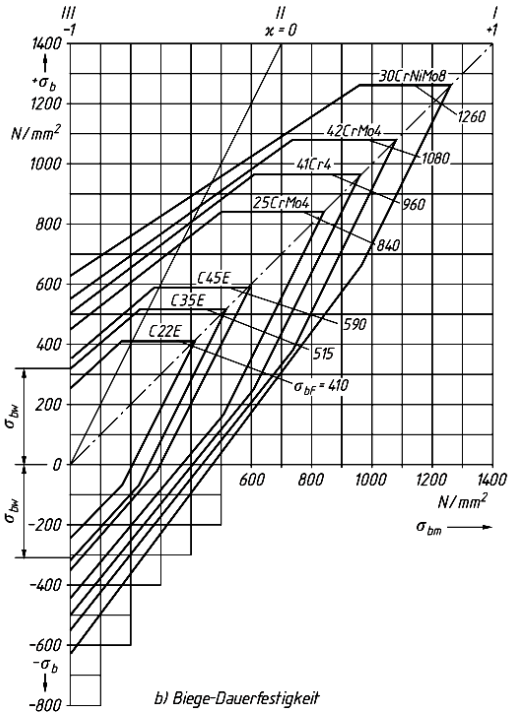

Figure 7: Smith diagram for different heat treated steels (diagram TB 3-1 in [23])

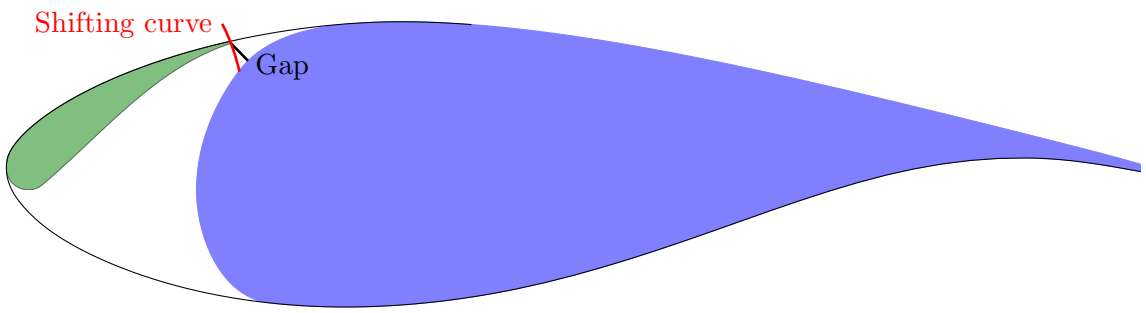

Figure 8: Resultant shifting curve of the slat's trailing edge due to different weight forces at the slats' force application point.

enlargement σ_{open} is $-450\,\mathrm{N/mm^2}$ and is also acquired from figure 7. The corresponding permitted gap enlargement u_{open} to the full closed gap is calculated approximately with a proportion equation of $u_{open} = (\sigma_{open}/\sigma_{close}) \cdot u_{close}$. Using this equation an additional gap enlargement u_{open} of approximately 5.7 mm directly at the force application point results.

5.4 Fatigue investigations

As described above the next step are fatigue investigations to ensure the fatigue strength during the wind tunnel measurements. Therefore a classic fatigue test up to $1 \cdot 10^6$ cycles is performed for the slat segments. The opening and closing of the gap, as sketched in figure 2, is one load cycle. The closing force F_{close} of 120 N is applied to simulate the complete closing of the gap. The used test rig simulates a continuous opening and closing of the gap. This is done by an eccentric shaft with a variable stroke that drives a connection rod, which is directly linked to the trailing edge of the slat. An electric motor drives the shaft at approximately 300 rpm, which leads to a loading frequency of 5 Hz. As the eccentric shaft induces a constant stroke within the fatigue test, the test is deflection controlled. The opening and closing force that must be reached have to be calibrated with a few cycles before the fatigue test starts. As the stroke is then locked, the resultant force is monitored during the fatigue test. Any change in the mechanical behaviour of the slat can then be seen in a change of the resultant force. Additionally several strain gauges were applied to the slats to monitor any changes in the strain distribution on the slats.

In total five slats were tested. Because of the limited amplitude of the used test rig each slat segment is investigated with different closing and opening forces to cover all expected fatigue loads. This paper presents the results of slat segment 4. This segment is tested with a maximum force F_{max} of 123 N (blue curve) which is close to the closing force F_{close} with 120 N and a minimum force F_{min} of -11 N (red curve). Figure 9 shows the resultant forces over the entire fatigue test up to $1 \cdot 10^6$ cycles.

It can easily be seen that the resulting force barely changes over the course of the test. Within the first hundred load cycles the resultant force changes the most. This is a result of the mechanical settling of the test rig. After that settling any barely change of the resultant force are visible. This behaviour was proven by examining the measurements of the strain gauges,

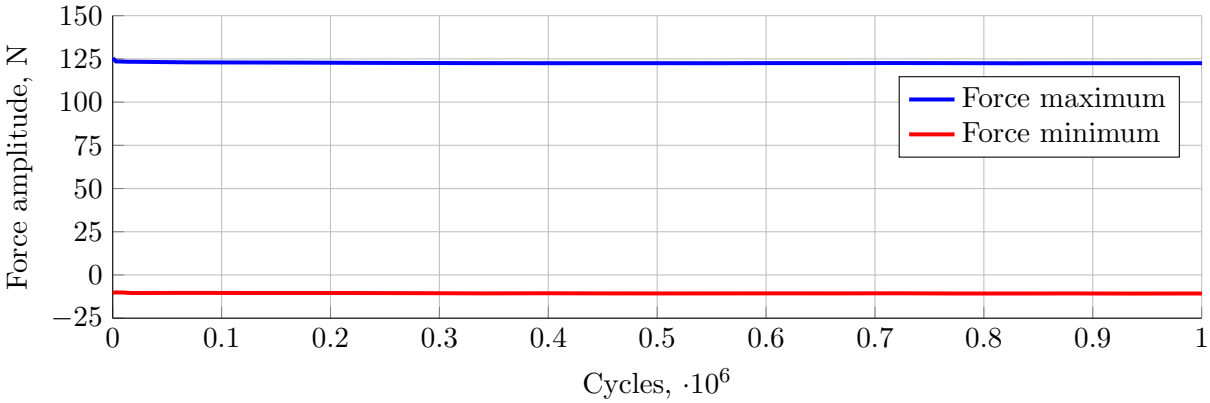

Figure 9: Envelope curve of the maximum and minimum forces that resulted from the fatigue loading of slat segment 4.

that were applied to the upper surface of the slat. Thereby and in combination with the results of the remaining four slat segments it can be stated, that no measurable damage occurred in the slat and the operational stability is given.

After the successful test, the strain gauges are removed from the slat to examine the surface in detail. A photograph of the slat is given in figure 10. The remnants on the surface are the soldering points from the strain gauges that could not be removed without damaging the slats' surface. No cracking or roughening is found on the slat. Severe mechanical damage due to fatigue could not be found. After the optical examination several bores are applied to the slat for installation tests of pressure taps. These bores can also be seen in figure 10.

In total, all slats showed this type of behaviour. No noticeable change in the resulting force was observed. In order to simulate an additional gap enlargement one slat segment is tested with a maximum force F_{max} of 77 N and a minimum force F_{min} of −75 N. The resultant stress ratio is $R = \sigma_{min} / \sigma_{max} \approx -1$, which is known to be a severe load case in fatigue. This proves, beyond the already shown operational stability, structural reserves against fatigue.

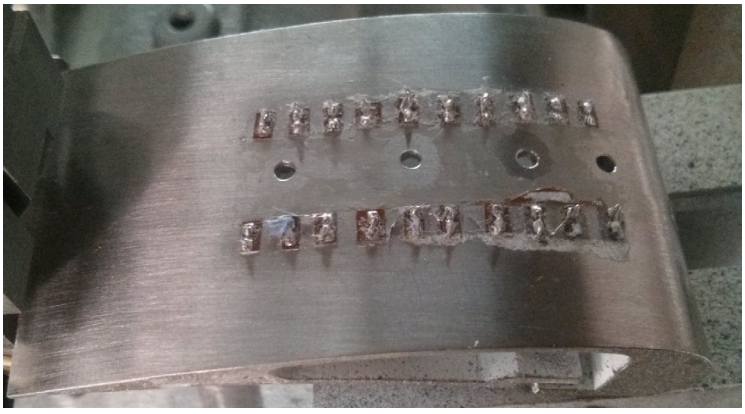

Figure 10: Slat segment 4 after the fatigue test with approximately $1 \cdot 10^6$ cycles. The bores visible in the picture were applied after the fatigue test.

6 WIND TUNNEL MODEL

Based on the results above the final wind tunnel model with the slat and the corresponding kinematics as well as additional parts are designed. Also the stepping motor to drive the shaft is selected. Afterwards the final wind tunnel model with a span s_{main} of 805 mm and the corresponding slat with a span s_{slat} of 803 mm are manufactured. The finally manufactured wind tunnel model with the shape-adaptive slat in front of the main profile is shown in figure 11.

Compared to the slat segments the slat's bearing is redesigned with the objective of reduced flow disturbances generated by the slat mounting itself. Hence two screws in chord direction instead of two bolts in span wise direction are used. An additional bolt in chord direction is used for deformation induced shear loads and to ensure identical slat position after possible reassemblies. The thickness at each slat mounting is 15 mm. The distance between the middle planes of the actuation stations is 200.75 mm.



Figure 11: Manufactured wind tunnel model with the non-deformed shape-adaptive slat in front of the main profile.

7 CONCLUSION

This paper gives an overview of the design of a shape-adaptive slat for scaled wind tunnel investigations at a wind energy profile. Based on the given geometry and requirements the structural concept of the slat is developed and described. In order to improve the fatigue behaviour of the slat's wind tunnel model the suction side's skin of the slat is designed in a parameter study with the objective to reduce the resultant strains in case of a deformed slat. In the case of a completely closed gap a maximum strain ε_{close} of 0.34 % results. The fatigue strength of the wind tunnel model is proven with experimental fatigue investigations with up to $1 \cdot 10^6$ cycles. Finally the wind tunnel model with the shape-adaptive slat and the corresponding kinematics is manufactured and presented.

As a next step the hardware to drive the stepping motors will be modified for controlled shape actuations. After that a wind tunnel campaign with controlled shape actuations as reaction of turbulent inflow conditions which are generated by an active grid will be done.

Furthermore, investigations to transfer the developed concept of the scaled slat to a full-scale slat are planned. Based on the changed dimension the main objective is to check the full-scale suitability of the selected concept and actuators. Another objective of interest is to use GFRP instead of metal as the slat's material.

ACKNOWLEDGEMENTS

This work was funded by the German Ministry of Economic Affairs and Energy (BMWi) on decision of the German Bundestag in the frame of the SmartBlades project (funding reference no. 0325601A/B/C/D).

REFERENCES

[1] Berry, D., *Design of 9-Meter Carbon-Fiberglass Prototype Blades: CX-100 and TX-100*, Sandia Report SAND2007-0201, USA, 2007.

[2] Ashwill, T., *Passive Load Control for Large Wind Turbines*, Sandia Report SAND2010-3276C, USA, 2010.

[3] Barlas, T.K. and van Kuik, G.A.M., *Review of state of the art in smart rotor control research for wind turbines*, Progress in Aerospace Science (2009), doi:10.1016/j.paerosci.2009.08.002, 2009.

[4] Barlas, A., Aagaard Madsen, H., Løgstrup Andersen, T., *Design and simulation of the rotating test rig in the INDUFLAP project*, DTU Wind Energy. (DTU Wind Energy E; No. 0063(EN)), 2014.

[5] Barlas, A., Bergami, L., Hansen, M.H., Pedersen, M.M., Verelst, D.R., Thomsen, K. Aagaard Madsen, H. *Load alleviation potential of active flaps and individual pitch control in a full design load basis*, In Proceedings of the EWEA Annual Event and Exhibition 2015, European Wind Energy Association (EWEA), 2015.

[6] Aagaard Madsen, H., Barlas, A., Løgstrup Andersen, T. *Testing of a new morphing trailing edge flap system on a novel outdoor rotating test rig*, In Scientific Proceedings, EWEA Annual Conference and Exhibition 2015. (pp. 26-30). European Wind Energy Association (EWEA), 2015.

[7] Berg, J. and Barone, M. and Resor, B. *Field Test Results from the Sandia SMART Rotor*, 51st AIAA Meet, AIAA 2013-1060, Texas, 2013.

[8] Pechlivanoglou, G. and Wagner, J. and Nayeri, C. and Paschereit, C., *Active aerodynamic control of wind turbine blades with high deflection flexible flaps*, in AIAA 2010-644, 48th AIAA Aerospace Sciences Meeting Including the New Horizons Forum and Aerospace Exposition, Orlando, Florida, USA 2010.

[9] Berg, D.E., Wilson, D.G., Resor, B.R., Barone, M.F., Berg J.C., Kota, S. and Ervin, G.*Active Aerodynamic Blade Load Control Impacts on Utility-Scale Wind Turbines*, Sandia National Laboratories, FlexSys Inc., 2009.

[10] Subramanian, B. and Kirtley, K. R. and Standish, K. J., *Method and apparatus for increasing lift on wind turbine blade*, Patent Application, No. US2010/0143152 A1.

[11] Larsen H., Mueller J.A., Larsen, L., *Blade for a rotor of a wind or water turbine*, Patent Application, No. WO2009/143846 A1.

[12] Mickeler, S., *Rotor blade for a wind power plant and wind power plant*, Patent application, No. WO 2009/146810 A2.

[13] Timmer, W.A. and van Rooij R.P.J.O.M., *Summary of the Delft University Wind Turbine Dedicated Airfoil*, Journal of Solar Energy Engineering, Vol. 125, Issue 4, Pages 488-496, Nov. 26 2003.

[14] Pechlivanoglou, G., Nayeri, C. N. and Paschereit, C. O., *Fixed leading edge auxiliary wing as a performance increasing device for hawt blades* DEWEK, Bremen, Germany, 2010.

[15] Gaunaa, M. and Zahle, F. and Sørensen, N. and Bal, C., *Quantification of the Effects of Using Slats on the inner Part of a 10MW Rotor*, EWEA 2012-European Wind Energy Conference & Exhibition, 2012.

[16] Monner, H.P., Huxdorf, O., Pohl, M., Riemenschneider, J., Homeyer, T. and Hölling, M. *Smart structures for wind energy turbines*, 25th AIAA/AHS Adaptive Structures Conference, AIAA SciTech Forum, AIAA 2017-0295, Grapevine, Texas, USA, 2017.

[17] Manso Jaume, A. and Wild, J., *Aerodynamic Design and Optimization of a High-Lift Device for a Wind Turbine Airfoil*, Springer Verlag. Pages 859-869, ISBN 978-3-319-27278-8.

[18] Gramüller, B., *Pressure-actuated Cellular Structures*, Dissertation, German Aerospace Center, Institute of Composite Structures and Adaptive Systems, Braunschweig, 2016.

[19] Vasista, S. and Tong, L., *Topology-Optimized Design and Testing of a Pressure-Driven Morphing-Aerofoil Trailing Edge Structure*, AIAA Journal, Vol. 51, No. 8 (2013), Pages 1898-1907.

[20] Krone, J.H., Huxdorf, O., Riemenschneider, J., Monner, H.P., Schur, F., Friedrichs, J. and Wiedemann, M., *Experimental investigation and design of a shape-variable compressor cascade*, CEAS Aeronautical Journal, doi:10.1007/s13272-016-0224-1, 2016.

[21] Monner, H. P., *Realization of an optimized wing camber by using formvariable flap structures*, Aerospace Science and Technology, Volume 5, Issue 7, Pages 445-455, 2001.

[22] GOM GmbH *ARAMIS - 3D Motion and Deformation Sensor*, `http://www.gom.com/metrology-systems/aramis.html`.

[23] Wittel, H. and Muhs, D. and Jannasch, D. and Voßiek, J., *Roloff/Matek Maschinenelemente*, 19th. edition, Vieweg + Teubner, Wiesbaden, 2009.

VIII ECCOMAS Thematic Conference on Smart Structures and Materials
SMART 2017
A. Güemes, A. Benjeddou , J. Rodellar and Jinsong Leng (Eds)

STRUCTURAL DESIGN OPTIMIZATION OF A MORPHING TRAILING EDGE FLAP FOR WIND TURBINE BLADES

THANASIS K. BARLAS*, YU-HUAN LIN* AND HELGE A. MADSEN*

* DTU Wind Energy
Technical University of Denmark (DTU)
Fredriksborgvej 399, Roskilde, Denmark
e-mail: tkba@dtu.dk, web page: http://www.vindenergi.dtu.dk

Key words: Morphing, flap, optimization, wind turbine

Abstract. A flap actuation system, the Controllable Rubber Trailing Edge Flap (CRTEF), for distributed load control on a wind turbine blade had been developed in the period from 2006 to 2013 at DTU (http://www.induflap.dk/). The purpose of the presented work is to optimize the structural design of the flexible part of the CRTEF based on a realistic blade section geometry in order to meet the required objectives and constraints. The objectives include the deflection requirements and the energy efficiency, while the constraints include the bending stiffness of the structure, the local shape deformations, critical material strength, and manufacturing limitations. A model with arches forming concave on the flap surface and enclosing the voids to be pressurized results in the bending movement of the flap when pressure is applied on the voids to straighten the arches. The model is designed using SolidWorks for the parameterization of the design and ANSYS Workbench for the static structural Finite Element Analysis (FEA) simulations. The built-in parametric optimizer of ANSYS Workbench, Direct Optimization of Design Exploration is used to optimize the design with the parameters of the geometry. The surface pressure loads during operation of the turbine with the flap installed are evaluated with XFOIL and included in the simulations. The model is developed first by qualitative analyses to obtain a reasonable preliminary design, and then by parametric optimization to have the final design. The parameterization of the design is improved on the way of optimizations, in order to expand the design space to solve the problem of stress concentration, so that it covers the design with an acceptable material safety factor. With the consideration of surface pressure loads during operation of the turbine, the optimum design fulfils the requirements for flap angle of 15deg and -15deg with the actuation pressure of 0.428 MPa and 0.386 MPa, and the material safety factor margins, respectively. The design also meets the objective for energy efficiency by the lower actuation pressure than in earlier designs and by the small volume of the voids. Besides, the constraint of the bending stiffness is fulfilled with the deflection of less than the flap angle of ±5deg when the turbine is operating without the actuation pressure, and the constraints of the local shape deformations and manufacturing limitations are also fulfilled.

1 INTRODUCTION

The size of wind turbines has increased steadily in the past decade. With a bigger rotor, the loads carried by all the components of a wind turbine have become an issue and consequently cost. Since the lower cost of energy per kWh is desired, reducing the loads on the blades is certainly one of the main focus of the research on wind turbines. One of the possible ways to reduce the loads without increasing the cost too much is to build blades with distributed local control surfaces and this concept is usually called 'smart rotor control'. Flaps, as one kind of the trailing edge aerodynamic devices, can serve as the control surface to reduce the loads on the blades [1]. A controllable flap can be actuated by different mechanisms. However, the strongest specifications for a robust control mechanism required by the wind turbine industry indicate no mechanical, metal and electrical parts in the blades. Therefore, the Controllable Rubber Trailing Edge Flap (CRTEF) has been designed, manufactured, and tested at Risø DTU in order to meet the requirements and realize the application in the industry of wind turbines [2, 3]. The CRTEF controls the flap by applying fluid or air pressure on the voids (chambers) in the rubber flap, and the geometry change of the voids results in the effect of the flap. Therefore, the geometry and distribution of the voids play important roles in the effect and efficiency of the flap mechanism. The presented work is focused on the optimization of the geometry and the distribution of the voids so that the desired flap angle can be met under several constraints, with the main design innovation being the use of only two actuation voids [4].

A conceptual prototype of the CRTEF has built and tested in the INDUFLAP project (Figure 1), the design of the geometry has to be further optimized. Instead of basing on a symmetrical airfoil, the present work is aimed at designing for the DTU 10MW reference turbine [5], and therefore FFA-W3-241 is the airfoil evaluated. Due to the feature of the extrusion process which is expected to be used in manufacturing, the project is focused on analyzing the 2D geometry of the flap with a span-wise constant cross section. The size of the chord to be analyzed is defined by the chord length of the DTU 10MW reference turbine at 80% rotor radius from the rotor center, which is the span-wise location that gives the optimum reduction in the blade root moment fatigue load. The ratio of the chord to be replaced with the rubber flap is determined to be 10% so that the flap is able to change the lift sufficiently to attenuate a big portion of the expected load fluctuation with insignificant drag penalty. There is a lot of literature covering different concepts of actuators for morphing or flap control. The biggest common challenge of the material and the structure in this application is the conflict between the requirement for low bending stiffness of the flap which leads to low actuation force and the requirement for high bending stiffness of the flap which is relevant to resisting the surface pressure loads during operation. The conflict is resolved by trying to balance the two requirements.

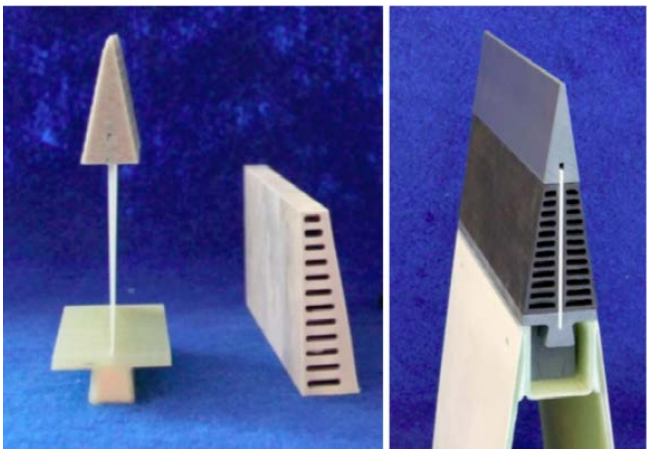

Figure 1: CRTEF design developed in the INDUFLAP project.

The presented work is structured as follows: In section 2, the objectives and constraints of the project are illustrated, followed by the methods, models and software used in the project. The load cases are determined and estimated in section 3. In section 4, the development of the preliminary design and its optimization is presented, and the design is then evaluated in section 5. Based on the evaluated results, the achievements and the disadvantages are concluded in section 6, followed by recommendations for future work.

2 OPTIMIZATION PROBLEM AND NUMERICAL TOOLS

Initially, the objectives of the design optimization include:

1. maximizing the effect of the flap angle
2. Maximizing the energy efficiency of the flap control system by minimizing the actuation pressure and the volume of the voids
3. maximizing the bending stiffness of the structure

The constraints include:

1. local shape deformations
2. the strength of the material
3. the manufacturing limitations

Although the overall objectives and the constraints are provided, the different objectives are actually contradicting. As a result, based on the priority and the extents to which the objectives are desired, some of the objectives and the constraints are quantified. The ideal goal of the flap angle is determined to be ±15deg, and ±10deg in a limited operation scenario. In order to evaluate the effect of flap angle more directly in the analyses, the equivalent tip deflection in the vertical direction of the flap angle is used as the measurement of the flap angle. In order to have a safe design which does not deflect too much when the actuator is not working, a flap angle within ±5deg during normal operation of the wind turbine without void pressure is set as the objective. The material used in the design is determined to be the thermoplastic Santoprene 101-73, due to the resistance of the material to the environment conditions which include UV radiation, fatigue, and lightening, and the fact that the material

is elastic with high strength and suitable for extrusion process. For strength analysis, the tensile stress at break σ_U = 8.8 MPa is used when evaluating the equivalent von Mises stress in the simulations. Due to the manufacturing efficiency in terms of time and cost, the flap is determined to be manufactured by extrusion which indicates a constant cross section, and this process limits the minimum wall or void thickness of the flap geometry to be 2 mm and the tolerance being no less than 0.1 mm.

In the work, several analysis tools were used. XFOIL [6] was used to estimate the static pressure on the surface of the flap, so that the loads during operation of the turbine can also be considered in the design process. SolidWorks [7] was used to design the geometry of the flap with the the built-in feature of parametric design. Static Structural analysis system in ANSYS 16.0 workbench [8] was then used to perform the simulations using the finite element method. With the results of the simulations, the performance of the designs was qualitatively analyzed, in order to have a better preliminary design. Finally, the Direct Optimization system, a built-in Design Exploration system in ANSYS 16.0, was used in combination with the parametric design in SolidWorks to conduct parametric optimizations.

The airfoil profile of FFA-W3-241 with 79 coordinate points and a unit chord was used in the analysis. After the profile was loaded, the desired flap angle was then added by modifying the geometry of the airfoil. The hinge point of the flap was added at 10% chord from the trailing edge and 50% thickness at the position. With the airfoil with desired flap, the viscous analysis with Reynold's number, Re = 5e6, was performed. The Reynold's number was calculated based on a kinematic viscosity of 1.456e−5 m2/s and a flow velocity of V = 72.6 m/s based on the 80% blade span section on the reference wind turbine at rated power operation. The pressure coefficient, Cp, distributed on the surface of the airfoil was calculated with the input angle of attack (AOA) in the analysis. The pressure coefficients were then used to calculate the static pressure loads on the surface of the flap.

SolidWorks is a 3-dimension (3D) computer-aided design (CAD) software. However, in the project, since the flap was determined to be designed with a constant cross section along the span due to the limitations of manufacturing, a 2-dimension (2D) analysis with the plane strain behavior should be as valid as a 3D analysis, and a 2D analysis is computationally cheaper. Therefore, the work is based on 2D analyses and the designed component in SolidWorks will be a 2D surface. SolidWorks was chosen as the CAD software to be used because of its friendly user interface, handy sketch tools, and most importantly, its feature of parametric design which can easily be coupled with the parametric analysis in ANSYS 16.0.

The finite element analysis (FEA) software to be used is ANSYS 16.0, which is powerful in parametric analysis. Static Structural analysis system in ANSYS 16.0 workbench is the system used. The non-linearity of the material is implemented with Mooney-Rivlin model with the coefficients provided by the material test data, and the material is assumed to be incompressible. The Mooney-Rivlin model with two parameters is used with different sets of parameters for different strain ranges, varying from 10-50%, depending on the simulated load case. The mesh settings of the simulations have been changed for different designs. The general idea is to have finer mesh at the edges with high curvature and large deformation, and coarser mesh for the rest of the model. Although a finer mesh gives more accurate solutions especially for stress values, it is more computationally expensive. Therefore, during the design process, the model is meshed fine enough to have valid results with acceptable computational cost. In order to make sure the mesh is fine enough, convergence tests are

carried out from time to time and most importantly, for the optimum model. The element types used in the simulations are 8-node quadrilateral (Quad8) and 6-node triangle (Tri6). The meshing tool first generate the mesh with all triangles and then converts most of the triangles to quadrilaterals, creating a quadrilateral dominant mesh. Due to the non-linear behavior of the design, large deflection calculations are enabled in Ansys, which includes stiffness changed resulting from changes in element shape and orientation due to large deflection, large rotation, and large strain. In terms of boundary conditions, the edge on the leading edge side of the flap is set to be fixed to simulate the connection to the main part of the blade, and the pressure is applied on the edge of the void, as well as a tip force at the trailing edge, equivalent to the aerodynamic pressure on the flap surface (Figure 2).

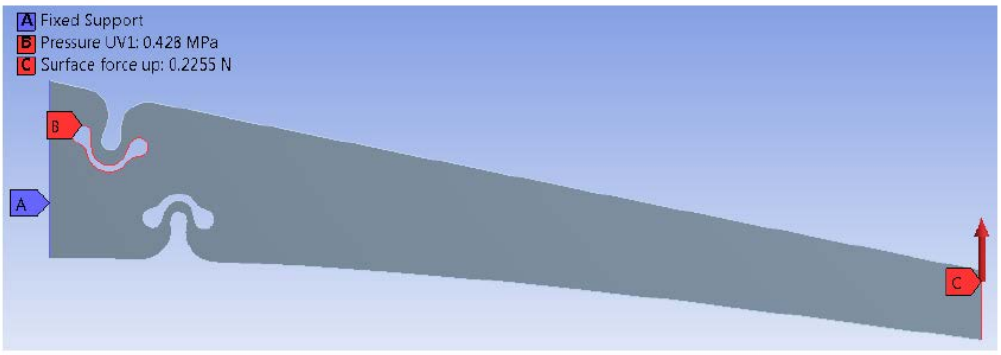

Figure 2: Boundary conditions on the flap geometry.

In order to perform parametric optimization, the built-in optimizer in ANSYS 16.0 is chosen, which is coupled with SolidWorks to change the parameters of the geometry and perform simulations automatically. In order to get the global optimum instead of local optimum, the direct optimization method 'Multiple-Objective Genetic Algorithm (MOGA)' is utilized. In the MOGA method, crossover and mutation are performed to generate a new population in every iteration, making it a more refined method than Screening. With the global optimum from MOGA as the starting point, the gradient-based approach 'Nonlinear Programming by Quadratic Lagrangian (NLPQL)', which is based on quasi-Newton methods is used to find the even more refined local optimum.

3 LOAD CASES

During the normal operation of the wind turbine installed with the flap, two load scenarios should be considered:

1. When the flap is not actuated, i.e. no void pressure.
2. When the flap is actuated with the desired effects.

Four load cases were designed using XFOIL and the equivalent tip forces were estimated for these two load scenarios. The equivalent tip force was obtained by applying the tip force which could result in approximately the same tip deflection (Figure 3).

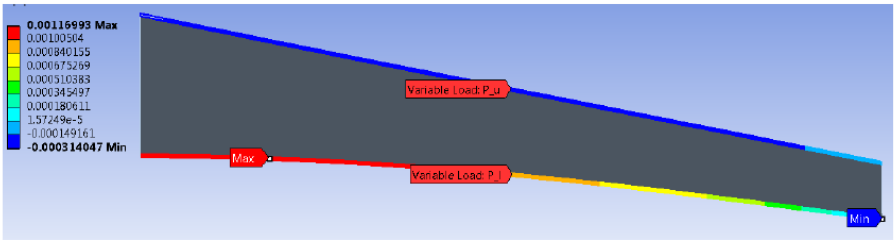

(a) When the surface pressure loads [MPa] of the case of stiffness up check were applied on the surface of the complete flap without voids, a tip deflection of flap was 5.79 mm.

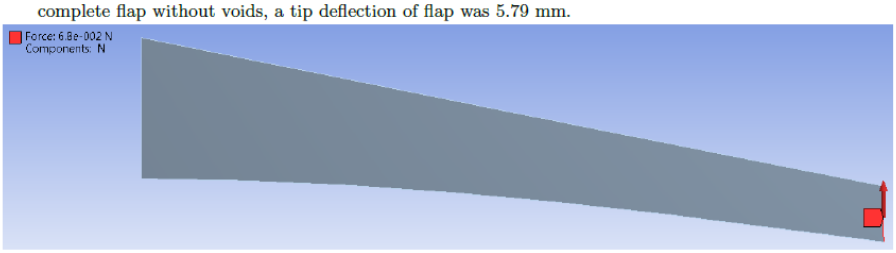

(b) A tip force of 0.068 N/mm causing a tip deflection of 5.87 mm was considered as the equivalent tip force in this case.

Figure 3: Surface pressure and equivalent tip force calculations.

In the first scenario, the flap is still carrying the surface loads during operation, and the stiffness of the flap without void pressure should be designed based on this scenario. In order to cover the operational range of the turbine, the two most extreme cases of the scenario should be considered.

1. The stiffness up load case: In this load case, the flap is deflected to -5deg under the maximum surface pressure load which corresponds to the AOA with the maximum Cl.
2. The stiffness down load case. In this load case, the flap is deflected to 5deg under the maximum surface pressure load which corresponds to the AOA with the minimum Cl.

The values of the AOA for these two load cases were then found with XFOIL to be 16deg for the first case and -20.4deg for the second case. These two cases were then defined as the first and second design load cases. In the second scenario, the desired flap angles are ±15deg. When the flap is actuated to such effects, it should reach the desired flap angles while carrying the surface loads. Therefore, two more extreme load cases were then defined.

1. The upper void effect load case: In this load case, the flap angle is actuated to 15deg, and the actuated structure is carrying the surface pressure load which corresponds to the AOA with the maximum Cl.
2. The lower void effect load case: In this load case, the flap angle is actuated to -15deg, and the actuated structure is carrying the surface pressure load which corresponds to the AOA with the minimum Cl within the operational range (AOA within ±15deg).

The values of the AOA for these two load cases were then found with XFOIL to be 14.9deg for the first case and -15deg for the second case.

For these four design load cases, the Cp values distributed on the airfoil were then output from XFOIL.

The pressure values to be applied on the surface of the flap were then calculated using the equations:

$$C_p = \frac{p - p_\infty}{q_\infty} \qquad \textbf{(Equation 1)}$$

$$q_\infty = \frac{1}{2}\rho_\infty {V_\infty}^2 \quad \textbf{(Equation 2)}$$

where V_∞ = 73 m/s is the freestream velocity approximated from the freestream velocity, ρ_∞ = 1.225 kg/m^3 is the freestream air density; q_∞ is the freestream dynamic pressure and can be calculated to be 3.267e3 Pa, p_∞ is the freestream static pressure; and p is the static pressure at the point where Cp is evaluated. The summary of load cases and equivalent tip force estimation are shown in Table 1.

Table 1: Summary of load cases and equivalent tip force estimation.

	Name	Stiffness up	Stiffness down	Upper void effect		Lower void effect	
Load Case	Flap Actuated	No	No	No	Yes	No	Yes
	Flap Angle [°]	-5	5	0	15	0	-15
	AOA [°]	16.0	-20.4	16	14.9	-20.4	-15.0
	Notes	Used	Ignored	Start	End	Start	End
	Tip Deflection at Flap Angle [mm]	26.03	-26.21	0	-79.64	0	79.26
Estimation	Tip Deflection with all loads [mm]	25.99	-26.07	-0.30	-80.08	0.47	79.29
	Counteracting Tip Force [N/mm]	-0.088	0.02	-0.108	-0.205	0.045	0.115
	Safety Factor	1.1	1.1	1.1	1.1	1.1	1.1
	Equivalent Tip Force [N/mm]	0.0968	-0.022	0.1188	0.2255	-0.0495	-0.1265

4 DEVELOPMENT OF THE DESIGN

Based on literature and previous work, an arch model with arches forming concave on the flap surface and enclosing the voids to be pressurized is expected to result in the bending movement of the flap when pressure is applied on the voids to straighten the arches. First, a qualitative investigation was performed with sweeping the main design parameters in order to have a preliminary design for the shape and location of the voids. The design is parameterized and the upper void of the design is analyzed qualitatively in order to have the preliminary design. With this preliminary design, the stiffness and the material safety factor of the upper void are parametrically optimized. Then, the design space is expanded with more parameters to deal with the problem of stress concentration. After the parametric optimizations within the expanded design space covering the design with acceptable safety factor, the lower void is then parametrically optimized followed by the determination of the locations of the voids. Another iteration of the estimation of the surface loads is then carried out, followed by the iterated optimization of the lower void. This gives the optimum design of the project. The geometry of the preliminary design is shown in Figure 4.



Figure 4: Geometry of the preliminary design.

The arch geometry of the voids is then parametrized using 10 geometrical variables, as shown in Figure 5 and Table 2.

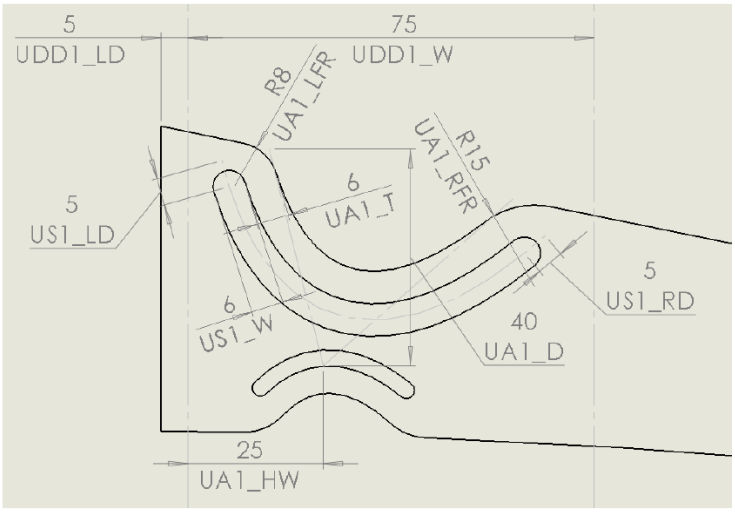

Figure 5: Parameterization of the design.

Table 2: Design parameters for the preliminary design.

Code	Value [mm]	Definition
UDD1_LD	5	Distance between the left end and the design domain
UDD1_W	35	Width of the design domain
UA1_D	30	Depth (of the control point) of the arch
UA1_T	4	Thickness of the arch
US1_W	3	Width of the slot
US1_LD/ US1_RD	10	Distance between the left/right end of the centerline and the center of the left/right cap of the slot
UA1_LFR/ UA1_RFR	11	Radius of the fillet of the left/right corner

In order to solve the stress concentration issues found in the preliminary design, the parts with stress concentration were trimmed with higher curvature. First, the diameter of the half-circle caps at the slot ends was increased. Second, the upper side of the arch was trimmed with a spline with lower curvature. Besides, the spline which constructs the arch was made perpendicular to the surface in order to have a symmetric stress distribution (Figure 6).

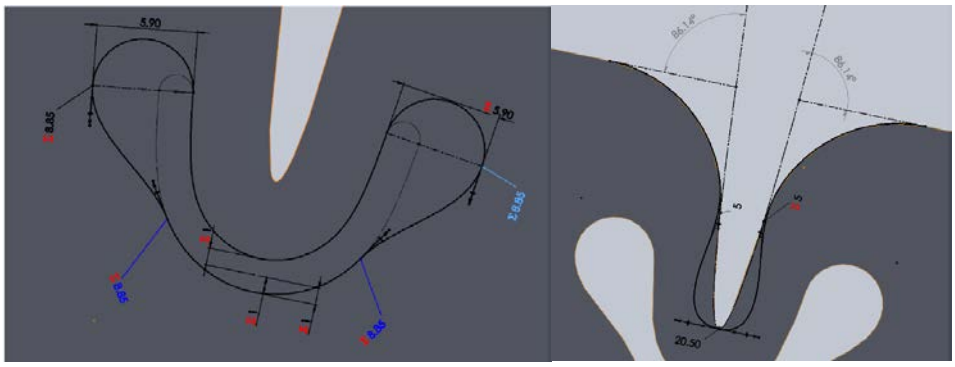

Figure 6: Parametrization of detailed design of slot ends.

The purpose of the optimization was to increase the safety factor to an acceptable value. In order to have a global optimum, a global optimization was first carried out, followed by the local optimization to refine the optimum. With the design with an acceptable safety factor, the optimizations for the lower void pressure were then performed, and finally the position of the voids. The optimization methods, objectives, constraints, input variables and results for the upper void can be found in Table 3.

Expanded Design Space Global Optimization for Safety Factor					
Method	MOGA				
Objectives	Maximize Safety Factor				
Constraints	Effect Tip Deflection ≤ -80 mm Arch location ≤ 62 mm Stiffness Tip Deflection ≤ 20 mm				
Converged	Yes				
		Units	Optimum	Lower bound	Upper bound
Input Variables	UDD1_W	mm	35.58	34.00	37.00
	UA1_T	mm	5.35	5.00	7.00
	US1_LD	mm	13.23	10.00	15.00
	UA1_D	mm	35.07	30.00	36.00
	UA1_LFR	mm	9.75	8.00	12.00
	UA1_UF_W	mm	26.30	15.00	30.00
	US1_End_Dia	mm	5.09	5.00	8.00
	US1_End_TF	mm	0.830	0.800	1.20
	Void Pressure	MPa	0.475	0.400	0.500
Results	Stiffness Tip Deflection	mm	19.93	-	-
	Effect Tip Deflection	mm	-90.30	-	-
	Arch Location	mm	61.20	-	-
	Safety Factor	-	0.92	-	-
	Minimum SF Location	-	Slot	-	-

Expanded Design Space Local Optimization for Safety Factor						
Method	NLPQL					
Objectives	Maximize Safety Factor					
Constraints	Effect Tip Deflection ≤ -80 mm Arch location ≤ 62 mm Stiffness Tip Deflection ≤ 20 mm					
Converged	No, but validated					
		Units	Start	Optimum	Lower bound	Upper bound
Input Variables	UDD1_W	mm	35.58	35.11	34.00	37.00
	UA1_T	mm	5.35	5.00	5.00	7.00
	US1_LD	mm	13.23	14.21	10.00	15.00
	UA1_D	mm	35.07	35.15	30.00	36.00
	UA1_LFR	mm	9.75	9.20	8.00	12.00
	UA1_UF_W	mm	26.30	27.61	15.00	30.00
	US1_End_Dia	mm	5.30	6.06	5.00	8.00
	US1_End_TF	mm	0.830	0.825	0.80	1.20
	Void Pressure	MPa	0.451	0.463	0.400	0.500
Results	Stiffness Tip Deflection	mm	20.00	20.00	-	-
	Effect Tip Deflection	mm	-80.44	-80.03	-	-
	Arch Location	mm	60.64	60.64	-	-
	Safety Factor	-	1.12	1.31	-	-
	Minimum SF Location	-	Slot	Slot	-	-

Table 3: Global and local optimization parameters and results.

The optimum design gives a minimum safety factor of 1.31, effect tip deflection of -80.06 mm, stiffness tip deflection of 20 mm and arch location of 60.64 mm. The lower void optimization gives similar results with an arch location of 19.77mm. The convex shape and the non-linearity of the design point were both considered to be acceptable.

4 EVALUATION OF THE DESIGN

The details of the final optimum design which fulfills the objectives of the project of having a flap effect of ±15deg with voids of small volume and achieving the stiffness requirement were examined. The mesh of the final design, consisting of 5000 elements is shown in Figure 7.

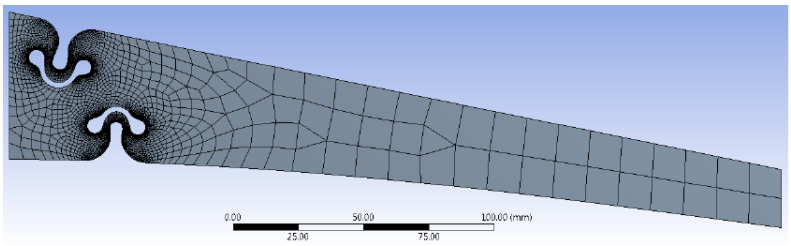

Figure 7: Mesh of the final design.

The deformed shape with the upper void activation, as well as the equivalent stress distribution is shown in Figure 8, showing an acceptable convex shape and stress distribution.

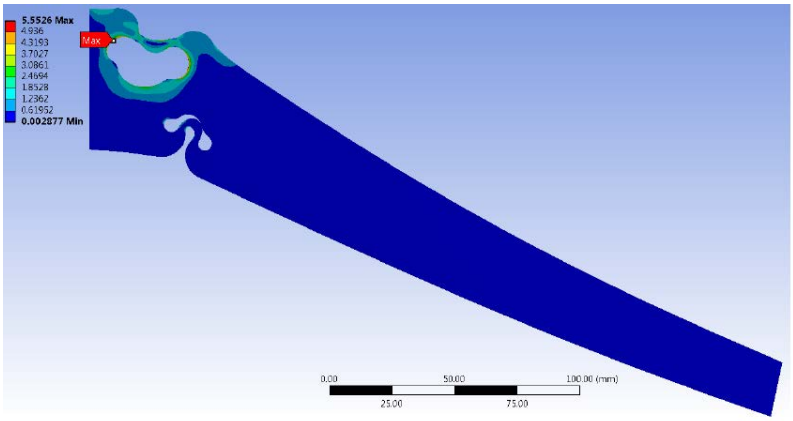

Figure 8: Deformed shape and equivalent stress of final design.

5 CONCLUSIONS

The flap design has been developed by using the qualitative analysis and parametric optimization, with the strategy of utilizing the allowable stiffness of the structure, while the desired deflection is fulfilled, to optimize for the material safety factor and the energy efficiency. The optimum design point fulfills the main objective of the project, which is having ±15deg flap angle under surface loads during operation of the turbine. It also meets the bending stiffness constraint of deflecting within ±5deg during operation of the turbine without actuation pressure, the local deformation constraint of having acceptable deformed shape locally and the material strength constraints by having a minimum safety factor, while respecting all manufacturing constraints. Further work includes developing the design solution for having a smooth aerodynamic surface on the deformed arch shape, and aerodynamically testing the developed design in the wind tunnel and rotating rig.

AKNOWLEDGEMENTS

The work has been funded by the Danish development and demonstration program EUDP under contract J.nr. 64015-0069 for the research project and research and development work Full scale demonstration of an active flap system for wind turbines.

REFERENCES

[1] Barlas T. K, and van Kuik G. A. M., *Review of state of the art in smart rotor control research for wind turbines*. Progress in Aerospace Sciences, Vol. 46:1, pp. 1–27, 2010.

[2] Madsen H. A. et al. *Towards an industrial manufactured morphing trailing edge flap system for wind turbines*. Proceedings of EWEA 2014. European Wind Energy Association (EWEA). 2014.

[3] Madsen H. A., Barlas T., Andersen T. L., *A morphing trailing edge flap system for wind turbine blades*. Proceedings of the 7th ECCOMAS Thematic Conference on Smart Structures and Materials (SMART 2015), IDMEC, 2015.

[4] Lin Y.-H., *Structural Design Optimization of the controllable rubber trailing edge flap (CRTEF)*, DTU Wind Energy Master Report, 2016.

[5] C. Bak, F. Zahle, R. Bitsche, T. Kim, A. Yde, L. Henriksen, A. Natarajan, and M. Hansen, *Description of the DTU 10 MW reference wind turbine*. DTU Wind Energy Report-I-0092, 2013.

[6] M. Drela. “XFOIL: An analysis and design system for low Reynolds number airfoils”. In: Low Reynolds number aerodynamics. Springer, pp. 1–12, 1989.

[7] Solidworks Premium 2016, Dassault Systemes, 2016.

[8] ANSYS Academic Research, Release 16.0, Help Viewer. ANSYS, Inc., 2016.

VIII ECCOMAS Thematic Conference on Smart Structures and Materials
SMART 2017
A. Güemes, A. Benjeddou , J. Rodellar and Jinsong Leng (Eds)

STRUCTURAL HEALTH MONITORING AND REPAIR OF THE BLADES FOR SMALL WIND TURBINES

NICOLAE CONSTANTIN AND ŞTEFAN SOROHAN

Laboratory for Integrity Evaluation of Composite Structures (LEISC)
The University "Politehnica" of Bucharest
Splaiul Independenței 313, 060042 Bucharest, Romania
e-mail: nicolae.constantin@upb.ro, www.pub.ro

Key words: small wind turbines, blades, Lamb waves, field inspection capabilities, repair patches.

Abstract. Small wind turbines are running in quite different conditions as compared to the big ones. Consequently, they need also a different approach concerning the structural health monitoring (SHM) issues. There are four main differences between the above mentioned categories: much smaller dimensions, considerably higher rotation speed, small distance, in most cases, between the turbine and the energy consumer, and SHM assumed generally by the owner. In such conditions, nondestructive inspections (NDI) have to be made as much as possible with affordable, yet effective techniques, requiring portable and accessible equipment. Additionally, the turbines and accessories should be easy to mount, dispose and repair. As the materials used for such unit can be metals, composites and combined, the technologies should be adapted accordingly. An example in which the two materials co-exist is the situation in which the damaged metallic skin of a blade is repaired with a composite patch. The paper presents the inspection of the bonding state/ quality of the patch, using portable ultrasonic equipment, able to put in place the Lamb wave method, which shows good efficiency for global and local inspections as well. The equipment is relatively easy to handle and can be borrowed from specialized laboratories or bought and used by a community of small wind turbine users, upon the case.

1 INTRODUCTION

The renewable or green energy sector is extensively using wind power, mainly produced by large units, grouped by many dozens in land or offshore wind farms. Such an approach created a distinct class of high technology producers, able to tackle the ever increasing challenges appearing on the structural side, concerning the huge blades, and the sensitive mounting, gear and automatic management aspects. These difficulties do not stop the continuous expansion in this sector, but, on another hand, encourage the development of the small wind turbine sector, more flexible and still facing its own challenges.

The small wind turbines have to be versatile in terms of energy output and storage, integration in local grids or in hybrid power units, but also in terms of easy assembling, repair and serviceability. The fact that such devices are running in most of the cases quite near

inhabited places and are in property of people not expert in technical issues is posing special problems with regard to in service reliability and unsophisticated maintenance In both issues, efficiency must meet non-prohibitive costs, even for powers above the quite modest figure of 2 kW, usually linked with small holiday chalets. Solution for these aspects resides in a sound SHM approach that means ensuring field effective NDI methods and damage tolerant materials for the critical structural components, mixed with adequate repair technology.

The small wind turbine blade consists generally of solid layered fibre reinforced plastics (FRP) or thin walled structures, both supported by a strong spar. The latter, using thin Al alloy or FRP skins, stiffened with foam core or ribs that keep the right shape of the airfoil all over the running envelope, decisive for ensuring the design power conversion factor [1], offers reduced weight and can be seen in Figure 1.

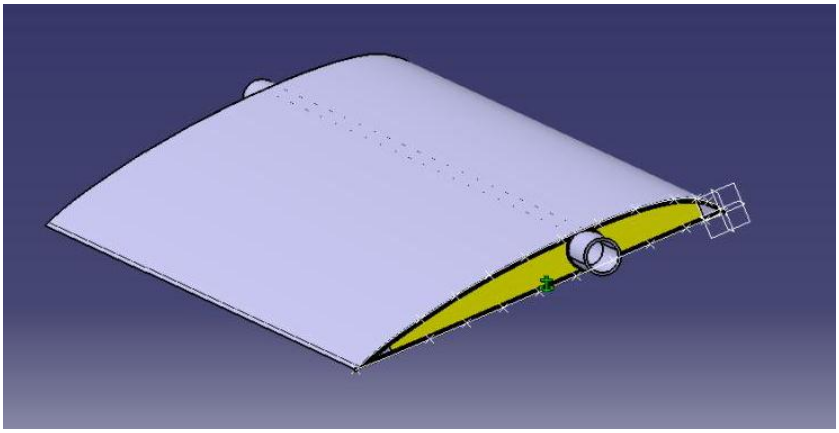

Figure 1: Thin walled structure for wind turbine blades

The use of Al skin is favouring the simple repair technology consisting in bonding composite patches over small damaged areas in order to restore the mechanical performance, technology applied on large scale in metallic aeronautical structures, as described in many reference works [2,3]. For this reason, the thin walled Al solution for blade manufacturing was considered by the authors for equipping a family of small wind turbines, with powers ranging from 2 to 10 kW, manufactured in enterprises with experience in such technologies.

The NDI technique considered for evaluating the structural integrity was the Lamb wave method, taking into consideration its capability of propagating on long distances in shells and plate thickness dependent propagation properties, leading to good results obtained in former research work in the same topic [4,5].

The present research work had two components:

a. A numerical simulation of the Lamb wave transmission in repaired panels;
b. Experiments aiming to assess the wave generation, transmission and reception, using PZT wafers or classical ultrasonic transducers.

The first component aimed to produce a robust numerical model, able to simulate different cases which might appear in the field: aluminium skins with various thicknesses, composite patches made of different composites, with different geometries and having also various thicknesses, with reference to previous research work [6,7].

The second component was intended to assess the various experimental techniques in view for performing NDI of repaired skin panels. The PZT wafers, solidly and permanently bonded in the composite patch neighbourhood, have the advantage to make possible both field inspections and on line inspections, with adequate links to adequate equipment. The classical ultrasonic transducers are better suited for wave generation and receiving [8], because the guided waves generated with such devices are better transmitted and easier to analyze than the non-guided and weaker waves generated by the PZT wafers. The possibility of having distortions in the wave transmission due to high stresses in the damaged area is also evaluated.

2 NUMERICAL SIMULATIONS

In order to perform the numerical simulation, FE models were created following the repaired panels used for experiments, with the composite patches covering cracks with extension-stop end holes. The repaired panels have been also tested in monotonic or fatigue tensile loading. The artificial cracks have been produced normal to the load direction, parallel with that (Figure 2), and on intermediate 45^0 direction, for assessing the behavior of the panel in each situation.

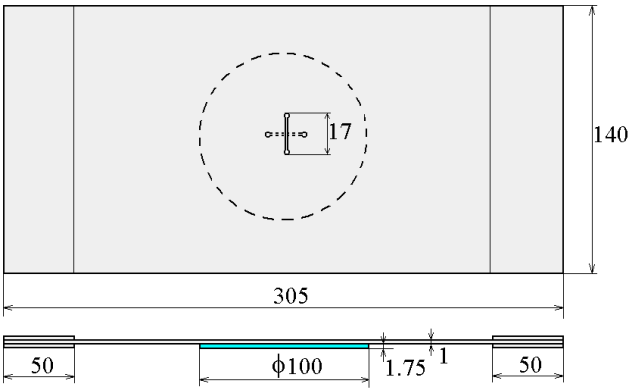

Figure 2: Physical model of a typical repaired panel

The composite patch was assimilated with an isotropic material characterized by E = 18 GPa; ν = 0.3 and ρ = 1800 kg/m^3. In order to include the strong damping in the composite patch [9], it was considered a Rayleigh type damping model ($C = \alpha M + \beta K$, where M is the composite mass matrix, K is the composite stiffness matrix, and C is the generated damping matrix of the composite), with $\alpha = 0$ and $\beta = 5 \cdot 10^{-5}$. The models were run by the ANSYS/LS Dyna code.

The frequency of the generated wave was chosen having as reference the dispersion curves for aluminum (Figure 3), obtained with the code lamb_izo.m, developed on a Matlab platform in our laboratory, and showing that under 1.5 MHz only S0 and A0 modes can be obtained.

Several 2D FE models in plane strain state (Figure 4), with meshing details shown in Figure 5, were created for simulating the transmission of a Lamb wave mode. The average element size was 0.15 mm, appropriate for a wave length higher than 1.5 mm. It was the case for the 1 MHz generated wave used in the 70 μs analysis. The burst signal is generated 25 mm rightwards point A and is received in point B (see Figure 4).

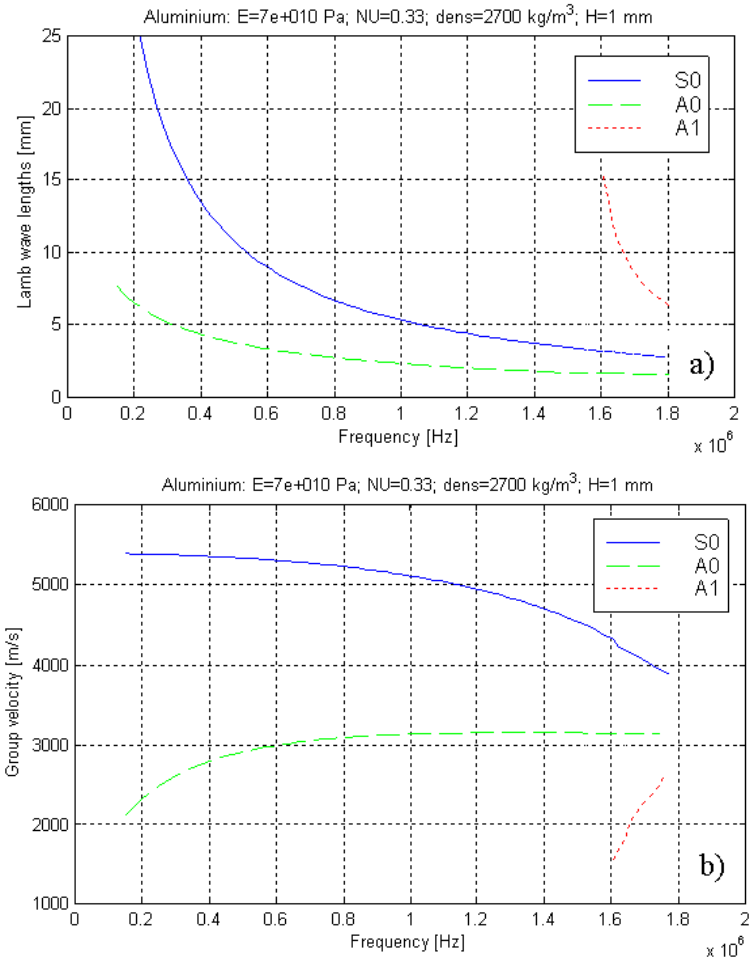

Figure 3: Dispersion curves for a 1 mm thick aluminum plate: a) wave length; b) group velocity



Figure 4: 2D FE models considered for the numerical analysis

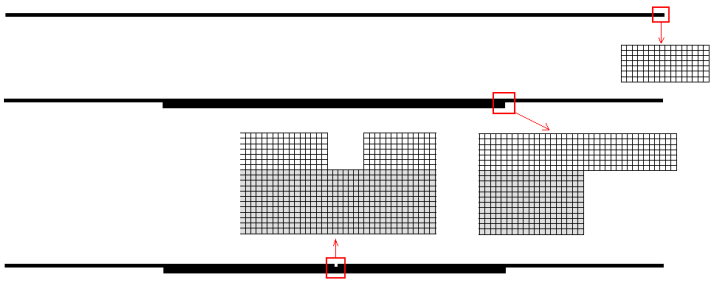

Figure 5: Meshing details of the 2D FE models

The generated and received signal is presented in Figure 6 for three different paths, considered for the FE models in Figure 4. It is to mention that by neglecting the damping effect of the composite patch in the second model, the generated signal will reach B point in a much stronger form than in Figure 6,b, but equally delayed.

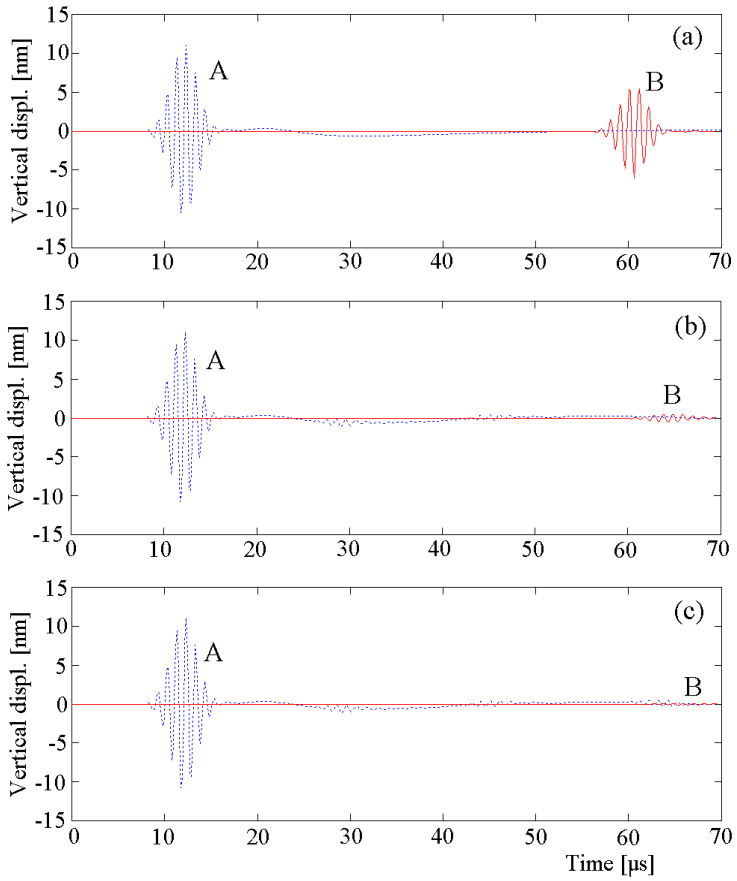

Figure 6: Signals got in point A and B: (a) transmission through the Al skin only; (b) transmission through the un-cracked Al skin and the composite patch; (c) transmission through the cracked Al skin and the composite patch

3 EXPERIMENTAL RESULTS

The experiments focusing the Lamb waves transmission through the patched panels have been carried out by using two types of transducers, with dedicated measuring chains.

3.1 Results obtained with surface bonded PZTs

Simple buzzers, solidly bonded on the Al skin, were used as wave generators and receivers, and the measurement chain is shown in Figure 7. The work frequency was 200 kHz.

In Figure 8,a and Figure 9,a is presented the positioning of identical PZTs on an Al repaired panel having a cross crack (normal to the long side), which was not loaded at all previously. The path of the transmitted signal, tangent to the composite patch or crossing it, is shown in each figure. In such a situation, only the composite patch bonding quality could have been assessed.

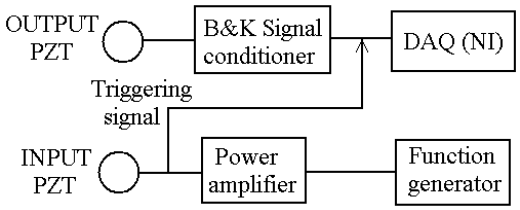

Figure 7: Measurement chain using PZT transducers

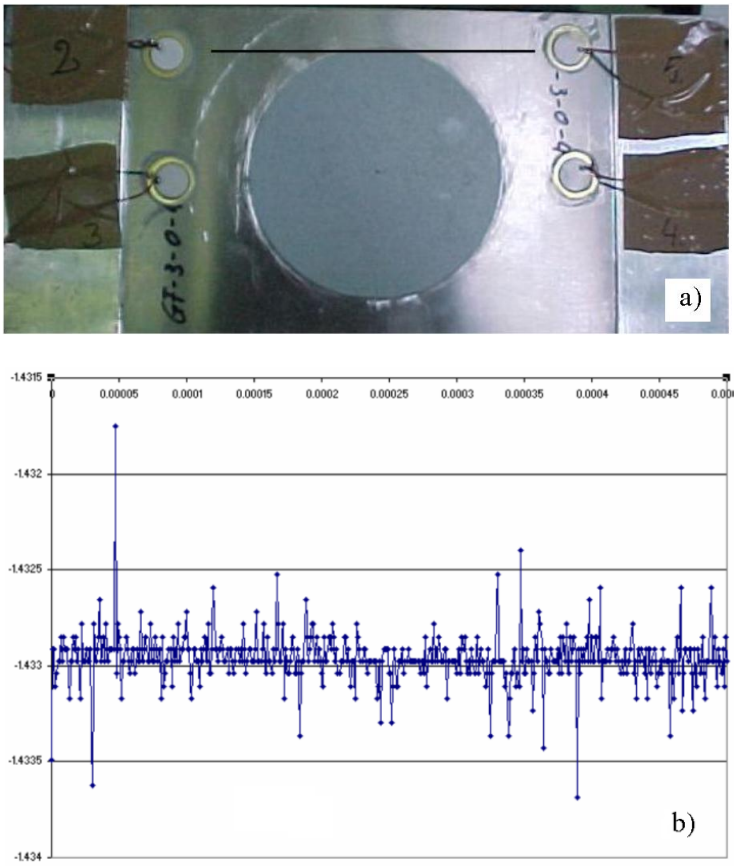

Figure 8: Signal transmission through a path tangent to the composite patch

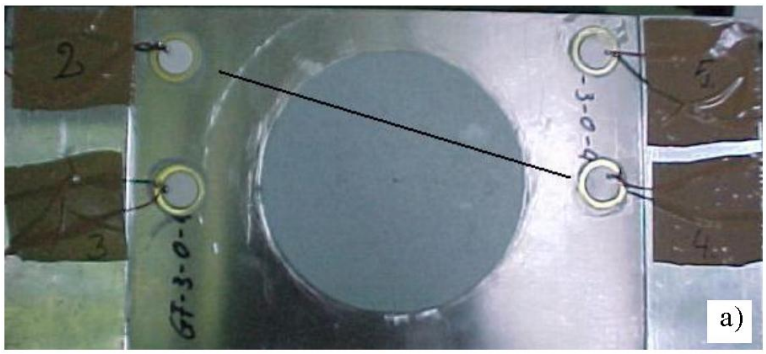

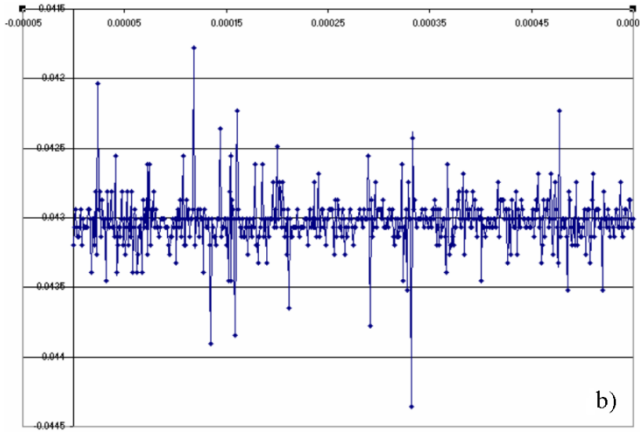

Figure 9: Signal transmission through a path crossing the composite patch

The signals obtained in the two cases (Figure 8,b and Figure 9,b have put in evidence only the quite more "noisy" signal transmitted through the composite patch. This fact can be explained by the more irregular path followed by the wave in this case, concerning both the material and the geometry, with step changes in the thickness.

The signal reception, made with a medium performance NI DAQ, could not be further filtered in this stage by hardware or software based methods, as it was reported in [10].

3.2 Results obtained with angle beam transducers

The classical ultrasonic transducers used in the next series of experiments were angle beam Krautkremer/GE transducers, accessories of a Phasor XS equipment. A similar repaired patch was inspected, with the only difference that the crack was made parallel with the long side.

The transducers were tuned at 1 MHz and oriented at slightly different angles (35^0 and 45^0). The shape of the transmitted signal, in three different situations, is shown in Figures 10, 11 and 12. The much better signal accuracy is clearly due to the much higher quality of the guided signal, but also to the fact that the transducers were placed, this time, on the reverse of the panel, the signal propagation being considerably improved. This solution, which is not possible to consider for field inspections, was imposed by the quite important dimensions of the transducers, which made almost impossible to place them on the averse. Anyway, the comparison between results, considering also the conditions in which they were obtained, emphasizes the damping effect of the composite patch (see Figure 10,b versus Figure 11,b) and the disruption got in the signal transmission when the crack is crossed (see Figure 12,b).

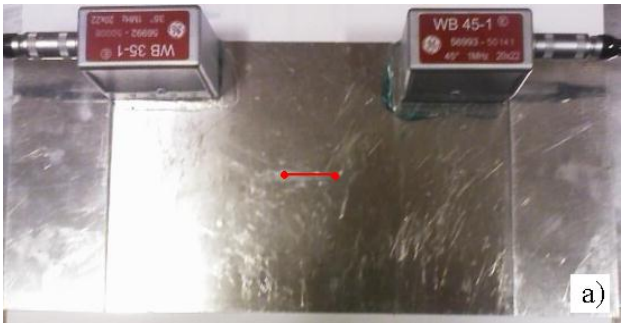

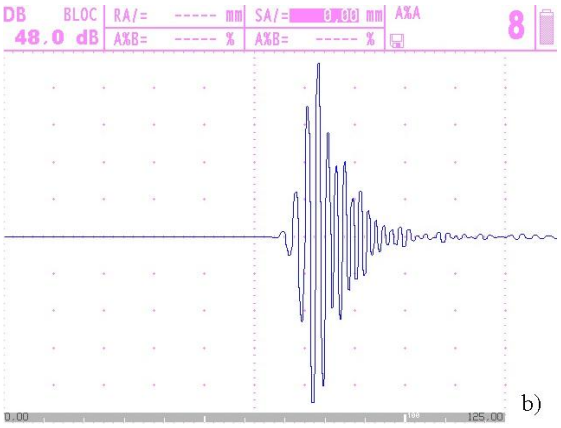

Figure 10: Signal transmission through a path tangent to the composite patch

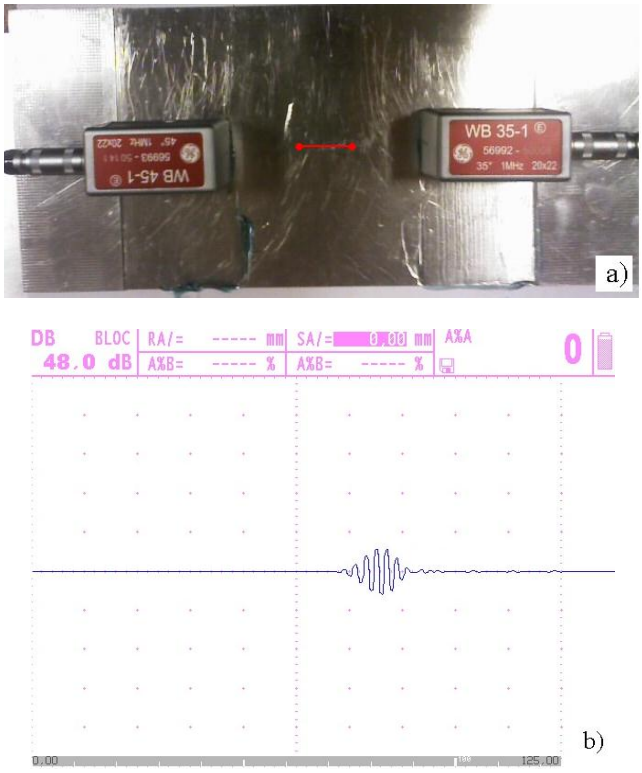

Figure 11: Signal transmission through a path crossing the composite patch, along the crack

4 EVALUATION OF THE STRESS STATE IN THE DAMAGED AREA

Having in view opinions expressed in the literature concerning the influence of the stress state upon the Lamb wave transmission in plates [11,12], a complementary study was performed on panel models, identical to those considered in the previous study (see Figure 1), stretched with a 14 kN tensile force along the big side of the panel. This force, uniformly distributed on the consolidated short sides, closely simulated the loading existing in the universal testing machines and on the real blade.

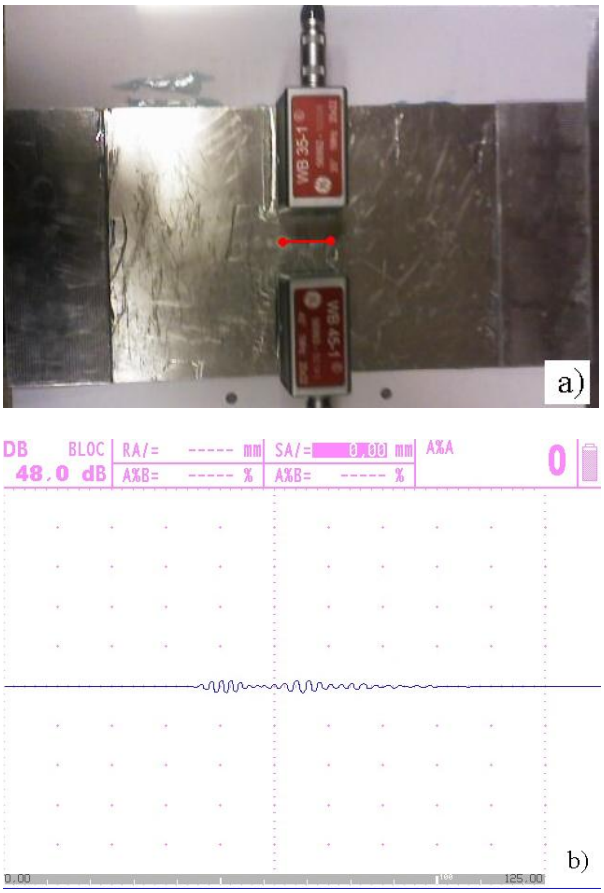

Figure 12: Signal transmission through a path crossing the composite patch and the crack

In this distinct simulation, different, adequate FE modelling was used. Having in view the symmetry, the model was halved and meshed with a graded mesh, with very fine grids around the crack (Figure 13), on the patched area, and coarser grids for the rest (Figure 14).

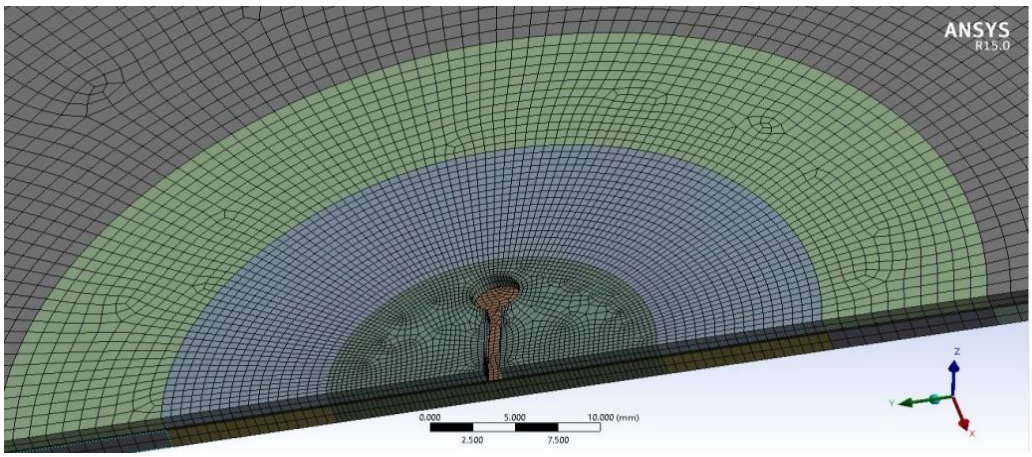

Figure 13: FE grid around the cracked area

The model used SOLID186 type elements, with material properties identical to those considered in the model dedicated to the Lamb wave transmission study, with adequate interface conditions simulating the bonding between the composite patch and the cracked Al panel. The same ANSYS platform was used.

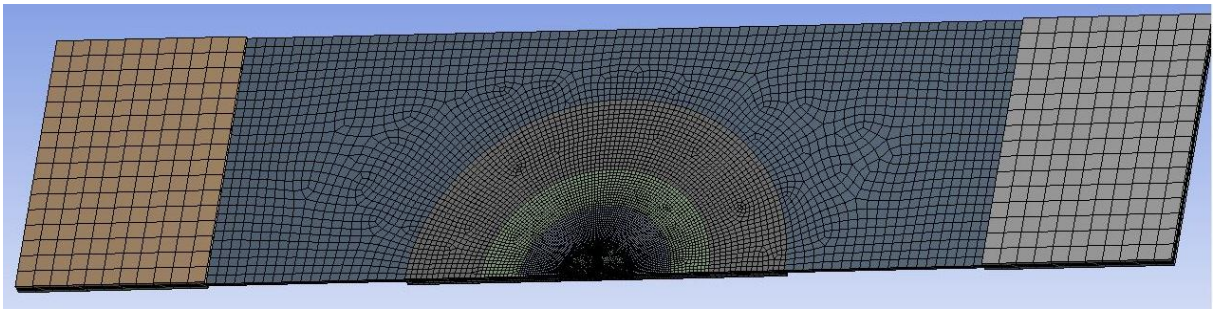

Figure 14: FE grid on the whole model

The results, in terms of stress distribution, are presented in Figure 15 and Figure 16, for the two orientations of the crack, respectively. Naturally, the highest stresses are reached in the case when the crack is normal to the long side, i.e. normal to the stretching force. Even in this case, stresses above 100 MPa are present on a small area around the crack tip ending in the small hole made in order to prevent its extension.

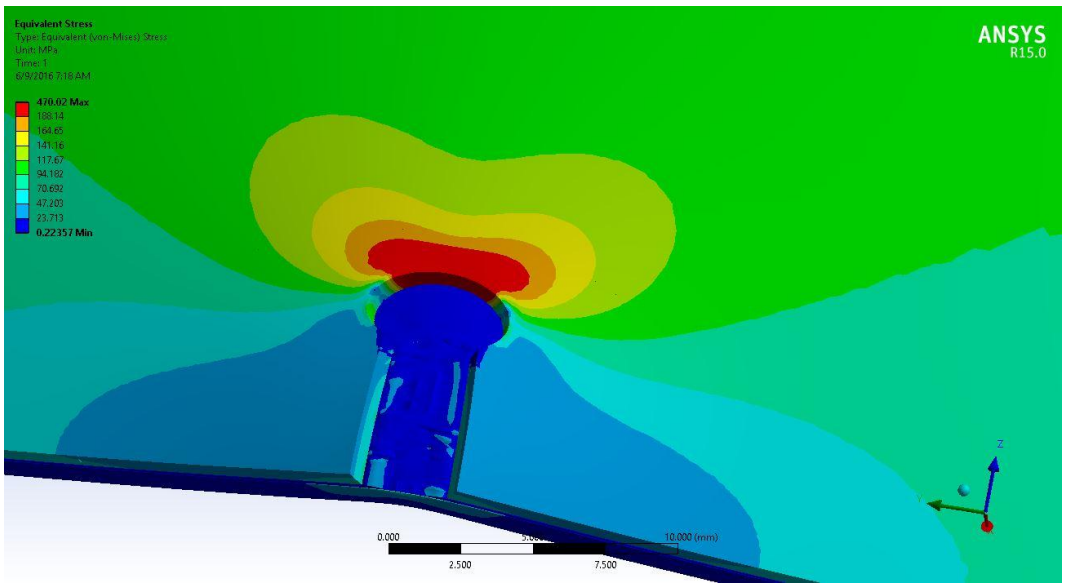

Figure 15: Stress distribution around the crack normal to the long side

A solution for keeping the stresses at lower levels and thus completely prevent undesirable effects on the wave transmission is proposed in [13]. Removal of the cracked area, eventually presenting some out-of-plane deformations, will prevent also possible, even probable crack extension, and will ease the patch bonding.

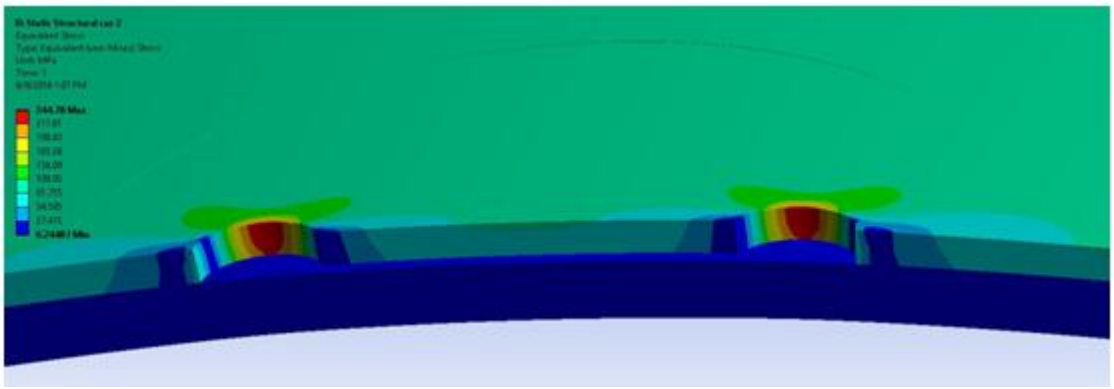

Figure 16: Stress distribution around the crack parallel with the long side

5 DISCUSSIONS AND CONCLUSIONS

The research made to date on the proposed subject outlines the various difficulties linked with Lamb wave inspections: the existence of at least two modes at any given frequency, the presence of more than one mode in the received signal, the modified shape of different modes due to mode conversion at imperfections, the highly dispersive nature of modes in anisotropic shells and the important damping effect produced by the presence of FRP patches on the signal path. Signal-to-noise problems are adding to signal treatment and, finally, to flaw detection. In the inspection made with PZTs, this last problem made impossible the mode identification. Efforts in filtering the signal will, most likely, significantly improve the situation. In the case of using classic ultrasonic transducers, the S0 wave, deducted by evaluating the group velocity, was clear for the first two inspections. In the third, a reflection and an additional damped delayed wave transmitted through the composite patch makes more difficult to interpret the transmission picture. In the first two inspections, good agreement was found with numerical approach.

The results obtained so far prove the potential of the Lamb wave method as a versatile and efficient NDI technique, provided a good understanding of the propagation characteristics of the wave over the repaired region is achieved. Due to the limited space, encouraging results proving the detection of a disbond suffered by a composite patch when the repaired panel was fatigue loaded were not reproduced. The detection was made with PZT wafers and, in spite of the ever present noise, the combination of the smaller amplitude signal, characterizing the transmission in the Al skin (see Figure 8.b), with the higher amplitude signal, characterizing the presence of the still bonded composite patch (see Figure 9.b), made rather clear the disbond extension. The stress distribution obtained in the damaged area under a load close to the one existing in usual in service conditions does not raise concerns about possible distortions of the Lamb wave transmission in the damaged and patched area.

Lamb wave global blade monitoring with smart positioned PZTs substantiates the perspective of achieving early warning through on-line SHM. The angle beam transducers, associated with versatile devices like the Phasor XS equipment, ensure rather quick field local inspections, able to more precisely localize the in service produced damage. When ambiguous results require cross-checking for higher reliability, a tandem with active infrared thermography (IRT) may be a wise decision to take in maintenance technology.

ACKNOWLEDGMENT

The research work was performed under project 258/2014, financed by the Romanian Ministry of Education and Scientific Research, through its dedicated body (MEN-UEFISCDI), in the "Partnership in priority domains – PN II" programme.

REFERENCES

[1] Ragheb, M. and Ragheb, A.M. Wind turbines theory – the Betz equation and optimal rotor tip speed ratio, in *Fundamental and Advanced Topics in Wind Power*, Carriveau, R. Ed., Rijeka, Shanghai, InTech (2011): 19–38.

[2] *Advances in the Bonded Composite Repair of Metallic Aircraft Structures*, Baker, A., Rose, L.R.L. and Jones, R. Eds., Vol. 1(2002), Amsterdam: Elsevier.

[3] Baker, A. and Jones, R. *Bonded Repair of Aircraft Structures* (1988), Dordrecht: Martinus Nijhoff Publishers.

[4] Chaudhry, Z., Lalande, F., Ganino, A. and Rogers, C. Monitoring the integrity of composite patch structural repair via piezoelectric actuators/sensors. *AIAA-1996-1074-CP* (1996).

[5] Rose, J.L. and Soley, L. Ultrasonic guided waves for the detection of anomalies in aircraft components. *Mat. Evaluation* (2000) **50**: 1080-1086.

[6] Moser, F., Jacobs, L.J. and Qu, J. Modeling elastic wave propagation in waveguides with the finite element method. *NDT&E Int.* (1999) **32**: 225-234.

[7] Constantin, N., Sorohan, Ş., Anghel, V. and Găvan M. Finite element analysis on the mechanism of Lamb wave generation with piezoelectric transducers. *Proc. 29th Int. Semiconductor Conf. - CAS 2006,* Sinaia, Romania, Vol. 2 (2006): 403-406.

[8] Lowe, M.J.S., Challis, R.E. and Chan, C.W. The transmission of Lamb waves across adhesively bonded lap joints. *The Journal of the Acoustical Society of America* (2000) **107**: 740–741.

[9] Neau, G., Lowe, M.J.S. and Deschamps, M. Propagation of Lamb waves in anisotropic and absorbing plates: theoretical derivation and experiments. *Review of Progress in Quantitative NDE* (2002) **21**: 1062-1068.

[10] Gubbala, R. and Rao, V.S. Health monitoring of adhesively bonded composite patch repair of aircraft structures using wavelet transforms of Lamb wave signals. *Proc. SPIE* (2003) **5056**: 33-40.

[11] Chakraborty, A. The effect of surface stress on the propagation of Lamb waves. *Ultrasonics* (2010) **50(7)**: 645-649.

[12] Mohabouth, M., Kotousov, A. and Ng, C.-T. Lamb waves in plates subjected to uniaxial stresses. *Int. J. Mech., Aerospace, Ind., Mechatronic and Manufacturing Engng.* (2015) **9(7)**: 1193-1198.

[13] Constantin, N., Sandu, M. and Sorohan, Ş. Restoration of the mechanical performance of damaged Al panels using bonded composite repair patches, *Int. J. Adhes. & Adhes.* (2013) **42**: 69-76.

Torque and Pitch Control for a Floating Offshore Wind Turbine

José Rodellar*, Christian Tutivén*, Yolanda Vidal* and Leonardo Acho*

* Control, Dynamics and Applications (CoDAlab)
Escola d'Enginyeria de Barcelona Est (EEBE)
Universitat Politècnica de Catalunya
Campus Diagonal-Besòs UPC, 08930 St. Adrià de Besòs, Barcelona, Spain
e-mail: {jose.rodellar,christian.tutiven,leonardo.acho,yolanda.vidal}.upc.edu,
web page: http://codalab.upc.edu

ABSTRACT

Wind power is one of the fastest growing power sources in the renewable energy field [1]. However, the future of wind energy industry passes through the use of larger and more flexible wind turbines (WT) in remote locations, which are increasingly offshore to benefit stronger and more uniform wind conditions. Onshore wind turbines technologies are not economically feasible in deeper water. Instead, space-frame substructures (as jacket-type) will be required to maintain the strength and stiffness requirements at the lowest possible cost [2]. However, floating support platforms will be the most economical at depths greater than 50m, approximately. In this work, new torque and pitch controllers for a barge-type floating wind turbine are proposed when operating in the full load region.

One of the main challenges is to reduce the platform pitch motions in a floating offshore wind turbine to guarantee its proper functioning under the constraints imposed by the floating support platforms, which are subjected to a greater range of motion than that of the conventional fixed platforms [3]. The main contribution of this work is to propose torque and pitch controllers whose main objective is to stabilize the WT tower against both the wind (WT tower top perturbation) and the platform movement (WT tower bottom perturbation due to the ocean waves). Additional objectives are to control the quality of the power energy generation and to keep the fore-aft and side-to-side accelerations inside acceptable levels. Because of the large dimensions of a commercial offshore WT, the above control objectives have to be correctly coordinated between appropriate torque and pitch control commands, which is an important control design challenge.

The proposed torque controller is based on the super-twisting algorithm with feedback of the fore-aft acceleration signals of the wind turbine tower [4]. The proposed pitch control is a PI-class controller that uses feedback of the generator shaft speed, feedback of the side-to-side acceleration signals of the wind turbine tower, and uses as reference generator speed a function of the platform pitch motion. The barge platform motions during normal operation with the proposed controllers are compared with respect to a well-known baseline controller [5] using a coupled non-linear aero-hydro-servo-elastic simulator of a barge-type offshore wind turbine [6].

Numerical experiments show that the proposed controllers improve the overall performance of the WT and also reduce fore-aft and side-to-side accelerations as well as reduce the platform pitch motions with respect to the baseline control, which is a significant problem for floating structures.

REFERENCES

[1] S. Gsanger and J. Pitteloud, *World wind energy report* 2011.World Wind Energy Association.
[2] J. M. Jonkman, *Dynamic modeling and loads analysis of an offshore floating wind turbine*, National Renewable Energy Laboratory, 2007.
[3] M.A. Lackner, "Controlling Platform Motions and Reducing Blade Loads for Floating Wind Turbines", *Wind Engineering*, Vol. **33**, pp. 541–554, (2009).
[4] C. Tutivén, Y. Vidal, J. Rodellar and L. Acho, "Acceleration-based fault-tolerant control design of offshore fixed wind turbines", *Structural Control and Health Monitoring,* (2016).
[5] J. M. Jonkman, *Influence of control on the pitch damping of a floating wind turbine*, National Renewable Energy Laboratory, 2008.
[6] J.M. Jonkman, P.D.S. *Development of Fully Coupled Aeroelastic and Hydrodynamic Models for Offshore Wind Turbines*, ASME Wind Energy Symposium, 2006.

VIII ECCOMAS Thematic Conference on Smart Structures and Materials
SMART 2017
A. Güemes, A. Benjeddou , J. Rodellar and Jinsong Leng (Eds)

UNMEASURED STRAIN ESTIMATION ON BOTTOM-FIXED OFFSHORE STRUCTURES BY MULTIMETRIC DATA FUSION AND KALMAN FILTERING WITH DATA BUFFER

RAJENDRA P. PALANISAMY[*], SUNG-HAN SIM[*], WONSUL KIM[†], JIN-HAK YI[†], AND WEON MU JEONG[†]

[*] School of Urban and Environmental Engineering
Ulsan National Institute of Science and Technology (UNIST), Republic of Korea
e-mail: prasath@unist.ac.kr, ssim@unist.ac.kr

[†] Coastal Engineering Division
Korea Institute of Ocean Science and Technology (KIOST), Republic of Korea
email: w.kim@kiost.ac.kr, yijh@kiost.ac.kr

Key words: Multimetric Data Fusion, Kalman Filter, Buffer, Response Reconstruction, Offshore Structures, Virtual Sensing.

Abstract. Offshore structures for tidal current energy converters and offshore wind turbines are always exposed to the much harsher environment with strong tidal current and wind loadings. While monitoring structural soundness and integrity is considered to be crucial to prevent catastrophic collapses and prolong lifetime, it is intrinsically challenging due to the difficulties in accessing to the critical structural members located under water for installing and repairing monitoring sensors and data acquisition systems. Virtual sensing technologies have the potential to alleviate such difficulties by estimating unmeasured structural responses at desired locations with other measured responses. This approach is particularly advantageous when (1) some sensors are malfunctioning and (2) sensor installation at critical members is difficult. Despite the usefulness of the virtual sensing, its performance and applicability for structural health monitoring of the offshore structures under non-stationary excitations has not been fully studied to date. This paper investigates the use of the virtual sensing for structural health monitoring of offshore structures for marine energy facilities rather for oil and gas exploitation. The Kalman filter is introduced for data fusion of different types of measured responses to produce estimated responses at structural members of interest. This study discusses how the non-stationary tidal current loading in the real-time response estimation is appropriately handled. Numerical analysis and laboratory experiment are conducted to verify the performance of the virtual sensing strategy using a bottom-fixed offshore structure model, showing that the unmeasured responses can be reasonably recovered from the measured responses.

1 INTRODUCTION

Bottom-fixed offshore structures such as monopiles, tripods, jackets, and gravity-based

structures have been widely utilized for the purpose of extracting oil and gas and supporting metrological towers and multipurpose ocean science platforms, and their applications are expanded for supporting ocean energy facilities (OEFs) including offshore wind turbines and tidal stream turbines. Indeed, in recent years, the number of bottom-fixed offshore structures has been increasing rapidly with the increase in the large-scale offshore wind farms [1]. Because these offshore structures are generally built in harsh environments, strong winds and tidal currents can cause structural degradation and critical damages. In addition, the quasi-periodic excitation forces due to the rotating devices including rotors, main shafts, and generators can be a source of fatigue. Being prone to the structural failures due to various external excitations, these offshore structures for OEFs are carefully maintained to prevent catastrophic collapses and to prolong their lifetime.

Structural health monitoring (SHM) provides an effective means of maintaining the offshore structures appropriately to assess the present status as well as the remaining lifetime. SHM is typically performed by collecting the response data measured from a limited number of accessible locations using sensors such as accelerometers and strain gauges. In the monitoring of the offshore structures of OEFs, most of the fatigue-sensitive spots and critical members are located in regions that are inaccessible for direct measurements (e.g., at the mudline several ten meters below the water level). Thus, the sensor installation at important regions deep inside the water can be quite challenging.

Recently, virtual sensing approaches are being actively developed for offshore wind turbines to indirectly obtain the responses at the unmeasured locations by using the measured responses such as acceleration and strain [2-4]. The model-based virtual sensing technology has been intensively studied for estimating the unmeasured responses from a limited set of response data based on the Kalman filter [5-11] and modal decomposition and expansion [12].

This study investigates a quasi-real time virtual sensing strategy based on Kalman filtering associated with an FE model tailored to the offshore structures under non-zero mean stochastic external loads. A multimetric data fusion technique is incorporated to overcome the difficulties related to the non-zero mean static response estimation. This technique is implemented by the fusion of different sensor data such as strain and acceleration for low and high-frequency regions.

The proposed method includes a buffering technique, which reduces the computation time significantly in contrast to any other real-time estimation techniques. Thus, this estimation technique can be easily implemented in wireless and mobile sensing technologies [13]. The proposed method is verified numerically using a four-legged portal frame under a certain level of nonstationary tidal current force and also dynamic force.

2 FORMULATION

Monitoring the offshore structures under water is unique in that the sensor installation and maintenance associated with the data acquisition systems are quite challenging because critical structural members are often inaccessible. Estimating structural responses at the important unmeasured locations can be a powerful alternative to the direct measurement when the direct measurement is impossible. Despite the usefulness of the response estimation technique, it has not been fully explored in the literature yet. This study investigates the Kalman filter-based data fusion technique to estimate the unmeasured non-stationary strain

data from an offshore structure, which can be subsequently used to assess structural conditions such as the fatigue remaining life of steel members in the offshore structure. As this study focuses on monitoring the offshore structures, we consider two major aspects that need to be addressed appropriately, i.e. 1) offshore structures for ocean energy facilities and offshore winds are continuously subjected to non-zero mean input excitations because of thrust force and tidal current and wind loadings, and 2) sensors are prone to damage because of the harsh environments or are difficult to install and manage in some hot spots.

The input forces, as well as the structural responses, have a large amplitude trend that varies slowly according to the changing speed and direction of the tidal current. Thus, the response estimation algorithm should be capable of handling non-zero mean inputs. Further, sensor malfunction and inaccessibility of some hot spots in offshore structures demand the algorithm to estimate complete responses with limited measurements [14].

The quasi-real time Kalman filter-based state estimator used to capture structural responses that are subjected to a non-stationary random input is outlined here. The Kalman filter provides an efficient computational means to estimate the state of a process in a way that minimizes the mean of the squared error [15]. This study uses the state estimation property of the Kalman filter to predict the unmeasured response of a structure.

The general Kalman filter-based state estimator requires a known input. Further, it assumes that the state disturbances and the sensor noise are stationary. In reality, offshore structures for OEFs and offshore winds are subjected to unknown non-stationary random inputs. Thus, the general Kalman filter is modified to perform the response estimation under unknown non-stationary random inputs using buffer method. Hence, the state estimator has three major parts including a plant, a buffer, and an observer. In this study, the plant is the actual structure, which is intractable, and the observer can be designed depending on the output of interest. The buffer is an addition to the typical Kalman estimator. This technique enables the estimator to handle non-stationary inputs in real time with a buffer delay.

The equation of motion of the considered linear system or plant is given as follows:

$$\mathbf{M}\ddot{\mathbf{x}}(t)+\mathbf{C}\dot{\mathbf{x}}(t)+\mathbf{K}\mathbf{x}(t)=\mathbf{u}(t) \tag{1}$$

where $\mathbf{x}(t)$ is the displacement, and $\mathbf{M}$, $\mathbf{C}$, and $\mathbf{K}$ are the mass, damping, and stiffness matrices of the dynamic system, respectively. $\mathbf{u}(t)$ is the input force vector applied to the system. Eqs. 2 and 3 express the state-space model of the system.

$$\dot{\mathbf{x}}(t)=\mathbf{A}\mathbf{x}(t)+\mathbf{B}\mathbf{u}(t) \tag{2}$$

$$\mathbf{y}_m(t)=\mathbf{C}\mathbf{x}(t)+\mathbf{D}\mathbf{u}(t)+\mathbf{v}(t) \tag{3}$$

where matrices $\mathbf{C}$ and $\mathbf{D}$ in Eq. (3) are selected depending on the output of interest $\mathbf{y}_m(t)$; input $\mathbf{u}(t)$ and measurement noises $\mathbf{v}(t)$ possess a covariance $\mathbf{Q}(t)=E[\mathbf{u}(t)\mathbf{u}(t)^T]$ and $\mathbf{R}(t)=E[\mathbf{v}(t)\mathbf{v}(t)^T]$, respectively. Matrices $\mathbf{A}$ and $\mathbf{B}$ are the system matrices.

As the input force vector, $\mathbf{u}(t)$, is unknown in this problem, the conventional Kalman estimator is slightly modified for quasi-real time application without the input, $\mathbf{u}(t)$. Eqs. 4 and 5 indicate the observer design.

$$\dot{\mathbf{x}}(t-\beta)=\mathbf{A}\mathbf{x}(t-\beta)+L(\mathbf{y}_m(t-\beta)-\mathbf{y}_{est}(t-\beta)) \tag{4}$$

$$\mathbf{y}_{est}(t-\beta) = \mathbf{C}\hat{\mathbf{x}}(t-\beta) \tag{5}$$

where β is the buffer time, $\hat{\mathbf{x}}$ is the estimated state, and L is the Kalman gain, which is selected to minimize the steady-state error covariance.

The followings explain how the buffer prepares the data and the Kalman gain for the observer to handle a non-stationary random input. The error dynamics of the complete system (plant + observer) without the buffer in real time is derived as

$$\dot{\mathbf{e}}(t) = (\mathbf{A} - L\mathbf{C})\mathbf{e}(t) + \mathbf{B}\mathbf{u}(t) - L(\mathbf{D}\mathbf{u}(t) + \mathbf{v}(t)) \tag{6}$$

where $\mathbf{e}(t)$ is the difference between the actual state and the estimated state, $\mathbf{e} = \mathbf{x} - \hat{\mathbf{x}}$. The objective of the Kalman filter is to minimize the covariance of $\mathbf{e}$.

$$\mathbf{P}(t) = E[\mathbf{e}(t)\mathbf{e}(t)^T] \tag{7}$$

The rate of change of error covariance is given as

$$\dot{\mathbf{P}}(t) = (\mathbf{A} - L\mathbf{C})\mathbf{P}(t) + \mathbf{P}(t)(\mathbf{A} - L\mathbf{C})^T + \mathbf{B}\mathbf{Q}(t)\mathbf{B} - \mathbf{P}(t)\mathbf{C}^T\bar{\mathbf{R}}(t)^{-1}\mathbf{C}\mathbf{P}(t) \tag{8}$$

To minimize error covariance $\mathbf{P}(t)$, $\dot{\mathbf{P}}(t)$ is equated to zero and solved using an algebraic Riccati equation. It is necessary that $\mathbf{Q}(t)$, $\mathbf{R}(t)$, and $\mathbf{P}(t)$ in Eq. 8 should be time invariant to equate $\dot{\mathbf{P}}(t)$ to zero. However, in the considered case, input covariance $\mathbf{Q}(t)$ is non-stationary, i.e., the statistical properties of the input changes over time. In order to solve this issue, a buffering technique is introduced where the measured data are preloaded and processed to estimate an input covariance $\mathbf{Q}$ during the complete time segment, β. The equation of input covariance after introducing the buffering technique is given as

$$\mathbf{Q}^S = E[(\mathbf{u}^S)(\mathbf{u}^S)^T] \tag{9}$$

where, $\mathbf{Q}^S$ is the input covariance between time t and $t+\beta$. $\mathbf{u}^S$ is the input between time t and $t+\beta$. As we have the complete knowledge of $\mathbf{Q}$ for the time segment β, we can safely assume that the input covariance is bounded and time invariant within the selected time segment β. Thus, $\dot{\mathbf{P}}(t)$ in Eq. 8 can be equated to zero, and it takes the form of a continuous-time algebraic Riccati equation (CARE).

$$0 = (\mathbf{A} - L\mathbf{C})\mathbf{P} + \mathbf{P}(\mathbf{A} - L\mathbf{C})^T + \mathbf{B}\mathbf{Q}\mathbf{B} - \mathbf{P}\mathbf{C}^T\bar{\mathbf{R}}^{-1}\mathbf{C}\mathbf{P} \tag{10}$$

where $\bar{\mathbf{R}} = \mathbf{D}\mathbf{Q}\mathbf{D} + \mathbf{R}$ and the solution, $\mathbf{P}$, from CARE is used to build the Kalman gain, L.

$$L = \mathbf{P}\mathbf{C}^T(\bar{\mathbf{R}} + \mathbf{D}\mathbf{Q}\mathbf{D}^T)^{-1} \tag{11}$$

The value of L behaves optimally within the time segment β. This enables the observer to handle the non-stationary input. It is important to note that Eqs. 10 and 11 should be recalculated for every time segment β. Further, while the observer is working on the offline data from the buffer, the buffer will load the data corresponding to the next time segment and estimate $\mathbf{Q}^S$. Thus, the overall system estimates the response in real time with a buffering time delay of β. These modifications in the Kalman filter are verified numerically as described in the following section.

3 NUMERICAL VALIDATION

3.1 Simulation setup

The model is composed of 24 frame elements, each of which has a length of 0.2 m as shown in Figure 1. The columns (C1, C2, C3, and C4) have the same circular cross section of radius 3 cm. The Young's modulus and the mass density of the columns presented here are 1,000 MPa and 953 kg/m^3, respectively. The Young's modulus and density of the four frame members on the top of the columns are 210 GPa and 7850 kg/m^3, respectively. The developed numerical model is used to simulate the acceleration and strain responses under the non-zero mean inputs that are applied to the first two nodes of each column as shown in Figure 1. Although all four columns are forced under a single stream, they may not have a similar stream velocity. The turbulence, stream direction, and structure complexity will change the stream velocity in each column, which in turn will change the input force at each column. However, the input forces are dependent on the speed and direction of the mainstream. Thus, for simulation, columns 1 and 2 in the downstream are assumed to experience a force 50% less than columns 3 and 4 in the upstream velocity. Responses are sampled at 150 Hz and the sampled acceleration data is artificially contaminated by 2% noise in the root mean square (RMS), whereas the strain is contaminated by 10% noise in the RMS based on the experience of higher noise on the actual strain measurement. These limited responses are used to predict the input covariance and the unmeasured responses.

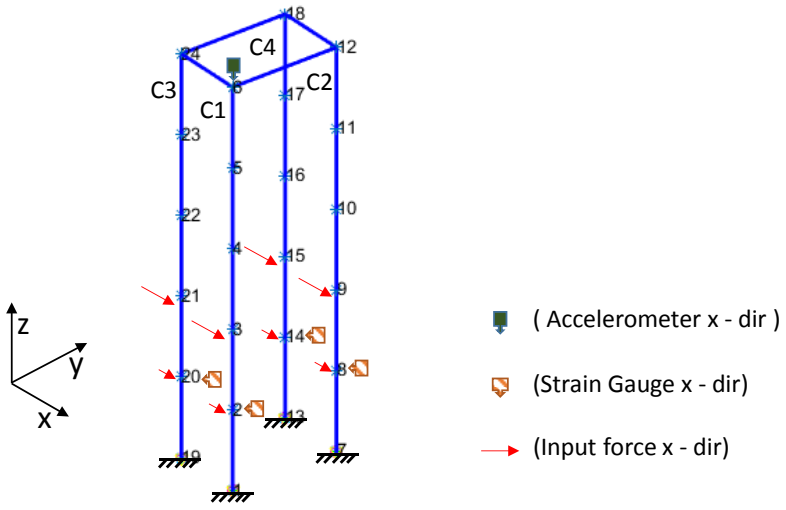

Figure 1: Numerical model

The input covariance estimation explained here is not a generic method; this is developed for the model and the loading conditions considered in this study. From the simulation setup, it can be understood that the input forces on each column are different but they are not independent. Using this idea, we calculated a strain relationship matrix as shown in Eq.12. This matrix is calculated when all the sensors are active. The Kalman state estimator estimates the input covariance $\mathbf{Q}^S$ in its buffer part using the available measurement $\mathbf{y}_m{}^S$. There are two

steps involved in estimating the input covariance. In Step 1, the missing strain data is estimated using the available strain data and strain relationship matrix $\boldsymbol{\varepsilon\varepsilon}$ (see Eq. 13). The estimated strain may not be accurate; the only purpose of this estimation is to estimate the input covariance in the next step. In Step 2, with the help of the numerical model, a flexibility matrix $\mathbf{K}_{sp}$ is constructed using strain $\boldsymbol{\varepsilon}^S$ and input force $\mathbf{u}^S$ as shown in Eq. 14. With this relation, the measured strain responses can be transformed to the input forces. The estimation may have a large error when the input forces are independent. Under such cases, the input estimation may not be reliable.

$$\boldsymbol{\varepsilon\varepsilon} = \begin{bmatrix} \left\{\dfrac{std(\varepsilon_i)}{std(\varepsilon_j)}\right\} & \left\{\dfrac{std(\varepsilon_i)}{std(\varepsilon_j)}\right\} & \cdots \\ \left\{\dfrac{std(\varepsilon_i)}{std(\varepsilon_j)}\right\} & \left\{\dfrac{std(\varepsilon_i)}{std(\varepsilon_j)}\right\} & \cdots \\ \vdots & \vdots & \ddots \end{bmatrix} \tag{12}$$

$$\boldsymbol{\varepsilon}^S = \boldsymbol{\varepsilon\varepsilon}\, \mathbf{y}_m^s \tag{13}$$

$$\mathbf{u}^S = \mathbf{K}_{sp}\boldsymbol{\varepsilon}^S \tag{14}$$

The accuracy of the estimated input, $\mathbf{u}^S$, depends on the accuracy of the FE model used. However, the observer gain, L, depends only on the covariance of input $\mathbf{Q}^S$ as shown in Eq. 11, which does not require an accurate FE model.

Further, to improve the accuracy of estimation, the multimetric data fusion technique is adopted. The acceleration and strain responses are chosen for data fusion. Unlike the accelerometer, strain gauges are sensitive to the electrical noise and local defects in a structure. Acceleration being a poor low-frequency observer, the quasi-static trend of non-zero mean responses is generally difficult to capture in comparison to the strain gauges. Thus, the fusion of the multimetric data (strain and acceleration) will enhance the accuracy of the response estimation [5-11].

Four different simulation cases are considered here. In each case, one of the strain responses is estimated with the help of other strain and acceleration responses (see Table 1). For example, in case 1, the strain measurements near the root of columns 2, 3, and 4 and the acceleration at the top of the columns (see Figure 1) are used to estimate the strain response of column 1.

Table 1: Measured and estimated response for each case

Case	Measured strain location	Measured acceleration location	Estimated strain location
1	8, 14, and 20	6	2
2	2, 14, and 20	6	8
3	2, 8, and 20	6	14
4	2, 8, and 14	6	20

3.2 Estimation result

Figure 2 shows the estimated strain in each case. As mentioned in Section 2, each case is processed in two steps including Step 1 for estimating the input covariance, Q, and calculate the Kalman gain, L and Step 2 for estimating the unmeasured responses using the Kalman gain, L, and the limited measurements in the Kalman filter-based state estimator.

In case 1, the strain response at nodes 8, 14, and 20 with the acceleration response at node 6 are used to estimate the strain at node 2. During the input covariance estimation, the strain response at unmeasured node 2 is replaced with that at node 8 because they experience a similar force. A similar procedure is followed to estimate the strain response at the other columns as shown in Table 1. From Figure 2, the estimated non-zero mean strain at each column is in good agreement with the reference strain. Because of the large upstream force, columns 3 and 4 experience a higher strain compared to columns 1 and 2. Figure 3 shows the capability of the algorithm to estimate the dynamic component of the response.

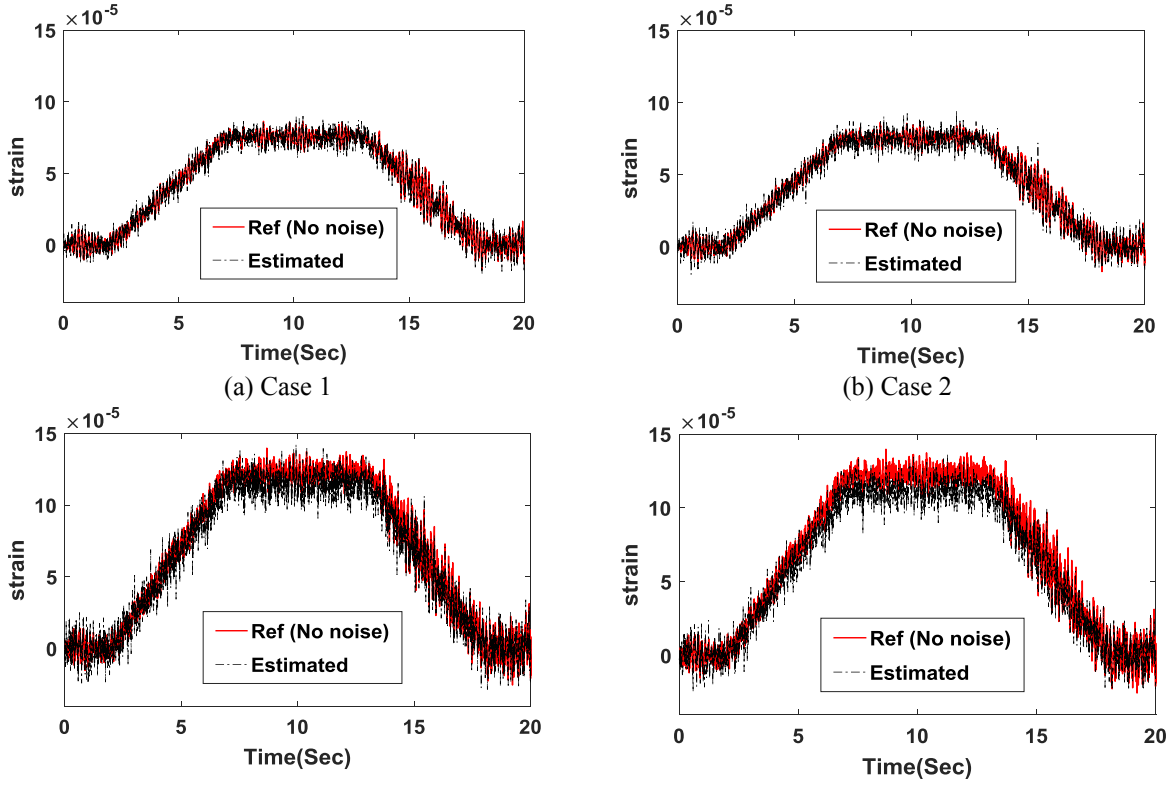

(a) Case 1 (b) Case 2

(c) Case 3 (d) Case 4

Figure 2: Estimated and reference strain responses in time domain

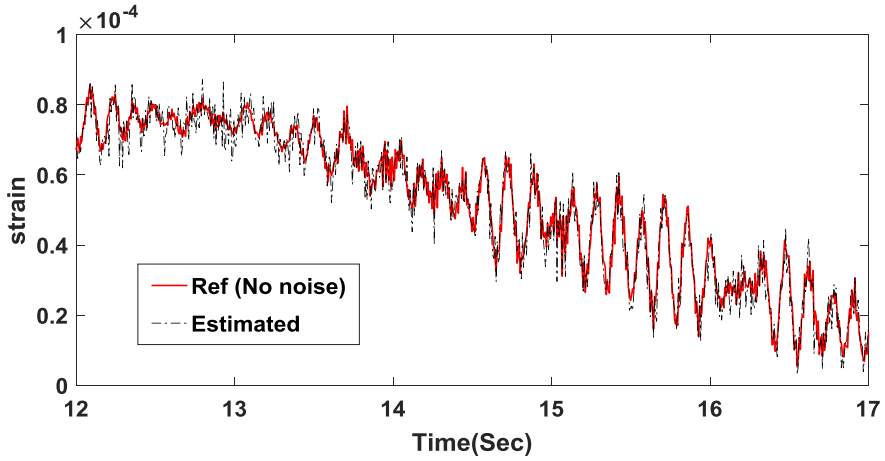

Figure 3: Estimated and reference strain response in column 1 (between 5 s and 9 s)

In addition to the comparison in the time domain, the estimated and measured strain responses are compared in the frequency domain by plotting their power spectra as shown in Figure 4. Note that only case 1 is shown as all the cases exhibit similar power spectra. From Figure 4, it can be observed that the estimated strain is in good agreement with the reference strain. Their strong agreement near 0 Hz shows the capability of the algorithm to handle non-stationary responses.

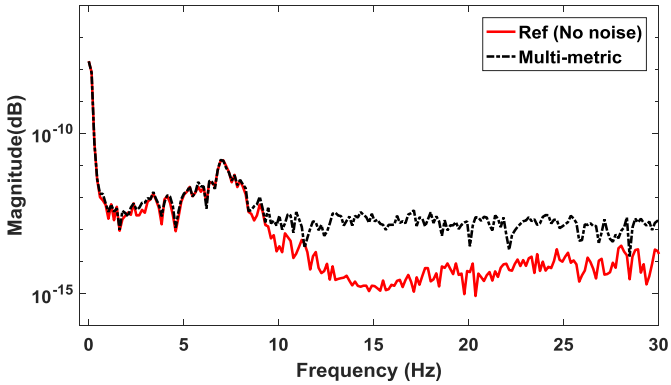

Figure 4: Estimated and reference strain response in frequency domain

To investigate the consistency of the response estimation, root mean square errors (RMSEs) between the reference and estimated strains were calculated as:

$$Error = \frac{\sqrt{\sum\left(\varepsilon_{est} - \varepsilon_{ref}\right)^2}}{\sqrt{\sum\left(\varepsilon_{ref}\right)^2}} \tag{15}$$

where ε_{ref} is the reference strain and ε_{est} is the estimated strain. Figure 5 shows the RMSEs calculated for each column. The error in the response estimation for each column is less than 2%. The estimation errors in columns 3 and 4 are relatively higher when compared to

columns 1 and 2. Because columns 3 and 4 experience a larger upstream force, the estimation error is also higher.

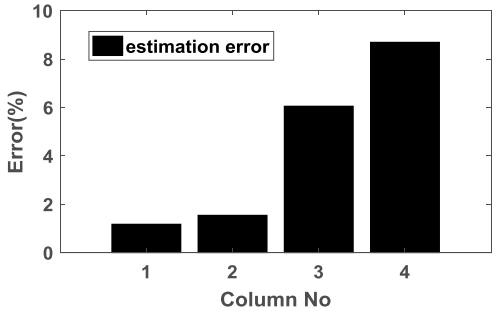

Figure 5: Estimation errors

Further, the estimation error corresponding to a different level of observation noise in the strain and acceleration data is tested. Figure 6 indicates that the estimation error increases with an increase in the measurement noise. A similar trend is observed in all the columns; thus, only the results corresponding to column 1 are shown. From Figure 6, it can be observed that the measurement noise in the strain has a larger influence on the estimation error when compared to the acceleration noise.

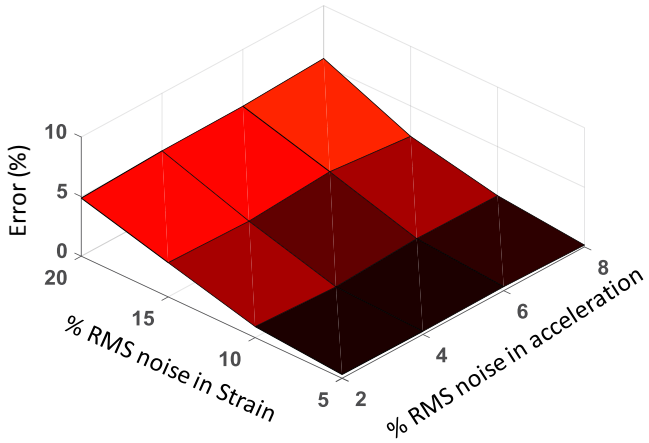

Figure 6: Estimation error in column 1 for different observation noise

4 CONCLUDING REMARKS

The virtual sensing strategy that is tailored to the SHM of offshore structures was investigated in this study. As the important structural members of offshore structures are located under water, the virtual sensing strategy can be a powerful alternative to the direct measurement, particularly when the structural responses are desired due to unavailable sensors. The problem formulation for the quasi-real time virtual sensing based on Kalman filtering was provided with how the non-stationary random excitation can be properly handled

for accurate response estimation. Two different types of data, acceleration and strain, were input to the state estimator. The strain response contributes to the low frequency, large amplitude trend in the estimation, whereas the acceleration with a high-frequency information is capable of reducing the random noise. The numerical simulation was conducted with the FE model of a small-scale offshore structure. The non-stationary input excitation that varies with time and height is introduced to simulate the tidal current. The simulation result indicated that the estimation was accurate with errors less than 2% and the following conclusions were obtained:

- The virtual sensing strategy has the potential to capture structural responses of the bottom-fixed offshore structures under the non-stationary tidal current loadings.
- The combined use of the different types of measurements (i.e., strain and acceleration) can help improve the estimation of the unmeasured strain response in lower and higher frequency regions.

The virtual sensing strategy is observed to be quite useful for monitoring offshore structures for OEFs and offshore winds with harsh environments. Based on the findings in this paper, further studies may use the estimated response for the SHM purposes such as fatigue estimation and damage detection.

ACKNOWLEDGMENT

This research was a part of the project titled “Development of active-controlled tidal stream generation technology” funded by the Ministry of Oceans and Fisheries, Korea (20110171) and KIOST R&D Program (project No. PE99521).

REFERENCES

[1] EWEA, *Aiming high rewarding ambition in wind energy*. The European Wind Energy Association (2015).

[2] Paust, H. S. *Finite element modeling and structural state estimation of a bottom fixed offshore wind turbine*. M.S. thesis, Department of Marine Technology Norwegian University of Science and Technology, June-2015.

[3] Iliopoulos, A. N., Weijtjens, W., Van Hemelrijck, D. and Devriendt, C., Prediction of dynamic strains on a monopile offshore wind turbine using virtual sensors. *Proceedings fo the* 11*th International Conference on Damage Assessment of Structures* (*DAMAS* 2015), *Journal of Physics: Conference Series* 628, 012108.

[4] Ren, P. and Zhou, Z., Strain response estimation for the fatigue monitoring of an offshore truss structure. *Pacific Science Review* (2014) **16**: 29-35.

[5] Kalman, R.E. A new approach to linear filtering and prediction problem. *Journal of Basic Engineering* (1960) **82**(1): 35-45.

[6] Van der Male, P. and Lourens, E. Operational Vibration-Based Response Estimation for Offshore Wind Lattice Structures. *Proceedings of the International Modal Analysis Conference* 2014.

[7] Papadimitriou, C., Fritzen, C-P., Kraemer, P., and Ntotsios, E. Fatigue predictions in entire body of metallic structures from a limited number of vibration sensors using

Kalman filtering. *Struct. Control Health Monit*. (2010) **18**(5): 554-573.
[8] Park, J.-W., Sim, S.-H., and Jung, H.-J. Displacement Estimation using Multimetric Data Fusion. *IEEE/ASME Transactions on Mechatronics* (2013) **18**(6): 1675-1682.
[9] Park, J.-W., Sim, S.-H., and Jung, H.-J., Wireless displacement sensing system for bridges using multi-sensor fusion. *Smart Materials and Structures* (2014) **23**(4): 045022.
[10] Cho S., Sim, S.-H., Park, J.-P., and Lee, J. Extension of indirect displacement estimation method using acceleration and strain to various types of beam structures. *Smart Structures and Systems* (2014) **14**(4): 699-718.
[11] Jo, H., and Spencer, B.F. Multimetric model based structure health monitoring. *Proc. of SPIE, Sensors and Smart Structures Technologies for Civil, Mechanical, and Aerospace Systems* 2014, *San Diego, California, USA*.
[12] Iliopoulos, A. N., Devriendt, C., Guillaume, P., Van Hemelrijck, D. Continuous fatigue assessment of an offshore wind turbine using a limited number of vibration sensors. *Proceedings of the 7th European Workshop on Structural Health Monitoring*, July 8-11, 2014. La Cite, Nantes, France.
[13] Lee, J.H., and Kim, S.-C. Mobile technology in the field data collection and management. *Journal of Structural Integrity and Maintenance*, (2016) **1**(3): 140-145
[14] Palanisamy, R. P., Cho, S., Kim, H., and Sim, S.-H., "Experimental validation of Kalman Filter-based strain estimation in structures subjected to non-zero mean input," *Smart Structures and Systems* (2015) **15**(2): 489-503.
[15] Crassidis, J. L. and Junkins, J. L. *Optimal Estimation of Dynamic Systems, Second edition*. CPC press, Taylor & Francis Group, ISBN -13: 978-1-4398-3986-7 (2012).

A BOUNDARY ELEMENT FORMULATION FOR MICROSTRUCTURAL MODELLING OF MULTILAYER ACTUATOR LAYERS

Mojtaba Biglar[a], Feliks Stachowicz[a], Tomasz Trzepieciński[a], Magdalena Gromada[b]

[a]Rzeszow University of Technology, Department of Materials Forming and Processing, Al. Powstancow Warszawy 8, 35-959 Rzeszów, Poland
e-mails : m_biglar@prz.edu.pl, stafel@prz.edu.pl, tomtrz@prz.edu.pl

[b]Institute of Power Engineering, Ceramic Department CEREL, ul. Techniczna 1, 36-040 Boguchwała, Poland
e-mail : gromada@cerel.pl

Key words: Multilayer Actuators, Piezoelectric Materials, Grain Boundary Formulations, Micromechanical Analysis, Crack Initiations and Evaluation.

Abstract. A two-dimensional grain boundary formulation is presented for the micromechanical analysis of multilayer barium titanate ceramics. The boundary element formulation of the elastic problem is generated for the single grains of the polycrystalline as well as heterogeneous aggregation and the assumption of tractions equilibrium and displacements compatibility are considered in this paper for expression of the intergranular variable which play an important role in elastic analysis of polycrystalline and heterogeneous micro-structures. However, these assumptions are valid only in undamaged areas. To model intergranular damage initiations and evaluations, a mixed mode effective traction as well as cohesive law is considered. The single crystals of homogenous $BaTiO_3$ are represented as anisotropic elastic regions and they are considered to be in contact with each other. So, the integrity of the collection must be guaranteed by applying equations on the interface of contiguous grains in different regions. The numerical modelling of the 2D polycrystaline has been done by developed technique and obtained results feats well with available data which confirm the reliability of the technique. Some numerical studies are provided to highlight the influence of piezoelectricity, metallic layers and predefined damages on the results.

1 INTRODUCTION

Micromechanical analysis has been converted to the most useful method in solid mechanics. Take stress –strain curve as an example, micromechanical analysis provide this opportunity for researchers to do some computational procedures and create this kind of curve and compare their results with experimental ones in order to make their numerical results valid. So, via these computational procedures, they are able to understand for example which kind of alleys have more effect on strange of materials or how much grains size and orientations can influence crack initiation or fracture criteria in composites.

In addition, the grain size and orientations as well as the structure of Representative Volume Elements (RVE) can have considerable effects on behaviour of materials. Some researchers showed that the specimen with different micro structure may experience different

crack initiation zone [1]. In the case of size of the grain it can be generally mentioned that the yield stress and the ultimate tensile strength decrease when the grain sizes increase. Off course the results depends on other factors such as back stress and strain rate [2].

Another advantage of micromechanical analysis is predicting the fracture behaviour of materials. In order to predict fracture behaviour of a composite, different cohesive law models or friction phenomena can be used [4-9]. Via cohesive low model, it possible to predict both intergranular or transgranular crack initiation. In other words, cohesive law is suitable tool in order to model interface where materials with different mechanical property are in contact together. However, it has this shortage that it is not possible to model singular crack field close to crack tip. There are two different kind of cohesive law based on which one is able to predict fracture and crack initiation, the potential-based law [5, 6], and the linear law [7, 8].

Precisely speaking, Most of the researchers have used cohesive law model and cohesive zone approach for crack nucleation and propagation in the polycrystalline materials. To achieve this important, they used different numerical model such as boundary element method or finite element method [9, 10]. Despite to this fact that some of the cohesive laws consider fracture criteria for first and second mode separately, some researcher proposed mixed mode relation to predict the location of cohesive zone in polycrystalline [11].

Alongside traditional cohesive approach, some researchers proposed modified rules to simulate fracture and fragmentation processes in various materials [12]. Snozzi et al. [13] presented a traction based law for modelling of deboning and frictional contact. This model combines interface separation and frictional contact. The nucleation of crack is modelled using this cohesive approach. While the separation process is controlled by a mix mode traction separation law which gives two separate values for energy dissipation in mode I and mode II loading.

The application of boundary element method in micromechanics and multistate modelling was studied by some researchers [14, 15]. In some of these works, researcher only modelled materials in micro scale and neither cohesive law nor averaging thorium was used. Off course these works were done many years ago and they could be a big step in micromechanical analysis in that time. However, several researchers utilized some basic concept of micro mechanical analysis such as representative volume element and grain boundaries in their studies. In these works, which are one of the earliest works in the area of polycrystalline analysis, a periodic arrangement of hexagonal grains was used to model micromechanical behaviour of polycrystalline. Then, through utilizing symmetry condition, they restricted the models to representative unit cell with special boundary conditions. However, Fotiu et al. [15] they used homogeneous materials property not composite for their investigation. Benedetti and Aliabadi [16] and Sfantos and Aliabadi [4] have done a comprehensive research in using boundary element method in micro-mechanical analysis. Their works contain modelling of grain boundaries as well as generating a numerical algorithm. However, the considering of piezoelectric effects is one of the important facts which they ignored in their studies, while piezoelectric materials have been studied by some researcher due to their alternative applications [17-22].

2 MICRO-MECHANICAL MODEL

2.1 Application of boundary element method in micro scale

In this work, the model of brittle materials is considered for representation of RVE and the basic assumption is that the every RVE consists of polycrystalline brittle materials. Generally, there are some researches which considered grain boundaries along with grain in their modelling and they assigned different properties in comparison with property of main grain for the boundaries [9]. However, due to small area of grain boundaries compared with grain, the modelling of them is ignored in current research and only the intergranular fracture is subject of current study. To investigate crack nucleation, propagation and branching in brittle polycrystalline, the boundary element method which was suggested in [4, 16] is being used here. Let us write the constitutive relation for piezoelectric ceramics in two dimensions namely 1-3 plane.

$$\begin{bmatrix}\sigma_{11}\\ \sigma_{22}\\ \sigma_{12}\end{bmatrix}=\begin{bmatrix}c_{11} & c_{13} & 0\\ c_{13} & c_{33} & 0\\ 0 & 0 & c_{44}\end{bmatrix}\begin{bmatrix}u_{1,1}\\ u_{2,2}\\ u_{1,2}+u_{2,1}\end{bmatrix}+\begin{bmatrix}0 & e_{31}\\ 0 & e_{33}\\ e_{15} & 0\end{bmatrix}\begin{bmatrix}\varphi_{,1}\\ \varphi_{,2}\end{bmatrix}$$
$$\begin{bmatrix}D_1\\ D_2\end{bmatrix}=\begin{bmatrix}0 & 0 & e_{15}\\ e_{31} & e_{33} & 0\end{bmatrix}\begin{bmatrix}u_{1,1}\\ u_{2,2}\\ u_{1,2}+u_{2,1}\end{bmatrix}+\begin{bmatrix}\kappa_{11} & 0\\ 0 & \kappa_{33}\end{bmatrix}\begin{bmatrix}\varphi_{,1}\\ \varphi_{,2}\end{bmatrix} \tag{1}$$

As it is known, there is an extra field in piezoelectric materials, namely electric displacement D_i and electrical potential φ which need to be considered. The displacement vector for piezoelectric materials can be written as

$$u_I=\begin{cases}u_i, & I=1,2\\ \varphi & I=3\end{cases} \tag{2}$$

In a similar way, the traction vector is shown like

$$\sigma_{iJ}=\begin{cases}\sigma_{ij}, & J=1,2\\ D_J & J=3\end{cases}\Rightarrow\quad t_I=\begin{cases}t_i=\sum_{j=1}^{2}\sigma_{ij}n_j, & I=1,2\\ D=\sum_{j=1}^{2}D_j n_j, & I=3\end{cases} \tag{3}$$

In Figure 1, the RVE is presented which is subject of current study. The procedure for obtaining this RVE via SEM photo. In this RVE, the basic assumptions are that for interface of two grains which are next to each other and are in undamaged regions, namely grain number 9 and 10, and are shown in Figure 1, the value of traction is equal and these two grains are completely attached to each other as follow,

$$\begin{aligned}&\mathbf{t}^9 = -\mathbf{t}^{10},\ \delta\mathbf{u}^I = \mathbf{u}^9 - \mathbf{u}^{10} = 0\\&\varphi^9 = \varphi^{10},\ D^9 = D^{10}\end{aligned} \tag{4}$$

where the value of $\mathbf{t}^I$ and $\delta\mathbf{u}^I$ are interface traction and relative displacement jump in global coordinates. The value of traction and displacement can be represented in two values, x direction ($\mathbf{t}_x^I, \mathbf{u}_x^I$) and y direction ($\mathbf{t}_y^I, \mathbf{u}_y^I$).

Fundamental boundary element equation the for each grain can be written as

$$\begin{aligned}&C_{ij}^k(z')u_j^k(z') + \int_{S_c^k} T_{ij}^k(z',z)u_j^k(z)dS_c^k + \int_{S_{nc}^k} T_{ij}^k(z',z)u_j^k(z)dS_{nc}^k =\\&\int_{S_c^k} U_{ij}^k(z',z)t_j^k(z)dS_c^k + \int_{S_{nc}^k} U_{ij}^k(z',z)t_j^k(z)dS_{nc}^k \qquad k = 1,...,number\ of\ \ grain\end{aligned} \tag{5}$$

In Eq. (5), $T_{ij}^k(z',z)$ and $U_{ij}^k(z',z)$ are fundamental solution for traction and displacement which can be obtained via Stroh formulation for each grain. C_{ij}^k refers to free term. The Eq. (5) is discretize in unique global coordinates, however, in order to simplify applying the boundary condition along with interface equations, it is better to convert the Eq. (5) into local coordinates. In next chapters examples of both local and global coordinates are provided.

It is worth mentioning that the transformation from global coordinate to local coordinate for boundary condition or free boundary can be done by;

$$\widetilde{\mathbf{t}}^I = \begin{bmatrix}\widetilde{\mathbf{t}}_s\\ \widetilde{\mathbf{t}}_n\\ \mathbf{D}\end{bmatrix} = \begin{bmatrix}-n_y & n_x & 0\\ n_x & n_y & 0\\ 0 & 0 & 1\end{bmatrix}\begin{bmatrix}\mathbf{t}_x\\ \mathbf{t}_y\\ \mathbf{D}\end{bmatrix} = \mathbf{R}\mathbf{t}^I,\ \widetilde{\mathbf{u}}^I = \begin{bmatrix}\widetilde{\mathbf{u}}_s\\ \widetilde{\mathbf{u}}_n\\ \varphi\end{bmatrix} = \begin{bmatrix}-n_y & n_x & 0\\ n_x & n_y & 0\\ 0 & 0 & 1\end{bmatrix}\begin{bmatrix}\mathbf{u}_x\\ \mathbf{u}_y\\ \varphi\end{bmatrix} = \mathbf{R}\mathbf{u}^I \tag{6}$$

where $\mathbf{R}$ denotes the local rotation matrix from global coordinates to local coordinates. The same procedure can be done for displacement and traction of internal grains. Now, the Eq. (5) can be rewritten as;

$$\begin{aligned}&\widetilde{C}_{ij}^k(z')\widetilde{u}_j^k(z') + \int_{S_c^k} \widetilde{T}_{ij}^k(z',z)\widetilde{u}_j^k(z)dS_c^k + \int_{S_{nc}^k} \widetilde{T}_{ij}^k(z',z)\widetilde{u}_j^k(z)dS_{nc}^k =\\&\int_{S_c^k} \widetilde{U}_{ij}^k(z',z)\widetilde{t}_j^k(z)dS_c^k + \int_{S_{nc}^k} \widetilde{U}_{ij}^k(z',z)\widetilde{t}_j^k(z)dS_{nc}^k \qquad k = 1,...,number\ of\ \ grain\end{aligned} \tag{7}$$

Where matrices in local coordinates can be defined in continuum form

$$\widetilde{C}_{ij}^k = C_{in}^k R_{nj}^k \quad \widetilde{U}_{ij}^k = U_{in}^k R_{nj}^k \quad \widetilde{T}_{ij}^k = T_{in}^k R_{nj}^k \tag{8}$$

2.2 The cohesive law model and grain boundary formulation

In the condition that node pairs are in undamaged zone, the following compatibility and equilibrium equations in local coordinates are governed

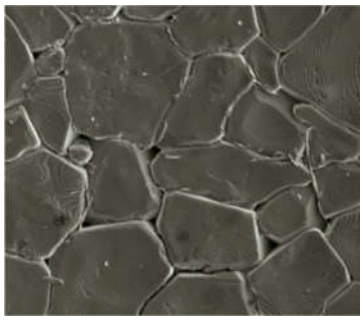

(a)

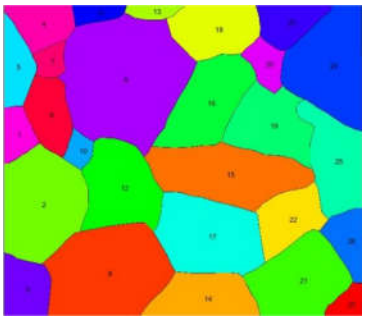

(b)

Figure 1: (a) The micro-mechanical model barium titante and (b) output of image processing algorithm.

$$\begin{aligned} &\tilde{u}_i^a + \tilde{u}_i^b = -\delta\tilde{u}_i^{ab} = 0 \\ &\qquad\qquad i = 1,2 \quad or\, i = t \;and\; n \\ &\tilde{t}_i^a - \tilde{t}_i^b = 0 \\ &\tilde{\varphi}^a = \tilde{\varphi}^b,\ \tilde{D}^a = \tilde{D}^b \end{aligned} \tag{9}$$

In this equation, $i = 1$ represents tangential components and $i = 2$ demonstrates normal components in local coordinates. Through components of normal and tangential traction, the effective traction can be defined as;

$$t_{eff} = \left[\left\langle \tilde{t}_n \right\rangle^2 + \left(\frac{\beta}{\alpha} \tilde{t}_s \right)^2 \right]^{\frac{1}{2}} \tag{10}$$

In this equation, the $\langle . \rangle$ denotes Mc-Cauley brackets which defined by $\langle x \rangle = max(0,x)$. In a glimpse to the Eq. (10) it can be understood that only tensile value of normal traction contributes in effective value of traction. β and α are suitable coefficient which determine the contribution of opening and sliding modes in damage process. As long as $t_{eff} < T_{max}$ the interface has undamaged status while T_{max} demonstrates the maximum value for traction.

Once effective traction exceed the maximum value, $t_{eff} \geq T_{max}$, the node pairs enter to the damaged zone and crack initiation starts at those node pairs. In this status, the node pairs experience displacement jump and one variable is needed to calculate the displacement jump in the cohesive zone and traction as well. In different works, some relations can be found in order to be applied for finding variables. The non-dimensional effective opening displacement can be introduced as;

$$d = \left[\left\langle \frac{\delta\tilde{u}_n}{\delta\tilde{u}_n^{cr}} \right\rangle^2 + \beta^2 \left(\frac{\delta\tilde{u}_s}{\delta\tilde{u}_s^{cr}} \right)^2 \right]^{\frac{1}{2}} \tag{11}$$

In this relation, $\delta\tilde{u}_n^{cr}$ and $\delta\tilde{u}_s^{cr}$ stand for critical values of displacement in normal and sliding modes in which interface failure or micro-crack can be happened. β is a weight which determines that which mode has more influence in effective displacement in mixed-mode condition. It is worth mentioning that the value of effective opening displacement varied between 0 and 1, $0 \le d \le 1$, which means that $d = 0$, there is no displacement jump and the interface is completely intact and, $d = 1$, stands for complete failure or cohesion in which micro-crack can be define.

The status of interface equation between two grain next to each other namely, *a* and *b*, can be shown in as

$$\begin{cases} \Omega_{ab}^{i}\left[\tilde{u}_j^a, \tilde{u}_j^b, \varphi^a, \varphi^b, \tilde{t}_j^a, \tilde{t}_j^b, D^a, D^b\right] = 0 \\ \Theta_{ab}^{i}\left[\tilde{t}_j^a, \tilde{t}_j^b, D^a, D^b\right] = 0 \end{cases} \tag{12}$$

In this equation, Ω_{ab}^{i} depends on status of interface, while Θ_{ab}^{i} stands for equilibrium equation in all regions. In the undamaged region, these two equations can be demonstrates as

$$\begin{cases} \Omega_{ab}^{i} = \tilde{u}_i^a + \tilde{u}_i^b = -\delta\tilde{u}_i^{ab} \\ \Omega_{ab} = \tilde{\varphi}^a - \tilde{\varphi}^b = \delta\tilde{\varphi}^{ab} \\ \qquad\qquad i = 1,2 \ \ or \ \ s \ and \ n \\ \Theta_{ab}^{i} = \tilde{t}_i^a - \tilde{t}_i^b \\ \Theta_{ab} = \tilde{D}^a - \tilde{D}^b \end{cases} \tag{13}$$

And when a node pairs enter to the cohesive region, these two equations can be represented by using cohesive law.

$$\begin{cases} \Omega_{ab}^{s} = C_s\left(d^*\right)\delta\tilde{u}_s^{ab} - \tilde{t}_s \\ \Omega_{ab}^{n} = C_n\left(d^*\right)\delta\tilde{u}_n^{ab} - \tilde{t}_n \\ \Omega_{ab} = \tilde{\varphi}^a - \tilde{\varphi}^b \\ \Theta_{ab}^{i} = \tilde{t}_i^a - \tilde{t}_i^b \qquad\qquad i = 1,2 \ or \ s \ and \ n \\ \Theta_{ab} = \tilde{D}^a - \tilde{D}^b \end{cases} \tag{14}$$

$$C_s\left(d^*\right) = \frac{1-d^*}{d^*}\frac{\alpha T_{max}}{\delta\tilde{u}_s^{cr}}$$

$$C_n\left(d^*\right) = \frac{1-d^*}{d^*}\frac{T_{max}}{\delta\tilde{u}_n^{cr}}$$

It is valuable to emphasize that all of the variables and equations are defined in local coordinates. In this paper uniform displacements boundary condition is applied to RVE which is represented as

$$u_i^m = \varepsilon_{ij}^M x_j^m \tag{15}$$

The linear relation for one single grain, namely grain number 10 in Figure 1, can be shown as follow,

$$\begin{bmatrix}\mathbf{H}_{\mathbf{nc}}^{\mathbf{10}} & \mathbf{H}_{\mathbf{c}}^{\mathbf{10}}\end{bmatrix}\begin{bmatrix}\mathbf{u}_{\mathbf{nc}}^{\mathbf{10}} \\ \mathbf{u}_{\mathbf{c}}^{\mathbf{10}}\end{bmatrix}=\begin{bmatrix}\mathbf{G}_{\mathbf{nc}}^{\mathbf{10}} & \mathbf{G}_{\mathbf{c}}^{\mathbf{10}}\end{bmatrix}\begin{bmatrix}\mathbf{t}_{\mathbf{nc}}^{\mathbf{10}} \\ \mathbf{t}_{\mathbf{c}}^{\mathbf{10}}\end{bmatrix} \tag{16}$$

Via applying the interface and boundary condition and generating the Eq. (16) for all of the grains in polycrystalline aggregate, the adaptive system of equation which contains boundary element method and grain interface equations can be written as

$$\begin{bmatrix}\mathbf{A}^{\mathbf{1}} & \mathbf{B}^{\mathbf{1}} & \mathbf{0} & \cdots & \mathbf{0} \\ \mathbf{0} & \mathbf{A}^{\mathbf{2}} & \mathbf{B}^{\mathbf{2}} & \cdots & \mathbf{0} \\ \vdots & \vdots & \vdots & \ddots & \vdots \\ \mathbf{0} & \cdots & \mathbf{0} & \mathbf{A}^{n_g} & \mathbf{B}^{n_g} \\ & \textit{Interface equation} & \Omega & & \\ & \textit{Interface equation} & \Theta & & \end{bmatrix}\begin{bmatrix}x_{nc}^{1} \\ x_{c}^{1} \\ \vdots \\ x_{nc}^{n_g} \\ x_{c}^{n_g}\end{bmatrix}=\begin{bmatrix}\begin{bmatrix}\mathbf{D}^{\mathbf{1}} & \mathbf{0} & \cdots & \mathbf{0} \\ \mathbf{0} & \mathbf{D}^{\mathbf{2}} & \cdots & \mathbf{0} \\ \vdots & \vdots & \ddots & \vdots \\ \mathbf{0} & \cdots & \mathbf{0} & \mathbf{D}^{\mathbf{2}}\end{bmatrix} \\ \begin{matrix}\mathbf{0} & & \mathbf{0}\end{matrix}\end{bmatrix}\begin{bmatrix}y_{nc}^{1} \\ y_{nc}^{2} \\ \vdots \\ \mathbf{0} \\ y_{nc}^{n_g}\end{bmatrix} \tag{17}$$

in this linear relation, the uniform displacement boundary condition is applied n_g represents for number of grains. $\mathbf{D}$ contains the value of matrix $\mathbf{H}_{nc}$ in Eq. (16) and $\mathbf{A}$ the value of matrix $\mathbf{G}_{nc}$ in Eq. (16), however, contrarily with Eq.(16), all of these matrices here are define in local coordinates. $\mathbf{B}$ is a matrix which has the form $\begin{bmatrix}\mathbf{G}_c & -\mathbf{H}_c\end{bmatrix}$. The vector, x_{nc} contains the unknown value of $\tilde{t}$ in non-contact or boundary condition area and x_c contains $\begin{bmatrix}\tilde{t} & \tilde{u}\end{bmatrix}^T$ which are traction and displacement in the contact area. y_{nc} contains the prescribed values of boundary condition in non-contact area. The Ω and Θ represented the interface status in Eq. (12) which contains a lot of zeros, some 1 and -1 in the undamaged areas, however, they can described through Eq. (12) in cohesive region. As it is clear, the total matrix of Eq. (17) are linear and it contains the nonlinear equations of cohesive law which can be solved in every iteration.

3 NUMERICAL SIMULATION OF MICRO-DAMAGE AND COHESIVE LAW

The specified value for parameters was introduced during last sections and subsections can be seen in Table 1. In this work the rest of the numerical examples are provided based on mechanical and electrical properties of barium titanate which are presented in Table 2.

Table 1: The property of PZT-4 piezoelectric ceramic

$T_{\max}(Mpa)$	α	β	d^*_{start}	ε_d
500	1	$\sqrt{2}$	0.5×10^{-5}	0.5×10^{-3}

Table 2: The property of PZT-4 piezoelectric ceramic

$c_{11}\left(\frac{N}{m^2}\right)$	$c_{13}\left(\frac{N}{m^2}\right)$	$c_{33}\left(\frac{N}{m^2}\right)$	$c_{44}\left(\frac{N}{m^2}\right)$	$e_{31}\left(\frac{C}{m^2}\right)$	$e_{33}\left(\frac{C}{m^2}\right)$	$e_{15}\left(\frac{C}{m^2}\right)$	$\kappa_{11}\left(\frac{C}{Vm}\right)$	$\kappa_{33}\left(\frac{C}{Vm}\right)$
9.54×10^{10}	3.26×10^{10}	7.57×10^{10}	2.56×10^{10}	-6.98	13.8	13.4	60×10^{-10}	54.7×10^{-10}

Figure 2 demonstrates the stress-strain curve for polycrystalline aggregate of Figure 1 with and without piezoelectric effects. It can be concluded that the piezoelectric coupling has significant influence on fracture criteria of aggregates which means that through considering the piezoelectricity and for a specified amount of strain, the polycrystalline aggregate without piezoelectric effect can experience more stress. It could be deduced that for a specific strain energy which is entered to the system, the piezoelectric aggregate, it should be divided between mechanical and electric effects, while in polycrystalline without piezoelectricity this energy can only have influence on mechanical properties. The fracture pattern of this example is shown in Figure 3. The difference between two patterns can be seen here with considering piezoelectric effects and without it. It can be concluded in this figure that by increasing the strain, the crack grows faster and faster.

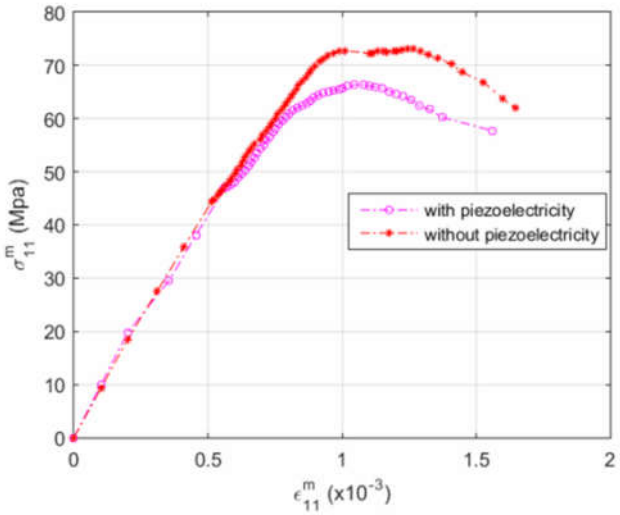

Figure 2: Normal strain and normal stress of polycrystalline aggregate of (Figure 1) in horizontal direction by considering piezoelectric effects and without piezoelectric effects.

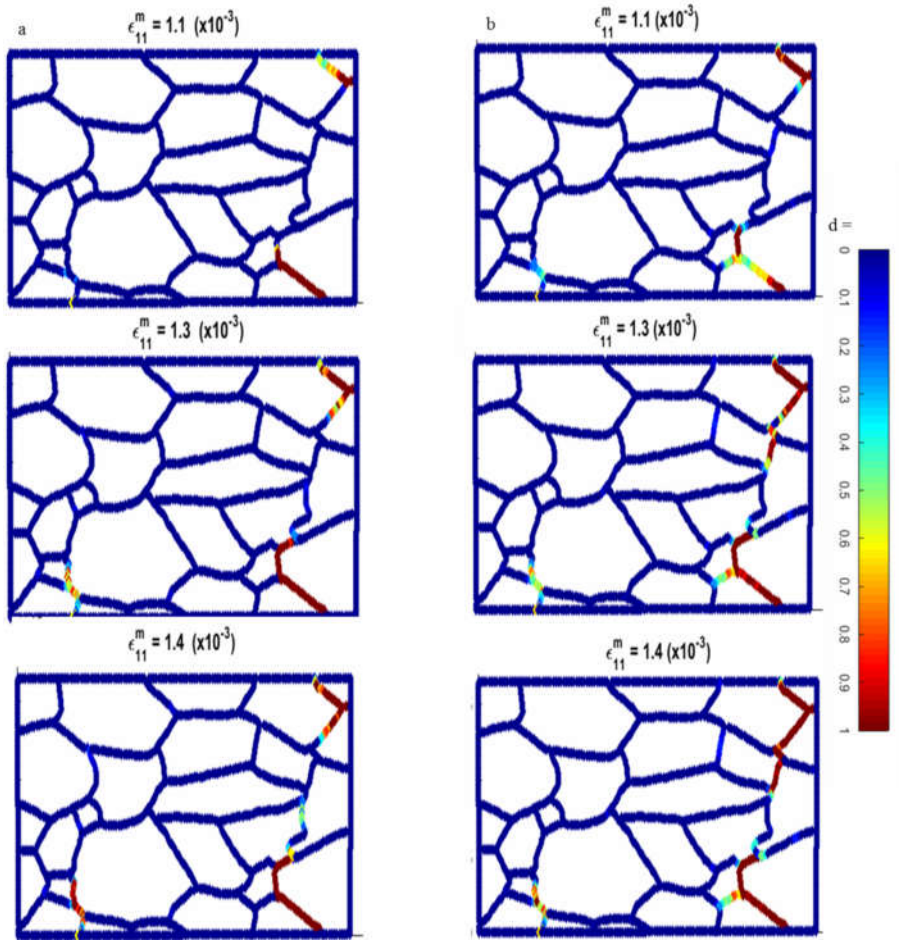

Figure 3: The fracture pattern for of polycrystalline aggregate of (Figure 1) without piezoelectric effects and (b) with piezoelectric effects.

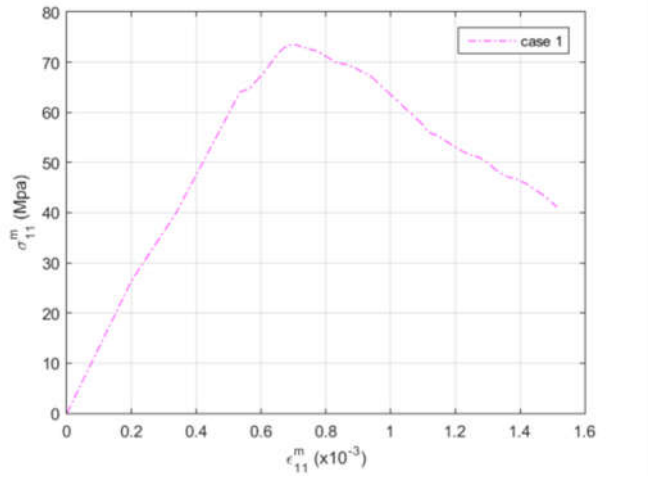

Figure 4: Normal stress versus normal strain in multilayer piezoelectric actuator.

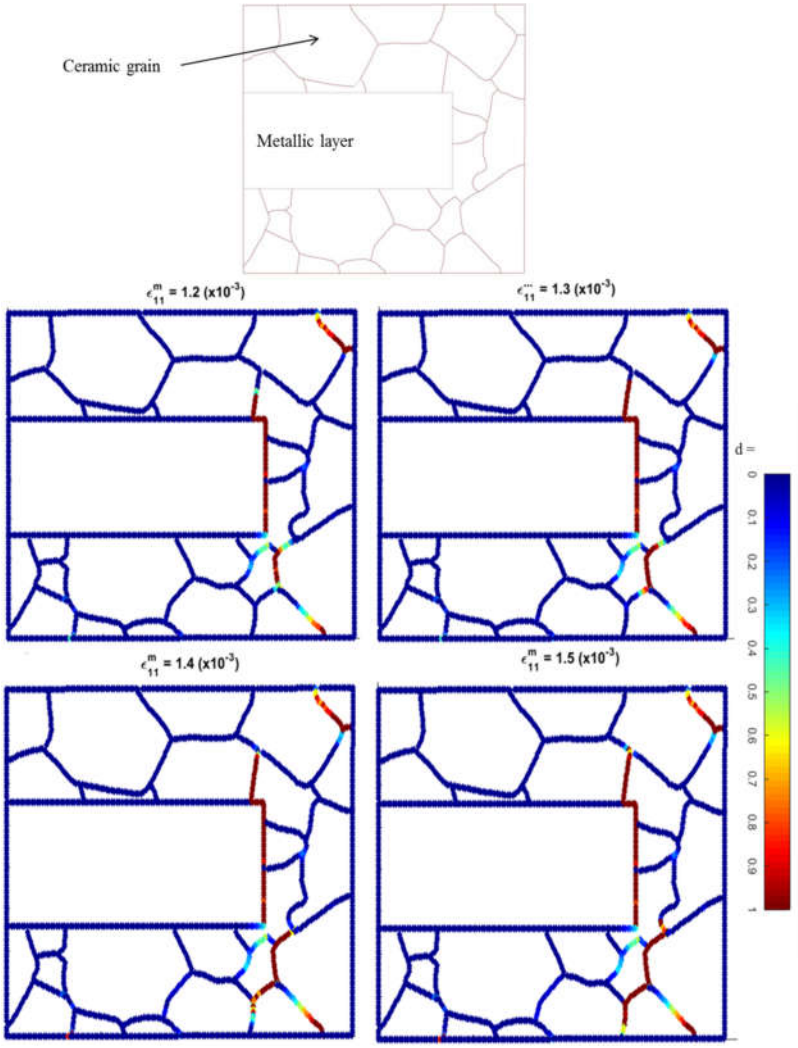

Figure 5: The fracture pattern of multilayer piezoelectric ceramics representative valume element.

One of the interesting results which can be visited in Figure 3 is that in the grain aggregate with piezoelectric effect, the fracture grows up faster. The reason that can justify this event is that after the crack is nucleated, the distant between two grains behaves like a capacitor and it injects opposite traction to the grains boundary. This traction can create the situation that the crack crow up faster than the time when there is no piezoelectric effects.

In order to increase the efficiency of piezoelectric ceramics, metallic layer can be applied inside of the homogeneous ceramics at different positions. This kind of technology can be used as actuator in fuel injector part of diesel engines. The mechanical behaviour of multilayer piezoelectric actuator is shown in Figure 4 and their fracture patterns are shown in Figure 5 for different values of strains. As can be noticed in this figure, the metallic interface has significant influence on micro-crack patterns of RVE of multilayer actuator and the fracture can happened near metallic interface. So, it can be deduced that near metallic interface is the most sensitive part of multilayer actuator. It is worth stressing that the ultimate

stress T_{max} between ceramic grains and metallic layer is lower than ceramic node pairs. However, in Figure 4 and Figure 5 it is assumed T_{max} = 80 MPa.

The influence of metallic interface on electrical behaviour of actuator is demonstrated in Figure 6. In the lower strain in the part that still there is no micro-crack, the multilayer actuator shows much more output than homogenous one which indicates the influence of metallic interface on output of piezoelectric ceramics.

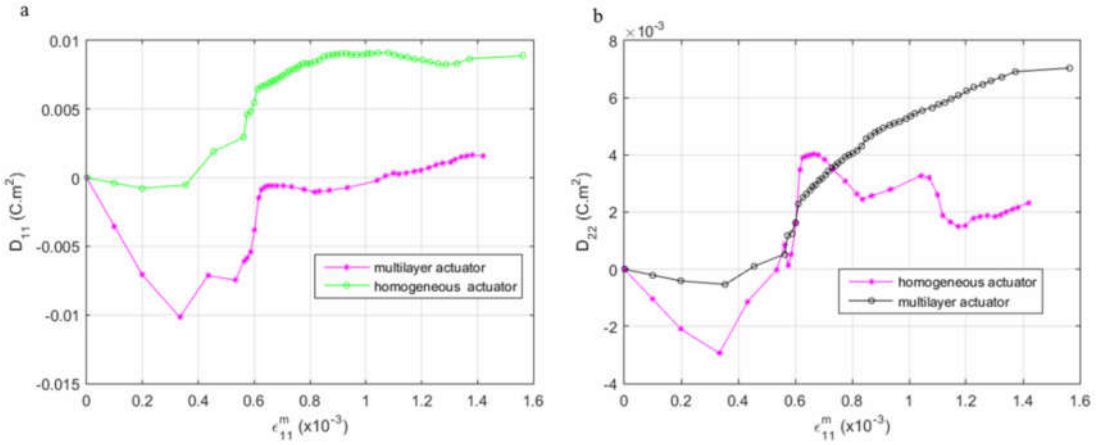

Figure 6: The electric displacement in (a) horizontal and (b) vertical direction versus horizontal strain.

4 CONCLUSIONS

The micro-mechanical analysis of multilayer and homogeneous actuator was done in this work. The grain boundaries were divided into two zones, namely undamaged zone and cohesive zone and suitable formulation for every zone were developed in order to study what is happening in the grain boundary.

The investigations indicate that the piezoelectricity can influence mechanical behaviour of materials. Moreover, adding metallic interface to the actuators can change their behaviour significantly.

ACKNOWLEDGEMENT

The research leading to these results has received funding from the People Programme (Marie Curie Actions) of the European Union's Seventh Framework Programme FP7/2007-2013/ under REA grant agreement No. PITN-GA-2013- 606878.

REFERENCES

[1] Jafari, M., Ziaei-Rad, S. and Noushin T. A dislocation density-based model for analyzing mechanical behavior of dual-phase steels. *Metallography Micro. Anal.* (2014) **3**:185-193.

[2] Ma, A., Roters F. and Raabe, D. Studying the effect of grain boundaries in dislocation density based crystal-plasticity finite element simulations. *Int. J. Solids Struct.* (2006) **43**:7287-7303.

[3] Lee, M.G., Lim, H., Adams, B.L., Hirth, J.P. and Wagoner R.H. A dislocation density-based single crystal constitutive equation. *Int. J. Plasticity* (2010) **26**:925-938.

[4] Sfantos, G.K. and Aliabadi, M.H. A boundary cohesive grain element formulation for modelling intergranular microfracture in polycrystalline brittle materials. *Int. J. Numer. Methods Engng.* (2007) **69**: 1590-1626.
[5] Espinosa, H.D., Zavattieri, P.D. and Emore G.L. Adaptive FEM computation of geometric and material nonlinearities with application to brittle failure. *Mech. Mater.* (1998) **29**:275-305.
[6] Ortiz, M. and Pandolfi A. Finite-deformation irreversible cohesive elements for three-dimensional crack-propagation analysis. *Int. J. Numer. Methods Engng.* (1999) **44**:1267-1282.
[7] Espinosa, H.D., Zavattieri P.D. and Dwivedi, S.K. A finite deformation continuum\discrete model for the description of fragmentation and damage in brittle materials. *J. Mech. Phys. Solids* (1998) **46**:1909-1942.
[8] Zavattieri, P.D., Raghuram, P.V. and Espinosa, H.D. A computational model of ceramic microstructures subjected to multi-axial dynamic loading. *J. Mech. Phys. Solids* (2001) **49**:27-68.
[9] Verhoosel, C.V., and Gutiérrez M.A. Modelling inter- and transgranular fracture in piezoelectric polycrystals. *Eng. Fract. Mech.* (2009) **76**:742-760.
[10] Galvis, A. F. and Sollero P. Boundary element analysis of crack problems in polycrystalline materials. *Procedia Mater. Sci.* (2014) **3**:1928-1933.
[11] Benedetti, I. and Aliabadi M.H. Multiscale modeling of polycrystalline materials: A boundary element approach to material degradation and fracture. *Comput. Method. Appl. Mech. Engng.* (2015) **289**:429-453.
[12] Lee, S.S., Heo, D.E. and Lee, J.K. Modified damage initiation criterion for the cohesive boundary element. *Int. J. Precis. Engng. Man.* (2010) **11**:577-581.
[13] Snozzi, L. and Molinari J.F. A cohesive element model for mixed mode loading with frictional contact capability. *Int. J. Numer. Methods Engng.* (2013) **93**:510-526.
[14] Goldberg, R.K. and Hopkins D.A. Application of the boundary element method to the micromechanical analysis of composite materials. *Comput. Struct.* (1995) **56**:721-731.
[15] Fotiu, P.A., Heuer, R. and Ziegler, F. BEM analysis of grain boundary sliding in polycrystals. *Engng. Anal. Bound. Elem.* (1995) **15**:349-358.
[16] Benedetti, I. and Aliabadi M.H. A three-dimensional cohesive-frictional grain-boundary micromechanical model for intergranular degradation and failure in polycrystalline materials. *Comput. Method. Appl. Mech. Engng*. (2013) **265**:36-62.
[17] Biglar, M., Mirdamadi H.R. and Danesh, M. Optimal locations and orientations of piezoelectric transducers on cylindrical shell based on gramians of contributed and undesired Rayleigh–Ritz modes using genetic algorithm. *J. Sound Vib.* (2014) **333**:1224-1244.
[18] Biglar, M. and Mirdamadi H.R. Integrated and consistent active control formulation and piezotransducer position optimization of plate structures considering spillover effects. *Shock Vib.* (2014) **2014**: article ID 276714.
[19] Biglar, M. And Mirdamadi H.R. Configuration optimization of piezoelectric patches attached to functionally graded shear-deformable cylindrical shells considering spillover effects. *J. Intel. Mat. Syst. Str.* (2015) **27**:295-313.
[20] Biglar, M., Gromada, M., Stachowicz, F. and Trzepieciński T. Optimal configuration of piezoelectric sensors and actuators for active vibration control of a plate using a genetic algorithm. *Acta Mech.* (2015) **226**:3451-3462.
[21] Biglar, M., F. Stachowicz, T. Trzepiecinski, and M. Gromada. "Micro-mechanical modelling of mechanical and electrical properties in homogeneous piezoelectric ceramic by using boundary integral formulations." In *IOP Conference Series: Materials Science and Engineering*, vol. 175, no. 1, p. 012040. IOP Publishing, 2017.
[22] Trzepieciński, Tomasz, Grażyna Ryzińska, Mojtaba Biglar, and Magdalena Gromada. "Modelling of multilayer actuator layers by homogenisation technique using Digimat software." *Ceramics International* 43, no. 3 (2017): 3259-3266.

A cohesive zone model for damage in multiferroic composites under magnetoelectromechanical loading

Alexander Schlosser* and Andreas Ricoeur†

* Institute of Mechanics, Chair of Engineering Mechanics / Continuum Mechanics
University of Kassel
Moenchebergstr. 7, 34109 Kassel, Germany
e-mail: alexander.schlosser@uni-kassel.de

† Institute of Mechanics, Chair of Engineering Mechanics / Continuum Mechanics
University of Kassel
Moenchebergstr. 7, 34109 Kassel, Germany
e-mail : andreas.ricoeur@uni-kassel.de

ABSTRACT

Exhibiting interactions between magnetical and electrical fields at room temperature makes magnetoelectric (ME) composites interesting for various applications in technical devices. The ferroelectric matrix as well as the magnetostrictive inclusions of those composites are mostly ceramics or other brittle materials, thus being prone to cracking. Due to this brittleness, the consideration of damage is crucial in numerical analyses of ferroelectric and ferromagnetic devices, too. Especially the delamination behaviour of boundary layers in ME composites is of a great interest due to its influence on coupling factors. In order to investigate delamination processes in ME composites, cohesive elements are being developed and applied in combination with nonlinear ME finite elements described in [1] and [2]. The mechanical behaviour of the cohesive zone is prescribed by a bilinear traction-separation-law. Magnetical and electrical fields are based on an approach of the potential gradient between the two phases. Electrical and magnetical properties change during damaging processes and are controlled by damage variables which themselves are determined by the separation between the boundaries. Some numerically calculated results with these cohesive elements are presented.

REFERENCES

[1] A. Avakian, R. Gellmann and A. Ricoeur, “Nonlinear modelling and finite element simulation of magnetoelectric coupling and residual stress in multiferroic composites”, *Acta Mechanica*, pp. 2789 - 2806, (2015).

[2] A. Avakian and A. Ricoeur, “Constitutive modelling of nonlinear reversible and irreversible ferromagnetic bahaviors and application to multiferroic composites”,*Journal of Intelligent Material Systems and Structures*, (2016).

VIII ECCOMAS Thematic Conference on Smart Structures and Materials
SMART 2017
A. Güemes, A. Benjeddou, J. Rodellar and J. Leng (Eds)

FORMULATION AND IMPLEMENTATION OF THERMO-ELECTRO-MAGNETO-ELASTOPLASTIC COUPLING FOR DIELECTRIC AND CONDUCTOR MATERIALS

ADNAN IBRAHIMBEGOVIC*, PABLO MORENO-NAVARRO* AND JOSÉ L. PÉREZ APARICIO†

*Laboratoire de Mécanique Roberval
Université de Technologie de Compiègne
Centre de Recherches Royallieu, 60200 Compiègne, France
e-mail: adnan.ibrahimbegovic@utc.fr, pablo.moreno-navarro@utc.fr

†Mecánica Medios Continuos
Universidad Politècnica de València
Camino de Vera s/n Valencia, Spain
e-mail: jopeap@mes.upv.es

Key words: Thermo-electro-magneto-mechanics coupling, Plasticity, Thermodynamics, Finite Element Formulation

Abstract. A consistent thermodynamic-based theoretical framework and three-dimensional finite element formulation is presented, capable of coupling thermal, electric, magnetic and mechanic fields. The complete set of governing equations are obtained from conservation principles. The constitutive relations are derived consistently from the Helmholtz free-energy potential for each corresponding dual variable in terms of the defined set of state variables. In the case of conductor formulation, the second principle of thermodynamics is taken into account to introduce the irreversible phenomena, such as plastic dissipation or Joule heating. The implementation is carried out in a research version of the well-known computer code FEAP. A numerical simulation is presented in order to illustrate the proposed model and formulation capabilities for providing an enhanced formulation of an important practical application in terms of Peltier cells.

1 INTRODUCTION

This work seeks to provide a consistent thermodynamic development for fully-coupled dielectric and conductor materials [1]. First a set of state variables and their corresponding dual ones are defined for each field in establishing the governing equations based on conservation principles. Second, by settling a full quadratic form of the free-energy potential, the linear constitutive equations can be derived from it in a consistent way, providing a hyperelastic response instead of a hypoelastic [2]. For the conductors formulation, the coupling is taken into inelastic

domain defined in terms of plasticity theory that accounts for mechanical, thermal and electric fields in defining the corresponding plasticity criterion. The latter is set in terms of intensive variables, dual to the chosen state (extensive) variables. The corresponding evolution equations for plastic part of state variables are obtained from maximum dissipation principle. Then, the theoretical formulation is accompanied by the discrete approximation, based upon 3D Finite Elements with thermo-electro-magneto-mechanic degrees of freedom, along with simultaneous solution procedures of the weak form for all governing equations. Finally, a numerical example with Peltier cells for the conductor formulation is shown.

2 FORMULATION

2.1 Kinematic equations

Four fields are considered in formulating the thermomechanics and electromagnetics coupling: displacement $\boldsymbol{u}$, temperature T, electric potential V and magnetic scalar potential φ. The state variables are obtained as the corresponding gradients of these fields. The set of resulting kinematic equations for both kind of materials can be written as:

$$\begin{aligned} \boldsymbol{\varepsilon} &= \frac{1}{2}\left[\nabla \otimes \boldsymbol{u} + (\nabla \otimes \boldsymbol{u})^{\mathsf{T}}\right] \\ \boldsymbol{E} &= -\nabla V \\ \boldsymbol{H} &= -\nabla \varphi \end{aligned} \tag{1}$$

where $\boldsymbol{\varepsilon}$ is the strain tensor, $\boldsymbol{E}$ is the electric field, $\boldsymbol{H}$ is the magnetic field, while $\nabla = [\partial/\partial x \quad \partial/\partial y \quad \partial/\partial z]^{\mathsf{T}}$ is a convenient notation for nabla operator of partial derivatives. With the hypothesis of small displacement gradient theory, we are limited here to strains defined in terms of the symmetric part of displacement gradient, hence the symmetric operator ∇^s can be used to define the strain tensor in Voigt notation:

$$\boldsymbol{\varepsilon} = \nabla^s \boldsymbol{u} \; ; \qquad \nabla^s = \begin{bmatrix} \dfrac{\partial}{\partial x} & 0 & 0 \\ 0 & \dfrac{\partial}{\partial y} & 0 \\ 0 & 0 & \dfrac{\partial}{\partial z} \\ \dfrac{\partial}{\partial y} & \dfrac{\partial}{\partial x} & 0 \\ 0 & \dfrac{\partial}{\partial z} & \dfrac{\partial}{\partial y} \\ \dfrac{\partial}{\partial z} & 0 & \dfrac{\partial}{\partial x} \end{bmatrix} \tag{2}$$

2.2 Constitutive equations

The constitutive equations relate the dual variables to the material properties. First, the equations for fully-coupled dielectric materials is presented in agreement with the chosen free energy potential; in this case, a simple quadratic form is chosen. Therefore, the constitutive

equations are obtained by deriving this potential as follows:

$$\begin{cases} \boldsymbol{\sigma} := & \dfrac{\partial \psi}{\partial \boldsymbol{\varepsilon}} = & \boldsymbol{\mathcal{C}}\boldsymbol{\varepsilon} - \boldsymbol{\beta}\,(T - T_0) - \boldsymbol{e}_{\mathrm{e}}\boldsymbol{E} - \boldsymbol{e}_{\mathrm{h}}\boldsymbol{H} \\ s := & -\dfrac{\partial \psi}{\partial T} = & \boldsymbol{\beta}\cdot\boldsymbol{\varepsilon} + \rho_m\; c_v \ln\left(\dfrac{T}{T_0}\right) + \boldsymbol{\pi}_{\mathrm{e}}\cdot\boldsymbol{E} + \boldsymbol{\pi}_{\mathrm{h}}\cdot\boldsymbol{H} \\ \boldsymbol{D} := & -\dfrac{\partial \psi}{\partial \boldsymbol{E}} = & \boldsymbol{e}_{\mathrm{e}}\boldsymbol{\varepsilon} + \boldsymbol{\pi}_{\mathrm{e}}\,(T - T_0) + \boldsymbol{\epsilon}\boldsymbol{E} + \boldsymbol{\upsilon}\boldsymbol{H} \\ \boldsymbol{B} := & -\dfrac{\partial \psi}{\partial \boldsymbol{H}} = & \boldsymbol{e}_{\mathrm{h}}\boldsymbol{\varepsilon} + \boldsymbol{\pi}_{\mathrm{h}}\,(T - T_0) + \boldsymbol{\upsilon}\boldsymbol{E} + \boldsymbol{\mu}\boldsymbol{H} \end{cases} \tag{3}$$

where $\boldsymbol{\sigma}$ is the mechanical stress, s the entropy per unit volume, $\boldsymbol{D}$ the electric displacement and $\boldsymbol{B}$ the magnetic induction. Also $\boldsymbol{\mathcal{C}}$ is the elasticity tensor, c_v the specific heat, $\boldsymbol{\beta} = \boldsymbol{\mathcal{C}}\alpha_{_T}\boldsymbol{I}$ the thermal isotropic stress tensor (with $\alpha_{_T}$ as the expansion coefficient), $\boldsymbol{e}_{\mathrm{e}}$ the piezoelectric tensor, $\boldsymbol{e}_{\mathrm{h}}$ the piezomagnetic tensor, $\boldsymbol{\pi}_{\mathrm{e}}$ the pyroelectric vector, $\boldsymbol{\pi}_{\mathrm{h}}$ the piezomagnetic vector and $\boldsymbol{\upsilon}$ the magnetoelectric tensor. The final ingredient left is to provide the definition of the heat flux through Fourier's law:

$$\boldsymbol{q} = -\kappa\;\nabla T \tag{4}$$

with κ as the thermal conductivity.

In the case of conductor materials, a step further on the mechanical model is taken to introduce plasticity. First, in the framework of linear kinematics (1), it is generally accepted to use the additive decomposition of the state variables into elastic and plastic parts:

$$\begin{aligned} &\boldsymbol{\varepsilon} = \boldsymbol{\varepsilon}^e + \boldsymbol{\varepsilon}^p\;; \\ &s = s^e + s^p\;; \\ &\boldsymbol{D} = \boldsymbol{D}^e + \boldsymbol{D}^p\;; \\ &\boldsymbol{B} = \boldsymbol{B}^e + \boldsymbol{B}^p \end{aligned} \tag{5}$$

The elastic part of these variables is obtained, as the previous material, from the free energy potential. For conductors, the constitutive equations derived are:

$$\begin{cases} \boldsymbol{\sigma} := & \dfrac{\partial \psi}{\partial \boldsymbol{\varepsilon}^e} = & \boldsymbol{\mathcal{C}}\,(\boldsymbol{\varepsilon} - \boldsymbol{\varepsilon}^p) - \boldsymbol{\beta}\,(T - T_0) + \epsilon\boldsymbol{E}\otimes\boldsymbol{E} + \mu\boldsymbol{H}\otimes\boldsymbol{H} - \dfrac{\boldsymbol{I}}{2}\,(\epsilon\;\boldsymbol{E}\cdot\boldsymbol{E} + \mu\;\boldsymbol{H}\cdot\boldsymbol{H}) \\ \boldsymbol{D}^e := & -\dfrac{\partial \psi}{\partial \boldsymbol{E}} = & \epsilon\,\{[1 + \mathrm{tr}\,(\boldsymbol{\varepsilon}^e)]\,\boldsymbol{E} - \boldsymbol{\varepsilon}^e\boldsymbol{E}\} \\ \boldsymbol{B}^e := & -\dfrac{\partial \psi}{\partial \boldsymbol{H}} = & \mu\,\{[1 + \mathrm{tr}\,(\boldsymbol{\varepsilon}^e)]\,\boldsymbol{H} - \boldsymbol{\varepsilon}^e\boldsymbol{H}\} \\ q := & -\dfrac{\partial \psi}{\partial \zeta} = & -K\zeta \\ s^e := & -\dfrac{\partial \psi}{\partial T} = & \rho_m\; c_p \ln\left(\dfrac{T}{T_0}\right) + \boldsymbol{\beta}\cdot(\boldsymbol{\varepsilon} - \boldsymbol{\varepsilon}^p) \end{cases} \tag{6}$$

where q is stress-like variable thermodynamically conjugate to ζ the isotropic hardening variable which controls the evolution of plasticity threshold. The coupling is introduced also in the

constitutive relations for fluxes through the generalized form of Ohm's and Fourier's laws, as suggested in [3] and [4]:

$$\begin{aligned} \boldsymbol{j} &= \gamma\ \boldsymbol{E} - \gamma\ \alpha\ \nabla T\ ; \\ \boldsymbol{q} &= -\kappa\ \nabla T + \Pi\ \boldsymbol{j} \end{aligned} \tag{7}$$

with γ as the electric conductivity, α the Seebeck coefficient and $\Pi = T\ \alpha$ the Peltier coefficient.

2.3 Equilibrium equations

These set of equations are the ones that the finite element program must ensure in the whole domain Ω and bounded by the surface Γ. Each kind of material has a different set of equilibrium equations. For the dielectric formulation, the set of equilibrium equations is:

$$\left\{ \begin{array}{rl} \rho_m \ddot{\boldsymbol{u}} = & \boldsymbol{\sigma}\nabla + \boldsymbol{b}_{\text{eh}} + \boldsymbol{b} \\ \nabla \cdot \boldsymbol{D} = & 0 \\ \nabla \cdot \boldsymbol{B} = & 0 \\ \rho_m c_v \dot{T} = & r - \nabla \cdot \boldsymbol{q} - T \left(\boldsymbol{\beta} \cdot \dot{\boldsymbol{\varepsilon}} + \boldsymbol{\pi}_{\text{e}} \cdot \dot{\boldsymbol{E}} + \boldsymbol{\pi}_{\text{h}} \cdot \dot{\boldsymbol{H}} \right) \end{array} \right. \tag{8}$$

The previous equations have been obtained from conservation principles of linear momentum, electric flux, magnetic flux and energy respectively. In the first one, the electromagnetic force $\boldsymbol{b}_{\text{eh}}$ is introduced, which accounts for the distributed electric and magnetic force that can arise due to the possible presence of a non-uniform electrical or magnetic field in the material [5].

Regarding the energy conservation, the entropy definition has been used to replace the time derivative of this variable; hence, this equation is in terms of temperature for the thermal field.

For the conductor materials the following set is taken into account:

$$\left\{ \begin{array}{rl} \rho_m \ddot{\boldsymbol{u}} = & \boldsymbol{\sigma}\nabla + \boldsymbol{b} \\ \nabla \cdot \boldsymbol{j} = & 0 \\ \nabla \cdot \boldsymbol{B} = & 0 \\ \rho_m c_v \dot{T} = & r - \nabla \cdot \boldsymbol{q} - T\ \boldsymbol{\beta} \cdot (\dot{\boldsymbol{\varepsilon}} - \dot{\boldsymbol{\varepsilon}}^p) + \mathscr{D} \end{array} \right. \tag{9}$$

The previous equations have been obtained from conservation principles of linear momentum, free electric charge, magnetic flux and energy respectively. In this case, $\boldsymbol{\sigma}$ is the sum of the Cauchy and the Maxwell parts of the stress tensor. $\mathscr{D}$ is the dissipation, obtained from the second principle of thermodynamics:

$$\mathscr{D} = \underbrace{q\ \dot{\zeta} + \boldsymbol{\sigma} \cdot \dot{\boldsymbol{\varepsilon}}^p + \boldsymbol{E} \cdot \dot{\boldsymbol{D}}^p + \boldsymbol{H} \cdot \dot{\boldsymbol{B}}^p}_{\mathscr{D}^p} + \boldsymbol{j} \cdot \boldsymbol{E} \tag{10}$$

where the thermal part of the of the plastic dissipation $\mathscr{D}^p$ is canceled when the entropy is eliminated from the energy conservation equation. The last term of (10) is the Joule heating.

2.4 Evolution equations for internal variables (conductor formulation)

We here use generalized form of von Mises criterion that builds upon the proposal in [6] for perfect plasticity, which allows to determine if the material is in elastic or plastic regime based upon its stress state and electric field values. This criterion can be recast in a more standard

format (e.g. [2]) by making the yield stress dependent upon thermal and electric field variations (not magnetic), which also allows to account for potential hardening effect in terms of isotropic hardening. Such a generalized von Mises criterion can be written as:

$$\phi\left(\boldsymbol{\sigma}, q, T, \boldsymbol{E}\right) = \|\mathrm{dev}(\boldsymbol{\sigma})\| - \sqrt{\frac{2}{3}}\left[\sigma_y\left(T, \boldsymbol{E}\right) - q\left(T, \boldsymbol{E}\right)\right] = 0 \; ; \quad q = -K\left(T, \boldsymbol{E}\right)\zeta \tag{11}$$

where $\mathrm{dev}(\boldsymbol{A}) = \boldsymbol{A} - \frac{1}{3}\left[\mathrm{tr}(\boldsymbol{A})\right]$ is the deviatoric part of the tensor $\boldsymbol{A}$, $\|\boldsymbol{A}\| = \sqrt{\mathrm{tr}\left(\boldsymbol{A}^{\mathsf{T}}\ \boldsymbol{A}\right)}$ is the Euclidean norm of $\boldsymbol{A}$, $\sigma_y(T)$ is the temperature dependent yield stress and E_0 a reference value. The yield stress and the isotropic hardening modulus are now assumed linearly dependent upon thermal and electric fields.

By using the principle of maximum dissipation [2], we will pick among all plastically admissible values of dual variables (which satisfy $\phi(\boldsymbol{\sigma}, q, T, \boldsymbol{E}) = 0$) the one which will maximize the plastic dissipation. We can further recast such a constrained optimization problem in terms of min-max problem of unconstrained minimization where the plastic admissibility constraint is enforced by using the method of Lagrange multipliers leading to plastic Lagrangian:

$$\max_{\phi(\boldsymbol{\sigma},q,T,\boldsymbol{E})=0} \mathscr{D}^p\left(\boldsymbol{\sigma}, q, T, \boldsymbol{E}\right) \Leftrightarrow \min_{\forall(\boldsymbol{\sigma},q,T,\boldsymbol{E})} \max_{\dot{\gamma}^p>0} \mathscr{L}^p\left(\boldsymbol{\sigma}, q, T, \boldsymbol{E}, \dot{\gamma}^p\right) \tag{12}$$

where the Lagrange multiplier is equal to the plastic multiplier $\dot{\gamma}^p$. The plastic Lagrangian will incorporate the yield criterion constraint $\phi = 0$, which can be written as:

$$\mathscr{L}^p\left(\boldsymbol{\sigma}, q, T, \boldsymbol{E}, \dot{\gamma}^p\right) := -\mathscr{D}^p\left(\boldsymbol{\sigma}, q, T, \boldsymbol{E}\right) + \dot{\gamma}^p\ \phi\left(\boldsymbol{\sigma}, q, T, \boldsymbol{E}\right) \tag{13}$$

The solution to such constrained minimization problem can be obtained by using the Kuhn-Tucker optimality conditions, which allows to write:

$$\begin{aligned}
\mathbf{0} &:= \frac{\partial \mathscr{L}^p}{\partial \boldsymbol{\sigma}} = \dot{\gamma}^p\ \frac{\partial \phi}{\partial \boldsymbol{\sigma}} - \dot{\boldsymbol{\varepsilon}}^p \; ; \\
0 &:= \frac{\partial \mathscr{L}^p}{\partial q} = \dot{\gamma}^p\ \frac{\partial \phi}{\partial q} - \dot{\zeta} \; ; \\
0 &:= \frac{\partial \mathscr{L}^p}{\partial T} = \dot{\gamma}^p\ \frac{\partial \phi}{\partial T} - \dot{s}^p \; ; \\
\mathbf{0} &:= \frac{\partial \mathscr{L}^p}{\partial \boldsymbol{E}} = \dot{\gamma}^p\ \frac{\partial \phi}{\partial \boldsymbol{E}} - \dot{\boldsymbol{D}}^p \; ; \\
&\dot{\gamma}^p \geq 0 \; ; \quad \phi \leq 0 \; ; \quad \dot{\gamma}^p\ \phi = 0
\end{aligned} \tag{14}$$

Using the first two previous equations, $\mathscr{D}^p_{\mathrm{m}}$ can further be simplified:

$$\mathscr{D}^p_{\mathrm{m}} = \dot{\gamma}^p \overbrace{\left[\underbrace{\boldsymbol{\sigma}\cdot\boldsymbol{\nu}}_{\|\mathrm{dev}(\boldsymbol{\sigma})\|} - \sqrt{\frac{2}{3}}\left(\sigma_y - q\right)\right]}^{\phi=0} + \dot{\gamma}^p\sqrt{\frac{2}{3}}\ \sigma_y = \dot{\gamma}^p\sqrt{\frac{2}{3}}\ \sigma_y \tag{15}$$

where $\boldsymbol{\nu} := \partial\phi/\partial\boldsymbol{\sigma} = \mathrm{dev}(\boldsymbol{\sigma})/\|\mathrm{dev}(\boldsymbol{\sigma})\|$.

3 FINITE ELEMENT IMPLEMENTATION

In this section we present the details of the discrete approximation constructed by the the finite element method, as a particular case of the Galerkin method. The starting point is provided by the weak form of the conservation equations for dielectric materials (**??**):

$$\begin{cases} -\displaystyle\int_\Omega \nabla^s \delta\boldsymbol{u}\cdot\boldsymbol{\sigma} + \delta\boldsymbol{u}\cdot(\rho_m\ddot{\boldsymbol{u}} - \boldsymbol{b}_{\rm eh} - \boldsymbol{b})\ \mathrm{d}\Omega + \displaystyle\int_\Gamma \delta\boldsymbol{u}\cdot\bar{\boldsymbol{t}}^c\ \mathrm{d}\Gamma = 0\ ; \\ \displaystyle\int_\Omega \nabla\delta V\cdot\boldsymbol{D}\ \mathrm{d}\Omega - \int_\Gamma \delta V\ \bar{D}\ \mathrm{d}\Gamma = 0\ ; \\ \displaystyle\int_\Omega \nabla\delta\varphi\cdot\boldsymbol{B}\ \mathrm{d}\Omega - \int_\Gamma \delta\varphi\ \bar{B}\ \mathrm{d}\Gamma = 0\ ; \\ \displaystyle\int_\Omega \nabla\delta T\cdot\boldsymbol{q} - \delta T\left[\rho_m\ c_v\ \dot{T} - r + T\left(\boldsymbol{\beta}\cdot\dot{\boldsymbol{\varepsilon}} + \boldsymbol{\pi}_{\rm e}\cdot\dot{\boldsymbol{E}} + \boldsymbol{\pi}_{\rm h}\cdot\dot{\boldsymbol{H}}\right)\right]\ \mathrm{d}\Omega \\ \qquad\displaystyle - \int_\Gamma \delta T\ \bar{q}\ \mathrm{d}\Gamma = 0 \end{cases} \tag{16}$$

and for conductors (9):

$$\begin{cases} -\displaystyle\int_\Omega \nabla^s \delta\boldsymbol{u}\cdot\boldsymbol{\sigma} + \delta\boldsymbol{u}\cdot(\rho_m\ddot{\boldsymbol{u}} - \boldsymbol{b})\ \mathrm{d}\Omega + \displaystyle\int_\Gamma \delta\boldsymbol{u}\cdot\bar{\boldsymbol{t}}^c\ \mathrm{d}\Gamma = 0\ ; \\ \displaystyle\int_\Omega \nabla\delta V\cdot\boldsymbol{j}\ \mathrm{d}\Omega - \int_\Gamma \delta V\ \bar{j}\ \mathrm{d}\Gamma = 0\ ; \\ \displaystyle\int_\Omega \nabla\delta\varphi\cdot\boldsymbol{B}\ \mathrm{d}\Omega - \int_\Gamma \delta\varphi\ \bar{B}\ \mathrm{d}\Gamma = 0\ ; \\ \displaystyle\int_\Omega \nabla\delta T\cdot\boldsymbol{q} - \delta T\left[\rho_m\ c_v\ \dot{T} - r + T\ \boldsymbol{\beta}\cdot(\dot{\boldsymbol{\varepsilon}} - \dot{\boldsymbol{\varepsilon}}^p) - \boldsymbol{j}\cdot\boldsymbol{E} - \dot{\gamma}^p\sqrt{\frac{2}{3}}\ \sigma_y\right. \\ \qquad\left. -\boldsymbol{E}\cdot\dot{\boldsymbol{D}}^p - \boldsymbol{H}\cdot\dot{\boldsymbol{B}}^p\right]\ \mathrm{d}\Omega - \displaystyle\int_\Gamma \delta T\ \bar{q}\ \mathrm{d}\Gamma = 0 \end{cases} \tag{17}$$

where $\delta\bullet$ denotes a virtual field or variation and the overbar, prescribed magnitudes. We can readily obtain the discrete approximations for all the fields, along with their space and time derivative by appealing to separation of variables in Einstein's notation:

$$\bullet \approx \mathcal{N}_a\ \mathfrak{a}_a^\bullet\ ; \qquad \delta\bullet \approx \mathcal{N}_a\ \mathfrak{w}_a^\bullet\ ; \qquad \nabla\bullet \approx \boldsymbol{\mathcal{B}}_a\ \mathfrak{a}_a^\bullet\ ; \tag{18}$$

where $\mathfrak{a}$ represent the nodal values of different fields (yet called degrees of freedom), whereas $\mathfrak{w}$ represent the nodal values of their variations. In last expression, $\mathcal{N}_a$ denotes the standard isoparametric shape function for node a (e.g., [2]), with their gradients gathered in matrix form as:

$$\begin{aligned} \boldsymbol{\mathcal{B}}_a &= \nabla\mathcal{N}_a\ ; \\ \boldsymbol{\mathcal{B}}_a^s &= \nabla^s\mathcal{N}_a \end{aligned} \tag{19}$$

The final form of the residuals is obtained by introducing the approximations of all field variables and by considering that the nodal values of virtual field $\forall\mathfrak{w}$ can be picked up arbitrarily and the common factor of the weak form can be nullified.

4 TIME DISCRETIZATION

For the finite element computation, two different computation phases have to be performed for the conductor formulation and only the global phase for the dielectric formulation.

4.1 Global solution step by Newmark scheme

The Newmark scheme is used for the time discretization of the global solution step. This scheme requires two parameters γ and β that will determine the numerical damping and order of the scheme (e.g. [2]).

Thus, the time stepping scheme of this kind will render the set of nonlinear algebraic equations. To solve such a nonlinear problem, we use Newton's iterative method where at each iteration $(i+1)$ we perform the consistent linearization of residual leading to:

$$\boldsymbol{\mathcal{R}}_{a,n+1}^{(i+1)} = 0 \quad \Rightarrow \quad \boldsymbol{\mathcal{R}}_{a,n+1}^{(i)} + \left.\frac{\partial \boldsymbol{\mathcal{R}}_{a,n+1}}{\partial \mathfrak{a}_{b,n+1}}\right|^{(i)} \Delta \mathfrak{a}_{b,n+1}^{(i)} = 0 \; ; \quad \boldsymbol{\mathcal{R}}_{a,n+1}^{(i)} = \left[\boldsymbol{\mathcal{R}}^{U}, \mathcal{R}^{V}, \mathcal{R}^{\varphi}, \mathcal{R}^{T}\right]_{a,n+1}^{\mathsf{T},(i)} \tag{20}$$

where $\Delta \mathfrak{a}_b$ are iterative contributions to nodal values of temperature, electric field, along with displacements, velocities and accelerations. At each iterative sweep, we can then perform the corresponding state variable updates according to:

$$\mathfrak{a}_{b,n+1}^{(i+1)} = \mathfrak{a}_{b,n+1}^{(i)} + \Delta \mathfrak{a}_{b,n+1}^{(i)} \tag{21}$$

In the first iteration within each time step we will take the starting guess equal to the converged value at the previous step:

$$\mathfrak{a}_{b,n+1}^{(0)} = \mathfrak{a}_{b,n} \tag{22}$$

The residual derivative in (20) can be reduced to so-called effective tangent stiffness for mechanical part, which is directly used to compute the iterative contributions to displacement increments:

$$\boldsymbol{\mathcal{S}}_{ab}^{U,(i)} = \boldsymbol{\mathcal{K}}_{ab}^{(i)} + \frac{\gamma}{\beta\ \Delta t}\ \boldsymbol{\mathcal{D}}_{ab}^{(i)} + \frac{1}{\beta\ \Delta t^2}\ \boldsymbol{\mathcal{M}}_{ab}^{(i)} \tag{23}$$

where $\boldsymbol{\mathcal{K}}_{ab} = -\dfrac{\partial \boldsymbol{\mathcal{R}}_a}{\partial \mathfrak{a}_b}$ is the elastoplastic tangent stiffness matrix, $\boldsymbol{\mathcal{D}}_{ab} = -\dfrac{\partial \boldsymbol{\mathcal{R}}_a}{\partial \dot{\mathfrak{a}}_b}$ is the damping matrix and $\boldsymbol{\mathcal{M}}_{ab} = -\dfrac{\partial \boldsymbol{\mathcal{R}}_a}{\partial \ddot{\mathfrak{a}}_b}$ is the mass matrix.

Given the solution for displacement increment at iteration (i), we proceed to compute the displacement updates $\mathfrak{a}_{n+1}^{(i+1)}$ by using the result in (21).

4.2 Local iterative solution for plasticity with isotropic hardening

This local computation has to be performed for every Gauss point in agreement with the corresponding result $\mathfrak{a}_{n+1}^{(i)}$ obtained in the global phase. For proposed generalization of von Mises plasticity, we first define the yield function for coupled problem of this kind:

$$\phi_{n+1}\Big|_{\mathfrak{a}_{n+1}^{(i)}} = \|\mathrm{dev}(\boldsymbol{\sigma}_{n+1})\| - \sqrt{\frac{2}{3}}\left(\sigma_y\left(T_{n+1}, \boldsymbol{E}_{n+1}\right) - q_{n+1}\right) \tag{24}$$

The elastic trial step is computed first, with the zero value of plastic multiplier $\gamma_{n+1}^{p,\mathrm{tr}} = 0$. This result with:

$$\boldsymbol{\varepsilon}_{n+1}^{p,\mathrm{tr}} = \boldsymbol{\varepsilon}_n^p \; ; \qquad \zeta_{n+1}^{\mathrm{tr}} = \zeta_n \; ; \qquad s_{n+1}^{p,\mathrm{tr}} = s_n^p \; ; \qquad \boldsymbol{D}_{n+1}^{p,\mathrm{tr}} = \boldsymbol{D}_n^p \tag{25}$$

These results are exploited in computation of the corresponding trial values of stress and hardening stress-like variable:

$$\begin{aligned} &\boldsymbol{\sigma}_{n+1}^{\mathrm{tr}} = \boldsymbol{\mathcal{C}} \left(\boldsymbol{\varepsilon}_{n+1} - \boldsymbol{\varepsilon}_n^p\right) - \boldsymbol{\beta} \left(T_{n+1} - T_0\right) + \epsilon \boldsymbol{E}_{n+1}^{\otimes} - \frac{\mathbf{1}}{2} \boldsymbol{E}_{n+1} \cdot \boldsymbol{E}_{n+1} \; ; \\ &q_{n+1}^{\mathrm{tr}} = q_n = -K \; \zeta_n \end{aligned} \tag{26}$$

To ensure that the elastic step is acceptable, the trial value of yield function must remain negative or zero

$$0 \geq \phi_{n+1}^{\mathrm{tr}} = \left\| \mathrm{dev} \left(\boldsymbol{\sigma}_{n+1}^{\mathrm{tr}}\right) \right\| - \sqrt{\frac{2}{3}} \left(\sigma_y(T_{n+1}, \boldsymbol{E}_{n+1}) - q_{n+1}^{\mathrm{tr}}\right) \tag{27}$$

If such a condition is not verified, the step is plastic. The latter implies that all the internal variables must be recomputed by integrating the evolution equations in (14):

$$\begin{aligned} &\boldsymbol{\varepsilon}_{n+1}^p = \boldsymbol{\varepsilon}_n^p + \gamma_{n+1}^p \; \boldsymbol{\nu}_{n+1} \; ; \\ &\zeta_{n+1} = \zeta_n + \sqrt{\frac{2}{3}} \; \gamma_{n+1}^p \; ; \\ &s_{n+1}^p = s_n^p + \gamma_{n+1}^p \sqrt{\frac{2}{3}} \; \omega_{\mathrm{t}} \left(\sigma_{y_0} + K_0 \; \zeta_{n+1}\right) \; ; \\ &\boldsymbol{D}_{n+1}^p = \boldsymbol{D}_n^p + \gamma_{n+1}^p \frac{\boldsymbol{E}}{\|\boldsymbol{E}\|} \sqrt{\frac{2}{3}} \; \omega_{\mathrm{e}} \left(\sigma_{y_0} + K_0 \; \zeta_{n+1}\right) \; ; \end{aligned} \tag{28}$$

The plastically admissible value of stresses can be computed as:

$$\begin{aligned} &\boldsymbol{\sigma}_{n+1} = \boldsymbol{\sigma}_{n+1}^{\mathrm{tr}} - \gamma_{n+1}^p \; \boldsymbol{\mathcal{C}} \; \boldsymbol{\nu}_{n+1} \\ &q_{n+1} = -K \; \zeta_{n+1} \end{aligned} \tag{29}$$

We note that the final value of plastic multiplier γ_{n+1}^p can be obtained from $\phi_{n+1} = 0$, by taking into account that:

$$\begin{aligned} &\boldsymbol{\nu}_{n+1} = \boldsymbol{\nu}_{n+1}^{\mathrm{tr}} \; ; \\ &\|\mathrm{dev} \left(\boldsymbol{\sigma}_{n+1}\right)\| = \left\| \mathrm{dev} \left(\boldsymbol{\sigma}_{n+1}^{\mathrm{tr}}\right) \right\| - 2\mu \; \gamma_{n+1}^p \end{aligned} \tag{30}$$

where μ is the shear modulus. We finally obtain:

$$\gamma_{n+1}^p = \frac{\phi_{n+1}^{\mathrm{tr}}}{2\mu + \frac{2K}{3}} \tag{31}$$

5 NUMERICAL EXAMPLE

5.1 Peltier cells with stress evolution under plasticity constraint

In this numerical example, we simulate the behavior of half a thermocouple of a pulsed Peltier cell, representing a cooler based on the Peltier effect under the action of an electric flux. This cell consists of four different materials: thermoelectric material (here chosen Bi_2Te_3), copper, alumina and a tin-lead solder.

A complete simulation for elastic regime can be found in [7]. The material properties for this problem are presented in Table 1. Moreover, some of these properties for the Bi_2Te_3 are chosen as temperature dependent:

$$\begin{aligned} \alpha(T) &= 1.988 \times 10^{-4} + 3.353 \times 10^{-7}\ T + 7.52 \times 10^{-10}\ T^2 \\ \kappa(T) &= 1.663 - 3.58 \times 10^{-3}\ T + 3.195 \times 10^{-5}\ T^2 \\ \gamma(T) &= 1.096 \times 10^{5} - 5.59 \times 10^{2}\ T + 2.498\ T^2 \end{aligned} \tag{32}$$

Finally, the alumina is considered to remain elastic material (setting very high value for yield stress) because the plasticity begins well after the ultimate stress is reached. The same values for the Newmark parameters are chosen as in the last example.

Property	**Units**	**Alumina**	**Copper**	**Tin-Lead**	**Bi_2Te_3**
Hardening modulus K	GPa	5	5	5	1
Yield stress σ_y	MPa	15,400	100	180	55
Mass density ρ	kg/m^3	3,570	8,960	7,310	7,530
Specific heat c_v	J/kg K	837	385	226	544
Expansion coefficient α_T	1/ °C	5.00×10^{-6}	1.70×10^{-5}	2.70×10^{-5}	1.68×10^{-5}
First Lam parameter λ	N/m^2	1.63×10^{11}	7.16×10^{10}	3.25×10^{10}	6.71×10^{10}
Shear stress μ	N/m^2	1.51×10^{11}	4.39×10^{10}	1.68×10^{10}	1.68×10^{10}
Thermal conductivity κ	W/K m	35.3	386	48	$\kappa(T)$
Electric conductivity γ	A/V m	0	5.81×10^{7}	4.72×10^{6}	$\gamma(T)$
Seebeck coefficient α	V/K	0	0	0	$\alpha(T)$

Table 1: Material properties for every material used in the Peltier Cell

The finite element mesh constructed with the hexaedral 8-node finite elements used for computing the solution to this problem is shown in Figure 1. Different materials are presented in different colors. The boundary conditions are shown in Figure 1 right. We fix the displacements in direction x and z at the respective end faces, along with the symmetry condition in the plane $y = 0$. The temperature is prescribed at the top face $\bar{T}_t = 50$ °C (called hot side) along with a zero heat flux imposed at the bottom (cold side) where the temperature T_b is left free. The electric flux is introduced at the bottom left end of the copper while ground voltage is assumed at the top right end copper.

The applied loading is presented in Figure 2 top. First, an electric flux $|\boldsymbol{j}_{ss}| = I_{op}/A$ is introduced, where I_{op} is an optimal electric current that maximizes the temperature difference $\bar{T}_t - T_b$ in steady-state (more details in [7]) with A as the transversal area of the copper. This electric flux value is kept fixed until evolution for all the degrees of freedom have been stabilized,

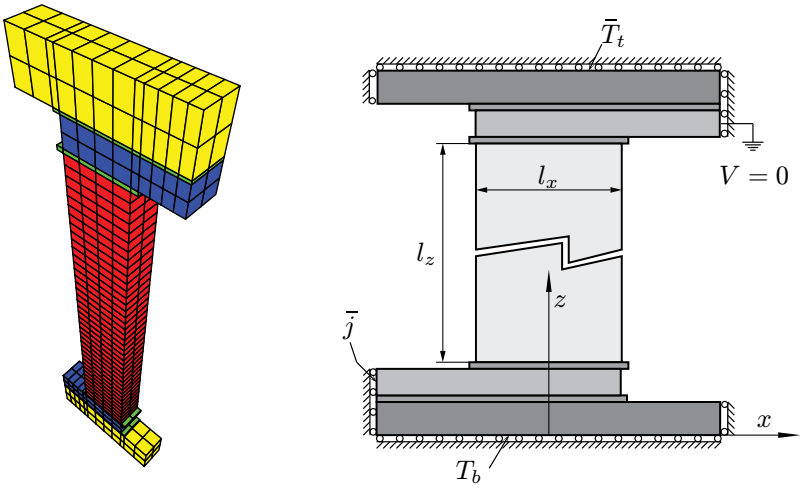

Figure 1: Left, mesh used in this numerical example, each material represented in a different color: Bi_2Te_3 in red, copper in blue, solder in green and alumina in yellow. Right, boundary conditions imposed in this problem.

and a steady-state has been reached. After this moment, the flux is incremented P times, where $P = |\boldsymbol{j}| \,/\, |\boldsymbol{j}_{ss}|$ is the pulse gain, which implies automatically that T_b decreases until a minimum is reached, but with an overheating penalty reached right afterwards. The steady-state temperature is reached eventually after reimposing $P = 1$ if no other pulse is introduced.

Figure 2 provides the representation of the maximum von Mises stress values calculated in Gauss points for each material in both elastic and plastic regime. In the steady-state, the maximum stresses are similar since the yield stress has not been reached yet. However, with the increase of electric flux, the stress increments seen in [7] due to accumulation of Joule heating, are no longer the same.

When the pulse is introduced reaching the yield stress σ_y, the subsequent stress-rate increase is reduced, due to the corresponding increase in plastic strains. These changes result in a noted decrease of the maximum stresses computed with activated plasticity constraint compared to the elastic case, specially in the copper and in the thermoelectric material. Once the steady-state gain is restated, the asymptotic stresses are reduced as a result of the plastic deformation in the copper and the solder. Moreover, due to the stresses redistribution, enforced by plasticity constraint, the stresses are increased in the Bi_2Te_3.

In Figure 3 the nodal von Mises projection distribution is shown at the end of the pulse $t = 130$ s, when the maximum stresses take place, along with a detailed zoom of the cold side, the most stressed part of the structure. The alumina has been omitted in order to show more clearly the differences with respect to the plastic materials.

In both cases the maximum is located at the bottom since this side has a bigger difference with respect to the reference temperature than the hot side. The maximum values are rather similar in both regimes. This is due to the influence of alumina that remains elastic, which stabilizes the corresponding stress distribution inside with no marked changes.

The first noticeable difference is that the stress distribution of the lower values is quite different. This can be appreciated specially for the copper, where the part on the bottom left

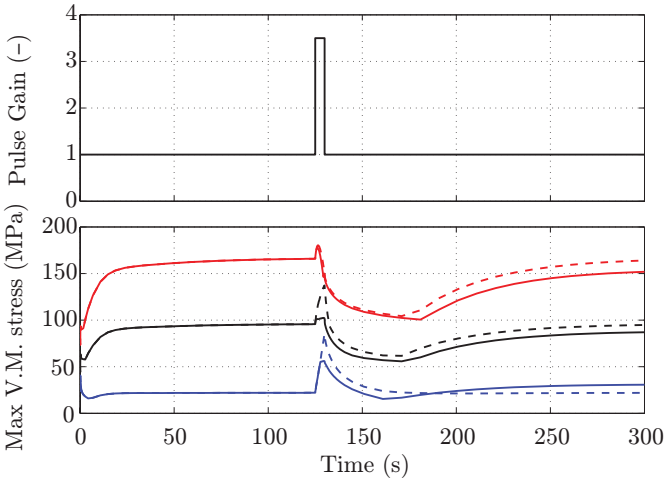

Figure 2: Maximum von Mises stress for solder (red), copper (black) and Bi_2Te_3 (blue) when an electric square pulse of gain $P = 3.5$ and duration $\Delta t_p = 5$ s is applied at $t = 125$ s. Full line, computed result with elastoplastic response; dashed line, computed results for elastic response.

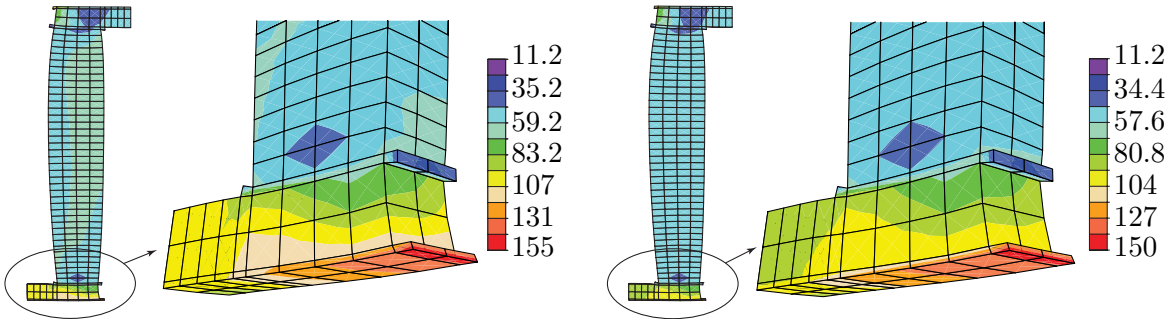

Figure 3: Von Mises stress [MPa] contour in deformed configuration for elastic (left) and plastic regime (right). All materials but the alumina. Detailed zoom at the bottom side of the Peltier cell.

has quite reduced values of stress, and in the Bi_2Te_3 where they have increased in average in a homogenization process. This further explains what was already observed in Figure 2, as in general in the copper the stresses in steady-state will be reduced and the opposite for the thermoelectric material. In this particular example, the temperature evolution is not very affected by the presence of plasticity unlike the stress distribution due to rather small contribution of the plastic dissipation towards total power sources, especially compared against the Joule dissipative term or Peltier cooling. Thus, it would appear that if the main goal in this problem concerned the temperature evolution, the plasticity would not have decisive role for computing the sufficiently good results.

6 CONCLUSIONS

A number of novelties for solving the coupled thermo-electro-magneto-mechanic problems for dielectric and conductor materials are presented in this work. In particular, two complete

formulations for thermo-electro-magneto-elastic and plastic behavior has been developed in a consistent manner by using conservation principles along with the definition of a free-energy potential leading to corresponding constitutive relations. This formulation has been implemented in the most general 3D framework, by using 8-node hexahedral finite element for constructing semi-discretization, along with the global phase of time discretization by the Newmark scheme and local computation of the internal variables for plasticity.

This development provides the sound basis to analyze practical examples for dielectric and conductor materials. For the former, the formulation goes beyond the classical applications such as piezoelectric, thermoelastic or magnetostrictive towards more complex combinations of the coupled fields; for the latter, allows to analyze application which either did not include an electric coupling to the thermomechanical formulation or have not implemented a plastic model in a thermo-electro-elastic framework. Moreover, the proposed formulation provides the starting point for further developments in plasticity that would include non-negligible magnetic field contribution.

ACKNOWLEDGMENTS

This work was supported jointly by Haut-de-France Region (CR Picardie) (120-2015-RDISTRUCT-000010 and RDISTRUCT-000010) and EU funding (FEDER) for Chaire-de-Mécanique (120-2015-RDISTRUCTF-000010 and RDISTRUCTI-000004). This support is gratefully acknowledged.

REFERENCES

[1] P. Moreno-Navarro, A. Ibrahimbegovic, and J.L. Pérez-Aparicio. Plasticity coupled with thermo-electric fields: Thermodynamics framework and finite element method computations. *Computer Methods in Applied Mechanics and Engineering*, 315:50–72, 2017.

[2] A. Ibrahimbegovic. *Nonlinear solid mechanics: theoretical formulations and finite element solution methods*, volume 160. Springer Science & Business Media, 2009.

[3] L.I. Anatychuk and O.J. Luste. *Modern Thermodynamic Theory of Thermoelectricity. Thermoelectrics Handbook*, chapter 2. CRC Press, 2006.

[4] J.L. Pérez-Aparicio, R. Palma, and R.L. Taylor. Multiphysics and thermodynamic formulations for equilibrium and non-equilibrium interactions: Non-linear finite elements applied to multi-coupled active materials. *Archives of Computational Methods in Engineering*, pages 1–49, 2015.

[5] Alessandro Ferrari and Antonio Mittica. Thermodynamic formulation of the constitutive equations for solids and fluids. *Energy Conversion and Management*, 66:77 – 86, 2013.

[6] C.M. Landis. Non-linear constitutive modeling of ferroelectrics. *Current Opinion in Solid State and Materials Science*, 8(1):59–69, 2004.

[7] J.L. Pérez-Aparicio, R. Palma, and P. Moreno-Navarro. Elasto-thermoelectric non-linear, fully coupled, and dynamic finite element analysis of pulsed thermoelectrics. *Applied Thermal Engineering*, 107:398 – 409, 2016.

Modeling Performance of Particulate Magnetoelectric Composites and Devices

Ever J. Barbero and T.I. Muchenik
West Virginia University, USA

Magnetoelectric composites generate electricity when exposed to a magnetic field. The composite is made of two phases: piezoelectric (PE) and piezomagnetic (PM). When the PM is exposed to a magnetic field it expands/contracts. The deformation is passed onto the PE, which when it is subjected to such deformation produces a current/voltage. In this work, magnetoelectric (ME) properties of particulate composites are calculated using a combination of Eshelby and Mori-Tanaka mean field theory. Limiting cases for low/high volume fractions of PM phase are corroborated using dilute approximation. All relevant ME properties (voltage, current, and power conversion) can be calculated by this method and for any boundary conditions (free standing, thin film on a rigid substrate, etc.). Predictions are compared with calculations reported by Harshe et al. and Nan et al. and good correlation is obtained with those previous results. Prior models neglected the conductivity of the PM phase and thus are unable to obtain good correlation with experimental data. Since conductivity is an essential component, the present model takes it into account, good comparison is obtained with available experimental data. The proposed model is further validated by considering two extreme scenarios. First, some researchers performed calculations assuming the PM phase is used as matrix, which in reality would give no ME output because the current generated in the PE inclusions will be shunted by the conductive PM matrix. However, prior calculations did not account conductivity. By temporarily shutting down the conductivity in our model, we are able to reproduce prior results. Then, enabling conductivity, the proposed model shows that no current/voltage/power is generated. Once the model is validated, we are able to evaluate the effect of PE and PM properties, volume fraction, particle size and topology. To account for device geometry, we calculate demagnetization. In this way, we are able to evaluate actual device performance as a function of geometric aspect ratio, direction of polarization, as well as direction of magnetic (H) and electric (E) fields, and device boundary conditions such as thin film clamped to a substrate, etc.

VIII ECCOMAS Thematic Conference on Smart Structures and Materials
SMART 2017
A. Güemes, A. Benjeddou, J. Rodellar and J. Leng (Eds)

FINITE ELEMENT SIMULATION OF THERMO-ELECTRO-MECHANICAL COUPLING IN FERROELECTRIC MATERIALS

MARIUS WINGEN*, ANDREAS RICOEUR†

*Institute of Mechanics, Chair of Engineering Mechanics / Continuum Mechanics
University of Kassel
Moenchebergstr. 7, 34109 Kassel, Germany
e-mail: marius.wingen@uni-kassel.de

† Institute of Mechanics, Chair of Engineering Mechanics / Continuum Mechanics
University of Kassel
Moenchebergstr. 7, 34109 Kassel, Germany
e-mail: ricoeur@uni-kassel.de

Key words: ferroelectrics; electrocaloric effect; domain switching

Abstract. In this paper, the theoretical background and a Finite Element (FE) approach based on a micromechanically and physically motivated constitutive model are presented. The model considers the mutual nonlinear coupling of thermal and electromechanical fields. Numerical calculations show the effects of temperature on the electromechanical field quantities and vice versa. They also reveal switching processes in ferroelectrics and associated heating, taking into account phase transitions and their dependence on tempeature changes.

1 INTRODUCTION

Due to their special electromechanical properties, nowadays ferroelectric materials are widely used in many technical applications, mostly as actuators or sensors. Advantages compared to other smart devices are their extremely fast reaction times in a range of μs - ms and large actuation forces. In the past, temperature changes inside the material were rather disturbing during the investigation and usage of these materials and were mostly neglected in numerical models, although they may have a non-negligible impact on issues like phase transitions, domain wall motion or reliability and lifetime.
Experiments have shown, that transient electromechanical fields in ferroelectric materials lead to two types of temperature changes [1, 2]. Technically, there is a reversible temperature change, which can heat up or cool down the material and much stronger irreversible temperature change caused by domain switching. The primary goal of this paper is to set up the thermodynamical framework of domain switching and related changes of entropy and temperature, in order to clarify opposing observations of heating and cooling.

2 THEORETICAL FRAMEWORK

2.1 Nonlinear thermo-electro-mechanical constitutive law

The electromechanical constitutive equations, which have been presented e.g. in [3], must be extended to include the temperature T as third independent variable. The thermodynamic potential $\bar{\Omega}(\epsilon, E, T)$ is obtained applying a Legendre transformation to the internal energy $\bar{U}(\epsilon, D, \bar{S})$, ths Gibb's fundamental equation reads:

$$\dot{\bar{\Omega}}(\dot{\epsilon}, \dot{E}, \dot{T}) = \sigma_{ij}\dot{\epsilon}_{ij} - D_i\dot{E}_i - \bar{S}\dot{T}, \tag{1}$$

where σ_{ij} and ϵ_{ij} are stresses and strains, D_i and E_i the electric displacement and electric field, respectively and $\bar{S}$ is the specific entropy. With Θ = T - T_0, the thermo-ferroelectric bahavior is governed by the potential:

$$\bar{\Omega} = \frac{1}{2}C_{ijkl}\epsilon_{ij}^{rev}\epsilon_{ij}^{rev} - \frac{1}{2}\kappa_{il}E_iE_l - \frac{1}{2}\gamma\Theta^2 - e_{lij}E_l\epsilon_{ij}^{rev} - \beta_{ij}\Theta\epsilon_{ij}^{rev} - k_l\Theta E_l - P_i^{irr}E_i - \bar{S}^{irr}\Theta, \tag{2}$$

where the superscript "rev" referes to reversible quantities and "irr" indicates irreversible changes of state. The material tensors C_{ijkl}, κ_{il}, γ, e_{lij}, β_{ij} and k_l denote the elasticity tensor, the dielectric tensor, the thermal coefficient, the piezoelectric tensor, the thermal stress and the pyroelectric coefficients. Together with $\epsilon_{ij}^{rev} = \epsilon_{ij}^{tot} - \epsilon_{ij}^{irr}$, Eqs. (1) and (2) lead to the rate dependent constitutive equations of a nonlinear ferroelectric material with thermal properties:

$$\dot{\sigma}_{ij} = C_{ijkl}(\dot{\epsilon}_{kl}^{tot} - \dot{\epsilon}_{kl}^{irr}) - e_{lij}\dot{E}_l - \beta_{ij}\dot{\Theta}, \tag{3a}$$

$$\dot{D}_i^{tot} = e_{ikl}(\dot{\epsilon}_{kl}^{tot} - \dot{\epsilon}_{kl}^{irr}) + \kappa_{il}\dot{E}_l + k_i\dot{\Theta} + \dot{P}_i^{irr}, \tag{3b}$$

$$\dot{\bar{S}}_i^{tot} = \beta_{kl}(\dot{\epsilon}_{kl}^{tot} - \dot{\epsilon}_{kl}^{irr}) + k_l\dot{E}_l + \gamma\dot{\Theta} + \dot{\bar{S}}^{irr}. \tag{3c}$$

The superscript "tot" referes to total and is equal to the sum of the reversible parts "rev" and the irreverible parts "irr".

2.2 Balance of momentum, charge and energy

In addition to the static mechanical and electrostatic balance equations, stemming from the momentum balance and the Maxwell equations:

$$\begin{aligned} \sigma_{ij,j} &= 0, \\ D_{i,i} &= 0, \end{aligned} \tag{4}$$

where volume forces and charges have been neglected, a third field equation balancing the energy is needed to describe the thermoelectromechanical three-field problem.
The equation is obtained considering the 1st law of thermodynamics, reading

$$\dot{\bar{U}} + \dot{\bar{K}} = \dot{\bar{W}}^{rev} + \dot{\bar{Q}} + \dot{\bar{\chi}}, \tag{5}$$

postulating for a quasistatic case, where the kinetic energy is equal to zero ($\bar{K} = 0$), that the change of internal energy is equal to the sum of the specific reversible electromechanical work rate

$$\dot{\bar{W}}^{rev} = \sigma_{ij}\dot{\epsilon}_{ij}^{rev} + E_i\dot{D}_i^{rev}, \tag{6}$$

the specific heat flow rate

$$\dot{\bar{Q}} = \dot{q}_v - \dot{q}^A_{j,j}, \tag{7}$$

where $\dot{q}_v$ is an internal heat source and $\dot{q}^A_{j,j}$ a heat flux across the boundary, and the dissipative work rate $\dot{\bar{\chi}}$ describing the non-conservative processes within the ferroelectric material such as domain switching. The latter requires some considerations on its interpretation.

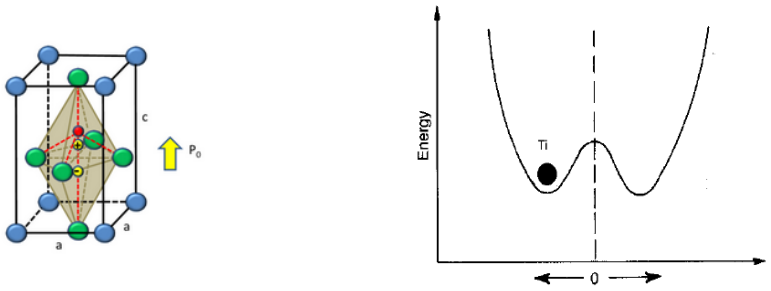

Figure 1: a) Tetragonal unit cell of $BaTiO_3$ [4]; b) Stable positions of the Ti^{4+}-ion in a tetragonal unit cell of $BaTiO_3$ [5].

Fig. 1 shows in a) a tetragonal unit cell of bariumtitanate and in b) the energy depending on the Ti^{4+}-ion-position with two stable positions in a tetragonal unit cell of $BaTiO_3$. The Ti^{4+}-ion is in the upper stable position, thus the polarization of the cell is upwards (Fig. 1 b)). If there is an electric field applied antiparallel to the polarization of the cell, the ion needs much more energy to fill the current gap. In the energy-diagramm, the ion is climbing up the local maximum between the two stable positions. At a certain point, the ion can not provide more energy to fill the current gap and jumps into the other stable lower energy position. A similar switching procedure is observed with the oxygen octahedron, moving to the opposite side. A simple approach to quantify the switching energy is given in [6]:

$$\dot{\bar{\chi}} = \sigma_{ij}\dot{\epsilon}^{irr}_{ij} + E_i\dot{P}^{irr}_i. \tag{8}$$

The ion jumps into a lower energy gap, where it does not need the high energy level anymore to fill the gap in the new stable position. Due to this energy loss, the entropy of the medium increases to exactly that amount:

$$\dot{\bar{S}}^{irr} = \frac{\dot{\bar{\chi}}}{T} = \frac{\sigma_{ij}\dot{\epsilon}^{irr}_{ij} + E_i\dot{P}^{irr}_i}{T} = -\dot{\bar{S}}^{irr}. \tag{9}$$

The material is heating up due to irreversible switching events.
With Eqs. (5), (6), (7), the Gibbs fundamental equation for the internal energy

$$\dot{\bar{U}}^{tot}(\dot{\epsilon}^{tot}_{ij}, \dot{D}^{tot}_i, \dot{\bar{S}}^{tot}) = \sigma_{ij}(\dot{\epsilon}^{rev}_{ij} + \dot{\epsilon}^{irr}_{ij}) + E_i(\dot{D}^{rev}_i + \dot{P}^{irr}_i) + T_0\dot{\bar{S}}^{tot}, \tag{10}$$

Eq. (3c) and Fourier's isotropic law $\dot{q}^A_j = -\lambda\Theta_{,j}$, the energy balance for a nonlinear thermo-electro-mechanical field problem is obtained as

$$\lambda\Theta_{,jj} = \beta_{ij}T_0\dot{\epsilon}_{ij}^{rev} + k_iT_0\dot{E}_i + \gamma T_0\dot{\Theta} - \sigma_{ij}\dot{\epsilon}_{ij}^{irr} - E_i\dot{P}_i^{irr}. \tag{11}$$

The same equation is derived assuming reversible behavior in connection with a heat source $\dot{q}_v = \sigma_{ij}\dot{\epsilon}_{ij}^{irr} + E_i\dot{P}_i^{irr}$.

2.3 Finite element formulation

The matrix representation of a nonlinear thermo-electro-mechanical field problem reads

$$\begin{bmatrix} 0 & 0 & 0 \\ 0 & 0 & 0 \\ [D_{\Theta u}] & [D_{\Theta\phi}] & [D_{\Theta\Theta}] \end{bmatrix} \begin{bmatrix} \{\dot{u}\} \\ \{\dot{\phi}\} \\ \{\dot{\Theta}\} \end{bmatrix} + \begin{bmatrix} [K_{uu}] & [K_{u\phi}] & [K_{u\Theta}] \\ [K_{\phi u}] & [K_{\phi\phi}] & [K_{\phi\Theta}] \\ 0 & 0 & [K_{\Theta\Theta}] \end{bmatrix} \begin{bmatrix} \{u\} \\ \{\phi\} \\ \{\Theta\} \end{bmatrix} = \begin{bmatrix} \{f_u\} + \{f_u^e\} \\ \{f_\phi\} + \{f_\phi^e\} \\ \{f_\Theta\} + \{f_\Theta^e\} \end{bmatrix} \tag{12}$$

with the abbreviations

$$\begin{aligned}
[K_{uu}] &= \int_V [B_u]^T[C][B_u]dV, & [K_{\phi u}] &= \int_V [B_\phi]^T[e][B_u]dV, \\
[K_{u\phi}] &= \int_V [B_u]^T[e]^T[B_\phi]dV, & [K_{\phi\phi}] &= -\int_V [B_\phi]^T[\kappa][B_\phi]dV, \\
[K_{u\Theta}] &= -\int_V [B_u]^T\{\beta\}[N_\Theta]dV, & [K_{\phi\Theta}] &= -\int_V [B_\phi]^T\{k\}[N_\Theta]dV, \\
[K_{\Theta\Theta}] &= \int_V [B_\Theta]^T[\lambda][B_\Theta]dV, & [D_{\Theta\Theta}] &= \int_V [N_\Theta]^T T_0[\gamma][N_\Theta]dV, \\
[D_{\Theta u}] &= \int_V [N_\Theta]^T[N_\Theta]T_0[\beta]^T[B_u]dV, & [D_{\Theta\phi}] &= -\int_V [N_\Theta]^T[N_\Theta]T_0\{k\}^T[B_\phi]dV, \\
\{f_u^e\} &= \int_V [B_u]^T[C]\epsilon^{irr}dV, & \{f_\phi^e\} &= \int_V [B_\phi]^T([e]\epsilon^{irr} - \{P^{irr}\})dV, \\
\{f_\Theta^e\} &= \int_V [N_\Theta]^T([\sigma]\frac{\Delta\{\epsilon^{irr}\}}{\Delta t} + \{E\}\frac{\Delta\{P^{irr}\}}{\Delta t}dV.
\end{aligned} \tag{13}$$

Neglecting nonlinear ferroelectric terms, Eq. (12) is also found in [7]. For the quasistatic calculation of $\{f_\Theta^e\}$ a parameter Δt for the switching time is introduced.
The mass matrix $[M_{uu}]$ is neglected.
For numerical calculations, the introduction of parameters λ_1 and λ_2 for the reduction of irreversible values is inevitable [3]. The nonlinear parts in Eq. (12) are thus modified as:

$$
\begin{aligned}
\{f_u^e\} &= \int_V [B_u]^T [C] \lambda_1 \epsilon^{irr} dV, \\
\{f_\phi^e\} &= \int_V [B_\phi]^T ([e] \lambda_1 \epsilon^{irr} - \lambda_2 \{P^{irr}\}) dV, \\
\{f_\Theta^e\} &= \int_V [N_\Theta]^T \Big(\lambda_1 [\sigma] \frac{\Delta \{\epsilon^{irr}\}}{\Delta t} + \lambda_2 \{E\} \frac{\Delta \{P^{irr}\}}{\Delta t} \Big) dV.
\end{aligned}
\tag{14}
$$

The microphysical model of domain wall motion and its algorithmic implementation is outlined in [3] and [8].

3 Numerical examples

The two-dimensional boundary value problem of a plate is considered according to Fig. 2. The model consists of 200 finite elements with 4 integration points each, thus representing a system of 800 grains. In this example, the plate is poled upwards at the beginning of the calculation, so that residual stresses due to the poling process have only a little influence on the temperature change. An alternating electric field is applied. In this calculation, the time dependent term in Eq. (12), representing the linear transient elasto- and electrocaloric effects is neglected ($[D_{\theta u}] = 0$, $[D_{\theta \phi}] = 0$, $[D_{\theta \theta}] = 0$), so the switching process is assuemed to be dominant for temperature changes of the material under electric loading.

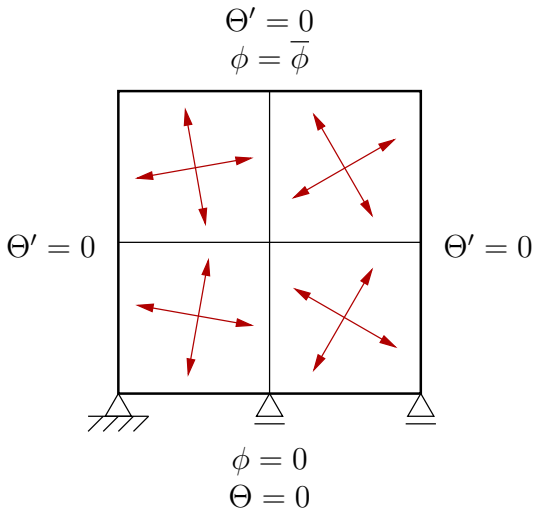

Figure 2: Boundary value problem for numerical calculation. The arrowed crosses schematically indicate the orientations of domains in each grain.

For the results presented in Fig. 3, the material data of C_{ijkl}, e_{lij} and κ_{il} for barium titanate have been used [3]. For a poling in x_1- and x_2-direction, the other material tensors are introduced as:

$$
\begin{aligned}
\{\beta\}^{x_1} &= \begin{bmatrix} \beta_{33} \\ \beta_{11} \\ \beta_{11} \\ 0 \\ 0 \\ 0 \end{bmatrix}, & \{\beta\}^{x_2} &= \begin{bmatrix} \beta_{11} \\ \beta_{33} \\ \beta_{11} \\ 0 \\ 0 \\ 0 \end{bmatrix}, \\
\{k\}^{x_1} &= \begin{bmatrix} k_3 \\ 0 \\ 0 \end{bmatrix}, & \{k\}^{x_2} &= \begin{bmatrix} 0 \\ k_3 \\ 0 \end{bmatrix}, \\
[\lambda]^{x_1} &= \begin{bmatrix} \lambda_{33} & 0 & 0 \\ 0 & \lambda_{11} & 0 \\ 0 & 0 & \lambda_{11} \end{bmatrix}, & [\lambda]^{x_2} &= \begin{bmatrix} \lambda_{11} & 0 & 0 \\ 0 & \lambda_{33} & 0 \\ 0 & 0 & \lambda_{11} \end{bmatrix},
\end{aligned}
\tag{15}
$$

with $\beta_{11} = 3.53 \cdot 10^6 \frac{J}{m^3 K}$, $\beta_{33} = 3.16 \cdot 10^6 \frac{J}{m^3 K}$, $k_3 = -5.48 \cdot 10^{-6} \frac{J}{V m^2 K}$ and $\lambda_{11} = \lambda_{33} = 14 \frac{W}{mK}$. The numerical parameters λ_1, λ_2 and Δt have been chosen λ_1=0.1, λ_2=0.3 and Δt=0.6s. Fig. 3a) shows a comparison of experimental [1] and simulated results of the temperature depending on loading cycles. For the chosen parameters, the plots are very similar. In the calculation, the heat flux across the surface is suppressed. Therefore, the intermediate temperature reductions observed experimentally are not present in the simulations.

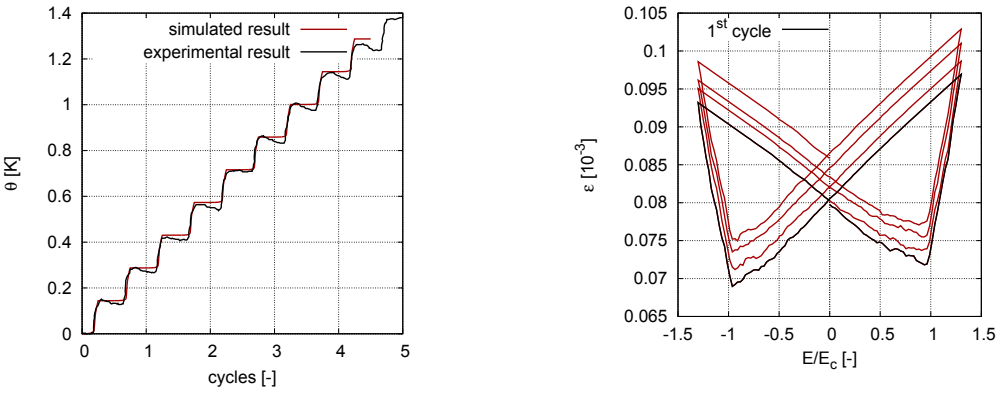

Figure 3: a) Comparison of the temperature between experimental [1] and simulated results. b) Butterfly hysteresis depending on temperature changes.

Fig. 3 b) shows the butterfly hysteresis depending on the temperature changes. The userelement does not consider the temperature dependency of the material parameters and the other material poperties so far. The effect, one can see in Fig. 3 b), is the thermal expansion. If the temperature rises, the strain undergoes a positive shift.

Fig. 4 shows, that the numerical parameter Δt has a non-negligible influence on the temperature. With Δt=0.6s for realistic results according to Fig. 3 a), the parameter is too large to be interpreted as switching time, which would be a physical parameter. However, the calculation is

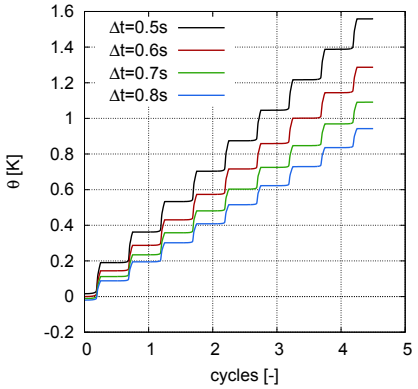

Figure 4: Influence of the numerical parameter Δt on the the temperature.

still static at the moment. The temperature jumps from one to the next value instantaneously due to the lack of a finite heat capacity. If the heat capacity is taken into account in the future, the parameter has to be reset again. Δt is expected to be much smaller then, which would be similar to a realistic switching or domain wall motion time.

4 CONCLUSIONS

- This paper extended a ferroelectric model to a nonlinear thermo-ferroelectric model.
- The temperature increases due to switching processes and is in good agreement with experimental findings.
- It shows the influence of the temperature change on the butterfly loop due to thermal expansion.
- It gives an idea for the determination of a switching or domain wall motion time.

REFERENCES

[1] Hao-Sen Chen, Yong-Mao Pei, Bin Liu and Dai-Ning Fang. *Rate dependent heat generation in single cycle of domain switching of lead zirconate titanate via in-situ spontaneous temperature measurement.* Applied Physics Letters 102, 242912 (2013); doi: 10.1063/1.4811702.

[2] Molin, C., Sanlialp, M., Shvartsman, V. V., Lupascu, D. C., Neumeister, P., Schönecker, A. and Gebhardt, S. *Effect of dopants on the electrocaloric effect of 0.92 $Pb(Mg_{1/3}Nb_{2/3})O_3$-0.08 $PbTiO_3$ ceramics.* Journal of the European Ceramic Society, Volume 35, Issue 7, p. 2065-2071 (2015).

[3] Lange, S. and Ricoeur, A. *A condensed microelectromechanical approach for modeling tetragonal ferroelectrics.* International Journal of Solids and Structures 54 (2015), pp. 100-110.

[4] Schwaab, H. *Nichtlineare Modellierung von Ferroelektrika unter Berücksichtigung der elektrischen Leitfähigkeit.* Dissertation, Schriftreihe des Instituts fr angewandte Materialien, Band 5, Karlsruher Institut fr Technologie, 2012.

[5] Gauckler, L. J. *Funktionskeramik III*. ETH, Eidgenössische Technische Hochschule Zürich, Professur fr nichtmetallische Werkstoffe, 2001.

[6] Hwang, S. C., Lynch, C. S. and McMeeking, R. M. *Ferroelectric/ferroelastic interactions and a polarization switching model*. Acta Metall. Mater. 43(5), 2073-2084 (1995).

[7] Görnandt, A. and Gabbert, U. *Finite element analysis of thermopiezoelectric smart structures*. Acta Mechanica 154, 129-140 (2002).

[8] Gellmann, R. and Ricoeur, A. *Continuum damage model for ferroelectric materials and its application to multilayer actuators*. Smart Materials and Structures. doi: 10.1088/0964-1726/25/5/055045, 2016.

VIII ECCOMAS Thematic Conference on Smart Structures and Materials
SMART 2017
A. Güemes, A. Benjeddou , J. Rodellar and Jinsong Leng (Eds)

NONLINEAR NUMERICAL SIMULATION OF MULTIFERROIC COMPOSITES: PREDICTION OF MAGNETOELECTRIC COUPLING AND DAMAGE

ARTJOM AVAKIAN[*] AND ANDREAS RICOEUR[†]

[*, †] Institute of Mechanics, University of Kassel, Mönchebergstr. 7, 34125 Kassel, Germany
e-mail: [*]artjom.avakian@uni-kassel.de, [†]ricoeur@uni-kassel.de
web page: [*, †] http://www.ifm.uni-kassel.de

Key words: Magnetoelectric composites, multiferroic magnetoelectric coupling, ferromagnetics, ferroelectrics, hysteresis loops, nonlinear constitutive modeling

Abstract: Magnetoelectric composites are investigated by numerical simulation. Nonlinear material models describing the magneto-ferroelectric or electro-ferromagnetic behaviors of the two constituents are presented. The ferroelectric model additionally accounts for damage evolution due to micro crack growth. The constitutive equations and weak forms of balance equations have been implemented within a finite element framework. Numerical simulations focus on the prediction of local domain orientation, the calculation of magnetoelectric coupling coefficients, and the investigation of damage processes predominantly during magnetoelectric poling as well as mutual interactions of these aspects. A particle and a laminated composite are compared as examples.

1 INTRODUCTION

The coupling of magnetic and electric fields due to the constitutive behavior of a material is commonly denoted as magnetoelectric (ME) effect. The latter is only observed in a few crystal classes exhibiting a very weak coupling, mostly at low temperatures, which can hardly be exploited for technical applications [12,15,18]. Much larger coupling coefficients are obtained at room temperature in composite materials with ferroelectric and ferromagnetic constituents. The ME effect is then induced by the strain of matrix and inclusions or of different constituents, respectively, converting electrical and magnetic energies based on the piezoelectric and magnetostrictive effects. From the engineering point of view, this kind of quasistatic conversion of magnetic to electric energy and vice versa is extremely interesting, giving rise to various technical applications. Promising examples are the monitoring of brain activity from weak magnetic fields generated by neuronal activity (magnetoencephalography, MEG) or the storage of digital data based on the principle of electric writing – magnetic reading [23].

Some ferromagnetic materials exhibit a pronounced hysteresis behavior, others show an almost reversible nonlinear characteristic. Even two specimens with an identical chemical composition can exhibit qualitatively different features [5-7], depending e.g. on the milling of the powder, the sintering conditions or particle diameters. The reason for the different behaviors is found on the micro scale of domain or Bloch walls [4,8]. In this paper, two approaches are presented for the constitutive modelling of ferromagnetic materials. The one is akin to a model for ferroelectrics and is based on microphysical considerations [1,17]. It takes advantage of the fact that some aspects of ferromagnetic and ferroelectric behaviors, although originating from completely different processes on the atomic scale, show comparable fea-

tures on the meso and macro levels. The other approach is purely phenomenological starting from a thermodynamical potential and providing a reversible nonlinear behavior.

The finite element (FE) method is adopted to solve complex boundary value problems based on weak formulations of multiphysical balance laws in connection with the constitutive laws outlined above. So-called User Elements have been developed, which are integrated into the commercial FE code ABAQUS providing the solver tool. Additionally, an own pre-and postprocessor has been developed for the sake of conveniently displaying the results of simulations. Due to the brittleness of the investigated materials, large deformations do not appear, thus the FE framework is restricted to linear kinematics.

Among various possible configurations of multiferroic composites, two compositions have been chosen in this paper, to demonstrate the potential of numerical simulation in the design process. One consists of a ferroelectric matrix with embedded soft ferromagnetic particles, the other is a laminated structure with ferroelectric and hard ferromagnetic layers. The prediction and comparison of ME coupling coefficients is in the focus of the investigations, providing the possibility of functional optimization. These coefficients turn out to be subject to a variety of influencing factors, e.g. the way of magnetoelectric poling, geometrical features or volume fractions of constituents.

One important and inevitable aspect is the cracking of the structure in terms of micro crack initiation in the ferroelectric and ferromagnetic materials, as well as delamination of the constituents. The related stress relief reduces the piezoelectric and magnetostrictive coupling, the domain activities and thus the ME coupling efficiency. A second aspect, of course, is the reduction of strength and lifetime of the smart devices. In order to include cracking into the simulations, damage evolution has been incorporated into the ferroelectric constitutive model, accounting for micro crack growth, predominantly driven by residual stresses due to ferroelectric domain switching. Cracking of the ferromagnetic constituent and delamination are not considered so far.

An overview on the state of the art in ferroic constitutive modelling and FE simulation of ME composites is given in [1,6,3].

2 CONSTITUTIVE BEHAVIOR: COMPILATION OF MODELS

The constitutive frameworks of ferroelectric and reversible and irreversible ferromagnetic behaviors are summarized and compared to each other. Ferroelectric materials exposed to electromagnetic fields are described by the following constitutive equations [1]:

$$\begin{aligned} \sigma_{ij} &= c_{ijkl}\left(\varepsilon_{kl} - \varepsilon_{kl}^{irr}\right) - e_{lij}E_l\,, \\ D_l &= e_{lij}\left(\varepsilon_{ij} - \varepsilon_{ij}^{irr}\right) + \kappa_{ln}E_n + P_l^{irr}, \\ B_k &= \mu_{km}H_m\,. \end{aligned} \tag{1}$$

Within a microphysical framework, the irreversible strain ε_{kl}^{irr} and polarization P_l^{irr} are due to domain wall motion. Considering plane problems, a grain consists of four domain species separated by 90° - and 180° - domain walls, see Fig. 1. The formulation of a nonlinear constitutive law thus requires four internal variables $v^{(i)}, i = 1, \ldots, 4$ and associated evolution equations describing the switching of unit cells on the micro level [14,17]. Due to intended applications within a multiferroic framework, the ferroelectric material is allocated a magnetic permeability expressed by the third equation relating the magnetic field H_m and the induction B_k. The elastic, piezoelectric, dielectric and magnetic permeability tensors $c_{ijkl}, e_{lij}, \kappa_{ln}$ and μ_{km} also depend on the internal variables $v^{(i)}$, giving rise to an additional source of non-

linearity, even in the magnetic properties. The other quantities in Eq. (1) are stress σ_{ij}, electric field $E_l = -\phi_{,l}$ and electric displacement D_l.

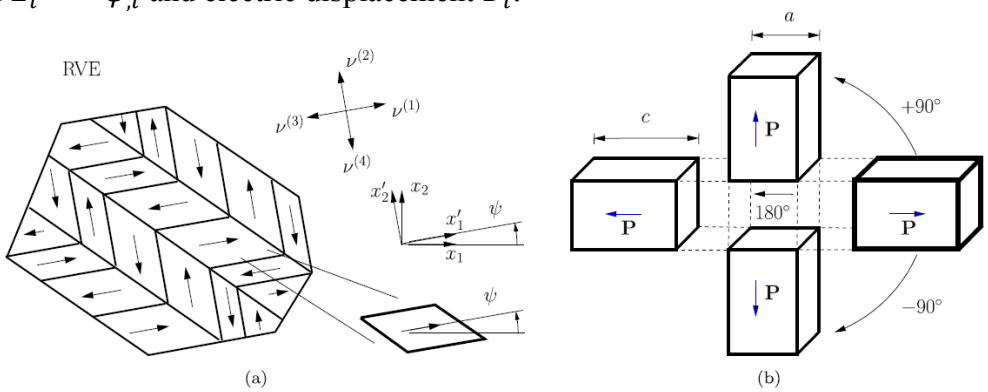

Fig. 1: Grain with tetragonal domain species in the plane represented by four internal variables $\nu^{(i)}$ and a single domain with poling direction ψ in the global $x_1 - x_2$ – plane; (b) possible switching variants of a tetragonal crystal unit cell [14]

Based on the same ideas as Eq. (1), the ferromagnetic constitutive equations read [2]

$$\begin{aligned} \sigma_{ij} &= c_{ijkl}\left(\varepsilon_{kl} - \varepsilon_{kl}^{irr}\right), \\ D_l &= \kappa_{ln} E_n, \\ B_k &= \mu_{km} H_m + M_k^{irr}. \end{aligned} \tag{2}$$

Here, irreversible strain and irreversible magnetization M_k^{irr} or magnetic polarization, respectively, are likewise governed by four internal variables describing Bloch wall motion due to magnetomechanical driving forces. The affinity to ferroelectricity on the macro- and mesoscales allows for a similar modeling of ferromagnetism covering the essential phenomena. Anyway, in the constitutive framework both physical processes merge into an evolution law for the internal variables, which is based on the magnetoelastic or electroelastic energies, respectively, going along with the changes of the directions of magnetic or electric dipoles.

In contrast to ferroelectricity, piezomagnetic coefficients relating magnetic field and stress or strain and magnetic induction are not involved, accounting for the saturation at larger fields. As a second consequence, the irreversible strain does not directly induce a magnetic induction B_k. Magnetostriction is rather induced by the irreversible part of the strain, which in turn is controlled by the magnetic field but also by mechanical loads. The same way, a strain field has an impact on the magnetic induction via M_k^{irr}. Dielectric properties are allocated by the second equation in (2) which is linear only at the first glance, since the dielectric constants κ_{ln} are controlled by the internal variables in a nonlinear manner. Ferromagnetic materials exhibiting a significant electric conductivity are excluded by the model.

Whereas Eq. (2) generates hysteresis loops, the constitutive equations of nonlinear reversible soft ferromagnetic behavior are given by

$$\begin{aligned} \dot{\sigma}_p\left(\dot{\varepsilon}_q, \dot{H}_k\right) &= c_{pq}\dot{\varepsilon}_q - q_{kp}(\varepsilon_q, H_k)\dot{H}_k, \\ \dot{D}_l\left(\dot{E}_n\right) &= \kappa_{ln}\dot{E}_n, \\ \dot{B}_k\left(\dot{\varepsilon}_p, \dot{H}_m\right) &= q_{kp}(\varepsilon_p, H_m)\dot{\varepsilon}_p + \mu_{km}(\varepsilon_p, H_m)\dot{H}_m, \end{aligned} \tag{3}$$

where a rate dependent depiction has been chosen. The nonlinearity is completely included in the material coefficients depending on the independent variables strain and magnetic field. Due to the reversibility of the constitutive behavior, these functions are unique, not involving any internal variables. The coefficient functions including the magnetostrictive tensor

$q_{kp}(\varepsilon_q, H_k)$, have to be chosen in a way to reflect experimental observations. A thermodynamical potential

$$\psi(\sigma_p, E_l, H_k) = -\frac{1}{2}s_{11}\sigma_1\sigma_1 - s_{12}\sigma_1\sigma_2 - \frac{1}{2}s_{22}\sigma_2\sigma_2 - s_{66}\sigma_6\sigma_6 - \frac{1}{2}\kappa_{11}E_1E_1 - \frac{1}{2}\kappa_{22}E_2E_2 - \frac{1}{2}\bar{\mu}_{11}^0 H_1H_1 - \frac{\eta_1}{1+\zeta_1 H_1^{-3}}\sigma_1 - \frac{\eta_2}{1+\zeta_2 H_1^{-3}}\sigma_2 - \rho\{H_1 - \xi\, ln(\xi + H_1)\} \tag{4}$$

has been identified in that context, yielding all the coefficient functions by differentiation [2,3]. This purely phenomenological approach involves several parameters, which are adjusted to specific material behaviors.

3 CONTINUUM DAMAGE MODEL FOR THE FERROELECTRIC PHASE

Two fundamental damage mechanisms are observed in a ME composite: cracking of the two constituents and delamination. The latter will not be considered at this point and cracking will be only allowed in the ferroelectric material. In Fig. 2 the micromechanical motivation of the model is depicted using the example of a particle composite with a ferroelectric matrix. The representative volume element (RVE) of the composite shows a few particles and the multiphysical boundary conditions. In the third sketch, the RVE of the ferroelectric matrix with statistically distributed cracks is shown, where the principal stresses σ_I and σ_{II} are the relevant loading quantities, being controlled by magnetic and electric fields as well. Those are part of the driving force being responsible for ferroelectric domain wall motion, giving rise to residual stress. In the model, only cracks being perpendicular to the maximum principal stress are allowed to grow following a classical K-factor-based fracture criterion. Assuming a dilute crack distribution, crack interactions can be neglected, thus leaving a single Griffith crack to be considered, as depicted in the last sketch of Fig. 2.

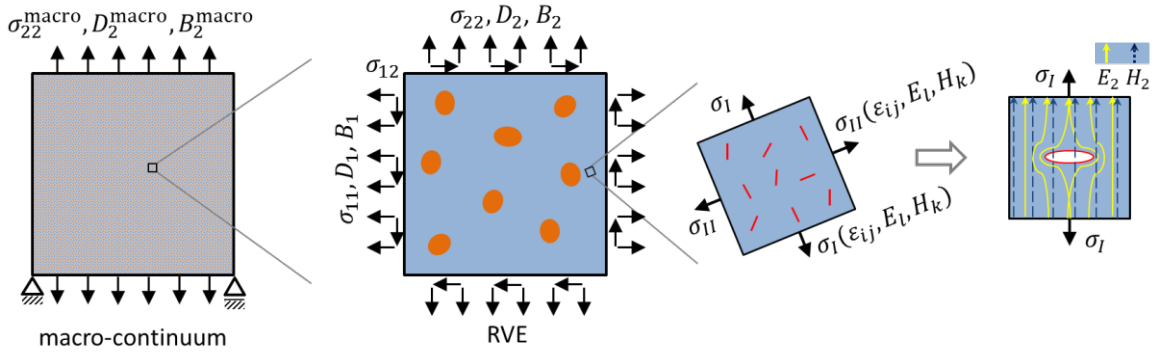

Fig. 2: Damaging of a ME particle composite: micro crack initiation perpendicular to the maximum principal stress σ_I, magnetic field penetrating the crack, electric field circumventing it

One essential issue in the fracture mechanics of multifunctional materials is the choice of boundary conditions at the crack faces. A comprehensive model is complex, including induced Maxwell tractions and finite electrical permeabilities [21,26-28]. A simple model is implemented here, where the crack is assumed traction-free and electrically impermeable, in Fig. 2 indicated by the solid yellow lines circumventing the crack. Concerning the magnetic field, the crack is assumed to be fully permeable, indicated by the dashed blue lines penetrating the crack. This is justified since, in contrast to the dielectric properties, the magnetic permeabilities of air and of a ferroelectric material are similar by order of magnitude.

In the following, some basic equations of the model are introduced, while the extended theory can be looked up in [14,29]. Introducing the compressed notations $\boldsymbol{\Pi} = (\sigma_{kl}, D_n)^T$ and

$\boldsymbol{Z} = \left(\varepsilon_{ij}, -E_l\right)^T$ for generalized stresses and electric displacements, the constitutive equations, linearized with respect to an operating point, are given as

$$\left.\begin{aligned}\langle\sigma_{ij}\rangle &= c^*_{ijkl}\langle\varepsilon_{kl}\rangle - e^*_{lij}\langle E_l\rangle \\ \langle D_l\rangle &= e^*_{lij}\langle\varepsilon_{ij}\rangle + \kappa^*_{ln}\langle E_n\rangle\end{aligned}\right\} \rightarrow \langle\boldsymbol{\Pi}\rangle = \boldsymbol{C}^*\langle\boldsymbol{Z}\rangle\,, \qquad \left.\begin{aligned}\langle B_k\rangle &= \mu^*_{km}\langle H_m\rangle\end{aligned}\right\} \rightarrow B_k = \mu_{km}H_m\,, \tag{5}$$

where angled brackets denote average fields and superscript asterisks represent effective material coefficients. The effective quantities have to be determined from homogenization of the crack RVE, thus the magnetic quantities remain unaffected due to the permeability of the crack. $\boldsymbol{C}^*$ is the effective generalized stiffness matrix, comprising homogenized elastic, dielectric and piezoelectric tangent modules. The inverse formulation of the effective constitutive law introduces the generalized stiffness $\boldsymbol{S}^* = [\boldsymbol{C}^*]^{-1}$:

$$\langle\boldsymbol{Z}\rangle = \boldsymbol{S}^*\langle\boldsymbol{\Pi}\rangle\,. \tag{6}$$

The generalized strain is decomposed as

$$\langle\boldsymbol{Z}\rangle = \boldsymbol{Z}_M + \boldsymbol{Z}_C \tag{7}$$

with $\boldsymbol{Z}_M = \boldsymbol{S}_M\boldsymbol{\Pi}^{\boldsymbol{0}}$ for the matrix and $\boldsymbol{Z}_C = \boldsymbol{S}_C\boldsymbol{\Pi}^{\boldsymbol{0}}$ for the defect phase**.** Assuming a generalized Reuss approximation, the average stress is introduced as a constant field, i.e. $\langle\boldsymbol{\Pi}\rangle = \boldsymbol{\Pi}^{\boldsymbol{0}}$. Stresses and electric displacements at the boundary of the crack RVE ∂V^C are thus coincident with the average quantities σ^0_{kl} und D^0_n in the domain V^C.

The generalized compliance is likewise decomposed in matrix and defect phase:

$$\boldsymbol{S}^* = \boldsymbol{S}_M + \boldsymbol{S}_C\,. \tag{8}$$

The contribution of micro cracks to the averaged strain and electric field is comprised in $\boldsymbol{Z}_C$ and reads

$$\varepsilon^C_{ij} = \frac{1}{2A}\int_{-a}^{+a}\left(\Delta u_i\, n_j + \Delta u_j\, n_i\right) dx^C_1\,, \tag{9}$$

$$E^C_i = -\frac{1}{A}\int_{-a}^{+a}\left(\Delta\phi\; n_i\right) dx^C_1 \tag{10}$$

where Δu_i and $\Delta\phi$ are jumps of displacement and electric potential accross the crack faces and n_j is the unit normal. The area of the plane RVE is denoted as A and a is half the crack length. The Griffith crack RVE and related quantities are depicted in Fig. 3, where x^C_i is the crack coordinate system.

The jumps in Eqs. (9) and (10) are determined from the closed-form solutions of the piezoelectric Griffith crack problem (see e.g. [21]), accounting for impermeable electric crack boundary conditions. The generalized effective compliance $\boldsymbol{S}^*$ according to Eq. (8) is then obtained as

$$\boldsymbol{S}_M = \begin{pmatrix} c_{ijkl} & e_{lij} \\ e_{lij} & -\kappa_{ln} \end{pmatrix}^{-1}, \qquad \boldsymbol{S}_C = \frac{f\pi}{4} \begin{pmatrix} 0 & 0 & 0 & 0 & 0 & 0 & 0 & 0 & 0 \\ 0 & Y_{22} & 0 & Y_{12} & 0 & Y_{23} & 0 & Y_{24} & 0 \\ 0 & 0 & 0 & 0 & 0 & 0 & 0 & 0 & 0 \\ 0 & Y_{12} & 0 & Y_{11} & 0 & Y_{13} & 0 & Y_{14} & 0 \\ 0 & 0 & 0 & 0 & 0 & 0 & 0 & 0 & 0 \\ 0 & Y_{23} & 0 & Y_{13} & 0 & Y_{33} & 0 & Y_{34} & 0 \\ 0 & 0 & 0 & 0 & 0 & 0 & 0 & 0 & 0 \\ 0 & Y_{24} & 0 & Y_{14} & 0 & Y_{34} & 0 & Y_{44} & 0 \\ 0 & 0 & 0 & 0 & 0 & 0 & 0 & 0 & 0 \end{pmatrix}. \tag{11}$$

The matrix is valid for the crack coordinate system (x_1^c, x_2^c) defined by the local principal stress axes see Fig. 3 a). The local polarization, being subject to continuous ferroelectric domain evolution, is associated with the local coordinate system (x_1, x_2), see Fig. 3 b). The Irwin matrix Y_{MN} in Eq. (11) is a material property, depending on the direction of polarization.

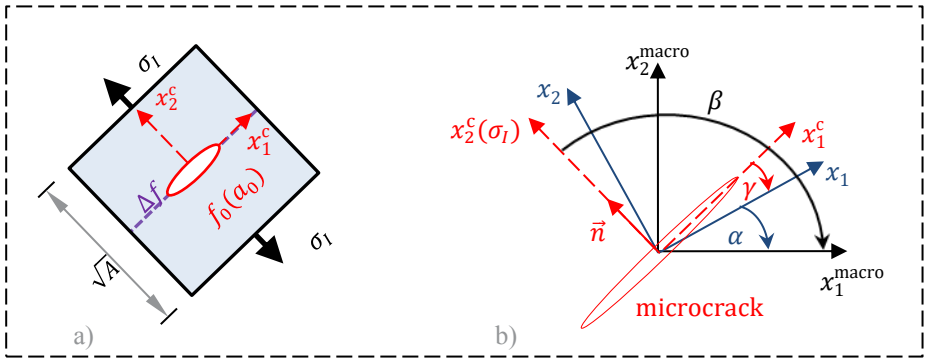

Fig. 3: a) Dilute crack RVE loaded by principal stress σ_I, initial crack length $2a_0$ and damage parameter f_0; b) crack with global $(x_1^{\text{macro}}, x_2^{\text{macro}})$, local material related (x_1, x_2) and crack (x_1^c, x_2^c) coordinate systems

The local degree of damage is described by the crack density or damage parameter f. Being defined as

$$f = \frac{4a^2}{A} \tag{12}$$

it takes the value $f = 1$ if the crack tips reach the boundary of the RVE, the extension of the latter $\sqrt{A}$ being a model parameter. The mode-I stress intensity factor $\mathrm{K}_I^{(n)}$ is applied to quantify the loading, and the related fracture criterion is

$$\sigma_I \sqrt{\pi a_n} = \mathrm{K}_I^{(n)} = \mathrm{K}_{IC}\,. \tag{13}$$

The fracture toughness K_{IC} can be chosen constant or account for an R-curve behavior, where the crack resistance is controlled by the electric field due to small scale switching at the crack tip [13]. The index n indicates an incremental crack growth in such a way that

$$a_n = a_0 + n \cdot \Delta a, \; f_n = f_0 + n \cdot \Delta f. \tag{14}$$

Eq. (14) is repeated at one external load step as long as the criterion Eq. (13) claims for crack growth, finally initiating the next load step. If $f = 1$ the elastic stiffness is locally reduced to 5% of the undamaged material, the dielectric properties of air are adopted and the piezoelectric coefficients are set to zero.

4 RESULTS

Based on the material models, in particular nonlinear simulations have been done in order to predict magnetoelectric (ME) coupling coefficients. First of all, however, linear calculations provide lower limiting values to demonstrate the essential role of nonlinear effects stemming from domain switching or damage. Two kinds of composites will be considered: one with a matrix of barium titanate (BT, $BaTiO_3$) with embedded elliptic soft ferromagnetic particles of cobalt ferrite (CF, $CoFe_2O_4$) and a laminated one consisting of three layers of BT and the hard ferromagnetic 0,2AlNiCo 35/5. The particle composite accounts for statistical distributions of particle sizes, shapes and positions. Fig. 4 shows a representative volume element (RVE) with a magnified excerpt on the right hand side including the finite element (FE) mesh. Periodic boundary conditions are generally imposed in the FE analyses prior to calculating the coupling coefficients.

Coefficients	Linear FEM	Experiment [10,11]
$g_{11}^{(R)^*} = \left.\frac{\Delta\langle D_l\rangle}{\Delta H_k^0}\right\|_{\sigma_{ij},E_n} = \left.\frac{\Delta\langle B_k\rangle}{\Delta E_l^0}\right\|_{\sigma_{ij},H_m} \left[{}^{\mathrm{Ns}}/_{\mathrm{VC}}\right]$	$148E-12$	$4{,}4E-12$

Table 1: Effective magnetoelectric coupling coefficients of a $0{,}2CoFe_2O_4 - 0{,}8BaTiO_3$ particle composite, where the simulation accounts for linear constitutive relations for both constituents

For the particle composite experimental values [10,11] are taken for comparison, where the composition is 80% BT and 20% CF. Table 1 shows a comparison with calculations based on linear piezoelectric and –magnetic constitutive laws. The values differ by two orders of magnitude, the larger coefficient belonging to the calculation.

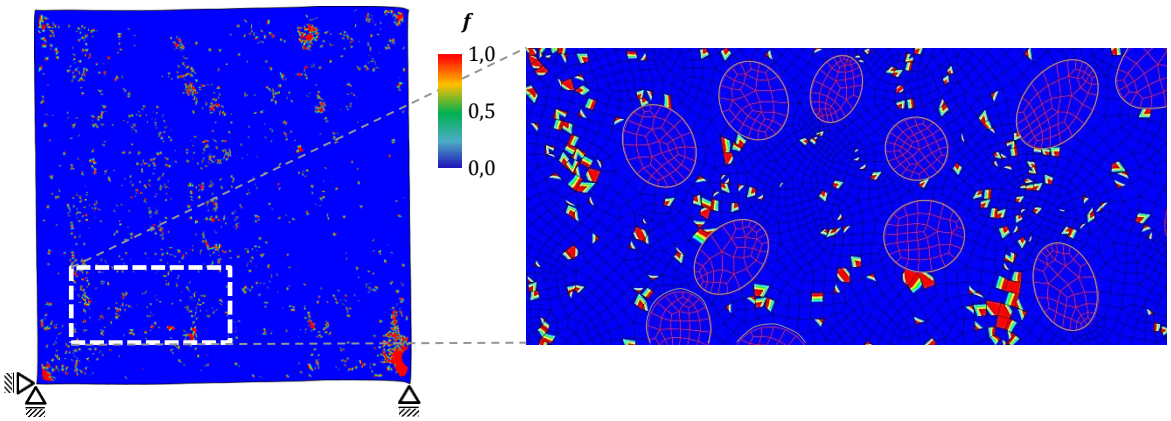

Fig. 4: Damage pattern of a ME particle composite ($0{,}2CoFe_2O_4 - 0{,}8BaTiO_3$, matrix: BT) right after electric poling with $E_1 = 5E_C$ and magnetic loading with $H_1 = 1000\,\mathrm{kA/m}$, see Fig. 6. The local damage parameter $f = 1$ indicates full damage and thus macro crack formation.

Several aspects are responsible for this overestimation. First of all, the constitutive laws for both constituents imply perfect poling along the transversal axes, which is far from reality. Fig. 5 shows the real state of polarization and magnetization in an example representing a periodic particle composite with hard ferromagnetic inclusions. It is obvious, that right after the poling, according to the magnetoelectric loading scheme in the left sketch, the vectors of magnetization and polarization are far from being perfectly aligned. Second, the residual stresses induced during the poling process will lead to substantial cracking and delamination

between matrix and particles, thus further reducing the ME coupling. A possible crack pattern in the matrix after the magnetoelectric poling is indicated in Fig. 4 by the red regions.

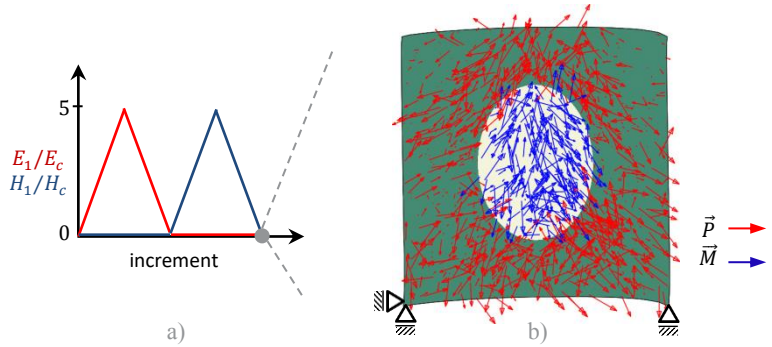

Fig. 5: RVE of an electrically and magnetically poled ME compound with periodically distributed ferromagnetic particles in a ferroelectric matrix ($0{,}2\mathrm{AlNiCo}\ 35/5 - 0{,}8\mathrm{BaTiO_3}$): a) poling load history and b) vectors of polarization and magnetization

Nonlinear simulations are shown next, where the ferroelectric matrix is modelled by the microphysically motivated constitutive law and the particle behavior is described by the phenomenological magnetostrictive law. Calculations are presented, accounting for damage evolution in the matrix on the one hand side and neglecting it on the other. Cracking of the particles and delamination are not considered in any case. The poling process of the initially unpoled materials has to be considered first, in order to induce a piezoelectric effect in the matrix. The magnetostrictive phase, following a nonlinear reversible material law, does not require a magnetic pre-poling. The loading scheme for calculating the ME coupling coefficients is depicted in a small sketch in Fig. 6, whereupon an electric half-cycle with a maximum load of $5\mathrm{E_c}$ is followed by a linearly increasing magnetic field up to $H_1 = 1000\ \mathrm{kA/m}$.

The coupling coefficient $g_{11}^{(R)^*}$ in Fig. 6 is determined in the interval of magnetic loading and plotted vs. the magnetic field H_1. The right plot is an excerpt of the left one, where the scaling of $g_{11}^{(R)^*}$ along the ordinate is different. The red crosses illustrate the scope of experimental results for coupling coefficients. The solid lines represent average electric displacements $\langle D_1 \rangle$. Green symbols and lines generally indicate results neglecting damage, blue ones emanate from simulations with damage. The electric displacement is non-zero at $H_1 = 0$ due to the electric poling, in the absence of free charges, leading to a remanent polarization. A depolarization along the x_1-axis is observed already at low magnetic fields. The reason is the magnetostriction, leading to a compression in the x_1-direction and an extension in x_2. The stress release due to damage on the one hand reduces the slope of reduction in $\langle D_1 \rangle$ for very small magnetic loads, on the other fosters the drop to a stationary value.

The coupling coefficients are calculated from the local derivatives of the $\langle D_1 \rangle(H_1)$-function. Averaging within intervals is necessary to smoothen the results which are depicted by the squared dots. Still there is a considerable scattering, in particular when damage is neglected, whereas the simulation with damage exhibits comparable variance just in the range of small magnetic fields. A general observation is that the ME coupling is obviously reduced by the damage, whose patterns are shown in Fig. 4, where the red regions with $f = 1$ indicate the formation of macro cracks. These are widely dispersed in the ferroelectric matrix, however most of them not being located at the interfaces of matrix and inclusions. Looking at the experimental values of coupling coefficients, they are within the range of those predicted from the model accounting for damage evolution.

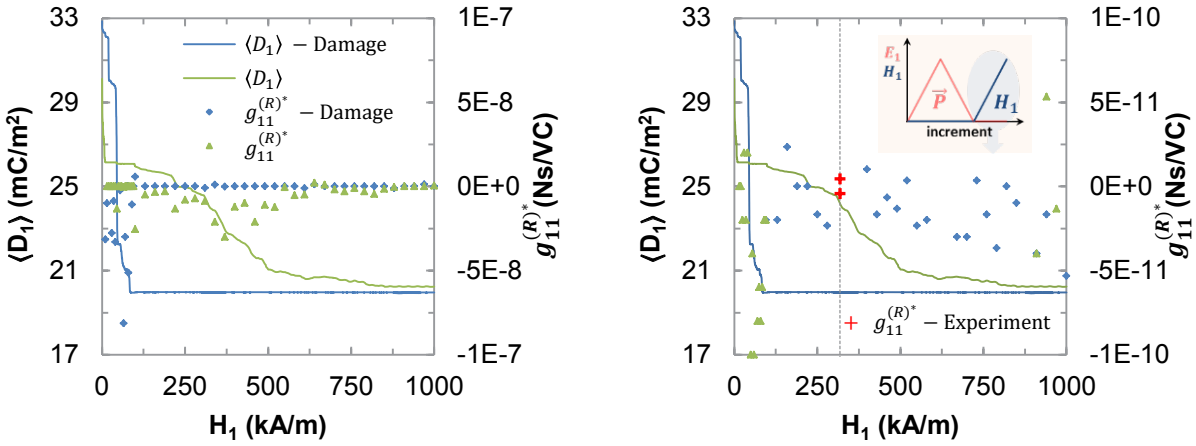

Fig. 6: Average electric displacement $\langle D_1 \rangle$ and ME coupling coefficient $g_{11}^{(R)^*}$ for a $0{,}2CoFe_2O_4 - 0{,}8BaTiO_3$ particle composite, see Fig. 4, from numerical simulation; experimental values from [10,11]

Results for the layered composite are considered next. Fig. 7 c) shows the three layers and the mechanical boundary conditions. The middle layer consisting of AlNiCo 35/5 is ferromagnetic, while the outer layers are made of BT. In contrast to the previous simulations of the particle composite, the microphysically motivated constitutive approaches are employed for both ferroelectric and ferromagnetic constituents. In d) an excerpt illustrates the damage pattern, the red dots again being interpreted as macroscopic crack formation. On the left hand side of Fig. 7 the ME loading scheme is depicted, starting with an electric poling by a field of strength $5E_c$, followed by a magnetic poling with $5H_c$. The ME coupling coefficients are calculated after the poling increasing an electric field linearly. The reason for imposing the fields along the longer edges is due to the fact that the simulation of the poling process is easier that way than for a perpendicular loading. In reality the middle layer will be poled before assembling the composite. The simulation, however, is based on the whole composite, so the magnetic poling field would have to penetrate the non-ferromagnetic layers, thus being too weak. The ME coupling coefficients might be even larger for fields along the shorter edges.

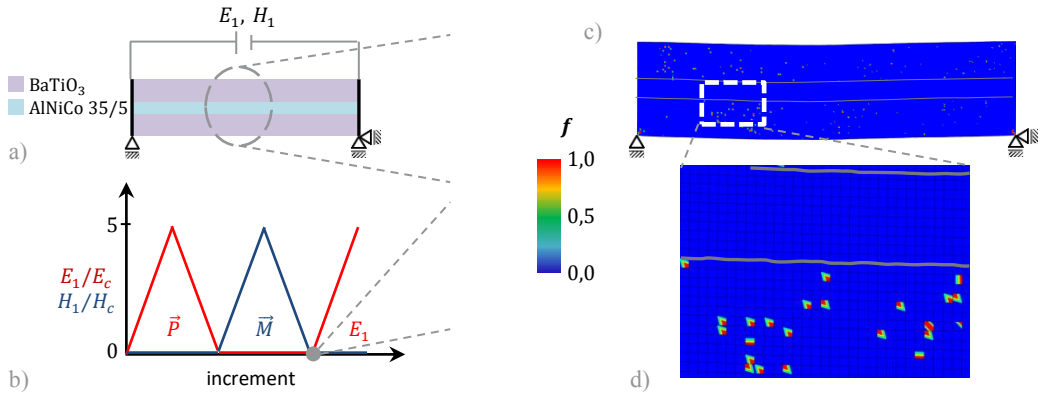

Fig. 7: a) laminated ME composite ($0{,}2AlNiCo\ 35/5 - 0{,}8BaTiO_3$) and boundary conditions, b) load history, c) FE analysis of displacement ($\times\ 10$) and damage pattern ($f = 1$: macro crack) right after poling

In Fig. 8 the average magnetic induction (solid lines) and the ME coupling coefficient (symbols) are plotted vs. the electric field. Both magnetic and electric fields are those along the longer edges denoted as x_1-direction. The blue color represents the results including dam-

age, again just in the ferroelectric layers, the green color stands for simulations neglecting damage. The right graph in Fig. 8 magnifies the scaling of the coupling coefficient.

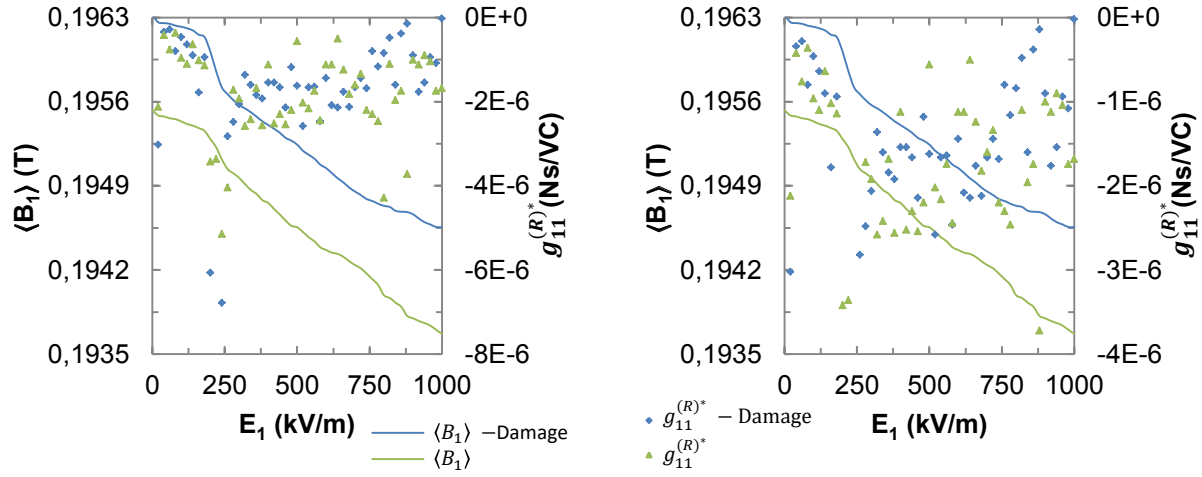

Fig. 8: Laminated composite according to Fig. 7: average magnetic induction $\langle B_1 \rangle$ and effective ME coupling coefficient $g_{11}^{(R)^*}$ with different scalings

Compared to the particle composite, a first observation is that the range of the induced field, i.e. the magnetic induction, is relatively small, barely exceeding one percent of its total magnitude. The regression caused by electric loading, however, is monotonous, reducing the initial magnetic poling. Comparing the ME coupling efficiency, the coefficients of the laminated composite exceed those of the one with embedded particles by several orders of magnitude, which is the most important outcome at this point. The cracking of the ferroelectric layers, on the other hand, doesn't have a significant impact, neither on the magnetic flux nor on the coupling coefficient. In the plots, the magnetic induction from poling seems to be slightly larger due to damage, the magnitudes, however, indicating a negligible effect.

5 CONCLUSIONS

Nonlinear constitutive models for ferroelectric and ferromagnetic materials have been presented within a magneto-electro-mechanical multifield context. The associated finite element implementation enables the simulation of multiferroic composites, in order to determine e.g. the magnetoelectric coupling coefficients or residual stresses due to domain switching. A simple micromechanically motivated damage model has been developed and included, since cracking turns out to have an essential impact, not only on life time but also on the functionality in terms of coupling efficiency. The present damage model thus has to be extended towards cracking in the ferromagnetic phase and delamination of the constituents. The latter aspect will be crucial for laminated composites, where cracking of the material itself turns out to have minor influence on the coupling coefficient. The numerical investigations confirm the common experience that the coupling efficiency of laminated composites is much larger compared to embedded particle composites. Nevertheless, more configurations will have to be investigated numerically, including variations of magnetoelectric poling procedures playing a crucial role. An important aspect, not yet considered in the constitutive and balance equations, is the flux of electric charge. In particular for ferromagnetic materials, the assumption of a dielectric medium often is not quite appropriate.

6 APPENDIX

The coefficients of cobalt ferrite and barium titanate are listed in Table 2.

	$BaTiO_3$	$CoFe_2O_4$
c_{11} (GPa)	162^{*}	$269{,}5^{***}$
c_{12} (GPa)	$77{,}5^{*}$	170^{***}
c_{22} (GPa)	166^{*}	286^{***}
c_{23} (GPa)	$76{,}6^{*}$	173^{***}
c_{44} (GPa)	$42{,}9^{*}$	$45{,}3^{***}$
κ_{11} (C/Vm)	$12{,}57\mathrm{E}-9^{*}$	$0{,}093\mathrm{E}-9^{***}$
κ_{22} (C/Vm)	$11{,}16\mathrm{E}-9^{*}$	$0{,}08\mathrm{E}-9^{***}$
μ_{11} ($\mathrm{Ns^2/C^2}$)	$1{,}26\mathrm{E}-6^{**}$	$2{,}71\mathrm{E}-6$
μ_{22} ($\mathrm{Ns^2/C^2}$)	$1{,}12\mathrm{E}-6$	$2{,}33\mathrm{E}-6$
e_{11} ($\mathrm{C/m^2}$)	$18{,}6^{*}$	0
e_{12} ($\mathrm{C/m^2}$)	$-4{,}4^{*}$	0
e_{24} ($\mathrm{C/m^2}$)	$11{,}6^{*}$	0

Table 2: Material properties of $BaTiO_3$ *[16,25], **[24] and $CoFe_2O_4$ ***[19,25]

Moreover, the quantities in Table 3 have been applied for the physically motivated model.

Parameter	Unit	$BaTiO_3$	AlNiCo 35/5
E_c	MV/m	$0{,}2^{*}$	–
$H_c = H_{cB}$	kA/m	–	47^{**}
P^0	$\mathrm{C/m^2}$	$0{,}26^{*}$	–
M^0	T	–	1,90
μ^r	–	–	5^{**}
ε_D	–	$0{,}01^{*}$	0,04
a_0	µm	5	–
f_0	–	0,005	–
K_{IC}	$\mathrm{MPa}\sqrt{\mathrm{m}}$	1,4	–

Table 3: Parameters of the physically based model adapted to the constitutive behavior of $BaTiO_3$ *[9,16,22] and AlNiCo 35/5 [20] (μ^r is denoted in [20] as μ_{rec})

Due to the lack of elastic and dielectric constants in literature, the values of Table 2 have been taken for AlNiCo 35/5 as well, assuming the same orders of magnitude.

REFERENCES

1 Avakian A, Gellmann R und Ricoeur A (2015) Nonlinear modeling and finite element simulation of magnetoelectric coupling and residual stress in multiferroic composites. *Acta Mechanica* 226 (8): 2789-2806.

2 Avakian A und Ricoeur A (2016) Constitutive modeling of nonlinear reversible and irreversible ferromagnetic behaviors and application to multiferroic composites. *Journal of Intelligent Material Systems and Structures* 27 (18): 2536–2554.

3 Avakian A und Ricoeur A (2017): An extended constitutive model for nonlinear reversible ferromagnetic behaviour under magnetomechanical multiaxial loading conditions. *Journal of Applied Physics* 121: 053901.

4 Bergmann L und Schaefer C (2005) *Lehrbuch der Experimentalphysik*. 6: Festkorper. Berlin / New York: de Gruyter.

5 Bhame SD und Joy PA (2006) Tuning of the magnetostrictive properties of $CoFe_2O_4$ by Mn substitution for Co. *Journal of Applied Physics* 100 (11): 113911.
6 Bhame SD und Joy PA (2007) Magnetic and magnetostrictive properties of manganese substituted cobalt ferrite. *Journal of Physics D: Applied Physics* 40 (11): 3263–3267.
7 Bhame SD und Joy PA (2008) Effect of Sintering Conditions and Microstructure on the Magnetostrictive Properties of Cobalt Ferrite. *Journal of the American Ceramic Society* 91 (6): 1976–1980.
8 Bozorth RM (1951) *Ferromagnetism*. New York: Van Nostrand.
9 Enderlein M (2007) *Finite-Elemente-Verfahren zur bruchmechanischen Analyse von Rissen in piezoelektrischen Strukturen bei transienter elektromechanischer Belastung*. Dissertation, Freiberg: TU Bergakademie.
10 Etier MF, Gao Y, Shvartsman VV, Lupascu DC, Landers J und Wende H (2012) Magnetoelectric properties of $0.2CoFe_2O_4 - 0.8BaTiO_3$ composite prepared by organic method. In: *Joint 21st IEEE ISAF/11th IEEE ECAPD/IEEE PFM (ISAF/ ECAPD/PFM)*, Aveiro, Portugal: 1–4.
11 Etier MF, Shvartsman VV, Salamon S, Gao Y, Wende H, Lupascu DC und Raveau B (2016) The Direct and the Converse Magnetoelectric Effect in Multiferroic Cobalt Ferrite-Barium Titanate Ceramic Composites. *Journal of the American Ceramic Society,* DOI: 10.1111/jace.14362.
12 Fiebig M (2005) Revival of the magnetoelectric effect. *Journal of Physics D: Applied Physics* 38 (8): R123 – R152.
13 Gellmann R und Ricoeur A (2012) Extended semi-analytical investigations of crack growth resistance behavior in ferroelectric materials. *Acta Mechanica* 223 (11): 2357-2368.
14 Gellmann R and Ricoeur A (2016) Continuum damage model for ferroelectric materials and its application to multilayer actuators. *Smart Materials and Structures* 25 (5): 055045.
15 Hill N (2000) Why are there so few magnetic ferroelectrics? *Journal of Physical Chemistry B* 104 (29): 6694–6709.
16 Jaffe B, Cook WR, Jaffe H (1971) *Piezoelectric ceramics*. London: Academic Press.
17 Lange S und Ricoeur A (2015) A condensed microelectromechanical approach for modeling tetragonal ferroelectrics. *International Journal of Solids and Structures* 54: 100–110.
18 Lee KY, Zong XC (2011) Dielectric crack problem for a magnetoelectroelastic strip with functionally graded properties. In: Archive of Applied Mechanics, Springer.
19 Li JY und Dunn ML (1998) Micromechanics of Magnetoelectroelastic Composite Materials: Average Fields and Effective Behavior. *Journal of Intelligent Material Systems and Structures* 9 (6): 404–416.
20 Plassmann W (2013) *Handbuch Elektrotechnik. Grundlagen und Anwendungen für Elektrotechniker*. 6., neu bearb. Aufl., Wiesbaden: Springer.
21 Ricoeur A und Kuna M (2003) Influence of electric field on the fracture of ferroelectric ceramics. *Journal of the European Ceramic Society* 23 (8): 1313-1328.
22 Rödel J und Kreher WS (2003) Modelling linear and nonlinear behavior of polycrystalline ferroelectric ceramics. *Journal of the European Ceramic Society* 23 (13): 2297-2306.
23 Scott JF (2007) Data storage: Multiferroic memories. *Nat Mater* 6 (4): 256–257.
24 Stevens D, Schweinler H, Sturm W und Sonder E (1956) The magnetic susceptibility of barium titanate. *Solid State Division Semiannual Progress Report* 30: 13–14.
25 Tang T und Yu W (2009) Micromechanical modeling of the multiphysical behavior of smart materials using the variational asymptotic method. *Smart Materials and Structures* 18 (12): 125026.
26 Ricoeur, R. Gellmann, Z. Wang: Influence of inclined electric fields on the effective fracture toughness of piezoelectric ceramics. Acta Mechanica, 226 (2015), 491-503.
27 R. Gellmann, A. Ricoeur: Some new aspects of boundary conditions at cracks in piezoelectrics. Archive of Applied Mechanics, 82 (2012), 841-852.
28 A. Ricoeur, M. Kuna: Electrostatic tractions at crack faces and their influence on the fracture mechanics of piezoelectrics. International Journal of Fracture, 157 (2009), 3-12.
29 S. Lange, A. Ricoeur: High cycle fatigue damage and life time prediction for tetragonal ferroelectrics under electromechanical loading. International Journal of Solids and Structures, 80 (2016), 181-192.

Aluminum Die Castings with the Property of active Vibration Damping - Process Technology and Functional Verification -

D. Himmler[a*], M. Schwankl[a], C. Pohle[a], C. Körner[a], S. Kimme[b], W. Drossel[bc]

[a] Chair of Metals Science and Technology
Department of Materials Science, Faculty of Engineering,
Friedrich-Alexander-University Erlangen-Nürnberg
Martensstrasse 5, 91058 Erlangen, Germany
E-Mail: david.himmler@fau.de, web page: http:// http://www.wtm.fau.de

[b] Department Mechatronics and Lightweight Design
Fraunhofer Institute for Machine Tools and Forming Technology
Nöthnitzer Strasse 44, 01187 Dresden, Germany
web page: https://www.tu-chemnitz.de/mb/adaptronik/

[c] Institute for Machine Tools and Production Processes
Chemnitz University of Technology
Reichenhainer Strasse 70, 09126 Chemnitz, Germany
web page: https://www.iwu.fraunhofer.de

ABSTRACT

This study deals with the process to integrate piezoelectric modules into high pressure die castings. The module functionality is demonstrated by active vibration damping of a structural aluminum part.

Due to weight-optimized design strong vibrations may occur. Hereby, the integration of smart materials can be used to avoid noise exposure. Additionally the piezoelectric module is protected against external influences by completely embed it within the component with the help of a hybrid fixing technology developed in prior works. The Al support structure has to be firmly bonded to the cast alloy Al-9Si-3Cu(Fe). A pre-processing before the actual casting process has to be applied. Active vibration damping is characterized by 3D laser scanning vibrometry (LSV).

The pre-processing of the support structure consists out of sandblasting and a subsequent active Zn-coating of the surface. Scanning electron microscope shows the influence of different process steps during sandblasting and coating. Microprobe analysis shows the diffusion of Zn atoms during casting in both directions (Pure Al and Al-9Si-3Cu) to create a firmly bonded compound.

X-ray analysis is used to check the casting quality and to investigate the damage free integration of the modules despite of severe thermal and mechanical loads during the casting process. Several information about the mode shapes of the casted part are offered by finite element simulations which could also be verified by measurements using LSV.

The present work shows the possibility to integrate a piezoelectric module in a die casted part. Finally, it is demonstrated that an actively induced vibration signal in the casting can be reduced by creating a phase-shifted counteracting vibration which is produced by the integrated module.

VIII ECCOMAS Thematic Conference on Smart Structures and Materials
SMART 2017
A. Güemes, A. Benjeddou , J. Rodellar and Jinsong Leng (Eds)

EFFECT OF THE INTEGRATION OF PIEZOCERAMIC COMPOSITES INTO STRUCTURAL COMPONENTS ON THEIR POLING CONDITION AND POLARIZABILITY

KAI HOHLFELD[*], SOPHIA EßLINGER[†], AGNES EYDAM[‡], ANJA WINKLER[+], TONY WEBER[+], MAIK GUDE[+], NILS MODLER[+], GERALD GERLACH[‡], GUNNAR SUCHANECK[‡], ALEXANDER MICHAELIS[†,*], ANDREAS SCHÖNECKER[†], SYLVIA GEBHARDT[†] AND PETER NEUMEISTER[†]

[*] Technische Universität Dresden (TUD)
Institute of Material Science (IfWW)
01062 Dresden, Germany
e-mail: kai.hohlfeld@tu-dresden.de, www.tu-dresden.de/ing/maschinenwesen/ifww

[†] Fraunhofer Institute for Ceramic Technologies and Systems (IKTS)
Winterbergstraße 28, 01277 Dresden, Germany
email: sophia.esslinger@ikts.fraunhofer.de, www.ikts.fraunhofer.de

[‡] Technische Universität Dresden (TUD)
Solid State Electronics Laboratory (IFE)
01062 Dresden, Germany
email: agnes.eydam@tu-dresden.de, www.tu-dresden.de/ing/elektrotechnik/ife

[+] Technische Universität Dresden (TUD)
Institute of Lightweight Engineering and Polymer Technology (ILK)
01062 Dresden, Germany
email: anja.winkler@tu-dresden.de, www.tu-dresden.de

Key words: Piezofiber composites, Integration, Polarization state, Polarizability

Abstract. In lightweight construction, integrated piezoelectric sensors and actuators find application for structural health-monitoring, vibration control, reduction of noise emission and condition monitoring. In order to create such smart components, we embedded piezofiber composites into thermoplastic structures. Thermal and mechanical loads during the integration process can lead to partial depolarization and thus degradation of the piezoelectric properties. In the present work, we investigate the effect of the integration on the poling condition and polarizability of piezofiber composites.

1 INTRODUCTION

Smart components are gaining high interest in the fields of lightweight construction, automotive, and aerospace design. Piezoelectric sensors and actuators are combined with

passive structures to utilize multi-functional applications like structural health monitoring, vibration control, noise emission reduction or condition monitoring in structures. Recently, a process chain for the direct integration of functional components into thermoplastic sheet structures has been developed, which allows for series production of active light weight structures at low costs [1].

Electromechanical properties of piezoelectric sensors and actuators are affected by temperature as well as applied electrical and mechanical loads which may occur during integration [2-5]. Therefore, we investigated the effect of fabrication processes on poling state and polarizability of integrated piezoceramic composites. Thereby, the natural aging without the influence of fabrication processes and re-poling was deduced from the capacitance of the samples by means of impedance measurement (IM). The poling state was evaluated by the Laser Intensity Modulation Method (LIMM). The pyroelectric current was analyzed by heating with an intensity-modulated laser beam [6]. Bipolar large signal polarization hysteresis measurements (HM) were performed to determine the effect of the integration on the polarizability.

1-3 piezofiber composites (PFC) consisting of a monolayer of PZT fibers embedded in epoxy resin were used as starting material [7]. In the first integration step, they were positioned between two transparent thermoplastic carrier films and consolidated by hot-pressing, forming the thermoplastic-compatible piezoceramic module (TPM). In the second integration step, these TPMs were integrated into a fiber reinforced plastic (FRP) structure [8]. Furthermore, the investigated samples were divided into three groups:

I. reference samples, which were poled but not integrated,
II. pre-poled samples, which were poled and integrated,
III. re-poled samples, which were additionally poled after each processing step.

Integration and investigation of the different sample groups was performed according to the experimental procedure depicted in Figure 1.

2 SAMPLE FABRICATION

2.1 Piezofiber composites (PFCs)

Piezoceramic fibers were fabricated from PZT powder (SONOX® P505 CeramTec GmbH, Germany) by means of the polysulfone spinning process [9]. The fibers with approximately 300 µm diameter were then arranged in parallel as a monolayer and embedded into epoxy resin (Araldite 2020). After curing the resulting piezofiber composite (PFC) with lateral dimensions of 35 mm × 22 mm was grinded to 250 µm thickness. Subsequently, continuous gold electrodes were deposited on top and bottom sides of the PFC by sputtering to enable poling and measuring. According to the fiber direction and the electrode design the PFC utilizes a lateral d_{31} functionality.

2.2 Thermoplastic-compatible piezoceramic-modules (TPMs)

In the thermoplastic-compatible piezoceramic-module (TPM) manufacturing process two thermoplastic films were functionalized with silver conductor by a screen printing process (see Figure 2). Both films have to be precisely positioned if congruent alignment between the upper and lower electrode is to be achieved. The aligned components were then fixed with the

aid of a thermal pressing step and trimmed as converted TPM: First, two functionalized foils were positioned and fixed by a local thermal welding process. As foil material a 100 µm thick PA6 material was used. After fixation of the foils two self-adhesive copper strips were positioned and fixed as contact element on the upper and lower layer. The assembly was finalized by inserting the PFC between the functionalized foils. Finally the prepared structure was positioned between the sliders of an interval hot pressing system and consolidated at 270°C with a pressure of 3 bar over 15 s.

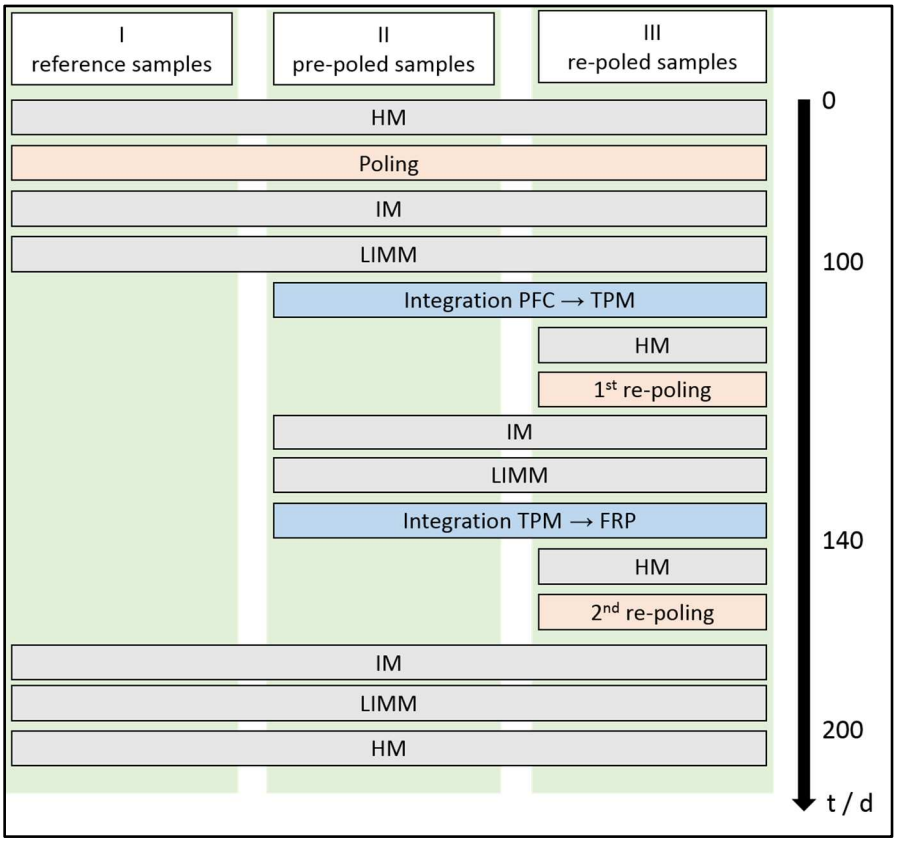

Figure 1: Experimental procedure

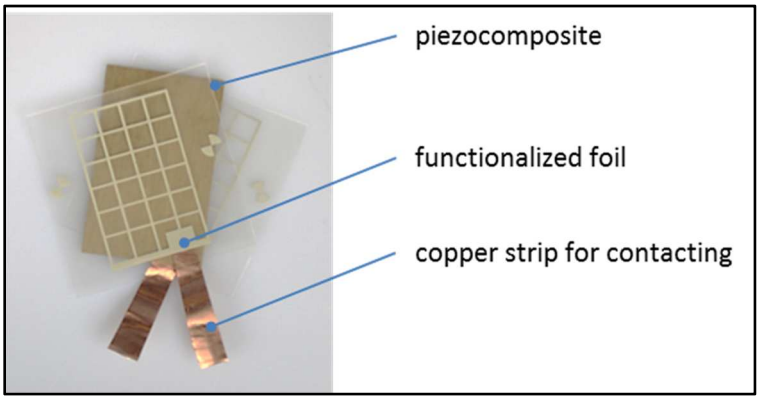

Figure 2: Structure of the thermoplastic-compatible piezoceramic-module (TPM)

2.3 Fiber-reinforced plastics (FRP) with thermoplastic matrices

The FRP samples were manufactured using an adapted thermoforming technology (see Figure 3). Pre-consolidated textile reinforced composites, so called organic sheets, were clamped in a tentering frame. This frame allows for proper handling through the entire process. The organic sheet was heated in an infrared preheating station over melting temperature of the thermoplastic component. Afterwards it was transferred into the pressing die. There, a thermoplastic film assembled with a TPM was fixed in the upper die and heated to the temperature of the constantly tempered pressing die. The surface of the pressing die was coated with a silicone layer (thickness 2 mm) in order to reduce stresses in the piezoceramic during the pressing process. After the insertion of the organic sheet into the press, the tool was closed immediately and a predefined pressure was applied to the components. Thus, the thermoplastic components of the organic sheet, the thermoplastic foil and the carrier films of the TPM melt together. After cooling to tool temperature, the press was opened and the FRP with integrated TPM was removed.

In the here presented studies organic sheets with a matrix made of polyamide 6 (PA6) and a glass fiber-reinforcement (TEPEX ®102-RG600(x)/47%, Bond Laminates GmbH) with a thickness of 2 mm were used. Preheating temperatures of 290°C were chosen and the pressing tool was tempered to 110°C. The transfer from the preheating station to the pressing die takes 6 s. Thus, the organic sheet has a temperature of approx. 270°C at the beginning of the pressing process, which is significantly higher than the melting temperature of the PA 6 matrix (T_M = 223°C). For the consolidation a predefined pressure of 0.01 MPa was used. The dwell time in the press was 130 s. The consolidated composite cools down to the tool temperature in about 80 s and remains there while the pressing pressure is still applied.

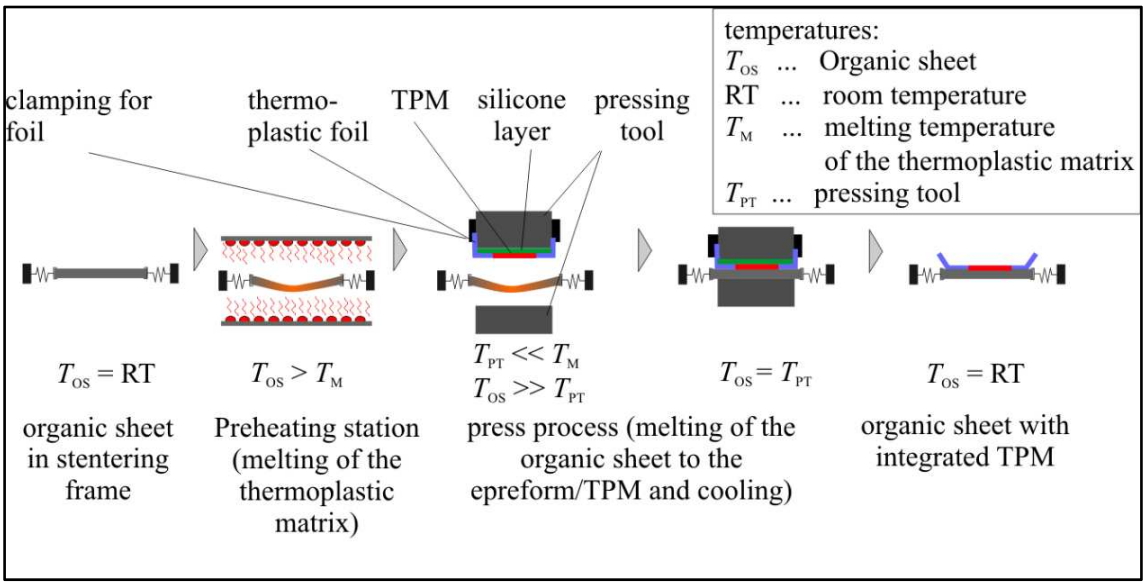

Figure 3: Schematic thermoforming process for the integration of TPM in FRP with thermoplastic matrices

2.4 Poling

Initial poling was performed by exposing each PFC to an electrical field of 2 kV/mm for 5 minutes at 80°C temperature. For group III samples additional re-poling procedures with identical parameters were executed after the two integration steps (see Figure 1).

3 MEASUREMENTS

3.1 Electrical Capacity

The electrical capacity of the samples was determined with an impedance analyzer (HP 4194A with test fixture 16034E) at room temperature. A sinusoidal voltage signal with a frequency of 1 kHz and a voltage amplitude of 0.5 V is applied.

3.2 Polarization State

The polarization state of the samples was evaluated nondestructively by Laser Intensity Modulation Method (LIMM) [10-16].

The value of the absorbed laser radiation within LIMM measurements can only be estimated so that an absolute value of the pyroelectric current cannot be calculated. The laser radiation is absorbed by the gold electrode of the PFC. This fact applies also to the integrated samples because the top PA 6 film is almost translucent. Consequently, the same amount of laser radiation is absorbed by the samples in the three states PFC, TPM and FRP, enabling a direct comparison of the pyroelectric current.

The thermal relaxation time of PZT fibers embedded in epoxy resin exceeds a few seconds. Thus, the thermal losses occur in a frequency range below 0.1 Hz. The pyroelectric current yields in the frequency region from 0.1 Hz to 100 Hz:

$$I(\omega) \approx \frac{\Phi_0 A}{c\rho \cdot d} p_0 . \tag{1}$$

At higher frequencies, the piezoelectric material causes also piezoelectric resonances.

The ratio of the pyroelectric currents of two samples is equal to the ratio of their average pyroelectric coefficients when neglecting heat transfer into the changing cover layers. The pyroelectric coefficient p is proportional to the remanent polarization P_r [17]:

$$p = \frac{P_r \cdot \varepsilon_r}{C_C} , \tag{2}$$

where ε_r is the dielectric constant and C_C the Curie constant. This leads to the following relation:

$$\frac{P_{r,1}}{P_{r,2}} = \frac{I_1 \cdot \varepsilon_{r,2}}{I_2 \cdot \varepsilon_{r,1}} . \tag{3}$$

LIMM measurements were performed by heating the samples periodically by a single laser diode (LCU98A041A, Laser Components GmbH, Olching, Germany) square-wave-modulated in the frequency range from 100 mHz up to 1 kHz with a power of 12 mW at a wavelength of 980 nm. The complex pyroelectric current was determined by an impedance/gain-phase analyzer (Solartron 1260, Solartron Analytical, Farnborough, UK) with

DC coupling. In order to reduce noise, 30 measurement repetitions were used for averaging. Furthermore, the relative dielectric constants ε_r were derived from the electrical capacity measurements.

3.3 Polarizability

Polarization hysteresis measurement was conducted on the different samples at room temperature. For the measurement, a Sawyer-Tower circuit was used. The material was cycled 10 times with 1 Hz and ±2 kV/mm maximum electric field amplitude. Always the 10th loop was evaluated. PZT classified as 200 in accordance with EN 503234-1, such as the PZT ceramic used in this investigation, show a more complex behavior: the hysteresis is shifted horizontally against the direction of the initial poling field (see Figure 4). This leads to a non-symmetric hysteresis loop for symmetric bipolar loading. Therefore, when evaluating a pre-poled sample, it is not possible to determine the absolute polarization. Hence, only the changes in remanent polarization can be evaluated.

For the evaluation of the remanent polarizability of the piezoceramic we propose the use of the change in remanent polarization due to re-poling ΔP_r at zero electric field. It is calculated as follows:

$$\Delta P_r = P_r^+ - P_r^- \tag{4}$$

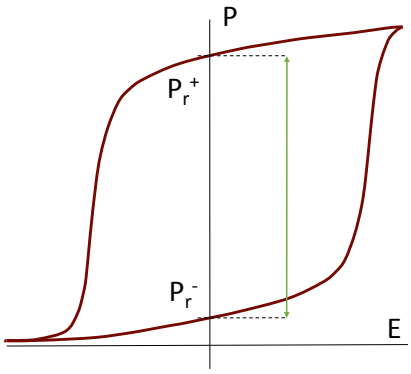

Figure 4: Schematic polarization hysteresis loop of a PZT ceramic classified as 200 that shows a hysteresis shift (initial poling in negative electric field direction).

4 RESULTS

Electrical capacity was determined by means of impedance measurements (IM) for the different sample groups before as well as after the integration steps. The results are depicted in Table 1. Time distance (in days) to initial poling (first) and re-poling (second) are mentioned in parenthesis.

Reference samples, which were not integrated, show a slight decrease of capacity values over time (< 4% in 122 d). This is assumed as natural degradation of the used PFC or piezo material respectively. Capacity of pre-poled samples remains stable for the first integration step (PFC→TPM) and undergoes a slight decrease (< 4%) for the second one (TPM→FRP), which is in the range of natural degradation. Re-poled samples exhibit decrease of capacity

values of < 4% for the first integration as well as approximately 6% in sum after the second integration, which is also in the natural degradation range. Thus, no negative influence of integration on sample capacity could be stated. Further, results of impedance measurements indicate that the utilized piezofiber composites work properly while being integrated.

Figures 5 and 6 show the pyroelectric current spectra of a pre-poled and a re-poled sample in the three states PFC, TPM and FRP, respectively as result of LIMM measurements. In the frequency range from 1 Hz to 100 Hz, the real part is almost constant and the imaginary part can be neglected.

Table 1: Change in capacity for sample groups I, II, III at different process steps

	C / nF (mean value ± standard deviation)		
Sample group	Initial IM	IM after Integration PFC→TPM	Final IM / IM after Integration TPM→FRP
I - reference samples	17.6 ± 1.9 (1 d)		17.0 ± 1.6 (122 d)
II – pre-poled samples	18.7 ± 0.8 (1 d)	18.6 ± 0.9 (34 d)	18.0 ± 0.7 (78 d)
III – re-poled samples	18.2 ± 1.0 (1 d)	17.6 ± 0.9 (43 d, 1 d)	17.1 ± 0.9 (78 d, 1 d)

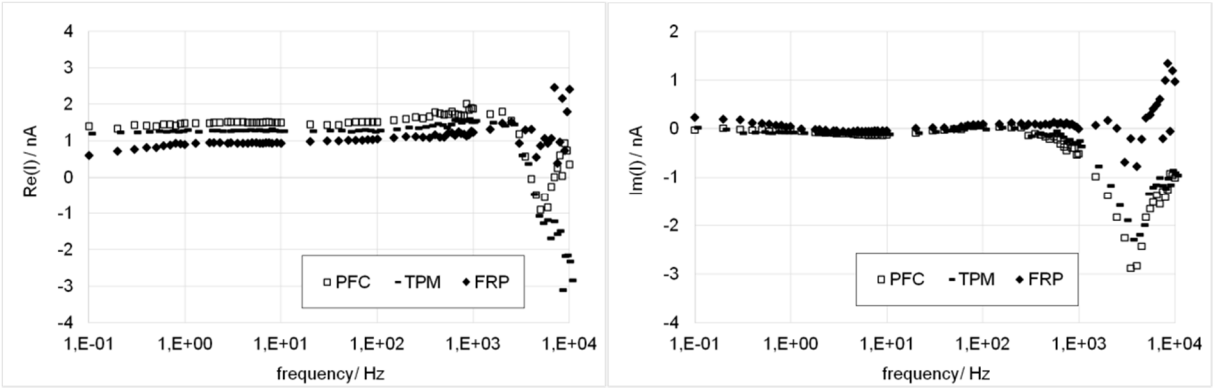

(a) (b)

Figure 5: (a) Real and (b) imaginary parts of the pyroelectric current spectra for a pre-poled sample in the three states PFC, TPM and FRP.

Table 2 presents the ratios of the remanent polarization after a process step to that before for the pre-poled and the re-poled samples as well as the polarization ratio over time for the reference samples according to Equation (3). The values (of one group) were not averaged due to the observed sample variation. The remanent polarization of the reference samples (I) remained stable over time. One sample exhibited an increase of 11%. All pre-poled samples (II) showed a degradation of the remanent polarization after each integration step. The range of degradation varied widely between 1% and 23% for one integration step. The measurement

uncertainty of $P_{r,1}/P_{r,2}$ amounted to ± 4% for a confidence interval of 95%. However, the observed depolarization of the pre-poled samples was within the variation of the polarization state of the PFC and thus, negligible. Furthermore, the polarization of the re-poled samples (III) was increased after the first integration and slightly decreased after the second one. Overall polarization ratios of re-poled samples were observed to be higher (97% - 111%) than those of pre-poled samples (64%-83%).

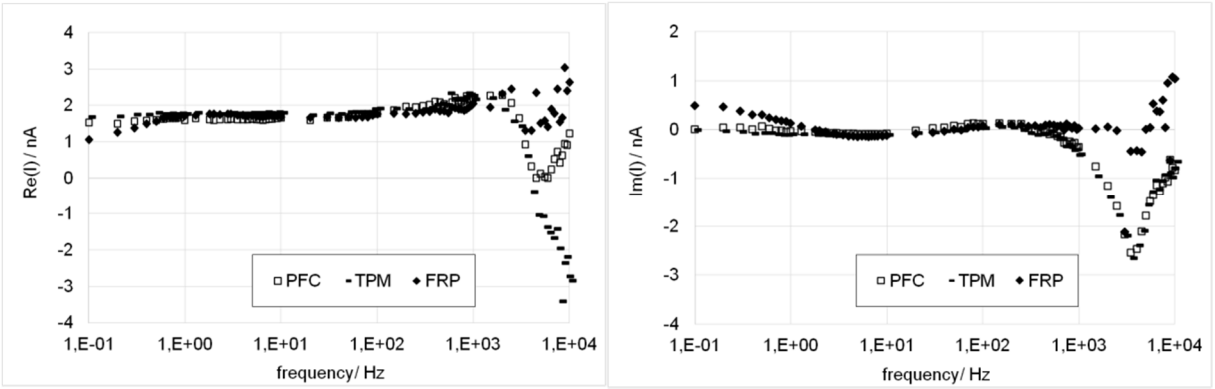

(a) (b)

Figure 6: (a) Real and (b) imaginary parts of the pyroelectric current spectra for a re-poled sample in the three states PFC, TPM and FRP.

Table 2: Ratios of the remanent polarization after integration (group II, III) as well as over time (group I).

		$P_{r,1}$ / $P_{r,2}$ (%)			
Sample group	No.	After Integration PFC→TPM	After Integration TPM→FRP	Overall PFC→TPM TPM→FRP	Final PFC/ Initial PFC
I – reference samples	3				101
	4				100
	5				111
II – pre-poled samples	6	99	82	81	
	7	83	77	64	
	8	97	86	83	
	10	81	94	75	
III – re-poled samples	14	113	99	111	
	17	125	78	97	
	18	113	91	103	
	19	113	97	110	

Table 3 shows the change in remanent polarization ΔP_r for the sample groups derived from hysteresis measurements. The reference samples (I) show an increase in polarization to 108% from the initial hysteresis measurement compared to the final hysteresis measurement, while the pre-poled (II) and re-poled (III) samples both show a decrease to 95%. This can be

attributed to the mechanical constraints due to the integration state [2, 3, 4]. The re-poled samples (III) show an increase of ΔP_r after the first integration step. For sample group III, the integration state not only affects the poled state of the PZT but also the poling process.

Table 3: Change in remanent polarization for sample groups I, II, III at different process steps

ΔP_r / µC/cm² (mean value ± standard deviation)				
Sample group	Initial HM	HM after Integration PFC→TPM	HM after Integration TPM→FRP	Final HM
I - reference samples	22.0 ± 3.8			23.7 ± 2.8
II – pre-poled samples	22.4 ± 1.6			21.2 ± 1.3
III – re-poled samples	21.5 ± 1.4	22.1 ± 1.4	20.7 ± 1.4	20.3 ± 1.4

5 CONCLUSIONS

- Changes in electrical capacity of integrated samples were observed to be in the range of natural degradation.
- LIMM experiments showed a degradation of the remanent polarization after integration. The range of degradation of pre-poled samples varied widely between 1% and 23% for each integration step. In contrast, the polarization of the re-poled samples was increased or only slightly decreased. The results indicate that the first integration step (PFC→TPM) has less impact on the remanent polarization than the second one (TPM→FRP).
- The attainable remanent polarization charge was decreased after integration. The remanent polarizability of the integrated composites reached 95% of the initial value.
- During integration the polarization state was preserved for the most part. However, re-poling promises an increase of remanent polarization and thus piezoelectric performance.

ACKNOWLEDGMENT

This research is supported by the Deutsche Forschungsgemeinschaft (DFG) in context of the Collaborative Research Centre/Transregio 39 PT-PIESA, subprojects A01, A05, B04, C03 and C08.

REFERENCES

[1] Hufenbach, W. A.; Modler, N.; Winkler, A.; Ilg, J. and Rupitsch, S. J. *Smart Mater. Struct.* **23** 025011, (2014).
[2] Zhou, D.; Kamlah, M.; Munz, D. *J. Europ. Ceram. Soc.* 25 (4), 425–432, (2005).
[3] Neumeister, P.; Eßlinger, S.; Gebhardt, S.; Schönecker, A. and Flössel, M. *Int. J. Appl. Ceram. Technol.* 11 (3), 422–430, (2014).

[4] Nicolai, M. *Dissertation*, Technische Universität Dresden, (2012).
[5] Winkler, A. *Dissertation*, Technische Universität Dresden, (2016).
[6] Eydam, A.; Suchaneck, G.; Hohlfeld, K.; Gebhardt, S.; Michaelis, A. and Gerlach, G. *IEEE Joint ISAF-PFM 2013, Electronic Proc.* 190-193.
[7] Hohlfeld, K.; Neumeister, P.; Gebhardt, S. and Michaelis A. *Proc. ACTUATOR 16*. Bremen, Germany, June 13-15, 2016. 69-72. www.actuator.de.
[8] Hufenbach, W.; Gude, M.; Modler, N.; Heber, Th.; Winkler, A. and Weber T. *Smart Mater. Res.* Vol. 2013, 201631, (2013).
[9] Hohlfeld, K.; Gebhardt, S.; Schönecker, A. and Michaelis, A. *Advances in Applied ceramics*, vol. 114 (4), 231-237, 2015.
[10] Bauer, S. and Ploss, B. *J. Appl. Phys.* Vol. 68, 6361-6367, (1990).
[11] Carslaw, H. S. and Jaeger, J. C. *Conduction of Heat in Solids.* 2nd ed., New York, NY: Oxford University Press, 1959.
[12] Eydam, A.; Suchaneck, G.; Esslinger, S.; Schönecker, A.; Neumeister, P. and Gerlach, G. *AIP Conf. Proceedings*. vol. 1627, 31-36, 2014.
[13] Bauer, S. and Bauer-Gogonea, S. *IEEE Trans. Diel. Electr. Insul.* vol. 10, No. 5, 883-902, 2003.
[14] Suchaneck, G.; Eydam, A.; Hu, W.; Krantz, B.; Drossel, W.-G. and Gerlach, G. *IEEE Tran Ultrason Ferroelectr Freq Control*. vol. 59, 1950-1954, 2012.
[15] Suchaneck, G.; Eydam, A.; Rübner, M.; Schwankl, M. and Gerlach, G. *Ceram. Int*. vol. 39, 587 590, 2013.
[16] Eydam, A.; Suchaneck, G.; Schwankl, M.; Gerlach, G.; Singer, R.F. and Körner, C., *Advances in Applied ceramics*, vol. 114 (4), 226-230, 2015.
[17] Liu, S. T. and Zook, J. D. *Ferroelectrics*. vol. 7, no. 1, 171-173, 1974.

VIII ECCOMAS Thematic Conference on Smart Structures and Materials
SMART 2017
A. Güemes, A. Benjeddou , J. Rodellar and Jinsong Leng (Eds)

EXPERIMENTAL AND NUMERICAL STUDY ON INHERENT SENSORY CHARACTERSITICS OF PIEZOCERAMIC MICRO PARTS DURING JOINING BY FORMING IN METAL SHEETS

WELF-GUNTRAM DROSSEL[1,2], ANDREAS SCHUBERT[1,3], MATTHIAS PUTZ[1,4], HANS-JOACHIM KORIATH[1], VOLKER WITTSTOCK[4], SIEGFRIED PETER[5], SEBASTIAN HENSEL[1], ALEXANDER PIERER[1], BENEDIKT MÜLLER[3] AND MAREK SCHMIDT[4*]

[1]Fraunhofer Institute for Machine Tools and Forming Technology,
Reichenhainer Str. 88, 09126 Chemnitz, Germany

[2]Professorship for Adaptronics and Lightweight Design, Chemnitz University of Technology,
Reichenhainer Str. 70, 09126 Chemnitz, Germany

[3]Professorship Micromanufacturing Technology, Chemnitz University of Technology,
Reichenhainer Str. 70, 09126 Chemnitz, Germany

[4]Professorship for Machine Tools and Forming Technology, Chemnitz University of Technology,
Reichenhainer Str. 70, 09126 Chemnitz, Germany
E-mail: marek.schmidt@mb.tu-chemnitz.de

[5]Professorship of Technical Physics, Chemnitz University of Technology,
Reichenhainer Str. 70, 09126 Chemnitz, Germany

Key words: Impedance spectroscopy, Joining by forming, Process monitoring, Sensitivity

Abstract.

A new approach for producing intelligent lightweight materials is the integration of prefabricated batches of piezoceramic micro parts in locally microstructured metal sheets by a joining by forming operation. In this way, semi-finished metal sheets with sensor and actuator functions can be manufactured in high-volume production cycles. Ensuring the component function of the piezoceramic parts in the form of parallel interconnected lead zirconate titanate (PZT) fibres is a key aspect during the forming process. Previous investigations at single PZT fibres have shown that the inherent sensor characteristics can be used for in-process monitoring by impedance spectroscopy during the forming process.

This paper deals with the electromechanical characterisation of the complete batch of interconnected PZT fibres before, during and after the joining process. For this purpose, experimental tests are carried out using fabricated test samples. Based on the gained findings from the experiments the preload state of the interconnected PZT fibres during the joining process can be specifically controlled and a fibre overload can be avoided. In addition, a numerical sensitivity analysis about the geometric scattering confirms the need for a controlled joining by forming process.

1 INTRODUCTION

The intelligent lightweight construction, which combines sensors and actuators with passive structural components, becomes increasingly important. This provides components with additional features, which are mainly concerned to vibration control [1], energy harvesting [2] and structural health monitoring [3]. Besides, material can be saved, thus reducing weight and costs as well as increasing the safety and running performance of products. In general, piezoelectric transducers are applied with adhesive layers onto the surface of metallic structural components. As a result, a polymer interlayer is located between the active element and the passive component. This layer influences the performance by damping. Moreover, adhesive layers exhibit signs of aging and are sensitive to weathering during outdoor use. This influences the properties of the complete system of transducer and structural component. A developed process chain enables the direct integration of piezoceramic elements in metal sheets by a forming operation. Consequently, polymer interlayers can be avoided. In addition, this technique allows to manufacture piezoelectric semi-finished products, with which further processing steps (e.g. shaping) can be performed. Subsequent bonding of sensors or actuators with the finished products is no longer necessary. The feasibility of the technology has already been demonstrated in previous investigations [4].

A compatible process chain for high-volume production was developed in order to transfer the technology in industrial sectors [5]. The schematic sequence of the process chain is shown in Figure 1. First step (ⓐ) is the generation of micro channels in an aluminium sheet by micro impact extrusion. The next step (ⓑ) involves the micro assembly of prefabricated PZT-fibre-array transducers in form of interconnected lead zirconate titanate (PZT) fibres. In the third step (ⓒ), the PZT fibres are connected form-fit and interference-fit with the aluminium sheet by forming. Finally, the piezo-metal substructure or also called piezo-metal module can be shaped by another forming operation (ⓓ). The process chain is to be further expanded for achieving the high-volume production.

Therefore, the research is particularly focused on the process step (ⓒ) joining by forming of the PZT fibres in the aluminium sheet. An implemented monitoring method is intended to ensure the component function and adjust a uniform preload of the PZT fibres. Initial preliminary studies with single fibres have already been carried out. It could be shown that the inherent sensory characteristics can be used to infer the preload situation [6]. According to single PZT fibre, the complex electromechanical behaviour of electrical interconnected fibres is subject of current investigations. Hereinafter, the structure of piezo-metal module will be presented as well as the theoretical approaches for use the impedance spectrum.

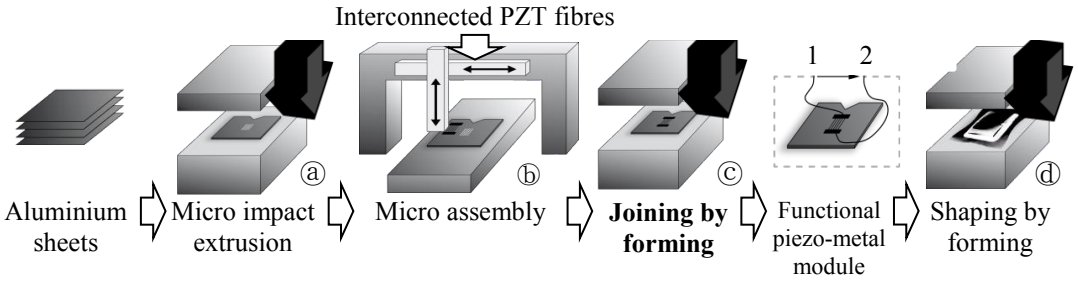

Figure 1: Process chain for manufacturing of shaped structures with integrated PZT fibres [5]

2 STRUCTURE OF PIEZO-METAL MODULES

A schematic structure of a single PZT fibre (dimensions: 0.58 x 0.46 x 10 mm³) and a single micro channel (dimensions: 0.6 x 0.6 x 10 mm³) in the aluminium sheet is shown in Figure 2 a). The widths of PZT fibres and the micro channels results in an assembly clearance of about 0.02 mm. The aluminium material is deformed by the joining tool until the assembly clearance is closed, which is shown in Figure 2 b). The fibres are subsequently integrated in form-fit and interference-fit with the metal sheet. The surfaces of the PZT fibres with contact to the channel walls are metallised. Furthermore, the fibre has a centre interface electrode (CIE). The CIE is necessary for the realisation of the electrical connection and polarisation for the d_{33} effect according to the Figure 2 b). In order to avoid an electrical short circuit between the PZT fibre and the aluminium sheet, the bottoms of the channels are coated with an insulating layer. The complete piezoceramic transducer is an array of parallel interconnected PZT fibres each with CIE. For the experiments five PZT fibres are used.

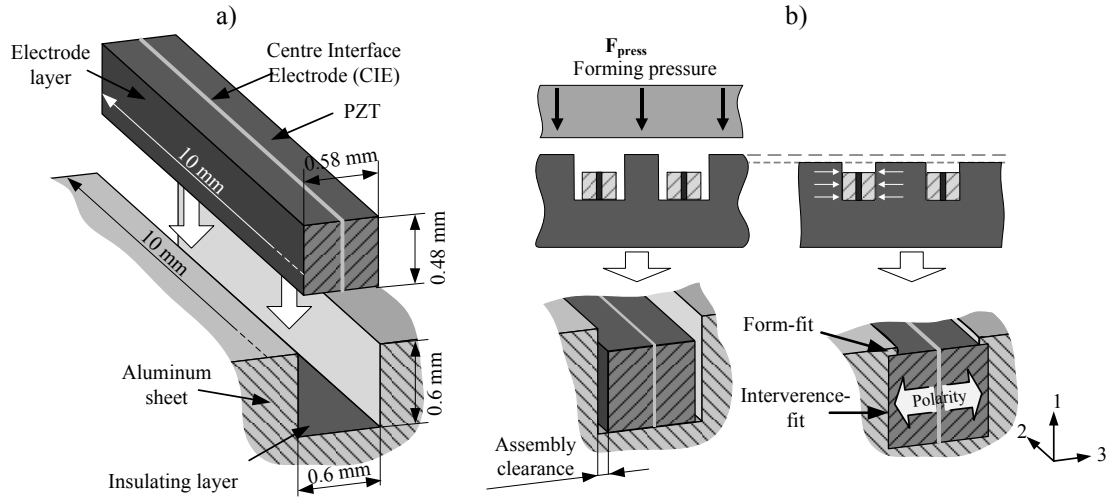

Figure 2: Principle for the integration of PZT fibres in aluminium sheets, a) schematic design of PZT fibre with CIE and micro channel in aluminium sheet, b) joining by forming operation

3 ELECTRICAL IMPEDANCE OF ELECTRICALLY IN PARALLEL CONNECTED PZT FIBRES WITH CHANGING MECHANICAL LOADS

The approximation of the electrical impedance of a single fibre in the vicinity of a resonance mode can be performed by the simplified equivalent circuit model with lumped parameters. Hence, the over-all impedance of the piezoelectric transducer can be descripted by a parallelisation of single fibres, which is illustrated in Figure 3. The capacitance $C_{1,i}$ represents the true electrical capacity and $R_{1,i}$ the true electrical contact resistance to the PZT fibre, whereas i is the index of the fibre. The parallel RLC-branch embodies the mechanical impedance of the first mechanical resonance mode of the fibre. Thereby the resistance $R_{2,i}$, capacitance $C_{2,i}$ and inductance $L_{2,i}$ are equivalent to the mechanical damping, mechanical stiffness and inertial mass. The higher resonance modes can be represented by additional parallel RLC-branches. In [7] proportionalities between the lumped parameters of the equivalent circuit and mechanical coupling factor α_i were found. Thereby the coupling factor

α_i indicates the effectiveness of the piezoelectric conversion between electrical energy $W_{\mathrm{el},i}$ and mechanical energy $W_{\mathrm{mech},i}$ of the fibre:

$$C_{2,i} \sim \alpha_i^{\,2},\ L_{2,i} \sim \frac{1}{\alpha_i^{\,2}},\ R_{2,i} \sim \frac{1}{\alpha_i^{\,2}} \text{ and } \alpha_i^{\,2} = \frac{W_{mech,i}}{W_{el,i}}. \tag{1}$$

As shown in Equation 2 the electrical impedance of the piezoelectric transducer can be changed by a variation of the coupling factor α_i. In [8] the authors showed that the coupling factor α_i can be changed by axial forces which cause destabilization or stiffening of a piezo patch. By applying of these proportionalities to the lumped parameters in Equation 1 the complex impedance $\underline{Z}_\mathrm{i}$ of a fibre i can be calculated as function of the frequency f and the coupling factor α_i:

$$\underline{Z}_i(f,\alpha_i) = R_{0,i} + \frac{1}{j\cdot 2\pi\cdot f\cdot C_{1,i}} \parallel \left(\left(\frac{1}{j\cdot 2\pi\cdot f\cdot C_{2,i}} + j\cdot 2\pi\cdot f\cdot L_{2,i} + R_{2,i} \right) \cdot \alpha_i^{\,2} \right). \tag{2}$$

The over-all impedance of the transducer can be descripted by a parallelization of the single fibre models as shown in Figure 3 a) and b). Hence, the impedance of a transducer with n=5 PZT fibres can be descripted with Equation 3.

$$\frac{1}{\underline{Z}_{Array}(f,\alpha_i)} = \sum_{i=1}^{n} \frac{1}{\underline{Z}_i(f,\alpha_i)} \tag{3}$$

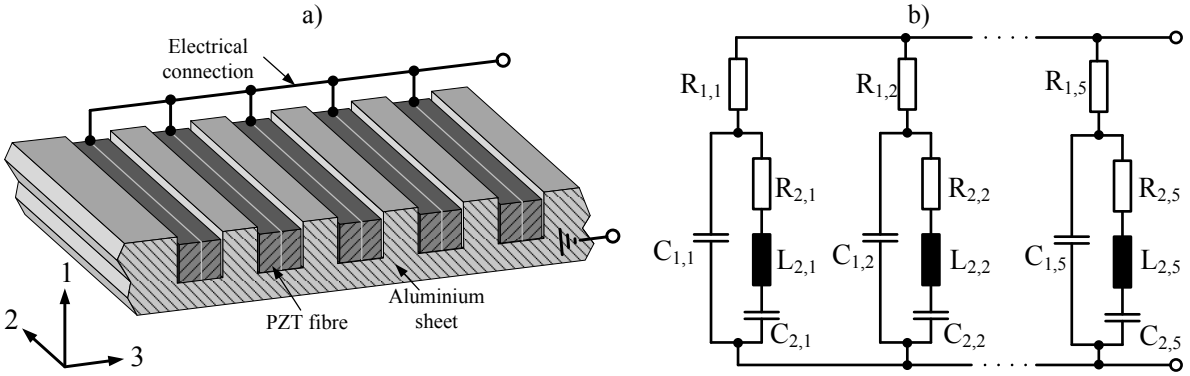

Figure 3: a) Electrical connection of piezo-metal modules, b) equivalent electrical circuit of parallel PZT fibres in vicinity of the first resonance mode as schematic

In a simulative study, the coupling factor α^*_i is normalised to the load-free state of the fibres and stepwise varied between 60 % and 100 %. The lumped parameters of the simulated equivalent circuit where estimated at load-free conditions in the d_{33}-direction of a single fibre from characteristic points of the impedance spectrum based on the experimental method introduced by DeAngelis and Schulze [9]. The simulation yields an impedance change driven by the electrical coupling factor as depicted in Figure 4 and demonstrates the feasibility of mechanical load estimation by impedance spectroscopy.

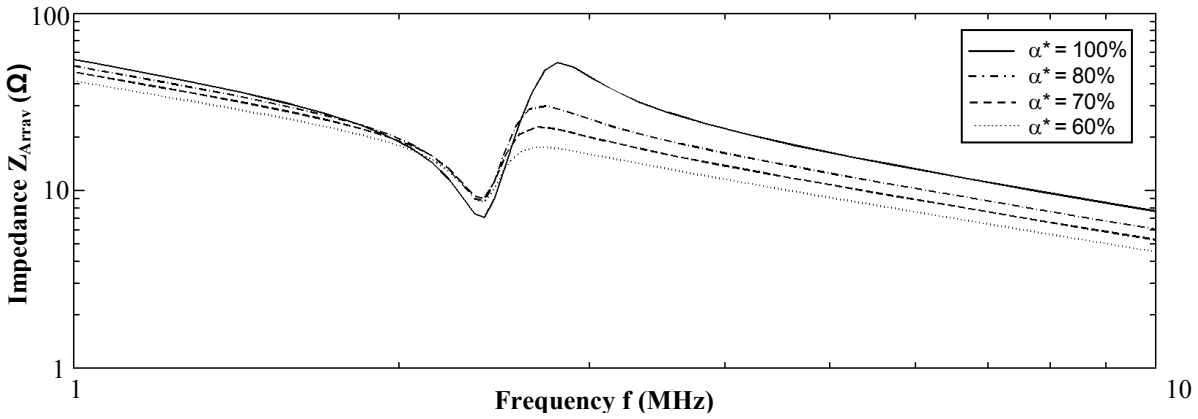

Figure 4: Simulated shift of impedance spectrum of PZT-fibre-array in dependency of mechanic coupling where α* is the normalised coupling factor

4 EXPERIMENTAL

10

4.1 Sample preparation

For preparing the PZT fibres, two PZT plates (type M1100 from Johnson Matthey Piezo Products) are bonded together with an epoxy resin adhesive (J-B Weld) and with a wire mesh between them. The thickness of the PZT plates is 0.26 mm and the surfaces are metallised with electrode layers. A schematic structure of the compound is represented in Figure 5 a). The electrode layers and the wire mesh ensure the electrical connection. The thickness of the CIE results in 60 µm. The bonded plates are separated in equally sized fibres by precision cut-off grinding, which is also illustrated in Figure 5 a). Wires get attached to each CIE and interconnected together and a PZT fibre array transducer is produced.

Micro channels in the aluminium sheets are generated by a micro-milling process. Afterwards, the bottom sides of the channels are coated with an insulating layer. A wire is connected to the aluminium sheet. The dimensions of all produced samples are measured using a digital microscope (Keyence VHX-600) for the numerical study on geometrical process sensitivity. Finally, the prepared PZT fibre array transducers are assembled in the microstructure, which is shown in Figure 5 b) and subsequently placed in the joining tool.

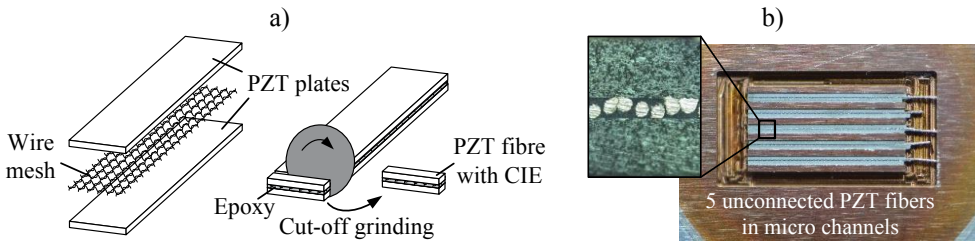

Figure 5: a) Manufacturing process of PZT fibres with CIE, b)assembled in the micro channels of an aluminium sheet

4.2 Experimental setup

All experiments are done with the d_{33}-effect of the PZT fibres. The wires at the test samples are electrically connected to a vector network analyser (OmicronLab Bode 100). The flat upper joining tool is insulated with polyimide tape (Kapton KL-KAPT) to prevent short-circuiting of the CIE against the aluminium sheet and ground potential of the machine equipment. Experiments are performed on a material testing machine (Hegewald & Peschke Inspekt 150 kN). During the joining operation the upper tool moves downwards and applies stepwise a rising pressing force F_{Press} to the webs of the microstructure. Hence, the fibres are continuously clamped through narrowing the channels as illustrated in Figure 2 b).

In order to locate the expected frequency range for the resonance mode, the series resonant frequency f_s for the longitudinal mode is calculated according to Equation 4. Using the frequency constant N_3 of 1870 m/s (manufacturer data) and the active length l in the d_{33}-direction of 0.52 mm, a series resonant frequency f_S of 3.6 MHz is obtained.

$$f_s = \frac{N_3}{l} \tag{4}$$

Whilst the joining operation the impedance spectra are measured at different levels of the uprising pressing force F_{Press} and after the joining with lifted upper joining tool. During the rising of the pressing force F_{Press} a decreasing of the impedance spectra over the measured frequency range, an increased damping and a frequency shifting of resonance-modes are observed. The resonance mode around 3.5 MHz shows a good sensitivity of the frequency shift and damping to the applied pressing force F_{Press}. The value is close to the calculated frequency for f_s. Based on this observation, this resonance mode can be utilised as monitoring indicator for the joining process. A series of joining with eight specimens reveals that a good clamping of the fibres is achieved when the resonance peak at around 3.5 MHz disappears. Figure 6 and Figure 7 exemplarily shows impedance spectra of two different transducers during the joining by forming operation at different pressing forces F_{Press}.

In the first case a good joining result is obtained by applying a maximum pressing force of 8 kN. The decreasing of the impedance (see Figure 6) during the joining indicates a good clamping of the fibres with the aluminium microstructure. The resonance-peak at around 3.5 MHz shifts from 3.47 MHz at 500 N pressing force F_{Press} to 3.55 MHz at 8 kN. At 8 kN the resonance peak disappears. A microscopic inspection (see Figure 8 a)) after the joining shows a completely closed assembly gap and good fit between the fibres and the webs of the microstructure. Even no visible fibre-cracks or damages are found.

In the second case the pressing force is increased up to 16 kN. Until 8 kN the impedance behaviour is similar to the previous example. The resonance peak at around 3.5 MHz shifts from 3.53 MHz at 500 N pressing force F_{Press} to 3.62 MHz at 8 kN. At 8 kN the resonance-peak disappears again. Beyond 10 kN a drastic drop-down of the impedance is observed in the range of 0.1 MHz and 0.8 MHz. This indicates for example a damaging of the insulation film of the CIE. After joining, a microscopic inspection shows a number of visible fibre cracks in the range of the channels as illustrated in Figure 8 b). Nevertheless, the proposed impedance analysis proves its feasibility for failure mode detection during the joining process in this case. The Figure 8 c) shows a micrograph for integrated PZT fibres. The fibres are well

clamped, only the form-fit has not yet been fully achieved. To this end, the process parameters must be adjusted, whereby the load limits of the fibres have to be considered.

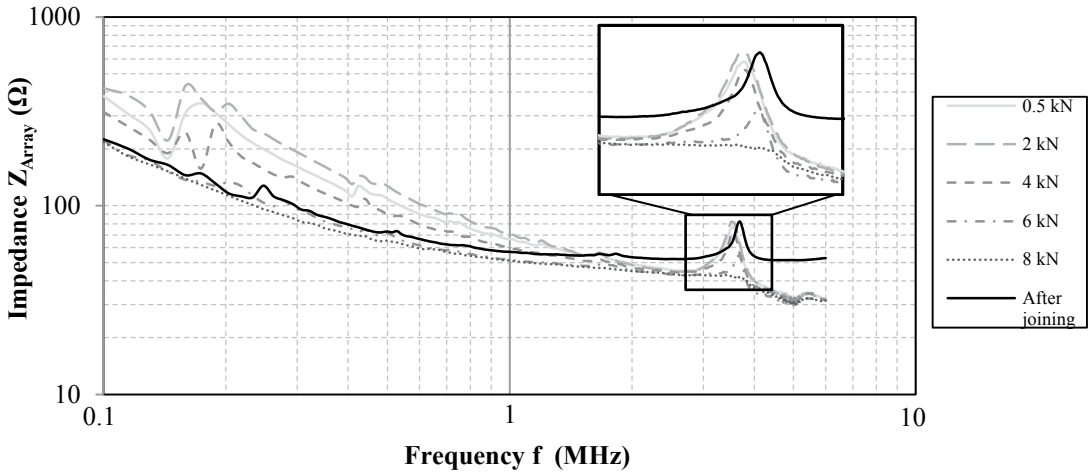

Figure 6: Measured impedance spectra of PZT-fibre-arrays during joining by forming at different pressing forces F_{Press} up to 8 kN and after joining

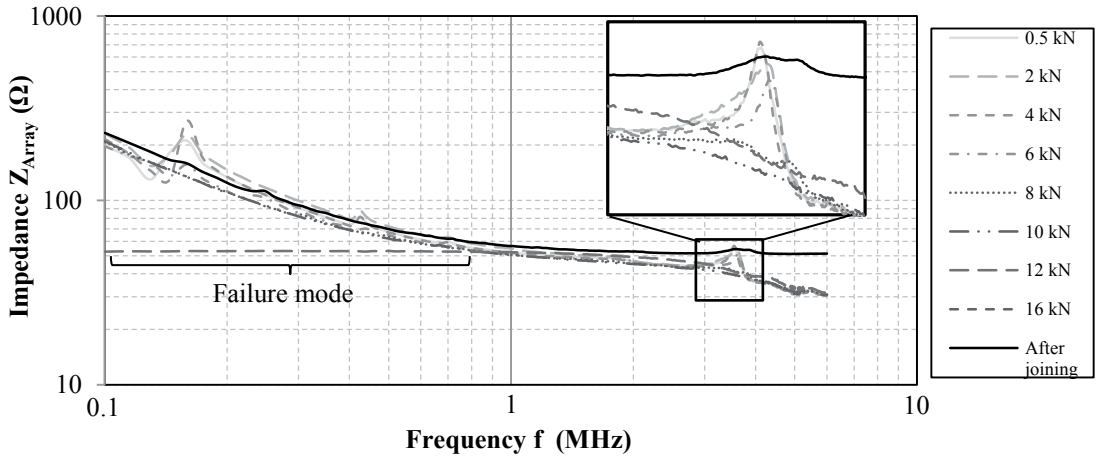

Figure 7: Measured impedance spectra of PZT fibre arrays during joining by forming at different pressing forces F_{Press} and after joining with failure mode due to excessive pressing forces up to 16 kN

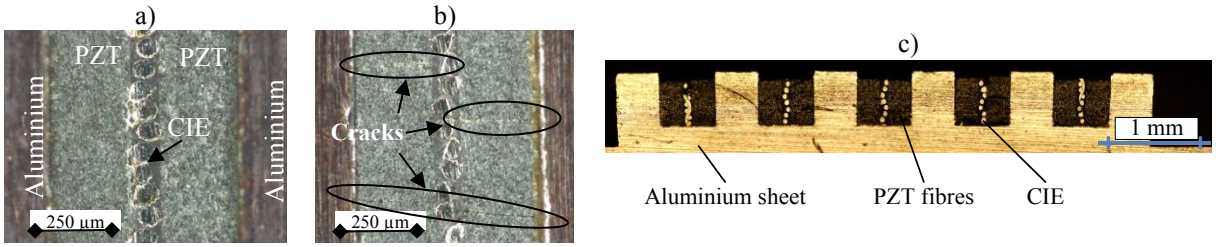

Figure 8: Microscopic inspection results after joining, a) forming up to 8 kN (top view), b) failure mode due to excessive pressing forces up to 16 kN (top view), c) micrograph of integrated PZT fibres (sectional view)

5 NUMERICAL STUDY ON GEOMETRICAL PROCESS SENSITIVITY

Typically, a critical fibre overload can be avoided by using a conservative upper joining force limit that is never reached. Maybe this limit has to be elevated to ensure a secure fibre clamping. Thus an efficient process monitoring is necessary. Furthermore, in cases where a force controlled process leads to high complexity or a displacement controlled process is advantageous for geometrical accuracy, a fibre overload may also occur due to inconvenient combinations of scattering of fibre dimensions and micro channel dimensions.. With numerical simulations the resulting maximum fibre stresses are investigated to evaluate the influence of geometric scattering. Figure 9 shows the two-dimensional plain strain model of the forming zone. LS-Dyna Implicit with release SMP R9.1.0 (double precision) is used as solver. The forming load is applied with a control of the displacement until a maximum value. In a final step the geometry is unloaded to investigate the remaining clamping stresses in the fibres. Maximum and final stresses are monitored in the middle of each fibre (Figure 9). The geometric scattering is determined by the optical scan of fibres as well as micro channels geometry before joining. Table 1 gives the mean values with scattering range. In the model the mean value for channels width is shifted to 0.609 mm to avoid an overlapping of fibre and channel. The centre interface electrode, described above, is not considered in the geometry model. In a first step only the influence of the dimensions of fibres and channels is included. The scattering of CIE thickness as well as irreversible deformation of CIE during joining is not part of the present study.

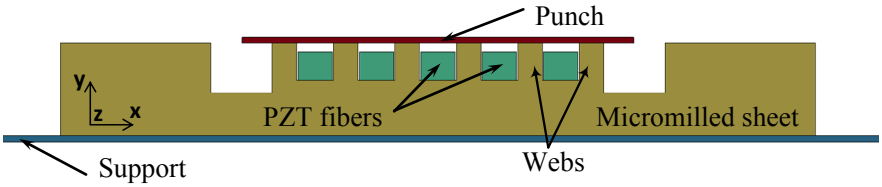

Figure 9: Geometry model for the sensitivity study

Table 1: Mean values and scattering range of fibre dimensions and channel dimensions

	Mean value (mm)	Scattering range (mm)
Channel width	0.607	±0.009
Channel height	0.600	-
Fibre width	0.580	±0.020
Fibre height	0.477	±0.024
Web width	0.396	±0.014

With a parameterised model an automatic geometry generation is realised to investigate the sensitivity of the chosen parameters channel width, fibre width and web width. Channel height and fibre height are excluded in the present study because of the reproducible results of the micro-milling process for the channels. The parameter space is covered with a reference state and two additional simulations for upper and lower scattering limit. For the web width only the extremal values are considered. Hence a total amount of 17 simulations are computed (Figure 10). Especially the outer parameter-space border where fibre width equals channel

width is only of theoretical interest. Due to the fitting difficulties during micro-assembly, the fibre width has to be smaller than the channel width.

For the isotropic hardening aluminium material model a true stress / true strain curve is determined in compression tests with cylindrical specimens. The parameters for the anisotropic elastic material model of the piezoceramic material are taken from [10].

In each calculation the stresses in the middle of all fibres are monitored. In the following only the third principle stress in the middle of the centre fibre is discussed. The stress is always lower zero due to clamping of the fibre (the channel walls act as punch) and its orientation is always perpendicular to the side walls. Two points of the stress curves over process time are evaluated. First point: the stress minimum occurs when the maximum pressure is applied by the side walls. Second point: the residual stress in the fibre after joining and unloading gives the remaining pressure that clamps the fibre. In the study the absolute value of the third principle stress is used to account for the pressure load nature of the resulting stress component.

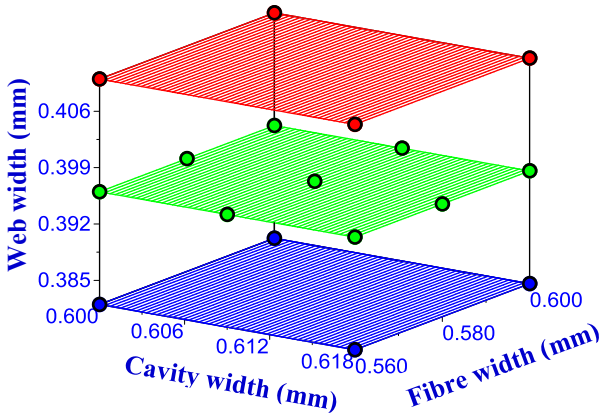

Figure 10: Distribution of geometric parameters in parameter-space

Figure 11 a) shows the stress maxima reached in the process dependent on the geometric parameters micro channel width and fibre width. Figure 11 b) gives the according residual stresses after unloading. The occurring clamping forces rise with lower gaps between fibre and channel. This is also valid for the residual stresses. While this correlation conforms to the expectations, the stress ranges (fibre pressure between channel walls) are unexpected high. A gap reduction from nearly 60 µm to zero results in an increase of 200 % in stress. The channel walls pressure dependency on channel width and fibre width is significant.

Figure 12 shows the same relation between fibre pressure and web width. There exists no dependency neither for the stresses at pressure maximum (Figure 12 a)) nor for the residual stresses (Figure 12 b)).

As a result, unfavourable combinations of channel and fibre width may cause high clamping stresses in some fibres. This leads to higher final clamping situations on the one hand. On the other hand, it is possible that a critical fibre loading is reached, which has to be avoided to maintain the part functionality. Hence, a fibre status monitoring as mentioned above supports the process reliability. The scattering ranges considered in the present study base on measurements of channels and fibres produced in the current investigations. It is expected that the variances can be reduced within a further process optimisation.

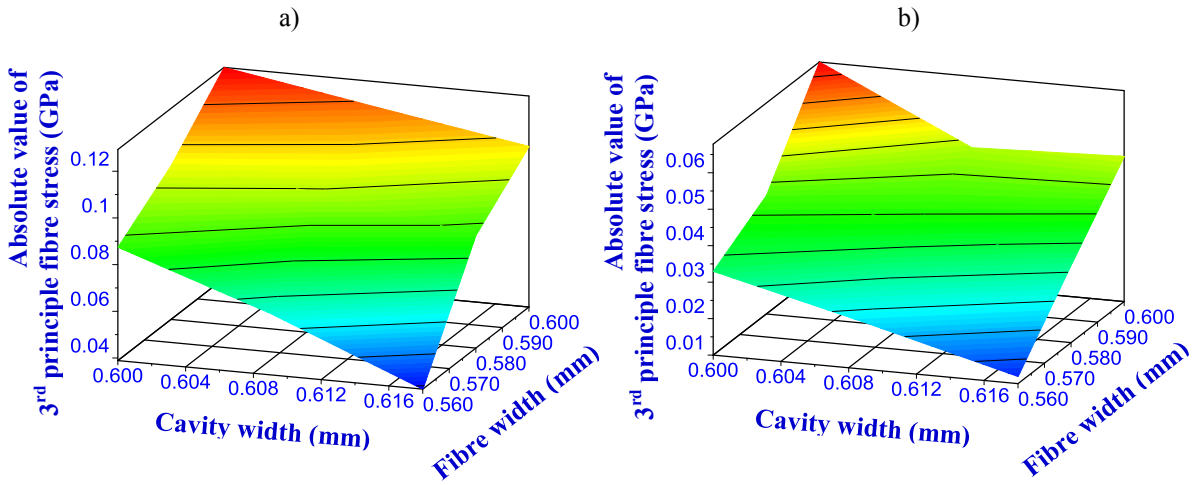

Figure 11: Distribution of absolute value of 3rd principle fibre stress in GPa dependent on channel width and fibre width, a) at pressure maxima, b) residual stresses after unloading

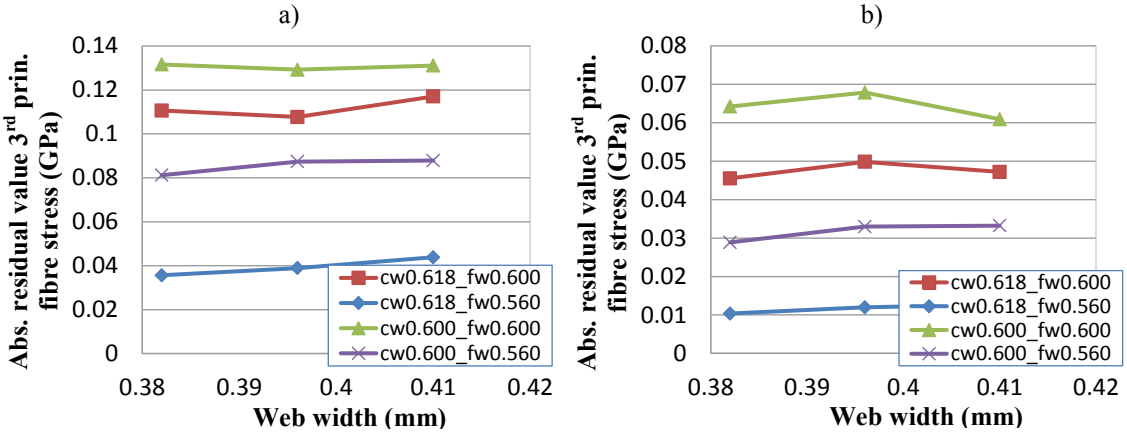

Figure 12: Absolute values of 3rd principle fibre stress in GPa dependent on web width, a) at pressure maxima, b) residual stresses after unloading

6 CONCLUSION

A new concept enables the structural integration of PZT fibres into aluminium sheets and thus the production of so-called piezo-metal modules. After the presentation of the production steps for piezo-metal modules, the main focus of the paper is on ensuring the functional reliability of the PZT fibre array transducers during the joining process as well as the adjustment of a defined preload via impedance spectroscopy. For this purpose, parallel interconnected PZT fibres and microstructured aluminium were prepared as test samples. Electrical impedance spectra are recorded during the joining process via the inherent sensor characteristics of the piezoceramic and finally evaluated. The impedance spectra of the interconnected fibres show a shift of the resonance point into higher frequencies as well as an attenuation of the signal. These findings enable the development of a novel monitoring method for the adjustment of a defined pretension and avoiding an overload.

The necessity of this new method is shown by a numerical study of the geometric process sensitivity. Already differing tolerances with a span of 60 µm result in a 200% increase in pressure with the same joining force. Further work is intended to secure statistically the results of the monitoring method. Additional, efforts are being done to minimize the manufacturing tolerances of the joining partners.

ACKNOWLEDGEMENT

This research is supported by the Deutsche Forschungsgemeinschaft (DFG) in context of the Collaborative Research Centre/Transregio 39 PT-PIESA, subprojects A02, A03 and B01.

REFERENCES

[1] Koszewnik, A. *The Optimal Vibration Control of the Plate Structure by using piezo-actuators.* 17th International Carpathian Control Conference (ICCC) (2016) 358-363

[2] Naveet, K. and Suresh, B. *Feasibility of energy harvesting from thin piezo patches via axial strain (d31) actuation mode.* Journal of Civil Structural Health Monitoring (2014) 1-15

[3] Glushkov, E.; Glushkova, N.; Lammering, R.; Eremin, A. and Neumann, M.N. *Lamb wave excitation and propagation in elastic plates with surface obstacles: proper choice of central frequencies*. Smart Materials and Structures, 20, (2011) 1-11

[4] Schubert, A; Wittstock, V.; Jahn, S.F.; Müller, B. and Müller, M. *Joining by forming of piezoceramic macro-fiber arrays within micro-structured surfaces of aluminum sheets*. Production Engineering Research and Development (2014) 195-205.

[5] Müller, M.; Müller, B.; Hensel, S.; Nestler, M.; Jahn, S.F.; Wittstock, V.; Schubert, A. and Drossel, W.-G. *Structural integration of PZT fibers in deep drawn sheet metal for material-integrated sensing and actuation*. Procedia Technology (2014) 659-668.

[6] Drossel, W.-G.; Schubert, A.; Putz, M.; Koriath, H.-J.; Wittstock, V.; Peter, S.; Hensel, S.; Nestler, M.; Jahn, S.F.; Müller, R.; Pierer, A.; Müller, B. and Schmidt, M. *Inherent process monitoring for piezoceramic transducer integration*, EUSPEN 16th International Conference & Exhibition, Nottingham (2016).

[7] Tilmans, H.A.C. *Equivalent circuit representation of electromechanical transducers: II. Distributed parameter systems*. Journal of Micromechanics and Microengineering 7 (1998) 285-309.

[8] Lesieutre, G. and Davis, C. *Can a coupling coefficient of a piezoelectric device be higher than those of its active material?*. Journal of Intelligent Material Systems and Structures 8 (1997) 859-867.

[9] DeAngelis, D.A. and Schulze, G.W. *Optimizing piezoelectric crystal preload in ultrasonic transducers.* 38th Annual Symposium of the Ultrasonic Industry Association (UIA), Canada (2009).

[10] Hosseini-Hashemi, S.; Es'haghi, M. and Rokni Damavandi Taher R.D., H. *An exact analytical solution for freely vibrating piezoelectric coupled circular/annular thick plates using Reddy plate theory.* Composite Structures (2010), 92(6): 1333-1351

Integration of Piezoceramic Composites in Aluminium Die Casting Structures and their Functional Characterization

Sebastian Rhein[a,*], Jonathan Wedler[b], Stefan Stein[c], Carolin Körner[b], Michael Schmidt[c], Alexander Michaelis[a,d], Sylvia Gebhardt[d]

[a] Dresden University of Technologies, Institute of Material Science, 01062 Dresden, Germany
e-mail: Sebastian.Rhein@ikts-extern.fraunhofer.de, web page: www.tu-dresden.de/ifww

[b] Friedrich-Alexander-University Erlangen-Nürnberg, Institute for Material Science, Chair of Metals Science and Technology, Martensstr. 5, 91058 Erlangen, Germany
e-mail: jonathan.wedler@fau.de, web page: www.ww.tf.fau.de

[c] Bayerisches Laserzentrum Erlangen, Konrad-Zuse-Straße 2-6, 91052 Erlangen, Germany
e-mail: s.stein@blz.org, web page: www.blz.org

[d] Fraunhofer Institute for Ceramic Technologies and Systems (IKTS), Winterbergstraße 28, 01277 Dresden, Germany
e-mail: Sylvia.Gebhardt@ikts.fraunhofer.de, web page: www.ikts.fraunhofer.de

ABSTRACT

Smart structures are using integrated sensors and actuators in combination with modified drive and control electronics for the active influence of dynamic structural characteristics, like noise control, vibration damping or structural health monitoring [1]. The direct integration of sensors and actuators into structural body parts possess some benefits concerning process efficiency and margin but demand in return resilient sensor-actuator modules, which can withstand the forming process. For integration into metal structures, electrical isolation against the matrix has to be solved. We developed a fully inorganic module consisting of piezoceramic plates (PZT) embedded in an LTCC (low temperature co-fired ceramic) multilayer [2] which could be successfully integrated into aluminium die casting parts for the first time. The LTCC/PZT modules are connected internally by screen-printed silver electrodes and pathways, and externally by a laser-based droplet joining method (LDJ) [3]. A hybrid support structure is used for the die casting process [4], in order to protect the braze joints and prevent drifting of the LTCC/PZT modules during melt immersion. The functionality of the embedded LTCC/PZT modules was determined by electro-mechanical methods like impedance analysis, ferroelectric hysteresis and deflection measurements. Permittivity and remnant polarization decreased slightly during the integrations steps: 1) laminating and 2) die casting. Measurement of deflection of a cantilever with integrated LTCC/PZT modules proved the actuator performance after die casting.

REFERENCES

[1] E. Garcia, “Smart structures and actuators: past, present, and future”, *Proc. SPIE **4698**, Smart Structures and Materials 2002: Industrial and Commercial Applications of Smart Structures Technologies*, pp. 1 (July 9, 2002), doi:10.1117/12.475054.

[2] M. Flössel et al. “Development of a Novel Sensor-Actuator-Module with Ceramic Multilayer Technology”, *J. Ceram. Sci. Tech.,* Vol. **1**, pp. 55–58, (2010), doi:10.4416/JCST2010-00010.

[3] S. Stein et al. “High Temperature Laser Based Drop on Demand Micro Joining of Thin Metallic Layers or Foils using Bronze Braze Preforms LAMP 2016”, *JLMN Journal of Laser Micro/Nanoengineering*, Vol. **11**, pp. 111–116, (2016), doi:10.2961/jlmn.2016.01.0021.

[4] M. Rübner et al. “Integration of Piezoceramic Modules into Die Castings - Procedure and Functionalities“, *Advances in Science and Technology*, Vol. **56**, pp. 170–175, (2008), doi:10.4028/www.scientific.net/AST.56.170.

VIII ECCOMAS Thematic Conference on Smart Structures and Materials
SMART 2017
A. Güemes, A. Benjeddou , J. Rodellar and Jinsong Leng (Eds)

INVESTIGATIONS ON LASER ASSISTED WIRE BONDING BY MEANS OF DROPLET BRAZING OF NOVEL THERMOPLAST-COMPATIBLE PIEZOCERAMIC MODULES

STEIN[*,‡], T. WEBER[†], A. WINKLER[†], M. SCHMIDT[*,‡,•] AND M. GUDE[†]

[*] Bayerisches Laserzentrum Erlangen (blz),
D-91052 Erlangen, Germany
Email: s.stein@blz.org

[†] Institute of Lightweight Engineering and Polymer Technology (ILK)
Technische Universität Dresden
D-01307 Dresden, Germany
Email: tony.weber@tu-dresden.de

[‡]Erlangen Graduate School in Advanced Optical Technologies (SAOT)
Friedrich-Alexander-Universität Erlangen-Nürnberg, 91052 Erlangen, Germany

[•] Institute of Photonic Technologies (LPT)
Friedrich-Alexander-Universität Erlangen-Nürnberg, 91052 Erlangen, Germany

Key words: smart structures, piezoceramic modules, laser brazing, wire bonding

Abstract. Active noise reduction, health monitoring and energy harvesting are some applications of piezo actuators, particularly in automotive and aeronautic industry [1].

Since piezoceramic modules are commonly soldered manually, a low reproducibility and high cycle times are the result, which is restricting a widespread application of such modules. Further, soldered joints do not withstand the temperatures occurring during the integration of actuators into e.g. polyphenylene sulfide (PPS) structures, which require processing temperatures of about 320 °C. Thus, a demand in developing a novel joining method arises, which has potential of automation and large scale production and further providing joints with high thermal stability.

In the presented work, a joining method is discussed, which is based on melting a spherical CuSn12 braze preform and is referred to as laser drop on demand brazing (LDB) for the application of joining novel thermoplastic compatible piezoceramic modules for integration in fibre-reinforced thermoplastic composites for high volume applications [2,3]. The paper is focusing on the diffusion processes introduced by the interaction between CuSn melt droplets and the Ag-electrode structure of the piezoceramic module. Furthermore different piezoceramic module layouts, with focus on the fusion zone, are investigated by means of digital image correlation due to the qualitative characterization of module performance.

1 INTRODUCTION

The integration of sensors or actuators into laminate lightweight structures offers high potential regarding lightweight design, by integrating several functionalities into one structure. Those so called adaptronic devices can be manufactured by integrating e.g. piezo actuators into the laminate lay-up of fibre reinforced plastics (FRP). This enables to provide functionalities like structural health monitoring, active vibration damping or sensor applications in one single structure. State of the art assembling process is the downstream attachment of such modules after the manufacturing process of the structural parts e.g. by gluing. Restrictions are process time, costs, and limitations in positioning accuracies as well as design restrictions preventing the placement of the actuator at the position of highest yield for the desired functionality. As a result, a direct integration of piezoelectric sensors and actuators during manufacturing of composite structures proposes significant advantages in comparison with the current state of the art and will be addressed in this work. Thus, this paper focuses on the process chain from manufacturing of thermoplastic piezo modules (TPMs) over electrical contacting of the TPM to its electromechanical characterisation. For electrical contacting, a laser droplet based joining method is applied, which is described in [4,5,6,7] The joining process is capable of joining Cu conductors with Ag-foils or solder pads with thicknesses below 20 µm, being able to prevent damaging foil, respectively electrode structure and substrate. Yet the joints can withstand significant temperatures, due to the solidus temperature of 830 °C and liquidus temperature of 1000 °C of the used CuSn12 filler material [8], which is exceeding the liquidus temperature of standard SAC-solders used in the electronics industry by a factor of 3.

2 MATERIALS AND METHODS

2.1 TPM DESIGN AND MANUFACTURING

In regard to fiber-reinforced thermoplastic composites, new piezoceramic module designs are required, since the processing temperatures of the used polymer matrix is increasing in recent years due to the widespread application of high performance polymers. Using for instance polyamide 6 as matrix material, processing temperatures above 240 °C are necessary for the production of composite components. Due to the allowed max. processing temperature of 130 °C for Macro Fiber Composites (MFC), commercially available modules will not withstand the processing temperatures for the manufacturing of fiber-reinforced thermoplastic composites [9]. As a consequence, novel thermoplastic compatible piezoceramic modules (TPMs) have been developed, which consist of two thermoplastic carrier films metalized with an electrode structure and a piezoelectric layer in the middle (see Fig. 1). Additionally, metallic foils are implemented, serving as electrode structures to be joined with Cu-wires in order to realize the electrical contact between the electrode structures and signal generators respectively sensors. Within this paper d_{31}-TPM are used to investigate different electrical contact layouts. This kind of module consists of a PZT-wafer as piezoelectric layer (see Fig. 1 a). In regard to a high volume production, a tailored manufacturing process for TPMs is developed. It bases on a roll-to-roll process (see Fig. 1 b).

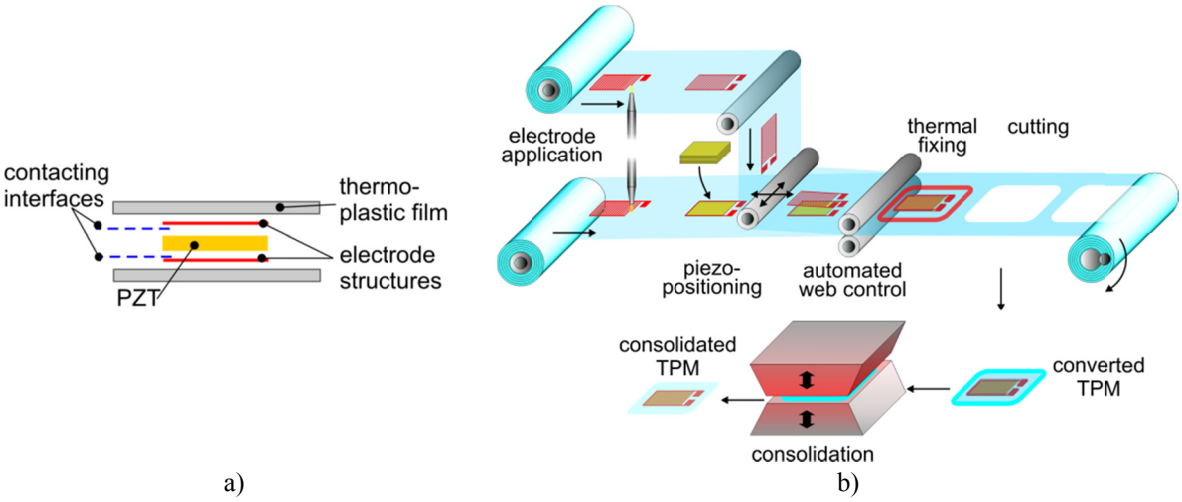

Fig. 1: Schematic of TPM, TPM manufacturing process

By applying this process chain, a continuous metallization of the carrier films and subsequent assembly of the TPM can be achieved, resulting in short cycle times. During the first step of manufacturing, the electrode structures are printed to the thermoplastic carrier film webs using screen printing techniques. Subsequently the ink is dried and the piezoelectric layer is inserted between the two webs. The electrode structures are aligned congruently to each other, which is controlled by an optical inspection system. After the assembly of the thermoplastic films and piezoelectric layer, the TPMs are fixed thermally, cut out and transferred into a hot press for subsequent consolidation by applying temperature and pressure. In order to achieve material homogenous integration of the TPMs into structural composite parts, a processing into PA6 composite structures would require consolidation temperatures of 250 °C to 270 °C and pressures of 5 bars. Further, an extension of the material range towards higher melting polymers e.g. polyphenylene sulfide (PPS) requires significantly higher processing temperatures of about 320 °C. Those processing parameters cannot be withstood by standard Sn96.5Ag3Cu0.5 lead free solders, due to the melting temperature of 219 °C [10]. Thus the modules will be electrically contacted by a laser droplet based brazing process (LDB) and polarized by applying an electric field in a final processing step to ensure polarization of the piezoceramics.

2.2 Electrical joining via laser droplet brazing (LDB)

The joining of the TPMs electrode structure to a Cu-wire is carried out using a laser assisted wire bonding process, referred to as laser droplet brazing, which is based on the melting of spherical CuSn12 braze preform using a laser pulse as described in [4,6,7]. The LDB process can be divided into four different phases. First the braze preform is introduced into a ceramic capillary. Subsequently the preform is irradiated by a laser pulse, resulting in its melting and ejection from the capillary by inert gas overpressure. After a flight phase, the molten droplet wets electrode structure of the piezo ceramic and Cu-wire, resulting in a firm joint (Fig. 2).

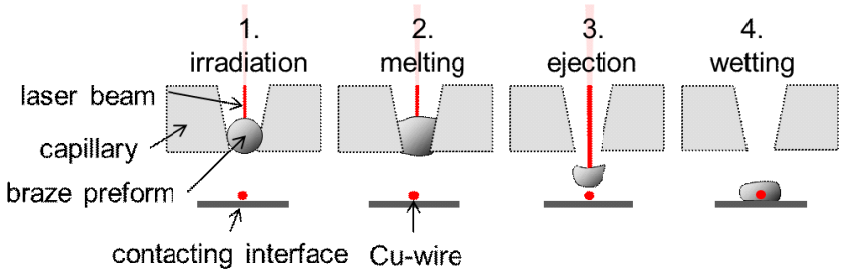

Fig. 2: Process phases of the laser droplet brazing process: 1. Irradiation of the braze preform with a laser pulse, 2. Wetting of capillary with braze melt, 3. Braze ejection by gas overpressure, 3. Metallurgic bond of Cu-conductor and electrode after wetting and solidification of the braze droplet

For the laser droplet joining process, a fiber laser with a wavelength of 1070 nm is used. Further, a nitrogen feed, which is attached to a pressure regulator, supplies a defined nitrogen overpressure, which is necessary to eject the braze preform, since the surface tension of the braze melt exceeds the force of gravity inside the capillary [11]. Fig. 3 shows a sketch of the experimental setup.

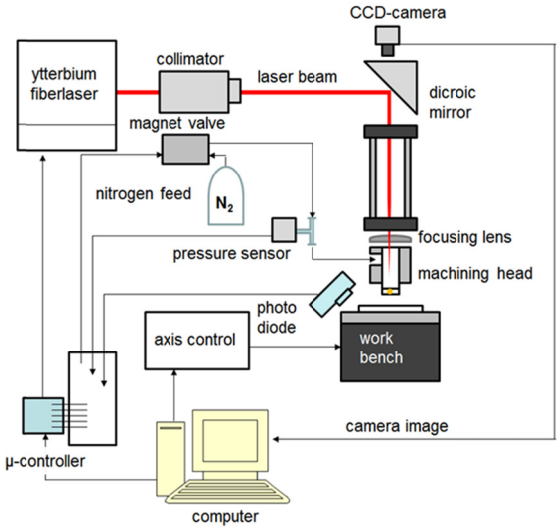

Fig. 3: Schematic of experimental setup [7]

3 METHODS AND EXPERIMENTAL INVESTIGATIONS

3.1 TPM manufacturing

Due to the aspects of joining with LDB processes TPMs with different electrode configurations were investigated. Therefore, TPM with metallic foils, protruding the thermoplastic carrier films were manufactured, which provide a free metal surface, suitable for the LDB process (see Fig. 4 b). In addition, TPMs with cutouts in the thermoplastic carrier films directly above the embedded conducting foils (see Fig. 4 a) were manufactured. Thus, the influence of soldering positions outside of the piezoceramic module and directly above the ceramic layer according to different thicknesses of the contact interface is investigated.

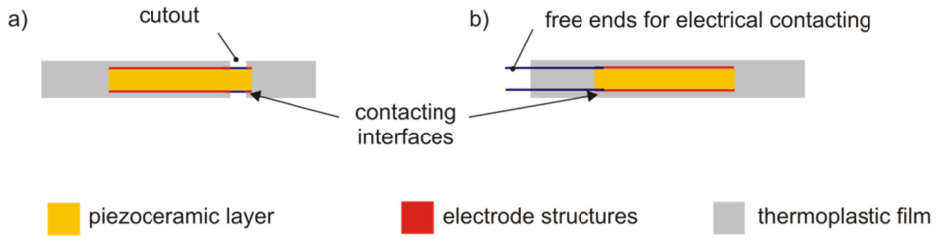

Fig. 4: Investigated configuration of contacting areas: a) TPM with cutout, b) TPM with free contacting foils

In regard to the brazeability, different foil materials and dimensions are used. The selected configurations consist of silver foils (Goodfellow Cambridge Limited, type AG000250 and AG000280) with a thickness of 0.15 and 0.35 µm. Table 1 shows the thicknesses and configurations of the used foil materials. The cutouts are generated by a punching tool with a diameter of 3 mm before the TPM is being laminated. During the assembly of the TPM, the silver-foils are positioned between thermoplastic carrier film and ceramic layer and the modules are consolidated in a laboratory hot press by applying 250 °C and a pressure of 5 bars for a dwell time of 10 s. Fig. 5 shows the details of the module configurations.

Table 1:-Specimen designation

Interface material	Inter-face	Free/Cutout	Thick-ness in mm
AgF-0.035	Silver-foil	Free	0.035
AgF-0.015	Silver-foil	Free	0.015
AgC-0.035	Silver-foil	Cutout	0.035
AgC-0.015	Silver-foil	Cutout	0.015

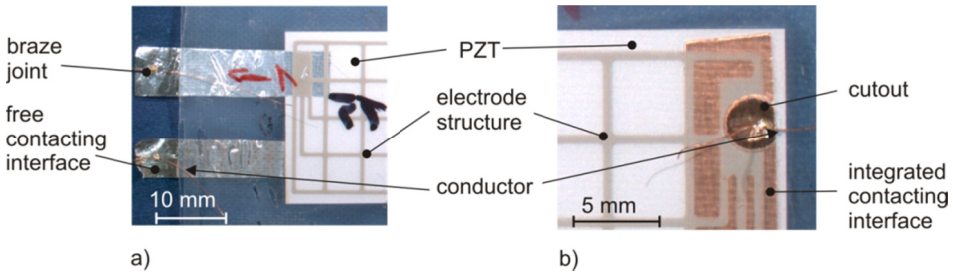

Fig. 5: Exemplary details of investigated TPM configurations: a) TPM with free contacting foils, b)TPM with cutout

3.2 Laser drop on demand joining process

The overpressure inside the machining head is being monitored in situ by a pressure sensor. A coaxially aligned CCD-camera enables a precise alignment of machining head to the Cu-conductor respectively the metallisation. In addition, the CCD can be used for optical monitoring and evaluation of the capillary by image processing algorithms as described in [7]. Additionally, a photodiode (PD) directed at the joint position enables the determination of the exact time of braze detachment by detecting scattered laser radiation on the joining area enabling an interruption of the laser pulse after droplet detachment, which is crucial to avoid substrate perforations. A maximum optical output power of 200 W and a raw beam diameter

of 6.9 mm is used. The raw beam is being focused by a lens of focal length f = 50 mm to form a laser spot of $2w_0$ = 10.9 µm.

3.3 Long-term thermal cycle test

Temperature changes can result in mechanical stress on the electrical joints due to a mismatch of thermal expansion (CTE mismatch) of the used braze material, the conductor and the conducting foils of the TPM. This CTE mismatch may cause cracks in the contact points and thus a failure of the joint. By using a climate simulation chamber, thermal cycle tests were performed to investigate the resistance of the brazing joints during the application of thermal loads. The joints were exposed to periodic temperature fluctuations in accordance with the standard ISO 16750-4. The individual joints consisting of the TPMs conducting foil, Cu-conductor and the connecting filler material were exposed to temperatures ranging from -40 to 150 °C in accordance to industrial standard DIN EN 60749-6 for a period of 10 days [12]. Table 2 shows the time temperature interval applied on the specimens:

Table 2:-Time temperature profile applied according to DIN EN 60749-6

time [min]	0	60	150	210	300	410	480
temp [°C]	20	-40	-40	20	150	150	20

This method enables the evaluation of material failure caused by CTE mismatch and to quantify the influence of temperature cycles on the diffusion between Ag-foil and the braze filler material. The magnitude of occurring diffusion can be evaluated by EDX element analysis (see chapter 4.1).

3.4 Diffusion

Diffusion is defined as mass transport by atom movement and can be described by the diffusion equation, which is given here for the two dimensional case:

$$\frac{\delta C}{\delta t} = D\frac{\delta C^2}{\delta x^2} \tag{1}$$

One solution of the diffusion equation (eq. 1) is Fick's second law, which will be used in the scope of this paper to evaluate the magnitude of occurring diffusion between Ag filler material and the Cu based braze during the laser drop on demand joining process. The formula used for describing unidimensional concentration gradients in the scope of this paper is proposed by [13]and [14] in slightly modified form:

$$C(x,t) = C_2 + \frac{C_1 + C_2}{2}\left[1 \pm erf\left(\frac{x}{2\sqrt{D \cdot t}}\right)\right] \tag{2}$$

Whereas C_1 is the concentration in wt% of element 1, which is in the described case Ag of the electrode structure. C_2 is the concentration of Cu in wt%, x is the coordinate where the measurement is carried out along the x-axis, respectively perpendicular to the interface between braze material and Ag-electrode structure of the TPM. Further, D is the diffusion coefficient and t the residence time.

Whereas the error function is a mathematic standard function defined as:

$$erf(z) = \frac{2}{\sqrt{\pi}} \int_0^z \exp(-\eta^2) \quad d\eta \tag{3}$$

Eq. 2 is used for fitting the element distribution in the joining area in order to acquire the diffusion length which is describing the magnitude of occurring diffusion during joining and calculated according to Eq. 2 as supposed by [15]

$$l_d = 2\sqrt{D \cdot t} \tag{4}$$

In order to evaluate the concentration distribution in the joining area, the element distribution has been measured using EDX analysis. In the scope of the measurements the elements Ar and Au have not been taken into consideration for evaluation during EDX analysis, since the presence of Ar is unlikely, yet large amounts of Ar would be detected and result in errors due to its electron shell configuration which leads to a superposition of Ar and Ag spectra during measurement. Since sputtered gold layers have been applied on each specimen in order to increase the electrical conductivity the element Au has been neglected in the measurements since the sputtered Au layers can be considered uniform in the area of interest of 50 x 50 µm. It can be assumed, that the diffusion length is a function of the Ag-foil thickness, since the foil thickness determines the time temperature evolution of the joining process, respectively the heat dissipation during cooling. A higher foil thickness would result in in faster droplet solidification, which would reduce the magnitude of occurring diffusion. In order to be able to quantify the influence of the foil thickness on the diffusion length, joints on 15 µm Ag-foil and 35 µm Ag-foil have been analysed.

3.5 Functional tests of laser joined TPM

In order to evaluate functionality of the manufactured TPMs, said were polarized for 5 minutes applying an electric field of 2 kV/mm. After 24 hours, the specimens were investigated regarding the strain hysteresis by a saw tooth excitation signal. Therefore, an input voltage of 0 V to 360 V and a frequency of 0.01 Hz was used, which is generated by a function generator (Agilent 33220A) and amplified by a high voltage power amplifier (Model 2205, TREK, INC.; amplification factor 50 V/V). Due to the changing electric field, the deformation of the piezoceramic layer of the TPM can be detected using high resolution optical metrology. In the presented paper contactless stereoscopic 3-D deformation measurements using a ARAMIS system (GOM GmbH) are used to observe the deformation of the TPM induced by the piezoelectric effect. . The specimens were coated by a stochastic pattern of black and white pixels to enable an evaluation of deformation via image processing algorithms. By the use of two cameras, the position and deformation of characteristic patterns (facets) are detected. Due to the fragmentation of the points of interest (POIs) of the facets, the deformation behaviour of the specimen according to applied loads (voltage) is measured by stereoscopic reconstruction of the images. Thus a 3-D deformation of the specimen can be calculated by the ARAMIS Software, which allows characterizing the TPM by a voltage-strain curve. Figure 6 a) shows the test set-up for the voltage-strain analysis of the TPM.

4 RESULTS AND DISCUSSION

4.1 Experimental investigation of diffusion at the filler/electrode interface during drop on demand joining

Due to the novel nature of the joining process it is vivid to understand how the electrode constellation influences the occurring diffusion during joining. In earlier investigations a significant amount of silver was found to diffuse into the CuSn braze material [7]. In order to quantify the occurring diffusion cross sections of the joining interface between Ag-electrode and CuSn-braze have been investigated by means of EDX measurements as described in chapter 3.4. Fig. 6 b) shows a SEM-BSE-image of a polished cross section at the interface of Ag-electrode and CuSn filler (P_{Laser} = 145 W; $p_{Nitrogen}$ 120 mbar). All elements were evaluated in such a way that the individual share of each element concentration adds up to 100 wt%. In order to quantify diffusion of Ag into the Cu-based filler material and vice versa, the element distribution perpendicularly to the joining interface has been evaluated using EDX line scans on the polished cross sections indicated by the dashed lines in Fig. 6 b).

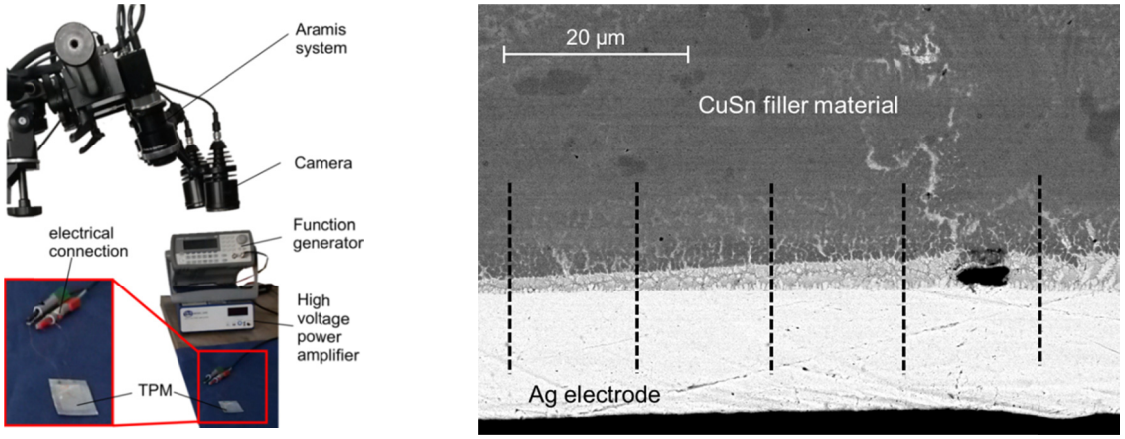

a) Test set-up for the stereoscopic measurements of the TPM strain-hysteresis

b) SEM-BSE-image of a polished cross section

Fig. 6: Test set-up for measuring the voltage-strain curve (a) and image of a polished cross section (b)

In Fig. 7 a) the discrete measured values results of a single line scan with equation 4 fitted to it using the Levenberg–Marquardt algorithm (Fig. 7 b) is shown. As a degree of freedom, the diffusion length was used for optimization.

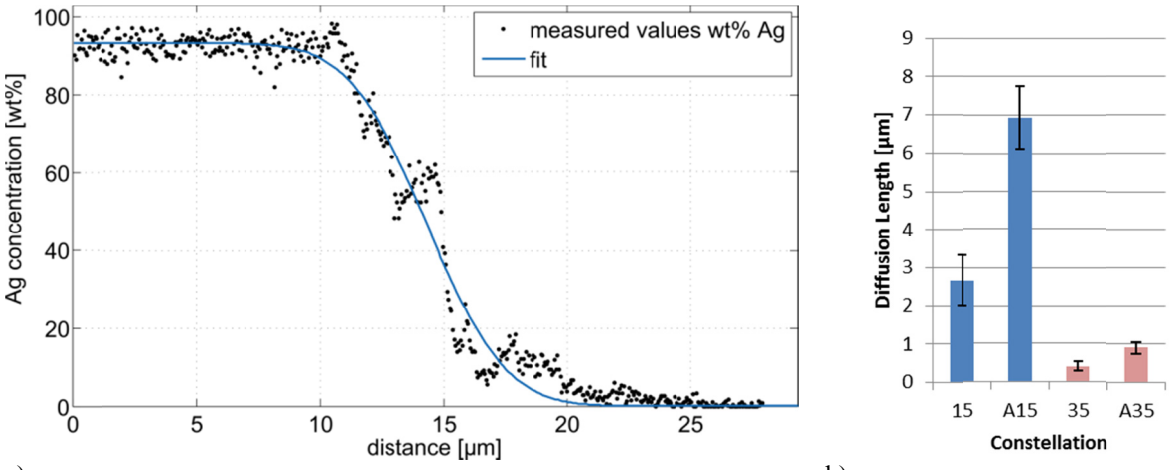

a) b)

Fig. 7: Discrete measured Ag-Values at the joining interface together (a). For fitting Eq 2 was used using the sum of least squares fitting method, giving the diffusion length as a degree of freedom (b).

The described approach enables the determination of the diffusion lengths for different electrode structure constellations. In order to obtain results with statistical significance, for each interface constellation, five line scans have been evaluated in the described way. Further, the joints have been evaluated in the described manner before and after thermal cycle tests in order to do statements regarding the influence of thermal cycles during the module lifetime in respect to the degeneration of the joints. Also the standard deviation of the measured values in respect to the fit has been evaluated in order to enable a statement regarding measurement reliability. In table 3, the fitting results of the four described constellations are displayed.

Table 3:-Diffusion length in dependency of the different joining constellations

	15 µm Ag		15 µm Ag after thermal aging		35 µm Ag		35 µm Ag after thermal aging	
Sample	σ_{fit}	l_{Diff}	σ_{fit}	l_{Diff}	σ_{fit}	l_{Diff}	σ_{fit}	l_{Diff}
	[wt%]	*[µm]*	*[wt%]*	*[µm]*	*[wt%]*	*[µm]*	*[wt%]*	*[µm]*
1	3.88	2.80	7.1	6.83	3.02	0.33	3.02	0.84
2	3.58	1.68	6.79	5.88	4.61	0.63	4.61	1.01
3	3.49	2.17	6.65	6.52	2.47	0.35	2.47	0.75
4	4.79	3.14	8.15	8.38	2.65	0.32	2.65	1.13
5	5.09	3.54	7.62	7.03	2.42	0.41	2.42	0.81
mean	**4.17**	**2.67**	**7.26**	**6.93**	**3.04**	**0.41**	**3.04**	**0.91**
σ	**0.65**	**0.67**	**0.55**	**0.82**	**0.82**	**0.12**	**0.82**	**0.14**

It can be stated, that the diffusion length can be used to describe the magnitude of occurring diffusion and thus quantify the metallurgical bond quality. The diffusion length is 6.5 times larger for 15 µm electrode structures than for 35 µm electrode structures before thermal cycle test. After thermal cycling the effects increases, exhibiting a 7.62 times higher diffusion length for the 15 µm Ag-foil. Thus it can be stated, that thinner electrode structures favour the formation of metallurgical bonds. This must be accounted to the larger amount of

heat accumulation in the 15 µm Ag electrode structure whereas the 35 µm Ag structure conducts the heat of the droplet better, resulting in faster solidification and thus reducing the occurring diffusion. In addition, applying periodic temperature changes did increase the diffusion lengths, however no degeneration of the joints have been observed, regardless the foil thickness. Yet, especially for the 15 µm Ag foil a significantly increased diffusion length after thermal cycle test was observed (see Fig. 8).

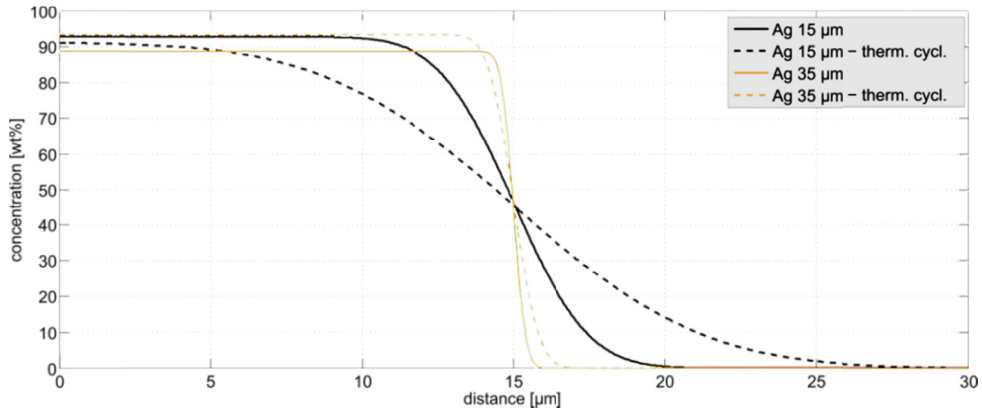

Fig. 8: Mean lines of fit for the carried out line scans at the interface of Ag-foil and CuSn12 braze on a 15 µm Ag-foil (black) and 35 µm Ag-foil (orange) without thermal cycling (solid) and after thermal cycling (dotted)

4.2 Functional test

In order to prove the functionality of the manufactured TPMs a stereoscopic analysis of voltage induced strain has been carried out in the scope of this paper. The designation of the specimens is listed in Table 1. Fig. 9 shows the determined voltage-strains behaviour of the investigated configurations in x- and y-direction. The optical strain analysis of the TPM indicates slight variations in deformation behaviour for different TPM configurations. Due to an improved clarity one characteristic hysteresis per configuration is shown in voltage-strain diagram (Fig. 9). It can be caused that there is no relevant influence by the different bonding methods on a static stimulation (0.1 Hz) of the TPM.

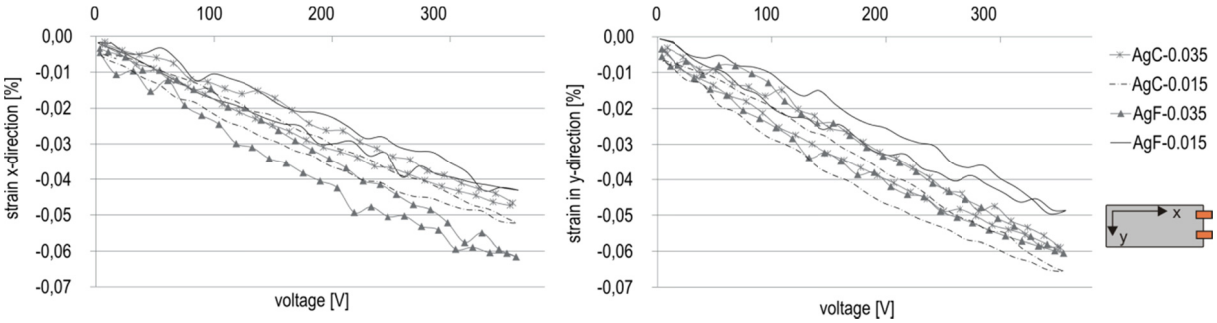

Fig. 9: Strain hysteresis the investigated TPM for the strain in x- and y-direction

By exploiting the d_{31}-effect of the TPM, a homogeneous allocation of the in plane strain results. Differences between the configurations can be caused by deviations in the PZT material. The silver foils enable only a loose contact, caused by external pressure due to the

embedding in the thermoplastic carrier films of the TPM. The differences between the configurations “free” or “cutout” are not significant. In regard to the relatively high deviations between the investigated specimens, statistical investigations are planned for future work to determine the influences of material deviations and the joining method. Furthermore a dynamic stimulation is necessary to characterize the bonding quality under realistic operational scenarios.

5 CONCLUSION

In the scope of this paper, a manufacturing process of TPMs has been introduced, which is capable of material homogeneous integration of piezoelectric actuators into CFRP structural parts and thus enabling functionalities like structural health monitoring, energy harvesting and sensor-/ actuator operations of lightweight structures. Further, an extension of the material range towards high performance polymers e.g. polyphenylene sulfide (PPS) was achieved, which requires significantly higher processing temperatures of about 320 °C. Thus a novel contacting method was developed to substitute standard soldering, which is restricted to process temperatures below 230 °C. The laser drop on demand joining process was proven to be suitable to withstand the occurring temperatures and pressures during manufacturing of PPS TPMs. Further, it was shown, that the electrode structure constellation of the TPM is crucial for metallurgic bonding between electrode and Cu-wire. In order to do a statement regarding resistance of the generated joints to cyclic thermal loads, the joints have been exposed to thermal loads according to industrial standard ISO 16750-4 for 20 days (corresponding to 60 cycles) in a climate simulation chamber. Except for a slight growth of the diffusion zone between filler material and Ag-electrode structure, no degenerations of the joint such as cracks or delamination could be detected which can be attributed to the ductile behaviour of the foil, which prevents stresses induced by CTE mismatch.

Due to the results of the functional test no relevant quality difference between the bonding configurations could be measured. Thus there is a need of extended investigations with help of dynamic stimulation to characterize the bonding configurations under realistic operational scenarios.

6 ACKNOWLEDGEMENT

This research is supported by the Deutsche Forschungsgemeinschaft (DFG) in context of the Collaborative Research Centre/Transregio 39 PT-PIESA, subproject A04 and A05. In addition, the authors gratefully acknowledge cooperation with the Erlangen Graduate School in Advanced Optical Technologies (SAOT) by the German Research Foundation (DFG) in the framework of the German excellence initiative.

REFERENCES

[1] Williams R. B., Park G., Inman D. J. and Wilkie W. K., “ An overview of composite actuators with piezoceramic fibers”, *Proceedings of SPIE, the International Society for Optical Engineering* 4753, pp. 421 – 427, (2002).

[2] Weber T., Gude M, Kastner T., "Experimental and Numerical Studies on Integration Thermoplastic Composite Compatible Piezoelectric Ceramics for Actuatory Application of Cylindrical Hollow Structures", *Materials Science Forum*, Vols. 825-826, pp. 556-562, (2015).

[3] Quentin, U.; Heberle, J.; Held, C.; Schmidt, M.: Laser Droplet Brazing for Electrical Contacting of Composite Materials with Integrated Active Elements, *Procedia Materials Science 2*, pp. 181–88, (2013).

[4] Stein, S.; Heberle, J.; Gürtler, F. J.; Cvecek, K.; Roth, S.; Schmidt, M.: Influences of Nozzle Material on Laser Droplet Brazing Joints with Cu89Sn11 Preforms. 8th International Conference on Laser Assisted Net Shape Engineering LANE 2014. *Physics Procedia* (2014) 56, S. 709–19.

[5] Quentin, U.; Heberle, J.; Held, C.; Schmidt, M.: Laser Droplet Brazing for Electrical Contacting of Composite Materials with Integrated Active Elements. *Procedia Materials Science 2* (2013), S. 181–88.

[6] Stein, S. Heberle, J.; Hugger, F.; Roth, S.; Schmidt, M.: Düsenbasiertes Laserstrahl-Löten mit Formteilen zur hochtemperaturfesten Kontaktierung piezokeramischer Substrate. LEF 2014. *Laser in der Elektronikproduktion & Feinwerktechnik Tagungsband: LEF 2014*.

[7] Stein Stefan; Johannes Heberle; Michael Suchy; Felix Tenner; Florian Hugger; Stephan Roth; Michael Schmidt: High Temperature Laser Based Drop on Demand Micro Joining of Thin Metallic Layers or Foils using Bronze Braze Preforms. LAMP 2016. *JLMN Journal of Laser Micro/Nanoengineering 11* (2016) 1, S. 111–16.

[8] Deutsches Kupfer-Institut Berlin, West: DKI Werkstoff-Datenblätter - CuSn12.

[9] Smart Material Macro Fiber Composite. URL: http://www.smart-material.com/MFC-product-main.html. Abrufdatum 14.07.2015.

[10] Albert, F.; Pfeiffer, C.; Michael Schmidt; Manfred Geiger; Markus Flössel; Alexander Michaelis: Laser Soldering and Laser Droplet Joining for Mechanical and Electrical Contacting of LTCC/PZT Laminates. *JLMN-Journal of Laser Micro/Nanoengineering Vol. 6* (2011) Vol. 6 No. 1.

[11] Jeromen, A.; Held, C.; Govekar, E.; Roth, S.; Schmidt, M.: Modelling of droplet detachment in the laser droplet brazing process. *Journal of Materials Processing Technology 214* (2014) 4, S. 737–49.

[12] Spraul, M.: Lebensdauerprognosen für gelötete Bauteile mit Zinn-Blei und Zinn-Silber-Kupfer Lot für Temperaturwechselprüfungen 2007.

[13] Oettel, H.; Schumann, H.: Metallografie. Mit einer Einführung in die Keramografie, 15., überarb. und erw. Aufl. Weinheim 2011.

[14] Sarafianos, N.: An analytical method of calculating variable diffusion coefficients. *Journal of Materials Science 21* (1986) 7, S. 2283–88.

[15] Bird, R. B.; Stewart, W. E.; Lightfoot, E. N.: Transport phenomena, Rev. 2nd ed. New York 2007.

VIII ECCOMAS Thematic Conference on Smart Structures and Materials
SMART 2017
A. Güemes, A. Benjeddou, J. Rodellar and J. Leng (Eds)

NON-DESTRUCTIVE CHARACTERIZATION OF FIBER-REINFORCED THERMOPLASTIC COMPONENTS WITH EMBEDDED PIEZOCERAMIC MODULES

ANJA WINKLER*, MICHAEL WUEST†, STEFAN J. RUPITSCH† AND NIELS MODLER*

*Institute of Lightweight Engineering and Polymer Technology (ILK)
Technische Universitaet Dresden
D-01307 Dresden, Germany
e-mail: anja.winkler@tu-dresden.de, web page: http://www.tu-dresden.de/mw/ilk

† Chair of Sensor Technology
Friedrich-Alexander-Universitaet Erlangen-Nuernberg
D-91052 Erlangen, Germany
e-mail: michael.wuest@fau.de - Web page: http://www.lse.fau.de

Key words: Piezoceramic Module, Smart Structures, Ultrasonic Testing, Computed Tomography, Fiber-Reinforced Polymer

Abstract. The contribution presents a manufacturing technology for the integration of piezoceramic modules into fiber-reinforced thermoplastic parts ready for series production. In regard to the assessment of the integration quality and the damage of the piezoceramic modules non-destructive testing methods like computed tomography and ultrasonic microscopy were used. In the case of acoustic microscopy, a novel 3D-scanning measuring system is introduced, which enables the scanning of curved surface structures. Commercial acoustic microscopes are only designed for investigations of plane surfaces. In order to achieve sufficient results in the image, the ultrasonic transducer axis has to be orientated orthogonally to the specimen surface for every scan position [12]. For this purpose, a 6DoF hexapod robot system is used to perform a matched angle adjustment. Acoustic microscopy is suitable for high-density materials and provides 3D data of the investigated area. The results show that a precise detection of cracks in the piezoceramic layers, trapped air between the fiber-reinforced composite and the piezoceramic modules as well as the localization of conductive paths and electrodes are possible and the ultrasound imaging data show a good accordance to those of the computed tomography.

1 INTRODUCTION

Fiber-reinforced polymers (FRP) show a high potential for innovative function-integrating lightweight constructions. In the case of textile-reinforced composites the textile structure, the layered build-up, and the associated specific production processes offer the possibility for the

integration of functional elements, like sensors, actuators or even electronic circuit boards [1, 2, 3]. Such components can be used for example for ultrasonic based radiation or measuring tasks, condition monitoring or structural health monitoring [4, 5].

The integration of the functional elements, e. g. piezoceramic modules, strain gauges, temperature sensors, can be realized already in the manufacturing process of the composite structures. Thus, time consuming additional processing steps can be avoided and the elements can be embedded inside the structure. Additionally, the influence of environmental conditions and manipulation from outside to the functional elements will be reduced. Process conditions for the manufacturing of thermoset composite structures are usually suitable for the integration of a large number of functional elements [5, 14]. By the utilization of thermoplastic matrices in composite structures, the integration of additional elements becomes more difficult. The processing temperatures and pressures are even higher than those for thermoset composites [8, 4]. Thus, adapted functional elements and an adjustment of the manufacturing processes is necessary for a non-destructive embedding of functional elements into composite structures with thermoplastic matrices.

In this context, the characterization of such function integrative structures is necessary for the evaluation of the integration quality, the determination of damages and the derivation of the elements performance. Besides destructive methods like microscopic analysis, non-destructive characterization methods like computed tomography and ultrasonic scanning methods are common. Due to the use of piezoceramic material (lead zirconium titanate – PZT), which shows a very high attenuation of X-rays, the computed tomography leads often to unsufficient resolved images. For a spatially resolved representation of the embedded functional elements and the surrounding FRP suitable testing methods have to be evaluated. Therefore, three non-destructive testing methods, two dimensional radiography, computed tomography, and acoustic microscopy were investigated and evaluated in regard to damage detection and spatial resolution at selected specimen.

2 FIBER-REINFORCED THERMOPLASTIC COMPOSITES WITH EMBEDDED PIEZOCERAMIC-MODULES

A major precondition for a series capable integration of piezoceramic modules into fiber-reinforced composites with thermoplastic matrices is a new generation of modules. These modules will not be damaged by the relatively high processing temperatures, which are necessary to melt the thermoplastic matrix of the composites. So-called thermoplastic compatible piezoceramic modules (TPM) enable a material homogeneous integration of piezoceramic transducers into fiber-reinforced composites [6, 7]. They consist of a piezoceramic functional layer in the middle and two carrier layers made of thermoplastic films, which are metallized with a surfacial or interdigitated electrode (see figure 1 a).

In regard to a precise and simple positioning of the TPM in the composite lay-up, the use of pre-assembled thermoplastic carrier foils, which contain the TPM and conductive paths (so-called ePreforms) are advantageous (see figure 1 b) [15]. For the realization of a material homogeneous embedding the thermoplastic materials of the TPM carrier films, the ePreform, and the matrix of the FRP have to be identical. This enables a melting of these components by an adapted hot pressing or autoclave process to one fiber-reinforced composite structure (see

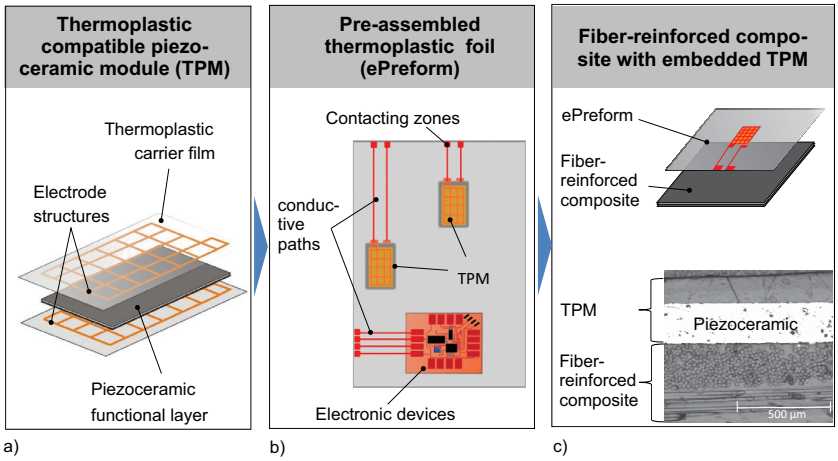

Figure 1: Schematic of a thermoplastic compatible piezoceramic module (TPM), ePreform and FRP with embedded TPM

figure 1 c). In regard to a manufacturing capable for series production an adapted thermoforming process is developed.

3 MANUFACTURING TECHNOLOGY

Thermoplastic composites reinforced with textile or endless fibers are often processed by thermoforming processes of semi-finished parts, so-called organic sheets. In regard to the integration of functional elements, these process variations offer several advantages. Pressing tools for thermoforming are often open, so that conductors can be lead outside of the mold. Furthermore, the organic sheets – preconsolidated fiber-reinforced thermoplastic composite plates – are melted in a separated preheating station. Thus, the functional elements can be inserted even in the pressing mold into the composite build-up. Due to that, long dwell times at higher temperatures for the functional elements are not necessary, which leads to less failures of the elements. The pressing pressures are also relatively low compared to injection molding or film-stacking processes. Figure 2 shows a conceptual schema of the developed thermoforming process for thermoplastic FRP with integrated TPM. The ePreform, consisting of a thermoplastic foil made of a matrix-identical thermoplastic material which is assembled with TPM and conductors, is fixed in a stentering frame and transferred into the mold. Simultaneously the composite build-up is stacked in the organic sheet stentering frame (OSF) and transferred into the preheating station. After the thermoplastic matrix is melt, the OSF is also put in the mold and the press will close and melt the composite build-up and the ePreform with applied TPM together. During this step an online polarisation of the piezoceramic elements takes place. Thereby, a high-voltage electrical field – in general field strengths of 2 kV/mm are used – up to a dwell time of 30 s is applied to the TPM, so that an active FRP component is produced.

For the investigations curved active FRP specimen made of a polyamide 6 matrix and glass fiber-reinforcement (TEPEX®102-RG600(x)/47 %, Bond Laminates GmbH) with surfacially embedded TPM are chosen (see figure 3). The curvature of the samples is 250 mm. They show different damages in accordance to different pressures in the thermoforming process.

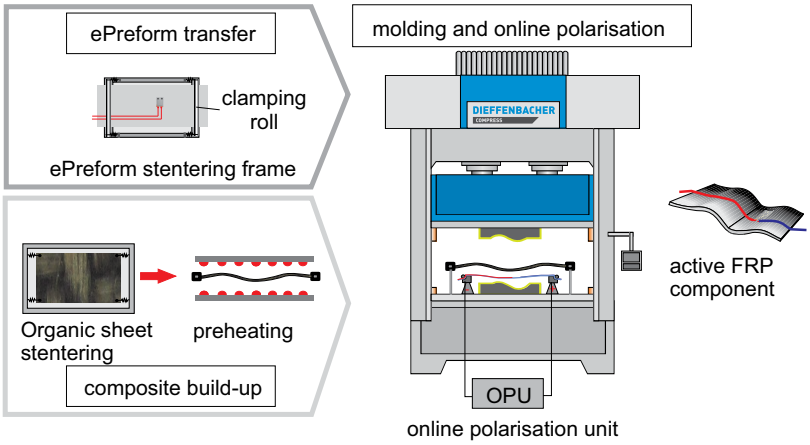

Figure 2: Schematic of an adapted thermoforming process for the integration of TPM into FRP with thermoplastic matrices

Table 1: example of the construction of one table

Specimen number	74	76	91
Pressure in MPa	4.55	0.57	4.55
Mold temperature in °C	100	100	60
Preheating temperature of the organic sheet in °C		270	

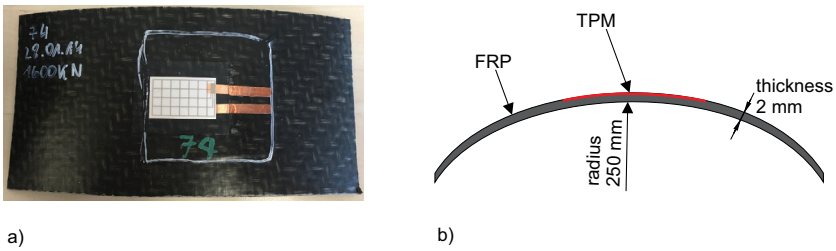

Figure 3: Exemplary shape of test specimen: a) photo of specimen number 74, b) schematic specimen geometry

4 NON-DESTRUCTIVE TESTING

The selected samples show typical failures of the piezoceramic (TPM) and in the connection of the TPM to the composite, like trapped air, cracks in the ceramic layer, and inhomogenities in the embedding. For the non-destructive testing conventional radiography (2D), computed tomography and an adapted device for 3D scanning acoustic microscopy were used.

4.1 Conventional radiography and computed tomography

Radiography and computed tomography (CT) are non-destructive test methods, which can be utilized for the examination of inner structures and defects. Due to the fact that fiber-reinforced composites show a very complex build-up and difficult failure behavior, these two methods are outstanding for the determination of the material or parts condition. X-ray imaging is based on the absorption properties of the investigated material. High-density materials show high absorptions in the resulting image. After the irradiation of the sample the X-radiation shows the energy J_1, which can be determined by the input energy J_0, the sample thickness h and the attenuation coefficient μ which depends on the order number and the density of the sample material [13]:

$$J_1 = J_0 e^{-\mu h} \tag{1}$$

In the case of conventional radiography a X-ray image is generated, which enables only a 2D illustration of the sample in general in thickness direction. The computed tomography does not provide a flat image, but a spatial image of the examined sample. For this purpose, a series of two-dimensional images is produced, whilst the sample is incrementally rotated by 360° in several hundred steps using a positioning unit. Figure 4 shows schematically the experimental setup for the investigation of samples by cone-beam CT. The radiation emitted by the X-ray tube is partially transmitted through the sample and the residual intensity is measured with a detector. After that, the resulting signal values can be used for a gray scale coded image. Subsequently, the three-dimensional sample geometry can be reconstructed out of the imaging data. For the investigation of the failure pattern of the selected samples the CT system phoenix V|tome|x-L 450 (General Electric) is used.

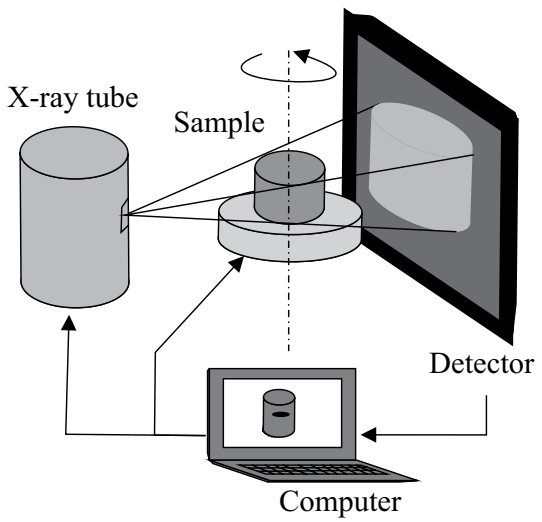

Figure 4: Schematic of computed tomography

4.2 3D scanning acoustic microscopy

Acoustic microscopy is often exploited for NDT in chip technology. Common acoustic microscopes utilize the so-called pulse-echo mode for data acquistion, i. e., the system collects reflections from boundaries between different materials [9]. The received echo data can be converted into a 3D image dataset. Acoustic microscopes normally consist of an ultrasonic transducer with a focusing lens and two linear stages, which move the transducer in a meandering pattern in the lateral plane [10]. The main disadvantage of conventional microscopes is, however, that they can not be applied to investigate curved surfaces. In case of curved surfaces, the incident sound wave should be orientated orthogonally to the surface in each scan position [11]. Otherwise, inner reflections may not be detected by the transducer. That was the reason why we developed a special 3D scanning acoustic microscope (see fig. 5) [12]. We realized a meandering scan with the linear stages while the specimen is rotated synchronously by a 6DoF hexapod robot system.

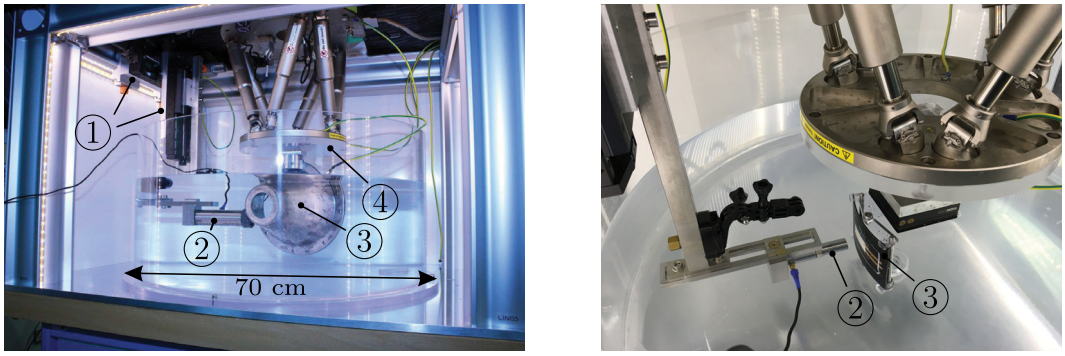

Figure 5: 3D scanning acoustic microscope at the Chair of Sensor Technology at the University of Erlangen (① linear stages, ② ultrasonic transducer, ③ exemplary specimen, ④ hexapod robot system)

In order to execute the rotational moves of the specimen precisely, the microscope's kinematic unit has to be calibrated. Our calibration method is based on a previous pure lateral scan without rotating the specimen to acquire the specimen's contour [12]. Thereby, the scan step size is about ten times greater than the step size of the imaging scan (fig. 6 (a)). After that, the contour shape has to be smoothed by a decimation filter to avoid large steps (fig. 6 (b)), which would lead to high rotation angles. The hexapod system's angle limits are $\pm 15°$ in vertical direction and $\pm 30°$ in horizontal direction. Basically, the contour measurement provides a shape of the surface, but the location in space is unknown first. In a second step, we determine the absolute coordinates of one point of the surface area and calculate the absolute coordinates for the whole contour shape. For this purpose, we execute an iterative algorithm. It performs a rotatory motion around a center point. The center point gets closer to the point of intersection of the transducer's mid-axis and the specimen's surface successively. If the center point is equivalent to the intersection point, a rotatory motion will not lead to a displacement of the reflected echo. By means of this calibration method, we obtain the surfaces coordinates with respect to the coordinates of the linear stages. The calibration method's accuracy is roughly equivalent to the ultrasonic transducer's axial resolution. Resulting images feature a uniform spatial resolution all over the measured area. The maximum achievable lateral resolution in the images for the investigated

specimen in this contribute is far below the scan step size of 0.1 mm. A lateral resolution of 50 µm is a typical value for the utilized transducer type.

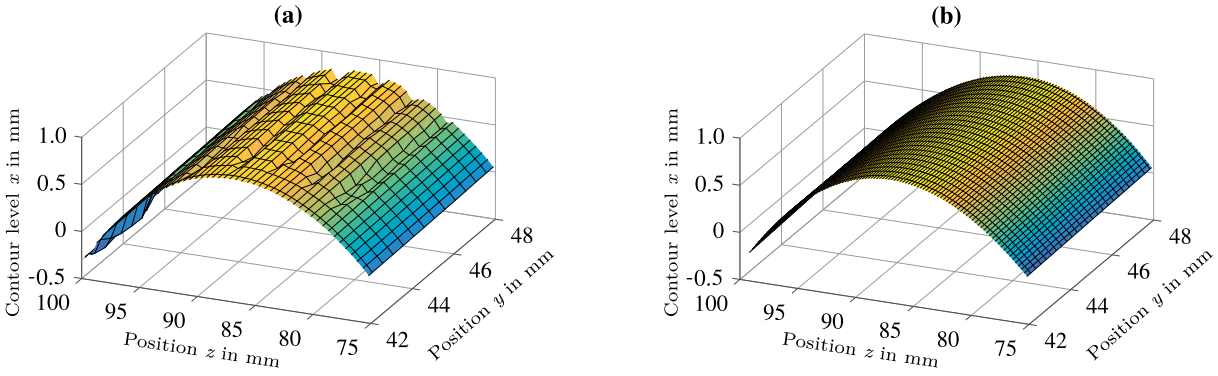

Figure 6: Exemplary contour scan of a metal strip surface with grooves (a) and the filtered and interpolated calculation of the positions of the imaging scan (b)

5 RESULTS

A comparison of the mentioned test methods provide a good correlation. Figure 7 shows the results of the evaluated specimen number 74. There, different materials (piezoceramic, printed silver electrodes, copper contacts) are very well detectable with all methods. Cracks are reliably determinable by acoustic microscopy. In regard to the conventional radiography and the CT method, the detection of cracks is more difficult. They will only be surely detected if they are opened, which can be realized by a prestress (tension load) of the specimen in the mounting. Otherwise, especially small cracks will not be detected (see figure 7 d). In regard to trapped air between the composite and the ceramic layer, the CT shows artifacts due to the high density of the piezoceramic material. Thus, these artifacts reduce the spatial resolution, so that regions with trapped air are not properly detectable by CT .

By the use of the ultrasonic microscopy regions of trapped air are detectable as a veiling glare (see figure 8).

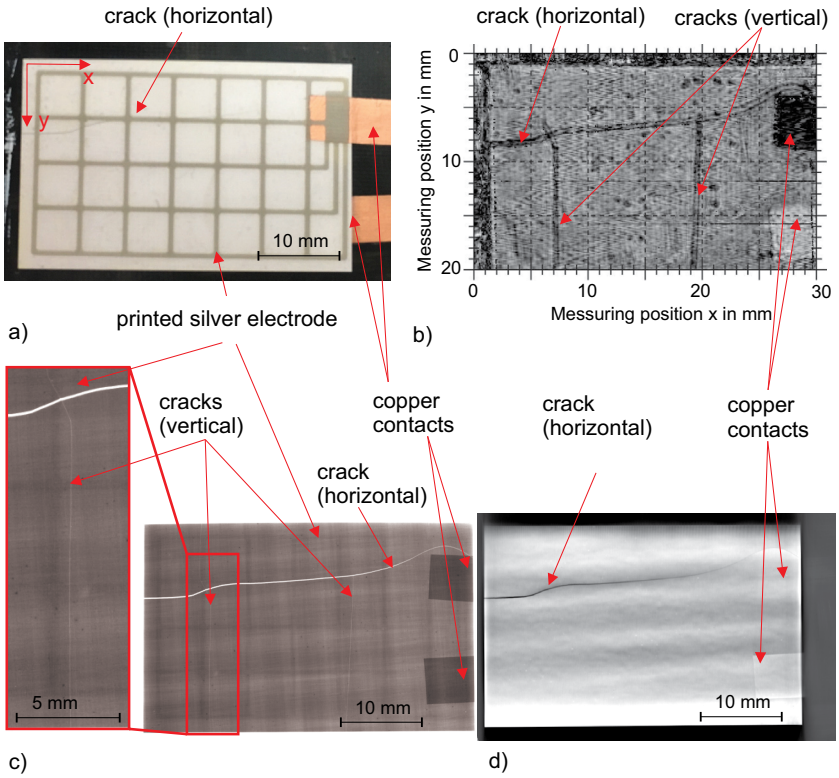

Figure 7: Comparison of the test methods for selected specimen (specimen number 74): a) photo with obvious horizontal crack, b) acoustic microscopy, c) conventional radiography (prestressed specimen), d) CT

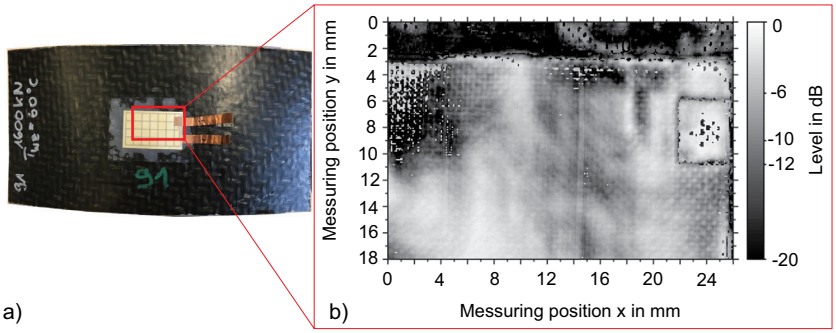

Figure 8: Detection of trapped air: a) photo with obvious regions of trapped air (specimen number 91), b) acoustic microscopy illustration

6 SUMMARY

Fiber-reinforced composites show a high potential for the integration of additional functional elements, like piezoceramic modules. By the use of thermoplastic matrices, a material homogeneous embedding of thermoplastic compatible piezoceramic modules (TPM) is possible. The introduced technology enables a manufacturing capable for series production of such composites.

Unfortunately, piezoceramics show a very low fracture strain, which often causes cracks during the forming of the function-integrative parts. Due to an incomplete melting of the TPM and the thermoplastic matrix trapped air occurs in the melting zone. The cracks and trapped air are often not obvious detectable. Therefore, non-destructive testing methods like conventional radiography, CT and acoustic microscopy are absolutely necessary. The presented contribution shows that all methods are suitable for the detection of cracks, whereby the ultrasonic microscopy showed the best results and additionally enable the detection of regions with trapped air. One disadvantage of the acoustic microscopy is the investigation of the specimen in water or in another coupling medium to get sufficient acoustic power into the specimen and receive enough echo power. This is not necessary for the X-ray methods.

7 ACKNOWLEDGEMENTS

This research is supported by the Deutsche Forschungsgemeinschaft (DFG) in context of the Collaborative Research Centre/Transregio 39 PT-PIESA, subprojects B04 and C09.

REFERENCES

[1] Dumstorff, G.; Paul, S. and Lang, W. Integration without disruption: The basic challenge of sensor integration. *IEEE Sensors Journal* (2014) **14**: 2102–2111

[2] Reddy, J.N. On laminated composite plates with integrated sensors and actuators. *Eng. Struct.*, (1999), **21**: 568–593.

[3] Zysset, C.; Kinkeldei, T.W.; Mnzenrieder, N.; Cherenack, K. and Trster, G. Integration method for electronics in woven textiles. *Compon. Packag. Manuf. Technol. IEEE Trans.* (2012) **2**: 1107–1117

[4] Holeczek, K.; Starke, E.; Winkler, A.; Dannemann, M. and Modler, N. Numerical and Experimental Characterization of Fiber-Reinforced Thermoplastic Composite Structures with Embedded Piezoelectric Sensor-Actuator Arrays for Ultrasonic Applications. *Applied Sciences* (2016) **6, 55**: doi:10.3390/app6020055

[5] Kostka, P.; Holeczek, K. and Hufenbach, W. Structure-integrated active damping system: Integral strain-based design strategy for the optimal placement of functional elements. *International Journal of Composite Material* (2013) **3**: 53–58.

[6] Hufenbach, W.; Gude, M. and Heber, T. Design and testing of novel piezoceramic modules for adaptive thermoplastic composite structures. *Smart Materials and Structures* (2009) **18**: 045012 (7pp).

[7] Hufenbach, W.; Gude, M.; Modler, N. and Heber, T. Consolidation behaviour during manufacture of adapted piezoceramic modules for functional integrated thermoplastic composite structures. *International Journal of Materials Research* (2011) **102**: 1021–1026

[8] Hufenbach, W.; Modler, N.; Winkler, A.; Ilg, J. and Rupitsch S.J. Fibre-reinforced composite structures based on thermoplastic matrices with embedded piezoceramic modules. *Smart Materials and Structures* (2014) **23**: 025011

[9] Lerch, R., Sessler, G. and Wolf, D. Technische Akustik: Grundlagen und Anwendungen. Springer, Berlin (2009).

[10] Rupitsch, S.J. and Zagar B.G. Acoustic Microscopy Technique to Precisely Locate Layer Delamination. *IEEE Transactions on Instrumentation and Measurement* (2008) **56**

[11] Maev, R.Gr. Advances in Acoustic Microscopy and High Resolution Imaging. Wiley-VCH, Weilheim, (2013).

[12] Wuest, M.; Eisenhart, J.; Rief, A. and Rupitsch, S.J. System for acoustic microscopy measurements of curved structures. *tm - Technisches Messen* (2017): https://dx.doi.org/10.1515/teme-2016-0085.

[13] Ochelski S. Experimental methods for composite mechanics. *WNT*, Warsaw 2004

[14] Ye L.; Lu Y.; Su Z. and Meng G. Functionalized composite structures for a new generation airframes: a review. *Composite Science and Technology* (2005) **65**: 1436-1446.

[15] Winkler, A. *Dissertation*, Technische Universitaet Dresden (2016).

VIII ECCOMAS Thematic Conference on Smart Structures and Materials
SMART 2017
A. Güemes, A. Benjeddou , J. Rodellar and Jinsong Leng (Eds)

PIEZOCERAMICS IN SHEET-METAL COMPOUNDS FOR ICING DETECTION

W.-G. DROSSEL, M. NESTLER, T. MÄDER AND J. SCHÖNHERR

Fraunhofer Institute for Machine Tools and Forming Technology,
Reichenhainer Str. 88, 09126 Chemnitz, Germany
e-mail: thomas.maeder@iwu.fraunhofer.de, web page: http://www.iwu.fraunhofer.de

Key words: Icing detection, Impedance analysis, Forming, Macro Fibre Composite, Sandwich material, Smart Structures.

Abstract. Icing detection and de-icing techniques play an important role to assure a safe operation of airplanes and wind turbines [1, 2]. Integration of piezoceramics in structural parts allow for additional functionalities like health monitoring, impact detection and even to solve icing problems. The paper deals with innovative sheet-metal compounds, consisting of a piezomodule in a layer of adhesive embedded between two aluminum sheets. An airfoil demonstrator structure with integrated piezomodules is used for icing detection. A special production and forming technology was presented in earlier studies, where forming takes place in a viscous condition of adhesive. This concept allows for a forming of brittle piezoceramic fibers inside the compound. This demonstrator structure was built with this production technology. The integrated sensor is used for a detection of additional local masses. Aim is the implementation for aerodynamic icing detection and a vibration assisted de-icing. Within the paper preliminary tests for an icing detection are described. Therefore impedance and loss angle of an integrated piezomodule are measured for a broad frequency range under variation of additional masses and temperature. Icing was performed inside a cold chamber at -40 °C. It is shown that the impedance is significantly influenced by additional masses at room temperature, by a reduction of temperature without additional masses and by additional masses (ice) at reduced temperatures. The results imply that the assumptions are correct and the continuative investigations are worthwhile to potentially develop an icing detection technology.

1 INTRODUCTION

Icing during a flight can change shape of airfoil leading to a decrease of aerodynamic performance of aircrafts. In worst case an accident can occur. Ice adhesion is also a major challenge of wind turbines, especially in icy Nordic environments [3]. The detection of icing is important, hence typically one or more ice detectors are used in aircrafts. These detectors are often coupled with de-icing systems [4]. De-icing systems remove the ice-layer from the subject whereas anti-icing strategies are used to prevent ice to accrete on the airfoil [5]. In aircrafts today typical means for a prevention or a control of ice formations are: heating surfaces with hot air, heating by electrical elements, breaking up ice formations (e.g. by inflatable boots) or chemical applications [4]. Often high amounts of energy are needed.

Aiming on a reduction of energy consumption for de-icing a vibration assisted de-icing is under investigation [6]. Electrical impulses achieved by a spiral coil placed near the surface allow an expulsion of the ice [2]. Disadvantage of this method is the weight of the impulse generating device [7]. Because of that the ability of piezoelectric actuators for a de-icing is investigated. Several studies deal with piezoelectric actuators and show the potential for de-icing [7, 8].

2 INNOVATIVE PRODUCTION TECHNOLOGY FOR PIEZO-METAL-COMPOUNDS

The authors propose the use of aluminum sheets with a local sandwich buildup and integrated piezomodules for a detection of icing and a support of the de-icing process. The process chain for the manufacturing of these piezo-metal-compounds was developed and described in earlier studies [9, 10]. Piezo-metal-compounds consist of two aluminum sheets joint with an adhesive. A piezomodule is positioned in the adhesive layer. Forming is performed with a viscous adhesive. This allows for a relative movement between the brittle piezomodule and the surrounding sheet metal layers and prevents critical elongations of the piezomodule. After forming the adhesive completely cures. An airfoil demonstrator structure was designed and manufactured, including a Macro-Fibre-Composite (MFC) integrated in a local sandwich buildup. Figure 1 (a, b) shows the manufacturing and the finished part (Figure 1 c).

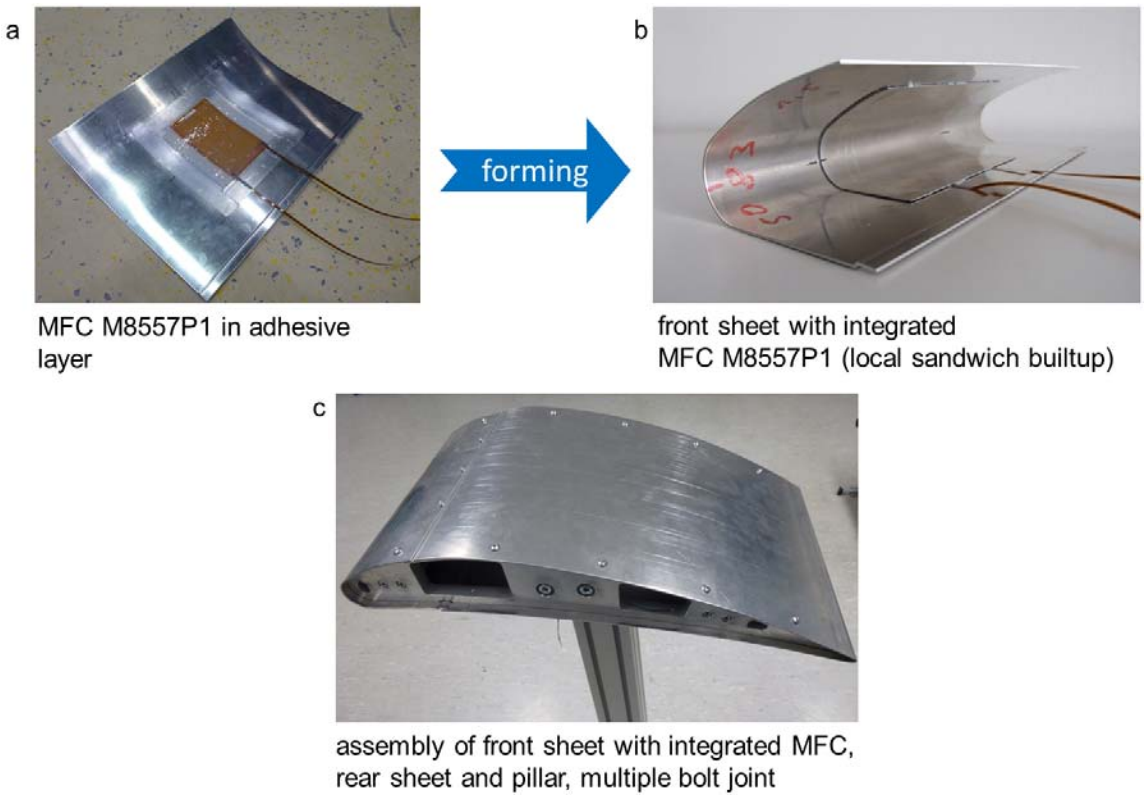

Figure 1: (a) MFC in adhesive layer before cover layer application ; (b) front sheet with integrated MFC after forming ; (c) assembly of demonstrator airfoil with integrated MFC

3 ICING-DETECTION EXPERIMENTS

The experimental approach includes the definition and determination of natural frequencies and natural modes with shifts of local maxima, which are appropriate for a detection of icing and de-icing processes. The targeted positioning of piezo elements allows stimulating selected frequencies, while shifts of resonance frequencies are induced by mass increase of local icing. The resonance frequencies are detected by the integrated piezo modules.

3.1 Experimental setup

In order to verify the icing detection capability of material integrated MFCs experiments were conducted using the above described demonstrator. Therefore the airfoil demonstrator structure with integrated MFC (Figure 1) was subjected to different surrounding conditions. An experimental series with the variation of temperature and using additional masses was carried out. Four principle set-ups and conditions were tested: 1st naked wing panel at room temperature, 2nd wing panel at room temperature with additional mass installed, 3rd wing panel at -40°C without an additional mass and 4th wing panel at -40°C covered with locally grown ice (Figure 2 left to right).

The room temperature experiments were carried out under regular laboratory conditions. A steel plate (about 50 g) was used as additional mass. This plate was fixed using reinforced adhesive tape. The low temperature experiments were realised in a Binder MKF 240 climate chamber. The wing panel was placed inside the chamber and cooled down to -40°C. Water was dropwisely injected through an insulated tube so as to create an ice cover on the wing panel. This tube was led through an opening in the wall of the climate chamber. Due to the low temperature of the wing panel in the chamber, the water drops froze almost instantaneously.

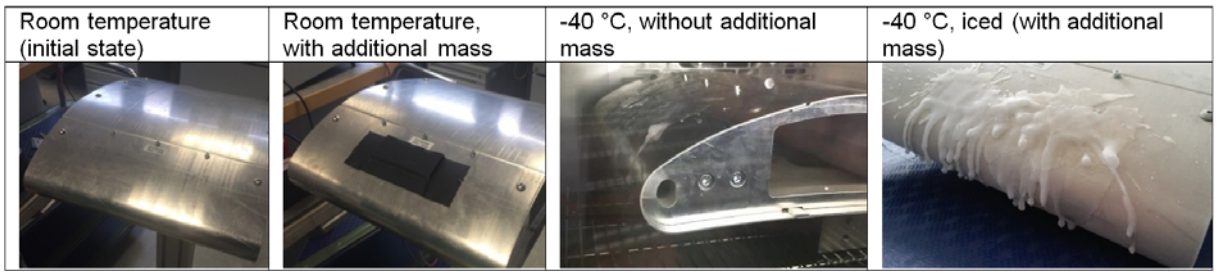

Figure 2: Experimental set-ups of wing panel test series with temperature and mass variation to verify the icing detection capability of integrated MFCs.

3.2 Measurement of Impedance and Phase Angle

The local magnitudes of the impedance and the phase angle between voltage and current over the excitation frequency both of the integrated MFC are a measure for resonance of the structure. The resonance frequency of the structure should shift, when additional mass is fixed to the structure. The impedance and the phase angle are therefore eligible parameters for icing detection.

In order to measure both parameters in the test series a LCR meter (Sourcetronic ST2826) was used. An excitation voltage of 5 V was implemented to stimulate the structure. The MFC was connected with a 4-wire fixture. The frequency response characteristic and monitoring of

the test parameters were realised within the frequency range between 18 kHz and 50 kHz with frequency steps of 10 Hz. The frequency response characteristic was recorded for all of the above mentioned set-ups. Characteristic frequency spectra were used for the further evaluation and the comparison of the set-ups with mass and temperature variation.

4 RESULTS

The results of the frequency response measurements of impedance and phase angle are shown below. The fixation of an additional mass to the wing panel structure at room temperature clearly shifts the resonance frequency of the structure. Certainly in the frequency range between 20 kHz and 25 kHz the frequency change of the local maximum can be seen for the impedance and the phase angle (Figure 3). The additional mass lowers the resonance frequency, as expected. Especially between 20 kHz and 21 kHz a distinct shift of about 140 Hz of the resonance frequency can be found. The magnitude of this change is stronger for the phase angle than for the impedance signal. The frequency shift can also be seen for higher vibration modes, but is comparibly smaller (Figure 3). The general idea of measuring mass increase by means of mechanical-electrical parameters of MFCs could be verified by the tests at room temperature. Further experiments are necessary to identify the best frequency spectrum. The scanning of the whole frequency band between 18 kHz and 50 kHz would take too long for practical monitoring applications.

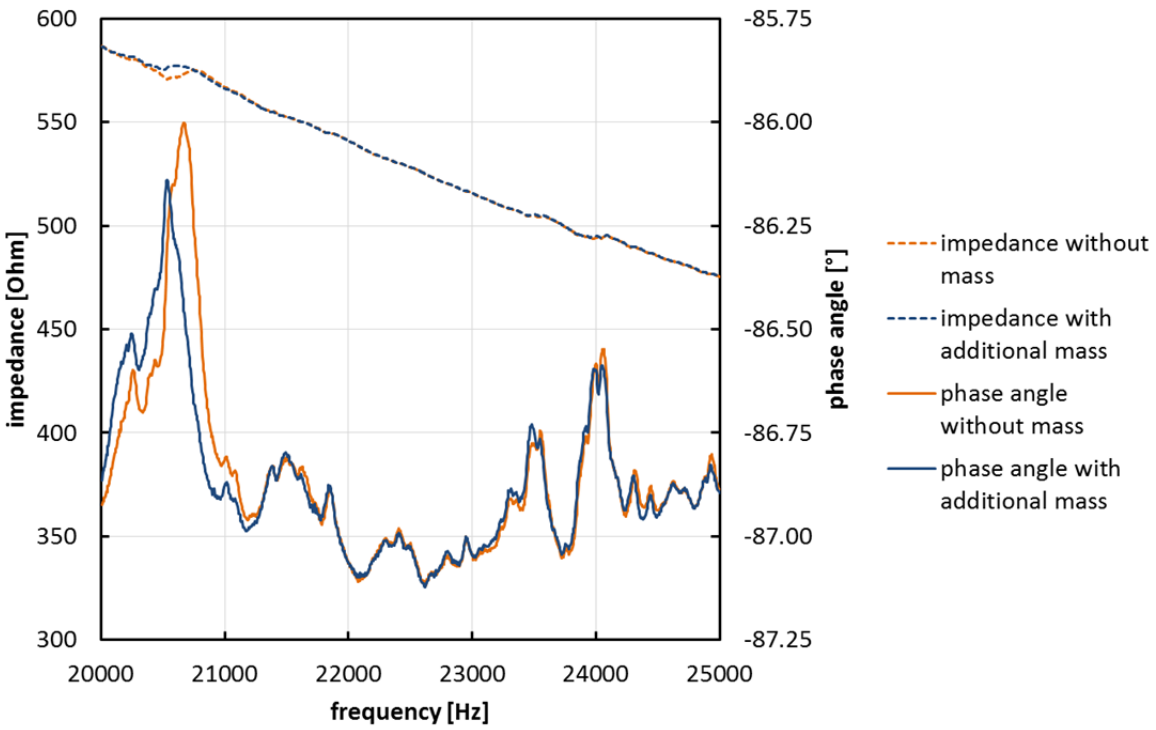

Figure 3: Comparison of the frequency response characteristic of impedance and phase angle of an integrated MFC in a wing panel structure at room temperature with and without an additional mass fixed to the structure.

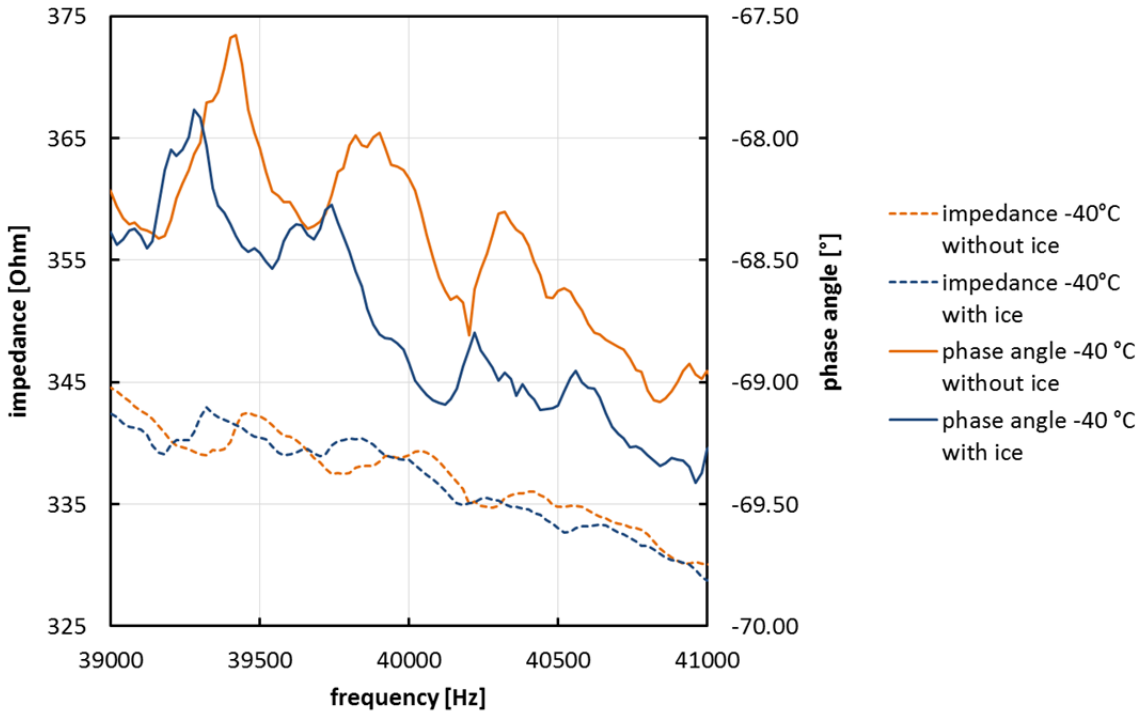

Figure 4: Comparison of the frequency response characteristic of impedance and phase angle of an integrated MFC in a wing panel structure at -40°C with and without additional ice cover.

A similar frequency shift can be found for the addition of an ice cover to the surface of the wing panel at -40 °C compared to the panel without ice on the surface (Figure 4). In the frequency range between 39 kHz and 41 kHz several local maxima of the phase angle and the impedance are shifted to lower frequencies due to the additional ice mass. Three distinct resonance frequencies can be found in the specified range. They represent a pattern. This whole pattern is shifted to a lower frequency by the ice. This frequency shift has a value of about 120 Hz and is similar to the shift at room temperature. In comparison to the impedance the frequency response pattern for the phase angle is also stronger, like it was for the test at room temperature. In the frequency range of about 20 kHz to 21 kHz, no distinct pattern or frequency shift could be found in the low temperature set-up. This means, that the monitored frequency range strongly depends on the temperature. An additional temperature monitoring is probably necessary to control the excitation frequency range for the MFCs.

The addition of ice to the surface also reduced the average phase angle in the frequency response characteristic (Figure 4). This reduction needs to be distinguished from the frequency shift. It is necessary to find mathematical methods to identify the resonance frequency pattern and the influence of additional masses to it. Out of these first results an icing detection method by means of integrated MFCs seems to be feasible.

The comparison of the frequency response characteristic of impedance and phase angle singly depending on the surrounding temperature shows a strong influence of the temperature to both parameters (Figure 5). The wing panel was tested at room temperature and at -40 °C both without additional mass. With lowering of the temperature, the average impedance reduces. The average phase angle increases with decreasing temperature (Figure 5).

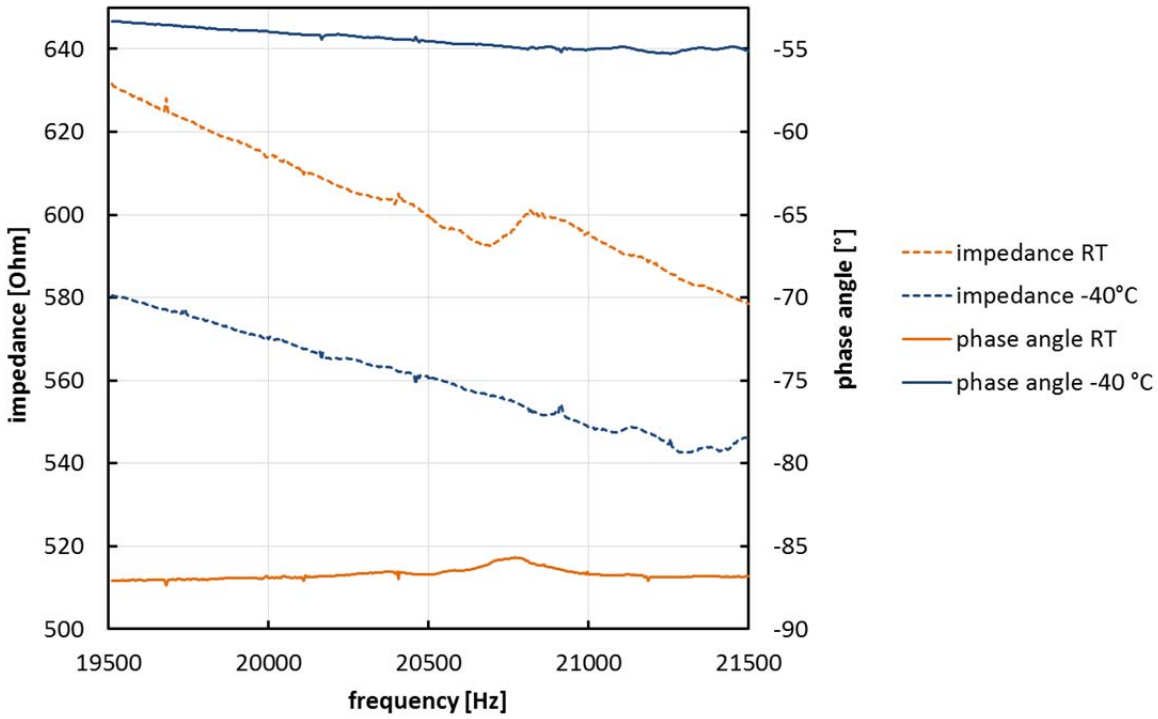

Figure 5: Comparison of the frequency response characteristic of impedance and phase angle of an integrated MFC in a wing panel structure at room temperature (RT) and at -40 °C.

The resonance frequencies also shift due to the singly temperature change (Figure 5). This effect challenges the icing detection monitoring method in specific applications. A calibration technology needs to be found in order to distinguish temperature change and icing. An additional monitoring of the temperature therefore seems to be important to successfully realise an MFC based icing detection system. The observed frequency range should be as narrow as possible to accelerate the identification of resonance frequencies. The excitation frequency range has to be adjusted to the actual temperature of the structure.

5 SUMMARY AND OUTLOOK

The possibility of icing detection using integrated MFCs and monitoring the frequency response of phase angle and impedance could be verified. The results show that mass increase at room temperature and down to temperatures of -40 °C can be detected by means of integrated piezo elements. The challenge for further development to a practical icing detection technology is the strong temperature dependence of the frequency response. It is therefore necessary to find a calibrating method to distinguish the effects of temperature and additional masses.

Another challenge for the further development is the use of MFCs for de-icing. De-icing could potentially be realised by vibration assistance by means of vibrational excitation of the MFCs with higher voltages. The further development concept comprises the structural integration of multiple piezo modules into the demonstrator structure and their sensor and

actuator usage. The necessary tasks to further develop the sensor and actuator function contains FE simulations to find suitable positions for sensors and actuators, manufacturing of demonstrator structures with optimum positions for the MFCs by forming technologies, the functional characterization of demonstrator, i. e. detection of natural frequencies and vibration forms by vibrometer measurements. This will be followed by functional tests of icing detection, i. e. targeted stimulation of resonance frequencies and detection of response signal by local icing. The conceptual development and functional test of the de-icing process enhanced by vibration as well as the avoidance of icing will then finish the investigations. Vibrations will be initiated for a mechanical de-icing process or to sustain the de-icing process with thermal heating elements.

ACKNOWLEDGEMENT

This research is supported by the Deutsche Forschungsgemeinschaft (DFG) in context of the Collaborative Research Centre/Transregio 39 PT-PIESA, subprojects K06 and B01.

REFERENCES

[1] Homola, M.C.; Nicklasson, P.J. and Sundsbø, P.A. Ice sensors for wind turbines. Cold regions science and technology, 46(2), 2006, 125-131.

[2] Parent, O. and Ilinca, A. Anti-icing and de-icing techniques for wind turbines: Critical review. Cold regions science and technology, 65(1), 2011, 88-96.

[3] Dalili, N., Edrisy, A., Carriveau, R. A review of surface engineering issues critical to wind turbine performance. Renewable and Sustainable Energy Reviews 13 (2009) 428–438.

[4] U.S. Department of Transportation, Federal Aviation Administration: Aviation Maintenance Technician Handbook Airframe, Vol. 2, Chapter 15, 2012

[5] Ilinca, A., 2011. Analysis and Mitigation of Icing Effects on Wind Turbines. Wind Turbines, Dr. Ibrahim Al-Bahadly (Ed.), ISBN: 978-953-307-221-0, InTech, 187, Available from: http://www.intechopen.com/books/windturbines/analysis-and-mitigation-of-icing-effects-on-wind-turbines

[6] Schütteln statt Schmelzen: Neue Methoden zur Flugzeug-Enteisung in der Luft. 02.03.2017, http://www.airliners.de/schuetteln-schmelzen-neue-methoden-flugzeug-enteisung-luft/34701, 2015

[7] Wan, W. and Yang, Z. Asymmetric Temperature Load Method for Simulation Study of Wing Leading Edge in Flight Deicing with MFC. International Journal of Control and Automation Vol.6, No.6 (2013), 359-370

[8] Ramanathan, S. An investigation on the deincing of helicopter blades using shear horizontal guided waves, Thesis, Pennsylvania State University, 2005.

[9] Nestler, M. Umformung metallbasierter Mehrschichtverbunde mit Sensor- und Aktorfunktionalität. Berichte aus dem IWU Band 93, Dissertation, Verlag Wissenschaftliche Scripten, 2016

[10] Nestler, M., Drossel, W.-G., S. Hensel, R. Müller, Fabrication method for series production of sheet metal parts with integrated piezoelectric transducers. Proc. Technol. 15 (2014) 494-502.

ADAPTATIVE CONTROL FOR BIOINSPIRED MICRO AIR VEHICLES

Javier Crespo-Moreno[*], Miguel A. Barcala-Montejano[*], Ángel A. Rodríguez-Sevillano[*], José Félix Alonso-Alarcón[*], Rafael Bardera-Mora[†], Denis Shportenko[*] and Alberto Romero-García[*]

[*] Escuela Técnica Superior de Ingeniería Aeronáutica y del Espacio
Universidad Politécnica de Madrid.
Plaza del Cardenal Cisneros, 28040 MADRID, Spain.

[†] Instituto Nacional de Técnica Aeroespacial (INTA)
Carretera de Ajalvir, km 4,5. 28850 Torrejón de Ardoz (MADRID), Spain

Key words: Control Law, Adaptive Control, Wing morphing, Wing-grid.

Abstract. The amazing world of drones supposes a field of aerospace research really exciting for universities and centers of excellence, and practically without technological limitations. Perhaps the reality is that the use of these drones is less glamorous than the media suggest. And, on the other hand, its operations are still limited by pending aspects of aeronautical regulation. But in the field of aerospace research the previous arguments are weak compared to the potential of new aerospace designs and developments.

The authors have been carrying out several research projects in the field of micro air vehicles. In addition, last researches have been outstanding in the analysis of bioinspired micro air vehicles (MAVs). Experimental and theoretical studies have been developed and aircraft prototypes based on morphing wings and wing-grids have been designed. For the design of this type of non-conventional geometry it is essential to select the appropriate materials that will meet the initial design specifications. And when the geometry and materials are finally defined, the next essential step is the design of the wing geometry control system. This system will allow to fulfilling the flight requirements. This paper shows the methodology of design for the flight control system carried out on these vehicles. The initial basis begins from our development in traditional flight control for guidance, navigation and control systems in conventional geometry airplanes. Subsequently, the foundations of adaptive and optimal control will be shown. Finally, the results of flight control over micro air vehicles' prototypes will be analyzed in the current design phase.

1 INTRODUCTION

A good interpretation of the term morphing may be understood referred as to both small and large aircraft scales. At least two approximation of wing morphing may be identified such as morphing for flight mission and morphing for control. In the context of this paper morphing is applied to control any aircraft aerodynamic surface to fulfill flight envelop and applied it to micro air vehicles, MAV [1].

In the context of this paper, morphing aircraft is understood as changes in the camber of the aircraft wings or the installation of special devices used to reduce induced drag as wing-grids. Both of them underlie in the use of new materials suitable to change the main dimension of any aircraft wings and improve the flight qualities [2], [3].

In the case of wing morphing, the modifications are related to changes in the external aspect of wing by electromechanical actuation. The focus of this technique is to modify the external aspects of wings to improve the flight performance.

The second device is the wing-grid. One of the problems limiting the aircraft performance is the drag produced. The aircraft´s wings may produce some vortices and at same time increase the aircraft drag. In this sense, it is interesting explore new concepts to reduce the drag and make flight more efficient and less costly [4].

The wing-grid device mainly is set up of surfaces make up of polymer to reduce the induced drag on wings. The performance of the wing-grids relative to installation, their shape and the control must be investigated.

The onboard system that controls the flight of any aircraft is the flight control computer. This computer is in charge of control the movement of aerodynamic and aircraft control surfaces. Additionally to that, and depending of the size of the aircraft, this computer may have the responsibility of manage the flight.

As new functions are appearing in the context of flight control, these must be given to any on board computer to be successfully executed. The case is focused on give morphing and wing-grid movements to the flight control computer. The surfaces movement control is based on some control laws calculated in the flight control computer. The complexity of the calculus of the control law will depend on the control surfaces installed on board, on their actuators and sensors, and also on the precision required.

The focus of this paper is analyzing the possibilities of exploring and applying the control laws by means of different engineering techniques. The paper also will include some experiences carried out in wing-grid design and test [5].

2 THEORETICAL ASPECTS OF WING MORPHING

Morphing research to date addressed the control aspects of shape changing or morphing like any other system. In this context may be found several control functionalities in performance values like range and speed at specific flight conditions related to wind speed, altitude, angle of attack and sideslip angle [6].

If the aerodynamic performance is taken as primary consideration, and flight successfully can be attributed to wing shape, a wing control system reveals a main activity in flight control. The flight may be considered in several phases introducing different control strategies depending on the flight phase flown. In this case, the flight problem becomes a flight reconfiguration taking sensing, actuation and control law as flight control activity.

3 THE COMMAND AND CONTROL CONCEPT

In terms of the controller, must be sufficiently robust to manage wide flight variations, such as time-varying moments and products of inertia of the aircraft that produce new configuration parameters of aircraft system. So, may be said that morphing wing control must know how to learn to reconfigure in multiple flight scenarios.

The control concept applied to these systems may be any of those applied to any other systems. In the case of wing morphing control several technics and practical control issues may be applied to obtain the optimal configuration of morphing commanded.

The level of actuation, the energy and the control technique used in any morphing aircraft will be suitable to the level of sensors, wing actuators and computing capacity of the main onboard computer.

The traditional control of aircraft attitude is performance by flaps, ailerons, elevators and rudders and control surfaces in general attached to the wing on a fixed-wing aircraft. All of the aircraft maneuvers are managed by such as control surfaces, managed as same time by a flight control computer on board aircraft.

In the morphing concept the aircraft is controlled by varying mechanical aspects of the wings, such us leading and trailing edge´s configuration and position related to their initial positions or simply varying wing camber. Therefore, the morphing airfoil technique may be suitable to replace some of the traditional aircraft control surfaces and control aircraft attitude and speed.

In terms of the controller, several controls techniques for automatic systems can be taken into account to design a flight control computer and move the morphing areas set up in aircraft. From the point of view of the controller the design method should allow to flexibility in internal adjustment of aircraft surface as a complex and nonlinear dynamics. To achieve satisfactory aircraft control and a fine wing morphing, some aspects will be faced, such as nonlinear and linear systems, their errors, the operating point, the aircraft performances and flight uncertainties. Added to that are the natural strong non-linear character of the smart materials and actuator used to obtain the required wing morphing.

3.1 Control Methods

The first approximation to calculate the control law is based on PID estimation. The tuning of PID controller is the process of finding the constants for proportional, integral and derivative gains to meet design requirements and desired performance. To find out the gains of this controller is not an easy task. Usually the tuning requires time consuming and may cause problems to the system. Tuning methods based on Ziegler-Nichols method is a good approximation to obtain the final controller. Figure 1 shows the feedback system in which controller is PID.

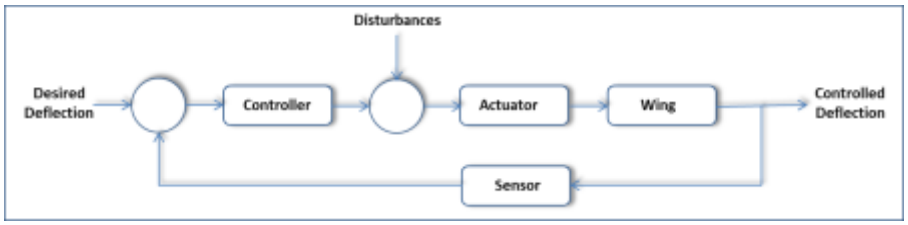

Figure 1: Feedback Control.

The second one suggested method to control wing shape is the adaptive control. This method is a good control technique to deal with uncertainties. Adaptive control has the ability to adjust itself to manage unknown model and environment uncertainties and to adapt to the flight requirements. In this sense, adaptive control direct methods allows to estimate parameters that will be used in the adaptive controller, and indirect methods are ones wherein the estimated model data are used to tuning the controller.

3.2 Morphing Control Law

A six degree of freedom dynamical system may represent the equations of motion for the morphing wing of any aircraft. The dynamics of most systems may be represented as a set of second order differential equations if the system is expressed in body axes.

To calculate the morphing control law the system states which will be the feedback information from sensors installed on the aircraft. It should be suitable to get information from velocities, acceleration level, and position of the aircraft surfaces.

All the information provided by sensors will be used to calculate system error according to the requirement of the system.

In the case of morphing wing several control techniques candidates will be assess to design the control law.

Adaptive control, Figure 2, has as objective to adjust to changing system parameters to minimize system error, or estimate to change the control law signal. Several approaches of adaptive control may be considered, such as, least square estimation adaptive control, model reference o dynamic inversion.

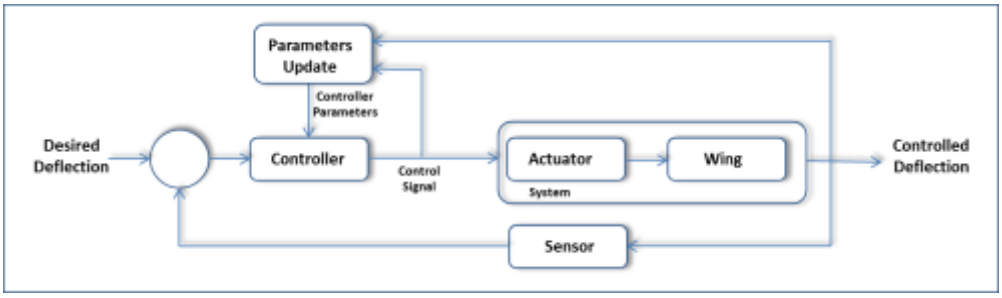

Figure 2: Adaptive Control.

3.3 The Feedback System

The feedback system is a set of different sensors adapted to the wing system, either wing morphing or wing-grid.

In the case of wing morphing, the wing shape control of the aircraft is obtained by means of piezoelectric actuators. The use of piezoelectric actuators for wing shape control and correction of static deformations is considered in this aircraft as the main option to achieve the desired wing shape. The most common methods to control the shape of a structure are based on using embedded piezoelectric materials. A straightforward method based on a feedback controller has been used to obtain the optimal wing position and the optimal actuation voltages of the piezoceramics elements. The voltages applied to the piezoceramic elements are induced in a defined way to avoid saturation voltages, which are one of the main constraints in controlling them.

The voltages applied to the piezoelectric are considered as an open loop system, where no sensor is set to check them. An optimization algorithm has been implemented to calculate the optimal voltages and control the saturation voltages.

The purpose of the actuator and sensor set in the wing is to bend it and to maintain the preferred shape. This sensor together with the wing shape control must be considered as a closed loop system. The main function of this system is to maintain the wing shape in presence of unknown aerodynamic loads. Thus position sensors at many wing locations are not required in this design for closed loop shape control.

In the case of wing-grid several surfaces will be added to the original wing to generate the aircraft attitude, so the actuator will be based on a mechanical screw rotation to move them. Comparing wing camber by means of piezoelectrical actuators and wing-grid and their surfaces, the actuator and the sensors will be different. But the technique to design the control may be based on same control theory adapted to the specific flight requirements.

5 PRACTICAL ASPECTS

The prototype built try to demonstrate the benefits of wing-grids to reduce the induce drag. To reduce induced drag on wings several techniques may be applied [1]:

- Wing with fanned partial wing.
- Wings with slotted edges.
- Simple wings with wingtip and endplates.
- Contouring plane wings.
- Planar straight wings.

The technique used in this prototype is the planar straight wings. The prototype is a set of a computer, some actuators, some motion sensors and the modified wings. The physical aspects of the prototype are described as follows.

5.1 Configuration and Dimensions

In this case the geometrical aspects are the main criteria lead to several wing-grid configurations. The possible configurations investigated in the wing prototype are presented next:

- Non-cruise configuration: Both wing-grids are completely retracted. This is the Base configuration (non-cruise). In this configuration there is neither effect on induced drag nor on lift. The MAV performs as if it were a planar geometry. It is important to notice the lack of roll control on this configuration.
- Cruise configuration: Both wing-grids completely unfolded. David Bennett in 2001 [4] proved testing on wind tunnel that "at high angles, the wing was half as efficient as at low angles, implying that this wing-grids may be better suited to cruise conditions". An increase on span and therefore aspect ratio and lift is obtained as well as a reduction on induced drag.
- Roll configuration: One of the wing-grids partially or completely unfolded, the other completely retracted: The wing which wing-grids is unfolded generates more lift than the other, producing roll. It provides the MAV with the control that would be normally provided by aerofoils.
- Yaw and pitch configuration: A V tail was chosen to control yaw and pitch instead of using horizontal and vertical stabilizers and a propeller was the preferred option for the generation of traction. The dimensions and main characteristics of the MAV are shown in the table below [1]:

Table 1: Characteristics of the original MAV model.

Magnitude	Wing	Winggrid (1 winglet)	Wing+Winggrid	V tail
Span (mm)	540	180	720	250
SMC (mm)	90	20	90	60
Area (mm^2)	48600	3600	64800	15000
AR	6	9	8	3
$\Lambda_{1/4}$ (°)	0	0	0	6

The approximated dimensions and main characteristics of the test model are shown in the table below, based on [5]:

Table 2: Characteristics of the modified MAV model

Magnitude	Wing 1A	Wing 1B	Wing 1C	Wing-grid (1 winglet)	Winglets' base
Span (mm)	63	66.3	63	149.7	9.75
SMC (mm)	191.73	191.73	191.73	51.78	157.41
Maximum thickness (mm)	30.87	30.87	30.87	15.37	25.13
Weight (g)	45.55	48.38	45.55	16.94	8.64
Material cost (€)	2.28	2.42	2.28	0.85	0.43

There are 3 winglets and 1 base per wing-grid. The fraction of wing is divided in 3 parts: 1A, 1B and 1C.

5.2 Hardware Configuration

The control system was designed to provide the MAV with the capacity of modifying its configuration as detailed above. Next, a brief description of the elements of hardware and software used is given.

The project is mainly underlying on Arduino technology. "Arduino is an open-source electronics platform based on easy-to-use hardware and software. Arduino boards are able to reading an input (e.g. finger on a button) and turn it into an output (e.g. activating a motor)". The software used to write and implement the code was the Arduino programming language, and the Arduino Software (IDE).

The model chosen was Arduino Uno due to its reduced dimensions, but Arduino Mega may be a better option regarding future progress owing to its higher number of pins. Technical specifications of Arduino Uno are shown in the table below, based on [6]:

Table 3: Technical specifications of Arduino Uno

Length/ Width	68.6 mm / 53.4 mm
Weight	25 g
Operating voltage	5 V
Input voltage (recommended)	7-12 V
Input voltage (limit)	6-20 V
Digital I/O pins	14 (of which 6 provide PWM output)
Analog input pins	6
DC current per I/O pin	40 mA
DC current for 3.3V pin	50 mA
Flash memory	32 KB (ATmega328P) of which 0.5 KB used by bootloader.
SRAM	2 KB (ATmega328P)
EEPROM	1 KB (ATmega328P)
Clock speed	16 MHz
Cost	24 € per unit (1 unit in total)

Various alternatives were considered to choose the motor for winggrid control. The one selected is a bipolar stepper motor NEMA 14 of Pololu®. The test model is bigger than the original design to avoid problems caused by the dimensions of the motor. This type of electric motor has two main features: the precision to stop its movement at any given angle (like a servomotor); and the capability of changing the direction of the rotation (like a DC motor).

The motor was chosen bipolar instead of unipolar due to its greater torque. The technical specifications of the NEMA 14 are shown in the table below, based on [9]:

Table 4: Technical specifications of the NEMA 14 of Pololu®

Size	35 mm x 35 mm x 36 mm
Weight	180 g
Shaft diameter	5 mm
Shaft type	5 mm "D"
Steps per revolution	200
Current rating	1000 mA (not including the shaft)
Voltage rating	2.7 V
Holding torque	1.4 Kg-cm
Resistance	2.7 Ω (per coil)
Inductance per phase	4.3 mH
Number of leads	4 (2 per coil)
Cost	13.10 € per unit (2 units in total)

However, the bipolar stepper motor has an issue that has to be mentioned here. The current flow on these motors needs to change its direction through the coils in a certain sequence. To solve this difficulty both coils could be connected in a configuration called H-bridge which would distribute the pulses appropriately. The coding of the H-bridge is very complex but it is solve by means of the driver. A driver is a controller that not only covers the problem but also has some crucial advantages incorporates a current regulator (chopper), it allows supplying the motors with higher nominal voltages than that admissible because of its resistance and maximum current (otherwise the motors could not start moving); it also allows working with steps smaller than the nominal of the stepper motor. This technique is called microstepping. Smaller steps favour quieter and smoother rotations, but on the other hand the torque is weaker. The driver set up was selected following manufacturer recommendation. Technical specifications are shown in the table below, based on:

Table 5: Technical specifications of driver A4988 of Pololu®

Length/ Width	20.32mm/15.24mm
Weight	1.3 g
Minimum and maximum operating voltage	8-35 V (supply for the motors)
Continuous current per phase	1 A (without a heat sink or forced air flow)
Maximum current per phase	2 A (with sufficient additional cooling)
Minimum and maximum logic voltage	3-5.5 V (supply for the driver)
Microstep resolutions	Full, 1/2, 1/4, 1/8 and 1/16

With regard to future progress a DC motor is proposed for the propeller and servomotors for the rudders on the V tail.

5.3 Hardware Supply

The supply of the elements requires a detailed analysis. The power source may adopt different forms depending on the development stage. A computer, a DC/DC converter was the source chosen in the tests, because of suitability to be tested at laboratory.

The A4988 works at 8-35 V while the stepper NEMA 14 works at 2.7 V. This presumed incompatibility can be overcome thanks to the current regulator integrated in the driver. It is needed to limit the maximum current allowed by the driver. To set this limit the first step is to determine the current that will be used in the motor and the best starting point for it is to know the motor's current per phase, which is 1A. To get full torque from the stepper the driver has to fulfil the following condition: driver continuous current must greater than motor current rating. The A4988 has a maximum current per phase of 2A with sufficient additional cooling, so the condition is fulfilled. After setting the current limit at 1A the following step is using the current limiting equation of the A4988. Current limit = Vref / (8·Rcs). For this driver Rcs = 50mΩ so Vref has to be set at 400mV. In order to do so, the potentiometer integrated in the driver has to be rotated while measuring the voltage with a multimeter. This technique allows supplying the driver with 12V for instance, which implies supplying the motors with 12V also, without exceeding the current limit of 1A.

One last consideration, if the driver is set to operate in full step mode, the coils are energized at 70% of the current limit (in this case, 700mA). If the only mode used is full step, it is convenient to set the current limit at 1A/0.7 = 1.43A, so the current flowing through the coils is 1A. Now, Vref = 570mV (using the current limiting equation).

In a real flight situation the recommendation is an external LiPo battery with 3 cells (11.1V of voltage in total considering that every cell has 3.7V) because Arduino Uno needs a voltage of 7-12V while the A4988 needs 8-35V. As advantages is worth noting that they are light, variable in shape and size, and have high capacity which implies high endurance.

5.4 Transmission Mechanism

To transform the rotation into a translation, a mechanism of nut and threaded spindle was proposed, bases on a threaded rod. The rod is joined to the stepper's shaft with an aluminium coupler. It is a standard M6 and its length is ~20 cm. However, there is a problem with the rod, its thread pitch (p) is 1mm and it has only 1 entrance (e), so the wing-grids will unfold slowly. Given the length of the wing-grids (L≈150mm) the time needed to change the configuration from entirely retracted to entirely unfold is calculated as following:

Table 6: Configuration data.

Variable	Data
n (rotational speed of the motor)	150rev/20s = 450 rpm
A (feed) = p·e	1mm
Va (feed rate) = A·n	7.5mm/s
t (time)= L/Va	20s

This time 20 seconds is unacceptable in a real flight, a spindle with 2mm of pitch and 2 entrances could reduce the time to 3 seconds (following the same calculations). The nut is also a standard M6 and it is fixed to the wing-grid to transmit the movement of the motors.

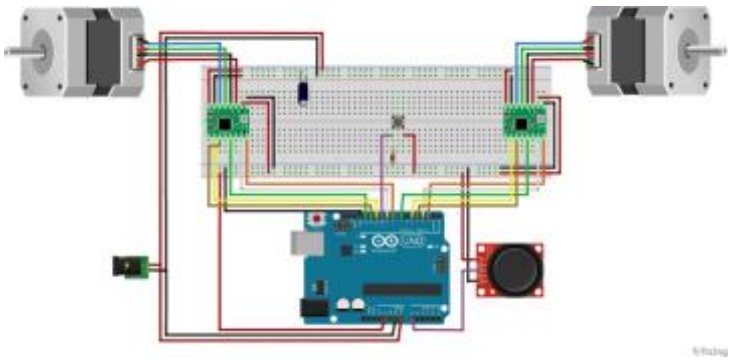

Figure 3: Wiring diagramme.

Figure 3 is an electric schematic representation of the wiring diagram designed to control the wing-grids. On one hand, the power source supplies Arduino Uno connecting the positive electrode with Vin pin and the negative with GND pin. To supply the motors the source is connected to the drivers in Vm and GND pins (positive and negative electrodes respectively) and they in turn are connected from pins 1a, 1b, 2a and 2b to the stepper terminals. The operating voltage of the motors should be within the interval 8-35V and that of the Arduino Uno within the interval 7-12V. 12V is the supply voltage used in the tests (the motors work at 2.7V, but there is compatibility due to the current limiting feature of the drivers, as explained above.

On the other hand Arduino Uno works as power source for some elements. The logical supply for the drivers (3-5.5V) is provided by the 5V pin of Arduino Uno, connected to Vdd pin of the drivers. It also supplies the joystick and the switch. A breadboard is used to make the majority of the connections.

There is a group of connections between Arduino Uno and the driver needed to configure the steppers: Rotation direction, microstepping and pulse control essentially.

Finally, it is important to note the 100µF capacitor connected between VMOT and GND. It protects the driver from LC voltage spikes that could exceed 35V, damaging the A4988.

5.5 Software

In the tests, a joystick was proposed to transmit the commands to Arduino Uno. The idea was to correspond linearly the position of the joystick with the position of the wing-grids, which is the number of steps of the motors. To avoid precision problems a margin of error (±50 steps) was set, so small variations of the joystick's position may not produce variations in the wing-grids' position. Furthermore, by means of a switch the configuration can be changed from cruise to non-cruise or vice versa.

A brief explanation of the program is needed. The code is divided for two base configurations: wing-grids completely retracted and completely unfolded. From each base configuration, every possible combination of the wing-grids' position is covered by means of conditional loops. To change the two base configurations, the value of the switch changes

from 0 to 1 or vice versa when it is pressed, giving Arduino Uno information of the current configuration.

5.6 Model Assembly

The design of the wings and wing-grids was based in a previous project [1]. Additive technology (3D printing) was used to make the model. Due to the limits in size of the printing machine, few modifications in the original design were needed (see configuration and dimensions section). Polymeric adhesive was used to join the structural elements together.

In addition, to integrate the structure of wing and wing-grids and the hardware elements and facilitate its use, a wood base was designed and built. The final result is shown in Figure 4.

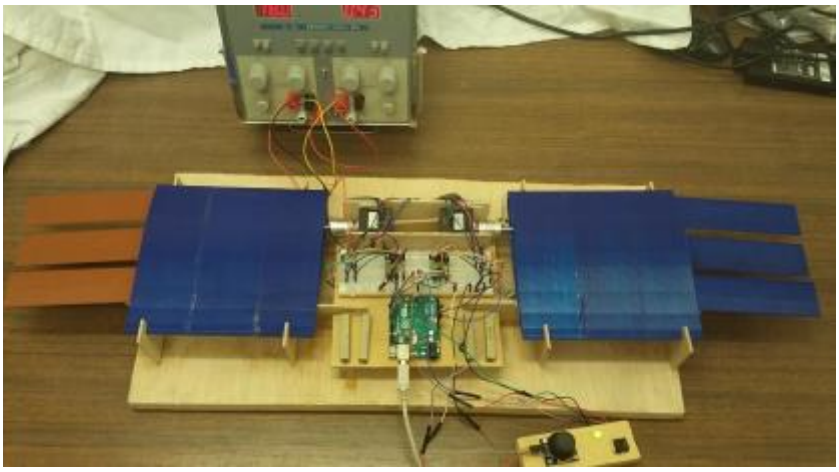

Figure 4: Prototype and control system.

7 CONCLUSIONS

Basically in this paper has been presented the main features related to modify the external aspects of wings and how to adapt them to the flight requirements by means of specific controllers. The vehicles considered in this paper are those named biometics aircraft, although small aircrafts are also included in this study.

The materials used to include modifications on wings are polymers well adapted to change their external configuration and strong to fly the required flight conditions. In the sense of move the wing devices to acquire the flight qualities, several control techniques were introduce to design a suitable control laws. Both PID techniques and adaptive techniques were included as candidates to design the controller.

Future work will focus on increase the size of the model, on carry out the aerodynamic test in wind tunnel, on calculating the mathematical model of the system and a deep formulation of the control law.

8 REFERENCES

[1] Barcala-Montejano, M. A., Rodríguez-Sevillano, A. A., Bardera-Mora, R., García-Piqueras, M. D. "Fabricación mediante prototipado rápido de un micro UAV (MAV) biomimético controlado por wing grids". Congreso CivilDRON'16. 26-27 January 2016. Minutes Book.

[2] La Roche, U. and La Roche, H. L. (2004): "Induced Drag Reduction Using Multiple Winglets, Looking Beyond the Prandtl-Munk Linear Model". AIAA Paper No. AIAA-2004-2120.

[3] Tucker, V. A. (1993): Gliding Birds: "Reduction of Induced Drag by Wing Tip Slots Between the Primary Feathers". Department of Zoology, Duke University, Durham.

[4] Bennett, D. (2001): "The Wing Grid: A New Approach to Reducing Induced Drag".

[5] Shportenko, D. (2016): "Sistema de Control por Wing Grids de un Micro RPAS". Unpublished end-of-degree project. Speciality of aircraft and spacecraft, Universidad Politécnica de Madrid.

[6] John Valasek. "Morphing Aerospace Vehicles and Structures", John Wiley and Sons, 2012.

[7] Roger W. Pratt. "Flight Control Systems, practical issues in design and implementation". The Institution of Electrical Engineering.

[8] ARDUINO. Technical specs: https://www.arduino.cc [Search: 08/02/2017].

[9] POLOLU. Robotics & Electronics. Stepper Motor: Bipolar, 200 Steps/Rev, 35×36mm, 2.7V, 1 A/Phase [online]. < https://www.pololu.com/product/1209/specs>. [Search: 08/02/2017].

Ballistic impact response of a new smart structure material designed by fibre metal laminates

XiaoWei Xie, SuJun Wu*

College of Material Science & Technology, Beihang University, Beijing 100191, PR China

ABSTRACT

Traditionally, monolithic metal materials are widely used as military armor for its relative high mechanical strength, however, the disadvantages of reduced maneuverability due to heavy weight and the phenomenon of adiabatic shear which may result catastrophic accidents, make it hard to meet the requirement of modern military materials. The transformation induced plasticity (TRIP) steel has good ballistic impact performance resulting from high strength and plasticity, absorbing more impact kinetic energy induced by high strain rate and temperature. In this paper, we designed a new smart structure material consisting of a series of TRIP steel sheets and glass fibre reinforced composite layers based on fibre metal laminates(FMLs), the embedded lightweight composite sharply decreases areal density and hinders metal petalling. The mechanical behavior of TRIP steel under the circumstance of high strain and high strain rate is investigated by Hopkinson test, then ABAQUS/Explicit is used to simulate ballistic impact performance of a new structure material by simplifying the mechanical properties of TRIP steel. Moreover, the contribution of both TRIP steel and composite under ballistic impact is also discussed by damage mechanisms.

Key Words: TRIP steel, FMLs, Hopkinson test, ballistic impact

BIOMIMETIC MICRO AIR VEHICLE CONTROLLED BY WING-GRIDS

ÁNGEL A. RODRÍGUEZ-SEVILLANO1*, MIGUEL A. BARCALA-MONTEJANO[1], RAFAEL BARDERA-MORA[2], MARINA LEÓN-CALERO[2], JAIME GARCÍA-RAMÍREZ[1], AND JOAQUÍN DE NOVA-TRIGUEROS[1]

[1] Escuela Técnica Superior de Ingeniería Aeronáutica y del Espacio
Universidad Politécnica de Madrid.
Plaza del Cardenal Cisneros, 28040 MADRID, Spain.

[2] Instituto Nacional de Técnica Aeroespacial (INTA)
Carretera de Ajalvir, km 4,5. 28850 Torrejón de Ardoz (MADRID), Spain

Keywords: wing-grid, micro air vehicle (MAV), force measurements, particle image velocimetry.

Abstract. Over the last years, the experience of the authors has focused on the design of micro unmanned aerial vehicles (RPAS or drones), but whose most important and distinguishing feature of this research has been the concept of bioinspiration. This paper shows the analysis and feasibility of wing-grids that emulate the wingtip feathers of birds. In aerospace design, these wing-grids are applied to modify the lift distribution over the wing; beside this, it is possible to reduce induced drag. These wing-grids will be deployed in loiter and cruise phases of the profile mission; with this deployment, the total drag of the airplane will be reduced, and the endurance or the range will be increased. Asymmetrically deployment of the wing-grids will be developed in order to turn the drone along the roll axis, such an aileron actuator. Based on this proposal, a conceptual prototype was designed and built. This prototype has been manufactured in a 3D printer, and a testbed for the wing-grids performance have been also carried out. As a result, this work focuses on the development of a versatile and low cost control system for a micro unmanned aircraft. In the present paper, force measurements and particle image velocimetry wing tunnel tests have been developed to study the aerodynamic effect of wing-grid technology.

1 INTRODUCTION

Unmanned Aerial Vehicles present interesting advantages to deal with dull activities, dirty environment, dangerous missions or deep profiles (long endurance or range) [1]. Furthermore, UAVs are an encouraging solution to prevent human from risky situations. A high demand of smaller vehicles to satisfy these missions have led designers to focus on micro air vehicles. Hence, engineers must find solutions to compensate the limits generated by low-aspect-ratio wings at low Reynolds number [2].

Drag is one of the primary drawbacks which limits aircraft performances [3]. Along years, induced drag reduction without wing-span increment has been investigated by several authors [4]. Solutions to several problems have resulted from nature observation [5]. Biologist found that birds such as eagles, hawks, condors, vultures and ospreys have high lift wings with

slotted feathers at the ends which allow drag reduction during gliding performances [4].

Notice that, the induced drag results from the vortices shed by the wing and it is proportional to the spacing and radii of them. One promising biomimetic design is the wing grid based on La Roche investigations in 1993 [6]. Wing grid solution forces the vortices farther apart and creates larger core radii [3]. Hence, while the wing span is increased by winglets deployment, the induced drag is reduced [7, 8]. In other words, wing-grid technology has a lower induced drag than a rectangular wing with the same wingspan [9].

Although few aircraft present this kind of design, several experimental studies have been developed to demonstrate the effectiveness of these devices [10]. Bennett tests [3] showed that wing-grids improve aerodynamic performances at low angle of attack (AoA) and at condition above the critical Reynolds number up to a certain value of velocity (27 m/s). Hence, it is a good approach for cruise and loiter phase, as well as gliding performances [11].

Regarding attitude control, modern designs with in-flight configuration variation have been developed recently [12, 13]. Wing-grid configuration also presents rolling performances capability by performing an antisymmetric deployment of the winglets [14]. These second skill allow to control the UAV with no need of aileron devices.

The preliminary aerodynamic study [14] of the wing-grid analysed in this paper was based on computational method. Vortex lattice method, lift line theory and panels' method (by means of XFLR5 software) were used to determine the aerodynamic performances of the wing-grid retracted case. In the present study, experimental aerodynamic results are presented to study the effectiveness of wing-grid technology at different configurations (wing-grid retracted and deployed) by incrementing the AoA. In addition, a rectangular wing with the same wing-span as the wing-grid extended case has been analysed. Six-axis force/torque transducer was used to show the lift and drag improvements obtained with wing-grid extended state. Particle image velocimetry tests were also developed to determine the flow structure at 2/3 of the half-wing which is known as the point where the lift is maximum.

2 WING GRID DESIGN

The wing-grid model studied in this paper is the result of a preliminary design developed recently at Universidad Politécnica de Madrid (Spain). Regarding drag reduction [6-11] which can be obtained with this configuration, a wing-grid with three-winglet were constructed. As stated, the possibility to develop flight performances without lift surface control add another advantage to carry out investigations in this field. In this preliminary design, winglets are expected to perform rolling control as well as improve UAV efficiency by increasing the total wing-span of the wing (see Table 1) and reducing the induced drag.

Table 1: Wing-grid dimensions

Configuration	Wing-grid retracted	Wing-grid extended
Aspect Ratio	6	8
Wing span (m)	0.54	0.72
Chord (m)	0.09	0.09
Wing area (m^2)	0.0486	0.0648

Regarding the small size of micro-UAVs, an electrical engine with a tractor propeller have

been installed as Figure 1.a shows. Notice that the V-tail is also based in birds' constitution. The winglets of the wing-grid are three small semi-wings (see Figure 1.b) with zero sweep and taper ratio and with the same angle of attack as the wing.



Figure 1. (a) Wing-grid preliminary design; (b) wing-grid winglets detail.

The winglets, which have a gap of 5 mm between them, are manufactured with a mounting and moved linearly with an engine located inside the fuselage. The wing inner design has been developed taking into account the room required to accommodate the winglets when they are retracted.

3 EXPERIMENTAL SETUP

3.1 Force measurements

Wind tunnel and wing-grid model

Force measurements were carried out in the wind tunnel A112 of Universidad Politécnica de Madrid (Spain) which is an Eiffel-type. The open return wind tunnel has a rectangular closed test section of 1 × 1.2 m^2. Four axial power units with 15 CV provide a maximum speed of 50 m/s and the stabilization section allows to reduce the maximum turbulence intensity up to 0.5 % of the freestream. The wind tunnel design was based on the criterion to allow an easy access to locate the model in the testbed. In addition, a positioning system integrated by a strut and an engine to select the yaw and pitch angle is installed in the floor of the test section.

Three different configurations were tested: retracted wing-grid, extended wing-grid and a rectangular wing with the same wing span as the extended wing-grid case. Regarding the wind tunnel limitations (0.8 m maximum span), it is possible to test a full scaled model. The 1:1 models tested was made of acrylonitrile butadiene styrene (ABSplus) which is a thermoplastic commonly used in additive manufacturing. This technique presents encouraging advantages such as time-saving, cost-effective and accuracy for preliminary aerodynamic investigation [16, 17].

Tests were conducted at 16 m/s (Reynolds number of 9.2 × 10^4, based on the chord of the wing). Figure 3 shows the rectangular wing model installed in the wind tunnel test section. The model is located in the strut which includes a fairing structure to reduce the interference

with the flow and avoid force error measurements.

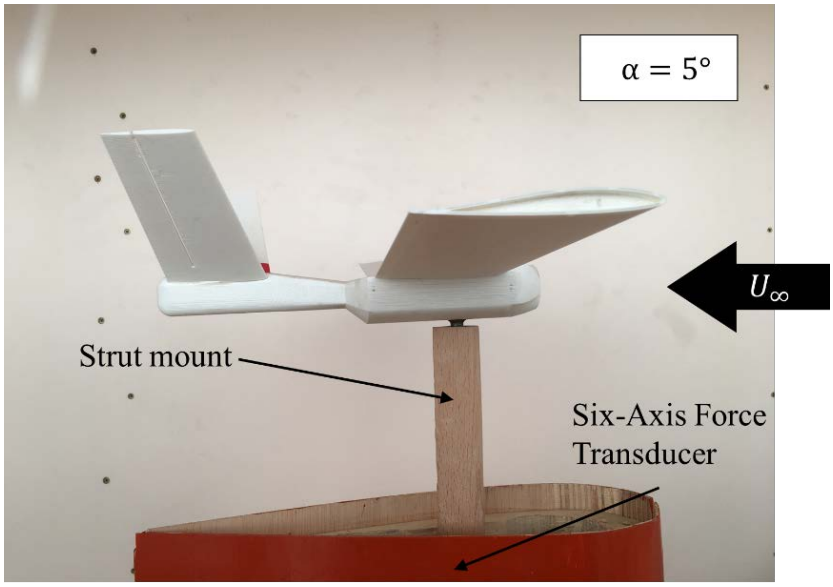

Figure 2. Rectangular wing at α = 5° installed in the fairing pod.

Six-axis force/torque transducer

A Six-Axis Force/Torque Transducer is a load cell made of sensitive silicon strain gauges which measure force and torque loads. The high accuracy, sensitivity and the capability to provide force and torque measurements make it an instrument widely used throughout industry [17].

An ATI Mini40 was used to obtain lift (L) and drag (D) of the wing-grid model. The transducer is connected to a signal amplifier, so the output values are in voltage. A Labview software was developed to record the data acquisition which includes a post-processing algorithm to transform the electrical signal into force/torque taking into account a calibration matrix provided by the manufacturer. The recording time was 4 minutes with a sampling time of 1993 Hz, so an average value of the forces is calculated.

Notice that, the transducer was linked to the gravity centre of the model, so the reference frame of the force resulted is body axis. Hence, the forces L and D are computed by projecting in wind axis the recorded values. Furthermore, the weight load was removed at the initial state when the speed of the tunnel is zero.

The results have been presented in non-dimensional parameters by using the classical procedure to determine the aerodynamic coefficients,

$$C_L = \frac{L}{\frac{1}{2}\rho V^2 S_{ref}} \tag{1}$$

$$C_D = \frac{D}{\frac{1}{2}\rho V^2 S_{ref}} \tag{2}$$

Where C_L and C_D are the lift and drag coefficients, L and D are the lift and drag forces, ρ is the density of the flow, V is the velocity of the tunnel and S_{ref} is the reference surface (wing area).

3.1 Flow field velocity measurements

Wind tunnel and wing-grid model

The experiments to study the flow field velocity at 2/3 of the wing were carried out in a low-speed wind tunnel at the facilities of Instituto Nacional de Técnica Aeroespacial (INTA), located in Madrid (Spain). The wind tunnel INTA-T1 has a closed-circuit and an open test section with an elliptical nozzle of 2 × 3 m^2. The maximum freestream velocity is 60 m/s and the turbulence intensity is lower than 0.5 %.

The 1:1 half-model was also made of ABSplus which was installed over a vertical wall based on the aerodynamics images method as a mirror image. The tests were conducted at 10 m/s which implies that the Reynolds number of the experiments is 6.2 × 10^4 based on the chord of the wing (0.09 m), so the results obtained in both wind tunnels can be compared. Figure 2 shows the wing grid aircraft half-model located in the vertical wall in test section. Experimental tests imply that the wall generates a shear layer which perturbs the results. However, the wing section investigated is far from the wall so it can be assumed that it is not affected by that region.

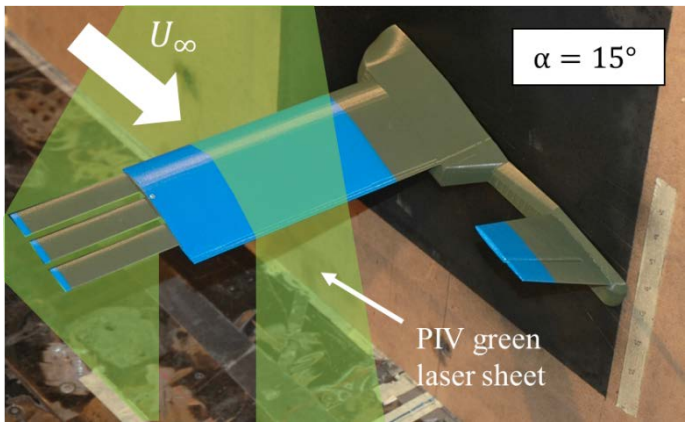

Figure 3. Extracted wing-grid model located in the vertical wall at α = 15°.

Particle image velocimetry

Particle Image Velocimetry (PIV) is a technique which uses instantaneous flow field information to obtain flow characteristics. The flow information was obtained by using Laskin nozzle atomizers [18] which generate olive oil tracer particles with a diameter of the order of 1μm [19]. These particles were illuminated with two Neodymium: Yttrium Aluminium Garnet (Nd:YAG) lasers with a maximum energy of 190 mJ per pulse and a pulse separation time (Δt) of 25 μs.

A total of 200 pair of images were recorded by a high-resolution CCD camera (2048 × 2048 pixels) which captured the scattered light by the tracers. These images were subsampled into small interrogation windows of 32 × 32 pixels in size [20] and an overlapping of 50 % in

both directions following the Nyquist sampling criteria [21-23]. The camera Field of View (FOV) was 250 × 250 mm^2. The spurious vectors were eliminated by using a post-processing analysis with a local mean filter of 3 × 3 pixels in size.

The velocity vectors in each interrogation window were computed based on the particle displacement and the pulse separation time. The particle displacement was computed implementing a cross-correlation analysis between each pair of images using a 2D fast Fourier transform (FFT) to simplify and speed up the computational process [20]. The stronger peak obtained with this algorithm corresponds to the averaged motion of the particles within the interrogation window. This correlation peak is located with sub-pixel accuracy by fitting a Gaussian curve [20].

The results will be represented in non-dimensional variables as Eq. 3 and 4 shows.

$$V^* = \frac{\sqrt{u^2 + v^2}}{U_\infty} \tag{3}$$

$$TI = \frac{\sqrt{\sigma_u^2 + \sigma_v^2}}{U_\infty} \tag{4}$$

Where V^* is the non-dimensional velocity, u and v are the horizontal and vertical velocity components, U_∞ is the freestream velocity (wind tunnel for this case), TI is the turbulence intensity and σ_u and σ_v are the standard deviation of the horizontal and vertical velocity components.

4 RESULTS

Figure 4 shows the lift coefficient versus angle of attack (AoA) for three tested configurations. Two regimes can be differentiated: above and below zero degrees of angle of attack. Positive angle of attack provides higher lift for the rectangular wing case as expected, but slightly difference is found with wing grid case. The lower lift coefficient is generated for the retracted wing-grid configuration. Opposite trend is observed for negative angles of attack.

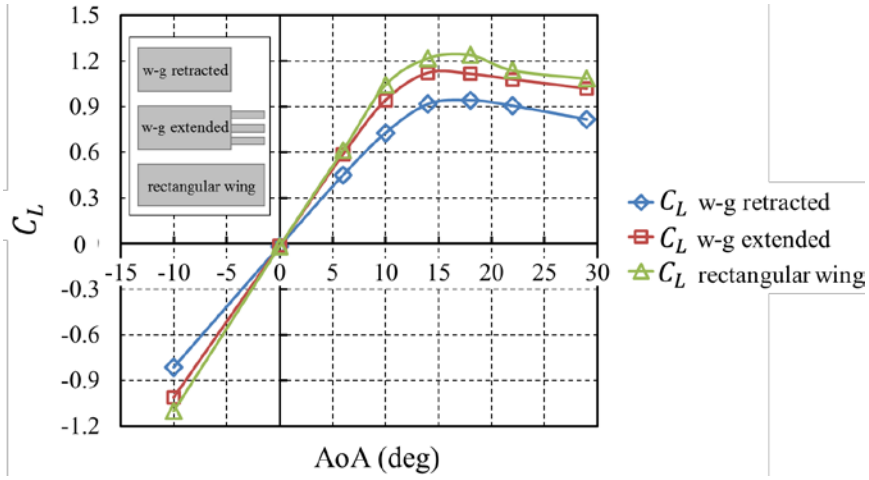

Figure 4. Lift coefficient at different AoA for each wing-grid configuration.

In addition, it is interesting to say that the critical angle of attack (stall condition) is lower than 15° for the extended wing-grid. The critical angle of attack (stall condition) of the retracted wing-grid and rectangular wing is higher than 15°.

Figure 5 shows polar curve plotted as the drag coefficient versus lift coefficient. As it can be expected, the drag coefficient increases for rectangular wing with the maximum wing span and extended wing-grid configuration. However, the extended wing-grid shows lower increment than rectangular wing.

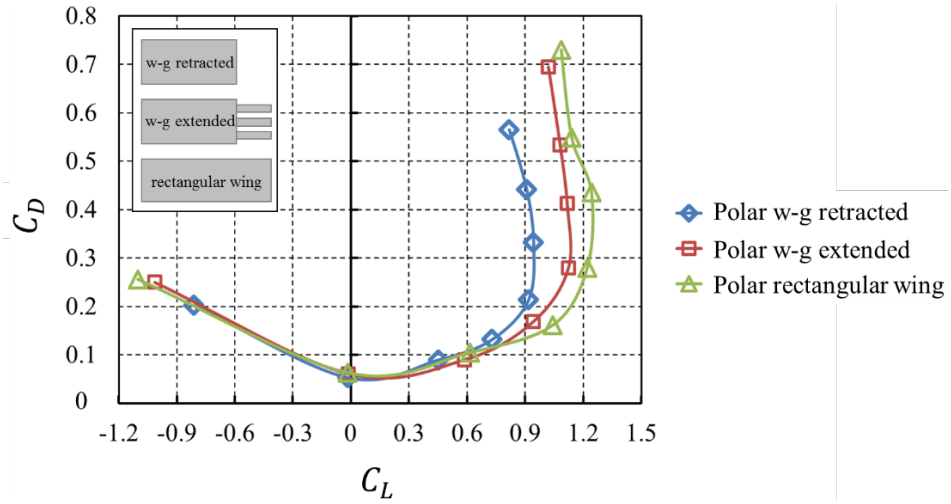

Figure 5. Polar curve for each wing-grid configuration.

Variables resulted from velocity measurements obtained with the PIV technique are presented in Figure 6. The non-dimensional velocity (V^*) indicates that the increment of the angle of attack (AoA) has worse adverse effect for extended wing-grid case. However, at low angle of attacks (α = 0 - 10°), it is observed a velocity increment that can be associated to the lift increment obtained during force measurements.

Regarding massive flow detachment, extended wing-grid case presents earlier stall generation (α = 15°) as indicated with lift coefficient curves.

Figure 6 also provides turbulence intensity maps which show the velocity variation regions. The high turbulence values allow to figure out the area with separation flow known as stall. The high turbulence intensity values can be associated with the drag increment observed during force measurements.

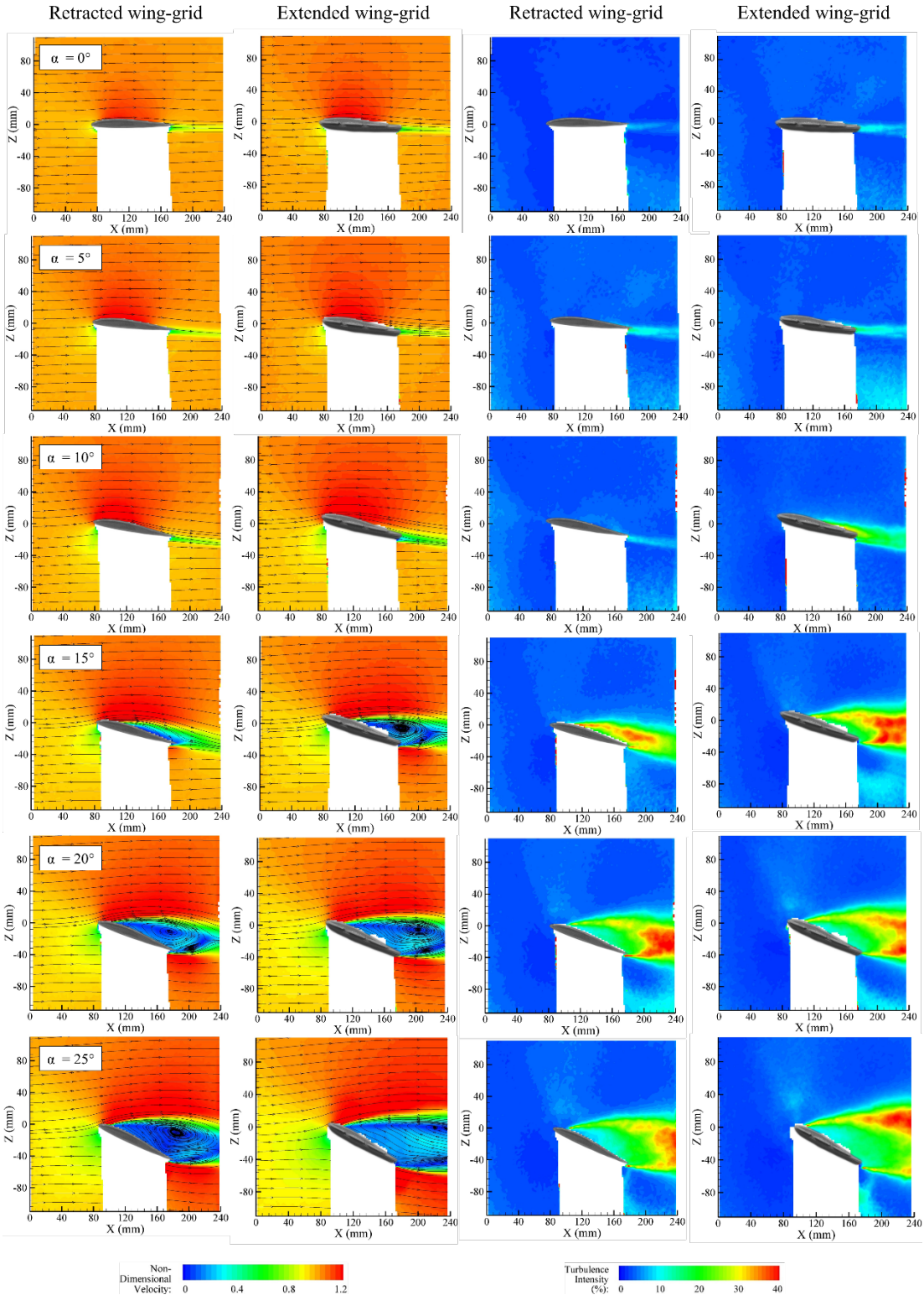

Figure 6. Non-dimensional velocity and turbulence intensity maps for retracted and extended wing-grid configurations at different AoA.

6. CONCLUSIONS

Unmanned Aerial Vehicles present interesting advantages to deal with dull activities, dirty environment, dangerous missions or deep profiles (endurance or range) [1]. Drag is one of the primary drawbacks which limits aircraft performances [3]. Wing-grid technology appeared from nature observation as a solution to reduce induced drag without increasing the wing-span.

The wing-grid model studied in this paper is the result of a preliminary design developed recently [14] at Universidad Politécnica de Madrid (Spain). Regarding birds' complexion, the wing-grid model studied in this paper is characterized by a three-winglets and a V-tail. Furthermore, the low weight implies that an electrical engine with a tractor propeller can be used for thrust generation.

In the present paper, three different wing configurations have been analysed: retracted wing-grid, extended wing-grid and rectangular wing. Although the later has the same top view as the retracted wing-grid, they differ in the aspect ratio for the same chord length. Hence, the rectangular wing configuration means that it has the same wing span as the retracted wing-grid case.

Force measurements were carried out by means a six force/torque transducer. Lift and drag coefficient were obtained with the aim to study the effect of changing the wing span and the winglets presence. The results showed that for a higher the wing span the lift and the drag are increased as it can be expected. However, the lift generated at the winglets case is close to the value obtained for the extended wing-grid case but a drag reduction is also obtained as other authors indicated [6-11].

Finally, particle image velocimetry technique was used to obtain flow field information at 2/3 of the half-wing span known as the point where the maximum lift is obtained. The results showed that, at high angle of attacks, extended wing-grid case has a higher massive detachment flow than at the retracted case as expected [3]. However, at low angles of attack (0° - 10°) it is observed a velocity increment which can be associated to the lift increment. In addition, turbulence intensity maps show the stall region which can be associated with drag increments for the extended wing-grid configuration.

7. ACKNOWLEDGEMENTS

The researcher team would like to thank to the undergraduate students who have taken part in the wind tunnel test campaign: D. Arrones, E. Sánchez and C. Cabaleiro.

REFERENCES

[1] Austin, R. (2011). *Unmanned aircraft systems: UAVS design, development and deployment* (Vol. 54). John Wiley & Sons.

[2] Torres, G. E., & Mueller, T. J. (2004). Low aspect ratio aerodynamics at low Reynolds numbers. *AIAA journal*, *42*(5), 865-873.

[3] Bennett, D. (2001). The Wing Grid: A New Approach to Reducing Induced Drag.

[4] Smith, M., Komerath, N., Ames, R., Wong, O., & Pearson, J. (2001). Performance analysis of a wing with multiple winglets. In *19th AIAA Applied Aerodynamics Conference* (p. 2407).

[5] Meseguer, J., & Sanz-Andrés, A. (2007). Aerodinámica del vuelo: aves y aeronaves. *Cuadernos Aena*, *9*.

[6] La Roche, U. y La Roche, H. L. (2004).: "Induced Drag Reduction Using Multiple Winglets, Looking Beyond the Prandtl-Munk Linear Model". AIAA Paper No. AIAA-2004-2120.

[7] Kroo, I. (2001). Drag due to lift: concepts for prediction and reduction. *Annual Review of Fluid Mechanics*, *33*(1), 587-617.

[8] Bushnell, D. M., & Moore, K. J. (1991). Drag reduction in nature. *Annual Review of Fluid Mechanics*, *23*(1), 65-79.

[9] La Roche, U., & Palffy, S. (1996, September). Wing-grid, a novel device for reduction of induced drag on wings. In *ICAS PROCEEDINGS* (Vol. 20, pp. 2303-2309).

[10] Tucker, V. A. (1993). Gliding birds: reduction of induced drag by wing tip slots between the primary feathers. *Journal of Experimental Biology*, *180*(1), 285-310.

[11] Thiede, P. (2001). Aerodynamic Drag Reduction Technologies: Proceedings of the CEAS/DragNet European Drag Reduction Conference, June 2000, Potsdam.

[12] Barcala-Montejano, M. A., Rodríguez-Sevillano, A. A., Crespo-Moreno, J., Bardera-Mora, R., & Silva-González, A. J. (2015, June). Optimized performance of a morphing micro air vehicle. In *Unmanned Aircraft Systems (ICUAS), 2015 International Conference on* (pp. 794-800). IEEE.

[13] Jones, K. D., Bradshaw, C. J., Papadopoulos, J., & Platzer, M. F. (2005). Bio-inspired design of flapping-wing micro air vehicles. *The Aeronautical Journal*, *109*(1098), 385-393.

[14] Barcala-Montejano, M. A., Rodríguez-Sevillano, A. A., Bardera-Mora, R., García-Piqueras, M. D. Fabricación mediante prototipado rápido de un micro UAV (MAV) biomimético controlado por wing grids. Congreso CivilDRON'16. 26-27 enero 2016. Libro de actas. (spanish).

[15] Springer, A. (1998). Evaluating aerodynamic characteristics of wind-tunnel models produced by rapid prototyping methods. *Journal of Spacecraft and rockets*, *35*(6), 755-759.

[16] Tyler, C., Braisted, W., & Higgins, J. (2005). Evaluation of rapid prototyping technologies for use in wind tunnel model fabrication. In *43rd AIAA Aerospace Sciences Meeting and Exhibit* (p. 1301).

[17] Rodriguez Sevillano, A. A., Barcala Montejano, M. A., & Sacristán Callejo, S. (2014). The development of a wind tunnel DAQ system by using Labview tools. *Applied Mechanics and Materials*, *629*, 467-474.

[18] Echols, W.H., and Young, J., "Studies of portable air-operated aerosol generator," Studies of Portable Air-Operated Aerosol Generators, 1963,

[19] Kähler, C., Sammler, B., and Kompenhans, J., "Generation and control of tracer particles for optical flow investigations in air," Experiments in Fluids, Vol. 33, No. 6, 2002, pp. 736-742.

[20] Prasad, A.K., "Particle image velocimetry," Current Science-Bangalore-, Vol. 79, No. 1, 2000, pp. 51-60.

[21] Raffel, M.,Willert, C. E.,Wereley, S. T.,Kompenhans, J. Particle ImageVelocimetry: A Practical Guide. Springer, 2007.

[22] Adrian, R. J. Particle-imaging techniques for experimental fluid mechanics. Annual Review of Fluid Mechanics 1991, 23: 261-304.

[23] Adrian, R. J., Westerweel, J. Particle Image Velocimetry, Cambridge University Press, 2011.

VIII ECCOMAS Thematic Conference on Smart Structures and Materials
SMART 2017
A. Güemes, A. Benjeddou , J. Rodellar and Jinsong Leng (Eds)

PIEZOELECTRIC TRANSDUCER ARRAY OPTIMIZATION THROUGH SIMULATION TECHNIQUES FOR GUIDED WAVE TESTING OF CYLINDRICAL STRUCTURES

XUDONG NIU[1,2], HUA-PENG CHEN[1]* AND HUGO R. MARQUES[2]

[1]Department of Engineering Science
University of Greenwich
Chatham Maritime, Kent ME4 4TB, UK
E-mail: x.niu@gre.ac.uk

[2]TWI Ltd. Granta Park, Cambridge, Cambridgeshire, CB21 6AL, UK

*Corresponding author: E-mail: h.chen@gre.ac.uk

Key words: Piezoelectric Transducer Array, Finite Element Modelling, Ultrasonic Guided Wave, Guided Wave Testing, Pipe Inspection, Structural Health Monitoring

Abstract. Guided wave testing as an advanced non-destructive method is a fast-growing field in structural health monitoring of engineering structures. Oil and gas pipelines are one of the major applications where the technology is particularly attractive. This is mainly due to the ability of guided waves to propagate over long distances (up to tens of meters) with a high sensitivity to changes in the structure on the propagation path. Guided wave testing enables the identification of defects and its location on the pipe circumference. Commonly a circumferential array of piezoelectric transducers clamped around the surface of the pipe is used to transmit and receive guided waves. The sensitivity of the operation is of 3 - 9 % of cross–sectional area reduction, depending on the signal-to-noise ratio. Optimisation of the transducer array design to increase performance in pipe inspection without significant increase in manufacturing and testing costs, is an area of interest for the industry. In this paper is presented part of the on-going research been carried out focusing on ultrasonic guided wave inspection of steel pipe structures. Here is described the propagation characteristics of an individual transducer and the propagation and defect sensitivity of a circumferential array design using finite element analysis (FEA) models with excitation of the axisymmetric torsional wave mode T(0,1).

1 INTRODUCTION

Pipeline transportation is a useful method to transport goods or materials through a pipe in an industrial setting. There are over 3 million kilometres of pipeline in the world. Many of these pipelines carry explosive and flammable material such as oil or natural gas. Serious incidents of structural failure have occurred owing to loss of pipe wall thickness by corrosion, fatigue cracks or manufacture anomalies. To reduce these, non-destructive testing (NDT) and structural health monitoring (SHM) systems have been used in engineering applications. NDT techniques are used to evaluate the properties of a specimen without causing damage.

Commonly used technologies include X-ray inspection, ultrasonic testing (UT), and guided wave (GW) testing, among others. GW testing has however a significant advantage over other techniques for pipeline inspection. GW testing makes use of lower frequency elastic waves when compared with UT, typically from 20 *kHz* to 100 *kHz* [1], which allows for propagation of guided waves for many tens of metres with minimal attenuation (depending of the structure condition and surrounding environment), making it ideal for pipeline screening. The main advantage of guided waves is that they can in principle propagate over a long distance with a high susceptibility to interference on a propagation path [2].

Sharan et al [3] described that some main features of GW pipe inspection systems are high sensitivity (3 - 9 % of cross – sectional area) depending on the signal-to-noise ratio (SNR)) and the operating frequency (10 to 100 *kHz*). Piezoelectric transducers are commonly used in GW pipe inspection system as the devices that convert electrical signals into vibrations and vice-versa. These are attached to pipes in groups (transducer arrays) working together to manipulate the transmission and reception of ultrasonic guided waves.

In this paper, is presented the first steps towards optimisation of transducer arrays for pipe inspection with the study of GW propagation on a 3 *m* long, 6-inch (168.3 *mm* outer diameter), schedule 120 (14.27 *mm* wall thickness) steel pipe modelled using FEA. A simulated pipe inspection setup with 1 transducer operating as transmitter exciting the T(0,1) mode (0 is the zeroth circumferential order, 1 is the first torsional wave mode) and an array of 24 transducers operating as receivers was modelled and then verified through empirical validation. Also evaluated was the defect detection sensitivity of an array of 24 transducers operating as transmitters and as receivers on a pipe model with a notch.

2 FREQUENCY RANGE AND WAVE MODE CHARACTERISTICS

Ultrasonic GWs have been widely-used to measure at frequencies ranging approximately between 20 *kHz* and 100 *kHz*. Løvstada & Cawley [4] described that a selection of excitation GW mode and frequency range is essential for an effective function of ultrasonic guided waves in defect sizing. The relation between GW modes and frequency is commonly presented in so-called dispersion curves. Wilcox et al. [5] discussed the effects of dispersion on a long-range inspection system using ultrasonic GWs. With a high number of GW modes with variable displacement characteristics in existence, Silk and Bainton [6] established a nomenclature of X (*n*, *m*) to describe these. The X represents a letter (L, T, or F, for longitudinal, torsional or flexural, respectively) that relates to characteristics of the individual GW modes. The *n* is a positive integer giving an identification of harmonic variation of displacement around the circumference of the pipe or pipeline (the circumferential order), and *m* is an index which indicates the mode order of occurrence.

Figure 1 presents the phase and group velocity dispersion curves for a 6-inch (168.3 *mm* outer diameter) and schedule 120 (14.27 *mm* wall thickness) steel pipes. These dispersion curves were generated by DISPERSE [7] version 2.0.20a. Figure 2 shows displacement shapes of some guided wave modes (axisymmetric and non- axisymmetric modes) at 60 kHz. The T(0,1) mode is the first torsional axisymmetric mode with zeroth circumferential order. Longitudinal axisymmetric modes of L(0,1) and L(0,2) are also a zeroth circumferential order with first and second mode shapes, respectively. Non-axisymmetric flexural modes (up to n = 1) of F(1,1), F(1,2) and F(1,3) are a first circumferential order with a first, a second and a

third mode shapes, respectively. The effective characteristics of displacement shapes are generated using DISPERSE [7] software.

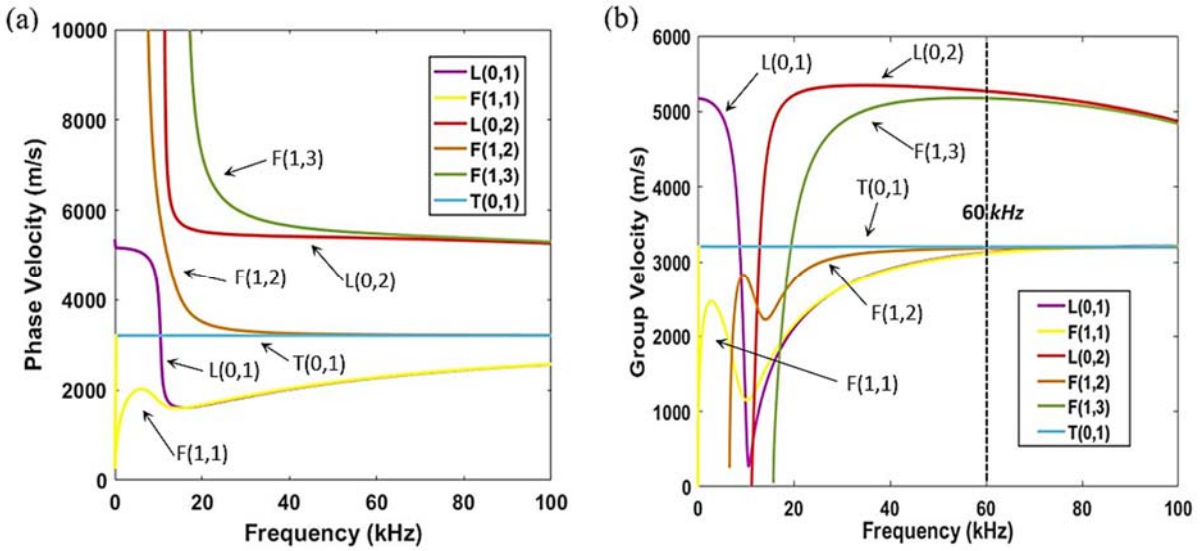

Figure 1: (a) Phase & (b) Group velocity dispersion curves for a 6-inch (168.3 *mm* outer diameter), schedule 120 (14.27 *mm* wall thickness) steel pipe

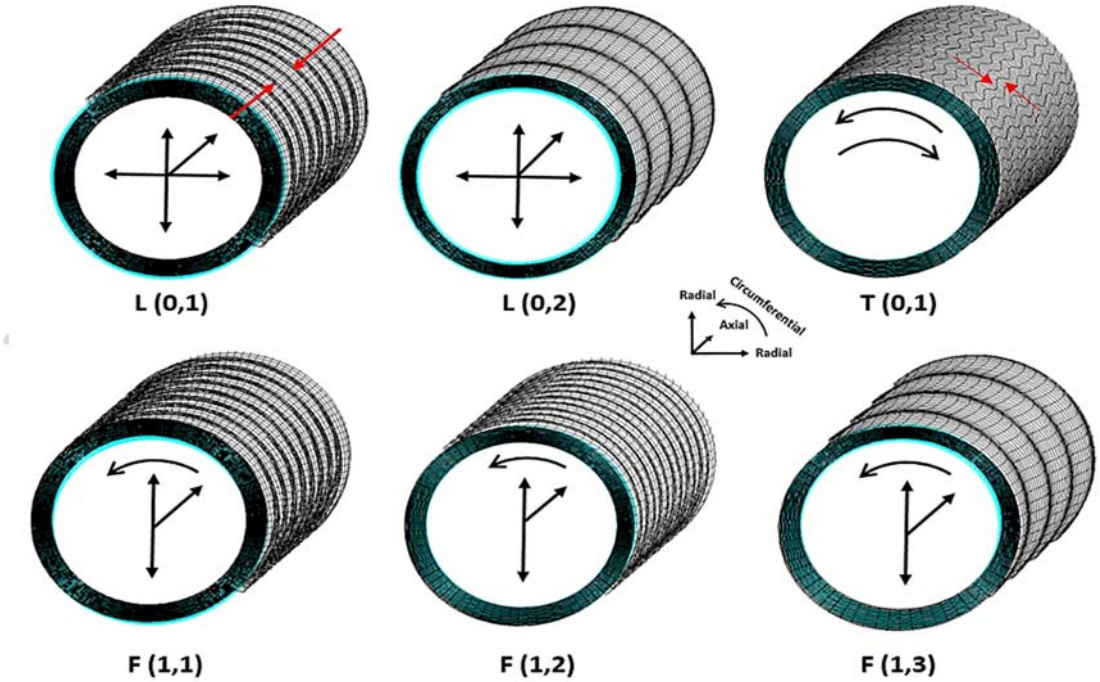

Figure 2: Selection of displacement shapes of guided wave modes in a 6-inch (168.3 *mm* outer diameter), schedule 120 (14.27 *mm* wall thickness) steel pipe at 60 *kHz*

3 THEORY

The wave mode selected for excitation by the system is the axisymmetric T(0,1) mode at 60 *kHz*. This mode is attractive for testing because it is non-dispersive, that is, with a velocity independent of frequency. However, a relatively narrow bandwidth signal was used to limit the dispersion of the other modes present within the frequency bandwidth over the propagation distance. The transmission signal is an n-cycle Hanning windowed tone burst given by Equation (1)

$$F(t) = \begin{cases} 0.25A\left[1 - \cos\left(\frac{2\pi ft}{n}\right)\right]\sin(2\pi ft) & 0 < t < t' \\ 0, & t > t' \end{cases} \tag{1}$$

where A is the amplitude, f is the centre frequency of the wave mode, and n is the number of the signal cycles. $t' = n/f$ is the signal impulse time.

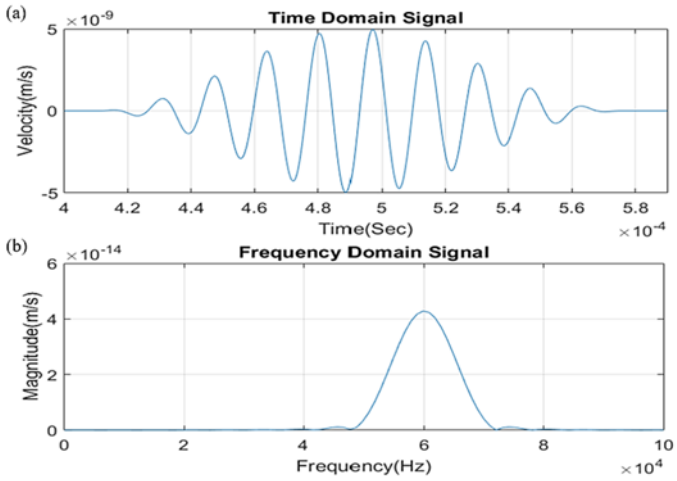

Figure 3: Ultrasonic guided wave signal: excitation (a) time record; (b) frequency spectrum

Shown in Figure 3 is the 60 kHz, 10-cycle Hann windowed signal in the time and frequency domain. The wave mode T(0,1) was excited by circumferential motion. The issue of circumferential wave propagation was researched by Viktorov [8]. The boundary values of a hollow cylinder structure were first described by Gazis [9]. The assumed particle displacement components (u_r, u_θ and u_z) are expressed [10]

$$\begin{aligned} u_r &= U_r(r)\cos n\theta\cos(\omega t + kz), \\ u_\theta &= U_\theta(r)\sin n\theta\cos(\omega t + kz), \\ u_z &= U_z(r)\cos n\theta\sin(\omega t + kz), \end{aligned} \tag{2}$$

where the terms u_r, u_θ, u_z are the components of displacement in the radial, circumferential and axial directions, respectively. The terms of $U_r(r)$, $U_\theta(r)$ and $U_z(r)$, which are the corresponding displacement amplitudes composed of Bessel functions in the out-of-plane. n (0, 1, 2, 3, …) is the circumferential order, kz is named the angular wavenumber in the axial (z) direction.

4 FINITE ELEMENT NUMERICAL MODELLING

4.1 Numerical modelling (1 transmitter - 24 receivers)

Finite element analysis has been widely used to simulate propagation of GW mode shapes [11] and their interaction with defects in pipes [12]. ABAQUS as a full 3D model software is used to build all FEA modelling in this paper. All FEA have been undertaken on a 3 *m* long 6 inches (168.3 *mm* outer diameter), schedule 120 (14.27 *mm* wall thickness) steel pipe model. The material properties of the steel pipe model include a mass density (ρ) of 7850 kg/m^3, a Young's modulus (E) of 210 *GPa* and a Poisson's ratio (υ) of 0.3. The single transducer was excited by a 10-cycle Hanning windowed sinusoidal tone burse with the centre frequency of 60 *kHz*, giving a ±12 *kHz* bandwidth. Specific mesh size and time step were selected. The technique aims to simulate pitch-catch setup of ultrasonic GW signals on the steel pipe.

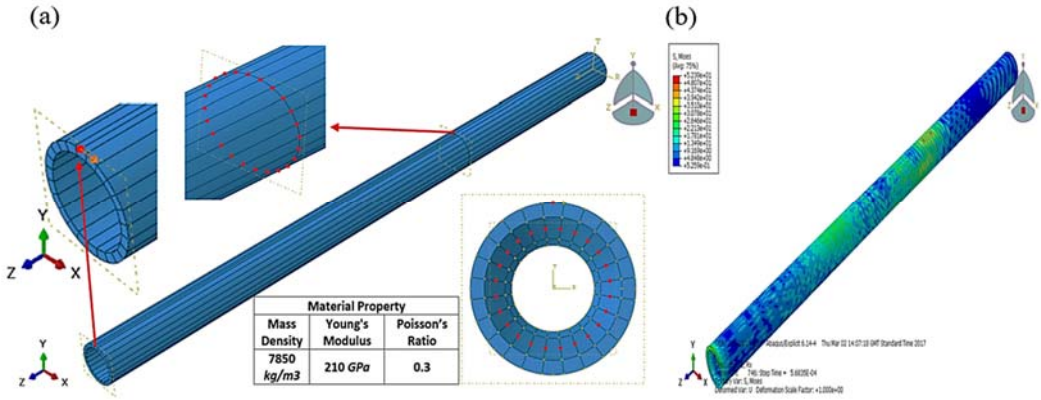

Figure 4: Pitch-catch setup of FEA model for a 6-inch (168.3 *mm* outer diameter), schedule 120 (14.27 *mm* wall thickness) steel pipe (a) placement of single transmitter and of 24 receivers (b) GW modes propagation on steel pipe

The transmitter is placed at the top part of the pipe end while the 24 receivers are placed 2 *m* away from the transmitter, as shown in Figure 3(a). All transducers are modelled as points. The 24 receivers are uniformly distributed around the circumference at the surface of steel pipe. A concentrated force of 10000 *kN* in the circumferential direction is loaded on the transmitter point. A total number of 1382400 elements were generated with a mesh size of 2.5 *mm*. A step time of 380 *ns* was used. Figure 4(b) shows the GW modes generated with relevant amplitude propagating on the pipe. Using the dispersion curves, a time window was determined were the T(0,1) would be received by the transducer array. From the FEA results at the determined time window, the data was collected with the default cartesian coordinate system X (horizontal), Y (vertical), Z (out-of-plane). These were then transformed to cylindrical coordinate system R (radial), T (circumferential), Z (axial) and analysed using MATLAB software. The FEA results can be provided to verify finite element model with a related experiment. The empirical work will be described in the next section.

4.2 Transducer array modelling (24 transmitters - 24 receivers)

Aimed at suppressing undesired GW modes a model was completed using an array of 24

transducers as transmitters. This is a common an effective technique used to reduce the number of undesired GW modes and simultaneously increase the amplitude of desired GWs.

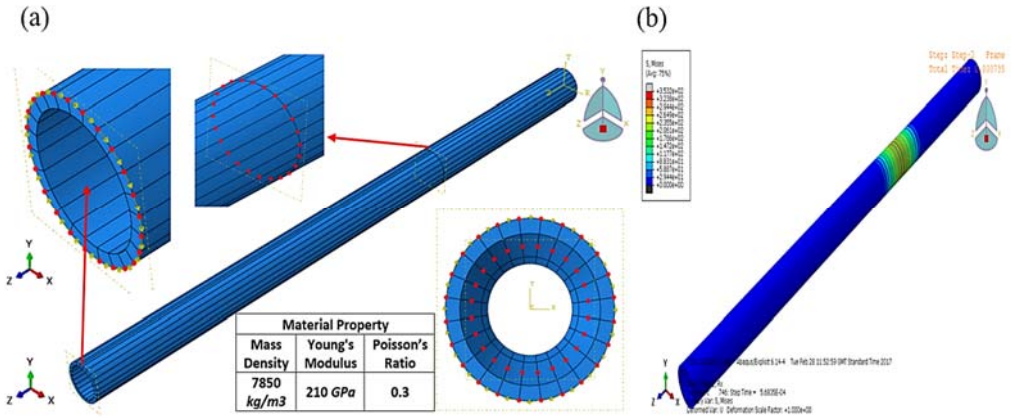

Figure 5: Pitch-catch setup of FEA model for a 6-inch (168.3 *mm* outer diameter), schedule 120 (14.27 *mm* wall thickness) steel pipe (a) placement of array of 24 transmitters and of array of 24 receivers (b) GW modes propagation on steel pipe

Figure 5(a) shows a pitch-catch setup of FEA model for a 6-inch (168.3 *mm* outer diameter), schedule 120 (14.27 *mm* wall thickness) steel pipe. The 24 transmitters (each excited by a tone burst under as a concentrated force of 10000 *kN*) are located uniformly on the pipe end and 24 receivers are placed 2 *m* away from the transmitters. A total number of 172800 mesh elements were generated. A mesh size of 5 *mm* and a step time of 762 *ns* were used. Figure 5(b) shows the GW mode T(0,1) propagating along the steel pipe model, with a significantly high amplitude relatively to other GW modes .

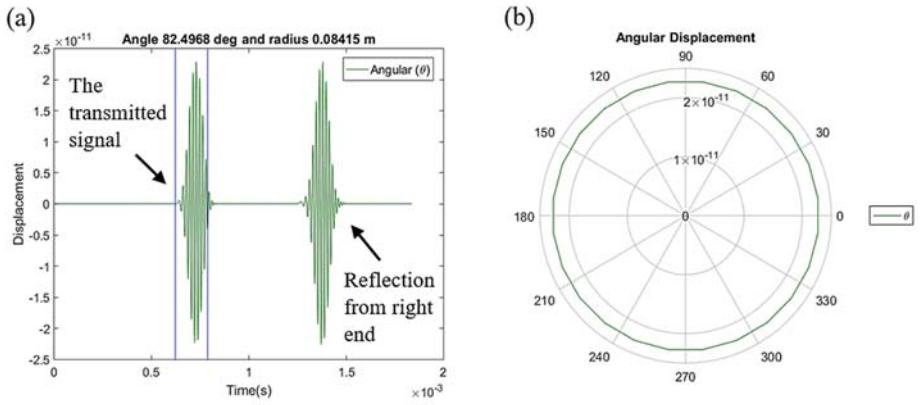

Figure 6: FEA output results for array of 24 transmitters - 24 receivers (a) displacement/time plot (b) polar plot of all maximum displacements in the circumferential direction measured at each of the 24 receivers

The results shown in Figure 6(a). indicate that a high purity torsional wave mode of T(0,1) was generated by the array of 24 transducers when excited by a 10-cycle Hanning windowed sinusoidal tone burse with the centre frequency of 60 *kHz.* Figure 6(b) presents a polar plot of

the maximum values for displacement in the circumferential direction at each of the transducer in the array of receivers. Is noted that completed circle as a plot shape was generated, when no defect in present in the structure.

4.3 Numerical simulation with notch

A FEA of a pipe with a circumferential notch has been set up. The FEA model is a 6-inch (168.3 *mm* outer diameter), schedule 120 (14.27 *mm* wall thickness) steel pipe with a notch 66×10 *mm* in circumferential direction. The notch is located 1.5 *m* away from the array of 24 transmitters. A total number of 830720 elements were generated with a mesh size 2.854 *mm*. A step time of 165 *ns* was used.

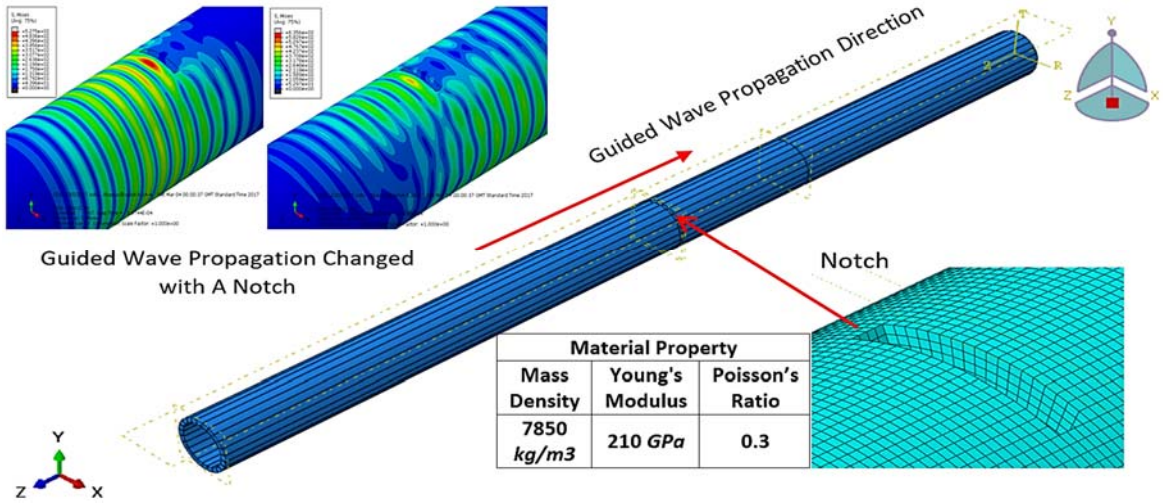

Figure 7: FEA model of steel pipe with a notch in the circumferential direction

The FEA model with the notch location and the T(0,1) wave mode interaction with a notch is presented in Figure 7. The upper-left corner part of Figure 7 shows detail of the T(0,1) propagation and its interaction with notch. A total of four notch sizes were simulated and their details are described in Table 1.

Table 1: Simulated 3D defects for different notch sizes

Section profile of the notch	Surface profile of the notch
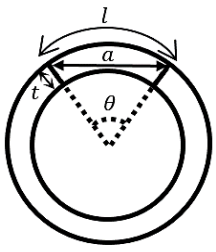	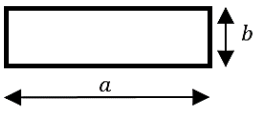 $l_1 = 22\text{mm}, \theta_1 = 15^\circ, b_1 = 10\text{mm}, t_1 = 14.27\text{mm};$ $l_2 = 66\text{mm}, \theta_2 = 45^\circ, b_2 = 10\text{mm}, t_2 = 14.27\text{mm};$ $l_3 = 66\text{mm}, \theta_3 = 45^\circ, b_3 = 1\text{mm}, t_3 = 14.27\text{mm};$ $l_4 = 110\text{mm}, \theta_4 = 75^\circ, b_4 = 10\text{mm}, t_4 = 14.27\text{mm};$

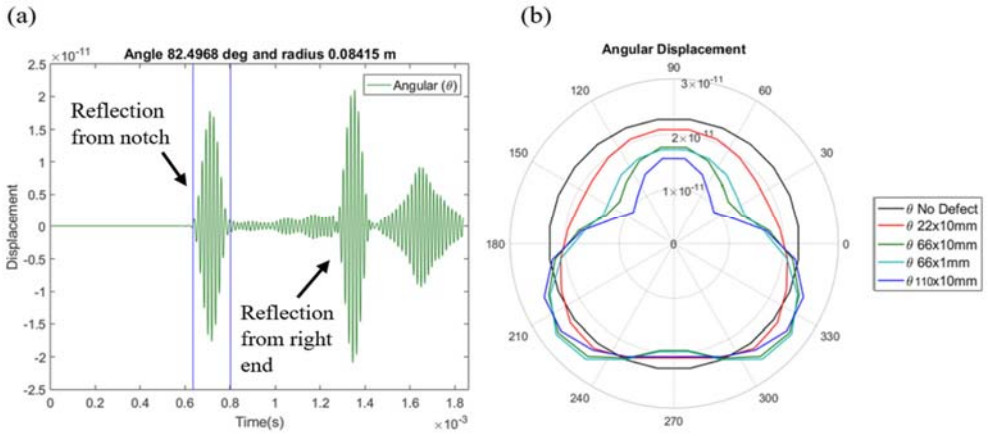

Figure 8: Displacement/time plot (a) and polar plot of angular displacement amplitude (b) when in pitch-catch operation

Evaluating the amplitude of angular displacements in the pitch-catch operation, shown in Figure 8(b) is noted that the pattern of maximum amplitudes of T(0,1) wave mode have different angular distributions with respect to the notch size. In the pitch-catch operation, the results indicate that the angular displacement amplitude at approximately 30 degrees and 150 degrees reduces as function of the notch growth in the circumferential direction. At 270 degrees, an amplitude reduction is noted for when the notch is present, but this is independent of notch growth. It is of note that in both modes of operation, notch growth in the longitudinal direction from 1 to 10 *mm* produces non-significant T(0,1) amplitude changes.

5 EXPERIMENTAL STUDY

An experiment was carried out on one 6 *m* long 6-inch schedule 120 steel pipe (outer diameter 168.3 *mm*, wall thickness 14.27 *mm*). Some defects are located on around 4.5 *m* from pipe end. The experiment had been performed by TWI Ltd as shown in Figure 9.



Figure 9: Set up of vibrometer pipe experiment [13]

Guided wave mode of T(0,1) was excited by a transmitter on the pipe end. It was set up 118 receivers located on 2 *m* away from the transmitter. The experimental result was collected from 3 *m* long distance of this steel pipe without any defect and picked up data of 24 receivers using MATLAB software.

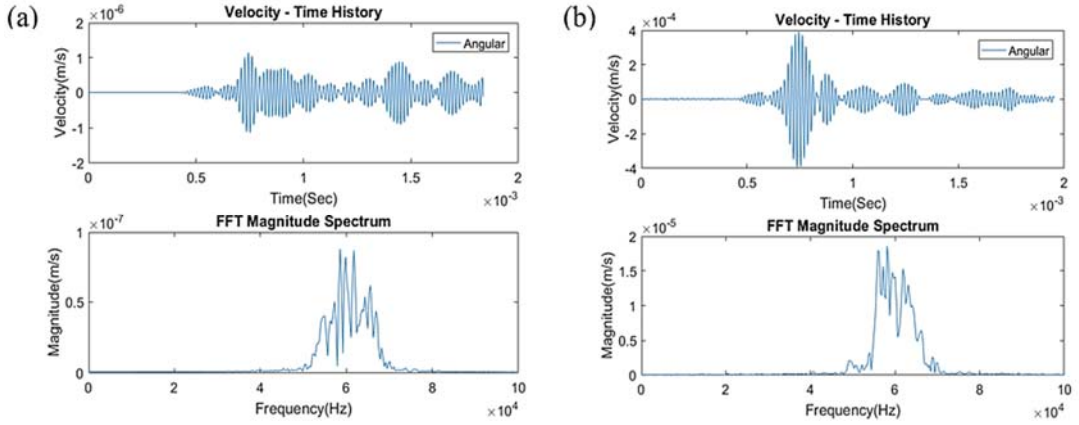

Figure 10 Velocity/time plot and its FFT frequency spectrum (a) FEA result, (b) Experimental result

The Fast Fourier Transform (FFT) was used to verify frequency function for the FEA modelling and experiment. Figure 10 shows that velocity/time plot of No.1 receiver and the corresponding FFT frequency spectrum. Figure 10(a) presents FFT analysis for finite element analysis and the FFT analysis of experimental result as shown in Figure 10(b). The frequency spectrum of these two results has a high similarity. Furthermore, it also was found that 24 receivers captured random synthesised 60 *kHz* signal and their frequency spectrums contain some random/coherent noise. Next, there are two groups of values have been described and compared between FEA results and experimental results. One is a group of velocity amplitudes/time output on 24 receivers through cylindrical coordinate system. Another is polar plot of their results for angular maximum displacement amplitude in time window. Its purpose is to further verify the validation of FEA modelling.

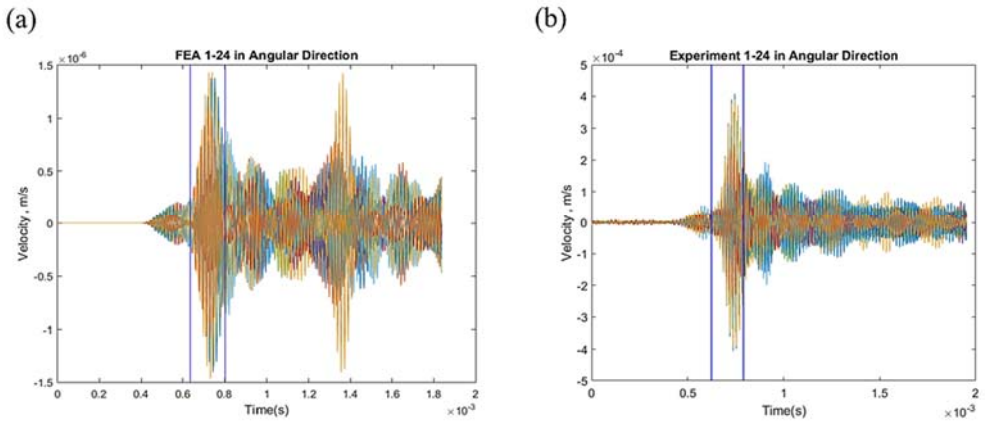

Figure 11: Velocity/time plot on 24 receivers (a) FEA results & (b) Experimental results (1 transmitter and 24 receivers) output in the circumferential direction

It is more distinct dispersed for FEA results after 1.2 *ms* as shown in Figure11(a). Because the experimental model is a 6 *m* long pipe, so the wave propagation did not reflect in 3 *m* distance. However, the FEA model is a 3 *m* long pipe and there had a reflection on the pipe end. Before 1.2 *ms*, there has a good agreement between FEA results and experiment results without considering amplitude values.

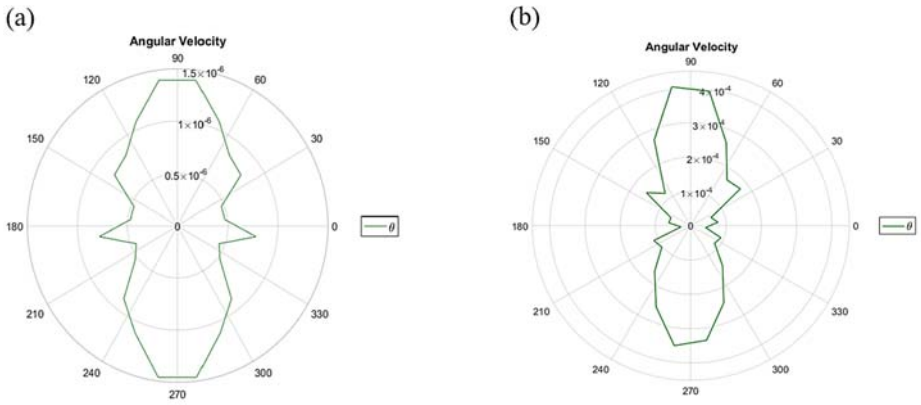

Figure 12: Polar plot of angular displacement amplitude (a) FEA output result (b) Experimental output result

Figure 12 presents a comparison between FEA results and experimental results in polar plots for maximum amplitude values of velocity on the 24 receivers. The output results were performed by MATLAB software. The predicted way has been done to excite the T(0,1) for ultrasonic GW testing and other wave modes are suppressed in Section 4.2.

Because values of each excited load were not considered. Therefore, there is a good agreement with the simulated FE results and experimental results for velocity/time plots and distribution trend of polar plots. Based on these results, further research of FEA modelling can be performed to use this FE model with T(0,1) excitation. The amplitude of T(0,1) has a more effective behaviour in circumferential direction.

6 CONCLUSIONS

This paper presents the characterisation of individual transducer's performance (1 transmitters - 24 receivers) and of a circumferential array design (24 transmitters - 24 receivers) using finite element analysis models with wave mode T(0,1) at the centre frequency of 60 *kHz*. The models are based on one 3 *m* long 6-inch schedule 120 (outer diameter 168.3 *mm*, wall thickness 14.27 *mm*) steel pipe.

From the preliminary numerical and experimental studies, following conclusion are noted: (1) The proposed transducer array of 24 transducers is a feasible method to excite the T(0,1) wave mode with significant purity for ultrasonic GW testing. (2) FEA has an effective function to simulate guided wave testing with defects, such as the represented notch. (3) The guided wave mode T(0,1) has shown high sensitivity to notch growth in the circumferential direction, but poor sensitivity to notch growth on the longitudinal direction. (4) Distinct angular displacement amplitude patterns at produced upon notch detection in pitch-catch operation.

Further work is considered to simulate more models with different kinds of defects and

undertake experiments for empirical validation. Numerical linear superposition analysis method will also be used through using MATLAB software.

7 ACKNOWLEDGE

This publication was made possible by the sponsorship and support of TWI Ltd. and University of Greenwich. The work was enabled through, and undertaken at, the National Structural Integrity Research Centre (NSIRC), a postgraduate engineering facility for industry-led research into structural integrity established and managed by TWI through a network of both national and international Universities. Furthermore, many thanks to Matthew Deere, my colleague who works in Plant Integrity Ltd. He provided the experimental data to support the FEA model verification.

REFERENCES

[1] P. Mudge, "Field application of the Teletest long-range ultrasonic testing technique," *Insight - Non-Destructive Testing and Condition Monitoring ,* vol. 43, no. 2, pp. 74-77, February 2001.

[2] P. W. Tse and X. Wang, "Semi-quantitative Analysis of Defect in Pipelines through the use of Technique of Ultrasonic Guided Waves," *Key Engineering Materials,* Vols. 413-414, pp. 109-116, 24 June 2009.

[3] P. K. Sharan, S. S, S. K. Chaitanya and H. K. Maddi, "Long Range Ultrasonic Testing - Case Studies," 2015. [Online]. Available: http://www.nde2015.com/papers-1/paper-83.pdf. [Accessed 17 11 2016].

[4] A. Løvstada and P. Cawley, "The reflection of the fundamental torsional guided wave from multiple circular holes in pipes," *NDT & E International,* vol. 44, no. 7, p. 553–562, November 2011.

[5] P. Wilcox, M. Lowe and P. Cawley, "The effect of dispersion on long-range inspection using ultrasonic guided waves," *NDT & E International,* vol. 34, no. 1, pp. 1-9, January 2001.

[6] M. G. Silk and K. F. Bainton, "The propagation in metal tubing of ultrasonic wave modes equivalent to lamb waves," *Ultrasonics,* vol. 1, pp. 11-19, 1979.

[7] B. P. with, "Disperse: A General Purpose Program for Creating Dispersion Curves," in *Review of Progress in Quantitative Nondestructive Evaluation*, vol. 16, D. O. Thompson and D. E. Chimenti, Eds., New York, Springer US, 1997, pp. 185-192.

[8] I. Viktorov, Rayleigh and Lamb Waves, New York: Plenum Press, 1967.

[9] D. C. Gazis, "Three□Dimensional Investigation of the Propagation of Waves in Hollow Circular Cylinders. I. Analytical Foundation," *J. Acoust. Soc. Am.,* vol. 31, no. 5, pp. 568-573, 1959.

[10] J. L. Rose, Ultrasonic Waves in Solid Media, Cambridge: Cambridge University Press, 2004.

[11] P. S. Lowe, S. Fateri, R. Sanderson and N. V. Boulgouris, "Finite element modelling of the interaction of ultrasonic guided waves with coupled piezoelectric transducers,"

Insight - Non-Destructive Testing and Condition Monitoring, vol. 56, no. 9, pp. 505-509, September 2014.

[12] M. J. S. Lowe, D. N. Alleyne and P. Cawley, “The Mode Conversion of a Guided Wave by a Part-Circumferential Notch in a Pipe,” *Journal of Applied Mechanics,* vol. 65, no. 3, pp. 649-656, 1998.

[13] M. Deere, "Guided Wave Eva;uation of Pipes using the First and Second Order Torsional Wave Modes," Ph.D. Thesis, Brunel University, London, 2017.

VIII ECCOMAS Thematic Conference on Smart Structures and Materials
SMART 2017
A. Güemes, A. Benjeddou , J. Rodellar and Jinsong Leng (Eds)

DAMAGE INDEXES COMPARISON FOR THE STRUCTURAL HEALTH MONITORING OF A STIFFENED COMPOSITE PLATE

N. MECHBAL* **& M. REBILLAT***

*PIMM – ENSAM/CNAM/CNRS,
151, Bd de l'Hôpital, 75013 Paris, France
e-mail: nazih.mechbal@ensam.eu & marc.rebillat@ensam.eu

Keywords: Structural Health Monitoring, Smart Structures, Composite Materials, Stiffener, Damage Detection, Lamb Waves, Performance Assessment, Robustness.

Abstract: Stiffened composite structures are very appealing in aeronautic applications due to their unique stiffness to mass ratio. However, they are also prone to various and complex damage scenario (stiffener debonding, impact damage...) and to complex wave propagation phenomena due to the presence of the stiffener. Consequently, autonomous monitoring of such structure is still a real issue. The process of monitoring in real-time a structure is referred to structural health monitoring (SHM) and consists of several steps: damage detection, localization, classification, and quantification. The focus is put here on the damage detection step of SHM. To detect damages, stiffened composite structures are equipped with piezoelectric elements that act both as sensors and actuators. A database at the unknown (and possibly damaged state) is then compared to a healthy reference database. Several damage indexes (DIs) designed for detection are extracted from this comparison. The SHM process classically relies on four sequential steps: damage detection, localization, classification, and quantification. The most critical step of such process is the damage detection step since it is the first one and because performances of the following steps depend on it. A common method to design such a detector consists in relying on a statistical characterization of the damage indexes available in the healthy behavior of the structure. On the basis of this information, a decision threshold can then be computed in order to achieve a desired probability of false alarm (PFA). In this paper, the performances of these DIs with respect to damage detection in a stiffened composite plate are studied. Results show that DIs based on energy consideration perform better than the ones based on cross-correlation. Furthermore Fourier-transform based DIs appear to be insensitive to the presence of damage in such structure.

1. INTRODUCTION

In aeronautic industry, composite materials are increasingly used due to their high strength properties. Because of their multilayer structure, they are inherently suitable to host smart materials. Indeed, embedded sensors and actuators (like piezoelectric transducers) can be permanently incorporated during the manufacturing process into the composite [1]. They can then be used to collect information about the structure through the analysis of guided waves signals in order provide a diagnosis of its current health and a prognosis of its remaining life [2]. This approach is called Structural Health Monitoring (SHM) and offers a new approach to interrogate

the integrity of structures in real-time, unlike traditional techniques such as Non-Destructive Testing (NDT) which require operators to perform the inspection [3, 4].

However, fiber reinforced materials are more complex than traditional materials such as metals. Their structural anisotropy and the fact that they contain different phases of material (fibers and matrix) generally results in various types of damage with different evolution characteristics. Damage detection and determination of the remaining strength and life of the structure remains a challenging task in that context. This is particularly the case when dealing with composite structures with complex geometry and co-bonded stiffeners as frequently applied in aircraft components. In this case, attenuation and dispersion of Lamb waves induced by reinforced stiffeners must be evaluated [5] in order to enhance the probability of detection (PoD) and to ensure a given probability of false alarm (PFA) in the context of the detection step of a SHM process [6, 7, 8].

To detect damages, smart-structures are equipped with piezoelectric elements that act both as sensors and actuators. A database at the unknown (and possibly damaged state) is then compared to a healthy reference database. Several damage indexes (DIs) designed for detection are extracted from this comparison. To date, most service life predictions are based on measurements of DIs and their growth towards criticality or failure, e.g. fatigue crack length, material loss due to corrosion or wear, etc… However, the dissemination of instrumentation technologies, complex structures, harsh environments, and operational variability has led to the development of a large variety of DIs [6].

The aim of the present paper is to compare the performances of several families of classical DIs for the challenging task of damage detection in a stiffened composite plate. The paper is organized as follows: the experimental setup is first presented in Section 2, before in traducing the proposed damage detection methodology in Section **Erreur ! Source du renvoi introuvable.**. Results are then presented in Section 0 and discussed in Section **Erreur ! Source du renvoi introuvable.**.

2. EXPERIMENTAL SETUP

The composite structure we are interested in is a composite stiffened plate (see Figure 1). This structure is geometrically complex and is made of composite monolithic carbon epoxy. It is a multilayered structure consisting of 4-plies oriented along $[0°/\,45°/\,-45°/\,0°]$. This structure is 400 mm in width for a height of 300 mm.

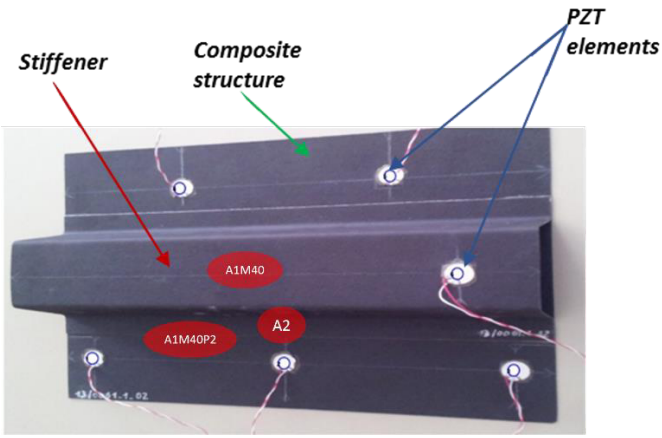

Figure 1: Stiffened composite plate under study

A network of 6 piezoelectric elements used as actuators and sensors has been bonded to the surface of the stiffened plate and is used to emit and collect signals. The PZT elements used are numbered from 1 to 6 and mounted at specific positions on the composite plate's surface as shown in Figure 1. The PZT elements have a diameter of 20 mm, a thickness of 0.1 mm and have been manufactured by Noliac.

Three types of damage are considered in the present study. The first two damages are made using Neodymium magnets placed on both sides of the composite: one is located on the monolithic part of the composite plate (A1M40) and the other one is located on the stiffener (A1M40P2). Finally, damage 3 corresponds to a real debonding on the center of the bottom part of the stiffener (A2).

3. DAMAGE DETECTION METHODOLOGY

The methodology proposed for the detection of the damage appearing on the stiffened composite structure is summarized in Figure 2.

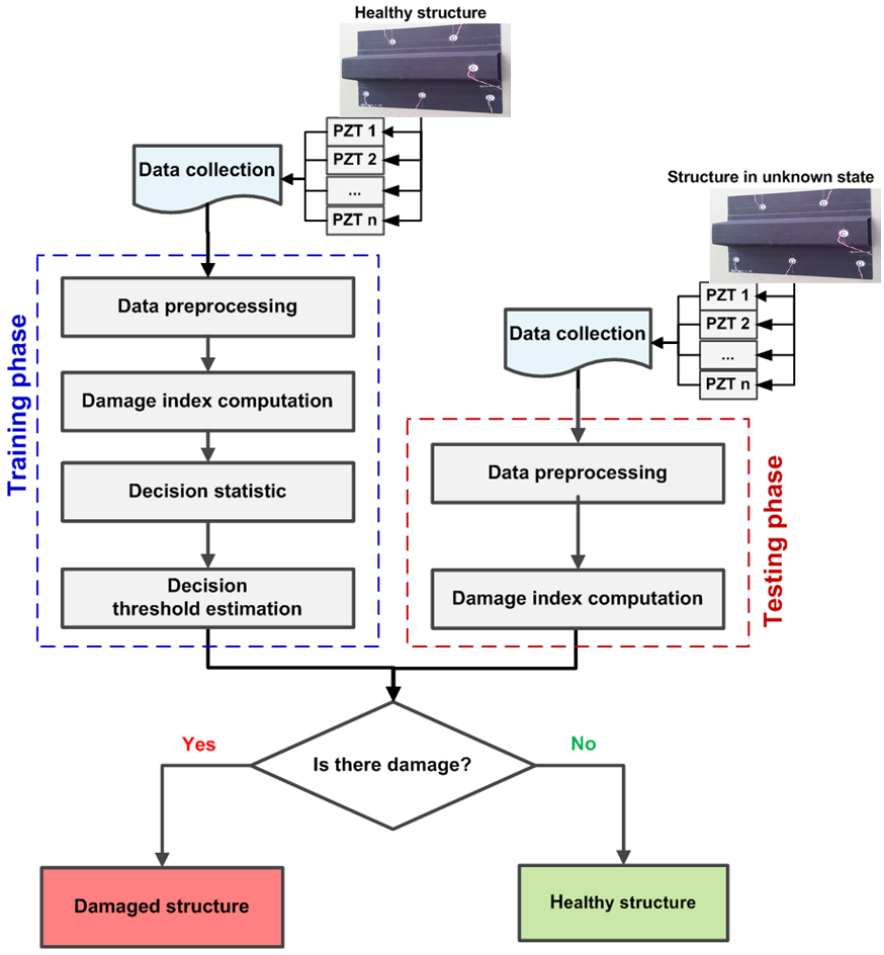

Figure 2: Damage detection methodology.

a. Data preprocessing

Structural health monitoring is achieved here by means of Lamb waves [9, 10]. This method is based on the principle that Lamb waves can propagate in the structure and will thus necessarily interact with damage. Information is then extracted from the waves diffracted by the damage for detection purposes. The excitation signal sent to the PZT element is a 5 cycles *"burst"* with a central frequency of $200\,kHz$ and with an amplitude of $10\,V$. In each phase of the experimental procedure, one PZT is selected as the actuator and the other act as sensors. All the PZTs act sequentially as actuators. Resulting signals are then simultaneously recorded by the others piezoelectric element and consist of 1000 data points sampled at $1\,MHz$. For all configurations 100 repetitions are performed to have enough data for a statistical approach.

As pre-processing steps, the measured signals are first denoised by means of a discrete wavelet transform up to the order 4 using the *"db40"* wavelet. Those signals are then filtered around their center frequency using a continuous wavelet transformation based on *"morlet"* wavelets and with a scale resolution equals to 20. The diaphonic part present in the measured signals (*i.e.* the copy of the input signals that appears on the measured signal due to electromagnetic coupling in wires) has been previously eliminated on the basis of the knowledge of the geometrical positions of the PZT and of the waves propagation speed in the material.

b. Damage Index (DI) computation

The damage index represents a crucial step for the design of the detector as this feature must correctly reflect the effect of the damage on the structure. The DIs chosen for this study are obtained as follows given a reference healthy signal $x_{ij}(t)$ and a signal $y_{ij}(t)$ corresponding to an unknown state for the path from actuator i to sensor j are given in Figure 3.

DI name	*Comments*	*Definition*
CCA	MATLAB based implementation of the maximum of the correlation	$1-\max\left(xcorr\left[x_{ij}(t),y_{ij}(t)\right]\right)$
CC0	MATLAB based implementation of the zero-lag correlation	$1-xcorr\left[x_{ij}(t),y_{ij}(t)\right](0)$
CRC	MATLAB-based implementation of the correlation coefficient	$1-corrcoeff\left[x_{ij}(t),y_{ij}(t)\right]$
NRE	Normalized residual energy	$\int_0^T \left(x_{ij}(t)-y_{ij}(t)\right)^2 dt$
MA	Maximum amplitude of the difference	$\max\left[x_{ij}(t)-y_{ij}(t)\right]$
FFT	FFT of the difference signal at f_0	$\max\left[x_{ij}(t)-y_{ij}(t)\right]$
ENV	Maximum envelope of the difference	$\max\left[ENV(x_{ij}(t)-y_{ij}(t))\right]$

Figure 3: Implemented damage indexes

These DIs belong to three families. DIs CC, CCA, CC0 and CR are all based on the notion of correlation. DIs NRE, MA and ENV are all based on an energy based processing of the difference signal. The last one, FFT, is based on a frequency analysis of the signals around the center frequency.

The damage indexes DI_{ij} computed for each path "actuator i to sensor j" are then integrated together. This leads to a global damage index DI_G defined as follows:

$$DI_G = \sum_{i=1}^{N_{act}=6} \sum_{j=1}^{N_{sen}=6} DI_{ij}$$

By rotating the reference healthy signal and the signal corresponding to an unknown state (healthy or damaged), important DI-databases are obtained. Among these different databases, the one obtained by comparing the healthy set to itself is very interesting as it allows characterizing the healthy behavior of the structure and to compute the decision thresholds. This database will be the input of the detector design methodologies presented in the next section.

c. Damage detector design using Parzen window estimator

We considered the decision thresholds estimated based on a nonparametric Parzen window estimator [10] as reference. The Parzen window adjustment is a nonparametric mean to estimate the probability density function of a random variable x known on N samples. It is commonly referred to as "kernel density estimator" because kernel functions are used to estimate the probability density function [11]. The analytical expression of the nonparametric Parzen window probability density function is [12]:

$$\hat{f}_{N,h}(x) = \frac{1}{Nh} \sum_{i=1}^{N} K\left(\frac{x - x_i}{h}\right) \quad (1)$$

where $K(.)$ and h are the kernel function and the window width respectively. The idea behind the Parzen window is to estimate the density probability function on N sample values thanks to a kernel function $K(.)$ which is most of the time a probability density function. The closer the observation x is to training samples x_i the larger is the contribution to $\hat{f}_{N,h}$ of the kernel function centered on x_i. Conversely, training observations x that are far from x_i have a negligible contribution to $\hat{f}_{N,h}$. This estimator of the probability density function is formed by averaging of the kernel function values (see Figure 4).

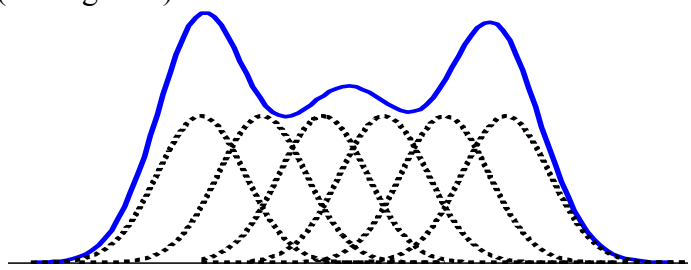

Figure 4: Probability density function of a random variable and some Gaussian kernels

This estimator is governed by the smoothing parameter h called window width. Under some non-binding restrictions on h, the Parzen window estimator is consistent. It exists several kernel functions (Gaussian, box, triangle…) but the Parzen window performances depend mainly on the choice of the window width h. It exists several methods to choose h. In this study, a Gaussian kernel has been used according to Eq. (*2*). Silverman [13] has determined an optimal window width value used a so-called "rule of thumb" when the distribution is Gaussian. This window width depends on an estimation of the variance $\hat{\sigma}$ and the learning data set size N according to Eq. (3).

$$K(x) = \frac{1}{\sqrt{2\pi}} \times e^{\left(\frac{x^2}{2}\right)} \tag{2}$$

$$h = \hat{\sigma}\left(\frac{4}{3\times N}\right)^{\frac{1}{3}} \tag{3}$$

According to the nonparametric Parzen window probability density function, $\hat{f}_{N,h}$, presented above in Eq. (*1*), and after the choice of the window width h using Eq. (3), the decision threshold, S, may be determined according to a requested probability of false alarm (PFA) and given a learning sample size N using Eq.(4).

$$S = \left\{ S \text{ such that } \int_{S}^{+\infty} \hat{f}_{N,h}(x)dx = \frac{1}{Nh}\sum_{i=1}^{N}\int_{S}^{+\infty} K\left(\frac{x - x_i}{x}\right)dx = \text{PFA} \right\} \tag{4}$$

4. RESULTS

This section presents the results obtained when computing the DIs defined in Figure 3 for the different damage cases depicted in Section 2. Their performances are assessed with respect to a decision threshold determined accordingly with the procedure described in Section **Erreur ! Source du renvoi introuvable.**.

a. Normalized probability density functions

The normalized probability functions (PDF) for the different DIs described in Figure 3 for different damage scenario are presented in

Figure 5. From this figure, the behavior of the three DIs families previously mentioned can be clearly identified. The correlation based DIs all provide PDF that are above the decision threshold for the case A2 but that are very close or below it for the two other cases. The energy based ones all perform very well for each case. Finally, the frequency based one do not perform well at all as the PDFs corresponding to the different damage cases are not separated at all.

a. Receiver Operating Characteristic

The Receiving Operator Characteristic (ROC) for the different DIs described in Figure 3 for different damage scenario are presented in Figure 6. From this figure, the performances of the three DIs families previously mentioned can again clearly be stated. The correlation based DIs all provide ROC curves that highlight good performances for the case A2 but poor ones for the two

other cases. The energy based ones all perform very well for each case. Finally, the frequency based one do not perform well at all as the ROC corresponding to the different damage cases are close to the diagonal.

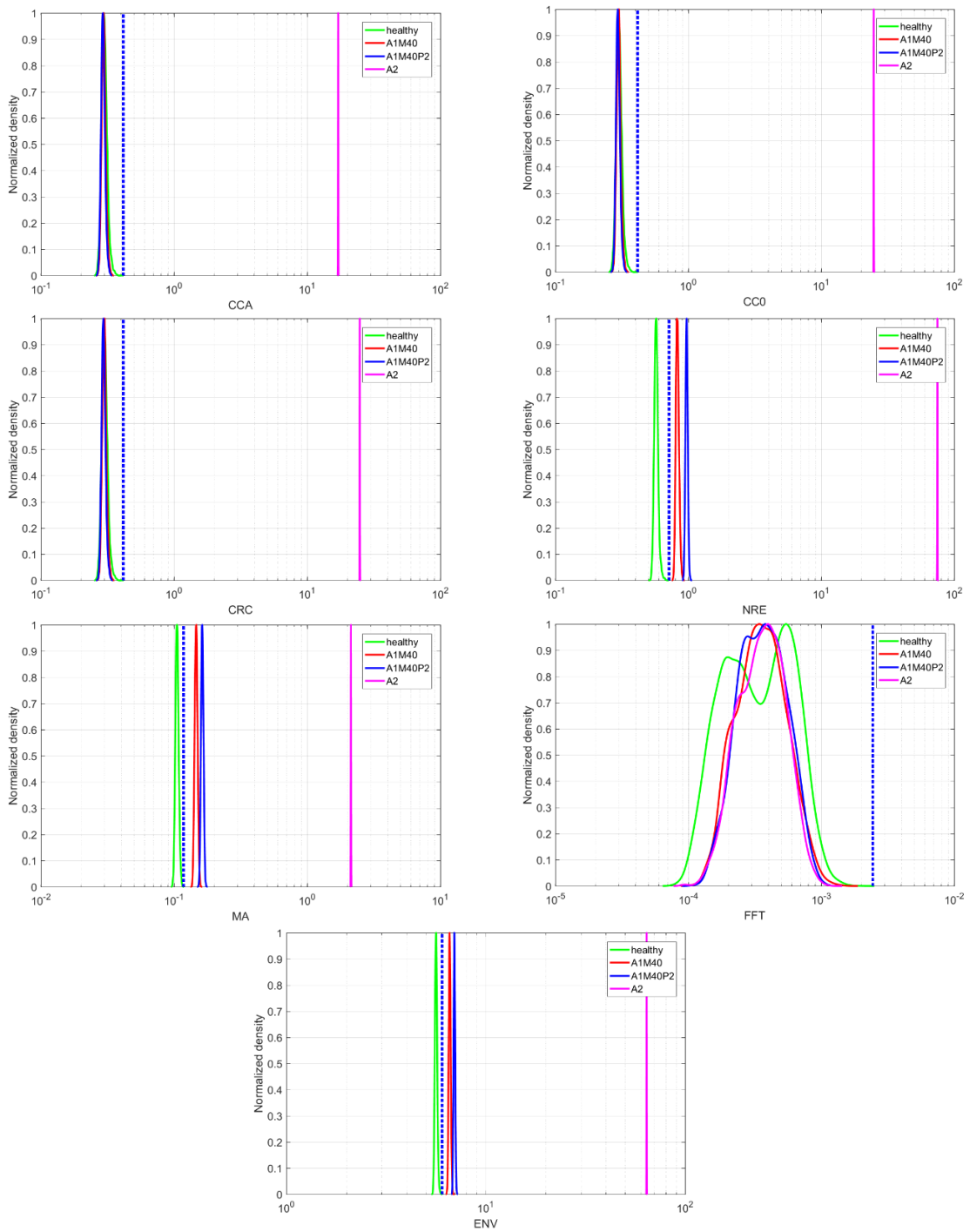

Figure 5: Normalized probability density functions for the different DIs and for the different damage cases.

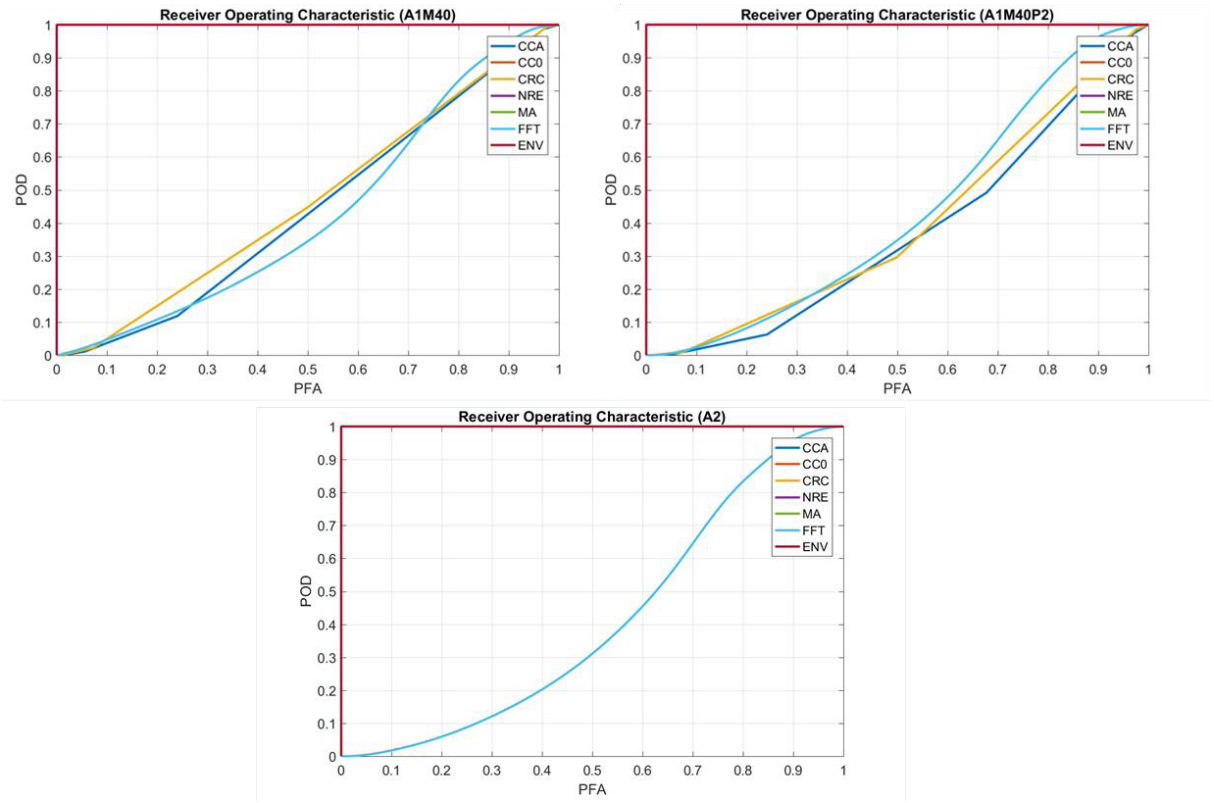

Figure 6: Receiving Operator Characteristic for the different DIs and for the different damage cases.

5. CONCLUSION

The aim of the present paper is to compare the performances of several families of classical DIs for the challenging task of damage detection in a stiffened composite plate. It appears that the correlation based DIs all provide good performances for the case A2 which corresponds to a real debonding of the stiffener but poor ones for the two other cases which correspond to a simulated damage case using magnets as damages. The energy based ones all perform very well for each case, real as well as simulated ones. Finally, the frequency based one do not perform well at all. Results provided here can thus help in designing an efficient SHM process for stiffened composite structures.

6. REFERENCES

[1] I. Chopra and J. Sirohi, Smart Structures Theory, New York: Cambridge University Press, 2013, p. 905.

[2] Z. Su and L. Ye, Identification of Damage Using Lamb Waves, Springer-Verlag London, 2009.

[3] K. Worden, C. R. Farrar, G. Manson and G. Park, "The fundamental axioms of structural health monitoring.," *Proceeding of the Royal Society,* vol. 463, pp. 1639-1664, 2007.

[4] W. Ostachowicz and A. Guemes, New Trends in Structural Health Monitoring,, I. 978-3-7091-1389-9, Ed., Springer,, 2013.

[5] Y. Lu, L. Ye, D. Wang and Z. Zhong, "Time-domain Analyses and Correlations of Lamb Wave Signals for Damage Detection in a Composite Panel of Multiple Stiffeners," *Journal of Composite Materials,* vol. 43, no. 26, 2009.

[6] O. Hmad, C. Fendzi, N. Mechbal and M. Rebillat, "Verification and Validation of Structural Health Monitoring Algorithms: A Maturation Procedure.," in *9th IFAC Symposium SAFEPROCESS'15*, Paris, 2015.

[7] O. Hmad, N. Mechbal and M. Rebillat, "Peaks Over Threshold Method for Structural Health Monitoring Detector Design," in *International Workshop on Structural Health Monitoring, IWSHM*, Standford, 2015.

[8] M. Rébillat, O. Hmad, F. Kadri and N. Mechbal, "Peaks Over Threshold Based Detector Design for Structural Health Monitoring: application to aerospace structures," *Structural Health Monitoring an international journal,* 2017.

[9] Z. Su and L. Ye, Identification of damage using Lamb waves: from fundamentals to applications, vol. 48, Springer Science & Business Media, 2009.

[10] H. Sohn, D. W. Allen, K. Worden and C. R. Farrar, "Structural damage classification using extreme value statistics," 2005.

[11] L. De Haan and H. Rootzén, "On the estimation of high quantiles," *Journal of Statistical Planning and Inference,* vol. 35, no. 1, pp. 1-13, 1993.

[12] E. Parzen, "On estimation of a probability density function and mode," *The Annals of Mathematical Statistics,* vol. 33, no. 3, pp. 1065-1076, 1962.

[13] B. W. Silverman, Density estimation for statistics and data analysis, vol. 26, CRC press, 1986.

[14] C. Fendzi, N. Mechbal, M. Rebillat and M. Guskov, "A General Bayesian Framework for Ellipse-based and Hyperbola-based Damage Localisation in Anisotropic Composite Plates," *Journal of Intelligent Material Systems and Structures,* vol. 27, no. 3, pp. 350-374, 2016a.

VIII ECCOMAS Thematic Conference on Smart Structures and Materials
SMART 2017
A. Güemes, A. Benjeddou, J. Rodellar and J. Leng (Eds)

DETECTION AND LOCALISATION OF WATER INTRUSION IN GLASS FIBRE REINFORCED COMPOSITE USING THZ SPECTROSCOPY

MAGDALENA MIELOSZYK*,[1], KATARZYNA MAJEWSKA[1] AND WIESLAW OSTACHOWICZ[1,2]

[1]Institute of Fluid Flow Machinery, Polish Academy of Sciences,
Fiszera 14, 80-231 Gdansk, Poland
* e-mail: mmieloszyk@imp.gda.pl

[2] Warsaw University of Technology,
Narbutta 84, 02-524 Warsaw, Poland

Key words: THz spectroscopy, glass fibre composite, Structural Health Monitoring, moisture

Abstract. Glass fibre reinforced composites are recently very popular in marine or wind energy industries. One of problems that can occur during manufacturing process is introducing of a contamination e.g. in a shape of a water drop. In such case the moisture is captured and cannot evaporate from the composite element during its exploitation. This discontinuity can be a damage origin (e.g. delamination, matrix cracking or fibre-matrix debonding) that significantly decreasing mechanical properties of composite element. It is important to have a method to inspect an internal structure of an element just after manufacturing process and also during its exploitation.

One of the non-destructive methods allow to observe and evaluate the internal structure of glass fibres reinforced composite is terahertz time-domain spectroscopy (THz-TDS). In the technique the properties of a material are probed with short pulses of THz radiation. The technique can be used for defects identifications like voids, delaminations, mechanical damage or burning [1] in non-conductive materials. The THz method allows to determine material structural disintegration that results in changes of absorption and refraction index of examined material. The limitations of THz propagation through water (absorption) allowed to detect water layer between two thin elements made out of glass fibre reinforced composite [2].

The paper presents an application of THz spectroscopy for observation and evaluation of the internal structure of glass fibres reinforced composite sample with a water intrusion. The relatively high permittivity of water compared to other materials enables a contrast mechanism for the detection and imaging of moisture even in a form of a water drop. The experimental investigation is performed on four-layered rectangular sample manufactured using infusion method.

1 INTRODUCTION

In recent years, composite elements have been widely used in many industrial branches: aviation [3], marine [4] or civil engineering [5]. Composite structures are exploited in different environmental and loading conditions. Monitoring of its influence using different Non-Destructive Techniques (NDT) or Structural Health Monitoring (SHM) methods is very important to increase the safety.

Among many environmental factors (moisture, temperature, ultra violet (UV) radiation, etc.) that can affect the durability of composite structures moisture is one of the most important [6]. Moisture absorption reduces the glass transition temperature T_g and tensile strength. It also lowers the ultimate elongation of the adhesive and increases the formation of cracks [6]. Due to this the composite elements are protected against post manufacturing sources of moisture by appropriate covers or painting layers. On the other hand a small amount of moisture/ water can be also introduced into composite element during its manufacturing process due to malfunction of the production line or human fault. Such water cannot be removed from the composite material and is trapped by surrounded epoxy resin. This produces discontinuity in the material and can be an origin of different damage types like delamination or crack. Due to this a NDT that allows to determine the location and size of water drop embedded into material during manufacturing process is an area of high interest in the field of composite material applications.

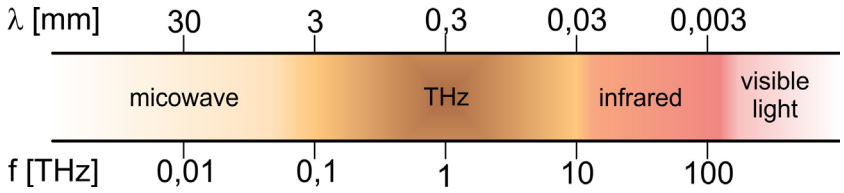

Figure 1: Electromagnetic waves range

The internal structure of a composite element can be inspected using different techniques based on electromagnetic radiation. Due to interaction between wave and inspected material structure the spectral range of electromagnetic radiation is divided into several ranges (Fig 1). One of them, that can be used for inspection of non-conductive materials, are THz waves with typically frequency range 0.1 – 10 THz (3 mm – 30 μm). The power generated by THz beam is very low and typically the mean power is below 1 μW [1] so risk of destroying sensitive materials is strongly limited [7]. THz radiation can be used in analysis of materials that affects minimum one of three THz wave parameters: refractive index, absorption coefficient or wave scattering referred to roughness of the material surface. The THz technique working both in transmission and reflection mode has unique capacity for examining composite materials and identification of mechanical defects like voids [8], delaminations [9] or burning on the material surface [8].

The relatively high permittivity of liquid water compared to other materials in the THz range enables a contrast mechanism for the detection and imaging of moisture. Water is highly absorptive in the THz range, while most materials which absorb moisture are either very transparent (e.g. paper, epoxy) or reasonably transparent to THz wave [3]. The first demonstration of THz imaging of moisture distribution is a moisture map of a drying leaf [3, 10]. The THz spectroscopy based method was also used for a determination of water layer (with a thickness

of 100 – 200 μm) on the surface of glass fibre reinforced polymer (GFRP) composite element. Additionally two water layers (with a thickness of 50 – 100 μm and 100 – 300 μm) in joint between two GFRP elements were investigated. The experimental analysis was performed in both transmission and reflection mode [2].

The paper presents an application of THz spectroscopy for observation and evaluation of the internal structure of GFRP sample with a water intrusion. The relatively high permittivity of water compared to other materials enables a contrast mechanism for the detection and imaging of moisture even in a form of a water drop. The experimental investigation was performed on four-layered rectangular sample manufactured using infusion method.

The paper is organised as follow. Firstly GFRP sample with water drop intrusion are described. Then the THz spectroscopy analysis results are presented and discussed. Finally some conclusions are drawn.

2 EXPERIMENTAL INVESTIGATION

The measurements were performed on four-layered rectangular GFRP sample with a dimension of 70 mm x 200 mm x 1.6 mm. The laminate was manufactured using infusion method for bidirectional material (glass SGlass) and epoxy resin. Between 1st and 2nd layer counting form the bottom of the sample two fibre optic with FBG sensors were embedded. Between them a water drop was introduced that was surrounded by epoxy resin during the manufacturing process and permanently trapped when the curing process was finished – Fig. 2(a)-(b). The sample was previously examined using active infrared thermography method. Both vibro- and pulse thermography allow to determine the location and size of the water drop intrusion [11]. Although the limitation of the thermography method do not allow to determine the thickness of the intrusion and its exact location between layers.

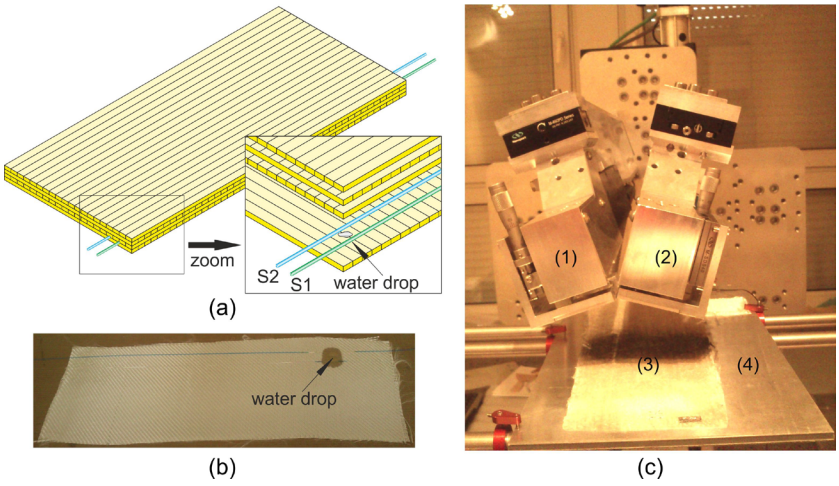

Figure 2: Sample with water drop intrusion: (a) schema, (b) photograph during manufacturing process; (c) THz equipment: (1) - emitting head, (2) - receiving head, (3) - GFRP sample, (4) - metal table

The internal structure of the sample was examined using THz spectrometer (TPS Spectra 300 THz Pulsed Imaging and Spectroscopy from TerraView®) in reflection mode (Fig. 2(c)).

The measuring heads were arranged in a angle of 22° between them. The system contains scanning unit (Gantry Imaging System) with moving platform that allows to scanning chosen area of samples. During scanning process of the investigated sample the measurement step was equal to 0.2 mm and THz signals were registered with 10 averaging. As the THz waves are sensitive on moisture in the ambient all measurements were performed with air dryer that removes moisture from the working heads area and air condition that stabilise laboratory temperature on assumed level equal to 20°C.

3 EXPERIMENTAL RESULTS

First of all the material part of the sample was examined in transmission mode to determine its absorption coefficient (κ_S) and refractive index (n_S). The complex refractive index (N_S) of the sample for 0.5 THz is equal to

$$\begin{aligned} N_S &= n_S + i\kappa_S \\ n_S &= 1.69 \\ \kappa_S &= 0.055 \end{aligned} \tag{1}$$

Due to determine sensitivity of THz spectrometry on water intrusion water absorption coefficient (κ_W) and refractive index (n_W) were also presented according to results achieved by Bertie and Lan [12]. The values, also for 0.5 THz, are equal to

$$\begin{aligned} N_W &= n_W + i\kappa_W \\ n_W &= 2.4 \\ \kappa_W &= 0.81 \end{aligned} \tag{2}$$

The differences between refractive indexes of those two materials (GFRP composite and water) are high enough to allow the THz spectrometry to detect and localize the water drop. The higher value of absorption coefficient for water indicated that the THz wave is more attenuated propagating throughout water than composite material. The main problem in the research presented in the paper is that the water is not in a form of a layer with equal thickness but because it was embedded in composite material its thickness vary.

In the reflection mode the majority of the signal energy is contained by signal for frequency values smaller than 3 THz. 90% of energy is achieved for frequencies up to 2 THz, while 80% – in a range up to 1.2 THz. This information was used to filter the waveforms and to remove noise.

A comparison of filtered and normalised waveforms for GFRP material with and without water intrusion is presented in Fig. 3. The disturbances in waveform due to water occurrence are denoted by 'W' and blue ellipse. The water intrusion method results in its not equal distribution and do not forming a layer with equal thickness. It results in propagating of THz wave throughout mix of glass fibres, epoxy resin and water. Due to this it is harder to determine the water drop location and size. During constructing of the sample the water drop was introduced as in Fig. 2 (b), but due to evaporation process and influence of epoxy resin flow its shape was changed. Due to thinness of the water drop and its character its influence is mostly local and it is visible as attenuation of the reflection from the 2nd layer. This effect for the next layers of the sample is neglected.

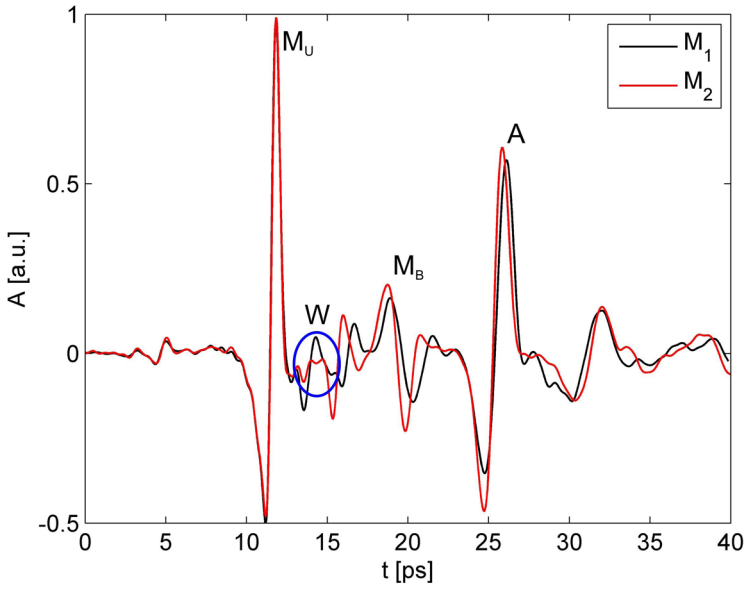

Figure 3: A comparison of waveforms for intact (M_1) material and with the water inclusion (M_2); M_U, M_B - reflections of upper and bottom surfaces of the sample, A - reflection from the metal table

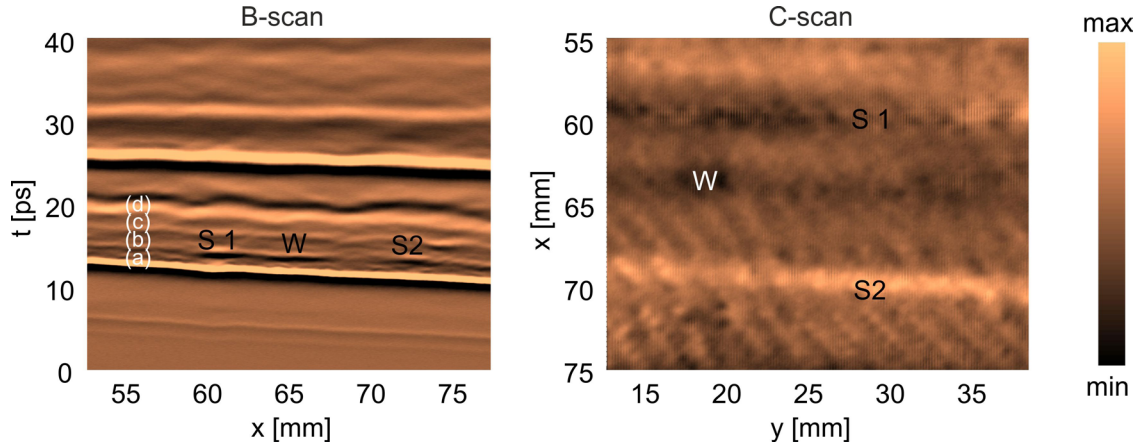

Figure 4: B-scan and C-scan presenting localisation of the water drop intrusion (W) and two fibre optics with FBG sensors (S1, S2): (a)-(d) – composite layers

B-scan and C-scan of the sample part are presented in Fig. 4. The B-scan, that was made for y = 20.03 mm, allows to count the sample layers as well as determine the location of the water drop and two fibre optics between 1st and 2nd layer. It also allows to determine the thickness of all presented elements. It can be observe that the water drop disturbance thickness is about two times smaller than the fibre optics which thickness is equal to 250 μm. Roughly it can be written that the drop thickness is similar to the distance between 1st and 2nd layer, because during the manufacturing process the glass material behave like limitation.

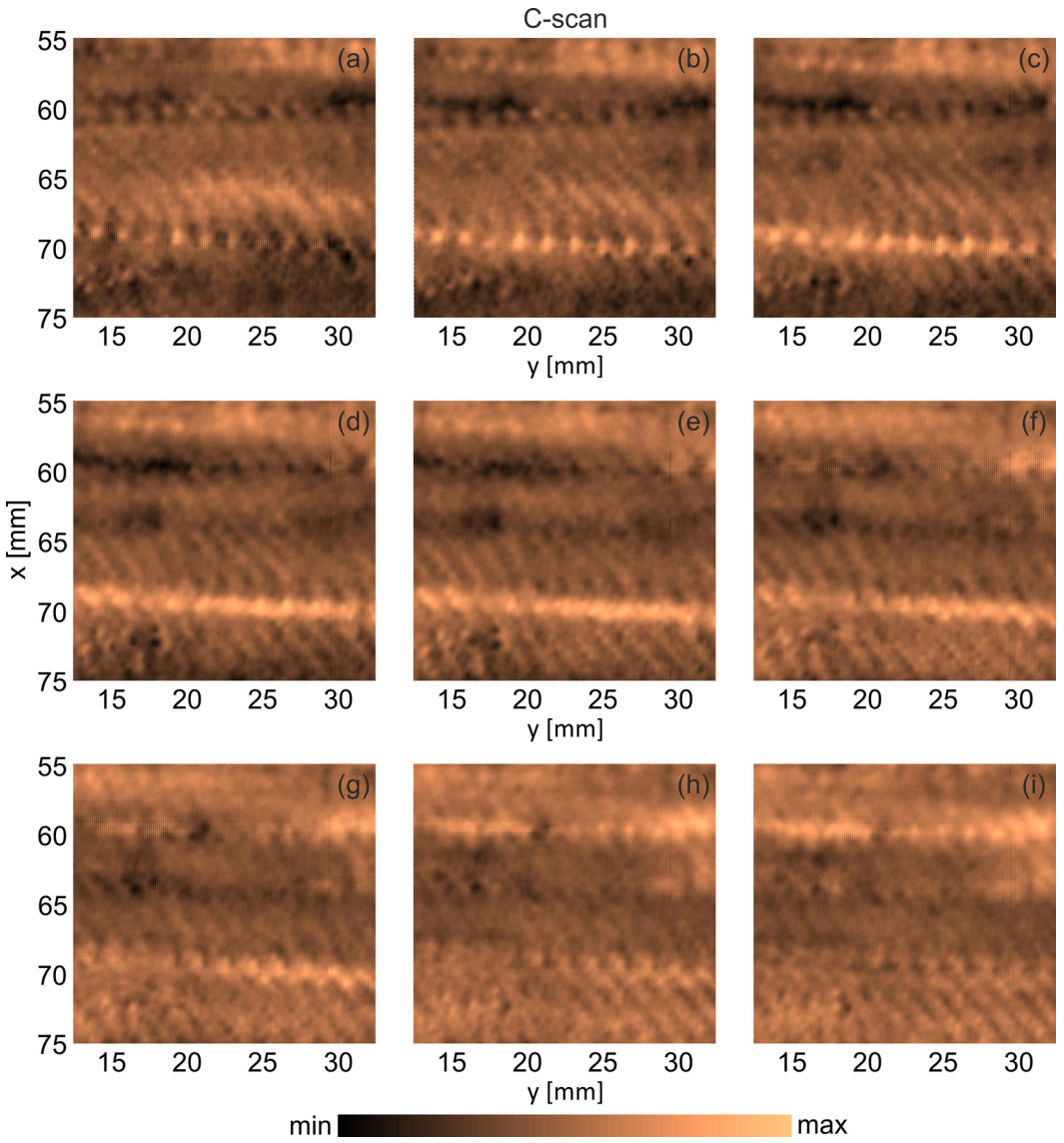

Figure 5: Sequence of C-scans on the water drop intrusion location for time step equal to 0.05 ps

C-scan, that was made for t = 15.39 ps, allows to determine the water drop shape and size. Comparing those two sizes of the same intrusion it is well visible that it differ – Fig. 4. The main reason could be that the water drop shape changes in the sample thickness direction. Due to this a sequence of C-scans in a range from 15.12 ps to 15.48 ps on the water drop intrusion location was made, as presented in Fig. 5.

The water intrusion is visible on C-scans in Fig. 5(b)-(h) as a local minimum with different shape. The maximum size of the intrusion is 2.5 mm x 5 mm. It confirms that the water drop intrusion was not in a form of a layer with stable thickness. Due this its influence is very local and is not noticed on C-scans made for time before and after the moment when THz wave

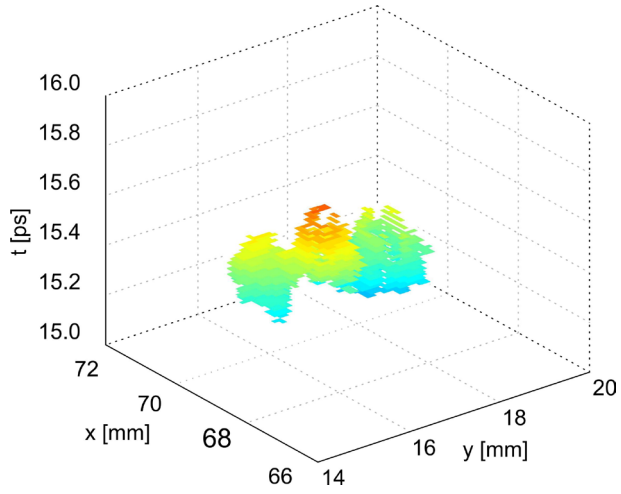

Figure 6: 3-D image of the water drop intrusion

propagates throughout the water area.

This characteristic interaction between THz wave and water embedded in composite material allows to propose a filtering method. It was mostly based on differences observed on the THz wave reflection from the 2nd layer that is denoted by the blue ellipse in Fig. 3. The filtering method allows to remove the material influence and present the 3D shape of the water drop intrusion – Fig. 6. It is observed that the shape of the intrusion vary in all directions.

4 CONCLUSIONS

The paper presents an application of THz spectrometry method for determination of location and size of the water drop intrusion that was introduced into composite sample during its manufacturing process. It is possible due to differences between GFRP and water parameters for electromagnetic waves in a THz range allows. Those differences in THz wave propagation in GFRP material with or without water allows to determine the water drop location between the 1st and the 2nd layer. The proposed filtering method allows to remove the surrounding material influence and determine the intrusion shape shape in all directions in space.

ACKNOWLEDGMENTS

The research in this paper was partially supported by the projects entitled:

- (PBS1/B6/8/ 2012) Non-invasive Methods for Assessment of Physicochemical and Mechanical Degradation granted by National Centre for Research and Development in Poland,
- (MARTECII/RAMMS/1/2016) Reliable and Autonomous Monitoring System for Maritime Structures granted by National Centre for Research and Development in Poland.

REFERENCES

[1] Mittleman D. *Sensing with Terahertz Radiation*. Springer-Verlag Berlin Heidelberg, ISBN 978-3-540-43110-7, (2003).

[2] Malinowski P., Pałka N., Opoka S., Wandowski T. and Ostachowicz W., Moisture detection in composites by terahertz spectroscopy. *J Phys Conf Series* (2015) **628**:012100 (8).

[3] Kahandawa G.C., Epaarachchi J., Wang H. and Lau K.T., Use of FBG Sensors for SHM in Aerospace Structures. *Photonic Sensors* (2012) **2**:203-214.

[4] Wang G., Pran K., Sagvolden G., Havsgard G.B., Jensen A.E., Johnson G.A. and Vohra ST. Ship hull structure monitoring using fibre optic sensors. *Smart Mater Struct.* (2001) **10**:472-8.

[5] Gebremichael Y.M., Li W., Boyle W.J.O., Meggitt B.T., Grattan K.T.V., McKinley B., Fernando G.F., Kister G., Winter D., Canning L. and Luke S., Integration and assessment of fibre Bragg grating sensors in an allfibre reinforced polymer composite road bridge. *Sensors Actuators A* (2005) **118**:78-85.

[6] Budhe S., Banea M.D., de Barros S. and da Silva L.F.M., An updated review of adhesively bonded joints in composite materials, *International Journal of Adhesion & Adhesives* (2017) **72**:30–42.

[7] Cai Y., Brener I., Lopata J., Wynn J., Pfeiffer L., Federici J., Design and performance of singular electric field terahertz photoconducting antennas. *Appl. Phys. Lett.* (1997) **71**:276–278.

[8] Stoik C.D., Bohn M.J. and Blackshire J.L., Nondestructive evaluation of aircraft composites using transmissive terahertz time domain spectroscopy, *Optics Express* (2008) **16**:17039–17051.

[9] Majewska K., Soman R., Mieloszyk M. and Ostachowicz W., Assessment of delamination in composite beam using infrared thermography, optical sensors and terahertz technique, *Proc. of SPIE*, 2017.

[10] Federici J.F., Review of Moisture and Liquid Detection and Mapping using Terahertz Imaging, *J Infrared Millim Te* (2012) **33**:97–126.

[11] Majewska K., Mieloszyk M. and Ostachowicz W.: Glass fibre composite elements with embedded fibre Bragg grating sensors inspected by thermography techniques, *Proc. of EWSHM*, 2016.

[12] Bertie J.E. and Lan Z., Infrared Intensities of Liquids XX: The Intensity of the OH Stretching Band of Liquid Water Revisited, and the Best Current Values of the Optical Constants of H_2O(I) at 25°C between 15,000 and 1 cm^{-1}, *Applied Spectroscopy* (1996) **50**(8):1047–57.

GAIN-SCHEDULING H_∞ CONTROL OF A SMART BEAM WITH PARAMETER VARYING

CEM ONAT[*], MELIN SAHIN[†] AND YAVUZ YAMAN[†]

[*] Department of Mechanical Engineering
Engineering Faculty, Inonu University, Malatya, Turkey
e-mail: cem.onat@inonu.edu.tr

[†]Department of Aerospace Engineering
Engineering Faculty, Middle East Technical University, Ankara, Turkey
e-mail: msahin@metu.edu.tr, yyaman@metu.edu.tr

Key words: Smart Beam, H_∞ Control, Gain Scheduling, PZT.

Abstract. The use of smart structures provides more efficient solutions to most of the active vibration control problems in flexible systems due to the significant advances in sensor and actuator technologies. This paper presents a novel design approach of a gain scheduling H_∞ controller for a parameter varying smart beam having surface bonded piezoelectric sensors and actuators. The robust approach intends to suppress the vibrations of the first flexural resonance of the smart beam which has a servo actuated end mass. The smart beam studied is a cantilever aluminum beam with four surface bonded Lead-Zirconate-Titanate (PZT) patches in bimorph configuration. In the design procedure, first, the parameter uncertain modeling of the flexible cantilever aluminum beam with a piezoelectric sensor and actuator is created by means of an analogical approach. Hence, the uncertain model was achieved from the simulation of the experimentally obtained beam model with a mass-spring-damper system having the equivalent smart beam characteristics. Then, the generalized plant model of the uncertain model is constituted, and a Linear Time Invariant (LTI) H_∞ controller is computed. Finally, a gain scheduling H_∞ controller was obtained by adapting a variable parameter filter to the LTI H_∞ controller. The developed gain scheduling H_∞ controller and its corresponding conventional H_∞ controller are applied on the smart system with parameter varying. The obtained experimental results in time and frequency domain reveal that the proposed controller is able to suppress the vibrations of the smart beam at the first flexural mode. In addition to this, the experimental results show that proposed gain scheduling H_∞ controller's performance is superior then conventional LTI H_∞ controller.

1 INTRODUCTION

The recent developments in sensor and actuator technologies allows the usage of Smart structures in the active vibration control of light and flexible structures; especially inaeronautical structures. The piezoelectric materials can serve both as sensor and actuator. The PZT (Lead-Zirconate-Titanate) piezo ceramic smart materials are widely used both as

embedded within the passive composites and/ or being surface bonded to the passive metals and/ or composites in order to form a smart structure.

The research for the active vibration control of smart beams can be broadly classified into three main categories as classical, adaptive and robust [1] among those the relatively straightforward PD and PID classical controller designs are the most widely encountered studies [2-8]. Fractional derivative effects in the controller designs of a smart beam are also investigated [9]. High performance requirements, uncertainties in the system model and different operating conditions require more effective control algorithms such as adaptive ones [10-16]. The adaptive control architecture on the other hand has its own requirements such as the application of an adaptation scheme which makes the controller a complicated one to design. If one would like to avoid the performance losses due to the system and the modeling uncertainties, then he inevitably resort to use robust control methodologies. Robust control can appropriately handle the parameter uncertainties and nonlinearities in the system model as well. Nestorovicand Oveisibyare proposing a combined H2/H_∞ approach, experimentally proved the efficacy of their design [17]. They obtained the system model through Finite Element Method (FEM) and successfully suppressed the vibration level at the first resonance frequency of the beam by 20 dB. The used a laser displacement sensor in the experiments. Sridevi and Madhavasarma designed an H_∞ controller and compared with an LQG (Linear Quadratic Gussian) controller [18]. In their experiment they used PZT patches. They showed that the developed controller was efficient at high frequencies when the closed loop responses were considered. They also showed that an H_∞ controller gave better performance as compared to an LQG controller. Omidi and Mahmoodi designed and applied controller for the active vibration control of smart structures [19]. In the study, H_∞ MPPF (H_∞ Modified Positive Position Feedback) and H_∞MPVF (H_∞ Modified Positive Velocity Feedback) designs were implemented. In that study where PZT patches were used as actuators H_∞ MPVF controller performer superior to H_∞ MPPF controller. In all the aforementioned smart beam studies, the beam had almost constant mass and stiffness properties; hence fall short of providing variable system parameters. If one considers an aircraft wing, the problem becomes more self-explanatory. Due to the fuel consumed during the flight, both mass and stiffness properties of the wing continuously change and this will reflect itself in changing values of resonance frequencies and respective mode shapes of the wing. Akın attempted to model such a problem by adding a mass-servo mechanism towards the tip of a cantilever smart beam [20]. The servo-mechanism changes the position of the mass for five different position and hence modifies the mass characteristics of the smart beam. The study conducted by developing an LQR controller together with neural network for robustness.

Gain scheduling controllers are especially suitable for systems in which the system parameters can vary [21-23]. This study presents a gain scheduling H_∞ controller which was designed to suppress the flexural vibrations of a system with varying parameters. The controller was designed and implemented to a smart cantilever beam. In order to design a reduced order H_∞ controller a, the lowest possible order, second order analytical model was obtained from the experiments. Therefore for each five position of the servo mechanism second order system model were obtained. Then the numerator polynomial equations, which actually represent the antiresonance frequencies, were omitted and the system was simulated as if it was a mass-spring-damper system. The analogical model corresponding to the mean value of servo bar position is perturbed and, crude H_∞ controller K(s) is computed by using that model. In the final

stages of the design, the anti-resonance polynomial which was previously neglected is suitably included into K(s). If only the polynomial having the highest antiresonance frequency is used then the LTI H_∞ controller is synthesized. If a parameter varying polynomial including all the antiresonance frequencies is used the gain scheduling H_∞ controller is synthesized.

It is believed that the developed controller is superior to other H_∞ controller designs in literature and advantageous in terms of the following criteria:

- ✓ The anti-resonance frequency which complicates the controller design had been successfully omitted.
- ✓ The synthesis of gain scheduling H_∞ controller follows the same methodology of conventional H_∞ controller.
- ✓ A lowest possible order of second order can successfully be used in the design.
- ✓ No reduction has been attempted for the implication of the developed controller.
- ✓ No additional compensator has been utilized for performance increase.

2 BEAM MODEL WITH PARAMETER UNCERTAINTY

Figure 1 gives the smart beam used in the study. It is an aluminum, cantilever beam with dimensions of 350x30x2 mm. Four BM500 PZT patches having dimensions of 25.4x25.4x0.50 mm stuck in bimorph condition. The details of the experimental set-up is given in [20].

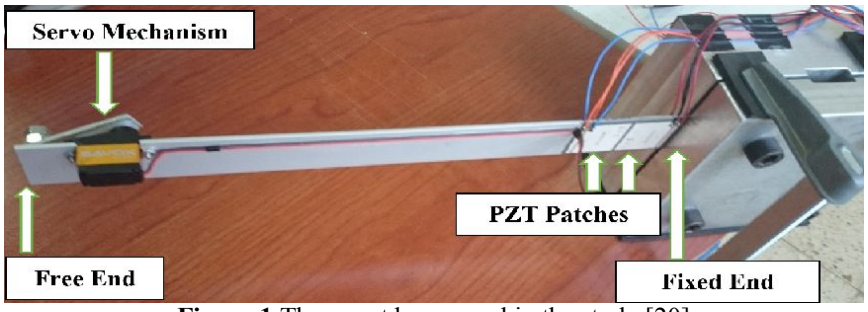

Figure 1:The smart beam used in the study [20]

The variations in system physical parameters were represented by different angles at which the servo mechanism arm assumed. Hence the cases of +64º, +32º, 0º, -32º and -64ºwere considered in order. For each case the actuator PZT patches were given a chirp sine wave with a range of 5 Hz to 30 Hz and the system response were measured by using from sensor PZT patches. These input-output data have been converted to frequency response function through a FFT by using MATLAB. Then second order transfer functions were fitted to these frequency response functions in the form of $G_n(s)=A_n(s)/B_n(s)$. Equations 1 to 5 represent the transfer functions of these five cases where the equation number gives the case considered.

$$\boldsymbol{G_1(s)} = \frac{\boldsymbol{A_1(s)}}{\boldsymbol{B_1(s)}} = \frac{\boldsymbol{0.0182s^2+0.3710s+251.1245}}{\boldsymbol{s^2+1.5255s+7193.2}} \quad (1)$$

$$\boldsymbol{G_2(s)} = \frac{\boldsymbol{A_2(s)}}{\boldsymbol{B_2(s)}} = \frac{\boldsymbol{0.0176s^2+0.3923s+264.4334}}{\boldsymbol{s^2+1.5840s+7604.7}} \quad (2)$$

$$\boldsymbol{G_3(s)} = \frac{\boldsymbol{A_3(s)}}{\boldsymbol{B_3(s)}} = \frac{\boldsymbol{0.0169s^2+0.4183s+283.0299}}{\boldsymbol{s^2+1.6754s+8175.1}} \quad (3)$$

$$\boldsymbol{G_4(s)} = \frac{\boldsymbol{A_4(s)}}{\boldsymbol{B_4(s)}} = \frac{\boldsymbol{0.0162s^2+0.4459s+303.3521}}{\boldsymbol{s^2+1.7759s+8796.6}} \quad (4)$$

$$\boldsymbol{G_5(s)} = \frac{\boldsymbol{A_5(s)}}{\boldsymbol{B_5(s)}} = \frac{\boldsymbol{0.0158s^2+0.4624s+317.3042}}{\boldsymbol{s^2+1.8454s+9216.7}} \quad (5)$$

3 GAIN SCHEDULING H_∞ CONTROLLER DESIGN

The proposed gain scheduling H_∞ controller design methodology is composed of 6 steps.

Step 1. First the second order transfer functions which correspond to the five different positions of the servo actuator arm were obtained. ($\mathbf{G_1(s)} = \frac{\boldsymbol{A_1(s)}}{\boldsymbol{B_1(s)}}$, $\mathbf{G_2(s)} = \frac{\boldsymbol{A_2(s)}}{\boldsymbol{B_2(s)}}, \dots, \mathbf{G_n(s)} = \frac{\boldsymbol{A_n(s)}}{\boldsymbol{B_n(s)}}$) The reason stems from the well-known fact that the lowest order transfer function which represents a resonance and an anti-resonance condition is a transfer function of second order polynomials of both numerator and the denominator.

Step 2. The numerator polynomial which is related to the anti-resonance value is omitted and the analogical transfer functions of $G_1^l(\mathbf{s}) = \frac{\mathbf{1}}{\boldsymbol{B_1(s)}}$, $G_2^l(\mathbf{s}) = \frac{\mathbf{1}}{\boldsymbol{B_2(s)}}, \dots, G_n^l(\mathbf{s}) = \frac{\mathbf{1}}{\boldsymbol{B_n(s)}}$ can be obtained. It can be seen that the resultant transfer functions are in the form of $\frac{1}{\bar{m}s^2+\bar{c}s+\bar{k}}$.

Step 3. By considering the range and values of the analogical model parameters corresponding to the mean value of servo bar position the perturbed analogical model is obtained. In this study, the servo arm has five different positions and the system model which corresponds to the mean value of 0° is $G_3^l(\boldsymbol{s}) = \frac{\mathbf{1}}{\boldsymbol{B_3(s)}} = \frac{\mathbf{1}}{\boldsymbol{s^2+1.6754s+8175.1}} = \frac{\mathbf{1}}{\bar{m}s^2+\bar{c}s+\bar{k}}$.

The physical mass, damper and spring terms in the denominator polynomial can be taken into the consideration as:

$$m = \bar{m}(1 + p_m\delta_m),\ c = \bar{c}(1 + p_c\delta_c),\ k = \bar{k}(1 + p_k\delta_k) \quad (6)$$

where, $\bar{m} = 1$, $\bar{c} = 1.6754$ and $\bar{k} = 8175.1$ represent the nominal values of m, c and k. p_m, p_c, p_k and $\delta_m, \delta_c, \delta_k$ if represent the probable perturbations of the physical parameters. In this study, $p_m = 0.1,\ p_c = 0.3,\ p_k = 0.3$ ve $-1 \le \delta_m, \delta_c, \delta_k \le 1$ values were assigned. These values correspond to a change of $\pm$%10 in m, $\pm$%30 in c and, $\pm$%30 in k. The uncertainties in the parameters are taken into account by the use of linear fractional transformations (LFTs) and the perturbed analogical model is obtained [24].

Step 4. The designed controller should provide the required closed loop performance and should make the system stable. The performance criterion for the closed loop system is the so-called *S* over *KS* design and is described by

$$\left\| \begin{bmatrix} W_P S(G_S) \\ W_u KS(G_S) \end{bmatrix} \right\|_\infty < 1 \quad (7)$$

where $S(G_s)=(I+G_sK)^{-1}$ is the output sensitivity function of the nominal system, and W_p, W_u are the weighting functions chosen to represent the frequency characteristics of the external disturbance d and performance requirement level.

H_∞ controller $K(s)$ is crudely computed by means of the perturbed analogical model. The required condition given in Equation 7 is satisfied and thus the closed loop system achieves nominal performance requirements.

The block diagram of the closed loop system showing the feedback structure and including the elements reflecting model uncertainty and performance requirements (e_p, e_u), is given in Figure 2. The rectangle with dashed lines in Figure 2 represents the transfer function matrix G. Inside the rectangle is the nominal model G_s of the analogical system and the uncertainty matrix Δ that includes the model uncertainties.

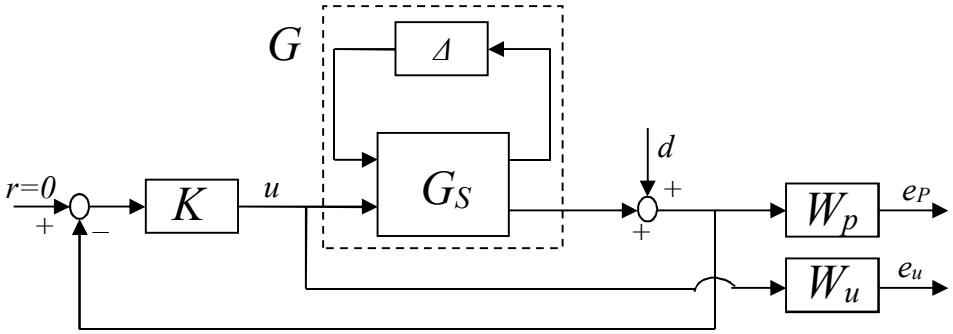

Figure 2:Generalized system architecture

The weight functions W_p and W_u used in this study are given in Equation 8 and Equation 9 respectively

$$W_p = \frac{15s^2+500s+14\cdot10^4}{s^2+0.018s+8172.2} \tag{8}$$

$$W_p = 1\cdot10^{-3} \tag{9}$$

$d$being the disturbance, the generalized system transfer function can be represented in a form which is given in Equation 10.

$$\begin{bmatrix} e_p \\ e_u \end{bmatrix} = \begin{bmatrix} W_p(I+GK)^{-1} \\ W_uK(I+GK)^{-1} \end{bmatrix} d \tag{10}$$

Hence, the crude H_∞ controller $K(s)$ providing the performance criterion is that the transfer functions from d to e_p and e_u should be small in terms of the infinity norm, for all the possible values of the uncertainty transfer matrix Δ.

Step 5. The numerator polynomials which were omitted in Step 2,$A_1(s),A_2(s),\ldots,A_5(s)$,were taken into the consideration in the controller dynamics as $K(s)/A_5(s)$ and then the classical H_∞ controller was synthesized. This controller is called the Linear Time Invariant (LTI) H_∞

controller. Note that $A_5(s)$ is the polynomial among the experimentally obtained models with the highest anti resonance frequency.

Step 6. The numerator polynomials which were omitted in Step 2, $A_1(s), A_2(s), \ldots, A_5(s)$,can be curve-fitted and can be represented as a function of servo arm angular position θ like $A(s,\theta)$. These polynomials were taken into the consideration in the controller dynamics as $K(s)/A(s,\theta)$ and then the gain scheduling H_∞ controller was synthesized. It can be easily understood that since $A_5(s)$ is close to $A_5(s,\theta)$; then for fifth case, the resonance suppression performances of LTI H_∞ and gain scheduling H_∞ controllers will be very close.

4 EXPERIMENTAL STUDY

Experiments were conducted in order to evaluate the effectiveness of the developed gain scheduling H_∞ controller. The experiments considered five different cases which corresponded to five different assigned angular positions of the servo actuator arm. The cases were $+64^o$, $+32^o$, 0°, -32° and -64° positions. The comparison of time domain responses of free vibrations of open and closed loop cases of gain scheduling H_∞ and LTI H_∞ controllers are shown in Figure 3. Table 1 details the suppression times for the free vibration responses of closed loop cases. Figure 4 represents the time domain responses of forced vibrations of closed open/ loop cases of gain scheduling H_∞ and LTI H_∞ controllers. After an initial 2 seconds, the controller was switched on. The comparison of frequency domain responses of closed loop cases of gain scheduling H_∞ and LTI H_∞ controllers together with the open loop response are shown in Figure 5. It can be seen from Figure 5 that except case five, in all the other cases the developed gain scheduling H_∞ controller outperform the LTI H_∞ controller. In the fifth case, as expected, both controllers perform nearly equally.

Table 1: Free vibrations suppression times of the controllers

	Case 1	**Case 2**	**Case 3**	**Case 4**	**Case 5**
LTI H_∞	0.51 s	0.50 s	0.41 s	0.38 s	0.35 s
Gain scheduling H_∞	0.49 s	0.41 s	0.35 s	0.25 s	0.35 s

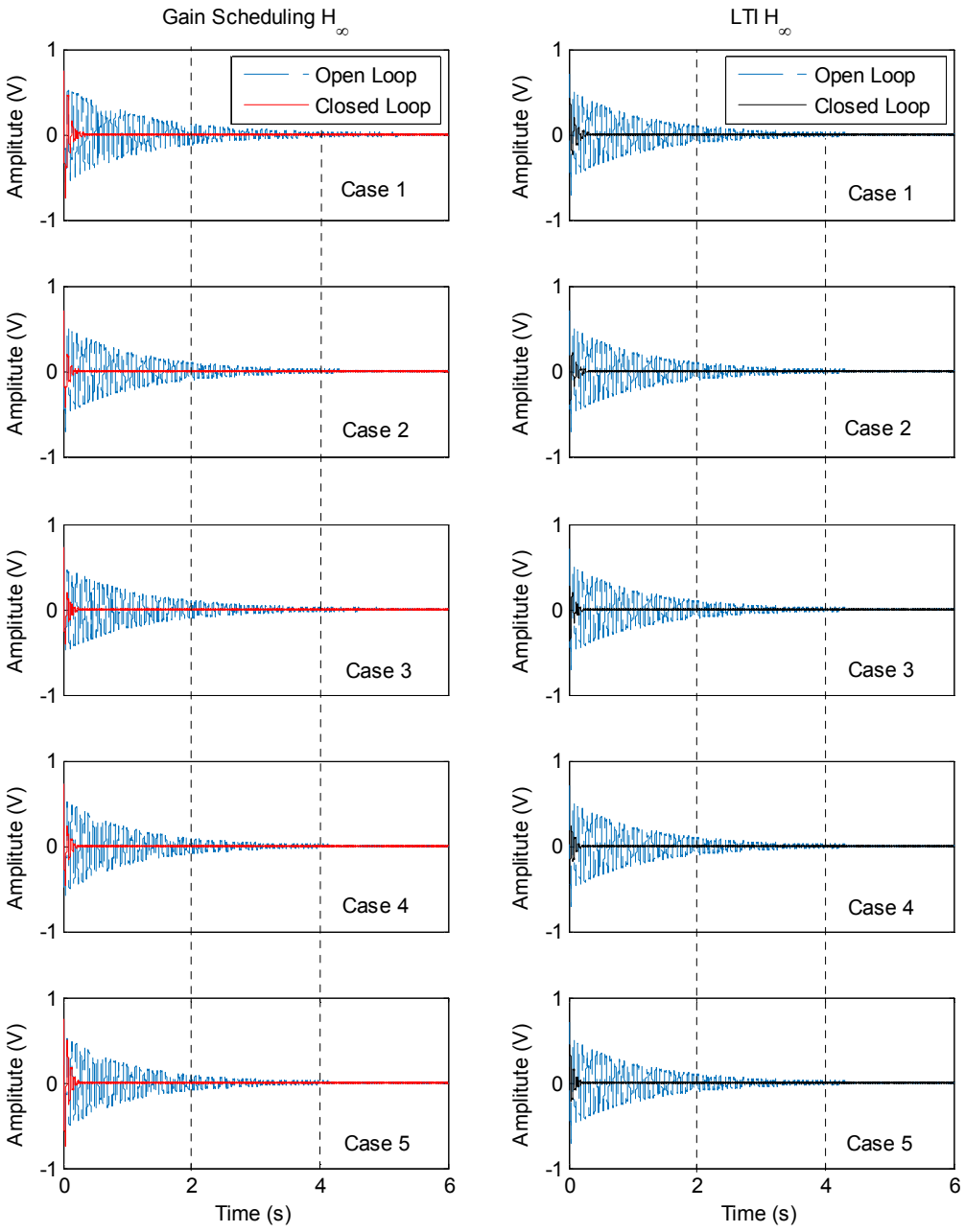

Figure 3: Time domain free vibration responses of the smart beam

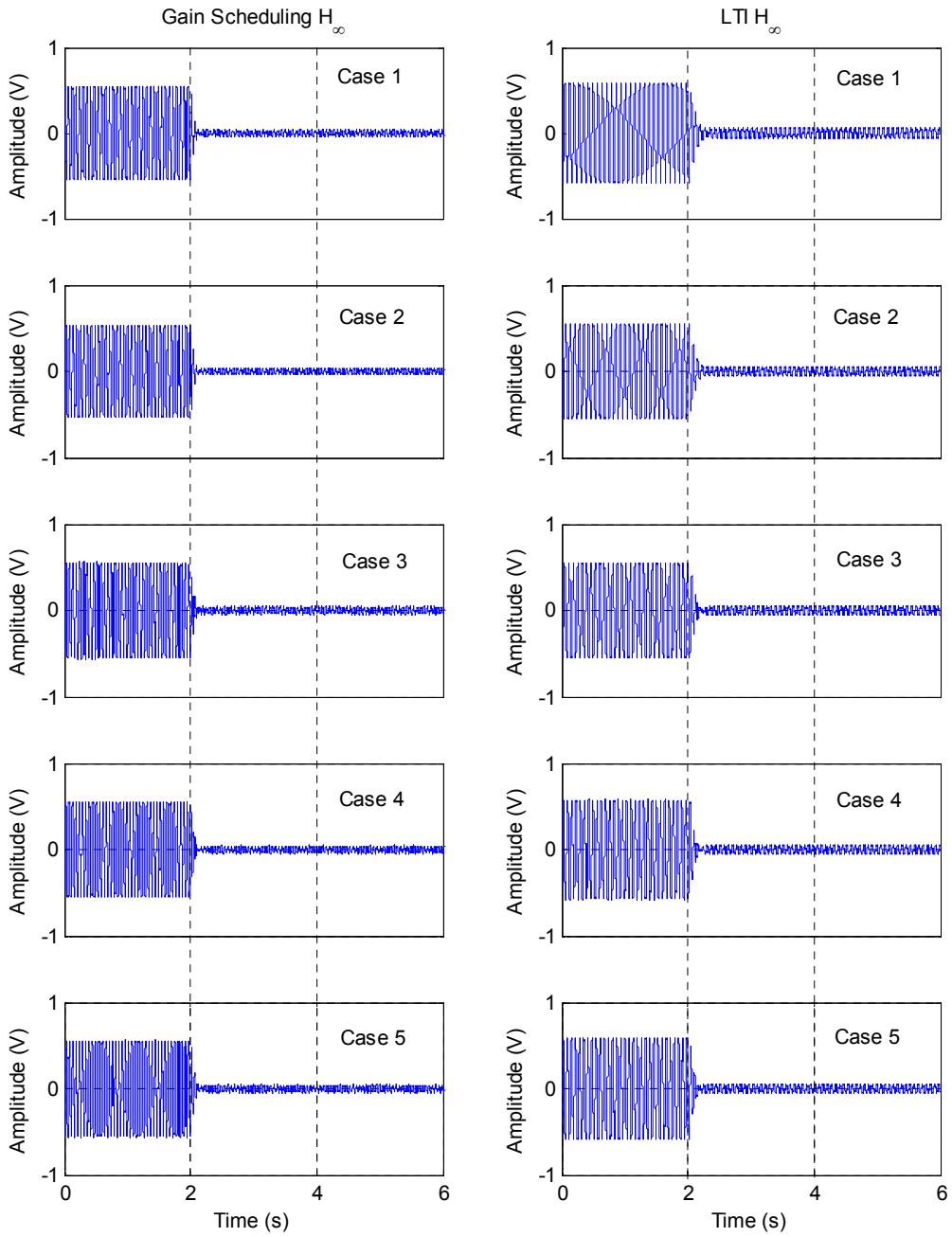

Figure 4: Time domain forced vibration responses of the smart beam

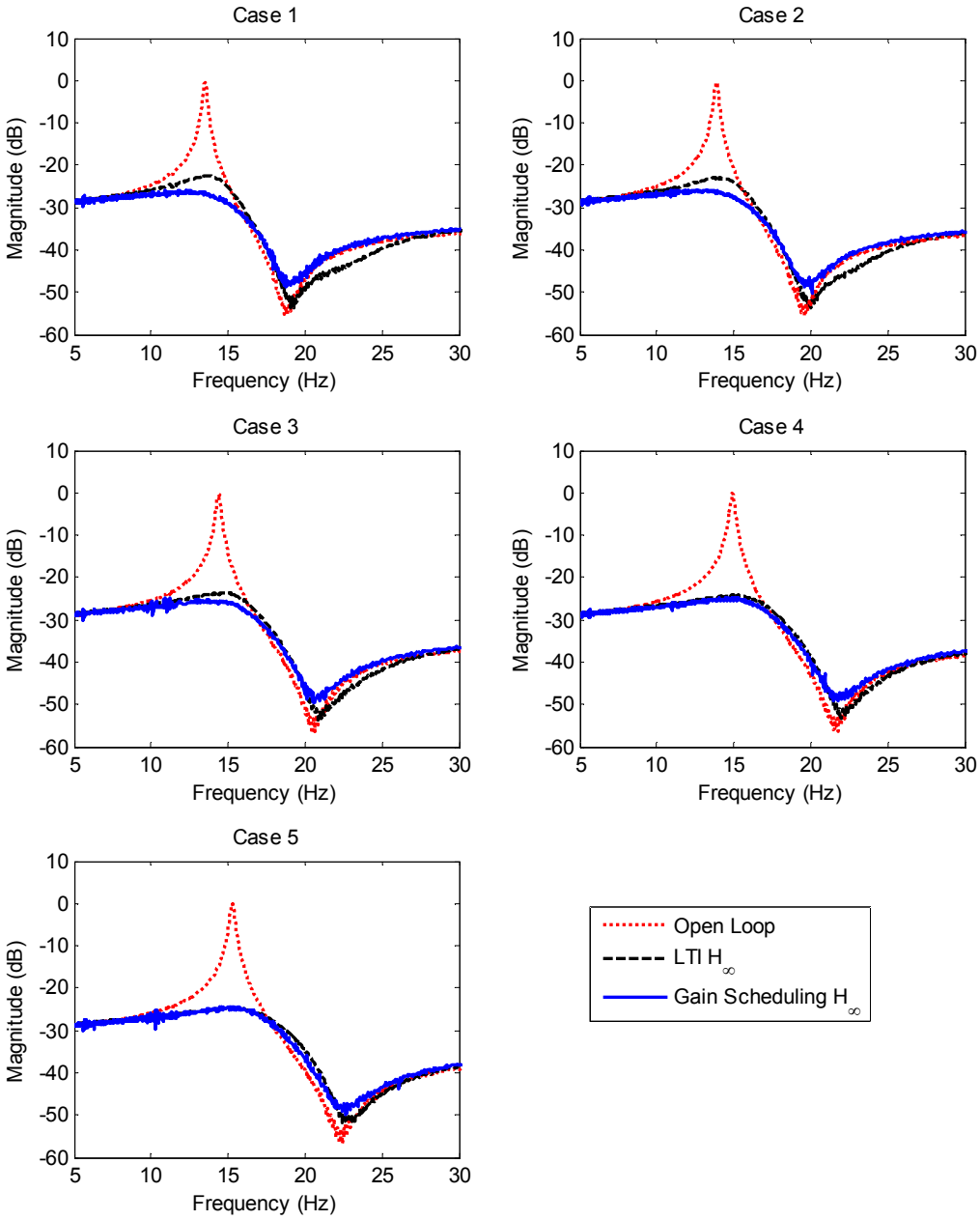

Figure 5: Frequency domain forced vibration responses of the smart beam

5 CONCLUSIONS

This study presented a new gain scheduling H_∞ controller design. The first flexural vibrations of a smart beam with varying physical parameters were tried to be suppressed. The design procedure is composed of six steps. At the fifth step a LTI H_∞ controller and at the sixth and last step a gain scheduling H_∞ controller was synthesized. The time domain and frequency domain experiments conducted for five different cases had revealed that the designed gain scheduling H_∞ controller performed satisfactorily for all the cases and controlled the effects of changes of system physical parameters.

It is believed that the systems where their physical parameter changes can be measured and/ or can be observed and/or can be estimated by an artificial network are suitable candidates for the efficient application of gain scheduling H_∞ controllers.

REFERENCES

[1] Ros, N.F.M., Saad M.S. and Darus I.Z.M. Dynamic Modeling and Active Vibration Control of a Flexible Beam: A Review.*Int. Journal of Engineering & Technology* (2015), 15:12-17.

[2] Saad, M.S., Jamaluddin, H. and Darus I.Z.M.Active Vibration Control of Flexible Beam System Using Proportional Control Scheme In Finite Difference Simulation Platform,*Fourth International Conference on Modeling, Simulation and Applied Optimization* (2011)1-5.

[3] Kumar, S.,Srivastava, R. and Srivastava, R.K. Active Vibration Control of Smart Piezo Cantilever Beam Using PID Controler. *Int. Journal of Research in Engineering and Technology* (2014)3:392-399.

[4] Fei, J., Fang, Y. and Yan, C. The Comparative Study of Vibration Control of Flexible Structure Using Smart Materials, *Mathematical Problems in Engineering* (2010)1-13.

[5] Alam, M.N. and Rahman, N.U. Active Vibration Control of a Piezoelectric Beam Using PID Controller: Experimental Study,Latin American Journal of Solids Structure, (2010) 9:657- 673.

[6] Khot, S., Yelve, N.P., Tomar, R., Desai, S. and Vittal, S. Active Vibration Control of Cantilever Beam By Using PID Based Output Feedback Controller,*Journal of Vibration and Control*, (2012) 18:366-372.

[7] Chhabra, D., Narwal, K. and Singh, P. Design and Analysis of Piezoelectric Smart Beam For Active Vibration Control,*International Journal of Advance Research and Technology*, (2012) 1:1-5.

[8] Fadil, M. A. and Darus, I. Z. M. Evolutionary Algorithms For Self- Tuning Active Vibration Control of Flexible Beam. *Australian Control Conference,* (2013) 104-108.

[9] Onat, C., Sahin, M. and Yaman, Y., *Fractional Controller Design for Suppressing Smart Beam Vibrations* Aircraft Engineering and Aerospace Technology: An International Journal (2012) 84/4:203-212.

[10] Onat, C., Sahin, M. and Yaman, Y. Active Vibration Suppression of a Smart Beam by Using a Fractional Control. *2nd International Conference of Engineering Against Fracture (ICEAF II)*, (2011) 22-24 June 2011, Mykonos, Greece.

[11] Onat, C., Sahin, M., Yaman, Y., Prasad, E. and Nemana, S. Design of an LPV Based Fractional Controller for the Vibration Suppression of a Smart Beam. *International Workshop on Smart Materials&Structures and NDT in Aerospace (CanSmart2011),* (2011) 02-04 November 2011, Montreal, Canada.

[12] Onat, C., Sahin, M., Yaman, Y. Optimal Control of a Smart Beam by Using a Luenberger Observer, *3rd International Conference of Engineering Against Failure (ICEAF III),* (2013) 26-28 June 2013, Kos, Greece.

[13] Fadil, M.A., Jalil, N.A. and Darus, I. Z.M. Intelligent PID Controller Using Iterative Learning Algorithm For Active Vibration Controller of Flexible Beam, *IEEE Symposium on Computer and Informatics*, (2013) 80-85.

[14] Saad, M.S., Jamaluddin, H. and Darus, I.Z.M. Active Vibration Control of Flexible Beam Using Differential Evolution Optimisation, *World Academy of Science and Technology*, (2012) 419-426.

[15] Zorić, N.D., Simonović, A.M., Mitrović, Z.S., Stupar, S.N., Obradović, A.M. and LukićN.S.Free Vibration Control of Smart Composite Beams Using Particle Swarm Optimized A.M. Self- Tuning Fuzzy Logic Controller, *Journal of Sound Vibration,* (2014) 333:5244-5268.

[16] Shouwei, G., Zhiyuan, G., Yong, S., Jincong, Y. andXiaojin, Z. Performance Analysis and Comparison of FXLMS and FULMS Algorithm For Active Structure Vibration Control, *International Conference of Advance Computer Control*, (2010) 1:197-201

[17] Nestorovic, T. and Oveisi, A. Robust Controller for The Vibration Suppression of an active Piezoelectric Beam.*7th ECCOMAS*, Smart (2015).

[18] Sridevi, M. and Madhavasarma, P. Model Identification and Smart Structural Vibration Control Using H_∞Cotroller,*Int. Journal on Smart Sensing and Intelligent Systems*, (2010) 3:655-671.

[19] Omidi, E. and Mahmoodi,S.N.Vibration Control of Collocated Smart Structures Using H_∞ Modified Positive Position and Velocity Feedback.*Journal of Vibration and Control*, (2014) 22:2434-2442.

[20] Akın, O. Active Neuro-Adaptive Control of a Smart Beam Having Uncertainties in Structural Dynamics. *Master Thesis*, Aerospace Engineering, METU, Ankara (2015).

[21] Onat, C., Kucukdemiral, I.B., Sivrioglu, S. and Yuksek, I. LPV model based gain-scheduling controller for a full vehicle active suspension system", *Journal of Vibration and Control*(2007)13:1629-66.

[22] Onat, C., Kucukdemiral, I.B., Sivrioglu, S., Yuksek, I. and Cansever, G. LPV gain-scheduling controller design for a nonlinear quarter-vehicle active suspension system, *Transactions of the Institute of Measurement and Control* (2009) 31:71-95.

[23] Onat, C. WGC Based Robust and Gain Scheduling PI Controller Design for Condensing Boilers.*Advances in Mechanical Engineering*(2014):1-13.

[24] Gu, D.W., Petkov, P.H. and Konstantinov, M.M. *Robust Control Design with Matlab*, Springer (2005).

VIII ECCOMAS Thematic Conference on Smart Structures and Materials
SMART 2017
A. Güemes, A. Benjeddou , J. Rodellar and Jinsong Leng (Eds)

HYDROGEN PERMEATION OF DLC-COATED STAINLESS STEELS

M. TAMURA*

* University of Electro-Communications
Chofu, Tokyo, Japan
e-mail: tamura@uec.ac.jp

Key words: Hydrogen Permeation, DLC Coatings, Stainless Steels, Hydrogen Trap Sites.

Abstract.
In many metallic materials hydrogen present in the material is well known to have a negative impact on the mechanical properties of the material. It is reported that the deposition of ceramic coatings such as Al_2O_3, TiN, and BN with a thickness of several micrometers can decrease hydrogen attack by a few orders of magnitudes.

In this study, the hydrogen barrier properties of the coatings of diamond-like amorphous carbon (DLC) were evaluated. The hydrogen permeation test was implemented under a differential hydrogen pressure of 400 k Pa and temperatures of 573 K to 773 K, and the amount of hydrogen that permeated a sample was measured. It was confirmed that DLC coatings have an impact on decreasing the hydrogen permeation rate. The hydrogen permeation rate was reduced to 1/1000 or lower. DLC coatings with high hydrogen content had high hydrogen barrier function.

For hydrogen diffusion in coatings, the movement of atoms through hydrogen trap sites such as pores in coatings, and crystal defects such as dislocations, are important. DLC coating is amorphous, and there are both sp^3 and sp^2 bonds, and excess hydrogen may be found in the interstitial space and the above-mentioned hydrogen trap sites. In a DLC coating with high hydrogen content, these hydrogen trap sites are likely already filled with hydrogen atoms, and the movement of new hydrogen atoms could be limited.

1 INTRODUCTION

Studies on hydrogen barrier coatings that prevent hydrogen attack have been conducted by researchers in various fields. Ceramic coatings such as Al_2O_3, TiC, TiN, and BN have been reported to be suitable as a hydrogen barrier [1-3]. There are various methods of generating these coatings such as chemical vapor deposition (CVD), physical vapor deposition (PVD), and plasma-spray, and the deposition of ceramic coatings with a thickness of several micrometers can decrease hydrogen attack by several orders of magnitudes.

Diamond-like carbon (DLC) coatings have superior properties such as high hardness, high resistance to abrasion, low friction, low aggressiveness against mating materials, seize resistance, high insulation, infrared transparency, high gas barrier properties, and biocompatibility [4-5]. Utilizing its low friction and low aggressiveness against mating materials, its application to sliding parts, such as in automobiles, is dominant. For protecting

the global environment and reducing CO_2 emission, methods for improving fuel efficiency, preventing abnormal noise, reducing oil usage, and improving the durability of automobiles are being investigated.

DLC is an amorphous coating that is a mixture of a diamond structure (sp^3 bond) and a graphite structure (sp^2 bond). The fraction of sp^3 bonds in DLC varies from 10–70%, and it also contains 0–60 at% hydrogen; therefore, its density varies from 1.1–3.0 g/cm^3, leading to a variety of characteristics. If the amount of hydrogen is less than 25 at%, the density, hardness, and abrasion resistance are high; therefore, these materials are used as cutting tools, molds, machinery parts, hard-disk heads, and magnetic tapes. DLC, with high hydrogen content have a lower density and polymer-like characteristics [4-5].

There is an example of DLC coating the insides of a polyethylene terephthalate (PET) bottle, acting as a gas barrier, through which permeation of oxygen and moisture is suppressed. This helps long-term maintenance of the quality of the products in the bottle.

As such, a DLC coating has a wide range of applications, but clinical trials on hydrogen barrier functions are quite limited and the hydrogen gas barrier function has still not been studied. In this study, the relationship among each structure of a DLC coating, the hydrogen content, and the hydrogen gas barrier function was investigated.

2 EXPERIMENTAL DETAILS

2.1 Deposition process

Coatings were prepared using plasma CVD and a sputtering method. DLC coatings, and ZrN, TiAlN, and AlCrN coatings with a thickness of about 3 μm were deposited on Type 316L stainless steel. About 0.6 μm thick Cr-N coating (Cr+CrN) was used as a buffer layer under DLC coatings. This buffer layer is necessary to increase the adhesiveness of the DLC coating to the stainless steel substrate. A Cr layer (0.1 μm) was deposited immediately above the stainless steel, and a CrN (0.5 μm) coating was deposited on top of this buffer-layer. We prepared three DLC coatings with different hydrogen content (20%, 10%, and 8%). DLC coatings with a hydrogen content of 20% and 10% were prepared using plasma CVD, and the coating with a hydrogen content of 8% was prepared using sputtering.

The composition of TiAlN (atomic molar ratio) was Ti:Al = 1:1. The AlCrN composition was Al:Cr = 7:3.

2.2 Hydrogen-permeation tests

Hydrogen-permeation tests were performed on the coated stainless steel samples [3]. The sample had a diameter of 35 mm and thickness of 0.1 mm. The coated samples were set on a susceptor made of silicon fiberglass and it could be held in place without bending at temperatures up to 773 K. The apparatus was evacuated to ~10^{-6} Pa. After the test temperature had become stable, hydrogen (purity of 99.995%) was introduced into one side (susceptor side) in a sequence of increasing filling pressures (400 kPa). The other side of the apparatus (stainless-steel-sample side) was continuously evacuated. The samples were affixed with a metallic seal made of gold and could be heated by an electric furnace to 773 K without oxidation. The permeation area was 6.6 cm^2.

3 RESULTS AND DISCUSSION

3.1 Hydrogen permeation characteristics of each type of coating

Hydrogen permeation test results for each type of coating are shown in Figure 1. ZrN, TiAlN, AlCrN, and DLC films that contains 20% hydrogen (DLC(20%H_2) in the Figure) lower the hydrogen permeation rate by two orders of magnitude (1/100 or lower) compared to the base material (SUS316L in the Figure). Specifically, DLC (20%H_2) lowered the hydrogen permeation rate by three orders of magnitudes (1/1000 or lower) at measurement temperatures of 573 K, 673 K, and 773 K.

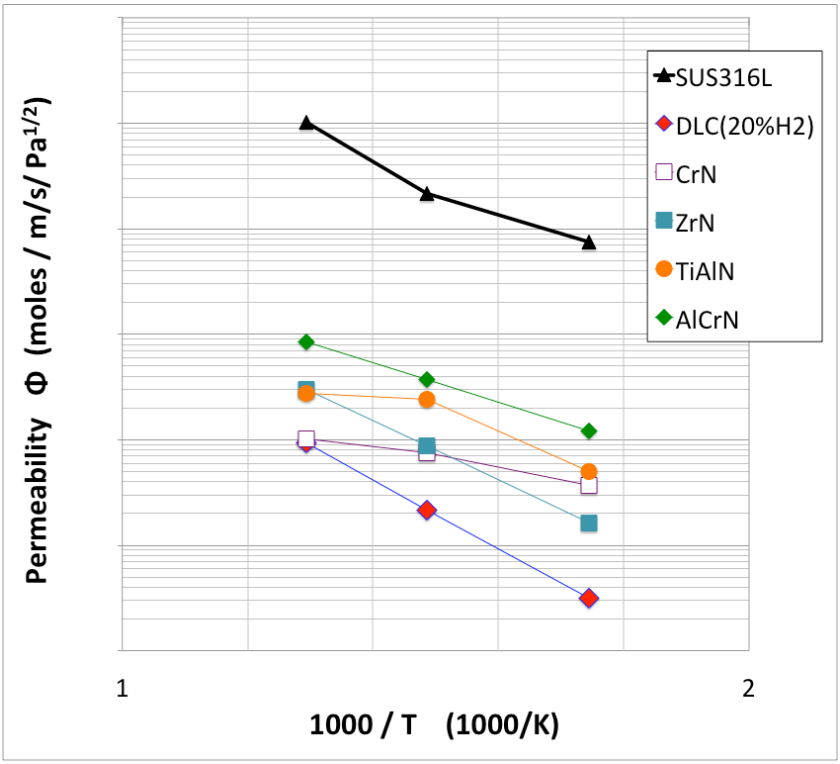

Figure 1: Arrhenius plot of hydrogen permeability of each type of coating

3.2 Characteristics and hydrogen barrier function of DLC coating

Hydrogen permeation test results for the DLC coating are shown in Figure 2. DLC coatings with varying hydrogen content (20, 10, and 8 at%), pre-coat only, and a DLC coating without buffer layer with 20% hydrogen content (DLC (20% H_2) in the Figure) were compared.

Compared to the base material, all coatings reduced the hydrogen permeation rate by two or more orders of magnitude, showing a superior hydrogen barrier function. The DLC coating with higher hydrogen content has lower hydrogen permeation rate.

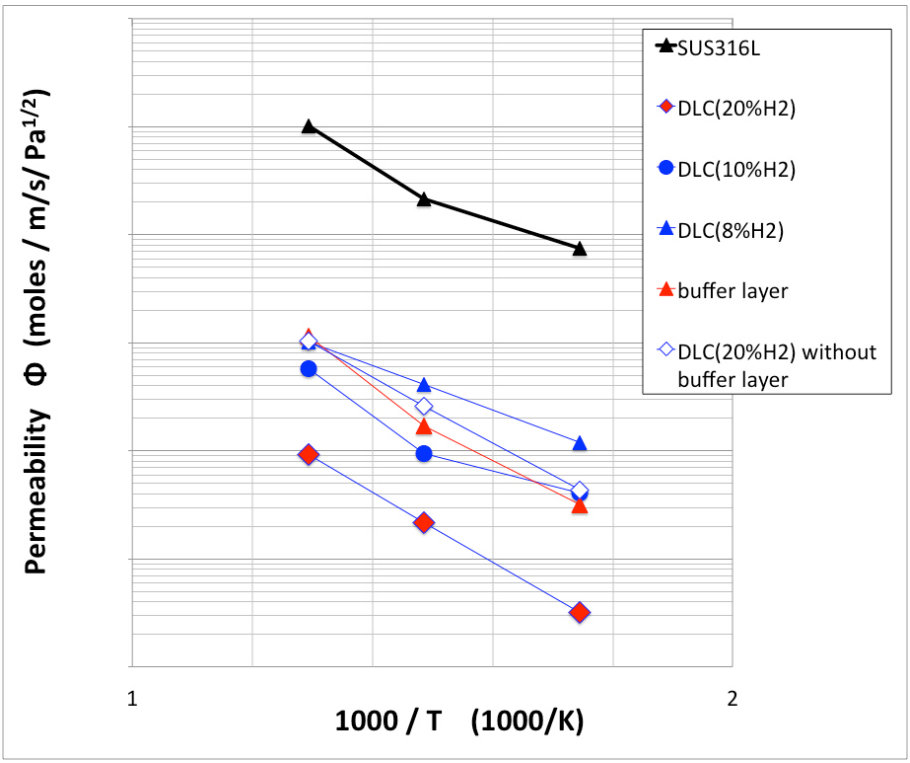

Figure 2: Arrhenius plot of hydrogen permeability of DLC coatings

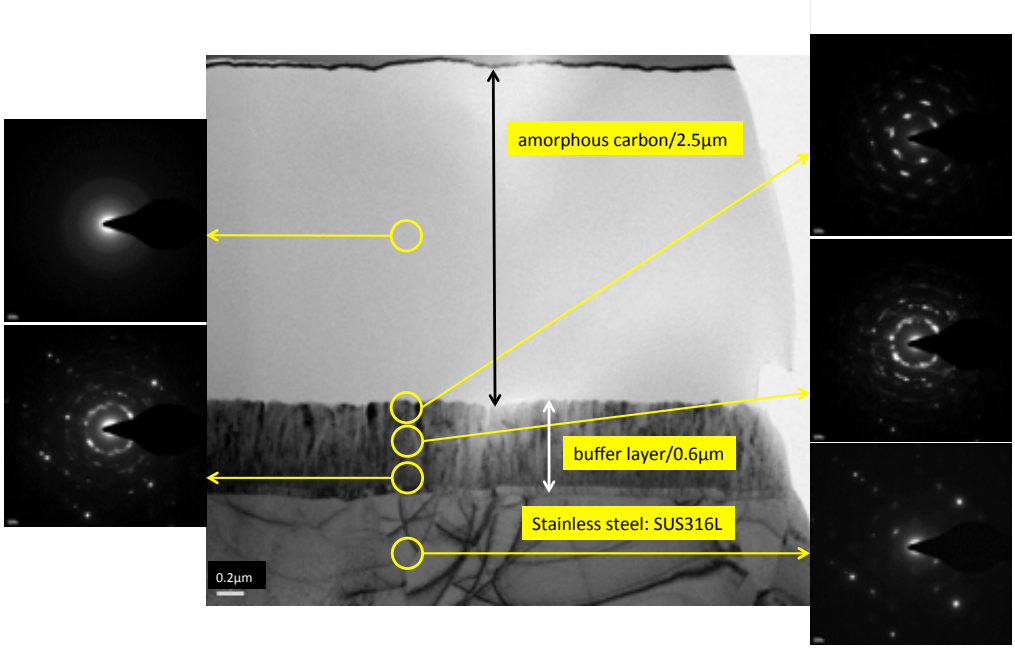

Figure 3: TEM image of cross section of DLC coated stainless steel

The TEM cross-sectional observation results of the DLC coating with a hydrogen content of 20% (DLC(20%H_2)) are shown in Figure 3. The observed thickness of the DLC film was 2.5 μm, and there was no diffraction pattern that indicates crystallinity; thus, the coating was confirmed to be amorphous. The pre-coat consists of two layers, and there is a 0.1 μm thick metallic Cr coating immediately above the substrate, and above this coating, there is a 0.5-μm thick CrN coating.

Figure 2 shows that even with only a buffer layer, it was effective in decreasing the hydrogen permeation rate. The CrN film is dense and consists of fine crystals. Crystals grow perpendicular to the substrate, and the diameter of the crystals in the cross-sectional direction parallel to the substrate is 20–30 μm. The buffer layer with a thickness of 0.6 μm also shows a hydrogen barrier function. When there is no pre-coat, the hydrogen permeation rate differs by an order of magnitude, and the combination of the buffer layer and the DLC film (DLC(20%H_2) in the Figure) had the lowest hydrogen permeation rate.

When considering the hydrogen diffusion in DLC coatings, the structure of the DLC coating, the conditions of the hydrogen atoms, and the mechanism of hydrogen diffusion need to be considered. When considering the structure of a DLC coating based on the local structure at the atomic level of the coating, it was determined that carbon atoms with a sp^3 hybrid orbit corresponding to the diamond structure, and carbon atoms with a sp^2 hybrid orbit corresponding to the graphite structure are mixed together.It is known that the ratio of these sp^2 and sp^3 hybrid atoms strongly affects the various properties of the DLC coatings. The bond ratio of sp^2 and sp^3 atoms in DLC coatings is a strong indicator of the structure of DLC coatings.

Because of the heating up to 773 K in the hydrogen permeation test, the graphite structure increased in all the coatings. The obtained Raman spectral waveforms are separated into the G-band peak near 1350 cm^{-1}, derived from the graphite structure and a D-band peak near 1550 cm^{-1}, derived from disordered graphite, and the I(D)/I(G) intensity ratio was compared. Visible light Raman spectroscopy has low sensitivity to the sp^3 bond, and can be considered as an evaluation of the sp^2 bond. However, in a sample after the hydrogen permeation rate test, with heating up to 773 K, the G-band peak increased notably, and fraction of graphite structure increased. Even when the hydrogen content is different, by heating to 773 K, it stabilizes into similar structures (i.e., the same I(D)/I(G) ratio).

As described above, when the DLC coating is heated at 773 K, the fraction of graphite structure increases. This is consistent with existing reports [6-7]. However, even when the structure changes, the hydrogen content does not change significantly. As hydrogen is assumed to be widely distributed in hydrogen trap sites such as interstitial spaces, pores, and dislocations in addition to bonding with carbon in the DLC coatings, even if part of the carbon structure changes, it likely does not have a strong impact on the overall hydrogen content.

Generally, similar to elemental diffusion in metals [8-9], the rate of hydrogen diffusion in coatings is limited by the movement of atoms through hydrogen trap sites such as crystal defects (pores, dislocations, and crystal grain boundaries).

Studies on hydrogen diffusion in the material, associated with the state of hydrogen in iron steel and hydrogen embrittlement mechanism are common, and there have been active studies since 1970s. The pathway for elemental diffusion in materials may include surface diffusion, lattice diffusion, grain boundary diffusion, and dislocation diffusion. Surface diffusion and

grain boundary diffusion often have higher diffusion coefficients than lattice diffusion and dislocation diffusion. Studies on the state of hydrogen in metallic materials and the diffusion mechanism [8-9] indicate that hydrogen diffusion progresses through hydrogen trap sites in materials. Surface diffusion and grain boundary diffusion often have higher diffusion coefficients than lattice diffusion and dislocation diffusion. Lattice defects (atomic pores, dislocations, and crystal grain boundaries), impurity atoms, precipitates, and interfaces with inclusions are proposed as hydrogen trap sites.

In ionic and shared bonds such as ceramic coatings, hydrogen diffusion in iron steel is several orders of magnitudes lower, and it contains more lattice defects and impurity atoms than metallic materials. Hydrogen trap sites may function in ceramic films as well.

A DLC coating is an amorphous material with mixed sp^3 and sp^2 bonds, but there also are pores and dislocations, which can be considered as a type of crystal defect [5, 10]. In a DLC coating with high hydrogen content, hydrogen atoms have likely already filled these crystal defects, and the movement of new hydrogen atoms through the hydrogen trap sites in the coating could be limited.

Studies focused on crystal defects will be important for hydrogen diffusion in DLC coatings in the future.

4 CONCLUSIONS

With austenitic stainless steel Type 316 L, which is used as materials for hydrogen, as the base material, we evaluated the hydrogen barrier properties of samples coated with a nitride coating and a DLC coating.

Using plasma CVD and sputtering, we prepared ZrN, TiAlN, AlCrN, and DLC coatings with a thickness of about 3 μm. For the DLC coating and samples with varying hydrogen content, we examined the effect of the presence of a buffer layer (CrN), used for improving the adhesiveness, on the hydrogen barrier properties. The results showed that all films lowered the hydrogen permeation rate significantly. By applying a buffer layer of a CrN layer, the hydrogen barrier properties were improved. In particular, by depositing a DLC coating, the hydrogen permeation rate was reduced to 1/1000 or lower. A DLC coating with high hydrogen content was shown to have especially high hydrogen barrier properties.

Hydrogen in the DLC coating has an impact on the bonding state of carbon, and as a result, it changes its density and hardness. When the hydrogen content is low, the density and hardness increases. Since its resistance to abrasion is also high, it is widely used in cutting tools, molds, machinery parts, hard-disk heads, magnetic tapes, etc. The industrial application of DLC coatings with high hydrogen content was previously limited, but new applications as a coating with hydrogen barrier properties is expected to be developed in the future.

REFERENCES

[1] G. W. Hollenberg, E. P. Simonen, G. Kalinin, A. Terlain, "Tritium/hydrogen barrier development", *Fusion Eng. Des.* 28, 190-208, (1995).

[2] J. Yamabe, S. Matsuoka, Y. Murakami,"Surface coating with a high resistance to hydrogen entry under high-pressure hydrogen-gas environment", *Int. J. Hydrogen*

Energy, 38, 10141-10154, (2013).

[3] M. Tamura, M. Noma, M. Yamashita, "Characteristic change of hydrogen permeation in stainless steel plate by BN coating", *Surface and Coatings Technology*, 260, 148-154, (2014).

[4] A. Zeng, V. F. Neto, J. J. Gracia, Q. H. Fan, "Diamond-like carbon (DLC) films as electrochemical electrodes", *Diamond and Related Materials,* 43, 12-22, (2014).

[5] J. Robertson, "Diamond-like amorphous carbon", *Mater. Sci. Eng.* R37, 129-281, (2002).

[6] A. Shimizu, M. Kawaguchi, "The effect of heat treatment on the hydrogen content of DLC films", *Bulletin of TIRI*, 9, 68-69, (2014).

[7] P. Yang, S. C. H. Kwok, R. K. Y. Fu, Y. X. Leng, J. Wang, N. Huang, Y. Leng, P. K. Chu, "Structure and properties of annealed amorphous hydrogenated carbon (a-C:H) films for biomedical applications", *Surface and Coatings Technology* , 177-178, 747-751, (2004).

[8] M. Nagumo, "Conformity between mechanics and microscopic functions of hydrogen in failure", *ISIJ International*, Vol. 52, No. 2, pp. 168-173, (2012).

[9] B. A. Szost, R. H. Vegter, P. E. J. Rivera-Diaz-del-Castillo, "Hydrogen trapping mechanism in nanostructured steels" *Metallurgical & Materials Transactions,* A Vol. 44, No. 10, pp. 4542-4550, (2013).

[10] N. Terayama, "DLC coating technology by PIG-Plasma CVD method", *J. Plasma and Fusion Research*, 87, 8, 548-555, (2011).

VIII ECCOMAS Thematic Conference on Smart Structures and Materials
SMART 2017
A. Güemes, A. Benjeddou, J. Rodellar and Jinsong Leng (Eds)

LATERAL-TORSIONAL BUCKLING OF PULTRUDED FIBER-REINFORCED POLYMER CANTILEVER ANGLE BEAMS

JAKSADA THUMRONGVUT*

* Innovation and Sustainability in Structural Engineering (ISSE) Research Group
Department of Civil Engineering, Faculty of Engineering and Architecture,
Rajamangala University of Technology Isan, Nakhon Ratchasima 30000, Thailand.
e-mail: jaksada.th@rmuti.ac.th

Key words: Pultruded Fiber-Reinforced Polymer (PFRP), Angle Section, Cantilever Beam, Lateral-Torsional Buckling, Pultrusion.

Abstract. This paper focuses on the cantilever beam tests of pultruded fiber-reinforced polymer (PFRP) angle sections. The structural performance and buckling behaviors of PFRP angle section beams under tip concentrated loads are studied. A total of fifteen beams considering the following primary parameters are tested: three dimensions and five span-to-width ratios (L/b) per cross-section. The dimensions of the angle sections are 50×6.4 mm, 76×6.4 mm and 102×6.4 mm. The span-to-width ratios of the specimens are in the range of approximately 10 to 50. The E-glass/polyester angle specimens are evaluated to investigate the effect of unbraced length of the beams on the critical buckling loads and buckling responses. The experimental segment of this study begins with an evaluation of the pultruded FRP angle cross-section geometry and its elastic and shear modulus. The cantilever beam tests setup and the instrumentation for recording load and deformation are described. The load-deformation relationships and failure modes of beams are presented. Then, the experimental buckling loads are compared to critical buckling loads calculated by using AISC-LRFD design equation in order to check the adequacy of the equation. From the load-deformation curves show that the specimens have linear elastic responses up to 90-95% of their buckling loads. The mode of failure of the specimens is in the form of lateral-torsional buckling. Tests also showed that the buckling load decreases as the span-to-width ratio increases, and with the span-to-width ratio increasing, the lateral-torsional buckling is more outstanding. Based on the results of this study, the AISC-LRFD approach unsatisfactorily predicts the critical buckling loads of pultruded FRP cantilever angle beams. Finally, a modification factor is appropriately proposed to calculate the buckling loads.

1 INTRODUCTION

Fiber-reinforced polymer (FRP) composite materials have been widely used for over the past few decades in marine applications, military, aerospace industry, but they have only seen limited application in the construction of buildings, bridges and other civil structures [1]. Civil structures made of the FRP composites have been shown to provide efficient and economical

applications in new structural construction, and in the rehabilitation and strengthening of imperfect structures [2]. FRP structural members are a smart choice because they have many advantageous engineering properties over the conventional civil engineering materials such as light-weight of the material allows for easier transport and installation, high strength-to-weight ratio, outstanding durability and high corrosion resistance in the harshest environments and chemical exposures, excellent fatigue resistance, reduce or eliminate the need for heavy maintenance, and being strongly directional in nature allowing them to be custom-tailored to specific engineering applications [3-8]. One of the most basic of FRP manufacturing processes, the pultrusion process is a very efficient way to manufacture fiber-reinforced composite products. The FRP manufactured by this process is called pultruded fiber-reinforced polymer (PFRP). It allows pultrusion manufacturers to produce continuous lengths and excellent dimensional tolerance of FRP profile shapes. Generally, the standard PFRP structural profiles are usually produced in a variety of cross-sectional shapes, including wide-flange sections, I-sections, angles, channels and etc.

However, since they are typically orthotropic materials, their analysis and design are much more complex [9]. Due to relatively low stiffness of the material and thin-walled sectional geometry, the strength is not usually the governing design parameter of the PFRP structural profiles. Mostly, their design is governed by the serviceability parameters such as large deflection or buckling instability, depending on the material properties, the geometry of the cross-section, and the loading conditions [10]. In addition, the critical obstacles to their widespread applications in construction are still limited due to the lack of information on the material properties, structural behaviors and reliable design criteria. Over the last 50 years, the research and development of PFRP profiles in civil engineering have progressed considerably in several countries, especially in United States and Europe [11]. Several theoretical and experimental studies have been conducted on the PFRP structural members subjected to flexure. In particular, most of them have emphasized on the lateral buckling performance of the members for doubly symmetric cross-sections such as wide-flange, I-shapes, and box profiles [12-16]. Only few research works have explored the experimental and theoretical evaluations of lateral-torsional buckling for mono-symmetric angle profiles. In general, angle profiles have been used as braces, purlins, trusses and struts. Angles also have been used retrofitting for distortion-induced fatigue problems in steel bridge girders [17]. Therefore, in order to create further confidence in the application of the angle profile, it is necessary to enhance knowledge of its structural performance, particularly the lateral-torsional buckling behaviors. This paper is intended to satisfy a portion of that need. The aims of this paper are to present the experimental results on the buckling behaviors and failure mode of the PFRP angle beams subjected to tip end load under the cantilevered configuration, and to compare the obtained critical buckling load with those obtained from the AISC-LRFD steel design equation of single-angle members [18] in order to check the adequacy of the equation.

2 TEST DESCRIPTION

The PFRP angle section specimens used in this investigation were made of E-glass fiber-reinforced with polyester resin, and manufactured by pultrusion process. The nominal dimensions, including the nominal leg width (b) and leg thickness (t) are shown in Table 1. Single angles have three nominal sizes of 50×6.4 mm, 76×6.4 mm and 102×6.4 mm with span-

to-width ratio (L/b) ranging approximately from 10 to 50. Unlike doubly symmetric wide-flanges and box profiles, single angles have principal axis that do not coincide with their geometric axis, as shown in Figure 1. Measurements of b and t differed from nominal values by no more than 3.2%. The coupon specimens of angle profiles with the same nominal thickness were cut from the same 6 m stock sections in order to determine the mechanical properties of the materials used in the test programme. To correlate the analytical results with the obtained test results, the values of the averaged longitudinal tensile strength (F_L) and averaged longitudinal modulus (E_L) were determined from the tension test in accordance with ASTM D3039. From the coupon tests, it was found that the average values of F_L and E_L were 218 MPa and 17.5 GPa, respectively.

Table 1: Geometry characteristics of the pultruded FRP angle specimens

Specimens	$b \times t$ (mm × mm)	L (m)	L/b	y_w (mm)	y_z (mm)	$I_x = I_y$ (mm^4)	I_z (mm^4)	I_w (mm^4)
L50-C-0.5	50.8×6.35	0.5	9.8	35.4	21.2	144,680	59,416	229,944
L50-C-1.0	50.8×6.35	1.0	19.7	35.4	21.2	144,680	59,416	229,944
L50-C-1.5	50.8×6.35	1.5	29.5	35.4	21.2	144,680	59,416	229,944
L50-C-2.0	50.8×6.35	2.0	39.4	35.4	21.2	144,680	59,416	229,944
L50-C-2.5	50.8×6.35	2.5	49.2	35.4	21.2	144,680	59,416	229,944
L76-C-1.0	76.2×6.35	1.0	13.1	53.7	30.3	517,890	200,315	835,465
L76-C-1.5	76.2×6.35	1.5	19.7	53.7	30.3	517,890	200,315	835,465
L76-C-2.0	76.2×6.35	2.0	26.2	53.7	30.3	517,890	200,315	835,465
L76-C-2.5	76.2×6.35	2.5	32.8	53.7	30.3	517,890	200,315	835,465
L76-C-3.0	76.2×6.35	3.0	39.4	53.7	30.3	517,890	200,315	835,465
L102-C-1.0	101.6×6.35	1.0	9.8	72.1	39.3	1,265,060	505,013	2,025,107
L102-C-1.5	101.6×6.35	1.5	14.8	72.1	39.3	1,265,060	505,013	2,025,107
L102-C-2.0	101.6×6.35	2.0	19.7	72.1	39.3	1,265,060	505,013	2,025,107
L102-C-2.5	101.6×6.35	2.5	24.6	72.1	39.3	1,265,060	505,013	2,025,107
L102-C-3.0	101.6×6.35	3.0	29.5	72.1	39.3	1,265,060	505,013	2,025,107

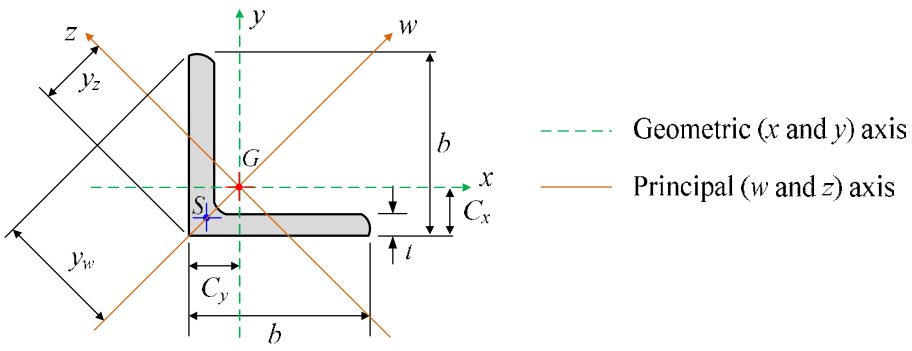

Figure 1: Geometric axis bending and principal axis bending of equal-leg angle

A total of 15 equal-leg angle specimens were tested under cantilevered configuration. Details of the test profiles are presented in Table 1. The specimen numbers were denominated in the form of "L*b*-C-*L*". For example, the specimen number L76-C-3.0 is the PFRP angle beams,

having the leg width (b) of 76 mm and the unbraced length (L) of 3.0 m, respectively. The typical test set-up in the form of cantilever beam is shown in Figure 2. The fixed end was set-up by using wood clamp. At the free end, a part of steel angle with notched groove was firmly installed so that the tip vertical load can be applied directly through the shear center of the cross-section in order to provide the flexural and transverse shear stress to the beams. The loads were applied by successive adding of steel plates on a loading platform. The incremental loads were added until reaching the failure of the beams. After each load increment, the vertical end displacement was measured with linear variable differential transducers (LVDTs) and was automatically recorded by a MW100 YOKOGAWA data acquisition unit. For each span the test was carried out two times in order to determine the average obtained buckling load.

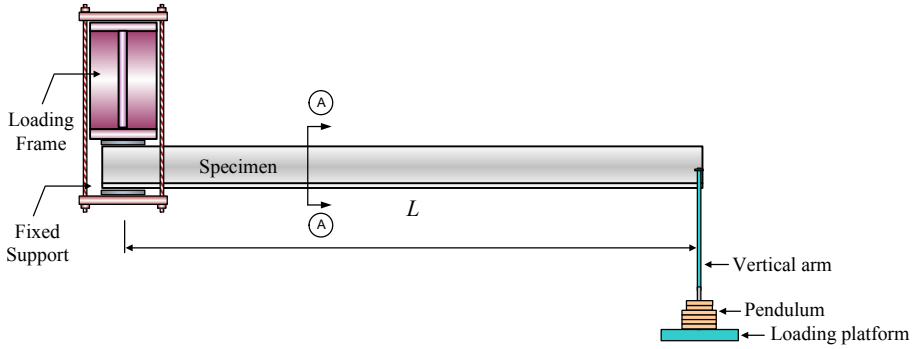

(a) Schematic view of PFRP angle beams with tip point load : Cantilever beam support

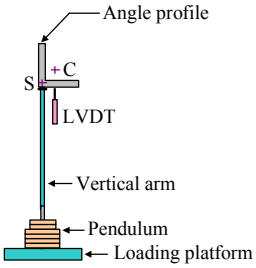

(b) Load application system (section A-A)

Figure 2: Schematic overview of test setup

3 EXPERIMENTAL RESULTS AND DISCUSSIONS

3.1 Structural Behaviors and Modes of Failure

The experimental results in terms of load versus vertical tip displacement curves of the PFRP cantilever angle beams are given in Figure 3. It can be seen that the specimens have a linear elastic response up to 90-95% of the obtained buckling load. After that, the load and displacement responses are gradually becoming nonlinear, leading to the lateral-torsional buckling failure in the form of twisting and large lateral displacement occurred simultaneously. Also, it is noticed that the buckling loads are very susceptible to the large span-to-width ratio (L/b). With the increasing span-to-width ratio, the failure mode is more outstanding and no

external material damage is observed. Figure 4(a)-4(c) show the failure modes of the specimens with the nominal sizes of 50×6.4 mm, 76×6.4 mm and 102×6.4 mm, respectively.

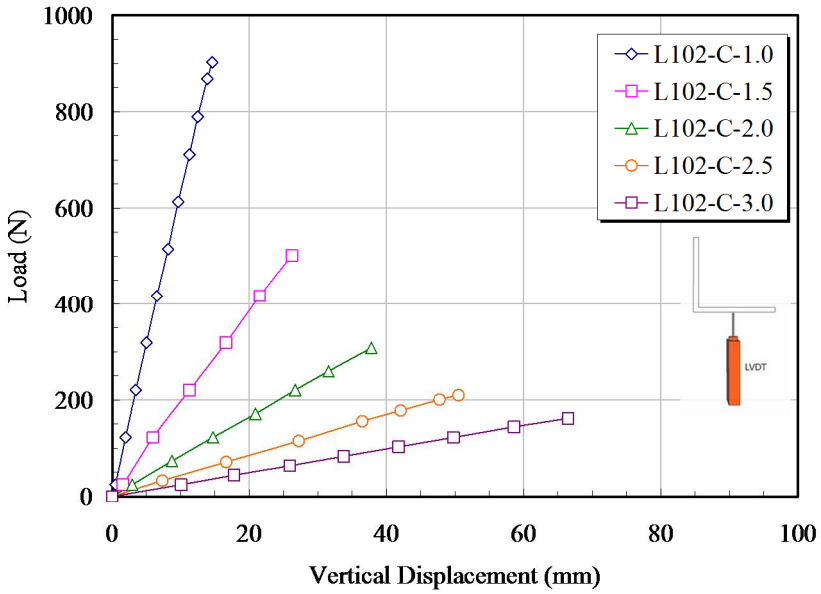

Figure 3: Typical loads versus vertical tip displacement curves of PFRP angle beam

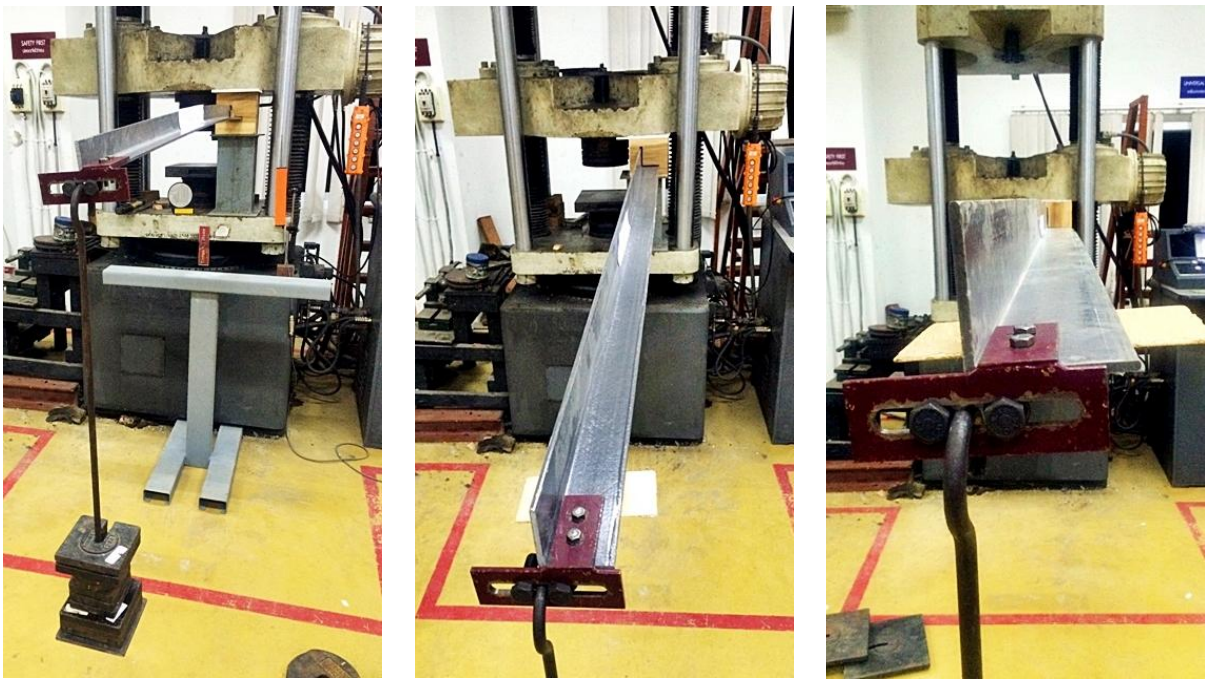

(a) L50×6.4 mm (b) L76×6.4 mm (c) L102×6.4 mm

Figure 4: Typical modes of failure

3.2 Buckling Load and Comparison with LRFD approach

The experimentally obtained critical buckling load (P_{EXP}) are summarized in Table 2. It can be seen that the critical load increases as the span-to-width ratio decreases. Thus, the degree of lateral-torsional buckling depends on the unbraced length of the beam specimens. The general practice for designing members against biaxial bending is to consider the separate failure modes of either in-plane bending or lateral buckling under bending about the major principal axis and bending about the minor principal axis [18]. Also, fiber-reinforced plastic (FRP) structural angle sections are often subjected to biaxial bending in real structural engineering applications. For single-angle members without lateral-torsional restraints, the LRFD specification [19] have proposed an equation used to calculate the elastic buckling with load applied to shear center of the cross-section. For the comprehensive design approach for single-angle members subjected to biaxial bending failing in elastic buckling, the buckling load for cantilevered configuration can be calculated from interaction equation to combine the two principal axis strengths:

$$P_{\text{LRFD}} = \frac{\phi\sqrt{2}}{L}\left(\frac{1}{1/M_{nz} + 1/M_{nw}}\right) \tag{1}$$

where

ϕ = resistance factor for flexure = 0.90

M_{nw} = nominal flexural strength about major principal axis (LRFD [19], Section 5.3.1a)

M_{nz} = nominal flexural strength about minor principal axis (LRFD [19], Section 5.3.1b)

Table 2: Experimental critical buckling loads and comparison with LRFD approach

Specimens	L (m)	L/b	P_{EXP} (N)	P_{LRFD} (N)	$\frac{P_{\text{EXP}}}{P_{\text{LRFD}}}$	$P_{mo,\text{LRFD}}$ (N)	$\frac{P_{\text{EXP}}}{P_{mo,\text{LRFD}}}$
L50-C-0.5	0.5	9.8	546.7	1186.3	0.46	474.5	1.15
L50-C-1.0	1.0	19.7	207.3	460.1	0.45	184.0	1.13
L50-C-1.5	1.5	29.5	106.8	248.9	0.43	99.6	1.07
L50-C-2.0	2.0	39.4	68.8	157.0	0.44	62.8	1.10
L50-C-2.5	2.5	49.2	48.1	108.3	0.44	43.3	1.11
L76-C-1.0	1.0	13.1	502.6	1062.6	0.47	425.0	1.18
L76-C-1.5	1.5	19.7	259.0	571.9	0.45	228.8	1.13
L76-C-2.0	2.0	26.2	164.2	359.4	0.46	143.7	1.14
L76-C-2.5	2.5	32.8	119.5	247.3	0.48	98.9	1.21
L76-C-3.0	3.0	39.4	90.4	180.8	0.50	72.3	1.25
L102-C-1.0	1.0	9.8	902.9	1968.8	0.46	787.5	1.15
L102-C-1.5	1.5	14.8	502.2	1051.0	0.48	420.4	1.19
L102-C-2.0	2.0	19.7	308.4	656.8	0.47	262.7	1.17
L102-C-2.5	2.5	24.6	210.2	450.2	0.47	180.1	1.17
L102-C-3.0	3.0	29.5	162.2	328.2	0.49	131.3	1.24

Table 2 also presents the obtained critical buckling load (P_{EXP}) compared with those predicted load (P_{LRFD}) with LRFD design equation. The P_{EXP}/P_{LRFD} ratios are presented to show the correlation between the experimental results and the predicted results by Eq. (1). Based on the analytical results, the P_{EXP}/P_{LRFD} ratios are in the range of 0.43 to 0.46 for the 50×6.4 mm specimens. Similarly, for the specimens with 76×6.4 mm and 102×6.4 mm, the P_{EXP}/P_{LRFD} ratios are in the range of 0.45 to 0.50 and 0.46 to 0.49, respectively, indicating that the LRFD design equation overestimates the critical buckling load of the PFRP angle section beams by approximately 50-57%. Therefore, a further modification on the proposed equation is needed.

Based on the scope of this study, it is proposed that the LRFD design equation should be modified by adjusting on buckling load. To study the relationship between P_{EXP}/P_{LRFD} ratios and L/b ratios, the values of P_{EXP}/P_{LRFD} ratios are numerically calculated and plotted for L/b ratios in the range of 10 to 50, as shown in Figure 5. Thus, to make the design equation conservative due to a limit in the number of tested beams, the modification factor (α) is proposed of 0.40 in the present study, and Eq. 1 can be rewritten in the form of Eq. 2.

$$P_{mo,\mathrm{LRFD}} = \alpha P_{\mathrm{LRFD}} \tag{2}$$

Based on the analytical results in Table 2, the $P_{EXP}/P_{mo,LRFD}$ ratios are also presented to show the correlation between the test results and the predicted results. The average $P_{EXP}/P_{mo,LRFD}$ value is 1.16 with coefficient of variation (COV) equal to 0.043. In addition, all values of the $P_{EXP}/P_{mo,LRFD}$ ratios show the values more than 1.0. This indicates that the proposed design equation is conservative and underestimate the critical buckling load of the PFRP angle beams by 7% to 25%.

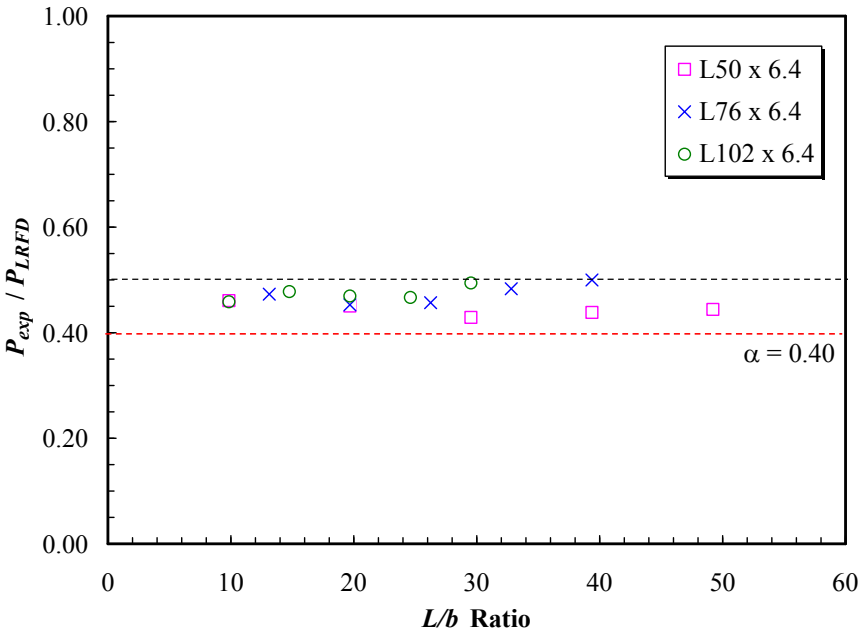

Figure 5: Normalized critical buckling load and L/b ratio

4 CONCLUSIONS

Based upon the results, the following conclusions derived from this research are listed as follows:

- The structural responses of the PFRP angle beams subjected to tip end load under the cantilevered configuration are linear elastic up to 90-95% of the buckling loads. Subsequently, the responses are gradually becoming nonlinear, leading to the buckling failure of the beam specimens.
- All of the specimens were failed in the form of twisting and large lateral displacement occurred simultaneously in the form of the lateral-torsional buckling mode of failure.
- Based on the test results, the critical buckling load increases as the span-to-width ratio of beam decreases.
- By comparing the test results with analytical results, the modified design equation based on the LRFD design equation of single-angle members is proposed by introducing the modification factor of 0.40. Finally, the proposed design equation is conservative and underestimate the critical buckling load of the PFRP angle beams.

ACKNOWLEDGMENTS

The author is thankful for the financial support provided by the Rajamangala University of Technology Isan and National Research Council of Thailand (NRCT), which is a part of the research project "Development of Design Equations for Pultruded Fiber-Reinforced Plastic Angle Beams under Flexure".

REFERENCES

[1] Ellingwood, B.R. Toward load and resistance factor design for fiber-reinforced polymer composite structures. *Journal of Structural Engineering* (2003) **129(4)**:449-458.

[2] Thumrongvut, J. and Seangatith, S. Responses of PFRP cantilevered channel beams under tip point loads. *Key Engineering Materials* (2011) **471-472**:578-583.

[3] Barbero, E.J., Lopez-Anido, R. and Davalos, J.F. On the mechanics of thin-walled laminated composite beams. *Journal of Composite Materials* (1993) **27(8)**:806-829.

[4] Davalos, J.F. and Qiao, P.Z. Analytical and experimental study of lateral and distortional buckling of FRP wide-flange beams. *Journal of Composites for Construction* (1997) **1(4)**:150-159.

[5] Qiao, P., Zou, G.P. and Davalos, J.F. Flexural-torsional buckling of fiber-reinforced plastic composite cantilever I-beams. *Composite Structures* (2003) **60(2)**:205-217.

[6] Ascione, L., Giordano, A. and Spadea, S. Lateral buckling of pultruded FRP beams. *Composites: Part B* (2011) **42**:819-824.

[7] Thumrongvut, J. and Seangatith, S. Influences of concentric and eccentric loads on buckling of fixed-end supported pultruded FRP channel beams. *Advanced Materials Research* (2015) **1119**:721-725.

[8] Turvey, G.J. Testing and analysis of pultruded GFRP continuous beams for the deflection serviceability limit state. *Composite Structures* (2016) **141**:213-220.

[9] Thumrongvut, J. and Seangatith, S. Experimental study on lateral-torsional buckling of PFRP cantilevered channel beams. *Procedia Engineering* (2011) **14**:2438-2445.

[10] Kim, N.I., Shin, D.K. and Kim, M.Y. Exact lateral buckling analysis for thin-walled composite beam under end moment. *Engineering Structures* (2007) **29(8)**:1739-1751.
[11] Bakis, C.E., Bank, L.C., Brown, V.L., Cosenza, E., Davalos, J.F., Lesko, J.J., Machida, A., Rizkalla, S.H. and Triantafillou, T.C. Fiber-reinforced polymer composites for construction - state-of-the-art review. *Journal of Composites for Construction* (2002) **6(2)**:73-87.
[12] Hai, N.D., Mutsuyoshi, H., Asamoto, S. and Matsui, T. Structural behavior of hybrid FRP composite I-beam. *Construction and Building Materials* (2010) **24**:956-969.
[13] Ascione, L., Berardi, V.P., Giordano, A. and Spadea, S. Buckling failure modes of FRP thin-walled beams. *Composites Part B: Engineering* (2013) **47**:357-364.
[14] Nguyen, T.T., Chan, T.M. and Mottram, J.T. Influence of boundary conditions and geometric imperfections on lateral-torsional buckling resistance of a pultruded FRP I-beam by FEA. *Composite Structures* (2013) **100**:233-242.
[15] Pekbey, Y. and Ghanbari, E. Flexural-torsional buckling of FRP thin-walled composite with various sections. *Science and Engineering of Composite Materials* (2014) **21(4)**:537-549.
[16] Ascione, F., Feo, L., Lamberti, M., Minghini, F. and Tullini, N. A closed-form equation for the local buckling moment of pultruded FRP I-beams in major-axis bending. *Composites Part B: Engineering* (2016) **97**:292-299.
[17] Ghahremani, K., Walbridge, S. and Topper, T. Inhibiting distortion-induced fatigue damage in steel girders by using FRP angles. *Journal of Bridge Engineering* (2015) **20(6)**:04014085.
[18] Trahair, N.S. Biaxial bending of steel angle section beams. *Journal of Structural Engineering* (2004) **130(4)**:554-561.
[19] American Institute of Steel Construction. *Specification for Load and Resistance Factor Design of Single-Angle Members*. American Institute of Steel Construction, Inc. Chicago, IL (2000)

VIII ECCOMAS Thematic Conference on Smart Structures and Materials
SMART 2017
A. Güemes, A. Benjeddou , J. Rodellar and Jinsong Leng (Eds)

MODELING OF DISSIPATIVE DIELECTRIC ELASTOMERS AFFECTED BY VISCOELASTICITY AND CURRENT LEAKAGE

CHOON CHIANG FOO*, JUN LIU AND ZHI-QIAN ZHANG

Institute of High Performance Computing (IHPC)
1 Fusionopolis Way, #16-16 Connexis, Singapore 138632, Singapore
*e-mail: foocc@ihpc.a-star.edu.sg, www.keithfoo.com

Key words: Dielectric elastomers transducers, Dissipation, Finite-element method, ABAQUS

1 INTRODUCTION

Dielectric elastomers are a popular class of electroactive polymers, which are capable of large deformation under voltage, fast speed, and high energy density [1]. Such characteristics have led these materials to be used as smart transducers for wide-ranging applications, such as artificial muscles [2], soft sensors [3], and power harvesters [4].

Despite their popularity, dielectric elastomers are imperfect; dissipative processes such as viscoelasticity and current leakage are known to affect the electromechanical performance of these dielectric elastomers. An elastomer consists of a network of polymer chains, connected by crosslinks. A polymer chain that is sufficiently flexible may twist, coil, and entangle with other chains. Subject to a force, entangled polymer chains may undergo sliding and localized slipping. Consequently, viscoelastic relaxation occurs when the elastomer relaxes to a new state of deformation over time. In actuators, viscoelasticity reduce actuation stresses [5-8] and strains [9]. In generators, viscous losses increase the mechanical input work, which result in lower conversion efficiencies and specific electrical energy output [10,11].

Current leakage, a phenomenon well-known in several insulator and semi-conductors systems [12,13], occurs when charges comprising of electrons, ions, or both flow through the dielectric under the electric field. This phenomenon is often linked to the presence of impurities and imperfections in the elastomer [14,15]. In experiments on dielectric elastomers, surges of leakage current and increasing volume conductivities have been observed to precede imminent electrical breakdown [15,16]. Current leakage affects the ability of the dielectric elastomer generators to store charges in an open-circuit condition, resulting in a lower voltage boost and energy density [4]. In extreme cases, the DEG may even operate at negative efficiency in very slow cycles under large strains; in other words, the DEG is wasting energy instead of generating it [17].

Beyond the analytical methods developed for viscoelastic dielectrics used in simpler configurations [5,17,18], simulation capabilities based on the finite element method have extended the design capability for dissipative dielectric elastomers. Till date, these simulations largely focus on the effect of viscoelasticity on actuation [19,20] and instabilities [21,22]. In this paper, we report a finite element simulation capability for dissipative dielectric elastomers accounting for viscoelasticity and current leakage. Based on a nonequilibrium thermodynamics framework, we construct a continuum theory that accounts for

electromechanical coupling, large deformation, viscoelasticity, and current leakage. To illustrate our approach, we use simple descriptions of viscoelasticity and current leakage, previously calibrated with widely-used dielectric elastomers. This model is implemented in a commercial finite element solver ABAQUS by developing new user-defined elements. Our simulations are used to highlight the significance and effects of these dissipative process for dielectric elastomers.

2 SUMMARY OF THEORY FOR DISSIPATIVE DIELECTRIC ELASTOMERS

In this section, we summarize the nonlinear field theory of dissipative dielectric elastomers specified within a framework of nonequilibrium thermodynamics, which follows closely our earlier work in [5,19]. We consider a body of a dielectric elastomer in three dimensions. When the dielectric is in the reference state, we denote an element of volume by $dV(\mathbf{X})$. In the reference state, denote an element area of the surface of the dielectric by $dA(\mathbf{X})$, and denote the unit vector normal to the element surface pointing outward by $\mathbf{n}$.

Kinematics. In the reference state, the elastomer is undeformed, with each material particle labeled by its coordinates $\mathbf{X}$. In the deformed state at time t, the particle $\mathbf{X}$ moves to a place with coordinates $\mathbf{x}(\mathbf{X}, t)$. The deformation gradient is defined by:

$$\mathbf{F} = \nabla\mathbf{x} \tag{1}$$

Imagine that every material particle with coordinates $\mathbf{X}$ is attached with a battery of electric potential $\Phi(\mathbf{X}, t)$. Define the nominal electric field by:

$$\tilde{\mathbf{E}} = -\nabla\Phi \tag{2}$$

Governing partial differential equations. Local force balance for the first Piola-Kirchoff stress $\mathbf{P}$ requires that:

$$\mathrm{Div}\mathbf{P} + \mathbf{B} = \mathbf{0} \tag{3}$$

in the volume where $\mathbf{B}$ is a body force, and that

$$(\mathbf{P}^{-} - \mathbf{P}^{+})\mathbf{n} = \mathbf{T}(\mathbf{n}) \tag{4}$$

on the part of the surface of the elastomer where $\mathbf{T}$ is a surface traction force applied, which is the difference between the stress exerted on the side of $dA(\mathbf{X})$ out of which $\mathbf{n}$ points ($\mathbf{P}^{-}$) and the stress exerted across the side of $dA(\mathbf{X})$ into which $\mathbf{n}$ points ($\mathbf{P}^{+}$).

Similarly, the nominal electric displacement obeys that:

$$\mathrm{Div}\tilde{\mathbf{D}} = \tilde{q} \tag{5}$$

in the volume of the body, where $\tilde{q}$ is the volumetric charge density in the reference configuration, and:

$$(\tilde{\mathbf{D}}^{+} - \tilde{\mathbf{D}}^{-})\mathbf{n} = \tilde{\omega}(\mathbf{n}) \tag{6}$$

on the surface of the body, where $\tilde{\omega}$ is the surface charge density in the reference configuration. These equations express Gauss's law in every current state in terms of nominal quantities.

In the deformed state, let the charge per unit time pumped into a volume element be $\mathbf{r}(\mathbf{X}, t)dV(\mathbf{X})$ and the charge into an interface element be $\mathbf{i}(\mathbf{X}, t)dV(\mathbf{X})$. Let $\mathbf{J}(\mathbf{X}, t)dA(\mathbf{X})$ be the charge per unit time crossing an area element. The conservation of charge then requires,

$$\frac{\partial\tilde{q}}{\partial t} + \nabla\mathbf{J} = \mathbf{r} \tag{7}$$

in the volume and,

$$\frac{\partial \widetilde{\omega}}{\partial t} + (\mathbf{J}^{+} - \mathbf{J}^{-})\mathbf{n} = \mathbf{i} \tag{8}$$

on the part of the surface of the elastomer where the battery injects charges. In (8), the current in the conducting wire should equal the sum of the rate of change of the polarizing charge on the electrodes and the current leaking through the membrane.

3 A MODEL OF DISSIPATIVE DIELECTRIC ELASTOMER

We specify a set of constitutive equations for the dissipative DE, which is assumed to be isotropic and nearly-incompressible. We consider a model of viscoelastic dielectric elastomer [5,19], where we adopt a rheological model of two parallel units: one unit consists of a spring, α, and the other unit consists of another spring, β, and a dashpot (Fig. 1a).

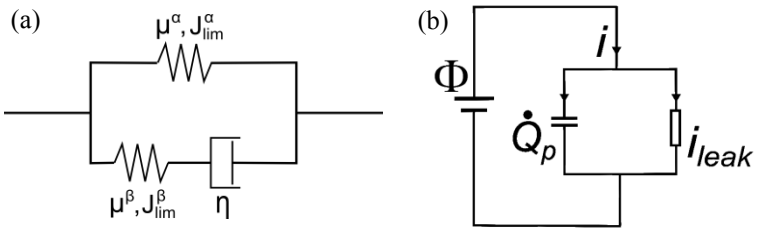

Figure 1. (a) A model of viscoelastic DE considers two parallel units of springs and dashpot, which comprise spring α in the top unit, and spring β and a dashpot of viscosity η in the bottom unit. (b) Current leakage is modeled using a resistor in parallel to a capacitor to represent the dielectric elastomer. Due to charge conservation, the current consumed by the battery i is the sum of the charge flow rate $\dot{Q}_p$ and the current leakage through the resistor i_{leak} [5].

Multiplicative decomposition. In this model, the deformation gradient $\mathbf{F}$ is decomposed into the elastic and viscous components with the multiplication rule: $\mathbf{F} = \mathbf{F}^{e}\mathbf{F}^{v}$. Here, $\mathbf{F}^{e}$ is the elastic component which corresponds to the deformation in the bottom spring. Conversely, $\mathbf{F}^{v}$ is the deformation gradient associated with the dashpot; $\mathbf{F}^{v}$ forms the viscous component and represents the internal variable.

Free-energy function. We adopt the model of ideal dielectric elastomers, which assumes the permittivity of the elastomer is independent of deformation [23]. To account for this stress-stiffening effect in the dielectric elastomer, we represent both springs (Fig. 1a) using the Gent hyperelasticity model [24], and write the Helmholtz free energy density as:

$$\begin{aligned} W(\mathbf{C},\mathbf{E},\mathbf{C}^{\mathrm{e}}) = &-\frac{\mu^{\alpha}J_m^{\alpha}}{2}\ln\left(1-\frac{\bar{I}_1-3}{J_m^{\alpha}}\right)+\frac{K^{\alpha}}{2}\left(\frac{J^2-1}{2}-\ln J\right)-\frac{\varepsilon}{2}J\mathbf{C}^{-1}:(\tilde{\mathbf{E}}\otimes\tilde{\mathbf{E}}) \\ &-\frac{\mu^{\beta}J_m^{\beta}}{2}\ln\left(1-\frac{\bar{I}_1^{e}-3}{J_m^{\beta}}\right)+\frac{K^{\beta}}{2}\left(\frac{J^{e2}-1}{2}-\ln J^{e}\right). \end{aligned} \tag{9}$$

Following usual computational practice, we use the right Cauchy-green deformation tensor to ensure that W is invariant under a rigid-body rotation, where $\mathbf{C} = \mathbf{F}^{\mathrm{T}}\mathbf{F}$ and $\mathbf{C}^{e} = \mathbf{F}^{v-\mathrm{T}}\mathbf{C}\mathbf{F}^{v-1}$. In Eq. (12), $J = \det(\mathbf{F})$, $J^{e} = \det(\mathbf{F}^{e})$, $\bar{I}_1 = J^{-2/3}\mathrm{tr}(\mathbf{C})$, $\bar{I}_1^{e} = J^{e-2/3}\mathrm{tr}(\mathbf{C}^{e})$, and $\mathbf{C}^{-1}$ is the inverse of $\mathbf{C}$. We use superscripts α and β to differentiate between the material parameters of the top and bottom springs, respectively, where μ is the shear modulus, J_m is the parameter in the Gent model associated with the limiting stretch [24], K is the bulk modulus, ε is the

dielectric permittivity. The elastomer is nearly incompressible with its bulk modulus much greater than the shear modulus ($K/\mu \sim 10^5$).

Constitutive equations for Cauchy stress. With the free-energy function W, the Cauchy stress is given as,

$$\begin{aligned}\boldsymbol{\sigma} = &\overbrace{\frac{\mu^\alpha}{J}\frac{\overline{\mathbf{B}} - (\bar{I}_1/3)\mathbf{I}}{1-(\bar{I}_1-3)/J_m^\alpha} + \frac{K^\alpha}{2}\left(J-\frac{1}{J}\right)\mathbf{I}}^{\boldsymbol{\sigma}^\alpha} + \varepsilon\left(\mathbf{E}\otimes\mathbf{E} - \frac{1}{2}(\mathbf{E}\cdot\mathbf{E})\mathbf{I}\right) \\ &+ \underbrace{\frac{\mu^\beta}{J}\frac{\overline{\mathbf{B}}^e - (\bar{I}_1^e/3)\mathbf{I}}{1-(\bar{I}_1^e-3)/J_m^\beta} + \frac{K^\beta J^e}{2J}\left(J^e-\frac{1}{J^e}\right)\mathbf{I}}_{\boldsymbol{\sigma}^\beta}.\end{aligned} \tag{10}$$

where on the RHS of (10), the first two terms $\boldsymbol{\sigma}^\alpha$ and last two terms $\boldsymbol{\sigma}^\beta$ are the stresses carried by the springs α and β, respectively, and the remaining components are the Maxwell stress produced by the electric field. Here $\overline{\mathbf{B}} = J^{-2/3}\mathbf{F}\mathbf{F}^{\mathrm{T}}$, $\overline{\mathbf{B}}^e = J^{e-2/3}\mathbf{F}^e\mathbf{F}^{e\mathrm{T}}$, and $\mathbf{I}$ is the Kronecker delta.

Evolution law for the internal variable. We specify the evolution law for the viscous deformation $\mathbf{F}^v$. Following [19], we model the dashpot as Newtonian fluid and write specifically the kinetic model as:

$$\frac{d\mathbf{F}^v}{dt} = \frac{1}{2\eta}\mathrm{dev}\left(\boldsymbol{\sigma}^\beta\right)\cdot\mathbf{F}^v \tag{11}$$

where $\eta = \tau_V\mu^\beta$ is the viscosity of the dashpot and $\boldsymbol{\sigma}^\beta$ is the state of stress acting across the spring β and the dashpot in (10).

Current leakage model. We represent the current leakage model as a capacitor in parallel with a resistor (Fig. 1b). Define the leakage current flux [5] as:

$$\mathbf{J} = \sigma_c(\mathbf{E})\mathbf{E} \tag{12}$$

where the conductivity $\sigma_c(\mathrm{E})$ depends on the electric field. We assume an exponential relationship:

$$\sigma_c(\mathbf{E}) = \sigma_0\exp(|\mathbf{E}|/E_B) \tag{13}$$

where σ_0 is the conductivity at low field, and E_B is an empirical constant. When $|\boldsymbol{E}| << E_B$, the elastomer behaves like an Ohmic conductor; as $|\boldsymbol{E}| \to E_B$, the conductivity increases exponentially [15,16].

4 NUMERICAL SOLUTION PROCEDURE

Given the strong form of the boundary-value problem in (3-6), we ignore the body forces and volumetric charges, and write the corresponding weak form as:

$$\int\left(\mathbf{P}:\frac{\partial\mathbf{w}_1}{\partial\mathbf{X}}\right)dV = \int(\mathbf{T}\cdot\mathbf{w}_1)dA \tag{14a}$$

$$-\int\left(\widetilde{\mathbf{D}}\cdot\frac{\partial\mathbf{w}_2}{\partial\mathbf{X}}\right)dV = \int(\tilde{\omega}\mathbf{w}_2)dA\,. \tag{14b}$$

where $\mathbf{w}_1$ and $\mathbf{w}_2$ are arbitrary test functions.

We approximate the body with finite elements, where the displacement and electrical potential are discretized using standard FE shape functions:

$$\mathbf{u} = \sum\mathbf{u}^A N^A \quad ; \quad \Phi = \sum\Phi^A N^A \tag{15}$$

with A denoting the nodes of the element, $\mathbf{u}^{\boldsymbol{A}}$ and $\boldsymbol{\Phi}^{\boldsymbol{A}}$ are the nodal displacements and electric potentials, and $\boldsymbol{N}^{\boldsymbol{A}}$ are the shape functions corresponding to node **A**. Applying discretization to (14) with a standard Galerkin approach, we obtain the residuals for the element:

$$(\mathbf{R}_u)^A = -\int \left(\mathbf{P} : \frac{\partial N^A}{\partial \mathbf{X}}\right) dV + \int (\mathbf{T} N^A) dA\,. \tag{16a}$$

$$(\mathbf{R}_\Phi)^A = \int \left(\widetilde{\mathbf{D}} \cdot \frac{\partial N^A}{\partial \mathbf{X}}\right) dV + \int (\widetilde{\omega} N^A) dA. \tag{16b}$$

with corresponding tangents:

$$(\mathbf{K}_{\mathbf{uu}})^{AB} = -\frac{\partial (\mathbf{R}_\mathbf{u})^A}{\partial \mathbf{u}^B}, (\mathbf{K}_{\mathbf{u}\Phi})^{AB} = -\frac{\partial (\mathbf{R}_\mathbf{u})^A}{\partial \Phi^B} \tag{17a}$$

$$(\mathbf{K}_{\Phi\mathbf{u}})^{AB} = -\frac{\partial (\mathbf{R}_\Phi)^A}{\partial \mathbf{u}^B}, (\mathbf{K}_{\Phi\Phi})^{AB} = -\frac{\partial (\mathbf{R}_\Phi)^A}{\partial \Phi^B} \tag{17b}$$

The finite element procedure is implemented in ABAQUS/Standard using a user-defined subroutine (UEL). During the analysis, the user subroutine UEL is called for each iteration in an increment. The residuals (16) and tangents (17) are required to be provided. To avert issues related to volumetric locking, we adopt the F-bar method [25] for fully integrated elements, following the approaches in [26].

5 NUMERICAL SIMULATIONS

We demonstrate the effect of dissipation on dielectric elastomers in various examples. In our previous work [5], we have calibrated material parameters for the commonly-used VHB (Fig. 1): $\mu^\alpha = 18$ kPa, $J_m^\alpha = 110$, $\mu^\beta = 42$ kPa, $J_m^\beta = 55$, $\eta = 16.8$ MPa. s, $\sigma_{c0} = 3.23 \times 10^{-14}$ S/m, $E_B = 40$ MV/m, $\varepsilon = 3.98 \times 10^{-11}$ F/m. To verify the numerical implementation of our user elements, we first compare single-element simulations of homogeneous actuation (Fig. 2) of a viscoelastic dielectric elastomer with analytical predictions [5].

We first consider equal-biaxial deformation (Fig. 2b) to verify our four-noded axisymmetric element and eight-noded brick element. In the reference state, consider an elastomer cube with dimensions dimensions L_1, L_2 and H (where $L_1 = L_2 = H$) as shown in Fig. 2a. In our simulations (Figs 3a and 3c), we consider the electromechanical response under various prestretches. Each prestretch λ_p is the stretch due to a preload P and at which $\Phi = 0$. The prestretched membrane is then left to relax for a long time. Subsequently the electric potential is then ramped up at a rate $\dot{\Phi} = 10^6$ V/s. It is well-known that the electromechanical instability can occur for low λ_p [5,8,23]. The FE simulations compare well with the analytical solutions [5], which demonstrate the validity of the axisymmetric and brick elements.

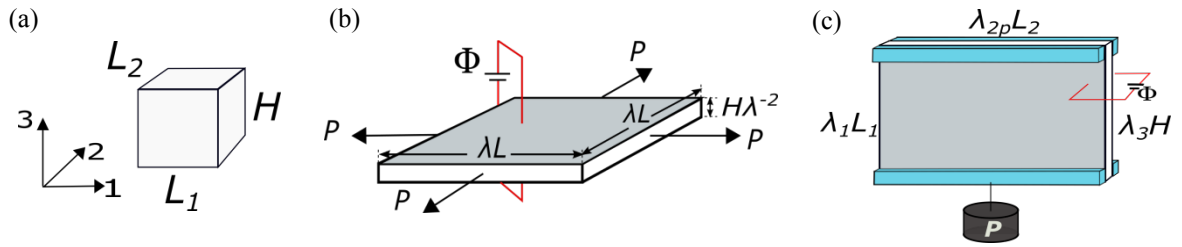

Figure 2. (a) An undeformed elastomer of dimensions L_1, L_2 and H. (b) The elastomer undergoes equal-biaxial deformation under forces P and voltage Φ. (c) The elastomer is prestretched and fixed in the 2-dir, while also subject to a constant load P in the 1-dir. In the actuated state, the elastomer undergoes plane-strain deformation under both force P and voltage Φ, with its dimensions $\lambda_1 L_1$, $\lambda_2 L_2$, and $\lambda_3 H$.

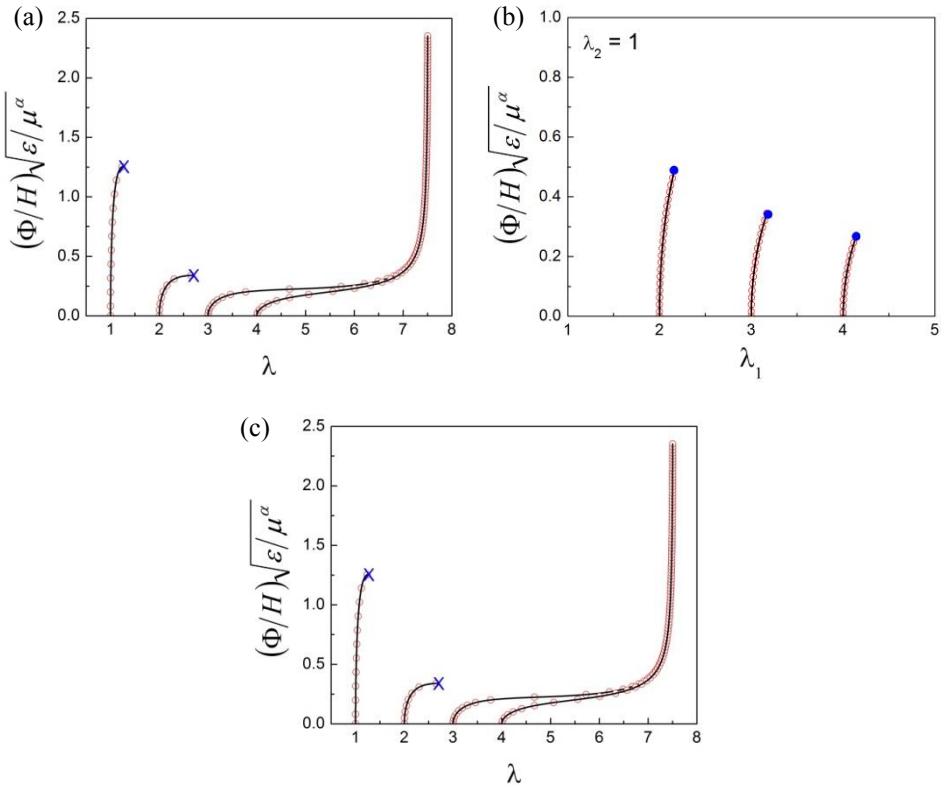

Figure 3. Simulated voltage-stretch response using user elements (UEL) for (a) 2D 4-noded axisymmetric element, (b) 2D 4-noded plane strain element, (c) 3D 8-noded hexagonal element, compared with theoretical predictions. Crosses denote electromechanical instability; filled circles denote loss of tension. FE simulations in symbols; analytical predictions in lines.

Next we consider a clamped elastomer under plane-strain deformation (Fig. 2c) to verify our four-noded plane-strain element. We prescribe the mechanical and electrical boundary conditions as described earlier, and set $\lambda_2 = 1$ with various prestretches λ_{1p} which are attained with specific preloads P. As voltage is applied, the actuation stretch λ_1 increases and the tensile stress σ_2 decreases and eventually becomes compressive at a specific voltage marked by a bold circle. After the loss of tension, the elastomer essentially becomes unclamped [18,27], such that the plane-strain element is no longer physically appropriate for

the simulations. For this reason, we ignore the case for $\lambda_{1p} = 1$, where any voltage application drives it to LT. In Fig. 3c, we plot the FE simulation for the four-noded plane-strain element and compare it with analytical predictions [18].

In the next example, we consider a loading case to verify the implementation of our current leakage model. The elastomer is first prestretched and then held until equilibrium is reached. Subsequently, the prestretched elastomer is held fixed such that it is unable to deform, which prevents creep from occuring. Charge is then ramped up on the top surface and held for a short time, before being switched to an open-circuit condition. In the open-circuit condition, the current i drops to zero over a time scale on the order of $\tau_c = \varepsilon/\sigma_{c0}$ [5], as shown in Fig. 4 for the axisymmetric and plane-strain elements.

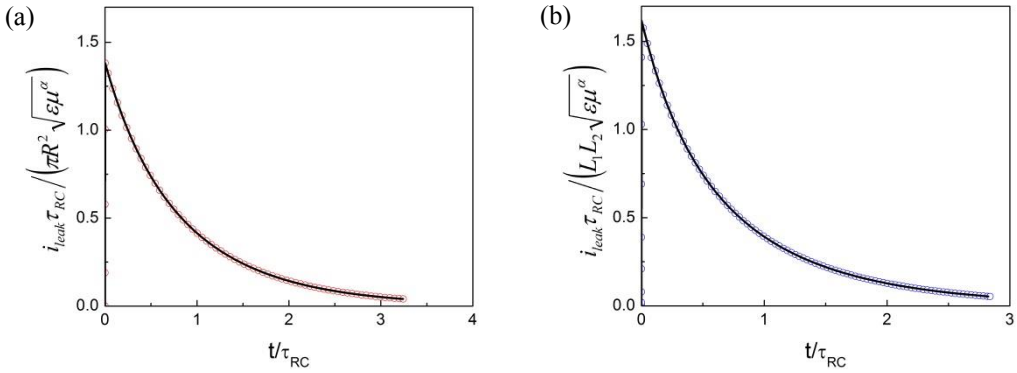

Figure 4. Validation of current leakage model. (a) axisymmetric, and (b) plane strain elements. FE simulations in symbols; analytical predictions in lines.

Next, with the verified elements, we consider a few cases to analyze the performance of dissipative dielectric elastomer actuators. We first study current leakage in an prestretched actuator $(\lambda_p = 3)$ undergoing equal-biaxial deformation subject to various voltage ramping rates. We simulate this loading case with axisymmetric elements (Fig. 5). Under actuation, the leakage current increases with the electric field. At slower ramping rates, the leakage current is higher due to viscoelasticity; the longer the loading takes, the longer viscoelastic relaxation is allowed to occur. Consequently, the leakage current accumulates due to a higher electric field.

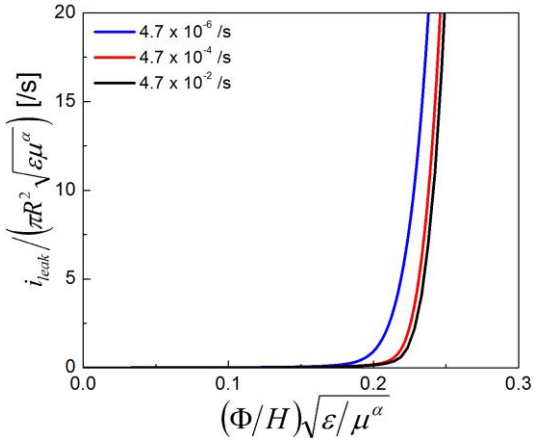

Figure 5. Current leakage in actuator subject to various voltage ramping rates $\left(\dot{\Phi}/H\right)/\sqrt{\varepsilon/\mu^{\alpha}}$ under equal-biaxial loading.

Current leakage under actuation increases the amount of charge delivered from the battery during actuation. On the other hand, when the actuator is put in an open-circuit condition, charge leakage leads to a different consequence. In this example, we consider a constrained actuator $\left(\lambda_{1p}=2,\lambda_{2p}=1\right)$, which is subject to a constant voltage Φ for a long time, before being switched to an open-ciruit condition. As charges leak through the membrane, we observe a contraction in the stretch of the actuator over time. This contraction occurs on the scale of the conduction time for various Φ, with a faster charge leakage rate at elevated electric fields.

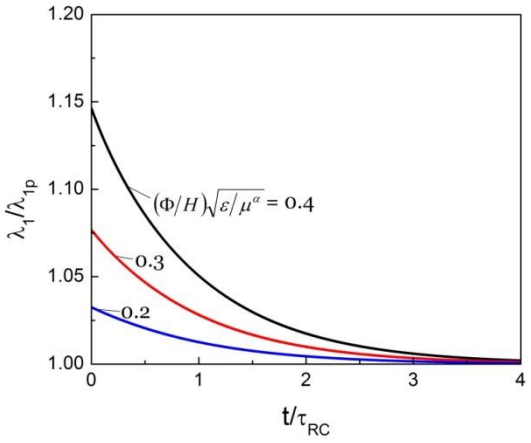

Figure 6. Current leakage results in stretch contraction of a DE actuator with various prestretches λ_{1p}.

6 CONCLUSIONS

In this paper, we describe a method to construct a model of dissipative dielectric elastomers on the basis of nonequilibrium thermodynamics. We implement the theory into a widely-used commercial FE software ABAQUS by implementing new user elements. The method is illustrated with examples to discuss the effect of viscoelasticity and current leakage on the performance of dielectric elastomers. Current leakage is significant under large actuation strains and at slow loading rates. Current leakage can also result in stretch contraction for precharged dielectric elastomers. We anticipate this method to be used for the design of practical dielectric elastomer transducers.

REFERENCES

[1] Carpi, F., Rossi, D. D., Kornbluh, R., Pelrine, R. E., & Sommer-Larsen, P. [2008]. *Dielectric Elastomers as Electromechanical Transducers: Fundamentals, Materials, Devices, Models and Applications of an Emerging Electroactive Polymer Technology*. Elsevier.
[2] Keplinger, C., Sun, J.-Y., Foo, C. C., Rothemund, P., Whitesides, G. M., & Suo, Z. (2013). Stretchable, Transparent, Ionic Conductors. Science, 341(6149), 984–987.
[3] Sun, J.-Y., Keplinger, C., Whitesides, G. M., & Suo, Z. (2014). Ionic skin. *Advanced Materials*, *26*(45), 7608–7614.

[4] Kaltseis, R., Keplinger, C., Koh, S. J. A., Baumgartner, R., Goh, Y. F., Ng, W. H., Kolger A., Trols, A., Foo, C. C., Bauer, S. (2014). Natural rubber for sustainable high-power electrical energy generation. *RSC Adv.*, *4*(53), 27905–27913.
[5] Foo, C. C., Cai, S. Q., Koh, S. J. A., Bauer, S., & Suo, Z. (2012). Model of dissipative dielectric elastomers. *Journal of Applied Physics*, *111*, 034102.
[6] Plante, J.-S., & Dubowsky, S. (2007). On the performance mechanisms of Dielectric Elastomer Actuators. *Sensors and Actuators A*, *137*, 96–109.
[7] York, A., Dunn, J., & Seelecke, S. (2010). Experimental characterization of the hysteretic and rate-dependent electromechanical behavior of dielectric electro-active polymer actuators. *Smart Materials and Structures*, *19*, 094014.
[8] Bozlar, M., Punckt, C., Korkut, S., Zhu, J., Chiang Foo, C., Suo, Z., & Aksay, I. A. (2012). Dielectric elastomer actuators with elastomeric electrodes. *Applied Physics Letters*, *101*(9), 091907.
[9] Bai, Y., Jiang, Y., Chen, B., Foo, C. C., Zhou, Y., Xiang, F., Suo, Z. (2014). Cyclic performance of viscoelastic dielectric elastomers with solid hydrogel electrodes. *Applied Physics Letters*, *104*(6), 062902.
[10] Kaltseis, R., Keplinger, C., Baumgartner, R., Kaltenbrunner, M., Li, T., Mächler, P., … Bauer, S. (2011). Method for measuring energy generation and efficiency of dielectric elastomer generators. *Applied Physics Letters*, *99*, 162904.
[11] Huang, J., Shian, S., Suo, Z., & Clarke, D. R. (2013). Maximizing the Energy Density of Dielectric Elastomer Generators Using Equi-Biaxial Loading. *Advanced Functional Materials*, *23*(40), 5056–5061.
[12] Seanor, D. A. (1965). Charge transfer in polymers. *Adv. Polymer Sci.*, *4*, 317–352.
[13] Raju, G. G. (2003). Field enhanced conduction. In *Dielectrics in Electric Fields* (pp. 329–382). New York: Marcel Dekker.
[14] Blythe, A. R., & Bloor, D. (2005). Electronic conduction in polymers. In Electrical Properties of Polymers (pp. 111–153). Cambridge University Press.
[15] Gisby, T. A., Xie, S. Q., Calius, E. P., & Anderson, I. A. (2010). Leakage current as a predictor of failure in dielectric elastomer actuators. Proc. of SPIE, 7642, 764213.
[16] Hammami, S., Jean-Mistral, C., Jomni, F., Gallot-Lavallée, O., Rain, P., Yangui, B., & Sylvestre, A. (2015). Leakage current and stability of acrylic elastomer subjected to high DC voltage. Proc. of SPIE, 9430, 943015.
[17] Foo, C. C., Koh, S. J. A., Keplinger, C., Kaltseis, R., Bauer, S., & Suo, Z. (2012). Performance of dissipative dielectric elastomer generators. *Journal of Applied Physics*, *111*(9), 094107.
[18] Kollosche, M., Kofod, G., Suo, Z., & Zhu, J. (2015). Temporal evolution and instability in a viscoelastic dielectric elastomer. *Journal of the Mechanics and Physics of Solids*, *76*, 47–64.
[19] Foo, C. C., & Zhang, Z.-Q. (2015). A Finite Element Method for Inhomogeneous Deformation of Viscoelastic Dielectric Elastomers. *International Journal of Applied Mechanics*, *07*(05), 1550069.
[20] Wang, J., Nguyen, T. D., & Park, H. S. (2013). Electrostatically Driven Creep in Viscoelastic Dielectric Elastomers. *Journal of Applied Mechanics*, *81*(5), 051006.

[21] Park, H. S., Wang, Q., Zhao, X., & Klein, P. A. (2013). Electromechanical instability on dielectric polymer surface: Modeling and experiment. *Computer Methods in Applied Mechanics and Engineering*, *260*, 40–49.
[22] Wang, S., Decker, M., Henann, D. L., & Chester, S. A. (2016). Modeling of dielectric viscoelastomers with application to electromechanical instabilities. *Journal of the Mechanics and Physics of Solids*, *95*, 213–229.
[23] Zhao, X., Hong, W., & Suo, Z. (2007). Electromechanical hysteresis and coexistent states in dielectric elastomers. *Physical Review B*, *76*(13), 134113.
[24] Gent, A. N. (1996). A new constitution relation for rubber. *Rubber Chemistry and Technology*, *69*, 59–61.
[25] de Souza Neto, E. A., Perić, D., Dutko, M., & Owen, D. R. J. (1996). Design of simple low order finite elements for large strain analysis of nearly incompressible solids. *International Journal of Solids and Structures*, *33*(20–22), 3277–3296.
[26] Chester, S. A., Di Leo, C. V., & Anand, L. (2015). A finite element implementation of a coupled diffusion-deformation theory for elastomeric gels. *International Journal of Solids and Structures*, *52*, 1–18.
[27] Kollosche, M., Zhu, J., Suo, Z., & Kofod, G. (2012). Complex interplay of nonlinear processes in dielectric elastomers. *Physical Review E*, *85*(5), 051801.

VIII ECCOMAS Thematic Conference on Smart Structures and Materials
SMART 2017
A. Güemes, A. Benjeddou , J. Rodellar and Jinsong Leng (Eds)

OPTIMAL ACTIVE TWIST COMPARATIVE DESIGN AND TESTING OF HELICOPTER ROTOR BLADES WITH C AND D-SPARS

EVGENY BARKANOV[*], ANDREY KOVALOV[*], PETER WIERACH[†] AND JOHANNES RIEMENSCHNEIDER[†]

[*] Institute of Materials and Structures
Riga Technical University
Kalku St. 1, LV-1658, Riga, Latvia
e-mail: barkanov@latnet.lv, www.ims.rtu.lv

[†] Institute of Composite Structures and Adaptive Systems
German Aerospace Centre
Lilienthalplatz 7, 38108 Braunschweig, Germany
e-mail: Peter.Wierach@dlr.de, www.dlr.de

Key words: Helicopter Rotor Blade, Macro-Fibre Composite (MFC), Active Twist, Finite Element Method, Quasi-Static Test, Optimisation.

Abstract. An application of macro-fibre composite (MFC) actuators for the active twist control of helicopter rotor blades leads to significant vibration and noise reduction without the need for complex mechanisms in the rotating systems. To optimise an active twist of rotor blades with C and D-spar, new 3D finite element models and corresponding piezoelectric, static torsional and modal analyses are developed for two variants of application of active materials. Due to a large dimension of the numerical problem to be solved, an optimisation methodology is developed employing the method of experimental design and response surface technique. The comparative analysis is carried out to choose an appropriate optimal solution from rotor blades with C and D-spar and two variants of application of MFC actuators in the examined design space. The results of quasi-static tests made on demonstration blade confirm high accuracy of the developed 3D finite element models and corresponding analyses.

1 INTRODUCTION

During flight, helicopter rotor blades produce significant vibration and noise as a result of variations in rotor blade aerodynamic loads with blade azimuth angle. Likely, significant vibration and noise reduction can be achieved without the need for complex mechanisms in the rotating system using active twist control of helicopter rotor blades by an application of MFC actuators. In this case MFC actuators are implemented in the form of active plies within the composite skin of the rotor blade with orientation at 45^0 to the blade axis to maximize shear deformations in the laminated skin producing a distributed twisting moment along the blade.

A number of theoretical and experimental studies were performed to estimate an active twist of helicopter rotor blades required for the reduction of noise and vibration, and

improvement of the overall performance of helicopters. The early studies were mostly experimental in nature and were undertaken to prove the concept of an active twist control using piezoceramic materials [1, 2]. Most present numerical investigations are based on simple box–beam blade models or combination of 2D cross–section analysis and 1D beam analysis along the blade span [3, 4]. Recently, using these approaches, optimisation methodologies were developed to maximise an active twist response for some rotor blade models [5, 6].

The present investigations demonstrate the optimal design of an active twist of helicopter rotor blades with C and D-spar developed by using new 3D finite element models and verified by the testing of demonstrator blade. Two design solutions for an application of active materials were studied to estimate their effectiveness.

2 CONSTRUCTION OF HELICOPTER ROTOR BLADES

The investigated helicopter rotor blades (model scale) presented in Fig. 1 are not pre-twisted, equipped with NACA23012 airfoil and have the radius of 2 m and chord length of 0.121 m. They consist of C or D-spar made of unidirectional GFRP, skin made of $+45^0/-45^0$ GFRP with the thickness of separate layer of 0.125 mm, foam core, balance weight and MFC actuators located on the skin. It is necessary to note that rib in the D-spar design presents continuation of C-spar ”moustaches” and, for this reason, has the same thickness with them.

MFC actuators used consist of rectangular piezoceramic fibres embedded into the epoxy matrix and sandwiched between polyamide films that have attached interdigitated electrode patterns as shown in Fig. 2. The direction of piezoceramic fibres in MFC coincides with the direction of outside GFRP skin layers to maximise the twist actuation capabilities. The thickness of MFC actuators is 0.3 mm, their operational voltage is from -500 till +1500 V and the spacing between electrodes is 0.5 mm. MFC actuators are applied as an active rectangular shape layer with the length of 1.56 m. Two design solutions for a best application of active materials (Fig. 3) were chosen from the previous study [7] for the present investigations. The material properties of the rotor blade components are given in Table 1.

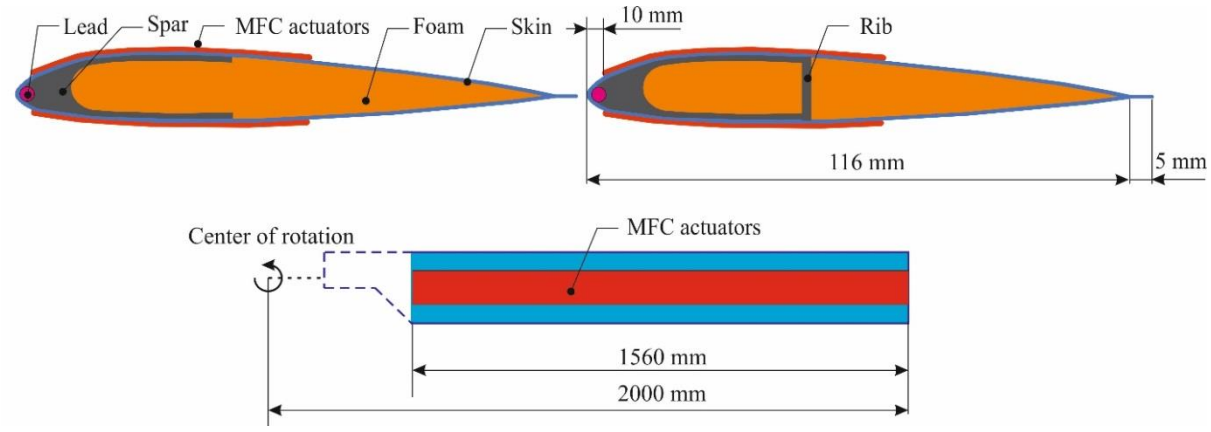

Figure 1: Helicopter rotor blades with C and D-spars

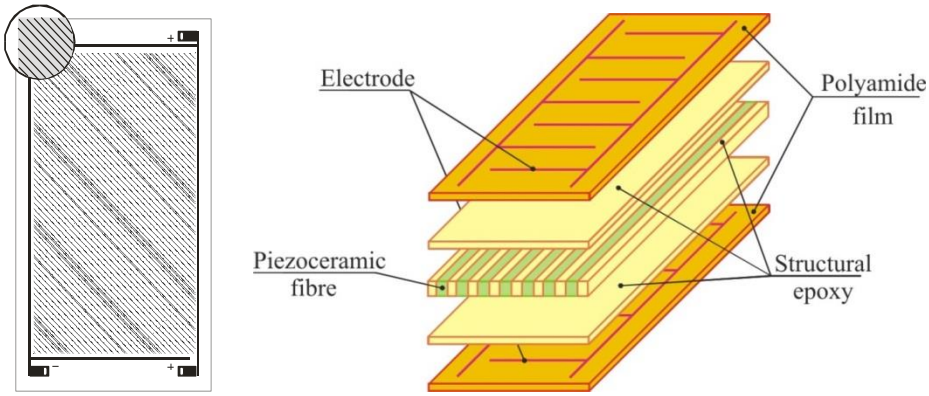

Figure 2: MFC actuator

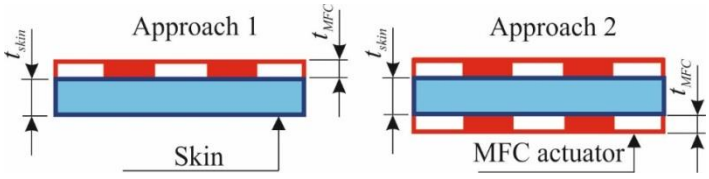

Figure 3: Application of active material

3 FINITE ELEMENT ANALYSIS

The finite element method is used for the modelling and piezoelectric, static torsional and modal analyses to determine active twist angle, strains arising in the rotor blades, location of centre of gravity and elastic axis, blade mass per unit span length and first torsional frequency.

Table 1: Material properties of rotor blade components

	MFC	GFRP	Rohacell 51FX	Lead	Wolfram
E_x, GPa	30.0	45.166	0.035	13.79	400
$E_y = E_z$, GPa	15.5	11.981	0.035	13.79	400
G_{yz}, GPa	5.7	1.289	0.014	2.00	160
$G_{xy} = G_{xz}$, GPa	10.7	4.583	0.014	2.00	160
ν_{yz}	0.35	0.325	0.25	0.44	0.28
$\nu_{xy} = \nu_{xz}$	0.4	0.238	0.25	0.44	0.28
ρ, kg/m^3	4700	2008	52	11300	19400
d_{33}, m/V	$4.18 \cdot 10^{-10}$	–	–	–	–
$d_{31} = d_{32}$, m/V	$-1.98 \cdot 10^{-10}$	–	–	–	–

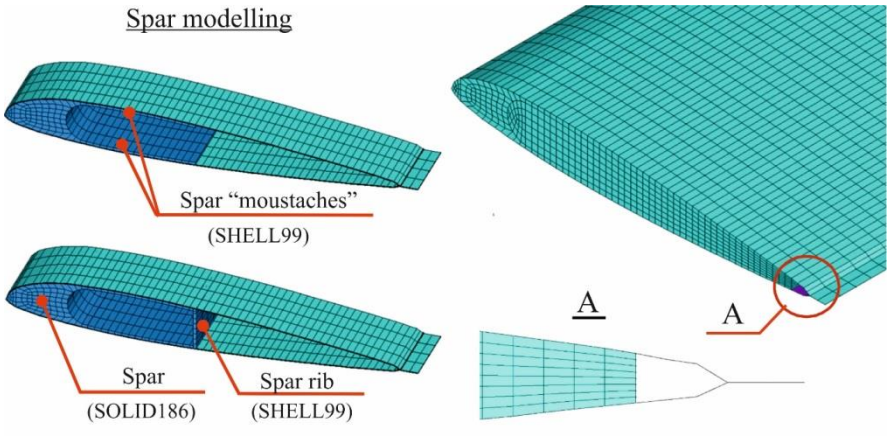

Figure 4: Finite element models of helicopter rotor blades

New 3D finite element models of the rotor blades with C and D-spar (Fig 4) are built using ANSYS code [8], where the rotor blade skin with MFC active layer, spar "moustaches" and rib in D-spar design are modelled by the linear layered structural shell elements SHELL99, but the spar, foam and balance weight by 3D 20 node structural solid elements SOLID186. Some model simplification was done, namely foam material was removed from the rotor blade tile. This gives the possibility to decrease the dimension of the finite element model and to preserve a proportional mesh for the blade skin without an accuracy loss for the obtained results. The node offset option is applied for the joint MFC-skin-spar "moustaches" structure to preserve the rotor blade profile. In this case the finite element nodes are located at the top surface of laminate. The adhesive layer between MFC actuators and skin is ignored and clamped boundary conditions are applied from one side of the rotor blade.

4 EXPERIMENTAL CHARACTERISATION

To validate the developed 3D finite element models, the demonstration rotor blade with MFC actuators was designed, produced and tested. The main characteristics of the demonstrator are taken from the well-known BO 105 model rotor blade consisting of unidirectional GFRP C-spar, laminated composite skin and foam core. The chord length of 121 mm and the radius of 2 m are in agreement with the original whereas, due to manufacturing reasons, the profile was slightly modified into a symmetrical NACA 0012 which does not really change the blade from a structural point of view. The demonstrator is not pre-twisted and its dimensions are presented in Fig. 5. The material properties of the rotor blade components are given in Table 1 where the wolfram material should be chosen for a balance weight in the demonstration blade.

MFC actuators used for an active twist of the rotor blade have the angle of piezoelectric fibres equal to +40° and the inner surface of skin is made of two GFRP layers with fibres angle of –30° (Fig. 5). In the areas outside actuators, two GFRP layers with the angle of +40° are added to the outer surface of skin in order to carry loads of actuators and to decrease the change of stiffness in this transition region between skin and actuator. Finally, 12 MFC actuators with operating voltage of -500 … +1500 V are implemented from both sides of the blade, resulting approximately in a total active area of 3200 cm^2. All MFC actuators are

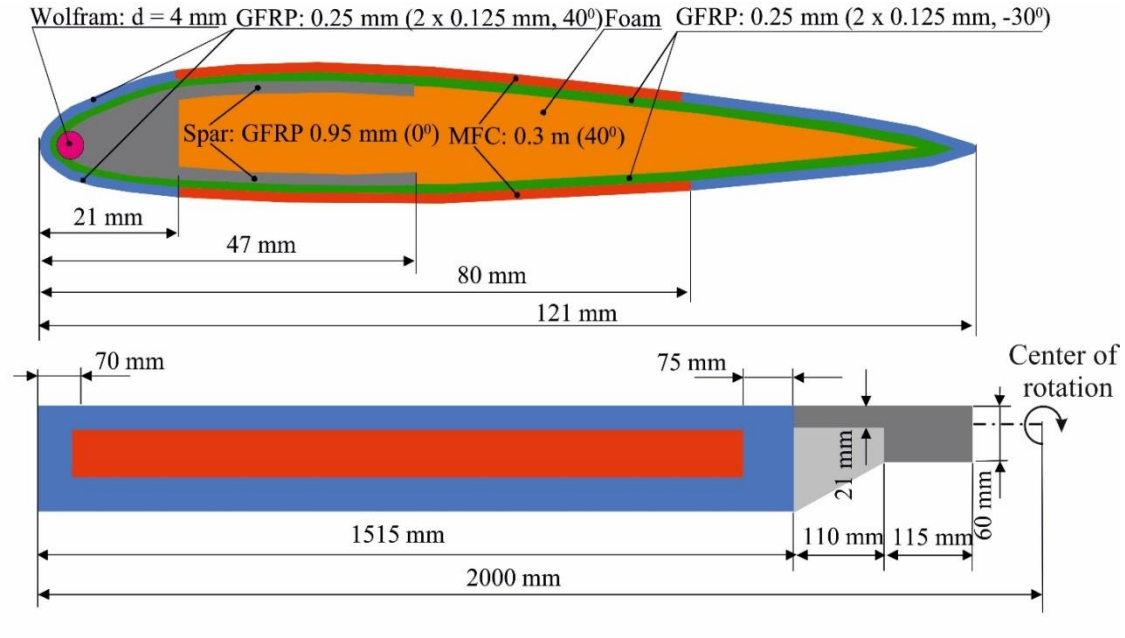

Figure 5: Cross-section and plan-form of the demonstration rotor blade

placed into the mould and then cured together with GFRP. The details of manufacturing process could be found in [9].

The quasi-static tests for the demonstrator blade were carried out to measure an active twist angle. For such measurements rotor blades are usually clamped at the root standing upright. This is done to avoid any influence of flap bending, which would occur just by the weight of the blade itself, if tested horizontally. The developed special test rig (Fig. 6) allows location of sensors and actuators close to the rotor blade and simple installation of the rotor blade shape clamp for a twist measurements in a certain area of the blade. It is necessary to note that the test rig is also useful for the blade stiffness measurements.

In order to measure the tip deflection, two different techniques were tested. The first assumes an application of laser beam on the blade tip. When the blade is twisted, this beam is also twisted and the beam's projection on a wall located several meters away from the test rig gives the possibility to determine the blade twist. The second technique utilizes a set of laser displacement sensors to measure the tip deflection at leading and trailing edge of the blade tip which results in the tip twist angle. MFC actuators were used with the voltage range of –500 … +1300V for a quasi-static excitation with the frequency of 0.15 Hz. Small voltage's reduction was applied to avoid any electrical overloads. The tip twist measured experimentally is given in Table 2 together with the results of the finite element analysis. It is

Table 2: Verification of numerical model

Active twist angle φ, °		Δ, %
Experiment	FEM	
3.93	4.06	3.3

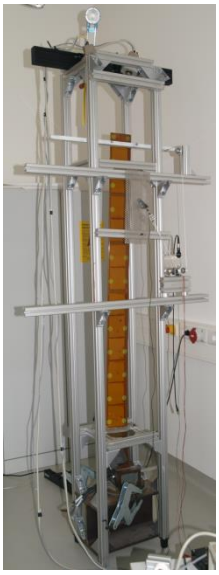

Figure 6: An experimental set-up

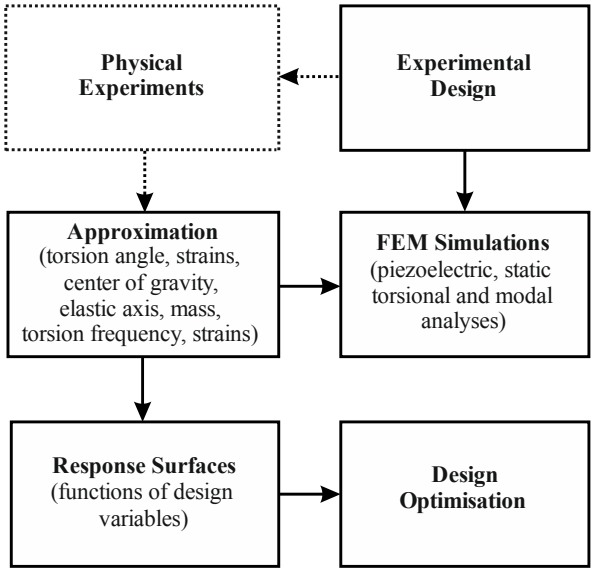

Figure 7: Optimisation procedure

seen that the difference between active twist angles obtained experimentally and numerically is 3.3% that confirms high accuracy of the developed 3D finite element model and corresponding analysis.

5 OPTIMAL DESIGN

Due to the large dimension of numerical problem to be solved, an optimisation methodology is developed employing the method of experimental design and response surface technique (Fig. 7). It is necessary to note, that in each of these stages, it is possible to solve the problem by different methods. The basic idea of this approach is that simple mathematical models (response surfaces) are determined only using the finite element solutions in reference points of experimental design. The significant reduction in calculations is achieved in this case in comparison with conventional optimisation methods.

An active twist optimisation problem for helicopter rotor blades with C and D-spar is formulated based on the results of parametric study. In this case the objective function is the torsion angle maximisation

$$\varphi(\{X\}) \Rightarrow \max \tag{1}$$

where $\{X\} = \{l, t_{spar} = t_{rib}, t_{skin}, L\}$ is the vector of design parameters (Fig. 8) with the following boarders in mm:

$$\begin{gathered} 16 \le l \le 24, \quad 0.50 \le t_{spar} = t_{rib} \le 2.50 \\ 0.25 \le t_{skin} \le 1.25, \quad 0 \le L \le 100 \end{gathered} \tag{2}$$

It is necessary to note that the skin thickness t_{skin} is a discrete value design parameter with the step of $\Delta t_{(+45/-45)} = 0.25$ mm. Taking into account the producers requirements, the following constraints are defined for the present optimisation problem:

$$22 \le y_{cg} \le 30, \;\; 10 \le y_{ea} \le 25 \tag{3}$$

$$m \le 1.35, \;\; f_{T_1} \ge 59.15, \;\; \varepsilon_{\max} \le 4000/k \tag{4}$$

where $k = 1.4$ is the safety coefficient.

The plan of experiments, where the points of experiments in the domain of factors are distributed as regularly as possible, was developed for $n = 4$ design parameters and $k = 30$ experiments. The piezoelectric, static torsional and modal analyses determining active twist angle, strains arising in the rotor blades, location of centre of gravity and elastic axis, blade mass per unit span length and first torsional frequency were applied in separate points of the developed plan of experiments. By using approximations of the numerical results, corresponding response surfaces were built for the active torsion angle with correlation coefficient of 94 % and for other behaviour functions with the correlation coefficients higher than 90 % for both rotor blades. They were verified successfully by the finite element solutions using the design parameters not presented by the points of the plan of experiments. The formulated optimisation problem is solved by the random search method [10] using EDAOpt optimisation software [11] and the response surfaces obtained.

The optimisation results for two rotor blades and two different MFC applications are given in Table 3. Since these results were obtained using approximations instead of original functions, they are verified by the corresponding finite element analysis in the optimal points. Table 3 shows that all the residuals Δ for objective and other behaviour functions determined as the relative errors between the response surfaces (RS) and original finite element solutions (FEM) are lower than 2 % in most cases that talks about high accuracy of the present optimal design. The optimisation results (Table 3) were obtained with 1000 V and linear piezoelectric analysis. Using linearity, the maximal torsion angle could be easily interpolated in the bounds of -500 … +1500 V. Strains arising in the rotor blades in the present diapason are lower than admissible and for this reason they are absent in Table 3. It is necessary to note that the maximal torsion angle desirable for the vibration and noise control applications is ±2º.

Clearly one can say from Table 3 that, due to the very close maximal torsion angles obtained for both spar optimal designs (difference around 2.5%), D-spar design could be examined like more preferable since it gives smaller distance between location of the centre of gravity and elastic axis, and at the same time does not considerably contribute to an increasing of the rotor blade mass (around 3.2% from C-spar design). Obviously also that approach 2, due to its ability of higher actuation energy application, is more effective than approach 1 concerning the maximal torsion angle. However, this approach gives the rotor blade design with biggest mass and larger distance between location of the centre of gravity and elastic axis that does not contribute to an improvement of the rotor-dynamic behaviour.

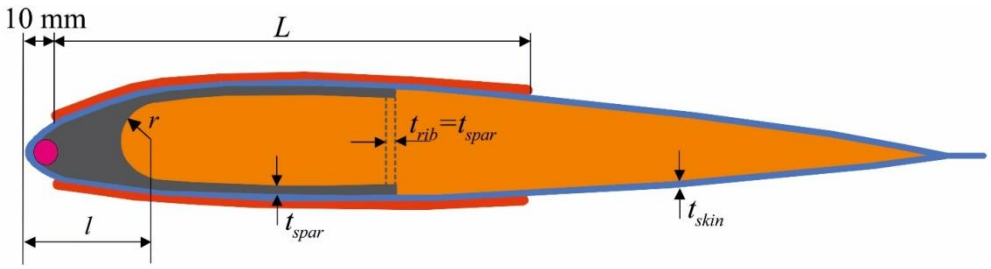

Figure 8: Design parameters

Table 3: Optimisation results

Optimal design		C-spar						D-spar					
		Approach 1			Approach 2			Approach 1			Approach 2		
		RS	FEM	Δ, %	RS	FEM	Δ, %	RS	FEM	Δ, %	RS	FEM	Δ, %
Design parameters	l, mm	24.0	24.0	–	16.0	16.0	–	16.0	16.0	–	22.0	22.0	–
	t_{skin}, mm	0.25	0.25	–	0.25	0.25	–	0.25	0.25	–	0.25	0.25	–
	t_{spar}, mm	0.50	0.50	–	1.50	1.50	–	1.00	1.00	–	0.50	0.50	–
	L, mm	91.0	90.0	–	77.0	76.0	–	89.0	88.0	–	82.0	82.0	–
Constraints	y_{cg}, %	26.5	26.7	0.7	28.9	29.2	1.0	29.7	29.4	1.0	29.4	29.0	1.4
	y_{ea}, %	16.3	16.6	1.8	15.7	16.0	1.8	22.1	21.9	0.9	18.1	17.7	2.3
	m, kg/m	0.99	0.99	0	1.16	1.14	1.7	0.96	0.95	1.0	1.20	1.23	2.5
	f_{T_1}, Hz	59.2	57.9	2.2	59.3	59.8	0.8	59.2	58.1	1.8	59.8	58.9	1.5
Objective function	φ,°	3.91	3.88	0.7	5.52	5.56	0.7	4.01	4.04	0.7	5.39	5.39	0.0

Additionally, it is necessary to note that very strong constraint narrowing borders of the optimal solution search is the fundamental torsion eigenfrequency since all optimisation results come on its boarder or very close to it.

To find a compromise between minimal distance of the centre of gravity and elastic axis, and maximal torsion angle and minimal rotor blade mass, multiple optimisation problems were solved with the same objective function maximising the torsion angle (Eq. (1)) under constraints described by Eq. (4) and presented below

$$\left|y_{cg} - y_{ea}\right| = const \tag{5}$$

In this case optimal solutions were obtained for the constant minimal distances of the centre of gravity and elastic axis taken with the step of 0.5%. The value of step was reduced till 0.1% only approaching the minimal and maximal possible boarders where the optimal solution still exists. The optimal results for all steps are presented in Figs 9-10 for two spar designs and two approaches presenting different MFC applications. It is seen from Figs 9-10 that D-spar design is more effective in most cases since gives the possibility to obtain higher values of torsion angle and to build rotor blades with the smaller distance between location of the centre of gravity and elastic axis. It is interesting to note that optimal solutions for the rotor blades with C-spar design do not exist already for the minimal distances of the centre of gravity and elastic axis lower than 6.7% for approach 1 and 12.1 % for approach 2. At the same time, D-spar design allows obtaining considerably lower values especially for approach

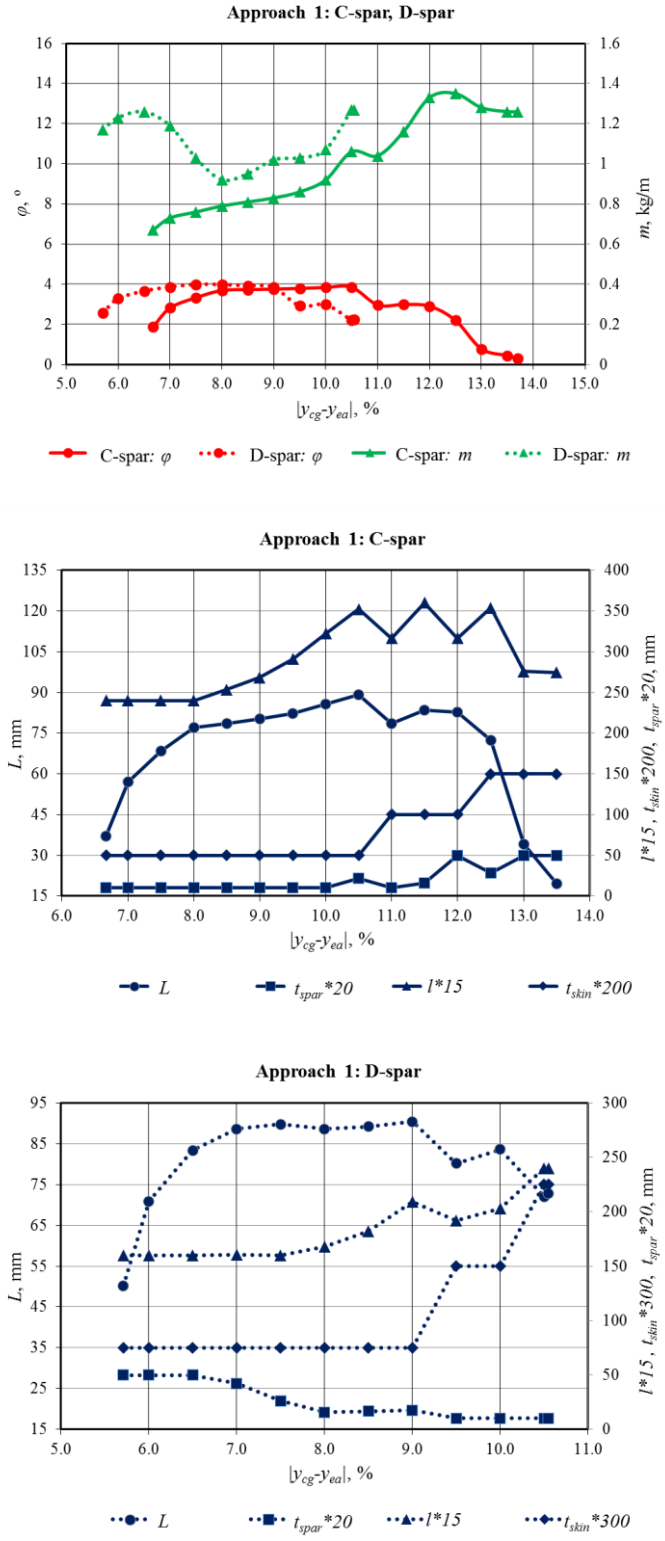

Figure 9: Optimal solutions for Approach 1

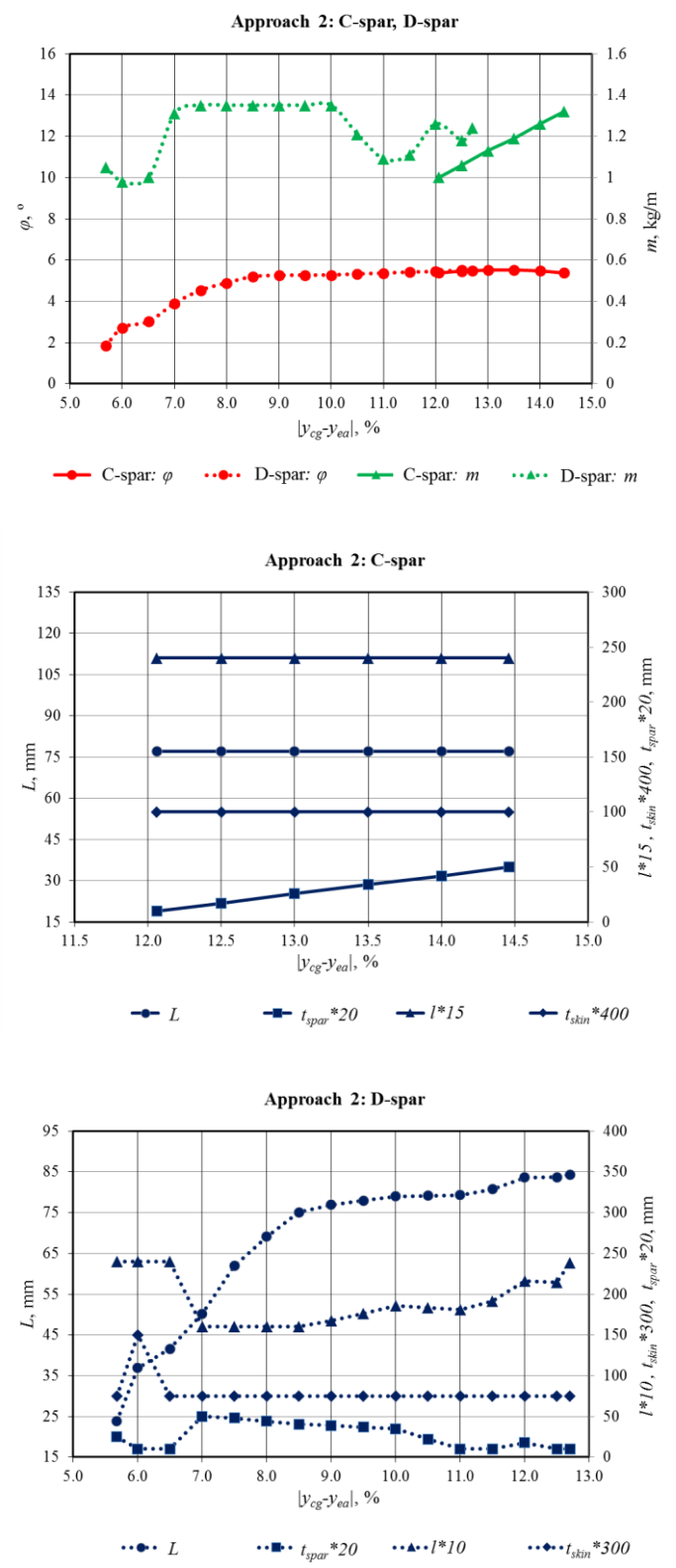

Figure 10: Optimal solutions for Approach 2

2. As expected, approach 2 is more effective than approach 1 concerning the maximal torsion angle but it considerably narrows application boarders of C-spar design and increases the weight of rotor blades. It is necessary to note also that approach 1 allows finding the optimal solutions in wider boarders for both spar designs.

6 CONCLUSIONS

Optimal design of helicopter rotor blades for an active twist application was developed by using simple plan of experiments with a regular distribution of sample points and accurate response surfaces obtained with high correlation coefficients. New 3D finite element models and corresponding piezoelectric, static torsional and modal analyses carried out in the points of experiments were successfully validated by the quasi-static tests made on demonstration blade. Optimisation problems were solved for two spar designs and two variants of application of MFC actuators to maximise an active twist angle. The comparative analysis was carried out to find a compromise between minimal distance of the centre of gravity and elastic axis, and maximal torsion angle and minimal rotor blade mass.

For an improvement of the rotor blade active control, D-spar design could be examined as more effective since allows smaller distance between location of the centre of gravity and elastic axis. At the same time it preserves high value of the active twist angle and does not considerably contribute to an increasing of the rotor blade mass. Moreover, D-spar design allows the obtaining of optimal solutions in such regions of the examined design space where C-spar optimal design is completely impossible.

As expected, approach 2 is more effective than approach 1 concerning the maximal torsion angle since it allows an application of higher actuation energy. However, at the same time this approach gives the rotor blade design with the biggest mass.

REFERENCES

[1] Chen, P. and Chopra, I. Induced strain actuation of composite beams and rotor blades with embedded piezoceramic elements. *Smart Materials and Structures* (1996) **5(1)**: 35-48.

[2] Riemenschneider, J. and Opitz, S. Measurement of twist deflection in active twist rotor. *Aerospace Science and Technology* (2011) **15(3)**: 216-223.

[3] Chandra, R., Stemple, A.D. and Chopra, I. Thin-walled composite beams under bending, torsional, and extensional loads. *Journal of Aircraft* (1990) **27(7)**: 619-626.

[4] Ghiringhelli, G.L., Masarati, P. and Mantegazza, P. Analysis of an actively twisted rotor by multi–body global modelling. *Composite Structures* (2001) **52(1)**: 113-122.

[5] Shin, S., Cesnik, C.E.S., Wilkie, W.K. and Wilbur, M.L. Design and manufacturing of a model–scale active twist rotor prototype blade. *Journal of Intelligent Material Systems and Structures* (2008) **19(12)**: 1443-1456.

[6] Park, J.S., Shin, S.J. and Kim, D.K. Design and vibratory loads reduction analysis of advanced active twist rotor blades incorporating single crystal piezoelectric fibre composites. *International Journal Aeronautical and Space Sciences* (2008) **9(2)**: 18-33.

[7] Barkanov, E., Gluhih, S. and Kovalov, A. Optimal design of the active twist for helicopter rotor blades with C-spar. *Mechanics of Advanced Materials and Structures* (2008) **15(3-4)**: 325-334.

[8] *ANSYS Mechanical User's Guide*. Release 16.2. ANSYS, Inc.

[9] Wierach, P., Riemenschneider, J., Opitz, S. and Hoffmann, F. Experimental investigation of an active twist rotor under centrifugal loads. In: *Adaptive, Tolerant and Efficient Composite Structures*, Springer–Verlag: Berlin, Heidelberg (2013) 391-407.

[10] Rao, S.S. *Engineering optimization: theory and practice*. John Wiley & Sons, Inc.: New York (2009).

[11] Auzins, J., Janushevskis, A., Janushevskis, J. and Skukis, E. Software EDAOpt for experimental design, analysis and multi-objective robust optimization. In: *Proceedings of the International Conference on Engineering and Applied Sciences Optimization*, Kos Island, Greece (2014) 23 P.

VIII ECCOMAS Thematic Conference on Smart Structures and Materials
SMART 2017
A. Güemes, A. Benjeddou , J. Rodellar and Jinsong Leng (Eds)

SIMPLE AUXETIC TUBULAR STRUCTURES

Xin Ren[1,2*], Jianhu Shen[1], Hongqi Tian[2] , and Yi Min Xie[1,3]

[*] 1. Centre for Innovative Structures and Materials (CISM)
School of Engineering, RMIT University
GPO Box 2476, Melbourne 3001, Australia
e-mail: s3460277@student.rmit.edu.au, www.rmit.edu.au

2. Key Laboratory of Traffic Safety on Track
School of Traffic & Transportation Engineering
Central South University, Changsha 410075, Hunan Province, China
e-mail: hongqitian.csu@gmail.com, www.csu.edu.cn

3. XIE Archi-Structure Design (Shanghai) Co., Ltd.,
Shanghai 200433, China
e-mail: mike.xie@rmit.edu.au, www.xieym.com

Key words: Auxetic, Poisson's ratio, tubular structure, tube, stent, random cut, pattern scale factor (PSF).

Abstract. Auxetic materials and structures have attracted significant interest because of their uncommon behaviour, i.e. they will shrink (expand) laterally under compression (tension). Auxetic tubular structures have been used as oesophageal stents. Inspired by the recent kirigami method and the pattern scale factor (PSF) adjustment method, we generated several tubular structures. The tensile auxetic performance of these tubes was investigated using validated finite element analysis (FEA) to explore their properties. The results demonstrated that the random cut method was unsuitable for generating auxetic tubular structures. Vertical and horizontal (VH) cut approach was suitable, but the change of the tubular diameter was lower than the tubular structures generated by the PSF adjustment method.

Highlights:

1) The auxetic performance of tubular structure generated by using random cut method is studied for the first time.
2) It is found that the random cut method is unsuitable for generating auxetic tubular structures.
3) It is found that the auxetic tubular structure generated by the pattern scale factor (PSF) adjustment method have a larger expansion ratio of diameter than that generated by cutting method.
4) The auxetic performance of tubular structure generated using PSF adjustment method is more stable than that of tubular structure generated using the Vertical and horizontal (VH) cut method.

1. INTRODUCTION

The term of "auxetic" is firstly proposed by Evans [1] to represent a cumbersome phrase of "negative Poisson's ratio", which is used to describe materials and structures with a counter-intuitive behaviour, i.e. under uniaxially vertical compression (tension), these materials and structures contract (expand) transversely.

Because of the uncommon behaviour, auxetics have been widely explored ever since Lakes [2] reported the first re-entrant foam with negative Poisson's ratio (NPR) in 1987. Compared with traditional materials and structures, the superior properties of auxetics include shear resistance [3], indentation and fatigue resistance [4-9], energy absorption [1, 10, 11], synclastic behaviour [2], improved resilience [2], fracture toughness [12], acoustic absorption [13], vibration control [14] and smart filters [15].

As foldable and expandable devices, auxetic tubular structures or auxetic stents have attracted significant interest because of their important role in the medical field, e.g. aunnuloplasty rings [16], angioplasty stents [17-19] and oesophageal stents [20, 21]. However, for the patterns of the most existing auxetic tubular structures, the cellular configuration is predesigned. Recently, Grima et al. [22] reported an interesting work. Using a random cut method, they successfully converted a non-auxetic conventional sheet of rubber-like material to an auxetic metamaterial with a large negative Poisson's ratio. In our previous paper[23], we also suggested that random cut method could be used to generate auxetic tubular structures.

In this paper, two kinds of tubular structural models utilizing random cut method [22] and vertical-horizontal (VH) cut method were firstly generated, respectively. Then validated FEA was carried out to explore the mechanical properties of the designed tubular structures under quasi-static tension. Lastly, the auxetic performance of the VH cut tubular structure was compared with an auxetic tubular structure [23] generated using PSF adjustment method [23-26].

2. DESIGNING AUXETIC TUBULAR STRUCTURES

2.1 Designing auxetic planar sheet using cutting method

Similar to the work of Grima et al. [22], two slit perforated planar sheets were generated, one with a highly ordered pattern of alternating vertical and horizontal slits, the other one with a disordered pattern of randomly oriented slits.

The geometries of the slit perforated sheets are shown in Fig. 1, where L is the length of the unit cell equals 20 mm; l is the length of the cutting slit equals 18 mm; t is the thickness of the cutting slit equals 0.2 mm; s0 is separation between the slits in the ordered system equals 0.9 mm. For the disordered planar sheet, same as [22], the disorder is introduced to the sheet by a random change in the angular orientation of the cutting slit. The rotational angle is defined by d where $-30° \leq d \leq 30°$, with 5° as an increment. That means d is set to 0°, ±5°, ±10°, ±15°, ±20°, ±25°, ±30°. It should be noted that s0 is always larger than 0, i.e., none of slits are overlapped with each other.

2.2 Converting sheets to auxetic tubular structures

According to the work from Grima et al. [22], the planar sheets shown in Fig. 1 have auxetic behaviour under quasi-static tension. But how these planar sheets would behave under tension when they were transformed to tubular structures was still unknown. Same as our previous work [23], a coordinate transformation method was used so that the planar sheets could be transferred into tubular structures as shown in Fig. 2.

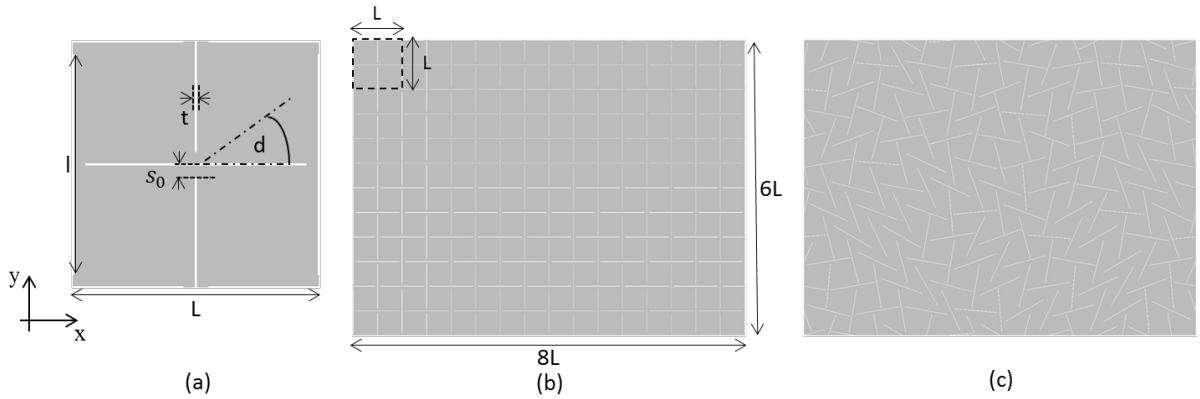

Figure 1. Planar sheets with perforated slits: (a) the representative unit cell of an auxetic perforated sheet consisting of perpendicularly arranged alternating slits; (b) the ordered perforated sheet made up of 8×6 representative unit cell using VH cut method; (c) the disordered perforated sheet with $d_{max} = 30°$ using random cut method.

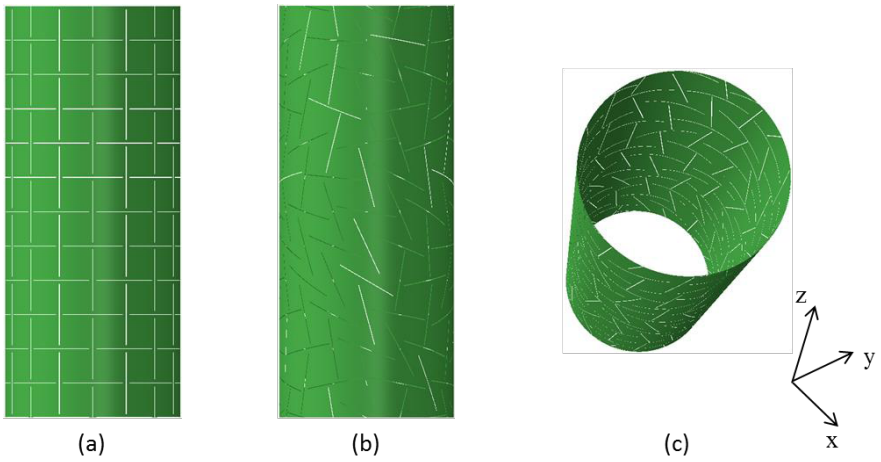

Figure 2. Cutting patterns of the tubular structures from different views: (a) the front view of the tubular structure generated using VH cut method; (b) the front view of the tubular structure generated using random cut method; (c) the perspective view of the tubular structure generated using random cut method.

3. FINITE ELEMENT ANALYSIS

3.1 FE model for tubular structures

ABAQUS/Explicit solver was employed for the large deformation. Shell elements (ABAQUS element type S4) with the thickness of 2 mm were adopted for large deformation analysis. In order to minimize the inertia effect of the models, a gradually increased velocity on the top layer of the models was applied to guarantee its zero acceleration at the beginning of the loading process. Similar to the rubber material setup in our previous work [27], the linear elastic material was used with an isotropic Young's modulus of 1 MPa and Poisson's ratio of 0.47. All freedoms of nodes on the bottom and top layer were constrained except for the loading direction on the top layer which was set as z = 1. The loading rate and mesh density were determined by a convergence check.

3.2 Comparisons of auxetic performance of tubular structures in tension

According to the work of Grima et al. [22], planar sheets with ordered or disordered random cuts have an auxetic behaviour under axially quasi-static tension. To extend their

work from planar sheets to tubular structures, the FEA method was implemented and the FE results of deformation processes both for VH cut and randomly cut tubular structures were shown in Fig. 3. The normalized strain was defined by the vertical displacement of the top layer of tubular structure divided by the initial height of the tubular structure.

As can be seen from Figs. 3(a) and 3(b), both of the two tubular structures seemed to exhibit auxetic behaviour because the overall diameters of these two tubular structures increased when compared with the initial diameters. It should be noted that the diameters at the different height of the tubular structure with ordered slits increased identically, as shown in Fig. 3(a). However, the diameters at different height of the tubular structure with random slits increased non-uniformly, as shown in Fig. 3(b).

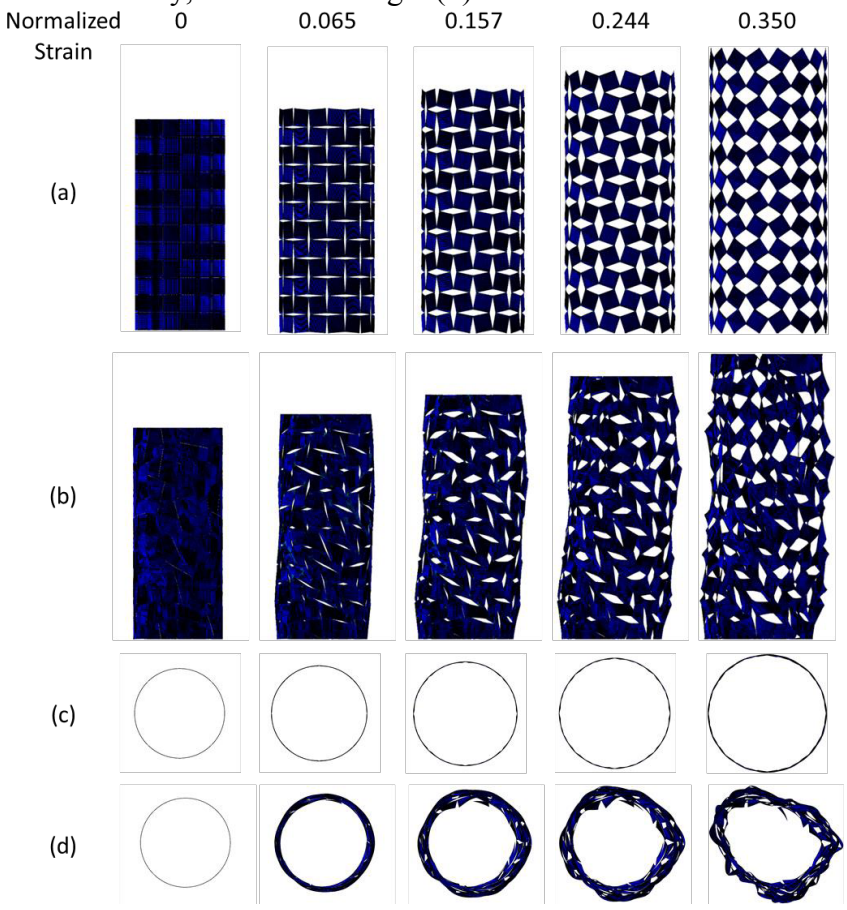

Figure 3. Deformation processes for two tubular structures under quasi-static tension from two views: (a) the front view of tubular structure generated using VH cut method; (b) the front view of tubular structure generated using randomly cut method; (c) the top view of tubular structure generated using VH cut method; (d) the top view of tubular structure generated using random cut method.

When observed from the top view, the differences of the deformation processes for the two tubular structures became more obvious, which can be seen in Figs. 3(c) and 3(d). The tubular structure with ordered slits was auxetic, which was confirmed by its deformation process from two different views, as shown in Figs. 3(a) and 3(c). Interestingly, we found that the diameter of the tubular structure with disordered slits was not increased with the tensile deformation which could be clearly seen from the top view, as shown in Fig. 3(d). This FE result indicated that the tubular structure generated from the randomly cut method was non-auxetic, or at least, not the strictly auxetic.

For the planar sheet with perpendicular ordered slits, as shown in Fig. 1(b), the planar system itself made up a rotating square system. For the planar sheet with disordered slits, as shown in Fig. 1(c), the system was no longer a uniformly shaped rotating square system under tensile deformation, and it could be regarded as a system consisting of irregular quadrilaterals rotating units. The irregularity of the rotating unit was not an important factor for the 2D planar sheet with disordered slits, because the auxetic performance for the two planar sheets was very close, which was concluded in Ref [22].

For a 3D tubular structure, although it could be generated by rolling a planar sheet, one more constraint was implemented, e.g., the previous two unconnected vertical edges of a planar sheet were merged when the planar sheet was transferred to form a tubular structure. Attributed to this extra constraint, the mechanical effect of irregularity of the rotating units was enlarged for a 3D tubular structure resulted in a out-of-plane deformation. It is beyond the scope of this work to fully understand the enlarging effect of irregularity of rotating units on 3D tubular structure, but we could still conclude that the random cut method is unsuitable for generating auxetic tubular structures.

3.3 Comparisons of auxetic performance for the tubular structures generated by VH cut method and PSF adjustment method

To evaluate the performance of VH cut auxetic tubes, deformation of the tubular structures generated by VH cut method was compared with that by PSF adjustment method. Followed by our previous work [23], an auxetic tubular structure with PSF of 100% was generated as shown in Fig. 4. And the same Abaqus configrations as the previous two tubular structures were used for exploring its auxetic performance under tension. The mesh density was determined by an independent convergence analysis for this FE model. The deformation process for the tubular structure generated by PSF adjustment method under quasi-static tension, with a PSF=100% is shown in Fig. 5.

The auxetic performance of two kinds of tubular structures, which were generated by VH cut method and PSF adjustment method, with a PSF=100%, is demonstrated in Fig. 6.

As can be seen in Fig. 6(a), the Poisson's ratio for the tubular structure with a PSF=100% was nearly constant over the normalized strain range of -0.9 to -0.6. The Poisson's ratio value for the VH cut tubular structure decreased dramatically at the beginning of the tensile deformation, with a maximal negative Poisson's ratio of -3.8. Then this value increased rapidly to -1.2, then the Poisson's ratio value increased moderately at the following normalized strain. At the normalized strain of 0.339, this value exceeded that of the tubular structure with a PSF=100%.

For the auxetic tubular structure, the uniformed expansion ratio of diameter was a significant factor to estimate its auxetic performance. As can be seen in Fig. 6(b), the expansion ratio of diameter for tubular structure with VH cut was larger than that of a tubular structure with a PSF=100% before the normalized strain reached 0.355. After this normalized strain point, the expansion ratio of diameter for the tubular structure with a PSF=100% exceeded the value of tubular structure with VH cut until the end of the given normalized strain. The maximal expansion ratio of diameter for the tubular structure with a PSF=100% was around 1.35 which was higher than the value of VH cut tubular structure around 1.30. It should be noted that the right part of the curve for VH cut tubular structure was unsmooth, but the overall curve for a tubular structure with a PSH=100% was very smooth.

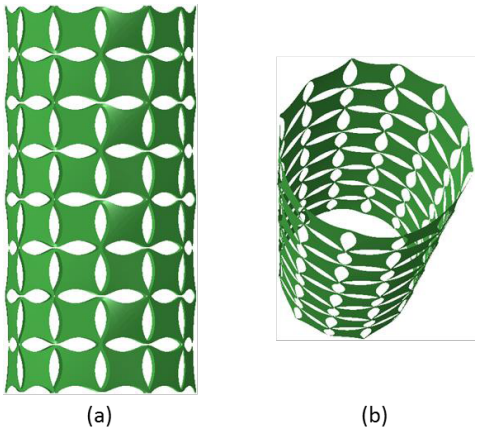

Figure 4. Geometries of the tubular structure generated by PSF adjustment method, with a PSF=100%: (a) the front view; (b) the perspective view.

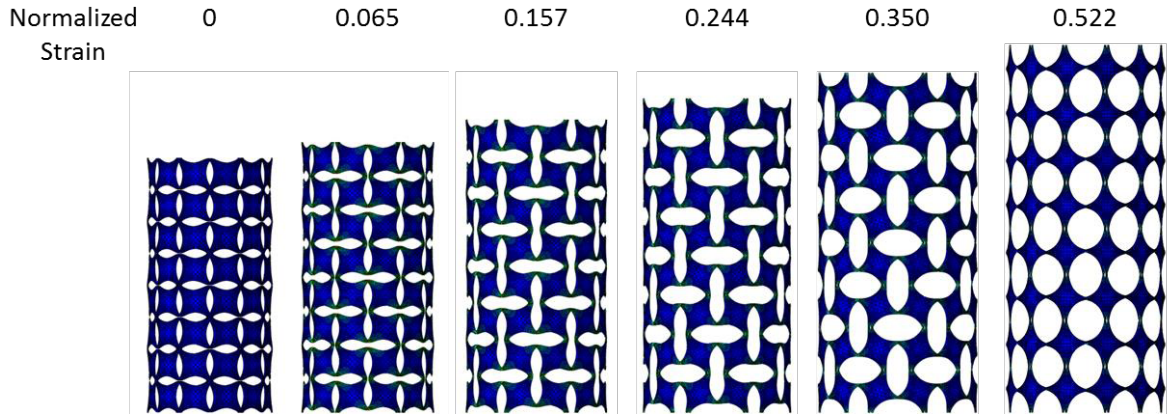

Figure 5. Deformation process for the tubular structure generated by PSF adjustment method under quasi-static tension, with a PSF=100%.

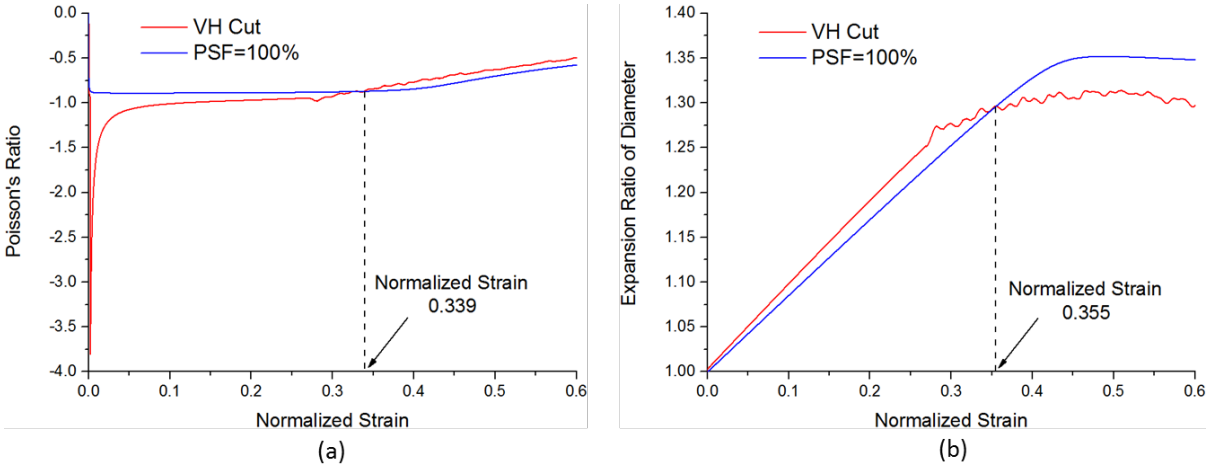

Figure 6. Curves of auxetic performance as a function of normalized strain for two kinds of tubular structures: (a) curves of Poisson's ratio as a function of normalized strain; (b) curves of expansion ratio as a function of normalized strain.

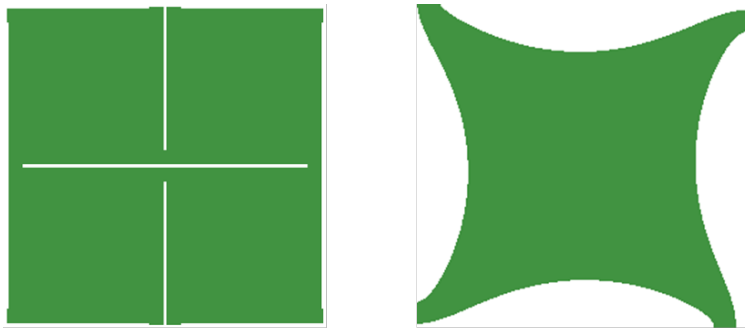

Figure 7. Configurations of rotating unit cells generated using two methods: (a) PSF adjustment method; (b) VH cut method.

We attributed the considerable turbulence of the curve for the VH cut tubular structure in Fig. 6(a) and the unsmooth curve for the VH cut tubular structure in Fig. 6(b) to the unsmooth transition of the geometry of the unit cell, as can be seen in Fig. 7(a). Compared with the geometry of unit cell for VH cut tubular structure, the unit cell for the tubular structure with a PSF=100% has a smooth transition at the joint rotating parts, as can be seen in Fig. 7(b). Therefore, the overall tensile deformation of the tubular structure with PSF=100% is more moderate and result in the smooth curves as shown in Fig. 6.

4. CONCLUDING REMARKS

Inspired by the latest work of Grima et al. [22], where they reported that a conventional non-auxetic sheet could be transformed into an auxetic metamaterial through a random cut method. As an extension work, we investigated the auxetic performance of the tubular structures generated by cutting technique through FEA method. Also, we compared the auxetic performance of the vertical and horizontal (VH) cut tubular structure with our designed auxetic tubular structure [23] using the pattern scale factor (PSF) adjustment method [24], with a PSF=100%. From the obtained FEA results, the following conclusions could be drawn:

a) The tubular structure generated using the random cut method has been investigated for the first time. It is found that the random cut method is unsuitable for generating auxetic tubular structures.
b) The tubular structure with PSF=100% has a larger maximal expansion ratio of diameter than the tubular structure generated using the VH cut method.
c) The unit cell of the tubular structure generated using PSF adjustment method has smoother transition curves than that of the tubular structure generated using the VH cut and the random cut methods.
d) The auxetic performance of tubular structures generated using the PSF adjustment method is more stable than that of tubular structures generated using the VH cut method.

ACKNOWLEDGEMENTS

This work was supported by the Australian Research Council (LP150100906, DP160101400), the China Scholarship Council (201306370057), the Major Program of the National Natural Science Foundation of China (U1334208).

REFERENCES

[1] Evans K E, Auxetic polymers: a new range of materials. *Endeavour*, **15** (1991) 170-174.

[2] Lakes R, Foam structures with a negative Poisson's ratio. *Science*, **235** (1987) 1038-1040.

[3] Choi J B and Lakes R S, Non-linear properties of polymer cellular materials with a negative Poisson's ratio. *Journal of Materials Science*, **27** (1992) 4678-4684.

[4] Argatov I I, Guinovart-Díaz R and Sabina F J, On local indentation and impact compliance of isotropic auxetic materials from the continuum mechanics viewpoint. *International Journal of Engineering Science*, **54** (2012) 42-57.

[5] Coenen V L and Alderson K L, Mechanisms of failure in the static indentation resistance of auxetic carbon fibre laminates. *Physica Status Solidi B*, **248** (2011) 66-72.

[6] Alderson K L, Simkins V R, Coenen V L, Davies P J, Alderson A and Evans K E, How to make auxetic fibre reinforced composites. *Physica Status Solidi B*, **242** (2005) 509-518.

[7] Bezazi A and Scarpa F, Mechanical behaviour of conventional and negative Poisson's ratio thermoplastic polyurethane foams under compressive cyclic loading. *International Journal of Fatigue*, **29** (2007) 922-930.

[8] Bezazi A and Scarpa F, Tensile fatigue of conventional and negative Poisson's ratio open cell PU foams. *International Journal of Fatigue*, **31** (2009) 488-494.

[9] Evans K E and Alderson A, Auxetic materials: Functional materials and structures from lateral thinking! *Advanced Materials*, **12** (2000) 617-628.

[10] Imbalzano G, Tran P, Ngo T D and Lee P V, A numerical study of auxetic composite panels under blast loadings. *Composite Structures*, **135** (2016) 339-352.

[11] Alderson A and Alderson K L, Auxetic materials. *Proceedings of the Institution of Mechanical Engineers, Part G: Journal of Aerospace Engineering*, **221** (2007) 565-575.

[12] Choi J B and Lakes R S, Fracture toughness of re-entrant foam materials with a negative Poisson's ratio: experiment and analysis. *International Journal of Fracture*, **80** (1996) 73-83.

[13] Bertoldi K, Reis P M, Willshaw S and Mullin T, Negative Poisson's ratio behavior induced by an elastic instability. *Advanced Materials*, **22** (2010) 361-366.

[14] Chen C P and Lakes R S, Micromechanical analysis of dynamic behavior of conventional and negative Poisson's ratio foams. *Journal of Engineering Materials and Technology*, **118** (1996) 285-288.

[15] Alderson A, Rasburn J, Ameer-Beg S, Mullarkey P G, Perrie W and Evans K E, An auxetic filter: A tuneable filter displaying enhanced size selectivity or defouling properties. *Industrial & Engineering Chemistry Research*, **39** (2000) 654-665.

[16] Burriesci G and Bergamasco G 2011, Annuloplasty prosthesis with an auxetic structure. *US Patent* 8034103B2.

[17] Kuribayashi K, Tsuchiya K, You Z, Tomus D, Umemoto M, Ito T and Sasaki M, Self-deployable origami stent grafts as a biomedical application of Ni-rich TiNi shape memory alloy foil. *Materials Science and Engineering: A*, **419**(2006) 131-137.

[18] Kuribayashi K and You Z 2006, Deployable stent. *US Patent* 7060092B2.

[19] Ley T J, Kveen G L, Her T G J, Brown B J and Friesen D L 2002 Stent configurations. *US Patent* 6416538B1.

[20] Ali M N and Rehman I U, An auxetic structure configured as oesophageal stent with potential to be used for palliative treatment of oesophageal cancer; Development and in vitro mechanical analysis. *Journal of Materials Science: Materials in Medicine*, **22** (2011) 2573-2581.

[21] Ali M N, Busfield J J C, and Rehman I U, Auxetic oesophageal stents: Structure and mechanical properties. *Journal of Materials Science: Materials in Medicine*, **25**(2014) 527-553.

[22] Grima J N, Mizzi L, Azzopardi K M and Gatt R, Auxetic perforated mechanical metamaterials with randomly oriented cuts. *Advanced Materials*, **28** (2016) 385-389.

[23] Ren X, Shen J, Ghaedizadeh A, Tian H and Xie Y M, A simple auxetic tubular structure with tuneable mechanical properties. *Smart Materials and Structures*, **25** (2016) 065012.

[24] Ren X, Shen J, Ghaedizadeh A, Tian H and Xie Y M, Experiments and parametric studies on 3D metallic auxetic metamaterials with tuneable mechanical properties. *Smart Materials and Structures,* **24** (2015) 095016.

[25] Ren X, Shen J, Ghaedizadeh A, Tian H and Xie Y M, Numerical simulations of 3D metallic auxetic metamaterials in both compression and tension. *Applied Mechanics and Materials*, **846** (2016) 565-570.

[26] Ghaedizadeh A, Shen J, Ren X and Xie Y M, Tuning the performance of metallic auxetic metamaterials by using buckling and plasticity. *Materials*, **9** (2016) 54

[27] Shen J, Zhou S, Huang X and Xie Y M, Simple cubic three-dimensional auxetic metamaterials. *Physica Status Solidi B*, **251** (2014) 1515-1522.

VIII ECCOMAS Thematic Conference on Smart Structures and Materials
SMART 2017
A. Güemes, A. Benjeddou , J. Rodellar and Jinsong Leng (Eds)

SMART CELLULOSE-HYDROGEL COMPOSITES FOR 4D PRINTING

MANU C. MULAKKAL [*], RICHARD S. TRASK [+] AND ANNELA M. SEDDON [†‡]

[*] Advanced Composites Centre for Innovation and Science (ACCIS), University of Bristol, Queen's Building, University Walk, Bristol BS8 1TR, UK
e-mail: manu.mulakkal@bristol.ac.uk

[+] Department of Mechanical Engineering, University of Bath, Bath, BA2 7AY, UK

[†] School of Physics, HH Wills Physics Laboratory, Tyndall Avenue, University of Bristol, Bristol, BS8 1TL, UK

[‡] Bristol Centre for Functional Nanomaterials, HH Wills Physics Laboratory, Tyndall Avenue, University of Bristol, Bristol, BS8 1TL, UK

Key words: 4D Materials, Composite Morphing, Stimuli-responsive, Cellulose-Hydrogel

Abstract. In nature, versatility and functionality is a consequence of controlled placement of 'building blocks' at nano and micro-scale and the resulting multifunctional hierarchical structures. This approach to manufacturing and philosophy is gaining interest among researches as it offers many advantages over traditional top down manufacturing. Latest developments in 3D printing (3DP) technology allows one to have control over the placement of building materials in 3D space. This paper focus on the development of a cellulose hydrogel composite that can be adapted for 3D printing. This system preserves the functionality of cellulose while enabling printing through a syringe extrusion system. Unlike conventional 3DP materials, this bespoke bio-inspired composite is sentient and can morph along the design rules we observe in nature such as pinecones in response to the stimuli of water. This paper presents the development and characterisation of the cellulose hydrogel composite.

1. INTRODUCTION

Sentient structures which incorporate sensory functions and proportionate mechanical responses within itself are touted to be the systems for the future. There have been a multitude of approaches in order to realise the goal of developing such smart structures. Whether it be the miniaturisation of existing sensory, electrical and mechanical systems by virtue of the advancements in robotics and nanotechnology or through development of novel material chemistries, the research community has been actively looking for solutions to tackle this particular challenge. Fortunately nature has already solved this challenge as evidenced by a myriad of examples [1]. The hygroscopic response of pinecones, Sun tracking of Cornish Mallow (*Lavatera cretica*) and the tactile response of 'touch-me-not' plant (*Mimosa pudica*) are some examples of sentient structures that respond to an array of stimuli. Nature has devised these sentient systems by controlled arrangement of materials and simple responsive processes such as swelling. Consequently there are significant research efforts and large body of scientific

literature [2–9] pertaining towards realising sentient systems akin to systems found in nature as opposed to just ‘smart’ materials or structures.



Figure 1: Examples of actuation in plant kingdom (a) Pinecone (b) Touch-me-not plant (*Mimosa pudica*)

Following nature’s design principles, two main parameters can be identified in order to realise smart systems, (a) a compliant stimuli responsive material and (b) a process emulating growth which enable controlled placement of the compliant stimuli responsive material so as to achieve the desired response from the system. This paper presents our efforts in developing a compliant stimuli responsive material that can enable 3D printing of responsive forms. The responsiveness of the material to the stimuli of water would enable the time dependant transformation of the printed 3D shape. The fabrication of such sentient forms that can transform in the time domain is termed as 4D printing.

2. CELLULOSE AS SMART MATERIAL

The potential of paper as a precursor for cost effective, renewable, bio-degradable and programmable smart material have been previously demonstrated by the authors [10]. Cellulose is the most abundant bio-macromolecule in nature with desirable properties such as renewability, environmental friendliness and biodegradability [11–13]. Therefore using cellulose and its derivatives in the manufacturing of engineering polymers have been rigorously investigated and implemented due to aforementioned benefits over traditional materials. Cellulose molecules consist of β -1,4-linked anhydro-D-glucose units in which every unit is corkscrewed 180° with respect to its adjacent unit [14,15]. The presence of hydroxyl groups (OH) in the molecule results in hydrogen bonding between molecules leading to the formation of fibrils which further associate to form fibres in a true hierarchical fashion. The nature of

hydrogen bonding results in crystalline and amorphous phases within cellulose structure [15]. Water can plasticise the amorphous regions by weakening or relaxing hydrogen bonding by forming competitive hydrogen bonds. These intercalating water molecules result in swelling throughout the material, which can be used to drive actuations of specific architectures created with them.

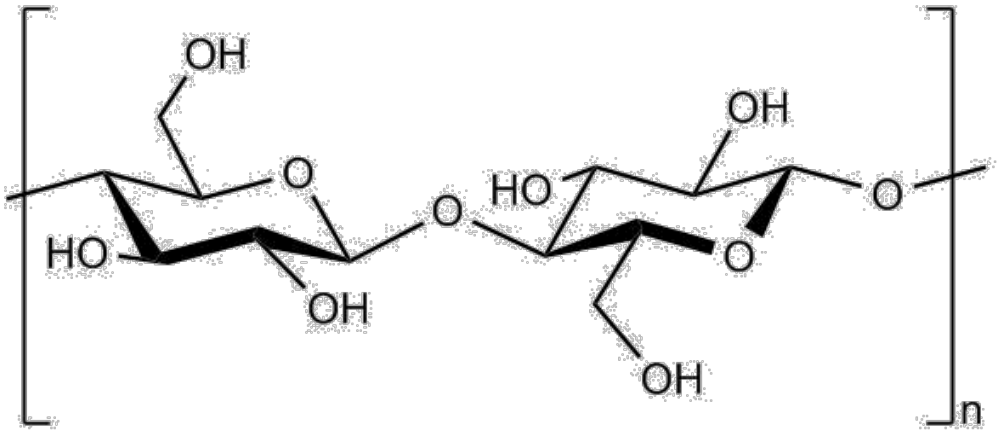

Figure 2: Structure of cellulose (Produced in Chem Draw)

Enabling functional Cellulose 3D printing

Cellulose cannot be used with current additive layer manufacturing systems in its native form because it cannot be melted and extruded like typical plastics. There are examples of commercially available 3D printing filaments with cellulosic materials such as saw dust and recycled wood forming fillers (≈40%) within a polymer matrix such as PLA (Poly lactic acid) [16–18]. This method however limits the exposure of cellulosic components to the environment/ stimuli and such approaches are not suitable for sentient-morphing applications. Markstedt *et.al* 3D printed cellulose by dissolution in ionic liquids followed by coagulation in non-solvents such as water resulting in 2D and multilayer 3D gel structures on a coagulating bed [19]. Håkansson *et.al* from Chalmers University of technology created composite printing inks by mixing cellulose nanofibrils in a hydrogel consisting of 95-99 % water. The 3D shape in dry state was achieved by means of freeze drying the water from the final print [20]. Similar approaches in cellulose printing were also reported from Aalto University (Finland) and VTT research (Finland) as part of their joint DWOC (Design Driven Value Chains in the World of Cellulose) program [21]. Even though these approaches enabled 3D printing of cellulose, the final shapes which could be achieved were fixed and their applications limited. Recent work from Gladman *et.al* from Lewis lab at Harvard University demonstrated the fabrication of plant-inspired architectures using cellulose microfibrils within a thermo-responsive acrylamide ink. The final 3D shape was not fixed in this case, but capable of transforming in the time domain as envisaged in 4D printing. These architectures actuated as a result of preferential swelling in an acrylamide gel when restricted by the alignment of cellulose microfibrils [22]. As such, research shows that adapting cellulosic materials to the 3D printing domain can be achieved but there is scope for discovery especially with regard to enabling 3D printing of cellulosic smart materials.

The design of cellulosic fibrils to preferentially control the swelling of an embedding matrix is inspired by nature's design of pinecones [23,24]. The significance of porosity and the resulting network structure of pulp fibres in controlling the opening and closing of folds in paper architectures has been previously established [10]. Such a network structure would not only enhance the mechanical properties of hydrogel substrate but also provide additional parameters such as porosity and anisotropic stiffness which can be programmed to tailor the response to stimuli. Combining a cellulose derived hydrogel with pulp fibres will permit the development a cost effective, cellulosic smart material. This approach will also aid in bypassing the undesirable shear thickening behaviour observed in pulp suspensions. Some examples of cellulose derived polymers forming hydrogels are hydroxypropyl cellulose (HPC), hydroxypropyl methylcellulose or hypomellose (HPMC), carboxymethyl cellulose (CMC), hydroxyethyl cellulose (HEC), methyl cellulose (MC) and ethyl cellulose (EC) [13,25].

Sodium Carboxymethyl cellulose (CMC-Na/ CMC) is a hydrophilic cellulose derivative with carboxymethyl groups bound to the hydroxyl groups of glucose unit and was chosen for this study. The functional properties of this biocompatible carbohydrate depends on its degree of substitution. The polar nature of carboxylic group makes CMC soluble in water resulting in the formation of gel. This polymer is widely used in food, skin care and drug industry as a thickening agent/ rheological modifier and is bio-compatible. In this work we have developed a stimuli (water) responsive cellulosic pulp-hydrogel composite which enables programmable transformation. This smart composite is formulated to be adapted for 3D printing, facilitating functional microstructures and increasingly complex shapes and forms. Furthermore the smart composite is also cost effective and bio-degradable.

3. DEVELOPMENT OF HYDROGEL COMPOSITE

3.1. Materials and Formulation

Reagent grade water from Fisher Scientific was used as received. CMC-Na with degree of substitution (DS) of 0.9 in molecular weight (Mw) of 700k and 250k were obtained from Arcos Organics. HEC was obtained from Merck Millipore. Montmorillonite (naturally occurring powder) and Citric acid (99%) were purchased from Alfa Aesar and Sigma Aldrich respectively. Poly acrylic acid (PAA) was purchased from Sigma Aldrich. All materials were used as supplied.

Nomenclature shown in **Figure 3** was used to indicate the respective ingredients (in grams) in each formulations.

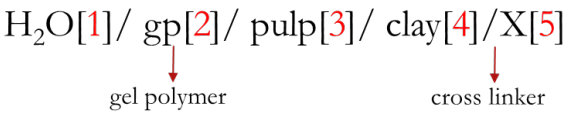

Figure 3: Formulation key

For example a sample [1]/[2]/[3]/[4]/[5] = 30 / 1.5 / 0 / 0 / 0.15 indicates that the formulation contains 30 g of water, 1.5 g of gel polymer, 0 g of dried pulp, 0 g of clay and 0.15 g of crosslinking agent. For samples crosslinked with citric acid, [2] the total amount of polymers, CMC and HEC were in 3:1 ratio.

3.2. Processing

Pressed pulp linters for papermaking was obtain from **www.georgeweil.com** and was saturated in water for ≈24 hrs. This was followed by breaking up of linters into smaller pieces using a spatula and drying at room temperature. The uniform dispersion of pulp in water is crucial for smooth extrusion through syringe heads without clogging - dispersion of pulp for paper making processes also requires large amount of water followed by mechanical agitation to separate the fibres from each other. The caveat here is that such amount of water would prevent the formation of hydrogels when CMC-Na is added. The gel nature is crucial to enable extrusion as suspensions tend to exhibit shear-thickening which hinders the flow under stress [26]. As such a balance is required so as to maximise the fibre V_f (volume fraction) without compromising the gel nature of the composite. Based on preliminary dispersion trials it was deemed that within a laboratory environment only minimal amount of pulp fibres could be evenly dispersed in a beaker before starting to compromise the gel nature of the composite. A 50% fibre V_f of final composite (i.e. half fibre - half CMC polymer) was desired based on the assumption that this would give a balance between benefits of fibrous network without compromising the gel.

A number of mixing strategies were trialled ranging from sonication and shear mixing but yielded less than ideal results. However adding a hydrocolloid such as CMC before and during the mixing of pulp in water showed promising results (**Figure 4** (c)). This strategy was further refined to yield improved extrusion results. The recipe for the hydrogel composite is as follows; 0.025 g each of pulp and CMC polymer per 1 ml of water. The best dispersion results (**Figure 4** (d)) for this formulation was obtained with a planetary mixer[1] (Thinky Mixer, USA). This was due to the efficient shear transfer of centrifugal forces facilitated by the addition of gel forming polymer in separating and dispersing the pulp fibres. The mixing procedures with Thinky mixer is as follows: The pulp, water and CMC were added in small quantities and mixed for 30 seconds at 1600 rpm before adding further up to the required amount as per the recipe. Once all the ingredients are in, the mixture is further mixed for 3-4 minutes (depending on the total volume) till a uniform paste was formed. The cellulose-hydrogel composite would then be manually extruded through a syringe (as in a 3D printer print head) and dried to form films. **Figure 4** shows the improvements in pulp dispersion in hydrogel composite and clog free extrusion as a result of optimised mixing strategies.

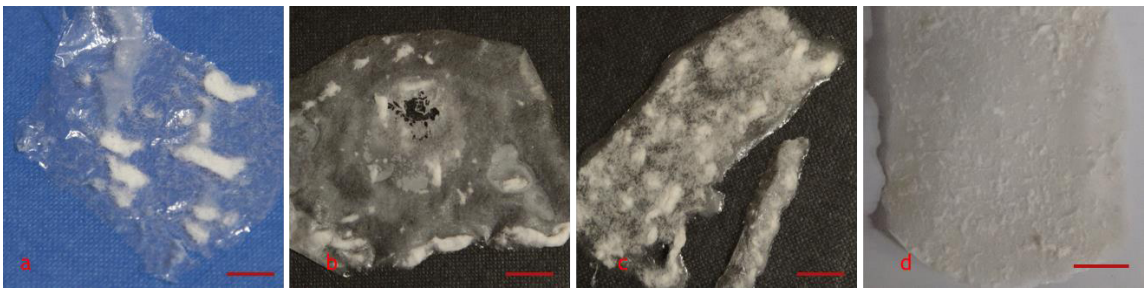

Figure 4: Improvements in pulp dispersion in CMC polymer as a result of optimised mixing strategies (Scale bar: 10 mm)

[1] Planetary mixer – A centrifugal mixer that mixes materials employing "rotation" and "revolution".

3.3. Stability of hydrogel composites

Stability of the gel formed is also important with regard to the ability to extrude through the syringe. A significant reduction in prepared composites gelling properties and viscosity was observed after a week. Clay (montmorillonite) was added (0.5% of water) as a filler in order to stabilise the hydrogel. An inversion test on one week old samples proved the effectiveness of clay in stabilising hydrogel. An off-white colour was imparted to hydrogel composite when clay was added. The molecular weight (M_w) of CMC used was also increased from 250,000 to 700,000 to improve viscosity and stability.

The stability in aqueous medium is paramount for hydrogel based actuators. Standard films (dry) of CMC polymer disintegrated (soluble) in water when left overnight. Whereas films of cellulose-hydrogel composite retained 'shape' in aqueous medium overnight but disintegrated when handled validating that just the pulp network is insufficient in holding shape. In order to provide aqueous stability it was decided to crosslink the hydrogels. Crosslinking reactions involving self-crosslinking [27], with PAA (poly acrylic acid) [28,29] and citric acid [30–32] as crosslinking agents were carried out and evaluated. The reaction involving citric acid (CA) was chosen as the way forward as it was more environmentally friendly and benign. The crosslinking reactions were successfully carried out at 120 °C for 10 minutes as opposed to 180 °C for 30 min for self-crosslinking and 140 °C for 30 minutes when PAA was used. Reaction parameters were obtained from [30] and adapted for the synthesis of hydrogel composites. A mixture of CMC-Na and HEC (Hydroxyethyl cellulose), with weight ratio equal to 3:1 was used to form Hydrogel. The presence of HEC is necessary to promote intermolecular rather than intramolecular crosslinking [30]. The formulations containing 10% (of total polymer content) CA was chosen in this study.

4. HYDROGEL COMPOSITE CHARACTERISATION

The formulations with citric acid as crosslinking agents were considered for full characterisation.

4.1 Rheology

The protocol used to characterise the rheological behaviour and consequently mechanical properties of the hydrogel and composites are outlined as follows. (i) Amplitude sweep (ii) Frequency sweep and (iii) Steady-state shear tests were carried out. This protocol was adapted from [33,34] and the gelation times were not determined using rheological parameters as the gel formation with CMC was observed as a function of loading capacity and constantly resulted in the formation of gels during the synthesis step for the formulations (**Table 1**) investigated. A rheometer (Kinexus Pro) from Malvern Instruments with a parallel plate geometry (PU20) of diameter 20 mm was used and all the samples were tested at 25 °C. Each sample was used only once and the tests were performed in triplicate and error bars represents the corresponding standard deviation. A standard loading sequence was used to guarantee reliable and precise loading protocol.

Table 1: Sample nomenclature and respective formulations

Gel+CA (low)	Gel+CA	Gel+Clay+CA	Composite+CA	Composite+Clay+CA
30/0.75/0/0/0.15	30/1.5/0/0/0.15	30/1.5/0/0.15/0.15	30/0.75/0.75/0/0.15	30/0.75/0.75/0.15/0.15

Gel+CA (low) has the same gel content (gel V_f) as the composite samples and the polymer content in other two gel samples equals the solid content (polymers and pulp) of the composite samples. This spectrum of samples would demonstrate the effect of pulp, clay and polymers forming the gel in governing the rheological characteristics of these samples. The effect of amplitude, frequency and shear rate on Elastic (storage) modulus G′ and Viscous (loss) modulus G″ will give a good indication of the nature and flow characteristics of the samples. The elastic modulus represents the solid-like characteristics whereas the viscous modulus represent the liquid-like characteristics of the samples tested.

The relative importance of G′ and G″ is represented by phase angle (δ) as follows:

$$\tan(\delta)=\frac{G''}{G'} \quad (1)$$

When $\delta > 45°$ (i.e. G″/G′ >1), it can be said that liquid like behaviour dominates within the sample.

Strain-Sweeps

A strain sweep from 0.01%-100% at a frequency of 1Hz was performed on gelled samples. **Figure 5** shows the elastic modulus (G′) as a function of shear strain for the samples tested. The loss modulus (G″) values were not presented for clarity but is embodied in the phase angle (δ) data presented. The solid line (—) and dotted line (…) represents data on primary axis and secondary axis respectively. The phase angle (δ) data also demonstrates that G′>G″ for most of the applied strain regime indicating that the samples are highly structured (gel). Elastic modulus values measured within the LVER (linear visco-elastic regime) shows highest value for Gel+Clay+CA (1.15 KPa) samples as expected. The presence of clay results in a higher elastic modulus and viscosity when compared to Gel+CA (0.9 KPa) samples. Contrary to what was observed in gel samples, the addition of clay in composites does not increase the elastic modulus (≈0.7 KPa) but resulted in gradual decay of modulus and viscosity at lower strains followed by a rapid decay of modulus which signified the critical strain %. It is assumed that the structural interactions of intercalated of clay and dispersed pulp fibres resulted in this flow behaviour. As the sampled gels were not chemically crosslinked, the gel nature was by virtue of physical crosslinks such as hydrogen bonds. Montmorillonite is of layered structure and could reduce the effective hydrogen bonding between cellulosic pulp, polymers and water by intercalating between them. This is reflected in the δ data as a rapid rate of increase in phase angle indicate more fluid like behaviour under increasing applied strain. Although further investigations as to why this behaviour arises are necessary, these characteristics are ideal for the proposed composite extrusion system as it not only provides long term stability to the material system but also flows easier when compared to other formulations in this study. It is also noted that the modulus and thus the δ data for Gel+CA (low) are particularly noisy at strain (0.01%-0.1%) as expected due to weaker signal at this strain range from the sample.

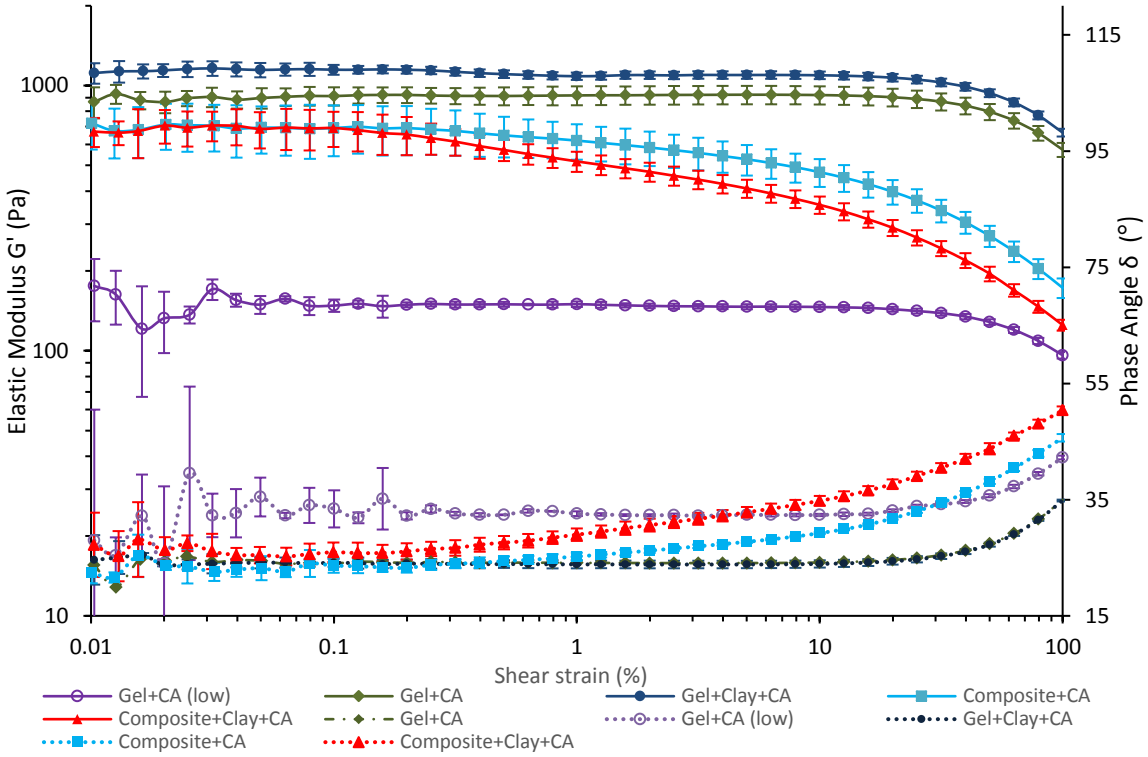

Figure 5: Amplitude sweep data showing Elastic modulus (G') and phase angle (δ) as the function of shear strain

Frequency sweeps

Frequency sweeps from 0.1 Hz-10Hz were conducted on formed gel samples at 0.5 % strain and the results are presented in **Figure 6**. Loss Modulus (G") values were omitted for clarity. It can be seen that the elastic modulus values at 1Hz matches the G' values in LVER regime in amplitude sweep results presented in **Figure 5**. **Figure 6** represents the G' variation and phase angle (δ) across the frequency range where solid line (—) and dotted line (…) represents data on primary axis and secondary axis respectively . The slope in G' suggests that the modulus is dependent on the frequencies probed and implies some structural relaxation where stored elastic energy is dissipated with time (i.e. higher frequencies). This implies a more fluid like nature of the samples when subjected to the frequency sweep.

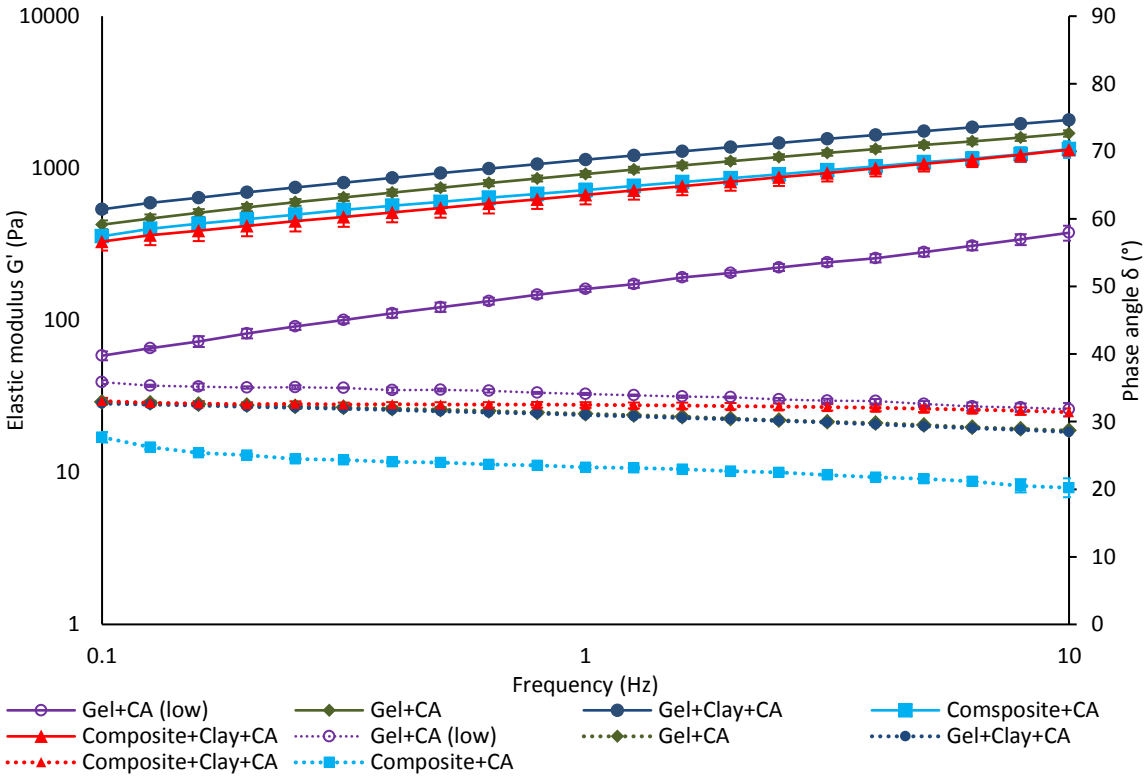

Figure 6: Frequency sweep data showing Elastic modulus (G') and phase angle (δ) as a function of frequency

Shear rate

The results of the steady state shear measurement are presented in **Figure 7** with solid line (—) and dotted line (…) representing data on primary axis and secondary axis respectively. It can be seen that the samples are highly shear thinning from the shear viscosity–shear rate plot. The relationship between shear stress developed and the applied shear rate is also presented. It can be seen that viscosity and stresses of Composite+Clay+CA samples are closer to the Gel+CA (low) samples especially at higher shear rates even though the solid content in them is twice as much. The comparison of viscosity and shear stress developed in Composite+Clay+CA, Gel+CA and Gel+Clay+CA confirms the observation made in amplitude sweep analysis regarding the combined effect of pulp and clay in facilitating better extrusion. These results shows the effectiveness of pulp-gel composite system in having ideal extrusion characteristics as a homogenous phase of either of the two would not have yielded necessary high viscosity (solid-like) at rest and decreasing at higher shear rates (i.e. when deformed).

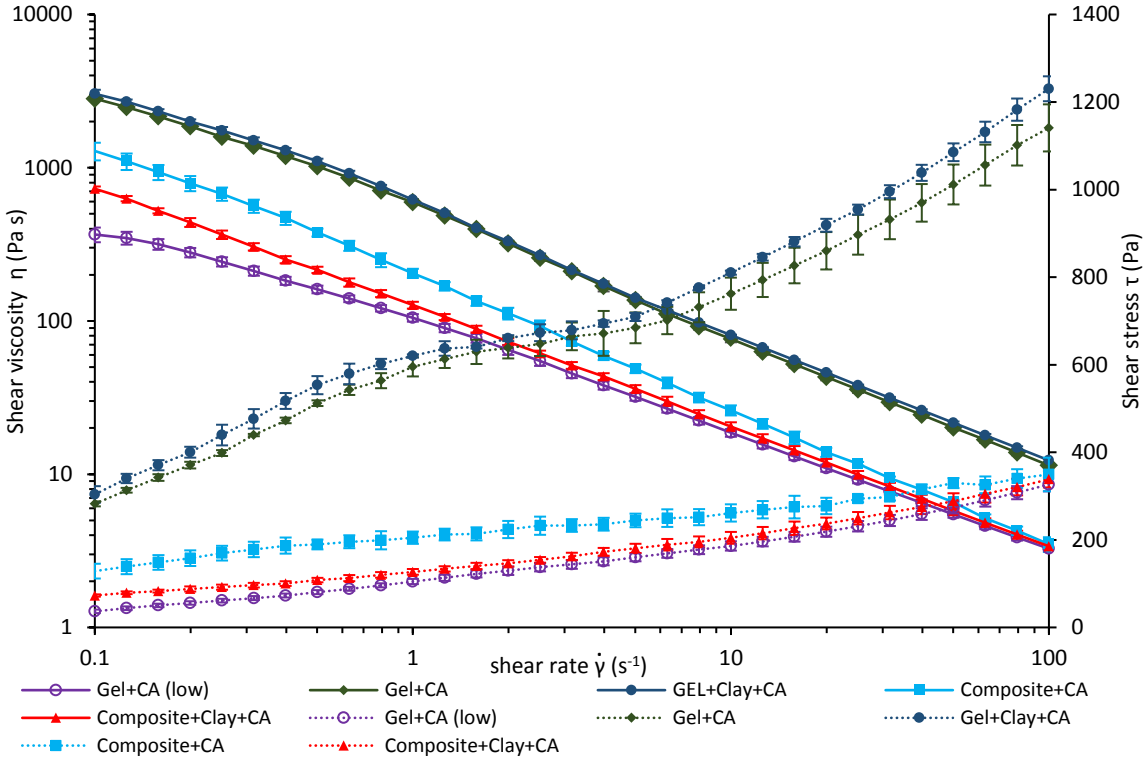

Figure 7: Steady state shear viscosity (η) and shear stress (τ) as a function of shear rates

4.2 Swelling Ratio

The equilibrium swelling ratio (SR) of the hydrogels and composites containing CA were investigated in de-ionised water. The samples (minimum of 3) were weighed and immersed in de-ionised water for 24 hrs to reach equilibrium swelling at room temperature (21 °C). The samples were recovered from water and weighed after removing excess water from the surface.

The SR was calculated as follows:

$$SR=\left(\frac{W_s-W_d}{W_d}\right) \quad (2)$$

where W_s is the weight of the swollen hydrogel/ composite, and W_d is the weight of the dried sample. **Table 2** summarises the results of swelling ratio investigation. The standard deviation is presented as error. The swelling ratios of comparable self-crosslinked samples (without CA) are also presented to better understand the effect of crosslinking agent. The effectiveness of CA in crosslinking at relatively lower temperature is clear when compared to self-crosslinked samples. The effect of pulp fibres on the swelling ratio is also evident. This confirms the presence of pulp network that restricts the swelling of hydrogel matrix resulting in a lower swelling ratio. The addition of montmorillonite clay was found to have no impact on swelling ratio. In swelling induced shape transformations, the SR results presented can be viewed as a concern. The versatility of this approach is that the amount of crosslinking agent or the ratio of cellulosic polymers (CMC-Na:HEC) can be varied so as to achieve desirable swelling specific for a structure.

Table 2: Equillibrium swelling ratio of formulations with CA after crosslinking

Crosslinked with CA	10 min @ 120 °C	Self-crosslinked	30 min @ 180 °C
30/1.5/0/0/0.15	2.62±0.20	30/1.5/0/0/0	38.30±1.4
30/1.5/0/0.15/0.15	2.79±0.14		
30/0.75/0/0/0.15	1.39±0.32		
30/0.75/0.75/0/0.15	0.85±0.02	30/0.75/0.75/0/0	4.10±0.15
30/0.75/0.75/0.15/0.15	0.82±0.03	30/0.75/0.75/0.15/0	6.20±0.25

5. DISCUSSION AND CONCLUSIONS

The main hurdle in the development of the 3D printable cellulosic fibres was the dissociation of pulp fibres. The strong hydrogen bonding between them could only be relaxed with large quantity of water as in a traditional paper making process which resulted in a shear thickening suspension that frequently clogged when attempted to extrude with precision. The addition of cellulosic hydrogels not only imparts necessary shear thinning properties but also aids in the dissociation and distribution of pulp fibres through optimised mixing strategies. This directly results in higher loading capacity of pulp fibres without clogging. Granting the crosslinking of these composites does not affect the extrusion characteristics, it is imperative that the shapes produced are stable in an aqueous environment and do not disintegrate over the duration of experiments. The choice of citric acid as cross-linker enables lower crosslinking temperatures (after printing of the shape) and a more eco-friendly direction for further material development.

The rheological characterisation of the formulations containing citric acid confirmed that the samples are shear thinning which is essential for smooth and controlled extrusion in any syringe based 3D printing extrusion set up. The low critical strains for composite samples indicate that they flow readily when deformed which is ideal. Even though montmorillonite clay was added to stabilise the formulations for long term storage, the complimentary effect it had on composite formulation is advantageous. The addition of filler materials usually results in increased solid like characteristics and viscosity hindering the flow but as demonstrated in the amplitude sweep and shear rate results, the combination of pulp and clay resulted in a more liquid like behaviour when deformed. It is believed that the intercalating clay platelets inhibits or even cleaves hydrogen bonding between pulp, CMC and water when deformed. Further understanding of the pulp-clay interaction and micro-structure in Composite+Clay+CA samples are required.

The swelling ratio of samples were determined after crosslinking as it would not only determine the swelling potential of the samples but also a measure of aqueous stability. As expected the citric acid formulations have considerably lower swelling ratio when compared to self-crosslinked samples. However it is paramount to generate controllable swelling without degrading the material. The role of pulp network in restricting the swelling of gel matrix was also noted.

It is envisaged that in conjunction with the versatility of additive layer manufacturing/ 3DP methods varying microstructure within an overall shape can be achieved. Whereas the sentient nature of material along with its tuneable parameters would result in hierarchical structures within a global form that can actuate in complex forms. The natural progression of the work presented here would be attempting to control the microstructure and final form through 3D printing where specific 3D printed actuation pathways within a global architecture or form

could lead to more complex actuating forms capable of sequential multi-stage deployment. Some preliminary results demonstrating the actuation of a manually fabricated flower architecture is presented in **Figure 8**. This architecture has a programmed actuation pathway (**Figure 8** (a) highlighted in yellow) around the base of petals where an additional layer of hydrogel-composite and gel are deposited. The drying of samples at room temperature (RT-21 °C) initiate the transformation (**Figure 8** (b)) which was maximised by drying at elevated temperature (140 °C for 5 minutes) fixing the new configuration (**Figure 8** (c)). This transformed shape is deployed back to the flat configuration by placing on a water bath at RT (**Figure 8** (d)). Asymmetric folding and waviness in dried petals are attributed to uneven amount of composite and hydrogel deposited during hand-held syringe extrusion.

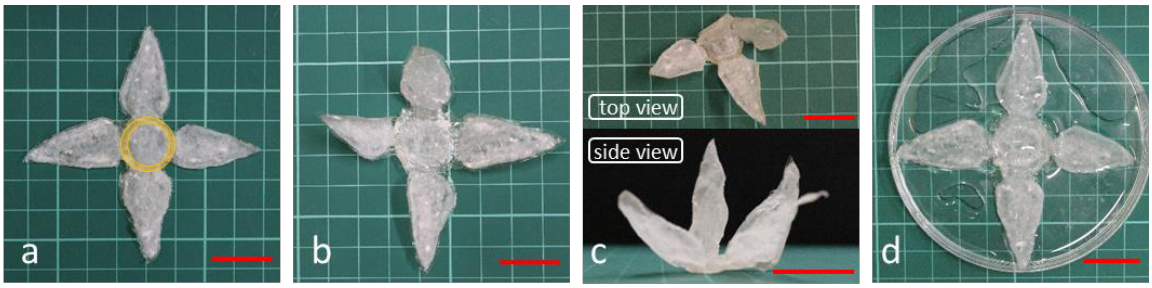

Figure 8: Actuation of flower architecture. (a) During drying at RT (21 °C) (b) dried at RT –initiation (c) after drying at elevated temperature– fixing shape (d) deployed back to flat configuration in water at RT. (Scale bar: 10 mm)

The development of pulp-hydrogel composite will further the prospective of cellulose as a smart material. As the previous work [10] from authors demonstrated the potential cellulose within an already an already existing fibrous architecture (i.e. paper), this work aims to enable designers to create bespoke architectures with varying microstructure. The adoption of pulp and cellulosic hydrogel in a composite form enabled integration of the cellulosic material into the domain of 3DP materials without compromising its functionality whilst retaining the tuneable parameters such as varying micro-structure porosity, temperature and fibre volume fraction. Implementation of 3D printing will not only ensure greater precision in the placement of materials but also facilitate the realisation of more complex architectures and actuation pathways for 4D printing.

6. ACKNOWLEDGEMENTS

This work was supported by the Engineering and Physical Sciences Research Council through the EPSRC Centre for Doctoral Training in Advanced Composites for Innovation and Science [grant number EP/G036772/1]. The author would also like to acknowledge Mr Ed Aldred (School of Chemistry, University of Bristol) for his help in providing the training and facilitating the use of Rheometer. The Thinky Mixer was purchased thanks to a donation from Renee Bates Legacy Fund from the School of Physics, University of Bristol.

7. REFERENCES

[1] Burgert I and Fratzl P 2009 Actuation systems in plants as prototypes for bioinspired devices. *Philos. Trans. A. Math. Phys. Eng. Sci.* **367** 1541–57

[2] Studart A R and Erb R M 2014 Bioinspired materials that self-shape through programmed microstructures *Soft Matter* **10** 1284–94

[3] Martone P T, Boiler M, Burgert I, Dumais J, Edwards J, MacH K, Rowe N, Rueggeberg M, Seidel R and Speck T 2010 Mechanics without Muscle: Biomechanical inspiration from the plant world *Integr. Comp. Biol.* **50** 888–907

[4] Kim S, Laschi C and Trimmer B 2013 Soft robotics: A bioinspired evolution in robotics *Trends Biotechnol.* **31** 287–94

[5] Schmitt S, Haeufle D F B, Blickhan R and Günther M 2012 Nature as an engineer: one simple concept of a bio-inspired functional artificial muscle. *Bioinspir. Biomim.* **7** 36022

[6] Daynes S, Trask R S and Weaver P M 2014 Bio-inspired structural bistability employing elastomeric origami for morphing applications *Smart Mater. Struct.* **23** 125011

[7] Dicker M P M, Rossiter J M, Bond I P and Weaver P M 2014 Biomimetic photo-actuation: sensing, control and actuation in sun-tracking plants. *Bioinspir. Biomim.* **9** 36015

[8] Capadona J R, Shanmuganathan K, Tyler D J, Rowan S J and Weder C 2008 Stimuli-Responsive Polymer Nanocomposites Inspired by the Sea Cucumber Dermis *Science (80-.).* **319** 1370–4

[9] Chen X, Mahadevan L, Driks A and Sahin O 2014 Bacillus spores as building blocks for stimuli-responsive materials and nanogenerators *Nat. Nanotechnol.* **9** 137–41

[10] Mulakkal M C, Seddon A M, Whittell G, Manners I and Trask R S 2016 4D fibrous materials: characterising the deployment of paper architectures *Smart Mater. Struct.* **25** 95052

[11] Azizi Samir M A S, Alloin F and Dufresne A 2005 Review of Recent Research into Cellulosic Whiskers, Their Properties and Their Application in Nanocomposite Field *Biomacromolecules* **6** 612–26

[12] Malmström E and Carlmark A 2012 Controlled grafting of cellulose fibres – an outlook beyond paper and cardboard *Polym. Chem.* **3** 1702

[13] Kang H, Liu R and Huang Y 2016 Cellulose-Based Gels *Macromol. Chem. Phys.* 1–13

[14] Zhang K, Geissler A, Standhardt M, Mehlhase S, Gallei M, Chen L and Marie Thiele C 2015 Moisture-responsive films of cellulose stearoyl esters showing reversible shape transitions *Sci. Rep.* **5** 11011

[15] Habibi Y, Lucia L A and Rojas O J 2010 Cellulose nanocrystals: Chemistry, self-assembly, and applications *Chem. Rev.* **110** 3479–500

[16] Wood Filament - 3D Printing Blog [online] available (http://3dprinting-blog.com/tag/wood-filament/) (accessed : 01-Mar-2017)

[17] 3D Printing Wood - Try These Sweet Finishing Techniques! [online] available (https://pinshape.com/blog/3d-printing-wood-finishing-techniques/) (accessed : 01-Mar-2017)

[18] 3D Printing Filament Tech Specs [online] available (http://www.printme3d.com/filament-tech-specs) (accessed : 01-Mar-2017)

[19] Markstedt K, Sundberg J and Gatenholm P 2014 3D Bioprinting of Cellulose Structures

from an Ionic Liquid *3d Print. Addit. Manuf.* **1** 115–21
[20] Håkansson K M O, Henriksson I C, de la Peña Vázquez C, Kuzmenko V, Markstedt K, Enoksson P and Gatenholm P 2016 Solidification of 3D Printed Nanofibril Hydrogels into Functional 3D Cellulose Structures *Adv. Mater. Technol.* **1**1600096--n/a
[21] 3D-printing of cellulose-based materials [online] available (http://cellulosefromfinland.fi/3d-printing-of-cellulose-based-materials/) (accessed : 01-Mar-2017)
[22] Sydney Gladman A, Matsumoto E A, Nuzzo R G, Mahadevan L and Lewis J A 2016 Biomimetic 4D printing *Nat. Mater.* 1–7
[23] Ibrîm Q, Peakman T M, Biddle M, Dawson C, Vincent J F V and Rocca A-M 1997 How pine cones open *Nat.* **390** 668
[24] Reyssat E and Mahadevan L 2009 Hygromorphs: from pine cones to biomimetic bilayers. *J. R. Soc. Interface* **6** 951–7
[25] Chang C and Zhang L 2011 Cellulose-based hydrogels: Present status and application prospects *Carbohydr. Polym.* **84** 40–53
[26] Menard K P 1999 *Dynamic Mechanical Analysis: A Practical Introduction*
[27] Borůvková K, Wiener J and Kukreja S 2012 Thermal Self Cross-Linking of Carboxymethylcellulose *Academic Coordination Centre at the Euroregion Neisse (ACC) Journal* **XVIII** 6–13
[28] Spoljaric S, Salminen A, Luong N D and Seppälä J 2013 Crosslinked nanofibrillated cellulose: poly(acrylic acid) nanocomposite films; enhanced mechanical performance in aqueous environments *Cellulose* **20** 2991–3005
[29] Cook J P, Goodall G W, Khutoryanskaya O V. and Khutoryanskiy V V. 2012 Microwave-assisted hydrogel synthesis: A new method for crosslinking polymers in aqueous solutions *Macromol. Rapid Commun.* **33** 332–6
[30] Demitri C, Del Sole R, Scalera F, Sannino A, Vasapollo G, Maffezzoli A, Ambrosio L and Nicolais L 2008 Novel superabsorbent cellulose-based hydrogels crosslinked with citric acid *J. Appl. Polym. Sci.* **110** 2453–60
[31] Hashem M, Sharaf S, Abd El-Hady M M and Hebeish A 2013 Synthesis and characterization of novel carboxymethylcellulose hydrogels and carboxymethylcellulolse-hydrogel-ZnO-nanocomposites *Carbohydr. Polym.* **95** 421–7
[32] Zheng W J, Gao J, Wei Z, Zhou J and Chen Y M 2015 Facile fabrication of self-healing carboxymethyl cellulose hydrogels *Eur. Polym. J.* **72** 514–22
[33] Zuidema J M, Rivet C J, Gilbert R J and Morrison F A 2014 A protocol for rheological characterization of hydrogels for tissue engineering strategies *J. Biomed. Mater. Res. - Part B Appl. Biomater.* **102** 1063–73
[34] Evaluating the rheological properties of hyaluronic acid hydrogels for dermal filler applications [online] available (http://www.malvern.com/en/support/resource-center/application-notes/AN150112-prop-HA-hydrogels-Dermal-Filler.aspx) (accessed: 05 -Feb-2017)

VIII ECCOMAS Thematic Conference on Smart Structures and Materials
SMART 2017
A. Güemes, A. Benjeddou, J. Rodellar and J. Leng (Eds)

STRUCTURAL OPTIMIZATION OF A FIVE-UNIT SINGLE-BRANCH TRUSS-Z MODULAR STRUCTURE

MACHI ZAWIDZKI, ŁUKASZ JANKOWSKI and JACEK SZKLARSKI

Institute of Fundamental Technological Research of the Polish Academy of Sciences
Pawinskiego 5B, 02-106 Warsaw, Poland
e-mail: zawidzki@mit.edu, ljank@ippt.pan.pl, jszklar@ippt.pan.pl

Key words: Extremely Modular System, Truss-Z, Structural optimization, Effective stress

Abstract. Truss-Z (TZ) is an Extremely Modular System (EMS). Such systems allow for creation of structurally sound free-form structures, are comprised of as few types of modules as possible, and are not constrained by a regular tessellation of space. Their objective is to create spatial structures in given environments connecting given terminals without self-intersections and obstacle-intersections. In an EMS, the assembly, reconfiguration and deployment difficulty is moved towards the module, which is relatively complex and whose assembly is not intuitive. As a result, an EMS requires intensive computation for assembling its desired free-form geometrical configuration, while its advantage is the economization of construction and reconfiguration by extreme modularization and mass prefabrication. TZ is a skeletal modular system for creating free-form pedestrian ramps and ramp networks among any number of terminals in space. TZ structures are composed of four variations of a single basic module (Truss-Z module, TZM) subjected to affine transformations (mirror reflection and rotation). The previous research on TZ focused on global discrete optimization of the spatial configuration of modules. This contribution reports on the first attempts at structural optimization of the TZM for a single-branch TZ. Namely, the internal topology of a TZM and sizing of its elements are subject to optimization. An important challenge is due the fact that TZM is to be *universal*, i.e., it must be designed for the worst case scenario. There are four variations of each module, and due to symmetries there are thus $4^4 = 256$ unique 5-unit configurations. The structural performance of all of them needs to be evaluated in terms of a typical structural criterion (the maximum von Mises effective stress), and used for structural optimization at the level of a single TZM.

1 INTRODUCTION

A stairway is the most common means of pedestrian vertical transportation used in the built environment. Elevators and escalators are relatively expensive to install and maintain, and their traffic flow capacity is much lower than that of stairs. Moreover, it is not always possible to install an elevator or escalator due to limited space. However, most people occasionally or temporarily cannot use stairs, as when riding a bicycle, pushing a baby stroller or carrying heavy luggage. For elders and people in wheelchairs, stairs form a permanent and impassable barrier.

This is an important social issue, especially since the proportion of elderly people in society is higher than in the past, and some predict that this tendency will continue [1]. A comprehensive literature review for elderly pedestrians is carried out in [2].

Truss-Z (TZ) is a modular skeletal system for creating free-form ramps and ramp networks among any number of terminals in space. The concept has been introduced in [3]. The motivation for TZ in the context of human mobility, and in particular the mobility problems of elders is discussed in [4]. The underlying idea of this system is to create structurally sound provisional or permanent structures using the minimal number of types of modular elements. Further discussion on modularity vs. free-form can be found in [4].

TZ is comprised of Truss-Z modules, TZMs for short. In principle, TZ connects two points in space, called terminals. Constructing an efficient TZ can be formally expressed as a constrained discrete multicriterial optimization problem. In the previous research only the geometrical properties, such as the total number of modules (n), "geometrical simplicity" (GS) and "number of turns" (NT), have been minimized. The criteria GS and NT measure how many units do not follow a straight line, and how many continuous turns there are in the path, respectively. Common constraints have been the locations of terminals, positions and shapes of obstacles in the environment, etc. This paper reports on the first attempts at the structural optimization of TZM for a single-branch TZ, which focuses on structural performance of the resulting TZs. The following assumptions have been made:

1. The maximal span of TZ is five modules;
2. The TZM mass is constant;
3. The outer shape of TZM is fixed.

Subject to optimization is the internal topology of a TZM and sizing of its elements.

2 THE CONCEPT OF TRUSS-Z

In geometrical terms, all TZ structures are composed of only four variations of a single basic unit or module (R). Figure 1 shows the geometrical properties of R which have been set arbitrarily and used in theretofore research. Unit L is a mirror reflection of the unit R. By rotation, they can be assembled in two additional ways (R_2 is the rotated R, and L_2 is the rotated L), effectively giving four types of units. Some examples are shown in Figure 2. Figure 3 shows an example of a TZ underpass installation.

The structural rigidity of the TZ module has been demonstrated in [5], along with other topological properties such as *nullity*, degree of static indeterminacy (DSI = 0), etc. Due to the modularity of this system, it is natural to apply discrete optimization methods for creating TZ connectors and networks. Such structures can be optimized for various criteria: the minimal number of modules, the minimal number of changes in direction, and in a case of multiple branches, the minimal network distance, etc. Various deterministic and meta-heuristic methods have been successfully implemented for single TZ paths, including backtracking [6], evolution strategy [3], and evolutionary algorithms [7]. These methods produced usually good, but not ideal, solutions. A graph-theoretical exhaustive search method, which produces the best allowable, that is ideal solutions, has been described in [8].

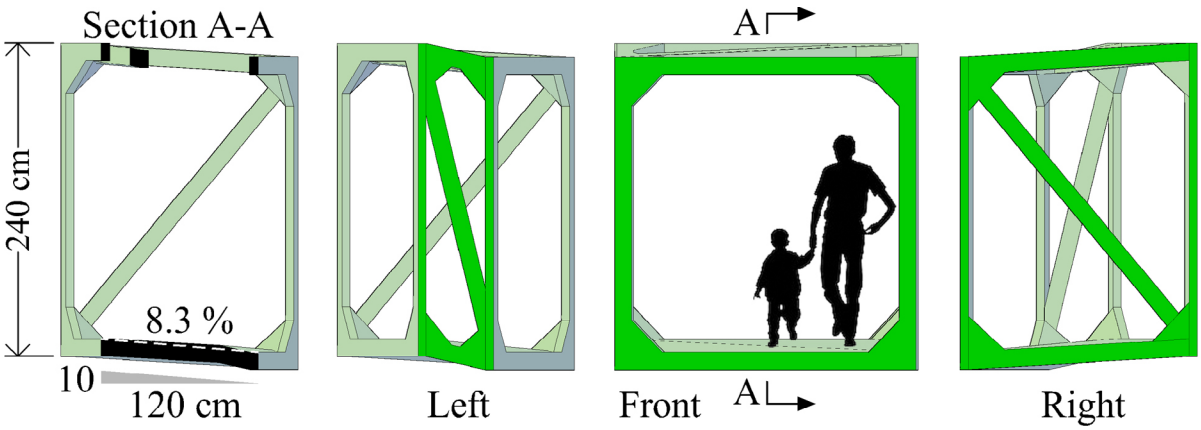

Figure 1: The original TZ basic unit (R). From the left: section A-A showing the slope, and three orthographic views.

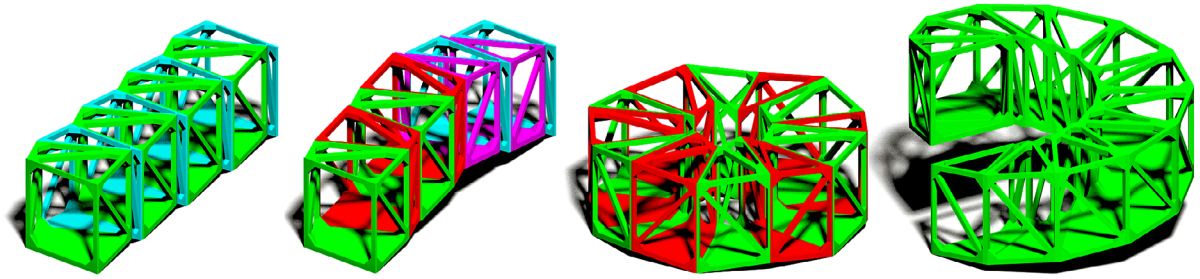

Figure 2: Four basic examples of various sequences of TZMs. From the left: flat and pitched ramps, circle and spiral. The color convention is: R, R_2, L and L_2 are shown in: green, cyan, red and magenta, respectively.



Figure 3: Visualization of retrofitting of a cycling/pedestrian path which continuity has been interrupted by a railway. The lightweight TZ could be partially suspended from the existing bridge. Without the necessity of heavy equipment, TZ is a feasible solution for countless situations.

3 TZ MODULE GEOMETRY

The geometry of the module is determined by the parameters: planar angle θ, width r, "slenderness" s, vertical displacement δ_{Z}, and height h, as shown in Figure 4. The slenderness s is the ratio between the offset from the apex d to the width r. For the three cases of $s = 0$, $0 < s < \infty$ and $s = \inf$, the corresponding projections of TZM form a triangle, a trapezoid, and a rectangle, respectively.

In this paper, the outer shape of TZM is based on functional considerations, and it the same as presented in theretofore investigations. It is defined by the following parameter values: $\theta_0 = 30°$, $r = 2.4$ m, $s = 0.5$, $\delta_{\mathrm{Z}} = 0.1$ m, and $h = 2.4$ m.

4 STRUCTURAL OPTIMIZATION OF A TRUSS-Z MODULE

4.1 Optimization variables

The outer geometry of a Truss-Z module has been proven in earlier research to be flexible enough to create free-form shaped ramps in complex environments. Thus, the geometry of a module is treated as fixed, and the structural optimization process is limited to two factors:

- *Placement of the diagonals of a module* (d). Since there are four module faces with a diagonal (floor, ceiling and two side walls), and since each diagonal can be placed in two configurations, there are a total of 16 different possible configurations of the diagonals.

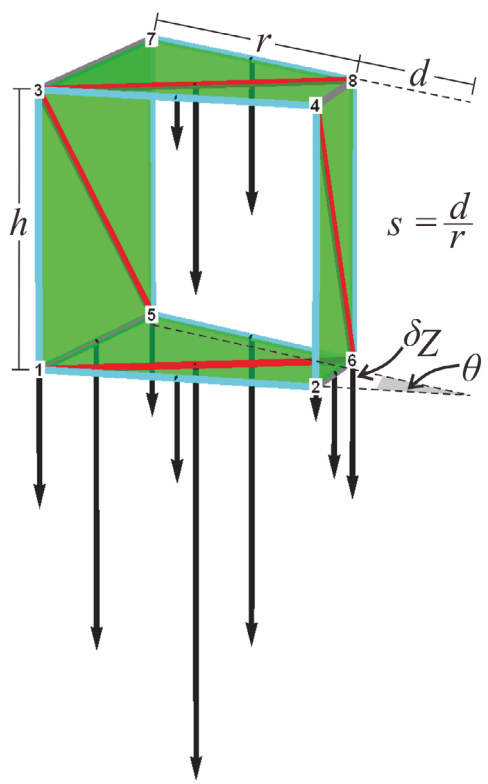

Figure 4: The topological and geometrical parameters of the original TZM. The main frame and the diagonal members are shown in cyan and red, respectively. Black arrows indicate the distribution of the static load (5000 N/m^2) used in the optimization process. The total load is distributed in proportion 4:1 between the ceiling and floor levels, and allocated to the end- and midpoints of the respective horizontal beams in proportion to the area of the neighboring floor/ceiling triangles.

They are denoted by a sequence d of four binary digits (or alternatively, the corresponding decimal number) that denote the configuration of the diagonal within the floor, the right-hand side wall (the longer wall), the left-hand side wall (the shorter wall), and the ceiling, respectively. For example, the specific configuration shown in Figure 4 is denoted by the binary sequence $d = 0101$, that is the decimal number 5.

- *Cross-sections of the module beams* ($\mathbf{x}$). Each TZM is modeled as a 3D frame and consists of 16 beams. The material parameters are assumed to correspond to steel with the density of 7850 kg/m^3, Young's modulus 210 GPa, and the shear modulus of 81 GPa. For optimization purposes, it is assumed here that each beam is a circular hollow section with the width of the wall equal to 5 mm, and that only the outer diameters of the sections are subject to optimization. The corresponding 16-element vector is denoted by $\mathbf{x}$,

$$\mathbf{x} = (\phi_1, \phi_2, \ldots, \phi_{16})\,. \tag{1}$$

There is an obvious non-negativity constraint, as well as a single linear constraint that

fixes the total mass m of the module at the level of 150 kg. The successive parameters in the vector $\mathbf{x}$ describe respectively the sections that join the following pairs of nodes of the module, as numbered in Figure 1: (1, 2), (5, 6), (1, 3), (2, 4), (5, 7), (6, 8), (3, 4), (7, 8), (1, 5), (2, 6), (3, 7), (4, 8), (1, 6) or (2, 5), (4, 6) or (2, 8), (3, 5) or (1, 7), and (3, 8) or (4, 7), where the last four pairs depend on the specific configuration d of the diagonals.

4.2 Static load scheme

The optimization is performed in the static case, in which the entire Truss-Z structure is subjected to a certain static load $\mathbf{F}(d)$. The load is assumed to correspond to the static vertical load of 5000 N/m^2, which is distributed in proportion 4:1 between the ceiling and floor levels, and then allocated to the end- and midpoints of the respective horizontal beams proportionally to the area of the neighboring triangles, as shown in Figure 4. Given a TZ structure, each its module is subjected separately to such a load, which are then all assembled into the global load of the entire structure.

4.3 Assessment criterion

The structural quality of a TZ structure constructed using modules of given cross-sections $\mathbf{x}$ and with diagonal configuration d is quantified here in terms of the maximum von Mises effective stress $\sigma_s^{\max}(\mathbf{x}, d)$ of the TZM sections that occurs in the entire TZ structure under the assumed load vector $\mathbf{F}(d)$. The subscript s denotes a specific configuration of modules that uniquely determines the entire Truss-Z, for example configurations see Figure 2.

The TZ system has a modular character, so that the ultimate configuration s used in specific conditions is not known in advance. As a result, one needs to assess structurally not a single specific configuration s of the modules, but rather the worst case scenario of a certain set S of configurations that are expected to be used in real environments [9]. In practice, a TZ ramp can be assumed to be supported not sparser than every five modules, thus the set S considered here contains all possible configurations of five TZMs with fixed supports in all degrees of freedom of the entrance and exit square plane frames. In general, the total number of such configurations is $5^4 = 1024$, but the left–right and entrance–exit structural symmetries yield 256 essentially different 5-module configurations. The assessment criterion for a TZ module is thus defined based on the worst case among all 256 possible scenarios: it is the maximum effective stress of the beams in all modules in all possible configurations $s \in S$ subjected to the assumed static load $\mathbf{F}(d)$,

$$\sigma_S^{\max}(\mathbf{x}, d) = \max_{s \in S} \sigma_s(\mathbf{x}, d). \tag{2}$$

4.4 Optimization process

During the optimization, the maximum effective stress $\sigma_S^{\max}(\mathbf{x}, d)$ is minimized with respect to the variables $\mathbf{x}$ and d, of which only $\mathbf{x}$ has a continuous character. Due to the discrete nature of the variable d, the optimization process with respect to the vector $\mathbf{x}$ is repeated 16 times,

that is separately for each possible configuration d of diagonals, to yield 16 optimized values:

$$\bar{\mathbf{x}}_d = \arg\max_{\mathbf{x}} \sigma_S^{\max}(\mathbf{x}, d), \tag{3}$$

$$\sigma_S^{\max}(d) = \max_{\mathbf{x}} \sigma_S^{\max}(\mathbf{x}, d) = \sigma_S^{\max}(\bar{\mathbf{x}}_d), \tag{4}$$

which are then used to find the best configuration of diagonals and the ultimate minimum,

$$\bar{d} = \arg\max_d \sigma_S^{\max}(d), \tag{5}$$

$$\sigma_S^{\max} = \max_d \sigma_S^{\max}(d) = \sigma_S^{\max}(\bar{d}). \tag{6}$$

Additionally, each of the 16 diagonal configurations d is assessed in terms of the maximum vertical displacement $h(d)$ of the TZ structure composed of the stress-optimized modules (as defined by $\mathbf{x}_d$) under the considered load $\mathbf{F}(d)$.

5 OPTIMIZATION RESULTS

5.1 Configuration of diagonals

The results of the optimization with respect to $\mathbf{x}$, see Eqs. (3) and (4), are shown Figure 5. The horizontal axis represents the maximum effective stress $\sigma_S^{\max}(\bar{\mathbf{x}}_d)$ under the test load, while the vertical axis represent the maximum vertical displacement under the same load, which might possibly occur in a TZ of another configuration s. Each point corresponds to a specific configuration d of the diagonals, which is printed in the point label. It should be emphasized that the objective function is multimodal and has several local minima, and consequently some of the points shown in Figure 5 might represent only local and not global minima.

With respect to the criterion of the maximum effective stress, the best diagonal configuration is found for $d = 15$ (the left-most point in Figure 5). It corresponds to a specific configuration of the diagonals used in the TZs shown in Figure 7. The diagonals join the nodes (2, 5), (4, 6), (1, 7) and (3, 8), as numbered in Figure 1. Notice that each node joins the same number of four beams.

5.2 Diameters of the beams

Figure 6 shows the optimized diameters of the beams $\bar{\mathbf{x}}_{15}$, as computed for the optimum configuration of the diagonals $d = 15$. The starting point of the optimization was the design with all diameters approximately equal to 40 mm, which resulted in the maximum effective stress at the critical level of 519 MPa. In the course of optimization, the maximum effective stress has been reduced to approximately 104 MPa, which is safely below the yield strength of steel and which indicates that the total mass of the module can be significantly decreased. The optimized values of the diameters $\bar{\mathbf{x}}_{15}$ of the beams are shown in Figure 6.

For each beam, the maximum effective stress occurs under the same load $\mathbf{F}(d)$, but it might occur in a different 5-module configuration s of the TZ structure. Figure 7 shows these 16 worst-case configurations for the successive beams. Each beam is drawn using its scaled optimized diameter.

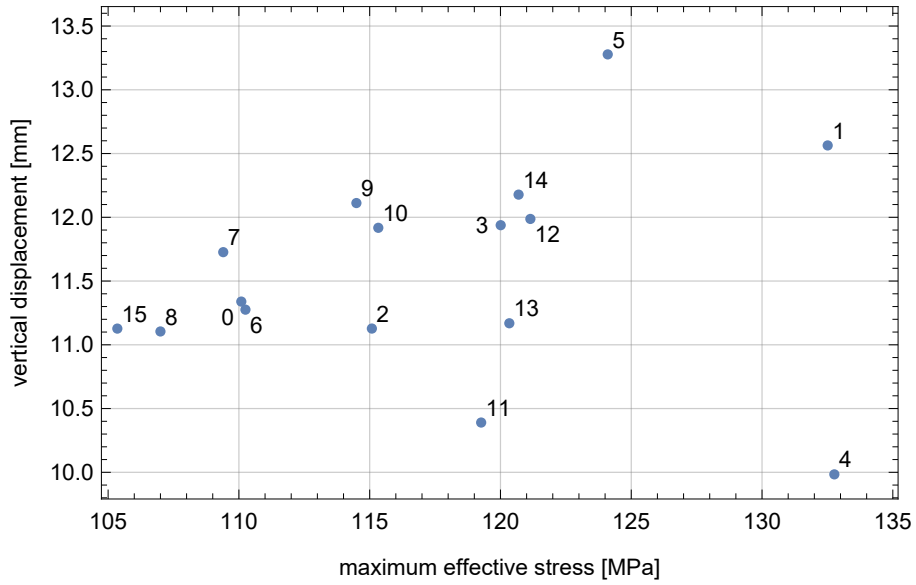

Figure 5: The 16 optimized modules that correspond to the 16 possible configurations of the diagonals, shown in the space of maximum effective stress vs. maximum vertical displacement. The specific configuration of the diagonals is shown in the label of each point.

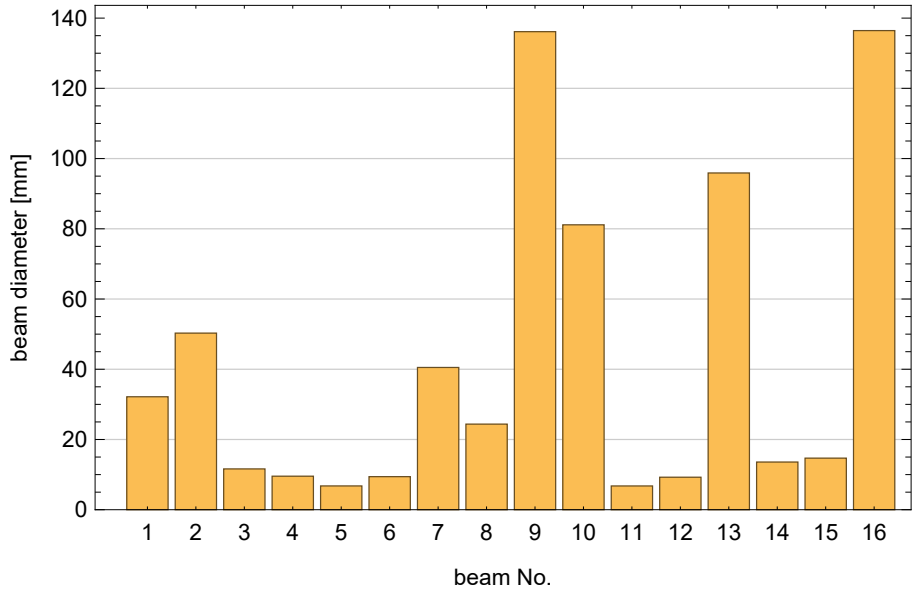

Figure 6: The optimized values $\bar{\mathbf{x}}_{15}$ of the beam diameters obtained in the optimum configuration of diagonals $d = 15$. The corresponding maximum effective stress has been reduced to 104 MPa from the initial critical level of 519 MPa (for the design with all diameters equal).

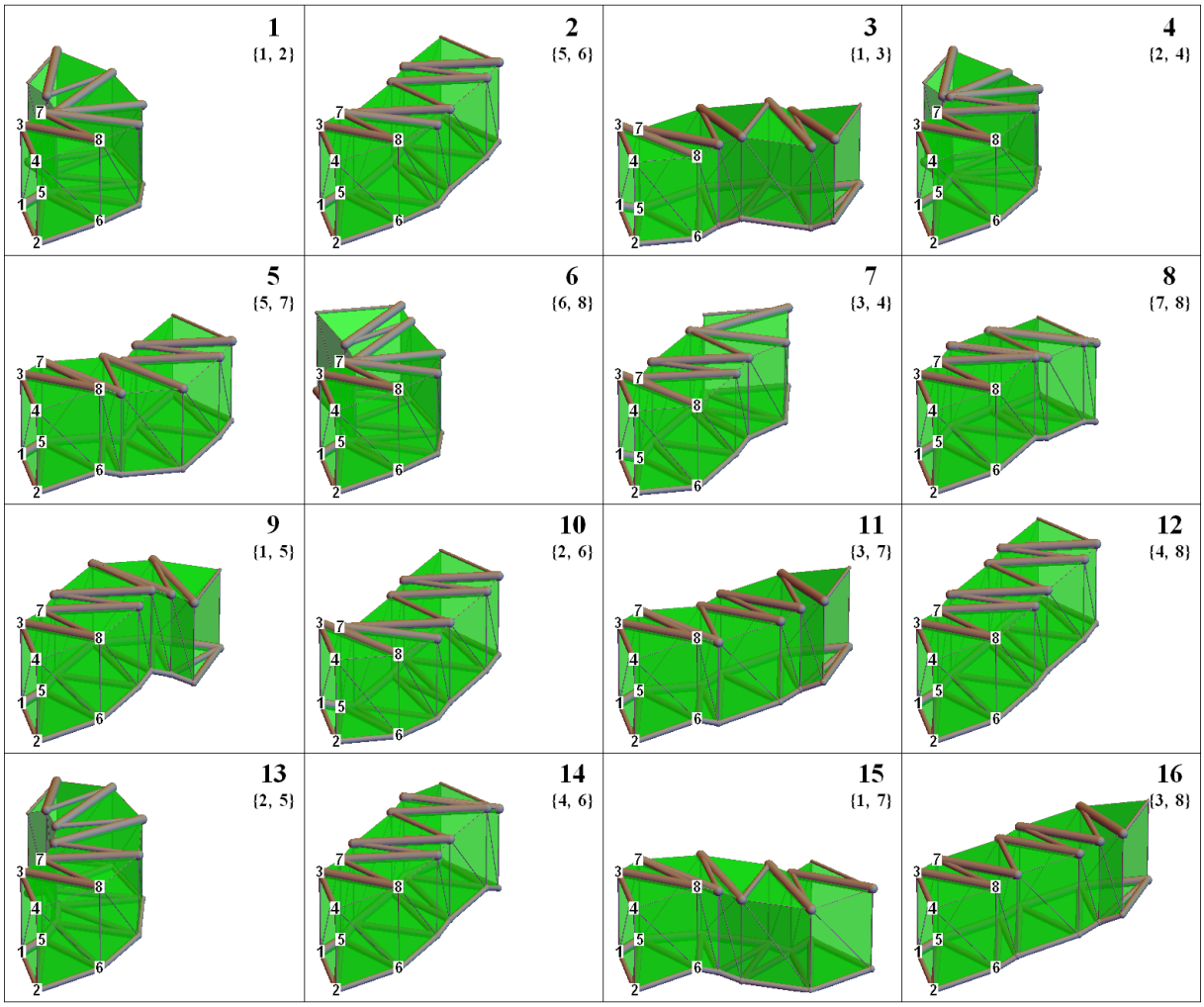

Figure 7: The 16 worst-case TZ configurations s that correspond to the optimum diagonal configuration $d = 0$. Each beam is drawn using its optimized diameter. The vertices defining beams are displayed at the first TZM in a sequence. The vertices identifying the most stressed beam are displayed for each case.

6 CONCLUSIONS

This contribution presents a preliminary study on structural optimization of the Truss-Z module. The outer geometry of the module is assumed fixed, and it is subjected to a static vertical load of 5 kN/m^2. The optimization variables are the diameters of the beams, as well as the internal topology of the module (configuration of its diagonals), as constrained by the assumption of the constant mass of the module. The optimization goal is to minimize the maximum effective von Mises stress that occurs in all 16 beams in all 5 modules in all 256 possible 5-module configurations. For the resulting optimized module, the maximum effective stress in each of the beams equals approximately 104 MPa, which is well below the yield strength of steel and which indicates that the mass of the module can be safely decreased. In future work, multicriterial optimization will be performed with respect to geometric parameters of the module, and the buckling effects will be taken into account.

Acknowledgments

This work was completed as part of the project titled: *"Extremely Modular Systems for temporary and permanent deployable structures and habitats: development, modeling, evaluation & optimization"*. It was funded by *"Polonez 2"* research grant no. 2016/21/P/ST8/03856 supported by the National Science Centre, Poland.

REFERENCES

[1] Pollack M.E. Intelligent Technology for an Aging Population: The Use of AI to Assist Elders with Cognitive Impairment. *Artificial Intelligence Magazine* (2005) **26**(2):9–24.

[2] Dunbar G. and Holland C. Road Safety Research Report No. 37. Older Pedestrians: A Critical Review of the Literature. *Department of Transport*: London, England, (2004).

[3] Zawidzki M. and Tateyama K. Application of Evolution Strategy for Minimization of the Number of Modules in a Truss Branch Created with the Truss-Z System, in Y. Tsompanakis, B.H.V. Topping (Eds.), Proceedings of the *Second International Conference on Soft Computing Technology in Civil, Structural and Environmental Engineering*, Civil-Comp Press, Stirlingshire, UK, Paper 9, doi:10.4203/ccp.97.9, 2011.

[4] Zawidzki M. Retrofitting of pedestrian overpass by Truss-Z modular systems using graph-theory approach. *Advances in Engineering Software* (2015) **81**:41–49.

[5] Zawidzki M. and Nishinari K. Modular Truss-Z system for self-supporting skeletal free-form pedestrian networks. *Advances in Engineering Software* (2012) **47**(1):147–159.

[6] Zawidzki M. "Tiling of a Path with Trapezoids in a Constrained Environment with Backtracking Algorithm", *Wolfram Demonstrations Project* [published: 20.09.11].

[7] Zawidzki M. and Nishinari K. Application of evolutionary algorithms for optimum layout of Truss-Z linkage in an environment with obstacles, *Advances in Engineering Software* (2013) **65**:43–59.

[8] Zawidzki M., Creating organic 3-dimensional structures for pedestrian traffic with reconfigurable modular "Truss-Z" system. *International Journal of Design & Nature and Ecodynamics* (2013) **8**(1):61–87.

[9] Calafiore G.C. and Dabbene F. Optimization under uncertainty with applications to design of truss structures *Structural and Multidisciplinary Optimization* (2008) **35**:189–200.

Theoretical and experimental study on silicone pneumatic artificial muscles

R. Soleymani*, H. Khajehsaeid†

* School of Engineering–Emerging Technologies
University of Tabriz, Tabriz, Iran
E-mail: ramin.soleymani93@ms.tabriz.ac.ir
† School of Engineering–Emerging Technologies
University of Tabriz, Tabriz, Iran
Email: khajehsaeid@tabrizu.ac.ir

ABSTRACT

Pneumatic artificial muscles (PAMs) are used to convert pneumatic power to pulling force. They have been widely used in industrial, medical and rehabilitation robots owing to their high power-to-weight ratio, natural compliance and flexible structure. However, PAMs exhibit highly non-linear characteristics due to compressibility of air and use of viscoelastic material as the inner tube[1]. The inner tube usually is made of elastomeric materials which undergo large deformation under relatively small stresses. Due to non-linear behavior of elastomers at large deformations, stiffness of these actuators would depend on the applied pressure. Therefore, it is important to obtain a precise mechanical model for these actuators. In this paper, based on the Exp-Ln hyperelastic strain energy function [2], a new mechanical model is developed for elastomeric pneumatic artificial muscles to predict stiffness and output parameters along actuation course. Two silicone PAMs are designed and tested at 0-100 psi pressure under the action of different axial forces. Results of the model are compared with those of experiments for actuation pressure threshold, muscle stiffness, produced pulling force and contraction ratio of the muscle.

REFERENCES

1. Wickramatunge, K.C. and T. Leephakpreeda, *Study on mechanical behaviors of pneumatic artificial muscle.* International Journal of Engineering Science, 2010. 48(2): p. 188-198.

2. Khajehsaeid, H., J. Arghavani, and R. Naghdabadi, *A hyperelastic constitutive model for rubber-like materials.* European Journal of Mechanics - A/Solids, 2013. 38(0): p. 144-151.

Vibration Control of Smart composite beam

Kouider. Bendine, Zouaoui. Satla Farouk Benallel Boukhoulda, and Nouari mohammed

ABSTRACT: In the present paper, the active vibration control of a composite beam using piezoelectric actuator. The space state equation is determined using system identification technique Based on the structure responses developed in Ansys finite element analysis package. Using ANSYS parametric design language (APDL) The Linear Quadratic (LQR) control law is designed and integrated into the ANSYS to perform closed loop simulations. Numerical examples have proved the efficiency of the proposed model.

VIII ECCOMAS Thematic Conference on Smart Structures and Materials
SMART 2017
A. Güemes, A. Benjeddou , J. Rodellar and Jinsong Leng (Eds)

A FUSED FILAMENT FABRICATION PROCEDURE FOR SMART COMPONENTS WITH EMBEDDED ELECTRONICS

G. GRATEROL NISI[*], M. EUGENI[†], S. ATEK[*], AND P. GAUDENZI [†]

[*] Smart Structures Solutions S.r.l
Via Luciano Manara, 51 – 00153 Rome
E-mail: gabriel.graterol@smartstru.com – sofiane.atek@smartstru.com
web page: http://www.smartstru.com

[†] University of Rome – La Sapienza,
Dept. of Mechanical and Aerospace Engineering, Italy.
Email: paolo.gaudenzi@uniroma1.it – marco.eugeni@uniroma1.it
Web page: http://www.dima.uniroma1.it/dima/

Key words: Fused Filament Fabrication, Smart Components, Embedded Electronics, Additive Manufacturing, Capacitive Sensors.

Abstract. In the present paper, the realisation of smart components by means of an Additive Manufacturing process is analysed. In particular, the possibility to build sensorised components with embedded electronics using the Fused Filament Fabrication additive technique without the intervention of any other manufacturing machine is studied. The feasibility of production by Additive Manufacturing of a smart component is demonstrated through a series of experiments where different filament types and design strategies are considered and compared. Finally, a methodology for the inclusion of electronic components in the manufacturing process is presented and discussed.

1 INTRODUCTION

Smart components are of great interest for advanced industrial applications. In fact, they offer the possibility to integrate additional functionalities into structural components such as actuation, sensing and energy harvesting. An important application of smart components is structural monitoring where, thanks to the presence of integrated sensors, they allow an evaluation of the status of the structure during its actual operative conditions and at the same time, due to the presence of actuators, they are able to control the dynamic response [1, 2].

Additive Manufacturing (AM) is a set of manufacturing technologies based on the sequential deposition of layers of material. Thus, it differs from the traditional manufacturing process, which is, usually, subtractive. In fact, the progressive addition of material in layers allows the production of components with complex geometry without compromising time and costs in the production stage.

AM with polymeric filament was initially used as a method for rapid prototyping, although recent advances in fabrication techniques have provided much more promising material properties, enabling the technology to include a wide range of materials, such as metals and ceramics. Currently, different techniques are used to create parts layer by layer with an additive principle, including material extrusion, stereolithography, selective laser sintering (SLS), and

direct laser metal sintering (DLMS) [3]. Fused Filament Fabrication (FFF), is an additive manufacturing technology, which consists of the extrusion of a fused thermoplastic filament. By depositing the molten material following a particular toolpath, the parts of the component are built up layer by layer from a digital Computer Aided Design (CAD) model. The inclusion of components inside FFF printed parts and the possibilities to create electronic circuits inside polymeric elements, have been actively studied by researchers, demonstrating the capabilities of the AM in the fabrication of sensorised elements [4]. The implementation of AM for the production of elements with embedded components (mechanical or electronic) has gained wide terrain in the research field, demonstrating applications from electronics and mechatronics to aerospace [5]. The feasibility of the fabrication of components with embedded micro-electronics has been demonstrated through the implementation of a multifunctional 3D system [6]. In this case, the manufacturing process has been enhanced by implementing different technologies such as micro-machining, CNC routing, and direct print. In the present paper a modification of the typical workflow procedure used for FFF technology is performed that allows the production of sensorised components without the intervention of any other manufacturing process and thanks to the use of conductive materials. The proposed methodology is first illustrated in comparison with the traditional one. Then, a case study is performed for two applications that demonstrate the suitability of the process in real cases.

2 FUSED FILAMENT FABRICATION

Since early 2000 when the RepRap© project came to life a proliferation of low cost desktop machines took place. To avoid legal issues with the trademark Fused Deposition Modeling (FDM) owned by Stratasys©, the name of the technology, which these desktop machines uses, is changed to Fused Filament Fabrication (FFF), although both FDM and FFF are essentially the same. The characteristics of this technology, such as the range of working temperature, the accessibility of materials and the simplicity of the hardware, as well as the characteristics resulting from the mentioned proliferation, such as open source system, hardware low cost, and available bibliography, makes FFF the optimal candidate for the objectives of this work.

2.1 Production line and materials

FFF is an additive manufacturing process based on the deposition of thermoplastic filaments. The polymeric material considered for the production of the required parts to fulfil the objectives of this work, is polylactic acid (PLA). This material is a biodegradable and bioactive thermoplastic aliphatic polyester derived from renewable resources, such as corn starch, tapioca roots, or sugarcane. The polymeric filament works on a temperature of 230 °C when deposited by the nozzle. The adherence of the material to the building plate in the machine is managed through the heating of the printing plate.

2.2 Standard FFF manufacturing process

The standard methodology of the FFF manufacturing process is structured in three main tasks, which take place after the identification of the part or product to be manufactured. These are pre-processing, manufacturing and post-processing. Each of these tasks is subdivided into different steps and each step represents a group of operations to be carried out before proceeding to the next one. In **Figure 1,** a schematic image of the FFF standard manufacturing process is shown.

In the pre-processing task, there are two main steps to carry out: 1) the design of a digital model using a Computer Aided Design (CAD) software and the subdivision of this model in printable parts. After the final form is defined, the model is analysed in order to check the shape-regularity (the so-called manifold object condition). The file is then exported in stereolithography (STL) format to proceed to the next step: 2) the intervention with a Computer Aided Manufacturing (CAM) software. In this step, the model is prepared for production through a process of "slicing" into printable layers. Moreover, the position and orientations of the component in the printer plate are defined together with the support structures. Once the printing parameters are established the file G-code is exported.

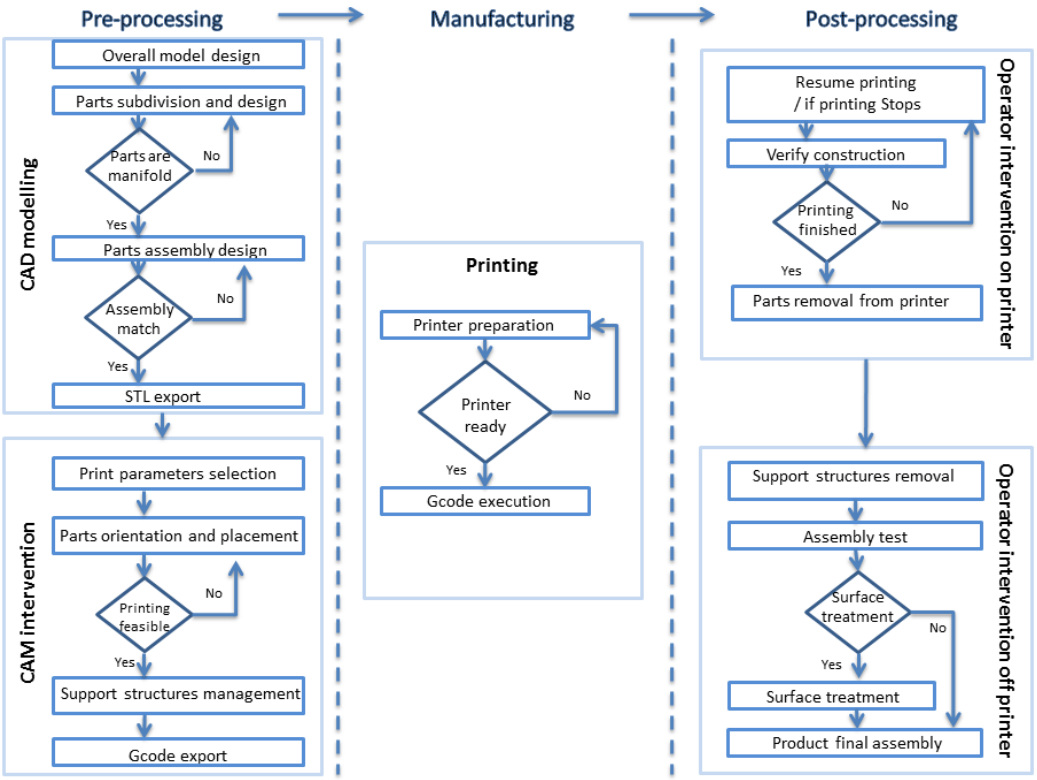

Figure 1: Standard workflow implemented for the creation of a 3D printed part

The G-code is a text file containing instructions for the numerical control of the AM machine, which is the most widely used Numerical Control (NC) programming language. For the manufacturing task, the machine is prepared and the file G-code must be loaded. The plate calibration is done by determining the distance between the extruder and the plate in several

positions on the X-Y axes. The intervention of the operator may be required on the plate to ensure that the first layer of molten material will adhere properly to it and also to load the filament on the machine. Consecutively the file G-code file is loaded and the manufacturing process begins. In the current methodology of manufacturing, no human intervention is required during the printing process apart from filament change.

The post-processing task starts when the part fabrication is complete. The part is carefully removed from the plate and the support structures are detached. The process is done by using appropriate tools. Once residual material is cleaned from the part, the finishing treatment begins if any particular superficial texture is desired.

The standard manufacturing process methodology does not take into account a pause in the manufacturing process or the inclusion of external elements during the production session. Thus, it is necessary to define a suitable procedure, which will be studied and presented in this paper.

3 A NEW WORKFLOW PROCESS FOR THE PRODUCTION OF SMART COMPONENTS BY FFF TECHNOLOGY

In the present work, a smart sensorised component with embedded electronics is created by using a stand-alone commercial FFF desktop machine. In order to do that, in this work a new workflow methodology is proposed by studying the FFF work logic and by identifying the key elements of the process: CAD design, CAM procedures and manufacturing equipment. In order to make the most of the FFF technology for the production of a smart component, different studies are performed. The analysis of conductive materials -with particular emphasis on conductive filaments- allows the exploration of different designs strategies for connections and circuitry traces. By experimenting the inclusion of components in the manufacturing process, thermal issues and material compatibility issues are identified. The experimental campaign allows the proposal of a new logic for the manufacturing process. Different tests are designed in order to demonstrate the feasibility of the production of a sensorised component implementing the proposed new workflow methodology by this work.

4 EXPERIMENTAL CAMPAIGN

A series of experiments are established in order to confirm the feasibility of the idea, and to propose a methodology for the use of a stand-alone commercial FFF machine for the production of smart components. In particular, conductive materials and embedded electronics in the printing process are studied thoroughly to acquire the expertise necessary for the fulfillment of the scope of the research.

4.1 Experimental Setup

In order to perform the series of experiments a specific experimental approach is followed. First, three different conductive materials are studied through a series of tests performed on produced specimens to identify conductivity characteristics and determine the choice of the material that will be implemented in the successive tests. After the material selection, a test board, with circuitry made of conductive filament is realized to demonstrate the possibility using such material for conductive tracks. The same material is also tested as a capacitive

sensor. Then, the inclusion of electronic components is studied through the realization of a specimen with an embedded button battery.

The machine used for the realization of specimens and prototypes is a Sharebot42©, a fourth generation professional desktop AM machine with single extruder and erectable heated bed, see **Table 1** for the machine specifications.

Table 1: Sharebot42 technical data

Parameter	Description
Printing volume	250 mm x 220 mm x 200 mm
Maximum printing speed	24 mm^3/sec
Heated printing plate max temperature	90°C
Minimum layer thickness	0.05 mm
Nozzle	0.4 mm (interchangeable)
Compatible filaments (1.75 mm diameter)	PLA-S, Nylon-Carbon, Thermoplastic Polyurethane

4.2 Conductive materials

Two types of materials are selected and studied. Commercial conductive paint and commercial conductive graphene filament. The two materials were selected due to the accessibility, simplicity to work with and the possibilities to include them in the parts during the manufacturing process. In **Table 2**, the main characteristics of the materials from the manufacturers datasheets are enlisted together with their possible applications.

Table 2: Conductive materials characteristics

Material	Characteristic	Aprox. Volume resistivity	Working temperature °C	Applications
PMNK_P00 02879	Nontoxic, water based, water soluble	0.1 ohm-cm	0°C -25°C	Painted resistor, capacitive electrode, conductor in low DC voltages circuits
AlfaOhm	Modified PLA conductive filament. With electrical non-ohmic behaviour	10 ohm-cm	10°C -225°C	Transfer of small currents, signals and information, worked by any 3D printer
Black Magic	PLA based material enhanced with Graphene traces	0.6 ohm-cm		Capacitive (touch) sensors, used to measure proximity, position, humidity, fluid levels, and acceleration, conductive traces, electromagnetic interference (EMI) and radio frequency (RF) shielding, high strength mechanical and functional parts, worked by any 3D printer.

The materials are analysed separately through a series of tests to understand their behaviour and conductive characteristics. The observations are compared among each other. Important manufacturing aspects such as simplicity of manipulation and deposition in the printing process are included in a final evaluation to select one subject to be implemented for the case study.

4.3 Specimens production for conductivity experiments

The specimens were produced following the phases described below.

1. Specimens for conductive filament test
    a. A printed volume of un-conductive material is deposited by the machine
    b. A filament change is required to charge the conductive filament
    c. The conductive samples are deposited by the machine following the specific toolpath.
2. Specimens for conductive paint tests
    a. A printed volume of un-conductive material with specific grooves is deposited by the machine
    b. The grooves are filled manually with the conductive paint.

Once the production of the specimens is completed, conductivity tests are performed.

4.4 Electrical conductivity tests on specimens

To measure the resistance of the samples a Metex M-3850D© multimeter is used. To avoid human factor influence on tests Schutzinger© clamps, connected to the multimeter, were used to hold onto the samples while measuring resistance.

These tests allows the analysis of the electric behaviour of the conductive materials as well as the deposition process in:

1) Samples with different sections so that the resistance of the material according to the dimensions can be identified,

2) Samples with same geometry in order to proceed to a comparison between them can be done to understand the range of repeatability, and

3) Samples deposited on layers of 0.25mm thickness to study the behaviour of the material in minimal layer thickness.

The tests are done for each type of material and they are named with letters a) for the conductive paint, b) for the Black Magic© conductive filament developed by Graphene 3D Lab©, and c) for the AlfaOhm© conductive filament developed by FiloAlfa© in partnership with LATI©.

In **Figure 3** a comparison among the test results is done in order to apprehend the behaviour of the materials when implemented.

For the conductive paint samples, the material is spread on the grooved models. This also allows evaluate the compatibility between the PLA and the paint and the difficulty related to the deposition process.

The conductive filament instead, can be extruded from a common extruder of a FFF machine, by changing the filament reel. The conductive filament is a PLA based polymeric material with traces of Graphene. This material has been revolutionary due to the mechanical and electric properties. The two selected filaments shown in Table 2 are tested for this experiment.

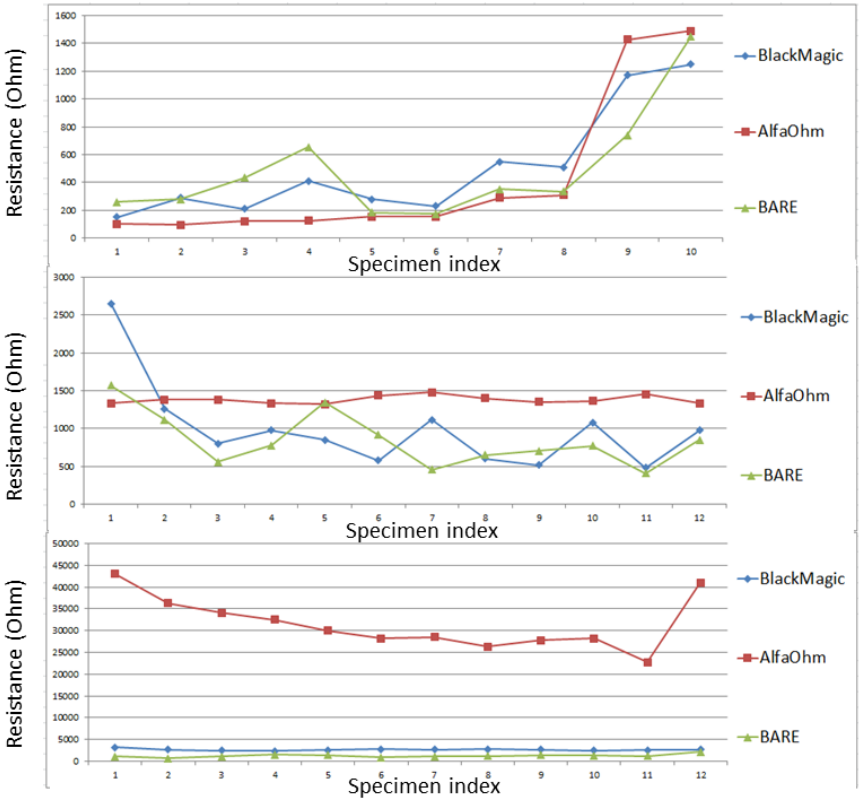

Figure 3: Samples resistance characteristics. Up test 1) Center test 2) Down test 3)

The results from the conductive materials are correlated in order to compare them in **Table 3**. In the material selection criteria, some parameters are included, such as design freedom and effort level of inclusion in the production process. For each material a score from 1 to 3 is assigned, 1 being the lowest rank and 3 the highest. The scores are assigned in the following way:

- For the conductivity parameter the score is assigned as 3 for the one with the less resistance, 2 the medium and 1 the one which presents high resistance, considering the average conductivity in the samples ranging from 1 to 10.
- For the repeatability parameter, the score is assigned by the variance of the resistance in each type of material. For this case, 1 is for the material with a high variance and 3 for the one with the minor variance.
- Design freedom and deposition effort are scored as 3 for "easy to deposit" and 1 for "difficult to deposit".

Table 3: Conductive materials comparison

Material	Conductivity	Repeatability / Conductive stability	Reduced qty. conductivity	Design freedom	Deposition effort	Total
a	1	1	3	1	1	7
b	1	1	2	3	3	10
c	3	3	1	3	3	13

In the previous tests, the paint shows better conductivity performances than the filament, when applied at a thickness of 0.25mm. Although, during the experimentation, some observations were made; the paint takes time to be deposited. The more complicated the circuit, the harder it was to include the paint during the printing process, risking unfeasibility. Another observation regards the current flow, which resulted as very unstable due to cracks formed in the samples when the deposited material dried. The conductive filaments of "AlphaOhm©" show better performances in repeatability, stability and geometrical-conductive relation. It was found during the experiments that the minimum thickness of the "AlphaOhm©" conductive layer must be at least 4 mm to ensure a good conductivity. Moreover, the filament is easy to be deposited in their respective places during the manufacturing process no matter how complex the geometry is. The filament has shown optimal malleability allowing design freedom when modelling with the CAD software. Even if the studied conductive materials have shown the capability to be implemented as current carriers in specific simple circuits as the one in **Figure 4** (left), the performances are still too poor (when compared to traditional copper wires) for complex circuit designs. For this reason, the conductive material implemented in this work is "AlphaOhm©".

The implementation of the conductive filament for the present work has the following advantages:

a. The deposition process is made directly by the desktop printer in the same temperature range as the already implemented regular PLA,
b. The amount of operator efforts required for the inclusion of the material during the printing process is reduced,
c. The conductive molten filament adherence to the PLA base is optimal due to the compatibility between the two materials,
d. The freedom of design is enhanced, even more, when using a dual extruder machine.

In order to explore the applications of the PLA based Graphene filament for the scope of manufacturing smart components where the circuitry and eventual sensors are also realized by the same machine, two simple experiments are established. 1) a basic photoresistor circuit is designed and printed with conductive traces and 2) a printed plate is connected to an "Arduino©" to test the conductive filament as a capacitive sensor. **Figure 4** shows the conductive-capacitive experiment carried out.

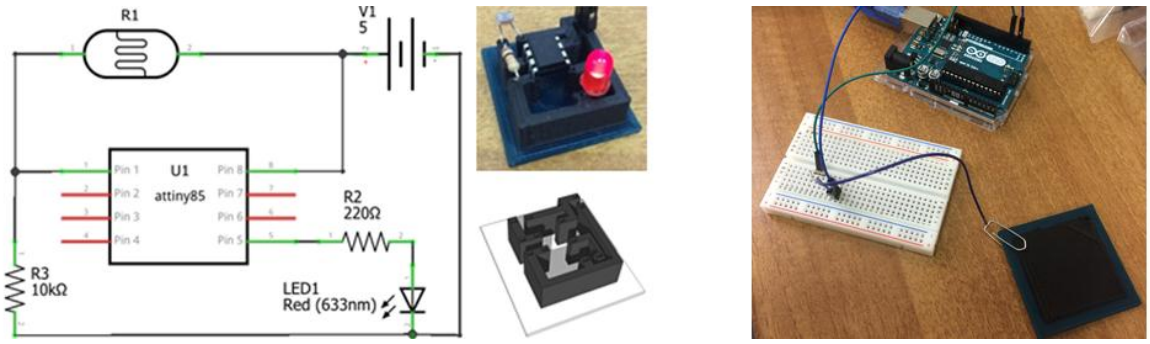

Figure 4: Left 1) conductive test. Right 2) capacitive test

4.5 Tests on embedded electronics

The embedding of electronics in the material requires the study of the optimal phasing of the process, mainly a specific study on how to stop the material deposition, place the electronic components and then start again the deposition.

The pre-processing and manufacturing tasks and can be subdivided into a series of phases:

1) Design of the placement of the components (CAD)
   a) Creation of cavities and tracks
   b) Distribution and interconnections design
   c) Individuation and design of thermal protection
2) Pausing the printer (CAM and Manufacturing)
   a) Precise layer individuation
   b) Components placement
   c) Temperature control
   d) Change of filament if single extruder

Figure 5 shows two tests carried out in order to implement the proposed strategy. The first test regards the adaptation of the basic photoresistor circuit described above to a particular geometry. The second test deals with the insertion of a button battery and copper wires. The component chambers and traces are designed in the CAM model and the precise layers are individuated in the CAM software.

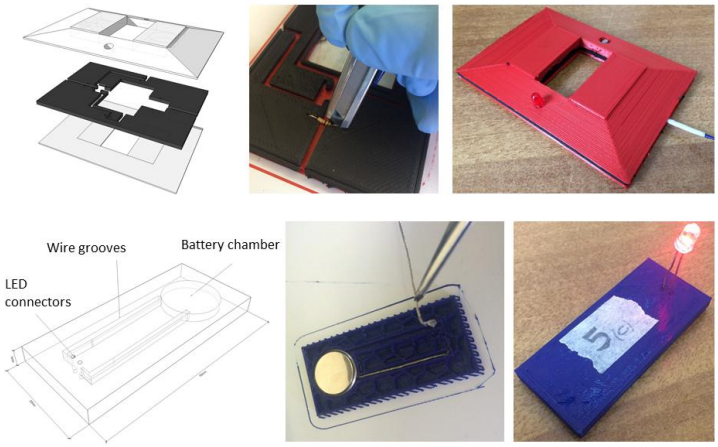

Figure 5: Inclusion experiment steps. Left CAD. Centre component inclusion. Right finished printed parts

When the printer is paused, a manual operation is performed to place the components in the respective positions. The temperature of the surroundings is usually near 50°C -60°C in the lower layers. When the polymer is deposited, it is over 200 °C, which can represent a problem for some components. In those cases it is necessary to apply thermal prevention strategies such as covering the chip or the battery with appositely printed protection covers.

4.6 Feasibility and functionality tests

Through the production of the parts with embedded electronics shown in **Figure 5**, the feasibility of the inclusion of electronic components during the manufacturing process has been

demonstrated and the functionality of the component once included has been proved. Through the experience of the tests shown in **Figure 4** and **Figure 5** a new fabrication process may be proposed. In **Figure 6** a diagram demonstrates the proposed fabrication process timeline is presented. Specifically, in **Figure 6** the model is divided into the different sections, which correspond to each manufacturing interruption. The fabrication timeline lists the different pauses of the process and in the section details the respective description. Moreover the diagram shows two strategies for the conductive traces, one in which the PLA grapheme filament is implemented and another where the interconnections are established by the inclusion of common copper wires during the manufacturing process.

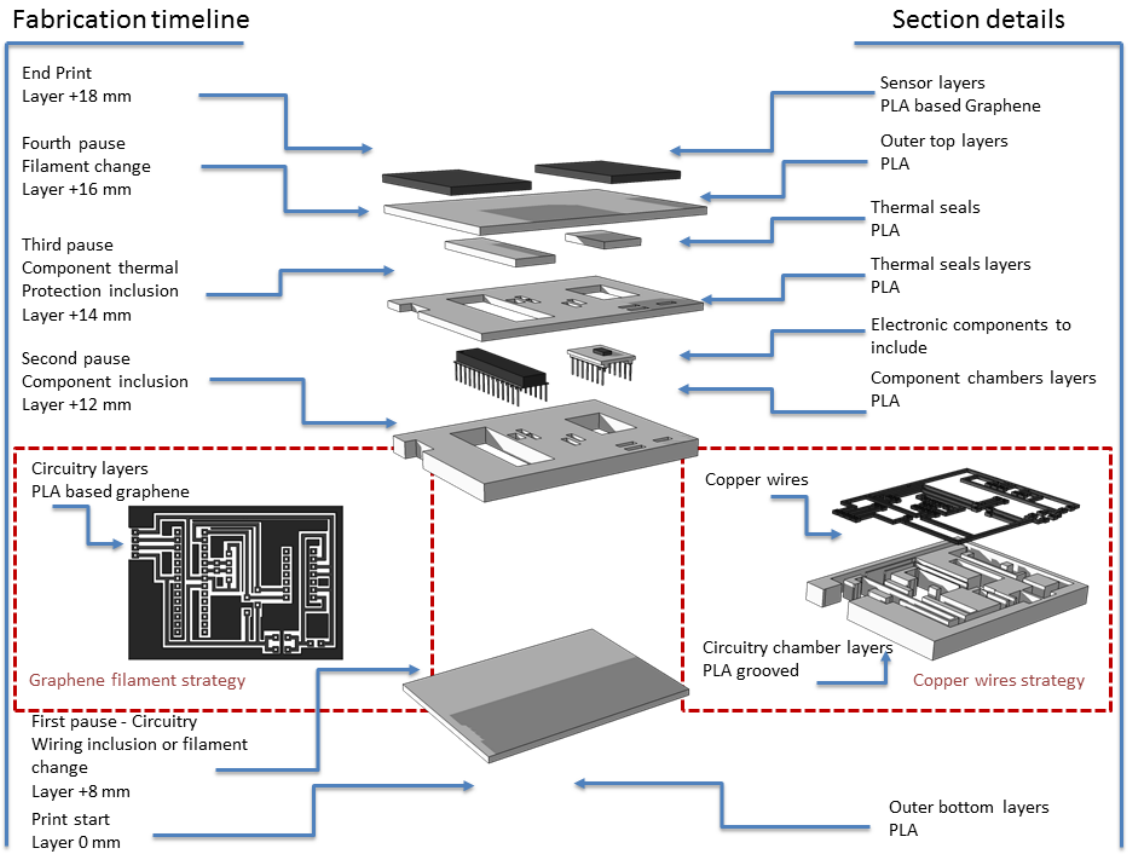

Figure 6: Fabrication procedure diagram

5 PROPOSED NEW WORKFLOW

The proposed process allows the production of components with functional embedded systems using a commercial desktop AM machine. In **Figure 7**, a schematic image shows the resulting workflow.

The methodology assumes some changes compared to the one used for typical components which does not consider either electronics nor circuitry. New steps which are the results of the experimental experiences done during this work are included. In the pre-processing task, two steps are included. While the model is being designed using a CAD software, the part design is merged with the circuit design considering interconnections and component cavities. The

circuitry design is made by implementing an electronic prototyping software. The modelling of the conductive layers takes into account the conductive characteristics of the material obtained by using the experimentation campaign presented in **Sec. 3.1**.

After the design of the embedded system takes place, the part subdivision and assembly strategy is done and the STL geometric representation file is exported to feed the CAM software, see **Sec. 2.1**. The second step of this task is the CAM intervention. In this step, the orientation and positioning of the parts on the building bed are studied. A critical point of this manufacturing step is the correct orientation of the model in the machine plate, as shown in the fabrication process diagram in **Figure 6**.

Moreover, the support structure parameter is turned off to avoid the deposition of material inside the components cavities, and the layers where an intervention occurs are individuated. When the file G-code is exported, it must be edited to include the code for the printing pause on the layers noted earlier. By following the numerical instruction in the G-code the machine pauses the manufacturing process according to the decided design strategy illustrated in the fabrication timeline shown in **Figure 6**. When the printing process is paused, the operator adds the components in their respective places, see section details in **Figure 6**.

After the printing is complete, the post-processing task remains the same as in the standard methodology. It is worth to note that the post-processing must take into account the presence of electronic components, which can be jeopardized.

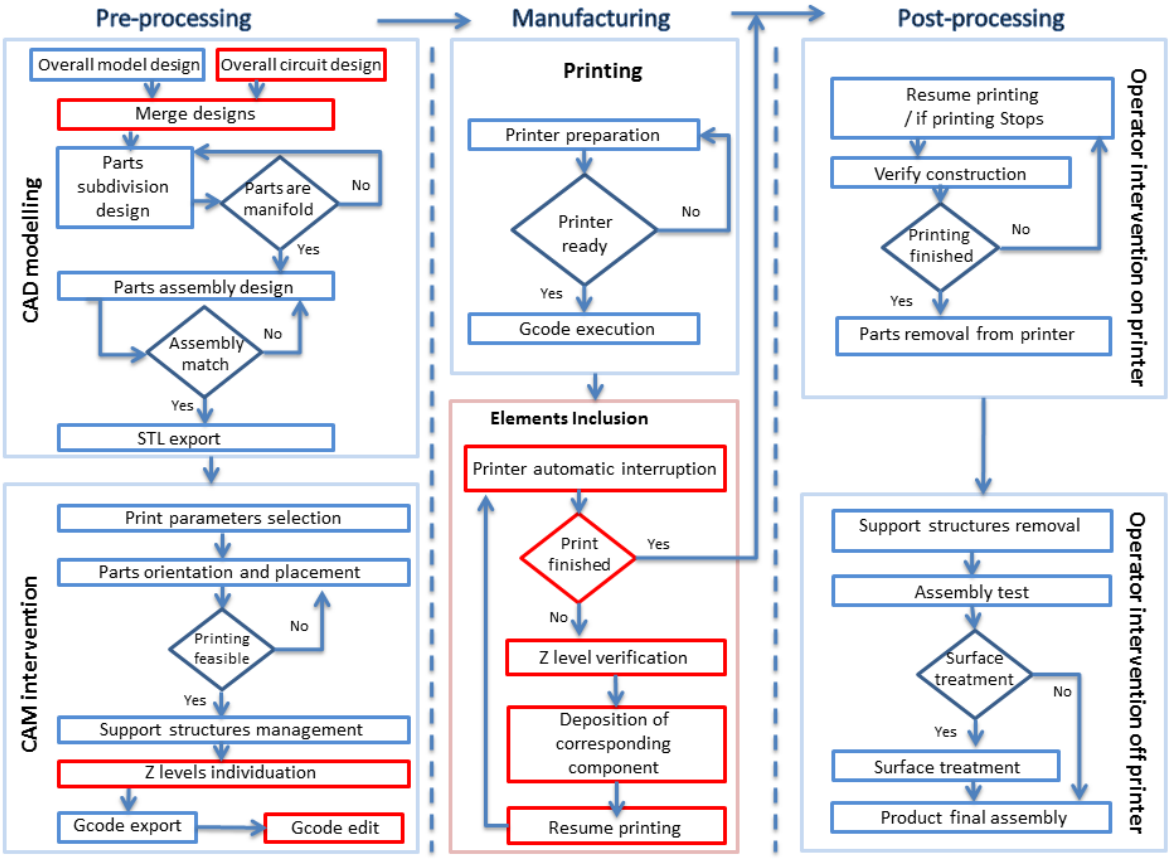

Figure 7: The proposed new methodology

6 CONCLUSIONS

In the present paper, the realisation of smart components in the framework of additive manufacturing has been analysed. In particular, the possibility to build smart sensorised components with embedded electronics using the Fused Filament Fabrication additive technique without the intervention of any other manufacturing machine has been studied. A methodology for the inclusion of electronic components in the manufacturing process has been presented and discussed. Moreover, experiments have been conducted in order to choose the conductive material to be used in the printing process: different materials have been evaluated in terms of conductivity, repeatability, deposition effort and design freedom. It is important to point out that, the presented new methodology of design and manufacturing allows the production of a smart component without the need of any hardware modification to the manufacturing machine or the implementation of additional manufacturing technologies. Moreover, the new methodology enables the FFF technology to embedded circuits and sensors which can adapt to the structures geometry.

The obtained results pave the way for further developments in the production of smart components with low cost commercial technology. A possible application may regard the manufacturing of smart printed tools; where conductive filament may be used as capacitive sensors to allow interaction with the tool holder.

REFERENCES

[1] P. Gaudenzi. Smart Structures: Physical Behaviour, Mathematical Modelling and Applications. Wiley and sons (2009)

[2] Luca Lampani, Paolo Gaudenzi. Composite Structure of a CubeSat Satellite with Embedded Sensors for structural monitoring experiment. 66th International Astronautical Congress, Jerusalem, Israel. (2015). IAC-15-C2.5.5

[3] Kaufui V. Wong and Aldo Hernandez, “A Review of Additive Manufacturing,” ISRN Mechanical Engineering, vol. 2012, Article ID 208760, 2012.

[4] Sung-Yueh Wu, Cheng Yang, Wensyang Hsu, Liwei Lin. 3D-printed microelectronics for integrated circuitry and passive wireless sensors. Microsystems & Nanoengieneering , (2015) 1, 15013.

[5] William M. Marshall, Michael Zemba, Corey Shemelya, Ryan Wicker, David Espalin, Eric MacDonald, Creig Keif and Andrew Kwas. Using Additive Manufacturing to Print a CubeSat Propulsion System. AIAA Propulsion and Energy Forum. 27-29 July 2015.

[6] David Espalin, Danny W. Muse, Eric MacDonald, Ryan B. Wicker. 3D Printing multifunctionality: structures with electronics. Int J Adv Manuf Technol (2014) 72: 963-978.

VIII ECCOMAS Thematic Conference on Smart Structures and Materials
SMART 2017
A. Güemes, A. Benjeddou , J. Rodellar and Jinsong Leng (Eds)

Cast metal with intelligence – from passive to intelligent cast components

RAUL CARLSSON[*], LENNART ELMQUIST[*], CHRISTER JOHANSSON[†]

[*]Swerea SWECAST
P.O. Box 2033, SE-550 02 Jönköping, Sweden
e-mail: raul.carlsson@swerea.se*, lennart.elmquist@swerea.se, www.swerea.se
[†]RISE Acreo
P.O. Box 53071, SE-400 14 Göteborg, Sweden
e-mail: christer.johansson@ri.se, www.acreo.se

Key words: cast metal, integrated sensors, digitalized cast metal, smart castings, interdisciplinary research, intelligent cast components

Summary. *The paper describes an innovation project aiming to embed sensors into cast metal during the casting process. Important measurands are e.g. elongation, shear, temperature and vibration. In practice this means to turn metal components into also being digital components. This will respond to some of metal industry´s challenges; resource efficient design, increased value added for the casting sector, and general access to different possibilities of digitalization. Technical challenges lie in choices of sensor material to integrate during the casting process that maintains its sensor functionality after casting processing without degrading the mechanical strength of the metal component. Other challenges relate to signal interaction and interference between sensor and metal. To handle the technical challenges the innovation project gathers competence about metal casting and sensor technology. One goal of this innovation project is to develop an innovation platform that elevates the material based casting industry into a wholly or partially value and service based industry. Integration of sensors into cast components makes sensing functionality a natural property of metal, which in turn may turn metal into key components for the industrial digitalization.*

1 INTRODUCTION

1.1 What the research develops

This paper presents the current development of a new technology that can reduce costs for a wider integration of robust sensors into machine parts that has the potential to revolutionize the digitalization of all sorts of machinery. Figure 1 presents the generic approach; a wire of deviating material is embedded in the cast metal. Changes in the cast metal will also affect the wire. Changes in the signal through the wire will reflect changes in the cast metal. The wire may be a metal or any other material that can carry a signal.

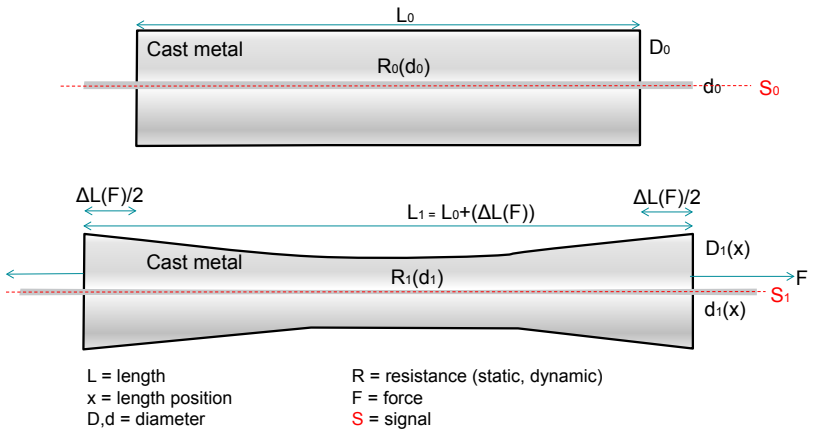

Figure 1: Initial simple approach; an embedded wire (sensor material) that changes it dimensions and/or properties when the cast metal is subjected to external stimuli such as mechanical and/or thermal changes.

Digitalization is the new market potential and consequently impregnates all aspects of industrial production, products, business and markets. The evolution of Internet into Internet of Things (IoT) takes the next step towards Internet of Materials (IoM) (Figure 2). This paper presents current research and findings towards evolving cast metal in that direction.



Figure 2: The strategic advance of Internet of Materials. The strategic and evolutional path from Internet of Things to Internet of Materials.

Transforming these electronically passive cast metal elements into sensors have a huge potential to significantly accelerate all the digitalization of all applications where cast metals today are used as construction or otherwise mechanically active elements. As a direct consequence, it may also have a huge potential to revolutionize the cast metal industry. Our research is practical and pragmatic and starts with the clear task of transforming a construction material into a digitally able sensor.

1.2 What are the market drivers

The goal is to achieve effective and robustly cast metal components that can work as electronically active sensor components, with low total weight and high total cost efficiency. If designed correctly this technology has the potential to reduce environmental impact over their product life cycle, as well as provide effective contributions to several of the sustainability goals. By achieving this there will be many benefits for metal based industries, ranging from metal producers and suppliers, recycling business, machinery, equipment and

construction, infrastructure and many more sectors. It is probably not an exaggeration to label it a revolution for metal based industry.

Today, the cast metal industry produces mechanically active but electronically passive metal components, with high mechanical, dynamic, chemical and thermal quality requirements for different advanced applications in constructions, electronics, vehicles, medical equipment, etc. Electronically active cast components will open for entirely new and widespread applications for embedded robust and cost-efficient sensor systems in machinery, equipment and constructions.

The potential for digitalization can efficiently and effectively control and monitor machines in rough and/or remote environments to reduce energy losses from friction and non-optimal operations of a wide range of machines that transforms motion into electric energy, or that transforms static, electric or chemical energy into motion. It can also support reducing extra material marginals included by design in buildings and machine constructions by instead enabling feedback from the metal to avoid stress forces, as well as to save resource needed for redundant equipment due to service stops and break downs.

Examples are sensors in bearings inside windmills at remotely placed sea based wind farms. By robustly and continuously monitoring the health of the bearings, breakdowns can be avoided and service interval can be reduced. Other examples are in widely distributed products, such as machinery and tools used globally in remote locations in harsh and widely different situations. Knowing that the moving parts inside the machine are in good order and that the machine can even avoid breaking down if temperature, vibrations or tensions may indicate any risks is an extra added value for an exposed user. In addition, by cost-efficiently providing sensor functionality throughout the use phase, many sorts of valuable information may be provided back to the drawing board to be used during design of the next version of the product

Beyond the immediate technical benefits, it also intends to meet some of metal industry´s challenges; increased value added for the casting sector, resource efficient cast component design and general access for cast components in any application to all possibilities of digitalization. Castings are used in a wide range of applications in the society and the concept will therefore add value far outside of the casting industry. It is anticipated that the greatest value of cast metal integrated sensors will come to the end users. Most likely they will never know about it, but most of their cast metal products will provide valuable services to them.

Embedded sensors may enable a wide introduction of digitally controlled and monitored machinery, hence opening for a much larger impact enabled by digitalization on resource and energy efficiency and on improvement of external and work environments.

Today some cast metal components are supplied with after mounted sensors, glued, drilled or screwed onto the metal. The extra cost associated with these manufacturing steps is a major threshold for digitalizing the metal industry. After-mounting also introduces weaknesses during the product life. For example, tensions, vibrations and temperature changes may lead to corrosions, cracks and wear, which together decreases the robustness and increase the product life cycle cost.

In addition to robustness and cost-efficiency, the potentials of embedding sensors into cast metal components may also lower weight, result in smaller component size, enable new design alternatives, open for many more sensors inside each component, allow for entirely new physical locations to sense at, present new properties to sense, and provide entirely new

and innovative product concepts based on defined or standardized digitalization component interfaces, services etc.

It is believed that this new technology may revolutionize the business path for the cast metal component supplying industries, today sometimes struggling with competing with price, into a business based on value added innovation, digitalization and services.

1.3 How we develop the technology

Our research develops the cast metal components into also being electronically active components by integrating sensor functionality into the metal during the casting process. This will enable cast metal components to provide data about e.g. the component's elongation, shear, temperature and vibrations, with purpose to monitor and control systems based on one or several of these components. The initial simple approach is to embed a wire as signal conductor and sensor, as was shown in figure 1.

Table 1: Research challenges and general approach.

CHALLENGES	TYPE OF CHALLENGES	PRINCIPLES OF APPROACH
Metallurgical	Sensor material choice, production, material properties	Systematic knowledge build-up, interdisciplinary research and development
Mechanical	Material properties, sensor connectors, impact on design	Systematic knowledge build-up, interdisciplinary research and development, invite technology providers early, new design alternatives
Sensor methods	Sensor signal interpretation and isolation, electromagnetic interference, short circuits	Systematic knowledge build-up, interdisciplinary research and development, invite technology providers early, new design alternatives
Signal analysis	Choice of signal, signal filtering and parameter interpretation	Systematic knowledge build-up, interdisciplinary research and development, invite technology providers early
Data science	Signal analysis, relevant feedback	Systematic knowledge build-up, interdisciplinary research and development, invite technology providers early
Commercial	Component supply-chain, commercial eco-system, standardization, product added value	Establish innovation platform of interested component and competence suppliers, initiate standardization, establish user-driven research routines to quickly reach market

By focusing practically and starting with simple shapes and materials of the cast component, we introduce controlled variations of different variables, such as material choices and signals. The general approach is to create internal solidified structures for both sensing and traversing sensor signals. Such structures may be introduced as wires of gradually deviating material integrated during the casting process, or as identifiable boundaries between differently solidified areas that are either induced or that naturally arise during the casting process within the cast metal structure.

Anticipated challenges identified are metallurgical, mechanical, sensor choices/sensing methods, signal analysis and data science as well as commercial exploitation due to lack of supply chains and standardization. In Table 1 the challenges and its related approaches are

listed.

2 THE KNOWN RESEARCH FRONT

Some ongoing research activities and development in the field of integrating sensors with materials were presented at the bi-yearly International Conference on System-Integrated Intelligence [1], and by some of the core activities of The European Technology Platform on Smart Systems Integration – EpoSS [3]. In particular a compiled state of the art and visionary outlook has been presented by Lehmus at the EpoSS in 2013 [2]. But there is very limited work on merging sensors with metal. Nothing can be found where this is done with ferro metal casting, but one related, and well-developed technique is marketed by Fraunhofer IFAM, in which they encapsulate piezo-electric sensors and RFID antennas into aluminum [4]. This is the most similar approach we can find. There is also research aiming at integrating sensor materials into metals during additive manufacturing [5,6], which to some respect is related. There is also a patent describing a technique to mount optical fibers into metal [7], which may be of relevance. However, the clear distinction between the identified existing published research and technologies and the research project presented in this paper, is that our research takes its starting point in the potentials, properties and challenges of the cast metal material itself, and the production methods of casting metal. The integration is not limited to integrating sensors, but to transform cast metal into also being active sensors, not by adding strange material and technology to the cast components, but by developing the cast material and the casting production processes.

3 CHOICE OF RESEARCH QUESTIONS

The research started with two core questions, the metallurgical challenges associated with integrating a sensor media into molten metal, and the sensor challenges of identifying appropriate sensor signals for different types of metals and potential sensor materials. The next level of research questions addresses the challenges of the surface between cast metal and sensor material.

Each of these metallurgical and sensor related challenges are associated with casting technology related challenges, such as positioning of sensors inside the casting molds, before and during casting, handling and preparation of any isolation material between sensor material and cast metal, shrinking phenomena during cooling and other practical matters. Once the new cast component with sensor functionality is produced, there are still the core challenges of ensuring that the mechanical and corrosive properties of the cast component are not adversely affected. And increasingly important is to ensure that this new technology does not also introduce new threats to the environment and to global sustainability.

4 THE RESEARCH APPROACH

4.1 General research capacity

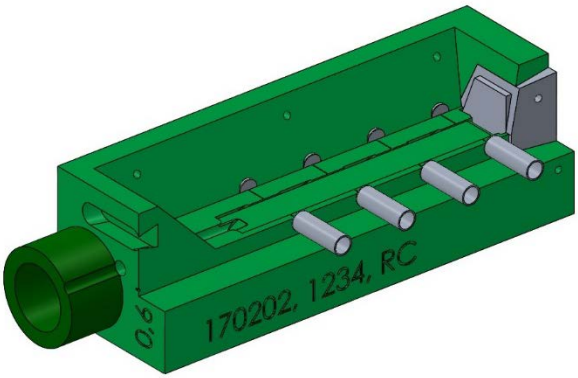

Figure 3: The CAD drawing of the mold, with sensor inserts and special mold closing to maintain a good metal flow and easy mounting of sensor wires.

The research is based on a serial production of sensor based cast metal prototypes. The design, production, resulting properties and functionlity are throroughly tested at each iteration, and all learnings from the previous iteration is being fed back as new requirements for the next version of prototypes. The ability to quickly serial produce and test cast metal prototypes is based on the casting research institute's modern full scale 3-D sand mould printer directly from a CAD-drawing like the one presented in figure 3. In addition, the sensor research institute has equipment and competence for advanced testing of different sensor functionality. This combined laboratory and production equipment enables production of entirely new prototypes every second day if necessary.

4.2. Early research approach

The different design parameters are chosen and tested in different ways, interdisciplinary and interorganisational. Fundamentally the cast metals to use for integration of sensors are chosen based on the cast metals used by the industries participating in the research. Currently this means that ductile cast iron and different forms of machinery type alumnium prototypes are being developed. Choices for sensor materials are based on the combined requirements of potential sensor signals and of other relevant physical properties.

Much of the early research focuses on practical aspects, such as how to design the sand molds to allow for precise positioning of sensors, and on early analysis of signal identification and materials defects.

4.3 Serial prototype testing and development

The large scale serial prototyping include a number of testing and development iterations, based on the core results of the early research. This empirical research intends to fine tune a number of foreseen aspects and challenges of the research work.

4.4 Metallurgy challenges

In addition to the metallurgical challenges presented already, there are detailed aspects regarding:

- Volume changes during solidification, which may adversely impact the sensor
- Material defects impacting mechanical strength and metal properties at micro level
- Defects in the surface between cast material and sensor or isolator, such as gas bubbles
- Intermetallic phases, carbides, brittle structures
- Diffusion and/or reactions between cast material and sensor or isolator
- Unwanted solidification structures, such as degenerated graphite

Metals inevitably shrink during solidification and the cooling down to room temperature. One challenge is how the surface between cast material and sensor system will withstand differences in thermal expansion coefficients. A sensor without or in combination with insulation will create a discontinuity in the cast metal, and as such it might be considered a defect in the structure. Another source for the defects is the interaction between cast material and sensor/insulator system. Casting defects is already a problem, with issues such as porosities and gases formed due to chemical reactions in combination with reduced solubility as temperature decreases.

By the introduction of sensors this complexity will increase. Other challenges are related to the formation of unwanted solidification structures such as intermetallic phases and carbides, constituents in the microstructure that are known to adversely decrease and deteriorate the expected properties. A sensor inside a mold will in practice represent a surface which will impact the solidification structure in the bulk of the cast metal. These challenges are related to traditional casting metallurgy competence and challenges, typically dealt with by prototype, metallurgical analysis, detailed simulations and thorough theory build-up. Having these main challenges identified and listed is already a great leap towards solving them, though the research needed shall of course not be underestimated or ignored.

4.5 Sensor signal challenges

Due to different electromagnetic properties of different cast metals, there is also a need for different sensing techniques:

- Electric sensing is possible if interference can be avoided with for example isolation of the integrated wire.
- Magnetic sensing is possible if electromagnetic disturbances can be ignored and an appropriate integrated magnetic wire material is used.
- Electromagnetic, up until optical sensing (optical fibers) may be possible if sensor material withstands production temperatures.
- Ultrasound sensing methods may be an option for specific applications.

Dependig on sensing methos and porperties of the cast metal the isolation kayer between signal conductor (wire) nd construction metal may can either be an isolator with a defined minimum resistance, or no isolation layer at all or be mediated in the form of diffraction index for electromagnetic waves or sound waves.

4.6 Casting technology



Figure 4: The sand mold during preparation before casting.

To prepare for industrial scale serial production, research will include:

- Prepared sensor inserts, which can easily be added into serial production sand molds, as well as protects the sensor during the production step.
- Simple production step that takes no time.

Introducing sensors during serial production based on sand molds would not introduce problems. Current sand mold casting is made by introducing several different production related components into the mold cavity before closing it before pouring the molten metal into it. For example, filters, in-mold inoculation and the application of mold wash are done in that way. Adding also a sensor to position in the mold before closing it will be integrate well with current production technique. Figure 4 shows one of the prototype molds, which is still not ready for serial production. Much manual detailed labor is still needed. Other factors that must be considered as challenges during mold filling are the high temperatures and forces acting by the melt. Also, when moving the research forward, towards high pressure die casting, new challenges will rise, related to forces and related to very high pressure and liquid metal turbulence to fill the mold.

4.7 Cost

Three major components are intended as cost reduction drivers for integrated sensors:

- By integrating sensor functionality during the casting additional mounting and manufacturing costs will be kept at a minimum.
- By developing sensor material with properties similar to the cast metal, rather than with advanced electronic components, material costs will be kept at a minimum
- The production and material costs will be only marginally higher for each additional integrated sensor into a component, enabling either redundancy or higher measurement precision, or both.

4.8 Recyclability of sensor and isolator material

The technology is general and is expected to spread globally. It is therefore important to consider the environmental consequences from a high scale production, and to design a technology with lowest possible environmental impact.

- Seek technologies with environmentally neutral sensor conductor material, preferably with alloys similar to the cast metal itself.
- When deviating materials are added, seek ways to simplify recycling of the digitalized metal cast component.

5 FINDINGS

5.1 Practical potential

The research is developed in close cooperation with large industrial companies with products based largely on cast components. This ensures the relevance and the progressive focus of the project.

Efforts have been spent to secure a clear view on end-user needs and on rough market analyses. Suitable products and applications have been identified as targets for prototype specifications, and for first pilot testing.

5.2 Early findings

Metallurgic research findings are not yet conclusive in any direction. Current prototypes indicate positive mechanical properties. Micro defects, such as gas bubbles around metal surfaces, intermetallic phases and unwanted solidification structures have not been thoroughly assessed at moment of writing.

Several valuable findings have already been made about the sensors and sensor integrations, though also those cannot be considered conclusive. There are several different sensor materials and combined sensor signals appropriate for the development.

All initial assessments of the potential sensor technologies include not only the technical potentials, but also cost estimates of the included parts for each type of sensor technology. These figures are yet rough, and will be continuously monitored and updated during as the research progresses towards more and more specific choices of technologies.

The research have a long term target how the intregrated sensors will lead to improved environmental benefits, in particular to low or no metal recycling contamination of the sensor to be included in the cast metal. The general approach is that the sensor material should be very small amounts of integratred materal, and that they should preferrably be based on the same metals already occuring the cast metal alloy. However, the first prototypes and product versions will likely be based on clearly deviating material, and further combined metallurgical and sensor research will be needed to achieve the full capability of environmentally sustainable integrated sensors.

6 DISCUSSIONS AND CONCLUSIONS

Cast metal components with integrated sensors will contribute with an innovative approach to solve some of metal industry´s challenges, by increasing the value added for the casting sector, possibilities for resource efficient design, and general access to the digital revolution

for cast metal components. Integrated sensors will significantly accelerate digitalization of all applications where cast metals today are used. As a direct consequence, it may also revolutionize the casting industry and its web of customers.

The combination of materials, signal and prototype still need to be balanced further for the correct sensing signal is stable in the chosen application prototypes. The interdisciplinary collaboration between Swerea SWECAST and RISE Acreo, combining casting technology and sensor technology, is necessary for the innovation area. The research is done in close cooperation with industrial partners that both produce products based on cast components and who see a high commercial potential in sensors in cast metal components. Their active role is to focus each research step onto specific customer added values of each technological advance.

7 NEXT STEP

Next steps are three paths on different levels, technical development, development of research and innovation platforms and ecosystems, and a long term strategic choice of a research agenda.

7.1 Technology

The current research project will be followed by a cascade of research projects focusing on different aspects of the integration of sensors into cast metal. This research strategy will both allow for in depth research in specific technological questions, as well as give opportunities to multiply the number of interdisciplinary and inter-organisational combinations that work on each different subject. There are several different examples. One example is the development of both wire based and wireless connections between sensing cast metal and the signal processing computing units. Another example is the specific development of high pressure die casting technology solutions, where speed and very high pressure are key technological challenges. Yet other examples are the different challenges related to sensor signals in ferrous metals in applications with electromagnetic surroundings, such as in electric engines or power transformers.

7.2 Ecosystems and platforms

It is expected that research projects will identify new knowledge and technology. In many situations there are other competences and organizations than the ones who identified the need for these, that are better suited to develop some of these results. By acknowledging this fact, the research intends to gradually establish a research and innovation eco-system, where several highly skilled competence organizations, such as academia, institutes and companies, work together to quickly and effectively producing solutions. This is a deliberate idea of the design of the research projects and of the dissemination of the results.

As the research projects are cascading into different specific research aspects and applications, well-established platforms intend to contribute to catalyze the development.

As technologies and solutions become market ready, it is important also to ensure that suppliers of competence, components and services are established at industrial scales. This will partly be handled in the research strategies by to greatest possible extent build the different parts of the new technology on available technologies. If that is not possible, a

combination of educational strategies and licensing to specific commercial actors will be prioritized.

To reach full technological breakthrough it is also important to initiate standardization of both signals and of connectors. Such standards will be needed to make different components work together in systems such as building constructions, vehicles and medical equipment.

ACKNOWLEDGEMENT

The project Cast metal with intelligence – METALIQ is financed by Vinnova. Vinnova is a Swedish government agency working under the Ministry of Enterprise and Innovation

REFERENCES

[1] International Conference on System-Integrated Intelligence, www.sysint-conference.org, March 7 2017

[2] D. Lehmhus, W. Lang, S. Bosse Material-Integrated Sensing and Intelligent Systems. A Review, EPoSS Annual Forum, Cork, September 26th, 2013

[3] European Technology Platform on Smart Systems Integration, www.smart-systems-integration.org, March 7 2017

[4] Fraunhofer IFAM, www.ifam.fraunhofer.de, March 7 2017

[5] De Baere D. et al., Effective Structural Health Monitoring with Additive Manufacturing, EWSHM - 7th European Workshop on Structural Health Monitoring, Jul 2014, Nantes, France. 2014

[6] Kobliska, J. et al, Rapid Fabrication of Smart Tooling with Embedded Sensors by Casting in Molds Made by Three Dimensional Printing, Department of Mechanical Engineering, University of Wisconsin-Madison, USA, Madison, 2005

[7] US Patent Apparatus and method for embedding optical fibers in metal, US 5283852 A, 1994

VIII ECCOMAS Thematic Conference on Smart Structures and Materials
SMART 2017
A. Güemes, A. Benjeddou, J. Rodellar and J. Leng (Eds)

DETECTION AND LOCALISATION OF FIBRE OPTICS EMBEDDED INTO GLASS FIBRE REINFORCED COMPOSITE SAMPLES USING INFRARED THERMOGRAPHY

KATARZYNA MAJEWSKA[*,1], MAGDALENA MIELOSZYK[1] AND WIESLAW OSTACHOWICZ[1,2]

[1]Institute of Fluid Flow Machinery, Polish Academy of Sciences,
Fiszera 14, 80-231 Gdansk, Poland
[*] e-mail: k.majewska@imp.gda.pl

[2] Warsaw University of Technology,
Narbutta 84, 02-524 Warsaw, Poland

Key words: thermography, glass fibre composite, Structural Health Monitoring, optical fibre

Abstract. Composite materials are used extensively in many industry area e.g. marine, aerospace, automotive, railway, wind energy. Due to their wide applicability the high need of safety is required. Any failure occurrence can result in costs of the damaged structures repairs as well as in environmental contamination (ecological catastrophe). To overcome the problem of safeness is to install permanently so called structural health monitoring (SHM) systems on/ into a structure. The SHM systems can contain various types of sensors and their configurations. Recently the SHM systems are based on fibre optics embedded into the structures for continuously monitor its behaviour. Due to fibre optics diameter slightly thicker than a human hair the development of optical time domain reflectometry, Brillouin scattering or fibre Bragg grating methods is observed [1]. The composite internal discontinuity caused by embedding fibre optics can be a damage origin (e.g. delamination, matrix cracking or fibre-matrix debonding) that significantly decreasing mechanical properties of composite. On the other hand it is important to know the fibre optics arrangement in the elements to not destroy them during structures maintenance.

It is important to have a non-destructive method to inspect an internal structure of an element just after manufacturing process and also during its exploitation. Infrared thermography (IRT) is a non-destructive testing technique that monitors heat distribution using vibration and/or ultrasonic excitation and/or light impulse in order to evaluate the structural health of analysed element [2]. IRT can be divided into two approaches: passive and active thermography. Passive thermography measures thermal variations of a material using an infrared vision device without external thermal sources. Contrary to passive thermography, active thermography requires an external heat sources to stimulate the materials under tests [2]. The common type of active thermography which can be particularly used for fragile, brittle and thin structures is pulsed thermography (PT) in both transmission and reflection modes.

The paper presenting an application of IRT (especially PT) for observation and evaluation of the internal structure of glass fibres reinforced composite samples with embedded fibre optics. The experimental investigation is performed on four-layered rectangular samples manufactured using infusion method with different arrangement of fibre optics. The goal of this paper is to study if it is possible applying PT to distinguish optical fibres to matrix fibre bundles as well as to track the arrangement of the optical fibres. Additionally the time and power of light signal for PT will be established.

1 INTRODUCTION

Composite materials are used extensively in many industry areas, so there is an increasing need of studying their mechanical behaviour in a case of damage occurrence as well as for the non-destructive testing methods for detection of damage initiation and subsequent tracking of its evolution. Composites reliability guarantee safety of mankind and nature. Nonetheless, structure damage in composite can appear in two ways: by external impacts or by internal failure (delamination, water ingress, dust, finger print, sensors etc.) originated from manufacturing. To overcome the problem is to installed permanently so called structural health monitoring (SHM) systems on/into structure. Due to optical fibre (with fibre Bragg grating sensors, FBG) diameter slightly thicker than a human hair it is possible to embed an optical fibre (OF) into a composite matrix. And it is extremely important to avoid failure while embedding an OF into composite.

IRT is very useful method used for diagnosis of structures. Infrared thermograpy methods can be divided into passive and active ones [3]. Passive thermography measures thermal variations of a material using an infrared vision device without external thermal sources. Contrary to passive thermography, active thermography requires an external heat sources to stimulate the materials under tests. The common types of active thermography are pulsed thermography (PT), stepped thermography (ST), lock-in thermography (LT), modulated thermography (MT), pulsed phase thermography (PPT) and frequency modulated thermography (FMT) [4]. Optical based excitation method have such advantages that allow to avoid modifications of temperature field of structures due to the contact of exciting transducer (ultrasound based methods). In the case of PT choice of the proper pulse parameters is a key issue. The two types of excitation pulse shapes are investigated: rectangular and exponential [5, 6] as well as very interesting approach based on frequency modulated thermal excitation was used [7].

In PT two approach can be distinguished. First is based on heat reflection (thermal excitation source and IR camera on the same side of sample) and second on heat transmission (thermal excitation source and IR camera on opposite side of sample) [3].The PT method is widely utilized for damage detection in metallic structural elements especially in aerial structures [3] as well as parts made out of carbon fibre reinforced polymer (CFRP) [8] and glass fibre reinforced polymer GFRP composites [9]. In composite materials IRT allows to detect delamination [10, 11], water ingress [12], matrix cracking [13] or thermal degradation [14].

The state of art shows that problem of composite material inspection is very important. It is caused by fact that composite elements are more and more used in our everyday life. The motivation of the research was a lack of literature related to the PT method applying for for observation and evaluation of the internal structure of glass fibres reinforced composite samples

with embedded fibre optics.

In the paper authors applied pulse thermography for observation and evaluation of the internal structure of GFRP samples with embedded OF. The paper is organised as follow: firstly the GFRP sample with embedded FBG sensors as well as manufacturing process is described. Then the thermography imaging results for the samples are presented. At the end some conclusions and methods limitation is discussed.

2 EXPERIMENTAL INVESTIGATION

2.1 Samples preparation

The laminates were manufactured using infusion method (Fig. 1) for bidirectional material (glass SGlass) and epoxy resin. During preparation process the material was laying on a metal plate covered by PTFE (*polytetrafluoroethylene*) layer allowing easy removing sample. The material plies were covered by additional material layer in a purpose of an equal distribution of the resin during the manufacturing process. Due to this the bottom surface of every sample is smooth while the top one is rough.

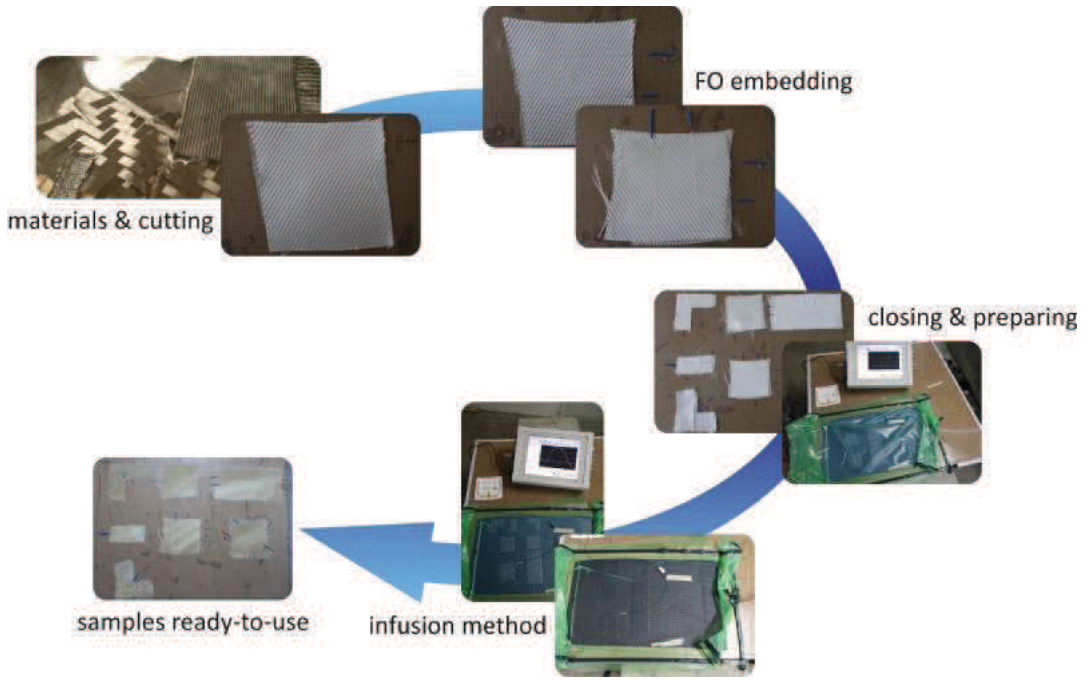

Figure 1: Schema of sample manufacturing.
Special thank you to CreeYach for helping with manufacturing the samples.

2.2 Sample & set-up

The measurements were performed on selected square GFRP (*Glass Fiber Reinforced Polymer*) sample. The dimensions of a sample were as follow 60 mm x 60 mm x 1 mm. The sample was made out of four layers of GFRP with four OF (*Fibre Optic*). Two of OF between 1st

and 2nd layer and two other between 3rd and 4th leyer counting form the bottom of the sample (Fig. 2 (a)). The physical parameters of a glass material and bare OF are similar. The main difference is that the glass fibres are intertwined making one textile while OF is separated. The dimension of OF is about 0.25 mm and is smaller than the thickness of textile (0.4 mm) used for making one layer of the composite sample.

The internal structure of prepared composite sample was examined using pulse thermography method (reflection mode). The experimental set up is presented in Fig 2 (b). Measurements were conducted using two halogen lamps (marked as L, R) 150 W each, infrared camera Flir SC-5600, dedicated support frame and PC computer for infrared camera software operation. Light from lamps changed the temperature field of the sample in the places where any discontinuities like OF were introduced. Temperature changes were registered using infrared camera (measurement frequency 100 Hz) and PC computer.

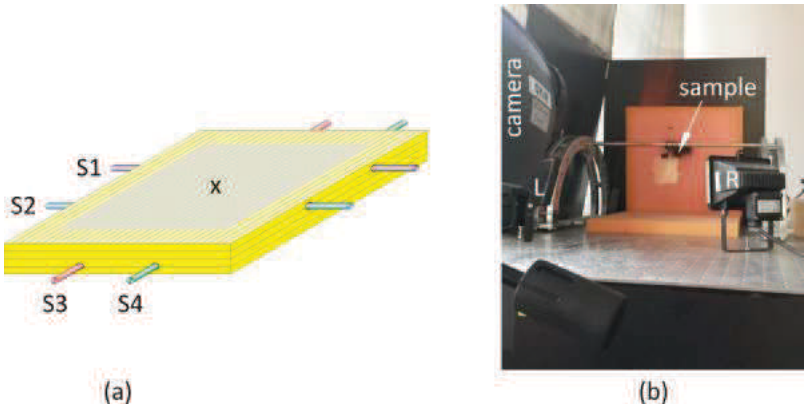

Figure 2: Sample and set-up.

2.3 Experiment details

The main purpose of this experimental investigations was to study if it is possible applying PT technique to distinguish OF to matrix fibre bundles, to track the arrangement of the OF into the sample as well as to establish the power of light signal. For this the following scenario of measurement was proposed. During the experiment the smooth face of the sample was excited using optical source (two halogen lamps, 150 W each) and also the infrared response was observed on the same face of the sample using infrared camera. The results recording was begun before the light excitation started and finished when the sample was cooled down. The light heating least 5 s. The light delivered to the sample changed local temperature field which was observed due to IR camera and registered in 1250 frame movie due to camera software installed on PC.

To achieve the challenges, the authors decided to propose 3 measurement cases (Fig. 2 (b)):

- B - using both lamps,
- L - using left lamp,
- R - using right lamp.

3 RESULTS

Timing graphs for selected point (x) in the middle of the sample (Fig. 2 (a)) for three exciting cases (B, L, R – meaning like above) with marked analysed frames are presented in Fig. 3. The frames were chosen for every 1 s where the I was for heating start moment and V - for heating end moment. It is clearly visible that for both (B) lamps the registered values of termogram / timimg graph DL (called *digital level*) is almost 2 times higher then for one lamp (L or R). Also the process of heating / cooling sample is easy to observe.

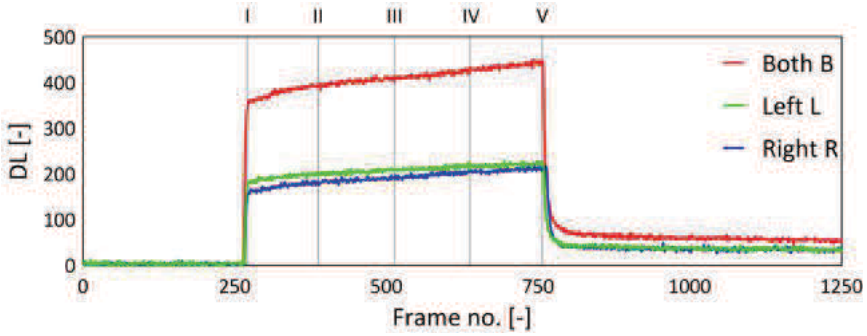

Figure 3: Timing graph with marked I-V analysed frames.

In Fig. 4, Fig. 5 and Fig. 6 the thermograms (a) of selected frames I-V and corresponding maps (b) achieved using own filtering algorithm are presented for three cases B, L, R, respectively. The termograms presents the sample together with fixing elements (see Fig. 2 (b)) and the background. On all of thermograms the sample surface pattern (due to used glass fibre textile) is well visible and the OF locations are only gentle marked. The filtering method was focused on the sample part of frame only (grey rectangular on sample in Fig. 2 (a)). It allows to distinguish all OF and they arrangement, although the effect of the textile pattern was not removed completely. Also it is impossible to distinguish between which layers OF is located. Comparing three presented excitation cases (B, L, R) it is possible to observe that the OF are the best visible in the B case. It is due to amount of energy achieved by the sample and the uniformity of thermal excitation distribution on the sample surface. On the other hand in the B case the textile pattern is highly visible and it is a problem to remove it completely and to see anything more (FO or any other discontinuities in the sample material). Due to this the cases R and L can be treated as a optimal choice for such purpose because it allows to distinguish OF without such strong excitation of sample roughness.

The differences in energy achieved by the sample during excitation using one (R, L) halogen lamp in comparison to two halogen lamps is presented in the following formulas. The differences are due to not symmetric position of lamps to the main axis of the sample.

$$\frac{case\ B - case\ L}{case\ B} * 100 = 51\% \tag{1}$$

$$\frac{case\ B - case\ R}{case\ B} * 100 = 48.5\% \tag{2}$$

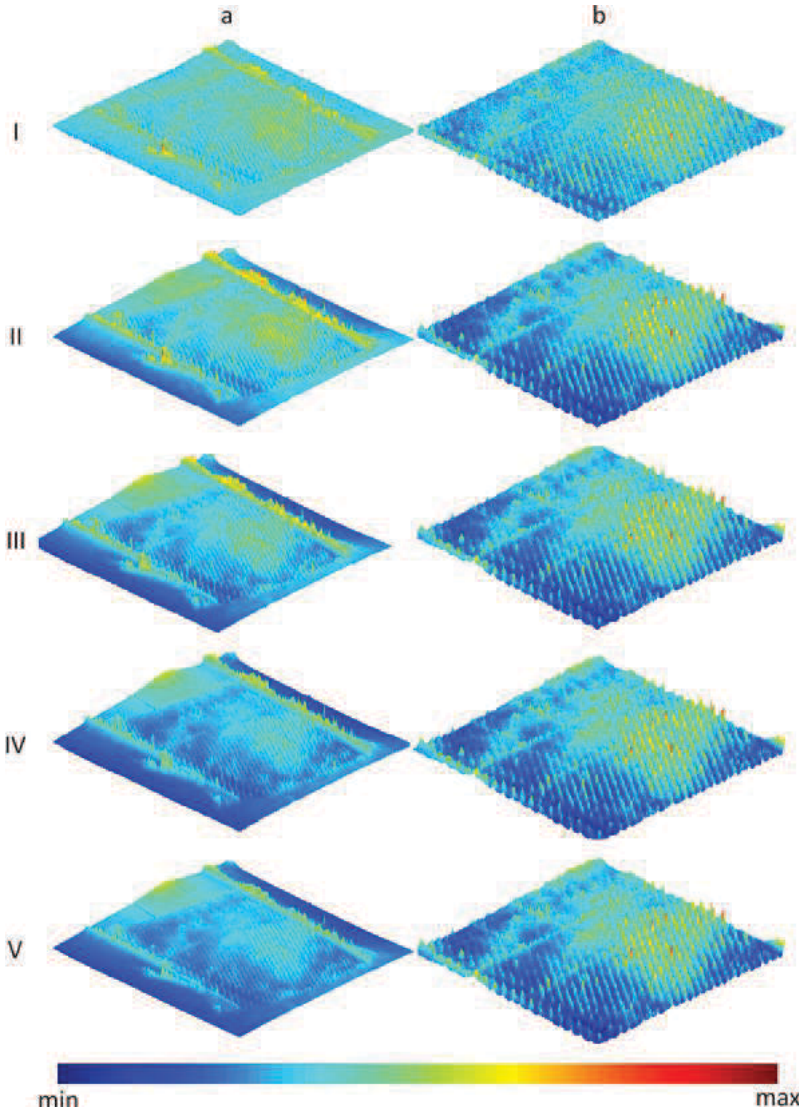

Figure 4: Analysed frames without (a) and with (b) applied own filter for case B.

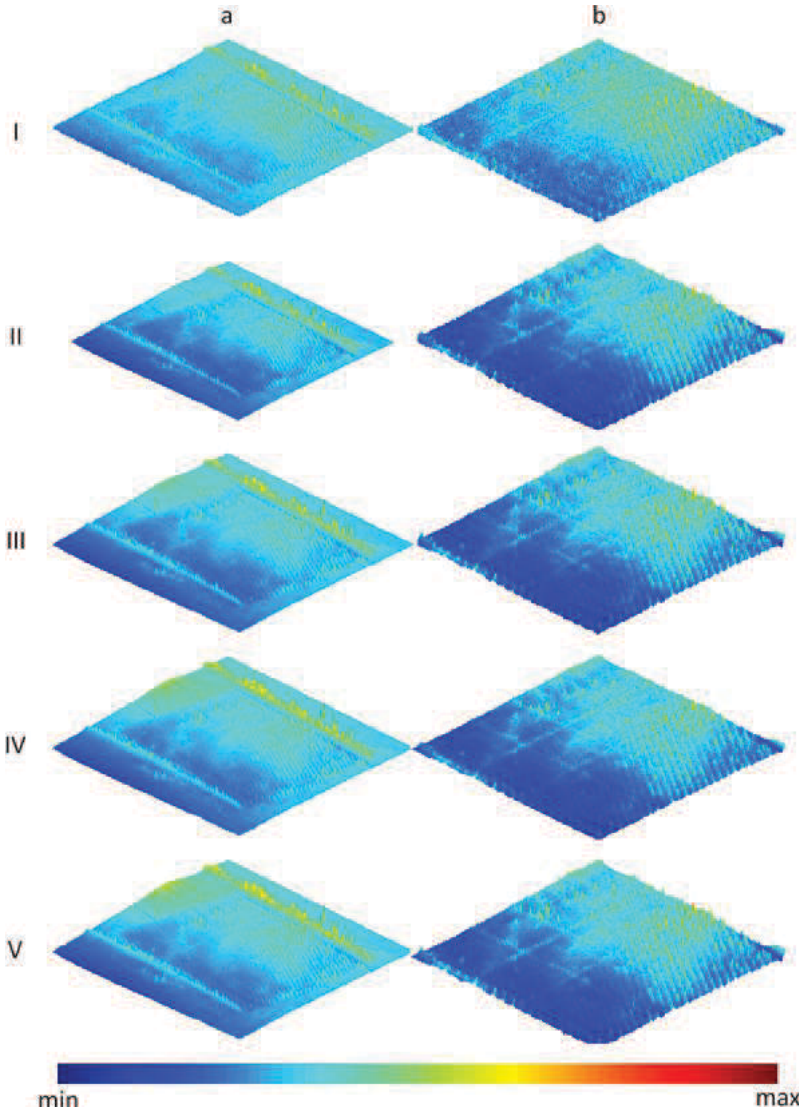

Figure 5: Analysed frames without (a) and with (b) applied own filter for case L.

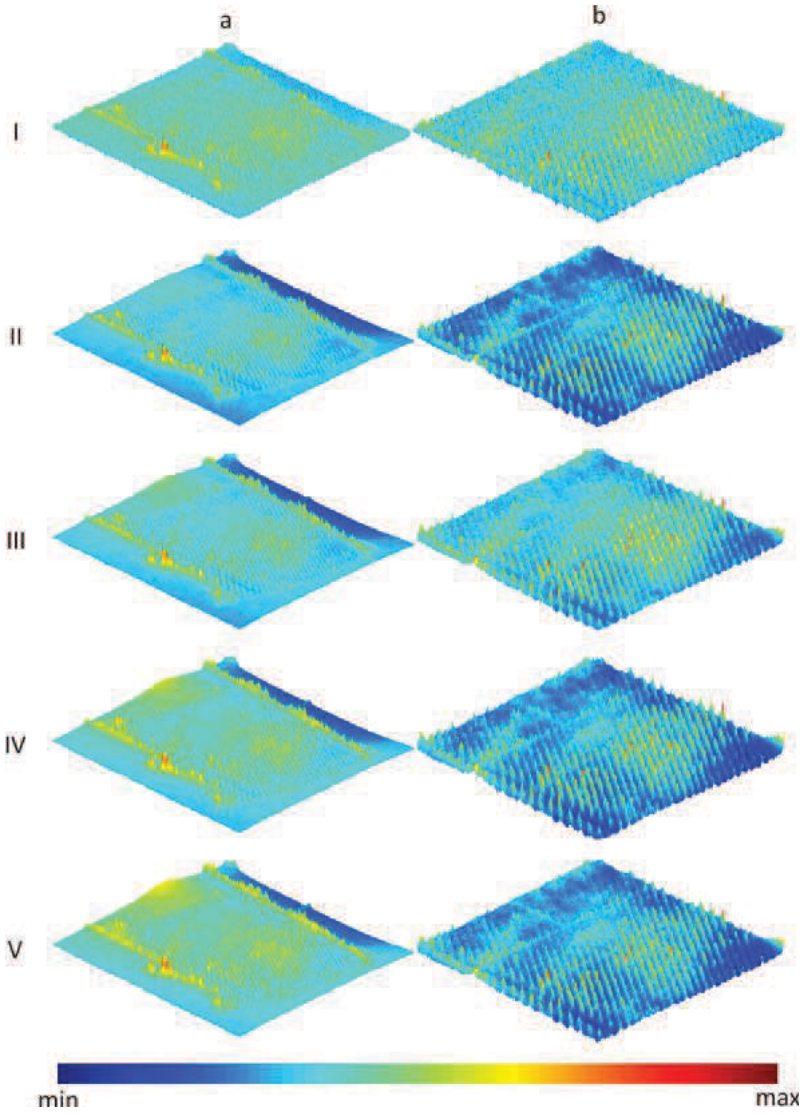

Figure 6: Analysed frames without (a) and with (b) applied own filter for case R.

Table 1: The optical fibre influence in comparison to averaged value of composite material for PT.

	B				L				R			
	S1	S2	S3	S4	S1	S2	S3	S4	S1	S2	S3	S4
I	137	155	140	156	144	165	123	152	150	173	160	171
II	123	131	116	129	138	148	113	138	132	140	139	144
III	120	129	115	129	136	148	110	137	129	137	134	139
IV	120	130	114	126	135	148	107	134	130	137	136	139
V	120	127	113	127	132	143	111	132	128	134	135	136

The Tab. 1 presents differences between thermal energy emitted/reflected by the optical fibre in comparison to averaged thermal energy for whole sample. The differences decreasing with heating time. The best chose is III – IV frame where time of the excitation is about 3-4 s. It means the sample is not cold and not overheated.

4 CONCLUSIONS

The paper investigates practical aspects of pulse thermography technique for observation and evaluation of an internal structure of glass fibre reinforced polymer sample with embedded optical fibre. The main conclusion is that it is possible to find and localise an optical fibres into the sample. It is possible to distinguish OF in all analysed excitation cases, although due to excitation of the sample roughness (glass fibre textile pattern) the best choice seems to be one halogen lamp instead of two. Also the distance between light source and sample as well as angle at which light is delivered to the sample can be an issue in PT (compare case L and case R). It is possible that such an effect (pattern sample) is not observed for painted samples. It will be analysed in future investigations.

ACKNOWLEDGMENTS

The research in this paper was partially supported by the projects entitled:

- (MARTECII/RAMMS/1/2016) Reliable and Autonomous Monitoring System for Maritime Structures granted by National Centre for Research and Development in Poland,
- (DEC-2013/10/A/ST8/00071) Excitation and control of mechanical waves in nonlinear media granted by Polish National Science Center,
- (PBS1/B6/8/ 2012) Non-invasive Methods for Assessment of Physicochemical and Mechanical Degradation granted by National Centre for Research and Development in Poland.

REFERENCES

[1] Udd E., Spillman Jr W.B. *Fiber Optic Sensors: An Introduction for Engineers and Scientists*. Wiley & Sons Inc., New Jersey, ISBN 978-0-470-12684-4, (2011).

[2] Ruddock R.W. *Basic Infrared Thermography Principles*. Reliabilityweb.com Press, USA, ISBN 978-1-939740-01-4, (2010).

[3] Vollmer M., Mllman K.-P. *Infrared Thermal Imaging*. Wiley-Vch, ISBN: 9783527407170, (2010).

[4] Yang R. & He Y., Optically and non-optically excited thermography for composites: A review. *Infrared Physics & Technology* (2016) **75**:26-50.

[5] Netzelmann U., Optimized temporal excitation profiles in active thermography, *Analytical Sciences -Special Issue* (2001) **17**:432-435.

[6] Netzelmann U., Heeg R. and Walle G., Pulsed Thermal Methods for Materials Characterization, *Proc. of NDE2002, National Seminar of ISNT*, Chennai, 2002.

[7] GhaliV.S., Mulaveesala R., Takei M., Frequency-modulated thermal wave imaging for nondestructive testing of carbon fiber-reinforced plastic materials. *Measurement Science and Technology* (2011) **22**:104018 (4pp).

[8] Susa M., Castanedo C.I., Maldague X. and Bendada A., Pulse thermography applied on a complex structure sample: comparison and analysis of numerical and experimental results, *Proc. of IV Conferencia Panamericana de END*, Buenos Aires, 2007.

[9] Shepard S.M., Flash Thermography of Aerospace Composites, *Proc. of IV Conferencia Panamericana de END*, Buenos Aires, 2007.

[10] Mieloszyk M., Krawczuk M., Malinowski P., Wandowski T., Ostachowicz W., Active Thermography Method for Delamination Detection and Localisation in Composite Structures, *Proc. of EWSHM*, Drezno, 2012.

[11] Majewska K., Soman R., Mieloszyk M., Ostachowicz W., Assessment of delamination in composite beam using infrared thermography, optical sensors and terahertz technique, *Proc. of SPIE*, Portland, 2017.

[12] Majewska K., Mieloszyk M. and Ostachowicz W., Glass fibre composite elements with embedded fibre Bragg grating sensors inspected by thermography techniques, *Proc. of EWSHM*, Bilbao, 2016.

[13] Adda-bedia E.A., Bouazzaa M., Tounsia A., Benzaira A., Maachouc M., Prediction of stiffness degradation in hygrothermal aged $[_m/90_n]_S$ composite laminates with transverse cracking. *Journal of Materials Processing Technology* (2008) **199(1-3)**:199-205.

[14] Muramatsu M., Harada Y., Suzuki T., Niino H., Infrared stress measurements of thermal damage to laser-processed carbon fiber reinforced plastics. *Composite Part A* **68**:242-250.

VIII ECCOMAS Thematic Conference on Smart Structures and Materials
SMART 2017
A. Güemes, A. Benjeddou , J. Rodellar and Jinsong Leng (Eds)

EXPERIMENTAL STUDY OF NON-UNIFORM STRAINS IN COMPOSITES WITH EMBEDDED FIBER BRAGG GRATING

A.N. ANOSHKIN[†], V.P. MATVEENKO[†], I.N. SHARDAKOV[††], N.A. KOSHELEVA[†], E.M. SPASKOVA[†], A.A. VORONKOV[†], G.S. SHIPUNOV[†], V.YU. ZUIKO[†] AND D.S. LOBANOV[†]

[†] Perm National Research Polytechnic University, 29, Komsomolski Ave., Perm, 614990, Russian Federation
e-mail: anoshkin@pstu.ru, www.pstu.ru

[††] Institute of Continuous Media Mechanics of the Ural Branch of Russian Academy of Science, ICMM UB RAS, 1, Academician Korolev St., Perm, 614013, Russian Federation
e-mail: mvp@icmm.ru, www.icmm.ru

Key words: polymeric composite material, fiberglass, optical fiber sensors, fiber Bragg grating (FBG), smart composite, experiment.

Abstract. This work presents the results of the experimental studies of strain distribution in the composite specimens using optical sensors based on fiber Bragg gratings (FBG) embedded into the material. Both flat bar and V-notch specimens were taken for tensile tests which were carried out on Instron 5982 machine. Also the optical system Vic-3D was used for independent registration of strain fields on the specimen surface. The results of tensile testing of flat specimens showed the general possibility of uniform strain measurement and were used for calculation of calibration factor for the next following tests. A series of repeated uniaxial tension and compression tests was performed on flat bar samples to determine the material modulus of elasticity using FBG sensors. The tension of V-notch specimen leads to occurrence of non-uniform fields of strain. The results of the strain gradient registration in the V-notch composite specimen using FBG sensors were compared with the digital images received from the optical system Vic-3D. The difference between the results of strain measurement obtained with the different approaches did not exceed 5%.

1 INTRODUCTION

One of the main issues in the development of advanced aviation and aerospace composite is a providing of design reliability during long-term operation especially for civil aviation. The composite material is a more complex object for studying mechanical properties because of anisotropy, an essential dependence of properties on temperature and manufacturing technology. In some cases, the material properties within the construction can not be determined on standard specimens, and the influence of technological factors, such as the characteristics of raw materials and the parameters of manufacturing processes, can hardly be predicted.

However, the solution of the problem of providing of design reliability can be found in the creating principle of composite material and construction [1, 2]. This is the creation of materials with the ability to diagnose and monitor its state during the short-term tests or continuous service using the fiber-optic sensors [3, 4]. Optical fibers can be used as sensors to measure strain, temperature, pressure and other physical quantities and capable of withstand strains comparable to strains of the composite structure. One of the main problems when using fiber optic sensors in composite materials is related to the strain measurement.

World experience of using fiber optic sensors viewed in a sufficiently large number of papers. In [5, 6] the possible problems in measuring the strain of structures made of composite materials are considered. The issues of the influence of optical fiber on the properties of polymer composite material, embedding technologies of fiber-optic sensors in composites and the problem of calibration are also touched upon. There are some publications devoted to the methods and measuring devices [7-9]. The multi-functional capability of the fiber optic sensors is analyzed in [10]. The capability of

interlaminar defects determination by the embedded fiber Bragg grating (FBG) sensors is viewed in [11]. An example of the effective use of FBG sensors in practical applications is [12], which describes the use of FBG sensors for monitoring composite road bridge.

2 EXPERIMENTAL STUDY

To carry out the experimental studies to assess the ability of fiber-optic sensors to register a non-uniform strain field, the composite flat bar and V-notched specimens made of fiberglass with embedded FBG sensors were manufactured using pre-preg technology (Figure 1,a). Schemes of optical fibers mounted in the specimens are shown on the Figure 1,b. The signals from FBG sensors are registered by ASTRO X 327 interrogator.

The flat bar samples were used for calibration of optical fiber sensors embedded in the composite material. The V-notched specimens were used for measuring of non-uniform fields of strain. The strain measurements were performed taking into account the results of calibration experiments. Furthermore, a series of uniaxial tension and compression tests was performed on flat bar samples to determine the material modulus of elasticity using FBG sensors.

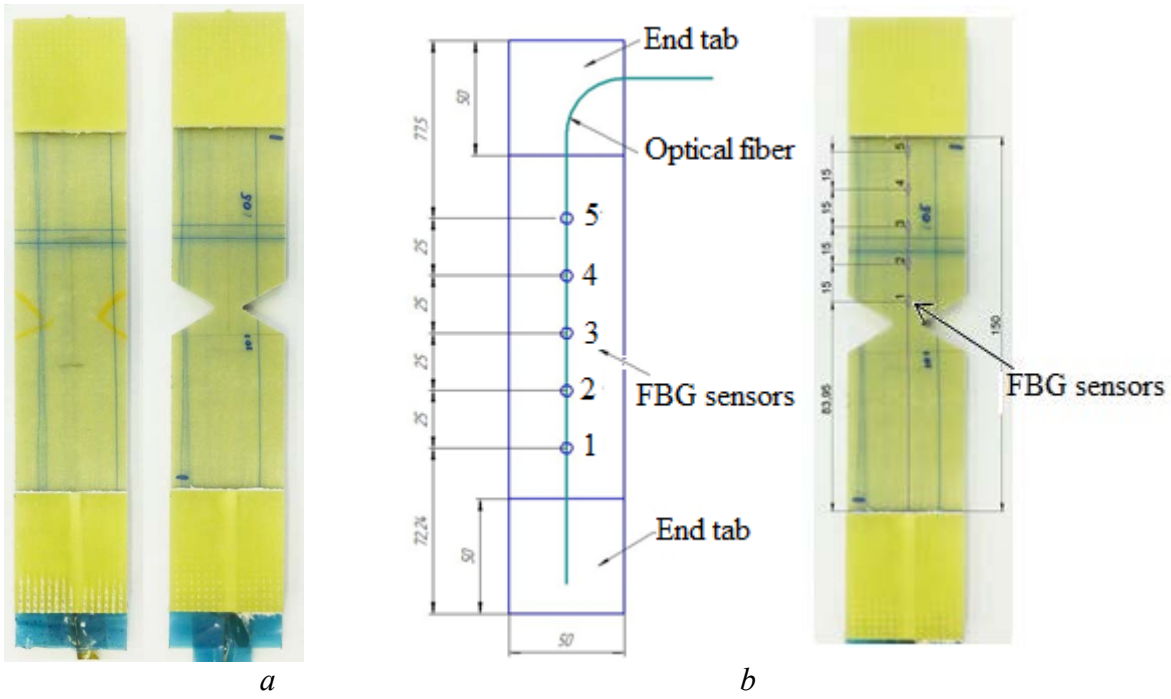

Figure 1: (a) Fiberglass specimens with embedded FBG sensors, (b) scheme of optical fibers mounted in the specimen

The mechanical tests were carried out on the universal Instron 5982 machine. The optical system Vic-3D was used for independent registration of strain fields on the specimen surface. It was especially necessary for calibration tests. Figure 2 shows the scheme for uniaxial strain measuring in a flat specimen using embedded FBG sensors.

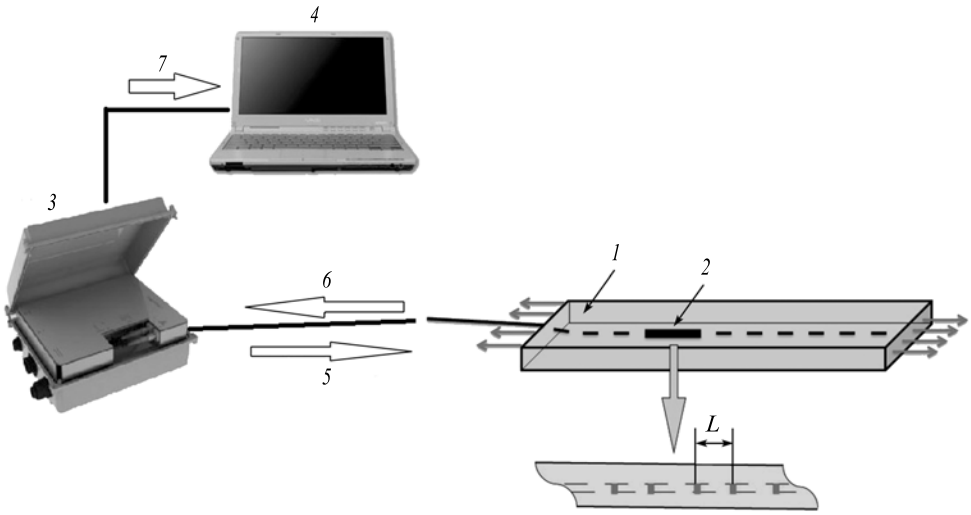

Figure 2: Scheme for uniaxial strain measuring in a flat specimen using embedded FBG sensors.
1 – specimen, 2 – FBG sensor, 3 – interrogator, 4 – PC, 5 – the input broadband spectrum, 6 – the spectrum reflected by an FBG, 7 – FBG sensor data recording.

3 TEST RESULTS ANALYSIS

At the first stage, a series of tests for uniaxial tension of specimens with a V-shaped notch was carried out. This shape of the sample provides non-uniform fields of strain along the center line, which was determined by the results of preliminary numerical simulation. The experiment was carried out at a speed of 2 mm/min, under a load of 10 kN.

In addition, the strains at the location of FBG sensors were measured using a three-dimensional digital optical system Vic-3D, with a frequency of 15 frames per second.

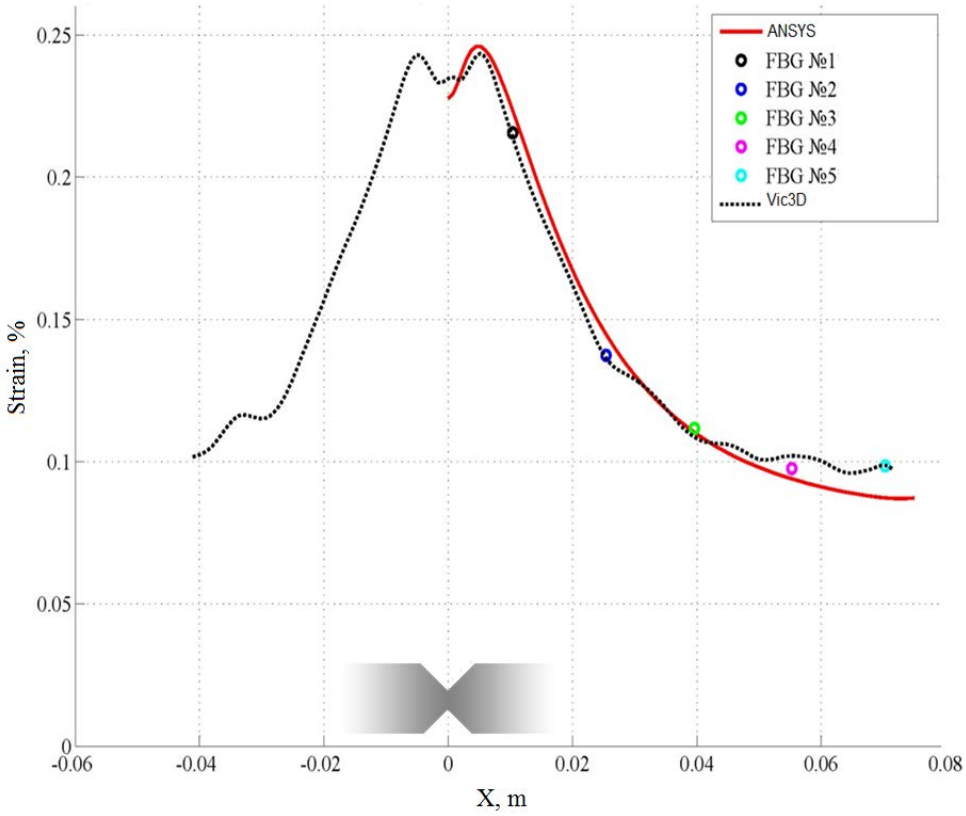

Figure 3: The results for the longitudinal strain distribution along the centerline of the specimen on the loading time t = 18.9 sec

Figure 3 shows the results for the longitudinal strain distribution along the centerline of the specimen on the loading time t = 18.9 sec., obtained by using the optical system and FBG sensors. The results of the measurements are presented taking into account the calibration factors. Also the results obtained by numerical simulation are shown on Figure3. The experimental data for all times of loading is compared to data obtained with the mathematical modeling - the difference between the results does not exceed 5%.

At the second stage of experimental research, the evaluation of Young's modulus by uniaxial tension and compression tests was performed on flat bar samples with embedded FBG sensors. Also, the modulus of elasticity was controlled using a standard test machine and a Vic-3D system.

The experiment was carried out according to the following scheme: preload up to 20% of Fmax (20 kN) with subsequent unloading up to 5% (5 kN), then thrice-repeated loading / unloading (5..30 kN). Then change to the compression: preload up to -11 kN with unloading up to -7 kN, then thrice-repeated loading / unloading (-7..-14 kN).

The results obtained by using the optical system and FBG sensors are shown on Figure 4.

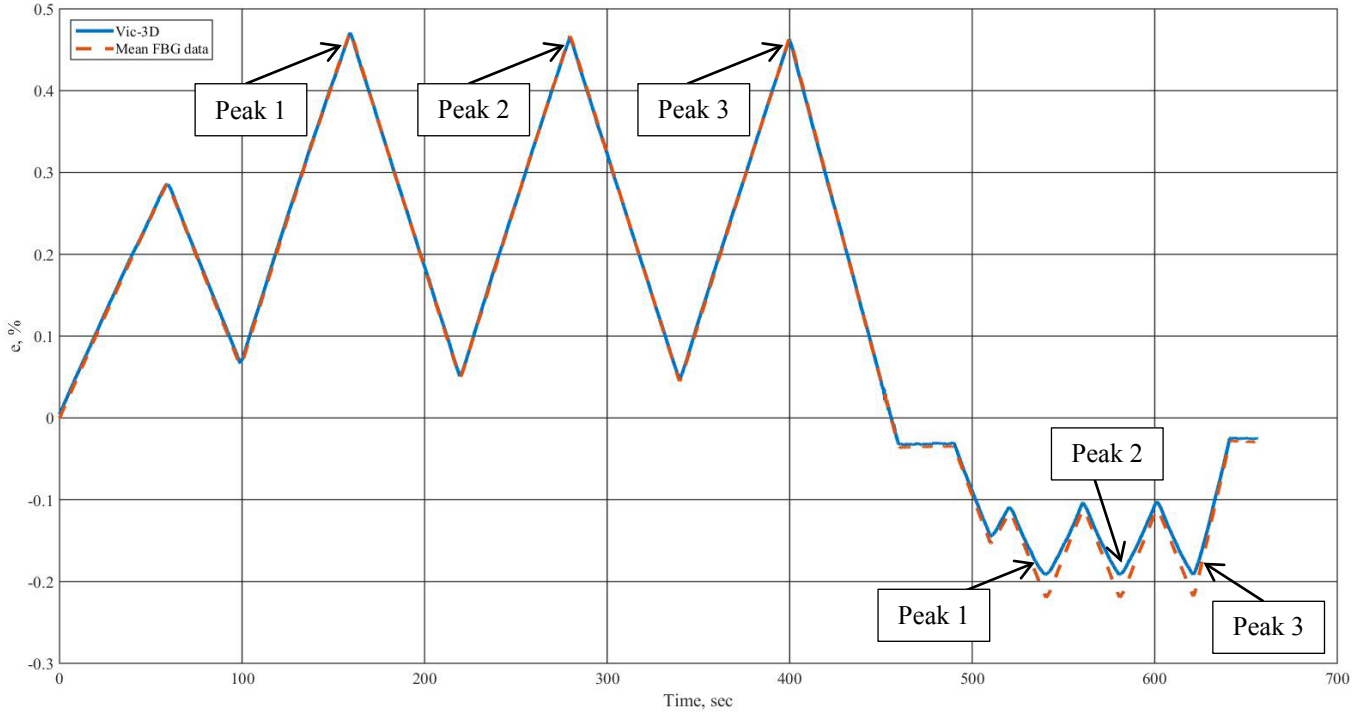

Figure 4: Strain of the specimen under uniaxial tension and compression

Experimental studies show that fiber-optic sensors describe the process of a repeated load in the tension region quite correctly. In the case of compression loading the difference between optical system data and signals from FBG sensors is about 10%. Figure 5 shows the load-strain curves where the strain was obtained with the help of the Vic-3D optical system and time synchronized signals from FBG sensors. The force was recorded from the Instron force transducer. The difference between Vic-3D data and signals from FBG sensors is about 10%.

The results of Young's modulus evaluation are given in table 1. It can be seen that the difference between the modulus of elasticity determined by the optical system and FBG sensors under the tensile loads does not exceed 6%.

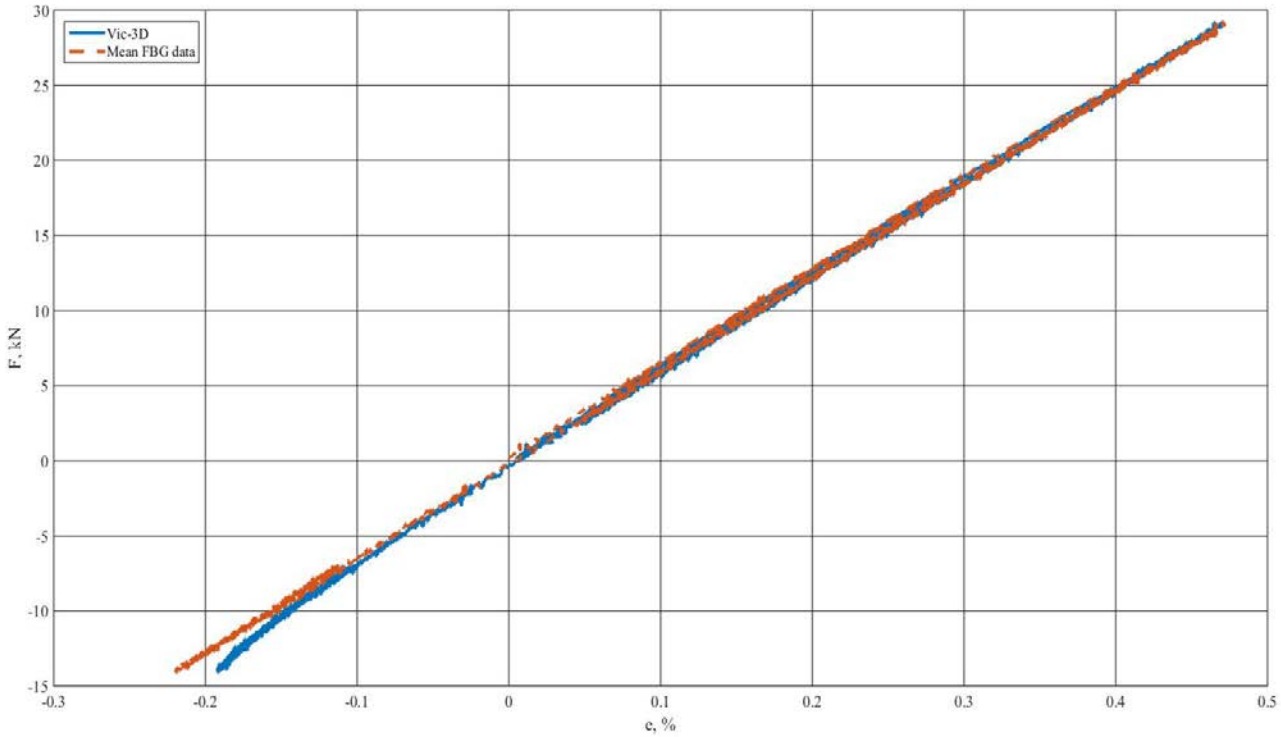

Figure 5: Load-strain curves obtained by Vic-3D data and signals from FBG sensors

Table 1: Experimental modulus of elasticity

	Modulus of elasticity, GPa						
	Vic3D	FBG №1	FBG №2	FBG №3	FBG №4	FBG №5	Vic3D vs. FBG,%
				Tension			
Peak 1	25.98	25.35	25.65	25.48	25.45	25.35	1.80%
Peak 2	26.50	24.94	24.93	25.13	24.72	24.94	5.97%
Peak 3	26.68	25.95	25.94	26.25	25.71	25.95	2.77%
				Compression			
Peak 1	34.47	28.20	26.67	26.83	28.49	28.20	20.40%
Peak 2	31.13	26.63	26.63	26.91	24.59	26.63	15.34%
Peak 3	36.62	26.27	25.62	25.92	27.28	26.27	28.46%

In the case of compression loading the difference between Young's modulus exceeds 25%. This may be due to the fact of occurring flexural strain caused by the non-standard geometrical dimensions. For more accurate evaluation of the modulus of elasticity, it is necessary to carry out the compression tests on standardized test specimens. Then, it is possible to refine the material modulus of elasticity using fiber-optic sensors.

4 CONCLUSIONS

This work presents the experimental results demonstrating the efficiency of the FBG sensors for registration of non-uniform fields of strain. The validity of these results is confirmed by the numerical calculations and measurements of the strain fields by the digital optical system Vic-3D. The results of the strain gradient registration in the V-notch composite specimen using FBG sensors were compared with the digital images received from the optical system. The difference between the results of strain measurement obtained with the different approaches did not exceed 5%.

The possibility of determining the material modulus of elasticity with the use of embedded fiber-optic sensors was evaluated. The difference between the modulus of elasticity determined by the optical system and FBG sensors under the tensile loads does not exceed 6% and in the case of

compression loading this difference exceeds 25%. To refine these results, it is necessary to carry out an additional set of experimental studies.

The results of this work will be used for fundamental investigation devoted to the development of experimental and theoretical principles of the mechanical analysis of smart materials with embedded fiber Bragg grating (FBG) sensors for structural health monitoring (SHM)

5 ACKNOWLEDGMENTS

The study was performed in Perm National Research Polytechnic University with support of the Russian Science Foundation (project №15-19-00243).

REFERENCES

[1] Kelly, A. (ed.) (1994), *Concise encyclopedia of composite materials (Advances in materials sciences and engineering)*, England: Revised Edition.

[2] Committee on new materials for advanced civil aircraft, national materials advisory board, aeronautics and space engineering board, commission on engineering and technical systems, national research council. New materials for next-generation commercial transports (1996), Washington, D.C: National academy press.

[3] Lee D., Lee J., Kwon I., Seo D. Monitoring of fatigue damage of composite structures by using embedded intensity-based optical fiber sensors. *Smart Mater. Struct.* (2001) **10**: 285–292.

[4] Leung C.K., Yang Z., Xu Y., Tong P., Lee S.K. Delamination detection in laminate composites with an embedded fiber optical interferometric sensor. *Sensors and Actuators A: Phys.* (2005) **119(2)**: 336–344.

[5] Makhsidov V.V., Fedotov M.Yu., Shiyonok A.M., Zuev M.A. For an issue of embedded optical fibre in CFRP and strain measurement with fibre Bragg gratings sensors. *Journal on Composite Mechanics and Design* (2014) **20(4)**: 568–574.

[6] Bosia F., Giaccari P., Botsis J., Facchini M., Limberger H., Salathe R. Characterization of the response of fibre Bragg grating sensors subjected to a two-dimensional strain field. *Smart Mater. Struct.* (2003) **12**: 925–934.

[7] Kanga D., Parkb S., Hongb C., Kimb C. The signal characteristics of reflected spectra of fiber Bragg grating sensors with strain gradients and grating lengths. *NDT&E International* (2005) **38(8)**: 712–718.

[8] Luyckx G., Voet E., De Waele W., Degrieck J. Multi-axial strain transfer from laminated CFRP composites to embedded Bragg sensor: I. Parametric study. *Smart Mater. Struct*. (2010) **19 (10)**, Art. ID 105017.

[9] Mawatari T., Nelson D. A multi-parameter Bragg grating fiber optic sensor and triaxial strain measurement. *Smart Mater. Struct*. (2008) 17, Art. ID 035033.

[10] Takeda N., Okabe Y., Kuwahara J., Kojima S., Ogisu T. Development of smart composite structures with small-diameter fiber Bragg grating sensors for damage detection: quantitative evaluation of delamination length in CFRP laminates using lamb wave sensing. *Compos. Sci. Technol* (2005) **65**: 2575–2587.

[11] Dai Y., Liu Y., Leng J., Deng G., Asundi A. A novel time-division multiplexing fiber Bragg grating sensor interrogator for structural health monitoring.*Opt. Lasers Eng*. (2009) **47**: 1028–1033.

[12] Gebremichaela Y., Lia W., Boylea W., Meggittb B., Grattana K., McKinleya B., Fernandoc G., Kisterc G., Winterc D., Canningd L., Luke S. Integration and assessment of fibre Bragg grating sensors in an all-fibre reinforced polymer composite road bridge. *Sensors and Actuators A*. (2005) **118(1)**: 78–85.

VIII ECCOMAS Thematic Conference on Smart Structures and Materials
SMART 2017
A. Güemes, A. Benjeddou , J. Rodellar and Jinsong Leng (Eds)

FIBRE OPTIC SENSOR EMBEDDING IN METALS USING LOW COST TIG WELDING AND HIGH PRECISION LASER BRAZING

TANIA GRANDAL[*†ª], SERGIO FRAGA[†], GEMMA CASTRO[†], ESTEBAN VAZQUEZ[†], JOSE A. VAZQUEZ[‡] AND ANDER ZORNOZA[†]

[†]AIMEN Technology Center,
Laser Application Centre
C/Relva, 27 A, 36410 O Porriño (SPAIN)
tania.grandal@aimen, http://www.aimen.es

[ª] City University London
School of Engineering and Mathematical Sciences
London EC1V0HB, UK, http://www.city.ac.uk/

[‡] Wärtsilä Ibérica S.A.
S&B Spain, Pol. Industrial As Gándaras, parcela 206, nave B-3
36475 O Porriño (SPAIN), http://www.wartsila.com/esp

Key words: Smart Metals, Embedded fiber optic sensors, Laser Brazing, TIG welding, Optical fiber sensor, Fiber optic sensors, Fiber Bragg gratings.

Abstract: Smart metallic specimens (ST-52 steel coated with Tin alloy), with embedded optical fiber sensors are manufactured using two techniques: Tungsten Inert Gas welding and Laser Brazing. Two specimens, each manufactured with one of the previous techniques for embedding a Fiber Bragg Grating, are studied, by tensile tests and metalographic imaging. In both cases the smart materials are sensible to axial strain, and the bond between the sensor and the embedding metal is very good.

1 INTRODUCTION

Fiber optic sensors present benefits when compared to other kind of sensors, as electromagnetic immunity, small size, possibility of multiplexing many sensors, monitoring several parameters in different positions in one single fiber, etc. These properties make this kind of sensors ideal for creating smart materials just by embedding them. In this work, Fiber Bragg Grating (FBG) sensors are the fiber optic sensors chosen to be embedded. An FBG sensor is a filter inside a small section of fiber optic which reflects certain wavelengths and transmit the others. The reflected wavelength depends of the period of the grating written in the fiber and is named Bragg grating. FBG sensors have a length around 5 mm and are the most used fiber optic sensors for different applications, because many parameters such as temperature, strain, pressure, erosion, detection of cracks, etc., can be monitored.

There is a large tradition embedding fiber optic sensors and, in particular, FBG sensors in different materials to monitor them. That kind of sensors are specially used in concrete to

monitoring the structural health of civil constructions [1]. Moreover, fiber optic sensors are embedded into composite materials too, for monitoring and control their manufacturing process and operation work [2]. In the case of metallic structures, the embedding process is more troubling than the previously explained, because of high temperatures achieved during manufacturing and the fragility of the fiber. In this case, melting the metallic material is needed to bond the fiber optic sensor to the metallic structure. Smart metallic parts with embedded optical fiber sensors are very riveting. they open the possibility to build smart materials and tools having overall control during their manufacturing and operation life. Moreover, it presents higher advantages when working with additive manufacturing techniques or repairing process where metallic material is added. Also, because of the embedded sensors in these structures, it is possible to know the interlayer and union condition and the temperature contribution during the manufacturing process, mainly when different materials are involved which potentially would allow rectifying and correcting any fail or inaccuracy [3]. Another great advantage of embedding fiber optic sensors into metallic materials, is the possibility of installing fiber optic sensors in structures which withstand harsh environments usually high temperature. In that environments the fiber optic or the coating of the fiber suffers a progressive deterioration process which weaken its mechanical properties or even sometimes an adhesive that supports these adverse conditions is hard to achieve. For these cases, the best option is embedding or welding the fiber to the metallic structure. Although, embedding fiber optic sensors into metallic structures is a research line which is still in development, there are works in which different embedding techniques are studied based on deposition techniques, ultrasonic welding, brazing techniques or Selective Laser Melting (SLM) [3-4]. Note that for metallic embedding the fiber must always have a metallic coating to protect it during the embedding process.

In this work two techniques for embedding fiber optic sensors into metallic structures are compared: Tungsten Inert Gas welding (TIG) [5] and Laser Brazing welding [6]. Although both techniques are capable of embedding fiber optic sensors to metallic structures, they present many differences. TIG welding is a cheap technique, easily accessible and being a manual process is easy to adapt and correct as required. In contrast, Laser brazing, though is an expensive process, is very repeatable, offers a high control over the process and allows embedding in selected areas. Previous both embedding process, the FBG sensors were metallic coated by sputtering and electroplating techniques as in previous works is described [7] to protect the fiber sensor. Two Ni coated FBG sensors with around 650µm of total fiber diameter, were embedded, each by one of mentioned technique, using the same metal; a tin alloy with a low melting point. The advantages from one to other, embedding technique, are in the advantages of the manufacturing process itself. The sensors were embedded in similar specimens constructed *ad hoc* to be tested in tensile tests for characterization.

2 FIBER OPTIC SENSOR EMBEDDING WITH TIG WELDING

TIG welding is a well-known and widely-adopted welding technique, where the weld is produced by a non-consumable tungsten electrode. Therefore, TIG welding is one of the simplest and cheapest techniques to embed optical fibers into metallic structures as we showed in [2]. While embedding optical fibers with TIG, the optical fiber is placed on top of the material to be welded on, and the wire is welded on top of the fiber. This process is carefully performed by an operator. Being a man-made process, the operator hast the possibility to make small

manual adjustments during the embedding process. Therefore, the experience and know-how of the operator is key for successfully embedding the optical fibers and optical fiber sensors to the metallic parts. The optical fiber or sensor to be embedded needs to be protected with a metallic coating, and a coating thickness of near 500µm (total diameter of the coated fiber) has been found to be necessary for successful embedding of optical fibers and sensors when Tin alloy wires are used in TIG [2].

A smart metallic specimen is manufactured with TIG welding. The FBG sensor embedded, shown in figure 1 (a) has been coated for a total diameter of 619µm with a 1µm Au layer and a 246.5µm Nickel layer by sputtering and electroplating deposition techniques respectively. The specimen with the embedded optical fiber is shown in figure 1 (b).

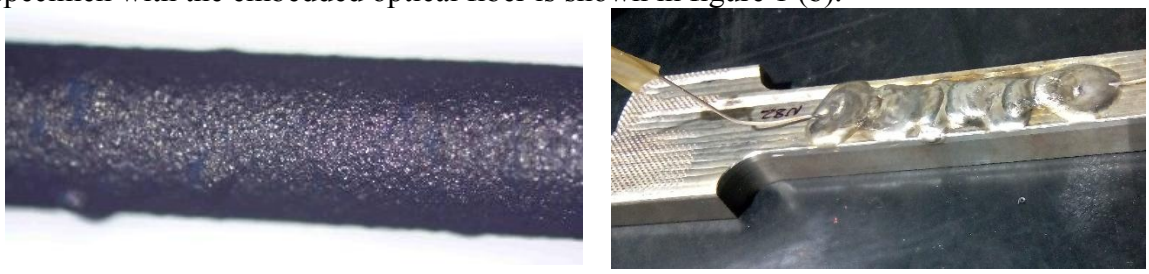

(a) **(b)**

Figure 1: (a) Nickel-coated FBG and (b) smart metallic specimen with embedded FBG manufactured with TIG.

3 FIBER OPTIC SENSOR EMBEDDING WITH LASER BRAZING

For the smart metallic specimen manufactured with laser Brazing, our previously developed technique and experimental setup, presented in [3], was used. The technique consists on placing the fiber well attached and slightly pre-strained on the top of a ST-52 specimen with a tin-alloy coating. The laser performs longitudinal wires, at least two at each side of the fiber and one on the center to embed de fiber. Our previous results show that Nickel coated fibers for a total diameter of 237µm can be embedded, although more research is conducted in this matter to embed less invasive (thinner coating) optical fibers. The total diameter of the Nickel coated optical fiber was 653µm, with a 1µm thick Gold layer and a 263.5µm thick Nickel layer. Figure 2 (b) shows the manufactured specimen.

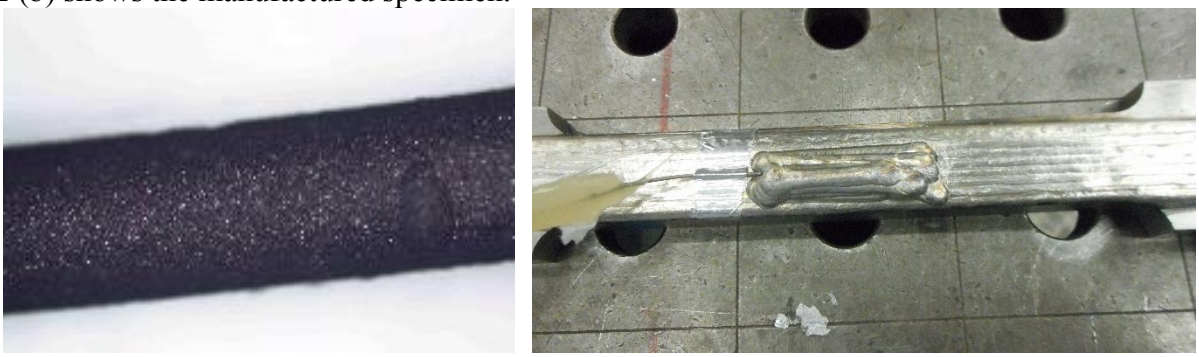

(a) **(b)**

Figure 2: (a) Nickel-coated FBG and (b) smart metallic specimen with embedded FBG manufactured with Laser Vrazing.

4 RESULTS AND DISCUSSION

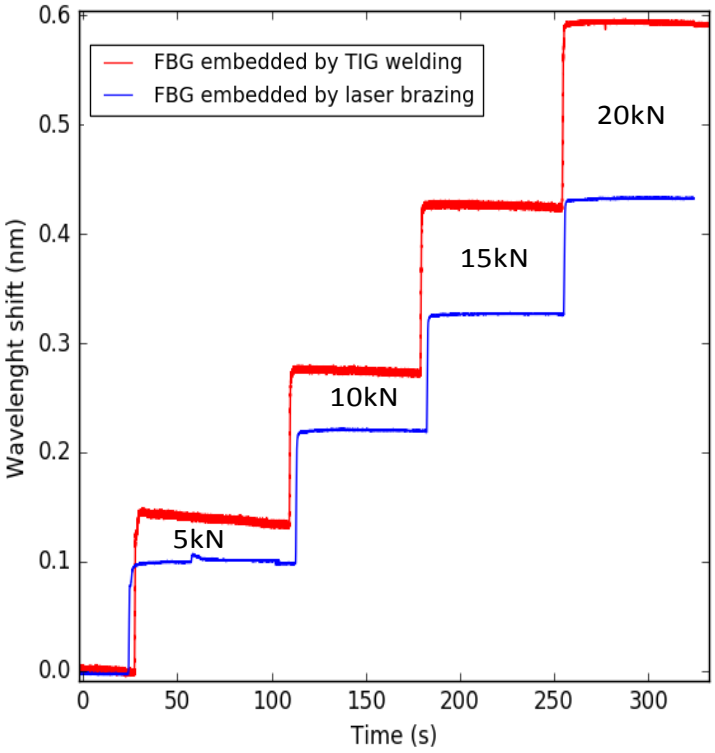

Figure 3: Tensile tests performed in both specimens and the response of the FBG to the load.

Tensile tests were performed with both smart specimens, where an axial force of up to 20kN was applied in 5kN steps, shown in figure 3. We can see that the response of the TIG welded specimen is greater to load, which is attributed to small differences in the geometry of the specimens, since for example, the Tin-alloy coatings where of different thickness and both specimen's steel was cut manually. Each specimen was provided with an electrical strain gauge, placed and attached on its side. The strain response of each specimen, comparing the output of the FBG to the strain gauge, is shown in figure 4. Both embedded FBGs show a similar response to the sensibility before coating or embedding, but still, very different one from another. This is attributed to misalignment of FBGs and strain gauges and errors of the measurements, although further studies are being conducted.

After the tensile tests, destructive metallographic imaging was performed, which is shown in figure 4 (a) for the TIG embedded FBG and in figure 4 (b) for the Laser Brazing embedded FBG. The inner black circle, is the optical fiber, the clear concentric bigger circle corresponds to the Nickel coating, and the rest is the embedding Tin-alloy. The darker section in the lower left side of the TIG embedded fiber coating, is just a defect created during cutting the specimen. So, it is clear there is very good bond between all layers.

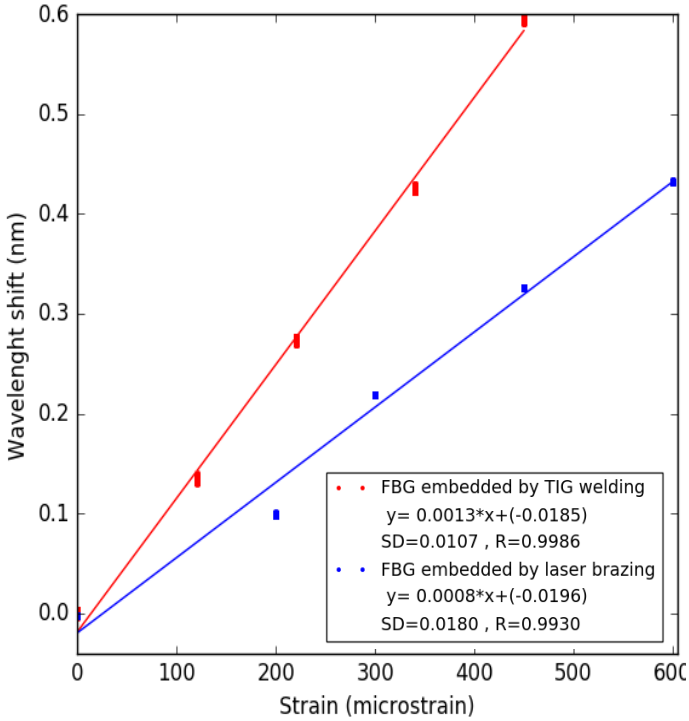

Figure 4: Strain characterization of the embedded FBGs.

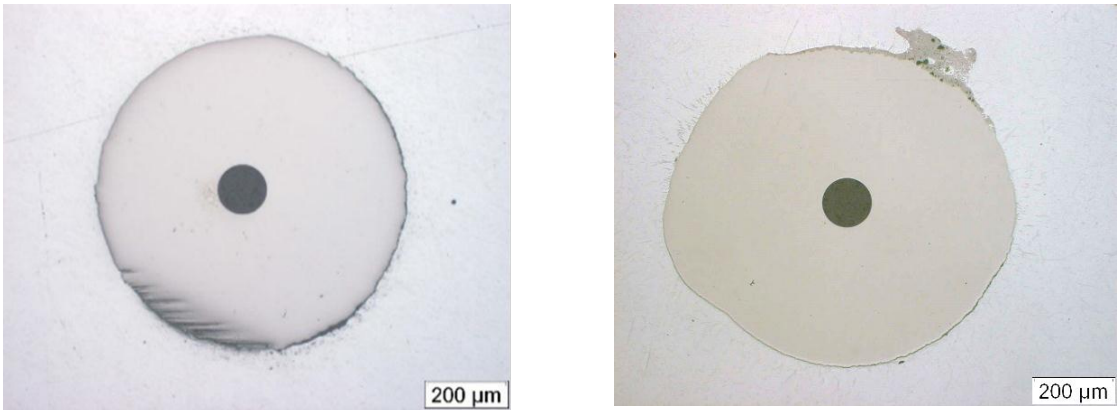

(a) (b)

Figure 5: (a) Metalography of the transversal cut of the FBG embedded with TIG and (b) Laser Brazing embedded FBG.

5 CONCLUSIONS

Smart metallic specimens manufactured with TIG and Laser Brazing have been compared. The quantitative parameters used for this comparison were the sensitivity of embedded fibre Bragg gratings (FBG) to strain characterised in tensile tests. Also, metallographic tests were performed to estimate the quality of the bond of the fibre and fibre coating to the embedding metal. The performance of the manufactured sensors is good in both cases, and strain sensibility

is close to the given by the original FBG sensibility. The difference in sensibility of both techniques is attributed to measurement error and uncertainties of the employed strain gauge, although further details are being currently investigated in this matter. The bond is also very good, as there are no pores. Note that the placing of the optical fibre prior to the embedding is crucial for this point, since the fibre must be pre-strained and placed in contact with the specimen. Regarding the manufacturing process, specimens manufactured with TIG welding need optical fibres with thicker protective Ni-coatings, of the order of 500µm, but the low cost of the manufacturing technique opens the possibility for the widespread manufacturing of smart metallic materials and structures. In the case of Laser Brazing, the precision of the technique allows a more controlled and successful embedding in critical SMART metallic materials or structures.

6 ACKNOWLEDGEMENTS

This paper was supported by the project *Unidad mixta de investigación* NEXT-BEARINGS with reference IN853A 2015/2, funded by the Spanish general government administration and the Xunta de Galicia through GAIN and the Ministry of Industry, Energy and Tourism of Spain. As requested by the sponsors, the logos are depicted in Figure 6. The authors would also like to acknowledge the help from Miguel Angel Suarez during the TIG welding tests, Santiago Pais for his help in the tensile tests and Patricia Vazquez for her help in metallographic imaging.



Figure 6: logos of supporting sponsors.

REFERENCES

[1] Leung CKY, Wan KT, Inaudi D, . Review: optical fiber sensors for civil engineering applications. Mater Struct 2013; 48(4): 871–906.

[2] Chiesura, G.; Lamberti, A.; Yang, Y.; Luyckx, G.; Van Paepegem, W.; Vanlanduit, S.; Vanfleteren, J.; Degrieck, J. RTM Production Monitoring of the A380 Hinge Arm Droop Nose Mechanism: A Multi-Sensor Approach. *Sensors* 2016, *16*, 866.

[3] Dirk Havermann, Jinesh Mathew, William N. MacPherson, Duncan P. Hand, Robert R. J. Maier; Measuring residual stresses in metallic components manufactured with fibre Bragg gratings embedded by selective laser melting. Proc. SPIE 9634, 24th International Conference on Optical Fibre Sensors, 96340T (September 28, 2015);

[4] Saheb, N., Mekid, S. "Fiber-Embedded Metallic Materials: From Sensing towards Nervous Behavior". Materials 2015, **8**: 7938-7961.

[5] Grandal, T., Fraga, S., Vazquez, J.A., Zornoza, A., "Technique for embedding fiber optics in metallic structures for smart material applications"; 8th European Workshop On Structural Health Monitoring (EWSHM 2016), 5-8 July 2016, Spain, Bilbao

[6] Grandal, T., Fraga, S., Castro, G., Vazquez, E., Zornoza, A., "Laser Brazing metallic embedding technique for fiber optic sensors"; Optical fiber sensors conference, April 24-28, 2017, Jeju (Korea). Accepted for publication.

[7] E. Piñeiro, T. Grandal, A. Asensio, F. Rodriguez; Coating process of Fiber Bragg Grating sensors for SHM applications in metallic structures Proc. SPIE 9157, 23rd International Conference on Optical Fibre Sensors, 9157A7 (June 2, 2014);

VIII ECCOMAS Thematic Conference on Smart Structures and Materials
SMART 2017
A. Güemes, A. Benjeddou , J. Rodellar and Jinsong Leng (Eds)

IMPLEMENTATION OF FBG OPTICAL SENSORS WITHIN A LASER-ASSISTED FIBER PLACEMENT PROCESS FOR ON-LINE MONITORING OF HIGH TEMPERATURE THERMOPLASTIC MATERIALS CONSOLIDATION

D. SAENZ-CASTILLO[*], F. RODRIGUEZ-LENCE[*] A.GÜEMES[†]

[*]Fundación para la Investigación y Aplicación en Materiales Compuestos (FIDAMC) Avda.
Rita Levi Montalcini, 29
Getafe 28906 SPAIN
www.fidamc.es
e-mail: Diego.Saenz@fidamc.es

[†] Universidad politécnica de Madrid (UPM)
Escuela Técnica Superior Ingeniería Aeronáutica y el Espacio (ETSIAE)
Departamento Materiales. Plaza Cardenal Cisneros, 3
Madrid 28040 SPAIN
e-mail: Alfredo.guemes@upm.es

Key words: Thermoplastic, Automatic Fiber Placement, Process monitoring, FBG, optical sensors.

Abstract. Smart processes and thermoplastics materials are two of the most active research lines nowadays in order to be incorporated into the aeronautical industry. Process monitoring is a key aspect for the next industrial revolution. Having real-time data of the process parameters is a target pursued by the industry.
Within this framework, Automatic Tape Placement (ATP) with a laser-assisted heating technology emerged as an alternative technique to the typical autoclave processes. This technology unifies the process automation and the use of high-performance thermoplastic polymers which do not require curing step. Heat transfer is the key parameter that rules the process together with other parameters such as pressure or roller compaction.
The present work attempts to show the successful implementation of the Fiber Bragg Grating sensors (FBG) into the AFP In-Situ consolidation manufacturing process. FBG sensors appear as the strongest display to monitor the process parameters. This is due to their low intrusiveness level into the material and their high sensitivity to temperature and strains.

1 INTRODUCTION

Weight reduction of aeronautical structures is a claimed target for every aircraft manufacturer. Carbon Fiber Reinforced Plastics (CFRP) emerged as a powerful alternative to the traditional metallic structures more than two decades ago. Composite materials have been intensively researched worldwide since then. A high rate of productivity has been achieved,

especially regarding thermoset matrix composites. Within this context thermoplastic matrices also appeared promising noteworthy advantages such as recyclability, high mechanical performance, high impact resistance and the lack of chemical reaction.

Besides the material science progress, the aeronautical industry has experienced an evolution during the last decades in terms of manufacturing processes. Composite parts need to be produced following an additive manufacturing philosophy to select every ply orientation. The lamination technology has evolved from manual hand-lay up to sophisticated automated processes with CNC systems such as Automatic Tape Lay-up (ATL) or Automatic Fibre Placement (AFP).

The automation of the laying processes lead to several advantages as material and labour time reductions, accuracy of the final shape and the angle position of the tape. Thermoplastic materials also open a wide range of opportunities for out of autoclave (OoA) technologies and reduced cycle times since a curing step is not required.

Due to the combination of promising materials and automatic lamination, the Thermoplastic Automatic Fiber Placement technology arose as a powerful combination in the 90's. Many technological centres have been investing in this technology for its optimization and industrialization [1]. The process is based in the automatic fibre placement of thermoplastic material whilst a heat source melts the resin. A compaction elastomeric roller presses the incoming tow against the tolling once the resin is melted.

Laser-assisted AFP with thermoplastic matrix has been under research in FIDAMC during the last decade with the support of AIRBUS Group and different European projects, besides internal investment. The main challenge in FIDAMC regarding the thermoplastic AFP is to create a robust process which allows the industry to create large-scale structures such as wing and fuselages; stringer reinforced structures or curved parts [2]. For the optimization of the process is mandatory to model the phenomena which take place in the process [3-4] and to monitoring and control of the key parameters of the process [5].



Figure 1 Machine head and compaction roller of the AFP thermoplastic system

Within the framework of process automation, process monitoring is also in the spotlight of the aerospace industry. The so-called 4th industrial revolution trends to both automation and

monitoring of all the manufacturing processes. Composite manufacturing is affected by several parameters that may lead to defects in the final part. Process monitoring allows to have knowledge about the critical parameters and to be able to prevent possible defects that may lead to a structural fail.

Optical based sensors as Fiber Bragg Grating (FBG) are a potential tool for monitoring due to their small size and low intrusiveness within the final specimen. The reason is that FBG sensors are highly sensitive to temperature, elongation, vibration, strain. Other institutions have used optical based sensors for process monitoring of thermoplastic AFP with different polymers with lower melting temperatures as made by Oromiehie *et al*. [6].

FBG sensors have been also used in other processes such as Resin Transfer Moulding (RTM) [7-9] with the aim of monitoring the resin flow and the degree of cure (DOC) and have also been used in adhesive bonding to know the quality of the bonding itself.

The aim of this document is to show the works performed related to the incorporation of FBG optical sensors inside thermoplastic structures while being manufactured by Laser-assisted AFP. Single and double FBG sensors have been used in different cases to monitor temperature and strain. Temperature compensation has been performed by using a double FBG sensor and an extra thermocouple to monitor the thermal history. An extra experiment has been carried out with a Hot-Plates Press to correlate both scenarios.

2 OPTICAL FBG SENSORS.

A FBG sensor is created inside a single-mode silica optical fiber. It is created by imprinting periodical patterns within the optical fiber core with a laser-beam striking the core through a grating. The ultraviolet light from the source causes a periodic perturbation in the refractive index in the fiber core along several millimeters of the length.

A broadband light source is connected to the optical fiber. The light is strongly reflected back when the light meets the grating (Figure 2). The light is reflected with Bragg wavelength λ_B according to the eq. 1, where Λ is the grating period and n_{eff} is the effective index of refraction.

$$\lambda_B = 2n_{eff}\Lambda \tag{1}$$

The basic principle of the interrogator system is to monitor the shifts of the reflected Bragg wavelength. Any future environmental perturbation that interacts with the optical fibre will cause a change in the received wavelength (Figure 2) because the periodic spacing between the grating planes is modified by the alteration. FBG optical sensors are developed to monitor phenomena such as strains, temperature, vibration or pressure.

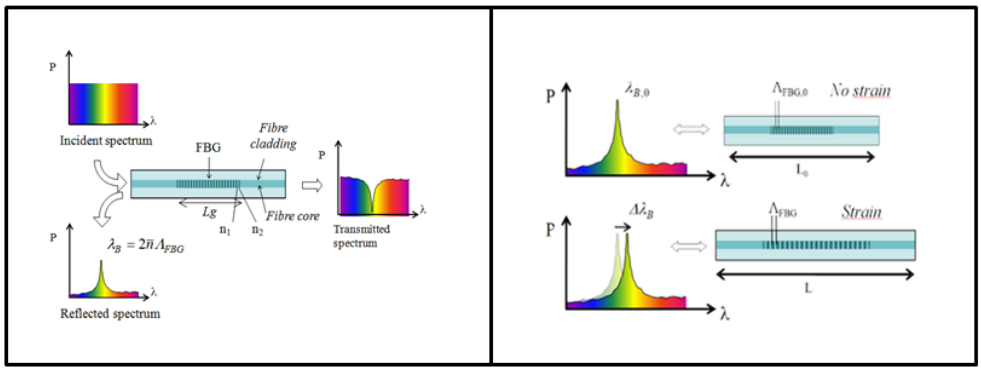

Figure 2 FBG sensors principle (left). Wavelength shift due to strains (right)

A wavelength shift occurs when an external distortion corresponding to a mechanical or thermal distortion interacts with the FBG sensor.

$$\Delta\lambda_B = \lambda_0[(\propto +\xi)\Delta T + (1 - p_e)\Delta\varepsilon] = k_\varepsilon\Delta\varepsilon + k_T\Delta T \quad (2)$$

As it can be seen in Eq.2 the wavelength shift is directly proportional to changes in the strain or the temperature. In the equation; $\Delta\lambda_B$ corresponds to the wavelength shift; α is the coefficient of thermal expansion of FBG; ξ is the Bragg grating's thermos-optical coefficient, p_e is the photoelastic constant of the fiber; ΔT is the change of the temperature and $\Delta\varepsilon$ is the strain change. In the second part of the equation, the expression is simplified by grouping the different parameters into K_ε and K_T: which are the sensitive coefficients of the strain and temperature, respectively.

Temperature and strain should be discriminated when both phenomena are taken place simultaneously. They could be compensated by means of knowing the temperature of the process at real time. Eq.3 is used to discriminate strain and temperature which are monitored by the same FBG sensor.

$$\Delta\varepsilon = \frac{\Delta\lambda_B - K_T\Delta T}{K_\varepsilon} \quad (3)$$

In the experimental method, the experimental expressions that can be found in throughout bibliography [10-11] are used and inserted into the software.

3 ON-LINE MONITORING OF THERMOPLASTIC LASER-ASSISTED AFP WITH SELF-HEATED TOOLING

3.1 Thermoplastic Automatic Fiber Placement.

Thermoplastic AFP is a manufacturing technology under research with the aim of being implemented in composite production lines. It may provide thermoplastic aerospace components avoiding extra autoclave cycles being replaced by In-situ Consolidation while the tapes is being laid-up.

Due to the nature of the process, every tow is melted and consolidated individually one after another. The head machine delivers an incoming tow which is melted by the heat source and then pressed by the compaction roller against the previously consolidated substrate.

The thermoplastic part under fabrication is experimenting critical events as melting, crystallization, intimate contact and internal stresses as it is shown in Figure 3.

Self-heated tooling is used with a base temperature of 200°C to favor a minimum temperature impact when the material cools-down; thereby reducing the residual stresses appearing inside the structure.

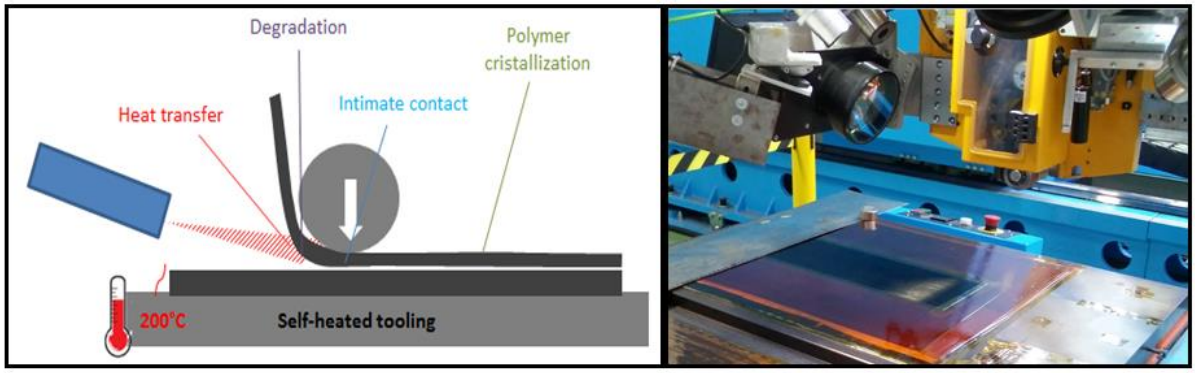

Figure 3 Laser-assisted thermoplastic Automatic Fiber placement scheme (left). Real machine set-up (right).

Heat transfer is the most relevant physical phenomenon which takes place in the process as is explained in Figure 4. It leads the temperature to be the key parameter ruling the entire process. Laser irradiation is the heat transfer method used in the performed experiments.

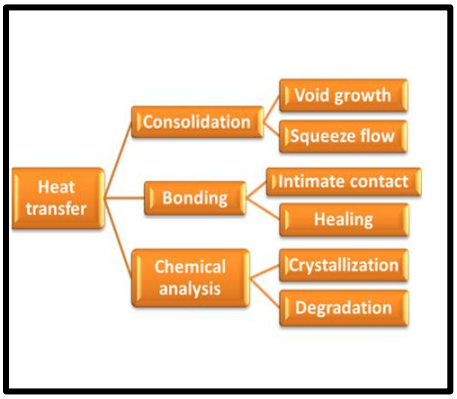

Figure 4 Physico-chemical phenomena related to thermoplastic AFP

To be able to optimize and industrialize the process, the physico-chemical phenomena need to be understood and the key parameters need to be monitored and controlled. That is the reason why important efforts need to be carried out regarding modelling and process monitoring.

3.2 Process monitoring. Experimental set-up

The experiments are performed using APC2-AS4 composites supplied by Cytec®. It is an unidirectional preimpregnated with Polyether ether ketone (PEEK) matrix. The processing temperature is based in 400°C.

The monitored process consists of a laminate of 10 plies taped by the ATP machine on a self-heated tool. The lamination tooling is pre-heated up to 200°C, thereby improving the consolidation between plies and ensuring a homogenous temperature in the part during fabrication. Tows are 6.35mm wide. The optical sensor is installed between the substrate and the 1st ply to monitor the the lamination of all the plies. Two Fiber Bragg Grating sensors have been engraved in the optical fiber. To avoid direct laser irradiation on the optical fiber which can lead to erroneous temperature interpretations, the first CFRP tow has been located manually with the help of a welder. It has been then consolidated with the laser and the compaction roller sensors. Final geometries of the specimens are 300x6.35x1.35mm. Experimental set-up is shown in Figure 5.

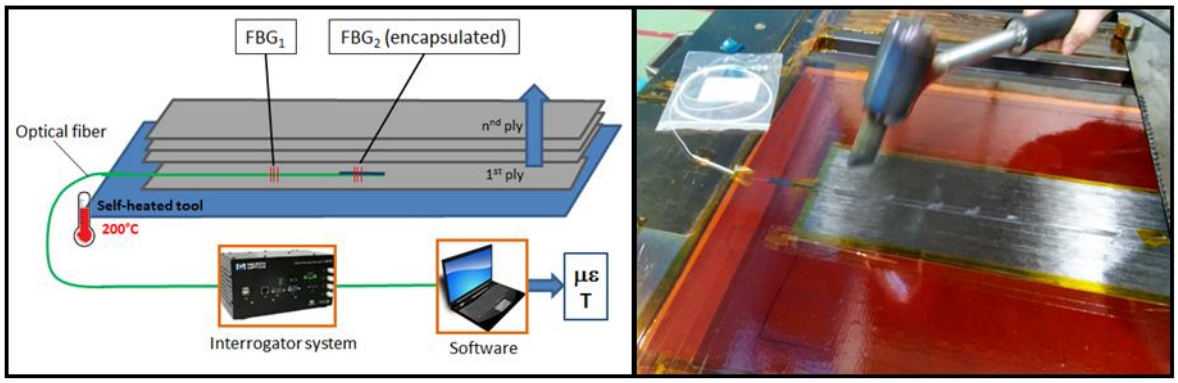

Figure 5 Thermoplastic AFP process monitoring and sensor installation diagram (left).Experimental set-up (right)

The FBG sensors are 10mm long centered at λ_B of 1549.4 and 1558.2 nm respectively. One of the sensors is located at the end of the optical fiber. It has been encapsulated within a brass cylinder to make that sensor being isolated to the strains effects Figure 6.

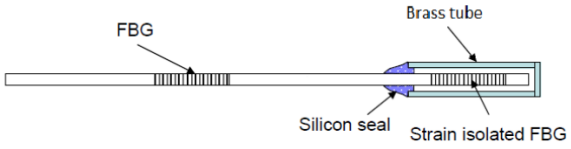

Figure 6 Dual grated sensors in an optical fiber. Covered sensor with a metallic cylinder

The optical interrogator system is a Micron Optics® SM 130 dynamic which uses a Gaussian algorithm system for the peak tracking. The final complete experimental monitoring set-up is shown in Figure 7.

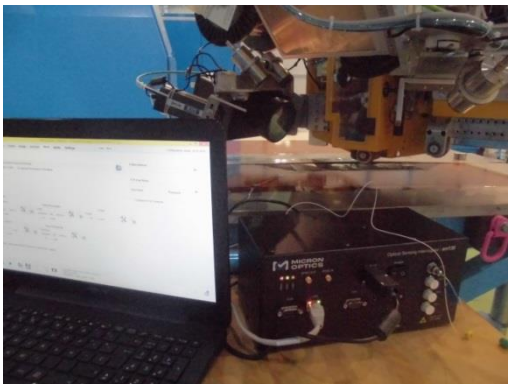

Figure 7 Monitoring experimental set-up

3.3 Results

The data obtained from the two FBG's implemented inside the thermoplastic AFP in-situ consolidation process have been processed and studied in order to obtain information of both manufacturing process and process monitoring. The data collected by the software is wavelength tracking (nm) which can be then transferred to other parameters such as temperature or strain through analytical equations. The equations are obtained from the literature. Figure 8 shows the data obtained from the FBG_1 (left) and the FBG_2 (right) during the experiment consisting of the automatic fiber placement and consolidation of the 10 plies of APC-2 AS4 PEEK material. A horizontal line has been drawn to represent the initial baseline wavelength for both sensors.

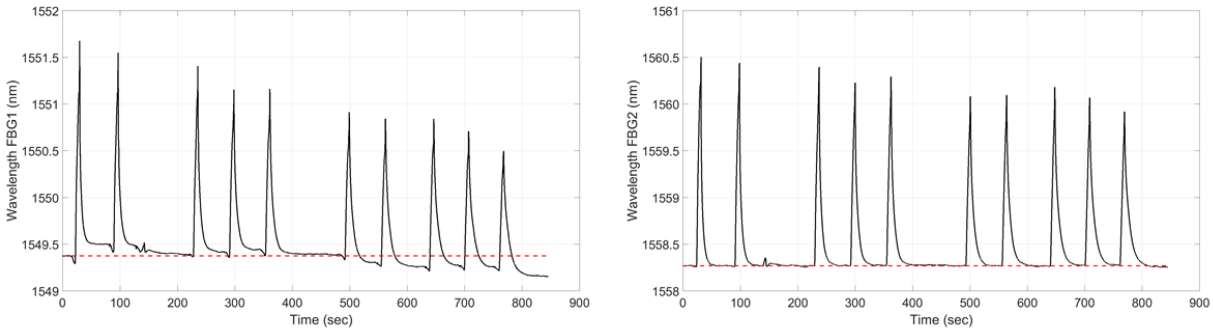

Figure 8 Wavelength profile by FBG1 (left) and by FBG2(right)

Temperature compensation is performed by knowing the temperature profile from the FBG_2 which is only affected by thermal changes. The temperature profile is shown in Figure *9*. A horizontal line has been drawn at 400°C to represent the optimal temperature of the process. The maximum temperature observed by the FBG is decreasing with time as the plies are consolidated increasing the material between the heat radiation and the sensor. It is important to note that the inner plies are still being heated beyond their melting temperature when external plies are taped and consolidated. This results correlates with the results published by Martin, I. *et al* [3]

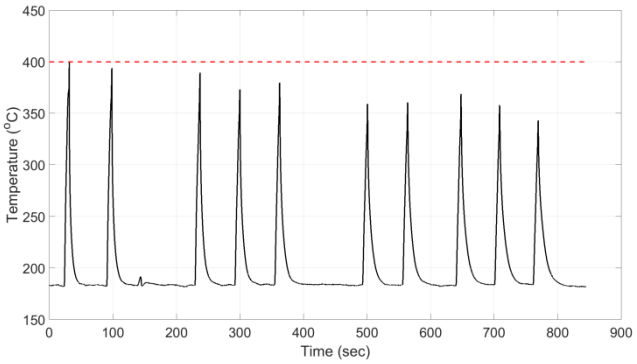

Figure 9 Temperature profile monitored by FBG2

After the temperature profile is obtained, the temperature compensation can be performed with the data obtained by FBG1 which is affected by both combined effects of strain and temperature. The strain profile of the test is shown in Figure 10. The study of the strain profile reveal that the sensor is subjected to tensile and compression stresses with the lamination of every incoming ply. It can be deducted that this effect is induced by the compaction rolling passing through the FBG. This effect is also attenuated with the numbers of plies as it occurred with the temperature. It is due as well to the increasingly distance from the sensor to the surface with the time. It is important also to observe that the strain level does not come back to the baseline level with the progression of the test. The baseline has been indicated with a red dotted line.

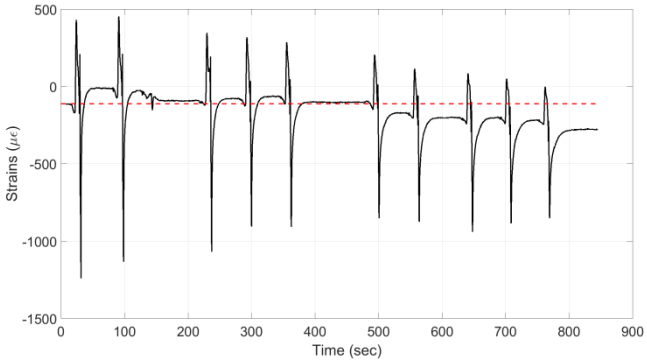

Figure 10 Strain profile obtained after temperature compensation

4 MONITORING OF THERMOPLASTIC PROCESSING IN HOT-PLATES PRESS

4.1 Experimental set-up.

The aim of this test is to monitor the strain and temperature profiles along a consolidation cycle of a thermoplastic flat panel manufactured via hot-plates press. The specimen configuration is $[0]_{10}$ (a ten plies stacking with 0º direction) to simulate the conditions of the previous AFP process. The material used is APC-2 AS4 PEEK in UD (unidirectional) format. The panel dimensions are 300x300mm. The test conditions correspond to the supplier

instructions. The processing temperature is 400°C with 15 min of consolidation time. Consolidation pressure is applied during the whole process.
The test has been carried out in the UPM laboratory. The experimental set-up can be seen in Figure 11.

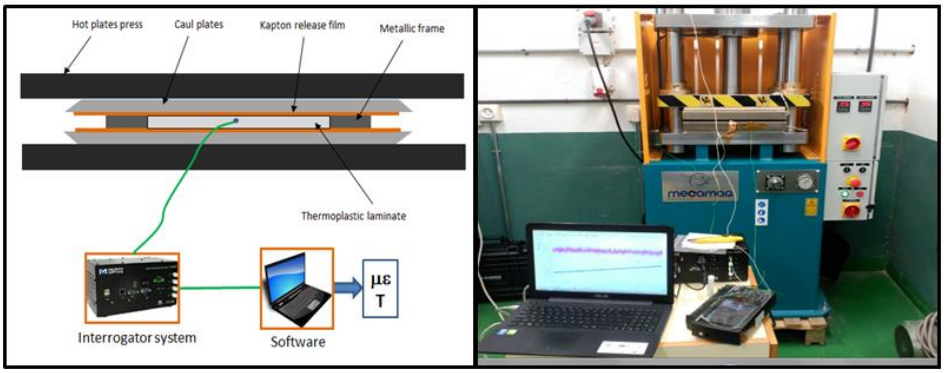

Figure 11 Hot-press plates monitoring experimental set-up

An optical fiber with dual FBG sensors has been located in the middle plane of the structure; between the 5th and 6th ply and it has been centered. The sensors are called FBG1 and FBG2. The latest sensor has been located in the edge of the optical fiber and a brass metallic cylinder has been located surrounding the sensor as in the AFP monitoring process. FBG2 is isolated from external strains being only affected by temperature changes. FBG sensors are centered at 1547.90nm and 1556.67nm respectively. A thermocouple has been embedded in the structure in the proximities of the optical sensors to monitor the temperature as a second thermal control apparatus. A top view of the embedding of the instrumentation in the laminate can be seen in Figure 12.

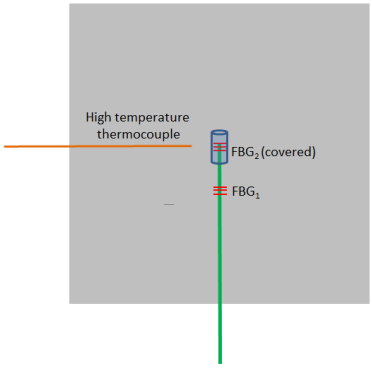

Figure 12 Top view of the location of FBG_1, FBG_2 and thermocouple in the structure

4.3 Results

The data obtained from the two FBG's implemented inside the thermoplastic hot-plates press process has been processed. The temperature compensation is performed with the temperature collected by the thermocouple due to the fact that it is a temperature control robust system.

Temperature has been also monitored by FBG_2. Strain profile along the hot press cycle is obtained from the compensation to obtain the strain changes.
Temperature and strain profiles can be observed in Figure 13

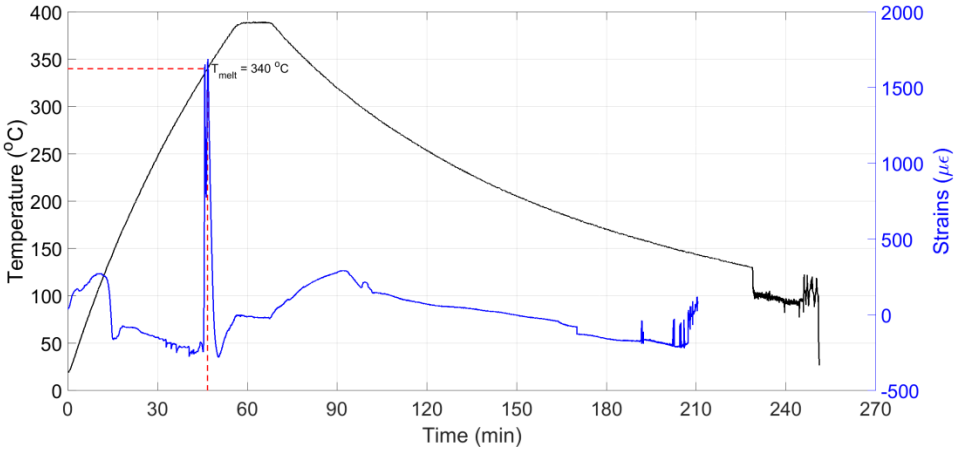

Figure 13 Hot-press process monitoring. Temperature (thermocouple) and strain (FBG) profiles

A red-dotted line has been placed to point out when the system has reached the melting point of the PEEK polymer. According to the strain profile obtained by the sensors, there is a considerable variation in the strain field corresponding to the melting point.

5 CONCLUSIONS

This paper describes that FBG sensors have been successfully incorporated in different thermoplastic manufacturing processes corresponding to laser-assisted Automatic Fiber Placement and hot-plates press consolidation systems. APC-2 AS4 coupons have been manufactured to monitor the consolidation process. Temperature and strain profiles from both processes have been monitored and discriminated with promising results. FBG sensors have proven to be a powerful instrument for thermoplastic process monitoring purposes.

The method of temperature monitoring was validated with the support of external temperature control methods such as thermographic camera and thermocouples. Specific events such as melting point of the resin or tensile-compression strains due to the compaction roller have been successfully observed.

Further experiments are required to be carried out in order to determine the scope of FBG sensors as instrument for on-line process monitoring and defectology detection.

REFERENCES

[1] August, Z.; Ostrander, G.; Michasiow, J. and Hauber, D. *Recent developments in Automated Fiber Placement of thermoplastic composites.* SAMPE, 2013.

[2] Black, S. and Rodriguez-Lence, F., *Thermoplastic composite wings on the horizon?* CompositesWorld

[3] Martin, I.; Rodriguez-Lence, F.; Fernandez, A. and Sánchez, J. *Automatic lamination and in-situ consolidation with thermoplastic composite materials-heat transfer model*. COMPTEST 2015

[4] Martin, I.; Rodriguez-Lence, F.; Fernandez, A. and Sánchez, J. *Simulación del problema térmico en procesos de laminación y consolidación in-situ con materiales termoplásticos reforzados.* MATCOMP 2015

[5] Saenz-Castillo. D.; Martin, I.; Rodriguez-Lence, F. and Güemes, F. *On-line monitoring of a laser assisted fiber placement process with CFR thermoplastic matrix by using Fiber Bragg Gratings*. European Workshop on Structural Healt Monitoring (EWSHM) 2016.

[6] Oromiehie E., Prusty B.G., Compston P. and Rajan G., Structural Health Monitoring and *Processing of Composites using Photonic Sensing Technology*, Proceedings of the 20th International Conference on Composite Materials, Copenhagen, Denmark, July 19-24, 2015.

[7] Hak-Sung Kim, Seong-Hwan Yoo, Seung-Hwan Chang. *In situ monitoring of the strain evolution and curing reaction of composite laminates to reduce the thermal residual stress using FBG sensor and dielectrometry* . Composites: Part B 44 (2013) 446–452

[8] Khoun, L.; de Oliveira, R.; Michaud, V. and Hubert, P.; *Investigation of process-induced strains development by fibre Bragg grating sensors in resin transfer moulded composites*. Composites: Part A 42 (2011) 274–282

[9] Garschke, C.; Weimer , C.; Parlevliet, P. and Fox, B.L. *Out-of-autoclave cure cycle study of a resin film infusion process using in situ process monitoring*. Composites: Part A 43 (2012) 935–944

[10] Yoona, H-J.; Costantini D., Michaud, V. ; Limbergerb, H-G ; Månson, A. ; Salathé, R.P. ; Kim, C-G. Hong, C-S.*In-situ simultaneous strain and temperature measurement of adaptive composite materials using a fiber Bragg grating based sensor*. Proc. SPIE 5758; Smart Sensor Technology and Measurement Systems, 62 (May 20, 2005).

[11] Marin, E. and Ouerdane, Y. *Dual Fibre Bragg Grating sensor for simultaneous temperature and strain sensing of composite materials manufacturing*. 7th European Workshop on Structural Health Monitoring. July 8-11, 2014. La Cité, Nantes, France

VIII ECCOMAS Thematic Conference on Smart Structures and Materials
SMART 2017
A. Güemes, A. Benjeddou , J. Rodellar and Jinsong Leng (Eds)

LAMINATES WITH INTEGRATED PIEZOELECTRIC TRANSDUCERS: INFLUENCE OF THE TRANSDUCERS LOCATION ALONG THE THICKNESS-AXIS ON THE STRUCTURAL PERFORMANCE

XIANLONG CHEN[1,3], YANN MEYER[1]*,REMY LACHAT[2] & MORVAN OUISSE[3]

[1] Univ. Bourgogne Franche-Comté, UTBM, Belfort, FRANCE
Email: xianlong.chen@utbm.fr, yann.meyer@utbm.fr

[2] ICB UMR 6303, CNRS Univ. Bourgogne Franche-Comté, UTBM, Belfort, FRANCE
Email: remy.lachat@utbm.fr

[3] Univ. Bourgogne Franche-Comté, FEMTO-ST Institute, CNRS/UFC/ENSMM/UTBM, Besançon, FRANCE
Email: morvan.ouisse@femto-st.fr

Key words: Composite material, Laminates, Smart structures, Piezoelectric implants, Embedding parameters.

Abstract. The composite structures embedding piezoelectric implants are able to modify their mechanical properties with respect to their environment (e.g. active vibration control), to interact with other structures (e.g. mechatronic) or with human beings (e.g. Human-Machine Interaction). Conventionally, to functionalize a mechanical device, the piezoelectric transducers are glued on the top surface of the structure and the power and control electronics are away. To protect the transducers and their electric connections and develop some industrial products in "plug and play" mode, it is necessary to be able to embed a wide distributed network of piezoelectric implants into the heart of the composite material during the manufacturing process of the products.

However, if these adaptive structures are widely studied in the literature in a numerical point of view, there is no experimental research about the influence of the embedding parameters on the overall performance of the final structures. The idea of this study is to create a benchmark. In this paper, a set of beams (around 50 mm wide and 715 mm long) made of glass fiber composite with six plies (around 2.5 mm thick) are manufactured, with three piezoelectric elements embedded at a specific depth. This parameter is modified for each beam. At first, the material parameters of each beam are characterized, then a modal analysis is used to extract the key parameters of the final products. At the end, the different parameters and test results of each beam are compared and discussed.

* Research Associate at Sorbonne Universités, Université de Technologie de Compiègne, CNRS, UMR 7337 Roberval, Centre de recherche Royallieu, CS 60 319 Compiègne cedex, France

1 INTRODUCTION

Currently, in different industrial fields as transport or aerospace, a research effort is conducted to reduce the structural weight [1, 2]. One of the most promising solutions is the use of composite structures [3], especially the fibres-based composite structures [4], due to their high stiffness and low mass density. At the same time, there is an intensification of the operational dynamic environment and an increase of durability requirements [5]. These different expectations seem to be contradictory. One solution to manage these points is to design and manufacture smart composite structures with a fully distributed set of integrated piezoelectric transducers [6]. These structures are able to modify their mechanical properties with respect to their environment (e.g. active vibration control), to interact with other structures (e.g. mechatronic) or with human beings (e.g. Human-Machine Interaction).

Conventionally, to functionalize a mechanical part made of composite, the piezoelectric transducers are glued on the surface of the structure and the power and control electronics are away. Our approach is significantly different. We want to develop a wide distributed network of piezo-ceramics and embed them into the heart of the composite material. The idea is to protect the transducer elements and their connections and develop some industrial products in "plug and play" mode.

To place these new elements at the heart of the composite material, it is necessary to embed the transducers during the manufacturing process of composite structures. To meet this requirement, specific manufacturing methods have been developed at the Belfort-Montbéliard University de Technology (UTBM), France.

The ability of embedding the transducers is however not sufficient to guarantee the effectiveness of the approach. A specific preliminary design strategy has then been developed. The idea is to be able to predict the final behaviour of the structure. The determination of the useful design parameters is based on an experimental approach [7]. It is necessary to develop:

- A characterization of piezoelectric ceramics. It corresponds to the input control of piezo-ceramics [8].
- A characterization of the fabricated composite. Once the manufacturing process is stabilized, the composite must be fully characterized by a set of tests, which get access to the nominal material parameters and the uncertainty of manufacturing process [9].
- A characterization of "integrated" piezo-ceramics. The idea is to develop a behaviour model, which can evaluate the drift of the electro-mechanical coupling coefficients from the input control data.
- A characterization of the electrical interfaces. The method of electrical connection, particularly between the transducers and the electrical grid, needs to assess the influence of process parameters on the quality of the contacts. Indeed, the electrical connection by welding technology is not used in our manufacturing process [10].
- A characterization of the inter-element coupling. It is necessary to evaluate the mechanical and electrical couplings between the transducers, according to the distance and connection technology, to establish dedicated design rules, an evaluation of the influence of the different manufacturing parameters with respect to the final performance of the smart material structures that we have produced.

This paper is focused on a part of the last point: the influence of the location of piezoelectric

elements along the thickness axis on the final performance of the structure. This point is widely studied in the literature in a numerical point of view. However, there is few experimental researches to validate the theoretical results. The idea of this study is to create a benchmark.

The paper is organised as follows. The process of the composite manufacturing is introduced in Section 2. Section 3 shows the experimental activities applied to the samples. Two different identification methods are used to extract the composite material parameters (Resonalyser Method and Time-of-flight Method). Then, the approach by modal analysis is investigated to characterize the final performance of these samples. In Section 4, the results are presented, compared and discussed. Finally, concluding remarks are given.

2 SMART COMPOSITE BEAMS

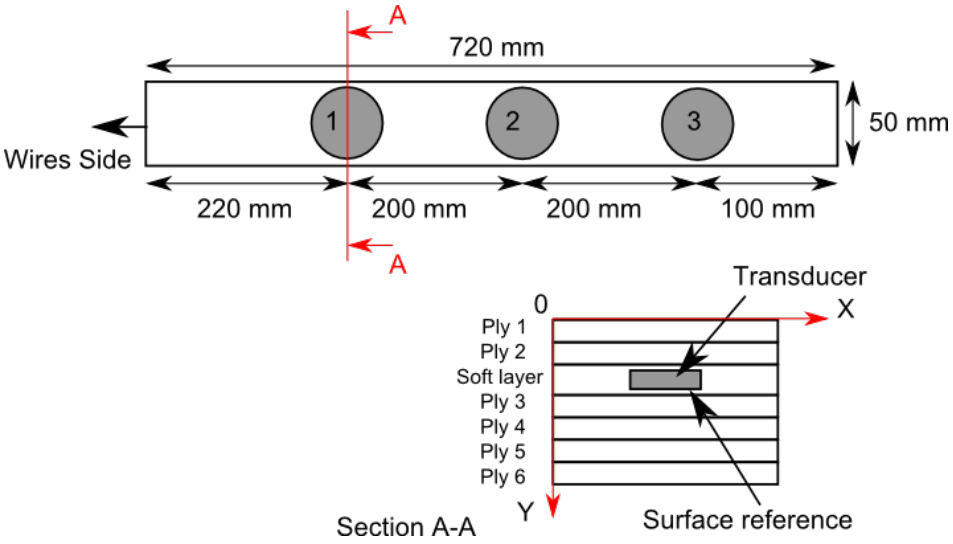

Figure 1: Smart composite beam specifications

The beams, manufactured for the tests, are around 50 mm wide, 715 mm long and 2.5 mm thick. As presented in Figure 1, the composite material consists of fiberglass-reinforced-polyester laminate. It was prepared from 6 plies of chopped strand mat. The matrix is a thermosetting plastic (polyester resin). The used composite manufacturing process is a Vacuum Assisted Resin Transfer Molding (VARTM). To avoid the variability due to the electric connections, an intermediate structure, called “soft layer” is used to embed the electrical conductors and the transducers. This layer is 0.5mm thick and mainly made of polyester resin. A ply is 0.33mm thick. The transducers are 135 µm thick. The piezoelectric transducers have been completely characterized in [8]. The fiber volume ratio is about 35%. For each beam, three piezoelectric elements are embedded inside the beams at a specific depth. This last parameter is modified for each beam.

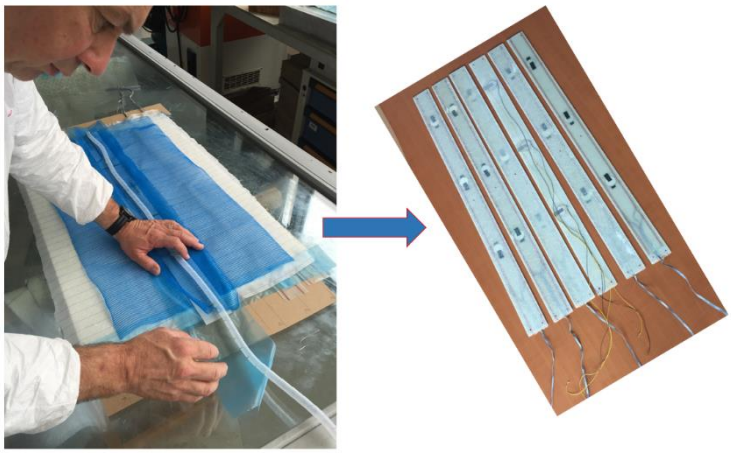

Figure 2: Manufacturing of the beams to be tested

As shown in Figure 2, the 6 beams are manufactured all at once in order to guarantee the repeatability of the beam parameters (like thickness, density, etc.). The only difference is that the piezo-ceramics for each beam are located at different depth. The information in detail are shown in Table 1. The beam a, because it has no soft layer inside, so it has a thickness of 2mm.

Table 1: Location of the piezoelectric transducteurs for each beam reference. (The reference surface for the specfic depth is the bottom electrode of the transducers)

Beam ref.	Specific depth (mm)	Comments
a	0	Piezo glued on the top surface of the beam
b	0.32	Piezo embedded between the top surface and Ply1
c	0.65	Piezo embedded between Ply 1 and Ply 2
d	0.98	Piezo embedded between Ply 2 and Ply 3
e	1.32	Piezo embedded between Ply 3 and Ply 4
f	1.98	Piezo embedded between Ply 5 and Ply 6

3 EXPERIMENTAL STUDIES

In this paper, two different identification methods are used to extract the composite material parameters (Resonalyser Method [11, 12] and Time-of-flight Method [9, 13]). Then, the approach by modal analysis is investigated to characterize the final performance of these samples.

3.1 Composite material characterization

First of all, the mass density is measured at 1660kg.m^{-3} +/-2.4%. The Young's modulus is 14.6 GPa +/- 6.2 % and the shear modulus 5.9 GPa +/- 6.6% with the Resonalyser method. As the composite material can be considered as a transversely isotropy material along the thickness axis, the Poisson ratio is 0.24 +/- 17.5%. The Resonalyser technique is a good method to extract overall material parameters at relative low frequencies. The Time-of-Flight technique is based on the duration measurements of wave propagation with a simple and low cost experimental

setup. The results obtained are more local and related to the wave path. For the moment, the Poisson's ratio is evaluated at 0.32 with the classical rule of mixtures. We have assumed that the Poisson's ratio of the fibreglass is around 0.23 and those of the thermosetting plastic around 0.37. By measuring the S_0 group velocity and using the formulas of extraction of the materials parameters developed for the phase velocity [9, 13], it is possible to extract the Young's Modulus.

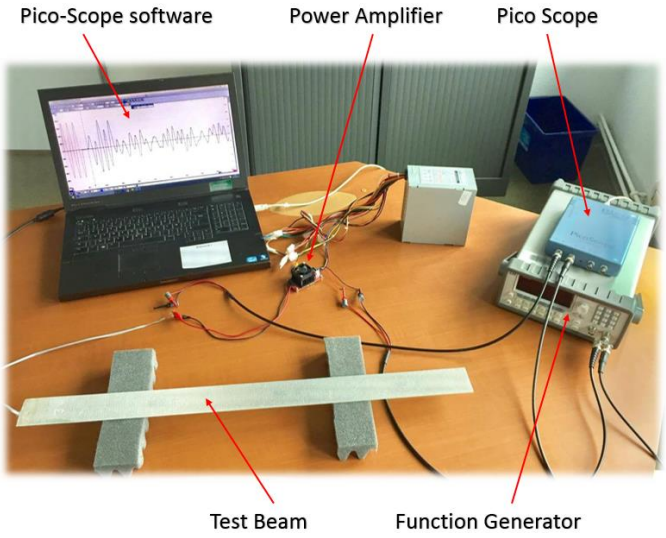

Figure 3: Experimental setup for Time-of-Flight method

Figure 3 shows the experimental setup to measure the wave trains. A function generator (Keithley, 3390) is used to generate excitation signals via a miniature power amplifier (PiezoDrive, PDM200B). The signals are then captured via a pico-scope (PicoScope, 4424), the signals are analyzed by Pico-Scope software.

One of the piezo electric transducers is used as an actuator, after a set of optimization tests, a short number of sinusoidal bursts (1 to 3 cycles) are chosen as the excitation signals [14]. Another piezo electric transducer is used as a sensor, the time-of-flight from the actuator to the sensor has been recorded for each beam. Finally, we have obtained a Young's modulus of 15 GPa+/-1.5%.

3.2 Modal Analysis

In Figure 4, the experimental setup for characterization is presented. The test beams are hanged by two wires in order to guarantee the free boundary conditions. The deflection shapes of the beams are determined with a scanning vibrometer. (Polytec, PSV-500-3D). The frequency range is from 1Hz to 1200Hz. 105 scan points (21 by 5 points) are measured.

The piezo-ceramics are used both as actuator and sensor. The measurement process is as follows:

1. One of the piezo-ceramics (i.e. Piezo 1) is used as an actuator and the two others are used as transducers (i.e. Piezo 2 and Piezo 3), the transducers are open-circuited (OC situation).
2. The same piezo-ceramics is used as an actuator, the other two piezo-ceramics are short-

cut (SC situation).

3. Piezo 2 is then selected and Step 1 and Step 2 are repeated.
4. Piezo 3 is finally selected and, once again, Step 1 and Step 2 are repeated.

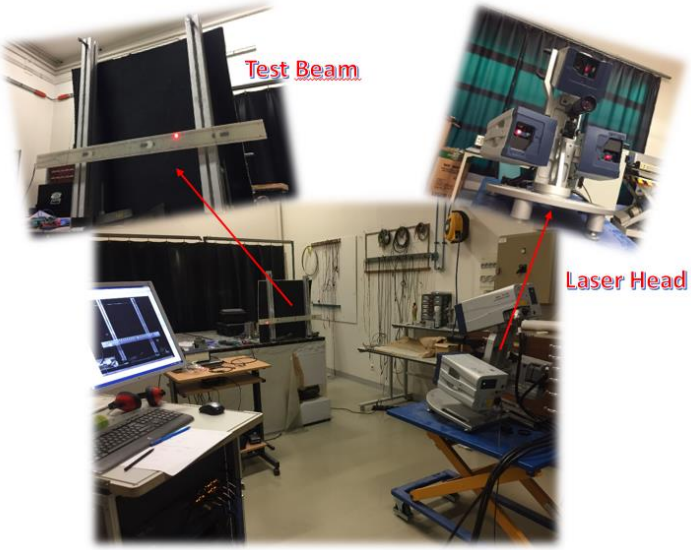

Figure 4: Experimental setup for Modal Analysis

4 RESULTS & DISCUSSION

Only the first five natural bending modes are investigated in this section. The mode shapes of these modes are presented in Figure 5. All the results from the modal analysis and the ToF method measurement are shown and discussed. To extract the relevant data from the measurements, a modal analysis software package called MODAN is used [15].

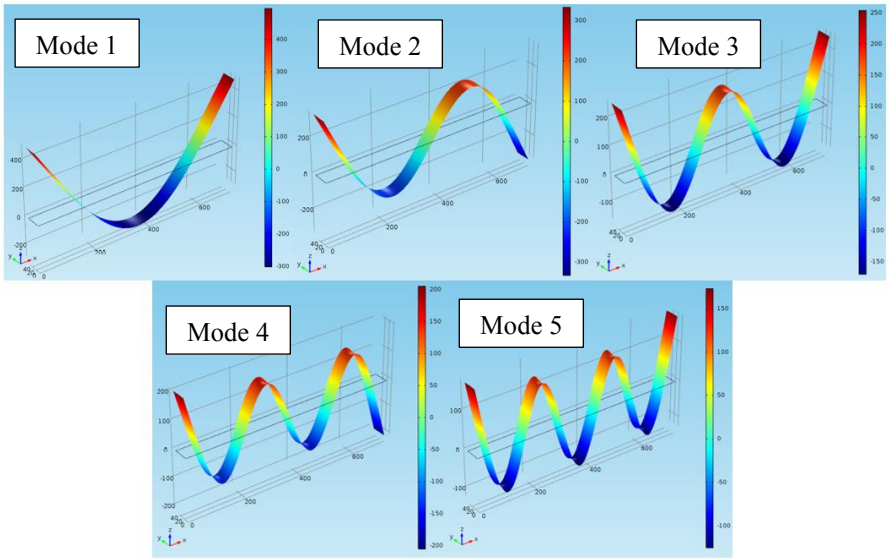

Figure 5: First five natural bending mode shapes of the beams

4.1 Data correction

To ensure the accuracy of the results and keep the possibility to compare them, it is necessary to correct the deviation due to the geometric uncertainty. For this, two measures are adopted:

1. Repeat the experiments 3~5 times in the same situation, the same beam, the same piezo-ceramic as actuator or sensor, the same excitation signals, etc. Then the Repeatability Standard Deviation (RSD) of the results is calculated, as shown in Table 2. The phenomenon observed must be much high than this value in order to be relevant and representative.
2. A finite element model is built with the modeling software COMSOL Multiphysics, which is used to correct the data from each beam, ensure that all the beams have the same length, width and thickness.

4.2 Natural bending frequencies

At first, the Eigen-frequency and the standard deviation of each selected mode are concerned, after data correction the results are shown in Table 2.

Table 2: Eigenfrequency and standard deviation of each mode

Beam reference / Eigen-frequency (Hz)	a	b	c	d	e	f	RSD(%)
Mode 1	13,8	14,4	14,1	14,7	15,2	14,0	0,12
Mode 2	39,5	40,5	39,4	41,2	42,9	39,5	0,05
Mode 3	78,2	78,9	78,0	81,5	85,7	78,0	0,08
Mode 4	128,3	130,1	128,7	135,6	140,5	130,1	0,04
Mode 5	189,4	195,0	200,5	202,9	211,1	196,0	0,08

The tendency of each Eigen-frequency is equivalent. In Figure 6, the tendency of the fifth natural mode is presented as an example. The numerical evolution with respect to the location of the "soft layer" is obtained by simulation with Comsol Multiphysics. For the modeling, the material parameters are from the resonalyser method for the composite material. Concerning the "soft layer", the isotropy of the layer is assumed and the material parameters are 0.24 for the Poisson's coefficient, 7 GPa for the Young's modulus and 1200 $kg.m^{-3}$ for the mass density. The tendency is strong, especially the Beam-e, while the piezo-ceramics are embedded in the middle of the composite, the eigen-frequencies are higher than other situations. This fact is clearly explained by the modification of the theoretical middle plane due to the variation of the material parameters. This tendency is confirmed by the theoretical data. The gap between Beam a and Beam b is huge, the reason is the soft layer, there is no soft layer in Beam a, the piezo-ceramics are just glued on the surface of the beam.

Furthermore, only Beam d and Beam e can get the torsion mode, the frequency of this mode is respectively 124.3 Hz and l32.4 Hz.

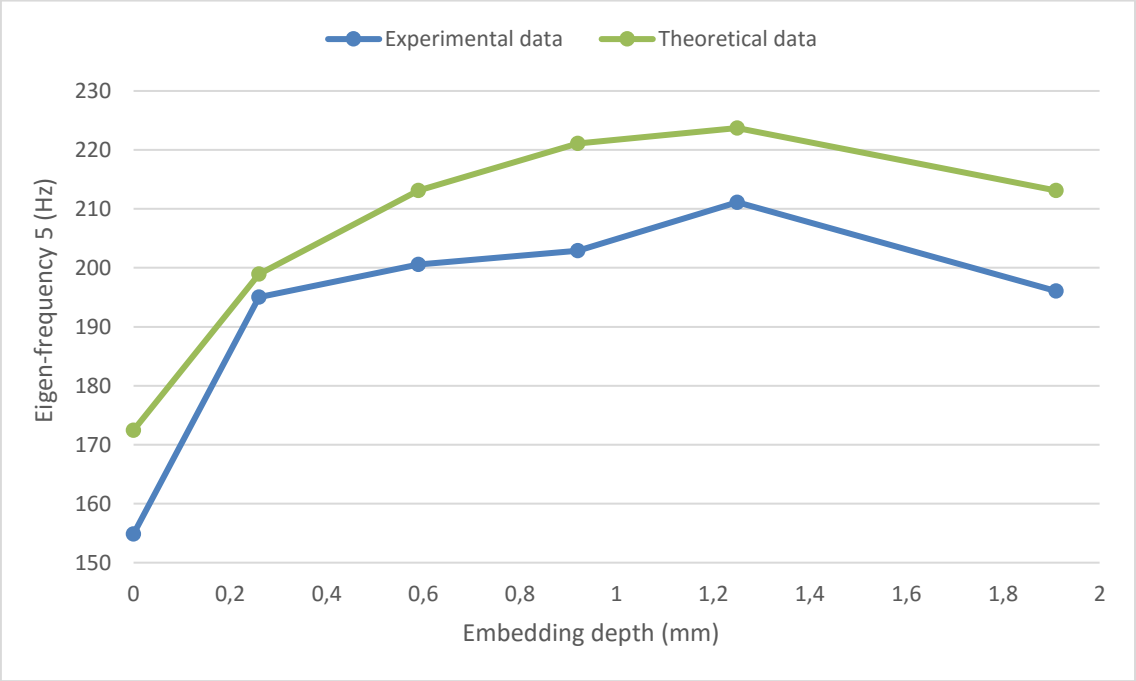

Figure 6: Tendency of the fifth natural frequency

4.3 Damping ratio and vibration amplitude

Then, for each beam, the maximum amplitudes of each Eigen-mode are captured, the data is shown in Table 3. At the same time, the damping ratios of each beam are measured also, the results are shown in Table 4.

The tendency of the first natural mode is presented as an example, in this mode, the damping ratios of each beam are not quite different. The tendency is shown in Figure 7.

Table 3: Maximum amplitude of each mode (Piezo 1 as actuator, the others piezo open-circuited)

Beam reference / Maxi amplitude (μm/V)	a	b	c	d	e	f	RSD(%)
Mode 1	32. 7	14.6	6.5	7.06	0.49	3.27	3.42
Mode 2	11.9	6.03	4.83	2.21	0.16	5.46	3.44
Mode 3	4.37	5.47	2.76	0.7	0.08	1.24	3.84
Mode 4	2.69	1.81	0.91	0.95	0.09	1.61	0.91
Mode 5	1.95	1.36	0.67	0.5	0.04	1.11	0.43

Table 4: Damping ratio of each beam (Piezo 1 as actuator, the others piezo open-circuited)

Beam reference / Damping ratio	a	b	c	d	e	f	RSD(%)
Mode 1	0. 58	0. 47	0. 55	0. 51	0. 53	0. 32	4. 93
Mode 2	0. 51	0. 51	0. 5	0. 65	0. 41	0. 5	2. 02
Mode 3	0. 53	0. 38	0. 41	0. 84	0. 42	0. 88	4. 39
Mode 4	0. 25	0. 44	0. 44	0. 43	0. 39	0. 48	≈0. 00
Mode 5	0. 47	0. 61	1. 2	0. 4	0. 37	0. 44	1. 21

As shows in Figure 7, the tendency of each mode for the beams is quite clear. The amplitutde of each Eigen-mode is much smaller when the piezo-ceramics locate at the middle of the luminate, like Beam-e. The deeper piezo-ceramics locate, the smaller the amplitutde will be.

Especially, from Beam-a and Beam-b, it shows that when the piezo-ceramics are just glued on the surface of the beam, the vibration is much larger than that when the piezo-ceramics located inside of the beam. This fact shows clearly that the influence of the location of the soft layer is quite significant. However, the impact of the soft layer on the damping ratio is limited.

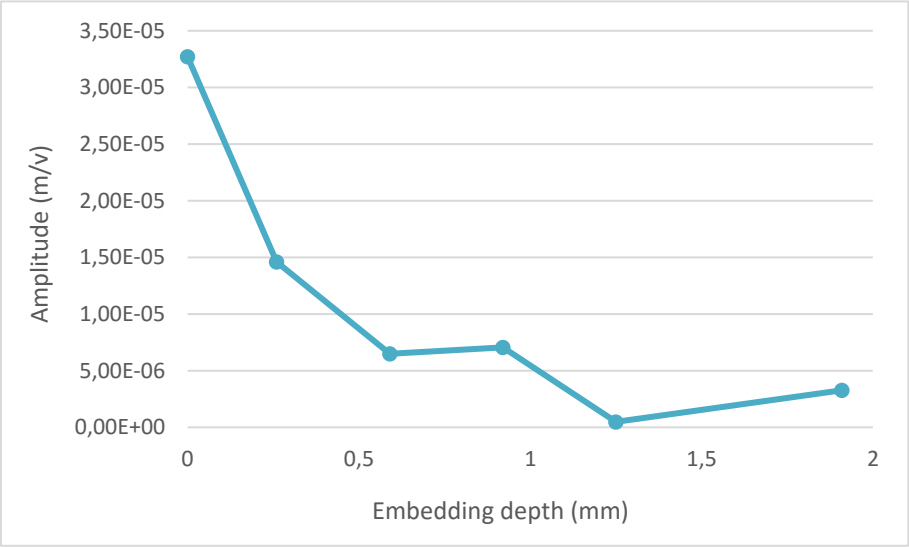

Figure 7: Tendency of each Eigen-mode

4.4 Modal effective electromechanical coupling coefficient

Probably the most interesting method to evaluate the effective electromechanical coupling coefficients (EMCC) is based on the effective energy conversion from mechanical to electrical and vice-versa for the whole system. [16] For this part, the Eigen-frequency of SC or OC state is captured. Beam d is chosen as an example, Piezo 1 is used as an actuator, the results are shown in Table 5, as well as the deviation of the repetition experiments.

Table 5: Eigen-frequency of OC/SC mode

Eigen-frequency (Hz)	OC	SC	Error(%)	RSD(%)
Mode 1	14.18	14.16	2	2
Mode 2	39.88	39.83	5	2
Mode 3	78.93	78.86	7	6
Mode 4	131.24	131.16	8	5
Mode 5	196.41	196.24	17	17

When short-cuting the circuit of the piezo-ceramics, the Eigen-frequency of the beam can change a bit, but when compare the error with the Repeatability Standard Deviation, the difference of the amplitude is not significant enough, so it is impossible to evaluate the EMCC in this situation.

4.5 Time-of-Flight measurements

Lamb wave techniques provide more information about damage presence and severity than previously tested methods (frequency response techniques), and provide the possibility of determining damage location due to their local response nature [17], hence the Time-of-Flight method is widely used in Structural Health Monitoring (SHM). Thus, it is quite necessary to well know if the location of piezoelectric elements along the thickness axis has an influence on the time-of-flight. For this part, two piezo-ceramics are used, one as an actuator and the other as sensor, the time-of-flight of the signal from actuator to sensor is captured.

In addition, in order to investigate the influence of the location of piezoelectric elements along the thickness axis, the Young's modulus (E) is a quite interesting parameter. So the Young's modulus of each beam is calculated with the T-o-F method, which is more convenient than Resonalyser method to calculate the Young's modulus. [9] The data is shown in Table 6. The Repeatability Standard Deviations of both the Time-of-Flight and the Young's modulus are quite good, both RSD≈0 with a measurement accuracy of 0.1 μs.

Table 6: Results of T-o-F method

Beam reference	Time-of-Flight (μs)	Young's modulus (GPa)
a	126	14.6
b	125	14.8
c	126	14.5
d	126	14.5
e	128	14.2
f	127	14.3

The tendency of Time-of-Flight and Young's modulus for each beam is shown in Figure 8. The tendency is quite clear. The location of piezoelectric elements along the thickness axis has

an influence on the time-of-flight and Young's modulus, especially for Beam-e, while the piezo-ceramics are embedded in the middle of the composite, the time-of-flight is the longest, and the Young's modulus of the beam is the smallest. The deeper the piezo-ceramics locate, the smallest the measured Young's modulus of the beam obtained by the T-o-F method will be, so the location of piezoelectric elements along the thickness axis can influence the accuracy of the T-o-F method.

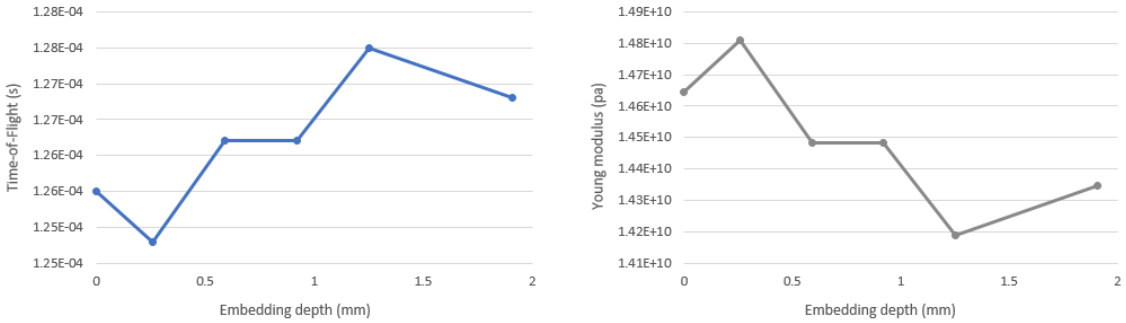

Figure 8: Impact of embedding depth of the piezo in the composite layers on time-of-flight and estimated Young's modulus

5 CONCLUSIONS

- The deeper the piezo-ceramics locate in the composite, the higher the Eigen-frequency of the beam will be. Only when the piezo-ceramics locate in the middle of the composite, the beam can get the torsion mode.
- The deeper the piezo-ceramics locate in the composite, the weaker the amplitude of vibration will be. But the open circuit & short circuit states are not adapted to this kind of situation.
- The deeper the piezo-ceramics locate, the smaller the measured Young's modulus of the beam will be.

ACKNOWLEDGEMENT

This project has been performed in cooperation with the Labex ACTION program (contract ANR-11-LABX-0001-01). This work was partly supported by a financial support from the UTBM, France. The authors are grateful to Mr Romain Viala from the FEMTO-ST Institute for his help and his fruitful assistance on modal analysis.

REFERENCES

[1] Lynette W Cheah. *Cars on a diet: the material and energy impacts of passenger vehicle weight reduction in the US.* PhD thesis, Massachusetts Institute of Technology, (2010).

[2] Karen Taminger. Technical challenges to reducing subsonic transport weight. In *AIAA Aerospace Sciences Meeting,* (2012).

[3] Georgios Koronis, Arlindo Silva, and Mihail Fontul. Green composites: a review of adequate materials for automotive applications. *Composites Part B: Engineering,* 44(1):120–127, (2013).
[4] Sujit Das. Life cycle assessment of carbon fiber-reinforced polymer composites. *The International Journal of Life Cycle Assessment,* 16(3):268–282, (2011).
[5] Air Resources Board. Preliminary discussion paper - amendments to California's low-emission vehicle regulations for criteria pollutants - lev iii. Strate of California, (2010).
[6] E.F. Crawley & J. De Luis. Use of piezoelectric actuators as elements of intelligent structures. *AIAA journal*, *25*(10), 1373-1385, (1987).
[7] T. Dessolier, R. Lachat, and Y. Meyer. Fibers-based composite structures with integrated piezo-ceramics. design approach of smart devices. In *International Conference on Dynamics of Composite Structures (Dyncomp'2015), Arles, France,* (2015).
[8] Y. Meyer and R. Lachat. Vibration characterization procedure of piezoelectric ceramic parameters. In *Proc.4eme Colloque francophone d'Analyse Vibratoire Expérimentale (AVE 14),* Blois, France, (2014).
[9] X.L. Chen, R. Lachat, S. Salmon, M. Ouisse and Y. Meyer. Complex Composite Structures with Integrated Piezoelectric Transducers. *International Journal of Computational Methods and Experimental Measurements*, 5(2): 125-134, (2017).
[10] R. Lachat and Y. Meyer. Structures composites adaptatives conception et fabrication d'un aileron automobile instrumenté. In *Congrès Français de Mécanique (CFM 2015), Lyon, France,* (2015).
[11] H. Sol and C. Oomens, *Material Identification Using Mixed Numerical Experimental Methods,* Kluwer Academic Publishers, (1997).
[12] T. Lauwagie. *Vibration-based methods for the identification of the elastic properties of layered materials*. PhD thesis, Katholieke Universiteit Leuven, (2005).
[13] B. J. Tucker. *Ultrasonic plate waves in wood-based composite panels*. PhD thesis, Washington State University, (2001).
[14] R. Sicard, *Nouvelles méthodes d'imagerie acoustique pour l'inspection par ondes de Lamb et ondes de volume* (Doctoral dissertation, Université du Québec à Trois-Rivières), (2000).
[15] E. Foltête, G. M. L. Gladwell and G. Lallement: On the reconstruction of a damped vibrating system from two complex spectra, part 2: experiment, *Journal of Sound and Vibration*, 240:2, 219-240, (2001).
[16] M. A. Trindade and A. Benjeddou. Effective electromechanical coupling coefficients of piezoelectric adaptive structures: critical evaluation and optimization. *Mech. Adv. Mater. Struct*. 16:210–23, (2009).
[17] S. S. Kessler, S. M. Spearing and C. Soutis. Damage detection in composite materials using Lamb wave methods, *Smart Mater. Struct*. 11:269-78, (2002).

REGISTRATION OF TECHNOLOGICAL STRAIN IN POLYMER COMPOSITE SAMPLES USING EMBEDDED FIBER - OPTIC STRAIN SENSORS

VALERII P. MATVEENKO[1], NATALIA A. KOSHELEVA[2], IGOR N. SHARDAKOV[3] AND ANDREY A. VORONKOV[4]

[1,2,4] Perm National Research Polytechnic University (PNRPU)
29 Komsomolsky prospekt, 614990, Perm, Russia
e-mail: nataly.kosheleva@gmail.com, web page: http://pstu.ru/en/

[3] Institute of Continuous Media Mechanics of the Ural Branch of Russian Academy of Science
1 Akademika Koroleva str., 614013, Perm, Russia
e-mail: shardakov@icmm.ru, web page: https://www.icmm.ru/en/

Key words: Polymer composite materials, Fiber-optic strain sensors, Technological strains, Smart-materials.

Abstract. The presence of technological strains induced by various manufacturing and operational factors is one of the characteristics of polymer composite materials (PCM). Conventional methods of registration and evaluation of residual strain are laborious, time-consuming and require a large amount of measurement procedures with special equipment. The idea of employing embedded fiber-optic strain sensors (FOSS) offers a real prospect for measuring residual strain.

The possibility of using embedded FOSS was demonstrated and implemented by the example of PCM samples obtained with the prepreg technology and compression molding method. In this method, the prepared reinforcing package is placed inside mold, heated and exposed to compaction pressure. Pressing process parameters (pressure, temperature and time) depend on material grade. The examined technology can be used for positioning fiber-optic strain sensors between the corresponding layers of the composite material.

In the process of PCM production, FOSS data were recorded with interrogator ASTRO X 327. Fiber optic sensors, interacting with the material of the examined object, allow registering the history of the strain process during all stages of polymer composite formation.

1 INTRODUCTION

Polymer composite materials (PCM) have a number of advantages over traditional materials: the ability to create different shapes of details with desired properties, high resistance to fatigue and corrosion, low specific gravity. However, during exploitation multi-layer composites have high probability of defects and damages development, which, among the other factors, determined by technological process of PCM creation and the presence of technological strains in the material. Traditional methods of assessing technological strain are laborious, time-consuming and require a large amount of measuring work using special

equipment.

Fiber-optic strain sensors (FOSS) have a special place among the various sensors for measuring mechanical damages of the material. The advantages of FOSS based on Bragg grating include a particular sensitivity, in comparison with other sensors, immunity to electrical noise, availability, easy integration with other equipment, remote control, as well as the ability to measure various physical and mechanical values. Additionally, for composite materials there is possibility of FOSS embedding into material during their manufacturing. Such material with embedded sensors is one of the sorts of SMART-materials. The FOSS embedding during PCM manufacture allows registering technological strains and offers control capabilities.

The ability of the technological strains measurement during manufacturing process of the mast of a sail boat in the autoclave molding is shown in work [1]. Research [2] provides experimental comparison between FOSS measurements and conventional resistive strain gages. During static tensile tests, the possibility of strain monitoring using FOSS, their sensitivity and accuracy were demonstrated. The emphasis of [3] is placed on the fact that the fiber-optic strain sensors with Bragg gratings are an excellent non-destructive tool to measure internal strains in the composite material. In the work [4] as one of the causes of FOSS spectrum distortion indicated the presence of residual stresses which appeared during the manufacturing process. The presence of residual stresses which appeared during the manufacturing process was indicated as one of the causes of FOSS spectrum distortion in the work [4]. The ability to use information about the internal and surface strains, obtained by FOSS with the aim to quantify damage and residual performance designs, are given in [5].

The small size and shape of the FOSS allows to embed them directly between the composite layers. This makes the possibility to monitor the composite structure from the beginning of the composite production to its operating conditions [6], [7]. FOSS embedding into the composite system potentially may let to eliminate the defects directly during production process [8]. Methods for efficient and reliable FOSS embedding into composite structure were studied. It was shown that the same sensors can be used for verifying the compliance with the specifications of elements or recognition of the quality assessment as well as for monitoring of structural integrity for its service life with the help of structural monitoring systems which operate in real time.

The possibility of usage fiber-optic strain sensors embedded between the layers of the formed composite material for strain registration was demonstrated at this work. The process of FOSS embedding into PCM was described. The history of the strain process of the polymer composite material formation at all stages of its manufacturing process was shown.

2 PREPREG TECHNOLOGIES AND METHODS FOR COMPRESSION MOLDING

This section contains a description of the technological process of FOSS embedding into PCM. One of the important conditions of this process is to ensure the entirety of the fiber material during manufacturing process.

A distinctive feature of the designs which is made from polymer composite materials is that materials and products are created simultaneously. The predefined geometrical dimensions and shape are given to this design. As a result, the physical and mechanical

characteristics of the product depend on the design features and technological features of the manufacturing process. Taking into account these features of PCM designs, the issue of control of the stress-strain state in the process of manufacturing products as well as in the subsequent operation of the structure become relevant.

The polymer composite material consists of high-impact (medium or high modulus) fibers (filler) and the polymer matrix (the cured binder). Prepreg is prepared for processing product that based on prepregged reinforcing material with woven and nonwoven structures. The process of creating products from polymer composite materials consist of several basic steps: laying out a reinforcing material into the specialized form, technology package assembly, the polymerization process, details removal. These technological steps are present in each technology of detail design from PCM with some additional items depending on the particular type. The most common technique is called: "Prepreg technology and autoclave molding".

Technology of details manufacturing occurs as semi-finished products, made from prepreg that was laying out, give a good account of the products that was made from PCM. This method consists of laying out the prepregged reinforcing material on special form-building equipment followed by curing in autoclave with overpressure. This provides a high level of physical and mechanical properties and low porosity of derived plastics.

In this paper, the possibility of measuring the technological strains with the help of FOSS, considered on an example of manufacturing process of standard samples for testing and demonstrated using contact pressing method.

Pressing technology is similar to the method of stamping, when prepared reinforcement package is placed into a mold, heated and exposed to compression pressure. The parameters of pressing process includes pressure, temperature and time that depend on the material grade. Pressing technology has high performance and possibility of full process mechanization, the ability to manufacture complex details with high precision implementation and with surface that does not require a mechanical treatment [9]. This technology can be applied with prepreg made from composite material based on thermosetting and thermoplastic matrices. During the manufacturing process of samples there is the possibility of control the product status in real time using embedded FOSS.

However, due to the fact that every process of manufacturing products from PCM arise with temperature and overpressure, the problems connecting with protection entirety of optical fibers in the material as well as protection fiber exits from the product are occurred. In the pressing process a number of adjustments that take into account technological features of FOSS based on the Bragg grating were done. Let’s consider the PCM manufacturing process with embedded FOSS.

The technological process of FOSS embedding into composite material includes a number of basic steps. First, the reinforcing material cutting on the plotter Zund G3 L-2500 is done. Further 20 layers of reinforcing material are laying out on special form-building equipment. In this paper stack of layers as an object forming is used. Stack of layers consists of 20 layers of fiberglass prepreg named as VPS-48. The characteristics of this material are presented in Table 1.

Predefined scheme of cutting samples is used while two optical fibers with five FOSS on each were embedded between 10 and 11 layers of reinforcing material. The assembly of technology package is held for material premolding. After performing all the operations above polymerization process is carried out. The process of polymerization of the samples with

embedded FOSS was carried out in the Langzauner press that was connected with interrogator ASTRO X327. During polymerization process control of pressure and temperature was derived by control computer as well as by FOSS. After the polymerization process was carried out the removal of technological package was done.

Table 1: Material characteristics

Name	VPS-48
Material	Fiberglass
Test temperature, °C	20
Tensile strength, MPa	710
Compressive strength, MPa	870
Bending strength, MPa	1100
Shear strength, MPa	75
Tensile modulus, GPa	33

For the curing process the recommended regime according to the specifications of the material has been selected:

- Temperature rise till 120°C with speed 3°C/min;
- Delay 0,4 hours with temperature 120°C;
- Molding pressure rise till 0,3 MPa;
- Temperature rise till 180°C with speed 3°C/min;
- Delay 1,5 hours with temperature 180°C;
- Cooling with speed 3°C/min till temperature 55°C;
- Decompression.

After the main polymerization process was carried out the temperature stabilizing of the workpiece during 4 hours at the temperature of 120°C was done.

3 ACTION PRINCIPLE OF FIBER-OPTIC STRAIN SENSOR BASED ON BRAGG GRATING

Fiber-optic Bragg gratings (FBG) are created by periodically changing in the core refractive index of the fiber (Figure 1). Such diffraction gratings are fully adapted to the conditions of waveguide propagation of emission and are capable to perform various operations on light signals.

Although fiber-optic communication is the most significant area of application for FBG, nevertheless they are widely used for creation concentrated and distributed fiber-optic sensors [10].

As a rule, for sensing element FBG formed in the photosensitive core of a single-mode lightguide at a small (~ 1-10 mm) section with a help of an interference pattern of coherent UV radiation are used. The main characteristic of FBG is the presence of a resonance reflection peak at the wavelength, determined by the relation [11]:

$$\lambda_{BG} = 2n\Lambda \tag{1}$$

where λ_{BG} – resonant (Bragg) wavelength, n – effective refractive index of lightguide at a given

wavelength, Λ – period of FBG.

The fiber deformation effect or temperature variation causes changes in the Bragg wavelength, which is used in fiber-optic sensor systems based on FBG.

From the relation (1) follows the expression for changing λ_{BG} with help of temperature variation or deformation effect. Thus, for the intrinsic temperature sensitivity of the FBG can be obtained [11]:

$$\frac{1}{\lambda_{BG}}\frac{d\lambda_{BG}}{dT}=\frac{1}{\Lambda}\frac{d\Lambda}{dT}+\frac{1}{n}\frac{dn}{dT}=\alpha+\frac{1}{n}\frac{dn}{dT} \tag{2}$$

where T – temperature FBG; α - coefficient of linear temperature expansion (CLTE) of quartz glass. This CLTE can be neglected cause of its smallness. The main contribution to the temperature sensitivity is made by $\frac{dn/dT}{n}$, which is called as thermo-optic coefficient. Usually it's assumed that the grating embedding into ambient with thermal expansion coefficient which is different from α leads to a longitudinal strain of the FBG when temperature changes.

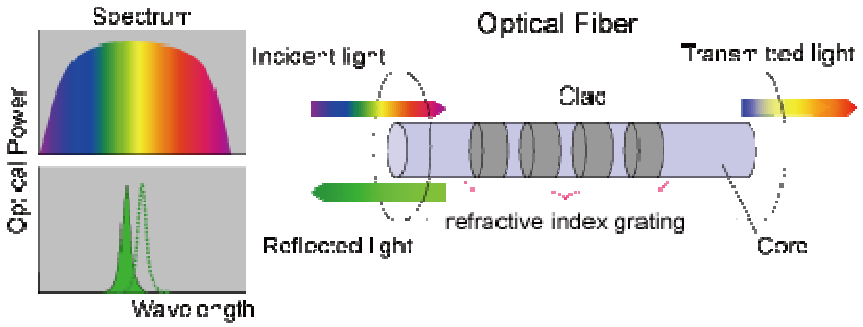

Figure 1: Fiber Optic Bragg Grating

Similarly, for strain sensitivity [11]:

$$\frac{1}{\lambda_{BG}}\frac{d\lambda_{BG}}{d\varepsilon}=\frac{1}{\Lambda}\frac{d\Lambda}{d\varepsilon}+\frac{1}{n}\frac{dn}{d\varepsilon}=\left(1-\frac{n^2}{2}\left(p_{12}-\nu\left(p_{11}+p_{12}\right)\right)\right)\times 10^{-6}\,\mu\varepsilon^{-1} \tag{3}$$

where ε - longitudinal strain of a lightguide part with FBG; ν - Poisson's ratio of quartz glass; p_{11} and p_{12} - Pockels coefficients in the optical stress tensor. This value of the strain sensitivity of FBG is usually equal to [11]:

$$\frac{1}{\lambda_{BG}}\frac{d\lambda_{BG}}{d\varepsilon}\approx 0.787\times 10^{-6}\,\mu\varepsilon^{-1} \tag{4}$$

The shift of the spectral position of the resonant wavelength of a fiber Bragg grating, $\Delta\lambda_{Br}$ linearly depends on the ambient temperature changes, ΔT, and strains, ε, which is occurred in the process when mechanical action is applied to fiber lightguide. Dependence of the shift $\Delta\lambda_{Br}$ from these parameters can be described [11]:

$$\Delta\lambda_{Br}=2n\Lambda\left(\left\{1-\left(\frac{n^2}{2}\right)\left[p_{12}-\nu\left(p_{11}+p_{12}\right)\right]\right\}\varepsilon+\left[\alpha+\frac{1}{n}\frac{dn}{dT}\right]\Delta T\right) \tag{5}$$

where n – effective refractive index of mane mode of fiber lightguide; $\Lambda \le 1$ μm refractive index modulation period; p_{11} and p_{12} - Pockels coefficients of the elastic-optical tensor; ν - Poisson's ratio; α - CLTE of quartz glass.

When temperature is constant ($T = const$), the expression (5) will take the following form:

$$\Delta\lambda_{Br} = 2n\Lambda\left\{1-\left(\frac{n^2}{2}\right)\left[p_{12}-\nu\left(p_{11}+p_{12}\right)\right]\right\}\varepsilon \tag{6}$$

Taking into account that when temperature is constant the ε equal:

$$\left(\frac{n^2}{2}\right)\left[p_{12}-\nu\left(p_{11}+p_{12}\right)\right] = 0.22 \tag{7}$$

The following expression can be obtained:

$$\Delta\lambda_{Br} = 2n\Lambda\cdot(1-0.22)\varepsilon \tag{8}$$

and

$$\varepsilon = \frac{\Delta\lambda_{Br}}{\lambda_{Br}\cdot 0.78} \tag{9}$$

According to the relation (9), the coefficient $\frac{1}{\lambda_{Br}\cdot 0.78}$ is unique for each FBG.

4 PROCESSING DATA OBTAINED FROM FOSS

The process of recording data during the manufacturing process, which includes compression molding process and was described in section 2 of this paper, was done. In order to ensure the completeness and objectivity of the recorded data from two lines with embedded FOSS, a single FBG was also used. This single FBG was located outside the material. This FBG is used for compensation of the resonant wavelength displacement that caused by a changes in temperature during the forming process. To assess the correctness of the data from single FBG, as independent and autonomous temperature record in the molding process record EClerk-USB-2Pt was used. The accuracy of this independent temperature record of temperature measuring is ± 0.04°C. Also as a sensitive element the thermal resistance device ТСПг-К2-Pt1000-В2 was used.

During the measurement, the interrogator determines the strongest peak of the reflected signal in the measuring zone that was tuned before test began, and calculates the deviation of the Bragg wavelength. Due to the distinctive features of realization the technological process of PCM production, in the process of sensor loading there is a redistribution of the intensity in the spectrum of the reflected signal. Cause of this reason interrogator begins to estimate the deviation along the neighboring peak, which leads to appearance of sharp "jumps" in the signal. Changes in the spectrum of reflected signals from the FBG caused by the effect of transverse pressure during the forming process are shown in Figure 2 and Figure 3.

These spectrum changes of the reflected signal occurred during the cooling of the material into which the line with FBG was embedded. And this spectrum changes reflected in the data that was taken from the FBG as a constant displacement. In order to compensate these changes, during data analysis a correction algorithm is used. The example of the algorithm is

shown in Figure 4.

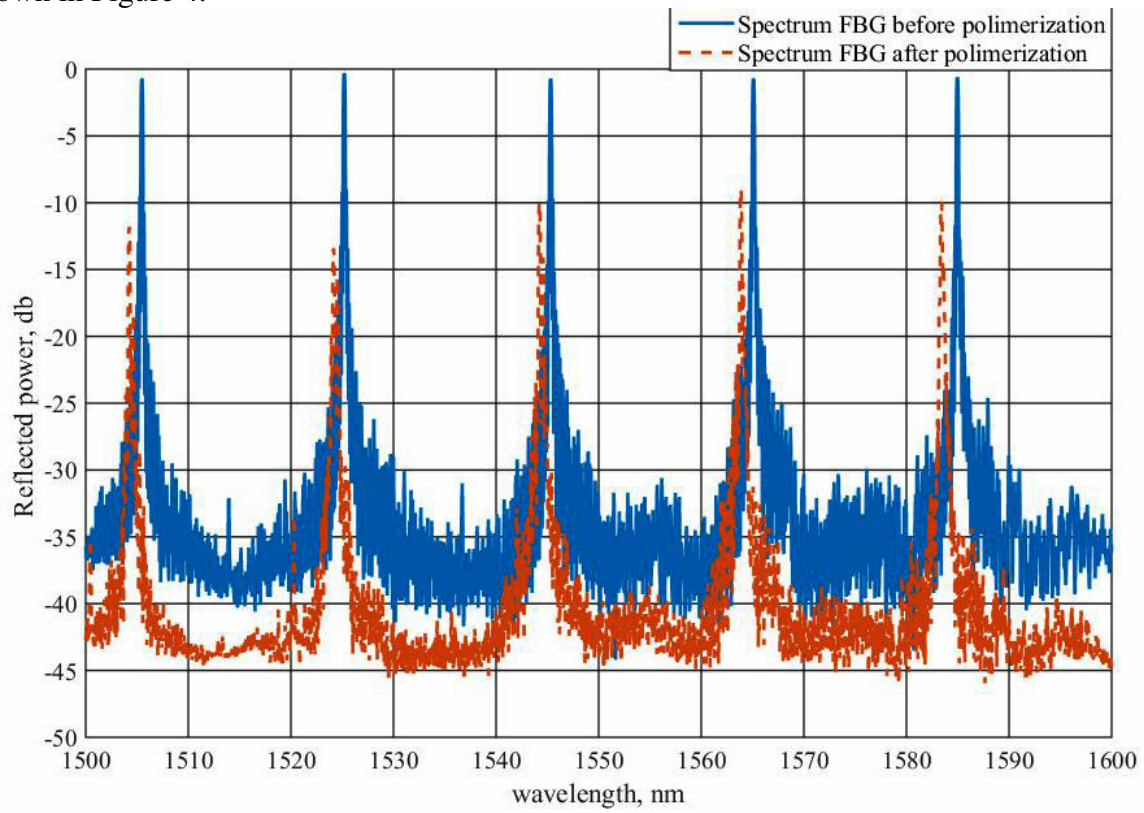

Figure 2: Changes in the total spectrum of the reflected signal of the FBG line

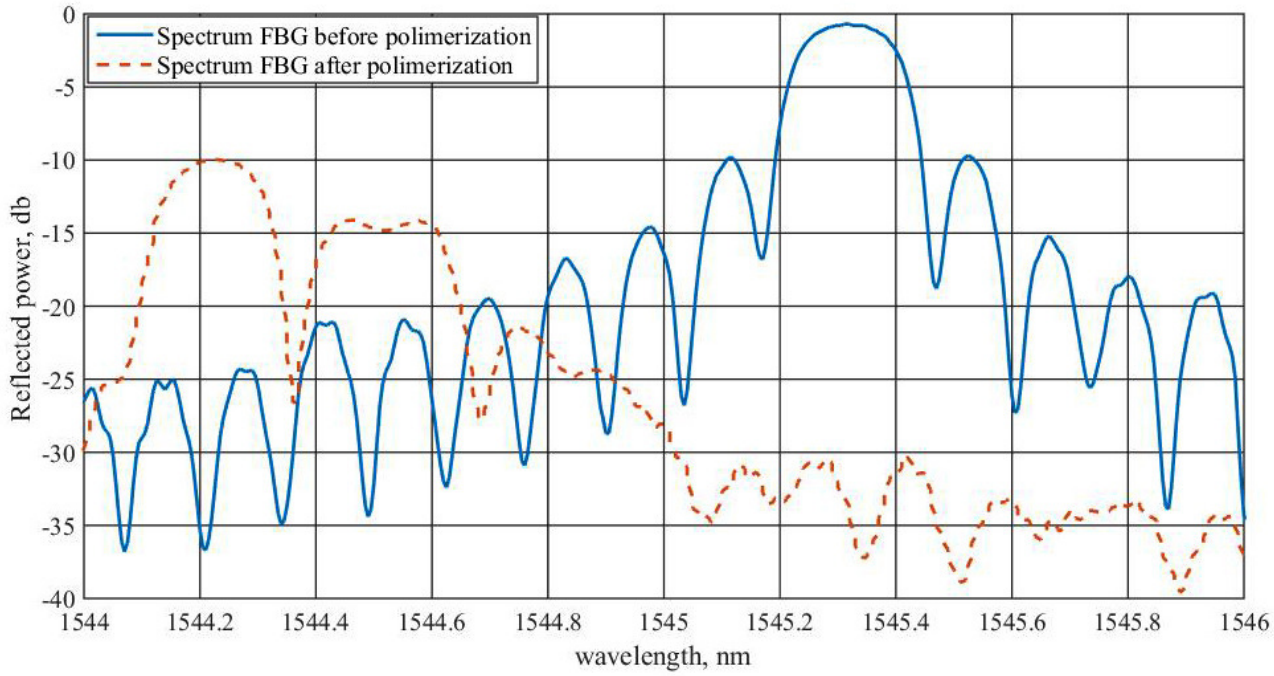

Figure 3: Changes in the reflected spectrum of second FBG line

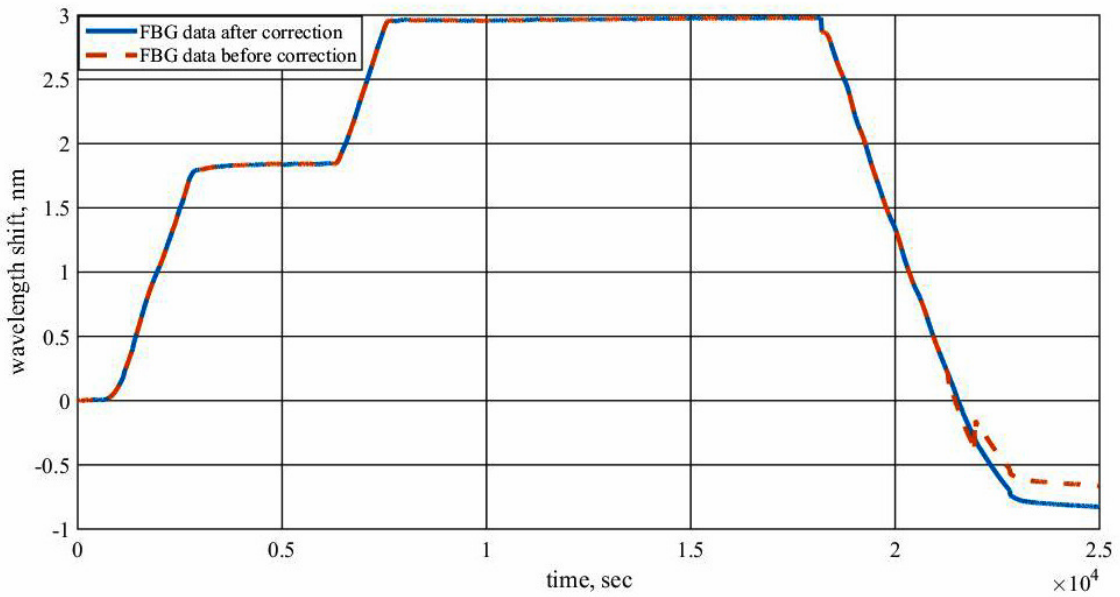

Figure 4: The example of the correction algorithm

The correction algorithm works as:

1. The value of the deviation (sensitivity to displacement) is introduced to the algorithm;
2. The number of measurements (window) on the basis of which the estimate will be done is entered;
3. The array of data is checked and the time when the displacement occurs is determined;
4. Based on the window, the value is interpolated to the displacement point;
5. The deviation is estimated;
6. All subsequent data are corrected by the value of this deviation.

5 DATA REGISTRATION IN REAL TIME

Figure 5 shows the registration scheme of technological strains in PCM in real time that was received from FOSS, where 1 – sample, 2 – segment of optical fiber with FOSS, 3 – interrogator, 4 – computer, 5 – broadband spectrum, 6 – reflected spectrum, 7 – output to computer, 8 – single FBG, acting as a temperature sensor.

To calculate the temperature according to the FBG data, the following dependence was used:

$$\Delta\lambda = K_2 \Delta T^2 + K_1 \Delta T \tag{10}$$

where $\Delta\lambda$ – changes in the Bragg resonant wavelength; ΔT – temperature changes.

From the relation (10), the following expression is obtained for calculating the temperature changes according to the FOSS data with respect to ΔT:

$$\Delta T = \frac{-K_1 + \sqrt{K_1^2 + 4K_2\Delta\lambda}}{2K_2} \tag{11}$$

or

$$T = \frac{-K_1 + \sqrt{K_1^2 + 4K_2\Delta\lambda}}{2K_2} + T_0 \tag{12}$$

where T_0 - initial temperature value.

The missing coefficients are found from FOSS data at the time of the molding process at temperatures of 120°C and 180°C, starting from the system of equations obtained from expression (10).

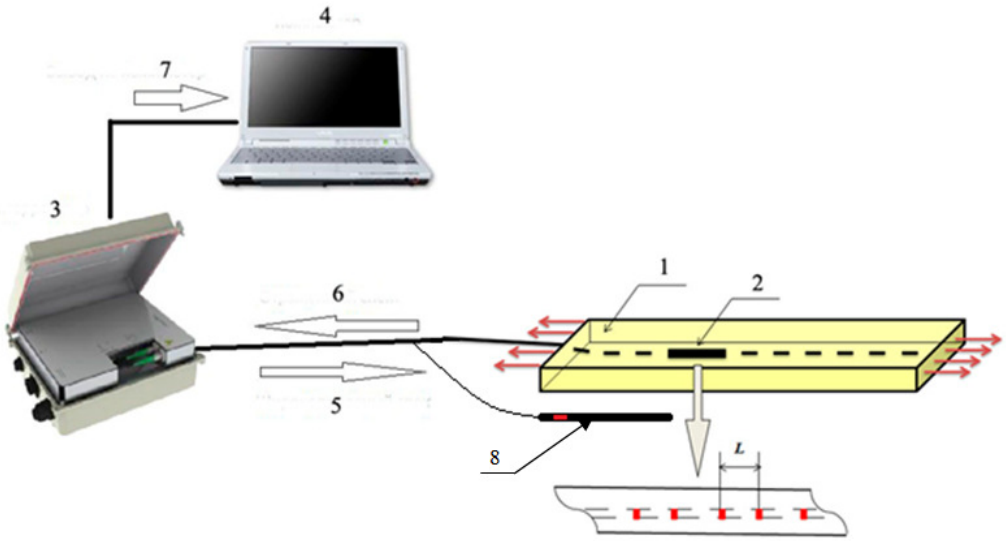

Figure 5: Scheme of data registration in real time

Figure 6 shows the graphical dependencies that were obtained with the help of a single FBG, acting as a temperature sensor, and also with the help of an independent temperature recorder EClerk-USB-2Pt. It should be noted that the data from single FBG (that was located near to the PCM) are correlated well with the data from independent temperature recorder EClerk-USB-2Pt. The fiber-optic sensor, interacting together with the material, allows to record the changes in the wavelength of the reflected spectrum using interrogator.

The history of the strain process in the polymer composite material formation at all technological stages of its production is presented in Figure 7. The red line marks the temperature sensor. Here: 1 - dotted blue curve is the averaged results for the five sensors on the first fiber; 2 - dash-dotted crimson curve – on the second fiber.

From relation (5) it follows that the detected change in the wavelength of the reflected spectrum is determined not only by technological strains, but also by temperature deformations due to temperature $\Delta T = T(t) - T_0$. Here $T(t)$, T_0 - system temperature "fiber optic sensor - the material in the vicinity of the sensor" respectively, at time *t* and at the time when sensor is mounted on the object of study.

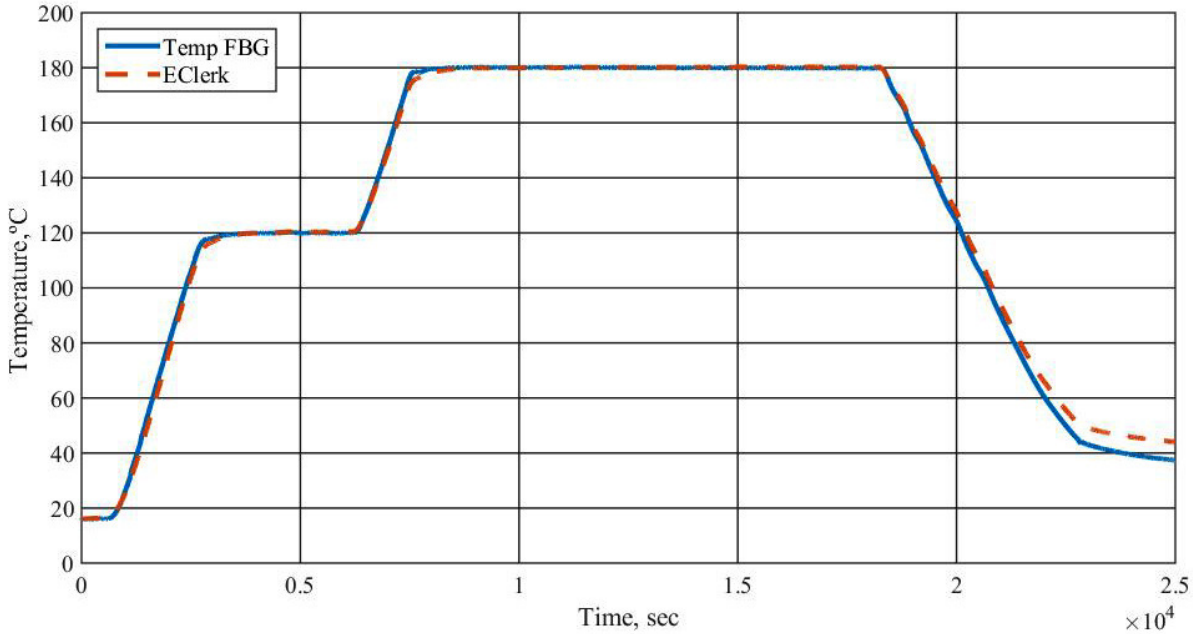

Figure 6: Temperature data from single FBG and independent recorder EClerk-USB-2Pt.

Applying to the relation (9) recorded data during the whole process of PCM forming, and subtracting the temperature component, the technological strains was obtained.

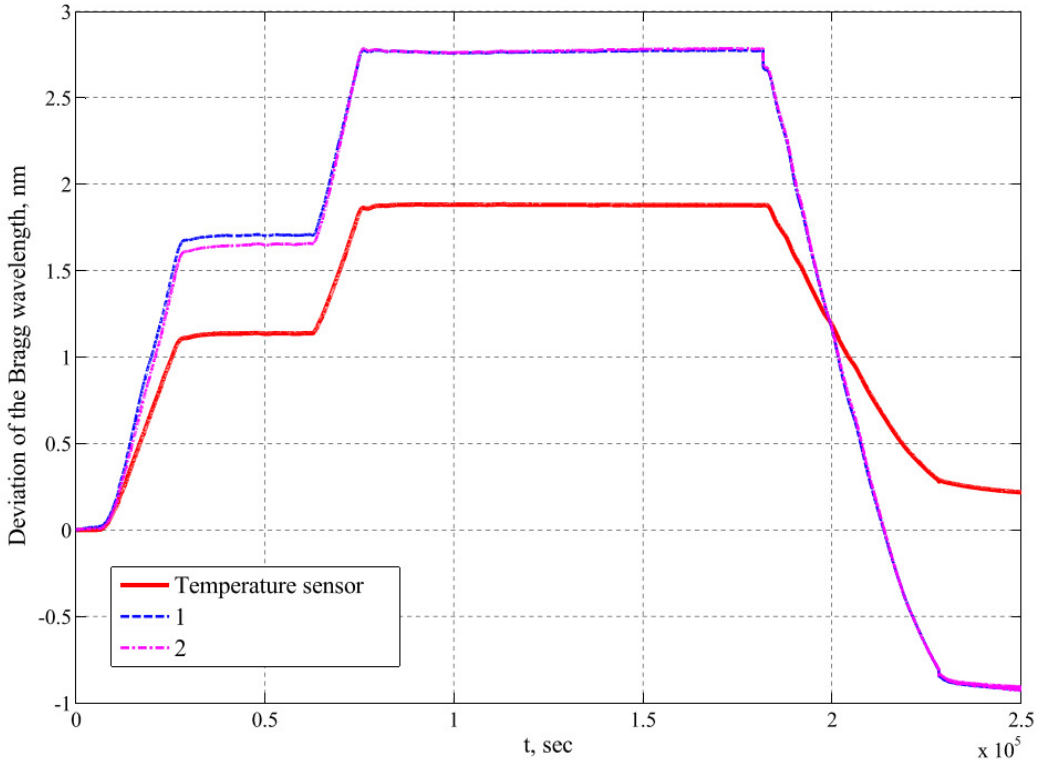

Figure 7: FOSS data during the whole process of molding PCM

Figure 8 shows the strain dependencies in the form of the average values obtained from FOSS that was located on the first (dashed blue curve) and second (dash-dotted crimson curve) optical fiber.

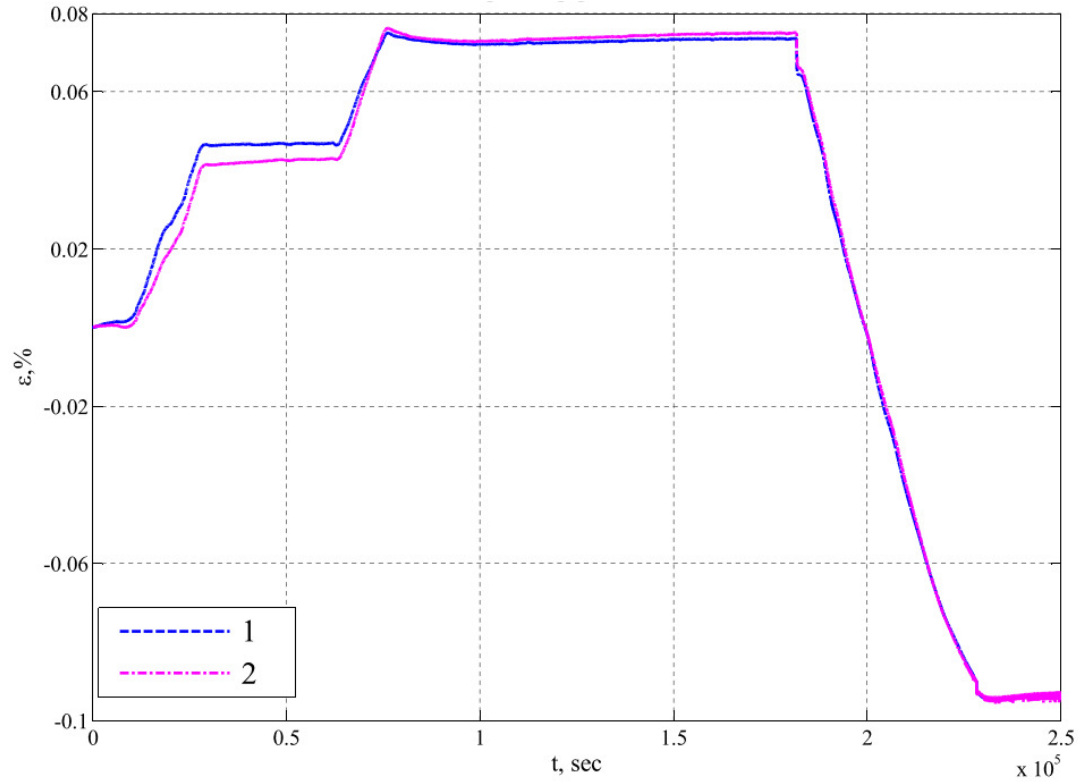

Figure 8: FOSS data in the strain

These dependences indicate the presence of technological strains in the PCM after molding. In addition, the obtained results allow to trace the evolution during all technological process of PCM manufacturing. Residual strain accounting allows to raise the operational properties at the complex objects designing. In addition, thanks to these relationships, there is an opportunity to assess the stress-strain state of structures during manufacturing process.

6 CONCLUSIONS

- In the paper the technology of FOSS embedding into PCM is described. Technological regimes of forming a material that includes 20 layers of prepreg (VPS-48) are given. The physical and mechanical characteristics for this material are provided.
- The principle of the FOSS action based on Bragg gratings is described. The features of real-time data recording with the help of FOSS are given. A data correlation algorithm for compensating of displacements in the FOSS data is presented.
- Dependences for the temperature calculation obtained from FOSS data are given. The reliability of these results was confirmed with the help of an independent temperature recorder EClerk-USB-2Pt.
- The history of technological strains in the PCM during the process of its

manufacturing and the presence of residual (technological) strains are shown.

The research was performed at Perm National Research Polytechnic University with support of the Russian Science Foundation (project №15-19-00243).

REFERENCES

[1] Di Sante, R. and Donati, L. Strain monitoring with embedded Fiber Bragg Gratings in advanced composite structures for nautical applications. *Meas* (2013) **46**:2118–2126.

[2] Guemes, J. and Menendez, J. Response of Bragg grating fiber-optic sensors when embedded in composite laminates. *Compos. Sci. Technol* (2002) **62**:959–966.

[3] Colpo, F., Humbert, L. and Botsis, J. Characterisation of residual stresses in a single fibre composite with FBG sensor. *Compos. Sci. Technol* (2007) **67**:1830–1841.

[4] Kuanga, K., Kennyb, R., Whelanb, M., Cantwella, W.and Chalkera, P. Embedded fibre Bragg grating sensors in advanced composite materials. *Compos. Sci. Technol* (2001) **61**:1379–1387.

[5] Bosia, F., Botsisa, J., Facchinia, M. and Giaccari, P. Deformation characteristics of composite laminates—part I: speckle interferometry and embedded Bragg grating sensor measurements. *Compos. Sci. Technol* (2002) **62**:41–54.

[6] Kang, H.-K., Kang, D.-H., Bang, H.-J., Hong, C.-S. and Kim, C.-G. Cure monitoring of composite laminates using fiber optic sensors. *Smart Mater. Struct* (2002) **11**:279.

[7] Khoun, L., De Oliveira, R., Michaud, V.and Hubert, P. Investigation of process-induced strains development by fibre Bragg grating sensors in resin transfer moulded composites. *Composites Part A* (2011) **42**:2011.

[8] Minakuchi, S., Umehara, T., Takagaki, K., Ito,Y. and Takeda, N. Life cycle monitoring and advanced quality assurance of L-shaped composite corner part using embedded fiber-optic sensor. *Composites Part A* (2013) **48**:153-161.

[9] De Oliveira, R., Lavanchy, S., Chatton, R., Costantini, D., Michaud, V., Salath, R. and Menson, J.-A. Experimental investigation of the effect of the mould thermal expansion on the development of internal stresses during carbon fibre composite processing. *Composites Part A* (2008) **39**:1083–1090.

[10] Kulchin, I.N. *Distributed fiber-optic measure systems.* Moscow: Fuzmatlit (2001).

[11] Kablov, E., Sivakov, D., Guliaev, I., Sorokin, K., Fedotov, M., Dianov, E., Vasilev, S., and Medvedkov, O. The use of optical fiber as strain gauges in polymer composite materials. *Encyclopedic Guide* (2010) **3**:10-15.

An asymptotically correct beam type piezoelectric energy harvester model

Shreya Banerjee*, Sitikantha Roy†

*, † Department of Applied Mechanics
Indian Institute of Technology-Delhi
Hauz Khas, New Delhi
India 110016
e-mail: shreyabanerjee002@gmail.com

ABSTRACT

There has been an increasing demand for wireless electronic devices which led to substantial research efforts in major fields like energy storage and energy harvesting. Among all other materials mostly piezoelectrics has grabbed attention for energy harvesting application because of its high electromechanical coupling property. The present study talks about developing an asymptotically correct electromechanical model of a vibration based piezoelectric energy harvester model and validate it with experimental studies published in past literature. The present study is based on a well renowned theory Variational Asymptotic Method (VAM). This theory is a rigorous mathematical technique which asymptotically split the original three dimensional electromechanical problem into two dimensional electromechanical cross sectional analysis and one dimensional beam analysis. As an example problem a bimorph configured energy harvester under a harmonic base excitation has been studied. Coupled voltage, power and current response under a harmonic base acceleration has been mathematically derived and obtained. The model is also capable of analysing the system response with varying load resistance. Close circuit and open circuit voltage are obtained and validated. Thus the present study is all about developing an efficient and reliable mathematical technique which can capture all the important multiphysics involved in any kind of a generalized piezoelectric energy harvester model.

Keywords: Piezoelectric energy harvester, Variational asymptotic method, Bimorph.

REFERENCES

[1] Roy S, Yu W and Han D 2007 An asymptotically correct classical model for smart beams International Journal of Solids and Structures 44 8424–8439

[2] Erturk A and Inman D J 2009 An experimentally validated bimorph cantilever model for piezoelectric energy harvesting from base excitations Smart Materials and Structures 18 1-18

[3] Banerjee S and Roy S 2016 Multiphysics analysis of an asymptotically correct piezoelectric sensor under static and dynamic load International Journal of Solids and Structures 92-93 64-75

DEVELOPMENT OF $LI_{1.4}AL_{0.4}TI_{1.6}(PO_4)_3$ SOLID ELECTROLYTE-BASED POWER COMPOSITES: CHARACTERISATION OF ELECTRICAL AND MECHANICAL PROPERTIES

G. LIAO*, S. GEIER, T. MAHRHOLZ, P. WIERACH, M. WIEDEMANN

* Institute of Composite Structures and Adaptive Systems, German Aerospace Center (DLR e.V.)
Lilienthalplatz 7, 38108 Braunschweig, Germany
guangyue.liao@.dlr.de

Key words: Multifunctional power composite, $Li_{1.4}Al_{0.4}Ti_{1.6}(PO_4)_3$ solid electrolyte, electrical properties, mechanical properties.

Abstract. This paper introduces a method of producing power composites which can store (and deliver) electrical energy whilst bearing mechanical loads simultaneously. The composite system in the present work based on all-solid-state supercapacitors by using $Li_{1.4}Al_{0.4}Ti_{1.6}(PO_4)_3$ solid electrolyte which is synthesized by conducting a sol-gel method. The as-prepared samples are embedded into commercial available glass fibre reinforced plastics (GRFP). Cyclic voltammetry tests characterize the double layer behaviour combined with galvanostatic charge-discharge measurements for capacitance calculation. The capacitance is still unchanged after 1500 charge-discharge cycles showing a promising potential for future applications, such as power supplier for electrical vehicles, airplanes and satellites. The mechanical properties of composite materials with and without solid electrolytes are characterized by four-point-bending tests. The influence of loads on electrical properties is also investigated by coupling tests which combine the electrical measurements during stepwise bending loads. The conducted tests reveal slightly reduced bending strength, ductility and Young's modulus for the specimens with embedded solid electrolytes compared to the pure composite specimen. Besides, the capacitance values remain constantly under different bending loads.

1 INTRODUCTION

The service time of space applications such as satellites depends exclusively on the lifetime of their electrical power source. Long active shelf life up to years and diver of planet probes are 30,000 life cycles. Batteries usually applied as the electrical energy storage device, however, are limited by their recharge cycle lifetimes. Besides, in space the batteries have to withstand hot and cold conditions radiation of the sun and work in a vacuum without leaking or exploding.

Furthermore the battery is designed for power peaks of very shortly used applications such as lidar, radar, repulsion or robotic systems. In these cases an alternative system such as a supercapacitor can handle these power peaks. As result the battery as main energy system can be downsized therefore weight and volume can be reduced whereas the lifetime of the battery and the whole operation time of a satellite can be extended.

A further challenge is the integration of the supercapacitors within the bearing structure of the satellite. Asp et al. [1] already presented how to use structural materials such as carbon fibers and ionic conductive resins as energy devices and structure at the same time. Unfortunately neither the mechanical nor the electrical performance was on a comparable level to the results of the individual systems. However this kind of combination has the potential to save volume (smaller size may open space for other devices) and weight (less propulsive power needed or more possible payload).

In previous research [2,3], we already reported a new approach of multifunction material integration. The investigation based on an all-solid-state structural supercapacitor of the NASICON-type $Li_{1.4}Al_{0.4}Ti_{1.6}(PO_4)_3$ ceramic electrolyte embedded in composite materials by means of Differential Pressure Resin Transfer Moulding (DP-RTM). The electrolyte was embedded in laminates made of fleece and metalized fleeces used as collectors, afterwards injected by using the resin RTM-6 (Hexcel® PRODUCTS INC., US). Using non liquid components, this energy storage device reduces the leakage problem induced by particle impacts. In this paper, Hexply® 913 GFRP-prepregs (Hexply® 913, Hexcel® Corporation, US) are used as semi-finished products processed by autoclave in vacuum bag. The glass fibre reinforced plastic (GFRP) composites are used because which improves the mechanical properties comparing with composites only with polyester fleece. In addition Hexply® 913 is a proven modified epoxy matrix which exhibits outstanding environmental resistance, whilst retaining good mechanical performance. Comparing with injection process, the manufacture with prepregs is more convenient. The electrical properties of this structural supercapacitor are characterised by cyclic voltammetry test and galvanostatic charge-discharge measurement, meanwhile the mechanical characterisation is demonstrated by four-point-bending tests in the present work.

2 EXPERIMENTAL PART

2.1 Synthesis process of $Li_{1.4}Al_{0.4}Ti_{1.6}(PO_4)_3$ (LATP) solid electrolyte

The $Li_{1.4}Al_{0.4}Ti_{1.6}(PO_4)_3$ (LATP) solid electrolyte was synthesised by a sol-gel method with citric acid. Stoichiometric amounts of 0.8 mol/L Titanium (IV) t-butoxide (≥99.9%, Alfa Aesar) were dissolved in 0.2 mol/L citric acid (>99%, Merck KGaA), heated and stirred at 95°C for 20h. Then stoichiometric amounts of $LiNO_3$ (>99%, ReagentPlus®), $NH_4H_2PO_4$ (>98.5%, ReagentPlus®) and $Al(NO_3)_3{\cdot}9H_2O$ (99.2%, VWR chemicals) were added, dissolved and stirred at the same temperature for 30 min until a homogeneous solution was obtained. After that, ethylene glycol (≥99.9%, Merck Schuchardt OHG) with a molar ration of citric acid at 1:1 was added. Then the solution was heated up to 120°C with stirring for 30 min and heated up to 170°C for 2h to evaporate the water and obtain the polymer precursor. The dried gel was milled by hand to a powders and transferred to a ceramic crucible, heated up to 600°C for 5 h with 5 °C/min to complete pyrolysis process and calcined in open air at 800°C for 5h. The acquired powder was milled by a mechanical milling method with ethanol for 2 h and pressed into pellets (thickness 1 mm) under the pressure of 180MPa. The pellets were sintered at 950°C for 8h (heating rate from ambient temperature to 600°C is 2°C/min, from 600°C to 950°C is 5°C/min).

2.2 Manufacturing of $Li_{1.4}Al_{0.4}Ti_{1.6}(PO_4)_3$ solid electrolyte-based multifunctional power composites

The solid electrolyte pellets were polished and sputtered with gold in thickness of about 90 nm. Hexply® 913 GFRP-prepreg (Hexply® 913, Hexcel® Corporation, US) was used as insulation materials and metalized polyester layers were used as electronic conductive materials.

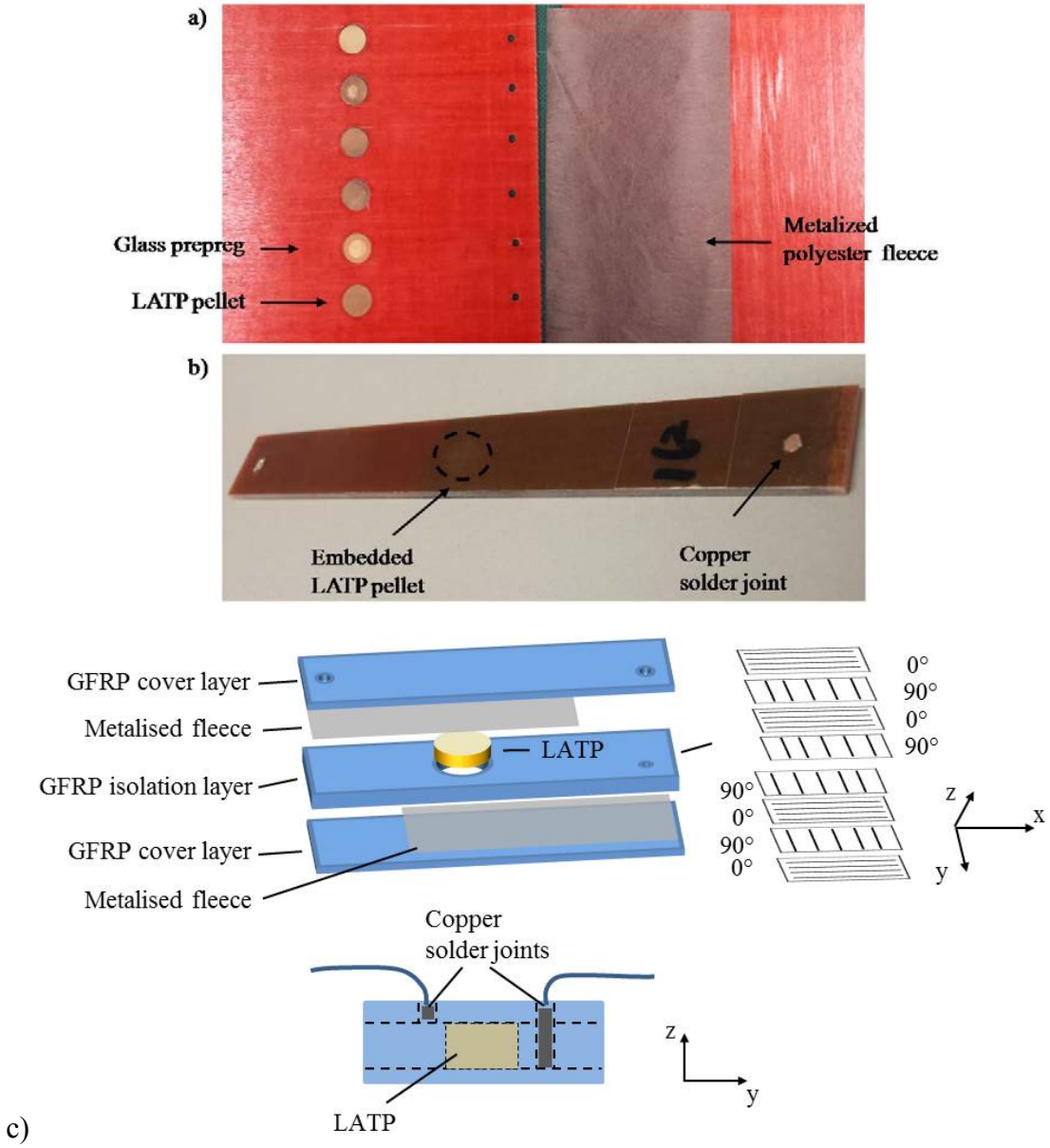

Figure 1 a) Layer configuration of LATP composite; b) Four point bending test sample with bond points for electrical measurements; c) configuration's sketch

The middle layer is made of eight layers GFRP-prepreg with a ply thickness of 0.125mm. The lay-up is designed in symmetrical manner with the two outer most layers oriented in 0°-direction while the internal four layers are alternately 0° and 90° oriented. The two cover layers are four layers with 0° and 90° oriented separately. All specimens are manufactured by hand using a one-step curing process under pressure (3 h 120 °C at 3 bars). The whole composite is consolidated within one process step. After curing, the plate was cut into samples of 100×15×2 mm for four-point-bending tests according to standard DIN EN ISO 14125:1988, class IV. Bonding points for cables were inserted for the electrical tests.

2.3 Characterization of microstructure, electrical and mechanical properties

A computerized tomography scan (CT, GE phoenix v|tome|x s) was used to exhibit the morphology condition of LATP composite samples before the mechanical tests.

The cyclic voltammetry (CV) test and galvanostatic charge-discharge measurements were conducted at room temperature by an electrochemical workstation (Vertex, IVIUM TECHNOLOGIES) for the LATP composite samples without and under mechanical load. The measurements were carried out at a voltage range of 0-0.5V by CV with different scan rates of 5 mV/s, 10 mV/s, 20 mV/s, 50 mV/s and 100 mV/s and galvanostatic charge-discharge measurement with different current density of 0.1 µA/g, 0.2 µA/g, 0.5 µA/g, 0.8 µA/g, 1 µA/g, 2 µA/g, 3 µA/g, 4 µA/g and 5 µA/g. To calculate the capacitances 1500 charge-discharge cycles are measured with a current density of 2 µA/g.

Mechanical properties were investigated by four-points-bending test and tensile test with a universal testing machine (Zwick 1484, Zwick GmbH & Co. KG). Both of the tests were conducted at a rate of 1 mm/min with a pre-load of 5N to ensure that the sample was under flat condition. A 20 kN load cell (Z4, Hottinger Baldwin Messtechnik GmbH, Germany) was used as well as a transducer. The bending force and deformation were recorded by the software Test-Expert II V3.31 (Zwick GmbH & Co. KG).

a) 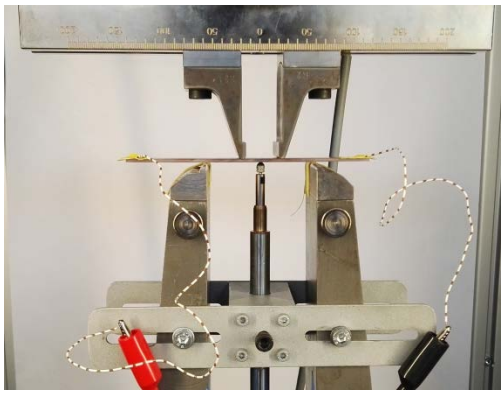 b) 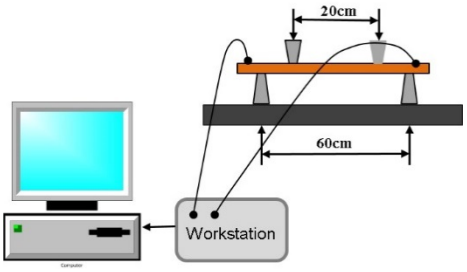

Figure 2 (a) Universal testing machine for four-point-bending tests; (b) sample is connected to electrochemical workstation.

Coupling tests were realized by combining mechanical test samples with the electrochemical workstation. A schematic picture of test set-up is showed in Fig. 2 b). A step

bending load was used with an interval of 120MPa, therefore the static electrical properties were tested under the bending loads of 120MPa, 240MPa, 360MPa, 480MPa and 600MPa.

2.4 MATHEMATICAL FORMULARS

2.4.1 Equations for capacitance calculation

Galvanostatic charge-discharge tests are executed by charging and discharging the device in between a set-up potential window with a constant current and the time of the corresponding process is recorded. Specific capacitance is calculated [4] by:
Specific capacitance:

$$C_m = \frac{Q}{U} = \frac{I_m \Delta t}{\Delta U} \quad (1)$$

C_m- Specific capacitance, µF/g;
U-Potential window, V;
ΔU - the potential window in discharge process excluded voltage drop, V;
Q - The capacitor's charge, C;
 t- Time of a measurement cycle, total time of discharge;
I_m– charge-discharge current density, µA/g
m – Weight of LATP electrolyte, g.

2.4.3 Equation for bending strength and Young's modulus

The bending strength and Young's modulus are calculated by force and deformation recorded by test machine during four-points-bending test. According to DIN EN ISO 14125 the equation is given by [5]:

$$\sigma = \frac{FL}{bh^2} \quad (2)$$

$$E_f = \frac{0.21L^3}{bh^3}\left(\frac{\Delta F}{\Delta s}\right) \quad (3)$$

σ - Bending stress, MPa;
E_f – Bending modulus, MPa;
 s – Deviation difference of s" and s' in the middle of sample, mm;
 F – Force difference of F" and F' according to s" and s', N;
b – Width of samples; h – Thickness of samples.

3. RESULT AND DISCUSSIONS

3.1 Electrochemical Tests

The LATP composite is firstly used as electrical energy storage device. Hence, the electrical properties are demonstrated.

Cyclic voltammetry curves for the LATP electrical energy storage system are shown in Fig. 3 obtained at room temperature (24 °C) between a potential of 0 to 0.5 V and at a scan rate of 5-100 mV/s. No visible peaks in the 0-0.5 V potential range are observed from the CV curves indicating an absence of Faradic current over this potential region. This reveals that charge and discharge occur reversibly at the Au/LATP interface. The curves are more close to a rectangular shape at low scan rate (5-20 mV/s), and tent to tilt toward vertical axis as the

scan rate increased above 20 mV/s. This result indicates that the influence of system resistance is stronger at high scan rate.

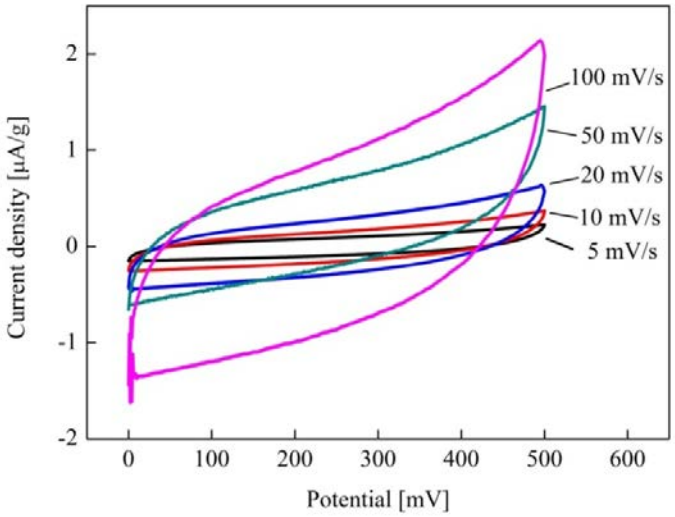

Figure 3 Cyclic voltammetry curves of LATP sample measured with different scan rates.

To investigate the storage ability of the LATP electrical energy storage device, the galvanostatic charge-discharge measurements are executed with different charge-discharge current density from 0.1 to 5 µA/g (seen in Fig. 4 a)). Only slight voltage drop caused by internal resistance could be observed at charge-discharge current density of 0.1 µA/g during discharge. The specific capacitances are calculated from discharge lines shown in Fig. 4 b). At values lower than 1µA/g the specific capacitance decreases very strongly with an increasing current density. At values higher than 2 µA/g the specific capacitance approaches asymptotically a constant value of 10-14 µA/g. The highest specific capacitance is achieved with 35.98 µF/g at a current density of 0.1 µA/g.

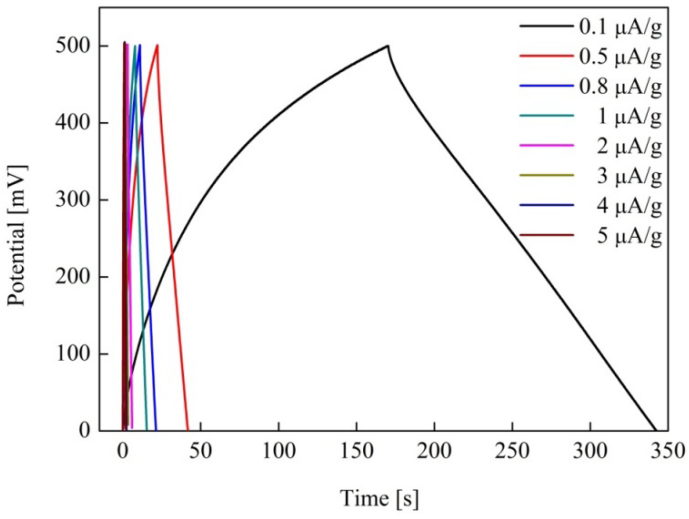

a)

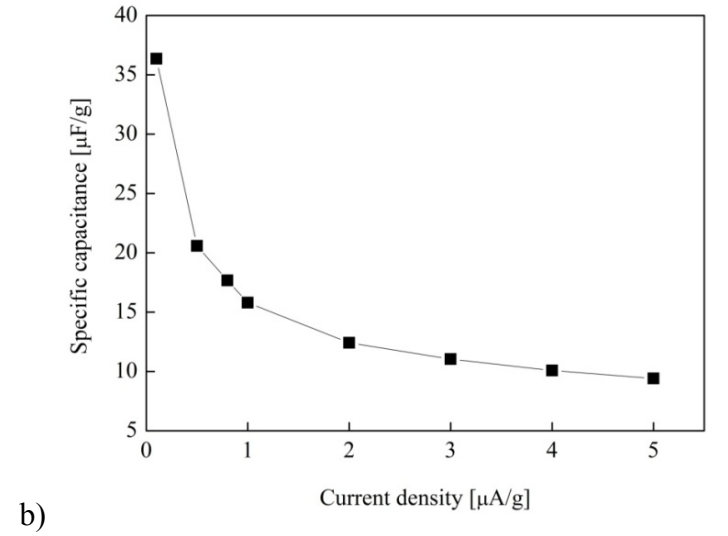

b)

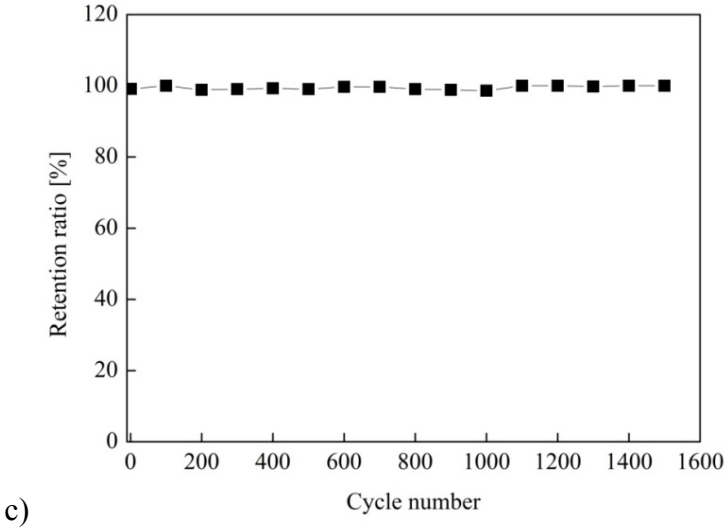

c)

Figure 4 a) Galvanostatic charge-discharge curves of LATP composite with different current densities; b) the specific capacitances of LATP composite calculated from galvanostatic charge-discharge measurements; c) change of capacitance during 1500 cycles of charge-discharge in 0-0.5 V potential window with current density of 2 µA/g.

Furthermore the LATP electrical energy storage system is characterized with respect to cycle life stability using galvanostatic charge-discharge cycling at a constant current density of 2 µA/g during 1500 cycles. The results are shown in Fig 4 c) revealing excellent cyclic properties because the pristine specific capacitance of 12.99 µF/g did not change during cyclicing.

3.2 Morphological Investigations

The solid electrolyte $Li_{1.4}Al_{0.4}Ti_{1.6}(PO_4)_3$ belongs to the class of ceramic materials, which have different mechanical properties compared with GFRP. The LATP as embedded element interrupts the continuity of fibres and matrix. Thus, it is worth being investigated, how the mechanical behaviour is affected by the combination of the two different components.

Before mechanical testing, the embedding quality of the LATP pellet inside laminates is characterized by CT scanning. In Fig. 5, cross section photos from three directions are displayed. The images are taken form the middle position of the layers indicating the absence of any macro-fractures in the LATP pellets.

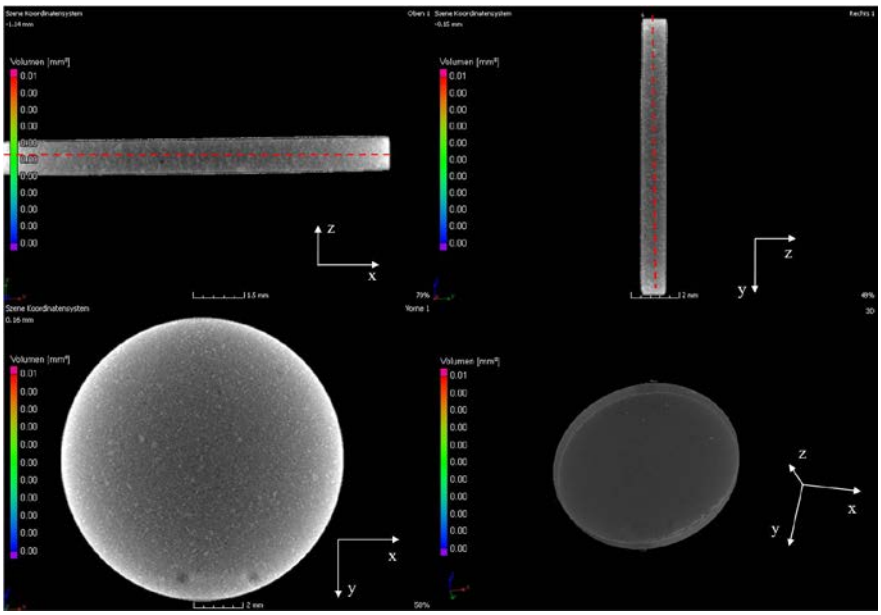

Figure 5 CT photos of LATP pellet after embedding, pictures from the middle position of each axis are displayed.

3.3 Mechanical tests

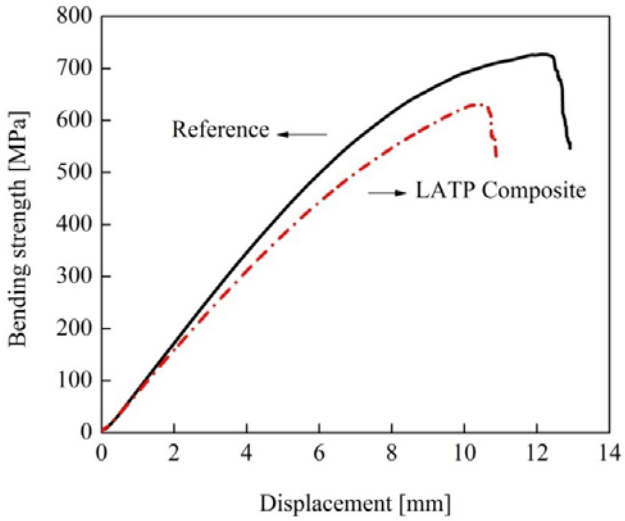

Figure 6 Curves of four-point-bending tests between LATP composite and GFRP sample without LATP.

Table 1 Mechanical properties of the reference specimens and LATP composites

Sample	σ_b [MPa]	Standard deviation of σ_b [%]	E [GPa]	Standard deviation of E [%]	ε_f [%]
Reference	735.113	2.4%	29.772	7.40%	26.17%
LATP-C	664.093	6.9%	28.722	16.70%	23.14%

To investigate the mechanical properties of the LATP electrical energy storage system, four-point-bending tests are conducted with samples of the embedded LATP pellets and ones without pellets as reference. Representative Strength-displacement curves of one sample per type are shown in Fig. 6. The flexural strength, elastic modulus as well as flexural deformation are shown in Table 1, in which the standard deviation is calculated by 4 specimens.

Usually, the presence of the embedded devices causes material and geometrical discontinuities of the fibre reinforced composites, which are responsible for unwanted peak values of stress/strain concentration with consequences on the stiffness reduction and the overall material performance. However, in the present work the elastic modulus of LATP composites decreases around 3.5% comparing with reference specimens. Flexural strength decreases slightly of 9.7% in the electrical energy storage system due to the decrease of ductility.

The two surfaces of a specimen with embedded LAPT-pellets after conducted bending test is shown in Fig.7. The photos are taken from the lower and upper side of the specimen where tensile and compressive stresses occur (see Fig. 2 b)). As result of a symmetrical lay-up it can be presumed that the bending-line is positioned in the middle of the specimen. Therefore the upper side is compressed which can be seen by cracks of the matrix and delamination between the layers transversely to the specimen-geometry. In contrast on the underside tensile-stress occurs on the outer most layers of the specimen. Here the glass-fibres are extremely stretched that way that the matrix failed between the fibres longitudinal to the specimen geometry. Figure 7 b) shows the failed fibres which were first stressed plastically failed after relieving the load as result of sharp bending.

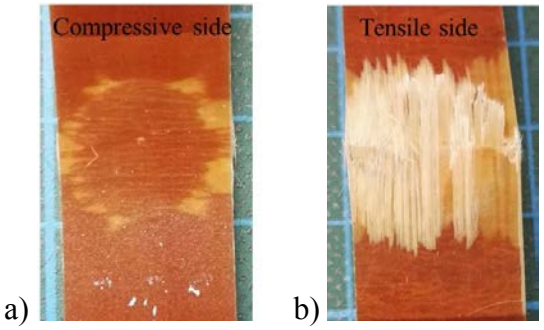

Figure 7: Photos of LATP composite sample after four-point-bending tests: a) compressive side; b) tensile side.

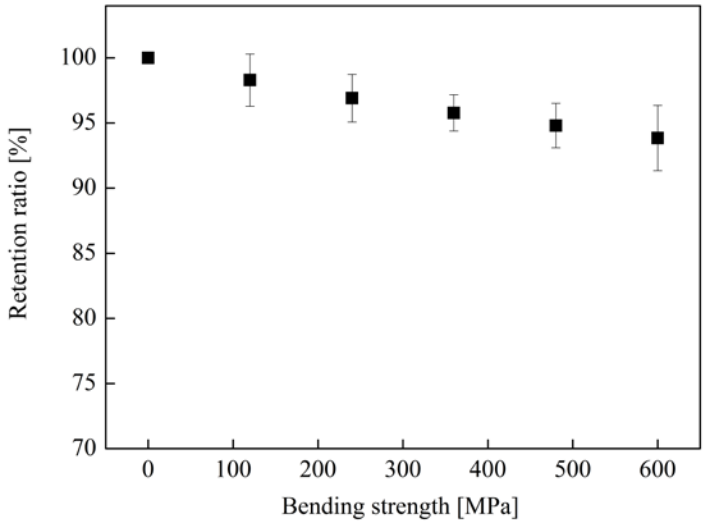

Figure 8: The retention ratios of capacitance ($C_{under\ loads}/C_{pristine}$) at different bending strength from 120 MPa to 600 MPa, which are calculated from CV measured at a voltage range of 0-0.5 V at 10 mV/s scan rate.

The investigation on the influence of mechanical loads on the capacitance of the LATP electrical energy storage system is tested by step loading measurements. The samples are bended at the first strength step of 120 MPa. Keeping this load, the capacitances of the specimen are measured by CV at scan rate of 10 mV/s. In a further step the bending strength is increased to 240 MPa and kept constant until the CV measurements have been finished. Capacitances are calculated and compared with the original capacitance before loading. The retention ratios of capacitance ($C_{under\ loads}/C_{pristine}$) at different bending strengths are shown in Fig. 8. The result shows no obvious decrease as value of 6.1% reduce of capacitance until 600 MPa. The demonstrated capacitance stability is important because the LATP electrical energy storage system should usually work under loading conditions.

4 CONCLUSIONS

A new method of producing structural supercapacitors is introduced, which uses NASICON-type $Li_{1.4}Al_{0.4}Ti_{1.6}(PO_4)_3$ as solid electrolyte embedded into glass fibre reinforced plastics. The curves of cyclic voltammetry show a nearly rectangular shape indicating a double layer behavior. The electrical storage ability is measured by galvanostatic charge-discharge tests showing specific capacitance values of 35.98 µF/g at 0.1 µA/g. The capacitance is still constant after 1500 cycles of charge and discharge. The mechanical properties are characterized by four-point-bending tests. The results show that the embedding of a capacitor only slightly decrease the mechanical properties of continuous composite materials compared with reference samples. The influence of bending loads on capacitance has also been studied indicating no obviously change of capacitance under bending loads. The present work demonstrates the multifunctional properties of this power composite which could store electrical energy and bear mechanical loads simultaneously. Meanwhile it exhibits a stability of capacitance during charge-discharge cycles and under mechanical loads. Beside the benefit of using solid state electrolyte for structural supercapacitors also the leakage problem caused by liquid electrolytes is avoided.

ACKNOWLEDGEMENT

This work was supported by Mrs. A.Viandier of the Technical University of Braunschweig, Institute of Adaptronics and Function Integration for using her analyzing methods and expertise.

REFERENCES

[1] Asp, L.E. and Greenhalgh, E.S. Structural Power Composites, Composites Science and Technology, (2014) 101: 41-61.

[2] Liao, G.Y., Geier, S., Mahrholz, T., Wierach, P. and Wiedemann, M. $Li_{1.4}Al_{0.4}Ti_{1.6}(PO_4)_3$ used as solid electrolyte for structural supercapacitors. Proceedings of the ASME Conference on Smart Materials, Adaptive Structures and Intelligent Systems, SMASIS 2015 , Colorado Springs, USA, September 21-23 (2015).

[3] Liao, G.Y., Geier, S., Mahrholz, T., Wierach, P. and Wiedemann, M. Electrical and Mechanical Properties of LiAlTi(PO4)3 Solid Electrolyte Based Power Composites. Proceeding of the 17th European Conference on Composite Materials. ECCM 2016, Munich, Germany, 26-30 June (2016).

[4] Pope, A.M., Korkut, S., Punckt, C. and Aksay, I.A. Supercapacitor Electrodes Produced through Evaporative Consolidation of Graphene Oxide-Water-Ionic Liquid Gels, J. Electrochem. Soc. (2013) 160 (10):A1-A8.

[5] Evaluation of bending properties, DIN EN ISO 14125, Berlin: DIN German Institute of Standards (1998)

VIII ECCOMAS Thematic Conference on Smart Structures and Materials
SMART 2017
A. Güemes, A. Benjeddou, J. Rodellar and J. Leng (Eds)

EXPERIMENTAL VALIDATION OF A POROUS PIEZOELECTRIC ENERGY HARVESTER

GERMÁN MARTÍNEZ-AYUSO*, HAMED HADDAD KHODAPARAST*,YAN ZHANG†, CHRISTOPHER R. BOWEN†, MICHAEL I. FRISWELL*, ALEXANDER D. SHAW*, HADI MADINEI* AND JAMES I. ROSCOW†

* Swansea University
College of Engineering, Bay Campus
Fabian Way, Crymlyn Burrows,
Swansea SA1 8EN, UK

† University of Bath
Department of Mechanical Engineering
Claverton Down, Bath, BA2 7AY, UK

Key words: Energy Harvesting, Porous material, Piezoelectricity, Model Validation, Physical Experiment

Abstract. In this paper, a homogenised finite element model is developed to predict the energy harvesting capabilities of a porous piezoelectric energy harvester. The harvester consists of a porous piezoelectric patch bonded to a cantilever beam. The material properties of the porous piezoelectric material are estimated by the *Mori-Tanaka* homogenisation method, which is an analytical method that provides the material properties as a function of the porosity of the piezoelectric composite. These material properties are then used in a finite element model of the harvester that predicts the deformation and voltage output for a given base excitation of the cantilever beam, onto which the piezoelectric element is bonded. Experiments are performed to validate the numerical model, based on the fabrication and testing of several demonstrators composed of porous piezoelectric patches with different percentages of porosity bonded to an aluminium cantilever beam. The electrical load is simulated using a resistor and the voltage is measured to estimate the energy generated. The beam is excited in a range of frequencies close to the first and second modes using base excitation. The effects of the porosity and the assumptions made for homogenisation are discussed.

1 INTRODUCTION

Piezo-electric materials can act as sensors or actuators in engineering structures. Embedded sensors in structures are an important application of piezo-electric materials and are used to track strain and damage in structures such as buildings, aircraft and bridges. Wireless sensor networks

are increasingly being used in areas such as the aerospace industry, where control and monitoring of slender and light-weight structures is becoming more important. Furthermore, these sensors can also harvest energy, in addition to measuring the deformation. The energy harvesting capability of these sensors must be optimised by carefully selecting their configuration and appropriate materials selection. Porous piezoelectric materials have shown promise as sensors and energy harvesters due to their beneficial figures of merit when the porosity is increased.

Traditionally, porosity has been considered a defect in the fabrication process or a non valuable property in many applications, such as concrete fabrication, steelworks industry, etc. Recent scientific advances in last decades are changing the perception of porosity by both scientists and engineers [10]. Different authors have points regarding the possible applications of porosity in different fields, from construction using porous metals [14] to bioengineering using porous titanium in bones implants [2]. The aerospace industry is interested in such materials for their good thermal isolation properties and reduced weight [8]. Porous silicon has been proposed for important electronic applications [4]. Some authors [20, 23, 19, 22] have studied porous ceramics from different points of view such as thermal shock isolation, catalyst supports, etc. However, less attention has been given to porous ceramics for energy harvesting. Energy harvesting is the capability of devices to scavenge energy from the surrounding environment from energy sources such as vibrations, light, thermal gradients, etc. Piezoelectric ceramics have been studied in last decades not only for its energy harvesting capabilities but also for their sensor and actuator capability. These materials have important applications such as ink-jet printers, sonar transducers, heart rate monitors, hydrophones, air bag sensors, etc. When acting as a sensor they can be used for structural health monitoring (SHM) or to power small devices. Sodano et al. [21] presented an extensive review of the applications of piezoelectric materials to energy harvesting. Friswell and Adhikari have explored the possibilities of piezoelectric devices to harvest energy from non-linear vibration [7] and from broadband excitation [1]. Bowen et al. [3] studied how the porosity affect the piezoelectric and dielectric coefficients. Roscow [17] has reviewed the manufacturing process of porous piezoelectric materials.

In this paper the capability of the porous piezoelectric material for energy harvesting is assessed by comparing the predictions from a homogenised numerical model with those obtained experimentally. The composite material is homogenized using analytical theories such as *Mori-Tanaka* and included in a numerical model based on the finite element method which includes the geometry of the energy harvester. The porous piezo patches used for experimental demonstrators, are fabricated using two different methods, Burnt polymer spheres (Bur-PS) and freeze-casting. These patches are bonded to an aluminium beam and tested with a shaker which provides harmonic base excitation in a wide range of frequencies to the beam. The spectrum of the voltage outputs are measured and compared with those obtained by numerical model predictions.

The structure of this paper is summarised as follows. The porous material manufacture process is detailed in section 2. Given the composite nature of the porous material, a homogenization process has to be performed to obtain the material properties. An analytical homogenization method known as *Mori-Tanaka* method is presented in Section 4. The obtained properties are used in the next section to create a finite element model of the cantilever beam demonstrator. The demonstrator fabrication, as well as the testing parameters, are presented in the next section. Finally, the results and discussion are presented followed by the conclusions of the present

study.

2 MANUFACTURE OF POROUS MATERIAL

In this study, commercial available barium titanate powders ($BaTiO_3$, d_{33}=147 pC/N, relative permittivity $\epsilon_{33}^T/\epsilon_0$ =1470 [18, 17] , deionized water and poly(acrylic acid) (PAA, Mv 100,000, Sigma Aldrich) and polyethylene glycol (PEG, Mv 8,000, Sigma Aldrich) are used as starting materials, freezing vehicle, dispersant and binder/pore forming agent (PFA), respectively.

For the burned out polymer spheres (BURPS) method, barium titanate powders mixed with PEG in different proportions by weight are uniaxially pressed at 300MPa to form the disks. For freeze casting, suspensions with barium titanate powders, 3 wt.% dispersant and 3 wt.% binder are ball-milled for 24 h in zirconia media and de-aired by stirring in a vacuum desiccator until complete removal of air bubbles. Freezing of the suspension and aqueous solution are carried out as described previously in [26, 25] by pouring them into a transparent aligned cylindrical polydimethylsiloxane (PDMS) mould, which is then transported to a copper cold finger and placed in a liquid nitrogen container. The frozen barium titanate pillars are then freeze-dried to remove the ice dendrites. The disks and freeze-dried barium titanate pillars are heat-treated at 500 °C for 2h to remove the organic additives, followed by heat-treatment at 1200 °C for 2h and then finally allowed to cool down naturally in the closed furnace. The sintered ceramics are then cut to a diameter of 10 mm and thickness of 1 mm by a cutting machine.

After the manufacture of the porous disks, the piezoelectric strain coefficient, d_{31}, was measured using a Berlincourt Piezometer (PM25, Take Control, UK), which applies an alternating force of 0.1 N at a frequency of 97 Hz. Measurements of the relative permittivity of the sintered porous barium titanate were carried out at room temperature using an impedance analyzer (Solartron 1260, Hampshire, UK). However, not all the material properties required to model the composite using FE method can be obtained without more advanced test. For example, the elastic modulus cannot be measured using widely used resonance technique because of the air in the porous attenuate the resonance making the reading not reliable. Other methods to measure these elastic properties might destroy the disk tests. Therefore, to avoid these problems, an homogenization process is proposed in the next section to predict the complete set of material properties.

3 THEORETICAL HOMOGENIZATION

The porous piezoelectric material is composed of two phases; air and piezoelectric material. For each phase the material constants are well known, but the set of homogenized material constants must be calculated for the resultant composite. As it is stated in Section 2, not all the material properties can be obtained with accuracy or without compromising the health of the porous ceramic disk. Hence, some material properties have to be predicted using a homogenization approach.

One of the most commonly used approaches is to homogenize the material using analytical methods. Analytical methods have been used extensively to homogenize composites because of their accuracy and speed with respect to other approaches such as computational homogenization using finite element methods (FEM). One of the most well-known and validated approach is the

Mori-Tanaka method [15]. This method improves the Eshelby solution [6] given for ellipsoidal inclusions in elastic mediums. The approach may be used in multi-field physics analysis, for example for general composite materials [16, 24] and for porous piezoelectric materials [5, 12]. To perform a Mori-Tanaka homogenization, the calculation of the Eshelby tensor, $\boldsymbol{S}^*$, is required and depends on the shape of the inclusion which is spherical in this case. The procedure to obtain this tensor is comprehensively detailed in [13] and hence is not explained here. In the Mori-Tanaka method, each inclusion with properties $\boldsymbol{E}^{\mathrm{I}}$ where $\boldsymbol{E}^{\mathrm{I}}$ is composed of the elastic stiffness matrix ($\boldsymbol{C}$), the piezoelectric matrix ($\boldsymbol{e}$) and the permittivity matrix at constant strain ($\boldsymbol{k^s}$). This tensor behaves as an isolated inclusion, embedded in an infinite matrix with properties $\boldsymbol{E}^{\mathrm{M}}$, that is loaded remotely by an applied strain, therefore, each inclusion is subjected to the averaged stress fields acting on it from all of the other inclusions, through the superposition of stresses. The application of this method in porous piezoelectric material is demonstrated in [11] and is compared with other homogenization methods such as self-consistent and computational homogenization method using FEM. In this paper, the Mori-Tanaka homogenization is presented as an accurate method to predict the material properties. The homogenization procedure of this method is summarized as follows: First, an influence tensor $\boldsymbol{A}_0^{\mathrm{I},r}$ has to be calculated for every phase r ($\boldsymbol{A}_0^{\mathrm{I},r}$) and percentage. This concentration tensor is written in terms of the Eshelby tensor as shown in equation 1a. These concentration tensors are then averaged to obtain the general influence tensor, $\boldsymbol{A}_{(\mathrm{MT})}^{\mathrm{I,r}}$ and finally, the effective electro-elastic material tensor ($\boldsymbol{E^*}$) using equation 1c.

$$\boldsymbol{A}_0^{\mathrm{I},r} = \left[\boldsymbol{I} + \boldsymbol{S}^* \left(\boldsymbol{E}^{\mathrm{M}}\right)^{-1} \left(\boldsymbol{E}^{\mathrm{I},r} - \boldsymbol{E}^{\mathrm{M}}\right)\right]^{-1} \tag{1a}$$

$$\boldsymbol{A}_{(\mathrm{MT})}^{\mathrm{I},r} = \left[c^{\mathrm{I},r}\boldsymbol{I} + c^{\mathrm{M}}(\boldsymbol{A}_0^{\mathrm{I},r})^{-1} + \sum_{j=1}^{N} c^{\mathrm{I},r}\boldsymbol{A}_0^{\mathrm{I},j}(\boldsymbol{A}_0^{\mathrm{I},r})^{-1}\right]^{-1} \tag{1b}$$

$$\boldsymbol{E}_{(\mathrm{MT})}^{*} = \boldsymbol{E}^{\mathrm{M}} + \sum_{r=1}^{N} c^{\mathrm{I},r}\left(\boldsymbol{E}^{\mathrm{I},r} - \boldsymbol{E}^{\mathrm{M}}\right)\ \boldsymbol{A}_{(\mathrm{MT})}^{\mathrm{I},r} \tag{1c}$$

This method is self-consistent, since the inverse of the electromechanical matrix $\boldsymbol{E}^*$ is equal to the compliance electromechanical matrix $\boldsymbol{F}^*$, which is composed by the elastic compliance ($\boldsymbol{S}$), the piezoelectric matrix ($\boldsymbol{d}$) and the permittivity matrix at constant stress ($\boldsymbol{k^T}$).

4 NUMERICAL MODEL

In order to design efficient porous material energy harvesters, a reliable and accurate modelling technique is needed. Today, one of the most powerful tools to represent complex multiphysics is the Finite Element Method. This method is based on discretization of partial differential equations that govern the problem. It can model complex geometries as well as complex material properties. The porosity in piezoelectric material allows a smart distribution of the piezoelectric mass in the energy harvester, removing piezoelectric material from the places where the strain is lower and reallocating it where higher strains are located. The graded distribution of porosity generates functionally graded material which can maximize the power output for a given quantity of piezoelectric ceramic. This distribution can be accurately modelled using finite element methods. Therefore FE technique is used here although this study does not include

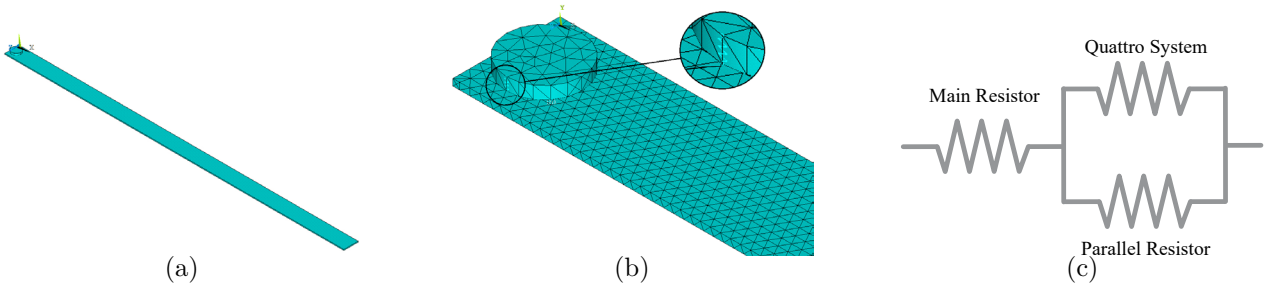

Figure 1: Finite element model. (a) General view of the cantilever beam energy harvester with the left side clamped. (b) Detailed view of the clamped side and the porous piezoelectric patch as well as the the resistor which connects the top surface with the bottom surface of the porous piezoelectric disk. (c) Schematic view of the external circuit connected to the harvester.

Sample number	**Porosity (%)**	**Thickness (mm)**	**Diameter (mm)**	**Fabrication method**	**Piezoelectric coeff.** d_{31} (pC/N)	**Relative Permittivity** ϵ_{33}/ϵ_0
1	66.0	2.073	11.137	BURPS	-10	290
2	55.0	2	11.24	BURPS	-60	445
3	50.0	1.86	11.273	BURPS	-120	526
4	32.0	1.5	11.247	BURPS	-190	808
5	20.0	1.27	11.26	BURPS	-250	1199
6	45.0	1.78	9.94	Freeze cast	-340	563
7	35.0	2.06	10.23	Freeze cast	-390	702
8	31.0	1.7	10.64	Freeze cast	-300	788

Table 1: Demonstrator patches properties using barium titanate.

functionally graded materials. In future studies, the porosity distribution will be optimised in order to maximize the power output.

In this study, the finite element package called ANSYS® is used in order to model the harvester. The material properties are modelled in the linear elastic range and using 3D elements. The element type used for the whole model is SOLID 227. The external resistors are modelled using the element CIRCU94, connecting the top surface of the disk and the bottom surface.

The FE model is coupled with Matlab® which performs the homogenization process and provides the material properties and geometrical parameters to ANSYS ®. An in-house Matlab® code has been developed to link ANSYS to MATLAB and can be used for optimisation/model updating purposes. The porous material is modelled using the homogenized parameters obtained in Section 3.

5 EXPERIMENTAL VALIDATION

In order to validate the finite element model, a set of experiments are designed. Several piezoelectric patches with different percentages of porosity are prepared at the University of Bath. The percentages of the test disk range between 20% and 66% with different values of thickness and radius, as shown in table 1.

In addition, some non-porous piezoelectric patches are used in order to compare the accuracy of the model with traditional lead zirconate titanate (PZT). These non-porous square patches are PZT-5A1 and supplied by Morgan Advanced Ceramics. Their properties and dimensions

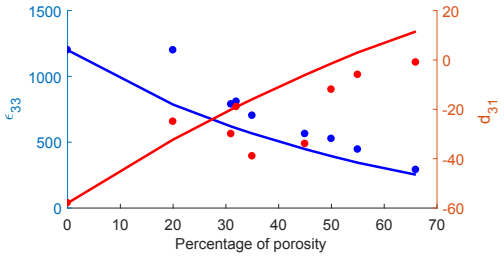

(a) (b) (c)

Figure 2: (a) Material coefficients d_{31} (red) and ϵ_{33} (blue) predicted by homogenization theory "Mori-Tanaka" (solid line) compared with the values measured experimentally (dots). (b) View of the lab setup. (c) Detailed view of a porous patch attached to the aluminium beam.

are shown in table 2.

The patches are attached to aluminium beams using conductive glue which acts also as electrode. These aluminium beams have the properties specified in table 2. These piezoelectric demonstrators are tested using an APS Dynamics Model 113-HF electrodynamic shaker (APS Dynamic Juan Capistrano, CA) as an excitation source, powered by an APS amplifier Model 125-230. The type of testing is a sin-step analysis for a range of frequencies between 5 Hz and 42Hz which includes the first two modes and anti-resonance mode. Two measurements are obtained, the base acceleration through an accelerometer located in shaker, and the voltage difference between the top and bottom electrode of the piezoelectric patch using Data Physics Quattro analyser, which is a usb powered data acquisition.

6 RESULTS AND DISCUSSION

As it is stated in Section 2, an homogenization method for the porous piezoelectric ceramic is used to obtain the complete set of material properties of the porous PZT. In Figure 2 the results obtained in the homogenization process for the piezoelectric coefficient d_{31} and the dielectric coefficient ϵ_{33} are compared with the values measured on the patches after its fabrication. The homogenized values of these coefficients indicate an overestimation of the measured values. Further examinations of the disk reveal some cracks which potentially could decrease the piezoelectric values.Also it has been observed that not all the inclusions are spherical as it is assumed in Section 3. In the case of the disk manufactured using free-casting method, the shape

PZT-5A		**Aluminium**	
Density (kg/m^3)	7750	Density (kg/m^3)	2700
S_{33}^E $(10^{-12}m^2/N)$	17.2	Young Modulus (GPa)	70
S_{11}^E $(10^{-12}m^2/N)$	16.7	Poisson Ratio	0.3
d_{33} (pC/N)	409		
d_{31} (pC/N)	176	**Beam Dimensions**	
$\epsilon_{33}^T/\epsilon_0$	1800	Length x Width x Thickness (mm)	375 x 16 x 1

Table 2: Material properties of the non-porous piezoelectric patch supplied by Morgan Advance Ceramics PLC and the aluminium used for the beams.

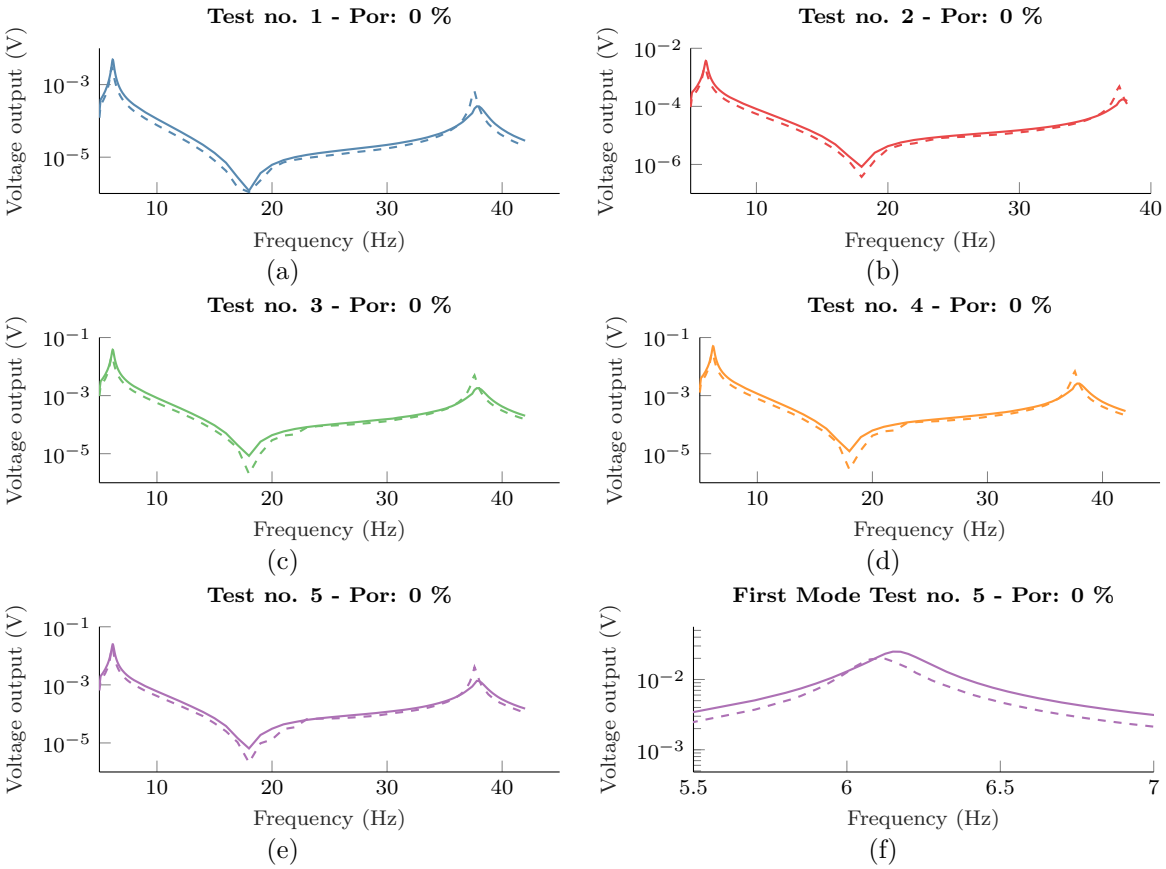

Figure 3: Dynamic test results performed on the non-porous patches.

of the inclusions tends to be more cylindrical than spherical. The cylindrical inclusions reduce in-plane properties whilst maintaining the benefits through thickness properties and this causes the differences between the values of the material coefficients in different directions. In other words, in-plane properties of the porous piezo with spherical inclusion shapes deemed to be larger than their corresponding values for the ones with cylindrical inclusion shapes [9]. Using the assumption of spherical inclusions could lead to overestimate some parameters especially in direction perpendicular to the cylinders as shown in Figure 2 presented. It is observed that the main piezoelectric coefficient for the voltage output in a cantilever energy harvesting device is the d_{31} which could be potentially greatly affected by the shape inclusions.

Once the material coefficients are obtained and validated, the dynamic tests are performed as stated in Section 5. In table 3 the experiment setup is shown for each test. The dynamic test are designed to account for the different fabrication methods (Free-Casting or BURPS) and percentages of porosity (it is tested disk from 20% to 66% porosity). In any harvester the external circuit has a strong impact on the power output. Therefore, the resistance has to be optimized for each level of porosity to obtain the maximum power. In [12] it was probed that the porosity does not have too much impact on the optimal resistance, being almost the same as the non-porous optimal resistance, defined by $\omega_n RC = 1$. This value for a natural frequency

of 5.84 Hz (obtained from FE model) is approximately 10 MΩ. The resistors configurations are detailed in table 3 for all the dynamic test performed.

Test number	Sample number	Method fabrication	Porosity	Main Resistor in series	Resistor in parallel
1	#Ref	–	0.0%	10.042 MΩ	0.9951 kΩ
2	#Ref	–	0.0%	14.677 MΩ	0.9951 kΩ
3	#Ref	–	0.0%	14.677 MΩ	9.987 kΩ
4	#Ref	–	0.0%	10.042 MΩ	9.987 kΩ
5	#Ref	–	0.0%	10.042 MΩ	9.987 kΩ
6	7	Free-casting	35.0%	10.042 MΩ	9.987 kΩ
7	8	Free-casting	31.0%	10.042 MΩ	9.987 kΩ
8	3	BURPS	50.0%	10.042 MΩ	9.987 kΩ
9	1	BURPS	66.0%	10.042 MΩ	9.987 kΩ
10	2	BURPS	55.0%	10.042 MΩ	9.987 kΩ
11	7	Free-Casting	35.0%	10.042 MΩ	9.987 kΩ
12	2	BURPS	55.0%	10.042 MΩ	0.9951 kΩ
13	6	Free-Casting	45.0%	10.042 MΩ	9.987 kΩ
14	5	BURPS	20.0%	10.042 MΩ	9.987 kΩ

Table 3: Dynamic tests performed for the different values of porosity, fabrication method and resistance configuration.

Figure 4: Test no. 9 which got detached during dynamic experiment.

In order to validate the FE model, non-porous patches are tested and compared with numerical predictions. This comparison is presented in Figure 3. Good agreement is obtained between the numerical model and the voltage output obtained in the lab for different values of resistance connected to the harvester (see Table 3). The FE model accurately predicts the values of the resonance frequencies for all the tests performed. For example, in test no. 1 the difference in frequencies of the first mode is lower than 0.5 Hz. The antiresonance frequencies slightly decreased with respect to the experimental values but the impact of this difference is negligible for energy harvesting. The amplitudes of the voltage output are predicted with a good accuracy especially around the first mode as Figure 3f presents. The difference between test no. 4 and 5, observed in Figures 3d and 3e, is due to differnet leveels of the amplitude of base excitation. This was achieved by increasing the acceleration from 0.0885 g (test no.5) to 0.1824 g for test no. 4 in order to identify possible sources of non-linearities. Nevertheless no sources of non-linearities were identified, confirming that the energy harvester behaviour will remain linear in the ranges of base excitation amplitude tested. The damping ratio is obtained experimentally from half power point test and its values oscillate between 0.06 and 0.085.

To assess the reliability of the numerical model for non-porous patches, the analysis of the dynamic results are presented. In Figure 5, a comparison between the numerical model prediction (solid line) and the experimental values (dashed line) is presented. The experimental voltage output of porous demonstrator is, in general, lower than the non-porous ones because the matrix material is different for non-porous (PZT-5A1) and porous ones ($BaTiO_3$). Test no. 9 is not presented in this figure because the disk detached during the dynamic test due to crack propagation and the formation of cracks are an issue when manufacturing or testing porous material. The fabrication of the porous disk presents important stability problems when fabricating thin patches (less than 2 mm) or high porosities (over 55%). The collapsing of the disk is ensured for percentages over 70%. In test no. 9, the porosity is 66% which is the highest

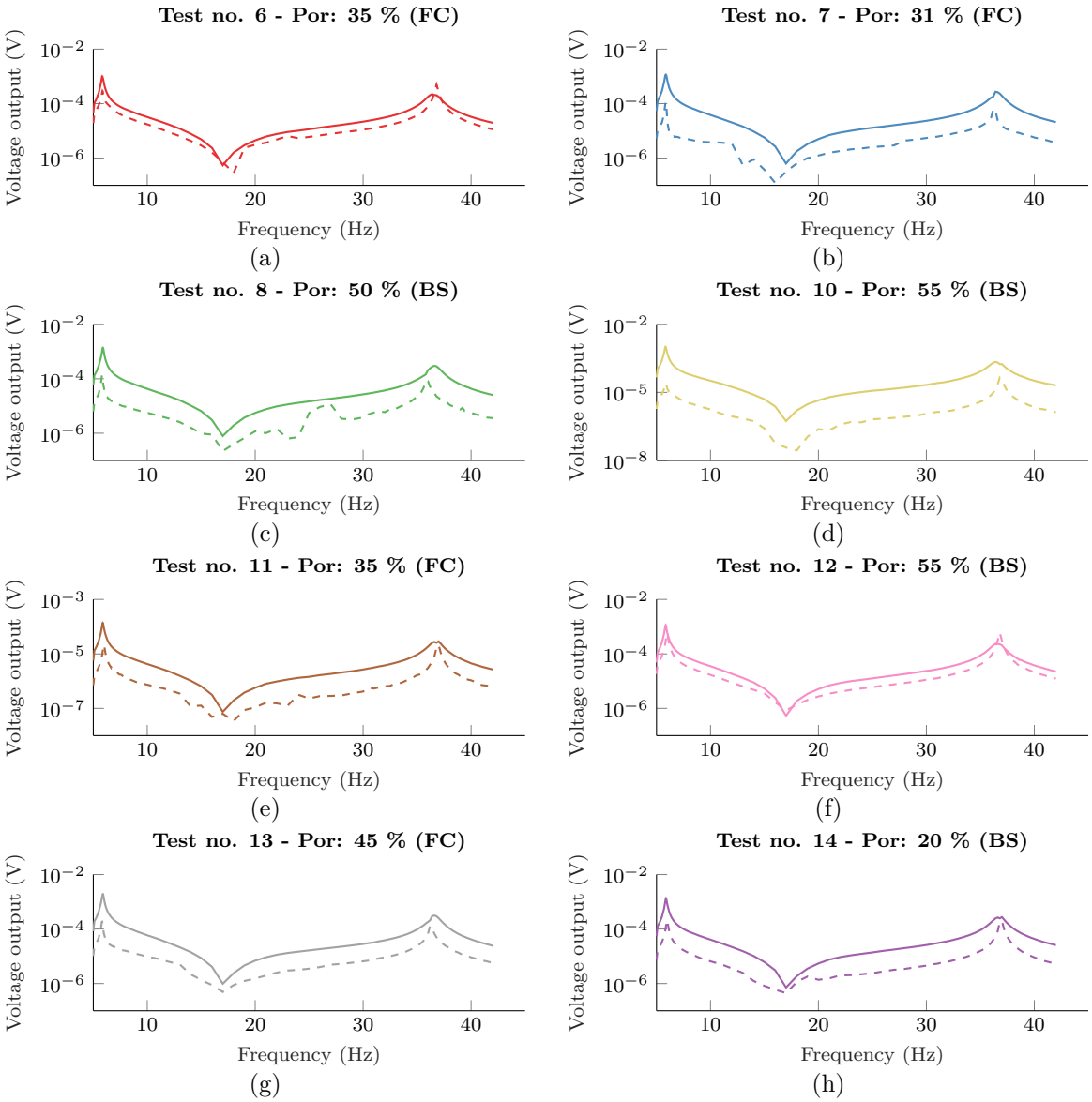

Figure 5: Dinamic test results performed on the porous piezoelectric disks. FC= Free-casting, BS=BURPS.

porosity achieved in the lab.

In general, the results show good agreement between FE model predictions and measurements. This is an indicator that the stiffness and mass matrix reflect the physics of the problem and hence the geometry and material properties of the porous material. The amplitude of the voltage output varies according to the porosity and manufacturing process. For example tests no. 6 and 12 show an acceptable degree of agreement between the predicted voltage output in the numerical model and the experimentally measured voltage. In particular, the predicted and measured voltages have similar values around the first resonance frequency. In general there is

a shift in the voltage output between the predictions and the experimental results. Test nos. 10, 7 and 8 present the greatest shifts. A general shift in the voltage output can be possibly related to wrong values of the piezoelectric coefficients. As it is mentioned in Sections 2 and 3, the values used in the FE model are obtained with Mori-Tanaka method which assumes spherical inclusions and no cracks inside the matrix. These cracks could decrease the piezoelectric coefficients and the dielectric coefficients, generating the shift presented in the graphs. This also might be seen as an indicator of the health of the disks. It is already pointed out the fragility of the disks and the tendency to cracks growth, hence measuring the coefficients before and after the dynamic tests could be an approximate way to quantify damage in piezoelectric porous material. It is important to notice that the experimental values of the voltage output are quite similar for both modes. In other words, the second mode voltage level is almost the same as the first mode voltage level (see Figure 5d). This is clearly different than the non-porous ones where the second mode harvest less power than the first mode (see Figure 3a). The lower mass per unit of length seems to benefit the power output in the second mode. This effect is interesting for designing wide range energy harvester which their frequency range spans through multiple modes.

Some experimental data present important changes in the voltage output close to the anti-resonance frequency, for example test nos. 7, 8 and 11. This variability is attributed to the noise due the voltage reading resolution of the Quattro data acquisition system which does not read accurately voltage outputs which round the microvolts (μV). This indicates the importance of the fabrication method. The BURPS manufacture processing is a more developed technique for porous piezoelectric material than free-casting. Therefore higher percentages of porosity could be achieved using this method.

7 CONCLUSIONS

A validation scheme for porous piezoelectric energy harvesters is presented. A numerical model based on finite element method which account for porous using analytical "Mori-Tanaka" homogenization theory is developed and validated by comparison of voltage output with dynamic tests performed on porous piezoelectric energy harvesters. This scheme shows promising results for predicting power output of energy harvester. Nevertheless more research is needed to optimise the piezoelectric material in terms of the electrical and mechanical requirement for energy harvesting applications. Future work will involve modelling cylindrical inclusion shapes in the numerical model of porous piezo-material and stochastic modelling to take account of manufacturing variabilities of porous piezo-materials.

ACKNOWNLEDGES

This research is supported by Aerospace Technology Institute in the framework of "Exploiting Aeroelastic Deflections For Improved Aircraft Performance" project.

The authors acknowledge the financial support from the Sêr Cymru National Research Network and Swansea University through a Postgraduate Scholarship NRN-103.

The authors would like to acknowledge the support from Morgan Advanced Ceramics PLC.

REFERENCES

[1] S. Adhikari, M. I. Friswell, and D. J. Inman. Piezoelectric energy harvesting from broadband random vibrations. *Smart Materials and Structures*, 18(11):115005, 2009.

[2] J. Bobyn, R. Pilliar, H. Cameron, and G. Weatherly. The optimum pore size for the fixation of porous-surfaced metal implants by the ingrowth of bone. *Clinical orthopaedics and related research*, 150:263–270, 1980.

[3] C. R. Bowen, A. Perry, A. C. F. Lewis, and H. Kara. Processing and properties of porous piezoelectric materials with high hydrostatic figures of merit. *Journal of the European Ceramic Society*, 24(2):541–545, 2004.

[4] L. T. Canham. Silicon quantum wire array fabrication by electrochemical and chemical dissolution of wafers. *Applied Physics Letters*, 57(10):1046–1048, 1990.

[5] M. L. Dunn and M. Taya. Electromechanical properties of porous piezoelectric ceramics. *Journal of the American Ceramic Society*, 76(7):1697–1706, 1993.

[6] J. D. Eshelby. The determination of the elastic field of an ellipsoidal inclusion, and related problems. In *Proceedings of the Royal Society of London A: Mathematical, Physical and Engineering Sciences*, volume 241, pages 376–396. The Royal Society, 1957.

[7] M. I. Friswell, S. F. Ali, O. Bilgen, S. Adhikari, A. W. Lees, and G. Litak. Non-linear piezoelectric vibration energy harvesting from a vertical cantilever beam with tip mass. *Journal of Intelligent Material Systems and Structures*, 23(13):1505–1521, 2012.

[8] P. Göransson. Tailored acoustic and vibrational damping in porous solids–engineering performance in aerospace applications. *Aerospace Science and Technology*, 12(1):26–41, 2008.

[9] S. Iyer and T. Venkatesh. Electromechanical response of (3-0) porous piezoelectric materials: Effects of porosity shape. *Journal of Applied Physics*, 110(3):034109, 2011.

[10] A. Kelly. Why engineer porous materials? *Philosophical Transactions of the Royal Society of London A: Mathematical, Physical and Engineering Sciences*, 364(1838):5–14, 2006.

[11] G. Martinez-Ayuso, M. I. Friswell, S. Adhikari, H. H. Khodaparast, and H. Berger. Homogenization of porous piezoelectric materials. *International Journal of Solids and Structures*, 2017.

[12] G. Martinez-Ayuso, M. I. Friswell, S. Adhikari, H. H. Khodaparast, and C. A. Featherston. Porous piezoelectric materials for energy harvesting. In *International Conference on Noise and Vibration Engineering*, 2016.

[13] Y. Mikata. Determination of piezoelectric eshelby tensor in transversely isotropic piezoelectric solids. *International Journal of Engineering Science*, 38(6):605–641, 2000.

[14] T. Miyoshi, M. Itoh, S. Akiyama, and A. Kitahara. Alporas aluminum foam: production process, properties, and applications. *Advanced engineering materials*, 2(4):179–183, 2000.

[15] T. Mori and K. Tanaka. Average stress in matrix and average elastic energy of materials with misfitting inclusions. *Acta Metallurgica*, 21(5):571–574, 1973.

[16] O. Pierard, C. Friebel, and I. Doghri. Mean-field homogenization of multi-phase thermo-elastic composites: a general framework and its validation. *Composites Science and Technology*, 64(10):1587–1603, 2004.

[17] J. I. Roscow, J. Taylor, and C. R. Bowen. Manufacture and characterization of porous ferroelectrics for piezoelectric energy harvesting applications. *Ferroelectrics*, 498(1):40–46, 2016.

[18] J. I. Roscow, V. Y. Topolov, C. R. Bowen, J. Taylor, and A. E. Panich. Understanding the peculiarities of the piezoelectric effect in macro-porous batio3. *Science and Technology of advanced MaTerialS*, 17(1):769–776, 2016.

[19] J. S. Seo, D. Whang, H. Lee, S. Im Jun, J. Oh, Y. J. Jeon, and K. Kim. A homochiral metal–organic porous material for enantioselective separation and catalysis. *Nature*, 404(6781):982–986, 2000.

[20] J. She, J. Yang, and T. Ohji. Thermal shock resistance of porous silicon nitride ceramics. *Journal of materials science letters*, 22(5):331–333, 2003.

[21] H. A. Sodano, D. J. Inman, and G. Park. A review of power harvesting from vibration using piezoelectric materials. *Shock and Vibration Digest*, 36(3):197–206, 2004.

[22] W. Staszewski, C. Boller, and G. R. Tomlinson. *Health monitoring of aerospace structures: smart sensor technologies and signal processing*. John Wiley & Sons, 2004.

[23] R. J. White, R. Luque, V. L. Budarin, J. H. Clark, and D. J. Macquarrie. Supported metal nanoparticles on porous materials. methods and applications. *Chemical Society Reviews*, 38(2):481–494, 2009.

[24] T. T. Wu. The effect of inclusion shape on the elastic moduli of a two-phase material. *International Journal of Solids and Structures*, 2(1):1–8, 1966.

[25] Y. Zhang, Y. Bao, D. Zhang, and C. R. Bowen. Porous pzt ceramics with aligned pore channels for energy harvesting applications. *Journal of the American Ceramic Society*, 98(10):2980–2983, 2015.

[26] Y. Zhang, L. Chen, J. Zeng, K. Zhou, and D. Zhang. Aligned porous barium titanate/hydroxyapatite composites with high piezoelectric coefficients for bone tissue engineering. *Materials Science and Engineering: C*, 39:143–149, 2014.

VIII ECCOMAS Thematic Conference on Smart Structures and Materials
SMART 2017
A. Güemes, A. Benjeddou, J. Rodellar and Jinsong Leng (Eds)

FLYWHEEL PROOF MASS TRANSDUCER FOR ENERGY HARVESTING APPLICATIONS

ALEKSANDER KRAS*, PAOLO GARDONIO

* Dipartimento Politecnico di Ingegneria e Architettura (DPIA)
University of Udine
Via delle Scienze 206, 33100 Udine, Italy
e-mail: aleksander.kras@uniud.it, paolo.gardonio@uniud.it

Key words: Inerter, proof mass transducer, energy harvesting.

Abstract. This paper introduces a new flywheel coil–magnet proof mass transducer for vibration energy harvesting. The seismic transducer presented in this paper includes an additional flywheel element that produces three effects on the elastically suspended proof mass: firstly, it lowers the fundamental resonance frequency, secondly it lowers the static displacement and thirdly it lowers the mechanical damping effect. The combination of all three effects is beneficial for vibration energy harvesting applications. In fact, having a low resonance frequency transducer facilitates the tuning of the harvester to a low frequency band where ambient vibration energy is normally higher. Also, having a low static displacement of the proof mass element allows the construction of a device robust to shocks and fast movements despite it has a low fundamental resonance frequency. Finally, having a low internal mechanical damping leaves more energy for the conversion to electrical energy. The paper presents both simulations and experimental results that contrast the principal electro-mechanical properties and the energy harvesting effects of classical and proposed flywheel coil–magnet proof mass transducers connected to a purely resistive load.

1 INTRODUCTION

During the past two decades, coil–magnet proof mass transducers have been extensively studied for vibration energy harvesting applications [1-6]. This paper presents simulation and experimental results for the characterisation of the energy harvesting properties of a new coil–magnet proof mass transducer, which is equipped with a flywheel element and is connected to a resistive load. This new proof mass transducer was first introduced in Refs. [7-9] for the implementation of feedback vibration control systems. As discussed in details in Ref. [9], the flywheel element produces an apparent mass effect without increasing the suspended mass. This results into three important effects on the elastically suspended proof mass: firstly, it lowers the fundamental resonance frequency, secondly it lowers the static displacement and thirdly it lowers the mechanical damping effect. All three effects concur to enhancing the efficiency and robustness of the energy harvesting since the transducer can be: a) tuned to low frequencies where the energy of ambient vibration is normally concentrated; b) made resistant to shocks and c) made more efficient in converting mechanical to electrical energy.

The paper is structured into two parts. The first part derives from simplified lumped

parameter models the mechanical and electric impedance functions and the electrical to mechanical and mechanical to electrical transduction functions that characterise the electro-dynamic response of a classical and of the proposed flywheel proof mass transducer. Simulated frequency response functions (FRFs) are contrasted with measured FRFs taken on a classical coil-magnet proof mass transducer and on a prototype coil-magnet proof mass transducer equipped with a flywheel element. The second part, uses the lumped parameter model to derive simple expressions of the energy harvested with the classical and with the proposed transducers connected to a purely resistive load. Simulated and measured spectra of the energy harvested by the classical and by the prototype transducers are then presented and analysed.

The paper is structured in 6 sections. Section 2 describes the proposed flywheel proof mass transducer. Section 3 presents a concise summary of the mathematical formulations used to derive the FRFs that characterise the response of a classical and of the proposed proof mass transducer and to derive power harvested per unit base excitation of a classical and of the proposed proof mass transducer connected to a purely resistive load. Section 4 contrasts the simulated and measured mechanical and electric impedance FRFs and electrical to mechanical and mechanical to electrical FRFs of the classical and of the proposed proof mass transducers. Section 5 presents simulation and experimental measurements of the energy harvested per unit base vibration produced by the classical and of the proposed proof mass transducers. Finally, section 6 presents the concluding remarks of the work presented in this paper.

2 FLYWHEEL PROOF MASS ACTUATOR

Classical proof mass transducers used for energy harvesting applications are often made with a coil–magnet linear transducer. This study considers the reference coil–magnet proof mass transducer shown in Fig. 1a, which has been studied with the lumped elements model shown in Fig. 1c. The transducer is formed by an inner cylindrical magnet and an outer cylinder that hosts the coil, which are connected to each other by two springs, which are characterised by soft axial stiffness and comparatively much higher transverse stiffness. The system is therefore modelled with a base mass m_b, for the inner cylinder magnet, and a proof mass M_a, for the outer cylinder, which are connected by an equivalent spring, of stiffness k, and equivalent damper, of damping c, connected in parallel. The electro-magnetic effect of the actuator is modelled in terms of transduction coefficient ψ_a, which produces either a pair of reactive forces F_a between the base mass (magnet) and proof mass (coil) proportional to the current i_a flowing in the coil, that has its resistance R and inductance L, or a back electromotive force u_{em} at the terminals of the coil proportional to the relative velocity $\dot{w}_m - \dot{w}_b$ between the proof mass (coil) and the base mass (magnet) of the actuator.

The new proof mass transducer considered in this study is based on the reference coil–magnet proof mass transducer, which has been equipped with the additional flywheel element shown in Fig. 1b, which has mass m_w and polar moment of inertia I_w. As depicted in the lumped elements model shown in Fig. 1d, the flywheel is connected by two frictionless pivot bearings of torsional stiffness k_w to the proof mass (coil). Also, it is connected to the case of the actuator (magnet) with a pushing pin and third frictionless pivot bearings that was mounted on one of the flywheel arms. The pushing pin was mounted to the base mass (magnet) with an offset r_w from the flywheel horizontal axis of rotation, which was set to intersect the vertical axis of the

transducer to keep the whole system in balance. This pushing pin linkage was used to convert the relative oscillations between the two masses $\dot{w}_m - \dot{w}_b$ into angular oscillations of the flywheel.

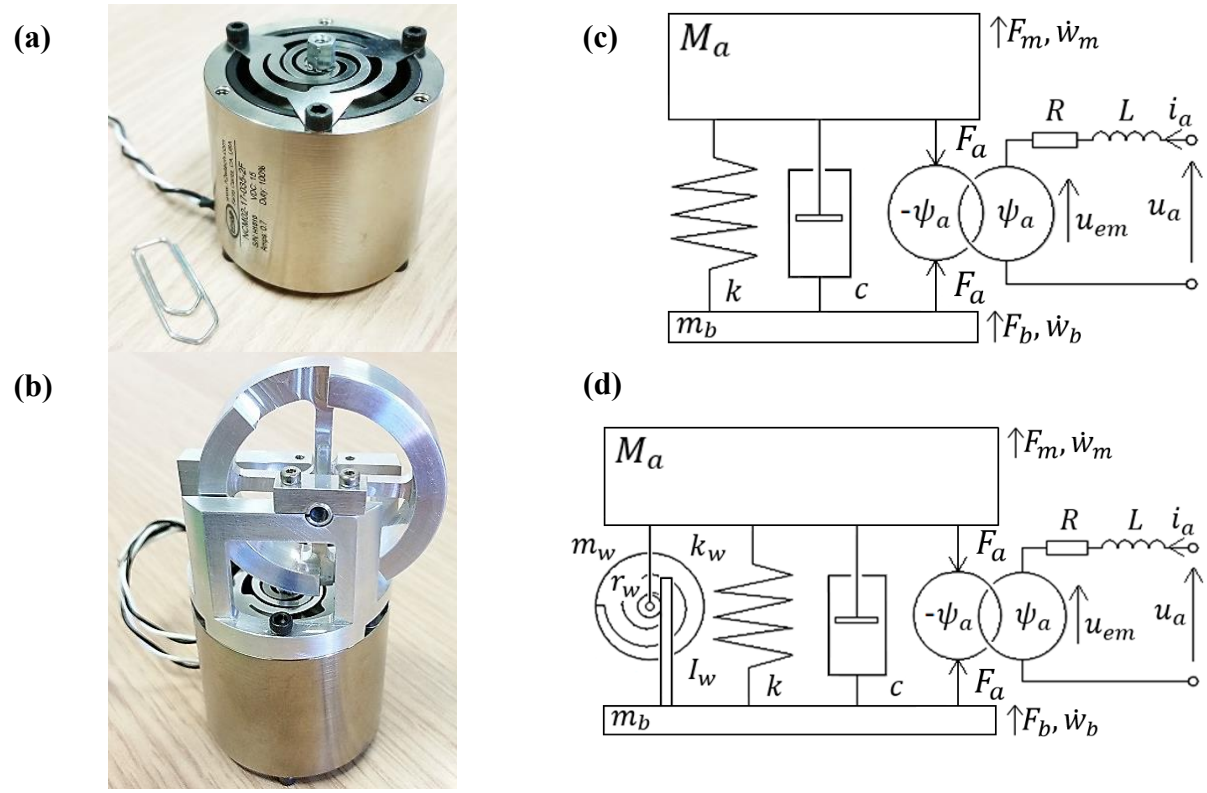

Figure 1: Pictures (a,b) and schemes (c,d) of the tested classical (a,c) and the flywheel proof mass actuator (b,d).

Table 1: Mechanical parameters of the proof mass actuators.

Parameter	Value
Proof mass / Coil mass	$M_a = 0.203$ kg
Case mass / Magnet mass	$m_b = 0.117$kg
Flywheel mass	$m_w = 0.027$kg
Axial stiffness	$k = 2950\text{Nm}^{-1}$
Damping ratio	$\zeta = 0.2$
Flywheel moment of inertia	$I_w = 6.81 \cdot 10^{-6} kgm^2$
Pushing pin radius	$r_w = 6.4$mm
Axial mass effect of the flywheel	$I_w/r_w^2 = 0.166$kg
Torsional stiffness	$k_w = 0.003\text{Nmrad}^{-1}$
Coil resistance	$R = 23.5\Omega$
Coil inductance	$L = 4.35 \cdot 10^{-3} H$
Transduction coefficient	$\psi_a = 22.5\ \text{NA}^{-1}$

The dimensions of the flywheel and the offset of the pushing pin used to convert axial to rotational motion were chosen based on results of parametric studies presented in Refs. [7-9].

More specifically, as shown in Fig. 1b, the dimensions of the flywheel element were optimised in such a way as to minimise weight and to maximise the polar moment of inertia. Compared to classical hinges the pivot bearings adopted in this prototype minimise stick-slip effects and reduce the backlash effects that could be generated by the linkage system used to convert the axial oscillations into angular oscillations.

The physical properties of the reference and of the new proof mass transducer with the flywheel element are summarised in Table 1. The flywheel element makes the proposed transducer 27g heavier compared to the reference proof mass transducer.

3 MATHEMATICAL MODEL

This section presents the mathematical formulations, which has been derived starting from Ref. [10], used to derive the FRFs that characterise the response of the classical (Figs 1a,c) and of the proposed (Figs 1b,d) proof mass transducer and to derive power harvested per unit base excitation with the classical and the proposed proof mass transducer. The frequency domain formulations presented in this section consider the complex amplitudes $g(\omega)$ of time–harmonic functions given in the form $g(t) = Re\{g(\omega)\exp(j\omega t)\}$, where ω is the circular frequency and $j^2 = -1$.

3.1 Constitutive equations

The constitutive equations that characterise the electro – mechanical response of the classical and proposed proof mass transducers have been expressed with the following two equations:

$$F_b = Z_{f\dot{w}}\dot{w}_b + T_{fi}i_a \tag{1}$$

$$u_a = T_{u\dot{w}}\dot{w}_b + Z_{ui}i_a \tag{2}$$

where, according to Eqs. (A.10) and (A13) given in appendix A,

$$Z_{f\dot{w}} = \frac{-F_b}{\dot{w}_b}\Big|_{i_a=0} = \frac{Z_b + Z_b Y_m Z_a + Z_a}{1 + Y_m Z_a} \tag{3}$$

is the mechanical impedance of the open circuit transducer,

$$T_{fi} = \frac{F_b}{i_a}\Big|_{\dot{w}_b=0} = \frac{\psi_a}{1 + Y_m Z_a} \tag{4}$$

is the electromechanical coupling coefficient, which gives the force produced by the blocked transducer per unit current,

$$T_{u\dot{w}} = \frac{u_a}{\dot{w}_b}\Big|_{i_a=0} = \frac{\psi_a}{1 + Y_m Z_a} \tag{5}$$

is the electromechanical coupling coefficient, which gives the electric voltage at the terminals per unit velocity,

$$Z_{ui} = \frac{u_a}{i_a}\Big|_{\dot{w}_b=0} = \frac{Z_e + Z_e Y_m Z_a + Y_m \psi_a^2}{1 + Y_m Z_a} \tag{6}$$

is the electrical impedance of the blocked transducer.

3.2 Energy harvesting

To harvest vibration energy, the electromagnetic transducer presented in figure 1 is connected to an electrical impedance Z_h. Considering the lumped parameter model shown in figure 1 the voltage across two terminals u_a is equal to:

$$u_a = -Z_h i_a \tag{7}$$

since i_a is defined to flow onto the transducer. Substituting equation (7) into equation (2), the current flowing in the coil and impedance load is given by:

$$i_a = \frac{-T_{u\dot{w}}}{Z_h + Z_{ui}} \dot{w}_c \tag{8}$$

When the electromagnetic transducer is exposed to harmonic vibrations the time averaged harvested power is given by:

$$\bar{P}_h = \frac{1}{2} Re\{i_a^* u_a\}. \tag{9}$$

Using Eqs. (7) and (8) the harvested power results:

$$\bar{P}_h = \frac{1}{2} \mathrm{Re}(Z_h) \left| \frac{T_{u\dot{w}}}{Z_h + Z_{ui}} \dot{w}_c \right|^2 \tag{10}$$

Now, assuming a purely resistive electrical load, i.e. $Z_h = R_h$, and recalling the expressions given in Eqs. (5) and (6) the harvested power can be rewritten in the following form:

$$\bar{P}_h = \frac{1}{2} R_h \left| \frac{\psi_a}{R_h + Z_e + (R_h + Z_e) Y_m Z_a + Y_m \psi_a^2} \right|^2 |\dot{w}_c|^2 \tag{11}$$

This equation indicates how both the electrical and mechanical parameters of the harvester influence the energy harvesting with either the classical or the proposed flywheel proof mass transducer. This study is indeed focused on the use of the additional flywheel element in the proof mass transducer to increase the energy harvesting of classical proof mass actuators.

4 ELECTROMECHANICAL PROPERTIES

This section presents simulation and experimental results for the mechanical and electrical impedance functions and transduction functions for the classical and the proposed flywheel proof mass actuators.

4.1 Base impedance

The Bode plots in Fig. 2 show the experimental (solid lines) and the simulation (dash-dotted lines) base impedance $Z_{f\dot{w}}$ FRFs for the classical (plot a) and for the flywheel (plot b) proof mass transducers. The simulated (dash-dotted line) base impedance of the classical proof mass transducer (plot a) is characterised by a marked resonance peak, at about 19 Hz and an antiresonance low, at about 34 Hz. The phase of the base impedance shifts from +90° to around -5° at the resonance frequency and form -5° to +90° at the antiresonance frequency. The base impedance is also characterised by low and high frequency mass-laws represented by two parallel asymptotes. The asymptote below resonance frequency is proportional to the total mass of the transducer ($M_a + m_b$), while the asymptote above antiresonance low is proportional to the case mass of the transducer (m_b). These results agree with similar studies carried out on

coil – magnet proof mass transducers used for the implementation of feedback vibration control systems [11].

The simulated (dash-dotted line) base impedance of the proposed flywheel proof mass transducer (plot b) presents similar features to those of the classical configuration. However, thanks to the flywheel element, the fundamental resonance peak is at about 14 Hz while the antiresonance low, is at about 20 Hz. Moreover, the phase shifts between +90° to around +15°. Compared to the classical configuration, the asymptotes below resonance frequency and above antiresonance low are slightly higher. This is due to the fact that, below the fundamental resonance frequency the flywheel element increments the total mass of the transducer from $M_a + m_b$ to $M_a + m_b + m_w$, while above the antiresonance frequency the flywheel increase the seismic mass effect from m_b to $m_b + I_w/r_w^2$.

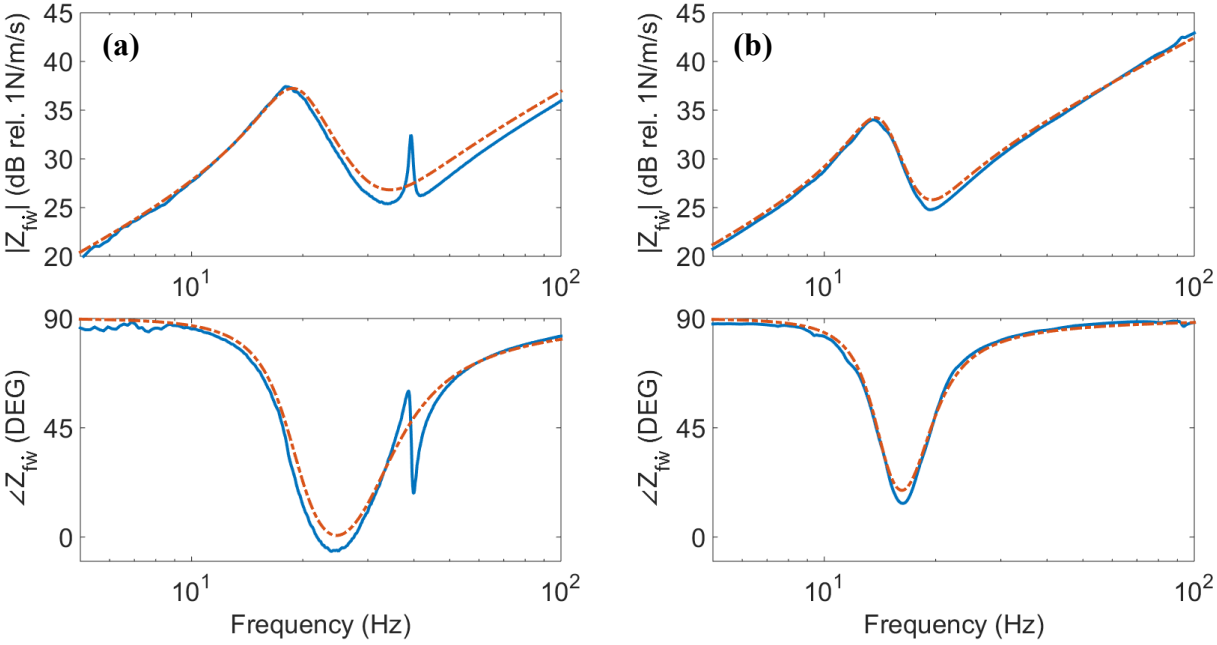

Figure 2: Base impedance for the reference transducer (a) and for the flywheel proof mass transducer (b). Experimental results (solid blue lines). Simulations (dashed-dotted red lines).

The measured base impedances (solid lines) for the classical configuration (plot a) and for the proposed flywheel configuration (plot b) agree quite well with the simulated values. The impedance measured on the classical transducer is characterised by a sharp peak at about 39Hz which is not predicted in the simulation. This feature is likely to be due to the measurement setup, which has introduced additional dynamic effects, such as for example a rocking mode of the transducer mounted on the shaker, which is not taken into consideration in the model. This sharp peak is however not visible in the measured impedance of the proposed proof mass transducer.

4.3 Transduction coefficient

The Bode plots in Fig. 3 show the experimental (solid lines) and the simulation (dash-dotted lines) of the transduction function $T_{u\dot{w}}$ for the classical (plot a) and the flywheel (plot b) proof

mass transducers, which according to Eqs. (4) and (5) should be equal to the transduction function T_{fi}. Considering first plot for the classical transducer, at flow frequencies the transduction effect rises proportionally with frequency and has phase +180°. At the fundamental resonance frequency, the transduction effect peaks and undergoes a -180° lag. At frequencies above the resonance frequency, the transduction approximates to a constant value with phase equal to 0°. The transduction coefficient of the proposed flywheel proof mass transducer is characterised by a similar FRF except that the fundamental resonance peak occurs at lower frequency and that the amplitude of the FRF is about 4 dB lower.

The measured FRFs of the transduction function agree rather well with the simulated ones both in the cases of the classical and proposed proof mass transducers. There is a glance at about 40 Hz, which, as discussed above, may be due to the test setup used for the measurement. Also the transduction function for the proposed flywheel transducer shows a low at about 100 Hz, which instead is due to the design of the setup considered in this study.

It is important to note that the plotted transduction FRF $T_{u\dot{w}}$, is bound to be equal to the transduction FRF T_{fi}, which gives the base force produced per unit current fed to the coil. Indeed the bode plots shown in Figure 3 resemble the so called "blocked force" FRFs, which are normally used to describe the actuation properties of coil – magnet proof mass transducers [11-14].

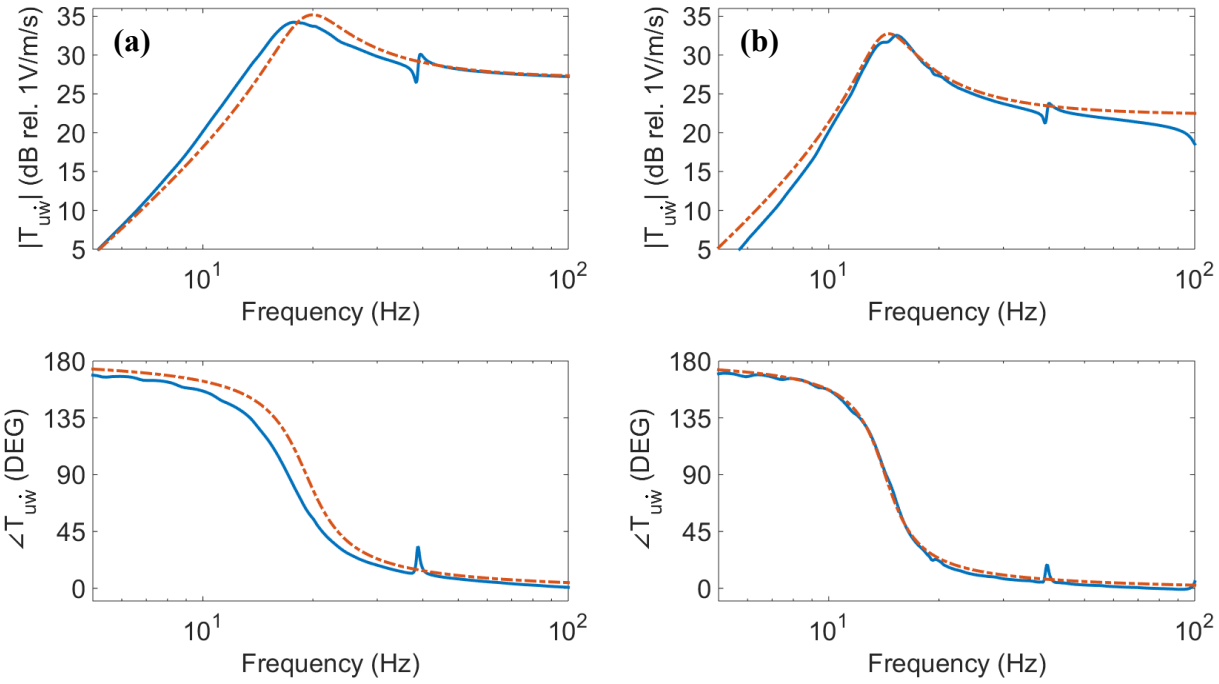

Figure 3: Electromechanical transduction coefficient for the reference transducer (a) and for the flywheel proof mass transducer (b). Experimental results (solid blue lines). Simulations (dashed-dotted red lines).

4.3 Electrical impedance

The Bode plots in Fig. 4 show the experimental (solid lines) and the simulation (dash-dotted lines) of the electrical impedance Z_{ui} of the classical (plot a) and the flywheel (plot b) proof mass transducer. The FRFs of the electrical impedance are characterised by low and high

frequency horizontal asymptotes with phase 0° separated by a wide peak at the resonance frequency of the transducer where the phase rises to +30°, then falls to -30° and finally return to 0°. Both asymptotes have amplitude equal to the transducer coil resistance (27.5 dB). At the resonance frequency of the transducer, the electrical impedance has phase 0°, that is the driving voltage is in phase with the current. In this case, the electrical impedances of the classical and proposed proof mass transducers are very similar, since the two transducers are made with identical coil – magnet components. The principal difference remains the lower resonance frequency due to the additional mass effect produced by the flywheel element.

Comparing experimental results for both configurations it can be observed that there is an additional peak that appears at about 40Hz. In results for the flywheel configuration, this peak appears at the same frequency but is much smaller. The measured FRFs of the electrical impedance also agree well with the simulated ones both in the cases of the classical and proposed proof mass transducers.

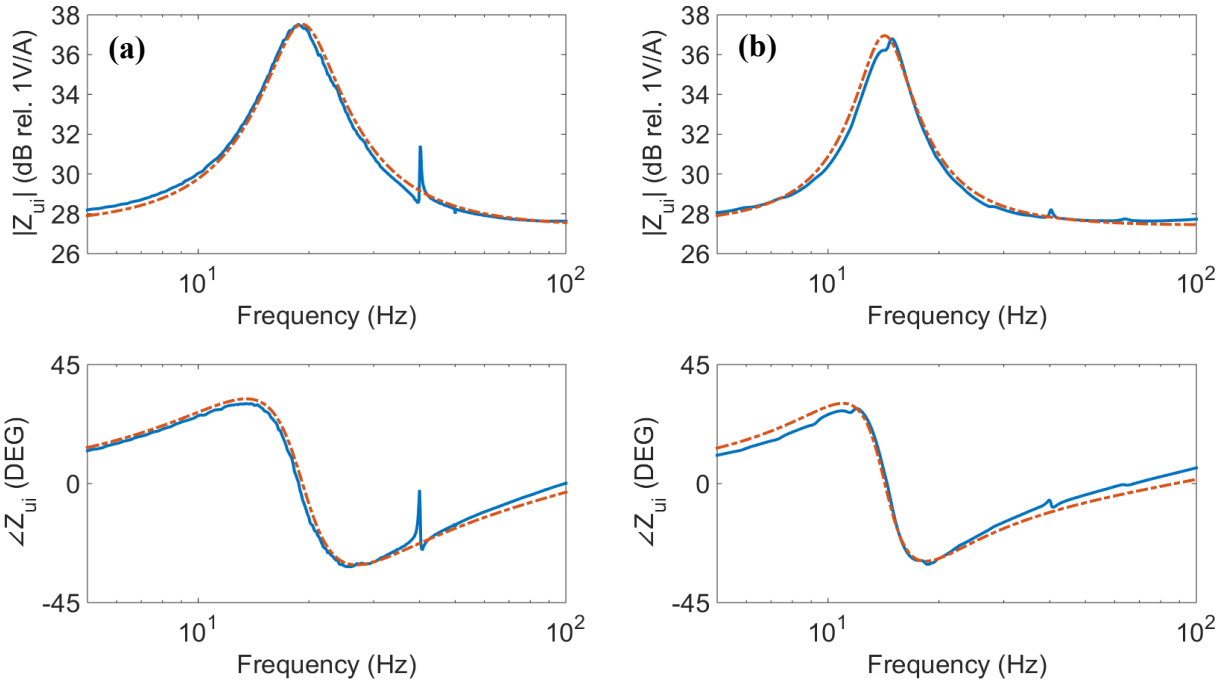

Figure 4: Electrical impedance for the reference transducer (a) and for the flywheel proof mass transducer (b). Experimental results (solid blue lines). Simulations (dashed-dotted red lines).

5 ENERGY HARVESTING

As discussed in Ref. [10], a key factor that determines the harvested power from a coil–magnet proof mass transducer connected to a purely resistive load is the internal losses in the transducer, that is mechanical damping and electrical dissipation. The mechanical damping is primarily due to the viscous losses in the air gap between the coil and the magnet. The electrical losses are instead generated by the resistive effect of the coil. While the electrical losses can be easily modelled considering the resistance of the coil, the mechanical dissipation is somewhat more complex to handle. This is particularly the case with the proposed proof mass transducer comprising the flywheel element, which is both hinged to the case and connected to the moving

coil-armature component via pivot bearings. Thus a preliminary experimental study was put in place to identify the most appropriate expression for the critical damping to be used in a classical viscous damping model. The power harvested per unit base acceleration was therefore measured with the flywheel proof mass transducer shown in Figure 1b connected to a purely resistive load $Z_h = 68\Omega$. The solid blue line in plots a-c of Fig. 6 shows the spectrum of the measured power harvested. The dash-dotted red line in the same plots a-c of Fig. 6 shows the power harvested simulated using Eq. (11), where the damping term c in the mechanical impedance Z_a given in Eq. (A3) has been taken equal to

$$c = \zeta c_c \tag{12}$$

considering a damping ratio equal to $\zeta = 0.2$. Plot a shows the simulated power harvested assuming the critical damping is derived from the classical definition given in literature for the inerter transducers [15,16]:

$$c_c = 2\sqrt{\left(k + \frac{k_w}{r_w^2}\right)\left(M_a + \frac{I_w}{r_w^2} + m_w\right)} \tag{13}$$

Alternatively, plot b shows the simulated power harvested assuming the critical damping is equal to that for the proof mass transducer without flywheel:

$$c_c = 2\sqrt{kM_a} \tag{14}$$

Finally, plot c shows simulated power harvested assuming the critical damping is given by:

$$c_c = 2\sqrt{\left(k + \frac{k_w}{r_w^2}\right)(M_a + m_w)} \tag{15}$$

Contrasting the results plotted in Fig 6a-c it is noted that the expression for the critical damping given in Eq. (15) is the most appropriate to derive the damping factor to be used in the calculus of the mechanical impedance Z_a in order to derive correctly the energy harvested with Eq. (11). This result indicates that, although the axial mass effect produced by the flywheel element I_w/r_w^2 reduce the fundamental resonance frequency of the transducer, it does not influence the mechanical damping, which, as discussed above, plays a key role in the disposal of the absorbed mechanical vibration energy to electrical energy, which is then harvested.

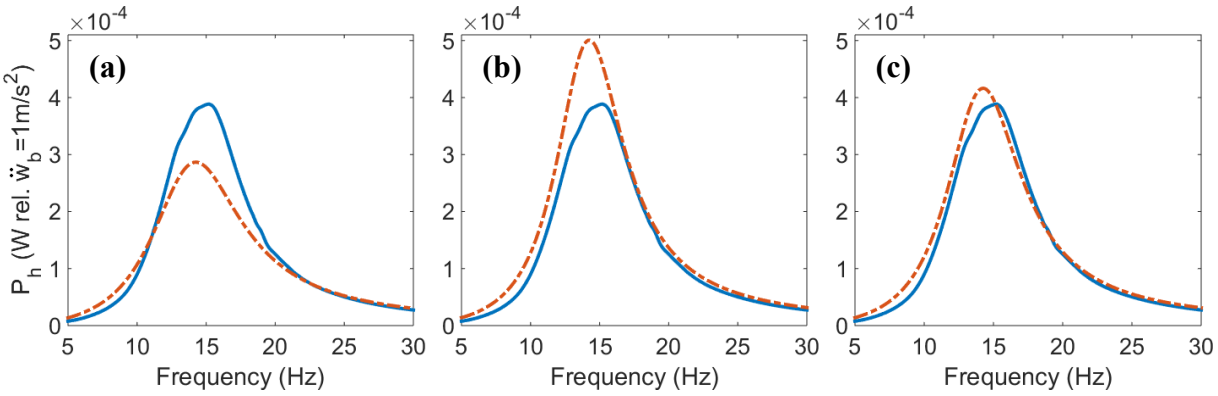

Figure 5: Frequency response function of the harvested power to a resistive load $Z_h = 68\Omega$ for the flywheel proof mass transducer with the constant damping ratio (a), with the constant damping coefficient (b), with the optimal damping (c). Experimental results (solid blue lines). Simulations (dashed-dotted red lines).

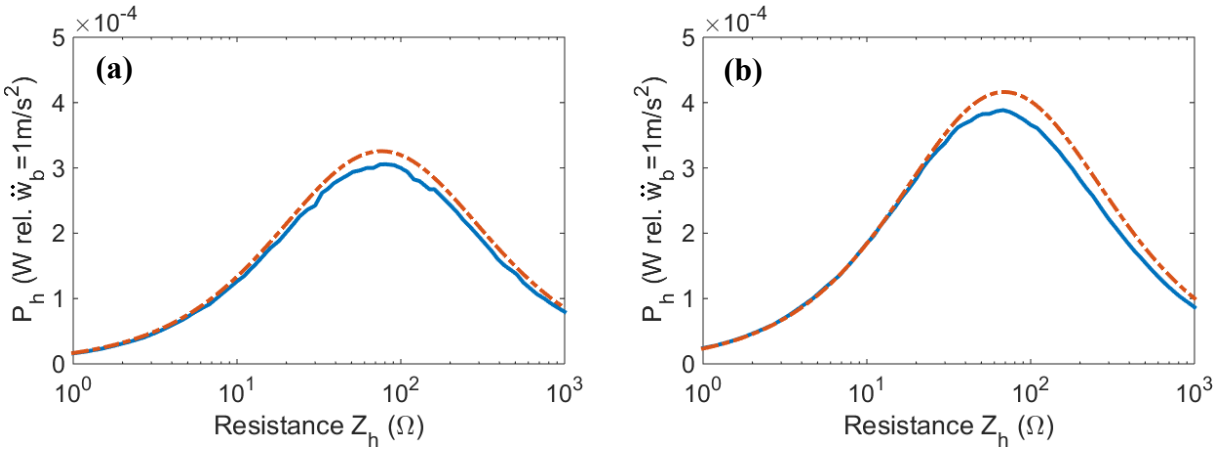

Figure 6: Maximum harvested power at the resonance frequency with varying resistive load Z_h for the classical transducer (a) and flywheel proof mass transducer (b). Experimental results (solid blue lines). Simulations (dashed-dotted red lines).

Having established the correct model for the mechanical damping, the measured (solid blue lines) and simulated (dash-dotted red lines) energy harvested with the classical proof mass transducer (Fig. 1a) and with the proposed flywheel proof transducer (Fig. 1b) are shown respectively in plot a and plot b of Fig. 6. Since the two transducers are characterised by different mechanical damping factors, the maximum energy harvesting at the resonance frequency is obtained with different resistive loads. The result in plot a shows that maximum power can be harvested by applying to the classical proof mass transducer a resistive load of $R_h = 75\Omega$. Alternatively, the result in plot b shows that maximum power can be harvested by applying to the proposed flywheel proof mass transducer a resistive load of $R_h = 68\Omega$.

The two plots clearly show that the simulation results agree well with the experimental tests carried out either with the classical (plot a) or with the flywheel (plot b) proof mass transducers.

6 CONCLUSIONS

This paper has presented simulation and experimental results on the electro-mechanical characteristics and the energy harvesting properties of a new coil-magnet proof mass transducer with a flywheel element. The experimental testes were successfully matched with numerical results obtained from a lumped parameter scheme, which included a specific model for the damping coefficient of the new transducer. Also, the results for the new configuration were compared with those obtained with a classical coil-magnet proof mass transducer.

The results presented in this paper have shown that the flywheel element reduces the fundamental resonance frequency of the actuator without significantly increasing the total mass of the transducer, without increasing the damping coefficient of the transducer and without increasing the static displacement. Moreover, the simulation and experimental results have shown that the proposed transducer increases the harvested energy by about 30%. The study considered an existing coil-magnet proof mass transducer equipped with the flywheel element. Thus, it may be possible that a proper design of the new transducer may lead to a device with even higher energy harvesting capabilities.

APPENDIX A

A.1 Derivation of the first constitutive equation

The first constitutive equation given in Eq. (1) is derived here considering the lumped parameter models shown in Figs. 1c, 1d, which indicates that the complex force at the base of the transducer is given by:

$$F_b = -(Z_b + Z_a)\dot{w}_b + Z_a\dot{w}_m - F_a \tag{A1}$$

where Z_a for the classical and proposed flywheel proof mass transducer is respectively given by:

$$Z_a = c + \frac{k}{j\omega} \quad \text{and} \quad Z_a = c + \frac{k}{j\omega} + j\omega\frac{I_w}{r_w^2} + \frac{k_w}{j\omega r_w^2}. \tag{A2,A3}$$

Also, the impedance of the base mass is given by:

$$Z_b = j\omega m_b \tag{A4}$$

Finally, the reactive force generated by the coil–magnet is given by:

$$F_a = -\psi_a i_a \tag{A5}$$

The complex velocity of the proof mass is given by the following mobility relation:

$$\dot{w}_m = Y_m F_m \tag{A6}$$

Where, considering the classical and proposed flywheel proof mass actuator:

$$Y_m = \frac{1}{j\omega M_a} \quad \text{or} \quad Y_m = \frac{1}{j\omega(M_a + m_w)}. \tag{A7}$$

The complex force acting on the proof mass can be expressed with the following impedance relation:

$$F_m = Z_a\dot{w}_b - Z_a\dot{w}_m + F_a. \tag{A8}$$

Substitution of Eq. (A8) into Eq. (A6) gives:

$$\dot{w}_m = \frac{Y_m Z_a}{1 + Y_m Z_a}\dot{w}_b - \frac{Y_m\psi_a}{1 + Y_m Z_a} i_a \tag{A9}$$

At this point, Eqs. (A5) and (A9) can be substituted into Eq. (A1) to give:

$$F_b = -\left(\frac{Z_b + Z_b Y_m Z_a + Z_a}{1 + Y_m Z_a}\right)\dot{w}_b + \frac{\psi_a}{1 + Y_m Z_a} i_a \tag{A10}$$

A.2 Derivation of the second constitutive equation

The second constitutive equation given in Eq. (2) is also derived here considering the lumped parameter models shown in Figs. 1c, 1d, which indicates that the complex voltage at the terminals of the coil is given by:

$$u_a = Z_e i_a + \psi_a\dot{w}_b - \psi_a\dot{w}_m \tag{A11}$$

where Z_e is the coil electrical impedance:

$$Z_e = j\omega L + R \tag{A12}$$

Substitution of Eq. (A9) into Eq. (A11), gives:

$$u_a = \frac{\psi_a}{1 + Y_m Z_a} \dot{w}_b + \frac{Z_e + Z_e Y_m Z_a + Y_m \psi_a^2}{1 + Y_m Z_a} i_a \tag{A13}$$

ACKNOWLEDGMENTS

The authors gratefully acknowledge the European Commission for its support of the Marie Skłodowska-Curie program through the ITN ANTARES project (GA 606817).

REFERENCES

[1] Priya, S. and Inman, D.J. *Energy harvesting technologies*. Springer, London (2009).
[2] Spreemann, D. and Manoli, Y. *Electromagnetic, vibration energy harvesting devices architectures, design, modeling and optimization,* Springer, London (2012).
[3] Khaligh, A. Peng, Z. and Cong, Z. Kinetic energy harvesting using piezoelectric and electromagnetic technologies—state of the art, *IEEE Trans. Ind. Electronic*, (2010) **57** (3):850-860.
[4] El-Hami, M. Glynne-Jones, P. White, N.M. Hill, M. Beeby, S. James, E. Brown, A.D. and Ross, J.N. Design and fabrication of a new vibration-based electromechanical power generator, *Sens Actuators A Phys* (2001) **92**:335–342.
[5] Glynne-Jones, P., Tudor, M.J., Beeby, S.P. and White, N.M. An electromagnetic, vibration-powered generator for intelligent sensor systems, *Sens Actuators A Phys* (2004), **110**(1-3):344-349.
[6] Elliott, S.J. and Zilletti, M. Scaling of electromagnetic transducers for shunt damping and energy harvesting. *J Sound Vib* (2014) **333**:2185-2195.
[7] Kras, A. and Gardonio, P. Flywheel proof mass actuator for velocity feedback control. *Proc. of the MoViC–RASD 2016 Int. Conf.* Southampton, UK, 3-6 July (2016).
[8] Kras, A. and Gardonio, P. Flywheel inertial actuator for velocity feedback control: parametric study. *Proc. of the ISMA2016 Int. Conf.* Leuven, Belgium, 19-21 September (2016).
[9] Kras, A. and Gardonio, P. Velocity feedback control with a flywheel proof mass actuator. *J Sound Vib* (2017) **In press**
[10] Dal Bo, L. and Gardonio, P. Comparison between electromagnetic and piezoelectric seismic vibration energy harvesters. *Proc. of the MoViC–RASD 2016 Int. Conf.* Leuven, Belgium, 19-21 September (2016).
[11] Rohlfing, J., Gardonio, P. and Elliott, S.J. Base impedance of velocity feedback control units with proof-mass electrodynamic actuators. *J Sound Vib* (2011) **330**:4661-4675.
[12] C.G. Diaz, P. Gardonio, Feedback control laws for proof-mass electro-dynamic actuators, *Smart Mater Struct* (2007) **16**:1766–1783.
[13] C.G. Diaz, C. Paulitsch, P. Gardonio, Active damping control unit using a small scale proof mass electrodynamic actuator, *J. Acoust. Soc. Am.* (2008) **124**(2):886–897.
[14] Fahy, F. and Gardonio, P. *Sound and structural vibration. Radiation, Transmission and Response 2nd ed*. Academic Press, Oxford, (2007).
[15] Smith, M. Synthesis of mechanical Networks: The Inerter. *IEEE Trans Automat Contr* (2002) **47**:1648–1662.
[16] Salvi, J. and Giaralis, A. Concept study of a novel energy harvesting-enabled tuned mass-damper-inerter (EH-TMDI) device for vibration control of harmonically-excited structures. *J. Phys. Conf. Ser.* (2016) **744**:1-12.

INVESTIGATION OF INTERFACIAL CONDITION FOR $LI_{1.4}AL_{0.6}TI_{1.4}(PO_4)_3$ SOLID ELECTROLYTE BASED MULTIFUNCTIONAL ENERGY STORAGE DEVICES

G. LIAO*, S. GEIER, T. MAHRHOLZ, P. WIERACH, M. WIEDEMANN

* Institute of Composite Structures and Adaptive Systems, German Aerospace Center (DLR e.V.)
Lilienthalplatz 7, 38108 Braunschweig, Germany
guangyue.liao@.dlr.de

Key words: Multifunctional composite, supercapacitor, interfacial condition, electrical properties.

Abstract. In the present research, a multifunctional composite is manufactured which is based on the mechanism of supercapacitor by using $Li_{1.4}Al_{0.4}Ti_{1.6}(PO_4)_3$ (LATP) ionic conductor as solid electrolyte. This device could store electrical energy, meanwhile bearing the mechanical loads. The LATP solid electrolyte is sintered and both round surfaces of the pellet are sputtered with gold in 90nm of thickness. Then, samples are embedded into composite systems by using RTM-6 as resin matrix. The capacitances of the sample before and after embedding are measured by cyclic voltammetry method. The results show a significant decrease of capacitance after embedding process. The reasons for this are systematically investigated by different methods, for example, electrochemical impedance spectroscopy, scanning electron microscopy and energy-dispersive X-ray spectroscopy. Different sputter methods are used for preparing the electrodes. Using various resins the impact of different thermal expansion coefficients and curing temperatures on the capacity is also investigated. The results indicate that the decrease should mainly come from the degradation of interfaces between LATP, sputtered gold layer and electrical collector. Finally, magnetron sputtering shows an obvious advantage in comparison to common deposition sputter methods, because the former one results in a stronger adhesion between sputtered metal layer and LATP pellet surface.

1 INTRODUCTION

Multifunctional power composites that have the ability to store or generate energy have recently been developed and have attracted a great deal of attention, because the increased demanding for lightweight, green and safe productions in transportation modes. One type of these multifunctional composites is a structural supercapacitor which combines the function as supercapacitor and can bear mechanical load simultaneously [1]. Supercapacitors are also called double layer capacitors, which possess high capacity, high power efficiency and long cycle life [2], usually consisted of two electrodes with high surface area, a separator avoiding short-cutting between two electrodes and electrolyte providing ions to build up the ‘double layer’. With respect to safety issues, solid state electrolytes are preferred.

The common approaches for the development of structural supercapacitors use carbon fibre weaves as electrodes with glass fibre in between as separators and injected by polymer solid

electrolytes, which are used as electrolytes and matrixes at the same time [3]. The multifunctional electrolyte may be even more challenging since it needs to combine high ionic conductivity with excellent rigidity and strength. However, ionic conductivity and mechanical performance usually have an inverse relationship. For example, Ji et al. [4] developed a ternary polymer electrolyte as poly(ethylene oxide)-block-polyethylene (PEO-b-PE) which enhances the ionic conductivity of pure PEO from 4.05×10^{-10} S/cm to 5.51×10^{-8} S/cm. However, the ultimate strength decreased from around 8.5 MPa to 7.29 MPa after addition of the copolymer. N. Shirshova [5] proposed a multifunctional polymer matrix which was manufactured by mixing a solid polymer electrolyte (poly (ethylene glycol) diglycidylether and diglycidylether of bisphenol-A) with a more rigid matrix formulation (epoxy resins with trademarks MVR444, MTM57 and VTM266). It was observed when increasing the content of the rigid matrix polymer from 30 wt. % to approx. 50 wt. %, the conductivity of the mixture dramatically decreases from 8×10^{-4} S/cm to 7×10^{-6} S/cm. The conflict between electrical and mechanical properties restricts the application of this kind of polymer solid electrolyte for structural supercapacitors.

Another type of solid electrolyte is based on ceramic materials. Ceramic electrolytes are also called fast ion conductors and possess relatively high ionic conductivity ($>10^{-5}$ S/cm) compared to regular crystalline solids ($\sim10^{-12}$ S/cm, NaCl [6]). In particular, lithium ion conductors are widely used for Li^+ ion batteries because of their relative high energy density and high ion conductivity at room temperature. Great attention is focused on the Li_2S-based solid electrolytes because of their extremely high ionic conductivity of 10^{-3}-10^{-2} S/cm. However, because of its hygroscopic character this kind of ceramic electrolyte is unstable under normal environmental conditions. $Li_{1.4}Al_{0.4}Ti_{1.6}(PO_4)_3$ (LATP) is a type of lithium ion conductor with a $Na_3Zr_2PSiO_{12}$ (NASICON) structure and relative high conductivity of 7×10^{-4} S/cm at room temperature. Both easy processability and high stability in different environmental conditions make this solid electrolyte interesting for application in structural supercapacitors [7–9].

With respect to the manufacturing process, the preparation of the fibre reinforced composite combined with the simultaneous embedding step of supercapacitors is favoured. In particular, liquid composite moulding (LCM) techniques such as RTM, VARI and DP-RTM are well established as manufacturing processes for fibre composites. Low manufacturing costs achieved through a combination of inexpensive resins and semi-finished fibre materials are decisive advantages compared with prepreg technology. Future composite lightweight structures are targeted for cost savings of 40% and weight reductions of 30%. These challenges can be met best by employing LCM techniques.

The present paper describes the manufacturing process of multifunctional power composites embedding LATP ceramic pellets into a polyester fibre laminate, using RTM-6 resin as a matrix and injected by means of the Differential Pressure Resin Transfer Moulding technique (DP-RTM). The DP-RTM is used, ensuring high quality and reproducibility of composites [10]. The process of embedding ceramic into a composite has already been successfully demonstrated using piezo-ceramic foils [11]. The embedded capacitors are analyzed by electrochemical impedance spectroscopy, scanning electron microscopy and energy-dispersive X-ray spectroscopy. Furthermore computerised tomography scan has been used to observe the condition of LATP pellet after embedding.

2 MATERIALS AND METHODS

2.1 Synthesis of $Li_{1.4}Al_{0.4}Ti_{1.6}(PO_4)_3$ solid electrolyte

The LATP solid electrolyte was synthesised (with nominal stoichiometric amount as $Li_{1.4}Al_{0.4}Ti_{1.6}(PO_4)_3$) by means of a sol-gel method [12]. Firstly, 0.8 mol/L Titanium (IV) t-butoxide (≥99.9%, Alfa Aesar, UK) was dissolved in 0.2 mol/L citric acid (>99%, Merck KGaA, Germany), heated and stirred at 95°C for 20h. Then, stoichiometric amounts of $LiNO_3$ (>99%, Sigma-Aldrich, US), $NH_4H_2PO_4$ (>98.5%, Sigma-Aldrich, US) and $Al(NO_3)_3 \cdot 9H_2O$ (99.2%, VWR International, Germany) were added, dissolved and stirred at the same temperature for 30 min until a homogeneous solution was obtained. After that, ethylene glycol (≥99.9%, Merck KGaA, Germany) was added to the solution with a molar ration of citric acid at 1:1. The solution was then heated to 120 °C in an oil bath and stirred with a magnetic stirrer for 30 min, and afterwards heated to 170 °C for 2h to evaporate the water and to obtain the polymer precursor. The dried gel was milled by hand in a porcelain mortar for 15 min and sieved through a porcelain sieve (holes in range of 1 mm) to obtain a powder, and then transferred to a ceramic crucible and heated to 500 °C for 5 h at a heating rate of 5 °C/min to complete the pyrolysis process. The calcination process was finished in the open air at 800 °C for 5 h. Afterwards the powders were milled in the presence of ethanol in an 80 mL steel jar with ZrO_2 balls (5 mm) by a planetary ball mill (PULVERSETTE 7, FRITSCH GmbH, Germany). The weight ration of mill balls and powders was 6:1. The powders with ethanol were milled for 2 h at a rotation speed of 400 rpm, and the powders were then dried in an oven at 80 °C for 5 h. At a final step the powders were milled in a glass mortar for 5 min and pressed into pellets (thickness 1 mm) under a pressure of 180 MPa. The pellets were sintered at 950 °C for 8 h at 5 °C/min.

2.2 Manufacture of $Li_{1.4}Al_{0.4}Ti_{1.6}(PO_4)_3$ (LATP) solid electrolyte- power composites

The solid electrolyte pellets were sputtered with gold in a thickness of approx. 90 nm using sputtering devices (POLARON E5100, LOT Quantum Design, Germany). Polyester fibre layers (Type Viledon T 1702, Freudenberg & Co. KG, Germany) were hot pressed in one layer of 1 mm and two layers of 0.7 mm thickness, used as an insulation layer in the middle and cover layers outwards (to reach the required thickness according to the standard). The metalised polyester fleece layers (0.2 mm in thickness) were used as an electronic conductor. In the middle, isolation layer holes of 12 mm in diameter were punched out for placing the LATP pellets. Holes of 3 mm in diameter were also punched out at both edges of the samples and Cu slips were placed into the holes to be used as bolt points for electrical measurement. The lay-up procedure is shown in Figure 1.

The composite samples were produced by DP-RTM injection technology using RTM-6 (Hexcel® Composites). After curing at 180 °C, the plate was cut into samples of 10.0×1.5×0.2 cm (according to four-point-bending test standard DIN EN ISO 14125:1988, class IV). It was important to ensure that the LATP-Ps were placed in the centre of each sample. Electric wires were then bolted onto the Cu slips.

2.3 Microstructure characterisation and measurement of electrical properties

A computerised tomography scan (GE phoenix v|tome|x s, GE Measurement & Control, USA) was used to investigate the inner morphology of the LATP composite samples. The interface between the LATP electrolyte and the metalised polyester collector was observed using a scanning electron microscope (LEO 1550, Zeiss Jena AG, operating voltage of 5 kV, 8 mm). The linear thermal expansion coefficient of LATP was measured by thermal mechanical analysis.

Gold was sputtered on both sides of the polished surfaces of the LATP pellets to work as the electrode. The electrical measurements of LATP pellets were carried out in a Swagelok@ PTFE cell, which ensured that the pressure upon samples was nearly the same at each measurement. Cyclic voltammetry (CV) test and electrochemical impedance spectroscopy (EIS) were performed at room temperature by an electrochemical workstation (Vertex, IVIUM TECHNOLOGIES, France) for the electrolyte samples. The voltage range of the CV was 0–0.5V with a scan rate of 10 mV/s and the capacitance of every sample was calculated from the CV curves. The EIS was carried out in the frequency range of 1 MHz to 1 Hz with voltage amplitude of 10 mV to calculate the ionic conductivity. An equivalent circuit, describing electrochemical processes in the solid supercapacitor, was simulated by EC-lab® software.

Two kinds of samples are analysed:

a. LATP pellet after sinter process, abbreviated as LATP-P;

b. LATP-P embedded into a composite using a DP-RTM process, abbreviated as LATP-C.

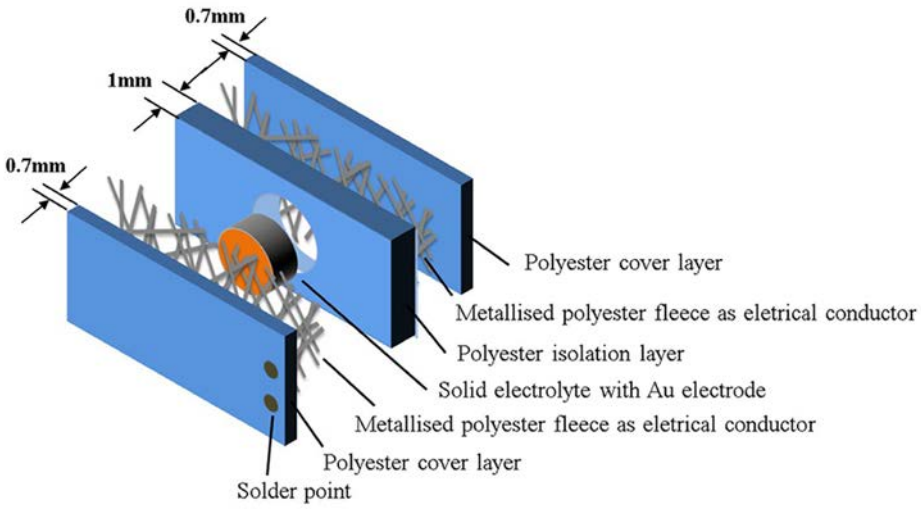

Figure 1: Configuration of LATP-C

The capacitances of LATP-P and LATP-C have been measured by means of cyclic voltammetry (CV). The specific capacitances have been measured and calculated at different scan rates of 10 mV/s, 20 mV/s, 50 mV/s and 100 mV/s to certify a portable scan rate which ensures a sufficient ion transfer for building up double layers. The capacitance is calculated from the CV curve, in which the current is detected responding to voltage change [13].

Capacitance:

$$C = \frac{Q}{U} = \frac{1}{\tau(\Delta U)} \int_{Ua}^{Uc} iUdU \tag{1}$$

Specific capacitance: $C_m=C/m$
here, C – Capacitance, [F]; C_m – Specific capacitance per unit weight, [F/g]; ΔU – The applied potential window (from minimum voltage Ua to maximum voltage Uc), [V]; τ – Scan rate, [mV/s]; Q – The capacitor's charge, [C]; m – Weight of LATP electrolyte, [g].

The conductivity is calculated by adding together the values of bulk resistance and grain boundary resistance, which are calculated from the equivalent circuit [14]. Ionic conductivity:

$$\sigma = \frac{l}{(R_b+R_{gb})A} \quad (2)$$

Here, σ – Ionic conductivity, [S/cm]; l – Sample thickness, [cm]; A – Electrode area, [cm^2]; R_b – Grain resistance, [Ω]; R_{gb} – Grain boundary resistance, [Ω].

3 RESULTS

The highest specific capacitance value of about 33.7 µF/g is achieved at the lowest scan rate of 10 mV/s. The near rectangular shape of CV curves obtained from each sample at the scan rate of 10 mV/s represents the formation of double layers; see Figure 2 a). However, more than 90% of the capacitance is lost after embedding the pellet into composite materials; see Figure 2 b).

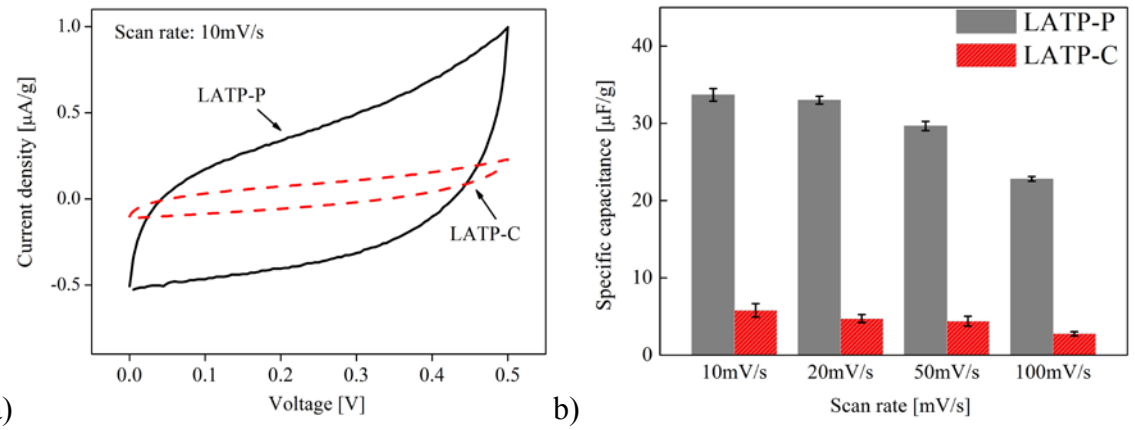

Figure 2: Capacitance measurement results: a. CV curve of LATP-P and LATP-C from same sample at scan rate 10mV/s; b. capacitances comparison under different scan rates

In Figure 3 a), Nyquist plots of the complex impedance Z*(□) = Z'(□) + jZ□(□) of LATP samples before and after embedding at room temperature are presented. According to previous publications about LATP [15], the EIS is usually divided into two semicircles due to bulk and grain boundary resistances. However, the grain semicircle shifts out of the frequency window, and only the total resistance of the sample can be determined. In order to calculate the values for the total resistances, an equivalent circuit is extracted from the EIS plots by EC-lab® software, shown in Figure 3 b).

The total conductivity of the LATP sample is measured to be 4.99×10^{-4} S/cm and is reduced after embedding to a value of 1.57×10^{-4} S/cm. In the low frequency range (10 kHz-1 Hz), the impedance of LATP-C obviously increases in comparison to LATP-P. This indicates

an increased resistance at interfaces between electrolytes, sputtered Au layer and metalised fleece layer.

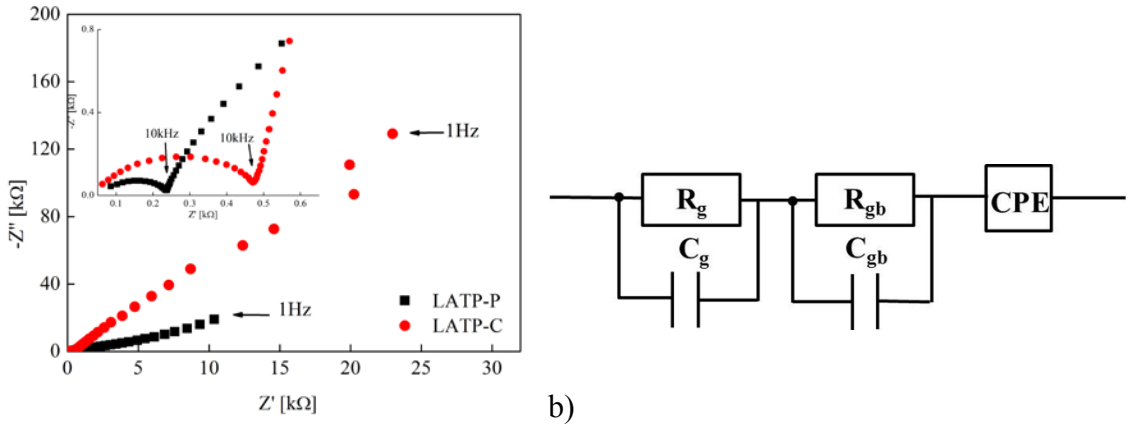

Figure 3: a) Nyquist plot of LATP-P and LATP-C from the same sample; b) equivalent circuit

CT measurements are utilised to analyse the LATP samples non-destructively after the embedding process. Sectional images exhibit two layers of the sample as shown in the Figure 4 indicating the appearance of fractures at the edge areas of the LATP-P. Ceramics contain unavoidable microscopic flaws (micro-cracks, internal pores and atmospheric contaminants) resulting from the manufacturing process (hand press, sintering). These defects could increase to form large cracks under inhomogeneous pressure resulting from the evacuation process and/or various stress concentration at the edges of the pellets because of slight differences in thickness. Another possible reason for flaw growth could be the thermal treatment. The LATP-C is heated to 180°C with a relative high heating rate during DP-RTM. This high heating rate could result in non-uniform thermal expansion inside the ceramic, which usually induces crack propagation. However, the cracks are not observed in all samples of LATP-C. The reason for the capacitance decrease will be discussed subsequently.

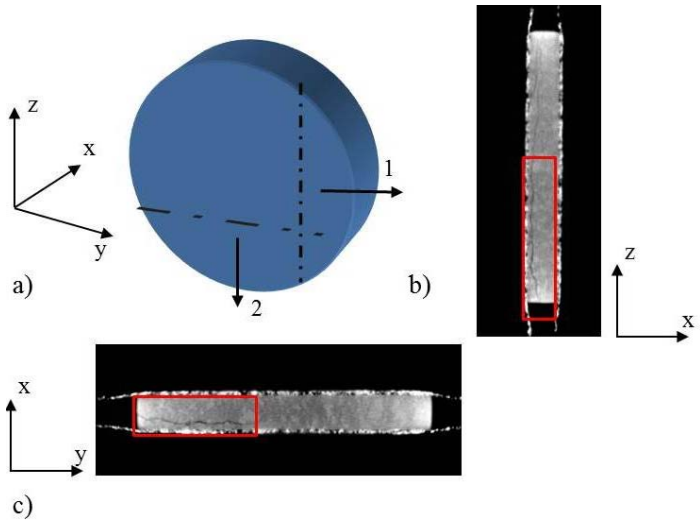

Figure 4: CT images of a LATP sample after embedding: a) Drawing of LATP sample with the selected cross sections 1 and 2; b) CT image of cross section 1 with fracture; c) CT image of cross section 2 with fracture.

4 DISCUSSIONS

The observed decrease of capacitance after embedding the LATP in the composite is analysed by taking some assumptions into consideration: Beside cracks in the pellets induced during or after embedding, also the influence of electrical conductive material, the temperature cycling during injection, the adhesion between sputtered metal layer and ceramic as well as the resin infiltration into surface or bulk of pellets itself are investigated.

4.1 Influence of fracture on electrical properties

The electrical properties of samples are measured in dependency of the fracture degree. Therefore the capacitance of pristine sample and the corresponding broken sample are analysed. After cutting the sample, the pieces are put together and the electrical properties are measured again illustrated in in Figure 5 a). The capacitance of pellets after breaking remains at a value of 93.39±6.4 % in comparison with the starting reference capacitance. In Figure 5 b), the radius of semi-circle shifts to higher resistance value at real impedance axis indicating a decrease of total conductivity, which is attributed to the fractures blocking the ion transport at grain boundaries. This could explain the impedance increase in high frequency range corresponding to Figure 3 a), however it doesn´t exhibit the drastic increase of impedance in low frequency range in Figure 3 a), meanwhile the fractures are also not the reason for capacitance reduce.

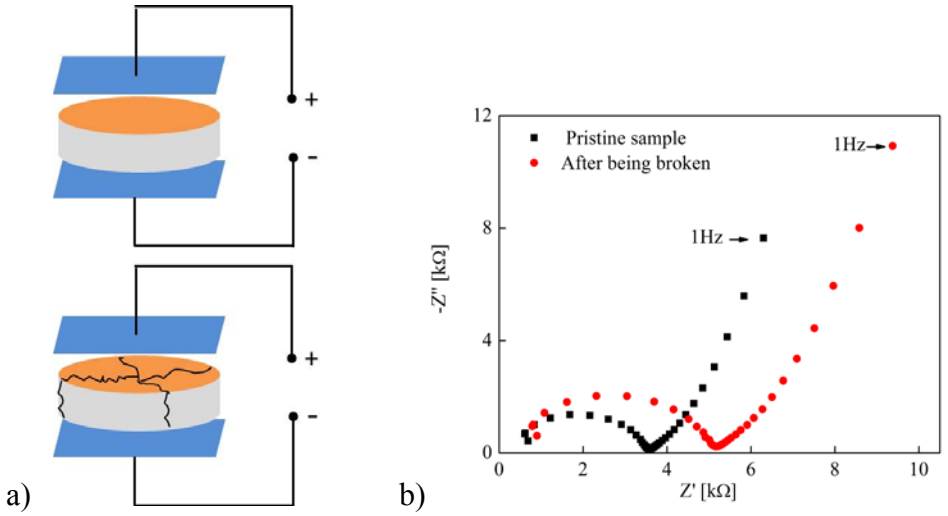

Figure 5: a) sketch of electrical measurements for pristine and broken sample; b) comparison of Nyquist plots of pristine and broken sample.

4.2 Influence of different electrical conductive materials

For connecting the metalized polyester fleece and the ceramic LATP sample different materials are used as electrical conductive materials like copper mesh, steel band (0.05 mm) and silver glue. The result in Figure 6 a) shows that all the pellets' capacitance remains around 10 % and no obvious difference between those conductive materials is observed.

4.3 Influence of sputtered metal layers

4.3.1 Thermal cycling effect

The manufacturing of the composite sample by DP-RTM technique based on a curing process at temperatures of 120 °C to 180 °C,. Thus temperature cycling could be one of the influence factors controlling the value of capacity. To verify this influence, the LATP-P is sputtered with Au following with measurements of electrical properties. As the second step, the LATP-P is placed into a glass tube which is connected with a vacuum pump to exclude any side reaction induced by atmosphere. Then the whole glass tube is subjected to a thermal treatment at 120 °C for 5 min. After cooling down to room temperature, the electrical properties are measured again. This procedure is repeated 3 times in 30 min steps. The trend of line (in Figure 6 b)) shows a great reduce of capacitance. Then the Au layers are polished off from ceramic surface with 5000# polish paper and, dried in desiccator for 12 h. Interestingly, after sputtering a new Au layer of 90nm thickness on both round surface the capacitance is comparable with the pristine sample. Starting the same thermal cycling again with 30 min intervals, the capacitance reduces dramatically. The impedances in low frequency range increase obviously (Figure 6 c)), even after 5 min thermal treatment. This could explain as the temperature cycling result in a release of sputtered Au layer which is one of the reasons resulting in capacitance decrease.

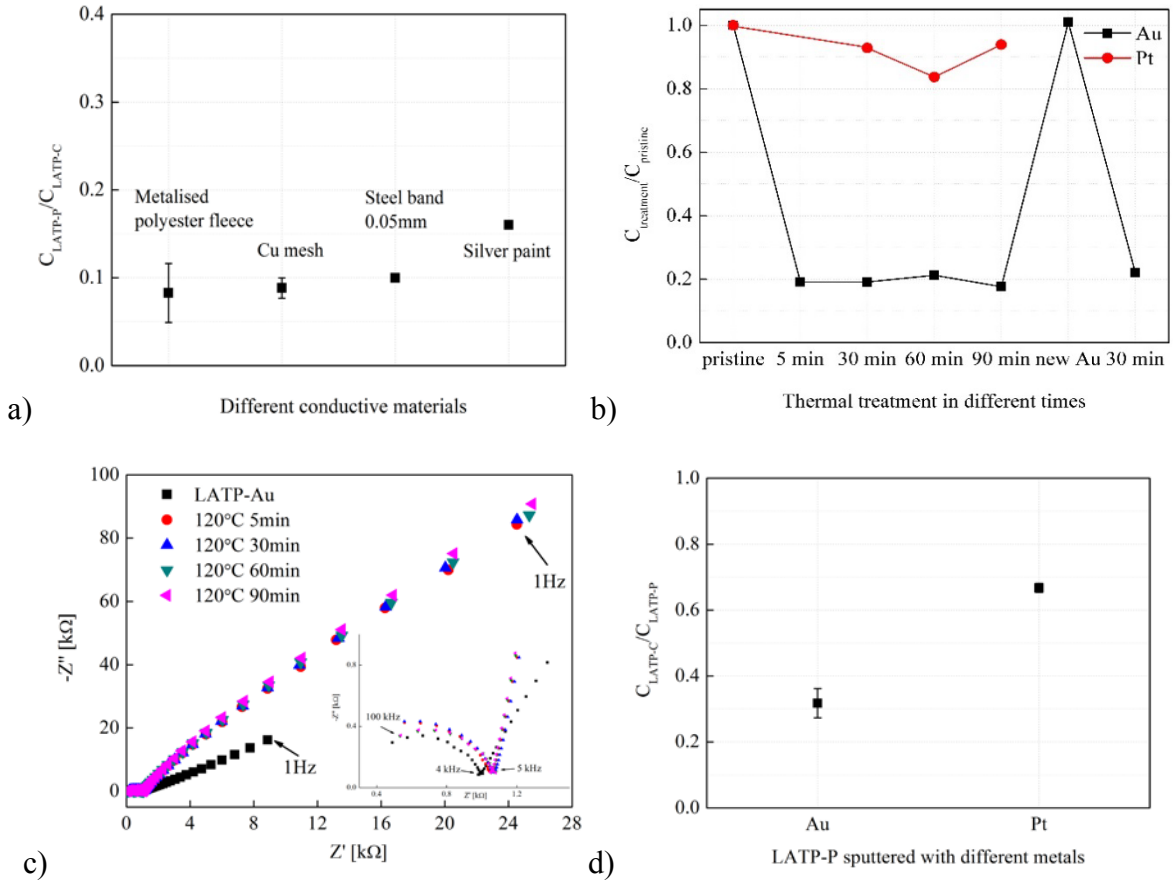

Figure 6: the capacitance ratio C_{LATP-C}/C_{LATP-P} is measured from the same LATP pellets before and after treatment (embedding or thermal treatment) a) capacitance ratio between LATP-C with different conductive

materials; b) the capacitance ratio after different thermal treatment times of two sputtering processes and materials; c) Nyquist plots of LATP-P with Au electrodes after different thermal treatment times; d) the capacitance ratio of LATP-P sputtered with Au and Pt before and after embedding.

4.3.2 Interface strength resulted from resin during curing

The assumption (described in Figure 7 a)) of this phenomenon resulted from two processes could be described as follow:

1. During chemical reaction of resin in curing temperature (here in 180 °C), the resin has a volume shrinkage associated to shrinkage of the polymer chains [16]. This results in an adhesion force between resin and metal. Consequently, the residual stresses would transfer to the metal surface which causes the dissolve of the gold layer from the LATP.
2. During the cooling process (from curing temperature to ambient temperature) after curing, the materials contract with different volumetric shrinkage because of different coefficient of thermal expansion (resin > 70×10^{-6} K^{-1}, Au~14.5×10^{-6} K^{-1}, Pt~9×10^{-6} K^{-1} [17] and LATP ~ 4×10^{-6} K^{-1}). This different volumetric shrinkage could result in a friction at the interface which results in a peel-off of Au layer on LATP surface.

To improve this, magnetic sputtering technique (Magnetron sputtering system LEYBOLD LH Z400S) combined with Pt as sputtering material is used. The metal layers of 100 nm platinum (Pt) are sputtered on the both round surfaces of LATP. Usually this sputtering technique results in higher adhesion between coating and substrate. It can be expected that Pt bonds more strongly to ceramic substrate than Au layers as underlined by literature [18]. The samples with Pt are also treated with different temperature (in Figure 6 b)). The capacitance remains constantly, which means an improvement of adhesion between ceramic and sputtered metal layer at the surface.

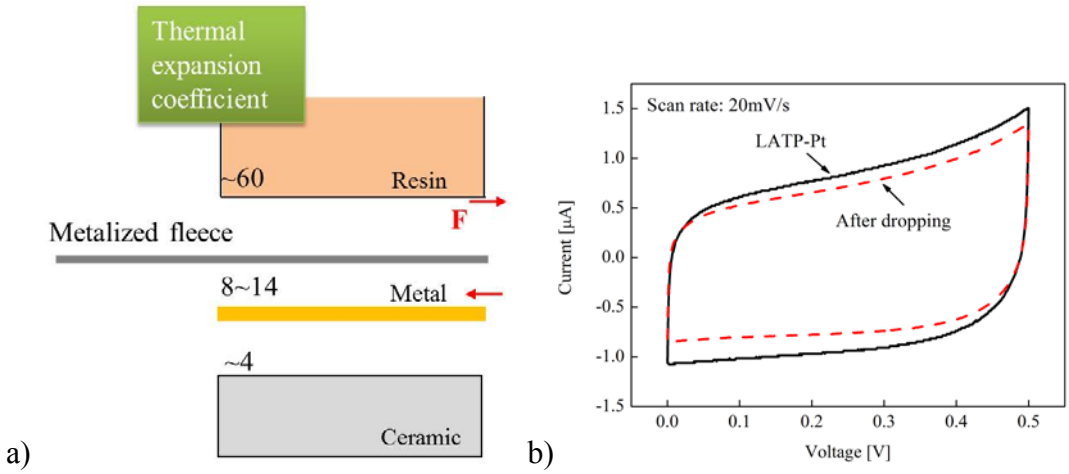

Figure 7: a) Sketch of interface between LATP, sputtered metals and resin; b) CV curves of the same sample before and after resin dropping at scan rate 20 mV/s.

To exclude the temperature factor, we choose Airstone 880/886H (Olin^{tm} EPOXY) as resin matrix because the resin could be cured at ambient temperature. As seen in Figure 6 d), the capacitance of LATP-P with Au decreases around 70 %. However, the capacitance of LATP-P with magnetron sputtered Pt (are shown in Figure 6 d)) only have around 30 % reduction.

This implies that the release of metal layer caused by volumetric shrinkage is one of the causes of capacitance decrease.

4.5 The influence of resin infiltration into pellets during embedding

The improved sputtering method and material have partially solved the degradation of electrical properties after embedding; however, there still exists a 30% reduction in capacitance. An explanation is given by the assumption of resin infiltration into the LATP-pellets. Therefore, samples of LATP-P and LATP-C are broken in the middle separately and EDX measurements are executed at different areas (for example, shown as the circle in Fig.8 a) and b)). The weight proportion of carbon in the pellet before embedding is 4.37±0.79 wt. % and 28.43±0.31 wt. % in LATP-C, respectively. A reasonable deduction could be drawn as the resin immerses into the pellets during injection process because of the pellet itself containing many pores. To confirm this assumption, the Airstone 880/886H is dropped directly on both surfaces of LATP-P magnetron sputtered with Pt. It is observed that 0.03 g resin immerses into the samples, and after 24 h curing in ambient temperature, the capacitances are measured again. In comparison with the untreated sample, the capacitance reduces by 16.9±1 % (seen in Figure 7 b)).

a)

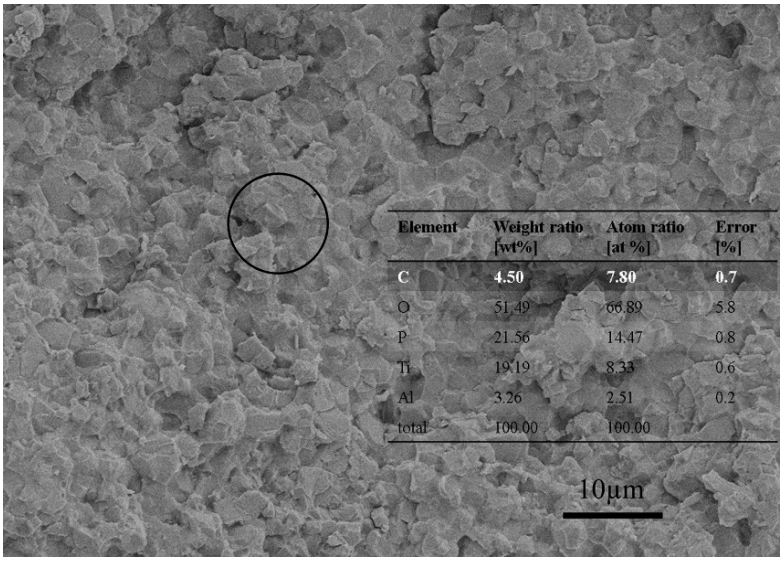

b)

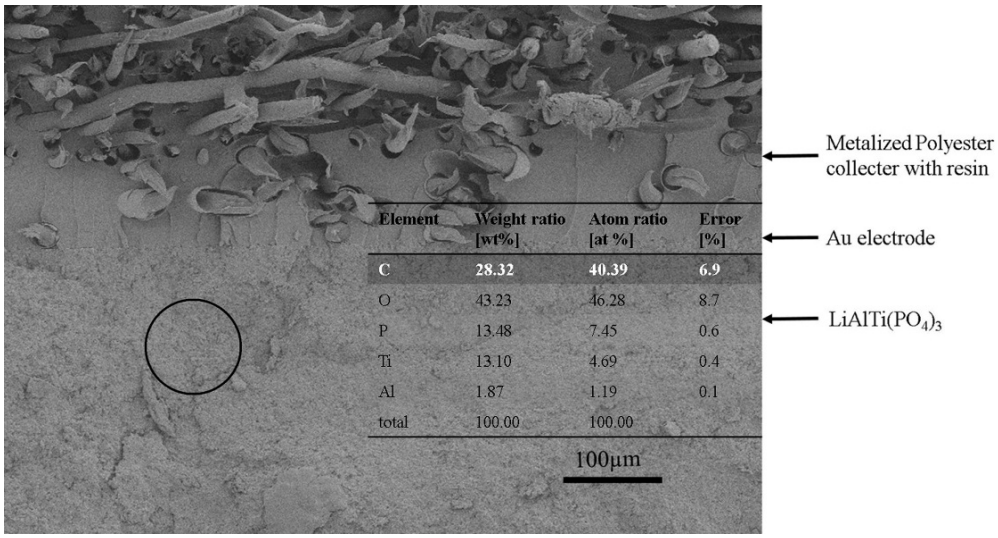

Figure 8: Cross section of the samples broken in the middle measured by SEM: a) LATP-P; b) the LATP after embedding.

5 CONCLUSIONS

In the present research, a method of manufacturing multifunctional power composites has been developed, which uses the NASICON-type $Li_{1.4}Al_{0.4}Ti_{1.6}(PO_4)_3$ as solid electrolytes embedded in a fibre composite by a DP-RTM process. The capacitance of samples before embedding is measured by CV tests. The capacitance is about 33.7 µF/g calculated at a scan rate of 10 mV/s and a voltage range of 0–0.5 V. Experimental results exhibit losses in capacitance for the prepared LATP composites of about 80 % compared to the LATP pellets before being embedded. There are three main causes identified and discussed:

Temperature cycling induces interface stresses between the gold layer and LATP surface because of different coefficient of thermal expansion resulting in a detaching of gold electrode. Moreover, the volume shrinkage of resin, after reaching the gel point, might also induce interface stress to the gold layer. In addition, porous pallet surfaces are infiltrated by the resin resulting in a reduced capacity.

By using improved sputtering techniques as magnetic sputtering of Pt could partially avoid this decrease. However, it is necessary to manufacture LATP pellets with high density smooth surfaces and without pin holes in future work.

ACKNOWLEDGEMENT

This work is supported by Ms A. Viandier, Dipl.-Ing. (Technical University of Braunschweig, Institute of Adaptronics and Function Integration) for use of her analysis methods and expertise. And thanks also to M.Sc Y. Dai (Jülich Research Centre) for supporting magnetron sputtering process.

REFERENCE

[1] Shirshova, N., Qian, H., Houllé, M., Steinke, J., Kucernak, A. et al. Multifunctional Structural Energy Storage Composite Supercapacitors. *FARADAY Discuss.* (2014) **172**: 81–103.

[2] Simon, P. and Gogotsi, Y. Materials for electrochemical capacitors. *Nature Mater.* (2008) **7**:845–854.

[3] Goodenough, J.B. and Kim, Y. Challenges for rechargeable Li batteries. *Chem. Mater.* (2010) **22**: 587.

[4] Ji, J., Li, B., Zhong, W. Simultaneously enhancing ionic conductivity and mechanical properties of solid polymer electrolytes via a copolymer multi-functional filler. *Electrochem. Acta* (2010) **55**(28): 9075–9082.

[5] Shirshova, N., Bismarck, A., Carreyette, S. Structural supercapacitor electrolytes based on bicontinuous ionic liquid-epoxy resin systems. *J Mater. Chem. A*. (2013) **1**:15300.

[6] West, A. *Solid state chemistry and its applications.* John Wiley & Sons, 450, (2014).

[7] Fu, J. Superionic conductivity of glass/ceramics in the system Li_2O-$A1_2O_3$-TiO_2-SiO_2-P_2O_5. *Solid State Ionics* (1997) **96**:195–200.

[8] Fu, J. Fast Li^+ ion conduction in Li_2O-$A1_2O_3$-TiO_2-SiO_2-P_2O_5 glass-ceramics. *J. Am. Ceram.* (1997) **80**: 1901–1903.

[9] Wen, Z.Y., Xu, X.X. and Li, J.X. Preparation, microstructure and electrical properties of $Li_{1.4}Al_{0.4}Ti_{1.6}(PO_4)_3$ nanoceramics. *J Electroceram.* (2009) **22**:342–345.

[10] Kleineberg, M., Pabsch, A., Siegle, C. *Ermittlung und Charakterisierung der Prozeß parameter eines weiterentwickelten RTM-Verfahrens*. DLR-Braunschweig, IB 131-95/34, (1995).

[11] Wiedemann, M. and Sinapius, M. *Adaptive, tolerant and efficient composite structures* .Springer-Verlag Berlin Heidelberg, 37-38, (2013).

[12] Takahashi, K., Ohmura, J., Im, D. A super high lithium ion conducting solid electrolyte of grain boundary modified $Li_{1.4}Ti_{1.6}Al_{0.4}(PO_4)_3$. *J Electrochem Soc.* (2012) **159**(4):A342-A348.

[13] Bard, A.J. and Faulkner, L.R. *Electrochemical methods, fundamentals and applications.* Hoboken, Wiley, (2001).

[14] Mariappan, C., Gellert, M., Yada, C. Grain boundary resistance of fast lithium ion conductors: Comparison between a lithium-ion conductive Li-Al-Ti-P-O-type glass ceramic and a $Li_{1.5}Al_{0.5}Ge_{1.5}P_3O_{12}$ ceramic. *Electrochem. Commun.* (2012) **14**: 25-28.

[15] Xu, X.X., Wen, Z.Y., Wu, J.G. and Yang, X.L. Preparation and electrical properties of NASICON-type structured $Li_{1.4}Al_{0.4}Ti_{1.6}(PO_4)_3$ glass-ceramics by the citric acid-assisted sol–gel method. *Solid State Ionics* (2007) **178**:29–34.

[16] Hill, R.R., Shailesh, J.R., Muzumdar, V. and Lee, L.J. Analysis of volumetric changes of unsaturated polyester resins during curing. *Polym. Eng. Sci.* (1995) **35** (10):852-859.

[17] Taylor, R.E. CINDAS Data Series on Materials Properties, Thermal Expansion of Solids, *ASM International* (1998) **1–4**.

[18] Buckley, D. H. *Friction Behavior of Members of the Platinum Metals Group with Gold.* NASA TN D-7896, (1975).

VIII ECCOMAS Thematic Conference on Smart Structures and Materials
SMART 2017
A. Güemes, A. Benjeddou, J. Rodellar and Jinsong Leng (Eds)

PHASE FIELD STUDY OF STRESS-INDUCED POLARIZATION SWITCHING FOR VIBRATION ENERGY HARVESTING: MATERIAL INFLUENCE

DAN WANG*†, LINXIANG WANG* AND RODERICK MELNIK†

* State Key Laboratory of Fluid Power and Mechatronic Systems
Zhejiang University, Hangzhou, 310027, China

† MS2Discovery Interdisciplinary Research Institute
Wilfrid Laurier University, Waterloo, ON N2L 3L5, Canada
email: rmelnik@wlu.ca

Key words: Vibration Energy Harvesting, Material Influence, Phenomenological Thermodynamic Analysis, Phase Field Model.

Abstract. Recently, a novel method for vibration energy harvesting has been proposed, which is based on stress-induced polarization switching. A huge improvement in the energy output associated with this new method has been theoretically demonstrated. In the current paper, the influence of different materials on the energy harvesting performance is studied. Firstly, a phenomenological thermodynamic analysis based on a Landau-type elastic Gibbs energy is carried out, which gives a guidance for further investigations. Then, the state-of-the-art phase field model is implemented to study the hysteretic nonlinear phenomena involved in the energy harvesting process. The influence of different materials is carefully compared and discussed. Furthermore, the combined effects of the bias electric potential and bias resistance in different materials are presented and discussed in the context of future real implementations.

1 INTRODUCTION

In the past two decades, vibration energy harvesting has emerged as a promising method to power wireless sensor networks and implantable biomedical devices, generating great interest from researchers around the world [1-3]. Generally, there are three principal ways to convert the ambient vibrational energy into useful electricity---through electromagnetic, electrostatic and piezoelectric effects [4-6]. However, the energy density harvested via these three traditional approaches is still not sufficient, especially for applications in low-frequency vibrational environments. Different methods have been proposed in the literature to improve the energy harvesting performance, including but not limited to designing different mechanical structures to lower the natural frequency of the systems to meet the frequency range of the vibration sources , introducing nonlinear effects into the energy harvesting structures to broaden the resonate frequency range, and employing materials with better properties, e.g., using single-crystal ferroelectric materials in piezoelectric vibration energy harvesting, which has a supreme piezoelectric coefficient over commonly-used ceramics[7-9].

In addition, several innovative physics-based methods have also been proposed, such as those based on triboelectric nanogenerators [10, 11].

Recently, a new method has been proposed, which is based on stress-induced polarization switching phenomena in ferroelectric materials [12, 13]. Different from the traditional piezoelectric vibration energy harvesting, which is confined to the linear piezoelectric region, a non-180° ferroelastic polarization switching is induced in this new method to seek more polarization variations. The huge polarization changes associated with stress-induced polarization switching process result in a great improvement of the energy output. The energy density, which is several orders of magnitude higher than its counterpart harvested by traditional linear piezoelectric effect, has been theoretically demonstrated. In Ref. [13], by introducing a bias electric field, the robustness deficiency problem associated with the original prototype has been successfully tackled. Due to its great potential in real applications and the complicated nonlinear hysteretic phenomena involved, this new method requires a more detailed analysis.

In the current paper, the influence of different materials on the energy harvesting performance is under investigation. The differences between single crystal $BaTiO_3$ and $PbTiO_3$ ferroelectrics are carefully studied and discussed. Firstly, a phenomenological thermodynamic analysis based on a Landau-type elastic Gibbs energy is carried out, which gives a basic understanding of the differences between these two single crystals and their effects on the energy harvesting performance. Secondly, the energy harvesting process is studied via the state-of-the-art phase field model. The phase field simulations confirm the predictions from the thermodynamic analysis. Furthermore, the combined effects of the bias resistance and bias electric potential on the energy harvesting performance in these two cases are presented and discussed.

2 PHENOMENOLOGICAL THERMODYNAMIC ANALYSIS

To analyze the influence of different materials on the energy harvesting performance, $BaTiO_3$ and $PbTiO_3$ ferroelectric single crystals are considered. Firstly, a phenomenological thermodynamic analysis is carried out, which is based on a Landau-type elastic Gibbs energy that can be given as follows:

$$G(\boldsymbol{P},\boldsymbol{\sigma}) = a_1(P_1^2+P_2^2+P_3^2) + a_{11}(P_1^4+P_2^4+P_3^4) + a_{12}(P_1^2P_2^2+P_1^2P_3^2+P_2^2P_3^2) + a_{111}(P_1^6+P_2^6+P_3^6) + a_{112}[P_1^4(P_2^2+P_3^2)+P_2^4(P_1^2+P_3^2)+P_3^4(P_1^2+P_2^2)] + a_{123}P_1^2P_2^2P_3^2 - \tfrac{1}{2}s_{11}(\sigma_{11}^2+\sigma_{22}^2+\sigma_{33}^2) - s_{12}(\sigma_{11}\sigma_{22}+\sigma_{11}\sigma_{33}+\sigma_{22}\sigma_{33}) - \tfrac{1}{2}s_{44}(\sigma_{12}^2+\sigma_{13}^2+\sigma_{23}^2) - Q_{11}(\sigma_{11}P_1^2+\sigma_{22}P_2^2+\sigma_{33}P_3^2) - Q_{12}[\sigma_{11}(P_2^2+P_3^2)+\sigma_{22}(P_1^2+P_3^2)+\sigma_{33}(P_1^2+P_2^2)] - Q_{44}(\sigma_{12}P_1P_2+\sigma_{13}P_1P_3+\sigma_{23}P_2P_3). \quad (1)$$

The associated material parameters, taken from Ref. [14] (for temperature 25℃), are listed in Table 1. The contour plots of the two-dimensional free energy without external stress are presented in Figure 1. The spontaneous polarizations of the materials can be deduced by minimizing the elastic Gibbs energy with zero stress. The corresponding values for $BaTiO_3$ and $PbTiO_3$ are $0.27C/m^2$ and $0.757C/m^2$, respectively. Therefore, it is reasonable to expect that the output electric current of $PbTiO_3$ is approximately 3 times larger than that of $BaTiO_3$, as long as complete stress-induced polarization switching is induced at the same rate in both materials ($I = \frac{dQ}{dt}$, $Q \propto P$). With the same external resistance, the energy output will be about

9 times larger ($W = I^2Rt$). On the other side, the critical input stress, which is required to complete a ferroelastic polarization switching, is also very important in real applications. To give an approximation, a strategy based on the energy barrier theory is adopted:

$$\sigma_c = G_{barrier}/\varepsilon^0_{diff}, \quad (2)$$

where $G_{barrier}$ is the energy barrier between states before and after the stress-induced polarization switching process. It can be approximated by the energy difference between the saddle point and the minimum point (as shown in Figure 1); ε^0_{diff} is the associated spontaneous strain change during the polarization switching process, which equals to the longitudinal spontaneous strain ε^0_{11} minus the transvers spontaneous strain ε^0_{22}.

With simple calculations, the critical values required to induce polarization switching for $BaTiO_3$ and $PbTiO_3$ are 35.4MPa and 625.6 MPa respectively, which means, approximately, a 20 times larger stress is required for $PbTiO_3$. In addition to the critical stress, several other important material-specific results are also provided, as listed in Table 2. It is noticed that the energy barrier for $PbTiO_3$ is more than 100 times larger than that for $BaTiO_3$, which can be used to estimate the inherent energy dissipation during the polarization switching process. Considering the fact that the energy output is only about 9 times larger, the energy efficiency of $PbTiO_3$ suffers. In conclusion, $PbTiO_3$ can give a larger energy output but requires a significantly larger critical stress. The choice of the material depends on application condition. For example, when a strong enough stress can be assessed and the energy density is the prime target, $PbTiO_3$ is always the first choice. It needs to be pointed out that the exact value obtained here is served only as an estimation. No bias electric field is taken into consideration, and the influence of domain walls or material defects are not considered either. Furthermore, the polarization switching phenomenon involved in this method is intrinsically nonlinear and hysteretic. Instead of a simple homogeneous switching, very complicated stress and electric field states can be present. Thus a more robust and detailed investigation is needed.

Table 1: Material parameters for the elastic Gibbs energy

Material parameters	a_1	a_{11}	a_{12}	a_{111}	a_{112}	a_{123}
$BaTiO_3$	-2.8e7	-5.4e8	4.9e8	6.6e9	2.9e9	3.7e10
$PbTiO_3$	-1.7e8	-7.3e7	7.5e8	2.6e8	6.1e8	-3.7e9
Material parameters	Q_{11}	Q_{12}	Q_{44}	s_{11}	s_{12}	s_{44}
$BaTiO_3$	0.11	-0.043	0.059	8.3e-12	-2.7e-12	9.24e-12
$PbTiO_3$	0.089	-0.026	0.0675	8e-12	-2.5e-12	9e-12

Table 2: Some important material-specific calculated results

	Spontaneous polarization $\boldsymbol{P_0}$	Spontaneous strain (longitudinal) $\boldsymbol{\varepsilon_{11}^0}$	Spontaneous strain (transverse) $\boldsymbol{\varepsilon_{22}^0}$	Spontaneous strain change $\boldsymbol{\varepsilon_{diff}^0}$
$BaTiO_3$	0.27	0.0074	-0.0029	0.0103
$PbTiO_3$	0.757	0.051	-0.015	0.066
	Energy barrier I $\boldsymbol{G_{barrier}}$	Critical stress $\boldsymbol{\sigma_c}$	Energy barrier II $\boldsymbol{G'_{barrier}}$*	Critical electric field $\boldsymbol{E_c}$**
$BaTiO_3$	3.65e5	3.54e7	2.36e6	4.53e6
$PbTiO_3$	4.12e7	6.256e8	7.39e7	4.88e7

*Energy barrier II is the energy barrier involved in 180° ferroelectric polarization switching, which can be approximated by the energy difference between the local maximum and minimum points.
**Critical electric field is an important constant in capturing 180° ferroelectric polarization switching phenomenon, which can be approximated by using the energy barrier II through the relation: $E_c = G'_{barrier}/(2 \cdot P_0)$

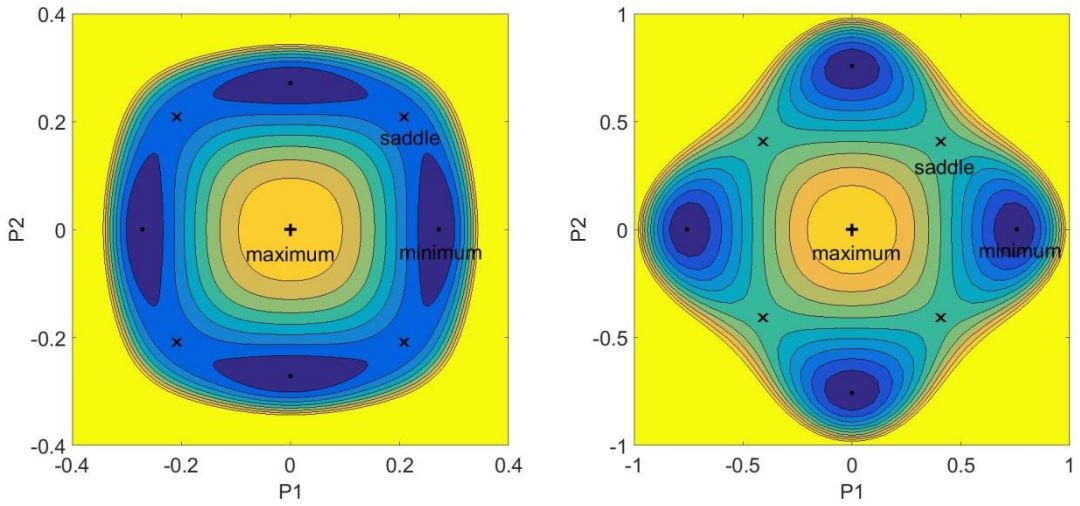

Figure 1: Contour plots of the two-dimensional free energy without external stress: (a) for $BaTiO_3$; (b) for $PbTiO_3$.

3 PHASE FIELD STUDY AND DISCUSSION

To further analyze the influence of materials, the state-of-the-art phase field model is implemented to study the energy harvesting process. The governing equation can be obtained as the gradient flow associated with the potential energy based on the Landau theory:

$$\mu \dot{P}_i = \left(\frac{\partial \Psi}{\partial P_{i,j}}\right)_{,j} - \frac{\partial \Psi}{\partial P_i} - \varphi_{,i}. \tag{3}$$

Here, $1/\mu > 0$ is the mobility; φ denotes the electric potential and Ψ is the potential energy in the following form:

$$\Psi(\boldsymbol{\nabla P}, \boldsymbol{P}, \boldsymbol{\varepsilon}) = \alpha_0\left(P_{1,1}^2 + P_{1,2}^2 + P_{1,3}^2 + P_{2,1}^2 + P_{2,2}^2 + P_{2,3}^2 + P_{3,1}^2 + P_{3,2}^2 + P_{3,3}^2\right) + \tilde{G}(\boldsymbol{P}, \boldsymbol{\varepsilon}), \tag{4}$$

where

$$\tilde{G}(\boldsymbol{P},\boldsymbol{\varepsilon}) = \alpha_1(P_1^2+P_2^2+P_3^2)+\alpha_{11}(P_1^4+P_2^4+P_3^4)+\alpha_{12}(P_1^2P_2^2+P_1^2P_3^2+P_2^2P_3^2)+ \alpha_{111}(P_1^6+P_2^6+P_3^6)+\alpha_{112}[P_1^4(P_2^2+P_3^2)+P_2^4(P_1^2+P_3^2)+P_3^4(P_1^2+P_2^2)]+ \alpha_{123}P_1^2P_2^2P_3^2+\tfrac{1}{2}C_{11}(\varepsilon_{11}^2+\varepsilon_{22}^2+\varepsilon_{33}^2)+C_{12}(\varepsilon_{11}\varepsilon_{22}+\varepsilon_{11}\varepsilon_{33}+\varepsilon_{22}\varepsilon_{33})+2C_{44}(\varepsilon_{12}^2+\varepsilon_{13}^2+ \varepsilon_{23}^2)-q_{11}(\varepsilon_{11}P_1^2+\varepsilon_{22}P_2^2+\varepsilon_{33}P_3^2)-q_{12}[\varepsilon_{11}(P_2^2+P_3^2)+\varepsilon_{22}(P_1^2+P_3^2)+\varepsilon_{33}(P_1^2+P_2^2)]- 2q_{44}(\varepsilon_{12}P_1P_2+\varepsilon_{13}P_1P_3+\varepsilon_{23}P_2P_3). \quad (5)$$

The expression for $\tilde{G}(\boldsymbol{P},\boldsymbol{\varepsilon})$ is derived following the Legendre transformation of the elastic Gibbs energy $G(\boldsymbol{P},\boldsymbol{\sigma})$. It needs to be pointed out that in the literature some misconceptions exist about the coefficients in the free energy. In Ref. [15, 16], the authors stated that the Landau coefficients were taken directly from Ref. [14]. However, it is noticed that the coefficients in Ref. [14] are for the elastic Gibbs free energy, rather than for the free energy used in the phase field model. Thus, a Legendre transformation is necessary. That is why the simulated normalized spontaneous polarization shown in Ref. [15] is around 1.5. The material parameters after the Legendre transformation are listed in Table 3. The gradient energy coefficient α_0, taken in the current simulations for $BaTiO_3$ and $PbTiO_3$, is 2.8×10^{-10} Vm^3/C and 1×10^{-10} Vm^3/C respectively. The corresponding characteristic length scales ($l_0 = \sqrt{\alpha_0 P_0^2/E_{Barrier}}$, which can be used as an approximation for the domain wall thickness) are 4.3nm and 2.0nm. In the simulation, the governing equation (3) is solved together with the elasticity and Maxwell equations. For simplicity, the simulations have been carried out for a two dimensional case. The computational domain is 160nm×20nm for both cases. The boundary conditions taken in the current simulations are the same as those used in Ref. [13]. The resulting model has been numerically implemented and solved in Comsol Multiphysics [17].

Firstly, simulations without external bias electric potential and resistance have been carried out to determine the critical stress value that is required to complete the stress-induced polarization switching process. The results for $BaTiO_3$ and $PbTiO_3$ are 32Mpa and 514Mpa respectively, which are consistent with the predictions from the energy barrier theory, as listed in Table 2. Further, some additional simulations have been carried out to determine the critical bias electric potential values for 180° ferroelectric switching. The results are 0.029V and 0.21V, respectively, for $BaTiO_3$ and $PbTiO_3$. The corresponding electric field values are 1.45MV/m and 10.5MV/m, which are approximately one fourth of the predicted values listed in Table 2.

Next, a series of simulations with different bias electric fields and different bias resistances have been carried out to investigate their combined effects. The external stress amplitudes for $BaTiO_3$ and $PbTiO_3$ in the simulations are 48Mpa and 740Mpa respectively, which are 1.25 times of the critical values for ferroelastic switching. The bias electric potential values are around one half of the critical values for 180° ferroelectric switching. To present combined effects, the bias resistance range has been determined based on numerical experiments.

The simulated results are shown in Figure 2 and Figure 3. With a constant bias electric potential, the energy output increases first, reaches its peak and then decreases, as the bias resistance increases. This behavior is observed in both cases. Further, we note that the energy peak will be improved when the bias electric potential increases, so will the associated bias resistance values. However, it does not mean that we can increase the bias electric potential without limit to improve the energy output. The material will break down with extreme electric fields and excessive stress. The peak energy output in the current simulations for

$PbTiO_3$ is approximately 100 times bigger than that for $BaTiO_3$, which is different from the thermodynamic prediction. This can be explained by the fact that the optimized bias resistance values are used here. Instead, in the above thermodynamic analysis, the same resistance value is assumed. It needs to be pointed out the unit for the bias resistance in the results is the parameter μ instead of a real value. Moreover, for different materials, the parameter μ will be different. Indeed, the parameter μ is related to the relaxation phenomena and frequency-dependent properties in ferroelectric materials. We will address this issue in a separate publication. In addition, it is also noticed that, there is no big difference between the energy efficiency for both materials, which is around 30%. As pointed out, the internal energy dissipation is about 100 times bigger for $PbTiO_3$. With a similar relationship in the energy output, it is reasonable to produce similar energy efficiency.

4 CONCLUSIONSS

In the current paper, the influence of different materials on the energy harvesting performance of a new method based on stress-induced polarization switching, has been carefully investigated. Firstly, a phenomenological thermodynamic analysis has been carried out, which has provided a primary guidance for further investigations. Then, the state-of-the-art phase field model has been implemented to analyze the energy harvesting processes and the involved hysteretic nonlinear phenomena. Finally, the combined effects of bias electric potential and bias resistance in both materials have been demonstrated and discussed in detail in the context of potential applications.

ACKNOWLEDGEMENTS

This work has been supported by the National Natural Science Foundation of China (Grant No. 51575478 and Grant No. 61571007). DW acknowledges the financial support from Zhejiang University for his visit to Wilfrid Laurier University. RM acknowledges the support from the NSERC and CRC program.

Table 3: Updated parameters for the phase field model

Updated parameters	α_1	α_{11}	α_{12}	α_{111}	α_{112}	α_{123}
$BaTiO_3$	-2.8e7	1.9e8	1.5e7	6.6e9	2.9e9	3.7e10
$PbTiO_3$	-1.7e8	4.2e8	7.3e8	2.6e8	6.1e8	-3.7e9
Updated parameters	q_{11}	q_{12}	q_{44}	c_{11}	c_{12}	c_{44}
$BaTiO_3$	1.3e10	--9.7e8	3.2e9	1.3e11	4.4e10	2.7e10
$PbTiO_3$	1.1e10	2.5e8	3.8e9	1.4e11	4.3e10	2.8e10

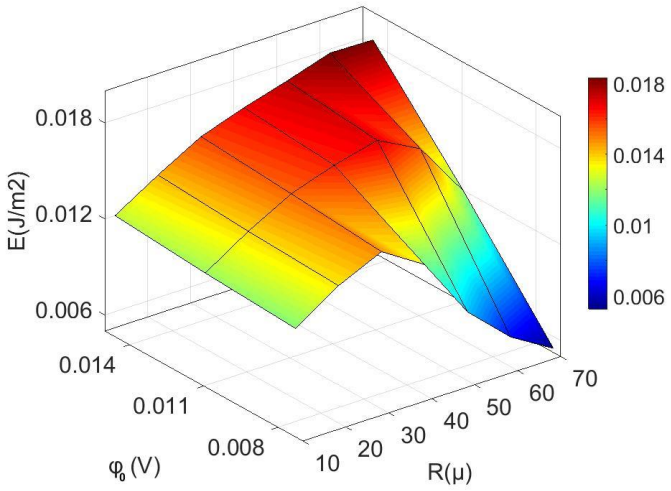

Figure 2: Energy output with respect to bias electric potential and bias resistance for $BaTiO_3$.

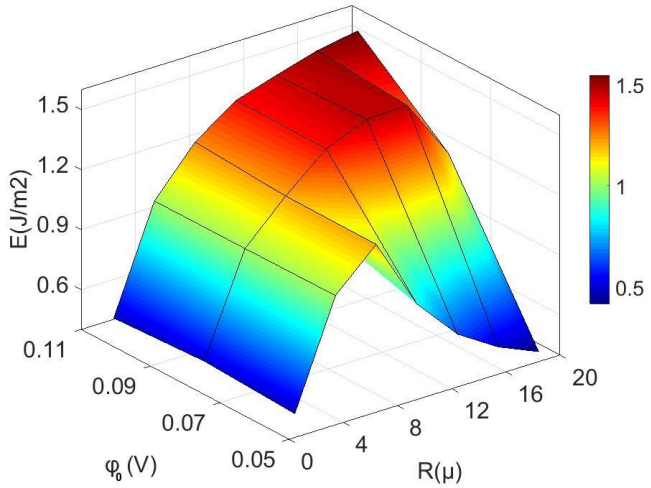

Figure 3: Energy output with respect to bias electric potential and bias resistance for $PbTiO_3$.

REFERENCES

[1] Shaikh, F. K., & Zeadally, S. (2016). Energy harvesting in wireless sensor networks: A comprehensive review. Renewable and Sustainable Energy Reviews, 55, 1041-1054.

[2] Babayo, A. A., Anisi, M. H., & Ali, I. (2017). A Review on energy management schemes in energy harvesting wireless sensor networks. Renewable and Sustainable Energy Reviews, 76, 1176-1184.

[3] Amin Karami, M., & Inman, D. J. (2012). Powering pacemakers from heartbeat vibrations using linear and nonlinear energy harvesters. Applied Physics Letters, 100(4), 042901.

[4] Roundy, S., Wright, P. K., & Rabaey, J. (2003). A study of low level vibrations as a power source for wireless sensor nodes. Computer communications, 26(11), 1131-1144.

[5] Invernizzi, F., Dulio, S., Patrini, M., Guizzetti, G., & Mustarelli, P. (2016). Energy

harvesting from human motion: materials and techniques. Chemical Society Reviews, 45(20), 5455-5473.
[6] Wang, W., Cao, J., Zhang, N., Lin, J., & Liao, W. H. (2017). Magnetic-spring based energy harvesting from human motions: Design, modeling and experiments. Energy Conversion and Management, 132, 189-197.
[7] Li, H., Tian, C., & Deng, Z. D. (2014). Energy harvesting from low frequency applications using piezoelectric materials. Applied Physics Reviews, 1(4), 041301.
[8] Yang, Z., & Zu, J. (2016). Toward harvesting vibration energy from multiple directions by a nonlinear compressive-mode piezoelectric transducer. IEEE/ASME Transactions on Mechatronics, 21(3), 1787-1791.
[9] Yang, Z., & Zu, J. (2016). Comparison of PZN-PT, PMN-PT single crystals and PZT ceramic for vibration energy harvesting. Energy Conversion and Management, 122, 321-329.
[10] Fan, F. R., Tian, Z. Q., & Wang, Z. L. (2012). Flexible triboelectric generator. Nano Energy, 1(2), 328-334.
[11] Niu, S., & Wang, Z. L. (2015). Theoretical systems of triboelectric nanogenerators. Nano Energy, 14, 161-192.
[12] Balakrishna, A. R., & Huber, J. E. (2016). Nanoscale domain patterns and a concept for an energy harvester. Smart Materials and Structures, 25(10), 104001.
[13] Wang, D., Wang, L., & Melnik, R. N. Vibration energy harvesting based on stress-induced polarization switching: a phase field approach, submitted, 2017.
[14] Pertsev, N. A., Zembilgotov, A. G., & Tagantsev, A. K. (1998). Effect of mechanical boundary conditions on phase diagrams of epitaxial ferroelectric thin films. Physical review letters, 80(9), 1988.
[15] Wang, J., & Kamlah, M. (2009). Three-dimensional finite element modeling of polarization switching in a ferroelectric single domain with an impermeable notch. Smart Materials and Structures, 18(10), 104008.
[16] Van Lich, L., Shimada, T., Nagano, K., Hongjun, Y., Wang, J., Huang, K., & Kitamura, T. (2015). Anomalous toughening in nanoscale ferroelectrics with polarization vortices. Acta Materialia, 88, 147-155.3341.
[17] Comsol multiphysics finite element analysis software. http://www.comsol.com.

VIII ECCOMAS Thematic Conference on Smart Structures and Materials
SMART 2017
A. Güemes, A. Benjeddou , J. Rodellar and Jinsong Leng (Eds)

PRELIMINARY INVESTIGATION OF THE ENERGY HARVESTING SYSTEM INTENDED FOR USE ON AN ORC MICROTURBINE

TOMASZ Z. KACZMARCZYK*[1], GRZEGORZ ŻYWICA[1], EUGENIUSZ IHNATOWICZ[1], MICHAŁ LUBIENIECKI[2] AND JAKUB ROEMER[2]

[1] Department of Turbine Dynamics and Diagnostics
Institute of Fluid Flow Machinery, Polish Academy of Sciences
Fiszera 14, 80-231 Gdańsk, Poland
Email: * tkaczmarczyk@imp.gda.pl, gzywica@imp.gda.pl, gieihn@imp.gda.pl,
web page: http://www.imp.gda.pl/en/

[2] Department of Robotics and Mechatronics, AGH University of Science and Technology,
Mickiewicza 30, 30-059 Kraków, Poland
Email: lubienie@agh.edu.pl, jroemer@agh.edu.pl

Key words: microturbine, organic Rankine cycle, energy harvesting, TEG.

Abstract. The article presents the preliminary results of the experimental research carried out on a cascade energy harvesting system that utilizes low-temperature (below 200 °C) waste heat. The system consists of thermoelectric generators (TEGs) mounted on the casing of a radial microturbine operating in the organic Rankine cycle (ORC) with a low-boiling working medium (HFE7100). Waste heat is passed to the evaporator in the ORC system where it heats up the working medium until it is vaporous. The generated vapour is used to drive the microturbine. The radial microturbine has the electric power of about 3 kW_e at a rated speed of 24000 rpm. The working fluid vapour (operating in the closed cycle) after expansion travels to the regenerator, then flows into the condenser and into the evaporator again. It has been shown that a suitably configured thermoelectric system generates electricity by taking in waste heat from the microturbine casing. The thermoelectric system consisted of Peltier modules connected in series, water cooling blocks and an aluminium block acting as a heat spreader and providing flat mounting surfaces for the modules. The idea of designing and constructing a thermoelectric system resulted from the need of a power supply for a self-sufficient remote control system. The microturbine wheel is connected to the shaft of a synchronous 3-phase generator. The generator's stator is situated in the casing. The generator operates effectively up to the temperature of 120 °C and the working medium temperature is approximately 170 °C at the microturbine inlet. This explains why the generator has to be externally cooled. The water jacket cooling system was mounted on the microturbine casing. The cooling system draws heat away from the inside of the generator and it can be partially recovered using a thermoelectric system that enables conversion of thermal energy into electrical energy. In this way, we were able to improve the thermal efficiency of the cycle by limiting heat losses. Electrical energy produced by a thermoelectric system can be used to power the sensors or other subassemblies of the control and measurement system, improving efficiency and operational safety of the entire ORC system.

1 INTRODUCTION

The past few years have witnessed an increased interest in developing new technologies based on renewable energy sources, in particular thermoelectric (TE) materials that enable a direct conversion of the thermal energy into the electrical energy and can be employed as alternative energy sources [1]. TE technology is applied for generation of electrical energy (TEGs – thermoelectric generators) using waste heat, e.g. from machinery and is used in submarines, satellites, medical transportation (for cooling purposes), smartphones and heart pacemakers [2,3]. TE systems are applied in energy efficient buildings, e.g. in Active Building Envelope (ABE) systems that convert the solar energy into the electrical energy to power heat pumps. Peltier modules are applied in both heating and cooling systems in a single installation. Such modules are characterised by a long-lasting (approx. 30 years) life cycle with a high reliability, low maintenance costs and a carbon-free operation. Peltier modules have the following disadvantages: a relatively narrow range of the temperature for effective operation, a low productivity and a high price [2]. TE modules are applied in energy harvesting (EH) systems used in micro-/nanosystems (MNSs), which are popular on the wireless sensor networks (WSNs) market. Micro-/Nano-devices are characterised by lower electrical/thermal time constants, a better sensitivity, a faster response time and higher energy density than their larger counterparts. The projections show that the electric efficiency of a solar cell based on an array of InP nanopillars will be approximately 8.1% and another based on an array of Si NWs will be around 17.4%. Nanoparticles are used to produce nanofluids, which improve heat transfer conditions [4,5] and can increase the overall thermal efficiency of systems that are equipped with heat recovery systems. Solar thermoelectric generators (STEGs) based on bulk nanostructured Bi_2Te_3 alloys have the efficiency in the conversion of the solar/thermal energy into the electrical energy of around 4.6% [6]. Piezoelectric systems AC NGs enable to generate a voltage of 50 mV at the deformation within the range of 0.05% – 0.1% with the efficiency of energy conversion of about 6.8%. The hybrid cell (HC) was created by the integration of a DSSC (dye-sensitized solar cell) and a piezoelectric NG using a serial connection, which causes the efficiency increase by approximately 13%. However, the systems based on photovoltaics, thermoelements and piezoelectrics are characterised by the following power density ranges: 10-100 mW/m^2, 10-100 $\mu W/m^2$ and 1-10 m/Wm^2, respectively. Triboelectric nanogenerators (TENGs) have output voltages of around 18 V and current densities of approximately 0.13 $\mu A/m^2$ [6]. Such generators are used for constructing energy harvesting (EH) systems intended for use in wireless electronic devices [7] and they utilise energy from human and machine motion [8,9]. For instance, the electromagnetic generators at the frequencies within the range from 50 Hz to 4.4 kHz produce the electric power within the range from 0.33 μW_e to 7.4 W_e, as the result of vibrations of the generator parts of the mass within the range from 2.4 mg to 38 kg [10-13]. The electrostatic generators, at the frequencies within the range from 4.67 Hz to 743 Hz, can produce the power within the range from 5 nW_e to 58 μW_e [10,14-16]. In the case of piezoelectric generators, the electric power outputs are within the range from 1.5 μW_e to 5 mW_e, and such generators use energy from the vibrations of their elements or from wind. Generators that utilise the vibrations of machinery may be applied, for instance, to CHP systems with scroll expanders, the RMS vibration velocity of which is within the range of 3.4 ÷ 6.4 mm/s [17] and may be used to produce electrical energy and power sensors. The literature gives a lot of examples of the

usage of TE systems for the production of electrical energy. For example, Jamal et al. [18] presented a system for the production of electrical energy using waste heat from a commercial gas stove. The system consisted of an aluminium ring on which 400 thermocouples of the K-type were mounted and their outputs were connected to an adder IC LM324-N. Two types of the load were tested on the TE system. The first one comprised six LED bulbs with a total power of 3 W_e. And the second load was a 6 V battery of 300 mAh rating. The output terminal of the TE system was used to charge this battery, with a charging current of 30 mA. The investigation shows that the maximal voltage generated by a single thermocouple was 20 mV, and the whole set of thermocouples provided around 8 V of voltage. Yang et al. [19] presented a TREC (thermally regenerative electrochemical cycle) system consisting of a $Fe(CN)_6^{3-/4-}$ redox pair and solid Prussian blue particles as active materials for the two electrodes. The system can achieve the heat-to-electricity conversion efficiency of around 2.0% (i.e. the thermoelectric figure of merit is approximately 0.9) for its operational temperature range of 20 °C – 60 °C. For the same temperature range and at the heat recovery of 50%, the heat-to-electricity conversion efficiency is approx. 1.2%. The authors of the article found that the maximal voltage generated by the TREC system was about 55 mV.

Martin-Gómez et al. [2] presented the prototypical cooling unit with Peltier modules, which has the potential to be applied to air-conditioning systems in residential buildings and computer server rooms. The TE HVAC (thermoelectric, heating, ventilation and air-conditioning) system removes the heat from its surroundings, and by means of Peltier modules, converts it into electricity that is used to power the fans of the air conditioner. The system comprise 84 Peltier modules of the type RC12-8, with a maximal power of 78 W_e. The system consists of 21 sets, with 4 modules connected in series in each set. At the thermal power of 3 kW_t and the supply voltage of 50 V, the temperature of the hot side was 50 °C. The radiators and the heat pipe technology were used for cooling purposes. The investigation shows that in a room with dimensions of 4m x 2.4m x 2.6m, the coefficient of performance (COP) of the system was approximately 0.6. Maharaj and Govender [1] presented a system for the production of electricity from heat, which they used to power low voltage receivers such as cell phone battery chargers, LED lighting and small devices that are powered from the USB port. The system was constructed using a module of the type TEG 127-50D, which was cooled by a heatsink and an axial-flow fan. At the temperature of the warm side of 165 °C and the temperature difference of 99.7 °C, the researchers obtained the maximal current of 3.07 A. However, at the temperature of the warm side of 202.6 °C and the temperature difference of 119.3 °C, they obtained the maximal voltage of 3.45 V. After the replacement of the blower fan with the extractor in the cooling system, the maximal voltage of 2.69 V was obtained at the temperature of the warm and the cold side of respectively 202.1 °C and 89.1 °C. The maximal current of 2.981 A was obtained at the temperature of the warm and the cold side of 207.1 °C and 90.8 °C, respectively. In the cooling system with the heatsink and the blower fan the maximal average temperature difference between the warm and cold sides of the device was approximately 92 °C, and after the replacement of the blower fan with the extractor this difference was 80 °C. Kamelia et al. [20] presented the results of the investigation on a system for the recovery of heat generated from a motorcycle (exhaust gas) and the production of electrical energy. The system comprised a Peltier module of the type TEC1-12706, a voltage regulator of the type LM2952 and a battery of the type MF 12 V (3.5Ah). After being tested for 60 minutes, the system generated the maximum voltage of 2.89 V at the maximum

temperature of the warm and cold sides of the module of respectively 579.8 °C and 18.9 °C. The maximum charging current of the battery was 0.22 A. The authors found that the system enables to charge the battery up to 12.8 V of voltage. In and Lee [21] constructed a system with a thermoelectric module of the type ZC-20 for the recovery of heat from the exhaust gas generated by Diesel engines and for the production of electrical energy. The module had the parameters: power 19 W_e, load voltage 2.38 V, current 8 A and efficiency 4.5%. For the cooling purposes of the module, the researchers applied a water system (CPT Inc., CDRC-8) with the nominal flow rate of 720 kg/h. They measured the power produced by the TEG by means of a charger of the type PLZ334W (manufactured by Kikush). The flow of air which heats the module, the temperatures and the voltage were measured using a system of the type cDAQ-9178 (produced by National Instruments). The combustion engine had the volume of 2.2 litres, the maximum power of 200 hp (at 3800 rpm) and the compression ratio of 16. The heat from the warm side of the module was transferred using a radiator. The exhaust gas temperature was within the range from 200 °C to 560 °C, and at the warm side of the module, the temperature was within the range from 130 °C to 450 °C. The module was tested at the value of the load/external resistance within the range from 0.25 Ω to 22 Ω. The researchers found that the maximum voltage measured at the module terminals was approximately 2.8 V. They observed that along with the increase in the load resistance, there was an increase in the generated voltage, and that was accompanied by a drop in the current and electric power produced by the module. The maximum produced current and power were respectively 5 A and 8.3 W_e. Nesarajah et al. [22,23] carried out the analysis of a cooling system for the EHS with TEGs heated by exhaust gas from a domestic oil boiler operating at the temperature within the range from 120 °C to 200 °C. Eight TEG modules (of the type 199-200-5 from Thermalforce) were applied to the system. Four modules were liquid cooled and the other ones were air cooled (using a fan), and in order to feed a single cooling component the powers of respectively 12.2 W_e and 2.04 W_e were needed. The researchers determined that the type of the cooling system and the way of its controlling have a significant impact on the electric power consumption of these systems. In the air-cooled system, the total produced power, with a controlled cooling rate, is approximately 34.1 W_e – and around 30.7 W_e without a control. However, using a liquid cooling, the maximal power was 34.7 W_e, regardless the system was controlled or not. Miller et al. [24] presented the results of the analysis of a system used for the recovery of heat from an exhaust gas, which consisted of an ORC system and a system with TEGs. The analysis was carried out using EES software. It resulted from the simulation that when the exhaust gas temperature at the outlet of the heat exchanger was remaining within the range of 480–600 °C, the power generated by the ORC system was stable at around 19.3 kW_e. However, the maximum electric power of approximately 3.6 kW_e, produced by the system with TEGs, was noted at the temperature of 540 °C. It was found that at the exhaust gas temperature of 400 °C at the inlet of the heat exchanger, 90% of the total production of electrical energy was produced by the ORC system, and the remaining 10% by the system with TEGs. However, along with the increase in the exhaust gas temperature, the share of the ORC system in the total energy production decreased and at the temperature of 800 °C was around 80%, and the share of the system with TEGs was 20%. It was determined that along the increase in the overheating degree of the R245fa working medium up to the temperature of 40 °C, the electric power produced by the ORC system increased from 19.3 kW_e to 27 kW_e, i.e. by approximately 40%. However, the electric power produced by the system with

TEGs decreased by approximately 27% (i.e. from 3.4 kW_e to 2.5 kW_e). Along with the increase in the pressure ratio (PR) from 4.0 to 5.75, the electric power produced by the ORC system increased from 21.0 kW_e to 22.8 kW_e, and with a further increase in the pressure ratio it started to decrease and dropped to 17.5 kW_e at the PR of 7.75. In the case of the system with TEGs, the electric power was stable at around 3.6 kW_e, irrespective of the value of the PR. It was found that along with the increase in the thermoelectric figure of merit (ZT) from 0.25 to 2.0, the power generated by the system with TEGs increased from 1.1 kW_e to 4.3 kW_e and the power of the ORC system was stable at around 19.3 kW_e.

The paper presents the preliminary results of the experimental research carried out on a cascade energy harvesting system that utilizes low-temperature (below 200 °C) waste heat. The system consists of thermoelectric generators (TEGs) mounted on the casing of a radial microturbine operating in the organic Rankine cycle (ORC) with a low-boiling working medium. Waste heat is passed to the evaporator in the ORC system where it heats up the working medium until it is vaporous. The generated vapour is used to drive the microturbine. The radial microturbine has the electric power of about 3 kW_e at a rated speed of 24000 rpm. The thermoelectric system consisted of Peltier modules connected in series, water cooling blocks and an aluminium block acting as a heat spreader and providing flat mounting surfaces for the modules. Electrical energy produced by a thermoelectric system can be used to power the sensors or other subassemblies of the control and measurement system, improving efficiency and operational safety of the entire ORC system.

2 TEST RIG

The ORC installation consists of three basic cycles: heating cycle, cooling cycle and working fluid cycle. The measurement scheme of the ORC system cooperating with a microturbine is shown in Fig. 1.

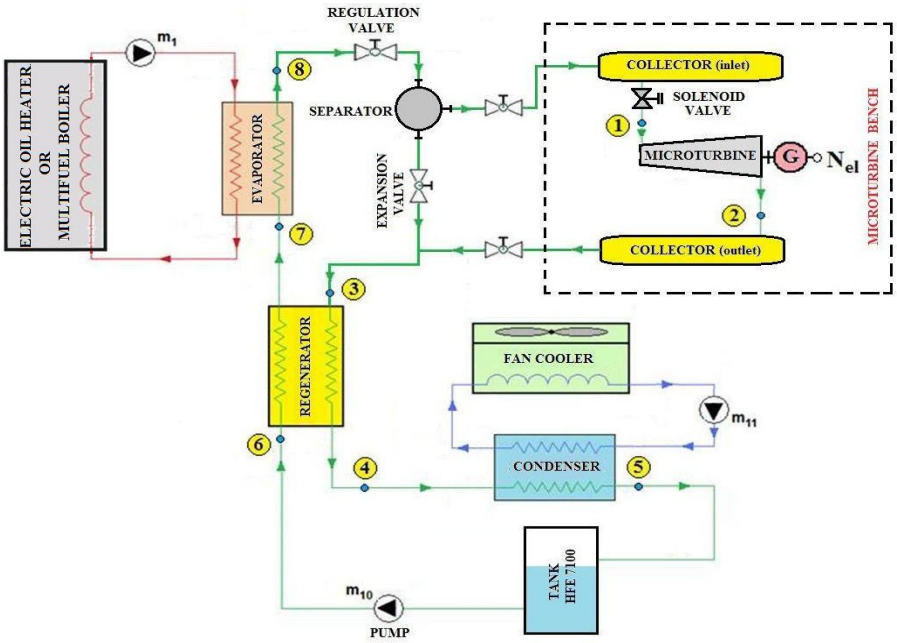

Figure 1: Scheme of the ORC with a radial microturbine

The test rig is equipped with a droplet separator that is used for the removal of liquid droplets from HFE7100 vapour streams, and its task is to protect the microturbine from erosion. The heating cycle comprises a set of oil pumps and two independent heat sources: a multi-fuel boiler and a set of two electric heaters—being capable of operating independently or in series/in parallel— that are used to heat the thermal oil as it flows through them. The structure of the multi-fuel boiler (with a thermal power of 30 kW_t) allows different types of fuel such as natural gas, syngas or biomass in the form of wood pellets. The electric heater consists of two modules, each of which has an electric power of 24 kW_e. The ORC installation can be run both with passive (e.g. expansion valves, throttle valves) and active expansion devices, i.e. the so-called expanders (e.g. turbines, scroll expanders, etc.). A fan cooler with a thermal power of 50 kW_t was used to dissipate heat energy. In the system, a 35% propylene glycol solution was employed as a cooling agent, which performs well even in winter conditions.

2.1 Radial-flow microturbine

The four-stage radial-flow microturbine is fed with the working medium (HFE7100) in the form of vapour. It was designed and constructed for the purposes of operating in the micro-CHP ORC power plant. At full load, rotating at the nominal rotational speed of 24000 rpm, the microturbine has an electric power of 2.5 kW_e. The turbine shaft is integrated with a high-speed electric energy generator and embedded in a hermetically sealed casing. The machine uses gas bearings that are lubricated by the HFE7100 vapour and no additional lubrication system is required. The nominal flow rate of the working medium is 0.17 kg/s, and the pressures at the microturbine inlet and outlet are 10 bar and 1.2 bar, respectively.

2.2 Thermoelectric system with Peltier modules

Six Peltier modules of the type TEC1-12710 (manufactured by Hebei I.T. Co., Ltd) [25] were employed for the construction of the thermoelectric (TE) system. They were connected to water cooling blocks, i.e. heat exchangers of the type WBA-1.62-0.55-CU-01 (produced by Custom Thermoelectric) [26]. The thermoelectric modules are connected in series. The scheme of the TE system with TEC modules and water cooling blocks is shown in Fig. 2.

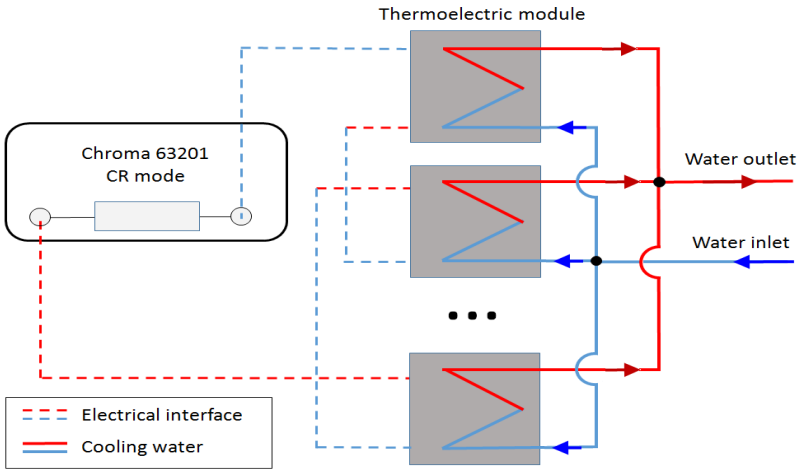

Figure 2: Wiring diagram of the thermoelectric system with TEC modules

Selected technical parameters of a Peltier module of the type TEC1-12710 are demonstrated in Table 1.

Table 1: Basic technical parameters of a Peltier module of the type TEC1-12710 [25]

Hot side temperature – $\mathbf{T_h}$ **[°C]**	25	50
Maximal power – $\mathbf{Q_{max}}$ **[W]**	85	96
Maximal temperature difference – $\mathbf{\Delta T_{max}}$ **[°C]**	66	75
Maximal current – $\mathbf{I_{max}}$ **[A]**	10.5	10.5
Maximal voltage – $\mathbf{U_{max}}$ **[V]**	15.2	17.4
Module resistance – **R [Ω]**	1.08	1.24

The cooling blocks were supplied with cold water from the municipal water supply and connected in parallel to ensure a uniform temperature at the cold sides of all Peltier modules. The temperature difference between the warm and the cold side of a module was regulated by changing the flow rate of cooling water. It was being done through the use of a ball valve installed at the water inlet to the cooling blocks. The warm sides of the modules absorb heat from the microturbine casing. The connection between the TE system and the microturbine was implemented by means of a specially designed block (adapter) made of aluminium alloy. The photo of the TE system mounted on the microturbine casing is shown in Fig. 3.

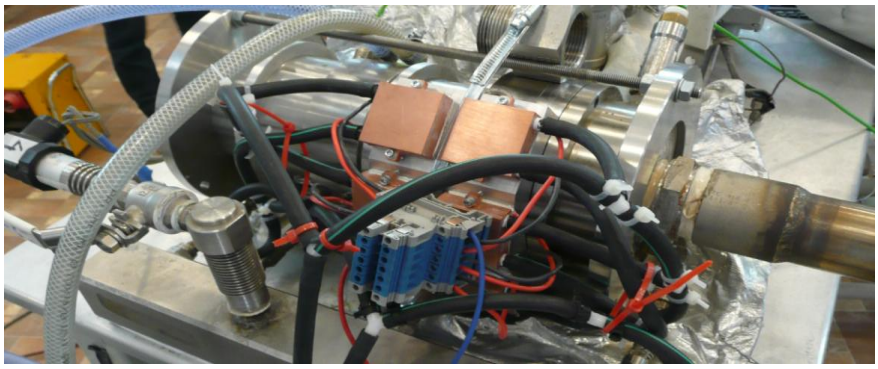

Figure 3: Photo of the thermoelectric system mounted on the microturbine casing

In order to ensure a proper contact between the adapter and the microturbine casing (at the warm side) and to decrease the thermal resistance, a heat conducting paste was applied. The heat conducting paste was also used at the cold side, in order to ensure that there is adequate contact between the surfaces of the Peltier module and the water cooling block.

The selection of the initial load resistance of the TE system was done, after the microturbine reached a steady state. This value was determined by searching for the maximal power within an assumed resistance range around the equivalent resisntace of the in series connection of the modules with known nominal ACR value given by the producer. The tested modules were chosen so that their ACR resistance and the characteristics number ZT match closely. The mesurement were taken with Z-Meter DX4090 (manufactured by RMT Ltd.). The Chroma 63201 device operating in the CR (constant resistance) mode was used as a load for the TE system. A compensation and a correction of the load resistance were carried out after each change in the operational conditions of the TE system applying the abobementioned

procedure. The changes in the operational conditions of the TE system were caused by the regulation of the flow rate of water flowing through the cooling system of the microturbine and the cooling blocks for Peltier modules, which resulted from the change in temperature of the working medium (HFE7100) that feeds the micro turbogenerator. Temperatures of the surfaces at the warm and the cold side were measured using a contact sensor of the type EMT-08 with a K-type thermocouple (from Czaki Thermo-Product) and a thermal imaging camera of the type T650sn (manufactured by FLIR) [27].

3 EXPERIMENTAL RESULTS

The idea of the construction of a thermoelectric system resulted from the need of cooling some components of the radial micro turbogenerator. The rotor of a three-phase synchro transmitter is mounted on the micro turbogenerator shaft and the stator is enclosed in the casing. The generator can operate up to a temperature of 120 °C, and the temperature of the working medium (HFE7100) at the microturbine inlet is approximately 170 °C (Fig. 4a). Therefore, the cooling system in the form of a water jacket was mounted on the microturbine casing. As a result of cooling the generator, heat is removed and it is partly recovered by the thermoelectric system and then the thermal energy is converted into electrical energy increasing the thermal efficiency of the ORC. The temperature of the working medium at the microturbine inlet has to be higher than 120 °C to ensure the adequate pressure of HFE7100 vapour and the operational safety of the fluid-flow machine. At the average HFE7100 temperature of approx. 170 °C, the average pressures of the working medium at the microturbine inlet and outlet of, respectively, approx. 650 kPa and 190 kPa (Fig. 4b) as well as the HFE7100 flow rate of approx. 0.13 kg/s (Fig. 5a), the microturbine reached the average electric power of approx. 900 W_e (Fig. 5b). The average flow rate of the glycol solution in the cooling system was approx. 0.175 kg/s (Fig. 5a).

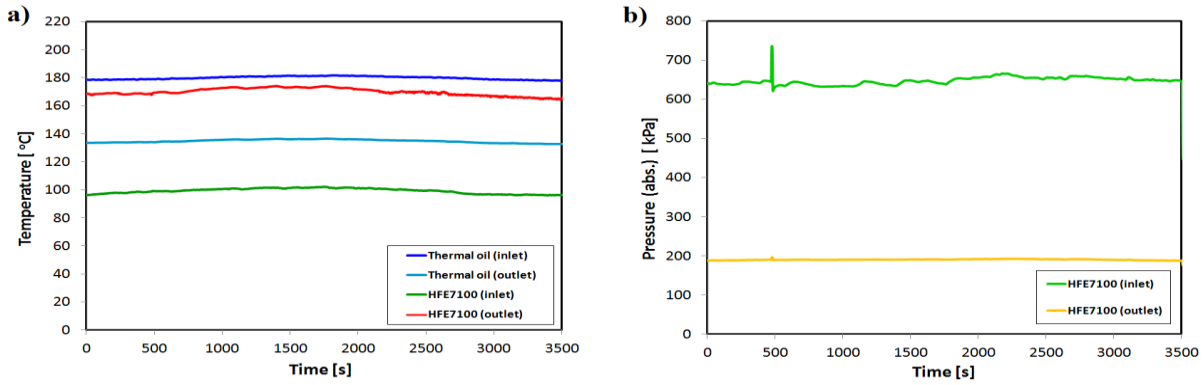

Figure 4: Graphs showing a) temperatures of the working mediums at the evaporator inlet and outlet vs. time, b) HFE7100 medium pressure at the microturbine inlet and outlet vs. time

It should be noted that the study presented herein does not show the maximal operational performance of the ORC. What the study shows is how additional electric energy can be produced by harvesting the thermal energy from the cooling system for the microturbine generator. It also examines the validity of using the thermoelectric system at a set power level. The additional energy can be used e.g. for supporting cooling system of high-speed bearings

or feeding some components of the automatic system, the control system or the measurement system (e.g. sensors).

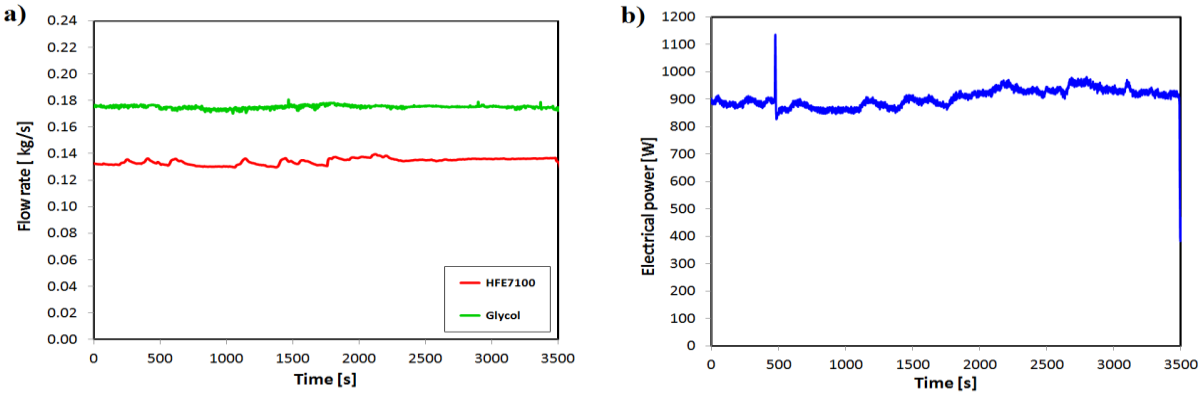

Figure 5: Graphs presenting a) flow rates of the working mediums vs. time, b) power produced by the microturbine vs. time

Within the framework of the research, the microturbine-on which the thermoelectric system with Peltier modules was mounted-was subjected to thermal imaging measurements and their exemplary results are demonstrated in Fig. 6 – 8.

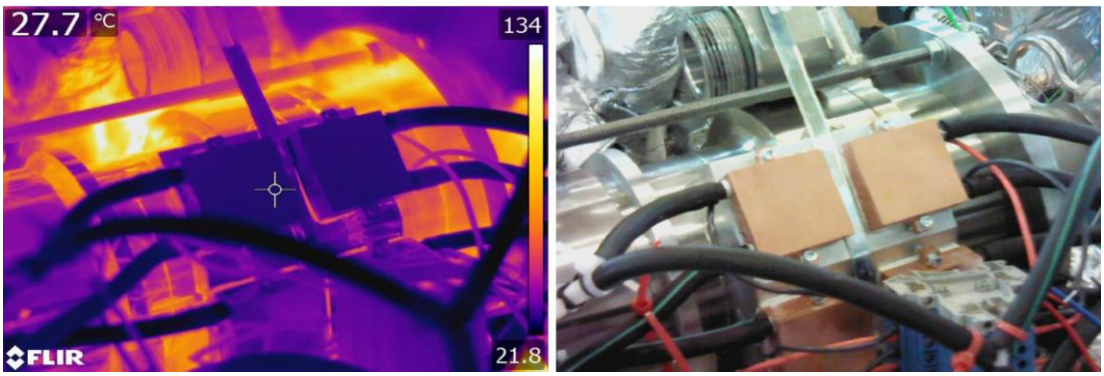

Figure 6: The thermal image and the photo (taken during tests) of the microturbine with the TE system

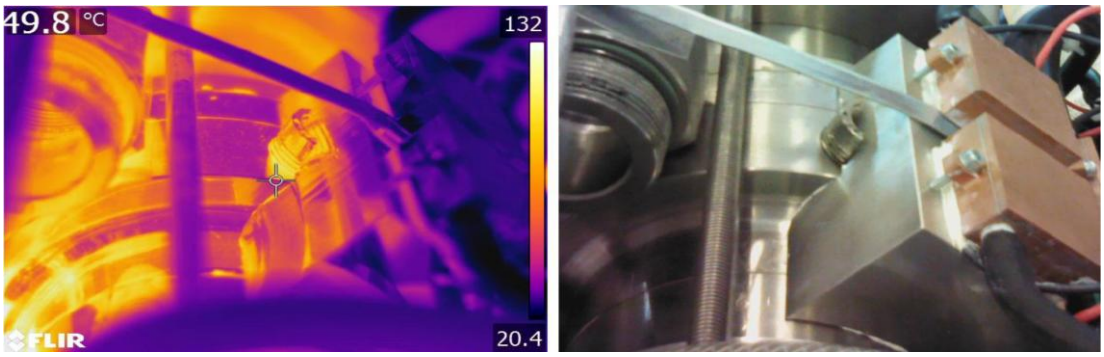

Figure 7: The thermal image and the photo (taken during tests) of the microturbine with the TE system

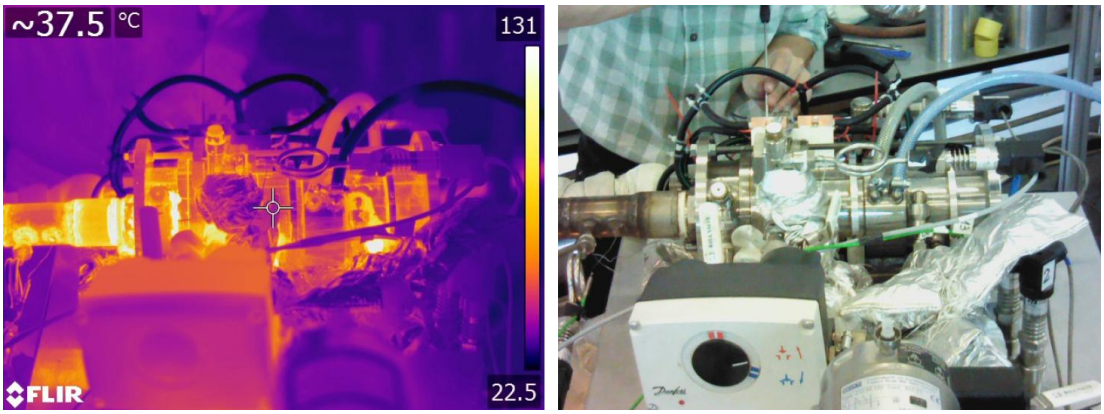

Figure 8: The thermal image and the photo (taken during tests) of the microturbine with the TE system

On the basis of the analysis of measurement results, it has been found that in the state of a steady load of the TE system and at the maximal flow rate of water flowing through the cooling blocks the electric power of this system was approximately 5 W_e. It should be noted that there was no measurement of the flow rate of water travelling through the cooling blocks. Moreover, the lowest electric power produced by the thermoelectric system was approx. 4.15 W_e and was obtained after the flow rate of water that cools the thermoelectric system was dramatically decreased. The voltage of a single loaded module was around 2.1 V, i.e. about half of the voltage value of the open circuit. As mentioned before, the Peltier modules (six pieces of the type TEC1-12710) were connected thermally in parallel. The average temperature of the surface of the water block was 20.5 °C - from the module side, and from the outside it was 17.5 °C. Furthermore, the mean temperature of the warm side of the module was approx. 65 °C. The temperature of the casing was approximately 100 °C on average, resulting in very large heat losses due to poor surface contact of the aluminium adapter (on which the modules were mounted) with the casing of the radial microturbine. It was observed that the highest impact on the obtained results is by the flow of the cooling water, but not by variable operational parameters of the microturbine. Therefore, the correlation of the power produced by the TEG modules and the operational state of the microturbine over time was not necessary. It was stated that the temperature difference between the warm and the cold side of the Peltier module is the deciding factor of the value of electric power generated at the module terminals.

4 CONCLUSION

Reassuming, it can be stated that, when the system was running in the steady state at the average flow rate of 0.134 kg/s and the average temperature of the working medium of 170 °C, the microturbine was generating about 900 W_e of electric power. However, at the mean temperatures at the warm and the cold side of the modules of respectively 65 °C and 20.5 °C, the maximal average power produced by the TE system was approximately 5 W_e. It should be noted that the Peltier modules were mounted on roughly 1/6 of the available surface of the microturbine casing, excluding the surface of the ports. Mounting the modules on all the available surface of the casing would allow to generate around 30 W_e of electric power (under the same operating conditions).The power obtained from the thermoelectric system

was below 1% of the average power generated by the microturbine. It should be noted that it was the first attempt to investigate the operation of a thermoelectric system. During the investigation, a lot of problems of a technical nature have been encountered, including the high contact resistance causing large heat losses, the lack of a proper thermal insulation of the thermoelectric system and also the lack of a suitable measurement system (lack of a measurement of the flow rate of the cooling water) which would enable to determine the operational characteristics of the thermoelectric system. Nevertheless, the application of a system that performs a direct conversion of the thermal energy into the electrical energy is an interesting topic to which more attention needs to be paid. Further attempts will be necessary in order to better adapt the system to its operating conditions, which in turn will make it possible to achieve a higher energy level.

REFERENCES

[1] Maharaj, S. and Govender, P. *Waste energy harvesting with a thermoelectric generator*. Energize, August (2013): 50-53.

[2] Martin-Gómez, C. Ibáñez-Puy, M. Bermejo-Busto, J. Fernández, J.A.S. Ramos, J.C. and Rivas, J. *Thermoelectric cooling heating unit prototype*. Building Services Engineering Research & Technology (2016), Vol. 37(4) 431–449, DOI: 10.1177/0143624415615533

[3] Nimbalkar, R.R. and Kshirsagar, S.S. *Thermoelectric Power Generation as an Alternative Green Technology of Energy Harvesting.* International Journal of Advanced Computer Research, Vol. 3, No.3 Issue-11, September-2013: 368-373.

[4] Cieslinski, J.T. and Kaczmarczyk, T.Z. *The effect of pressure on heat transfer during pool boiling of water-Al_2O_3 and water-Cu nanofluids on stainless steel smooth tube*. Chemical and Process Engineering - Inżynieria Chemiczna i Procesowa 2011, Vol. 32, Issue 4: 321-332, DOI: 10.2478/v10176-011-0026-2

[5] Cieslinski, J.T. and Kaczmarczyk, T.Z. *Pool Boiling of Water-Al_2O_3 and Water-Cu Nanofluids Outside Porous Coated Tubes*. Heat Transfer Engineering 2015, Vol. 36, Issue 6: 553-563, DOI: 10.1080/01457632.2014.939046

[6] Wang, Z.L. and Wu, W. *Nanotechnology-Enabled Energy Harvesting for Self-Powered Micro-/Nanosystems.* Angew. Chem. Int. Ed. 2012, 51: 2–24.

[7] Mitcheson, P.D. Yeatman, E.M. Rao, G.K. Holmes, A.S. and Green, T.C. *Energy Harvesting From Human and Machine Motion for Wireless Electronic Devices*. Proceedings of the IEEE 2008, Vol. 96, No. 9: 1457-1486.

[8] Rome, L.C. Flynn, L. Goldman, E.M. and Yoo, T.D. *Generating electricity while walking with loads.* Science 2005, vol. 309, p. 1725–1728.

[9] Roundy, S. Wright, P.K. and Rabaey, J.M. *Energy Scavenging for Wireless Sensor Networks*. 1st ed. Boston, MA: Kluwer Academic, 2003.

[10] Williams, C.B. and Yates, R.B. *Analysis of a micro-electric generator for microsystems.* Proc. 8th Int. Conf. Solid-State Sensors Actuators 1996, 52, p. 8-11.

[11] Shearwood, S. and Yates, R.B. *Development of an electromagnetic micro-generator*. Electron. Lett., vol. 33, p. 1883–1884, Oct. 1997.

[12] James, E.P. Tudor, M.J. Beeby, S.P. Harris, N.R. Glynne-Jones, P. Ross, J.N. and White, N.M. *An investigation of self-powered systems for condition monitoring applications*. Sensors Actuators A, Phys., vol. 110, p. 171–176, Feb. 2004.

[13] Torah, R.N. Beeby, S.P. O'Donnell, T.J.T. and Roy,, S. *Development of a cantilever beam generator employing vibration energy harvesting*. in Proc. 6th Int. Workshop Micro Nanotechnol. Power Generation Energy Conversion Applicat., Berkeley, CA, 2006, p. 181–184.

[14] Tashiro, R. Kabei, N. Katayama, K. Ishizuka, Y. Tsuboi, F. and Tsuchiya, K. *Development of an electrostatic generator that harnesses the motion of a living body*. JSME Int. J., ser. C, vol. 43, no. 4, pp. 916–922, 2000.

[15] Sterken, T. Fiorini, P. Baert, K. Puers, K. and Borghs, G. *An electret-based electrostatic μ-generator*. Proc. 12th Int. Conf. Solid State Sensors, Actuators Microsyst. (Transducers), Boston, MA, Jun. 2003, p. 1291–1294.

[16] Mizuno, M. and Chetwynd, D.G. *Investigation of a resonance microgenerator*. J. Micromech. Microeng., vol. 13, p. 209–216, 2003.

[17] Kaczmarczyk, T.Z. Żywica, G. and Ihnatowicz, E. *Vibroacoustic diagnostics of a radial microturbine and a scroll expander operating in the organic Rankine cycle installation*. Journal of Vibroengineering, Vol. 18, Issue 6, 2016, p. 4130-4147.

[18] Jamal, G.R.A. Masumuzzaman, A.N.M. Hossain, M.A. Kaysher, A.R. and Rashid, H. *Production of Low Scale Electric Power from Waste Heat of Conventional Kitchen Stoves*. American Journal of Renewable and Sustainable Energy 2015, Vol. 1, No. 2: 21-25.

[19] Yang, Y. Lee, S.W. Ghasemi, H. Loomis, J. Lia X. Kraemer, D. Zheng, G. Cui, Y. and Chen, G. *Charging-free electrochemical system for harvesting low-grade thermal energy*. Proceedings of the National Academy of Sciences of the United States of America (PNAS) 2014, December 2, Vol. 111, no. 48: 17011–17016.

[20] Kamelia, L. Faroqi, A. Muajianisan, A.A. *The Conversion of Waste Heat From Motorcycle Into Small Power Plant.* OIDA International Journal of Sustainable Development (2016), Vol. 09, No. 01: 79-84.

[21] In, B.D. and Lee, K.H. *A study of a thermoelectric generator applied to a diesel engine.* Proceedings of the Institution of Mechanical Engineers, Part D: Journal of Automobile Engineering 2016, Vol. 230(1): 133–143, DOI: 10.1177/0954407015576440

[22] Nesarajah, M. Felgner, F. and Frey, G. *Model-based System Assessment of Thermoelectric Energy Harvesting from the Exhaust Gas Pipe of Oil-fired Heatings*. Modern Machinery Science Journal, ISSN 1803-1269, p. 570-575, Mar. 2015.

[23] Nesarajah, M. Felgner, F. and Frey, G. *Modeling and simulation of a thermoelectric Energy Harvesting System for control design purposes*. Proceedings of the 16th International Conference on Mechatronics - Mechatronika 2014*,* Brno, 2014, p. 170-177. doi: 10.1109/MECHATRONIKA.2014.7018254

[24] Miller, E.W. Hendricks, T.J. Wang, H. and Peterson, R.B. *Integrated dual-cycle energy recovery using thermoelectric conversion and an organic Rankine bottoming cycle*. Proceedings of the institution of mechanical engineers, part A Journal of Power and Energy 2011, 225 (1), p. 33–43.

[25] http://www.hebeiltd.com.cn/peltier.datasheet/TEC1-12710.pdf

[26] http://www.customthermoelectric.com/Water_blocks.html

[27] http://www.flirmedia.com/MMC/THG/Brochures/RND_015/RND_015_US.pdf

VIII ECCOMAS Thematic Conference on Smart Structures and Materials
SMART 2017
A. Güemes, A. Benjeddou , J. Rodellar and Jinsong Leng (Eds)

VIBRATION ENERGY HARVESTING WITH ELECTROMAGNETIC AND PIEZOELECTRIC SEISMIC TRANSDUCERS: SIMULATION AND EXPERIMENTAL RESULTS

L. DAL BO*, P. GARDONIO

Università degli Studi di Udine, DPIA,
Via delle Scienze,208-33100 Udine, Italy
e-mail: dalbo.loris@spes.uniud.it

Key Words: energy harvesting, harmonic ambient vibrations, electromagnetic, piezoelectric, transducers

Abstract. This paper presents both simulation and experimental results on the principal characteristics of vibration energy harvesting with electromagnetic and piezoelectric seismic transducers. The electromagnetic seismic transducer is formed by coil-magnet components connected via soft springs. The piezoelectric seismic transducer is made by a thin cantilever beam with piezoelectric patches bonded on the top and bottom sides and a block mass fixed at the free end. The two transducers are design and built in such a way as they have the same weights of the base and suspended masses and the same fundamental natural frequency. A unified lumped parameter model based on the frequency response functions of the electro-mechanical transduction coefficients and mechanical and electrical impedances is derived and validated experimentally. A formulation is thus introduced for the energy harvested with the two transducers. The spectra of the power harvested per unit base vibration of the two harvesters are simulated and validated experimentally.

1 INTRODUCTION

In recent years, there has been a global trend towards the use of large amount of information collected from vehicles, machineries, buildings, the environment, etc., which has resulted into an exponential increment for the use of sensors that often require autonomous energy supply. As a result, there has been an intensive research activity on energy harvesting systems. Many technologies have been investigated, which cover a vast range of energy densities, dimensions and weights. Of particular interest are ambient vibration energy harvesting systems, which can be used in many applications and can provide enough energy to power low consumption sensors and wireless communication systems. In this respect, researchers have put a lot of effort into studying a variety of designs (inertial, strain, etc.) [1-14] and energy conversion mechanisms [15-18] for new vibration energy harvesters. For example, as shown in refs. [11,19,20] innovative vibration energy harvesting systems have been developed to collect energy from shocks produced by human motion, which can be worn by people in the form of clothes, footwear or watches and can be used to power portable electronic devices or medical aids. Also,

vibration energy harvesting applications have been developed to power condition monitoring sensors to be used in industrial machinery [11]. Finally, ambient vibration energy harvesting systems have been conceived, which, for example, extract energy from air and fluid flows [19,20,21]. According to literature, the most common methods to convert vibration energy into electrical energy use either electromagnetic [2, 14, 22-24] or piezoelectric [3,5,6,24,25] transducers. Most of current research has been focussed on tonal and broad-band energy harvesting using either strain or seismic transducers. Hoverer, recently, new harvesting systems exhibiting nonlinear properties have been investigated to amplify the stroke and the operation frequency band of the harvesting transducer [26-29].

This paper aims to validate experimentally the theoretical study presented in in ref. [30], which contrasted the constitutive equations and the energy harvesting properties of two seismic energy harvesting systems using either a coil-magnet proof mass transducer or a piezoelectric patch transducer bonded on a cantilever beam equipped with a tip mass. Therefore, this paper is characterised by two contributions. First, the validation with measured data of the constitutive mechanical, electrical and transduction functions that characterise the two seismic harvesters. Second, the experimental measurement of the energy harvested by the two seismic harvesters. The experimental measurements are taken on a coil-magnet proof mass and on a piezoelectric cantilever beam with tip mass prototype seismic harvesters, which have been designed in such a way as they have the same weighs of the case and moving masses and have the same fundamental resonance frequency. The measured results have been contrasted with simulation results obtained from the unified mathematical formulation developed for these two seismic transducers in ref. [30].

The paper is structured in 4 Sections. Section 2 briefly recalls the unified formulation used to model the electromagnetic and piezoelectric seismic harvesters considered in this study. In addition, it contrasts the simulated and measured frequency response functions (FRFs) that characterise the constitutive equations of the two seismic transducers. Section 3 introduces the energy formulation, which is then used to study the conditions to maximise the vibration energy absorption for tonal vibrations of the base structure and then presents simulated and measured spectra of the energy harvested per unit base vibration of the two seismic transducers. Finally, Section 4 summarises the main results of this study.

2 SEISMIC TRANSDUCERS

Figure 1 shows a) the pictures, b) the schematics and c) the lumped parameter models of I) the coil-magnet and II) the piezoelectric patch seismic transducers for vibration energy harvesting considered in this study. As shown by the drawing Ib, the electromagnetic seismic transducer is composed by a coil–magnet transducer, with the magnet mounted via soft spiral springs and the coil rigidly fixed to the case. The relative motion between the magnet and coil elements produces a back electromotive force, i.e. a voltage, at the terminals of the coil; vice versa, the current flow in the coil generates a pair of reactive forces on the magnetic and on the coil-armature elements. As shown by the drawing IIb, the piezoelectric seismic harvester is composed by a thin beam with one end fixed to the case and the other end connected to a tip block mass: The beam is equipped on the top and bottom side with two rectangular piezoelectric patches connected in parallel. In this case, the relative motion between the case and the block mass produces a bending strain of the cantilever beam, which, in turn, produces a separation of

electric charge in the electrodes of the piezoelectric patches. Alternatively, a bending strain effect is produced on the cantilever beam when a voltage is applied at the terminals of the piezoelectric patches.

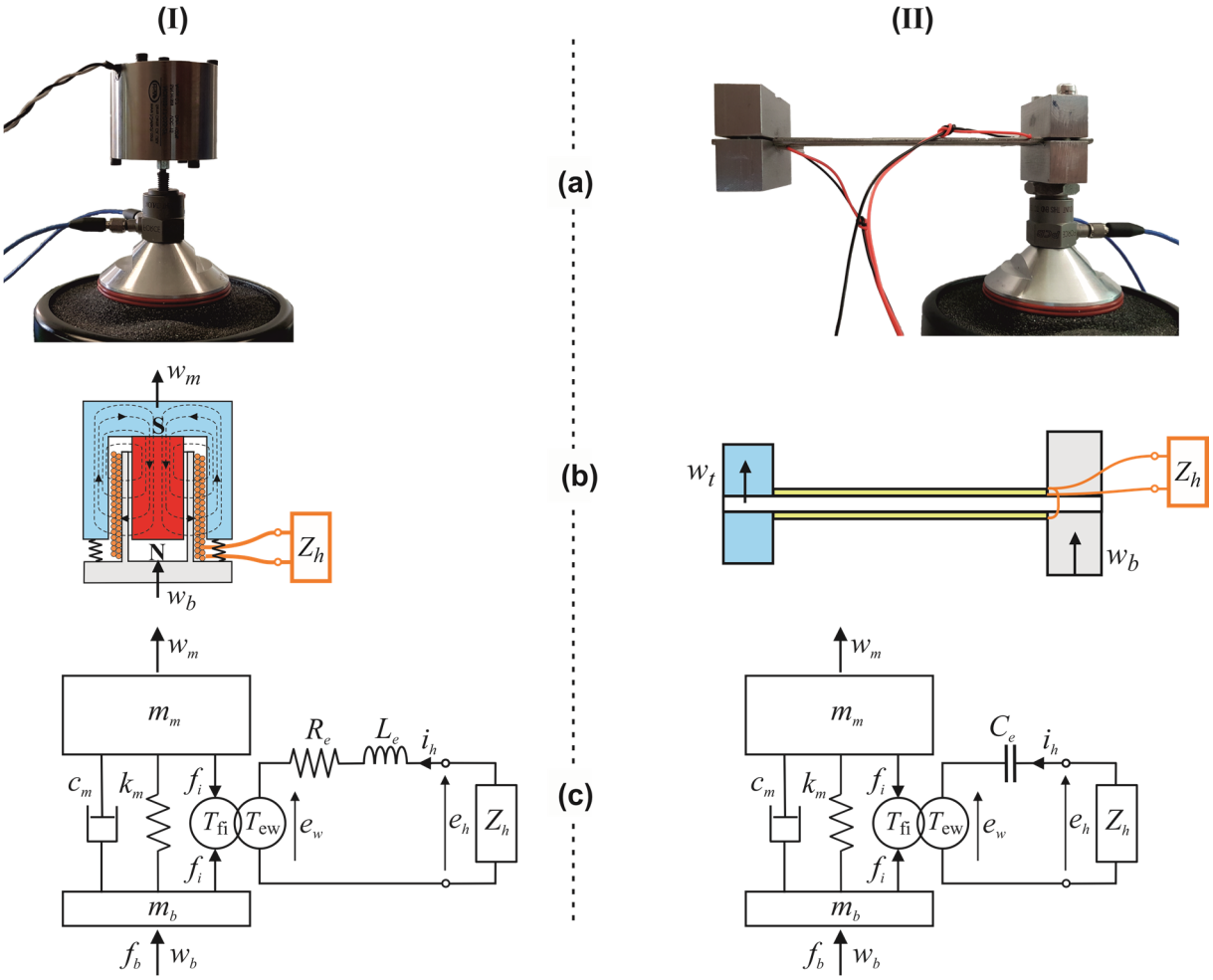

Figure 1: Electro-magnetic (I) and piezoelectric (II) proof mass vibration energy harvesters. (a) Pictures, (b) schematics, (c) lumped paramenter models

2.1 Lumped parameter models

The dynamic response of the two inertial transducers derived in ref. [30] is briefly revised here considering the two equivalent lumped parameter models shown in the schemes Ic and IIc. These models are characterised by equivalent mechanical and by equivalent electrical parts. The mechanical part is composed by a base mass and a proof mass connected via spring and damper elements, with in parallel an idealised actuator that produces a reactive force per unit current flowing into the coil proportionally to a force-current transduction transfer function. The electrical part is composed by an idealised generator that produces a voltage per unit relative velocity between the coil and the magnet proportionally to a voltage-velocity transduction transfer function. The voltage source is connected in series with resistor and inductor components for the coil-magnet transducer and with a capacitor component for the

piezoelectric transducer. For the piezoelectric transducer, the masses-spring-damper lumped elements and the transduction transfer function are derived considering only the first flexural mode that characterise the flexural response of the beam-piezoelectric patches laminate. As discussed in ref. [30], this requires the introduction of a virtual displacement w_m for the modal proof mass, which does not correspond to the effective displacement of the tip mass w_t but it refers to a particular coordinate $\bar{x}$ with respect to the clamped end of the beam (See Table 2). Tables 1 and 2 summarise the principal lumped parameters of the electro-magnetic and piezoelectric seismic harvesters considered in this study.

Table 1: Lumped parameters for the electro-magnetic seismic harvester

Parameter	Value
Base mass	$m_b = 115 \cdot 10^{-3}\ kg$
Proof mass	$m_m = 185 \cdot 10^{-3}\ kg$
Spring stiffness	$k_m = 2921\ N/m$
Damping coefficient	$c_m = 7.4$ Ns/m
Natural frequency	$f_n = 20$ Hz
Damping ratio	$\xi = 0.16$
Transduction coefficient	$Bl = 22.5\ N/A$
Resistance	$R_e = 22\ \Omega$
Inductance	$L_e = 4.35$ mH

Table 2: Lumped parameters for the piezo-electric seismic harvester

Parameter	Value
Base mass	$m_b = 126 \cdot 10^{-3}\ kg$
Proof mass	$m_m = 215 \cdot 10^{-3}\ kg$
Spring stiffness	$k_m = 3515\ N/m$
Damping coefficient	$c_m = 1.26$ Ns/m
Natural frequency	$f_n = 20.4$ Hz
Damping ratio	$\xi = 0.005$
Transduction coefficient	$\psi = -0.0025\ N/V$
Capacitance	$C_p = 1.68 \cdot 10^{-7}$ F
Equivalent coordinate	$\bar{x} = 135 \cdot 10^{-3}$ m

2.2 Constitutive equations

The constitutive equations for the two transducers are here recalled using the unified formulation derived in ref. [30]. Considering time-harmonic vibrations described with phasors given in the form $w(t) = w(\omega)\exp(j\omega t)$, where $w(\omega)$ is the complex amplitude, ω is the circular frequency and $j = \sqrt{-1}$, the electromechanical response of the two lumped parameter models can be expressed in the frequency domain with the following two equations [21]

$$f_b = Z_{mi}\dot{w}_b + T_{fi}i_h\,, \tag{1}$$

$$e_h = T_{ew}\dot{w}_b + Z_{ei}i_h\,, \tag{2}$$

where f_b, $\dot{w}_b$ are respectively the complex amplitudes of the force and velocity at the base of the transducer and e_h, i_h are the complex amplitudes of the voltage and current across the terminals of the transducer. The mechanical and electrical impedance FRFs and the two-electromechanical transduction FRFs are given by:

$$Z_{mi} = \frac{f_b}{\dot{w}_b}\Big|_{i_h=0} = Z_b + \frac{Z_{mm}Z_m}{Z_a}, \qquad T_{fi} = \frac{f_b}{i_h}\Big|_{\dot{w}_b=0} = \Psi_{fi}\frac{Z_{mm}}{Z_a}, \tag{3,4}$$

$$Z_{ei} = \frac{e_h}{i_h}\Big|_{\dot{w}_b=0} = Z_e + \frac{\Psi_{fi}\Psi_{ew}}{Z_a}, \qquad T_{ew} = \frac{e_h}{\dot{w}_b}\Big|_{i_h=0} = -\Psi_{ew}\frac{Z_{mm}}{Z_a}, \tag{5,6}$$

The terms Z_{mi} and Z_{ei} are respectively the mechanical impedance of the open circuit seismic transducer and the electrical impedance of the blocked seismic transducer. The two terms T_{fi} and T_{ew} represent the electromechanical coupling coefficients for both seismic transducers, which give the base force effect produced by the transducer per unit current of the blocked

seismic transducer and the electric voltage at the terminals of the transducer per unit velocity at the base of the open circuit seismic transducer. As shown in ref. [30], for the coil magnet

$$\Psi_{fi} = Bl \,, \quad \Psi_{ew} = Bl \,, \tag{7,8}$$

where B is the magnetic field in the gap where the coil is housed and l is the length of the wire. Also, for the piezoelectric transducer

$$\Psi_{fi} = Z_e \psi \,, \quad \Psi_{ew} = -Z_e \psi \,, \tag{9,10}$$

where ψ is the piezoelectric transduction coefficient and Z_e is the capacitive electric impedance. All the other coefficients in Eqs. (3-6) can be found in ref. [30].

2.3 Mechanical-electrical-transduction FRFs

Figures 2 and 3 show the simulated and measured 8 Hz – 1 kHz spectra of the mechanical impedance and electrical impedance FRFs and of the two-electromechanical transduction FRFs that form the constitutive Eqs. (1) and (2) for the electromagnetic and the piezoelectric seismic transducers shown in Figure 1.

Considering first the simulated FRFs for the electro-magnetic seismic transducer shown with the solid black lines in Figure 2, the mechanical impedance Z_{mi} given in Eq. (3) is characterised by low- and high-frequency asymptotic mass behaviours, which are proportional respectively to the total mass of the transducer $m_m + m_b$ and to the mass of the host element m_b. These two asymptotic behaviours converge to a peak at the fundamental resonance frequency of the transducer (at about 20 Hz) and to a trough at the close by antiresonance (at about 35 Hz). The electrical impedance Z_{ei}, given by Eq. (5) is characterised by two components: first the electrical impedance of the coil Z_e and second the electro-mechanical impedance $\Psi_{fi}\Psi_{ew}/Z_a$. The electrical impedance of the coil Z_e is characterized by a resistive effect at low frequencies and by an inductive effect at frequencies above the cut off frequency at about 800 Hz. The electro-mechanical impedance $\Psi_{fi}\Psi_{ew}/Z_a$ becomes relevant in correspondence to the transducer fundamental resonance frequency, where it produces a smooth resonance peak. The electromechanical transduction coefficients T_{fi} and T_{ew} in Eqs. (4) and (6) have the same modulus and opposite phase. At low frequencies, the modulus rises proportionally to ω^2 towards a resonance peak at the fundamental resonance frequency of the seismic transducer. At frequencies above 50 Hz, the modulus levels to a constant value, such that the seismic transducer both generates a constant force per unit current and produces a constant voltage source per unit relative velocity of the proof mass with respect to the case. The phase spectra of T_{fi} and T_{ew} start respectively at $+\,180°$ and 0°, and in correspondence to the resonance frequency undergo through a $-180°$ phase lag. Thus, at frequencies higher than the fundamental resonance frequency, the constant force-current transduction and voltage-relative velocity transduction effects are characterized respectively by a positive and negative sign with respect to the notation indicated in the lumped parameter model Ic of Figure 1.

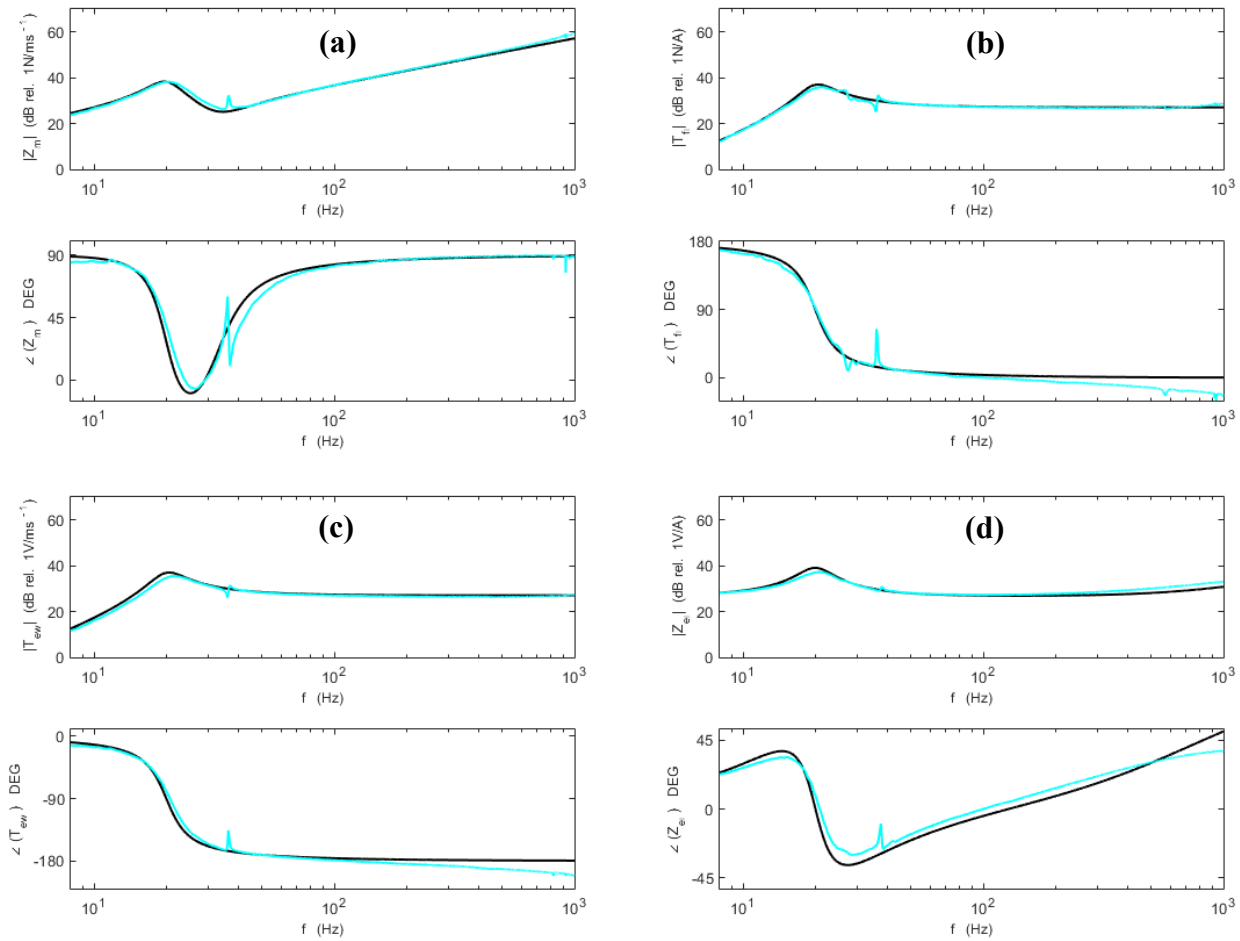

Figure 2: mechanical impedance (a), electrical impedance (d) and electromechanical transduction (b), (c) FRFs for the electromagnetic seismic transducer. Simulated (solid black line) and measured (solid cyan line) FRFs.

The validity of these simulation results was verified against measured FRFs taken on the prototype transducer shown in Figure 1a. The mechanical and electrical impedances, Z_{ei} and Z_{mi}, and the two transduction coefficients, T_{fi} and T_{ew}, were measured in the frequency range 8 Hz – 1 kHz. As can be noticed by contrasting the solid cyan lines (measurements) and the solid black lines (simulations) in Fig. 2, the measured FRFs agree quite closely with the simulated FRFs. The measured FRFs show an additional glance at about 30 Hz, which is probably caused by the dynamics of the mechanical setup used for the measurements. Another difference can be noticed at high frequencies, where the phase of T_{fi}, T_{ew} and Z_{ei} tends to drop at a slightly higher rate than in the simulations. This is probably due to the measurement chain that introduces a small time delay, which turns into the additional phase lag.

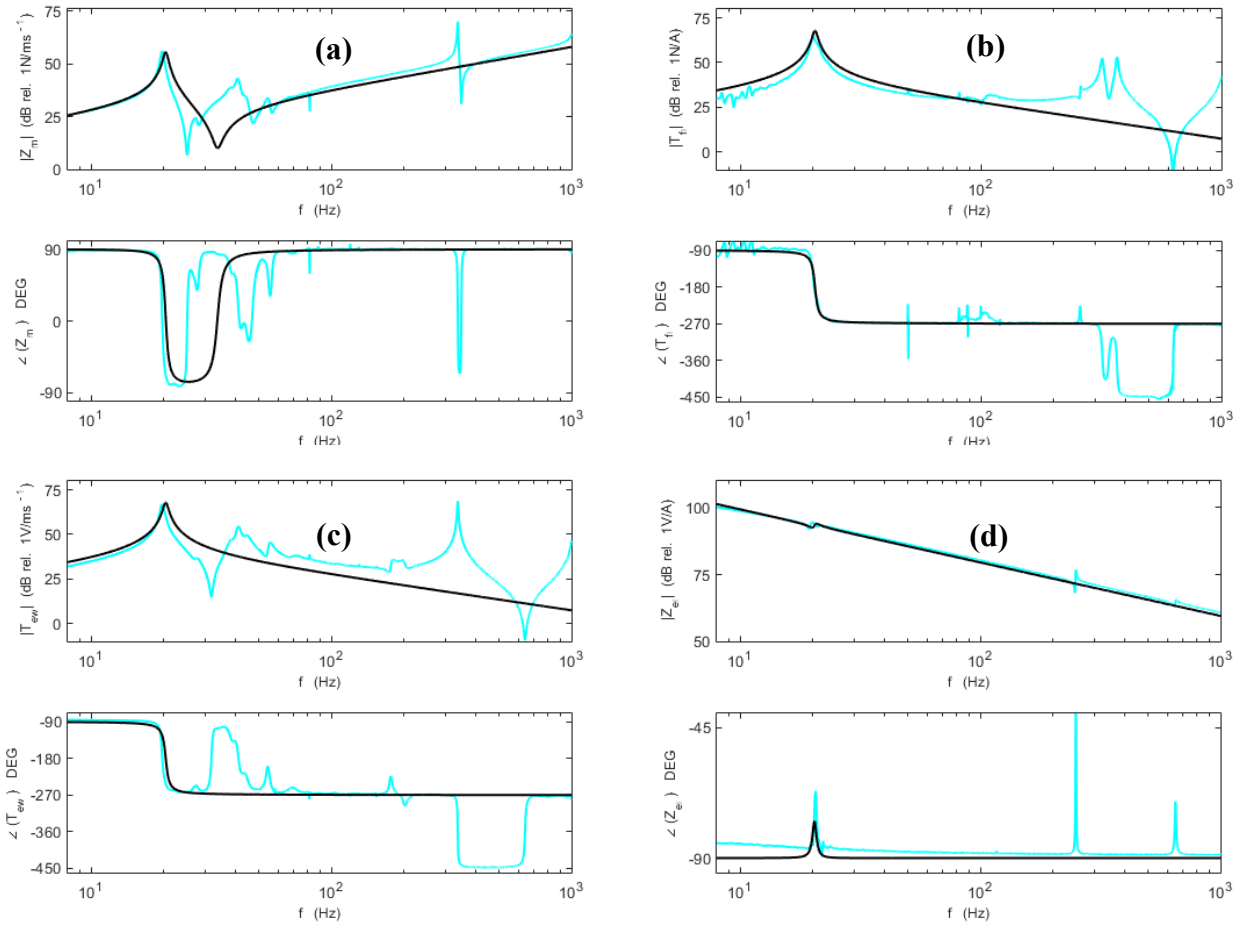

Figure 3: mechanical impedance (a), electrical impedance (d) and electromechanical transduction (b), (c) FRFs for the piezoelectric seismic transducer. Simulated (solid black line) and measured (solid cyan line) FRFs.

Considering now the simulated FRFs for the piezoelectric seismic transducer, the mechanical impedance Z_{mi} given in Eq. (3) is very similar to that of the electromagnetic transducer. Thus, it characterised by low- and high-frequency asymptotic mass behaviours, proportional respectively to $m_m + m_b$ and to the m_b, which are linked via a close by resonance peak and antiresonance low, respectively at about 20 Hz and 35 Hz. As found for the electromagnetic transducer, the electric impedance is characterized by the superposition of the piezoelectric patch electrical impedance Z_e and the electromechanical impedance $\Psi_{fi}\Psi_{ew}/Z_a$. The former is a capacitive impedance, which, as can be noted in Figure 3, dominates the whole spectrum apart from a small resonance peak at about 20 Hz due to the latter electromechanical component. The electrical capacitive component is characterised by a modulus that drops proportionally to ω^{-1} and phase -90°. At first sight the spectra of the two-transduction coefficients T_{fi} and T_{ew} seem quite different from those found for the electromagnetic transducer. However, after a closer view, it can be noticed that the principal difference is given by a factor $j\omega$. In fact, piezoelectric transducers convert strain into electricity and vice versa. Thus, for the unified formulation considered in this paper, the moduli of the two transduction

coefficients T_{fi} and T_{ew} are characterised by a low frequency rising behaviour proportional to ω^1 and a higher frequency falling behaviour proportional to ω^{-1}, which are joined by a resonance peak at about the fundamental natural frequency of the transducer at 20 Hz. The phase starts at -90° and undergoes a -180° phase lag in correspondence to the resonance frequency so that, at higher frequencies, the phase drops to -270°.

As done for the coil-magnet transducer, the validity of these simulation results was verified against measured FRFs taken on the prototype transducer shown in Figure 1b. Thus, the mechanical and electrical impedances, Z_{ei} and Z_{mi}, and the two transduction coefficients, T_{fi} and T_{ew}, were measured in the frequency range 8 Hz – 1 kHz. In this case, contrasting the solid cyan lines (measurements) and the solid black lines (simulations) in Fig. 1, it is noted that the simulated FRFs reproduce quite closely the measured FRFs up to about 30 Hz, that is up to the fundamental resonance frequency of the transducer. At higher frequencies the measured FRFs reproduce the asymptotic behaviour of the simulated FRFs, although new resonance peaks appear, particularly in the Z_{mi}, T_{fi}, T_{ew} FRFs, which are due to the dynamics of higher order flexural modes as well as to the dynamics of the mechanical setup used for the measurements. Nevertheless, these initial measurement results indicate that the proposed model accurately reproduce the mechanical and electrical impedances, Z_{ei} and Z_{mi}, and the two transduction coefficients, T_{fi} and T_{ew} of the piezoelectric transducer up to about the fundamental resonance frequency of the transducer. Thus, the model accurately reproduce the electro-mechanical response of the transducer up to the working frequency of an seismic energy harvester. Indeed as discussed in ref. [16] for example, and as shown in Section 3 below, the maximum energy harvesting occurs at the fundamental resonance frequency of seismic transducers. The FRFs shown in this paper were measured using a small shaker with relatively soft rotational stiffness. Thus it is likely, that measurements taken with a moving table device may be more accurate.

3 ENERGY ANALYSIS

The energy harvested is now derived with a common formulation for the two transducers using the unified constitutive equations (1), (2). As shown in the two schemes c of Fig. 1, the two seismic transducers are connected to a purely resistive load, which could represent the effect of a battery or a low power consumption electronic circuit. Assuming harmonic vibrations, the time averaged harvested power can be expressed as follows

$$\overline{P_h} = \lim_{T\to\infty} \frac{1}{T} \int_0^T P_h(t) dt. \tag{11}$$

Here, the instantaneous harvested power is given by

$$P_h(t) = e_h(t) i_h(t)\,, \tag{12}$$

where $e_h(t)$, $i_h(t)$ are the voltage across and current through the harvesting load. Considering the sign convention shown in the two schemes c of Fig. 1, the two electrical signals are linked by the electrical impedance of the harvesting circuit Z_h as follows:

$$e_h = -Z_h i_h\,. \tag{13}$$

According to the constitutive Eqs. (1), (2), the transducers yield a voltage

$$e_w = T_{ew} \dot{w}_b. \tag{14}$$

Thus, the harvesting current can be derived straightforwardly by analysing the electric meshes of the harvesters shown in Figure 1c with Kirchhoff's voltage law, which gives

$$i_h = -\frac{T_{ew}}{Z_h+Z_{ei}}\dot{w}_b. \tag{15}$$

In conclusion, for harmonic vibrations, the time average harvested power can be derived from Eqs. (11) to (15) as follows:

$$\overline{P_h} = \frac{1}{2}R_e\{Z_h\}|i_h|^2 = \frac{1}{2}R_e\{Z_h\}\left|\frac{-T_{ew}}{Z_h+Z_{ei}}\right|^2|\dot{w}_b|^2. \tag{16}$$

As derived in ref. [31] for example, the optimal resistive impedance of the harvesting circuit that maximizes the harvested power at each frequency is given by:

$$Z_{h,R} = |Z_{ei}|, \tag{17}$$

Thus, after substitution of Eq. (17) into Eq. (16), the maximum harvested power is derived as follows:

$$\overline{P_h} = \frac{1}{4}\frac{|T_{ew}|^2}{|Z_{ei}|+R_e\{Z_{ei}\}}|\dot{w}_b|^2. \tag{18}$$

This expression can be equally used to calculate the maximum harvested power by the electromagnetic and by the piezoelectric seismic harvesters provided the pertinet expression of Ψ_{ew} is used in the electromechanical FRF T_{ew}, i.e. Eq. (8) for the electromagnetic seismic transducer and Eq. (10) for the piezoelectric seismic transducer. The two plots in Figure 4 show the simulated (solid black lines) and simulated from measured FRFs (solid cyan lines) spectra of the optimal resistive (i.e. real) impedances for the electromagnetic (Plot a) and piezoelectric (Plot b) seismic harvesters. The solid black line in Plot (a) shows that the optimal resistive impedance for the electromagnetic seismic harvester is characterised by a marked peak at about 20 Hz that matches the electromechanical resonating effect of the electrical impedance. Also, above about 500 Hz, the optimal impedance tends to rise proportionally to ω^1 to match the the coil inductive effect that controls the electrical impedance at higher frequencies. The solid black line in Plot b shows the optimal resistive impedance for the piezoelectric seismic harvester, which, apart from a small glance in correspondence to the fundamental resonance frequency at about 20 Hz, is characterised by a constant drop roportional to ω^{-1} to match the capacitive effect of the piezoelectric patch. In general, the solid black and cyan lines in Plots a and b show a rather good matching between the simulated and simulated from measured FRFs optimal resistive impedances for the electromagnetic and piezoelectric seismic harvesters. There is a mismatch for the amplitude of the resonance peak of the optimal impedance for the electromagnetic seismic harvester, which is overestimated by about 25% in the simulation. The amplitude of this peak depends on the damping effect produced by the relative motion between the coil and the magnet, whose magnitude is rather difficult to estimate. Also the rising effect above 500 is slightly under estimated in the simulation. In this case this is due to the difficulty to correctly estimate the inductive effect of the coil.

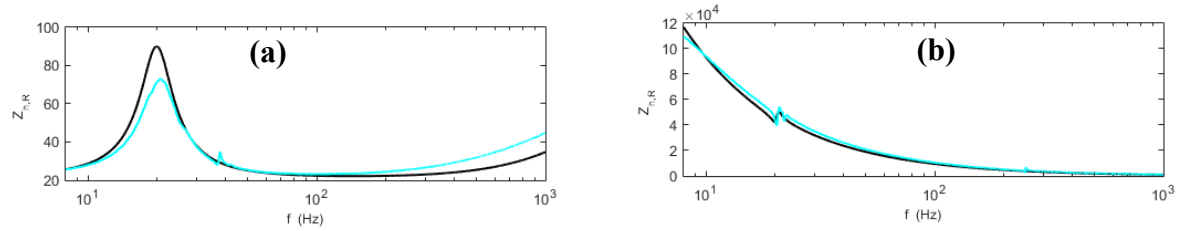

Figure 4: Optimal real impedance for (a) the electromagnetic and (b) the piezoelectric seismic harvesters. Simulated, solid black line; simulated from measured FRFs, solid cyan line

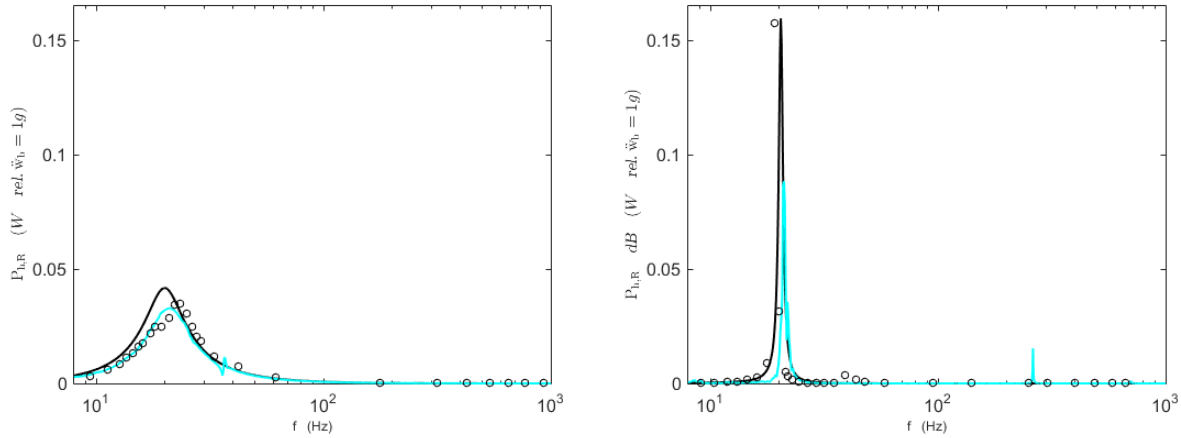

Figure 5: Power harvested with reference to a 1 g base acceleration for (a) the electromagnetic and (b) the piezoelectric seismic harvesters with optimal harvesting impedances. Simulated, solid black line; simulated from measured FRFs, solid cyan line; measured, dots.

Figure 5 shows the simulated (solid black lines) and the simulated from measured FRFs (solid cyan lines) spectra of the power harvested by the electromagnetic seismic harvester (Plot a) and by the piezoelectric seismic harvester (Plot b), with reference to a 1 g base acceleration, when the harvesting circuits are characterised by the optimal complex impedance $Z_{h,R} = |Z_{ei}|$. The two plots show that the spectra of the harvested power are characterised by a distinct peak at the fundamental resonance frequency of the two transducers. The peak for the piezoelectric seismic harvester is rather sharp and it is about four times higher than that of the electromagnetic seismic harvester. Considering the peak values, the electromagnetic seismic harvester produces about 0.04 W while the piezoelectric seismic harvester produces about 0.16 W. The simulated spectra derived from measured FRFs agree quite well with the simulated spectra. There is just a visible mismatch for the peak value of the energy harvested by the piezoelectric seismic harvester.

To substantiate the results presented above, single frequency experiments were carried out by connecting to the seismic transducers shown in Figure 1a the resistances indicated by the yan lines in Fig. 5. The dots in Plots a and b of Figure 5 indicate that the simulated spectra agree rather well with the measured spectra of the harvested power. It is interesting to note how the peak value of the simulated power harvested by the piezoelectric seismic harvester precisely corresponds to the measured one. Thus, it is likely that the mismatch found between the spectra simulated and simulated using measured FRFs is due to a rounding off effect due to the method used to measure the FRFs used to simulate the spectrum of the harvested power.

4 CONCLUSIONS

This paper has presented a comparative simulation and experimental study on the energy harvested by electromagnetic and piezoelectric equivalent seismic harvesters. The two systems were modelled with consistent electro-mechanical lumped parameter models to enable the derivation of a unified formulation for the energy harvesting and thus to allow the direct comparison of the electro-mechanical response and energy harvesting properties of the two harvesters. The study was limited to energy harvesting from tonal ambient vibrations.

The study has shown that the proposed models accurately reproduce the principal characteristics of electro-mechanical constitutive relations of the two seismic transducers. The piezoelectric transducer is characterised by higher order dynamic effects, which however occur at higher frequencies than the fundamental resonance frequency where the peak power harvesting occurs. The electromagnetic harvester produces a peak energy value of $0.04\,\mathrm{W}$. In contrast the piezoelectric harvester generates a four time higher peak energy value of $0.16\,\mathrm{W}$. This is due to the lower inherent damping of the piezoelectric seismic transducer.

REFERENCES

[1] S. Priya, D. J. Inman, Editors *Energy Harvesting Technologies*, Springer, London (2009).

[2] D. Spreemann, Y Manoli Electromagnetic, *Vibration Energy Harvesting Devices Architectures*, *Design, Modeling and Optimization,* Springer, London (2012).

[3] A.Erturk**,** D.J. Inman**,** *Piezoelectric Energy Harvesting*, John Wiley & Sons, (2011).

[4] T. Hehn, Y. Manoli, CMOS Cir*cuits for Piezoelectric Energy Harvesters Efficient Power Extraction, Interface Modeling and Loss Analysis,* Springer, London (2012).

[5] H.A. Sodano, D.J. Inman and G. Park, *A Review of Power Harvesting from Vibration using Piezoelectric Materials*, The Shock and Vib. Digest, Vol. 36, No. 3, (2004), pp. 197–205.

[6] S. R. Anton, H. A. Sodano, *A review of power harvesting using piezoelectric materials 2003–2006*, Smart Materials and Structures, Vol. 16, No. 3, (2007), pp. R1.

[7] A. Khaligh, Z. Peng and Z. Cong, *Kinetic energy harvesting using piezoelectric and electromagnetic technologies—state of the art*, IEEE Trans. Ind. Electronic, Vol. 57, No. 3, (2010), pp. 850-860.

[8] D.P. Arnold, *Review of microscale magnetic power generation*, IEEE Transactions on Magnetics, Vol. 43, No. 11, (2007), pp. 3940–3951.

[9] Y. Naruse, N. Matsubara, K. Mabuchi, M. Izumi, K. Honma, *Electrostatic micro power generation from low-frequency vibration such as human motion*, *Proceedings of Power MEMS 2008+ micro EMS 2008, Sendai, Japan, 2008 November 9-12*, pp. 19-22.

[10] P. Glynne-Jones, N.M. White, *Self-powered systems, a review of energy sources*, Sensor Review, Vol. 21, No. 2, (2000), pp. 91–98.

[11] P.D. Mitcheson, E.M. Yeatman, G. Kondala Rao, A. S. Holmes, T.C. Green, *Energy harvesting from Human and Machine Motion for Wireless Electronic Devices*, Department of Electrical and Electronic Engineering, Imperial College London, Vol. 96, No.9 (2008).

[12] C.B. Williams, R.B. Yates, *Analysis of micro – electric generator for microsystems, Proceedings of the Transducers*, Sensors and Actuators A 52 8-11, (1996).

[13] S. Roundy, P.K. Wright, J. Rabaey, *A Study of Low Level Vibrations as a Power Source for Wireless Sensor Nodes*, Computer Communications, vol. 26, no. 11, (2003).

[14] M. El-Hami, P. Glynne-Jones, N.M. White, M. Hill, S. Beeby, E. James, A.D. Brown, J.N. Ross, *Design and fabrication of a new vibration-based electromechanical power generator*, Sensors and Actuators A 92, (2001), 335–42.
[15] P.D. Mitcheson, T.C. Green, E.M. Yeatman, A.S. Holmes, *Architectures for vibration driven micropower generators*, IEEE J. Microelectromech. Sys., Vol. 13, No. 3, (2004).
[16] S. J.Elliott, M. Zilletti, *Scaling of electromagnetic transducers for shunt damping and power harvesting*, Journal of sound and vibration, Vol. 333, No. 8, (2014), pp. 2185-2195.
[17] B. S. Hendrickson, S. B. Brown, *Harvest of motion*, Mechanical Engineering-CIME, (2008).
[18] I. L. Cassidy, J. T. Scruggs, S. Behrens, *Design of electromagnetic energy harvesters for large-scale structural vibration applications*, Active and Passive Smart Structures and Integrated Systems, Proceedings of SPIE, Vol. 7977, (2011), pp. 79770P (11 pp).
[19] N. G. Stephen, *On energy harvesting from ambient vibration*, J. of Sound and Vibration, Vol. 293, (2006), pp. 409-425.
[20] P. Gardonio and M. Zilletti. *Vibration Energy harvesting from an array of flexible stalks exposed to airflow*, J. Smart Materials and Structures, 25, (2016).
[21] J. D. Hobeck and D. J. Inman, *Artificial Piezoelectric Grass for Energy Harvesting from Turbulence-induced Vibration*, Smart Materials and Structures, Vol. 21, No. 10, (2012).
[22] F.V Hunt, *The analysis of transduction, and its historical background: electroacoustic* , 2nd edition, Harvard University Press , Cambridge, MA (1982).
[23] Crandall S H, Karnopp D C, Kurtz J E F and Pridmore-Brown D C, *Dynamics of Mechanical and Electromechanical Systems,* Krieger Pub Co. Malabar, (1982).
[24] A Preumont,*Mechatronic dynamics of electromechanical and piezoelectric systems,* Springer, Dordrecht, (2006).
[25] G. Poulin, E. Sarraute, F. Costa, *Generation of electrical energy for portable devices, comparative study of an electromagnetic and a piezoelectric system*, Sensors and Actuators A, Vol. 116, Elsevier (2004), pp. 461- 471.
[26] E. Lefeuvre, A. Badel, C. Richard, L. Petit, D. Guyomar, *A comparison between several vibration-powered piezoelectric generators for standalone systems*, Sensors and Actuators A, Vol. 126, No. 2, Elsevier (2006), pp. 405-416.
[27] P.L. Green, K.Worden, K. Atallah, N.D. Sims, *The modelling of friction in a randomly excited energy harvester*, *International Conference on Noise and Vibration Engineering (ISMA 2012), Katholieke Universiteit Leuven, Belgium, 2012 17–19 Sept.* Leuven (2012).
[28] K. Nakano, M. P. Cartmell, H. Hu and R. Zheng, *Feasibility study on energy harvesting using stochastic resonance, Eleventh International Conference on Recent Advances in Structural Dynamics, Pisa, Italy, 2013 July 1-3*, Pisa (2013).
[29] G. Sebald, H. Kuwano, D. Guyomar and B. Ducharne1, *Experimental Duffing oscillator for broadband piezoelectric energy harvesting*, Smart Materials and Structures, Vol. 20, (2011), pp. 102001 (10 pp).
[30] D. Zhu, M. J. Tudor, S. P. Beeby, *Strategies for increasing the operating frequency range of vibration energy harvesters: a review*, Meas. Science and Technology, Vol. 21, (2010).
[31] L. Dal Bo, P. Gardonio, *Comparison between electromagnetic and piezoelectric energy harvesters*, ISMA 2016, Belgium.

VIII ECCOMAS Thematic Conference on Smart Structures and Materials
SMART 2017
A. Güemes, A. Benjeddou, J. Rodellar and J. Leng (Eds)

A MACHINE LEARNING METHODOLOGY FOR STRUCTURAL DAMAGE CLASSIFICATION IN STRUCTURAL HEALTH MONITORING

Francesc Pozo[†], Diego A. Tibaduiza[*], Maribel Anaya[II] and Jaime Vitola[†‡]

[†] Control, Dynamics and Applications (CoDAlab), Departament de Matemàtiques, Escola d'Enginyeria de Barcelona Est (EEBE), Universitat Politècnica de Catalunya (UPC), Campus Diagonal-Besòs (CDB), Eduard Maristany, 6–12, Sant Adrià de Besòs (Barcelona) 08930, Spain; e-mail: francesc.pozo@upc.edu, jaime.vitola@estudiant.upc.edu; web page: https://codalab.upc.edu/en/

[*] Departamento de Ingeniería Eléctrica y Electrónica, Universidad Nacional de Colombia, Cra 45 No. 26-85, Bogotá, Colombia; e-mail: dtibaduizab@unal.edu.co

[II] Facultad de Ingeniería, Fundación Universitaria Los Libertadores, Carrera 16 No. 63 A - 68, Bogotá, Colombia;e-mail: maribel.anaya@libertadores.edu.co

[‡] MEM (Modeling-Electronics and Monitoring Research Group), Faculty of Electronics Engineering, Universidad Santo Tomás, Cra. 9 No, 51 - 20. Bogotá, Colombia; jaimevitola@usantotomas.edu.co

Key words: machine learning; principal component analysis; piezoelectric sensors; temperature variations, damage classification

Abstract. One of the goals of structural health monitoring (SHM) applications is to determine the presence and the severity of a damage. In some cases, this is an element to forecast the behaviour and take decisions to allocate maintenance or replace the structure or the piece. An appropriate decision can reduce the risk of an accident, making more efficient the management of maintenance tasks and reducing the costs while improving the performance of a system. In this way, the development of a good SHM system is a need. Through the use of: (i) advanced methodologies of digital signal processing; (ii) the acquisition of information from a set of piezoelectric sensors appropriately placed in the surface of a structure; and (iii) the use of techniques such as principal component analysis (PCA) [1, 2, 3] and machine learning, it is possible to generate a solution that meets the necessity about the knowledge of the structural state.

This work presents a methodology which allow to determine the presence of a structural damage and its classification in spite of temperature changes. The methodology is tested with a composite plate instrumented with a PZT sensor network and some added masses as damages. The whole system is validated to different temperatures.

1 INTRODUCTION

Damage detection and classification are some of the tasks to consider in the damage identification process [4]. These task can be tackled from different points of view, however pattern recognition is one of the most used because it allows to work directly whit the acquired data from the structure [5]. Compared with the use of model-based methodologies, the use of data driven algorithms adds advantages such as the use of data directly from the structure by avoiding the development of a complex mathematical model to analyze the information. Among the disadvantages with the use of data are the variations in environmental and operational conditions to the structures and sensors are subjected what can result in errors in the damage identification process [6, 7].

There are many magnitudes to consider in the design of a structural health monitoring system (SHM). For instance, temperature, temperature gradients, humidity, wind or traffic [8]. When these factors are not considered, the results may mask or conceal the changes of the structure. Therefore, the diagnosis provided by the structural health monitoring system will not be accurate and can produce some false alarms. In this sense, the development of any SHM system requires the consideration of these variables to provide a robust analysis and confident results. As contribution to solve the stated problem, this work introduces a damage detection and classification methodology based on the use of data from a piezoelectric sensor network permanently installed over the structure under test, principal component analysis and machine learning approaches for detecting and classifying damages. The methodology considers two steps: training and testing. During the first, data from different temperatures under different structural states are considered to produce a robust training and testing process is after used to evaluate the results in the detection and classification. The experimental validation is performed with data from a composite plate subjected to temperature variations. Results show a good performance in the development of both processes.
This work is organized in five sections starting with this introduction and following with a theoretical background, a damage detection and classification methodology description, the experimental setup and results and closing with the conclusions.

2 THEORETICAL BACKGROUND

This section exposes some basic concepts about the methods and techniques included in the methodology such as principal component analysis and machine learning.

2.1 Principal Component Analysis (PCA)

PCA was described by Pearson in the year 1901, as a Mechanism of Multivariate analysis. It is mainly used to pre-process very large data from multiple sources with no apparent relationship between them. Principal component analysis allows to reduces the size of a dataset by finding relevant information that identify the reason for the variation between them and qualify through indices [5, 9]. In many applications, PCA is used as a tool to reduce the dimensionality of the data to be applied in a subsequent process to work with a reduced number of data. Currently,There are many useful toolbox to apply PCA and analyze the reduced data provided by the technique [10], this is one of the reasons about PCA still being used. Most information about PCA and the normalization process can be consulted in [9] and [11].

In a general case, typical data from a batch process may consist of N variables measured at L time instants for n batches or experimental trials. This data can be easily arranged in a three-way matrix

$\mathbf{Z} \in \mathcal{M}_{n\times N\times L}(\mathbb{R})$ as represented in Figure 1 (top, left). However, to apply multivariate statistical techniques, such as principal component analysis (PCA), this three-way matrix $\mathbf{Z}$ must be unfolded to a two-way array. Westerhuis *et al.* [12] discussed profoundly how to unfold this three-way matrix and what were the effects of data normalization on the multivariate statistical techniques. One of the possibilities that are presented in [12] is depicted in Figure 1 (right), where the three-way matrix $\mathbf{Z} \in \mathcal{M}_{n\times N\times L}(\mathbb{R})$ is unfolded to a two-way matrix with $n \cdot L$ rows and N columns. This way, each of the N columns in the unfolded matrix still represent the N variables that are measured in the process.

However, in our application, we propose a quite different approach to unfold the original three-way matrix $\mathbf{Z}$. As it can be observed in Figure 1 (bottom, left), the three-way matrix $\mathbf{Z} \in \mathcal{M}_{n\times N\times L}(\mathbb{R})$ is unfolded to a two-way matrix with n rows and $N \cdot L$ columns. This way, the columns of the unfolded matrix no longer represent the variables but the measures of the variables at the different time instants. More precisely, the submatrix defined by taking the n rows and the first L columns represent the discretized measures of the first variable for the n batches or experimental trials; similarly, the submatrix defined by taking the n rows and columns $L+1$ to $2L$ represent the discretized measures of the second variable for the n batches or experimental trials. In general, then, the submatrix defined by taking the n rows and columns $(l-1)\cdot L+1$ to $l \cdot L$ represent the discretized measures of the $l-$th variable for the n batches or experimental trials.

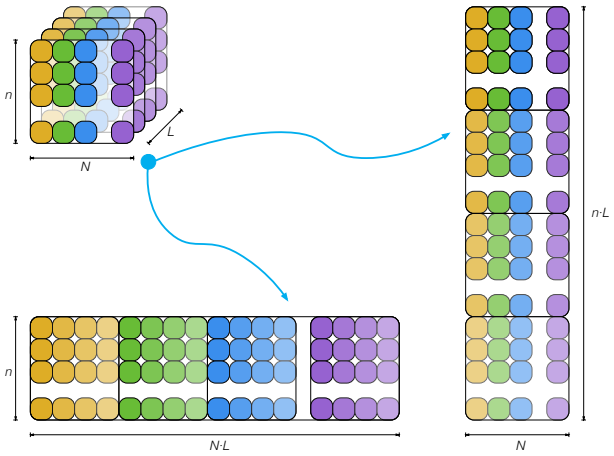

Figure 1: The three-way matrix $\mathbf{Z}$ can be unfolded to a two-way array in several ways.

2.2 Machine learning

The solution of complex problems can be tackled form different approaches in computer science, however machine learning has demonstrated to be a very useful tool to analyse data by providing a quite remarkable set of strategies for pattern recognition. More precisely, when a deterministic mathematical model is difficult to define and data has, at first glance, no correlation, these pattern recognition techniques are generally able to find some kind of relationship. Machine learning strategies allow to avoid this difficulty through mechanisms designed to find the answer by themselves. Some examples of its use in SHM includes problem detection such as breaks, corrosion, cracks, impact damage, delamination, disunity, breaking fibers (some pertinent to metals and the others to composite materials) [13] and the

evaluation of structure under extreme events such as earthquakes [14].

Machine learning approaches can be classified in two main groups: unsupervised and supervised learning depending on the training process. In the first case, the information is grouped and interpreted using uniquely the input data. However, to perform the learning task in the second case, information about the output data is required. Figure 2 shows this classification and includes information about the kind of tasks that can be performed –clustering, classification, regression–.

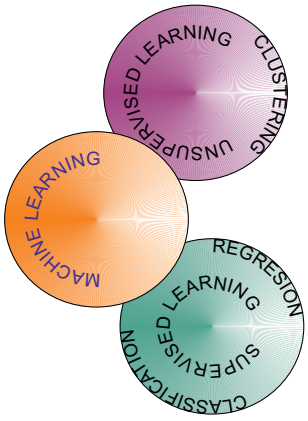

Figure 2: Classification of the Machine learning approaches according to the learning.

Some of the machines available for classification and regression processes are nearest neighbor, decision trees and support vector machines. More information about these approaches can be found in [15].

3 DAMAGE CLASSIFICATION METHODOLOGY

The structural health monitoring system described on this work, is composed by two elements, the first corresponds to the data acquisition system, this allows collecting data with information about the state of the structure under test. Second element corresponds to the pre-procesing, feature extraction and data analysis and it is a procedure that includes the use of digital signal processing techniques and statistical pattern recognition approaches to determine the health of the structure. This is aimed to the system should decide autonomously whether the host structure is damaged or not [4].

3.1 Data acquisition system

This subsystem let obtain information about the element under inspection by means of the data from the sensors attached to the structure. It is composed by two processes (transmission an reception), one of that generates stimulus signal by using aTie Pie HS5 - arbitrary generator. This signal is applied to one piezoelectric sensor in the sensor network which acts as actuator. The applied signal is transfered to the structure and the propagated signal is collected by an osciloscope Tie Pie HS4 from the rest of the sensors in the network as is shown in Figure 3.

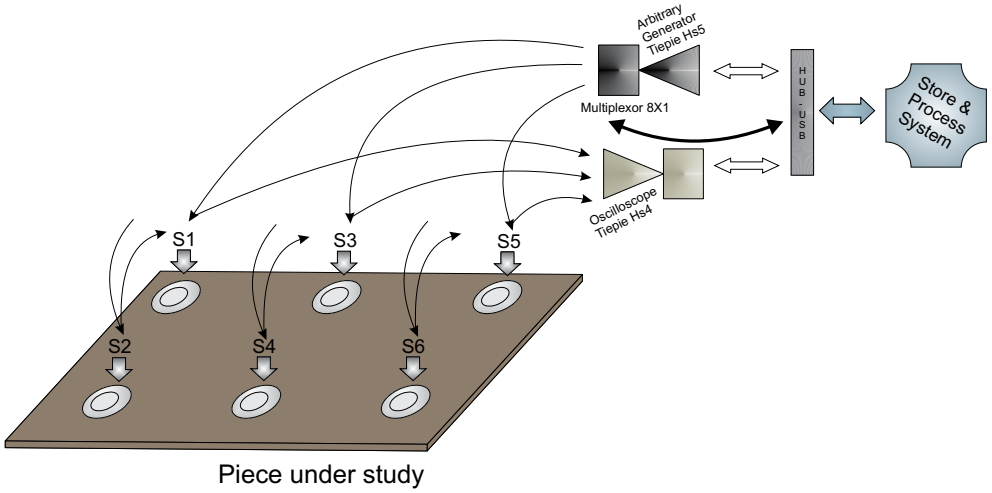

Figure 3: Data acquisition system

3.2 Pre-processing, feature extraction and data analysis

This subsystem is the core of the methodology, because allows to create a pattern and define the state of a structure based on the analysis of data. The developed methodology is shown in figure 4. After, data acquisition, the digitized signals are organized and pre-processed using the golay filter to reduce the noise, afterward, PCA is applied for data reduction and feature extraction. Here, three scores per experiment and per structural state and temperature are obtained and used to train the machine. In this case, training is performed with 80 experiments in each temperature in each damage and without damage, this is 1920 experiments in total (without damage and three structural states by 6 temperatures and 80 experiments) and the test is made with 480 experiments, 120 per damage.

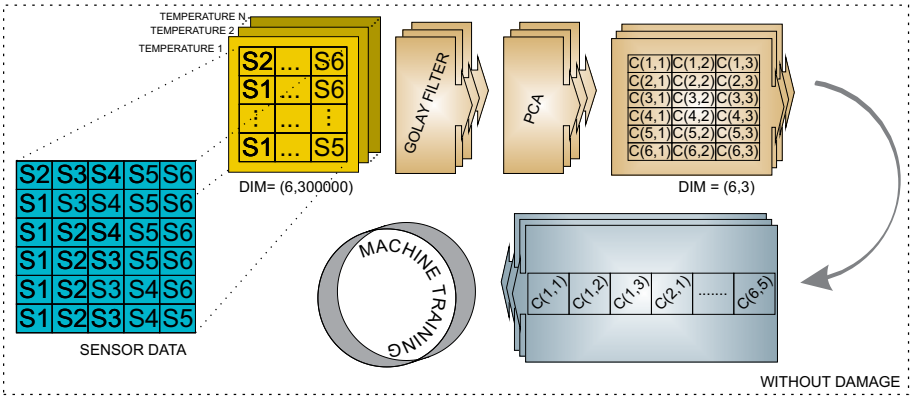

Figure 4: Methodology

The machines are trained using twenty one different algorithm provided by the toolbox of classification learner of Matlab with the main objective of finding best results in the classification.

4 EXPERIMENTAL SETUP AND RESULTS

The validation of the methodology is performed by means of a carbon fiber plate instrumented with six piezoelectric sensors. To change the temperature, this plate was introduced in a climatic chamber with reference Faithful HWS-250BX , this is shown in the figure 5, in this case six different values of temperature (0, 10, 20, 30, 40, 50 ° C) were evaluated.



Figure 5: Composite plate in the climatic chamber

4.1 Composite Plate

As structure, a carbon fiber composite plate is used. Figure 6 shows the dimensions and distributions of the six piezoelectric sensors attached to its surface, also shows the position of three damages (adding mass in different positions) used for this purpose.

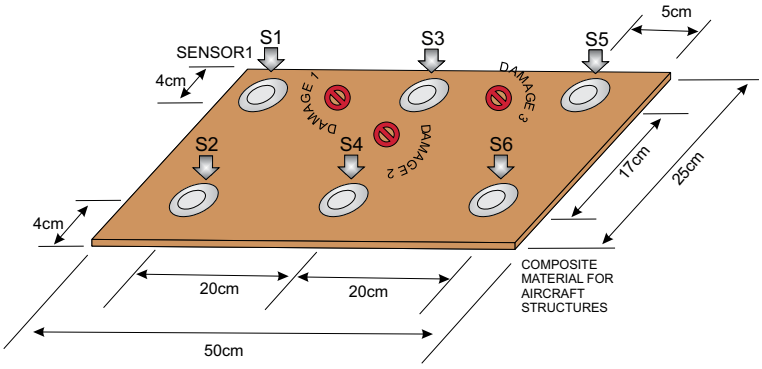

Figure 6: Experimental setup for the composite plate

Figure 7, shows some photos of the experiments for the three damages, as it is possible to observe, structure was isolated by means of rubber tapes, to reduce the external vibrations.

Figure 8(a) shows the changes over the collected signals with temperature variations viewed from a sensor. In this case three different values of temperature (0, 30 and 50 ° C) are considered for the same

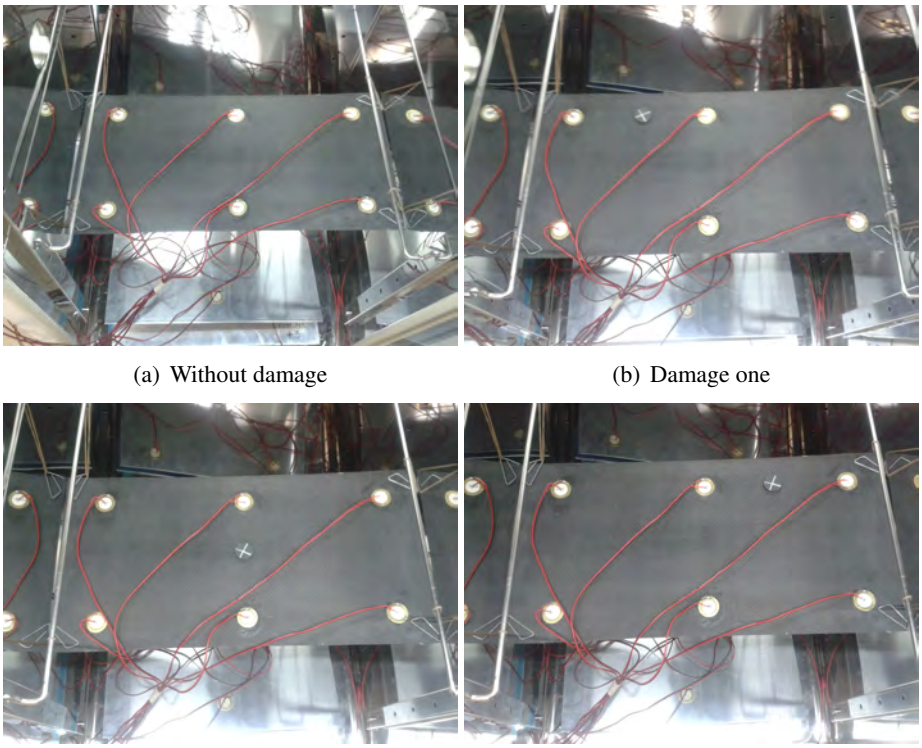

(a) Without damage (b) Damage one

(c) Damage two (d) Damage three

Figure 7: Experiment photographs

experiment. Figure 8(b), shows three captures of the same experiment under 20 ° C, as it is expected the signal varies slightly. These figures demonstrate the effect of the temperature in the captured data.

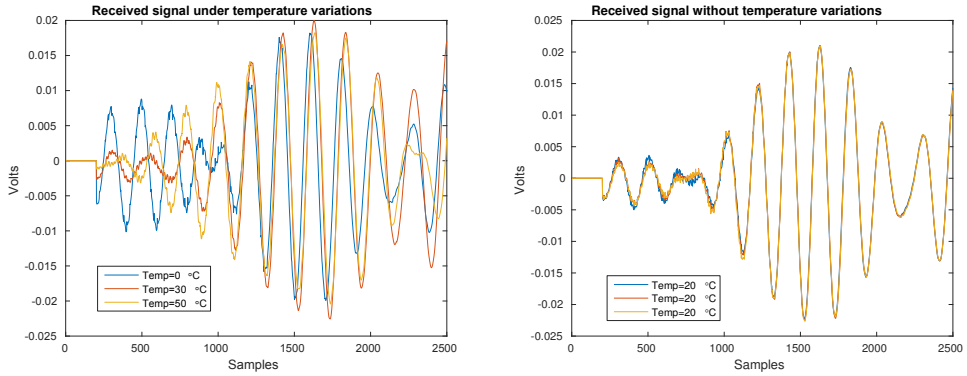

(a) Received signal with temperature variations (b) Received signal without temperature variations

Figure 8: Received signal by the sensor number 2, sensor 1 work as actuator, under and without temperature variations

As it was previously explained, after pre-processing step, PCA is applied to the data. Figure 9 shows

simple 2D plots by considering just two components. Figure 9a shows the result by using the first two scores, Figure 9b shows fourth vs fifth score. The use of these plots could be taken advantage for damage detection when the cumulative variance contained into the components is higher to 80 or 90%, in other case, datasets cannot be identified as in this case.

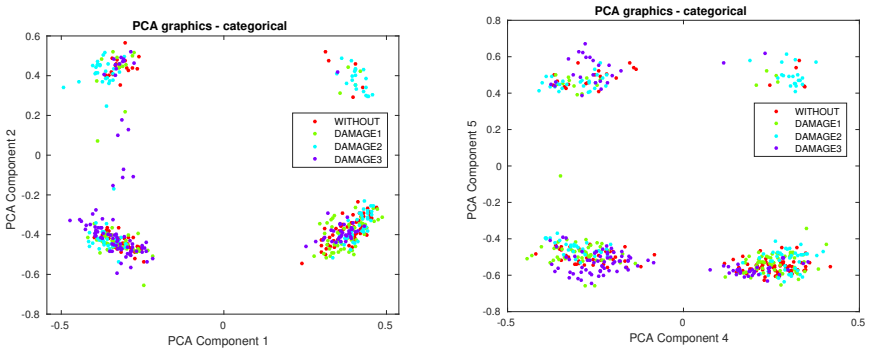

(a) Two first components of PCA (b) Fourth and fifth components

Figure 9: Principal Component Analysis

To define the number of principal components, a cumulative variance analysis is performed, in this case, three PCA scores per actuation phase were considered (this means eighteen scores for all the actuation phases) these values have an accumulated variance closed to 80 percent, this is shown in Figure 10, nevertheless, it is necessary to bear in mind that the use of the 100 percent of accumulated variance allows more sensitivity to small changes in the input signals.

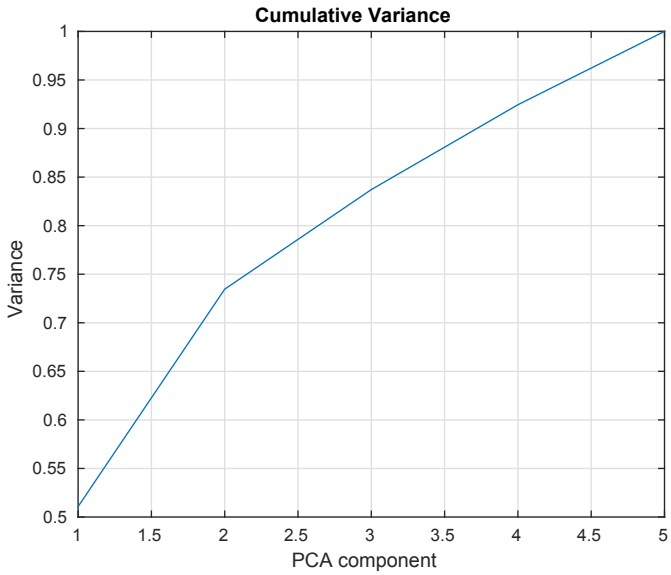

Figure 10: Cumulative variance for scores of PCA

Finally, to perform the classification, different machines are trained as it was explained in previous sections, as result, the confusion matrices for Subspace KNN, Weighted KNN, are presented in Figure 11. Only these machines are presented because are the machines with the best behavior in the classification process.

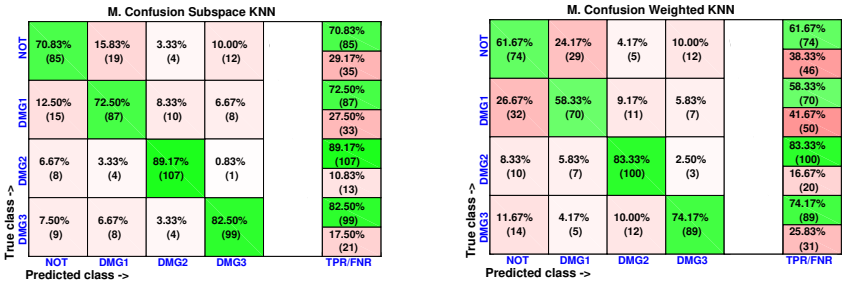

(a) Subspace KNN (b) Weighted KNN

Figure 11: Confusion matrix machines with good behavior

In the case of Cosine KNN, and Weighted KNN an intermediate behavior is obtained. Confusion matrices are shown in Figure 12.

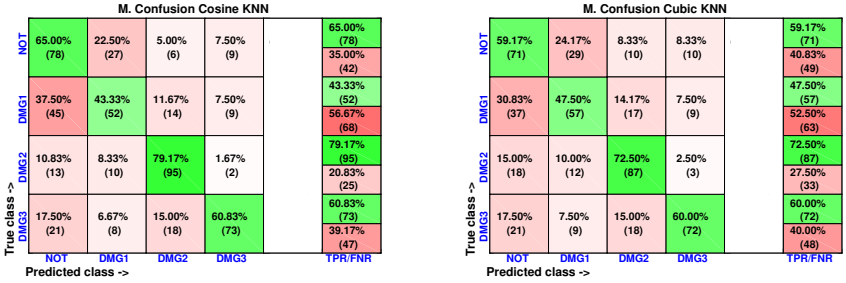

(a) Cosine KNN (b) Weighted KNN

Figure 12: Confusion matrix machines with intermediate behavior

Worst results were obtained with Rusboosted tree and Boosted trees which are presented in Figures 13.

5 CONCLUSIONS

Machine learning offers an interesting and sophisticated way to solve complicated problems, in this case, the detection of four structural states (three different damages and healthy state) under different temperatures was performed with excellent results. Among them, subspace KNN and Weighted KNN presented best results while rusboosted and boosted trees have worst results.

Acknowledgments: This work has been partially funded by the Spanish Ministry of Economy and

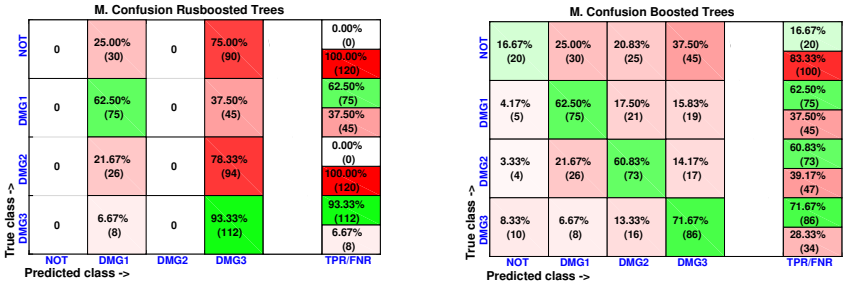

(a) Rusboosted trees (b) Boosted trees

Figure 13: Confusion matrix machines with bad behavior

Competitiveness through the research project DPI2014-58427-C2-1-R, and by the Catalonia Government (Generalitat de Catalunya) through the research project 2014 SGR 859. This work also is supported by Universidad Santo Tomás through grant FODEIN 2017, project code FODEIN 17545020-47.

REFERENCES

[1] L. Mujica, J. Rodellar, A. Fernandez, and A. Güemes, "Q-statistic and t2-statistic pca-based measures for damage assessment in structures," *Structural Health Monitoring*, vol. 10, no. 5, pp. 539–553, 2011.

[2] L. Mujica, M. Ruiz, F. Pozo, J. Rodellar, and A. Güemes, "A structural damage detection indicator based on principal component analysis and statistical hypothesis testing," *Smart materials and structures*, vol. 23, no. 2, p. 025014, 2013.

[3] F. Pozo and Y. Vidal, "Wind turbine fault detection through principal component analysis and statistical hypothesis testing," in *Advances in Science and Technology*, vol. 101, pp. 45–54, Trans Tech Publ, 2017.

[4] M. A. Torres-Arredondo, I. Buethe, D. A. Tibaduiza, J. Rodellar, and C.-P. Fritzen, "Damage detection and classification in pipework using acousto-ultrasonics and non-linear data-driven modelling," *Journal of Civil Structural Health Monitoring*, vol. 3, no. 4, pp. 297–306, 2013.

[5] M. Anaya, D. A. Tibaduiza, and F. Pozo, "A bioinspired methodology based on an artificial immune system for damage detection in structural health monitoring," *Shock and Vibration*, vol. 501, p. 648097, 2015.

[6] H. Sohn, "Effects of environmental and operational variability on structural health monitoring," *Philosophical Transactions of the Royal Society of London A: Mathematical, Physical and Engineering Sciences*, vol. 365, no. 1851, pp. 539–560, 2007.

[7] M. Anaya, D. Tibaduiza, M. Torres, F. Pozo, M. Ruiz, L. Mujica, J. Rodellar, and C. Fritzen, "Data-driven methodology to detect and classify structural changes under temperature variations," *Smart Materials and Structures*, vol. 23, pp. 1–15, 2014.

[8] A.-M. Yan, G. Kerschen, P. De Boe, and J.-C. Golinval, "Structural damage diagnosis under varying environmental conditions - part i: a linear analysis," *Mechanical Systems and Signal Processing*, vol. 19, no. 4, pp. 847–864, 2005.

[9] D. A. T. Burgos, "DESIGN AND VALIDATION OF A STRUCTURAL HEALTH MONITORING SYSTEM FOR AERONAUTICAL STRUCTURES," *PhD thesis*, vol. 1, 2012.

[10] D. H. Jeong, C. Ziemkiewicz, B. Fisher, W. Ribarsky, and R. Chang, "iPCA: An Interactive System for PCA based Visual Analytics," vol. 28, no. 3, pp. 767–774, 2009.

[11] D. A. Tibaduiza, L. E. Mujica, J. Rodellar, and A. Guemes, "Structural damage detection using principal component analysis and damage indices," *Journal of Intelligent Material Systems and Structures*, vol. 27, no. 51, pp. 233–248, 2015.

[12] J. A. Westerhuis, T. Kourti, and J. F. MacGregor, "Comparing alternative approaches for multivariate statistical analysis of batch process data," *Journal of Chemometrics*, vol. 13, no. 3-4, pp. 397–413, 1999.

[13] C. R. Farrar and K. Worden, *Structural health monitoring: a machine learning perspective*. John Wiley & Sons, 2012.

[14] C. C. Ciang, J.-R. Lee, and H.-J. Bang, "Structural health monitoring for a wind turbine system: a review of damage detection methods," *Measurement Science and Technology*, vol. 19, no. 12, p. 122001, 2008.

[15] J. Vitola, F. Pozo, D. A. Tibaduiza, and M. Anaya, "A sensor data fusion system based on k-nearest neighbor pattern classification for structural health monitoring applications," *Sensors*, 2017.

VIII ECCOMAS Thematic Conference on Smart Structures and Materials
SMART 2017
A. Güemes, A. Benjeddou, J. Rodellar and J. Leng (Eds)

ADVANCED VIBRATION CONTROL OF LARGE STRUCTURES WITH DISTRIBUTED MULTI-ACTUATOR SYSTEM AND PARTIAL STATE INFORMATION

F. PALACIOS-QUIÑONERO*, J. RUBIÓ-MASSEGÚ*, J.M. ROSSELL* AND J. RODELLAR†

*Universitat Politècnica de Catalunya (UPC)
Department of Mathematics
EPSEM. Av. Bases de Manresa 61-73, 08242 Manresa, Spain
e-mail: {francisco.palacios, josep.rubio, josep.maria.rossell}@upc.edu

† Universitat Politècnica de Catalunya (UPC)
Department of Mathematics
EEBE. C. Eduard Maristany 10-14, 08019 Barcelona, Spain
e-mail: jose.rodellar@upc.edu

Key words: Structural vibration control, Output-feedback control, Multi-actuator systems, Seismic protection

Abstract. In this paper, the design and performance of partial-state controllers with incomplete multi-actuation systems for the seismic protection of tall buildings is investigated. The proposed approach considers a partially instrumented multi-story building with an incomplete system of interstory force-actuation devices implemented at selected levels of the building, and an associated set of collocated sensors that measure the interstory drifts and velocities corresponding to the instrumented stories. The main elements of the proposed controller design methodology are presented by means of a twenty-story building with two different actuation schemes. For these control configurations, partial-state controllers are designed following a static output-feedback H_∞ controller design approach, and the corresponding frequency and time responses are investigated. The obtained results clearly indicate that the proposed partial-state controllers are effective in mitigating the building seismic response. They also show up that a suitable distribution of the instrumented stories is a relevant factor in the control system design.

1 INTRODUCTION

Protection of large buildings and civil structures against the damaging effects of seismic excitations is an important issue that has attracted increasing research attention over the last years. In some advanced approaches, complex and sophisticated vibration control systems are considered. These control configurations involve a large set of sensors and actuation devices, which are widely distributed throughout the structure, and work coordinately to mitigate the structure

vibrational response [1, 2]. Overall, the controlled structure can be seen as a huge mechatronic system, which is able to produce an intelligent reaction to mitigate the negative effects of external disturbances. In this work, we present a controller design methodology for the seismic protection of tall buildings equipped with a distributed set of actuators and sensors. More specifically, we assume that some of the building stories are equipped with an interstory force-actuation device and a sensing unit that can measure the corresponding interstory drift and velocity [3]. We also assume that the building is only partially instrumented and, consequently, the available state information is incomplete. Using a distributed set of small actuation devices instead of a single large actuator allows reducing the structural loads produced by the control system, and helps to provide a more balanced control action. A distributed set of collocated sensors is a natural and technically convenient choice. Additionally, considering a partially instrumented scheme is a realistic approach for tall buildings with a large number of stories. It should be noted that, in this context, the control system design comprises two different problems: (1) computing an effective controller for a given distribution of the instrumented stories (controller design), and (2) determining an optimal distribution of the instrumented stories (optimal control configuration). Obviously, a computationally efficient solution to the first problem can help to explore the effectiveness of different control configurations and, consequently, can contribute to obtain an optimal solution to the second problem. Due to the high dimensionality and information constraints, the considered controller design problem leads to serious issues, both theoretical and computational. The solution proposed in this work is based on an output-feedback H_∞ approach, and allows obtaining effective controllers with incomplete state information by solving a two-step Linear Matrix Inequality (LMI) optimization problem [4]. The main results are presented by means of a twenty-story building with two different actuation schemes. The obtained results confirm the effectiveness of structural vibration control strategies with incomplete multi-actuator systems and partial state information. They also point out that an enhanced performance can be achieved by a suitable distribution of the instrumented stories.

The rest of the paper is organized as follows: In Section 2, a state-space model for the twenty-story building with incomplete actuation schemes is presented. In Section 3, full-state and partial-state controllers are designed for the different control configurations and the corresponding frequency characteristics are investigated. In Section 4, numerical simulations of the time responses are conducted and illustrative peak-value plots of the interstory drifts, story absolute accelerations and control efforts are presented and compared. Finally, in Section 5, some conclusions and future research directions are briefly discussed.

2 BUILDING MODEL

Let us consider an n-story building whose lateral displacement can be described by the second-order differential equation

$$M\,\ddot{q}(t) + C_d\,\dot{q}(t) + K_s\,q(t) = T_u u(t) + T_w w(t), \tag{1}$$

where $q(t) = \big[q_1(t), \ldots, q_n(t)\big]^T$ is the vector of story displacements with respect to the ground, $w(t)$ is the seismic ground acceleration and $u(t)$ is the vector of control actions. M, C_d and K_s are the mass, damping and stiffness matrix, respectively, which model the mechanical characteristics of the building, T_u is the control location matrix and T_w is the disturbance input matrix. The

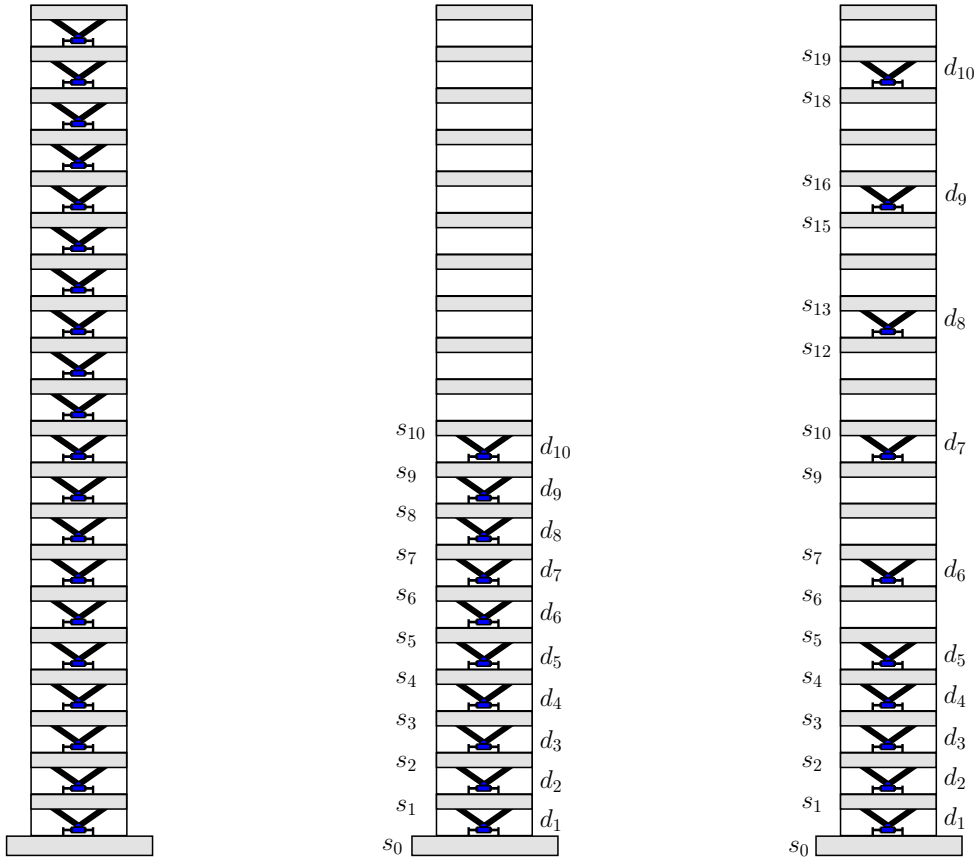

(a) Complete actuation scheme (b) Partial actuation scheme 1 (c) Partial actuation scheme 2

Figure 1: Interstory actuation schemes. (a) Complete actuation scheme. (b) Partial actuation scheme AS1, with $m = 10$ actuators located at positions $P_1 = [1, 2, \ldots, 10]$. (c) Partial actuation scheme AS2, with $m = 10$ actuators located at positions $P_2 = [1, 2, 3, 4, 5, 7, 10, 13, 16, 19]$.

mass matrix is a diagonal matrix $M = \text{diag}(m_1, m_2, \ldots, m_n)$, and the stiffness matrix has the following tridiagonal structure:

$$K_s = \begin{bmatrix} k_1 + k_2 & -k_2 & & & & & \\ -k_2 & k_2 + k_3 & -k_3 & & & & \\ & \cdots & \cdots & \cdots & & & \\ & & \cdots & \cdots & \cdots & & \\ & & & -k_{n-1} & k_{n-1} + k_n & -k_n & \\ & & & & -k_n & k_n \end{bmatrix}, \tag{2}$$

where m_i and k_i, $i = 1, \ldots, n$, denote the mass and stiffness coefficient of the i-th story, respectively. The damping matrix C_d can be computed from M and K by setting a proper damping ratio on the building modes [5]. The disturbance input matrix has the form $T_w = -M[1]_{n\times 1}$, where $[1]_{n\times 1}$ denotes a vector of dimension n with all its entries equal to 1. The structure of the control location matrix depends on the considered actuation scheme. In this work, we assume that the control forces are exerted by a system of m devices $d_1, \ldots, d_m$, where d_i is an interstory

actuator implemented at position p_i, which produces a force of magnitude $u_i(t)$ on the story number p_i (upper story), and an opposite force of magnitude $-u_i(t)$ on the story number $p_i - 1$ (lower story). An actuation scheme is determined by a list of positions $P = [p_1, \ldots, p_m]$. If the actuation scheme is complete, as the one schematically depicted in Fig. 1(a), then the list of positions is $P_c = [1, 2, \ldots, n]$ and the corresponding control location matrix is a square matrix of size n with the following upper-diagonal band form:

$$T_u^{P_c} = \begin{bmatrix} 1 & -1 & & & & \\ & 1 & -1 & & & \\ & & \cdots & \cdots & & \\ & & & \cdots & \cdots & \\ & & & & 1 & -1 \\ & & & & & 1 \end{bmatrix}. \tag{3}$$

For an incomplete actuation scheme with a list of positions $P = [p_1, \ldots, p_m]$, $m < n$, the corresponding control location matrix T_u^P is a rectangular matrix of size $n \times m$ that can be obtained by extracting the corresponding columns from $T_u^{P_c}$, that is:

$$T_u^P = T_u^{P_c}(1, 2, ..., n; p_1, \ldots, p_m). \tag{4}$$

Thus, for the actuation scheme AS1 in Fig. 1(b), the list of positions is $P_1 = [1, 2, \ldots, 10]$ and the control location matrix

$$T_u^{P_1} = T_u^{P_c}(1, 2, \ldots, 20; 1, 2, \ldots, 10) \tag{5}$$

can be obtained by selecting the first 10 columns of $T_u^{P_c}$, which in this case is a square matrix of size 20. For the actuation scheme AS2 in Fig. 1(c), the list of actuator positions is $P_2 = [1, 2, 3, 4, 5, 7, 10, 13, 16, 19]$ and the corresponding control location matrix has the following form:

$$T_u^{P_2} = T_u^{P_c}(1, 2, ..., 20; P_2) = \begin{bmatrix} 1 & -1 & 0 & 0 & 0 & 0 & 0 & 0 & 0 & 0 \\ 0 & 1 & -1 & 0 & 0 & 0 & 0 & 0 & 0 & 0 \\ 0 & 0 & 1 & -1 & 0 & 0 & 0 & 0 & 0 & 0 \\ 0 & 0 & 0 & 1 & -1 & 0 & 0 & 0 & 0 & 0 \\ 0 & 0 & 0 & 0 & 1 & 0 & 0 & 0 & 0 & 0 \\ 0 & 0 & 0 & 0 & 0 & -1 & 0 & 0 & 0 & 0 \\ 0 & 0 & 0 & 0 & 0 & 1 & 0 & 0 & 0 & 0 \\ 0 & 0 & 0 & 0 & 0 & 0 & 0 & 0 & 0 & 0 \\ 0 & 0 & 0 & 0 & 0 & 0 & -1 & 0 & 0 & 0 \\ 0 & 0 & 0 & 0 & 0 & 0 & 1 & 0 & 0 & 0 \\ 0 & 0 & 0 & 0 & 0 & 0 & 0 & 0 & 0 & 0 \\ 0 & 0 & 0 & 0 & 0 & 0 & 0 & -1 & 0 & 0 \\ 0 & 0 & 0 & 0 & 0 & 0 & 0 & 1 & 0 & 0 \\ 0 & 0 & 0 & 0 & 0 & 0 & 0 & 0 & 0 & 0 \\ 0 & 0 & 0 & 0 & 0 & 0 & 0 & 0 & -1 & 0 \\ 0 & 0 & 0 & 0 & 0 & 0 & 0 & 0 & 1 & 0 \\ 0 & 0 & 0 & 0 & 0 & 0 & 0 & 0 & 0 & 0 \\ 0 & 0 & 0 & 0 & 0 & 0 & 0 & 0 & 0 & -1 \\ 0 & 0 & 0 & 0 & 0 & 0 & 0 & 0 & 0 & 1 \\ 0 & 0 & 0 & 0 & 0 & 0 & 0 & 0 & 0 & 0 \end{bmatrix}. \tag{6}$$

The interstory drift $r_i(t)$ is the relative displacement between the consecutive stories located at the building levels i and $i-1$ (denoted as s_i and s_{i-1} in Fig. 1). The vector of interstory drifts $r(t) = [r_1(t), r_2(t), \ldots, r_n(t)]^T$ can be computed as follows:

$$\begin{cases} r_1(t) = q_1(t), \\ r_i(t) = q_i(t) - q_{i-1}(t), \quad \text{for} \;\; i = 2, \ldots, n. \end{cases} \tag{7}$$

Table 1: Twenty-story building model. Mass, stiffness and damping characteristics.

story	1–5	6–11	12–14	15–17	18–19	20
mass ($\times 10^6$ Kg)	1.10	1.10	1.10	1.10	1.10	1.10
stiffness ($\times 10^8$ N/m)	8.62	5.54	4.54	2.91	2.56	1.72
relative damping	2%					

By considering the state vector $x(t) = [r_1(t), \dot{r}_1(t), r_2(t), \dot{r}_2(t), \ldots, r_n(t), \dot{r}_n(t)]^T$, we obtain a first-order state-space model

$$\dot{x}(t) = A\,x(t) + B\,u(t) + E\,w(t), \tag{8}$$

with

$$A = \mathcal{C}\,\widehat{A}\,\mathcal{C}^{-1}, \quad B = \mathcal{C}\,\widehat{B}, \quad E = \mathcal{C}\,\widehat{E}, \tag{9}$$

$$\widehat{A} = \begin{bmatrix} [0]_{n\times n} & I_n \\ -M^{-1}K_s & -M^{-1}C_d \end{bmatrix}, \quad \widehat{B} = \begin{bmatrix} [0]_{n\times m} \\ M^{-1}T_u \end{bmatrix}, \quad \widehat{E} = \begin{bmatrix} [0]_{n\times 1} \\ -[1]_{n\times 1} \end{bmatrix}, \tag{10}$$

where I_n is the identity matrix of dimension n, $[0]_{n\times m}$ represents a zero-matrix of the indicated dimensions, and $\mathcal{C}$ is the change-of-basis matrix corresponding to the state transformation

$$x(t) = \mathcal{C} \begin{bmatrix} q(t) \\ \dot{q}(t) \end{bmatrix}. \tag{11}$$

In the controller designs and numerical simulations presented in this paper, we consider a twenty-story building model with the mass, stiffness and damping parameters collected in Table 1 [3].

3 CONTROLLERS DESIGN

3.1 Controllers with full state information

Assuming that the control objective is to reduce the building vibrational response by means of moderate control actions, we consider the controlled-output vector

$$z(t) = C_z\,x(t) + D_z\,u(t), \tag{12}$$

defined by the matrices

$$C_z = \begin{bmatrix} I_{2n} \\ [0]_{m\times 2n} \end{bmatrix}, \quad D_z = \alpha \begin{bmatrix} [0]_{2n\times m} \\ I_m \end{bmatrix}, \tag{13}$$

where α is a scaling factor that can be used to adjust the intensity of the control action. If the full state information is available, we can consider a state-feedback controller $u(t) = Gx(t)$, defined by the state gain matrix $G \in \mathbb{R}^{m\times 2n}$, which produces the closed-loop system

$$\begin{cases} \dot{x}(t) = A_G\,x(t) + Ew(t), \\ z(t) = C_G\,x(t), \end{cases} \tag{14}$$

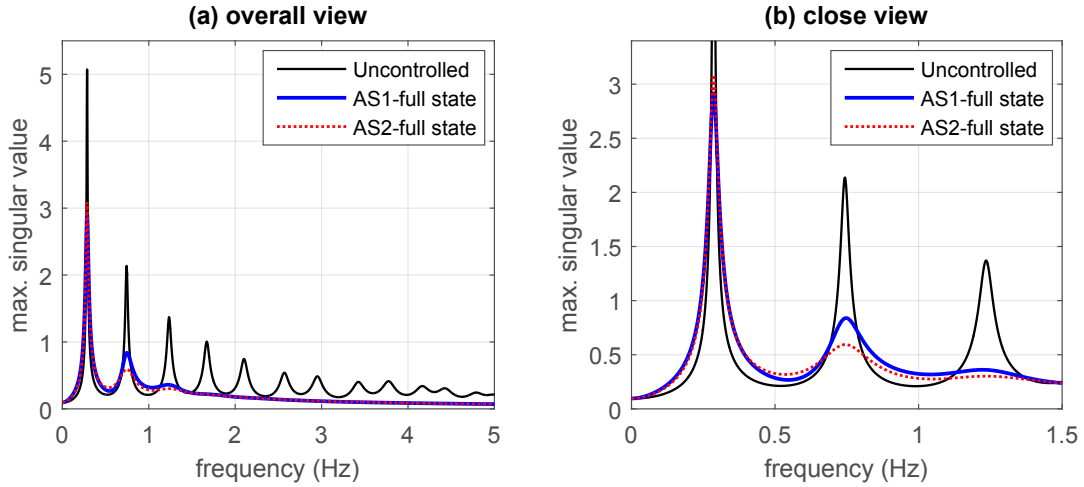

Figure 2: Frequency response of the controllers with full state information. Maximum singular values of the closed-loop transfer function $T_{\widetilde{G}_1}(\omega)$ (thick blue solid line), the closed-loop transfer function $T_{\widetilde{G}_2}(\omega)$ (red dotted line) and the open-loop transfer function $T(\omega) = C(2\pi\omega j I_{2n} - A)^{-1}E$ (thin black solid line).

with $A_G = A + BG$ and $C_G = C + DG$. The H_∞ controller design methodology considers the system norm

$$\gamma_G = \sup_{\|w\|_2 \neq 0} \frac{\|z\|_2}{\|w\|_2}, \tag{15}$$

where $\|f\|_2 = \left[\int_0^\infty f^T(t)\, f(t)\, dt\right]^{1/2}$ is the usual continuous 2-norm. The value γ_G represents the worst-case gain from the disturbance-input to the closed-loop controlled-output defined by the control gain matrix G. The value γ_G can be computed by solving the optimization problem

$$\gamma_G = \sup_{\omega}\ \sigma_{\max}\big[T_G(\omega)\big], \tag{16}$$

with

$$T_G(\omega) = C_G(2\pi\omega j I_{2n} - A_G)^{-1}E, \tag{17}$$

where $j = \sqrt{-1}$, ω is the frequency in hertz, and $\sigma_{\max}[\,\cdot\,]$ denotes the maximum singular value. The controller design objective is obtaining an optimal state-feedback controller $u(t) = \widetilde{G}x(t)$ that produces an asymptotically stable matrix $A_{\widetilde{G}}$ and attains a minimum H_∞-norm value $\gamma_{\widetilde{G}}$. Using an LMI formulation, the optimal state-feedback H_∞ controller can be obtained by solving the following optimization problem [6]:

$$\mathcal{P}: \begin{cases} \text{maximize } \eta \\ \text{subject to } X > 0,\ \eta > 0, \\ \qquad \begin{bmatrix} AX + XA^T + BY + Y^TB^T + \eta EE^T & * \\ C_zX + D_zY & -I_{2n+m} \end{bmatrix} < 0, \end{cases} \tag{18}$$

where $*$ denotes the transpose of the symmetric entry and $X = X^T \in \mathbb{R}^{2n\times 2n}$, $Y \in \mathbb{R}^{m\times 2n}$ are the optimization variables. If an optimal value $\widetilde{\eta}$ is attained in $\mathcal{P}$ for the pair $\left(\widetilde{X}, \widetilde{Y}\right)$, then the

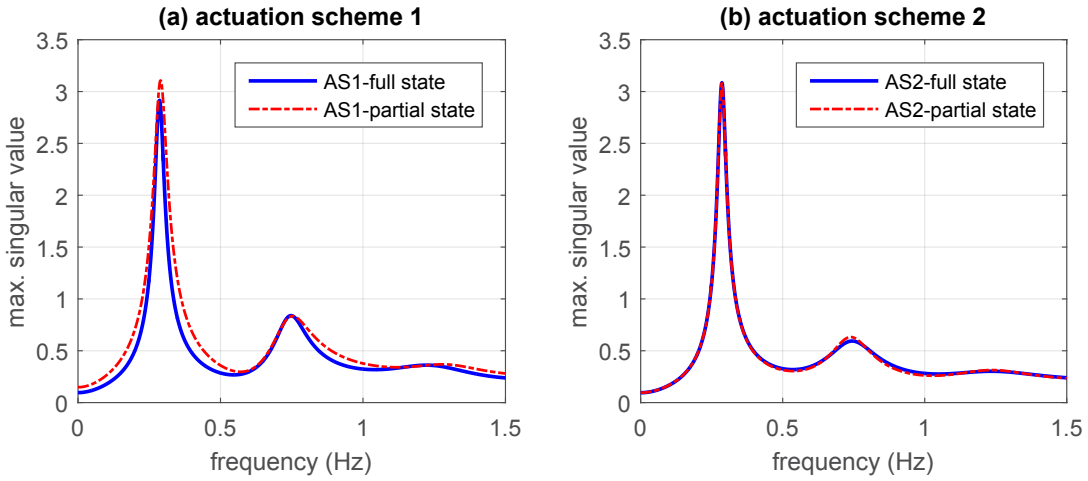

Figure 3: Frequency response of the controllers with full and partial state information. (a) Maximum singular values of the closed-loop transfer function $T_{\widetilde{G}_1}(\omega)$ (blue solid line) and the closed-loop transfer function $T_{\widetilde{K}_1}(\omega)$ (red dotted line). (b) Maximum singular values of the closed-loop transfer function $T_{\widetilde{G}_2}(\omega)$ (blue solid line) and the closed-loop transfer function $T_{\widetilde{K}_2}(\omega)$ (red dotted line).

state-feedback gain matrix $\widetilde{G} = \widetilde{Y}\widetilde{X}^{-1}$ is an optimal solution to the H_∞ controller synthesis problem and the corresponding γ-value can be computed as $\gamma_{\widetilde{G}} = \left(\widetilde{\eta}\right)^{-1/2}$.

To obtain a state-feedback control gain matrix $\widetilde{G}_1$ for the actuation scheme AS1, we solve the LMI optimization problem $\mathcal{P}$ with the values $n = 20$, $m = 10$; the matrices A, B, E in Eq. (9) corresponding to the values in Table 1 and the control location matrix $T_u^{P_1}$ in Eq. (5); and the controlled-output matrices C_z, D_z in Eq. (13) with the scaling factor $\alpha = 10^{-7.4}$. We also compute a state-feedback control gain matrix $\widetilde{G}_2$ for the actuation scheme AS2, using this time the control location matrix $T_u^{P_2}$ in Eq. (6). The γ-values of the obtained controllers are

$$\gamma_{\widetilde{G}_1} = 2.9153,\ \gamma_{\widetilde{G}_2} = 3.0850, \tag{19}$$

and the corresponding frequency responses are displayed in Fig. 2. Looking at the overall view presented in Fig. 2(a), it can be appreciated that both controllers produce a significant reduction of the building resonant peaks. In accordance with the obtained γ-values, the plots in Fig. 2(b) show that a slightly higher performance is attained by the actuation scheme AS1 with the controller $\widetilde{G}_1$ in the main resonant peak. However, a better behavior is exhibited by the actuation scheme AS2 with the controller $\widetilde{G}_2$ in the second resonant peak.

3.2 Controllers with partial state information

In this section, we assume that the available feedback information is reduced to a vector of measured outputs $y(t) = [y_1(t), y_2(t), \ldots, y_{2m-1}(t), y_{2m}(t)]^T$, where $y_{2i-1}(t) = r_{p_i}(t)$ and $y_{2i}(t) = \dot{r}_{p_i}(t)$ are, respectively, the interstory drift and velocity associated to the interstory actuation device d_i implemented at the building position p_i (between the stories s_{p_i-1} and s_{p_i}). Using a measured-output matrix $C_y \in \mathbb{R}^{2m\times 2n}$, the vector $y(t)$ can be written in the form $y(t) = C_y\, x(t)$. For a complete actuation scheme, C_y is an identity matrix of dimension $2n$. For

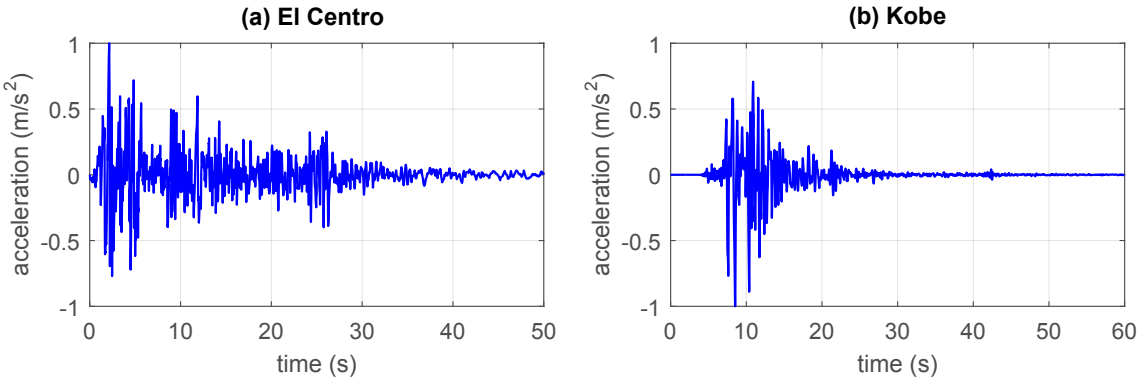

Figure 4: Ground acceleration disturbances. (a) North-South El Centro 1940 seismic record scaled to an acceleration peak-value of 1m/s^2. (b) North-South Kobe 1995 seismic record scaled to an acceleration peak-value of 1m/s^2.

an incomplete actuation scheme defined by a list of positions $P = [p_1, \ldots, p_m]$, the corresponding measured-output matrix C_y^P can be obtained by selecting the rows in positions $2p_i - 1$, $2p_i$ from the identity matrix I_{2n}, that is:

$$C_y^P = I_{2n}(2p_1 - 1, 2p_1, \ldots, 2p_m - 1, 2p_m; 1, 2, \ldots, 2n). \tag{20}$$

Thus, for example, the measured-output matrix corresponding to the actuation scheme AS1 is $C_y^{P_1} = \big[I_{20}, [0]_{20\times 20}\big]$. Considering the imposed constraints on the feedback information, we are interested in designing a static output-feedback controller $u(t) = Ky(t)$, defined by a constant output-feedback gain matrix $K \in \mathbb{R}^{m\times 2m}$, that allows computing the vector of control actions from the vector of measured-outputs by means of a simple matrix multiplication. Now, the closed-loop system has the following form:

$$\begin{cases} \dot{x}(t) = A_K\, x(t) + Ew(t), \\ z(t) = C_K\, x(t), \end{cases} \tag{21}$$

with $A_K = A + BKC_y$ and $C_K = C_z + D_zKC_y$, and the associated H_∞-norm takes the value $\gamma_K = \sup_\omega \sigma_{\max}\big[T_K(\omega)\big]$, with $T_K(\omega) = C_K(2\pi\omega j I_{2n} - A_K)^{-1}E$. In this new context, the H_∞ controller design aims at obtaining an optimal static output-feedback controller $u(t) = \widetilde{K}y(t)$ that produces an asymptotically stable closed-loop matrix $A_{\widetilde{K}}$ and, simultaneously, attains a minimum H_∞-norm value $\gamma_{\widetilde{K}}$. The effective computation of this kind of optimal controllers for large-scale systems is a very difficult problem that still remains unsolved. However, according to the results presented in [7, 8], a suboptimal static output-feedback H_∞ controller can be designed by solving the following LMI optimization problem:

$$\mathcal{P}_o : \begin{cases} \text{maximize } \eta \\ \text{subject to } X_Q > 0,\ X_R > 0,\ \eta > 0 \text{ and the LMI in (23)}, \end{cases} \tag{22}$$

$$\begin{bmatrix} AQX_QQ^T + QX_QQ^TA^T + ARX_RR^T + RX_RR^TA^T + BY_RR^T + RY_R^TB^T + \eta EE^T & * \\ C_zQX_QQ^T + C_zRX_RR^T + D_zY_RR^T & -I_{2n+m} \end{bmatrix} < 0, \tag{23}$$

where $*$ denotes the transpose of the symmetric entry, X_Q, X_R and Y_R are the optimization variables, Q is a matrix whose columns contain a basis of $\mathrm{Ker}(C_y)$, and the matrix R has the form $R = C_y^{\dagger} + QQ^{\dagger}\widetilde{X}C_y^T\left(C_y\widetilde{X}C_y^T\right)^{-1}$, where $C_y^{\dagger} = C_y^T\left(C_y\,C_y^T\right)^{-1}$ and $Q^{\dagger} = \left(Q^TQ\right)^{-1}Q^T$ are the *Moore-Penrose* pseudoinverses of C_y and Q, respectively, and $\widetilde{X}$ is the optimal X-matrix obtained in the LMI optimization problem $\mathcal{P}$ corresponding to the state-feedback design. If an optimal value $\widetilde{\eta}_{\mathrm{o}}$ is attained in $\mathcal{P}_{\mathrm{o}}$ for the triplet $\left(\widetilde{X}_Q, \widetilde{X}_R\,, \widetilde{Y}_R\right)$, then the matrix $\widetilde{K} = \widetilde{Y}_R\left(\widetilde{X}_R\right)^{-1}$ defines a static output-feedback controller $u(t) = \widetilde{K}y(t)$ with asymptotically stable closed-loop matrix $A_{\widetilde{K}}$, and the value $\widetilde{\gamma}_{\widetilde{K}} = \left(\widetilde{\eta}_{\mathrm{o}}\right)^{-1/2}$ provides an upper bound of the associated H_∞-norm value $\gamma_{\widetilde{K}}$.

To design a partial-state controller for the proposed twenty-story building model with the actuation scheme AS1, we consider the measured-output vector

$$y^{(1)}(t) = [r_1(t), \dot{r}_1(t), r_2(t), \dot{r}_2(t), \ldots, r_{10}(t), \dot{r}_{10}(t)]^T, \tag{24}$$

and solve the LMI optimization problem $\mathcal{P}_{\mathrm{o}}$ in Eq. (22) with the same matrices A, B, E, C_z and D_z used in the design of the state-feedback gain matrix $\widetilde{G}_1$, and the matrices Q, R defined by the measured-output matrix $C_y^{P_1} = \left[I_{20}, [0]_{20\times 20}\right]$ and the optimal X-matrix computed in the associated full-state controller design. As a result, we obtain an output-feedback gain matrix $\widetilde{K}_1$ with a γ-value upper bound $\widetilde{\gamma}_{\widetilde{K}_1} = 3.3846$. The frequency response of the partial-state controller $u(t) = \widetilde{K}_1\, y^{(1)}(t)$ and the associated full-state controller $u(t) = \widetilde{G}_1\, x(t)$ are displayed in Fig. 3(a). The plots in the figure show a small (but clearly appreciable) loss of performance of the partial-state controller (red dash-dotted line) with respect to the full-state controller (blue solid line). Using the closed-loop transfer function $T_{\widetilde{K}_1}(\omega)$, we obtain that the actual γ-value of the partial-state controller is $\gamma_{\widetilde{K}_1} = 3.1072$, which represents an increment of 6.58% with respect to the optimal value $\gamma_{\widetilde{G}_1} = 2.9153$.

For the distributed actuation scheme AS2, the vector of measured outputs $y^{(2)}(t)$ contains the interstory drifts and velocities indicated in the list of positions $P_2 = [1, 2, 3, 4, 5, 7, 10, 13, 16, 19]$. In this case, we obtain an output-feedback gain matrix $\widetilde{K}_2$ with a γ-value upper bound $\widetilde{\gamma}_{\widetilde{K}_2} = 3.0857$ by solving the LMI optimization problem $\mathcal{P}_{\mathrm{o}}$ with the same matrices A, B, E, C_z and D_z used in the design of the state-feedback gain matrix $\widetilde{G}_2$, and the matrices Q and R defined by the measured-output matrix $C_y^{P_2}$ and the corresponding auxiliary X-matrix. Comparing the value of the upper bound $\widetilde{\gamma}_{\widetilde{K}_2}$ with the optimal value $\gamma_{\widetilde{G}_2} = 3.0850$, it can be seen that the static output-feedback controller $u(t) = \widetilde{K}_2\, y^{(2)}(t)$ is practically optimal. In fact, the plots presented in Fig. 3(b) show that the frequency response of the partial-state controller defined by the output-feedback gain matrix $\widetilde{K}_2$ (red dash-dotted line) is practically equal to the frequency response of the optimal full-state controller defined by the state-feedback gain matrix $\widetilde{G}_2$ (blue solid line).

4 NUMERICAL RESULTS

To further illustrate the behavior of the proposed partial-state controllers, a suitable set of numerical simulations has been carried out using the scaled North-South components of El Centro 1940 and Kobe 1995 seismic records as ground acceleration inputs (see Fig. 4). For the El Centro seismic disturbance, the absolute peak-values of the interstory-drifts, the story absolute

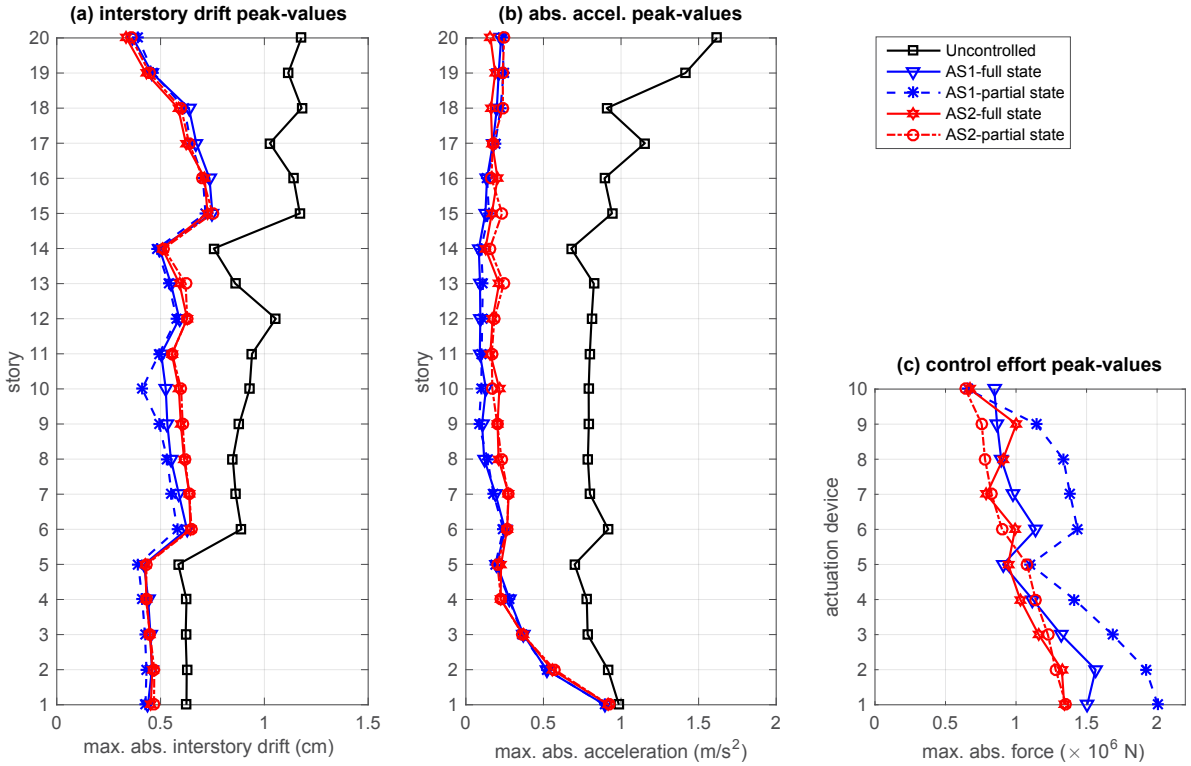

Figure 5: Response of the twenty-story building model corresponding to the scaled North-South El Centro 1940 seismic record for the uncontrolled configuration (black line with squares), the actuation scheme AS1 with the full-state controller defined by the state-feedback gain matrix $\widetilde{G}_1$ (blue solid line with triangles), the actuation scheme AS1 with the partial-state controller defined by the output-feedback gain matrix $\widetilde{K}_1$ (blue dashed line with asterisks), the actuation scheme AS2 with the full-state controller defined by the state-feedback gain matrix $\widetilde{G}_2$ (red solid line with hexagrams), and the actuation scheme AS2 with the partial-state controller defined by the output-feedback gain matrix $\widetilde{K}_2$ (red dash-dotted line with circles). (a) Interstory drift peak-values. (b) Absolute acceleration peak-values. (c) Control effort peak-values.

accelerations and the actuation control efforts corresponding to the different control configurations are presented in Fig. 5, where the black lines present the response of the uncontrolled building, the blue lines correspond to the controllers of the actuation scheme AS1, and the red lines represent the controllers of the distributed actuation scheme AS2. Also, solid lines are used for the full-state controllers and discontinuous lines for the partial-state controllers. Looking at the plots in the figure, the following facts can be appreciated: (i) All the proposed controllers provide a good level of reduction in the interstory drift and absolute acceleration peak-values with respect to the uncontrolled response. (ii) For the distributed actuation control scheme AS2, the behavior of the full-state controller and the partial-state controller (red lines) are very similar. (iii) For the concentrated actuation scheme AS1, the interstory drift peak-values produced by the partial-partial state controller (blue dashed line with asterisks) are slightly smaller that those attained by the full-state controller controller (blue solid line with triangles). However,

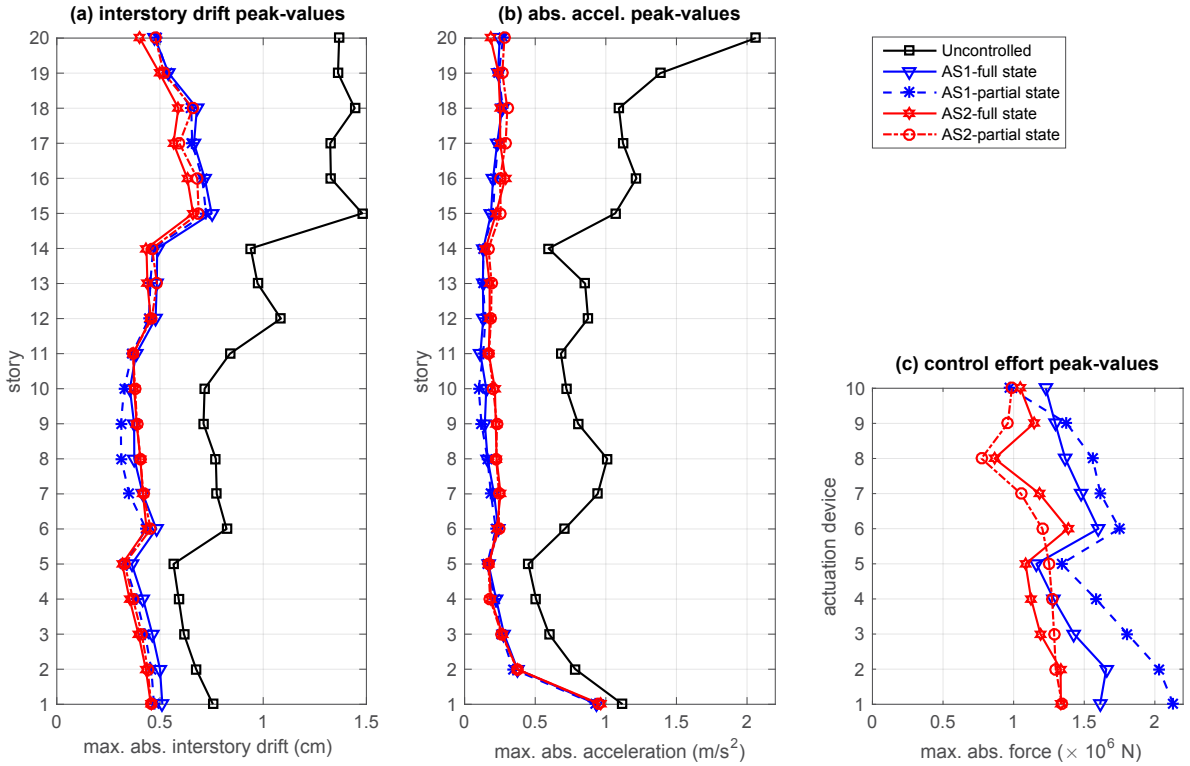

Figure 6: Response of the twenty-story building model corresponding to the scaled North-South Kobe 1995 seismic record for the uncontrolled configuration (black line with squares), the actuation scheme AS1 with the full-state controller defined by the state-feedback gain matrix $\widetilde{G}_1$ (blue solid line with triangles), the actuation scheme AS1 with the partial-state controller defined by the output-feedback gain matrix $\widetilde{K}_1$ (blue dashed line with asterisks), the actuation scheme AS2 with the full-state controller defined by the state-feedback gain matrix $\widetilde{G}_2$ (red solid line with hexagrams), and the actuation scheme AS2 with the partial-state controller defined by the output-feedback gain matrix $\widetilde{K}_2$ (red dash-dotted line with circles). (a) Interstory drift peak-values. (b) Absolute acceleration peak-values. (c) Control effort peak-values.

significantly larger control-effort peak-values are also required by the partial-state controller. Looking at the graphics in Fig. 6, the same facts can be appreciated in the peak-value plots obtained for the Kobe seismic disturbance. These time-response results are entirely consistent with the frequency-response characteristics observed in Section 3, and indicate that a similar performance level is attained by the full-state controllers in both actuation schemes. For the partial-state controllers, the situation is clearly different. In the distributed actuation scheme AS2, the partial-state controller is not affected by the reduced feedback information, and it attains practically the same level of performance as the full-state controller. In contrast, an evident loss of effectiveness can be observed in the partial-state controller corresponding to the concentrated actuation scheme AS1.

Remark. All the computations in this paper have been carried out using Matlab© R2015b on a regular laptop with an Intel© Core™ i7-2640M processor at 2.80 GHz. The LMI optimization problems have been solved with the function `mincx()` included in the Robust Control Toolbox™.

5 CONCLUSIONS AND FUTURE DIRECTIONS

In this paper, the design of partial-state controllers with incomplete multi-actuation systems for the seismic protection of large buildings has been investigated. The proposed approach considers a partially instrumented building with a system of interstory force-actuation devices implemented at selected levels of the building, and an associated set of collocated sensors that provide the interstory drifts and velocities corresponding to the instrumented stories. Using a static output-feedback H_∞ controller design methodology, partial-state controllers have been designed for a twenty-story building with two different actuation schemes, and the corresponding frequency and time responses have been investigated. The obtained results confirm the effectiveness of the proposed partial-state controllers and indicate that a suitable distribution of the instrumented stories is a relevant factor in the control system design. After these positive outcomes, further research effort should be invested in finding a suitable methodology to determine the optimal configuration of distributed multi-actuation systems with partial state information. This is certainly an important and challenging problem, specially for large-scale structures.

Acknowledgments

This work was partially supported by the Spanish Ministry of Economy and Competitiveness under Grant DPI2015-64170-R/FEDER.

REFERENCES

[1] Spencer, B.F. and Nagarajaiah, S. State of the art of structural control, *Journal of Structural Engineering* (2003) **129**:845–856.

[2] Thenozhi, S. and Yu, W. Advances in modeling and vibration control of building structures, *Annual Reviews in Control* (2013) **37**:346–364.

[3] Wang, Y., Lynch, J.P. and Law, K.H. Decentralized H_∞ controller design for large-scale civil structures, *Earthquake Engineering and Structural Dynamics* (2009) **38**:377–401.

[4] Palacios-Quiñonero, F., Rubió-Massegú, J., Rossell, J.M. and Karimi, H.R. Vibration control strategy for large-scale structures with incomplete multi-actuator system and neighbouring state information, *IET Control Theory and Applications* (2016) **10**:407–416.

[5] Chopra, A.K. *Dynamics of Structures. Theory and Applications to Earthquake Engineering 3rd ed.* Prentice Hall (2007).

[6] Boyd, S., Ghaoui, L.E., Feron, E. and Balakrishnan, V. *Linear Matrix Inequalities in System and Control Theory.* SIAM Studies in Applied Mathematics (1994).

[7] Rubió-Massegú, J., Rossell, J.M., Karimi, H.R. and Palacios-Quiñonero, F. Static output-feedback control under information structure constraints, *Automatica* (2013) **49**:313–316.

[8] Palacios-Quiñonero, F., Rubió-Massegú, J., Rossell, J.M. and Karimi H.R. Feasibility issues in static output-feedback controller design with application to structural vibration control. *Journal of the Franklin Institute* (2014) **351**:139–155.

VIII ECCOMAS Thematic Conference on Smart Structures and Materials
SMART 2017
A. Güemes, A. Benjeddou , J. Rodellar and Jinsong Leng (Eds)

APPLICATION OF ADVANCED TECHNOLOGIES IN CONSTRUCTION OF CONCRETE DAMS USING WIRELESS TEMPERATURE MEASURING AND MONITORING SYSTEMS

JAVAD MAJROUHI SARDROUD

Assistant Professor, Department of Civil and Construction Engineering, Central Tehran Branch, Islamic Azad University
Nyayesh University Complex, Emam Hasan Blv., Ponak Sq., Tehran, Iran
Email: j.majrouhi@iauctb.ac.ir, Web page: http://j-majroohis-civil.iauctb.ac.ir/faculty/

Key words: Concrete Dam, Lifecycle Assessment and Management, Wireless Temperature Measuring.

Abstract. Concrete dams are constructed for a wide range of water storage functions such as hydropower. The internal temperature of concrete dams is commonly measured both during and after construction. Temperature measurements are important both to determine causes of movement due to expansion or contraction and to compute actual movement. Temperature may be measured using any of several different kinds of embedded thermometers, embedded fibre optic sensors or by simultaneous temperature readings on devices such as stress and strain meters. This paper investigates an integrated application of Radio Frequency Identification (RFID) and sensor technology connected to GSM technology for accurate and timely temperature measuring and monitoring of concrete dams both during and after construction. The RFID tags can log, and wirelessly transmit, the concrete temperature. In this approach, the combination of RFID, sensor, and GSM technologies as a powerful data collection tool enables collection, storage, sharing, and reuse of temperature data accurately, completely, and almost instantaneously. Thus, the proposed system secures rapid notification of potentially hazardous condition and alarm. The proposed system provides an opportunity to measure and transmits real time concrete temperature using minimal or no worker inputs which leads to conduct quality assessment and management in dams' structures.

1 INTRODUCTION

Dams are constructed for a specific purpose such as water supply, flood control, irrigation, navigation, sedimentation control, and hydroelectricity generation. Concrete dams are used for a wide range of water storage functions including water supply, and hydropower. The performance of these structures under operational and environmental loads may decrease over time due to age related deterioration, floods and other factors. If concrete dams are not well managed and maintained, failure may occur leading to economic and life losses[1]. The construction process and the change of surrounding temperature outside of dams, especially for a high RCC dam, have an important influence on the temperature and stress fields[2].

The internal temperature of concrete dams is commonly measured both during and after construction. During construction, the heat of hydration of freshly placed concrete can create

high stresses which can result in cracking later. Therefore well controlling of difference in temperature and temperature strain are important measures on concrete cracking control.

In fact, what is called cement hydration reaction for cementitious materials (cement + water ---> hydrates + calcium hydroxide + heat) is the combination of hydration reactions that takes place when concrete is becoming mature[3,4]. For Portland cement hydration, the main reactions are based on the mineral compounds of the clinker[3].

After construction is completed and a dam is in operation, very significant temperature differentials are not uncommon, depending on the season. By the other words, extreme external actions in the surrounding geological system involving the dam are causes of possible structural damage[5]. Temperature measurements are important both to determine causes of movement due to expansion or contraction and to compute actual movement.

Structural Health Monitoring (SHM) is the science and technology of monitoring and assessing the condition of civil and mechanical infrastructures which controls, verifies and informs about the condition or changes in the condition of a structure using a sensing system integrated into the structure[6]. The monitoring can be continuous or periodic, short-term or long term, local or global and the monitoring system can consist of a few sensors up to hundreds or even thousands of them depending on the demands of the monitoring object. Health monitoring of dams plays an essential role in securing their structural integrity and maintaining their longevity. This is divided into static and dynamic monitoring. Static monitoring involves measurement of static factors such as ambient temperatures, reservoir level, opening and closing of joints, crack opening, displacements and strains which are measured accurately by instruments, and dynamic monitoring is used to determinate resonant frequencies, damping ratio and mode shapes by running forced vibration testing and ambient vibration testing[1].

The parameters that are to be monitored is the most important task in SHM and the whole concept may fail if it is not performed appropriately. Although the development of structural health monitoring technology such as fibre optic sensors[7] for surveillance, evaluation and assessment of existing or newly built structures has now attained some degree of maturity, the development and implementation of a structural health monitoring system capable of fully achieving the objectives and benefits is still a challenge at present[8]. The network of wires may easily loose connections. Therefore, maintaining the wire network on construction sites while concrete is being cured is a challenge[9].

Radio Frequencies (RF) based information and communication technologies, such as Radio Frequency Identification (RFID) tags have matured and become commercially available to potentially support automated data collection in construction. A RIFD system consists of tags (transponder) with an antenna, a reader (transceiver) with an antenna, and a host terminal. The RFID reader acts as a transmitter and receiver and transmits an electromagnetic field that ‘‘wakes-up’’ the tag and provides the power required for the tag to operate[10]. RFID technology provides a solution for the wiring issue because of its ability of sending data wirelessly[11]. One of the recent developments is the use of the RFID tags integrated with the temperature sensor. An RFID tag integrated with a temperature sensor and placed within fresh concrete may be able to read temperatures of concrete and transmit them to an RFID reader wirelessly in real-time[12].

This research investigates an integrated application of Radio Frequency Identification technology and sensor technology for accurate and timely temperature measuring and

monitoring of concrete dams both during and after construction. In other words, RFID-facilitated automated data collection system will provide an opportunity to measure and transmits real time concrete temperature using minimal or no worker input which leads to conduct Structural Health Monitoring (SHM) in dams' structures. Although the proposed system can be used to cover all aspect of structural health monitoring by using appropriate sensor embedded to RFID system, this paper explained just cracks control of concrete structure by temperature monitoring of concrete.

2 LITERATURE REVIEW

Monitoring of civil infrastructure and operational systems can be divided to time schedule, sampling, object, phenomenon, instruments and response. For this research, monitoring system is continuous in its time schedule, low speed sampling, for structural, materials and other components of dam with environmental parameters for phenomenon which uses electrical instruments and responses static[13].

The determination of bulk material properties, e.g., compressive stress in concrete structures, across a large material volume remains a necessary job in the concrete evaluation industry or Non-Destructive Testing (NDT) applications. However, for a long time, it has been disturbing that piezoelectric transducers are sensitive not only to mechanical settings but also to a lot of surrounding factors such as temperature and humidity[14].

Structural health especially temperature may be measured using any of several different kinds of embedded thermometers[15], embedded fibre optic sensors[16,17] or by simultaneous temperature readings on devices such as stress and strain meters. Management workload, involving such activities as measurement and collecting and classifying data, can be reduced by information technology because of automatic sensing technology[18].

In Concrete structure such as dams, Cracks can adversely affect structural performance in various ways such as durability and serviceability[19]. If the initial cracks are not carefully handled, they will grow till one of them reaches the critical dimension, which makes extreme structural damage and may directly result in the entire collapse. Therefore, crack monitoring is one of the most important steps to prevent the collapse of concrete structures[20]. Temperature gradients and differential thermal expansions can have damaging effects on structures. Globally, temperature variations may generate stresses that facilitate mechanical cracking in statically indeterminate structures. Locally, they can change the mechanical properties of the material and lead to its deterioration[21].

Distributed and quasi-distributed fibre optic systems for large-scale monitoring have been developed and commercialised in recent years. Large-scale structures like dams, pipelines, concrete columns, tunnels, dykes, piles and roadbeds have been instrumented and monitored for temperature and strain changes[22].

Some studies have found that changes in structural vibration properties because of temperature variations could be more significant than those caused by a medium degree of structural damage[23]. A sensor that monitors the hydration process would provide information on instantaneous condition of the concrete and when critical actions can be taken, for example, formwork removal[24].

In order to conduct effective structural health monitoring system, the system should support continuous monitoring, early alarm of any incipient damage, and data acquisition

even in harsh environmental conditions. This system can be called remote structural monitoring. Remote structural monitoring methodology requires an interdisciplinary approach integrating areas such as structural engineering, sensor technology, communication technology, statistical mechanics, information technology for online data transmission (over larger distances) and damage detection/health assessment of the structure[25]. Many researchers over the past decade have proposed passive wireless strain sensors, also known as radio frequency identification (RFID) - based sensors, to eliminate the need for cables and collocated power sources, thereby opening the possibility of densely instrumented embedded monitoring systems[26].

Smart sensors with embedded microprocessors and wireless communication links have the potential to change fundamentally the way civil infrastructure systems are monitored, controlled, and maintained[27]. RFID technology has recently matured due to industrial development, costing as little as $0.50 per tag, allowing for many such devices to be placed on a large structure at numerous critical junctures[28].

3 AIMS AND OBJECTIVES

The goal of the research is to assess RFID application for effective structural health monitoring of concrete dams by measurement of concrete temperature both during and after construction. This suggested way for monitoring and measuring temperature with RFID-enabled system is an actual solution for structural health monitoring with minimum staff and financial outlay and maximum accuracy. It means that by using RFID technology and with a high degree of accuracy we are able to assess structure's condition in terms of cracks. Automated data collection for cracks control, furthermore, enables structural health of concrete dams to be controlled and managed in a real-time base. This research will focus mainly on evaluating the potential for utilising RFID-based techniques to monitor and capture data for all cracks related to temperature. Figure 1 shows an RFID-based SHM typical system.

4 ARCHITECTURE OF THE PROPOSED INTEGRATED RFID-BASED SYSTEM

Although measurement of concrete temperature could eventually be achieved with other systems, this paper introduces the pioneering combination of RFID and sensor technologies for this purpose. Even though each of them can be used as a stand-alone system in dam construction, the combination of them will significantly raises the consistency and reliability of the system as a whole, thus greatly alleviate the data collection process.

In this research, RFID-based sensor system was developed to measure concrete temperature in its lifecycle. This system was divided into two main parts, namely hardware and a server. The hardware of the system mainly consists of two types of hardware components; namely:

- RFID technology (RFID readers, antenna), RFID was selected as the technology in Identification segment and RFID active tag (containing a data logger) connected to temperature sensor was used for identifying and monitoring the concrete temperature by using RFID reader which is connected to the system; and
- GSM technology, the system is then synchronised over GSM network via SIM card, and the information (ID, date, and temperature) retrieved from RFID readers is

transferred to the server in the form of GPRS. Therefore, data collection and transmission are done continuously and autonomously.

The server can consist of two parts: application server and database server (information database). The application server could use different software for collecting, storing, updating, modifying, filtering, and sharing this data to act as a structural health monitoring system. Figure 2 is a schematic representation of the RFID-based temperature monitoring tool's architecture.

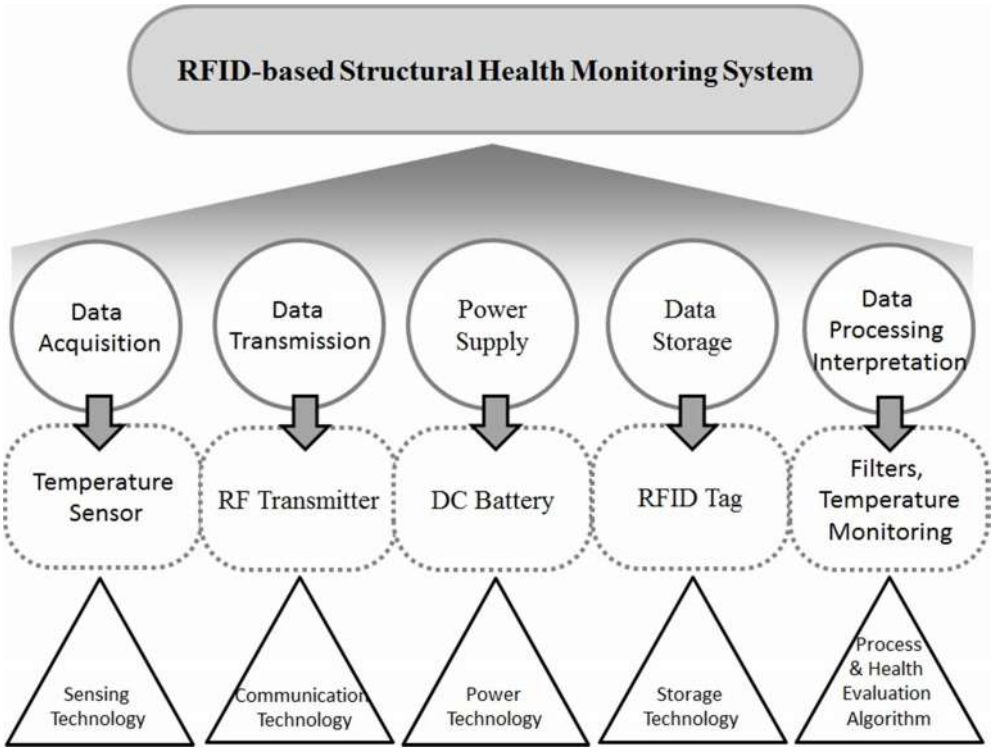

Figure 1: RFID-based SHM typical system

In this system, RFID tags which are connected to temperature sensors can be placed in any element of structure. In other words, the RFID tag is embedded in concrete at the time of placement, and the system provides wireless communication between the tag and reader. Tags are equipped with unique ID number. The sensors may need to be placed in different depths at the same location. The reader system can be mounted on any specific place and people. RFID tags are scanned 24 hours a day, 7 days a week by each reader's and information gathered from RFID-based system is then transmit to the server using GPRS. If temperature of concrete is changed, this system can effectively monitor its value. These advantages are due to the flexibility of the proposed integrated RFID-based system.

5 IMPLEMENTATION PROCESS AND GUIDELINES

In order to achieve success with the proposed temperature monitoring system using the RFID-based automated data collection system: first, a management team must be created at early phase of the project and the team is to be responsible for purchasing and implementing

the system. The team may be from the owner side, from the main contractor, or both of them. Second, necessary training is required for construction workers and managers to ensure successful implementing and running the system. Third, a pilot test should be run before the actual implementation of the system to identify any malfunction issue.

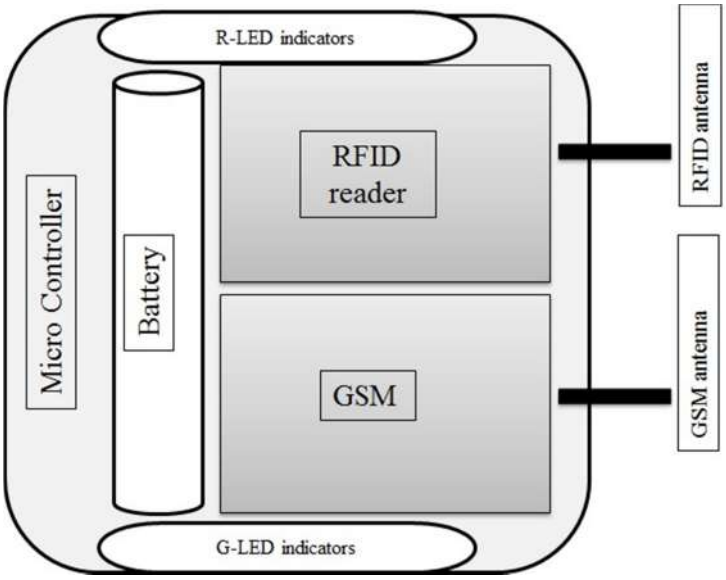

Figure 2: A schematic representation of the RFID-based temperature monitoring architecture

This system could be programmed to generate reports and alerts. The report of measuring temperature for a specific location is usually based on the tag identity code which is unique. The reports include history of temperature for any specific tag. The alerts include a list of tags with high temperature that should be checked. The proposed system has the flexibility of monitoring temperature just placing a tag without investing in additional fixed infrastructure. Figure 3 represents temperature monitoring of concrete dams during and after construction.

Automated structural health monitoring which relies on real-time and accurate information necessitates collection of data automatically, continuously and almost instantaneously. Hence, the main benefit from the use of the proposed integrated system is to guarantees the availability of the accurate information related to the concrete temperature. Collective information is sent automatically to the database. This means that all the information is available in one place so that construction players (including contractors and clients) can access in a cost-effective way and almost instantly. Thus, an electronic exchange of information is created in this research, which provides real-time information and wireless communication among all players. An adequate data structure needed to be identified in order to store, share, and manage large amounts of collected data and to integrate the collected information with other project management tools.

5.1 Tagging any element of structure

Tagging recognised as one of the multi-phase process and requires co-operation of various parties to guarantee its functionality during the project life-cycle. Although, tagging any element of structure would occur at the construction phase, the process has to be taken into

consideration already during design and modelling. As discussed earlier in this paper, they are many factors which affect the performance of the tags, for example: RF transmission power on readable distance and failure of readings. The RFID active tags which are used in this research have longer reading ranges and can act as self-signalling tags working on their own batteries. These tags also are space tags which attached to any element of space to represent the three-dimensional positions of the point which tag is attached.

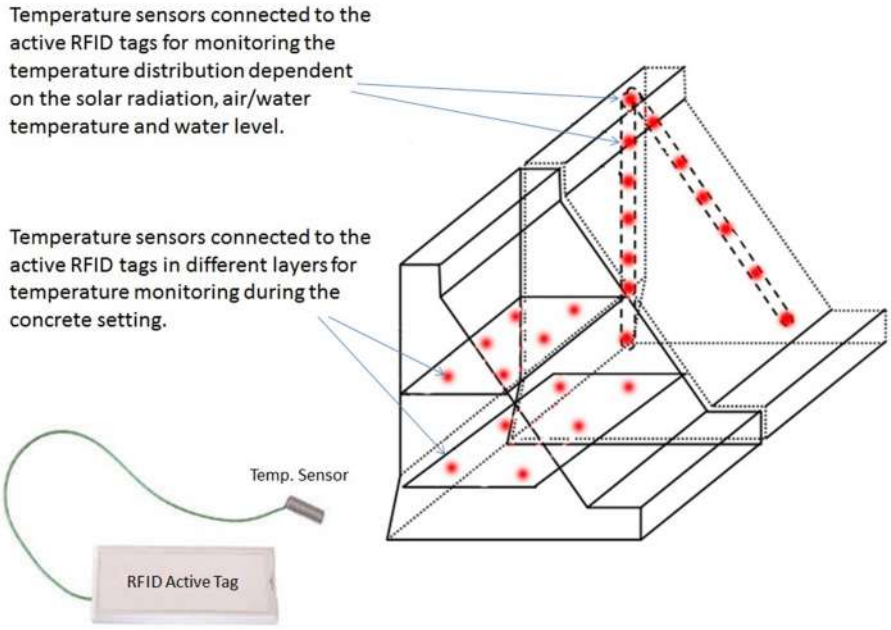

Figure 3: Temperature monitoring

Tag needs to be attached to clearly defined location into any element of structure. Considering the various types and sizes of concrete members, it would not be possible to produce a generalized outcome unless a significant amount of cases were tested. Instructions and the position of the tags need to be saved in the server. Some common rules and best practices about the location should be agreed to guarantee the readability of tags and ease the later reading process.

As stated earlier, considering the limited memory of the tags, in addition to collected temperature data, the subset of information stored on the RFID tags has to be chosen based on the requirements. Types of information that need to be stored on the tags or remote databases could be divided into following groups:

- Identification-related information which is a serial number or unique ID.
- Place-related information which are longitude, latitude, and height.

5.2 System installation management

A management team must be created at early phase of the project and the team is to be responsible for purchasing and implementing the system. The size of the installation team depends on the size of the project. In order to be sure that the outcome will be adequate for all partners, implementation team could be from the owner side, from the construction contractor,

from the design consultant and instrumentation consultant (Table 1). The temperature data should be collected until the dam has been in satisfactory service for several years. Thus, the choice of system and sensors should be done in cooperation by different kind of experts as several fields of engineering are involved.

Table 1: System installation and implementation team

Activity	Owner	Design Consultant	Instrumentation Consultant	Construction Contractor
Monitoring design and planning	✓	✓	✓	
Instrument procurement		✓	✓	
Instrument installation			✓	✓
Instrument calibration and maintenance			✓	✓
Preparation of the plan to collect data		✓	✓	
Data collection			✓	✓
Data analysis and offering			✓	
Data interpretation and report		✓	✓	
Decision making about using data	✓	✓		

6 BENEFITS AND CHALLENGES OF USING TEMPERATURE MONITORING SYSTEM

In general, the following benefits can be achieved by using temperature monitoring systems, depending on the applications:

- Data is available real time with alarms increase the safety for the end-uses.
- Constantly monitoring the in-situ temperature which leads to identify a change and to verify, control, assess and understand the actual behaviour of the structure.
- Temperature monitoring can continue for years.
- Data can be transferred, analysed and archived.
- Documents proof of quality assurance.
- Eliminates concerns of weather and construction problems.
- Decreased maintenance costs.

In order to face any problems or challenges, adapting the technology in the most suitable way and to prove the system practicality a pilot application is necessary. It is also necessary to provide guidelines to run inspection and monitoring processes for the RFID technology itself during the implementation phase. Thus, extra efforts and training are needed. Hence, it is important to provide strong incentives for enterprises for adoption of new technologies.

Even though power efficient technique, such as sleep mode, can provide possible solution to better performance of battery's life cycle, limitation of battery operation time is exist. Thus, power can be identified as another challenge. Although, in active RFID system the reader can be set to be triggered wake-up on a set time interval if desired, for low power RFID systems, the tag goes to sleep in between transmissions, so the reader needs to be on at all time listening for tags to wake up and transmit. Other key challenges could be the following issues:

- Selection of monitoring location. Number of sensors and importance of sensor locations can be studied to optimize number of sensors used per cubic meter of concrete.

- Need to operate during power outages.
- Sensor installation.

7 CONCLUSIONS

This research presented a new approach for integrating RFID technology with sensor technology that address a clear path to automate measuring and monitoring of temperature in concrete dams using minimal or no human effort. The selected technologies involve the use of combined RFID and GSM technologies to obtain real-time and accurate information about thermal condition of concrete dams. The RFID tags can log, and wirelessly transmit, the concrete temperature. In this approach, the combination of RFID, sensor, and GSM technologies as a powerful data collection tool enables collection, storage, sharing, and reuse of temperature data accurately, completely, and almost instantaneously. Thus, the proposed system secures rapid notification of potentially hazardous condition and alarm.

REFERENCES

[1] Bukenya, P., Moyo, P., Beushausen, H. and Oosthuizen, C. Health monitoring of concrete dams: a literature review, *Journal of Civil Structural Health Monitoring*, (2014) 4(4): 235-244.

[2] Zhang, X.F., Li, S.Y., Chen, Y.I. and Chai, J.R. The development and verification of relocating mesh method for the computation of temperature field of RCC dam, *Adv Eng Softw,* (2009) 40:1119-1123.

[3] Evsukoff, A.G., Fairbairn, E.M.R., Faria, E.F., Silvoso, M.M. and Toledo Filho, R.D. Modelling adiabatic temperature rise during concrete hydration: A data mining approach, *Comput Struct*, (2006) 84:2351-2362.

[4] Azenha, M. and Faria, R. Temperatures and stresses due to cement hydration on the R/C foundation of a wind tower-A case study, *Eng Struct*, (2008) 30: 2392-2400.

[5] Ardito, R., Maier, G. and Massalongo, G. Diagnostic analysis of concrete dams based on seasonal hydrostatic loading, *Eng Struct*, (2008) 30: 3176-3185.

[6] Zhou, D., Sam Ha, D. and Inman, D.J. Ultra low-power active wireless sensor for structural health monitoring, *Smart Struct Syst, An Int'l Journal*, (2010) 6(5): 675-687.

[7] Mehrani, E., Ayoub, A. and Ayoub, A. Evaluation of fiber optic sensors for remote health monitoring of bridge structures, *Mater Struct*, (2009) 42:183-199.

[8] Ko, J.M. and Ni, Y.Q. Technology developments in structural health monitoring of large-scale bridges, *Eng Struct*, (2005) 27: 1715-1725.

[9] Majrouhi Sardroud, J. Towards linking islands of information within construction projects utilizing RF technologies, *Electrical Engineering and Applied Computing,* Springer Netherlands, (2011) 197-207.

[10] Wang, L.C., Lin, Y.C. and Lin, P.H. Dynamic mobile RFID-based supply chain control and management system in construction, *Adv. Eng. Inform.*, (2007) 21(4): 377-390.

[11] Majrouhi Sardroud, J. Developing RFID-Based Electronic Specimen and Test Coding System in Construction Quality Management, *Iran J Sci Technol, Transactions of Civil Engineering*, (2013) 37(C^{+}): 469-478.

[12] Kang, J.H. and Gandhi, J. Readability Test of RFID Temperature Sensor Embedded in Fresh Concrete, *Journal of Civil Engineering and Management*, (2010) 16: 412-417.

[13] Bergmeister, K. and Santa, U. Global monitoring concepts for bridges. *Structural Concrete*, (2001) 2(1): 29-39.
[14] Wen, Y., Chen, Y., Li, P., Jiang, D. and Guo, H. Smart Concrete with Embedded Piezoelectric Devices: Implementation and Characterization, *J Intel Mat Syst Str*, (2007) 18:265-274.
[15] Antczak, E., Defer, D., Elaoami, M., Chauchois, A. and Duthoit, B. Monitoring and thermal characterisation of cement matrix materials using non-destructive testing, *NDT&E International*, (2007) 40: 428-438.
[16] Li, H.N., Li, D.S. and Song, G.B. Recent applications of fiber optic sensors to health monitoring in civil engineering, *Eng Struct*, (2004) 26: 1647-1657.
[17] Kesavan, K., Ravisankar, K., Parivallal, S., Sreeshylam, P. and Sridhar, S. 2010, Experimental studies on fiber optic sensors embedded in concrete, *Measurement*, 43, 157-163.
[18] Lee, U.K. and Kang, K.I. Mass Concrete Curing Management Based on Ubiquitous Computing, *Comput-Aided Civ Inf*, (2006) 21: 148-155.
[19] Farhidzadeh, A., Salamone, S. and Singla, P. A probabilistic approach for damage identification and crack mode classification in reinforced concrete structures, *Journal of Intelligent Material Systems and Structures*, (2013) 24:1722-1735.
[20] Zhou, Z., Zhang, B., Xia, K., Li, X., Yan, G. and Zhang, K. Smart film for crack monitoring of concrete bridges, *Struct Health Monit*, (2010) 10: 275-289.
[21] Yao, Y., Tung, S.T.E. and Glisic, B. Crack detection and characterization techniques-An overview, *Struct Control Hlth*, (2014) 21(12): 1387-1413.
[22] Enckell, M., Glisic, B., Myrvoll, F. and Bergstrand, B. Evaluation of a large-scale bridge strain, temperatureand crack monitoring with distributed fibre optic sensors, *Journal of Civil Structural Health Monitoring*, (2011) 1: 37-46.
[23] Xia, Y., Chen, B., Weng, S., Ni, Y.Q. and Xu, Y.L. Temperature effect on vibration properties of civil structures:a literature review and case studies, *Journal of Civil Structural Health Monitoring*, (2012) 2: 29-46.
[24] Quinn, W., Kelly, G. and Barrett, J. Development of an embedded wireless sensing system for the monitoring of concrete, *Struct Health Monit*, (2011) 11: 381-392.
[25] Sridhar, S., Ravisankar, K., Sreeshylam, P., Parivallal, S., Kesavan, K. and Murthy, S.G.N. Development of a Real-time Remote Structural Monitoring Scheme for Civil Infrastructural Systems, *Struct Health Monit*, (2009) 8: 509-513.
[26] Loh, K.J., Lynch, J.P., Shim, B.S. and Kotov, N.A. Tailoring Piezoresistive Sensitivity of Multilayer Carbon Nanotube Composite Strain Sensors, *Journal of Intelligent Material Systems and Structures*, (2008) 19: 747-764.
[27] Spencer Jr, B.F., Ruiz-Sandoval, M.E. and Kurata, N. Smart sensing technology: opportunities and challenges, *Struct Control Hlth*, (2004) 11: 349-368.
[28] Farrar, C.R., Park, G., Allen, D.W. and Todd, M.D. Sensor network paradigms for structural health monitoring, *Struct Control Hlth*, (2006) 13:210-225.

Continuous dynamic monitoring of a stone-masonry tower using a few accelerometers: from automated OMA to damage assessment

Alessandro Cabboi*, Carmelo Gentile† and Antonella Saisi†

* University of Cambridge, Engineering Department
Trumpington Street, CB2 1PZ Cambridge, UK
e-mail: alexcabboi@gmail.com

† Politecnico di Milano, ABC Department
P.za Leonardo da Vinci 32 – 20133 Milan, Italy
e-mail: carmelo.gentile@polimi.it, antonella.saisi@polimi.it

ABSTRACT

The full-scale experiences recently carried out on two Italian masonry towers [1]-[2] provided the evidence that the use of simple monitoring systems, consisting of a few accelerometers installed in the upper part of the building, combined to state-of-art processing tools may detect the onset of damage. However, the damage detection represents the first level (Level 1) of damage assessment in the classification originally proposed by Rytter [3] and does not answer important questions on the damage localization (Level 2) and the evaluation of its severity (Level 3).

Within the framework of historic towers, the paper aims at extending the capability of the SHM based on the use of few accelerometers, moving a step towards damage localization. To this purpose, it is proposed to extend, after a training period, the automated identification of natural frequencies to the "updating" of a baseline FE model. The automatically tuned model, in turn, might provide information on possible location of damage and its severity. Of course, removing the effects of unmeasured (environmental/operational) factors from natural frequencies is necessary to avoid the propagation of the frequencies variability associated with changing environment through the structural identification process. In case damage occurs, it should be localized – in principle – if some of the updated structural parameters exhibit clear variation with respect to the values identified during the training period.

The proposed methodology is exemplified on a historic bell-tower placed in the town of Arcisate (Northern Italy), which has been extensively studied by Politecnico di Milano between 2007 and 2012.

REFERENCES

[1] A. Saisi, C. Gentile and M. Guidobaldi, "Post-earthquake continuous dynamic monitoring of the *Gabbia* Tower in Mantua, Italy", *Meccanica*., Vol. **81**, pp. 101-112, (2015).

[2] F. Ubertini, G. Comanducci and N. Cavalagli, "Vibration-based structural health monitoring of a historic bell-tower using output-only measurements and multivariate statistical analysis", *Structural Health Monitoring,* Vol. **15**(4), pp. 438-457, (2016).

[3] T. Rytter, *Vibration based inspection of civil engineering structure*, Ph.D. Thesis, Aalborg University, Denmark, 1993.

VIII ECCOMAS Thematic Conference on Smart Structures and Materials
SMART 2017
A. Güemes, A. Benjeddou , J. Rodellar and Jinsong Leng (Eds)

CONTINUOUS DYNAMIC MONITORING OF LARGE CIVIL STRUCTURES: DIFFERENT PERSPECTIVES OF APPLICATION

Á. CUNHA*, E. CAETANO*, C. MOUTINHO* AND F. MAGALHÃES*

* CONSTRUCT-ViBest, Faculty of Engineering (FEUP), University of Porto
R. Dr. Roberto Frias, 4200-465 Porto, Portugal
e-mail: acunha@fe.up.pt, web page: http://www.fe.up.pt/vibest

Key words: Dynamic Monitoring, Bridges, Stadia, Wind Turbines, Dams.

Abstract. The Laboratory of Vibrations and Structural Monitoring (ViBest) of FEUP has been implementing, since 2007, a significant set of long-term dynamic monitoring systems in large Civil structures with different typologies (e.g. roadway, railway and pedestrian bridges, stadia suspension roofs, wind turbines, concrete dams or high voltage transmission lines). This paper briefly describes some of these applications, clearly illustrating the interest and potential of the developed technology, as well as of the huge high quality database created, which can now be used for joint collaborative research at European level.

1 INTRODUCTION

Continuous dynamic monitoring of large Civil Engineering structures has gained an increasing interest and potential in recent years, enabling the assessment of different problems, such as:

- The accurate characterization of human induced vibrations, supporting the verification of safety with regard to vibration serviceability limit states in lively structures and of the efficiency of vibration control devices;
- The accurate evaluation of dynamic effects induced by traffic loads on roadway and railway bridges;
- The fatigue assessment of old metallic railway bridges, as well as of onshore and offshore wind turbine towers;
- The accurate evaluation of the influence of environmental (e.g. temperature, wind) and operational factors (e.g. traffic intensity, water level) on the modal variability of bridges and concrete dams;
- The vibration based early detection of structural changes (e.g. damage);
- The dynamic characterization of wind effects in slender structures based on in-situ measurements.

In this context, the Laboratory of Vibrations and Structural Monitoring (ViBest) of FEUP has been implementing, since 2007, a significant set of long-term dynamic monitoring systems in large Civil structures with different typologies (e.g. roadway, railway and pedestrian bridges,

stadia suspension roofs, wind turbines, concrete dams or high voltage transmission lines).

This paper briefly describes some of these applications, clearly illustrating the interest and potential of the developed technology, as well as of the huge high quality database created, which can now be used for joint collaborative research at European level.

2 CONTINUOUS DYNAMIC MONITORING OF CIVIL STRUCTURES

2.1 Monitoring of human induced vibrations for vibration serviceability safety checking

The continuous dynamic monitoring of human induced vibrations can be useful to support the verification of safety with regard to vibration serviceability limit states in lively structures and of the efficiency of vibration control devices.



(a)



(b)

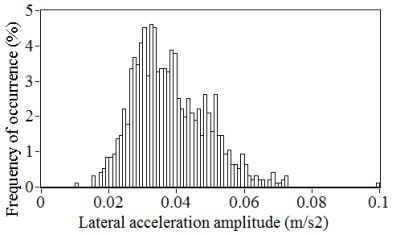

(c)

Figure 1. (a) Lateral view of Pedro e Inês footbridge; (b) TMD units for control of lateral vibrations; (c) Histogram of maximum daily lateral accelerations (June 2007 – May 2010).

This is the case, for instance, of Pedro e Inês footbridge (Fig. 1(a)), where ViBest/ FEUP implemented a long-term continuous dynamic monitoring to check the real efficiency of a set of tuned mass dampers (TMDs, Fig. 1(b)) installed at different points of the deck to control excessive lateral and vertical accelerations.

This bridge is a slender structure 275m in length and 4m wide, except in the central square with dimensions of 8mx8m. The metallic arch spans 110m and rises 9m and has a rectangular box cross-section with 1.35m x 1.80m. The deck has a L-shaped box cross-section, the top flange being formed by a composite steel-concrete slab 0.11m thick. In the central part of the bridge, each L shaped box cross-section and corresponding arch "meet" to form a rectangular box cross-section 8m x 0.90m. In the lateral spans, arch and deck generate a rectangular box cross-section 4m x 0.90m. The significant slenderness of the bridge and the geometric characteristics lead to a complex structural behavior. A key factor for the bridge global stiffness is the structural behavior of its foundations, which are formed by vertical piles deep about 30m.

Dynamic studies developed at the design stage could anticipate that this bridge would be prone to high levels of vibration induced by pedestrians, owing to the existence of a

fundamental lateral bending mode with a frequency close to one half of the mean pacing rate, easily inducing a lateral synchronization phenomenon (lock-in), as well as several natural frequencies associated to vertical bending modes susceptible to be excited by pedestrians walking, running or under rhythmic jumping. Therefore, ViBest/ FEUP, under contract with the designer (AFAssociados), and subsequently with the construction company (Soares da Costa/ Socometal), developed during the design phase a preliminary design of a set of TMDs to control the critical modes of vibration. After the end of construction, it was made a final design, which required the performance of a series of dynamic tests (ambient and free vibration tests and tests with pedestrians), which enabled an accurate updating and experimental validation of a sophisticated finite element model, that was used for an accurate evaluation of the modal masses in correspondence with the modes of vibration to be controlled. All this extensive work is described in detail in [1][2]. After installation of TMDs, forced vibration tests were also performed to accurately measure the levels of damping achieved. In the meanwhile, the owner also required a continuous dynamic monitoring of the footbridge during a period of 5 years to confirm the good performance of the vibration control devices used.

The monitoring system, described in detail in [2], is composed by 6 piezoelectric accelerometers, a signal conditioning system and an industrial PC, with an ADSL connection to the Internet. Every 20 minutes, all the collected time series are transmitted to FEUP, becoming available to the constructer, designer and owner through a website supported by a LabVIEW application, and allowing to issue alert messages in case any lateral or vertical vibration comfort level is exceeded.

Fig. 1(c) shows, for instance, a histogram associated to maximum daily lateral accelerations at midspan during a period of 3 years, which clearly shows that, after implementation of the lateral TMD, no situation of excessive lateral vibrations was recorded in that period.

2.2 Monitoring of dynamic effects of traffic loads in roadway and railway bridges

The dynamic monitoring of bridges also enables an accurate evaluation of dynamic effects induced by traffic loads on roadway or railway bridges.

This kind of study was for instance developed by ViBest/ FEUP on Salgueiro Maia bridge (Fig. 2a)), a single-plane cable-stayed bridge over Tagus river, upstream the Vasco da Gama bridge. The main objective of this study, described with more detail in [3][4][5], was the experimental evaluation of dynamic effects induced by the passage of heavy trucks using a monitoring system based on strain gages embedded in the concrete and load cells in the stay-cables.

This system was used during the static load tests involving 20 heavy trucks with total mass of 38-40t each in different loading configurations. Afterwards, dynamic tests were performed in which some of those trucks crossed the bridge at different velocities (15, 30, 45, 60, 75 and 90km/h), and along different lanes, alone or in groups. As an example, Figure 2b) shows a dynamic response recorded during the passage of a heavy truck crossing the bridge at 90km/h along a lateral lane, as well as the quasi-static response obtained by digital filtering. The dynamic amplification factors obtained (DAFs) reached, in this case, about 1.20. It's worth noting however that the induced dynamic effects are significantly dependent upon the pavement roughness conditions, which were characterized in this case by a spatial laser scanning.

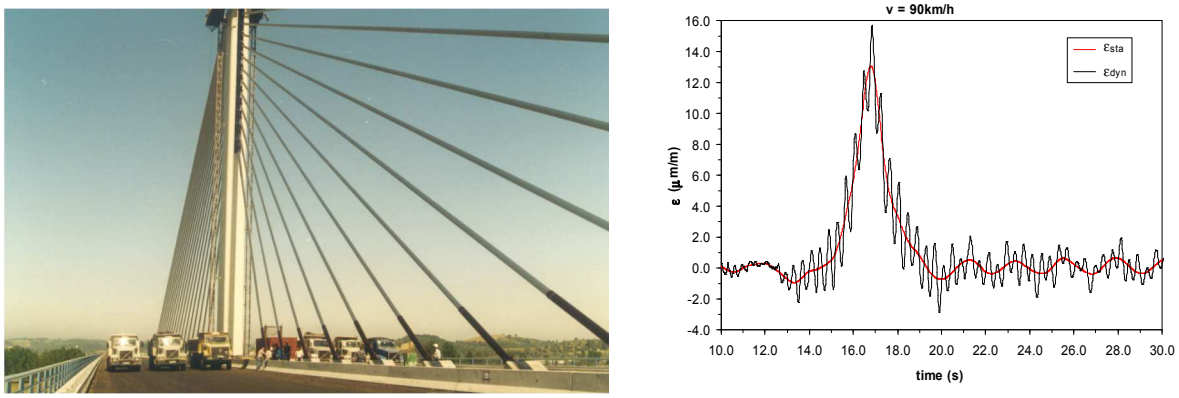

(a) (b)

Figure 2. (a) Salgueiro Maia bridge during the static load tests; (b) Record from embedded strain gage (vehicle speed of 90 km/h).

Another interesting example regards the experimental evaluation of the dynamic effects induced by traffic loads on the Trezói railway bridge (Fig. 3). This bridge is a single track metallic riveted structure with three spans of 39m, 48m and 39m, supported by two intermediate trapezoidal metallic piers and two masonry abutments at the extremities.



(a) (b)

Figure 3. Trezói bridge: (a) lateral view; (b) view inside the deck.

A temporary monitoring campaign (Fig. 4) [6] was also developed at this bridge by ViBest/ FEUP so as to characterize the global and local structural behavior, enabling the calibration and validation of numerical models used in numerical simulations.

2.3 Monitoring for fatigue assessment of railway bridges and wind turbine towers

The temporary monitoring campaign of Trezói railway bridge was also used for the analysis of stress distributions in critical elements and connections, the construction of histograms of stress cycles suitable for fatigue assessment, and collecting reliable information regarding the characteristics of real traffic crossing the bridge in terms of velocity, axle loads, number of axles and axles distances [6][7].

In a first instance, measurements were performed during two days of higher level of traffic. During that period, the bridge was crossed by 8 freight trains and 16 passenger trains. Fig. 4b) shows the very good agreement between measured and calculated stresses at an inferior chord of the truss at midspan, which is the element subjected to higher traction stresses. These results provided a higher confidence on the developed numerical simulations, as well as on the trains characteristics obtained. The fatigue damage was then evaluated for the 14 instrumented sections and for each train.

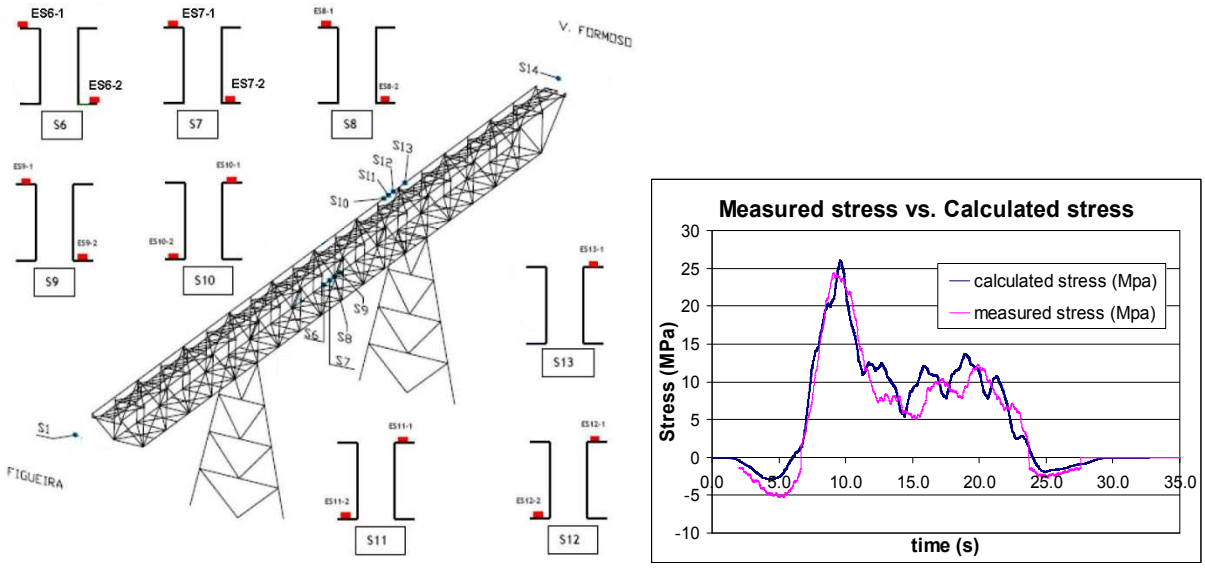

(a) (b)

Figure 4. (a) Instrumentation with strain gages; (b) Measured vs calculated stresses.

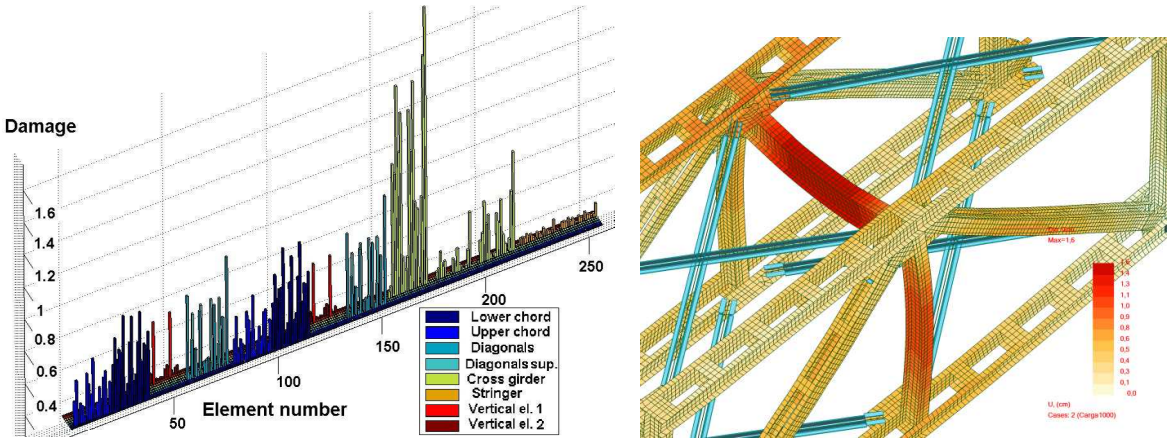

(a) (b)

Figure 5. (a) Evaluation of fatigue damage for real traffic; (b) Shell finite element modelling.

This investigation was subsequently extended to all structural elements of the bridge, which led to the conclusion that the most susceptible elements to fatigue damage are the transversal stringers (Fig. 5), which are affected by local vibrations. This aspect motivated a new research component specifically focused on these local effects, which involved also the development of

more sophisticated numerical models (Fig. 5b)) and the continuous dynamic monitoring of two transversal stringers [6][7].

A different approach has been also developed for the fatigue assessment of wind turbine towers essentially based on the use of accelerometers [8]. This methodology, illustrated and validated with the help of a numerical example developed with the HAWC2 code, is based on the decomposition of the acceleration data records in modal acceleration responses. After this step, the fatigue stress due to each vibration mode or stationary responses to harmonic exciations is computed.

2.4 Dynamic monitoring for modal variability analysis of bridges, stadia suspension roofs, wind turbines and concrete dams

Continuous dynamic monitoring can also be used to evaluate the modal variability induced by environmental and operational factors, such as temperature, traffic intensity, wind speed or water level in reservoirs.

For instance, a 12-channel continuous monitoring system installed at Infante D. Henrique bridge (Figure 6) [9], in Porto, Portugal, in 2007, has been used to track since then the time evolution of the corresponding modal estimates, by automated processing of the acceleration time series collected every half an hour using very robust home-made software (DYNAMO) for output-only modal identification based on the most advanced methods (SSI and p-LSCFD) [10][11].

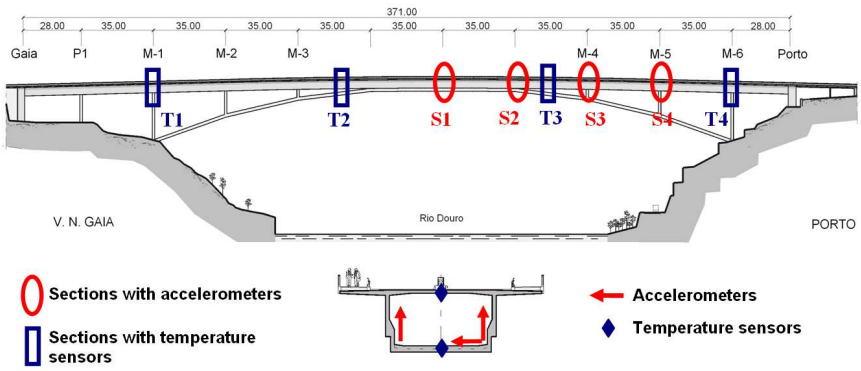

Figure 6. Position of accelerometers and temperature sensors at Infante D. Henrique bridge.

Figure 7 shows the time evolution of the estimates of the first 12 natural frequencies along one year, by application of the p-LSCF method. Though these estimates look rather stable at a first glance, an appropriate zoom of this plot for each natural frequency clearly shows the existence of daily and seasonal variations (Figure 8), which are mainly motivated by oscillations of temperature and intensity of traffic. Figure 9 (left) shows, for instance, the good correlation between the estimates of the first natural frequency and measured temperature at the top of section T3. On the other hand, Figure 9 (right) illustrates the influence of the increase of traffic intensity at the beginning of each morning on the estimates of the second natural frequency.

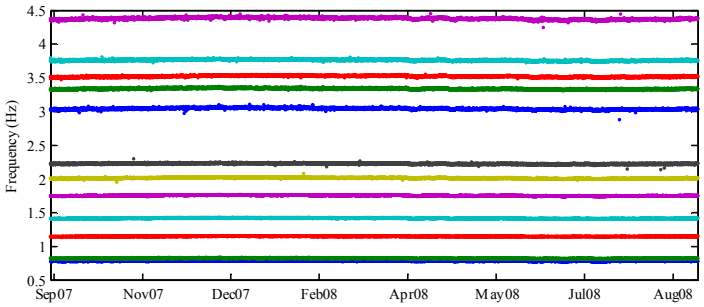

Figure 7. Time evolution of the estimates of the first 12 natural frequencies along one year, by application of the p-LSCF method.

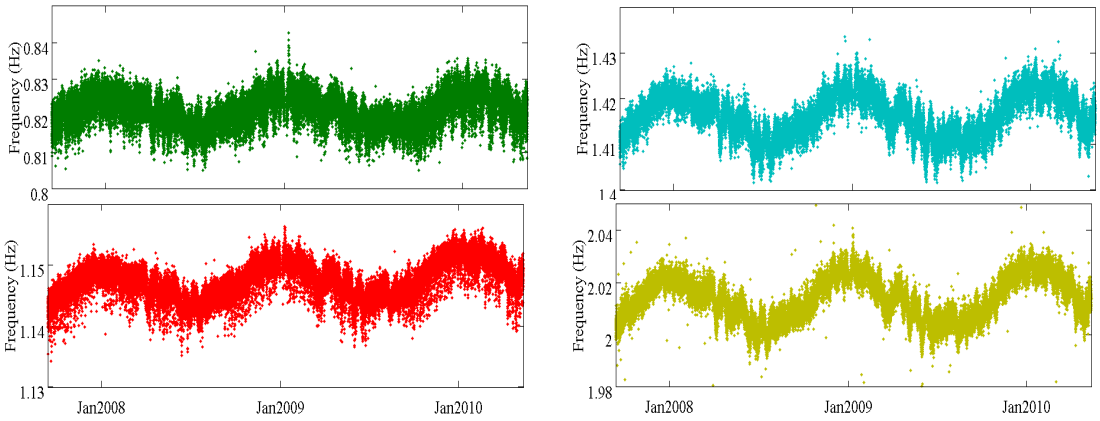

Figure 8. Time evolution of the estimates of the first 4 natural frequencies along three years, by application of the p-LSCF method.

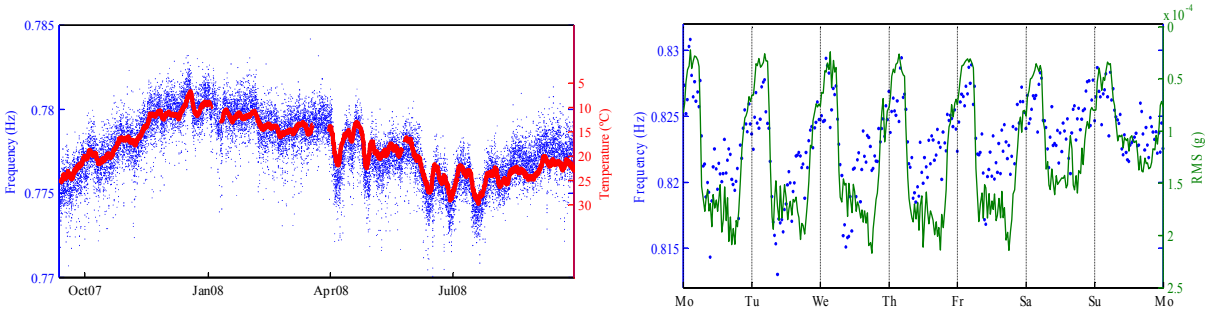

Figura 9. (Left) Variation of the estimates of the first natural frequency (blue dots) *vs* measured temperature at the top of section T3 (red line); (Right) Time evolution of the second natural frequency vs RMS values of vertical acceleration time series collected at section S3 during one week (03/03/2008 - 09/03/2008).

In structures with clear linear behaviour under ambient excitation, as is the case of Infante D. Henrique bridge, the increase of temperature usually induces a decrease of natural frequencies according to some linear relation. However, in some structures some form of non-linear behaviour can cause a non-linear relation. This fact can stem either from some type of material non-linearity (e.g. sudden variation of the stiffness of the asphalt layer for negative temperatures) or from different forms of geometrical non-linearity (e.g. induced by temperature joints or long suspension cables). As an example, we can mention the case of the Braga Stadium

suspension roof (Figure 10), where a 6-channel continuous dynamic monitoring system has been installed in 2009, enabling the tracking of a large number of modal frequencies in the range 0-1 Hz (Figure 11) [12]. However, careful inspection of the zoom shown in Figure 11 shows the occurrence of some non-linear correlation between frequencies and temperature induced by the non-linear geometrical characteristics of the suspension roof, and in some cases the increase of temperature leads even to an increase of modal frequency [13][14].

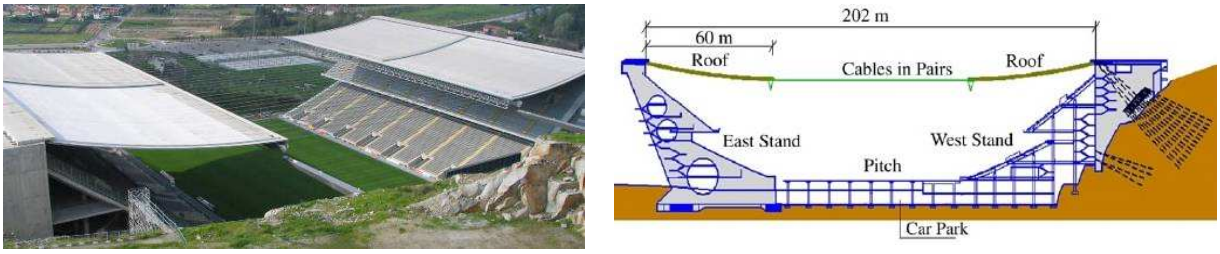

Figure 10. Braga stadium suspension roof: View from the west side; Cross-section.

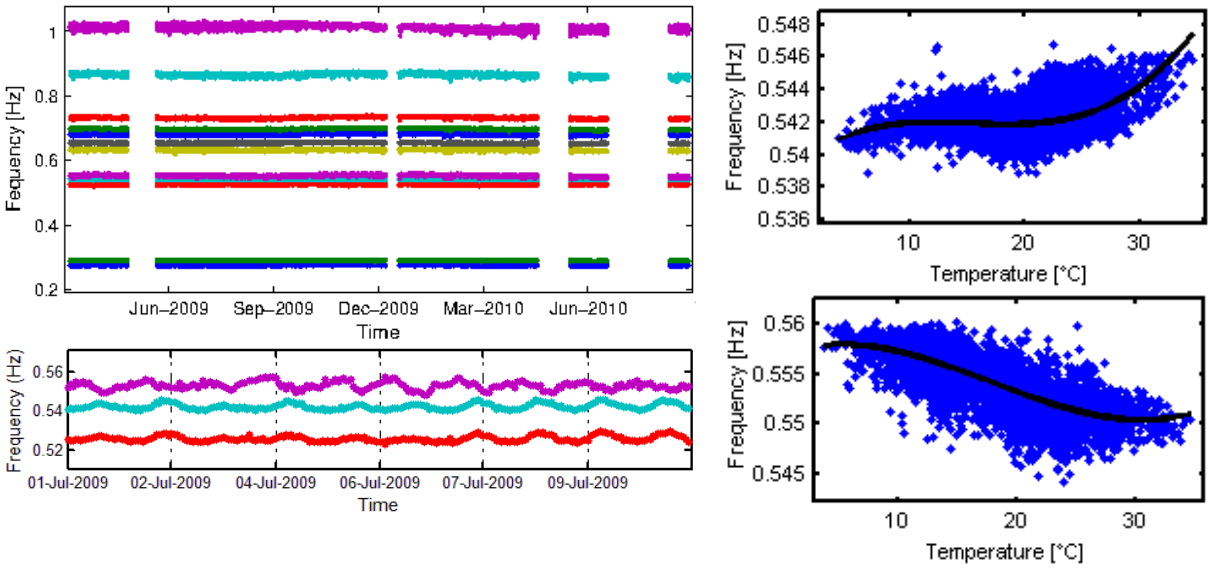

Figure 11. (Left) Temporal evolution of identified natural frequencies: (top) from 25/03/2009 to 27/09/2012 in the range 0-1.1 Hz; (bottom) from 1/07/2009 to 10/07/2009 for modes 3, 4 and 5; (Right) Correlation between modal frequencies and measured temperatures in the period 1/07/2009 to 31/12/2009.

Wind can also play an important role in terms of inducing significant variations in the modal parameters. This has been noticed for instance processing data from one year of continuous monitoring at Torrão wind turbine [8] and observing the Campbel diagram achieved relating frequency estimates with the rotor speed (Figure 12). It is however particularly interesting to show the significant increase of modal damping of the 1st FA mode induced by the increase of wind speed along the different operating regimes of the wind turbine (Figure 13).

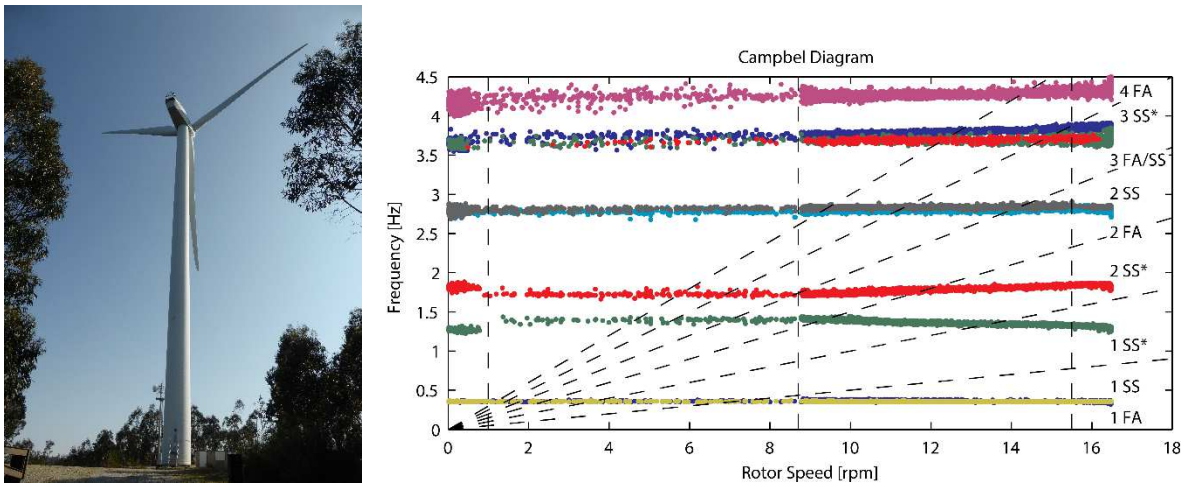

Figure 12. (Left) Torrão wind turbine; (Right) Campbel diagram after one year of continuous monitoring and removal of the estimates corresponding to excitation harmonics.

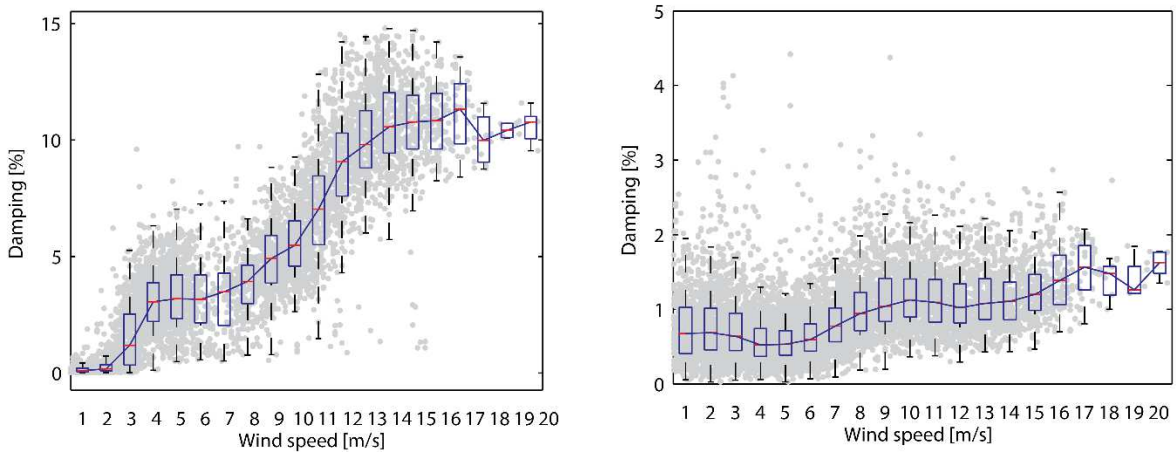

Figure 13. Evolution of damping with the wind speed: (Left) 1st FA tower mode; (Right) 1st SS tower mode.

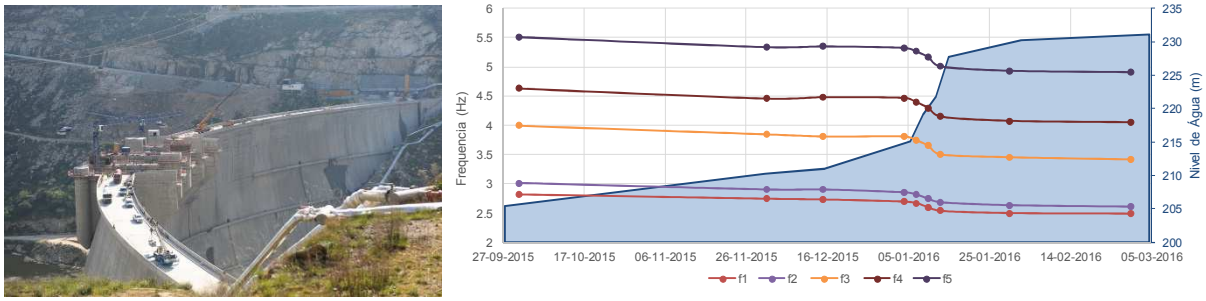

Figure 14. Variation of identified natural frequencies of Baixo Sabor dam with the water level in the reservoir.

At last, it's still worth mentioning the influence of the water level in the reservoir on the natural frequencies of Baixo Sabor dam recently detected by processing the data from a 20-channel continuous dynamic monitoring system installed after construction to follow the first filling of the reservoir (Figure 14) [15].

2.5 Monitoring for vibration based early detection of structural changes

Although the variations of modal frequency estimates induced by environmental and operational factors are in general relatively small, they can clearly disturb any attempt of detecting structural damages on the basis of the analysis of natural frequency shifts.

Therefore, it is of utmost importance to remove or mitigate the effect of such factors on the modal variability by applying appropriate statistical methods (e.g. multiple linear regression or PCA methods) and building suitable control charts that may flag the occurrence of slight damage [16][17].

Figure 15(a) shows, for instance, the temporal evolution of the estimates of the first natural frequency of Infante D.Henrique bridge before and after the removal of the environmental/ operational effects. Inspection of this figure shows the high efficiency of such correction, most of the estimates being then located in a very narrow frequency range with an amplitude of about 0.005 Hz. This means that relatively small damage can be detected in the future provided that the variations of modal frequencies induced are higher than that order of magnitude. This conclusion has been better confirmed analysing different damage scenarios idealized numerically and building appropriate control charts, as illustrated in Figure 15(b) [16][8], both in bridges and in wind turbines.

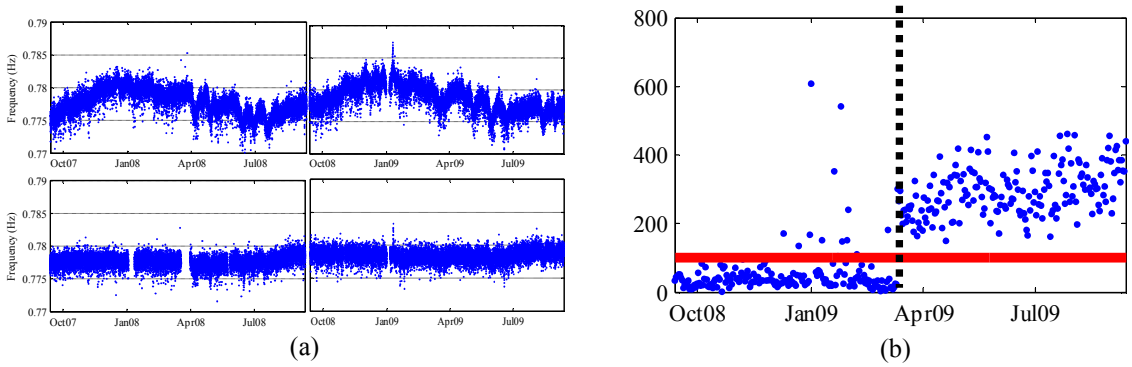

(a) (b)

Figure 15. (a) Temporal evolution of the first natural frequency estimates before and after the removal of environmental/ operatioanl effects; (b) Control chart used for damage detection.

2.6 Dynamic monitoring of wind effects on large bridges and suspension roofs

Continuous dynamic monitoring can also play an interesting role in Wind Engineering studies developed on prototypes, specially in the case bridges located in zones with high susceptibility to the occurrence of extreme events, such as cyclones or typhoons, demanding an adequate characterization of loads and an accurate assessment of the corresponding response.

Such type of research has been carried out by ViBest/ FEUP on the Grande Ravine viaduct (Fig.16), which is a slender girder bridge crossing a volcanic breach of 320m width and 170m depth, at the Reunion Island. This viaduct is located in an area frequently affected by tropical cyclones and has a particular structural configuration that, although stiff when compared to cable-stayed and suspended bridges, is slender in comparison to ordinary girder bridges.

These aspects led the Designer SETEC tpi [18] to idealise a continuous monitoring system with aerodynamic character, grouping a set of anemometers, pressure cells, temperature sensors and accelerometers (Fig.16). Collaboration between the Designer, ViBest/FEUP and CSTB was

established for the processing and analysis of recorded data, in order to validate the wind studies carried out during the design stage. Several other experimental tests were also conducted. In particular, ambient vibration tests were performed to characterise the bridge structure after construction, and detailed wind tunnel tests were developed, using simultaneous measurement of aerodynamic forces with balance and through pressures on the surface of cross section of the deck model, in order to characterise the aerodynamic forces acting on the viaduct model [19].

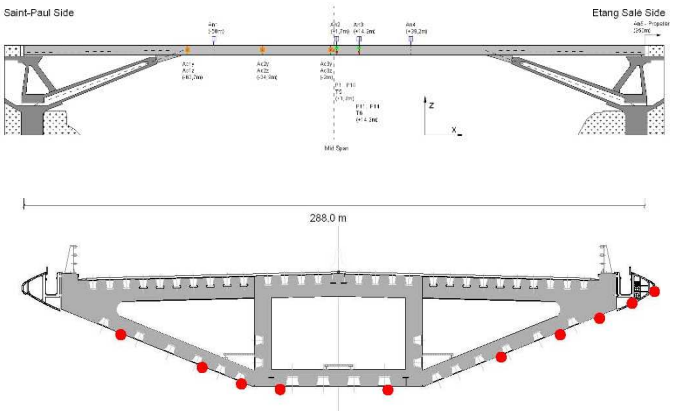

Figure 16. Monitoring of Grande Ravine viaduct: Location of (a) anemometers and accelerometers; (b) pressure cells.

3 CONCLUSIONS

This paper briefly refers a set of long-term dynamic monitoring systems implemented by the Laboratory of Vibrations and Structural Monitoring (ViBest) of FEUP in large Civil structures with different typologies (e.g. roadway, railway and pedestrian bridges, stadia suspension roofs, wind turbines or concrete dams). These applications clearly illustrate the interest and potential of the developed technology in different perspectives, as well as the huge high quality database created, which can now be used for joint collaborative research at European level.

ACKNOWLEDGEMENTS

This work was financially supported by: PTDC/ECM-EST/0805/2014|16761 – DAM_AGE - Advanced Online Dynamic Structural Health Monitoring of Concrete Dams, funded by FEDER funds through COMPETE2020 - Programa Operacional Competitividade e Internacionalização (POCI) – and by national funds through FCT - Fundação para a Ciência e Tecnologia.

REFERENCES

[1] Caetano E., Cunha A., Magalhães F. and Moutinho C., Studies for controlling human-induced vibration of the Pedro e Inês footbridge, Portugal. Part 1: Assessment of dynamic

behavior. *Engineering Structures* (2010) **32**: 1069-1081.
[2] Caetano E., Cunha A., Moutinho C. and Magalhães F., Studies for controlling human-induced vibration of the Pedro e Inês footbridge, Portugal. Part 2: Implementation of tuned mass dampers. *Engineering Structures* (2010) **32**: 1082-1091.
[3] Cunha A., Caetano E., Calçada R., De Roeck G. and Peeters B., Dynamic Measurements on Bridges. Design, Rehabilitation and Monitoring. *Bridge Engineering*. ICE Proceedings of the Institution of Civil Engineers. (2003) **156**: issue BE3 135-148.
[4] Calçada R., Cunha A. and Delgado R., Analysis of Traffic Induced Vibrations in a Cable-Stayed Bridge. Part I: Experimental Assessment. *Journal of Bridge Engineering*. ASCE. (2005) **10**: No.4 370-385.
[5] Calçada R., Cunha A. and Delgado R., Analysis of Traffic Induced Vibrations in a Cable-Stayed Bridge. Part II: Numerical modeling and stochastic simulation. *Journal of Bridge Engineering*. ASCE (2005) **10**: No.4 386-397.
[6] Marques F., Cunha A., Caetano E., Moutinho C., Magalhães F., Analysis of dynamic and fatigue effects in a old metallic riveted bridge. *Journal of Constructional Steel Research*. (2014) **99C** 85-101.
[7] Marques F., Moutinho C., Hu W.-H., Cunha A. and Caetano E., Weigh-in-motion implementation in an old metallic railway bridge. *Engineering Structures*. (2016) **123**: 15–29.
[8] Oliveira G. (2016). *Vibration-Based Structural Health Monitoring of Wind Turbines* (in English), PhD Thesis, FEUP, (2016).
[9] Magalhães F., Cunha Á. and Caetano E., Dynamic Monitoring of a Long Span Arch Bridge, *Engineering Structures* (2008) **30**: (11) 3034-3044.
[10] Magalhães F., Cunha Á. and Caetano E., Online automatic identification of the modal parameters of a long span arch bridge. *Mechanical Systems and Signal Processing* (2009) **23**: (2) 316-329.
[11] Magalhães F., Cunha A. and Caetano E., Vibration based structural health monitoring of an arch bridge: from automated OMA to damage detection, *Mechanical Systems and Signal Processing*. Special issue on interdisciplinary and integration aspects in structural health monitoring (2012) **28**: 212-228.
[12] Martins N. , Caetano E., Diord S., Magalhães F. and Cunha, Dynamic monitoring of a stadium suspension roof: wind and temperature influence on modal parameters and structural response, *Engineering Structures* (2014) **59C**: 80-94.
[13] Amador S., Magalhães F., Cunha A. and Caetano E., High spatial resolution modal identification of a stadium suspension roof: assessment of the estimates uncertainty and of modal contributions, *Engineering Structures* (2017) in press.
[14] Amador S., Magalhães F., Cunha A., Caetano E. and Martins N., Automated modal tracking in a football stadium suspension roof for detection of structural changes, *Structural Control and Health Monitoring* (2017) in press.
[15] Pereira S., Magalhães F., Gomes J., Cunha A. and Vieira de Lemos, J., Installation and Results from the first 6 months of operation of the Dynamic Monitoring System of Baixo Sabor arch dam. 10th International Conference for Structural Dynamics. EURODYN 2017, Rome, Italy, (2017).
[16] Magalhães F. *Operational Modal Analysis for Testing and Monitoring of Bridges and Special Structures* (in English), PhD Thesis, FEUP, (2008).

[17] Hu W.-H. *Operational Modal Analysis and Continuous Dynamic Monitoring of Footbridges* (in English), PhD Thesis, FEUP, (2011).
[18] Croiset J. E., Ryckaert J., Spielmann A. and Viel G., Viaduc de la Grande Ravine, *Travaux* (2205) **823**: 110-116.
[19] Bastos F. *Aerodynamic Behaviour of Long Span Structures. Numerical Analysis and Experimental Validation based on Full-Scale Measurements* (in English), PhD Thesis, FEUP, (2015).

VIII ECCOMAS Thematic Conference on Smart Structures and Materials
SMART 2017
A. Güemes, A. Benjeddou , J. Rodellar and Jinsong Leng (Eds)

DAMAGE EVALUATION BASED ON THE FLEXIBILITY MATRIX

BERTHA A. OLMOS[*], JOSÉ M. JARA[†] AND GUILLERMO MARTÍNEZ[†]

[*] División de Estudios de Posgrado, Facultad de Ingeniería Civil
Universidad Michoacana de San Nicolás de Hidalgo
Ciudad Universitaria, 58040 Morelia, Michoacán, México
e-mail: ba.olmos@gmail.com

[†] División de Estudios de Posgrado, Facultad de Ingeniería Civil
Universidad Michoacana de San Nicolás de Hidalgo
Ciudad Universitaria, 58040 Morelia, Michoacán, México
e-mail: jmjara60@gmail.com; guillermo.mtzruiz@gmail.com

Key words: Damage evaluation, Flexibility matrix, Damage detection, Bridges.

Abstract. During the last decades, researchers have developed several methodologies to locate and identify damage in structures due to the continuous action of the service load, and to the combined action of the service and accidental loads, as well. The damage detection techniques are attractive due to the fact that they allow to study the continuous behavior of structures such as bridges, hospitals, schools, and historic buildings, among others. These tools are very helpful to evaluate the actual capacity of the structure and to determine if it can sustain current loads when extreme events as earthquakes, hurricanes or tornados occur. These techniques belong to the group of nondestructive tests, and play an important role in the engineering area. Among the methodologies proposed in the literature, one of them is the flexibility difference method. This theory is based on the study of eigenvectors, looking for a vector that shows changes in flexibility that reflects damage. The objective of this work is to assess the damage location using the flexibility matrix. For the study, ambient vibration campaigns were led on two existing bridges, one pedestrian and other for vehicles, in order to measure the structures' dynamic properties under different loading scenarios that will allow to detect the presence of possible damage through the identification of changes in the flexibility matrixes. The results show the location where there are changes in the flexibility matrix along the bridges, showing the zones where structural elements can have been damaged along their cycle of life.

1 INTRODUCTION

Around the world, road bridges play an important role for the economic development of any country since they are the instrument that permit the communication among cities; furthermore, they allow the rural communities to have access to hospitals, schools, and other vital services that would be unavailable if they would not exist. Pedestrian bridges are a fundamental part of the infrastructure of a city, allowing that people have access to different places where the rods or highways are wide or have to cross rivers or street with heavy traffic. For any town or village, pedestrian bridges allow an easy and faster way for communicating places. The system identification technique is an excellent tool for continuously monitoring the health state of a bridge in a short period of time, which is important in maintenance and rehabilitation projects to prevent excessive damage of the structure due to accidental loads and, at the same time, allows the protection of people that daily make use of the infrastructure.

Based on the important tool that system identification is, it was determined the dynamic characteristics of two bridges, one highway bridge located on the Morelia´s loop and a pedestrian bridge located close to the Morelia's University city, both in Mexico, by using the frequency domain decomposition technique (FDD) [1]. The structures' system identification was obtained with data measured from ambient vibration studies. The data acquisition were recorded using digital accelerometers with twelve channels, locating the sensors at different points along the structures.

The present work describes the methodology used to detect damage on the bridges' structure by implementing the flexibility difference method for locating damage in structures [2]

2 FLEXIBILITY DIFFERENCE METHOD FOR LOCATING DAMAGE IN STRUCTURES [2]

The methodology proposed by Pandey and Biswas [2] to detect and to locate damage on structures only requires to know modal shapes and their frequencies that are associated to different scenarios along the service life of the structures. The dynamic properties are measured at different periods of time or under different load condition of the structures where it is desired a health monitoring. So by using the ambient vibration technique, it is possible to determine the information needed to implement the Pandey and Biswas' method to identify damage with a very less computational effort. In the present work, for implementing the methodology, first the modal shapes and frequencies were measured through an ambient vibration tests, the following steps to estimate the flexibility changes and to locate damage are numbered in the next lines:

1. Normalization of the modal shapes with respect to the mass.

$$M_{ni} = \int_0^L \Phi_i(x)^2 m(x) dx \tag{1}$$

where M_{ni} is the generalized mass at mode i, Φ_i is the ith mode shape, and m is the mass of the structure. For a structure with continuous mass, the normalized mode shapes correspond to the estimated ones divided by the squared root of the generalized mass.

2. Evaluation of the undamaged flexibility matrix

$$[F] = \Phi \overline{K}^{-1} \Phi^T = \sum_{i=1}^{n} \left({}^{1}/_{\omega_i^2} \right) \phi_i \phi_i^T \tag{2}$$

3. Evaluation of the flexibility matrix at a damage condition

$$[F^*] = \Phi^* \overline{K^*}^{-1} \Phi^{*T} = \sum_{i=1}^{n} \left({}^{1}/_{\omega^{*2}_i} \right) \phi^*{}_i \phi^{*T}_i \tag{3}$$

4. Estimation of the change in flexibility

$$[\Delta F] = [\mathrm{F}] - [\mathrm{F}^*]^T \tag{4}$$

5. Detection of the flexibility changes at each measurement location

$$\delta_j = max_i \left| \delta f_{ij} \right| \tag{5}$$

where F, K, Φ, ω are respectively the flexibility matrix, the stiffness matrix, the mode shapes, and the frequencies for the undamaged structure; F^*, K^*, ϕ^* and ω^*, are the same parameters but for the damaged condition, ΔF is the change in the flexibility matrix, and δf_{ij} are the elements of ΔF. To locate damage the quantity δ_j is used as the measure of change in flexibility for each measurement location.

3 CASES OF STUDY

Two bridges built in Morelia city, Mexico, designed to fulfill two different load demands were selected to conduct the present work, the first one is a highway bridge and the second one is a pedestrian bridge. The main idea for studying different classes of structures is to explore the accuracy of the flexibility difference method to locate damage in structures excited by different dynamic loading since the first structure is subjected to heavy transit loads whereas the second is under small dynamic loads due to walking people crossing a river, so they have different frequency content.

For the damage identification first of all it is needed to know the modal properties of the structures at different times along their service life time. In this work, modal shapes where measured trough an ambient vibration campaign by using sets of uniaxial and triaxial Kinemetrics accelerometers that measured the ambient vibrations in two orthogonal and a vertical directions. The recording console is a Kinemetricks K2 with 12 channels with nine force balanced unidirectional sensors and one Episensor triaxial force balanced instrument. The data acquisition consisted in recording 200 samples per second in windows of 10 minutes for each measurement. Figure 1 shows the equipment used with full-scale range of ±0.20 to ±4 g and extended bandwidth –DC to 200 Hz. The signals were processed using the ARTEMIS software [3], selecting the frequency domain decomposition technique for the system identification. The description and results obtained for each of the bridges are described in the following sections.



Figure 1: Unidirectional and triaxial force balance sensors.

3.1 Highway Bridge

La Central Bridge is composed by five-span simply supported, two of 30.3 m and three of 30.6 m long. It is conformed by two-parallel structures with a bridge deck of 12.3 m wide and 0.20 m thick, supported on nine AASHTO type IV girders resting on elastomeric bearings. The substructure is a RC three-column bent designed for a concrete strength of 24.5 MPa (Figure 2). The same concrete strength was used in the bent caps, diaphragms and slabs. AASHTO prestressed girders were designed for a concrete strength of 39.2 MPa. Figure 2 shows that the deck slab is continuous over piers 2 and 5, and it has an expansion joints at abutments and piers 3 and 4.

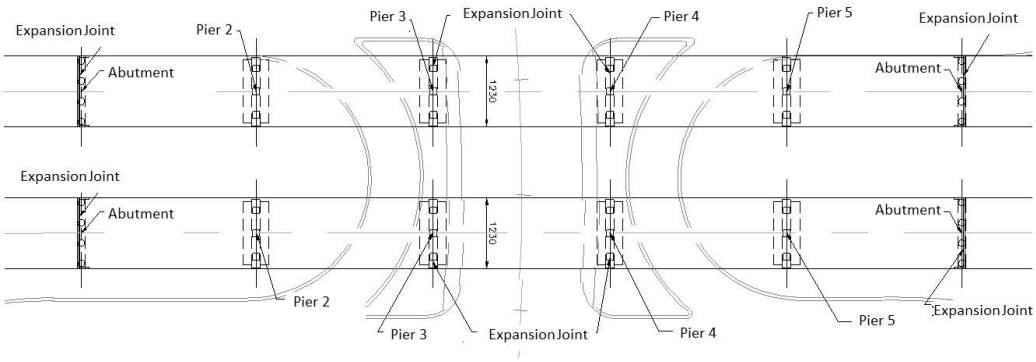

Figure 2: Plan view of La Central Bridge

Figure 3 shows a picture of the bridge during the construction process in 2014. RC rectangular columns composed the piers and the arch shape displayed in Figure 3 was built with light non-structural elements and it only has decorative purposes.



Figure 3: Longitudinal view of La Central Bridge

Until now, the ambient vibration campaigns on the Central Bridge were led in a period of two years under different load scenarios. Two measurements were made on 2014, one when the bridge construction was finished but not the asphalt overlay, the following at the beginning of the traffic circulation along the bridge, and the third one a year after the structure started to be on full operation. For the ambient vibration campaign, the sensors were located at several positions covering the length and wide of the bridge, with the aim to cover several modal shapes for their identification. The data recorded were processed with the ARTEMIS software where it was possible to identify the mode shapes in 3D, thanks to wide range of points cover with the ambient vibration work. The signal process allowed to define several mode shapes of the bridge, from them only two were selected to implement the flexibility difference method to detect damage in the structure since these were the best correlated among all the measurements achieved and the real behavior expected in the bridge. Figure 4 shows the modes shapes used to achieve the objective of this work.

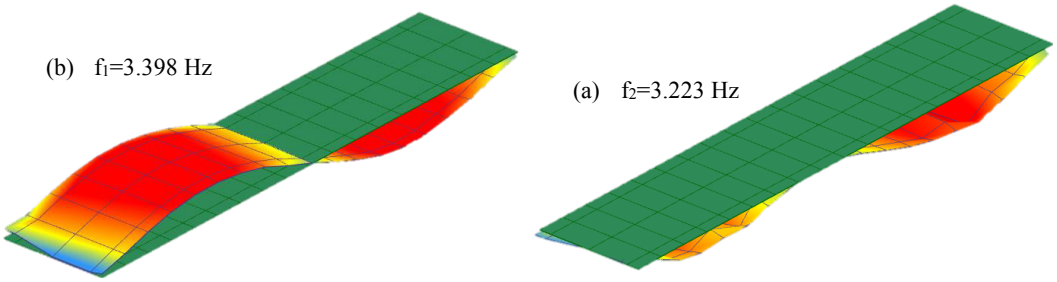

Figure 4: (a) First and (b) second mode shapes for La Central bridge identified with ARTEMIS [3].

When implementing the flexibility difference method to locate damage on the Central Bridge, the structure was discretized in 160 elements along its length where it was estimated the changes in flexibility reported in Figure 5; this figure presents in the horizontal and vertical axes, respectively, the position along the bridge length and the change in flexibility at each element represented by bars defining the elements' start and end. The results show the presence of damage in locations where there are expected the maximum deformations for a continuous deck, at this point the changes in flexibility are small, representing small cracking present on

deck and beams located at the distances identify on the ordinate axes along the bridge. These results indicate that a continuous health monitoring must be carefully led over the segments presenting the higher picks along the bridge's length. Following the same idea and given the fact that the bridge can be considered still as a new structure, there will be a continuous study of the health monitoring of the bridge, conducting new ambient vibration campaigns; it is expected to make at least one ambient vibration campaign per year, in order to opportunely prevent damage on the Central Bridge.

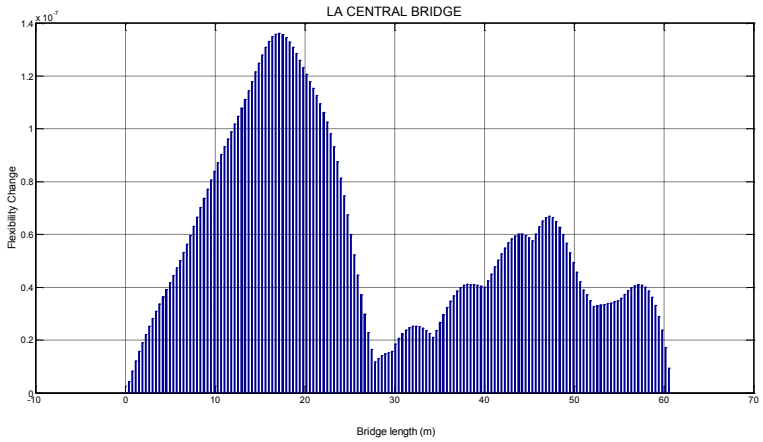

Figure 5: La Central bridge damage location.

3.2 Pedestrian bridge

The pedestrian bridge is composed by a reinforced concrete deck supported on a metallic truss (Figure 6). The bridge crosses a small river in Morelia, México (Figure 7). The webs and bottom chord have a box cross section composed by two channel cold-formed steel elements. Over the deck slab, along both longitudinal edges, there are metallic handrails for protecting pedestrians from possible falls.

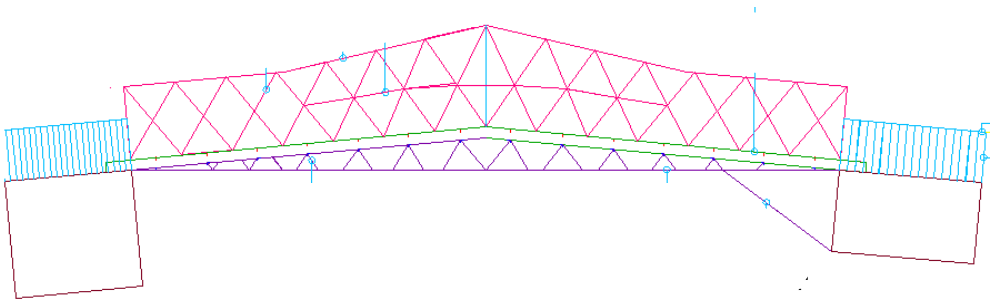

Figure 6: Pedestrian Bridge



Figure 7: Longitudinal view of the pedestrian Bridge and damage on the top chord.

The bridge presents several pathologies in structural and non-structural elements (handrails). The most important damage in structural elements is observed in the top chord and bottom of the truss where the visual inspection showed, in some parts, loss of the cross section and at others loss of welding, as well as corrosion in several structural elements (Figures 7 and 10). The handrail presents some unwelded joints and some elements with evident corrosion. The bridge is of easy accessibility to lead at any time ambient vibration tests, and it is also a small structure that is easy to move under forced vibration where there are people walking all days and almost most of the time; further, because the structure exhibit damage, it was selected to study the accuracy of the change in flexibility method to locate damage.

As explained before, to implement the methodology selected for damage detection, it is needed to know the modal shapes of the structure. Since the interest for this bridge came after known its actual condition, first a topographic study was led in order to correctly identify the geometry, structural and nonstructural elements that conform the bridge; based on this study, a numerical model was developed in the software SAP2000 [4] developed in order to determine the analytical mode shapes of the original bridge. The ambient vibration campaign was led on the damaged structure where the sensors were located along the bridge with two different positions, one locating the sensors at the fourths of the length, and another at the span center with sensors at 0.60 m from the end supports. The data recorded were processed with the ARTEMIS software and the mode shapes were identified in 2D since the sensors cover only the length and not the wide of bridge, mainly because the intensive pedestrian circulation. Figure 8 shows two of the mode shapes identified and correlated with the analytical model, the first and five modes were used in the flexibility difference method to detect damage in the pedestrian bridge.

The damage located on the pedestrian bridge is reported in Figure 9 where the horizontal and vertical axes, respectively, correspond to the position along the bridge length and to the change in flexibility at each element represented by bars that define the elements' start and end. The results show the presence of damage in locations where physically can be distinguished the damage, for example Figure 10 shows some damaged elements, as well the longitudinal view of the truss show the presence of corrosion along the bridge. The changes in flexibility are larger in locations where it is expected the larger vertical deflections and visually detected damage in structural elements. Following the same idea and having easy accessibility to the bridge, it is

planned to make a continuous study on the health monitoring of this bridge by conducting new ambient vibration campaigns, in order to measure continuously the progress of damage, and also to study other methodologies to detect damage with the aim to determine their accuracy.

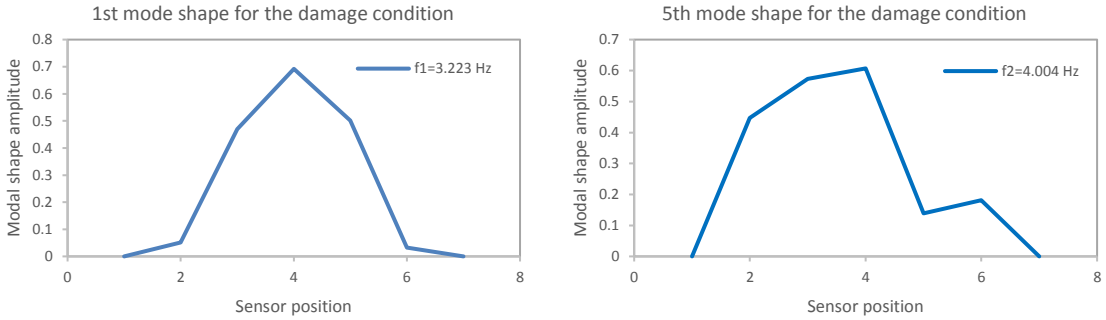

Figure 8: (a) First and (b) five mode shapes for the pedestrian bridge identified with ARTEMIS.

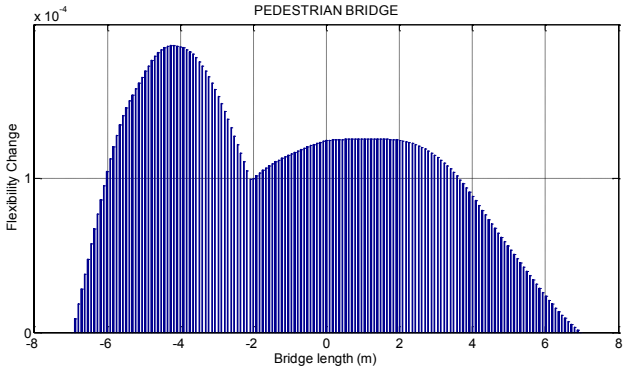

Figure 9: Pedestrian bridge damage location.



Figure 10: Visual identification of damage on the Pedestrian bridge.

11 CONCLUSIONS

The present work reports the results of a study focused in determining the accuracy of the difference flexibility method for locating damage on structures. The methodology was applied for two bridges working under completely different loads scenarios: a highway bridge and a pedestrian bridge. In both cases, ambient vibration campaigns that allow to determine the mode shapes of the structures and their respective frequencies were developed. The results presented and discussed let us to conclude the following:

- The change in flexibility method for detecting damage in structures is effective and accurate to detect damage using few mode shapes.
- The methodology is easy to implement allowing an easy interpretation of results; changes in flexibility, which are easy to present in graphs, correlate the position along the structure where it is expected the presence of damage.
- The efficacy of the method depends on the quality of the data used to identify modal shapes and frequencies, as well as the different load and damage scenarios used.
- The methodology demands small computational efforts, what is desired particularly for big structures.

REFERENCES

[1] Zhang, Y., Zhang, Z., Xu, X. and Hua, H. Modal parameter identification using response data only. *Journal of Sound and Vibration* (2005) **282**:367-380.
[2] Pandey, A.K. and Biswas, M. Experimental verification of flexibility difference method for locating damage in structures. *Journal of Sound and Vibration* (1995) **184(2)**:311-328.
[3] SVS, ARTEMIS Modal Pro 3.6. 2014.
[4] SAP2000 Nonlinear 19.0. Computers and Structures Inc.

VIII ECCOMAS Thematic Conference on Smart Structures and Materials
SMART 2017
A. Güemes, A. Benjeddou, J. Rodellar and J. Leng (Eds)

DAMAGE IDENTIFICATION IN VIBRATING RODS UNDER UNCERTAIN ELASTICALLY RESTRAINED END CONDITIONS

M. DILENA, M. FEDELE DELL'OSTE AND A. MORASSI

Polytechnic Department of Engineering and Architecture
University of Udine
Via Cotonificio 114, 33100 Udine, Italy
e-mail: antonino.morassi@uniud.it

Key words: Damage identification, End conditions, Cracks, Natural frequencies, Beams

Abstract. We consider the identification of a single open crack in a uniform elastic cantilever with elastic support of unknown stiffness by minimal resonant frequency data. The damage is modelled by inserting a localized flexibility at the cracked cross-section. The flexibility of the end constraint and the additional flexibility induced by the crack are assumed to be small and of the same order of smallness. We establish conditions for the unique identification of the position and severity of the crack and of the stiffness of the elastic support in terms of the first three resonant frequencies of either the axial or the bending vibrations. Numerical simulations support the theory.

1 INTRODUCTION

The inverse problem of determining a crack in a beam from natural frequency measurements has attracted a lot of attention in the last decades [1, 4]. The prototype of these inverse problems is the determination of a single open crack in a straight thin elastic beam from measurement of natural frequencies of the longitudinal vibration. The crack can be modelled by means of a massless translational elastic spring located at the damaged cross-section, with stiffness depending on the geometry of the cross-section and on the mechanical properties of the material. Assuming that the undamaged configuration of the defected rod is completely known, that is the rod profile, material properties and end conditions are given, the diagnostic problem consists in determining the position of the crack and the stiffness of the elastic spring simulating the crack by minimal (two) natural frequency measurements. A well-established theory has been developed since the middle of 90's for uniform rods with small crack [5, 7]. More recently, the Lambda-Curves Method has been proposed to deal with the general case in which the crack is not necessarily small and the rod has variable profile [8].

With the exception of the paper [9], which, however, deals with a cantilever beam under bending vibration, all the results available in literature hold under the assumption that the boundary conditions at the ends of the beam are ideal, that is either the end is perfectly clamped

or the end is free. Supported end conditions can be considered as a simplified model of real end conditions, since, for example, the perfect clamp may soften due to loosening or local weakening during the service of the structure. These structural changes result in not negligible frequency variations, which could erroneously be considered induced by damage when the system is monitored over a long period of time.

Main goal of this paper is to reconsider the method presented in [6] and present a theory for the identification of a single small crack in a longitudinally vibrating cantilever in presence of unknown elastically restrained end condition. On assuming that end condition involves low flexibility and causes frequency variations of the same order as those induced by the damage, we prove in Section 2.1 that the measurement of the first three natural frequencies in a uniform rod allows for unique identification of the position and severity of the crack, and for unique determination of flexibility of the elastic support. Closed-form expressions are deduced for the unknowns in terms of the natural frequency shifts. The analogous problem for a cracked cantilever with elastically restrained clamped support and under bending vibration is analyzed in Section 2.2. Numerical applications and a study of the stability of the method to errors on the data are presented in Section 3.

2 IDENTIFICATION: THEORY

2.1 Cracked cantilever under axial vibration

Consider a thin, straight uniform rod of length ℓ, cross-section area A, mass per unit length ρ, and Young's modulus of the material E. Assume that the right end of the rod, at $x = \ell$, is free, whereas the left end, at $x = 0$, is clamped. The infinitesimal, free, undamped longitudinal vibration of the cantilever, with radial frequency ω_n and amplitude $u_n = u_n(x)$, is governed by the eigenvalue problem

$$\begin{cases} EAu_n'' + \lambda_n \rho u_n = 0, & x \in (0, \ell), \\ u_n(0) = 0, \\ u_n'(0) = 0, \end{cases} \tag{1}$$

where $\lambda_n = \omega_n^2$ is the eigenvalue associated to the nth eigenfunction $u_n = u_n(x)$, $n \geq 0$. Problem (1) can be considered as the *reference* eigenvalue problem of the rod. Hereinafter, $f'(x)$ denotes the first derivative of the function $f = f(x)$.

We assume that, during its service, the rod is simultaneously affected by the degradation of the ideal constraint at $x = 0$, and by the occurrence of a localized damage - a crack - at the cross section $x = s$, $s \in (0, \ell)$. The end condition at $x = 0$ is modelled by means of an elastic spring of stiffness $K_0 > 0$ connecting the end of the rod and the support. Moreover, following an approach commonly adopted in damage identification, the crack at s is assumed to remain open during vibration and it is modelled by inserting a translational spring, of stiffness $K > 0$, at the damage cross-section. The value of K can be expressed in terms of the geometry of the cracked cross-section and the properties of the material, as explained, for example in [10]. Therefore, the free longitudinal vibration of the elastically restrained cracked rod is governed by the eigenvalue

problem

$$\begin{cases} EA\widetilde{u}_n'' + \widetilde{\lambda}_n \rho \widetilde{u}_n = 0, & x \in (0,s) \cup (s,\ell) \\ K_0 \widetilde{u}_n(0) = EA\widetilde{u}_n'(0), \\ K[\![\tilde{u}_n(s)]\!] = EA\tilde{u}_n'(s), \\ [\![\tilde{u}_n'(s)]\!] = 0, \\ \widetilde{u}_n'(\ell) = 0, \end{cases} \tag{2}$$

where $(\widetilde{\lambda}_n, \widetilde{u}_n)$ is the nth eigenpair, $n \geq 0$. The eigenvalue problem (2) will coincide with the reference problem (1) as, simultaneously, K and K_0 tend to ∞. Here, $[\![\widetilde{u}_n(s)]\!] = (\lim_{x\to s^+} \widetilde{u}_n(x) - \lim_{x\to s^-} \tilde{u}_n(x))$.

In real situations, the deviation of the end condition at $x = 0$ from the ideal case (with $K_0 = \infty$) is generally small, namely the deviation from the ideal support condition involves low flexibility K_0^{-1}. Moreover, the identification of small cracks is the main issue in structural diagnostics. Therefore, it is reasonable to assume that both K_0^{-1} and K^{-1} are *small* and *of the same order of smallness*. Under the above assumption, our inverse problem consists in determining the flexibility of the support K_0^{-1}, and the damage location s and severity K^{-1} by measuring the variations in the first three natural frequencies of the cantilever from the reference to the perturbed state.

By adapting the approach proposed in [11], the first order change in the nth eigenvalue $\delta\lambda_n \equiv \widetilde{\lambda_n} - \lambda_n$ is given by

$$\delta\lambda_n = -\frac{N_n^2(0)}{K_0} - \frac{N_n^2(s)}{K}, \tag{3}$$

where $N_n(x) = EAu_n'(x)$ is the axial force associated with the nth eigenfunction of the unperturbed system, normalized as $\int_0^\ell \rho u_n^2(x)\,dx = 1$. A direct calculation shows that

$$\lambda_n = \frac{EA}{\rho\ell^2}\left(\frac{\pi}{2}(1+2n)\right)^2, \quad u_n(x) = \sqrt{\frac{2}{\rho\ell}}\sin\left(\frac{\pi}{2}(1+2n)\frac{x}{\ell}\right), \quad n \geq 0. \tag{4}$$

By writing (3) for $n = 1, 2, 3$, we obtain the following system of three nonlinear equations in the three unknowns K_0, K, s:

$$\begin{cases} C_1 = \xi\cos^2(\frac{\pi}{2}\frac{s}{\ell}) + \mathscr{F}, \\ C_2 = \xi\cos^2(\frac{3\pi}{2}\frac{s}{\ell}) + \mathscr{F}, \\ C_3 = \xi\cos^2(\frac{5\pi}{2}\frac{s}{\ell}) + \mathscr{F}, \end{cases} \tag{5}$$

where

$$C_n = -\frac{\delta\lambda_n}{2\frac{EA}{\ell}\lambda_n}, \quad \xi = \frac{1}{K}, \quad \mathscr{F} = \frac{1}{K_0}. \tag{6}$$

Let us introduce the position variable $x = \cos(\frac{\pi s}{\ell})$, $x \in (-1,1)$ and let $\mathscr{C}_1 = 2(C_2 - C_1)$, $\mathscr{C}_2 = 2(C_3 - C_1)$. One can prove the following result:

i) if $\mathscr{C}_1 = 0$, then $x = 0$, that is $s = \frac{\ell}{2}$;

ii) if $\mathscr{C}_1 \neq 0$, then x solves the second degree polynomial equation $x^2 = \frac{1}{4} + \frac{\mathscr{C}_2}{\mathscr{C}_1}$, that is

$$x_1 = -\sqrt{\frac{1}{4} + \frac{\mathscr{C}_2}{\mathscr{C}_1}}, \qquad x_2 = \sqrt{\frac{1}{4} + \frac{\mathscr{C}_2}{\mathscr{C}_1}}. \tag{7}$$

One of the two solutions (7) can always be excluded. To show this, it is enough to recall the following identity deduced from (5):

$$C_1 = \xi(1+x)((2x-1)^2 - 1). \tag{8}$$

The third factor in the right end side of (8) takes positive or negative value when it is evaluated either for $x = x_1$ or for $x = x_2$, respectively. Therefore, since ξ must be positive quantity, if $C_1 > 0$ then the solution x_2 is discarded and, vice versa, if $C_1 < 0$ then the solution x_1 is excluded. In conclusion, since the function $x = x(s)$ is one-to-one in $(0, \ell)$, the crack is uniquely localized. Once s and ξ have been uniquely determined, also K_0 can be uniquely identified, and the problem is solved. It should be noticed that, quite remarkably, closed-form solutions for the three unknowns are provided.

2.2 Cracked cantilever under bending vibration

In this section we shall consider the inverse problem discussed in Section 2.1 for a cantilever under bending vibration. We will see that closed form solutions are not longer available in this case.

The model is a uniform cantilever under non-perfect clamped end condition at the left end $x = 0$ and with an open crack at $x = s$. The infinitesimal, undamped, free bending vibration, of radian frequency $\sqrt{\widetilde{\lambda}_n}$ and amplitude $\widetilde{v}_n = \widetilde{v}_n(x)$, of the elastically restrained cracked cantilever is governed by the eigenvalue problem

$$\begin{cases} EI\widetilde{v}_n'''' - \widetilde{\lambda}_n \rho \widetilde{v}_n = 0, \quad x \in (0,s) \cup (s,\ell), \\ \widetilde{v}_n(0) = 0, \\ K_0 \widetilde{v}_n'(0) = EI\widetilde{v}_n''(0), \\ [\![\widetilde{v}_n(s)]\!] = 0, \\ K[\![\widetilde{v}_n'(s)]\!] = EI\widetilde{v}_n''(s), \\ [\![\widetilde{v}_n''(s)]\!] = 0, \\ [\![\widetilde{v}_n'''(s)]\!] = 0, \\ \widetilde{v}_n''(\ell) = 0, \\ \widetilde{v}_n'''(\ell) = 0, \end{cases} \tag{9}$$

where I is the moment of inertia of the cross-section, K_0 is the stiffness of the elastic rotational spring modelling the elastic constraint, and K is the stiffness of the rotational spring modelling the open crack at $x = s$ (see [10]). The eigenpairs $\{(\lambda_n, v_n)\}_{n=1}^{\infty}$ of the *reference* system, e.g., the cantilever without damage and with ideal clamped end, can be obtained as limit of the problem

(9) as, simultaneously, K_0 and K tend to ∞. The eigenvalues λ_n are the roots of the reference frequency equation

$$1 + \cos(\sqrt[4]{\lambda_n}\ell)\cosh(\sqrt[4]{\lambda_n}\ell) = 0, \tag{10}$$

and the eigenfunction $v_n(x)$, normalized such that $\int_0^\ell \rho v_n^2(x)\,dx = 1$, has the expression

$$\frac{1}{\sqrt{\rho\ell}}\left(\cos(\sqrt[4]{\lambda_n}x) - \cosh(\sqrt[4]{\lambda_n}x) + \frac{\sin(\sqrt[4]{\lambda_n}\ell) - \sinh(\sqrt[4]{\lambda_n}\ell)}{\cos(\sqrt[4]{\lambda_n}\ell) - \cosh(\sqrt[4]{\lambda_n}\ell)} \cdot (\sin(\sqrt[4]{\lambda_n}x) - \sinh(\sqrt[4]{\lambda_n}x))\right) \tag{11}$$

As before, we assume that the elastically restrained cracked cantilever is obtained as perturbation of the reference cantilever, that is we assume that K_0^{-1} and K^{-1} are small and of the same order of smallness. Following [11], and using the above notation, we have

$$\delta\lambda_n = -\frac{M_n^2(0)}{K_0} - \frac{M_n^2(s)}{K}, \tag{12}$$

where $M_n(x) = -EI\,v_n''(x)$ is the bending moment associated to the normalized eigenfunction $v_n(x)$. The diagnostic problem consists in determining the position s and the flexibility $\xi = K^{-1}$ of the crack, and the flexibility $\mathscr{F} = K_0^{-1}$ of the elastic support at $x = 0$ from the knowledge of the shifts in the first three eigenvalues of the cantilever. By writing equation (12) for $n = 1, 2, 3$ we obtain the following system of nonlinear equations

$$\begin{cases} C_1 = \xi {\lambda_1}^{-1} M_1^2(s) + 4\mathscr{F}, \\ C_2 = \xi {\lambda_2}^{-1} M_2^2(s) + 4\mathscr{F}, \\ C_3 = \xi {\lambda_3}^{-1} M_3^2(s) + 4\mathscr{F}, \end{cases} \tag{13}$$

where $C_n = \frac{\delta\lambda_n}{\lambda_n}$, $n = 1, 2, 3$. After some algebraic transformations, one can prove that the possible positions of the crack are the solution of the following equation

$$\frac{C_3 - C_1}{C_2 - C_1} = \frac{M_3^2(s)\lambda_3^{-1} - M_1^2(s)\lambda_1^{-1}}{M_2^2(s)\lambda_2^{-1} - M_1^2(s)\lambda_1^{-1}} \equiv f(s), \tag{14}$$

where $s \in (0, \ell)$ and the difference $C_2 - C_1$ is supposed to be different from zero. Equation (14) may be used to solve the damage identification problem for given (measured) value of the ratio $(C_3 - C_1)(C_2 - C_1)^{-1}$. More precisely, the only possible locations of the crack are the abscissas of the intersection points between the function $y = f(s)$ and the straight line $y = (C_3 - C_1)(C_2 - C_1)^{-1}$, see Figure 1. It should be noticed that in practical applications the function $f(s)$ is known from the solution of the free vibration problem of the undamaged ideal cantilever. Once the admissible crack locations are determined numerically, the stiffnesses K_0 and K can be identified via (13).

3 APPLICATIONS

In this section, some numerical applications for the cantilever either under axial or bending vibration are presented. For the sake of simplicity, we shall consider a uniform cantilever with unitary values of the physical parameters, i.e. $E = A = I = \ell = \rho = 1$. The identification problem is formulated by using pseudo-experimental frequency data, that is, the resonant frequencies

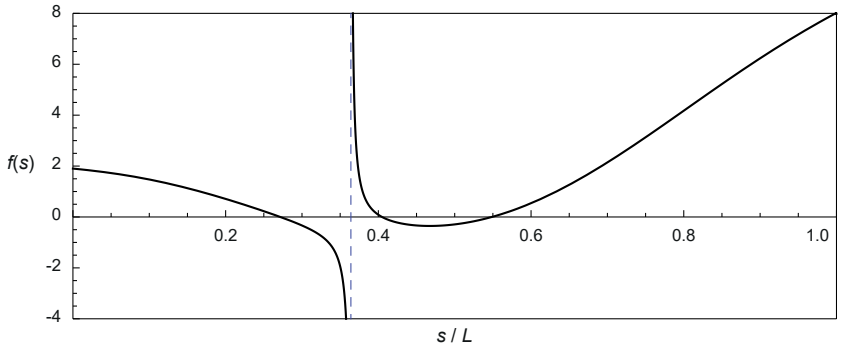

Figure 1: Plot of the function $y = f(s)$ defined in (14) for cracked cantilever in bending vibration.

are obtained by solving the direct eigenvalue problem in referential and perturbed configuration for different flexibilities of the support and different positions and severity of the crack. In a first stage, simulations have been performed with error-free data. Then, to test the robustness of the proposed method to errors on the data, the eigenvalue shifts have been perturbed as follows

$$\delta\lambda_n^{err} = \delta\lambda_n(1+\tau), \tag{15}$$

where τ is a Gaussian variable with vanishing mean and standard deviation σ given by $\sigma = \Pi/3$. Here, Π is the maximum error on the eigenvalue shift, and simulations have been performed for $\Pi = 0.05, 0.10, 0.20$.

3.1 Axial vibration

Among an extensive series of simulations, Table 1 collects the results of identification in absence of errors for three positions of the crack, namely, $s = 0.30$, $s = 0.60$ and $s = 0.90$, and for a selected set of flexibilities $\mathscr{F}$, ξ of the elastic support and of the crack, respectively. The flexibilities $\mathscr{F}$, ξ have the same order of magnitude, and have been chosen so that the shifts in the first three radian frequencies of the cantilever are of the order $1 - 5\%$ of the unperturbed initial value.

Identification errors are generally small and of order of few per cent of the target values. The accuracy of identification decreases as the flexibility of the support and the severity of the damage increase, and maximum errors, up to 15 per cent of the actual values, are attained for the damage severity when the crack is close to the free end of the cantilever. Finally, the estimate of the crack position turns out to be generally more accurate than the corresponding estimates of the two flexibilities.

In presence of errors, 500 simulations have been performed for each level of error Π. Table 2 shows a typical result obtained for the target values $s = 0.3$, $\xi = 0.004$ and $\mathscr{F} = 0.004$. It can be seen that the errors on the input data are not amplified by the identification algorithm, and the average of each unknown parameter differs from the target values by few points per cent. As before, the estimate of the crack position seems to be less sensitive to errors than the estimates of the two flexibilities.

Table 1: Axial vibrations: percentage errors in the determination of the position s and flexibility ξ of the crack, and of the flexibility $\mathscr{F}$ of the elastic support by using free-of-error data. $e_s = 100 \times (s_{exact} - s_{ident})/s_{exact}$, $e_{\mathscr{F}} = 100 \times (\mathscr{F}_{exact} - \mathscr{F}_{ident})/\mathscr{F}_{exact}$ and $e_\xi = 100 \times (\xi_{exact} - \xi_{ident})/\xi_{exact}$.

Actual values		$s = 0.30$			$s = 0.60$			$s = 0.90$		
$\mathscr{F}$	ξ	e_s	$e_{\mathscr{F}}$	e_ξ	e_s	$e_{\mathscr{F}}$	e_ξ	e_s	$e_{\mathscr{F}}$	e_ξ
0.004	0.004	−1.1	0.5	1.8	−0.1	0.6	1.6	−0.2	0.6	−2.3
	0.010	−1.3	0.2	2.6	0.0	0.6	2.3	−0.5	0.6	−8.1
	0.020	−1.7	−1.1	4.0	0.3	0.7	3.4	−0.9	0.8	−18.3
0.010	0.004	−2.3	1.6	3.3	−0.3	1.7	2.8	−0.3	1.5	1.0
	0.010	−2.7	1.4	4.2	−0.3	1.6	3.9	−0.6	1.5	−5.7
	0.020	−3.1	1.0	5.6	−0.1	1.5	5.1	−1.0	1.5	−16.3
0.020	0.004	−3.5	3.3	4.9	0.5	3.6	1.0	0.0	2.9	14.5
	0.010	−4.5	3.2	6.5	−0.4	3.5	5.1	−0.6	2.9	1.4
	0.020	−5.1	3.1	7.9	−0.5	3.4	7.3	−1.1	3.0	−11.6

Table 2: Axial vibrations: determination of the position s and flexibility ξ of the crack, and of the flexibility $\mathscr{F}$ of the elastic support by using frequency data with errors. Actual values of the identification parameters: $s = 0.3$, $\xi = 0.004$ and $\mathscr{F} = 0.004$.

	$\Pi = 0.05$			$\Pi = 0.10$			$\Pi = 0.20$		
Stat. Property	s	ξ	$\mathscr{F}$	s	ξ	$\mathscr{F}$	s	ξ	$\mathscr{F}$
Max	0.315	0.0045	0.0042	0.325	0.0050	0.0044	0.364	0.0057	0.0049
Min	0.295	0.0034	0.0038	0.287	0.0029	0.0034	0.267	0.0018	0.0033
Average value	0.303	0.0039	0.0040	0.304	0.0039	0.0040	0.305	0.0039	0.0040
% error average	−1.0	2.5	0.0	−1.3	2.5	0.0	−1.7	2.5	0.0
Std. dev.	0.004	0.0002	0.0001	0.007	0.0004	0.0001	0.015	0.0007	0.0003
Ident. without errors	0.303	0.0039	0.0040	0.303	0.0039	0.0040	0.303	0.0039	0.0040
Actual value	0.300	0.0040	0.0040	0.300	0.0040	0.0040	0.300	0.0040	0.0040

3.2 Bending vibration

Numerical simulations without errors analogous to those described in previous section have been carried out for the bending problem. However, it should be noticed that, in the present case, the inverse problem is more complicated due to the intrinsic non-uniqueness of the solutions of equation (14) governing the crack location problem. Two cases are considered in detail in Table 3. They refer to crack position either at $s = 0.33$ (Case 1) or at $s = 0.60$ (Case 2), and flexibilities are chosen such that typical radian frequency shift ranges between 0.5 and 2.0 per cent of the reference value. In Case 1, equation (14) has exactly one solution, whereas in Case 2 three distinct solutions $\{s_i\}_{i=1}^3$ of the equation (14) do exist, namely, $s_1 \simeq 0.20$, $s_2 \simeq 0.40$ and $s_3 = 0.60$. The latter value is the actual position of the crack, whereas the former two are spurious solutions due to the mathematical nature of the inverse problem. It is interesting to

notice that, in spite of the non uniqueness of the crack location problem, only one solution of the identification problem is attained in Case 2. In fact, the two spurious solutions $s_1 \simeq 0.20$ and $s_2 \simeq 0.40$ are excluded because they lead to negative value of the flexibility either of the crack or of the rotational spring modelling the elastic support at $x = 0$. This peculiarity of the inverse problem has been checked on the basis of numerical simulations only, and needs further theoretical investigation. Table 3 shows that the determination of the crack position is rather accurate, with percentage errors up to 6%, whereas deviations from the actual value are significantly larger for the two flexibilities.

Finally, the sensitivity of the method to the presence of errors on the data has been investigated in Table 4 for the case with $s = 0.33$, $\xi = 0.005$ and $\mathscr{F} = 0.001$. As in the axial vibration case, 500 numerical simulations have been performed for each level of error $\Pi = 0.05, 0.10, 0.20$. It is confirmed that the errors on the input data are not strongly amplified by the identification method, and the determination of the crack position is more stable than the estimates of the two flexibilities.

Table 3: Bending vibrations: percentage errors in the determination of the position s and flexibility ξ of the crack, and of the flexibility $\mathscr{F}$ of the elastic support by using free-of-error data. $e_s = 100 \times (s_{exact} - s_{ident})/s_{exact}$, $e_{\mathscr{F}} = 100 \times (\mathscr{F}_{exact} - \mathscr{F}_{ident})/\mathscr{F}_{exact}$ and $e_\xi = 100 \times (\xi_{exact} - \xi_{ident})/\xi_{exact}$.

Actual values		$s = 0.33$			$s = 0.60$		
$\mathscr{F}$	ξ	e_s	$e_{\mathscr{F}}$	e_ξ	e_s	$e_{\mathscr{F}}$	e_ξ
0.001	0.004	−0.4	3.7	−5.6	0.0	−0.3	−1.7
	0.008	−0.6	11.1	−8.6	0.0	0.1	−2.4
	0.020	−1.7	40.6	−19.9	−0.2	2.6	−5.1
0.002	0.004	−0.8	3.0	−10.5	−0.1	−0.7	−2.9
	0.008	−0.7	6.9	−11.4	0.0	−0.5	−3.3
	0.020	−1.6	26.1	−21.6	−0.1	0.7	−5.8
0.005	0.004	−5.6	3.2	−46.2	−0.7	−1.9	−10.2
	0.008	−2.6	5.3	−30.3	−0.2	−1.8	−7.7
	0.020	−1.9	14.3	−31.2	−0.1	−1.3	−8.4

4 CONCLUSIONS

We have considered the inverse problem of determining the position and severity of an open crack in a longitudinally vibrating uniform cantilever with elastic support of unknown stiffness by minimal eigenfrequency data. Under the assumption that the flexibility introduced by the crack and the flexibility of the support are small and are of the same order of smallness, it is possible to show that the knowledge of the first three eigenfrequencies guarantees for the unique solution of the identification problem by means of closed form expressions. The stability of the method to errors on the frequency data has been investigated within an extensive series of numerical simulations. The analysis of the corresponding problem for an elastically restrained cracked cantilever has been also discussed.

The details of the proofs and extension of the results to different set of boundary conditions

Table 4: Bending vibrations: determination of the position s and flexibility ξ of the crack, and of the flexibility $\mathscr{F}$ of the elastic support by using frequency data with errors. Actual values of the identification parameters: $s = 0.33$, $\xi = 0.005$ and $\mathscr{F} = 0.001$.

	$\Pi = 0.05$			$\Pi = 0.10$			$\Pi = 0.20$		
Stat. Property	s	ξ	$\mathscr{F}$	s	ξ	$\mathscr{F}$	s	ξ	$\mathscr{F}$
Max	0.343	0.0065	0.00149	0.353	0.0082	0.0018	0.361	0.0153	0.0019
Min	0.304	0.0032	0.00055	0.291	0.0022	0.0000	0.243	0.0016	−0.0020
Average value	0.328	0.0047	0.00105	0.327	0.0049	0.0010	0.325	0.0053	0.0009
% error average	0.6	6.0	−5.0	0.9	2.0	0.0	1.5	−6.0	10.0
Std. dev.	0.006	0.0005	0.00016	0.011	0.0011	0.0003	0.023	0.0021	0.0006
Ident. without errors	0.329	0.0047	0.00105	0.329	0.0047	0.0011	0.329	0.0047	0.0011
Actual value	0.330	0.0050	0.00100	0.330	0.0050	0.0010	0.330	0.0050	0.0010

will be presented in a forthcoming paper.

Acknowledgement

This work has been developed within the National Research Project PRIN2015 'Identificazione e diagnostica di sistemi strutturali complessi', whose financial support is gratefully acknowledged.

REFERENCES

[1] Adams, R.D., Cawley, P., Pye, C.J. and Stone, B.J. A vibration technique for non-destructively assessing the integrity of structures. *J. Mech. Eng. Sci.* (1978) **20**: 93–100.

[2] Hearn, G. and Testa, R.B. Modal analysis for damage detection in structures. *J. Struct. Eng.-ASCE* (1991) **117**:3042–3063.

[3] Vestroni, F. and Capecchi, D. Damage evaluation in cracked vibrating beams using experimental frequencies and finite element models. *J. Vib. Control* (1996) **2**:69–86.

[4] Caddemi, S. and Caliò, I. Exact reconstruction of multiple concentrated damages on beams. *Acta Mech.* (2014) **225**:3137–3156.

[5] Narkis, Y. Identification of crack location in vibrating simply supported beams. *J. Sound Vib.* (1994) **172**:549–558.

[6] Morassi, A. Identification of a crack in a rod based on changes in a pair of natural frequencies. *J. Sound Vib.* (2001) **242**:577–596.

[7] Dilena, M. and Morassi, A. The use of antiresonances for crack detection in beams. *J. Sound Vib.* (2004) **276**:195–214.

[8] Rubio, L., Fernández-Sáez, J. and Morassi, A. Identification of an open crack in a non-uniform rod by two frequency data. *Int. J. Solids. Struct.* (2015) **75-76**:61–80.

[9] Narkis, Y. and Elmalah, E. Crack identification in a cantilever beam under uncertain end conditions. *Int. J. Mech. Sci.* (1996) **38**:499–507.

[10] Freund, L.B. and Herrmann, G. Dynamic fracture of a beam or plate in plane bending. *J. Appl. Mech.-T. ASME* (1976) **76-APM-15**:112–116.

[11] Morassi, A. Crack-induced changes in eigenparameters of beam structures. *J. Eng. Mech.-ASCE* (1993) **119**:1798–1803.

VIII ECCOMAS Thematic Conference on Smart Structures and Materials
SMART 2017
A. Güemes, A. Benjeddou, J. Rodellar and J. Leng (Eds)

DESIGNING A SMART TMD FOR A COMPOSITE STEEL-CONCRETE SLENDER SLAB

José M. Soria*, Iván M. Díaz*, Jaime H. García-Palacios*, Gonzalo Marinas-Sanz* and Emiliano Pereira†

*ETS Ingenieros de Caminos, Canales y Puertos
Universidad Politécnica de Madrid
28040 Madrid, Spain
e-mail: jm.soria@upm.es

† Escuela Politécnica Superior
Universidad de Alcalá de Henares
28805 Alcalá de Henares, Spain

Key words: structural control, semi-active vibration control, smart TMD

Abstract. This paper explores different vibration control strategies for the cancellation of human-induced vibration on a slender structure. More concretely, the performance of semi-active control is compared with passive control for a time-varying modal parameters structure numerically, as a previous step to the experimental implementation. The structure is a composite steel-concrete slender slab with its first vibration mode at 5.51 Hz which may change up to 25%. In order to find a solution for this case, this paper takes the modal parameter estimates from the Frequency Response Function and designs three control strategies: a) a tuned mass damper (TMD) tuned to the aforementioned mode, b) two semi-active TMD strategies, one with an on-off control law for the TMD damping, and other with frequency and damping tuned by updating the damper force. All strategies have been carefully compared considering two structure models: a) the nominal case of the aforementioned mode and b) the same mode but with different frequency. The results have been compared using predictors for human-induced vibrations.

1 INTRODUCTION

The continuous development of structural materials and construction techniques is leading to lighter and slender structures, which may be susceptible of experiencing excessive vibrations due to human-induced loading. These results show that this kind of structures might not fulfill vibration serviceability requirements. Then, the inclusion of a device to reduce vibration levels may be a recommendable action [1]. Within then, it can be found passive, semi-active and active devices. When structures show modal properties changing over time, and/or several vibration

modes must be canceled by the same device [2], passive devices may detune and experience a significant loss of efficacy. Under these circumstances, the use of semi-active devices is a solution to be explored [3].

Lightweight floors and only footbridges can suffer excessive vibration compromising Vibration Serviceability Limit State (VSLS). The research group has recently built a composite steel-concrete slender slab of a span-to-depth ratio of only 1/40 (1/20 is the commom value) and weights 3000 kg. The presence of users onto the structure changes drastically the modal parameters (up to 30%, from bare structure to 10 spectators). Thus, the objective of this paper is to test two different laws of semi-active TMD (STMD) that should be easy to implement practically. The following steps are carried out:

1. The structure modal properties are studied for different configurations.
2. A TMD is designed for a nominal model of the structure. The CAD model is carried out including magneto-rheological (MR) dampers. The TMD is proved for different structure models.
3. The TMD is upgraded to a STMD. For these purpose, the laws proposed by Moutinho [4] (STMD 1) and Weber [5] (STMD 2) are explained and used due to their simplicity and ease of implementability in practice.

The STMDs are tested for different configurations. No more modes have been studied because their vibration frequencies are far away from the range of interest (tipically modes $\leq$ 10 Hz). The loading case used to excite the first mode simulates the magnitude of a person bouncing that excite the structure with the second harmonic. The paper continues with the structure description and its model, describing the different configurations. In section 3, the load case and the three control strategies are described. Finally, the results are presented in section 4. The paper ends with a conclusion section.

2 STRUCTURE DESCRIPTION AND THE MODELS FOR DIFFERENT CONFIGURATIONS

The lab structure is a composite steel-concrete slender slab (see Figure 1) resulting in a very light structure that does not fulfill the VSLS, as expected when it was designed. The structure has 5.5 m span, 14 cm depth and weights only 3000 kg.

The nominal case is the first configuration with the structure with two electrodynamic shakers onto it weighting approximately 210 kg. Apart from this configuration, other two configurations are studied. The second configuration consists of adding masses (4 blocks of 150 kg, a total mass of 600 kg). The latter configuration is obtained changing the support conditions (reducing 30 cm the span of the slab). Figure 2 shows a picture of each one illustrating the structure modification.

The modal parameters are obtained with the estimator H_v of the Frequency Response Function (FRF) at the point of maximum amplitude of the mode. The modal properties estimated for each configuration are shown in Table 1 and Figure 3.



(a) Before casting.



(b) After casting.

Figure 1: Composite steel-concrete slender slab.



(a) Second configuration.



(b) Third configuration.

Figure 2: Details of modified configurations.

As usual, the Transfer Function between the structure acceleration and the applied force in the Laplace domain is as follows:

$$G(s) = \frac{s^2/m}{s^2 + 2\,\zeta\,\omega\,s + \omega^2}, \tag{1}$$

in which $s = j\omega$, $\omega = 2\pi f$ being the circular frequency (rad/s) and f the natural frequency (Hz), ζ is the damping ratio and m is the modal mass.

Table 1: Modal parameters of each configuration.

	Conf. 2	Nominal	Conf. 3
f_1 (Hz)	4.81	5.51	6.90
ζ_1 (%)	0.98	0.76	1.08
M_1 (kg)	2343	1714	1559

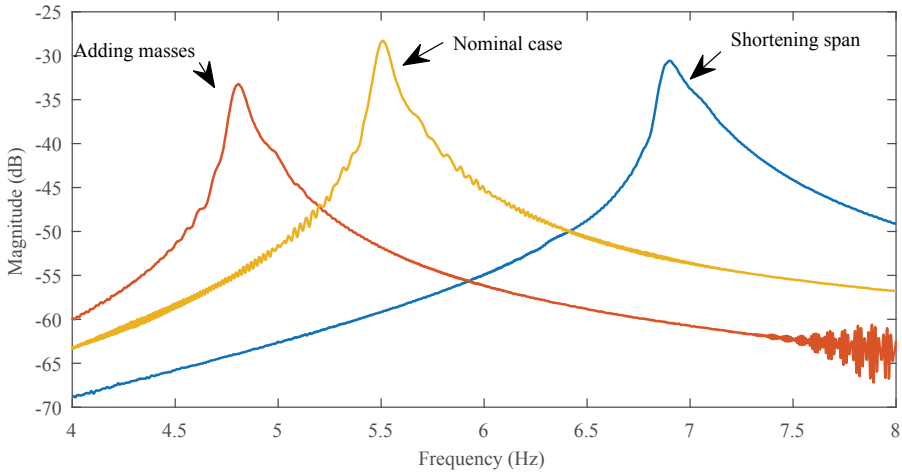

Figure 3: Amplitude of Frequency Response Functions of each configuration.

3 VIBRATION CONTROL STRATEGIES

3.1 Loading case

The force used to evaluate the vibration control strategies has been a chirp waveform whose frequency increases at a linear range with time, $f(t)$, as follows

$$\begin{aligned} &F(t) = F_0 \cdot \sin(2\pi\, f(t)), \\ &\text{with} \;\; f(t) \in (3,\, 7)\,\text{Hz}, \;\; \text{and} \;\; t \in [0,\, T_f]\,\text{s}. \end{aligned} \tag{2}$$

The frequency range has been chosen in order to excite first vibration mode. The final time, T_f, has been 500 s. This value was chosen to ensure that sweeping at each frequency is sufficiently slow so that the results do not depend on the final time. The force amplitude, F_0, of 400 N is representative of bouncing force.

3.2 Passive control: Tuned Mass Damper

A TMD consists of a secondary mass (also called moving or inertial mass) attached to the structure by means of springs and dampers. The TMD mass is fixed as a fraction of the modal mass of the targeted vibration mode; the stiffness of the springs is selected to obtain the optimum TMD frequency, and the viscous dampers ensure the operation of the TMD in a range of frequencies around the tuning frequency.

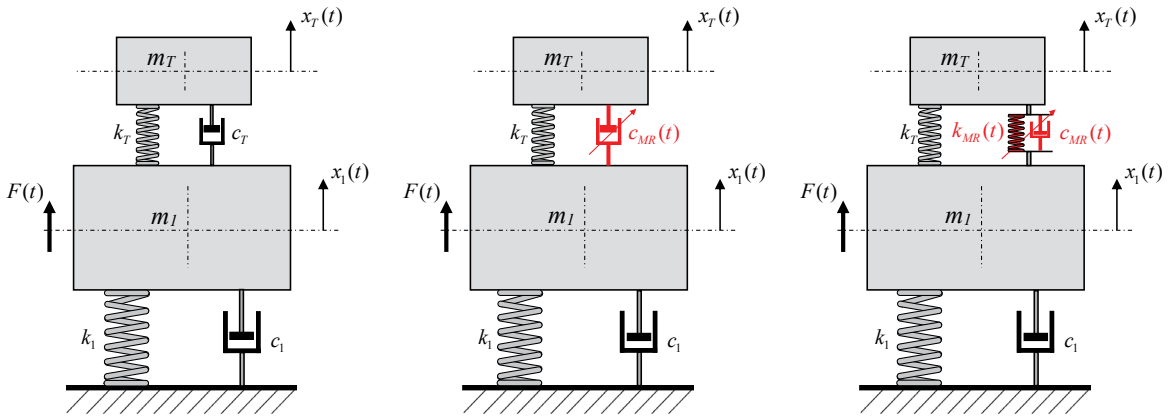

(a) Passive (b) STMD 1 (c) STMD 2

Figure 4: Model of the devices installed on a primary structure. Red symbol (↗) means changing over time.

Figure 4a shows the model of a classical TMD composed of an inertial mass m_T attached to a primary system by means of a spring of constant k_T and a viscous damper of constant c_T. The primary system is the structure modeled as a SDOF system, which is composed of a mass m_1, a spring of constant k_1 and a viscous damper of constant c_1.

The TMD has been designed using the [6] formulas and only the first mode is considered for TMD design and tuned according to the frequency value of the nominal case. The second mode is considered that its frequency is far enough and furthermore it is not so representative in the response of the structure. It is well known and widely used in real structures for the mitigation of resonance vibration problems and it is chosen in this study as a benchmark damper, as it is also done in [5], for instance.

The TMD properties are

$$m_T = \mu\, m_1 \tag{3}$$

$$\eta = \frac{1}{1+\mu} \tag{4}$$

$$\zeta_T = \sqrt{\frac{3\mu}{8(1+\mu)^3}}, \tag{5}$$

in which $\mu = m_T/m_1$ is the mass ratio, which is estimated to be 2.85% ($m_T = 49\,\text{kg}$), $\eta = \omega_T/\omega_1$ is the frequency ratio and the stiffness and damping ratio for the TMD are obtained from

$$k_T = \omega_T^2 m_T \tag{6}$$

$$c_T = 2\zeta_T m_T \omega_T, \tag{7}$$

respectively.

3.3 Semi-active control 1

Figure 4b shows a STMD (hereafter denoted as STMD 1) in which the TMD damper is suposed to be a MR-damper ($c_{\text{MR}}(t)$), whose damping can be changed continously. A phase control strategy for the TMD damping is considered here. More concretely, the adapted version from [7] proposed by [4] has been adopted since this is clearly geared to practical implementation due to the quantities employed: the structure acceleration instead of displacement and the TMD mass velocity instead of the relative velocity, as usual [8]. The control law achieves a phase lag between the control force (the force coming from the TMD) and structure displacement close to 90° even in situation of significant detuning. The control law adopted is of ON/OFF type due to its simplicity. Thus, the adopted control law is defined as follows [4]:

$$\begin{cases} \ddot{x}_1 \cdot \dot{x}_{_T} \leq 0 \quad \Rightarrow \quad c_{\text{MR}} = c_{min} & \text{(normal functioning)} \\ \ddot{x}_1 \cdot \dot{x}_{_T} > 0 \quad \Rightarrow \quad c_{\text{MR}} = c_{max} & \text{(blocking functioning),} \end{cases} \tag{8}$$

in which $c_{max} = 50 \cdot c_{min}$, c_{min} is the optimal damping obtained from equation (7), $\ddot{x}_1$ is the structure acceleration (obtain by an accelerometer) and $\dot{x}_{_T}$ is the absolute velocity of the TMD mass (which might be obtained from the integration of an accelerometer signal installed on the TMD mass).

3.4 Semi-active control 2

Figure 4c depicts the STMD strategy proposed by [5] and denoted as STMD 2 hereafter. The key feature of this control law is that the energy dissipation and natural frequency of the STMD, respectively, are adjusted according to Den Hartog's formula in real time to f_w instead of f_1, f_w being the actual instantaneous frequency of the vibration response, independently if this frequency corresponds to the resonant frequency of the targeted vibration mode or represents an excitation frequency due to forced excitation out of resonance. The MR damper works in parallel with a passive spring designed according to Den Hartog's formula (see Figure 4c), denoted by $k_{_T}$.

The MR damper emulates the sum of a controllable stiffness force (positive or negative), F_k, and a controllable dissipative force, F_c, as follows

$$F = F_k + F_c. \tag{9}$$

These forces are clipped to zero, which yields to the semi-active force, F_{MR}, as follow

$$F_{\text{MR}} = \begin{cases} F, & \text{sgn}(\dot{x}_1 - \dot{x}_{_T})\, F \geq 0 \\ 0, & \text{sgn}(\dot{x}_1 - \dot{x}_{_T})\, F < 0 \end{cases}, \tag{10}$$

in which $\text{sgn}(\dot{x}_1 - \dot{x}_{_T})$ is the sign of the relative velocity between the structure and TMD mass.

The actual frequency, f_w, is estimated from the zero-crossings of the relative displacement,

$x_S - x_T$, through the half period time, T_{half}. The actual frequency is then estimated as follows:

$$f_w = \frac{1}{2\,T_{\text{half}}}. \tag{11}$$

Thus, the stiffness and energy dissipation of the STMD2 are tuned to the actual frequency of vibration f_w by the modified mass ratio $\widetilde{\mu}$ that depends on the frequency shift between f_w and f_1 as follows

$$\widetilde{\mu} = \mu \left(\frac{f_w}{f_1} \right), \tag{12}$$

and then, the damper properties are derived as

$$k_{\text{MR}} = k_1 \frac{\widetilde{\mu}}{(1+\widetilde{\mu})^2} - k_T, \tag{13}$$

$$\zeta_{\text{MR}} = \sqrt{\frac{3\,\widetilde{\mu}}{8\,(\widetilde{\mu}+1)^3}}, \tag{14}$$

$$c_{\text{MR}} = 2\,\zeta_{\text{MR}}\,m_T\,(2\pi f_w). \tag{15}$$

Finally, the control forces to compute (9) and apply the semi-active control law (10) are,

$$F_k = k_{\text{MR}}\,(x_1 - x_T), \tag{16}$$

$$F_c = \text{sgn}(\dot{x}_1 - \dot{x}_T)\,\left\{ \frac{\pi}{4} c_{\text{MR}} (2\pi f_w)\,(x_1 - x_T) \right\}. \tag{17}$$

The reader can consult the article of [5] to go deeper into the algorithm. It should be mentioned that this algorithm requires measuring the relative displacement as well as knowing the sign of relative velocity. This might be undertaken using a displacement transducer between the structure and TMD mass. It is worth mentioning that the implementation of the control law of STMD 2 is is more complicated than the implementation of the one of STMD 1.

3.5 Mechanical design of Tuned Mass Damper

It has been designed a physical model that consists of four springs with a stiffness of 16.5 kN/m each one, two sponge-type magneto-rheological dampers from Lord Corporation company, vibrating box with adjustable height and modular weights. The final CAD solution of TMD is shown in Figure 5 and it has a vibrating mass of 49 kg to be tuned with the frequency of the nominal case. It intends to study this solution numerically, functioning as passive control and also with two laws of semi-active control. In this way, conclusions can be drawn before being constructed and tested in practice.

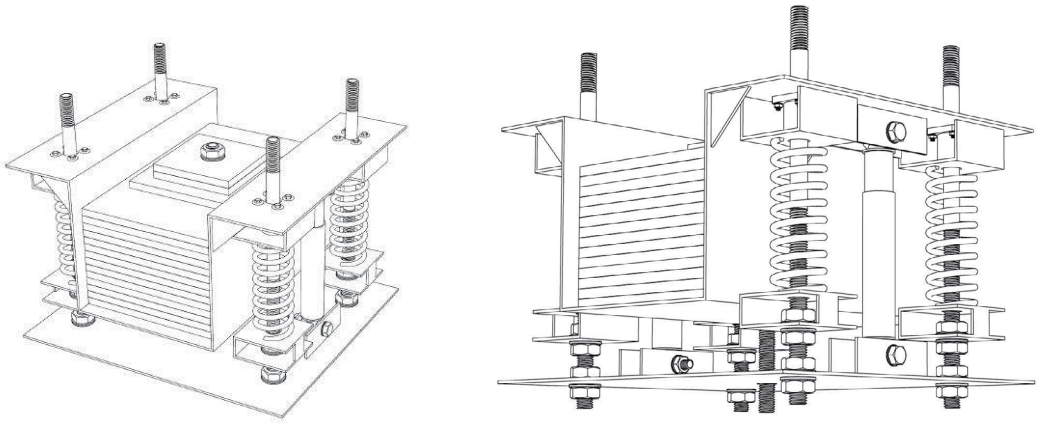

(a) View 1. (b) View 2.

Figure 5: Different views of TMD.

Table 2: MTVV accelerations in (m/s^2) for the nominal case and the other two configurations.

	Uncontr.	TMD	STMD 1	STMD 2
Nominal case	1.99	0.25 (87.41%)	0.23 (88.40%)	0.22 (88.71%)
Conf. 2	1.17	0.51 (55.98%)	0.27 (76.59%)	0.25 (78.70%)
Conf. 3	1.66	0.76 (53.99%)	0.34 (79.58%)	0.36 (78.47%)

4 RESULTS

Figure 6 shows the frequency response spectra under loading described in 3.2 for the nominal configuration. The control performance of these three strategies are compared in time with the Maximum Transient Vibration Value (MTVV). The MTVV is calculated from the 1s running root-mean square acceleration and it is adopted for current standards [9] as vibration predictor for the serviceability assessment. In this case, the performance of the three devices (TMD, STMD 1 and STMD 2) and the vibration reduction are quite similar (87.41%, 88.40% and 88.71%, respectively) although STMDs show a broader band performance. Figure 7*a* and *b* show also the spectra of configuration 1 and 2, respectively. Although in these other two cases none of the control devices works as in the nominal case, the semi-active control devices show less performance degradation than the passive solution (55.98%, 76.59% and 78.70% for the configuration 2 and 53.99%, 79.58% and 78.47% for the configuration 2, respectively). Table 2 summarizes the results.

4.1 Degrading by MR-damper behavior

Bingham model is used to illustrate the different behavior obtained when a real MR-damper is used and the results are compared between the passive solution. The stress-strain behavior of the Bingham vistoplastic model is often used to describe the behavior of MR fluids. In this

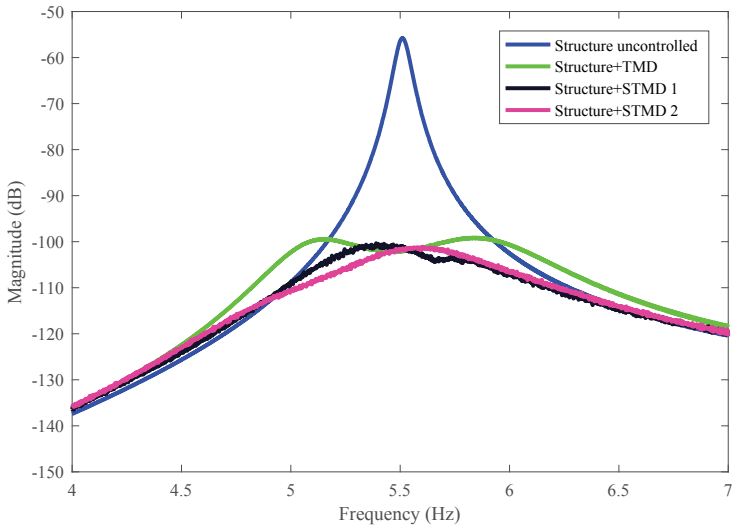

Figure 6: Frequency response spectra for nominal configuration.

model, the plastic viscosity is defined as the slope of the measured shear stress versus shear strain rate data. Thus, for positive values of the shear rate, $\dot{\gamma}$, the total stress is given by

$$\tau = \tau_\gamma \, \mathrm{sgn}(\dot{\gamma}) + \eta \, \dot{\gamma} \tag{18}$$

where τ_γ is the yield induced by magnetic field and η is the viscosity of fluid. Based on this model, the Bingham model consists of a Coulomb friction element placed in parallel with a viscous damper. In this model, for nonzero piston velocities, $\dot{x}$, the force generated by the device is given by

$$F = f_c \, \mathrm{sgn}(\dot{x}) + c_0 \, \dot{x} + f_0 \tag{19}$$

where c_0 is the damping coefficient, f_c is the frictional force, which is related to fluid yield stress. An offset in the force f_0 is included to account for the nonzero mean observed in the measured force due to the presence of the accumulator. Values according to the size of a possible MR-damper for the TMD of this structure have been used in the modeling carried out.

Although this model is not advisable to use for control, its simplicity allows to highlight, in a simple way, the degradation that is obtained when TMD does not have a damping model perfectly linear and viscous. Figure 8 shows the frequency responses of the different cases: uncontrolled structure, structure with TMD and structure with MR-TMD, MR modeled by Bingham model.

5 CONCLUSIONS

A complete study has been carried out in order to study a feasible-to-be-implementable semi-active control strategies to reduce vibrations in a frequency varying structure taking into account only one mode and different configurations.

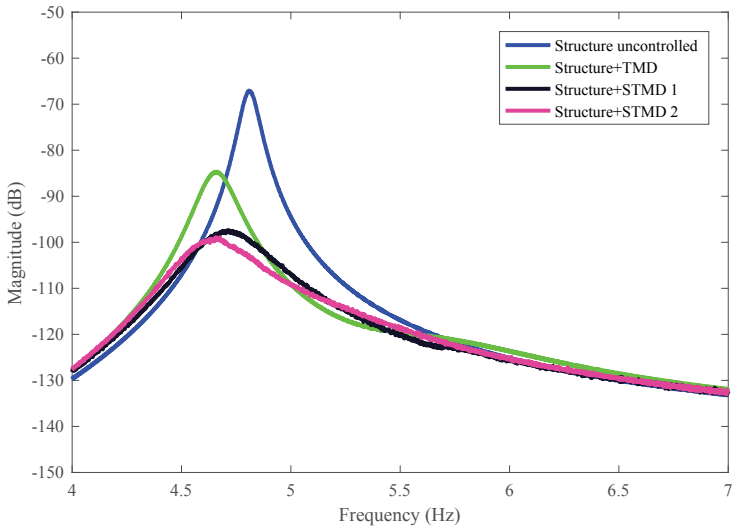

(a) Configuration 2.

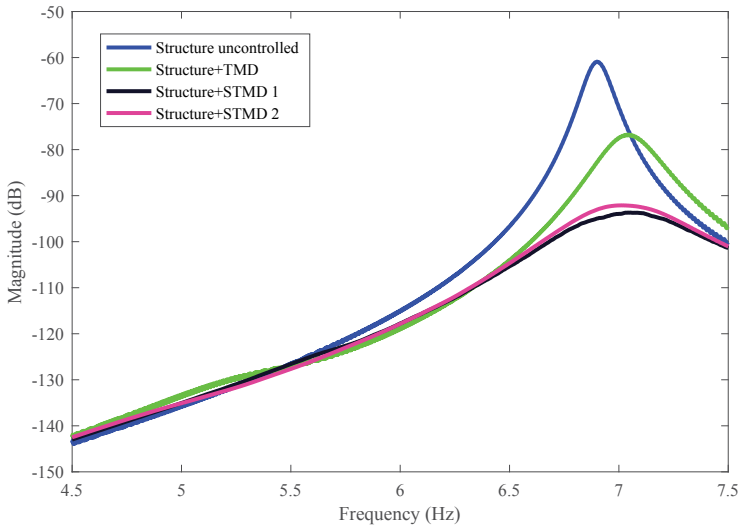

(b) Configuration 3.

Figure 7: Frequency response spectra for other configurations different from nominal case.

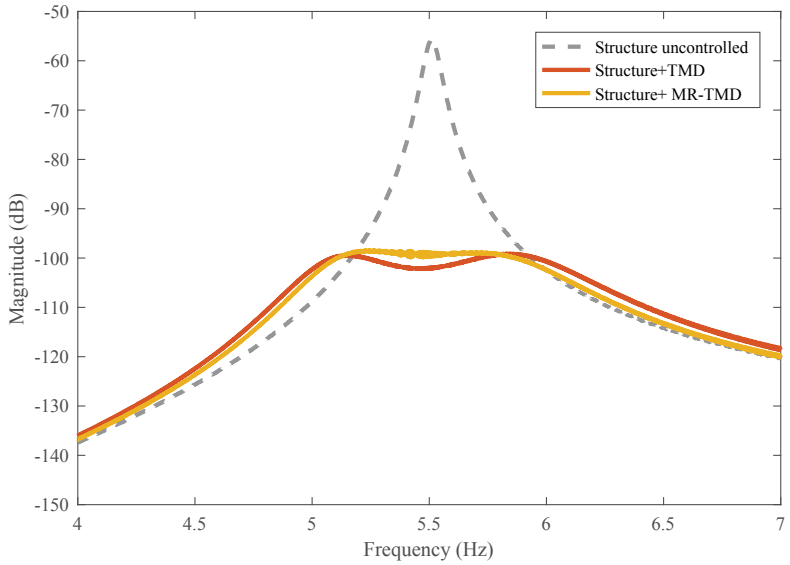

Figure 8: Frequency spectra of nominal configuration of TMD and MR-TMD modeled by Bingham model.

From the preceding discussions, the following conclusions can be drawn:

- The TMD, even though it behaves quite well, its performance degrades significantly when model frequencies of tuned vibration mode move away from the nominal case.
- STMDs have been shown to be less sensitive to its initial tuning and able to cancel effectively the vibration independently of the modal properties of the tuned vibration mode. It is able to cope with changing model parameters with less degrading of its behavior.
- For the passive case, it has shown the comparison between having modeling the MR-damper and not having it, affecting slightly to the response. Obviously, for semi-active cases, the worsening will be much greater.

Future work should be to test the real TMD (see Figure 9) on the slender slab and compare the practical results with the numerical one. It will also be necessary to study how the semi-active control laws should be modified to take into account the non-linear behavior of MR-damper.

6 ACKNOWLEDGMENTS

The authors acknowledge the financial support provided by the Ministry of Economy and Competitiveness of the Government of Spain to make this work possible by funding from the REVES-P Research Project, with reference DPI2013-47441. The authors also acknowledge the financial support provided by Project VibraStruNET with reference BIA2015-71942-REDT.



(a) MR-TMD. (b) Movie of a first test without MR-damper.

Figure 9: Tuned Mass Damper built.

REFERENCES

[1] C. M. Casado, I.M. Díaz, J.D. Sebastián, A.V. Poncela, and A. Lorenzana. Implementation of passive and active vibration control on an in-service footbridge. *Structural Control and Health Monitoring*, 20:70–87, 2013.

[2] J.M. Soria, I.M. Díaz, J.H. García-Palacios, and N. Ibán. Vibration monitoring of a steel-plated strees-ribbon footbridge: uncertainties in the modal estimation. *Journal of Bridge Engineering*, 108(5):1175–1183, 2016.

[3] J.M. Soria, I.M. Díaz, E. Pereira, J.H. García-Palacios, and X. Wang. Exploring vibration control strategies for a footbridge with time-varying modal parameters. In *MOVIC & RASD 2016*, Southampton, 2016.

[4] C. Moutinho. Testing a simple control law to reduce broadband frequency harmonic vibrations using semi-active tuned mass dampers. *Smart Materials and Structures*, 24(5):964–1726, 2015.

[5] F. Weber. Dynamic characteristics of controlled MR-STMDs of wolgograd bridge. *Smart Materials and Structures*, 22(095008):16pp, 2013.

[6] J.P. Den Hartog. *Mechanical vibrations*. Courier Corporation, 1985.

[7] L. Chung, Y. Lai, and C.W. Yang. Semi-active tuned mass dampers with phase control. *Journal of Sound and Vibration*, 332(15):1–16, 2013.

[8] J.H. Koo, M. Ahmadian, M. Setareh, and T. Murray. In Search of Suitable Control Methods for Semi-Active Tuned Vibration Absorbers. *Journal of Vibration and Control*, 10(2):163–174, 2004.

[9] ISO 10137. *Bases for Design of Structures – Serviceability of Buildings and Walkways against Vibrations*, international organization for standardization edition, 2007.

VIII ECCOMAS Thematic Conference on Smart Structures and Materials
SMART 2017
A. Güemes, A. Benjeddou , J. Rodellar and Jinsong Leng (Eds)

DYNAMIC PROPERTIES EVOLUTION OF MEDIUM-LENGTH RC BRIDGES

JOSÉ M. JARA*, URIEL GALVÁN†, GUILLERMO MARTÍNEZ† AND BERTHA A. OLMOS†

* División de Estudios de Posgrado, Facultad de Ingeniería Civil
Universidad Michoacana de San Nicolás de Hidalgo
Ciudad Universitaria, 58040 Morelia, Michoacán, México
e-mail: jmjara70@gmail.com

† División de Estudios de Posgrado, Facultad de Ingeniería Civil
Universidad Michoacana de San Nicolás de Hidalgo
Ciudad Universitaria, 58040 Morelia, Michoacán, México
e-mail: uriel_1020@hotmail.com; guillermo.mtzruiz@gmail.com; ba.olmos@gmail.com

Key words: Dynamic Properties, Ambient Vibration Measurements, Medium-length Bridges, Frequency Domain Decomposition.

Abstract. Many countries of the world have an important family of medium-length RC bridges. In Mexico, it is very common to find in highways and urban areas simply-supported RC bridges. This study evaluates the evolution of dynamic properties of a group of existing typical RC bridges in Mexico based on ambient vibration tests. The measurements campaign started during the construction process and continued after the bridges were finished. The bridges are 30-m span simply supported structures with superstructure composed by reinforced concrete slab resting on prestressed concrete AASTHO girders. In the transverse direction, the AASHTO beams are connected with diaphragms to provide lateral stiffness to the superstructure. The bridges have two lanes of circulation and the substructure consists of frame type piers with three rectangular columns of constant cross section. The girders are supported on the piers and abutments through elastomeric bearings. The dynamic properties were assessed by using the Frequency Domain Decomposition (FDD) and they were used to calibrate several numerical models. The results show that in a period of one year, the change in dynamic properties of the bridges is around 10% of the initial measurements. The implication of these results are also discussed.

1 INTRODUCTION

A very common technique to assess dynamic properties of a structure is by conducting ambient vibration measurements. The source of the ambient vibration is the wind and traffic among other sources [1-2]. Since several decades ago, diverse structures, as bridges, have been studied by determining their dynamic properties through ambient vibration measurements [3-4]. Ambient vibration tests are also the basis to calibrate numerical models that allow to evaluate the vulnerability of structures and, when is required, to select a retrofit

technique to improve the structural capacity. Bridges are usually exposed to increments of dead and live loads during their useful life and sometimes are also located in sites of aggressive environment. Load increments induce cracking, not always easily exposed, in girders, deck and sometimes in piers. Changes in dynamic properties, can be the evidence of damage. Health monitoring [5] is a technique used to assess variations of the dynamic characteristics of bridges and based on that locate damage of structural elements. Starting in 2014 several ambient vibration measurements were conducted in three RC bridges since the construction stage. This study analyses the results of ambient vibration measurements in two of these bridges located in Mexico. The vibration records are used to evaluate dynamic properties of the bridges before the opening to traffic and after that, during a year period.

2 AMBIENT VIBRATION MEASUREMENTS

2.1 Measurement campaign

The equipment used for the ambient vibration measurements is a Kinemetrics K2 recording console with 12 channels, nine force balanced unidirectional sensors and one Episensor triaxial force balanced instrument. Figure 1 shows the unidirectional and triaxial sensors, both with a full-scale range of ±0.20 to ± 4 g and extended bandwidth – DC to 200 Hz.



Figure 1: Unidirectional and triaxial force balance sensors.

The ambient vibration measurements started in 2014 during the stage of construction and finished at the end of 2015 when the bridges were finished.

2.2 La Central Bridge

This bridge is located in Morelia, a city in the central zone of Mexico. It is a five-span simply supported bridge with span lengths of 30.6 m. The 0.20 m thick deck slab rests on nine AASHTO type IV girders supported on elastomeric bearings. The deck width is of 12.3 m. The substructure is a RC three-column bent (Figure 2). The design concrete strength was of 24.5 MPa in bent caps, diaphragms, slabs and piers. In AASHTO prestressed girders, the design concrete strength was of 39.2 MPa. Even though the girders are simply supported on bent caps, the deck slab is continuous between spans 1-2 and 4-5. Conversely, an expansion joint exists at approaches and between spans 2-3.

Figure 3 shows a bridge elevation along the central axis. All piers and abutments have

similar length and rest on continuous RC footing.



Figure 2: La Central Bridge

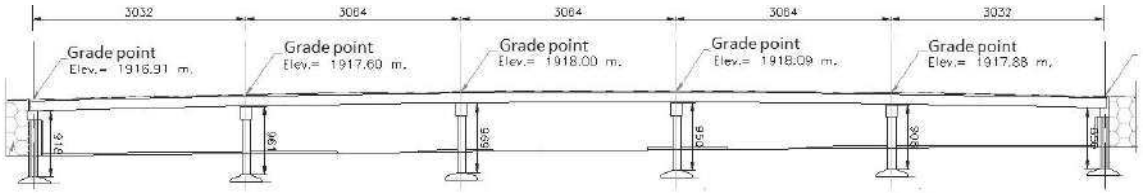

Figure 3: La Central Bridge elevation.

Figure 4 displays an elevation view of Pier 2. The concrete elements on cap beam give a cross slope to the right of the figure.

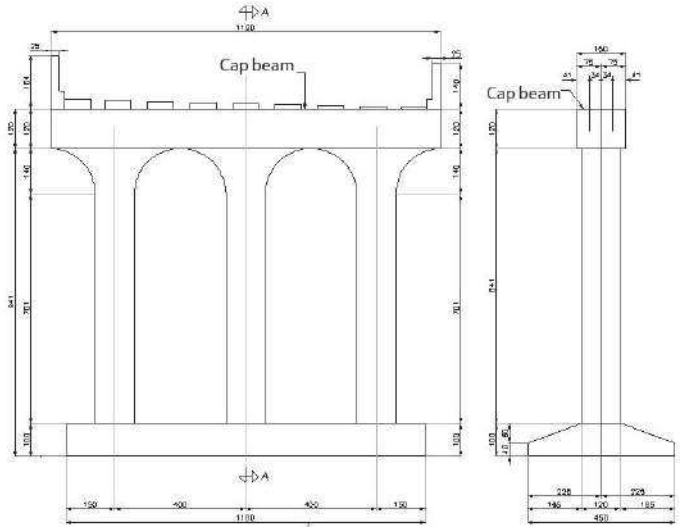

Figure 4: Elevation view of Pier 2 of La Central Bridge.

During a year period, ambient vibration measurements were recorded. The first one in November 2014 without asphalt overlay and the last one in operation. Figure 5 shows the sensor arrangement along the bridge in the 2014 campaign. The sensors were located in the first and second spans between the expansion joint of the approach slab and the expansion joint of pier 3. These two spans have a continuous deck slab. Each empty circle represents

unidirectional sensors in three directions of analysis and the black circle is a triaxial sensor. The latter was the reference sensor that kept a fixed position for all positions of the unidirectional sensors. The sensor separation was always less than 4 m.

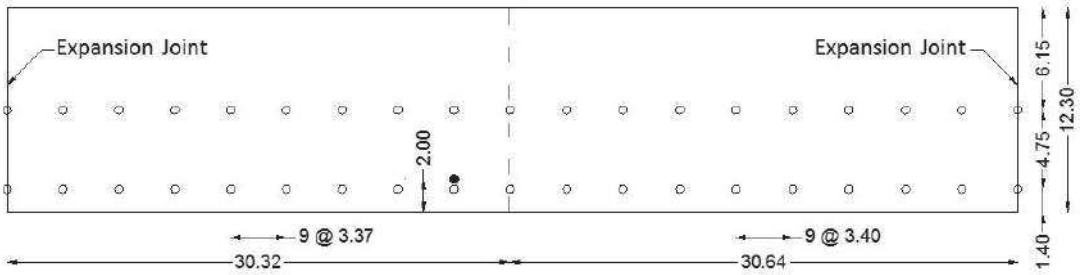

Figure 5: Sensor location for the ambient vibration measurements of La Central Bridge in November 2014.

Figure 6 displays pictures of the process of vibration measurements during the November 2014 campaign. In this stage, the bridge had the deck slab without asphalt overlay.



Figure 6: Ambient vibration measurements of La Central Bridge in November 2014.

The last vibration measurement was completed in December 2015. As observed in Figure 7, the bridge had already asphalt overlay and it was in operation. The intense vehicle circulation prevented the sensor locations transversely. Consequently, the sensors were placed in only one lane.



Figure 7: Ambient vibration measurements of La Central Bridge in December 2015.

2.2 Pedregal Bridge

This skewed bridge is also located in Morelia, about 1.5 km away from La Central Bridge. It is also a five-span simply supported bridge with span lengths in the range of 30.4-30.8 m. The 0.20 m thick deck slab rests on nine AASHTO type IV girders supported on elastomeric bearings. The deck width is of 12.3 m. The substructure is a RC four-column bent skewed 39.6° (Figure 8). The design concrete strength was of 24.5 MPa in bent caps, diaphragms, slabs and piers. In AASHTO prestressed girders, the design concrete strength was of 39.2 MPa. Even though the girders are simply supported on bent caps, the deck slab is continuous between spans 1-2 and 4-5. Conversely, an expansion joint exists at approaches and between spans 2-3.



Figure 8: Pedregal Bridge

Figure 9 shows a bridge elevation along the longitudinal central axis. All piers and abutments have similar length and because of the soil characteristics, the bridge is over a pile foundation system.

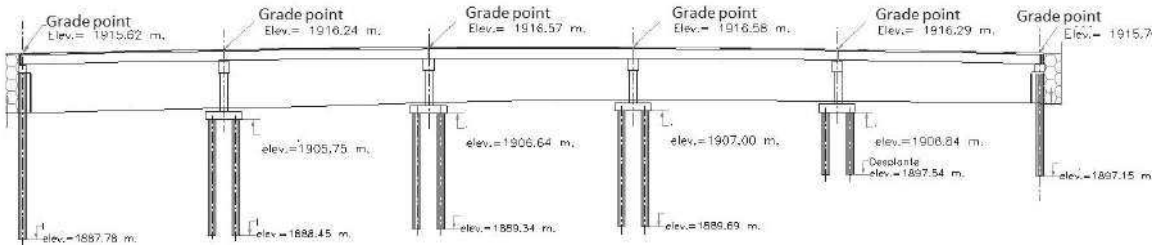

Figure 9: Pedregal Bridge

Figure 10 displays an elevation view of Pier 2 of the Pedregal Bridge. The bridge has a cross slope to the right of the figure draining the rainwater to that side of the superstructure. The first ambient vibration measurement was accomplished in January 2015 without asphalt overlay and the last one in operation. Figure 11 shows the sensor arrangement along the bridge spans 1-3, in the January 2015 measurement. The sensors were located in the first and second spans between the expansion joint of the approach slab and the expansion joint of pier 3. These two spans have a continuous deck slab. Each empty circle represents unidirectional sensors in three directions of analysis and the black circle is a triaxial sensor. The triaxial sensor was the reference sensor with a fixed position for all positions of the unidirectional sensors. In this case, the reference sensor is located 5.1 m from the Pier 3 axis and

unidirectional sensors separate each other around 7 m. The sensor placement follows the skewness angle of the bridge.

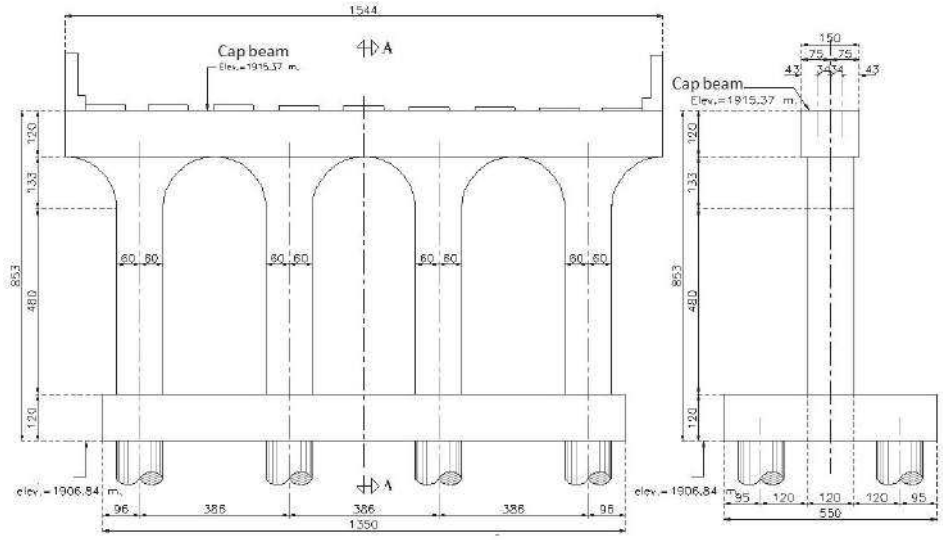

Figure 10: Elevation view of Pier 2 of Pedregal Bridge.

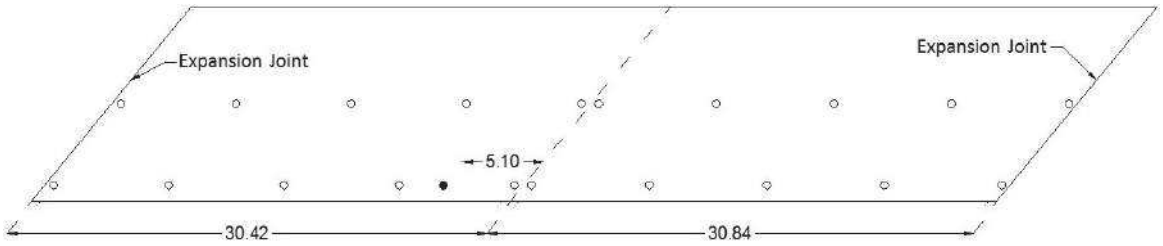

Figure 11: Sensor location for the ambient vibration measurements of Pedregal Bridge in January 2015.

Figure 12 displays two pictures of the measurement campaign in January 2015. The bridge was at that period in a construction phase that allow placing sensors in the longitudinal and the transverse directions of the deck slab.

3 SYSTEM IDENTIFICATION

To identify the dynamic properties of the bridges this study employs the frequency domain decomposition technique (FDD) with the use of singular value decomposition [6]. The vibration measurements of the Central Bridge allowed identifying six modal shapes in the first measurement campaign; five in the vertical and one in the longitudinal directions (Figure 12).

Figure 13 shows in green color the undeformed shape and in yellow and red colors the deformed shape of the two first spans of the bridge. It is important to mention again that the deck slab is continuous in these two spans.

The identified frequencies are in the range of 3.2 Hz (T=0.31 s) to 13.9 Hz (0.07 s). The first three modes are in the vertical direction, the four mode in the longitudinal direction and the last two modes in the vertical direction as well.



Figure 12: Ambient vibration measurements of Pedregal Bridge in January 2015.

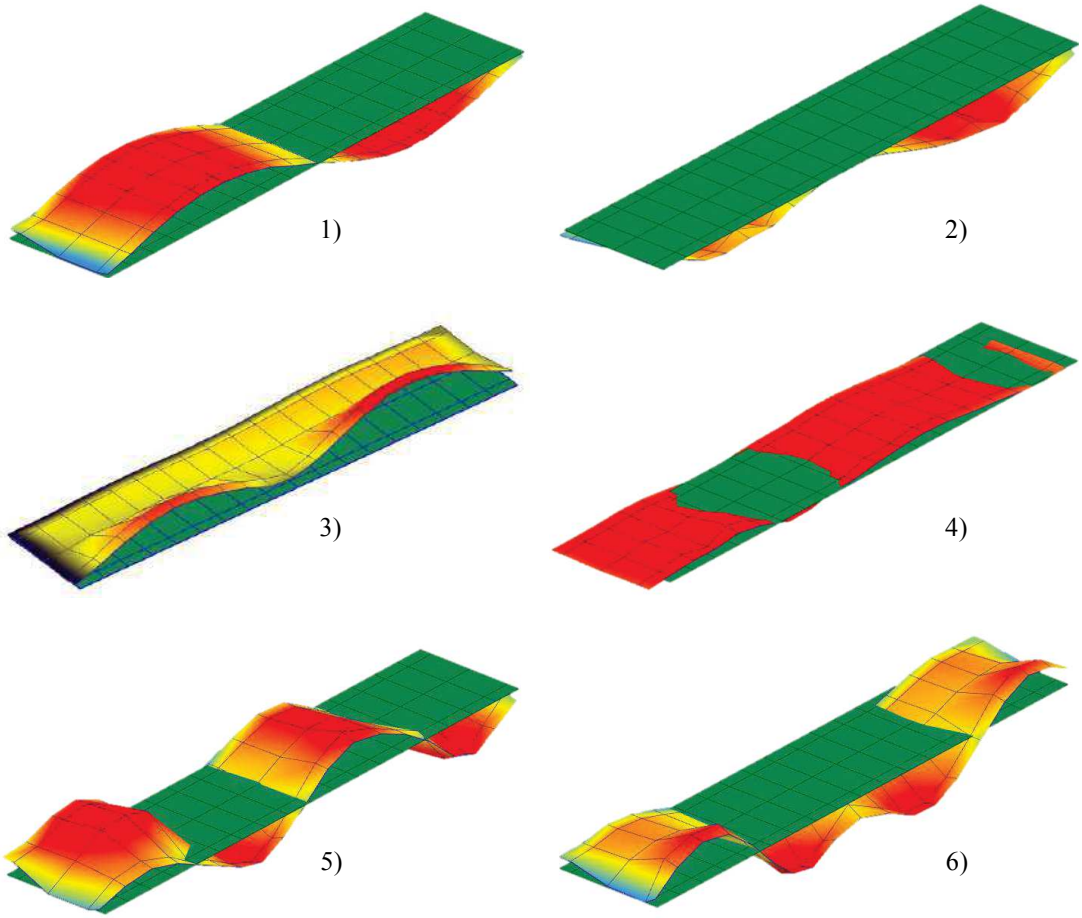

Figure 13: Modal shapes of La Central Bridge identified with the ambient vibration measurements.

Table 1 presents the first six frequencies of La Central Bridge assessed after three ambient vibration measurements conducted in November 2014, December 2104 and November 2015. The first instrumental measure corresponds to the bridge state without asphalt overlay; in the second one the bridge had partially asphalt overlay and during the third one the bridge was in operation.

The differences in frequency values among the November and December 2014 campaigns

are in the range of 4%-13%. The highest frequency reduction between a year period measurements was 16%.

Table 1: Frequencies of the first six modes in La Central Bridge.

Mode	Nov-14	Dec-14	Nov-15
	(Hz)	(Hz)	(Hz)
1	3.398	3.238	3.223
2	4.648	4.375	4.004
3	5.117	4.922	
4	7.305	6.484	
5	12.541	12.031	11.816
6	13.906	12.891	12.500

Table 2 displays the results of processing two ambient vibration measurements of the Pedregal Bridge conducted in January 2015 and November 2015.

Table 2: Frequencies of the first three modes in Pedregal Bridge.

Mode	Jan-15	Nov-15
	(Hz)	(Hz)
1	3.345	3.174
2	3.906	3.809
3	12.012	12.158

All the identified frequencies are in the vertical direction and the frequency of the first mode decrease 5% between both measurements. The second and third mode remain practically the same. The time interval between both measurements was of eight months.

4 CONCLUSIONS

- The study presents the results of ambient vibration measurements conducted in two typical RC bridges in Mexico. The measurements campaign was one year period in one bridge and eight months in the other.
- Both bridges reduce slightly the initial modal frequency after some months and particularly after the vehicle circulation.
- The reduction in the frequency values was in the range of 3% to 13% that suggests load-induced cracking in structural elements because of the truck loads circulation on the bridges.
- The vibration measurements will continue and these results will be also valuable to calibrate numerical models to assess the seismic vulnerability of the structures.

REFERENCES

[1] Ivanovic, S.S., Trifunac, M.D. and Todorovska, M.I. Ambient vibration tests of structures – a review. *J of Earthquake and Technology* (2000) **407**: 165-197.

[2] Wenzel, H. and Furtner, P. Damage detection and bridge classification by ambient vibration monitoring – application of BRIMOS at two stay cable bridges in China. *Proc. 4th China-Japan-US Symposium on Structural Control and Monitoring* (2006) Hangzhou, China.

[3] Afdel-Ghaffar, A.M. and Housner G.W. An analysis of the dynamic characteristics of a suspension bridge by ambient vibration measurements. *Earthquake Engineering Research Laboratory* (1977). CALTECH. Report EERL.

[4] Chang, C.C., Chang T.Y.P. and Zhang Q.W. Ambient vibration of long-span cable-stayed bridge, *J of Bridge Engng* (2001) **6**: 46-53.

[5] Gastineau A., Johnson T. and Schultz A. Bridge Health Monitoring and Inspections – A Survey of Methods. *Department of Civil Engineering University of Minnesota* (2009). Report MN/RC 2009-29.

[6] SVS, ARTeMIS Modal Pro 3.6. 2014.

VIII ECCOMAS Thematic Conference on Smart Structures and Materials
SMART 2017
A. Güemes, A. Benjeddou , J. Rodellar and Jinsong Leng (Eds)

ENERGY CAPACITY INFLUENCE ON MODAL PARAMETERS OF PRESTRESSED CONCRETE BOX GIRDERS

OSCAR S. LUNA VERA[*], CHUL-WOO KIM[*] AND YOSHINOBU OSHIMA[†]

[*] Department of Civil and Earth Resources Engineering
Graduate School of Engineering, Kyoto University
Katsura Campus, 615-8540 Kyoto, Japan
Email: kim.chulwoo.5u@kyoto-u.ac.jp - Web page: http://infra.kuciv.kyoto-u.ac.jp

[†] Center for Advanced Engineering Structural Assessment and Research (CAESAR)
Public Works Research Institute
305-8516 Tsukuba, Japan
Web page: https://www.pwri.go.jp/caesar/index-e.html

Key words: Concrete Box Girder, Energy Capacity, Experimental Modal Analysis, Tendon Breakage.

Summary: *This paper investigates the relationship between modal parameters and energy capacity of PC box girders by means of laboratory experiments. The girders were tested under different loading-unloading scenarios and tendon cuts. Along the whole process, vibration tests were performed before and after each loading and damage event such as tendon cuts and static-loading steps. Static and dynamic responses of the girders were measured and collected by several instruments consisting of accelerometers, displacement transducers and temperature gauges. Moreover, cracks were also measured and details of crack growth are presented. The performance of the PC box girders was investigated utilizing the energy absorbed and the energy dissipated as well as the modal parameters obtained from vibration responses. Finally, the change in modal parameters is explained by a correlation with the energy capacity of the PC box girders.*

1 INTRODUCTION

Extensive works have been done recently to describe precisely the structural performance of major civil infrastructures, such as concrete bridges. However the huge amount of bridges in a highway system makes it difficult to apply conventional inspections to all the bridges. The use of structural health monitoring (SHM) to describe the current performance of a structure will improve efficiency in bridge maintenance. The purpose of finding the link between SHM and structural performance is to have tools for decision making in maintenance and judgment of the bridge condition. Data collected from bridges with 50 years of service life showed that the natural frequency is a good strength parameters for deteriorated concrete beams. Thus, it might be possible to use modal parameters as indicators in bridge health monitoring [1]. Moreover, in different field experiments, damping ratio was identified as a damage feature for concrete structures. The rate increase of modal damping ratio could be a sign of structural deterioration [2]. All the previous outcomes sometimes disagrees with expected concepts. Some

discrepancies between assumed models and results from experimental testing come about due to different reasons that needs to be faced [3].

This paper investigates the relationship between modal parameters and energy capacity of PC box girders by means laboratory experiments. The performance of the PC box girders is investigated utilizing the energy absorbed and energy dissipated as well as modal parameters.

2 EXPERIMENTAL SET-UP AND PLAN

The experiments were carried out in the Center for Advanced Engineering Structural Assessment and Research (CAESAR), one of the four research institutes and centers of Japan's Public Works Research Institute. The 30-MN Universal Structural Testing Machine, largest of its kind in Japan, was used for bending tests in prestressed concrete (PC) box girders to evaluate the ultimate strength and the behavior until failure. The control accuracy of this machine is ±1% of loading range (3MN-30MN) for the loading control and ±0.1mm for the displacement control. The span length of two PC box girders (G1 and G2) have a total length of 7.5 meters and all their geometric details with the post-tensioned tendons are described in Figure 1. Ten accelerometers were allocated evenly under the two webs of the box section (5 accelerometers under the front side web and another 5 under the back side web). The accelerometers are piezoelectric type ONOSOKKI NP-2120 with a maximum acceleration of 8000 m/s2 and a sensitivity of 5pC/ (m/s2) +/-2dB. Similarly, 4 displacement transducers were deployed on the supports vertically, other 8 transducers under the two webs and 4 more in the upper surface. In total, 16 transducers were used to measure the change in displacements of the PC box girder along the whole experiment tests. In addition, each PC box girder has 14 post-tensioned tendons (seven each side: from C1 to C7 in "cross-section" from Figure 1). In specimen G1, the tendons in the back side web are not completely grouted for experiment purposes, except tendon C7. In girder G2, all tendons within the webs, except both C7, have been partially grouted so as to cut the tendons. Similar tendon configurations were placed in earlier research for PC beams to study the evaluation of grout failure process by means of acoustic emission [4].

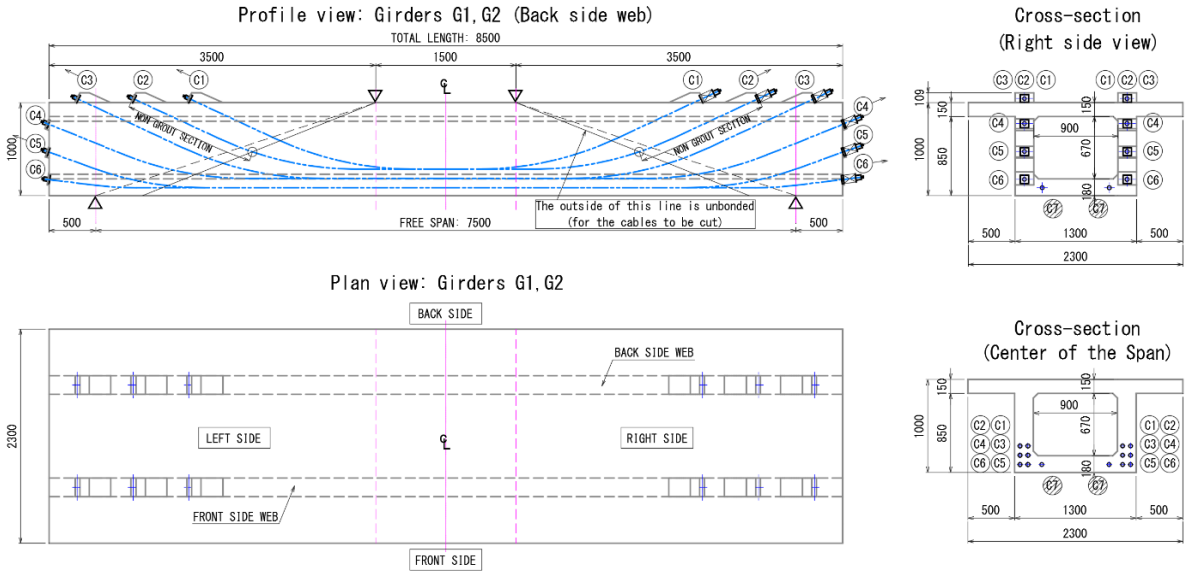

Figure 1: Concrete box girders description (distance in millimeters)

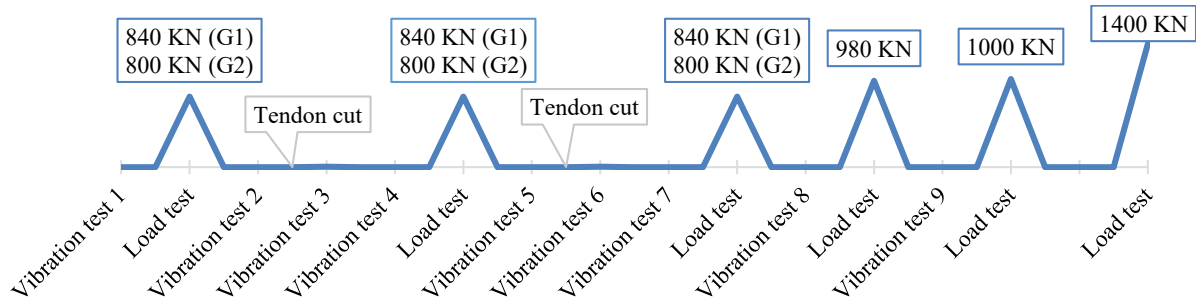

Figure 2: Experiment plan

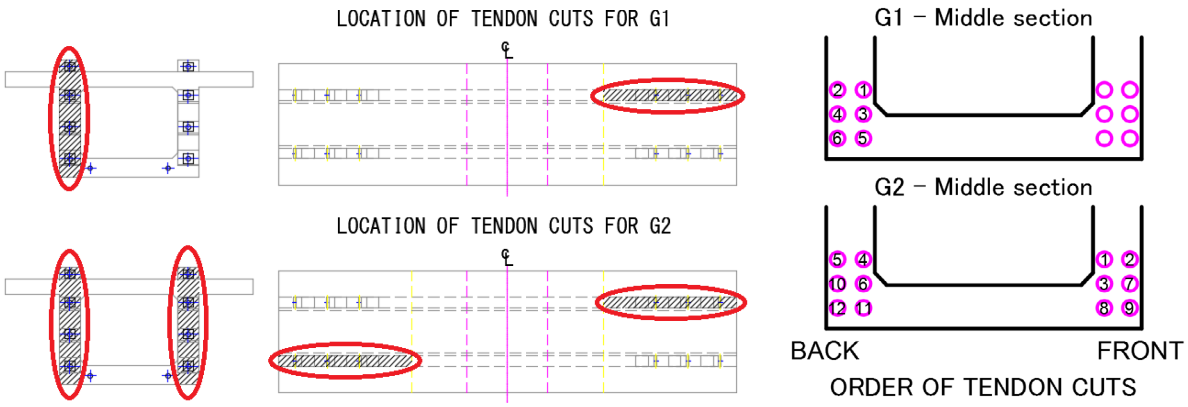

Figure 3: Plan for the tendon severing

All the experiment events are summarized using a timeline in Figure 2. Along all the procedures for each PC box girder, nine vibration tests were performed. Besides, the static loading plan consists of six load tests, from which the first three are the same load level (840kN for G1 and 800kN for G2). The reason that the first three load levels are the same, is in order to study the effect of tendon breakage in between these static tests. The following load increment is to provoke the growth of cracks and test the specimens' ultimate strength.

Figure 3 shows the severing plan for both PC box girders. An unbalanced damage is planned for PC box girder G1, reason why only 6 tendons from the back side web were cut in two steps: three tendon cuts after the first static test and another three after the second loading-unloading step. For the PC box girder G2 a similar plan that of the G1 girder was carried out, but the difference is that this time the tendons in the two side webs were cut simultaneously (see "order of tendon cuts" in Figure 3).

3 STATIC LOAD TESTING AND DAMAGE MONITORING

The purpose of the static load testing is to change the stiffness of the PC box girders due to crack growth by increasing load levels. It is expected that monitoring the growth of cracks can explain changes in structural performance of the PC box girders. It is also expected that influence of tendon cuts on the growth of cracks in each side of the PC box girders might be observed. The damage monitoring will consist primarily on the crack growth and decrease of the structural performance. The structural performance is examined utilizing a specific damping capacity and energy capacity which will be explained in 3.2.

3.1 Cracks monitoring

The growth of cracks is clearly affected by the location of the tendon cut. In the G1 girder, the back side of the girder shows larger amount of cracks since the tendon cut was made only in that side web. The growth of cracks in the back side is considerable larger than those of the front side (see Table 1). Besides, there is also a higher concentration of cracks in the left flank, adjacent to the severing location (see Figure 4). In girder G2, the cracks occurrence is more equally distributed along both sides, compared to girder G1, since the severing was made to both sides. At this time, the right flank showed to be more affected by cracks occurrence. In addition, the cracks' length when loading until failure converges to similar values in both sides of the two concrete box girders.

Table 1: Total length of cracks after load stages

Stage	G1 total cracks length (mm)				G2 total cracks length (mm)			
	Front	Back	Top	Bottom	Front	Back	Top	Bottom
840/800 KN (1)	160	794	0	2633	347	296	0	1339
840/800 KN (2)	452	1086	0	2956	1034	1152	0	3763
840/800 KN (3)	772	1086	0	2980	1446	1422	0	3763
980 KN	5202	7881	0	14378	6285	6747	0	15478
1000 KN	6741	10934	0	15385	10126	11557	0	18811
Ultimate	29859	30836	730	29825	34704	32455	6795	31970

The ratio between the cracks' length in both sides of G1 girder under the first time loading is almost five times. The value drops to 2.4 times after the second loading and 1.4 times when loading for the third time. Then, when increasing the load level to 980 kN, the ratio increase to 1.5 times and to 1.6 times after 1000 kN loading. This verifies the damage produced by the unbalanced tendon cuts.

For the G2 girder, the length ratio from the cracks in both sides varies from 1.2 times to 1.0 times in all loading stages. This is a corroborating evidence of difference with the G1 girder, and shows a balanced damage in both sides, cause of the tendon cut in the two webs.

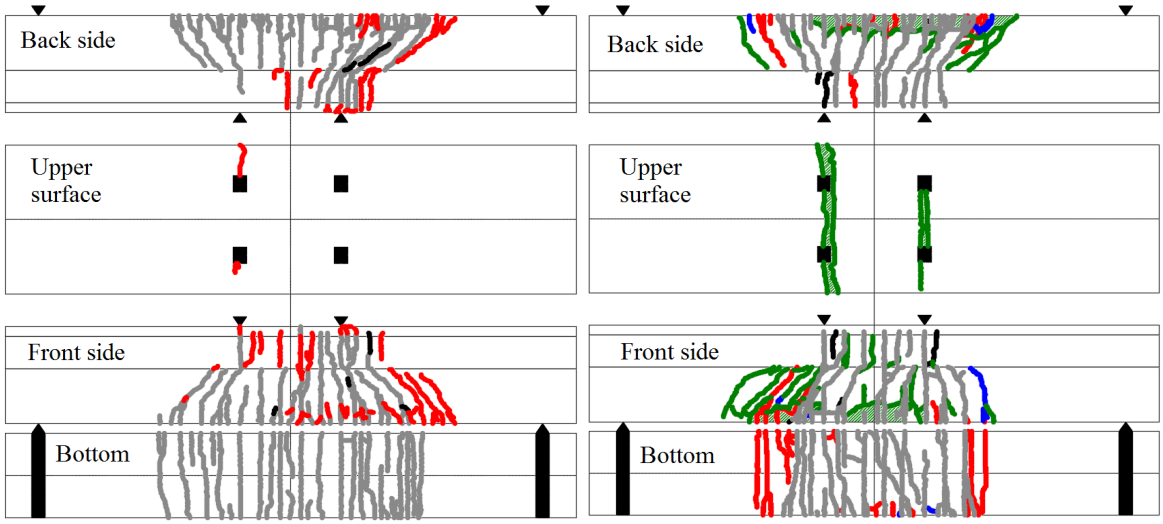

Figure 4: Cracks after ultimate load stage (left: G1 girder – right: G2 girder)

3.2 Energy calculation

In order to describe the change in performance, two energy concepts are used for this aim (see Figure 5). The energy dissipated ΔW is the enclosed area in the load-displacement graph when the specimen is tested in a specific loading-unloading step. On the other hand, the energy absorbed, or work applied W, is the area below the curve in the same graph, but this time considering only the loading process. The summary of the energy concepts, introduced before, are shown in Table 2 where the calculations were made for each web (front side and back side).

Once the dissipated and absorbed energy are calculated, the specific damping capacity ψ and the energy capacity Z can be defined as:

$$\psi = \frac{\Delta W}{W} \tag{1}$$

$$Z = (1 - \psi) \cdot 100\% \tag{2}$$

where the specific damping capacity ψ is the ratio between the amount of energy dissipation ΔW in each loading stage and the work W applied to it. The energy capacity $Z\ (\psi)$ is in function of the damping described before. When the girder behaves elastically and no damage is occurred, the energy dissipation is zero and the energy capacity will remain 100 % theoretically. Conversely, if damage is introduced or the girder reaches its plastic range, the energy dissipation should be different from zero and the energy capacity value should be changed. The energy capacity will be used to assess the change in natural frequencies and also the damping capacity for the damping ratio variation.

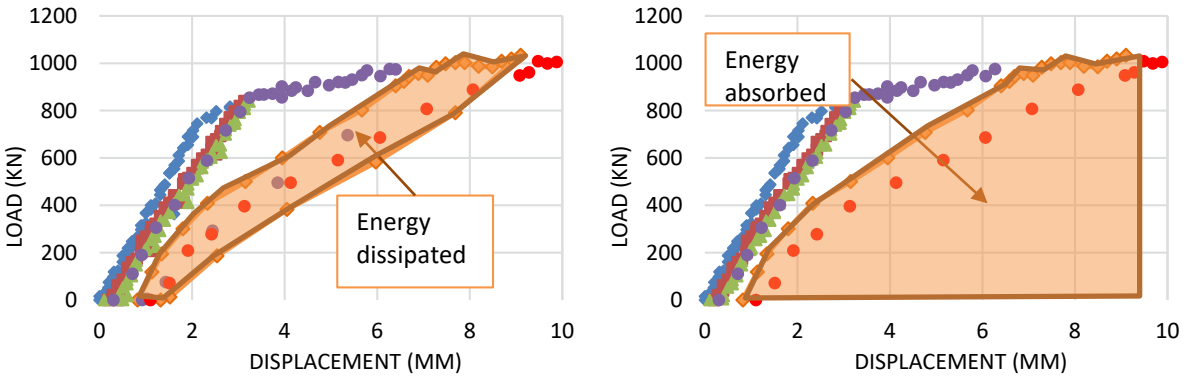

Figure 5: Energy calculation from one displacement transducer in a specific load event

Table 2: Energy dissipated and absorbed from all loading stages

G1 Stage	Energy dissipated (Joule)		Energy absorbed (Joule)		*G2 Stage*	Energy dissipated (Joule)		Energy absorbed (Joule)	
	Front	Back	Front	Back		Front	Back	Front	Back
840 KN (1)	179	184	729	759	*800 KN (1)*	111	110	598	622
840 KN (2)	99	92	693	723	*800 KN (2)*	160	166	554	571
840 KN (3)	51	98	667	747	*800 KN (3)*	158	158	759	785
980 KN	819	864	2147	2233	*980 KN*	1702	1759	3470	3730
1000 KN	798	831	2880	2999	*1000 KN*	3340	3348	6074	6183
Ultimate	70669	71737	74175	75981	*Ultimate*	46071	47059	48348	49314

4 DYNAMIC TESTING AND VIBRATION MONITORING

By using a Modal sledge hammer with a 3-pound head, the impact test was performed to obtain the modal parameters. Ten impact points were located in the opposite face (upper) of the accelerometers location. Then, the single-input multiple-output (SIMO) was used to estimate the frequency response functions (FRF) since hammer and accelerometers were synchronized.

4.1 Frequency monitoring

Structural damage is defined as a decrease of mechanical properties of the structure such as stiffness reduction. Thus, decrease of the natural frequencies is expected due to structural damage. However sometimes in experiments, the trend of frequencies according to the growth of damage shows an anomalous increase from one damage configuration to the next one [5]. Figure 6 shows changes in frequencies of two PC box girders, G1 and G2 girders. Those identified frequencies up to the 4th mode are summarized in Table 3. On one hand, it can be observed in the same table that there is a decrease whenever cracks started or growth. On the other hand, an increase took place some days after the tendon's severing (before loading and after the tendons cut).

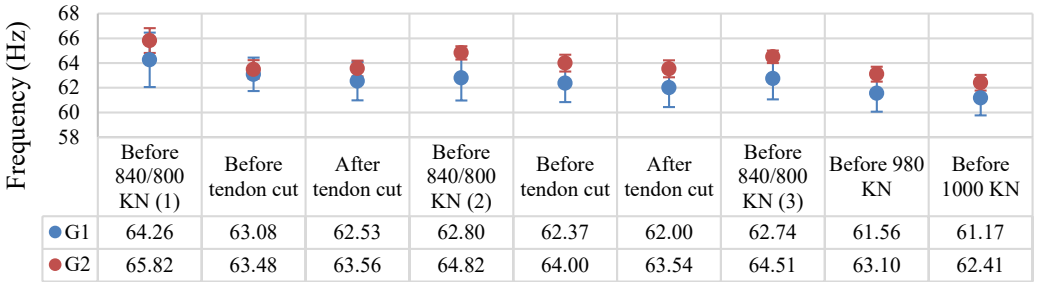

Figure 6: Progress of the natural frequency (2nd bending mode)

Table 3: Frequency development of the two girders (first 4 bending modes)

			Before 840/800 KN (1)	Before tendon cut	After tendon cut	Before 840/800 KN (2)	Before tendon cut	After tendon cut	Before 840/800 KN (3)	Before 980 KN	Before 1000 KN
1st freq. (Hz)	G1	mean	31.00	30.00	30.00	30.50	30.00	30.00	30.05	30.00	29.01
		std	0.00	0.00	0.00	0.00	0.00	0.00	0.15	0.00	0.07
	G2	mean	29.55	30.00	30.16	30.50	30.00	30.00	30.50	29.96	28.98
		std	0.57	0.00	0.23	0.00	0.00	0.00	0.00	0.21	0.10
2nd freq. (Hz)	G1	mean	64.26	63.08	62.53	62.80	62.37	62.00	62.74	61.56	61.17
		std	4.40	2.71	3.11	3.67	3.07	3.12	3.37	2.99	2.81
	G2	mean	65.82	63.48	63.56	64.82	64.00	63.54	64.51	63.10	62.41
		std	2.00	1.50	1.26	1.08	1.36	1.37	1.01	1.20	1.27
3rd freq. (Hz)	G1	mean	233.79	235.18	234.32	234.32	234.35	234.27	235.10	234.88	234.29
		std	2.65	3.73	3.56	2.52	2.48	2.49	3.10	2.88	2.50
	G2	mean	233.49	233.05	233.71	234.27	233.97	233.88	234.60	234.25	233.39
		std	2.11	2.12	2.12	2.99	2.30	2.24	2.73	2.55	2.30
4th freq. (Hz)	G1	mean	282.82	282.23	280.82	282.07	282.62	282.71	282.58	282.54	283.43
		std	4.98	6.62	6.25	5.86	5.66	5.38	5.74	5.77	4.89
	G2	mean	283.80	282.35	282.82	283.80	282.92	283.44	283.06	282.54	282.82
		std	3.78	3.74	3.81	3.67	3.80	5.08	5.06	4.61	4.16

4.2 Damping ratio monitoring

The damping ratio was estimated by identifying the half power points of the magnitude of the frequency response function, so called -3dB points. Once having the approximate frequency bandwidth between the two half power points, the damping ratio is the bandwidth value divided by two times the frequency resonance. Figure 7 shows the progress of the damping ratio of the second natural frequency with respect to the experiment plan. Table 4 shows the summary of the damping ratio up to the 4th mode. An inconsistent increment was observed when damage is introduced. Even if considering only occurrence of cracks or tendons' cut, there is no clear pattern like the frequencies.

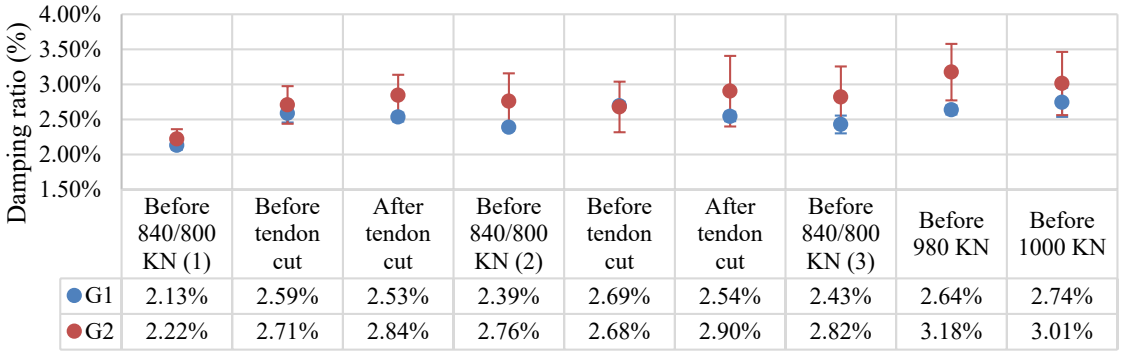

Figure 7: Progress of the damping ratio (second bending mode)

Table 4: Damping ratio development of the two girders (first 4 bending modes)

			Before 840/800 KN (1)	Before tendon cut	After tendon cut	Before 840/800 KN (2)	Before tendon cut	After tendon cut	Before 840/800 KN (3)	Before 980 KN	Before 1000 KN
1st damp. ratio	G1	mean	2.16%	1.75%	1.82%	1.88%	1.73%	1.64%	2.02%	2.55%	3.07%
		std	0.03%	0.06%	0.04%	0.10%	0.05%	0.03%	0.03%	0.06%	0.06%
	G2	mean	5.11%	4.20%	4.22%	3.67%	3.69%	3.12%	2.89%	3.92%	3.50%
		std	0.07%	0.16%	0.17%	0.28%	0.15%	0.19%	0.08%	0.18%	0.13%
2nd damp. ratio	G1	mean	2.13%	2.59%	2.53%	2.39%	2.69%	2.54%	2.43%	2.64%	2.74%
		std	0.12%	0.26%	0.13%	0.10%	0.12%	0.13%	0.25%	0.13%	0.41%
	G2	mean	2.22%	2.71%	2.84%	2.76%	2.68%	2.90%	2.82%	3.18%	3.01%
		std	0.28%	0.54%	0.58%	0.79%	0.72%	1.01%	0.87%	0.81%	0.90%
3rd damp. ratio	G1	mean	0.64%	0.64%	0.66%	0.80%	0.68%	0.70%	0.69%	0.64%	0.73%
		std	0.03%	0.02%	0.02%	0.04%	0.04%	0.04%	0.07%	0.03%	0.03%
	G2	mean	0.65%	0.69%	0.59%	0.60%	0.59%	0.61%	0.60%	0.63%	0.73%
		std	0.03%	0.05%	0.02%	0.02%	0.03%	0.02%	0.02%	0.05%	0.02%
4th damp. ratio	G1	mean	0.66%	0.81%	0.83%	0.62%	0.66%	0.69%	0.68%	0.69%	0.70%
		std	0.03%	0.08%	0.11%	0.06%	0.11%	0.13%	0.14%	0.07%	0.07%
	G2	mean	0.66%	0.66%	0.69%	0.73%	0.73%	0.77%	0.79%	0.82%	0.78%
		std	0.15%	0.13%	0.07%	0.06%	0.10%	0.06%	0.06%	0.09%	0.05%

4.3 Mode shapes monitoring

The changes in mode shapes from stage to stage are shown in Figure 8, which shows small changes even under cracks. Only 4th mode shape started to show more changes between stages,

but considered not reliable when checking its other normalized modal parameters in chapter 5.

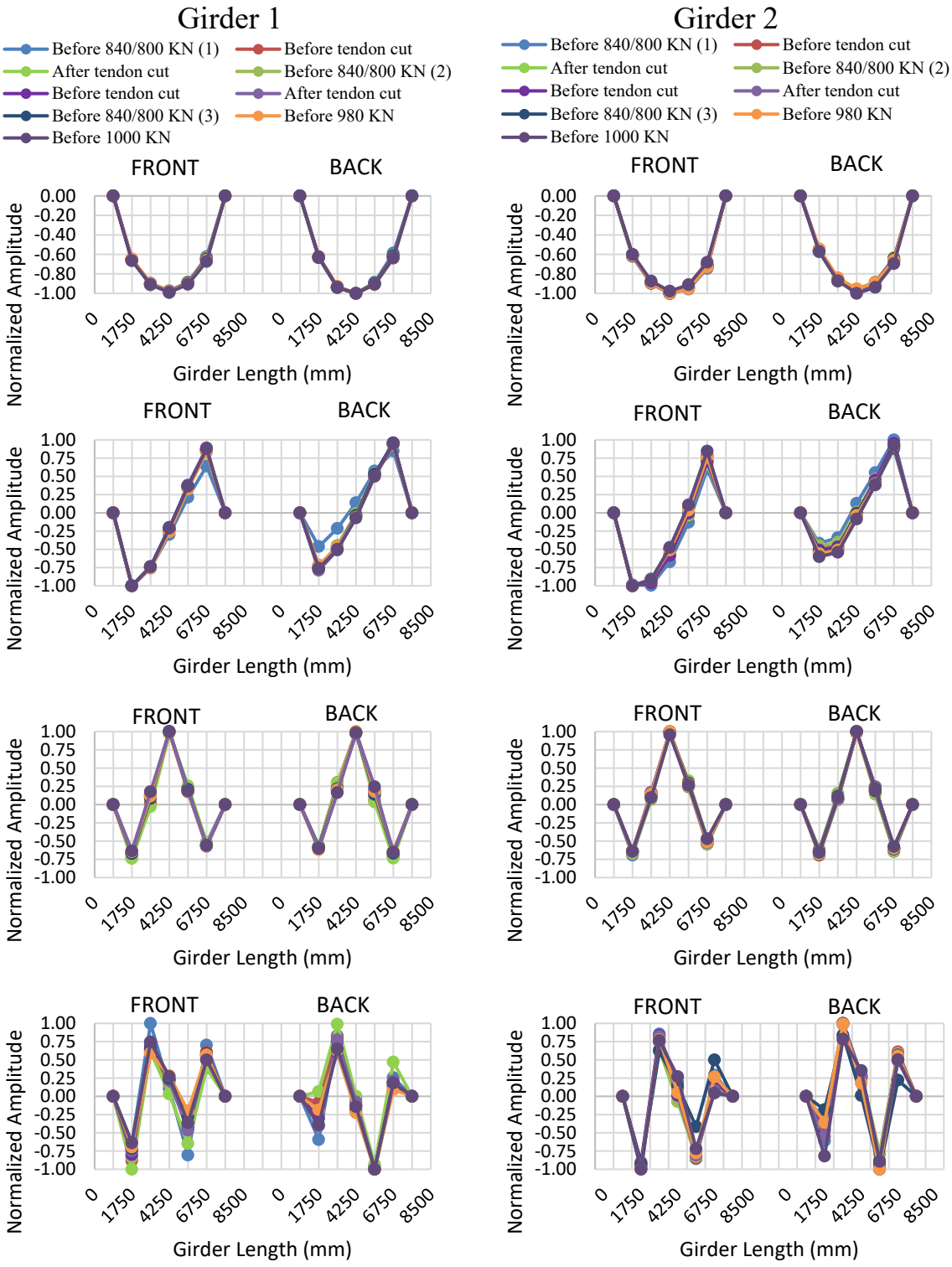

Figure 8: Evolution of all mode shapes (1st to 4th bending mode)

5 DISCUSSIONS ON EXPERIMENTAL RESULTS

Figure 9 and Figure 10 shows similar outcomes than in previous researches carried out in concrete bridges, where an increase of the damping ratio indicates deterioration [2]. This study normalized all modal parameters in order to determine a correlation between frequency and damping ratio. An interesting observation from the normalization was that parameters of the second mode have a better fit compared to the rest. It is also evident that the higher the mode is, the more unreliable the values of modal parameters become. Thus, the modal parameters of the second mode of the box girders are investigated in more detail as shown in Figure 11. The trend of the frequency shows decrease under tendon breakage or occurrence of cracks. However it increases in case of an elastic recover as shown in green arrows in Figure 11.

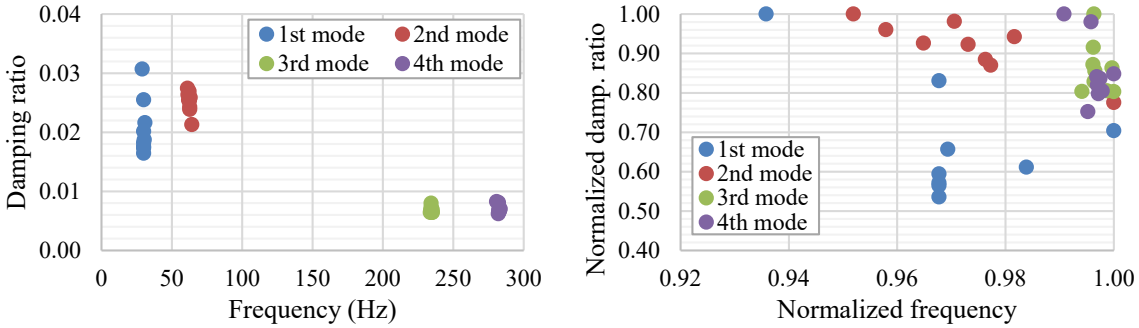

Figure 9: Correlation between frequency and damping ratio – G1

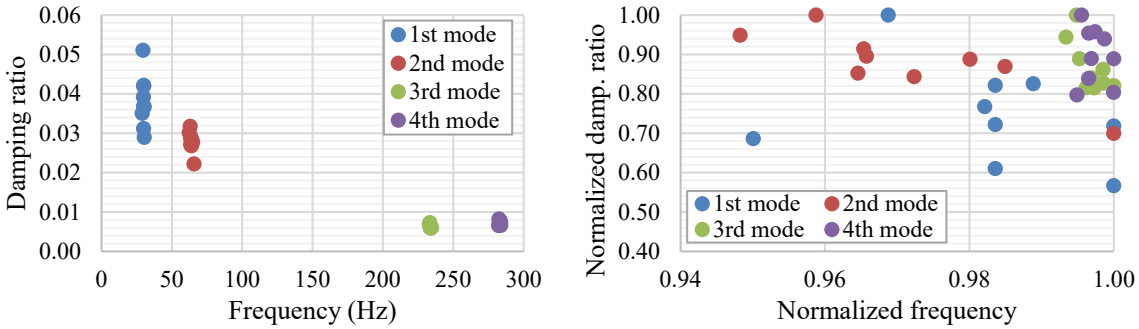

Figure 10: Correlation between frequency and damping ratio – G2

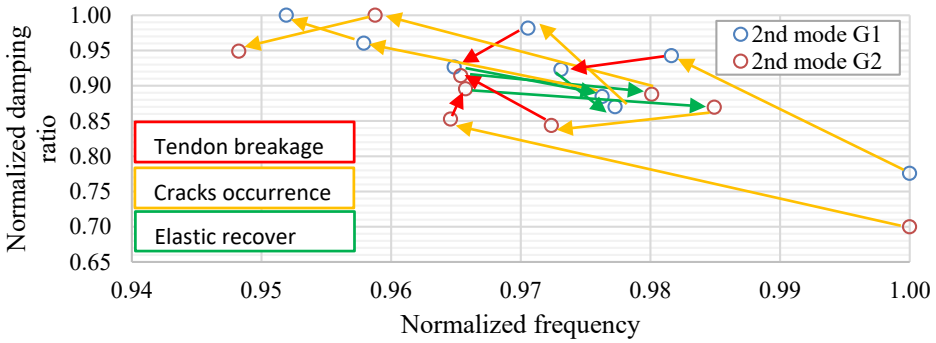

Figure 11: Comparison of 2nd mode correlations

The trend of the damping ratio is opposite to the ones of frequency. It is noteworthy that the damping ratios under balanced damage (G2 girder) and unbalanced damage (G1 girder) show contrary trends as shown in red arrows in Figure 11. Figure 12 shows the relation between the cracks length and the energy capacity. The more increase the cracks length, the more it decrease the energy capacity or performance.

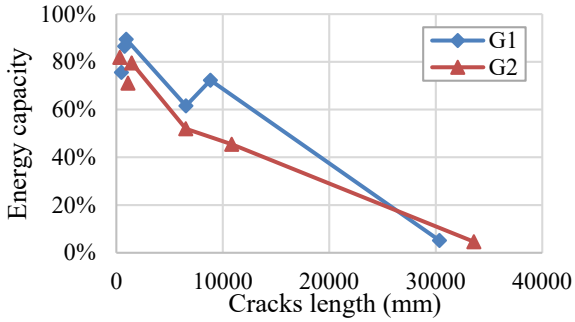

Figure 12: Ratio between cracks length and energy capacity

The effect of the tendon damage did not have a relevance on the modal parameters as happened in previous studies where the tension of tendons of a post-tensioned concrete beam and a concrete bridge were altered to check alterations in modal parameters [6], [7] and it also verifies that prestressing measurement force is not possible through frequencies only, because changes in modal parameters are minor [8]. Lastly, the correlation from static test data could be corroborated with the ones obtained from dynamic tests (see Figure 13). Figure 13 a) shows clear trends about frequency and energy capacity, as well as the effect of balance damage (G2 girder: red triangular) and unbalanced damage (G1 girder: blue diamond). In Figure 13 b) unclear correlations between the damping ratio and damping capacity were observed.

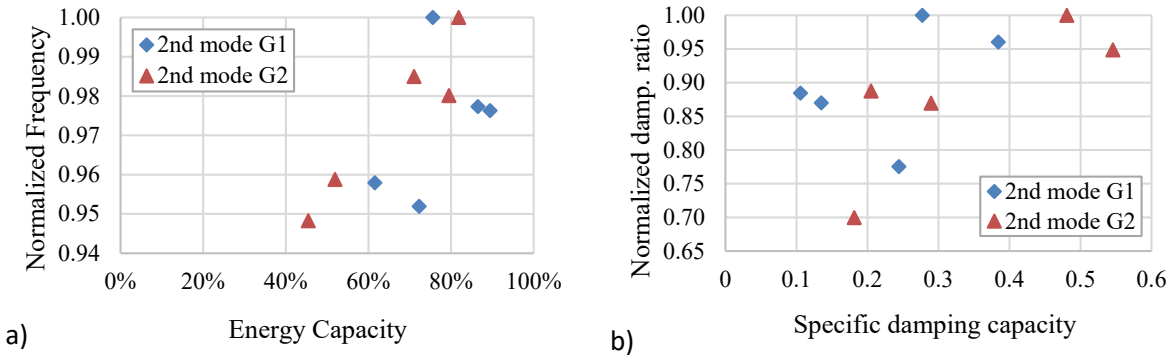

Figure 13: Energy capacity and specific damping capacity influence on modal parameters (2nd mode only)

6 CONCLUSIONS

This paper investigates the relationship between modal parameters and energy capacity of PC box girders by means of laboratory experiments. The summarized results are as follows.

- The second mode showed a better fit between frequency and damping ratio.
- A linear relationship between crack length and energy capacity was observed.

- Balanced and unbalanced damage, when severing the tendons, gave inconsistent trends between damping capacity and damping ratio.
- A clear relationship between normalized frequency and energy capacity was observed.
- The decrease of the performance (energy capacity) was mainly due to the growth of cracks.
- The tendon breakage clearly affected the growth of cracks.

REFERENCES

[1] Quattrone, A. et al. Vibration tests on dismounted bridge beams and effects of deterioration. *Journal of Physics: Conference Series* (2012) **382**

[2] Dammika, A. J. et al. *Proc. Int. Symp. on Life-Cycle Civil Engineering.* London, Taylor & Francis Group (2015) pp. 404-410

[3] Udwadia, F. E. Structural Identification and Damage Detection from Noisy Modal Data. *Journal of Aerospace Engineering* (2005) **18**:3, pp. 179-187.

[4] Shiotani, T., Oshima, Y., Goto, M. & Momoki, S. Temporal and spatial evaluation of grout failure process with PC cable breakage by means of acoustic emission. *Construction and Building Materials* (2013) **48**, pp. 1286-1292.

[5] Dilena, M. & Morassi, A. Dynamic testing of a damaged bridge. *Mechanical Systems and Signal Processing* (2011) **25**:5, pp. 1485-1507.

[6] Limongelli, M. P. et al. Damage detection in a post tensioned concrete beam - Experimental investigation. *Engineering Structures* (2016) Volume **128**, pp. 15-25.

[7] Döhler, M., Hille, F., Mevel, L. & Rücker, W. Structural health monitoring with statistical methods during progressive damage test of S101 Bridge. *Engineering Structures* (2014) Volume **69**, pp. 183–193.

[8] Noble, D., Nogal, M., O'Connor, A. J. & Pakrashi, V. The effect of prestress force magnitude and eccentricity on the natural bending frequencies of uncracked prestressed concrete beams. *Journal of Sound and Vibration* (2016) Volume **365**, pp. 22-44.

Estimating the tensile force in ancient metallic tie-rods from vibration measurements

Carmelo Gentile* and Antonello Ruccolo†

* Politecnico di Milano, ABC Department
P.za Leonardo da Vinci 32 – 20133 Milan, Italy
e-mail: carmelo.gentile@polimi.it,

† Politecnico di Milano, ABC Department
P.za Leonardo da Vinci 32 – 20133 Milan, Italy
e-mail: antonello.ruccolo@polimi.it

ABSTRACT

The Milan Cathedral, constructed over a period of more than 400 years, is one of the few Gothic cathedrals where permanent metallic tie-rods are installed under all naves to support a portion of the lateral thrust exerted by vaults and arches.

During the maintenance interventions preceding EXPO 2015, all tie-rods of the Milan Cathedral underwent visual inspection, geometric characterization and hammer tests to evaluate their dynamic characteristics. Since about 30 tension elements supported heavy lamps at the time of the first survey and the recorded signals clearly indicated anomalous behaviour conceivably associated to the presence of additional masses, more recently the experimental survey was completed after the removal of the lamps from the metallic elements and both hammer and ambient vibration tests were performed.

A first vibration-based assessment of the tensile forces in the tie-rods [1] was performed using the methodology described in [2]. According to this procedure: (a) an analytical model is established for each tie-rod with the geometric characteristics, the Young's modulus and the mass density being assumed as known; (b) the tensile force and the boundary conditions (represented by unknown rotational springs) of the model were identified using the dynamic parameters (i.e. natural frequency and mode shape) of the first mode. Since the correlation between the experimentally observed natural frequencies and the corresponding parameters of the identified analytical model tends to worsen with increased mode order, an enhanced version of the basic procedure [1] was developed.

After a brief summary of the experimental procedures adopted for testing the tie-rods of the Milan Cathedral, the paper mainly focuses on presenting and exemplifying the enhanced procedure, which differs from the original one as: (1) the Young's modulus of the metallic material is assumed to be unknown as well and (b) the natural frequencies of upper modes are used to solve the inverse problems.

REFERENCES

[1] M. Vasic, *A multidisciplinary approach for the structural assessment of historical constructions with tie-rods*, Ph.D. Thesis, Politecnico di Milano, Italy, 2015.

[2] N. Tullini and F. Laudiero, "Dynamic identification of beam axial loads using one flexural mode shape", *J. of Sound and Vibration*, Vol. **318**(1-2), pp. 131-147, (2008).

VIII ECCOMAS Thematic Conference on Smart Structures and Materials
SMART 2017
A. Güemes, A. Benjeddou , J. Rodellar and Jinsong Leng (Eds)

EXPERIMENTAL DYNAMIC CHARACTERIZATION OF THE MORELIA CATHEDRAL USING OPERATIONAL MODAL ANALYSIS

GUILLERMO MARTINEZ[*], JOSE M. JARA[†], BERTHA A. OLMOS[†] AND LIDIA MEJIA[††]

[*] Civil Engineering School
Universidad Michoacana de San Nicolás de Hidalgo
Universitary City, 58040 Morelia, Mexico
e-mail: guillermo.mtzruiz@gmail.com, www.posgfic.estructuras.umich.mx

[†] Civil Engineering School
Universidad Michoacana de San Nicolás de Hidalgo
Universitary City, 58040 Morelia, Mexico
e-mail: jmjara70@gmail.com, ba.olmos.gmail.com, www.posgfic.estructuras.umich.mx

[††] Master student at the Civil Engineering School
Universidad Michoacana de San Nicolás de Hidalgo
Universitary City, 58040 Morelia, Mexico
e-mail: elmo_lidia@hotmail.com

Key words: Morelia, Cathedral, Modal Analysis, Frequency, Operational Modal Analysis.

Abstract. This document deals the experimental dynamic characterization of the Morelia Cathedral in Mexico using ambient vibration records and Operational Modal Analysis. Measurements of ambient vibration were performed over 172 points on the main and processional naves, the dome, transept, the two bell towers and the Mithra building for this emblematic structure of the XVII-XVIII centuries.

1 INTRODUCTION

The Morelia cathedral (Figure 1) is one of the most emblematic historic buildings in Mexico. The construction of this magnificent structure started in 1660 and was concluded in 1744 by the Italian architect Vicenzo Barrochio. Since 1991 Morelia city has been distinguished by UNESCO as one of the World Heritage Sites and the cathedral can be considered as one the main listed buildings. Such architectural beauty unfortunately was built in a high seismic zone and since then it has been striked by several earthquakes, so degradation in strength and stiffness can be supposed without no fear to get wrong. In the middle of such scenario it is crucial to preserve this building to the following generations, so the knowledge of the future structural behavior implies a deep research. Is at this moment

when the experimental non-destructive techniques are a well-known path to success in that complex and demanding task, so the present paper presents a part of an ongoing research focused in the correct preservation of this magnificent building.

2 BUILDING GEOMETRICAL CHARACTERISTICS

The Morelia cathedral was built using pink quarry stone jointed with lime and sand mortar. The building plan is a three nave configuration connected with lateral chapels, the chapter room and the Mithra building (Figure 2). The in-plan dimensions are 77,1m long and 30,5m wide in the transept zone (Figure 2), the height of the main nave are 20,60m and the corresponding lateral naves height reaches the 14,35m (Figure 3). The cimborrio height reaches 40,3m at the top of the dome cross (Figure 3) and the bell towers are 64m height.



Figure 1: Morelia cathedral main façade.

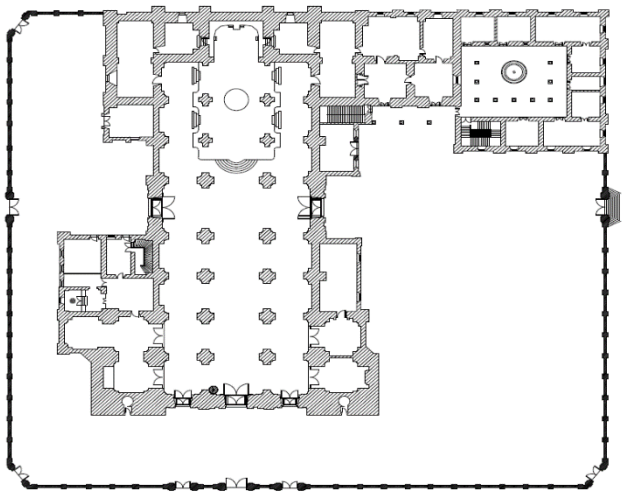

Figure 2: Plan view including the cloister limits.

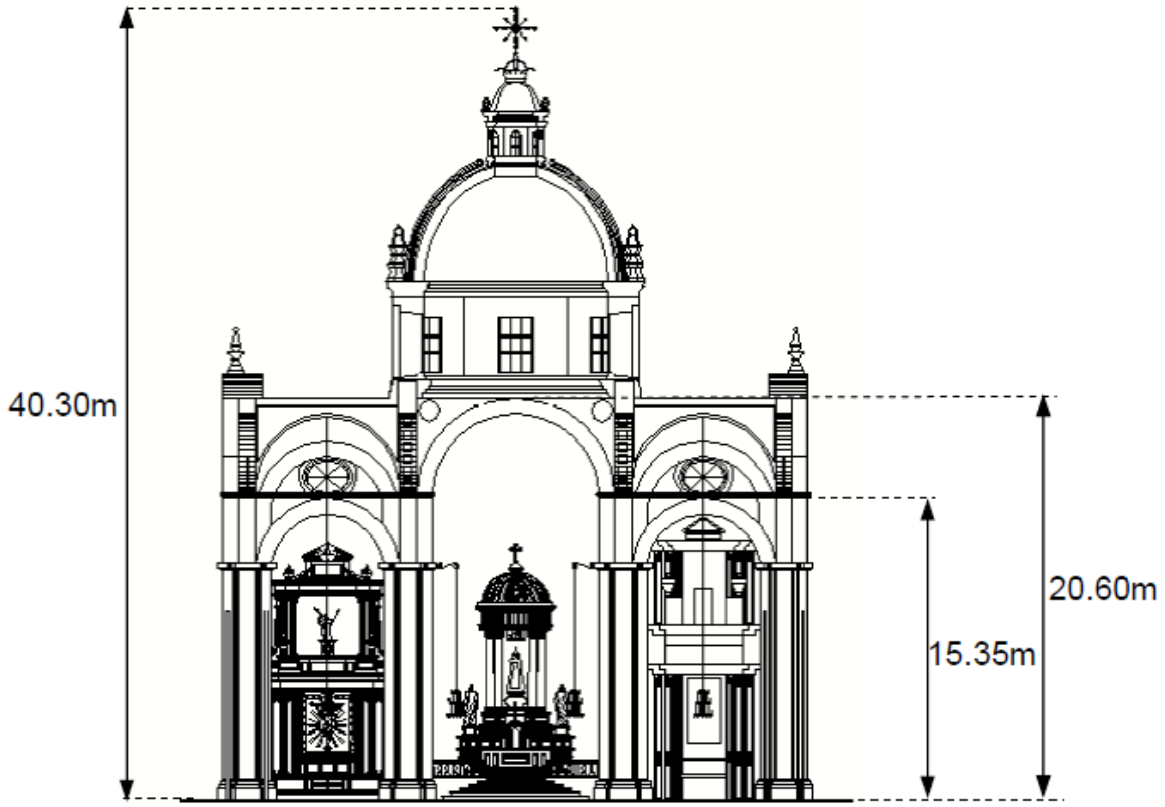

Figure 3: Transept transversal section.

3 EXPERIMENTAL DYNAMIC CHARACTERIZATION

In the conservation practice and research a proper insight to the mechanical and dynamic properties of ancient buildings has starting to become a widespread practice thanks to the new non-destructive techniques available, which are the commonly allowed for these structures. The International Council on Monuments and Sites (ICOMOS) trough It´s Scientific Committees has been the main reference to deal with this complex task. In the structural field the ISCARSAH Committee Recommendations [1] stablished the necessity of deep experimental campaigns focused on the correct estimation of structural mechanical and dynamic properties for the calibration of numerical models. The updated numerical models together with a deep qualitative historical and architectural analysis has become one of the best procedures to the best understanding of these complex buildings.

3.1 Accelerometric equipment

The used equipment in the whole experimental campaigns were two Basalt Accelerographs (Figure 4) of the Kinemetrics company. The key features of this accelerograph are a 3+1 sensor channels digital recorder w/internal Episensor triaxial deck, a 24-bit Delta Sigma converter per channel together with a built-in GPS [2]. Additionally, it can record ad communicate multiple sample rates in multiple data formats and telemetry protocols. The

compact physical dimensions were a key factor in some positions with a reduced space introducing a good stability during the measurements.



Figure 4: Basalt Accelerograph of Kinemetrics.

3.2 Sensor setups

Because the used two accelerometric sensors for the ambient vibration tests were much less than the set of measured points along the whole building, several setups were considered. A master accelerograph was fixed on the extrados main vault near by the cimborrio and the slave accelerograph was changed of position along the highest levels of the building (Figure 5).



Figure 5: Sensor setup 1. Master acceleroghap (red circle) and slave accelerograph (blue circle).

Each simultaneous measurement was triggered using the internal GPS of the two accelerographs and each record of ambient vibrations was 3-minute-long at 200 samples per second, so the complete campaign included 172 points on the main and processional naves, the dome, transept, the two bell towers and the Mithra building (Figure 6).

3.3 Operational Modal Analysis

Because modal information is derived from structural responses (outputs) while the

structure is in operation this process is usually called Operational Modal Analysis (**OMA)** or Output-only Modal Analysis in opposition to input-output modal analysis [3]. Therefore, for large heavy masonry structures where it is quite complex to introduce an input signal (e.g. shakers) the **OMA** seems to be one of the most adequate techniques for dynamic characterization of these type of structures using ambient vibration records, condition which will be analyzed in the present article.

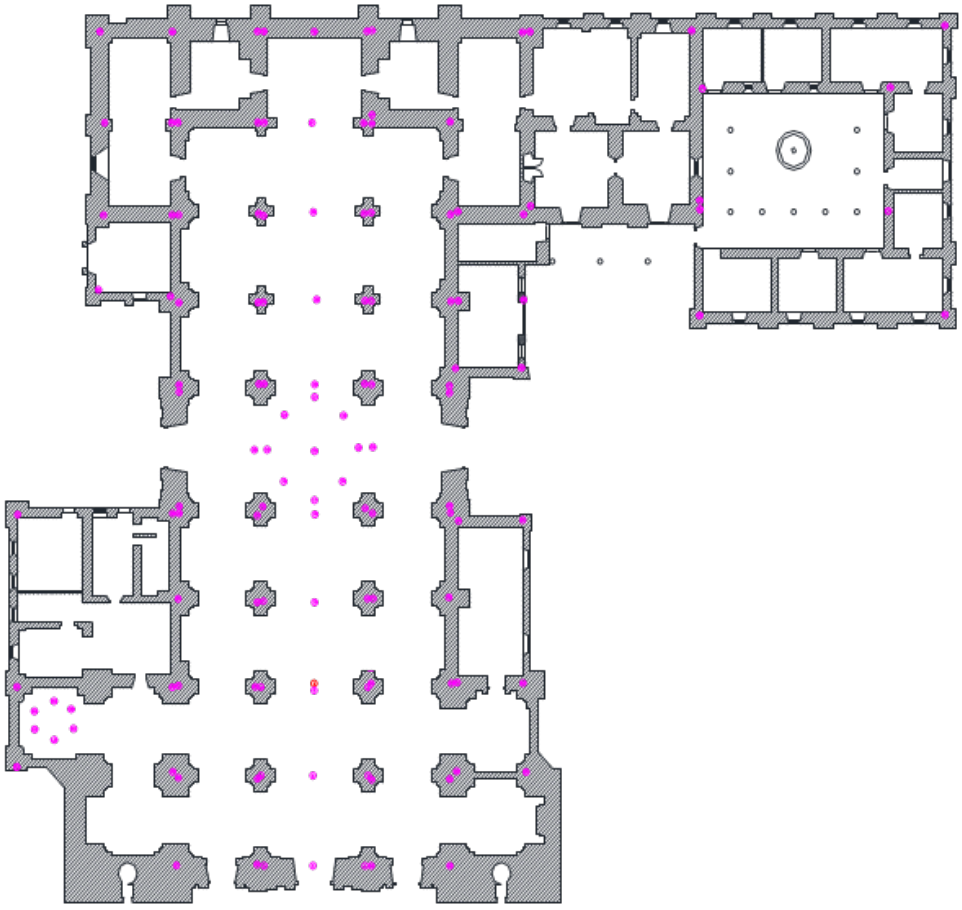

Figure 6: Measured points (pink dots) along the cathedral.

3.4 Modal Parameters Identification

In the present work to obtain the modal parameters based on the response to ambient vibration the non-parametric Frequency Domain Decomposition method (FDD) [4] was applied using the ARTeMIS Modal software [5]. This method is a simple technique that allows the separation of closely spaced modes and the identification of modal damping ratios, interpreting output spectrum matrices previously calculated with the Welch method [6]. The average of normalized singular values spectra covering all setups in the X (transversal) and Y (longitudinal) directions are presented in Figures 7 and 8.

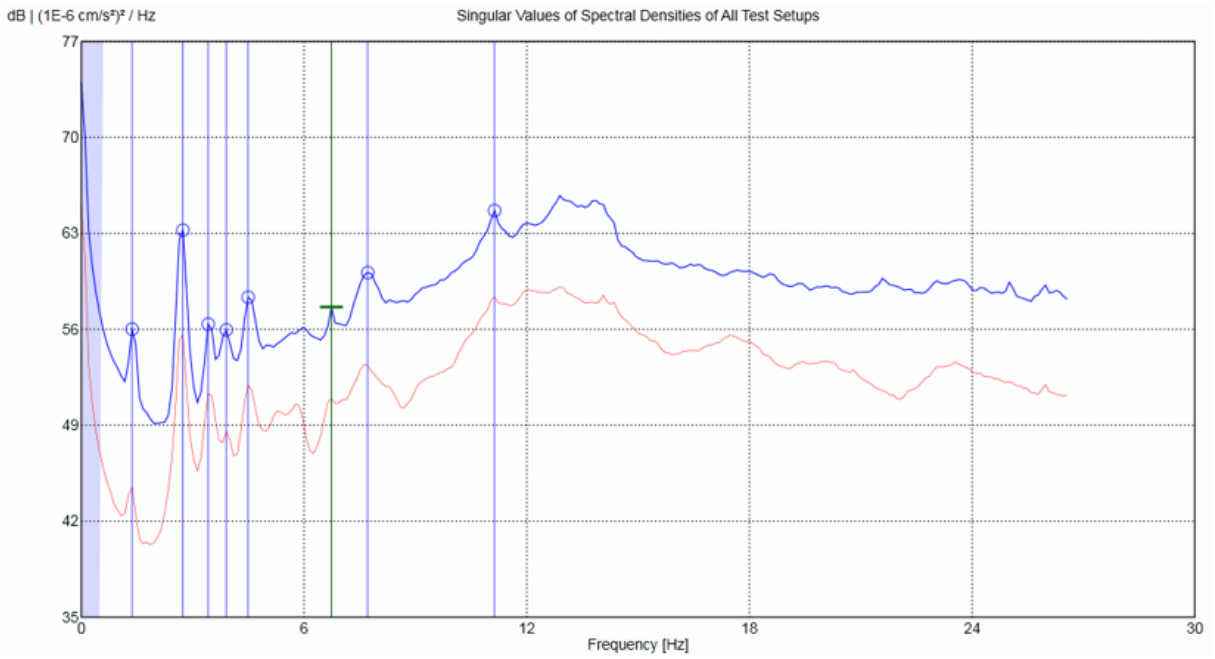

Figure 7: Average normalizaed singular values in the X (transversal) direction.

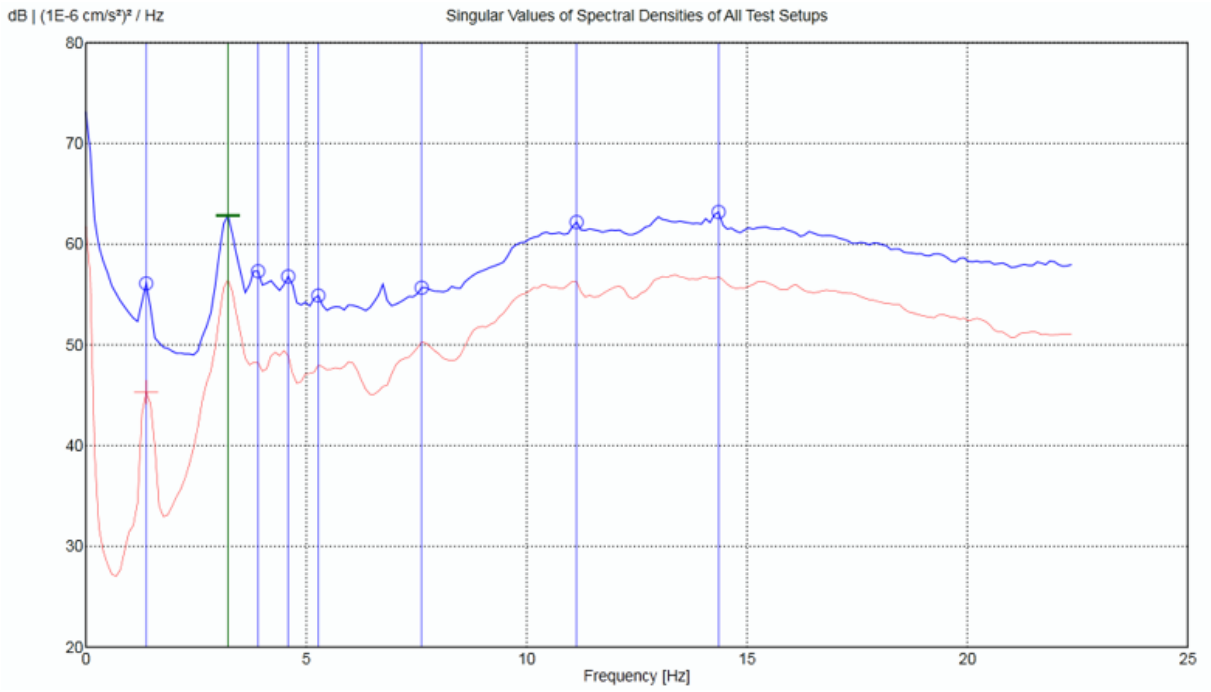

Figure 8: Average normalized singular values in the Y (longitudinal) direction.

Table 1 show the frequencies and periods associated to each analysis direction and it can

be noted a major number of identified frequencies in the X direction mainly attributed to the absence of buttresses usually stiffening the longitudinal walls of the cathedrals.

Table 1: Obtained frequencies and periods of all setups

Transversal direction		Longitudinal direction	
Frequency (Hz)	Period (Sec)	Frequency (Hz)	Period (sec)
1,367	0,7315	1,367	0,7315
2,734	0,3658	-	-
3,418	0,2926	3,223	0,3103
3,906	0,2560	3,906	0,2560
4,492	0,2226	-	-
6,738	0,1484	5,273	0,1896
7,715	0,1296	7,617	0,1313
11,133	0,0898	11,133	0,0898

3.5 Identified modes of vibration

The complete sensor location setup in both directions is shown in Figure 9. Modal shapes obtained with the ARTeMIS Modal software are shown in Figures 10 to 13.

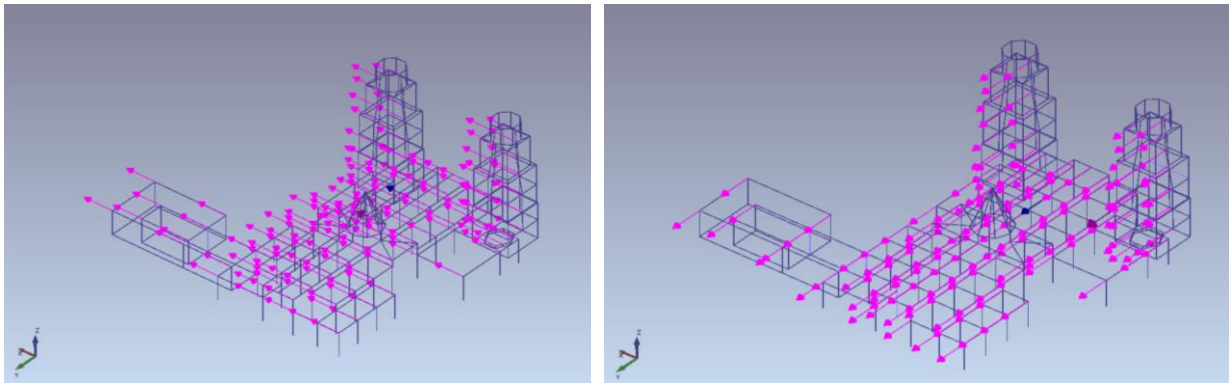

Figure 9: Sensor location setup. X acceleration (left) and Y acceleration (right).

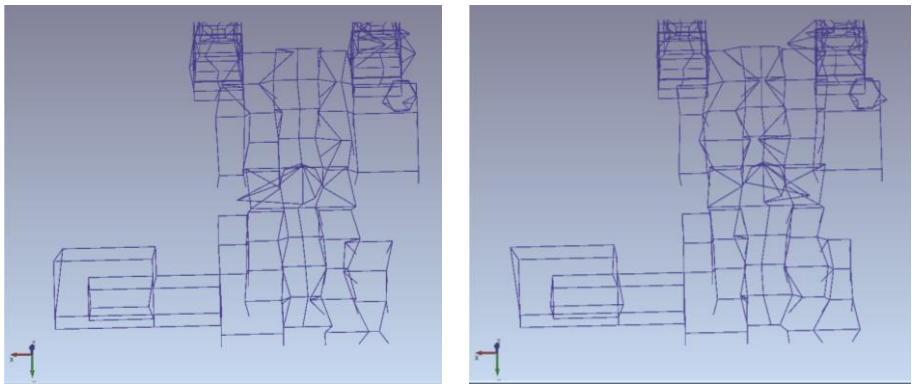

Figure 10: Plan view vibration mode 1 in X direction.

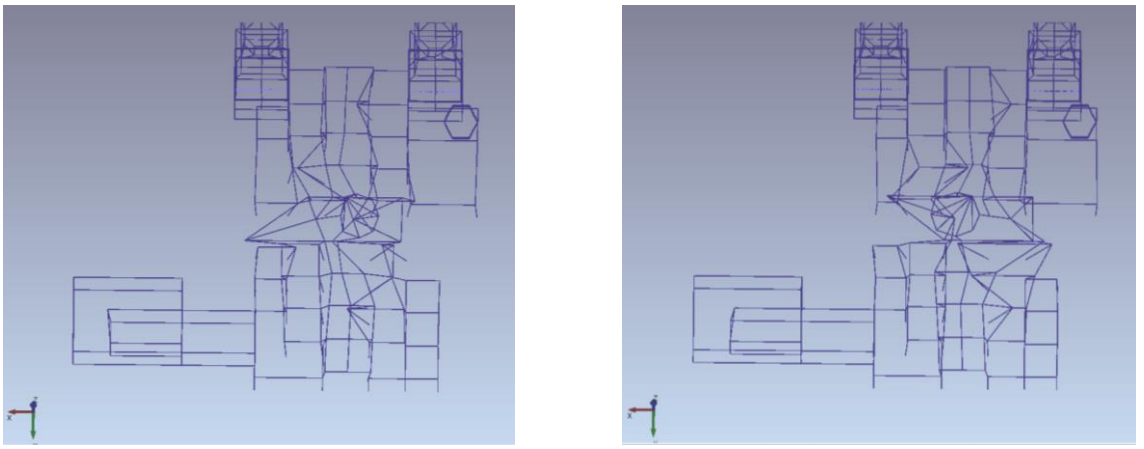

(a)

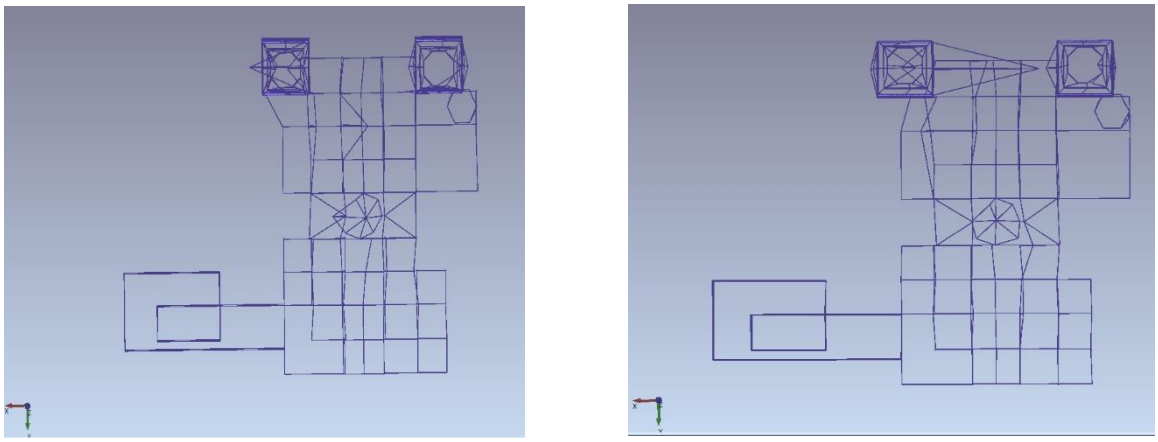

(b)

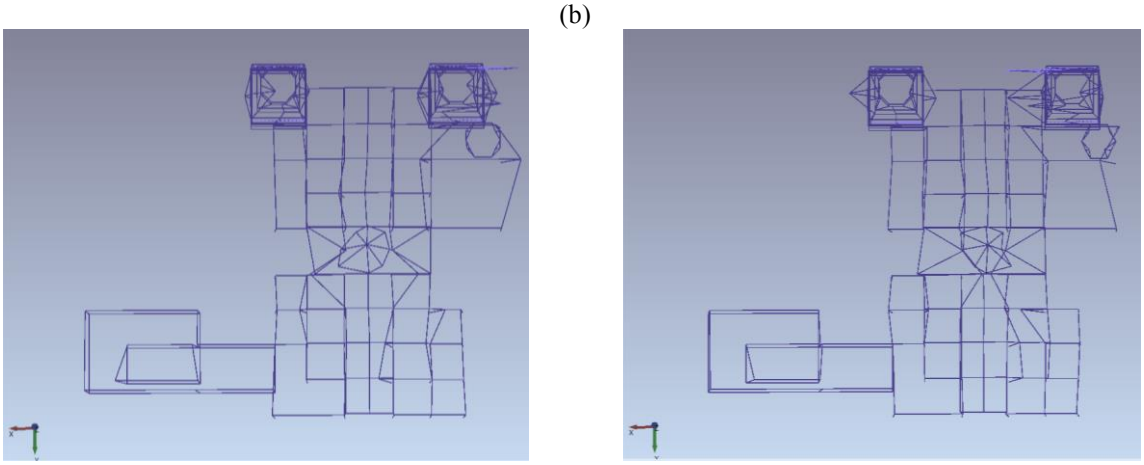

(c)

Figure 11: Plan view vibration modes 2 (a), 3 (b) and 4 (c) in X direction.

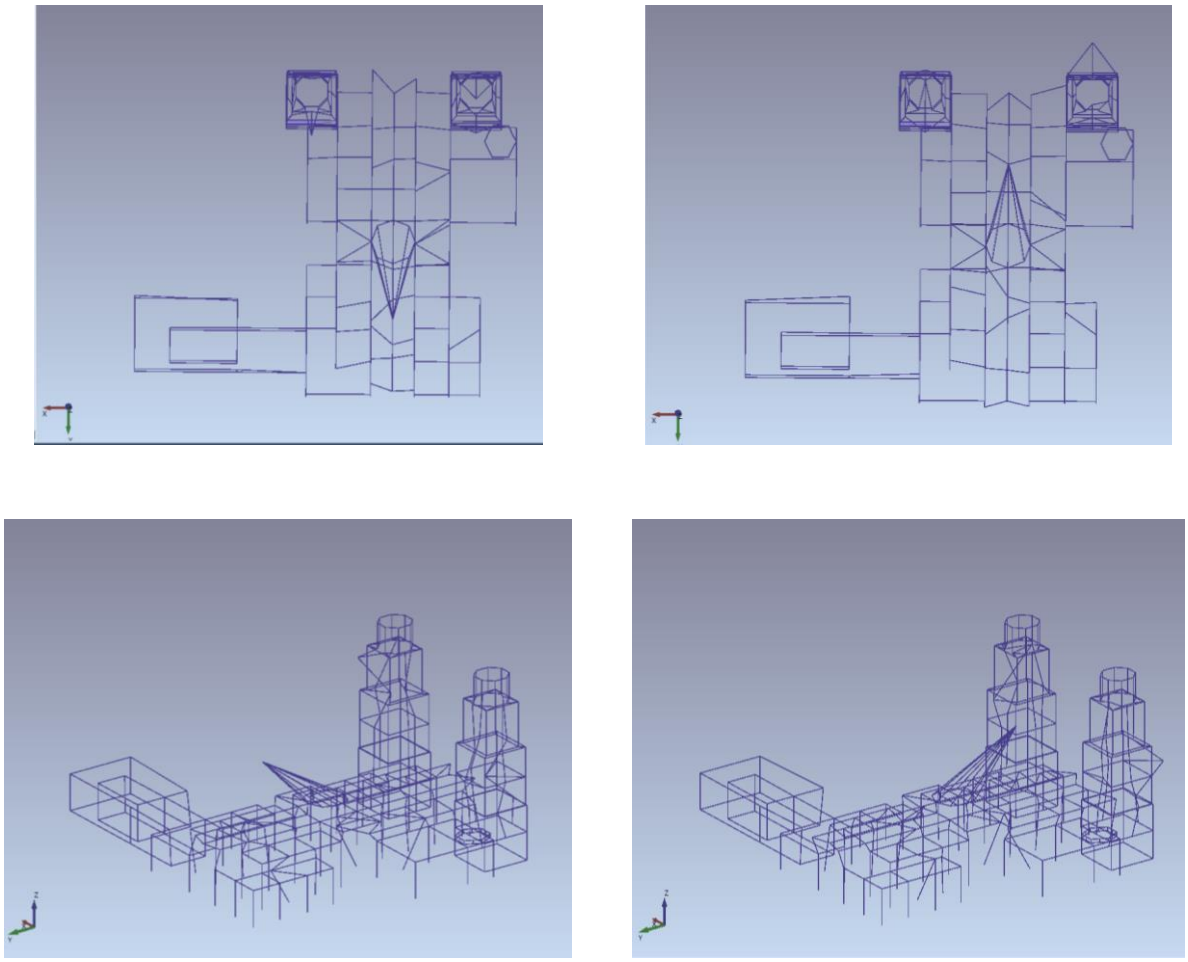

(a)

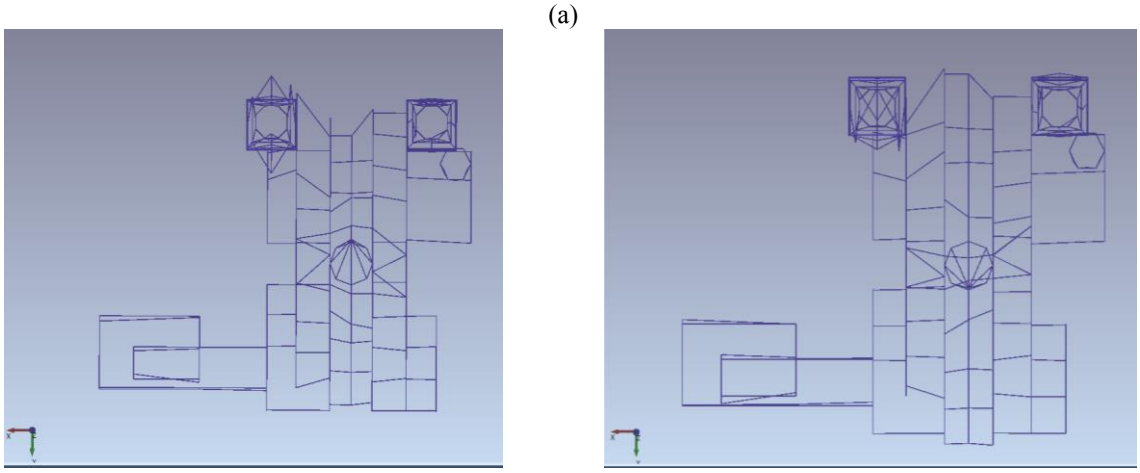

(b)

Figure 12: Plan view and isometric view vibration mode 1 in Y direction (a). Plan view of mode 2 in Y direction (b).

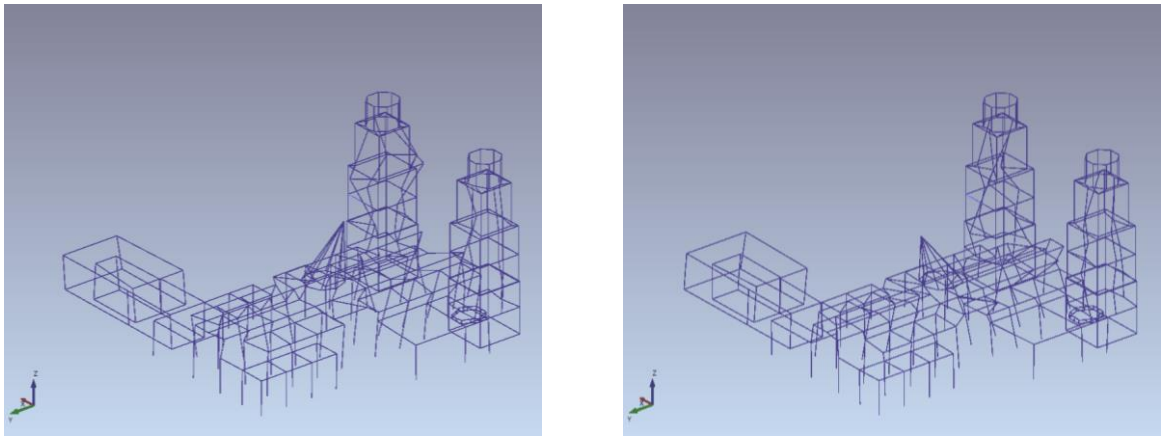

(a)

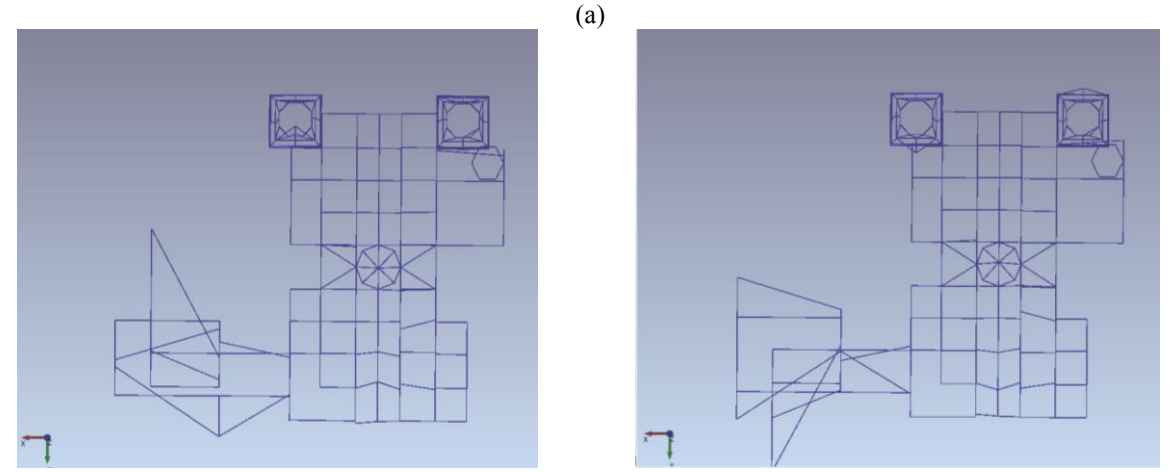

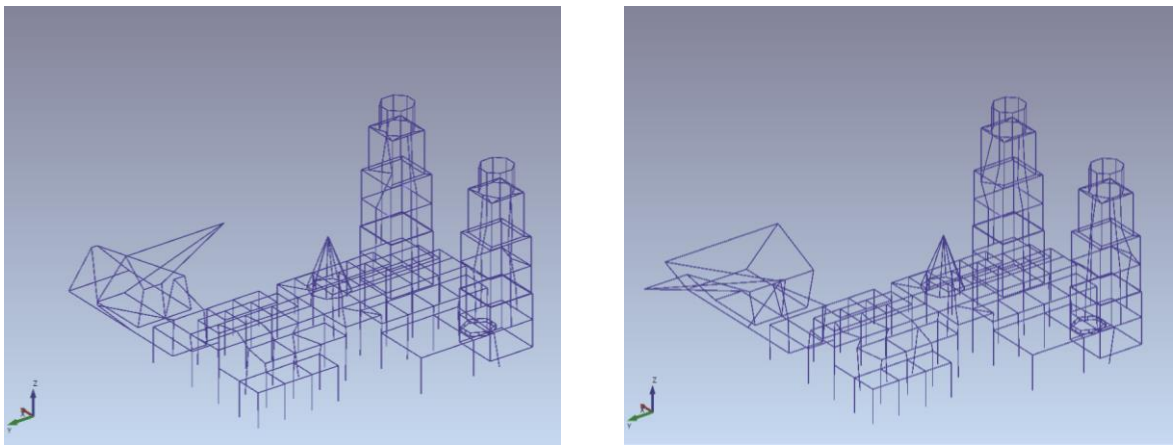

(b)

Figure 13: Isometric view for vibration mode 2 in Y direction (a). Plan and isometric view for mode 3 in Y direction (b).

4 CONCLUSIONS

Regarding to the most relevant modal shapes in both analysis directions the following conclusions can be done:

- Mode 1 (1,367Hz) X direction: The larger modal amplitudes can be observed on the main and lateral naves, this behavior is associated to the lower stiffness in this direction of the cathedral. Regarding to the east bell tower it presents a larger modal amplitude than the west one, this can be associated to the internal changes of the vaults stiffness located on each one of the five vaulted levels. The north is located to the front façade of the cathedral.
- Mode 2 (2,734Hz) X direction: The largest modal amplitude can be observed on the transept zone including the top of the cimborrio. In this case, the modal displacement was smaller than the observed in the first modal shape.
- Mode 3 (3,418Hz) X direction: A large modal amplitude can be noticed on the north-west zone of the lateral nave. The transept presents a lower amplitude than the observed in the mode 2 but it's very significate for the cimborrio and the triumphal arches. Regarding to the west tower the vault on the clock level shows a larger amplitude than the observed for the second mode at the same location.
- Mode 4 (3,906Hz) X direction: In this case, the naves again exhibit a larger amplitude in the transept zone but an overall more uniform amplitude. On the other hand, both bell towers show large modal amplitudes.
- Mode 1 (1,367Hz) Y direction: The main nave exhibits a larger amplitude than the lateral naves and the cimborrio presents the largest amplitudes of all the building, even this amplitude exceed the observed in the same zone for the X direction.
- Mode 2 (3,223Hz) Y direction: Again, the cimborrio shows larger amplitudes and the façade denote amplitudes out of plane. The west bell tower shows larger amplitudes than the east tower in its whole height.
- Mode 3 (3,906Hz) Y direction: The naves and the towers exhibits small and uniform amplitudes. The Mithra building on the contrary shows the largest modal amplitudes.
- Operational Modal Analysis together with three minutes' ambient vibration measurements were enough to get a reasonable insight to the dynamic behavior of this building.
- According to the obtained modal shapes a quite complex dynamic behavior can be noticed where de combined flexural and torsional modes are the most predominant. This behavior can be associated to the high geometrical irregularities in plan and elevation typical of the religious architecture, increased in this specific case for the high interaction with posterior structures with a smaller height (e.g. lateral chapels and the Mithra building). It can be noted than the cimborrio is the most flexible macroelement in the building and this must be taken into account for the future vulnerability and risk studies.
- Such complex modal shapes on the other hand could be produced as well by inner hidden cracks, strength and stiffness variations, age effects, accumulated damage and temperature influence. All these and other possible effects increase the uncertainty towards updating numerical models, so, it's necessary to increase these kinds of

studies to stablish better methodologies for the correct conservation of these amazing architectural beauties for the joy and identity preservation of the next generations.

REFERENCES

[1] ICOMOS. *Recommendations for the Analysis, Conservation and Structural Restoration of Architectural Heritage*. International Scientific Committee for the Analysis and Restoration of Structures of Architectural Heritage, (2001).

[2] Kinemetrics, [online]. Available: www.kmi.com/uploads/PDFs/Basalt.pdf. [Accessed April 2017].

[3] Rodrigues Leite de Magalhães, F.M. *Operational Modal Analysis for Testing and Monitoring of Bridges and Special Structures.* Ph.D. Thesis, Faculty of Engineering of the University of Porto, Portugal, (2010).

[4] Brincker, R., Andersen, P. and Jacobsen, N.J. *Automated Frequency Domain Decomposition for Operational Modal Analysis.* In Proceedings of *IMAC 25*, *International Modal Analysis Conference,* Orlando, Florida, USA. (2007).

[5] Svibs. ARTeMIS Modal 4.0. Structural Vibration Solutions, Aalborg, Denmark. (2015).

[6] Welch, P.D. The use of Fast Fourier Transform for the Estimation of Power Spectra: A Method based on Time Averaging over short Modified Periodograms. *IEEE Transaction on Audio and Electro-Acoustics,* AU-15 (2). (1967).

VIII ECCOMAS Thematic Conference on Smart Structures and Materials
SMART 2017
A. Güemes, A. Benjeddou , J. Rodellar and Jinsong Leng (Eds)

PROPOSAL AND COMPARISON OF DIFFERENT OPTIMAL TUNING CRITERIA FOR TMDS

A. MAGDALENO[*], J. FERNÁNDEZ[†], J.M. GARCÍA-TERÁN[*], M. CACHO-PEREZ[*] AND A. LORENZANA[*]

[*] ITAP – Universidad de Valladolid (UVa)
Paseo del Cauce, 59, 47011 Valladolid, Spain
e-mail: alvaro.magdaleno@uva.es, teran@uva.es, cacho@eii.uva.es, ali@eii.uva.es

[†] CEMIM – Universidad Politécnica de Madrid (UPM)
Calle José Gutiérrez Abascal, 2, 28006 Madrid, Spain
email: jfernandezm@etsii.upm.es – http://cemim.etsii.upm.es

Key words: Tuned Mass Damper, seismic excitation, shear building model, optimization.

Abstract. Lively structures subjected to excitations such as wind, earthquake or human-induced forces can undergo relevant stresses and accelerations that can compromise some limit state criteria. Passive, semi-active and active vibration control devices have been proposed as possible solutions to reduce the level of vibration in civil structures such as bridges, multi-storey buildings or thin floor structures, among others [1]. Tuned Mass Dampers (TMD) are usually installed in order to mitigate structural vibrations by increasing its damping through the application of inertial forces generated in response to the movement of the structure [2]. It is known that different algorithms can be used to improve their tuning. When more than one TMD is advisable, in the case of structures with spatially distributed and closely spaced natural frequencies, the TMDs design may not be obvious because simplified tuning concepts [3] cannot consider the coupling effects that appear [4]. In such cases, different criteria lead to different tuning parameters.

In this work, different scalar values (called "indicators", evaluated according to different response considerations) are proposed to find the optimum tuning of two TMDs installed in a two-storey building model. Some of these indicators are based on the frequency response of the structure but others are evaluated according to the time response under a reference excitation. In all cases the tuning parameters are obtained by minimizing the selected indicator. The obtained solutions are compared in order to show the importance of making a good choice of the indicator when designing vibration control devices. Some practical limitations are also discussed through an experimental setup (two-storey building model) that provides the means to test some of the solutions obtained.

1 INTRODUCTION

During the past decades, enormous improvements have taken place in the structural and construction industries, resulting in lighter and more slender structures. Consequently, higher displacements and accelerations appear when they are subjected to a dynamic load such as wind, earthquake or human-induced forces. Many devices have been already designed to cope with this problem including passive, semi-active and active ones. In this work, only the passive control device known as Tuned Mass Damper (TMD) is considered for mitigating the vibrations induced by a quake-like acceleration applied on the basement of a two-storey building model.

The concept of TMD is already a century old, presented for the first time by the naval engineer Hermann Frahm in 1911 [5]. Since then, much effort has been made to understand the coupling effects between TMDs and structures leading to more efficient designs. One of the most important works in this area is the one conducted by J.P. Den Hartog in 1928 which ended by establishing the basics to understanding the behavior of TMDs [3]. His research was entirely based on the Frequency Response Function of a SDOF undamped model subjected to multiple kinds of loads. With the approach of Den Hartog [3], some decades later G.B. Warburton [6] developed a set of closed-form formulae to calculate the optimum properties of a single TMD.

Since then, and following the path opened by Den Hartog and Warburton, FRFs of more complex structural models have been developed to carry out different types of optimizations of one or multiple TMDs properties [7][8][9]. However, the time domain behaviour has had very little impact on the further development of the state of the art. In this work, two simple time domain indicators are proposed and compared with the traditional optimization approach: the maximum of the acceleration responses $\ddot{x}(t)$ and the area under $\ddot{x}(t)$ curve. Both indicators are obtained by simulating the response of the two-storey building model subjected to the El Centro (1940) earthquake accelerogram (Figure 1). Another two timed-based indicators are evaluated in order to compare the solutions: the total amount of energy dissipated by the TMDs and the Maximum Transient Vibration Value of the acceleration response of the model. Some conclusions will be obtained concerning the benefits of using one approach or the other.

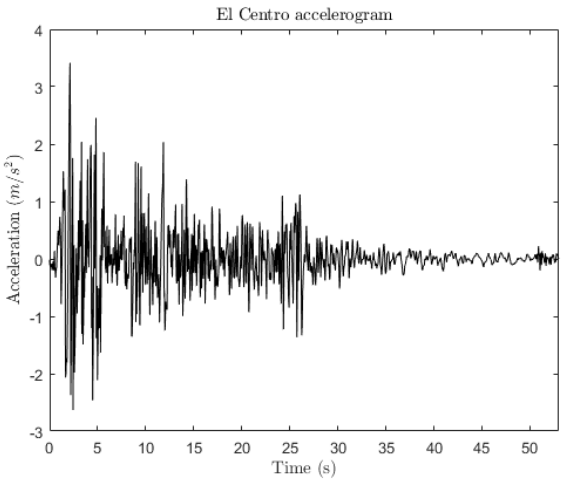

Figure 1: El Centro accelerogram.

2 MODEL DESCRIPTION AND IDENTIFICATION

A two-storey building model has been manufactured (Figure 2, right) in the laboratory to perform some experimental tests. It comprises of two units joint together, one of 0.5 m and the other 0.75 m height. The assembly is placed in a moving table to perform the modal analysis and to obtain its physical and modal properties. The test is carried out by applying an impact to the base and measuring both input and output accelerations. The correlation between basement and 1st floor accelerations and basement and 2nd floor accelerations gives the two FRFs of the model used to update the computational model.

To obtain the physical properties of the model a curve fitting procedure to the experimental FRFs must be done. The analytical FRFs are obtained through the state-space model of the system, which is schematically represented in Figure 1, left. Its mass and stiffness matrices are shown in Equation 1 and, with them, the eigenproblem $(-\omega_i^2 M + K)\phi_i = 0$ can be solved to obtain the natural modes and frequencies, ϕ_i and ω_i respectively. The damping matrix C is defined in this work (without loss of generality) upon the modal damping ratios ξ_i as stated in Equation 2, where $\tilde{C}$ modal damping matrix containing the products $2\xi_i\omega_i$ in its diagonal and V is the modal matrix whose columns are the natural modes.

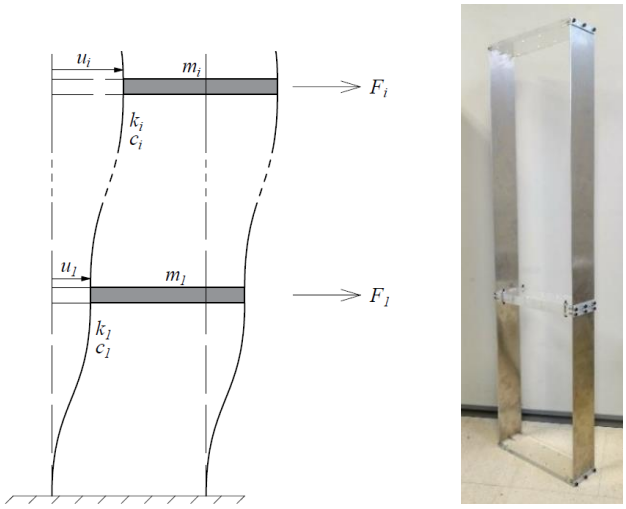

Figure 2: Scale structure: left, the 2-floor schematic model; right, actual 2-floor building.

$$M = \begin{bmatrix} m_1 & 0 \\ 0 & m_2 \end{bmatrix} \qquad K = \begin{bmatrix} k_1 + k_2 & -k_2 \\ -k_2 & k_2 \end{bmatrix} \tag{1}$$

$$C = V^{-T}\,\tilde{C}\,V^{-1} \tag{2}$$

The four matrices of the state-space model can be obtained by rewriting the equations of motion system (Equation 3) properly. In this equation, r is a vector of ones which distribute the base excitation through the structure and a_b is the basement acceleration. Considering the accelerations of both floors of the model as the output and being q_i the displacement of the i-th floor relative to the ground, the four matrices A to D of the state-space equations can be written as shown in Equation 4, where x is the state vector containing displacements and accelerations of the model ($x = [q\ \dot{q}]^T$), u is the input vector ($u = a_b$), y is the output vector ($y = [\ddot{q}_1\ \ddot{q}_2]^T$), I_{nxn} is the n by n identity matrix and $\emptyset_{nxn}$ is the n by n zeros matrix.

$$M\ddot{q} + C\dot{q} + Kq = -Mr\, a_b \tag{3}$$

$$\begin{cases} \dot{x} = Ax + Bu \\ y = Cx + Du \end{cases} \tag{4}$$

$$A = \begin{bmatrix} \emptyset_{2x2} & I_{2x2} \\ -M^{-1}K & -M^{-1}C \end{bmatrix} \qquad B = \begin{bmatrix} \emptyset_{2x1} \\ r \end{bmatrix} \qquad C = [-M^{-1}K \quad -M^{-1}C] \qquad D = \emptyset_{2x1}$$

Programming this approach in Matlab and making use of its state-space functions *tf()* and *lsim()*, both frequency and time responses can be calculated. The six properties of the model $(m_1, m_2, k_1, k_2, \xi_1, \xi_2)$ can be obtained by minimizing the error between the analytical state-space model and the experimental FRFs. The result is shown in Figure 3, leading to the set of properties in Table 1

Table 1: Properties of the identified model

$M_1 =$ 2.17 kg	$K_1 =$ 1210 N/m	$\xi_1 =$ 0.41 %
$M_2 =$ 1.76 kg	$K_2 =$ 341.4 N/m	$\xi_2 =$ 0.11 %

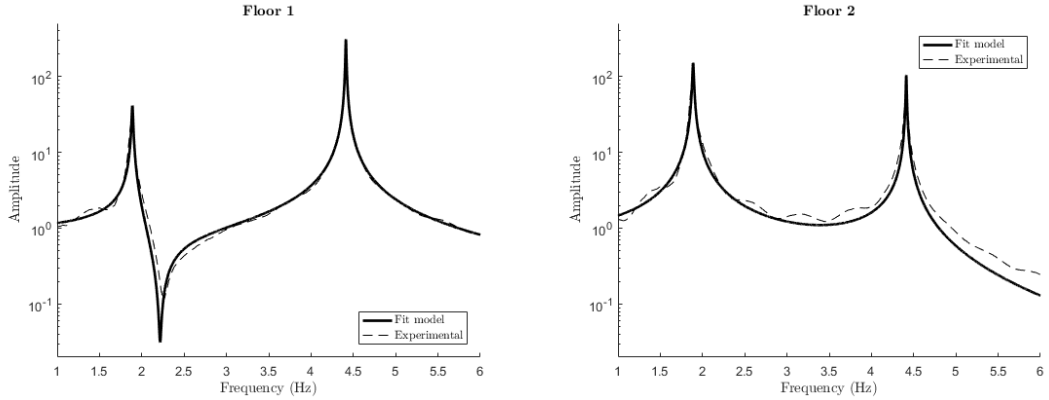

Figure 3: Result of the curve-fitting of the experimental FRF

These properties lead to the natural frequencies $f_1 = 1.89\, Hz$ and $f_2 = 4.41\, Hz$ and the natural modes shown in Figure 4.

2.1. Model of the TMD

A TMD is modelled as shown in Figure 5 and is included directly in the mathematical model presented above. When adding a single TMD, the three matrices M, C and K grow by a row and a column. The mass m_j of the TMD is put in the new diagonal position of the mass matrix. The stiffness k_j is put in the new diagonal position of the stiffness matrix, summed up to the corresponding diagonal position of the floor to which the TMD is attached and two more negative terms $(-k_j)$ are placed in the intersections of the rows and columns affected. Finally, the TMD damper constant c_j is added in a similar way. In order to add a second TMD, the same procedure must be followed.

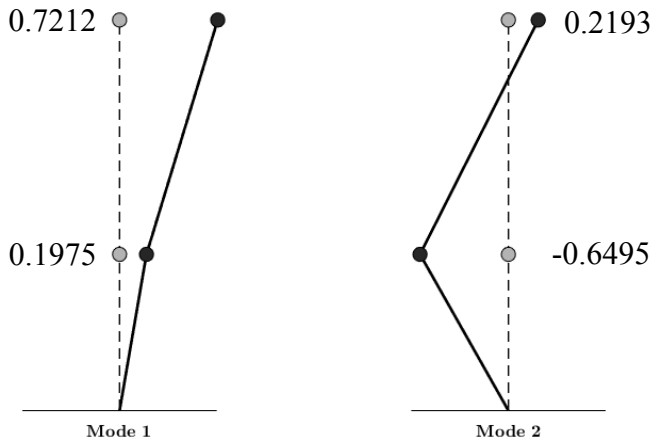

Figure 4: Natural modes of the model

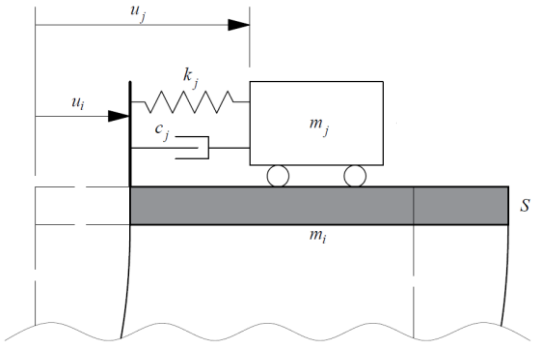

Figure 5: TMD number j attached to the floor number i

The model presented here is used through the entire paper to perform the corresponding optimizations and it is programmed in all the cost functions to obtain the value of the indicator for a set of properties of the TMDs.

3 FREQUENCY DOMAIN INDICATORS

In this section, only the standard frequency domain indicator in is considered, that is, the maximum peak value of a FRF. Regarding only the accelerances of the system, different combinations can be considered: maximum of a single FRF in a limited range of frequency, maximum of every FRF in a limited range, maximum of a single FRF in the whole range and maximum of all the FRFs in the whole range of frequencies. In addition, when multiple FRFs are taken into consideration the sum of all maxima may be also minimized. That makes a lot of different scenarios as the optimizations can be carried out for one or two TMDs. To simplify the task, the cases to discuss will be named after the number of FRFs taken into account (‘Si’ for a single, i-th floor, and ‘A’ for both floors) and the range of frequency considered (‘Lj’ for limited range around the j-th natural frequency and ‘W’ for the whole range), preceded by an ‘F’ (from Frequency domain).

The limited ranges are established around the original natural frequencies of the model and

including the possible double peaks after splitting by the addition of the TMDs. As there are only two natural frequencies, only two limited ranges will be considered: L1 will cover from 0.5 to 3 Hz and L2 will cover from 3 to 6 Hz.

The case in which one TMD is tuned to reduce the FRF peak in a limited range of frequencies is the problem solved by Den Hartog and Warburton [3][6]. For this, the next terminology will be used: DH_{ij}, where i means where the TMD is placed and j which mode is to be reduced.

4 TIME DOMAIN INDICATORS

Regarding the time domain indicators, two different sets will be proposed: the maximum of the response acceleration of some floor (TM) and the area under its curve (TA).

4.1. Peak acceleration response

The first indicator follows the same philosophy than the frequency indicators: minimizing the peak of the response but, this time, in the time domain. An appreciable reduction of the response is expected, especially in the regions of higher accelerations, but, globally, the response may not be minimal. This indicator is named here TM and can be computed for a single response ('S1','S2') or for all of them ('A'). In the latter situation, the indicator may contain the maximum of all the maximum values of each floor ('AM') or, alternatively, the sum of them all ('AS'). Equation 5 provides the definitions for these concepts:

$$TMSj = \max(\ddot{x}_j) \quad ; \quad TMAM = \max\left(\max_{j}(\ddot{x}_j)\right) \quad ; \quad TMAS = \max\left(\sum_{j}\max(\ddot{x}_j)\right) \tag{5}$$

4.2. Area under the acceleration response

To ensure a global reduction of the response, the areas under the time histories are also calculated and minimized. With this procedure, the maximum values of the responses may not be minimal but rather the total amount of movement during the whole simulation. The indicator is named TA and, once again, it can be computed for a single floor ('S1','S2') or the sum of them all ('AS').

$$TASj = \int_0^T \ddot{x}_j(t)dt \quad ; \quad TAAS = \sum_j \int_0^T \ddot{x}_j(t)dt \tag{6}$$

Once these four criteria (F, DH, TM, TA) are used to tune the TMDs, their performance is compared by evaluating two standard quality indicators: the dissipated energy and the maximum transient vibration value.

4.3. Dissipated energy

It is well known that one of the aims of a TMD is to absorb part of the energy of the structure where it is attached. It also helps to redistribute the energy flow in the system, increasing the quantity of energy transmitted through the spring (k_j) up to the mass (m_j). As a way for evaluating the performance of each optimization the total amount or energy dissipated by the

damper (c_j) of the TMD can be computed with Equation 7, where $\dot{x}_j$ is its velocity relative to the ground, $\dot{x}_i$ is the velocity of the floor where the TMD is attached to (also relative to the ground) and T is the total simulation time.

$$W_{Cj} = \int_0^T c_j \left(\dot{x}_j(t) - \dot{x}_i(t)\right)^2 dt \tag{7}$$

The equation shows that the energy dissipated by the TMD increases with its damping constant. However, it depends also on the relative velocity between the TMD and its floor. If the damper constant is too high it is expectable to obtain little relative velocities and, thus, small values for the dissipated energy.

This indicator will be named W_C and followed by a number indicating the number of the TMD to which it refers in the considered scenario.

4.4. Maximum Transient Vibration Value

Finally, the Maximum Transient Vibration Value (MTVV) will also be used to compare performances. This indicator is defined in the ISO 2631 in the context of human perception of structural vibrations. It is evaluated as the maximum of the RMS trend curve of the response in terms of accelerations. RMS trend curve is obtained, point by point, as the root mean square (RMS) of a one second window of the acceleration response with an overlapping of 50% (0,5 s) between each pair of points (Equation 8). As an example, Figure 6 shows the acceleration (grey) and its RMS trend curve (black), being its maximum the MTVV value sought.

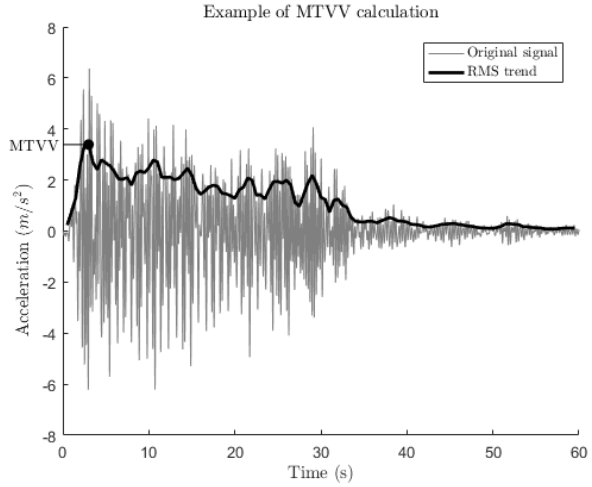

Figure 6: Example of RMS trend and MTVV calculation

$$MTVV = \max_{j} \sqrt{\frac{1}{N}\sum_{i} \ddot{x}\left(\Delta t_j\right)^2} \qquad with\ \Delta t_j = [t_1 \quad \dots \quad t_i \quad \dots \quad t_N] \tag{8}$$

This indicator represents in some way the amplitude of the maximum of the response and so it is closely related to the TM indicator. Low values of MTVV are expected when the TM criteria will be used.

5 RESULTS

The whole optimizations are carried out using the genetic algorithm included in Matlab (*ga()* function) with each cost function programmed separately. Two types of situations are considered: the installation of one TMD (denoted by '_1T') or two TMDs (denoted by '_2T'). In all cases, the algorithm itself puts the TMDs in the best locations. Thus, the optimization contains, apart from the 6 properties of both TMDs, 2 more integer values indicating the floor p_j to which they are attached to.

In the case of frequency domain, one TMD is first tuned to minimize the FRF of the 2nd floor (S2) around first mode (L1) (FS2L1_1T) and another TMD for the second mode (L2) in the 1st floor (S1) (FS1L2_1T). Both solutions can be compared with those obtained via Den Hartog formula (DH12 and DH21). Then, two TMDs are considered to minimize at the same time the first mode in the 2nd floor and the second mode in the 1st floor (FS2L1_S1L2_2T). Then, two TMDs are designed for minimizing the whole 2nd floor FRF (FS2W_2T) and another two TMDs for reduce the first mode in all FRFs as much as possible (FAL1_2T). Finally, two TMDs are obtained to minimize the maximum of all the FRFs in the whole range (FAWM_2T) and another two to minimize the sum of all those maxima (FAWS_2T). Solutions are shown in Table 2.

Table 2: Solutions from optimizations in the frequency domain

Case	$m_j\ (kg)$	$f_j\ (Hz)$	ξ_j (%)	p_j	$W_{Cj}\ (J)$	$MTVV_j\ (m/s^2)$
FS2L1_1T	0.119	1.79	14.63	2	2.51	8.08 ; 6.07
FS1L2_1T	0.119	4.21	13.04	1	0.31	3.97 ; 12.64
DH12	0.119	4.15	13.55	1	0.87	5.39 ; 13.44
DH21	0.119	1.75	15.01	2	2.50	8.10 ; 6.10
FS2L1_ S1L2_2T	0.064 0.055	1.83 4.31	10.79 9.26	2 1	2.50 0.22	3.66 ; 6.80
FS2W_2T	0.115 0.004	1.79 4.40	14.7 2.66	2 1	2.45 0.22	4.10 ; 6.13
FAL1_2T	0.038 0.081	1.98 1.71	9.83 10.93	2 2	0.82 1.70	8.25 ; 5.94
FAWM_2T	0.087 0.032	1.81 4.36	12.66 7.18	2 1	2.46 0.21	3.72 ; 6.47
FAWS_2T	0.069 0.050	1.83 4.32	11.66 8.67	2 1	2.50 0.22	3.68 ; 6.73

Table 3: Solutions from optimizations in the time domain

Case	$m_j\ (kg)$	$f_j\ (Hz)$	ξ_j (%)	p_j	$W_{Cj}\ (J)$	$MTVV_j\ (m/s^2)$
TMS2_1T	0.119	1.85	2.87	2	1.94	8.59 ; 5.42
TMS2_2T	0.011 0.108	4.39 1.81	0.0 11.99	1 2	0.0 1.53	7.04 ; 5.91
TMAM_1T	0.119	1.86	29.45	2	2.75	7.54 ; 6.53
TMAM_2T	0.107 0.012	1.81 4.40	1.34 0.07	2 1	1.51 0.07	5.92 ; 5.97
TMAS_2T	0.105 0.014	1.80 4.24	2.02 4.82	2 1	0.19 1.65	3.46 ; 5.54
TAS2_1T	0.119	1.81	23.87	2	2.69	7.75 ; 6.38
TAS2_2T	0.112 0.007	1.83 4.36	12.22 2.56	2 1	2.41 0.20	3.77 ; 6.05
TAAS_1T	0.119	2.08	47.42	2	2.78	7.01 ; 8.61
TAAS_2T	0.091 0.028	1.83 4.36	11.04 5.37	2 1	2.42 0.21	3.71 ; 6.33

Concerning the solutions in the time domain, one and two TMDs have been sought to reduce the maximum of the 2nd floor's response (TMS2_1T and TMS2_2T). In the case of two TMDs, also the stroke of the TMDs has been minimized because the optimization led to zero damping and, consequently, very high strokes. After that, one and two TMDs are designed to reduce the maximum of both responses (1st and 2nd floors simultaneously, TMAM_1T and TMAM_2T). The sum of all of them is also minimized but only with two TMDs (TMAS_2T). Then, one and two TMDs are considered to reduce the area under the curve response of the top floor (TAS2_1T and TAS2_2T) and finally one and two TMDs have been put on the structure to reduce the total area of all responses (TAAS_1T and TAAS_2T).

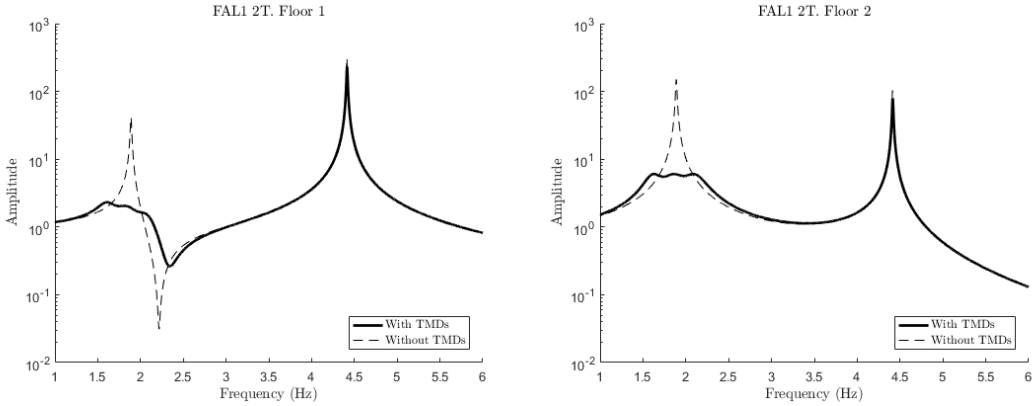

(a) (b)

Figure 7: FRFs of the FAL1_2T case. (a) floor 1; (b) floor 2

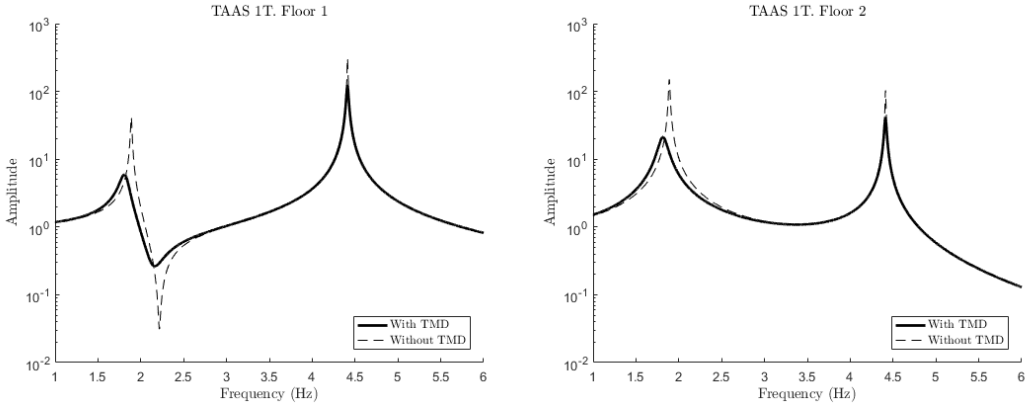

(a) (b)

Figure 8: FRFs of the TAAS_1T case. (a) floor 1; (b) floor 2

As it can be stated by observing the whole set of results is that all TMDs frequencies are focused to one of the two natural frequencies of the structure, no matter what the objective to minimize was. In fact, TMDs placed on the top floor have their natural frequency a little below 1.89 Hz and the others, placed on the 1st floor have their frequency close to 4.41 Hz. There is only two exceptions. The first one is FAL1_2T case, that has two TMDs placed on the 2nd floor and tuned to the first mode, one of them over 1.89 Hz. This is because of the *Multi TMD* effect: instead of resulting in a couple of peaks, this optimization leads to three perfectly levelled maxima in the proximity of the first natural frequency (Figure 7). The other exception is TAAS_1T, with the only TMD tuned at 2.08 Hz. (Figure 8) and with a very high damping ratio (0.4742).

6 CONCLUSIONS

To show the time responses, TAAS_2T case has been taking as reference (Figure 9). Figure 9a and 9b show (black line) the accelerations in the 1st and 2nd floor (respectively), compared with the response of the building without TMDs. Figure 9c shows the energy dissipated by both TMDs.

According to frequency domain indicators, the solution for the FS2L1_S1L2_2T case is the one that dissipates more (2.72 J), together with FAWS_2T case, being both cases very similar in tuning parameters. FS2W_2T case is the design with less maximum MTVV (6.13 m/s^2). Note that in this case, although two TMDs are found, most of the mass is placed in the one tuned to the first mode.

FS1L2_1T and DH12 cases (TMD tuned to mode 2) are the worst, according not only to their low dissipation of energy (less than 0.88 J) but also to the high values for the MTVV (more than 12.6 m/s^2). From this point of view, both indicators seem to be correlated. Also, almost the rest of the "F" cases dissipate the same amount of energy (around 2.6 J) and the maximum MTVV value is around 6 m/s^2.

Regarding time domain indicators, TMAS_2T case is the one with less maximum MTVV (5.54 m/s^2) and, unexpectedly, TAAS_1T is the design that dissipates the most (2.78 J). However, TMAS_2T dissipates only 1.89 J and maximum MTVV value is the corresponding

to TAAS_1T case (8.61 m/s^2), which is contradictory and shows that both indicators are not correlated.

For both types of indicators, table 2 and 3 show that several designs dissipate the same amount of energy (around 2.7 J). According to Figure 9c, where W_{Cj} curves became asymptotic, that seem to be the total energy available in the structure after the earthquake. This result reveal that W_{Cj} indicator should be replaced by another one accounting not for the dissipation in the whole time (60 s) but for the dissipation ratio, being preferable to dissipate energy the more quickly the better.

Finally, TMAS_2T case is the one with less maximum MTVV (5.54 m/s^2) so, for the El Centro loading, it is the best design, but it remains to be check if it is also the best solution for other types of earthquakes. There are 9 cases (FS2L1_S1L2_2T, FS2W_2T, FAWM_2T, FAWS_2T, TMS2_2T, TMAM_2T, TMAS_2T, TAS2_2T and TAAS_2T) where the maximum MTVV values are under 7.1 m/s^2 and all of them resolve to 2 TMDs, being the one with more mass tuned to mode 1 and placed in the 2nd floor and the other tuned at mode 2 and placed in the 1st floor. This is a reasonable strategy, having in mind that the 2nd floor has the maximum modal coordinate for mode 1, 0.7212 and the 1st floor the maximum for mode 2, 0.6495.

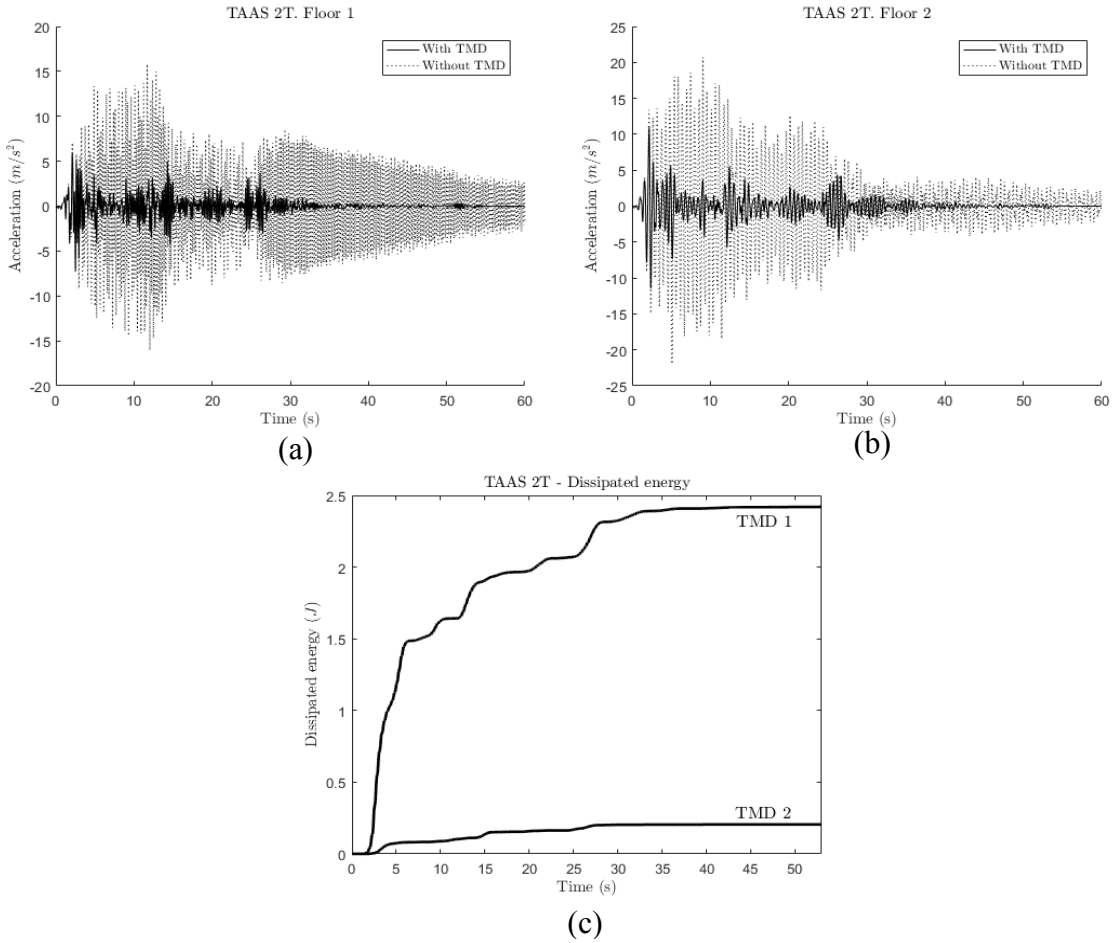

Figure 9: Example for time responses in terms of acceleration (m/s^2) and dissipation of energy (J)

ACKNOWLEDGEMENTS

The authors wish to acknowledge to the partial support through Research Projects BIA2014-59321 and BIA2015-71942-REDT (Ministerio de Economía y Competitividad, Spanish Goverment).

REFERENCES

[1] G. W. Housner, L. A. Bergman, T. K. Caughey, A. G. Chassiakos, R. O. Claus, S. F. Masri, R. E. Skelton, T. T. Soong, B. F. Spencer, and J. T. P. Yao, "Structural control: past, present and future.," *J. Eng. Mech.*, vol. 127, pp. 887–971, 1997.

[2] M. D. Symans and M. C. Constantinou, "Semi-active control systems for seismic protection of structures: a state-of-the-art review," *Eng. Struct.*, vol. 21, pp. 469–487, 1999.

[3] J. P. Den Hartog, *Mechanical vibrations*. New York: McGraw-Hill Book Company, 1934.

[4] M. Abé and T. Igussa, "Tuned Mass Dampers for structures with closely spaced natural frequencies.," *Earthq. Eng. Struct. Dyn.*, vol. 24, pp. 247–261, 1995.

[5] H. Frahm, "Device for damping vibrations of bodies." Google Patents, 1911.

[6] G. B. Warburton, "Optimum absorber parameters for various combinations of response and excitation parameters," *Earthq. Eng. Struct. Dyn.*, vol. 10, no. 3, pp. 381–401, 1982.

[7] H. Yamaguchi and N. Harnpornchai, "Fundamental characteristics of Multiple Tuned Mass Dampers for suppressing harmonically forced oscillations," *Earthq. Eng. Struct. Dyn.*, vol. 22, no. 1, pp. 51–62, 1993.

[8] F. Sadek, B. Mohraz, A. W. Taylor, and R. M. Chung, "A method of estimating the parameters of tuned mass dampers for seismic applications," *Earthq. Eng. Struct. Dyn.*, vol. 26, no. 6, pp. 617–635, 1997.

[9] J. C. Miranda, "On tuned mass dampers for reducing the seismic response of structures," *Earthq. Eng. Struct. Dyn.*, vol. 34, no. 7, pp. 847–865, 2005.

VIII ECCOMAS Thematic Conference on Smart Structures and Materials
SMART 2017
A. Güemes, A. Benjeddou , J. Rodellar and Jinsong Leng (Eds)

STATIC AND DYNAMIC ANALYSIS OF MASONRY TOWER OF ALLAHABAD UNIVERSITY, INDIA

Ambareesh Kumar*, Kumar Pallav†

*Research Scholar, Civil Engineering Department, Motilal Nehru National Institute of Technology Allahabad-211004, Uttar Pradesh, India
Email: ambar006@gmail.com

†Assistant Professor, Civil Engineering Department, Motilal Nehru National Institute of Technology Allahabad-211004, Uttar Pradesh, India
Email: kpallav@mnnit.ac.in

Key words: Unreinforced Masonry Tower, Historic Structure, Static Analysis, Modal Analysis, Geometric survey.

Abstract. This paper aims to present static and dynamic analysis of 102-year-old masonry tower (28.5 m high and 6.7m square base) of Senate Hall, Allahabad University, which was constructed during British era. The tower walls are modeled in ANSYS-14 using ten-degree tetrahedral SOLID 187 Element. The top dome of tower is modeled using SURF (3 noded with 6 degrees of freedom at each) element. The static analysis shows that, in general, the structural arrangement of the masonry tower is adequate to take care of gravity loads comprises of self-weight and live load. Most stress region is at base of the structure with maximum value of compressive stress of about 1.295 MPa. The displacement distribution shows that a maximum displacement of 0.55 mm occurs at top dome. Further, the results of modal analysis of the tower are also shown.

1 INTRODUCTION

The Allahabad city is one of the oldest Holi city of India, also known as Prayag (*place of offering)*. This city is known for *Kumbha Mela*, one of the largest gathering of people during the month of *Magh* (January and February of every year), is having the buildings of different era *viz*., Allahabad Fort (1583), Khusro Bagh (1622), Ulta Qila (1855), The Allahabad high court (1869), Allahabad Public Library (1878), Allahabad University (1887), all Saints Cathedral Church (1887), Allahabad Museum (1931) etc. These buildings were constructed of thick brick masonry and stone masonry and they are not in good condition due lack of proper maintenance work. The senate hall building of Allahabad university was constructed in 1887 is fourth the oldest university after Bombay, Madras and Calcutta in India. Senate hall was established in 1905 is a load bearing masonry structure. Stones were used in ground floor verandah and balcony of structure. Minor damage was observed in upper portion and in decorating materials during 2015 Nepal earthquake. Further minor cracks were generated in floorings, stone piers, masonry walls, and connections on the roof of masonry bricks. The towers are important vertical structures in old buildings. They were built either isolated or commonly included in with respect to the urban content, such as built as a part of churches,

castles, municipal buildings and city walls. In this case the masonry tower was constructed, isolated from the other building part of the University. The proper assessment of these structures against various forces (Gravity, load and dynamic load) is a relevant importance for historical, social and artistic reasons.The present study is limited to Gravity and modal analysis of Masonry tower.

Literature are available on historical structures for in-situ surveys [1, 2], geometric survey and architectural features of masonry structure [3] were widely discussed by many researchers. The static and seismic analysis of masonry towers [5–9], experimental works [10–17], dynamic identification [4, 16], study on structure damaged due to past earthquakes [18-20], and its post-earthquake investigation (including direct survey, historic and documentary research, testing of materials and ambient vibration tests) [21], were investigated to know the critical location in the structure and to improved them. Complex non-linear static (pushover) and dynamic analyses [8, 22] were also perform to asses the behaviour of structure. Researcher has also reported about the collapsed and damage of historical masonry structure [5-8]. Structural retrofitting and retrofitting of traditional materials (mortar and bricks) on the collasped and damaged old buildings along with its structural upgrading mechanisum was discussed by Salvatori [23]. The modal pushover analysis was performed on historical masonry tower [24]. In view of above, an important university building is taken for detailed analysis. In this reconnisance survey, modelling and analysis (static and dynamic) has been performed on masonry tower of Allahabad university.

2 MASONRY TOWER

The masonry tower is 28.5m high with base width of 7.0m, located in front right side of senate hall building which was constructed in 1915 by British engineer *Sir Swinton Jacob*. It is three-floor masonry structure having dome at top, that is rested on stone arch panel supported by twelve columns as shown in **Figure 1**. The tower is basically used for stair.



(a) Senate hall with view of masonry tower (b) Masonry tower of 28.5m high

Figure 1: Masonry tower of Senate Hall of Allahabad university, India

In detailed geometric study of Senate hall building is performed and discussion with

engineer in-charge (Civil works), it is reported that the masonry wall thickness is varying from 1.5m to 0.6m in ground floor and first floor respectively. The sandstone is used in the front of the ground floor, backside of the verandah, stairs and in the canopies of the masonry tower. **Figure 2** shows some of the snapshots which state the condition of the tower.

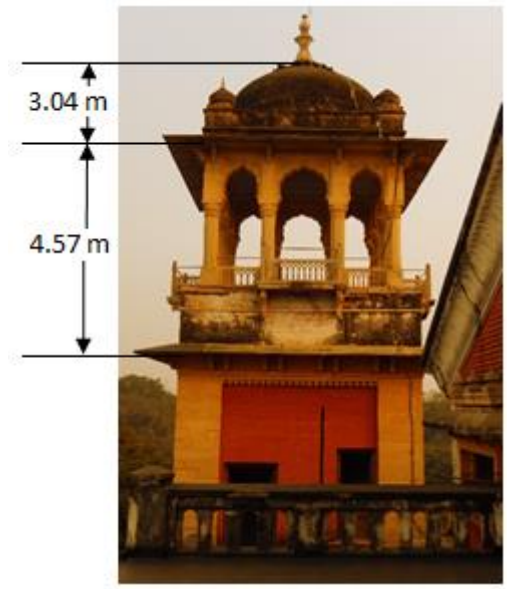

(a) Dome supported on 12 Column



(b) Detoriation of material on stair case

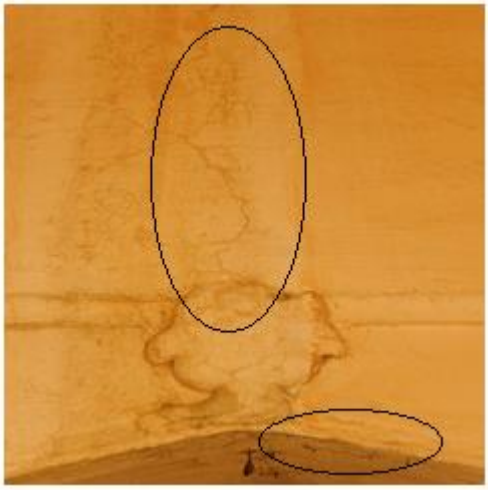

(c) Visible Crack in the middle of arch.



(d) Patch work in wall and column

Figure 2: Geometric survey for masonry tower

The load bearing masonry tower is constructed of brick masonry and stone, with a regular texture, is 1.07m above ground level. The wall of the tower is up to the height of 28.5m. The opening at the entrance to the stairs and windows are made up of stone arches. The ratio between the overall height of the structure and the smallest dimension of the base cross section is equal to 4.07. The tower is internally subdivided into three storeys, which is

connected vertically by a stone staircase. Each level of the story is square plan and consists of a unique space, which is partly occupied by the staircase. The first and second floor has same floor height of 6.10m and thickness of the wall varying from 0.76m and 0.61m respectively. The third-floor height is 7.62m of wall thickness 0.46m. The stone arch Gumbaj (Dome shape, structure) above third floor is supported on twelve numbers of stone arch column having height of 4.57m. The column is octagonal in shape with each side of 0.305m and height 2.13m, they are supported on rectangular stone base cross section of 0.31m x 0.31m and height 0.46m. The radius of the dome is 4.88m having crown height of 3.04m, that is a beautiful example of Mughal architecture. The arch is made up of stone column, which is resting on brick masonry. **Figure 3(a)** show the elevation of masonry tower with all the dimensions. **Figure 3(b)** shows the plan of each floor level along with stone staircase of masonry tower. First and second floor stair width is the same 1.83m, rise 0.305m and trade 0.23m. Third floor stair is designed open well shape with outside edge is support on continuous stone beam, stair width 1.22m and rise and trade is same as first storey stair. Most openings are located on the internal side of the tower. A general view along with relevant geometrical features of the masonry tower are presented in **Figure 3**.

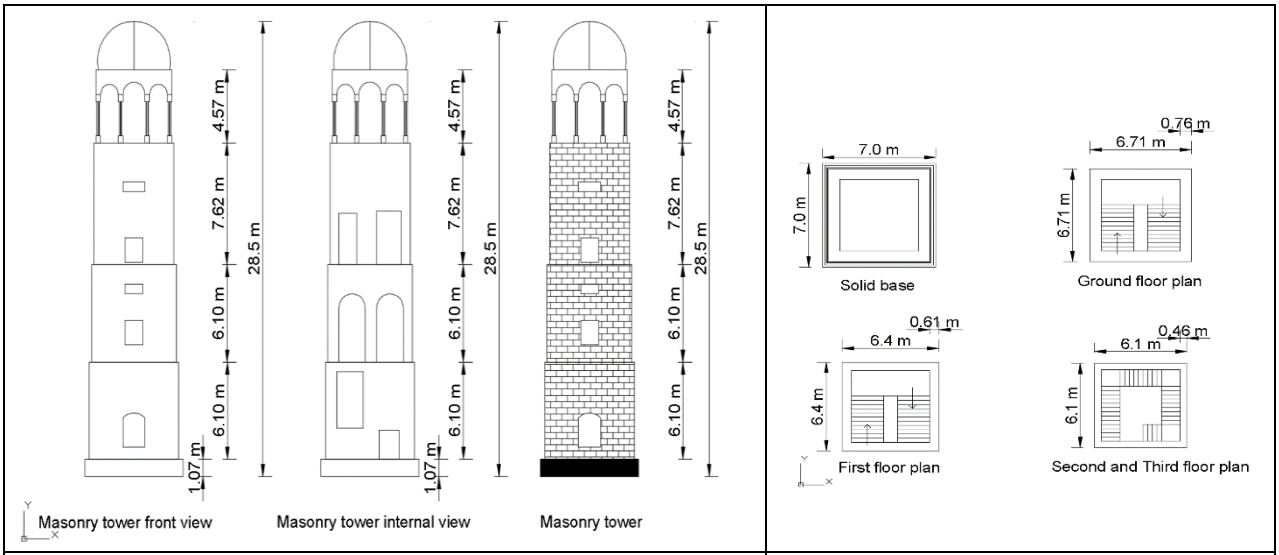

(a) Front and Back elevation view | (b) Floor plan of tower

Figure 3: Geometric view of masonry tower senate hall

3 FINITE ELEMENT MODELLING

A numerical 3D finite element model of the masonry tower modelled in commercial finite element ANSYS workbench 14.0 [27]. The geometry is based on the geometric survey. The macro modelling approach was used, and the masonry was modelled as an isotropic continuum. Masonry tower is modelled by using, *Solid 186, Solid 187* elements (10-Noded 3D solid elements) in the masonry walls and stairs and Surf-*154* used in the dome. *TARGE 170,* and *CONTA 174* used contact and connections of tower components. The main region to choose 3D 10-noded solid element, it exhibits the quadratic displacement behavior, the element supports plasticity, hyper-elasticity, creep, stress stiffening, large deflection and large

strain capabilities. The major openings of the masonry tower were reproduced together with the vaults at first floor level. The specific attention was paid in the modelling of the multi leaf masonry walls for each floor level. The numerical analysis aims to investigate the stress distribution due to static load and to identify the dynamic behavior of the masonry tower. The model is developed assuming a linear behavior of masonry material.

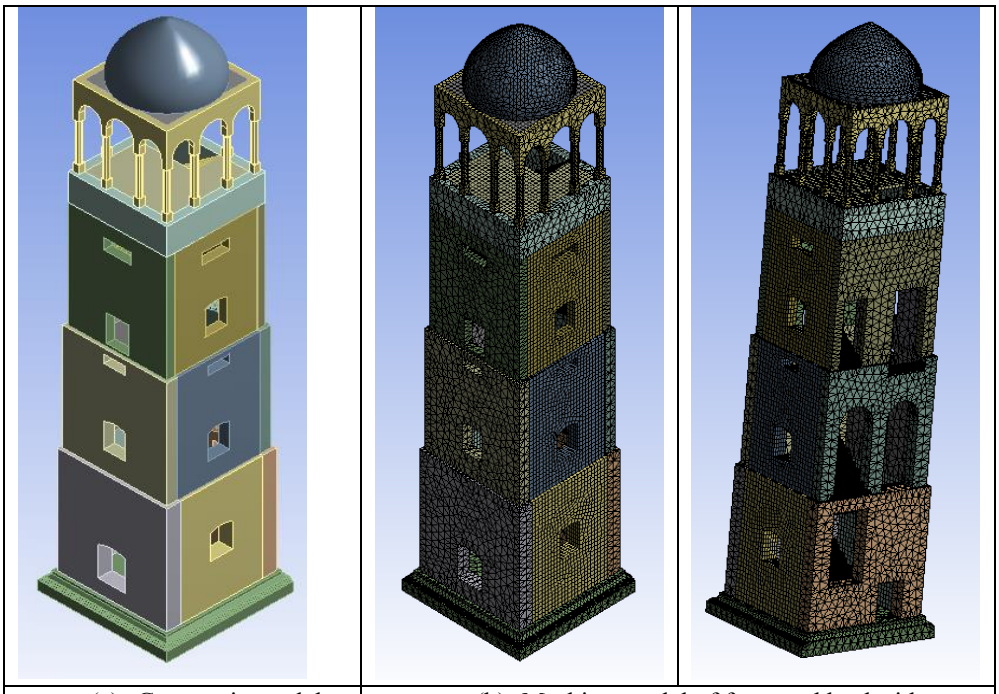

(a) Geometric model | (b) Meshing model of front and back side

Figure 4: Finite element modelling of masonry tower

4 ANALYSIS OF TOWER

The static and dynamic analysis of the monumental masonry tower has been performed by applying gravity load as per IS: 875 (Part 1) 1987. The elastic material behavior Young's modulus, E equal to 3000 MPa and 11000 MPa, mass density, ρ equal to 1800 kg/m3 and 2400 kg/m3 of masonry and stone respectively, the poisons modulus, ν equal to 0.2 [11]. The mechanical properties are used in the present study is based on a literature survey of historical monument structures. The results of static and dynamic analyses on the masonry tower in term of Von-Mises stress distribution and model behavior are shown **Figure 5 to 7**.

4.1 Standard gravity analysis

The static analysis of the masonry tower under standard gravity loads has been performed with fixed base. The high stress of 1.295MPs is localized at the ground level closed to first floor level. The bottom of the tower where stresses are localized agrees well with the observation of cracks shown in **Figure 5**. This was predictable considering that the masonry tower has several openings at first floor and second floor, the maximum stresses in generated in the first-floor masonry wall, middle portion of arch and the corner or near the openings on

stairs at high concentration is developed. Firstly, stress is developed at the first-floor vault at shown **Figure 2(b)** and **Figure 2(c)**. The maximum stress is generated at a masonry wall of the first floor and bottom slab of stairs to second floor and third floor. The minor cracks are visible on the bottom side of third floor stairs, and joints between stairs and wall are closely spaced. The dome has performed well in gravity load condition. The maximum deformation 0.54mm is produced at the top of dome shown **Figure 6**. The deformation at the first-floor is 0.2mm. The small crack is observed in the masonry tower wall and buttress wall, which shows good agreement with the results obtained. The total deformation distributed is shown in masonry tower **Figure 6**. **Table 1** shows the deformation and stress at different level of masonry tower.

Table 1: Floor wise deformation and Stress of Masonry under gravity loading

Floor	Deformation (mm)	Stress (MPa)
1st	0.0692	1.2953
2nd	0.2254	0.8723
3rd	0.38068	0.5326
Dome	0.5469	0.0864

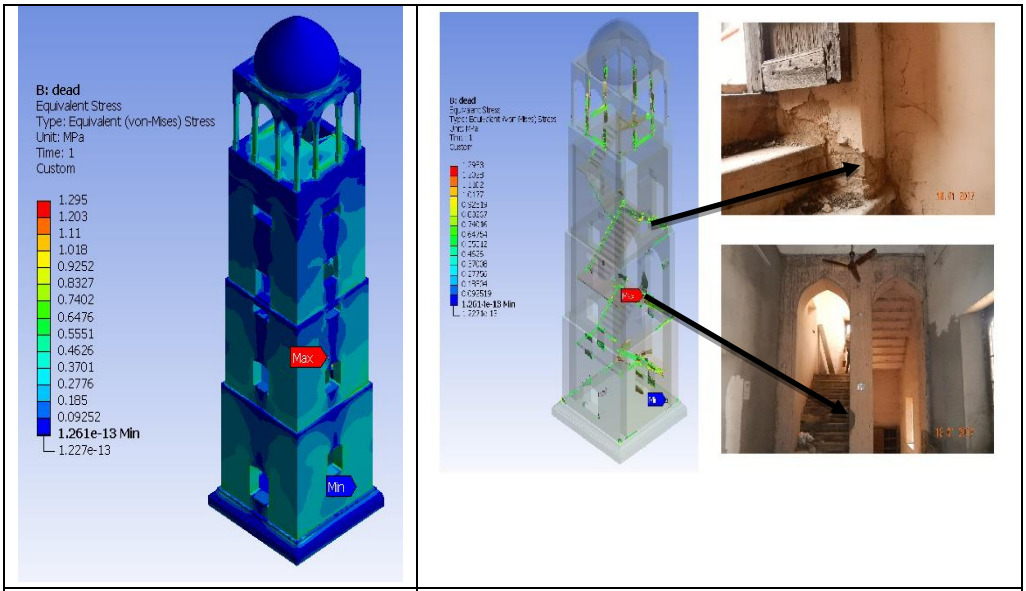

(a) Maximum stress at first floor | (b) Stress show in internal side of tower

Figure 5: Maximum stress shown in masonry tower

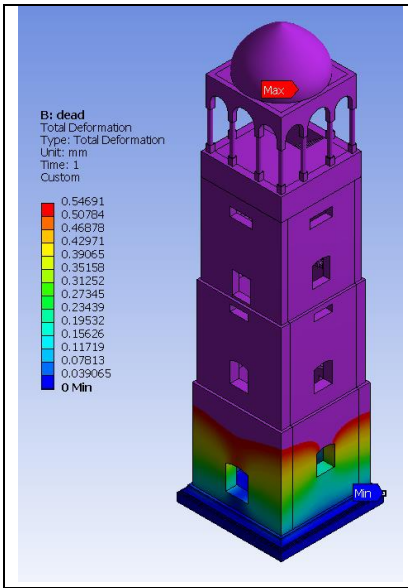

(a) Dead load deformation

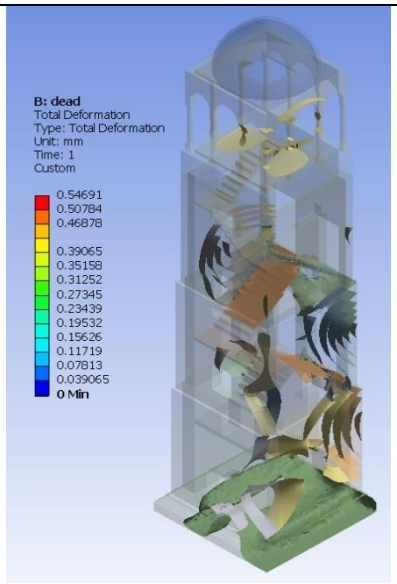

(b) Maximum deformation observed in floor

Figure 6: Total deformation of masonty tower

4.2 Dynamic model analysis

The dynamic modal analysis of masonry tower has been performed by 3D finite element model for linear elastic behavior materials. The dynamic analysis has been considered to evaluate the response of masonry tower. The free vibration analysis of the tower shows of first six natural modes, shown in **Figure 7**. The fundamental frequency is 2.27Hz. **Table 2**: shown the frequencies (f) and periods (T) of the first six vibration modes evidencing that the period increases when configuration is more deformable. The deformation in first and second modes is 4.41mm and 4.72mm respectively. In discussion with engineer in-charge it is confirmed that the tower was originally built separately from the other buildings particularly from senate hall structure. It is therefore interesting to understand if the strength increase is sufficient to secure an increase of safety with the higher stresses state induced.

Table 2: Mode shape and frequency of masonry tower

Mode	Frequency (Hz)
1	2.27
2	2.37
3	4.34
4	4.79
5	4.95
6	7.56

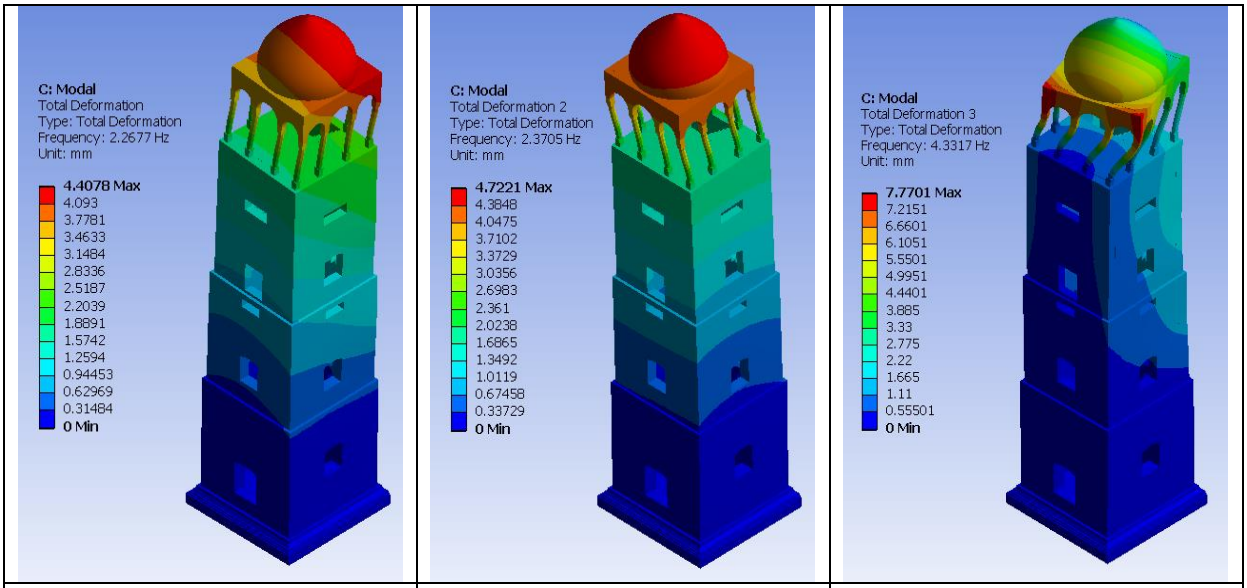

Mode 1	Mode 2	Mode 3
Mode 4	Mode 5	Mode 6

Figure 7: Dynamic modal analysis of masonry tower

5 CONCLUSIONS

A numerical study performed by means of FE simulations on masonry towers located in the Allahabad university, India. The aims of this work are to discuss some general geometrical characteristics, such as openings, wall thickness, top domes and staircase and modelled them in Ansys. Further to perform gravity and model analysis of the masonry tower. The survey of a masonry tower, reveals that the structure is stable and only some of the minor cracks were observed at the openings of doors, windows and near the staircase. The bricks and stone are well intact with the structure. In general tower is in good conditions, but some part of the tower is closed for access due to some structural deformations. The masonry tower

performs well under gravity load and the maximum stress is 1.295MPa. The fundamental frequency of the tower is 2.27Hz.

Acknowledgement:

We sincerely thanks to Er. Naveen Kumar of Allahabad university for his unconditional support for performing the survey of the building as and when required. Also, we are thankful to the administration of Allahabad university for giving the permission.

REFERENCES

[1] Casolo, S. Milani, G. Uva, G. and Alessandri, C. *Comparative seismic vulnerability analysis on ten masonry towers in the coastal Po Valley in Italy*. Engineering Structures 49 (2013) 465–490.

[2] Valente M. and Milani G. *Seismic assessment of historical masonry towers by means of simplified approaches and standard FEM.* Construction and Building Materials, 108 (2016) 74–104.

[3] Valente, M. and Milani, G. *Non-linear dynamic and static analyses on eight historical masonry towers in the North-East of Italy.* Engineering Structures 114 (2016) 241–270.

[4] D'Ambrisi, A. Mariani, V. and Mezzi, M. *Seismic assessment of a historical masonry tower with nonlinear static and dynamic analyses tuned on ambient vibration tests*. Engineering Structures 36 (2012) 210–219.

[5] Pena, F. Lourenco, P.B. Mendes, N. and Oliveira, D.V. *Numerical models for the seismic assessment of an old masonry tower*. Engineering Structures 32 (2010) 1466–1478.

[6] Colapietro, D. Fiore, A. Netti, A. Fatiguso, F. Marano, G.C. Fino, M.D. Cascella, D. and Ancona A. *Dynamic Identification and Evaluation of the Seismic Safety of a Masonry Bell Tower in the South of Italy*. COMPDYN 2013, 4th ECCOMAS Thematic Conference on Computational Methods in Structural Dynamics and Earthquake Engineering, Kos Island, Greece, 12–14 June 2013.

[7] Acito, M. Chesi, C. Milani, G. and Torri, S. *Collapse analysis of the Clock and Fortified towers of Finale Emilia, Italy, after the 2012 Emilia Romagna seismic sequence: Lesson learned and reconstruction hypotheses.* Construction and Building Materials 115 (2016) 193–213.

[8] Acito, M. Bocciarelli, M. Chesi, C. and Milani G. *Collapse of the clock tower in Finale Emilia after the May 2012 Emilia Romagna earthquake sequence: Numerical insight.* Engineering Structures 72 (2014) 70–91.

[9] Preciado, A. *Seismic vulnerability and failure modes simulation of ancient masonry towers by validated virtual finite element models*. Engineering Failure Analysis 57 (2015) 72–87.

[10] Camata, G. Cifelli, L. Spacone, E. Conte, J. and Torrese, P. *Safety Analysis of the Bell Tower of S. Maria Maggiore Cathedral in Guardiagrele (Italy)*. The 14th World Conference on Earthquake Engineering October 12-17, 2008, Beijing, China.

[11] Bartoli, G. Betti, M. and Giordanom S. *In situ static and dynamic investigations on the ''Torre Grossa'' masonry tower*. Engineering Structures 52 (2013) 718–733.

[12] Saisi, A, and Gentile, C. *Post-earthquake diagnostic investigation of a historic masonry tower*. Journal of Cultural Heritage 16 (2015) 602–609.

[13] Speranza, E. Viskovic, A. and Sepe, V. *Integrated Methods for the Assessment of the Structural Vulnerability of Historic Towers.* Structural Analysis of Historical Constructions, New Delhi 2006.
[14] Ceroni, F. Pecce, M. Palmaccio, F. and Manfredi, G. *Structural investigations and modelling of the Bell Tower of Santa Maria del Carmine*. WIT Transactions on The Built Environment, Vol 95, 2007 WIT Press.
[15] Russo, G. Bergamo, O. Damiani, L. and Lugato, D. *Experimental analysis of the ''Saint Andrea'' Masonry Bell Tower in Venice. A new method for the determination of ''Tower Global Young's Modulus E''*. Engineering Structures 32 (2010) 353–360.
[16] Gentile, C. and Saisi, A. *Ambient vibration testing of historic masonry towers for structural identification and damage assessment*. Construction and Building Materials 21 (2007) 1311–1321.
[17] Beconcini, M.L. Bennati, S. and Salvatore W. *Structural characterisation of a medieval bell tower: First historical, experimental and numerical investigations*. Historical Constructions, P.B. Lourenco, P. Roca (Eds.), Guimaraes, 2001.
[18] Soyluk, A. and Ilerisoy, Z.Y. *Dynamic analysis of Dolmabahce masonary clock tower*. GRADEVINAR **65** (2013) 4, 345-352.
[19] Preciado, A. Orduna, A. Bartoli, G. and Budelmann, H. *Facade seismic failure simulation of an old Cathedral in Colima, Mexico by 3D Limit Analysis and nonlinear Finite Element Method*. Engineering Failure Analysis 49 (2015) 20–30.
[20] Minghini, F. Milani, G. Tralli, A. *Seismic risk assessment of a 50 m high masonry chimney using advanced analysis techniques*. Engineering Structures 69 (2014) 255–270.
[21] Saisi A, Gentile C, Guidobaldi M. *Post-earthquake continuous dynamic monitoring of the Gabbia Tower in Mantua, Italy*. Construction and Building Materials 81 (2015) 101–112.
[22] Pineda P. *Collapse and upgrading mechanisms associated to the structural materials of a deteriorated masonry tower. Nonlinear assessment under different damage and loading levels*. Engineering Failure Analysis 63 (2016) 72–93.
[23] Salvatori. L. Marra, A.M. Bartoli, G. and Spinelli, P. *Probabilistic seismic performance of masonry towers: General procedure and a simplified implementation*. Engineering Structures 94 (2015) 82–95.
[24] Minghini, F. Bertolesi, E. Grosso, A. D. Milani, G. and Tralli, A. *Modal pushover and response history analyses of a masonry chimney before and after shortening.* Engineering Structures 110 (2016) 307–324.
[25] Pieraccini, M. Dei, D. Betti, M. Bartoli, G. Tucci, G. and Guardini, N. *Dynamic identification of historic masonry towers through an expeditious and no-contact approach: Application to the "Torre del Mangia" in Siena (Italy)*. Journal of Cultural Heritage 15 (2014) 275–282.
[26] IS: 875-Part I, (1987), Indian standard criteria for earthquake resistant design of structures, fifth revision, part-1, Bureau of Indian Standards, New Delhi.
[27] Finite element modelling software ANSYS workbench 14.0.

VIII ECCOMAS Thematic Conference on Smart Structures and Materials
SMART 2017
A. Güemes, A. Benjeddou , J. Rodellar and Jinsong Leng (Eds)

TAKING INTO ACCOUNT THE UNCERTAINTY IN THE TMD DESIGN FOR THE VIBRATION SERVICEABILITY OF A FOOTBRIDGE

J.F. JIMÉNEZ-ALONSO[*] AND A. SÁEZ[†]

[*] Department of Building Structures and Geotechnical Engineering
Universidad de Sevilla
Avenida de Reina Mercedes 2, 41012 Seville, Spain
e-mail: jfjimenez@us.es, web page: www.us.es

[†] Department of Continuum Mechanics and Structural Analysis
Universidad de Sevilla
Camino de los Descubrimientos s/n, 41092 Seville, Spain
e-mail: andres@us.es, web page: www.semni.org

Key words: footbridge, passive structural control, tuned mass dampers, uncertainty, genetic algorithms

Abstract. Tuned mass dampers (TMDs) are control devices widely used to reduce the pedestrian induced vibrations on footbridges. The TMD parameters are designed according to the requirements demanded for the structure. One of the main factors to be overcome for the TMD design is the change of the modal parameters of the structure associated with the modification of its operational and environmental conditions. The main purpose of this study is to analyze the effect of this uncertainty in the TMD design for the vibration serviceability of footbridges. The sensitivity of three well-known constraints under these uncertainty conditions is analyzed. The variability of the modal parameters is simulated by a probabilistic approach based on previous results reported in literature. A robust method is implemented in order to ensure an adequate behavior of the structure under these stochastic conditions. As an example, a benchmark footbridge is considered to assess numerically the performance and accuracy of the different methods. The pedestrian action is simulated according to the recommendations of the Synpex guidelines. The results show which the most adequate constraint is (among the three studied cases) to control the pedestrian induced vibrations on footbridge under stochastic conditions.

1 INTRODUCTION

Nowadays the use of the tuned mass dampers (TMDs) has become a usual tool to reduce the vibrations of civil engineering structures induced by dynamic loads [1]. Several design methods [2] have been proposed in order to constrain the frequency response function of the structure, H_a, under the different type of dynamic actions. One of the main limitations of these damping devices (passive damping) is that these only can be tuned to a fixed frequency (normally around the affected natural frequency of the structure) and thus a reduction of their performance is experienced if for any reason the natural frequency of the structure varies [3].

As it is reported in the literature [4] the change of the operational and environmental conditions are the main cause of the modification of the modal frequencies of footbridges. It is therefore interesting to find out: (i) if it is possible to determine a set of TMD parameters that ensures the mitigation of the vibration under these stochastics conditions and (ii) to check which the best constraint is to deal with the uncertainty among the existing mentioned requirements. For this purpose, a robust design method is proposed in this manuscript. This method is based on a probabilistic approach where the uncertainty associated with the modification of the modal parameters of the structure is simulated by a probabilistic distribution function [5]. The proposal is implemented in a numerical example, reported in literature [6], in order to reflect as the uncertainty influences the TMD design. Three different constraints have been considered to define the resultant frequency response function of the structure [2]: (i) H_∞ optimization, (ii) H_2 optimization and (iii) H_{max} optimization.

The pedestrian action is simulated according to the recommendations of the Synpex guidelines [7]. The study is restricted to walking pedestrian induced vibration on footbridges in vertical direction. As result of the study the constrained optimization method under the robust approach that better adjusts the uncertainty conditions is determined. Further, the need to consider the uncertainty associated with the modification of the modal parameters of the structure is revealed.

2 TMD-STRUCTURE INTERACTION MODEL

The TMD-structure interaction model may be formulated from the application of the dynamic equilibrium equation [8] to the different masses of a model with two degrees of freedom. As an assumption for this study, only one vibration mode is considered to be affected by the pedestrian-structure interaction and it is assumed that the damping device is located at the position with the maximum modal deflection. Figure 1 illustrates the TMD-structure interaction model and the definition of its main parameters.

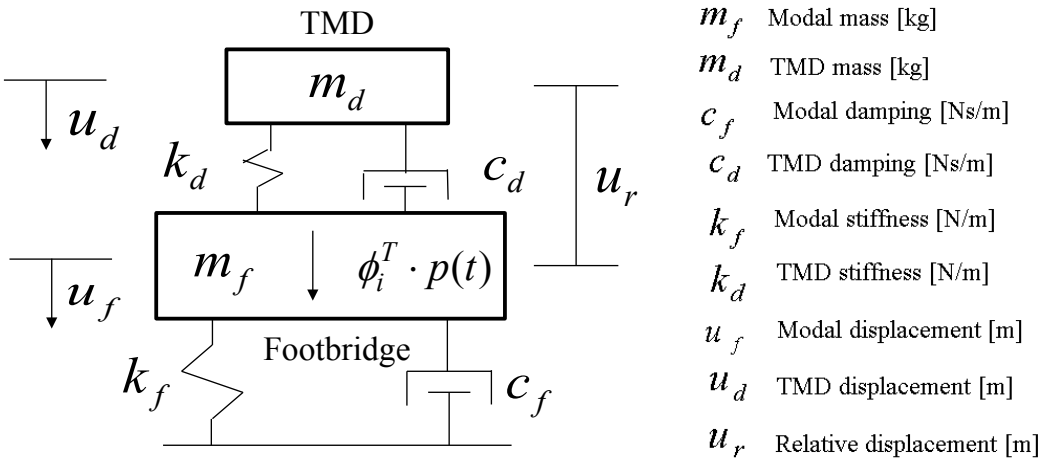

Figure 1: TMD-structure interaction model.

The following coupled equations govern the TMD-structure interaction:

$$m_f \cdot \ddot{u}_f + c_f \cdot \dot{u}_f + c_d \cdot (\dot{u}_f - \dot{u}_d) + k_f \cdot u_f + k_d \cdot (u_f - u_d) = \phi_i^T \cdot p(t) \quad (1)$$

$$m_d \cdot \ddot{u}_d + c_d \cdot (\dot{u}_d - \dot{u}_f) + k_d \cdot (u_d - u_f) = 0 \quad (2)$$

where $\dot{}$ and $\ddot{}$ reflects respectively the first and second derivatives respect to time and $\emptyset_i^T$ the transpose of the affected numerical vibration mode.

The proposed equations may be reorganized in matrix form and subsequently, this system may be integrated using a β–Newmark method (with parameters β=1/4 and γ=1/2 in order to ensure an unconditionally stable system). The equivalent pedestrian load, $p(t)$, and the required comfort level, a_{lim}, are simulated following the model proposed by the Synpex guidelines [7].

3 ROBUST TMD DESIGN

The modal parameters of the structure may vary due to the modification of its operational and environmental conditions. A robust design of the TMD parameters is need in order to ensure an adequate behavior of the structure under these conditions [3]. In order to simulate these stochastic conditions the Monte Carlo method is considered in this study [5]. Thus, the modal parameters of the structure are assumed to be random variables that follow normal probabilistic distributions according to previous results reported in literature [4]. Several 'states' are generated (sets of natural frequencies and damping ratios), simulating the response of the structure under each 'state'. The robust TMD parameters may be selected in terms of the number of cases that after the TMD installation does not meet the required comfort criteria [3].

The robust TMD design may be formulated as a constrained single-objective optimization problem as follows:

$$\text{find } \mu, \text{ optimize } f = \mu, \text{ subject to } \begin{matrix} A(a_{max}) = \frac{a_\infty}{a_{lim}} - 1 \leq 0 \\ A(u_{r.max}) = \frac{u_\infty}{u_{lim}} - 1 \leq 0 \\ H(\delta_{opt} \quad \zeta_{opt}) \end{matrix} \quad (3)$$

where

$\mu = m_d / m_f$ is the mass ratio.

f is the objective function.

$A()$ are the inequality constraints.

$H(\delta_{opt} \quad \zeta_{opt})$ is an additional constraint considered for the adjustment of the frequency response function of the structure (Table 1).

a_{max} is a vector that contains the maximum vertical acceleration of the structure under each simulated 'state'.

$u_{r,max}$ is a vector that contains the maximum vertical relative displacement of the structure

under each simulated 'state'.

$a_{\propto}$ is the percentile α^{th} of the probability distribution of the maximum vertical accelerations of the structure.

$u_{\propto}$ is the percentile α^{th} of the probability distribution of the maximum vertical relative displacements of the structure.

a_{lim} is the limit vertical acceleration according to the required comfort level.

u_{lim} is the limit vertical relative displacement provided by the manufactured.

Table 1: Optimum TMD frequency and damping ratios according to different criteria [2]

	H_∞	H_2	$H_{\max}$
δ_{opt}	$\frac{1}{1+\mu}$	$\frac{1}{1+\mu}\sqrt{1+\frac{\mu}{2}}$	$\frac{1}{1+\mu}$
ζ_{opt}	$\sqrt{\frac{3\mu}{8(1+\mu)}}$	$\sqrt{\frac{\mu(4+3\mu)}{8(1+\mu)(2+\mu)}}$	$\sqrt{\frac{\mu}{1+\mu}}$

The method provides the TMD parameters that reduce the acceleration response of the structure minimizing the TMD mass. This procedure may be summarized as follows [7]:

(i) Choice of TMD mass, m_d, based on the mass ratio.

(ii) Calculation of the optimum TMD ratios: frequency ratio, δ_{opt}, and damping ratio, ζ_{opt} (Table 1).

(iii) Calculation of the TMD constants: spring and damping constant.

$$k_d = m_d \cdot (2 \cdot \pi \cdot \delta_{opt} \cdot f_f)^2 \tag{4}$$

$$c_d = 2 \cdot m_d \cdot 2 \cdot \pi \cdot \delta_{opt} \cdot f_f \cdot \zeta_{opt} \tag{5}$$

(iv) Checking of the comfort requirements.

(v) Repeating the process if the comfort requirements are not met.

As global optimization method, genetic algorithms have been used. In order to take into account the effect of the uncertainty the search domain of the mass ratio is increased, $\mu \in [0.01 - 0.15]$. Both the population size and the maximum number of iterations were set to 100. Each individual modified through the operation of reproduction, crossover and mutation its value in order to minimize the value of the objective function.

4 NUMERICAL EXAMPLE

As numerical example, the study of effect of the uncertainty on the dynamic response of a numerical footbridge, provided in the French standard [6] has been considered. Figure 2 shows the main geometrical and mechanical characteristics of the footbridge.

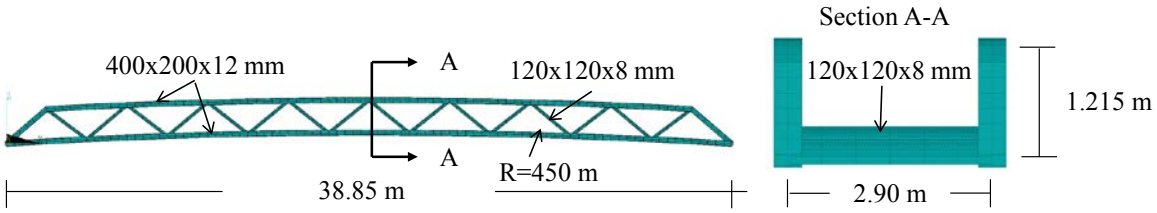

E_s=210 GPa; ν_s=0.3; ρ_s=7850 kg/m^3
E_c=31 GPa; ν_c=0.2; ρ_c=2500 kg/m^3

Figure 2: Finite element model of the numerical example [6]

The numerical natural frequencies of the structure have been obtained from a numerical model analysis [9]. It has been verified that the first vertical natural frequency of the structure, f_f, is affected by the pedestrian-structure interaction (Table 2). The method proposed by the Synpex guidelines [7] has been used to check the comfort requirements of the structure. Five different load cases have been considered in terms of the pedestrian density on the footbridge (Table 2). The maximum accelerations on the structure exceed the medium comfort degree for all the load case.

Table 2: Comfort level of the numerical example

Load Cases	d [P/m^2]	n [P]	m_f [kg]	f_f [Hz]	a_{max} [m/s^2]	Comfort degree	Comfort level
I	<0.20	15	34706	2.14	1.05	Minimum	CL3
II	0.20	19	34706	2.14	1.16	Minimum	CL3
III	0.50	48	37710	2.05	1.74	Minimum	CL3
IV	0.80	76	39500	2.00	2.08	Minimum	CL3
V	1.00	96	40750	1.97	4.96	Discomfort	CL4

In order to improve the behavior of the structure a TMD is installed. Two design scenarios (D.S.) are considered to design the TMD parameters: (i) $a_{lim} = 0.50$ m/s2 for load cases I-IV and $a_{lim} = 1.00$ m/s2 for load case V; and (ii) $a_{lim} = 0.50$ m/s2 for all the load cases. Additionally, the relative displacement between the TMD and the deck of the structure is limited to $u_{lim} = 20$ mm.

For our purpose, it is assumed that the first natural frequency and associated damping ratio may vary randomly considering a variation range of ± 10 % [4]. 10000 possible 'states' are generated considering uncorrelated normal distribution functions and the Latin Hypercube

Sampling method [5]. The robust design method is implemented considering that the maximum vertical acceleration of the Monte Carlo simulation may be considered a random variable and modifying the constraint equations for each design scenario. The three mentioned constraints (H_∞, H_2 and H_{max}) have been considered. The design process has been performed using the software Matlab [10]. Four uncertainty levels have been taken into account during the design process (50th, 67th, 95th and 99th percentile). The TMD parameters designed according to the three mentioned criteria under stochastic conditions are shown in Table 3.

Table 3: TMD parameters versus the uncertainty level for each desing method and design scenario

		μ [%]			δ_{opt}			ζ_{opt} [%]		
D.S.	α [%]	H_∞	H_2	$H_{\max}$	H_∞	H_2	$H_{\max}$	H_∞	H_2	$H_{\max}$
1	50	1.00	1.19	1.54	0.990	0.991	0.985	6.09	5.43	12.32
	67	1.28	1.56	2.04	0.987	0.988	0.980	6.88	6.21	14.14
	95	2.19	2.69	2.38	0.978	0.980	0.977	8.96	8.12	15.25
	99	2.79	3.45	2.41	0.973	0.975	0.976	10.09	9.17	15.34
2	50	3.50	4.43	7.21	0.966	0.968	0.933	11.26	10.35	25.93
	67	4.04	5.14	9.09	0.961	0.963	0.917	12.07	11.12	28.87
	95	5.62	7.21	10.50	0.947	0.949	0.905	14.13	13.08	30.83
	99	6.63	8.54	10.57	0.938	0.941	0.933	15.27	14.17	30.92

Additionally, the frequency response function in terms of accelerations ratio, H_a, of the TMD-footbridge system is shown in Figure 3 for the three considered design criteria and the two design scenarios. The effect of the different uncertainty levels in the frequency response function is also shown in Figure 3.

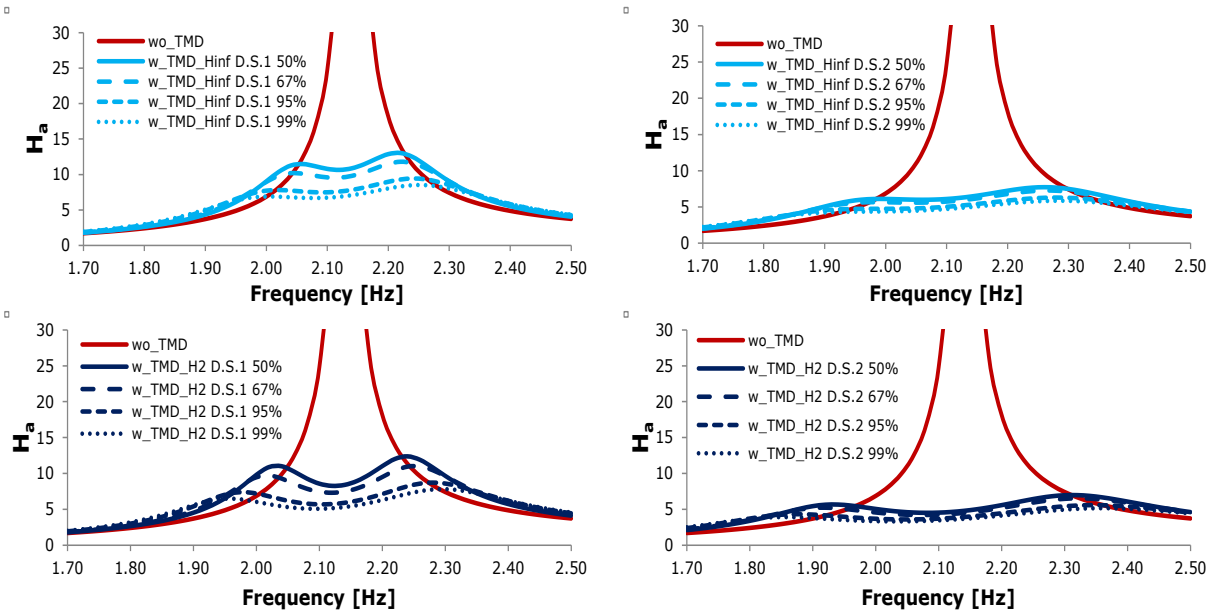

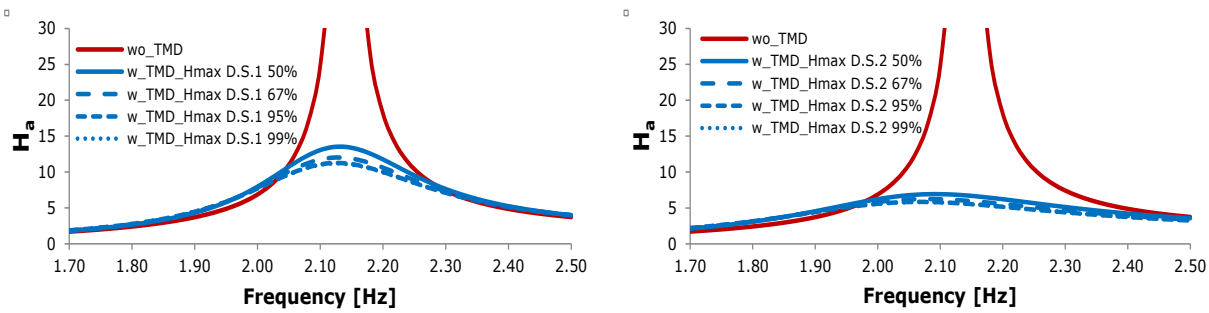

Figure 3: Frequency Response Function, H_a, for the different design methods, uncertainty levels and design scenarios.

As Figure 3 shows, the H_{max}criterion present a worse adjustment to the stochastics conditions than the other two criteria. It is clear as the uncertainty influences the parameters design especially when the comfort requirements are lower.

Finally, Figure 4 shows the TMD mass designed according to the three mentioned constraints, the two design scenarios and the different uncertainty levels. A clear tendency, an increase of the TMD mass in terms of the uncertainty levels, is shown in Figure 4. The constrained criterion that shows the best performance is the H_∞ criterion, except in the design scenario 1 under high uncertainty where the H_{max} criterion reduces the TMD mass.

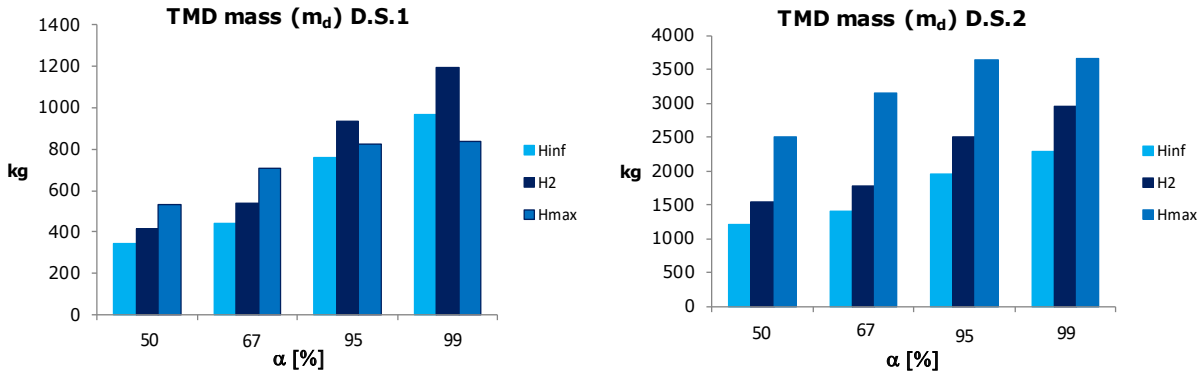

Figure 4: TMD mass versus de uncertainty level for each design criterion and design scenario.

5 CONCLUSIONS

The main purpose of this manuscript is to determine the robust parameters of a TMD under uncertainty conditions in order to control the dynamic response of footbridges under pedestrian flows. The uncertainty associated with the change of the modal parameters of the structure due to the modification of its operational and environmental conditions is taken into account. A constrained single-objective optimization method is used to obtain the parameters of a TMD. The different design criteria, H_∞, H_2 and H_{max}, have been considered for the TMD design in terms of inequality constraints. The response of a numerical footbridge under a pedestrian flow is checked during the design process considering only the walking pedestrian action in vertical direction. This action is simulated via an equivalent harmonic load according to the Synpex guidelines. The study was performed under a stochastic

approach. In this way, the natural frequencies and the damping ratios of the footbridge are supposed to vary randomly due to the change of the operational and environmental conditions. A variation range is established by previous results reported in literature. In order to guarantee the robustness of the TMD parameters, under the stochastic approach, a robust design procedure is implemented. The performance of the method and the effect of the uncertainty in the TMD design are assessed comparing the results between the three mentioned design criteria (H_∞, H_2 and H_{max}) under the two design scenarios. The H_∞ constraint shows the better adjustment under the stochastics conditions. The effect of the uncertainty in the TMD parameters is clear, showing an increasing trend to the uncertainty level. Nevertheless, further studies are recommended to find a design constraint that optimizes the TMD parameters under stochastics conditions.

ACKNOWLEDGEMENTS

This work was partially supported by the Ministerio de Economía y Competitividad of Spain under project BIA2015-71942-REDT.

REFERENCES

[1] Caetano, E., Cunha, A., Raoul, J., Hoorpah, W.. Footbridge Vibration Design p. 192. Leuden (The Netherlands). CRC Press, Taylor and Francis Group, 2009.

[2] Asami, T., Nishihara, O., Baz, A.M.. Analytical solutions to H_∞ and H_2 optimization of dynamic vibration absorbers attached to damped linear systems. *Journal of Vibration and Acoustics*, (2002); 124(2): 284-295.

[3] Jiménez-Alonso J.F., Sáez, A., Robust optimum design of TMDs to mitigate pedestrian induced vibrations using multi-objective genetic algorithms. *Structural Engineering International* (2017) (in press).

[4] Hu, W.H., Caetano, E., Cunha, A.. Structural health monitoring of a stress-ribbon footbridge. *Eng. Struct*. (2013); 57: 578-593.

[5] Bucher, C.. Computational Analysis of Randomness in Structural Mechanics. London (U.K.). CRC Press Taylor & Francis Group, 2009.

[6] SETRA/AFGC. Guide méthodologique passerelles piétonnes (Technical Guide Footbridges: Assessment of vibration behaviour of footbridge under pedestrian loading), 2006.

[7] Butz CH., Heinemeyer, CH.; Goldack, A.; Keil, A.; Lukic, M.; Caetano, E.; Cunha, A.. Advanced Load Models for Synchronous Pedestrian Excitation and Optimised Design Guidelines for Steel Footbridges (SYNPEX). RFCS-Research Project RFS-CR-03019, 2007.

[8] Clough, R.W., Penzien J.. Dynamics of structures, p. 634. New York (EEUU). McGraw-Hill Book Company, 1993.

[9] ANSYS Mechanical Release

[10] Matlab R2011a. . http://www.mathworks.com/.

VIII ECCOMAS Thematic Conference on Smart Structures and Materials
SMART 2017
A. Güemes, A. Benjeddou, J. Rodellar and J. Leng (Eds)

VIBRATION CONTROL OF A DINING HALL: MIMO AND SISO DESIGN

Emiliano Pereira†, Xidong Wang*, Cristina Alén†, Jaime H. García-Palacios* and Iván M. Díaz*

† Escuela Politécnica Superior
Universidad de Alcalá de Henares
28805 Alcalá de Henares, Spain

*ETS Ingenieros de Caminos, Canales y Puertos
Universidad Politécnica de Madrid
28040 Madrid, Spain
e-mail: ivan.munoz@upm.es

Key words: Active vibration control; human-induced vibrations; MIMO control

Abstract. Active vibration control (AVC) via inertial-mass actuators is a viable technique to mitigate human-induced vibrations in civil structures. A multi-input multi-output (MIMO) AVC has been previously proposed in the literature to simultaneously find the sensor/actuator pairs' optimal placements and tune the control gains. However, the application examples are simple and/or they do not correspond with real structures. This work considers the previously proposed methodology to design an AVC for a typical floor structure with multiple vibration modes locally spatially distributed and with similar natural frequencies, which is where MIMO strategies are really of interest.

1 INTRODUCTION

Every day it is more common to find light and slender structures with vibration serviceability problems. These structures satisfy ultimate limit state criteria but they have the potential of attracting complaints coming from excessive human-induced vibrations [1]. Examples and solutions to these problems can be found in pedestrian bridges or long-span office floors (see for example [2]). Passive dampers, such as tuned mass dampers (TMDs) are commonly used to reduce the vibration level of these structures. These solutions can only cope with one vibration mode and with modal properties which do not change over time. When several vibration modes have to be cancelled and modal properties may change, an active solution may be a competitive alternative. Moreover, if the structure is only used during a short period of time (like concert hall, dining hall, etc.), the solution of active vibration control (AVC) via inertial mass actuators is quite attractive (since no significant structure modifications are needed, i.e., reduction costs). In addition, AVC has been shown to significantly reduce the level of response, allowing structures to satisfy vibration serviceability limits [3].

The authors have been recently proposed AVC solutions ([4], [5]) where multi-input multi-output (MIMO) control strategies have been used. In addition, sensor/actuator placement and gain matrix are designed considering how humans perceive the vibration [6]. However, these applications examples are quite simple [4] and/or they do not correspond with real structures [5].

A finite element model (FEM) of a steel-concrete composite dining room floor sited in Spain is considered in this work. This structure is a good example of floor with vibration modes with closely-spaced natural frequencies, where MIMO strategies are of special interest.

The structure of this work is as follows: next section describes the generalized framework used to obtain the optimal design of MIMO AVC and location of sensors and actuators. This section also describes the structural model of the application example used in Section 3. Section 3 presents a comparison between two SISO and one MIMO in order to evaluate the application of MIMO control for real complex structures. Section 4 closes the paper by giving some conclusions and remarks on this research.

2 Problem definition

The problem tackled in this paper consists of designing two SISO and one MIMO strategies by considering the methodology presented in [4]. This section also briefly explains the general scheme shown in Figure 1. In addition, the FEM, the AVC design methodology and the optimization problem are also described in this section.

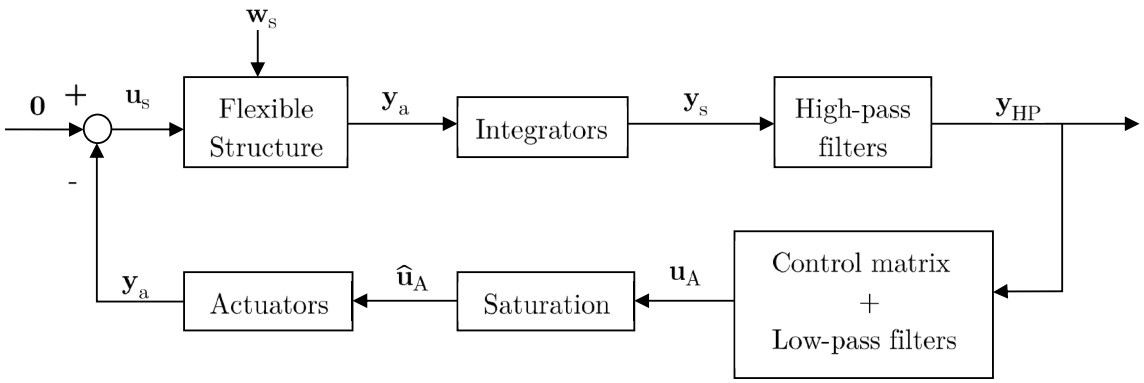

Figure 1: General control scheme.

2.1 Floor structure

The structure considered in this paper is a dining room floor of a primary-secondary school sited in Madrid (Spain). The general arrangement of beams and columns is shown in Figure 2. The FEM was created in ANSYS [7] using shell elements with 449 nodes. It is an irregular rectangular composite floor with dimension of 25.5 m×20 m. The material properties considered are: modulus of elasticity $E = 20 \times 10^9$ N/m^2, Poisson's ratio $\nu = 0.15$ and density $\rho = 3000$ kg/m^3. The density has been increased from 2500 kg/m^3 to 3000 kg/m^3 in order to include

a portion of the imposed load (approximately 30%) and the total dead load [8]. The effective depth has been taken as 0.3 m. The modal shapes, natural frequencies, damping ratios and modal masses of the first ten vibration modes can be seen in Figure 3. Natural frequencies and damping ratios were experimentally validated through an operational modal analysis. As it can be observed, the structure shows several vibration modes under 10 Hz, which are likely to be excited by users.

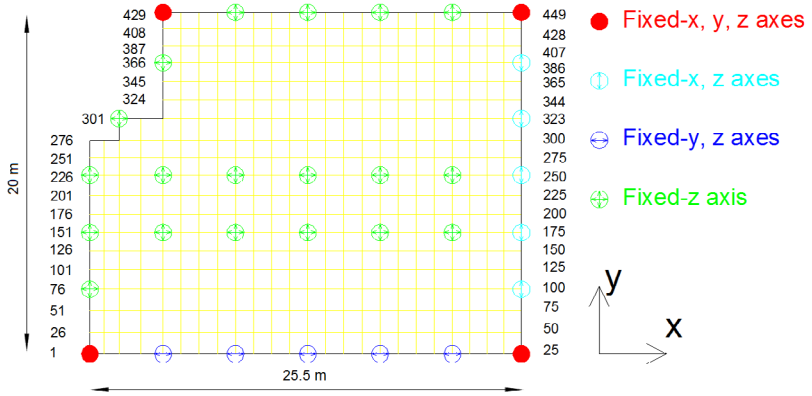

Figure 2: Floor structure considered.

For the sake of simplicity, the flexible structure and the integrators are grouped, so that the output of the resulting system is $\mathbf{y}_s$, which is the velocity at q locations. Thus, the standard state-space representation of the model for this flexible structure (with n vibration modes, p actuators, q sensors and r perturbations) is represented as follows (see Figure 1):

$$\begin{aligned} \dot{\mathbf{x}}_s =& \mathbf{A}_s\mathbf{x}_s + \mathbf{B}_{s_1}\mathbf{u}_s + \mathbf{B}_{s_2}\mathbf{w}_s, \\ \mathbf{y}_s =& \mathbf{C}_s\mathbf{x}_s, \end{aligned} \tag{1}$$

If Equation (1) is defined in modal coordinates, the state-space matrices are as follows [9]:

$$\begin{aligned} \mathbf{A}_s &= \begin{bmatrix} \mathbf{0} & \mathbf{I} \\ -\mathbf{\Omega}^2 & -2\mathbf{Z}\mathbf{\Omega} \end{bmatrix}, \mathbf{B}_{s_1} = \begin{bmatrix} \mathbf{0} \\ \mathbf{\Phi}_u \end{bmatrix}, \\ \mathbf{B}_{s_2} &= \begin{bmatrix} \mathbf{0} \\ \mathbf{\Phi}_w \end{bmatrix}, \mathbf{C} = \begin{bmatrix} \mathbf{\Phi}_y & \mathbf{0} \end{bmatrix}, \end{aligned} \tag{2}$$

in which $\mathbf{\Omega}$ and $\mathbf{Z}$ are, respectively, the diagonal matrices formed by the natural frequencies ($[\omega_1, \cdots, \omega_n]$) and the damping ratios ($[\xi_1, \cdots, \xi_n]$); and the matrices $\mathbf{\Phi}_u$, $\mathbf{\Phi}_y$ and $\mathbf{\Phi}_w$ are matrices with dimensions $n \times p$, $q \times n$ and $n \times r$. It is important to highlight that each kth column of $\mathbf{\Phi}_u$ and $\mathbf{\Phi}_w$ and each row of $\mathbf{\Phi}_y$ is formed by the kth vibration mode values at the positions of the actuators ($\mathbf{\Phi}_u$), perturbations ($\mathbf{\Phi}_w$) and sensors ($\mathbf{\Phi}_y$), respectively. The state vector is defined as: $\mathbf{x}_s = [x_{s_1}, \cdots, x_{s_n}, \dot{x}_{s_1}, \cdots, \dot{x}_{s_n}]$, where $[x_{s_1}, \cdots, x_{s_n}]$ are the modal coordinates of the structure, and $[\dot{x}_{s_1}, \cdots, \dot{x}_{s_n}]$ are their derivatives.

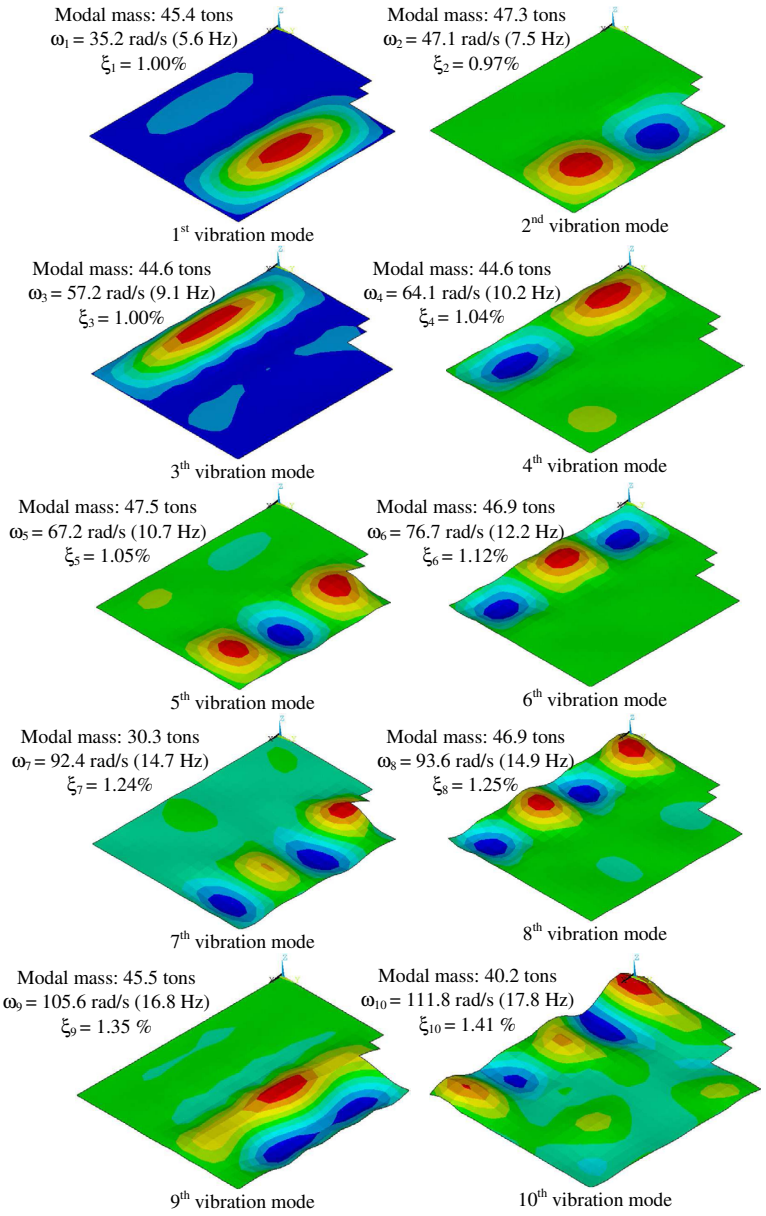

Figure 3: Floor mode shapes, natural frequencies, damping ratios and modal masses.

2.2 AVC methodology

The AVC is implemented by using (see Figure 1): i) inertial actuators to generate the forces through the acceleration of inertial masses to the structure on which they are placed, ii) second-order Butterworth high-pass filters to reduce the gain of the loop at low-frequencies, which can saturate the actuator, iii) second-order Butterworth high-pass filters to reduce the gain of the loop at high-frequencies, reducing thus the risk of spillover problems [10], and iv) force saturation blocks to simulate the maximum voltage inputs of the inertial actuators. Note that if the cut-off frequencies of the filters are separated from the vibration modes, the AVC can be approximated by a direct velocity feedback (DVF).

The AVC methodology consists of these main steps: i) defining the cut-off frequencies of the filters according to the vibration modes of the structure and to the bandwidth of the actuators and ii) deciding the locations of p inertial actuators and q sensors (i.e., the values of $\mathbf{\Phi}_u$ and $\mathbf{\Phi}_y$ in Equation (2)) and iii) tuning the gain matrix in order to minimize a cost function.

The state-space equation of the closed-loop system is obtained from Figure 1 and is as follows (see references [4] and [5] for more details):

$$\begin{aligned} \dot{\mathbf{x}}_{CL} = &\quad \mathbf{A}_{CL}\mathbf{x}_{CL} + \mathbf{B}_{CL}\mathbf{w}_s, \\ \mathbf{y}_s = &\quad \mathbf{C}_{CL}\mathbf{x}_{CL} + \mathbf{D}_{CL}\mathbf{w}_s, \end{aligned} \tag{3}$$

where the state vector is $\mathbf{x}_{CL} = [\mathbf{x}_s, \mathbf{x}_I, \mathbf{x}_{LP}, \mathbf{x}_A]$ and the state matrices are:

$$\mathbf{A}_{CL} = \begin{bmatrix} \mathbf{A}_s & \mathbf{0} & \mathbf{0} & -\mathbf{B}_{S_1}\mathbf{C}_{A_T} \\ \mathbf{B}_{I_T}\mathbf{C}_s & \mathbf{A}_{I_T} & \mathbf{0} & \mathbf{0} \\ \mathbf{B}_{LP_T}\mathbf{D}_{I_T}\mathbf{C}_s & \mathbf{B}_{LP_T}\mathbf{C}_{I_T} & \mathbf{A}_{LP_T} & \mathbf{0} \\ \mathbf{0} & \mathbf{0} & \mathbf{B}_{A_T}\mathbf{K}\mathbf{C}_s & \mathbf{A}_{A_T} \end{bmatrix}, \tag{4}$$

$$\mathbf{B}_{CL} = \begin{bmatrix} \mathbf{B}_{s_1} \\ \mathbf{0} \\ \mathbf{0} \\ \mathbf{0} \end{bmatrix}, \mathbf{C}_{CL} = [\mathbf{C}_s\mathbf{A}_s, \mathbf{0}, \mathbf{0}, -\mathbf{B}_{s_1}\mathbf{C}_{A_T}] \text{ and } \mathbf{D}_{CL} = \mathbf{B}_{s_1},$$

and the gain matrix, defined in a general form, is as follows:

$$\mathbf{K} = \begin{bmatrix} K_{11} & K_{12} & \cdots & K_{1q} \\ K_{21} & K_{22} & \cdots & K_{2q} \\ \vdots & \vdots & \ddots & \vdots \\ K_{p1} & K_{p2} & \cdots & K_{pq} \end{bmatrix}, \tag{5}$$

in which K_{ij} is the control gain applied at control input i due to control output j. Sensor/actuator locations and gain matrix are tuned considering the human vibration perception. This perception depends on the direction of incidence to the human body, the frequency content of the vibration (for given amplitude) and the duration of sustained vibration, among other factors.

The human vibration perception is considered in the controller design by weighting the state vector of the structure $\mathbf{x}_s$ (see Equation (4)) as follows

$$x_{s_{W_l}} = \left(e^{\alpha t} x_{s_l}(t)\right) * g_{FW}(t),\ l \in [1, \cdots, 2n], \tag{6}$$

where (*) denotes the convolution process and $g_{FW}(t)$ is the impulse response function corresponding a frequency domain filter that account for the different human perception of different frequencies of excitation (see references [4] and [6]). Note that the weighted vector $\mathbf{x}_{s_W}$ is only used to calculate the PI used to derive the optimal sensor/actuator locations and the gain matrix. In other words, the weighting functions are neither included into the closed-loop system of Figure 1 nor into the Equations (3) and (4).

Finally, the optimal control design proposed in [4] is based on minimizing the following cost function:

$$g(\mathbf{z}) = \max\left\{\frac{1}{2}\int_0^{t_f} \mathbf{x}_{sw}^T(\mathbf{z})\mathbf{Q}\mathbf{x}_{sw}(\mathbf{z})\mathrm{d}t\right\}, \tag{7}$$

by finding the optimal parameters of $\mathbf{z} = [\mathbf{K}, \mathbf{\Lambda}]$, where the matrix $\mathbf{Q}$ is a $2n \times 2n$ positive definite matrix, which is taken as [11]

$$\mathbf{Q} = \begin{bmatrix} \omega_1^2\phi_{1,\max}^2 & \cdots & 0 & 0 & \cdots & 0 \\ \vdots & \ddots & \vdots & \vdots & \ddots & \vdots \\ 0 & \cdots & \omega_n^2\phi_{n,\max}^2 & 0 & \cdots & 0 \\ 0 & \cdots & 0 & \phi_{1,\max}^2 & \cdots & 0 \\ \vdots & \ddots & \vdots & \vdots & \ddots & \vdots \\ 0 & \cdots & 0 & 0 & \cdots & \phi_{n,\max}^2 \end{bmatrix}, \tag{8}$$

in which $\phi_{k,\max}$ is the maximum value of the kth eigenvector ϕ_k. Note that the displacement states are weighted by the natural frequencies, thus making the displacement states comparable to velocity states. The variable $\mathbf{\Lambda}$ contains the locations of a set of p actuators and q sensors (i.e., $\mathbf{\Lambda}$ is a vector of $p = q$ components, whose values indicate the node number where each pair sensor/actuator is placed). Finally, the value of t_f is the simulation time to obtain the PI, which must be large enough to achieve the steady state of $g(\mathbf{z})$ (i.e., the weighted vector $\mathbf{x}_{s_W} \cong 0$).

3 Simulation results

Note that the problem of finding $\mathbf{z} = [\mathbf{K}, \mathbf{\Lambda}]$, which minimizes $g(\mathbf{z})$ is a hard optimization problem, in which the traditional optimization method (gradient-based approaches or similar) used in [4] presents these main problems: ii) solution may be local, advising the optimization of each possible sensor-actuator configuration and with a set of initial condition for gain matrix, ii) unlike reference [11], where the cost function can be obtain analytically for a set of initial condition (i.e., the computation time for each iteration is negligible), the control scheme of Figure 1 must simulate since it considers the stroke and force saturation of actuator together with high and low pass filters and iii) computation time may be unaffordable for complex applications, like the presented herein.

Therefore, in order to limit the computation time and to guarantee a good enough solution, the nodes to place the actuator/sensors pairs have been previously selected based in our experience. Thus, the two chosen nodes are 369 and 82. Note that the node 369 is good to cancel 1st,

2nd, 5th, 7th and 9th mode whereas node 82 is good to cancel 3rd, 4th, 6th, 8th and 10th mode (see Figure 3).

The common design parameters are: i) the cut-off frequencies are 2 Hz and 20 Hz for the low and high pass filters, respectively, ii) the actuator used is the APS Dynamics Model 400 Shaker, where the stroke and voltage saturation are 7.9 mm and 2 V, respectively, and iii) $\alpha = 0.3547$ (see Equation (6)).

The MATLAB function *fminsearch* is used to find the optimal value of $\mathbf{K}$ for: i) a SISO AVC with the pair sensor/actuator located at node 369, ii) a SISO AVC with the pair sensor/actuator located at node 82 and iii) a MIMO AVC with the two pairs of sensor/actuator located at nodes 369 and 82. The results are

$$\text{SISO at node 369: } \mathbf{K} = 2214.9,\ g(\mathbf{z}) = 2.2210^{-5} \tag{9}$$

$$\text{SISO at node 82: } \mathbf{K} = 2423.4,\ g(\mathbf{z}) = 9.0610^{-5} \tag{10}$$

$$\text{MIMO at nodes 369 and 82: } \mathbf{K} = \begin{bmatrix} 1992.9 & 0 \\ \cong 0 & 1234.2 \end{bmatrix},\ g(\mathbf{z}) = 1.6710^{-5} \tag{11}$$

Note that the functional $g(\mathbf{z})$ is minimum when MIMO AVC is used. In addition, the 1st, 2nd, 5th, 7th and 9th mode are more important in the system response since that the SISO at node 369 can obtain a value of $g(\mathbf{z}) = 2.2210^{-5}$. However, the reduction of MIMO respect to SISO at node 369 is of 24.77 %, which shows that a MIMO is necessary to reduce the vibration of all floor (i.e., the vibration level due to 3rd, 4th, 6th, 8th and 10th mode).

This issue can be also illustrated by checking time responses. Five nodes (82, 88, 327, 355 and 360) are chosen to excite (with a normalized heel-drop) the first five vibration modes in order to show the performance of the controllers (SISO at nodes 369 and 82 and MIMO). The nodes 333 and 90 are monitored to show the vibration level (peak acceleration and settling time). The settling time is defined as the time taken for the response to fall and remain within some specified percentage of the maximum peak value of the acceleration response. For the sake of simplicity, here it is calculated as the time taken for the acceleration response to fall and remain within the range of 0.005 m/s^2. Note that nodes 333 and 90 show the vibration level corresponding to the 1st, 2nd, 5th, 7th and 9th mode and to the 3rd, 4th, 6th, 8th and 10th mode, respectively.

Figure 4 shows the simulated time response of node 333 for a normalized heel-drop excitation at nodes 82, 88, 327, 355 and 360 for: no controlled case, the SISO AVC at node 369, the SISO AVC at node 82 and the MIMO AVC at nodes 369 and 82. Note that the vibration reduction level is only significant when SISO at node 369 and MIMO AVC is used. In addition, the SISO at node 82 has a small effect at vibration reduction since this SISO AVC can only reduce the vibration of 3rd, 4th, 6th, 8th and 10th mode, which cannot be cancelled from node 82.

Figure 5 shows the simulated time response of node 90 for a normalized heel-drop excitation at nodes 82, 88, 327, 355 and 360 for: no controlled case, the SISO AVC at node 369, the SISO AVC at node 82 and the MIMO AVC at nodes 369 and 82. Note that the vibration reduction level is only significant when SISO at node 82 and MIMO AVC is used. In addition, the SISO at node 369 has a small effect at vibration reduction since this SISO AVC can only reduce the vibration of 1st, 2nd, 5th, 7th and 9th mode, which cannot be cancelled from node 369.

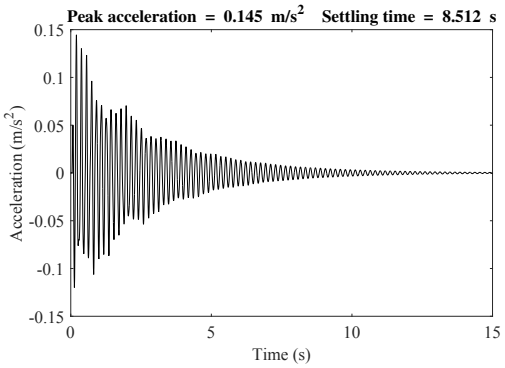

(a) Without AVC

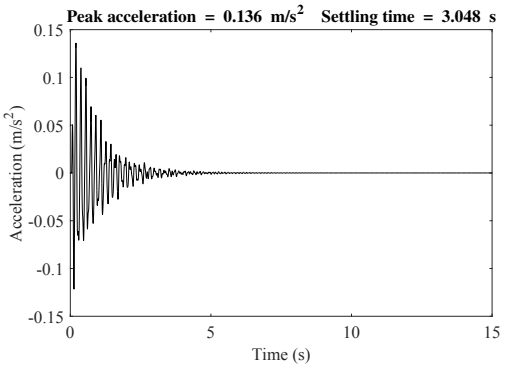

(b) SISO at node 369

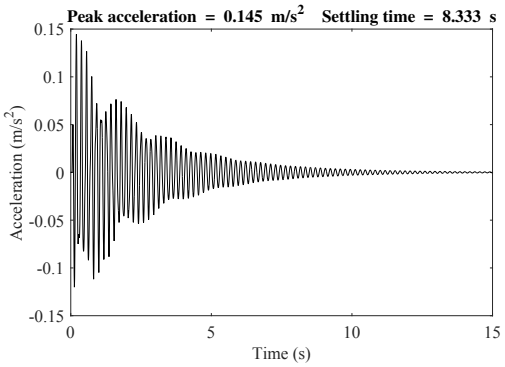

(c) SISO at node 82

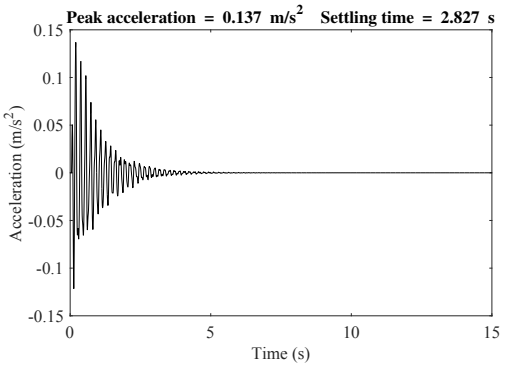

(d) MIMO at nodes 369 and 82

Figure 4: Simulated time response of node 333 for a normalized heeldrop excitation at nodes 82, 88, 327, 355 and 360.

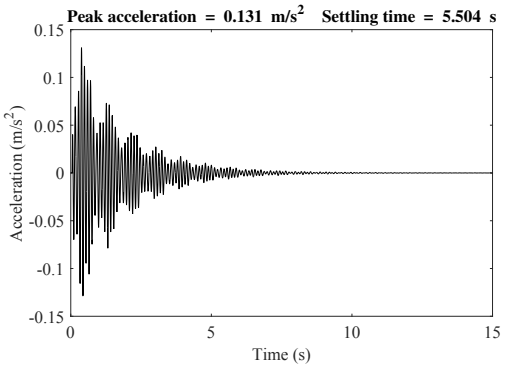

(a) Without AVC

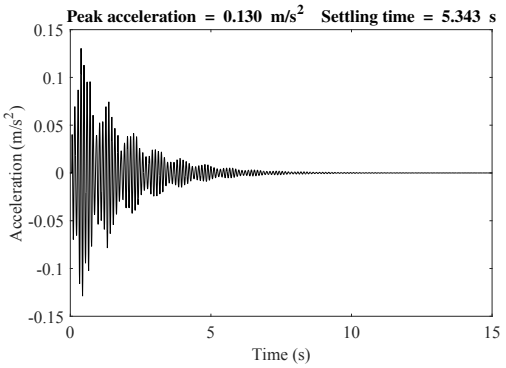

(b) SISO at node 90

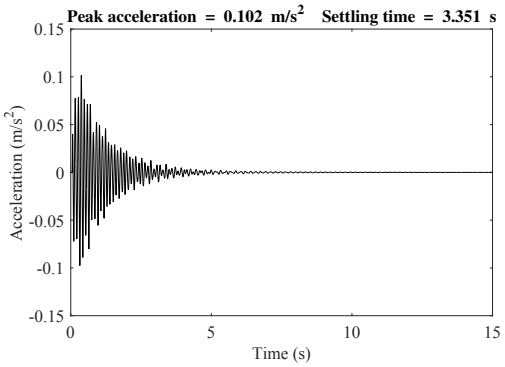

(c) SISO at node 82

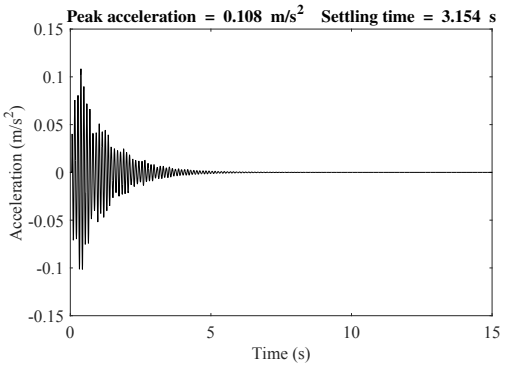

(d) MIMO at nodes 369 and 82

Figure 5: Simulated time response of node 90 for a normalized heeldrop excitation at nodes 82, 88, 327, 355 and 360.

4 Conclusions

This work has shown an example of a multi-input multi-output (MIMO) active vibration control (AVC) applied to a dining room floor of a primary-secondary school sited in Madrid (Spain), where the use of MIMO AVC shows a significant advantage as compared to single-input single-output AVCs. The floor structure model has been obtained with ANSYs, where the finite element model has been validated experimentally. The structure controlled by SISO and MIMO has been simulated with MATLAB-SIMULINK.

Finally, this work has shown the limitation of using traditional optimization method (gradient-based approaches or similar) since that it was practically impossible to analyze all the structures nodes. Therefore, the location of the pairs of actuator/sensor was decided by the authors' experience.

Therefore, two future works should be done. The first one must consider modern global optimization method, which can solve this optimization problem in affordable computation time. The second one must be the real implementation of this MIMO AVC in this dining room floor.

5 ACKNOWLEDGMENTS

The authors acknowledge the financial support provided by the Ministry of Economy and Competitiveness of the Government of Spain to make this work possible by funding from the REVES-P Research Project, with reference DPI2013-47441. The authors also acknowledge the financial support provided by Project VibraStruNET with reference BIA2015-71942-REDT.

REFERENCES

[1] Ebrahimpour A. and Sack R.L.. A review of vibration serviceability criteria for floor structure. *Comput. and Struct.*, 83(28-30):2488-2494, 2005.

[2] Maraveas C., Fasoulakis Z.C. and Tsavdaridis K.D. A Review of Human Induced Vibrations on Footbridges. *Am. Jour. of Engng. and Appl. Scien.*, 8(4):422-433, 2015.

[3] Hudson M.J. and Reynolds P. Implementation considerations for active vibration control in the design of floor structures. *Engng. Struct.*, 80:153-162, 2012.

[4] Pereira E., Díaz I.M., Hudson E.J. and Reynolds P.. Optimal control-based methodology for active vibration control of pedestrian structures. *Engng. Struct.*, 80:153-162, 2014.

[5] Wang X., Díaz I.M. and Pereira E. MIMO control design including input-output frequency weighting for human-induced vibrations, *EACS 2016(6th European Conference on Structural Control)*, Sheffield, England: 11-13 July 2016.

[6] ISO2631-1. *Mechanical vibration and shock evaluation of human exposure to whole-body vibration. Part 1: General requirements.* International Organization for Standardization, 1997.

[7] ANSYS Multiphysics, Release 10.0, Help System, Ansys Elements Reference, ANSYS, Inc.

[8] Smith A.L., Hicks S.J. and Devine P.J. Design of floors for vibration: a new approach (P354). The Steel Construction Institute; 2007.

[9] Gawronski W. K. *Advanced Structural Dynamics and Active Control of Structures*. Mechanical Engineering Series, Springer Link, 2004.

[10] Griggs W.M., AndersonB.D. and Lanzon A. A "mixed" small gain and passivity theorem in the frequency domain, *Systems & Control Letters*, 56(9-10):596-602, 2007.

[11] Hanagan L.M., Kulasekere E.C., Walgama K.S. and Premaratne K. Optimal Placement of Actuators and Sensors for Floor Vibration Control, *Journal of Structural Engineering*, 126(12):1380-1387, 2000.

Vibration control of a dining hall: structure modelling

Jaime H. García-Palacios*, José M. Soria[*], Xidong Wang[*], Iván M. Díaz[*] and Emiliano Pereira[†]

[*] ETSI de Caminos, Canales y Puertos
Universidad Politécnica de Madrid (UPM). Prof. Aranguren s/n. 28040. Madrid, Spain
e-mail: jaime.garcia.palacios@upm.es, jm.soria@upm.es, ivan.munoz@upm.es, wangxidong@caminos.upm.es. web page: http://www.upm.es

[†]Universidad de Alcalá de Henares
Escuela Politécnica Superior, 28805, Alcalá de Henares (Madrid), Spain
e-mail: emiliano.pereira@uah.es

ABSTRACT

The dining hall studied through this paper is consider to be a lively structure, In an attempt of designing vibration control strategies, the research group have been testing experimentally the structure in order to update a finite element model (FEM) to be used for control design. The control strategies will include passive and active mass dampers [1] considering multi-input and multi-output based-design [2].

The following steps are carried out: first, architectural drawings have been used to sketch up a finite element model of the structure (FEM). However, some uncertainties remain unsolved due to the difficulties to determine the joint between the different structural components as well as some structural dimensions that were hiding to visual inspection.

Second, an experimental campaign is undertaken with two different tests. The Operational Modal Analysis (OMA) with high sensitivity PCB accelerometers is carried out to extract the fundamental frequencies, damping ratios and modal shapes of the structure. Special care is taken with modal frequencies smaller than 10 Hz within the range of human perception. With these results, a first calibration of the FEM is carried out and the second experimental test is planned. To overcome the limitation introduced by the OMA to obtain the associated mass of each identified frequency a frequency-response-function test analysis is conducted. AnAPS400 shaker is placed at maximum modal identified displacements and a chirp signal in the range if interest is used as the excitation input. Measurements were carried out using a NI CompactRIO platform. These data is necessary for the design of the control system, and adds important information to the calibration process

Thirdly, the FEM is finally calibrated according to the results of both tests. This process requires identifying the variables associated to possible uncertainties, geometrical, materials and boundary conditions, as well as their allowed range of variation. For each one of this set a sensitivity analysis is performed to discard some of the variables according to its influence in the calibration. The most sensible ones are used in a Montecarlo simulation on the parameter set to identify the best calibrated model according to a predefined objective function that takes into account the modal frequencies and modal shapes. The structural model is defined in ANSYS where the modal estimators are for each defined set of variables. The set of variables for the different models and the evaluation of the objective function are programmed into Matlab. An interface between both programs is also developed.

The obtained model accurately represents the dynamic behaviour of the floor under study.

REFERENCES

[1] X. Wang, I. M. Díaz, E. Pereira and Q. Xu, "Optimal TMD-based control for human-induced vibration", 3rd International Conference on Mechanical Models in Structural Engineering, Seville, Spain: 24-26 June 2015.

[2] X. Wang, I. M. Díaz, E. Pereira, "MIMO control design including input-output frequency weighting for human-induced vibrations", EACS 2016 – 6th European Conference on Structural Control, Sheffield, England: 11-13 July 2016.

A Soft Electromagnetically Controlled Robotic Gripper to Manipulate Delicate Food Products

Young T. Choi, Christine M. Hartzell, and Norman M. Wereley*

*Department of Aerospace Engineering
University of Maryland, College Park, Maryland, USA 20742
Email: wereley@umd.edu - Web page: http://aero.umd.edu/faculty/wereley

ABSTRACT

This study addresses the design and testing of a novel soft robotic gripper actuated by an electromagnet with which to handle of unpackaged delicate fruits in the food industry. Traditional rigid mechanical grippers are not applicable to manipulate delicate food products because their gripping action can easily bruise or damage fragile food products during handling due to hard contacts. In addition, the size, shape and weight of individual food items can vary widely. Because of this statistical variation and the need for delicate handling, the system integration and control requirements for a soft gripper are sufficiently complex that conventional rigid mechanical grippers are not a practical solution when handling delicate food products. To overcome the disadvantages of rigid mechanical grippers, a soft robotic gripper, which can softly and gently hold fragile objects by inflating flexible compliant elastomeric fingers, have been recently developed. The compliance of the soft grippers can be controlled by adjusting a pressure level of air and safe grasping of sensitive objects can be achieved because excessive gripping force is intrinsically avoided. In addition, when using pressurized air as an actuating source, hygienic risks during handling of food products is minimized. But, soft pneumatic grippers require a bulky and noisy compressor to supply pressurized air to the soft elastomeric fingers. In this study, the design of a soft robotic gripper, operated by an electromagnet, is proposed and its feasibility for soft gripping action were validated experimentally. A soft gripper configured as two opposing fingers, was designed in this study to achieve compactness, lightness, simple design, and to reduce system complexity. The flexible two-finger appendages were 3D printed via fused filament fabrication (FFF) method using soft elastic thermoplastic polyurethane (TPU) filament material. Thus, the manufacturing process was simple and quick, and production cost was low. The soft electromagnetic gripper was constructed by mounting the flexible two-finger appendage atop an electromagnet. A permanent magnet was attached to the bottom center of the two-finger part. When the electromagnet is activated by applied current input, the attractive electromagnetic force pulls the magnet attached to the two-finger part toward the electromagnet. As a result, the two opposing fingers are closer against each other and a pinch grasp occurs when an object is placed between these two fingers. In the absence of current input, these two fingers act like passive flexible elastomeric fingers, thus releasing the object. If the polarity of the electromagnet is reversed by changing the direction of current input, the repulsive force pushes the magnet against the electromagnet, thereby letting the two fingers opened wider so as to accommodate larger object. In this study, the gripping displacement and the holding force of the soft gripper will be experimentally evaluated by different initial gaps between the magnet and the electromagnet. In addition, feasibility of the soft electromagnetic gripper will be demonstrated by grasping a population of different sizes, shapes and weights of delicate fruit items.

REFERENCES

[1] G. Rateni, M. Cianchetti, G. Ciuti, A. Menciassi, and C. Laschi, "Design and development of a soft robotic gripper for manipulation in minimally invasive surgery: a proof of concept," *Meccanica*, Vol. **50**, pp. 2855-2863, (2015).

[2] T. Weyrauch, "Development of novel elastomer grippers for a flexible and hygienic handling of unpackaged food," *iFood Conference 2013*, Hannover, Germany, 8-10 October, (2013).

[3] R. Sam and S. Nefti, "Design and feasibility tests of flexible gripper for handling variable shape of food products," *10th International Conference on Control, Automation, Robotics and Vision*, ICARCV 2008, pp. 1684-1689 (2008).

VIII ECCOMAS Thematic Conference on Smart Structures and Materials
SMART 2017
A. Güemes, A. Benjeddou , J. Rodellar and Jinsong Leng (Eds)

AGGREGATION KINETICS OF CARBONYL IRON PARTICLES UNDER MAGNETIC FIELDS: INFLUENCE OF PARTICLE-WALL INTERACTIONS AND CONFINEMENT

KESHVAD SHAHRIVAR*, ELIZABETH CARREÓN-GONZÁLEZ*, RODRIGO AGÍS† AND JUAN DE VICENTE*

*Department of Applied Physics, University of Granada,
Faculty of Science, 18071-Granada, Spain

†Department of Computer Architecture and Technology, ETSI Informática y de Telecomunicación,
CITIC-UGR CIC, University of Granada, Granada, Spain

emails: kshahrivar@ugr.es, invasor_cat@hotmail.com, ragis@ugr.es, jvicente@ugr.es

Key words: Magnetorheological fluids, aggregation kinetics, microchannels, carbonyl iron, magnetic latex

Abstract. Magnetorheological (MR) fluids are smart colloids that exhibit a dramatic rheological change upon the application of a magnetic field as a result of the field-promoted interparticle aggregation. In this presentation we show our most recent work on the aggregation kinetics of carbonyl iron particles of use in the formulation of MR fluids of commercial interest. First, we demonstrate the importance of experimental conditions in the aggregation kinetics. In particular, we demonstrate the effect of the carrier fluid viscosity and surfactant addition. Second, we demonstrate the importance of magnetic field strength. In particular, we demonstrate that mean cluster size versus time curves can be re-scaled following a purely deterministic aggregation process. Finally, we show that the confinement of the field-induced structures results in a long-time plateau in the mean cluster size presumably as a result of the predominant lateral repulsive interactions between the chain like structures.

INTRODUCTION

Materials whose properties (mechanical, optical, etc…) vary considerably in the presence of an external stimulus are known as smart materials. Magnetic suspensions are a subclass of smart materials whose rheological characteristics remarkably change in the presence of a magnetic field. In particular, magnetorheological fluids (MRFs) are (magnetic) suspensions of magnetizable micron-sized particles dispersed in a carrier fluid. Typically, these micronsized particles are made of iron coming from the thermal decomposition of iron pentacarbonyl (so called carbonyl iron). This is so because of their large purity and therefore large saturation magnetization. MRFs can exhibit changes in apparent viscosity of several orders of magnitude for fields of the order of a few kA/m. Recently, MRFs have received considerable attention in the field of mechanical engineering for actuation and motion control.

Some examples are shock absorbers, dampers, clutches and rotary brakes. However, interest from other research areas such as thermal energy transfer, precision polishing, chemical sensing and biomedical applications shows the potential of these materials to be employed in many other different disciplines [1, 2].

In the linear magnetization regime, under a magnetic field H_0, an isolated magnetizable sphere of diameter d and relative permeability μ_{pr}, suspended in a media of relative permeability μ_{cr}, acquires a magnetic moment:

$$m = \frac{\pi \mu_0 \mu_{cr} \beta d^3 H_0}{2} \tag{1}$$

Here, $\beta \equiv (\mu_{pr} - \mu_{cr})/(\mu_{pr} + 2\mu_{cr})$ is the contrast factor. In the case of carbonyl iron suspensions $0 < \beta < 1$.

Once the particles become magnetized, they interact forming elongated structures in the field direction. The total interaction energy between two linear magnetic moments reads as follows:

$$U = \frac{Cm^2}{r^3}(1 - 3cos^2\theta) \tag{2}$$

Where $C = \frac{1}{4\pi\mu_0\mu_{cr}}$, r is the center-to-center distance and θ is the angle between the dipole moment vector.

The magnitude of the magnetic interaction energy between two parallel magnetic moments ($r = d, \theta = 90°$) relative to the thermal energy ($\kappa_B T$) is the so-called λ ratio or coupling coefficient:

$$\lambda \equiv \frac{Cm^2}{d^3 \kappa_B T} \tag{3}$$

When $\lambda \gg 1$, magnetostatic particle interactions overcome thermal motion, resulting in the formation of field induced structures. However, for very small λ values, Brownian motion dominates and field-induced aggregates are absent. In this work, we are specifically interested in carbonyl iron suspensions where $\lambda \gg 1$, because they serve as a basis for commercial MRFs formulations.

BACKGROUND AND MOTIVATION

The aggregation kinetics of carbonyl iron particles in suspension has not been reported in the literature yet. Instead, there are plenty of experimental and simulation data available in the literature on magnetic latex suspensions and inverse ferrofluids (i.e. magnetic holes) for a wide range of magnetic field strengths (typically in the range $1 < \lambda < 100$). Available reports

describe the aggregation process in terms of the evolution of the probability density of clusters of size s at time t, $n_s(t)$. The most frequently used statistical variable, derived from the cluster size distribution, is the so-called mean cluster size (i.e. weight average cluster size):

$$S(t) = \sum_s s^2 n_s(t) \Big/ \sum_s s n_s(t) \tag{4}$$

Experiments, theoretical developments and simulation data demonstrate that, once the tip-to-tip aggregation process begins, the mean cluster size follows a power-law behavior as a function of time, $S(t) \sim t^z$. Theories and simulations predict $z = 0.5 - 0.6$ [3-5]. However, experimental z values are typically lower and the scatter observed in the different publications available is generally unacceptably large [5, 6]. It seems that the particular z value is strongly sensitive to the experimental conditions. In this work we will carefully tune the suspension formulation in order to elucidate its impact in the aggregation kinetics. In particular, we will explore the influence of the carrier fluid viscosity and surfactant concentration.

Additionally, most of the previous works demonstrate that the aggregation process involved in the case of magnetic latexes and inverse ferrofluids is reasonably well described by Scaling Theories where Brownian motion plays a crucial role in the diffusion of the particles [7]. However, in the case of interest in the work, carbonyl iron particles are too big in size and Scaling Theory is not expected to be applicable. Instead, a deterministic aggregation theory should be capable to explain the experimental observations [8, 9]. In this work, we will demonstrate that carbonyl iron suspensions are very well described using a deterministic aggregation theory and particle-level simulations.

Finally, most of the previous works reported in the literature focus on the aggregation kinetics of magnetic particles in open domains. However, in any commercial application, suspensions are confined in narrow gaps. Therefore, in this work, we will study the aggregation process in rectangular PDMS microchannels of different widths.

MATERIALS AND METHODS

Carbonyl iron particles used in this work where obtained from BASF SE Germany (Grade EW). These particles are 3.0 microns diameter and contain 96.8 % iron in the bulk. A thin silica layer exists surrounding the particles to facilitate their dispersion in solution. The suspensions were prepared by mechanical dispersion of the carbonyl iron powder in glycerol (Sigma Aldrich). In some cases, sodium dodecyl sulfate SDS (1 wt%) was also added to the suspensions. We worked at a low particle concentration (volume fraction $\phi \approx 5 \times 10^{-4}$, surface fraction $\phi_{2D} \approx 0.02$).

The carbonyl iron suspensions were confined in polydimethylsiloxane (PDMS) microchannels prepared using conventional Soft Lithography techniques. The microchannels used had a constant depth of 25 microns and their width changed between 75 and 1000

microns. Once the suspensions were introduced in the microchannels, they were allowed to settle to get a 2D monolayer. The aggregation process was monitored in an inverted optical microscope (Leica DMI 3000B) and the magnetic field was superimposed in the transversal direction to the microchannel. Finally, image analysis was carried out using a Matlab subroutine.

Particle level simulations were also carried out assuming non-Brownian buoyant Hard Spheres interacting through dipolar magnetostatic forces under Stokes' drag approximation. In more detail, forces acting on the particles were:

$$F^{rep} = -\frac{3Cm^2}{d^4} exp\left(-\frac{r-d}{0.01d}\right)\hat{e}_r \tag{5}$$

$$F^{mag} = \frac{3Cm^2}{r^4}[(3cos^2\theta - 1)\hat{e}_r + sin(2\theta)\hat{e}_\theta] \tag{6}$$

$$F^{drag} = -3\pi\eta d\frac{dx}{dt} \tag{7}$$

Here η represents the carrier fluid viscosity. The equation of motion was solved in the dimensionless form using the following characteristic length, force and time scales: $l_c = d$, $f_c = \frac{3Cm^2}{d^4}$, and $t_c = \frac{\pi\eta d^6}{Cm^2}$ [10, 11]. The dimensionless variables are denoted with an asterisk (e.g. $t^* \equiv t/t_c$).

Simulations were carried out in rectangular domains in 2D using Non-slip Boundary Conditions on the confining walls and Periodic Boundary Conditions in the direction perpendicular to the magnetic field. The equations of motion for each particle are integrated numerically using an explicit Euler method with a dimensionless time step $\Delta t = 1 \times 10^{-3} t_c$.

RESULTS AND DISCUSSION

Figure 1a shows the mean cluster size as a function of time, $S(t)$, for carbonyl iron suspensions in glycerol:water mixtures. It is clear that the initial aggregation state is strongly affected depending on the glycerol concentration in the formulation. Bigger aggregates are observed at the beginning of the aggregation process the smaller the amount of glycerol in the suspension. This is something expected because increasing the glycerol concentration results in a more viscous carrier and therefore a slower diffusion of the particles.

Figure 1b shows the influence of SDS concentration in the aggregation kinetics. In the absence of SDS the mean cluster size remains essentially constant suggesting that carbonyl iron particles are stuck on the bottom wall. Interestingly, upon increasing the SDS concentration, the mean cluster size increases suggesting that the particles are capable to slide/roll along the wall forming the chain-like structures. The saturation for SDS

concentrations above 0.7 wt% suggest that particles are free to move for so high concentrations.

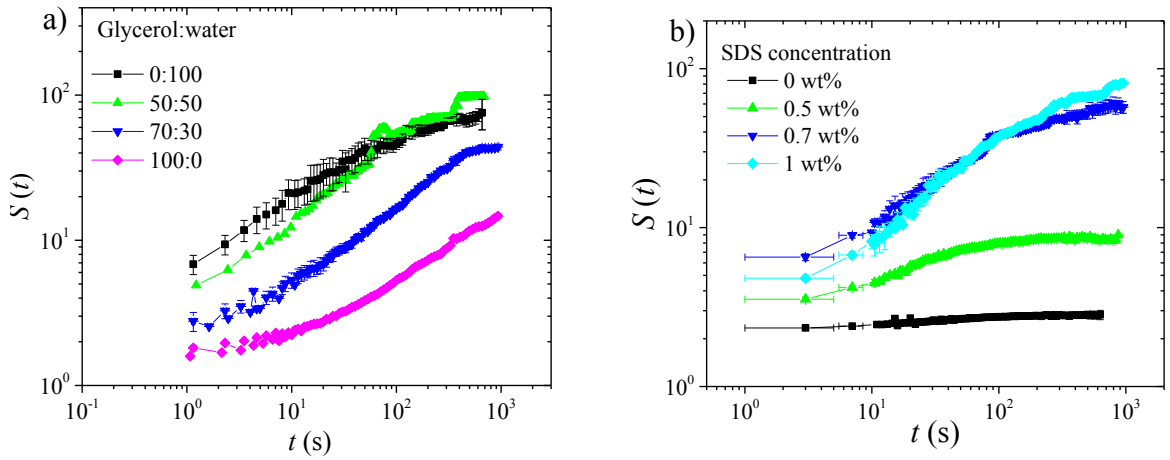

Figure 1. Evolution of mean cluster size. a) Different glycerol/water mixtures (no SDS). b) Glycerol:water 100:0 and different SDS concentrations.

Simulations were carried out for a wide range of microchannel widths $W^* \epsilon [25 - 100]$ and surface fractions $\phi_{2D} \epsilon [0.01 - 0.05]$. Results demonstrate that the mean cluster size can be simply scaled as follows:

$$S(t) = 1 + (t/t_s)^b \tag{8}$$

with $t_s = 1.07 \times 10^{-2} \phi_{2D}^{-2.61} W^{*-0.23} t_c$ and $b = 0.55$.

Simulation results are shown in Figure 2 together with experimental data in dimensionless form. As observed a very good agreement is found whatever the glycerol:water concentration for the larger SDS concentrations studied.

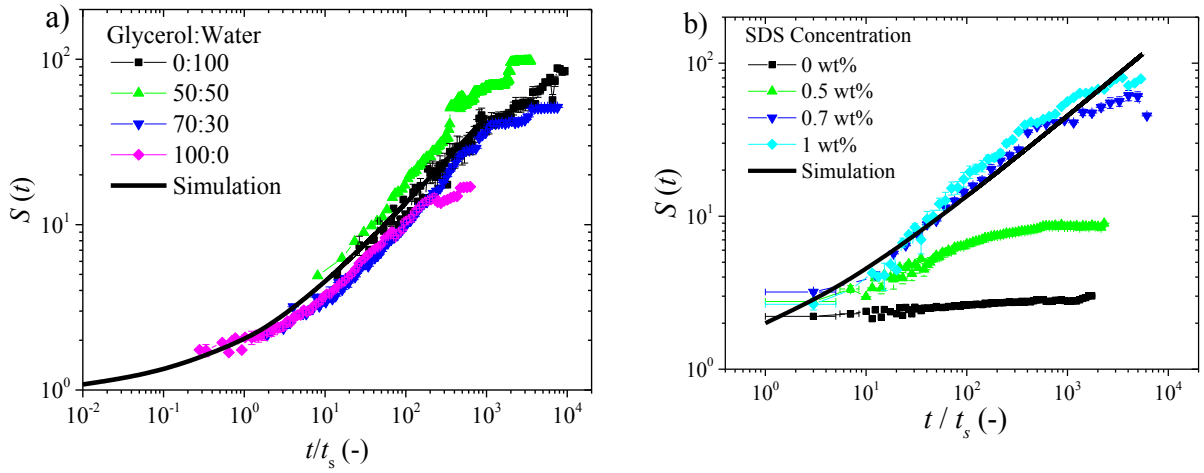

Figure 2. Mean cluster size as a function of scaling time obtained from molecular dynamic simulation. a) Glycerol/water mixture. b) Different SDS concentrations.

The influence of the microchannel width is demonstrated in Figure 3a. When the width is small enough, the mean cluster size is observed to reach a long-time plateau. This is expected because the chain-like aggregates do not have sufficient space to grow up. Interestingly, a similar observation comes from particle level simulations (see Figure 3b). Obviously, in this case, Equation (8) is not capable to predict the long-time plateau. In an attempt to capture the full aggregation curve we propose a semiempirical expression:

$$S(t) = 1 + (S_{max} - 1)(1 + (t/t_d)^{\alpha})^{\omega} \tag{9}$$

Here, t_d is a deviation time corresponding the point where the mean cluster size $S(t)$ levels off to saturation. The parameter α represents the width of the transition region ($t = t_d$): the slope decreases when $|\alpha|$ decreases. Finally, the slope of power-law region is described by ω. Equation (9) was fitted to the simulation data for a range of particle concentrations and microchannel widths. The resulting best fitting parameters -S_{max}, t_d, α, and ω- as obtained from simulations are included in Table 1. As expected, in view of Table 1, the critical time t_d is strongly dependent on area fraction and dimensionless microchannel width. On the other hand, the slope of $S(t)$ in log-log scale corresponds to the dynamic exponent z. In this case, $z = 0.89\phi_{2D}^{0.2}W^{*0.05}$.

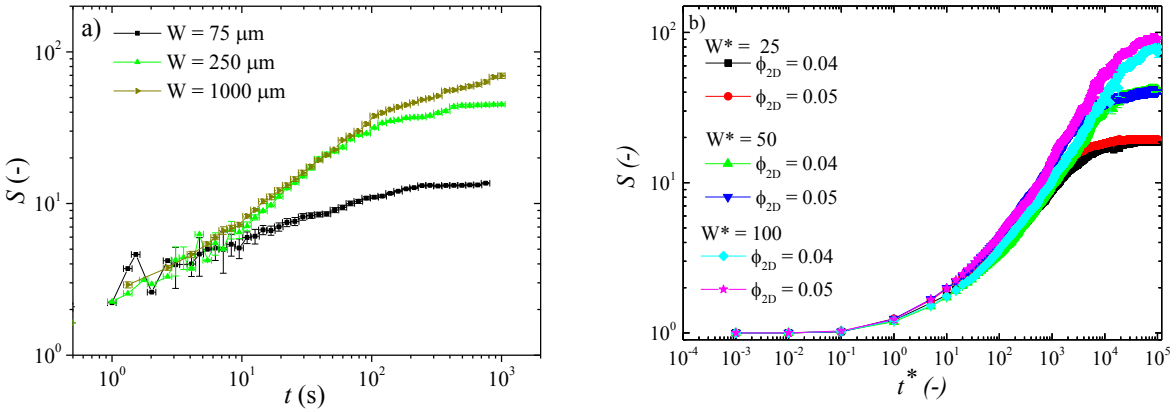

Figure 3. Influence of microchannel width. a) Experimental results. b) Molecular dynamic simulations. In experiments and simulation long-time plateau is observed.

Table 1. Best fitting parameters to the simulation curves using Equation 9.

$\boldsymbol{S(t) = 1 + (S_{max} - 1)(1 + (t/t_d)^{\alpha})^{\omega}}$	
$\boldsymbol{S_{max}}$	$0.97W^* - 5.98$
$\boldsymbol{t_d}$	$2.3 \times 10^{-4}\phi_{2D}^{-3.2}W^{*1.91}t_c$
$\boldsymbol{\alpha}$	$-2.4 \times 10^{-2}\phi_{2D}^{-1.05}W^{*0.2}$
$\boldsymbol{\omega}$	$-36.26\phi_{2D}^{1.25}W^{*-0.15}$

In Figure 4 we plot the experimental data for a wide range of microchannel thicknesses together with predictions from Equation (9). Interestingly, it is observed a reasonably good collapse between experiments and simulations without any free fitting parameters.

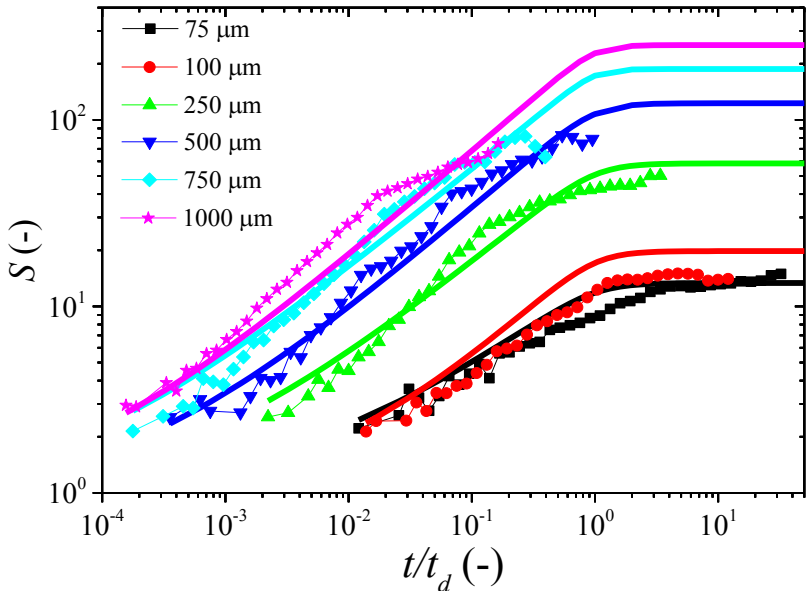

Figure 4. Mean cluster size of carbonyl iron as a function of reduced time for experiments (symbols) and theoretical prediction (lines) for different channel widths.

CONCLUSIONS

We study the aggregation kinetics of dilute carbonyl iron suspensions in rectangular microchannels at $\lambda \gg 1$ using video-microscopy, image analysis and particle-level dynamic simulations. We show that the carrier fluid viscosity determines the time scale for aggregation. On the other hand, friction strongly determines the aggregation rate. Moreover, we also studied the influence of microchannel width (75-1000 μm) in the aggregation process. The effect of channel width is found to be crucial in the dynamic exponent and in the saturation (long time) mean cluster size. On the contrary, it has no effect in the onset of the tip-to-tip aggregation process.

REFERENCES

[1] Wereley, N. *Magnetorheology: advances and applications*, Royal Society of Chemistry, Vol. 6., (2013).

[2] de Vicente, J., Klingenberg, D. J. and Hidalgo-Alvarez, R. Magnetorheological fluids: a review. *Soft Matter* (2011) **7(8)**:3701–3710.

[3] Fermigier, M. and Gast, A. P. Structure evolution in a paramagnetic latex suspension.

J. Colloid Interface Sci. (1992) **154(2)**:522–539.

[4] Dominguez-Garcia, P., Melle, S., Pastor, J. M. and Rubio, M. A. Scaling in the aggregation dynamics of a magnetorheological fluid. *Phys. Rev. E* (2007) **76(5)**: 051403.

[5] Černák, J., Helgesen, G. and Skjeltorp, A. T. Aggregation dynamics of nonmagnetic particles in a ferrofluid. *Phys. Rev. E* (2004) **70(31)**:031504.

[6] Erb, R. M., Krebs, M. D., Alsberg, E., Samanta, B., Rotello, V. M. and Yellen, B. B. Beyond diffusion-limited aggregation kinetics in microparticle suspensions. *Phys. Rev. E* (2009) **80(5)**:051402.

[7] Vicsek, T. and Family, F. Dynamic scaling for aggregation of clusters. *Phys. Rev. Lett.* (1984) **52(19)**:1669.

[8] See, H. and Doi, M. Aggregation Kinetics in Electro-Rheological Fluids. *J. Phys. Soc. Jpn.* (1991) **60(8)**:2778–2782.

[9] Reynolds, C. P., Klop, K. E., Lavergne, F. A., Morrow, S. M., Aarts, D. G. A. L. and Dullens, R. P. A. Deterministic aggregation kinetics of superparamagnetic colloidal particles. *J. Chem. Phys.* (2015) **143(21)**:214903.

[10] Klingenberg, D. J. and Zukoski, C. F. Studies on the steady-shear behavior of electrorheological suspensions. *Langmuir* (1990) **6(1)**:15–24.

[11] Kittipoomwong, D., Klingenberg, D. J. and Ulicny, J. C. Simulation of Bidisperse Magnetorheological Fluids. *Int. J. Mod. Phys. B* (2002) **16(17n18)**:2732–2738.

CHARACTERIZATION OF CARBON BLACK-FILLED NATURAL RUBBER AND SILICONE MAGNETORHEOLOGICAL ELASTOMERS UNDER PURE SHEAR LOADING

Siddaiah Yarra[a], Gokhan Pekcan[a], Majid Behrooz[b] and Faramarz Gordaninejad[b]

[a] Civil and Environmental Engineering Department and [b] Mechanical Engineering Department
University of Nevada, Reno, Nevada 89557, USA
e-mail: faramarz@unr.edu

Keywords: magnetorheological elastomers, natural rubber, platinum silicone.

Abstract. This study presents a mechanical characterization of carbon black-filled natural rubber and silicone magnetorheological elastomers (MREs). ASTM standard MRE samples with silicone matrix and carbon black fillers are fabricated and their properties are compared with those of carbon black-filled natural rubber-based isotropic MREs. The mechanical properties of the MREs are investigated with a double-lap shear experimental setup. The effect of loading parameters such as shear strain, loading frequency, and magnetic field on the shear moduli of MRE are presented. Experimental results show that adding carbon black improves not only the passive modulus of MRE, but also the MR effect.

1. INTRODUCTION

Magnetorheological elastomers are a class of materials whose properties can be regulated with an applied external magnetic field. MREs are fabricated by adding micron-sized iron particles to a polymeric matrix. If a magnetic field is not used during the curing process, MRE material maintains an isotropic structure. Isotropic MREs with large and irregular shaped iron particles are known to show a higher MR effect (percentage change in moduli due to magnetic field) due to smaller distance between particles compared to isotropic MREs with regular carbonyl iron [1]. Pre-compressed isotropic MREs show higher elastic modulus when compared to isotropic MREs without pre-compression [2]. The MR effect of an isotropic MRE increases due to an increased magnetic field and loading frequency [3]. Gong et al. [4] showed that shear modulus of isotropic MREs can be increased up to 60% when subjected to 1.0 T magnetic field intensity. Furthermore, MREs with carbon black show higher tensile strength (56.8% increase) compared to MREs with no carbon black [5]. It was also demonstrated by [5] that MREs with carbon black can operate at higher temperatures due to their higher thermal stability. Isotropic MREs show a linear shear stress-strain behavior when the applied strain is less than 10% [6].

When a MRE is cured under a magnetic field, particles form chain-like structures that will result in an anisotropic MRE. Shear modulus and hysteresis damping of an anisotropic silicone MRE increases with an increased magnetic field [7-9]. Anisotropic MREs made of polyurethane shows 20% higher MR effect than anisotropic natural rubber MRE under a varying magnetic field of 0 to 0.395T [8]. Non-magnetic fillers in MRE mixtures can be used to modify the properties to achieve desired passive stiffness and damping levels. Chen et al. [10] concluded that adding carbon black to MRE improves the microstructure bonding, MR effect, and tensile

strength. Thickness and length of iron particle chains increase with an increased magnetic field; therefore, anisotropic MREs fabricated in a higher magnetic field show higher MR effect [11]. MRE has a short response time, in the order of milliseconds, with a reversible behavior under a magnetic field. Therefore, static and dynamic properties of MRE can be controlled in real time. Both isotropic and anisotropic MREs were studied experimentally as well as analytically and used in different vibration absorption applications such as adaptive tunable energy absorbers, isolators, and tunable stiffness engine mounts. MRE layers have been proposed in vibration absorbers for structural applications that can reduce the vibration transmissibility [12]. Also, using MRE isolators with an appropriate control strategy results in a reduction of acceleration and displacement in a scaled model of a building structure [13]. Lateral stiffness of a MRE base isolator can be increased up to 1,630% from quasi-static tests with increased electric current from 0 to 3 amp [14]. An isolator made with anisotropic MRE performs better under combined shear-compression than shear or compression only [15]. The natural frequency, stiffness, and damping of an anisotropic MRE isolator can be controlled by an applied current to electromagnets that supply magnetic field through MRE material. When the current increases from 0 amp to 1.5 amp, the natural frequency increases 103%, stiffness increases 330%, and damping increases 180%, respectively [15]. In the present study, two different MREs with different curing conditions, additives, and matrices are fabricated. The mechanical properties of MREs are experimentally evaluated under quasi-static monotonic and cyclic loadings. Experimental results demonstrate that adding carbon black improves the MR effect and the shear modulus of MREs.

2. FABRICATION OF NATURAL RUBBER AND SILICONE MREs

Elastomeric matrix was created by mixing TAP platinum silicone side A base and side B catalyst with a weight ratio of 1:1. Carbonyl iron particles (Grade-R-2410; High purity micro powder iron) of average sizes ranging from 5 to 8 microns were used for magnetic permeability, SR303 carbon black (provided by Sid Richardson) was used as an additive. Silicone-based anisotropic MREs are fabricated by mixing 80.5g of iron particles, 0.5g of carbon black and 18g of platinum silicone side A and side B in a beaker. After thoroughly mixing, the mixture was placed into a mold designed to produce ASTM standard size [16] MRE samples with the geometrical dimensions presented in Table 1. To remove air bubbles, the mold with mixture went through a two-step vacuum process. First, the mold was placed into a vacuum chamber without the top until the pressure reaches -70 kPA, and then with top the vacuum process was repeated. Finally, the mold was placed into the electromagnet and cured under 1.2 T magnetic field. Figure 1 (a) shows a sample of the aligned silicone MRE sample.

Isotropic MREs slabs with natural rubber (254 mm x 254 mm x 12.7 mm) were fabricated using milling technique with different carbon black percentages (0, 1, 2, 3, 4 and 5) at Akron Rubber Development Laboratory (Akron, OH, USA). The samples were cut to the ASTM standard size by Scougal Rubber Corp. (McCarran, NV, USA). Figure 1 (b) shows an isotropic rubber MRE sample. Recipe of different MRE samples is summarized in Table 2.



Figure 1. MRE samples using different polymeric material with: (a) silicone rubber and (b) Natural rubber.

Table 1: ASTM Standard Size of Specimens' Dimensions [16]

Units	Length	Width	Thickness
mm	40	16	5
Inches	1.6	0.625	0.2

Table 2: Chemical Composition of MRE Samples

Test ID	IP% (w/w)	CB% (w/w)	A% (w/w)	B% (w/w)	NR-TSR20 (w/w)
MRE-S-1	80.5	0.5	9.5	9.5	N/A
NR-S-2	76.0	5.0	N/A	N/A	19

3. MRE MICROSTRUCTURE ANALYSIS

Scanning Electron Microscope was used to observe the microstructure of silicone and rubber MREs. The samples were dipped in liquid nitrogen to achieve smooth sectional surface for imaging purposes. Then, the surface was coated with a thin layer of platinum and finally placed in the SEM machine. Accelerating voltage of 20 kV was used while taking pictures. Figure 2(a) demonstrates the iron particle chains in a 40%wt. iron particles and 15%wt. carbon black. SEM picture of isotropic rubber MRE sample with 80%wt. natural rubber and 5% carbon black is shown in Figure 2 (b). The anisotropic silicone MRE has the particle chains while in the rubber MRE particles are randomly dispersed that results in an isotropic MRE.

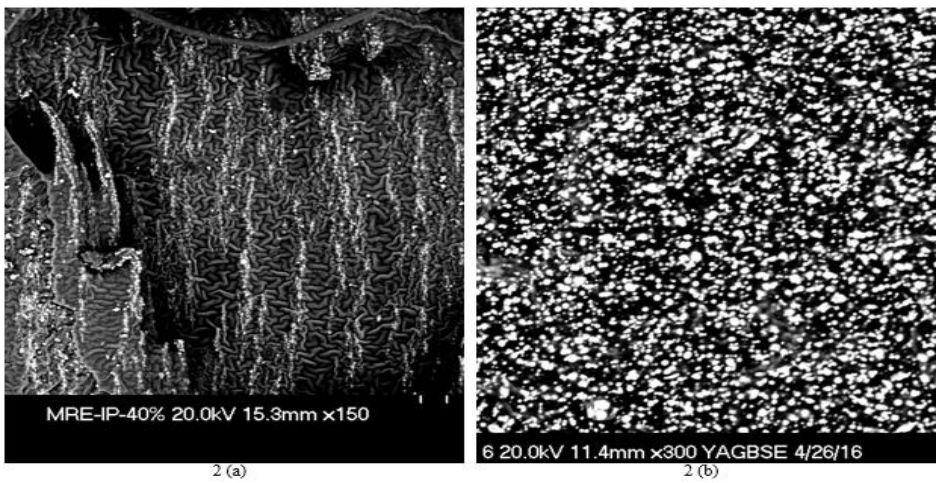

Figure 2. SEM image of the MREs fabricated at different curing conditions: (a) with a magnetic field; (b) without a magnetic field.

4. EXPERIMENTAL SETUP

To characterize the mechanical properties of MREs with different matrices, a special test setup was designed and fabricated as shown in Figure 2. This test setup was used for the application and control of shear strains with different loading frequencies and magnetic field intensities. As shown in Figure 2, electromagnets were used to apply the magnetic field.

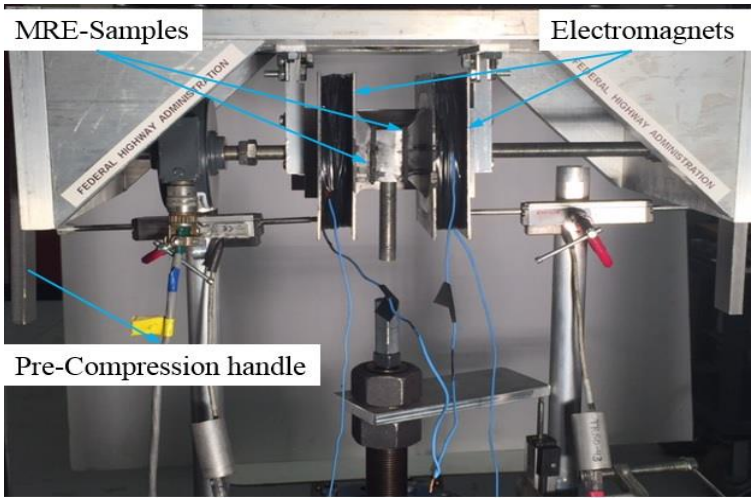

Figure 3. Double-lap shear test setup.

Experiments are performed with monotonic and cyclic tests under pure shear loading, different magnetic field intensities, and loading frequencies. Results are used to compute shear moduli of ASTM standard size samples. Table 3 shows test protocol of experiments.

Table 3: Test Protocol for Monotonic and Cyclic Tests

Strain (%)	Frequency (Hz)	Magnetic field intensities (Tesla) (Amp)
10, 20, 30, 40 and 50	0.1	0.0 (0)
	0.5	0.3 (1)
	1.0	0.5 (2)
	3.0	0.6 (3)
	5.0	0.7 (4)
	10.0	0.8 (5)

Magnetorheological effect (MR effect) was calculated as the ratio of absolute relative magnetic field to the modulus measured with zero magnetic field. The absolute relative magnetic field was calculated as difference between modulus measured at certain magnetic field and the modulus measured under no magnetic field.

$$MR\ effect = \frac{G_m - G_0}{G_0} \tag{1}$$

4.1. Monotonic experiments

Monotonic tests were conducted to characterize mechanical properties such as shear modulus of both isotropic and anisotropic MRE's. The effect of magnetic field on shear modulus of MRE-S-1 and NR-S-2 is shown in Figure 4. As can be seen, the anisotropic silicone MRE (MRE-S-1) sample shows 11%, 11%, and 6% MR effect at 10%, 30%, and 50% strain amplitudes, respectively. The isotropic natural rubber MRE (NR-S-2) sample achieved 11%, 51%, and 38% MR effect at 10%, 30%, and 50% strain amplitudes, respectively. The effective shear modulus values are summarized in Table 4.

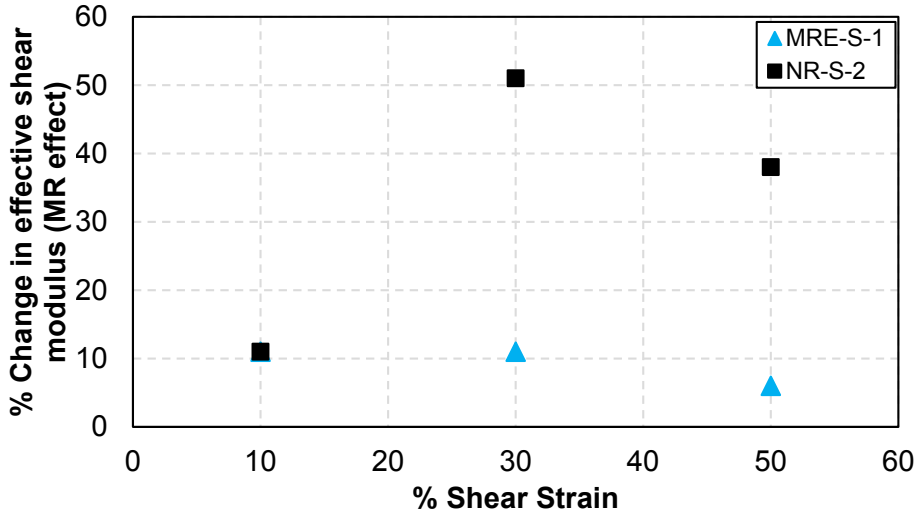

Figure 4. Experimentally determined MR effect.

Table 4: Effective Shear Modulus Values

Effective shear modulus (psi)	MRE-S-1			NR-S-2		
	10% Shear strain	30% Shear strain	50% Shear strain	10% Shear strain	30% Shear strain	50% Shear strain
G_0	160.0	137.0	129.0	78.0	33.3	29.0
G_4	178.0	152.0	137.0	86.5	50.2	40.0
% Change in effective shear modulus	11	11	6	11	51	38

G_0 - Shear modulus under no magnetic field, and G_4 - Shear modulus under 0.7 Tesla magnetic field

4.2 Cyclic experiments

MRE samples were subjected to six cycles of strain-controlled sinusoidal motions to study viscoelastic properties under varying shear loading frequencies and magnetic field intensities. The storage and loss moduli were calculated by using Eqs. (2) and (3), respectively, as follows:

$$G' = \tau/\gamma \cos\delta \quad (2)$$

$$G'' = \tau/\gamma \sin\delta \quad (3)$$

where δ is the phase lag measured from the reordered the shear stress and shear strain responses.

The effect of frequency on storage and loss moduli of MRE-S-1 is shown in Figure 5. Both moduli increase with increasing test frequency. As can be seen in the Figure 6, the MRE-S-1 sample show various levels of MR effect due to the applied magnetic field. In general, an increase in magnetic field results in larger storage and loss moduli for any given strain amplitude. However, while the MR effect associated with the storage modulus decreases with increasing strain amplitudes, MR effect for loss modulus increases with increasing strain amplitudes. Table 5 summarizes the measured MRE effects. Accordingly, the storage modulus of MRE-S-1 sample achieved approximately 68%, 42% and 24% MR effect at 10%, 30% and 50% strain amplitudes, respectively. The loss modulus of MRE-S-1 show 40%, 111%, and 119% MR effect at 10%, 30%, and 50% strain amplitudes, respectively, which implies a higher damping capacity at larger strain amplitudes. Figure 7 shows a sample of cyclic force-displacement response of silicone MRE under different strains and magnetic field intensities.

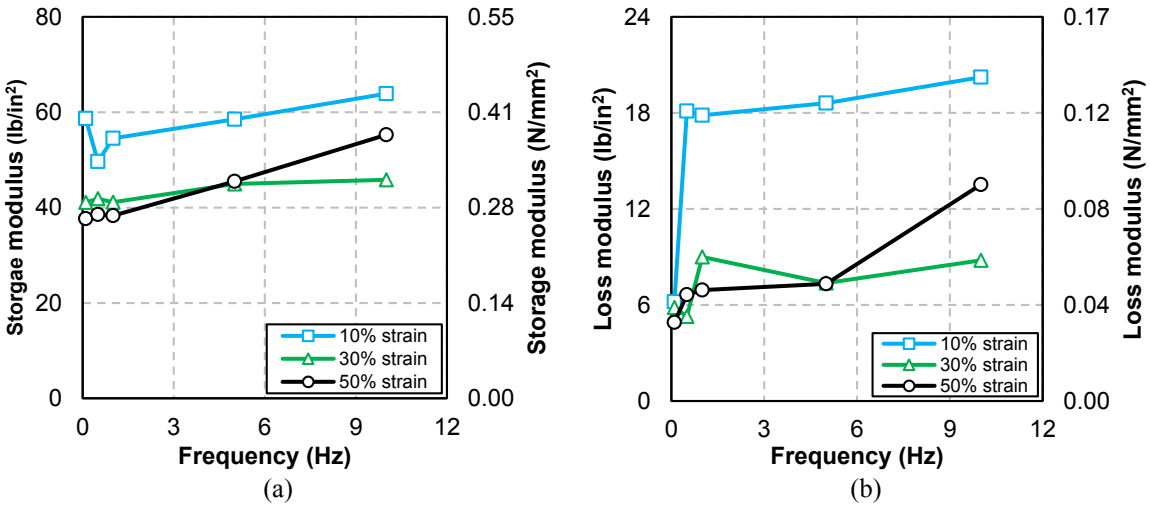

Figure 5. Effect of frequency on the rheological properties of MRE-S-1 at zero magnetic field: (a) Storage modulus (b) Loss modulus.

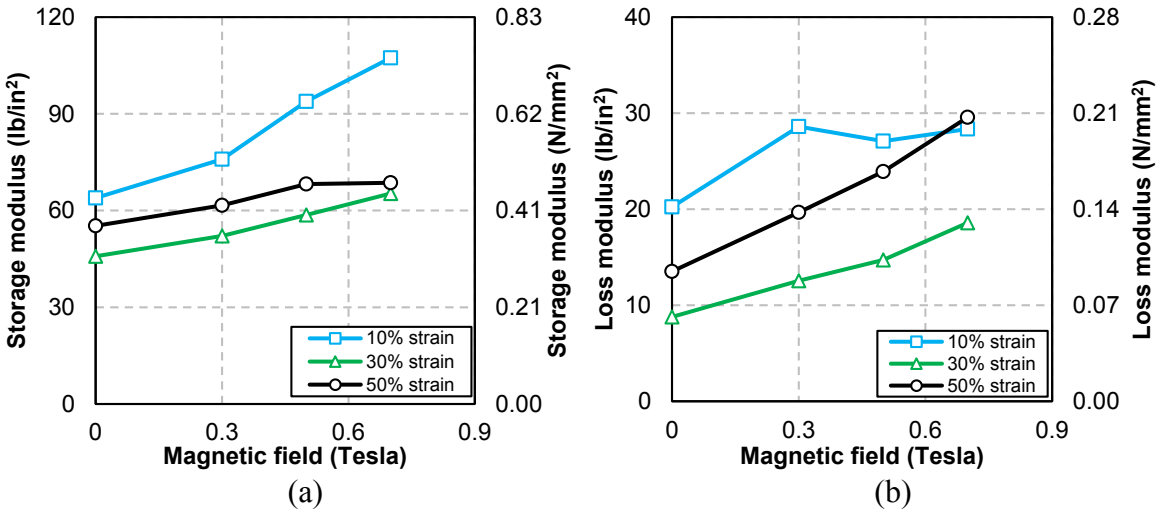

Figure 6. Effect of magnetic field on the rheological properties of MRE-S-1 at frequency of 10Hz: (a) Storage modulus (b) Loss modulus.

Table 5: Storage and loss modulus values of MRE-S-1

Magnetic field (Tesla)	Shear strain					
	10%	30%	50%	10%	30%	50%
	Storage modulus			Loss modulus		
	G'	G'	G'	G"	G"	G"
0	63.9	45.8	55.3	20.2	8.8	13.5
0.3	75.9	52.1	61.6	28.6	12.6	19.7
0.5	93.8	58.6	68.2	27.1	14.7	23.9
0.7	107.4	65.3	68.6	28.3	18.6	29.6
MR effect	68%	42%	24%	40%	111%	119%

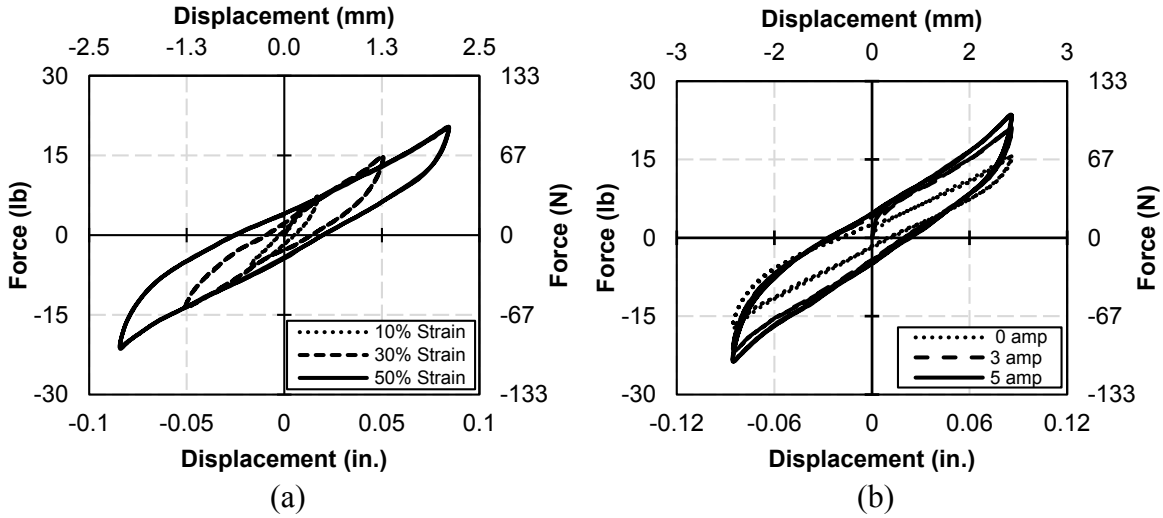

Figure 7. Platinum silicone MRE force-displacement results under varying: (a) Strains and (b) Magnetic field.

As shown in Figure 8, storage loss moduli of the isotropic natural rubber-based MRE (NR-S-2) show an increasing trend with increasing frequency for any given strain amplitude. Also, from Figure 8, it can be seen that both storage modulus and loss modulus show a decreasing trend with increasing strain amplitudes. Figure 9 shows magnetic field effect on storage and loss modulus of NR-S-2. As can be seen in the Figure, both storage modulus and loss modulus increase with increasing magnetic field. The storage modulus of NR-S-2 exhibits 35%, 24%, and 24% MR effect at 10%, 30%, and 50% strain amplitudes, respectively. The loss modulus of NR-S-2 show 45%, 19%, and 26% MR effect at 10%, 30%, and 50% strain amplitudes. Table 6 summarizes the measured storage and loss modulus values and corresponding MR effects. Figure 10 shows the shear force–displacements hysteresis of natural rubber-based isotropic MRE under different loading conditions.

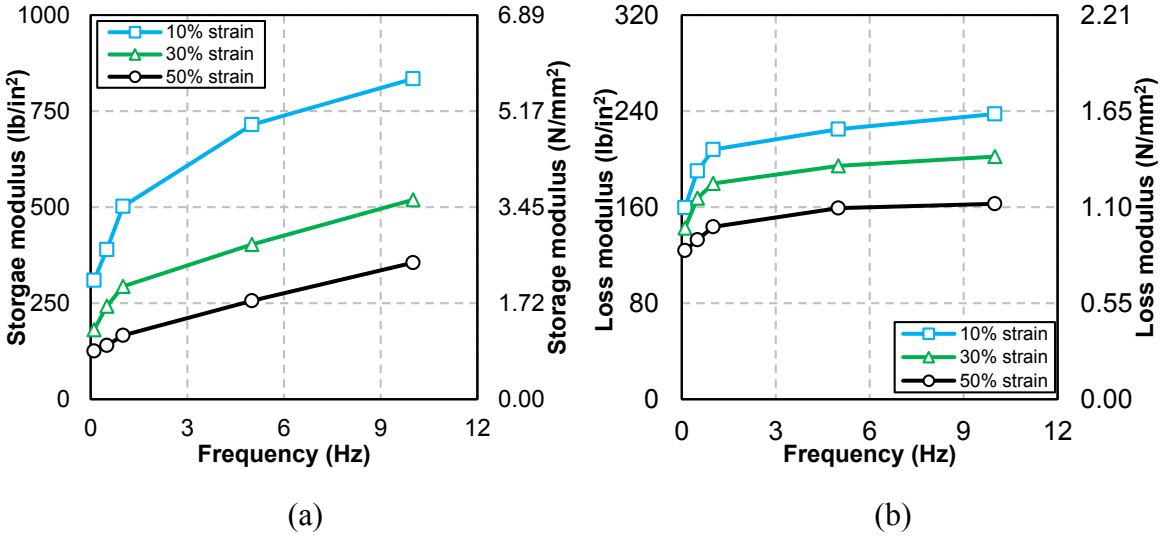

Figure 8. Effect of frequency on the rheological properties of NR-S-2 at zero magnetic field: (a) Storage modulus (b) Loss modulus.

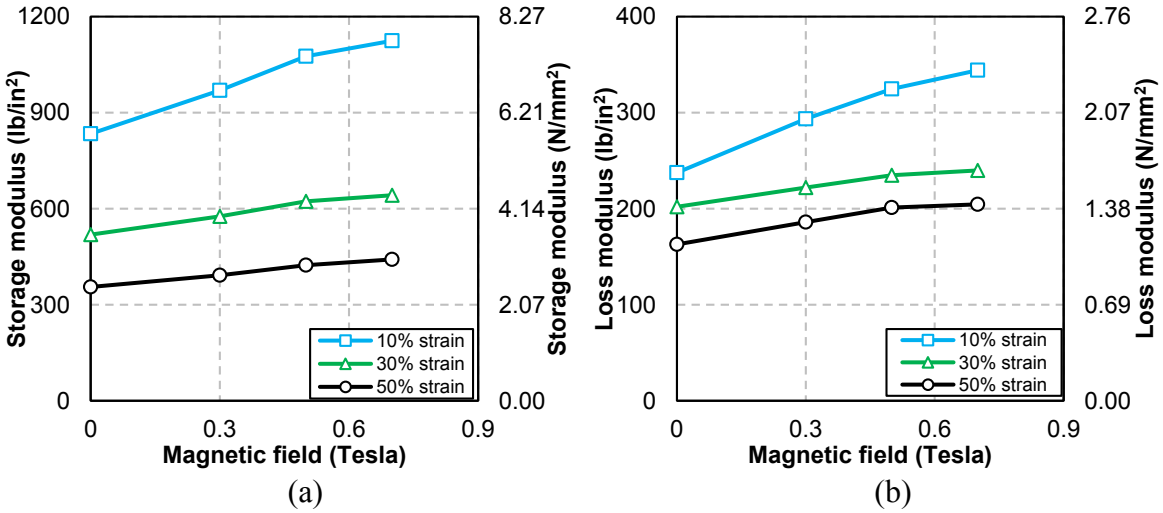

Figure 9. Effect of magnetic field on the rheological properties of NR-S-2 at frequency of 10Hz: (a) Storage modulus (b) Loss modulus

Table 6: Storage and loss modulus values of NR-S-2

Magnetic field (Tesla)	Shear strain					
	10%	30%	50%	10%	30%	50%
	Storage modulus			Loss modulus		
	G'	G'	G'	G"	G"	G"
0	834.3	519.2	355.5	237.6	202.1	162.8
0.3	969.7	576.3	392.3	293.5	222.1	186.0
0.5	1076.0	623.0	423.7	324.8	234.9	201.3
0.7	1124.9	642.0	441.7	344.2	239.9	204.5
MR effect	35%	24%	24%	45%	19%	26%

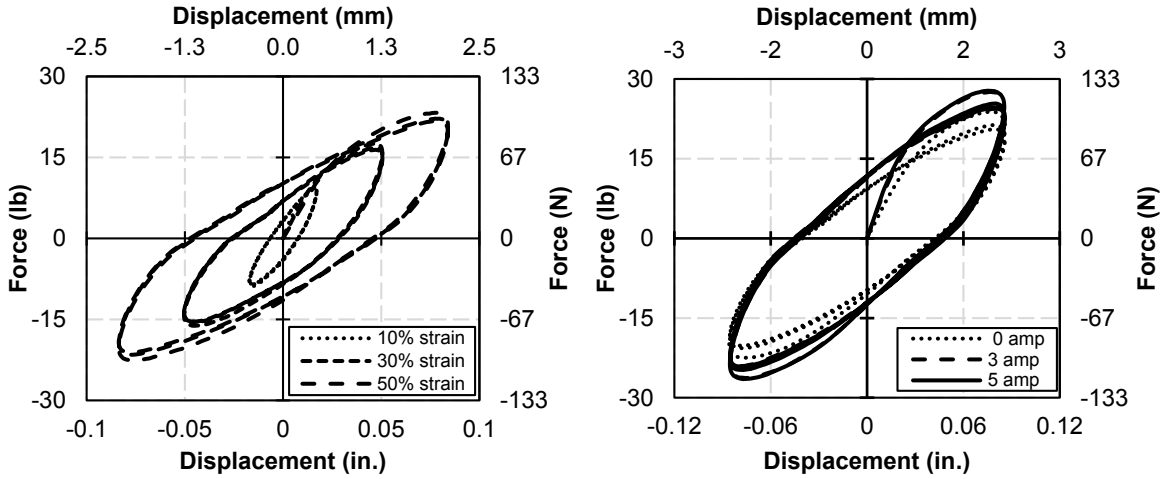

Figure 10. Natural rubber MRE force-displacement results under varying: (a) Strains and (b) Magnetic field.

5. CONCLUSIONS

In this study, different MRE samples are characterized using a double-lap shear test setup that is designed for combined shear and compression experiments. Experiments were carried out for anisotropic and isotropic MRE samples. The silicone MRE (MRE-S-1) sample were characterized as anisotropic (cured under magnetic field) and Natural rubber-based MRE (NR-S-2) samples were characterized as isotropic (cured without magnetic field). Both samples demonstrated varying levels of MR effect ranging between 11%-6% for MRE-S-1 and 11%-38% for NR-S-2 at 0.7 Tesla (4amp). It is important to note that NR-S-2 sample achieved a higher MR effect which tends to increase with larger strains. Additional material tests are planned for further investigation under various loading conditions and larger strain amplitudes.

ACKNOWLEDGMENTS

The authors would like to express their gratitude to the U.S. Federal Highway Administration for their support under contract # DTFH61-13-C-00020 under the exploratory Advanced Research Program. Also, the authors would like to thank undergraduate assistant Nathan Pinuelas for his assistance.

REFERENCES

[1] Lokander, M. and Stenberg, B. Performance of isotropic magnetorheological rubber materials. *Polymer Testing* (2003) **22**: 245–251.

[2] Jung, H. J., Lee, S. J., Jang, D. D., Kim, I. H., Koo, J. H. and Khan, F. Dynamic characterization of magneto-rheological elastomers in shear mode. IEEE *Trans Magn*, (2009), 40:39303933.

[3] Koo, J. H., Khan, F., Jang, D. D. and Jung, H. J., Dynamic characterization and modeling of magneto-rheological elastomers under compressive loading, *Smart Mater. Struct.*, (2010) **19**, pp. 1–6, 2010.

[4] Gong, X. L., Zhang, X. Z. and Zhang, P. Q., Fabrication and characterization of isotropic magnetorheological elastomers. *Polymer Testing*, (2005) **24**, 669-676.

[5] Nayak, B., Dwivedy, S. K. and Murthy, K. S., Fabrication and characterization of magnetorheological elastomer with carbon black. *J. Intll. Matl. Sys. Struct* (2014) **26** 830–9.

[6] Li. W. H., Zhou. Y. and Tian. T. F., Viscoelastic properties of MR elastomers under harmonic loading, *Rheologica Acta*, (2010) **49**, 733-740.

[7] Behrooz, M., Yarra, S., Mar, D., Pinuelas, N., Muzinich, B., Publicover, N. G., Pekcan, G., Itani, A. and Gordaninejad, F. A self-sensing magnetorheological elastomer-based adaptive bridge bearing with a wireless data monitoring system. *Proc. SPIE 9803, Sensors and Smart Structures Technologies for Civil, Mechanical, and Aerospace Systems* (2016), 98030D; doi:10.1117/12.2218691.

[8] Shen Y., Golnaraghi, M. F. and Heppler, G. R., Experimental research and modeling of magnetorheological elastomers. *J. Intell. Matl Sys. and Structures* (2004) **15**: 27–35.

[9] Zhou, G. Y., Complex shear modulus of a magnetorheological elastomer, *Smart Materials and Structures*, (2004) **13**, 1203-1210, 2004.

[10] Chen, L., Gong X. L. and Li, W. H., Effect of carbon black on the mechanical performances of magnetorheological elastomers, *Polymer Testing*, (2008) **27**, 340-345.

[11] Chen, L., Gong X. L. and Li W. H., Microstructures and viscoelastic properties of anisotropic magnetorheological elastomers, *Smart Materials and Structures*, (2007)**16**, 2645-2650.

[12] Behrooz, M., Wang, X., and Gordaninejad, F., A new semi-active/passive isolator," *Proceedings 5th World Conf. on Structural Control and Monitoring*, (2010), 10308, Tokyo, Japan.

[13] Behrooz, M., Wang, X. and Gordaninejad, F., Seismic control of base isolated structures using novel magnetorheological elastomeric bearings. *Proceedings of ASME*

Conference on Smart Materials, Adaptive Structures and Intelligent Systems, SMASIS 2013, Snowbird, UT, (2013) 16–18 September. New York: American Society of Mechanical Engineers.

[14] Li, Y., Li. J., Tian, T. and Li, W., A highly adjustable magnetorheological elastomer base isolator for applications of real-time adaptive control. *Smart Mater Struct.* (2013) **22**:095020

[15] Yang, C., Fu, J., Yu, M., Zheng, X. and Ju, B., A new magnetorheological elastomer isolator in shear–compression mixed mode. *J. Intell. Mater. Syst. Struct.* (2014) doi:10.1177/ 1045389X14541492

[16] ASTM D5992-96 Standard Guide for Dynamic Testing of Vulcanized Rubber and Rubber-Like Materials Using Vibratory Methods, ASTM International, West Conshohocken, PA, (2011),http://dx.doi.org/10.1520/D5992-96R11.

Compressive Properties of Adaptive Magnetorheological Impact Foams

Norman M. Wereley* and Young T. Choi

*Department of Aerospace Engineering
University of Maryland, College Park, Maryland, USA 20742
Email: wereley@umd.edu - Web page: http://aero.umd.edu/faculty/wereley

ABSTRACT

Flexible elastomeric foams have been widely used as packaging and cushioning materials in many engineering fields and sports areas because of lightweight, simple configuration, and freedom of geometric design. They can provide good vibration damping, sound and thermal insulation, and also protect delicate instruments from impact and prevent human from a danger of severe injury in critical areas through collision and fall. The crashworthiness protection performance of flexible elastomeric foams strongly depends on their energy absorption and dissipation capabilities. But, because of relatively lower generated force levels and limited energy absorption and dissipation capabilities, flexible elastomeric foams are mainly effective in the protection for low-velocity impacts. To improve crashworthiness performance for higher-velocity impacts, the flexible elastomeric foams need to be designed in fashion of much thicker and denser forms, thereby being less flexible, stiffer, heavier, and eventually impairing the protection performance at low-velocity impacts. This disadvantage is possible to be surmounted by adaptive cushioning materials that are soft and flexible for light compressive loads and low strain, but stiffen for higher impact loads and high strains.[1,2] Thus, in this study, the magnetorheological elastomeric foam (MREF) was developed as an adaptive cushioning material. The isotropic MREF which has no oriented particle structure was synthesized by randomly dispersing micron-sized carbonyl iron particles in an uncured silicone elastomeric foam in the absence of magnetic field. To evaluate the effect of the particle concentrations, five different iron particle volume fractions (hereinafter vol%) of 0, 2.5, 5, 7.5, and 10% were chosen. The MREF samples were placed between two flexible multipole strip magnets, and their quasi-static and dynamic compressive properties were conducted by using an Instron servo-hydraulic testing machine. From these tests, magnetic field-sensitive compressive properties such as compression stress, energy absorption capability, complex modulus, and equivalent viscous damping, were measured. In addition, the variation of the compressive properties of the MREFs due to the magnet placement directions (0° and 90°) was also experimentally investigated.

REFERENCES

[1] S. S. Deshmukh and G. H. McKinley, "Adaptive energy-absorbing materials using field-responsive fluid-impregnated cellular solid," *Smart Materials and Structures*, Vol. 16, pp. 106-113, (2007).

[2] M. D'Auria, D. Davino, R. Pantani and L. Sorrentino, "Polymeric foam-ferromagnet composites as smart lightweight materials," *Smart Materials and Structures*, Vol. 25, 13 pages, (2016).

[3] W. H. Li, X. Z. Zhang and H. Du, *Advances in Elastomers I: Blends and Interpenetrating Networks*, Berlin, Germany, Springer, pp. 357-374 (2013).

VIII ECCOMAS Thematic Conference on Smart Structures and Materials
SMART 2017
A. Güemes, A. Benjeddou , J. Rodellar and Jinsong Leng (Eds)

DEVELOPEMNT AND OPTIMIZATION OF A NOVEL MAGNETORHEOLOGICAL FLUID BRAKE WITH NO ZERO-FIELD VISCOUS TORQUE FOR AUTOMOTIVE APPLICATIONS

HADI SHAMIEH[*] AND RAMIN SEDAGHATI[†]

Department of Mechanical and Industrial Engineering,
Concordia University, Montreal, QC, H3G 1M8, Canada

[*]Graduate Student, h_sham@encs.concordia.ca
[†]Professor, ramin.sedaghati@concordia.ca

Key words: Magnetorheological (MR) Fluids, MR Brake, Multidisciplinary Design Optimization, Automotive.

Abstract. The magnetorheological brake (MRB) is an electromechanical brake containing smart magnetorheological (MR) fluid which provides adaptive braking torque by varying the applied magnetic field. This is due to the inherent characteristics of MR fluids which their apparent viscosity changes rapidly and reversibly from free-flowing fluid to semi-solid through application of an external magnetic field. The main purpose of this study is to propose and develop a novel real-size vehicle model of the MRB design with absolutely no energy loss in terms of viscous torque generation in the absence of applied magnetic field. The Herschel-Bulkley constitutive model is utilized to develop the mathematical equations governing the system's braking torque as a function of the rotational speed, geometrical and material properties, and the applied magnetic field (electrical current). Magnetic circuit analysis of the MRB design allowed the derivation of the relation between the applied magnetic field intensity and the electric current as a function of number of coil turns and the brake's geometrical variables. Subsequently, a multidisciplinary design optimization problem has been formulated to identify the optimal brake geometrical parameters to maximize the dynamic range while minimizing the response time and weight of the MRB under different constraints. The optimization problem has been solved using Genetic Algorithm (GA) followed by Sequential Quadratic Programming (SQP) in the MATLAB environment to achieve the true global optimal design. The optimal MRB design proved to be suitable for application in real commercial vehicles by having a maximum braking torque of 1802 *Nm*, a response time of 150 *ms* and an overall weight just under 37 *kg*.

1 INTRODUCTION

Research on implementing electromechanical systems in the automotive industry has been given specific attention by researchers around the world. Such systems allow better vehicle control through fast and direct electric actuation. Smart devices with MR fluids offer a remarkable potential in the electro-mechanical interface. Some applications of these devices are dampers, valves, clutches and brakes [1]. The focus of this research is advancing the vehicle braking system through the modelling and design optimization of an innovative MRB design.

The MRB actuator was proposed in 1998 by J. David Carlson of LORD Corporation [2]. Later, a double-disk MRB design was introduced to further enhance the performance of the MRB [3]. Several other design concepts have been projected for the MRB, like the drum type, inverted drum type and T-shape MRB designs [4]. Park et al. in [5] proposed the application of the MRB in the automotive industry. They utilized a sliding mode controller to evaluate the performance of the designed MRB. Later in 2008 [6, 7], the design was improved through multidisciplinary considerations with a major focus on the geometry of the MRB in which optimal design parameters were obtained using the Simulated Annealing algorithm.

The Bingham mathematical model was adopted in the MRB models proposed by Park et al. [5, 6]. The Bingham model may not accurately estimate the braking torque in high shear rates due to shear thickening/thinning effect. Also, the formulate optimization strategy did not involve the zero-current viscous torque. Nguyen and Choi [8] addressed some of these issues and considered the Herschel-Bulkley mathematical model in their study.

The major limitation of the conventional MRB design is the viscous torque generation due to the contact between the MR fluid and its interacting surfaces. In addition to the loss of energy, the continuous fluid-surface shearing in the idle condition can negatively affect the fluid's lifetime [9]. Several innovative ideas have been proposed to limit this contact and to reduce the viscous torque generation. The general concept of the designs is to control the location of the MR fluid and allow it to alternate to different positions between the idle and the braking states.

One such design to separate the MR fluid in the idle state of the MRB employ earth's gravitational force [10] and another utilizes the centrifugal forces [11]. In addition, the use of permanent magnets was introduced to control the location of the MR fluid at different states [12]. Figure 1 shows the concept in which a permanent magnet (PM) in the rotor ensures that the fluid is locked with the rotor and not touching the stator. When braking is required, the electromagnet (EM) that is mounted with the casing is supplied with electric current. By modelling and simulation, it was concluded that the design with one PM and one EM has significantly reduced the torque losses in the off-state and maintained a smooth control of the generated torque in the on state.

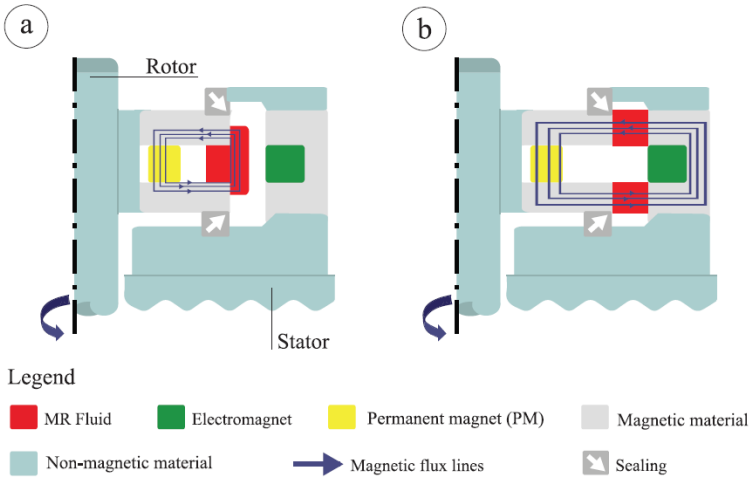

Figure 1: MRB design with PM in (a) off and (b) on states.

The objective of this research is to design and optimize an innovative automotive MRB design with no viscous torque in the off state considering multiple disciplines. The design is

achieved using permanent magnets to allow the MR fluid volume to shift locations between the brake's operating modes – 'on' and 'off' – to allow complete de-coupling. In this study, a two disk MRB design is considered. It is also assumed that proposed MRB generates a retarding torque through employing MRF-132DG from Lord Corporation. First, braking torque equations based on the Herschel-Bulkley model for the MR fluid have been presented for the 2-disk-type MRB. A magneto-static analysis of the magnetic circuit of the MRB brake has been conducted to derive an approximate analytical relation to evaluate the magnetic field intensity in MR fluid gaps with respect to the applied current. The inductive time constant of the magnetic circuit has been analyzed and an arrangement to decrease the time response has been suggested. A multidisciplinary design optimization problem has been formulated to identify the optimal brake geometrical parameters to simultaneously maximize the dynamic range while minimizing the inductive time constant and of the magnetic circuit and the MRB's weight subject to weight, size and magnetic flux density constraints. The optimization problem has been solved using combined Genetic Algorithm and Sequential Quadratic Programming techniques.

2 NOVEL DECOUPLED DESIGN

Here, an MRB design that may be practical for use in the automotive industry has been proposed. The main purpose of this design is to completely eliminate the MR fluid–rotor surface contact in the off state. The decoupling of MR fluids with rotor surface in the off-state can be achieved by integrating permanent magnets (PM) on parts of the casing as shown in Figure 2.

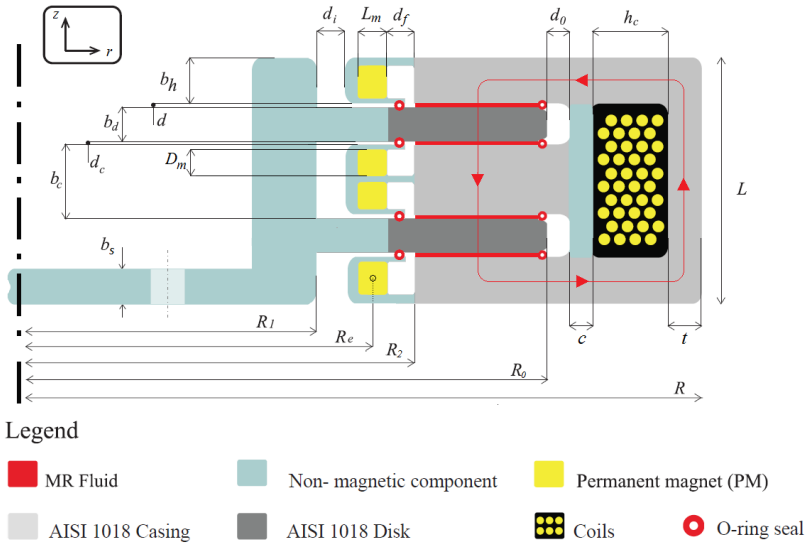

Figure 2: Proposed Decoupled Design.

The PM can practically attract the specified volume of the MR fluid into a neighboring gap to lock them with the stator and prevent their contact with the rotor. O-ring seals are placed at the edges of the active region to insure the fluid remains in the active shear gap region.

The design parameters presented in Figure 2 for this proposed design are equivalent to those of the conventional MRB design proposed in [13] with the addition of three new parameters: L_m, D_m and R_2. The parameters L_m and D_m are length and thickness, respectively, of the permanent magnets. The variable R_2 is introduced to define the lower radius of the shear gap

region, where the MR fluid are situated in the 'on' state. R_e is the effective radius of the permanent magnets; calculated as: $R_e = R_2 - d_f - L_m/2$. Figure 2 demonstrates the on-state configuration of the proposed novel MRB design. The configuration of the MRB in the off-state is presented in Figure 3.

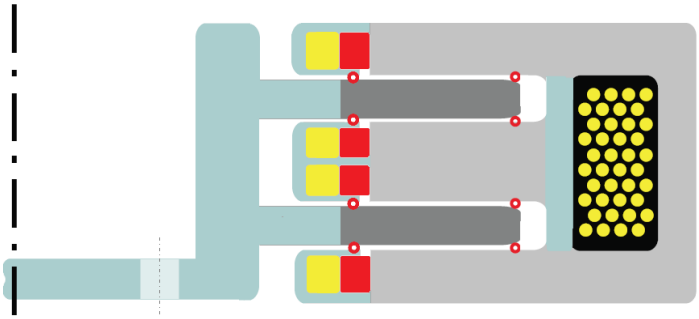

Figure 3: Novel de-coupling design in the off-state.

As it can be seen in Figures 2 and 3, four permanent magnets are embedded in the side walls and core section of the stator casing. The role of the magnets is to attract the MR fluids to fill the neighboring gaps in the off-state. In this case, the MR fluid will be merged with the casing and completely separated from the brake's rotor. However, in the on-state configuration, the main large electromagnet embedded in the outer radial surface of the casing is supplied with the current creating a strong magnetic field that will pull the MR fluid out of the gaps and into the shear gap region. In this research study, the transition phase between the on and off state is assumed to be perfect. The complete separation in this design leads to near elimination of viscous torque through preventing any friction in the shear gap region in the idle state. The torque equations for this designs are estimated using a similar approach to that of the conventional MRB in [13] and the total braking torque using Herschel-Bulkley model can be given as:

$$T_b = \frac{8\pi}{3}\left(R_0^3 - R_2^3\right)\tau_y + \frac{4\pi K\left(R_0^{3+n} - R_2^{n+3}\right)}{n+3}\left(\frac{1}{d^n} + \frac{1}{d_c^n}\right)\dot{\theta} \tag{1}$$

According to the Herschel-Bulkley model, the shear stress developed in the MR fluid can be represented as:

$$\tau = (\tau_y + K|\dot{\gamma}|^n)\,\mathrm{sgn}(\dot{\gamma}) \tag{2}$$

where τ_y is the field dependent yield strength which is the function of the applied magnetic field intensity, H, and $\dot{\gamma}$ is the shear strain rate of the MR fluid, which can be approximated as:

$$\dot{\gamma} = \frac{r\dot{\theta}}{d_{MR}} \tag{3}$$

where $\dot{\theta} = \omega$ is the angular velocity of the shaft and the d_{MR} is the MR fluid gap; d and d_c.

The parameters K and n are the consistency and flow behavior indices. They are properties of the MR fluid and may vary as a function of the surrounding magnetic flux density. In the Herschel-Bulkley model, the variation of the field-dependent rheological properties, K, n and τ_y for different magnetic flux densities, B, may be expressed as [14]:

$$K = K_\infty + (K_0 - K_\infty)(2e^{-B\alpha_{SK}} - e^{-2B\alpha_{SK}}) \tag{4}$$

$$n = n_\infty + (n_0 - n_\infty)(2e^{-B\alpha_{Sn}} - e^{-2B\alpha_{Sn}}) \tag{5}$$

$$\tau_y = \tau_{y_\infty} + (\tau_{y_0} - \tau_{y_\infty})(2e^{-B\alpha_{STy}} - e^{-2B\alpha_{STy}}) \tag{6}$$

where K_0, n_0 and τ_{y0} are the properties at zero magnetic field and K_∞, n_∞ and $\tau_{y\infty}$, are the saturation values of the properties and α_{SK}, α_{Sn} and α_{STy} are related to the torque.

For Lord`s MRF-132DG these parameters are reported by [8] to be 0.22 $Pa.s^n$ and 0.917 for K_0 and n_0, 3900$Pa.s^n$ and 0.25 for K_∞ and n_∞, and 5 T^{-1} and 32 for α_{SK} and α_{Sn}, respectively. For MR fluid MRF-132DG, yield stress in the absence of magnetic field, $\tau_{y0,}$ is10.821Pa, as obtained in [13] and yield saturation limit, $\tau_{y\infty}$, and α_{STy} are also reported to be 50kPa and $2T^{-1}$, respectively [8]. Equations (4), (5) and (6) can be utilized to obtain the shear stress as a function of shear rate at different magnetic flux densities.

3 MAGNETIC CIRCUIT ANALYSIS

For the proposed novel MRB design, a similar magnetic circuit formulation conducted in Ref. [13] can be derived under the assumption of perfect decoupling between MR fluids and the rotor in off-state configuration.

$$H = \frac{N_c}{\left(\frac{\mu_f}{\mu_s}\right)\left(\frac{l_1 A_3}{A_1} + \frac{2l_2 A_3}{A_2} + 2l_3 + 2l_5 + l_7\right) + 2l_4 + 2l_6} i \tag{7}$$

The effective lengths of the twelve links considered in the magnetic circuit with respect to geometrical parameters can be described as:

$$\begin{aligned} &l_1 = L - b_h; \quad l_2 = l_{12} = R - R_2 - \frac{g_a + t}{2}; \quad l_3 = l_{11} = \frac{b_h}{2} \\ &l_4 = l_{10} = d; \quad l_5 = l_9 = b_d; \quad l_6 = l_8 = d_c; \quad l_7 = b_c \end{aligned} \tag{8}$$

where g_a is the length of the shear gap region as shown in Figure 4.

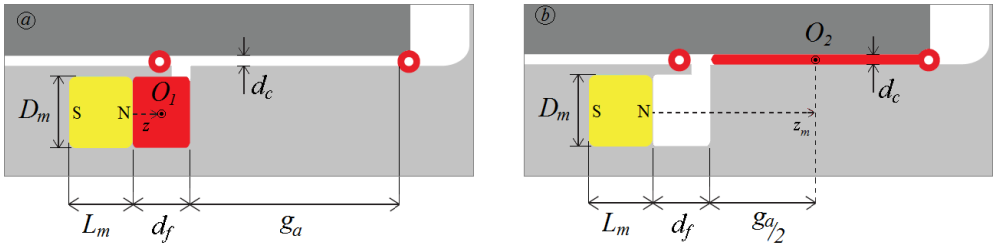

Figure 4: Section sketch of the shear gap region the proposed MRB design in (a) OFF and (b) ON modes.

The links' corresponding cross-sectional areas for the proposed design are:

$$\begin{aligned} A_1 &= \pi\left[R^2 - (R-t)^2\right] \\ A_2 &= A_{12} = \pi b_h (R - t + R_2) \\ A_3 &= A_4 = \ldots = A_{11} = \pi\left[R_0^2 - {R_2}^2\right] \end{aligned} \tag{9}$$

Furthermore, to examine the ability of the permanent magnets in the current MRB design to completely pull the volume of the MRF into its adjacent gap, the Maxwell equation is adopted to define the permanent magnet's pull force as:

$$F_{PM} = \frac{{B_{PM}}^2 A_{PM}}{2\mu_{sp}} \tag{10}$$

where B_{PM} is the magnetic flux density (*Tesla*) exerted by the permanent magnet, A_{PM} is the cross-section area (m^2) of the of the pole and μ_{sp} is the permeability of free space. The magnetic flux density for a block type magnet is defined as [15]:

$$B_{PM} = \frac{B_r}{\pi}\left[\arctan\left(\frac{L_m W}{2z\sqrt{4z^2 + L_m^2 + W^2}}\right) - \arctan\left(\frac{L_m W}{2(D_m + z)\sqrt{4(D_m + z)^2 + L_m^2 + W^2}}\right)\right] \quad (11)$$

where B_r is the remanence field of the permanent magnet – a property of the magnet that is independent of its geometrical dimensions. The permanent magnet chosen for this design is the Neodymium magnet N30EH. They are composed of neodymium, iron and boron (NdFeB). For N30EH, B_r is between 1.08 to 1.13 *Tesla* [16]. The average value, 1.1 *Tesla*, is assumed for the current analysis. L_m, D_m and W are the length and thickness and width of the block magnet, respectively. The width, W, of the PM in the current brake design is estimated as $W=2\pi R_e$. The parameter z is the distance of the attracted object from the pole face on the symmetry axis, as seen in the section drawing of Figure 4. The PM is desired to sufficiently pull the whole MR fluid volume. The maximum distance for z would be the distance from the face of the PM pole to the center of gravity, O_2, of the MR fluid volume (on-state mode). It is expressed as:

$$z_m = d_f + \frac{g_a}{2} \quad (12)$$

In Figure 4, the cavity next to the permanent magnet is expected to hold the volume of the MR fluid. This geometric constraint allows the estimation of the required size of the corresponding cavity, d_f, as:

$$d_f = g_a d_c / D_m \quad (13)$$

The forces acting on the MR fluid inside the MRB are the gravitational force, F_{gf}, due to the weight of the MR fluid, and the centrifugal force, F_{cf}, due to its rotation inside the MRB. A free body diagram (FBD) of the forces acting on an MR fluid particle is presented in Figure 5.

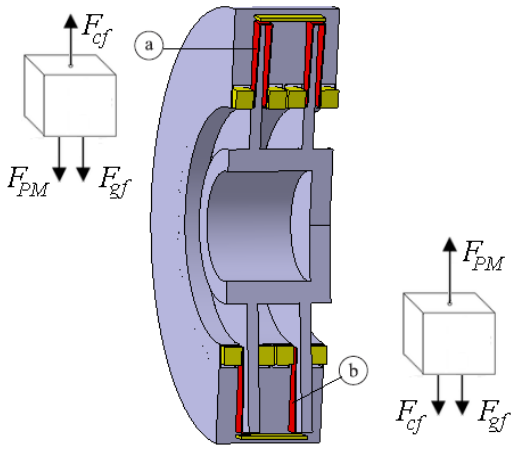

Figure 5: FBD of MR fluid situated on (a) top end and (b) bottom end of the MRB.

In case (a), the MRF on the top of the brake are subject to a centrifugal force pushing it upwards while the forces from the PM and gravity are exerted downwards. In case (b) where the MRF is on the lower end of the brake, the centrifugal force would be pushing the fluid in the same direction as the gravitational force. The pull force of the PM must be sufficient enough

to attract the full amount of MRF into the cavity despite the two opposing forces. Hence, the condition for the pull force of the permanent magnet is represented as:

$$F_{PM} > F_{gf} + F_{cf} \tag{14}$$

$$\frac{B_{PM}^2 A_{PM}}{2\mu_{sp}} > m_f g + m_f \dot{\theta}^2 R_0 \tag{15}$$

where m_f and $\dot{\theta}$ are the MR fluid's mass and shaft's angular velocity, respectively. Thus, the minimum magnetic field density required by the permanent magnet to attract and fully pull the MR fluid can be calculated by:

$$B_{\min} = \sqrt{\frac{2\mu_{sp} m_f}{A_{PM}}\left(g + \dot{\theta}^2 R_0\right)} \tag{16}$$

Using the above formula, the proper permanent magnet with the required properties is selected and employed in the design. After this condition is met, to simplify the finite element analysis problem, it can be assumed that the transition between the "on" and the "off" state is instantaneous and the two cases are examined independently.

4 RESPONSE TIME ANALYSIS

For an electric circuit with a resister and an inductor, a property called the inductive time constant is defined as the time required for the applied current passing through the circuit wires to reach 63.2% of its maximum value. After five time constants, the electric current applied in the circuit reaches nearly 99.5% of its final value. A similar behavior also takes place when the current source is switched off. The lower is the inductive time constant, the faster is the response of the system. The inductive *TC* of the magnetic circuit of the MRB can be written as:

$$TC = \frac{L_{in}}{R_{AWG}} \tag{17}$$

where L_{in} is the inductance of the coil, described as:

$$L_{in} = \frac{N_c \Phi}{i} = \frac{N_c B A_c}{i} = \frac{N_c B \pi \bar{R}_w^2}{i} \tag{18}$$

and R_{AWG} is the electric resistance of the AWG21 wire, which can be calculated [17] as:

$$R_{AWG} = \frac{2\pi\left(R - t - {}^{h_c}\!/_{2}\right) N_c r_{AWG}}{S_w} \tag{19}$$

The term r_{AWG} is the resistivity of the AWG wire. Here, the copper alloy AWG21 with resistivity of 1.724×10^{-8} *Ohms-m* is chosen. S_w is the cross-sectional area of the AWG wires. The inductive time constant for the MRB design is expected to be higher than 500 *ms*. due to the size of the coil of the electromagnet. This value is exceedingly high compared with that of conventional hydraulic braking systems, which demonstrate a total response time (equivalence of 5*TC*) of around 300 *ms*. The inductive time constant is inversely proportional to the resistance of its electric circuit. A suggestion to decrease the response time of the brake is to increase the equivalent resistance of the circuit by adding a resistor in series to the car battery – MRB electric circuit, as shown in the Figure 6. Knowing that after 3*TC*, the applied current is at around 95% of its final value, a constraint is formed to equate the required response time, 3*TC*, to 300 *ms*

(TC=100 ms). Thus, the required resistance, R_{es}, may be calculated by:

$$TC = \frac{L_{in}}{R_{AWG} + R_{es}} = 100ms\ ; \quad \rightarrow \quad R_{es} = \frac{L_{in}}{100ms} - R_{AWG} \tag{20}$$

An increase in the added resistance would contribute to an increase in the MRB design's power consumption ($PC = i^2 R_{AWG}$). The response time of the MRB, RT, is estimated as:

$$RT = 3TC + t_e \tag{21}$$

The additional term, t_e, considers the time required by the MR fluid to activate and completely decouples. The response time of the MR fluid to the applied magnetic field is less than 1 ms [18]. The time required for the MR fluid to be transmitted to the shear gap region is adopted from [12] to be around 25 ms; thus, the total response time is estimated as t_e = 26 ms.

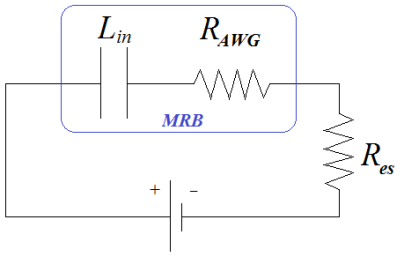

Figure 6: MRB electric circuit with added R_{es}.

5 MULTI-OBJECTIVE DESIGN OPTIMIZATION

For the proposed MRB design shown in Figure 2, the geometrical parameters related to the permanent magnets and their gaps are also considered as design variables. The design variable vector, X, for the optimization is:

$$X = [R_1, R_d, c, d, d_c, d_0, d_i, h_c, t, b_h, b_d, b_c, r_e, d_m, L_m\ ]^T \tag{22}$$

It is noted that the variables r_e and d_m are used to calculate the effective radius of the permanent magnet, R_e, and the depth of the magnet, D_m, using the following relations:

$$R_e = R_1 + r_e R_d \tag{23}$$

$$D_m = d_m b_h \tag{24}$$

The optimization problem can be formally formulated as to find design variable vector to:

Minimize: $f(x) = \alpha_d \frac{T_{b_{ref}}}{T_b} + \alpha_t \frac{RT}{RT_{ref}} + \alpha_w \frac{W_{MRB}}{W_{ref}}$; (25)

Subject to the following constraints:

Generated Torque:	$T_b \geq 1300\ Nm$;	Weight:	$W_{MRB} \leq 60\ kg$;	
Magnetic Field:	$H \leq 300\ kA/m$;	$B_{\min} \leq 4\, B_{PM}$		
Geometric:	$L \leq 0.1\ m$;	$R \leq 0.2\ m$;	$L_m \leq 2(R_e - R_1)$;	$b_c \geq 2b_h$
Side Constraints:	$X_{\min} \leq X \leq X_{\max}$;			

The variables α_d, α_t and α_w are weighting factors chosen for each of the three specifications and are selected to be 0.4, 0.5 and 0.1, respectively. The highest weighting is given to the response time of the brake because the faster the vehicle brakes, the safer the ride is. $T_{b,ref}$, RT_{ref}

and W_{ref} are reference values of each performance measure, equated to their values in an ideal case: 1300, 300 *ms* and 30 *kg*, respectively.

With respect to the constraints, the limiting braking torque that would allow the MRB to be applied in vehicles is 1010 *Nm*. In this paper, the torque constraint is set at 1300 *Nm* to give the brake a 30% advantage in braking power for safety and performance purposes. The weight constraint is set at 60 *kg* since it is almost equivalent to the weight of the conventional hydraulic brake system. W_{MRB} is calculated as a function of the brake's geometric dimensions and its materials' densities. With respect to *H,* as the magnetic field increases, the magnetic material gets closer to its magnetic saturation limit and the ability to polarize it weakens. The saturation limit of MRF-132DG is obtained from its non-linear *B-H* curve and is found to be 300kA/m. *L* and *R* are the total width and radius of the MRB, respectively. Their constraints are based on the available space inside the vehicle wheel. They are chosen in comparison with the conventional hydraulic brake dimensions. It is noted that the second magnetic constraint (for $B_{\min}$) is to ensure that the magnetic flux densities of the four permanent magnets satisfy the condition of being over the limiting value B_{min} of Eq. (16) that they would completely draw the full MRF volume to the gap region. Additionally, geometric constraints are added to restrict the MRB geometry from overlapping. Finally, the side constraints are provided in Table 1.

Table 1: Design variables and their ranges for the conventional MRB design.

X *(unit)*	R_1 *(cm)*	R_d *(cm)*	c *(cm)*	d, d_c, d_0, d_i *(cm)*	h_c *(cm)*	t *(cm)*	b_h *(cm)*	b_d *(cm)*	b_c *(cm)*	r_e, d_m *(%)*	L_m *(cm)*
X_{min}	3.00	2.00	0.25	0.10	0.25	0.50	0.25	1.00	1.00	10.00	0.50
X_{max}	12.00	12.00	1.00	0.50	2.50	3.00	3.00	5.00	5.00	90.00	2.50

6 MULTI-OBJECTIVE OPTIMIZATION RESULTS

The optimization algorithm used to solve the defined optimization problem is based on combined global (Genetic Algorithm) and local (Sequential Quadratic Programming) optimizers in order to catch the "True Global" minimum of the objective function [13]. The Genetic Algorithm (GA) is a stochastic based optimization algorithm that is capable of catching the near global optimum solution. On the other hand, the Sequential Quadratic (SQP) Algorithm is a powerful gradient based optimization algorithm capable of catching local optimum solutions. The SQP algorithm requires an initial point from which it starts its first iteration and stops when the objective function reaches the closest minimum.

The multi-objective optimization algorithm, carried out in the MATLAB environment, starts by implementing the Genetic Algorithm to solve the optimization problem stated in Eq. (25). After only five generations, GA reached to the minimum value for the cost function $f(x)$ = 0.76088. To complete the optimization, optimal design point obtained from GA was fed into the SQP algorithm as the starting point to accurately catch the true global solution. Eight additional iterations performed by the SQP local optimizer decreased the objective function to f(x) = 0.66805. The resulting *True Global* vector along with the major specifications of the optimal MRB are presented in Table 3.

It should be noted that the values for r_e and d_m, the components of X used to calculate R_e and D_m, were obtained to be 28.18% and 90%, respectively. At a driving speed of 70 *km/hr*, the maximum braking torque of the proposed MRB design is 1802 *Nm*, which is significantly larger

than the initial referenced value. The addition of a 200 Ohm resistor reduced the inductive time constant by nearly 93% while maintaining reasonable power consumption. The full response time of the MRB is around 150 *ms*; making it nearly twice as fast in response as the conventional hydraulic system. The overall weight of the MRB is much less than the referenced value. Finally, the geometric (R and L) and magnetic specifications (B_{PM}) of the optimal MRB meet their corresponding constraints.

Table 2: Geometric variables and specifications for the optimal MRB design.

MRB Geometry			*MRB Specs*		
R_1	*(cm)*	7.86	$\boldsymbol{T_b}$	***(Nm)***	**1,802**
R_d	*(cm)*	11.04	T_{vis}	*(Nm)*	0
c	*(cm)*	0.25	TC_0	*(ms)*	606.3
d	*(cm)*	0.10	R_{es}	*(Ohms)*	200
d_c	*(cm)*	0.10	TC	*(ms)*	41.5
d_0	*(cm)*	0.10	***RT***	***(ms)***	**150.4**
d_i	*(cm)*	0.50	PC_0	*(watts)*	58.74
h_c	*(cm)*	0.25	PC	*(watts)*	858.74
t	*(cm)*	0.50	$\boldsymbol{W_{MRB}}$	***(kg)***	**36.61**
b_h	*(cm)*	1.35	R_2	*(cm)*	14.15
b_d	*(cm)*	1.00	R	*(cm)*	20.00
b_c	*(cm)*	2.70	L	*(cm)*	7.79
R_e	*(cm)*	10.97	B_{min}	*(Tesla)*	0.3587
D_m	*(cm)*	1.21	$4B_{PM}$	*(Tesla)*	0.4005
L_m	*(cm)*	5.56	N_c	*(turns)*	288

7 CONCLUSIONS

The aim of this paper is to fundamentally study and enhance the automotive Magnetorheological Brake design. An innovative design was proposed that employs permanent magnets to allow full separation of the operating modes. The braking torque equations were derived based on the Herschel-Buckley mathematical model. Magnetostatic analysis has been conducted to find the approximate relation between the induced magnetic field in the MR gap and the applied current and electromagnet geometrical parameters. This is followed by the formulation of a formal multi-objective design optimization problems to identify the optimal parameters of the MRB. A combined Genetic Algorithm and Sequential Quadratic Programming technique have been utilized to solve the optimization problem. The final optimal MRB design demonstrated a decent braking torque capacity with no residual viscous torque generation. In addition, the quick response time contributes to the braking performance through enhanced safety, enriched ride stability and reduced braking time and distance while providing a smooth and comfortable controlled deceleration. In short, the proposed MRB design demonstrated improved specifications for automotive applications.

REFERENCES

[1] Mohammad, A. Yao X. L. C. and Deng J. Review of Magnetorheological (MR) fluids and its applications in vibration control. *J. Mar. Sci. Appl.* (2006) **5**: 17-29.

[2] Carlson, D. J. Magnetorheological brake with integrated flywheel. United States Patent Office Patent US Patent 6,186,290 Bl, 2001.
[3] Zhou, W. Chew, C. M. and Hong G. S. Development of a compact double-disk magnetorheological fluid brake *Robotica* (2006) **25:** 493-500.
[4] Avraam, M.T. MR-fluid brake design and its application to a portable muscular rehabilitation device. PhD thesis, Universitè Libre de Bruxelles, Bruxelles, Belgium (2009).
[5] Park, E.J. Stoikov, D. Falcao da Luz, L. and Suleman, A. A performance evaluation of an automotive magnetorheological brake design with a sliding mode controller. *Mechatronics* (2006) **16**: 405–416.
[6] Park, E.J. Falcao da Luz, L. and Suleman, A. Multidisciplinary design optimization of an automotive magnetorheological brake design. *Computer and Structures* (2008) **86**: 207-216.
[7] Karakoc, K. Park, E.J. and Suleman, A. Design considerations for an automotive magneto-rheological brake. *Mechatronics* (2008) **18**(8): 434−447.
[8] Nguyen, Q. and Choi, S. Optimal design of an automotive magnetorheological brake considering geometric dimensions and zero-field friction heat. Smart Materials and Structures (2010) **19**: 115024 (11pp)
[9] Carlson, J. D. What makes a good MR fluid? *J. Intell. Mater. Syst. Struct.* (2002) **13**: 431.
[10] Usoro, P. B. Smith, A. I. C-K, K. Moser, G. and Sommer, G. Magnetorheological fluid clutch. Patent US Patent Specification 6,318,531 B1 (2001).
[11] Guth, D. and Maas, J. Magnetic fluid control. Patent DE Patent Specification 10 2011 119 919.9 (2011).
[12] Guth, D. Schamoni, M. and Maas, J. Magnetic fluid control for viscous loss reduction of high-speed MRF brakes and clutches with well-defined fail-safe behavior. *Smart Mater. Struct.* (2013) **22:** 094010.
[13] Shamieh, H. and Sedaghati, R. Design Optimization of a Magneto-Rheological Fluid Brake for Vehicle Applications. In: ASME Conference on Smart Materials, Adaptive Structures and Intelligent Systems, Stowe, VT, USA, 28-30 September (2016).
[14] Zubieta, M. Eceolaza, S. Elejabarrieta, M. J. and Bou-Ali, M. M. Magnetorheological fluids: characterization and modeling of magnetization. *Smart Mater. Struct.* (2009) **19**: 095019.
[15] Supermagnete. How do you calculate the magnetic flux density? [Retrieved Online on June 11, 2016]. Available on: https://www.supermagnete.de/eng/faq/How-do-you-calculate-the-magnetic-flux-density#ring-magnet.
[16] Supermagnete, "Physical Magnet Data," [Retrieved Online on June 12, 2016]. Available on: https://www.supermagnete.de/eng/data_table.php.
[17] Rossa, C. Jaegy, A. Lozada, J. and Micaelli, A. Design Considerations for Magnetorheological Brakes. In: IEEE ASME Transactions on Mechatronics (2014) **19**(5): 1669-1680.
[18] Webb, G. M. Exercise Apparatus and Associated Method Including Rheological Fluid Brake. United States Patent Office Patent US Patent No. 5810696, (1998).

VIII ECCOMAS Thematic Conference on Smart Structures and Materials
SMART 2017
A. Güemes, A. Benjeddou , J. Rodellar and Jinsong Leng (Eds)

FINITE ELEMENT METHOD SIMULATIONS IN MAGNETORHEOLOGY

JOSE R. MORILLAS AND JUAN DE VICENTE

Department of Applied Physics, University of Granada,
Faculty of Science, 18071-Granada, Spain

emails: jmorillas@ugr.es, jvicente@ugr.es

Key words: Magnetorheological fluids, finite element method simulations, yield stress

Abstract. Finite Element Methods have been thoroughly used in the past to simulate the yield stress and storage modulus in model magnetorheological fluids. There are essentially two approaches, involving the calculation of the magnetostatic force between two isolated particles or within a cubic array of single particle-width chains. Eventually, the yield stress (storage modulus) is calculated from the maximum (initial slope) of the simulated shear stress versus shear strain curves. Current simulation methodologies have two important limitations: i) a pure shearing flow is not actually imposed; instead the particle chains are stretched and forces/fields are projected along the flow direction, ii) the field boundary conditions are not correctly applied; instead the magnetic field is fixed as a constant (i.e. the external field) at the boundaries of the computational domain. These two limitations make the current models invalid for medium-to-large concentrations that are of interest in commercial applications. In this communication we propose a novel and very simple Finite Element Method that grounds on a reduced field formulation with periodic boundary conditions. On the one hand, the reduced field formulation allows us to set the applied magnetic field as a domain property so it is not necessary to impose it at the boundaries. On the other hand periodic boundary conditions allow us to reproduce a truly three dimensional network of particles. As a result, the kinematics is simply created by shearing the unit cell and simulations are not restricted anymore to dilute suspensions involving single particle-width chains.

INTRODUCTION

Magnetorheological (MR) fluids are field-responsive suspensions that exhibit a liquid-to-solid transition upon the application of an external magnetic field. In the absence of a magnetic field they behave as nearly Newtonian liquids. Contrarily, in the presence of a magnetic field, the particles become magnetized and interact forming chain-like structures. As a consequence of the formation of these elongated structures, the suspensions exhibit a yield stress (i.e. a minimum stress is needed to make the suspensions flow under field)[1,2].

For simplicity, magnetostatic interactions between particles are typically considered under the dipolar approximation. However, a dipolar approximation is only valid under two particular scenarios: (1) very dilute suspensions and/or (2) saturating fields. However, as stated above, particles get into close contact under structuration and typically the magnetic fields applied are not large enough to ensure the full saturation of the particles. As a result, a dipolar approximation is a rude one and multipoles are definitely needed if we aim for a precise determination of the properties of the suspensions (e.g. yield stress).

Among the techniques available to incorporate multipolar interactions we are particularly interested in Finite Element Method (FEM) simulations. This numerical method provides the magnetic field distribution in a space domain by directly solving Maxwell's equations. For this, the simulation box is divided in subdomains having different magnetic properties (specified by the constitutive equation of each material) and properly delimited by a set of boundary conditions.

Previous studies on MR fluids using FEM simulations can be classified in two groups: i) those papers focused on the calculation of two-body interparticle interactions with emphasis in the influence of magnetic field strength[3], morphology and particle surface characteristics[4,5], and ii) those papers interested in the (multibody) calculation of the yield stress and storage modulus of prescribed arrays of particles in single-width particle chains[6-9]. In this manuscript we are interested in precisely simulating the yield stress and storage modulus of preassembled structures.

Currently, MR fluids of interest in the vast majority of commercial applications are necessarily concentrated. However, FEM simulations reported to date on the yield stress of MR structures are not accurate enough and definitely fail for large particle concentrations. On the one hand, the magnetic field strength on the boundaries of the simulation box is assumed to be the external one and this is not an acceptable assumption for large packing fractions (narrow simulation boxes)[6-9]. On the other hand, the affine deformation of the structure is not appropriately implemented in the simulation by simply decomposing in elongation + rotation movements[8,9]. In this communication we propose a novel approach that grounds on a reduced field formulation with periodic boundary conditions. This novel approach allows us to overcome these two limitations.

SIMULATION METHODOLOGY

The magnetic field was obtained by numerically solving Maxwell's equations for magnetostatics (COMSOL Multiphysics). In the steady state without free currents -from Ampere law equation- it can be deduced that the magnetic field is derivable from a scalar potential:

$$\vec{H} = -\nabla V \tag{1}$$

At this point, a reduced field formulation is introduced that allows us to split total magnetic field in two contributions: (i) a homogenous background field that is set as the external magnetic field and (ii) a perturbation due to the presence of the magnetizable particles. Therefore, equation (1) is rewritten as

$$\vec{H} = \vec{H}_{ext} - \nabla V_p \tag{2}$$

where $\vec{H}_{ext} = H_{ext}\hat{z}$ is the external applied field and V_p is the perturbation scalar potential. The main advantage of this formulation is that the external magnetic field can be set in the model as a domain property (not a boundary property).

Next, equation (2) is solved together with Gauss law for magnetic field flux density:

$$\nabla \cdot \vec{B} = \mu_0 \nabla \cdot \left(\mu_r \vec{H}\right) = 0 \tag{3}$$

Here μ_r is the relative magnetic permeability of each simulated subdomain. In the case of the carrier fluid $\mu_r = 1$. On the other hand, the non-linear magnetization of particles is modeled using the Frölich-Kennelly equation for the permeability:

$$\mu_r = 1 + \frac{(\mu_i - 1)M_s}{M_s + (\mu_i - 1)H} \tag{4}$$

In the evaluation of equation (4) we take $\mu_i = 1000$ as the initial permeability and $M_s = 1600\ kA/m$ as the saturation magnetization.

We further assume that in the quiescent state particles aggregate forming single-width chains along the field direction in an infinite tetragonal lattice (Figure 1a). Next, when the MR fluid is strained in the perpendicular direction to the external field (for example, in the $\hat{y}$ direction, see Figure 1b), particles are supposed to deform affinely with the commanded strain γ. As a consequence, the initial tetragonal lattice becomes a monoclinic one whose inclination angle θ verifies $\gamma = \tan\theta$.

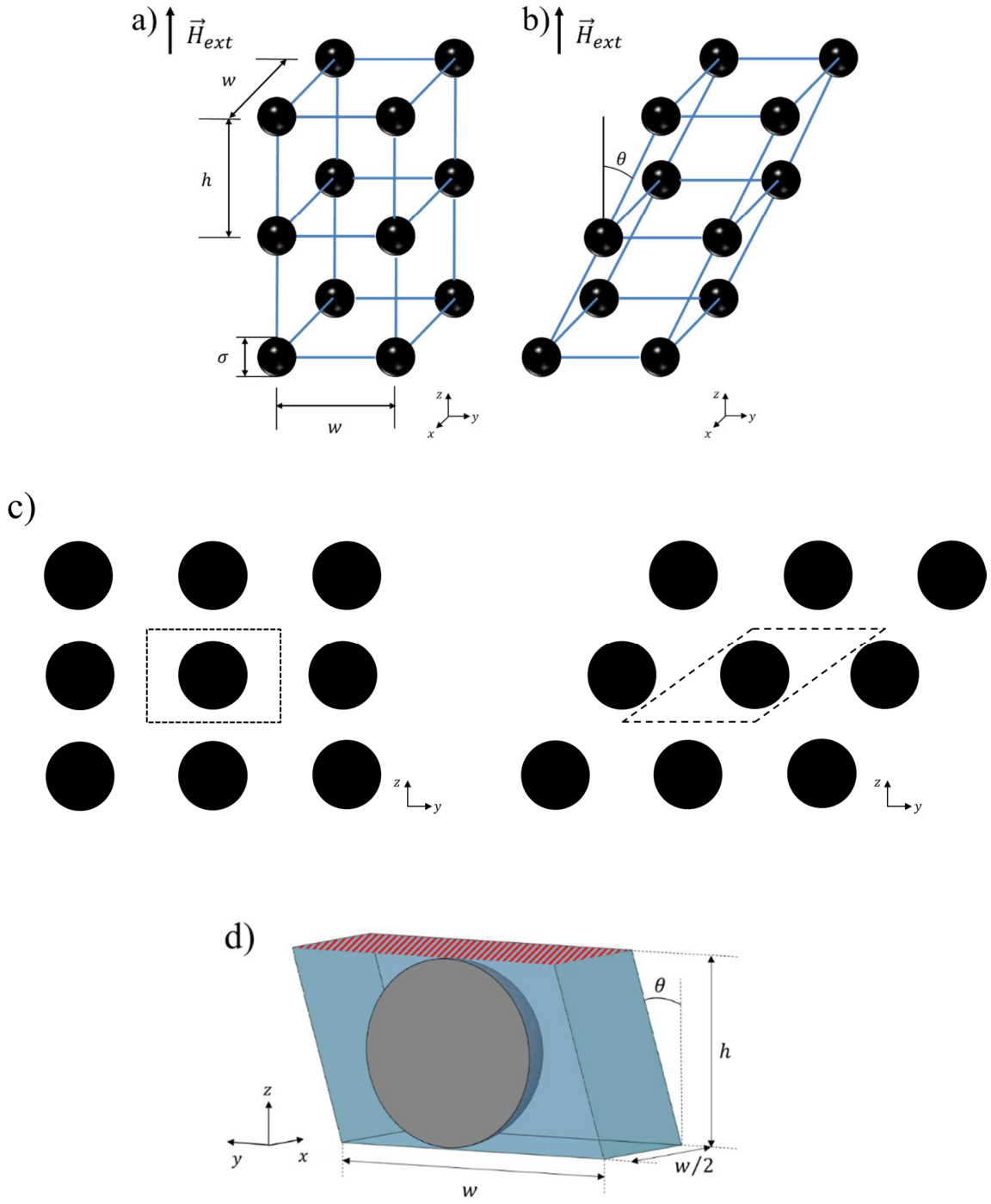

Figure 1: (a) Under the presence of an external field particles are supposed to be arranged in a tetragonal lattice. (b) A monoclinic lattice is generated under affine deformation with a shear strain $\gamma = \tan\theta$. (c) Unit cell in tetragonal and monoclinic lattices (dashed lines). (d) Strained computational domain in 3D. Symmetric boundary conditions are imposed in faces perpendicular to x direction while periodic boundary conditions are set in the rest of the faces.

The size of the unit cell is given by the particle diameter σ and the volume fraction ϕ. Theoretically, its height (dimension in the direction of the applied field) should be σ, however this would imply a tangential point between top/bottom faces of the unit cell and the particle. As tangential points are not allowed in FEM due to meshing requirements, necessarily an interparticle gap Δ had to be added, therefore the cell height is given by $h = \sigma + \Delta$. The lateral distance between chains in the lattice (or equivalently the width of the unit cell w) was selected in order that the particle volume fraction is ϕ. In the case of a tetragonal lattice $w = \sqrt{\sigma^3 \pi / 6\phi h}$.

Once the magnetic field distribution is solved for different strains, the shear stress is determined from the magnetic force acting on the particles. The force in the strain direction, acting on the particles placed in the upper half of the lattice due to the bottom ones, is calculated by integrating the corresponding Maxwell's stress tensor components over the top boundary of the unit cell for our simple tetragonal lattice (see the red striped surface in Figure 1d). Next, the shear stress is obtained by dividing the magnetic force by the area of the top face:

$$\tau = \frac{F_y}{w^2/2} = \frac{2}{w^2 \mu_0} \int B_y B_z ds \tag{5}$$

Finally, yield stress is identified as the maximum in shear stress versus shear strain curves.

RESULTS AND DISCUSSION

A key publication on FEM applied to MR fluids is undoubtedly the classical paper by Ginder and Davis[8]. Therefore, we start our discussion with a direct comparison of the results obtained using the proposed method with the one by Ginder and Davis[8]. The curves corresponding to the normalized shear stress versus shear strain are shown in Figure 2 together with the original results obtained by Ginder and Davis[8] for the same tetragonal lattice. We follow their normalizations using our parameters (in our case $\vec{H}$ is imposed instead of $\vec{B}$).

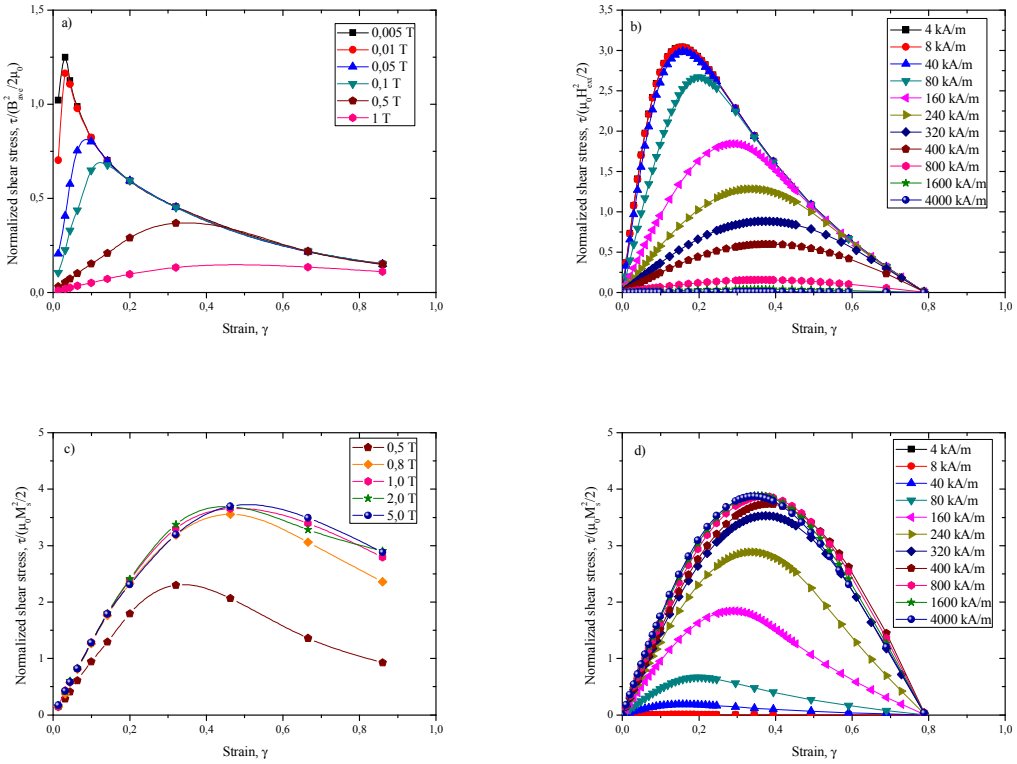

Figure 2: Shear stress as a function of the applied shear strain for different external magnetic fields and a fixed volume fraction of $\phi = 0.2$. The yield stress is identified as the maximum of each curve. The shear stress is normalized by the external field squared (a and b, note different y-axis scales are used) and by saturation magnetization squared (c and d). Graphs a and c come from Ginder and Davis[8] whereas graphs b and d are results from the proposed method. The equivalence between Tesla in the manuscript by Ginder and Davis[8] and our work is as follows: 0.005 T = 4 kA/m, 0.01 T = 8 kA/m, 0.05 T = 40 kA/m, 0.1 T = 80 kA/m, 0.5 T = 400 kA/m, 1 T = 800 kA/m, 2 T = 1600 kA/m, 5 T = 4000 kA/m.

As it was expected, for the smaller magnetic fields the normalization by H_{ext}^2works well due to the fact that there are not saturated poles within the particle and they behave in the linear magnetization regime. On the other hand, for large magnetic fields the yield stress is appropriately normalized by M_S^2. Although the obtained yield stress values are similar to those published by Ginder and Davis[8], it can be observed that the shape of the stress (τ) vs. strain (γ) curves are clearly different. The reason for this resides in the method used in Ginder and Davis[8] to implement the applied strain. In their work, the strain is approximated by an elongation -of the chains- followed by a rotation -of the elongated chains- an angle $\theta = \tan^{-1}\gamma$. The axial force is calculated during the chain elongation and corrected by a factor that is dependent on the strain, $\sin\theta\cos\theta = \gamma/(1+\gamma^2)$, to take into account the rotation. The approach followed by Ginder and Davis[8] retains symmetry and therefore permits a 2D calculation but does not produce the true strain experimented by the chains. In order to see

this, in Figure 3 we schematically depict together the real and simulated strains acting on the chain.

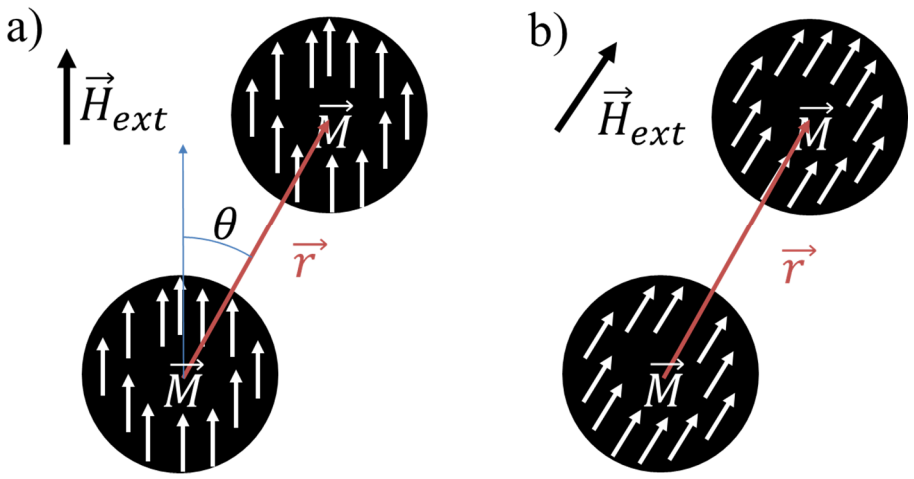

Figure 3: Under a real strain γ (a), mean magnetization vector forms an angle $\theta = \tan^{-1}\gamma$ with the position vector of the neighboring particle. However under the approximation of Ginder and Davis[8], the mean magnetization vector is aligned with the axis of the chain (b) to keep the cylindrical symmetry of their model.

A major difference between our simulations and those performed by Ginder and Davis[8] is that in their simulations the magnetization vector within the particles is always aligned with the vector position under straining. As a result, the magnetostatic force between the particles is always attractive and when it is corrected by the rotation force keeps its sign because of $\sin\theta\cos\theta$ is positive in the range 0º to 90º. In contrast, in our simulations magnetostatic forces between the particles can be negative depending on their arrangement.

The major achievement of our model is that, due to the imposed periodic boundary conditions, it is not needed to rotate nor elongate the system since the true real strain is simply modeled by straining the computation domain (see Figure 1c and 1d). Going back to Figure 2 it can also be seen that the critical strain γ_c (associated to the yield stress) increases with the applied field. Even more interesting is the fact that γ_c exhibits a lower threshold limit ($\gamma_c \sim 0.15$) at small H_{ext} in clear contrast to Ginder and Davis[8] where γ_c asymptotically reaches zero with smaller B_{ave}. In addition, our simulations predict a negative stress for sufficiently large strain levels. This is expected not only due to the anisotropic behavior of the magnetic force but also because of the proximity of neighboring particles. The calculated critical strain for sign reversal is $\gamma_c = \sqrt{\pi/24\phi}$ in good agreement with simulations data. This result is again in clear contrast with the data obtained by Ginder and Davis[8] where the shear stress tends to zero for large strains.

Finally, in Figure 4 we show the yield stress dependence on the external magnetic field for two volume fractions. Together with these simulation data we also include experiments from Ruiz-López et al.[10]. As observed, a reasonably good qualitative agreement is obtained. Experimental and simulation results show the same tendency although the

simulations overestimate the experimental data. At this point it is worth to remark that conventional MR fluids used for comparison were based on carbonyl iron microparticles with an initial permeability of 8.9 ± 0.7 and a saturation magnetization of 1820 ± 40 kA/m (both parameters were obtained by fitting equation 4 to the magnetization curve of iron powders). Clearly, the initial permeability is different from that taken in simulations (1000) and this could explain the overestimation of simulations for small fields. Nevertheless, saturation magnetization levels are similar in both cases and we would expect a similar yield stress for experiments and simulations. The discrepancy at large fields suggests that, in the real systems, more complex and less energetically favorable structures form under fields in contrast to the proposed model lattice.

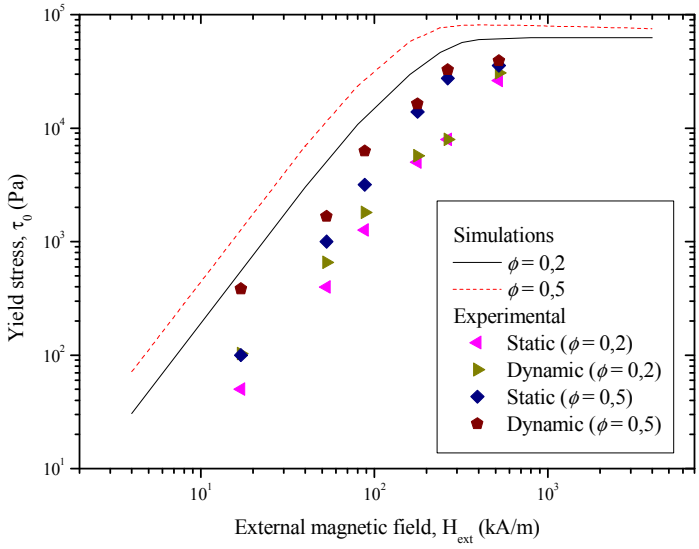

Figure 4: Yield stress as a function of the external field for volume fractions of 0.2 and 0.5. Together with simulation data we also plot experiments from Ruiz-López et al.[10] corresponding to static and dynamic yield stresses.

CONCLUSIONS

We propose a novel Finite Element Method simulation approach for the precise computation of interparticle (multipolar and multibody) magnetostatic forces on preassembled structures. The referred approach grounds on a reduced field formulation with periodic boundary conditions. It satisfactorily captures the real strain experienced by the particle array and is capable to simulate large packing fractions. The yield stress results obtained using the proposed model are thoroughly compared to previous FEM results by Ginder and Davis[8] and experimental data by Ruiz-López et al.[10]. The methodology can be easily extended to other lattices such as body centered BCT and the results are expected to be of interest for the design of novel MR elastomers.

REFERENCES

[1] Ginder, J.M. Behavior of magnetorheological fluids. *MRS Bull*. (1998) **23(8)**: 26-29.

[2] Bossis, G., Lacis, S., Meunier, A. and Volkova, O. Magnetorheological fluids. *J. Magn. Magn. Mater*. (2002) **252**: 224-228.

[3] Klingenberg, D.J., Ulicny, J.C. and Golden, M.A. Mason numbers for magnetorheology. *J. Rheol*. (2007) **51**: 883-893.

[4] Vereda, F., Segovia-Gutiérrez, J.P., de Vicente, J. and Hidalgo-Alvarez, R. Particle roughness in magnetorheology: effect on the strength of the field-induced structures. *J. Phys. D: Appl. Phys*. (2015) **48**: 015309 (11pp).

[5] Vereda, F. de Vicente, J. and Hidalgo-Alvarez, R. Effect of surface roughness on the magnetic interaction between micron-sized ferromagnetic particles: Finite element method calculations. *Journal of Intelligent Material Systems and Structures* (2016) Special Issue Article (7pp).

[6] Davis, L.C. Finite-element analysis of particle-particle forces in electrorheological fluids. *Appl Phys Lett*. (1992) **60**: 319-321.

[7] Davis, L.C. Polarization forces and conductivity effects in electrorheological fluids. *J Appl Phys.* (1992) **72**: 1334-1340.

[8] Ginder, J.M. and Davis, L.C. Shear stresses in magnetorheological fluids: Role of magnetic saturation. *Appl Phys Lett*. (1994) **65**: 3410-3412.

[9] Ginder, J.M., Davis, L.C. and Elie, L.D. Rheology of magnetorheological fluids: Models and measurements. *Int. J. Mod. Phys. B*. (1996) **10**: 3293-3303.

[10] Ruiz-López, J.A., Fernández-Toledano, J.C., Hidalgo-Alvarez, R. and de Vicente, J. Testing the mean magnetization approximation, dimensionless and scaling numbers in magnetorheology. *Soft Matter* (2016) **12**: 1468-1476.

Impact responses of a magnetorheological energy absorber

Xian-Xu 'Frank' Bai, Sheng Shen, Fei-Long Cai and Sen Yang

Laboratory for Adaptive Structures and Intelligent Systems (LASIS),
Department of Vehicle Engineering, Hefei University of Technology, Hefei, 230009, China
Email: bai@hfut.edu.cn - Web page: http://www.hfut.edu.cn

ABSTRACT

Magnetorheological (MR) fluids are a kind of smart material with a reversible rheological property in milliseconds and large range of controllability. The controllable actuators-energy absorbers (EAs) based on MR fluids have prospect to be applied to the control systems to mitigate the high-speed impact. To verify the feasibility of MREAs for high-speed impact, a MREA utilizing an internal bypass that we proposed earlier is further investigated in this paper. The MREA is a linear configuration with double cylinders. The piston connected with a piston rod divides the inner cylinder into two chambers. Inlets/Outlets set at the upper/lower of inner cylinder are used to connect the inner cylinder chambers and the MR fluid flow channel sandwiched between the inner and outer cylinders into a whole. Based on the flow properties between parallel plates, the mathematical model of mechanical properties of MREA under impact loads is established, and the flow model of MREA is constructed in software ANSYS/Fluent. The damping force characteristics of the MREA prototype are tested under different impact loads based on our test bench in Hefei University of Technology. The research results, including controllable damping force range, constant stroking load velocity range (which is defined by the controllable velocity range that can be adapted by tuning the applied current to the MREA to have the damping force achieve a specific damping force level), and response time, are analysed and compared with the mathematical model.

Figure 1 presents the comparison of constant stroking load velocity ranges of MREA with an internal bypass and conventional MREA. As shown in figure 1, for various damping forces, 1 kN, 2 kN, and 3 kN, the constant stroking load velocity ranges of the MREA with an internal bypass are much wider than those of the conventional MREA. For the conventional MREA case, the smaller the specified damping force level is, the wider the constant stroking load velocity range is.

Figure 2 presents the mechanical response of MREA with an internal bypass under different exciting current levels and different impact excitations.

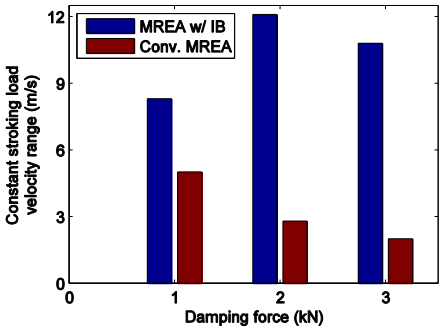

Figure 1. Constant stroking load velocity ranges of the MREA with an internal bypass and conventional MREA for specific damping forces.

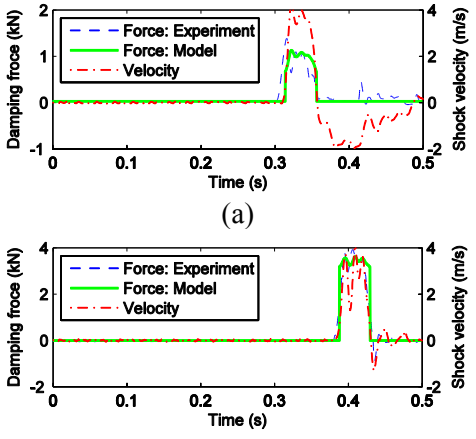

Figure 2. Impact response of the MREA with an internal bypass at initial impact velocity of 4 m/s: (a) $I = 0$ A and (b) $I = 4$ A.

VIII ECCOMAS Thematic Conference on Smart Structures and Materials
SMART 2017
A. Güemes, A. Benjeddou , J. Rodellar and Jinsong Leng (Eds)

Inverse Modelling of Magnetorheological Elastomer Isolator with Recurrent Neural Network and Genetic Algorithms for Real-time Control

Guanyao Liao[†], Jie Fu[*] , Junjie Lai[†], Junfeng Bai[†] and Miao Yu[†]

[*] Key Lab for Optoelectronic Technology and Systems, Ministry of Education, College of Optoelectronic Engineering, Chongqing University, Chongqing 400044, China
e-mail: fujie@cqu.edu.cn

Key words: Magnetorheological Elastomer Isolator, Hysteresis, Inverse Model, Jordan Network, Genetic Algorithm.

Abstract. Due to the controllability of stiffness and damping under the applied external magnetic field, magnetorheological elastomer (MRE) isolator has been proved effectively in the field of vibration control. For the realization of vibration control system, an accurate inverse model of MRE isolator is particularly important. However, the existing researches mainly focus on forward model for MRE isolators, including parametric and non-parametric models. But to date, there are few papers published on the inverse modelling of a MRE isolator. Feedforward neural networks have been applied to emulate the inverse dynamic behaviours of magneto-rheological dampers due to their good learning capability. But the data used for the training and validating of neural network is generated from numerical simulation of the parametric models proposed for an MR damper, which may be great differences from the practical application. In addition, the feedforward neural network is a static network, and has lower accuracy and poorer capacity of resisting disturbance. In this paper, a recurrent neural network (RNN) named Jordan network is proposed to approximate the inverse dynamic behaviours of a MRE isolator in shear-compression mixed mode by combining the genetic algorithms to search for the optimal network configuration. The dynamic characterization test system of the MRE mixed mode isolator is established, and the output forces of the isolator are obtained under different loading conditions (variable displacement with amplitudes and frequencies). Different from the direct current in forward mode of MRE isolator, the current used for training and validating of the network model is sinusoidal signal, which is also approximate to the real-time control application well. Experimental results show that the proposed Jordan network with genetic algorithms can represent inverse dynamic behaviours of the MRE isolator satisfactorily.

1 INTRODUCTION

As a kind of semi-active isolator, MRE isolators have the advantages of reversibility, fast response, and wide variation range of operation frequency [1], so they have been paid more and more attention in the engineering fields of civil structure [2-4], vehicle seat suspension [5], precision fabrication vibration isolation [6, 7].

The inverse model of MRE isolator is critical element in real time control application. If the

inverse model is not described accurately, it will lead to unsatisfied control result. However, in published paper there are few papers to establish the inverse model of MRE isolator. In general, there are two approaches to obtain the inverse models of systems. One is inverting the derived forward model. Some papers on the forward MRE isolator modelling are reported in [8-13] which are all focused on parametric models. Due to the highly nonlinearity of MRE isolator, their parametric models are complex and there are too many parameters to be identified. Moreover, if the inverse models are to be derived from these forward parametric models, the invertibility and zero dynamics of these models must be investigated first. Therefore, it is difficult to obtain the corresponding inverse dynamic model by inverting the derived forward model. The other is directly identifying the inverse model from the input and output data set without relying on a precise mathematical model.

Neural network (NN) is an effective non-parametric modelling method to approximate any nonlinear mapping relationship between input and output, which is not able to be solved by a mathematical model. Yu et al. [14] proposed a feedforward NN with ant colony algorithm to model the laminated MRE base isolator. Fu et al. [15] employed NARX network to identify the model of MRE mixed mode isolator. The results show that NARX network has higher accuracy and stronger robustness than BP network. This identification method by using neural network model provides possibility for the establishment of inverse MRE isolator models. However, the current used in above papers is constant current, it does not approximate the time-vary continuous current well in real time control system. In addition, the repetitive test condition is also a challenge. Moreover, the NARX network structure in [15] is determined by trial and error method, which cannot guarantee the optimal network structure found. The genetic algorithm (GA) [16-19] is a kind of optimization algorithm based on the mechanism of natural selection and evolution. It encodes the parameters to be solved and do some basic genetic operations on these codes, such as reproduction, crossover and mutation. Since the ability of GA to make a robust search for a global optimum in complex space, it has been applied in many applications. It has been shown that GA is quite well in identifying the NARX network model for a wide class of non-linear systems [20, 21]. Therefore, GA is employed in this paper to optimize the structure of Jordan network model for MRE isolation system.

In this paper, the inverse model of MRE isolator is established by employing Jordan RNN and GA. Different from the training data produced by parametric model, such as a Bouc-Wen model [22], the data is obtained by experimental tests under different sinusoidal excitation displacement with variable amplitudes and frequencies in this paper. In addition, exciting current in the test is a sinusoidal wave signal, not constant current, which are more approximate accurately to the real application. Based on the experimental data, the Jordan RNN is employed to identify the inverse model of MRE isolator. Meanwhile, the GA is used to optimize the structure of the Jordan network. The training and generalization of network show that the proposed Jordan RNN with GA can approximate the MRE isolation inverse model accurately.

2 DYNAMIC CHARACTERISTIC EXPERIMENT OF MRE ISOLATOR

2.1 Experimental setup

The structure of mixed mode MRE isolator in this paper is shown in Figure 1. The material used in this testing is silicone rubber MRE, in which the mass fraction of carbonyl iron particles, silicon rubber and silicone oil is 70%, 15% and 15%, respectively. The MRE material is cut into two pieces, one of which operates on shear mode with the size of 40×4×4mm, and the other works on compression mode with the size of ϕ20×4mm.

Considering the practical application of control system, the output of controller is usually an alternating current for MRE isolator. Therefore, in order to characterize the performance of the MRE isolator under the alternating current, a series of experimental tests are conducted. The experimental system is shown in Figure 2. The MRE isolator is installed on the electromagnetic vibration table (model MPA406/M232A; ETS Solutions (Beijing) Led, China) which supplies an excitation signal for the isolator. A load cell (BISE5110，No.0748) is connected to the top of the MRE isolator and the other end is fixed to the three-jaw chuck to measure the output force generated by the isolator. A laser displacement sensor (model LK-H025; KEYENCE, Japan) used to measure the excitation displacement signal of the base is mounted on the vibration table. The desired voltage signal waveform output by dSPACE AutoBox (Model DS1005, dSPACE, Germany) is applied to the current driver to generate corresponding exciting current signal for MRE isolator. The voltage and current signals are converted by current driver in the ratio of 1:1. A current probe is used to measure the current signal output from the current driver. The excitation displacement signal, exciting current signal and output force signal are collected simultaneously by a data acquisition instrument (model MDR-05, Beijing Aerostandard New Technology Company, China) and transferred to the computer for processing and analyzing.

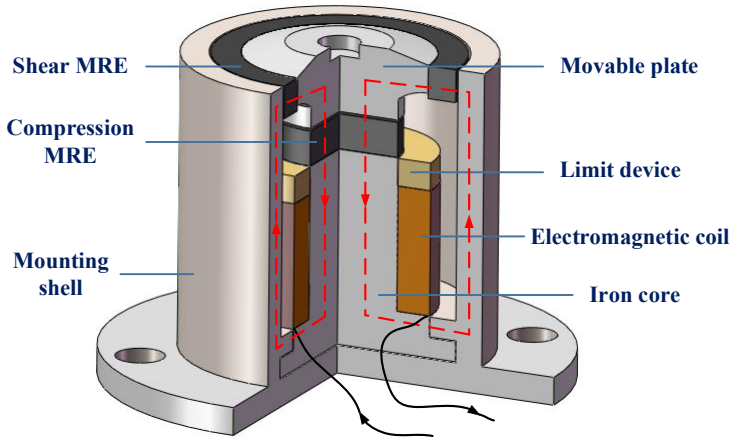

Figure 1. Structure of MRE isolator with shear-compression mixed mode

By applying various harmonic inputs of excitation displacement and exciting currents, the response forces of the isolator can be recorded. To make the identified model fully represent the MRE isolation system, the test condition should cover the work frequency and amplitude ranges of input variables. As a result, three displacement amplitudes of 0.045 mm, 0.09 mm and 0.13 mm (corresponding to 2.3%, 4.5% and 6.5% shear strain) are selected for the tests

under different loading frequencies (40, 60 and 80 Hz). The corresponding harmonic current signals with three frequencies (40Hz, 60Hz and 80Hz) and four level*s (0A, 0-0.6*A, 0-1.0A and 0-1.5A) are applied to the isolator to characterize the dynamic performance. In each test, the sampling frequency is set to 2048Hz. The velocity responses are obtained by deriving the measured displacements.

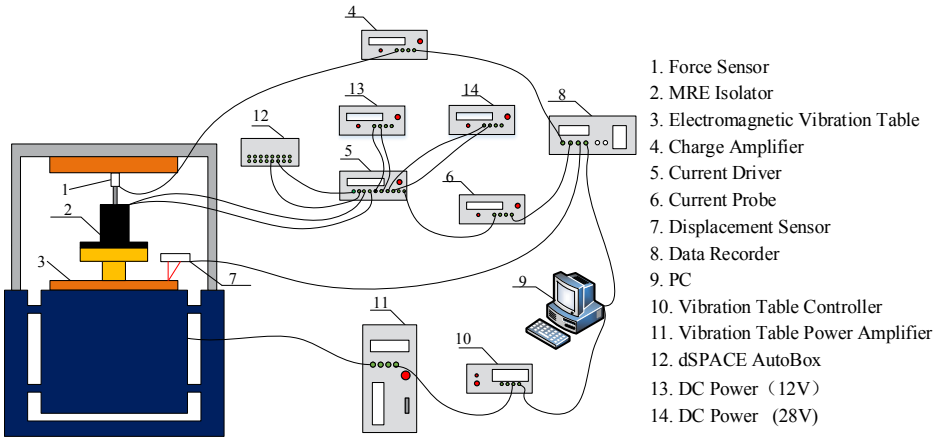

(a)



(b)

Figure 2: Experimental equipment: (a) sketch (b) picture

2.2 Experimental results and analysis

The exciting currents and the corresponding force responses of the MRE isolator under the different applied sinusoidal currents (0A, 0-0.6A, 0-1.0A and 0-1.5A, respectively) with sinusoidal excitation displacement (0.09mm amplitude and 40Hz frequency) are shown in Figure 3. The frequency of applied current is corresponding to the excitation displacement. From the figure, it can be seen that the measured force has a significant increase with increasing of applied currents. The force-displacement curves of the isolator under different loading conditions are shown in Figure 4. As the applied current increases, the slope and area of the force-displacement loop grow. Based on the identification theory in [15] and measured

force-displacement curves of the isolator, the identified parameters including maximum force, effective stiffness and equivalent damping are listed in table 1. The maximum force is directly proportional to the excitation displacement amplitude, while the effective stiffness and equivalent damping are inversely proportional to that one.

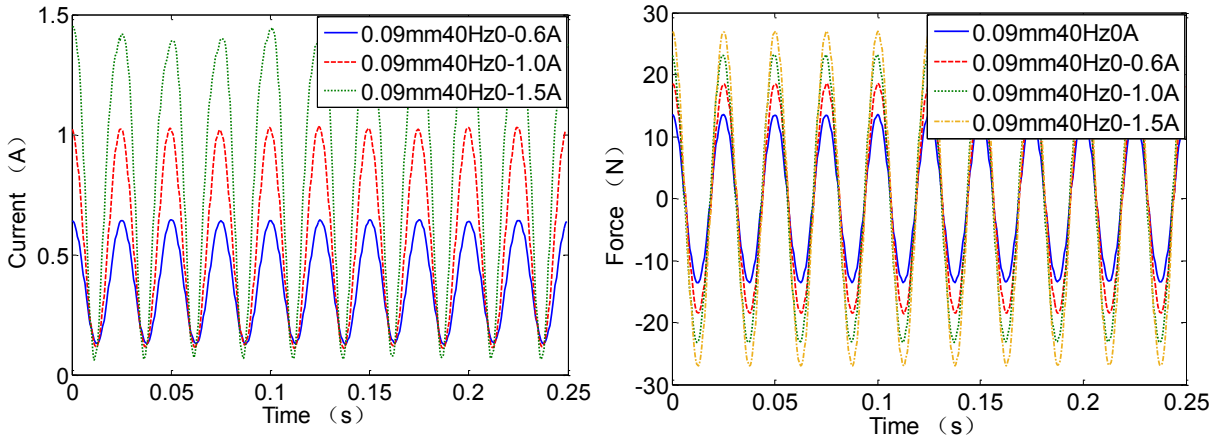

(a) (b)

Figure 3: The measured signal of the isolator under different currents with sinusoidal excitation (0.09mm-40Hz): (a) Exciting currents; (b) corresponding forces

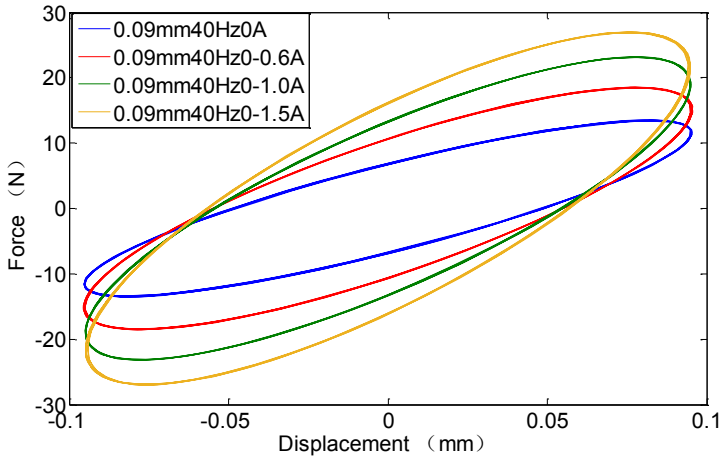

Figure 4: Force-displacement loops of the isolator under different currents with sinusoidal excitation (0.09mm-40Hz)

Table 1: Indentified parameters of the MRE isolator under different loading conditions with the excitation frequency of 40Hz

		0A	0-0.6A	0-1.0A	0-1.5A
Maximum Force (N)	0.045mm	13.57	18.34	19.12	19.13
	0.09mm	23.16	30.37	37.90	43.16
	0.135mm	32.14	40.48	45.00	60.00
Effective Stiffness(kN/m)	0.045mm	142.85	192.53	200.49	200.72
	0.09mm	121.58	159.38	199.73	227.99
	0.135mm	112.32	141.91	158.01	211.70

Equivalent Damping(N*s/m)	0.045mm	291.62	550.23	651.76	653.40
	0.09mm	286.04	443.46	556.13	676.25
	0.135mm	268.44	414.19	543.74	534.02

3 INVERSE MODELING AND VALIDATION FOR MRE ISOLATOR

In the practical vibration control application, the inverse model of isolator is more practical than the forward model. The Jordan network based on GA is employed to describe the relationship between applied current and displacement, velocity and force in this paper.

3.1 Optimization network structure by real-coded genetic algorithm

The structure and learning algorithm of Jordan network have been described in detail in the literature [15]. Before training the Jordan network, the structure of the network needs to be determined which has a great influence on the training results. While, there is no clear functional relationship between the structure of network and the training results so far. The structure of RNN is usually determined by trial and error. This approach leads to tremendous amount of work and not smart enough. Hence, the real-coded GA is adopted to optimize the configuration of Jordan network to obtain an optimal network structure.

In the proposed method, for reducing the amount of computation, the network is assumed that contains two hidden layers and the number of hidden neurons is the same. The external input delay value d_e ($d_e \in [0,3]$), feedback input delay value d_f ($d_f \in [0,3]$) and hidden neuron number n are in sequential order. The range of hidden neuron number is set $[1,25]$. Each parameter to be optimized is an integer. The performance index (fitness value) defined for Jordan network is

$$F_{in} = 1/\mathrm{MSE}(e) \tag{1}$$

In equation (1), F_{in} is the fitness value in real-coded GA, and e is the error value between experimental value and predicted value. The initiation and update of GA parameters which is based on the literature work are listed in table 2. The flowchart of GA optimization process is shown in Figure 5.

At subroutine GA program, the parameters of Jordan network involving delay value and hidden neuron number have been optimized sequentially. The obtained design parameters of Jordan network using real-coded GA are given in table 2. Consequently, a four-layer network structure with two hidden layers is determined, which contains 7 input neurons, 20 hidden neurons in each hidden layer, 1 output neuron and 1 delay of external and feedback input.

Table 2: Initiation and update of GA parameters

maximum generation number	30
population number	20
mutation probability	0.01
crossover probability	0.8

Table 3: Optimized values of Jordan network

external input delay	1

feedback input delay	1
hidden neuron number	20

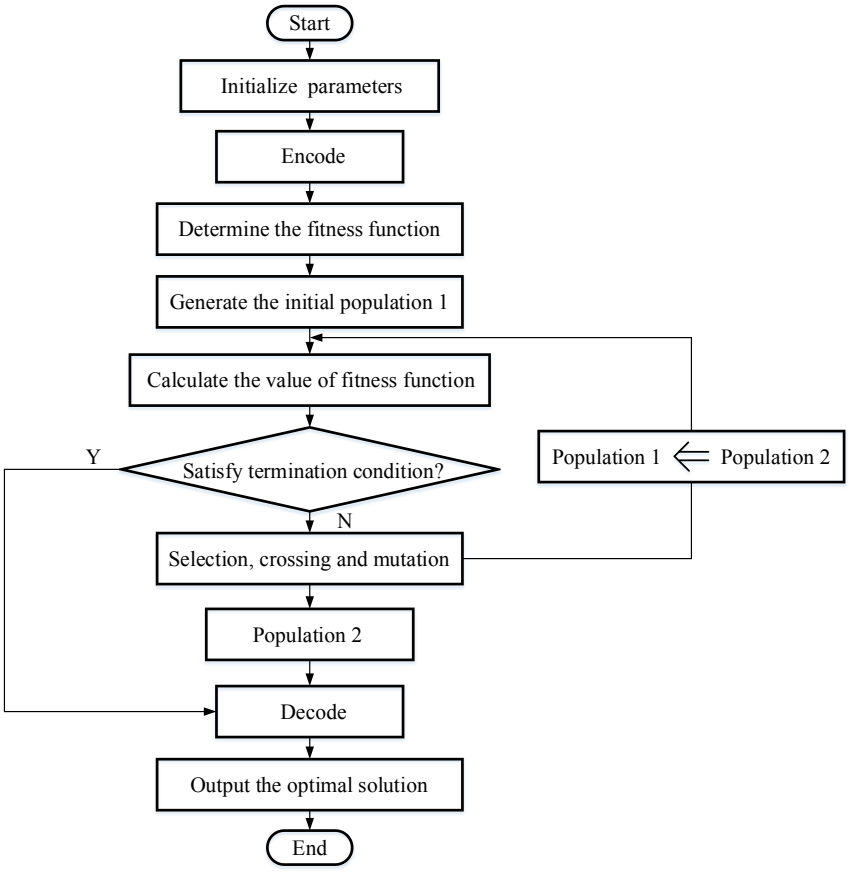

Figure 5: Flowchart of GA optimization process

3.2 Inverse modeling of MRE isolator

The inverse model identification scheme of MRE isolator with Jordan network is shown in Figure 6. The inputs of the network are displacement, velocity and force together with their delay values and previous force, while the output variable is applied current. The training sample data which comes from the experimental results in section 2 is used to train the determined network. The training results under the alternating current amplitude of 0A-0.6A are shown in Figure 7. The comparison between predicted current and measured current is shown in Figure 7(a). It can be observed that the predicted current and measured current can be well consistent. The mean squared error (MSE) between the predicted and measured currents is calculated as 7.6152e-06, which is small enough. Figure 7(b) shows the error distribution of training results with the range of [-0.00841, 0.007571]. It is apparent that the error is small and most of them are mainly distributed near the value of zero.

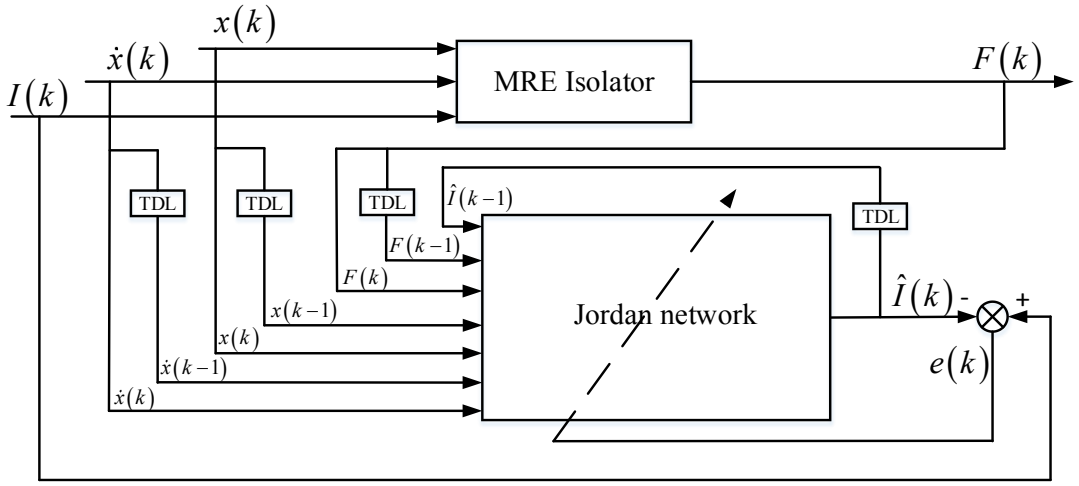

Figure 6: Inverse model identification scheme of the MRE isolator with Jordan network

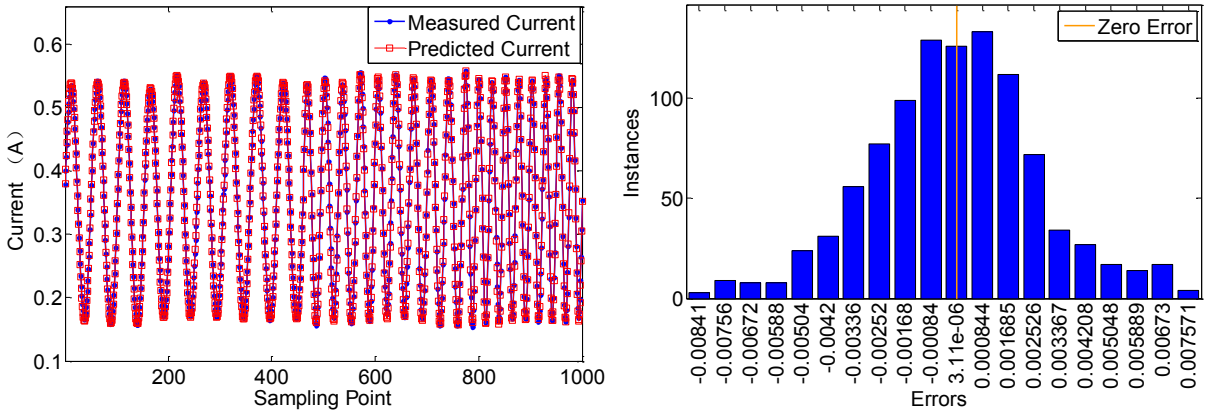

(a) (b)

Figure 7: Training results: (a) comparison between predicted values and experimental values; (b) error distribution

3.3 Model validation

Although the approximation capability of the Jordan network for training data is proved well, the generalization capacity of network is more emphasis in practice. In order to demostrate the generalization ability of the trained network, a new data set which is different from the training data is used to test the perfomance of the network. The test results are shown in Figure 8. In the comparison between predicted current and measured current as shown in Figure 8(a), it can be seen that the predicted value can be good match for the measured value. The MSE of test result is 2.8384e-04 which is also very small. But there are some small errors at some peak points. The error range of the network lies in [-0.08071, 0.06559] as shown in Figure 8(b). The regression value R is 0.99264 which is closer to 1. It demonstrates that the network has a better approximation capability to generalize.

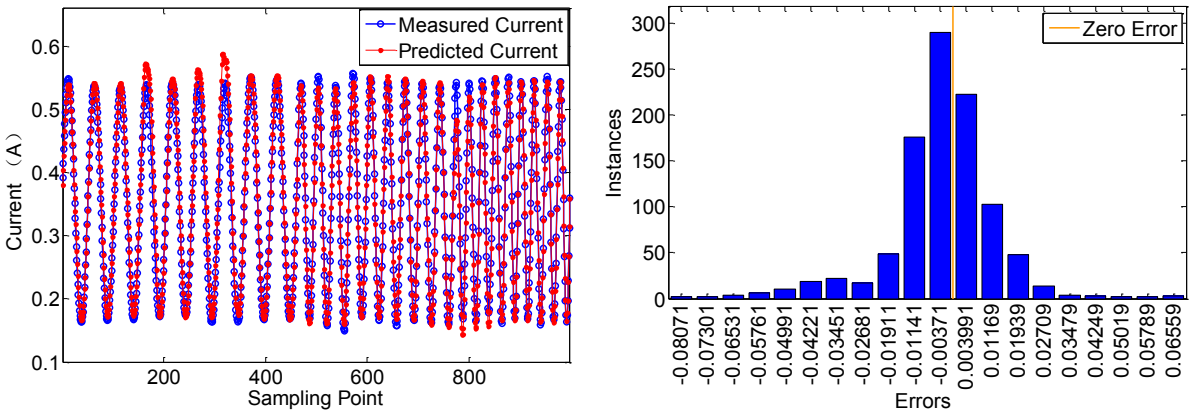

(a)

(b)

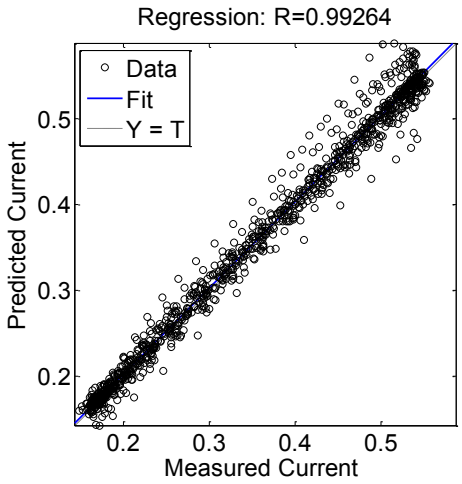

(c)

Figure 8: Generalization results: (a) comparison between predicted current and measured current; (b) error distribution; (c) regression

4 CONCLUSIONS

In this paper, the Jordan network is proposed to identify the inverse model of MRE mixed mode isolator. Considering the exciting current continuously varies with time in real time control system, the dynamic characteristic experiments of the isolator under different alternating currents are conducted to obtain the training and testing sample data. The real-coded GA is adopted to optimize delay value and hidden neuron number to obtain the optimal configuration of the Jordan network for the isolator. The training and generalization results of the network show that the proposed network with 7-20-20-1 neurons and 1 input delay can approximate the isolator's inverse model well according to MSE, error distribution and regression value. It provides the possibility for the application of the MRE isolator inverse model in vibration control applications.

REFERENCES

[1] Li, Y.C. Li, J.C. Li, W.H. et al 2014 A state of the art review on magnetorheological elastomer devices. *Smart Mater. Struct*. (2014) 23:1-24

[2] Yang, J. Sun, S.S. Tian, T.F. Li, W.H. Du, H.P. etc. Development of a novel multi-layer MRE isolator for suppression of building vibrations under seismic events. Mechanical Systems and Signal Processing, (2016) 70-71: 811-820.

[3] Behrouz, M. Wang, X. J. Gordaninejad, F. Performance of a new magnetorheological elastomer isolation system. Smart Mater. Struct. (2014) 23:494-501.

[4] Li, Y.C. Li, J.C. Li, W.H. et al Development and characterization of a magnetorheological elastomer based adaptive seismic isolator. Smart Mater. Struct. (2013) 22:035005.

[5] Du, H. P. Li, W.H. Zhang, N. Semi-active variable stiffness vibration control of vehicle seat suspension using an MR elastomer isolator. Smart Mater. Struct. (2011) 20:105003.

[6] Yang C.Y. and Fu, J. et al, A new magnetorheological elastomer isolator in shear-compression mixed mode. J. Intel Mat Syst. Str. (2015) 26: 1290–300.

[7] Fu, J. Li, P.D. Wang, Y. Liao, G.Y. Yu, M. Model-free Fuzzy Control of Magnetorheological Elastomer Vibration Isolation System: Analysis and Experimental Evaluation. Smart Mater. Struct. (2016) 25: 035030.

[8] Yang, J. and Du, H.P. et al Experimental study and modeling of a novel magnetorheological elastomer isolator. Smart Mater. Struct. (2013) 22: 117001.

[9] Behrooz M, Wang X.J. Gordaninejad F. Modeling of a new semi-active/passive magnetorheological elastomer isolator. Smart Mater. Struct. (2014) 23:045013.

[10] Li, Y.C. Li, J.C. A highly adjustable base isolator utilizing magnetorheological elastomer: experimental testing and modelling. J. Vib. Acoust. (2015) 137:011009.

[11] Yu Y. Li, Y.C. Li, J.C. A new hysteretic model for magnetorheological elastomer base isolator and parameter identification based on modified artificial fish swarm algorithm. International Symposium for Automation and Robotics in Construction. (2014) 176-183

[12] Yu Y. Li, Y.C. Li, J.C. Parameter identification of an Improved Dahl model for magnetorheological elastomer base isolator based on enhanced genetic algorithm. 23rd Australasian Conference on the Mechanics of Structures and Materials. (2014) 2:931-936.

[13] Yu Y. Li, Y.C. Li, J.C. Parameter identification and sensitivity analysis of an improved LuGre friction model for magnetorheological elastomer base isolator. Meccanica. (2015) 50:2691-2707.

[14] Yu Y. Li, Y.C. Li, J.C. Nonparametric modeling of magnetorheological elastomer base isolator based on artificial neural network optimized by ant colony algorithm. J. Intel Mat Syst. Str. (2015) 26:1789–98.

[15] Fu, J. Liao, G.Y. et al, NARX neural network modeling and robustness analysis of magnetorheological elastomer isolator. Smart Mater. Struct. (2016) 25:125019.

[16] Goldberg, D. E. Genetic Algorithms in Search, Optimization, and Machine Learning. Addison-Wesley, Reading, Massachusetts, (1989)

[17] Holland, J. H. Adaptation in Natural and Artificial Systems: An Introductory Analysis with Application to Biology, Control, and Artificial Intelligence. MIT Press, Cambridge, Massachusetts, (1993)

[18] Gen, M. and Cheng, R. Genetic Algorithms and Engineering Design. John Wiley, New York, (1997)

[19] Man, K. F., Tang, K. S. and Kwong, S. Genetic Algorithms, Concepts and Designs. Springer-Verlag, London, (1999)

[20] Luh, G.-C. and Wu, C.-Y. Non-linear system identification using genetic algorithms. Proc. Instn Mech. Engrs, Part I, Journal of Systems and Control Engineering, (1999) 213: 105–117.

[21] Li, C. J. and Jeon, Y. C. Genetic algorithm in identifying nonlinear auto regressive with exogenous input models for nonlinear systems. In Proceedings of the American Control Conference, San Francisco, California, (1993) 2–4: 2305–2309.

[22] Du, H.P. and Lam, J.et al, Modelling of a magneto-rheological damper by evolving radial basis function networks. Eng. Appl. Artif. Intel. (2006)19:869–881.

Monitoring Sedimentation of Magnetorheological Fluids Using a Vertical Axis Inductance Monitoring System with a Low Aspect Ratio Sensing Coil

Mingfu Wen[1,2], Jonathan Chambers[1], Stephen Sherman[1], Norman Wereley[1], Miao Yu[2]

[1]Department of Aerospace Engineering, University of Maryland
College Park, Maryland, USA 20742.
Email: wereley@umd.edu - Web page: http://aero.umd.edu/faculty/wereley
[2]College of Optoelectronic Engineering, Chongqing University,
Chongqing, China.
Email: yumiao.cqu@gmail.com

ABSTRACT

Adaptive energy absorbers (EAs) utilizing magnetorheological fluids (MRFs) to adjust stroking load to account for severity of impact, and payload mass, are currently being investigated for a number of severe impact or shock mitigation problems. Utilizing MRFs in such EAs requires a highly stable suspension that maintains a uniform concentration. Such suspension stability can be studied using a MRF column and a vertical axis inductance monitoring system (VAIMS), as shown in Figure 1, where an inductance sensor is translated along a vertical MRF column to track the mudline, which is defined as the boundary between the clarified fluid above, and the concentrated MRF below, the mudline. The rate of descent of the mudline is typically referred to as the sedimentation rate of the MRF. Prior work used a high aspect ration (tall) sensor coil [1-2], so that mudline location had to estimated. Therefore, key goals of this inductance sensor design were to: reduce magnetic flux leakage, apply lower magnetic flux, achieve higher spatial resolution to better locate mudline. A low aspect ratio inductance sensor was designed, fabricated and used to measure particle concentration in an MRF column. Using the low aspect ratio sensor coil, the magnetic flux applied to the MRF in the sensing volume was decreased by 20%. Using the VAIMS with the low aspect ratio coil, the inductance was measured as a function of MRF column height, and its spatial derivative was then calculated. The spatial derivative of inductance was used to more accurately determine the mudline in the MRF column. Discrimination of the mudline facilitated using the low aspect ratio sensor coil, resulting in more accurate tracking of mudline location, and shorter transition zones due to the increased spatial resolution.

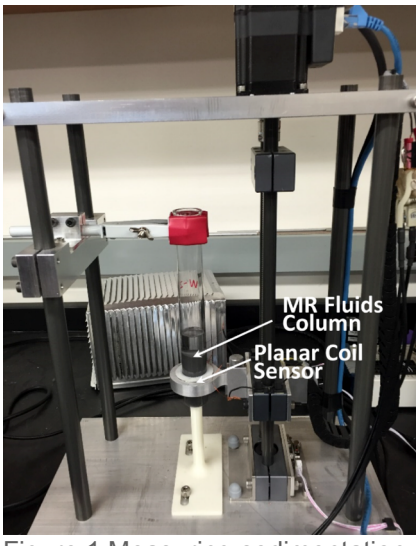

Figure 1:Measuring sedimentation in MRFs

REFERENCES

[1] Y.-T. Choi, L. Xie, and N.M. Wereley, Smart Materials and Structures., 25(4): 04LT01(2016).
[2] S. Gorodkin, W. Kordonski, A. Shorey and S. Jacobs, Review of Scientific Instruments., 71(6): 2476-2480(2000).

The influence of a surface molecular structure on the stability of magnetorheological fluids

Haibin Cheng*, Ming Wang†, Chaosheng Liu†, Hong Shu† and Norman M. Wereley†
* State Key Laboratory of Advanced Technology for Materials Synthesis and Processing
Wuhan University of Technology
122 Luo Shi Road,Wuhan 430070, China
e-mail: chenghbok@163.com
†State Key Laboratory of Advanced Technology for Materials Synthesis and Processing
Wuhan University of Technology
122 Luo Shi Road,Wuhan 430070, China
e-mail: mwang@whut.edu.cn
† Department of Aerospace Engineering
University of Maryland
3179F Martin Hall College Park MD 20742,USA
Email: wereley@umd.edu

ABSTRACT

Magnetorheological fluids (MRFs) have proven to be advantageous for adaptive energy absorption systems, for such applications as occupant protection and antivibration, for both vehicles and seismic mitigation. However, a remaining key challenge is to develop MRF formulations that minimize or even eliminate sedimentation of MRFs. In our prior work, we investigated several methods with which to minimize sedimentation of MRFs, while retaining high yield stress. In this study, we investigate the effect of surface molecular structure on the stability of MRFs. At first, a chelating organic chain molecule (N-nonyl acyl ethylenediamine triacetate, NED3A) was synthesized and the molecular structure of the synthesis products was characterized using FTIR. Secondly, NED3A was grafted onto the surface of carbonyl iron particles to modify the surface molecular structrure of the particles. Then MR fluids were prepared by silicone oil and the as-synthesized particles with different surface molecular structure. Finally, sedimentation behavior of the MRF samples were quantitatively evaluated using a thermal conductivity method. Measurements show that sedimentation rate of these MRF samples are reduced using this surface coating. Sedimentation rates of the MRFs were decreased by 70.3% as the organic molecular chains grafted onto the surface of the carbonyl iron particles increased from 0% to 3.0%. In addition, the organic molecular chain induces apparent thixotropy. The off-state viscosity of the MRFs decreased steadily with shear rate, that is, the MRFs are shear thinning, and the MRFs exhibit the magnetorheological yield stress effects. In summary, the organic molecular chain grafted onto the surface of the carbonyl iron particles significantly reduces sedimentation rates in MRFs. In particular, modifying the surface molecular structure of the particles can greatly improve the sedimentation stability of MRFs.

Acknowledgment: This work was supported by a grant from Natural Science Foundation of China (No. 51372189).

REFERENCES

[1] Cheng HB, Wang JM, Zhang QJ and Wereley N M. “Preparation of composite magnetic particles and aqueous magnetorheological fluids,”*Smart Mater. Struct.* , Vol. 18, pp. 530-603, (2009).

[2] Cheng HB, Zuo L, Song J H, Zhang QJ and Wereley N M., ”Magnetorheology and sedimentation behavior of an aqeuous suspension of surface modified carbonyl iron particles,” *J. Appl. Phys*., Vol.107, pp.507-510, (2010).

[3] Cheng HB, Zhang XP, Liu GZ, Ma WT, and Wereley N M., “Measuring the sedimentation rate in a magnetorheological fluid column via thermal conductivity monitoring,”*Smart Mater. Struct.,* Vol. 25, pp. 055007 (8pp), (2016).

VIII ECCOMAS Thematic Conference on Smart Structures and Materials
SMART 2017
A. Güemes, A. Benjeddou , J. Rodellar and Jinsong Leng (Eds)

SOUND TRANSMISSION LOSS OF SANDWICH PANELS PARTIALLY TREATED WITH MR FLUID AND VISCOELASTIC CORE LAYER

MASOUD HEMMATIAN * AND RAMIN SEDAGHATI†

Department of Mechanical and Industrial Engineering,
Concordia University, Montreal, QC, H3G 1M8, Canada

* PhD Candidate, e-mail: m_hemmat@encs.concordia.ca

† Professor, e-mail: ramin.sedaghati@concordia.ca

Abstract. This study aims to investigate the acoustical behavior of a sandwich panel partially treated with Magnetorheological (MR) fluid core layer. MR fluids are smart materials with promising controllable rheological characteristics in which the application of an external magnetic field instantly changes their rheological properties. Finite element (FE) method is utilized to obtain the equation of motion of a clamped circular sandwich panel radially treated with MR fluid and viscoelastic rubber core layer. Solving the equations of motion, the transverse velocity of the panel is converted to the radiated sound and utilized to calculate the Sound Transmission Loss (STL). Three cases are selected to investigate the behavior of radial treatment of the core with MR fluid and the STL, first natural frequency and mode shapes of the panel are calculated and compared for those cases.

Key words: Magnetorheological fluid, Finite element method, Sound transmission loss, Clamped circular sandwich panel, Partial treatment.

1 INTRODUCTION

Light weight and high flexural to weight ratio are encouraging properties of sandwich panels when vibration of the structure is the issue. Contrariwise, the acoustical characteristics of the structures is directly correlated with its areal density and as the areal density increases, the sound transmission loss (STL) of the structure enhances. The STL of sandwich panels passively treated with viscoelastic and honeycomb core layer has been widely studied during last decades. Utilizing smart materials as the core layer is a new methodology to control the acoustical properties of sandwich structures by changing the characteristics of the core layer. The possibility of controlling the transmitted noise in wide frequency range and also low required power are the advantages of the proposed approach. Magnetorheological (MR) and Electrorheological (ER) fluids are smart materials that their rheological properties can be controlled by controlling the external magnetic/electric fields. Using MR fluid as the core layer, the stiffness and damping and consequently the vibration and noise characteristics of the sandwich panel can be controlled. Limited studies have been investigated the noise control

behavior of sandwich structures treated with smart materials [1-8]. Hasheminejad and Shabanimotlagh [1] studied the sound transmission properties of an infinite sandwich panel treated with magnetorheological elastomer core layer. They investigated the effect of applied magnetic field on the STL of the panel for all angles of incident in the audible frequency range. Choi et al [2] fabricated an experimental setup to investigate the STL of a sandwich panel treated with ER fluid core layer. The ER sandwich panel was fabricated as one of the sides of a rectangular closed cabin and a microphone was used to measure the transmitted sound into the cabin. They studied the performance of a fuzzy controller in enhancing the STL of the panel. Tang et al. [3, 4] studied the STL of the sandwich panels treated with ER fluid as the core layer. They mentioned that the tunable characteristics of the flexible, thin ER fluid layer at low frequencies including the possibility of adjusting the sound pressure level and the phase angle by varying the electrical field provides an opportunity to utilize the thin ER layer in manufacturing low frequency tunable phononic crystals and other acoustic devices. The effect of magnetic field on the STL of MR sandwich panels was studied by Mahjoob et al [8]. The MR layer was modeled as a linear viscoelastic material and a model was developed for the STL of an infinite sandwich panel. Moreover, they fabricated an experimental setup including an impedance tube equipped with a magnetic chamber and measured the STL of MR sandwich panels to validate the theoretical model. Previous studies mostly focused on the infinite MR/ER sandwich panels and some of them just experimentally investigated the effect of electric/magnetic field on the acoustical behavior of MR/ER structures. The authors recently studied the STL of clamped circular sandwich panel fully treated with MR fluid core layer. They investigated the influence of magnetic field on the natural frequency and the STL of the panel using Ritz method and compared the results with the experimental measurements [9].

This study aims to investigate the STL of sandwich panels partially treated with MR fluid. The equation of motion of a clamped circular sandwich panel with elastic face sheets is modeled using finite element (FE) method. The core layer is radially divided into viscoelastic rubber and MR fluid segments with complex frequency dependent shear moduli. The STL of the panel is calculated utilizing the transverse velocity of the structure. Three different cases are considered for the distribution of the MR fluid and the viscoelastic rubber in the core layer and the STL of the panel is investigated for these cases. Moreover, the changes in the first natural frequency of the panel as function of applied magnetic field is studied for the three cases.

2 FINITE ELEMENT FORMULATION

Figure 1 shows a circular sandwich panel comprising two elastic face sheets and the core layer which has been partially treated with MR fluid. The FE model is developed considering following assumptions: (1) the ratio of the thickness to radius of the face sheets is considered to be small and the classical plate theory is used to obtain the displacements of the face sheets, (2) The transverse displacements are the same for the face sheets and the core layer, (3) There is no slippage between the face sheets and core layer and the compatibility conditions is used to obtain the displacements of the core layer in terms of those of the face sheets, (4) The stress components of the face sheets and the core layer are obtained utilizing the Hooke's law. The

schematic of the finite element model and the degrees of freedom of each element is shown in Figure 2. The circular panel is divided into a circular element at the center and 4 node elements circumferentially and radially connected to each other. The circular element comprising a node at the edge and four degrees of freedom, $\left[w \quad \frac{\partial \mathrm{w}}{\partial r} \quad \mathrm{u}_1^0 \quad \mathrm{u}_3^0\right]^T$, as it was presented in [10]. The 4-node element is defined by two i_1 and i_2 nodes at the inner radious and two j_1 and j_2 nodes at the outer radius. Seven degrees of freedom have been considered for each of the nodes as follows:

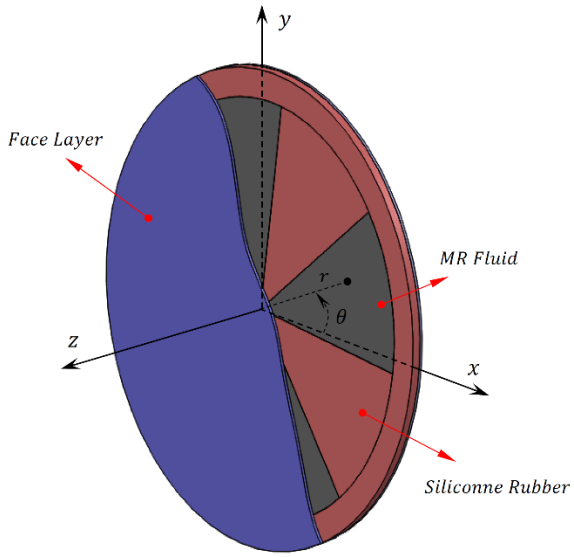

Figure 1. Schematic of sandwich panel partially treated with MR fluid core layer.

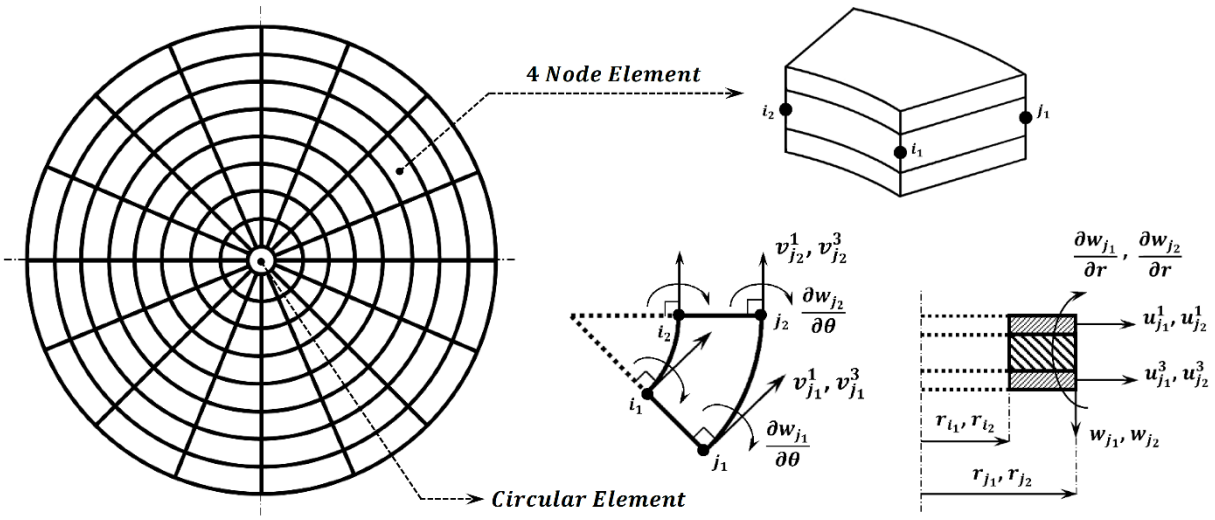

Figure 2. Schematic of the finite element model.

$$\delta_n = \begin{bmatrix} w_n & \dfrac{\partial w_n}{\partial r} & \dfrac{\partial w_n}{\partial \theta} & u_{1_n}^0 & u_{3_n}^0 & v_{1_n}^0 & v_{3_n}^0 \end{bmatrix}^T \qquad n = i_1, i_2, j_1, j_2 \tag{1}$$

where w_n, $\frac{\partial w_n}{\partial r}$ and $\frac{\partial w_n}{\partial \theta}$ are the transverse displacement, radial and circumferential rotations, respectively. $u_{1_n}^0$, $u_{3_n}^0$ and $v_{1_n}^0$, $v_{3_n}^0$ are the in-plane radial and circumferential displacements of the mid-plane of the face sheets in r and θ directions, respectively. Now considering Figure 2, the nodal displacement vector is expressed as:

$$\delta_e = \begin{Bmatrix} \delta_{i_1} \\ \delta_{i_2} \\ \delta_{j_1} \\ \delta_{j_2} \end{Bmatrix} \tag{2}$$

The nodal displacement vector can then be utilized to express the transverse and in-plane displacements of the face sheets' mid-plane as a function of shape functions:

$$\begin{Bmatrix} w \\ u_{\mathrm{i}}^0 \\ v_i^0 \end{Bmatrix} = \begin{bmatrix} L_w \\ L_{u_i}^0 \\ L_{v_i}^0 \end{bmatrix}_{3\times 28} \{\dot{\delta}_e\}_{28\times 1} \quad \& \quad i = 1,3 \tag{3}$$

where L_w, $L_{u_i}^0$ and $L_{v_i}^0$ are the shape functions. The strain-displacement relations are then written using Eq. (3) to obtain the strain and subsequently kinetic and strain energies of the 4-node element:

$$T_e = T_{e_1} + T_{e_2} + T_{e_3} \tag{4}$$

$$V_e = V_{e_1} + V_{e_2} + V_{e_3} \tag{5}$$

where subscripts 1, 2 and 3 refer to the front face sheet, the core layer and back face sheets, respectively. T_{e_1} , T_{e_2}, T_{e_3} and V_{e_1} , V_{e_2}, V_{e_3} are defined as:

$$T_{e_i} = \frac{1}{2} \int_{-\frac{h_i}{2}}^{\frac{h_i}{2}} \iint_{A_e} \rho_i \{\dot{\delta}_e\}^T [L_i]^T [L_i] \{\dot{\delta}_e\} dA\, dz \quad \& \quad i = 1,3 \tag{6}$$

$$T_{e_2} = \frac{1}{2} \iint_{A_e} I_2 \{\dot{\delta}_e\}^T [B_2]^T [B_2] \{\dot{\delta}_e\} dA + \frac{1}{2} \iint_{A_e} \rho_2 h_2 \{\dot{\delta}_e\}^T [L_w]^T [L_w] \{\dot{\delta}_e\} dA \tag{7}$$

$$V_{e_i} = \frac{1}{2} \int_{-\frac{h_i}{2}}^{\frac{h_i}{2}} \iint_{A_e} \{\dot{\delta}_e\}^T [B_i]^T [D_i][B_i]\{\dot{\delta}_e\} dA\, dz \quad \& \quad i = 1,3 \tag{8}$$

$$V_{e_2} = \frac{1}{2} \int_{-\frac{h_2}{2}}^{\frac{h_2}{2}} \iint_{A_e} \{\dot{\delta}_e\}^T [B_2]^T [G_2][B_2]\{\dot{\delta}_e\} dA\, dz \tag{9}$$

where ρ_i and h_i are the mass density and the thickness of the face sheets, respectively, and ρ_2, h_2 and $I_2 = \frac{\rho_2 h_2^3}{12}$ are the mass density, the thickness and the moment of inertia of the core layer, respectively. $[L_i]$, $[B_i]$, $[D_i]$ and $[G_2]$ are defined as:

$$[L_i] = \begin{bmatrix} L_w \\ L_{u_i}^0 - z_i \dfrac{\partial L_w}{\partial r} \\ L_{v_i}^0 - z_i \dfrac{\partial L_w}{r\partial \theta} \end{bmatrix} \quad \& \quad i = 1,3 \tag{10}$$

$$[B_i] = \begin{bmatrix} -z_i \dfrac{\partial^2}{\partial r^2} & \dfrac{\partial}{\partial r} & 0 \\ -\dfrac{z_i}{r^2}\dfrac{\partial^2}{\partial \theta^2} - \dfrac{z_i}{r}\dfrac{\partial}{\partial r} & \dfrac{1}{r} & \dfrac{1}{r}\dfrac{\partial}{\partial \theta} \\ -\dfrac{2z_i}{r}\dfrac{\partial^2}{\partial r \partial \theta} + \dfrac{2z_i}{r^2}\dfrac{\partial}{\partial \theta} & \dfrac{1}{r}\dfrac{\partial}{\partial \theta} & \dfrac{\partial}{\partial r} - \dfrac{1}{r} \end{bmatrix} \begin{bmatrix} L_w \\ L_{u_i}^0 \\ L_{v_i}^0 \end{bmatrix} \quad \& \quad i = 1,3 \tag{11}$$

$$[B_2] = \begin{bmatrix} \dfrac{d}{2h_2} & \dfrac{\partial}{\partial r} & 1 & 0 \\ \dfrac{d}{2h_2} & \dfrac{\partial}{r\partial \theta} & 0 & 1 \end{bmatrix} \begin{bmatrix} L_w \\ L_{u_1}^0 \\ L_{v_1}^0 \end{bmatrix} + \begin{bmatrix} \dfrac{d}{2h_2} & \dfrac{\partial}{\partial r} & -1 & 0 \\ \dfrac{d}{2h_2} & \dfrac{\partial}{r\partial \theta} & 0 & -1 \end{bmatrix} \begin{bmatrix} L_w \\ L_{u_3}^0 \\ L_{v_3}^0 \end{bmatrix} \tag{12}$$

$$[D_i] = \frac{E_i}{1 - v_i^2} \begin{bmatrix} 1 & v_i & 0 \\ v_i & 1 & 0 \\ 0 & 0 & \dfrac{1 - v_i}{2} \end{bmatrix} \quad \& \quad i = 1,3 \tag{13}$$

$$[G_2] = \begin{bmatrix} G & 0 \\ 0 & G \end{bmatrix} \tag{14}$$

where $d = \frac{h_1}{2} + h_2 + \frac{h_3}{2}$ and E_i and v_i are the Young's modulus and the Poisson's ratio of the

face sheets, respectively and z_i denotes the transverse coordinate in the local coordinate system of each layer considering the origin at the mid-plane of each layer. G is the shear modulus of the core layer comprising the silicone rubber and MR fluid in the present study. Considering the MR fluid to operate in pre-yield region, both MR fluid and the silicone rubber can be described as a linear viscoelastic material with complex shear modulus.

The work done by the acoustic pressure on the MR sandwich panel might then be described as:

$$\pi_{ext} = \{\dot{\delta}_e\} \iint_{A_e} P_b [L_w]^T dA \tag{15}$$

where P_b is the blocked pressure obtained as twice of the incident pressure. Considering the strain and kinetic energies and the work done by the acoustic pressure and using Lagrange's equations, the mass and stiffness matrices and the vector of nodal forces for the 4-node element are obtained. Assembling the mass, stiffness and the nodal force matrices of the circular and the 4-node elements, the governing equation of motion of the panel can be expressed as:

$$[M]\{\ddot{\delta}\} + [K]\{\delta\} = \{f\} \tag{16}$$

where $[M]$, $[K]$ and $\{f\}$ are the mass, stiffness and force vector of the system, respectively, and $\{\delta\}$ is the global nodal displacement vector.

The transverse velocity of the panel can then be used to calculate the sound radiated from the panel using the Rayleigh integral approach as [11]:

$$P_{rad} = \iint_{A} j\omega\rho_f v\, G\, dA \tag{17}$$

where ρ_f, ω and G are the density of the medium, the incident sound frequency and the half-space free field Green's function, respectively. v is the velocity of the structure which is substituted by $j\omega w$ for harmonic excitation.

Finally, the STL can be written as:

$$STL = 10 \log_{10} \frac{\Pi_{\text{inc}}}{\Pi_{\text{rad}}} \tag{18}$$

where the incident power, Π_{inc}, and the radiated power, Π_{rad}, are described as a function of the amplitude of the incident and radiated pressures.

3 RESULTS

In order to examine the accuracy of the developed finite element model, the STL and first axisymmetric natural frequency of the clamped circular sandwich panel fully treated with MR fluid core layer was compared with the experimental results presented in [9] by authors and the results matched with the experimental measurements. Figure 3 shows the three cases that is

considered in the present study. The core layer of the panel is comprised of silicone rubber and MR fluid that radially distributed among the surface. Considering that the surface area of the MR fluid and the silicone rubber are equal in the three cases, the mass per unit area is the same for all the cases and only the damping and the stiffness of the panel are affected by different distributions.

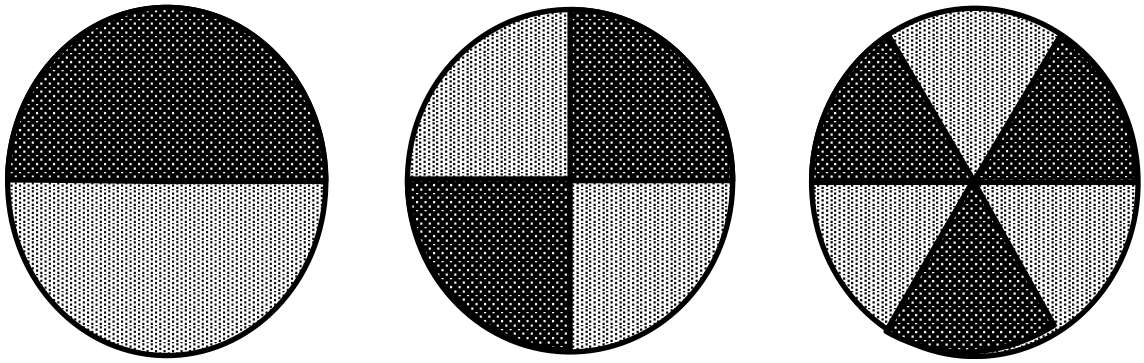

Figure 3. Schematic of circular sandwich panel partially treated with MR fluid;
MR Fluid: ▓; Silicone Rubber: ▒.

The STL of the partially treated MR sandwich panels is presented in Figure 4. It can be seen in this figure that matching the frequency of the incident sound with the natural frequency of the panel causes the panel to resonate and reduces the STL. Comparing the STL of the three cases shows that changing the position of the MR fluid affects the stiffness of the panel and consequently the natural frequency of the case #1 is less than the natural frequency of the cases #2 and #3. The first natural frequency of the cases #2 and #3 are almost equal to each other. This is due to the fact of symmetric distribution of the MR fluid in the core layer for these two cases. Figure 5 shows the first mode shape of the panel for three cases. As it can be seen in this figure, the asymmetric distribution of the MR fluid and silicone rubber for case #1 causes the half of the panel that is treated with MR fluid to oscillate with larger magnitude compare to the other half and the mode shape to be asymmetric. On the other hand, the symmetric treatment of the cases #2 and #3 provides their first mode shapes to be almost the same and this may interpret the equality of their STL near to the first natural frequency.

The first natural frequency of the three cases for different current inputs is presented in Table 1. It is clear that the stiffness and consequently the natural frequency of the panel increases as the applied magnetic field enhances. The increase rate of natural frequency with respect to the current input is $21.0\ Hz/A$ for case #1 and this rate decreases to $19.4\ Hz/A$ and $19.2\ Hz/A$ for cases #2 and #3, respectively. This shows that concentrating MR fluid in larger segments enhances its effectiveness to further change the stiffness and natural frequency of the panel utilizing current input.

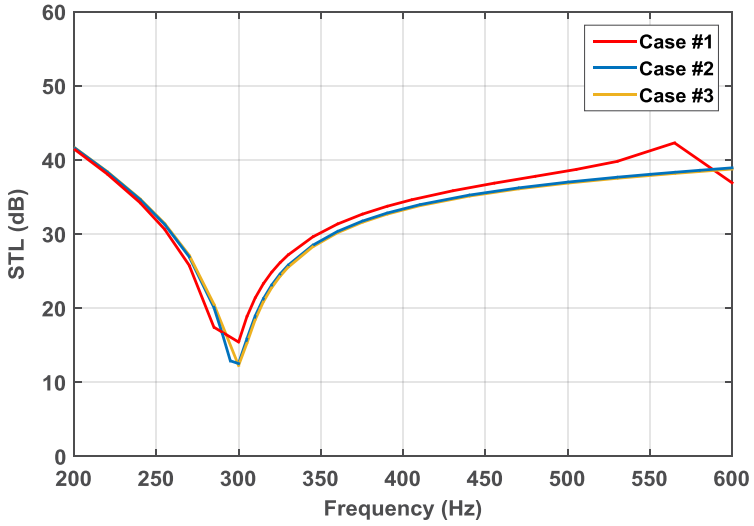

Figure 4. STL of partially treated MR sandwich panels with $0.4\ mm$ thickness aluminum face sheets and $1.35\ mm$ thickness core layer in absence of magnetic field ($I = 0\ A$).

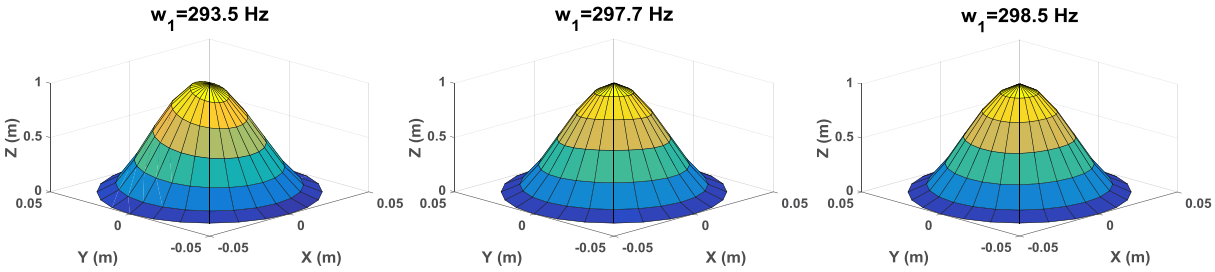

Case #1 Case #2 Case #3

Figure 5. First mode shape of a clamped sandwich panel partially treated with MR fluid and silicone rubber core layer.

Table 1. The first natural frequency of the panel with $0.4\ mm$ thickness aluminum face sheets and $1.35\ mm$ thickness core layer.

Input Current (A)	Case #1 - $NF\ (Hz)$	Case #2 - $NF\ (Hz)$	Case #3 - $NF\ (Hz)$
0	293.5	297.7	298.5
0.6	304.0	307.3	307.9
1.2	316.5	318.8	319.3
1.8	331.5	332.7	333.0

4 CONCLUSIONS

Sound transmission of a circular sandwich panel partially treated with MR fluid and viscoelastic core layer was studied. The FE model of the panel has been developed using 4-node elements and solved using clamped boundary condition. Then, the Rayleigh integral approach has been used to calculate the STL as a function of the transverse velocity of the panel and the incident sound. Three cases have been selected to investigate the influence of radial distribution of MR fluid and viscoelastic rubber on the behavior of the circular sandwich panel. The STL, first natural frequency and mode shapes of the three cases have been presented. Asymmetric distribution of the MR fluid causes the stiffness of the panel and consequently its natural frequency to reduce. In addition, the first mode shape of the panels symmetrically treated with MR fluid are almost the same and this is a reason for the equality of their first natural frequency and STL.

REFERENCES

[1] Hasheminejad, S. M., and Shabanimotlagh, M., Magnetic-field-dependent sound transmission properties of magnetorheological elastomer-based adaptive panels *Smart Materials and Structures* (2010) **19(3)**:035006.

[2] Choi, S., Seo, J., Kim, J. *et al.*, An electrorheological fluid-based plate for noise reduction in a cabin: experimental results *Journal of sound and vibration* (2001) **239(1)**:178-185.

[3] Tang, H., Luo, C., and Zhao, X., Tunable characteristics of a flexible thin electrorheological layer for low frequency acoustic waves *Journal of Physics D: Applied Physics* (2004) **37(16)**:2331.

[4] Tang, H., Zhao, X.-p., and Luo, C.-r., Sonic responses of an electrorheological layer with one side of grating electrodes *Journal of Physics D: Applied Physics* (2006) **39(3)**:552.

[5] Zielinski, T. G., and Rak, M., Acoustic Absorption of Foams Coated with MR Fluid under the Influence of Magnetic Field *Journal of Intelligent Material Systems and Structures* (2010) **21(2)**:125-131.

[6] Mahjoob, M., Mohammadi, N., and Malakooti, S., An investigation into the acoustic insulation of triple-layered panels containing Newtonian fluids: theory and experiment *Applied Acoustics* (2009) **70(1)**:165-171.

[7] Mohammadi, N., and Mahjoob, M., Transmission loss of multilayer panels containing a fluid using progressive wave model: comparison with impedance progressive model and experiments *Comptes Rendus Mécanique* (2009) **337(4)**:198-207.

[8] Mahjoob, M. J., Mohammadi, N., and Malakooti, S., Analytical and experimental evaluation of magnetic field effect on sound transmission loss of MR-based smart multi-layered panels *Applied Acoustics* (2012) **73(6)**:614-623.

[9] Hemmatian, M., and Sedaghati, R., Effect of applied magnetic field on sound transmission loss of MR-based sandwich panels *Smart Materials and Structures* (2017) **26(2)**:025006.

[10] Hemmatian, M., and Sedaghati, R., Sound transmission analysis of partially treated MR fluid based-sandwich panels using finite element method *SPIE Smart Structures and Materials+ Nondestructive Evaluation and Health Monitoring.* (2017).

[11] Baumann, W. T., Saunders, W. R., and Robertshaw, H. H., Active suppression of acoustic radiation from impulsively excited structures *The Journal of the Acoustical Society of America* (1991) **90(6)**:3202-3208.

Time-dependent viscoelastic properties of magnetorheological paste with cement as carrier

Yancheng Li*, Wengui Li and Jianchun Li

Centre for Built Infrastructure Research, Faculty of Engineering and Information Technology, University of Technology Sydney, Ultimo, NSW 2007, Australia

Email: Yancheng.li@uts.edu.au

Website: http://www.uts.edu.au/research-and-teaching/our-research/built-infrastructure

ABSTRACT

This paper reports an investigation on the viscoelastic properties of a new magnetorheological (MR) material, i.e. magnetorheological cement paste. The MR cement paste is mainly composed of cement based carrier and carbon iron particles (CIP). During the solidifying process of the cement carrier, the viscoelastic properties of the MR cement paste under various harmonic loading were examined under different solidifying periods, i.e. 0 minute, 5 minutes, 30 minutes and 60 minutes, and applied magnetic field, i.e. 0 mT, 0.1 mT, 0.2 mT, 0.3mT, 0.4 mT and 0.5 mT. The rheological properties were explained by chemical process of cement and water, as well as magnetorheological effect. A viscoelastic model was developed to portray the rheological behavior of the MR cement paste.

REFERENCES

[1] S D Nair and R D Ferron, "Real time control of fresh cement paste stiffening: Smart cement-based materials via a magnetorheological approach", Rheological Acta, Vol.55, pp.571-579, (2015).

[2] W. H. Li, Y. Zhou and T. F. Tian, "Viscoelastic properties of MR elastomers under harmonic loading", Rheologica Acta, Vol. 49, pp. 733-740, (2010).

[3] G. M. Kamath and N. M. Wereley, "A nonlinear viscoelastic-plastic model for electrorheological fluids", Smart Materials and Structures, Vol.6, pp. 351, (1997)

VIII ECCOMAS Thematic Conference on Smart Structures and Materials
SMART 2017
A. Güemes, A. Benjeddou, J. Rodellar and Jinsong Leng (Eds)

3D DESIGN OF A LARGE-DISPLACEMENT DROOP-NOSE WING DEVICE

SRINIVAS VASISTA* AND HANS PETER MONNER*

* Institute of Composite Structures and Adaptive Systems
German Aerospace Center (DLR)
Lilienthalplatz 7, 38108, Braunschweig, Germany
E-mail: srinivas.vasista@dlr.de, www.dlr.de/fa/en

Key words: Morphing Wing, Droop-nose, High-lift, Structural Optimization.

Abstract. The 3D structural design of a morphing droop-nose device for a new high-lift system is presented in this paper. This new type of high-lift system is anticipated to reduce airframe noise, takeoff and landing speeds and thus runway length, and be capable of actively producing a range of lift coefficients as per demand. A structural design process using optimization tools was further developed and applied to the case of large target deflections required for this high-lift system. The results of the 3D optimization of thickness distribution, stringer position, and force introduction points on a hybrid fiberglass-elastomeric composite skin showed close agreement to the target shapes under different aerodynamic load cases. The design of a kinematic system of linkages was also performed and upon input actuation the outer surface conformed to the target aerodynamic shapes. Required actuator torque in this design was shown to be high in the order of 3600 Nm thought actuators are available which meet the internal space requirements. Reported strains were within design limits in the order of 1.5%. The design is set to be refined in the near future with manufacturing and ground tests to follow.

1 INTRODUCTION

A large-displacement morphing wing droop-nose device with smooth shape variation is a mandatory component of the novel high-lift system for the future aircraft design investigated in the German Collaborative Research Center 880 (SFB880 for “Sonderforschungsbereich 880” in German). [1] The motivation for the research in this project stems from the need to improve aircraft flying efficiency, generate large lift coefficients with low noise thereby enabling operations from smaller less congested airports closer to neighborhoods and thus reducing door-to-door travel times, and to allow flexibility to changes in the design over the aircraft lifetime. With such enhancements to aircraft, growth of the industry can be ensured in a sustainable manner. A number of technologies, including the droop-nose device, are being investigated in the project and for more information the reader is referred to Refs. [1–3]. The droop-nose device under research is gapless and therefore quieter than current slats, and smoothly varying thereby ensuring a good pressure gradient delaying stall and reducing the demand on the internal compressor system. With such qualities the droop-nose device is a

mandatory component of this new high-lift system. Further advantages could include increased laminarity due to the droop-nose being stepless.

The design of the droop-nose device is largely driven through structural optimization tools given the large number of design variables and whose optima are non-intuitive. The development of the tools and the design itself follows on from previous works. Kintscher et al. [4] developed a fiberglass droop-nose device in the SADE project which was manufactured at 1:1 scale and wind tunnel tested, and Kintscher et al. [5] in a separate project (SARISTU) considered aspects of anti/de-icing, lightning protection, erosion, and bird-strikes in the droop-nose design. Rudenko et al. [6] developed a 2D section of a droop-nose demonstrator composed of a hybrid fiberglass-elastomer material to enable large deflections also as part of the SFB880 project [7]. Vasista et al. manufactured and wind tunnel tested a 3D droop-nose for a wingtip featuring a flexible skin and superelastic compliant mechanism as part of the NOVEMOR project [8–10]. Radestock et al. [11] manufactured a droop-nose for a UAV which was flight tested as part of the CHANGE project. Other works on morphing droop-nose devices can be found in Refs. [12–14].

This paper presents the design of the droop-nose device as it nears completion and the manufacturing stage. The aircraft geometry, and aerodynamic and spar bending loads is first presented, followed by intermediate results of the design. A discussion on the design and roadmap to manufacture are subsequently presented.

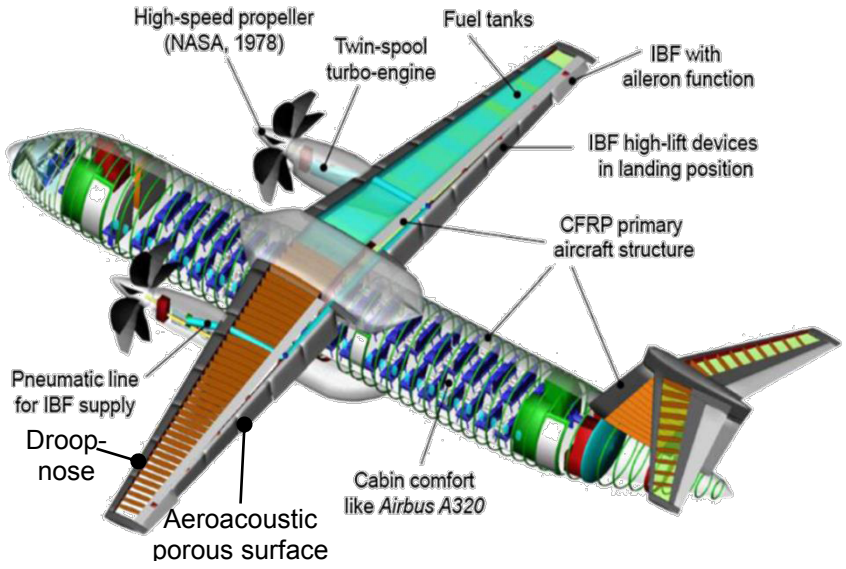

Figure 1 One of the reference aircraft configurations investigated in the SFB880 project.

2 DESIGN CHAIN, GEOMETRY, AND LOADS

A high-wing turboprop aircraft considered as one of multiple reference configurations in the project is shown in Fig. 1 and is designed for a range of 2,100 km for a payload of 12,000 kg. The 2D geometry of the droop-nose in clean (cruise) and droop (approach) configurations is shown in Fig. 2a-c. The droop-nose requires a camber variation of 90° at the leading edge point and the magnitude of curvature change is shown in Fig. 2d, with a maximum value of

0.017 mm^{-1}. The overall process chain of the droop-nose design is presented in Fig. 3. Geometry and loading calculated by project partners is transferred to the skin optimization tool in which the skin thickness distribution and locations and magnitudes of forces acting on the stringer load introduction points are determined. The design of the internal kinematic mechanisms is subsequently performed and reintegrated with the skin finite element model. Upon a successful design, the droop-nose is then manufactured.

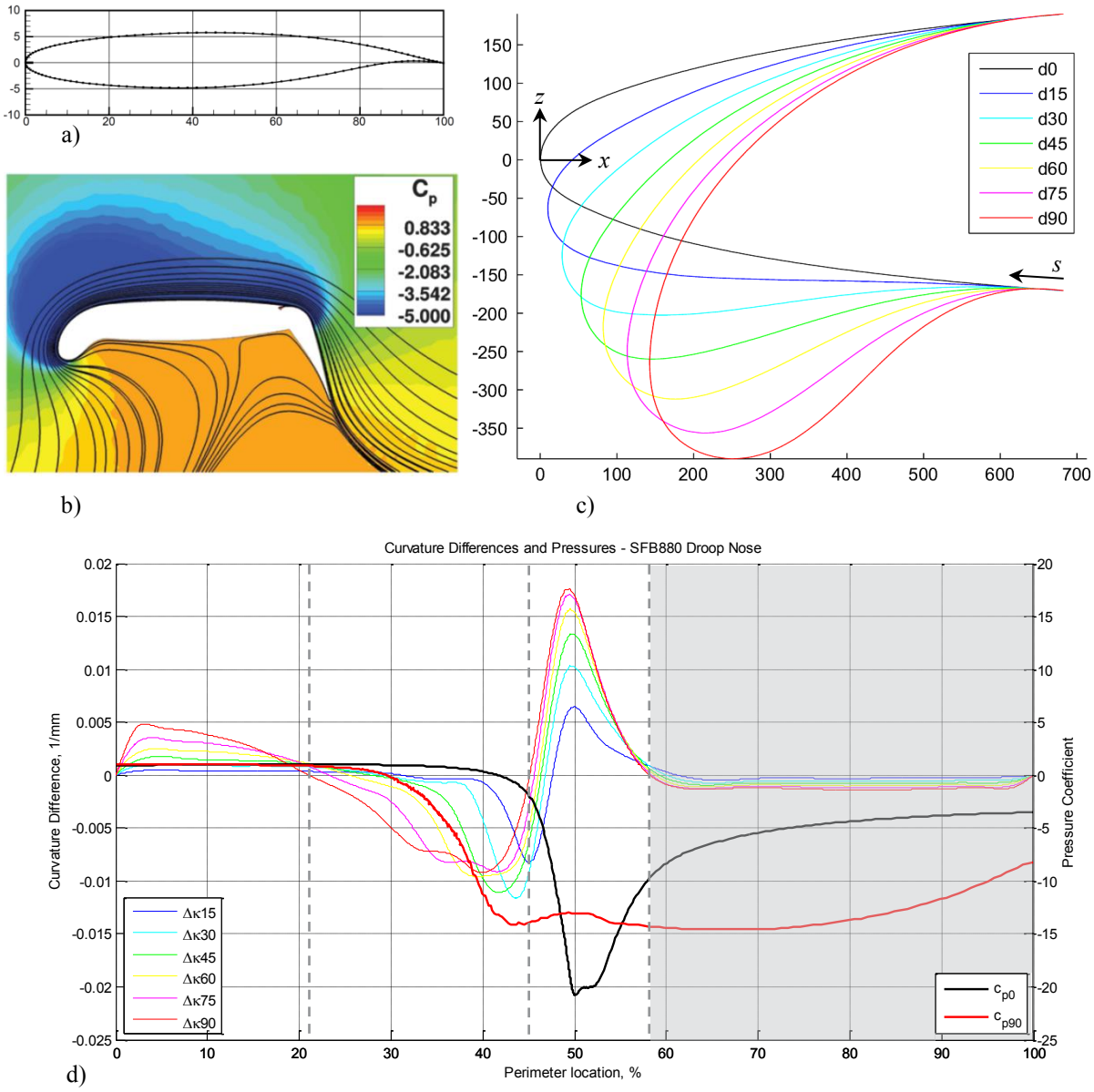

Figure 2. a) DLR F15 aerofoil. b) CFD result presented in Ref. [2]. c) Droop target deflections. d) Shape change and loading requirements along the 2D leading edge profile. The grey dashed lines and area where Δκ is zero or low and pressure is high show potential locations for stringers.

The starboard wing 3D geometry of the leading edge is shown in Fig. 4 and is segmented along the span. The droop-nose segments have been taken perpendicular to the front spar and normal to the dihedral angle to minimize stresses. A number of aerodynamic load cases at various angles of attack (AoA) and inertial load cases (calculated by project partners) have been considered in the design as shown in Table 1. A radial basis function (RBF) tool was used to transfer the pressures and bending on to the mesh for the droop-nose finite element analysis as shown in Fig. 5 as an example.

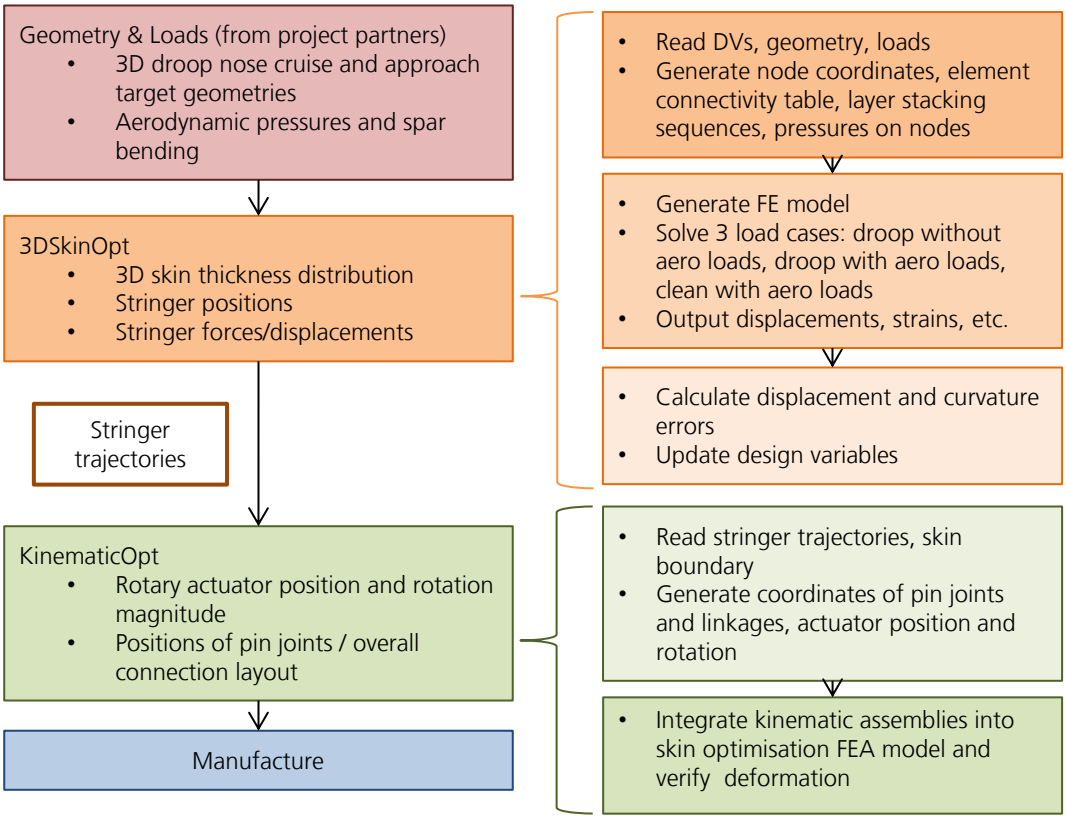

Figure 3 Design chain of the droop-nose device with supporting kinematic mechanisms.

Table 1. Summary of load cases considered.

Aerodynamic Pressures
cruise (clean shape) 3 deg. AoA
approach (droop shape) 0 deg. AoA
approach (droop shape) c_{Lmax}
Spar Bending
cruise (clean shape) 1 g
approach (droop shape) 1 g
landing (droop shape) 4 g
maneuver (clean shape) 2.5 g

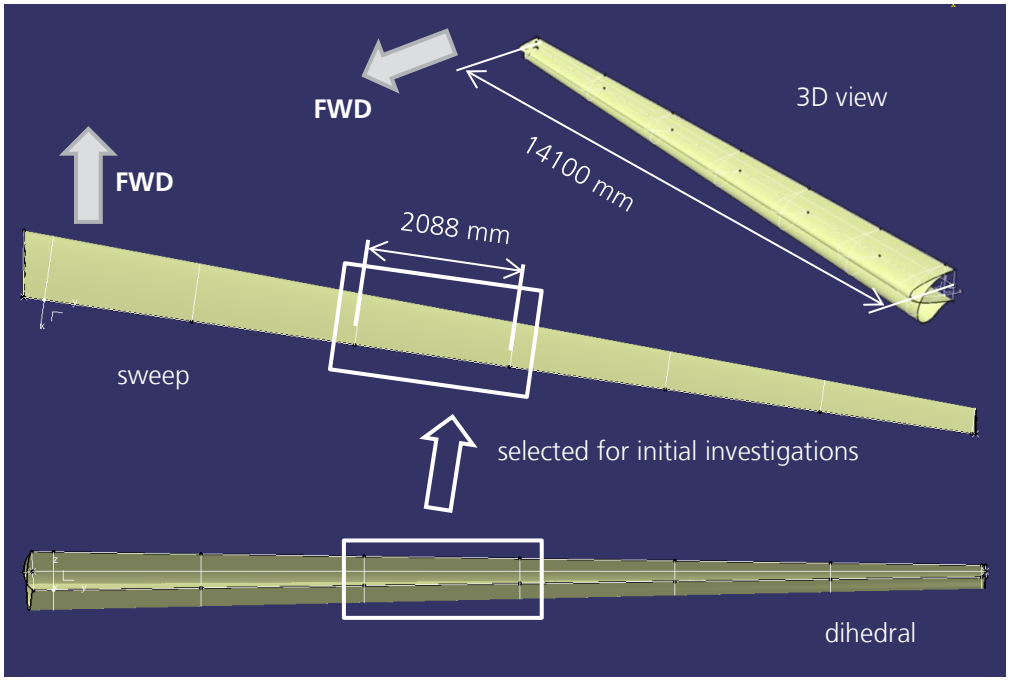

Figure 4 3D geometry of the droop-nose segments on the starboard wing.

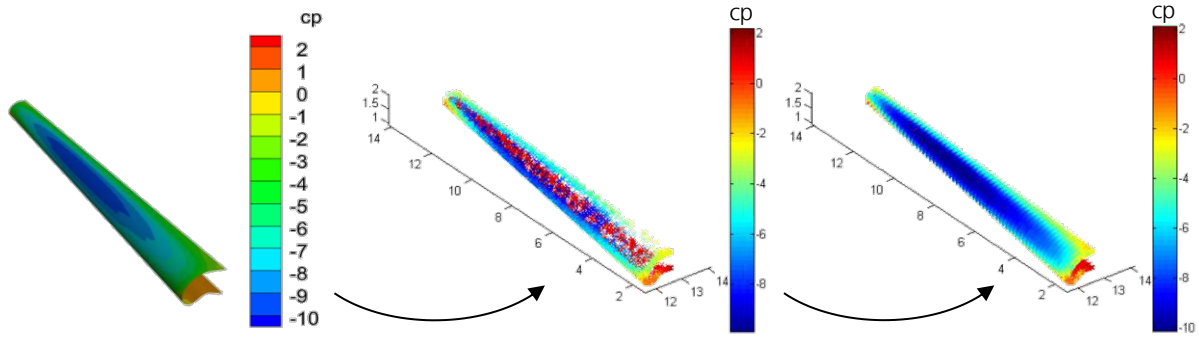

a) surface contour display of CFD results

b) point cloud display of CFD results

c) c_p values at FEA nodes

Figure 5 Example of mapping approach c_{Lmax} pressure loads from CFD to FEA meshes through a radial basis function tool.

3 SKIN DESIGN

The selected droop-nose segment is shown in Fig. 6 with clean and droop surfaces and is intended to be produced with a composite skin attached to kinematic mechanisms at three spanwise stations through stringers at various locations along the profile perimeter. The composite skin is composed of HexPly® 913 fiberglass prepreg layers in combination with ethylene propylene diene monomer (EPDM) elastomer as shown in Fig. 7 and was previously designed in this project. Stiffness can be tailored by determining the best thickness distribution of the material over the full surface and physically captured by dropping-off plies with corresponding geometries. More details on this hybrid material combination are provided

in Ref. [7] and such a hybrid lay-up was used to ensure sufficient stiffness in the spanwise direction and sufficient flexibility in the chordwise morphing direction. Material characterization was performed and orthotropic properties were generated from homogenization procedures. This material information was used in the finite element analysis subroutines where layered shell elements with multiple plies in orientations as specified by a plybook were used. The optimization procedure and the ensuing results are presented in this section.

3.1 3D Skin Optimization Method

The optimization method is based on that of Refs. [4,8] with modifications necessary for the large displacements and 3D analysis made in this work. The optimization solver is the Nelder - Mead Simplex local method [15] and is suited given the non-differentiable nature of this optimization problem. In total 24 design variables were used which included 14 skin thickness points (7 at the inboard and outboard aerofoil profiles and bilinearly interpolated between to map the thickness over the entire droop-nose surface), 5 stringer position points, and 5 force values (scaled along the span and applied at the 15 force application points i.e. 5 stringers × 3 ribs). It should be noted that modifications to the optimization tool included the ability to easily change mesh fidelity as the computation time is high, and easily change the number of stringers. The overall process is shown in Fig. 3. The objective function was to minimize the combined displacement and curvature error over the droop-nose surface over three different load cases, namely droop under actuation load without aerodynamic load, droop under actuation load with aerodynamic load, and clean under blocked actuator with aerodynamic load. Spar bending was omitted at this stage and is checked at the end of the optimization procedure.

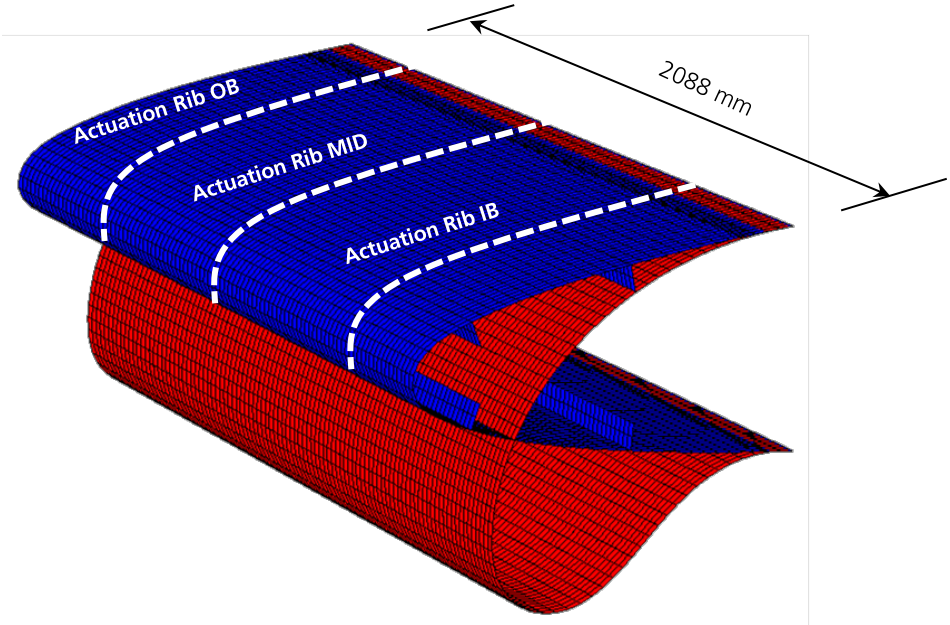

Figure 6 Concept of a single droop-nose segment showing kinematic rib stations.

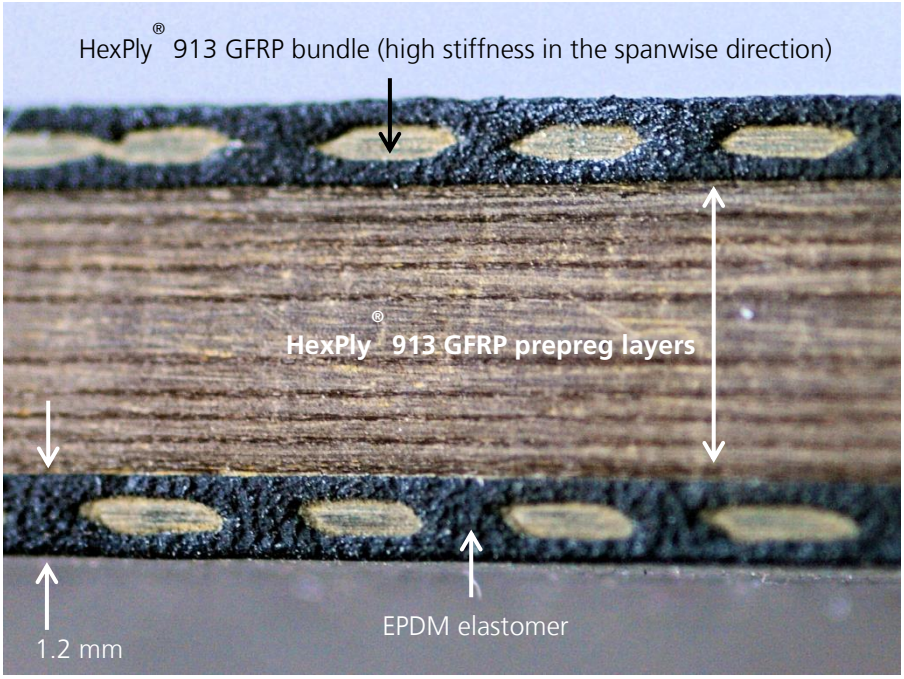

Figure 7 Cross-section view of the hybrid GFRP-EPDM composite skin

3.2 3D Skin Optimization Results

Displacement, curvature, strain and reaction forces output by the skin optimization tool are presented in this section. Fig. 8 shows the resultant profile shapes under the different load cases at the root and tip locations of the droop-nose segment. It is clear that the target shape is appropriately met under all load cases thus verifying the suitability of the optimization tool to find optimum values of the design variables. The mean curvature errors presented in Fig. 9a further confirms this with the errors being in the range of 1.5×10^{-3} mm^{-1}. The thickness distribution shown in Fig. 9b depicts higher thickness towards to the spar and root and lower thickness towards the leading edge and tip section. This is expected given the target curvature difference function shown in Fig. 2d and the taper in chord and profile height along the span. The strain results in Fig. 9c show that maximum strain occurs due to the straightening of the leading edge line from the clean configuration to droop configuration. The contours are shown for the outer EPDM layers and for the outermost GFRP layers the strain was in the order of 1.5%. The strains for the cruise configuration in Fig. 9d show low holding strains even in the outermost EPDM layers at 0.3%.

4 KINEMATIC MECHANISM DESIGN

It is envisaged that the skin is supported by a set of metallic mechanical linkages and pin joints connected to rotational actuators. The kinematic linkages need to move in the paths the stringers would assume as calculated in the skin optimization stage. An additional optimization tool has been used to determine the kinematic mechanism design.

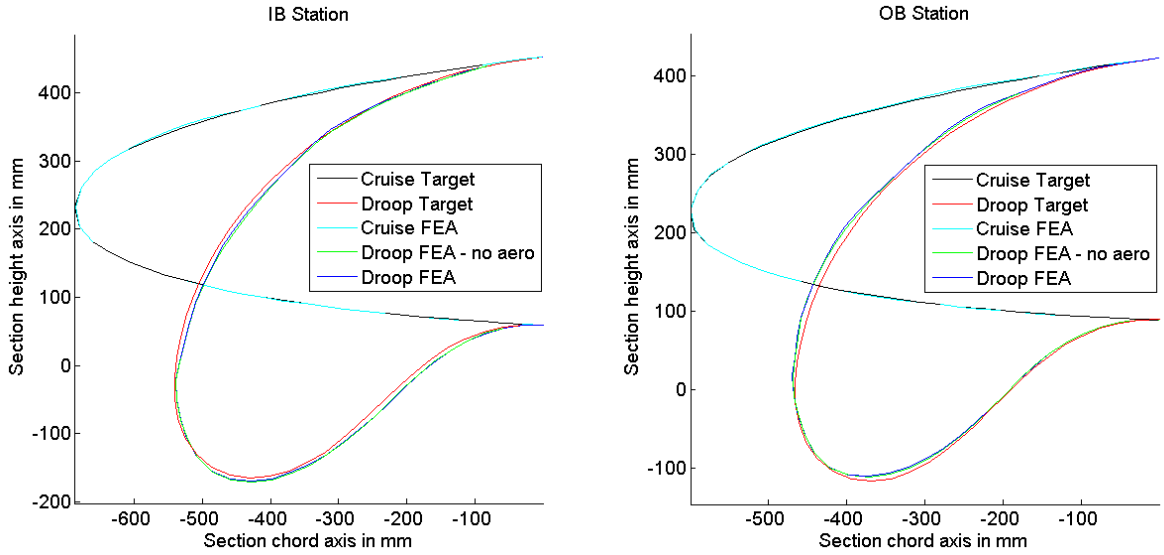

Figure 8 Root (IB) and tip (OB) profile shape results under different load cases.

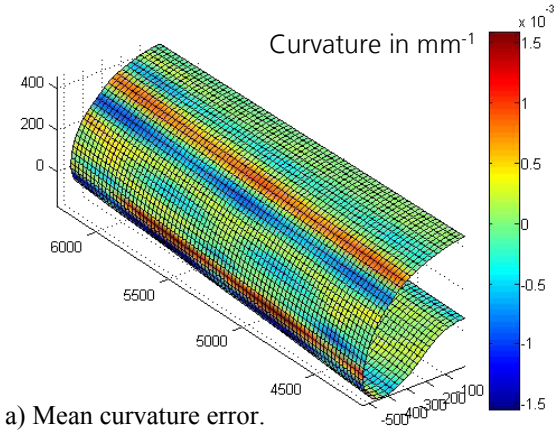

a) Mean curvature error.

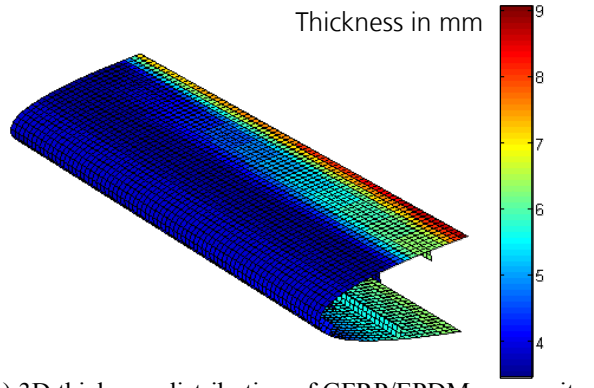

b) 3D thickness distribution of GFRP/EPDM composite.

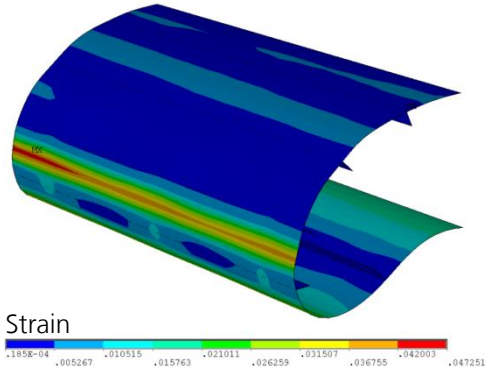

b) Outer layer strain results at approach $c_{L\max}$.

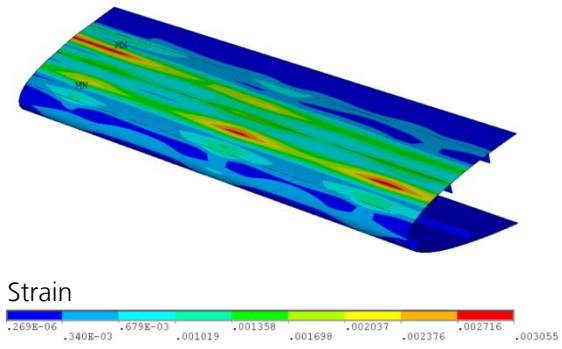

b) Outer layer strain results at cruise, 3 deg. AoA.

Figure 9 Results of the 3D skin optimization stage.

4.1 Kinematic Optimization Method

The kinematic optimization tool uses a local optimization solver to determine the locations of pin joints and linkage lengths. The tool cycles over the number of stringers and for each stringer a single joint in the connection between actuator and stringer is used. In this way, the path to each stringer is independently calculated though using the same actuator position and magnitude of rotation for all actuator-stringer paths. The design variables are the positions of the pin joints $P(x, z)$, the actuator position (x_d, z_d) and the actuator rotation angle ϕ as shown in Fig. 10. The objective function is to minimize the length error between the moving pin joint-target trajectory point $(L_i - L_1)$ over all m target trajectory points.

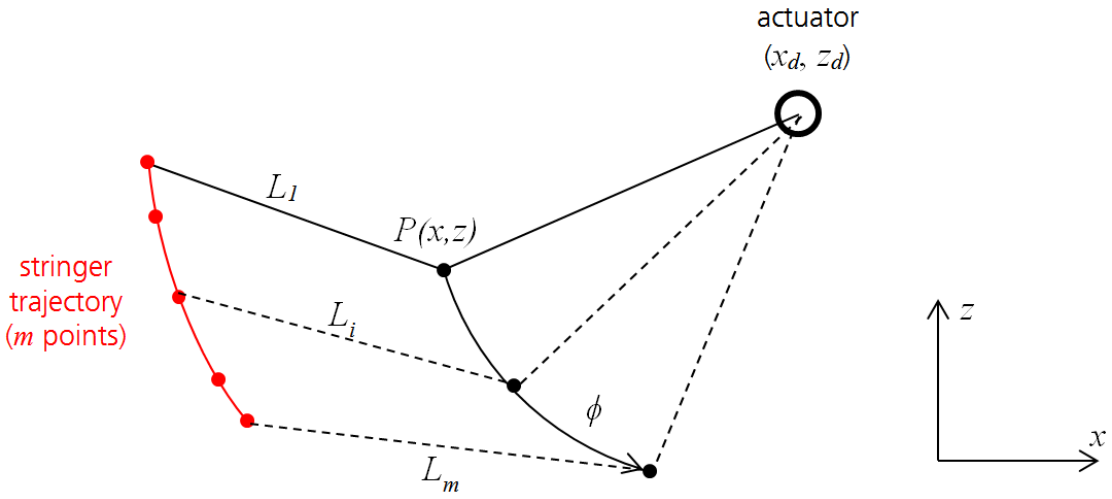

Figure 10 Kinematic mechanism optimization tool design variables.

4.2 Kinematic Optimization Results

The resultant inboard kinematic design is shown in Fig. 11a as an example. The mid span and outboard kinematic stations featured similar results. An example search history of the pin joint for stringer 2 is shown in Fig. 11b with dark red being the worst location and dark blue and the overlaid green cross being the best location of the pin joint. In this case the maximum length error over the trajectory points was 0.62 mm. One drawback of the method is that given the skin is flexible, the actual assumed point by the stringer may fall anywhere on the circle prescribed by the linkage from the pin joint to the stringer. This needs to be addressed in future work.

4.3 Integration into the Skin Model

The resulting kinematic linkages were input into the existing skin finite element model as multipoint constraint rigid link and spherical joint elements. The strain results in Fig. 12 and show that the deformation under actuation load and transmission through the kinematic linkages results in appropriate droop deformation. The strain values remain in the order of 1.5% for the outermost GFRP layers and the actuator torque for the different load cases are shown in Table 2. It can be seen that actuator torque requirements are relatively high with

maximum values of 1765, 3587 and 527 Nm for the cases of droop without aerodynamic loads, droop with maximum approach loads, and clean with cruise aerodynamic loads respectively. From the difference with and without approach loads, it can be seen that the external pressure loading itself requires approximately 2000 Nm of torque. Whilst these values are high, they are producible through actuators such as harmonic drives or traditional torque tube and reduction gearbox transmission systems as used in conventional aircraft. Reduction in actuator torque could be possible by positioning the actuator closer to the foremost stringers thereby reducing the moment arm and thus torque.

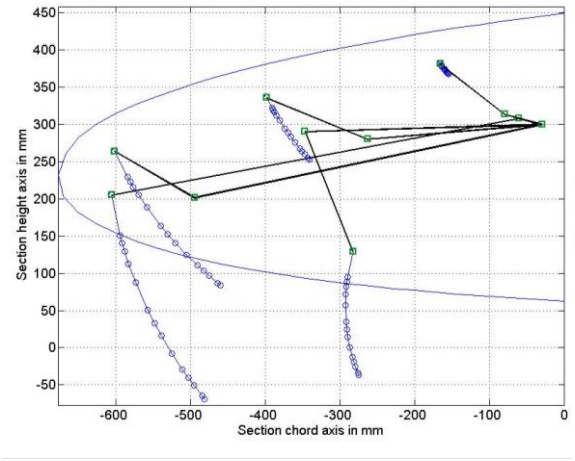

a) Kinematic design of the inboard station.

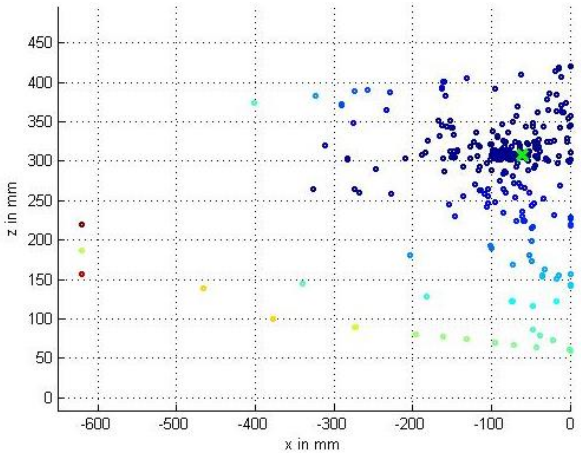

b) Sampled search points with length error for stringer 2. Red points have large errors and blue points have low. The green cross is the best found location.

Figure 11 Results of the kinematic optimization stage.

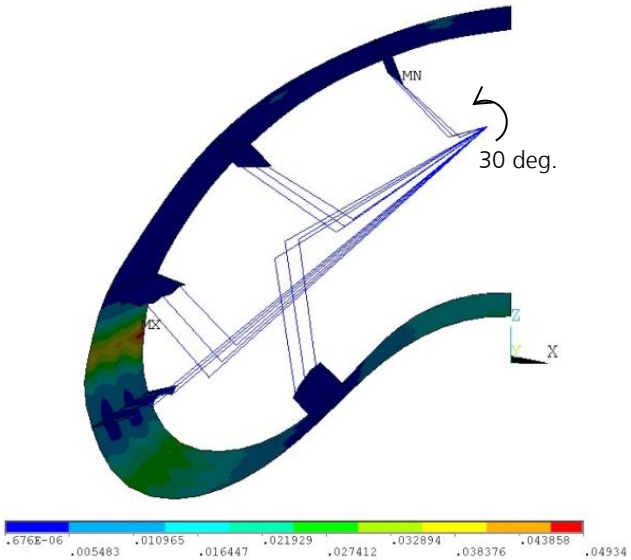

Figure 12 Finite element strain results at outer EPDM layers with kinematic linkages and actuator rotation.

Table 2 Actuator rotation and torque results.

Station	Rotation, deg.	Torque, N·m
Droop, no aeroload		
IB	30	910
MID	30	1765
OB	30	1323
Droop, c_{Lmax} approach		
IB	30	2782
MID	30	3587
OB	30	2535
Clean, 3 deg. AoA cruise		
IB	0	527
MID	0	431
OB	0	164

5 CONCLUSIONS AND FUTURE WORK

The procedure of the structural design of a large displacement morphing wing leading edge was presented in this work and intermediary results show the validity of the methods used. A number of tasks are required to refine the design before the manufacture stage, namely the post-optimization validation with bending loads applied, the inclusion of draping effects along the 3D surface and orientation of the stackings of individual elements, the improvement of the kinematic optimization procedure to ensure kinematic trajectories match the targets, and the inclusion of strap material for the connection of the linkages to the stringers as this will be necessary in the manufactured part. Parallel to this design, the design of compliant substructures is also being investigated for comparison purposes.

ACKNOWLEDGMENTS

The authors are grateful for the financial support from the German Research Foundation (Deutsche Forschungsgemeinschaft DFG) for funding as part of the Collaborative Research Center 880 (Sonderforschungsbereich SFB880).

REFERENCES

[1] Radespiel, R., and Heinze, W., "SFB 880: Fundamentals of High Lift for Future Commercial Aircraft," *CEAS Aeronautical Journal*, Vol. 5, No. 3, 2014, pp. 239–251, DOI: 10.1007/s13272-014-0103-6.

[2] Burnazzi, M., and Radespiel, R., "Design and Analysis of a Droop Nose for Coanda Flap Applications," *Journal of Aircraft*, Vol. 51, No. 5, 2014, pp. 1567–1579, DOI: 10.2514/1.C032434.

[3] Seume, J., Teichel, S., Burnazzi, M., Schwerter, M., Behr, C., Rudenko, A., Schmitz, A., Dörbaum M., and Atalayer, C., "SFB 880 - Efficient High Lift," *Deutscher Luft- und Ramfahrtkongress*, 2013.

[4] Kintscher, M., Wiedemann, M., Monner, H. P., Heintze, O., and Kühn, T., "Design of a

Smart Leading Edge Device for Low Speed Wind Tunnel Tests in the European Project SADE," *International Journal of Structural Integrity*, Vol. 2, No. 4, 2011, pp. 383–405, DOI: 10.1108/17579861111183911.

[5] Kintscher, M., Kirn, J., Storm, S., and Peter, F., "Assessment of the SARISTU Enhanced Adaptive Droop Nose," *Smart Intelligent Aircraft Structures (SARISTU): Proceedings of the Final Project Conference*, P.C. Wölcken and M. Papadopoulos, eds., Springer International Publishing, Switzerland, 2016, pp. 113–140, DOI: 10.1007/978-3-319-22413-8_6.

[6] Rudenko, A., Monner, H. P., and Rose, M., "A Process Chain for Structural Optimization of a Smart Droop Nose for an Active Blown High Lift System," *22nd AIAA/ASME/AHS Adaptive Structures Conference (SciTech 2014)*, January 13-17, AIAA Paper 2014-1414, National Harbor, Maryland, 2014, DOI: 10.2514/6.2014-1414.

[7] Schmitz, A., and Horst, P., "A New Curvature Morphing Skin: Manufacturing, Experimental and Numerical Investigations," *European Conference on Composite Materials*, 22-26 June 2014, Seville, Spain, 2014.

[8] Vasista, S., De Gaspari, A., Ricci, S., Riemenschneider, J., Monner, H. P., and van de Kamp, B., "Compliant Structures-Based Wing and Wingtip Morphing Devices," *Aircraft Engineering and Aerospace Technology*, Vol. 88, No. 2, 2016, DOI: 10.1108/AEAT-02-2015-0067.

[9] Vasista, S., Riemenschneider, J., van de Kamp, B., Monner, H. P., Cheung, R. C. M., Wales, C., and Cooper, J., "Lessons Learned from Wind Tunnel Testing of a Droop-Nose Morphing Wingtip," *SPIE Proceedings Active and Passive Smart Structures and Integrated Systems 2016*, Vol. 9799, 2016, pp. 1–9, DOI: 10.1117/12.2219163.

[10] Vasista, S., Riemenschneider, J., van de Kamp, B., Monner, H. P., Cheung, R. C. M., Wales, C., and Cooper, J. E., "Evaluation of a Compliant Mechanism-Based Droop-Nose Morphing Wingtip via Experimental Tests," *Journal of Aircraft*, 2017.

[11] Radestock, M., Riemenschneider, J., Monner, H. P., and Rose, M., "Structural Optimization of an UAV Leading Edge with Topology Optimization," *DeMEASS*, 2014.

[12] De Gaspari, A., and Ricci, S., "A Two-Level Approach for the Optimal Design of Morphing Wings Based On Compliant Structures," *Journal of Intelligent Material Systems and Structures*, Vol. 22, No. 10, 2011, pp. 1091–1111, DOI: 10.1177/1045389X11409081.

[13] Sodja, J., Martinez, M. J., Simpson, J. C., and De Breuker, R., "Experimental Evaluation of the Morphing Leading Edge Concept," *23rd AIAA/AHS Adaptive Structures Conference (SciTech 2014)*, January 5-9, AIAA Paper 2015-0791, 2015, DOI: 10.2514/6.2015-0791.

[14] Weber, D., Mueller-Roemer, J. S., Simpson, J. C., Adachi, S., Herget, W., Landersheim, V., and Laveuve, D., "Smart Droop Nose for Application to Laminar Wing of Future Green Regional A/C," *Greener Aviation*, Brussels, Belgium, 2014.

[15] Lagarias, J. C., Reeds, J. A., Wright, M. H., and Wright, P. E., "Convergence Properties of the Nelder--Mead Simplex Method in Low Dimensions," *SIAM Journal on Optimization*, Vol. 9, No. 1, 1998, pp. 112–147, DOI: 10.1137/S1052623496303470.

A multistable helical structure enabled by Automated Fibre Placement

R. Telford, P.M. Weaver

Varicomp, Bernal Institute, University of Limerick, Ireland

Significant opportunity exists to exploit composite materials for enabling morphing structures. Morphing structures are capable of undergoing large, controlled and seamless shape changes to adapt to changing requirements [1, 2]. Potential beneficiaries of such technology include the aerospace and wind-energy industries, where there is a premium on lightweight and efficient structures. Morphing airfoils increase aerodynamic efficiency by changing shape without creating aerodynamic gaps, as currently occurs with hinged surfaces. This leads to a reduction in drag, fuel usage, emissions and noise. In addition, reductions in system weight are possible through active load alleviation and reduced actuator requirements. Likewise, spacecraft frequently employ deployable structures to minimise payload volume during transport. Increasing the shape changing configurations possible while minimising the weight of deployable structures results in valuable additional capabilities for such applications.

Maximising the potential of morphing structures is currently hindered by the opposing requirements of a flexible surface capable of large strains (enabling morphing), structural rigidity (reducing deformation under in-service loads) and low weight (to achieve efficiency goals)[3-5]. The properties of composite materials provide solutions to these challenges. Firstly, by exploiting the anisotropic material properties and pre-stress of fibre-matrix composites, novel morphing structures with large deformations and tailored energy landscapes become possible. Secondly, the high strength-to-weight ratio of composite materials allows for strong, yet lightweight structures. Combined, these properties enable lightweight yet stiff structures that can morph through careful control of their flexural stiffness.

This work aims to enable new highly adaptable and lightweight morphing structures through the use of Automated Fibre Placement (AFP). By utilising fibre steering, highly complex geometries with local variations in stiffness become possible, allowing for new morphing concepts to be developed. The accurate fibre placement possible also allows for precise control of the energy landscapes, resulting in highly-optimised morphing structures.

A multistable helical structure (as in Figure 1) was manufactured. The composite flanges were manufactured through winding on a cylindrical tool before being assembled into the helical structure using rigid spokes. By controlling the critical length L, (as described by $\sqrt{\varepsilon L} \gg 1$, where ε is a material parameter) a previously analytically predicted shape configuration (see [6]) was experimentally verified.

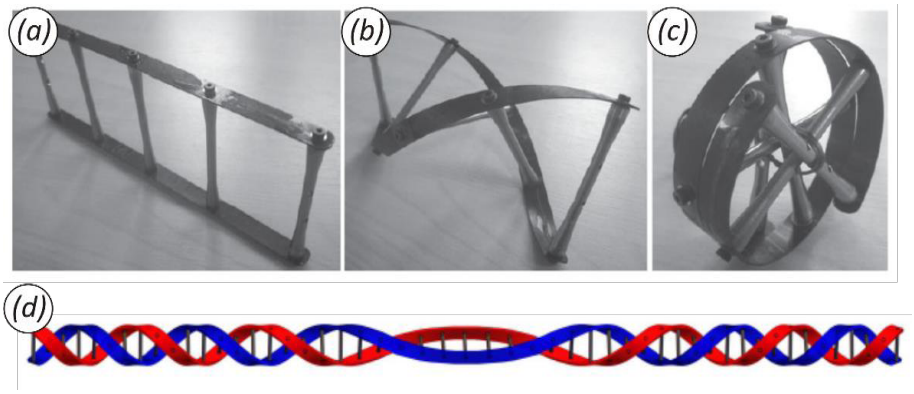

Figure 1 Multistable twisting structure in (a) the straight, (b) the twisted, (c) the coiled configuration (reproduced from [7]) and (d) example of a stable perversion of a long ladder (eproduced without permission from [9])

Acknowledgements

This work has been undertaken as part of the Bernal Project, with funding from Science Foundation Ireland.

References

1. Lachenal, X., S. Daynes, and P.M. Weaver, *Review of morphing concepts and materials for wind turbine blade applications.* Wind Energy, 2013. **16**(2): p. 283-307.
2. Daynes, S. and P.M. Weaver, *A morphing trailing edge device for a wind turbine.* Journal of Intelligent Material Systems and Structures, 2012. **23**(6): p. 691-701.
3. Ursache, N.M., A.J. Keane, and N.W. Bressloff, *Design of Postbuckled Spinal Structures for Airfoil Camber and Shape Control.* AIAA Journal, 2006. **44**(12): p. 3115-3124.
4. Davis, L.P., et al., *The application of thermally induced multistable composites to morphing aircraft structures.* 2008. **6930**: p. 693012.
5. Schultz, M.R., *A Concept for Airfoil-like Active Bistable Twisting Structures.* Journal of Intelligent Material Systems and Structures, 2008. **19**(2): p. 157-169.
6. Lessinnes, T. and A. Goriely, *Design and stability of a family of deployable structures.* Preprint: http://arxiv.org/abs/1604.07014v1, 2016.
7. Lachenal, X., P.M. Weaver, and S. Daynes, *Multi-stable composite twisting structure for morphing applications.* Proceedings of the Royal Society A: Mathematical, Physical and Engineering Sciences, 2012. **468**(2141): p. 1230-1251.

VIII ECCOMAS Thematic Conference on Smart Structures and Materials
SMART 2017
A. Güemes, A. Benjeddou, J. Rodellar and J. Leng (Eds)

A SPANWISE TWISTING MORPHING FLAP DEVICE FEATURING MULTISTABILITY

QING AI* AND PAUL M. WEAVER†

*Advanced Composites Centre for Innovation and Science (ACCIS),
Queen's Building, University Walk,
University of Bristol, BS8 1TR, UK
e-mail: qa12090@bristol.ac.uk

† Advanced Composites Centre for Innovation and Science (ACCIS),
Queen's Building, University Walk,
University of Bristol, BS8 1TR, UK
e-mail: Paul.Weaver@bristol.ac.uk

Key words: Morphing, Control Surface, Stiffness Tailoring, Multistability

Abstract. A novel span-wise twist morphing flap device is presented in this paper which provides smooth trailing edge deflection variation along the wing span. The span-wise morphing trailing edge proposed consists of carbon fibre reinforced plastic laminate spars and ribs which are assembled in a grid pattern. The composite laminate spar strips are manufactured in a stress free state with an initial curvature and are prestressed by flattening before assembly, which provides a heightened strain energy state of the structure. The prestress effects in the spar strips lead to structural stiffness tailorability and multistability. Design parameters including laminate layups of the spar and rib and the initial curvature in the spar strips are investigated in a preliminary optimization study using an analytical model. Results show that by tailoring the structural design, the stable equilibria configuration of the span-wise morphing trailing edge can be set over a wide range of torsion angles and a zero torsional stiffness span-wise morphing trailing edge design can be achieved as well. Results are verified against finite element analysis and good correlation is found.

1 Introduction

Morphing structures have been considered as promising high-lift devices of the next generation aircraft and have received significantly growing attention. Due to the intrinsic conformality of morphing structures, they are believed to be more efficient and quieter compared to the mechanical control surfaces used on aircraft and wind turbine blades[1].

Airfoil morphing concepts are primarily classified into two main categories: in-plane morphing and out-of-plane morphing with the latter predominantly studied in research. Chord-wise, span-wise profile change and twist are the three different ways of enabling out-of-plane morphing structures[3]. Chord-wise morphing structures have received growing interest in recent decades.

Campanile *et al.*[5] developed a chord-wise morphing airfoil concept, the Belt-Rib, consisting of a closed belt and spokes. Experimental studies have successfully confirmed the feasibility of the concept for airfoil flow control purposes and was shown that careful tailoring of the structural stiffness of the Belt-Rib can lead to significant aerodynamic and aeroelastic amplification effects minimising the external actuation requirement. However even though a continuous chord wise structural surface is achieved with the morphing trailing edge concepts, span-wise end gaps remain between the discrete morphing trailing edges that could lead to increased noise emission and drags. To address the issue, different flap transitions span-wisely linking flaps have been proposed recently[7, 8, 9, 10]. Woods *et al.* [10] proposed an elastically lofted transition control surface for wings which covers the gaps between span-wise ends of adjacent control surfaces. The proposed morphing transition control surface constitutes a series of stacked ribs with skewed corrugations along the wing span which combines material and geometric compliance with bend-twist coupling. Desired span-wise deformation can be obtained with carefully selected corrugation skewing angles in the ribs.

In this paper, a novel span-wise twist morphing trailing edge (SMTE) concept is proposed which features prestressed composite laminate spar strips. Prestress effects in structures have been widely used to adaptively change the structural stiffness[13] and the proposed SMTE concept draws on previous research work by Daynes and Weaver[12] and Lachenal *et al.*[11]. The paper is organised as follows: firstly, the spanwise morphing flap design is introduced followed by an analytical model to describe the mechanical behaviours of the flap; then, a preliminary optimization study is carried out in terms of the spar laminate ply angle and the initial curvature of the strips and verification studies are done using a commercial software, ABAQUS; the paper is finished by presenting conclusions and future work.

.

2 The span-wise morphing flap design

A SMTE provides smooth span-wise change of wing shape and can also be used as a smooth transition between span-wise ends of flaps and morphing trailing edges, as shown in Figure 1. Drag and wing noise emission then can be reduced by removing flow vortices around the flap ends from the pressure side to the suction side. In this section, a SMTE consisting of CFRP laminate spars and ribs is introduced and an analytical model is developed to describe the mechanical behaviours of the structure.

The proposed SMTE concept consists of two main types of components: ribs along chord and spars in the span direction, which are assembled in a grid pattern. A NACA 0012 airfoil is chosen in this study. The wing has a chord c, of 500 mm and the trailing edge length b is 100 mm (20% of the chord of the airfoil, c). The span length, L, is 600 mm and five ribs are evenly arranged. Three rows of spar strips are used: the rear, middle and tip spars, as shown in Figure. 2 and the spar strip length, l is 150 mm. Distances from rear spar to middle spar, R_1 and from middle spar to tip spar, R_2, are 30 mm and 40 mm respectively. The paper focuses on describing a generic concept of a twist morphing trailing edge instead of developing a product for any specific application and as such, the geometric parameters used are for general purposes and not optimized. All the rib and spar strips are made of composite laminates using Hexcel 8552/IM7 CFRP prepreg[15] with mechanical properties given in Table 1. All ribs have the

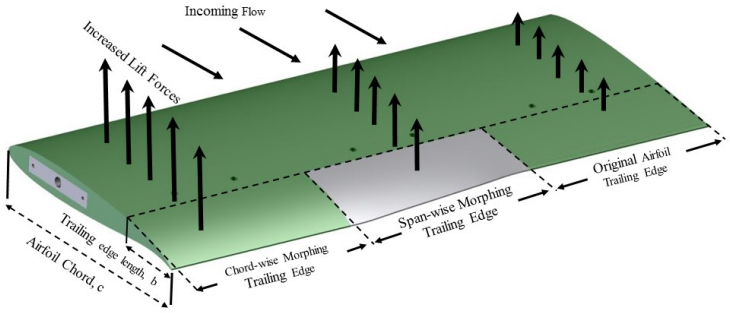

Figure 1: Wing with a chord-wise and span-wise morphing trailing edge

Table 1: Material properties of prepreg material [15]

Material	E_{11} (GPa)	E_{22}(GPa)	G_{12}(GPa)	$\nu_{12}(--)$	$\nu_{21}(--)$	Thickness (mm)
8552/IM7	135	9.5	5	0.3	0.021	0.125

same laminate layup of $[0_4]$ with 0° along chord and the spar ribs ply angle β is considered as a design parameter for a layup of $[\beta_8]$ with 0° along span. It is worth noting that prestress effects are only introduced in to the middle and tip spar strips with an initially manufactured curvature before assembly (see Figure 2). Morphing skins are not included in this section and are discussed briefly in a later section.

The twist axis is positioned at the centroid of the rear spar and does not coincide with the shear centre of the structure. The offset between the selected twist axis and the structural shear centre leads to span-wise bending deformation and such effects can be minimised by optimizing the positions of the middle and tip spar, *i.e.* R_1 and R_2, which is not considered in detail in this paper. The rear spar strips are manufactured flat without an initial curvature while the middle and tip spar laminate strips are manufactured in a stress free state with an initial curvature $\kappa_{x,initial}$ along its local x axis (see the coordinate system in dashed line Figure 2). The grid structure is then constructed in a heightened energy state and the pre-stored energy in the flattened spar strips can be released during the twist deformation to reduce the work done by the actuation force.

3 Mechanics

3.0.1 Strain energy Π

The internal grid structure of the SMTE is similar to the morphing airfoil device by Daynes *et al.*[12]: two prestressed spars are kept at a distance R_i from the twist axis at the centroid of the rear spar and are subject to twist deformation about the twist axis under twist moment. In this paper, the inextensible model developed in Ref. [12] is adopted and assumptions are: the

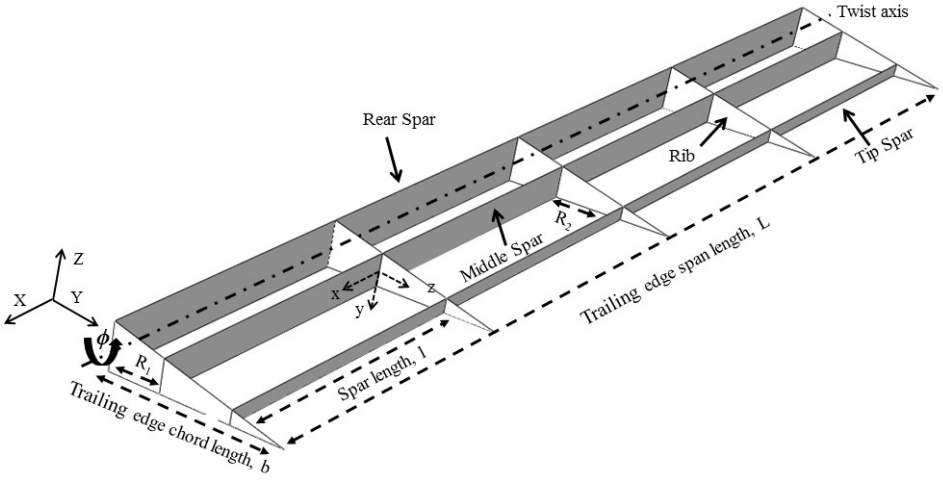

Figure 2: Schematic of the span-wise morphing trailing edge design

laminate strip deformation is inextensible and the curvature is uniform across the mid-surface of the strips. When the SMTE is subject to a twist angle ϕ at the span-wise end as shown in Figure 2, the curvature change $\triangle\kappa$ of a spar strip with respect to its local coordinate (see coordinate system in dashed line in Figure 2) is expressed as follows[12]:

$$\triangle\kappa = \begin{bmatrix} \triangle\kappa_x \\ \triangle\kappa_y \\ \triangle\kappa_{xy} \end{bmatrix} = \begin{bmatrix} \dfrac{R_i \cdot \phi^2}{2L^2} - \kappa_{x,initial} \\ 0 \\ 2\dfrac{\phi}{L} \end{bmatrix} \tag{1}$$

where R_i refers to R_1 and R_2 for middle and tip spars respectively and is zero for rear spar and L is the SMTE span length; $\kappa_{x,initial}$ is the initial bend curvature in the middle and tip spar strips, defined as $\kappa_{x,initial} = 1/\rho$ with ρ denoting the initial radius of curvature in the pre-bend strips. An assumption is made that the transverse curvature is negligible in the model, which is valid for slender strips where strain energy from longitudinal curvature and twist are dominant. However, a thorough study has been carried out by Lachenal *et al.*[14] to investigate the effects of the transverse curvature on the stability of helix structures and it was found that membrane stretching occurs when the transverse curvature is considered and a two-dimensional, extensional model can provide explicit insight into the mechanical behaviours. In the following sections, investigations are carried out with the analytical formulations in Ref. [12] owing to its simplicity.

The structural strain energy Π is expressed as:[16]

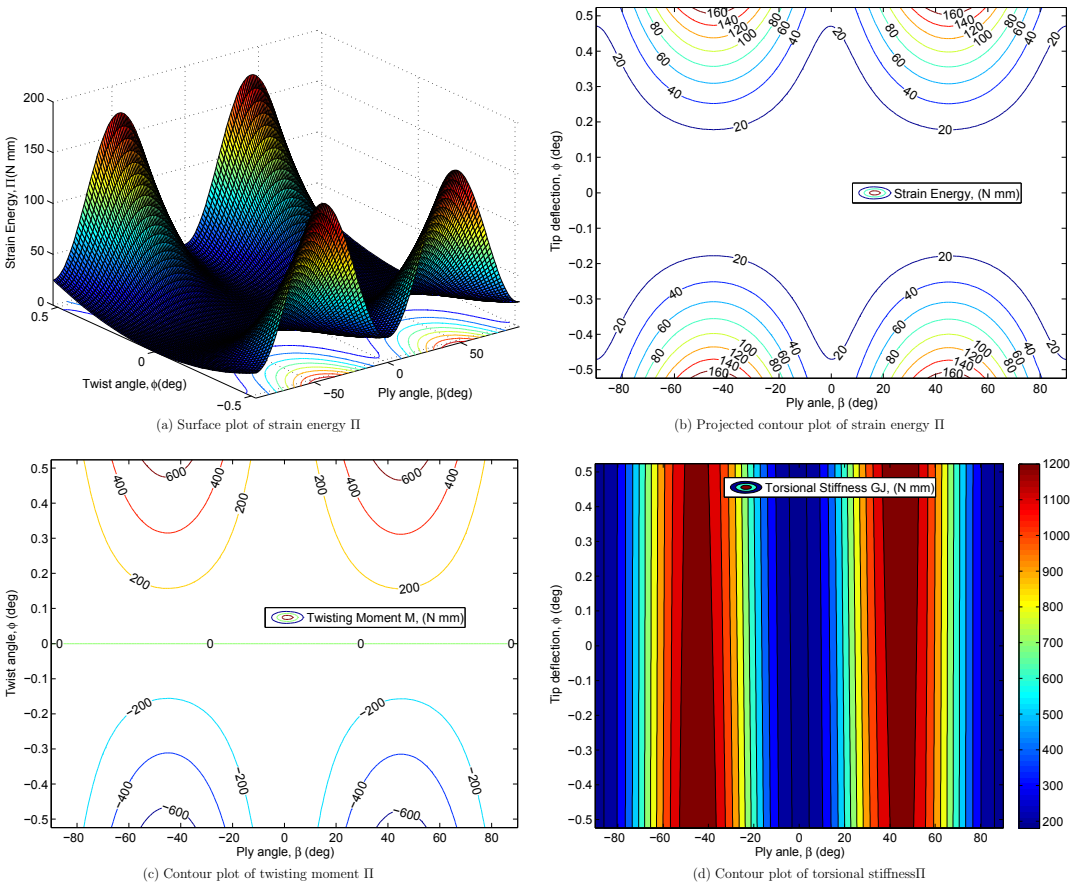

(a) Surface plot of strain energy Π

(b) Projected contour plot of strain energy Π

(c) Contour plot of twisting moment Π

(d) Contour plot of torsional stiffnessΠ

Figure 3: Surface and contour plot of strain energy Π, twisting moment M and torsional stiffness GJ as a function of ply angle β and twist angle ϕ for $\alpha = 0$

$$\Pi = \frac{1}{2}\sum_{i=1}^{N} l_i H_i \triangle\kappa_i^T D_i^* \kappa_i \tag{2}$$

where N is the total number of spar strips in the structure while l_i and H_i denote the length and width of the ith strip respectively; $\triangle\kappa_i^T$ refers to the transpose of the curvature change tensor $\triangle\kappa_i$; D_i^* represents the reduced flexural stiffness matrix of the composite laminate spar strips and is defined as: $D^* = D - BA^{-1}B$ where A, B and D are the in-plane, coupling and flexural stiffness matrices in classic laminate theory[17].

Combining Eq. 1 and 2, the strain energy is calculated as:

$$\begin{aligned}\Pi &= \frac{1}{2}\sum_{i=1}^{N} l_i H_i \triangle\kappa_i^T D_i^* \kappa_i \\ &= \frac{1}{2}\sum_{i=1}^{N} l_i H_i \{D_{11,i}^*(\triangle\kappa_{x,i})^2 + 2D_{16,i}^*(\triangle\kappa_{x,i}\triangle\kappa_{xy,i}) + D_{66,i}^*(\triangle\kappa_{xy,i})^2\} \\ &= \frac{1}{2}\sum_{i=1}^{N} l_i H_i \{D_{11,i}^*(\frac{R_i\cdot\phi^2}{2L^2} - \kappa_{x,initial})^2 + 2D_{16,i}^*(\frac{R_i\cdot\phi^2}{2L^2} - \kappa_{x,initial})(2\frac{\phi}{L}) + D_{66,i}^*(2\frac{\phi}{L})^2\}\end{aligned} \tag{3}$$

where $D_{11,i}^*$ $D_{16,i}^*$ and $D_{66,i}^*$ are the stiffness components of the reduced flexural stiffness matrix of the ith laminate spar strip. As the spar laminate strips are constrained from warping at both ends, the torsional stiffness has been effectively increased and the new stiffness is expressed as:[12]

$$D_{66,new}^* = \frac{D_{66}^*}{1 - \frac{H_i}{12l_i}\sqrt{\frac{10E_{11}}{G_{12}}}} \tag{4}$$

where E_{11} and G_{12} are the longitudinal Young's modulus and in-plane shear modulus and given in Table 1.

3.0.2 Structural stability

The stable equilibria of the SMTE can be found by seeking the minimum strain energy state in terms of the design parameters *i.e.* the laminate ply angle β for all the spar strips, the initial pre-bend curvature $\kappa_{initial}$ in the middle and tip spars and the twist angle ϕ[12, 18]. Stable equilibrium configurations are determined when the first derivative of the strain energy Π is zero and the second derivative of Π is greater than zero. The first derivative of the strain energy with respect to the twist angle ϕ is the twisting moment M and the second derivative of Π to ϕ is the torsional stiffness GJ. Expressions of M and GJ and the structural stability criteria are expressed as:

$$\begin{aligned}M &= \frac{\partial\Pi}{\partial\phi} = 0 \\ GJ &= \frac{\partial M}{\partial\phi} = \frac{\partial^2\Pi}{\partial\phi^2} > 0\end{aligned} \tag{5}$$

4 Preliminary optimization studies

With the developed formulations of the strain energy and the stable equilibria conditions in Eq.3 and 5, a preliminary optimization study is carried out to investigate the stability of the SMTE. The design parameters considered in this study are the initial pre-bend radius of curvature ρ of the middle and tip spar strips, the spar laminate strip stiffness matrix D^* and the twist angle ϕ applied to the SMTE. In order to simplify the analysis, only symmetric laminates

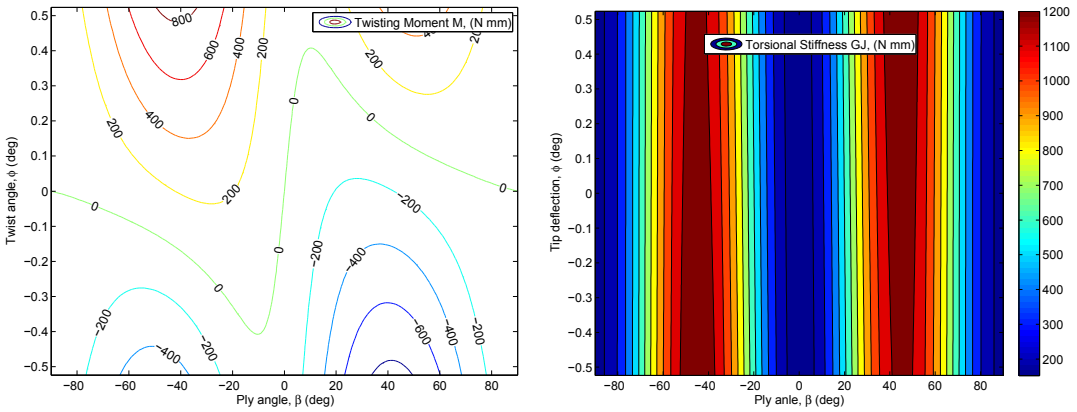

(a) Contour plot of twisting moment Π

(b) Contour plot of torsional stiffnessΠ

Figure 4: Plots of twisting moment M and torsional stiffness GJ as a function of ply angle β and twist angle ϕ for $\alpha = 0.2$

with the same orientation angle β (defined in the local coordinate system shown in dashed lines in Figure. 2) with constant thickness of 1 mm are considered for all the spar strips, *i.e.* a layup of $[\beta_8]$. Ply angle varies from $-90°$ to $90°$ to cover the whole ply angle range. The twist angle ϕ is selected to change from $-30°$ to $30°$, which provides a large deformation capability for the SMTE. A parameter α, is defined as the ratio of the spar length l to the initial pre-bend radius of curvature ρ, *i.e.* $\alpha = l/\rho$. After a parametric sensitivity study, a range of [0,1.5] is selected for α. Effects of the ply angle β and α on the stability of SMTE are studied and discussed in detail in the following sections.

4.1 Ply angles

Figure 3 presents the surface representation and contour plot of strain energy Π, twisting moment M and torsional stiffness GJ of the SMTE as a function of ply angle β of the laminate spar strips for a zero initial curvature in the middle and tip spars (see Figure 2). Without the prestress effects in the spars, the strain energy Π increases with the twist angle ϕ for all ply angles and peaks are found at ply angles $\beta = \pm 45°$ and twist angle $\phi = \pm 30°$. A unique stable equilibrium is found at $\phi = 0°$ where the condition $M(0) = \partial\Pi/\partial\phi = 0$ (Figure 3(c)) and $GJ(0) = \partial^2\Pi/\partial\phi^2 > 0$ (Figure. 3(d)) are satisfied. As expected, a ply angle of $\beta = \pm 45°$ provides the highest torsional stiffness and hence requires greatest twist moment. Without any pre-stored strain energy, the neutral position of the SMTE is only possible with $\phi = 0°$, which corresponds to a minimum strain energy state for the SMTE.

Twist moments and torsional stiffness of the SMTE for non-zero initial curvature $\kappa_{x,initial}$ ($\alpha = 0.2$, 0.6 and 1.3) are shown in Figures 4 to 5. As the SMTE begins being assembled in a heightened energy state, the stable equilibria configurations become dependent on the ply angle β and α. The lines where the twisting moment is zero ($M = 0$) in Figure 4(a) indicate that the stable equilibria configurations of the SMTE, corresponding to positive stiffness GJ in Figure 4(b). In Figure 4(a), for $\alpha = 0.2$, the stable configuration varies from $\phi = -0.4$ rad with a ply angle of $\beta \approx -10°$ to $\phi = 0.4$ rad with a ply angle of $\beta \approx 10°$. Interestingly, one stable configuration corresponds to two different ply angles. As the initially stored energy

further increases to $\alpha = 0.6$ and more energy can be released in the twisting deformation, the stable twist angle of the SMTE further increases to $\pm 0.524\ rad$ ($\pm 30°$). Similarly, every stable equilibrium corresponds to two ply angles, one of which is in a narrow range about $\beta = 0°$. It is worth noting that the stable neutral position of the SMTE proposed can be predefined in a wide range of twist angles ϕ (in this case, $\phi_{stable} = \pm 0.524$ is achievable) by selectively designing the ply angle and the initial curvature in the middle and tip spar laminates.

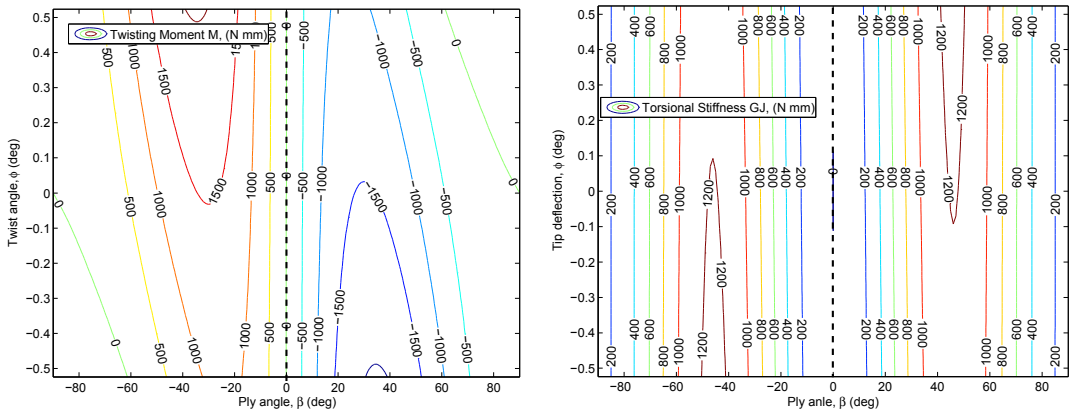

(a) Contour plot of twisting moment Π

(b) Contour plot of torsional stiffnessΠ

Figure 5: Plots of twisting moment M and torsional stiffness GJ as a function of ply angle β and twist angle ϕ for $\alpha = 1.3$

Particular attention is paid to a design case of $\alpha = 1.3$ where a zero torsional stiffness (ZTS) SMTE is observed. As shown in Figure 5(a) and 5(b), the dotted line at a ply of angle $\beta = 0°$ shows that for all the twist angle from $\phi = -0.524$ to $\phi = 0.524$, the twisting moment M and torsional stiffness GJ remain unchanged at zero and the required actuation twist moment hence becomes zero. The ZTS SMTE observed is discussed in detail in a later section with finite element method (FEM).

4.2 Initial curvatures

In this section, three ply angles β of 0°, 45° and 90° are selected to investigate effects of initial curvature in the middle and tip spar strips on the twist moment, torsional stiffness and stability of the SMTE. It has been noticed that effects of α on twist moment and torsional stiffness change significantly as the ply angle increases from 0° to 90°. As shown in Figure 6, for a ply angle $\beta = 0°$, the twist moment for a certain twist angle ϕ decreases to zero while α increases from 0 to 1.3. The torsional stiffness also reduces from 180 Nmm for $\alpha = 0$ to zero for $\alpha = 1.3$ and increases again to 20 Nmm for $\alpha = 1.5$. The ZTS SMTE case is also observed in Figure 6 and marked by the dotted line in the plots. For ply angles of β of 45° and $\beta = 90°$, however, no ZTS SMTE design is found.

It is shown that changes to material stiffness and initial curvature in the prestressed spar strips significantly affects the structural elastic strain energy, torsional stiffness as well as the stable equilibria configuration. The neutral stable position of the SMTE can be pre-defined

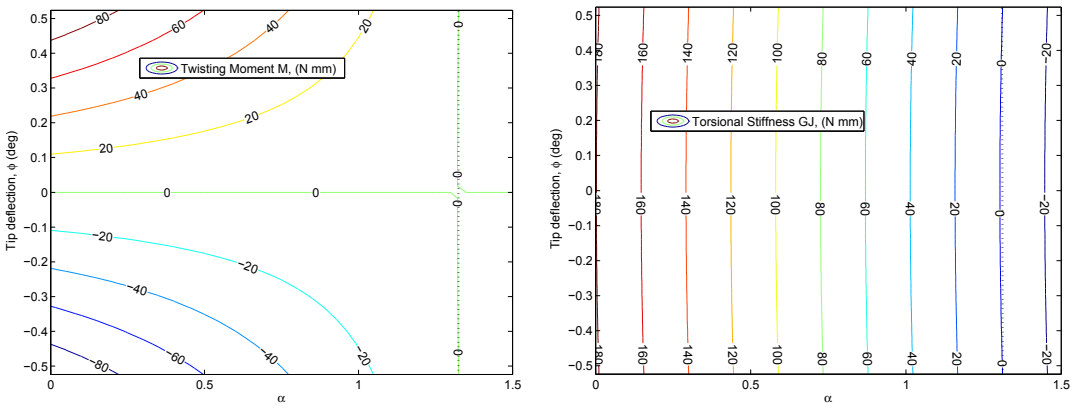

(a) Contour plot of twisting moment Π

(b) Contour plot of torsional stiffnessΠ

Figure 6: Plots of twisting moment M and torsional stiffness GJ as a function of α and twist angle ϕ for ply angle $\beta = 0°$

by carefully selecting the spar strip ply angle β and the initial curvature in the prestrssed strips. This functionality provides a new design freedom of control over the SMTE concept and particularly, a ZTS SMTE is also obtained minimising the actuation force.

5 Results validation

5.1 Finite element method

Commercial software package ABAQUS/CAE (ABAQUS 6.12, Dassault Systems Inc., VV, France) was used to verify the analytical model. All the spars and ribs were modelled with S4R shell elements and after a mesh convergence analysis, a mesh seed size of approximate 4 mm was chosen for the model. The 8552/IM7 CFRP mechanical properties in Table 1 were used and the laminates were modelled with 'Composite Layups' in Abaqus. One span-wise end of the rear spar was clamped as boundary conditions while twist deformation was applied as displacement boundary conditions at the centroid of the other end where the reaction twist moment was measured.

The ZTS SMTE design found in Section 4 was modelled, which has a layup of $[0_8]$ for all the spar strips with 0° along span-wise direction and ribs are CFRP laminates of layup $[0_4]$ with with 0° along chord-wise direction. With the analytical model, it is found that an initial manufactured radius of curvature $\rho = 115.1$ mm (corresponding to $\alpha = 1.3$) in the prestressed middle and tip spar strips (see Figure. 2) leads to the ZTS of the SMTE. In this study, an equivalent gradient temperature field across the laminate thickness is modified to model the prestress strain caused by flattening the initial pre-bend laminates[19].

Figure 7 shows that the developed analytical model provides accurate predictions of twist moment for the SMTE compared to FEM. It is noticed that for the ZTS design, discrepancy between the analytical model results and FEM increases for larger twist angles. However, significant reduction in torsional stiffness and twist moment is still observed for $\alpha = 1.3$ for both the analytical model and FEM. A parametric study with FEM shows that a further increased $\alpha = 1.62$ shows a ZTS performance in FEM, as presented by the dashed black line in the

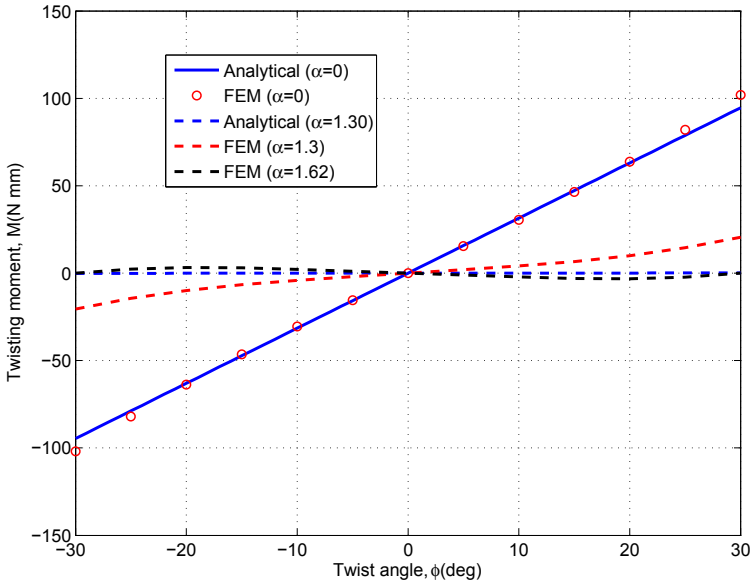

Figure 7: Verification of the analytical model–plot of twist moment M as function of twist angle ϕ

plot. The difference is believed to be due to the simplicity of the analytical model and also the models used to capture the restrained warping, as the airfoil thickness varies along the chord and in the analytical model only an averaged spar strip thickness is used to model the warping restraint effects[12]. Furthermore, the stress concentration and redistribution caused by the prestress at the corners between spar strips and ribs are not modelled in the analytical model, which contributes to the discrepancies too. Furthermore, it is noticed that the proposed SMTE trailing edge deflection features a typical shear/torsion deformation shape along the span with a constant slope of ϕ/L.

6 Conclusions

A novel span-wise twist morphing trailing edge device consisting of CFRP ribs and spars are proposed in this paper and preliminary optimization studies are carried out. In the developed SMTE concept, the middle and tip spar strips are prestressed by flattening a manufactured initial curvature before the structure is assembled. This way, the SMTE grid structure is built to a heightened strain energy state and yields different stable equilibrium configurations depending on the laminate layups, prestress and geometric parameters. Investigations using an analytical model are carried out and thorough parametric studies show that by selectively changing the spar laminate layups and the initial curvature in the prestressed spar strips, stable neutral position of the SMTE can be pre-defined over a wide range of twist angles ($\pm 30^\circ$ has been achieved in the current design). In particular, a zero torsional stiffness design is found for spar strips with layup of $[0_8]$ and $\alpha = 1.3$ corresponding to an initial radius of curvature of 115.5 mm in the pre-stressed spars. Our analytical model is verified using commercial FEM and good correlation was found. With the ZTS SMTE, the torsional stiffness is significantly reduced and hence the required actuation force are decreased greatly, even to zero. Though some relative

minor discrepancy is observed between the proposed analytical model and FEM yet, the current model can be used for preliminary optimization studies. Future work may include:

- integrity design between the SMTE and leading edge body of wing;
- studies on actuation method using smart materials including piezoelectric and shape memory alloy material;
- morphing skin selections.

Acknowledgments

This work was supported by the Engineering and Physical Sciences Research Council through the EPSRC Centre for Doctoral Training in Advanced Composites for Innovation and Science [grant number EP/G036772/1]. Assistance from Dr. Stephen Daynes with the FEM is much appreciated.

REFERENCES

[1] Dobrzynski, W. Almost 40 Years of Airframe Noise Research: What did We Achieve?. *J Aircraft*, 2010, **47(20)**:353-367.

[2] Campanile L.F. *Adaptive Structures: Engineering Applications*, Wiley:Chichester, 2007.

[3] Lachenal, X., Daynes, S., Weaver, P. Review of Morphing Concepts and Materials for Wind Turbine Blade Applications,. *Wind Energy*, 2013, **16**:283-307.

[4] Daynes, S., Weaver, P.M. Review of Shape-morphing Automobile Structures: Concepts and Outlooks, *P I MECH ENG D-J AUT*, 2013, **227**:1603-1622.

[5] Campanile, L.F., Anders, S., Aerodynamic and Aeroelastic Amplification in Adaptive Beltrib Airfoils, *AEROSP SCI TECHNOL*, 2004, **9**:55-63.

[6] Ai, Q., Azarpeyvand, M., Lachenal, X., Weaver, P. Aerodynamic and Aeroacoustic Performance of Airfoils Using Morphing Structures, *Wind Energy*, 2016, **19**:1325-1339.

[7] Kunz, R., *Apparatus for Closing an Air Gap between a Flap and an Aircraft*, US Patent No. US4471925A. Issued Sep 18, 1984.

[8] Diller, J.B., Miller, N.F., *Elastomeric Transition for Aircraft Control Surfaces*, US Patent No. US6145791A. Issued Nov 14, 2000.

[9] Etling, K.A., *Morphing Control Surface Transition*, US Patent No. US8342447B2, Issued Jan 1, 2013.

[10] Woods, B., Parsons, L., Coles, A.B., Fincham, J.H.S., Frishwell, M.I., Morphing Elastically Lofted Transition for Active Control Surfaces, *ICAST 2015: 26th International Conference on Adaptive Structures and Technologies*, October 14-16th, 2015, Kobe, Japan.

[11] Lachenal, X., Daynes, S., Weaver, P.M. A Zero Torsional Stiffness Twist Morphing Blade as a Wind Turbine Load Alleviation Device, *Smart Mater. Struct*,2013, **22**:065016(13pp).

[12] Daynes, S., Lachenal, X., Weaver, P.M. Concept for Morphing Airfoil with Zero Torsional Stiffness , *THIN WALL STRUCT*, 2015, **94**:129-134.

[13] Daynes, S., Weaver, P. Stiffness Tailoring Using Prestress in Adaptive Composite Structures, *Compos. Struct.*, 2013. **106**:282-287.

[14] Lachenal, X., Weaver, P.M., Daynes, S. Influence of Transverse Curvature on the Stability of Pre-stressed Helical Structures, *Int J Solids Struct* , 2014, **51**:2479-2490.

[15] Daynes, S., Weaver, P.M. Analysis of Unsymmetric CFRP-Metal hybrid laminates for Use in Adaptive Structures, *COMPOS PART A-APPL S*, 2010, **41**:1712-1718.

[16] Kollar, L.P., Springer, G.S. *Mechanics of Composite structures*, Cambridge, Uk, Cambridge University Press, 2003.

[17] Jones, RM. *Mechanics of Composite Materials*, 2nd edn; Taylor and Francis:Philadelphia, 1999.

[18] Lachenal, X., Weaver, P.M., Daynes, S. Multi-stable Composite Twisting Structure fro Morphing Applications, *Proc Math Phys Eng Sci*, 2012, **468**:1230-1251.

[19] Mansfield, E.H. *The Bending and Stretching of Plates*, Cambridge, UK, Cambridge University Press, 22 Aug 2005.

[20] Thill, C., Etches, J., Bond, I., Potter, K., Weaver, P. Morphing skins. *The Aeronautical Journal*, 2008, **112**:117-139.

VIII ECCOMAS Thematic Conference on Smart Structures and Materials
SMART 2017
A. Güemes, A. Benjeddou , J. Rodellar and Jinsong Leng (Eds)

BEHAVIOR CHARACTERIZATION OF MACHINE-KNIT SMA

LUCY (YUZHOU) ZHUANG[*], JONATHAN LUNTZ[*], DIANN BREI[*], SEAN AHLQUIST[†], PAUL ALEXANDER[+]

[*] Department of Mechanical Engineering
University of Michigan
Ann Arbor, Michigan 48109
e-mail: jluntz@umich.edu

[†] Architecture and Urban Planning
University of Michigan
Ann Arbor, Michigan 48109

[+] Research and Development
General Motors Corp.
Warren, Michigan 48092

Key words: Knitted fabrics, shape memory alloy, shape changing, bistable behavior.

Abstract. Fabrics using a knitted architecture can provide interesting structural characteristics like stiffness, bi-stability and textured surfaces, but using only traditional fibers renders these textiles passive and unresponsive. Shape memory alloy (SMA) is an accessible and bendable smart material with the advantage of its reversible thermally induced change of state between austenite and martensite, which can be used in a knitted structure to create shape changing surfaces. Active SMA knits offer the potential of designing flexible actuators and interactive surfaces in products to provide adaptive textures and haptic feedback to fully engage customers with the product, which will revolutionize user experience. Recent research has demonstrated that fabrics hand knitted from SMA wires can produce interesting shapes and motions when heated, but the samples have loose and inconsistent knitting patterns. This project aims to quantify and characterize the mechanical behaviors of knitted SMA samples fabricated by an industrial flat bed knitting machine, which provides a more consistent and reliable structure with denser knitting patterns than can be achieved by hand knitting. When heated, a knitted SMA sample using single-jersey stitch forcefully deforms out of plane into a curved shape with a height which varies with an applied compressive load. Unlike previous hand knitted samples, these dense, machine-knitted samples exhibit bi-stability, where the knits deform in either course-wise axial curling or wale-wiselongitudinal rolling depending on the boundary conditions. This bi-stable actuation is often biased towards one of the two directions depending on the overall geometry of the sample, but the two actuation modes are generally interchangeable by setting boundary conditions. Force-deflection properties of the samples were experimentally characterized on a specifically designed test rig, by measuring the compressive force as a function of displacement at both low (~25 °C) and high (~100 °C)

temperatures, below and above the SMA transition temperature. A parameter study is done to quantify the scaling effect of geometry on actuation force and displacement, demonstrating that the displacement scales linearly with sample width. The quantified actuation curves of curling and rolling actuation modes can allow designers to distinguish between the two different behaviors of the bi-stable samples based on measurement data. The ranges of the achievable actuation force (up to 1600 gram-force) and displacement (up to 5mm) are of levels useful for interactive surfaces, the motions and shapes of which can be experienced by customers. This quantitative study of actuation performance and bi-stability of SMA wire knitted structures will be a foundation of designing future interactive surfaces in products.

1 INTRODUCTION

Automotive manufacturers have been continually developing advanced technology for vehicles, especially focusing on functionality, safety, and performance. Recently this focus has increasingly been emphasizing the customer-vehicle interaction. Customers interact with many components within their vehicle including the steering wheel, seats, entertainment controls, etc. Some features within the vehicle, however, remain completely passive, particularly the many smooth, featureless surfaces visible to and accessible by the customer. Unexplored opportunities exist in this area of future vehicle design to creating interactive surfaces in vehicles to revolutionize the user experience. From the steering wheel, the inner surfaces of car doors, to any surface that the users touch by the hands and the body, if those otherwise passive surfaces can be controlled to change shape, texture, and appearance to provide visual and haptic feedback, they will fully engage both drivers and passengers, providing exciting new experiences with such new design features.

Most vehicle interior surfaces are relatively smooth and featureless. Knitted fabrics, however, provide the potential for creating a huge variety of different textures and appearances. A knitted structure is constructed by repeated single basic loops (Figure 1) of either knit loops (loop legs in front of ridges) or purl loops (loop legs behind ridges). The length of each loop is referred to as the stitch length. This unique structure is used extensively in the fashion industry and more recently in the area of architecture [1] where knitted surfaces provide interesting mechanical characteristics such as corrugated surfaces, bi-stability and extra stiffness (Figure 2).

However, knitted surfaces made from traditional fabrics like wool, cotton, and synthetic yarns are still unchanging and unresponsive. Recent research has explored the use of active material fibers in a knitted structure to create interactive surfaces by leveraging the base

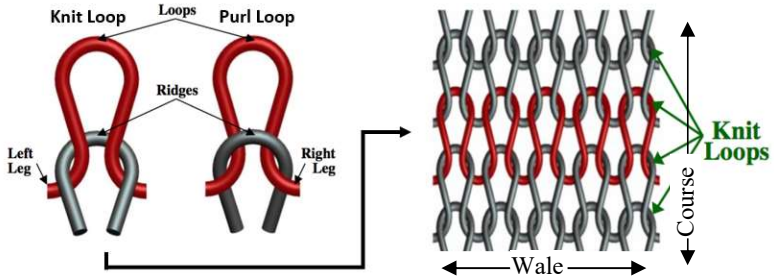

Figure 1. Knitted structures consist of interlocked knit and/or purl loops. A single-jersey (stockinette) stitch pattern is shown [3].



Figure 2. Knitted fabrics can create corrugated surfaces, surfaces with extra stiffness and elasticity, and bi-stable surfaces [1].

material's own behaviors. Smart textiles have been developed using shape memory alloy (SMA) [2], [3], piezoelectric fibers [4], and electroluminescent yarns [5]. Prior research of SMA knitted fabrics [3] has shown hand-knitted SMA samples, which demonstrated outstanding mechanical behaviors and motions that produced a wide variety of bumpy and shape-changing surfaces. Of these three materials, the texture and shape changing capabilities demonstrated by knitted SMA combined with its commercial availability and off-the-spool functionality make it particularly promising for interactive surface technologies

Shape memory alloy, transforms between soft, deformable martensite to stiff austenite in response to heating above its transition temperature. In a knit structure, the stiffening of the wire upon heating causes the knit loops to attempt to straighten to their memorized straight shape, pushing against the neighboring loops into which they are interlocked. The result is a bulk deformation of the entire fabric depending on the structure of the knitting pattern, boundary conditions, and hierarchical textile structure [3]. For example, samples with a Stockinette pattern roll into a tube after heated (Figure 3(a)), and samples with a Rib knit patterns deform into a W-shaped bumpy surface (Figure 3(b)). The deformation of these active knitted structures shows the potential to create interactive surfaces and adaptive textures.

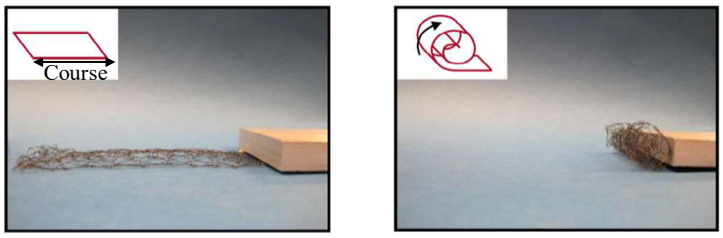

a) Stockinette pattern

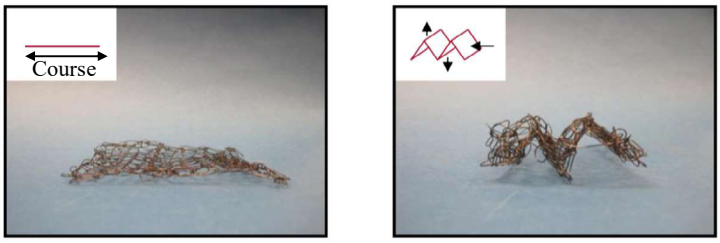

b) Rib knit pattern

Figure 3. . Hand knitted samples move and change shape when heated [3].

In these earlier studies, however, these samples were knitted by hand and therefore loose and inconsistent with uneven stitch lengths, loop diameters and loop shapes (Figure 4), making it somewhat difficult to quantify their behavior. In addition, the looseness of the knit limits the mechanical interaction between adjacent loops since there is significant freedom of motion within each loop. These hand-knit samples are not representative of future knitted products in mass production which can be knit much more densely with extreme consistency.

This paper examines machine-knit SMA samples, characterizing and quantifying their mechanical behaviors. Densely knit single-jersey (equivalent to Stockinette stich in hand-knitting) samples are produced from commercial SMA wire on an industrial knitting machine. Their course-wise curling and wale-wise rolling behaviors upon heating are examined, and a geometry-dependent bistable actuation behavior is identified. The ability of the samples to actuate against a load is measured and a parameter study quantifies the scaling effect of geometry and sheds light on the ranges of geometries under which the two modes of the bistable behavior are exhibited. By characterizing the actuation behavior of machine-knit SMA samples, this study provides an initial basis for the identification of potential applications for the use of such smart textiles for interactive surfaces in future vehicle interior design.

2 QUALITATIVE SMA MACHINE-KNIT BEHAVIOR

Since the behavior of an SMA knitted sample depends on the mechanical interactions between adjacent loops, it is expected that the density of knitting has a significant impact on the behavior of an SMA knit sample. To understand the types of behaviors produced by the extremely dense machine knit SMA samples, and to guide the quantitative measurement of actuation behaviors, a qualitative examination of the SMA knit behaviors is necessary. SMA knit samples were produced on an industrial knitting machine and heated under a variety of initial and boundary conditions to expose the variety of accessible behaviors.

2.1 Machine-Knit Fabrication

Machine knit samples were fabricated on a Stoll CMS 822 HP knitting machine [6] (Figure 5). SMA wires (0.010'' Dynalloy FLEXINOL® Actuator Wire) are used for the main body of the sample with traditional yarn used at the two ends of the sample to aid in fixturing when characterizing the samples. The desired single-jersey knitting program is loaded into the machine controller and the machine proceeds with the automatic knitting process. When the machine is running, the knitting carriage moves forward and backward repeatedly to create

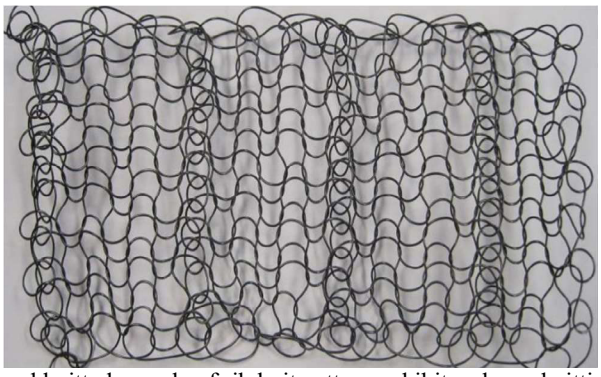

Figure 4. A hand knitted sample of rib knit pattern exhibits a loose knitting desnity [3].

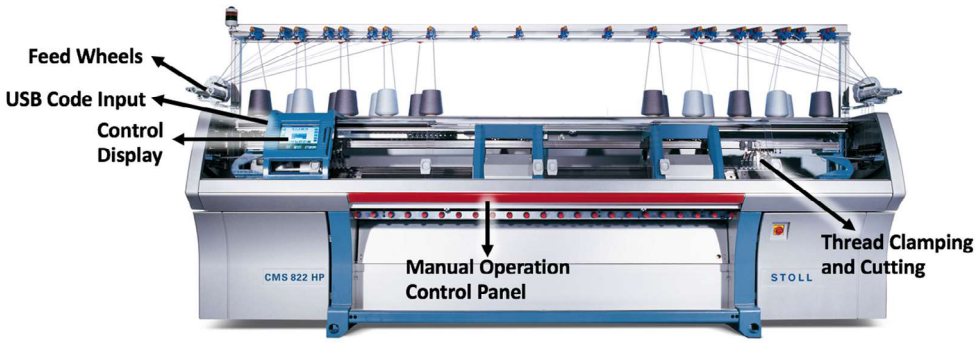

Figure 5. All the samples are fabricated on a Stoll CMS 822 HP knitting machine, providing a consistent and dense knitting pattern [6].

loops in the knitted structure. Each pass of the knitting carriage creates a course: a horizontal row of kitted loops or stitches. The number of courses (rows) and wales (columns) along with the stitch length correspond to the relative length and width of the sample, which are important geometric parameters of the SMA active knit. A completed rectangular knit sample is shown in Figure 6 with black SMA wire knit in the body, and brown traditional yarn fixturing patches at each end.

2.2 Qualitative Observations of Mechanical Behavior

Initially, all samples, as knitted, tended to naturally roll into a coiled shape with the axis perpendicular to the knitting direction, a nature typical of all single-jersey knits. The behavior of samples was observed when heated with a heat gun above their transition temperature (~90 to 100°C). When heated from the initial state, all samples rolled more tightly into a smaller diameter tube under free loading. However, by manually flattening the sample and then forcefully bending it in the perpendicular direction the sample can be switched from the rolling mode to a curling mode. All samples exhibited this bistable behavior with two different actuation modes – longitudinal rolling and axial curling (Figure 7). Rolling actuation occurs around an axis perpendicular to the knitting direction starting with the edge course (Figure 8 (left)), while curling actuation occurs around an axis parallel to the knitting direction starting

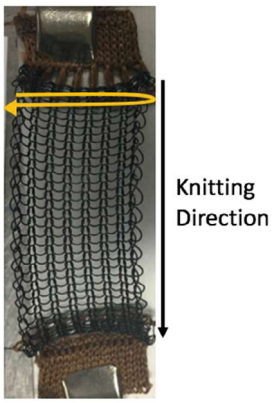

Figure 6. Completed single jersey knit simple with SMA (middle) and yarn fixturing attachments (ends).

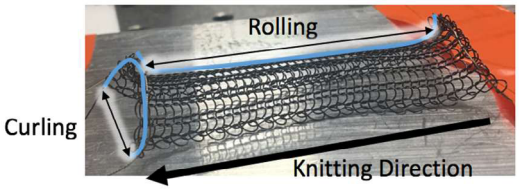

Figure 7. Both course-wise curling and wale-wise rolling actuation modes can occur on the same knitted sample. The thick blue curves dwarn on the photo show the sectional arcs for rolling and curling. The arrows show the motion direction of the edges.

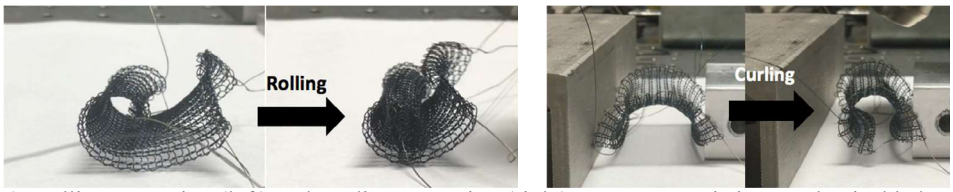

Figure 8. Rolling Actuation (left) and Curling Actuation (right) are two co-existing mechanical behaviors on the active SMA knitted structure depending on boundary conditions.

with the edge wale (Figure 8 (right)). All samples can be forced to actuate in either the rolling mode or curling mode by setting initial boundary conditions (for example, placing it between two rigid blocks to hold it in a partially curled shape before heating induces the curling mode). Generally, wider samples have stronger tendencies towards rolling, while longer samples have stronger tendencies towards curling. In either case, samples demonstrated forceful deformation when heated.

In the rolling mode, the samples roll from a two-dimensional flat surface to a three-dimensional coil; In the curling mode, the samples form a hump up to a higher and stiffer surface. Therefore, the curling mode is more interesting for interactive surface design and testing because it retains the shape of a deformed two-dimensional surface when heated, which can be directly used to design shape-changing surfaces.

3 QUANTITATIVE BEHAVIOR STUDY

The primary action of the curling mode is to forcefully deform out of plane. Quantitative measurement of this actuation behavior focuses on measuring the out-of-plane force-deflection properties of a sample when cold and when heated. A set of four single-jersey knit samples spanning a range of widths and lengths were characterized on a planar compression experimental setup which measures the force required to compress the sample between two plates (Figure 9). All samples used the same stitch length of 12.5 (units are specific to the STOLL software and knitting machines). The resulting force-deflection behavior provides an understanding of the geometric scaling of force and deflection and of the dependence of the bistable behavior on sample geometry.

3.1 Experimental Design

Because the difference between rolling and curling mode is that either the edge course or the edge wale has a stronger tendency of moving, the width and the length of the sample has a strong effect to determine the preferred tendency of motion. Therefore, in determining the set of sample geometries to characterize, the control parameters of the experimental design of

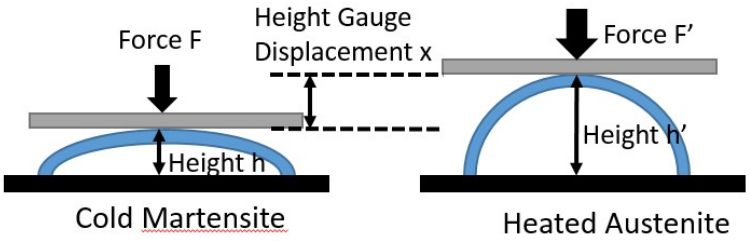

Figure 9. A flat plate on the top of the sample is used to measure the total compression force on the sample as a function of the sample height which is the gap between the top plate and the bottom plate.

experiments are the number of courses and number of wales. Starting with a particular shape, by doubling the number of courses (length) and/or doubling the number of wales (width), this experimental design explores the geometric and scaling effects of the actuation force and displacement. A baseline sample was knitted from 0.010'' diameter SMA wire with a geometry of 8 columns and 26 rows. A sample with double the rows (longer aspect ratio), a sample with double the columns (wider aspect ratio), and a sample with both double the rows and double the columns (same aspect ratio, double the size) were knitted (Figure 10).

3.2 Experimental Testing Method

An experimental setup was fabricated (Figure 11) to measure a sample's compressive force as a function of sample height in the vertical direction. A load cell is mounted onto a height gauge with a 3d printed fixture screwed on the gauge. A flat metal plate is used to compress the sample and is mounted to a wood block directly attached to the bottom of the load cell. Since a heat gun is used to heat the sample, the wood block, combined with a cardboard heat deflecting shroud attached to the block, insulates and deflects the hot air from the temperature-sensitive load cell to provide consistent force measurement. The sample is compressed between the upper metal plate and a stationary lower plate, and is loosely taped down to the bottom plate at one end to prevent the hot air from dislodging the sample while ensuring free sideways deformation of the sample while it is compressed.

Before measuring the force-deflection properties of a sample, the load cell and the height gauge are zeroed by measuring the load reading with only the wood block and cardboard shroud

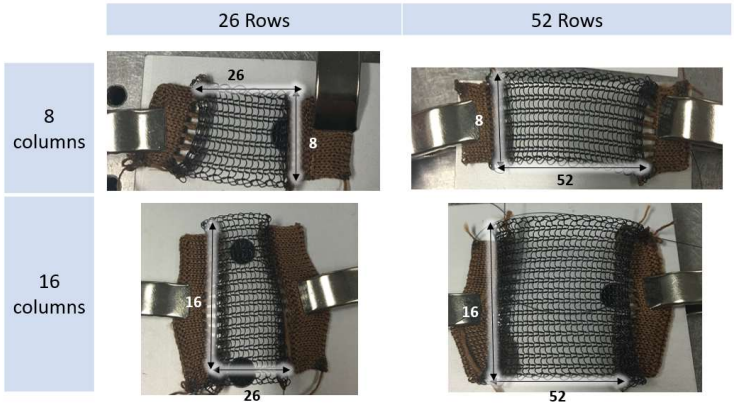

Figure 10. Parametric study DOE explores aspect ratio and scale relative to a baseline 8x26 sample.

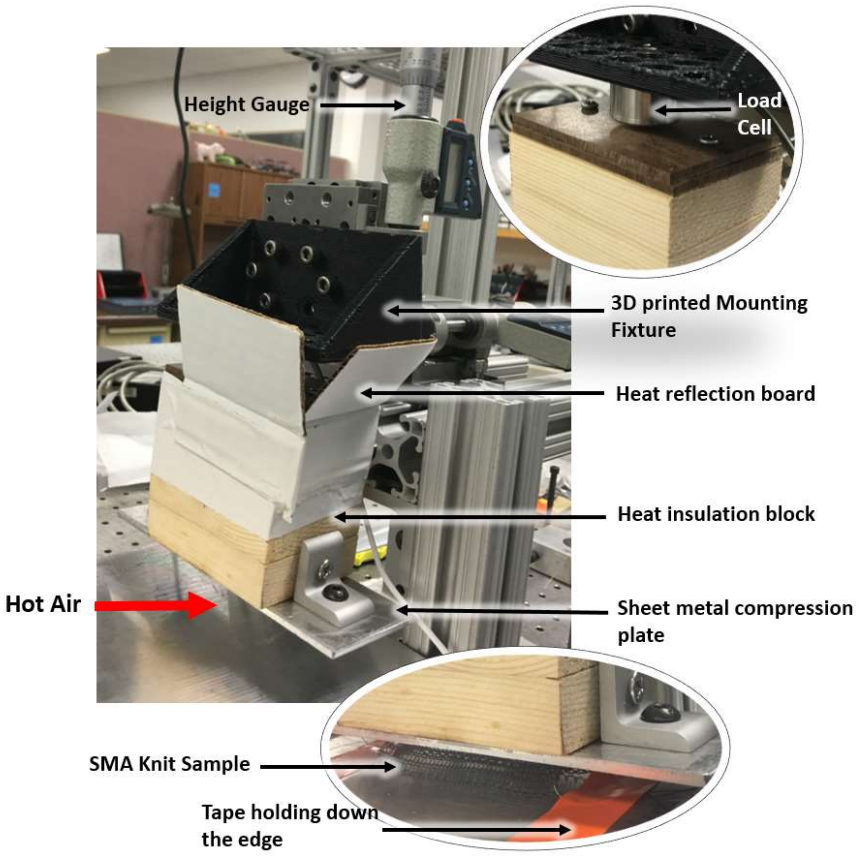

Figure 11. The experimental fixture contains the height gauge, load cell, 3D printed mounting fixture, wood block with the heat reflection cardboard shroud, sheet metal compression plate.

hanging from the load cell, and by lowering the height gauge until the upper and lower plates touch. The upper plate is then raised and a sample placed between the plates set into an initial arched condition conducive to either curling or rolling, depending on the state being tested. The sample is held in its initial shape by slight compression between the upper and lower plates at the largest height possible before the sample curls or rolls back on itself.

To measure the martensitic force-deflection behavior, at room temperature, the height gauge is incrementally lowered and the reading from the load cell and the height gauge is recorded at each increment as the sample is compressed. This is continued until the force level increases dramatically with a small additional displacement, indicating that the sample is compressed completely flat. The measurement process is reversed, decompressing the sample until the measured load reaches zero. Both the compression and decompression force-deflection data are plotted.

A similar procedure is followed to measure the austenite force-deflection behavior where hot air is blown from a heat gun onto the sample as the data is recorded. Since blowing hot air heats the sample inconsistently, and overheating the sample can damage the SMA material's shape memory effect, the load cell reading is carefully monitored while heat is applied. As the sample heats, the force measurement increases until the SMA fully transforms into austenite. At this point the force measurement remains constant with additional applied heat. Heating is

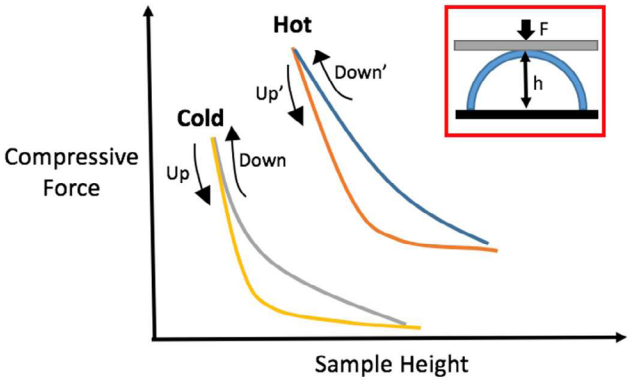

Figure 12. The testing cycles under low and high temperatures for the characterization of actuation performances of the SMA knitted samples.

then reduced and this maximum force level is recorded. To avoid hysteresis effects due to the austenite to martensite transformation, between compression and decompression displacement increments, the heat is not completely removed so that the sample does not begin to transform into martensite. Like the martensite measurements, this process produces two curves when plotted, one during compression and one during decompression which differ due to both the hysteretic nature of SMA and due to the internal friction between the knit loops as the sample deforms. Figure 12 shows the expected resulting load paths for the two curves generated for each of the two material states, austenite and martensite. While all four curves are useful for characterizing behavior, when characterizing the actuation capabilities of a sample, the cold compression (down) curve and the hot decompression (up) curve are most relevant. This is because when acting as an actuator, the sample expands upward when heated and is compressed downward when cooled.

Typical force-deflection curves obtained from this process are shown in Figure 13. Each of the four curves exhibits a characteristic "J" shape with a lower initial stiffness at high heights (small amount of compression) and an increasingly higher stiffness at larger compression. The austenite force is generally larger than the martensite force. For example, at 7mm of sample height, when the sample is only lightly compressed, there is a gain of 160 gram-force after heating the SMA knit. At 4mm of height when the sample is in the stiffer region, there is a gain of 1000 gram-force gain at the high temperature. This substantial force difference is available as useful out-of-plane actuation and is large enough to provide strong pushing tactile interactions with a user.

The stiffness of the surface also increases from low temperature to high temperature in the slightly compressed region. Above 6 mm height, the surface stiffness is 106 gram-force/mm at high temperature, which is much larger than the 19 gram-force/mm above 5mm height at low temperature. In the highly compressed region, however, the stiffnesses are nearly equal, with 492 gram-force/mm when hot below 5 mm height and 494 gram-force/mm when cold below 4 mm height. Thus, the sample stiffness when lightly compressed comes mainly from the bending stiffness of the wires themselves which changes between austenite and martensite, whereas the sample stiffness when highly compressed comes mainly from the compressive interactions between the overlapping wires and the knit geometry and is largely independent of the material stiffness.

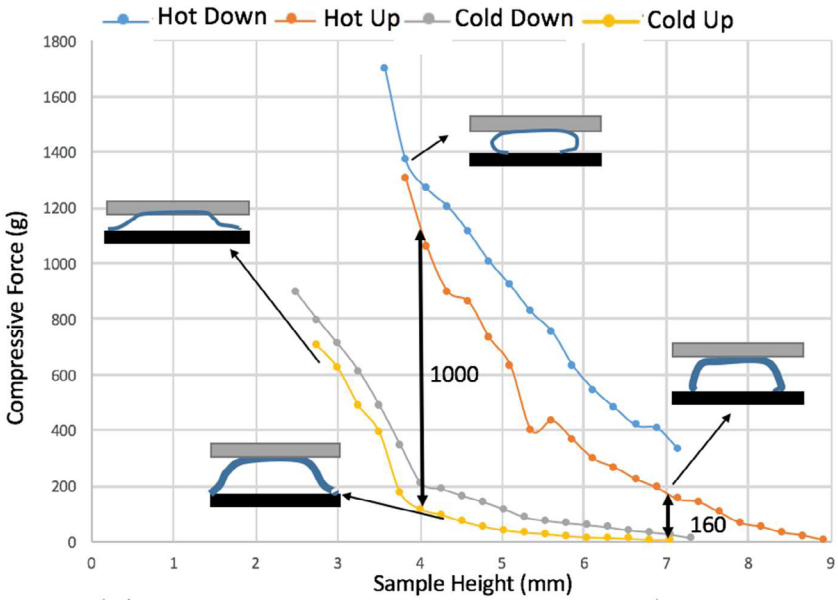

Figure 13. Typical testing results under low and high temperatures for the characterization of curling actuation performances of an 8-column by 52 row sample knitted from 0.010" diameter SMA wire.

The samples show good cycle repeatability under both low temperature and high temperature (Figure 14) with no visible trend after several cycles. Thus, the SMA knitted surface appear to be able to actuate repeatedly without losing its stiffness and actuation force (although more cyclic testing is required), aiding characterization and enhancing the reliability of operation of interactive surfaces which will not lose its features and stiffness over time.

3.3 Effect of Geometric Scaling in Curling

The scaling effect for the curling actuation mode is investigated by testing three different knit samples (width × length): 8×52, 8×26, 16×52. The up actuation curves (most relevant to characterizing actuation performance) under high temperatures of different samples are compared in Figure 15. Comparing 8×52 and 16×52 curves, when the width is doubled,

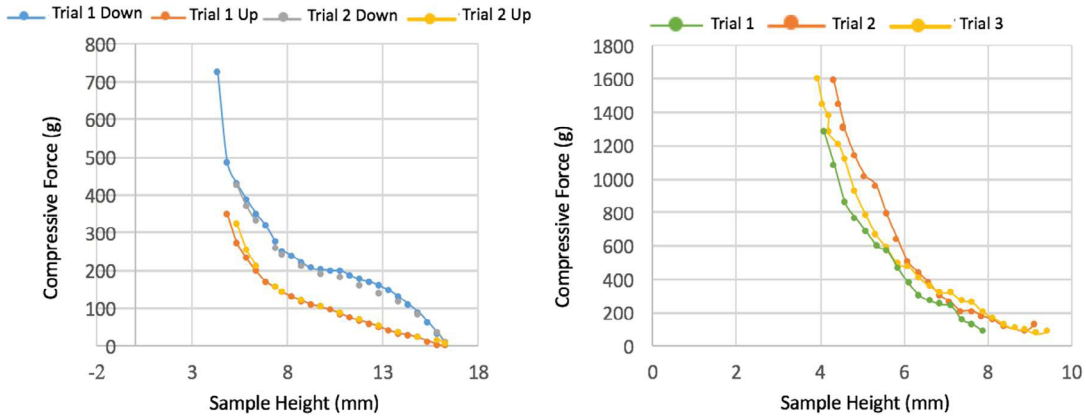

Figure 14. Cycle repeatability test results show that the surface actuation performance is reliable and consistent after two to three cycles under low temperature (left) and high temperature (right).

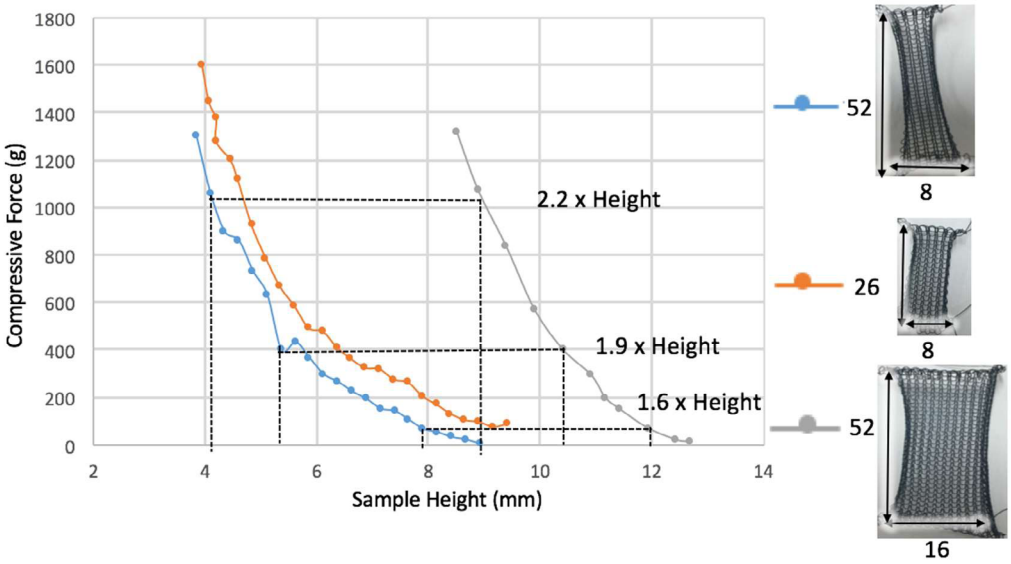

Figure 15. Up actuation force-deflection curves in curling for three different samples with either doubling the width or doubling the length. The displacement approximately doubles when the width of the sample is doubled, but there is no linear relationship found when the length of the sample doubles..

doubles, the sample height approximately doubles throughout the entire actuation curve. This scaling effect with length is expected since for a given shape, the height of an arch formed by curling actuation scales with the width of the sample (i.e. arch perimeter). However, comparing the actuation performances of 8×26 the 8×52 samples, the displacements and forces are approximately the same when the length of the sample doubles. This is not expected since a longer sample should act like two shorter samples acting in parallel, producing twice the force at the same displacement. One possible explanation for this lack of linear relationship is that the edge effects overweighs the linear tendency, where rolling observed at the ends of the sample adds to the displacement, bending the ends upward. This occurs more relative to its curling actuation in the shorter sample than it does to the longer sample where the overall length softens these edge effects. Thus, the shorter sample has a slightly larger deflection at a given load than does the longer sample rather than a larger force at a given displacement as expected.

3.4 Rolling Mode Actuation

Although the rolling actuation mode, which turns the sheet into a coil, doesn't directly produce out-of-plane actuation, the potential exists to add boundary constraints to use this actuation mode for interactive surfaces. The actuation force deflection data for rolling of a 16x26 sample is recorded to produce behavior curves which distinguish the two different actuation modes directly from the measurement data. Figure 16 shows that for this rolling actuation, there is 310 gram-force increase when heated in the slightly compressed region and a 1125 gram-force increase in the fully compressed region. This actuation force gain is slightly larger than that in the curling mode actuation because the tube shape it forms can withstand a heavier load.

The 16x26 sample used to test the rolling actuation mode has a much larger width then length, leading to a natural rolling motion. Although the sample can be forced to actuate in the

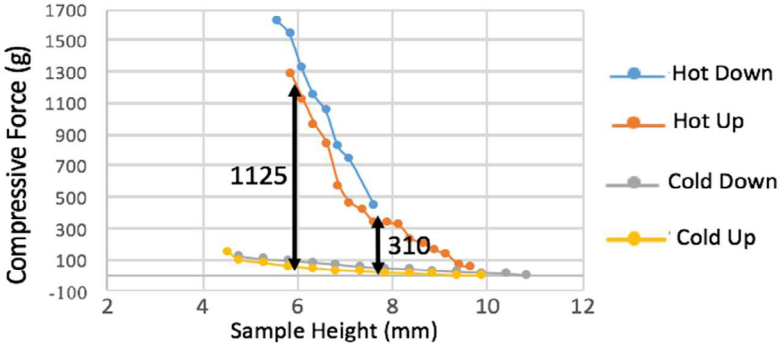

Figure 16. Rolling actuation performance for the 16x26 SMA sample.

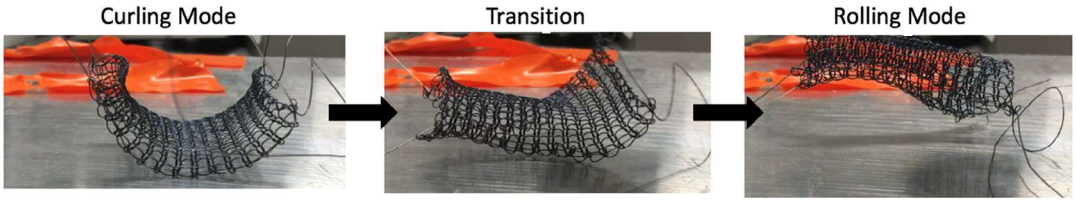

Figure 17. The 16x26 SMA simple naturally transitions from curling to Rolling under free loading.

curling mode, the sample naturally transitions to rolling mode under free loading (Figure 17). Depending on which actuation mode the sample is started in, the actuation curves behave differently depending on the original state. Figure 18 shows both the rolling and curling actuation heated up actuation curves of the same 16x26 sample which were induced by forcing the original state. In the highly compressed region, the rolling mode produces a significantly larger force at the same displacement: 500 gram-force larger at 6mm height representing an 80% increase. This larger force makes sense because in rolling, the actuator has a longer support surface with shorter moment arms to leverage the bending in the sample to an upward force. However, as the sample is decompressed in the up-direction, the rolling and curling forces become identical above 7 mm. In this case, it was observed that as the sample was decompressed, the curling mode transitioned to rolling as the vertical constraint was relaxed.

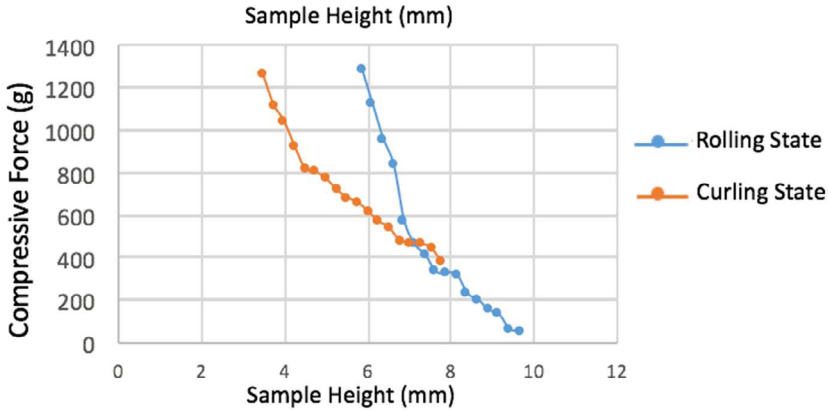

Figure 18. Rolling and curling heated up actuation performance curves for the 16x26 SMA sample. Rolling produces a significantly larger force at the same displacement.

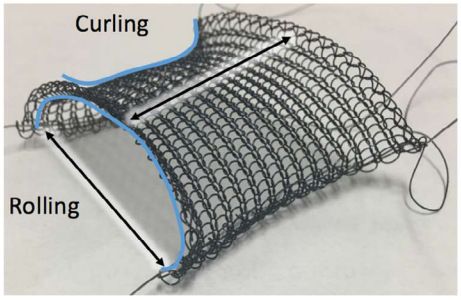

Figure 19. The 16 x 52 sample has a square shape that it can be easily set to either curling and rolling state without a strong bias.

3.5 Bistable Performance

The 16x52 sample is unusual among the four samples in that it has a square aspect ratio. When heated, this sample can easily be set into either the rolling mode or the curling mode without a strong preference in either direction (Figure 19). This, this square sample has a bi-stable operation and will actuate stably in whichever of the two modes it is started. This bistable operation gives the sample interesting properties, particularly at low loads. Most of the samples exhibit a forceful deformation and an actuation force increase when heated. However force measurement of the 16x52 sample (Figure 20) shows a unique trend that the heated compressive forces at lower compression are lower than the forces at low temperature. This unusual phenomenon is likely due to the rolling actuation and curling actuation interfering with each other, holding the sample flat, and reducing the compressive load. The 16x52 sample with a square aspect ratio is unbiased toward either curling or rolling making the rolling actuation significant even in the curling mode, rather than simply just an edge effect.

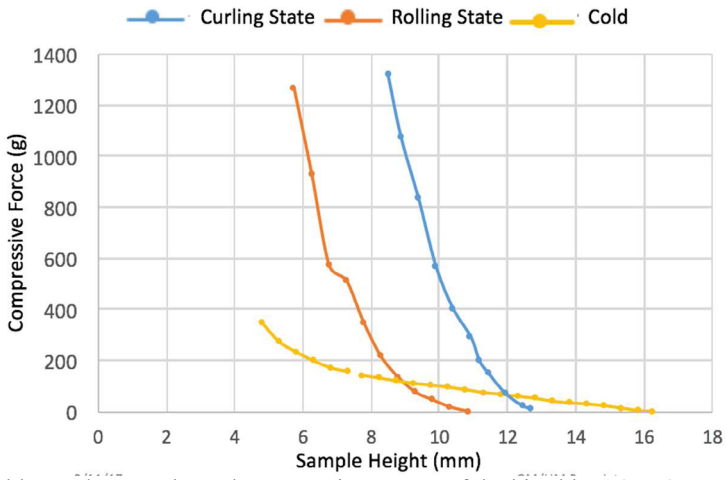

Figure 20. The blue and orange heated up-actuation curves of the bistable 16 x 52 sample. The yellow actuation curve is under low temperatura which crosses the heated curves.

4 CONCLUSIONS

Machine-knit SMA fabrics are a promising technology for interactive surface design. The dense and regular structure of single-jersey machine knit with SMA wire makes it capable of producing large out-of-plane forces and displacements with a variety of behaviors. Actuation forces were observed to be as large as 1600 gram-force with net actuation displacements of 5 mm, which are useful levels of magnitude for customers to feel the shape changes and interact with the surfaces. Two different modes of actuation were observed, wale-wise rolling and course-wise curling, depending on the sample geometry and the initial conditions.

The samples can be scaled in width and length by increasing the number of columns or rows, changing the performance properties both quantitatively and qualitatively. The displacement increases approximately linearly with the width of the samples in the curling mode, while the length of the sample shows no significant scaling effect in the experiments due to edge effects. The geometric parameters play a significant role in actuator performance and are important parameters when designing interactive surfaces to produce appropriate actuation forces.

A new bi-stable characteristic is observed in these machine-knit single jersey SMA samples which provides the potential of designing shape-changing surfaces and actuators with two different motions. However, the boundary conditions, the original state, and the geometry of the sample are all important factors to take into consideration when designing different actuation motions.

Further exploration is necessary to explore the quantitative dependencies of these factors on the resulting actuation mode and performance. In addition, controlled parameters such as wire diameter, stitch length and knitting patterns can be altered to further explore the important design factors as many other behaviors and ranges of performance are possible. The unique and powerful shape changing actuation performance of these knitted structures is highly promising as the basis for interactive surface technologies to add new and exciting functionality to the many otherwise plain, passive surfaces existing in automobiles and in many other fields.

REFERENCES

[1] S. Ahlquist, “Sensory material architectures: Concepts and methodologies for spatial tectonics and tactile responsivity in knitted textile hybrid structures,” *Int. J. Archit. Comput.*, vol. 14, no. 1, pp. 63–82, Mar. 2016.

[2] M. Hatamura and T. Wada, “Huge Shape Recovery of the Knitting actuators made by TiNi Shape Memory Alloy Wires,” *Trans. Mater. Res. Soc. Jpn.*, vol. 40, no. 3, pp. 281–285, 2015.

[3] J. Abel, J. Luntz, and D. Brei, “Hierarchical architecture of active knits,” *Smart Mater. Struct.*, vol. 22, no. 12, p. 125001, 2013.

[4] I. Patel, E. Siores, and T. Shah, “Utilisation of smart polymers and ceramic based piezoelectric materials for scavenging wasted energy,” *Sens. Actuators Phys.*, vol. 159, no. 2, pp. 213–218, 2010.

[5] B. Hu *et al.*, “Textile-Based Flexible Electroluminescent Devices,” *Adv. Funct. Mater.*, vol. 21, no. 2, pp. 305–311, 2011.

[6] K. + F. G. M. und Kommunikation, “STOLL - Flachstrickmaschinen, CMS Flachstrickmaschinen, CMS, Flat knitting machines, CMS Flat knitting machines - Reutlingen, Deutschland.” [Online]. Available: http://stoll.com/stoll-produkte/cms-822-hp-en/2_1. [Accessed: 15-Mar-2017].

VIII ECCOMAS Thematic Conference on Smart Structures and Materials
SMART 2017
A. Güemes, A. Benjeddou , J. Rodellar and Jinsong Leng (Eds)

CLOSED-LOOP CONTROL OF THE SMART SPRING – AN ANALYTICAL SOLUTION FOR THE ACTUATOR MODEL

FRED NITZSCHE,[*] MELISSA ARRAS AND GIULIANO COPPOTELLI[†]

[*] Department of Mechanical and Aerospace Engineering
Carleton University
1125 Colonel By Drive, ME 3135, Ottawa, Ontario, Canada, K1S 5B6
e-mail: fred.nitzsche@carleton.ca

[†] University of Rome "La Sapienza"
Department of Mechanical and Aerospace Engineering
Via Eudossiana 18, 00184 Rome, Italy
e-mails: melissa.arras@uniroma1.it and giuliano.coppotelli@uniroma1.it

Key words: Smart Spring, periodic systems, vibration reduction, actuator model, stiffness modulation, morphing.

Abstract. The analytical modeling of the Smart Spring actuator for vibration reduction of periodically excited systems is performed. The mathematical model is developed in the frequency domain using the harmonic balance method, assuming that the solution is harmonic on the exciting frequency. Both the fixed-base and base-excited configurations are studied. It is shown that the Smart Spring transmissibility at the target frequency depends on only three dimensionless parameters associated with the stiffness modulation characteristics of the device for the fixed-base configuration and five dimensionless parameters for the base-excited configuration. The fundamental values for the Smart Spring closed-loop control are discussed.

1 INTRODUCTION

Reduction of vibration is one of the most challenging requirements in many engineering applications, especially for periodically excited systems. Rotating shafts, propellers and helicopter rotors are examples of such systems. In steady-state forward flight, the cyclic variation of the aerodynamic loads acting on the helicopter blades generate harmonic loads that are transmitted to the fuselage. The vibratory hub loads are transmitted especially at their nN_b/rev harmonics, where n is an arbitrary integer, N_b is the number of blades and 1/rev is the fundamental frequency of the rotor. [1] This reduces the comfort of passengers, causes crew long-term health problems, and leads to the decrease in the fatigue life of airframe structural components.

Different approaches for vibration control, either *passive* or *active*, have been proposed over the past years. [2,3] Specifically, passive control systems alter the structure by adding vibration absorbers or isolators, with the advantage to not require an external power source to operate. However, they are effective only at a specific frequency. On the other hand, closed-loop control systems can act over a broadband of frequencies by using actuators powered by

an external source that apply forces to the structure adaptively, based on the response measured by sensors. The development of active materials and morphing techniques allowed the advance of active control techniques as these materials can directly convert electrical energy into mechanical deformation that can be used for structural actuation. Active control systems are usually classified into direct active and indirect active, or semi-active. In direct-active schemes vibration is controlled by acting directly against the excitation force, thus requiring high actuation forces to counteract the vibratory forces. This issue is overcome by the other indirect active or semi-active concepts such as the Smart Spring that reduces vibrations by modulating the stiffness properties of the system. [4] This results in lower actuation forces and displacements with respect to the direct-active schemes. This device allows leveraging the micro displacements produced internally by a typical piezoelectric actuator to generate actuation that can mitigate large external vibratory loads. The Smart Spring has been extensively studied both theoretically and experimentally over the past years. [5,6] The objective of this paper, however, is to develop the mathematical model of the device both in its fixed-base and the base-excited configurations. The model, developed in the frequency domain considering the excitation force and the displacement solution as a combination of harmonics of the fundamental frequency, enables an insight into the capabilities of the device and, more importantly, the development of closed-loop control algorithms.

2 THE SMART SPRING CONCEPT

For the sake of completeness, the Smart Spring concept is introduced. More detailed information can be found in the referred previous publications. [5,6] The conceptual drawing of the Smart Spring is shown in Fig. 1, where it is modeled as two mass-spring systems denoted with subscripts 1 and 2. Specifically, k_1 and m_1 represent the *primary load path* system stiffness and mass, respectively, whereas the *secondary load path* system is characterized by k_2 and m_2. The primary load path is attached to the main structure subjected to the external vibratory force, $F(t)$ and the base, at which low vibration transmissibility is sought. There is a built-in sleeve in the main structure that is simply a conceptual representation for the Smart Spring stiffness-switching element. Following this schematic, a piezoceramic stack actuator is attached to the secondary load path system, which is inserted into the sleeve.

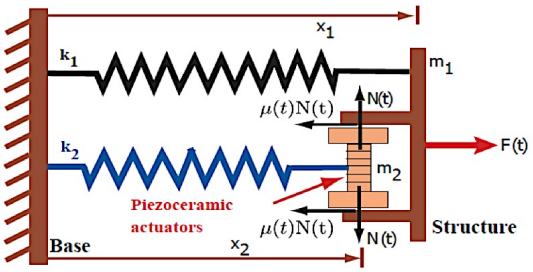

Figure 1: Fixed-base Smart Spring concept.

When the actuator is *off*, the sleeve can move freely and only the primary load path determines the transmissibility of the loads from the main structure to the Smart Spring base; the two load paths are totally decoupled. Instead, when the actuator is powered *on*, the normal

force, $N(t)$ that engages the two systems is generated; the two load path systems are fully coupled if the resultant friction force $\mu(t)N(t)$, $\mu(t)$ being the kinematic friction coefficient, is sufficiently large. Therefore, activating the piezoelectric actuator, the resulting stiffness of the system increases from k_1 to $k_1 + k_2$. It is worthwhile to stress that the present is a cartoonish representation for the Smart Spring stiffness-switching element. The basic elements of any Smart Spring are the multiple load paths and the corresponding switching devices for engaging and disengaging these load paths.

3 MATHEMATICAL MODELS OF THE SMART SPRING CONFIGURATIONS

The conceptual model presented in the previous section will be next used to derive the equations of the motion in the Smart Spring both in its fixed-base and based-excited configurations. The common objective of the two configurations is to reduce the transmissibility of the dynamic loads throughout the primary load path. In the case of the fixed-base configuration, the loads are applied to mass m_1 and low transmissibility is sought at the base of the Smart Spring. In the case of the base-excited configuration, the excitation is applied to the base of the Smart Spring and the objective is to reduce the transmissibility of the vibrations to mass m_1. In the latter case, the system represented by k_3 and m_b are identified to the modal characteristics of a natural mode of the rotating structure for which the minimization of its transmissibility to a supporting structure is sought. Therefore, these two parameters can be associated with the targeted mode generalized stiffness and mass, respectively, whose ratio produces the square of the natural frequency of the targeted mode.

3.1 Fixed-base Smart Spring

The equations of motion for the system shown in Fig. 1 are:

$$\begin{cases} m_1\ddot{x}_1(t) + k_1 x_1(t) = F(t) \mp \mu(t)N(t) \\ m_2\ddot{x}_2(t) + k_2 x_2(t) = \pm\mu(t)N(t) \end{cases} \tag{1}$$

When the Smart Spring is *unlocked*, its two mass-spring systems are decoupled, and (1) becomes:

$$\begin{cases} m_1\ddot{x}_1(t) + k_1 x_1(t) = F(t) \\ m_2\ddot{x}_2(t) + k_2 x_2(t) = 0 \end{cases} \tag{2}$$

Therefore, the dynamic response is determined by the primary load path system. When the Smart Spring is *completely locked*, the two mass-spring systems move in unison and, thus, their displacement and acceleration are identical. In this case, the summation of the two equations in (1) reduces to:

$$(m_1 + m_2)\,\ddot{x}_1(t) + (k_1 + k_2)\,x_1(t) = F(t) \tag{3}$$

However, in the *general case*, even if the two mass-spring systems are never completely locked, the summation of the two equations in (1) yields:

$$m_1\ddot{x}_1(t)\left(1 + \frac{m_2}{m_1}\frac{\ddot{x}_2(t)}{\ddot{x}_1(t)}\right) + k_1 x_1(t)\left(1 + \frac{k_2}{k_1}\frac{x_2(t)}{x_1(t)}\right) = F(t) \tag{4}$$

or, simply:

$$m(t)\ddot{x}_1(t) + k(t)x_1(t) = F(t) \tag{5}$$

where:

$$m(t) = m_1\left(1 + \frac{m_2}{m_1}\frac{\ddot{x}_2(t)}{\ddot{x}_1(t)}\right) \quad k(t) = k_1\left(1 + \frac{k_2}{k_1}\frac{x_2(t)}{x_1(t)}\right) \tag{6}$$

Taking into consideration that the effective mass of the secondary path in the Smart Spring, m_2 is negligible with respect to the mass of the main structure, $|m_2\ddot{x}_2(t)| \ll |m_1\ddot{x}_1(t)|$, and the device turns out to be a stiffness modulation device:

$$m_1\ddot{x}_1(t) + k(t)x_1(t) = F(t) \tag{7}$$

3.2 Base-excited Smart Spring

The equations of motion of the base-excited Smart Spring are here derived by an energy approach. Hence, the generalized coordinates, i.e. the degrees of freedom of the system, are introduced. Referring to Fig. 2, they correspond to the displacements x_1, x_2, and x_b.

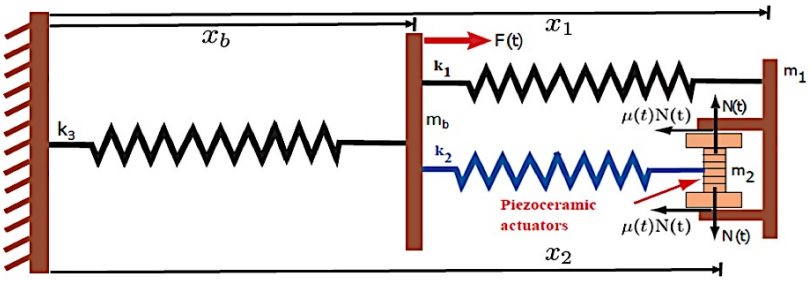

Figure 2: Base-excited Smart Spring concept.

The kinetic and potential energies of the system are obtained as follows:

$$\begin{aligned} T &= \frac{1}{2}m_1\dot{x}_1^2 + \frac{1}{2}m_2\dot{x}_2^2 + \frac{1}{2}m_b\dot{x}_b^2 \\ U &= \frac{1}{2}k_1(x_1 - x_b)^2 + \frac{1}{2}k_2(x_2 - x_b)^2 + \frac{1}{2}k_3x_b^2 \end{aligned} \tag{8}$$

whereas the generalized forces that are associated with the corresponding degrees of freedom non-conservative forces are written as:

$$\begin{aligned} Q_{x_1} &= \mp\mu(t)N(t) \\ Q_{x_2} &= \pm\mu(t)N(t) \\ Q_{x_b} &= F(t) \end{aligned} \tag{9}$$

Applying Lagrange's equations,[i] the equations of motion of the system are derived:

[i] The general form of Lagrange's equation on the generalized coordinate q_i is $\frac{d}{dt}\left(\frac{\partial T}{\partial \dot{q}_i}\right) - \frac{\partial T}{\partial q_i} + \frac{\partial U}{\partial q_i} = Q_{q_i}$

$$m_1\ddot{x}_1(t) + k_1x_1(t) - k_1x_b(t) = \mp\mu(t)N(t)$$

$$m_2\ddot{x}_2(t) + k_2x_2(t) - k_2x_b(t) = \pm\mu(t)N(t) \tag{10}$$

$$m_b\ddot{x}_b(t) - k_1x_1(t) - k_2x_2(t) + (k_1 + k_2 + k_3)x_b(t) = F(t)$$

Summing the first two equations, this system can be rearranged as follows:

$$\begin{cases} m_1\ddot{x}_1(t)\left(1 + \dfrac{m_2}{m_1}\dfrac{\ddot{x}_2(t)}{\ddot{x}_1(t)}\right) + k_1x_1(t)\left(1 + \dfrac{k_2}{k_1}\dfrac{x_2(t)}{x_1(t)}\right) - (k_1 + k_2)x_b(t) = 0 \\ m_b\ddot{x}_b(t) - k_1x_1(t)\left(1 + \dfrac{k_2}{k_1}\dfrac{x_2(t)}{x_1(t)}\right) + (k_1 + k_2 + k_3)x_b(t) = F(t) \end{cases} \tag{11}$$

Considering again that $|m_2\ddot{x}_2(t)| \ll |m_1\ddot{x}_1(t)|$ and the former definition of $k(t)$ in (6), (11) reduces to:

$$\begin{cases} m_1\ddot{x}_1(t) + k(t)x_1(t) - (k_1 + k_2)x_b(t) = 0 \\ m_b\ddot{x}_b(t) - k(t)x_1(t) + (k_1 + k_2 + k_3)x_b(t) = F(t) \end{cases} \tag{12}$$

4 FREQUENCY DOMAIN MATHEMATICAL MODELS

In this work mathematical model of the Smart Spring operation in the frequency domain will be derived for both the fixed-base and the base-excited configurations. The device control function in both configurations will be the same, as discussed in Section 4.1.

4.1 The Smart Spring control function

It has been determined that only the stiffness of the Smart Spring system is a function of time (through the ratio between the displacement of the secondary and primary path systems). The control function that modulates this ratio from the value of the main spring k_1 to the value of the coupled systems, $k = k_1+k_2$, is now introduced. The control function model depends fundamentally on the design of the switching mechanism of the Smart Spring. In the cartoonish scheme presented in this paper, a friction-based mechanism is represented. In previous works this system was numerically simulated by a typical representation of the dry (Coulomb) friction effect where the *dynamic friction coefficient*, $\mu(t)$ is a function of the material and the absolute value of the relative speed between the two elements of the sleeve, $|\dot{x}_1 - \dot{x}_2|$. [7] In these time-domain simulations that were supported by experimental verifications, [8] it was determined that if the normal force (controlled by the piezoelectric stack) is sufficient large to guarantee perfect locking between the primary and the secondary load paths during the operation of the Smart Spring, a square wave is a good approximation for this type of switching mechanism following an *on-off control law*. Hence, the square-wave control function shown in Fig. 3 is considered to perform such a modulation of the stiffness by the Smart Spring in this work. When the control function, $f(\alpha) = x_2/x_1$ is equal to 0 (or 1), the stiffness of the system assumes the value of k_1 (or $k = k_1+k_2$), as it can be verified from (6). In this case, a perfect unlocking of the secondary path is also assumed in the present model.

This has been verified in experiments to be a concern in the design of the switching element, thereof requiring the necessary attention in the selection of the piezoelectric material and stacking procedure. [8]

The time dependence of the control function is introduced by the angular parameter, $\alpha = \omega t$ in the frequency domain:

$$\alpha = r\psi + \phi \tag{13}$$

and the system stiffness in the frequency domain is modulated as $k(\alpha) = k_1 + k_2 f(\alpha)$, where $\psi = \Omega t$ is the non-dimensional time (azimuth angle), Ω the reference frequency (fundamental rotor frequency, for example) and ϕ the control phase angle (angular delay from a reference azimuth value). In (13) the parameter r represents the harmonic of the fundamental frequency, Ω targeted for the Smart Spring control action (i.e. the transmissibility reduction). However, *not necessarily the Smart Spring control is frequency-tuned (synchronized)* to the periodic excitation produced by $F(t)$. In the case of *asynchronous control*, the harmonic control number, r either must be allowed to assume values different from integers or, alternatively, Ω must be regarded as the Smart Spring control frequency and, thus, $\alpha = \Omega t + \phi$ ($r = 1$). Also, in the latter case, the harmonics n in the subsequent frequency-domain analyses must be likewise regarded as the multiples of the Smart Spring control frequency, Ω.

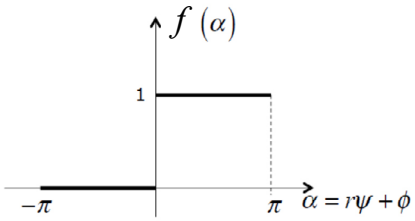

Figure 3: Smart Spring control function.

4.2 Fixed-base Smart Spring

The harmonic balance method is the basis for the mathematical model of the Smart Spring in the frequency domain derived in this work, allowing the study of the response of the system in terms of its harmonic components. Assuming the following complex Fourier series representations for the exciting force and for the response of the primary load path system, respectively:

$$\begin{aligned} F(t) &= \sum_{n=-\infty}^{+\infty} F_n e^{in\psi} \\ x_1(t) &= \sum_{n=-\infty}^{+\infty} x_{1_n} e^{in\psi} \end{aligned} \tag{14}$$

The square-wave control function can be likewise represented as:

$$f(\alpha) = \frac{1}{2} + \frac{1}{i\pi} \sum_{p=\pm 1, \pm 3, \ldots}^{+\infty} \frac{1}{p} e^{ip\alpha} \tag{15}$$

From which,

$$k(\alpha) = k_0 + \frac{k_2}{i\pi} \sum_{p=\pm1,\,\pm3,\,\ldots}^{+\infty} \frac{1}{p} e^{ip\alpha} \tag{16}$$

where $k_0 = (2k_1 + k_2)/2$. Using (14) and (15), the equation of motion for the fixed-base Smart Spring, (7) can be converted into the frequency domain:

$$\begin{aligned} -m_1\Omega^2 \sum_{n=\pm1,\,\pm2,\,\ldots}^{+\infty} n^2 x_{1_n} e^{in\psi} + \left[k_0 + \frac{k_2}{i\pi} \sum_{p=\pm1,\,\pm3,\,\ldots}^{+\infty} \frac{1}{p} e^{ip\alpha}\right] \\ \cdot \left[x_{1_0} + \sum_{n=\pm1,\,\pm2,\,\ldots}^{+\infty} x_{1_n} e^{in\psi}\right] \\ = F_0 + \sum_{n=\pm1,\,\pm2,\,\ldots}^{+\infty} F_n e^{in\psi} \end{aligned} \tag{17}$$

where $x_{1,0}$ represents the new static equilibrium of the primary load path due to the operation of the Smart Spring, that is slightly changed from its former value, F_0/k_1. Using (13) and the identity $1/i = e^{-i\pi/2}$, (17) is rewritten as:

$$\begin{aligned} \sum_{n=-\infty}^{+\infty} \sum_{p=\pm1,\,\pm3,\,\ldots}^{+\infty} \Big[\left(-m_1\Omega^2 n^2 + k_0\right) x_{1_n} e^{in\psi} + \\ + \frac{k_2}{\pi} \frac{1}{p} x_{1_n} e^{i(pr+n)} e^{i(p\phi - \frac{\pi}{2})} \Big] = \\ = \sum_{n=-\infty}^{+\infty} F_n e^{in\psi} \end{aligned} \tag{18}$$

Noting that $(pr + n) \to \pm\infty$ as $n \to \pm\infty$ and $p \to \pm\infty$, and that both p and n are dummy indices:

$$\sum_{n=-\infty}^{+\infty} \sum_{p=\pm1,\,\pm3,\,\ldots}^{+\infty} x_{1_n} e^{i(pr+n)\psi} = \sum_{n=-\infty}^{+\infty} \sum_{p=\pm1,\,\pm3,\,\ldots}^{+\infty} x_{1_{(pr+n)}} e^{in\psi} \tag{19}$$

(18) is rearranged as:

$$\begin{aligned} \sum_{n=-\infty}^{+\infty} \sum_{p=\pm1,\,\pm3,\,\ldots}^{+\infty} \Big[\left(-m_1\Omega^2 n^2 + k_0\right) x_{1_n} + \\ + \frac{k_2}{p\pi} x_{1_{(pr+n)}} e^{i(p\phi - \frac{\pi}{2})} \Big] e^{in\psi} = \\ = \sum_{n=-\infty}^{+\infty} F_n e^{in\psi} \end{aligned} \tag{20}$$

which corresponds to an infinite set of complex frequency response relationships, as follows:

$$\left(-m_1\Omega^2 n^2 + k_0\right) x_{1_n} + \frac{k_2}{\pi} \sum_{p=\pm1,\,\pm3,\,\ldots}^{+\infty} \frac{1}{p} e^{i(p\phi - \frac{\pi}{2})} x_{1_{(pr+n)}} = F_n \tag{21}$$

$$n = 0,\ \pm1,\ \pm2,\ \ldots$$

It is convenient to obtain the non-dimensional form of (21) by dividing the expressions by k_1, the primary path stiffness and recalling that the natural frequency of the primary path is given by $\omega_1 = \sqrt{k_1/m_1}$. Introducing the dimensionless parameter $\kappa = k_2/k_1$:

$$\left[-\left(\frac{\Omega}{\omega_1}\right)^2 n^2 + 1 + \frac{\kappa}{2}\right] x_{1_n} + \frac{\kappa}{\pi} \sum_{p=\pm1,\pm3,\ldots}^{+\infty} \frac{1}{p} e^{i(p\phi - \frac{\pi}{2})} x_{1_{(pr+n)}} = \frac{F_n}{k_1} \tag{22}$$

$$n = 0, \pm1, \pm2, \ldots$$

The summation in the second term of (22) is related to the spillover harmonics excited by the operation of the Smart Spring control function (in this case the square wave). Because the harmonics amplitude decrease as p^{-1}, this summation is explicitly shown below for the first $N = n + 5r$ harmonics ($p_{max} = 5$):

$$\begin{aligned} \sum_{p=\pm1,\pm3,\ldots}^{+\infty} \frac{1}{p} e^{i(p\phi - \frac{\pi}{2})} = \ldots &- \frac{1}{5} e^{i(-5\phi - \frac{\pi}{2})} x_{1_{-5r+n}} + \\ &- \frac{1}{3} e^{i(-3\phi - \frac{\pi}{2})} x_{1_{-3r+n}} + \\ &- e^{i(-\phi - \frac{\pi}{2})} x_{1_{-r+n}} + \\ &+ e^{i(\phi - \frac{\pi}{2})} x_{1_{r+n}} + \\ &+ \frac{1}{3} e^{i(3\phi - \frac{\pi}{2})} x_{1_{3r+n}} + \\ &+ \frac{1}{5} e^{i(5\phi - \frac{\pi}{2})} x_{1_{5r+n}} + \ldots \end{aligned} \tag{23}$$

Introducing Euler's formula, $e^{i\theta} = \cos\theta + i\sin\theta$ in (23), and considering the real and imaginary parts of each harmonic in (22), the complex-value relationship between the nth harmonic of the dynamic response associated with the primary path transmissibility, $x_{1,n}$ and the corresponding exciting force, F_n is obtained:

$$\begin{aligned} &\left[-\left(\frac{\Omega}{\omega_1}\right)^2 n^2 + 1 + \frac{\kappa}{2}\right] [\mathrm{Re}(x_{1_n}) + i\,\mathrm{Im}(x_{1_n})] + \frac{2\kappa}{\pi}\Bigg[\cdots + \\ &+ \frac{1}{5} cos(5\phi)\,\mathrm{Im}(x_{1_{5r+n}}) + \frac{1}{5} sin(5\phi)\,\mathrm{Re}(x_{1_{5r+n}}) + \\ &+ \frac{1}{3} cos(3\phi)\,\mathrm{Im}(x_{1_{3r+n}}) + \frac{1}{3} sin(3\phi)\,\mathrm{Re}(x_{1_{3r+n}}) + \\ &+ cos(\phi)\,\mathrm{Im}(x_{1_{r+n}}) + sin(\phi)\,\mathrm{Re}(x_{1_{r+n}})\Bigg] = \\ &= \frac{1}{k_1} [\mathrm{Re}(F_n) + i\,\mathrm{Im}(F_n)] \end{aligned} \tag{24}$$

Equation (24) can be expressed in the matrix form:

$$[A(n)]\ \{z\} = \{b\} \tag{25}$$

If $N = n + rp_{max}$, the $2N\times1$ vectors $\{z\}$ and $\{b\}$ in (25) collect the real and the imaginary parts of the harmonics of x_1 and F, in their upper and lower halves, respectively:

$$\{z\}^T = \lfloor \cdots, \mathcal{R}e(x_{1,n+1}), \mathcal{R}e(x_{1,n}), \mathcal{I}m(x_{1,n}), \mathcal{I}m(x_{1,n+1}), \cdots \rfloor_{1\times 2N}$$
$$\{b\}^T = \frac{1}{k_1} \lfloor \cdots, \mathcal{R}e(F_{n+1}), \mathcal{R}e(F_n), \mathcal{I}m(F_n), \mathcal{I}m(F_{n+1}), \cdots \rfloor_{1\times 2N} \tag{26}$$

$[A(n)]$, for $n = 0, \pm 1, \pm 2, ...$, are the following square matrices of dimension $2N$:

$$[A(n)] = \left(1 + \frac{\kappa}{2}\right)[I] - \left(\frac{\Omega}{\omega_1}\right)^2 [n]^2 + \frac{2\kappa}{\pi}\begin{bmatrix}[A_{11}] & [A_{12}]\\ [0] & [0]\end{bmatrix} \tag{27}$$

where $[n]$ is the diagonal matrix:

$$[n] = \begin{bmatrix} \ddots & 0 & \vdots & & & \\ 0 & n+1 & 0 & \vdots & & \\ \cdots & 0 & n & 0 & \cdots & \\ & \vdots & 0 & n & 0 & \cdots \\ & & \vdots & 0 & n+1 & 0 \\ & & & \vdots & 0 & \ddots \end{bmatrix} \tag{28}$$

and $[A_{11}]$ and $[A_{12}]$ are square of dimension N, following the multiple diagonal structure seen in (29) and (30), respectively, $[I]$ being the identity matrix and $s_\theta = \sin\theta$ and $c_\theta = \cos\theta$:

$[A_{11}] =$

$$\begin{bmatrix} \cdots & \ddots & \cdots & \ddots & \cdots & \ddots & \cdots & \ddots & \cdots & \ddots & \cdots & \ddots & \cdots & & \\ \ddots & \cdots & \frac{1}{3}s_{3\phi} & \cdots & s_\phi & \cdots & 0 & \cdots & s_\phi & \cdots & \frac{1}{3}s_{3\phi} & \cdots & \frac{1}{5}s_{5\phi} & \cdots & \\ \cdots & \frac{1}{5}s_{5\phi} & \cdots & \frac{1}{3}s_{3\phi} & \cdots & s_\phi & \cdots & 0 & \cdots & s_\phi & \cdots & \frac{1}{3}s_{3\phi} & \cdots & \frac{1}{5}s_{5\phi} & \cdots \\ & \cdots & \frac{1}{5}s_{5\phi} & \cdots & \frac{1}{3}s_{3\phi} & \cdots & s_\phi & \cdots & 0 & \cdots & s_\phi & \cdots & \frac{1}{3}s_{3\phi} & \cdots & \ddots \\ & & \cdots & \ddots & \cdots & \ddots & \cdots & \ddots & \cdots & \ddots & \cdots & \ddots & \cdots & \ddots & \cdots \end{bmatrix} \tag{29}$$

$[A_{12}] =$

$$\begin{bmatrix} & & \cdots & \iddots & \cdots & \iddots & \cdots & \iddots & \cdots & \iddots & \cdots & \iddots & \cdots & \iddots & \cdots \\ & \cdots & \frac{1}{5}c_{5\phi} & \cdots & \frac{1}{3}c_{3\phi} & \cdots & c_\phi & \cdots & 0 & \cdots & c_\phi & \cdots & \frac{1}{3}c_{3\phi} & \cdots & \iddots \\ \cdots & \frac{1}{5}c_{5\phi} & \cdots & \frac{1}{3}c_{3\phi} & \cdots & c_\phi & \cdots & 0 & \cdots & c_\phi & \cdots & \frac{1}{3}c_{3\phi} & \cdots & \frac{1}{5}c_{5\phi} & \cdots \\ \iddots & \cdots & \frac{1}{3}c_{3\phi} & \cdots & c_\phi & \cdots & 0 & \cdots & c_\phi & \cdots & \frac{1}{3}c_{3\phi} & \cdots & \frac{1}{5}c_{5\phi} & \cdots & \\ \cdots & \iddots & \cdots & \iddots & \cdots & \iddots & \cdots & \iddots & \cdots & \iddots & \cdots & \iddots & \cdots & & \end{bmatrix} \tag{30}$$

It should be noted that when the Smart Spring is operating in its asynchronous mode (where Ω is the control frequency and $r = 1$) the dimension of the matrix system in (25) is considerably smaller ($N = p_{max} + n$), and the matrices become very condensed as well (with a much lesser number of interpolation zeros).

4.3 Base-excited Smart Spring

In the case of the base-excited Smart Spring, a similar procedure as in the previous section is followed with (12), observing that the base displacement is also expanded in Fourier series:

$$x_b(t) = \sum_{n=-\infty}^{+\infty} x_{b_n} e^{in\psi} \tag{31}$$

This results in the following expressions in the frequency domain:

$$\begin{cases} \left[-\left(\frac{\Omega}{\omega_1}\right)^2 n^2 + 1 + \frac{\kappa}{2} \right] x_{1_n} + \frac{\kappa}{\pi} \sum_{p=\pm1,\pm3,\dots}^{+\infty} \frac{1}{p} e^{i(p\phi - \frac{\pi}{2})} x_{1_{(pr+n)}} - (1+\kappa) x_{b_n} = 0 \\ \left[-\kappa_b \left(\frac{\Omega}{\omega_b}\right)^2 n^2 + 1 + \kappa + \kappa_b \right] x_{b_n} - \left(1 + \frac{\kappa}{2}\right) x_{1_n} + \frac{\kappa}{\pi} \sum_{p=\pm1,\pm3,\dots}^{+\infty} \frac{1}{p} e^{i(p\phi - \frac{\pi}{2})} x_{1_{(pr+n)}} = \frac{F_n}{k_1} \\ n = 0, \pm1, \pm2, \dots \end{cases} \tag{32}$$

where the dimensionless parameters, $\omega_b = \sqrt{k_3/m_b}$ and $\kappa_b = k_3/k_1$ were introduced. Solving the first equation for $x_{b,n}$ and substituting it into the second, a similar relationship as (24) is obtained for the nth harmonics of $x_{1,n}$ and F_n of the based-excited Smart Spring:

$$\begin{aligned} &\left\{ n^4 \left(\frac{\Omega}{\omega_b}\right)^2 \left(\frac{\Omega}{\omega_1}\right)^2 - n^2 \left[\left(\frac{\Omega}{\omega_b}\right)^2 \left(1 + \frac{\kappa}{2}\right) + \left(\frac{\Omega}{\omega_1}\right)^2 \left(1 + \frac{\kappa}{\kappa_b} + \frac{1}{\kappa_b}\right) \right] + \left(1 + \frac{\kappa}{2}\right) \right\} \\ &[\mathrm{Re}(x_{1_n}) + i\,\mathrm{Im}(x_{1_n})] + \left[-\left(\frac{\Omega}{\omega_b}\right)^2 n^2 + 1 \right] \frac{2\kappa}{\pi} \Big[\cdots + \\ &+ \frac{1}{5} cos(5\phi)\,\mathrm{Im}(x_{1_{5r+n}}) + \frac{1}{5} sin(5\phi)\,\mathrm{Re}(x_{1_{5r+n}}) + \\ &+ \frac{1}{3} cos(3\phi)\,\mathrm{Im}(x_{1_{3r+n}}) + \frac{1}{3} sin(3\phi)\,\mathrm{Re}(x_{1_{3r+n}}) + \\ &+ cos(\phi)\,\mathrm{Im}(x_{1_{r+n}}) + sin(\phi)\,\mathrm{Re}(x_{1_{r+n}}) \Big] = \\ &= \frac{1}{k_1} [\mathrm{Re}(F_n) + i\,\mathrm{Im}(F_n)] \left(\frac{1+\kappa}{\kappa_b} \right) \end{aligned} \tag{33}$$

It can be seen that structure of the current system of equations, (33) is similar to the one obtained in Section 4.2. However, in the present case, $[A(n)]$ in (27) become quartic functions of the harmonic numbers; for $n = 0, \pm1, \pm2, \dots$:

$$\begin{aligned} [A(n)] = \left(1 + \frac{\kappa}{2}\right)[I] + \left(\frac{\Omega}{\omega_b}\right)^2 \left(\frac{\Omega}{\omega_1}\right)^2 [n]^4 - \left[\left(\frac{\Omega}{\omega_b}\right)^2 \left(1 + \frac{\kappa}{2}\right) + \left(\frac{\Omega}{\omega_1}\right)^2 \left(1 + \frac{\kappa + \kappa_b}{\kappa_b}\right) \right] [n]^2 \\ + \frac{2\kappa}{\pi} \left([I] - \left(\frac{\Omega}{\omega_b}\right)^2 [n]^2 \right) \begin{bmatrix} [A_{11}] & [A_{12}] \\ [0] & [0] \end{bmatrix} \end{aligned} \tag{34}$$

5 OPEN-LOOP NUMERICAL SIMULATIONS – NEED FOR CLOSING THE LOOP

The mathematical models derived in the previous section were implemented to analyze the harmonic response of the fixed-base and the based-excited Smart Spring. For the fixed-base case, the harmonic response was calculated for certain values of Ω/ω_1 as a function of κ and ϕ. For the base-excited configuration, it was obtained as a function of κ_b and ϕ for selected values of κ, Ω/ω_1 and Ω/ω_b. In both cases, a flat unitary spectrum for the excitation force was considered, $\{b\} = \{1\}$, and (25) was solved for $\{z\}$. In Figs. 4 and 5, results of a parametric study for the two Smart Spring configurations are presented: magnitude plots of the harmonics $|x_{1,3}|$, $|x_{1,4}|$, $|x_{1,5}|$ (for the fixed-base) and $|x_{1,3}|$, $|x_{1,4}|$ (for the base-excited)

are exhibited as a function of the control parameters.

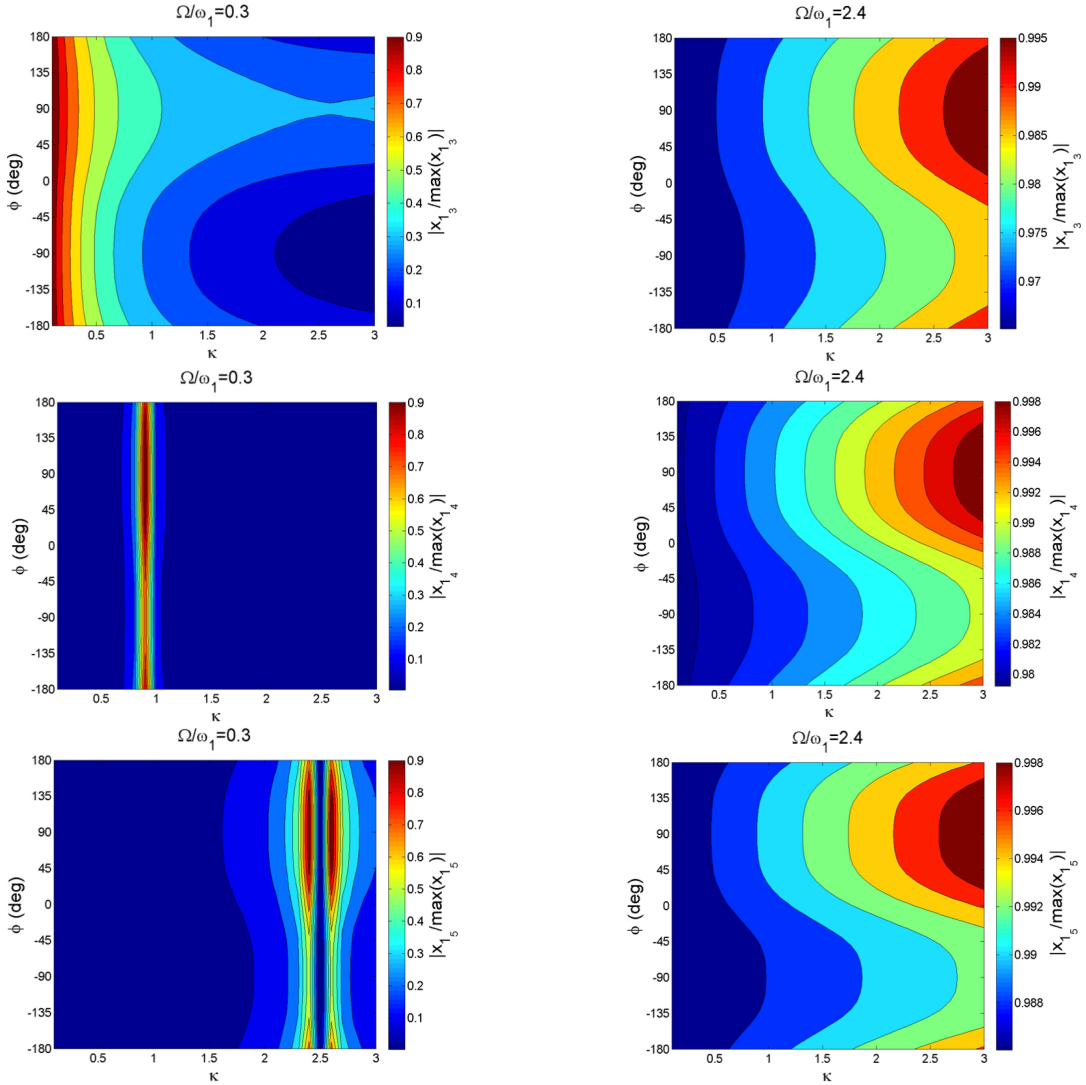

Figure 4: Parametric studies: fixed-base configuration – 3rd to 5th harmonics magnitudes.

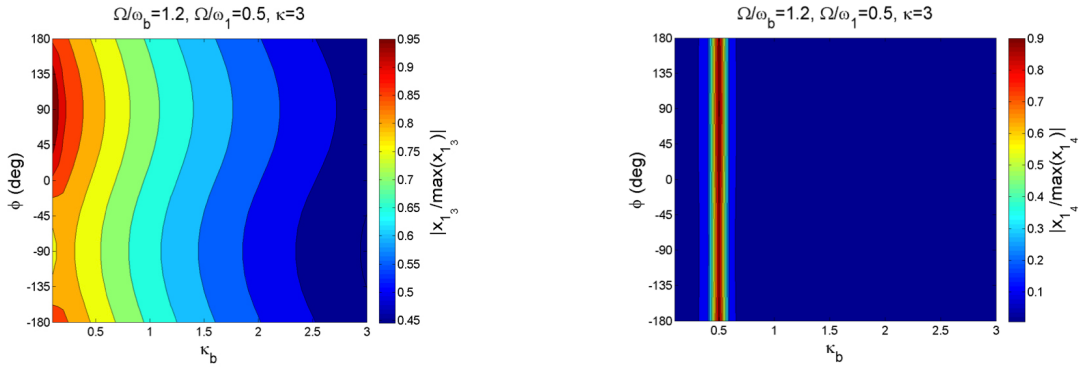

Figure 5: Parametric studies: base-excited configuration – 3rd and 4th harmonics magnitudes.

In all cases, synchronous operation of the Smart Spring was considered. The 4th harmonic was

targeted for control ($r = 4$). It is verified that substantial reductions in the harmonic response, notably at the harmonic targeted for control occur if the right combination of the Smart Spring control parameters is chosen. However, it is also seen that ample spillover happens at harmonics not targeted by the control action. High sensitivity of the response to the control parameters is also noticeable. This was verified in supporting experimental work conducted with a helicopter blade model as well. [8] All results stress the fact that a closed-loop action that searches for a combination of the control parameters that provides continuous reduction in the transmissibility of the target harmonic without producing important spillover at other harmonics needs to be developed.

6 CONCLUSIONS

The present work developed the actuator model for the Smart Spring device in the frequency domain using the harmonic balance method. The closed mathematical forms of this model for the fixed-based and base-excited device configurations were established. Numerical simulations with the model support previous experimental results and indicate that the Smart Spring accomplishes substantial transmissibility reduction of the periodic excitations at the harmonic targeted for control. Large spillover to non-targeted harmonics and high sensitivity of the Smart Spring to its control parameters are detected from the simulations as well, indicating that a closed-loop control approach is necessary to enhance the concept.

REFERENCES

[1] Johnson, W., *Helicopter Theory*, Dover Publications, 1994.

[2] Inman D. J., *Vibration with control*, John Wiley & Sons, 2006.

[3] Bielawa, R. L., *Rotary Wing Structural Dynamics and Aeroelasticity*, AIAA Education Series, 1992.

[4] Nitzsche, F., Grewal, A., and Zimcik, D. G., *Structural component having means for cyclically varying its stiffness to control vibrations - Smart Spring*. Patents: 1999 USA (5,973,440), 2001 European Community (EP-996570-B1), and Canada (2,242,214).

[5] Yong, C., Zimcik D. G., Wickramasinghe, V. K. and Nitzsche, F., "Development of the Smart Spring for Active Vibration Control of Helicopter Blades", *Journal of Intelligent Material Systems and Structures*, Vol. 15, 2004, pp. 37-47.

[6] Nitzsche, F., Feszty, D., Grappasonni, C., and Coppotelli, G., "Whirl-tower Open Loop Experiments and Simulations with an Adaptive Pitch Link Device for Helicopter Rotor Vibration." In 54th AIAA/ASME/ASCE/AHS/ASC Structures, Structural Dynamics and Materials Conference, Paper No. AIAA-2013-1711, Boston, MA, April 8-11, 2013.

[7] Wickramasinghe, V. K., Yong, C., Zimcik D. G., Harold T., and Nitzsche, F., "Smart Spring: A Novel Impedance Control Approach for Active Vibration Suppression Applications", *Smart Structures and Materials 2004: Smart Structures and Integrated Systems, Proc. of SPIE*, Vol. 5390, 2004.

[8] Nitzsche, F. et al, "Developments on the Hybrid Stiffness - Flow Control Active System for Rotor Vibration Attenuation Project – SHARCS," Paper No. 010. In 38th European Rotorcraft Forum, Amsterdam, The Netherlands. September 4-7, 2012.

VIII ECCOMAS Thematic Conference on Smart Structures and Materials
SMART 2017
A. Güemes, A. Benjeddou , J. Rodellar and Jinsong Leng (Eds)

COMPLIANCE AND INSTABILITY IN MORPHING STRUCTURES

ANDRES F. ARRIETA[*], FALK RUNKEL[†], GIULIO MOLINARI[†] AND PAOLO ERMANNI[†]

[*]School of Mechanical Engineering
Purdue University
585 Purdue Mall, West Lafayette, Indiana, 47907, USA
e-mail: aarrieta@purdue.edu

[†] Laboratory of Composite Materials and Adaptive Structures
ETH Zurich
Leonhardstrasse 21, CH-8092 Zurich, Switzerland

Key words: Morphing, Selective Stiffness, Compliant Structures, Nonlinearity, Instability.

Abstract. Morphing structures continue to attract significant attention as a potential technology for increasing efficiency, multi-functionality and performance for aeronautical systems. In this respect, contemporary morphing systems have departed from a mechanistic approach [1] to embrace compliant based systems achieving the desired deformations with actively controlled actuators [2, 3, 4]. Compliant structures allow for maintaining a smooth aerodynamic profile eliminating gaps and discontinuities, reducing part count and limiting maintenance due to the robustness of monolithic designs [5, 6]. These advantages currently come at the cost of increased actuation needs due to the energy spent deforming the structure [6, 7], which typically results in added actuator-related weight. The aforementioned advantages and costs broadly exemplify the main problem at the heart of morphing structures design: namely, the intimate trade-off between the load-carrying (stiffness) and shape adaptation (compliance) functions. Therefore, to fully exploit the superior performance and augmented functionality promised by morphing, a new class of systems is required in which the load-carrying, deformation and actuation functions are more intimately coupled. The possibility to alter on-demand the stiffness of the structure to enable deformation when needed can offer a very interesting solution to the mentioned trade-off. A particularly interesting methodology to achieve selective stiffness adaptation is to utilise structural nonlinearity and instability carefully design to augment the morphing capabilities [8], while maintaining the load-carrying function of the structures.

This paper presents a review of the efforts in utilising structural nonlinearity and instability in the design of morphing structures conducted by the researchers in the past 5 years [9, 10, 11, 11, 12, 13, 14, 15, 16]. First, a general introduction to the specific challenges regarding compliant-based morphing is presented. Two different avenues describing alternative methodologies for realising selective stiffness adaptation in morphing systems are presented, namely, via aeroelastically driven morphing and by profiting from geometrically multi-stable local elements within compliant structures. The presented results highlight the challenges to

find solutions to the trade-off between load-carrying capacity high shape adaptability, while maintaining light weight at the heart of morphing structures.

REFERENCES

[1] J. W. Smith, W. P. Lock and G. A. Payne, "Variable-Camber System Integration and Operational Performance of the AFT1/F111 Mission Adaptive Wing," 1992.

[2] T. A. Weisshaar, "Morphing Aircraft Systems: Historical Perspectives and Future Challenges," Journal of Aircraft, vol. 50, no. 2, pp. 337-353, 2013.

[3] S. Barbarino, O. Bilgen, R. M. Ajaj, M. I. Friswell and D. J. Inman, "A Review of Morphing Aircraft," Journal of Intelligent Material Systems and Structures, vol. 22, no. 9, pp. 823-877, 2011.

[4] J. C. Gomez and E. Garcia, "Morphing unmanned aerial vehicles," Smart Materials and Structures, vol. 20, no. 10, p. 103001, 2011.

[5] G. Molinari, A. F. Arrieta and P. Ermanni, "Aero-Structural Optimization of Three-Dimensional Adaptive Wings with Embedded Smart Actuators," AIAA Journal, vol. 52, no. 9, pp. 1940-1951, 2014.

[6] F. Previtali, A. F. Arrieta and P. Ermanni, "Performance evaluation of a Three-Dimensional morphing wing and comparison with a conventional," AIAA Journal, vol. 52, no. 10, pp. 2101-2113, 2014.

[7] M. I. Frecker, "Recent advances in optimization of smart structures and actuators," Journal of Intelligent Material Systems and Structures, vol. 14, pp. 207-216, 2003.

[8] I. K. Kuder, A. F. Arrieta, W. E. Raither and P. Ermanni, "Variable stiffness material and structural concepts for morphing applications," Progress in Aerospace Sciences, vol. 63, pp. 33-55, 2013.

[9] A. F. Arrieta, I. K. Kuder, M. Rist, T. Waeber and P. Ermanni, "Passive load alleviation aerofoil concept with variable stiffness multi-stable composites," Composite Structures, vol. 116, pp. 235-242, 2014.

[10] A. F. Arrieta, I. K. Kuder, T. Waeber and P. Ermanni, "Variable stiffness characteristics of embeddable multi-stable composites," Composites Science and Technology, vol. 97, no. 16, pp. 12-18, 2014.

[11] I. K. Kuder, A. F. Arrieta, M. Rist and P. Ermanni, "Aeroelastic response of a selectively compliant morphing aerofoil featuring integrated variable stiffness bi-stable laminates," Journal of Intelligent Material Systems and Structures, vol. in Press, 2015.

[12] I. K. Kuder, A. F. Arrieta and P. Ermanni, "Design Space Exploration of Embeddable Variable Stiffness Bi-Stable Composites," Composite Structures, vol. 122, pp. 445-455, 2015.

[13] F. Previtali, A. F. Arrieta and P. Ermanni, "Double-walled corrugated structure for bending-stiff anisotropic morphing skins," Journal of Intelligent Material Systems and Structures, vol. 26, no. 5, pp. 599-613, March 2014.

[14] F. Runkel, A. F. Arrieta and P. Ermanni, "Design of passive morphing wing structures using elastic instabilities," in 20th International Conferences on Composite Materials, ICCM 2015, Copenhaguen, Denmark, July 19 - 24, 2015.

[15] F. Runkel, A. Reber, A. F. Arrieta and P. Ermanni, "Passive Twisting of Composite Beam Structures by Elastic Instabilities," Composite Structures, vol. Accepted, 2016.

[16] W. Raither, E. Furger, M. Zündel, A. Bergamini and P. Ermanni, "Variable-stiffness skin concept for camber-morphing airfoils," Journal of Intelligent Material Systems and Structures, pp. 1-13, 2014.

VIII ECCOMAS Thematic Conference on Smart Structures and Materials
SMART 2017
A. Güemes, A. Benjeddou, J. Rodellar and J. Leng (Eds)

DESIGN AND FABRICATION OF A SHAPE MEMORY-BASED BIO-INSPIRED MORPHING WING

Pedro B. C. Leal, Hannah R. Stroud and Darren J. Hartl*

Department of Aerospace Engineering
Texas A&M University
College Station, TX, 77843, USA
*e-mail: darren.hartl@tamu.edu, web page: http://maestrolab.tamu.edu/

Key words: Smart Structures, Bio-inspired, and Prototyping

Abstract. Aircraft wings utilizing continuous morphing controls surfaces and bio-inspired geometries can increase aircraft performance for certain flight conditions. This potential increase in aerodynamic performance motivates the use of shape memory alloy-based (SMA) actuators, which mimic bird muscles and generate new outer mold lines (OML) while requiring a minimal interior volume for actuator installation. To experimentally demonstrate ex situ the capabilities of morphing technology, the design problem of morphing a bio-inspired wing for lower Reynolds numbers (e.g., landing flight) is considered. The geometric properties of avian-inspired airfoils harshly differ from more traditional airfoils in the sense that, for example, the maximum thickness of avian airfoils is far forward. Therefore, different aerodynamic analysis methods are necessary to evaluate aerodynamic properties of the wing. Potential flow and Reynolds-averaged Navier–Stokes (RANS) equations are utilized to evaluate the geometry and a wind tunnel prototype is fabricated. A novel fabrication method is proposed and demonstrated for elastomeric SMA composite actuators, which are then utilized in a morphing wing concept. Preliminary results for the morphing wing prototype using an SMA composite actuator generates trailing edge deflections equivalent to 3.5% of the chord.

1 INTRODUCTION

Most bird wings are the result of natural selection where the evolutionary objectives include reduced energy consumption via aerodynamic efficiency, especially for low Reynolds numbers [1]. Such wing sections may not be appropriate for high Reynolds numbers typical for modern aircraft. However, it may be advantageous to morph from an OML more suited to high Reynolds numbers when flying at cruise to a more avian-inspired profile for take-off and landing conditions. This work builds upon previous numerical studies [2] where a suitable low-camber OML and elastomeric composites including shape memory alloy (SMA) wires were designed. The objective in that initial work was to morph the baseline OML into a hawk-inspired wing via localized temperature induced actuation. This work focuses in fabricating prototypes for validating the performance of avian-inspired wings, composite actuators, and morphing wings in support of

this overall concept.

Previous studies evaluated the aerodynamic performance of bird wings in a wind tunnel environment [1, 3, 4, 5] and have highlighted the advantages and drawbacks of such designs. Lees *et al.* [3] and Withers [4] evaluated the aerodynamic performance of wings from different bird species, including common snipes, wood ducks, American woodcocks, red-shouldered hawks, black vultures, and many others. The main metrics for both studies were the platform lift and drag coefficients (C_L and C_D). Although all species differ in regards to aspect ratios, wingspan, and other geometric properties, all studies indicate that bird and insect wings have low efficiency factors at high Reynolds numbers compared to conventional airfoils [4]. Therefore, the use of such wing geometries with high camber and maximum thickness so close to the leading edge is unsuitable for the typical cruise velocity of modern aircraft. Moreover, results indicate that general wing-morphological measures based upon platform cannot predict the gliding performance of avian wings as fixed surfaces [3].

The work of Bansmer *et al.* [1] and Liu *et al.* [5] developed avian-inspired airfoils based on the wing section geometry of ducks, seagulls, mergansers, teals, owls, and hawks. Typically avian airfoils have the maximum thickness located close to the leading edge. Because of this, the aerodynamic performance of the OMLs calculated via a potential flow solver [6] indicate that avian inspired airfoils may offer extended laminar flow regions. This also allows for a delay of boundary layer separation at higher angles of attack. However, the numerical solver utilized is based upon inviscid flow theory and semi-empirical correlations developed for low camber airfoils [6]. Since avian-inspired airfoils tend to have high camber, there is a critical need to verify the low-fidelity results with high-fidelity and experimental results. To verify the advantages and disadvantages of an avian-inspired airfoil, this work provides a novel comparison between the results from potential flow analysis and CFD simulations, and develops new hardware for wind tunnel experiments.

As stated by Withes [4], avian wings are only suitable for low-Reynolds flight conditions. Therefore for a large aircraft designed for high speed flight conditions, a method to change the OML is necessary to enable the use of avian wings. Geometrically continuous morphing provides a higher lift-to-drag ratio than the use of discrete surface actuators [7]. Because of these advantages, morphing capabilities are herein explored. Previous experimental work from Strelec *et al.* [8] indicates that SMA wires can be utilized for morphing the OML, though in that example, substantial structural compliance of the airfoil section was required to enable morphing, and a large portion of the wing volume was occupied by the actuator mechanism. To minimize the loss of internal volume when using SMA actuators while also maintaining wing rigidity, a novel concept using monolithic SMA actuators embedded at the wing skin was proposed by Leal *et al.* [9]. The use of elastomers embedded with SMA wires proposed by Peraza Hernandez *et al* [10] enables tailoring of generated force and power consumption to the local actuation needs. As a consequence of the inherent advantages of these composite actuators and of morphing, the fabrication and implementation of the actuators is also assessed herein.

The work is organized as follows: the concepts for the bio-inspired wing, composite actuators, and morphing wing are introduced in section 2; the numerical results for a potential flow and CFD are provided in section 3; the fabrication and assembly of all components are depicted in section 4; the preliminary results for a morphing wing prototype are described in section 5; and finally the conclusions are summarized at section 6.

2 BIO-INSPIRED DESIGN

By taking into consideration the morphological properties of bird wings, bio-inspired wing geometries and actuators are herein explored. The characterization of the aerodynamic properties of the fixed and morphing avian wings is planned for the closed-loop 3x4 ft (0.9144x1.219 m) wind tunnel located at Texas A&M University, with a maximum velocity of approximately 50 m/s. Wind tunnel testing expertise is also leveraged from previous work [11], where 3D printed structure with an SMA-driven mechanism was built and tested in the same facility.

2.1 Avian-inspired wing

The avian-inspired wing considered herein utilizes the F0808 airfoil developed by Bansmer *et al.* [1] as depicted in figure 1. Compared to other airfoils such as the seagull-inspired SG04 [1] and SD7003 [12] airfoils, there is a larger range of angles of attack for which the hawk airfoil performs well, even up to 15°. Thus, the F0808 has the advantage of a more extensive range of lift. As a drawback, the hawk-inspired wing has higher drag coefficient. A prototype with a 4 ft (1.219 m) span and 1.18 ft (0.36 m) chord is designed for experiments in the wind tunnel of figure **??**. The assembly of the model is depicted in figure 2. The model consists primarily of a steel spar supporting 3D printed components with no external fasteners. This will be described in section 4.1.

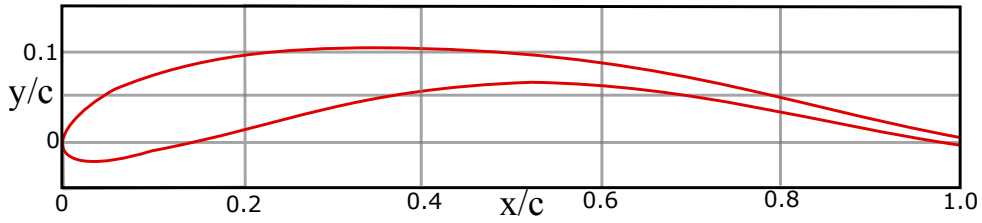

Figure 1: Hawk-inspired airfoil (F0808) [1].



Figure 2: Assembly of 3D printed avian wing model.

2.2 SMA composite actuator

To produce the desired morphing effect on the wing, a robust actuator is required. This actuator must generate a force capable of inducing necessary displacements to achieve a desired OML. Other requirements for the actuators are that they must be easily attached to the wing itself, present a continuous and smooth OML, be easy to manufacture, and allow local tailoring of actuator thermomechanical properties. An actuator solution that satisfies all requirements consists of SMA wires embedded in an elastomeric matrix. The SMA wires were provided by SAES [13], have a 0.5 mm diameter and can generate up to 33 N when fully actuated. To increase the amount of force generated, the periodic design depicted in figure 3 is implemented, allowing the required local force for actuation to be achieved based on the number of tines the SMA wire traverses the actuator for a given actuator width. For the elastomeric matrix, the polymer polydimethylsiloxane (PDMS) [14] is utilized for its rheological properties as well as its heat resistivity. Ease of manufacturing is achieved through a molding technique whereby PDMS is poured over pre-tensioned wires secured with metal dowels as depicted in figure 3. The pre-tensioning of the wires is necessary so that the individual segments are straightend but the SMA is not detwinned. This design also allows for ease of assembly, in that the wing has matching metal dowels to allow the actuator to be installed on the final morphing wing.

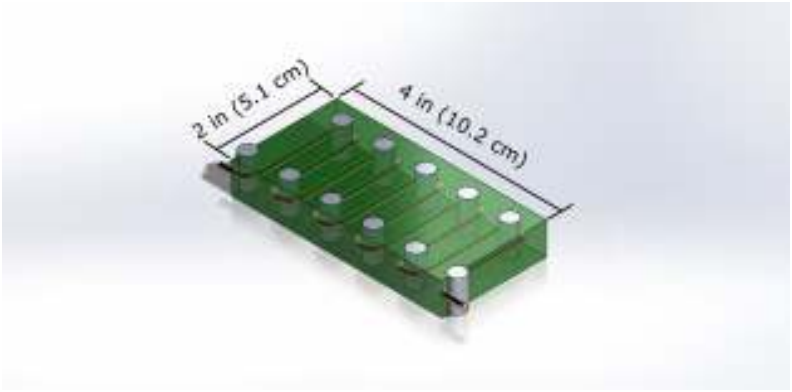

Figure 3: SMA embedded elastomeric actuator [2].

2.3 Morphing wing

This effort expands upon initial studies [2, 9] that numerically explored the feasibility of utilizing SMA actuators to produce an active wing skin. Leal *et al.* [2] demonstrated that with only three SMA embedded actuators on the bottom surface, sufficient OML morphing was obtained. An optimization algorithm was implemented to obtain a low-camber, high Reynolds airfoil that could approximately but repeatably morph to an avian wing. Without yielding or buckling, one of the optimal solutions is provided in figure 4. Because of these promising results, a morphing wing prototype similar to figure 5 with a 4 in (.1016 m) span has been fabricated for preliminary analysis, as will be discussed at section 4.3.

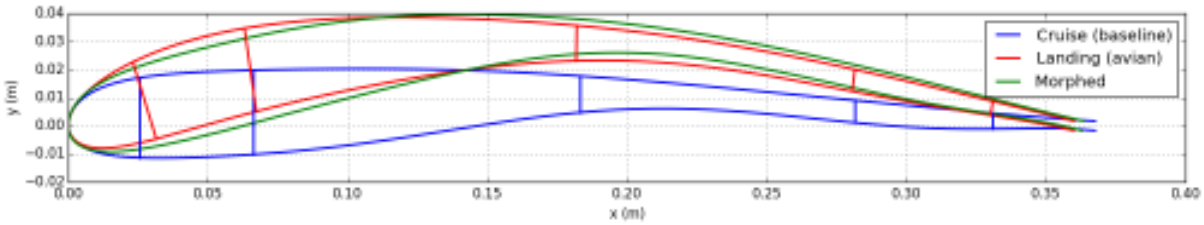

Figure 4: Optimization results that depict a low camber wing morphing into an avian wing [2].

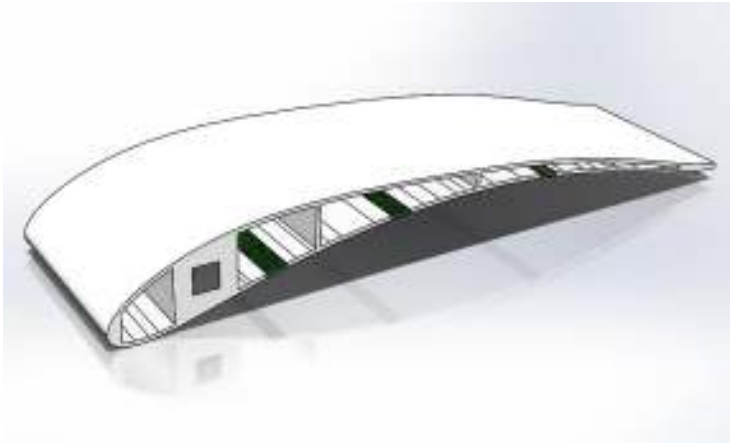

Figure 5: Avian wing with actuators [2].

3 NUMERICAL FLUID ANALYSIS

To develop a greater understanding of the advantages and disadvantages of avian wings, two analysis techniques varying fidelity were utilized for the numerical fluid analysis. The implemented low-fidelity potential fluid solver Xfoil [6] considers inviscid flow coupled with a built-in semi-empirical correction for viscous effects. Although the model is of lower fidelity and limited to conditions prior to stall, it has low computational cost and is a robust tool for preliminary design. For high fidelity results, a Reynolds-averaged Navier−Stokes (RANS) simulation utilizing CRADLE [15] is employed. In each case, the boundary conditions utilized are: inlet fluid velocity is 30 m/s at a 2° angle of attack, static pressure at the outlet is zero, and no-slip conditions on airfoil walls for the RANS analysis. A k-ω turbulence model is used with a time step of .02 miliseconds, air density of 0.9398 kg/m^3, and dynamic viscosity 1.6922 Pa-a. The fluid dimensions are 11x8 chords. The mesh consists of three mesh regions in order to refine the mesh near the airfoil while enabling a coarse mesh far from the airfoil. In total, 665,052 elements were utilized.

The results for both methods are depicted in figure 6, and a summary of the aerodynamic metrics is provided in table 1. Both methods agree in regards to the lift coefficient calculations as the calculated aerodynamic pressures are qualitatively similar. However, the drag coefficient predictions strongly disagree, with the high-fidelity method giving a value 115% higher than the low-fidelity method. This result supports the notion that the use of potential flow solvers for the

calculation of drag effects on high camber airfoils may not be advisable, even at low Reynolds and angles of attack. However, Xfoil predicts lift with an accuracy approaching a RANS simulation while having a much smaller computational time (Xfoil: 10 seconds; CRADLE: 35 hours with four cores until pressure and viscous forces fluctuation where of the order of 0.1 mN). This study and the need to verify drag results for high cambered airfoils motivates the experimental aerodynamic characterization of the avian wing to verify the results obtained.

	Xfoil	RANS	Relative difference (Xfoil/RANS)
c_l	1.088	1.018	7%
c_d	0.01035	0.02229	115%

Table 1: Summary of numerical results at 30 m/s and $\alpha = 2°$.

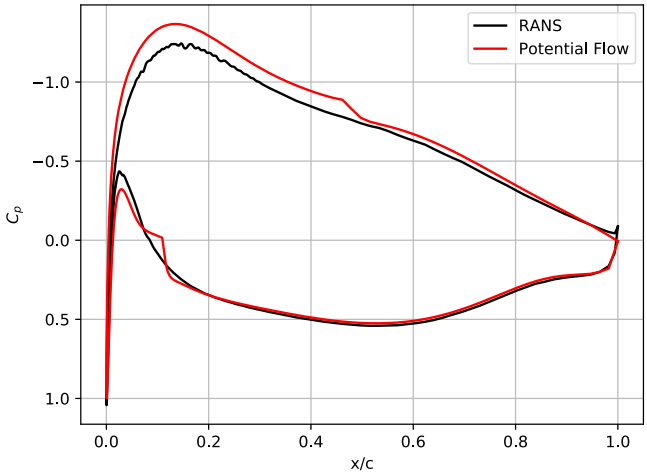

Figure 6: Numerical fluid analysis utilizing low and high fidelity solvers.

4 FABRICATION OF AVIAN-INSPIRED PROTOTYPES

In the previous section, the two flow solvers utilized in the numerical analysis disagree in regards to the drag coefficient of the avian wing. Experimental evaluation is necessary to fully assess the aerodynamic performance of the hawk-inspired airfoil. The fabrication method for the avian wing is described in section 4.1. Furthermore, the results from previous studies [2] for SMA composite actuators and an associated morphing wing also motivate the production of prototypes to validate this concept.

4.1 Avian wing

The avian wing for wind tunnel testing consists primarily of additively manufactured thermoplastic components. Due to build volume restrictions, the four foot wing is sectioned into

eight parts, the largest of which measures 9 in (.229 m). The layout for all components and their labels are depicted at figure 7. Sections 3 and 6 are modified internally to accommodate a network of tubes connected to a pressure transducer; section 3 directs the tubing to the upper surface for low pressure measurements while section 6 is designed to allow similar assessment of the lower surface. These two sections along with sections 2, 4, 5 and 7 are slid onto a solid steel spar and connected to each other using steel dowels fore and aft of the steel spar; an extrusion along the trailing edge matches a female cavity on the neighboring part such that all sections are nested together and cannot move relative to each other under lifting loads. The end sections are designed to allow easy installation into the tunnel without the need for external fasteners of any kind, accomplished through a carefully designed series of part slide and snap operations.

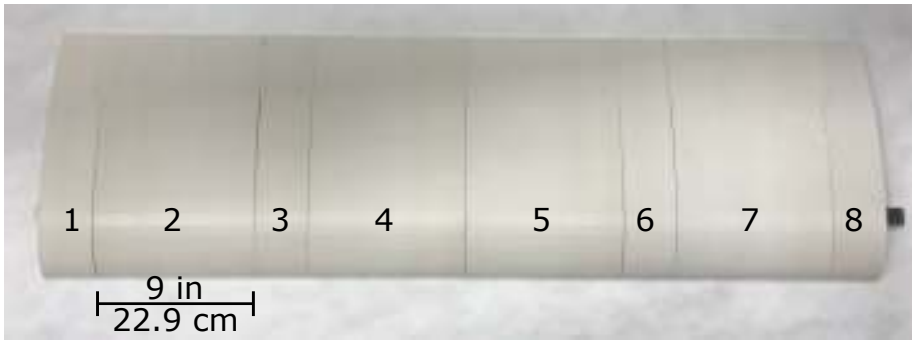

Figure 7: Assembled 3D printed avian wing prototype.

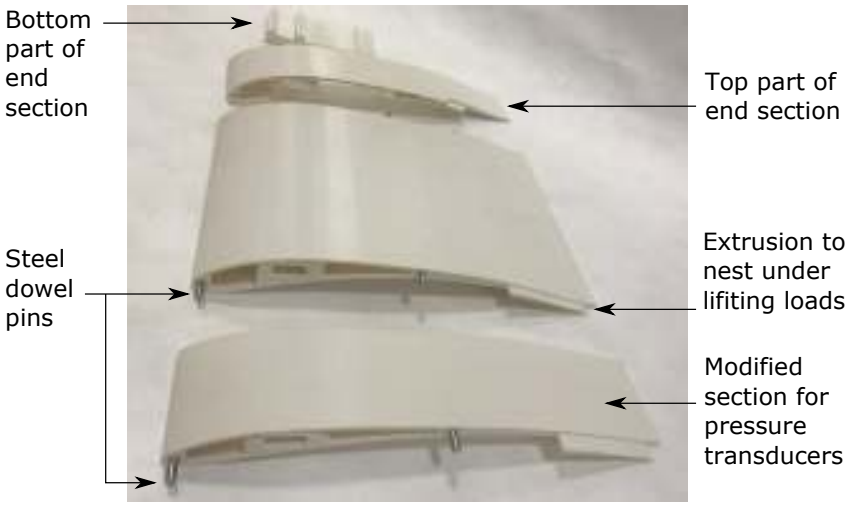

Figure 8: Sections 1, 2, and 3 for the avian wing in further detail.

Because the method of manufacturing used is fused filament fabrication (FFF), some amount of post-processing was required in fabricating the wing. FFF characteristically results in "ridging" along the build axis of the part, resulting in non-negligible surface roughness. The surface is therefore sanded with the appropriate grit until a satisfactory finish was achieved. Figure 8

depicts the inner structure and steel dowel pins for sections 1, 2, and 3. The final assembly depicted in figure 7 has good surface quality, is stiff, and is easy to assemble without the need for fasteners. The prototype was assembled inside the wind tunnel (figure 9a), and preliminary lift results were obtained (figure 9b). The comparison between potential fluid results, RANS, and experimental demonstrate that a similar lift curve is obtained for all method. However, further work is necessary for a quantitative comparison of drag.



(a) Avian wing prototype assembled in wind tunnel.

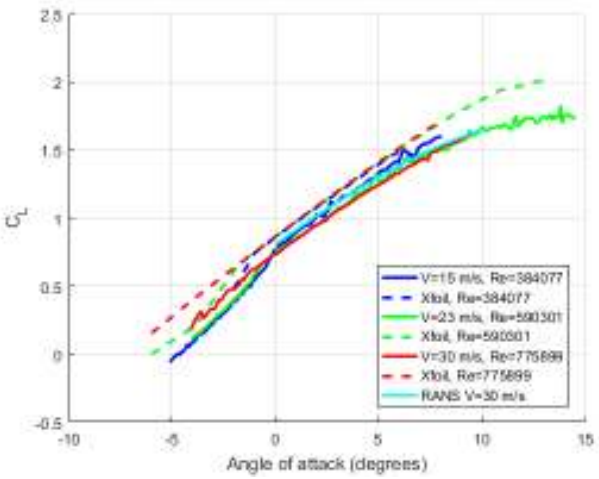

(b) Lift coefficient v. angle of attack.

Figure 9: Avian wing prototype and obtained results in wind tunnel

4.2 SMA composite actuator

The SMA composite actuator is manufactured using a mold casting method. The cast part is designed such that its outer surface is flush with the wing surface when installed and also features a method of attachment to the wing via dowel pins. The pins are inserted into the mold through a clearance fit hole, allowing them to be to be easily removed for cured part removal from the mold. SMA wire is cooled to ensure a complete martensite state before it is then wrapped around the dowels, manually tensioned, and secured. Once secure, liquid PDMS is poured into the mold and set to cure as depicted in figure 10a, forming a compliant matrix that surrounds the wire tensile actuators. The curing process is accelerated by heating the casting in an oven at 60°C, a temperature which increases curing speed but is insufficient to actuate the SMA wires. The cured part is then released from the mold by depressing the dowels fully through the aluminum mold and separating the cured composite actuator from the mold. The final result is depicted in figure 10b. The manufactured actuator is stiff along the intended actuation direction and compliant in the transverse direction.



(a) Fabricated actuator inside mold.

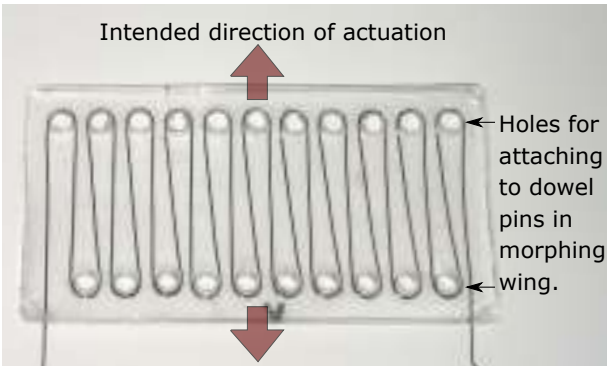

(b) Fabricated actuator outside mold.

Figure 10: Fabricated SMA composite actuator

4.3 Morphing wing

The theory of operation of the morphing wing concept is first verified using one actuator before considering the three actuator design from figure 5. This preliminary test serves to evaluate the ability of the actuators to morph the wing. To accommodate the actuator, the following modifications are made to the avian airfoil as can be seen in figure 11: part of the wing skin is removed to fit the actuator without creating a discontinuity at OML, two cavities are placed to allow the passage of SMA wires to the voltage source, and two extra inner surfaces extend from the lower surface to attach the actuator to the wing structure. Dowel pins are driven into the inner surfaces, allowing the actuator to be mounted easily by pressing each of the molded holes over the dowel pins. The morphing wing section prototype, like the avian airfoil, is also additively manufactured using FFF.

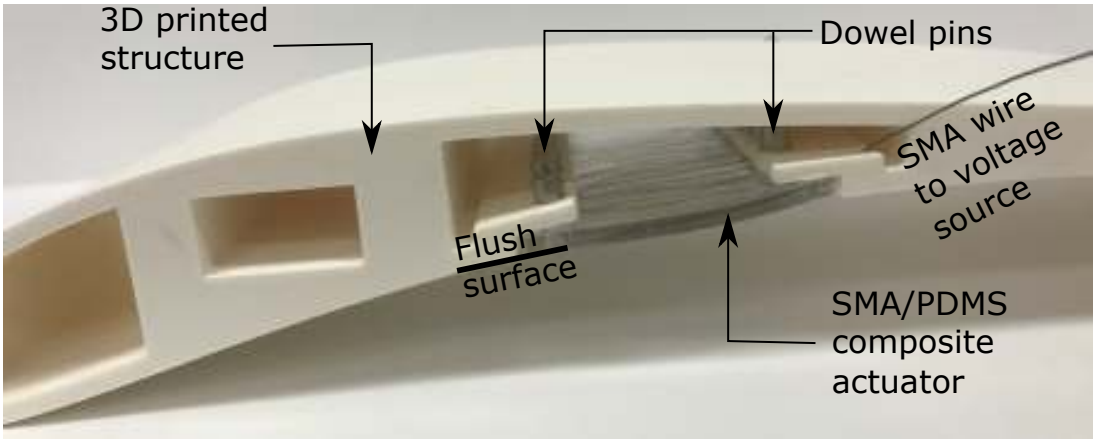

Figure 11: Prototype of avian wing with an SMA embedded actuator.

5 PRELIMINARY RESULTS FOR MORPHING WING

To demonstrate the capabilities of the SMA composite actuator and the morphing wing concept in a preliminary manner, experiments were undertaken to evaluate the actuation of the fabricated prototype (c.f. section 4.3). The prototype was fixed to the optic table via a grip near the leading area in such a way that the deflection of the trailing edge and the actuation were not hindered. The free SMA wire ends were connected to a voltage source, a laser displacement sensor and a ruler were also placed on the optic table to measure the trailing edge displacement. The setup and results obtained are depicted in figure 12 and 13. After four seconds with voltage applied, the original configuration in figure 13a morphs into the configuration in figure 13b. The obtained trailing edge displacement is .5 in (12.7 mm) which is 3.5% of the chord. After 40 seconds cooling down, the prototype recovers the initial configuration (c.f. figure 13).

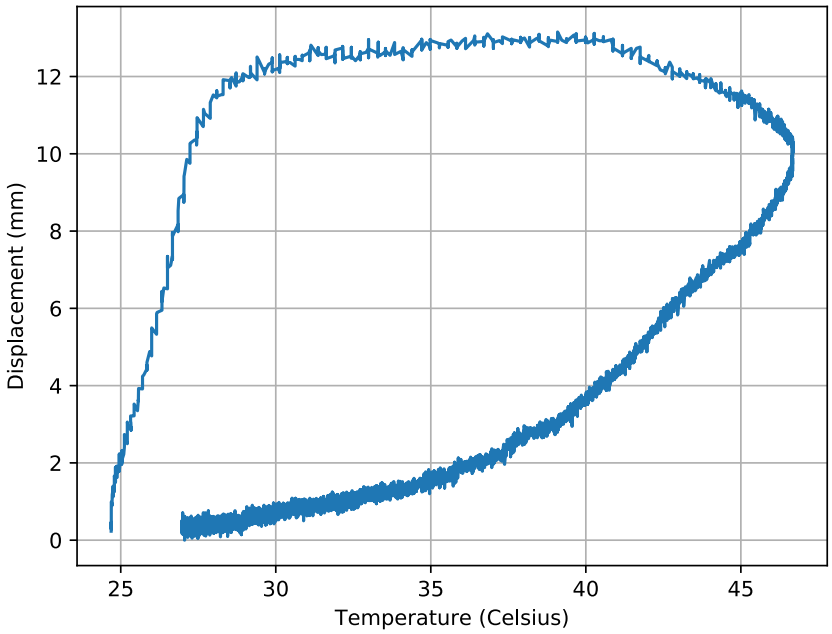

Figure 12: Displacement of trailing edge as a function of temperature for a full actuation cycle.

Compared to an equivalent monolithic actuator, the heat necessary for full actuation is considerably smaller because the SMA wires are a small fraction of the total actuator volume, and PDMS is a poor thermal conductor. As a result most of the power utilized is used to heat the SMA wires. The cooling process was also considerably fast because SMA wires have a high area to volume ration, and the wires are directly exposed to air at room temperature (the wires are located at the surface). Results demonstrate in a preliminary way the advantages and possibilities of the novel SMA composite actuators.

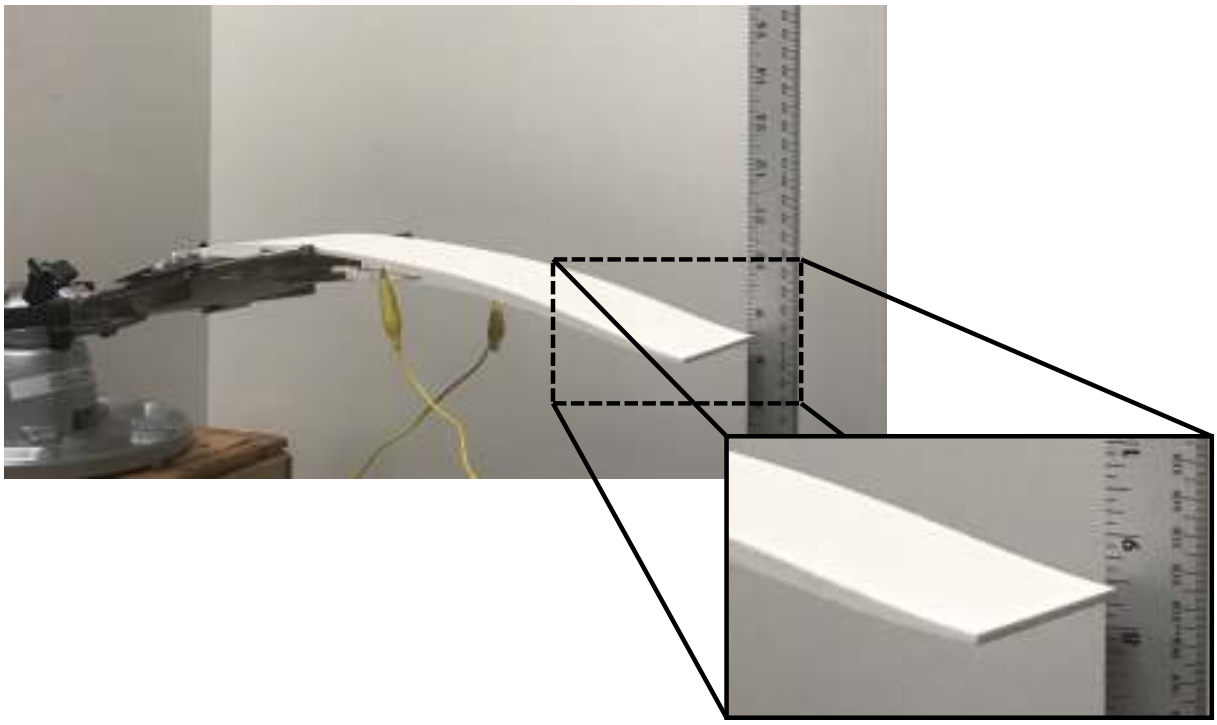

(a) Morphing wing and amplified view of trailing edge position before actuation.

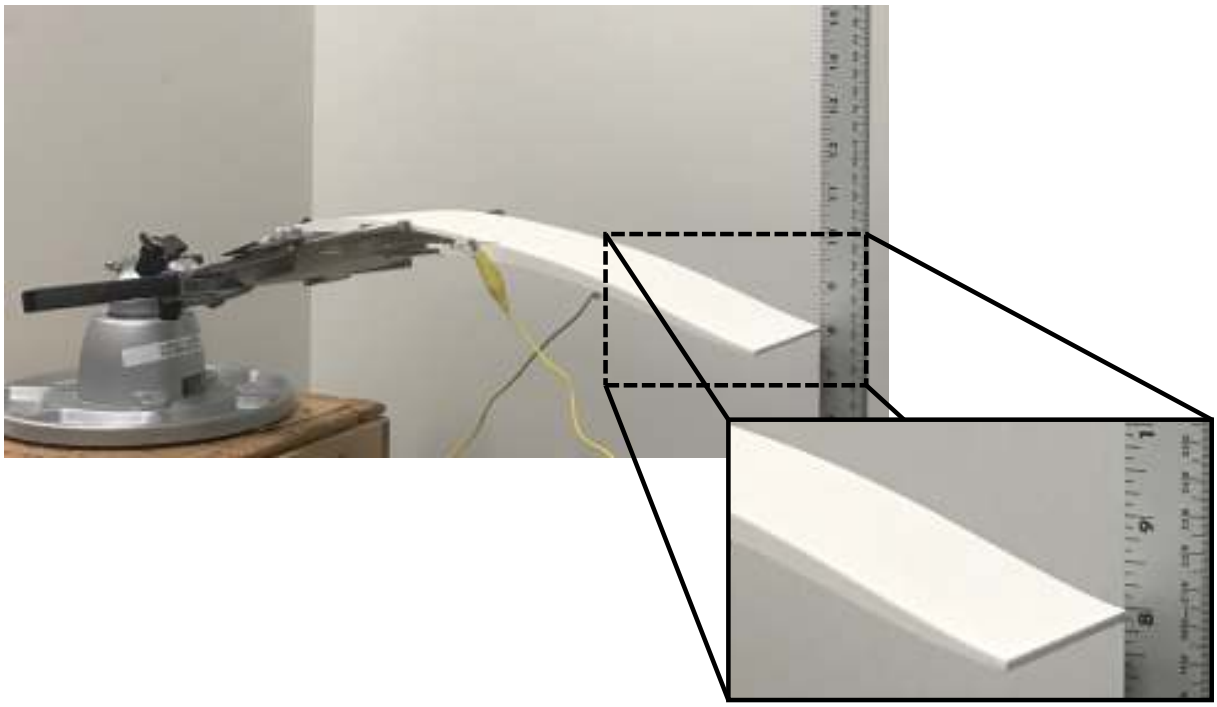

(b) Morphing wing and amplified view of trailing edge position after actuation.

Figure 13: Results of morphing wing utilizing SMA composite actuators.

6 CONCLUSIONS

In this work a bio-inspired morphing wing design is proposed, numerically evaluated in its low Reynolds configuration, and associated prototypes fabricated. The bio-inspired wing consists of an hawk-inspired airfoil (F0808) and SMA/PDMS composite actuators. As the SMA wires are heated, the contraction of the actuators modifies the outer mold line of the wing; the new geometry will improve aerodynamic performance in other flight conditions. The numerical analysis undertaken uses a low fidelity (potential flow) and high fidelity (RANS) solvers to assess the aerodynamic performance of the avian wing. Results show that both methods converge to similar lift coefficients, but the drag coefficient for the high fidelity is 115% higher. Therefore experimental results are necessary to truly qualify the advantages and disadvantages of an avian wing. An easily fabricated and deconstructable, constant section avian wing prototype is designed and fabricated via 3-D printing. New SMA actuators are also designed to be easily manufactured. Finally, an example prototype of the avian wing section with the composite actuators attached is manufactured. An experiment was undertaken to evaluate ex situ the capabilities of the morphing wing utilizing SMA composite actuators. Results demonstrate in a preliminary way that considerable trailing edge deflections are obtained through the use of the novel SMA composite actuators. It also also demonstrates that it is feasible to fabricate shape memory-based morphing wings.

The next steps in this research are the wind tunnel experiments for the avian wing and further improvements of the manufacturing process to guarantee repeatability. An in situ multidiciplinary characterization of the morphing wing is planned, whereby a 3D-DIC system with an infrared camera will be used to obtain displacements and temperature measurements of the morphing wing inside a wind tunnel environment during morphing operation.

7 ACKNOWLEDGMENTS

This work is supported in part by the US Air Force Office of Scientific Research under a grant number FA9550-16-1-0087, titled Avian-Inspired Multifunctional Morphing Vehicles monitored by Dr. BL Lee. The technical help from William Scholten and Ryan Patterson is appreciated.

REFERENCES

[1] Stephan Bansmer, Nadine Buchmann, Rolf Radespiel, Ralf Unger, Matthias Haupt, Peter Horst, and Ralf Heinrich. Aerodynamics and structural mechanics of flapping flight with elastic and stiff wings. In *Nature-Inspired Fluid Mechanics*, pages 331–354. Springer, 2012.

[2] Pedro B. Leal, Ryan Petterson, and Darren J. Hartl. Design optimization toward a shape memory alloy-based bio-inspired morphing wing. American Institute of Aeronautics and Astronautics, January 2017.

[3] John J. Lees, Grigorios Dimitriadis, and Robert L. Nudds. The influence of flight style on the aerodynamic properties of avian wings as fixed lifting surfaces. *PeerJ*, 4:e2495, October 2016.

[4] Philip C. Withers. An aerodynamic analysis of bird wings as fixed aerofoils. *Journal of Experimental Biology*, 90(1):143–162, 1981.

[5] Tianshu Liu, Kathryn Kuykendoll, Ray Rhew, and Shirley Jones. Avian Wing Geometry and Kinematics. *AIAA Journal*, 44(5):954–963, May 2006.

[6] Mark Drela. *XFOIL 6.9 User Primers*. MIT AERO and Astro, Harold Youngren, Aerocraft, Incl, 2001.

[7] B. Sanders, F. E. Eastep, and E. Forster. Aerodynamic and Aeroelastic Characteristics of Wings with Conformal Control Surfaces for Morphing Aircraft. *Journal of Aircraft*, 40(1):94–99, January 2003.

[8] Justin K. Strelec, Dimitris C. Lagoudas, Mohammad A. Khan, and John Yen. Design and implementation of a shape memory alloy actuated reconfigurable airfoil. *Journal of Intelligent Material Systems and Structures*, 14(4-5):257–273, 2003.

[9] Pedro B. C. Leal, Christopher L. Bertagne, and Darren J. Hartl. Aero-structural Optimization of Shape Memory Alloy-based Wing Morphing via a Class/Shape Transformation Approach. American Institute of Aeronautics and Astronautics, 2015.

[10] Edwin A. Peraza Hernandez, Bjoern Kiefer, Darren J. Hartl, Andreas Menzel, and Dimitris C. Lagoudas. Analytical investigation of structurally stable configurations in shape memory alloy-actuated plates. *International Journal of Solids and Structures*, 69-70:442–458, September 2015.

[11] William D. Scholten, Ryan Patterson, Quentin Chapelon, Darren J. Hartl, Thomas W. Strganac, and Travis L. Turner. Experimentation and Computational Assessment of an SMA-Based Slat-Cove Filler For Noise Reduction in a High Lift Wing. American Institute of Aeronautics and Astronautics, January 2017.

[12] Michael S. Selig, editor. *Summary of low speed airfoil data*. SoarTech Publications, Virginia Beach, Va, 1995.

[13] SAES group. SmartFlex Wires. Technical report.

[14] Dow corning. Sylgard 184 Silicone Elastomer. Technical report, 2014.

[15] SC/Tetra. User's Manual, 2015.

VIII ECCOMAS Thematic Conference on Smart Structures and Materials
SMART 2017
A. Güemes, A. Benjeddou , J. Rodellar and Jinsong Leng (Eds)

DESIGN AND MANUFACTURING OF A MORPHING TRAILING EDGE USING A 3D-PRINTED PIEZOELECTRIC POLYMER

AMIN MOOSAVIAN[*], MOHAMMAD H. MALAKOOTI[*], JIAJUN LIN[†],

HENRY A. SODANO[*] AND DANIEL J. INMAN[*]

[*] Department of Aerospace Engineering
University of Michigan
Ann Arbor, MI 48109, USA
e-mail: amoosavi@umich.edu, www.aimslabumich.com

[†] Department of Macromolecular Science and Engineering
University of Michigan
Ann Arbor, MI 48109, USA

Key words: Morphing Wing, 3D Printing, Piezoelectric Polymer, Polyvinylidene Fluoride.

Abstract. With the advent of smart materials technologies, there has come a multitude of ideas and concepts for morphing structures. Some of the simpler geometries can be obtained with one mode of actuation, such as shape memory alloys, or piezoelectric materials. However, more complex geometries typically rely on more complex approaches, requiring combining multiple actuation modes. The ability to 3D print a piezoelectric polymer in a desired configuration allows for the generation of more complex geometries and designs that could solely rely on piezoelectric actuation. In this work, we attempt to utilize the direct write and fused deposition approaches to print polyvinylidene fluoride (PVDF) into a section of the wing trailing edge. The section would take on a morphed cambered shape when subjected to an electric field, and some nominal shape when the electrical input is taken away. The topological design and the fabrication process are discussed herein, followed by the presentation of some preliminary results.

1 INTRODUCTION

Morphing aircraft technologies have recently moved to the forefront of modern aerospace innovation due to the simultaneous advancements in smart materials and investigations into avian flight. Inspired by birds, bats, and insects, a benefit of morphing aircraft is their ability to adapt to a variety of flight conditions by changing the underlying geometry, unlike their traditional counterparts, which remain designed and optimized for a single flight condition. In nature, particularly in birds, this is predominantly achieved through changes in the wing geometry achieved using the underlying wing structure and the feathers, decreasing drag and

allowing for high speed maneuvers. One particular shape change which is of great interest to the morphing field is the change in the camber of the airfoils, making up the cross sections of the wing. One such change in camber is known as reflexed camber. Reflexed airfoils have been shown to have substantial benefits at stall due to their ability to generate comparable lift with substantially less drag compared to conventionally cambered airfoils [1]. It is believed that high angles of attack passively induce reflex in the trailing edge feathers of bird wings.

In a previous work, a hybrid concept that utilizes shape memory alloys (SMAs) and macro fiber composites (MFCs), which are piezoelectrically actuated, was proposed and demonstrated to achieve the reflexed shape [2]. The capabilities of the proposed design, called the synergistic smart morphing aileron (SSMA) were demonstrated in [1]. Furthermore, this concept was used as the basis for investigating the effect of combining the changes in the airfoil shape and wing sweep [3], as well as studying the impact of variations in speed on the effectiveness of the changes in the airfoil shape and the sweep [4].

Figure 1 illustrates the SSMA concept and the components that allow shape morphing in the wing structure. Figure 2 shows two of the airfoil shapes achieved using the SSMA: the unmorphed shape, which is simply a NACA 0012 airfoil and the reflexed shape. Due to the relatively complex geometry of the reflexed shape, the shape memory actuation as well as piezoelectric actuation are required to achieve the desired profile. The piezoelectric actuation is enabled by the use of MFCs, that are commercially available in patches of varying areas manufactured by Smart Material Corp[1]. Figure 3 illustrates a typical MFC patch. Although MFCs function robustly, they can be hard to integrate into complex geometries and used to achieve more complex morphing shapes. Thus, they need to be combined with other means of actuation, such as SMAs, to obtain more complex shapes.

In the current work, we use an approach to obtain more complex geometries, such as the reflexed shape solely using piezoelectric actuation. This is done via 3D printing a piezoelectric polymer laid out in a particular geometric configuration. More specifically, we attempt to utilize the direct write and fused deposition modeling approaches to print polyvinylidene fluoride (PVDF) into a section of the wing trailing edge. The section would take on a reflexed shape when subjected to an electric field, and some nominal shape when the electrical input is taken away.

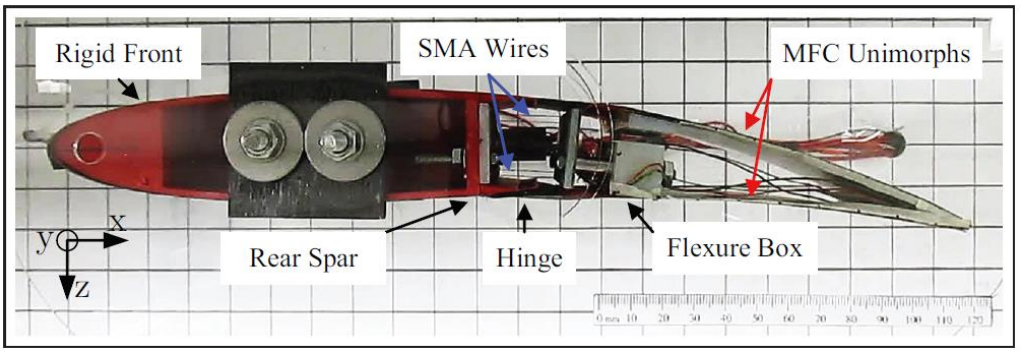

Figure 1: Synergistic smart morphing aileron [2].

[1] http://www.smart-material.com

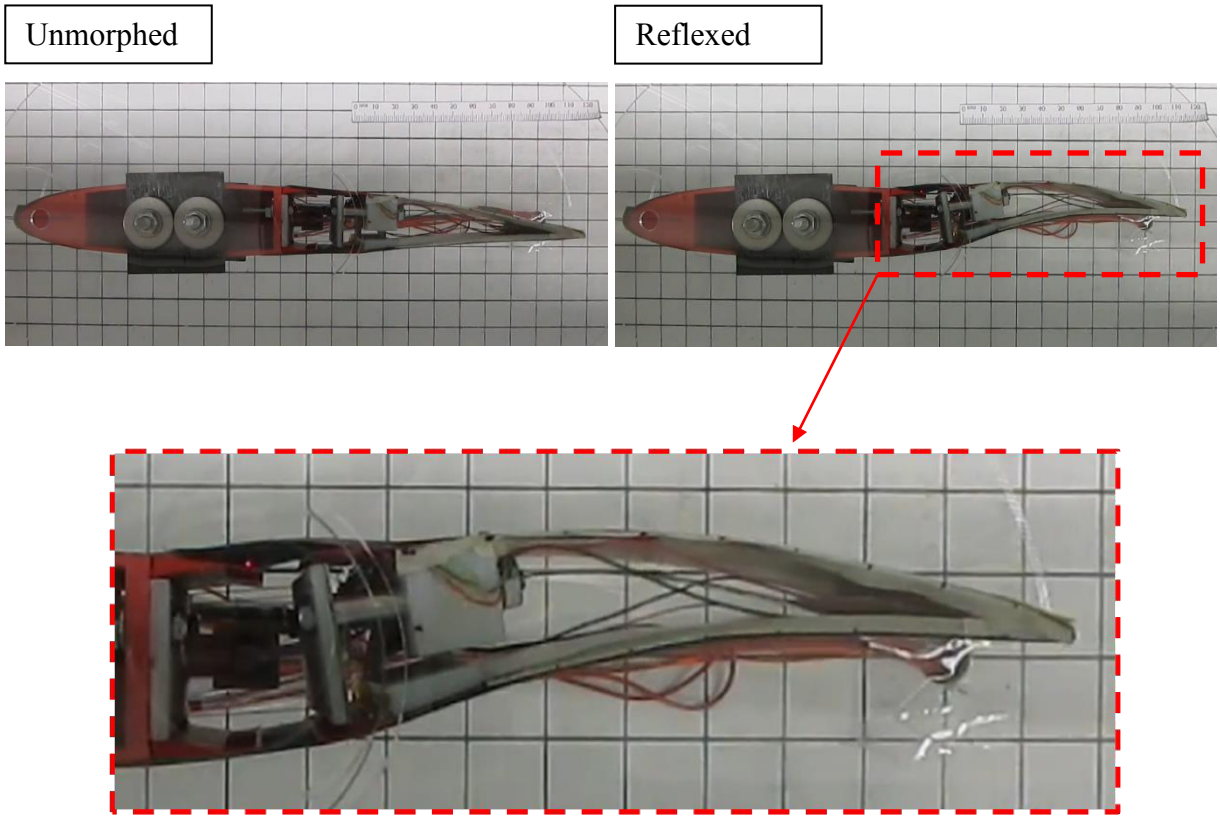

Figure 2: SSMA shown in the unmorphed and reflexed positions.

For the purpose of this study, a NACA 0012 airfoil is used as the unmorphed geometry. With the two shapes, that is, unactuated and actuated, known a priori, and the mechanical properties of the printed material established, the placement of the material can be set up as a topology optimization problem, and solved using the finite element method, using a two-dimensional mesh, as schematically presented in Fig. 4. This will be discussed in more detail in Sec. 2. Furthermore, Sec. 3 will cover the fabrication process, while Sec. 4 will present the findings to date.



Figure 3: Macro fiber composite (MFC) patch from Smart Material Corp.

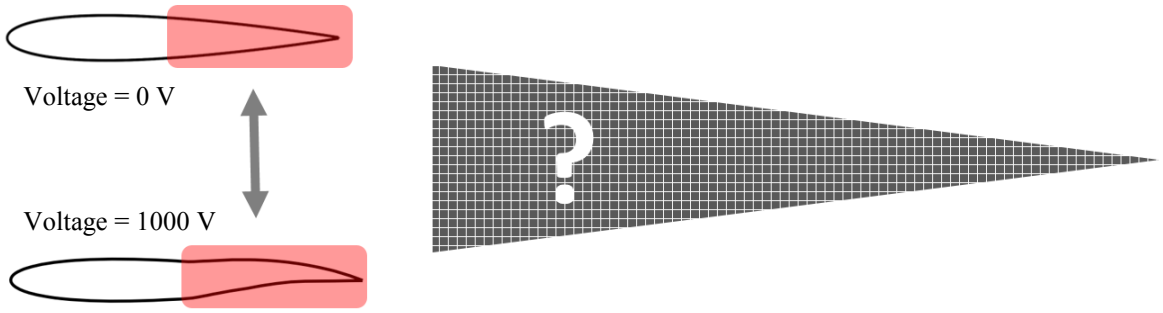

Figure 4: The design problem can be defined as a material placement problem with geometric constraints imposed to control the morphed shape.

2 DESIGN

The problem of placing the appropriate piezoelectric material, whose strain can be controlled using a voltage input, can be set up as a material placement problem, which could be solved using topology optimization. The basis of most topology optimization problems revolves around minimizing the potential energy of the system, more specifically, its internal strain energy, limited to the elastic range. Broken down into finite elements, the total strain energy of the system can be expressed as

$$U = \sum_{i=1}^{N} \frac{1}{2} \int_{V_i} \boldsymbol{\varepsilon}_i^T \mathbf{E}_i(x_i) \boldsymbol{\varepsilon}_i dV_i \tag{1}$$

where $\mathbf{E}_i(x_i)$ represents the constitutive matrix of the *i*th element; $\boldsymbol{\varepsilon}_i$ is the strain tensor for the *i*th element; V_i is the volume of the *i*th element; N is the total number of elements in the problem; and x_i, the design variable, is the element density of the *i*th element. The element density can take one of two forms: 1 or 0, with 1 representing the existence of a finite element and 0 representing a void. Although, an optimization problem with large number of discretized design variables is generally ill-posed and difficult to solve by mathematical programming, there are ways of dealing with this problem by means of relaxing the problem or introducing continuum-type design variables via penalization. One of the most widely used methods of penalization is the solid isotropic material with penalization (SIMP) interpolation scheme [5,6]. In this method, the density of the material is manipulated using a design variable, with the design variable taking a value between 0 and 1. To avoid the formation of an ill-conditioned stiffness matrix, a minimum density is typically specified. The elements that are contributing to the minimum strain energy design will take higher densities and as a result a higher modulus of elasticity will be assigned to them. Equation (2) describes the relationship between the element density and the modulus of elasticity, which makes up $\mathbf{E}_i(x_i)$, along with the Poisson's ratio, ν:

$$E_i(x_i) = E_{min} + x_i^p (E_{max} - E_{min}) \tag{2}$$

where E_{max} represents the material modulus of elasticity at 100% density, while E_{min} is added to the equation for numerical stability and typically takes a relatively low vlaue of $E_{max}/1000$ [7]; p is the penalization factor. The penalization is used to encourage the algorithm to form more discrete load paths, by having a design variable be closer to 0 or 1, as opposed to intermediate values, which would be hard to interpret using typical fabrication processes. To learn more about penalization methods, see [8].

The topology optimization problem here was set up with the objective to minimize the total strain energy of the system. Given the goal for this design is to morph from one geometric shape to another, displacement vectors were used to define the constraints imposed on the shape of the trailing edge. The electrically-induced strains were simulated using thermal loading applied at the grids of the entire design space. The variation in the density of the material was then used to figure out where to place the piezoelectric materials. Figure 5 illustrates the results, where the two colors represent materials with similar stiffness properties, but with different sensitivities to the electrical input.

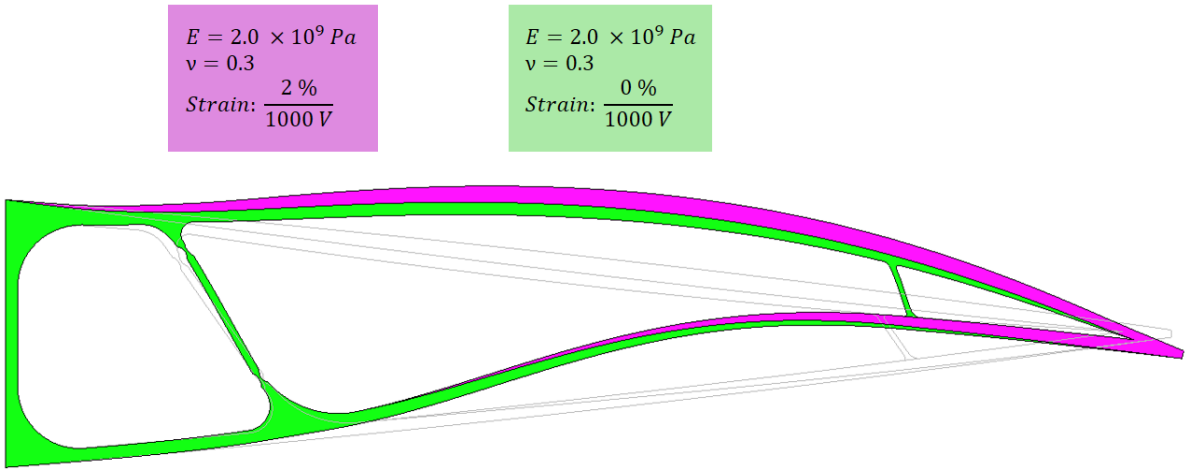

Figure 5: The proposed topology can be used to obtain the reflexed shape using solely the piezoelectric actuation. The grey lines show the unactuated shape, while the colored geometry shows the actuated configuration under 1000 V. The green and the purple areas are identical in stiffness; however, only the purple portion is sensitive to a voltage input.

3 FABRICATION

Piezoelectric ceramics are the most common piezoelectric materials used in actuators due to their high electromechanical coupling. However, piezoelectric polymers are becoming more popular for actuation applications because of their toughness, mechanical flexibility, lightweight, and chemical resistance. Among other piezoelectric polymers, PVDF is the most renowned polymer that exhibits promising potential in applications such as sensing, actuation, and energy harvesting. PVDF is a transparent semi-crystalline polymer that shows a good combination of structural properties, feasible processing, and cost-effective manufacturing. Although there are different crystalline phases in PVDF, the amount of the polar β phase in PVDF correlates to the piezoelectric response of this polymer. Conventionally, the crystalline phase transformation of PVDF is engineered during the manufacturing process. Annealing,

drawing, and electric poling are common processes that have been commonly used to increase the polar β phase in PVDF and consequently produce piezoelectric polymers [9-11].

In this study, piezoelectric PVDF powders have been transformed to printable forms to be used in additive manufacturing processes. Two different approaches were taken to print the desired wing trailing edge structure presented in Sec. 2. In fused deposition modeling (FDM) approach, the PVDF powder was transformed to PVDF filament using a small twin screw extruder (Filabot EX2) and printed on a custom-built 3D printer. As an alternative approach, the PVDF powder was dissolved in dimethylformamide (DMF) solvent to be utilized by an air-powered solution dispenser (Ultimus™ V High Precision Dispenser, Nordson EFD) assembled on the customized 3D printer. Figure 6 shows the controlled moving stage (Aerotech Gantry system) equipped with the extruder head and the solution dispenser for 3D printing of the PVDF filament and direct-writing (DW) of the PVDF solution.

The additive manufacturing of the morphing trailing edge began by converting the digital models of the designed structure into G-code for the 3D printer. Here, Slic3r, which is an open source software, was used to convert the CAD model presented in Fig. 5 to horizontal layered structures and generate the toolpath for the 3D printer. Initially, a set of printing parameters and settings should be determined in a way to accomplish the fabrication of the designed trailing edge continuously without defects. Depending on the resolution of the printed components, the feasibility of the design is evaluated and modifications will be applied to the morphing structure.

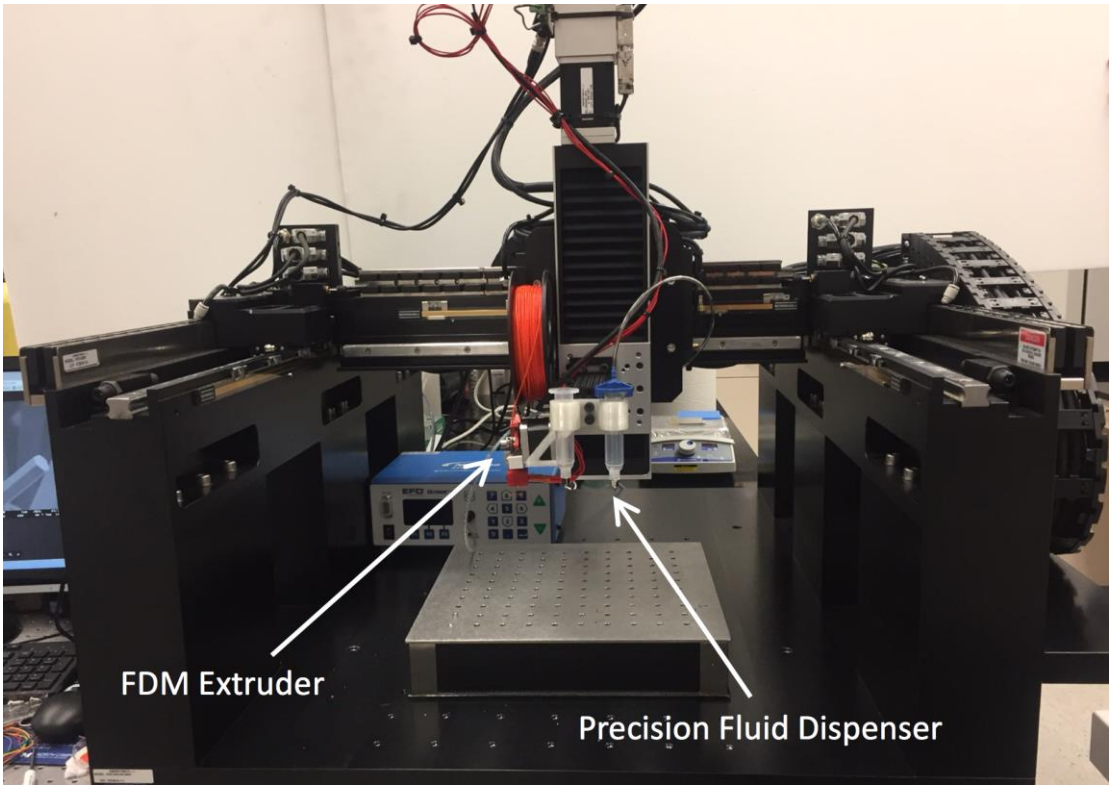

Figure 6: Custom-built 3D printer for fused deposition modeling (FDM) and direct-writing (DW) of piezoelectric polyvinylidene fluoride (PVDF).

3.1 Fused deposition modeling of PVDF

The popular fused filament modeling technique was used to fabricate three-dimensional trailing edge structures. The PVDF filament with a diameter of 1.75 mm made by the Filabot EX2 single screw extruder was fed into the FDM extruder. The temperature of the nozzle was adjusted to be in the range of 270 – 285 °C to accomplish a heat-assisted fabrication process of PVDF structures. A glass substrate was used as the printing bed which was placed on a hot plate at a temperature of 150 – 170 °C to facilitate building a flat layer of the trailing edge structure. In this case, the resolution of the printed object was controlled by tailoring the height of layers as well as the infill percentage of the structure in the slicing software, Slic3r. By adjusting the thermal and rheological properties of the PVDF, trailing edges composed of 1 to 2 layers were fabricated. Due to the large thickness of the printed layers, a high voltage was required to actuate the structure. Alternatively, the same geometry was fabricated using the DW technique which can produce structures with smaller thicknesses.

3.2 Solution-based direct-writing of PVDF

Alternatively, PVDF films with the desired geometry were fabricated using a solution-based direct-write technique. In this approach, a PVDF solution with a concentration of 20 wt% in MDF solvent was used to print PVDF films with a thickness of 30 to 100 microns. The thickness of the films was controlled by tuning the speed of the moving dispenser and the level of air pressure required to deposit the PVDF solution. Additionally, the size of the nozzle can be utilized to fabricate a layer-by-layer structure or even complex, self-supported, three dimensional geometries. In all different scenarios, during the direct-write process, the solvent evaporates at elevated temperatures to form a solid film or three-dimensional structures. Here, gauge 22 blunt stainless steel dispensing needles were used to write the PVDF solution on a glass substrate. The speed of the moving nozzle was adjusted to remain between 10 - 20 mm/s and the solution was delivered with an air pressure of 4 - 8 psi.

Upon the fabrication of the trailing edge structures with PVDF, the samples were annealed and electrically poled to be prepared for actuation. In order to allow the polymer chain to align and reorganize in the PVDF, corona poling at 14 kV was applied to the specimens at an elevated temperature. The poling was continued in this condition for at least 30 minutes. Subsequently, the active sections of the structure, that is, the purple colored parts of the structure as shown in Fig. 5, were electroded by sputtering a thin layer of gold on both sides of the printed object. After completing this process, the samples were ready to be tested in order to evaluate the performance of the structure and feasibility of the designed morphing trailing edge.

4 RESULTS AND DISCUSSION

Figure 7 demonstrates the 3D printed trailing edge structures made from PVDF. The parts fabricated using the FDM technique are shown in Fig. 7a. The small defects between extruded filaments in these structures can cause current leakage and make a short circuit when subjected to an electric field. Therefore, the size of the parts can be increased in order to avoid this resolution limitation. Another challenge in exciting 3D printed wing trailing edges was the relatively large electric field required to generate visible morphing shapes in the structure. The large thickness of the fabricated PVDF parts also added extra rigidity to the structure and limited the flexibility of the printed objects. Due to the resolution of the printer, the compliant

linkages connecting the upper and the lower surfaces of the trailing edge had to be increased in size, increasing their stiffness drastically. It was observed that the stiff linkages of the designed trailing edge effectively eliminated the deformability of the entire structure. In order to modify the current design and overcome the high stiffness of the printed PVDF parts, structural joints should be integrated into the design to allow on-demand movement of the part without having to overcome the structural rigidity.

As mentioned earlier, PVDF films with similar geometries of the designed trailing edge were fabricated as an alternative approach to determine the feasibility of the design and PVDF materials to be used in morphing wing structures. Figure 7b shows four specimens fabricated through direct writing of the PVDF solution. After evaporation of the solvent, the films were annealed, poled and electroded. The biggest challenge in actuating these PVDF specimens was the abrupt electric discharge between the top and bottom electrodes of the specimens. Because of the high electric field and small thickness of the specimens, the air was ionized at the edge of the electrodes and electric sparks were observed during the actuation testing. This design can be improved by adding inactive borders around the electrodes or packaging the electrodes with a thin layer of a nonconductive polymer. However, altering the current design requires conducing simulations to ensure that the reflexed shape of the trailing edge will be favorable. It can be concluded that these preliminary results provided better insight to this design problem and suggested possible solutions to overcome current limitations in the fabrication of morphing structures composed of piezoelectric polymers.

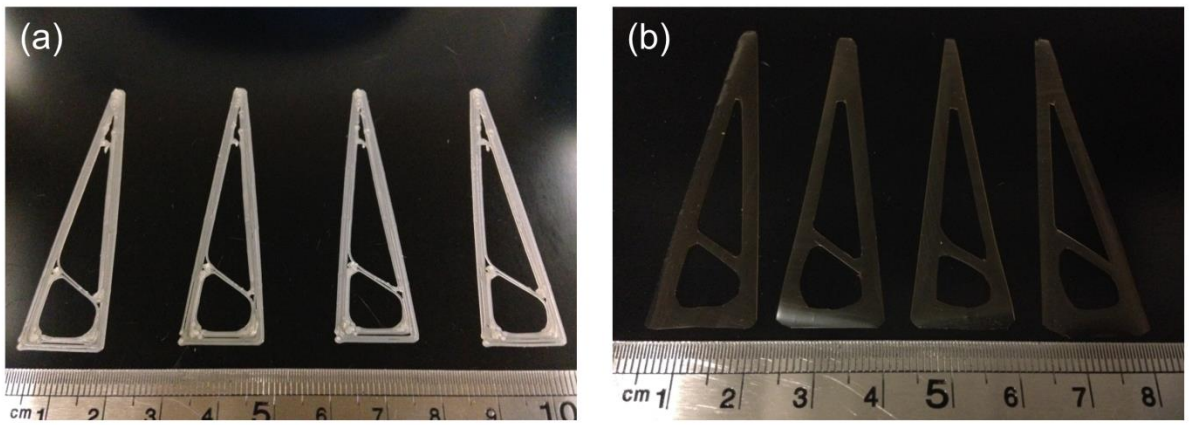

Figure 7: Photos of 3D printed designed trailing edge structures with piezoelectric polyvinylidene fluoride (PVDF) to produce desired morphing shape (a) PVDF films fabricated by solution-based direct-write technique (b) PVDF parts fabricated by fused deposition modeling (FDM).

5 CONCLUSION

The freedom to 3D print piezoelectric polymers allows for the generation of complex morphing structures that rely solely on piezoelectric actuation. In this work, we generated and presented a design for a wing morphing application designed for additive manufacturing. This design would allow for the generation of reflexed camber, which could enhance the aerodynamic characteristics of the wing at near-stall conditions. The details of the fabrication process, as well as the current limitations were then discussed. As future work, minor

modifications to the design are planned to enhance its printability without adversely affecting the desired morphed shape.

ACKNOWLEDGMENTS

This work was supported in part by the US Air Force Office of Scientific Research (AFOSR) under grant number FA9550-16-1-0087, titled "Avian-Inspired Multifunctional Morphing Vehicles" monitored by Dr. B.L. Lee, and in part by the Natural Sciences and Engineering Research Council of Canada (NSERC).

REFERENCES

[1] Pankonien, A.M., Gamble, L.L., Faria, C.T., and Inman, D.J., Synergistic Smart Morphing Aileron: Capabilities Identification. *Proceedings of the 24th AIAA/AHS Adaptive Structures Conference*, San Diego, California (2016).

[2] Pankonien, A.M., Faria, C.T., and Inman, D.J., Synergistic Smart Morphing Aileron: Experimental Quasi-static Performance Characterization. *Journal of Intelligent Material Systems and Structures*, 26.10 (2014): 1179-1190.

[3] Moosavian, A., Gamble, L.L., Pankonien, A.M., and Inman, D.J., Bio-inspired Coupling of Camber and Sweep in Morphing Wings. *Proceedings of the 2016 ASME Conference on Smart Materials, Adaptive Structures and Intelligent Systems*, Stowe, Vermont (2016).

[4] Gamble, L.L., Moosavian, A., and Inman, D.J., Effects of Speed on Coupled Sweep and Camber in Morphing Wings. *Proceedings of the 55th AIAA Aerospace Sciences Meeting*, Grapevine, Texas (2017).

[5] Bendsøe, M.P. Optimal Shape Design as a Material Distribution Problem. *Structural Optimization*, 1.4 (1989): 193-202.

[6] Bendsøe, M.P., and Sigmund, O., Material Interpolation Schemes in Topology Optimization. *Archive of Applied Mechanics*, 69.9 (1999): 635-654.

[7] Luo, Z., Yang, J., and Chen, L., A New Procedure for Aerodynamic Missile Designs Using Topological Optimization Approach of Continuum Structures. *Aerospace Science and Technology*, 10.5 (2006): 364-373.

[8] Sigmund, O., and Petersson, J., Numerical Instabilities in Topology Optimization: A Survey on Procedures Dealing with Checkerboards, Mesh-dependencies and Local Minima. *Structural Optimization*, 16.1 (1998), 68-75.

[9] Lovinger, A.J., Ferroelectric Polymers. *Science*, 220.4602 (1983): 1115-1121.

[10] Kepler, R.G., and R.A. Anderson, Ferroelectric Polymers. *Advances in physics*, 41.1 (1992): 1-57.

[11] Lee, C.B., and Tarbutton, J.A., Electric Poling-assisted Additive Manufacturing Process for PVDF Polymer-based Piezoelectric Device Applications. *Smart Materials and Structures*, 23.9 (2014): 095044.

DEVELOPMENT OF A MORPHING WING IN A MICRO AIR VEHICLE

MIGUEL A. BARCALA-MONTEJANO[*], ÁNGEL A. RODRÍGUEZ-SEVILLANO[*], RAFAEL BARDERA-MORA[†], JAIME GARCÍA-RAMÍREZ[*], MARINA LEÓN-CALERO[†], JOAQUÍN DE NOVA-TRIGUEROS[*]

[*] Escuela Técnica Superior de Ingeniería Aeronáutica y del Espacio
Universidad Politécnica de Madrid.
Plaza del Cardenal Cisneros, 28040 MADRID, Spain.

[†] Instituto Nacional de Técnica Aeroespacial (INTA)
Carretera de Ajalvir, km 4,5. 28850 Torrejón de Ardoz (MADRID), Spain

Keywords: Smart Structures, Morphing wing, micro air vehicle (MAV), particle image velocimetry (PIV), macro fiber composites (MFC).

Abstract. The paper presents a research in the field of morphing wings (adaptive wing geometry) developed over a prototype of micro unmanned air vehicle. This morphing wing will optimize the aircraft performance features. Modifying the curvature of the wing, the micro-UAVs will adjust its performance in an optimum mode to cruise flight condition as well as in the phases of takeoff and landing. The installation of mechanical elements for control surfaces in small size aircraft means, on some occasions, an additional complexity. In addition, it takes into account an increase in aircraft weight. In this research, the adaptive wing geometry is based on MFC (macro fiber composites), so that its position on the inner surfaces of the wing allows the appropriate modification of the curvature, adapting them to the flight profile. This research will present the conceptual design of the vehicle, computational calculations, experimental results of the wind tunnel testing and validations using non-intrusive techniques (PIV). The control parameters of the MFC deformation are performed by an Arduino board. With these analytical, computational, and experimental results, the most relevant performances are estimated. From all these set of results obtained, it will be a good start to prepare the maiden flight of the micro air vehicle for carrying out the flight tests campaign.

1 INTRODUCTION

In the last decade, a new variety of unmanned vehicles has been developed to perform different missions. These types of vehicles are used in missions that do not require human performance for their success. Furthermore, they allow the automation of processes that have a high level of development.

A high demand for smaller vehicles to satisfy these missions has led designers to focus on a specific type of unmanned vehicle, namely, the micro air vehicle. The design of this kind of

vehicles is restricted by the not well known aerodynamics phenomena of low-aspect-ratio wings operating at low Reynolds numbers [1]. Moreover, their reduced development cost has allowed universities and research centres to explore a wide variety of designs. This is the case of morphing, which has enhanced innovation in MAVs. These wings help to develop multi-role MAVs by optimizing their overall performance [2].

A particular case of morphing is based on an in-flight camber profile change. In this way, the increased lift coefficient reached with an increment in camber would allow the aircraft to perform at lower speeds. Consequently, it would be possible to obtain better conditions for a real-time video recording, decreased values of camber would provide higher lift to drag ratios and therefore higher values for range and endurance. It is widely known that one of the main effects of modifying an airfoil's camber is to vary the zero-lift angle of attack, airfoil efficiency and also stall pattern. Furthermore, maximum lift increases with camber [3]. The scope of this research is to study the effects of performing in-flight camber variations by means of smart structures, such as Macro Fiber Composites (MFCs) [4].

2 INTRODUCTION TO SMART MATERIALS

Materials which are able to vary one or several of their properties as a result of external stimulus, such as voltage and temperature, are called intelligent materials.

The development of these materials has increased significantly in recent years, as they show new capabilities within industries such as aeronautics, aerospace and biomedical.

The classification of these kinds of materials is very wide. For this reason, the following report shall focus on only one of them: the piezoelectric materials. One of the main properties of this material is the ability to modify its shape when it is exposed to an electric field. Therefore, piezoelectricity can be considered as a bridge between electrical and mechanical components.

Within the great variance of piezoelectric devices, the focus of this research is the MFC (Macro-Fiber Composite).

2.1 Macro–Fiber Composites actuators

The MFC is an innovative low-cost piezoelectric device designed by NASA to control vibrations, noise and deflections in composite structures. The figure 1 shows the MFC profile that has been considered in this research.



Figure 1: MFC device

It consists of rods of piezoceramic material interspersed between layers of an adhesive film which contains a number of minute electrodes. These electrodes transfer the voltage to actuators, which will be deformed when an electric field works in them [4]. These embedded layers of different materials which provide a uniaxial performance along its length. Extensive information of these can be found in [5].

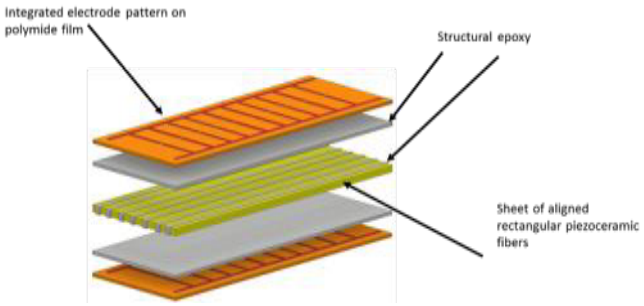

Figure 2: Schematic view of a Macro Fiber Composite device

The assembly of MFCs enables in-plane poling. They use the d33 piezoelectric effect, which is an elongating effect [6]. The strain generation is anisotropic so that the transversal strain could be assumed to be zero. Normally, there should be slight contraction, but due to the matrix effects, negative strain becomes negligible. These devices can be attached to different types of materials such as aluminum or composites. However, it is believed that MFCs tend to perform better when attached to materials with higher elastic modulus [7].

One of their main advantages is the capability to achieve a continuous deformation, instead a flapped deformation, which means an increase in the mechanical complexity. Parameters such as the lift to drag ratio, lift to weight ratio, and power to weight ratio could be reduced by conventional servo-linkage actuators. Furthermore, due to the volume occupied by these servos, less volume is left in the fuselage for allocating electronic systems. Moreover, MFCs allow controlled morphing to be performed, something that cannot be achieved with self-deformable systems [6].

3 CONCEPTUAL DESIGN OF MAV

This study is focused on the aerodynamic characterization of a morphing micro air vehicle (MAV). Unmanned aircraft are being developed to perform different types of missions. Morphing wings can help to improve mission efficiency and perform a wider variety of tasks. The MAV normally performs at low Reynolds numbers and generally with low aspect ratio (LAR) wings and there is actually scarce knowledge about this flight regime. Thus, a detailed aerodynamic investigation has to be performed for each new design.

This particular MAV was designed in Technical University of Madrid (UPM) (Figure 3).



Figure 3: Morphing MAV prototype.

It can perform in-flight camber profile changes without varying any other geometric parameters (Figure 4) in order to improve the lift to drag ratio or increase the maximum lift coefficient. This improvement in aerodynamic efficiency increases the aircraft range and endurance while a higher maximum lift coefficient helps the aircraft to perform at lower speeds. Morphing is performed by Macro Fiber Composite (MFC) piezoelectric actuators attached inside the wing.

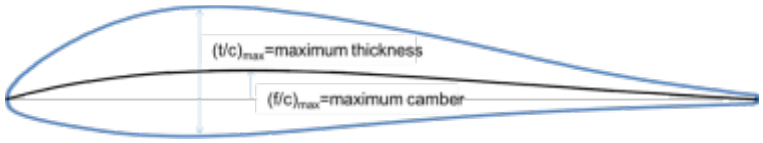

Figure 4: Geometrical airfoil characteristics: maximum camber and maximum thickness

The Eppler 61 airfoil is an airfoil which at low Re (which extends to $\mathrm{Re} \approx 1 \cdot 10^5$) performs mostly with a turbulent boundary layer. In spite of the drawback of producing a high skin-friction drag, it has been observed that a turbulent boundary layer is more predictable than a laminar boundary layer for low Reynolds numbers [8]. Moreover, and in order to achieve continuous camber variations, a concave-low surface airfoil is required.

This preliminary aerodynamic research has focused on wind tunnel tests of our first prototype. In this first set of tests, experimental data about lift and profile stall behavior have been obtained. Using the results of the experimental study carried out in this research, a relationship between airfoil geometrical parameters which have an optimum response in the maximization of the lift has been obtained.

The researches carried out in [1] demonstrated how this planform provided one of the highest lift to drag ratio for an Aspect Ratio of two, only overtaken by an elliptical planform with the same Aspect Ratio. This increase supposes an overall optimization in performance which is considered to be a major aspect in MAV's development.

Moreover, in the range of Low Aspect Ratios (LAR), a value for this parameter higher than 1.5 has shown to make aerodynamic behave more linearly. As a consequence, it becomes more predictable, enabling designers to draw further conclusions about its performance than for a lower Aspect Ratio wing.

Zimmerman Wing (Figure 5) has been selected over elliptical wing since the latter has been researched for decades and no further information can be drawn from it. However, Zimmerman Wings reached its summit in the 50's but they were rapidly abandoned. Projects being currently developed are trying to recover this configuration and it is inside this project to research their performance at low Reynolds numbers.

The aerodynamic benefits of an elliptical wing planform are well known. The Zimmerman and inverse Zimmerman wing planforms consists of two half-ellipses joined at either the c/4 location or at the 3c/4 location.

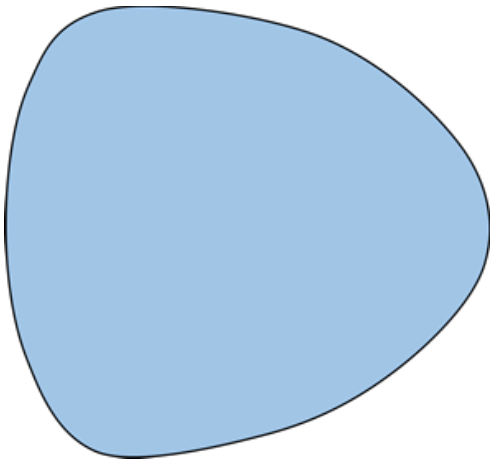

Figure 5: Typical Zimmerman wing configuration

The wing is designed with Eppler E61 airfoils and a Zimmerman wing planform with an AR of 2.3 which has high aerodynamic efficiency only surpassed by the elliptic form.

4 VOLTAGE DEFORMATION TESTBED

In this section, we will present the voltage-deformation test of the Zimmerman half-wing, in which the entire aerodynamic study has been carried out, in order to observe the MFC deformation capacity of the wing intrados. In order to achieve this, two power supplies were used, as shown in the figure 6.

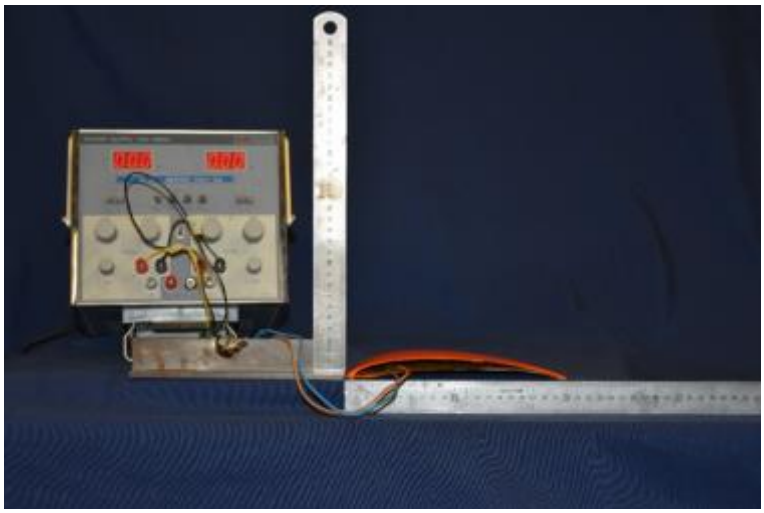

Figure 6: Voltage – Deformation test facility

As it can be observed in Figure 6, the MFC was connected to a main power source, so that different variants of voltage could be emitted within the actuator.

According to experimental data measured in previous tests, the maximum voltage which causes a significant deformation in the half-wing is 5 V. Thus, for this test, voltage margins between 0 and 5 V were supplied, so that it could be possible to obtain the voltage/deformation curves along the main airfoil (which corresponds to the socket) of the intrados as well as the extrados. It is important to remember that the wing's original aerodynamic profile is the Eppler E61 airfoil.

For the purpose of this report, only the results obtained for the 0 and 5 V tests will be shown, since these are the aircraft configurations analyzed in wind tunnel aerodynamic tests. Despite this, it is important to emphasize that there are two different curvature variations: a softer distribution (less variation of curvature) for voltages between 0 and 2.5 V, and another one which is more pronounced (greater variation of curvature) for higher voltages than 2.5 V.

Figure 7 shows two images corresponding to the main airfoil indicated above, for a voltage of 0V (left) and for a voltage of 5V (right).



Figure 7: Stages of airfoil deformation from 0 V to 5 V

In order to make the control process more intuitive, the wing geometry is supposed to be modified by means of a control device. This control device consists of two potentiometers which transform the x and y axes movement in an electric signal proportional to its position. This signal will be in a range of 0 to 5 V range of the output signal. In order to obtain a relationship between voltage and maximum camber, the wing will be tested for different values of the input voltage and the changes in the geometry will be measured. In particular, the maximum profile camber for each value of the voltage has been determined. The results obtained are presented in the following graph:

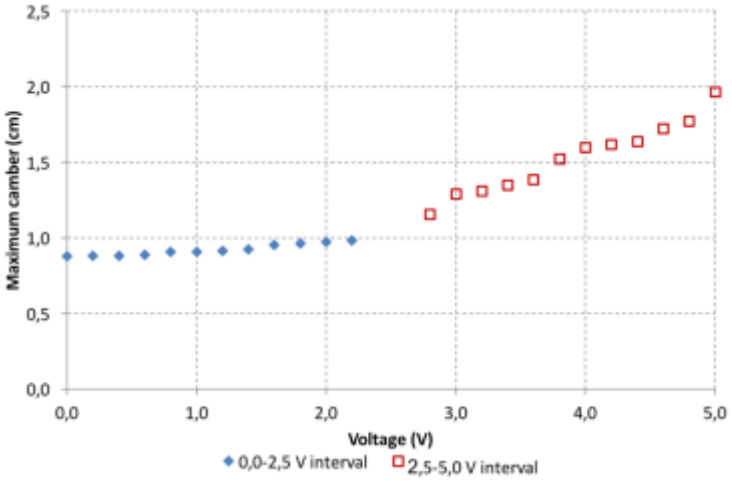

Figure 8: Airfoil camber variation as a function of voltage control

From the experimental data, several fitting curves have been obtained in order to get the better fitting which relates the input voltage with the wing's maximum curvature. Two functions for each range have been finally chosen, a linear and an exponential one.

Exponential fitting curves:

$$f/c\big|_{e1} = 0.8589 \times e^{(0.0664 V)}$$
$$f/c\big|_{e2} = 0.6348 \times e^{(0.2215 V)} \quad (1)$$

Where ' $f/c|_1$ ' indicates that it is referred to the first range (from 0 to 2.5 V) and ' $f/c|_2$ ' to the second one (from 2.5 to 5 V).

Linear fitting curves:

$$f/c\big|_{l1} = 0.0629 \cdot V + 0.8500$$
$$f/c\big|_{l2} = 0.3240 \cdot V + 0.2631 \quad (2)$$

We concluded that the exponential fitting curve adjusts more precisely to the experimental data. Nevertheless, although the exponential function provides a slightly better approach, the average error obtained for each one of them is quite acceptable for a first model of the control system. As a result, the ease of programming this curve has been the main criterion taken into account for the final decision to implement the linear function.

A graph showing the comparison between the upper and lower profile coordinates for 0 and 5 V is presented in Figure 9. When results are analyzed, significant differences between the curvatures of the original and modified airfoils become apparent.

As observed, during the tests carried out, the airfoil chord at wing root in the testbed does not change. This is so important, because it will allow its application in a complete aircraft which, if the airfoil chord at wing root varied, it would be more complicated to establish a reliable joint between the wing and the fuselage of an aircraft. Furthermore, a great variation

of the airfoil curvature is noteworthy as it will give the aircraft greater lift allowing distribution of the lift coefficient across the linear zone, which is of great relevance in the case of aircraft flight.

5 WIND TUNNEL TESTS

The test campaign was developed by means of experimental wind tunnel testing at National Institute of Aerospace Technology (INTA) in Spain. Velocity measurements were taken using the Particle Image Velocimetry (PIV) in five sections along the wingspan in order to understand the three-dimensional behavior of the airflow.

The tests were carried out using a 1:2 scaled half-model of the MAV attached to a wall to simulate the symmetric half of the model. Two different models were used, one corresponding to the unmodified configuration of the wing (Eppler E61 airfoil) and other which corresponds with the modified configuration with highest camber increase (up to 10% of maximum airfoil camber) (Figure 9).

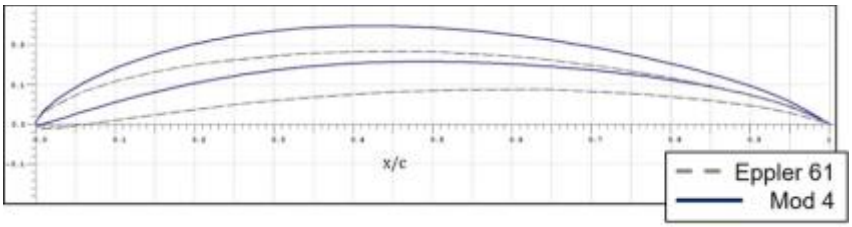

Figure 9: Two different airfoil configurations tested

The wind tunnel has an open test section of 2×3 m^2 with a platform to place the experiment aligned with the flow (zero yaw angle). The model was tested with a freestream velocity of 10 m/s ($Re \approx 6.5 \cdot 10^4$) and a turbulence intensity less than 0.5%. The flow was seeded with olive oil tracer particles and illuminated with two Nd:YAG (Neodymium: Yttrium Aluminum Garnet) lasers with a pulse separation of 25 μs. The mean flow velocity field was calculated over a total of 200 instantaneous maps.

The non-dimensional mean velocity flow for the unmodified configuration is shown in Figure 10 for different angles of attack (AoA) for the section corresponding to 75% of the wingspan. Streamlines are superimposed on to the velocity maps. The values of C_L where measured from the unmodified vehicle for a Reynolds number of $6.5 \cdot 10^4$ for previous researches [9]. Detachment of the flow appears for an AoA of 25°. This is shown by a massive low wind speed region in the trailing edge of the airfoil.

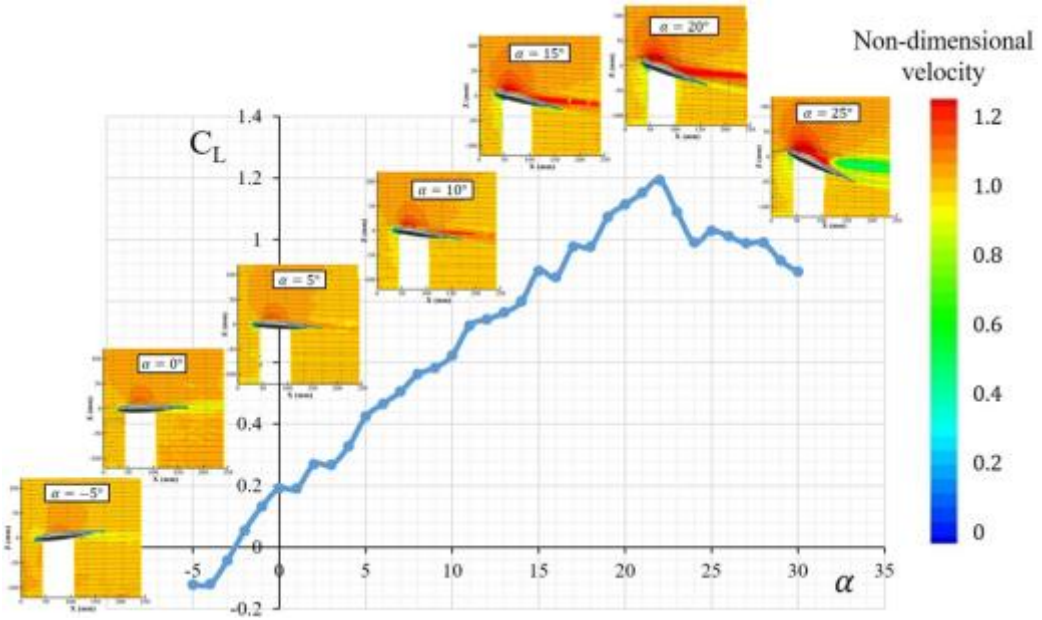

Figure 10: Non-dimensional mean velocity flow field at 75% of the wingspan for the unmodified MAV over the C_L vs **α** curve for Re≈$6.5 \cdot 10^4$.

Figure 11 shows the five measurement sections along the wingspan for the unmodified MAV for an angle of attack of 25°. A wide detachment region appears throughout the wingspan which confirms that the wing is fully stalling. The structure of this low velocity area suggests a strong three-dimensional behavior of the flow, typical of LAR wings performing at low Reynolds numbers.

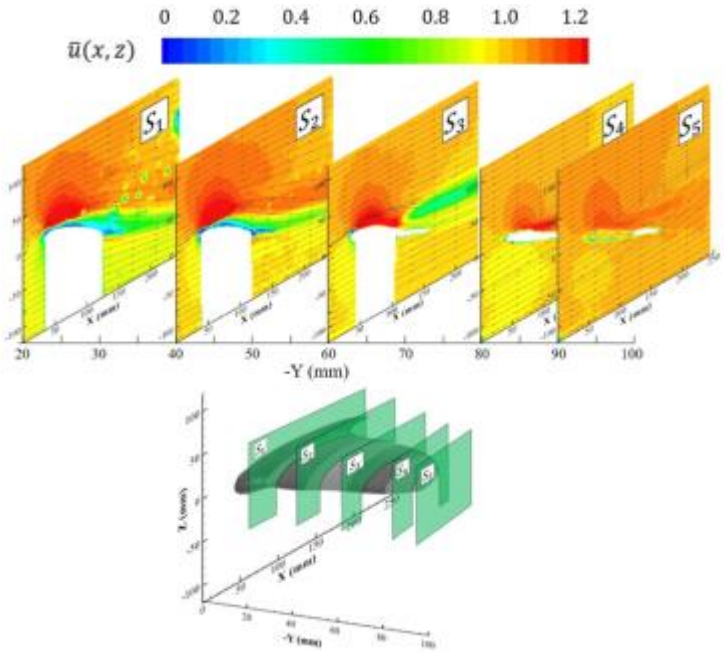

Figure 11: Non-dimensional velocity flow around the unmodified MAV along the wingspan.

Very significant differences appeared for the Mod4 configuration of the wing, mostly at higher angles of attack closer to the stall of the vehicle. In Figure 12 it is shown the non-dimensional mean velocity flow field for both aircraft configurations for an AoA of 25° at 75% of the wingspan. The Mod4 configuration shows no detachment region. The higher camber value for the Mod4 configuration allows the aircraft to increase the stall angle of attack and improve the maximum lift coefficient of the wing. This can be deduced because of the higher acceleration of the flow in the upper side of the wing shown in Mod4 configuration.

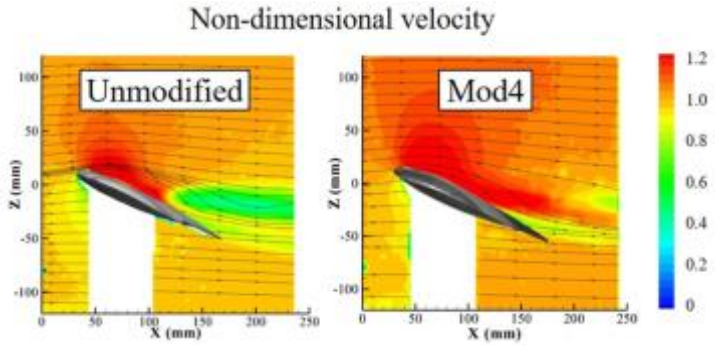

Figure 12: Non-dimensional mean velocity flow field for both MAV configurations and AoA of 25° at 75% of the wingspan.

Turbulence intensity distribution can be derived from the velocity measurements. Figure 13 is showing the turbulence intensity distribution for both MAV configurations at 75% of the wingspan for 25° of AoA. The Mod4 configuration reduces the high turbulent region in the air wake of the wing. This is very important for the stability of the vehicle. This unsteady turbulent flow might produce vibrations in the wing and result in dynamic instability and fatigue problems in the structure.

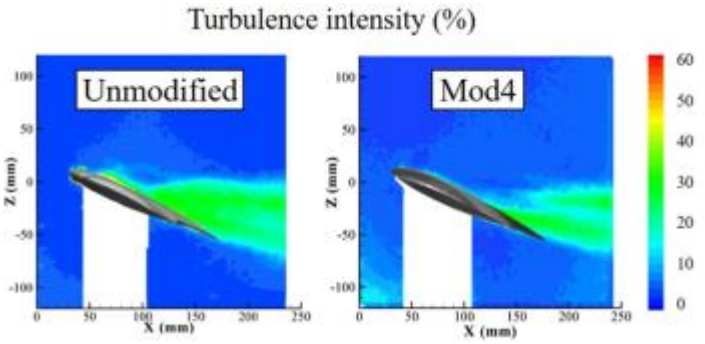

Figure 13: Turbulence intensity distribution for both MAV configurations and AoA of 25° at 75% of the wingspan.

6 CONCLUSIONS

The objective of this research was to develop a conceptual model and, as a result, a prototype of an unmanned aerial vehicle of reduced dimensions (micro air vehicle, MAV)

based on adaptive wing geometry (morphing concept). This innovative proposal will optimize the performances on the aircraft mission profile. Morphing wings can provide a wide range of configurations that rigid ones are not able to.

Throughout this paper, the highlights of the project are presented: the main conceptual design features, the effect of the voltage variation over the curvature, and experimental wind tunnel tests.

The flow around the morphing micro air vehicle was measured by means of PIV technique and wind tunnel testing. Two different configurations of the MAV were studied: the unmodified configuration and the Mod4 configuration, which consists of a higher cambered Eppler E61 airfoil with the same chord and thickness. The Mod4 wing showed better performance at high angles of attack delaying stall up to higher AoA and therefore obtaining higher maximum lift coefficient ($C_{L\ max}$). This design will help the aircraft to have a wider range of maneuver during the mission. Further investigations should be focused in the other configurations of the vehicle and the study of the transient states during the change of configurations of the wing.

REFERENCES

[1] Torres GE, Mueller TJ. Low aspect ratio aerodynamics at low Reynolds numbers. AIAA J 2004;42(5):865-873.

[2] Weisshaar TA. Morphing aircraft technology-new shapes for aircraft design 2006.

[3] Jones RT. The minimum drag of thin wings in frictionless flow. Journal of the Aeronautical Sciences (Institute of the Aeronautical Sciences) 2012;18(2).

[4] Williams RB, Park G, Inman DJ, Wilkie WK. An overview of composite actuators with piezoceramic fibers. Proceeding of IMAC XX 2002:4-7.

[5] Smart Material Corporation
. Available at: www.smart-material.com.

[6] Ohanian III O, Hickling C, Stiltner B, Karni ED, Kochersberger KB, Probst T, et al. Piezoelectric morphing versus servo-actuated MAV control surfaces. AIAA Paper 2012;1512:23-26.

[7] Design, manufacturing, and verification of piezoceramics embedded in fiber-reinforced thermoplastics. Smart Structures & Materials' 95: International Society for Optics and Photonics; 1995.

[8] Anderson Jr JD. Fundamentals of aerodynamics. : Tata McGraw-Hill Education; 1985.

[9] Barcala-Montejano, M. A., Rodríguez-Sevillano, A. A., Crespo-Moreno, J., Bardera-Mora, R., & Silva-González, A. J. (2015, June). Optimized performance of a morphing micro air vehicle. In Unmanned Aircraft Systems (ICUAS), 2015 International Conference on (pp. 794-800). IEEE.

VIII ECCOMAS Thematic Conference on Smart Structures and Materials
SMART 2017
A. Güemes, A. Benjeddou , J. Rodellar and Jinsong Leng (Eds)

A ROBUST FLUID STRUCTURE INTERACTION NUMERICAL TOOL FOR THE ANALYSIS OF AIRFOIL MORPHING STRUCTURES WITH SHAPE MEMORY ALLOY ACTUATORS

ANARGYROS KARAKALAS[*], THEODOROS MACHAIRAS[*], ALEXANDROS KONTOGIANNIS[*], ALEXANDROS SOLOMOU[‡], VASILIS RIZIOTIS[†] and DIMITRIS SARAVANOS[*]

[*] Dept. of Mechanical Engineering and Aeronautics
University of Patras
University of Patras Campus, 26500, Rion, Greece
e-mail: saravanos@mech.upatras.gr

[‡] Dept. of Aerospace Engineering
Texas A&M University

[†] Dept. of Mechanical Engineering
National Technical University of Athens

Key words: Fluid Structure Interaction, Shape Memory Alloys, Morphing, Wind Turbines

Abstract. In the present paper, a Fluid Structure Interaction (FSI) numerical tool is presented for the rapid simulation of morphing structures with implemented Shape Memory Alloy (SMA) actuators if form of wires. The tool consists of two main components: (1) the fluid simulation tool and (2) the structural analysis tool. The former consists of an inviscid model as a preliminary step for the development of a Viscous-Inviscid Interaction (VII). Firstly, the panel method for the purely inviscid flow is described as well as the viscous displacement model for the Equivalent Inviscid Flow (EIF). Due to the low computational cost and required solution time of VII methods, the present method is promising for fluid-structure interaction computations where multibody assemblies are considered and the numerical model involves thousands of Degrees of Freedom (DoFs). The structural model is developed using the commercial finite element software ABAQUS which offers the ability to develop and implement user subroutines for the numerical simulation of the shape memory alloys adopting well established material models. An articulated, finger-like, morphing mechanism for load alleviation in horizontal axis wind turbine (HAWT) blades, consisting of three pairs of antagonistic actuators to control bilateral morphing shapes is presented and investigated. The FSI numerical model is used to quantify the effect of the aerodynamic pressure on the SMA actuator wires in terms of developed stresses as well as to prove the variations in the aerodynamic characteristics of the airfoil in terms of changes on the coefficient of pressure. A number of different possible activation cases are selected and assessed to compare between flap and morphing operation of the mechanism.

1 INTRODUCTION

Development of high fidelity numerical tools with low computational time and improved accuracy is the most essential prerequisite for the design and realization of new engineering applications with enhanced capabilities. Morphing applications' potential is constantly growing as new materials and techniques are emerging. While these structures augur more efficient operation than conventional solutions in the fields of aerospace industry [1] and wind turbines [2] the prediction of the accurate response of the whole system remains an open and quite challenging field because of the number of the different scientific areas and problems that have to be addressed and solved. Thus, multidisciplinary approaches that combine the individual scientific problems into a single model offer more realistic solutions. FSI is such a technique that considers the effect that a fluid domain has on a structure immersed inside the domain. FSI techniques can be used for both determining the response of a structure under the influence of a flow but also in the efficient design of structures that will interact or affect a flow.

An example of design of adaptive structures oriented in the field of aerospace applications is the work of Bilgen et. al. [3] who proposed a variable-camber and variable twist morphing wing using piezocomposites to induce surface deformations. Their design was based on a coupled static FSI problem. Moreover, Willis and his coworkers [4] developed a multi-fidelity computational framework capable of analyzing and designing flapping wing. A different aerospace application is the use of chevrons activated by SMA actuators on the circumference of jet engine outlets for aircraft noise reduction [5].

In the field of renewable energy and more specifically in the design of new generation wind turbines, morphing is considered as a possible solution to reduce aerodynamic loads or improve the efficiency of the machine. The effect of adaptive airfoil geometries has been demonstrated in several studies implementing FSI techniques for both HAWT [6], [7] and Vertical Axis Wind Turbines (VAWT) [8]. Srinivas Vasista and Liyong Tong [9] have used a FSI analysis to create a topology-optimized design of a morphing trailing edge structure capable for providing the flexibility for variations in airfoil shape and the stiffness to carry the aerodynamic loads.

University of Patras (UPAT) and National Technical University of Athens (NTUA) have already developed a morphing airfoil section [10], [11] to reduce the loads acting on the root of a 10 MW HAWT blade. The morphing of the airfoil section changes the flow field around it, thus it affects significantly its aerodynamic performance in terms of variations of the coefficients of lift, drag and pressure. In this paper, a fluid structure interaction scheme is developed for the numerical investigation of the aerodynamic response of an airfoil with an adaptive trailing edge actuated by shape memory alloy wires designed for a 20MW HAWT blade.

2 MODELING BACKGROUND

In this section, the main theoretical background and methods used for the numerical simulation of the complex thermomechanical response of shape memory alloys and the simulation of viscous-inviscid fluid flow around an airfoil are described concisely.

2.1 Thermomechanical Behavior of Shape Memory Alloys

Shape memory alloys belong to the category of smart materials and present a very particular type of diffusionless displacive phase transformation. When transformation occurs the parent phase called Austenite (high temperature phase) is transformed to the product phase called Martensite (low temperature phase) under applied stress or variations of temperature. The martensitic transformation is the key to the Shape Memory Effect (SME) [12] a unique phenomenon that is depicted schematically in the diagram of Figure 1 A.

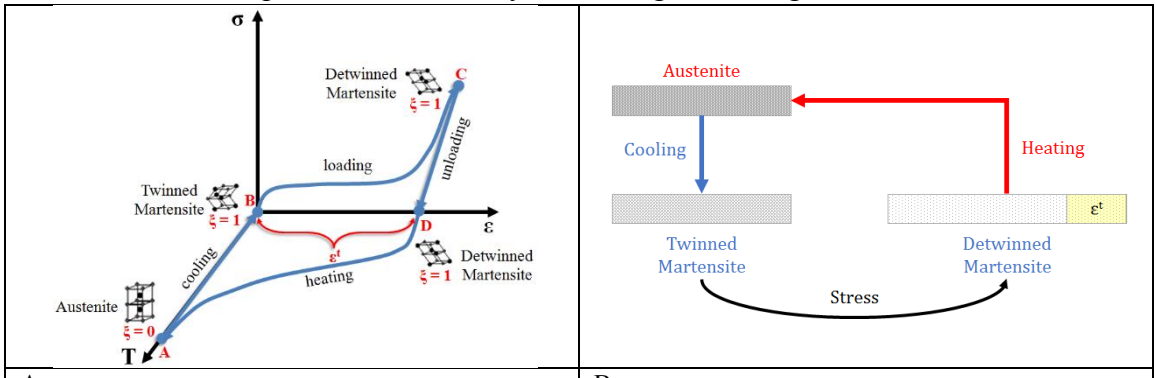

A. B.

Figure 1: Shape Memory Effect shown in a A. Stress – Strain – Temperature Space Diagram and a B. Ribbon Representation

Figure 1 A denotes the starting state where the material is considered in the phase of Austenite thus the martensitic volume fraction (represented with letter ξ) equals 0. While under cooling the material's atoms undergo a displacive reorganization until a preferred arrangement, or ordered lattice structure is obtained. This microstructure is highly twinned and completely martensitic self-accommodated groups are formed (point B). After application of a mechanical load beyond a particular limit the martensite will be detwinned a process that is described as a stress induced transformation (point C). Upon unloading an inelastic strain denoted as ε^t, remains (point D) and can be recovered by heating the detwinned martensite. Applied heat generates a reverse phase transformation to the parent phase (point A). The described thermomechanical loading cycle is known as shape memory effect due to the inherent ability of the material to "remember" a crystal structure which can be recovered after a thermomechanical loading process. This behavior can be deployed in applications where solid state actuators with low volume characteristics are required such as satellite solar panel hinges, safety valves, chevrons etc.

Many mathematical models have been proposed in order to describe the complex nonlinear thermomechanical behavior of SMAs and they can be categorized in three main categories: (i) macro-mechanical phenomenological models, (ii) micromechanical models and (iii) macro-mechanical based on micromechanics and thermodynamics [13]. The models of category (i) appear to address adequately the outline of the response of SMAs but their capabilities are limited and case oriented as they are based on experimental observations. Thus, the micromechanical models were considered to predict the response of these polycrystalline materials by accounting for their granular microstructure. Although these models are accurate

they are not optimal for engineering applications due to the requirement of modeling of the entire microstructure which concludes to extreme computational cost when feasible. Consequently, the macro-mechanical models emerged because of the need for low computational cost constitutive equations that are based on micromechanics and thermodynamics. The model adopted in the present study is the 1D version of the model developed by Lagoudas et.al. [14] considering the extension proposed by Darren et. al. [15].

2.2 Aerodynamic Analysis Method

For the prediction of the aerodynamic loads acting on the morphing airfoil, a viscous-inviscid interaction (VII) method was adopted since it requires incredibly lower computational time than alternative Reynolds-Averaged Navier-Stokes (RANS) methods for comparative accuracy. Using a panel method for the inviscid flow field the problem involves 1/100 fewer unknowns for obtaining results within the same accuracy level, as space-filling grid generation can be avoided [16].

In the present formulation, a Hess-Smith panel method describes the inviscid flow field while a wall-transpiration method is used to model the displacement thickness due to the viscous effects. The wall-transpiration boundary condition is dictated by the boundary layer properties which are calculated by integrating a simplified form of Navier-Stokes equations along the thickness of the boundary layer at the surface of the airfoil and the upper/lower wakes. The two-equation integral boundary layer method is comprised of the integral momentum and kinetic energy equations whilst semi-empirical velocity profiles are used for the turbulence closure. One supplementary equation is solved, which depends on the state of the flow and can be either (i) an equation for the transition criterion (e^n) for the laminar regime or (ii) a simplified stress-transport equation (lag-entrainment method) to account for rapidly changing flows. The set of equations for the inviscid and viscous flow is solved fully simultaneously using a Newton-Raphson (N-R) method, and because of that strong interaction local regions of separated flow such as laminar separation bubbles can be well predicted. The previously described method hinges on the work of Drela [17] and Drela and Giles [18] which has been implemented in the XFOIL code. An extension of this work has been performed by Riziotis and Voutsinas [19] to model dynamic stall behavior (double wake concept) in FOIL2W numerical tool and by Kontogiannis for the analysis of two element airfoils in FOIL2E numerical tool. In the present context, the FOIL2E numerical tool was loosely coupled with a commercial finite element software and to develop a fluid-structure interaction analysis scheme.

3 IMPLEMENTATION OF THE FSI ANALYSIS

Having described the dominant phenomena that take place and will be numerically investigated during the FSI analysis the developed subroutines and numerical tools are presented in the following paragraphs. The FSI scheme consists of a commercial finite element software for the 2.5D FE modeling of the airfoil and the morphing mechanism with the implemented actuators, a user material subroutine for the description of the thermomechanical response of shape memory alloys, a user load subroutine for the extraction of the airfoil's

geometry during each increment and the application of pressure distribution and an in-house viscous-inviscid code for the solution of the flow problem around the airfoil and the extraction of the pressure distribution. The selected airfoil is located at the 77% of a 20MW blade's length.

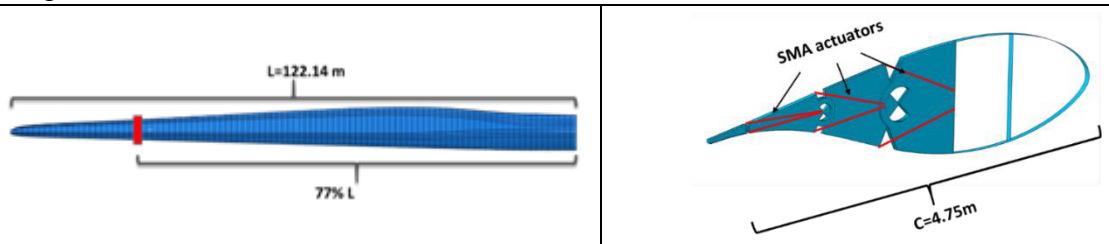

A. B.

Figure 2: 20MW wind turbine blade; A) Basic Dimensions and B) Morphing Concept

3.1 Material Subroutine for SMAs

The constitutive equations describing the complex thermomechanical response of SMA actuator wires were implemented into a commercial finite element (FE) software [20] via a User MATerial subroutine (UMAT). At the beginning of each time step the values of total strain ($\varepsilon_{t+\Delta t}$) and temperature ($T_{t+\Delta t}$) are known based on the guesses of N-R process of the global solver of FE software. The aforementioned quantities are provided to the UMAT as input. In the same manner, the chosen state variables, which include (i) the martensitic volume fraction (ξ) and the transformations stain (ε^t) that describe changes in the microstructure of the material, are considered equal to their values on the last converged time step. At this time, the thermo-elastic prediction step begins, which as a trial step, verifies whether the trial values of the internal state variables comply with a set of time discrete conditions. To this end the stress (σ) and the transformation function (Φ) are calculated. If transformation function Φ is greater than zero then the transformation takes place and the corrected values of ε^t and ξ are calculated according to an approach usually referred in computational plasticity as closest projection return mapping algorithm [21].

3.2 FOIL2E Tool for Fluid Flow Simulation

The aerodynamic analysis method described in section 2.2 was based on the well-established and validated numerical tool FOIL2W that has been developed by the researchers of Laboratory of Aerodynamics of NTUA. The FOIL2E tool has been developed for cases of two-element high-lift airfoil analysis for aeronautical applications but it is also suitable for one-element airfoils commonly used in the wind energy sector as well as more advanced blade designs involving biplane configurations [22]. The numerical tool provides rapid results for 2D steady flows and angles of attack up to stall whilst the results are dubious for post-stall conditions. Lastly, the present method is promising for quasi-3D (2.5D) aerodynamic analysis of blades since it is computationally efficient and thus attractive to wind turbine applications.

3.3 Middleware Subroutine DLOAD

DLOAD subroutine was considered as a middleware which was responsible for the communication between the structural and the aerodynamic analysis tools. This subroutine writes in an appropriate file the coordinates of the nodes on the outer aerodynamic surfaces, the number of each element and the number of the load integration point that is called for and the respective increment. These data are stored during every iteration of the global N-R solver of ABAQUS. It also identifies when a convergence has been reached and targets the last iteration of the converged increment to extract the coordinates of only one point from each element. The file containing the coordinates of each point is passed to the aerodynamic code at the first iteration of the next increment only. Once the new pressure data are calculated, at each iteration for every point DLOAD is called and another subroutine is used to locate the current point and find the respective pressure supplied by the aerodynamic code.

3.4 Fluid Structure Interaction

The numerical tools described in the previous subsections were combined to compose the FSI analysis scheme. In the flow chart of Figure 3 the interaction between the subroutines the numerical tools is briefly outlined. The ABAQUS structural model contains the geometry of the airfoil with the implemented morphing mechanism and the shape memory alloy actuators. In the model the initial thermomechanical conditions describing actuators' initial state and the boundary conditions representing supports are defined. During the initialization of the FSI analysis the aerodynamic pressure acting on the airfoil is considered equal to zero. Temperature variation is considered as the input for the activation of the proper actuator. When temperature input is passed into the model, UMAT subroutine is called to determine the changes in actuators state in terms of stress, temperature and transformation strain. If transformation takes place the airfoil is morphed and the coordinates describing the current geometry are extracted through the DLOAD subroutine. The coordinates of the morphed airfoil are then passed into FOIL2E code to determine the pressure distribution acting on the whole structure. Before the calculation of the new pressure field, FOIL2E checks if the maximum displacement variation in order to ensure that convergence between the structural and fluid model has been achieved. If the solution has not converged to a predefined tolerance value, the output of FOIL2E is the same pressure distribution provided in the previous increment. If the solution has converged then the pressure field is read by DLOAD subroutine and then it is applied to the airfoil's aerodynamic surfaces. During the next increment a new temperature variation is considered and the process is repeated until the end of the analysis.

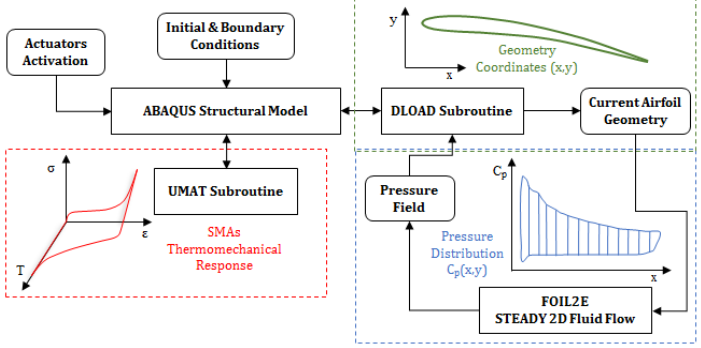

Figure 3: Brief Operational Flow Diagram of FSI Procedure

4 CASE STUDY DESCRIPTION & RESULTS

The presented case study is a 2.5D model of a morphing airfoil section of a 20 MW HAWT blade designed for load alleviation purposes. Load alleviation is performed by adoption of two different concepts: (i) the morphing mechanism acts like a flap representing 30% of the chord's length and (ii) two equivalent flaps of the morphing mechanism are entailed in a combined rotation to achieve a smoother camber line adaptation. For each one of the morphing cases the SMA wire actuators are modelled as thin wires of circular cross section (D = 3 mm) and three different analyses are considered: a. absence of aerodynamic pressure effects on the airfoil, b. constant aerodynamic pressure field acting on the airfoil and c. fluid structure interaction defines the aerodynamic loading. In b. and c. the pressure field is calculated by considering a wind velocity of 10 m/s and a.o.a. 4º. Furthermore, the activation of the actuators has for each analysis subcase has been considered the same and it is presented in FIGURE in terms of temperature variation.

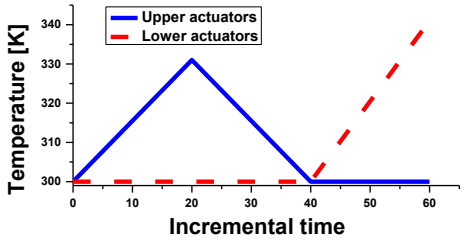

Figure 4: Temperature Variation of the Actuators

4.1 Flap Activation

In this section, the simulation results of the morphing concept entailing a single flap with 30% chordal length are presented for the three different subcases of aerodynamic loading. As it can be seen in Figure 5 the pressure application on the flap rotation cannot be neglected as it affects significantly its response. However small difference is observed between the constant pressure field and the varying aerodynamic pressure field predicted during the FSI analysis. This can be attributed to the small extent of flap movement that is confined between -1º and +1.52º rotation.

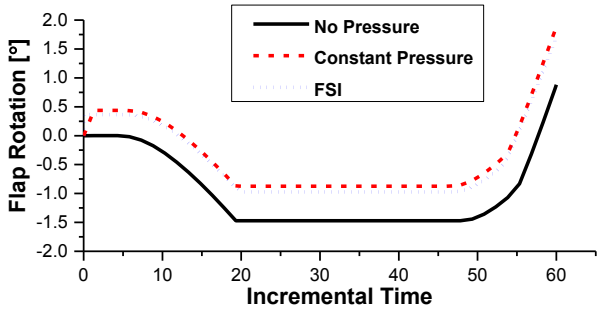

Figure 5: Angular Rotation of the 30% Chordal Length Flap for the Three Load Cases

In Figure 6 the developed stresses on the SMA actuators are presented. As it can be seen the application of pressure cannot be omitted as it changes significantly the predicted results. However there is no significant difference between the constant and the time varying time distribution fields. The same, holds true for the martensitic volume fraction evolution as presented in Figure 7.

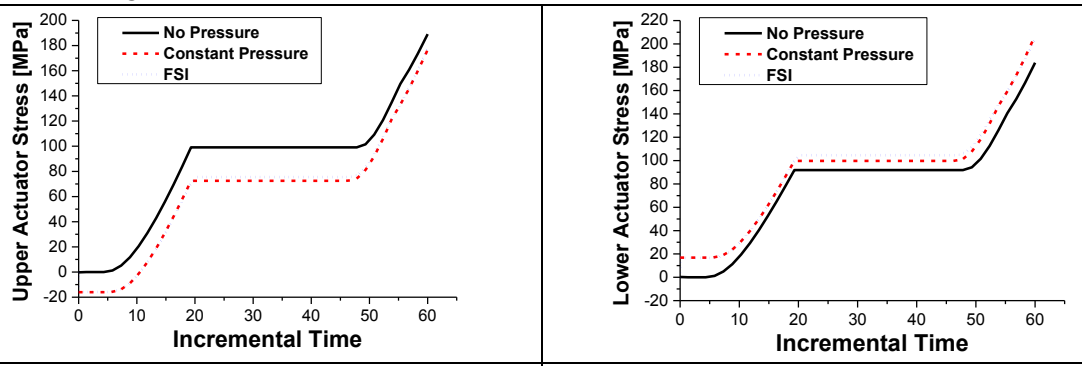

A. B.

Figure 6: Stress of Actuators for the 30% Chordal Length Flap A. Upper Actuator and B. Lower Actuator

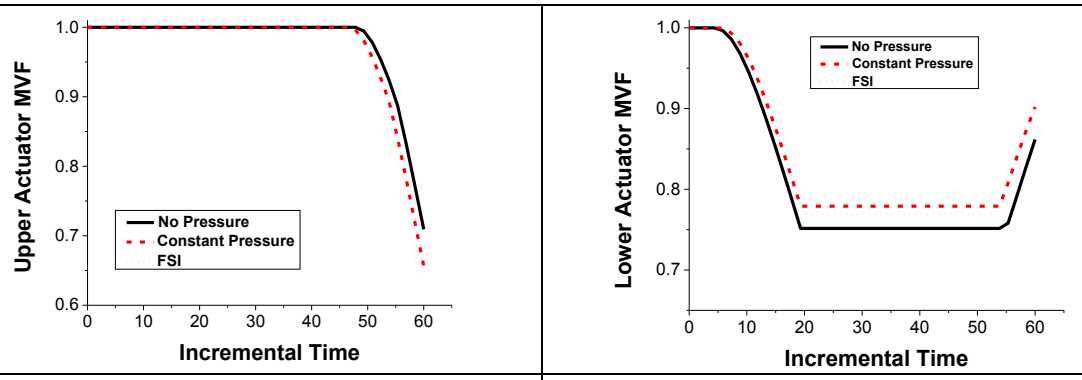

A. B.

Figure 7: Martensitic Volume Fraction of Actuators for the 30% Chordal Length Flap A. Upper Actuator and B. Lower Actuator

The aerodynamic performance of the morphing concept with the flap with 30% chordal length is assessed during the FSI analysis. In Figure 8 the distribution of pressure coefficient along the

chord of the airfoil is presented along with the values of lift and drag coefficients at the baseline state and the two extreme positions.

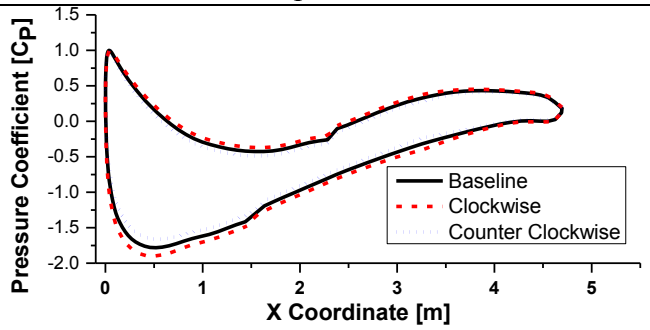

C_l	ΔC_l	C_d	ΔC_d
0.8975	-	0.0081	-
1.0068	12.2%	0.0085	5.1%
0.7825	12.8%	0.0077	4.2%

Figure 8: Pressure Coefficient Distribution during FSI Analysis and Aerodynamic Characteristics

4.2 Morphing Operation

In order to extend the morphing of the airfoil and to achieve a smoother deformed profile, a combined movement of the 10% and 30% chord length flap is attempted. Both actuators responsible for either the clockwise or the counter clockwise rotation are activated simultaneously to deflect the 30% and the 10% chord length flaps. The temperature of each set of actuators follows the profile depicted Figure 4. As it can be seen in Figure 9 the pressure application on the flap rotation cannot be neglected as it affects significantly its response. Additionally, there exists a non-negligible difference between the response predicted for the constant and the time varying pressure field predicted via the FSI analysis.

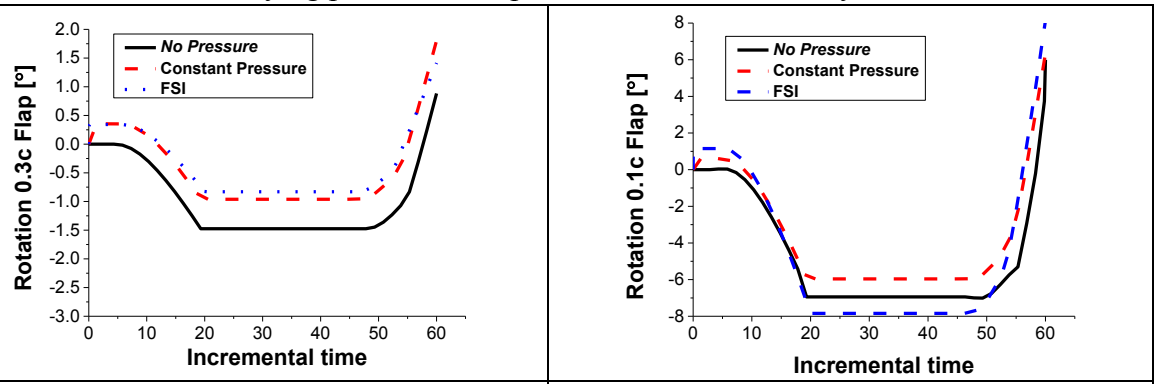

A. B.

Figure 9: Flap rotations of morphing airfoil. A. Rotation of 30% Chordal Length Flap and B. Rotation of 10% Chordal Length Flap.

In Figure 10 A the developed stress of the upper actuator responsible for the movement of the 30% chordal length flap is depicted while in Figure 10 B the stress for the upper actuator for the movement of the 10% chordal length flap is shown. Additionally, Figure 11 A presents the developed stresses on the lower SMA actuator responsible for the movement of the 30% chordal length flap while Figure 11 B depicts the stress of the lower actuator responsible for the clockwise movement of the 10% chordal length flap. As it can be seen the application of pressure cannot be omitted as it changes significantly the predicted results. The difference

between the constant and the time varying pressure field on the developed actuator stresses is considerable.

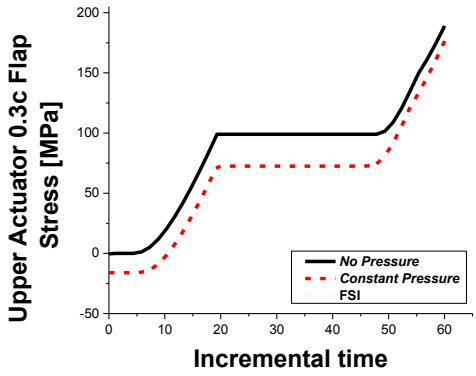

A.

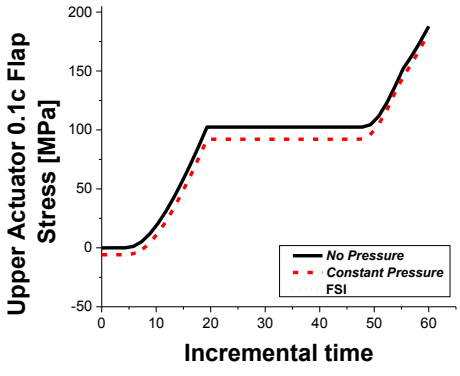

B.

Figure 10: Stress of Upper Actuators responsible for the Rotation of A. 30% Chordal Length Flap and B. 10% Chordal Length Flap

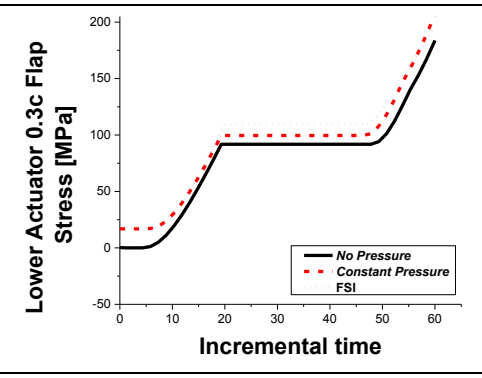

A.

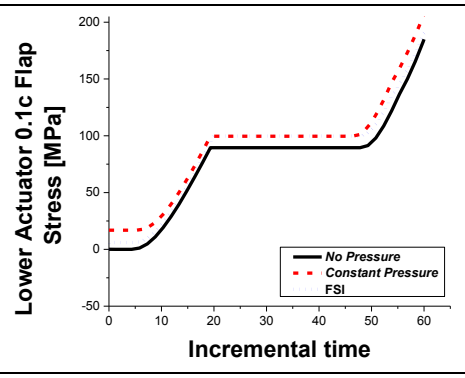

B.

Figure 11: Stress of Lower Actuators responsible for the Rotation of A. 30% Chordal Length Flap and B. 10% Chordal Length Flap

In Figure 12 and Figure 13 the evolution of the martensitic volume fraction for the upper and lower actuator sets respectively are presented. The effect of time varying aerodynamic pressure field is occasionally significant especially for the actuator responsible for the clockwise rotation of the 10% chordal length flap.

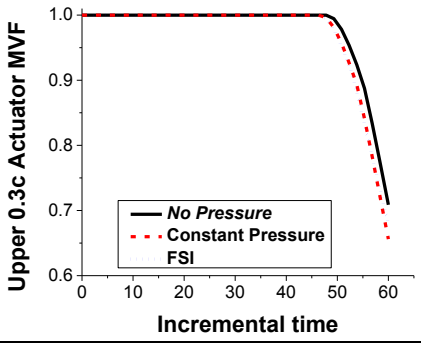

A.

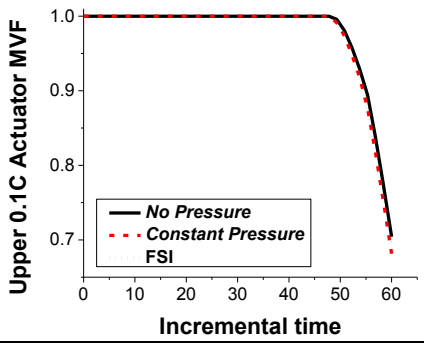

B.

Figure 12: Martensitic Volume Fraction of Upper Actuators responsible for the Rotation of A. 30% Chordal Length Flap and B. 10% Chordal Length Flap.

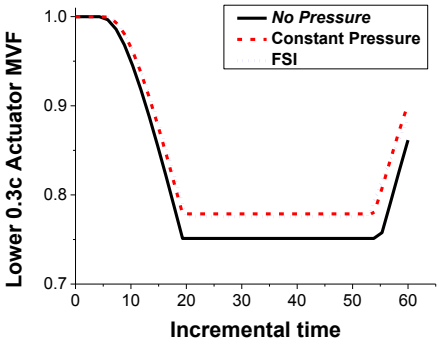

A.

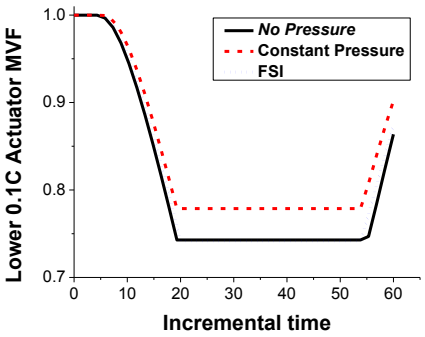

B.

Figure 13: Martensitic Volume Fraction of Lower Actuators responsible for the Rotation of A. 30% Chordal Length Flap and B. 10% Chordal Length Flap.

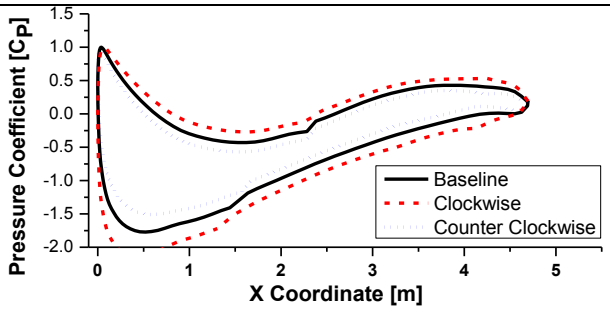

C_l	ΔC_l	C_d	ΔC_d
0.8978	-	0.0081	-
1.2245	36.4%	0.0095	17.6%
0.6190	31.1%	0.0074	8.5%

Figure 14: Pressure Coefficient Distribution calculated during FSI Analysis for the Combined Movement of 10% and 30% Chordal Length Flaps

5 CONCLUSIONS

In the work presented in this paper, a method to implement loosely coupled fluid structure interaction has been described and performed on a 20MW WTB morphing section to evaluate

its performance. During the study two cases and three subcases have been numerically tested. The two cases involved the operation of the morphing mechanism and the subcases the consideration of aerodynamic pressure through fluid structure interaction between a structural and a fluid flow numerical tool.

The produced results show that the FSI method has been successfully developed and allows for more reliable predictions and accurate estimation of the structural response of the morphing concept and the evaluation of its aerodynamic performance. The estimation of the change of lift coefficient due to morphing can be successfully predicted for the actual achieved morphed shape. Also the varying aerodynamic pressure field due to shape morphing can be taken into account to assess its effect on the structural performance of the morphing concept. Numerical predictions indicate that the aerodynamic pressure acting on the airfoil can affect significantly the developed stress on the actuators and consequently their performance and effectiveness.

A comparison performed between the consideration of flap and morphing operation proved that morphing can produce greater effects on the aerodynamic performance of an airfoil while keeping the developed actuator stresses on the vicinity of 200MPa and without overstressing the rest of the structural components. The percentage of the variations on the coefficient of lift and the coefficient of drag are more than doubled when the flap at 30% and the flap at 10% are activated in a combined operation. Morphing entails a smoother change of the camber line of the airfoil by adapting its shape which leads to a more effective way to controlling its performance and therefore the produced loads on the whole blade structure.

6 ACKNOWLEDGEMENTS

Part of this work has been supported by the INNWIND.EU project (grand agreement No. 234313) funded by the European Union's Seventh Framework Program for research, technological development and demonstration. The Support is greatly appreciated by the authors.

X REFERENCES

[1] A. Y. N. Sofla, S. A. Meguid, K. T. Tan, and W. K. Yeo, "Shape morphing of aircraft wing: Status and challenges," *Mater. Des.*, vol. 31, no. 3, pp. 1284–1292, 2010.

[2] S. D. and P. M. W. Xavier Lachenal, "Review of morphing concepts and materials for wind turbine blade applications," *Wind Energy*, vol. 16, no. 2, pp. 283–307, 2012.

[3] O. Bilgen, M. I. Friswell, K. B. Kochersberger, and D. J. Inman, "Surface Actuated Variable-Camber and Variable-Twist Morphing Wings Using Piezocomposites," *Struct. Struct. Dyn. Mater. Conf.*, vol. 19, no. April, pp. 1–13, 2011.

[4] D. Willis *et al.*, "A Computational Framework for Fluid Structure Interaction in Biologically Inspired Flapping Flight," *25th AIAA Appl. Aerodyn. Conf.*, no. June, pp. 1–22, 2007.

[5] S. D. Oehler, D. J. Hartl, T. L. Turner, and D. C. Lagoudas, "Modeling Fluid Structure Interaction with Shape Memory Alloy Actuated Morphing Aerostructures," *Spie - Ind. Commer. Appl. Smart Struct. Technol. 2012*, vol. 8343, pp. 834305-834305–12, 2012.

[6] P. Krawczyk, A. Beyene, and D. MacPhee, "Fluid structure interaction of a morphed

wind turbine blade," *Int. J. Energy Res.*, vol. 37, no. 14, pp. 1784–1793, 2013.
[7] D. MacPhee and Asfaw Beyene, "Fluid-structure interaction of a morphing symmetrical wind turbine blade subjected to variable load," *Int. J. Energy Res.*, vol. 37, no. 1, pp. 69–79, 2011.
[8] D. W. MacPhee and A. Beyene, "Fluid-structure interaction analysis of a morphing vertical axis wind turbine," *J. Fluids Struct.*, vol. 60, pp. 143–159, 2016.
[9] S. Vasista and L. Tong, "Topology-Optimized Design and Testing of a Pressure-Driven Morphing-Aerofoil Trailing-Edge Structure," *AIAA J.*, vol. 51, no. 8, pp. 1–10, 2013.
[10] A. Karakalas, T. Machairas, A. Solomou, V. Riziotis, and D. Saravanos, "Design and Simulation of Morphing Airfoil Sections with SMA Actuators for Wind Turbine Rotors," *Proc. ICAST 2014*, no. 2, pp. 1–12, 2014.
[11] A. Karakalas, T. Machairas, A. Solomou, V. Riziotis, and D. Saravanos, "Development of SMA actuated morphing airfoil for wind turbine load alleviation," *Proc. TMS Middle East - Mediterr. Mater. Congr. Energy Infrastruct. Syst. MEMA 2015*, pp. 181–190, 2015.
[12] D. Stoeckel, "The Shape Memory Effect - Phenomenon, Alloys, and Applications," *Shape Mem. Alloy. Power Syst. EPRI*, pp. 1–13, 1995.
[13] C. Cisse, W. Zaki, and T. Ben Zineb, "A review of constitutive models and modeling techniques for shape memory alloys," *Int. J. Plast.*, vol. 76, pp. 244–284, 2016.
[14] D. Lagoudas, D. Hartl, Y. Chemisky, L. Machado, and P. Popov, "Constitutive model for the numerical analysis of phase transformation in polycrystalline shape memory alloys," *Int. J. Plast.*, vol. 32–33, pp. 155–183, 2012.
[15] D. J. . Hartl, A. . Solomou, D. C. . Lagoudas, and D. . Saravanos, "Phenomenological modeling of induced transformation anisotropy in shape memory alloy actuators," *Proc. SPIE 8342, Behav. Mech. Multifunct. Mater. Compos.*, vol. 8342, 2012.
[16] M. Drela, *Flight Vehicle Aerodynamics*. The MIT Press, 2014.
[17] M. Drela, "XFOIL: An analysis and design system for low Reynolds number airfoils," *Conference on Low Reynolds Number Airfoil Aerodynamics*, vol. Volume 54. p. pp 1-12, 1989.
[18] M. Drela and M. B. Giles, "Viscous-inviscid analysis of transonic and low Reynolds number airfoils," *AIAA J.*, vol. 25, no. 10, pp. 1347–1355, 1987.
[19] V. A. Riziotis and S. G. Voutsinas, "Dynamic stall modelling on airfoils based on strong viscous–inviscid interaction coupling," *Int. J. Numer. Methods Fluids*, vol. 56, no. 2, pp. 185–208, Jan. 2008.
[20] Simulia, "Abaqus 6.14 - User Subroutines Reference Manual." 2014.
[21] M. a Qidwai and D. C. Lagoudas, "Numerical implementation of a shape memory alloy thermomechanical constitutive model using return mapping algorithms," *Int. J. Numer. Methods Eng.*, vol. 47, no. 6, pp. 1123–1168, 2000.
[22] R. E. WIRZ, "Advanced aerodynamic and structural blade and wing design," 13/581,278, 2011.

VIII ECCOMAS Thematic Conference on Smart Structures and Materials
SMART 2017
A. Güemes, A. Benjeddou , J. Rodellar and Jinsong Leng (Eds)

MORPHING WINGLETS BASED ON COMPLIANT STRUCTURES

Chen Wang[*], Hamed Haddad Khodaparast[†], Michael I Friswell[†] and Alexander D Shaw[†]

[*]College of Engineering, Swansea University, Bay Campus
Fabian Way, Crymlyn Burrows, Swansea SA1 8EN, UK
Email: 804685@swansea.ac.uk

[†] College of Engineering, Swansea University, Bay Campus
Fabian Way, Crymlyn Burrows, Swansea SA1 8EN, UK

Key words: Morphing Winglet, Compliant Structure, Corrugated Panel, Flexible Honeycomb Structure

Abstract. Compliant structures, such as flexible corrugated panels and honeycomb structures, are promising structural solutions for morphing aircraft. The compliant structure can be tailored to carry aerodynamic loads and achieve the geometry change simultaneously, while the reliability of the morphing aircraft can be guaranteed if conventional components and materials are used.

In this paper, a compliant structure is proposed to change the dihedral angle of a morphing winglet. Unsymmetrical stiffness is introduced in the compliant structure to induce the rotation of the structure when it is actuated. Trapezoidal corrugated panels are used in the compliant structure, whose geometry parameters can be tailored to provide the stiffness asymmetry. An equivalent model of the corrugated panel is employed to calculate the deformation of the compliant structure, which improves the efficiency of the optimization. The optimization is performed to determine the optimum geometry variables, while also considering the actuator requirements and the available space to install the compliant structure.

To provide the airfoil shape a flexible honeycomb structure is integrated into the morphing skin panel. The stiffness of the honeycomb structure can be designed to be much smaller than the stiffness of the corrugated panel, which ensures the deformation of the corrugated panel will not be influenced significantly by the honeycomb structure, and the deflections of the morphing winglet can still be calculated preliminarily by the simplified model. An experimental prototype has been manufactured to demonstrate the deformation of the morphing winglet, and a detailed finite element analysis has further verified the morphing winglet model.

1. INTRODUCTION

The development of morphing aircraft is the subject of intensive research activity in recent years. The morphing winglet is one of the most promising concepts because small winglets give a relatively important aerodynamic influence.

The research into the morphing winglets (wing tip devices) has different motivations, such as the increase in the flight range [1, 2], the reduction of air pollution [3], the enhancement of the takeoff capability [4], and alleviating loads [5]. Despite the different motivations, reliable structural solutions will be required to achieve the shape change of the morphing winglet while simultaneously carrying the aerodynamic loads.

The conflicting relationship between the three requirements of the structure, i.e., 'light', 'load-carrying' and 'shape-adaptable', has been discussed in a requirement triangle [6]. From the pespective of the system level study, the philosophy dillema remaining in the design of the morphing structure is to satisfy the requirements of carrying aerodynamic load and being able to change its shape with the constraints of its additional weight, system complexity, stability and cost. Smart materials, e.g. shape memory alloys [7] or piezoeletric material [8], have been applied in morphing aircraft. The success of these designs relies on the novel active characteristics of the materials. Another apporach is using conventional materials, but adopting unconventional structural concepts to design the morphing structutrue.

Corrugated panels and honeycombs are two kinds of structures that have been in long-term use. However, they have been applied to new applications in the field of morphing aircraft. Flexible corrugated panels, and honeycomb structures have been used as morphing skins [9-12]. One common feature in these applications is the anistropic mechnical proterties of the entire structure, although the structure can be made of isotropic materials. With the equivalent anisotropic properties, stiffness tailoring can optimize design requirement of the morphing aircraft.

The authors have proposed a compliant structure, which uses an unsymmetrical stiffness allocation in the structure [13]. The unsymmetrical stiffness in the structure is able to induce a rotation of the structure when a linear actuation is applied. The induced rotation of the compliant structure enables the dihedral angle of the winglet to change if the compliant structure is installed spanwise as a winglet or as a transion section between the main wing and the winglet.

In this paper, a functional model based on the compliant structure is designed, manufactured and tested to validate the previous conceptual study. The trapezoidal corrugated panel is investigated for the compliant structure, which is optimized to minimize the required actuation force reducing the weight of the actuation system. The equivalent model of the trapzoidal corrugated panel is applied in the optimnization to reduce the calculation time.

To provide the aerodynamic shape, flexible honeycomb structures are employed in the leading and trailing edges of the winglet. There has been extensive research on honeycomb structures, including the use of flexible honeycomb structures as the skin to provide the airfoil shape in wing span morphing [14]. It is less common to combine the honeycomb structure and

a corrugated panel into one morphing aircraft design. The morphing winglet was manufactured using a 3D printer, and a static test was performed to demonstrate the deflection of the morphing winglet.

2. COMPLIANT STRUCTURES BASED ON UNSYMMETRICAL STIFFNESS

Corrugated panels may have different profiles, such as round, sinusoidal and trapezoidal. The current study selects the trapezoidal corrugated panel. In the 2-dimensional case, the profile of a trapezoidal corrugated panel has the peridoic unit as shown in Figure 1.

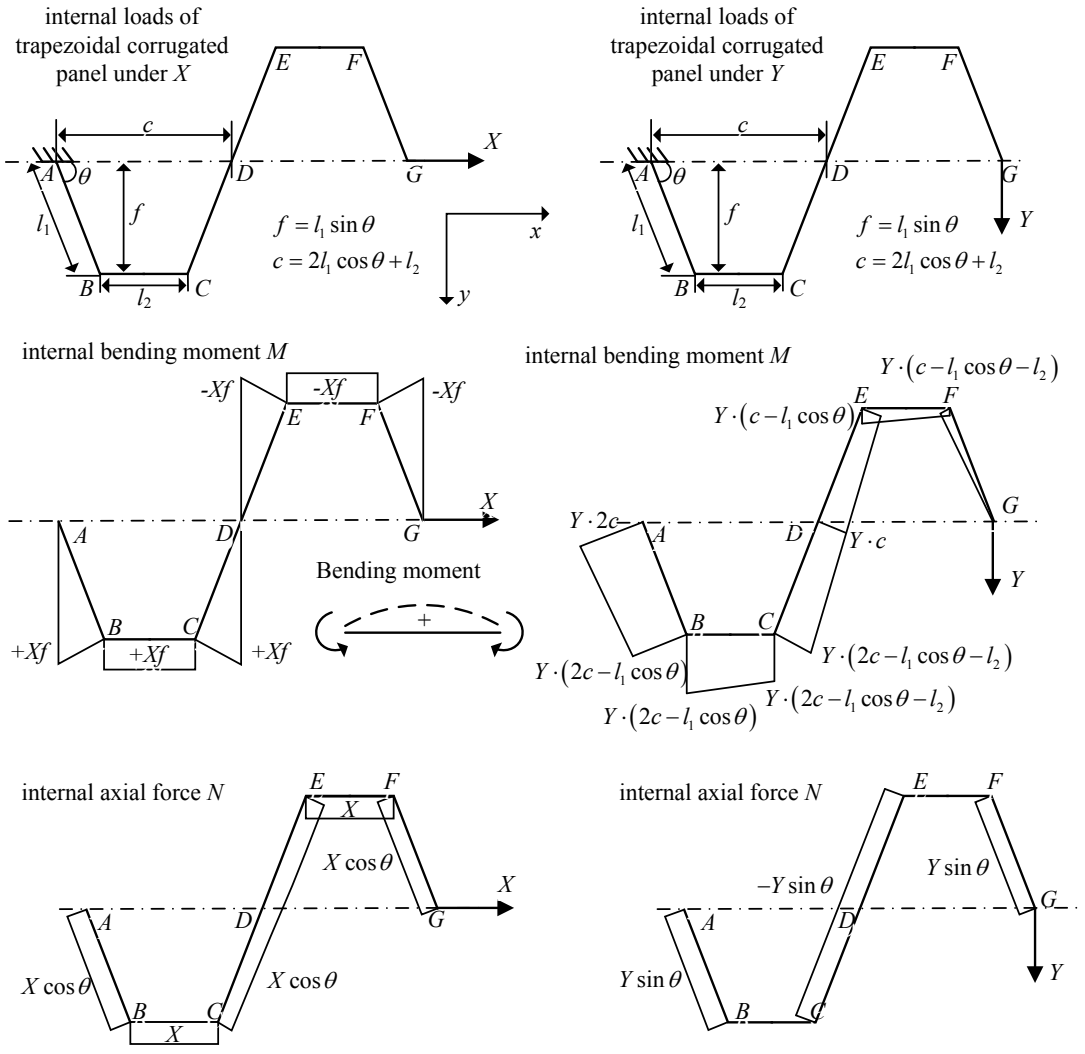

Figure 1. Internal loads of a trapezoidal corrugated panel

The corrugation unit consists of the rigid-connected beams, labelled by the points A, B, …, G. In the trapezoidal unit, the geometry variables l_1, l_2, t, θ are used to describe the length of beam AB, the length of beam BC, the thickness of the panel and the internal angle of the trapezoid ($0<\theta\leq 90$ degrees). The half height, and the half length of the corrugated panel are also represented by f and c respectively. The width along the z direction is denoted as w.

The internal loads in one trapezoidal unit are shown in Figure 1. Using the classical beam theory, the deflections of point G can be obtained by accumulating the deflections of the other points (A, B, …, F), including the rigid translations caused by the rotation angle of the beam cross section. The entire corrugated panel is then considered as an equivalent straight beam, which is fixed at one end and has the same deflections at the other end to the deflections of point G. The method to has been applied to find the deflections under the force in the x direction [15]. Using the same method, the deflections in response to the force in the y direction and the moment along the z direction have also been obtained. The deflection in the x direction u, the deflection in the y deflection v, and the rotation angle of the beam section along the z direction α, can then be expressed by the equivalent properties of the model as

$$\begin{bmatrix} u \\ v \\ \alpha \end{bmatrix} = \begin{bmatrix} \dfrac{L_n}{\overline{EA}} & \dfrac{1}{K_c} & 0 \\ \dfrac{1}{K_c} & \dfrac{L_n^3}{3\overline{EI}} + \dfrac{1}{K_{sy}} & \dfrac{L_n^2}{2\overline{EI}} \\ 0 & \dfrac{L_n^2}{2\overline{EI}} & \dfrac{L_n}{\overline{EI}} \end{bmatrix} \begin{bmatrix} X \\ Y \\ M \end{bmatrix} \tag{1}$$

where the equivalent properties are

$$\begin{aligned} \overline{EA} &= \frac{3\left(2l_1\cos\theta + l_2\right)EI \cdot EA}{l_1^2 \sin^2\theta\left(2l_1 + 3l_2\right)EA + 3\left(2\cos^2\theta l_1 + l_2\right)EI} \\ \overline{EI} &= \frac{2l_1\cos\theta + l_2}{2l_1 + l_2} \\ K_c &= \frac{EI}{l_1 \sin\theta\left(l_1 + l_2\right)\left(2l_1\cos\theta + l_2\right)n} \\ K_{sy} &= \frac{3}{2}\frac{EI}{l_1 l_2\left(1-\cos\theta\right)\left(l_1\cos\theta + l_2\right)n} \end{aligned} \tag{2}$$

The number of the corrugation units in the corrugated panel is represented by n, and the length of the entire corrugated panel is represented by L_n. The Young's modulus, area and second moment of area are denoted as E, A and I respectively. It should be noted that the axial extension is taken into account when calculating the deflection in x direction.

The equivalent beam element has two nodes i and j as shown in Figure 2. According to Equations (1) and (2), the deflections of the two nodes can be obtained in response to the external loads. Thus, the stiffness matrix of the beam can be built by considering the

equilibrium of the beam. For example, when node *j* is constrained, the deflections of node *i* can be written as

$$\begin{bmatrix} u_i \\ v_i \\ \alpha_i \end{bmatrix} = \begin{bmatrix} \frac{L_n}{\overline{EA}} & \frac{1}{K_c} & 0 \\ \frac{1}{K_c} & \frac{L_n^3}{3\overline{EI}} + \frac{1}{K_{sy}} & -\frac{L_n^2}{2\overline{EI}} \\ 0 & -\frac{L_n^2}{2\overline{EI}} & \frac{L_n}{\overline{EI}} \end{bmatrix} \begin{bmatrix} X_i \\ Y_i \\ M_i \end{bmatrix} \tag{3}$$

Inverting this equation will give the external loads on node *i* as

$$\begin{bmatrix} X_i \\ Y_i \\ M_i \end{bmatrix} = [K_{11}] \begin{bmatrix} u_i \\ v_i \\ \alpha_i \end{bmatrix} \tag{4}$$

Taking the equilibrium relationship of the beam element into consideration, we can obtain the loads at node *j* as

$$\begin{bmatrix} X_j \\ Y_j \\ M_j \end{bmatrix} = [K_{21}] \begin{bmatrix} u_i \\ v_i \\ \alpha_i \end{bmatrix} \tag{5}$$

Repeating the step when node *i* is constrained, and combining the results from the two cases will finally give the stiffness matrix of the beam element as

$$\begin{bmatrix} X_i \\ Y_i \\ M_i \\ X_j \\ Y_j \\ M_j \end{bmatrix} = \begin{bmatrix} K_{11} & K_{12} \\ K_{21} & K_{22} \end{bmatrix} \begin{bmatrix} u_i \\ v_i \\ \alpha_i \\ u_j \\ v_j \\ \alpha_j \end{bmatrix} \tag{6}$$

where K_{12}, K_{12}, K_{21}, K_{22} are sub-blocks (three-by-three) of the stiffness matrix of the equivalent beam element.

As illustrated in Figure 2, the compliant structure is composed of three parts: two corrugated panels with different extension stiffnesses, which are modelled by two equivalent elements, and a connection part between them, which can be modelled by normal beam elements. The stiffness matrix of the compliant structure is then assembled to calculate its deformation. For the compliant structure, two sets of geometry parameters are needed, in which the superscripts ‘1’ or ‘2’ before the variables represent the two corrugated panels. The

length and the height of the structure are represented by a and b. The actuation force and the concentrated aerodynamic force are represented by F and P respectively.

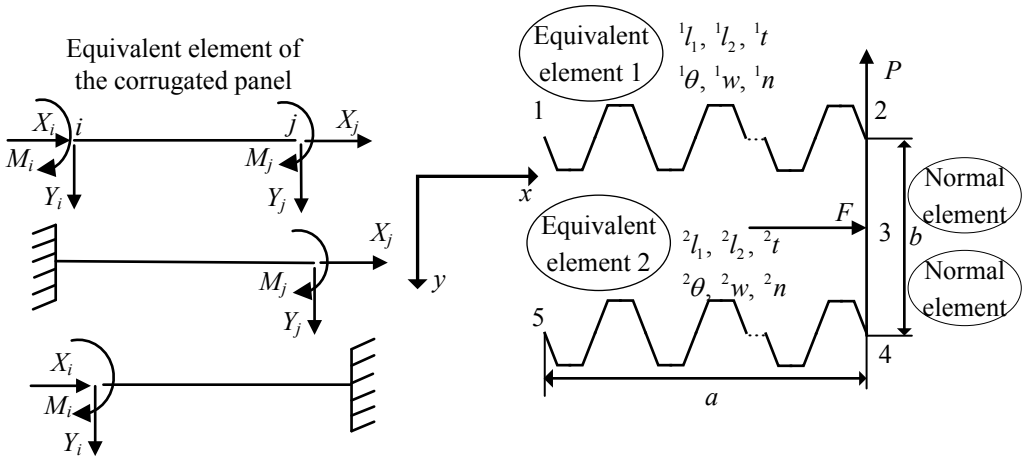

Figure 2. Compliant structures based on trapezoidal corrugated panels

3. DEVELOPMENT OF A DEMONSTRATION MODEL

3.1 General description

The structure of the morphing winglet consists of three main components: the leading edge, the compliant structure and the trailing edge as shown in Figure 3.

In this paper, the model is mainly for structural demonstration, thus the NACA 0024 airfoil is used and the chord is 0.25m, considering the manufacturing cost and convenience. The spanwise length of the structure, a, is 0.12m.

The compliant structure based on the unsymmetrical stiffness is supposed to carry the aerodynamic loads on the winglet, while the airfoil shape needs to be maintained especially in the leading and trailing edges. In the current study, flexible honeycomb structures are used to provide and maintain the aerodynamic profile in the leading and trailing edges. The zero Poisson's ratio honeycomb design is employed, which has been applied in wing span morphing [14]. The honeycomb structures are connected to the corrugated panels evenly in the spanwise direction. In this demosntration model, an eletrical linear actuator is used. The actuator is pinned at both ends, so that it can rotate with the structure. Part of the upper panel in the middle is removed to install the actuator and avoid interference. An elastomer skin, such as silicone rubber, will be used, which will be supported by the stringers. A fairing will also be added to provide an aerodynamic surface at the tip of the compliant structure.

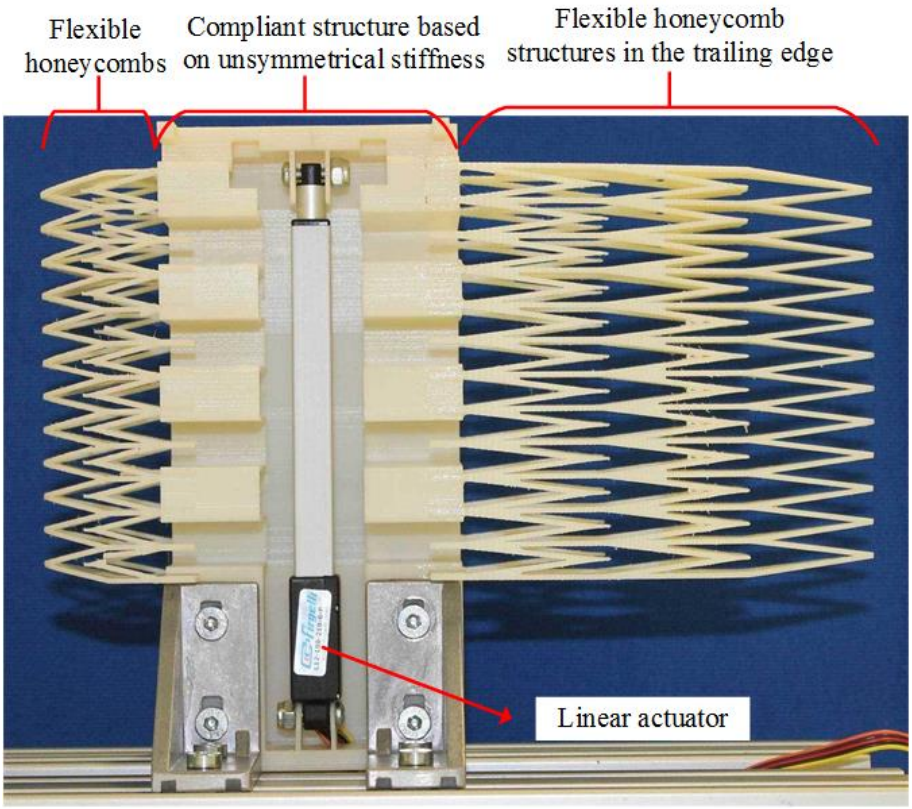

Figure 3. The morphing winglet demonstrator (stringers and fairing are not included)

3.2 Optimization of the compliant structure

By employing the equivalent model, the calculation time for the compliant structure is reduced significantly, which leads to a faster optimization. The compliant structure based on the unsymmetrical stiffness is optimized to reduce the actuation force, while the entire height of the compliant structure, B ($B=b+{}^{1}l_1\sin{}^{1}\theta+{}^{2}l_2\sin{}^{2}\theta$), should be constrained to fit within the thickness of the airfoil. A sequence of optimization is performed to find the fittest geometry variables. The ranges of the variables for the optimization are

$$\begin{cases} {}^{1,2}l_1 \left(0.01 \le {}^{1,2}l_1 \le 0.025 \text{ m}\right) \\ {}^{1,2}\theta \left(0 \le {}^{1,2}\theta \le 90\ ^{\circ}\right) \\ {}^{1,2}n \left(1 \le {}^{1,2}n \le 4,\ {}^{1,2}n = 1, 2\ldots\right) \\ {}^{1,2}t \ \left(0.0015 \le {}^{1,2}t \le 0.005 \text{ m}\right) \end{cases} \tag{7}$$

The variables need to satisfy the geometry constraints, which are

$$\begin{cases} \frac{1}{2}h_{act}Coeff_{safety} \le b \cdot LA^b + {}^1l_1 \sin {}^1\theta \\ \frac{1}{2}h_{act}Loc_{act}Coeff_{safety} \le b\left(1-Loc_{act}\right) - {}^2l_1 \sin {}^2\theta \\ {}^1l_1 \sin {}^1\theta + {}^2l_1 \sin {}^2\theta \le 0.75b \\ {}^1t \le \frac{1}{5}{}^1l_1; \quad {}^1t \le \frac{1}{5}{}^1l_2 \\ {}^2t \le \frac{1}{5}{}^2l_1; \quad {}^2t \le \frac{1}{5}{}^2l_2 \\ 2{}^1l_1 \cos {}^1\theta \le \frac{a}{2{}^1n} \\ 2{}^2l_1 \cos {}^2\theta \le \frac{a}{2{}^2n} \end{cases} \tag{8}$$

Here, the parameters h_{act}, $Coeff_{safety}$ and LA^b correspond to the height of actuator, the safety coefficient preventing the interference and the non-dimensional location of the actuator respectively. These parameters are fixed in the optimization with values of 0.02m, 1.5 and 0.3.

The maximum Von Mises stress σ_v in the compliant structure should not exceed the yield stress of the material σ_y. Thus another constraint is employed in the optimization as

$$\sigma_v \le \sigma_y \tag{9}$$

Here, the yield stress is 30 MPa is the current study.

The Matlab® GA optimization toolbox [16] is applied to find the minimum actuation force required for a specific rotation angle. The entire height of the compliant structure will be influenced by the optimal variables, and thus a series of optimization cases are performed to find the relationship between the height between the two corrugated panels b and entire height B. Before the height is determined, the width of the corrugated panels has been found irrelevant to the optimal variables since the equivalent model of the corrugated panel is inherently a 2-dimensional model. A sequence of optimization cases with the same Matlab GA setting and state is performed to verify the assumption. While the required actuation force changes with the width of the corrugated panels, the optimized variables have almost no differences. With this assumption, the relationship between the entire height of the compliant structure B and the distance between two corrugated panels b is shown in Figure 4(a), which gives a quite linear trend between them. Then, the compliant structure is accommodated within the airfoil, as shown in Figure 4(b). The parameter b can be interpolated according to the entire height B, and then the width of the corrugated panels can be determined according to the airfoil thickness. The width of the compliant structure is 0.0875m in these optimization cases.

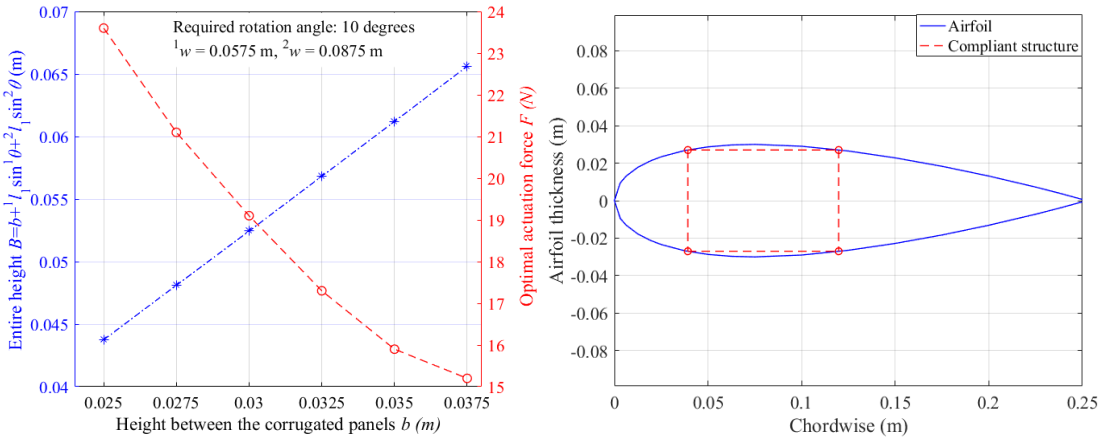

Figure 4. (a) Optimal height and actuation force, (b) Compliant structure in the airfoil.

In the current study, the entire height of the compliant structure is 0.054m, and the width of the compliant structure accounts for around 35% chord, which starts at 15%. Minor modifications are made considering the installation and the other details, which will not influence the focus of this paper. The optimized variables of the corrugated panels are listed in Table 1 and the geometry is plotted in Figure 5(a). The optimal results show that the optimization provides a much more flexible upper corrugated panel compared to the lower panel, which introduces a significant stiffness asymmetry in the compliant structure. The thicknesses of both panels are at their lower bounds, indicating the requirement of the smallest actuation force. Also, it can be seen the entire height of the structure will be increased by ${}^1l_1$ since the angle ${}^1\theta$ is around 90 degrees but ${}^2l_1$ has almost no influence on the entire height due to the small ${}^2\theta$.

Table 1: Optimal variables of the compliant structure

Upper corrugated panel		Lower corrugated panel	
${}^1l_1$	0.0213 m	${}^2l_1$	0.0115 m
${}^1\theta$	89.98 degree	${}^2\theta$	5.60 degree
${}^1n$	4	${}^2n$	1
${}^1t$	0.0015 m	${}^2t$	0.0015 m

The leading and trailing edges of the airfoil are provided by the flexible honeycomb structure, as shown in Figure 5(b). The equivalent modulus of the honeycomb in the transverse direction, E_x, has been derived in [14] as

$$E_x = E_m\left(\frac{t}{l}\right)^3 \frac{\sin\theta}{\frac{c}{l}\cos^2\theta} \tag{10}$$

A sequence of optimizations is performed to minimize the modulus. Except for the geometry constraints, the constraint of the connection to the corrugated panels is also included: the number of honeycomb units should be an integer multiple of the number of corrugation units to ensure the honeycombs are evenly connected to the corrugated panels at both leading and trailing edges, and the loads can be transferred evenly through the structure.

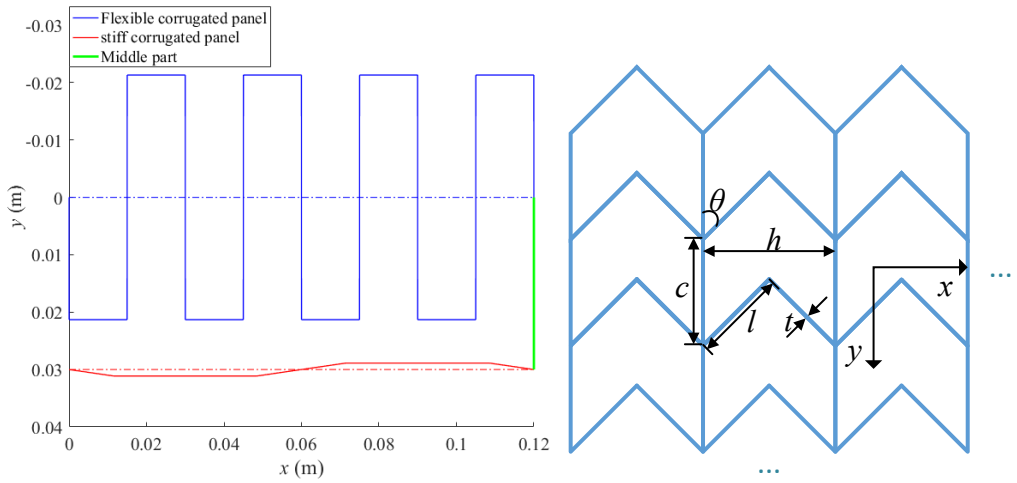

Figure 5. (a) Compliant structure based on corrugated panels, (b) Flexible honeycomb structure

3.3 Functional model test

A function model is fabricated using a 3D printer. Due to the limitation of the maximum size the printer can build, two parts of the morphing winglet are printed seperately and then assembled and glued together.

The linear actuator is controlled by a control board and powerd by a 6V DC battery. A 9% intial stroke is given to the actuator to reach its installation position. In the static test, the position of the actuator stroke varies from 9% to 29% and then back to 9%, which is recorded by a digital camera. As shown in Figure 6, the stiffness asymmetry leads to a rotation angle of the compliant structure, β, as well as a change of the dihedral angle, θ, if the compliant structure works as a transition section connected to an endboard fixed-geometry winglet. According to the geometry relationship in Figure 6, the introduced dihedral angle change θ is larger than the rotation angle β. The angles θ and β are measured from the pictures, which are equal to 23 degrees and 49 degrees respectively.

4. CONCLUSIONS

In this paper, the development of a compliant structure of a morphing winglet is introduced. Rotation deformation of the compliant structure can be induced by a linear actuator, and the current study integrates the compliant structure into an airfoil.

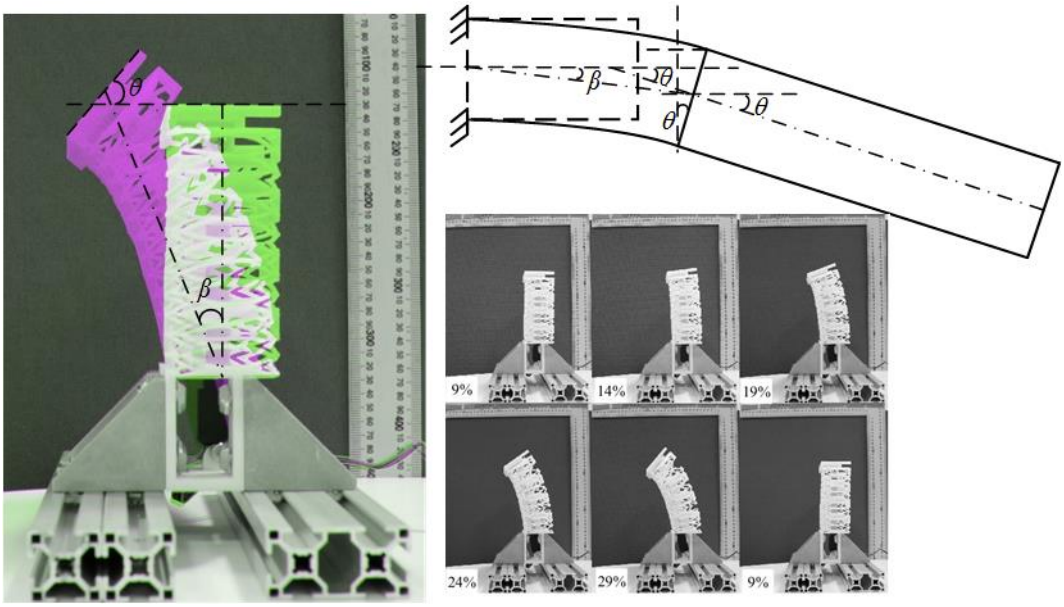

Figure 6. Static test demonstration when the actuator stroke position varies from 9% to 29%

Trapezoidal corrugated panels are used in the compliant structrues. An equivalent model of the corrugated panel is built, which is expressed by its stiffness matrix. The equivalent model is applied in the optimization to find the optimal stiffness allocation in the structure. To fit within the thickness of the airfoil, a sequence of optimization cases is performed to find the proper height of the compliant structure. To provide the airfoil shape, flexible honeycomb structures are used in the leading and trailing edges, which are evenly connected to the corrugated panels after the optimization of the honeycomb structures is performed.

A functional model is manufactured using 3D printing, and the static tests validate the deformation of the model, which is driven by a linear actuator. The rotation angle is recorded while a larger dihedral angle is found if the proposed model works as a transition section connected to an endboard of a fixed-geometry winglet, which shows a promising structural solution for a morphing winglet.

ACKNOWLEDGEMENTS

Chen Wang would like to thank the China Scholarship Council (CSC) and the College of Engineering of Swansea University for providing his PhD scholarship.

REFERENCES

1. Smith, D.D., Ajaj, R.M., Isikveren, A.T., et al., *Multi-objective optimization for the multiphase design of active polymorphing wings.* Journal of Aircraft, 2012. **49**(4): p. 1153-1160.

2. Falcão, L., Gomes, A.A., and Suleman, A., *Aero-structural Design Optimization of a Morphing Wingtip.* Journal of Intelligent Material Systems and Structures, 2011. **22**(10): p. 1113-1124.
3. Daniele, E., De Fenza, A., and Della Vecchia, P., *Conceptual adaptive wing-tip design for pollution reductions.* Journal of Intelligent Material Systems and Structures, 2012. **23**(11): p. 1197-1212.
4. Gatto, A., Mattioni, F., and Friswell, M.I., *Experimental Investigation of Bistable Winglets to Enhance Aircraft Wing Lift Takeoff Capability.* Journal of Aircraft, 2009. **46**(2): p. 647-655.
5. Castrichini, A., Siddaramaiah, V.H., Calderon, D.E., et al., *Preliminary investigation of use of flexible folding wing tips for static and dynamic load alleviation.* The Aeronautical Journal, 2017. **121**(1235): p. 73-94.
6. Campanile, L.F., *Initial thoughts on weight penalty effects in shape-adaptable systems.* Journal of Intelligent Material Systems and Structures, 2005. **16**(1): p. 47-56.
7. Richard Degenhardt, D.L.J.C., Prof, Karagiannis, D., Stamatelos, D., et al., *Airfoil morphing based on SMA actuation technology.* Aircraft Engineering and Aerospace Technology: An International Journal, 2014. **86**(4): p. 295-306.
8. Bilgen, O. and Friswell, M.I., *Implementation of a continuous-inextensible-surface piezocomposite airfoil.* Journal of Aircraft, 2012. **50**(2): p. 508-518.
9. Dayyani, I., Khodaparast, H.H., Woods, B.K., et al., *The design of a coated composite corrugated skin for the camber morphing airfoil.* Journal of Intelligent Material Systems and Structures, 2015. **26**(13): p. 1592-1608.
10. Bubert, E.A., Woods, B.K.S., Lee, K., et al., *Design and fabrication of a passive 1D morphing aircraft skin.* Journal of Intelligent Material Systems and Structures, 2010. **21**(17): p. 1699-1717.
11. Ermakova, A. and Dayyani, I., *Shape optimisation of composite corrugated morphing skins.* Composites Part B: Engineering.
12. Olympio, K.R. and Gandhi, F., *Flexible Skins for Morphing Aircraft Using Cellular Honeycomb Cores.* Journal of Intelligent Material Systems and Structures, 2010. **21**(17): p. 1719-1735.
13. Wang, C., Khodaparast, H.H., and Friswell, M.I., *Conceptual study of a morphing winglet based on unsymmetrical stiffness.* Aerospace Science and Technology, 2016. **58**: p. 546-558.
14. Vocke III, R.D., Kothera, C.S., Woods, B.K.S., et al., *Development and testing of a span-extending morphing wing.* Journal of Intelligent Material Systems and Structures, 2011. **22**(9): p. 879-890.
15. Wang, C., Khodaparast, H.H., Friswell, M.I., et al., *An equivalent model of corrugated panels with axial and bending coupling.* Computers & Structures, 2017. **183**: p. 61-72.
16. *Matlab R2014b*, 2014, The MathWorks Inc.

VIII ECCOMAS Thematic Conference on Smart Structures and Materials
SMART 2017
A. Güemes, A. Benjeddou, J. Rodellar and J. Leng (Eds)

NUMERICAL INVESTIGATION OF DAMPING OF TORSIONAL BEAM VIBRATIONS BY VISCOUS BIMOMENTS

David Hoffmeyer & Jan Høgsberg

Department of Mechanical Engineering, Technical University of Denmark
Nils Koppels Allé, building 404, DK-2800 Kongens Lyngby, Denmark
e-mail: davhoff@mek.dtu.dk, jhg@mek.dtu.dk, www.dtu.dk

Key words: Torsional beam vibrations, damping, warping, viscous bimoment, complex natural frequency, finite element method.

Abstract. Damping of torsional beam vibrations of slender beam–structures with thin–walled cross–sections is investigated. Analytical results from solving the differential equation gover–ning torsion with viscous bimoments imposed at the boundary, are compared with a numerical approach with three–dimensional, isoparametric elements. The viscous bimoments act on the axial warping displacements associated with inhomogeneous torsion, and are in a numerical for-mat realized by suitable configurations of concentrated, axial forces describing discrete dampers. It is illustrated by an example that significant damping ratios may be obtained for a beam with an open cross–section.

1 INTRODUCTION

Torsional vibrations may be induced in slender, thin–walled beam–structures by e.g. wind, if the loads on the beam act with a certain eccentricity relative to the shear center of the cross-section. For beams with asymmetric cross-sections the elastic and shear centers do not coincide, whereby the flexural and torsional vibrations couple. In both cases the total dynamic response may be damped by damping the torsional motion of the beam. Slender structures like long bridge decks, aircraft wings or wind turbine blades may be prone to aerodynamic instabilities like flutter, where flexural and torsional vibrations couple. Flutter is associated with apparent negative damping that cannot be sufficiently compensated by the inherent structural damping. To avoid flutter and e.g. to reduce fatigue stresses by aerodynamic forces, supplemental damping is therefore required.

Torsional vibrations of thin–walled beams are associated with inhomogeneous torsion which generates out-of-plane, axial warping displacements that are often significant at the boundaries of beams with open cross-sections. The free, torsional vibration characteristics including warping were originally investigated by Gere [1] who solved for the natural frequencies and mode shapes of beams with various boundary conditions, and by Carr [2] where an energy apporach was applied to obtain approximate frequency equations for a few combinations of boundary conditions.

Subsequently Gere and Lin [3] studied the coupling between flexural and torsional vibrations, and the coupling with restrained thin–walled beams by Lin [4]. Numerical results using a finite element approach were compared with analytical results by Mei [5], and Friberg [6] derived an exact dynamic element stiffness matrix, though without the effect of warping. Analytical solutions of frequencies and mode shapes for prismatic beams excited by harmonic, torsional loads have been derived by Augustyn and Kozién [7].

Damping of torsional vibrations has only briefly been addressed in the literature. Narayanan and Malik [8] attached viscoelastic layers to the flanges of a beam with an open cross–section; Jansen and van der Steen [9] considered damping of torsional vibrations in oil well drillstrings; and recently Augustyn and Kozién [10, 11] glued piezoelectric actuators to a beam to reduce the torsional vibrations. Christiano and Salmela [12] showed that the restraining of warping results in an often considerable increase in natural frequency and change in vibration characteristics. This localized effect of restrained warping was utilized to introduce a substantial amount of supplemental damping by Høgsberg et. al. [13], where viscous boundary conditions were applied through pure bimoments at the supports. They solved the eigenvalue problem associated with free vibrations with respect to the complex-valued natural frequency and corresponding damping ratio. They demonstrated that significant damping ratios could be realized by these viscous bimoments at the beam supports.
The present paper performs a numerical investigation of the changed dynamic behaviour of thin-walled beams with applied viscous bimoments at the boundaries. The results in terms of natural frequencies and damping ratios are compared with [13]. The numerical procedure is based on a linear finite element approach with three-dimensional, isoparametric elements. In a simple numerical code, the bimoments are easily represented by concentrated, axial forces distributed over the cross-section. These viscous forces are proportional to the velocity of the given node and are added to the equations of motion by an influence vector describing the points of application. As they are proportional with velocity, they constitute a damping term and result in a modified damping matrix. Setting up the equations of motion in a state-space format yields an eigenvalue problem, from which the corresponding complex natural frequencies and damping ratios are extracted.

2 UNCOUPLED TORSIONAL VIBRATIONS

Consider a beam element of length ℓ, axial coordinate x and transverse axes $\{y, z\}$. The axial displacement is $u(x, y, z, t)$ and the angle of twist is $\theta(x, t)$ as seen in Fig. $1a$. In the present analysis it is assumed that flexural and torsional vibrations uncouple because of coinciding elastic centers.
The differential equation governing the torsional vibration problem is set up by energy relations which require the elastic and kinetic energy. The elastic strain energy contains contribution from homogeneous and inhomogeneous torsion, respectively given as

$$U = \int_\ell \tfrac{1}{2}\, GK(\theta')^2\, dx + \int_\ell \tfrac{1}{2}\, EI_\psi(\theta'')^2\, dx \tag{1}$$

where G is the shear modulus, K is the torsion stiffness parameter, E is Young's modulus and I_ψ is the warping moment of inertia with ψ indicating the sector–coordinate or warping function.

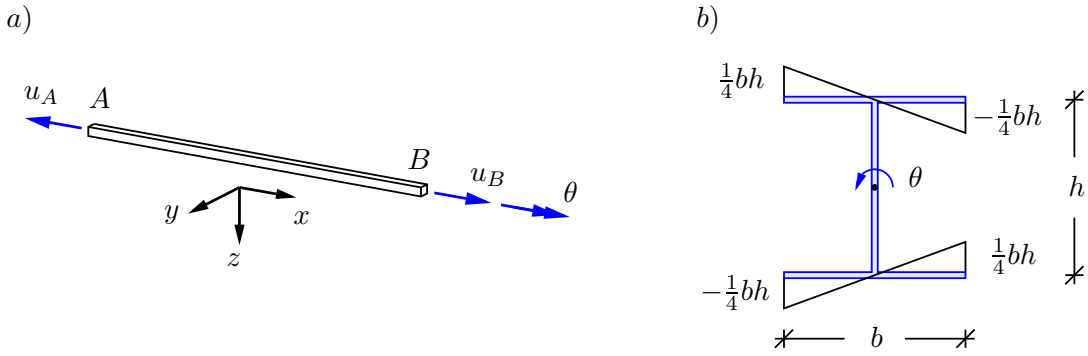

Figure 1: Degrees of freedom and coordinates a) and sector–coordinate ψ for an I–profile with a positive angle of twist b).

For an I–profile the distribution of the sector–coordinate is shown in Fig. 1b. The kinetic energy o the torsional motion is

$$T = \int_\ell \tfrac{1}{2}\,\rho J \dot{\theta}^2\,dx \tag{2}$$

where ρ is the mass density and J is the polar moment of inertia taking the distribution of the mass into account. Energy dissipation may be defined through a viscous damping coefficient either distributed along the beam by $c_0(x)$ or acting at discrete points via c described by Dirac's delta function δ. As dampers may be applied at discrete points the latter is relevant whereby the dissipated energy D then takes the form:

$$D = \int_\ell c_0(x)\,\dot{\theta}^2\,dx = \int_\ell c\,\delta(x - x_0)\,\dot{\theta}^2\,dx \tag{3}$$

where x_0 indicates the point of application of the discrete damper. In the case of damped vibrations the change in mechanical energy is balanced by the dissipated energy, $\dot{U} + \dot{T} = -D$. Performing the differentiation of the energy balance and using integration by parts yields the governing differential equation as

$$EI_\psi \theta'''' - GK\theta'' + \rho J\ddot{\theta} = 0 \tag{4}$$

As no continuous form of damping is intended, the last expression in (3) is instead applied as a boundary condition. Thus, (4) is valid between the points of application of external dampers. A time harmonic solution of the form $\theta = \varphi\,\mathrm{e}^{i\omega t}$ may be assumed with ω being the natural frequency and φ the spatial solution. Inserting the frequency solution into (4) and following the approach by Gere [1], the spatial solution may be expressed as

$$\varphi = D_1\cosh(\alpha x) + D_2\sinh(\alpha x) + D_3\cos(\beta x) + D_4\sin(\beta x) \tag{5}$$

introducing the four integrations constants D_1 to D_4 – determined by the boundary conditions – and the two apparent and real–valued wave numbers defined as

$$\alpha^2 = \sqrt{\tfrac{1}{4}k^4 + \lambda^4} + \tfrac{1}{2}k^2 \qquad , \qquad \beta^2 = \sqrt{\tfrac{1}{4}k^4 + \lambda^4} - \tfrac{1}{2}k^2 \tag{6}$$

This formulation of the solution introduces the warping length scale k, wave speed v and scaled wave number λ respectively as

$$k^2 = \frac{GK}{EI_\psi} \quad , \quad v^2 = \frac{GK}{\rho J} \quad , \quad \lambda^4 = \left(\frac{k\omega}{v}\right)^2 \tag{7}$$

It is noted that v represents the wave speed for the homogeneous torsion problem. The spatial solution to the torsion problem in terms of the vibration form is obtained from (5) by use of relevant boundary conditions. Applying the boundary conditions yields transcendental equations which must be solved iteratively for the combined set of α and β. One wave number is then given by the other through (6), and the use of the third expression in (7) determines the frequency ω. For more details see e.g. [1, 13].

2.1 Viscous Bimoment at the Boundary

A viscous condition on the boundary may be imposed in several ways. In [13] a viscous normal stress distribution was applied at the beam supports acting through the axial displacement producing a bimoment. This normal stress was distributed across the cross-section of the beam in a continuous manner. In the case of active control a discrete device would produce a concentrated force proportional to the velocity at specific points at the cross-section. A viscous, concentrated force $F_d(y, z, t)$ at the boundary is

$$F_d = \pm\, c\, \dot{u}_d \tag{8}$$

where c is a viscous damping coefficient and $\dot{u}_d(y, z, t)$ is the axial velocity, positive in the x–direction. The force is defined as positive in tension, whereby the "+" in (8) refers to the left end of the beam at $x = 0$ and the "−" refers to the right end at $x = \ell$. The axial displacement due to torsion is given through the sector–coordinate, and the corresponding velocity is

$$\dot{u}_d = -\psi\, \dot{\theta}'_d \tag{9}$$

see e.g. Vlasov [14]. A series of discrete dampers may be applied at the boundary each dissipating energy. Thus the second expression in (3) indicates a sum of the viscous damping coefficients associated with the given damper and the velocity at that particular point. In combination with (8) the rate of external work D produced by the dampers is formulated as the sum of the contributions of the viscous forces multiplied with the energy conjugate velocity by

$$D = \pm \sum_j F_{d,j}\, \dot{u}_{d,j} = \pm \sum_j c\, \dot{u}^2_{d,j} = \pm \big(\dot{\theta}'_d\big)^2 \sum_j c\, \psi_j^2 \tag{10}$$

where ψ_j is the sector–coordinate at the location of the j'th damper and c is here assumed to be constant for all dampers. A bimoment as shown in Fig. 2*a* is usually noted with a double arrow due to the classical example shown in Fig. 2*b*. Here two opposite bending moments are applied at the flanges. Vectorially they add up to zero, and a pure bimoment is thus a kinematic and not a static condition. It does not generate a resulting force (or moment) but acts as a concentrated change in rotation curvature. The bending moments, however, may be decomposed into force couples as seen in Fig. 2*c*. A given configuration of concentrated, axial forces therefore generates

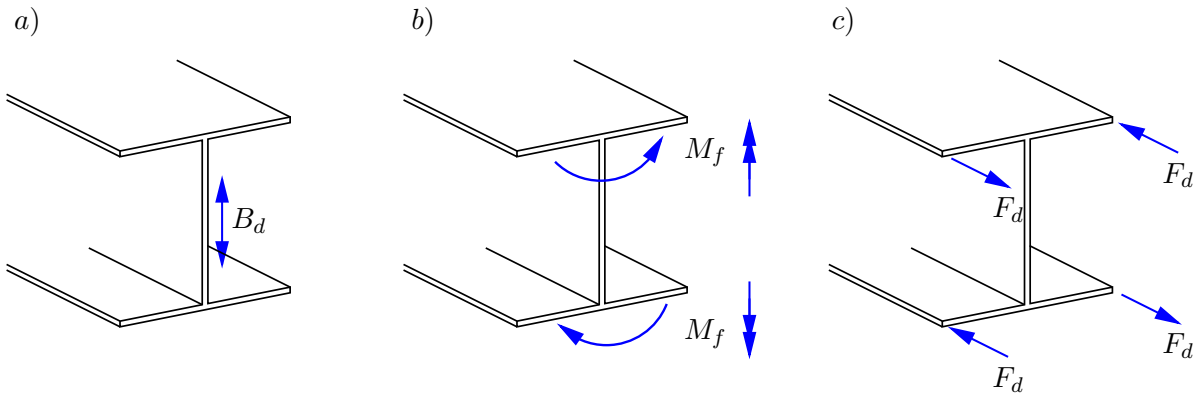

Figure 2: I–profile beam with a bimoment a), bending moments at the flanges generating the bimoment b) and equivalent configuration of concentrated, axial forces c).

a bimoment through the sector–coordinate. By definition the bimoment produces work through the negative gradient of the angle of twist, see e.g. Vlasov [14]. Thus, the rate of work produced by a bimoment is $D = -\dot{\theta}'_d\, B_d$. Equating this rate of work with (10) yields

$$B_d = \mp\, \dot{\theta}'_d \sum_j c\, \psi_j^2 \tag{11}$$

The bimoment produced by the dampers $B_d(t)$ must be balanced by the section bimoment at the boundary $B(x,t) = -EI_\psi \theta''(x,t)$. The dynamic boundary condition then takes the form

$$\theta''_d \mp \eta\, \dot{\theta}'_d = 0 \tag{12}$$

with the effective viscous damping parameter $\eta = \sum_j c\, \psi_j^2 / EI_\psi$. The form of (12) is identical to [13] with exception of the effective parameter η. Here the viscous damping coefficient c is scaled relative to the amount of dampers, the corresponding sector–coordinates at the points of application and the warping stiffness EI_ψ. Inserting the frequency solution $\theta = \varphi\, \mathrm{e}^{i\omega t}$ yields the harmonic boundary condition

$$\varphi'' \mp i\omega\eta\varphi' = 0 \tag{13}$$

which is directly applicable in connection with the transcendental equations governing the torsional vibration problem.

3 DAMPING OF TORSIONAL VIBRATIONS

When not considering a beam element but modelling the entire structure by a finite element procedure, a discretized, multi–degree–of–freedom system with n degrees of freedom may be assumed. The equations of motion are set up by the elastic, kinetic and dissipated energy. The elastic energy gives the stiffness contribution through the stiffness matrix $\mathbf{K}$, the kinetic energy gives the inertia contribution through the mass matrix $\mathbf{M}$ and the dissipated energy gives the applied, discrete viscous forces as described in (8) and in the second term in (10). The energy balance $\dot{T} + \dot{U} = -D$ then gives

$$\mathbf{M}\ddot{\mathbf{q}}(t) + \mathbf{K}\mathbf{q}(t) = -\mathbf{f}_d(t) \tag{14}$$

where $\mathbf{q}(t)$ is a column vector containing the degrees of freedom and $\mathbf{f}_d(t)$ are the externally applied viscous forces. In this case the inherent structural damping is neglected. Damping may be constituted as a series of dampers modelled as equivalent concentrated, viscous forces acting through a viscous damping coefficient c and the velocity of the corresponding nodes in the discretized system:

$$\mathbf{f}_d(t) = \left(\sum_j^{nd} c_j \mathbf{w}_j \mathbf{w}_j^T \right) \dot{\mathbf{q}}(t) = \widetilde{\mathbf{C}}\dot{\mathbf{q}}(t) \tag{15}$$

Here c_j is the viscous damping coefficient associated with the j'th damper and $\mathbf{w}_j$ is an influence vector describing the points in the structure connected to the damper. The column vector $\mathbf{w}_j$ thus contains 1 at the location of the damper and otherwise 0's. In this case, however, a constant viscous damping coefficient is used for all dampers. Inserting (15) into (14) yields the equations of motion with a modified damping matrix

$$\mathbf{M}\ddot{\mathbf{q}} + \widetilde{\mathbf{C}}\dot{\mathbf{q}} + \mathbf{K}\mathbf{q} = \mathbf{0} \tag{16}$$

These modified equations of motion with damping included yields a quadratic eigenvalue problem. However, they may be formulated in a state–space format

$$\frac{d}{dt}\begin{bmatrix}\mathbf{q} \\ \dot{\mathbf{q}}\end{bmatrix} = \begin{bmatrix}\mathbf{0} & \mathbf{I} \\ -\mathbf{M}^{-1}\mathbf{K} & -\mathbf{M}^{-1}\,\widetilde{\mathbf{C}}\end{bmatrix}\begin{bmatrix}\mathbf{q} \\ \dot{\mathbf{q}}\end{bmatrix} \tag{17}$$

where $\mathbf{I}$ is a $n \times n$ identity matrix. Assuming a time–dependent, partial solution the state–space format constitutes an ordinary eigenvalue problem, from which the eigenvalue $i\omega$ and corresponding eigenvector may be extracted. For damped vibrations the natural frequency ω is generally complex–valued and usually expressed as

$$\omega = |\omega| \left(\sqrt{1-\zeta^2} + i\zeta \right) \tag{18}$$

with ζ being the damping ratio defined by the imaginary part of the natural frequency

$$\zeta = \frac{\mathrm{Im}[\omega]}{|\omega|} \tag{19}$$

In the complex plane the natural frequency ω constitutes a semicircle between the undamped frequency ω_0 and the corresponding upper limit frequency ω_∞. In the former case the damper(s) have no effect and the viscous damping coefficient therefore is $c = 0$. In the corresponding extreme case where $c \to \infty$ the damper locks and the node, at which the damper is attached, simply becomes restrained against axial movement.

4 EXAMPLE

In the following an example is used to illustrate the theory from Section 2, the numerical procedure established in Section 3 and to illustrate the use of concentrated, axial forces as a measure of damping.

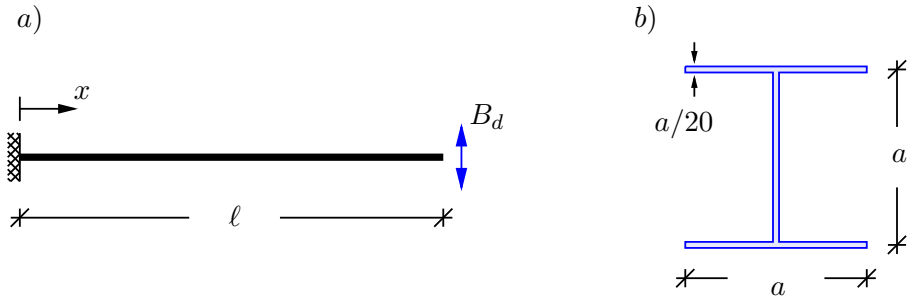

Figure 3: Fixed–free beam with viscous bimoment B_d at $x = \ell$ *a*) and I–profile cross–section *b*).

4.1 Damping of a fixed–free beam.

Consider the fixed–free beam in Fig. 3*a*. The beam has the length ℓ, is fixed at $x = 0$ with restrained rotation and warping and is free at $x = \ell$. The beam cross–section is an open I–profile with height and width a and thickness $t = a/20$, see Fig. 3b. With the chosen cross-section, material and length of the beam the warping length scale normalized with the length of the beam is $k\ell = 3$ and thus represents a slender structure. For a particular viscous bimoment at the boundary at $x = \ell$, the complex natural frequency ω and corresponding damping ratio ζ are obtained by determining the integration constants in (5) by use of the boundary conditions. For the fixed–free beam with damping at $x = \ell$ the boundary conditions are

$$\varphi(0) = 0 \quad , \quad \varphi'(0) = 0 \quad , \quad \varphi''(\ell) + i\omega\eta\varphi'(\ell) = 0 \quad , \quad k^2\varphi'(\ell) - \varphi'''(\ell) = 0 \tag{20}$$

With these homogeneous boundary conditions and the homogeneous differential equation (4) the torsion problem constitutes an eigenvalue problem where the spatial solution (5) leads to a transcendental equation. In [13] it is derived as

$$\begin{aligned} &\frac{(\alpha\ell)^4 + (\beta\ell)^4}{(\alpha\ell)^2(\beta\ell)^2}\cosh(\alpha\ell)\cos(\beta\ell) + \frac{(\alpha\ell)^2 + (\beta\ell)^2}{(\alpha\ell)(\beta\ell)}\sinh(\alpha\ell)\sin(\beta\ell) + 2 \\ &+ i\omega\eta\ell\frac{(\alpha\ell)^2 + (\beta\ell)^2}{(\alpha\ell)^2(\beta\ell)^2}\cosh(\alpha\ell)\cos(\beta\ell)\big[\alpha\ell\,\tanh(\alpha\ell) + \beta\ell\,\tan(\beta\ell)\big] = 0 \end{aligned} \tag{21}$$

This equation is solved iteratively for $\alpha\ell$ and $\beta\ell$, while the third expression in (7) determines the frequency and by (19) the damping ratio is found. In obtaining a semi–circle in the complex plane, illustrating the variation of the frequency, the viscous damping coefficient c – contained within the effective damping parameter η – is varied in the interval $c \in [0\,;\,\infty[$. In this example a series of configurations for the distribution of discrete dampers is applied, see. Fig. 4. The first configuration seen in Fig. 4*a* consists of a single damper applied at one corner of the I–profile, and the resulting warping of the cross–section is thus only partly restrained. The second configuration is a more effective measure of restraining warping as two dampers are located at opposite corners where the largest warping displacements occur, see Fig. 1*b*. The profile may though still warp, and thus the third configuration is applied which effectively prevents the cross–section from warping almost completely. The two configurations in Figs. 4*a* and 4*b* do not constitute pure bimoments as they generate a normal force – and in the first case also

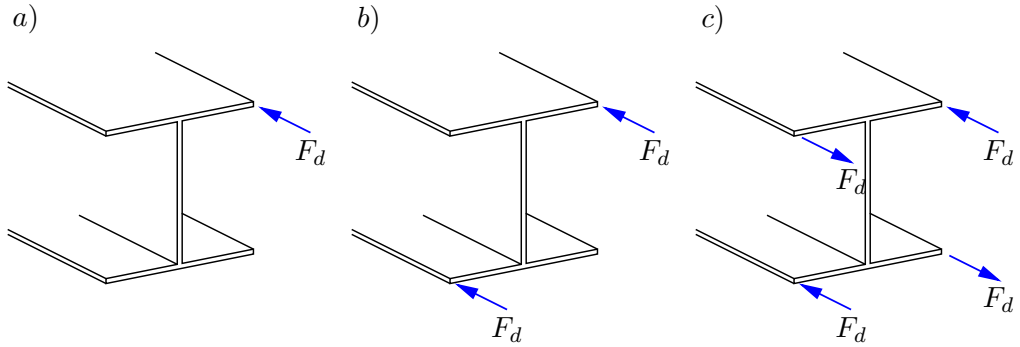

Figure 4: Three configurations of dampers; opposite corners a), all corners b) and distributed along flanges c).

bending moments – which must be accounted for. However, together with the third configuration they serve to illustrate the amount of damping that might by obtained by restraining at the right locations and with a proper number of dampers. The two configurations with non–pure bimoments may even serve to illustrate the possibility of damping coupled flexural vibrations, if the right structural set–up could be established.
The frequency loci and damping ratios for the three different configurations obtained by solving (21) are seen as the solid curves in Figs. 6a and 6b, respectively. By all three configurations of dampers the analytical model yields the same results in terms of undamped frequency ω_0 and the frequency with the dampers being locked ω_∞, corresponding to infinite damping. The dynamic boundary condition (12) restrains warping of the entire cross–section in a unified manner, and does not take the possible modes of warping with the dampers applied into account. The optimal value of the viscous damping parameter c_{opt} is therefore different in the three cases, but plotted as the effective damping parameter η the three sets of curves coincide as seen in Fig. 6b.

Frequencies and damping ratios

In the numerical comparison a standard finite element approach is used with solid, isoparametric elements. A special bi–cubic–linear element is exploited to model thin flanges and a cubic–bi–linear element for connections and corner – these are illustrated in Fig. 5.

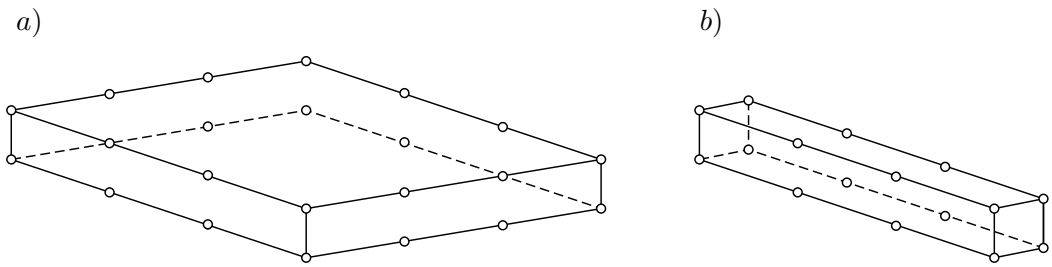

Figure 5: Isoparametric 24–node bi–cubic–linear a) and 16–node cubic–bi–linear b) element.

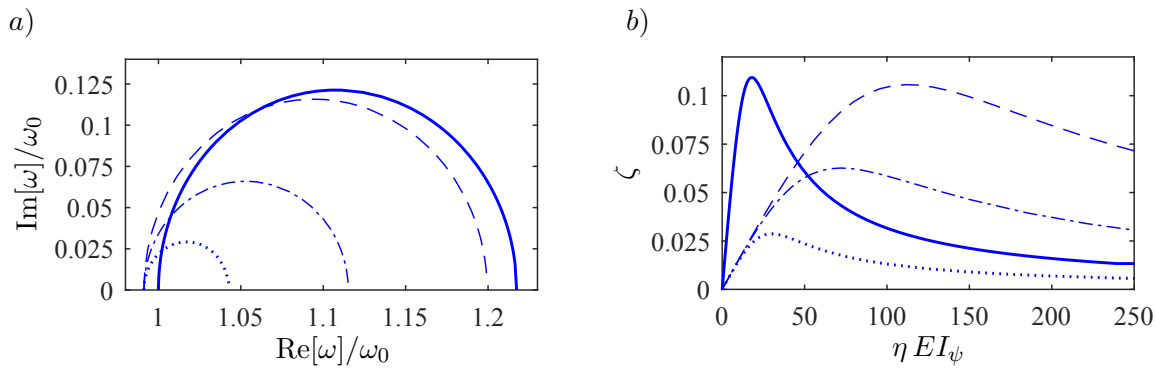

Figure 6: Frequency loci *a*) and damping ratios *b*) showing the results from (–) the analytical procedure and numerical procedure with (· · ·), (– · –) and (– –) representing the three bimoment configurations shown in Figs. 4*a*, 4*b* and 4*c* respectively.

The elements are intended for modelling of thin-walled beams where a linear interpolation across the thickness is sufficient and a cubic interpolation in the flange–wise direction to capture the parabolic stress variations associated with shear. The I–profile is thus sufficiently modelled with seven elements in the cross–section in the case of a simple static analysis. See e.g. Høgsberg & Krenk [15] for the use of a two–dimensional version of these elements for general cross–sectional analyses of thin–walled beams. In the present case, however, a further discretization of the cross–section is necessary in order to capture the warping effect. As two nodes across the thickness of the flanges are present, a damper at each node of the corners are applied in order to avoid any unnecessary distortion of the cross–section as the damping effect increases. Thus, the damping forces F_d in Fig. 4 constitute a set of two dampers.
Solving the eigenvalue problem in the state–space format for the complex frequency and corresponding damping ratio for the three configurations of dampers yield the frequency loci and distribution of the damping ratio illustrated with the non–solid curves in Fig. 6. As seen the undamped frequency ω_0^{FEM} is 0.9 % lower than the analytical solution. This may be due to the torsional mode in the numerical example not representing 'pure torsion' – as the analytical method requires – but contains some minor distortion, e.g. local deformations of the flanges. The analytical approach is independent of the shape of the cross–section and only works through the cross-sectional parameters, but a three–dimensional numerical model takes this into account. In the case of $c \to \infty$ the boundary condition (12) completely restrains the warping at the free end, and the increment, $(\omega_\infty - \omega_0)/\omega_0$, in the frequency is 0.217 in the analytical case. The numerical model, however, only requires an axial restraining of the nodes at the corners of the I–profile where the dampers are attached. As the largest warping displacements occur at the corners, restraining these will have an essential influence on the warping of the rest of the cross–section. As the cross–sections in the three cases in Fig. 4 still are able to warp locally when $c \to \infty$, the corresponding frequencies ω_∞^{FEM} will be lower compared to the analytical model, which is also seen in Fig 6a. For the configurations shown in Figs. 4*a*, 4*b* and 4*c* the increments in frequencies, $(\omega_\infty^{FEM} - \omega_0)/\omega_0$, are 0.043, 0.115 and 0.199 relative to the analytical ω_0, corre-

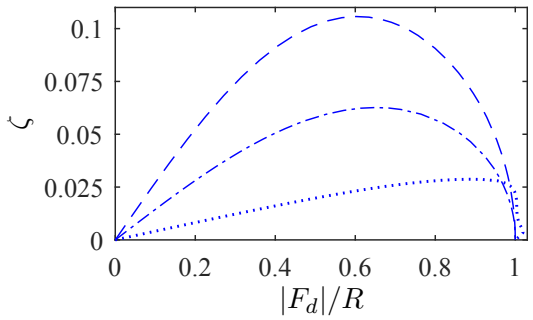

Figure 7: Damping ratio given as a function of damper force, for the three damper configurations.

sponding to an increase in stiffness from increased restraining of the warping. The increase in locked frequency has a direct consequence on the damping ratio; the bigger the frequency locus the more damping it is possible to obtain. This is also evident in Fig. 6*b* where the damping ratio ζ increases from 0.029 through 0.063 to 0.106 for the three configurations, compared to 0.109 in the analytical case. This should correspond to approximately half of the frequency increment, but due to ω_0^{FEM} not completely coinciding with ω_0 the values are just slightly off. By this it is noted that the numerical and analytical models match quite well, as the damping ratios are almost identical in the case 4*c* when restraining the entire cross–section.

In this example identical viscous damping coefficients c are used for all dampers. And larger damping ratios may be reached by application of different damping coefficients optimised for each damper. Different cross–sections where warping is more pronounced may equivalently result in even large damping ratios. However, for closed cross–sections associated with larger $k\ell$–values the obtainable damping ratios are limited due to the vanishing warping displacements. In that case an amplified warping displacement may be induced by including a slit along the beam, whereby non–vanishing, relative axial displacements occur.

Damper force

As damping of torsional vibrations by restraining of warping displacements prospectively is intended for beam–structures within civil or mechanical engineering, it is of interest to consider the magnitude of the forces occurring in the dampers. As the eigenvalue problem solved is complex, the force in the damper is also complex. Thus, the magnitude of the force vector for the j'th damper is $|F_{d,j}| = |c_j\, \mathbf{w}_j^T\, \dot{\mathbf{q}}|$. Assuming a time dependent solution of the form $\mathbf{q} = \mathbf{q}_0\, \mathrm{e}^{i\omega t}$ the force takes the form

$$|F_{d,j}| = |i\, c_j\, \omega\, \mathbf{w}_j^T\, \mathbf{q}_0| \tag{22}$$

This force, however, is scaled according to the corresponding eigenvector and does not represent the actual magnitude. But related to the reaction force R in the case of infinite damping, the relation between the two forces is comparable, provided that the eigenvectors are scaled identically. Fig. 7 shows the damping ratio given as a function of the force of the damper in a single corner of the I–beam, in Fig. 4. For the three configurations in Figs. 4*a*, 4*b* and 4*c* the force ratios $|F_d|/R$ corresponding to maximum damping are 0.887, 0.650 and 0.602 respectively.

It is seen that quite large portions of the reaction force must be realized at optimal damping, and for the single damper configuration almost 90 % of the reaction force is present in the damper. This indicates that a configuration of several dampers that effectively restrains warping is most advantageous.

5 CONCLUSION

A previously developed novel method for damping of torsional vibrations of thin–walled beams by control of warping displacements has been investigated and compared with a numerical finite element procedure. The torsional vibrations are damped by restraining the out–of–plane warping displacements by applying viscous bimoments at the boundary of the beam. These viscous bimoments are represented by axial, concentrated forces proportional with the velocity of a given node in the numerical model. By an example it is shown that restraining warping is associated with a significant increase in natural frequency depending on the part of the cross–section being restrained. A proper configuration of dampers results in a considerable amount of supplemental damping for a slender beam-structure, even though all dampers in the present paper are associated with identical viscous damping coefficients. The undamped and infinitely damped natural frequencies are however not exactly identical due to the numerical model taking the actual geometry of the beam into account. This suggests that a final design should be carried out by a numerical procedure to get accurate calibration of the dampers, as well as the forces in the dampers which may be close to the reaction force when locking the damper.

REFERENCES

[1] Gere, J. M., *Torsional vibrations of Beams of Thin–Walled Open Section*, ASME Journal of Applied Mechanics (1954), **21**, pp. 381–387.

[2] Carr, J. B., *The Torsional Vibration of Uniform Thin–Walled Beams of Open Section*, The Aeronautical Journal of the Royal Aeronautical Society (1968), vol. 73, pp. 672–674.

[3] Gere, J. M. & Lin, Y. K., *Coupled Vibrations of Thin–Walled Beams of Open Cross–Section*, ASME Journal of Applied Mechanics (1958), **25**, pp. 373–378.

[4] Lin, Y. K., *Coupled Bending and Torsional Vibrations of Restrained Thin–Walled Beams*, ASME Journal of Applied Mechanics (1960), **27**(4), pp. 739–740.

[5] Mei, C., *Coupled Vibrations of Thin–Walled Beams of Open Section using Finite Element Method*, International Journal of Mechanical Sciences (1970), vol. 12 no. 10.

[6] Friberg, P. O., *Coupled Vibrations of Beams – An Exact Dynamic Element Stiffness Matrix*, International Journal for Numerical Methods in Engineering (1983), vol. 19, pp. 479–493.

[7] Augustyn, E. & Kozień, M. S., *Analytical Solution of Excited Torsional Vibrations of Prismatic Thin–Walled Beams*, Journal of Theoretical and Applied Mechanics (2015), **53** no. 4, pp. 991–1004.

[8] Narayanan, S. & Malik, A. K., *Free Vibrations of Thin–Walled Open Section Beams with Constrained Damping Treatment*, Journal of Sound and Vibration (1981), **74**(3), pp. 429–439.

[9] Jansen, J. D. & van den Steen, L., *Active Damping of Self–Excited Torsional Vibrations in Oil Well Drillstrings*, Journal of Sound and Vibration (1995), **179**(4), pp. 647–668.

[10] Augustyn, E. & Kozień, M. S., *A Study on Possibility to Apply Piezoelectric Actuactors for Active Reduction of Torsional Beams Vibrations*, Acta Physica Polonica (2014), Vol. 125.

[11] Augustyn, E. & Kozień, M. S., *FEM Analysis of Active Reduction of Torsional Vibrations of Clamped–Free Beam by Piezoelectric Elements for Separated Modes*, Archives of Acoustics (2014), Vol. 39 no. 4, pp. 639–644.

[12] Christiano, P. & Salmela, L., *Frequencies of Beams with Elastic Warping Restraint*, Journal of the Structural Division (1971), **97** no. 6, pp. 1835–1840.

[13] Høgsberg, J., Hoffmeyer, D. & Ejlersen, C., *Damping of Torsional Beam Vibrations by Control of Warping Displacement*, Journal of Vibration and Acoustics (2016), vol. 138.

[14] Vlasov, V. Z., *Thin–walled Elastic Beams*, (1961) Israel Program for Scientific Translations, Jerusalem.

[15] Høgsberg, J. & Krenk, S., *Analysis of Moderately Thin–Walled Beam Cross–Sections by Cubic Isoparametric Elements*, Computers and Structures (2014), **134**, pp. 88–101.

VIII ECCOMAS Thematic Conference on Smart Structures and Materials
SMART 2017
A. Güemes, A. Benjeddou, J. Rodellar and Jinsong Leng (Eds)

BENCHMARK EXACT FREE VIBRATION SOLUTIONS FOR MULTILAYERED PIEZOELECTRIC COMPOSITE PLATES

F. MOLEIRO[*], C.M. MOTA SOARES[*], C.A. MOTA SOARES[*], A.L. ARAÚJO[*] AND J.N. REDDY[†]

[*] IDMEC, Instituto Superior Técnico, Universidade de Lisboa
Av. Rovisco Pais 1, 1049-001 Lisboa, Portugal
email: filipa.moleiro@tecnico.ulisboa.pt, cristovao.mota.soares@tecnico.ulisboa.pt, carlos.mota.soares@tecnico.ulisboa.pt, aurelio.araujo@tecnico.ulisboa.pt

[†] Texas A&M University
College Station, TX 77483-3123, USA
email: jnreddy@tamu.edu

Key words: Smart Structures, Multilayered Plates, Composite Layers, Piezoelectric Layers, Exact Free Vibration Solution.

Abstract. The development of advanced finite element models suitable for the analysis of smart structures depends on a comprehensive understanding of the behaviour of multilayered piezoelectric composite structures. In fact, an accurate electromechanical modelling of smart structures requires a correct description of both electrical and mechanical fields, particularly in the thickness direction. The assessment of recent and advanced models still continues to rely nowadays only on a few well-known benchmark three-dimensional (3D) exact solutions provided by pioneer works, namely, in the 1970s by Pagano [1,2] as well as Srinivas [3] for composite plates and later in the 1990s by Heyliger [4–6] for piezoelectric composite plates. To overcome the limited number of test cases whose 3D exact solutions have been published, the authors provided in a previous work [7] new additional benchmark 3D exact solutions for the static analysis of piezoelectric composite plates. The present work aims to complete this previous one by providing new benchmark 3D exact solutions for the corresponding free vibration analysis. The method introduced by Heyliger to derive the 3D exact solutions has been successfully implemented using symbolic computing and a number of new test cases for free vibration analysis are here presented. Specifically, two multilayered plates using PVDF piezoelectric material are chosen as test cases under two sets of electrical boundary conditions and considering three plate aspect ratios for thick, moderately thick and thin plate, in a total of 12 distinct test cases.

1 INTRODUCTION

Smart structures technology is nowadays growing constantly aiming to control actively structural vibration, damping, noise, aeroelastic stability, shape change or stress distribution, thus playing an important role in several engineering systems. A smart structure incorporates smart material sensors and actuators that enable it to monitor a change in its environment,

whether external (such as loads or shape change) or internal (such as damage or failure), and adapt to it by modifying the system characteristics (such as stiffness or damping) or the system response (such as strain or shape), in a controlled manner. Among smart materials, piezoelectric sensors and actuators are being used extensively due to their excellent electromechanical properties and design flexibility, such that they can be easily integrated in multilayered composite structures. In fact, smart composite structures offer the possibility to combine the lightweight, superior mechanical and thermal properties of composite materials with actuation, sensing and control. Due to their self-monitoring and self-adaptive capability, smart composite structures technology has an enormous potential to improve high performance engineering applications.

An accurate electromechanical modelling of these smart composite structures, which are inherently anisotropic multilayered structures, requires a correct description of both electrical and mechanical fields, particularly in the thickness direction. This is precisely demonstrated by pioneer works on 3D exact solutions that became paramount to the understanding of multilayered piezoelectric composite structures. In the 1970s, Pagano [1,2] derived the 3D exact elasticity solutions for the static analysis of simply supported cross-ply composite laminates and sandwich plates (i.e. multilayered orthotropic plates). Likewise, in that time, Srinivas and Rao [3] developed the corresponding 3D exact elasticity solutions for the free vibration and bucking analyses. Later in the 1990s, Heyliger [4,5] extended the work of Pagano to include piezoelectric layers and provided the 3D exact solutions for the static analysis of simply supported multilayered orthotropic piezoelectric plates. Heyliger and Saravanos [6] also developed the corresponding 3D exact solutions for the free vibration analysis. All these 3D exact solutions have been extremely useful in assessing the accuracy of numerous laminated plate theories and related finite element models. However, the limited number of test cases whose 3D exact solutions have been published has somewhat restricted the assessment of recent and advanced models to the same few test cases. To avoid redundancy and in the interest of this research area of modelling smart structures, the authors successfully implemented the method introduced by Heyliger using symbolic computing and provided in a previous work [7] additional test cases to serve as benchmark 3D exact solutions for the static analysis of multilayered piezoelectric composite plates. The implemented exact solution method has now been successfully extended to derive free vibration solutions as well. Hence, the present work aims to complete this previous one by providing new benchmark 3D exact solutions for the corresponding free vibration analysis of multilayered piezoelectric composite plates.

Assessments on the modelling and analysis of multilayered structures are available in some well-known excellent review papers, namely, by Saravanos and Heyliger [8], Benjeddou [9] and Carrera [10], as well as in the book of Reddy [11] devoted to composite structures. In overview, the models mostly differ in equivalent single layer (ESL) or layerwise (LW) variable descriptions as well as in the chosen unknown variables, consistent with classical (i.e. displacement-based) or mixed formulations. Some of the most relevant contributions are worth mentioning: the LW classical models developed by Heyliger, Saravanos and co-workers [12,13], the LW classical models of Semedo Garção et al. [14], the LW mixed models of Garcia Lage et al. [15], the classical and mixed models developed by Carrera and co-workers [16,17] using Carrera's unified formulation, and also the LW mixed least-squares models developed by the authors [18–20]; all of which use the 3D exact solutions for

assessment of the models predictive capabilities. More recently, advanced models especially devoted to free vibration analysis continue to be developed, such as the LW classical model of Araújo et al. [21] for smart sandwich plates and the 3D model approach developed by Messina and Carrera [22,23]. The analysis of free vibration of multilayered structures is still an area of much needed research that is of particular interest for smart composite structures growing technology.

2 GOVERNING EQUATIONS

Consider a multilayered plate of total thickness h and rectangular planar geometry $a \times b$ made of N generally orthotropic layers, either piezoelectric or composite layers, as illustrated in Figure 1. A Cartesian coordinate system (x,y,z) is used, with the z-axis taken positive upward from the midplane along the thickness direction.

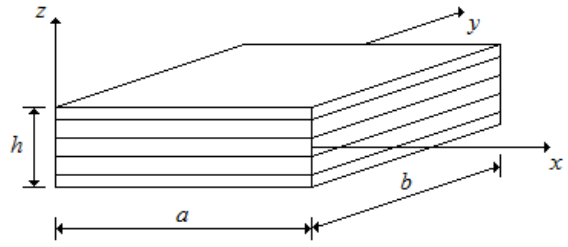

Figure 1: Configuration of a multilayered plate.

In agreement with linear elasticity and piezoelectricity the complete set of linear governing equations for each layer of the multilayered plate involves the following equations.

- The equations of motion and charge equation of electrostatics:

$$\frac{\partial \sigma_{ij}}{\partial x_j} = \rho \frac{\partial^2 u_i}{\partial t^2} \, , \frac{\partial D_i}{\partial x_i} = 0 \, , i,j = 1,2,3 \tag{1}$$

where σ_{ij} are the stress components, D_i are the electric displacement components, u_i are the displacement components with $u_1 = u$, $u_2 = v$ and $u_3 = w$, and similarly x_i are the coordinates with $x_1 = x$, $x_2 = y$ and $x_3 = z$;

- The constitutive equations (in the general case of a piezoelectric layer):

$$\sigma_i = C_{ij}\varepsilon_j - e_{ik}E_k \, , D_k = e_{ki}\varepsilon_i + \epsilon_{kl}E_l \, , i,j = 1,2,\dots 6 \, , k,l = 1,2,3 \tag{2}$$

where the standard engineering notation is used, and so here, σ_i are the stress components and ε_i are the strain components, C_{ij} are the elastic stiffness coefficients, e_{ik} are the piezoelectric coefficients, E_k are the electric field components, D_k are the electric displacement components (as before) and ϵ_{kl} are the dielectric constants;

- The strain-displacement equations (for infinitesimal strains) and field-potential equations:

$$\varepsilon_{ij} = \frac{1}{2}\left(\frac{\partial u_i}{\partial x_j} + \frac{\partial u_j}{\partial x_i}\right) \, , E_k = -\frac{\partial \phi}{\partial x_k} \, , i,j,k = 1,2,3 \tag{3}$$

where ε_{ij} are the strain components, ϕ is the electrostatic potential and the remaining variables as before.

The expanded form of this complete set of governing equations can be found in the authors previous works [19,20]. Note that in the layer constitutive equations C_{ij}, e_{ik} and ϵ_{kl} are already referred to the multilayered plate coordinate system (x,y,z), assuming that the transformation between the layer material coordinate system and the multilayered plate coordinate system is simply an in-plane rotation. See Reddy [11] for further details. Also, the 3D exact solutions as developed by Heyliger [4,5] assume that the most general conditions for the layer material properties are such that: the nonzero rotated elastic stiffness coefficients are C_{11}, C_{12}, C_{13}, C_{22}, C_{23}, C_{33}, C_{44}, C_{55} and C_{66}, the nonzero rotated piezoelectric coefficients are e_{31}, e_{32}, e_{33}, e_{24} and e_{15}, and the nonzero rotated dielectric constants are ϵ_{11}, ϵ_{22} and ϵ_{33}. Therefore, in respect to the material, the scope of the 3D exact solutions is limited to multilayered orthotropic piezoelectric plates.

Ultimately, substituting the constitutive equations, the strain-displacement equations and the field-potential equations into the three equations of motion and the charge equation gives the four governing equations for each layer, in terms of the displacement components u, v and w, and the electrostatic potential ϕ, as follows:

$$
\begin{aligned}
C_{11}\frac{\partial^2 u}{\partial x^2}+C_{12}\frac{\partial^2 v}{\partial x\partial y}+C_{13}\frac{\partial^2 w}{\partial x\partial z}+e_{31}\frac{\partial^2 \phi}{\partial x\partial z}+C_{66}\left(\frac{\partial^2 u}{\partial y^2}+\frac{\partial^2 v}{\partial x\partial y}\right)+C_{55}\left(\frac{\partial^2 u}{\partial z^2}+\frac{\partial^2 w}{\partial x\partial z}\right)+e_{15}\frac{\partial^2 \phi}{\partial x\partial z}=\rho\frac{\partial^2 u}{\partial t^2}\\
C_{66}\left(\frac{\partial^2 u}{\partial x\partial y}+\frac{\partial^2 v}{\partial x^2}\right)+C_{12}\frac{\partial^2 u}{\partial x\partial y}+C_{22}\frac{\partial^2 v}{\partial y^2}+C_{23}\frac{\partial^2 w}{\partial y\partial z}+e_{32}\frac{\partial^2 \phi}{\partial y\partial z}+C_{44}\left(\frac{\partial^2 v}{\partial z^2}+\frac{\partial^2 w}{\partial y\partial z}\right)+e_{24}\frac{\partial^2 \phi}{\partial y\partial z}=\rho\frac{\partial^2 v}{\partial t^2}\\
C_{55}\left(\frac{\partial^2 u}{\partial x\partial z}+\frac{\partial^2 w}{\partial x^2}\right)+e_{15}\frac{\partial^2 \phi}{\partial x^2}+C_{44}\left(\frac{\partial^2 v}{\partial y\partial z}+\frac{\partial^2 w}{\partial y^2}\right)+e_{24}\frac{\partial^2 \phi}{\partial y^2}+C_{13}\frac{\partial^2 u}{\partial x\partial z}+C_{23}\frac{\partial^2 v}{\partial y\partial z}+C_{33}\frac{\partial^2 w}{\partial z^2}+e_{33}\frac{\partial^2 \phi}{\partial z^2}=\rho\frac{\partial^2 w}{\partial t^2}\\
e_{15}\left(\frac{\partial^2 u}{\partial x\partial z}+\frac{\partial^2 w}{\partial x^2}\right)-\epsilon_{11}\frac{\partial^2 \phi}{\partial x^2}+e_{24}\left(\frac{\partial^2 v}{\partial y\partial z}+\frac{\partial^2 w}{\partial y^2}\right)-\epsilon_{22}\frac{\partial^2 \phi}{\partial y^2}+e_{31}\frac{\partial^2 u}{\partial x\partial z}+e_{32}\frac{\partial^2 v}{\partial y\partial z}+\epsilon_{33}\frac{\partial^2 w}{\partial z^2}-\epsilon_{33}\frac{\partial^2 \phi}{\partial z^2}=0
\end{aligned}
\tag{4}
$$

3 EXACT SOLUTION METHOD

Consider a multilayered plate with an arbitrary number of generally orthotropic layers that are assumed to be perfectly bonded together. The solutions for the displacement components and the electrostatic potential for each layer are determined by the abovementioned governing equations, while enforcing for both mechanical and electrical fields the required interface continuity conditions between adjacent layers and the specific boundary conditions imposed on the multilayered plate, whether a static or free vibration analysis is concerned.

3.1 Solution form for each layer

The solution general form assumed for the displacement components and the electrostatic potential for each layer is the following:

$$
\begin{aligned}
u(x,y,z,t)&=U(z)\exp(i\omega t)\cos(px)\sin(qx)\ ,U(z)=\overline{U}\exp(sz)\\
v(x,y,z,t)&=V(z)\exp(i\omega t)\sin(px)\cos(qx)\ ,V(z)=\overline{V}\exp(sz)\\
w(x,y,z,t)&=W(z)\exp(i\omega t)\sin(px)\sin(qx)\ ,W(z)=\overline{W}\exp(sz)\\
\phi(x,y,z,t)&=\Phi(z)\exp(i\omega t)\sin(px)\sin(qx)\ ,\Phi(z)=\overline{\Phi}\exp(sz)
\end{aligned}
\tag{5}
$$

where $p=p(n)=n\pi/a$ and $q=q(m)=m\pi/b$, with n and m positive integers.

Here the overbarred terms are constants, s is an unknown number that is generally complex and z represents the local layer thickness coordinate, whose origin is at the layer midplane.

3.2 Boundary and interface conditions

In view of this solution form, the plate is assumed to be simply supported and the vertical edges of the plate are also assumed to be grounded, which are conditions that are all satisfied *a priori*. Hence, the plate edge boundary conditions are:

$$\begin{aligned} \sigma_{xx} = v = w = \phi = 0 \text{ , at } x = 0, a \\ \sigma_{yy} = u = w = \phi = 0 \text{ , at } y = 0, b \end{aligned} \tag{6}$$

The boundary conditions on the plate top and bottom surfaces require the specification of one variable from each of the pairs: (u,σ_{xz}), (v,σ_{yz}), (w,σ_{zz}) and (ϕ,D_z). Of primary interest to the free vibration analysis are the cases in which both the plate top and bottom surfaces are traction free and the specified electrical boundary conditions on the plate top and bottom surfaces are either a homogenous potential or a homogenous transverse electric displacement. Specifically, the two sets of electric boundary conditions considered herein on the plate top and bottom surfaces are:

$$\begin{aligned} \sigma_{xz} = \sigma_{yz} = \sigma_{zz} = \phi = 0 \text{ , at } z = -h/2 \\ \sigma_{xz} = \sigma_{yz} = \sigma_{zz} = 0 \text{ and } \phi = 0 \text{ or } D_z = 0 \text{ , at } z = h/2 \end{aligned} \tag{7}$$

In addition, at the interface between adjacent layers, the interlaminar continuity conditions for the displacements components u,v,w, the potential ϕ, the transverse stresses σ_{xz},σ_{yz},σ_{zz} and the transverse electric displacement D_z must be enforced as well, due to compatibility and equilibrium conditions.

3.3 Solution for each layer

The substitution of the assumed solution form shown in Eq. (5) into the layer governing equations given by Eq. (4) results in the following system of equations for each layer:

$$\begin{bmatrix} A_{11} - C_{55}s^2 & A_{12} & A_{13}s & A_{14}s \\ A_{12} & A_{22} - C_{44}s^2 & A_{23}s & A_{24}s \\ -A_{13}s & -A_{23}s & A_{33} - C_{33}s^2 & A_{34} - e_{33}s^2 \\ -A_{14}s & -A_{24}s & A_{34} - e_{33}s^2 & A_{44} + \epsilon_{33}s^2 \end{bmatrix} \times \begin{Bmatrix} \overline{U} \\ \overline{V} \\ \overline{W} \\ \overline{\Phi} \end{Bmatrix} = \begin{Bmatrix} 0 \\ 0 \\ 0 \\ 0 \end{Bmatrix}$$

where,

$$\begin{aligned} A_{11} = C_{11}p^2 + C_{66}q^2 - \rho\omega^2 \text{ , } A_{12} = pq(C_{12} + C_{66}) \text{ , } A_{13} = -p(C_{13} + C_{55}) \text{ , } A_{14} = -p(e_{31} + e_{15}) \\ A_{22} = C_{66}p^2 + C_{22}q^2 - \rho\omega^2 \text{ , } A_{23} = -q(C_{23} + C_{44}) \text{ , } A_{24} = (e_{32} + e_{24}) \\ A_{33} = C_{55}p^2 + C_{44}q^2 - \rho\omega^2 \text{ , } A_{34} = e_{15}p^2 + e_{24}q^2 \text{ , } A_{44} = -\epsilon_{11}p^2 - \epsilon_{22}q^2 \end{aligned} \tag{8}$$

For a given resonant frequency ω, a nontrivial solution of this system of equations requires a zero determinant. The resulting characteristic equation is an eight-order polynomial in even powers of s, which can be rewritten as a fourth-order equation, as follows:

$$r^4 + cr^3 + dr^2 + er + f = 0 \text{ , with } r = s^2 \tag{9}$$

The four roots for r can be either real or complex in conjugate pairs. Depending on the nature of these roots, the solutions for the displacement components and the electrostatic potential for each layer, corresponding to each type of root, are developed separately. More details can be found in Heyliger [4,5] as well as in Heyliger and Saravanos [6]. Actually, for a nonpiezoelectric elastic layer the piezoelectric coefficients e_{ik} are zero and the electric and elastic fields uncouple. In this case, the four roots for r are real. For some piezoelectric materials with orthotropic behaviour, such as PVDF, the four roots for r are also real. For piezoelectric materials with transverse isotropy, such as PZT-4, there are two real roots and two complex conjugate roots for r. In any case, the solutions for the displacement components and the electrostatic potential for each layer are expressed in terms of 8 unknown constants.

3.4 Solution for the plate

For a multilayered plate with N layers there are subsequently $8N$ unknown constants to be determined by enforcing $8(N\text{-}1)$ interface continuity conditions and 8 boundary conditions on the plate top and bottom surfaces, resulting in a total system of $8N$ equations for the entire plate. For a given resonant frequency ω, a nontrivial solution of this total system (of size $8N$) requires a zero determinant. Since the solution for each layer, namely the roots and resulting through-thickness field distributions are, to begin with, a function of the resonant frequency ω, which is unknown *a priori*, the 3D exact free vibration solution for the entire multilayered plate ultimately requires an iterative procedure.

An initial low frequency is used first, which is then stepped through a series of frequencies iteratively, so that the determinant of the total system of equations (of size $8N$) for the entire plate can be evaluated in each iteration. The zero determinant requirement establishes the necessary relationships for the calculation of the natural frequencies and the modal shapes for the plate. Once the sign of the determinant changes (and a near zero eigenvalue is confirmed), the sign-change frequency values are used as a bounding interval for a classical minimization method to be employed and refine the value of the true natural frequency. In particular, the determinant is computed through the product of all eigenvalues of the total system matrix (of size $8N$), as described in Heyliger and Saravanos [6], to overcome the numerical difficulty of evaluating the determinant of a matrix as it becomes singular. Furthermore, it is recommended a preliminary balancing step to improve the conditioning of the total system matrix, which improves the eigenvalues accuracy as well as the computed determinant.

Once a natural frequency is found, the $8N$ constants that define the modal displacements and potential are readily computed by solving the corresponding total system of $8N$ equations for the entire plate with one constant arbitrarily set to one. Actually, all remaining mechanical and electrical field variables can be then be computed using the former Eq. (2) and Eq. (3), if necessary.

Note that the solution form for each layer in Eq. (5) uses a combination of p and q that describe the in-plane modal characteristics of the mechanical and electrical fields. For each combination of p and q there are an infinite number of natural frequencies corresponding to the through-thickness modes. Of primary interest to the 3D exact solutions considered herein are the thickness modes that correspond to the fundamental in-plane mode with $n = m = 1$.

3.5 Exact solution verification

As mentioned earlier, the exact solution method introduced by Heyliger [4,5], which is briefly described herein and in detail in Heyliger and Saravanos [6], has been successfully implemented using symbolic computing to derive the 3D exact solutions for the free vibration analysis of multilayered piezoelectric composite plates. The free vibration solutions obtained by the implemented method were primarily verified by direct substitution into the governing equations, to make sure of the intended high accuracy of the new test cases here presented to serve as benchmark 3D exact solutions. Furthermore, for the numerical examples shown, a series of finite element analyses with increasing refinement were performed as well, simply as a baseline reference, which also support the exact solutions here presented.

4 NUMERICAL EXAMPLES

To facilitate the assessment and comparison between recent and advanced models for the free vibration analysis of multilayered piezoelectric composite plates, new test cases are here presented to serve as benchmark 3D exact solutions that are based on two simply supported multilayered plates, as follows:

- Case (1): A square three-layer piezoelectric plate made entirely of PVDF piezoelectric material with equal thickness layers and a staking sequence (0/90/0). The plate thickness is fixed as $h = 0.01m$ and the plate side length a is varied to consider different aspect ratios;
- Case (2): A square four-layer piezoelectric composite plate with the top and bottom layers made of PVDF piezoelectric material, oriented at 0 degrees, and the core layers a cross-ply (0/90) composite of graphite-epoxy. The plate thickness is again fixed as $h = 0.01m$, such that each piezoelectric layer is $h/10$ and the core is $8h/10$ of equal thickness composite layers, and the plate side length a is also varied to consider different aspect ratios.

The material properties are taken from Heyliger and Saravanos [6] and shown in Table 1.

Table 1: Mechanical and electrical material properties.

Properties	PVDF	Graphite-Epoxy
E_1 $[GPa]$	237.0	132.38
E_2 $[GPa]$	23.2	10.756
E_3 $[GPa]$	10.5	10.756
G_{12} $[GPa]$	6.43	5.6537
G_{13} $[GPa]$	4.4	5.6537
G_{23} $[GPa]$	2.15	3.606
ν_{12}	0.154	0.24
ν_{13}	0.178	0.24
ν_{23}	0.177	0.49
e_{15} $[C/m^2]$	-0.01	0
e_{24} $[C/m^2]$	-0.01	0
e_{31} $[C/m^2]$	-0.13	0
e_{32} $[C/m^2]$	-0.14	0
e_{33} $[C/m^2]$	-0.28	0
ϵ_{11}/ϵ_0 †	12.50	3.5
ϵ_{22}/ϵ_0 †	11.98	3.0
ϵ_{33}/ϵ_0 †	11.98	3.0

† ϵ_0 stands for the vacuum dielectric constant.

For simplicity, the same density is used for both materials, chosen as a unit of their typical order of magnitude, i.e. $\rho = 1000 kg/m^3$.

For each multilayered plate, two sets of electrical boundary conditions are considered that differ on the specified condition imposed on the plate top surface: (*a*) a homogenous potential or (*b*) a homogenous transverse electrical displacement, as indicated in Eq. (7). Moreover, three plate aspect ratios are also considered: 4, 10 and 100, i.e. thick, moderately thick and thin plate, respectively. Hence, overall 12 distinct new test cases. Actually, both multilayered plates used as Case (1) and Case (2) have already been considered by the authors in a previous work [7] on benchmark 3D exact solutions for the static analysis of multilayered piezoelectric composite plates. Therefore, the present work aims to complete the previous one with the corresponding free vibration solutions. Since this work is still ongoing, the 3D exact free vibration solutions here presented for the natural frequencies and through-thickness modes focus only on the first mode, although it is intended to provide later on the free vibration solutions corresponding to the first few thickness modes for all 12 test cases.

4.1 Case (1): three-layer piezoelectric plate

The 3D exact free vibration solutions for the fundamental frequencies of the multilayered plate of Case (1) for each of the two sets of electrical boundary conditions and for each of the three plate aspect ratios are shown in Table 2. For argument purposes, Table 2 also includes the fundamental frequencies obtained using a standard 3D commercial finite element model, denoted basic FEM, to assess the eventual weaknesses of such models predictive capabilities.

Table 2: Case (1) 3D exact fundamental frequencies (in *rad*/*s*) for three plate aspect ratios and two sets of electrical boundary conditions.

Thickness Mode 1	$a/h = 4$		$a/h = 10$		$a/h = 100$	
	(*a*) $\phi = 0$	(*b*) $D_z = 0$	(*a*) $\phi = 0$	(*b*) $D_z = 0$	(*a*) $\phi = 0$	(*b*) $D_z = 0$
Basic FEM	129046.8149	129271.9355	36549.5523	36570.2995	486.9378	486.9379
3D Exact	142533.0089	142538.5755	37446.5847	37446.6995	486.6145	486.6145

As mentioned, the 3D exact solutions aim to be primarily useful in assessing the accuracy of finite element models and associated theories, even though their scope is limited to simply supported multilayered orthotropic piezoelectric plates. In fact, it is shown in Table 2 that as the plate aspect ratio decreases, its more complex solution may compromise the accuracy of standard models. Figures 2–3 show the through-thickness distributions of the first mode for the displacements and the potential precisely for the plate aspect ratio $a/h = 4$, with each set of electrical boundary conditions, revealing that only the potential mode shape is significantly affected by the different set of electrical boundary conditions. Note that in all plots shown, the displacement components are normalized with respect to the maximum value of u, v, or w, and the potential is also normalized with respect to its maximum value. A scaling factor ξ is defined to denote the relationship between the potential and the displacements, just as in [6].

4.2 Case (2): four-layer piezoelectric composite plate

The 3D exact free vibration solutions for the fundamental frequencies of the multilayered

plate of Case (2) for each of the two sets of electrical boundary conditions and for each of the three plate aspect ratios are now shown in Table 3. Likewise, it is also included in Table 3 the fundamental frequencies obtained by a standard 3D commercial FEM.

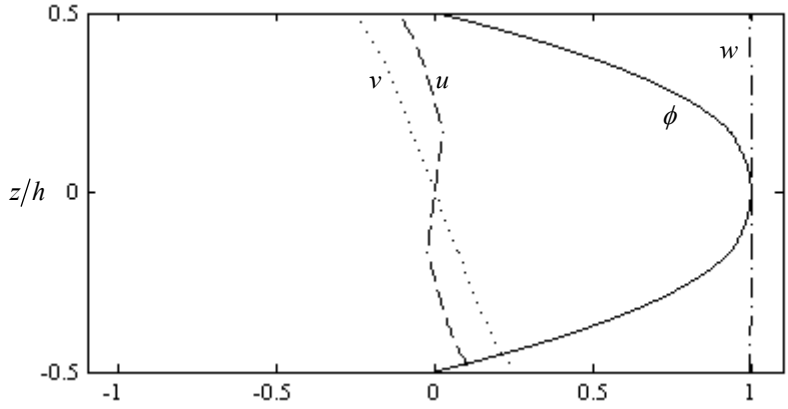

Figure 2: Case (1*a*) thickness distributions of mode 1 for $a/h = 4$ (scale factor $\xi = -0.3148e9$).

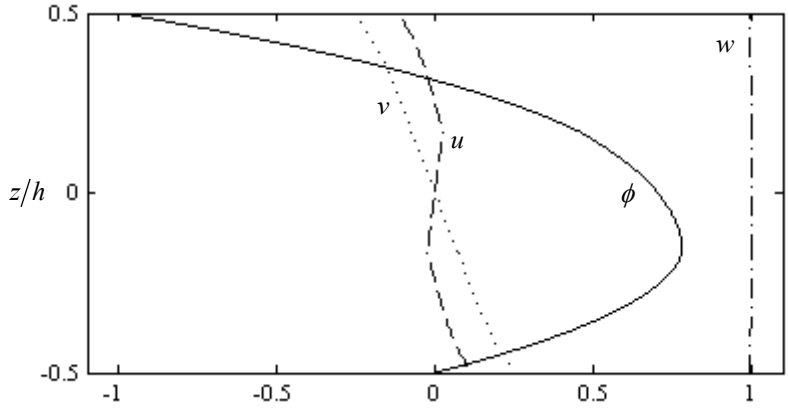

Figure 3: Case (1*b*) thickness distributions of mode 1 for $a/h = 4$ (scale factor $\xi = -0.1948e9$).

Examination of Table 3 indicates that for both extreme plate aspect ratios the accuracy of standard models may be compromised. This situation may be explained by the fact that the multilayered plate of Case (2) includes two piezoelectric layers that are much thinner than the elastic layers, which can be numerically complicated for both extreme plate aspect ratios.

Table 3: Case (2) 3D exact fundamental frequencies (in *rad*/*s*) for three plate aspect ratios and two sets of electrical boundary conditions.

Thickness Mode 1	$a/h = 4$		$a/h = 10$		$a/h = 100$	
	(*a*) $\phi = 0$	(*b*) $D_z = 0$	(*a*) $\phi = 0$	(*b*) $D_z = 0$	(*a*) $\phi = 0$	(*b*) $D_z = 0$
Basic FEM	137203.7594	137637.2943	34765.5267	34811.1699	542.6952	542.7465
3D Exact	156509.9416	156510.0511	35689.3355	35689.3360	403.5158	403.5158

Figures 4–5 show the thickness distributions of the first mode for the displacements and the potential for two different plate aspect ratios, $a/h = 4$ and $a/h = 10$, both with the same set of electrical boundary conditions. As expected, as the plate aspect ratio increases, all mode shapes become more linear (within each layer).

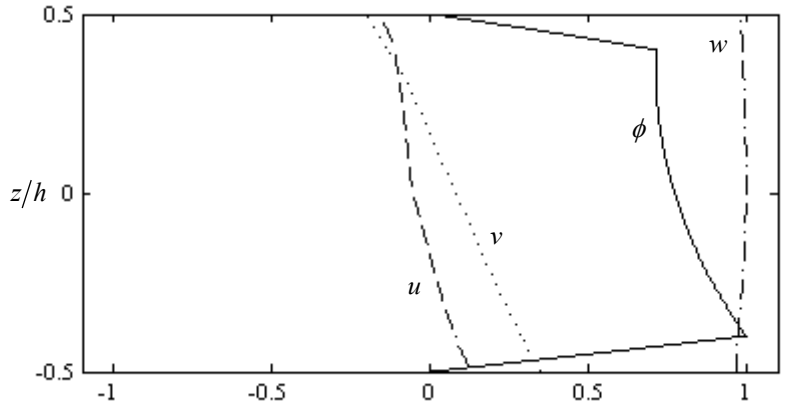

Figure 4: Case (2*a*) thickness distributions of mode 1 for $a/h = 4$ (scale factor $\xi = -0.1230e9$).

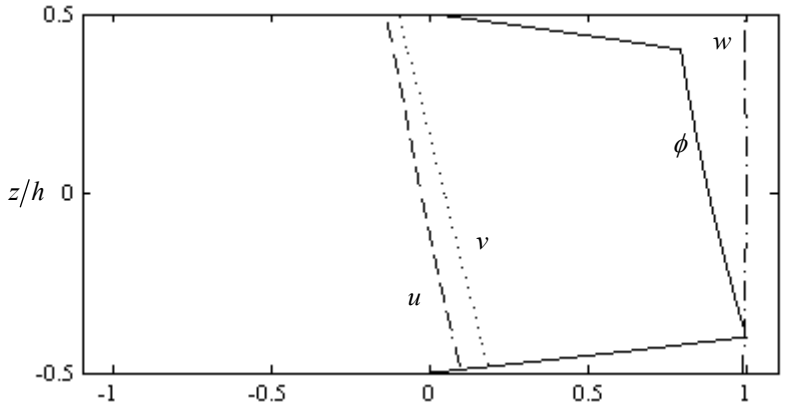

Figure 5: Case (2*a*) thickness distributions of mode 1 for $a/h = 10$ (scale factor $\xi = -0.0374e9$).

Furthermore, Tables 2–3 also show that the difference between the two sets of electrical boundary conditions on the plate natural frequencies becomes more pronounced as the plate aspect ratio decreases, with the homogenous potential providing smaller frequencies every time the distinction is noticeable.

5 CONCLUSIONS

The development and assessment of advanced finite element models particularly suitable for the analysis of smart composite structures still continues to rely nowadays mostly on benchmark 3D exact solutions, as derived by Heyliger [4,5] and also Heyliger and Saravanos [6]. In response to the limited number of well-known test cases whose 3D exact solutions have been published, this work provides new test cases to serve as benchmark 3D exact

solutions for the free vibration analysis of multilayered piezoelectric composite plates.

Specifically, two multilayered plates using PVDF piezoelectric material are chosen as test cases under two sets of electrical boundary conditions, i.e. either a homogenous potential or a homogenous transverse electric displacement, and considering three plate aspect ratios for thick, moderately thick and thin plate, in a total of 12 distinct test cases. Although this work is still ongoing, the presented 3D exact free vibration solutions for the fundamental frequencies, for all test cases, along with the through-thickness distributions of the first mode for the displacements and the potential, can already demonstrate the difference in the plate vibration response for the two sets of electrical boundary conditions as well as the effect of the plate aspect ratio. Ultimately, the 3D exact free vibration solutions here presented may prove to be quite useful to this research area that is of particular interest for smart composite structures growing technology.

ACKNOWLEDGEMENTS

The authors acknowledge the financial support received by means of National Funds from "Fundação para a Ciência e a Tecnologia" (FCT), through IDMEC, under the Associated Laboratory of Energy, Transports and Aeronautics (LAETA), Project UID/EMS/50022/2013.

REFERENCES

[1] Pagano, N.J. Exact solutions for rectangular bidirectional composites and sandwich plates. *Journal of Composite Materials* (1970) **4**:20-34.

[2] Pagano, N.J. and Hatfield, S.J. Elastic behavior of multilayered bidirectional composites. *American Institute of Aeronautics and Astronautics Journal* (1972) **10**:931-933.

[3] Srinivas, S. and Rao, A.K. Bending, vibration and buckling of simply supported thick orthotropic rectangular plates and laminates. *International Journal of Solids and Structures* (1970) **6**:1463-1481.

[4] Heyliger, P.R. Static behavior of laminated elastic/piezoelectric plates. *American Institute of Aeronautics and Astronautics Journal* (1994) **32**(12):2481-2484.

[5] Heyliger, P.R. Exact solutions for simply supported laminated piezoelectric plates. *Journal of Applied Mechanics* (1997) **64**:299-306.

[6] Heyliger, P.R. and Saravanos, D.A. Exact free-vibration analysis of laminated plates with embedded piezoelectric layers. *Journal of the Acoustical Society of America* (1995) **98**(3):1547-1557.

[7] Moleiro, F., Mota Soares, C.M., Mota Soares, C.A. and Reddy, J.N. Benchmark exact solutions for the static analysis of multilayered piezoelectric composite plates using PVDF. *Composite Structures* (2014) **107**:389-395.

[8] Saravanos, D.A. and Heyliger, P.R. Mechanics and computational models for laminated piezoelectric beams, plates and shells. *Applied Mechanics Reviews* (1999) **52**(10):305-320.

[9] Benjeddou, A. Advances in piezoelectric finite element modeling of adaptive structural elements: a survey. *Computers and Structures* (2000) **76**:347-363.

[10] Carrera, E. Theories and finite elements for multilayered anisotropic, composite plates and shells. *Archives of Computational Methods in Engineering* (2002) **9**(2):87-140.

[11] Reddy, J.N. *Mechanics of laminated composite plates and shells - theory and analysis*.

Boca Raton: CRC Press (2004).
[12] Heyliger, P.R., Ramirez, G. and Saravanos, D.A. Coupled discrete-layer finite elements for laminated piezoelectric plates. *Communications in Numerical Methods in Engineering* (1994) **10**:971-981.
[13] Saravanos, D.A., Heyliger, P.R. and Hopkins, D.A. Layerwise mechanics and finite element for the dynamic analysis of piezoelectric composite plates. *International Journal of Solids and Structures* (1997) **34**(3):359-378.
[14] Semedo Garção, J.E., Mota Soares C.M., Mota Soares C.A. and Reddy, J.N. Analysis of laminated adaptive plate structures using layerwise finite element models. *Computers and Structures* (2004) **82**:1939-1959.
[15] Garcia Lage, R., Mota Soares, C.M., Mota Soares, C.A. and Reddy, J.N. Modelling of piezolaminated plates using layerwise mixed finite elements. *Computers and Structures* (2004) **82**:1849-1863.
[16] Robaldo, A., Carrera, E. and Benjeddou, A. A unified formulation for finite element analysis of piezoelectric adaptive plates. *Computers and Structures* (2006) **84**:1494-1505
[17] Carrera, E. and Boscolo, M. Classical and mixed finite elements for static and dynamic analysis of piezoelectric plates. *International Journal for Numerical Methods in Engineering* (2007) **70**:1135-1181.
[18] Moleiro, F., Mota Soares, C.M., Mota Soares, C.A. and Reddy, J.N. Layerwise mixed least-squares finite element models for static and free vibration analysis of multilayered composite plates. *Composite Structures* (2010) **92**(9):2328-2338.
[19] Moleiro, F., Mota Soares, C.M., Mota Soares, C.A. and Reddy, J.N. Assessment of a layerwise mixed least-squares model for analysis of multilayered piezoelectric composite plates. *Computers and Structures* (2012) **108-109**:14-30.
[20] Moleiro, F., Mota Soares, C.M., Mota Soares, C.A. and Reddy, J.N. Layerwise mixed models for analysis of multilayered piezoelectric composite plates using least-squares formulation. *Composite Structures* (2015) **119**:134-149.
[21] Araújo, A.L., Carvalho, V.S., Mota Soares, C.M., Belinha, J. and Ferreira, A.J.M. Vibration analysis of laminated soft core sandwich plates with piezoelectric sensors and actuators. *Composite Structures* (2016) **151**:91-98.
[22] Messina, A. and Carrera, E. Three-dimensional free vibration of multi-layered piezoelectric plates through approximate and exact analyses. *Journal of Intelligent Material Systems and Structures* (2015) **26**(5):489-504.
[23] Messina, A. and Carrera, E. Three-dimensional analysis of freely vibrating multilayered piezoelectric plates through adaptive global piecewise-smooth functions. *Journal of Intelligent Material Systems and Structures* (2016) **27**(20):2862-2876.

VIII ECCOMAS Thematic Conference on Smart Structures and Materials
SMART 2017
A. Güemes, A. Benjeddou , J. Rodellar and Jinsong Leng (Eds)

DETERMINATION OF PASSIVE RL-CIRCUIT PARAMETERS FOR DAMPING VIBRATIONS ON THE BASIS OF THE SOLUTION OF THE PROBLEM ON NATURAL VIBRATIONS OF ELECTROELASTIC BODIES

NATALIIA A. IURLOVA*, VALERII P. MATVEENKO*, DMITRII A. OSHMARIN*, NATALIYA V. SEVODINA* AND MAKSIM A. IURLOV*

* Department of complex problems of deformable solidsmechanics
Institute of Continuous Media Mechanics of the Ural Branch of RAS (ICMM UB RAS)
Acad. Korolev str., 1, 613013 Perm, Russian Federation
e-mail: yurlova@icmm.ru, www.icmm.ru

Key words: Electroelasticity, External electrical circuit, Piezoelectric element, Natural vibrations, Damping, Numerical modeling.

Abstract. In this paper, a new approach is proposed for choosing optimal parameters for the external electric circuits, shunting the connected piezoelectric elements of the structure, and providing thereby a passive control over the structure vibration. The approach is based on the mathematical statement of the natural vibration problem. By solving this problem, we find complex eigenfrequencies, the real part of which represents the frequency of vibrations, while the imaginary part corresponds to the damping coefficient, which characterizes the rate of vibration damping. The analysis of the behavior of the real and imaginary parts of different complex frequencies as a function of the electric circuit parameters allowed us to derive the criteria for determination of the optimal parameters of the external passive shunting circuits, which will provide the system with the required dissipative characteristics. The efficiency of the proposed approach has been demonstrated by solving two example problems on the vibration of cantilevered plate and cylindrical shell for two types of external electric circuits: resistive circuit comprising only one resistor (*R*-circuit) and resonant *RL*-circuit (consisting of inductive and resistive elements). The validity of the selected optimal parameters has been supported by the results of solution of the steady-state forced vibration problem.

1 INTRODUCTION

Today, the operation of some hi-tech structures gives rise to a serious technological problem of controlling their dynamic behavior. Therefore, the elaboration and development of new techniques for vibration damping is the problem of current interest. A relatively new approach is incorporation of piezoelectric element into modern structures. One of the ways of damping the structure vibrations with the aid of piezoelectric elements is their connection to electrical impedance in the form of external passive electric circuits (also known as shunting). In this case, a piezoelectric element serves as a transformer of the mechanical energy of

vibrations into the electrical energy, which is then dissipated in the external circuit.

The early studies, which considered the possibility of controlling the dynamic characteristics of structures via connecting the attached piezoelectric element to additional electrical impedance, dated back to the end of 70-ies of the past century [1]. However, the first paper that really attempted a detailed study of this approach was written by Hagood N.W. and Von Flotow A. [2]. This work describes the key features of structure behavior in the presence of shunted piezoelectric elements, including the influence of the external circuits on the mechanical characteristics of the structure. It also presents an approach for selection of optimal parameters for the external circuits, which is based on the analysis of the transfer function of the system with a shunted piezoelectric element.

The analysis of literature [2-14] shows that this approach still remains the most popular one at analysis of dynamic behavior of systems with shunted piezoelectric from the optimal damping search point of view. When using this approach there are some ways for transfer function formulation. Apart of it there are some techniques to obtain optimal parameters of external circuit within this approach, such as optimization by $\mathcal{H}_2$- or $\mathcal{H}_\infty$-norms of transfer function [4, 13], optimization by equality of transfer function magnitudes at S and T points [2, 3, 6], optimization by transfer function pole placement [5, 6, 14]. All of these lead to difference in optimal values of circuit parameters for one and the same structure depending on choice of transfer function and optimization criterion [2, 6, 13].

The degree of damping vibrations of electromechanical systems with piezoelectric elements and external electric circuits can be determined by solving three types of problems: of forced steady oscillations, transient process with the initial conditions and natural vibrations. Finding amplitude at resonant modes require solving multiple times the problem of forced steady-state vibrations for a particular load at different frequencies of external disturbances, as well as the solution of dynamic problems with initial conditions allows us to estimate the rate of damping of oscillations only for the particular load and initial conditions.

The solution of problem of natural vibrations does not have these disadvantages, which making it more effective in the study of the dynamic behavior of structures. The result of solving this problem - complex natural frequencies $\omega = \omega_{\mathrm{Re}} + \mathrm{i}\omega_{\mathrm{Im}}$, where ω_{Re} corresponds to the natural frequency, ω_{Im} corresponds to damping ratio [15].

In this study, as a basis for developing one of such approaches we use the problem on natural vibrations of electroelastic bodies with external electric circuits. In a previous work [16], it was shown that for a structure with piezoelectric elements and external circuits the above problem is most convenient and informative from the viewpoint of optimization of its dynamic characteristics, because it allows getting relation of damping ratio on the external electric circuit parameters and then determining their optimal parameters.

2 MATHEMATICAL STATEMENT OF THE PROBLEM AND METHODS OF ITS SOLUTION

Consider a piece-wise homogeneous body (smart-structure) of volume $V = V_1 + V_2$, where V_1 consists of homogeneous elastic parts and volume V_2 - of piezoelectric elements. A part of the surface of the body volume V_2 is covered by electrodes. One of the electrode-covered surfaces is connected to the external passive electric circuit of arbitrary configuration

consisting of resistive elements (resistors) of resistance R, inductive elements (induction coils) of inductance L and capacitive elements (capacitors) of capacitance C.

The variational equation of natural vibrations for a body consisting of elastic and piezoelectric elements is formulated using the relations of the linear elasticity theory and quasi-static Maxwell equations [17-21]:

$$\int_{V_1}\left(\sigma_{ij}\delta\varepsilon_{ij}+\rho\ddot{u}_i\delta u_i\right)dV+\int_{V_2}\left(\sigma_{ij}\delta\varepsilon_{ij}-D_i\delta E_i+\rho\ddot{u}_i\delta u_i\right)dV+ \tag{1}$$

$$+\sum_{p=1}^{n_L}\frac{1}{L_p}\iint\left(\varphi_1^{L_p}-\varphi_2^{L_p}\right)\delta\varphi dtdt+\sum_{q=1}^{n_R}\frac{1}{R_q}\int\left(\varphi_1^{R_q}-\varphi_2^{R_q}\right)\delta\varphi dt+\sum_{r=1}^{n_C}C_r\left(\varphi_1^{C_r}-\varphi_2^{C_r}\right)\delta\varphi=0$$

Here D, E are the vectors of the electric inductance and electric field strength; σ_{ij} are the components of the symmetric Cauchy stress tensor; ε_{ij} are the components of the tensor of linear deformations; u_i are the components of the displacement vector; φ is the electric potential; $\varphi_1-\varphi_2$ - the potential difference in the external circuit element, n_L, n_R are the number of inductive and resistive elements, respectively, L_p, R_q, C_r - values of inductance, resistance and capacitance of the corresponding circuit element.

For electric field, the condition of equipotentiality is fulfilled

$$\varphi_{,i}=-E_i \tag{2}$$

For elastic parts (V_1), the physical equations of the linear elasticity theory hold true

$$\sigma_{ij}=C_{ijkl}\varepsilon_{kl} \tag{3}$$

For isothermal processesthe electroelastic parts (V_2) are governed by the following physical relations:

$$\left.\begin{aligned}\sigma_{ij}&=\overline{C}_{ijkl}\varepsilon_{kl}-\beta_{ijk}E_k\\ D_k&=\beta_{ijk}\varepsilon_{ij}+e_{ki}E_i\end{aligned}\right\} \tag{4}$$

where C_{ijkl}, $\overline{C}_{ijkl}$ are the tensors of elastic constants, β_{ijk} and e_{ki} are the tensors of piezoelectric and dielctric coefficients.

The constraints imposed on the examined system are given in the form of mechanical and electrical boundary conditions. The mechanical boundary conditions are defined as

$$u_i\big|_{\Gamma_u}=u_{i0}, \tag{5}$$

where Γ_u is the part of the surface of the body V_1, on which the displacements are prescribed.

The expressions for electrical boundary conditions on the piezoelectric parts of volume V_2 are written as

$$\varphi\big|_{\Omega_{el}^{\varphi}}=\varphi_0, \tag{6}$$

here Ω_{el}^{φ} is the part of the bounding electrode-covered surface of body volume V_2, on which

the electric potential is prescribed. In the absence of electrode covering all electrical boundary conditions take zero values.

The eigenvectors of vibrations are determined in the following form:

$$u_i(x,t) = \overline{u}_i(\vec{x})e^{i\omega t}, \varphi(x,t) = \overline{\varphi}(\vec{x})e^{i\omega t} \tag{7}$$

where $\omega = \omega_{\mathrm{R}} + \mathrm{i}\omega_{\mathrm{I}}$ is the complex eigenfrequency of vibrations. In this relation ω_{R} corresponds to the eigenfrequency and ω_{I} corresponds to the rate of vibration damping (damping coefficient), $\overline{u}_i(\vec{x})$, $\overline{\varphi}(\vec{x})$ are the vibration eigenmodes.

A complete mathematical formulation of the problem is presented in work [21]. The stated problem was solved using the finite element method (FEM). Its numerical implementationwas performed based on the new algorithm developed by the authors of the paper, in which, to derive benefits from the commercial ANSYS software package, the APDL macros and FORTRAN programs were incorporated. The obtained algebraic problem of complex eigenvalues was solved by the Muller method with a search through a variety of initial approximations.

3 NUMERICAL RESULTS

To verify the robustness of the proposed approach we considered two example problems:

1) a rigidly clamped elastic plate with a fastened piezoelectric element (figure 1(a)). The plate has the following dimensions: $l_1 = 210$ mm, $b_1 = 26$ mm, $h_1 = 0.5$ mm. The plate is made from material with the following mechanical characteristics $E = 2 \cdot 10^{11}$ Pa, ν=0.3, ρ=7800 kg/m^3. The piezoelectric element made in shape of rectangle with the dimensions $l_p = 50$ mm, $b_p = 20$ mm, $h_p = 0.36$ mm and located 12mm from the fixed plate edge symmetrically to the plate axis. It is made of the material PZT-4 with polarization in the z direction and the following mechanical characteristics: $C_{11} = C_{22} = 13.9 \cdot 10^{10}$ N/m^2, $C_{12} = 7.78 \cdot 10^{10}$ N/m^2, $C_{13} = C_{23} = 7.43 \cdot 10^{10}$ N/m^2, $C_{33} = 11.5 \cdot 10^{10}$ N/m^2, $C_{44} = 3.06 \cdot 10^{10}$ N/m^2, $C_{55} = C_{66} = 2.56 \cdot 10^{10}$ N/m^2, $\beta_{31} = \beta_{32} = -5.2$ C/m^2, $\beta_{33} = 15.1$ C/m^2, $\beta_{52} = \beta_{61} = 12.7$ C/m^2, $e_{11} = e_{22} = 6.45 \cdot 10^{-9}$ F/m, $e_{33} = 5.62 \cdot 10^{-9}$ F/m, $\rho = 7700$ kg/m^3. The upper and lower surfaces of the element are fitted with electrodes.

2) a thin-walled shell in the form of a semi-cylinder, which is rigidly clamped at the edges and is simply supported along the generatrix (figure 1(b)). The shell with $r_1 = 76$ mm, $l_1 = 300$ mm, $h_1 = 0.25$ mm is made from the elastic isotropic material showing the following mechanical properties: $E = 1.96 \cdot 10^{11}$ Pa, $\nu = 0.3$, $\rho = 7700$ kg/m^3. The shell structure comprises a piezoelectric element in the form of the ring segment, which is attached to the shell surface. The element has the following dimensions: $r_p = 76.25$ mm, $\varphi_p = 15.08^0$, $h_p = 0.36$ mm. The center of mass of the element is located at a distance of 15mm from the clamped edges of the shell and is shifted by 90° with respect to the angular coordinate from the simply supported generatrixes. The piezoelectric element is made of piezoceramics PZT-4 showing similar physic-mechanical characteristics, specified yet in the cylindrical coordinates. The direction of polarization coincides with the direction of the *r*–axis. The upper and lower surfaces of the element are fitted with electrodes.

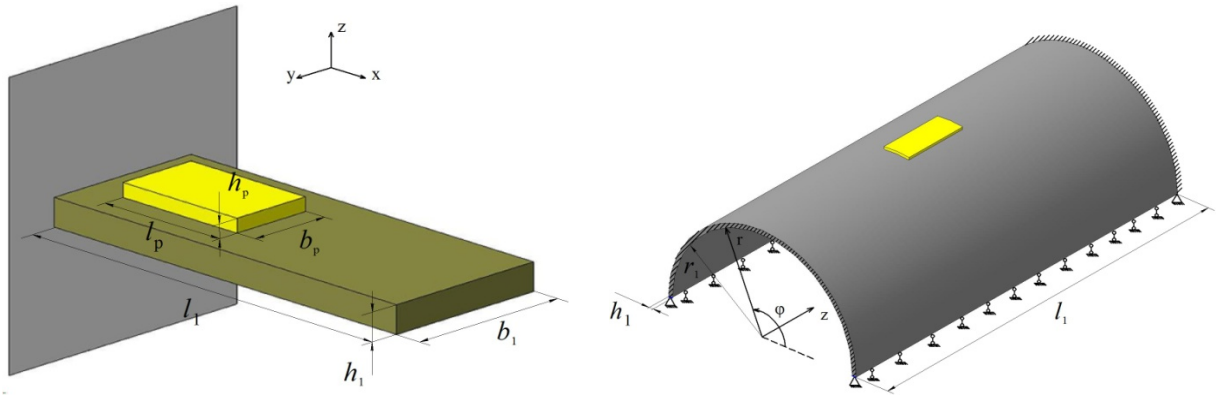

a b

Figure 1: Computational schemes of structures with piezoelectric elements: a) plate; b) shell.

Consider as the external electric circuit the series resonance *RL*-circuit consisting of series-connected resistance (*R*) and inductance (*L*). As an object, a piezoelectric element by virtue of its nature exhibits capacitive properties and in the presence of the external resonance *RL*-circuit it forms a series oscillatory *RLC*-circuit, which leads to the appearance of additional eigenfrequency in the frequency response of our base smart-structure. This means we have frequency response of full system - smart-structure with external electrical circuit. Involvement of the external electric *RL*-circuit into damping of structure vibrations at a specified frequency is accomplished by incorporating in the initial spectrum of eigenfrequencies a purposely-tuned additional frequency from the electric circuit. Tuning is achieved by varying value of external inductance, bringing frequency closer to the eigenfrequency of smart-structure, up to their match.

It has been recognized [22] that the coincidence of the damped eigenfrequency of smart-structure with the frequency of the electric circuit:

$$\omega_R^n = \omega_R^e \tag{8}$$

results in maximum damping of the system vibrations at this particular frequency.

Equation (8) defines the condition I, which the parameters of the external electric circuit must fulfill, to provide with the maximum vibration damping in the particular frequency.

However, the question remains. Does this condition fully define the parameters of the external electric circuit to ensure maximum damping vibrations of the structure at a given frequency?

To tune an oscillation circuit on required frequency it is necessary to choose the corresponding pair of the parameters of external *RL*-circuit. The investigations have shown that the coincidence of the above mentioned frequencies in the range of parameters *R* and *L* may not be singular. Figure 2 shows the line of equality of the first eigenfrequency of the plate with piezoelectric element connected to the shunting resonance *RL*-circuit and the frequency of the oscillatory circuit tuned to the first resonance in the range of parameters *R* and *L*.

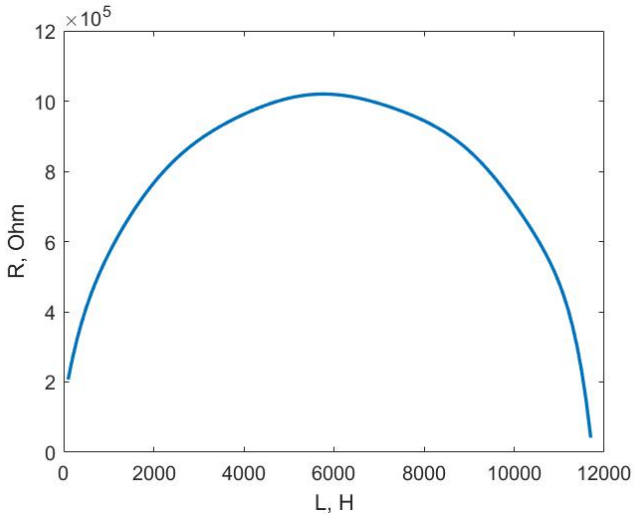

Figure 2: The line of equality of the first eigenfrequency of the plate with piezoelectric element connected in series to the resonant shunt electric *RL*-circuit and the vibration frequencies of the oscillatory circuit in the range of parameter *RL*

It is apparent that condition I is not sufficient for unique determination of the optimal parameters of the external electric circuit.

We can use the fact that the solution of the problem of natural vibrations smart-structure with an external electrical circuit provides a direct measure of damping ratio ω_{Im}^{n} on a particular frequency. It is possible to find such values of the parameters R and L of external electric circuit by scanning the field of circuit parameters, at which achieved the maximum value of the modulus of the imaginary part of the smart-structure's complex frequency (9):

$$\max\left|\omega_{\text{Im}}^{n}\right| \tag{9}$$

The values of R and L, at which the condition II, defined by (9), and will be optimal.

In the examples considered in this paper, ω_{I}^{n} has a unique maximal absolute value in the examined range of the circuit parameters R and L (figure 3): R=402 kOhm, L=11200 H for the plate and R=5.3 kOhm, L=6.93 H for the shell.

It should be noted that the obtained point of maximum ω_{Im}^{n} lies on the curve of coincidence of the real part of the first eigenfrequency of the smart-structure ω_{Re}^{n} and the real part of the additional frequency from circuit ω_{Re}^{e}, that is, a curve that reflects the condition (8). But at this point on this curve is no coincidence of maximum modules of imaginary parts of the eigenfrequency of smart-structure and additional frequency

$$\max\left|\omega_{\text{Im}}^{n}\right| \neq \max\left|\omega_{\text{Im}}^{e}\right| \tag{10}$$

Therefore, to really find the optimal parameters requires careful separation of eigenfrequency of smart-structure and additional frequency.

Thus, on the entire space of possible parameters R and L for the imaginary part of eigenfrequency of smart-strucutre ω_{Im}^{n} (damping ratio) exists only one maximum modulo

value corresponding to the optimal circuit parameters. This maximum point occurs only at the coincidence of the frequency of the oscillation smart-structure and additional frequency.

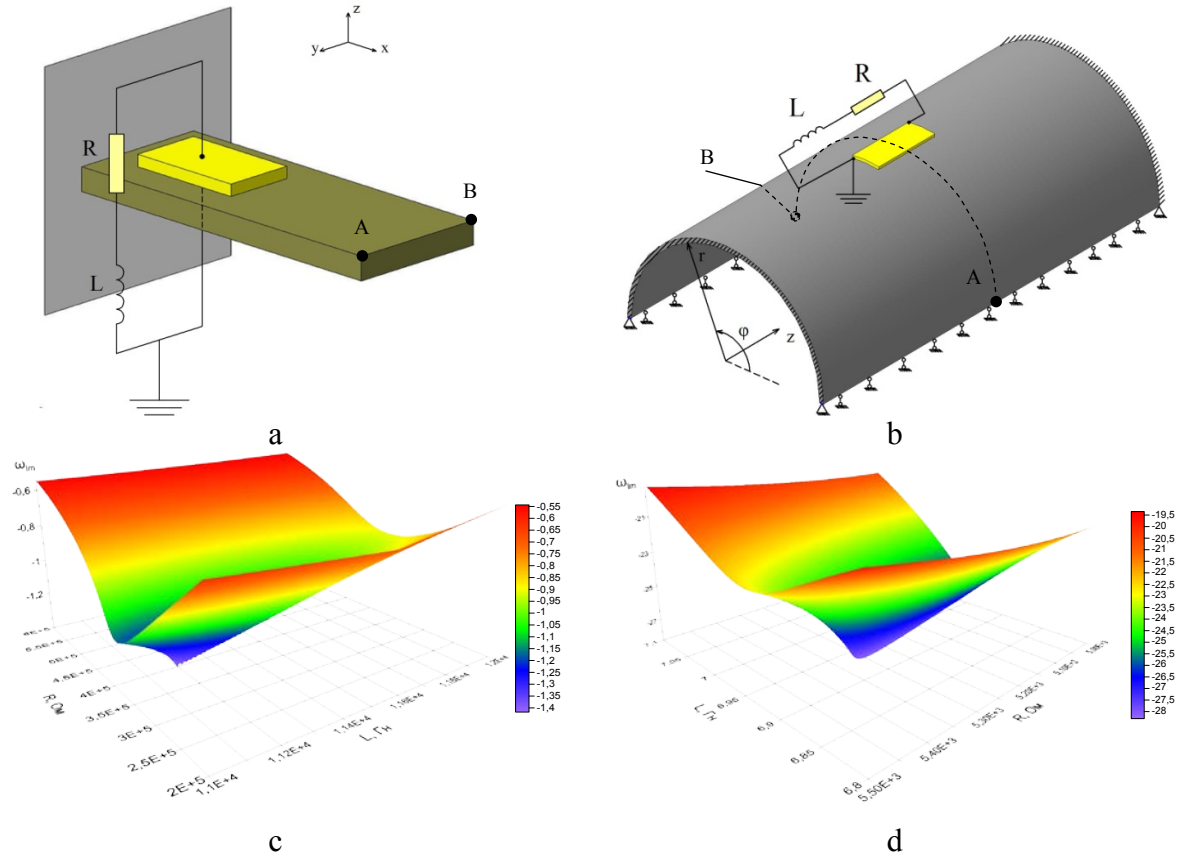

Figure 3: Computational schemes for structures with piezoelectric elements and resonant *RL*-circuit: a) plate, b) shell. The plots constructed for each type of the structure describes the behavior of the vibration damping coefficient of the structure with external circuit at the first eigenfrequency in the range of parameters *R* and *L*

Let us compare the obtained results with the amplitude frequency characteristic (AFC) of the system connected to resistive or resonant external circuits. The AFC of the displacement U_s ($U_s = \sqrt{U_x^2 + U_y^2 + U_z^2}$) of point A (figure 1(a,b)) was calculated as being produced by the external axial harmonic forces with the amplitude $P_X = P_Y = P_Z$=0.01 N applied at point B of the structure.

In the case of the resistive circuit (consisting only of a resistor with resistance *R*) for the first oscillation mode of both systems the maximum modulus value of the parameter vibration damping (condition II) is achieved when the value of the resistor *R* = 1000 Ohms (for the plate), and R = 25 Ohms (for the shell).

Figure 4 shows a comparison of the frequency response of the plate and the shell in the presence of resistive and resonant electric circuits, the optimum parameters are determined by conditions II.

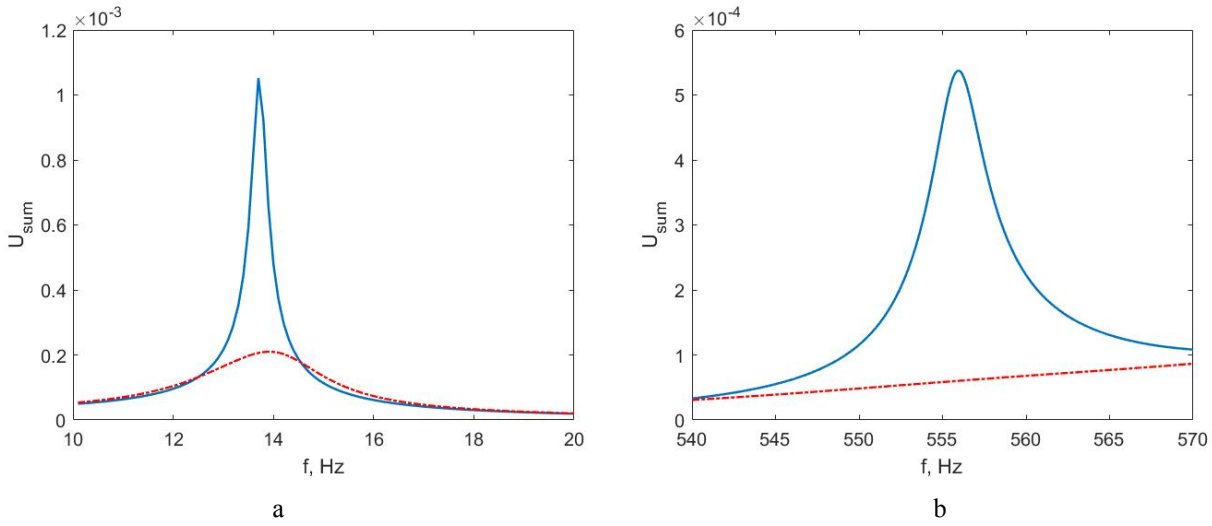

Figure 4: Comparison frequency response of structure's displacement at point A for a resistive and resonant circuits with the optimal parameters for a) plate, b) shell. Solid line - *R*-circuit, dot-dash - *R*L-circuit.

Selected based on the implementation of the proposed terms the parameters of resonant *RL*-circuit gives greater damping of vibration than with the resistive circuit only, and for the shell these parameters have led to the complete disappearance of the resonance peak in the frequency response.

4 CONCLUSIONS

- An approach to selection of optimal parameters for the external passive electric circuits ensuring maximum rate of vibration damping has been proposed based on the mathematical formulation of the problem on natural vibrations of electroelastic bodies with piezoelectric elements connected to external passive electric circuits.
- The condition allowing the evaluation of optimal parameters of the external electric circuits have been determined based on the analysis of the real and imaginary parts of complex eigenvalues of different structures.
- The effectiveness and robustness of the proposed approach have been demonstrated in the context of the example problems studying different structures with piezoelectric elements and two types of shunting external electric circuits: resistive *R*-circuit and series resonant *RL*-circuit.

The work is supported by the RFBR (projects No 15-01-03976-a, No 16-31-00094-mol-a) and UB RAS complex program (project No 15-10-1-18).

REFERENCES

[1] Forward, R.L. Electronic damping of vibrations in optical structures. *Appl. Optics*, (1979) **18:** 690-697.

[2] Hagood, N.W., von Flotow, A. Damping of structural vibrations with piezoelectric materials and passive electrical networks, *Journal of Sound and Vibration* (1991) **146** (2): 243–268.

[3] Park, C.H., Inman, D.J. Enhanced piezoelectric shunt design, *Shock and Vibration* (2003), **10** (2): 127–133.
[4] Fleming, A.J., Moheimani, S.O.R. Control Orientated Synthesis of High-Performance Piezoelectric Shunt Impedances for Structural Vibration Control, *IEEE Transactions on control systems technology* (2005) **13**(1): 97-113.
[5] Wu, D., Yang, Z., Sun, H. Vibration control efficiency of piezoelectric shunt damping system, *Front. Mech. Eng. China* (2009) **4**(4): 441–446.
[6] Thomas, O., Ducarne, J., Deü, J.-F. Performance of piezoelectric shunts for vibration reduction, *Smart Materials and Structures* (2012) **21** (1): 0150082012.
[7] Berardengo, M., Cigada, A., Manzoni, S., Vanali, M. Vibration Control by Means of Piezoelectric Actuators Shunted with *LR* Impedances: Performance and Robustness Analysis, *Shock and Vibration* (2015): 704265.
[8] Høgsberg, J., Le Cöent, A. Explicit solution format for complex-valued natural frequency of beam with R-shunted piezoelectric laminate transducer, *Proc IMechE Part C: J Mechanical Engineering Science* (2014) **228**(1): 31–44.
[9] Preumont, A. *Vibration control of active structures*. 3rd ed. Heidelberg: Springer (2011).
[10] Moheimani, S.O.R., Fleming, A.J. *Piezoelectric transducers for vibration control and damping*. London: Springer (2006).
[11] Delpero, T., Bergamini, A.E., Ermanni, P. Identification of electromechanical parameters in piezoelectric shunt damping and loss factor prediction, *Journal of Intelligent Material Systems and Structures* (2012) **11**: 287–298.
[12] Porfiri, M., Maurini C., Pouget, J. Identification of electromechanical modal parameters of linear piezoelectric structures, *Smart Mater Struct*. (2007) **16**: 323–331.
[13] Soltani, P., Kerschen, G., Tondreau, G., Deraemaeker, A. Piezoelectric vibration damping using resonant shunt circuits: an exact solution, *Smart Materials and Structures*, (2014) **23**: 125014.
[14] Heuss, O., Salloum, R., Mayer, D., Melz, T. Tuning of a vibration absorber with shunted piezoelectric transducers, *Arch. Appl. Mech.* (2016) **86** (10): 1715–1732.
[15] Kligman, E.P., Matveenko, V.P. Natural Vibration Problem of Viscoelastic Solids as Applied to Optimization of Dissipative Properties of Constructions, *International Journal of Vibration and Control* (1997) **3**(1): 87-102.
[16] Matveenko, V.P., Kligman, E.P., Yurlov, M.A., Yurlova, N.A. Simulation and optimization of dynamic characteristics of piezoelectric smart structures, *Physical Mesomechanics* (2012), **15** (3-4): 190-199.
[17] Washizu, K. *Variational Methods in Elasticity and Plasticity*. Pergamon Press, London (1982).
[18] Parton, V.Z., Kudryavtsev, B.A. *Electromagnetoelasticity of piezoelectric and electroconductive bodies*. Nauka, Moscow (1988).
[19] Karnaukhov, V.G., Kirichok, I.F. *Electrothermal Viscoelasticity*, Naukova Dumka, Kiev (1988).
[20] Matvvenko, V.P., Oshmarin, D.A., Sevodina, N.V., Iurlova, N.A. Natural vibration problem for electroviscoelstic body with external electric circuits and finite-element relations for its numerical implementation, *Computational Continuum Mechanics* (2016) **9**(4): 476-485.

[21] Matveenko, V.P., Yurlov, M.A., Yurlova, N.A. Optimization of the damping properties electro-viscoelastic objects with external electric circuits, *Mechanics of Advanced Materials,* Engineering Materials, Springer (2015): 79-100.

[22] Nashif, A.D., Jones, D.I.G., Henderson, J.P. *Vibration Damping*, John Wiley and Sons Inc. (1985).

VIII ECCOMAS Thematic Conference on Smart Structures and Materials
SMART 2017
A. Güemes, A. Benjeddou, J. Rodellar and J. Leng (Eds)

DYNAMIC CONTROL OF DEFORMABLE MIRRORS FOR ADAPTIVE OPTICS

Kainan Wang*, David Alaluf†, Bilal Mokrani*, André Preumont*

* Active Structures Laboratory
Department of Control Engineering and System Analysis
Université Libre de Bruxelles (ULB)
Avenue F.D. Roosevelt 50, CP.165/55, 1050 Brussels, Belgium
e-mail: Kainan.Wang@ulb.ac.be, web page: http://scmero.ulb.ac.be

† European Space Agency - ESA/ESTEC, Opto-Electronics Section
Keplerlaan 1, 2201 AZ Noordwijk ZH, The Netherlands
e-mail: David.Alaluf@esa.int

Key words: Adaptive Optics, Deformable Mirror, Control-Structure Interaction, Active/Passive Damping, Modal filter, Inductive shunt.

Abstract. This paper discusses the shape control of deformable mirrors in the dynamic range. The phenomenon of control-structure interaction which appears when the control bandwidth increases is described and the main parameters affecting it are highlighted. Finally, passive and active strategies for damping augmentation are proposed and tested in simulation.

1 INTRODUCTION

Adaptive optics (AO) has revolutionized astronomy by correcting in real-time the aberrations introduced by atmospheric turbulence using deformable mirrors with hundreds of actuators [1]. Several deformable mirror (DM) technologies are being used, employing piezoelectric, electrostatic or electromagnetic actuation; see e.g.[2] for a review of various technologies. The various aspects involved in the design of a AO deformable mirror are its size, the stroke, the number of actuators, the control bandwidth and, as we shall see, its natural frequency and damping.

- There are AO mirrors of all sizes, but a minimum size is generally required by the field of view of the telescope; typical DM diameter for a few hundred actuators is 150-200 mm.
- The stroke δ necessary to compensate the turbulent wave front may be estimated from the RMS phase error. A typical value would be 3 times the RMS wavefront error: Using Equ.(A.2) in the Appendix, $\delta = 3.\sigma_\phi.\lambda/2\pi$, where λ is the wavelength.
- The number of actuators depends on the required optical quality, the diameter of the primary mirror D, the telescope site and the wavelength. Equation (A.7) may help in this matter. Typical AO mirrors have hundreds of actuators.

- In addition to the "fitting" error resulting from the limited morphing capability of the mirror, there will be additional errors due to the limited bandwidth f_c of the control system; they will be analyzed below.

The control system requires a real-time measurement of the wavefront error, which is generally obtained with a micro-lenses array known as Shack-Hartmann (SH) sensor. Because of the complexity of the problem which involves hundred of inputs and hundred of outputs, the control problem is generally formulated as quasi-static, the system being defined by its Jacobian. However, deformable mirrors are flexible structures with flexible modes of natural frequencies f_i and modal damping ξ_i. When the damping is low and the control bandwidth increases, the system experiences *control-structure interaction* which is the subject of this paper.

To illustrate our discussion, we will consider the bimorph piezoelectric mirror of Figure 1. It is controlled by an array of 127 piezoelectric electrodes on the back, organized in honeycomb and the SH sensor consists of a square array of 17×17 lenslets (225 activated). The front side of the mirror is supplemented by a ring of piezoelectric material outside the pupil, whose double role is to improve the thermal balance and provide additional damping to the system (this will be clarified later). It is assumed that a separate mirror takes care of the tip-tilt disturbance, so that the control system discussed here handles the Zernike modes of radial order $n \geq 2$. Several boundary conditions are possible, which affect the Jacobian as well as the spectrum of natural frequencies of the mirror; in this study, the mirror is assumed simply supported on the edge.

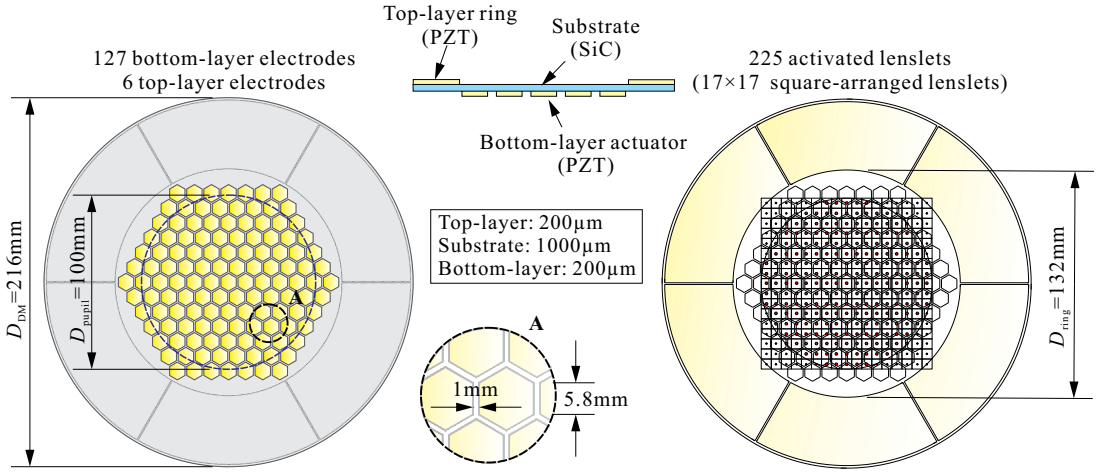

Figure 1: AO mirror configuration used in the simulations

The paper is organized as follows: section 2 discusses the quasi-static control of the mirror, section 3 discusses the feedback control assuming a quasi-static model of the mirror and analyzes the influence of the control bandwidth on the residual error. Section 4 introduces the control-structure interaction and the main parameters involved in it. Some concepts of Adaptive Optics which have been used are summarized in appendix.

2 QUASI-STATIC CONTROL

Once the number and shape of the actuators, the boundary conditions, and the configuration of the Shack-Hartmann sensor have been chosen, the quasi-static behaviour of the AO mirror is described by the linear equation

$$\mathbf{s} = J\,\mathbf{v} \tag{1}$$

where $\mathbf{s}$ is the vector of output of the SH sensor and $\mathbf{v}$ is the vector actuator input voltages applied to the piezoelectric actuators. The actuator input which cancels the sensor output is obtained as the pseudo-inverse:

$$\mathbf{v} = J^{\dagger}\,\mathbf{s} \tag{2}$$

If a Singular Value Decomposition (SVD) of J is carried out

$$J = U\Sigma V^T = \sum_{i=1}^{n} \sigma_i \mathbf{u}_i \mathbf{v}_i^T \tag{3}$$

($\mathbf{u}_i$ are the orthogonal sensor modes and $\mathbf{v}_i$ the orthogonal actuator modes), the pseudo-inverse reads

$$J^{\dagger} = V\Sigma^{\dagger}U^T = \sum_{i=1}^{n} \frac{1}{\sigma_i}\mathbf{v}_i\mathbf{u}_i^T \tag{4}$$

This solution is that minimizing $||\mathbf{s} - J\mathbf{v}||^2$. The sum normally extends to all singular values. However, because they appear as σ_i^{-1}, the smallest singular values tend to generate unnecessary large control inputs without bringing any contribution to improvement of the fitting error. The problem may be solved either by truncating the SVD expansion of $J^{\dagger}$ after r terms, to eliminate the smallest singular values, or to use a *Tikhonov regularization*, minimizing

$$min_{\mathbf{v}}[||\mathbf{s} - J\mathbf{v}||^2 + \alpha^2||\mathbf{v}||^2] \tag{5}$$

where α^2 is a tuning parameter (the method is also known as *damped least square*). The solution is

$$\mathbf{v} = (J^T J + \alpha^2 I)^{-1} J^T \mathbf{s} \tag{6}$$

The singular value expansion of $J^{\dagger}$ now reads

$$J^{\dagger} = V\Sigma^{\dagger}U^T = \sum_{i=1}^{n} \frac{\sigma_i}{\sigma_i^2 + \alpha^2}\mathbf{v}_i\mathbf{u}_i^T \tag{7}$$

Both methods have been found to reduce significantly the input voltage budget without affecting significantly the fitting error of the deformable mirror (see [3] for illustrations).

3 FEEDBACK CONTROL BASED ON QUASI-STATIC MODEL

3.1 Control of Zernike modes

In order to estimate the control bandwidth, consider the temporal Power Spectral Density (PSD) $\Phi(f)$ of a Zernike polynomial (see Appendix). It may be approximated as in Figure 2,

with a cut-off frequency $f^\star$ being given by Equ.(A.8). In order to analyze the residual error after feedback control, it is common practice in the optics community to assume an integral feedback control $H(f) = f_c/jf$ (where f_c is the cross-over frequency), leading to a closed-loop transfer function F and an *error transfer function* T of respectively

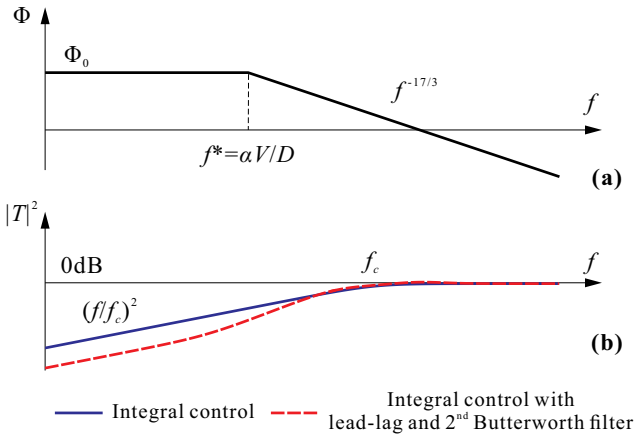

Figure 2: (a) Approximation of the PSD of a Zernike polynomial; $f^\star = 0.3(n+1)V/D$ where n is the radial order. (b) Squared magnitude of the error transfer function $|T|^2$.

$$F = \frac{H}{1+H} = \frac{1}{1+jf/f_c} \qquad \text{and} \qquad T = 1 - F = \frac{jf/f_c}{1+jf/f_c} \tag{8}$$

The closed-loop Mean square (MS) residual error in the Zernike mode i is given by

$$< |a_i|^2 >_{CL} = \int_0^\infty |T|^2 \Phi(f)\, df \simeq 0.708\, \Phi_0 f^\star \left(\frac{f^\star}{f_c}\right)^2 \simeq 0.585\ < |a_i|^2 > \left(\frac{f^\star}{f_c}\right)^2 \quad (f_c \gg f^\star) \tag{9}$$

after using Equ.(A.9). Since $f^\star$ increases with the radial order of the Zernike mode, the foregoing might suggest that f_c should be larger for higher order modes; however, as rightly observed by Conan [4], the contribution $< |a_i|^2 >$ of the Zernike modes with low radial orders to the total MS error is much larger than that of the higher modes, leading to a higher control bandwidth (f_c is also the control bandwidth in this case) for the low order modes. To illustrate this, consider the defocus mode Z_4 with radial order $n = 2$ and the spherical aberration Z_{11} with radial order $n = 4$. Their open-loop contributions to the overall MS phase error are respectively [5]: $< |a_4|^2 >= 0.023(\frac{D}{r_0})^{5/3}$ and $< |a_{11}|^2 >= 0.0024(\frac{D}{r_0})^{5/3}$ and their corner frequencies: $f_4^\star = 0.9\, V/D$ and $f_{11}^\star = 1.5\, V/D = 1.66 f_4^\star$. Reducing the closed-loop MS error of these two modes to, say $10^{-4}(\frac{D}{r_0})^{5/3}$, will require respectively $f_c = 11.6\, f_4^\star$ and $f_c = 3.75\, f_{11}^\star = 6.22\, f_4^\star$.

The integral controller used above is convenient for illustration purposes and computing orders of magnitude. More performing control laws are available; the compensator of Figure 3 will be used later in this study: the integral control has been supplemented with a lag filter at low frequency to magnify the gain (and lower $|T|^2$), a lead filter near crossover to increase the phase margin and a second-order Butterworth filter at high frequency to increase the roll-off. The controller may be scaled to the appropriate bandwidth by simply translating the Bode plots

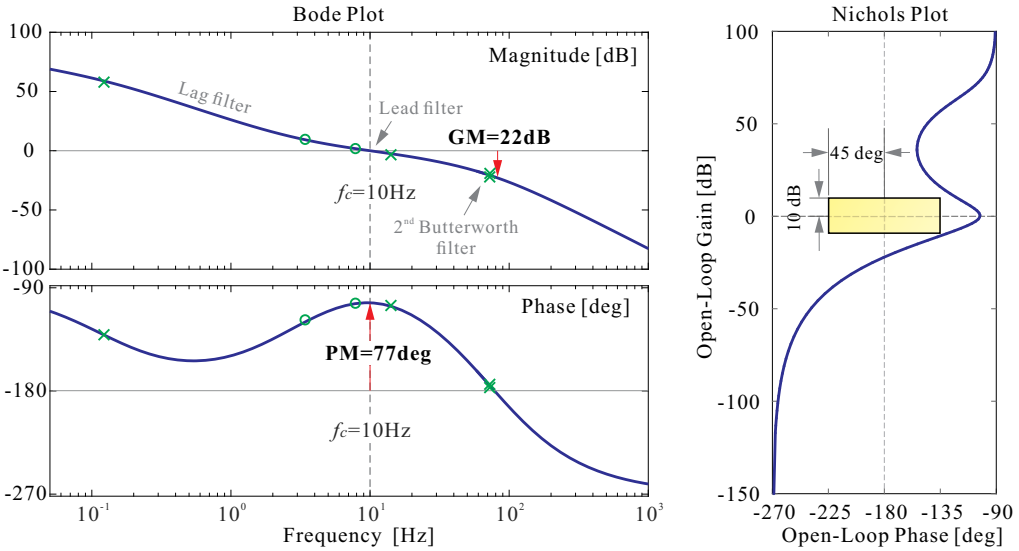

Figure 3: Compensator used in this study (normalized to $f_c = 10$ Hz). It consists of an integrator, a lag filter, a lead filter and a Butterworth second order filter. The position of the poles and zeros are indicated on the Bode plots (left). The bandwidth may be adjusted by translating the Bode plots along the frequency axis. This leaves the Nichols plot (Right) unchanged.

along the frequency axis until the cross-over frequency f_c has the appropriate value; this leaves the Nichols plot unchanged.

3.2 Control of the mirror based on the Jacobian

Figure 4 shows the block diagram of the control system. The input-output relationship between the voltages applied to the piezoelectric electrodes and the SH sensor outputs is assumed to be the Jacobian J (the dynamic response is ignored). A simulation code has been developed, which allows to generate turbulent screens with Kolmogorov distribution (see Appendix) and to calculate the time-history of the mirror response when the turbulent screen is transported by the wind with a velocity V. The SH sensor is assumed to have infinite bandwidth (no dynamics). Using this code, it is possible to study the influence of the feedback control law $H(s)$ on the performance of the control system; the residual MS phase error is estimated by statistical analysis of time-histories of the mirror response. The following data have been assumed in our calculations: telescope aperture: $D = 5m$, Fried coherence length $r_0 = 79\,cm$ (defined at $\lambda = 2.2\,\mu m$ for a 0.57 arcsec seeing), wind speed $V = 10m/s$. The *Greenwood frequency* is $f_G = 0.43\frac{V}{r_0} = 5.44$Hz. The controller bandwidth (approximated by the cross-over frequency f_c) is varied from 2Hz to 30Hz.

Figure 5 shows the cumulative phase variance in closed-loop

$$[\Delta_J]_{CL} = \sum_{i=J}^{\infty} < |a_i|^2 >_{CL}$$

as a function of the cross-over frequency f_c of the compensator of Figure 3; the figure starts at $J = 4$ because the tip-tilt modes are assumed to be controlled separately. The residual

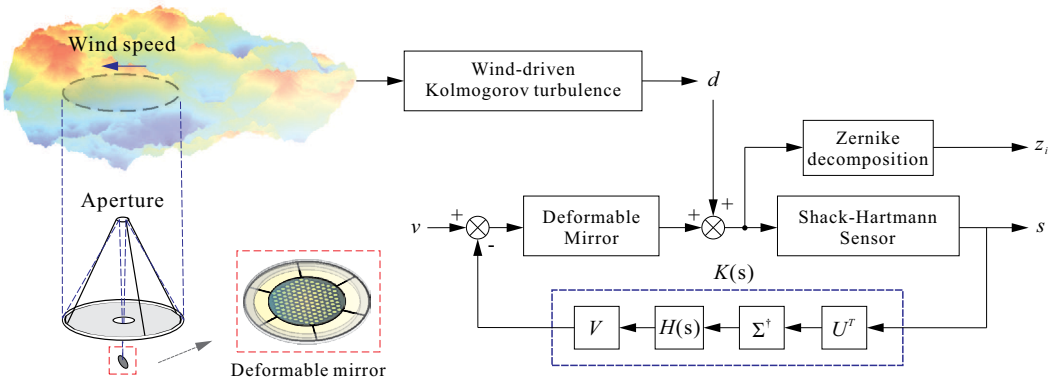

Figure 4: Block diagram of the control system. The input-output relationship is $s = Jv$. The feedback loop consists of the SVD controller $K(s) = VH(s)\Sigma^{\dagger}U^{T}$. The disturbance d consists of a frozen Kolmogorov turbulent screen transported by the wind at velocity V. The performance is measured by the Zernike expansion of the residual error.

phase variance may be transformed directly in optical quality using Equ.(A.3). The residual error includes the fitting error due to the finite resolution of the actuators and sensors and the dynamic error due to the finite bandwidth of the controller.

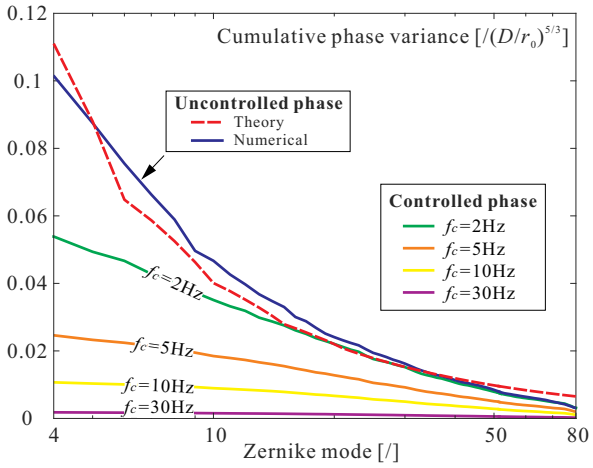

Figure 5: Cumulative phase variance scaled by $(\frac{D}{r_0})^{5/3}$ as a function of the cross-over frequency f_c of the compensator of Figure 3. Equ.(A.6) is shown in dash-dotted lines.

4 CONTROL-STRUCTURE INTERACTION

So far, it has been assumed that the mirror responds in a quasi-static manner to the voltage input. However, when the control bandwidth increases, the dynamics of the mirror can no longer be ignored and the closed-loop stability must be investigated with care.

4.1 Single axis piezoelectric actuator

In order to introduce the phenomenon of control-structure interaction, consider a single axis piezoelectric actuator acting on a mass m (Figure 6). If δ is the unconstrained piezoelectric displacement, it may be replaced by an equivalent piezoelectric force $f = K_a\delta$ where K_a is the stiffness of the piezoelectric element. The input-output relationship of the system is

$$\frac{x}{\delta} = G(s) = \frac{1}{1 + 2\xi\frac{s}{\omega_n} + \frac{s^2}{\omega_n^2}} \tag{10}$$

with $\omega_n^2 = K_a/m$ and $2\xi\omega_n = c/m$. We assume that the compensator is $H(f) = 2\pi f_c/s$ as previously. If the structure is assumed to behave quasi-statically, $G(s) = 1$ and $G(s)H(s) = 2\pi f_c/s$ which has infinite gain margin (GM) and 90^0 phase margin (PM). On the contrary, if the full dynamics is included, the amplitude Bode plot of the control system is that of Figure 6. Accordingly, the system stability requires that $f_n/f_c > 1/2\xi$ and the gain margin is expressed simply as

$$GM = 20\log[\frac{2\xi f_n}{f_c}] \qquad (\text{in dB}) \tag{11}$$

This formula points out the two parameters which control the control-structure interaction: the frequency ratio f_n/f_c and the structural damping ξ. Of course, the compensator used in this analysis is not the best one, and the situation may be improved by adding a Butterworth filter as the one of Figure 3, but the two parameters remain the same. Figure 7 gives the gain margin (in dB) as a function of the frequency ratio f_n/f_c for a few values of the damping ratio ξ, for the compensator of Figure 3. Equation (11) is represented in dashed lines. The interest of increasing the damping of the structure is obvious from this plot. This can be done passively or actively.

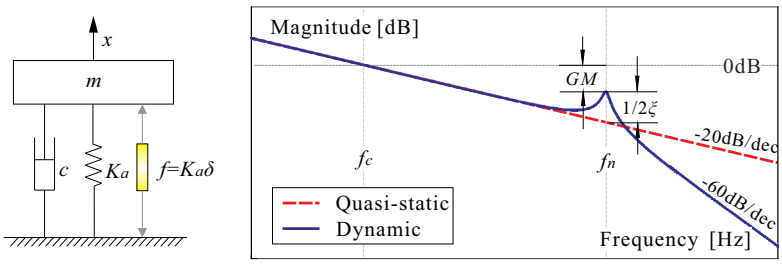

Figure 6: Position control of a mass with a single axis piezo-actuator; the compensator is $H(f) = 2\pi f_c/s$. The gain margin is GM $= 20\log[\frac{2\xi f_n}{f_c}]$.

4.2 Multi-Input-Multi-Output-System

The case of the full mirror cannot be treated as simply as that of the previous section; however, based on the *small gain theorem*, it is possible to develop a sufficient condition for stability (e.g. [6], Ch.10). The dynamic response of the system (mirror plus SH sensor) may be written with classical notations:

$$G(s) = S\Phi.diag[\frac{1}{s^2 + 2\xi_i\omega_i s + \omega_i^2}]\Phi^T K_a \tag{12}$$

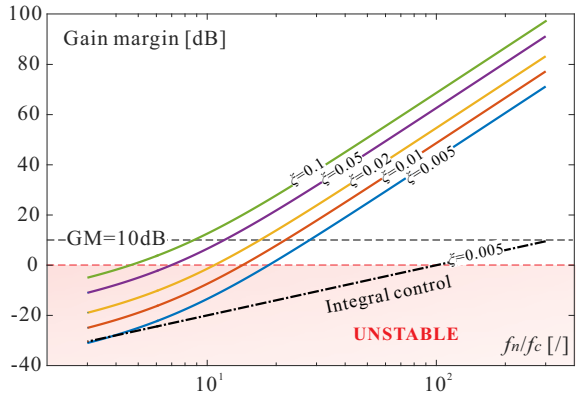

Figure 7: Single axis system with the compensator of Figure 3. Gain margin in dB as a function of the frequency ratio f_n/f_c for a few values of the damping ratio ξ. Equation (11) is represented in dashed line.

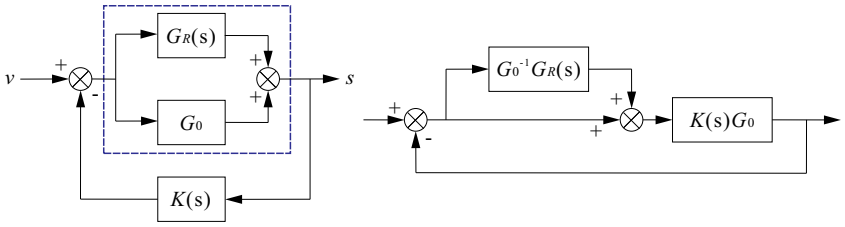

Figure 8: Left: Control structure of a flexible mirror: the nominal system is $G_0 = J$ and the residual system $G_R(s)$ includes all the dynamic deviation with respect to the nominal system. $K(s)$ is the SVD feedback controller. Right: Classical form of multiplicative uncertainty.

where Φ is the matrix of (normalized) mode shapes, S is the output matrix of the SH sensor and K_a is the matrix connecting the input voltages to the equivalent piezoelectric forces acting on the mirror. With these notations, the Jacobian describing the quasi-static response may be written

$$J = G(0) = S\Phi.diag[\frac{1}{\omega_i^2}]\Phi^T K_a \tag{13}$$

and the response may be decomposed in the *nominal* response $G_0 = J$ (quasi static) and the *residual* response $G_R(s)$:

$$G_R(s) = S\Phi.diag[\frac{1}{s^2 + 2\xi_i\omega_i s + \omega_i^2} - \frac{1}{\omega_i^2}]\Phi^T K_a \tag{14}$$

This control structure can be easily transformed into a classical form of multiplicative uncertainty (Figure 8) for which the following sufficient condition for stability applies :

$$\overline{\sigma}(G_0^{-1}G_R) < \underline{\sigma}[I + (KG_0)^{-1}] \tag{15}$$

where $\overline{\sigma}$ and $\underline{\sigma}$ stand respectively for the maximum and the minimum singular value. The left hand side $\overline{\sigma}(G_0^{-1}G_R)$ expresses the maximum relative value of the residual response with

respect to the quasi-static one; it is small at low frequency and becomes large in the vicinity of the vibration modes, where the amplitude of the peaks is governed by the structural damping; increasing the structural damping will lower the resonance peaks and increasing the natural frequencies of the structure will move them to the right. The right hand side of Equ.(15) is concerned only with the nominal system; the curve is essentially flat within the bandwidth of the control system. Figure 9 shows the result of the application of this test to our problem, a structural damping of 0.5% has been assumed; the distance between the two curves may be interpreted as a gain margin, if the two curves cross each other, there is a danger of instability.

Two ways of increasing the damping have been investigated: passive and active damping.

4.3 Passive Damping

The first option consists of using the piezoelectric ring on the front side of the mirror and connect it to an inductive shunt targeted at the most critical mode [7]. This technique is particularly adapted when the first mode is well separated from the other modes. With the geometrical arrangement of Figure 1 of the mirror supported on the edge, it is possible to achieve up to $\xi = 0.053$ with the 6 PZT patches shunted in parallel on an Inductive (RL) circuit. This reduces significantly the first peak of Figure 9. Note that, although this is outside the present discussion, the PZT ring on the front side of the mirror may be used to improve the thermal balance of the mirror, and to introduce a bias curvature which allows to operate the control electrodes with positive voltage only. These aspects are discussed in detail in [3].

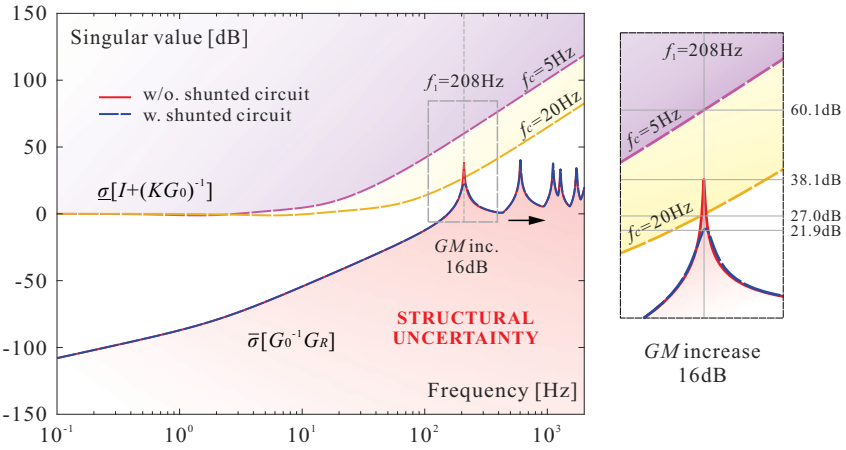

Figure 9: Stability robustness test for various crossover frequencies. A structural damping of 0.5% has been assumed. The effect of inductive shunt damping of the first mode of vibration is shown in dashed lines (a zoom in the vicinity of the first resonance is on the right side).

4.4 Active Damping

The second option is to supplement the shape control loop (High Authority Control - HAC) with an active damping loop (Low Authority Control - LAC). Both loops use the same actuators and sensors. The LAC loop takes advantage of the large sensor array of the SH and the large actuator array of the PZT actuators to do some modal filtering and apply modal active damping

to the critical modes [8] (Figure 10). If $\hat{\Phi}$ is the matrix of the mode shapes to be controlled actively (only very few modes will need to be damped actively), one can construct the matrices

$$C = S\hat{\Phi} \qquad \text{and} \qquad B = \hat{\Phi}^T K_a \tag{16}$$

their pseudo-inverse are respectively $C^\dagger$ and $B^\dagger$. The principle of the modal filter is as follows: If $\mathbf{s}$ is the SH sensor output, $\hat{\mathbf{z}} = C^\dagger \mathbf{s}$ is the vector of modal amplitudes of the modes to be controlled. The modal amplitudes are the inputs of independent active damping controllers $D(s)$; the controller output $\hat{\mathbf{u}}$ is projected onto voltages applied to the electrodes according to $\mathbf{v} = B^\dagger \hat{\mathbf{u}}$. Overall, the independent modal active damping loop reads:

$$\mathbf{v} = B^\dagger.D(s).C^\dagger\,\mathbf{s} = [(\hat{\Phi}^T K_a)^\dagger.D(s).(S\hat{\Phi})^\dagger]\,\mathbf{s} \tag{17}$$

A modal damping ratio ξ_d may be enforced by the controller

$$D(s) = diag(2\xi_d \omega_i s) \tag{18}$$

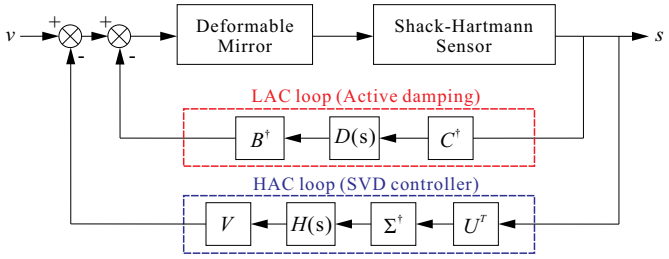

Figure 10: HAC/LAC strategy for active damping of the mirror. The shape control loop is supplemented by a modal active damping of the critical low frequency vibration modes.

Figure 11 illustrates the effect of active damping on the stability robustness test, when an active damping ratio $\xi_d = 0.05$ is requested.

5 CONCLUSION

This paper is an attempt to elucidate the control-structure interaction in AO mirrors; this phenomenon appears when the control bandwidth increases and interact with the flexible modes of the mirror. The main parameters affecting it have been highlighted and passive and active strategies for damping augmentation have been proposed and tested in simulation.

APPENDIX: EFFECT OF ATMOSPHERIC TURBULENCE ON IMAGE

The aim of this section is to introduce some concepts in adaptive optics which are necessary to discuss the control performance and bandwidth. The material below is taken from [4, 5, 9, 10]:

- The **Fried coherence length** r_0 is the aperture above which there is no improvement of the resolution without Adaptive Optics. If $D \leq r_0$, the telescope is diffraction limited; if $D \geq r_0$, the resolution is limited by the **seeing**: λ/r_0 (the seeing is a property of the telescope site). r_0 depends on the wavelength; typical values are $r_0 = 10 - 20\,cm$ at $\lambda = 0.55\mu m$ (visible) and $r_0 = 53 - 106\,cm$ at $\lambda = 2.2\,\mu m$ (infrared).

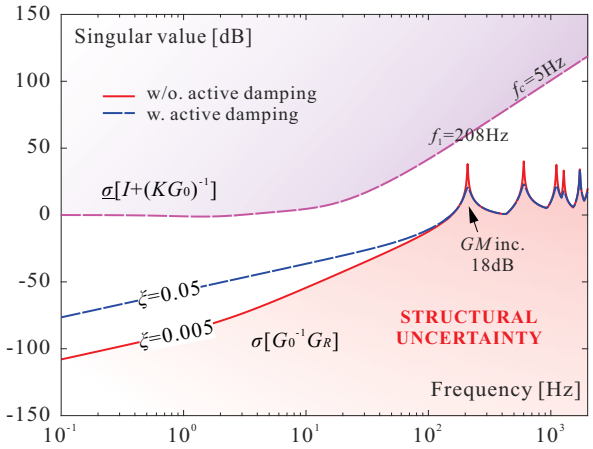

Figure 11: Effect of the active damping of the mirror on the robustness test.

- The atmospheric turbulence introduces a wavefront distortion w on an initially plane wave; this is responsible for a phase delay $\phi(\mathbf{x}) = 2\pi.(w/\lambda)$ which may be represented by the **Kolmogorov turbulence model**:

$$\Phi(\vec{\kappa}) = \frac{0.023}{r_0^{5/3}} |\vec{\kappa}|^{-11/3} \tag{A.1}$$

  where $\vec{\kappa}$ is the two dimensional spatial frequency vector. According to the Taylor assumption, the phase screen is transported as a frozen shape at the wind velocity V. The Mean-Square (MS) error of the phase for a telescope of diameter D is given by:

$$\sigma_\phi^2 = 1.03\,(\frac{D}{r_0})^{5/3} \tag{A.2}$$

  According to this formula, if $D = r_0$, $\sigma \simeq 1$ rad.

- The **Strehl Ratio** S is a measure of the image quality; it is equal to 1 for a perfect diffraction limited telescope. The threshold of image acceptability corresponds to $D = r_0$, thus $\sigma = 1$ rad, leading to $S \simeq 0.37$. The so-called *Marechal Approximation* relates S to the MS phase error by

$$S = e^{-\sigma^2} \qquad (S > 0.1) \tag{A.3}$$

  The approximation $S \simeq 1 - \sigma^2$ ($\sigma^2 \ll 1$) is also often used. A well corrected system has a Strehl ratio $S \geq 0.8$, corresponding to $\sigma_\phi^2 = 0.2$ rad^2, that is a wavefront aberration of $\sigma_w \simeq \lambda/14$. Since the effect of a deformable mirror is to introduce a modification of the wavefront twice that of the deformed mirror within the pupil, $\lambda/28$ is a typical value for the residual error on the deformed mirror after control.

- The **Zernike polynomials** $Z_i(\varrho, \theta)$ are a set of orthogonal functions defined on the unit circle which are used to characterize the phase aberration [9]. If the wavefront phase error

is expanded in the Zernike modes:

$$\phi(R\varrho) = \sum_{i=1}^{\infty} a_i Z_i(\varrho, \theta) \tag{A.4}$$

The MS phase error may be written

$$\sigma^2 = \sum_{i=1}^{\infty} < |a_i|^2 > \tag{A.5}$$

The Zernike modes with low radial order have the largest contribution to the MS error. If J Zernike modes have been perfectly corrected, the residual MS error is given by [9]

$$\Delta_J = \sum_{i=J+1}^{\infty} < |a_i|^2 > \simeq 0.29\, J^{-\frac{\sqrt{3}}{2}} (\frac{D}{r_0})^{5/3} \qquad \text{rad}^2 \qquad (J \gg 1) \tag{A.6}$$

The number J of Zernike modes which must be perfectly cancelled to achieve a given Strehl ratio (image quality), for a given value of D/r_0, is solution of the equation

$$S = 1 - 0.29\, J^{-\frac{\sqrt{3}}{2}} (\frac{D}{r_0})^{5/3} \tag{A.7}$$

The solution J gives the minimum number of degrees of freedom to achieve a given image quality; for example, if $D/r_0 = 10$ and $S = 0.8$, $J = 109$. Since a perfect cancellation of the low order modes will never be possible, the number of actuators is larger than this number.

The temporal Power Spectral Density (PSD) of the amplitudes of the Zernike polynomials expansion of the phase error has been studied by Conan [4]. For a given radial degree ($n > 1$), the PSD can be roughly approximated by a constant value Φ_0 until the cut-off frequency $f^\star$ followed by a decay according to $f^{-17/3}$ (Figure 2). The cut-off frequency depends on the radial order n and the wind velocity according to

$$f^\star = 0.3(n+1)V/D \tag{A.8}$$

The corresponding MS error (of Zernike polynomial of order i) without any control is

$$< |a_i|^2 >= 1.21\Phi_0\, f^\star \tag{A.9}$$

- For a single layer of turbulence, the **Greenwood frequency** is given by

$$f_G = 0.43\frac{V}{r_0} \tag{A.10}$$

For a first-order filter of bandwidth f_c, the closed-loop residual phase error is related to the Greenwood frequency by

$$\sigma^2_{CL} = (\frac{f_G}{f_c})^{5/3} \qquad \text{rad}^2 \tag{A.11}$$

REFERENCES

[1] Tyson, R.K. *Introduction to Adaptive Optics*. SPIE Press, 2000.

[2] Madec, P. Y. Overview of deformable mirror technologies for adaptive optics and astronomy. *SPIE Astronomical Telescopes+ Instrumentation* (2012).

[3] Alaluf, D. *Piezoelectric Mirrors for Adaptive Optics in Space Telescopes*. PhD thesis, Brussels, Belgium, 2016.

[4] Conan, J. M., Rousset, G., and Madec, P. Y. Wave-front temporal spectra in high-resolution imaging through turbulence. *JOSA A* (1995) **12**:1559–1570.

[5] Dainty, J. C. Optical Effects of Atmospheric Turbulence, Chapter 1 of *Laser Guide Star Adaptive Optics for Astronomy* Springer, (2010).

[6] Preumont, A., *Vibration Control of Active Structures, An Introduction*, 3rd Edition, Springer, 2011.

[7] de Marneffe, B. *Active and passive vibration isolation and damping via shunted transducers*. PhD thesis, Brussels, Belgium, 2007.

[8] Meirovitch, L. and Baruh, H. The implementation of modal filters for control of structures. *Journal of Guidance, Control, and Dynamics* (1985) **8**:707–716.

[9] Noll, R. J. Zernike polynomials and atmospheric turbulence. *JOSA* (1976) **66**:207–211.

[10] Greenwood, D. P. Bandwidth specification for adaptive optics systems. *JOSA* (1977) **67**:390–393.

VIII ECCOMAS Thematic Conference on Smart Structures and Materials
SMART 2017
A. Güemes, A. Benjeddou , J. Rodellar and Jinsong Leng (Eds)

EFFECT OF ADHESIVE LAYER PROPERTIES ON THE ENERGY HARVESTING PERFORMANCE OF A PLATE WITH TOPOLOGICALLY OPTIMIZED NETWORKS OF PIEZOELECTRIC PATCHES

JELDER Q. VELASQUEZ*, MARCELO A. TRINDADE†

Department of Mechanical Engineering, São Carlos School of Engineering,
University of São Paulo
Av. Trabalhador São-Carlense, 400, São Carlos, SP, 13566-590, Brazil
*e-mail: jequive@usp.br

† e-mail: trindade@sc.usp.br

Key words: Piezoelectric materials, Energy harvesting, Finite element, Smart structures.

Abstract. One of the key issues to improve the performance of piezoelectric energy harvesting devices is the increase the electromechanical coupling between host structure and piezoelectric patches. Thus some aspect affecting the electromechanical coupling, such as bonding effectiveness and patches positioning are investigate in this work. This is done by, first, analyzing the effect on the electromechanical coupling of successive segmentation of piezoelectric material and the number of piezoelectric patches covering the hos structure. Then a genetic algorithm optimization is used to determine the optimal distribution of a fixed number of patches to maximize the electromechanical coupling. Results are obtained using a custom finite element model that accounts for adhesive layer properties.

1. INTRODUCTION

Piezoelectric patches adhesively bonded on the surface of a vibrating structure are widely employed as sensors in structural health monitoring (SHM) applications [1]. This typically includes permanent mounted or embedded elements for sensing or data acquisition, signal processing and wireless communication [2]. Aimed at improving the performance of SHM systems, in recent years, recent researches have focused on the possibility of providing self-powering capabilities, leading to so-called autonomous sensors. Fortunately, piezoelectric materials high electromechanical coupling characteristic allows their use as sensor but also for micro power generation [3]. However, to improve the performance of piezoelectric energy harvesting of a sensors network, it is required to increase the electromechanical coupling between host structure and piezoelectric patches.

In the literature, few works focused on the optimization of distributed networks of piezoelectric sensors to maximize their energy harvesting capabilities [4 5]. Thus, some aspects affecting the electromechanical coupling of a piezoelectric sensors network, such as bonding effectiveness and patches positioning, are studied here. This is done by, first, analyzing the effect on the electromechanical coupling of successive segmentation of

piezoelectric material and the number of piezoelectric patches covering the host structure. Then, a genetic algorithm optimization is used to determine the optimal distribution of a fixed number of patches to maximize the electromechanical coupling. Results are obtained using a custom finite element model that accounts for adhesive layer properties.

2. FINITE ELEMENT MODELING

A generic plate-like elastic structure containing a discrete distribution of surface-bonded piezoelectric patches is modeled employing the finite element method (FEM). The developed mathematical model is thought to take into account important properties of the adhesive layer between the plate and piezoelectric patches such as thickness, Young's modulus and thickness non-uniformity. For this purpose, the adhesive layers and piezoelectric patches are modeled as solid materials, while the plate structure is modeled using a first-order shear deformation theory (FSDT) [6], offsetting the node plane up to top surface to guarantee the assembly between this and nodes of the solid elements.

2.1 Constitutive equations for piezoelectric materials

A strain-voltage model is proposed considering linear and orthotropic piezoelectric materials. Thermal coupling is neglected and Kelvin-Voigt notation is adopted. Mechanical stress and strain vectors are represented by $\boldsymbol{\sigma}$ and $\boldsymbol{\varepsilon}$, respectively, with six components each and electric field and displacement vectors by $\boldsymbol{E}$ and $\boldsymbol{D}$ respectively, with three components each. The electric enthalpy density for piezoelectric materials is written as

$$H_2(\boldsymbol{\varepsilon}, \boldsymbol{E}) = \frac{1}{2}\boldsymbol{\varepsilon}^T \boldsymbol{c}^E \boldsymbol{\varepsilon} - \boldsymbol{\varepsilon}^T \mathbf{e} \boldsymbol{E} - \frac{1}{2}\boldsymbol{E}^T \boldsymbol{\epsilon}^\varepsilon \boldsymbol{E} \tag{1}$$

where $\boldsymbol{c}^E$, $\mathbf{e}$ and $\boldsymbol{\epsilon}^\varepsilon$ are respectively the matrices of elasticity constants at constant electric field, piezoelectric constants and dielectric coefficients at constant strain field.

2.2 Variational formulation

The equations of motion for the elastic structure with piezoelectric patches adhesively bonded on its surface are obtained using the d'Alembert's principle

$$\delta T - \delta U + \delta W = 0 \tag{2}$$

where the virtual variation of the internal loads, that can be obtained from the virtual variation of the electromechanical potential energy from (1), and the virtual variation of the work done by inertial and external forces are, respectively:

$$\delta U = \delta H_2 = \int_\Omega (\delta\boldsymbol{\varepsilon}^T \boldsymbol{c}^E \boldsymbol{\varepsilon} - \delta\boldsymbol{\varepsilon}^T \mathbf{e}\boldsymbol{E} - \delta\boldsymbol{E}^T \boldsymbol{e}^T \boldsymbol{\varepsilon} - \delta\boldsymbol{E}^T \boldsymbol{\epsilon}^\varepsilon \boldsymbol{E})\, d\Omega\,; \quad \delta T = -\int_\Omega \delta\boldsymbol{u}^T \rho \ddot{\boldsymbol{u}}\, d\Omega\,; \quad \delta W = \int_\Omega \delta\boldsymbol{u}^T \boldsymbol{f}\, d\Omega \tag{3}$$

where δ is the variational symbol, $\boldsymbol{u}$ is the vector of generalized displacements, ρ is the material mass density, Ω is the structure volume and $\boldsymbol{f}$ is the vector of external applied mechanical forces per unit volume. The geometric relations provide the standard relations between displacements and infinitesimal strains field or displacement-strain equations

$$\boldsymbol{\varepsilon} = \boldsymbol{L}\boldsymbol{u} \tag{4}$$

where the differential operator matrix $\boldsymbol{L}$ is defined as

$$\boldsymbol{L} = \begin{bmatrix} \partial/\partial x & 0 & 0 \\ 0 & \partial/\partial y & 0 \\ 0 & 0 & \partial/\partial z \\ \partial/\partial y & \partial/\partial x & 0 \\ \partial/\partial z & 0 & \partial/\partial x \\ 0 & \partial/\partial z & \partial/\partial y \end{bmatrix} \tag{5}$$

similarly, the electric field is related to electric potential as

$$\boldsymbol{E}(x,y,z,t) = -\boldsymbol{\nabla} V(x,y,z,t) = -\begin{Bmatrix} \partial V/\partial x \\ \partial V/\partial y \\ \partial V/\partial z \end{Bmatrix} \tag{6}$$

such that, substituting (3), (4) and (6) in (2), leads to

$$\int_{\Omega} (\delta \boldsymbol{u}^T \rho \ddot{\boldsymbol{u}} + (\delta \boldsymbol{u}^T \boldsymbol{L}^T \boldsymbol{c}^E \boldsymbol{L}\boldsymbol{u} + \delta \boldsymbol{u}^T \boldsymbol{L}^T \mathbf{e} \boldsymbol{\nabla} V + \delta V \boldsymbol{\nabla}^T \mathbf{e}^T \boldsymbol{L}\boldsymbol{u} - \delta V \boldsymbol{\nabla}^T \boldsymbol{\epsilon}^{\boldsymbol{\varepsilon}} \boldsymbol{\nabla} V) - \delta \boldsymbol{u}^T \boldsymbol{f}) d\Omega = 0 \tag{7}$$

2.3 Finite element discretization

For a generic FE implementation, the mechanical displacements and electric potentials are written in terms of nodal quantities such that

$$\boldsymbol{u}(x,y,z,t) = \bar{\boldsymbol{N}}_u(x,y,z)\hat{\boldsymbol{u}}(t); \quad V(x,y,z,t) = \bar{\boldsymbol{N}}_V(x,y,z)\hat{\boldsymbol{V}}(t) \tag{8}$$

where $\bar{\boldsymbol{N}}_u(x,y,z)$ and $\bar{\boldsymbol{N}}_V(x,y,z)$ are the matrices of interpolation functions for mechanical displacements and electric potentials, respectively, and $\hat{\boldsymbol{u}}(t)$ and $\hat{\boldsymbol{V}}(t)$ are vectors containing their corresponding nodal values. Hence, substituting (8) in the equations of motion (2), yields

$$\int_{\Omega} \{\delta \hat{\boldsymbol{u}}^T [(\rho \bar{\boldsymbol{N}}_u^T \bar{\boldsymbol{N}}_u)\ddot{\hat{\boldsymbol{u}}} + (\boldsymbol{B}_u{}^T \boldsymbol{c}^E \boldsymbol{B}_u)\hat{\boldsymbol{u}} + (\boldsymbol{B}_u{}^T \mathbf{e} \bar{\boldsymbol{N}}_V)\hat{\boldsymbol{V}} - \bar{\boldsymbol{N}}_u^T \boldsymbol{f}] + \delta \hat{\boldsymbol{V}}^T [(\boldsymbol{B}_V^T \mathbf{e}^T \boldsymbol{B}_u)\hat{\boldsymbol{u}} - (\boldsymbol{B}_V^T \boldsymbol{\epsilon}^{\boldsymbol{\varepsilon}} \boldsymbol{B}_V)\hat{\boldsymbol{V}}]\} d\Omega = 0 \tag{9}$$

with $\boldsymbol{B}_u = \boldsymbol{L}\bar{\boldsymbol{N}}_u; \quad \boldsymbol{B}_V = \boldsymbol{\nabla}\bar{\boldsymbol{N}}_V$. For an arbitrary variation of displacement $\delta\hat{\boldsymbol{u}}$ and electric potential $\delta\hat{\boldsymbol{V}}$, which are compatible with the essential boundary conditions, expression in (9) can be written in matrix form as

$$\begin{bmatrix} \boldsymbol{M} & \boldsymbol{0} \\ \boldsymbol{0} & \boldsymbol{0} \end{bmatrix} \begin{Bmatrix} \ddot{\hat{\boldsymbol{u}}} \\ \ddot{\hat{\boldsymbol{V}}} \end{Bmatrix} + \begin{bmatrix} \boldsymbol{K}_u & \boldsymbol{K}_{uV} \\ \boldsymbol{K}_{uV}{}^T & -\boldsymbol{K}_V \end{bmatrix} \begin{Bmatrix} \hat{\boldsymbol{u}} \\ \hat{\boldsymbol{V}} \end{Bmatrix} = \begin{Bmatrix} \boldsymbol{F}_m \\ \boldsymbol{0} \end{Bmatrix} \tag{10}$$

where the elementary matrices of mass, elastic stiffness (for constant electric field), piezoelectric stiffness and dielectric stiffness (for constant strain field) and the elementary vector of external applied forces are, respectively

$$\begin{gathered} \boldsymbol{M}^e = \int_{\Omega} \rho \bar{\boldsymbol{N}}_u^T \bar{\boldsymbol{N}}_u d\Omega_e; \quad \boldsymbol{K}_u{}^e = \int_{\Omega} \boldsymbol{B}_u{}^T \boldsymbol{c}^E \boldsymbol{B}_u d\Omega_e, \quad \boldsymbol{K}_{uV}{}^e = \int_{\Omega} \boldsymbol{B}_u{}^T \mathbf{e} \boldsymbol{B}_V d\Omega_e; \\ \boldsymbol{K}_V{}^e = \int_{\Omega} \boldsymbol{B}_V^T \boldsymbol{\epsilon}^{\boldsymbol{\varepsilon}} \boldsymbol{B}_V d\Omega_e; \quad \boldsymbol{F}_m{}^e = \int_{\Omega} \bar{\boldsymbol{N}}_u^T \boldsymbol{f} d\Omega_e \end{gathered} \tag{11}$$

2.3.1 Solid element

An isoparametric hexahedron element with eight nodes [7] is used to discretize the regions modeled as solid material. The particular shape functions for the hexahedron solid element expressed in terms of its natural coordinates (ξ, η, ζ) and in the compact form are

$$N_i = 1/8\,(1+\xi_i\xi)(1+\eta_i\eta)\big(1+\zeta_j\zeta\big) \tag{12}$$

where ξ_i, η_i, ζ_j are the coordinates of i-th node of the element. Hence, the displacements $\boldsymbol{u}$ of any point within element can be interpolated from the nodal displacements values $\widehat{\boldsymbol{u}}$ from

$$\boldsymbol{u}(x,y,z,t) = \sum_{i=1}^{8} N_i(\xi,\eta,\zeta)\widehat{\boldsymbol{u}}_i(t) = \boldsymbol{N_u}(\xi,\eta,\zeta)\widehat{\boldsymbol{u}}(t) \tag{13}$$

2.3.2 Plate element

A quadrilateral plate element with four nodes is developed based in the FSDT and offsetting the node plane up to top surface. The displacements of any point within the plate domain are written in terms of those in the node plane $(z = \alpha)$, such that

$$\boldsymbol{u}(x,y,\bar{z},t) = \begin{Bmatrix} u(x,y,\bar{z},t) \\ v(x,y,\bar{z},t) \\ w(x,y,\bar{z},t) \end{Bmatrix} = \begin{Bmatrix} u_\alpha(x,y,t) + \bar{z}\phi_x(x,y,t) \\ v_\alpha(x,y,t) + \bar{z}\phi_y(x,y,t) \\ w_\alpha(x,y,t) \end{Bmatrix} \tag{14}$$

When the node plane is located on the top surface, $\alpha = h/2$ and $u_\alpha, v_\alpha, w_\alpha$ represent displacements in the x, y and z directions of a point located on this surface. Thickness coordinate is denoted $\bar{z}$, which is related with the original one by $\bar{z} = z - \alpha$ and it takes values $-h \le \bar{z} \le 0$, where h is the total thickness of the plate, and ϕ_x and ϕ_y denote the cross-section rotations about the y and x axes respectively. For this element, the in-plane displacements u_α and v_α, and the cross-section rotations ϕ_x and ϕ_y are interpolated by the linear Lagrange interpolation functions and, for transversal displacement, cubic Hermite interpolation functions are considered. Thus, the generalized displacements $\boldsymbol{u}$ of any point within element can also be expressed in terms of the interpolation function and the nodal displacements values $\widehat{\boldsymbol{u}}$:

$$\boldsymbol{u} = \sum_{i=1}^{4} N_u^i(\xi,\eta)\widehat{\boldsymbol{u}}_i(t) = \boldsymbol{N}_u(\xi,\eta)\widehat{\boldsymbol{u}}(t) \tag{15}$$

2.4 Electric boundary conditions

Two types of electric boundary conditions will be considered for the piezoelectric patches, depending on the connection between top and bottom electrodes: short circuit (SC), and open circuit (OC). Whichever, the electric boundary condition, in first instance, an equipotential state must be imposed on top and bottom electrodes. The vector of electric degrees of freedom (dof) can be written as: $\widehat{\boldsymbol{V}} = \{\widehat{\boldsymbol{V}}_i \quad \widehat{\boldsymbol{V}}_t \quad \widehat{\boldsymbol{V}}_b\}^T$, where $\widehat{\boldsymbol{V}}_i$, $\widehat{\boldsymbol{V}}_t$ and $\widehat{\boldsymbol{V}}_b$ are the vectors of electric potentials at internal, top surface and bottom surface nodes, respectively. Then, equal values of electric potential at top and bottom electrodes are imposed by, defining $\boldsymbol{V}_t$ and $\boldsymbol{V}_b$ and the Boolean matrices $\boldsymbol{L}_t$ and $\boldsymbol{L}_b$, such that

$$\widehat{\boldsymbol{V}}_t = \boldsymbol{L}_t\boldsymbol{V}_t; \quad \widehat{\boldsymbol{V}}_b = \boldsymbol{L}_b\boldsymbol{V}_b \tag{16}$$

Accounting for (16), the equation of motion (10) can be written as

$$\begin{bmatrix} \boldsymbol{M} & \mathbf{0} & \mathbf{0} & \mathbf{0} \\ \mathbf{0} & \mathbf{0} & \mathbf{0} & \mathbf{0} \\ \mathbf{0} & \mathbf{0} & \mathbf{0} & \mathbf{0} \\ \mathbf{0} & \mathbf{0} & \mathbf{0} & \mathbf{0} \end{bmatrix} \begin{Bmatrix} \ddot{\widehat{\boldsymbol{u}}} \\ \ddot{\widehat{\boldsymbol{V}}}_i \\ \ddot{\boldsymbol{V}}_t \\ \ddot{\boldsymbol{V}}_b \end{Bmatrix} + \begin{bmatrix} \boldsymbol{K}_u & \boldsymbol{K}_{uV_i} & \bar{\boldsymbol{K}}_{uV_t} & \bar{\boldsymbol{K}}_{uV_b} \\ \boldsymbol{K}_{uV_i}{}^T & -\boldsymbol{K}_{V_ii} & -\bar{\boldsymbol{K}}_{V_it} & -\bar{\boldsymbol{K}}_{V_ib} \\ \bar{\boldsymbol{K}}_{uV_t}{}^T & -\bar{\boldsymbol{K}}_{V_it}{}^T & -\bar{\boldsymbol{K}}_{V_tt} & -\bar{\boldsymbol{K}}_{V_tb} \\ \bar{\boldsymbol{K}}_{uV_b}{}^T & -\bar{\boldsymbol{K}}_{V_ib}{}^T & -\bar{\boldsymbol{K}}_{V_tb}{}^T & -\bar{\boldsymbol{K}}_{V_bb} \end{bmatrix} \begin{Bmatrix} \widehat{\boldsymbol{u}} \\ \widehat{\boldsymbol{V}}_i \\ \boldsymbol{V}_t \\ \boldsymbol{V}_b \end{Bmatrix} = \begin{Bmatrix} \boldsymbol{F}_m \\ \mathbf{0} \\ \mathbf{0} \\ \mathbf{0} \end{Bmatrix} \tag{17}$$

where the different sub-matrices are: $\bar{\boldsymbol{K}}_{uV_t} = \boldsymbol{K}_{uV_t}\boldsymbol{L}_t$; $\bar{\boldsymbol{K}}_{V_it} = \boldsymbol{K}_{V_it}\boldsymbol{L}_t$; $\bar{\boldsymbol{K}}_{V_tt} = \boldsymbol{L}_t{}^T\boldsymbol{K}_{V_tt}\boldsymbol{L}_t$; $\bar{\boldsymbol{K}}_{uV_b} = \boldsymbol{K}_{uV_b}\boldsymbol{L}_b$; $\bar{\boldsymbol{K}}_{V_ib} = \boldsymbol{K}_{V_ib}\boldsymbol{L}_b$; $\bar{\boldsymbol{K}}_{V_tb} = \boldsymbol{L}_t{}^T\boldsymbol{K}_{V_tb}\boldsymbol{L}_b$; $\bar{\boldsymbol{K}}_{V_bb} = \boldsymbol{L}_b{}^T\boldsymbol{K}_{V_bb}\boldsymbol{L}_b$. From the second row of (17), it is possible to express the vector $\widehat{\boldsymbol{V}}_i$ as a function of the remaining dof: $\widehat{\boldsymbol{V}}_i = \boldsymbol{K}_{V_{ii}}{}^{-1}\left[\boldsymbol{K}_{uV_i}{}^T \quad -\bar{\boldsymbol{K}}_{V_it} \quad -\bar{\boldsymbol{K}}_{V_ib}\right]\{\widehat{\boldsymbol{u}} \quad \boldsymbol{V}_t \quad \boldsymbol{V}_b\}^T$. Therefore, substituting this value in first, third and fourth rows of (17) and assuming that all electrodes on bottom surfaces of the piezoelectric patches are grounded, $\boldsymbol{V}_b = 0$, it is possible obtain

$$\begin{bmatrix} \boldsymbol{M} & \mathbf{0} \\ \mathbf{0} & \mathbf{0} \end{bmatrix} \begin{Bmatrix} \ddot{\widehat{\boldsymbol{u}}} \\ \ddot{\boldsymbol{V}}_t \end{Bmatrix} + \begin{bmatrix} \bar{\bar{\boldsymbol{K}}}_u & \bar{\bar{\boldsymbol{K}}}_{uV_t} \\ \bar{\bar{\boldsymbol{K}}}_{uV_t}{}^T & -\bar{\bar{\boldsymbol{K}}}_{V_tt} \end{bmatrix} \begin{Bmatrix} \widehat{\boldsymbol{u}} \\ \boldsymbol{V}_t \end{Bmatrix} = \begin{Bmatrix} \boldsymbol{F}_m \\ \mathbf{0} \end{Bmatrix} \tag{18}$$

where $\bar{\bar{\boldsymbol{K}}}_u = \boldsymbol{K}_u + \boldsymbol{K}_{uV_i}\boldsymbol{K}_{V_ii}{}^{-1}\boldsymbol{K}_{uV_i}{}^T$; $\bar{\bar{\boldsymbol{K}}}_{uV_t} = \bar{\boldsymbol{K}}_{uV_t} - \boldsymbol{K}_{uV_i}\boldsymbol{K}_{V_ii}{}^{-1}\bar{\boldsymbol{K}}_{V_it}$; $\bar{\bar{\boldsymbol{K}}}_{V_tt} = \bar{\boldsymbol{K}}_{V_tt} - \bar{\boldsymbol{K}}_{V_ti}\boldsymbol{K}_{V_ii}{}^{-1}\bar{\boldsymbol{K}}_{V_it}$. If the electrodes of piezoelectric patches are in SC, induced electric potential at the top electrodes are also null $\boldsymbol{V}_t = 0$, consequently (18) is reduced to

$$\boldsymbol{M}\ddot{\widehat{\boldsymbol{u}}} + \bar{\bar{\boldsymbol{K}}}_u\widehat{\boldsymbol{u}} = \boldsymbol{F}_m \tag{19}$$

On the other hand, if electrodes of the piezoelectric patches are in OC, the induced electric potential on top can be found from the second row of (18) as

$$\boldsymbol{V}_t = \bar{\bar{\boldsymbol{K}}}_{V_tt}{}^{-1}\bar{\bar{\boldsymbol{K}}}_{uV_t}{}^T\widehat{\boldsymbol{u}} \tag{20}$$

substituting (20) in first row of (18), equations of motion similar to (19) are obtained

$$\boldsymbol{M}\ddot{\widehat{\boldsymbol{u}}} + \boldsymbol{K}_{eq}\widehat{\boldsymbol{u}} = \boldsymbol{F}_m \tag{21}$$

where the equivalent stiffness $\boldsymbol{K}_{eq}$ is given by: $\boldsymbol{K}_{eq} = \bar{\bar{\boldsymbol{K}}}_u + \bar{\bar{\boldsymbol{K}}}_{uV_t}\bar{\bar{\boldsymbol{K}}}_{V_tt}{}^{-1}\bar{\bar{\boldsymbol{K}}}_{uV_t}{}^T$. Solving (21) for the mechanical dof $\widehat{\boldsymbol{u}}$, the induced electric potential on top electrodes may be evaluated through post-processing from (20).

3. PROBLEM DESCRIPTION

In the present work, it is considered that the potentially harvestable energy of a given piezoelectric element depends strongly on the effective electromechanical coupling coefficient (EMCCe) it provides to the structure. This represents the energy fraction that could be stored in the piezoelectric element when the structure vibrates in a given mode The EMCCe of the structure depends on the electromechanical coupling coefficient (EMCC ou k_{ij}^2) of the material and on the mechanical coupling between the piezoelectric element and the host structure, consequently it can be expected that the EMCCe will be smaller than the material EMCC [8].

On the other hand, previous works indicate a potential reduction on the mechanical coupling between host structure and piezoelectric element due to the presence of an adhesive layer between them [9-11]. To evaluate the effect of the adhesive layer on the performance of surface-bonded piezoelectric patches working as energy harvesting devices, two analyses were proposed. In the first one, the effect of successive segmentation is investigated, once it is expected that segmentation could have a positive effect of mitigating electric charge cancellation but also a negative one due to an increase of border effects in the adhesive layer. In the second analysis, an optimization procedure is proposed to find a distribution of mechanically and electrically uncoupled piezoelectric patches that maximizes the EMCCe of the first five vibration modes.

3.1 Calculation of the effective electromechanical coupling EMCCe

For a generic flexible structure with a discrete distribution of piezoelectric patches, it is possible to evaluate the structure's EMCCe provided by each piezoelectric patch. A general procedure to calculate the EMCCe based on modeling has been proposed [8]. The ith modal parameters, mode and natural frequency, of a structure with a discrete distribution of piezoelectric elements for SC and OC electric boundary conditions respectively can be found from (19) and (21) as

$$\left(\omega_{SC}^{i\,2}\boldsymbol{M}+\bar{\bar{\boldsymbol{K}}}_u\right)\boldsymbol{T}_{SC}^{i}=0;\quad \left(\omega_{OC}^{i\,2}\boldsymbol{M}+\boldsymbol{K_{eq}}\right)\boldsymbol{T}_{OC}^{i}=0 \tag{22}$$

assuming that the mode shapes of the structure are not affected by the electric boundary conditions of the piezoelectric elements $\left(\boldsymbol{T}_{SC}^{i}=\boldsymbol{T}_{OC}^{i}=\boldsymbol{T}_i\right)$, the ith natural frequency for SC and OC condition respectively, assuming mass normalized mode shapes, are given by

$$\omega_{SC}^{i\,2}=\boldsymbol{T}_i^t\bar{\bar{\boldsymbol{K}}}_u\boldsymbol{T}_i;\quad \omega_{OC}^{i\,2}=\boldsymbol{T}_i^t\boldsymbol{K}_{eq}\boldsymbol{T}_i \tag{23}$$

thus, the EMCCe of the structure, provided by a piezoelectric element, when it is vibrating in the ith mode shape is defined as

$$k_i^2=\frac{\omega_{OC}^{i\,2}-\omega_{SC}^{i\,2}}{\omega_{OC}^{i\,2}}=\frac{\boldsymbol{T}_i^t\left(\boldsymbol{K}_{eq}-\bar{\bar{\boldsymbol{K}}}_u\right)\boldsymbol{T}_i}{\boldsymbol{T}_i^t\boldsymbol{K}_{eq}\boldsymbol{T}_i} \tag{24}$$

3.2 Description of the proposed analyses

It is assumed that a network of piezoelectric patches is to be bonded to a flexible plate structure so that the network should be effective in harvesting energy from the structural vibrations within a frequency-range that contains the first five resonant frequencies. A rectangular aluminum plate with at all edges clamped and dimensions 420 x 320 x1 [mm^3] is considered. The material used for the piezoelectric patches is a piezoceramic **PZT-5H** with thickness $e_{Al}=0.5$ [mm], containing an adhesive layer with thickness $e_{Ad}=0.1$ [mm]. The electromechanical properties of the PZT-5H are listed in Table 1. Additionally, the aluminum properties are: Young modulus $E_{Al}=70$ [GPa], Poisson ratio $\nu_{Al}=0.34$ and mass density $\rho_{Al}=2700$ [Kg/m^3], and the adhesive layer properties are: Young modulus $E_{Ad}=2.7$ [GPa], Poisson ratio $\nu_{Ad}=0.4$ and mass density $\rho_{Ad}=1140$ [Kg/m^3]. A uniform mesh

of 42 x 32 elements has been used to discretize the aluminum plate and consequently adhesive layer and piezoelectric patches have also been discretized by a uniform mesh.

Table 1: Electromechanical properties of the PZT -5H [12]

Mechanical properties	Piezoelectric properties	Dielectric properties
$c_{11} = c_{22} = 127.2$ [GPa]		
$c_{12} = 80.2$ [GPa]		
$c_{13} = c_{23} = 84.7$ [GPa]	$e_{31} = e_{32} = -6.6$ [C/m^2]	$\epsilon_{11} = \epsilon_{22} = 15.09$ [nF/m]
$c_{33} = 117.4$ [GPa]	$e_{33} = 23.2$ [C/m^2]	$\epsilon_{33} = 12.69$ [nF/m]
$c_{44} = 23.5$ [GPa]	$e_{15} = e_{24} = 17.0$ [C/m^2]	
$c_{55} = c_{66} = 23$ [GPa]		
$\rho = 7500$ [Kg/m^3]		

A modal analysis has been performed and the first five mode shapes and natural frequencies of the clamped plate (without piezoelectric patches) are shown in Figure 1. The requirements of the system are defined as following: to maximize the global structure EMCCe for a band of frequencies between the first and fifth modes of vibration of the structure with the purpose of providing it self-powering capabilities in this band.

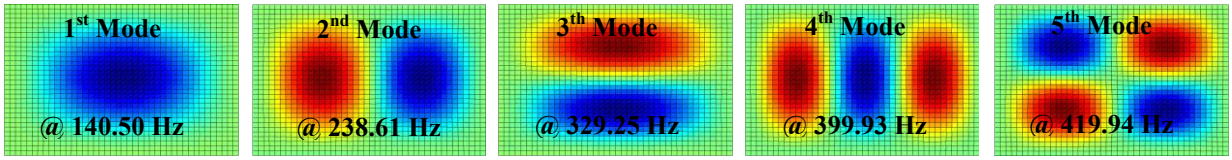

Figure 1: First five mode shapes of vibration and its natural frequencies for the clamped aluminum plate

3.2.1 Successive segmentation analysis

This analysis is thought to determine the effect of the piezoelectric material segmentation on the global structure's EMCCe for the first five modes of vibration. For an initial unique piezoelectric patch bonded on the plate's surface, which is centered and has rectangular shape, it is calculate the average of the EMCCe. Then, keeping the total area covered by the piezoelectric material, this patch is segmented into two parts symmetrically with respect to the y-axe and again the average EMCCe for this new configuration is evaluated. Next, the segmentation is done again, but this time symmetrically with respect to the x-axe, obtaining four patches at total. This procedure is performed for successive times aiming to obtain the EMCCe values for configuration with one, two, four, eight and sixteen patches. Afterwards, the completed described procedure is performed for reduced covered areas: 83.33%, 75.00%, 64.29%, 57.14%, 47.62%, 41.67%, 33.33%, 28.57%, 23.81%, 21.43% and 11.90%. The areas are shown schematically in Figure 2.

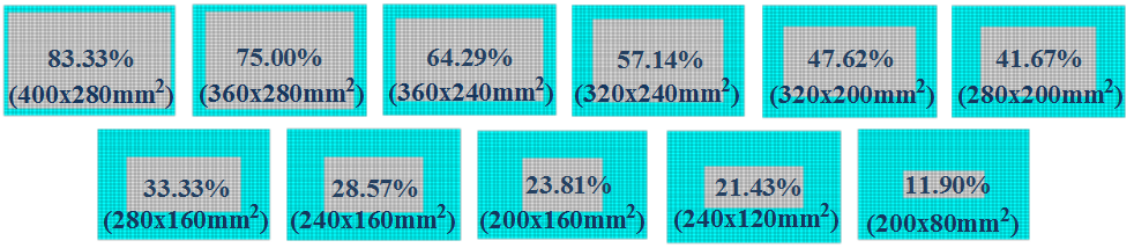

Figure 2: Schematic representation of evaluated areas in segmentation analysis

3.2.2 Analysis for fixed size of the piezoelectric patches

In the previous analysis the patch size is varied after each segmentation procedure while the total covered area is hold constant. Oppositely, it is interesting to hold constant the patch size in 40 x 40 [mm^2], while the total covered area will be varied by means of modifying the total number of piezoelectric patches.

3.3 Optimized network configuration

Based on results provided by the two previous analyses, it has been proposed to search for the optimal distribution of a network of piezoelectric patches, which maximizes the average of the first five modal EMCCe of the structure, using a genetic algorithms (GA) based optimization method. Thus, for this non-convex problem it is wanted to find the vector $\boldsymbol{x}_{Np}$, that represent the positions of the N_p piezoelectric patches; which maximizes the function cost gives by:

$$J(\boldsymbol{x}_{Np}) = \sum_{i=1}^{N_m=5} k_i(\boldsymbol{x}_{Np})^2 \tag{25}$$

4. NUMERICAL RESULTS

4.1 Successive segmentation analysis

Results for the segmentation test are listed in Tables 2 and 3. In penultimate row of the table it is computed the average EMCCe and in the last one it is computed the specific EMCCe by percentage of covered area, which is a more interesting parameter to evaluate the efficiency of adding mass to the structure. In Table 3, it is summarized the absolute average EMCCe and the specific one by percentage of covered area, for all tested areas. Generally, it is observed that segmentation of the piezoelectric patch increases EMCCe, since charge cancellation is limited. However, results also shows that excessive segmentation does not increase EMCCe. It is guessed here that this should be due to the adhesive layer shear loss at the borders.

Table 2: Modal, average and specific* by percentage of covered area values of EMCCe for 28.57 % of covered area segmented in 1, 2 4, 8 and 16 piezoelectric patches

	Number of Patches				
	1	**2**	**4**	**8**	**16**
Mode 01	9.9	9.6	9.2	9.1	8.8
Mode02	0.0	7.6	7.4	7.7	7.4
Mode03	0.0	0.0	5.4	5.3	5.6
Mode04	0.2	0.1	0.1	5.2	5.0
Mode05	0.0	0.0	4.3	4.6	5.0
$\boldsymbol{EMCCe_g}$	**2.0**	**3.5**	**5.3**	**6.4**	**6.4**
$\boldsymbol{EMCCe_g^*}$	7.1	12.2	18.5	22.3	22.3

Thus, for a determined number of patches forming a rectangular area, there is a patch size that maximizes the average EMCCe of the structure. On the other hand, the biggest EMCCe

value (9.0%) is found for 57.14% of covered area (320x240mm^2) with sixteen patches, but to obtain this value it is required adding around 297 [g] of additional mass to the structure, which can be non-convenient for certain applications. Whereas the biggest value of specific EMCCe (22.3%) it is found for 28.57% of covered area (240x160mm^2), and it is only required adding around 148 [g] of additional mass. This is shown in a graphical form in Figure 3.

Table 3: Average and specific percentage of covered area EMCCe values for 1, 2 4, 8 and 16 patches for all configurations of evaluated areas

Covered Area	Number of Patches									
	1		2		4		8		16	
	$k^2{}_g$	k_g^{2*}	$k^2{}_g$	k_g^{2*}	$k^2{}_g$	k_g^{2*}	$k^2{}_g$	k_g^{2*}	$k^2{}_g$	k_g^{2*}
83.33%	0.6	0.7	1.6	1.9	4.0	4.8	5.4	6.4	6.0	7.2
75.00%	1.0	1.4	2.4	3.2	5.4	7.2	6.6	8.8	7.4	9.9
64.29%	1.5	2.4	3.3	5.1	6.7	10.4	8.2	12.8	8.4	13.0
57.14%	1.7	3.0	3.6	6.3	7.2	12.6	8.8	15.5	9.0	15.7
47.62%	2.0	4.2	4.1	8.5	7.1	15.0	8.8	18.5	8.6	18.1
41.67%	2.0	4.9	3.9	9.4	6.9	16.6	8.4	20.2	8.2	19.8
33.33%	2.0	6.0	3.8	11.5	5.8	17.4	7.2	21.7	7.2	21.6
28.57%	2.0	7.1	3.5	12.2	5.3	18.5	6.4	22.3	6.4	22.3
23.81%	2.2	9.1	3.1	13.1	4.6	19.5	5.2	21.9	5.2	21.8
21.43%	1.7	7.9	3.0	13.8	3.8	17.7	4.7	22.1	4.2	19.7
11.90%	1.2	10.5	1.9	15.9	2.1	17.3	2.4	20.3	2.4	20.2

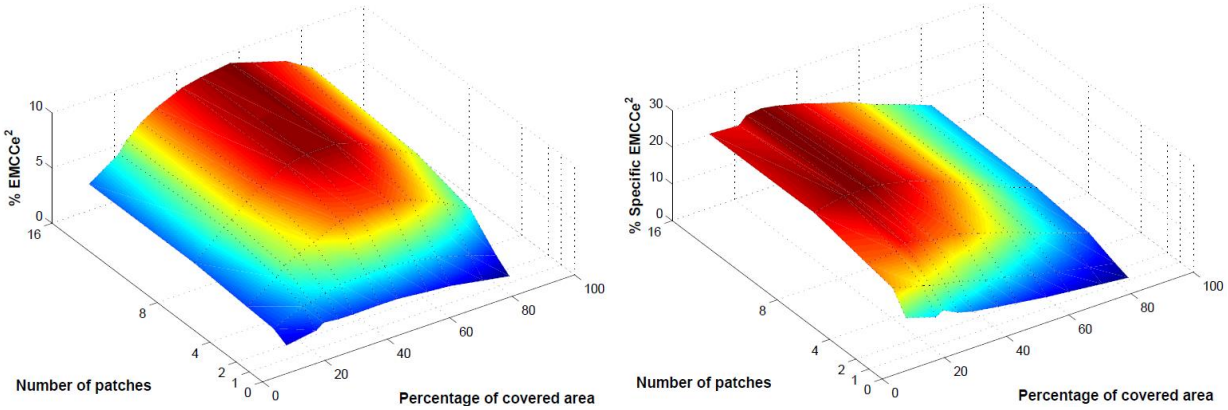

(a) (b)

Figure 3: Percentage of average global EMCCe of the structure for different configurations of size area and segmentations, (a) absolute average, (b) specific average by percentage of covered area

4.2 Analysis for fixed size of the piezoelectric patches

Results for the fixed patch size test are presented in the same way than previous ones. In Table 4, the modal, average and specific EMCCe by percentage of covered area are shown. Additionally, in the last one row it is computed the ratio of average EMCCe per patch, which is also an interesting parameter for comparison. Table 5 and Figure 4 summarize the average and specific values for all tested configurations.

Table 4: Modal, average and specific* by percentage of covered area values of EMCCe for 42, 36, 30,24, 18 and 12 piezoelectric patches of 40x40 [mm^2]

	42 (6x7)	**36 (6x6)**	**30 (6x5)**	**24 (6x4)**	**18 (6x3)**	**12 (6x2)**
Mode01	8.3	8.7	9.0	8.6	7.2	5.1
Mode02	7.2	7.6	7.7	7.4	6.5	4.9
Mode03	8.1	8.6	7.8	5.5	2.8	0.8
Mode04	5.5	5.7	5.7	5.4	4.7	3.6
Mode05	7.3	7.7	6.9	5.0	2.6	0.7
$EMCCe_g$	**7.3**	**7.7**	**7.4**	**6.4**	**4.8**	**3.0**
$EMCCe_g^*$	**14.6**	**17.9**	**20.8**	**22.4**	**22.3**	**21.2**
$EMCCe_g/P$	**0.2**	**0.2**	**0.2**	**0.3**	**0.3**	**0.3**

The biggest value of average EMCCe (9.2 %) found is for a configuration area with 48 patches (8x6), which correspond to the same area of the optimal configuration of the segmentation test, but the EMCCe is slightly better. In terms of efficiency, 24 patches (6x4), 20 patches (5x4) and 16 patches (4x4) have similar values of specific EMCCe.

Table 5: Average and specific by percentage of covered area EMCCe values for all configurations of tested areas holding constant the patch size (40x40mm^2).

Number of patches in y-direction	**Number of patches in x-direction**									
	8		**7**		**6**		**5**		**4**	
	$k^2{}_g$	k_g^{2*}	$k^2{}_g$	k_g^{2*}	$k^2{}_g$	k_g^{2*}	$k^2{}_g$	k_g^{2*}	$k^2{}_g$	k_g^{2*}
7	8.8	13.2	8.3	14.2	7.3	14.6	6.1	14.6	4.9	14.6
6	9.2	16.2	8.7	17.4	7.7	17.9	6.4	17.9	5.1	17.8
5	9.0	18.8	8.5	20.3	7.4	20.8	6.2	20.8	4.9	20.7
4	7.7	20.3	7.3	21.8	6.4	22.4	5.3	22.3	4.2	22.1
3	5.8	20.4	5.5	21.9	4.8	22.3	3.9	22.0	3.1	21.9
2	3.8	19.7	3.5	21.1	3.0	21.2	2.5	20.8	2.0	20.7

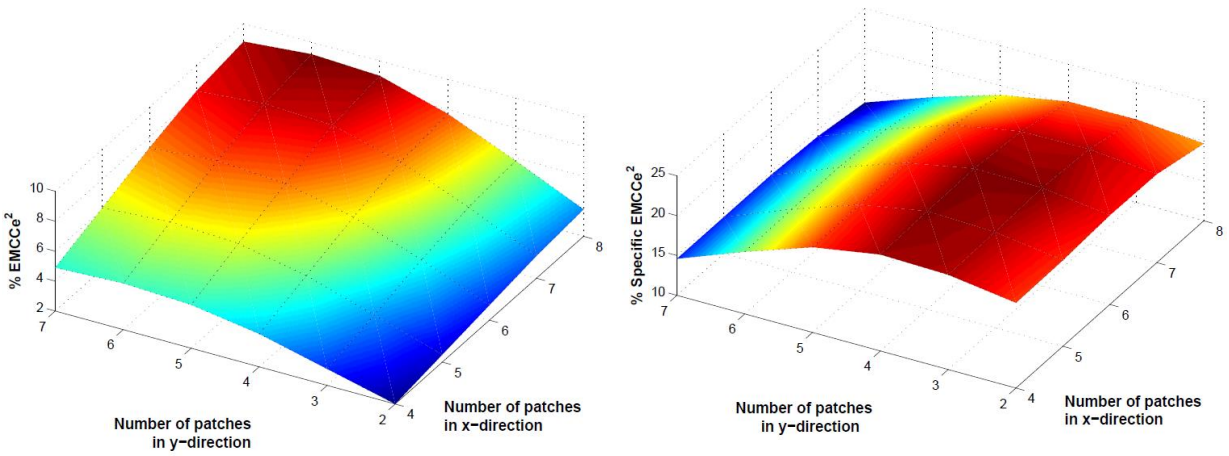

(a) (b)

Figure 4: Percentage of average global EMCCe of the structure for different configurations of size area holding fixed the patch size, (a) absolute average, (b) specific average by percentage of covered area

4.3 Optimized network configuration

Results obtained in the previous parametric analyses were used as initial data to search for optimal distributions of a network of piezoelectric patches that maximize the average EMCCe of the structure and consequently its expected harvesting performance when working in a frequency-range that contains the first five natural frequencies. Thus, it has been chosen to find the optimal distribution of a network with 16, 20 and 24 piezoelectric patches of 40x40 [mm^2]. Network distributions found with GA are shown in Figure 5. Modal and average EMCCe values are presented in Table 6. They are also compared with values found from a rectangular centered network distribution.

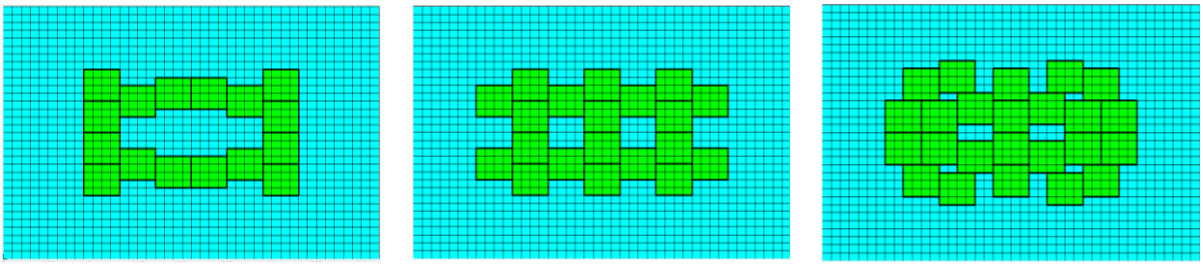

(a) (b) (c)

Figure 5: Optimized network configuration, with (a) sixteen, (b) twenty, and (c) twenty four patches

The GA optimization procedure has allowed to find several optimized network configurations for the proposed cases of 16, 20 and 24 patches. For the case of 16 patches a slight improve on the average EMCCe is obtained, but it is also worthwhile to notice a reduction on the difference between maximum and minimum modal values which could be valuable to improve the global efficiency of a multimodal device. A similar conclusion could be drawn for the network with 20 patches. On the other hand, for the network with 24 patches, it was not possible to improve the global EMCCe, but the difference between maximum and minimum modal values are reduced.

Table 6: Comparison between modal and average EMCCe values obtained from optimized location of the piezoelectric patch network and from a rectangular distribution of the network

	16 Patches		**20 Patches**		**24 Patches**	
	Optimized	**Rectangular**	**Optimized**	**Rectangular**	**Optimized**	**Rectangular**
Mode01	4.2	7.1	6.4	8.1	7.3	8.6
Mode02	5.7	3.3	6.5	5.4	7.9	7.4
Mode03	3.9	4.7	4.6	5.2	5.2	5.5
Mode04	4.0	3.7	5.3	4.1	6.1	5.4
Mode05	4.4	2.3	4.6	3.7	5.2	5.0
$\boldsymbol{EMCCe_g}$	4.4	4.2	5.5	5.3	6.4	6.4
$\boldsymbol{EMCCe_g^*}$	23.2	22.1	23.0	22.3	22.2	22.4
$\boldsymbol{EMCCe_g/P}$	0.28	0.26	0.27	0.26	0.26	0.27

5. CONCLUSION REMARKS AND FUTURE WORKS

Obtained results indicate, as expected, that the piezoelectric patch segmentation may improve potential energy harvesting performance since it reduces the electric charge cancellation phenomena. However, excessive segmentation is detrimental and it may be due

to border effects in adhesive layer that may diminish the mechanical coupling between patches and host structure. This suggests that for a given geometry and percentage of covered area, there is a specific patch size, which maximizes the efficiency of conversion energy. Another important aspect to take into account, for cases of multimodal harvesters, is the location of the piezoelectric patches when the quantity of patches are limited due to weight, costs or design limitations. In this case, a network distribution optimization may be worthwhile. Future works are being directed to a better understanding of the negative effects of excessive segmentation and other network optimization criteria including other energy harvesting important parameters.

ACKNOWLEDGEMENTS

Support of MCT/CNPq/FAPEMIG National Institute of Science and Technology on Smart Structures in Engineering, 574001/2008-5, and National Council for Scientific and Technological Development (CNPq), 306675/2011-0 and 309193/2014-1, is acknowledged.

REFERENCES

[1] Gilbert, J. M., and Balouchi, F., "Comparison of energy harvesting systems for wireless sensor networks," international journal of automation and computing, 5(4), pp. 334-347, 2008.

[2] Le, M. Q., Capsal, J. F., Lallart, M., Hebrard, Y., Van Der Ham, A., Reffe, N., Geynet, L., and Cottinet, P. J., "Review on energy harvesting for structural health monitoring in aeronautical applications," Progress in Aerospace Sciences, 79, pp. 147-157, 2015.

[3] Sodano, H. A., Inman, D. J., and Park, G., "A review of power harvesting from vibration using piezoelectric materials," Shock and Vibration Digest, 36(3), pp. 197-206, 2004.

[4] Nakasone, P. H., and Silva, E. C. N., "Dynamic Design of Piezoelectric Laminated Sensors and Actuators using Topology Optimization," Journal of Intelligent Material Systems and Structures, 21(16), pp. 1627-1652, 2010.

[5] Aghakhani, A., Basdogan, I., and Erturk, A., "Multiple piezo-patch energy harvesters integrated to a thin plate with AC-DC conversion: Analytical modeling and numerical validation," Proc. Conference on Smart Materials and Nondestructive Evaluation for Energy Systems 2016.

[6] Reddy, J. N., Mechanics of laminated composite plates and shells: theory and analysis, CRC press, 2004.

[7] Zienkiewicz, O. C., and Taylor, R. L., The finite element method for solid and structural mechanics, Butterworth-heinemann, 2005.

[8] Trindade, M. A., and Benjeddou, A., "Effective Electromechanical Coupling Coefficients of Piezoelectric Adaptive Structures: Critical Evaluation and Optimization," Mechanics of Advanced Materials and Structures, 16(3), pp. 210-223, 2009.

[9] Austin, E. M., and Inman, D. J., "Effects of modeling assumptions on loss factors predicted for viscoelastic sandwich beams," Proc. Smart Structures and Materials 1999 Conference, pp. 251-262, 1999.

[10] Tinoco, H. A., Serpa, A. L., and Ramos, A. M., "Numerical study of the effects of bonding layer properties on electrical signatures of piezoelectric sensors," Mecánica Computacional, 29(86), pp. 8391-8409, 2010.

[11] de Faria, A. R., "The impact of finite-stiffness bonding on the sensing effectiveness of piezoelectric patches," Smart Materials & Structures, 12(4), pp. N5-N8, 2003.

[12] Efunda Engineering Fundamentals, Piezo Data: PZT-5H, https://www.efunda.com/materials/piezo/material_data/matdata_output.cfm?Material_ID=PZT-5H

VIII ECCOMAS Thematic Conference on Smart Structures and Materials
SMART 2017
A. Güemes, A. Benjeddou, J. Rodellar and J. Leng (Eds)

EXTENSION TO PIEZOELECTRIC PLATES OF THE RITZ SUBLAMINATE GENERALIZED UNIFIED FORMULATION APPROACH

MICHELE D'OTTAVIO*, LORENZO DOZIO†, RICCARDO VESCOVINI† AND OLIVIER POLIT*

*Laboratoire Energétique Mécanique Electromagnétisme (LEME)
Univ Paris Nanterre, UPL
50 Rue de Sèvres, 92410 Ville d'Avray, France
e-mail: {michele.d_ottavio, olivier.polit}@u-paris10.fr

† Department of Aerospace Science and Technology
Politecnico di Milano
Via La Masa 34, 20156 Milano, Italy
e-mail: {lorenzo.dozio, riccardo.vescovini}@polimi.it

Key words: Piezoelectric Composites, Variable Kinematics Model, Ritz Method, Unified Formulation

Abstract. The Sublaminate Generalized Unified Formulation (SGUF) is a variable kinematics plate modeling approach and is here extended to composite plates including piezoelectric plies. The two-dimensional plate equations are obtained upon defining *a priori* the through-thickness distribution of the generalized displacements, i.e., the displacement field and the electric potential. According to SGUF, independent approximations can be adopted for the four components of the generalized displacements, which encompass: an Equivalent Single Layer (ESL) or Layer-Wise (LW) description over an arbitrary group of physical plies constituting the composite plate (the *sublaminate*) and the polynomial order that is employed in each sublaminate. The solution of the two-dimensional piezoelectric plate equations is subsequently sought in weak form by means of a Ritz method. Boundary functions are thus used in conjunction with the domain approximation, whose orthogonal basis may be spanned by trigonometric functions, Chebyshev polynomials or Legendre polynomials. Free-vibration problems as well as static problems involving actuator and sensor configurations are addressed. Three validation case studies are first presented, which demonstrate the high accuracy of the proposed Ritz method in conjunction with high order models. A model assessment is then proposed for showcasing to which extent the flexible SGUF approach allows a reduction of the number of unknowns with a controlled impact on the accuracy of the response.

1 INTRODUCTION

Composite structures with embedded piezoelectric sensors and/or actuators are among the most indicated solutions for implementing an adaptive strategy for, e.g., vibration suppression applications [1]. On the one hand, it is very important for a conservative design to have the possibility of accurately predicting the global and local electromechanical response of the structure. On the other hand, a reduced-order model is necessary in the control algorithm for allowing a real-time adaptation.

Unified formulations, pioneered by Reddy [2] and systematically developed by Carrera [3], allow constructing within a single computer program a variable-kinematics modeling approach with variable accuracy and computational cost, see also [4]. The importance of such an approach, in particular for coupled multi-field problems such as composite structures with piezoelectric elements, was early recognized [5–7]. Carrera Unified Formulation (CUF) was subsequently generalized by Demasi [8] (Generalized Unified Formulation, GUF). D'Ottavio [9] further extended the flexibility of GUF to include a sublaminate approach (SGUF): in SGUF, the composite stack is subdivided into an arbitrary number of laminates grouping adjacent physical plies, and a GUF variable-kinematics model can be employed for each sublaminate independently. Recently, the authors employed the displacement-based SGUF approach in conjunction with a Ritz method previously developed by Dozio and Carrera [10]: mechanical problems involving bending, buckling and free-vibration, including visco-elastic layers, have been addressed [11–13]. The proposed Ritz method is particularly useful as it provides sufficient flexibility for a rapid analysis of configurations involving arbitrary boundary and loading conditions as well as anisotropic coupling.

This paper presents the extension of the Ritz-SGUF approach to composite plates with piezoelectric coupling. Section 2 presents the principal steps of the modeling approach, where particular emphasis is given to the compact index notation typical of Unified Formulations. Section 3 presents preliminary results for validating the implemented software and showing the flexibility of the proposed approach. Section 4 summarizes the main conclusions.

2 MODELING APPROACH

2.1 Description of the geometry

A plate is considered that occupies the volume $V = \Omega \times \left[-\frac{h}{2} \leq x_3 \leq \frac{h}{2}\right]$, with h denoting the constant thickness and Ω the reference surface lying on the $(x_1, x_2)-$plane. The composite plate is composed of $p = 1, 2, \dots N_p$ homogeneous plies stacked along the thickness direction $x_3 \equiv z$, each of thickness h_p, see Figure 1. According to the SGUF approach, the laminate is subdivided into $k = 1, 2, \dots N_k$ sublaminates, each of constant thickness h_k and consisting of a stack of N_p^k adjacent plies. Throughout the paper, indexes p and k are related to the physical plies and the sublaminate, respectively, and quantities related to the ply p of the sublaminate k will be indicated by $()^{p,k}$. Local coordinates $z_p \in \left[-\frac{h_p}{2}, \frac{h_p}{2}\right]$ and $z_k \in \left[-\frac{h_k}{2}, \frac{h_k}{2}\right]$ are introduced along with the corresponding non-dimensional coordinates

$$\zeta_p = \frac{2z_p}{h_p}; \quad \zeta_k = \frac{2z_k}{h_k} \tag{1a}$$

These coordinates are linked through the relation

$$\zeta_p = \frac{h_k}{h_p}\zeta_k + \frac{2}{h_p}\left(z_{0k} - z_{0p}\right) \tag{1b}$$

where z_{0p} and z_{0k} are the midplane $z-$coordinates of the ply and sublaminate, respectively.

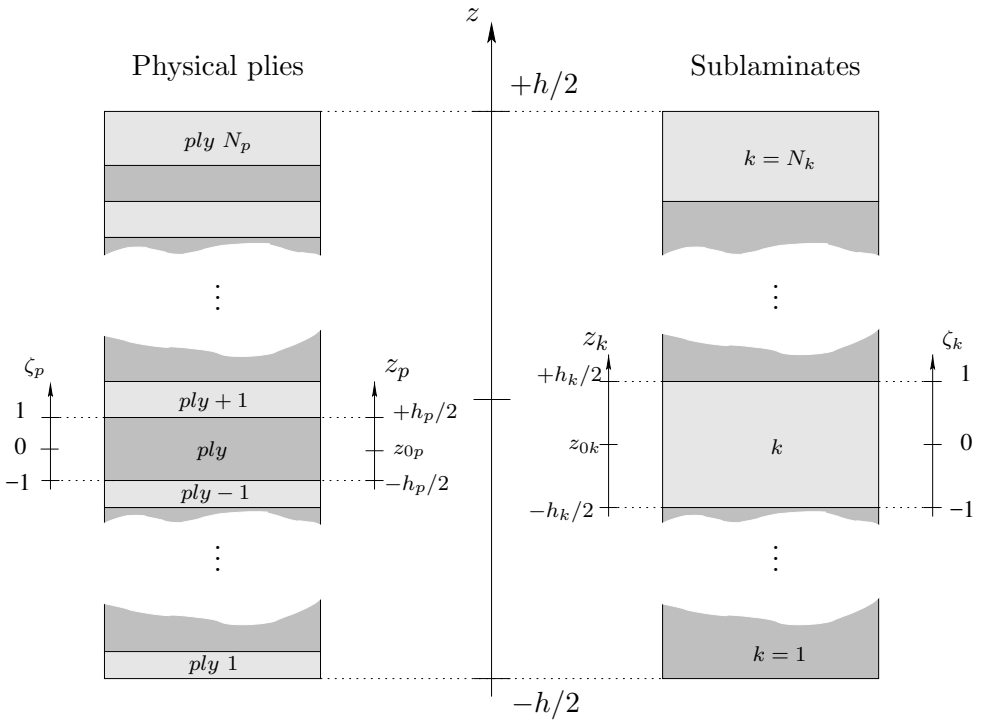

Figure 1: SGUF: geometry description

2.2 The variational approach based on generalized displacements

The two-dimensional (2D) model of the composite piezoelectric plate is obtained upon introducing *a priori* assumptions for the through-the-thickness behavior of the displacements u_i and the electrostatic potential Φ in a variationally consistent manner. Unless otherwise stated, Latin indexes range in $\{1, 2, 3\}$ while Greek indexes take values in $\{1, 2\}$. Adopting tensor notation and the repeated index summation convention, the weak form of the mechanical and electrical equilibrium equations is expressed by the following integral statement

$$\int_V \delta\epsilon_{ij}\,\sigma_{ij} - \delta E_i\,D_i + \delta u_i\,\rho\,\ddot{u}_i\,\mathrm{d}V = \int_{S_t} \delta u_i\,\bar{t}_i\,\mathrm{d}S - \int_{S_q} \delta\Phi\,\bar{q}\,\mathrm{d}S \tag{2}$$

where ϵ_{ij}, σ_{ij}, E_i and D_i represent the strain and stress tensors and the electric field and electric displacement vectors, respectively, ρ is the mass density, δ indicates an admissible virtual variation, $\bar{t}_i$ is the vector of external traction imposed at the boundary S_t and $\bar{q}$ is the imposed

electric charge density imposed at the boundary S_q. In this paper it shall be assumed without loss of generality that mechanical load and electric charge densities are imposed at the top and/or bottom surfaces of the plate, viz. $\{S_t, S_q\} = \Omega \times \pm\frac{h}{2}$, while essential boundary conditions specifying displacements and electric potential are defined at $\{S_u, S_\Phi\} = \partial\Omega \times \left[-\frac{h}{2} \leq z \leq \frac{h}{2}\right]$. Eq.(2) can be hence re-expressed upon separating in-plane and through-the-thickness integrals and introducing the definition of sublaminates:

$$\sum_{k=1}^{N_k}\sum_{p=1}^{N_p^k}\int_\Omega\int_{h_p} \delta\epsilon_{ij}^{p,k}\sigma_{ij}^{p,k} - \delta E_i^{p,k}D_i^{p,k} + \delta u_i^{p,k}\rho^{p,k}\ddot{u}_i^{p,k}\,\mathrm{d}z\,\mathrm{d}x_\alpha = \int_\Omega \left(\delta u_i\,\bar{t}_i - \delta\Phi\,\bar{q}\right)|_{z=\pm\frac{h}{2}}\,\mathrm{d}x_\alpha \quad (3)$$

The variations in Eq.(2) and Eq.(3) are to be taken under the following subsidiary conditions:

- the linearized gradient relations for small perturbations:

$$\epsilon_{ij}^{p,k} = \frac{1}{2}\left(u_{i,j}^{p,k} + u_{j,i}^{p,k}\right); \qquad E_i^{p,k} = -\Phi,_i^{p,k} \quad (4)$$

  where the notation $(),_i$ stays for partial derivative with respect to x_i.

- the piezoelectric constitutive equations in each ply:

$$\begin{aligned} \sigma_{ij}^{p,k} &= \tilde{C}_{ijlm}^{p,k}\,\epsilon_{lm}^{p,k} - e_{ijl}^{p,k}\,E_l^{p,k} \\ D_i^{p,k} &= e_{ilm}^{p,k}\,\epsilon_{lm}^{p,k} + \varepsilon_{il}^{p,k}\,E_l^{p,k} \end{aligned} \quad (5)$$

  where $\tilde{C}_{ijlm}$ is the stiffness coefficient at constant electric field, ε_{il} the dielectric coefficient at constant strain and e_{ijl} the piezoelectric stress coefficient. Elastic plies are represented by Eq.(5) with nil piezoelectric coupling, i.e., $e_{ijl}^{p,k} = 0$. Voigt compact notation is introduced based on the symmetry of the strain and stress tensors according to $\{\epsilon_i, \sigma_i\} = \{\epsilon_{ii}, \sigma_{ii}\}$ and $\{\epsilon_{9-i-j}, \sigma_{9-i-j}\} = \{2\epsilon_{ij}, \sigma_{ij}\}$ for $i \neq j$ [14]. Eq.(5) is thus expressed in terms of vectors and matrices as:

$$\begin{aligned} \sigma_P &= \tilde{C}_{PQ}\,\epsilon_Q - e_{Pl}\,E_l \\ D_i &= e_{iQ}\,\epsilon_Q + \varepsilon_{il}\,E_l \end{aligned} \quad (6)$$

  where uppercase Latin indexes $P, Q = 1, 2 \ldots 6$. Note that Eq.(5) and Eq.(6) are considered to hold in the global Cartesian reference frame employed for describing the plate geometry, i.e., the relations include the angle $\theta^{p,k}$ describing the orientation of the principal material axis X_1 with respect to the structural axis x_1, see also [14].

Note that the electric field is considered to be quasi-static compared to the mechanical wave propagation velocity.

2.3 Variable kinematics modeling in SGUF

Following the SGUF approach, each sublaminate is associated to a specific kinematic approximation, which is here extended for including the approximation for the electric potential

Φ. According to the compact index notation used in Unified Formulations, the generalized displacements are regrouped in one vector

$$\boldsymbol{\mathcal{U}}^{p,k} = \left\{ u_1^{p,k}, u_2^{p,k}, u_3^{p,k}, \Phi^{p,k} \right\} \tag{7}$$

In SGUF, the variation along the thickness direction z of each unknown function $\mathcal{U}_r^{p,k}$ is defined by a polynomial expansion of order $N_{\mathcal{U}_r}^k$ and by specifying whether the N_p^k plies of the sublaminate are described in an Equivalent Single Layer (ESL) or Layer-Wise (LW) manner. Therefore, the plate model is expressed in SGUF notation as

$$\mathcal{U}_r^{p,k}(x_1, x_2, z_p) = \sum_{\alpha_{\mathcal{U}_r}=0}^{N_{\mathcal{U}_r}^k} F_{\alpha_{\mathcal{U}_r}}(z_p)\, \hat{\mathcal{U}}_{\alpha_{\mathcal{U}_r}}^{p,k}(x_1, x_2) \tag{8}$$

where $r = 1, 2, 3$ for a displacement component and $r = 4$ for the electric potential, see Eq.(7). The thickness functions $F_{\alpha_{\mathcal{U}_r}}$ are expressed in terms of the ply-coordinates z_p if the plies of the sublaminate are described in a LW description; the approximation for the whole sublaminate is then obtained through the assembly of all plies upon enforcing the continuity of the function $\mathcal{U}_r$ at the interface between adjacent plies. However, if an ESL description is adopted for the sublaminate k, the thickness functions vary along z_k and the ply index p can be omitted in Eq.(8). If a constant approximation is used for a variable $\mathcal{U}_r^{p,k}$ within a sublaminate, one has $N_{\mathcal{U}_r}^k = 0$ and $F_{0_{\mathcal{U}_r}} = 1$. If a linear approximation is used, $N_{\mathcal{U}_r}^k = 1$ and the thickness functions correspond to the linear Lagrange polynomials that interpolate the values at the top and bottom of the ply (LW) or sublaminate (ESL). Higher-order approximations with $N_{\mathcal{U}_r}^k > 1$ are implemented through a hierarchic enrichment of the polynomial basis and employ Legendre polynomials. More details can be found elsewhere [9, 11].

In a sublaminate whose N_p^k plies are described in an ESL manner, a slope discontinuity can be introduced in the kinematics at the interface between adjacent plies by superposing a Zig-Zag function to the $C^1(z_k)$ polynomial expansion given by Eq.(8). the Zig-Zag function is constructed in such a manner that it vanishes at the top and bottom planes of the sublaminate and it varies linearly between -1 and +1 across each ply.

2.4 Ritz approximate solution

The weak form solution of the two-dimensional problem is sought within the space spanned by the global approximation (Ritz) functions, which can be expressed as

$$\hat{\mathcal{U}}_{r_{\alpha_{\mathcal{U}_r}}}^{p,k}(x_1, x_2) = \sum_{i=1}^{M} N_{\mathcal{U}_r i}(x_1, x_2)\, \mathcal{U}_{r_{\alpha_{\mathcal{U}_r}} i}^{p,k} \tag{9}$$

Different sets of Ritz functions can be used: $N_{\mathcal{U}_r i}$ can be a combination of trigonometric functions, or be the Legendre or Chebyshev polynomial of order i. In any case, a map between the physical $(x_1, x_2)-$plane and the computational $(\xi_1, \xi_2)-$domain is introduced, where $\xi_\alpha \in [-1, 1]$, for expressing the ith two-dimensional Ritz function as the product of two one-dimensional ("beam") functions according to

$$N_{\mathcal{U}_r i}(\xi_1, \xi_2) = \phi_{\mathcal{U}_r m}(\xi_1)\, \psi_{\mathcal{U}_r n}(\xi_2) \tag{10}$$

where $m = 1 \dots R$, $n = 1 \dots S$ (note that R and S may be, in general, different) and the relation between the ith function and the beam functions m and n has been chosen as $i = S(m-1)+n$.

In order to efficiently deal with various boundary conditions, such as clamped, free or simply-supported edges, the "beam" functions are expressed as a product between the polynomial spanning the complete field solution and an appropriate boundary function (pb2-Ritz approach):

$$\phi_{\mathcal{U}_r m}(\xi_1) = p_{\mathcal{U}_r m}(\xi_1)\, b_m(\xi_1); \qquad \psi_{\mathcal{U}_r n}(\xi_2) = p_{\mathcal{U}_r n}(\xi_2)\, b_n(\xi_2) \tag{11}$$

More details may be found in [10, 11]. As far as the boundary conditions for the electric potential are concerned, the plate edges may be grounded ($\Phi = 0$) or the potential may be let free.

2.5 The discrete system

The weak form of the equilibrium equation is formally expressed in terms of the generalized displacements by substituting Eq.(4) into Eq.(6), and both into Eq.(3). The through-the-thickness approximation and the Ritz solution are then introduced for the virtual and actual field variables according to following notation:

$$\begin{aligned} \delta\mathcal{U}_r^{p,k}(x_1,x_2,z_p) &= F_{\alpha_{\mathcal{U}_r}}(z_p)\, \delta\hat{\mathcal{U}}_{\alpha_{\mathcal{U}_r}}^{p,k}(x_\alpha) = F_{\alpha_{\mathcal{U}_r}}(z_p)\, \delta N_{\mathcal{U}_r i}(x_1,x_2)\, \mathcal{U}_{r_{\alpha_{\mathcal{U}_r}} i}^{p,k} \\ \mathcal{U}_s^{p,k}(x_1,x_2,z_p) &= F_{\beta_{\mathcal{U}_s}}(z_p)\, \hat{\mathcal{U}}_{\beta_{\mathcal{U}_s}}^{p,k}(x_\alpha) = F_{\beta_{\mathcal{U}_s}}(z_p)\, N_{\mathcal{U}_s j}(x_1,x_2)\, \mathcal{U}_{s_{\alpha_{\mathcal{U}_s}} j}^{p,k} \end{aligned} \tag{12}$$

where $r, s \in [1,4]$ according to Eq.(7), $\alpha_{\mathcal{U}_r} \in [0, N_{\mathcal{U}_r}^k]$ and $\beta_{\mathcal{U}_s} \in [0, N_{\mathcal{U}_s}^k]$ according to Eq.(8), and $i, j \in [1, M]$ according to Eq.(9). All integrals along z are explicitly carried out and are identified by the following notation:

$$\left\{ Z_{\mathcal{U}_r\mathcal{U}_s}^{p\,\alpha_{\mathcal{U}_r}\beta_{\mathcal{U}_s}}, Z_{\partial\mathcal{U}_r\mathcal{U}_s}^{p\,\alpha_{\mathcal{U}_r}\beta_{\mathcal{U}_s}}, Z_{\mathcal{U}_r\partial\mathcal{U}_s}^{p\,\alpha_{\mathcal{U}_r}\beta_{\mathcal{U}_s}}, Z_{\partial\mathcal{U}_r\partial\mathcal{U}_s}^{p\,\alpha_{\mathcal{U}_r}\beta_{\mathcal{U}_s}} \right\} = \int_{h_p} \left\{ F_{\alpha_{\mathcal{U}_r}} F_{\beta_{\mathcal{U}_s}}, F_{\alpha_{\mathcal{U}_r},z} F_{\beta_{\mathcal{U}_s}}, F_{\alpha_{\mathcal{U}_r}} F_{\beta_{\mathcal{U}_s},z}, F_{\alpha_{\mathcal{U}_r},z} F_{\beta_{\mathcal{U}_s},z} \right\} \mathrm{d}z \tag{13}$$

In a similar manner, the in-plane integrals of the Ritz functions are evaluated according to the following notation:

$$\mathcal{I}_{\mathcal{U}_r\mathcal{U}_s ij}^{degh} = \int_\Omega \frac{\partial^{d+e} N_{\mathcal{U}_r i}}{\partial x_1^d\, \partial x_2^e} \frac{\partial^{g+h} N_{\mathcal{U}_s j}}{\partial x_1^g\, \partial x_2^h}\, \mathrm{d}x_1\, \mathrm{d}x_2 \qquad (d,e,g,h = 0,1) \tag{14}$$

The discrete expression of Eq.(3) can be finally written as

$$\sum_{k=1}^{N_k} \sum_{p=1}^{N_p^k} \delta\mathcal{U}_{r_{\alpha_{\mathcal{U}_r}} i}^{p,k} M_{\circ\circ}^{p,k}\, Z_{(\partial)\mathcal{U}_r(\partial)\mathcal{U}_s}^{p\,\alpha_{\mathcal{U}_r}\beta_{\mathcal{U}_s}}\, \mathcal{I}_{\mathcal{U}_r\mathcal{U}_s ij}^{degh}\, \mathcal{U}_{s_{\beta_{\mathcal{U}_s}} j}^{p,k} + \delta u_{l_{\alpha_{u_l}} i}^{p,k}\, \rho^{p,k} Z_{u_l u_l}^{p\,\alpha_{u_l}\beta_{u_l}}\, \mathcal{I}_{u_l u_l ij}^{0000}\, \ddot{u}_{l_{\beta_{u_l}} j}^{p,k} = \sum_{\mathrm{intf}} \delta\mathcal{U}_{ri}^{\mathrm{intf}}\, \mathcal{I}_{\mathcal{U}_r \bar{P}_r i}^{\mathrm{intf}} \tag{15}$$

The left-hand side is the virtual internal work and includes the inertial terms, for which $l = 1, 2, 3$. $M_{\circ\circ}^{p,k}$ is one of the material parameters of Eq.(6) depending on the nature of the generic variables $\mathcal{U}_r$ and $\mathcal{U}_s$:

- if $r, s = 1, 2, 3$, i.e. $\mathcal{U}_r = u_r$ and $\mathcal{U}_s = u_s$, then $M_{\circ\circ}^{p,k} = \tilde{C}_{PQ}^{p,k}$ is an elastic stiffness coefficient;
- if $r = 1, 2, 3$ and $s = 4$, i.e. $\mathcal{U}_r = u_r$ and $\mathcal{U}_s = \Phi$, then $M_{\circ\circ}^{p,k} = e_{Pi}^{p,k}$ is a piezoelectric stress coefficient; analogously, if $r = 4$ and $s = 1, 2, 3$, then $M_{\circ\circ}^{p,k} = e_{iP}^{p,k}$
- if $r = s = 4$, i.e. $\mathcal{U}_r = \mathcal{U}_s = \Phi$, then $M_{\circ\circ}^{p,k} = \varepsilon_{ij}^{p,k}$ is a dielectric permittivity coefficient.

The right-hand side represents the virtual work done by the external loading:

- a mechanical loading if $r = 1, 2, 3$, i.e. $\mathcal{U}_r = u_r$, with

$$\mathcal{I}_{\mathcal{U}_r \bar{P}_r i}^{\text{intf}} = \int_\Omega N_{u_r i}(x_1, x_2)\, \bar{t}_r(x_1, x_2)\, \mathrm{d}x_1\, \mathrm{d}x_2$$

- an electrical loading if $r = 4$, i.e. $\mathcal{U}_r = \Phi$, with

$$\mathcal{I}_{\mathcal{U}_r \bar{P}_r i}^{\text{intf}} = \int_\Omega N_{\Phi i}(x_1, x_2)\, \bar{q}(x_1, x_2)\, \mathrm{d}x_1\, \mathrm{d}x_2$$

The electromechanical loading can be applied at several interfaces at the top/bottom of the plies: the pressure load is typically applied at the top and bottom surfaces of the plate, whereas electroded surfaces with prescribed electric charge or electric potential can be present also inside the composite stack, where an electric DOF is defined. Note that all natural boundary conditions, e.g., those specifying the electric charge density, are fulfilled in weak sense only.

After cycling over all indexes $\alpha_{\mathcal{U}_r}, \beta_{\mathcal{U}_s}$ of the thickness assumptions, assembly over all plies p and sublaminates k, and finally cycling over all Ritz expansion indexes i, j, the following discrete system is obtained:

$$\begin{bmatrix} \boldsymbol{M} & \boldsymbol{0} \\ \boldsymbol{0} & \boldsymbol{0} \end{bmatrix} \begin{bmatrix} \ddot{\boldsymbol{u}}(t) \\ \ddot{\boldsymbol{\Phi}}(t) \end{bmatrix} + \begin{bmatrix} \boldsymbol{K}_{uu} & \boldsymbol{K}_{u\Phi} \\ \boldsymbol{K}_{u\Phi}^T & \boldsymbol{K}_{\Phi\Phi} \end{bmatrix} \begin{bmatrix} \boldsymbol{u}(t) \\ \boldsymbol{\Phi}(t) \end{bmatrix} = \begin{bmatrix} \boldsymbol{T}(t) \\ \boldsymbol{Q}(t) \end{bmatrix} \tag{16}$$

Static problems are obtained by dropping out the time-dependency, while free-vibration responses are obtained by setting $\boldsymbol{T} = \boldsymbol{0}$ and $\boldsymbol{u}(t) = \boldsymbol{u}\, e^{i\omega t}$, where $i = \sqrt{-1}$ and ω is the eigenfrequency. Electrical open-circuit and short-circuit conditions can be taken into account as in [15].

3 NUMERICAL RESULTS

Before proceeding to the presentation of some numerical examples, the naming convention is introduced for identifying the variable kinematics models that can be implemented. For each sublaminate, the in-plane displacements u_α, the transverse displacement u_3 and the electric potential can be described in an ESL (E) or LW (L) manner, and with a specific polynomial order $N_{u_\alpha}^k$, $N_{u_3}^k$ and N_Φ^k. These informations are gathered for each sublaminate as follows:

$\mathrm{ED}_{N_{u_\alpha}\, N_{u_3}}^{N_\Phi}$ if all generalized displacements (u_α, u_3, Φ) are ESL

$\mathrm{LD}_{N_{u_\alpha}\, N_{u_3}}^{N_\Phi}$ if all generalized displacements (u_α, u_3, Φ) are LW

$\mathrm{D}_{\mathrm{L}N_{u_\alpha}\, \mathrm{E}N_{u_3}}^{\mathrm{L}N_\Phi}$ if u_α and Φ are LW, while u_3 is ESL

$\mathrm{D}_{\mathrm{E}N_{u_\alpha} Z\, \mathrm{E}N_{u_3}}^{\mathrm{L}N_\Phi}$ if u_α is ESL with ZigZag function, u_3 is ESL and Φ is LW

3.1 Validation: free-vibration analysis

In order to validate the formulation for the piezoelectric coupling, the fundamental frequencies of a square plate made of a homogeneous PZT-4 material is considered according to the classical benchmark of Heyliger and Saravanos [16]. Reference results are those provided by Messina and Carrera [17], which improve the early results published in [16]. Table 1 shows that the model accurately represents both conditions, the Short-Circuit (SC, top and bottom surfaces electrically grounded) and Open-Circuit (OC, top and bottom surfaces free of electric charge). A high-order ESL model $E^4_{6,6}$ is used for exactly recovering the reference 3D solution even for the very thick plate with $L/h = 1$, where L is the edges' length. The reported results are obtained with trigonometric Ritz functions of expansion orders $R = S = 8$, which provide converged results for the first flexural mode of the simply-supported plate.

L/h	1		4		10		50	
	SC	OC	SC	OC	SC	OC	SC	OC
3D [17]	713.0	724.6	96926.7	98227.7	18012.9	18077.2	746.7	746.9
$E^4_{6,6}$	713.0	724.6	96926.5	98227.8	18012.8	18077.2	746.7	746.8

Table 1: Fundamental eigenfrequencies of a simply-supported square PZT-4 plate

3.2 Validation: static analysis

An actuator case is considered by referring to the benchmark proposed by Heyliger [18]: a thick (L/h = 4) simply-supported square plate, consisting of a (0,90) Graphite-Epoxy basis structure with 2 piezoelectric plies bonded at its top and bottom surfaces, is subjected to a bi-sinusoidal electric potential at the top surface, with the bottom surface being grounded. Perfect electromechanical bond is modeled between the piezo-layers and the basis structure, which implies the continuity of displacement and electric potential. Figure 2 reports the generalized displacement components $u_1(x_1 = 0, x_2 = L/2, z)$ and $\Phi(x_1 = L/2, x_2 = L/2, z)$ and the stresses $\sigma_{11}(x_1 = L/2, x_2 = L/2, z)$, $\sigma_{13}(x_1 = 0, x_2 = L/2, z)$ and $\sigma_{33}(x_1 = L/2, x_2 = L/2, z)$. A perfect agreement is found, even for the very complex thickness distributions of the stress components. Note that the σ_{11} values reported in [18] for the bottom piezoelectric layer have been divided by a factor 10, as already discussed in [6].

The sensor response of a square thick plate (L/h=5) subject to a bi-sinusoidal pressure load is considered. The plate is composed of a $(0, 90)$ Graphite-Epoxy laminate with a piezoelectric PZT-5A layer on top of the 90-ply. The top and bottom surfaces of the PZT-5A ply are electroded and grounded. All data can be found in the paper by Vel and Batra [19], which provides reference 3D results also. This case study is here employed to demonstrate the convergence behavior of the proposed Ritz method and to show the capability of the method to represent different boundary conditions. Legendre polynomials are here employed in order to avoid the boundary conditions that are naturally fulfilled by trigonometric shape functions.

Figure 3 reports convergence plots for the generalized displacements (U_1, U_3, Φ) and some secondary variables (in-plane stress Σ_{11}, transverse shear stress Σ_{13} and transverse electric dis-

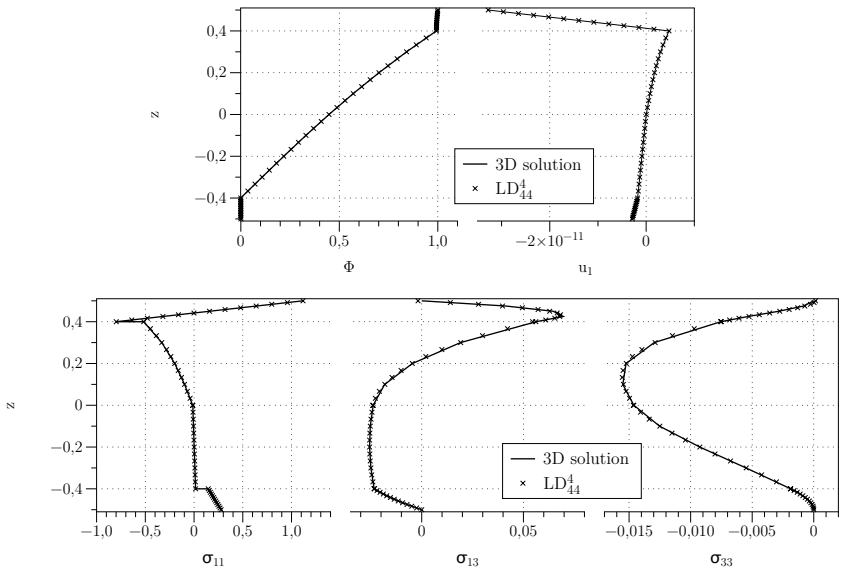

Figure 2: Generalized displacements (u_1, Φ) and stress components $(\sigma_{11}, \sigma_{13}, \sigma_{33})$ in a piezoelectric composite plate actuated by an electric potential.

placement D_3). All quantities are taken at specific points inside the laminate and are reported in non-dimensional form – all details can be found in [19]. The considered plate is mechanically simply-supported and electrically grounded at its four edges (SP-SP boundary conditions). The reference solutions is exactly recovered already with $R = S = 6$ functions.

Non-dimensional results for a different set of boundary conditions are reported in Table 2. The two edges $x_2 = 0, L$ are simply-supported and grounded, whereas the two edges $x_1 = 0, L$ are clamped and in open-circuit (nil electric charge) – in [19], this configuration is referred to as CD-CD. Very small discrepancies with respect to the reference 3D solution can be seen, which are attributed to the different manner the open-circuit boundary conditions are taken into account.

	U_1	U_3	Σ_{11}	Σ_{13}	Σ_{23}	Σ_{33}	Φ	D_3
3D [19]	-1.082	10.851	6.652	1.056	0.096	0.462	-3.020	13.301
$E^6_{6,6}$	-1.082	10.848	6.622	1.054	0.095	0.463	-3.014	13.286

Table 2: Nondimensional response at selected points of the square (0,90)/PZT-5A plate subjected to mechanical load and CD-CD boundary conditions

3.3 Model assessment

The latter example involving a thick piezoelectric laminate in sensor configuration with SP-SP boundary conditions [19] is considered for demonstrating the modeling flexibility of the SGUF

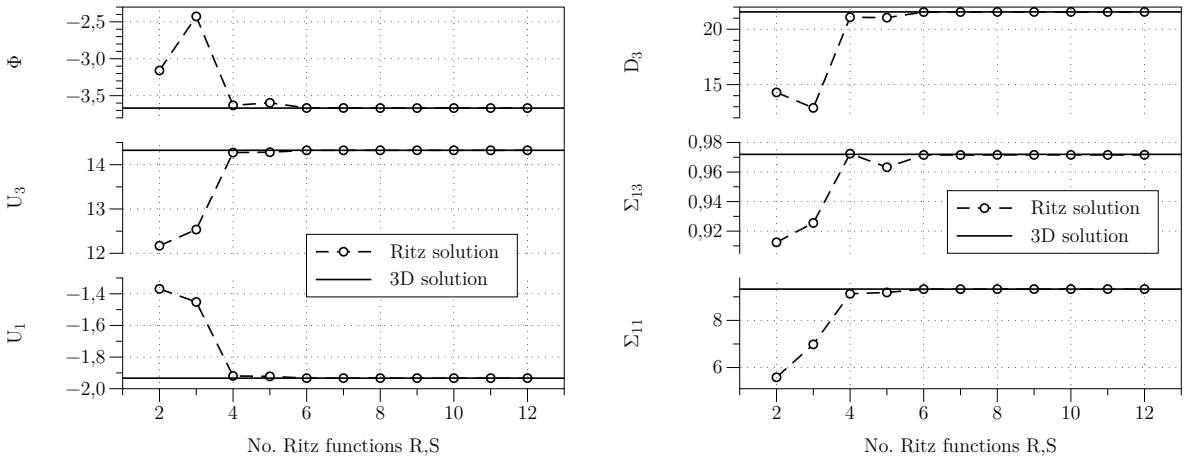

Figure 3: Convergence of the Ritz solution towards the exact 3D solution. Left: non-dimensional generalized displacements (U_1, U_3, Φ). Right: non-dimensional stress and dielectric displacement $(\Sigma_{11}, \Sigma_{13}, D_3)$

approach. Due to the grounded electrodes at the top and bottom faces of the piezoelectric ply, it is apparent that the electric field is confined inside the piezoelectric ply. The plate shall thus be conveniently modeled with 2 sublaminates, one for the piezoelectric ply and another for the basis laminate. While a quadratic approximation for $\Phi(z)$ should be used across the piezoelectric ply in order to capture the sensor effect, a constant electric potential $\Phi(z)$ can be assumed across the basis laminate. These approximations can be coupled with various kinematical models, such as simple FSDT (ED_{10}), an HSDT (ED_{30}), or the Lo-Christensen-Wu model (ED_{32}). A ZigZag function can be superimposed to the in-plane displacements (e.g., ED_{3Z2} or ED_{1Z0}). Table 3 compares the reference solutions of Vel and Batra [19] with those obtained with various models obtained by the present SGUF approach. One notices that the sublaminate approach can enhance the accuracy without increasing the DOF number (e.g., comparing $\mathrm{D}^{\mathrm{L2}}_{\mathrm{E3}Z2}$ and ED^{2}_{30} / ED^{0}_{3Z0}). One may also remark that the full 3D law including the transverse normal deformation is required for an accurate prediction of the electric displacement D_3.

4 CONCLUSIONS

A variable-kinematics modeling approach based on the Sublaminate Generalized Unified Formulation (SGUF) has been extended to piezoelectric coupling. A Ritz method has been used to solve in weak form the resulting two-dimensional differential equations, which may include anisotropic couplings and various types of essential boundary conditions. The SGUF-Ritz appears to be very flexible as it provides a valuable means for (i) investigating various piezoelectric plate problems, including static actuator or sensor applications and free-vibration analysis with open or short-circuit conditions; (ii) assessing a large number of models in view of a minimization of the number of DOF with a controlled accuracy.

	No. DOF	U_1	U_3	Σ_{11}	Σ_{13}	Σ_{23}	Σ_{33}	Φ	D_3
3D [19]	–	-1.933	14.325	9.329	0.972	0.384	0.419	-3.668	21.563
$\mathrm{LD}^4_{4,4}$	52	-1.933	14.325	9.329	0.972	0.384	0.419	-3.668	21.563
$\mathrm{LD}^2_{3,2}$	34	-1.933	14.323	9.365	0.971	0.384	0.426	-3.668	21.475
ED^2_{32} / ED^0_{3Z2}	24	-1.929	14.308	9.347	0.969	0.383	0.473	-3.660	21.437
ED^2_{32} / ED^0_{32}	22	-1.947	14.100	9.355	0.976	0.381	0.474	-3.605	21.478
ED^2_{32} / ED^0_{3Z0}	22	-1.947	14.342	9.379	0.983	0.386	–	-3.599	21.721
ED^2_{30} / ED^0_{3Z2}	22	-2.034	14.559	9.150	0.959	0.375	0.474	-3.804	25.203
ED^2_{30} / ED^0_{3Z0}	20	-2.052	14.591	9.183	0.973	0.378	–	-3.744	25.491
$\mathrm{D}^{\mathrm{L2}}_{\mathrm{E3}Z2}$	20	-1.872	14.215	9.757	1.332	0.484	0.143	-3.158	19.324
ED^2_{10} / ED^0_{3Z2}	18	-2.021	14.526	9.100	0.559	0.221	0.474	-3.797	25.027
$\mathrm{D}^{\mathrm{L2}}_{\mathrm{E32}}$	18	-2.011	13.222	9.935	3.142	0.694	0.091	-3.062	19.908
ED^2_{32} / ED^0_{10}	16	-2.171	12.712	9.744	1.090	0.387	–	-3.169	23.206
ED^2_{10} / ED^0_{1Z0}	12	-2.027	14.339	9.073	0.563	0.221	–	-3.680	25.299
$\mathrm{D}^{\mathrm{L2}}_{\mathrm{E10}}$	12	-2.121	11.201	8.628	2.347	0.584	–	-2.733	24.631
ED^2_{10} / ED^0_{10}	10	-2.261	12.937	9.491	0.608	0.218	–	-3.313	26.767

Table 3: Model assessment: nondimensional response at selected points of the square (0,90)/PZT-5A plate subjected to mechanical load (SP-SP boundary conditions)

References

[1] S. O. R. Moheimani and A. J. Fleming. *Piezoelectric Transducers for Vibration Control and Damping*. Springer-Verlag London, 2006.

[2] J. N. Reddy. An evaluation of equivalent-single-layer and layerwise theories of composite laminates. *Compos. Struct.*, 25:21–35, 1993.

[3] E. Carrera. Theories and finite elements for multilayered plates and shells: A unified compact formulation with numerical assessment and benchmarking. *Arch. Comput. Meth. Eng.*, 10:215–296, 2003.

[4] E. Carrera, M. Cinefra, M. Petrolo, and E. Zappino. *Finite Element Analysis of Structures through Unified Formulation*. John Wiley & Sons, Ltd, 2014.

[5] D. H. Robbins Jr and J. N. Reddy. An efficient computational model for the stress analysis of smart plate structures. *Smart Mater. Struct.*, 5:353–360, 1996.

[6] D. Ballhause, M. D'Ottavio, B. Kröplin, and E. Carrera. A unified formulation to assess multilayered theories for piezoelectric plates. *Comput. Struct.*, 83:1217–1235, 2005.

[7] E. Carrera, S. Brischetto, and P. Nali. *Plates and shells for smart structures. Classical and advanced theories for modeling and analysis*. John Wiley & Sons, Ltd, 2011.

[8] L. Demasi. ∞^3 hierarchy plate theories for thick and thin composite plates: The generalized unified formulation. *Compos. Struct.*, 84:256–270, 2008.

[9] M. D'Ottavio. A Sublaminate Generalized Unified Formulation for the analysis of composite structures and its application to sandwich plates bending. *Compos. Struct.*, 142:187–199, 2016.

[10] L. Dozio and E. Carrera. Ritz analysis of vibrating rectangular and skew multilayered plates based on advanced variable-kinematics models. *Compos. Struct.*, 94:2118–2128, 2012.

[11] M. D'Ottavio, L. Dozio, R. Vescovini, and O. Polit. Bending analysis of composite laminated and sandwich structures using sublaminate variable-kinematic Ritz models. *Compos. Struct.*, 155:45–62, 2016.

[12] M. D'Ottavio, R. Vescovini, L. Dozio, and O. Polit. A sublaminate generalized unified formulation for buckling and wrinkling of sandwich plates. In *2016 EMI - International Conference*, Metz, France, October 2016. ASCE Engineering Mechanics Institute.

[13] M. D'Ottavio, L. Dozio, R. Vescovini, and O. Polit. Dynamic analysis of multilayered plates with viscoelastic layers using a sublaminate generalized unified formulation. In A. J. M. Ferreira, editor, *19th International Conference on Composite Structures*, Porto, Portugal, 5 – 9 September 2016.

[14] J. N. Reddy. *Mechanics of Laminated Composite Plates and Shells: Theory and Analysis*. CRC Press, 2nd edition, 2004.

[15] A. Benjeddou and S. Belouettar. On the evaluation and application of piezoelectric adaptive structures modal properties. In B. H. V. Topping, G. Montero, and R. Montenegro, editors, *Innovation in Computational Structures Technology*, chapter 14. Saxe-Coburg Publications, 2006.

[16] D. A. Saravanos and P. R. Heyliger. Exact free-vibration analysis of laminated plates with embedded piezoelectric layers. *J. Acoust. Soc. Am.*, 98:1547–1557, 1995.

[17] A. Messina and E. Carrera. Three-dimensional free vibration of multi-layered piezoelectric plates through approximate and exact analyses. *J. Intellig. Mat. Sys. Struct.*, 26:489–504, 2015.

[18] P. R. Heyliger. Static behavior of laminated elastic/piezoelectric plates. *AIAA J.*, 32:2481–2484, 1994.

[19] S. S. Vel and R. C. Batra. Three-dimensional analytical solution for hybrid multilayered piezoelectric plates. *J. Appl. Mech.*, 67:558–567, 2000.

VIII ECCOMAS Thematic Conference on Smart Structures and Materials
SMART 2017
A. Güemes, A. Benjeddou, J. Rodellar and J. Leng (Eds)

FINITE ELEMENT TECHNIQUES FOR THE CHARACTERIZATION OF EFFECTIVE PROPERTIES OF TRANSVERSE PIEZOELECTRIC MACRO-FIBRE COMPOSITES

MARCELO A. TRINDADE[*] AND AYECH BENJEDDOU[†‡]

[*]Department of Mechanical Engineering, São Carlos School of Engineering,
University of São Paulo, Av. Trabalhador São-Carlense, 400, São Carlos, SP, 13566-590, Brazil
e-mail: trindade@sc.usp.br

[†] Sorbonne Université, Université de Technologie de Compiègne, CNRS, UMR 7337 ROBERVAL,
Centre de Recherche Royallieu, CS 60319, 60203 Compiègne CEDEX, France
e-mail: ayech.benjeddou@utc.fr

[‡] SUPMECA, 3 Rue Fernand Hainaut, 93407 Saint Ouen, CEDEX, France
e-mail: benjeddou@supmeca.fr

Key words: Piezoelectric materials, Macro-fibre composites, Effective properties characterization, Finite element method, Homogenization techniques

Abstract. Macro-Fibre Composites (MFC) have become very popular since they combine the conformability of epoxy-matrix composites and the electromechanical energy density of piezoceramic materials. The main difficulty in the study of MFC is that their behaviour may be much more complex since they are made of different materials (piezoceramic fibres, epoxy matrix, electrode layers and protective layers). Therefore, it is necessary to understand and model their behaviour to be able to quantify or characterize their effective material properties and, thus, their effectiveness as distributed sensors and actuators. Previous results have shown that the effective properties depend not only on the piezoceramic fibres and epoxy materials and fibre volume fraction but also on the geometrical and material properties of the other layers (Kapton, Acrylic, Electrodes). This work presents new results on finite element homogenization techniques used to relate individual material properties of piezoceramic fibres and effective material properties of the corresponding MFC. In particular, an enthalpy-based homogenization procedure, as proposed previously in the literature for a shear d_{15} MFC, is applied here to the characterization of a d_{31} MFC effective properties and compared to previously published results using average quantities homogenization. Results from both methods are also compared to available data from a MFC manufacturer.

1 INTRODUCTION

Piezoelectric Macro-Fibre Composites (MFC) are composed of piezoceramic macro-fibres, that are generally obtained through precision machining of piezoceramic patches, embedded in an Epoxy matrix to provide mechanical properties not found in piezoceramic patches, such as conformability and resilience. This composite so-called active layer is then covered on both faces by electrode and protective

layers. MFC transducers have extended the use of piezoceramic materials to applications in which conformable packaged transducers are more interesting, such as for controlling and/or monitoring flexible curved structures. Depending on poling and fibre orientation, these transducers can be made to operate in standard d_{33}, d_{31} [1] and d_{15} [2] modes.

Since MFC transducers are made of different materials with highly heterogeneous mechanical properties, some recent research works have focused on the characterization of MFC effective material properties using homogenization techniques, as in [3, 4, 5, 6, 7, 8] for MFCs in d_{31} and d_{33} operation modes and [2, 9, 10] for d_{15} MFCs. The general idea is to provide effective material constants that could be used in other analyses considering an equivalent homogeneous material transducer. Previous works have shown that the effective properties depend not only on the active layer characteristics (properties of piezoceramic fibres and epoxy material, and their distribution, that is the fibre volume fraction) but also on the electrode and protective layers (geometrical and material properties).

Most of the methods already available allow reasonable characterization of effective elastic properties. On the other hand, for the characterization of effective piezoelectric and dielectric properties, there are still some open issues, such as proper accountability for the electric boundary conditions and the effect of electrical assumptions on the effective material constants. Some recent works discussed these issues, such as the modeling of realistic electrode configurations inside the Representative Volume Element (RVE) [8] and the effect of considering the relation between RVE inner electrodes and global ones [11]. The latter reference also points out the necessity of accounting for an energetic equivalence between the heterogeneous RVE and the equivalent homogeneous material. This was done using a so-called Enthalpy-Based Homogenization Method (EBHM), in which the homogenization should lead to an equivalence between heterogeneous RVE and homogenized material enthalpies (as a measure of inner energy). This method differs from another more standard one, so-called Average Quantities Homogenization Method (AQHM), in which the homogenization leads to an equivalence between selected mechanical and electrical fields, when averaged over the heterogeneous RVE.

The main objective of this work is to present a comparison between AQHM and EBHM for the numerical characterization of the effective properties of a d_{31} MFC transducer. In both cases, a finite element model of a d_{31} MFC RVE is built and used to solve specially designed local static problems that allow to evaluate the effective elastic, piezoelectric and dielectric properties of a d_{31} MFC based on known material and geometrical properties of its constituents. Both techniques account for electrode and protective layers, realistic electrode configurations and proper electric boundary conditions.

2 EFFECTIVE CONSTITUTIVE EQUATIONS FOR d_{31} MFC

The d_{31} piezoelectric MFC considered in this work is schematically represented in Figure 1. It is made of an active layer, composed of piezoceramic macro-fibres embedded in an Epoxy matrix, which is then fully covered by electrode and protective layers. The macro-fibres are assumed poled in through-thickness direction (x_3). The same direction is considered as preferential or dominant for the applied/induced electric field. This is reinforced by an electrode layer that fully covers top (x_3^+) and bottom (x_3^-) surfaces. Thus, it can be assumed that in-plane electric fields vanish (that is, $E_1 = E_2 = 0$).

Starting from the general linear piezoelectric constitutive equations, in the so-called stress-charge or *e* form,

$$\left\{\begin{array}{c}\mathbf{T}\\ \hline \mathbf{D}\end{array}\right\} = \left[\begin{array}{c|c}\mathbf{c}^E & -\mathbf{e}^{\mathrm{t}}\\ \hline \mathbf{e} & \boldsymbol{\epsilon}^S\end{array}\right]\left\{\begin{array}{c}\mathbf{S}\\ \hline \mathbf{E}\end{array}\right\}, \tag{1}$$

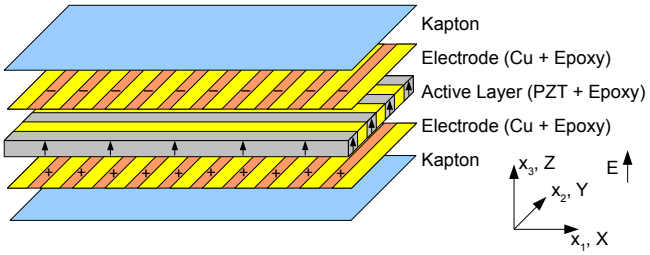

Figure 1: Schematic representation of a d_{31} Macro-Fibre Composite.

and accounting for electric field assumptions, reduced constitutive equations can be written as

$$\left\{\begin{array}{c} T_1 \\ T_2 \\ T_3 \\ T_4 \\ T_5 \\ T_6 \\ \hline D_3 \end{array}\right\} = \left[\begin{array}{cccccc|c} c_{11}^E & c_{12}^E & c_{13}^E & 0 & 0 & 0 & -e_{31} \\ c_{12}^E & c_{22}^E & c_{23}^E & 0 & 0 & 0 & -e_{32} \\ c_{13}^E & c_{23}^E & c_{33}^E & 0 & 0 & 0 & -e_{33} \\ 0 & 0 & 0 & c_{44}^E & 0 & 0 & 0 \\ 0 & 0 & 0 & 0 & c_{55}^E & 0 & 0 \\ 0 & 0 & 0 & 0 & 0 & c_{66}^E & 0 \\ \hline e_{31} & e_{32} & e_{33} & 0 & 0 & 0 & \epsilon_{33}^S \end{array}\right] \left\{\begin{array}{c} S_1 \\ S_2 \\ S_3 \\ S_4 \\ S_5 \\ S_6 \\ \hline E_3 \end{array}\right\}, \tag{2}$$

where T_p and S_q, with $p,q = 1,\ldots,6$, stand for the six components of mechanical stress and strain vectors in Kelvin-Voigt notation. D_3 and E_3 denote the transverse electric displacement and field. In the so-called e-form of the linear piezoelectric constitutive equations (2), c_{pq}^E, e_{3j} $(j = 1,2,3)$ and ϵ_{33}^S denote the short-circuit elastic stiffness (at constant electric fields), stress piezoelectric and blocked electric permittivity (at constant mechanical strains) coefficients.

Considering a d_{31} operation mode, the most important electromechanical coupling is between applied/induced through-thickness electric field and displacement, E_3 and D_3, and macro-fibre longitudinal applied/induced normal stress and strain, T_1 and S_1. However, in order to properly model the equivalent homogeneous material, it is also important to account for other deformation modes, such as width and thickness normal strains/stresses and shear strains/stresses. Hence, the only material constants that are not evaluated, and thus do not appear in (2), are those that relate to in-plane electric fields E_1 and E_2 that cannot be applied/induced due to the electrode configuration.

Besides those present in (2), other interesting material constants may be evaluated through post-processing. For instance, the corresponding material constants for the so-called strain-charge or d form linear piezoelectric constitutive equations are written as

$$[\mathbf{s}^E] = [\mathbf{c}^E]^{-1}, [\mathbf{d}] = [\mathbf{c}^E]^{-1}[\mathbf{e}], [\boldsymbol{\epsilon}^T] = [\boldsymbol{\epsilon}^S] + [\mathbf{e}][\mathbf{c}^E]^{-1}[\mathbf{e}]^{\mathrm{t}}. \tag{3}$$

The effective electromechanical coupling coefficients k_{3j}^2 of the MFC may be evaluated as

$$k_{3j}^2 = \frac{d_{3j}^2}{s_{jj}^E \epsilon_{33}^T}. \tag{4}$$

It is clear, though, that the behavior of a MFC transducer composed of different materials with highly heterogeneous material properties (not all piezoelectric) does not need to comply with constitutive equa-

tions (2). It can be only assumed that an equivalent homogeneous piezoelectric material could approximately behave according to (2). This is the baseline of the two finite element homogenization methods that are presented in the following.

3 FINITE ELEMENT HOMOGENIZATION THROUGH STATIC LOCAL PROBLEMS

In order to evaluate the effective material constants of an homogeneous material that could be equivalent, in some respect, to the d_{31} MFC schematically represented in Figure 1, two finite element homogenization techniques are presented. They are both based on the evaluation of mechanical stresses and strains and electric fields and displacements in a finite element model of a RVE of the MFC when its is subjected to a number of so-called static local problems. In each static local problem, mechanical and electrical boundary and periodicity conditions are imposed depending on the effective material constant that should be determined. In all cases, it is important to account for symmetric or periodic mechanical and electrical boundary conditions in longitudinal (x_1) and width (x_2) directions, since the RVE is obtained from a through-thickness cut of the real MFC.

Figure 2 depicts the RVE considered in this work for the d_{31} MFC. The RVE active layer is built with one longitudinal section of the piezoceramic macro-fibre (through-thickness poled and electroded) between two Epoxy inserts. Both upper and lower surfaces of the active layer are covered by a thin electrode layer each, composed of two Copper and one Epoxy layers representing a section of the fingered electrode layer. Finally, the electrode layers are covered by a homogeneous Kapton protective layer. The boundaries of the RVE are denoted X_1^-, X_1^+, X_2^-, X_2^+, X_3^- and X_3^+ according to Figure 2. To obtain a more realistic analysis, electric potential boundary conditions are imposed at the electrodes on surfaces Γ_e^- and Γ_e^+, which represent the areas covered by Copper electrodes and piezoceramic fibre electrodes.

To obtain the desired loading conditions for each local problem, average strains $\bar{S}_{ij}$ and electric field $\bar{E}_3$ are imposed to the RVE using displacements u_i and voltage ϕ boundary conditions, such that

$$u_i^{X_j^+} - u_i^{X_j^-} = \bar{S}_{ij}(x_j^{X_j^+} - x_j^{X_j^-}), \;\; i,j = 1,2,3, \tag{5}$$

$$\phi^{\Gamma_e^+} - \phi^{\Gamma_e^-} = -\bar{E}_3(x_3^{\Gamma_e^+} - x_3^{\Gamma_e^-}), \;\; \phi^{X_\alpha^+} - \phi^{X_\alpha^-} = 0, \;\; \alpha = 1,2. \tag{6}$$

Notice that, in all cases, symmetric boundary conditions for the electric potential along directions x_1 and x_2 for the corresponding X_1^-/X_1^+ and X_2^-/X_2^+ RVE surfaces are applied.

3.1 Average quantities homogenization method

In the case of the AQHM, the resulting average mechanical stresses and strains and electric fields and displacement over the RVE are evaluated and, then, used to determine the desired material constants in each local problem. Since the RVE is discretized in a number of finite elements, the average quantities are approximated by a sum of averaged element values multiplied by the respective element volume divided by the RVE total volume, such that

$$\bar{S}_q = \frac{\sum_{e=1}^N S_q^{(e)} V^{(e)}}{\sum_{e=1}^N V^{(e)}}, \; \bar{T}_p = \frac{\sum_{e=1}^N T_p^{(e)} V^{(e)}}{\sum_{e=1}^N V^{(e)}}, \;\; p,q = 1,\ldots,6, \tag{7}$$

$$\bar{E}_k = \frac{\sum_{e=1}^N E_k^{(e)} V^{(e)}}{\sum_{e=1}^N V^{(e)}}, \; \bar{D}_i = \frac{\sum_{e=1}^N D_i^{(e)} V^{(e)}}{\sum_{e=1}^N V^{(e)}}, \;\; i,k = 1,2,3. \tag{8}$$

where $V^{(e)}$ is the volume of the element e. $S_q^{(e)}$, $T_p^{(e)}$, $E_k^{(e)}$ and $D_i^{(e)}$ are the average strains, stresses, electric fields and electric displacements evaluated at element e. N is the total number of finite elements used to discretize the RVE.

Then, based on the effective constitutive equations of the MFC, a number of local problems were designed to determine the corresponding effective material constants. First, the short circuit (or constant electric field) elastic coefficients are determined using specific loading conditions in which each mechanical strain is imposed, one at a time, and the transverse electric field is set to vanish. The mechanical normal strains were imposed through relative normal displacements in the surfaces of the RVE (AQ01, AQ02 and AQ03 in Table 1), whereas mechanical shear strains were imposed through relative shear displacements in each of the three planes (AQ04, AQ05 and AQ06 in Table 1). To ensure that the other strains vanish, symmetric coupling of normal displacements between opposing surfaces were applied. To ensure a short circuit electric boundary condition, the electric potential degrees of freedom in the electrodes at surfaces Γ_e^- and Γ_e^+ are set to zero. This leads to the first six local problems presented in Table 1 that summarizes the boundary conditions and the expression considered to determine the corresponding effective material constants. Notice that the first three local problems also allow to determine the effective stress piezoelectric material constants, $e_{3j},\ j=1,2,3$, by dividing the average electric displacement $\bar{D}_3$ by the respective average normal strain $\bar{S}_j$.

To determine the blocked dielectric constant ϵ_{33}^S, another local problem (AQ07 in Table 1) is set up for which an electric potential $\phi^{\Gamma_e^+} = h_P$ (in value) is applied to the electrode at surface Γ_e^+ while the voltage at the opposite electrode (at surface Γ_e^-) is set to zero. This leads to a unitary electric field applied in the x_3 direction. The mechanically blocked condition (no strain) is approximated by ensuring that average normal strains S_1, S_2 and S_3 vanish. This is done through symmetric coupling of normal displacements between opposing surfaces. The last row of Table 1 summarizes this local problem and the expression considered to determine the dielectric constant.

A summary of the seven local problems used for determining the effective material properties of the d_{31} MFC RVE using the AQHM is presented in Table 1. In the table, u_j^{i-} and u_j^{i+} are the displacements in direction j and ϕ^{i-} and ϕ^{i+} are the electric potentials at i-th node of opposite surfaces. The dimensions of the RVE are $\Delta x_1 = L_T = 2L_C + L_E$, $\Delta x_2 = w_T = 2w_E + w_P$ and $\Delta x_3 = h_T = 2(h_K + h_C) + h_P$.

Table 1: Boundary conditions (displacement/electric potential) and relations used to evaluate the effective material properties of a d_{31} piezoelectric MFC using AQHM.

Problem	X_1^-/X_1^+	X_2^-/X_2^+	X_3^-/X_3^+	Γ_e^-/Γ_e^+	Effective material constant
AQ01	$u_1^{i+} - u_1^{i-} = L_T$	$u_2^{i+} - u_2^{i-} = 0$	$u_3^{i+} - u_3^{i-} = 0$	$\phi^{i+} - \phi^{i-} = 0$	$c_{1j}^E = \bar{T}_j/\bar{S}_1,\ e_{31} = \bar{D}_3/\bar{S}_1$
AQ02	$u_1^{i+} - u_1^{i-} = 0$	$u_2^{i+} - u_2^{i-} = w_T$	$u_3^{i+} - u_3^{i-} = 0$	$\phi^{i+} - \phi^{i-} = 0$	$c_{2j}^E = \bar{T}_j/\bar{S}_2,\ e_{32} = \bar{D}_3/\bar{S}_2$
AQ03	$u_1^{i+} - u_1^{i-} = 0$	$u_2^{i+} - u_2^{i-} = 0$	$u_3^{i+} - u_3^{i-} = h_T$	$\phi^{i+} - \phi^{i-} = 0$	$c_{3j}^E = \bar{T}_j/\bar{S}_3,\ e_{33} = \bar{D}_3/\bar{S}_3$
AQ04	$u_1^{i+} - u_1^{i-} = 0$	$u_3^{i+} - u_3^{i-} = w_T/2$	$u_2^{i+} - u_2^{i-} = h_T/2$	$\phi^{i+} - \phi^{i-} = 0$	$c_{44}^E = \bar{T}_4/\bar{S}_4$
AQ05	$u_3^{i+} - u_3^{i-} = L_T/2$	$u_2^{i+} - u_2^{i-} = 0$	$u_1^{i+} - u_1^{i-} = h_T/2$	$\phi^{i+} - \phi^{i-} = 0$	$c_{55}^E = \bar{T}_5/\bar{S}_5$
AQ06	$u_2^{i+} - u_2^{i-} = L_T/2$	$u_1^{i+} - u_1^{i-} = w_T/2$	$u_3^{i+} - u_3^{i-} = 0$	$\phi^{i+} - \phi^{i-} = 0$	$c_{66}^E = \bar{T}_6/\bar{S}_6$
AQ07	$u_1^{i+} - u_1^{i-} = 0$	$u_2^{i+} - u_2^{i-} = 0$	$u_3^{i+} - u_3^{i-} = 0$	$\phi^{i+} - \phi^{i-} = h_P$	$\epsilon_{33}^S = \bar{D}_3/\bar{E}_3$

3.2 Enthalpy-based homogenization method

The main idea of EBHM is to evaluate the effective material properties of the RVE, under different loading conditions, so that a homogeneous material with these effective properties would lead to the

same enthalpy as the RVE. This would then ensure energetic equivalence between the proposed RVE and the corresponding homogeneous material, at least for the loading conditions considered.

Let us consider the electromechanical enthalpy density for a linear and homogeneous piezoelectric material written as

$$\bar{H} = \frac{1}{2}(\bar{T}_p \bar{S}_p - \bar{D}_j \bar{E}_j), \tag{9}$$

where $p = 1,\ldots,6$, $j = 1,2,3$ and repeated index summation is assumed. In the case of a heterogeneous RVE, with expected linear piezoelectric effective material behavior, the electromechanical enthalpy density is obtained through summation of the local enthalpies for each finite element, such that

$$H_{RVE} = \frac{1}{2V}\sum_{e=1}^{N}\left(T_p^{(e)} S_p^{(e)} - D_j^{(e)} E_j^{(e)}\right) V^{(e)}, \tag{10}$$

where V is the total RVE volume and N is the number of finite elements considered for the RVE.

Expansion of (9) leads to the effective enthalpy written in terms of the individual effective material constants

$$\begin{aligned} 2\bar{H} = {} & \bar{c}_{11}^E \bar{S}_1^2 + \bar{c}_{22}^E \bar{S}_2^2 + \bar{c}_{33}^E \bar{S}_3^2 + \bar{c}_{44}^E \bar{S}_4^2 + \bar{c}_{55}^E \bar{S}_5^2 + \bar{c}_{66}^E \bar{S}_6^2 + 2\bar{c}_{12}^E \bar{S}_1 \bar{S}_2 + 2\bar{c}_{13}^E \bar{S}_1 \bar{S}_3 + 2\bar{c}_{23}^E \bar{S}_2 \bar{S}_3 \\ & - 2\bar{e}_{31} \bar{S}_1 \bar{E}_3 - 2\bar{e}_{32} \bar{S}_2 \bar{E}_3 - 2\bar{e}_{33} \bar{S}_3 \bar{E}_3 - 2\bar{e}_{24} \bar{S}_4 \bar{E}_2 - 2\bar{e}_{15} \bar{S}_5 \bar{E}_1 - \bar{\epsilon}_{11}^S \bar{E}_1^2 - \bar{\epsilon}_{22}^S \bar{E}_2^2 - \bar{\epsilon}_{33}^S \bar{E}_3^2. \end{aligned} \tag{11}$$

Based on this expansion, it is possible to observe that one may design loading conditions for which only selected effective material constants affect the effective enthalpy. Hence, each loading condition could allow the determination of desired effective material constants. One possible way to do this, as proposed in [10], is through 17 loading conditions, that is one for each effective material constant, in which unit strains $\bar{S}_p = 1$ and electric fields $\bar{E}_j = 1$ are imposed as loading conditions. In each case, the enthalpy of the RVE can be evaluated and, then, the effective material constant can be determined so that $\bar{H} = H_{RVE}$.

Table 2 summarizes the loading conditions and the corresponding expressions to determine the effective material constants. Numbering of the loading conditions follows [11] for clarity. However, since for the present case it is not possible to apply/induce electric fields in longitudinal (x_1) and width (x_2) directions, E_1 and E_2 respectively, loading conditions EB10, EB11, EB16 and EB17 are not possible and thus are not shown in Table 2. This means that effective stress piezoelectric constants $\bar{e}_{24}$ and $\bar{e}_{15}$ and blocked dielectric constants $\bar{\epsilon}_{11}^S$ and $\bar{\epsilon}_{22}^S$ cannot be evaluated. Since, in practice, operation through these two electric fields is not possible, these material constants should not affect any predictive model.

Notice that, compared to the Average Quantities Homogenization Method, the first six local problems are the same (AQ01/EB01, AQ02/EB02, AQ03/EB03, AQ04/EB04, AQ05/EB05, AQ06/EB06) . The main difference is that, for AQHM, the problems AQ01, AQ02 and AQ03 are also used to evaluate three other elastic constants, $\bar{c}_{12}^E$, $\bar{c}_{13}^E$ and $\bar{c}_{23}^E$, as well as the three piezoelectric constants, $\bar{e}_{31}$, $\bar{e}_{32}$ and $\bar{e}_{33}$, which, in EBHM, are all evaluated through separate local problems, namely, EB07, EB08 and EB09 for the three elastic constants, and EB14, EB15 and EB13, for the three piezoelectric constants. Therefore, these last six local problems are not necessary in AQHM. The local problem to evaluate the constant strain dielectric constant $\bar{\epsilon}_{33}^S$ is the same in both methods (AQ07/EB12).

Table 2: Loading conditions for evaluating effective material constants using enthalpy-based homogenization method.

Problem	X_1^-/X_1^+	X_2^-/X_2^+	X_3^-/X_3^+	Γ_e^-/Γ_e^+	Effective material constant
EB01	$u_1^{i+}-u_1^{i-}=L_T$	$u_2^{i+}-u_2^{i-}=0$	$u_3^{i+}-u_3^{i-}=0$	$\phi^{i+}-\phi^{i-}=0$	$c_{11}^E=2H_{RVE}$
EB02	$u_1^{i+}-u_1^{i-}=0$	$u_2^{i+}-u_2^{i-}=w_T$	$u_3^{i+}-u_3^{i-}=0$	$\phi^{i+}-\phi^{i-}=0$	$c_{22}^E=2H_{RVE}$
EB03	$u_1^{i+}-u_1^{i-}=0$	$u_2^{i+}-u_2^{i-}=0$	$u_3^{i+}-u_3^{i-}=h_T$	$\phi^{i+}-\phi^{i-}=0$	$c_{33}^E=2H_{RVE}$
EB04	$u_1^{i+}-u_1^{i-}=0$	$u_3^{i+}-u_3^{i-}=w_T/2$	$u_2^{i+}-u_2^{i-}=h_T/2$	$\phi^{i+}-\phi^{i-}=0$	$c_{44}^E=2H_{RVE}$
EB05	$u_3^{i+}-u_3^{i-}=L_T/2$	$u_2^{i+}-u_2^{i-}=0$	$u_1^{i+}-u_1^{i-}=h_T/2$	$\phi^{i+}-\phi^{i-}=0$	$c_{55}^E=2H_{RVE}$
EB06	$u_2^{i+}-u_2^{i-}=L_T/2$	$u_1^{i+}-u_1^{i-}=w_T/2$	$u_3^{i+}-u_3^{i-}=0$	$\phi^{i+}-\phi^{i-}=0$	$c_{66}^E=2H_{RVE}$
EB07	$u_1^{i+}-u_1^{i-}=L_T$	$u_2^{i+}-u_2^{i-}=w_T$	$u_3^{i+}-u_3^{i-}=0$	$\phi^{i+}-\phi^{i-}=0$	$c_{12}^E=H_{RVE}-\bar{c}_{11}^E/2-\bar{c}_{22}^E/2$
EB08	$u_1^{i+}-u_1^{i-}=L_T$	$u_2^{i+}-u_2^{i-}=0$	$u_3^{i+}-u_3^{i-}=h_T$	$\phi^{i+}-\phi^{i-}=0$	$c_{13}^E=H_{RVE}-\bar{c}_{11}^E/2-\bar{c}_{33}^E/2$
EB09	$u_1^{i+}-u_1^{i-}=0$	$u_2^{i+}-u_2^{i-}=w_T$	$u_3^{i+}-u_3^{i-}=h_T$	$\phi^{i+}-\phi^{i-}=0$	$c_{23}^E=H_{RVE}-\bar{c}_{22}^E/2-\bar{c}_{33}^E/2$
EB12	$u_1^{i+}-u_1^{i-}=0$	$u_2^{i+}-u_2^{i-}=0$	$u_3^{i+}-u_3^{i-}=0$	$\phi^{i+}-\phi^{i-}=h_P$	$\epsilon_{33}^S=-2H_{RVE}$
EB13	$u_1^{i+}-u_1^{i-}=0$	$u_2^{i+}-u_2^{i-}=0$	$u_3^{i+}-u_3^{i-}=h_T$	$\phi^{i+}-\phi^{i-}=h_P$	$\bar{e}_{33}=-H_{RVE}+\bar{c}_{33}^E/2-\bar{\epsilon}_{33}^S/2$
EB14	$u_1^{i+}-u_1^{i-}=L_T$	$u_2^{i+}-u_2^{i-}=0$	$u_3^{i+}-u_3^{i-}=0$	$\phi^{i+}-\phi^{i-}=h_P$	$\bar{e}_{31}=-H_{RVE}+\bar{c}_{11}^E/2-\bar{\epsilon}_{33}^S/2$
EB15	$u_1^{i+}-u_1^{i-}=0$	$u_2^{i+}-u_2^{i-}=w_T$	$u_3^{i+}-u_3^{i-}=0$	$\phi^{i+}-\phi^{i-}=h_P$	$\bar{e}_{32}=-H_{RVE}+\bar{c}_{22}^E/2-\bar{\epsilon}_{33}^S/2$

As previously discussed in [11], the effective dielectric constant depends on the distance considered between the electrodes of the 'equivalent homogeneous' material. This could be, for instance, the actual distance between electrodes (in the real transducer) or the total thickness of the transducer (which accounts also for the protective layers). The latter was considered in [11]. In the case of EBHM, the enthalpy for the local problem EB12, that is used for the determination of the blocked dielectric constant $\bar{\epsilon}_{33}^S$ may be written as

$$\bar{H}_{EB12}=-\frac{1}{2}\bar{\epsilon}_{33}^S\bar{E}_3^2=-\frac{1}{2}\bar{\epsilon}_{33}^S(\Delta\phi/\Delta x_3)^2, \tag{12}$$

where $\Delta\phi$ and Δx_3 are, respectively, the difference of electric potentials applied to the electrodes and the distance between the electrodes.

Since, in the local problem, the electric field is imposed through the difference of electric potential in the actual electrodes, that is at $x_3^{\Gamma_e^+}$ and $x_3^{\Gamma_e^-}$, the resulting electric field would be unitary over the active layer, and thus piezoceramic fibre, if the difference of electric potential is equal to h_P (in value). However, this would not lead to a unitary electric field over the entire MFC thickness and, thus, the average electric field is expected to be smaller than 1. As the expression used for the evaluation of the dielectric constant, $\epsilon_{33}^S=-2H_{RVE}$, considers a unitary electric field, over the 'equivalent homogeneous' material, the obtained effective dielectric constant will be directly proportional to the square of the actual distance between electrodes, Δx_3^2, in order to ensure the energy density equivalence (same enthalpy in both cases).

Notice that the procedure considered in AQHM is different in that the average electric displacement is divided by the average electric field over the RVE and, thus, electric field is not considered to be unitary, like in EBHM. This will lead to an apparent inconsistency between the two approaches. However, as shown in the next section, both approaches may be equivalent provided the material properties are adjusted to reflect the same electrical boundary conditions.

4 FINITE ELEMENT ANALYSIS AND VALIDATION

For both homogenization methods, AQHM and EBHM, the same Representative Volume Element (RVE) was considered to represent the studied d_{31} MFC. The RVE is shown in Figure 2. The dimensions considered for the RVE were based on the MFC transducer manufactured by Smart Material Co. [1] and also on previous works [3]. According to Figure 2, these are $h_P = 180$ μm, $h_K = 40$ μm, and $h_C = 18$ μm, $L_E = 420$ μm, $L_C = 80$ μm, $w_E = 28.35$ μm and $w_P = 348.3$ μm. This leads to a Fibre Volume Fraction (FVF) of 0.86 for the active layer.

In addition, the same finite element mesh was used for both AQHM and EBHM to solve the local problems in Ansys$^{(R)}$ and evaluate the effective material constants of the d_{31} MFC RVE. The 3D 20-Node coupled-field solid finite element SOLID226 was used to mesh all volumes. It has the three displacement translations along the Cartesian coordinate system and the electric potential as nodal degrees of freedom. A mesh of 3211 finite elements was used considering 19 divisions in x_1 direction (11 divisions for the Epoxy layer and 4 divisions for each electrode layer), 13 divisions in x_2 direction (9 divisions for the PZT fibre and 2 divisions for the Epoxy layer) and 13 divisions in x_3 direction (5 divisions for the PZT layer, 2 divisions for each electrode layer and 2 divisions for each protective layer). The finite element mesh considered is shown in Figure 3.

The material constituents of the MFC are Sonox P502, as the piezoceramic material in gray, Epoxy covering most of piezoceramic surfaces in yellow, Copper for the electrodes in orange, and Kapton for the protective layer in blue. The material properties for the piezoceramic material Sonox P502, in d-form, taken from [3], are: $s^E_{11} = s^E_{22} = 18.5$ pm^2/N, $s^E_{33} = 20.7$ pm^2/N, $s^E_{12} = -6.29$ pm^2/N, $s^E_{13} = -6.23$ pm^2/N, $s^E_{44} = s^E_{55} = 33.2$ pm^2/N, $s^E_{66} = 52.3$ pm^2/N, $d_{31} = d_{32} = -185$ pC/N, $d_{33} = 440$ pC/N, $d_{15} = d_{24} = 560$ pC/N, $\epsilon^T_{11} = \epsilon^T_{22} = 1950\epsilon_0$, $\epsilon^T_{33} = 1850\epsilon_0$. The material properties for the other constituents, taken from [10], are: Epoxy – $Y = 2.5$ GPa, $\nu = 0.42$ and $\epsilon = 4.25\epsilon_0$; Kapton – $Y = 2.5$ GPa, $\nu = 0.34$ and $\epsilon = 3.4\epsilon_0$; and Copper electrode – $Y = 110$ GPa, $\nu = 0.34$ and $\epsilon = 5\epsilon_0$. The vacuum electric permittivity is $\epsilon_0 = 8.854\ 10^{-12}$ F/m.

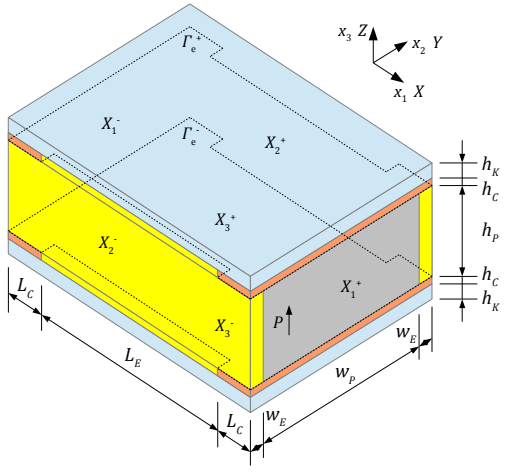

Figure 2: Representative volume element (RVE) of the d_{31} MFC.

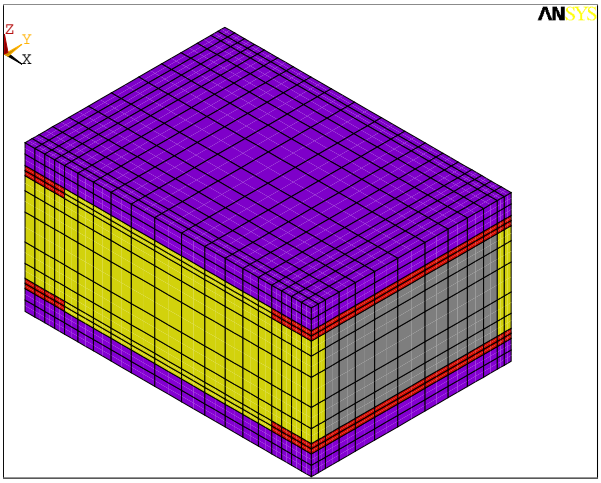

Figure 3: Finite element mesh for the 5-layered d_{31} MFC RVE with FVF=0.86.

Figures 4 shows the field distributions of normal stress T_1 and strain S_1 resulting from the first local

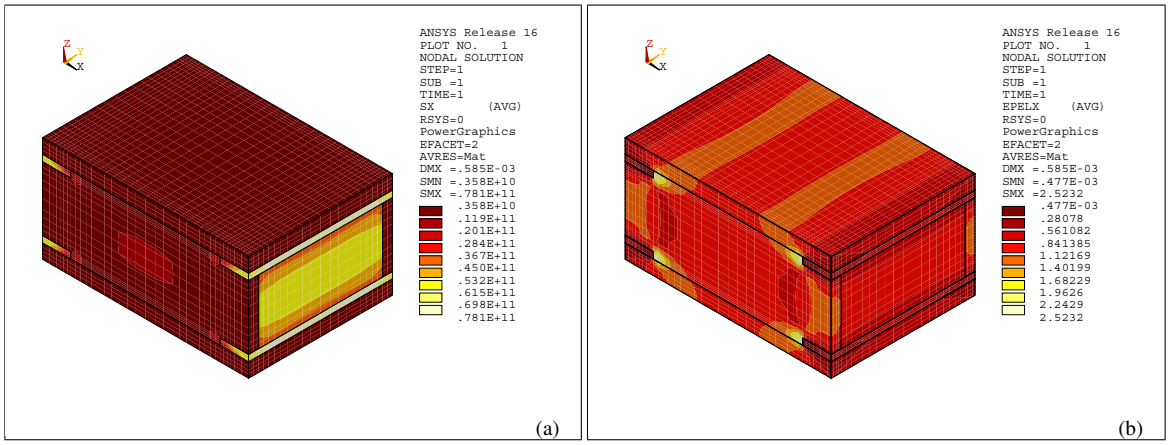

Figure 4: Stress T_1 (a) and strain S_1 (b) induced by normal displacements applied to the d_{31} MFC RVE (local problem AQ01/EB01).

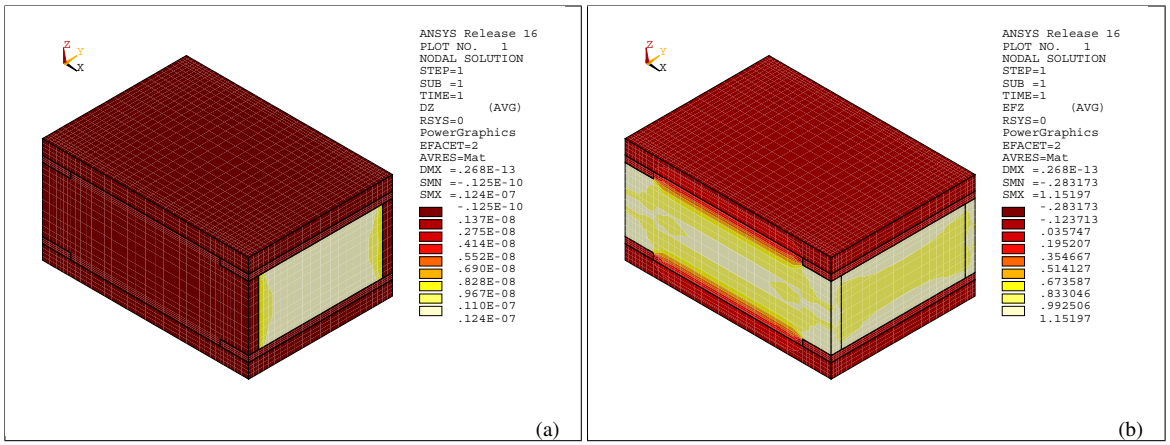

Figure 5: Electric displacement D_3 (a) and field E_3 (b) induced by electric potential applied to the blocked d_{31} MFC RVE (local problem AQ07/EB12).

problem (AQ01/EB01). It was used to evaluate the elastic constant c_{11}^E in the case of EBHM. For AQHM, it was also used to evaluate other elastic constants c_{12}^E and c_{13}^E and the stress piezoelectric constant e_{31}. It is remarkable in Figure 4 that, while the normal strain S_1 distribution is quite uniform, the normal stress T_1 is concentrated in the stiffer PZT fibre and Copper electrode.

The local problem (AQ07/EB12) is intended to evaluate the blocked dielectric constant, ϵ_{33}^S, by applying a difference of electric potential on the electrodes and, hence, a uniform through-thickness electric field. Thus, the distributions of electric field E_3 and displacement D_3 are of major interest and are shown in Figure 5. It is noticeable that the electric field in nearly uniform over the active layer and negligible over the electrode and protective layers (Figure 5b). On the other hand, the electric displacement is very much concentrated in the piezoceramic fibre (Figure 5a).

Following the same procedure, field distributions may be obtained for each local problem and allow to evaluate the uniformity and magnitude of the desired fields. However, for the sake of brevity, they are

not shown here.

Then, after carrying out the local problems required for the AQHM and EBHM methods, it was possible to determine the effective material constants. The results obtained for the d_{31} MFC RVE considered here with AQHM and EBHM approaches were compared to the available data provided by the manufacturer of a commercial d_{31} MFC (Smart Material Co.) [1]. The nominal geometrical and material properties for the MFC constituents were based on the best available information from the manufacturer and literature. Notice that not all coefficients are provided by the manufacturer. The effective material properties are shown in Table 3 which shows that both AQHM and EBHM approaches represent very well the actual (manufactured) d_{31} MFC.

Table 3: Effective material properties of d_{31} MFC (*: obtained post-processing data provided in reference; **: values adjusted to reflect the same electrical boundary conditions).

Coefficient	EBHM	AQHM	Manufacturer [1]
Y_1^E (GPa)	31.30	31.40	30.34
Y_2^E (GPa)	19.50	19.80	15.86
Y_3^E (GPa)	8.93	9.03	–
G_{23}^E (GPa)	2.15	2.17	–
G_{13}^E (GPa)	2.40	2.42	–
G_{12}^E (GPa)	5.24	5.34	5.52
ν_{12}^E	0.36	0.36	0.31
ν_{23}^E	0.38	0.37	–
ν_{13}^E	0.42	0.42	–
d_{31} (pC/N)	-173.2	-172.2	-170
d_{32} (pC/N)	-132.6	-133.8	–
d_{33} (pC/N)	310.0	310.0	–
e_{31} (C/m^2)	-6.01	-6.04	–
e_{32} (C/m^2)	-3.37	-3.47	–
e_{33} (C/m^2)	1.47	1.48	–
$\epsilon_{33}^T/\epsilon_0$	1394.4**	1401.4	1558.6
$\epsilon_{33}^S/\epsilon_0$	1175.0**	1179.7	–
k_{31}^2 (%)	7.6	7.5	6.4*
k_{31}	0.28	0.27	0.25*

The only elastic coefficient presenting a more important difference (10-11%) compared to the data from manufacturer is the transversal elastic modulus Y_2^E, but this may be explained by the fact that the actual width of the Copper electrode finger (L_C) is not known and was only visually approximated from a microphotography presented by the original prototype developers at NASA Langley Research Center [12]. A wider Copper electrode finger would lead to a higher transversal elastic modulus Y_2^E. It could also affect the transversal piezoelectric coefficients e_{32} and d_{32} (non provided by the manufacturer). The results obtained for the most important effective elastic and piezoelectric coefficients, Y_1^E and d_{31}, are below 4% error (3.0% EBHM - 3.5% AQHM and 1.9% EBHM - 1.3% AQHM, respectively) compared to the data provided by the Smart Material Corp. [1]. Unfortunately, the blocked dielectric constant ϵ_{33}^S is not provided by the manufacturer. The values obtained for this constant using AQHM and EBHM were then post-processed to obtain the equivalent free dielectric constant ϵ_{33}^T. Notice, though, that this transformation depends on the elastic and piezoelectric constants as shown in (3) and, thus, any difference between other constants may affect the transformation.

As mentioned in the previous section, the main difference between AQHM and EBHM is due to the difference between the actual (real) distance between electrodes and the corresponding distance in the 'equivalent homogeneous' material. In AQHM, since the average electric field in the RVE is used to divide from the average electric displacement, the effect of the difference between real and effective electrode distance is naturally corrected. However, in EBHM, it is considered that the effective average electric field is unitary, which is only approximately the case by considering a larger applied electric potential to account for the larger equivalent electrode distance. If, on the contrary, the electric potential is considered to be the thickness of the active layer, h_P (in value), as it is done here, the electric field is unitary over the active layer but not in the whole RVE, where in fact it should be smaller. Therefore, as explained in the previous section, the effective dielectric constant obtained using EBHM is smaller than the one obtained using AQHM. Indeed, EBHM yields $\epsilon_{33}^S/\epsilon_0 = 714.5$. This value can be corrected, or adjusted, to reflect the difference between electrodes' distance. By multiplying the obtained value by the ratio between RVE and active layer thicknesses $h_T/h_P = 1.644$, the value of $\epsilon_{33}^S/\epsilon_0 = 1175.0$ is obtained (which is the one presented in Table 3). This adjusted value is now very close to the one obtained using AQHM. If one chooses to apply a larger electric potential to account for the larger equivalent electrode distance, that is h_T in value instead of h_P, $\epsilon_{33}^S/\epsilon_0 = 1932.2$ is obtained. This is equivalent to the previous value (1175.0) multiplied once again by $h_T/h_P = 1.644$. However, in the last case, the piezoelectric constants are also affected by this electrode distance change, leading to larger values for them.

Therefore, as a conclusion of this analysis, it is suggested here that one should use the actual electrode distance and, thus, an applied electric potential equal in value to the active layer thickness. Then, in the case of EBHM, the effective dielectric constant should be corrected by multiplying it by the ratio between RVE and active layer thicknesses. Notice that this apparent inconsistency comes from the fact that to ensure energetic equivalence, in EBHM, the ratio between actual and equivalent electrode distances appears squared in the case of the dielectric constant.

Although the actual procedure to determine experimentally the free dielectric constant of the real MFC by the manufacturer is not known, it is guessed here that a measure of the effective capacitance is used. In this case,

$$C^T = Q/V = \epsilon_{33}^T A_E/h_E, \;\; \epsilon_{33}^T = C^T h_E/A_E, \tag{13}$$

where A_E and h_E are the electrodes area and distance. Notice that the measurement of the capacitance in the real MFC accounts for the electric potential applied to the actual electrodes and the charge accumulated on the actual electrodes. Therefore, the measured capacitance reflects the actual distance between electrodes. The only issue that remains is the value of h_E that is used by the manufacturer to determine the effective dielectric constant from the measured capacitance. It is clear that if the thickness of the active layer is used, the corresponding effective dielectric constant would be better represented by the procedure adopted here, either using AQHM or EBHM with correction. That is why, these are the values that are presented in Table 3 and compared to the data provided by the manufacturer.

5 CONCLUSIONS

New results were presented on finite element homogenization techniques to relate individual material properties of piezoceramic fibres and effective material properties of corresponding d_{31} MFC transducers. In particular, an enthalpy-based homogenization procedure was applied to the characterization of a d_{31} MFC effective properties and compared to previously published results using average quantities

homogenization. A detailed analysis on the differences between the two procedures was carried out and a technique to obtain a better consistency between them was proposed. Results from both methods were also compared to available data from a MFC manufacturer. Around 10% deviation was found between numerical (AQHM and EBHM) and manufacturer data for the transversal Young modulus and the free dielectric coefficient.

Acknowledgements

Support of MCT/CNPq/FAPEMIG National Institute of Science and Technology on Smart Structures in Engineering, grant 574001/2008-5, and of the National Council for Scientific and Technological Development (CNPq), grants 306675/2011-0 and 309193/2014-1, is acknowledged.

REFERENCES

[1] Smart Material Corp. Macro-fibre composites technical data, www.smart-material.com, Sarasota (2009).

[2] Trindade, M.A. and Benjeddou, A. Finite element homogenization technique for the characterization of d_{15} shear piezoelectric macro-fibre composites. *Smart Mater. Struct.* (2011) **20**(7):075012.

[3] Deraemaeker, A., Nasser, H., Benjeddou, A. and Preumont, A. Mixing rules for the piezoelectric properties of macro fiber composites. *J. Intell. Mater. Syst. Struct.* (2009) **20**(12):1475–1482.

[4] Deraemaeker, A., Nasser, H. Numerical evaluation of the equivalent properties of macro fiber composite (MFC) transducers using periodic homogenization. *Int. J. Solids Struct.* (2010) **47**(24):3272–3285.

[5] Biscani, F., Nasser, H., Belouettar, S., Carrera, E. Equivalent electro-elastic properties of macro fiber composite (MFC) transducers using asymptotic expansion approach. *Composites: Part B* (2011) **42**(3):444–455.

[6] Sreenivasa Prasath, S., Arockiarajan, A. Effective electromechanical response of macro-fiber composite (MFC): Analytical and numerical models. *Int. J. Mech. Sci.* (2013) **77**:98–106.

[7] Sreenivasa Prasath, S., Arockiarajan, A. Analytical, numerical and experimental predictions of the effective electromechanical properties of macro-fiber composite (MFC). *Sensors and Actuators A* (2014) **214**:31–44.

[8] Trindade, M.A. and Benjeddou, A. Finite element characterisation of multilayer d_{31} piezoelectric macro-fibre composites. *Composite Struct.* (2016) **151**:47–57.

[9] Benjeddou, A. and Al-Ajmi, M. Analytical homogenizations of piezoceramic d_{15} shear macro-fibre composites *Proceedings of the IUTAM Conference on Multiscale Modelling of Fatigue, Damage and Fracture in Smart Materials* ed M Kuna and A Ricoeur (Freiburg, Germany) Sept 1-4, 2009.

[10] Kranz, B., Benjeddou, A., Drossel, W.-G. Numerical and experimental characterizations of longitudinally polarized piezoelectric d_{15} shear macro-fiber composites. *Acta Mech.* (2013) **224**(11):2471–2487.

[11] Kranz, B., Benjeddou, A., Drossel, W.-G. Enthalpy-based homogenization procedure for composite piezoelectric modules with integrated electrodes. *Smart Struct. Syst.* (2013) **12**(5):579–594.

[12] Wilkie, W.K., Bryant, G.R., High, J.W. Low-cost piezocomposite actuator for structural control applications. *Proceedings of SPIE International Symposium on Smart Structures and Materials* (Newport Beach) 5-9 March, 2000.

VIII ECCOMAS Thematic Conference on Smart Structures and Materials
SMART 2017
A. Güemes, A. Benjeddou , J. Rodellar and Jinsong Leng (Eds)

MODELING OF DYNAMIC PROCESSES IN SYSTEMS WITH PIEZOELEMENTS AND EXTERNAL ELECTRIC CIRCUITS ON THE BASIS OF EQUIVALENT ELECTRIC CIRCUITS

MAKSIM A. IURLOV*, DMITRII A. OSHMARIN*, NATALIYA V. SEVODINA*, NATALIIA A. IURLOVA*

*Department of complex problems of deformable solids mechanics
Institute of Continuous Media Mechanics of the Ural Branch of RAS (ICMM UB RAS)
Acad. Korolev str., 1, 613013 Perm, Russian Federation
e-mail: yurlovm@icmm.ru, www.icmm.ru

Keywords: Smart structures, Electroelasticity, Piezoelectric elements, External circuits, Equivalent electric circuits, Natural vibrations.

Abstract. Optimization of dissipative properties of electromechanical systems with external electric circuits suggests the selection of parameters for these circuits, such that can provide the most effective damping of vibrations at the prescribed frequency. Since the external circuits can be represented as a set of elements with concentrated parameters connected to the system with distributed parameters, solving of electroviscoelastic problems for such systems using their full formulation requires high computational and time costs. In mechanics, there exist several approaches, which allow representation of the mechanical systems with distributed parameters as discrete systems with concentrated parameters of the spring-mass-damper type. In this paper, an approach to the analysis of the dynamic behavior of electromechanical systems with external electric circuits is developed based on the equivalent electric circuits representing discrete electric systems with concentrated parameters. The above discrete systems are complete analogues of the initial electromechanical systems in relation to frequency characteristics and electrical processes occurring in them.

1 INTRODUCTION

In the fields of high technology, the use of smart structures with constituent elements made of piezoelectric materials (piezoelectric ceramics, piezoelectric polymers) and showing therefore a strong piezoelectric effect, allows one to solve several engineering problems related to damping of vibrations of various origin, reducing the level of acoustic noise, increasing the level of dynamic stability, examining the mechanical state of the structure, etc. One of the approaches to solution of the above problems with the aid of piezoelectric elements is connection of such elements to the electrode-covered surfaces of external passive electric circuits. A successful implementation of this approach is impossible without clear understanding of how the variation of the environmental parameters or inherent characteristics of the system itself affects its mechanical behavior.

The dynamic characteristics of electromechanical systems with piezoelectric elements and external electric circuits, which are generally used in the analysis of their dynamic behavior,

can be determined by solving the problems of forced and natural vibrations or problems of transient process with initial conditions. From the viewpoint of effective estimation of dynamic characteristics and optimization of dissipative properties, the problem of natural vibrations is most convenient and informative, which was demonstrated in works [1, 2]. The complex eigenvalues obtained by solving this problem will define the frequencies of natural vibrations (real parts) and damping ratios (imaginary parts). The effectiveness of the above problem in determining the optimal dynamic characteristics can be attributed to their independence of loads.

Since a mathematical formulation of the problem on natural vibrations of electroelastic bodies with external electric circuits has some distinctive features, the numerical implementation of its solution algorithms by the finite element method is a non-trivial problem just because of the presence of the external electric circuit [3]. Moreover, the development of the solution itself using the above mentioned mathematical formulation is a time-consuming process due to a great size of the resultant system of equations.

One of the approaches, which could essentially simplify the procedure of evaluating the dynamic characteristics of the vibrating system, is the development of its discrete analogue, consisting of the elements with concentrated parameters. In the classical mechanics, such analogue is a single mass-spring system, which is generally used to describe the dynamic behavior of the system in the vicinity of some resonance frequency. On the other hand, the electrodynamics can offer a few other approaches to modeling the behavior of piezoelectric elements with equivalent electric circuits, for example, such as presented in works [4-6]. These models describe the behavior of piezoelectric materials in the frequency range lower than the ultrasonic frequency.

At present, the equivalent circuits, which can take into account the influence of the base structure, have found wide applications in the problems concerning the operation of energy harvesting devices with piezoelectric elements designed as small alternative sources of energy [7-8]. To estimate the efficiency of such devices, it is necessary to give a correct interpretation of their operating capacity determined by mechanical and electrical interactions. The device is generally modeled by a cantilevered beam [8-9] fitted with complicated equivalent electrical circuits.

The objective of this paper is to analyze the dynamic behavior of the electromechanical system with external electric circuits, using for this purpose the equivalent circuits, representing discrete electric systems with concentrated parameters.

2 EQUIVALENT ELECTRIC CIRCUIT REPRESENTATION OF ELECTROMECHANICAL SYSTEM

As was already mentioned above, to determine the dynamic characteristics of the electromechanical systems in the form of a structure with attached piezoelectric elements and external electric circuits, it is not always convenient and reasonable to solve the natural vibration problem based on its full mathematical formulation.

The external electric circuit is a set of elements with concentrated parameters and electrical degrees of freedom. Suppose that the electric current pulsations in such a circuit occur at a frequency of the entire electromechanical system. Eigenvectors of vibrations are found in the form of:

$$u_i(x,t) = \bar{u}_i(\vec{x})e^{i\omega t}, \quad \varphi(x,t) = \bar{\varphi}(\vec{x})e^{i\omega t} \tag{1}$$

where u_i – components of the displacement vector, φ - electric potential, $\omega = \omega_R + i\omega_I$ - complex natural frequency, wherein ω_R corresponds to the natural frequency, ω_I - oscillation damping rate, $\bar{u}_i(\vec{x}), \bar{\varphi}(\vec{x})$ - eigenforms of vibrations.

Therefore, it is reasonable to represent the initial structure with the attached piezoelectric element as a similar discrete system with electrical degrees of freedom, which in this case should properly describe the dynamics of the initial electromechanical system with concentrated parameters in terms of the eigenfrequency spectrum of vibrations and electrical processes occurring in its elements.

Connection of a structure with a piezoelectric element to a resonance circuit comprising inductor and resistor in series or in parallel leads to the appearance of additional frequency in the frequency response of the system [10]. The occurrence of additional frequency is attributed to the fact that intrinsic capacitance of the piezoelectric element together with the external inductance and resistance form, depending on the connection mode, a series or parallel oscillatory circuit, in which some energy is lost (fig.1).

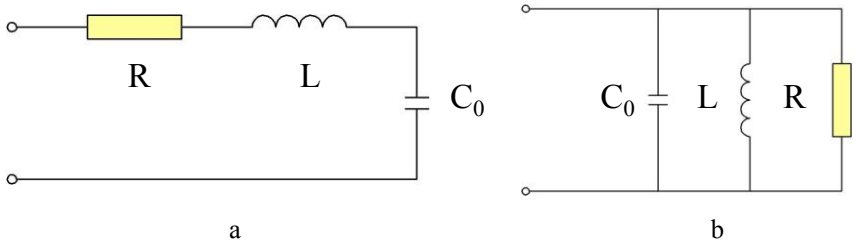

Figure 1: Series (a) and parallel (b) oscillatory circuits.

The value of additional frequency can be determined using the approach proposed in several previous works [11-15]. In these studies, as an electric analogue of the piezoelectric element the authors used its simplest model, including only one condenser with constant capacitance C_0. In this case, the oscillatory circuit formed by a piezoelectric element and external electric circuit (fig.1) represents a discrete electric oscillatory system with one degree of freedom. The vibration frequency of such simple electric circuit (for example, for the external series circuit) is calculated by the following equation [16]:

$$\omega = -\frac{R}{2L} \pm \sqrt{\frac{R^2}{4L^2} - \frac{1}{LC_0}} \tag{2}$$

However, recent investigations have shown that this model is inapplicable for evaluation of the add-in frequency within the entire frequency range considered in our study, although it operates well at some distance from the each eigenfrequency of the structure, which has a piezoelectric element, but not has an external electric circuit [17]. This can be explained that describing piezoelectric element with single capacitance is not enough.

A more adequate description of the piezoelectric element with distributed parameters can be obtained with the use of the equivalent electric model composed of electric elements with fixed parameters. One of the first models was proposed by Van Dyke [18]. This models is

schematically shown in fig.2 and represents parallel connection of series-connected capacitance C, inductance L, resistance R and inherit capacitance of piezoelectric C_0.

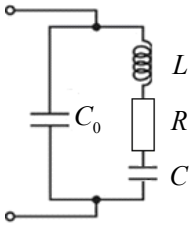

Figure 2: Equivalent circuit proposed by van Dyke in [17].

The above electrical analogue has one resonance frequency corresponding to the resonance frequency of mechanical vibrations of the piezoelectric element. Let us consider more carefully each element of the examined scheme. Here $C_0 + C$ – is the intrinsic capacitance of the piezoelectric element of the resonator. Series-connected inductance L and capacitance C provide a resonant nature of the process. Resistor R describes losses due to the passage of the electric current through the elements of the circuit. Thus, from the viewpoint of the electrical processes the examined electromechanical system behaves as a series electric oscillatory circuit with losses in the vicinity of resonance frequency and as a capacitor outside this frequency range.

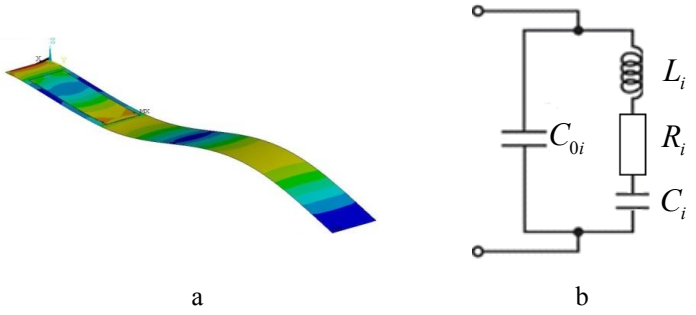

a b

Figure 3: The second vibration mode of electromechanical system in the form of a plate with the attached piezoelectric element (a) and its schematic representation as an equivalent electric circuit in the vicinity of this resonance frequency.

Equivalent circuit can be used to model the behavior of any electromechanical system, comprising a structure with piezoelectric element on its surface located in the vicinity of one of its resonance frequencies [17]. Figure 3a depicts the second vibration mode of the structure with the attached piezoelectric element as an example of the object, which is subject to the replacement by its electrical analogue in the form of equivalent circuits.

In the case when it is necessary to explore the dynamic behavior of the structure not in the vicinity of some separate resonance frequency, but in some frequency range, which can include several resonance frequencies, the equivalent model is modified by adding in parallel to the existing elements a set of series oscillatory circuits (fig. 4a). The resultant equivalent circuit can be used to describe the dynamics of the examined system in any frequency range.

Here, worthy of note is the following observation. As it was mentioned above, the loss or dissipation of energy occurs in the resistor of the branch, containing the oscillatory circuit. Thus, if the examined electromechanical system (the structure with piezoelectric element fixed to the surface) is elastic, the resistance R_i in the resonance branches is absent (fig.4b).

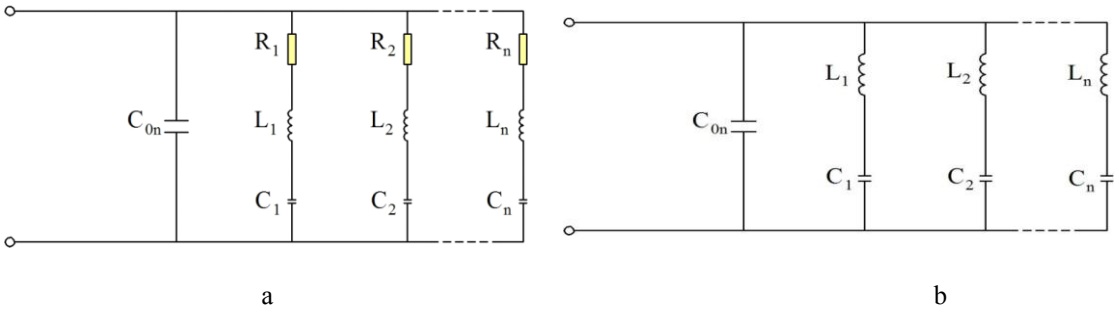

Figure 4: Equivalent circuits for electromechanical system with energy dissipation (a) and without energy dissipation (b).

3 MATHEMATICAL FORMULATION OF THE NATURAL VIBRATION PROBLEM FOR EQUIVALENT MODEL

Let us consider a mathematical formulation of the natural vibration problem for equivalent electric circuit, using as an example some oscillating system, comprising an electric structure with piezoelectric element attached to its surface. The electrode-coated surfaces of the piezoelectric element are connected to an arbitrary electric circuit with total electric impedance Z_{ext}, consisting of differently connected resistive (resistors R_i), inductive (inductors L_i) or capacitive (capacitors C_i) elements. This system, external circuit included, is modeled by the equivalent circuit, which can describe its behavior in the frequency range involving n resonance frequencies. The schematic of the equivalent circuit is given in fig.5. Here, capacitance C_{0n} and parallel branches L_iC_i refer directly to the structure with piezoelectric element, and element Z_{ext} describes the external electric circuit.

The equations, describing the dynamic processes in this system can be constructed by the standard technique, which is based on the first and second Kirchhoff's laws [16].

First, it is necessary to choose the basic electrical circuits and direction of the currents in these circuits. The circuits should be selected in such a way that each of them includes the branch with capacitance C_{0n}. Figure 6a shows schematically the selection of elementary circuits and indicates the direction of the electric current in these circuits.

The second step is to choose a node in the circuit for which the current balance equation will be constructed using Kirchhoff's first law (the sum of all currents entering the node is equal to the sum of currents escaping from the node.). In the examined equivalent circuit, such node is denoted as A in fig.6. Then, for the node A, considering the direction of the currents in the circuits, we can write the equation based on Kirhhoff's first law:

$$I_1 + I_2 + ... + I_n + I_{ext} = I_0 \tag{3}$$

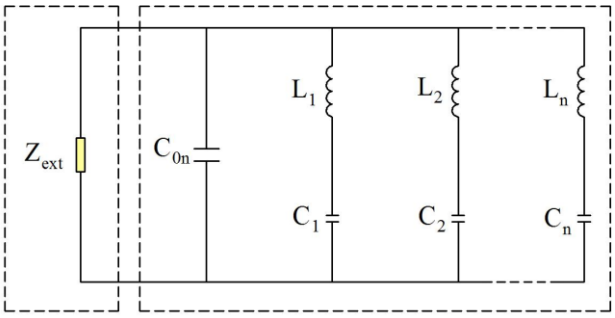

Figure 5: Equivalent circuits for elastic electromechanical system with external electric circuit.

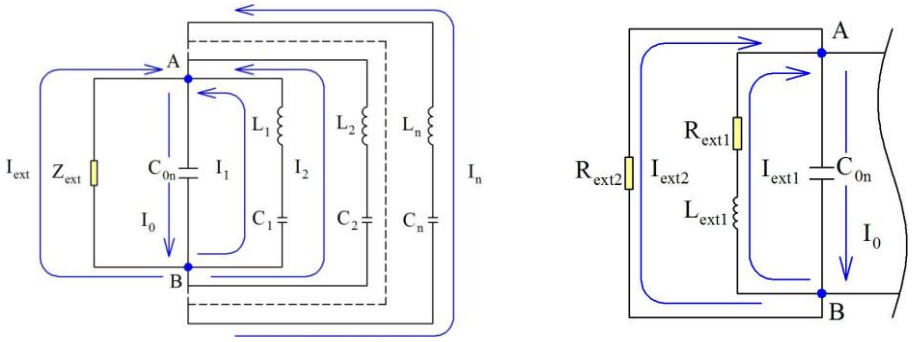

Figure 6: The method of constructing the elementary loops with indication of current directions for the entire electromechanical system with arbitrary external circuit (a) and specified type of the external circuit.

Thus, the total number of currents in the equivalent circuit is equal to $N = n_{ext} + n + 1$, where $n+1$ - is the number of currents in the circuits, corresponding to the structure with piezoelectric element (n currents in the branches $L_i C_i$ and the current in the branch C_{0n}), n_{ext} - is the number of currents in the branches corresponding to the external circuit.

The second equation to be constructed is the voltage balance equation, which is written for all selected elementary circuits based on the Kirchhoff's second law – the sum of potential differences (voltage) on all elements of the loop is equal to electromotive force (EMF) of the external source. The total number of circuits is $N-1$, since each elementary circuit includes two branches, one of which should necessarily be the branch with C_{0n}. Hence, for the section of the circuit simulating the structure with piezoelectric element the number of elementary circuits will be equal to n, whereas for the section simulating the external electric circuit it will be equal to n_{ext}. Taking for generalized coordinates the charges q_k, corresponding to the currents I_k (k - is the number of currents) and related to them by equation

$$I_k = \frac{dq_k}{dt}, \quad k = \overline{1, N}, \tag{4}$$

we can determine with the use of the known relation of electrical engineering [16] the electric potential on each element of the equivalent circuit (capacitance, resistance, inductance):

$$U_C = \frac{q_C}{C}, \quad U_R = R\frac{dq_R}{dt}, \quad U_L = L\frac{d^2 q_L}{dt^2} \quad . \tag{5}$$

First, let us write the voltage balance equation for each *i-th* circuit, related only to the structure with piezoelectric element. In the absence of external sources of EMF, these equations take the following form:

$$L_i \frac{d^2 q_i}{dt^2} + \frac{q_i}{C_i} + \frac{q_0}{C_{0n}} = 0, \quad i = \overline{1,n} \tag{6}$$

or with account of (3) and (4)

$$L_i \frac{d^2 q_i}{dt^2} + \frac{q_i}{C_i} + \sum_{j=1}^{N-1} \frac{q_j}{C_{0n}} = 0, \quad i = \overline{1,n} \tag{7}$$

Then, we build the equations for arbitrary external circuit Z_{ext}. For clarity, as an external electric circuit, we take the circuit consisting of a branch of series-connected resistance and inductance elements, which in its turn is connected in parallel with the branch comprising only one resistor (fig. 6b). In this case, the current I_{ext} (see (2)) is the sum of two currents $I_{ext} = I_{ext1} + I_{ext2}$, because the above-mentioned circuits are connected in parallel. Thus, the voltage balance equation for the external circuit will take the following form:

$$\begin{aligned} &L_{ext1} \frac{d^2 q_{ext1}}{dt^2} + R_{ext1} \frac{dq_{ext1}}{dt} + \sum_{j=1}^{N-1} \frac{q_j}{C_{0n}} = 0; \\ &R_{ext2} \frac{dq_{ext2}}{dt} + \sum_{j=1}^{N-1} \frac{q_j}{C_{0n}} = 0; \end{aligned} \tag{8}$$

where $n_{ext} = 2$ is the number of elemental circuits in the external circuit. Combining (7) and (8), we obtain the second system of $n+2$ differential equations, which in the absence of external EMF sources is a mathematical description of the natural vibration problem for electrical analogue of the initial electromechanical system in the form of equivalent electric circuit (9):

$$\begin{aligned} &L_i \frac{d^2 q_i}{dt^2} + \frac{q_i}{C_i} + \sum_{j=1}^{N-1} \frac{q_j}{C_{0n}} = 0, \quad i = \overline{1,n} \\ &L_{ext1} \frac{d^2 q_{ext1}}{dt^2} + R_{ext1} \frac{dq_{ext1}}{dt} + \sum_{j=1}^{N-1} \frac{q_j}{C_{0n}} = 0 \\ &R_{ext2} \frac{dq_{ext2}}{dt} + \sum_{j=1}^{N-1} \frac{q_j}{C_{0n}} = 0. \end{aligned} \tag{9}$$

Then, substituting the solution $q_i = \overline{q}_{0i} e^{\lambda t}$ into (9) we arrive at the system of linear algebraic equations (10) with respect to unknown charges on the branches of equivalent circuit where $\lambda = -\lambda_{\mathrm{Re}} \pm i\lambda_{\mathrm{Im}}$ – is the complex vibration frequency.

$$\begin{aligned} &\overline{q}_{0i} \lambda^2 L_i + \frac{\overline{q}_{0i}}{C_i} + \sum_{j=1}^{N-1} \frac{\overline{q}_{0j}}{C_{0n}} = 0, \quad i = \overline{1,n} \\ &\overline{q}_{0ext1} \lambda^2 L_{ext1} + \overline{q}_{0ext1} \lambda R_{ext1} + \sum_{j=1}^{N-1} \frac{\overline{q}_{0j}}{C_{0n}} = 0 \\ &\overline{q}_{0ext2} \lambda R_{ext2} + \sum_{j=1}^{N-1} \frac{\overline{q}_{0j}}{C_{0n}} = 0. \end{aligned} \tag{10}$$

After writing for this system the characteristic equations with respect to λ, we obtain $n+2$ pairs of complex conjugate eigenvalues. In view of physical grounds, we consider only the values with positive imaginary part λ_{Im}, which are the complex frequencies of vibration. Here the imaginary part of the complex frequency represents the angular frequency of vibrations λ_{Im} and the real part λ_{Re} corresponds to the damping ratio.

If the external circuit is a series resonance *RL*-circuit (including resistance *R* and inductance *L*-elements connected in series), the equivalent circuit will lack the branch with current I_{ext2}, and the system of equations (10) will lack the last equation. If the external circuit is a parallel resonance *RL*-circuit (resistance *R* and inductance *L*-elements are connected in series), the equivalent circuit will be free of the element R_{ext1}, and in the second equation of system (9) the term containing R_{ext1} will be absent.

4 DETERMINATION OF THE VALUES OF PARAMETERS FOR THE EQUIVALENT CIRCUIT

The main problem of using the equivalent circuits for the analysis of the dynamic behavior of electroelastic systems (fig.4b) is the evaluation of parameters C_i, L_i and C_{0n}. These parameters can be calculated using the following numerical algorithm.

At the first stage, we need to determine the statistic capacitance C_0 of piezoelectric element. To this end, it is necessary to solve the static problem of damping the structure with piezoelectric element due to potential difference V applied to the piezoelectric element considering grounding one of its electrode-covered surfaces. The solution of the problem allows us to remove the value of the total electric charge Q_s from the ungrounded electrode-covered surface of the piezoelectric element, after which the static capacitance is defined as

$$C_0 = \frac{Q_S}{V} \tag{11}$$

Then, we calculate the eigenfrequencies of the structure with piezoelectric element and without the external electric circuit under short-circuit conditions of the piezoelectric element. In this case, we solve the natural vibration problem, the detailed formulation of which was given in work [3]. As a result, we obtain the eigenfrequency spectrum, which will serve the basis for calculating the required parameters C_i, L_i and C_{0n}.

If the structure and piezoelectric element are made of elastic materials, all eigenfrequencies of such smart structure without the external circuit will be real. In this case, the parameters of the equivalent circuit C_i, L_i and C_{0n} for each resonance frequency are determined by:

$$C_i = \left(\frac{Q_i}{\omega_i}\right)^2, \quad L_i = \frac{1}{C_i \omega_i^2}, \quad C_{0n} = C_0 - \sum_{i=1}^{n} C_i \tag{12}$$

Here ω_i is the *i*-th eigenfrequency, Q_i is the total charge on the electrode-covered surface of the piezoelectric element at the *i*-th frequency, *n* is the number of considered eigenfrequencies.

Eventually, we obtain all equivalent characteristics, which are essential for modeling the electrical analogue to the electromechanical system.

5 THE RESULTS OF NUMERICAL CALCULATIONS

To demonstrate the applicability of the proposed electrical analogue for description of the dynamic behavior of the electromechanical system, we performed a series of numerical experiments. As an external circuit to the examined piezoelectric element, we used a series and parallel resonance *RL*-circuit.

The investigations were made for a cantilevered rectangular plate with piezoelectric element attached to its surface (fig.7a). The dimensions of the plate were as follows: $l_1 = 210$ mm, $b_1 = 26$ mm, $h_1 = 0.5$ mm. The plate was made of material with the following mechanical characteristics: $E = 2 \cdot 10^{11}$ Pa $\nu = 0.3$, $\rho = 7800$ kg/m^3. The piezoelectric element was rectangular in shape with $l_p = 50$ mm, $b_p = 20$ mm, $h_p = 0.36$ mm and located symmetrically about the plate axis at a distance of 12 mm from the clamped edge of the plate. The piezoelectric element was made of piezoceramics PZT-4 polarized in the direction of the z-axis and showing the following mechanical characteristics: $C_{11} = C_{22} = 13.9 \cdot 10^{10}$ N/m^2, $C_{12} = 7.78 \cdot 10^{10}$ N/m^2, $C_{13} = C_{23} = 7.43 \cdot 10^{10}$ N/m^2, $C_{33} = 11.5 \cdot 10^{10}$ N/m^2, $C_{44} = 3.06 \cdot 10^{10}$ N/m^2, $C_{55} = C_{66} = 2.56 \cdot 10^{10}$ N/m^2, $\beta_{31} = \beta_{32} = -5.2$ C/m^2, $\beta_{33} = 15.1$ C/m^2, $\beta_{52} = \beta_{61} = 12.7$ C/m^2, $e_{11} = e_{22} = 6.45 \cdot 10^{-9}$ F/m, $e_{33} = 5.62 \cdot 10^{-9}$ F/m, $\rho = 7700$ kg/m^3. The upper and lower surfaces of the piezoelectric element were covered with electrodes.

Table 1 presents the values of the first ten eigenfrequencies for the structure depicted in (fig.7) and the values of parameters C_{0n}, C_i and L_i of the equivalent electric circuit. In all further calculations, the equivalent circuit was assumed to have 10 L_iC_i-circuits. The higher number of circuits required for gaining desired accuracy of computation is the research topic in its own right.

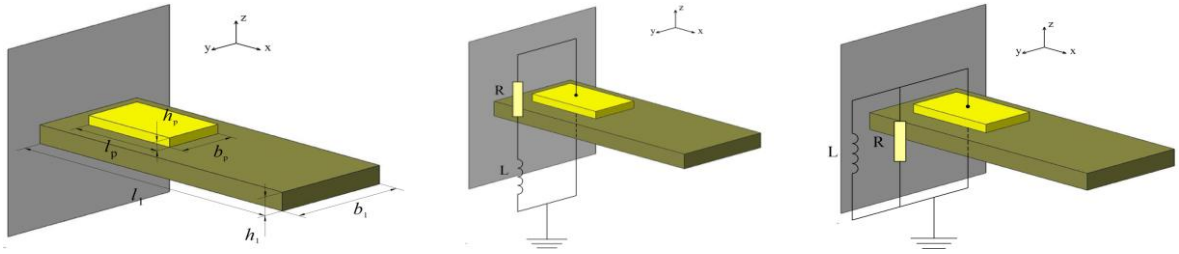

a b c

Figure 7: Computational schemes of a plate with piezoelectric element (a), which is connected to a series *RL*-circuit (b) or parallel *RL*-circuit (c)

Table 2 and 3 gives the values of eigenfrequencies for external circuits connected in series or in parallel for four variants of parameters of the external circuit. Two variants are for circuits connected in series: $L_1^{ser} = 11675$ H and $R_1^{ser} = 75$ kOhm, $L_2^{ser} = 413$ H and $R_2^{ser} = 6$ kOhm; and two variants are for circuits in parallel: $L_1^{par} = 11675$ H and $R_1^{par} = 14000$ kOhm, $L_2^{par} = 413$ H and $R_2^{par} = 6000$ kOhm. The tabulated results are the complex eigenfrequencies represented as $\omega = \omega_{\mathrm{Re}} - i\omega_{\mathrm{Im}}$, where ω_{Re} is the eigenfrequency, ω_{Im} is the damping ratio. The inset vibration

frequency resulting from connecting the external electric circuit to the smart structure is typed italic.

№ frequency	Eigenfrequencies of the plate with piezoelectric element in short circuit regime	Parameters of piezoelectric element for equivalent circuit		
		C_{0n}	C_i	L_i
1	13.86	$1.129 \cdot 10^{-8}$	$4.821 \cdot 10^{-10}$	$28.512 \cdot 10^{+4}$
2	72.33	$1.123 \cdot 10^{-8}$	$57.556 \cdot 10^{-10}$	$8.455 \cdot 10^{+4}$
3	198.33	$1.118 \cdot 10^{-8}$	$48.614 \cdot 10^{-10}$	$1.330 \cdot 10^{+4}$
4	204.45	$1.118 \cdot 10^{-8}$	$4.309 \cdot 10^{-24}$	$1.406 \cdot 10^{+17}$
5	404.15	$1.093 \cdot 10^{-8}$	$2.445 \cdot 10^{-10}$	$0.064 \cdot 10^{+4}$
6	489.41	$1.093 \cdot 10^{-8}$	$2.342 \cdot 10^{-29}$	$4.516 \cdot 10^{+21}$
7	584.11	$1.093 \cdot 10^{-8}$	$2.989 \cdot 10^{-26}$	$2.484 \cdot 10^{+18}$
8	674.97	$1.063 \cdot 10^{-8}$	$3.066 \cdot 10^{-10}$	$0.018 \cdot 10^{+4}$
9	928.29	$1.063 \cdot 10^{-8}$	$1.564 \cdot 10^{-28}$	$1.879 \cdot 10^{+20}$
10	990.66	$1.049 \cdot 10^{-8}$	$1.430 \cdot 10^{-10}$	$0.018 \cdot 10^{+4}$

Table 1: The values of parameters for branches of the equivalent circuit for the first ten eigenfrequencies of the plate with piezoelectric element under short circuit conditions.

№	$L_1^{ser} = 11675$ H, $R_1^{ser} = 75$ kOhm		$L_2^{ser} = 413$ H, $R_2^{ser} = 6$ kOhm	
	Eigenfrequencies, obtained from electromechanical problem solution	Eigenfrequencies, obtained from equivalent circuit problem solution	Eigenfrequencies, obtained from electromechanical problem solution	Eigenfrequencies, obtained from equivalent circuit problem solution
1	$12.40 - i\ 2.57 \cdot 10^{-1}$	$12.40 - i\ 2.57 \cdot 10^{-1}$	$13.56 - i\ 1.86 \cdot 10^{-3}$	$13.57 - i\ 1.79 \cdot 10^{-3}$
2	$15.17 - i\ 2.55 \cdot 10^{-1}$	$15.17 - i\ 2.55 \cdot 10^{-1}$	$70.39 - i\ 4.10 \cdot 10^{-1}$	$70.39 - i\ 4.10 \cdot 10^{-1}$
3	$72.34 - i\ 1.68 \cdot 10^{-4}$	$72.34 - i\ 1.04 \cdot 10^{-4}$	$75.71 - i\ 7.42 \cdot 10^{-1}$	$75.71 - i\ 7.42 \cdot 10^{-1}$
4	$198.32 - i\ 1.02 \cdot 10^{-5}$	$198.33 - i\ 1.08 \cdot 10^{-5}$	$198.39 - i\ 9.53 \cdot 10^{-4}$	$198.39 - i\ 9.19 \cdot 10^{-4}$

Table 2: Eigenfrequencies of the plate with piezoelectric element and series-connected *RL*-circuit

From the results summarized in Tables 2 and 3, it follows that eigenfrequencies obtained by solving the natural vibration problem in the framework of complete mathematical formulation and on the basis of its equivalent model are in good agreement, which reflects the adequacy of the proposed discrete model for interpretation of the behavior of the examined electromechanical system in terms of frequency characteristics.

	$L_1^{par} = 11675\,\text{H},\ R_1^{par} = 14000\,\text{kOhm}$		$L_2^{par} = 413\,\text{H},\ R_2^{par} = 6000\,\text{kOhm}$	
№	Eigenfrequencies, obtained from tromechanical problem solution	Eigenfrequencies, obtained from alent circuit problem solution	Eigenfrequencies, obtained from tromechanical problem solution	Eigenfrequencies, obtained from equivalent circuit problem solution
1	$12.40 - i\,2.01\cdot10^{-1}$	$12.40 - i\,2.01\cdot10^{-1}$	$13.56 - i\,9.33\cdot10^{-5}$	$13.57 - i\,6.17\cdot10^{-5}$
2	$15.17 - i\,3.03\cdot10^{-1}$	$15.17 - i\,3.02\cdot10^{-1}$	$70.39 - i\,3.78\cdot10^{-1}$	$70.40 - i\,3.78\cdot10^{-1}$
3	$72.34 - i\,2.79\cdot10^{-3}$	$72.34 - i\,2.78\cdot10^{-3}$	$75.71 - i\,7.98\cdot10^{-1}$	$75.70 - i\,7.98\cdot10^{-1}$
4	$198.32 - i\,2.18\cdot10^{-3}$	$198.33 - i\,2.18\cdot10^{-3}$	$198.39 - i\,6.74\cdot10^{-3}$	$198.39 - i\,6.77\cdot10^{-3}$

Table 3: Eigenfrequencies of the plate with piezoelectric element and parallel-connected *RL*-circuit.

6 CONCLUSIONS

- In this paper, an approach has been developed to analyze the dynamic processes in smart structures containing piezoelectric elements and external electric circuits. The approach is based on the equivalent electric circuits representing discrete electric systems with concentrated parameters.
- In the framework of this approach a version of equivalent electric circuit has been developed, using as a basis the van Dyke model. The proposed equivalent circuit allows us to describe adequately the behavior of the entire electromechanical system representing a structure with attached piezoelectric element and external electric circuit.
- A mathematical formulation of the natural vibration problem has been developed.
- It has been shown that the behavior of electromechanical systems with external electric circuits can be effectively modeled by an electrical analogue, in which the electric circuits including elements with concentrated parameters are used to describe the piezoelectric element. The efficiency of the electric analogue for the description of such systems has been verified by calculating the eigenfrequencies of the smart structure composed of a plate with piezoelectric element connected to a series or parallel resonance *RL*-circuit.

The work supported by RFBR (projects № 17-01-590152, 16-31-00094-mol_a) and UB RAS complex program (project 15-10-1-18).

REFERENCES

[1] Matveenko, V.P., Kligman, E.P., Yurlov, M.A., Yurlova, N.A. Simulation and optimization of dynamic characteristics of piezoelectric smart structures, *Physical Mesomechanics* (2012) **15** (3-4): 190-199.

[2] Matveenko, V.P., Yurlov, M.A., Yurlova, N.A. Optimization of the damping properties electro-viscoelastic objects with external electric circuits, *Mechanics of Advanced Mate-*

rials/ eds. V.V. Silberschmidt and V.P. Matveenko, Engineering Materials, Springer, (2015): 79-100.

[3] Matvvenko, V.P., Oshmarin, D.A., Sevodina, N.V., Iurlova, N.A. Natural vibration problem for electroviscoelstic body with external electric circuits and finite-element relations for its numerical implementation, *Computational Continuum Mechanics,* (2016) **9**(4): 476-485.

[4] Guan, M., Liao, W.-H. Studies on the circuit models of piezoelectric ceramics, *International Conference on Information Acquisition* (2004): 26-31.

[5] Sherrit, S., Wiederick, H.D., Mukherjee, B.K., Sayer, M. An accurate equivalent circuit for the unloaded piezoelectric vibrator in the thickness mode, *Journal of Physics D: Applied Physics* (1997) **30**(16): 2354-2363.

[6] Park, C.H. On the circuit model of piezoceramics, *Journal of Intelligent Material Systems and Structures* (2001) **12:** 515-522.

[7] Pang, S., Li, W., Kan, J. Optimization analysis of interface circuits in piezoelectric energy harvesting systems, *Journal of Power Technologies* (2016) **96** (1): 1–7.

[8] Kim, J., Grisso, B.L., Kim, J.K., Ha, D.S., Inman, D.J. Electrical modeling of piezoelectric ceramics for analysis and evaluation of sensory systems, *SAS 2008 - IEEE Sensors Applications Symposium Atlanta, GA, February 12-14, 2008* (2008): 122-127.

[9] Chen, Y.-Y., Vasic, D. Electrical interfacing circuit discussion of galloping-based piezoelectric energy harvester, *Physics Procedia* (2015) **70:** 1017-1021.

[10] Hagood, N.W., von Flotow, A. Damping of structural vibrations with piezoelectric materials and passive electrical networks, *Journal of Sound and Vibration* (1991) **146** (2): 243–268.

[11] Viana, F.A.C., Valder, S.Jr., Multimodal Vibration Damping through Piezoelectric Patches and Optimal Resonant Shunt Circuits, *J. of the Braz. Soc. of Mech. Sci. & Eng*. (2006) **XXVIII**(3): 293-310.

[12] Agneni, A., Mastroddi, F., Polli, G.M. Shunted piezoelectric patches in elastic and aeroelastic vibrations, *Computers and Structures* (2003) **81:**91–105.

[13] Fleming, A.J., Behrens, S., Moheimani, S.O.R. Reducing the inductance requirements of piezoelectric shunt damping systems, *Smart Mater. Struct*. (2003) **12:**57-64.

[14] Thomas, O., Ducarne, J., Deu, J.-F. Performance of piezoelectric shunts for vibration reduction, *Smart Mater. Struct*. (2012) **21**(1):015008.

[15] Caruso, G. A critical analysis of electric shunt circuits employed in piezoelectric passive vibration damping, *Smart Mater. Struct*. (2001) **10:**1059-1068.

[16] Popov, V.P. *Osnovy teorii cepej,* Moscow. Vysshaya Shkola (1985).

[17] Ivanov, A.S., Matvienko, V.P., Oshmarin, D.A., Sevodina, N.V., Yurlov, M.A., Yurlova, N.A. Justification of equivalent substitution circuits used to optimize the dissipative properties of electroelastic bodies with external electric circuits, *Mechanics of Solids* (2016) **51**(3): 273–283.

[18] Dyke, V. The electric network equivalent of a piezoelectric resonator, *Physical Review* (1925) **25:** 895A.

VIII ECCOMAS Thematic Conference on Smart Structures and Materials
SMART 2017
A. Güemes, A. Benjeddou , J. Rodellar and Jinsong Leng (Eds)

PASSIVE MULTIMODAL DAMPING OF VIBRATIONS OF STRUCTURES WITH PIEZOELECTRIC ELEMENTS AND EXTERNAL ELECTRIC CIRCUITS

DMITRII A. OSHMARIN*, MAKSIM A. IURLOV *, NATALIYA V. SEVODINA* AND NATALIIA A. IURLOVA*

*Department of complex problems of deformable solids mechanics
Institute of Continuous Media Mechanics of the Ural Branch of RAS (ICMM UB RAS)
Acad. Korolev str., 1, 613013 Perm, Russian Federation
e-mail: oshmarin@icmm.ru, www.icmm.ru

Key words: Electroelasticity, External electrical circuit, Piezoelement, Natural vibrations, Numerical modeling, Multimodal damping

Abstract. Under the operating conditions, many modern technical structures require complete elimination of vibrations at several certain frequencies or in the specified frequency range with the aid of the same technical facilities. In literature this problem is called the problem of multimodal damping. One of the approaches to the solution of this problem is to use special damping devices – piezoelectric elements connected with external electric circuit, which being attached to the initial mechanical structure form the so-called smart-structure. When using this kind of damping devices the problem of multimodal damping can be solved by one of the following methods: attaching to the initial structure an array of piezoelectric elements, each being connected to its own external electric circuit or to one common circuit, or connection of one piezoelectric element to a complicated branched multi-loop circuit. These approaches have serious drawbacks such as structural mass increase due to large number of piezoelectric elements, complexity of external circuit tuning, etc. In this paper, it was investigated the possibility of using one piezoelectric element and one external passive *RL*-circuit for damping the system vibrations at several frequencies due to appropriate selection of the external electric circuit parameters.

1 INTRODUCTION

The idea of using piezoelectric elements with connected external electric circuits for damping the vibrations of mechanical structures has proved highly efficient and attractive especially for engineering applications with strict size (miniaturization) and weight limits (elements of space and aircraft facilities). Piezoelectric elements connected with external electric circuits (shunted peizoelectric elements) being attached to the mechanical structure form the energy dissipation devices, which provide additional damping of vibrations. Due to the piezoelectric effect part of the mechanical vibration energy is transformed to the electric energy, which can be dissipated through the shunt circuit as heat or electromagnetic radiation, generating thereby the mechanism of passive control of vibration damping. Because of a

small weight of peizoelectric elements and components of the external electric circuits, such a system does not lead to serious changes in the spectral pattern of the initial structure and can be used as a complementary device to the developed technical solutions. For the first time the possibility of applying such devices to damping the vibrations of the mechanical structure has been demonstrated by Forward R.L. in work [1] and theoretically substantiated by Hagood N.W. and von Flotow A. in [2].

A key to the problem of vibration damping with shunted piezoelectric elements is to find the simplest shunt, which is most effective in damping the vibrations of a particular structure at the frequencies of a certain group in the specified frequency range. The shunt circuit should meet the following requirements: it should provide maximum damping of mechanical vibrations and preserve its stability; it should operate without power source; its design costs and weight should be reduced to a minimum; since the circuit is integrated in the structure, the size of its elements should be minimal [3].

Over the period of the last decade a lot of various passive shunt circuits have been designed and rated. According to classification presented in [3] passive shunts can be linear and nonlinear. Among the linear passive circuits one can distinguish between the resistive (including only resistors) and resonant (including resistors and inductors) circuits.

The resistive circuits used to shunt piezoelectric elements cause the structure to behave itself as if it is made of viscoelastic material.

The use of resonant *RL*-circuits consisting of parallel- or series-connected inductance coil and resistor leads to the creation of the electric oscillatory circuit due to the interaction of the external circuit inductance and inherent capacitance of the piezoelectric element. As a result, the frequency spectrum of the system (the structure with piezoelectric element and external electric circuit) extends to include an additional resonance frequency (eigenfrequency of the oscillatory circuit).

By varying the parameters of the elements of external electric circuit one can adjust this additional resonance to the frequency coincident with the natural vibration frequency of the structure. This allows the energy of vibrations to be transferred to the external electric circuit, which provides an effective suppression of the structure vibrations at a given frequency. In practice, the requirements commonly imposed on structures are the absence of vibrations at the frequencies of a certain group in some excitation frequency range. Therefore, the development of techniques for multimodal damping of structure vibrations is an urgent problem. At present, one can distinguish the following basic approaches to multimodal damping:

- employment of one piezoelectric element and complex external electric circuit, in which the possibility of damping several modes of vibrations is realized in one way or another [5-14];
- usage of several piezoelectric elements forming an integrated network and connected by one or another method to a single external electric circuit [15-19];
- usage of several piezoelectric elements, each having its own electric circuit, which is not coupled with others to form a joint circuit [20-22].

Each of these approaches has its own advantages and drawbacks. Thus, for example, in the presence of complicated branched circuits the complexity of their tuning increases, because each branch of the shunt circuit cannot be considered as a separate independent shunt [5]. In this case, it is advisable to use blocking or conducting circuits connected in series to shunt

branches [6, 9], which allows one to consider them as independent. However, in practice this leads to very cumbersome electric circuits due to the use of many inductive elements, which certainly affects the mass characteristics of damping devices. This problem can partially be solved with the use of electronic analogues of inductive elements. However, such a substitution is only an approximation to ideal inductive elements and does not completely eliminate the necessity of tuning the branches and determining the circuit parameters [11].

The difficulty with the circuit tuning can be readily solved with the use of several piezoelectric elements connected to simple *RL*-circuits, since in this case each piezoelectric element with connected circuit represents an isolated system and parameters of the shunt circuits can be selected independently. However, as it was shown in [14], in the case of multimodal damping this approach is not necessarily successful, because a great number of elements in the circuit can essentially increase the mass of the structure and have an ill-effect on its dynamic characteristics.

Hence, nowadays, a number of problems accosiated with the use of piezoelectric elements for damping several vibration modes invite further investigation and development of new approaches to implementation of multimodal damping.

In this paper, it was investigated the possibility of using one piezoelectric element and one external series *RL*-circuit for damping the vibrations at several by appropriate selection of parameters of the external electric circuit on the basis of natural vibration problem for electroelastic bodies with external electric circuits.

2 MATHEMATICAL STATEMENT OF THE PROBLEM ON NATURAL VIBRATIONS

Consider a piece-wise homogeneous body of volume $V = V_1 + V_2$, where volume V_1 is composed of homogeneous elastic parts and volume V_2 - of piezoelectric elements. Part of the surface of the volume V_2 is covered with electrodes. One of the electrode surfaces is connected to the external electric circuit of arbitrary configuration consisting of resistive elements (resistors) of resistance *R*, inductive elements (inductors) of inductance *L* and capacitive elements (capacitors) of capacitance *C*, and providing passive control of the dynamic behavior of the structure.

The variational equation for natural vibrations of the body consisting of elastic and piezoelectric elements is constructed based on the relations of linear theory of elasticity and quasi-static Maxwell equations [23-25]:

$$\int_{V_1}\left(\sigma_{ij}\delta\varepsilon_{ij}+\rho\ddot{u}_i\delta u_i\right)dV+\int_{V_2}\left(\sigma_{ij}\delta\varepsilon_{ij}-D_i\delta E_i+\rho\ddot{u}_i\delta u_i\right)dV+ \tag{1}$$

$$+\sum_{p=1}^{n_L}\frac{1}{L_p}\iint\left(\varphi_1^{L_p}-\varphi_2^{L_p}\right)\delta\varphi dtdt+\sum_{q=1}^{n_R}\frac{1}{R_q}\int\left(\varphi_1^{R_q}-\varphi_2^{R_q}\right)\delta\varphi dt+\sum_{r=1}^{n_C}C_r\left(\varphi_1^{C_r}-\varphi_2^{C_r}\right)\delta\varphi=0$$

Here D_i, E_i – are the components of electric flux density and electric field intensity vectors; σ_{ij} are the components of the symmetric Cauchy stress tensor, ε_{ij} are the components of the linear strain tensor, u_i are the components of the displacement vector, φ – electric potential, $\varphi_1 - \varphi_2$ - potential difference on external circuit element, n_L, n_R, n_C - the numbers of inductive,

resistive and capacitive elements respectively, L_p, R_q, C_r - inductance, resistance and capacitance values for corresponding circuit element.
For the electric field the potentiality condition is fulfilled:

$$\varphi_{,i} = -E_i \tag{2}$$

For elastic parts (V_1) the following physical equations of the linear theory of elasticity hold true:

$$\sigma_{ij} = C_{ijkl}\varepsilon_{kl} \tag{3}$$

For isothermal processes, the electroelastic parts (V_2) obey the following physical relations:

$$\left.\begin{aligned} \sigma_{ij} &= \overline{C}_{ijkl}\varepsilon_{kl} - \beta_{ijk}E_k \\ D_k &= \beta_{ijk}\varepsilon_{ij} + e_{ki}E_i \end{aligned}\right\} \tag{4}$$

where C_{ijkl} and $\overline{C}_{ijkl}$ are the tensors of elastic constants, β_{ijk} and e_{ki} are the tensors of piezoelectric and dielectric coefficients.

For the examined system the restrictions are set in the form of mechanical and electric boundary conditions. The mechanical boundary conditions are given as:

$$u_i\big|_{\Gamma_u} = u_{i0}, \tag{5}$$

where Γ_u is the part of the surface of volume V, on which the displacements are prescribed.

The expressions for electric boundary conditions on the piezoelectric parts confined in the volume V_2 read as follows:

$$\varphi\big|_{\Omega_{el}^{\varphi}} = \varphi_0, \tag{6}$$

here Ω_{el}^{φ} is the part of the electrode surface of the volume V_2, with the prescribed electric potential. In the absence of electrode covering all electric boundary conditions take zero values.

The eigenvectors of vibrations are sought in the following form:

$$u_i(x,t) = \overline{u}_i(\vec{x})e^{i\omega t}, \quad \varphi(x,t) = \overline{\varphi}(\vec{x})e^{i\omega t} \tag{7}$$

where $\omega = \omega_{\mathrm{Re}} + i\omega_{\mathrm{Im}}$ is the complex eigenfrequency, in which ω_{Re} corresponds to the vibration eigenfrequency itself, ω_{Im} corresponds to the rate of vibration damping (damping ratio), $\overline{u}_i(\vec{x})$, $\overline{\varphi}(\vec{x})$ are eigenmodes of vibrations.

A complete mathematical formulation of the problem is given in work [25]. The stated problem is solved by the finite element method (FEM), using the algorithm elaborated by the authors of this paper.

As it was shown in [2], the series resonant electric circuit, shunting the piezoelectric element can decrease oscillations for only one selected frequency, to which the external circuit is tuned by choosing the appropriate parameters *R* and *L*.

Since the dynamic processes are investigated by solving the natural vibration problem, it is convenient to use the imaginary parts of the complex eigenfrequencies ω_{Im} for the

formulation of optimality criterion for search the parameters of the external electric circuit, ensuring damping of several vibration modes.

The analysis of the behavior of the imaginary parts ω_{Im} of different complex eigenfrequencies $\omega = \omega_{\text{Re}} + i\omega_{\text{Im}}$ depending on variation of resistance R and inductance L of the external series resonant *RL*-circuit has shown that in the space of parameters R and L at some frequencies there exist a number of points, at which damping ratios of these frequencies coincide. Basing on this the criterion for external series *RL*-circuit was formulated in the following way: for damping of vibrations on several frequencies the values of parameters of external circuit should correspond the point in the *RL*-space where absolute values of damping ratios for several frequencies are equal and maximal.

Mathematically, the above criterion for two frequencies for instance can be formulated as follows:

$$\max\left(\left|\omega_{\text{Im}}^{k}\right| = \left|\omega_{\text{Im}}^{l}\right|\right) \tag{8}$$

where k, l are the numbers of frequencies, at which the vibrations can be damped with the use of a single external electric resonant circuit.

3 THE RESULTS OF NUMERIC COMPUTATIONS

The applicability of the proposed approach can be demonstrated in the context of the problem of a thin-walled shell in the form of semi-cylinder, which is clamped at the edges and simply supported along the generatrix (figure 1a).

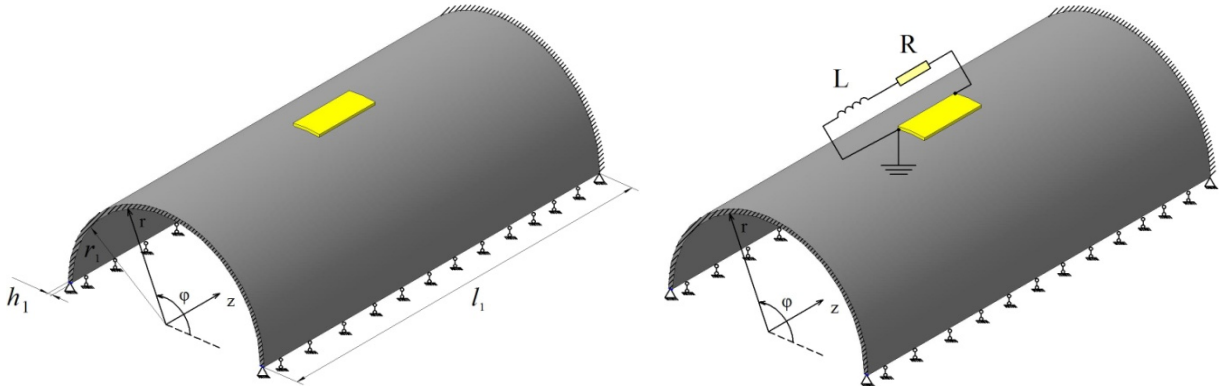

Figure 1: The design models of cylindrical shell with piezoelectric attached element (a) and cylindrical shell with attached piezoelectric element connected to series RL-circuit (b).

The geometrical dimensions of the shell are as follows: $r_1 = 76$ mm $l_1 = 300$ mm, $h_1 = 0.25$ mm. The shell is made of elastic isotropic material having the following characteristics: $E = 1.96 \cdot 10^{11}$ Pa, $\nu = 0.3$, $\rho = 7700$ kg/m^3. The piezoelectric element, which is attached to the surface of the shell has the shape of the ring segment with the following dimensions: $r_p = 76.25$ mm, $\varphi_p = 15.08°$, $h_p = 0.36$ mm. The center of mass of the piezoelectric element is 15

mm away from the clamped edges and is shifted by 90° from the simply supported generatrices along the angular coordinate. The piezoelectric element is made of peizoceramics PZT-4 polarized along the r-axis and having the following characteristics (in the cylindrical coordinate system): $C_{11} = C_{22} = 13.9 \cdot 10^{10}$ Pa, $C_{12} = 7.78 \cdot 10^{10}$ Pa, $C_{13} = C_{23} = 7.43 \cdot 10^{10}$ Pa, $C_{33} = 11.5 \cdot 10^{10}$ Pa, $C_{44} = 3.06 \cdot 10^{10}$ Pa, $C_{55} = C_{66} = 2.56 \cdot 10^{10}$ Pa, $\beta_{31} = \beta_{32} = -5.2$ C/m^2, $\beta_{33} = 15.1$ C/m^2, $\beta_{52} = \beta_{61} = 12.7$ C/m^2, $e_{11} = e_{22} = 6.45 \cdot 10^{-9}$ F/m, $e_{33} = 5.62 \cdot 10^{-9}$ F/m, $\rho = 7700$ kg/m^3. The upper and lower surfaces of the piezoelectric element are covered with electrodes. The external series *RL*-circuit is connected to piezoelectric element electrodes (figure 1b).

The chosen frequency range up to 1500 Hz contains 15 natural vibration frequencies of the structure. At current piezoelectric element location vibrations are possible to be suppressed by proposed technique at only five of them [26]. As the solution of problem on natural vibrations (1)-(7) natural frequencies of shell with attached piezoelectric element were obtained for the cases of no external circuit (real) and with external circuit (complex) tuned for maximal damping of corresponding frequency (single-mode damping). Table 1 presents the only 5 frequencies for which vibration damping of the structure under study is achievable.

Table 1. Natural vibration frequencies for the structure with no external circuit and with external circuit tuned to corresponding frequency

№ of frequency	Vibration frequencies for the case of no circuit f, Гц	Vibration frequencies for the case with circuit $f = f_{\mathrm{Re}} - if_{\mathrm{Im}}$
1	557.41	553.60 – *i* 29.55
2	759.57	750.59 – *i* 32.06
3	803.79	813.58 – *i* 31.12
4	1293.42	1282.19 – *i* 51.97
5	1482.21	1493.29 – *i* 81.48

On the basis of natural vibration problem solution for the system (shell with attached piezoelectric element and external circuit) the relationship surfaces for damping ratios depending on variation of *R* and *L* external circuit parameters were retrieved for the five frequencies under consideration (figure 2).

Based on the analysis of the obtained dependences two following groups can be distinguished:

1) damping ratios for the 2-nd and 3-rd frequencies (figure 3a)
2) damping ratios for the 4-th and 5-th frequencies (figure 3c).

Figures 3b and 3d show projections of the lines of coincidence of damping ratios in the space of *RL*-parameters. The value of damping ratio ω_{Im} along the lines correspond these projections changes. According to the criterion proposed (8) the external circuit parameters providing multimodal damping were defined for the abovementioned groups of frequencies.

A comparison between damping ratios for the frequencies from table 2 and corresponding maximum achievable values of the damping ratio presented in table 1 allows to draw a conclusion that with the use of one series resonant electric circuit connected to one piezoelectric element with parameters identified by the proposed criterion it is possible to achieve sufficient damping of vibrations for the examined pairs of adjacent frequencies.

Carrying on the analysis of relationships shown on figure 2 one can point out that in the *RL*-space exist the points where damping ratios are coincident for more than two frequencies.

Table 2. Optimal parameters for the series *RL*-circuit for the two groups of frequencies under study

№ of frequency to be damped	Optimal parameter values *R* (kOhm), *L* (H)	Complex eigemfrequencies values
2, 3	*R*=4.41 *L*=3.57	755.40 - *i* 23.76 791.50 - *i* 23.58
4, 5	*R*=2.45 *L*=1.19	1281.48 - *i* 25.43 1507.57 - *i* 25.76

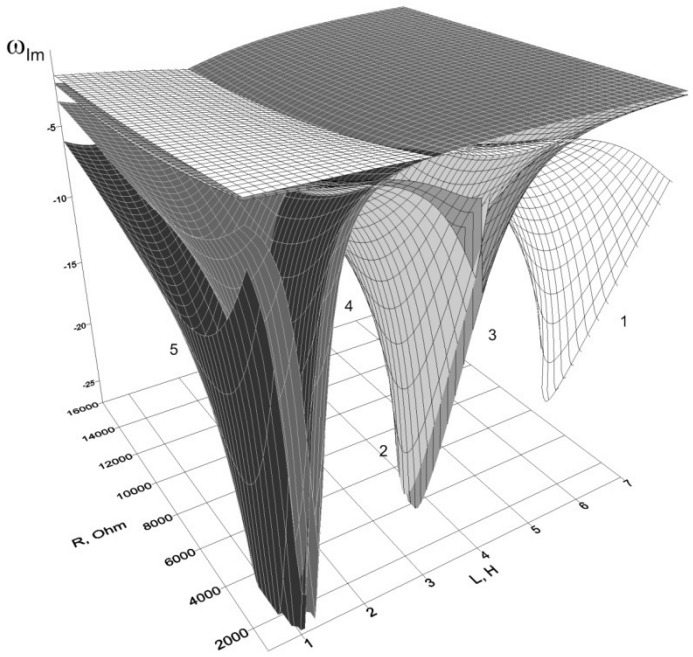

Figure 2: Damping ratios relationship surfaces in the *RL*- parameters space for the given five frequencies.

Figure 4 presents projections of all possible lines of pair-wise coincidence of damping ratios for the five frequencies under study. Analyzing these lines four points of coincidence were determined where damping ratios are equal for three frequencies:

- point I – intersection of lines 2-4, 2-5, 4-5 – ω_{Im} coincidence for the 2-nd, 4-th, 5-th frequencies;
- point II – intersection of lines 3-4, 3-5, 4-5 – ω_{Im} coincidence for the 3-rd, 4-th, 5-th frequencies;
- point III – intersection of lines 1-4, 1-5, 4-5 – ω_{Im} coincidence for the 1-st, 4-th, 5-th frequencies;

– point IV – intersection of lines 2-3, 2-5, 3-5 – ω_{Im} coincidence for the 2-nd, 3-rd, 5-th frequencies.

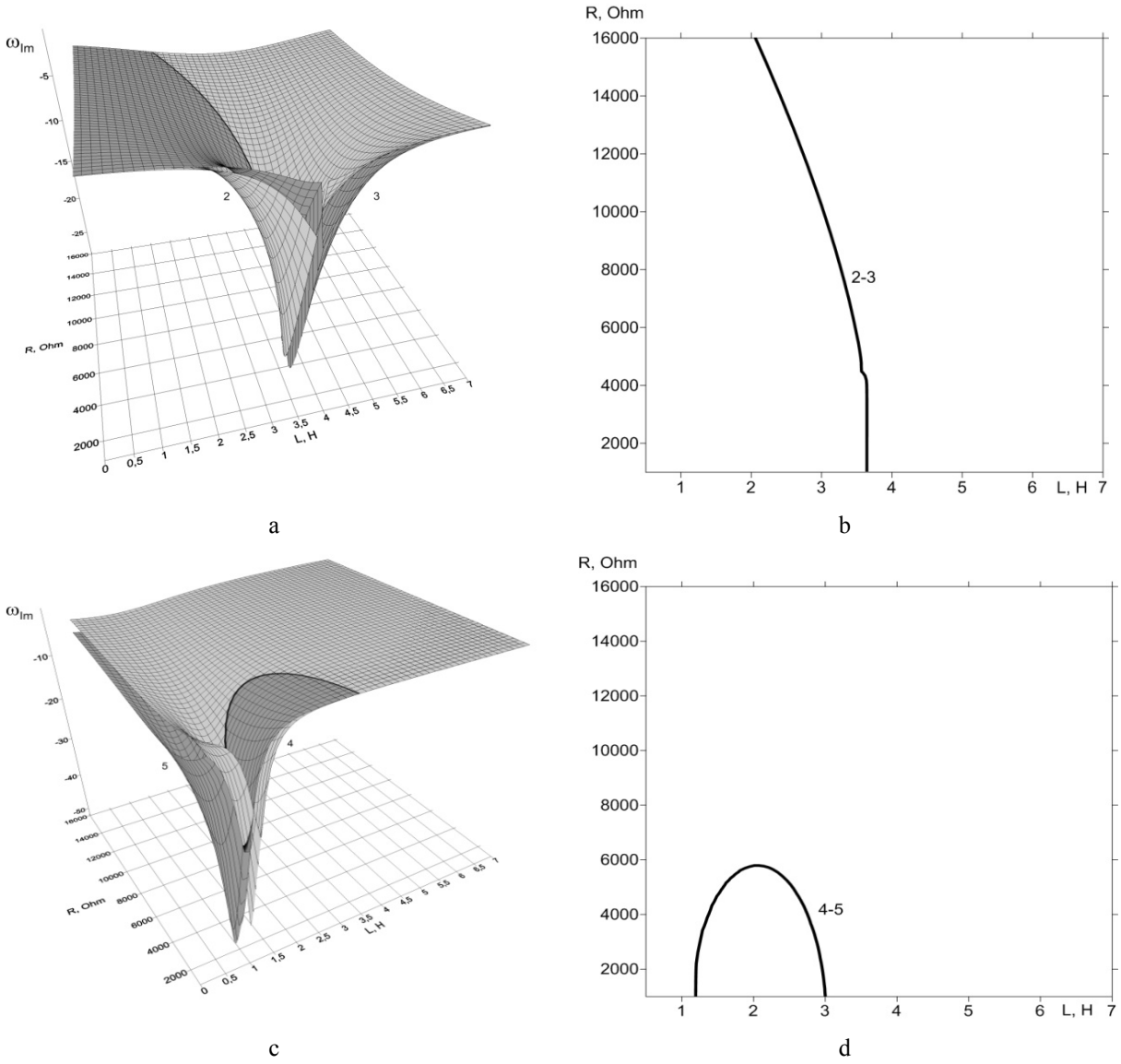

Figure 3: Damping ratios relationship surfaces and projections of their lines of intersection in the *RL*-parameters space: for 2-nd и 3-rd frequencies (a, b); for 4-th и 5-th frequencies (c, d).

Other intersections for projections of the lines of coincidence of damping ratios shown in 2D figure 4 do not have common points in a 3D space (figure 2).

For the above frequency groups Table 3 presents the values of parameters of the electric circuit, which were defined by the coordinates of points I–IV in figure 4 and complex frequencies of the system, corresponding to these parameters. The accuracy of the presented

results is determined by the precision of the computational methods and the errors of reading out the plot data.

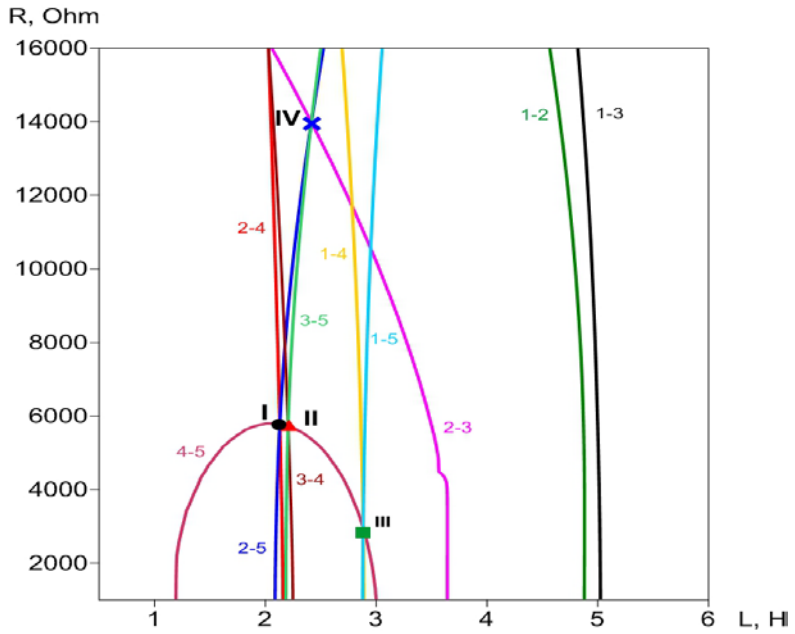

Figure 4: Projections of lines of pair-wise coincidence of damping ratios in the *RL*-space.

Table 3. External circuit parameter values and corresponding eigenfrequencies for the I-IV groups of frequencies.

Groups of frequencies	№ of frequencies to be damped	External circuit parameters *R* (kOhm), *L* (H)	Complex eigenfrequencies
I	2, 4, 5	*R* =5.77 *L* =2.14	2-nd: 753.82 - *i* 4.41 4-th: 1298.61 - *i* 4.12 5-th: 1489.72 - *i* 4.06
II	3, 4, 5	*R* =5.72 *L* =2.21	3-rd: 797.84 - *i* 3.95 4-th: 1298.54 - *i* 3.73 5-th: 1489.49 - *i* 3.68
III	1, 4, 5	*R* =2.94 *L* =2.88	1-st: 552.30 - *i* 1.01 4-th: 1297.78 - *i* 0.96 5-th: 1487.89 - *i* 0.95
IV	2, 3, 5	*R* =13.99 *L* =2.42	2-nd: 757.92 - *i* 4.10 3-rd: 801.76 - *i* 4.09 5-th: 1485.87 - *i* 3.90
D	2-5	*R* =5.75 *L*=2.20	2-nd: 753.73 - *i* 4.64 3-rd: 797.86 - *i* 3.94 4-th: 1298.53 - *i* 3.76 5-th: 1489.49 - *i* 3.71

Points I and II in figure 4 lays sufficiently close, which implies that at properly identified parameters of the external circuit damping of the structure vibrations can be achieved in the range from the 2-nd to the 5-th frequencies. The line D of table 3 contains the values of frequencies for circuit parameters taken arbitrarily from the interval limited by the values of R and L for groups I and II. The results from the line D of table 3 show that the imaginary parts ω_{Im} (damping ratios) for the frequencies under consideration are quite high and close to each other. Thus one can make a conclusion about possibility of damping of four vibration frequencies with single series RL-circuit.

In order to verify the results obtained the problem on forced, steady-state harmonic vibrations of the system consisting of a shell with piezoelectric element connected in the first case to a resistive R-circuit and in the second case to a series resonant RL-circuit was solved. The amplitude vs. frequency plot for the displacements U_s ($U_s = \sqrt{U_x^2 + U_y^2 + U_z^2}$) of point A (see fig.1b) of the above system was gained for the case of application of the harmonic force with the ampltude of $P_r = 0.01$ N to point B along the r-axis.

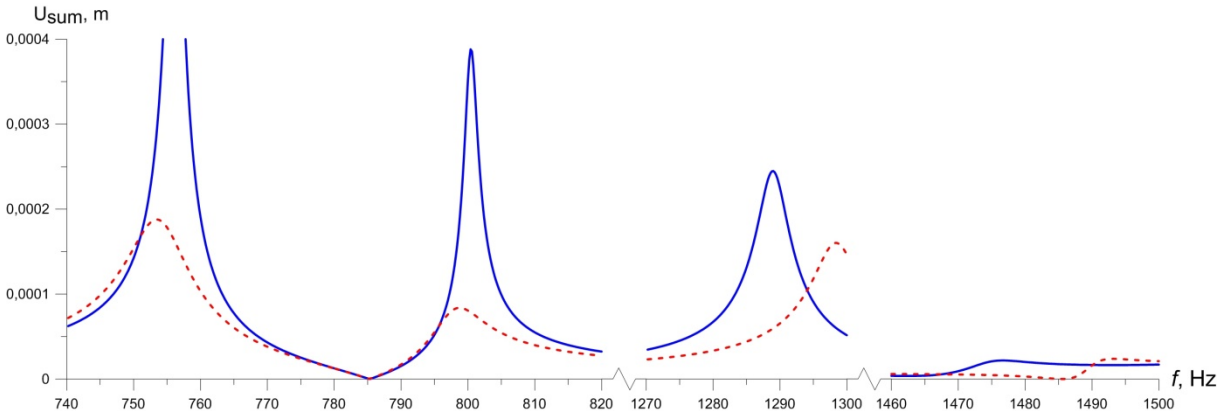

Figure 5: Amplitude vs. frequency plots in point A for the cases of resistive circuit (solid line) and resonant circuit tuned to damp frequencies from 2-nd to 5-th (dashed line).

Figure 5 presents amplitude vs. frequency plots for the displacements of point A of the examined structure (figure 1) connected to a resistive or resonance external electric circuit. In the calculations, the parameters of the resonant circuit take the values, corresponding to the line D of table 2 (R=5.750 kOhm, L=2.2 H.). The computations for the resistive circuit were made using the same value of resistance (R=5.750 kOhm).

4 CONCLUSIONS

- In the framework of mathematical statement of the natural vibration problem for electro-elastic bodies with external passive electric circuits, a new approach has been developed for identification of optimal parameters for a simple external passive electric circuit, which provides damping of vibrations at several frequencies for a given configuration of the smart-structure.
- The efficiency of the proposed approach was verified by making computations for a

semi-cylindrical shell with piezoelectric element connected to the external series resonant *RL*-circuit.

- It has been shown that pairs of parameters selected for the resonant *RL*-circuit on the basis of the proposed criterion allow damping of vibrations at several frequencies providing thereby multimodal damping.

The work is supported by the RFBR (projects No 15-01-03976-a, No 16-31-00094-mol-a) and UB RAS complex program (project No 15-10-1-18).

REFERENCES

[1] Forward, R.L. Electronic damping of vibrations in optical structures, *Journal of Applied Optics* (1979) **18** (5): 690-697.

[2] Hagood, N.W., von Flotow, A. Damping of structural vibrations with piezoelectric materials and passive electrical networks, *J. Sound Vib*. (1991) **146:** 243–268.

[3] Moheimani, S.O.R., Fleming, A.J. *Piezoelectric transducers for vibration control and damping*, Springer Science & Business Media, (2006).

[4] Wu, S.Y. Piezoelectric shunts with parallel R–L circuit for structural damping and vibration control, *Smart Structures and Materials, Passive Damping and Isolation. Proc. SPIE* (1996), **2720:** 259–269.

[5] Hollkamp, J.J. Multimodal passive vibration suppression with piezoelectric materials and resonant shunts, *J. Intell. Mater. Syst. Struct*. (1994) **5**: 49–56.

[6] Wu, S.Y. Method for multiple mode shunt damping of structural vibration using a single PZT transducer, *Smart Structures and Materials, Smart Structures and Intelligent Systems*, *Proc. SPIE* (1998) **3327:** 159–168.

[7] Wu, S.Y. Multiple PZT transducers implemented with multiple-mode piezoelectric shunting for passive vibration damping, *Smart Structures and Materials, Passive Damping and Isolation, Proc. SPIE* (1999) **672:** 112–122.

[8] Wu, S.Y., Bicos, A.S. Structural vibration damping experiments using improved piezoelectric shunts, *Smart Structures and Materials, Passive Damping and Isolation*, *Proc. SPIE* (1997) **3045:** 40–50.

[9] Behrens, S., Moheimani, S.O.R. Current flowing multiple mode piezoelectric shunt dampener, *Smart Materials and Structures*, *Proc. SPIE* (2002) 4697-24.

[10] Behrens, S., Moheimani, S.O.R., Fleming, A.J. Multiple mode current flowing passive piezoelectric shunt controller, *Journal of Sound and Vibration* (2003) **266**(5): 929–942.

[11] Fleming, A.J., Moheimani, S.O.R. Adaptive piezoelectric shunt damping, *Smart Mater. Struct.* (2003) **12**(1): 36–48.

[12] Behrens, S., Moheimani, S.O.R. Optimal resistive elements for multiple mode shunt damping of a piezoelectric laminate beam, *Proceedings of the 39th IEEE Conference on Decision and Control* (2000) **4:** 4018-4023.

[13] Cheng, T.H., Oh, I.K. A current-flowing electromagnetic shunt damper for multi-mode vibration control of cantilever beams, *Smart Materials and Structures* (2009) **18** (9): 095036.

[14] Viana, F.A.C., Valder, S.Jr. Multimodal Vibration Damping through Piezoelectric Patches and Optimal Resonant Shunt Circuits, *J. of the Braz. Soc. of Mech. Sci. & Eng*. (2006) **XXVIII** (3): 293-310.

[15] Vidoli, S., dell'Isola, F. Vibration control in plates by uniformly distributed PZT actuators interconnected via electric networks, *European Journal of Mechanics/A Solids* (2001) **20:** 435–456.
[16] Porfri, M., dell'Isola, F., Frattale, M.F.M. Circuit analog of a beam and its application to multimodal vibration damping, using piezoelectric transducers, *Int. J. Circ. Theor. Appl.* (2004) **32:** 167–198.
[17] dell'Isola, F., Henneke, E.G., Porfiri, M. Piezoelectromechanical structures: new trends towards the multimodal passive vibration control, *Smart Structures and Materials 2003: Damping and Isolation, Proceedings of SPIE* (2003) **5052:** 392-402.
[18] Maurini, C., dell'Isola, F., Del Vescovo, D. Comparison of piezoelectronic networks acting as distributed vibration absorbers, *Mechanical Systems and Signal Processing* (2004) **18** (5): 1243-1271.
[19] Giorgio, I., Culla, A., Del Vescovo, D. Multimode vibration control using several piezoelectric transducers shunted with a multiterminal network, *Arch. Appl. Mech.* (2009) **79** (9): 859–879.
[20] Casadei, F., Ruzzene, M., Dozio, L., Cunefare, K.A. Broadband vibration control through periodic arrays of resonant shunts: experimental investigation on plates, *Smart Materials and Structures* (2010) **19**(1): 015002.
[21] Guo, K.M., Jiang, J. Independent modal resonant shunt for multimode vibration control of a truss-cored sandwich panel, *Int. J. Dynam. Control* (2014) **2:** 326-334.
[22] Trindade, M.A., Maio, C.E.B. Multimodal passive vibration control of sandwich beams with shunted shear piezoelectric materials, *Smart. Mater. Struct.* (2008) **17:** 055015.
[23] Parton, V.Z., Kudryavtsev, B.A. *Electromagnetoelasticity: Piezoelectrics and Electrically Conductive Solids*, New York: Gordon and Breach Science Publishers Ltd. (1988).
[24] Karnaukhov, V.G., Kirichok, I.F. *Electrothermal viscoelasticity*, Kiev, Nauk. Dumka, (1988)
[25] Matvvenko, V.P., Oshmarin, D.A., Sevodina, N.V., Iurlova, N.A. Natural vibration problem for electroviscoelstic body with external electric circuits and finite-element relations for its numerical implementation, *Computational Continuum Mechanics* (2016) **9**(4): 476-485.
[26] Sevodina, N.V., Yurlova, N.A., Oshmarin, D.A. The optimal placement of the piezoelectric element in a structure based on the solution of the problem of natural vibrations, *Solid State Phenomena* (2015) **243**:67-74.

VIII ECCOMAS Thematic Conference on Smart Structures and Materials
SMART 2017
A. Güemes, A. Benjeddou, J. Rodellar and J. Leng (Eds)

SOME HOMOGENIZATION MODELS OF NANOSIZED PIEZOELECTRIC COMPOSITE MATERIALS OF TYPES CERAMICS PORES AND CERAMICS CERAMICS WITH SURFACE EFFECTS

ANDREY V. NASEDKIN

Institute of Mathematics, Mechanics and Computer Science
Southern Federal University
Miltchakova str., 8a,, 344090 Rostov-on-Don, Russia
e-mail: nasedkin@math.sfedu.ru

Key words: Piezoelectricity, Nanomechanics, Surface Effect, Gurtin–Murdoch Model, Porous Piezoelectric Composite, Nanosized Inclusion, Effective Moduli, Finite Element Method

Abstract. The paper presents mathematical and computer modelling of effective properties of two-phase composite piezoelectric materials of types piezoceramics - pores or piezoceramics - ceramics (inclusions) with a nanoscale random structure of porosity or inclusions. This integrated approach includes the effective moduli method of composite mechanics, the simulation of representative volumes with stochastic porosity or inclusions and the finite element method. In order to take into account nanoscale sizes of pores or inclusions, the generalized Gurtin-Murdoch model of coupled surface effects is used at the borders between material and pores or inclusions. The common methodology for determination of effective mechanical properties of piezoelectric composites is produced for a two-phase bulk (mixture) composite with special conditions for stresses and electric flux discontinuities at the phase interfaces. The mathematical statements of boundary value problems and the resulting formulas to determine the complete set of effective stiffness moduli, piezomoduli and dielectric permittivities of the two-phase composites with arbitrary anisotropy and with coupled surface effects are described; the generalized problem definitions are formulated and the finite element approximations are given. It is noted, that the homogenization procedures for porous composites with surface effects can be considered as special cases of the corresponding procedures for the two-phase composites with interphase boundaries if the moduli of the second phase (nanoinclusions) are negligibly small. These approaches have been implemented in the finite element package ANSYS. Model of representative volume was built in the form of a cube, evenly divided into cubic solid finite elements, some of which had been declared as pores or inclusions. Coupled surface effects on the boundaries between principal material and pores or inclusions were modeled by special quasi-shell piezoelectric finite elements. It has been noted that the magnitude of the area of the interphase boundaries has influence on the effective moduli of the composite materials with nanosized stochastic structure of pores or inclusions.

1 INTRODUCTION

Piezoelectric composite materials are widely used for the manufacture of high-tech devices for medical diagnostics and therapy, hydroacoustics, nondestructive testing and diagnostics, level and flow metering, consumer, automotive, biomedical and aerospace industries. Rapidly growing demand for efficiency, reliability and cost constantly stimulates the development of new and improved materials, devices and systems. The analysis shows that the properties of the electrically active material remain the limiting factor in the development of more effective piezoelectric transducers and devices. The simulation and experimental studies of electrically active materials at various scale levels help to enhance the technologies of directed changing of the properties of these materials and provide a qualitative improvement of their characteristics. The developed in the recent years new nanostructured piezoelectric composite materials have a range of important advantages, such as the possibilities of controllable variation of the functional characteristics within a wide range, the ultra-low mechanical quality factor, the large electromechanical anisotropy, the giant dielectric relaxation, and the electrocaloric and piezoelectric effects.

Furthermore, it should be noted that the modeling of micro- and nanomaterials and devices has some specific features. It is known that a range of nanomaterials have abnormal mechanical properties that considerably differ from the properties of ordinary macrosized bodies. Thus, the experimentally observed fact is the increasing of the stiffness with reducing the sizes of nanoobjects. One of the factors that are responsible for this behavior of nanomaterials can be surface effects. As research of the recent years shows, for the bodies of submicro- and nanosizes the surface stresses play an important role and influence the deformation of the bodies in general. In connection to this, the actual problem can be an extension of this approach to the nanoscale elements of piezoelectric composite materials [2, 9, 18, 19, 20]. Therefore, here it is logical to consider not only the mechanical surface effects, but also for the surface effects for electric fields.

Theoretical investigations of piezoelectric and magnetoelectric nanosized materials with surface effects and imperfect interface models were presented in [2, 3, 4, 6, 7, 8, 13, 18]. Formulae for the effective shear modulus of a fiber reinforced piezoelectric composite was obtained in [22] using a self-consistent method. Investigations of effective moduli for nanoisized piezoelectric composites were continued in [1, 5, 10, 21, 22, 23] and etc.

In present investigation the models of two-phase piezoelectric composite materials of types ceramics – pores and ceramics – ceramics account for their internal microstructure were developed in the framework of classic continuum approaches of solid mechanics and methods of composite mechanics. These models were used to construct new models of the micro- and nanosized bodies made of piezoelectric materials that were additionally take into account the surface effects and interphase boundary conditions.

We use an integrated approach to the determination of the material properties of nanoscale piezoelecrtric bulk (mixture) stochastically distributed composites with account for their internal microstructure. In order to take into account nanoscale level at the borders between material and pores or between two materials, the generalized Gurtin-Murdoch model of surface effects [3, 11] are used. ANSYS finite element package was used to simulate representative volumes and to calculate the effective moduli. This approach is based on the theory of effective moduli of composite mechanics, modeling of representative volumes and the finite element method. Here, the contact boundaries between material and pores or between two materials were covered by

the surface quasi-shell elements in order to take the surface effects into account.

2 EFFECTIVE MODULI METHOD FOR HOMOGENIZATION OF PIEZOELECTRIC MIXED TWO-PHASE NANOCOMPOSITES

Let Ω be a representative volume of piezoelectric two-phase composite body with nanodimensional pores or inclusions; $\Omega = \Omega^{(1)} \cup \Omega^{(2)}$; $\Omega^{(1)}$ is the volume occupied by the main piezoelectric materials of the first phase (matrix); $\Omega^{(2)}$ is the set of the volumes occupied by the materials of the second phase (pores or inclusions); $\Gamma = \partial\Omega$ is the external boundary of the volume Ω; Γ^s is the set of frontier surfaces of materials with different phases ($\Gamma^s = \partial\Omega^{(1)} \cap \partial\Omega^{(2)}$); $\boldsymbol{\nu}$ is the external unit normal vector to the boundary, outward with respect to the region $\Omega^{(1)}$ occupied by the material of the matrix; $\mathbf{x} = \{x_1, x_2, x_3\}$ is the vector of the spacial coordinates. We assume that the volumes $\Omega^{(1)}$ and $\Omega^{(2)}$ are filled with different piezoelectric materials. Then in the framework of linear static theory of piezoelectricity we have the following system of differential equations in vector-matrix symbols

$$\mathbf{L}^*(\nabla) \cdot \mathbf{T} = 0, \quad \nabla^* \cdot \mathbf{D} = 0\,, \tag{1}$$

$$\mathbf{T} = \mathbf{c} \cdot \mathbf{S} - \mathbf{e}^* \cdot \mathbf{E}, \quad \mathbf{D} = \mathbf{e} \cdot \mathbf{S} + \boldsymbol{\kappa} \cdot \mathbf{E}\,, \tag{2}$$

$$\mathbf{S} = \mathbf{L}(\nabla) \cdot \mathbf{u}\,, \quad \mathbf{E} = -\nabla\varphi\,, \tag{3}$$

where

$$\mathbf{L}^*(\nabla) = \begin{bmatrix} \partial_1 & 0 & 0 & 0 & \partial_3 & \partial_2 \\ 0 & \partial_2 & 0 & \partial_3 & 0 & \partial_1 \\ 0 & 0 & \partial_3 & \partial_2 & \partial_1 & 0 \end{bmatrix}, \quad \nabla = \begin{Bmatrix} \partial_1 \\ \partial_2 \\ \partial_3 \end{Bmatrix}, \tag{4}$$

$\mathbf{T} = \{\sigma_{11}, \sigma_{22}, \sigma_{33}, \sigma_{23}, \sigma_{13}, \sigma_{12}\}$ is the stress array; $\mathbf{S} = \{\varepsilon_{11},\ \varepsilon_{22},\ \varepsilon_{33},\ 2\varepsilon_{23},\ 2\varepsilon_{13},\ 2\varepsilon_{12}\}$ is the strain array; $\mathbf{D}$ and $\mathbf{E}$ are the electric flux density vector or the electric displacement vector and the electric field vector; $\mathbf{c} = \mathbf{c}^E$ is the 6×6 matrix of elastic stiffness moduli; $\mathbf{e}$ is the 3×6 matrix of piezoelectric moduli; $\boldsymbol{\kappa} = \boldsymbol{\kappa}^S = \boldsymbol{\epsilon}^S$ is the 3×3 matrix of dielectric permittivity moduli; $(...)^*$ is the transpose operation; and $(...)\cdot(...)$ is the scalar product operation.

For nanosized interphase boundaries we assume that on Γ^s the surface stress and surface electric flux exist. For these quantities we accept the Gurtin–Murdoch model:

$$\mathbf{L}^*(\mathbf{n}) \cdot [\mathbf{T}] = \mathbf{L}^*(\nabla^s) \cdot \mathbf{T}^s, \quad \mathbf{n} \cdot \mathbf{D} = \nabla^s \cdot \mathbf{D}^s, \quad \mathbf{x} \in \Gamma^s\,, \tag{5}$$

where $[\mathbf{T}] = \mathbf{T}^{(1)} - \mathbf{T}^{(2)}$; $[\mathbf{D}] = \mathbf{D}^{(1)} - \mathbf{D}^{(2)}$; ∇^s is the surface gradient operator, associated with nabla-operator by the formula $\nabla^s = \nabla - \mathbf{n}(\partial/\partial r)$, where r is the coordinate, measured by the normal Γ^s; $\mathbf{T}^s = \{\sigma^s_{11}, \sigma^s_{22}, \sigma^s_{33}, \sigma^s_{23}, \sigma^s_{13}, \sigma^s_{12}\}$ is the array of surface stresses σ^s_{ij}; $\mathbf{D}^s$ is the surface electric flux density vector.

For surface stress $\mathbf{T}^s$ and surface electric flux $\mathbf{D}^s$ in general case we take the coupled constitutive relations

$$\mathbf{T}^s = \mathbf{c}^s \cdot \mathbf{S}^s - \mathbf{e}^{s*} \cdot \mathbf{E}^s\,, \tag{6}$$

$$\mathbf{D}^s = \mathbf{e}^s \cdot \mathbf{S}^s + \boldsymbol{\kappa}^s \cdot \mathbf{E}^s\,, \tag{7}$$

where

$$\mathbf{S}^s = \mathbf{L}(\nabla^s) \cdot \mathbf{u}^s, \quad \mathbf{u}^s = \mathbf{A} \cdot \mathbf{u}, \quad \mathbf{A} = \mathbf{I} - \mathbf{nn}^*, \quad \mathbf{E}^s = -\nabla^s \varphi\,, \tag{8}$$

$\mathbf{I}$ is the identity matrix; $\mathbf{c}^s$, $\mathbf{e}^s$, $\boldsymbol{\kappa}^s$ are the surface tensors of elastic stiffness moduli, piezoelectric moduli and dielectric permittivity moduli, respectively.

We suppose that the matrix of surface material moduli have the similar properties that the matrix of volume material moduli, but relatively to surface strains $\mathbf{S}^s$ and surface electric field vector $\mathbf{E}^s$, i.e. $c^s_{\alpha\beta} = c^s_{\beta\alpha}$, $\kappa^s_{kl} = \kappa^s_{lk}$, and surface energy is positive definiteness ($\forall\ \varepsilon^s_{ij} = \varepsilon^s_{ji}$, $\mathbf{E}^s$), $\exists\, W_\Gamma > 0$:

$$\mathbf{S}^{s*} \cdot \mathbf{c}^s \cdot \mathbf{S}^s + \mathbf{E}^{s*} \cdot \boldsymbol{\kappa}^s \cdot \mathbf{E}^s \geq W_\Gamma \mathbf{S}^{s*} \cdot \mathbf{S}^s + \mathbf{E}^{s*} \cdot \mathbf{E}^s)\,.$$

Setting the appropriate boundary conditions at $\Gamma = \partial\Omega$, we can find the solutions of the problems (1)–(8) for heterogeneous medium in the representative volume Ω. Then the comparison of the solution characteristics averaged over Ω (such as stresses, electric flux densities, etc.) with analogous values for homogeneous comparison medium will permit to determine the effective moduli for the composite material. We note that for piezoelectric media in order to determine the full set of the effective moduli it is necessary to solve several problems of the considered types for different boundary conditions.

Here the main difficulties consist in the choice of the representative volume and boundary problems for the heterogeneous medium and the comparison medium, as well as the technologies for solving the problems for heterogeneous media. According to the previously developed methods of modeling the piezoelectric composite materials of ordinary sizes [12, 17], we consider analogous approaches for the problems of piezoelectricity with surface effects.

For piezoelectric homogeneous comparison medium we adopt that the same equations (1)–(8) are satisfied with constant effective moduli $\mathbf{c}^{\,\mathrm{eff}}$, $\mathbf{e}^{\,\mathrm{eff}}$ and $\boldsymbol{\kappa}^{\,\mathrm{eff}}$, which are to be determined.

For determination of the effective moduli let us assume that at the boundary Γ the following boundary conditions take place

$$\mathbf{u} = \mathbf{L}^*(\mathbf{x}) \cdot \mathbf{S}_0, \quad \varphi = -\mathbf{x} \cdot \mathbf{E}_0, \quad \mathbf{x} \in \Gamma\,, \tag{9}$$

where $\mathbf{S}_0 = \{\varepsilon_{011}, \varepsilon_{022}, \varepsilon_{033}, 2\varepsilon_{023}, 2\varepsilon_{013}, 2\varepsilon_{012}\}$; $\mathbf{E}_0 = \{E_{01}, E_{02}, E_{03}\}$; ε_{0ij}, E_{0j} are some values that do not depend on $\mathbf{x}$. Then $\mathbf{u} = \mathbf{L}^*(\mathbf{x}) \cdot \mathbf{S}_0$, $\mathbf{S} = \mathbf{S}_0$, $\varphi = \varphi_0$, $\mathbf{T} = \mathbf{T}_0 = \mathbf{c}^{\,\mathrm{eff}} \cdot \mathbf{S}_0 - \mathbf{e}^{\,\mathrm{eff}*} \cdot \mathbf{E}_0$, $\mathbf{D}_0 = \mathbf{e}^{\,\mathrm{eff}} \cdot \mathbf{S}_0 + \boldsymbol{\kappa}^{\,\mathrm{eff}} \cdot \mathbf{E}_0$ will give the solution for the problem (1)–(9) in the volume Ω for the homogeneous comparison medium.

Let us solve now problem (1)–(9) for heterogeneous medium and assume that for this medium and for the comparison medium the averaged stresses and electric flux densities are equal $\langle\sigma_{ij}\rangle = \langle\sigma_{0ij}\rangle$, $\langle D_j\rangle = \langle D_{0j}\rangle$, where hereinafter the angle brackets $\langle(...)\rangle$ denote the averaged by the volume Ω and by the surfaces Γ^s values

$$\langle(...)\rangle = \frac{1}{|\Omega|}\Big(\int_\Omega (...)\, d\Omega + \int_{\Gamma^s} (...)^s\, d\Gamma\Big)\,. \tag{10}$$

Therefore we obtain that for the effective moduli of the composite the equations $\mathbf{T}_0 = \mathbf{c}^{\,\mathrm{eff}} \cdot \mathbf{S}_0 - \mathbf{e}^{\,\mathrm{eff}*} \cdot \mathbf{E}_0 = \langle\mathbf{T}\rangle$, $\mathbf{D}_0 = \mathbf{e}^{\,\mathrm{eff}} \cdot \mathbf{S}_0 + \boldsymbol{\kappa}^{\,\mathrm{eff}} \cdot \mathbf{E}_0 = \langle\mathbf{D}\rangle$ are satisfied, where $\mathbf{S}_0$ and $\mathbf{E}_0$ are the given values from the boundary conditions (9). Hence, even in the assumption of the anisotropy

of the general form for the comparison medium, all the stiffness moduli $c_{\alpha\zeta}^{eff}$, piezomoduli $e_{i\zeta}^{\text{eff}}$ and dielectric permittivity moduli κ_{ij}^{eff} can be computed.

Indeed, setting in (9) $\mathbf{S}_0 = \varepsilon_0 \mathbf{h}_\zeta$, $\varepsilon_0 = \text{const}$, $\mathbf{E}_0 = 0$, where ζ is some fixed index mark ($\mathbf{h}_\zeta$ is the vector from six-dimensional basic set for the components for strain tensor basic set; $\mathbf{h}_j = \mathbf{e}_j\mathbf{e}_j$, $j = 1,2,3$; $\mathbf{h}_4 = (\mathbf{e}_2\mathbf{e}_3 + \mathbf{e}_3\mathbf{e}_2)/2$; $\mathbf{h}_5 = (\mathbf{e}_1\mathbf{e}_3 + \mathbf{e}_3\mathbf{e}_1)/2$; $\mathbf{h}_6 = (\mathbf{e}_1\mathbf{e}_2 + \mathbf{e}_2\mathbf{e}_1)/2$; $\mathbf{e}_j$ are the orts of the Cartesian coordinate system), from the solution of the boundary problem (1)–(9) we get the computation formulas for the elastic moduli $c_{\alpha\zeta}^{\text{eff}}$ and the piezomoduli $e_{i\zeta}^{\text{eff}}$:

$$\mathbf{S}_0 = \varepsilon_0 \mathbf{h}_\zeta,\ \mathbf{E}_0 = 0 \ \Rightarrow\ c_{\alpha\zeta}^{\text{eff}} = \langle T_\alpha \rangle / \varepsilon_0,\ e_{j\zeta}^{\text{eff}} = \langle D_j \rangle / \varepsilon_0,\ \alpha, \zeta = 1, 2, ..., 6,\ j = 1, 2, 3\,. \quad (11)$$

If in (9) we set $\mathbf{S}_0 = 0$, $\mathbf{E}_0 = E_0 \mathbf{e}_j$, $E_0 = \text{const}$, than from the boundary problem (1)–(9) the piezomoduli $e_{j\zeta}^{\text{eff}}$ and the dielectric permittivity moduli κ_{ij}^{eff} can be obtained:

$$\mathbf{S}_0 = 0,\ \mathbf{E}_0 = E_0 \mathbf{e}_j \ \Rightarrow\ e_{j\alpha}^{\text{eff}} = -\langle T_\alpha \rangle / E_0,\ \kappa_{ij}^{\text{eff}} = \langle D_i \rangle / E_0,\ \alpha = 1, 2, ..., 6,\ i, j = 1, 2, 3\,. \quad (12)$$

Note that the boundary value problems (1)–(9) differ from the usual problems of linear piezoelectricity by the presence of the interface boundary conditions (5)–(8) and average quantities (10) which are typical for the Gurtin–Murdoch model of surface stresses and the model of surface piezoelectricity for nanosized bodies.

3 WEAK STATEMENTS

For the numerical solution of the problems (1)–(9) we derive their weak or generalized statements. Previously we introduce the space of the functions θ and the vector functions $\mathbf{u}$, defined on Ω.

On the set of vector functions $\mathbf{u} \in C^1$ which satisfy the first homogeneous boundary condition (9), i.e. $\mathbf{u} = 0$ on Γ, we introduce the scalar product

$$(\mathbf{v}, \mathbf{u})_{H_u^1} = \int_\Omega \mathbf{S}(\mathbf{v})^* \cdot \mathbf{S}(\mathbf{u})\, d\Omega + \int_{\Gamma^s} \mathbf{S}^s(\mathbf{v})^* \cdot \mathbf{S}^s(\mathbf{u})\, d\Gamma\,.$$

The closure of this set of vector functions $\mathbf{u}$ in the norm generated by the indicated scalar product will be denoted by H_u^1.

For functions $\varphi \in C^1$ which satisfy second homogeneous boundary condition (9), i.e. $\varphi = 0$ on Γ, we introduce the scalar product

$$(\eta, \varphi)_{H_\varphi^1} = \int_\Omega \mathbf{E}^*(\eta) \cdot \mathbf{E}(\varphi)\, d\Omega + \int_{\Gamma^s} \mathbf{E}^{s*}(\eta) \cdot \mathbf{E}^s(\varphi)\, d\Gamma\,.$$

The closure of this set of functions φ in the norm generated by the indicated scalar product will be denoted by H_φ^1.

In order to formulate the generalized or weak solution we scalar multiply the first equations (1) by arbitrary vector function $\mathbf{v} \in H_u^1$, and we multiply the second equation (1) by some function $\eta \in H_\theta^1$. By integrating the obtained equations on Ω, and by using the standard technique of the integration by parts with Eqs. (1)–(8), we obtain the following integral relations

$$c(\mathbf{v}, \mathbf{u}) - e(\varphi, \mathbf{v}) = 0\,, \quad (13)$$

$$e(\eta, \mathbf{u}) + \kappa(\eta, \varphi) = 0\,, \quad (14)$$

where

$$c(\mathbf{v},\mathbf{u}) = c_\Omega(\mathbf{v},\mathbf{u}) + c_{\Gamma^s}(\mathbf{v},\mathbf{u}), \quad e(\varphi,\mathbf{v}) = e_\Omega(\varphi,\mathbf{v}) + e_{\Gamma^s}(\varphi,\mathbf{v}), \tag{15}$$

$$c_\Omega(\mathbf{v},\mathbf{u}) = \int_\Omega \mathbf{S}^*(\mathbf{v})\cdot\mathbf{c}\cdot\mathbf{S}(\mathbf{u})\,d\Omega, \quad c_{\Gamma^s}(\mathbf{v},\mathbf{u}) = \int_{\Gamma^s} \mathbf{S}^{s*}(\mathbf{v})\cdot\mathbf{c}^s\cdot\mathbf{S}^s(\mathbf{u})\,d\Gamma, \tag{16}$$

$$e_\Omega(\varphi,\mathbf{v}) = -\int_\Omega \mathbf{E}(\varphi)\cdot\mathbf{e}\cdot\mathbf{S}(\mathbf{v})\,d\Omega, \quad e_{\Gamma^s}(\varphi,\mathbf{v}) = -\int_{\Gamma^s} \mathbf{E}^s(\varphi)\cdot\mathbf{e}^s\cdot\mathbf{S}^s(\mathbf{v})\,d\Gamma, \tag{17}$$

$$\kappa(\eta,\varphi) = \kappa_\Omega(\eta,\varphi) + \kappa_{\Gamma^s}(\eta,\varphi), \tag{18}$$

$$\kappa_\Omega(\eta,\varphi) = \int_\Omega \mathbf{E}^*(\eta)\cdot\boldsymbol{\kappa}\cdot\mathbf{E}(\varphi)\,d\Omega, \quad \kappa_{\Gamma^s}(\eta,\varphi) = \int_{\Gamma^s} k^s_{ij}\mathbf{E}^{s*}(\eta)\cdot\boldsymbol{\kappa}\cdot\mathbf{E}^s(\varphi)\,d\Gamma. \tag{19}$$

Further, we present the solution $\{\mathbf{u},\,\varphi\}$ of the problem (1)–(9) in the form

$$\mathbf{u} = \mathbf{u}_d + \mathbf{u}_b, \quad \varphi = \varphi_d + \varphi_b, \tag{20}$$

where $\mathbf{u}_d$, φ_d satisfy homogeneous boundary mechanical and electric conditions and ad hoc fitted functions $\mathbf{u}_b$, φ_b satisfy the inhomogeneous boundary conditions on Γ, i.e.

$$\mathbf{u}_d = 0, \quad \varphi_d = 0, \quad \mathbf{u}_b = \mathbf{L}^*(\mathbf{x})\cdot\mathbf{S}_0, \quad \varphi_b = -\mathbf{x}\cdot\mathbf{E}_0, \quad \mathbf{x}\in\Gamma, \tag{21}$$

and therefore, $\mathbf{u}_d \in H^1_u$.

By using (20) we can rewrite equations (13), (14) in the form

$$c(\mathbf{v},\mathbf{u}_d) - e(\varphi_d,\mathbf{v}) = L_u(\mathbf{v}), \tag{22}$$

$$e(\eta,\mathbf{u}_d) + \kappa(\eta,\varphi_d) = L_\varphi(\eta), \tag{23}$$

where

$$L_u(\mathbf{v}) = -c(\mathbf{v},\mathbf{u}_b) + e(\varphi_b,\mathbf{v}), \quad L_\varphi(\eta) = -e(\eta,\mathbf{u}_b) - \kappa(\eta,\varphi_b). \tag{24}$$

Now we can define the generalized or weak solution of the static problem (1)–(9) of piezoelectricity with interphase boundaries using introduced functional space. Namely, the functions $\{\mathbf{u},\,\varphi\}$ in the form (20), (21) are the weak solution of the problem (1)–(9), if equations (22), (23) with (15)–(19), (24) are satisfied for $\forall\,\mathbf{v}\in H^1_u$, $\eta\in H^1_\theta$.

So far we have been discussing the two-phase piezoelectric composites. However, we can note that the presented models also describe homogenization procedures for porous piezoelectric composites with surface internal effects, if we put the stiffness and piezoelectric moduli negligible, and set the dielectric permittivity moduli equal to the dielectric permittivity of air.

4 FINITE ELEMENT SOLUTION

For solving problems (22), (23) for piezoelectri body with surface effects in weak forms we will use classical finite element approximation techniques. Let Ω_h be a region of the corresponding finite element mesh composed of volume elements, $\Omega_h \approx \Omega$, $\Omega_h = \Omega^{(1)}_h \cup \Omega^{(2)}_h$, $\Omega^{(j)}_h \approx \Omega^{(j)}$, $\Omega_h = \cup_k \Omega_{ek}$, where Ω_{ek} is a separate volume finite element with number k. Let also Γ^s_h be a finite element mesh of surface elements conformable with the volume mesh Ω_h, $\Gamma^s_h = \partial\Omega^{(1)}_h \cap \partial\Omega^{(2)}_h$, $\Gamma^s_h \approx \Gamma^s$, $\Gamma^s_h = \cup_m \Gamma^s_{em}$, Γ^s_{em} is a separate surface finite element with number m, and the elements Γ^s_{em} are the faces of the suitable volume elements Ω_{ek} located on the interface boundaries.

We will use the classic Lagrangian or serendipity volume finite elements with nodal degrees of freedom of displacements and electric potential. Note that due to the structure of surface mechanical and electric fields (6)–(8), for the elements Γ^s_{em} we can use special piezoelectric shell or plate elements only with nodal degrees of freedom of displacements and electric potential. For these elements we can take a fictitious unit thickness so that the surface moduli from (6), (7) can be determined by the product of specially defined volume moduli and shell thickness.

On these finite element meshes we will find the approximation to the weak solutions $\{\mathbf{u}_h \approx \mathbf{u}, \varphi_h \approx \varphi\}$ for static piezoelectric problem in the form

$$\mathbf{u}_h(\mathbf{x}) = \mathbf{N}^*_u(\mathbf{x}) \cdot \mathbf{U}, \quad \varphi_h(\mathbf{x}) = \mathbf{N}^*_\varphi(\mathbf{x}) \cdot \mathbf{\Phi}\,, \tag{25}$$

where $\mathbf{N}^*_u$ is the matrix of the shape functions for displacements, $\mathbf{N}^*_\varphi$ is the row vector of the shape functions for electric potential, $\mathbf{U}$, $\mathbf{\Phi}$ are the global vectors of nodal displacements and electric potential, respectively. Here, the surface shape functions are the reduction on the boundaries Γ^s_h of the volume shape functions.

According to conventional finite element technique, we approximate the continuous weak formulations of the piezoelectric problems by the corresponding problems in finite-dimensional spaces. Substituting (25) and similar representations for projection functions into integral relations (22), (23) for Ω_h, we obtain the following finite element system

$$\mathbf{K}_{uu} \cdot \mathbf{U} + \mathbf{K}_{u\varphi} \cdot \mathbf{\Phi} = 0\,, \tag{26}$$

$$-\mathbf{K}^*_{u\varphi} \cdot \mathbf{U} + \mathbf{K}_{\varphi\varphi} \cdot \mathbf{\Phi} = 0\,, \tag{27}$$

where

$$\mathbf{K}_{uu} = \mathbf{K}_{uu\,\Omega} + \mathbf{K}_{uu\Gamma}, \quad \mathbf{K}_{u\varphi} = \mathbf{K}_{u\varphi\,\Omega} + \mathbf{K}_{u\varphi\,\Gamma}, \quad \mathbf{K}_{\varphi\varphi} = \mathbf{K}_{\varphi\varphi\,\Omega} + \mathbf{K}_{\varphi\varphi\,\Gamma}\,, \tag{28}$$

$$\mathbf{K}_{uu\Omega} = \int_{\Omega_h} \mathbf{B}^*_u \cdot \mathbf{c} \cdot \mathbf{B}_u \, d\Omega, \quad \mathbf{K}_{uu\Gamma} = \int_{\Gamma^s_h} \mathbf{B}^{s*}_u \cdot \mathbf{c}^s \cdot \mathbf{B}^s_u \, d\,\Gamma\,, \tag{29}$$

$$\mathbf{K}_{u\varphi\,\Omega} = \int_{\Omega_h} \mathbf{B}^*_u \cdot \mathbf{e}^* \cdot \mathbf{B}_\varphi \, d\Omega, \quad \mathbf{K}_{u\varphi\,\Gamma} = \int_{\Gamma^s_h} \mathbf{B}^{s*}_u \cdot \mathbf{e}^{s*} \cdot \mathbf{B}^s_\varphi \, d\Gamma\,, \tag{30}$$

$$\mathbf{K}_{\varphi\varphi\,\Omega} = \int_{\Omega_h} \mathbf{B}^*_\varphi \cdot \boldsymbol{\kappa} \cdot \mathbf{B}_\varphi \, d\Omega, \quad \mathbf{K}_{\varphi\varphi\,\Gamma} = \int_{\Gamma^s_h} \mathbf{B}^{s*}_\varphi \cdot \boldsymbol{\kappa}^s \cdot \mathbf{B}^s_\varphi \, d\,\Gamma, \,, \tag{31}$$

$$\mathbf{B}^{(s)}_u = \mathbf{L}^{(s)*}(\nabla) \cdot \mathbf{A} \cdot \mathbf{N}^*_u, \quad \mathbf{B}^{(s)}_\varphi = \nabla^{(s)} \mathbf{N}^*_\varphi\,. \tag{32}$$

We note that in (28)–(32) the stiffness matrix $\mathbf{K}_{uu\,\Omega}$ is formed in the same way as for purely elastic body, and the matrices $\mathbf{K}_{u\varphi\,\Omega}$, $\mathbf{K}_{\varphi\varphi\,\Omega}$ are identical to the corresponding matrices for piezoelectric bodies. The matrices $\mathbf{K}_{\Gamma uu}$, $\mathbf{K}_{\Gamma u\varphi}$ and $\mathbf{K}_{\Gamma\varphi\varphi}$ are defined by the surface mechanical, piezoelectric and dielectric effects. The matrix $\mathbf{K}_{uu\,\Gamma}$ is analogous to the stiffness matrix for surface elastic membranes and the matrix $\mathbf{K}_{\varphi\varphi\,\Gamma}$ is the matrix of dielectric permittivities for surface dielectric films. Hence, for implementing the finite element piezoelectric analysis for the bodies with surface effects it is necessary to have surface piezoelectric elements with structural membrane option along with ordinary solid piezoelectric finite elements.

Also, we can represent the finite element solutions in the another variants considering the main boundary conditions: $\mathbf{u}_h = \mathbf{u}_{dh} + \mathbf{u}_{bh}$, $\varphi_h = \varphi_{dh} + \varphi_{bh}$, $\mathbf{u}_{dh} \approx \mathbf{u}_d$, $\mathbf{u}_{dh} = \mathbf{N}^*_{ud} \cdot \mathbf{U}_d$, $\mathbf{u}_{bh} \approx \mathbf{u}_b$,

$\mathbf{u}_{bh} = \mathbf{N}^*_{ub} \cdot \mathbf{U}_b$, $\varphi_{dh} \approx \varphi_d$, $\varphi_{dh} = \mathbf{N}^*_{\varphi d} \cdot \mathbf{\Phi}_d$, $\varphi_{bh} \approx \varphi_b$, $\varphi_{bh} = \mathbf{N}^*_{\varphi b} \cdot \mathbf{\Phi}_b$, $\mathbf{N}_u = \{\mathbf{N}_{ud}, \mathbf{N}_{ub}\}$, $\mathbf{N}_\varphi = \{\mathbf{N}_{\varphi d}, \mathbf{N}_{\varphi b}\}$,

$$\mathbf{K}_{uu} = \begin{bmatrix} \mathbf{K}^{dd}_{uu} & \mathbf{K}^{db}_{uu} \\ \mathbf{K}^{bd}_{uu} & \mathbf{K}^{bb}_{uu} \end{bmatrix}, \quad \mathbf{K}_{u\varphi} = \begin{bmatrix} \mathbf{K}^{dd}_{u\varphi} & \mathbf{K}^{db}_{u\varphi} \\ \mathbf{K}^{bd}_{u\varphi} & \mathbf{K}^{bb}_{u\varphi} \end{bmatrix}, \quad \mathbf{K}_{\varphi\varphi} = \begin{bmatrix} \mathbf{K}^{dd}_{\varphi\varphi} & \mathbf{K}^{db}_{\varphi\varphi} \\ \mathbf{K}^{bd}_{\varphi\varphi} & \mathbf{K}^{bb}_{\varphi\varphi} \end{bmatrix},$$

$$\mathbf{U} = \begin{Bmatrix} \mathbf{U}_d \\ \mathbf{U}_b \end{Bmatrix}, \quad \mathbf{\Phi} = \begin{Bmatrix} \mathbf{\Phi}_d \\ \mathbf{\Phi}_b \end{Bmatrix},$$

where $\mathbf{U}_b$, $\mathbf{\Phi}_b$ are the vectors, known from the main boundary conditions.

So, after using these expressions we can transform equations (26), (27) for the piezoelectric problem with interface bondaries in the form

$$\mathbf{K}^{dd}_{uu} \cdot \mathbf{U}_d + \mathbf{K}^{dd}_{u\varphi} \cdot \mathbf{\Phi}_d = \mathbf{F}^d_u\,, \tag{33}$$

$$-\mathbf{K}^{dd*}_{u\varphi} \cdot \mathbf{U}_d + \mathbf{K}^{dd}_{\varphi\varphi} \cdot \mathbf{\Phi}_d = \mathbf{F}^d_\varphi\,, \tag{34}$$

where

$$\mathbf{F}^d_u = -\mathbf{K}^{db}_{uu} \cdot \mathbf{U}_b - \mathbf{K}^{db}_{u\varphi} \cdot \mathbf{\Phi}_b\,,$$
$$\mathbf{F}^d_\varphi = \mathbf{K}^{db*}_{u\varphi} \cdot \mathbf{U}_b - \mathbf{K}^{db}_{\varphi\varphi} \cdot \mathbf{\Phi}_b\,.$$

Thus, the homogenizing problems for piezoelectric composite with interface boundaries can be solved by finite element approaches. The resulting finite element systems (33), (34) differ from similar systems for the bodies of usual sizes by the matrices $\mathbf{K}_{uu\,\Gamma}$, $\mathbf{K}_{u\varphi\,\Gamma}$, $\mathbf{K}_{\varphi\varphi\,\Gamma}$ in (28)–(31). These matrices arise due to the surface mechanical, piezoelectric and dielectric effects.

5 DISCUSSION AND CONCLUSION

For automated coating of internal boundaries of pores or inclusions in the cubic representative volume the following algorithm for finite element package ANSYS was used similarly [15, 16]. At the beginning, as a result of the formation of the structure of pores or inclusions, the finite element mesh from octanodal cubic elements was created, some of which had the material properties of primary piezoelectric material, and the other part of the elements had the material properties of the pores or inclusions. Further, only the finite elements with primary piezoelectric material properties were selected. The resulting elements on the outer boundaries were covered by four nodal target contact elements. Then, the contact elements, which were located on the external surfaces of the full representative volume, were removed, and the remaining contact elements were replaced by the octanodal quasi-shell elements with one edge on the interface bondaries. As a result, all the facets of the contact of piezoelectric structural elements with pores or inclusions were coated by quasi-shell elements imitating piezoelectric membrane finite elements. For imitation of membrane finite elements we coupled degrees of freedom located on the interface edges with corresponding degrees of freedom located on the contrary edges.

The next step consisted in solving the static problems for obtained representative volume with the main boundary conditions which were conventional for effective moduli method.

In the case of porous piezoceramics of $6mm$ class, in order to find its ten independent effective constants ($c^{E\,\mathrm{eff}}_{11}$, $c^{E\,\mathrm{eff}}_{12}$, $c^{E\,\mathrm{eff}}_{13}$, $c^{E\,\mathrm{eff}}_{33}$, $c^{E\,\mathrm{eff}}_{44}$, e^{eff}_{31}, e^{eff}_{33}, e^{eff}_{15}, $\epsilon^{S\,\mathrm{eff}}_{11}$, $\epsilon^{S\,\mathrm{eff}}_{33}$), following (11), (12) it is enough to solve five static problems (1)–(9) with various values of $\mathbf{S}_0$ and $\mathbf{E}_0$, having set one of

the component $S_{0\beta}$, E_{0k} ($\beta = 1, 2, ..., 6$; $k = 1, 2, 3$) in the boundary conditions (9) not equal to zero:

$$\text{I)}\ \ S_\beta = \varepsilon_0\delta_{1\beta},\ \mathbf{E}_0 = 0\ \Rightarrow\ c_{1j}^{E\,\text{eff}} = \langle\sigma_{jj}\rangle/\varepsilon_0,\ j = 1,2,3,\ e_{31}^{\text{eff}} = \langle D_3\rangle/\varepsilon_0\,,$$

$$\text{II)}\ S_\beta = \varepsilon_0\delta_{3\beta},\ \mathbf{E}_0 = 0\ \Rightarrow\ c_{j3}^{E\,\text{eff}} = \langle\sigma_{jj}\rangle/\varepsilon_0,\ j = 1,2,3,\ e_{33}^{\text{eff}} = \langle D_3\rangle/\varepsilon_0\,,$$

$$\text{III)}\ S_\beta = \varepsilon_0\delta_{4\beta}, \mathbf{E}_0 = 0\ \Rightarrow\ c_{44}^{E\,\text{eff}} = \langle\sigma_{23}\rangle/\varepsilon_0,\ e_{15}^{\text{eff}} = \langle D_2\rangle/\varepsilon_0\,,$$

$$\text{IV)}\ \mathbf{S}_0 = 0,\ E_k = E_0\delta_{1k}\ \Rightarrow\ e_{15}^{\text{eff}} = -\langle\sigma_{13}\rangle/E_0,\ \epsilon_{11}^{S\,\text{eff}} = \langle D_1\rangle/E_0\,,$$

$$\text{V)}\ \mathbf{S}_0 = 0,\ E_k = E_0\delta_{3k}\ \Rightarrow\ e_{3j}^{\text{eff}} = -\langle\sigma_{jj}\rangle/E_0,\ j = 1,2,3,\ \epsilon_{33}^{S\,\text{eff}} = \langle D_3\rangle/E_0\,.$$

Further, in the ANSYS postprocessor the averaged stresses and electric fluxes were calculated, both on the volume finite elements and on the surface finite elements. Finally, the effective moduli of two-phase composite with surface effects were calculated from the corresponding formulas of the effective moduli method by using the estimated average characteristics.

In the results of computational experiments, the following features were observed [15, 16]. If we compare two similar bodies, one of which has usual dimensions and the other is a nanoscale body, then for the nanosized body due to the surface stresses the effective stiffness will be greater than for the body with usual sizes. Furthermore, for the porous body of the usual size the effective elastic stiffness decreases with increasing porosity. Meanwhile, the effective stiffness of nanocomposite porous body with the same porosity may either decrease or increase depending on the values of surface moduli, dimensions and number of pores. This effect is explained by the fact that the sizes of the surface pore with surface stresses depend not only on the overall porosity, but also on the configuration, size and number of pores. We can observe similarly but more differ effects for the effective piezomoduli and dielectric permittivity coefficients.

The described methodology could be also applied for mixed anisotropic nanostructured composites with other type of connectivity for different physic-mechanical fields, such as thermoelastic, poroelastic, magnetoelectric (magnetoelectroelastic) and other nanocomposites ([4, 6, 7, 8, 13, 14, 22, 23], etc.)

ACKNOWLEDGMENTS

This work was supported by grants 16-01-00785 of the Russian Foundation for Basic Research.

REFERENCES

[1] Chen, T. Exact size-dependent connections between effective moduli of fibrous piezoelectric nanocomposites with interface effects. *Acta Mech.* (2008) **196**:205–217.

[2] Dai, Sh., Gharbi, M., Sharma, P. and Park, H.S. Surface piezoelectricity: Size effects in nanostructures and the emergence of piezoelectricity in non-piezoelectric materials. *J. Appl. Phys.* (2011) **110**:104305-1–7.

[3] Eremeyev, V.A. and Nasedkin, A.V. Mathematical models and finite element approaches for nanosized piezoelectric bodies with uncoulped and coupled surface effects. *Methods of wave dynamics and mechanics of composites for analysis of microstructured materials and metamaterials*, Ed. M.A. Sumbatyan, *Advanced Structured Materials*, **59**. Springer, Singapore, 1–18 (2017).

[4] Eremeev, V.A. and Nasedkin, A.V. Natural vibrations of nanodimensional piezoelectric bodies with contact-type boundary conditions. *Mech. Solids.* (2015) **50**(5):495–507.

[5] Gu, S.-T., He, Q.C. and Pensée V. Homogenization of fibrous piezoelectric composites with general imperfect interfaces under anti-plane mechanical and in-plane electrical loadings. *Mech. Mater.* (2015) **88**:12–29.

[6] Gu, S.-T., Liu, J.-T. and He. Q.-C. Piezoelectric composites: Imperfect interface models, weak formulations and benchmark problems. *Comp. Mater. Sci.* (2014) **94**:182–190.

[7] Gu, S.-T., Liu, J.-T. and He. Q.-C. The strong and weak forms of a general imperfect interface model for linear coupled multifield phenomena. *Int. J. Eng. Sci.* (2014) **85**:31–46.

[8] Gu, S.-T. and Qin, L. Variational principles and size-dependent bounds for piezoelectric inhomogeneous materials with piezoelectric coherent imperfect interfaces. *Int. J. Eng. Sci.* (2014) **78**:89–102.

[9] Huang, G.Y. and Yu, S.W. Effect of surface piezoelectricity on the electromechanical behaviour of a piezoelectric ring. *Phys. Status Solidi B.* (2006) **243**(4):R22–R24.

[10] Malakooti, M.H. and Sodano, H.A. Multi-Inclusion modeling of multiphase piezoelectric composites. *Composites: Part B.* (2013) **47**:181–189.

[11] Nasedkin, A.V. Models and finite element approximations for interacting nanosized piezoelectric bodies and acoustic medium. *AIP Conf. Proc.* (2017) **1798**:020181-1–7.

[12] Nasedkin, A.V. Finite element design of piezoelectric and magnetoelectric composites by using symmetric saddle algorithms. *Advanced Materials – Studies and Applications*, Eds. I.A. Parinov, S.-H. Chang, S. Theerakulpisut, Nova Science Publ., NY, 109–124 (2015).

[13] Nasedkin, A.V. and Eremeyev, V.A. Harmonic vibrations of nanosized piezoelectric bodies with surface effects. *ZAMM.* (2014) **94**(10):878–892.

[14] Nasedkin, A.V. and Eremeyev, V.A. Some models for nanosized magnetoelectric bodies with surface effects. *Advanced Materials – Manufacturing, Physics, Mechanics and Applications*, Eds. I.A. Parinov, S.-H. Chang, V.Y. Topolov, *Springer Proceedings in Physics*, **175**. Springer, 373–391 (2016).

[15] Nasedkin A.V. and Kornievsky A.S. Finite element modeling and computer design of anisotropic elastic porous composites with surface. *Methods of wave dynamics and mechanics of composites for analysis of microstructured materials and metamaterials*, Ed. M.A. Sumbatyan, *Advanced Structured Materials*, **59**. Springer, Singapore, 107–122 (2017).

[16] Nasedkin, A.V., Nasedkina, A.A. and Kornievsky, A.S. Modeling of nanostructured porous thermoelastic composites with surface effects. *AIP Conf. Proc.* (2017) **1798**:020110-1–10.

[17] Nasedkin, A.V. and Shevtsova, M.S. Improved finite element approaches for modeling of porous piezocomposite materials with different connectivity. *Ferroelectrics and Superconductors: Properties and Applications*, Ed. I.A. Parinov. Nova Science Publ., NY, 231–254 (2011).

[18] Pan, X.H., Yu, S.W. and Feng, X.Q. A continuum theory of surface piezoelectricity for nanodielectrics. *Science China: Physics, Mechanics & Astronomy.* (2011) **54**(4):564–573.

[19] Park, H.S., Devel, M. and Wang, Z. A new multiscale formulation for the electromechanical behavior of nanomaterials. *Comput. Methods Appl. Mech. Engrg.* (2011) **200**:2447–2457.

[20] Wang, K.F., Wang, B.L. and Kitamura, T. A review on the application of modified continuum models in modeling and simulation of nanostructures. *Acta Mech. Sin.* (2016) **32**(1):83-100.

[21] Wang, Z., Zhu, J., Jin, X.Y., Chen, W.Q. and Zhang, Ch. Effective moduli of ellipsoidal particle reinforced piezoelectric composites with imperfect interfaces. *J. Mech. Phys. Solids.* (2014) **65**:138–156.

[22] Xiao, J.H., Xu, Y.L. and Zhang, F.C. Size-dependent effective electroelastic moduli of piezoelectric nanocomposites with interface effect. *Acta Mechanica.* (2011) **222**(1–2):59–67.

[23] Xiao, J.H., Xu, Y.L. and Zhang, F.C. Evaluation of effective electroelastic properties of piezoelectric coated nano-inclusion composites with interface effect under antiplane shear. *Int. J. Eng. Sci.* (2013) **69**:61–68.

VIBRATION SUPPRESSION OF PLATES BY OPTIMALLY CALIBRATED PIEZOELECTRIC RL SHUNT DAMPING

JOHAN TOFTEKÆR*, JAN HØGSBERG*, AYECH BENJEDDOU†+ AND STEEN KRENK*

*Department of Mechanical Engineering
Technical University of Denmark
Nils Koppels All, Building 404, DK-2800 Kgs. Lyngby, Denmark
e-mail: jotof@mek.dtu.dk, sk@mek.dtu.dk, jhg@mek.dtu.dk/

† Sorbonne Universités, Université de Technologie de Compiègne, CNRS, UMR 7337 ROBERVAL
Centre de Recherche Royallieu, CS 60319, 60203 Compiègne CEDEX, France
e-mail: ayech.benjeddou@utc.fr
+SUPMECA, 3 Rue Fernand Hainaut, 93407 Saint Ouen CEDEX, France
e-mail: benjeddou@supmeca.fr

Key words: RL Shunts, Piezoelectric damping, Structural dynamics, Resonant calibration

Abstract. A calibration procedure for suppression of plate vibrations by means of piezoelectric RL shunt damping is developed, in which the spill-over from non-resonant vibration modes is included by a quasi-dynamic modal correction, taking both flexibility and inertia effects from the residual modes into account. The procedure includes the 2D behaviour of a shunted piezoelectric patch, represented in a finite element model with Kirchhoff plate kinematics. The calibration based on the plate model is compared to previous results for beams, illustrating the 2D effect of the patch and the influence from transverse contraction by the Poisson's ratio. Finally, the ability to reproduce the desired level of attainable damping for a plate structure is demonstrated.

1 INTRODUCTION

The paper concerns suppression of plate vibrations by means of resonant piezoelectric shunt damping. Piezoelectric patches with orthotropic material properties attached locally on a plate are beneficial due to their fairly large force-to-deflection ratio, [1]. Hereby, mechanical energy is effectively converted into electrical energy, which can be dissipated in supplemental resonant shunts.

Piezoelectric vibration damping by a resonant inductive-resistive (RL) shunt was originally suggested by Forward [2] and subsequently developed by Hagood and von Flotow [3], who proposed two calibration procedures based on minimization of response amplitudes and maximization of the damping characteristics, respectively. A corresponding calibration procedure for the parallel RL shunt was subsequently proposed by Wu [4], arguing that the series shunt

would be inappropriate for a large resistance. The series and parallel configurations have been compared by Park and Inman [5], revealing a larger attainable energy dissipation using the parallel configuration, while a summary of the calibration procedures is provided by Caruso [6]. Several alternative procedures for calibration of RL shunts have since been proposed, for instance based on the H_∞-norm of the response amplitude [7]. Recently a calibration procedure based on simultaneous conditions on the dynamic amplification of the structural motion and the relative voltage amplitude of the shunt circuit has been proposed by Høgsberg and Krenk [8], using principles originally developed for the tuned mass damper by Krenk [9]. The procedure has since been extended to include the effect from the non-resonant modes of the structure, initially by a quasi-static correction [10] and subsequently by a quasi-dynamic flexibility and inertia correction [11, 12]. The performance of piezoelectric shunt damping relies on a precise calibration of the shunt frequency, in particular for transducers or patches located indirectly with respect to the deformation pattern of the targeted mode. Thus, the ability to account for the energy spill-over from the non-resonant modes is an important aspect in the calibration of shunt damping of flexible plate structures, with multiple and closely spaced modes.

In the present paper, the calibration procedure described in [12] and illustrated for simple one-dimensional piezoelectric strips on beams is applied to optimal calibration of RL-shunted piezoelectric patches for vibration suppression of plates. Only the parallel RL shunt is considered, while the results may be readily transferred to the corresponding series version. The plate displacements are approximated by a developed finite element model with Kirchhoff plate kinematics, while the piezoelectric patch displacements are considered mainly in-plane with a coupling to the rotations of the plate element. A thorough review of piezoelectric finite elements is provided By Benjeddou [13]. The ability to reproduce the desired level of attainable damping by an optimally calibrated piezoelectric shunt system is demonstrated for beam-like and plate structures. For the beam example, the results obtained with the present plate model are compared to previous results for beams, investigating the contributions from non-resonant modes and the influence of in-plane contraction from the Poisson's ratio effect.

2 MECHANICAL SYSTEM

The dynamics of the considered plate structure is represented by a finite element model based on a Kirchhoff plate element, while a bonded piezoelectric patch acts as external forces at the nodes of attachment. The equation of motion of adaptive the structure can be written as

$$\mathbf{M}\ddot{\mathbf{u}}(t) + \mathbf{K}_0\mathbf{u}(t) + \mathbf{W}\mathbf{f}(t) = \mathbf{f}_e(t) \tag{1}$$

with host structure mass and stiffness matrices $\mathbf{M}$, $\mathbf{K}_0$, patch connectivity matrix $\mathbf{W}$ and force vector $\mathbf{f}(t)$ and external load vector $\mathbf{f}_e(t)$. The degrees of freedom of the structural plate model are contained in the vector $\mathbf{u}(t)$, while structural damping is omitted in the present analysis.

2.1 Structural plate

The plate model is based on Kirchhoff the plate pure bending theory and is discretised by four-node rectangular finite elements. Thus, coupling with an assumed rectangular piezoelectric patch is straightforward. Element-wise Hermitian cubic interpolation is obtained by choosing suitable shape functions for three nodal degrees of freedom (dofs), represented by the lateral

displacement w, and the rotations ϕ_x and ϕ_y about the x- and y-axis, contained in the vector

$$\mathbf{u} = \begin{bmatrix} w_1 & \phi_{x1} & \phi_{y1} & w_2 & \phi_{x2} & \phi_{y2} & \cdots & w_n & \phi_{xn} & \phi_{yn} \end{bmatrix}^T \tag{2}$$

where n is the total node number. The chosen interpolation order must secure C^1 continuity between the elements, associated with second derivatives in the strain definitions. Based on the strains definitions and a weak form representation of the governing equations of motion, the mass matrix $\mathbf{M}$ and stiffness matrix $\mathbf{K}_0$ are obtained for the discretized plate structure.

2.2 Piezoelectric patch

The piezoelectric patch is considered as thin, whereby a simple plane stress assumption is valid, in which transverse stresses are omitted. Further, the electric field is homogeneous through the patch thickness, as the electrodes are evenly distributed on the upper and lower in-plane surfaces. Hereby, the electromechanical coupling between mechanical stresses and strains in an in-plane isotropic patch is governed by the piezoelectric constant e^*, contained in the vector

$$\mathbf{e}_3 = e^*\mathbf{b}, \quad \mathbf{b} = \begin{bmatrix} 1 & 1 & 0 \end{bmatrix}^T \tag{3}$$

The coupled constitutive equations for a 2D plane stress piezoelectric patch can be written as

$$\begin{bmatrix} \boldsymbol{\sigma}_p \\ D_3 \end{bmatrix} = \begin{bmatrix} \mathbf{D}_p & -\mathbf{e}_3 \\ \mathbf{e}_3^T & \varepsilon_{33}^* \end{bmatrix} \begin{bmatrix} \boldsymbol{\varepsilon}_p \\ E_3 \end{bmatrix}, \quad \mathbf{D}_p = \frac{E}{1-\nu^2} \begin{bmatrix} 1 & \nu & 0 \\ \nu & 1 & 0 \\ 0 & 0 & (1-\nu)/2 \end{bmatrix} \tag{4}$$

Here D_3 is the electric displacement, ε_{33}^* is the (blocked) dielectric constant in plane stress, $\boldsymbol{\sigma}_p$ and $\boldsymbol{\varepsilon}_p$ contain the three plane stresses and strains, ν is Poisson's ratio and E is the elastic modulus. The in-plane patch deformations neglect contributions from bending, whereby they can be discretized by four-node rectangular element with two nodal dofs, represented by the in-plane displacements u and v. Thus, the displacement vector for the patch can be arranged as

$$\mathbf{u}_p = \begin{bmatrix} u_1 & v_1 & u_2 & v_2 & u_3 & v_3 & u_4 & v_4 \end{bmatrix} \tag{5}$$

The strains in the patch are now obtained by the first derivatives of the linearly interpolated in-plane displacements. By suitable shape functions N_i in the strain interpolation matrix $\mathbf{B}_p$, the strains can be determined from the nodal displacements as

$$\boldsymbol{\varepsilon}_p = \begin{bmatrix} \varepsilon_{11} \\ \varepsilon_{22} \\ 2\varepsilon_{12} \end{bmatrix} = \mathbf{B}_p\mathbf{u}_p, \quad \mathbf{B}_p = \begin{bmatrix} \partial u/\partial x \\ \partial v/\partial y \\ \partial u/\partial y + \partial v/\partial x \end{bmatrix} \begin{bmatrix} N_1 & 0 & \cdots & N_4 & 0 \\ 0 & N_1 & \cdots & 0 & N_4 \end{bmatrix} \tag{6}$$

The finite element (FE) formulation is now obtained by the so-called weak form of the system of equations in (4), obtained by pre-multiplication with a test function $[\delta\mathbf{u}_p^T \ \delta V]$, followed by integration across the patch area A_p. This weak form equation can be written as

$$\int_{A_p} \begin{bmatrix} \delta\mathbf{u}_p^T & \delta V \end{bmatrix} \begin{bmatrix} \mathbf{B}_p^T\mathbf{D}_p\mathbf{B}_p & \mathbf{B}_p^T\mathbf{e}_3/t_p \\ -\mathbf{e}_3^T\mathbf{B}_p/t_p & \varepsilon_{33}^*/t_p^2 \end{bmatrix} \begin{bmatrix} \mathbf{u}_p \\ V \end{bmatrix} dA_p = \int_{A_p} \begin{bmatrix} \delta\mathbf{u}_p^T & \delta V \end{bmatrix} \begin{bmatrix} \mathbf{B}_p^T\boldsymbol{\sigma}_p \\ -D_3/t_p \end{bmatrix} dA_p \tag{7}$$

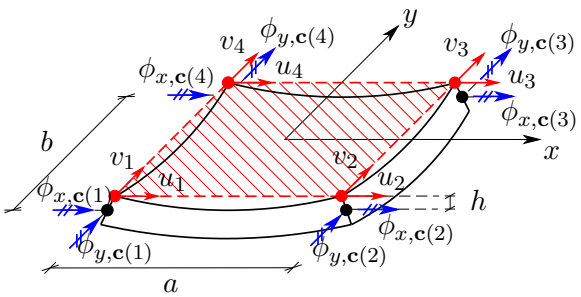

Figure 1: Connectivity between plate element and piezoelectric disk element

in which the electric field E_3 has been replaced by the voltage $V = -E_3 t_p$ across the electrodes. When evaluating the integral, the two coupled constitutive equations for the piezoelectric patch are obtained as

$$\mathbf{f} = \int_{A_p} \mathbf{B}_p^T \boldsymbol{\sigma} A_p = \mathbf{k}_p \mathbf{u}_p + \mathbf{T}_p^T \mathbf{b} k V \quad , \quad q = -D_3 A_p / t_p = -\theta \mathbf{b}^T \mathbf{T}_p \mathbf{u}_p + CV \tag{8}$$

where q is the charge. In these governing equations the piezoelectric element stiffness matrix $\mathbf{k}_p$, the integrated strain interpolation matrix $\mathbf{T}_p$, the electromechanical coupling coefficient θ and the capacitance C for blocked patch boundaries ($\mathbf{u}_p = \mathbf{0}$) have been introduced as

$$\mathbf{k}_p = \int_{A_p} \mathbf{B}_p^T \mathbf{D}_p \mathbf{B}_p dA_p, \quad \mathbf{T}_p = \int_{A_p} \mathbf{B}_p dA_p, \quad \theta = e^*/t_p, \quad C = A_p \varepsilon_{33}^*/t_p^2 \tag{9}$$

In (8a) the force vector $\mathbf{f}$ depends on both the patch stiffness $\mathbf{k}_p$ and the electromechanical coupling. The latter is in the following dynamic analysis represented by the piezoelectric force

$$f_p = \theta V \tag{10}$$

which is proportional to the voltage V across the electrodes.

2.3 Coupled piezo-structure system

The piezoelectric patch is now coupled with the structural plate model, as illustrated in Fig. 1, where $\mathbf{c}$ contains the particular nodes of the structural plate model that are connected to the piezoelectric patch. The distance from the midplane of the plate to the midplane of the patch is defined by h (positive upwards), whereby the rotations ϕ_x and ϕ_y of the plate generate in-plane displacements v and u in the patch, as given by the kinematic relation

$$u_i = h\phi_{y,\mathbf{c}(i)}, \quad v_i = -h\phi_{x,\mathbf{c}(i)}, \quad i = 1,2,3,4 \tag{11}$$

where the minus follows from the kinematics associated with a Kirchhoff plate. The relation between the in-plane patch displacements and the rotations of the plate in $\mathbf{u}$ are defined as

$$\mathbf{u}_p = \mathbf{W}^T \mathbf{u}, \quad \mathbf{W}^T = \begin{bmatrix} 0 & \cdots & 0 & 0 & 0 & h & \cdots & & & 0 & \cdots & 0 \\ 0 & \cdots & 0 & 0 & -h & 0 & \cdots & & & 0 & \cdots & 0 \\ \vdots & \ddots & \vdots & & & & \ddots & & & \vdots & \ddots & 0 \\ 0 & \cdots & 0 & & & & \cdots & 0 & 0 & h & 0 & \cdots & 0 \\ 0 & \cdots & 0 & & & & \cdots & 0 & -h & 0 & 0 & \cdots & 0 \end{bmatrix} \tag{12}$$

Node $\mathbf{c}(1)$ Node $\mathbf{c}(4)$

where the 12 non-zero columns in the connectivity matrix $\mathbf{W}$ uniquely establish the coupling in (11) with the structural plate model at the location of the patch. When substituting the force vector in (8a), the equation of motion (1) for the coupled piezo-plate system can be written as

$$\mathbf{M}\ddot{\mathbf{u}}(t) + \underbrace{(\mathbf{K}_0 + \mathbf{W}\mathbf{k}_p\mathbf{W}^T)}_{\mathbf{K}}\mathbf{u}(t) + \underbrace{\mathbf{W}\mathbf{T}_p^T\mathbf{b}}_{\mathbf{w}} f_p(t) = \mathbf{f}_e(t) \tag{13}$$

where the piezoelectric patch introduces a stiffness contribution $\mathbf{k}_p$ to the mechanical system, while the voltage dependent force f_p is determined by the shunt circuit impedance.

2.4 Shunt damping

The electromechanical properties of the piezoelectric patch depend on the apparent voltage V in the transverse 3-direction, governed by the shunt impedance $Z(\omega)$ via the relation

$$V = -i\omega Z(\omega)Q. \tag{14}$$

in the frequency domain, assuming a temporal dependence represented by the complex exponential factor $\exp(i\omega t)$ with assumed angular frequency ω. The charge in (8b) is now eliminated through this impedance relation, and the derived expression for the voltage is subsequently substituted into (10) to obtain the following flexibility relation,

$$u_p = \mathbf{w}^T\mathbf{u} = \left(\frac{C}{\theta^2} + \frac{1}{i\omega\theta^2 Z(\omega)}\right) f_p, \tag{15}$$

For the parallel RL-shunt circuit, the inverse of the impedance function is

$$\frac{1}{Z(\omega)} = \frac{1}{R} + \frac{1}{i\omega L} \tag{16}$$

and substitution of $Z(\omega)$ into (15) gives

$$u_p = \left(\frac{C}{\theta^2} + \frac{1}{i\omega R\theta^2} - \frac{1}{\omega^2 L\theta^2}\right) f_p \tag{17}$$

which represents a mechanical model of a spring (θ^2/C), damper ($R\theta^2$) and inerter ($L\theta^2$) placed in series. The coupled system equations are represented by (13) and (17) with $\mathbf{w} = \mathbf{W}\mathbf{T}_p^T\mathbf{b}$.

3 MODAL CALIBRATION PROCEDURE

The components of the RL shunt are calibrated with respect to a targeted vibration mode of the structure. With shorted transducer electrodes ($V = 0$), the homogeneous form of the equations of motion (13) reduces to this eigenvalue problem

$$(\mathbf{K} - \omega_j^2\mathbf{M})\mathbf{u}_j = \mathbf{0} \tag{18}$$

Based on the normalized mode shape $\mathbf{u}_j/(\mathbf{w}^T\mathbf{u}_j)$, the j'th equation of motion (13) becomes

$$(-\omega^2 m_j + k_j)u_j + f_p = f_j \tag{19}$$

where m_j, k_j and f_j are modal mass, stiffness and load, respectively. The resulting patch displacement u_p is now represented by the contribution u_r from the resonant mode ($j = r$) and an additional contribution from the non-resonant vibration modes ($j \neq r$). As shown in [11] the following approximate representation captures the contribution of higher and lower frequency modes around the resonant frequency,

$$u_p = u_r - \left(\frac{1}{k'_r} - \frac{1}{k''_r} \frac{\omega_r^2}{\omega^2} \right) f_p \tag{20}$$

where the contribution from the non-resonant resonant modes is represented by supplemental flexibility and inertia via the two modal coefficients [12]

$$\frac{1}{k'_r} = \mathbf{w}^T \mathbf{K}_r^{-1} \mathbf{K} \mathbf{K}_r^{-1} \mathbf{w} - \frac{1}{k_r} \quad , \quad \frac{1}{k''_r} = \mathbf{w}^T \mathbf{K}_r^{-1} \mathbf{K} \mathbf{K}_r^{-1} \mathbf{w} - \mathbf{w}^T \mathbf{K}_r^{-1} \mathbf{w} \tag{21}$$

using a frequency shifted form of the stiffness matrix

$$\mathbf{K}_r = \mathbf{K} - \omega_r^2 \mathbf{M}_r \quad , \quad \mathbf{M}_r = \mathbf{M} - \frac{(\mathbf{M}\mathbf{u}_r)(\mathbf{M}\mathbf{u}_r)^T}{\mathbf{u}_r^T \mathbf{M} \mathbf{u}_r} \tag{22}$$

in which case the inertia of the resonant modes is removed in the corresponding mass matrix $\mathbf{M}_r$. The resulting patch displacement determined by (17) can now be substituted into (20),

$$u_r = \left(\frac{C}{\theta^2} - \frac{1}{\omega^2 L \theta^2} + \frac{1}{i\omega R \theta^2} + \frac{1}{k'_r} - \frac{1}{k''_r} \frac{\omega_r^2}{\omega^2} \right) f_p \tag{23}$$

It is seen that the flexibility and inertia correction terms can be combined with the capacitance and inductance, respectively. The flexibility relation in (23) is then reduced to

$$u_r = \frac{C_r}{\theta^2} \left(1 - \frac{1}{\omega^2 L_r C_r} + \frac{1}{i\omega R C_r} \right) f_p \tag{24}$$

introducing a modal capacitance C_r and a modal inductance L_r as

$$C_r = (1 + \kappa'_r) C \quad , \quad L_r C_r = L \left(C_r + \frac{1}{\kappa''_r \omega_r L} \right) \tag{25}$$

where the non-dimensional correction coefficients are defined as

$$\kappa'_r = \frac{\theta^2}{k'_r C} \quad , \quad \kappa''_r = \frac{\theta^2}{k''_r C_r} \tag{26}$$

The balanced calibration with equal modal damping used in [12] is now used for the optimal tuning of the shunt inductance L and resistance R, which are obtained by the expressions

$$LC\omega_r^2 = \frac{1}{(1 + \kappa'_r)(1 - \kappa''_r)}, \quad RC\omega_r = \frac{1}{1 + \kappa'_r} \sqrt{\frac{1}{2\kappa_r}} \tag{27}$$

It is seen that the inductance depends both on the flexibility and inertia corrections, while the magnitude of the shunt resistance is only influenced by the flexibility coefficient κ'_r.

4 NUMERICAL EXAMPLES

In the following both a beam and a plate structure with piezoelectric patches are analyzed, demonstrating the influence from non-resonant modes in the calibration of RL-shunts.

4.1 Cantilever beam

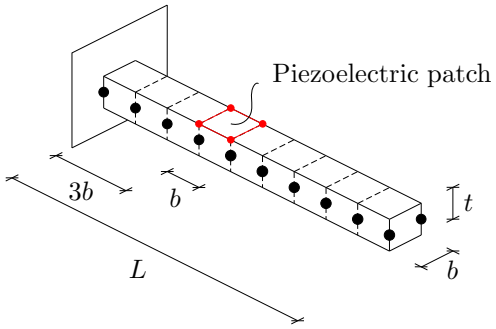

Figure 2: Geometry and discretization of cantilever beam by use of plate elements.

The first example concerns a cantilever beam with a piezoelectric patch shown in Fig. 2, which also indicates the discretisation and dimensions, where the width is given $b = L/10$ and the thickness is determined by $t = b/100$, hence the use of Kirchhoff plate bending theory appears valid. Initially a Poisson's ratio of $\nu = 0$ is considered for both plate and patch, chosen in order to compare with the results for a beam model. Both the thickness and elastic modulus of the patch are assumed to be $t_p = t/4$ and $E_p = E/4$, respectively. The natural frequencies for the beam without the patch (ω_0) and with shorted electrodes (ω_r) are in Table 1 normalized by the analytical value $\omega_a = (1.875)^2\sqrt{EI/(\rho AL^4)}$ for a cantilever. The table also provides the calibrated shunt components, the correction parameters and the attained damping ratios for the beam modeled by plate elements (ζ_r) and for a pure beam model [12]. The final column in the table presents the damping ratio ζ_{rb} for the plate model when using the calibrated parameters from the beam model. The first six mode shapes for the plate model are shown in Fig. 3. However, only results for the five bending modes are presented in Table 1, as the torsional mode (d) in Fig. 3 can not be attenuate by the present patch model.

Table 1: Optimal calibration of the electronic components, for respectively the beam and plate model

Mode	ω_0/ω_a	ω_r/ω_a	$LC\omega_r^2$	$1/(RC\omega_r)$	κ_r'	κ_r''	ζ_r		ζ_{rb}	
1	1.0000	1.0088	0.8771	0.1825	0.1405	0.0003	0.0400	0.0400	–	–
2	6.2671	6.3109	0.8561	0.1877	0.1733	0.0045	0.0400	0.0400	–	–
3	17.5519	17.7617	0.9314	0.1724	0.0772	0.0033	0.0400	0.0400	–	–
4	34.4188	34.4208	–	–	–	–	–	–	–	–
5	56.9859	57.5794	0.9225	0.1777	0.1104	0.0237	0.0401	0.0399	–	–
1	1.0000	1.0088	0.8031	0.1993	0.2457	0.0004	0.0400	0.0400	0.0237	0.0534
2	6.2661	6.3099	0.7754	0.2073	0.2958	0.0048	0.0400	0.0400	0.0216	0.0550
3	17.5313	17.7410	0.8919	0.1800	0.1252	0.0036	0.0400	0.0400	0.0291	0.0489
4	34.2787	34.2814	–	–	–	–	–	–	–	–
5	56.4311	57.0179	0.8880	0.1848	0.1552	0.0251	0.0402	0.0400	0.0313	0.0464

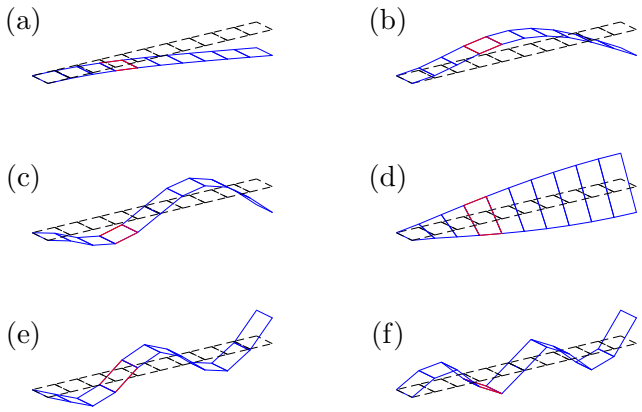

Figure 3: Vibration modes 1-6 ((a)-(f)) for the cantilever beam discretized by plate elements

Good agreement is observed when comparing the natural frequencies for the beam and plate models in Table 1. For each mode the shunt transducer parameters are determined by the balanced calibration formulae in (27) based on a desired damping ratio $\zeta_r^{\rm des}$, which can be predicted by the design expression $\kappa_r = 8(\zeta_r^{\rm des})^2 = 0.0128$, as explained in [12]. The normalized shunt parameters exhibit significant deviations, when comparing the beam and plate models, mainly due to the influence from the non-resonant modes. It is especially observed for the flexibility coefficient κ_r', which in Table 1 is larger for the plate model because of a more substantial contribution from non-resonant modes. The fourth bending mode can not be attenuated, as the patch is located at a nodal point of the vibration form shown in Fig 3(e).

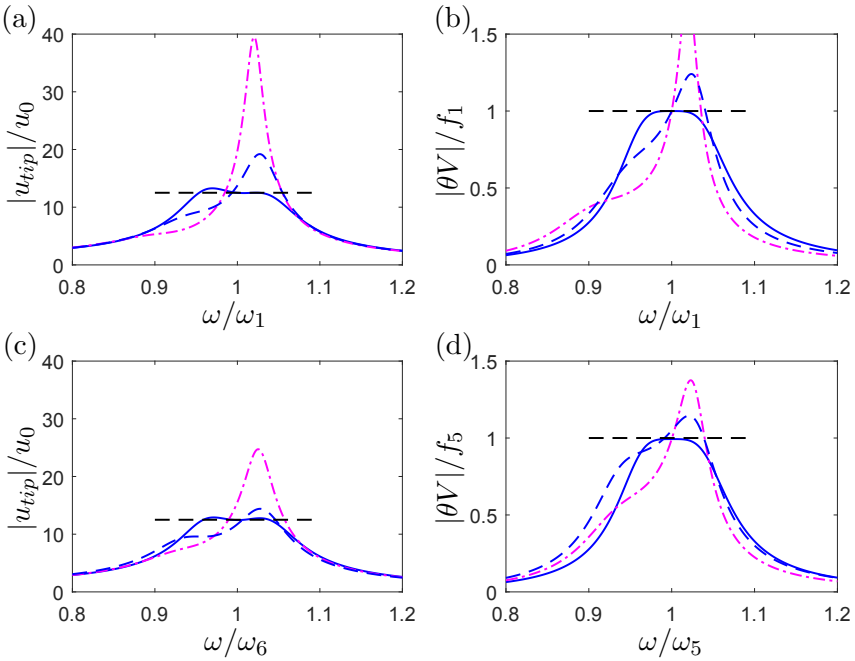

Figure 4: (a,c) Dynamic amplification, and (b,d) Voltage amplitude, calibrated for mode $r = 1, 5$

The dynamic amplification of the tip displacement and the frequency amplitude of the corresponding transducer force f_p is shown on Fig. 4 for bending modes 1 and 5. The (blue) solid curve represents the optimal calibration from the beam and plate models, the (blue) dashed curve represents the beam model calibration used in the plate model, and the (magenta) dashed-dotted curve represents the calibration where the residual mode correction is neglected ($\kappa_r' = 0$ and $\kappa_r'' = 0$). It is seen that the optimally calibrated models recover the desired level of vibration mitigation (horizontal dashed line), while when using the beam model calibration in the plate model a substantial off-tuning is observed, due to the apparent misrepresentation of the spill-over from the non-resonant modes. Furthermore, the calibration without residual mode correction also yields a large increase in vibration amplitude.

The effect of in-plane contraction, which in particular will cause significant contraction of the beam width, is now investigated for a Poisson's ratio of $\nu = 0.3$. The natural frequencies and calibration parameters are presented in Table 2. It is seen that the inclusion of this effect has a significant impact on the calibration results, while the changes in natural frequency are only moderate. The mistuning obtained by neglecting the Poisson's ratio effect is illustrated by the damping ratio $\zeta_{r,\nu=0}$ obtained when using the calibration determined for $\nu = 0$. It shows a considerable reduction in the attainable damping, and a sufficiently accurate model should therefore be used for calibration of piezoelectric shunts, see [14].

Table 2: Optimal shunt calibration for plate model of cantilever beam, with $\nu = 0.3$

Mode	ω_0/ω_a	ω_r/ω_a	$LC\omega_r^2$	$1/(RC\omega_r)$	κ_r'	κ_r''	ζ_r		$\zeta_{r,\nu=0}$	
1	1.0078	1.0169	0.6725	0.2380	0.4875	0.0004	0.0400	0.0400	0.0233	0.0584
2	6.3373	6.3806	0.6194	0.2597	0.6229	0.0052	0.0400	0.0400	0.0243	0.0577
3	17.8812	18.0972	0.8250	0.1947	0.2166	0.0037	0.0400	0.0400	0.0272	0.0537
4	35.4038	35.4101	–	–	–	–	–	–	–	–
5	59.5008	59.7209	0.8344	0.1971	0.2319	0.0272	0.0400	0.0403	0.0187	0.0633

4.2 Plate structure

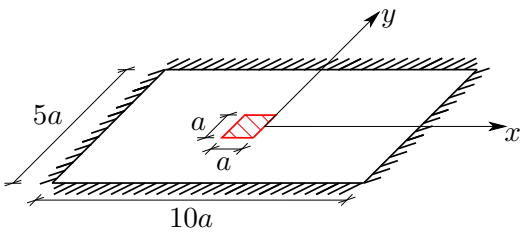

Figure 5: Geometry of simple plate structure with patch centred about the x-axis and right patch edge following the y-axis.

A piezoelectric patch is now coupled to a simple plate structure, see Fig. 5, with the patch placed with a small offset from the center, so that the right patch edge follows the central y-axis. This placement is chosen in order to avoid nodal points for the targeted vibration modes at the center of the plate. The plate thickness is $t = a/100$ and the patch thickness and elastic modulus are defined as in the previous example, while Poisson's ratio for both patch and plate are $\nu = 0.3$,

Table 3: Optimal shunt calibration for plate structure.

Mode	ω_0/ω_a	ω_r/ω_a	$LC\omega_r^2$	$1/(RC\omega_r)$	ζ_r		ζ_r^q		ζ_r^0	
1	0.9919	0.9968	0.9662	0.0829	0.0200	0.0200	0.0197	0.0202	0.0125	0.0268
2	1.5681	1.5688	0.6332	0.1360	0.0200	0.0200	0.0123	0.0255	0.0010	0.0314
3	2.5313	2.5399	0.9581	0.0839	0.0200	0.0200	0.0192	0.0206	0.0112	0.0278
4	3.3747	3.3748	–	–	–	–	–	–	–	–
5*	3.8869	3.8913	–	–	–	–	–	–	–	–
6*	3.8862	3.8924	0.8970	0.0920	0.0200	0.0200	0.0167	0.0224	0.0056	0.0316

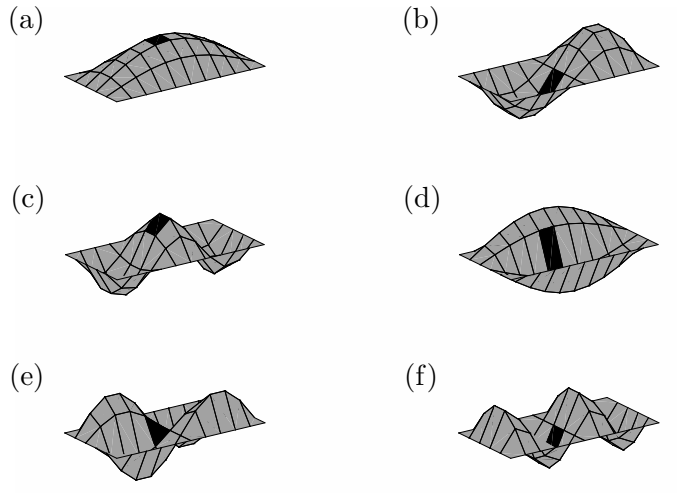

Figure 6: Vibration mode 1-6((a)-(f)) for the rectangular plate with piezoelectric patch

whereas the mass of the patch is neglected. The natural frequencies are again normalized by the analytical solution $\omega_a = \sqrt{D/(\rho t)}\left(\pi^2/(5a)^2 + \pi^2/(10a)^2\right)$ for the first plate vibration mode with bending stiffness $D = \frac{Et^3}{12(1-\nu^2)}$. The piezoelectric shunt is calibrated according to a desired damping ratio $\zeta_{des} = 0.02$, which gives the modal coupling coefficient $\kappa_r = 8(\zeta_r^{\rm des})^2 = 0.0032$. The plate has been discretized by 10×5 Kirchhoff plate elements and the piezoelectric patch is represented by a single element. The first six natural frequencies and corresponding mode shapes are investigated, and the optimal calibration for each mode is presented in Table 3. The mode shapes are shown in Fig. 6, where the black element indicates the patch position. Table 3 also presents the damping ratios ζ_r^q and ζ_r^0, achieved by a quasi-static correction ($\kappa_r'' = 0$) and without correction ($\kappa_r' = 0$ and $\kappa_r'' = 0$), respectively. It is found that when not including the full residual mode correction, with both flexibility and inertia contributions, substantial mistuning might occur. Thus, it is important to consider the spill-over effect from residual modes in the calibration procedure of RL shunts. For mode 4, the patch is located at a nodal point and can therefore not be attenuated. Vibration modes $r = 5$ and 6 have practically identical frequencies, and when attaching the piezoelectric patch they even interchange order. However, it is seen that mode 5 can not be attenuated because the patch is exposed to torsion deformations, thus is in pure shear.

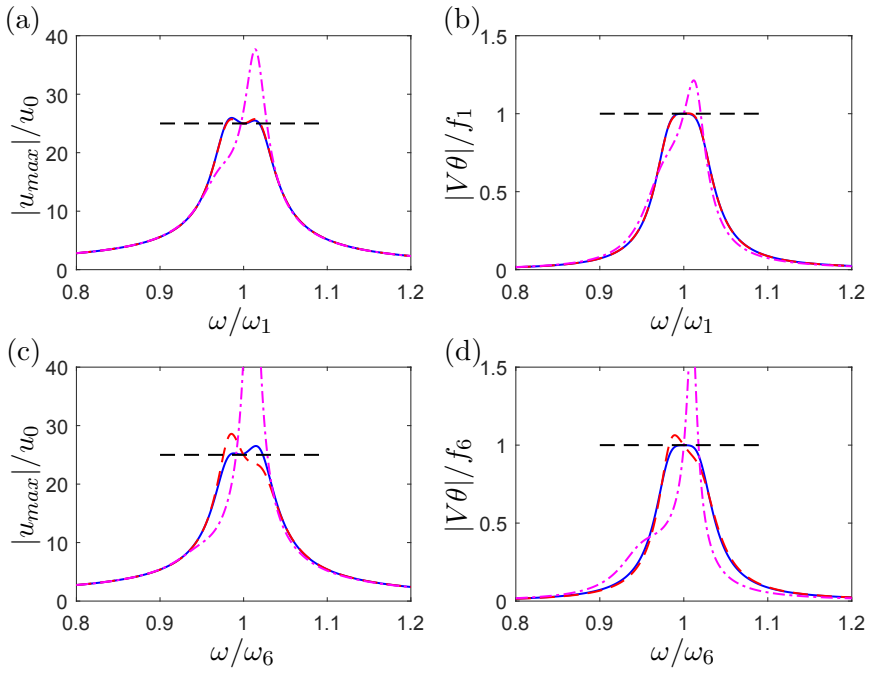

Figure 7: Dynamic amplification (a,c) and force amplitude (b,d) for modes $r = 1$ and 6.

Figure 7 shows the dynamic amplification of the plate structure at the specific position of maximum amplitude and the shunt force f_p for modes $r = 1$ and 6. The solid curve shows the response for the present calibration procedure, the dashed curve shows the case with only quasi-static correction ($\kappa_r'' = 0$), while the dotted-dashed curve shows the structural amplitude in the case without residual mode correction. The black dashed line indicates the desired amplitude level, which is attained by the fully corrected calibration, while substantial amplification is observed when the residual mode correction is not included.

5 CONCLUSIONS

The balanced calibration procedure based on equal modal damping and with compensation for spill-over from residual modes has been successfully implemented for plate structures with an RL shunted piezoelectric patch. The importance of a precise structural model has been shown by comparing results for a cantilever beam, modeled by beam and plate elements, respectively. For the plate model of the cantilever, the 2D behavior of the piezo-plate model captures additional dynamic effects that improve the accuracy of the calibration procedure. Furthermore, the inclusion of in-plane contraction from a non-vanishing Poisson's ratio is important in order to obtain a precise RL shunt calibration. Finally, a finite element scheme and calibration procedure has been investigated for piezoelectric shunt damping of plate structures, based on a desired level of damping in the targeted vibration mode. It has been demonstrated that a consistent correction with respect to the flexibility and inertia contributions from non-resonant modes is important. In future work, the contribution from the bending stiffness of the piezoelectric patch will be

included, improving the model accuracy. Furthermore, a refined mesh of the plate and patch is introduced to achieve full convergence of the natural frequencies, the residual mode corrections coefficients and the calibrated shunt components.

ACKNOWLEDGEMENT

This research has been supported by the Danish Council for Independent Research via the project 'Resonant Piezoelectric Shunt Damping of Structures'.

REFERENCES

[1] Preumont, A., *Vibration Control of Active Structures. An Introduction*, 3rd edition, Springer, Heidelberg, 2011.

[2] R.L. Forward, Electronic damping of vibrations in optical structures, *Applied Optics* (1979) **18**:690–697.

[3] Hagood, N.W., von Flotow, A., Damping of structural vibrations with piezoelectric materials and passive electrical networks, *Journal of Sound and Vibration* (1991) **146**:243-268.

[4] Wu, S.Y., Piezoelectric shunts with a parallel R-L circuit for structural damping and vibration control, *SPIE Proceedings* (1996) **2720**:259-269.

[5] Park, C.H., Inman, D.J. A uniform model for series R-L and parallel R-L shunt circuits and power consumption, *SPIE Proceedings*, (1999) **3668**:797804.

[6] Caruso, G., A critical analysis of electric shunt circuits employed in piezoelectric passive vibration damping, *Smart Materials and Structures*, (2001)**10**:1059-1068.

[7] Soltani, P., Kerschen, G., Tondreau, G., Deraemaeker, A., Piezoelectric vibration damping using resonant shunt circuits: an exact solution, *Smart Materials and Structures*, (2014) **23**:125014 (11pp).

[8] Høgsberg, J., Krenk, S., Balanced calibration of resonant shunt circuits for piezoelectric vibration control, *Journal of Intelligent Material Systems and Structures* (2012) **23**:1937-1948.

[9] Krenk, S. Frequency analysis of the tuned mass damper, *Journal of Applied Mechanics*, (2005) **72**:936-942.

[10] Høgsberg, J., Krenk, S. Balanced calibration of resonant piezoelectric RL shunts with quasi-static background flexibility correction, *Journal of Sound and Vibration* (2015) **341**:16-30.

[11] Krenk, S., Høgsberg, J., Tuned resonant mass or inerter-based absorbers: Unified calibration with quasi-dynamic flexibility and inertia correction, *Proceedings of the Royal Society A-Mathematical, Physical and Engineering Sciences* (2015) **472**:20150718 (23 pp).

[12] Høgsberg, J., Krenk, S., Calibration of piezoelectric RL shunts with explicit residual mode correction, *Journal of Sound and Vibration*, (2017) **386**:65-81

[13] Benjeddou, A., Advances in piezoelectric finite element modeling of adaptive structural elements: a survey, *Computers and Structures*, **76** (2000) 347-363.

[14] Benjeddou, A., Modal effective electromechanical coupling approximate evaluations and simplified analyses: Numerical and experimental assessments, *Acta Mechanica*, **225** (2014) 2721-2742.

VIII ECCOMAS Thematic Conference on Smart Structures and Materials
SMART 2017
A. Güemes, A. Benjeddou, J. Rodellar and J. Leng (Eds)

VIBROACOUSTIC ANALYSIS OF LAMINATED SANDWICH PANELS WITH VISCOELASTIC CORE AND PIEZOELECTRIC PATCHES

AURELIO ARAUJO*, JORGE BELINHA†, ANTONIO FERREIRA† AND CARLOS MOTA SOARES*

*IDMEC, Instituto Superior Tecnico
Universidade de Lisboa
Av. Rovisco Pais, 1049-001 Lisboa, Portugal
e-mail: aurelio.araujo@tecnico.ulisboa.pt, carlosmotasoares@dem.ist.utl.pt - Web page: http://www.idmec.ist.utl.pt/

† Department of Mechanical Engineering, Faculty of Engineering
Universidade do Porto
Rua Dr. Roberto Frias, 4200-465 Porto, Portugal
e-mail: jorge.belinha@fe.up.pt, ferreira@fe.up.pt - Web page: http://www.fe.up.pt

Key words: Sandwich Structures, Smart Structures, Viscoelasticity, Piezoelectricity, Vibroacoustics

Abstract. This paper addresses the issue of vibration and noise reduction in laminated sandwich plates using both passive and active elements. A finite element implementation of a laminated sandwich plate element with viscoelastic core and surface bonded piezoelectric patches is used to obtain the frequency response of the panels. The sound transmission characteristics of the panels are evaluated by computing their radiated sound power and radiation efficiency, using the Rayleigh integral method. Results are presented for illustration of the performance of the active sandwich panels in terms of their noise reduction efficiency.

1 INTRODUCTION

Noise and vibration reduction is a fundamental issue for the competitiveness in the transportation industry and the designed solutions should be as much integrated as possible in order to reduce manufacturing costs. These structures should be optimized for cost, weight, vibration and noise attenuation, subject to technological, failure and stress constraints. The generalized introduction of lightweight composites in the automotive and aerospace industries, while leading to significant weight reductions and associated fuel savings, pose a serious problem of low acoustic performance of these lightweight composites when subjected to mechanical or acoustic excitations. Passive damping technologies are nowadays frequently used to control sound and vibration levels through the use of viscoelastic materials, while active devices such as surface

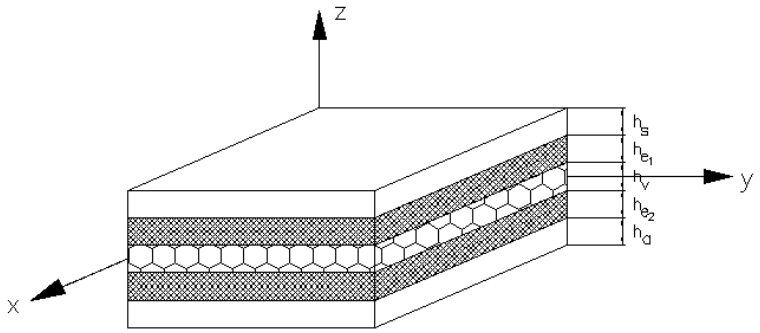

Figure 1: Sandwich plate

bonded piezoelectric patches can also be effectively used to control these undesired sound and vibration levels in lightweight composite structures. Sandwich composite panels may represent an optimized solution for both sound radiation and structural vibration for most frequency ranges. Viscoelastic materials are an efficient way of reducing structural vibrations and providing noise attenuation, which allied to active elements may lead to broader control capabilities regarding acoustic emissions.

The open literature regarding the subject of vibration and sound radiation from passive or active composite and sandwich structures is quite scarce. Regarding the vibration control using passive technologies, previous works have been presented for mechanical vibration suppression [1] and sound level attenuation [2, 3, 4, 5]. The vibrocoustic problem has been recently addressed by Larbi et al. in smart piezoelectric composite and sandwich plates [6, 7] and also in double-wall sandwich panels [8].

In the present work we apply a layerwise sandwich finite element model, previously developed by the authors [9], with frequency dependent viscoelastic core, composite laminated skin layers and piezoelectric patches with an associated feedback control law. The model is used to calculate the frequency response of sandwich panels and the structural results from the model are used to calculate the radiated sound power and radiation efficiency of the panel.

2 SANDWICH PLATE MODEL

The *layerwise* active sandwich finite element model is briefly described here, to analyse sandwich laminated plates with a viscoelastic (v) core, composite laminated face layers (e_1, e_2) and piezoelectric sensor (s) and actuator (a) layers, as shown in Figure 1.

The basic assumptions in the development of the sandwich plate model are: The origin of the z axis is the medium plane of the core layer; No slip occurs at the interfaces between layers; The displacement is C^0 along the interfaces; Elastic and piezoelectric layers are modeled with first order shear deformation theory (FSDT) and viscoelastic core with a higher order shear deformation theory (HSDT); All materials are linear, homogeneous and orthotropic and the elastic layers (e_1) and (e_2) are made of laminated composite materials; For the viscoelastic core, material properties are complex and frequency dependent; Upper and lower layers play the roles of sensor and actuator, respectively, and are connected via feedback control laws, considering

co-located control.

The FSDT displacement field of the face layers may be written in the general form:

$$\begin{aligned} u^i(x,y,z,t) &= u_0^i(x,y,t) + (z-z_i)\theta_x^i(x,y,t) \\ v^i(x,y,z,t) &= v_0^i(x,y,t) + (z-z_i)\theta_y^i(x,y,t) \\ w^i(x,y,z,t) &= w_0^i(x,y,t) \end{aligned} \tag{1}$$

where u_0^i and v_0^i are the in-plane displacements of the mid-plane of the layer, θ_x^i and θ_y^i are rotations of normals to the mid-plane about the y axis (anticlockwise) and x axis (clockwise), respectively, w_0^i is the transverse displacement of the layer, z_i is the z coordinate of the mid-plane of each layer, with reference to the core layer mid-plane ($z=0$), and $i = s, e_1, e_2, a$ is the layer index.

For the viscoelastic core layer, the HSDT displacement field is written as a series expansion of the displacements in the thickness coordinate:

$$\begin{aligned} u^v(x,y,z,t) &= u_0^v(x,y,t) + z\theta_x^v(x,y,t) + z^2 u_0^{*v}(x,y,t) + z^3\theta_x^{*v}(x,y,t) \\ v^v(x,y,z,t) &= v_0^v(x,y,t) + z\theta_y^v(x,y,t) + z^2 v_0^{*v}(x,y,t) + z^3\theta_y^{*v}(x,y,t) \\ w^v(x,y,z,t) &= w_0^v(x,y,t) + z\theta_z^v(x,y,t) + z^2 w_0^{*v}(x,y,t) \end{aligned} \tag{2}$$

where u_0^v and v_0^v are the in-plane displacements of the mid-plane of the core, θ_x^v and θ_y^v are rotations of normals to the mid-plane of the core about the y axis (anticlockwise) and x axis (clockwise), respectively, w_0^v is the transverse displacement of the core mid-plane. The functions u_0^{*v}, v_0^{*v}, w_0^{*v}, θ_x^{*v}, θ_y^{*v} and θ_z^v are higher order terms in the series expansion, defined also in the mid-plane of the core layer.

After enforcing displacement continuity at the layer interfaces we retain the translational degrees of freedom of the elastic and piezoelectric face layers, while eliminating the corresponding rotational ones. At the same time, the higher order terms in the transverse displacement expansion of the core are also eliminated. Hence, the generalized displacement field has 19 mechanical unknowns:

$$u_0^a \quad v_0^a \quad u_0^{e2} \quad v_0^{e2} \quad w_0^{e2} \quad u_0^v \quad v_0^v \quad w_0^v \quad \theta_x^v \quad \theta_y^v \quad u_0^{*v} \quad v_0^{*v} \quad \theta_x^{*v} \quad \theta_y^{*v} \quad u_0^{e1} \quad v_0^{e1} \quad w_0^{e1} \quad u_0^s \quad v_0^s \tag{3}$$

For more details on the model and its validation, the reader is directed to Araujo et al. [9].

2.1 Constitutive relations

We consider that fibre-reinforced laminae in elastic multi-layers (e_1) and (e_2), viscoelastic core (v), and piezoelectric sensor (s) and actuator (a) layers are characterized as orthotropic. However, due to the different nature of the displacement fields in the face layers and in the core, the constitutive relations are going to be different.

For the laminas in the elastic laminated face layers or in the piezoelectric layers, constitutive equations for each lamina may be expressed in the principal material directions, assuming zero transverse normal stress as [10]:

$$\begin{Bmatrix} \sigma_{11} \\ \sigma_{22} \\ \sigma_{23} \\ \sigma_{13} \\ \sigma_{12} \end{Bmatrix} = \begin{bmatrix} Q_{11} & Q_{12} & 0 & 0 & 0 \\ Q_{12} & Q_{22} & 0 & 0 & 0 \\ 0 & 0 & Q_{44} & 0 & 0 \\ 0 & 0 & 0 & Q_{55} & 0 \\ 0 & 0 & 0 & 0 & Q_{66} \end{bmatrix}^{E} \begin{Bmatrix} \varepsilon_{11} \\ \varepsilon_{22} \\ \gamma_{23} \\ \gamma_{13} \\ \gamma_{12} \end{Bmatrix} - \begin{bmatrix} 0 & 0 & e_{31}^{*} \\ 0 & 0 & e_{32}^{*} \\ 0 & e_{24} & 0 \\ e_{15} & 0 & 0 \\ 0 & 0 & 0 \end{bmatrix} \begin{Bmatrix} \mathcal{E}_1 \\ \mathcal{E}_2 \\ \mathcal{E}_3 \end{Bmatrix}$$
$$\begin{Bmatrix} D_1 \\ D_2 \\ D_3 \end{Bmatrix} = \begin{bmatrix} 0 & 0 & 0 & e_{15} & 0 \\ 0 & 0 & e_{24} & 0 & 0 \\ e_{31}^{*} & e_{32}^{*} & 0 & 0 & 0 \end{bmatrix} \begin{Bmatrix} \varepsilon_{11} \\ \varepsilon_{22} \\ \gamma_{23} \\ \gamma_{13} \\ \gamma_{12} \end{Bmatrix} + \begin{bmatrix} \epsilon_{11} & 0 & 0 \\ 0 & \epsilon_{22} & 0 \\ 0 & 0 & \epsilon_{33}^{*} \end{bmatrix}^{\varepsilon} \begin{Bmatrix} \mathcal{E}_1 \\ \mathcal{E}_2 \\ \mathcal{E}_3 \end{Bmatrix} \tag{4}$$

where σ_{ij} are stress components, ε_{ij} and γ_{ij} are strain components, $\mathcal{E}_i$ and D_i are the electric field and electric displacement components, respectively, Q_{ij}^{E} are reduced stiffness coefficients at constant electric field, e_{ij} and e_{ij}^{*} are piezoelectric and reduced piezoelectric constants, respectively, and $\epsilon_{ij}^{\varepsilon}$ and $\epsilon_{33}^{*\varepsilon}$ are dielectric and reduced dielectric constants, measured at constant strain. Expressions for the reduced quantities mentioned above can be found in [10]. The complete set of equations in (4) is only used for the piezoelectric sensor and actuator layers, while for the remaining elastic and viscoelastic layers, only the first equation is considered without the piezoelectric part.

For the viscoelastic core, a full 3D orthotropic stiffness matrix is used in the principal material directions [11] and the stiffness coefficients are complex quantities, since the complex modulus approach was used in this work, using the elastic-viscoelastic correspondence principle [12]. In this case, and for isothermal conditions, the usual engineering moduli may be represented by complex quantities:

$$\begin{aligned} E_1(i\omega) &= E_1'(\omega)(1 + i\eta_{E_1}(\omega)) \\ E_2(i\omega) &= E_2'(\omega)(1 + i\eta_{E_2}(\omega)) \\ E_3(i\omega) &= E_3'(\omega)(1 + i\eta_{E_3}(\omega)) \\ G_{12}(i\omega) &= G_{12}'(\omega)(1 + i\eta_{G_{12}}(\omega)) \\ G_{23}(i\omega) &= G_{23}'(\omega)(1 + i\eta_{G_{23}}(\omega)) \\ G_{13}(i\omega) &= G_{13}'(\omega)(1 + i\eta_{G_{13}}(\omega)) \\ \nu_{12}(i\omega) &= \nu_{12}'(\omega)(1 - i\eta_{\nu_{12}}(\omega)) \\ \nu_{23}(i\omega) &= \nu_{23}'(\omega)(1 - i\eta_{\nu_{23}}(\omega)) \\ \nu_{13}(i\omega) &= \nu_{13}'(\omega)(1 - i\eta_{\nu_{13}}(\omega)) \end{aligned} \tag{5}$$

where the prime quantities denote storage moduli, associated material loss factors are represented by the letter η, ω represents frequency of vibration and $i = \sqrt{-1}$ is the imaginary unit. Furthermore, in Equation (5), E, G and ν denote Young's moduli, shear moduli and Poisson's ratio, respectively.

The use of the complex modulus approach in linear viscoelasticity allows for the direct use of experimentally obtained frequency dependent material properties to obtain the frequency

domain response in steady state oscillatory conditions. Additionally, it is also possible to obtain transient responses from this approach, considering a trigonometric expansion of the excitation and Fourier analysis [12, 13]. Hence, time domain transient responses can be obtained by inverse Fourier analysis, as long as the viscoelastic material model is causal [12, 13], which is usually the case when frequency dependent experimental complex moduli are used.

2.2 Finite element formulation

The equations of motion for the plate are obtained by applying the extended Hamilton's principle, the solution of which was obtained through the finite element method, using an eight node serendipity element with 19 mechanical degrees of freedom per node, and one electric potential degree of freedom per piezoelectric layer. The system equilibrium equations are obtained in the usual way through assembly of the element equations, yielding:

$$\begin{bmatrix} \mathbf{M}_{uu} & \mathbf{0} \\ \mathbf{0} & \mathbf{0} \end{bmatrix} \begin{bmatrix} \ddot{\mathbf{u}} \\ \ddot{\boldsymbol{\phi}} \end{bmatrix} + \begin{bmatrix} \mathbf{K}_{uu} & \mathbf{K}_{u\phi} \\ \mathbf{K}_{u\phi}^T & \mathbf{K}_{\phi\phi} \end{bmatrix} \begin{bmatrix} \mathbf{u} \\ \boldsymbol{\phi} \end{bmatrix} = \begin{bmatrix} \mathbf{F}_u \\ \mathbf{0} \end{bmatrix} \tag{6}$$

where $\mathbf{u}$, $\ddot{\mathbf{u}}$, $\boldsymbol{\phi}$ and $\ddot{\boldsymbol{\phi}}$ are mechanical degrees of freedom and corresponding accelerations, electric potential and corresponding second time derivatives, respectively. $\mathbf{M}_{uu}$ and $\mathbf{K}_{uu}$ are the mass and complex stiffness matrices, respectively, corresponding to purely mechanical behavior, while $\mathbf{K}_{\phi\phi}$ is the dielectric stiffness matrix, $\mathbf{K}_{u\phi}$ is the stiffness matrix that corresponds to the coupling between the mechanical and the piezoelectric effects, and $\mathbf{F}_u$ is the externally applied mechanical load vector.

The feedback control law is based on a direct proportional or velocity feedback, and can be written in the following form:

$$\boldsymbol{\phi}_a = G_d \boldsymbol{\phi}_s + G_v \dot{\boldsymbol{\phi}}_s \tag{7}$$

where G_d and G_v are the constant displacement feedback gain and the constant velocity feedback gain, respectively, $\boldsymbol{\phi}_a$ and $\boldsymbol{\phi}_s$ are the vectors of actuator and sensor potentials, respectively, and $\dot{\boldsymbol{\phi}}_s$ is the vector of sensor potential time derivatives.

Now, Equation (6) can be rewritten in the following form:

$$\begin{bmatrix} \mathbf{M}_{uu} & \mathbf{0} & \mathbf{0} \\ \mathbf{0} & \mathbf{0} & \mathbf{0} \\ \mathbf{0} & \mathbf{0} & \mathbf{0} \end{bmatrix} \begin{bmatrix} \ddot{\mathbf{u}} \\ \ddot{\boldsymbol{\phi}}_s \\ \ddot{\boldsymbol{\phi}}_a \end{bmatrix} + \begin{bmatrix} \mathbf{K}_{uu} & \mathbf{K}_{u\phi_s} & \mathbf{K}_{u\phi_a} \\ \mathbf{K}_{u\phi_s}^T & \mathbf{K}_{\phi\phi_s} & \mathbf{0} \\ \mathbf{K}_{u\phi_a}^T & \mathbf{0} & \mathbf{K}_{\phi\phi_a} \end{bmatrix} \begin{bmatrix} \mathbf{u} \\ \boldsymbol{\phi}_s \\ \boldsymbol{\phi}_a \end{bmatrix} = \begin{bmatrix} \mathbf{F}_u \\ \mathbf{0} \\ \mathbf{0} \end{bmatrix} \tag{8}$$

The generated potential on the sensors is now given by:

$$\boldsymbol{\phi}_s = -\mathbf{K}_{\phi\phi_s}^{-1} \mathbf{K}_{u\phi_s}^T \mathbf{u} \tag{9}$$

Assuming harmonic vibrations, potentials in actuators can be written as:

$$\boldsymbol{\phi}_a = -\left(G_d + i\omega G_v\right) \mathbf{K}_{\phi\phi_s}^{-1} \mathbf{K}_{u\phi_s}^T \mathbf{u} \tag{10}$$

Hence, the final equilibrium equations are given by:

$$\left[\mathbf{K}^*(\omega) - \omega^2 \mathbf{M}_{uu}\right] \mathbf{a} = \mathbf{F}_u \tag{11}$$

where the non-symmetric condensed stiffness matrix is given by:

$$\mathbf{K}^*(\omega) = \mathbf{K}_{uu}(\omega) - \left[(G_d + i\omega G_v)\,\mathbf{K}_{u\phi_a} + \mathbf{K}_{u\phi_s}\right]\mathbf{K}_{\phi\phi_s}{}^{-1}\mathbf{K}_{u\phi_s}^T \tag{12}$$

and $\mathbf{K}_{uu}(\omega)$ is a complex matrix.

It is worthwhile noting that when electroded surfaces exist in a given patch or layer, equipotential conditions should be imposed before condensing the electric degrees of freedom.

The forced vibration problem is solved in the frequency domain, which implies the solution of the following linear system of equations for each frequency point:

$$\left[\mathbf{K}^*(\omega) - \omega^2\mathbf{M}_{uu}\right]\mathbf{u}(\omega) = \mathbf{F}_u(\omega) \tag{13}$$

where $\mathbf{F}_u(\omega) = \mathcal{F}\left(\mathbf{F}_u(t)\right)$ is the Fourier transform of the time domain force history $\mathbf{F}_u(t)$.

For the free vibration problem, Equation (13) reduces to the following non-linear eigenvalue problem:

$$\left[\mathbf{K}^*(\omega) - \lambda_n^*\mathbf{M}_{uu}\right]\mathbf{u}_n = \mathbf{0} \tag{14}$$

where, the complex eigenvalue λ_n^* is written as:

$$\lambda_n^* = \lambda_n\left(1 + i\eta_n\right) \tag{15}$$

and $\lambda_n = \omega_n^2$ is the real part of the complex eigenvalue and η_n is the corresponding modal loss factor.

The non-linear eigenvalue problem is solved iteratively using ARPACK [14] with a shift-invert transformation. The iterative process is considered to have converged when:

$$\frac{\|\omega_i - \omega_{i-1}\|}{\omega_{i-1}} \leq \epsilon \tag{16}$$

where ω_i and ω_{i-1} are current and previous iteration values for the real part of the particular eigenfrequency of interest, respectively, and ϵ is the convergence tolerance.

3 ACOUSTIC INDICATORS

When subjected to external excitation, the sandwich plate radiates noise into the surrounding acoustic medium. For a light fluid, the fluid mass may be neglected and both acoustic and structural problems can be solved independently, whereas for heavy fluids the problem is more complex owing to strong acoustic radiation damping and added mass effects which may significantly change the inertia of the coupled structure. In the present work we are concerned mainly with radiation involving light fluids such air. Hence, the fluid loading is neglected in the present approach, and in order to evaluate the acoustic performance of the active sandwich panels, the radiated sound power (Π) and the radiation efficiency (σ_{RAD}) are the acoustic indicators chosen in this work.

3.1 Radiated sound power

The sound power that is radiated through an area S of the panel is given by:

$$\Pi = \frac{1}{2}\Re\left(\int_S p(G)v_n^*(G)dS\right) \tag{17}$$

where G is a point on the plate surface, p is the sound pressure applied as an external loading and v_n is the normal velocity. The complex conjugate is denoted by * and $\Re$ denotes the real part of the integral.

For a flat plate embedded in an infinite rigid plane baffle and radiating in a semi infinite fluid, the pressure p can be obtained using the Rayleigh Integral [15]:

$$p(\omega, M) = \rho_0 \frac{i\omega}{2\pi}\int_S v_n(\omega, G)\frac{e^{-ikr}}{r}dS \tag{18}$$

where ρ_0 is the mass density of the external acoustic domain, k is the wave number expressed as ω/c_0, c_0 is the speed of sound in air, M is a point inside the external acoustic domain and $v_n(\omega, G)$ is the normal velocity at point G, which is easily obtained from the finite element formulation presented in the previous sections.

The sandwich panel is meshed into a grid of triangular elements, obtained by dividing the rectangular finite elements into four triangular elements each. The transverse vibration of the plate is then specified in terms of the normal velocities at the center positions of these triangles. We assume that the dimensions of these triangular elements are small when compared to the structural and acoustic wavelengths, so that the total radiated sound power in Equation (17) can be expressed as the sum of the powers radiated by each element:

$$\Pi = \frac{S_e}{2}\Re\left(\mathbf{v}_n^H\mathbf{p}\right) \tag{19}$$

where the superscript ^{H} denotes the hermitian transpose, $\mathbf{v}_n$ and $\mathbf{p}$ are the vectors of complex amplitudes of the normal velocity and acoustic pressure in all elements, respectively, and S_e is the area of each element. The pressure on each element is generated by the vibrations of all elements of the panel. The vector of sound pressure can therefore be obtained using the impedance matrix:

$$\mathbf{p} = \mathbf{Z}\mathbf{v}_n \tag{20}$$

where $\mathbf{Z}$ is the (symmetric) impedance matrix with components $Z_{ij} = \left(i\omega\rho_0 S_e/2\pi r_{ij}\right)e^{-ikr_{ij}}$ and r_{ij} is the distance between the centers of elements i and j. Substituting Equation (20) in Equation (19), we obtain:

$$\Pi = \frac{S_e}{2}\Re\left(\mathbf{v}_n^H\mathbf{Z}\mathbf{v}_n\right) = \frac{S_e}{4}\Re\left(\mathbf{v}_n^H\left[\mathbf{Z}+\mathbf{Z}^H\right]\mathbf{v}_n\right) = \mathbf{v}_n^H\mathbf{R}\mathbf{v}_n \tag{21}$$

where $\mathbf{R}$ is the radiation resistance matrix for the elementary radiators which is given by:

$$\mathbf{R} = \frac{\omega^2 \rho_0 S_e^2}{4\pi c_0} \begin{bmatrix} 1 & \frac{\sin(kr_{12})}{kr_{12}} & \cdots & \frac{\sin(kr_{1R})}{kr_{1R}} \\ \frac{\sin(kr_{21})}{kr_{21}} & 1 & \cdots \frac{\sin(kr_{2R})}{kr_{2R}} & \\ \vdots & \vdots & \ddots & \vdots \\ \frac{\sin(kr_{R1})}{kr_{R1}} & \frac{\sin(kr_{R2})}{kr_{R2}} & \cdots & 1 \end{bmatrix} \tag{22}$$

In this work, the finite element method is used to obtain the normal velocity distribution, assuming a sufficient number of discrete radiating elements, according to the smallest wavelength to be observed.

3.2 Radiation efficiency

The non-dimensional radiation efficiency of the plate-acoustic system characterizing the acoustic radiation is defined as non-dimensional ratio between the radiated sound power and the mean square velocity or potential energy of the plate:

$$\sigma_{RAD} = \frac{\Pi}{\frac{1}{2}\rho_0 c_0 \int_S \mathbf{v}_n^H \mathbf{v}_n dS} \tag{23}$$

Considering the above definition, the radiation efficiency expresses the portion of vibration energy transformed into sound.

4 APPLICATION

A laminated hybrid sandwich plate is considered with a viscoelastic core described by a fractional derivative constitutive law, and with four pairs of surface bonded co-located sensor-actuator patches, using the negative velocity feedback control law.

The plate is a 300 mm × 200 mm laminated sandwich with all edges simply supported and made of carbon fibre plies and a central isotropic viscoelastic damping material core. The stacking sequence for carbon fibre laminates is $[0°/90°/+45°]$ for (e_1) and $[+45°/90°/0°]$ for (e_2). The thickness of each carbon fibre ply is 0.5 mm, and the viscoelastic core is 2.5 mm thick.

Material properties for the isotropic viscoelastic damping polymer are described by a five parameter fractional derivative constitutive model [16], where $\nu = 0.49$ and $\rho = 1300$ kg/m^3, have been assumed here. The expression for the complex shear modulus is as follows:

$$G(j\omega) = G_0 + G_0(d-1)\frac{(j\omega\tau)^\alpha}{1+(j\omega\tau)^\beta} \tag{24}$$

where $G_0 = 0.8$ MPa is the static shear modulus, $d = 570$, $\alpha = 0.566$, $\beta = 0.558$, and $\tau = 7.23 \times 10^{-10}$ s is the relaxation time.

For the carbon fiber plies, material properties are $E_1 = 130.8$ GPa, $E_2 = 10.6$ GPa, $G_{12} = 5.6$ GPa, $G_{13} = 4.2$ GPa, $G_{23} = 3.0$ GPa, $\nu_{12} = 0.36$, and $\rho = 1543$ kg/m^3.

Four pairs of surface electroded 50 mm × 50 mm × 0.9 mm piezoelectric patches are also bonded to the upper and lower surface of the plate, as illustrated in Figure 2.

Material properties for the piezoelectric patches were taken as $E_1 = 50.9$ GPa, $E_2 = 46.1$ GPa, $G_{12} = 14.3$ GPa, $G_{13} = 8.0$ GPa, $G_{23} = 20.6$ GPa, $\nu_{12} = 0.29$, $\rho = 7800$ kg/m^3, $e_{31}^* = -17.0$ N/Vm, $e_{32}^* = -12.2$ N/Vm, and $\epsilon_{33}^{*\varepsilon} = 1.549 \times 10^{-8}$ F/m.

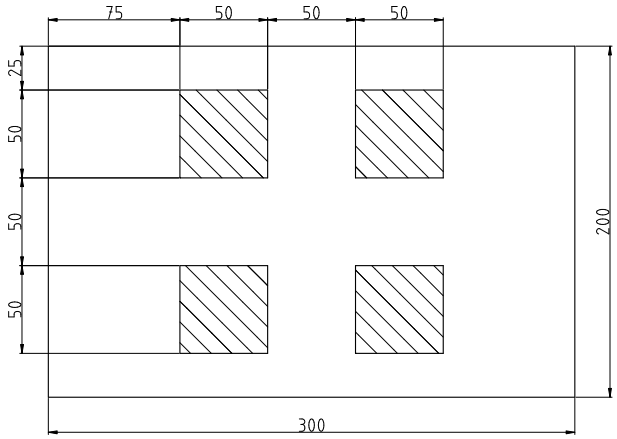

Figure 2: Laminated viscoelastic sandwich plate with piezoelectric patch positions (dimensions in mm)

A 10 N force is applied at $t = 0$ at the center of the plate and the magnitude of the frequency response of the central point of the plate is presented in Figure 3. The radiated sound power and the radiation efficiency of the plate are presented in Figures 4 and 5, respectively. The three situations plotted in Figures 3, 4 and 5 correspond to the situations where (a) **SC (undamped)**: damping is not considered for the viscoelastic core ($d = 1$ in Eq. (24)) and the electrodes on the piezoelectric patches are short circuited, (b) **SC (damped)**: viscoelastic core with damping included ($d = 570$ in Eq. (24)) and (c) $G_v = -0.001$ **(damped)**: active control with velocity feedback gain $G_v = -0.001$ in each patch, with damping in the viscoelastic core.

One can observe that the effect of the damping introduced by the viscoelastic core is determinant in reducing the amplitudes of vibration and consequently the radiated sound power up to 1 kHz. Regarding the active damping that is introduced with the negative velocity feedback control law, we observe that it is most effective for higher modes within the frequency range that was considered in the application. The radiation efficiency of the plate is affected only in the neighborhood of the structural modes.

5 CONCLUSIONS

A vibroacoustic analysis of laminated sandwich panels with surface bonded piezoelectric patches has been addressed in this paper. The frequency response, radiated sound power and radiation efficiency has been calculated for a sandwich panel with a viscoelastic core and a negative velocity feedback control law has been used to implement the additional active damping. The effect of both passive and active damping has been analyzed with respect to beoth vibration and sound radiation levels.

ACKNOWLEDGEMENTS

This work has been supported by National Funds through Fundação para a Ciência e Tecnologia (FCT), through IDMEC, under LAETA, project UID/EMS/50022/2013, and also funding provided by the inter-institutional projects from LAETA.

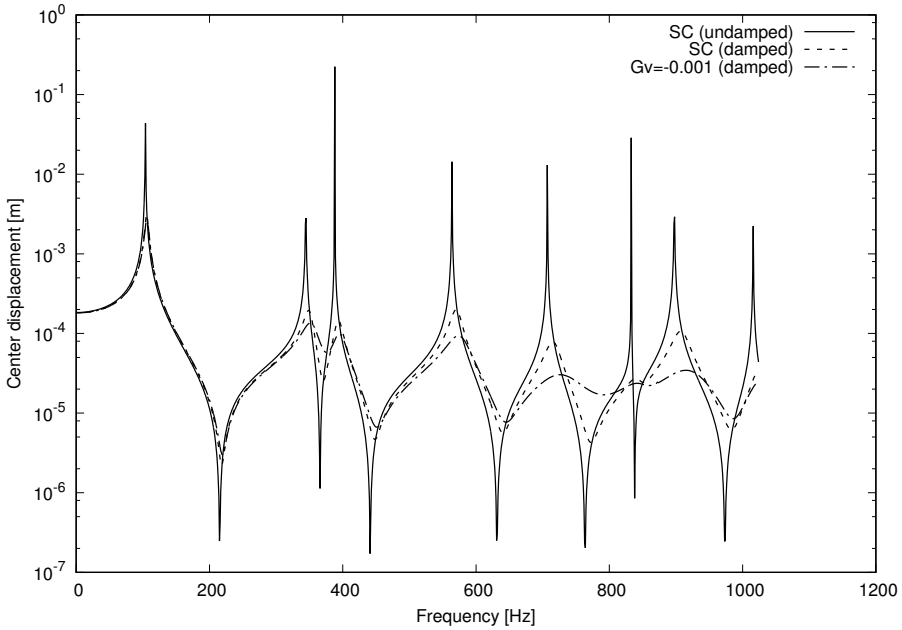

Figure 3: Magnitude of the frequency response of the sandwich panel.

REFERENCES

[1] M. D. Rao. Recent applications of viscoelastic damping for noise control in automobiles and commercial airplanes. *Journal of Sound and Vibration* (2003) **262**(3):457–474.

[2] O. Foin, J. Nicolas, and N. Atalla. An efficient tool for predicting the structural acoustic and vibration response of sandwich plates in light or heavy fluid. *Applied Acoustics* (1999) **57**(3):213–242.

[3] S. Subramanian, R. Surampudi, K. R. Thomson, and S. Vallurupalli. Optimization of damping treatments for structure borne noise reduction. *Sound and Vibration* (2004) **38**(9):14–18.

[4] S. Assaf, M. Guerich, and P. Cuvelier. Vibration and acoustic response of damped sandwich plates immersed in a light or heavy fluid. *Computers & Structures* (2010) **88**(13-14):870–878.

[5] A. Loredo, A. Plessy, A. El Hafidi, and N. Hamzaoui. Numerical vibroacoustic analysis of plates with constrained layer damping patches. *Journal of the Acoustical Society of America* (2011) **129**(4):1905–1918.

[6] W. Larbi, J.-F. Deu and R. Ohayon. Finite element formulation of smart piezoelectric composite plates coupled with acoustic fluid. *Composite Structures* (2012) **94**:501–509.

[7] W. Larbi, J.-F. Deu and R. Ohayon. Finite element reduced order model for noise and vibration reduction of double sandwich panels using shunted piezoelectric patches. *Applied Acoustics* (2016) **108**:40–49.

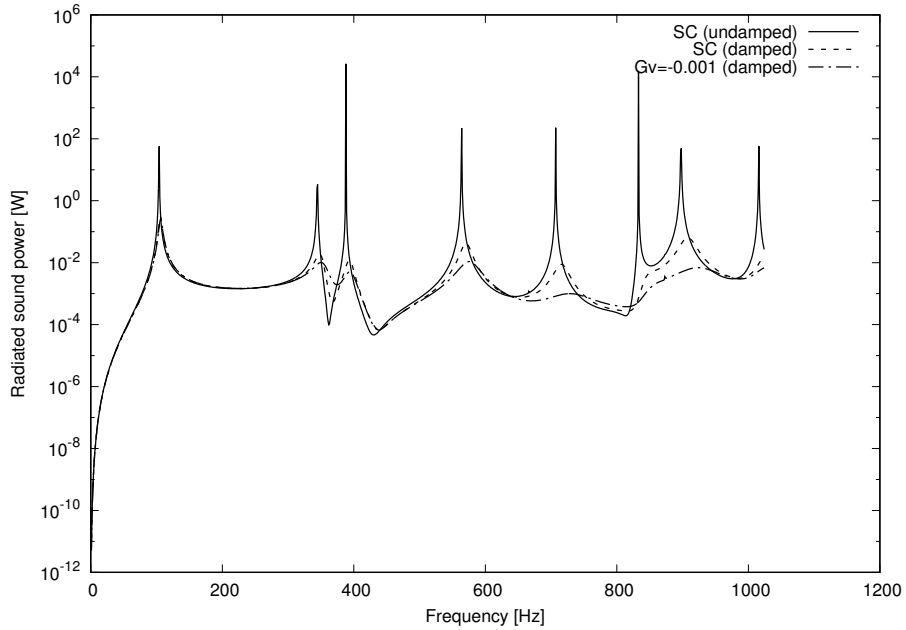

Figure 4: Radiated sound power of the sandwich panel.

[8] W. Larbi, J.-F. Deu and R. Ohayon. Vibroacoustic analysis of double-wall sandwich panels with viscoelastic core. *Computers & Structures* (2016) **174**:92–103.

[9] A.L. Araujo, V.S. Carvalho, C.M. Mota Soares, J. Belinha and A.J.M. Ferreira. Vibration analysis of laminated soft core sandwich plates with piezoelectric sensors and actuators. *Composite Structures* (2016) **151**:91–98.

[10] A.L. Araújo, H.M.R. Lopes, M.A.P. Vaz, C.M. Mota Soares, J. Herskovits and P. Pedersen. Parameter estimation in active plate structures. *Computers & Structures* (2006) **84**:1471–1479.

[11] J.N. Reddy. *Mechanics of Laminated Composite Plates and Shells: Theory and Analysis.* 2nd edition, CRC Press, Boca Raton, (2004).

[12] R.M. Christensen. *Theory of Viscoelasticity.* 2nd edition, Academic Press, New York, (1982).

[13] E. Barkanov. Transient response analysis of structures made from viscoelastic materials. *International Journal for Numerical Methods in Engineering* (1999) **44**:393–403.

[14] D.C. Sorensen. *Implicitly restarted Arnoldi/Lanczos methods for large scale eigenvalue calculations.* Technical Report TR95-13. Department of Computational and Applied Mathematics, Rice University, Houston, Texas, (1995).

[15] F. Fahy and P. Gardonio. *Sound and Structural Vibration: Radiation, Transmission and Response.* 2nd Edition, Academic Press, (2006).

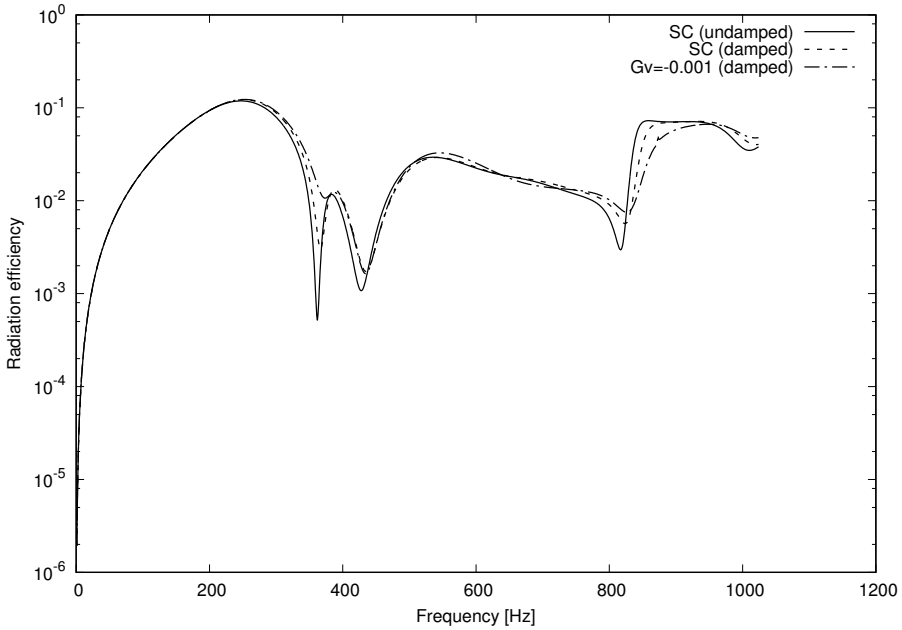

Figure 5: Radiation efficiency of the sandwich panel.

[16] T. Pritz. Five-parameter fractional derivative model for polymeric damping materials. *Journal of Sound and Vibration* (2003) **265**:935–952.

A NANOCOMPOSITE-INSPIRED SMART SENSING COATING FOR ACOUSTO-ULTRASONICS-BASED STRUCTURAL HEALTH MONITORING: *MODELING, VALIDATION AND APPLICATION*

YAOZHONG LIAO[*], MENGLONG LIU[*], HAO XU[†], LIMIN ZHOU[*] AND ZHONGQING SU[*]

[*]Department of Mechanical Engineering
The Hong Kong Polytechnic University
Hung Hom, Kowloon, Hong Kong SAR
e-mail: Zhongqing.Su@polyu.edu.hk (Prof. Zhongqing Su, *Ph.D.*),
web page: http://www.mypolyuweb.hk/mmsu/index.html

[†]School of Aeronautics and Astronautics
Dalian University of Technology
Dalian, P.R. China
e-mail: xuhao@dlut.edu.cn

Key words: Smart sensing coating, Carbon nanocomposites, Acousto-ultrasonics, Structural health monitoring

Abstract. An innovative smart sensing coating based on the nanocomposites made of carbon black (CB) and polyvinylidene fluoride (PVDF) is developed. This coating exhibits high fidelity, fast-response and high sensitivity to broadband acousto-ultrasonic waves (from static to high frequency up to 400 kHz). Making use of the tunneling effect [1], the nanostructure of the developed nanocomposites allows the coating to perceive low dynamic disturbance induced by acousto-ultrasonic waves. Morphological characterization is implemented on the prepared nanocomposites to reveal the sensing mechanism of the sensor. For the sake of balancing conductivity and sensitivity, 6.5 wt% of CB nanofiller is determined based on morphological characterization. Performance of the coating is demonstrated by using the sensing coating to capture acousto-ultrasonic waves from low-frequency vibration, through medium-frequency impact signals to high-frequency ultrasonic waves, to show good coincidence, frequency-independence and higher gauge factor compared with conventional piezoelectric transducers and strain gauges [2]. Lightweight and flexible, the developed sensing coating offers superior designability and tailorablilty, allowing it to be embedded in engineering structures of various geometries and materials, whereas with minimum weight penalty. In addition, a nano-scale model is developed, to facilitate understanding of the sensing mechanism and to corroborate experimental results. Last, the developed sensing coating is applied to acousto-ultrasonics-based structural health monitoring (SHM), including passive impact localization and active damage identification, highlighting that the coating has paved a new path for implementing *in-situ* SHM, by striking a compromise between "sensing cost" and "sensing effectiveness".

1 INTRODUCTION

The design and fabrication of high sensitive piezoresistive sensors that can be used to perceive broadband frequency waves and ultralow magnitude responses have been increasingly explored, to meet practical demand of structural health monitoring (SHM). Conductive polymer composites (CPCs), benefiting from excellent mechanical and electrical properties, have aroused a great deal of attention from engineering industry to develop new functional and structural materials, sensors, printing electronic circuits, and electro-magnetic shielding [3-6]. In fact, one of the most severe bottlenecks of CPCs-based sensors is that the sensors are not responsive to ultrahigh frequency (in an ultrasonic frequency regime) disturbance with ultralow magnitudes (of several micrometers or even nanometers).

Recently, the introduction of quantum mechanics has blazed a trail for developing nanocomposite-inspired smart sensors owing to the nanoscale fillers which can be dispersed uniformly in the matrix [1]. The microcosmic motion of the nanofillers can induce adjustments of internal conductive network resulting in resistivity change. Motivated by tunneling effect, a high sensitive and lightweight CPCs-based sensor made of CB and PVDF has been developed in this study for fulfilling structural health monitoring.

2 SENSOR FABRICATION AND CHARACTERIZATION

2.1 Sensor fabrication

CB (N220, with an average particle diameter of 80 nm, supplied by CABOT Corporation) and PVDF (Kynar k721, with a density of 1.74 g/cm^3, and a melting point of ~158 °C, supplied by ARKEMA Corporation) were chosen as fillers and matrix polymer, respectively to fabricate the nanocomposite. An internal mixer was employed to disperse CB particles uniformly in PVDF matrix by a standard melt-mixing process at 190 ºC and 50 rpm for 0.5 hour. Then the hybrids, with various mass ratio of nanofillers ranging from 5 to 30wt%, were cured under 20 MPa and 190 °C by hot-press method inside a two-steel-plate model. The fabricated sensors were tailored into rectangular flake-like sensing elements, each measuring 15 mm × 8 mm ×200 μm. A dual-component (polymer/silver powder) adhesive (D05001, Beijing Emerging Technology Co. Ltd., China) was deposited upon the flake for introducing electrodes to form a sensor. A light weight and flexibility sensor with silver pasted electrodes was developed as shown in Figure 1, and later the electrical resistivity and morphological characteristics were evaluated and represented.

2.2 Fundamental Characterizations

The conductivity of the fabricated sensors with various CB concentrations was measured. A dramatical conductivity enhancement can be observed between 5 wt% to 10 wt%, as shown in Figure 2, so that the percolation threshold of the hybrid sensor can be determined to be around 6.5 wt% where a sufficiently conductive network is formed.



Figure 1: A fabricated CB/PVDF nanocomposite sensor with silver pasted two electrodes (front and back view)

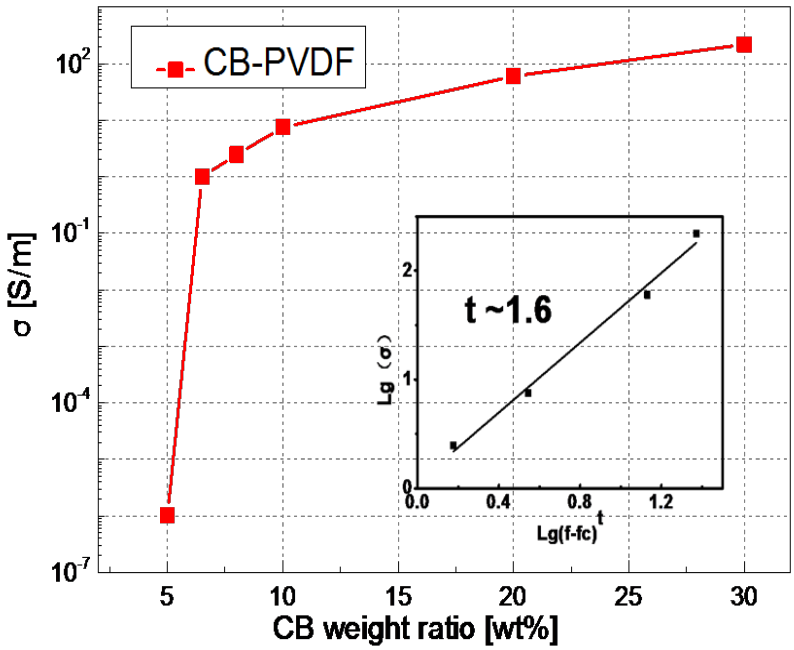

Figure 2: Electrical conductive of fabricated sensors with various CB concentration

In quest of the microstructure of the hybrid sensors, a scanning electron microscopy (SEM) (JSM-7500F, JEOL Ltd.) was used to reveal the dispersion status of CB in the matrix including the formation of conductive network and their aggregation. The hybrid sensor was treated by spray-gold for 30 s before scanning. It can be observed from Figure 3 that the CB nanofillers are dispersed uniformly in the PVDF polymer with sparse aggregation at the determined percolation threshold (~6.5 wt%).

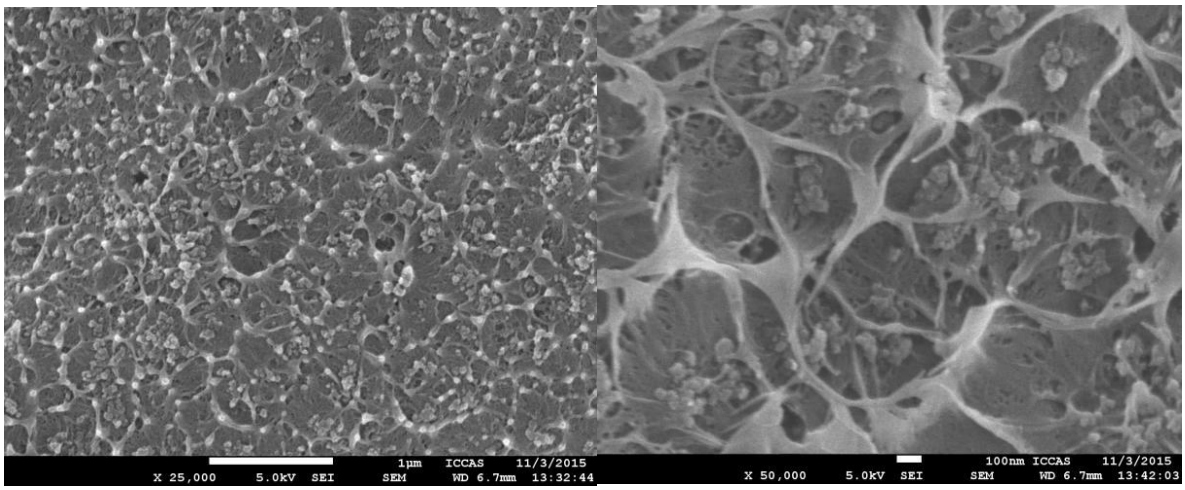

Figure 3: Nano-scalar structures of the fabricated 6.5 wt% nanocomposite (right: zoomed-in SEM image of the one on left)

The crystal characteristic of the hybrid sensor was confirmed by X-ray diffraction (XRD) analysis at room temperature on a XRD platform (X'Pert Pro, PANalytical, the Netherlands) at the determined percolation threshold. As seen in the Figure 4, this speculation shows that this hybrid sensor is mainly α-crystals with a non-polar structure, which manifests that the resistivity change should originate from PVDF matrix itself depending on piezoresistivity and has not relation with piezoelectricity because only a polar crystal (such as β-crystals) will induce piezoelectricity.

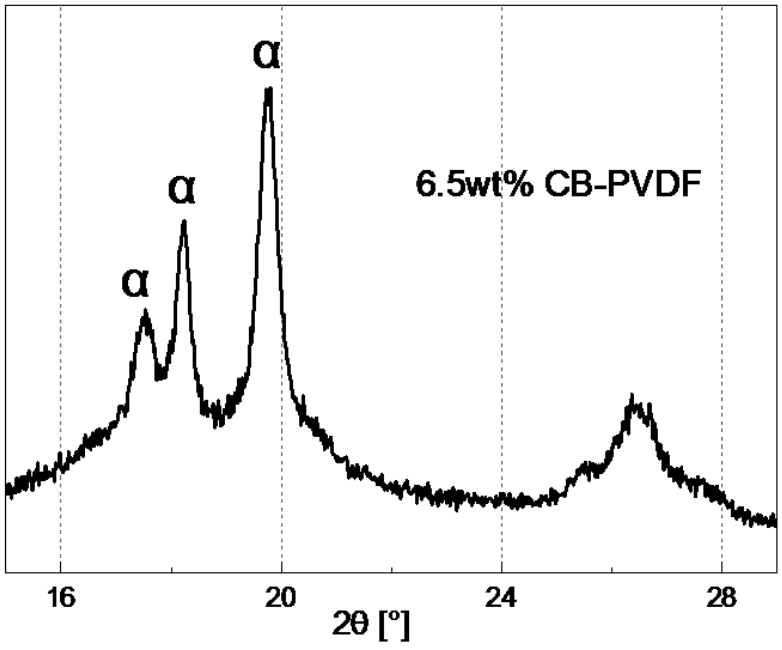

Figure 4: XRD pattern of the hybrid sensor

Static and dynamic electrical resistance (ER) change analysis were implemented to gain a further understanding of the sensing mechanism of the hybrid sensor with various CB concentrations. Static and dynamic electro-mechanical responses of the fabricated sensor were conducted by a dynamic mechanical testing platform (TA Q800, TA Instruments) and a semi-conductor characterization system (4200-SCS, Keithley Instrument, Inc., Cleveland, Ohio, the USA).

The static ER change ratio of the fabricated sensor, which has a CB concentration lower than 20 wt%, shows a linear relation with the strain change and a higher gauge factor (around 5) comparing with traditional metal-foil strain gauge as shown in Figure 5(a). Later, a cyclic tensile stress was applied to the sensor showing good consistency between response and dynamic load as seen in Figure 5(b).

Owing to the high aspect ratio of the CB particles, each CB particle can easily "communicate" with the neighbor particles to form a series of conductive paths resulting in resistivity increase. Tunneling effect, when the distance between two adjacent CB particles dispersed in the matrix is extremely close (of the order of several nano-meters), is the primary working mechanism.

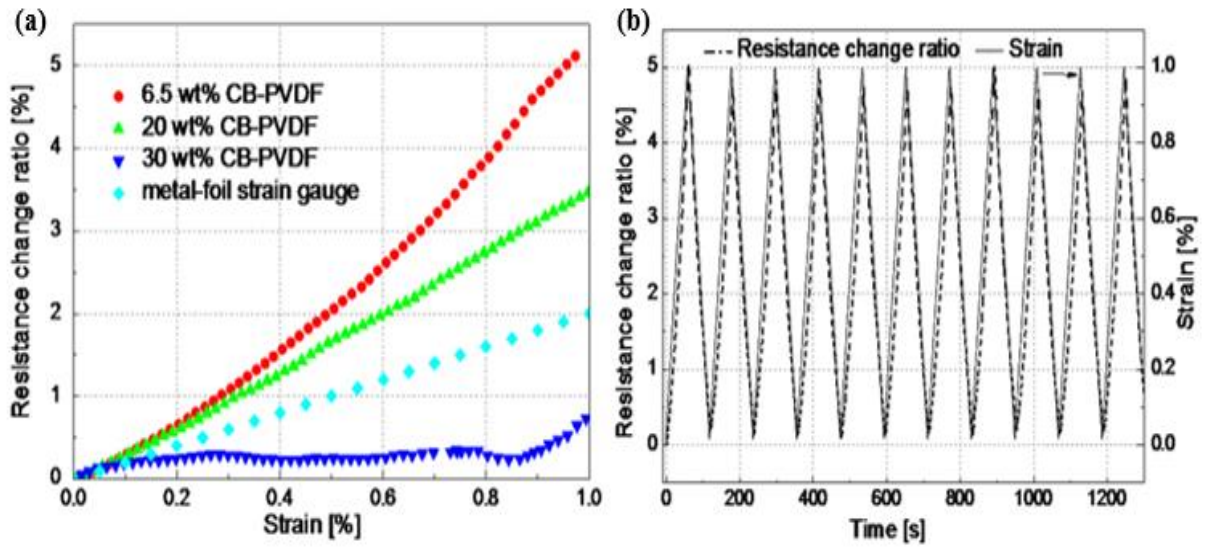

Figure 5: (a) ER response of the fabricated sensors at different CB concentrations under static load (b) ER response of the fabricated sensors at percolation threshold under cyclic load

3 PROOF-OF-PRINCIPLE TEST

On account of the different working mechanisms (strain change will result in electric potential adjustment for PZT wafers while resistance change for CB/PVDF sensors), two different acquisition methods were carried out: PZT could be directly connected to the oscilloscope (Agilent® DSO9064A) without any treatment, while CB/PVDF sensors would be connected into a self-developed electrical bridge system to transfer resistivity change into voltage change, whose output was displayed on the oscilloscope either.

3.1 Acquisition of Low-Frequency Vibration Signals

Owing to the high magnitude of excitation signal, a low-frequency structural vibration can be easily captured by the fabricated sensor bonded in a cantilever through a vibration shaker (B&K® 4809). The fabricated sensor can receive a stable and regular sinusoidal signal with obvious signal amplitude from 100 Hz to 3000 Hz as seen in Figure 6(a). Taking 100 Hz as an example, the response magnitude of the fabricated sensor with various CB concentrations shows a good linear relation with the excitation voltage as shown in Figure 6(b) and (c). A 2000 Hz sinusoidal signal was applied to the cantilever beam continuing about 100 million cycles and the result is shown in Figure 6(d), manifesting that the fabricated sensor possesses longer working life and more stable sensing performance than other reported sensors.

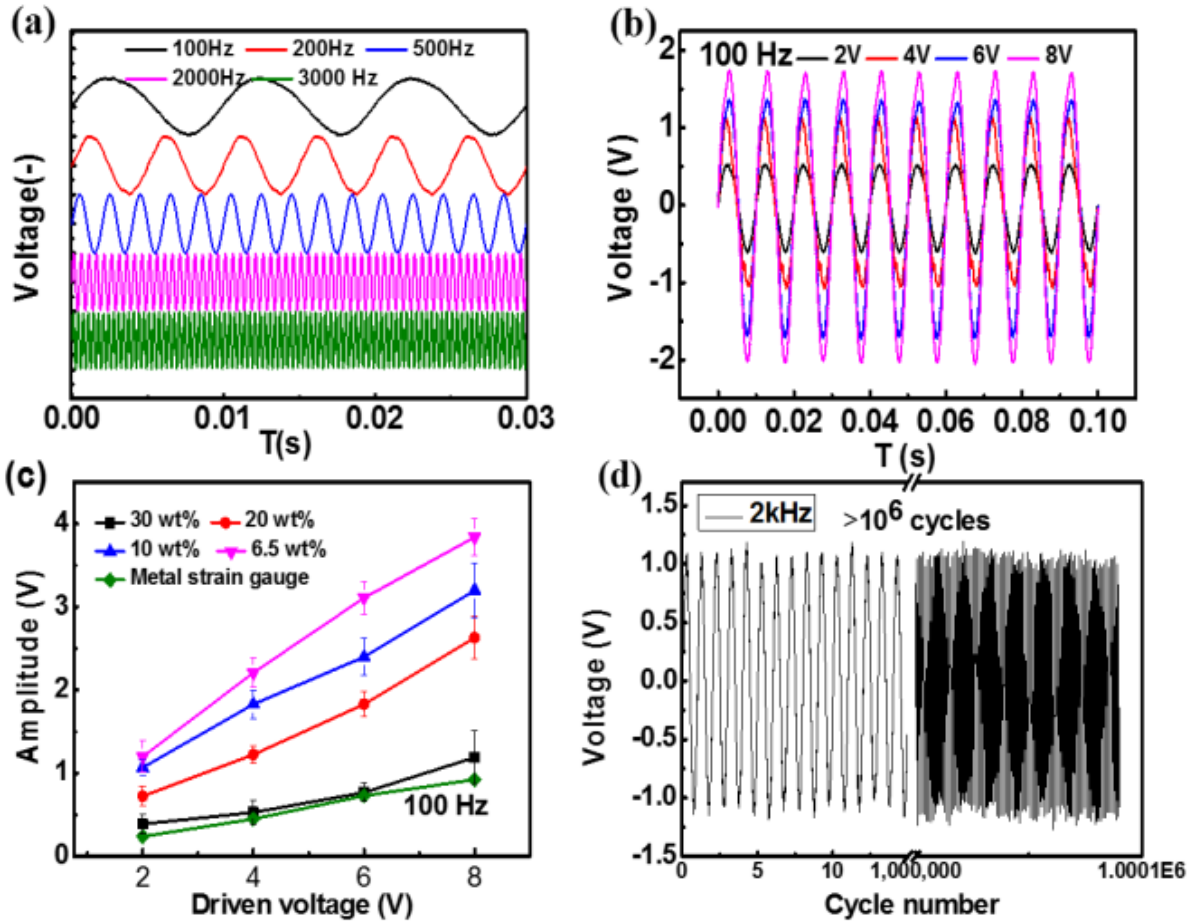

Figure 6: (a) vibration signals captured by 6.5 wt% CB/PVDF sensor at different central frequencies ranging from 100 to 3000 Hz, (b) response signals of 6.5 wt% CB/PVDF composites under 100 Hz with various excitation amplitude, (c) amplitudes of sensing signal for various concentrations of CB/PVDF composites under various excitation magnitudes at 100 Hz, (d) sensor stability test of the fabricated sensor with 6.5 wt% CB under 2000 Hz

3.2 Acquisition of Medium-Frequency Impact Signals

A drop test was conducted, in which a steel ball fell from a height of 15 cm, to impact a glass-fiber plate and then the signals were captured by the CB/PVDF sensor and compared

against the responses perceived with traditional PZT wafers. As seen in Figure 7(a), the two received signals are quite similar with a slight deviation in the time domain since the total propagation distances of PZT and the fabricated sensor are approximate and some manmade errors cannot be avoided. Simultaneously, the time domain response data is transferred into frequency domain data by Fourier transfer method, which reveals its potential applicability to sense medium frequency signal below 5 kHz as observed in Figure 7(b).

3.3 Acquisition of High-Frequency Ultrasonic Guided Wave Signals

Two PZT wafers were used to excite ultrasonic guided waves (GUWs) and acquire signals, separately. Five-cycle Hanning-windowed sinusoidal tone bursts were applied to the excited PZT wafer at a central frequency ranging from 50 to 400 kHz emitted by a waveform generator (NI® PXIE-1071). The CB/PVDF nanocomposite sensor and the acquisition PZT wafer, both having the same distance (150 mm) to the excited one, were deposited on the glass fiber plate to acquire GUWs simultaneously. Taking 175 kHz as an example, as observed in Figure 8, the first arrived wave (Lamb wave with zeroth-order symmetric mode, represented by S_0), which possesses remarkable amplitude and unambiguous waveform, was captured by PZT wafer and the CB/PVDF nanocomposite keeping consistent in terms of arrived time. Furthermore, the CB/PVDF nanocomposite can receive GUWs ranging from 50 to 400 kHz with distinguishable time information and signal intensity.

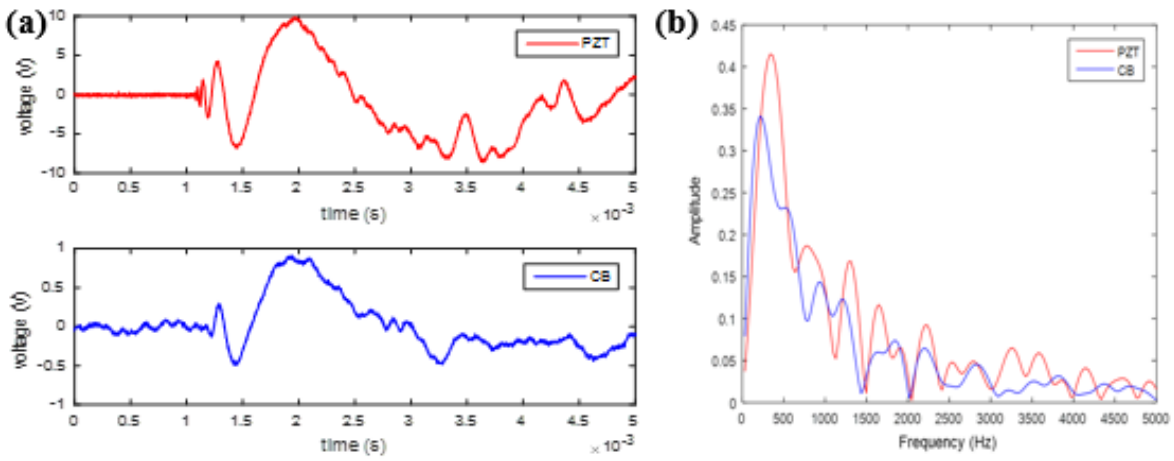

Figure 7: (a)Original impact signals acquired by PZT and CB/PVDF (b)Frequency spectrum by FFT of the normalized filtered impact signal acquired by PZT and CB/PVDF

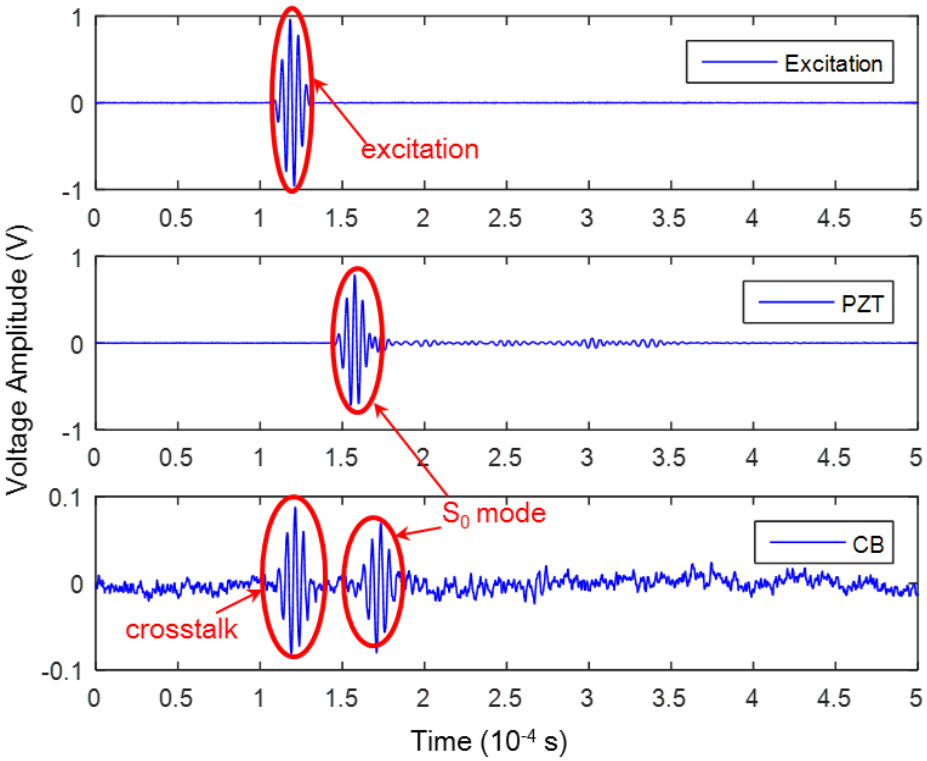

Figure 8: (a) Excitation signal (at 175 kHz); raw GUW signals captured by (b) PZT wafer, and (c) CB/PVDF nanocomposite sensor

4 SIMULATION AND 3D NANOSCAL MODELING

A 3D model was established to gain a further understanding of the working mechanism (tunneling effect) of the fabricated sensor. On the basis of the SEM image in Figure 3, the CB nanoparticles (diameter of each is 80 nm) are dispersed randomly to form a series of fractal aggregate containing 16 CB particles each as shown in Figure 9(a). As highlighted in the cubic model, several conductive paths are formed by the propagation of tunneling current through the CB aggregations. A 2D simplified view of the 3D model is also presented to ferret out the potential conductive path when the structure is subject to external pressure or interference. The piezoresistive response can be evaluated by the follow equation:

$$R_{Tunneling} = \frac{16\pi^2 h}{3e^2}\frac{d}{k_0 S}\exp(k_0 d) \quad (1)$$

In the above, k_0 denotes the potential barrier to be determined by $k_0 = \frac{2\sqrt{2m_e}}{h}\sqrt{V_e}$, in which V_e signified the potential height (0.2 eV) and me is the mass of an electron; h is the Planck constant, e the quantum of electricity, and d the shortest distance between two neighboring CB nanoparticles.

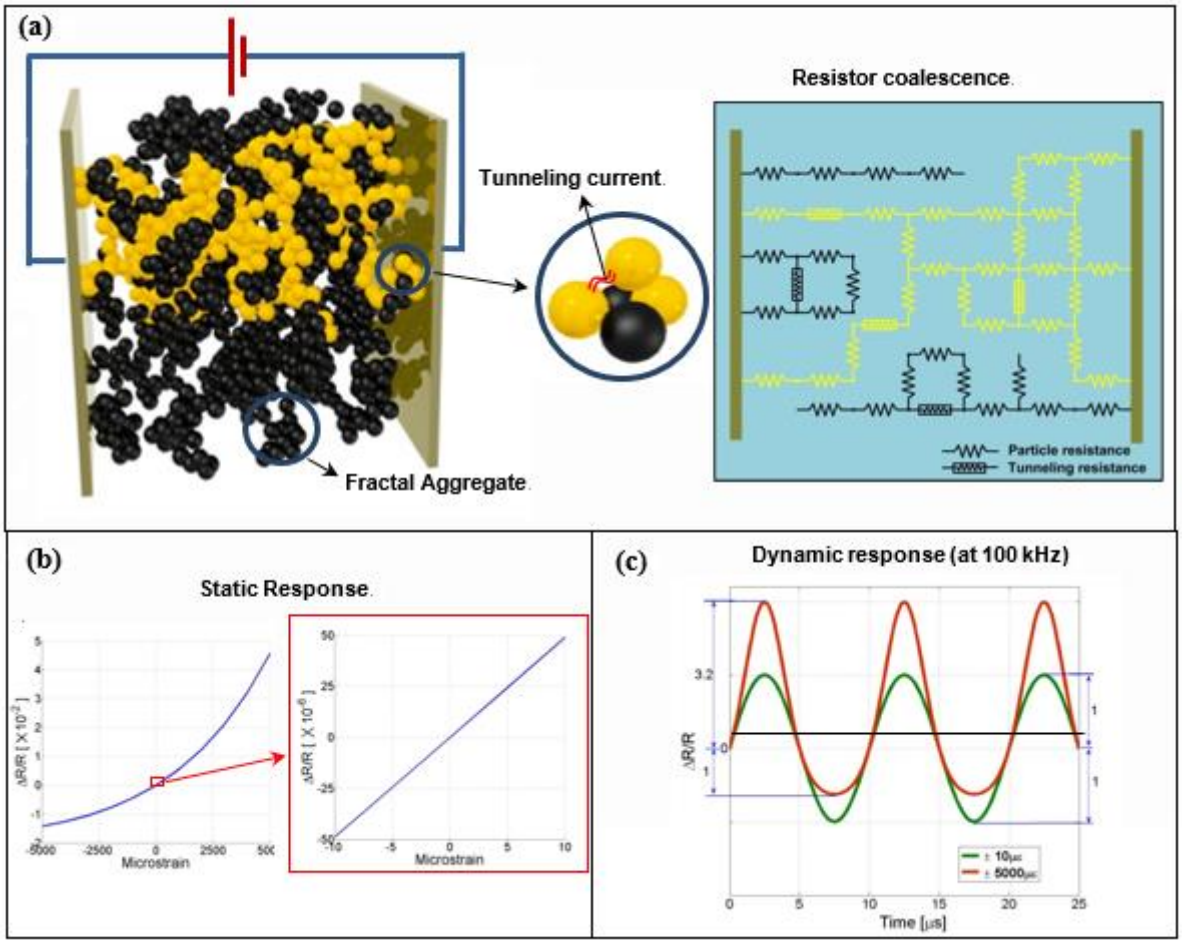

Figure 9: (a) 3D nanostructure model of the fabricated sensor and 2D simplified model; (b) static response under static strain; (c) dynamic response under 100 kHz GUWs

Furthermore, the static resistance change driven by a load ranging from -5000 to +5000 μm and dynamic resistance change under a 100-kHz sinusoidal excitation were simulated using this model. As showed in Figure 9(b), a nonlinear relation between the response and static strain alternation can be observed in a largescale strain range, but the change curve is still strictly linear within a small sub-range (±10 με - the excited amplitude for GUWs). And Figure 9(c) shows good consistence without any hysteresis between the excitation signal and the response. Those results verify the potential of the fabricated sensor to acquire structural disturbance and deformation in a broadband frequency range.

5 DAMAGE DETECTION

Eight fabricated sensors, representing by the yellow circle in Figure 10, were uniformly surface-mounted to four perpendicular sides of a square glass-fiber composite plate. Simultaneously, a PZT wafer, mounted at the center of the plate (green circle in Figure 10), was used to emit GUWs at a central frequency of 175 kHz which had been amplified to 400 Vp-p before applied on the wafer through a waveform generator. Then, the eight fabricated sensors

could be used to acquire the GUWs respectively and finally transfer into schematic diagram of damage location through a self-developed algorithm. From the figure, we can find that the true damage location is precise in the region of the prediction area.

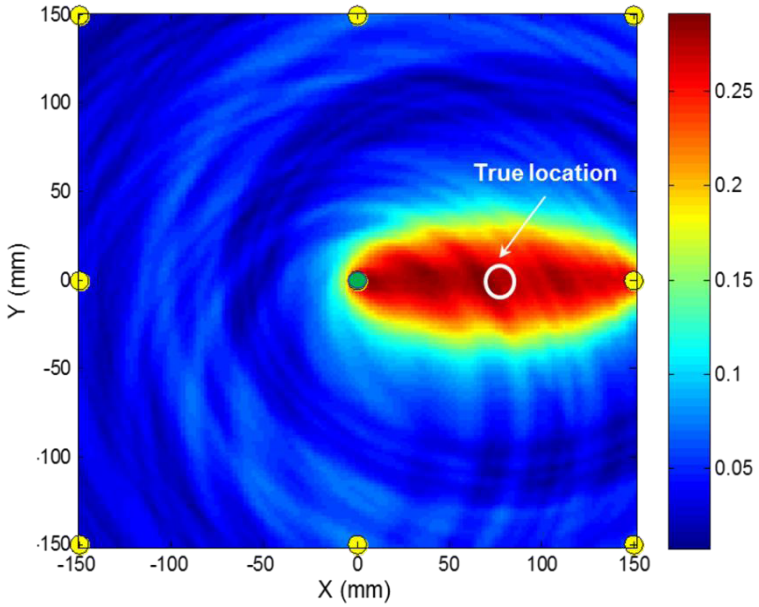

Figure 10: damage location using the fabricated sensors

6 CONCLUSIONS

In this study, the potential of sensing structural vibration and ultrasonic waves using the fabricated CB/PVDF nanocomposite sensor has been verified via experiment, through computational simulation, to practical application. Conclusions have been drawn that

- the fabricated nanocomposite sensor can perceive the acousto-ultrasonic signal favorably, comparable with traditional PZT wafers without any hysteresis;
- most importantly, this hybrid sensor can perceive the signal in an ultrawideband frequency range from static to 400 kHz, in virtue of the piezoresistivity and tunneling effect;
- numerical simulation further reveals the micro mechanism about how the conductive paths created under the GUWs with a micro-scale magnitude;
- the CB/PVDF sensor can be used to implement structural-vibration-based or ultrasonic-wave-based damage detection for engineering structures with minimum weight-penalty.

In conclusion, a lightweight and fast-response nanocomposite sensor has been developed to path a new way for structural health monitoring.

ACKNOWLEDGEMENTS

This project is supported by the Hong Kong Research Grants Council via General Research Funds (No. 15201416, 15214414, 523313). This project is also supported by National Natural Science Foundation of China (Grant No. 51375414).

REFERENCES

[1] Hu N, Karube Y, Yan C, Masuda Z and Fukunaga H. Tunneling effect in a polymer/carbon nanotube nanocomposite strain sensor. *Acta Mater.* (2008) **56**: 2929-36

[2] Zeng, Z., Liu M., Xu H., Liao Y., Su Z., et al. A coatable, light-weight, fast-response nanocomposite sensor for the in-situ acquisition of dynamic elastic disturbance: from structural vibration to ultrasonic waves. *Smart Mater. Struct.* (2016) **25(6)**: 065005.

[3] Hwang S-H, Park H W and Park Y-B. Piezoresistive behavior and multi-directional strain sensing ability of carbon nanotube–graphene nanoplatelet hybrid sheets. *Smart Mater. Struct.* (2013) **22**: 015013

[4] Parmar K, Mahmoodi M, Park C and Park S S. Effect of CNT alignment on the strain sensing capability of carbon nanotube composites. Smart Mater. Struct. (2013) **22**: 075006

[5] Gong L, Kinloch I A, Young R J, Riaz I, Jalil R and Novoselov K S. Interfacial stress transfer in a graphene monolayer nanocomposite" *Adv. Mater.* (2010) **22**: 2694-7

[6] Thomassin J-M, Jérôme C, Pardoen T, Bailly C, Huynen I and Detrembleur C. Polymer/carbon based composites as electromagnetic interference (EMI) shielding materials. *Mat. Sci. Eng. R.* (2013) **74**: 211-32

Application of carbon nanotubes-based hierarchical hybrids in damage sensing of structural composite materials

Delong He, Weikang Li, Benhui Fan and Jinbo Bai*

jinbo.bai@centralesupelec.fr

Laboratoire de Mécanique des Sols, Structures et Matériaux, UMR 8579 CNRS, Ecole CentraleSupelec, Université Paris-Saclay, Grande Voie des Vignes, 92290, Chatenay-Malabry, France

Advanced fiber-reinforced polymer composites are playing an increasingly important role in aerospace and aeronautics, due to their light weight, high specific modulus and strength, excellent fatigue and corrosion resistance. However, the widely-used thermosetting matrix-based composite structures are extremely sensitive to impact damage, which might result in significant degradation of composite properties, and even catastrophic failure in some cases. Therefore, in-situ damage sensing ability is highly desired to improve the composite structure security.

In this communication, carbon nanotubes (CNTs)-based hierarchical structures are integrated into glass fiber reinforced epoxy matrix composites. The improved composite electrical conductivity and the piezoelectric properties of CNTs allow *in-situ* monitoring the failures generated inside the composites under external mechanical load. Two kinds of nano/micro hybrids are studied, which include CNTs-grafted alumina microparticles (CNTs- uAl_2O_3) and CNTs-grafted glass fibers (CNTs-GF). These hybrids have aligned CNTs on the microparticles or fibers, which are in-situ synthesized by chemical vapor deposition method. The hybrids are introduced into the composites by the following two ways: directly mixing with polymer matrix for the CNTs-uAl_2O_3, and substituting conventional GF with hierarchical reinforcement for the CNTs-GF. The electrical resistance variation as a function of strain is investigated for the two kinds of composites. A detailed study has also been conducted on the correlation between the electrical resistance variation and the internal structural damages such as delamination and fiber/matrix interfacial debonding. The results demonstrate that the CNTs-based hybrid structures have great application potential in the fields of composite structure health monitoring.

Key word: Carbon nanotube, hybrid structure, glass fiber, composite, damage sensing

VIII ECCOMAS Thematic Conference on Smart Structures and Materials
SMART 2017
A. Güemes, A. Benjeddou , J. Rodellar and Jinsong Leng (Eds)

CRACK PROPAGATION MONITORING ON BONDED JOINTS WITH NOVEL CARBON NANOTUBE DOPED ADHESIVE FILMS

XOAN F. SÁNCHEZ-ROMATE[A,B,*], CLAUDIO SBARUFATTI[C] , MARÍA SÁNCHEZ[B], ANDREA BERNASCONI[C], DIEGO SCACCABAROZZI[C], ALFREDO GÜEMES[A] AND ALEJANDRO UREÑA[B]

[a] Department of Aerospace Materials and Processes, Escuela Técnica Superior de Ingenieros Aeronáuticos, Universidad Politécnica de Madrid, Plaza del Cardenal Cisneros 3, 28040 Madrid, Spain

[b] Materials Science and Engineering Area, Escuela Superior de Ciencias Experimentales y Tecnología, Universidad Rey Juan Carlos, Calle Tulipán s/n, 28933 Móstoles (Madrid), Spain
[c] Politecnico di Milano, Dipartimento di Meccanica, Via La Masa 1, 20156, Milano, Italy

*Corresponding author: xoan.fernandez.sanchezromate@urjc.es Tel: +34 91 488 82 52

Key words: Carbon nanotubes, fatigue tests, crack detection, SHM, electrical properties

An investigation on fatigue crack propagation on bonded joints has been carried out. For that purpose, a novel carbon nanotube (CNT) doped adhesive film has been used, exploiting CNT exceptional electrical sensitivity for fatigue damage monitoring. Single lap shear fatigue tests have been conducted at 7 kN load and 10 Hz frequency while the electrical response of the joints has been measured by means of voltage acquisition. In addition, crack length has been also monitored by optical analysis using a microscope camera. A clear correlation between the electrical response and the crack length has been highlighted during fatigue tests. In particular, it is possible to distinguish three different regions: the first, with no crack initiation and, thus, a stable measured electrical resistance; the second, where crack initiation and a first propagation take place, characterized by a slight increase of the electrical resistance; the third, including the final propagation to failure, where a sharp increase of the electrical resistance is observed. Moreover, the number of cycles to failure is not affected negatively by the addition of CNTs. Thus, CNT doped adhesive film capability to detect crack initiation and propagation has been demonstrated, proving their huge potential for Structural Health Monitoring (SHM) purposes.

1 INTRODUCTION

In the last decades, the use of composite materials has increased drastically as they generally exhibit better specific properties than conventional alloys. In addition, the demand for mechanical performance maximization has led to the increase of composite structure complexity, often involving the integration of multiple components. In this context, the selection of proper assembly techniques is crucial.

In particular, bonded joints present many advantages over bolted connections as they avoid

stress concentrations at bolt holes and lead to weight saving [1,2]. However, their inspection is not easy and the availability of real-time inspection techniques would ensure the structure reliability with reduced maintenance costs. Some potential real-time applications are based on FBG sensors [2,3] and guided Lamb Waves [4] but in many cases they do not provide an accurate analysis of crack propagation and the acquired signal is often difficult to analyze.

Carbon nanoparticles and, more specifically, carbon nanotubes (CNTs), have demonstrated their applicability for SHM purposes [5-7] by providing electrical pathways through the insulator resin [8,9]. Their piezoresistive behavior [10] and the tunneling effect between adjacent particles [11,12] lead to good electrical resistance change sensitivity [13]. Crack propagation in bonded joints can thus be monitored by taking advantage of the excellent electromechanical properties of CNTs. In previous works, electrical conductivity and sensing properties of bonded joints using CNT doped adhesive films have been demonstrated [14,15]. The increase of the electrical resistance as a function of crack length was observed. This rise was more unstable in the case of stick-slip behavior due to the instability of crack propagation, while a more stable sensitivity was observed for a smooth damage evolution.

This study aims to continue investigating sensing capabilities of CNT doped adhesive films. The main goal is to correlate crack length with the electrical response of Single Lap Shear (SLS) specimens subject to fatigue loads, eventually predicting the final failure in advance. Fatigue test on SLS specimens are carried out while the crack length and their electrical response are measured. In addition, the effect of CNTs on the fatigue properties of the adhesive film is also investigated in terms of the number of cycle to failure.

2 EXPERIMENTAL PROCEDURE

2.1 Manufacturing of adhesive joints

Adhesive joints were manufactured by secondary bonding of CFRP substrates, supplied by Fundación para la Investigación, Desarrollo y Aplicación de Materiales Compuestos (FIDAMC) using an adhesive film doped with CNTs. Adhesive film was an *FM 300KN* epoxy-based supplied by Cytec. It has a wide open knit tricot carrier, indicated to achieve a better thickness control. CNTs are supplied by Nanocyl, with a commercial name *NC7000*. They have an average diameter of 11 nm and a length up to 2 μm.

CNTs are dispersed in distilled water in a weight fraction of 0.1 wt. %. A surfactant sodium dodecyl sulfate (SDS) is used to improve CNT dispersion in a weight fraction of 0.25 wt. %, previously optimized [15]. Then, the aqueous dispersion is sonicated during 20 min at 0.5 cycles at 50 Hz using a horn sonicator *UP400S* supplied by Hielscher. Then, CNT dispersion was sprayed over the adhesive surface using an airbrush at 40 cm distance and a pressure of 1 bar during 0.5 s in order to achieve a good homogenization of CNT dispersion over the sample. Curing cycle of CFRP bonded joints was set as shown in Table 1.

2.2 Electromechanical tests

Four fatigue single lap shear tests were carried out for the CNT doped and the neat adhesives. They were performed in a test machine *MTS 810*. The peak load was set to 7 kN, with load ratio R=0.1 and the test frequency was set to 10 Hz. These parameters were selected in order to obtain a finite fatigue life of approximately 100000 cycles, according to S-N curves for similar

adhesives and substrates [16].

Table 1: curing cycle parameters of secondary bonding.

Parameter	First Stage	Second stage
pressure	Ramp from 0 to 0.6 MPa during 15 min	0.6 MPa during 90 min
temperature	Ramp from 25 to 175 ºC during 45 min	175 ºC during 60 min

The monitoring of fatigue tests was carried out by means of voltage measurements between two points through the thickness, as shown in the set-up of Figure 1. The electrodes were made of copper wire attached to the substrate surface with silver ink and sealed with an adhesive layer to protect them from environment. Current through the specimen (approximately 1 mA) was generated by means of a power supply *STAB AR60* connected with an integrated circuit. Voltage acquisition was performed using a *NI9234* module supplied by National Instruments with a sampling frequency of 5 kHz. Crack length was measured on the edges using a microscope camera. In addition, GFRP tabs were used in order to electrically isolate SLS specimens from the test machine.

(a) (b)

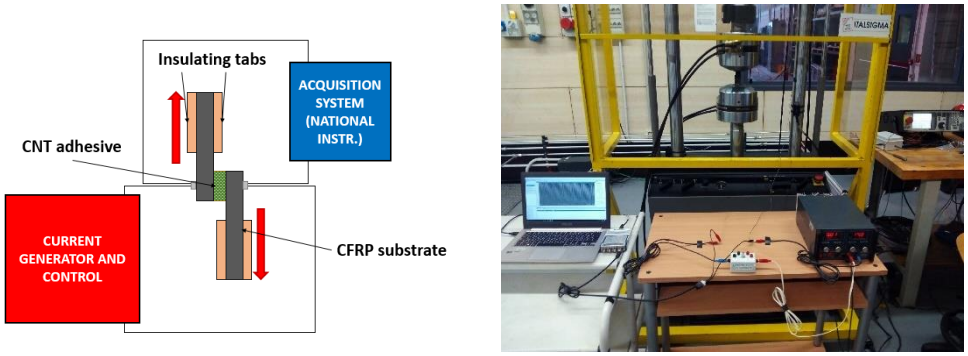

Figure 1: (a) schematics of fatigue test set-up and (b) image of the actual configuration.

3 RESULTS AND DISCUSSION

Figure 2 shows the voltage measurement as a function of time (and the number of cycles, considering the constant load frequency of 10 Hz) for a CNT-doped specimen. The normalized electrical resistance $\frac{\Delta R}{R_0}$ is directly calculated from the measured voltage by applying the Ohm's Law:

$$R = \frac{V}{I} \quad \rightarrow \quad \frac{\Delta R}{R_0} = \frac{R - R_0}{R_0} = \frac{\frac{V - V_0}{I}}{\frac{V_0}{I}} = \frac{V - V_0}{V_0} \tag{1}$$

Being R_0, V_0, R and V the resistance and the voltage at the initial acquisition frame (baseline) and at the generic time, respectively. Therefore, the variations of the electrical resistance are equal to the changes in the voltage.

On the other hand, Figure 3 shows a more detailed analysis of the electromechanical response, being correlated with the crack length determined by the microscope camera.

Focusing on Figure 2, the electrical response of single lap shear specimens during fatigue tests is affected by two contributions. The first corresponds to the variation of the electrical resistance within a single cycle (Figure 2 (b)), due to the CNT piezo-resistive behavior and the variation of tunneling distance as a function of the applied strain, similar to those observed in previous studies on quasi-static tests [17]. The second is related to the variation of the electrical resistance as a function of the number of cycles, associated to the fatigue crack evolution during the tests.

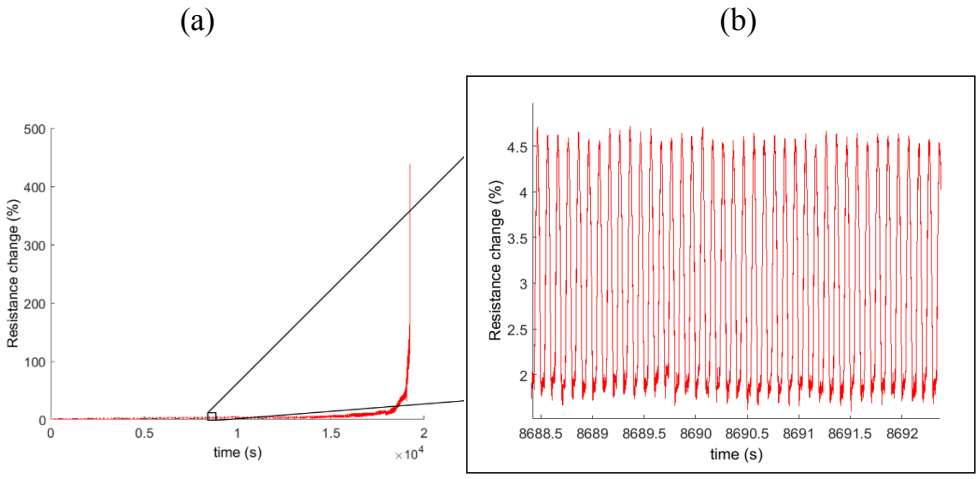

Figure 2: (a) variation of the electrical resistance as a function of the number of cycles and (b) detailed electrical response on repeated cycles.

Concerning the variation of the electrical resistance as a function of the number of cycles, three different regions can be highlighted in Figure 3, by observing the peak and valley trends, defined as the value of the normalized resistance when the maximum and minimum force is applied at each fatigue cycle, respectively. A simplified electrical sensitivity parameter is also defined, consisting in the difference between the maximum and the minimum normalized resistance for each cycle.

The first region is related to a quasi-stable electrical response. No variations are observed in the peak and valley trends and the sensitivity is almost constant, as shown in Figure 3 (b). The sensitivity is only including the effect of adhesive deformation, as no fatigue damage has nucleated yet, as observed in the left side TOM image (black rectangle) of Figure 3 (c).

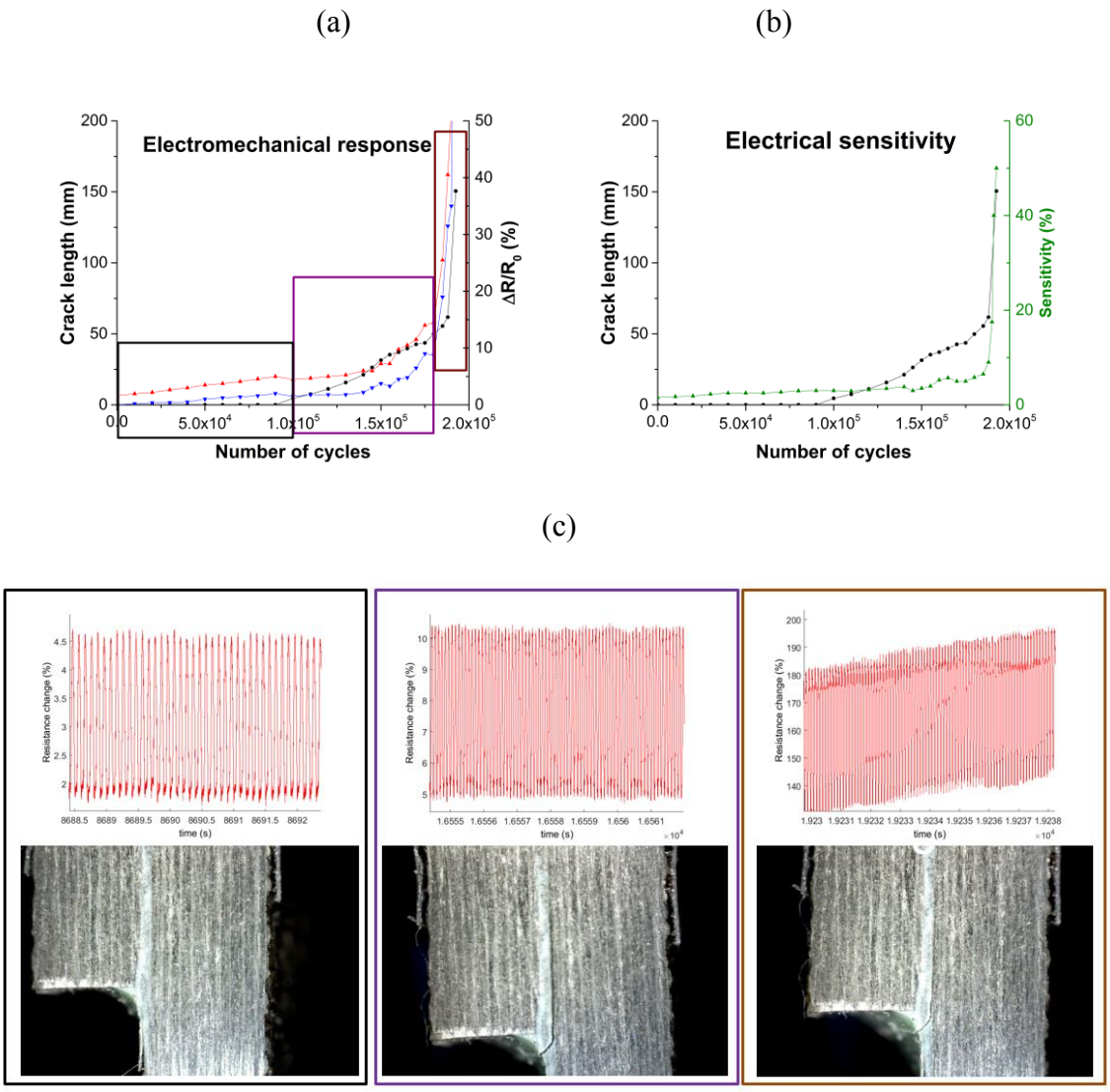

Figure 3: (a) detailed analysis of the electromechanical behavior during fatigue tests in which red and blue lines correspond to peak and valley normalised resistance, respectively; (b) analysis of sensitivity and (c) correlation with TOM images of crack length.

The second region corresponds to a slight variation of the electrical response. Both the peak and valley lines show a slight increase as a function of the cycle number, which is correlated to the crack initiation and a first stage of its propagation, as shown at Figure 3 (a) (purple rectangle). The modification of the sensitivity can be explained by observing Figure 4. When the minimum force is applied, the strain is lower and the crack is closed, while at peak force, the crack is wide open, due to a higher adhesive deformation. Thus, this difference on crack openings induces a higher variation of the electrical resistance (thus higher sensitivity) within

a single cycle. Obviously, the higher the crack length, the higher the change of the electrical resistance and, thus, the electrical sensitivity (Figure 3 (b))

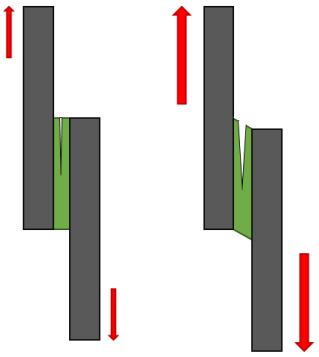

Figure 4: Effect of crack opening during a single cycle of fatigue test.

The third region is associated to the final propagation to failure. It is observed that both peak and valley lines present a much higher increase than for the second region and the sensitivity also suddenly increases. This is explained by a higher crack propagation velocity near failure, as observed in Figures 3 (a) and 3 (b) (brown region). Therefore, the proposed CNT doped adhesive films are able to properly monitor the crack evolution during a Single Lap Shear fatigue test. In addition, the variations observed in the sensitivity and the exponential behavior of the normalized resistance could lead to a better understanding of crack propagation during these tests, allowing to predict the onset of the final failure.

Finally, Figure 5 presents the mechanical behavior of neat and CNT doped adhesive joints, in terms of their fatigue life duration. It is observed that the mean value of the cycles to failure is considerably higher for the CNT doped adhesive joints than for the neat adhesive. However, the scattering is also higher in the first case, due to a non-uniform CNT dispersion over the adhesive surface, which induces preferential areas with CNT aggregates. Thus, it can be concluded that the addition of CNTs does not significantly worsen the number of cycles to failure during fatigue tests, thus confirming the lap shear strength results previously obtained in quasi-static tests [17].

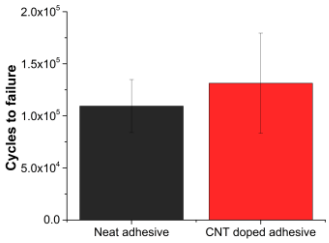

Figure 5: Number of cycles to failure for neat and CNT doped adhesive joints.

4 CONCLUSIONS

Fatigue tests on single lap shear specimens using CNT doped adhesive films have been carried out. It is observed that CNT doped adhesive films are able to properly monitor the crack evolution by means of electrical resistance measurements through thickness.

Crack propagation is correlated to the increase of the electrical resistance as a function of the number of cycles. This increase is higher with crack propagation velocity, that is, when the joint is close to final failure. Therefore, it is possible to predict the final failure by observing the changes of the electrical resistance.

In addition, no decrement of the fatigue life duration has been observed comparing the neat and CNT doped adhesive joints. Thus, it can be stated that the proposed CNT doped adhesive film does not affect negatively the mechanical behavior, showing a huge potential for SHM applications.

5 ACKNOWLEDGEMENTS

This work was supported by the Ministerio de Economía y Competitividad of Spanish Government [Project MAT2013-46695-C3-1R], Comunidad de Madrid Government [Project P2013/MIT-2862] and by the Department of Mechanical Engineering (DMEC) of Politecnico di Milano under the Young Researcher Program.

REFERENCES

[1] R. Hussey, J. Wilson, *Structural Adhesives: Directory and Databook*, Springer Science & Business Media, 1996.

[2] A. Bernasconi, M. Carboni, L. Comolli, Monitoring of fatigue crack growth in composite adhesively bonded joints using fiber Bragg gratings, *Procedia Engineering.* 10 (2011) 207-212.

[3] J. Palaniappan, S.L. Ogin, A.M. Thorne, G.T. Reed, A.D. Crocombe, T.F. Capell, S.C. Tjin, L. Mohanty, Disbond growth detection in composite-composite single-lap joints using chirped FBG sensors, *Composites Sci. Technol.* 68 (2008) 2410-2417.

[4] F. Habib, M. Martinez, A. Artemev, M. Brothers, Structural health monitoring of bonded composite repairs - A critical comparison between ultrasonic Lamb wave approach and surface mounted crack sensor approach, *Composites Part B-Engineering.* 47 (2013) 26-34.

[5] C. Li, E.T. Thostenson, T. Chou, Sensors and actuators based on carbon nanotubes and their composites: A review, *Composites Sci. Technol.* 68 (2008) 1227-1249. doi:10.1016/j.compscitech.2008.01.006.

[6] N. Hu, Y. Karube, M. Arai, T. Watanabe, C. Yan, Y. Li, Y. Liu, H. Fukunaga, Investigation on sensitivity of a polymer/carbon nanotube composite strain sensor, *Carbon.* 48 (2010) 680-687.

[7] Alamusi, N. Hu, H. Fukunaga, S. Atobe, Y. Liu, J. Li, Piezoresistive Strain Sensors Made from Carbon Nanotubes Based Polymer Nanocomposites, *Sensors.* 11 (2011) 10691-10723.

[8] C. Martin, J. Sandler, M. Shaffer, M. Schwarz, W. Bauhofer, K. Schulte, A. Windle, Formation of percolating networks in multi-wall carbon-nanotube–epoxy composites, *Composites Sci. Technol.* 64 (2004) 2309-2316.

[9] N. Hu, Z. Masuda, C. Yan, G. Yamamoto, H. Fukunaga, T. Hashida, The electrical properties of polymer nanocomposites with carbon nanotube fillers, *Nanotechnology.* 19 (2008) 215701.

[10] M.H.G. Wichmann, S.T. Buschhorn, J. Gehrmann, K. Schulte, Piezoresistive response of epoxy composites with carbon nanoparticles under tensile load, *Physical Review B.* 80 (2009) 245437.

[11] C. Li, E.T. Thostenson, T. Chou, Dominant role of tunneling resistance in the electrical conductivity of carbon nanotube-based composites, *Appl. Phys. Lett.* 91 (2007) 223114.

[12] N. Hu, Y. Karube, C. Yan, Z. Masuda, H. Fukunaga, Tunneling effect in a polymer/carbon nanotube

nanocomposite strain sensor, *Acta Materialia.* 56 (2008) 2929-2936.
[13] M.A. Cullinan, M.L. Culpepper, Carbon nanotubes as piezoresistive microelectromechanical sensors: Theory and experiment, *Physical Review B.* 82 (2010) 115428.
[14] C. Garcia, M. Sanchez, A. Urena, J. Rams, Carbon Nanotubes for Assessing the Structural Integrity of Composite Bonded Joints with Film Adhesives, *Structural Health Monitoring 2015: System Reliability for Verification and Implementation, Vols.1 and 2.* (2015) 2169-2176.
[15] X.F. Sánchez-Romate, M. Sánchez, C. García-Nieto, J. Molinero, A. Jiménez-Suárez, A. Güemes, A. Ureña, Structural health monitoring of bonded joints using carbon nanotube doped adhesive films, *Eur. Workshop Struct. Health Monit., EWSHM*. 4 (2016) 2450-2455.
[16] M. Quaresimin, M. Ricotta, Fatigue behaviour and damage evolution of single lap bonded joints in composite material, *Composites Sci. Technol.* 66 (2006) 176-187.
[17] X.F. Sánchez-Romate, M. Sánchez, C. García-Nieto, J. Molinero, A. Jiménez-Suárez, A. Güemes, A. Ureña, Structural health monitoring of bonded joints using carbon nanotube doped adhesive films, *Eur. Workshop Struct. Health Monit., EWSHM.* 4 (2016) 2450-2455.

GRAPHENE BASED CONDUCTING ARCHITECTURES TO MAKE QUANTUM RESISTIVE SENSORS (QRS) FOR HEALTH MONITORING

J. F. FELLER[*], S. NAG[*], M. CASTRO[*], T. T. TUNG[*] AND P. GUÉGAN[†]

[*] Université Bretagne Loire (UBL), Smart Plastics Group, IRDL CNRS 3744 - UBS, Lorient, France
e-mail: jean-francois.feller@univ-ubs.fr, mickael.castro@univ-ubs.fr
web page: http:// http://www.smartplasticsgroup.com/
[†] Sorbonne Universités, Chimie des Polymères, IPCM CNRS 8232 - UPMC, Paris, France
e-mail: philippe.guegan@upmc.fr
web page: http://www.ipcm.fr

Abstract: During the last decade, several nanocarbon species such as nanoparticles (CNP), nanotubes (CNT) or nanofoils (GR) have been synthesized allowing to design new functional conductive polymer nanocomposite (CPC) films able to react to their environment. In particular graphene based hierarchical conducting architectures can lead to quantum resistive sensors (QRS) able to detect tiny variations of strain [1] or volatile organic compounds VOC concentrations [2], thanks to respectively their original piezo- and chemo-resistive properties. When properly structured from the nano- to the macro-scale, these nanohybrids can meet promising applications such as human health monitoring by the prevention or non-invasive diagnosis of diseases derived from the analysis of VOC biomarkers emitted by the body (volatolomics). The best strategies used to control the different types of conductive architectures during their fabrication, and in particular the tailoring of the nano-junctions responsible for QRS sensitivity will be presented and discussed.

Keywords: Conductive Polymer nanoComposites; CPC; Smart Materials; Quantum Resistive Sensors; QRS; Chemo-Resistive; Piezo-Resistive; Human health monitoring; Graphene;

1 INTRODUCTION

During the last decade, several nanocarbon species such as nanoparticles (CNP) [3-4], nanotubes (CNT) [5-6] or graphene nanofoils such as (GR) [7,8] have been synthesized allowing to design new functional conductive polymer nanocomposite (CPC) films able to react to their environment providing a new class of smart materials. In particular graphene based hierarchical conducting architectures can lead to two categories of quantum resistive sensors (QRS) able to detect either volatile organic compounds VOC concentrations [2] or tiny variations of strain or pressure [1] thanks to respectively their original chemo- and piezo-resistive properties.

1.1 Graphene based materials with chemo-resistive properties

vQRS can bring a significant contribution to the new and active field of research studying the volatile organic compounds (VOC) produced by a biological system to investigate the metabolite differences between natural and perturbed systems (cells, organs and tissues).

Thus, metabolomics allows profiling diseases such as cancer from a VOC fingerprint found in breath, urine, faeces, saliva, nasal mucus or gaseous excretions of the skin [9] or combination of them [10]. Among these, exhaled breath is an excellent source containing several hundreds of VOC (including water) but at the ppm or ppb level, which makes their identification difficult. However, analysing VOC profiles with pattern recognition algorithms allows to efficiently discriminate between cancerous and healthy subjects [11–20]. Commonly used techniques for breath VOC analysis such as GC-MS [21], infrared spectroscopy [22], ion flow tube mass spectrometry [23], optical spectroscopy [24], suffer from several shortcomings such as high cost, low-portability, low sensitivity or high consumption. On the contrary, arrays of nonspecific sensors, i.e., electronic noses (e-nose), have demonstrated their effectiveness in the detection of VOC [25]. E-noses present in particular the advantage of being non-invasive, cost effective, quick and portable. Additionally they are allowing real time monitoring [26] and provide almost directly a pattern of exhaled biomarkers in the form of a VOC breath imprint [27]. Moreover, a wide choice of vapour sensors can be assemble in the array, depending on the nature of the transducer: metal oxides (MO) [20-21], intrinsically conductive polymers (ICP) [22-23], and functionalized carbon nanomaterials or nanocomposites [4,32–35]. However, e-noses have also some drawbacks, such as processing and performance reproducibility, drift in baseline and response of sensors requiring sometimes recalibration so that none of these strategies allows really to control at the same time the architecture of the conducting network and the physico-chemical properties of the junction's gap, optimizing at the same time sensitivity, stability and selectivity of the QRS. This communication aims at demonstrating that these parameters can be optimized, through the development of hybrid transducers, fabricated by supramolecular assembly of graphene and cyclodextrin. These two singular nanofillers, which combine steric and chemical effects, will allow reaching a positive synergy thanks to their complementary properties that will be shortly described in the following.

1.2 Graphene based materials with piezo-resistive properties

sQRS are piezo-resistive materials able to convert strain into an interpretable signal. They are finding applications in variety of areas such as automotive, aerospace, manufacturing plants, heavy machinery, and sport-wear products [36, 37, 38]. Doped silicone is a well-known piezo-resistive material for pressure sensors, because of its high piezo-resistive strain coefficient (gauge factor) [39]. However, silicon-based sensors have an issue on their reliability, because their sensing response is highly dependent on the environmental parameter such as temperature and moisture. The integration of silicon onto mechanically flexible substrates or flexible MEMS devices is also limited due to its high processing temperatures [40, 41, 42]. Thus, alternative piezo-resistive materials such as fibres (carbon, glass, aramid, etc.) reinforced polymer composites (FRPC) are being increasingly used in the industry [43, 44, 45, 46]. At present, carbon nanotubes (CNT) are particularly interesting for the next generation of piezo-resistive materials because of their possible local bonding change from sp^2 to sp^3 and the band gap opening [47, 48]. In particular conditions, CNT can lead to gauge factor as high as 100 or even 200, which surpasses those of doped Si and metals. However, CNT are still difficult develop in large-area devices because of variations in chirality [49], difficulty of dispersion and high cost of production, which limits their widespread use [50]. It has been reported that the high specific surface area along with two-dimensional geometry of

graphene is superior to one-dimensional nanotubes, which is a key enabler in enhancing the mechanical properties of polymer composites as compared to CNT [51, 52, 53, 54, 55-56]. Among various forms of graphene-based materials, chemically modified graphene has been widely explored for various applications including sensing devices because they possess chemically active sites and are available in a wide range of processible forms [57, 58, 59, 60, 61, 62]. In order to further explore its potential, the researchers are experimenting ways to functionalize graphene with nanoparticles (NP). Hybrid materials consisting of graphene and NP could potentially display not only the unique properties of NP and those of graphene, but also additional novel properties due to the synergistic interaction between them [63, 64]. In this respect, hybrids of chemically modified graphene with magnetic nanoparticles (i. e., Fe_3O_4 NP) are also a good option to produce a new type of sensing materials with tailored structures and functions [65, 66, 67, 68, 69, 70, 71].

In this communication, we have investigated the potentiality of graphene nanofoils to build an original conducting architecture with enhanced piezo-resistive properties for the design of tactile sensing skins. The idea was to use a poly(urethane) matrix to host and protect the percolated conducting network, and use poly(ionic liquid) to effectively disperse and stabilize carbon platelets preventing graphene aggregation, whereas 5-15 nm diameters Fe_3O_4 nanoparticles would act as nano-spacers increasing compression potential [72]. This strategy was expected to provide a thin film of hybrid nanomaterial combining robustness and high sensitivity to pressure.

2 MATERIAL & METHODS

2.1 Materials

For the synthesis of cyclodextrine functionalized graphene to develop vQRS we used the following reactants: 1-pyrenebutyric acid N-hydroxysuccinimide ester (ALDRICH, 95 %), 1-adamantanemethylamine (ALDRICH, 98%) triphenylphosphine (ALDRICH, 99 %), sodium azide (ALDRICH, 99.5 %), 2-propynyl-tetra-O-acetyl-β-D-glucopyranoside (ALDRICH, 97 %), ascorbic acid sodium salt (FLUKA, 99%), sodium methoxide (FLUKA, 97 %), cupric sulfate pentahydrate (FLUKA, 99%), iodine (ALFA AESAR, 99%), anhydrous pyridine (ALDRICH, 99.8 %), acetic anhydride (ALDRICH, 99%) were used as received without further purification. CH_2Cl_2 (VWR, 100 %) was dried over CaH_2 and distilled just before use. The deuterated solvents (D_2O, DMSO-d_6) were purchased from EURISOTOP. The β-CD (ROQUETTE, 98 %) was purified before use. A saturated solution of β-CD was prepared at 80 °C, then slowly cooled to room temperature and left at 0 °C for one night. The crystallized β-CD was then filtered and dried under vacuum at 80 °C over one night. All solvents ethanol, methanol, DMF, formaldehyde, acetone, toluene, benzene, propanol, isopropanol, o-xylene, from Acros Organics (Belgium) were used as received.

For the synthesis of magnetite decorated graphene to develop sQRS we used graphene oxide (GO) prepared by a modified HUMMER's method from graphite flake [73, 74]. PIL of poly(1-vinyl-3-ethylimidazolium) salts bearing the anion (Br^-) was synthesized according to the literature [75, 76, 77]. And Fe_3O_4 nanoparticle-decorated reduced graphene oxide mediated by PIL (Fe_3O_4@RGO-PIL) was prepared as described in our previous work [72].

To synthesize a nanocomposite from the dispersion of Fe_3O_4@RGO-PIL nanofillers in a TPU matrix, the as-prepared Fe_3O_4@RGO-PIL was transferred from aqueous into organic

phase using PIL as phase transferring medium. For this process, an aqueous suspension of Fe_3O_4@RGO-PIL was mixed with a saturate aqueous solution of lithium bis(trifluoro methyl sulfonyl)amide ($Li^+NTf_2^-$) for the anion exchange of PIL. The addition of $Li^+NTf_2^-$ leads to an immediate replacement of hydrophilic and water soluble Br^- anions in the PIL with hydrophobic and water-immiscible NTf_2^- anions. As-produced Fe_3O_4@RGO-PIL became readily dispersible in a range of low boiling-point organic solvent such as acetone, acetonitrile, methyl ethyl ketone (MEK). A TPU/Fe_3O_4@RGO-PIL nanocomposite was prepared with the concentrations of Fe_3O_4@RGO-PIL varied from 0.5 to 10 % by weigh (i. e., 0.5, 1, 3, 5, 8, 10 wt. %). In the typical procedure, 250 mg of Fe_3O_4@RGO-PIL were dispersed in 100 $cm^3$of MEK with the aid of 15 min ultra-sonication, followed by stirring with a magnetic bar for 2 h.

Thermoplastic poly(urethane) TPU (IROSTIC S9815, HUNTSMAN, Germany) pellets (2.5 g) were added to 100 cm^3 MEK and stirred at 30 °C for 1 day. This polymer solution was then mixed with the above Fe_3O_4@RGO-PIL suspensions and stirred at room temperature for additional 5 h to yield the homogeneous dispersion of Fe_3O_4@RGO in TPU solution.

2.2 Techniques

The NMR spectra were recorded on a BRUKER AV300 spectrometer, operating at 300 MHz. Electrospray-ionization mass spectra (ESIMS) was recorded with an API 2000 spectrometer. The thermo-gravimetric analysis was done using METTLER TOLEDO Star instrument. Samples were heated from 25 °C to 700 °C with 5 °C.min^{-1} heating rate in nitrogen atmosphere. UV-visible spectroscopy was done using CARY WinUV BIO-50 within 250-750 nm range.

Scanning electron microscopy (SEM) images were recorded using a JEOL JSM-700F microscope operated at 15.0 kV. Transmission electron microscopy (TEM) images were obtained using a TECNAI 20 operating at 200 kV. Atomic force microscopy (AFM) measurements were performed in tapping mode with an AFM XE-100. Thermo-gravimetric analysis (TGA) measurements were performed at a heating rate of 10 °C min^{-1} under nitrogen flow using a NETZSCH STA 409 PC/PG instrument. Dynamic mechanical analysis (DMA) was performed using a DMA 50N analyser from TA Instruments (USA). A three-point bending clamping geometry was used. DMA test was carried out from -100 to 80 °C at a heating rate of 5 °C.min^{-1} at 1 Hz. The surface resistance was obtained using a four-probe method (CMT-SR2000N) at room temperature.

3 RESULTS & DISCUSSION

When properly structured from the nano- to the macro-scale, graphene based nanohybrids can meet promising applications such as human health monitoring by the non-invasive diagnosis of diseases derived from the analysis of VOC biomarkers emitted by the body (volatolomics) Figure 1b or mobility monitoring resulting from the application of sensing skins on some parts of the body Figure 2c. For the two applications presented above, the best strategies used to control the different types of conductive architectures during their fabrication, and in particular the tailoring of the nano-junctions responsible for QRS sensitivity will be presented and discussed.

3.1 Chemo-Resistive behaviour of graphene based vQRS

Most of the problems met with traditional e-noses made of MO sensors come from their low sensitivity at room temperature, lack of selectivity, high operating temperature (several hundred degrees leading to high energy consumption) imposed by their too high sensitivity to water [29], or made with ICP sensors that are too sensitive to humidity, irradiation and oxido-reduction [78], can be overcome when using quantum resistive vapour sensors. vQRS are versatile nanomaterials obtained by structuring conductive nanofillers like carbon nanotubes (CNT) into an insulating matrix like a polymer of suitable functionality, provided that a control of both the conductive architecture [30-31] and the nanoswitching at junctions of percolated nanofillers [32-33] is ensured. In addition, the selectivity of vQRS can be easily adjusted by changing the chemical nature of the thin organic layer separating the conductive junctions [34-35]. The first problem can be fixed by using a process such as spray layer by layer (sLbL), which allows a step by step building of the transducers from the nano to the macro scale [76,82], whereas the second can find a solution through the tailoring of junction's gap [84,85]. This last parameter will determine both the selectivity (depending on the nature of intermolecular interactions between the organic layer and the biomarker) and the sensitivity (depending on the initial value and amplitude of the gap) of QRS. Several strategies have already been experimented to control the nano-switching of QRS involving exclusion volumes [33,80,86], functionalization of carbon nanofillers such as CNT [86,87] or graphene [76], with a polymer [4,5,88], an oligomer [87] or non-polymer organic/inorganic molecules [16,89–91], which could effectively modify the selectivity and sensitivity of chemo-resistive vapour sensors.

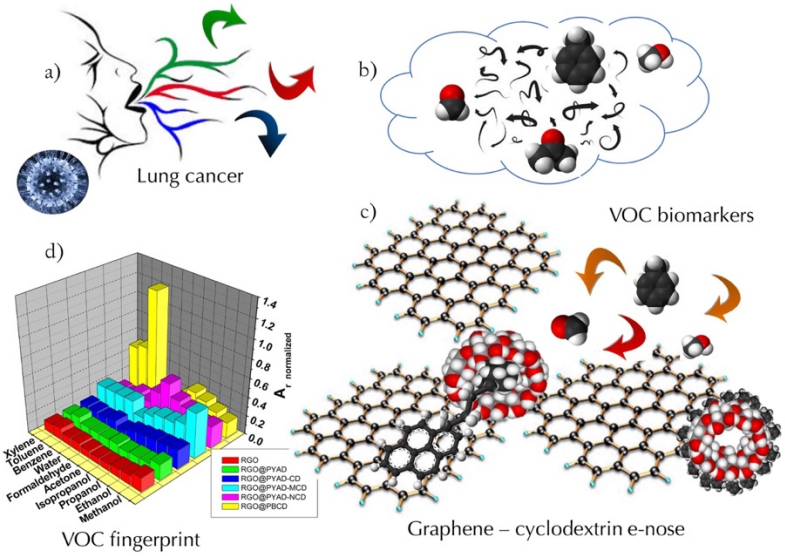

Figure 1: Principe of lung cancer biomarkers' detection with CD functionalized graphene vQRS, a) Breath contains hundreds of volatile organic compounds (VOC), b) The detection of variations of VOC biomarkers' composition allows to make an anticipated diagnostic of diseases such as lung cancer, c) Graphene foils separated with functionalized CD act as nano-switches, d) This kind of hierarchical architecture provides very sensitive and selective vQRS for e-noses [2]

However, non-covalent functionalization of nanofillers, which can also be obtained

through secondary interactions such as π-π stacking, charge-charge interaction and hydrogen bonding, is probably the most attractive approach to preserve the graphitic chemical structure, and hence, provide a positive synergy of properties [92]. This approach was used to synthesize ultrasensitive vQRS made of graphene foils interspaced with functionalized nanoswitches as presented in Figure 1c.

The sensing performances of the electronic nose composed of 3 types of functionalized CD wrapped graphene sensors along with one pristine graphene and one pyrene adamantan linked graphene sensors were analyzed, after being exposed to 10 selected cancer VOC biomarkers. The compilations of all chemoresistive responses lead to a unique fingerprint Figure 1d. The specific functionality of CD is found to be a predominant influencing parameter to tune the specific molecular selectivity of the sensors used in the electronic nose. The present study therefore opens a novel approach to achieve distinct selectivity of the chemical vapour sensors for specific VOC by employing functionalized CD modified reduced graphene oxide hybrid functional nano-material as chemical vapour sensor.

3.2 Piezo-Resistive behaviour of graphene based sQRS

As presented above, it is possible to synthesize strongly piezo-resistive nanostructured TPU/Fe_3O_4@RGO-PIL nanocomposites (sQRS) from the assembly of only 1 wt% of magnetite-decorated reduced graphene oxide mediated by poly(ionic liquid) and TPU matrix (Figure 2).

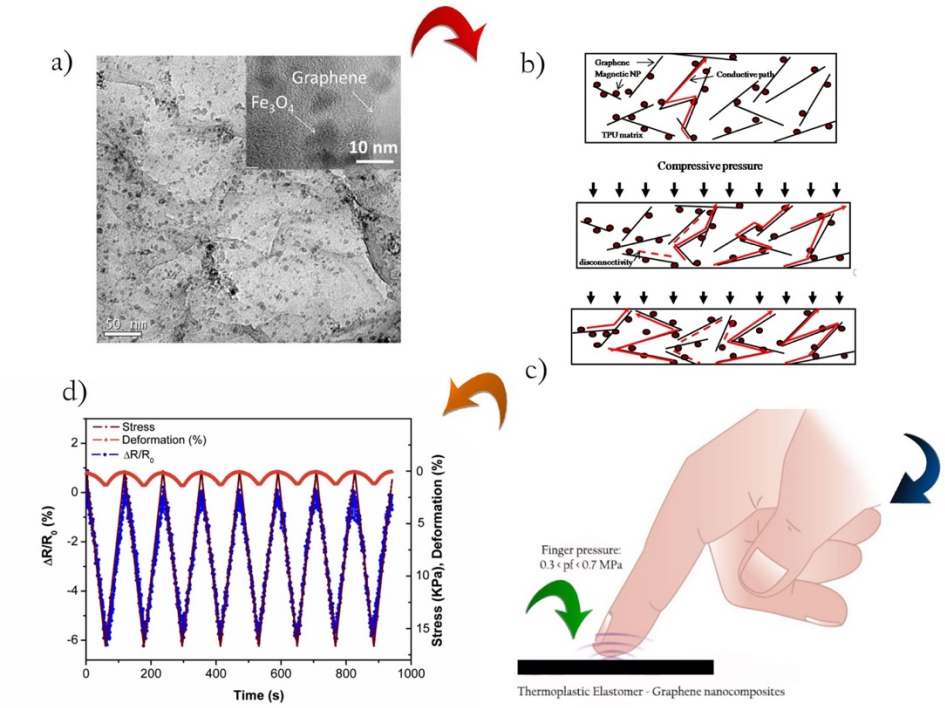

Figure 2: a) Transmission Electronic Micrograph (TEM) of graphene nanofoils (GR) decorated with magnetite nanoparticles (Fe_3O_4 NP) of about 5 nm diameter, b) House of cards architecture made of Fe_3O_4 NP decorated GR nanofoils dispersed in a thermoplastic polu(urethane) TPU matrix and assembled by spray layer by layer (sLbL), Principle of finger pressure sensing (tactile capacity) with TPU-GR piezo-resistive film, d) Piezo-Resistive $\Delta R/R_0$, stress σ and strain ε responses in cyclic mode [1].

This material structured with a house of cards morphology that exhibits high performances such as a gage factor of GF = 6.2, a minimum pressure threshold of P_s = 0.5 kPa, a linear response in a large range of pressures (10 - 200 kPa), low noise and loading/unloading reversibility, coming from its original 3D compressible and reversible conducting architecture.
The different steps of the development of the graphene based sQRS are given in Figure 2, starting from poly(ionic liquid) used effectively to exfoliated and stabilize graphene nanofoils whereas Fe_3O_4 NP preserve RGO sheets reconnection potential acting as nanospacers, thus enhancing the piezo-resistive effect of the nanocomposite, its reliability and decreasing its limit of detection.
Additionally, the thermoplastic poly(urethane) used fully satisfied the requirements associated to a good matrix in terms of processing, dispersion, protection. Finally, the sensing films have demonstrated that if synergistic interactions between compounds can be obtained, it is possible to develop a multifunctional nanomaterial, combining flexibility, resilience, piezo-resistive and magnetic properties, that should have a variety of applications in flexible and wearable electronics, such as tactile sensors, sensing skins and compressive strain sensors.

4 CONCLUSIONS

- Enhancing the quality of life by decreasing the impact of severe diseases is still a global challenge. According to the World Health Organization (WHO), cancers which are killing each year 7.6 million peoples, can be considered as a global priority [93]. The WHO has also projected that without immediate action, the global number of deaths from cancer will increase by nearly 80 % by 2030, with most occurring in low- and middle-income countries. Cancers could be more efficiently treated in case of an anticipated diagnosis, and from this point of view metabolomics can bring very promising solutions. A novel ultrasensitive vapour sensors for e-nose system comprising functionalized β-cyclodextrin wrapped reduced graphene oxide (RGO) sensors with distinct ability of discrimination of a set of volatile organic compounds, has been developed. Non-covalent modification of chemically functionalized cyclodextrin with RGO was carried out by using pyrene adamantan as a linker wherever necessary, in order to build a supramolecular assembly. The chemical functionality on cyclodextrin was varied utilizing the principle of selective chemical modification of cyclodextrin. In the present study, the combined benefits of host-guest inclusion complex formation ability and tuneable chemical functionality of cyclodextrin, as well as high surface area and electrical conductivity of graphene were utilized for the development of a set of highly selective chemical vapour sensors, which can be assembled in an electronic nose.
- A strongly piezo-resistive nanocomposite flexible sensor has been developed using an innovative combination of materials, i.e., magnetite-decorated graphene/poly(ionic liquid) compatibilized poly(urethane) (TPU/Fe_3O_4@RGO-PIL). The transducer has been fabricated by spray layer by layer (sLbL) to structure an original three-dimensional architecture in which: reduced graphene oxide (RGO) platelets are used to build the conducting network, PIL stabilizes this percolated assembly, Fe_3O_4 NP act as nano-spacers between platelets to prevent their stacking and facilitate their switching, and TPU matrix brings cohesion and flexibility to the whole. This strategy results in highly sensitive

TPU/Fe_3O_4@RGO-PIL flexible nanocomposite sensors (high gauge factor in compression up to 6.2, exceptionally low threshold pressure 0.5 kPa), yielding a linear response in a large range of pressures (10 - 200 kPa), with robust and reproducible piezo-resistive properties (weak hysteresis upon loading unloading cycling, no creep). These performances are promising for a variety of applications in flexible and wearable electronics, such as tactile sensors, sensing skins and compressive strain sensors.

- An ongoing project is attempting to use the capability of both vQRS and sQRS to prevent the development of

ACKNOWLEDGEMENTS

This work was supported by the University of South Brittany (UBS) and Brittany Region (France) and General Council of Morbihan (56). We are grateful to Hervé BÉLLEGOU, Isabelle PILLIN and Véronique BENNEVAULT for their contributions to this work.

REFERENCES

1 T. T. Tung, C. Robert, M. Castro, J. F. Feller, T. Y. Kim and K. S. Suh, *Carbon N. Y.*, 2016, **108**, 450–460.

2 S. Nag, L. Duarte, E. Bertrand, V. Celton, M. Castro, V. Choudhary, P. Guégan and J. F. Feller, *J. Mater. Chem. B Biol. Med.*, 2014, **2**, 6571–6579.

3 G. Droval, J. F. Feller, P. Salagnac and P. Glouannec, *e-Polymers*, 2009, 1–17.

4 A. Bouvrée, J. F. Feller, M. Castro, Y. Grohens and M. Rinaudo, *Sensors Actuators B Chem.*, 2009, **138**, 138–147.

5 B. Kumar, M. Castro and J. F. Feller, *Carbon N. Y.*, 2012, **50**, 3627–3634.

6 C. Robert, J. F. Feller and M. Castro, *ACS Appl. Mater. Interfaces*, 2012, **4**, 3508–3516.

7 T. T. Tung, M. Castro, J. F. Feller, T. Y. Kim and K. S. Suh, *Org. Electron.*, 2013, **14**, 2789–2794.

8 T. T. Tung, M. Castro and J. F. Feller, in *Proceedings of the IEEE Conference on Nanotechnology*, 2012.

9 B. de Lacy Costello, A. Amann, H. Al-Kateb, C. Flynn, W. Filipiak, T. Khalid, D. Osborne and N. M. Ratcliffe, *J. Breath Res.*, 2014, **8**, 14001.

10 Y. Y. Broza, L. Zuri and H. Haick, *Sci. Rep.*, 2014, **4**, 1–6.

11 A. Manolls, *Clin. Chem.*, 1983, **29**, 5–15.

12 M. Phillips, K. Gleeson, J. M. Hughes, J. Greenberg, R. N. Cataneo, L. Baker and W. P. McVay, *Lancet*, 1999, **353**, 1930–1933.

13 J. W. Gardner, H. W. Shin and E. L. Hines, *Sensors Actuators B Chem.*, 2000, **70**, 19–24.

14 G. Peng, U. Tisch, O. Adams, M. Hakim, N. Shehada, Y. Y. Broza, S. Billan, R. Abdah-Bortnyak, A. Kuten and H. Haick, *Nat. Nanotechnol.*, 2009, **4**, 669–673.

15 N. G. Hockstein, E. R. Thaler, D. Torigian, W. T. Miller, O. Deffenderfer and C. W. Hanson, *Laryngoscope*, 2004, **114**, 1701–5.

16 R. Ionescu, Y. Y. Broza, H. Shaltieli, D. Sadeh, Y. Zilberman, X. Feng, L. Glass-Marmor, I. Lejbkowicz, K. Müllen, A. Miller and H. Haick, *ACS Chem. Neurosci.*, 2011, **2**, 687–693.

17 M. McCulloch, T. Jezierski, M. Broffman, A. Hubbard, K. Turner and T. Janecki, *Integr. Cancer Ther.*, 2006, **5**, 30–9.

18 G. Peng, M. Hakim, Y. Y. Broza, S. Billan, R. Abdah-Bortnyak, A. Kuten, U. Tisch and H. Haick, *Br. J. Cancer*, 2010, **103**, 542–51.

19 C. L. Silva, M. Passos and J. S. Câmara, *Talanta*, 2012, **89**, 360–8.

20 A. P. F. Turner and N. Magan, *Nat. Rev. Microbiol.*, 2004, **2**, 161–166.

21 H. J. O'Neill, S. N. Gordon, M. H. O'Neill, R. D. GIbbons and J. P. Szldon, *Clin. Chem.*, 1988, **34**, 1613–1618.

22 G. Giubileo, in *Proceedings of SPIE*, eds. D. C. Dumitras, M. Dinescu and V. I. Konov, 2002, vol. 4762, pp. 318–325.

23 D. Smith, T. Wang, J. Sulé-Suso, P. Spanel and A. El Haj, *Rapid Commun. Mass Spectrom.*, 2003, **17**, 845–50.

24 M. J. Thorpe, D. Balslev-Clausen, M. S. Kirchner and J. Ye, *Opt. Express*, 2008, **16**, 2387.

25 A. D'Amico, G. Pennazza, M. Santonico, E. Martinelli, C. Roscioni, G. Galluccio, R. Paolesse and C. Di Natale, *Lung Cancer*, 2010, **68**, 170–176.

26 H. Troy Nagle, R. Gutierrez-Osuna and S. S. Schiffman, *IEEE Spectr.*, 1998, 22–31.

27 S. Dragonieri, M. P. van der Schee, T. Massaro, N. Schiavulli, P. Brinkman, A. Pinca, P. Carratú, A. Spanevello, O. Resta, M. Musti and P. J. Sterk, *Lung Cancer*, 2012, **75**, 326–31.

28 M. M. Arafat, B. Dinan, S. A. Akbar and A. S. M. A. Haseeb, *Sensors*, 2012, **12**, 7207–7258.

29 C. Wang, L. Yin, L. Zhang, D. Xiang and R. Gao, *Sensors*, 2010, **10**, 2088–2106.

30 J. Lu, B. J. Park, B. Kumar, M. Castro, H. J. Choi and J. F. Feller, *Nanotechnology*, 2010, **21**, 1–10.

31 Y. Dan, Y. Cao, T. E. Mallouk, S. Evoy and A. T. C. Johnson, *Nanotechnology*, 2009, **20**, 434014.

32 B. Kumar, M. Castro and J. F. Feller, *Sensors Actuators B Chem.*, 2012, **161**, 621–628.

33 J. Lu, J. F. Feller, B. Kumar, M. Castro, Y. S. Kim, Y. T. Park and J. C. Grunlan, *Sensors Actuators B Chem.*, 2011, **155**, 28–36.

34 G. Peng, E. Trock and H. Haick, *Nano Lett.*, 2008, **8**, 3631–3635.

35 G. Peng, U. Tisch and H. Haick, *Nano Lett.*, 2009, **9**, 1362–1368.

36 C. Pramanik, H. Saha and U. Gangopadhyay, *J. Micromechanics Microengineering*, 2006, **16**, 1340.

37 C. S. Park, B. S. Kang, D. W. Lee and Y. S. Choi, *Appl. Phys. Lett.*, 2006, **89**, 223516.

38 S. M. Shaby and A. V. Juliet, *Int. J. Comput. Appl.*, 2011, **34**, 1–4.

39 C. K. M. Fung, M. Q. H. Zhang, Z. Dong and W. J. Li, in *5th IEEE Conference on Nanotechnology, 2005.*, IEEE, 2005, vol. 1, pp. 353–356.

40 Y. Matsuoka, Y. Yamamoto, M. Tanabe, S. Shimada, K. Yamada, A. Yasukawa and H. Matsuzaka, *J. Micromechanics Microengineering*, 1995, **5**, 32–35.

41 J. Zavickis, M. Knite, G. Podins, A. Linarts and R. Orlovs, *Sensors Actuators A Phys. Actuators*, 2011, **171**, 38–42.

42 C. Gau, H. S. Ko and H. T. Chen, *Nanotechnology*, 2009, **20**, 185503.

43 S. Nauman, P. Lapeyronnie, I. Cristian, F. Boussu and V. Koncar, *IEEE Sens. J.*, 2011, **11**, 1329–1336.

44 Z. Wei, D. Song, Q. Zhao and H. L. Cui, *IEEE Sens. J.*, 2008, **8**, 1615–1619.

45 S. Nesson, M. Yu, X. Zhang and A. H. Hsieh, *J. Biomed. Opt.*, 2008, **13**, 44040.

46 C. Hierold, A. Jungen, C. Stampfer and T. Helbling, *Sensors Actuators A Phys.*, 2007, **136**, 51–61.

47 L. Liu, C. Jayanthi, M. Tang, S. Wu, T. Tombler, C. Zhou, L. Alexseyev, J. Kong and H. Dai, *Phys. Rev. Lett.*, 2000, **84**, 4950–3.

48 A. Bsoul, M. S. Mohamed Ali and K. Takahata, *Electron. Lett.*, 2011, **47**, 807–808.

49 K. Lee, S. S. Lee, J. A. Lee, K. C. Lee and S. Ji, *Appl. Phys. Lett.*, 2010, **96**, 13511.

50 S. Vadukumpully, J. Paul, N. Mahanta and S. Valiyaveettil, *Carbon N. Y.*, 2011, **49**, 198–205.

51 T. Ramanathan, A. A. Abdala, S. Stankovich, D. A. Dikin, M. Herrera-Alonso, R. D. Piner, D. H. Adamson, H. C. Schniepp, X. Chen, R. S. Ruoff, S. T. Nguyen, I. A. Aksay, R. K. Prud'Homme and L. C. Brinson, *Nat. Nanotechnol.*, 2008, **3**, 327–331.

52 W. Zhang, I. Srivastava, Y. F. Zhu, C. R. Picu and N. A. Koratkar, *Small*, 2009, **5**, 1403–1407.

53 M. A. Rafiee, J. Rafiee, I. Srivastava, Z. Wang, H. Song, Z. Z. Yu and N. A. Koratkar, *Small*, 2010, **6**, 179–183.

54 M. A. Rafiee, J. Rafiee, Z. Wang, H. Song, Z. Z. Yu and N. A. Koratkar, *ACS Nano*, 2009, **3**, 3884–3890.

55 M. A. Rafiee, J. Rafiee, Z. Z. Yu and N. A. Koratkar, *Appl. Phys. Lett.*, 2009, **95**, 223103.

56 S. S. Kandanur, M. A. Rafiee, F. Yavari, M. Schrameyer, Z. Z. Yu, T. A. Blanchet and N. A. Koratkar, *Carbon N. Y.*, 2012, **50**, 3178–3183.

57 J. T. Robinson, F. K. Perkins, E. S. Snow, Z. Wei and P. E. Sheehan, *Nano Lett.*, 2008, **8**, 3137–3140.

58 T. H. Han, Y. K. Huang, A. T. L. Tan, V. P. Dravid and J. Huang, *J. Am. Chem. Soc.*, 2011, **133**, 15264–15267.

59 S. Gilje, S. Han, M. Wang, K. L. Wang and R. B. Kaner, *Nano Lett.*, 2007, **7**, 3394–3398.

60 V. Dua, S. P. Surwade, S. Ammu, S. R. Agnihotra, S. Jain, K. E. Roberts, S. Park, R. S. Ruoff and S. K. Manohar,

Angew. Chemie - Int. Ed., 2010, **49**, 2154–2157.

61 R. K. Srivastava, S. Srivastava, T. N. Narayanan, B. D. Mahlotra, R. Vajtai, P. M. Ajayan and A. Srivastava, *ACS Nano*, 2012, **6**, 168–175.

62 F. Yavari and N. A. Koratkar, *J. Phys. Chem. Lett.*, 2012, **3**, 1746–1753.

63 G. Lu, S. Mao, S. Park, R. S. Ruoff and J. Chen, *Nano Res.*, 2009, **2**, 192–200.

64 H. Vedala, D. C. Sorescu, G. P. Kotchey and A. Star, *Nano Lett.*, 2011, **11**, 2342–2347.

65 O. C. Compton and S. T. Nguyen, *Small*, 2010, **6**, 711–723.

66 Y. Zhu, S. Murali, W. Cai, X. Li, J. W. Suk, J. R. Potts and R. S. Ruoff, *Adv. Mater.*, 2010, **22**, 3906–3924.

67 R. Verdejo, M. M. Bernal, L. J. Romasanta and M. A. Lopez-Manchado, *J. Mater. Chem.*, 2011, **21**, 3301–3310.

68 J. R. Potts, D. R. Dreyer, C. W. Bielawski and R. S. Ruoff, *Polymer (Guildf).*, 2011, **52**, 5–25.

69 H. Bai, C. Li and G. Shi, *Adv. Mater.*, 2011, **23**, 1089–1115.

70 X. Huang, Z. Yin, S. Wu, X. Qi, Q. He, Q. Zhang, Q. Yan, F. Boey and H. Zhang, *Small*, 2011, **7**, 1876–1902.

71 V. K. Rana, S. Akhtar, S. Chatterjee, S. Mishra, R. P. Singh and C. S. Ha, *J. Nanosci. Nanotechnol.*, 2014, **14**, 2425–2435.

72 T. T. Tung, J. F. Feller, T. Y. Kim, H. K. Kim, W. S. Yang and K. S. Suh, *J. Polym. Sci. A Chem.*, 2012, **50**, 927–935.

73 T. T. Tung, T. Y. Kim, J. P. Shim, W. S. Yang, H. Kim and K. S. Suh, *Org. Electron.*, 2011, **12**, 2215–2224.

74 T. Y. Kim, H. W. Lee, J. E. Kim and K. S. Suh, *ACS Nano*, 2010, **4**, 1612–1618.

75 R. Marcilla, J. A. Blazquez, J. Rodriguez, J. A. Pomposo and D. Mecerreyes, *J. Polym. Sci. A Chem.*, 2004, **42**, 208–212.

76 T. T. Tung, M. Castro, T. Y. Kim, K. S. Suh and J. F. Feller, *J. Mater. Chem.*, 2012, **22**, 21754–21766.

77 T. Y. Kim, T. H. Lee, J. E. Kim, R. M. Kasi, C. S. P. Sung and K. S. Suh, *J. Polym. Sci. A Chem.*, 2008, **46**, 6872–6879.

78 H. Bai and G. Shi, *Sensors*, 2007, **7**, 267–307.

79 J. Lu, B. Kumar, M. Castro and J. F. Feller, *Sensors Actuators B Chem.*, 2009, **140**, 451–460.

80 J. F. Feller, J. Lu, K. Zhang, B. Kumar, M. Castro, N. Gatt and H. J. Choi, *J. Mater. Chem.*, 2011, **21**, 4142–4149.

81 B. Kumar, M. Castro and J. F. Feller, *J. Mater. Chem.*, 2012, **22**, 10656–10664.

82 B. Kumar, M. Castro and J. F. Feller, *Chem. Sensors*, 2013, **3**, 1–7.

83 S. Chatterjee, M. Castro and J. F. Feller, *J. Mater. Chem. B*, 2013, **1**, 4563.

84 B. Kumar, M. Castro and J. F. Feller, *J. Mater. Chem.*, 2012, **22**, 10656–10664.

85 B. Kumar, M. Castro and J. F. Feller, *Carbon N. Y.*, 2012, **50**, 3627–3634.

86 J. F. Feller, N. Gatt, B. Kumar and M. Castro, *ChemoSensors*, 2014, **2**, 26–40.

87 M. Castro, J. Lu, S. Bruzaud, B. Kumar and J. F. Feller, *Carbon N. Y.*, 2009, **47**, 1930–1942.

88 B. Kumar, J. F. Feller, M. Castro and J. Lu, *Talanta*, 2010, **81**, 908–15.

89 N. Bachar, L. Mintz, Y. Zilberman, R. Ionescu, X. Feng, K. Müllen and H. Haick, *ACS Appl. Mater. Interfaces*, 2012, **4**, 4960–4965.

90 E. Massera, A. Castaldo, L. Quercia and G. Di Francia, *Sensors Actuators B Chem.*, 2008, **129**, 487–490.

91 Y. Zilberman, U. Tisch, G. Shuster, W. Pisula, X. Feng, K. Müllen and H. Haick, *Adv. Mater.*, 2010, **22**, 4317–4320.

92 N. G. Sahoo, S. Rana, J. W. Cho, L. Li and S. H. Chan, *Prog. Polym. Sci.*, 2010, **35**, 837–867.

93 *Cent. Dis. Control Prev.*, 2014.

Improving Dielectric Properties of Polymeric Matrix Composites by the Thermal Treatment

Benhui Fan[1], Fahmi Bedoui[2], Delong He[1]* and Jinbo Bai[1]*

[1]Laboratoire Mécanique des Sols, Structures et Matériaux (MSSMat), CNRS UMR 8579, Ecole CentraleSupelec, Université Paris Saclay, Grande Voie des Vignes, 92290, Chatenay-Malabry, France

[2]Sorbonne Universités, Université de Technologie de Compiègne, Roberval UMR-CNRS 7337, Compiègne, France

Corresponding author: Jinbo Bai, Delong He
Email: jinbo.bai@ecp.fr delong.he@ecp.fr
Tel : +33 (0)1 41 13 13 16

Abstract

Dielectric properties of the polymeric matrix composite reinforced by conductive fillers are usually sensitive to the external stimulation especially when filler's volume fraction is approaching to a certain value, known as the percolation threshold (f_c). This sensitivity is largely associated with the processing of the composite and the dispersing mode of conductive fillers. An appropriate thermal treatment enables to reduce the sensitivity of the conductive network and further improve dielectric properties of the composite. The method of thermal treat depends on polymeric matrix's molecular structure and rheological properties. Concretely, for a linear amorphous polymeric matrix composite, e.g. PMMA, the temperature of annealing is associated with the temperature of glass transition. For a linear semi-crystalline polymeric matrix composite, e.g. PVDF, it is associated with the crystallization temperature. For a non-linear cross-linking polymeric matrix composite, e.g. epoxy, it follows a continuous after-curing process. After the annealing and cooling, the average distance between adjacent conductive fillers is reduced by the shrinkage of polymer chains which strengthens interfacial polarization effect. Besides, for the semi-crystalline polymer, the transition of crystalline polymorph happens in the interfacial region of conductive fillers and matrix which strengthens dipole polarization effect. Therefore, the thermal treatment helps to modify the conductive network so that increase and stabilize dielectric properties in a wide frequency range of the composite.

VIII ECCOMAS Thematic Conference on Smart Structures and Materials
SMART 2017
A. Güemes, A. Benjeddou, J. Rodellar and J. Leng (Eds)

COMPOSITION- AND ION-DEPENDING ACTUATION MECHANISM OF CARBON NANOTUBE ARCHITECTURES

SEBASTIAN GEIER*, THORSTEN MAHRHOLZ*, PETER WIERACH* AND MICHAEL SINAPIUS†

* Institute of Composite Structures and Adaptive Systems
German Aerospace Center (DLR)
Lilienthalplatz 7, 38108 Braunschweig, Germany
e-mail: Sebastian.Geier@dlr.de, web page: http://www.dlr.de/FA

† Institute of Adaptronics and Function Integration
Technical University Braunschweig
Langer Kamp 6, 38106 Braunschweig, Germany

Key words: carbon nanotubes, actuators, carbon nanotube arrays, actuation mechanism

Abstract. Future adaptive applications such as morphing surfaces require materials featuring low density, high mechanical stiffness, high active strain but low energy consumption. These properties are well combined by carbon nanotubes (cnts)-based actuators which are typically made of paper-like mats. Two carbon nanotube-papers are arranged towards to each other within an electrolyte. The charging of these papers results in an electrical field which forms a double-layer of the electrolyte ions at the surface of the electrodes. During charging a deflection of the papers can be detected. Although various cnt-architecures have been extensively analysed there is still no generally accepted theory for the actuation mechanism. This paper focuses on investigations of the actuation mechanisms of cnt-papers in comparison to cnt-arrays. The cnt-papers represent architectures of randomly oriented and entangled cnts. The sample geometrie is formed by micro-sized cnts. In contrast cnt-arrays are based on multi-walled cnts whose length is as long as the sample length. Both sample types are tested within an actuated tensile test set-up under different conditions. The cnt-papers are tested in water-based electrolytes while the hydrophobic cnt-arrays need to be tested in ionic liquids. Furthermore different ions are used to investigate the influence of the ion-radius on the properties. Regarding the cnt-papers these tests are completed by in-plane actuation tests measuring the free strain. During the actuated tensile tests three parameters were indentified to influence the mechanical performance of cnt-papers decisively: the humidity of the conditions under which the papers are tested, a preloading of the sample and the electrical charging. All these influencing factors point at the weak inter-tube linking which seem to influence not only the actuation but also the mechanical properties of cnt-papers. Finding a general trend of influencing conditions on the mechanical behaviour of cnt-arrays turns out to be dfficult because of varying results. The mounting of the samples seems to be an important influence. However, the quadratic voltage-strain correlation

suggests an electrostatic effect maybe on a quantum-chemical level of the carbon structure.

1 INTRODUCTION

After Iijima's publication [1] extensive research revealed excellent properties such as a Young's modulus above 1 TPa [2], strength of 45 GPa ([3] regarding multi-walled cnts) a reversible structural elongation of 12 % ([2] regarding multi-walled cnts) and a thermal conductivity of 6000 W/Km [4]. Although the listed properties were measured experimentally their transfer into commercially available applications turns out to be extremely challenging. Beside the costs of mass-production and a poor quality of the supplied nanotubes [5] there is still no mesoscopic semi-finished material available which might close the performance gap between nano-scale theoretical and experimental results and macroscopic structures featuring incorporated nanoscopic cnts. Baughman [6] revealed 1999 their active behavior using mats made of randomly oriented single-walled carbon nanotubes (swcnts). In his presented set-up free strain of about 0.2 % was detected. This publication set the standard for the future experimental investigations of cnt-mats: two electrodes in capacitor mode, one working electrode and its counter electrode, both made of CNT-papers. These sheets are immersed in an electrically insulating but ionic conductive electrolyte. Furthermore the three electrode cell is completed by a Calomel reference electrode. The analyzed paper is activated via rectangular charge-pulses (maximum free strain) or triangular voltage (cyclovoltammetry) and shows an almost quadratic correlation between strain and voltage steps, independent of the polarity. Considering the mechanical and adaptive properties as well as the low actuation-voltage of 1V (regarding aqueous electrolytes) of this carbon-based actuator, cnts seem to be a promising material for future adaptive structures. The published results about free strain or actuation force of cnt-based actuators have to be treated with circumspection because the results can either depend on the composition of the analysed material or on the used analysis method which might detect secondary effects instead of the charge- or ion-induced reactions of the carbon structure itself. In this context the term *architectures* will be used in this paper representing macro-scale structures which are formed by nano-scale cnts. Usually the length of the individual single tubes is too small to form one dimension of a macroscopic architecture. Furthermore, due to their high specific surface, a single-walled nanotube tends to bundle with other cnts to reduce its surface energy. Thus, a cnt-bundle represents the first step towards an architecture. The carbon tubes within an architecture are entangled with each other and linked by van der Waals forces. This is the reason why results found by testing cnt-based architectures can only represent partially the active behaviour of the single tubes because the interlinking between the tubes represents the weakest part of the electromechanical system. Using out-of-plane set-ups to analyse cnt-papers in bending mode [6] give also rather qualitatively results because secondary effects like thermal- or diffusion-induced volume change can influence the findings extensively. For reducing these effects, the papers are pre-stressed and the measurements are carried out at the in-plane direction of the paper [7]. This test set-up requires a symmetrical composition of the tested samples. Beside the already mentioned publications [6, 7] only a few others [8, 9, 10] used similar in-plane test set-ups for characterising nanotube papers. However, similar trends were found referring to the correlation between voltage and strain but only the latter publication discussed the actuation mechanism.

Suppiger [10] supposed an electrostatic effect causing the strain of cnt-papers as result of an inverse correlation between Young's modulus and free strain. The less the cnts are linked to each other the more the charged tubes can repulse from each other creating the detected actuation. Whitten [11] found similar trends regarding the influences of test conditions on the mechanical properties of cnt-papers. The stiffness of a paper drops significantly under wet conditions compared to the results anaysed at dry conditions. Furthermore he can verify the influence of the ion size. Rather small ions (aqueous electrolytes) cause lower loss of mechanical stability compared to the larger ions of the ionic liquid (il). Another explanation for the actuation of cnt-papers was given by Spinks [12] suggesting that the lay-up architcture of cnt paper is similar to honycombs. Gas generation as result of irreversible chemical reactions takes place in the interspaces which causes a swelling of the whole cnt-structure measured as actuation. Another approach to verify the reason of the paper-actuation was carried out by Gupta [13] using Raman-spectroscopy. Raman-spectroscopy is a sensitive method for detecting changes in the atomic structure of a single carbon tube. His approach did not bring further details because the signals of too much different carbon walls overlapped each other disguising any significant detail. Specific methods for analysing single carbon nanotubes on nanoscopic level like atomic microscopy [14] or Raman-spectroscopy [15, 16, 17, 18] revealed a charge- or ion-induced dimensional change of the carbon structure itself. So, there is still the capability of cnts to work like an actuator.
This paper presents measurements of two different kinds of cnt-architectures: cnt-papers compared to cnt-arrays. An architecture formed by short single-walled nanotubes linked by entanglement and Van-der-Waals force compared to long multi-walled carbon tubes which are directly clamped at both ends. The results are compared in order to point out indications that every kind of mechanism can be addressed to its specific composition.

2 EXPERIMENTAL

The first chapter of this section describes the used samples. In the second chapter a brief overview of used test set-ups are given.

2.1 SAMPLE PREPARATION

In the presented paper two kinds of samples are analysed. The first type appears as paper-like sample of randomly oriented single-walled cnts, also called bucky-paper [6]. These papers are manufactured by a high pressure filtration process described elsewhere [6, 7]. The cnts are supplied by Thomas Swan (Elicarb P0925, Thomas Swan & Co. Ltd., UK). The geometry of the tested samples is 2 mm in width, 10 mm in length and feature a mean thickness of 150 μm. All samples are cut from the same circular master cnt-film (diameter of 30 mm) which is manufactured within the mentioned process. With respect of the quality management of Thmoas Swan the single-walled cnts consist of two walls (actually they should be called double-walled cnts), feature a purity of 95 %, a diameter of 1-3 nm and a length of several hundred nanometers. Within the paper the cnts are bundled (see fraction line in Fig. 1 b)) und several layers of sedimented carbon material build up the paper as it can be seen in Fig. 1 a).

The cnt-arrays are supplied by the Technical University of Hamburg-Harburg and consist of

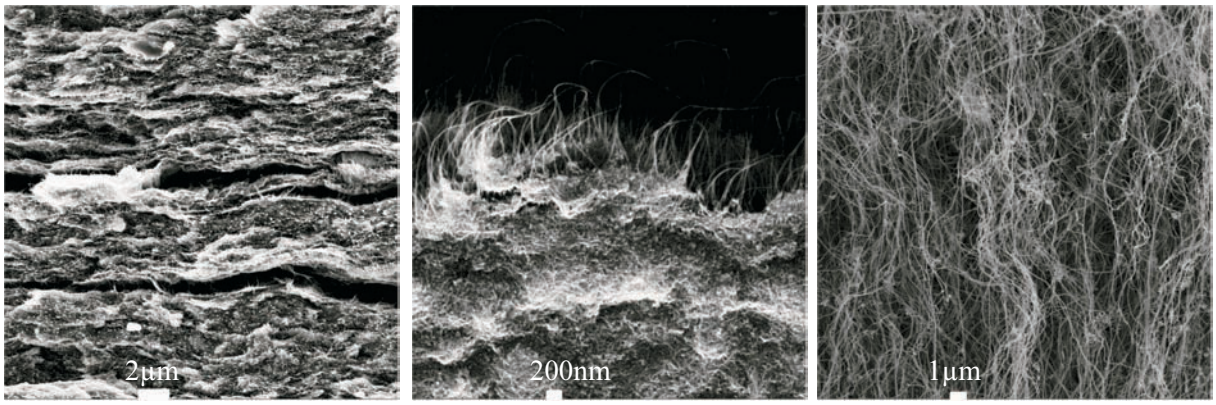

Figure 1: Analysed cnt-architectures: a) Cross section of a cnt-paper with layers of sedimented cnt-agglomerates. b) Top view onto a cnt-paper revealing bundled swcnts at the fraction line. c) Detailed view on alinged multi-walled cnts of the analysed array.

vertical free standing, unaffected cnts, typically grown on a silicon substrate. The tubes are grown during 5.5 hours using a thermal-induced chemical vapor deposition (cvd) method. Their geometry features a mean length of 2.8 mm (continuous tubes) with diameters in the range of 17 nm to 37 nm. Their orientation varies between an angle of 0 - 43 as result of an overall sinusoidal shape. The wavy shape might be a result of the low density of the arrays and fluctuation of the flow during processing the cvd in the furnace. Further process- and geometry-specifications of the mwcnt-arrays are presented in [21]. The tested specimens are manufactured from a slide of the whole array which is cut off using a sharp razor blade. The arrays are cut off the silicon wafer because in neat condition they can be analysed more exactly. The linking between tubes and silicon is rather weak and as the silicon features semiconducting properties it is less suitable for an electrical contact to the tubes. In a subsequent step the array-slide is divided into a set of specimens with almost the same width. The as-produced specimen thickness is about 1 mm which is manual compacted between two microscope slides so a final thickness of 20 μm can be achieved. The other geometries of the array specimens are a length of 2.8 mm and a width of 3-4 mm.

2.2 IN-PLANE FREE STRAIN SET-UP AND ACTUATED TENSILE TESTING

The in-plane free strain test set-up is similar to the published tests [6, 7] apart from using a platinum-plate a counter electrode for better reproducibility. Furthermore it is designed for better mounting and removal of the cnt-paper in order to reduce a damage of the samples and an easier and therefore higher number of measurements. As reference-electrode a calomel electrode (KE 10, Sensortechnik Meinsberg GmbH) is used. The three electrode cell is controlled by a potentiostat (1030 PC.T., IPS Elektroniklabor GmbH & Co. KG) and is charged via a function generator (FG 300, Yokogawa Deutschland GmbH). The results are recorded via a data acquisition system (SCM05, LMS International). The three electrode cell as well as the data acquisition system is used for both set-ups.

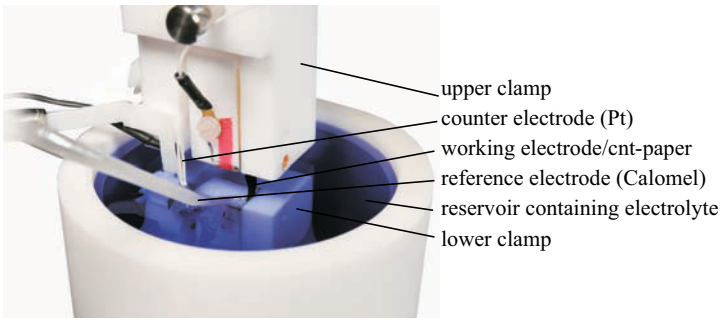

Figure 2: Details of the actuated tensile test set-up.

In general the actuated tensile-test, as shown in Fig. 2, is a modified version of the in-plane free strain set-up. The main difference is the PTFE-clamping and the testing method. Earlier published tests of cnt-arrays [19, 20] used arrays grown on a silicon substrate as test sample. During the tests the substrate was fixed and electrical connected. The linking between substrate and carbon tubes was assumed to be durable. The optical measurements were carried out at the free end on their top. Experiences with cnts grown on silicon revealed only a weak linking between both materials. This weak linking only allows the easy harvesting of arrays and enabling the spinning of cnt-yarns [23] or the manufacturing of highly aligned cnt-papers [24]. This situation resulted to the presented approach of harvesting the arrays from the substrate and clamping them with both ends into the mountings of the tensile testing set-up (see Fig. 2). Both clamping jaws are equipped with Pt-electrodes to measure the electrical resistivity of the sample and for charging the sample during the tests. The sample's resistivity indicates both a damage of the specimen caused during assembly and an inaccurate clamping. The set-up allows to test the samples in dry condition, wet condition immersed in their electrolyte and charged condition. The elastic behaviour (Young's modulus) of the papers operating at different conditions is measured and compared in order to find influences of the condition and the electrolyte on the mechanical behaviour of the cnt-paper.

2.3 ELECTROLYTES

The cnt-papers are immersed in aqueous one molar solutions of various salts for at least 30 minutes to guarantee saturation. Three different one molar, aqueous electrolytes are used: sodium chloride (NaCl, Merck KGaA), potassium chloride (KCl, Synopharm GmbH & Co. KG) and magnesium chloride ($MgCl_2$, Synopharm GmbH & Co. KG). The experiments focus on the differences of the electromechanical actuation using different ions. In this paper the negative ion Cl^- is kept constant while the three positive ions Na^+, K^+ and Mg^{+2} are compared. According to [22] the effective and hydrated ion radii are given in Tab. 1.

As a consequence of the high surface energy of the arrays resulting in extreme hydrophobicity only ionic liquids, in the case of the presented study, 1-ethyle-3-methylimidazolium bis(trifluormethyl-sulfonyl)imide (EMImTFSA, IoLiTec GmbH), can be used. Ionic liquids feature a higher chemical stability that is why a comparatively wide redox-window of ± 2 V (aqueous electrolytes provide a maximum voltage range of $\pm$ 1 V) can be used. Due to their higher molecular weight they feature a higher viscosity. This property reduces the feasible scan rates to archieve com-

Table 1: Effective and hydrated ion radii according to [22].

ion	effective ion size	hydrated ion size
	[pm]	[pm]
Na^+	95	358
K^+	133	331
Mg^{2+}	65	428
Cl^-	181	332

paratively capacities.

3 RESULTS AND DISCUSSION

This chapter presents the results of in-plane strain measurements and actuated tensile tests of swcnt-papers. The focus of this work is the identification of the influence of conditions and electrolyte on the mechanical properties of the cnt-papers. In contrast mwcnt-arrays are only tested in the actuated tensile test under similar conditions (dry, wet, wet and actuated) to compare the results. The cnt-arrays cannot be tested in the free strain set-up due to their small geometries.

3.1 MEASUREMENTS OF CNT-PAPERS

At first the results of the tensile testing are presented. The trend of mechanical loss by wetting the samples presented by Whitten [11] can be confirmed. Earlier studies showed a reduction 44 % [25] only by immersing the paper into the electrolyte. This finding indicates a detaching influence of water on the weakest part of the paper: the tube linking. In parallel when the connection between the tubes is reduced a swelling of the paper occurs causing the measured deflection. Van-der-Waals-forces seem to be reduced and water molecules make the single cnts become movable within the bundle or entanglement. A general negative effect of the positive Ions Na^+, K^+ or Mg^{2+} on the Young's modulus at -0.5 V cannot be seen (compare Tab. 2).

Table 2: Young's modulus of cnt-papers in various electrolytes.

ion	Young's modulus at 0 V [MPa]	Young's modulus at -0.5 V [MPa]
Na^+	529.7±1.7	531±3.6
K^+	572.4±6.2	559±5.2
Mg^{2+}	483.5±7.8	487±7.1

While the potassium-ion seems to reduce the paper stiffness by 2 % the other two ions sodium and magnesium do not affect the mechanical properties at this voltage step. There are two possible explanations for this result. On the one hand the potential may be too small to cause effects

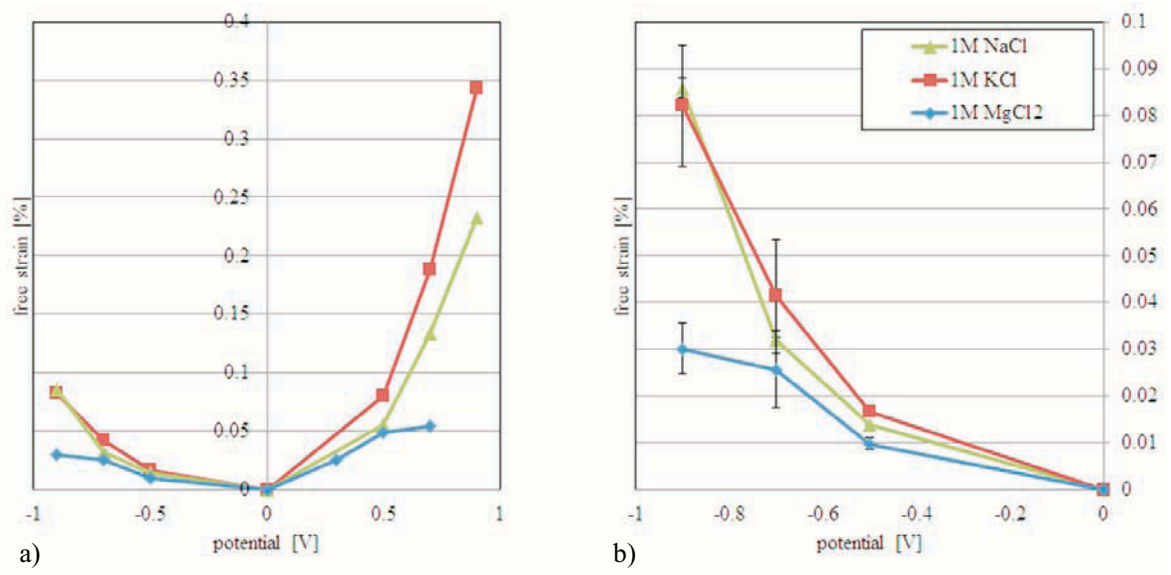

Figure 3: Results of the free strain measurements: a) Overview of the whole potential of ± 1 V. b) Detailed view on the strain generated by negative potentials.

which can be detected by the tensile testing machine. On the other hand earlier results [25] revealed the prestress of the set-up influencing significantly the stiffness of the paper. Due to the soft material PTFE and inaccuracies in manufacturing the mounting stresses or compresses the paper what closes or opens up the pores of the paper allowing the ions to move onto the charged surfaces. This movement weakens sustainably the interlinking of the cnts resulting in a reduced mechanical stiffness. The former stiffness cannot be reached again after uncharging or relaxation. A interesting result is the fact that although all samples are cut off the same master cnt-membrane the measured values of the Young's modulus vary of about ± 8 %.
The results of the free-strain measurements are presented in Fig. 3 a) und Tab. 3 and seem to correlate with the crystalline geometry of the ions. Most of the attention should be paid to the results of -0.5 V and -0.7 V. The results of -0.9 V have to be treated with circumspection because the redox window of ± 1 V is near to this test series. Impurities of the electrolyte or the electrode might cause irreversible chemical reaction such as ion absorption at the electrode surface. The bonded ions can cause a stronger swelling of the electrode which would be detected as strain.

Focusing on the mean strain results several explanations are possible. One the one hand a correlation to the crystalline ion geometry can be found. This effect would explain the actuation mechanism of cnt-papers if the papers are suggested to be flexible porous structures which are filled by ions via charging. It seems that the ions are highly compressed on the surface so that their hydrated shell is deformed or partly removed outside. Maybe this is a result of the pore-size and ion-density on the surfaces. A similar sieving effect of ions by poros carbon is described by Arruda [26]. Taking the standard deviation into account (see Fig. 3 b)) the discussed trend is not as strong.

Table 3: Results of free strain using different electrolytes.

ion	free strain at -0.5 V [%]	free strain at -0.7 V [%]	free strain at -0.9 V [%]
Na^+	0.014±0.0	0.032±0.001	0.086±0.002
K^+	0.016	0.041±0.012	0.082±0.013
Mg^{2+}	0.01±0.001	0.026±0.008	0.03±0.006

On the other hand if the degree of dissociation of $MgCl_2$ cannot be expected to be similar to the degrees of NaCl and KCl there would not be as much free ions available to take part in the electrochemical reactions. Especially the results of the negative ion Cl^- is surprising because the double molecular weight compared to the other electrolytes is present but the measured actuation is even lower. Therefore the assumption of high amount of still associated pairs of Mg^{2+}- and Cl^--ions which are not taking part in the electrochemical charging is justified and can also explain the effects.
A third explanation can be found taking the hydrated ion-radius as a strong, not removable shell into account. Due to the fact of the comparatively small hydrated radii of KCl and NaCl a higher amount of these ions are able to accumulate on the surface of the electrode resulting in higher capacities. This effect causes the higher actuation of both electrolytes.

3.2 RESULTS OF ARRAY-TESTING

In this section the results of the actuated tensile tests are discussed with a focus on the tests under different conditions. The results are presented in Fig. 4 a) and b) and in Table 4. Figure 4 b) reveals clearly an influence of the conditions on the Young's modulus. By wetting the Young's modulus is almost reduced by 90 %. Furthermore the appearance of the whole loading changes into a longer process with a flat section at the beginning of the test with a comparatively low Young's modulus (0.5 MPa).

In earlier publications [25] the results were quite different in terms of keeping the stiffness under various conditions. All in all a clear trend cannot be given but it has to be suggested, according to the current findings, that there is an influence of wetting the cnt-arrays. A possible explanation might be given by an additional result in Fig. 4 a). The Figure shows the results of a cnt-array sample which is fixed at its ends by an adhesive between two metal plates respectively. The so prepared sample was tested under dry conditions but can not be charged because the adhesive is not conductive. This experiments reveals that the sliding of the mwcnts within the mounting reduces the mechanical performance drastically. Typically the cnt-arrays are just clamped by the ptfe-mounting. A specific property of ptfe is a low friction coefficient. Especially within a mounting this is a adverse property but was conducted this way because for charging the cnts an adhesive can electrically insulate the tubes. However, the wetting might induce a further reduction of the friction between the clamps and cnts so that a sliding of the material was supported and the found measurements can be explained.

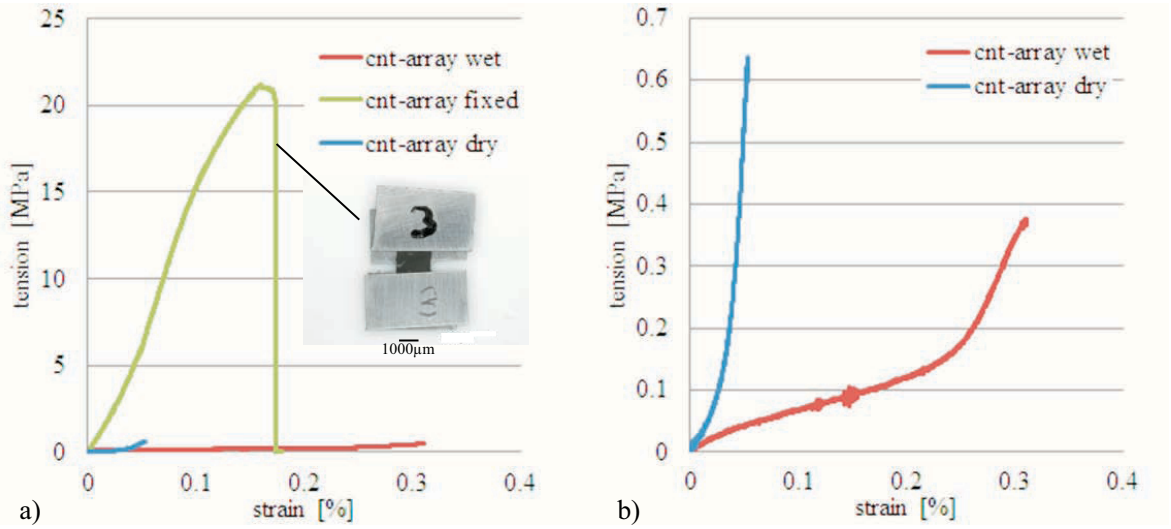

Figure 4: Results of the tensile measurements: a) Comparison of the results of dry (blue), wet (red) and fixed, dry (green) arrays b) Detailed view on the results of the dry and wet array.

Table 4: Results of the Young's modulus of a array at different conditions.

condition	Young's modulus [MPa]
dry	29.5±8.6
wet	3.8±1.1
dry+fixed	734.9

4 CONCLUSION

This paper compares the results of two different kinds of carbon nanotube-based architectures: cnt-papers and cnt-arrays. These architectures can be distinguished because of one significant detail, the cnt-arrays consist of tubes with a continuous length of 2.8 mm. So the tubes are tested parallel to each other clamped at theri both ends. In contrast the cnt-papers consist of nano-scale tubes which are too short for bridging the specimen dimensions. They are tesed in series connected by entanglement or Van-der-Waals-forces. Using in-plane measurements for detecting the free strain and actuated tensile tests for analysing the mechanical behaviour of the cnt-based material at different conditions, influencing parameters are identified which affect the actuation and reveal the actuation mechanism of both architectures. The reason of the cnt-actuation is of high interest because it may open the technology for numberless applications. The influence of the positive charged ions Na^+, K^+ and Mg^{2+} on the mechanical properties of cnt-papers using the tensile testing set-up could not be proven. Maybe settings of the test such as a clamping-induced prestressing or low voltage-pulses reduced the significance. Here the test method needs to be further improved. However, using the free strain set-up reveals a trend between radius and strain. However, there are several possible explanations for these findings;

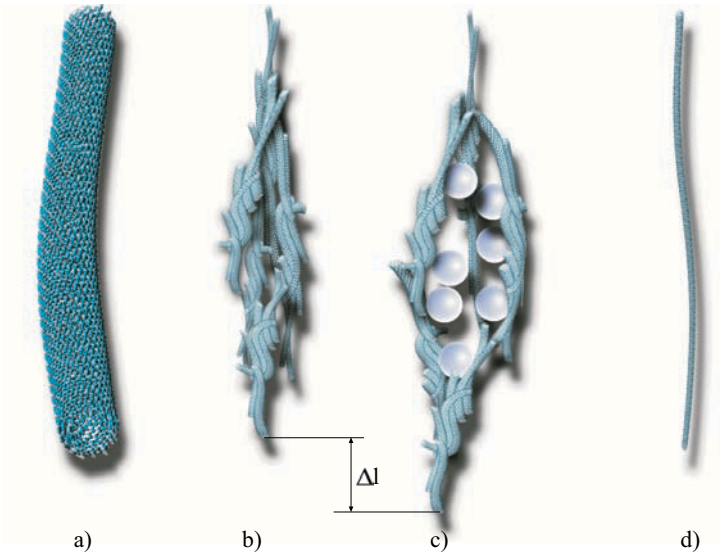

Figure 5: Actuation models of different cnt-achritectures: a) Mwcnt-model. b) Dry swcnt-paper model. c) Wet, actuated swcnt-paper model with intercalated ions. d) Single, long swcnt model.

Maybe the actuation mechanism of a cnt-paper can be understood as is presented in Fig. 5 b) and c) as an interaction of the charged, porous carbon structure and the ions which are able to move into the pores of the paper. The pores can be open and closed by compressing or stretching the paper. Corresponding to the size of the ions their intercalation causes a swelling of the paper and thus a detectable actuation Δ l. Nonetheless there are some uncertainties so that more tests have to be carried out.

The actuated tensile tests of long cnt-arrays (see Fig. 5 a)) did not bring a consistent trend. Some test-series appear to be mechanical unaffected by the different conditions (dry, wet, wet and actuated) others document a loss of stiffness. An actuation of the arrays was already demonstrated in earlier publications [25]. That is the reason why this paper focuses on the influence of the conditions on the mechanical behaviour. However, an important aspect and a possible explanation for the varying results might be the quality of clamping. It was demonstrated that a fixing of the cnt-arrays by an adhesive is feasible and results in significant higher test values which might be needed for better separation of the effects. In contrast to the used adhesive a future mounting by an adhesive requires also good conductivity for charging the tubes during the tests.
Future tests should be carried out using long single-walled tubes (such as it is shown in Fig. 5 d)). With this approach a comparison of the active behaviour to the current tested architectures are possible maybe revealing their individual actuation mechanism.

5 ACKNOWLEDGEMENTS

This work is part of the basic research on future smart materials at the DLR - Institute of Composite Structure and Adaptive Systems. It was supported by the German Research Council

(DFG) within the framework of the DFG PAK 355 - 'Basics for CNT-based Actuators' and the German Federal Ministry of Education and Research (BMBF) project 'Aktu_Komp'. Tribute has also to be paid to Prof. Karl Schulte and his assistant Dr. Thea Schnoor of the Institute of Composite Polymers at the Technical University of Hamburg-Harburg (TUHH) and Prof. Frank Endres and Dr. Timo Carstens of the Institute of Mechanical Process Engineering, department of Interface Chemistry, at the University of Clausthal-Zellerfeld for supporting the presented research with their analysis techniques and expertise in the fields of ionic liquids.

REFERENCES

[1] Iijima, S. Helical microtubules of graphitic Carbon. *Nature* (1991) **354**:56-58.

[2] Yu, M.-F., Lourie, O., Dyer, M. J., Moloni K., Kelly, T. F. and Ruoff, R. F. Strenght an Breaking Mechanism of Multiwalled Carbon Nanotubes Under Tensile Load. *Science* (2000) **287**:637–640.

[3] Walters, D. A., et al. Elastic strain of freely suspended single-wall carbon nanotube ropes. *Appl. Phys. Lett.* (1999) **74**:3803.

[4] Vohrer, U., Zschoerper, N. Kohlenstoff-Nanoröhren - Phönix aus der Asche. *Vakuum in Forschung und Praxis* (2007) **19(2)**:22–30.

[5] Grobert, N. Nanotubes - grow or go?. *Mater. Today* (2006) **9(10)**:64.

[6] Baughman, R. H. et. al. Carbon nanotube actuators. *Science* (1999) **284**:1340–1344.

[7] Riemenschneider, J., Temmen H. and Monner, H. P. CNT based actuators: Experimental and theoretical investigation of the in-plain strain generation. *J. Nanosci. Nanotech.* (2007) **7(10)**:3359–3364.

[8] Hughes, M., Spinks, G. M. Multiwalled Carbon-Nanotube Actuators. *Advanced Materials* (2005) **17(4)**:443–446.

[9] Ebron, H. et. al. Fuel-Powered Artificial Muscles. *Science* (2006) **311**:1580–1583.

[10] Suppiger, D., Busato, S., Ermanni, P., Motta, M. and Windle, A. Electromechanical actuation of marcoscopic carbon nanotube structures: mats and sligned ribbons. *Phys. Chem. Chem. Phys.* (2009) **11**:5180–5185.

[11] Whitten, P. G., Spinks, G. M. and Wallace, G. G. Mechanical properties of carbon nanotube paper in ionic liquid and aqueous electrolytes. *Carbon* (2005) **43**:1891–1896.

[12] Spinks, G. et. al. Pneumatic Carbon Nanotube Actuators. *Adv. Mater.* (2002) **14(23)**:1728–1732.

[13] Gupta, S., Hughes, M., Windle, A. H. and Robertson J. In situ Raman spectroelectrochemistry study of single-wall carbon nanotubes. *Diam. Relat. Mater.* (2004) **13**:1314–1321.

[14] Roth, S., Baughman, R. H. Actuators of individual carbon nanotubes. *Cur. App. Phy.* (2002) **2**:311-314.

[15] Kavan, L., Rapta, P. and Dunsch L. In situ Raman and Vis-NIR spectroelectrochemistry at single-walled carbon nanotubes. *Chem. Phy. Lett.* (2000) **328**:363–368.

[16] Corio, P., Santos, P. S., Brar, V. W., Samsonidze Ge. G., Chou. S. G. and Dresselhaus M. S. Potential dependent surface Raman spectroscopy of single wall carbon nanotube films on platinum electrodes. *Chem. Phy. Lett.* (2003) **370**:675–682.

[17] Murakoshi, K., Okazaki, K.-I. Electrochemical potential control of isolated single-walled carbon nanotubes on gold electrode. *Electrochimica Acta* (2005) **50**:3069–3075.

[18] Kalbac, M., Farhat, H., Kavan, L., Kong, J., Sasaki, K.-I., Saito, R. and Dresselhaus, M. Electrochemical Charging of Individual Single-Walled Carbon Nanotubes. *ACS Nano* (2009) **3(8)**:2320–2328.

[19] Yun, Y.H., Shanov, V., Tu, Y., Schulz, M. J., Yarmolenko, S., Neralla, S., Sankar, J. and Subramaniam, S. A Multi-Wall Carbon Nanotube Tower Electrochemical Actuator *Nano Lett.* (2006) **6(4)**:689–693.

[20] Geier, S., Mahrholz, T., Wierach, P. and Sinapius M. Carbon nanotubes array actuators *Smart. Mater. Struct.* (2013) **22(9)**:094003.

[21] Vainio, U., Schnoor, T., I., W., Vayalil, S., K., Schulte, K., Müller, M. and Lilleodden, E., T. Orientation Distribution of Vertcally Aligned Multiwalled Carbon Nanotubes *J. Phys. Chem. C* (2014) **118**:9507–9513.

[22] Nightingale, E., R. Phenomenological Theory of Ion Solvation. Effective Radii of Hydrated Ions *J. Phys. Chem.* (1959) **63(9)**:1381–1387.

[23] Mirfakhrai, T., Oh, J., Kozlov, M., Fok, E. C., Zhang, M., Fang, S., Baughman, R. H. and Madden, J. D. Carbon Nanotube Yarns as High Load Actuators and Sensors *Advances in Science and Technology* (2009) **61**:65–74.

[24] Wang, D. et. al. Highly oriented carbon nanotube papers made of aligned carbon nanotubes *Nanotechnologie* (2007) **19**:1–5.

[25] Geier, S., Mahrholz, T., Wierach, P. and Sinapius, M. Experimental Investigations of Actuators based on Carbon Nanotube Architectures in *Computational Methods in Applied Science, Smart Strctures and Materials* Springer International Publishing Araujo, A., L., Mota Soares, C., A. (Editors) Vol. I (2016):67–95.

[26] Arruda, T. M., Heon, M., Presser, V., Hillesheim, P. C., Dai, S., Gogotsi, Y., Kalinin, S. V. and Blake, N. In situ tracking of the nanoscale expansion of porous carbon electrodes *Energy Environ. Sci.* (2013) **6**:225–231.

VIII ECCOMAS Thematic Conference on Smart Structures and Materials
SMART 2017
A. Güemes, A. Benjeddou , J. Rodellar and Jinsong Leng (Eds)

Manufacture and characterization of transparent conductor polymer coatings doped with graphitic nanofillers for optoelectronic devices

S. G. Prolongo[1,*], N. Rolston[2], A. D. Printz[2], B. L. Watson[2], and R. H. Dauskardt[2,†]

[1,*]Materials Science and Engineering. Universidad Rey Juan Carlos
C/Tulipán, S/N, Móstoles, 28933, Madrid, Spain
e-mail: silvia.gonzalez@urjc.es, web page: http://www.urjc.es

[2]Department of Materials Science and Engineering. Stanford University
Durand Building, Rm. 121, CA 94305, Stanford, USA

[†]Email: dauskardt@stanford.edu - Web page: https://dauskardt.stanford.edu

Key words: Conductor polymer, optoelectronic device, graphitic nanoparticles

Abstract

The main goal of this work is the addition of electrically conductive nanofillers into a semiconducting polymer, poly(triarylamine) (PTAA), in order to increase its electrical conductivity, while retaining its transparency and mechanical behavior in order to enhance its applicability on photovoltaic and optoelectronic devices. This work consists on the optimization of the dispersion of graphitic nanofillers, using carbon nanotubes and graphene nanoplatelets. The dispersion degree is analysed by optical microscopy and image analysis software for the PTAA composite films doped with graphene. The transparency of the doped polymer films in the visible spectra range is further evidence of the dispersion quality. The obtained results confirm the importance and necessity to optimize the experimental conditions of manufacturing, such as the spin-coating conditions and type and concentration of graphene. The optimized procedure allows for manufacturing of transparent films with high nanofiller contents, close to 10 – 20% for polymer films doped with graphene nanoplatelets and 0.7 – 2% for polymer film doped with carbon nanoplatelets.

1 INTRODUCTION

Semiconducting polymers are being widely investigated due to their combination of low density, optical and mechanical properties, and their optoelectronic behavior for different applications [1-3]. Their main advantages are high flexibility and transparency, which significantly increase their range of applications. However, one of the limitations of these materials is low electrical conductivity, and, for this reason, the recent literature has focused on

the addition of electrically conductive fillers [2-3]. These polymer composite films generally exhibit high electrical conductivity, but their transparency is usually negatively affected.

The present work focuses on the addition of graphitic nanofillers into the organic semiconducting polymer poly(triarylamine) (PTAA). The graphitic nanofillers used are graphene nanoplatelets (GNP) and carbon nanotubes (CNT), whose intrinsic electrical conductivity is very high [1,2].

The aim was to manufacture a highly conductive transparent film with low cost, replacing expensive oxides (e.g. indium tin oxide) in different electrical applications, such as transparent electrodes, light emitting diodes, thermoelectric, or photovoltaic devices. In order to achieve this objective, it is necessary to optimize the dispersion process of nanofillers into the polymer solution. In the literature, the addition of high nanofiller content induces an important increment of the electrical conductivity, but this enhancement is usually accompanied with a decrease of the transparency. This phenomenon is caused by a poor dispersion, appearing agglomerates of large size, which decrease the transparency of film.

In this work, PTAA [3] was the studied organic semiconductor polymer, because it exhibits high optical transparency, relatively high hole mobility, and high air stability, making it an ideal material for photovoltaic devices. As electrically conductive filler, graphitic nanofillers, GNPs and CNTs, were used in two states: unmodified and amine-functionalized. The amine-functionalization was selected because it could possibly enhance the dispersion degree of nanofillers into the poly(triarylamine) due to stronger chemical interactions. It is worth noting, however, that a high interaction of nanofillers with the polymer matrix usually decreases the electrical conductivity of the composite due to the polymer forming a layer that surrounds the nanofiller. Additionally, chemical functionalization induces structural defects in the nanofillers, decreasing their intrinsic electrical conductivity.

In this paper, the authors report the optimization of experimental parameters for dispersing different graphitic nanofillers into PTAA. The dispersion degree is analysed by image analysis of optical micrographs and by high resolution scanning electron microscopy. Optical transparency was used to further confirm the dispersion quality.

2 EXPERIMENTAL

The organic semiconducting polymer used as the matrix was poly(triarylamine) (PTAA, Solaris Chem Inc.) with a molecular weight of 7000-10000 g/mol, as measured by gel permeation chromatography (GPC). Unmodified (NC3150, Nanocyl) and amine-functionalized (NC3152, Nanocyl) carbon nanotubes (CNTs) and graphene nanoplatelets (GNPs) were added to the PTAA in different concentrations. The average diameter of CNTs was 10 nm, measured by transmission electron microscopy (TEM) and their average length was less than 1 μm, measured by scanning electron microscopy of high resolution (FEG-SEM). The GNPs, powder grade M25 with an average thickness of 6–8 nm and an average lateral size of 20 μm, was provided by XGScience. Finally, amine-functionalized graphene nanoplatelets with a thickness of 4–6 nm and an average lateral size of 5 μm were supplied by Cheaptubes.

The optimization of the dispersion procedure was performed using 1,2-dichlorobenzene (ODCB), which was selected because it was a good solvent for both PTAA and the graphitic nanofillers. First, the nanofillers were dispersed into the solvent by ultrasonication using a probe sonicator at an amplitude of 30% and a frequency of 3 Hz. The ultrasonication was performed in an ice water bath to prevent extensive heating and damage of the graphitic nanofillers. The time to achieve a suitable dispersion varied as a function of nanofiller content, from 15 min for the lowest concentration to 2 h for highest concentrations. PTAA was subsequently added at a concentration between 10 and 20 mg/ml into the solution of graphitic nanofillers in ODCB. This solution was dispersed further by an additional 15 min in an ultrasonication bath. Finally, a composite film, formed by the graphitic nanofillers in a PTAA matrix, was fabricated by spin-coating on clean glass substrates. Different spin-coating conditions were utilized, with different numbers of steps, revolutions, and spinning time. Two procedures were finally selected, the first being a one-step treatment, at 500 rpm for 60 s, and the second was a two-step process, first at 500 rpm for 30 s, followed by 2000 rpm for 60 s. The fabricated films were subsequently dried in air with an oven at 100 ºC for 1 h.

PTAA composite films were fabricated with varying graphitic nanofiller concentrations. The higher GNP concentrations (1 – 50 wt %) tested in comparison with CNT percentages (0.3-10 wt %) is justified by the different specific area of both nanofillers, which was ~500 m^2/g for carbon nanotubes and ~150 m^2/g for graphene nanoplatelets. A higher specific area hinders the dispersion and thus limits the maximum concentration of the nanofiller allowable to obtain a well-dispersed solution.

Different experimental techniques were used to characterize the manufactured composites. Differential scanning calorimetry (DSC, TA Instrument Q2000) was used to measure the glass transition temperature (T_g) of neat PTAA and composites.

The thickness of each film was measured using a stylus profilometer (Bruker Dektak 150 profilometer). The dispersion quality was determined by UV/VIS spectroscopy, transmission optical microscopy (in the case of GNP/PTAA films), and scanning electron microscopy. The transparency of the films was measured by UV/VIS spectroscopy (Agilent Cary 6000i) from 300 to 800 nm. All films were deposited on glass and a blank glass slide was used as a background. The transmission optical microscopy was performed using a Leica microscope and the subsequent image analysis was performed with Image-J software. This technique allowed the study of the degree of dispersion for the PTAA films doped with GNPs due to their large lateral size. In contrast, the dispersion of CNT/PTAA films had to be analysed using Field Emission Gun Scanning Electron Microscope (FEG-SEM, Philips Nova NanoSEM FEI 230). To reduce surface charging, the samples were coated with a thin Pt layer (5–10 nm).

3 RESULTS

PTAA was characterized initially by DSC in order to analyse its thermal behavior, and visible spectroscopy to determine its transparency. A glass transition temperature of 119 ºC for neat PTAA was measured by DSC. PTAA was also highly transparent in the wavelength range from 400 – 750 nm. A slight decrease in the transparency of neat PTAA films with increasing film thickness was observed, with a transparency higher than 99% for films of ~10 nm and

close to 95% for films 50 nm thick.

In addition to the film thickness, the transparency of the PTAA nanocomposites films was also influenced by the nanofiller nature, its concentration, and functionalization. Table 1 shows the thickness and transparency of PTAA films doped with carbon nanotubes, unmodified (CNT) and amine functionalized ones (CNT-NH2). Similar results are obtained for PTAA composites doped with graphene nanoplatelets.

Table 1: Thickness and transparency at 600 nm of CNT/PTAA composites films as a function of the functionalization and concentration of carbon nanotubes, the PTAA concentration and spin-coating manufacturing conditions.

Transparency at 600 nm (%) and film thickness (nm)					
PTAA (mg/ml)		**10**		**20**	
Spin coating steps		**500**	**500/2000**	**500**	**500/2000**
Neat PTAA		98.81%	99.43%	95.79%	95.09%
		19.57 ± 2.70 nm	11.59 ±1.59 nm	48.69 ± 9.88 nm	51.49 ± 3.59 nm
CNT/PTAA	0.07 CNT	97.65%	96.62%	94.16%	94.44%
		28.66 ± 4.73 nm	25.81± 3.50 nm	56.58 ± 8.02 nm	71.02 ± 8.10 nm
	0.3 CNT	92.34%	90.37%	89.87%	90.09%
		53.22 ± 10.89 nm	12.74± 2.56 nm	83.11 ± 6.11 nm	81.51 ± 8.35 nm
CNT-NH2/PTAA	0.5 CNT-NH2	83.75%	84.45%	88.95%	89.69%
		52.11 ± 6.25 nm	31.04 ± 8.91 nm	88.19 ± 8.34 nm	83.12 ± 9.52 nm
	0.7 CNT-NH2	84.56%	83.69%	82.34%	80.80%
		36.50 ± 7.23 nm	20.56 ± 3.38 nm	57.54 ± 15.97 nm	53.26 ± 3.35 nm

At the same conditions of film fabrication, meaning the same concentration of PTAA and the same spin-coating procedure, the thickness of nanofilled films is higher than films of neat PTAA. Since the concentration of the nanofillers is relatively low, the reason for the increased thickness is likely due to an increase in the solution viscosity. As expected, in all cases, the increase of spin-coating speed reduces the film thickness. This effect is higher at low PTAA concentration. The homogeneity of film thickness, analyzed by error bars, was observed to be higher for the samples manufactured with the spin coating procedure based in two steps (500/2000).

The transparency of the composite films proportionally decreased as a function of GNP and CNT load, with a higher decrease observed for CNTs than for GNP, likely due to the higher specific area of CNTs. A higher decrease in transparency was also observed for unmodified

nanofillers in comparison with amine-functionalized ones because of the better chemical interactions between the amine groups of the nanofiller and PTAA matrix. Table 2 shows the decrease of transparency associated with the presence of graphitic nanofillers, calculated as the slope between the percentage of transparency at 600 nm and the nanofiller concentration as a weight load percentage. Also, this table presents the maximum nanofiller concentration to obtain films with 95 and 90% transparency, respectively.

Table 2: Decrease of transparency of PTAA composites films as a function of the nanofiller content.

Nanofiller	Slope (transparency/nanofiller content	Maximum nanofiller content for 95% transparency of doped PTAA film	Maximum Nanofiller content for 90% transparency of doped PTAA film
GNP	-0.6	10%	15%
GNP-NH2	-0.2	12%	20%
CNT	-5.4	0.7%	-
CNT-NH2	-2.0	2%	3.5%

Figure 1 shows the optical micrographs captured for GNP/PTAA films in order to analyse the quality of the nanofiller dispersion. This analysis could only be carried out for nanocomposites doped with GNPs (and not CNTs) due to their relatively large size, with micro-scale planar dimensions.

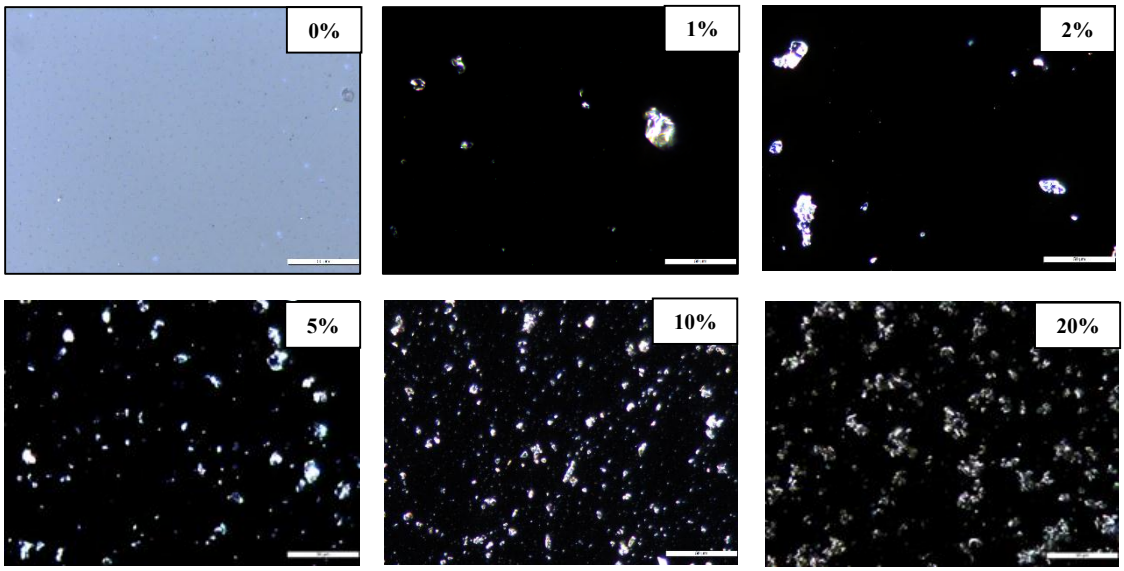

Figure 1: Optical micrographies of GNP/PTAA composite films

Table 3 shows the results of the image analysis of PTAA films doped with neat GNPs and amine functionalized GNPs. The image analysis determined the surface area occupied by nanofiller and the average lateral size of the nanoparticles. Figure 2 shows the comparison between the average lateral size of the nanoparticles or even agglomerations as a function of

nanofiller content. These results confirms the tendency observed by UV/Vis spectroscopy. The average size of the nanoparticles in the GNP/PTAA films was higher than the average size of the graphene nanoplatelets in powder, meaning poor dispersion and the presence of agglomerates of several nanoplatelets. In contrast, the lateral size of nanoparticles for PTAA composite films doped with amine-functionalized GNPs was similar to the average diameter of amine-functionalized GNPs in powder, confirming the lack of agglomerates. In this system it was also observed that the size of nanoparticles increased (i.e., the degree of dispersion decreased) with increasing amine-GNP content into PTAA matrix.

Table 3: Image analysis results of optical micrographies of GNP/PTAA composite films.

Sample	PTAA (mg/ml)	[GNP] (%)	% occuped area	Average lateral size (µm)
PTAA:GNP 10:0.1	10	1%	1.09	34.4
PTAA:GNP 10:0.2	10	2%	2.51	40.0
PTAA:GNP 10:0.5	10	5%	5.46	33.4
PTAA:GNP 100:10	100	10%	28.08	37.1
PTAA:GNP-NH2 10:0.1	10	1%	0.43	3.21
PTAA:GNP-NH2 10:0.2	10	2%	0.84	5.50
PTAA:GNP-NH2 10:0.5	10	5%	5.99	3.85
PTAA:GNP-NH2 10:5	10	20%	11.72	7.25
PTAA:GNP-NH2 100:5	100	5%	8.70	6.10

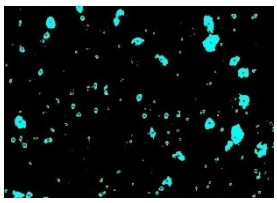

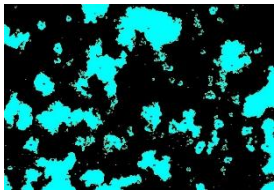

Because it was not possible to study the dispersion degree of CNT into PTAA matrix by optical microscopy, these samples were instead analysed by FEG-SEM. The high dispersion degree of carbon nanotubes in spite of the high load was confirmed, however, large agglomerates were observed (Figure 3). It is worth noting that the length of the pull-out of carbon nanotubes for fractured films was higher for neat carbon nanotubes than with amine-functionalized CNT, likely due to the stronger chemical interface between the functionalized nanotubes and the polymer matrix.

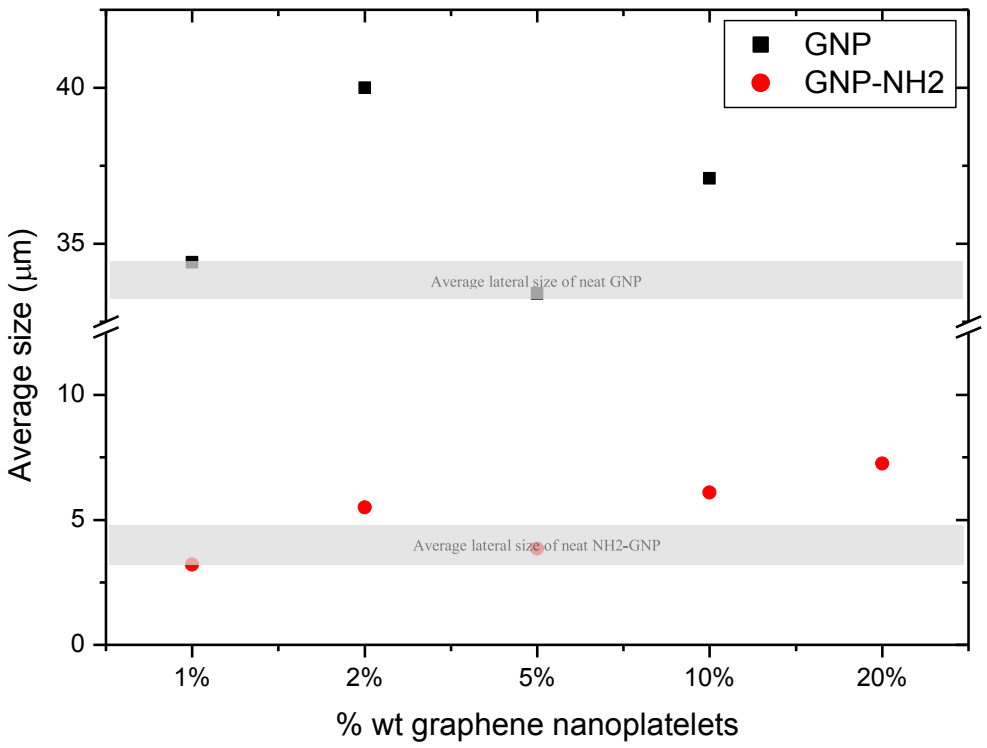

Figure 2: Average lateral size of nanoparticles for GNP/PTAA composite films.

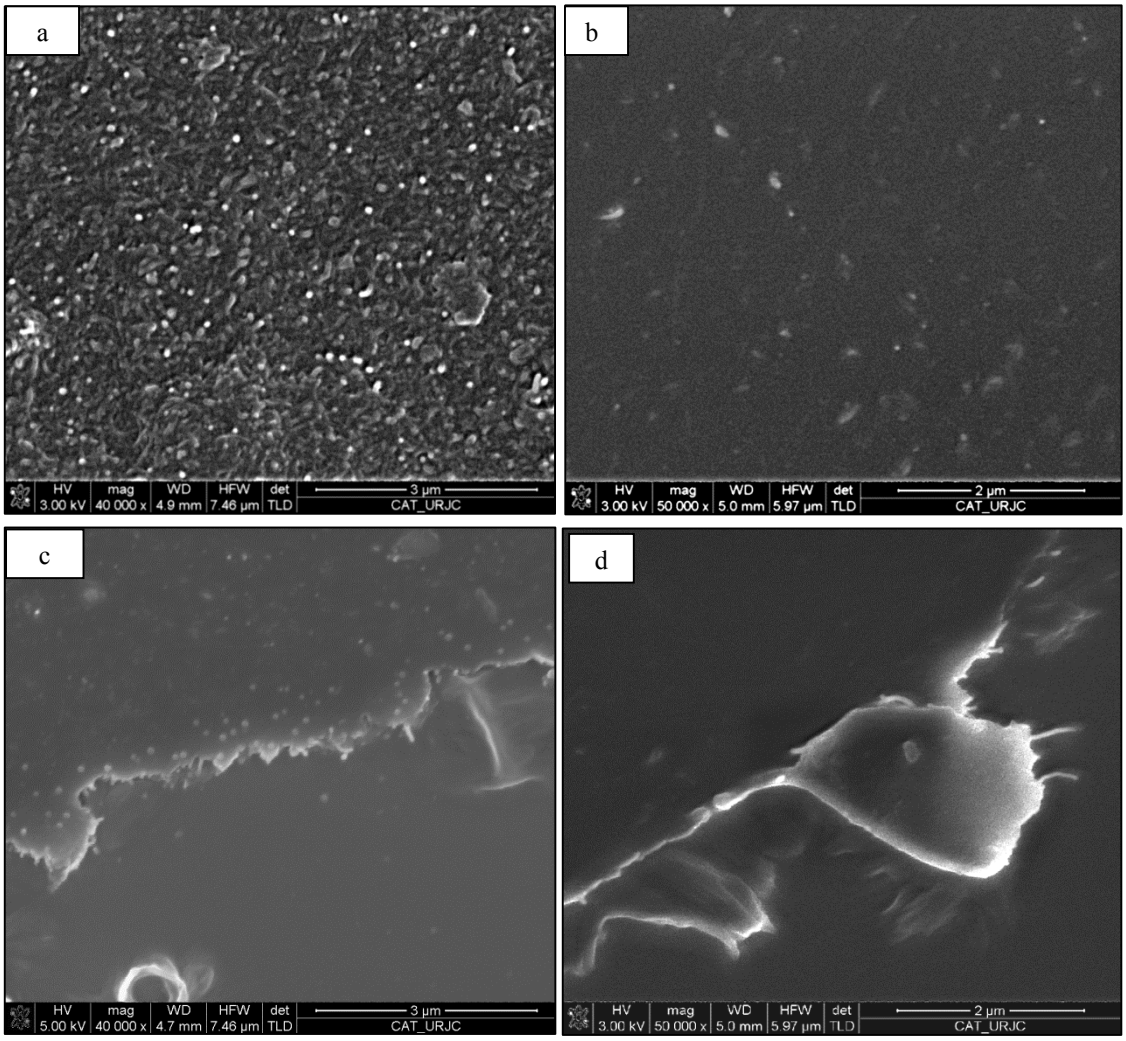

Figure 3: FEG-SEM micrographs of CNT/PTAA composite filmswith 5 wt % amino-functionalized CNT (a,c) and 1% neat CNT (b,d)

4. CONCLUSIONS

The present work consists of the optimization of the dispersion of graphitic nanofillers into the semiconducting polymer PTAA. Different parameters have been analysed, such as the geometry, nature, functionalization, and concentration of the nanofillers, as well as the spin coating procedure. Transparent films of PTAA composite films were successfully

manufactured with a high nanofiller load. The main conclusions from the present work are:

- The maximum nanofiller load on PTAA composite films is much higher for graphene nanoplatelets than nanotubes because of their lower specific area.
- Applying the same experimental spin-coating procedure, the thickness of nanofilled films is higher than neat PTAA, due to the increased viscosity of the doped solutions.
- The homogeneity of film thickness is higher for the samples manufactured with the spin coating procedure based in two steps (500/2000).
- The functionalization of graphitic nanofillers enhances the dispersion degree, inducing the formation of strong chemical interaction between the nanofiller and polymer matrix.

ACKNOWLEDGE

Silvia G. Prolongo thanks the financial support of USA Government, Fulbright program, for the research grant in Stanford University. The authors also thank the service and help of Gilberto Del Rosario in the technological Center Support (CAT).

REFERENCES

[1] Madec, M.B. Morrison J.J., Rabjohns, M., Turner, M.L. and Yeates, S.G. *Effect of ply(triarylamine) molar mass distribution on organic field effect transistor behavior*. Organic Electronics (2010) **11**: 686-691

[2] Dey, A., Bajpai, O.P., Sikder, A. K., Chattopadhyay, S. and Khan, M.A.S. *Recent advances in CNT/graphene based on thermoelectric polymer nanocomposite: A proficient move towards waste energy harvesting.* Renewable and Sustainable Energy Reviews (2016) **53**: 653-671.

[3] Behnam, A.V.K., Shanwan, X., Zhong., F., Lian, D., Estrada, D., Jariwala, A., Hoag J., Lauhon, L.J., Marks, T.J., Hersam, M.C. and Pop, E. *High-field transport and thermal reliability of sorted carbon nanotube network devices*. ACS Nano (2012) **7**: 482-490

VIII ECCOMAS Thematic Conference on Smart Structures and Materials
SMART 2017
A. Güemes, A. Benjeddou, J. Rodellar and Jinsong Leng (Eds)

NANOCOMPOSITES SPRAY QUANTUM RESISITVE SENSORS (QRS) FOR THE STRUCTURAL HEALTH MONITORING OF COMPOSITE WIND BLADE

A. LEMARTINEL[*, 1, 2], S. NAG-CHOWDHURY [2], M. CASTRO[2], O. FOUCHE[1], AND J. F. FELLER[2]

[1] Institut de Recherche Technologique Jules Verne (IRT Jules Verne)
Chemin du Chaffault, 44340, Bouguenais, France
e-mail: antoine.lemartinel@irt-jules-verne.fr, web page: http:// http://www.irt-jules-verne.fr/

[2] Smart Plastics Group
Université Bretagne Loire (UBL), IRDL CNRS 3744 - UBS, Lorient, France
e-mail: jean-francois.feller@univ-ubs.fr, web page: http:// http://www.smartplasticsgroup.com/

Key words: Carbon Nanotubes CNT, Composite, Structural Health Monitoring SHM, Smart Structure, Quantum piezo-resistive sensor QRS, Spray layer by layer.

Abstract. *The growing development of renewable energies leads to the fabrication of composite's parts with bigger dimensions or subjects to a severe environment. An optimization of the health monitoring of these systems is compulsory to estimate their damages and predict the associated maintenance. The development of nanocomposites Quantum Resistive Sensors (sQRS) for the monitoring of strain and damage of composite structures is presented. sQRS are based on the addition of carbon nanotubes (CNT) in an epoxy resin. Those sensors can be on the surface or embedded in the core of material during its fabrication. Due to their small dimensions (1-2 µm thick), they can provide an in situ monitoring without any loss of mechanical properties, without generating new defects, and preserving the matrix integrity. The characteristics of the sensor can be adjusted by the fraction of CNT in the resin or the amount of resin and CNT in the sensors. The fabrication steps of spray layer-by-layer (sLbL) sensors are explained in relation with the electrical response of the sensor due to a mechanical solicitation.*

1 INTRODUCTION

Over the last decade, the need for fibre reinforced polymers (FRP) has more than doubled and this growth is expected to continue. This affects the markets from civil engineering to transport and defence. The need for carbon fibre reinforced polymers should rise from 101 to 175 106 kg between 2016 and 2021 [1]. One of the main reasons is the better mechanical

properties/weight ratio of composites compare to others materials, which enables the construction of lighter structures.

At the same time, the will to decrease carbon emissions, in particular fossil energies has encouraged the examination of the renewable energy development in many countries [2]. For example, in France it is planned to increase between 2014 and 2023 from 9.3 GW to 26 GW of on-shore wind farms and to develop the off-shore wind farms up to 3 GW. To provide for this increase of wind energy, the size of the wind turbine are increased continuously, from a diameter of 15 m in the early 80's to 150 m nowadays, and they could be higher than 200 m in 2030 [3,4]. The lifetime of these structures is also expected to be improved, with less required planned maintenance. Nowadays, composites materials are taking an important part in wind turbines materials, since the blades are usually made of glass fibre and epoxy. However, composites are anisotropic or orthotropic materials, whose failure is a combination of various mechanisms like matrix cracking, delamination, fibre breakage, and interfacial debonding. Hence, the damage initiation and propagation remains difficult to predict. The detection of damages along with undergone strain could promote a better prediction of the ultimate failure of the structure, thus leading to a maintenance cost reduction, which is expected to be up to 30% of the total cost for off shore wind turbines [5].

In this frame, a Structural Health Monitoring (SHM) system, which would provide clues about the material's health state, comes out like a very interesting tool [6]. SHM systems have multiple objectives, such as allowing an optimal use of the structure, minimizing the downtime, and avoiding catastrophic failure. It should also help to replace the scheduled and periodic maintenances by performance based inspections; as well as to reduce the human involvement for less labour, human errors, and therefore higher reliability.

Among the requirements, such systems should have a non-destructive evaluation of strain, damages and failures in the structure. SHM involves the integration of sensors or sensing elements within the composite structure for prediction, localization, assessment and evaluation of various damages induced in the composites materials. It would therefore help to avoid the structure downtime, and the cost of maintenance. The interest for SHM is displayed in various fields: aeronautics [7,8], energy [9,10], or civil engineering [11,12]. Since the first construction of bridges equipped with monitoring devices in the 70' [13], SHM market gains momentum and expects an annual growth of nearly 25 % between 2015 and 2020. In 2020, it could reach 1.89 billion dollars [14].

Over the past decades various conventional SHM technics were developed like strain gauges, doped semi-conductors, piezo-electric sensors, optical fibre sensors (OF), Eddy-current sensors, and acoustic sensors. However, these kinds of sensors usually suffer from performance degradation over time due to temperature, moisture effects, or wiring issues [15] that are not correlated to the structure mechanical properties changes. These observations confirm the need for more reliable sensors, with clear correlation between the change of the structure and the output signal. This challenging task has recently raised interest in the research community, particularly through the use of nanoparticles.

Actually, the emergence of conductive polymer nanocomposites (CPC) is leading for the development of self-sensing materials [16–20]. Thanks to their unique mechanical [21], thermal [22] and electrical properties [23], carbon nanotubes (CNT) are one of the leading candidates for the development of nano composites. Since nanofillers can create a 3D conductive network in an insulating polymer matrix, the electrical recording of the

nanocomposites resistance can be used to detect and measure the undergone deformation and the induced damages [17,24,25]. Furthermore, the use of such materials leads to a concordance between the durability of the structure and the nano composite. Nano reinforced composites are therefore good candidates for SHM devices but still mainly remain at a laboratory scale.

In this paper, the use of Quantum Resistive Sensor (QRS), localized in the core of a composite structure for *in situ* strain and damage detection, is proposed. The QRS electrical behaviour is investigated, when embedded in glass fibre epoxy composite during mechanical testing in the elastic and plastic domains until ultimate failure. The fabrication by spray layer by layer allows controlling the sensor geometrical and electrical characteristics and enables to target specific areas of deposition.

2 SENSOR'S THICKNESS

The sensor's fabrication has been described in previous works [16,17,24]. SEM and AFM were used to measure the thickness of QRS, as shown on Figure 1.a for a 40 layers sensor. The measured thickness is comprised in 1.8 and 2.1 µm, which illustrates the thickness control by the spray deposition technic. Figure 1.b exhibits the sensor's thickness increase with the number of layers. Similar results are found with both SEM and AFM measurements. This fabrication technic enables to obtain sensor with a thickness lower than 1 µm, which is below the size of other strain monitoring technics as optical fibre, usually higher than 100 µm.

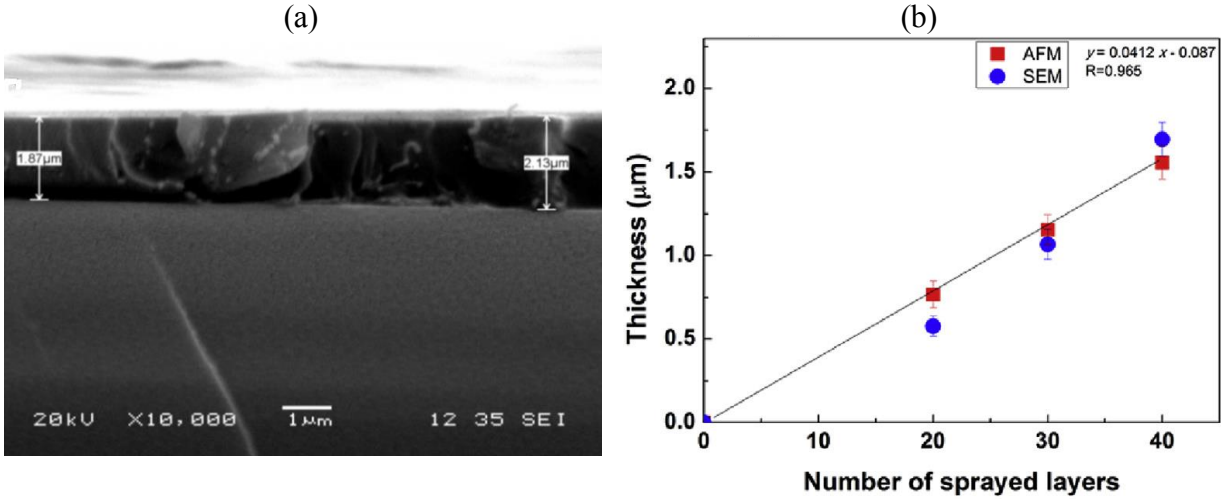

Figure 1: a) Thickness of CPC sensors measured by SEM for 40 sprayed layers of CPC solution. b) Evolution of sensors' thickness with number of sprayed layers (20, 30 and 40 layers), measured by SEM (circles) and AFM (squares) [26].

3 MECHANICAL AND PIEZO-RESISTIVE BEHAVIOURS

The piezo-resistive properties of QRS were determined by static tensile tests on glass fibre epoxy (GFEP) specimen with embedded QRS to characterize the mode of failure of the specimen. The figure 2 shows the 0/90° GFEP sample stress and the sensor change of resistance (A_r) versus strain during the tensile test. The mechanical behaviour exhibits a first elastic domain ($\varepsilon < 0.35\%$) with a 17.1 GPa Young Modulus. Then cracking initiates in the

90° plies and propagates in the adjacent 0° plies until the final brutal breakage. It results in a decrease of the stress slope with the strain. Concerning the electrical behaviour of the sensor, AR is linear in the elastic domain and a slope increase occurs afterwards until ε = 1.0%. A decrease in the slope occurs followed by an infinite increase. Hu *et al.* [27] had previously evidence that the tunnelling effect is a determining parameter controlling the electrical performance of CNT-epoxy nano composite especially close to the percolation threshold. The observed non-linear behaviour occurring over the elastic limit is induced by the tunnelling effect. The final infinite increase in A_r depicts the propagation of cracks in the CNT network and the breaking of the conductive paths, corresponding to the laminate breakage. Therefore, *in situ* QRS are able to monitor the damage status and monitor the health of a GFEP composite. The QRS could be implanted in a composite structure in chosen strategic or fragile locations to monitor a specific area.

The QRS sensitivity, named gauge factor (GF), is defined as the relative change in electrical resistance due to a mechanical solicitation and expressed as follows in Equation (1):

$$GF = A_R/\varepsilon \tag{1}$$

with $A_R = (R-R_0)/R_0$, ε is the deformation, A_R is the change of resistance, R_0 (Ω) is the resistance at ε=0 and R (Ω) is the resistance at ε

Experimentally the gauge factor (GF) is calculated from the slope of the electrical response versus strain curve, in the elastic domain (ε < 0.35%). In figure 2, the GF obtained is 6, which is 3 times higher than for usual commercial metallic strain gauges. Based on the QRS GF it is possible to determine the local strain of the sample with the measure of the QRS resistance. Therefore, QRS can detect as well strain and damage *in situ* of the composite structure.

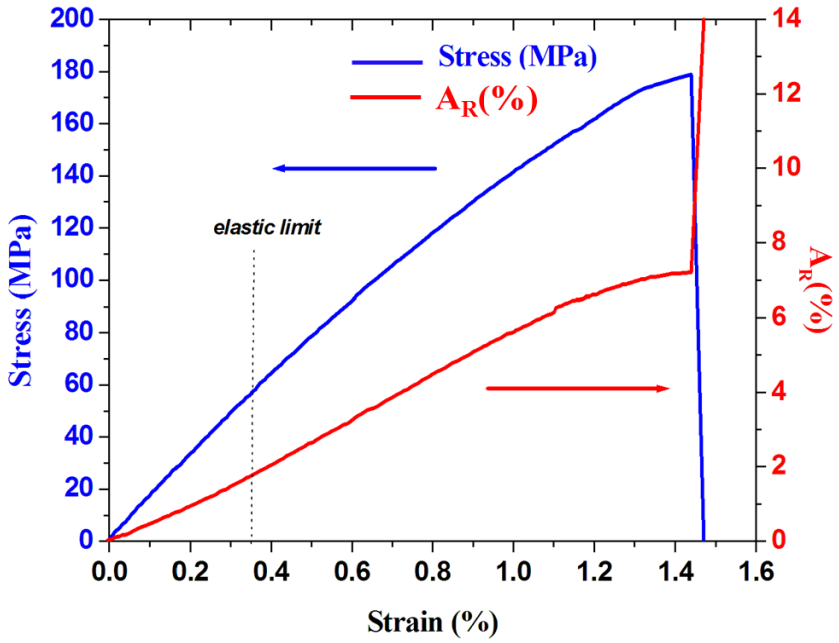

Figure 2: Evolution of stress and electrical response change (A_R) with strain during static tensile test, up to fracture [17].

4 EFFECT OF INITIAL RESISTANCE R_0 ON SENSITIVITY

To adapt the QRS sensitivity, the number of sprayed layers (20, 30 and 40) and the CNT content in the epoxy matrix (1, 2 and 3%) has been changed. The Figure 4 depicts the resulting gauge factor versus the initial resistance for the different each case. It can be seen that the resistance can be adjusted depending on the CNT content and the number of layers, and that the GF is determined by the initial resistance. Hu *et al.* [27] previously observed that the increase of the CNT content in the epoxy matrix decreased its resistance resulting in a decline of the GF. This increase of the CNT content favoured the formation of the percolated network and the reduction of the distance between two successive CNT. The decrease of the distance would reduce the tunnelling effect, and any variation in the network due to a deformation would lead to a lower change of resistance. On the other hand, close the percolation threshold, any disconnection in the CNT network would cause a large resistance increase. It is why for 1 wt% with 20 layers the initial resistance is 15 MΩ and the resulting GF of 11, while with 3 wt% and 30 layers the initial resistance has diminished to 30 kΩ and a GF of 4. Therefore, the QRS' CNT content and numbers of layers are adjusted depending on the targeted sensibility or initial resistance. In addition, the best compromise between the sensitivity and the signal noise has been found to be the 2 wt% of CNT with 40 layers.

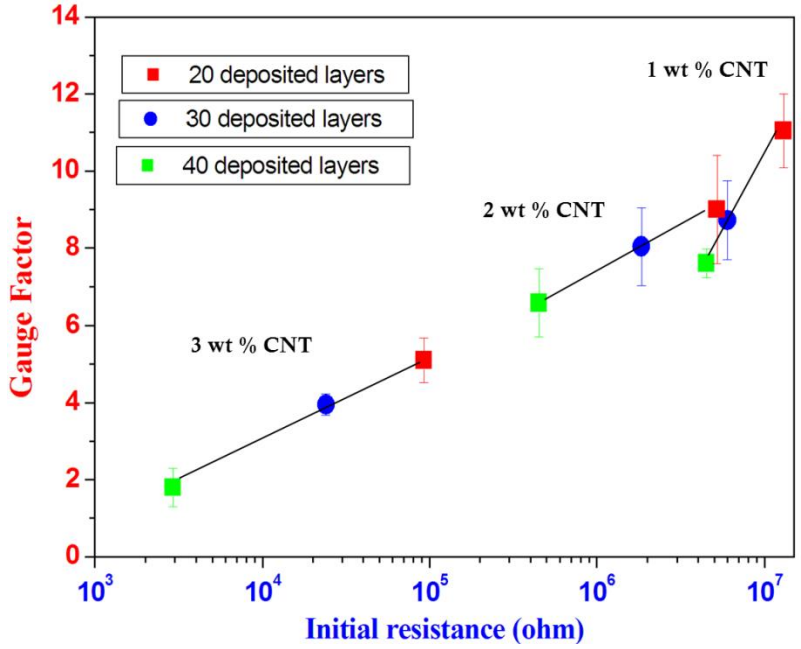

Figure 3: Gauge factor as function of QRS' initial resistance with various CNT content in the epoxy matrix and various spray layers [17].

5 DYNAMIC CYCLING BEHAVIOUR OF CPC SENSORS

To investigate on the electrical behaviour of QRS during the life of a composite structure like windmill blades, fatigue tests have been conducted. The QRS were embedded in GFEP samples in the tension side during bending fatigue with a frequency of 0.5 Hz. Two different levels of loading corresponding to nominal deformations of $\varepsilon = 0.4 \pm 0.2\%$ and $\varepsilon = 0.6 \pm 0.2\%$

were selected, and the results are presented in figure 4.a-b. The QRS response, after 3500 and 60000 cycles are compared in the two cases.

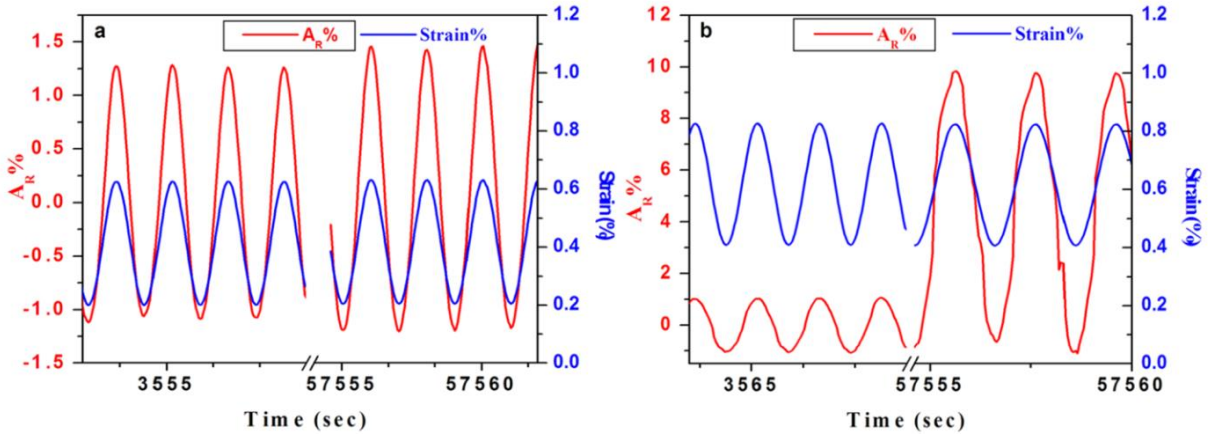

Figure 4: Variation of A_R and strain with time during fatigue bending test at 0.5 Hz (a) strain 0.4 +/- 0.2% (b) strain 0.6 +/- 0.2% [26].

The resistance is in phase with the strain for both cases from low to high number of cycles, which illustrates the ability of sQRS to monitor the fatigue behaviour. When the deformation is under the elastic limit, as in figure 4.a, a slight increase of A_R is visible after 25000 cycles, which may correspond to the formation of microcracks in the sample. At the beginning of the test, the GF measured is 5.6, which is in agreement with the static tensile test. For strain above the elastic limit, as in figure 4.b, the resistance displays at the beginning a similar behaviour than for a strain level under the elastic limit. Yet, a progressive increase of the A_R amplitude occurs to reach after 60000 cycles five times the initial value. Simultaneously, the resistance sinusoidal shape is modified. Thostenson *et al.* [25] have linked this kind of behaviour, during increasing tensile cycles, to the reopening of cracks and the formation of new ones. The QRS homogeneity with the sample allows the development of similar amounts of cracks than in the composite. Therefore, the degradation of the electrical response matches the development of damage in the composite laminate, and the measure of the A_R drift could provide an amount of damage accumulation.

The overall sQRS piezo-resistive behaviour for both cases is summarized in figure 5. The evolution of the average resistance value with the number of cycles is shown for both 0.4 and 0.6 average strain fatigue tests, as well as the nominal load for the 0.6 strain test. With the little development of damages in the 0.4 strain specimen, no drift in the average resistance can be noticed. For the 0.6 strain sample, in addition to the amplitude response with the numbers of cycles, the average resistance displays a sharp increase simultaneous to the loss of load applied on the sample. This degradation of mechanical properties corresponds to the development of cracks in the sample. The change of resistance is therefore correlated with the density of cracks in the composite structure. In this way, QRS appear to be a very promising for the detection and monitoring of damage at strategic location in GFRP structures.

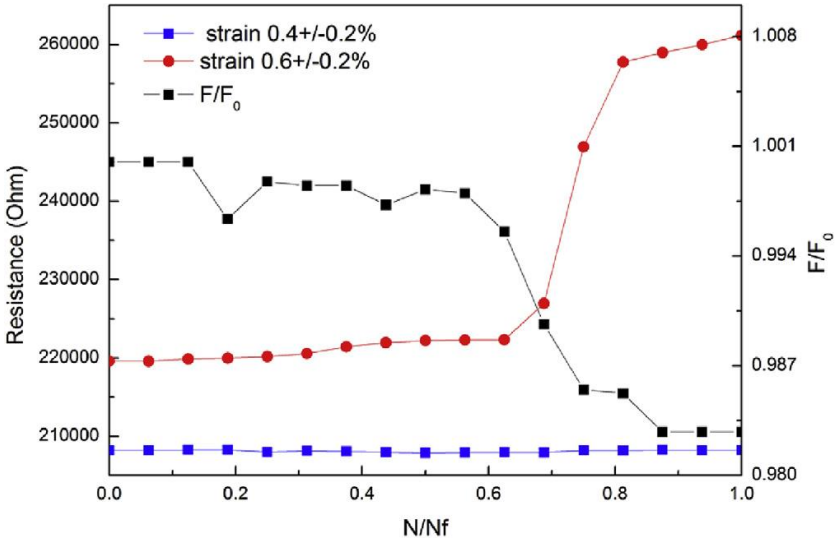

Figure 5: Variation of resistance along strain cycles for two different amplitudes: (a) strain 0.4 ± 0.2% (b) strain 0.6 ± 0.2% [17].

6 CONCLUSIONS

In the aim of developing new SHM systems for composite structures like windmill blades, Quantum Resistive strain Sensors (sQRS) appear to be very good candidates. The sensor is made of a CNT network nanostructured in an epoxy matrix by spray layer by layer fabrication process. sQRS have the advantages to be adaptable in dimensions and homogeneous with the composite matrix, and can therefore be embedded in defined locations in the core of composite structure. The adjustable sensor's resistance and sensibility with the CNT content and the number of sprayed layers enables to predict the QRS performance and afterwards the strain and damage of the composite from elastic deformation to ultimate failure. During fatigue experiments above the elastic limit, phenomena such as cracks' creation, closing/reopening and propagation, resulting in damage accumulation with increasing number of cycles, could be followed by the drift of A_R, thus showing the two steps of formation of microcracks and the delamination of plies. These tests are better fitting the real solicitations to which GFEP parts will be submitted to, in applications such as windmill blades, they have demonstrated that sQRS were perfectly able to monitor real time damage accumulation in GFEP composites and eventually anticipate and prevent the complete fracture of structures provided that the behaviour is known.

REFERENCES

[1] E. Witten, T. Kraus, M. Kühnel, Composites Market Report 2015 Market developments, trends, outlook and challenges, 2015.

[2] J. Burck, F. Marten, C. Bals, A. Dertinger, T. Uhlich, Climate Change Performance Index Results 2017, 2017.

[3] M.R. Islam, S. Mekhilef, R. Saidur, Progress and recent trends of wind energy technology, Renew. Sustain. Energy Rev. 21 (2013) 456–468.

[4] Y. Kumar, J. Ringenberg, S.S. Depuru, V.K. Devabhaktuni, J.W. Lee, E. Nikolaidis, et

al., Wind energy: Trends and enabling technologies, Renew. Sustain. Energy Rev. 53 (2016) 209–224.
[5] L. Castro-Santos, V. Diaz-Casas, Floating Offshore Wind Farms, Springer International Publishing, Cham, 2016.
[6] P.J. Schubel, R.J. Crossley, E.K.G. Boateng, J.R. Hutchinson, Review of structural health and cure monitoring techniques for large wind turbine blades, Renew. Energy. 51 (2013) 113–123.
[7] V. Giurgiutiu, Structural Health Monitoring of Aerospace Composites, Elsevier, 2016.
[8] M. Nicolas, R. Sullivan, W. Richards, Large Scale Applications Using FBG Sensors: Determination of In-Flight Loads and Shape of a Composite Aircraft Wing, Aerospace. 3 (2016) 18.
[9] M. Mitra, S. Gopalakrishnan, Guided wave based structural health monitoring: A review, Smart Mater. Struct. 25 (2016) 53001.
[10] M. Martinez-Luengo, A. Kolios, L. Wang, Structural health monitoring of offshore wind turbines: A review through the Statistical Pattern Recognition Paradigm, Renew. Sustain. Energy Rev. 64 (2016) 91–105.
[11] A. Diez, N.L.D. Khoa, M. Makki Alamdari, Y. Wang, F. Chen, P. Runcie, A clustering approach for structural health monitoring on bridges, J. Civ. Struct. Heal. Monit. (2016).
[12] W.L. Schulz, J.P. Conte, E. Udd, J.M. Seim, Static and dynamic testing of bridges and highways using long-gage fiber Bragg grating based strain sensors, Ind. Sens. Syst. 4202 (2000) 79–86.
[13] C. Yun, J.-J. Lee, S.-K. Kim, J.-W. Kim, Recent R&D activities on structural health monitoring for civil infra-structures in Korea, KSCE J. Civ. Eng. 7 (2003) 637–651.
[14] Structural Health Monitoring (SHM) Market by Technology, by Solution Type, by Application, and by Geography - Global Trend & Forecast to 2020, Markets and Markets, 2015.
[15] M. Ettouney, S. Alampalli, Infrastructure health in civil engineering, CRC Press, 2012.
[16] C. Robert, J.F. Feller, M. Castro, Sensing skin for strain monitoring made of PC-CNT conductive polymer nanocomposite sprayed layer by layer, ACS Appl. Mater. Interfaces. 4 (2012) 3508–3516.
[17] S. Nag-Chowdhury, H. Bellegou, I. Pillin, M. Castro, P. Longrais, J.F. Feller, Non-intrusive health monitoring of infused composites with embedded carbon quantum piezo-resistive sensors, Compos. Sci. Technol. 123 (2016) 286–294.
[18] L. Gao, E.T. Thostenson, Z. Zhang, T.-W.W. Chou, Coupled carbon nanotube network and acoustic emission monitoring for sensing of damage development in composites, Carbon N. Y. 47 (2009) 1381–1388.
[19] M.H.G. Wichmann, S.T. Buschhorn, J. Gehrmann, K. Schulte, Piezoresistive response of epoxy composites with carbon nanoparticles under tensile load, Phys. Rev. B. 80 (2009) 245437.
[20] F.H. Gojny, M.H.G. Wichmann, B. Fiedler, W. Bauhofer, K. Schulte, Influence of nano-modification on the mechanical and electrical properties of conventional fibre-reinforced composites, Compos. Part A Appl. Sci. Manuf. 36 (2005) 1525–1535.
[21] M.M.J. Treacy, T.W. Ebbesen, J.M. Gibson, Exceptionally high Young's modulus

observed for individual carbon nanotubes, Nature. 381 (1996) 678–680.
[22] J.D. Fidelus, E. Wiesel, F.H. Gojny, K. Schulte, H.D. Wagner, Thermo-mechanical properties of randomly oriented carbon/epoxy nanocomposites, Compos. Part A Appl. Sci. Manuf. 36 (2005) 1555–1561.
[23] T.W. Ebbesen, H.J. Lezec, H. Hiura, J.W. Bennett, H.F. Ghaemi, T. Thio, Electrical conductivity of individual carbon nanotubes, Nature. 382 (1996) 54–56.
[24] I. Pillin, M. Castro, S. Nag Chowdhury, J.-F. Feller, Robustness of carbon nanotube-based sensor to probe composites' interfacial damage in situ, J. Compos. Mater. 50 (2016) 109–113.
[25] E.T. Thostenson, T.-W.W. Chou, Real-time in situ sensing of damage evolution in advanced fiber composites using carbon nanotube networks, Nanotechnology. 19 (2008) 215713.
[26] S.N. Chowdhury, Conductive Polymer nanoComposite Quantum Resistive strain Sensors for structural composites' damage monitoring, UBS, 2014.
[27] N. Hu, Y. Karube, M. Arai, T. Watanabe, C. Yan, Y. Li, et al., Investigation on sensitivity of a polymer/carbon nanotube composite strain sensor, Carbon N. Y. 48 (2010) 680–687.

Figures reprinted from Composites Science and Technology, 123, S. Nag-Chowdhury, H. Bellegou, I. Pillin, M. Castro, P. Longrais, J.F. Feller, Non-intrusive health monitoring of infused composites with embedded carbon quantum piezo-resistive sensors, 286–294, Copyright (2016), with permission from Elsevier and S.N. Chowdhury, Conductive Polymer nanoComposite Quantum Resistive strain Sensors for structural composites' damage monitoring, UBS, 2014.

VIIIECCOMAS Thematic Conference on Smart Structures and Materials
SMART 2017
A. Güemes, A. Benjeddou , J. Rodellar and JinsongLeng (Eds)

PREPARATION, CHARACTERIZATION AND ANALYSES OF ALBUMIN NANOPARTICLES LOADED WITH ALUMINUM CHLORIDE PHTHALOCYANINE

TÁCILA GABRIELE LOPES[†], LEONARDO PEREIRA FRANCHI [†], ANTONIO CLAUDIO TEDESCO[†]AND ALAIN PONTON[*††]

[†]Center of Nanotechnology and Tissue Engineering- Photobiology and Photomedicine (CNET)
Department of Chemistry, FFCLRP, University of São Paulo
14040-901, RibeirãoPreto-SP, Brazil.
e-mail: tacila.glopes@gmail.com web page:sites.ffclrp.usp.br/nanotecnologiafomed
e-mail: leonardofranchi@yahoo.com.br web page: sites.ffclrp.usp.br/nanotecnologiafomed
e-mail: atedesco@usp.br, web page: sites.ffclrp.usp.br/nanotecnologiafomed

[††] Laboratoire Matière et Systèmes Complexes
UMR 7057, Université Paris Diderot-Paris 7 et CNRS
F-75205 Paris, France.
e-mail: alain.ponton@univ-paris-diderot.fr, web page: http://www.msc.univ-paris-diderot.fr/site/

Key words: Albumin Nanoparticles; Chemistry Cross-linking; Aluminum Chloride Phthalocyanine; Photodynamic Therapy, cell viability.

Abstract. The developments of albumin-based nanocarriers, which are nontoxic, biocompatible and biodegradable, have been extensively studied for seeking new alternatives of the treatment for numerous diseases. The most relevant characteristic of these protein-based systems are its capacity of the selectively achieve the target cells within of the brain. These nanocarriers are proteins-based and have covalent bonds, which, consequently, can be rapidly degraded through the proteolytic cleavage process on the inside of the cells. In this context, we propose to develop such nanocarriers for the treatment of Central Nervous System (CNS) by incorporating a free and pre-encapsulated photoactive agent aluminum chloride phthalocyanine (AlClPc) in albumin nanoparticles (HAS-NPs) with a chemistry cross-linking method. This later has been optimized by varying some relevant parameters such as Hydrogenionic potential (pH) and the stirring speed. From Scanning Electron Microscopy, Atomic Force Microcopy and Zeta potential measurements, we have clearly shown that the elaborated nanoparticles (NPs) have a smaller size with a spherical shape, are more homogeneous and have greater electronic repulsion (preventing their aggregation) compared to other synthesis methods allowing not only promising advances with the application of this technique in future to *in vivo* studies, as well as the availability, in the future, of a viable and low-cost drug for the treatment of CNS diseases. Preliminary results of rheological measurements of HAS-NPs incorporating magnetic nanoparticles (MNPs) are also presented.

1 INTRODUCTION

Systemic drug administration has shown a weak specificity to reach target cells, leading to a plethora of adverse side effects. Due to this, over the years, development of new drug delivery systems (DDS) has grown exponentially in the area of the nanotechnology to development of nanoparticles (NPs) like biodegradable and biocompatible nanocarriers with high potential in biomedical applications and diagnostics [1]. Besides they are used to improve treatment efficacy through controlled release of therapeutic agents inside the lesion, thus reducing the unwanted side effects [2].

Currently, the development of albumin-based nanoparticles, which are nontoxic, biocompatible and biodegradable, have been extensively studied for seeking new alternatives for treatments in several diseases, mainly because albumins are soluble in water and found abundantly in human plasma at a concentration of approximately 60 μM [3]. These albumin-based particles have already been approved for clinical practice by the Food and Drugs Administration (FDA) in the United States [4], with registration of commercial names as Albunex® and Abraxane® [5]. The most relevant characteristic, as evidenced by previous studies in our group, is that these protein-based systems can cross the blood-brain barrier (BBB) and selectively achieve the target cells within of the brain [6]

The importance of the development of these albumin-based nanoparticles basically due to the rapid and easy degradation of them within the human body which is performed by proteases [7]. Proteases rapidly degrade the albumin-based nanoparticles (HAS-NPs) through proteolytic cleavage which occurs by lysosomal pathway [8]. Thus, after cleavage the actives incorporated into this DDS are released inside of the cells [9], locally acting in these cells. In this sense, these NPs can be used to delivery photoactive molecules limiting the oxidative stress generated by their photo activation to a specific sick tissue. The use of photodynamic therapy (PDT) has proven to be a powerful tool in medicine, thanks to the numerous works and clinical protocols developed worldwide obtained in the last 40 years of research in this field. PDT has been used as an alternative form of treatment of innumerable diseased tissue by inducing cell death only in the photosensitized site, thus reducing and minimizing damage to neighboring healthy tissues and avoiding undesirable side effects common in classical treatments such as chemotherapy and radiotherapy [10, 11, 12]. Therefore, PDT is a clinical approved procedure that is minimally invasive and can be applied to several pathologies that do not yet present 100% effective treatment [13].

Besides of AlClPc, there are several iron oxide, in particular the magnetite (Fe_3O_4) and maghemite (γ-Fe_2O_3) that also have shown greatest interest for use in biomedicine, due their low toxicity, relative ease of functionalization and high magnetization [14, 15, 16]. Magnetic hyperthermia is a general factor that maximizes the action of MNPs added to the body, under external magnetic field with an alternating frequency, because it performed a treatment based on generation of heat where the temperature in tumor cells reach rates between 41 to 45 °C, causing magneto thermo cytolysis or cell death induced by magnetism [14, 15, 17]. These are a promising technique for cancer treatment, once that it is easy for the drug reach the cancerous tissue, with more reducing side effects than chemotherapy and radiotherapy, which is confirmed through of results clinical trials [18]. Given the importance of these nanocarriers as DDS and their effective permeation through blood-brain barrier, we proposed here a

multidisciplinary scientific development combining protocols, techniques and experimental tests of the areas of pharmaceutical technology, nanotechnology and chemistry.

The objective of the present study is thus to optimize the synthesis of albumin-based nanoparticles NPs by chemistry cross-linking with the incorporation of photoactives, as aluminum chloride phthalocyanine (AlClPc) or magnetic nanoparticles (MNPs) and to use them *in vitro* to probe the cell viability of U87MG cells.

2 MATERIALS AND METHODS

2.1 Materials

Human serum albumin (HSA) and aluminum chloride phthalocyanine (AlClPc) (85% pure) were purchased from Sigma-Aldrich; and functionalized magnetic nanoparticles (MNPs) was obtained at Laboratory Matièrie and Systèmes Complexes (University Paris 7 Diderot, France); Acetone analytical grade (J.T.Baker); Sodium chloride (Mallinckrodt Pharmaceuticals); Absolute ethyl alcohol analytical grade (J.T.Baker); 8% glutaraldehyde solution in water (Fluka) were all the reagents used in this work.

2.2 Methods

2.2.1 Nanoparticle preparations – chemistry cross-linking method

The HSA-NPs were prepared following the method of coacervation as described by Weber *et al.* [19]. An aqueous solution with NaCl (10 mM) and HSA at room temperature is first prepared. After, the pH was adjusted and MNPs were included into one part of the formulation while another part was kept without these additive. Subsequently, using a pump injection, it was added absolute ethanol with or without AlClPc. Next, the NPs were formed by addition of 8% glutaraldehyde followed by washing in water. Finally, they were lyophilized and stored at 4 °C. Thus, four different types of NPs were prepared and studied here, namely:

(1) HSA-NPs (Empty) – the empty serum albumin-based nanoparticles;
(2) HSA-NPs (AlClPc) – the HSA-NPs containing AlClPc;
(3) HSA-NPs (MNPs) – the HSA-NPs containing MNPs;
(4) HSA-NPs (AlClPc+MNPs) – the HSA-NPs containing AlClPc plus MNPs

For optimization of the NPs, the weight of the albumin and injection speed was kept constant, while two values of magnetic stirring (155 RPM and 380 RPM) and two values of pH (7.0 and 8.5) were studied.

2.2.2 Measurement of particle size and zeta potential

The measurements of particle size and zeta potential were carried out using a zetasizer Nano ZS, Zen 3600 (Malvern Instruments Ltd., Malvern, UK). For the analyses of average particle diameter, Polydispersity Index (PdI) and zeta potential, the samples were dissolved 1:1 in water.

2.2.3 Scanning Electron Microscopy (SEM) and Atomic-force microscopy (AFM)

The Scanning Electron Microscopy (SEM) analyses of solid samples were conducted on a Zeiss SEM microscope on Zeiss EVO® 50 model operating at 5 and 20 kV. Before image acquisition, the manufactured nanoparticles were coated by gold. In addition, Atomic-Force Microscopy (AFM) (Scanning Probe Microscope SPM-9600 model, Shimadzu and SPM software) was also used to characterize the samples prepared, detecting topographic surface images [21]. For AFM analysis, diluted samples were dropped onto mica surface.

2.2.4 Cells and cell culture conditions

The glioblastoma grade IV (U87 MG) cell line was purchased from American Type Culture Collection (ATCC® HTB-14™). The U87 MG cells were cultured in DMEM medium supplemented with 10% fetal bovine serum (FBS), 1% L-glutamine, and 1% penicillin-streptomycin. The cells were used in the logarithmic growth phase and cultured in a humidified incubator at 37°C and 5% CO_2.

2.2.4.1 Viability assay (MTT)

The MTT ((3-(4,5-dimethylthiazol-2-yl)-2,5-diphenyltetrazolium bromide)) assay was used to analyze the U87MG cell viability after treatments with all the nanoparticles. Briefly, cells were plated (1.0×10^4 cells/well) onto 96-well plates and grown by 24 h in humidified incubator; Following cell treatment by 3 h cells were washed with PBS and fresh culture medium added. Next day medium was carefully discarded and MTT solution (5 mg mL^{-1}) previously diluted in phenol red-free medium were applied to each well. The cells were then incubated at 37°C, under 5% CO_2, for 4 h. Following incubation, the medium containing the MTT solution was removed, and the formazan crystals were dissolved in isopropanol. The optical density was measured at 570 and 690 nm using a Safire^2 microplate reader (TECAN Group Ltd.). The results are presented as the percentage of survival relative to untreated control cells.

2.3 Data and statistical analysis

Data from spectrophotometer and spectrofluorometer were analyzed by IGOR pro version 6.0 software. Statistical analysis was performed using one-way ANOVA followed by Tukey test ($p<0.05$) comparing to negative control (untreated cells). All data are expressed as the mean ± SD from at least three independent measurements.

3 RESULTS

3.1 Preparation of albumin-based nanoparticles

3.1.1 Optimization of pH

First, HSA-NPs (AlClPc) were optimized using two different pHs (7.0 and 8.5), which were based on previous work described by Langer and their collaborators [20]. The zetasizer analysis allowed identifying a strong influence of pH in the stability of these nanoparticles. The average diameter was 1178 nm for pH 7.0 and 261 nm for pH 8.5 **(Figure 1A)**; Therefore, a fourfold decreased was detected when pH was increased from 7.0 to 8.5. Moreover, a lower Polydispersity index (PdI) and highly negative charge values were

obtained for preparation with pH 8.5 **(Figure 1B and C)**. We thus used the pH 8.5 in the others analyzed parameters.

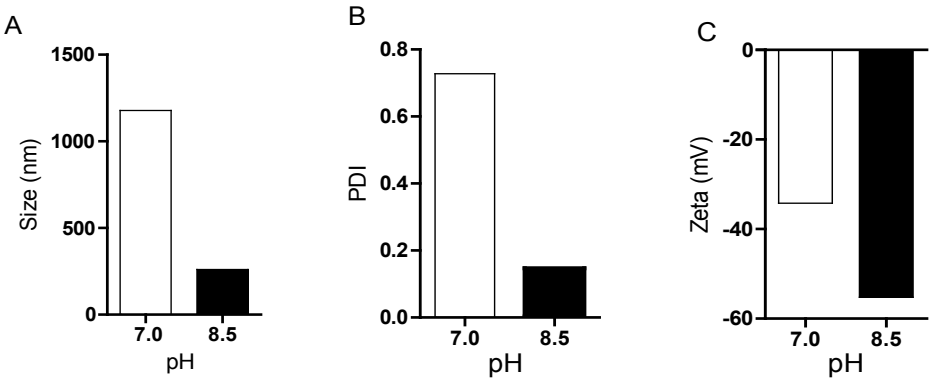

Figure 1: Characterization of HSA-NPs (AlClPc) as a function of pH using zetasizer Nano ZS. **A** – Average diameter; **B** – Polydispersity index (PdI) and **C** – Zeta potential

3.1.2 Optimization of stirring speed

The HSA-NPs (Empty) and HSA-NPs (AlClPc) were evaluated in relation to stirring speeds 155 RPM and 380 RPM, which were selected based on studies performed previously by our group [22]. A reduction of 2.5-fold in the diameter size and Polydispersity index was observed by increasing magnetic stirring speed during the preparations (**Figure 2A and B**). But, it is noteworthy that zeta potential does not change with the increasing of stirring speed. pH is then the main variable influencing the nanoparticle charges, as explained before **(Figure 1C vs. Figure 2C)**.

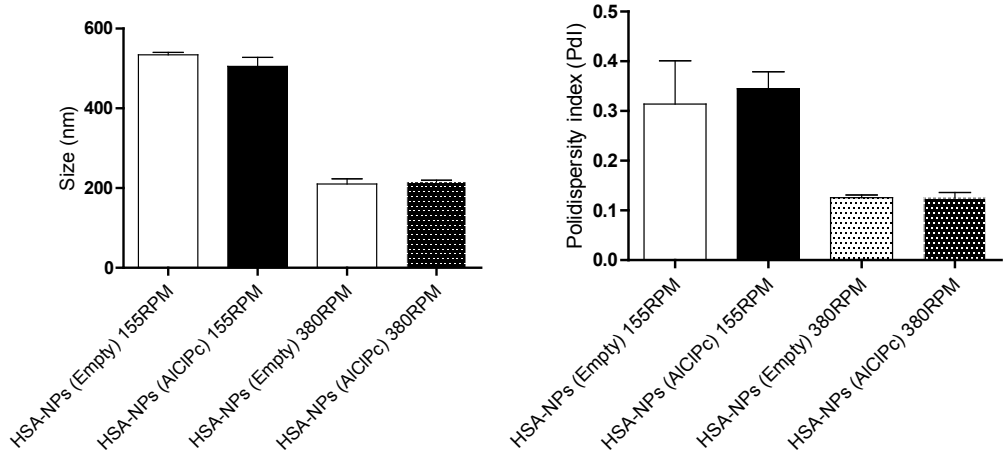

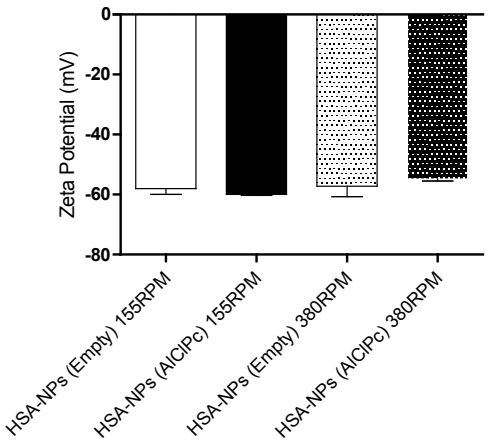

Figure 2: Characterization of HSA-NPs (Empty) and HSA-NPs (AlClPc) related to stirring speed (155 and 380 RPM) using zetasizer Nano ZS. **A** – Average diameter; **B** – Polydispersity index (PdI) and **C** – Zeta potential

3.2 Physical-chemical stability related to storage time

After lyophilization, a stability monitoring of the solid nanoparticles [HSA-NPs (Empty) and HSA-NPs (AlClPc)] were performed for a period of 60 days using the zetasizer parameters. First, it was not detected variations related to storage time in the size distribution of HSA-NPs (Empty) and HSA-NPs (AlClPc) which was approximately of 200 nm and 190 nm, respectively. Besides AlClPc inclusion does not affect the average size of the HSA-NPs (Empty) **(Figure 3A and B)**. In addition, low polydispersity index was detected at all times studied, showing the values of 0.172 and 0.174 to HSA-NPs (Empty) and HSA-NPs (AlClPc), respectively; thus these nanoparticles presented a high homogeneity in the distribution of the average diameter during the period of analysis. **(Figure 3C and D)**. Finally, it can be observed insignificant variation on zeta potential related to time that the values of zeta potential were kept around -56 mV and -57 mV to HSA-NPs (Empty) and HSA-NPs (AlClPc), respectively. These highly negative values cause electronic repulsion, not allowing the agglomeration of the manufactured samples **(Figure 3E and F)**. Together all these results states for a very stable preparation of albumin-based nanoparticles.

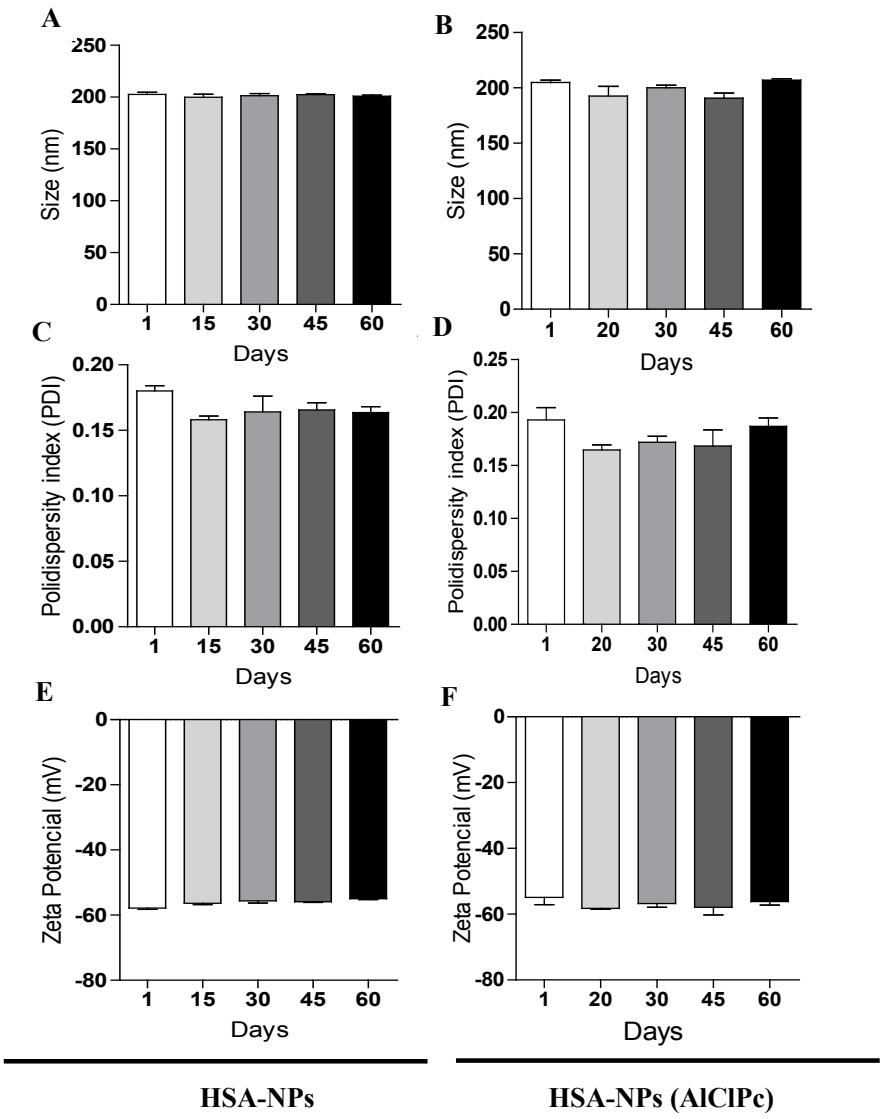

Figure 3: Characterization of HSA-NPs (Empty) and HSA-NPs (AlClPc) related to storage time (up to 60 days) using zetasizer Nano ZS. Average diameter **(A and B)**; Polydispersity index – PdI – (**C and D**); and zeta potential (**E and F**). All these data were evaluated by Tukey test.

3.3 Nanoparticle characterization of albumin based nanoparticles by SEM

From the SEM pictures, it can be observed at low magnification (1 K×) aggregated structure with highly irregular shape of about hundred microns probably due to the lyophilization process of HSA-NPs (Empty, **Figure 4A**) and HSA-NPs (AlClPc, **Figure 4B**). At higher magnification (50 K×) the presence of small agglomerated spheres with a diameter size from 80 nm to 360 nm is clearly evidenced for HSA-NPs (Empty, **Figure 4C**) and for HSA-NPs (AlClPc, **Figure 4D**).

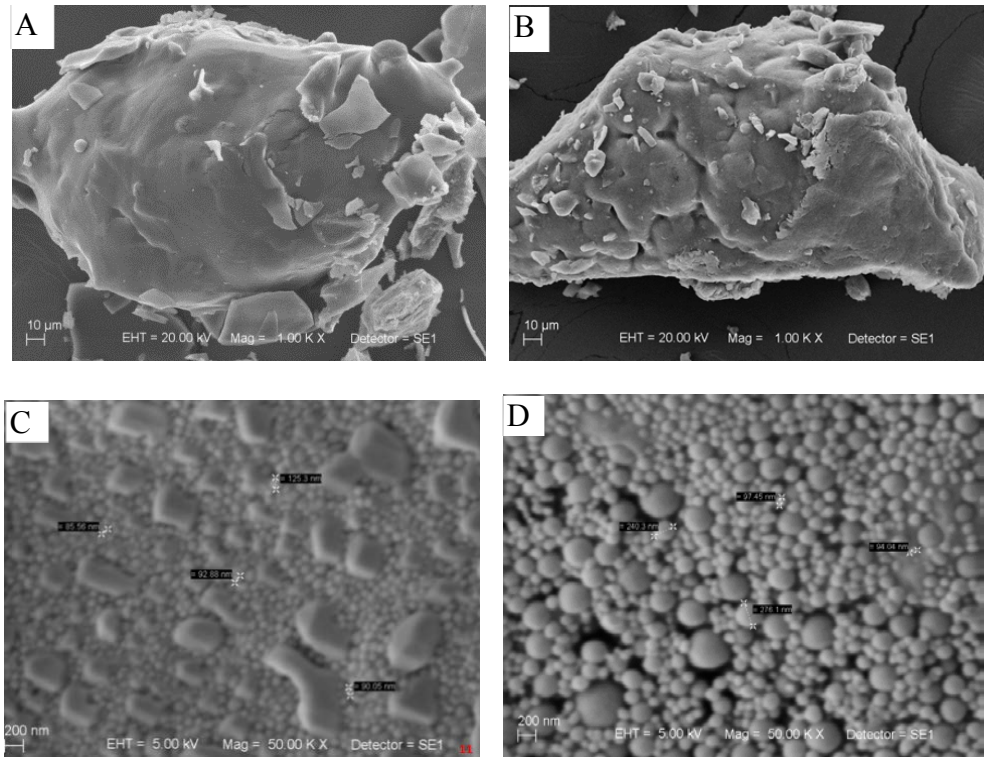

Figure 4: Nanoparticle characterizations by SEM. SEM photomicrographs at low magnification **(A and B)** and high magnification **(C and D)** of HSA-NPs (Empty) **(A and C)** and HSA-NPs (AlClPc) **(B and D)**

3.4 Nanoparticle characterization of albumin based nanoparticles by AFM

After diluted samples, the AFM analysis, showed spherical shaped nanoparticles separated in the range of 175 nm to 200 nm **(Figure 5A and B)**.

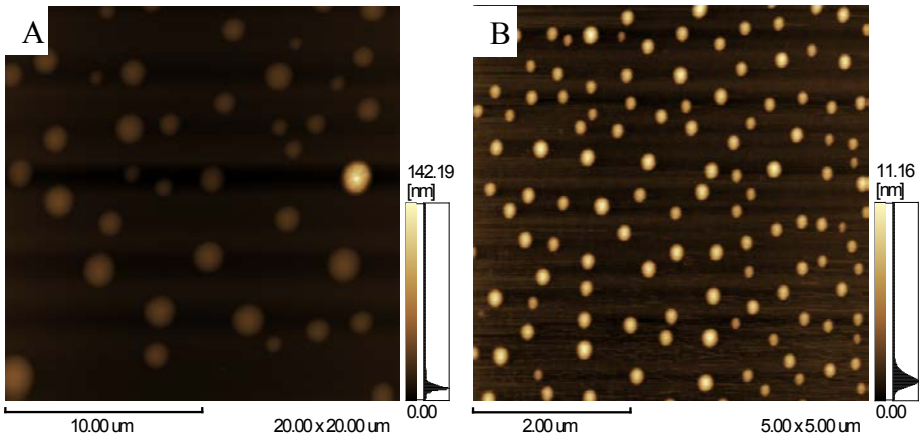

Figure 5: Nanoparticle characterizations by SEM. AFM photomicrographs of HSA-NPs (Empty) **(A)** and HSA-NPs (AlClPc) **(B and D)**

3.5 Cell viability of the U87MG cells evaluated by MTT assay

In order to detect cytotoxicity to U87MG cells induced by the albumin-based nanoparticles it was used the colorimetric assay; MTT salt that is metabolized by mitochondrial enzymes into a purple compound (formazan), and then detected by absorbance using a spectrophotometer.
It can be observed (**Figure 6**) that the incorporation of AlClPc and MNPS separately in HSA-NPs (HAS-NPs (AlClPc) and HSA-NPs (MNPs) has no effect on metabolic activity 24 h after incubation of the U87cell. However when AlClPc and MNPS are both incorporated in HSA-NPs (AlClPc+MNPs) the cell viability decreases up to of 82% and 80% ($p<0.05$) at concentrations of 0.25 μM and 0.5 μM.

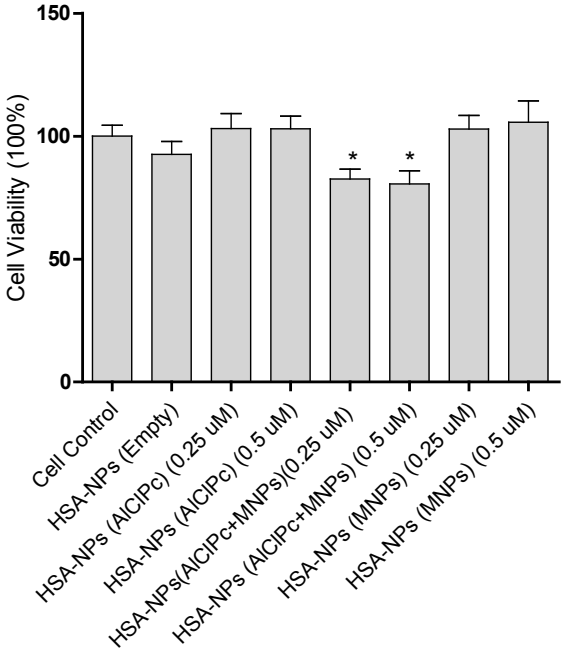

Figure 6: Viability analysis of U87MG cells by MTT assay, 24 h after incubation (3 hours of) with HSA-NPs (Empty); HSA-NPs (AlClPc); HAS-NPs (AlClPc+MNPs) and HSA-NPs (MNPs). Nanoparticle concentrations: 0.25 μM and 0.5 μM. The experiments were carried out with biological triplicate (ANOVA, Tukey Test; * $p\leq0.05$).

4 CONCLUSION

The synthesis of albumin-based nanoparticles (HAS-NPs) by cross-linking method has been optimized. We have clearly showed that pH and speed of magnetic stirring are relevant parameters. Smaller spherical particles with a lower polydispersity index, good homogeneity and high negative surface charge have been obtained at pH higher than neutral pH. Incorporation of photoactive agent aluminum chloride phthalocyanine (AlClPc) and magnetic nanoparticles (MNPs) in these albumin-based nanoparticles does not affect their physical-chemical characteristics. HAS-NPs with incorporated both AlClPc and MNPs have showed a mild effect on viability of glioma cells 24h after incubation. These promising first results

support the use of these nanoparticles to glioma treatments using photodynamic therapy and hyperthermia.

5 REFERENCE

[1] Assa, F.; Jafarizadeh-Malmiri, H.; Ajamein, H.; Vaghari, H.; Anarjan, N.; Ahmadi, O.; Berenjian, A. *Chitosan magnetic nanoparticles for drug delivery systems*, Critical reviews in biotechnologyp. (2016) 1-18.

[2] Stylianopoulos, T. *Intelligent drug delivery systems for the treatment of solid tumors*, european journal of nanomedicine, (2016) v. 8, p. 9-16.

[3] Ghuman, J.; Zunszain, P. A.; Petitpas, I.; Bhattacharya, A. A.; Otagiri, M.; Curry, S. *Structural basis of the drug-binding specificity of human serum albumin*, Journal of molecular biology, (2005) v. 353, p. 38-52.

[4] Misra, R.; Acharya, S.; Sahoo, S. K. *Cancer nanotechnology: application of nanotechnology in cancer therapy*, drug discovery today, v. 15, (2010) p. 842-850.

[5] Dreis, S.; Rothweiler, F.; Michaelis, M.; Cinatl, J.; Kreuter, J.; Langer, k. *Preparation, characterisation and maintenance of drug efficacy of doxorubicin-loaded human serum albumin (HSA) nanoparticles*, international journal of pharmaceutics, v. 341, (2007) p. 207-214.

[6] Silva, C.; de Oliveira, D.; Estevanato, I. L. C.; Simioni, A. R.; de Andrade, R.; Machado, M.; Lacava, B. M.; Lacava, Z. G. M.; Tedesco, A. C.; Morais, P. C. S. *Successful strategy for targeting the central nervous system using magnetic albumin nanospheres*, journal of biomedical nanotechnology, v. 8, (2012) p. 182-189.

[7] Sailaja, A.; Amareshwar, P.; Chakravarty, P. *Different techniques used for the preparation of nanoparticles using natural polymers and their application*, int j pharm pharmsci, v. 3, (2011) p. 45-50.

[8] Ai, X.; Ho, C. J. H.; Aw, J.; Attia, A. B. E.; Mu, J.; Wang, Y.; Wang, X.; Wang, Y.; Liu, X.; Chen, H. *In vivo covalent cross-linking of photon-converted rare-earth nanostructures for tumour localization and theranostics*, nature communications, v. 7, (2016).

[9] Jahanshahi, M.; Babaei, Z. *Protein nanoparticle: a unique system as drug delivery vehicles*, african journal of biotechnology, v. 7, (2008).

[10] Ferreira, M.; Saga, Y.; Aluicio-Sarduy, E.; Tedesco, A. C. *Chitosan nanoparticles for melanoma cancer treatment by photodynamic therapy and electrochemotherapy using aminolevulinic acid derivatives*, current medicinal chemistry, v. 20, (2013) p. 1904-1911.

[11] Primo, F. L.; de Paula, L. B.; de Siqueira-Moura, M. P.; Tedesco, A. C. *Photobiostimulation on wound healing treatment by clalpc-nanoemulsion from a multiple-wavelength portable light source on a 3d-human stem cell dermal equivalent*, current medicinal chemistry, v. 19, (2012) p. 5157-5163.

[12] Zhou, C. *New trends in photobiology: mechanisms of tumor necrosis induced by photodynamic therapy*, journal of photochemistry and photobiology b: biology, v. 3, (1989) p. 299-318.

[13] Agostinis, C.; Bossi, F.; Masat, E.; Radillo, O.; Tonon, M.; De, S. F.; Tedesco, F.; Bulla, R. *Mbl interferes with endovascular trophoblast invasion in pre-eclampsia*, clin. Dev. Immunol., v. 2012, (2012) p. 484321.

[14] De Paula, L. B.; Primo, F. L.; Pinto, M. R.; Morais, P. C.; Tedesco, A. C. *Combination of*

hyperthermia and photodynamic therapy on mesenchymal stem cell line treated with chloro aluminum phthalocyanine magnetic-nanoemulsion, journal of magnetism and magnetic materials, v. 380, (2015) p. 372-376.

[15] Feuser, P. E.; dos Santos Bubniak, L.; dos Santos Silva, M. C.; da CasViegas, A.; Fernandes, A. C.; Ricci-Junior, E.; Nele, M.; Tedesco, A. C.; Sayer, C.; de Araújo, P. H. H. Encapsulation *of magnetic nanoparticles in poly (methyl methacrylate) by miniemulsion and evaluation of hyperthermia in u87mg cells*, european polymer journal, v. 68, (2015) p. 355-365.

[16] Calero, M.; Gutirrez, L. A.; Salas, G.; Luengo, Y.; Lazaro, A.; Acedo, P.; Morales, M. P.; Miranda, R.; Villanueva, A. *Efficient and safe internalization of magnetic iron oxide nanoparticles: two fundamental requirements for biomedical applications*, nanomedicine: nanotechnology, biology and medicine, v. 10, (2014) p. 733-743.

[17] Kumar, C. S.; Mohammad, F. *Magnetic nanomaterials for hyperthermia-based therapy and controlled drug delivery*, advanced drug delivery reviews, v. 63, (2011) p. 789-808.

[18] Laurent, S.; Dutz, S.; Hfeli, U. O.; Mahmoudi, M. *Magnetic fluid hyperthermia: focus on superparamagnetic iron oxide nanoparticles*, advances in colloid and interface science, v. 166, (2011) p. 8-23.

[19] Weber, C.; Kreuter, J.; Langer, K. *Desolvation process and surface characteristics of hsa-nanoparticles, international journal of pharmaceutics*, v. 196, (2000) p. 197-200.

[20] Langer, K.; Balthasar, S.; Vogel, V.; Dinauer, N.; Von Briesen, H.; Schubert, D. *Optimization of the preparation process for human serum albumin (hsa) nanoparticles*, international journal of pharmaceutics, v. 257, (2003) p. 169-180.

[21] Reggente, M.; Rossi, M.; Angeloni, L.; Tamburri, E.; Lucci, M.; Davoli, I.; Terranova, M. L.; Passeri, D. *Atomic force microscopy techniques for nanomechanical characterization: a polymeric case study*, jom, v. 67, (2015) p. 849-857.

[22] Simioni, A. R.; Martins, O. P.; Lacava, Z. G. M.; Azevedo, R. B.; Lima, E. C. D.; Lacava, B. M.; Morais, P. C.; Tedesco, A. C. *Cell toxicity studies of albumin-based nanosized magnetic beads*, journal of nanoscience and nanotechnology, v. 6, (2006) p. 2413-2415.

[23] Preetz, C.; Hauser, A.; Hause, G.; Kramer, A.; Mader, K. *Application of atomic force microscopy and ultrasonic resonator technology on nanoscale: distinction of nanoemulsions from nanocapsules*, european journal of pharmaceutical sciences, v. 39, (2010) p. 141-151.

6 ACKNOWLEGEMENTS

We would like to thank Rodrigo Ferreira Silva and Ivana Aparecida Borin of FFCLRP-USP for technical support on SEM and AFM analysis. The authors also acknowledge the financial support from Brazilian agency CAPES and FAPESP Thematic Project # 2013/50181-1 and 2015/09125-6 (T.G.L) and 2016/21504-5 (T.G.L.).

VIII ECCOMAS Thematic Conference on Smart Structures and Materials
SMART 2017
A. Güemes, A. Benjeddou , J. Rodellar and Jinsong Leng (Eds)

HIGH-PERFORMANCE STRAIN SENSORS BASED ON FRAGMENTED CARBON NANOTUBE STRUCTURES

GILLES LUBINEAU*, JIAN ZHOU, YANGYANG XIN AND XUEZHU XU

*King Abdullah University of Science and Technology (KAUST), Physical Sciences and Engineering Division, COHMAS Laboratory, Thuwal 23955-6900, Saudi Arabia
e-mail: gilles.lubineau@kaust.edu.sa, www.cohmas.kaust.edu.sa

Key words: Strain sensors, Carbon nanotubes, Sensitivity, Stretchability.

Abstract. Stretchable strain sensors are needed for emerging applications like wearable electronics, artificial e-skins, bionic sensory systems as well as deployable structures. The crucial factors that govern the performance of such sensors are sensitivity, stretchability, and linearity. High gauge factor sensors are vital for small strain detection and open up opportunities for exploration of subtle strain detection. The stretchability determines the sensing strain range. Finally, despite it is needed for robust measurements and easy post processing, linearity of the response is challenging for stretchable strain sensors as severe changes in configuration might take place between the reference and the deformed configuration. Most of the developed sensors feature poor performance for at least one of these three criteria. We propose here to rely on cracked structures to solve all issues together. Cracks are considered detrimental to the overall mechanical and electrical properties of materials. However, if these cracks can be controlled, they also have the potential for use in mechanical sensing applications. In this study, we demonstrate that strain sensors based on fragmented single-walled carbon nanotube (SWCNT) assemblies embedded in poly (dimethyl siloxane) (PDMS) can maintain their sensitivity at very high strain levels. Our strategy here is to develop a new family of sensors taking advantage of the special properties of fragmented carbon-nanoparticles based structures (papers and wires). We systematically describe how to control the fragmentation of the conductive CNT papers or wires for achieving high-performance strain sensors. This fragmentation based sensing system brings opportunities to engineer highly sensitive stretchable sensors.

1 INTRODUCTION

Stretchable conductive materials have continued to receive considerable attention with the rapid development of stretchable electronic devices as they have bring new solutions to achieve both conductivity and stretchability.[1-6] The important factors that govern the performance of the strain sensor is sensitivity, stretchability and linearity. In detail, the sensitivity is represented by the gauge factor (GF) and evaluated by the relative resistance change versus applied strain. High GF sensors are vital for small strain detection and open up opportunities for exploration of subtle strain detection. The stretchability is the maximum uniaxial tensile strain of the sensor before failure, which will determine the sensing strain range. The linearity is significant for stretchable strain sensors because nonlinearity makes the calibration process difficult. However, conventional strain sensors cannot achieve the combination of high sensitivity (GF>100), high stretchability (strain >100%) and linearity. This will limit the development of application in wearable electronics.

One of the most effective approaches for bringing stretchability to highly conductive and brittle materials is the formation of cracks in the material on stretchable substrates.[7-10] Here, we introduce a new strategy[11-13], using fragmented SWCNT papers or wires, to construct

high-performance strain sensors. We first introduce cracks with controlled density to SWCNT assemblies by tuning the paper thickness, wire diameter, etc. The fragmented SWCNT assemblies embedded in PDMS substrate shows a maximum stretchability while maintaining a high sensitivity. Moreover, the dense and well-controlled network cracks enable a high linearity of the sensing response. The combination of high sensitivity, high stretchability and high linearity of the sensor will be vital for the development of stretchable electronics.

2 EXPERIMENTAL

2.1 Materials. SWCNTs with 2.7 wt % COOH groups were purchased from CheapTubes, Inc. at over 90 wt % purity and containing more than 5 wt % multiwalled CNTs (MWCNT). SWCNT length ranged from 5 to 30 μm and their outer diameter ranged from 1 to 2 nm. The true density of these SWCNTs was 2.1 g/cm^3. Methanesulfonic acid (CH_3SO_3H) and SYLGARD 184 PDMS were purchased from Sigma Aldrich.

2.2 Preparation of SWCNT paper-based strain sensor. 0.5 wt.% SWCNT dope was prepared by adding 0.2 g of SWCNTs into 40 g of CH_3SO_3H, sealed in a glass bottle, stirred for 5 min and bath sonicated using a Brason 8510 sonicator (250 W) (Thomas Scientific) for 60 min. The mixture was then stirred for 12 h at 500 rpm. SWCNT/CH_3SO_3H dispersions were vacuum filtrated through a ceramic filtration membrane (pore size: 20 nm, Whatman). Any remaining CH_3SO_3H was removed from the sample by washing it with water. The freestanding SWCNT paper was peeled away from the filter and cut into 30×3 mm^2 strips for producing the strain sensors. The first layer of 5.3 g PDMS (ratio of base to curing agent is 10:1) was poured onto a 10×10 cm^2 petri dish s and cured at 70 °C for 12 min to obtain a sticky substrate. The strips of SWCNT paper were transferred onto the 0.5-mm-thick sticky PDMS substrates; copper wires were connected to the SWCNT paper strips by silver epoxy. Next, the second layer of PDMS of equal weight was poured onto the sample and cured at 70 °C for 2 h to fully encapsulate the SWCNT paper.

2.3 Preparation of SWCNT wire-based strain sensor.
A 2 wt% SWCNT dope was prepared by adding 0.2 g of SWCNTs into 9.8 g of MeSO3H and stirred for 2 min, followed by bath sonication using a Branson 8510 sonicator (250 W) (Thomas Scientific) for 60 min. Then the mixture was further stirred for 24 hours, followed by passing through a 30 μm syringe filter (Pall Corporation) to remove aggregates. The SWCNT ink was loaded into a 5 ml syringe and spun into a water bath through stainless steel needles. The SWCNT wires were spun onto sticky PDMS substrates (5.3 g, 10 × 10 cm), which were made by mixing the PDMS base and a curing agent with a ratio of 2.5 to 1 and cured at 70 degrees for 12 min. After spinning, the wires were dried at 70 °C overnight to remove residual water. Then, two ends of the SWCNT wires were connected with copper wires and painted with silver epoxy. The SWCNT wires were sealed with 5.3 g of PDMS precursor, which was cured at 70 °C for 2 h.

2.4 Characterizations. Scanning electron microscopy (SEM) on SWCNT paper was performed using a Quanta 3D (FEI Company). The mechanical behavior of the SWCNT assemblies was measured by a 5944 Instron universal testing machine at a strain rate of 0.4 mm min^{-1} by a 5-N load cell. The reversible motion (stretching and relaxing) of the sample was controlled by a 5944 Instron machine. The whole sample region is glued except the 4-mm gap in the center. This 4-mm gap between the metal plates defines the effective length of

the sample for determining the strain during the stretching. The change in electrical resistance of the specimen was monitored using a U1252B digital multimeter. Fragmentation was generated on each sample by loading it to 50% strain at a speed of 0.4 or 1.2 mm min^{-1}.

3 RESULTS AND DISCUSSION

3.1 Sensing strategy and structure

Figure 1a and b show that the SWCNT assemblies are either prepared by vacuum filtration or wet-spinning to obtain SWCNT papers and wires, respectively. To achieve the desired low-strength, low-stiffness SWCNT assemblies, a mild acid, CH_3SO_3H, was used to disperse SWCNTs so that the tube-to-tube interactions are insufficient to induce alignment. A porous structure of the SWCNT papers or wires with randomly distributed SWCNT networks can be observed in the SEM images shown in Figure 1c and d, respectively. This randomly oriented structure results in low-strength SWCNT assemblies that facilitate breakage of the fragile wire. CNT papers or wires are typically not stretchable (strain to failure is less than 5%); therefore, to introduce stretchability of the material, we embedded them into a PDMS substrate. By fully embedding these SWCNT assemblies into PDMS substrates, and cutting the samples using a die, we were able to obtain standard dog-bone-shaped specimens (Figure. 1e and f).

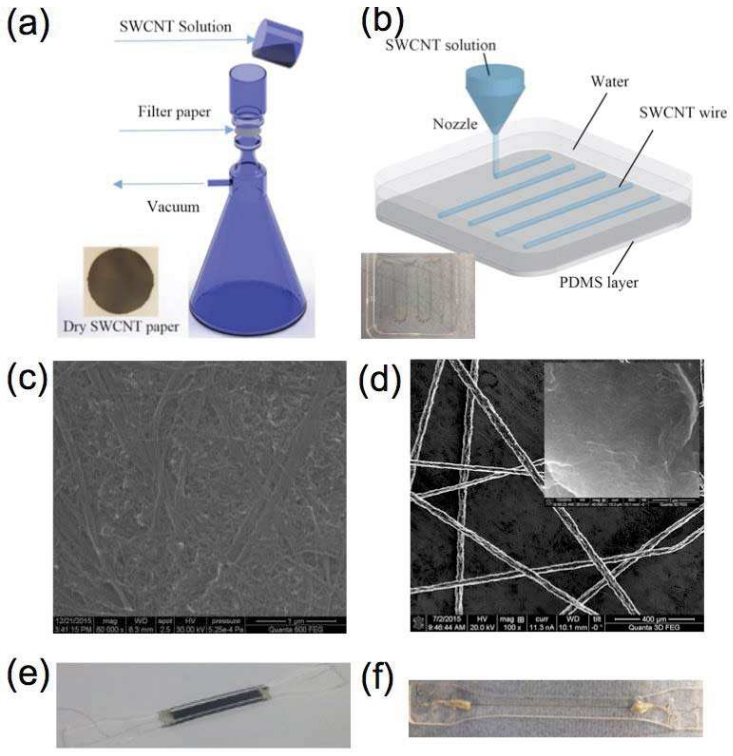

Figure 1: SWCNT paper or wire-based sensors. (a) Vacuum filtration of the SWCNT paper. (b) Wet-spinning of SWCNT wire. (c) and (d) SEM images of the SWCNT paper and wire shows random oriented SWCNTs in the assemblies, respectively. (e) and (f) PDMS encapsulated SWCNT paper strip and SWCNT wire, respectively.

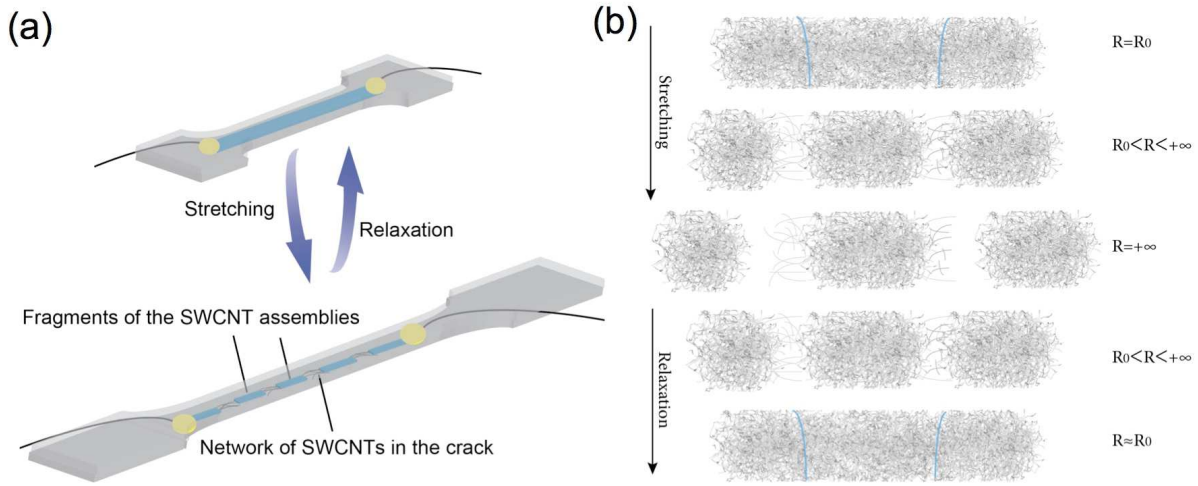

Figure 2: Strategy for fragmenting SWCNT assemblies in PDMS to produce high-sensitivity strain sensors. (a) A schematic presenting how SWCNT assemblies are fragmented in elastic substrates. (b) Illustrations of the mechanical sensing mechanism resulting from disconnection and connection of SWCNT networks in cracks.

Figure 2a demonstrates how a fragmented SWCNT-based sensor was stretched. When this sample is stretched, the SWCNT assemblies fragment, while the behavior of the surrounding PDMS remains reversible. When the strain is relaxed, cracks close but remains in the conductive medium. The disconnection and reconnection of SWCNT networks in cracks formed after stretching lead to sensing and resistance recovery, and become central to the sensing strategy.

3.2 Fragmented SWCNT paper for strain sensing

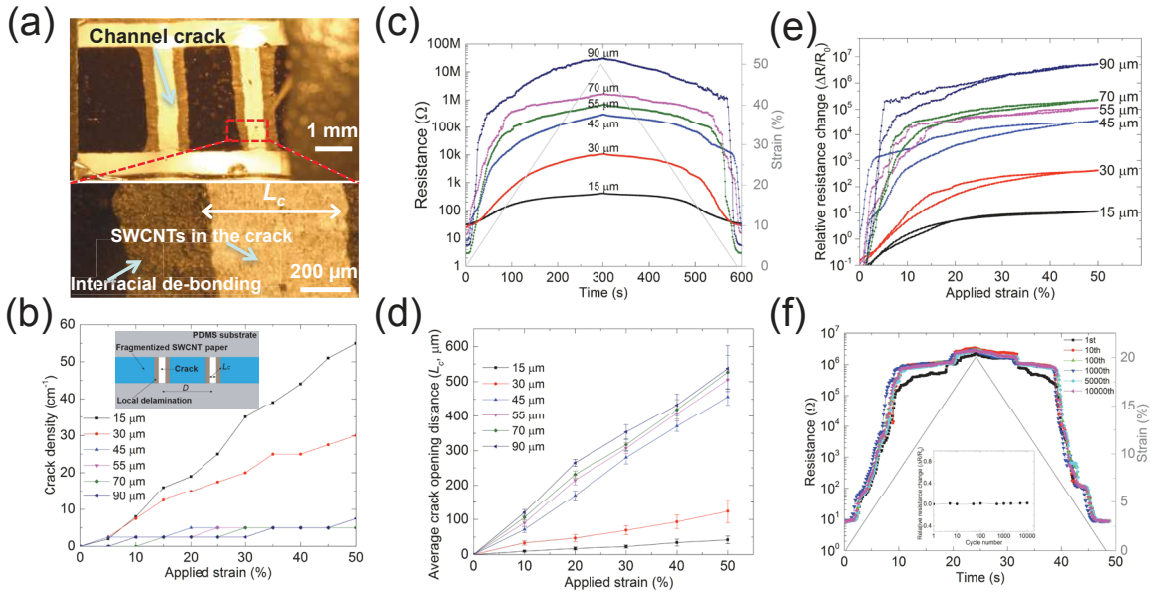

Figure 3:. Fragmented SWCNT paper in PDMS as a strain sensor. (a) Photograph of 45-μm-thick SWCNT paper embedded in elastic substrates after stretched to 50% strain. (b) Evolution of crack density with applied strain for samples of different thicknesses. We define in the inset image the average spacing (D) between the cracks. (c) Resistance changes by stretching and relaxing of strain sensors. (d) Increasing average crack opening distance (L_C) with increasing applied strain. (e) Relative resistance change versus applied strain of the SWCNT

paper in elastic substrates during loading and unloading with a maximum applied strain of 50%. (f) Resistance changes versus strain for long-term cycle test: 1, 10, 100, 1000, 5000 and 10000 cycles at 0-20% strain at 2 mm min^{-1}. The Inset shows that the relative resistance change after relaxation from each cycle for a total of 10000 cycles, showing excellent long-term repeatability of the sensor.

The cracking mechanism is typical of degradation phenomenology in laminated structures. We used an SWCNT paper with a random, porous structure because its low strength and toughness make it easy to fragment. When the tensile load is increased, a pseudo-periodical pattern of channel cracks develops perpendicular to the principal loading direction (see Figure 3a). This is similar to the "transverse" cracking mechanism well know in laminated composites and to the channel cracking mechanisms in thin coatings, for which there are well-established micromechanical models.

The first stage of the degradation is a fragmentation process that is strongly dependent on thickness. Let us define the crack density (i.e., the number of cracks per unit length about the loading direction) as *1/D*, where *D* is the average spacing between the cracks, as shown in the inset image of Figure 3b. The evolution of crack density with strain is reported for the sample with different thicknesses. Two regimes can be observed: for "thin" papers (15 and 30 μm), channel cracks generally go only partially through the width and for "thick" papers (45, 55, 70 and 90 μm), very few cracks are observed, but those do run through the whole width of the sample. This is consistent with the classical micromechanics of channel cracking, where the usual distinction is done between an energy-guided regime for thin plies and a strength-guided regime for thick plies. The second stage of the degradation is the development of local delamination between the SWCNT paper and the PDMS substrate. Local delamination can be expected around crack tips because channel cracks cause severe out-of-plane stresses at the interfaces between the tips and the substrate. This process is dependent on the thickness of the ply: delamination is difficult to observe in the thin papers but obvious on the thick papers (45, 55, 70 and 90 μm). Furthermore, the degree of delamination depends on the balance between the energy release rate for channel cracking and the energy release rate for local delamination, the latter of which is more favorable in thick plies.

Figure 3c presents the strain-sensing behavior of strips of the fragmented paper in PDMS when the strain ranges from 0 to 50%. The resistance of the paper increases with applied strain for all samples. Moreover, the range of relative change in resistance ($\Delta R/R_0$) can be thickness controlled. This is very important for engineering the sensitivity of the strain sensor. At 50 % strain, the increase in resistance ranges from 100 Ω to 30 MΩ for 15-μm to 90-μm thick paper. The evolution of average crack opening distance, L_c, with strain is almost linear (Figure 3d), testifying to the linear elastic response of the sensor after fragmentation and relaxation. As expected, samples with larger opening distances exhibit larger resistance under strain (Figure 3c and d). For example, the resistance at a strain of 50 % of 15-μm and 45-μm samples are 400 Ω and 300 kΩ, respectively. The relatively small change in resistance of thin samples is attributed mainly to small fragments connecting the cracks, ensuring residual electronic transport. We then plot the relative change in resistance ($\Delta R/R_0$) with respect to the strain on Figure 3e. The sizeable change in resistance of 90-mm-thick SWCNT paper in PDMS enables us to obtain a GF of 2×10^6 at $\varepsilon < 5\%$ and reach a record GF of 10^7 at $\varepsilon = 50\%$. The high sensitivities across the low and high strain levels are important for wearable applications. The repeated opening and closing of the cracks led to reversible strain sensing with high sensitivity. Figure. 3f shows that the sensor displays a very high repeatability at 1, 10, 100, 1000, 5000, and 10000 cycles. After 10000 cycles at 20% strain, the resistance of the strain sensor (SWCNT paper thickness: 90 μm) remained nearly unchanged (inset in Figure 3f).

The stretchability could be dramatically improved by bringing high density of cracks containing conductive networks. Therefore, how to obtain the SWCNT paper with controlled crack density within an elastic substrate is a crucial point. Figure 4a show that partial cracks (partial meaning non extending through the whole thickness) on a SWCNT paper were obtained by a laser-engraving process. This approach is crucial to control the location of the cracks and to maintain the integrity and functionality of the SWCNT networks below the surface cracks. By decreasing the average spacing, D, between the cracks, the crack density, 1/D, can be increased. After embedding the laser-engraved SWCNT paper into a PDMS substrate, a roll-to-roll pressing process was repeatedly applied in clockwise and counterclockwise directions to fully initiate the fragmentation of SWCNT papers guided by surface cracks (Figure 4b). Upon roll-to-roll pressing, cracks were opened and propagated through thickness The average spacing, D, between the cracks was controlled at 2.0, 0.9, 0.6, 0.5 and 0.3 mm, correspond to different crack densities, 1/D, at 0.5, 1.1, 1.7, 2.0 and 3.3 mm^{-1}. These results prove that the laser engraving and roll-to-roll process is effective to control the cracking pattern. These through-thickness cracks will be a key element for the strain sensing. The crack-guided fragmentation in this study is superior to previous method by using only stretching of the SWCNT assembly, for which the crack spacing can only be coarsely controlled by engineering the thickness of the SWCNT paper (Figure 3). It is also advantageous over previously reported metal nanofilm fragmentation, in which cracks were formed with an uncontrollable manner through bending deformation. The ability to control the crack density in the SWCNT paper will be a prerequisite for tuning the stretchability of the sensor. For the sample of PDMS-embedded SWCNT paper with high crack density (3.3 mm^{-1}) (Figure 4c), when the sensor undergoes stretching, distributed cracks develops with crack size correlated to the applied strain. These cracks act as "switches" to adjust the density of the conductive networks of the sensor. As the strain ranges from 0 to 150%, the resistance of the paper increases with applied strain from 15 Ω to 1.2 MΩ.

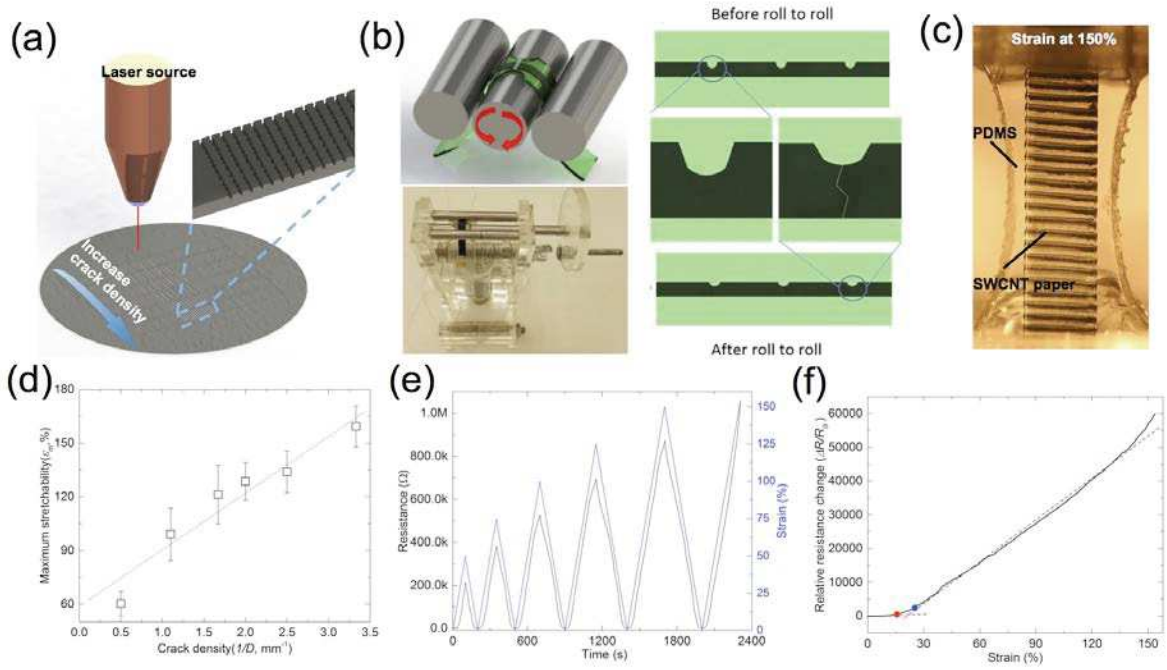

Figure 4:. Laser-engraved SWCNT paper for high-performance strain sensors. (a) Illustration image presents the laser-engraving process for generating partial cracks on the SWCNT paper. (b) An illustration and a real of roll-to-roll pressing device for the propagation of through-thickness cracks in SWCNT paper, respectively.

Graphs on the right show the partial and through-thickness cracks before and after the roll-to-roll pressing, respectively. (c) Images of a typical, high crack density SWCNT paper in PDMS when stretched to 150% strain. (d) The increase of maximum stretchability of the sensors with crack density. (e) Resistance changes under incremental cyclic stretching/relaxing of a high crack density sensor (1/D = 3.3 mm^{-1}). The maximum stretchability of the sensor is determined to be 153%. (f) Relative change in resistance versus strain of the high crack density sensor (1/D = 3.3 mm^{-1}). Red and blue dashed lines are the fitting slopes for strain from 0 to 15% with a linearity of 0.98 and strain from 22 to 150% with a linearity of 0.96, respectively.

Figure 4d presents the maximum stretchability, ε_m, of the sensor with different crack density. The ε_m increased from 60% to 153% by increasing the crack density from 0.5 to 3.33 mm^{-1}, indicating the working range of the sensors at various crack densities. This trend suggests that the increase in crack density in SWCNT paper will dramatically increase the stretchability. In Figure 3, the stretchability of the SWCNT paper-based sensor is limited to 50-60% at a low crack density (1/D=0.5 mm^{-1}) due to the high-stress concentration around the cracks. The stress concentration near the cracks was high enough to result in an early failure of the PDMS substrate. Moreover, the sensor was showing an obvious nonlinearity due to the previously uncontrolled and quasi-random network of cracks. However, by introducing high crack density (1/D=3.33 mm^{-1}) to the SWCNT paper through laser-engraving and roll-to-roll pressing, the sensor show a maximum stretchability of 153% and a high linearity (Figure 4e). We then plot the relative change in resistance ($\Delta R/R_0$) on strain for the sample with the highest stretchability on Figure 4f. The change in resistance of this high crack density SWCNT paper in PDMS is $\Delta R/R_0 = 6.1 \times 10^4$ at 150%. The sensing behavior of the sample was characterized by two linear regions with 2 different slopes (strain from 0 to 15% with linearity of 0.98 and strain from 22 to 150% with linearity of 0.96), which reflects the GF at different strain range: the GF was 2.2×10^3 (0 to 15%) and 4.2×10^4 (22 to 150%). In comparison, conventional metal gauges have a GF around 2.0 at low strain ($\varepsilon < 5\%$).[1,2] The value is also higher compare with the performance of metal nanomaterials based stretchable sensors in both GF and maximum stretchability

3.3 Fragmented SWCNT wire for strain sensing

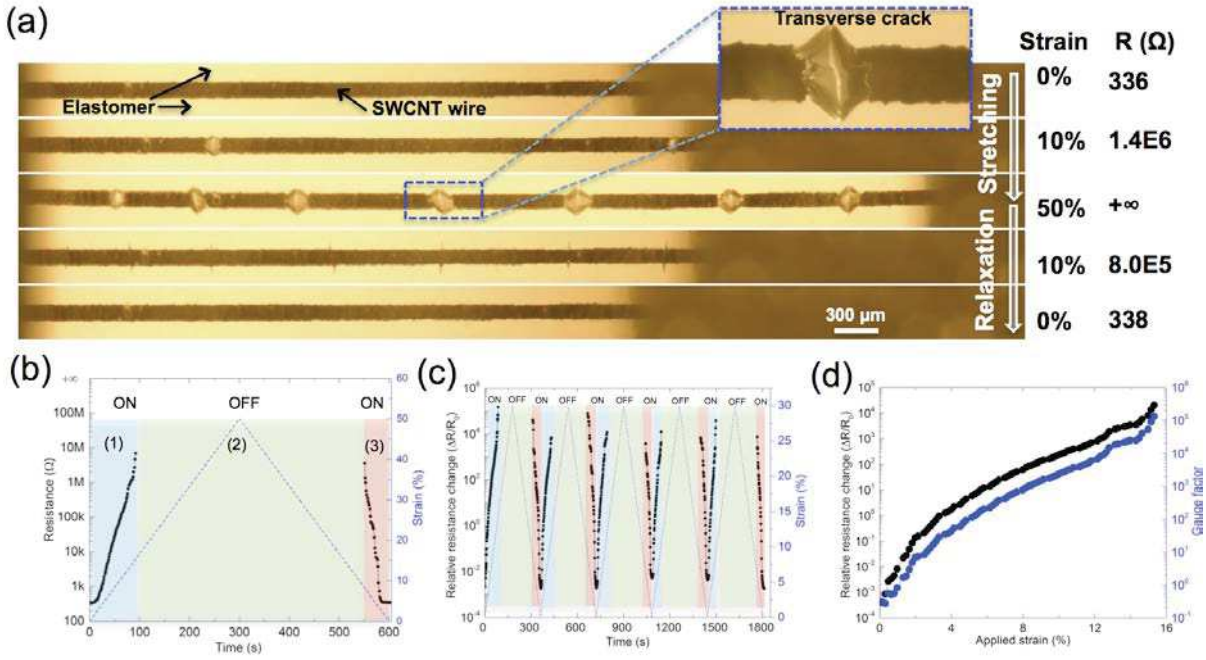

Figure 5: The Wet-spun SWCNT wire for resistance-recoverable strain sensor. (a) Optical images show the fragmentation and relaxation process of the SWCNT wire in PDMS under strain. The inset shows a transverse crack in the SWCNT wires at 50% strain. The resistance of the wire is recoverable after relaxation from a disconnected state. (b) Changes in the electrical resistance with strain indicate that the strain sensor goes through three regimes: (1) strain sensing regime (blue); (2) open circuit regime (green); (3) resistance recovery regime (orange). (c) Dynamic response of the sensor under cyclic loading/unloading conditions up to 30% strain. (d) The evolution of relative resistance change and the gauge factor with applied strain.

Figure. 5a shows the initiation, progression, and closing of transverse cracks during loading/unloading. By stretching the sample, the wire in the PDMS substrate fragments into many pieces, which is resulting from the porous structure of the SWCNT wire with randomly distributed SWCNT networks (Figure 1d). This randomly oriented structure results in low-strength SWCNT assemblies that facilitate breakage of the fragile wire in PDMS. The average crack density of the 60 μm-SWCNT wire is 1.8 ± 0.2 mm^{-1} at 50% strain. The resistance of the sample increases up to a non-measurable value (that we call practically infinity) on our measuring instrument, but the resistance can be recovered to its initial value after relaxation. It shows that the recoverability of resistance comes from the closure of the transverse crack.

Figure. 5b shows that changes in resistance can be divided into three regimes. (1) The strain sensing regime: $0 < \varepsilon < \varepsilon_c$, where ε_c is the critical strain, where resistance (R) increases to infinity. In this regime R increases from 336 Ω to 10 MΩ before the resistance increases to infinity. The circuit is in the "ON" state; we do not observe an increase in the number of cracks because the wire has already been fragmented. Only the average opening distance of

the cracks (L_C) increases with strain, which leads to the increase in the resistance. Even though large gaps can be seen at a relatively high strain (ε = 15%) in this regime, the resistance of the wire does not go to infinity (R = 10 MΩ). This observation suggests that there are SWCNT networks in the cracks that are connected to the fragments nearby. (2) The open circuit regime: $\varepsilon > \varepsilon_c$, the SWCNTs are completely disconnected from each other. We measured the average crack opening distance (L_C) to be longer than 50 μm, which is longer than the length of the SWCNTs (5–30 μm). The L_C of the SWCNT wire is long enough to result in an "OFF" circuit. (3) Resistance recovery regime: the resistance of the SWCNT wire recovers to its initial value after relaxation and the circuit recovers to the "ON" state. The L_C between the fragments reduces as the applied strain decreases. In the completely relaxed state, cracks are no longer visible. In this regime, PDMS obviously plays an important role in the recovery of the electrical resistance. We further tested the reproducibility of the strain sensor with repeated stretching/relaxation cycles. Figure. 5c presents five cycles of a strain to be 30%. The ΔR/R0 increased with almost complete reversibility even after the electrical disconnection. The conversion of "ON–OFF" states occurred at almost the same strain in all cycles. We then plot ΔR/R0 and the gauge factor (GF) on strain as shown in Fig. 2c. The operational strain range and GF are dramatically improved when compared with those of self-standing SWCNT fibers (GF = 1 at a maximum strain of 1.1%). The dramatic change in resistance ($\Delta R/R0 = 5 \times 10^4$) in the 60 μm-SWCNT wire enables us to obtain a GF of 105 at ε = 15%. This GF value is the highest value compared with the GF values recently reported for CNT, graphene, metal and other strain sensors at this strain level.

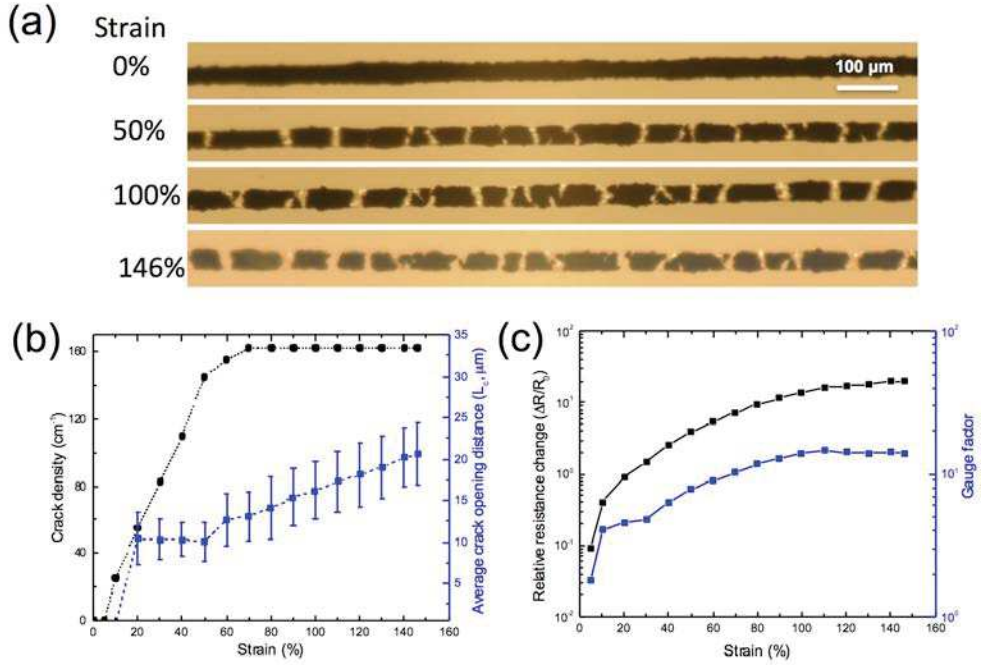

Figure 6: Highly stretchable strain sensors based on a fragmented thin 32 μm-SWCNT wire in PDMS. (a) Optical images show how the SWCNT wire is fragmented by stretching in the PDMS. (b) Crack density and average crack opening distance with applied strain. (c) Change in relative resistance and the gauge factor with

applied strain.

Although the GF in the results was high for 60 μm-SWCNT wire, the maximum stretchability of the sensor was limited to 15%. To obtain higher stretchability while maintaining a continuous resistance change in the operational range of the strain, we need to increase the crack density in the SWCNT wires. Figure. 6a shows that by reducing the diameter of the wire from 60 to 32 μm, we were able to obtain a higher crack density in the wire. Before the critical strain (60%), the crack density increases with the applied strain. After reaching the critical strain at 60%, the crack density remains constant, while L_c increases with the applied strain (Figure. 6b). The PDMS substrate breaks at 146% due to the concentration of stress near the cracks, suggesting that the stretchability of the sensor can be dramatically increased by using narrower SWCNT wires. However, the narrower wire had a small $\Delta R/R_0$ and a low GF of 15 at 146% (Figure. 6c). These characteristics can be ascribed to the high initial resistance 32 μm-SWCNT wire (10 ± 0.8 kΩ), which is more than one order of magnitude higher than that of the 60 μm-SWCNT wire (338 Ω) and to the maximum L_c, which is less than 25 μm, indicating that SWCNT networks remain in a percolated state. The fragmentation strategy can be modified to tune the GF and stretchability of the sensors. It can be realized by adjusting the crack density by using wires with different diameters and choosing substrates with different stretchability.

4 CONCLUSION

In summary, we have demonstrated that fragmented SWCNT paper in PDMS functioned as a ultrasensitive and stretchable strain sensor. Our experiments suggest a pathway towards the formation of fragmented SWCNT paper sensors with high sensitivity and high stretchability. The performance of such strain sensors could be tuned by changing the thickness of the SWCNT papers or the diameter of the SWCNT wire. Moreover, controlling crack patterns in SWCNT paper through laser engraving and roll-to-roll pressing can achieve the high-performance strain sensors features of high sensitivity, high stretch- ability, and high linearity. A sensitivity of 4.2×10^4 at a strain of 153% was achieved by using a high crack-density SWCNT paper (3.3 mm^{-1}). The tunability of these sensors relies mainly on the use of two very different strategies based on either intralaminar or interlaminar crack, each of which shows very different changes in conductivity when stretched. The controlled fragmentation process could potentially be applied to other nanomaterial-based structures for engineering the stretchability of material while maintaining sensitivity. We believe that these techniques can inspire various designs of other sensitive and reversible strain-responsive materials with widespread applications.

REFERENCES

[1] Amjadi, M.; Kyung, K.; Park, I.; Sitti, M. Adv. Funct. Mater 2016, 26, 1678.

[2] Park, J.; You, I.; Shin, S.; Jeong, U. Chemphyschem 2015, 16, 1155–1163.

[3] Chortos, A.; Liu, J.; Bao, Z. A. Nat. Mater. 2016, 15, 937–950.

[4] Zhou, J.; Li, E. Q.; Li, R.; Xu, X.; Aguilar Ventura, I.; Moussawi, A.; Anjum, D.; Hed- hili, M. N.; Smilgies, D.; Lubineau, G.; Thoroddsen, S. T. J. Mater. Chem. C. 2015, 3, 2528– 2538.

[5] Zhou, J.; Mulle, M.; Zhang, Y. B.; Xu, X. Z.; Li, E. Q.; Han, F.; Thoroddsen, S. T.; Lu- bineau, G. J. Mater. Chem. C. 2016, 4, 1238–1249.

[6] Miura, H.; Fukuyama, Y.; Sunda, T.; Lin, B.; Zhou, J.; Takizawa, J.; Ohmori, A.; Kimura, M. Adv. Eng. Mater. 2014, 16, 550–555.

[7] Park, B.; Kim, J.; Kang, D.; Jeong, C.; Kim, K. S.; Kim, J. U.; Yoo, P. J.; Kim, T. Adv. Mater.2016, 28, 8130–8137.

[8] Kang, D.; Pikhitsa, P. V.; Choi, Y. W.; Lee, C.; Shin, S. S.; Piao, L. F.; Park, B.; Suh, K. Y.;Kim, T. I.; Choi, M. Nature 2014, 516, 222–226.

[9] Yang, T.; Li, X.; Lin, S.; Lao, J.; Shi, J.; Zhen, Z.; Li, Z.; Zhu, H. Mater. Horiz. 2016, 3,248–255.

[10] Liu,Z.Y.;Qi,D.P.;Guo,P.Z.;Liu,Y.;Zhu,B.W.;Yang,H.;Liu,Y.Q.;Li,B.;Zhang,C.G.;Yu, J. C.; Liedberg, B.; Chen, X. D. Adv. Mater. 2015, 27, 6230–6237.

[11] Xin, Y.; Zhou, X.; Xu, X.; Lubineau, G. Submitted. (2017).

[12] Zhou, J.; Yu, H.; Xu, X.; Han, F,; Lubineau, G. *ACS Appl*. *Mater*. *Interfaces*, 2017, 9(5), 4835-4842.

[13] Zhou, J.; Xu, X.; Yu, H.; Lubineau, G.. *Nanoscale*, 2017, **9**, 604-612.

VIII ECCOMAS Thematic Conference on Smart Structures and Materials
SMART 2017
A. Güemes, A. Benjeddou, J. Rodellar and J. Leng (Eds)

A MIXED FINITE ELEMENT FORMULATION FOR MODELING THE VISCOELASTIC RESPONSE OF ELECTROACTIVE POLYMERS AT FINITE DEFORMATION

Dana Bishara[†] and Mahmood Jabareen[‡]

[†] Faculty of Civil and Environmental Engineering. Technion - Israel Institute of Technology, Haifa 32000, Israel.
[‡] Neubauer Assistant Professor. Faculty of Civil and Environmental Engineering. Technion - Israel Institute of Technology, Haifa 32000, Israel.
E-mail: cvjmah@technion.ac.il

Key words: Smart materials, Multiphysics problems, Electro-active polymers, Finite element, Electro-mechanical coupling, Visco-elasticity

Abstract. In this work, constitutive equations and proper finite element formulation for modeling electromechanical coupling including finite viscoelasticity have been developed. For this objective, tools from continuum mechanics have been adopted for developing a phenomenological model that accounts for large deformations combined with the electromechanical coupling and the viscous nature of EAPs. Moreover, polymers are nearly incompressible materials, thus, a mixed finite element formulation was developed and implemented in a finite element package (e.g. Abaqus) for realistic simulations of EAPs. Moreover, a material parameter identification procedure has been developed in order to specify a proper strain energy function for the acrylic elastomer "VHB".

1 Introduction

Electro-active polymers (EAPs) are soft, flexible and active materials, which are classified as smart materials due to their ability to undergo large deformations when they are subjected to electrical stimuli. Therefore, they have received an extensive attention among researchers in various fields such as robotics, optics, acoustics and biomimetics ([16], [14], [5], [6]). Moreover, EAPs possess the characteristics of polymeric materials, in particular, they are lightweight, elastic, fracture tolerant, inexpensive, and their chemical and physical structure is well understood. Thus, this class of materials is attractive and it has been integrated in several applications, which have been developed and discussed in the literature. For instance, biomimetic applications and artificial muscles have been developed, including: i) a four-finger EAP gripper ([5]); ii) a miniature robotic arm ([5]); iii) a fish-like airship [13] with planar membrane dielectric elastomer actuators; and iv) artificial muscles, which mimic natural masseter muscles (superficial portion), using dielectric elastomer actuators reinforced with plastic fibers [24] and more.

In addition, optical devices has been developed in [9], which enables the implementation of a revolutionary phase shifter and a lens with tunable focal length. The working principle of the lens is similar to that of the human eye, where the lens are controlled by the applied voltage. The advantage of this design of focus and zoom systems can be exploited in many applications, outperforming existing solutions in terms of size, cost and power consumption.

Due to the aforementioned applications, EAPs are promising materials with outstanding features, which have a great potential for further applications. The activation of the EAP based actuators is controlled by the potential difference applied on the the electrodes, which are smeared on the upper and the lower surfaces of the polymeric thin film, causing thinning of the film and lateral expansion ([8]). For optimal design of EAPs, there is a need of a computational model, which is able to predict the EAP based actuators behavior. For achieving this aim, several works in the computational mechanics realm have been dedicated for studying the electro-mechanical coupling in EAPs in the last two decades. However, It should be noted that different theories for electro-magnetic interactions can be found in the literature since the pioneering work of Toupin (1956)[18], in which the first theory for electro-elastic interactions had been developed and a weak formulation was presented.

Generally speaking, EAPs are nearly-incompressible materials due to the fact that polymeric materials have bulk modulus, which is much higher than the shear modulus, consequently, the developed finite element must be volumetric locking free. Moreover, typical EAPs are made of silicones, polyacrylics or polyurethanes, which exhibit a time dependent behavior, therefore, the viscous nature of EAPs should be taken into account in the implemented model. Referring to the literature, several research groups have computationally studied the EAPs, such as Wissler and Mazza([26],[28],[29],[27],[25]) have studied the so-called dielectric elastomer VHB, however in their works they have adopted a hyper-elastic behavior combined with the quasi-linear viscoelastic function. Ask et al.([2],[3],[1]) have studied the electro-viscoelastic behavior of polyurethane using the standard Bubnov-Galerkin approach, which is not appropriate for incompressible and nearly-incompressible materials. Later, Ask et al.(2013)[4] have presented a mixed finite element formulation eliminating the volumetric locking, but in this work, the viscous nature has not been considered. The research group of Steinmann ([19],[22],[21],[23],[20]) has developed several variational pronciples providing an important framework for developing finite elements and numerical schemes.

In order to study the mechanical and the electrical behavior of EAPs, various experimental works have been performed. Wissler and Mazza ([27],[26]) have carried out number of stretch controlled tensile tests and relaxation tests for characterizing VHB. A wide experimental work that provides mechanical characterization for VHB has been carried out by Hossain et al.(2012)[11] in which they have presented different standard experiments such as: single-step relaxation tests, multi-step relaxation tests, and loading-unloading cyclic tests. Moreover, multi-axial tests have been performed in the work of ([25]) including (i) aspiration tests, in which circular VHB actuators have been radially stretched and their centers subjected to an external pressure causing aspiration of the loaded port; and (ii) actuator tests, in which circular VHB actuators have been radially stretched and their centers have been coated with flexible electrodes and subjected to potential difference, leading to radial changes.

In view of the aforementioned, we aim in this work to provide a numerical formulation that enables modeling EAPs in general, while accounting for the electro-mechanical coupling, the

visco-elasticity and the volumetric locking elimination. Thus, the free strain energy is assumed to be composed of a hyperelastic function, a visco-elastic part and a term accounting for the electro-mechanical coupling. In addition, for tackling the volumetric locking a mixed finite element formulation is developed expanding the functional that has been proposed in [17] to account for the electromechanical coupling. Furthermore, the presented model is calibrated to predict the behavior of the widely-used elastomer VHB. The calibration procedure has been performed using various results of experimental works found in the literature.

2 Governing equations and Strain energy function

Here we consider a material body consisting of matter occupying its material configuration $\mathcal{B}_0$ in the undeformed state. Due to the deformation, the body will occupy spatial configurations $\mathcal{B}$. The boundary of the body $\partial\mathcal{B}_0$ in the material configuration defines the interface between free space and matter. Let $\mathbf{F} = \frac{\partial \mathbf{x}}{\partial \mathbf{X}}$ and $\mathbf{C} = \mathbf{F}^T\mathbf{F}$ be the deformation gradient tensor and the right Cauchy-Green deformation tensor, respectively, with $\{\mathbf{X}, \mathbf{x}\}$ being the location of a material point in $\mathcal{B}_0$ and $\mathcal{B}$ respectively. Also, let $\boldsymbol{e}$ and $\boldsymbol{d}$ be the electric field vector and electric displacement vector, respectively. Under a conservative electric field and by definition they are given by

$$\boldsymbol{e} = -\frac{\partial \phi}{\partial \mathbf{x}}, \quad \boldsymbol{d} = \epsilon_0 \boldsymbol{e} + \boldsymbol{p}, \tag{1}$$

where $\boldsymbol{p}$ is the polarization density vector in the current configuration and ϕ is the electric potential. Their counterparts in the reference configuration $\{\boldsymbol{E}, \boldsymbol{D}\}$ can be demonstrated using the "pull-back" operation as follows

$$\boldsymbol{E} = \mathbf{F}^T\boldsymbol{e}, \quad \boldsymbol{D} = J\mathbf{F}^{-1}\boldsymbol{d}. \tag{2}$$

The equilibrium equation, which is governing the body in the absence of body forces, and Maxwell's equations without free currents and free electric charges, are given in the reference configuration by

$$\mathrm{Div}\,(\mathbf{FS}) = \mathbf{0}, \quad \mathrm{Div}\,(\mathbf{D}) = 0. \tag{3}$$

In order to solve the boundary value problem, we need to specify boundary conditions, therefore, the mechanical and electric Neumann boundary conditions are, respectively, given by

$$(\mathbf{FS}) \cdot \mathbf{N} = \bar{\mathbf{T}}_0 \quad on \quad \partial\mathcal{B}_0^T, \quad \mathbf{D} \cdot \mathbf{N} = -\bar{Q}_0 \quad on \quad \partial\mathcal{B}_0^Q, \tag{4}$$

where $\mathbf{N}$ is the unit outward normal to the surface of the body in the reference configuration, $\mathbf{S}$ is the total second Piolla Kirchhoff tensor and $\left\{\bar{\mathbf{T}}_0, \bar{Q}_0\right\}$ are the external mechanical traction applied on $\partial\mathcal{B}_0^T$ and the electric charges at $\partial\mathcal{B}_0^Q$, respectively. For the derivation of the total second Piolla-Kirchhoff tensor $\mathbf{S}$, a constitutive law must be determined, including the viscous nature of EAPs and the electromechanical coupling. Referring to the work of [12], an invariant based strain energy function has been proposed, where the set of the invariants takes the form

$$\begin{aligned} &J = \det(\mathbf{F}), \quad \alpha_1 = \mathbf{C}' : \mathbf{I}, \quad \alpha_2 = \mathbf{C}' : \mathbf{C}' \\ &I_4 = \boldsymbol{E} \cdot \boldsymbol{E}, \quad I_5 = \mathbf{C}^{-1} : (\boldsymbol{E} \otimes \boldsymbol{E}), \quad I_6 = \mathbf{C}^{-2} : (\boldsymbol{E} \otimes \boldsymbol{E}), \end{aligned} \tag{5}$$

where $\mathbf{C}'$ is the uni-modular tensor, i.e., $\mathbf{C}' = J^{-2/3}\mathbf{C}$. The total strain energy can be written as

$$\mathcal{W}\left(\mathbf{C}, \boldsymbol{E}, \mathbf{Q}_1, ..., \mathbf{Q}_n\right) = \mathcal{W}^{hyper}\left(\mathbf{C}\right) + \mathcal{W}^{coup}\left(\mathbf{C}, \boldsymbol{E}\right) + \mathcal{W}^{viscus}\left(\mathbf{C}, \mathbf{Q}_1, ..., \mathbf{Q}_n\right), \tag{6}$$

where $\mathcal{W}^{hyper}\left(\mathbf{Q}\right)$ is the pure hyper-elastic energy, $\mathcal{W}^{coup}\left(\mathbf{C}, \mathbf{E}\right)$ is the energy stored as a result of the coupling and $\mathcal{W}^{viscus}\left(\mathbf{C}, \mathbf{Q}_1, ..., \mathbf{Q}_n\right)$ is the energy related to the viscus nature of EAPs. $\mathcal{W}^{hyper}\left(\mathbf{C}\right)$ is a phenomenological strain energy, and in this study, we chose the Yeoh strain energy function

$$\mathcal{W}^{hyper}\left(\mathbf{C}\right) = \frac{K}{4}\left(J^2 - 1 - 2\ln\left(J\right)\right) + \sum_{i=1}^{3} C_i \left(\alpha_1 - 3\right)^i. \tag{7}$$

For determining the coupling term, referring to the work of [12], assuming that for dielectric materials the current direction of the polarization (and thus the electric displacement) coincides with the current direction of the electric field, the strain energy function accounting for the coupling yields to

$$\mathcal{W}^{coup}\left(\mathbf{C}, \boldsymbol{E}\right) = -\frac{1}{2} J \epsilon_0 \epsilon_r \left(\mathbf{C}^{-1} : \left(\boldsymbol{E} \otimes \boldsymbol{E}\right)\right). \tag{8}$$

The phenomenological model proposed in the work of [12] lacks the effect of viscoelasticity. Using the Maxwellian type rheological model of the isochoric response of the material, which consists of a single elastic branch representing the elastic ground network as well as viscous branches each of them representing a single mobile viscous sub-network, the strain energy function can be extended to include the viscous branches. Using the work by [10] and [15], the free energy associated with the viscous is given by

$$\mathcal{W}^{viscus} = \sum_{i=1}^{n} \frac{1}{2} \mu_i^v \left[\mathbf{C}' : \mathbf{Q}_i - 3 - \ln\left(\det\left(\mathbf{Q}_i\right)\right)\right], \tag{9}$$

where $\{\mathbf{Q}_1, ..., \mathbf{Q}_n\}$ are strain-like internal tensorial variables associated with the viscous Maxwell branches and $\{\mu_1^v, ..., \mu_n^v\}$ are the viscous shear moduli of the branches. The evolution law of a single strain like internal variable is given by

$$\dot{\mathbf{Q}}_i = \frac{1}{\tau_i^v}\left(\mathbf{C}'^{-1} - \mathbf{Q}_i\right), \tag{10}$$

with $\{\tau_1^v, ..., \tau_n^v\}$ are the relaxation times of the different Maxwell branches.

3 Finite element formulation

EAPs belong to the class of nearly incompressible materials, thus, using the Bubnov-Galerkin approach will lead to volumetric locking. In order to tackle this limitation, we will use the mixed finite element formulation which has been developed for mechanical problems by [17], while expanding the functional to account for the electromechanical coupling. The total potential energy Π can be decomposed into an internal part due to the strain energy and external part

because of the external tractions and electrical fluxes, and it can be written as

$$\begin{aligned}\Pi = \Pi^{int} - \Pi^{ext} = &\int_{\Omega_0} \left(\mathcal{W}\left(\bar{\mathbf{C}}, \boldsymbol{E}, \mathbf{Q}_1..\mathbf{Q}_n\right) + \bar{p}\left(J - \Theta\right)\right) d\Omega_0 \\ &- \left[\int_{\partial\mathcal{B}_0^T} \mathbf{u}\cdot\bar{\mathbf{T}} d\Gamma_0 + \int_{\partial\mathcal{B}_0^Q} \phi\bar{Q} d\Gamma_0\right],\end{aligned} \tag{11}$$

where $\{\bar{p}, \Theta\}$ are the average pressure and the average dilatation properly, Ω_0 is the volume at reference configuration and $\bar{\mathbf{C}}$ is the modified right Cauchy-Green tensor, defined by

$$\bar{\mathbf{C}} = \bar{\mathbf{F}}^T\bar{\mathbf{F}}, \quad \bar{\mathbf{F}} = \left(\frac{\Theta}{J}\right)^{1/3}\mathbf{F} \tag{12}$$

Using the multi-field Hu-Washizu variational principle, the variation of the total potential energy (11) with respect to the different fields yields the following variational equations

$$\begin{aligned}\delta\Pi_{\bar{\mathbf{C}}} &= \int_{\Omega_0}\left[\bar{\bar{\mathbf{S}}} : \frac{1}{2}\left(\frac{\Theta}{J}\right)^{2/3}\delta\mathbf{C}\right] d\Omega_0, \quad \delta\Pi_{\boldsymbol{E}} = \int_{\Omega_0} -\boldsymbol{D}\cdot\delta\mathbf{E} d\Omega_0, \\ \delta\Pi_{\Theta} &= \int_{\Omega_0}\left[\left(\frac{\bar{\mathbf{S}}:\bar{\mathbf{C}}}{3} - \Theta\bar{p}\right)\frac{\delta\Theta}{\Theta}\right] d\Omega_0, \quad \delta\Pi_{\bar{p}} = \int_{\Omega_0}\left[\left(J-\Theta\right)\delta\bar{p}\right] d\Omega_0,\end{aligned} \tag{13}$$

where $\bar{\bar{\mathbf{S}}} = \bar{\mathbf{S}} - \frac{1}{3}\left(\bar{\mathbf{S}}:\bar{\mathbf{C}}\right)\bar{\mathbf{C}}^{-1} + \bar{p}\Theta\bar{\mathbf{C}}^{-1}$, and $\bar{\mathbf{S}}$ is the second Piolla-Kirchhoff calculated using the modified Cauchy-Green tensor. By vanishing the variational equations (13c) and (13d) at the element level, one can deduce the following results

$$\Theta = \frac{1}{\Omega_0}\int_{\Omega_0} J d\Omega_0, \quad \bar{p} = \frac{1}{\Omega_0}\int_{\Omega_0}\frac{\bar{\mathbf{S}}:\bar{\mathbf{C}}}{3\Theta} d\Omega_0. \tag{14}$$

It should be noted that $\delta\mathbf{C}$ can be written in terms of the virtual displacement $\delta\mathbf{u}$, and $\delta\mathbf{E}$ can be written using the virtual electric potential $\delta\phi$ as follows

$$\delta\mathbf{F} = \frac{d\delta\mathbf{u}}{d\mathbf{X}}, \quad \delta\mathbf{C} = \delta\left(\mathbf{F}^T\mathbf{F}\right), \quad \delta\mathbf{E} = -\frac{d\delta\phi}{d\mathbf{X}}. \tag{15}$$

Within the developed formulation, a three dimensional element with eight nodes and four degrees of freedom at each node (three nodal displacements, and one nodal electric potential) was developed and implemented in Abaqus (a commercial finite element package) for numerical simulations. For this aim, the well-known discretization of the displacements and the electric potential fields has been used as demonstrated

$$\mathbf{u} = \sum_{I=1}^{Nen} N_I\left(\mathbf{X}\right)\widehat{\mathbf{u}}_I, \quad \phi = \sum_{I=1}^{Nen} N_I\left(\mathbf{X}\right)\widehat{\phi}_I, \tag{16}$$

where $\widehat{\mathbf{u}}_I$ denotes the displacement vector of node I, $\widehat{\phi}_I$ denotes the electric potential of node I, $N_I\left(\mathbf{X}\right)$ the shape function I defined at the reference configuration, and Nen is the number of nodes in an element.

4 Parameter identification

A parameter identification procedure has been performed in order to determine the material's coefficients of VHB. Therefore, an objective function has been built for minimizing the difference between the numerical results obtained from the developed finite element and the experimental results. In this parameter identification process different experimental works, including both uniaxial and multi-axial tests ([26],[28],[29],[27],[25]) have been used to characterize the response of VHB under both mechanical and electrical stimuli. A detailed explanation about the parameter identification process of the material's coefficients of VHB can be found in [7]. Here we present the result of the parameter identification process for unixial stress case. Fig. 1 shows the nominal stress versus the applied axial stretch obtained from both the numerical model and experimental data ([11]). Specifically, the samples have been uniaxially stretched to a measured value, and the stretches have been hold fix for 2000 seconds. The forces have been measured at the tail of the time. The the nominal stresses have been calculated by dividing the measured force by the samples section's area and plotted against the applied stretches.

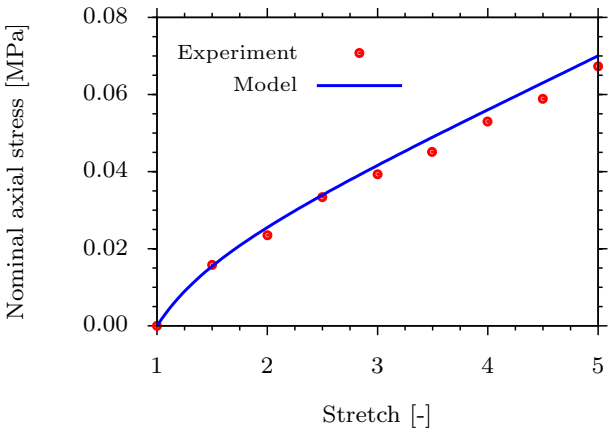

Figure 1: The nominal hyper-elastic stress plotted as a function of the applied stretch in uniaxial tests

5 Numerical Example

Here we present a numerical simulation, which has been conducted using the mixed FE formulation. In this example, we consider a bimorph bending actuator of a bi-layered thin film. In general, bending actuators are needed for simulating artificial muscles (such as muscles in the joints) and bending grippers ([6]). The actuator dimensions have been chosen as demonstrated in Fig. 2, where $L_1 = 20\text{mm}$, $L_2 = 5\text{mm}$ and $L_3 = 1\text{mm}$. The thickness consists of two thin layers, where each of them is $0.5mm$ thick. The bottom layer is sandwiched between a pair of compliant electrodes located at the composite's bottom and in the mid plane on which potential differences can be applied, and the upper layer is electrically passive. Applying voltage causes a reduction in the thickness of the bottom layer, and at the same time, a lateral expansion. Since the active layer is perfectly adhered to the passive layer, the structure gradually bends towards

the active layer.

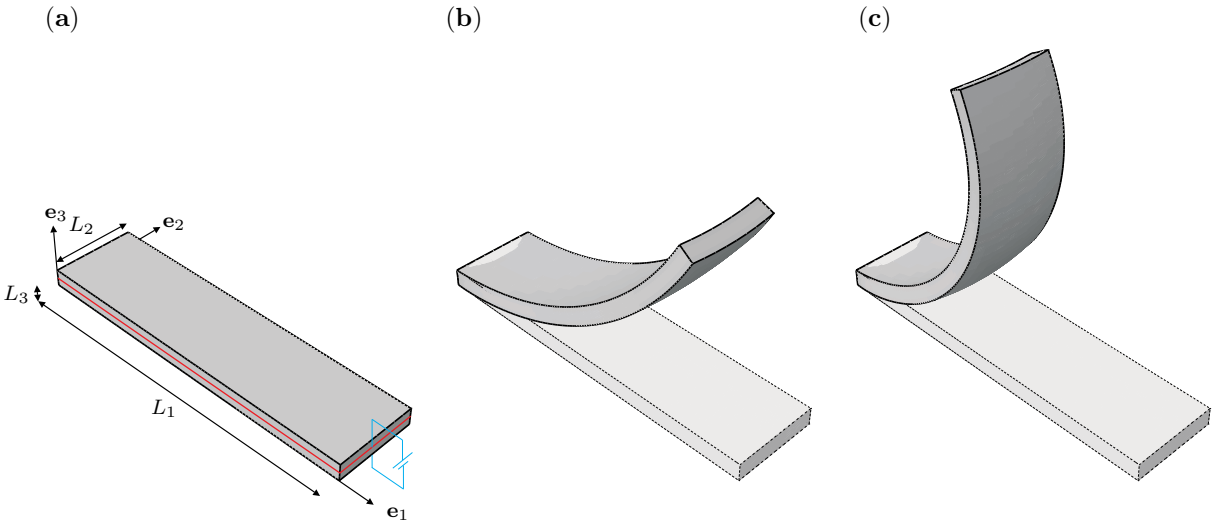

Figure 2: (a) The reference configuration of the actuator, $t = 0$ sec. (b) The actuator at $t = 50$ sec. (c)The current configuration of the actuator, $t = 150$ sec.

The actuator is subjected to a voltage of 5kV, which is linearly ramped over a time period of 50 sec and followed by a constant value for 100 sec (see Fig. 3). Both horizontal and vertical displacements of a selected point A (the tip of the beam) were calculated and plotted in Fig. 3. When the linear voltage load is applied, i.e, $t \leq 50$ sec, the actuator exhibits highly nonlinear deformations. The actuator undergoes additional deformations due to creeping when the voltage is hold fix. As shown in Fig. 3, the additional displacements while creeping are not negligible, and this is because of the highly viscoelastic response of EAPs.

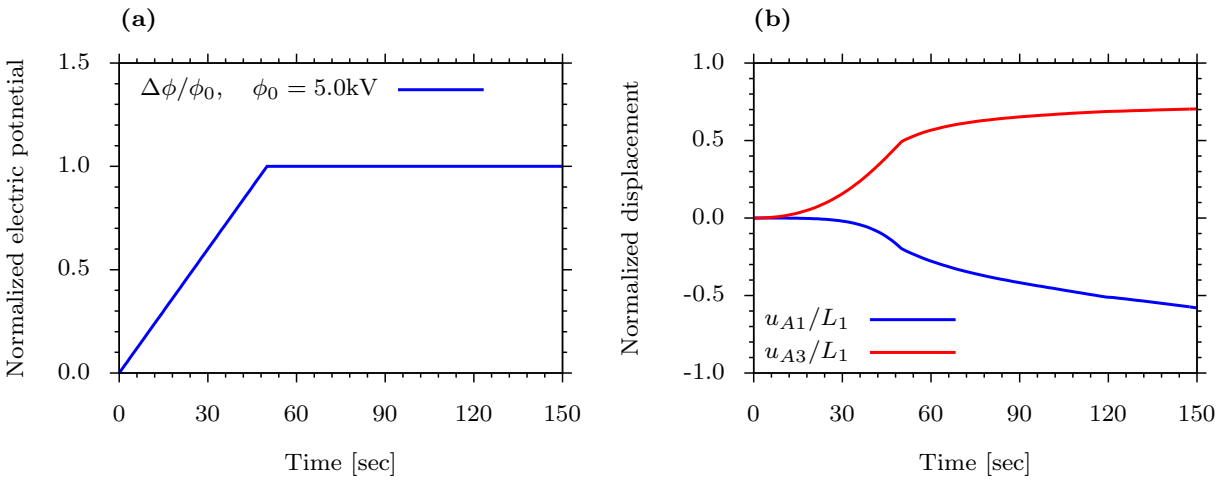

Figure 3: (a) The applied voltage. (b) The normalized displacements, in both horizontal and vertical directions.

6 Conclusions

In this work, a numerical scheme accounting for the electro-mechanical coupling, the time-dependent response and the incompressibility has been developed for modelling EAPs. For this objective, the strain energy function has been split into a hyper-elastic term, a visco-elastic term and a coupling term. The functional of the total potential energy has been written in terms of the right Cauchy-Green strain tensor, the electric field vector, the average pressure, and the average dilatation. With Hu-Washizu variational principle, the mixed finite element formulation has been developed, and the expressions for the average hydrostatic pressure and the average dilatation measurement have been derived. With the developed finite element, a parameter identification procedure has been performed for characterizing the so-called dielectric elastomer VHB using experimental result found in the literature ([11], [26],[28],[29],[27],[25]). As a result, the material's parameters have been specified considering both uniaxial and multi-axial experimental tests. With the derived set of material parameters, a numerical example has been presented for predicting a VHB based bimorph bending actuator.

In summary, EAPs have been computationally studied in this work, and a general numerical tool for EAPs and a specific energy function for VHB have been presented. In particular, a finite element formulation providing an efficient design tool for EAP based actuators has been implemented in a commercial finite element software namely, Abaqus for further simulations.

Acknowledgements

Financial support for this work was provided by the Israel Science Foundation under grant 1713/13, which is gratefully acknowledged.

References

[1] A. Ask, A. Menzel, and M. Ristinmaa. On the modelling of electro-viscoelastic response of electrostrictive polyurethane elastomers. In *IOP Conference Series: Materials Science and Engineering*, volume 10, page 012101, 2010.

[2] A. Ask, A. Menzel, and M. Ristinmaa. Electrostriction in electro-viscoelastic polymers. *Mechanics of Materials*, 50:9–21, 2012.

[3] A. Ask, A. Menzel, and M. Ristinmaa. Phenomenological modeling of viscous electrostrictive polymers. *International Journal of Non-Linear Mechanics*, 47(2):156–165, 2012.

[4] A. Ask, A. Menzel, and M. Ristinmaa. Inverse-motion-based form finding for quasi-incompressible finite electroelasticity. *International Journal for Numerical Methods in Engineering*, 94(6):554–572, 2013.

[5] Y. Bar-Cohen. *Electroactive Polymers as Artificial Muscles - Reality and Challenges*. SPIE press, 1 edition, 2001.

[6] Y. Bar-Cohen. Electroactive polymers as artificial muscles. *Journal of Spacecraft and Rockets*, 39:822–827, 2002.

[7] D. Bishara and M. Jabareen. A reduced mixed finite element formulation for modeling viscous electroactive polymers at finite deformations. *Submitted*.

[8] J. Blok and D. Legrand. Dielectric breakdown of polymer films. *Journal of Applied Physics*, 40(1):288–293, 1969.

[9] Empa. EAP Technology at Empa. `http://oldweb.empa.ch/plugin/template/empa/*/72289`, 2007. Online; accessed 14 January 2017.

[10] M. Green and A. Tobolsky. A New Approach to the Theory of Relaxing Polymeric Media. *The Journal of Chemical Physics*, 14:80–92, 1946.

[11] M. Hossain, D. Vu, and P. Steinmann. Experimental study and numerical modelling of VHB 4910 polymer. *Computational Materials Science*, 59:65–74, 2012.

[12] M. Jabareen. On the Modeling of Electromechanical Coupling in Electroactive Polymers Using the Mixed Finite Element Formulation. *Procedia IUTAM*, 12:105–115, 2015.

[13] C. Jordi, S. Michel, and E. Fink. Fish-like propulsion of an airship with planar membrane dielectric elastomer actuators. *Bioinspiration & biomimetics*, 5(2):026007, 2010.

[14] G. Kofod. *Dielectric Elastomer Actuators*. PhD thesis, The technical university of Denmark, 2001.

[15] J. Lubliner. A model of rubber viscoelasticity. *Mechanics Research Communications*, 12(2):93–99, 1985.

[16] R. Pelrine, R. Kornbluh, and J. Joseph. Electrostriction of polymer dielectrics with compliant electrodes as a mean of actuation. 64(97):77–85, 1998.

[17] J. Simo, R. Taylor, and K. Pister. Variational and projection methods for the volume constraint in finite deformation elasto-plasticity. *Computer Methods in Applied Mechanics and Engineering*, 51:177–208, 1985.

[18] R. Toupin. The elastic dielectric. *Journal of Rational Mechanics and Analysis*, 5:849–915, 1956.

[19] F. Vogel, R. Bustamante, and P. Steinmann. On some mixed variational principles in electro-elastostatics. *International Journal of Non-Linear Mechanics*, 47:341–354, 2012.

[20] D. Vu and P. Steinmann. Material and Spatial Motion Problems in Nonlinear Electro- and Magneto-elastostatics. *Mathematics and Mechanics of Solids*, 15:239–257, 2010.

[21] D. Vu and P. Steinmann. On 3-D coupled BEM-FEM simulation of nonlinear electro-elastostatics. *Computer Methods in Applied Mechanics and Engineering*, 201-204:82–90, 2012.

[22] D. Vu and P. Steinmann. On the spatial and material motion problems in nonlinear electro-elastostatics with consideration of free space. *Mathematics and Mechanics of Solids*, 17(8):803–823, 2012.

[23] D. Vu, P. Steinmann, and G. Possart. Numerical modelling of non-linear electroelasticity. 70:685–704, 2007.

[24] Z. J. Wang Y. Artificial muscles for jaw movements. *Extreme Mechanics Letters*, 6:88–95, 2016.

[25] M. Wissler. *Modelling dielectric elastomer actuators*. PhD thesis, Swiss federal institute of technology in Zurich, 2007.

[26] M. Wissler and E. Mazza. Modeling and simulation of dielectric elastomer actuators. *Smart Materials and Structures*, 14:1396–1402, 2005.

[27] M. Wissler and E. Mazza. Modeling of a pre-strained circular actuator made of dielectric elastomers. *Sensors and Actuators A*, 120:184–192, 2005.

[28] M. Wissler and E. Mazza. Electromechanical coupling in dielectric elastomer actuators. *Sensors and Actuators A*, 138:384–393, 2007.

[29] M. Wissler and E. Mazza. Mechanical behavior of an acrylic elastomer used in dielectric elastomer actuators. *Sensors and Actuators, A: Physical*, 134(2):494–504, 2007.

VIII ECCOMAS Thematic Conference on Smart Structures and Materials
SMART 2017
A. Güemes, A. Benjeddou, J. Rodellar and J. Leng (Eds)

CONSTITUTIVE MODELING OF HYSTERESIS IN NITINOL AND STEEL STRANDS THROUGH DATA-DRIVEN STRATEGIES

PATRICK BREWICK*, SAMI F. MASRI*, WALTER LACARBONARA†, AND BIAGIO CARBONI†

*Astani Department of Civil and Environmental Engineering
University of Southern California
Los Angeles, California, USA
e-mail: masri@usc.edu

† Department of Structural and Geotechnical Engineering
Sapienza University of Rome
Rome, Italy

Key words: Nonlinear Identification, Data-Driven Methods, Hysteresis, Neural Networks, Nonparametric Methods

Abstract. Data-driven strategies for nonlinear identification are applied to experimental data exhibiting various types of hysteretic behavior. The experimental data contain displacement and restoring force information for several tests conducted using different configurations of a unique rheological testing device with various assemblies of NiTiNOL and steel wire strands. Among the different configurations the response of the wire strands show distinct forms of nonlinear behavior, such as quasi-linear softening, pinching, and hardening. The data-driven methods applied for nonlinear identification include polynomial basis functions and neural networks. The polynomial basis nonlinear identification methods are used for the construction and characterization of reduced-order models in order to gain insight into the physical modeling of the hysteretic phenomena. The neural network methods are found to be more useful for predictive purposes, demonstrating an ability to produce accurate results on both training and testing data.

1 INTRODUCTION

Despite being better known for their axial load bearing capacity, the energy dissipation capabilities in short wires, ropes, cables and strands has been utilized in several applications, including vibration isolation [19], seismic protective systems [6], and tuned mass dampers [5, 8]. These various devices and technologies take advantage of inter-wire frictional forces to dissipate energy. Recently, a new device has been proposed by [3] that can potentially provide energy dissipation by exploiting the simultaneous occurrence of phase transformations and frictional hysteresis in wire ropes made of nickel titanium-Naval Ordnance Laboratory (NiTiNOL) and

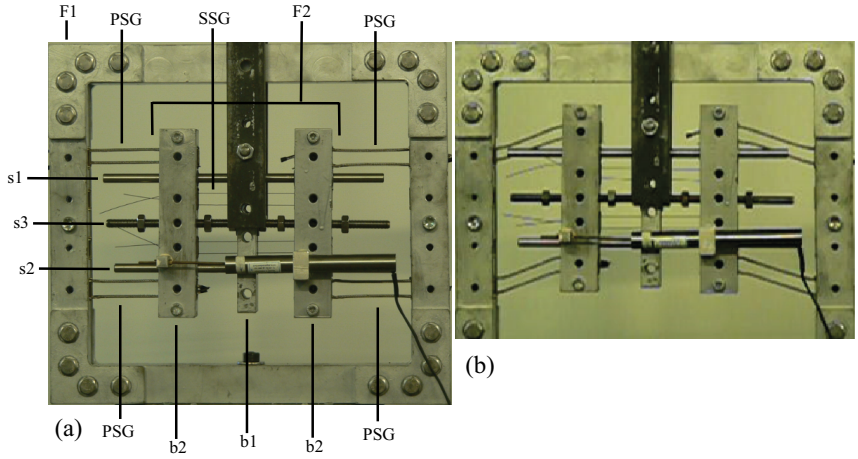

Figure 1: The device in its (a) reference and (b) deformed states

steel wires subjected to coupled shear-bending tension. In their work, [3] demonstrated how different assemblies of NiTiNOL and steel wire ropes, when integrated into a mechanism capable of providing geometric nonlinearities, produced different kinds of hysteretic behaviors, such as hardening, pinching, and quasi-linear hysteresis. The rich dynamical behavior of the proposed device [4] can be suitable for many engineering applications, which thus requires robust mechanical models and identification procedures.

Once observed experimentally, one of the foremost challenges is associated with devising a suitable constitutive model for the hysteretic behavior. One of the more well-known models for nonlinear hysteretic systems was developed by Bouc [2] and modified by Wen [20]. While such parametric models are extremely useful and can be fitted with very low error [3], there is also a need for data-based, or model-free, identification strategies that are not constrained by assumed models or model classes.

Applications for non-parametric methods have included identification for hysteretic systems under earthquake loading [1] and structural health monitoring and damage detection [11, 18]. Some of the more recent developments in non-parametric identification have focused on using neural networks [7, 9, 10, 12, 16, 17, 21]. This study will consider different polynomial basis functions, specifically power series [14, 15] and Chebyshev polynomials [13], and neural network approaches, both artificial neural networks (ANNs) [7] and the Volterra/Wiener neural network (VWNN) [9], as possible strategies for data-driven identification.

2 Experimental Data

This section will provide an overview of the NiTiNOL wire strands and the experimental set-up used to generate the data for this study; a more complete description of the experimental data may be found in [3].

Although several device configurations were tested, this study will focus on one (Configuration S1a) of the three configurations shown in Table 1, where the rope type, length (L), and number (n^0) are given for each of the primary stiffness group of wire ropes (PSG) and a secondary stiffness group of wire ropes (SSG). The wire rope cross sections are shown in Fig. 2, where NiTi7 and

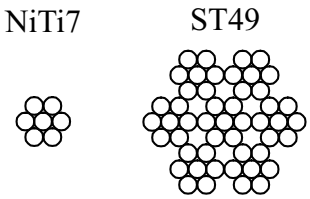

Figure 2: Wire rope cross sections

Table 1: Device configurations

Configuration	PSG			SSG			Hysteresis
	Type	L (mm)	n^0	Type	L (mm)	n^0	
S1a	NiTi7	56	8	–			STHP
S2a	ST49	100	8	–			QS
S3b	ST49	100	8	NiTi7	63	2	SLHP

ST49 denote a NiTiNOL seven-wire strand and a steel seven-strand rope with diameters of 1.8 mm and 6 mm, respectively. Within each device configuration, cyclic tests were conducted by prescribing sinusoidal vertical displacements and measuring the resulting restoring forces, as explained previously. A number of cyclic tests were performed for each configuration by varying the amplitudes of the sinusoidal displacement time history. In this study, four cyclic tests of increasing displacement amplitude were included for each device configuration shown in Table 1.

Each configuration produced a unique hysteretic behavior during the cyclic tests. These different hysteretic behaviors are classified in the last column of Table 1, where STHP stands for strongly hardening and pinched hysteresis, QS for quasilinear-softening hysteresis, and SLHP for slightly hardening and pinched hysteresis. The pinching at the origin of the force-displacement cycles is due to load-induced phase transformations of the shape memory material. The increase of the dissipated energy at large displacement amplitudes produces the pinching effect. Examples of each hysteresis type are shown in Fig. 3.

3 Nonlinear Identification Methods

Based on the experience of other researchers in the modeling of complex nonlinear systems, the present study will consider the Volterra/Wiener neural network, power series and Chebyshev polynomial estimators, and an adaptive neural network approach for nonlinear identification of the restoring forces. The technical details of the inner workings of these methods are available in [7], [9], [13], and [14].

4 Application to Configuration S1a

Due to page limitations, this study will only discuss results for Configuration S1a. The data with the largest amplitude from the cyclic tests was used as the *training* case for identification, meaning that the different nonlinear identification methods would fit their parameters to that data set. The largest amplitude test was chosen for parameter fitting because this data set

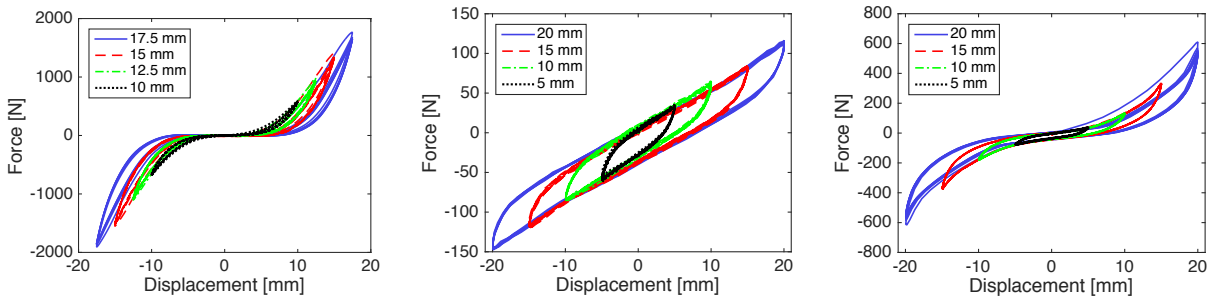

(a) S1a – STHP (b) S2a – QS (c) S3b – SLHP

Figure 3: Examples of the different hysteretic behaviors observed for device Configurations (a) S1a with strongly hardening and pinched hysteresis (STHP), (b) S2a with quasilinear-softening hysteresis (QS), and (c) S3b with slightly hardening and pinched hysteresis (SLHP)

Table 2: Relative RMS errors from polynomial basis identification strategies for Configuration S1a data

	Training (Fitting)	**Test Cases**		
ID Method	±17.5 mm	±15 mm	±12.5 mm	±10 mm
Power Series	13.94 %	9.55 %	19.81 %	46.89 %
Chebyshev	9.29 %	29.51 %	35.39 %	25.39 %

would include the largest possible range of restoring force and displacement values, making it the most likely to capture the nonlinear behavior of subsequent tests with smaller amplitudes.

4.1 Polynomial Basis Nonlinear Identification

The nonlinear identification methods using polynomial basis functions were first applied to the training data set from Configuration S1a. Once determined, the coefficients from each method were applied to the data from the other cyclic tests. The restoring forces for the training and testing cases are plotted against their respective relative displacements in Fig. 4. Both methods show a good fit for the training data in Fig. 4a, but the fits become progressively worse for the other tests as the amplitudes decrease. However, this result is not surprising given the corresponding phenomenological change with amplitude shown previously.

The accuracy of the restoring force estimates, as measured by the relative root-mean-square (RMS) error, is given in Table 2. The power series polynomial method actually performed slightly better on the ±15 mm amplitude test case than it did during training. Generally, the power series basis shows increase in error as the amplitudes decrease. In contrast, the Chebyshev polynomial basis method generated consistent RMS errors around $25-35\%$ for all test cases despite a good fit from training.

Chebyshev polynomials also offer potential physical insights into the hardening nonlinearities observed during the cyclic tests for Configuration S1a. The Chebyshev polynomials may be transformed from their orthogonal basis functions to a basis of normalized displacements and velocities $(x', \dot{x}')$, and the coefficients corresponding to these transformed Chebyshev polynomials

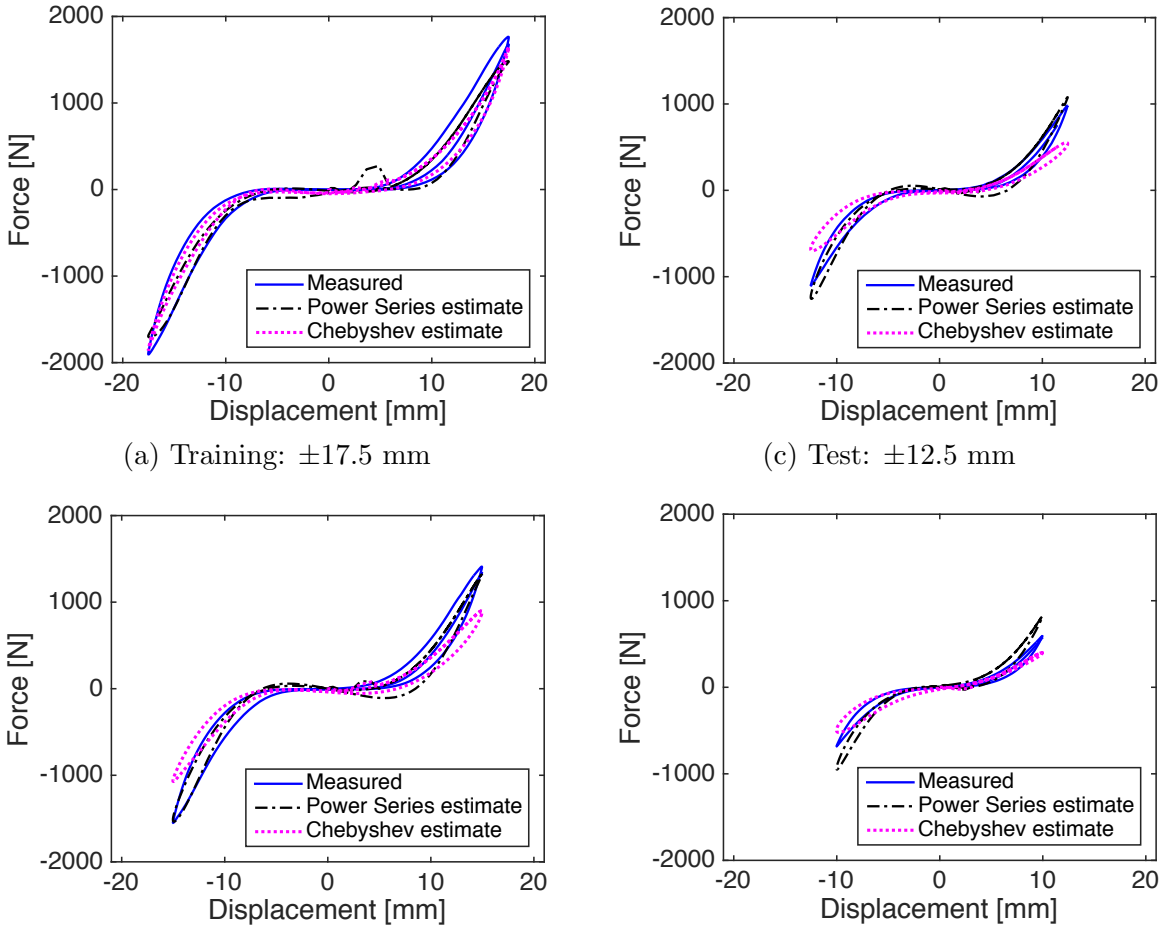

(a) Training: ±17.5 mm

(c) Test: ±12.5 mm

(b) Test: ±15 mm

(d) Test: ±10 mm

Figure 4: Force-displacement cycles for Configuration S1a, where (a) ±17.5 mm case was used for training (fitting), and (b) ±15 mm, (c) ±12.5 mm, and (d) ±10 mm were used as test cases

k \ l	$T_0(\dot{x}')$	$T_1(\dot{x}')$	$T_2(\dot{x}')$	$T_3(\dot{x}')$	$T_4(\dot{x}')$	$T_5(\dot{x}')$
$T_0(x')$	–15.33	44.11	25.24	–40.20	33.48	10.61
$T_1(x')$	1241.37	–1.83	–47.16	11.36	–11.00	–16.24
$T_2(x')$	–36.76	3.22	–0.32	–11.89	6.40	9.98
$T_3(x')$	446.58	4.06	76.36	–32.48	8.92	47.06
$T_4(x')$	–49.22	–39.05	–39.13	40.18	–17.29	4.10
$T_5(x')$	72.14	–0.95	–11.32	24.99	8.85	–32.89

Figure 5: Matrix of identified Chebyshev coefficients $C_{kl}^{(i)}$ from the ±17.5 mm training data for Configuration S1a

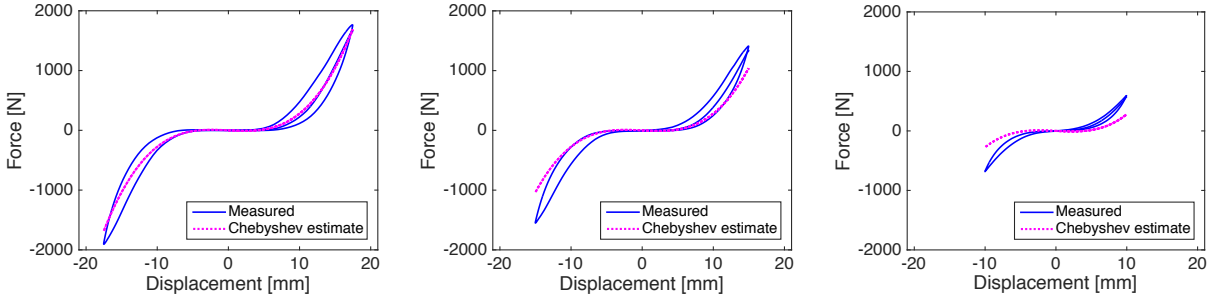

(a) Training: ±17.5 mm (b) Test: ±15 mm (c) Test: ±10 mm

Figure 6: Force-displacement cycles for Configuration S1a using only linear and cubic displacement terms from the Chebyshev polynomials, where (a) ±17.5 mm case was used for training (fitting), and (b) ±15 mm and (c) ±10 mm were used as test cases

are shown in Fig. 5. From the matrix in this figure it may be clearly seen that the largest coefficients, by orders-of-magnitude, are those for the linear and cubic displacement terms. The positive sign on the cubic displacement term implies a hardening behavior, which is precisely the type of behavior observed in the restoring force plots in Fig. 4.

Figure 6 shows representations of the restoring forces when the estimation is limited to only the linear and cubic displacement terms from the Chebyshev polynomial. The first observation is that the absence of velocity information prevents the accurate capture of the hysteresis phenomenon as the Chebyshev polynomial has become one-dimensional, creating a "backbone curve" representation of the restoring force. The backbone presents a very good fit for the training data and reasonable fit for the ±15 mm test case. The quality of the fit for the backbone curve drops sharply with decreasing amplitude for the remaining test cases; however, its quality is not significantly worse than that provided by the full Chebyshev polynomial representation. This demonstrates that, in a qualitative sense, a backbone curve comprised of linear and cubic displacement terms can be used to describe the general nonlinear behavior observed for Configuration S1a.

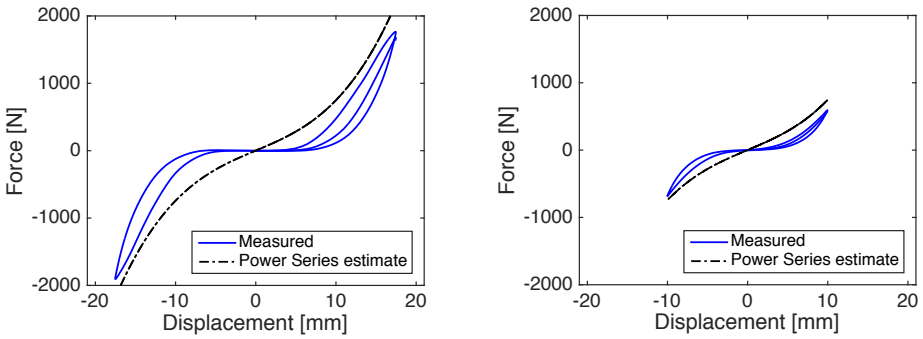

(a) Training: ±17.5 mm (b) Test: ±10 mm

Figure 7: Force-displacement cycles for Configuration S1a using only linear and cubic displacement terms from the power series basis functions, where (a) ±17.5 mm case was used for training (fitting), and (b) ±10 mm was used as a test case

Despite the relative similarity between the Chebyshev and power series estimates, the same backbone approximation cannot be made using the power series fit. Although the power series basis functions utilize the same normalization of terms, the linear and cubic displacement terms were not dominant, as several other terms had coefficients of comparable magnitude. (This is attributable to the fact that each transformed Chebyshev term contains "projections" of higher order terms from the original Chebyshev polynomial.) Figure 7 shows that the backbone curve created by linear and cubic displacement terms from the power series proves to be a poor approximation of the restoring force and does not capture its global behavior, *e.g.*, the backbone curve for the test case exhibits an almost purely linear behavior.

4.2 Neural Network Nonlinear Identification

The data from Configuration S1a was also subjected to neural network methods for nonlinear identification. The restoring force estimates produced by the VWNN and ANN are plotted against displacement in Fig. 8. Both methods provide very good fits for the training data, as the two curves produced by neural networks are essentially superimposed on the measured restoring force and display comparably accurate fits for the other testing data sets.

The RMS errors for the different neural network estimates are given in Table 3. Both methods display considerable improvements over the polynomial basis methods, but the VWNN clearly outperforms the ANN. Figure 8 demonstrates how slight this advantage in accuracy is to the naked eye, as there appears to be little perceptible difference in the two estimates. Although, this would be expected when comparing RMS errors on the order of 10% or less. The only real advantage to the VWNN is that its RMS errors remain consistent throughout the test cases, whereas the ANN shows a gradual increase in its RMS errors as the amplitudes decrease. It should be noted that the ANN gives slightly different estimates each time it is run, even for the same data set, due to its randomized initialization. However, the RMS errors reported in Table 3 may be considered as fully representative of its accuracy.

Despite the increased accuracy over the polynomial basis methods, neural networks expose their shortcomings when it comes to physical insight. Previous studies have shown that neural

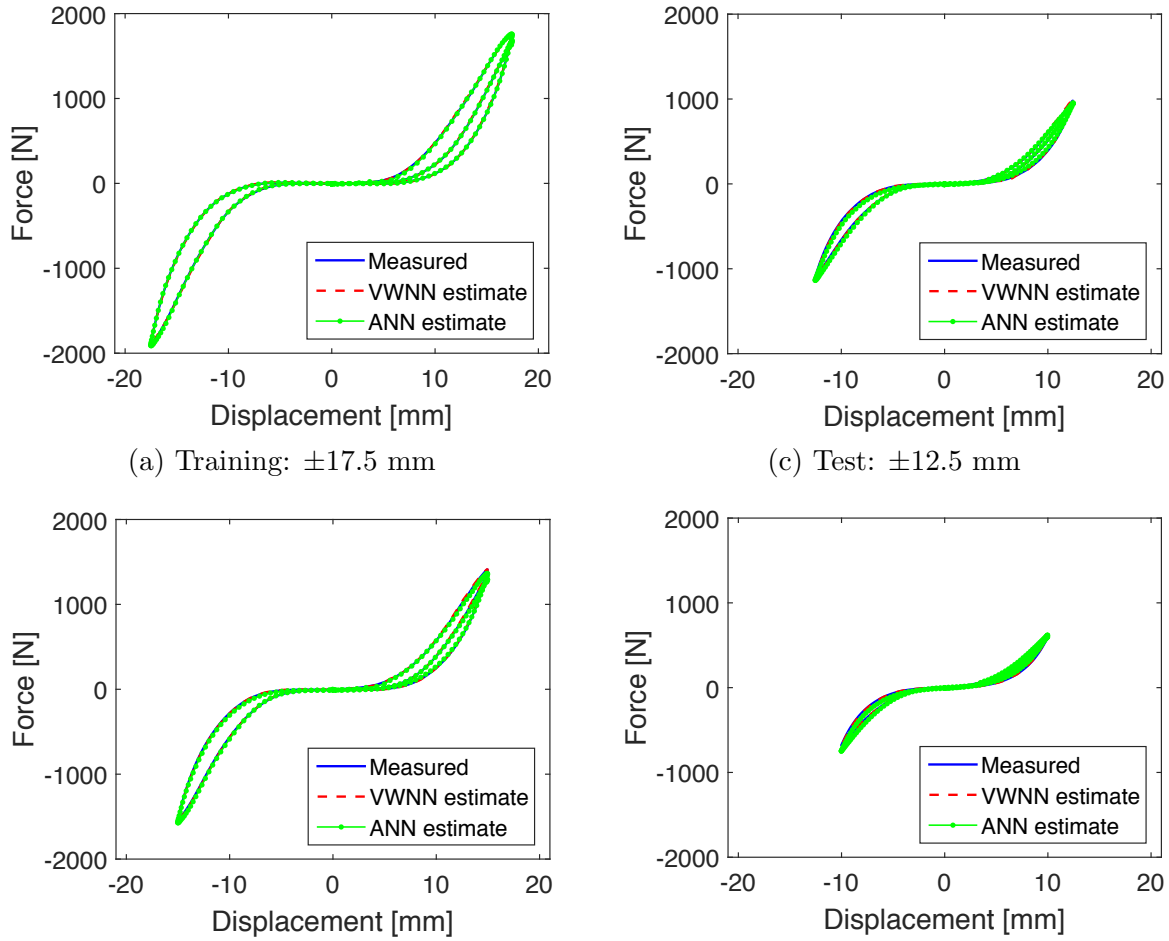

(a) Training: ±17.5 mm

(c) Test: ±12.5 mm

(b) Test: ±15 mm

(d) Test: ±10 mm

Figure 8: Force-displacement cycles for Configuration S1a using neural network methods, where (a) ±17.5 mm case was used for training (fitting), and (b) ±15 mm, (c) ±12.5 mm, and (d) ±10 mm were used as test cases

Table 3: Relative RMS errors from neural network identification strategies for Configuration S1a data

	Training (Fitting)	**Test Cases**		
ID Method	±17.5 mm	±15 mm	±12.5 mm	±10 mm
VWNN	0.85 %	2.86 %	2.16 %	2.05 %
ANN	0.47 %	3.02 %	4.97 %	10.58 %

networks are unable to provide physical understanding of the system parameters [18]. Unlike the Chebyshev polynomials, the weights and functions of a neural network cannot be easily connected to the system's states, such as displacement or velocity, nor its stiffness features or properties. Thus, while the VWNN and ANN offer clear advantages in identification, they lack clear connections to the physics or mechanics of the system.

5 CONCLUSIONS

Through this study, it was found that the several data-driven strategies considered could be successfully applied to identify the nonlinear hysteretic behavior observed in NiTiNOL and steel wire ropes, but each method displayed strengths and weaknesses. The polynomial-based methods were simple to implement and allowed for reduced-order modeling and physical parameter inference, but they were only moderately accurate during validation on the test cases. Conversely, the neural network approaches could not be used much beyond response prediction, but they exhibited high accuracy. This was especially true with respect to the amplitude-dependent aspects of the nonlinear behavior, as the neural networks better captured these phenomenological aspects of the hysteresis. The neural networks even managed to provide adequate identification using the small amplitude test as training data, but, owing to issues of clipping and normalization, the polynomial methods were generally unsuccessful in this case.

Perhaps the most important result of this study was the ability of the Chebyshev polynomials to produce reduced-order models that could represent the hysteretic behaviors. By reducing the models to only two or three terms, the generalizability of these models suffered, but they generally captured some, if not most, of the important aspects of the nonlinear restoring forces for both the training and testing data. Further, these reduced-order models could be connected to the physical system. This is significant, as it demonstrates that a physics-based model may be created for a system based on a data-driven identification strategy that assumes no model *a priori*. Future studies should go beyond quasi-static harmonic testing and look more into random dynamic excitation testing in order to determine whether the reduced-order models may become better generalized by using a more complete region of the phase-space for coefficient and parameter fitting.

6 ACKNOWLEDGMENTS

The first author would like to acknowledge the support of the Viterbi Postdoctoral Fellowship from the University of Southern California. The work of Walter Lacarbonara and Biagio Carboni was partially supported by the Italian Ministry of Education, University and Scientific Research (2010-2011 PRIN Grant No. 2010BFXRHS-002).

References

[1] F. Benedettini, D. Capecchi, and F. Vestroni. Identification of hysteretic oscillators under earthquake loading by nonparametric models. *ASCE Journal of Engineering Mechanics*, 121:606–612, 1995.

[2] R. Bouc. Forced vibration of mechanical systems with hysteresis. In *4th Conference on Nonlinear Oscillation*, Prague, Czechoslovakia, 1967.

[3] Biagio Carboni, Walter Lacarbonara, and Ferdinando Auricchio. Hysteresis of multiconfiguration assemblies of nitinol and steel strands: Experiments and phenomenological identification. *ASCE Journal of Engineering Mechanics*, 141(3):04014135, 2015.

[4] Biagio Carboni, Carlo Mancini, and Walter Lacarbonara. *Hysteretic Beam Model for Steel Wire Ropes Hysteresis Identification*, pages 261–282. Springer International Publishing, Cham, 2015. ISBN 978-3-319-19851-4.

[5] N. Carpineto, Walter Lacarbonara, and F. Vestroni. Hysteretic tuned mass dampers for structual vibration mitigation. *Journal of Sound and Vibration*, 333(5):1302–1318, 2014.

[6] G. F. Demetriades, M. C. Constantinou, and A. M. Reinhorn. Study of wire rope systems for seismic protection of equipment in buildings. *Engineering Structures*, 15(5):321–334, 1993.

[7] Armen Derkevorkian, Sami F. Masri, Yozo Fujino, and Dionysius M. Siringoringo. Development and validation of nonlinear computational models of dispersed structures under strong earthquake excitation. *Earthquake Engineering and Structural Dynamics*, 43:1089–1105, 2014.

[8] R. R. Gerges and B. Vickery. Parametric experimental study of wire rope spring tuned mass dampers. *Journal of Wind Engineering and Industrial Aerodynamics*, 91(12-15):1363–1385, 2003.

[9] E. B. Kosmatopoulos, A. W. Smyth, S. F. Masri, and A. G. Chassiakos. Robust adaptive neural estimation of restoring forces in nonlinear structures. *ASME Journal of Applied Mechanics*, 68:880–893, 2001.

[10] J.-W. Lin. Adaptive identification of structural systems by training artificial neural networks. *Advances in Information Sciences and Service Sciences*, 4:10–17, 2012.

[11] J.-W. Lin and R. Betti. On-line identification and damage detection in non-linear structural systems using a variable forgetting factor approach. *Earthquake Engineering and Structural Dynamics*, 33:419–444, 2004.

[12] J.-W. Lin and T.-H. Wu. Modeling and assessment of VWNN for signal processing of structural systems. *Structural Engineering and Mechanics*, 45:53–67, 2013.

[13] S. F. Masri and T. K. Caughey. A nonparametric identification technique for nonlinear dynamic problems. *ASME Journal of Applied Mechanics*, 46:433–447, 1979.

[14] S. F. Masri, J. P. Caffrey, T. K. Caughey, A. W. Smyth, and A. G. Chassiakos. A general data-based approach for developing reduced-order models of nonlinear MDOF systems. *Nonlinear Dynamics*, 39:95–112, 2005.

[15] S. F. Masri, F. Tasbihgoo, J. P. Caffrey, A. W. Smyth, and A. G. Chassiakos. Data-based model-free representation of complex hysteretic MDOF systems. *Structural Control and Health Monitoring*, 13:365–387, 2006.

[16] J.-S. Pei, A. W. Smyth, and E. B. Kosmatopoulos. Analysis and modification of Volterra/Weiner neural networks for the adaptive identification of non-linear hysteretic dynamic systems. *Journal of Sound and Vibration*, 275:693–718, 2004.

[17] J. S. Pei, E. C. Mai, J. P. Wright, and S. F. Masri. Mapping some functions and four arithmetic operations to multilayer feedforward neural networks. *Nonlinear Dynamics*, 71 (1-2):371–399, 2013.

[18] A. W. Smyth, S. F. Masri, T. K. Caughey, and N. F. Hunter. Surveillance of mechanical systems on the basis of vibration signature analysis. *ASME Journal of Applied Mechanics*, 67:540–551, 2000.

[19] M. L. Tinker and M. A. Cutchins. Damping phenomena in a wire rope vibration isolation system. *Journal of Sound and Vibration*, 157(1):7–18, 1992.

[20] Y.K. Wen. Method for random vibration of hysteretic systems. *Journal of the Engineering Mechanics Division, ASCE*, 102:249–263, 1976.

[21] T. Wu and A. Kareem. Modeling hysteretic nonlinear behavior of bridge aerodynamics via cellular automata nested neural network. *Journal of Wind Engineering and Industrial Aerodynamics*, 99:378–388, 2011.

VIII ECCOMAS Thematic Conference on Smart Structures and Materials
SMART 2017
A. Güemes, A. Benjeddou, J. Rodellar and J. Leng (Eds)

DESCRIPTION OF DAMAGE AND HEALING OF A SELF-HEALING ANISOTROPIC MATERIAL

STEFFEN SPECHT*, JOACHIM BLUHM† AND JÖRG SCHRÖDER‡

Institute of Mechanics
University of Duisburg-Essen
Campus Essen, 45141 Essen, Germany
web page: http://www.uni-due.de/mechanika
e-mail: *steffen.specht@uni-due.de, †joachim.bluhm@uni-due.de,
‡j.schroeder@uni-due.de

Key words: Theory of Porous Media, Phase Transition, Self-Healing Material, Anisotropy

Abstract. In this contribution the damage and healing behavior of a fiber reinforced self-healing composite is investigated. The considered underlying self-healing principle is based on microencapsulated healing agents (monomer) and catalysts (to initiate the polymerization) which are embedded in a polymeric matrix material. Thus, the overall material consists of five different phases: i.) solid matrix material; ii.) liquid healing agents; iii.) catalysts; iv.) solidified healed material; v.) air (inside the cracks). In order to model such a multiphase material, the Theory of Porous Media (TPM) is used in this contribution.

Furthermore, the composite is reinforced by one fiber family, which leads to a transversely isotropic material behavior on the macroscale. The damage behavior is described by a discontinuous damage model and the healing effect is modeled via a phase transition from liquid healing agents to solidified healed material.

At the end, the applicability of the developed model is shown by means of a numerical simulation of an initial boundary value problem.

1 INTRODUCTION

Usually, engineering materials are designed in order to resist damages or at least the growth of them. But due to load peaks or other environmental influences, like corrosion or UV radiation, they can fail. In case of polymers and polymeric composites microdamages inside the structure can lead to a spontaneous loss of the structural stability. The crucial point is that these microdamages are very hard to detect and more or less impossible to repair. Thus, even if microdamages are detected in a structural part before it has been already failed, the whole part has to be replaced, which can be very expensive, i.e., in case of aerospace applications or even offshore wind turbine blades.

In order to extend the structural lifetime and save maintenance costs, materials can be designed with respect to the damage management principle [1]. Here, the material can undergo

a certain amount of microdamages, i.e., due to load peaks, without a collapse of the structural integrity. During the usual working load, the material is able to repair its internal microdamages via self-healing.

In general, self-healing can be divided into autonomic and non-autonomic healing [2, 3]. Non-autonomic healing implies the usage of an external trigger like heat or UV radiation, whereas in case of autonomous healing, the damage itself triggers the onset of the healing mechanism. Furthermore, it is possible to divide also the healing mechanism into intrinsic and extrinsic [3, 4]. If the material is able to heal itself, e.g., by diffusion or reversible bonds, it is termed intrinsic healing. In contrast, extrinsic healing means that the healing mechanism is incorporated to the material, e.g., with embedded healing agents. An overview of different self-healing materials and principles is given in [5].

In the following, an extrinsic and autonomic self-healing system is considered, cf. [6], which is extended to an anisotropic model in the following. The considered system consists of a polymeric matrix material with dispersed catalysts and embedded, with monomer filled, microcapsules. If a crack propagates through the structure, the capsules rupture, the monomer flows into the crack due to capillary action and comes into contact with the catalysts. This leads to a polymerization of the monomer and thus, the structural integrity can be recovered up to a certain amount, cf. [7].

2 Theoretical Framework

For the description of the here considered multiphase material, the Theory of Porous Media (TPM) is used. This theory combines the mixture theory and the concept of volume fractions and is very suitable to model a porous solid material which is saturated with gas and/or liquid. Within the TPM every constituent has separate balance equations, which are extended by so-called total production terms, in order to consider internal interactions between the different constituents (i.e., heat exchange, phase transitions, moment exchange, etc.). But, the balance equations of the overall mixture, i.e., the summation over all constituents of the balance equations, leads to the balance equation of a one component material. For a more detailed introduction to the TPM and the historical development, the interested reader is referred to [8]. In the following the control space in the reference configuration (time $t = t_0$) is denoted by $\mathcal{B}_{0\mathrm{S}}$ with its surface $\partial\mathcal{B}_{0\mathrm{S}}$ related to the solid phase. The control space in the actual configuration (time t) is denoted by $\mathcal{B}_{\mathrm{S}}$ with its surface $\partial\mathcal{B}_{\mathrm{S}}$ also related to the solid phase. For the derivation of the equations we restrict ourselves to the actual configuration. The used literature for the theoretical basics, which are shortly presented in the following, is from [9, 10, 11, 12, 13].

2.1 Basics of the TPM

The idea of the TPM is to describe a saturated porous body, which consists of m different constituents, a solid phase and $m-1$ pore fluids, without the knowledge of the real microscopic structure. Therefore, the mixture theory is considered [14, 15]. Here, it is assumed that all constituents are statistically distributed over the whole control space and that all constituents φ^{α} ($\alpha = \mathrm{S}, \mathrm{H}, \mathrm{L}, \mathrm{G}, \mathrm{C}$) appear in every spatial point $\mathbf{x}$ of the control space $\mathcal{B}_{\mathrm{S}}$ simultaneously. Furthermore, all quantities, geometrical and physical ones (e.g., motion or deformation), are defined as statistical averages of the real quantities in the considered control space $\mathcal{B}_{\mathrm{S}}$.

In order to identify the different constituents, the concept of volume fractions is used, i.e.,

the amount of the individual constituent φ^α in a spatial point $\mathbf{x}$ can be expressed by its volume fraction $n^\alpha = \mathrm{d}v^\alpha/\mathrm{d}v$. The volume fractions are restricted by the so-called saturation condition, which states that in a spatial point x the sum over all m constituents φ^α of the volume fractions n^α has to be equal to one, i.e., $\sum_{\alpha=1}^{m} n^\alpha = 1$, cf. [8]. By use of the volume fraction, two different densities are introduced: the partial density ρ^α and the partial real density $\rho^{\alpha R}$ of the constituent φ^α. Both densities are connected by the volume fraction via $\rho^\alpha = n^\alpha \rho^{\alpha R}$. It is mentioned that even if the considered constituent is assumed to be incompressible ($\rho^{\alpha R} =$ const.), the partial density ρ^α can change due to a change of the volume fraction n^α.

2.2 Kinematics

Within the TPM the principle of superposition is applied, i.e., at a specific time t a spatial point x is simultaneously occupied by all m constituents φ^α. Furthermore, independent motions for each constituent are assumed, which leads to the fact that the material points X_α have been located in different reference positions at time $t = t_0$. Thus, independent deformation gradients $\mathbf{F}_\alpha = \partial\mathbf{x}/\partial\mathbf{X}_\alpha$ for each constituent φ^α can be defined. With that, the spatial velocity gradient is given by $\mathbf{L}_\alpha = \operatorname{grad}\mathbf{x}'_\alpha$, where $\mathbf{x}'_\alpha$ is the spatial form of the velocity, which can be additively decomposed $\mathbf{L}_\alpha = \mathbf{D}_\alpha + \mathbf{W}_\alpha$ into a symmetric part $\mathbf{D}_\alpha = 1/2(\mathbf{L}_\alpha + \mathbf{L}_\alpha^T)$ and a skew-symmetric part $\mathbf{W}_\alpha = 1/2(\mathbf{L}_\alpha - \mathbf{L}_\alpha^T)$, respectively. Due to the fact that the individual constituents perform different motions, different material time derivatives have to be taken into account. As an example, the material time derivative of an arbitrary scalar valued function is given by $\Gamma'_\alpha = \partial\Gamma/\partial t + \operatorname{grad}\Gamma \cdot \mathbf{x}'_\alpha$.

2.3 Assumptions

In order to develop a simplified five-phase model for the description of the self-healing material, some assumptions are made, cf. [6]: **1**.) Dynamic effects are neglected, i.e., the acceleration of the phases are set to be zero $\rightarrow \mathbf{x}''_\alpha = \mathbf{0}$, where $(\bullet)''_\alpha$ describes the second time derivative with respect to the corresponding constituent φ^α, in this case the acceleration; **2**.) The local temperatures of all constituents are equal and constant $\rightarrow \Theta^\alpha = \Theta$, $(\Theta^\alpha)'_\alpha = 0$; **3**.) Neglecting the volume-distributed heat supply and heat fluxes $\rightarrow r^\alpha = 0$ and $\operatorname{div}\mathbf{q}^\alpha = 0$; **4**.) Mass exchange occurs only between the liquid healing agents in connection with the catalysts and the healed material $\rightarrow \hat{\rho}^{\mathrm{H}} = -\hat{\rho}^{\mathrm{L}} - \hat{\rho}^{\mathrm{C}}$, $\hat{\rho}^{\mathrm{S}} = \hat{\rho}^{\mathrm{G}} = 0$ and $\hat{\rho}^{\mathrm{C}} =$ const.; **5**.) Only the gas phase is compressible, all other phases are assumed to be incompressible $\rightarrow \rho^{\mathrm{G}R} \neq$ const., $\rho^{\mathrm{S}R} = \rho^{\mathrm{H}R} = \rho^{\mathrm{L}R} = \rho^{\mathrm{C}R} =$ const.; **6**.) The amount of catalysts is very small in comparison to the other constituents, thus, the volume fraction of them is neglected $\rightarrow n^{\mathrm{C}} = 0$; **7**.) No diffusion of the catalyst inside the solid matrix is considered and therefore, the stress state (osmotic pressure) is neglected $\rightarrow \mathbf{x}'_{\mathrm{C}} - \mathbf{x}'_{\mathrm{S}} = \mathbf{w}_{\mathrm{CS}} = \mathbf{0}$ and $\mathbf{T}^{\mathrm{C}} = \mathbf{0}$; **8**.) The velocities of motion of the solid and healed material are equal $\rightarrow (\boldsymbol{\chi}_{\mathrm{S}})'_{\mathrm{S}} = (\boldsymbol{\chi}_{\mathrm{H}})'_{\mathrm{H}} = (\boldsymbol{\chi}_{\mathrm{H}})'_{\mathrm{S}}$; **9**.) The motion of the solid and healed material are identical except at an initial solid motion $\rightarrow \boldsymbol{\chi}_{\mathrm{H}} = \boldsymbol{\chi}_{\mathrm{S}} - \boldsymbol{\chi}_{\mathrm{S0}}$, where $\boldsymbol{\chi}_{\mathrm{S0}}$ is the solid motion before the onset of the healing process ($n^{\mathrm{H}} = 0$).

The last assumption leads to a multiplicative decomposition of the deformation gradient of the solid phase

$$\mathbf{F}_{\mathrm{S}} = \operatorname{Grad}\boldsymbol{\chi}_{\mathrm{S}} = \frac{\partial\boldsymbol{\chi}_{\mathrm{S}}}{\partial\mathbf{X}_{\mathrm{S}}} = \mathbf{F}_{\mathrm{H}}\,\mathbf{F}_{\mathrm{S0}}\,, \tag{1}$$

which was originally introduced within the framework of growth modeling in biological tissues [16, 17, 18]. Here, the decomposition is connected with the condition that the added solid like healed material is stress free as long as the body gets no further deformations after the healing started. In other words, if the specimen is healed in the deformed setting and then unloaded, the healed specimen would have remaining deformations in case of force driven deformations, or remaining stresses in case of displacement driven deformations. For further information about the multiplicative decomposition of the deformation gradient, the reader is referred to [19].

2.4 Field Equations

In the following the used field equations are shortly introduced. For a more detailed introduction see, e.g., [10, 12, 13, 20]. Due to the assumptions in section 2.3, the balance equations of energy is neglected. With respect to the balance equation of moment of momentum for non-polar continua, it turns out that the *Cauchy* stresses are symmetric, i.e., $\mathbf{T}^{\alpha} = (\mathbf{T}^{\alpha})^{T}$. Thus, the used field equations are given by the balance equations of mass of the individual constituents

$$\begin{aligned}
&(\mathrm{n}^{\mathrm{S}})'_{\mathrm{S}} + \mathrm{n}^{\mathrm{S}}\, \mathrm{div}\, \mathbf{x}'_{\mathrm{S}} = 0\,, \qquad (\mathrm{n}^{\mathrm{H}})'_{\mathrm{S}} + \mathrm{n}^{\mathrm{H}}\, \mathrm{div}\, \mathbf{x}'_{\mathrm{S}} = \frac{\hat{\rho}^{\mathrm{H}}}{\rho^{\mathrm{H}R}}\,,\\
&(\mathrm{n}^{\mathrm{L}})'_{\mathrm{L}} + \mathrm{n}^{\mathrm{L}}\, \mathrm{div}\, \mathbf{x}'_{\mathrm{L}} = -\frac{\hat{\rho}^{\mathrm{H}}}{\rho^{\mathrm{L}R}}\,, \qquad \mathrm{n}^{\mathrm{S}}\, (\mathrm{c}^{\mathrm{C}})'_{\mathrm{S}} = \hat{\rho}^{\mathrm{C}}\,,\\
&(\mathrm{n}^{\mathrm{G}})'_{\mathrm{G}} + \mathrm{n}^{\mathrm{G}}\, \mathrm{div}\, \mathbf{x}'_{\mathrm{G}} + \frac{\mathrm{n}^{\mathrm{G}}}{\rho^{\mathrm{G}R}}\, (\rho^{\mathrm{G}R})'_{\mathrm{G}} = 0\,,
\end{aligned} \tag{2}$$

the balance equations of momentum of the mixture, liquid and gas phase

$$\begin{aligned}
&\mathrm{div}\ \mathbf{T}^{\mathrm{SHLG}} + \rho^{\mathrm{SHLG}}\, \mathbf{b} = -\hat{\rho}^{\mathrm{H}}\, \mathbf{w}_{\mathrm{LS}}\,, \qquad \mathrm{div}\, \mathbf{T}^{\mathrm{L}} + \rho^{\mathrm{L}}\, \mathbf{b} = -\hat{\mathbf{p}}^{\mathrm{L}}\,,\\
&\mathrm{div}\, \mathbf{T}^{\mathrm{G}} + \rho^{\mathrm{G}}\, \mathbf{b} = -\hat{\mathbf{p}}^{\mathrm{G}}\,,
\end{aligned} \tag{3}$$

and the material time derivative of the saturation condition

$$\mathrm{div}(\mathrm{n}^{\mathrm{L}}\, \mathbf{w}_{\mathrm{LS}} + \mathrm{n}^{\mathrm{G}}\, \mathbf{w}_{\mathrm{GS}} + \mathbf{x}'_{\mathrm{S}}) + \frac{\mathrm{n}^{\mathrm{G}}}{\rho^{\mathrm{G}R}}\, (\rho^{\mathrm{G}R})'_{\mathrm{G}} - \hat{\rho}^{\mathrm{H}}\, (\frac{1}{\rho^{\mathrm{H}R}} - \frac{1}{\rho^{\mathrm{L}R}}) = 0\,. \tag{4}$$

Here, $\mathbf{b}$ denotes the body force vector and $\mathbf{w}_{\beta\mathrm{S}} = \mathbf{x}'_{\beta} - \mathbf{x}'_{\mathrm{S}}$ $(\beta = \mathrm{L}, \mathrm{G})$ is the so-called seepage velocity vector, which describes the relative velocity between the fluid phases and the solid. For the reformulation of the balance equation of mass of the catalysts $(2)_4$ as well as of the material time derivative of the saturation condition (4), it is referred to [6]. In contrast to one-component materials, the balance equations of the individual constituents φ^{α} are extended by the local production terms, denoted by the symbol $\hat{(\bullet)}$, in order to consider interactions between the different phases. But, as stated in *Truesdell's* third "metaphysical principle", cf. [21], the summation over all m constituents of the balance equations must lead to the balance equations of one component materials. Therefore, the total production terms of mass and momentum are introduced and restricted as follows:

$$\sum_{\alpha=1}^{m} \hat{\rho}^{\alpha} = 0\,, \quad \sum_{\alpha=1}^{m} \hat{\mathbf{s}}^{\alpha} = \hat{\mathbf{p}}^{\alpha} + \hat{\rho}^{\alpha}\, \mathbf{x}'_{\alpha} = 0\,. \tag{5}$$

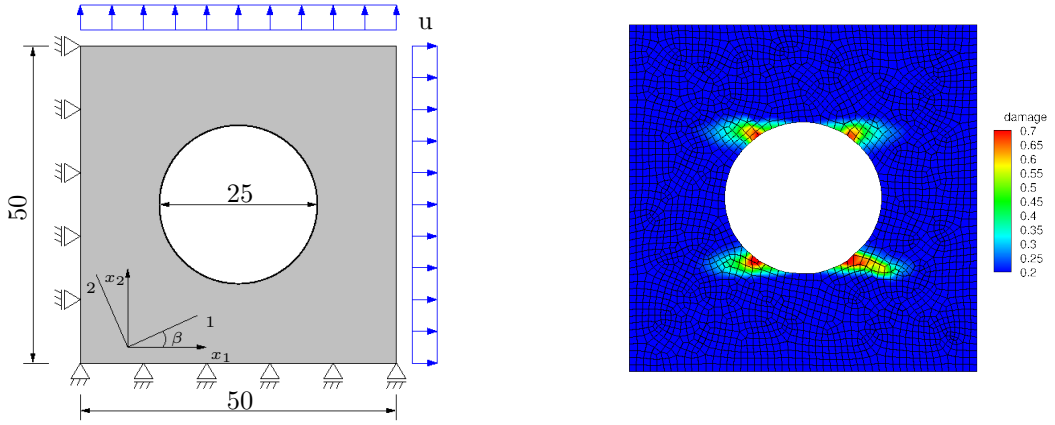

Figure 1: Illustrated boundary value problem. The applied displacement is u = 5, all dimensions are in mm (left); Plot of the damage variable at the end of the first loading cycle (right).

Here, the total production term of mass is equivalent to the local production term of mass. But, the total production term of momentum consists of the local production term of momentum $\hat{\mathbf{p}}^{\alpha}$ and an additional term, where the lower balances are exploited.

2.5 Anisotropic Material Model

To incorporate transversely isotropic behavior, the considered *Helmholtz* free energy function of the solid matrix material $\psi^{\mathrm{S}} = \psi^{\mathrm{S}}_{iso} + \psi^{\mathrm{S}}_{aniso}$ is additively split into an isotropic part ψ^{S}_{iso} and an anisotropic part $\psi^{\mathrm{S}}_{aniso}$, which are given by

$$\begin{aligned} \psi^{\mathrm{S}}_{iso} &= \frac{1}{\rho^{\mathrm{SR}}}(1 - D^{\mathrm{S}}) \left[\frac{1}{2}\,\lambda^{\mathrm{S}} (\log J_{\mathrm{S}})^2 - \mu^{\mathrm{S}} \log J_{\mathrm{S}} + \frac{1}{2}\,\mu^{\mathrm{S}} (\mathbf{C}_{\mathrm{S}} \cdot \mathbf{I} - 3) \right] , \\ \psi^{\mathrm{S}}_{aniso} &= \frac{1}{\rho^{\mathrm{SR}}} \left\{ \frac{k_1}{2\,k_2} \{ \exp[k_2 (I_4 - 1)^2] - 1 \} \right\} \qquad \text{with} \quad I_4 = \mathbf{a}_0 \cdot \mathbf{C}_{\mathrm{S}}\, \mathbf{a}_0 \,. \end{aligned} \tag{6}$$

Here, λ^{S} and μ^{S} are the *Lamé* parameters, $\mathbf{C}_{\mathrm{S}} = \mathbf{F}_{\mathrm{S}}^{T}\, \mathbf{F}_{\mathrm{S}}$ is the right *Cauchy-Green* deformation tensor, $J_{\mathrm{S}} = \det \mathbf{F}_{\mathrm{S}}$ is the *Jacobian*, k_1 and k_2 are material parameters, and $\mathbf{a}_0$ is the preferred direction vector. The term $(1 - D^{\mathrm{S}})$, where D^{S} is the internal damage variable, is used in order to take discontinuous damage behavior into account, cf. [22]. Damage is only considered in the isotropic part, i.e., damage takes only place in the matrix material and not in the reinforcement.

3 Example

As numerical example a plate with a hole is considered. The mechanical behavior is given as transversely isotropic, whereas the preferred fiber direction is in x_1-direction, i.e., $\beta = 0$. In Tab. 1 the initial material parameters are listed.

After 30 seconds the full displacement of u = 5 mm is applied to the specimen followed by an unloading down to 5 % of the total displacements. After that, the healing mechanism is active for three hours, before the full displacement is applied within 30 seconds for the second time.

Fig. 2 shows the anisotropic behavior of the specimen in x_1- and x_2-direction. In x_1-direction, the exponential behavior due to the reinforcement can be observed. In contrast, the slope of

Table 1: Initial material parameters.

	matrix S	healed material H	healing agents L	gas G	catalysts C	[–]
Young's modulus E^α	3.0e+9	3.4e+9	–	–	–	Pa
real density $\rho^{\alpha R}$	1.2e+3	0.98e+3	0.98e+3	1.2	–	kg/m^3
initial volume fraction n^α	0.69	0.0	0.3	0.01	–	–
initial concentration c^α	–	–	–	–	1.0	$\times$100 %
stress-like parameter k_1	1.0e+6	–	–	–	–	Pa
dimensionless parameter k_2	1.0e+1	–	–	–	–	–

the force-displacement curve in x_2-direction decreases due to the damage in the isotropic matrix material. Furthermore, the force-displacement curve in x_2-direction during the reloading is nearly the same as during the first loading, whereas in x_1-direction the reloading curve is just slightly higher than the unloading curve. Thus, the influence of damage and healing is higher in direction perpendicular to the reinforcement, as it was expected.

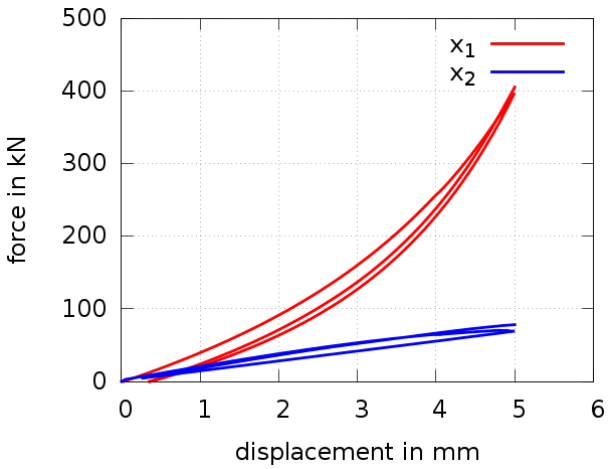

Figure 2: Diagram of force-displacement curves in x_1- and x_2-direction for a loading-unloading-healing-reloading cycle.

4 Conclusion

This work focuses on the numerical simulation of damage and self-healing effects in a fiber-reinforced polymer. The developed multiphase model, based on the Theory of Porous Media, consists of the following five phases: the solid matrix material with imbedded catalysts, the liquid healing material (healing agent), the solid healed material, and the gas phase. In order to take the unidirectional reinforcement into account, the polymeric matrix is considered as transversely isotropic material, i.e., the free energy function is additively decomposed into an isotropic and anisotropic part. Concerning the constitutive relations, the (1d) approach is used to describe

the damage behavior of the solid matrix material as well as of the solid-like healed material. It is mentioned that the damage function has only an influence on the isotropic part of the solid matrix material, because damage of the matrix material (like delamination or microcracks inside the polymer) is what happens first and leads to failure of the structural part.

The presented results show the strong anisotropic behavior of the fiber-reinforced self-healing polymer. Furthermore, due to the fact that damage and healing are subjected to the isotropic matrix material, distinct healing effects in x_1- and x_2-direction can be observed.

Acknowledgement This work has been supported by the German Research Society (DFG) within the Priority Program SPP 1568 "Design and Generic Principles of Self-healing Materials" under the grant numbers BL 417/7-2 and Schr 570/26-2.

REFERENCES

[1] S. van der Zwaag. *Self healing materials: an alternative approach to 20 centuries of materials science*. Springer, Dordrecht, 2007.

[2] S. K. Gosh. *Self-healing materials*, chapter Self-healing materials: fundamentals, design strategies, and applications, pages 1–28. WILEY-VCH, 2009.

[3] M. D. Hager, P. Greil, C. Leyens, S. van der Zwaag, and U. S. Schubert. Self-healing materials. 22:5424–5430, 2010.

[4] Y. C. Yuan, T. Yin, M. Z. Rong, and M. Q. Zhang. Self healing in polymers and polymer composites. concept, realization and outlook: a review. 2:238–250, 2008.

[5] S. Grigoleit. Überblick über Selbstheilende Materialien. Technical report, Frauenhofer-Institut für Naturwissenschaftlich-Technische Trendanalysen (INT), 2010.

[6] S. Specht, J. Bluhm, and J. Schröder. *Self-healing materials*, volume 273 of *Advances in Polymer Science*, chapter Continuum mechanical description of an extrinsic and autonomous self-healing material based on the theory of porous media, pages 143–184. Springer, 2016.

[7] S. R. White, N. R. Sottos, P. H. Geubelle, J. S. Moore, M. R. Kessler, S. R. Sriram, E. N. Brown, and S. Viswanathan. Autonomic healing of polymer composites. *Nature*, 409:794–797, 2001.

[8] R. de Boer. *Theory of porous media*. Springer, 2000.

[9] R. de Boer and W. Ehlers. Theorie der Mehrkomponentenkontinua mit Anwendung auf bodenmechanische Probleme. Technical report, Universität - Gesamthochschule - Essen, 1986.

[10] W. Ehlers. Grundlegende Konzepte in der Theorie Poröser Medien. *Technische Mechanik*, 16:63–76, 1996.

[11] J. Bluhm. *Porous media*, chapter Modelling of saturated thermo-elastic porous solids with different phase temperatures, pages 87–118. Springer, 2002.

[12] W. Ehlers. *Porous media*, chapter Foundations of multiphasic and porous materials, pages 3–86. Springer, 2002.

[13] W. Ehlers. *Poröse Medien - ein kontinuummechanisches Modell auf der Basis der Mischungstheorie*. Nachdruck der Habilitationsschrift aus dem Jahr 1989, Universität - Gesamthochschule - Essen, 2012.

[14] R. M. Bowen. Incompressible porous media models by use of the theory of mixtures. *International Journal of Engineering Science*, 18:1129–1148, 1980.

[15] R. M. Bowen. Compressible porous media models by use of the theory of mixtures. *International Journal of Engineering Science*, 20:697–735, 1982.

[16] E. Rodriguez, A. Hoger, and A. McCulloch. Stress-dependent finite growth in soft elastic tissues. *Journal of Biomechanics*, 27:455–467, 1994.

[17] J. Humphrey and K. Rajagopal. A constrained mixture model for growth and remodelling of soft tissues. 12:407–430, 2002.

[18] G. A. Ateshian and T. Ricken. Multigenerational interstitial growth of biological tissues. *Biomechanics and Modeling in Mechanobiology*, 9:689–702, 2010.

[19] J. Bluhm, T. Ricken, and W. M. Blossfeld. Dynamic phase transition border under freezing-thawing load in porous media – a multiphase description. Technical Report 47, Institut of Mechanics, University of Duisburg-Essen, Germany, 2009.

[20] A. Y. Acartürk. *Simulation of charged hydrated porous materials*. PhD thesis, Universität Stuttgart, 2009.

[21] C. Truesdell. *Rational thermodynamics*. Springer, 2nd edition, 1984.

[22] L. M. Kachanov. Time of the rupture process under creep conditions. *Izvestija Akademii Nauk Sojuza Sovetskich Socialisticeskich Republiki (SSSR) Otdelenie Techniceskich Nauk (Moskra)*, 8:26–31, 1958.

Finite element analysis of piezolaminated structures with both geometric and electroelastic material nonlinearities

Shun-Qi Zhang[*], Shu-Yang Zhang[*], Min Chen[†] and Jing Bai[*]

[*] School of Mechanical Engineering, Northwestern Polytechnical University,
West Youyi Road 127, 710072 Xi'an, P.R. China
e-mail: sqzhang@nwpu.edu.cn, http://www. nwpu.edu.cn

[†] Department of Industrial Design, Xi'an Jiaotong – Liverpool University,
Chongwen Road, 215123, Suzhou, China
e-mail: min.chen@xjtlu.edu.cn, web page: http://www.xjtlu.edu.cn

ABSTRACT

Piezoelectric laminated smart structures can be subjected to strong driving electric field, which may result in large displacements and rotations. In one hand, piezoelectric materials usually behave very significant material nonlinear effects under strong electric fields. On the other hand, thin-walled structures undergoing large displacements and rotations exist nonnegligible geometric nonlinearity.

In order to give a precise prediction of piezolaminated smart structures under large electric field, this paper develops a finite element (FE) model accounting for material nonlinearity (piezoelectric part) and geometric nonlinearity based on the first order shear deformation (FSOD) hypothesis. The proposed FE model is first validated by both experimental and numerical examples from the literature. Afterwards, it is applied to simulate for plate and shell structures with multiple piezoelectric patches under strong applied electric field. From the simulation results, it shows that large discrepancies occur between linear and nonlinear predictions for piezoelectric laminated structures driving at strong electric field. Therefore, both material and geometric nonlinearities should be taken into account for piezoelectric structures under strong electric.

REFERENCES

[1] S. Q. Zhang and R. Schmidt, "Static and dynamic FE analysis of piezoelectric integrated thin-walled composite structures with large rotations", Compos. Struct., Vol. 112, pp. 345-357, (2014).

[2] S. Kapuria and M.Y. Yasin, "Active vibration control of piezolaminated composite plates considering strong electric field nonlinearity", AIAA J., 53(3):603–616, 2015.

VIII ECCOMAS Thematic Conference on Smart Structures and Materials
SMART 2017
A. Güemes, A. Benjeddou, J. Rodellar and J. Leng (Eds)

LINEAR RESPONSE OF A PLANAR FGM BEAM WITH NON-LINEAR VARIATION OF THE MECHANICAL PROPERTIES

GIUSEPPE BALDUZZI*, MEHDI AMINBAGHAI*, AND JOSEF FÜSSL*

*Institute for Mechanics of Materials and Structures (IMWS)
Vienna University of Technology
Karlsplatz 13/202 A-1040 Vienna, Austria
e-mail: Giuseppe.Balduzzi@tuwien.ac.at, Mehdi.Aminbaghai@tuwien.ac.at,
Josef.Fuessl@tuwien.ac.at

Key words: Functionally Graded Material (FGM) beam, First order Shear Deformation Theory (FSDT), non-linear distribution of stiffness, enhanced beam constitutive relation

Abstract. This contribution aims at proposing an effective First order Shear Deformation Theory (FSDT) capable to tackle the non-trivial effects that a continuous variation of the mechanical properties induces on stresses, displacement, and stiffness distributions within a planar beam made of Functionally Graded Material (FGM). In greater detail, the beam model assumes the Timoshenko beam kinematics and it results naturally expressed by six Ordinary Differential Equations (ODEs) considering both cross-section displacements and internal forces as unknowns. Furthermore, exploiting a recently proposed analysis tool, the paper provides also effective tools for the accurate reconstruction of cross-section stress distributions (with special emphasis on shear stresses) and the beam stiffness estimation. A simple numerical example demonstrates that the proposed beam model can catch with good accuracy the main effects induced by variations of the mechanical properties, allowing for a simple and effective modeling of a large class of structures and opening the doors to a new family of enhanced beam models.

1 INTRODUCTION

Functionally Graded Material (FGM) beams and plates are more and more used in several engineering fields since they allow for a optimal distribution of strength and stiffness within the structure leading, as an example, to the maximal strength exploitation and significant cost saving. Furthermore, this trend benefits also from new additive-layer technologies that allow for complex object manufacture without significant increase of production costs. Conversely, also the presence of defects (e.g., a local deviation of fiber direction) could be seen as a smooth variation of the mechanical or geometrical properties of the structural element. In both cases, an effective modeling is mandatory for an accurate description of the structural element response.

According to a consolidated practice in engineering field, the most natural choice for the modeling of such structures is the usage of 1D (beam) or 2D (plate) Partial Differential Equations

(PDEs). Unfortunately, standard models are developed for prismatic bodies with constant mechanical properties along the axis/mid-plane and turn out to be too coarse and inadequate for enhanced engineering applications. As an example, a non-homogeneous and non-symmetric distribution of the mechanical properties within the beam body induces significant transversal displacements in a beam subjected to axial load. Since standard beams model separately the axial and the shear bending problem, they are not able to catch the so far described effect and, therefore, ad-hoc models must be developed.

Furthermore, even limiting to FGM beams where the mechanical properties vary only along the thickness, the shear stress distribution is significantly different from both homogeneous and layered beams [1, 2] and accurate evaluations of both the shear correction factor and the shear stiffness are required. Therefore, extending the attention to FGM beams where the mechanical properties vary both along the thickness and the axis, the shear stress distribution can vary significantly from one cross-section to the other [3, 4]. Consequently, also the shear correction factor varies along the beam axis leading the shear stiffness to have a non-trivial distribution along the beam axis [4].

Last but not least, a recent paper has highlighted that any variation of the geometry and/or mechanical properties along the beam axis deeply influences the cross-section shear stress distribution that, furthermore, turns out to depend on all the internal forces [5]. As a consequence, also the shear deformation depends on all internal forces and, for symmetry of the constitutive relations, both axial elongation and curvature depend on shear internal force [6, 5]. In other words, according to the notation introduced by [6], the beam's constitutive relations are represented by a full matrix whereas, for standard prismatic beams, they are represented by a diagonal matrix.

This paper aims at proposing a First order Shear Deformation Theory (FSDT) capable to tackle the non-trivial effects that a continuous variation of the mechanical properties induces on stresses, displacement and stiffness distributions within a planar FGM beam. In greater detail, the beam model assumes the Timoshenko beam kinematics and it results naturally expressed by six linear Ordinary Differential Equations (ODEs) with non-constant coefficients where both cross-section displacements and internal forces are the problem unknowns. Furthermore, exploiting a recently proposed modeling strategy [5], the paper provides also an effective tool for the beam stiffness estimation based on an accurate cross-section stress analysis.

The paper is structured as follows. Section 2 resumes the beam model's ODEs proposed in [5] and specializes the stress representation to FGM beams with general variation of mechanical properties. Section 3 discusses a simple numerical example that shows the main capabilities of the proposed beam model. Section 4 reports final remarks and delineate future research developments.

2 1D PLANAR BEAM MODEL

The model consists of 5 main steps detailed in the following subsections: (1) the beam's mechanical properties evaluation (2) the compatibility equations definition, (3)the equilibrium equations definition, (4) the stress representation, and (5) the simplified constitutive relations definition. The herein presented beam model ODEs was derived according to the procedure detailed in [6, 5]. For this reason, details on derivation path are not given in this section and

readers may refer to the cited literature for further details.

2.1 Beam's mechanical properties and loads

The object of our study is a planar rectangular beam with non-homogeneous and non-linear distribution of the mechanical properties both within the thickness and along the beam axis. Furthermore, we assume that it behaves under the hypothesis of small displacements and plane stress state.

The horizontal stiffness and the first order of stiffness are defined as

$$A^*(x) = b\int_{h_1}^{h_{n+1}} E(x,y)\,dy; \quad S^*(x) = b\int_{h_1}^{h_{n+1}} E(x,y)\,y dy \tag{1}$$

Consequently, the beam centerline reads

$$c(x) = \frac{S^*(x)}{A^*(x)} \tag{2}$$

Thereafter, the bending stiffness reads

$$I^*(x) = b\int_{h_1}^{h_{n+1}} E(y)\,(y - c(x))^2\,dy \tag{3}$$

Finally, we define the horizontal, vertical, and bending resulting loads acting on the cross-section as $q(x)$, $p(x)$, and $m(x)$, respectively.

2.2 Compatibility equations

We assume the kinematics usually adopted for prismatic Timoshenko beam models. Therefore, the 2D displacement field $\boldsymbol{s}(x,y)$ is approximated as

$$\boldsymbol{s}(x,y) \approx \left\{ \begin{array}{c} u(x) + (y - c(x))\,\varphi(x) \\ v(x) \end{array} \right\} \tag{4}$$

where $\varphi(x)$, $u(x)$, and $v(x)$ indicate the rotation, the horizontal, and the vertical displacements of the cross-section, respectively.

Furthermore, indicating the horizontal strain, the curvature, and the shear strain as $\varepsilon_0(x)$, $\chi(x)$, and $\gamma(x)$, respectively, the beam compatibility is expressed through the following ODEs

$$\varepsilon_0(x) = u'(x) - c'(x)\,\varphi(x) \tag{5}$$

$$\chi(x) = -\varphi'(x) \tag{6}$$

$$\gamma(x) = v'(x) + \varphi(x) \tag{7}$$

2.3 Equilibrium equations

Indicating the bending moment, the horizontal, and the vertical internal forces as, $M(x)$, $H(x)$, and $V(x)$, respectively, the equilibrium ODEs read

$$H'(x) = -q(x) \tag{8}$$

$$M'(x) - H(x)\cdot c'(x) + V(x) = -m(x) \tag{9}$$

$$V'(x) = -p(x) \tag{10}$$

2.4 Stress representation

Introducing the horizontal-stress distribution functions $d_\sigma^H(x,y)$ and $d_\sigma^M(x,y)$ defined as

$$d_\sigma^H(x,y) = \frac{E(x,y)}{A^*(x)}; \quad d_\sigma^M(x,y) = \frac{E(x,y)}{I^*(x)}(c(x)-y) \tag{11}$$

the horizontal stress distribution can be defined as follows

$$\sigma_x(x,y) = d_\sigma^H(x,y)\,H(x) + d_\sigma^M(x,y)\,M(x) \tag{12}$$

In order to recover the shear stress distribution within the cross-section we resort to a procedure similar to the one proposed initially by Jourawski [7], used among others by [8], and nowadays adopted in most standard literature [9]. After few simplifications and integration with respect to the y variable, the horizontal equilibrium of a slice of infinitesimal length dx of the FGM beam reads

$$\tau(x,y) = -\int_{h_1}^{y} \sigma_{x,x}(x,t)\,dt \tag{13}$$

where the notation $(\cdot)_{,x}$ indicates partial derivatives with respect to the x variable. Inserting the horizontal stresses definition (12) into Equation (13), calculating the derivative of σ_x, recalling the beam equilibrium equations (8) and (9), and neglecting the contributions of loads and beam eccentricity (i.e., assuming $q(x) = m(x) = c'(x) = 0$) yield the following expression

$$\tau(x,y) = -\int_{h_1}^{y} d_\sigma^H{}_{,x}(x,t)\,H(x)\,dt - \int_{h_1}^{y} d_\sigma^M{}_{,x}(x,t)\,M(x)\,dt - \int_{h_1}^{y} d_\sigma^M(x,t)\,V(x)\,dt \tag{14}$$

It is worth highlighting once more that Equation (14) leads the shear stress distribution to depend on all the internal forces.

Aiming at providing an expression of shear stress distribution similar to (12), we define the shear stress distributions induced by a unitary vertical internal force $V(x)$ as

$$d_\tau^V(x,y) = -\int_{h_1}^{y} d_\sigma^M(x,t)\;dt \tag{15}$$

Consistently, we define the shear stress distributions induced by a unitary bending moment $M(x)$ as

$$d_\tau^M(x,y) = -\int_{h_1}^{y} d_\sigma^M{}_{,x}(x,t)\,dt \tag{16}$$

Finally, we define the shear stress distributions induced by a unitary horizontal internal force $H(x)$ as

$$d_\tau^H(x,y) = \tilde{d}_\tau^H(x,y) - D_\tau^H(x)\,d_\tau^V(x,y) \tag{17}$$

where

$$\tilde{d}_\tau^H(x,y) = -\int_{h_1}^{y} d_\sigma^H{}_{,x}(x,t)\,dt \tag{18}$$

and its resulting area reads

$$D_\tau^H(x) = \int_{h_1}^{h_{n+1}} \tilde{d}_\tau^H(x,y)\,dy \tag{19}$$

According to all so far introduced definitions, the shear stress distribution can be defined as follows

$$\tau(x,y) = d_\tau^H(x,y)\,H(x) + d_\tau^M(x,y)\,M(x) + d_\tau^V(x,y)\,V(x) \tag{20}$$

2.5 Simplified constitutive relations

To complete the Timoshenko-like beam model we introduce some simplified constitutive relations that define the generalized strains as a function of the internal forces.

Therefore, we consider the stress potential, defined as follows

$$\Psi^{*}\left(x,y\right)=\frac{1}{2}\left(\frac{\sigma_{x}^{2}\left(x,y\right)}{E\left(x,y\right)}+\frac{\tau^{2}\left(x,y\right)}{G\left(x,y\right)}\right) \tag{21}$$

Substituting the stress recovery relations (12) and (20) in Equation (21), the strains $\varepsilon_{0}\left(x\right)$, $\chi\left(x\right)$, and $\gamma\left(x\right)$ result as the derivatives of the stress potential with respect to the corresponding internal forces $H\left(x\right)$, $M\left(x\right)$, and $V\left(x\right)$, respectively

$$\begin{aligned}\varepsilon_{0}\left(x\right)=&b\int_{h_{1}}^{h_{n+1}}\frac{\partial\Psi^{*}\left(x,y\right)}{\partial H\left(x\right)}dy=\\&\varepsilon_{H}\left(x\right)H\left(x\right)+\varepsilon_{M}\left(x\right)M\left(x\right)+\varepsilon_{V}\left(x\right)V\left(x\right)\end{aligned} \tag{22}$$

$$\begin{aligned}\chi\left(x\right)=&b\int_{h_{1}}^{h_{n+1}}\frac{\partial\Psi^{*}\left(x,y\right)}{\partial M\left(x\right)}dy=\\&\chi_{H}\left(x\right)H\left(x\right)+\chi_{M}\left(x\right)M\left(x\right)+\chi_{V}\left(x\right)V\left(x\right)\end{aligned} \tag{23}$$

$$\begin{aligned}\gamma\left(x\right)=&b\int_{h_{1}}^{h_{n+1}}\frac{\partial\Psi^{*}\left(x,y\right)}{\partial V\left(x\right)}dy=\\&\gamma_{H}\left(x\right)H\left(x\right)+\gamma_{M}\left(x\right)M\left(x\right)+\gamma_{V}\left(x\right)V\left(x\right)\end{aligned} \tag{24}$$

where

$$\varepsilon_{H}\left(x\right)=\quad b\int_{h_{1}}^{h_{n+1}}\left(\frac{\left(d_{\sigma}^{H}(x,y)\right)^{2}}{E(x,y)}+\frac{\left(d_{\tau}^{H}(x,y)\right)^{2}}{G(x,y)}\right)dy \tag{25}$$

$$\varepsilon_{M}\left(x\right)=\chi_{H}\left(x\right)=\quad b\int_{h_{1}}^{h_{n+1}}\frac{d_{\sigma}^{H}(x,y)d_{\sigma}^{M}(x,y)}{E(x,y)}dy+b\int_{h_{1}}^{h_{n+1}}\frac{d_{\tau}^{H}(x,y)d_{\tau}^{M}(x,y)}{G(x,y)}dy \tag{26}$$

$$\varepsilon_{V}\left(x\right)=\gamma_{H}\left(x\right)=\quad b\int_{h_{1}}^{h_{n+1}}\frac{d_{\tau}^{H}(x,y)d_{\tau}^{M}(x,y)}{G(x,y)}dy \tag{27}$$

$$\chi_{M}\left(x\right)=\quad b\int_{h_{1}}^{h_{n+1}}\left(\frac{\left(d_{\sigma}^{M}(x,y)\right)^{2}}{E(x,y)}+\frac{\left(d_{\tau}^{M}(x,y)\right)^{2}}{G(x,y)}\right)dy \tag{28}$$

$$\chi_{V}\left(x\right)=\gamma_{M}\left(x\right)=\quad b\int_{h_{1}}^{h_{n+1}}\frac{d_{\tau}^{M}(x,y)d_{\tau}^{V}(x,y)}{G(x,y)}dy \tag{29}$$

$$\gamma_{V}\left(x\right)=\quad b\int_{h_{1}}^{h_{n+1}}\frac{\left(d_{\tau}^{V}(x,y)\right)^{2}}{G(x,y)}dy \tag{30}$$

2.6 Remarks on beam model's ODEs

In is worth noticing what follows.

- Despite the beam body is rectangular (as usual for planar prismatic beams), the continuous variation of the mechanical properties leads the position of the cross-section centroid to change along the beams axis. As a consequence, the centerline definition (2) is non-trivial and leads the modeling of FGM beams to be closer to non-prismatic than to prismatic beams.

- Despite the strong analogy with prismatic beam coefficients, Definitions (1) and (3) are not sufficient to define the stiffness of the non-prismatic beam, as illustrated in Section 2.5.

- Definitions (16) (17) leads

$$\int_{h_1}^{h_{n+1}} d_\tau^H(x,y)\,dy = \int_{h_1}^{h_{n+1}} d_\tau^M(x,y)\,dy = 0 \tag{31}$$

  As a consequence, only the shear-stress distribution functions $d_\tau^V(x,y)$ depends on the vertical force $V(x)$, leading to a simpler stress representation.

- Equation (22) highlights that curvature and shear strains depend on both bending moment and vertical internal force through a non-trivial relation, substantially different from the one that governs the prismatic beam. Furthermore, Equation (22) also highlights that horizontal and bending stiffnesses depend on both the Young's E and the shear G moduli.

- Following the notation adopted by Gimena et al. [10] the beam model's ODEs (5), (8), and (22) can be expressed as

$$\begin{Bmatrix} H'(x) \\ V'(x) \\ M'(x) \\ \varphi'(x) \\ v'(x) \\ u'(x) \end{Bmatrix} = \left[\begin{array}{ccc|ccc} 0 & 0 & 0 & & & \\ 0 & 0 & 0 & & \mathbf{0} & \\ -c' & 1 & 0 & & & \\ \hline \chi_H & \chi_V & \chi_M & 0 & 0 & 0 \\ \gamma_H & \gamma_V & \gamma_M & -1 & 0 & 0 \\ \varepsilon_H & \varepsilon_V & \varepsilon_M & c' & 0 & 0 \end{array}\right] \begin{Bmatrix} H(x) \\ V(x) \\ M(x) \\ \varphi(x) \\ v(x) \\ u(x) \end{Bmatrix} - \begin{Bmatrix} q(x) \\ p(x) \\ m(x) \\ 0 \\ 0 \\ 0 \end{Bmatrix} \tag{32}$$

  The resulting ODEs have the same structure as the ones obtained by Balduzzi et al. [6], but differ due to a more complex definitions of both the centerline $c(x)$ and the constitutive relations. For further comments on the resulting ODEs, readers may refer to Balduzzi et al. [6, 5].

3 NUMERICAL RESULTS

Let us consider the layered FGM beam depicted in Figure 1 where $L = 500\,\text{mm}$, $h_1 = 0\,\text{mm}$, $h_2 = 4\,\text{mm}$, $h_3 = 96\,\text{mm}$, $h_4 = 100\,\text{mm}$, $M = 1\,\text{Nm}$, $E_{min} = 10\,000\,\text{MPa}$, $E_{max} = 500\,000\,\text{MPa}$, and $E_{core} = 5\,000\,\text{MPa}$. Specifically, in bottom and top layers the Young's modulus varies linearly between E_{max} and E_{min} and vice-versa whereas the core has constant mechanical properties. Finally, we assume that the Poisson's coefficient is constant within all the layers and $\nu = 0.25$.

In order to provide a reference solution, the whole beam body has been modeled with 2D Finite Element (FE), through the commercial software ABAQUS Sim [11]. Specifically, we approximate the bottom and top layers with a sequence of 21 equal overlapping wedges with piecewise constant mechanical properties. Furthermore, bottom and top layers are discretized with a un-structured mesh of triangles with characteristic element size of 1mm whereas the core is modeled with a structured mesh of squared elements with the edge size equal to 1mm. The resulting mesh turns out to be made of 56 560 elements.

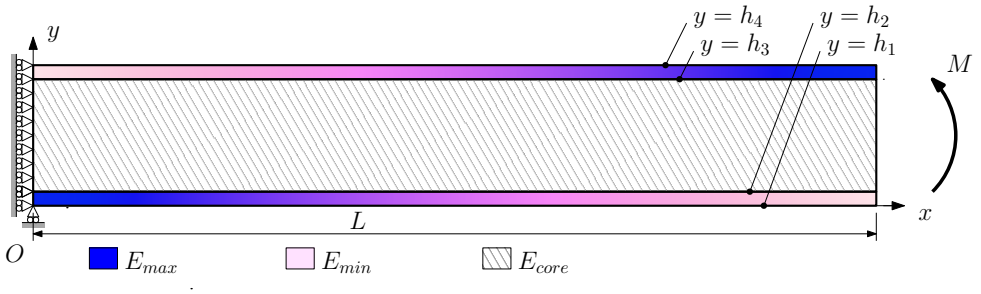

Figure 1: Multilayered FGM beam: geometry and mechanical properties definition.

3.1 Stress distribution

We focus on two cross-sections A_1 and A_2, located at $x = 150\,\text{mm}$ and $x = 250\,\text{mm}$. Figures 2 and 3 depict the cross-section distribution of axial and shear stresses.

It is worth noticing that the approximation of the FGM layers adopted in reference solution introduce some spurious oscillations in both bottom and top layers, nevertheless the proposed model and the reference solution are in good agreement in describing the stresses within these layers. In greater detail, the proposed model predicts the axial stress with errors smaller than 5% whereas the maximal error in shear stress estimation is near 15% (see Figure 3(a), interlayer surfaces).

It is worth recalling that the reference solution indicates that the shear stress is absolutely not-negligible since within the beam's core, the ratio between maximal shear and axial stresses is around 1/3. Conversely, the beam results to be under a simple bending load since the material weight is neglected and the initial cross-section is constrained as depicted in Figure 1. Therefore, according to both standard [12, 9] and advanced [3, 4] planar beam models, only axial stresses should resist to the applied load and shear stress should vanish at least in the region far from initial and final cross-sections. Roughly speaking, the presence of so big shear stresses within the considered beam body can be justified by the fact that axial stress migrates according to the stiffness variation along the beam axis and non-vanishing shear stress appears in order to guarantee local equilibrium (see Equation (13)).

As a consequence, it is evident that the prismatic homogeneous beam models existing in literature provide misleading information whereas the herein proposed one has the capability to provide a reasonable description of both axial and shear stresses, resulting therefore significantly more accurate.

3.2 Displacement distribution

Figure 4 depicts the mean vales of the displacements evaluated along the beam axis. It is worth noticing that the proposed beam model estimates the maximal absolute-value of both horizontal and vertical displacements (occurring at $x = 250\,\text{mm}$ and $x = 500\,\text{mm}$, respectively) with an error of 5%.

Once more, both standard and advanced beam models tackle separately the axial and the shear-bending problems. Therefore, for the considered load, they predict vanishing horizontal displacements. Conversely, the proposed beam model has the capability to effectively tackle the coupling between axial and shear-bending problems, providing more accurate displacement's

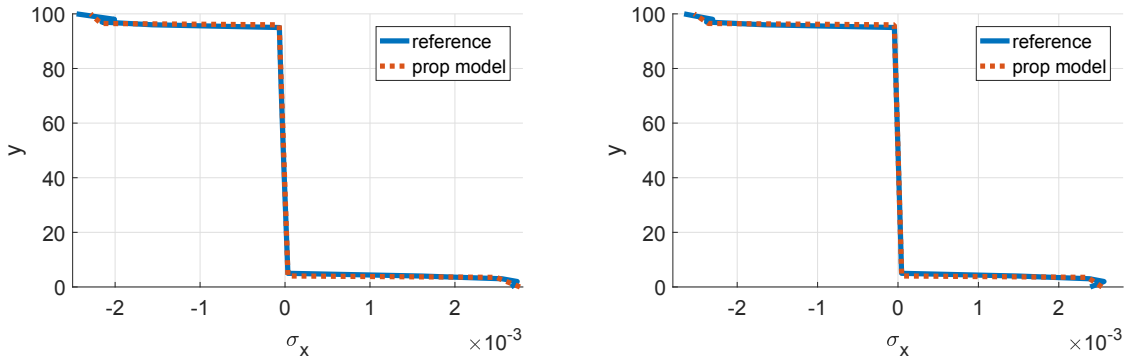

(a) A_1, $x = 150$ (b) A_2, $x = 250$

Figure 2: Axial-stress cross-section distributions

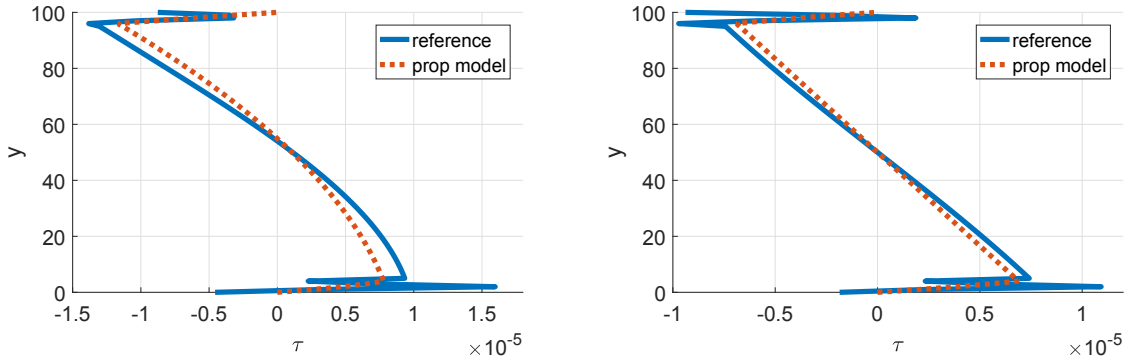

(a) A_1, $x = 150$ (b) A_2, $x = 250$

Figure 3: Shear-stress cross-section distributions

estimations.

This simple observation confirms that the prismatic homogeneous beam models provide misleading information whereas the herein proposed one has the capability to provide a reasonable description of displacements, resulting therefore significantly more accurate. Furthermore, the results so far illustrated highlights that, aiming at tackling effectively the variation of mechanical properties, prismatic homogeneous beam ODEs must be enriched with suitable additional terms and not only with varying coefficients.

Finally, Figure 5 depicts the cross-section distribution of both horizontal and vertical displacements evaluated at $x = 150\,\text{mm}$. It is evident that the distribution of vertical displacements (Figure 5(b)) is highly non-linear whereas the proposed model only has the capability to estimate the vertical-displacement's mean value. Since the Timoshenko kinematics does not allow to catch higher order effects (clearly not negligible in the considered example), it is reasonable to suppose that the model's fundamental hypothesis represents the most important error source that could be easily eliminated considering more refined kinematics.

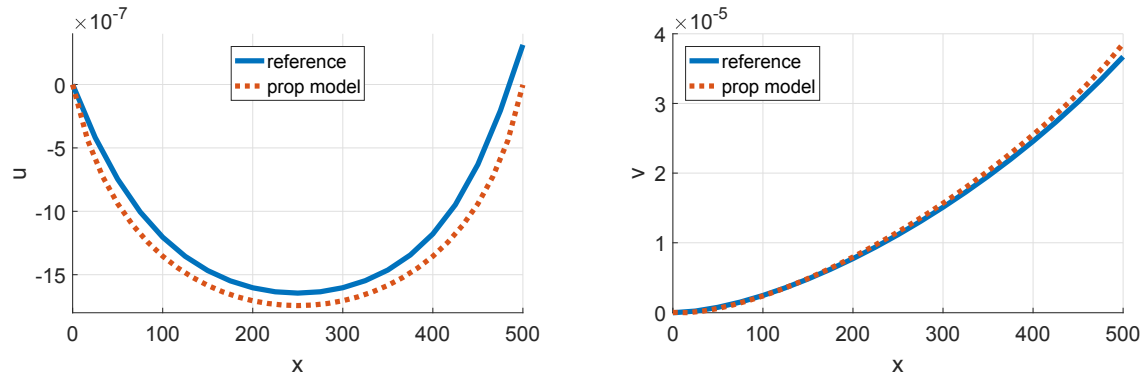

(a) $u\,(x)$ (b) $v\,(x)$

Figure 4: Mean value of cross-section displacements

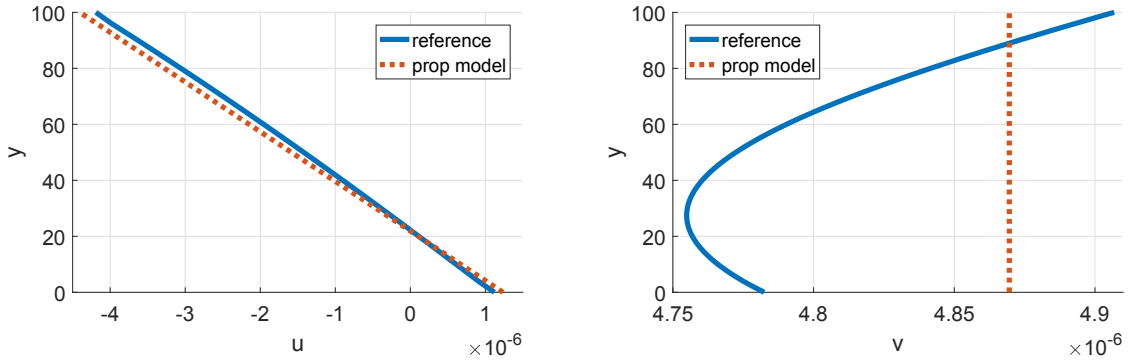

(a) $u\,(150, y)$ (b) $v\,(150, y)$

Figure 5: Distribution of cross-section displacements

4 FINAL REMARKS

This paper proposed a simple FSDT for a planar FGM beams with non-linear variation of the mechanical properties. The numerical results highlight that it has the capability to tackle effectively (i) the variations of the cross-section centroid position, (ii) the non trivial stress distribution, (iii) the complex beam constitutive relations, and (iv) the nontrivial distribution of stiffness and displacements. The main model limitations are strictly related to the hypotheses behind beam model. In particular, it neglects all the boundary effects and the higher order effects.

Further developments of the present work will include the generalization to plate models and the consideration of higher order kinematics.

ACKNOWLEDGMENTS

This work was funded by the Austrian Science Found (FWF): M 2009-N32.

References

[1] Vo, T.P., Thai, H.T., Nguyen, T.K., Inam, F., and Lee, J. Static behaviour of functionally graded sandwich beams using a quasi-3D theory. *Composites Part B*, 68:59–74, 2015.

[2] Giunta, G., Belouettar, S., and Ferreira, A.J.M. A static analysis of three-dimensional functionally graded beams by hierarchical modelling and a collocation meshless solution method. *Acta Mech.*, 227(4):969–991, 2016.

[3] Kutiš, V., Murin, J., Belak, R., and Paulech, J. Beam element with spatial variation of material properties for multiphysics analysis of functionally graded materials. *Comput. Struct.*, 89(11):1192–1205, 2011.

[4] Murin, J., Aminbaghai, M., Hrabovskỳ, J., Kutiš, V., and Kugler, S. Modal analysis of the FGM beams with effect of the shear correction function. *Composites Part B*, 45(1): 1575–1582, 2013.

[5] Balduzzi, G., Aminbaghai, M., Auricchio, F., and Füssl, J. Planar Timoshenko-like model for multilayer non-prismatic beams. *Int. J. Mech. Mater. Des.*, IN PRESS 1–20, 2017. doi: 10.1007/s10999-016-9360-3.

[6] Balduzzi, G., Aminbaghai, M., Sacco, E., Füssl, J., Eberhardsteiner, J., and Auricchio, F. Non-prismatic beams: a simple and effective Timoshenko-like model. *Int. J. Solids Struct.*, 90:236–250, 2016.

[7] Jourawski, D.J. Sur le résistance dun corps prismatique et dune piece composée en bois ou on tôle de fer à une force perpendiculaire à leur longeur. In *Annales des Ponts et Chaussées*, volume 12, pages 328–351, 1856.

[8] Bleich, F. *Stahlhochbauten*, chapter 16, pages 80–85. Verlag von Julius Springer, 1932.

[9] Bruhns, O.T. *Advanced Mechanics of Solids*. Springer, 2003.

[10] Gimena, L., Gimena, F.N., and Gonzaga, P. Structural analysis of a curved beam element defined in global coordinates. *Eng. Struct.*, 30:3355–3364, 2008.

[11] *ABAQUS User's and theory manuals - Release 6.16*. Simulia, Providence, RI, USA., 2011.

[12] Timoshenko, S. and Goodier, J.N. *Theory of Elasticity*. McGraw-Hill, second edition, 1951.

VIII ECCOMAS Thematic Conference on Smart Structures and Materials
SMART 2017
A. Güemes, A. Benjeddou, J. Rodellar and J. Leng (Eds)

NEW MIXED FINITE ELEMENTS FOR THE DISCRETIZATION OF PIEZOELECTRIC STRUCTURES OR MACRO-FIBRE COMPOSITES

ASTRID S. PECHSTEIN* AND ALEXANDER HUMER*

*Institute of Technical Mechanics
Johannes Kepler University Linz
Altenberger Str. 69, 4040 Linz, Austria
e-mail: astrid.pechstein@jku.at, alexander.humer@jku.at

Key words: mixed finite elements, piezoelasticity

Abstract. We propose a new three-dimensional formulation based on the mixed Tangetial-Displacement Normal-Normal-Stress (TDNNS) method for elasticity. In elastic TDNNS elements, the tangential displacement and the normal component of the stress vector are degreees of freedom and continuous across interfaces. These elements have been shown to be locking-free with respect to shear locking in thin elements, which makes them suitable for the discretization of laminates or macro-fibre composites. In the current paper, we extend the elements to piezoelectric materials by adding the electric potential as degree of freedom. We show that nonlinear material properties, as a nonlinear piezoelectric coefficient d_{15}, can be included into the framework.

1 INTRODUCTION

The simulation of smart, piezoelectric structures is of high interest in science and applications. A powerful method for the approximate solution of the underlying coupled electric-mechanical equations is the finite element (FE) method.

First FE simulations of piezoelectric structures were carried out by Allik and Hughes [1] and later Lerch [5, 6]. They provide volume elements based on the principle of virtual work where the mechanical displacement and the electric potential are chosen as degrees of freedom. These finite element methods are very flexible – in principle, they can be used to model almost any technical application. A severe drawback is the complexity of the underlying numerical system. Due to locking, flat layered piezoelectric structures have to be resolved by a sufficient number of well-shaped elements. This easily leads to computational systems with millions or billions of unknowns even for simple applications.

Two different ways to circumvent this problem are pursued nowadays: the design of locking-free volume elements and the derivation of equations for layered plates, beams and shells. For both categories, we distinguish methods based on the principle of virtual work, and so-called mixed methods based on Hellinger-Reissner type formulations. In the former class of methods,

usually displacement and electric potential are considered as unknowns, while in the latter class of methods the mechanical stress, and sometimes also the dielectric displacement, are added as degrees of freedom.

For both volume elements as well as layered plates, beam or shell elements, it has been shown experimentally that the mixed methods provide good results for coarse discretizations and independently of the layer thickness. We mention the volume element by Sze and Yao [14], the solid shell element by Klinkel and Wagner [4] and the geometrically nonlinear element by Ortigosa and Gil [10]. Reissner-type mixed zigzag formulations were successfully used by [2, 3, 16].

These experimental findings motivate our suggestion for a new family of piezoelectric elements. In [11, 12] the "Tangential Displacement Normal Normal Stress" (TDNNS) finite element method was introduced for linear elastic solids. The elements are based on a Hellinger-Reissner formulation, where the tangential component of the displacement as well as the normal component of the (normal) stress vector are considered as degrees of freedom. In [12] it was shown the these elements are locking-free when used as flat prismatic elements. In the current contribution, we propose an extension of these elements to piezoelectric materials.

We show the accuracy of the proposed elements for the case of a linear bimorph beam. We show how the method can be extended to nonlinear material laws by the example of a nonlinear d_{15} MFC.

2 THE PROBLEM OF LINEAR PIEZOELASTICITY

Let $\Omega \subset \mathbb{R}^3$ describe a solid made of elastic, in part piezoelectric material that is subjected to body forces $\vec{f}$ and boundary conditions. In linear piezoelasticity, we are concerned with finding the displacement field $\vec{u}$ and the electric potential ϕ. Derived of these fields are the electric field $\vec{E} = -\nabla\phi$ and the linear strain tensor $\varepsilon(\vec{u}) = \frac{1}{2}(\nabla\vec{u} + (\nabla\vec{u})^T)$. The displacement field $\vec{u}$ and the electric potential ϕ are the unknowns in the usual finite element formulation based on variational principles as the principle of virtual work or D'Alemberts principle. We call $\vec{u}$ and ϕ the *primal quantities*.

Opposed to the primal quantities, the *dual quantites* of interest are the Cauchy stress tensor $\underline{\sigma}$ and the dielectric displacement $\vec{D}$. Usually, these quantities $\underline{\sigma}$ and $\vec{D}$ are computed in a postprocessing step from $\vec{u}$ and ϕ, using the constitutive law.

In linear piezoelasticity, a linear relationship between the primal, derived quantities strain ε and electric field $\vec{E}$ and the dual quantities mechanical stress $\underline{\sigma}$ and dielectric displacement $\vec{D}$ is assumed. This linear relationship is described by three tensors, the mechanical stiffness tensor, the electric permittivity tensor and the piezoelectric permittivity tensor. We use the fourth order mechanical stiffness tensor $\underline{\underline{C}}^E$ or its inverse, the flexibility $\underline{\underline{S}}^E$, both measured at constant electrical field. The electric permittivity at constant mechanical stress is denoted $\underline{\epsilon}^\sigma$. Piezoelectric material further exhibits the third order piezoelectric permittivity $\underline{d}$ responsible for the electro-mechanical coupling. The constitutive equations for linear piezoelasticity read

$$\varepsilon(\vec{u}) = \underline{\underline{S}}^E\underline{\sigma} + \underline{d}^T\vec{E}, \tag{1}$$

$$\vec{D} = \underline{d\sigma} + \underline{\epsilon}^\sigma\vec{E}. \tag{2}$$

Both the mechanic balance equation and Gauss' law for the dielectric displacement are of diver-

gence form, reading

$$\begin{aligned} \operatorname{div} \underline{\sigma} &= \vec{f} && (3)\\ \operatorname{div} \vec{D} &= 0. && (4) \end{aligned}$$

For simplicity, we assume homogeneous boundary conditions, namely the mechanical conditions

$$\vec{u} = 0 \text{ on } \Gamma_1 \qquad \text{and} \qquad \vec{\sigma}_n = 0 \text{ on } \Gamma_2 = \partial\Omega \backslash \Gamma_1, \tag{5}$$

and the electrical conditions

$$\vec{E}_t = 0 \text{ on } \Gamma_3 \qquad \text{and} \qquad D_n = 0 \text{ on } \Gamma_4 = \partial\Omega \backslash \Gamma_3. \tag{6}$$

To develop a finite element method, we assume $\mathcal{T} = \{T\}$ to be a finite element mesh of the domain Ω, consisting of tetrahedral, prismatic or hexahedral elements. By $\vec{n}$ we denote the outward unit normal on the (element or domain) boundary ∂T or $\partial\Omega$. On each element or domain boundary surface, a general vector field $\vec{v}$ can be split into a normal and tangential component by $\vec{v} = v_n\vec{n} + \vec{v}_t$ with $v_n = \vec{v} \cdot \vec{n}$ and $\vec{v}_t = \vec{v} - v_n\vec{n}$. Note that the normal component v_n is scalar, while the tangential component $\vec{v}_t$ is vectorial. A tensor field $\underline{\tau}$ has a normal vector $\vec{\tau}_n = \underline{\tau}\vec{n}$ on a surface, which can again be split into a normal and tangential component $\tau_{nn} = \vec{\tau}_n \cdot n$ and $\vec{\tau}_{nt} = \vec{\tau}_n - \tau_{nn}\vec{n}$.

3 THE ELASTIC TDNNS METHOD

The TDNNS method is a mixed finite element method based on Reissner's principle. Displacement and stress are considered as unknowns, see [11, 13]. We will shortly introduce the method.

The tangential component of the displacement $\vec{u}_t$ and the normal component of the stress vector σ_{nn} are degrees of freedom of the finite element. We use finite element spaces for which these respective quantities are continuous across element interfaces. Note that, in general, the displacement field will be discontinuous.

Nédélec [8, 9] introduced tangential-continuous finite elements, which are commonly used to describe the electric field in Maxwell's equations. We use these elements for the displacement. For the stresses, we introduced normal-normal continuous elements in [11]. These finite element spaces can be shortly described by

$$\begin{aligned} \vec{u}, \delta\vec{u} \in V_h &= \{\vec{v} : \vec{v}|_T \in [P^k(T)]^3, \vec{v}_t \text{ cont.}, \vec{v}_t = 0 \text{ on } \Gamma_1\}, && (7)\\ \underline{\sigma}, \delta\underline{\sigma} \in \Sigma_h &= \{\underline{\tau} : \underline{\tau}|_T \in [P^k(T)]^{3\times 3}_{sym}, \tau_{nn} \text{ cont.}, \tau_{nn} = 0 \text{ on } \Gamma_2\}. && (8) \end{aligned}$$

Here, $P^k(T)$ denotes the space of polynomials of order at most k on element T. Shape functions for tetrahedral, prismatic and hexahedral elements are provided in [11], additionally two-dimensional triangular or quadrilateral elements exist. In [12] it was shown that the method works well for thin prismatic or hexahedral elements.

The variational formulation is based on Reissner's principle, and reads: find $\vec{u} \in V_h$ and $\underline{\sigma} \in \Sigma_h$ such that

$$\int_\Omega \underline{\underline{S}}\underline{\sigma} : \delta\underline{\sigma}\, dx - \langle \varepsilon(\vec{u}), \delta\underline{\sigma}\rangle - \langle \varepsilon(\delta\vec{u}), \underline{\sigma}\rangle = \int_\Omega \vec{f} \cdot \delta\vec{u}\, dx, \tag{9}$$

for all virtual displacements $\delta\vec{u} \in V_h$ and virtual stresses $\delta\underline{\sigma} \in \Sigma_h$. Note that, as $\vec{u}$ is not continuous, the strain $\varepsilon(\vec{u})$ does not exist in the classical sense, but as a distribution. It contains additional distributional terms on element interfaces.

In the variational principle (9), we see duality products of the form $\langle \varepsilon(\vec{u}), \underline{\sigma} \rangle$ instead of integrals of the form $\int_\Omega \varepsilon(\vec{u}) : \underline{\sigma}\, dx$ in common methods. This distinction is necessary to be mathematically correct, since the strain $\varepsilon(\vec{u})$ is a distribution. The duality product is well defined only if the stress field $\underline{\sigma}$ is normal-normal continuous. For finite element functions on the mesh $\mathcal{T}$, the duality product can be evaluated element-wise by volume and surface integrals. The surface integrals represent the distributional terms on element interfaces mentioned above. The following two formulas are equivalent, and motivate that the duality product can also be viewed as the (negative) distributional divergence of the stress tensor,

$$\langle \varepsilon(\vec{u}), \underline{\sigma} \rangle = \sum_{T\in\mathcal{T}} \Big(\int_T \underline{\sigma} : \varepsilon(\vec{u})\, dx - \int_{\partial T} \underline{\sigma}_{nn} \vec{u}_n\, ds \Big) \tag{10}$$

$$= \sum_{T\in\mathcal{T}} \Big(- \int_T \operatorname{div} \underline{\sigma} \cdot \vec{u}\, dx + \int_{\partial T} \underline{\sigma}_{nt} \vec{u}_t\, ds \Big) = -\langle \operatorname{div} \underline{\sigma}, \vec{u} \rangle. \tag{11}$$

The equivalence of formulas (10) and (11) can be shown by integration by parts on each element, and using the continuity of σ_{nn} and $\vec{u}_t$, respectively. For a more involved mathematical motivation see [11, 13].

4 MIXED FINITE ELEMENTS FOR PIEZOELECTRIC STRUCTURES

In the sequel, we present a piezoelectric finite element based on the elastic TDNNS method. The electric field $\vec{E} = -\nabla\phi$ is added by considering the electric potential ϕ as a further unknown.

The variational formulation above (9) is enriched by the piezoelectric coupling terms and the virtual change of electric energy under a virtual potential $\delta\phi$. We choose the electric potential in the standard continuous finite element space of order k,

$$\phi \in \Phi_h := \{\phi \in \mathcal{C}(\Omega) : \phi|_T \in P^k(T), \phi = 0 \text{ on } \Gamma_3\}. \tag{12}$$

To derive the variational formulation for piezoelectric materials, we insert the piezoelectric constitutive equation for the strain (1) into the TDNNS variational equation (9). Thus we arrive at

$$\int_\Omega (\underline{\underline{S}}^E \underline{\sigma} - \underline{d}^T \nabla\phi) : \delta\underline{\sigma}\, dx - \langle \varepsilon(\vec{u}), \delta\underline{\sigma} \rangle - \langle \varepsilon(\delta\vec{u}), \underline{\sigma} \rangle = \int_\Omega \vec{f} \cdot \delta\vec{u}\, dx. \tag{13}$$

Additionally, we insert the constitutive equation for the dielectric displacement vector (2) into the conservation of charge (4). We multiply with a virtual potential $\delta\phi$ and integrate over the domain,

$$\int_\Omega \operatorname{div}(\underline{d}\underline{\sigma} - \underline{\epsilon}^\sigma \nabla\phi)\, \delta\phi\, dx = 0 \tag{14}$$

Integration by parts in (14), using that either D_n or $\delta\phi$ is zero on the boundary leads to the well-known virtual change of the electric energy,

$$-\int_\Omega (d\underline{\sigma} - \underline{\epsilon}^\sigma \nabla\phi) \cdot \delta\nabla\phi\, dx = \int_\Omega \vec{D} \cdot \delta\vec{E}\, dx = 0. \tag{15}$$

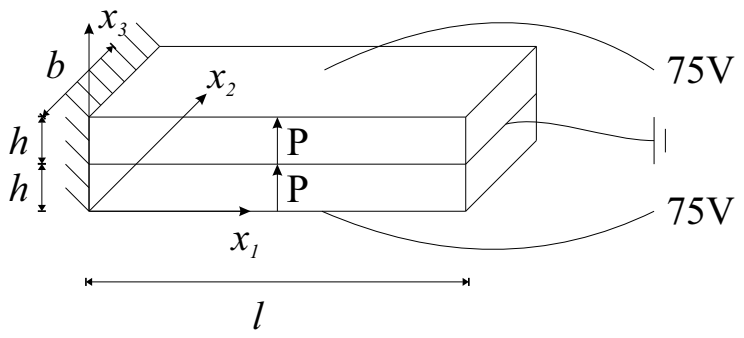

Figure 1: Setup of the bimorph beam

Adding (15) to (13) leads to a symmetric variational formulation

$$\int_\Omega (\underline{\underline{S}}^E \underline{\sigma} - \underline{d}^T \nabla\phi) : \delta\underline{\sigma}\, dx - \langle \varepsilon(\vec{u}), \delta\underline{\sigma}\rangle - \langle \varepsilon(\delta\vec{u}), \underline{\sigma}\rangle + \int_\Omega (-\underline{\underline{d}}\underline{\sigma} + \underline{\epsilon}^\sigma \nabla\phi)\cdot \delta\nabla\phi\, dx = \int_\Omega \vec{f}\cdot\delta\vec{u}\, dx. \tag{16}$$

Equation (16) in union with the finite element spaces V_h, Σ_h and Φ_h comprises the finite element formulation we propose. Its performance for thin prismatic elements is tested in the sequel. We shall see that it is free from locking for elements of order $k \geq 2$. For the lowest order case, the quadratic behavior of the electric potential in thickness direction cannot be represented by the degrees of freedom, as we have only a linear behavior of ϕ. Therefore, we expect a deterioration of accuracy when using only one layer of elements in thickness direction. However, for higher orders, the quadratic variation can be represented, and accurate results are obtained.

5 NUMERICAL RESULTS

5.1 Bimorph beam

The first example is a benchmark test of a piezoelectric bimorph beam. The beam is clamped at $x_1 = 0$. The length, width and height are $l = 100$mm, $b = 5$mm and $2h = 2 \cdot 0.5$mm. The two layers of the bimorph beam are both made from PZT and poled in x_3 thickness direction. The beam is electroded at the upper and lower surface, and in the interior between the layers. The material parameters are summarized in Table 1. A constant electric potential of $\phi = 75$V is applied to electrodes on the upper and lower surface of the beam, while the interior electrode is grounded. See Figure 1 for a sketch.

The beam is discretized using prismatic elements in the plane, where different in-plane meshes were used. In Table 2 we provide the relative error of the mean value of the tip displacement when using different finite element meshes in-plane and different polynomial orders of the finite elements. The relative error was obtained in comparison to a finite element solution on a fine grid using standard nodal elements of order 5 for displacement and electric potential. All computations were performed using the FE package Netgen/NGSolve (see `ngsolve.org`).

Table 1: Material constants used for the bimorph beam.

Parameter		Parameter	
S_{11}^E	16.4×10^{-12} m^2/N	d_{31}	-1.71×10^{-10} m/V
S_{33}^E	18.8×10^{-12} m^2/N	d_{33}	3.74×10^{-10} m/V
S_{12}^E	-5.74×10^{-12} m^2/N	d_{15}	5.84×10^{-10} m/V
S_{13}^E	-7.22×10^{-12} m^2/N	$\epsilon_{11}^\sigma/\epsilon_0$	1730
S_{44}^E	47.5×10^{-12} m^2/N	$\epsilon_{33}^\sigma/\epsilon_0$	1700
S_{66}^E	44.3×10^{-12} m^2/N		

Table 2: Relative error of the mean value of the tip deflection u_3 for the bimorph beam.

mesh size h	order k	relative error
5 mm	1	12.5%
	1, 2 layers	5.8%
	2	0.8%
	3	0.5%
2.5 mm	1	13.2%
	1, 2 layers	4.0%
	2	0.4%
	3	0.1%
1 mm	1	13.3%
	1, 2 layers	3.2%
	2	0.1%
	3	$< 0.1\%$

If not mentioned otherwise, only one layer of finite elements in each ply was used. This is enough if the finite element order is high enough to represent the linear variation of the electric field in thickness direction. We see fast convergence of the error for elements of order $k = 2$ and $k = 3$.

Only for elements of lowest order $k = 1$, the solution does not converge when using one layer of elements in each ply. In this case, the error due to the restriction to constant electric field in thickness direction dominates. Further subdivisions in thickness direction lead to an increase in accuracy.

5.2 Homogenization of a d_{15} MFC

As a second example, we compute the piezoelectric coefficient of a d_{15} MFC using the nonlinear material law [7]. The geometry and material properties of the MFC are taken from [15] and displayed in Figure 2.

The material parameters in the linear regime are displayed in Table 3. Note that the permittivity of the nickel electrodes is not needed, as the electric potential is assumed to take a given

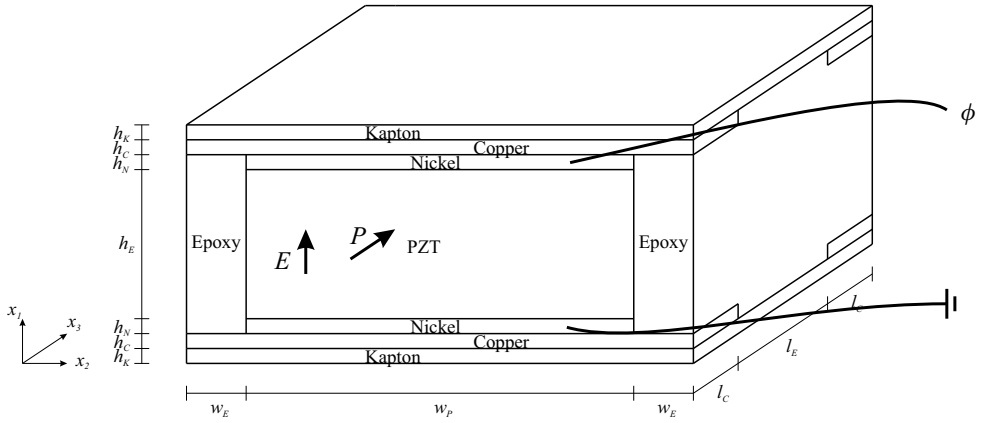

Figure 2: Unit cell of the d_{15} MFC. Dimensions: $h_P = 180\mu$m, $h_K = 25\mu$m, $h_N = 2\mu$m, $h_C = 18\mu$m, $l_E = 420\mu$m, $l_C = 80\mu$m, $w_E = 27.5\mu$m, $w_P = 350\mu$m.

Table 3: Material constants used for the d_{15} MFC.

SONOX P502			
S_{11}^E	18.5×10^{-12} m^2/N	d_{31}	-1.85×10^{-10} m/V
S_{33}^E	20.7×10^{-12} m^2/N	d_{33}	4.40×10^{-10} m/V
S_{12}^E	-6.29×10^{-12} m^2/N	d_{15}^{lin}	5.60×10^{-10} m/V
S_{13}^E	-6.23×10^{-12} m^2/N	$\epsilon_{11}^{\sigma,lin}/\epsilon_0$	1950
S_{44}^E	33.2×10^{-12} m^2/N	$\epsilon_{33}^{\sigma}/\epsilon_0$	1850
S_{66}^E	52.3×10^{-12} m^2/N		
Epoxy			
Y	2.5×10^9 N/m^2	ϵ/ϵ_0	4.25
ν	0.42		
Kapton			
Y	2.5×10^9 N/m^2	ϵ/ϵ_0	3.4
ν	0.0.34		
Copper			
Y	110×10^9 N/m^2	ϵ/ϵ_0	2000
ν	0.34		
Nickel			
Y	200×10^9 N/m^2	ν	0.31

input voltage there. The piezoelectric coefficient d_{15} and the permittivity ϵ_{11}^{σ} increase with the applied electric field in the piezoelectric material. We use the following power law taken from [15] based on [7],

$$d_{15}(E_1) = d_{15}^{lin}\big(1 + (\gamma E_1)^{\beta}\big), \qquad \epsilon_{11}^{\sigma}(E_1) = \epsilon_{11}^{\sigma,lin}\big(1 + (\gamma E_1)^{\beta}\big), \tag{17}$$

with $\gamma = 2.8$ and $\beta = 1.2$.

In a first, linear homogenization procedure, we compute the piezoelectric coefficient d_{15}^{MFC} and permittivity $\epsilon_{11}^{\sigma,MFC}$ for the MFC using the proposed TDNNS finite element method. This comprises a finite element computation on the unit cell assuming linear material behavior $d_{15}(E_1) = d_{15}^{lin}$ and $\epsilon_{11}^{\sigma}(E_1) = \epsilon_{11}^{\sigma,lin}$. The electric potential $\phi = 1\text{V}$ is prescribed on the electrodes. All boundary conditions are assumed periodic in the x_2x_3 plane, while stress-free conditions are assumed on the top and lower surface. From the finite element solution, the average shear strain $\bar{\gamma}_5$, the average electric field $\bar{E}_1$ and the average dielectric displacement $\bar{D}_1$ are computed by

$$\bar{\gamma}_5 = 2\int_\Omega \underline{\varepsilon}_{13}\,dx, \qquad \bar{E}_1 = \int_\Omega E_1\,dx, \qquad \bar{D}_1 = \int_\Omega D_1\,dx,. \tag{18}$$

Then the macroscopic piezoelectric and dielectric constants can be evaluated by

$$d_{15}^{MFC} = \bar{\gamma}_5/\bar{E}_1, \qquad \epsilon_{11}^{\sigma,MFC} = \bar{D}_1/\bar{E}_1. \tag{19}$$

We use a triangular finite element mesh in the x_2x_3 plane, which is extended to prismatic elements in x_1 direction. The electrode layer is resolved by the finite element mesh. Three different prismatic meshes are considered in computations: The *coarse mesh*, with 164 triangular elements and one element per ply in x_1 direction, the x_1 *refined mesh* using more layers of elements per ply, and the *fine mesh* using an in-plane mesh with 862 triangular elements additionally to the x_1 refinement. For the x_1 refinement, we use geometrically decreasing element heights in the active layer towards the electrodes. Fine and coarse mesh are depicted in Figure 3. We see, that the accuracy for one layer of elements per ply is already good, but can be improved by further subdivision. However, using a finer in-plane mesh does not lead to a significant increase of accuracy. The computation on the fine mesh with polynomial order $k = 2$ was not performed due to memory restrictions. In Figure 4 and Figure 5 we plot the strain and stress components γ_5 and σ_5, respectively, on the cut plane $x_3 = (2l_C + l_E)/2$, using the x_1 refined mesh.

In Table 4 we provide the coefficients d_{15}^{MFC} and $\epsilon_{11}^{\sigma,MFC}$ obtained from our computation and compare them to the values in [15]. We note that our computation converges to slightly different values, which may be due to the different setup concerning the electrodes and periodic boundary conditions.

In a second computation we find the nonlinear coefficients d_{15} and ϵ_{11}^{σ} as function of the electric field $\vec{E}$. The values are computed by a homogenization method with different input voltages, using the nonlinear material law (17). We perform a fully nonlinear computation, and observe a quick convergence of the fixed-point iteration. This is probably due to the fact that the computed electric field E_1 is nearly constant and close to the incident field ϕ/h_p. In Figure 6, the results are compared to the respective given values for the piezoelectric fibre, and to the values using the nonlinear material law and the linear coefficients d_{15}^{MFC} and $\epsilon_{11}^{\sigma,MFC}$ from [15] as given in Table 4.

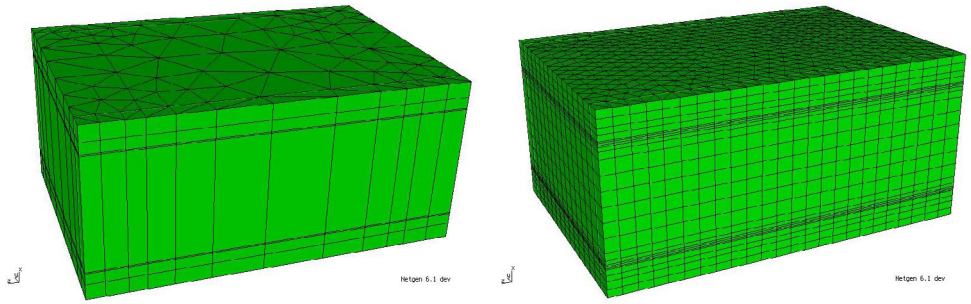

Figure 3: Different finite element meshes used: coarse mesh with 1148 elements (left) and fine mesh with 20688 elements (right).

Table 4: Piezoelectric coefficient d_{15} and permittivity ϵ_{11}^{σ} of the MFC in the linear regime, computed by a homogenization method, compared to the values provided in [15].

MFC	[15]	coarse mesh		coarse m., x_1 ref.		fine mesh
		$k=1$	$k=2$	$k=1$	$k=2$	$k=1$
d_{15}^{MFC} [pC/N]	554.02	552.384	551.364	549.213	549.522	549.121
$\epsilon_{11}^{\sigma,MFC}$ [nF/m]	15.02	14.888	14.912	14.923	14.953	14.928

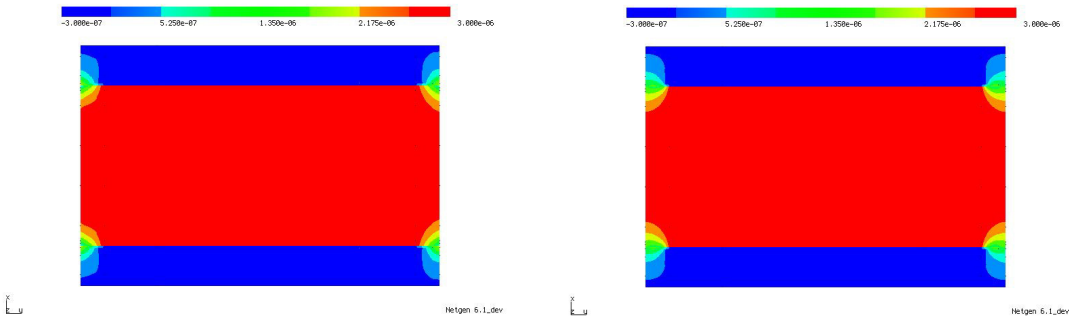

Figure 4: Strain γ_5 from the linear homogenization problem, polynomial order $k=1$ and $k=2$.

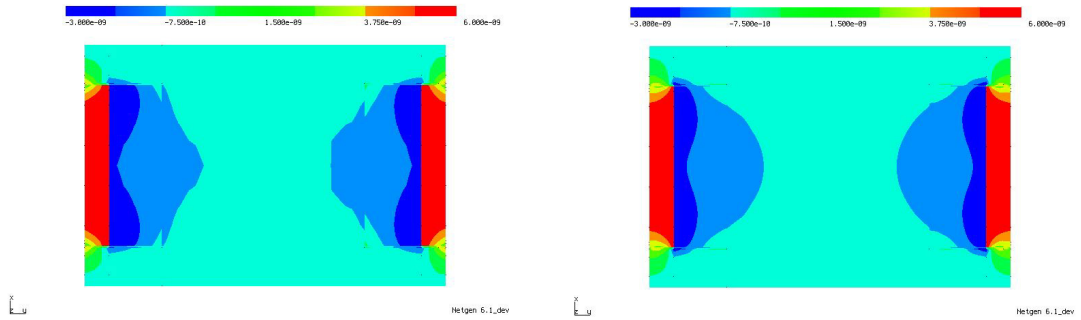

Figure 5: Shear stress σ_5 from the linear homogenization problem, polynomial order $k = 1$ and $k = 2$.

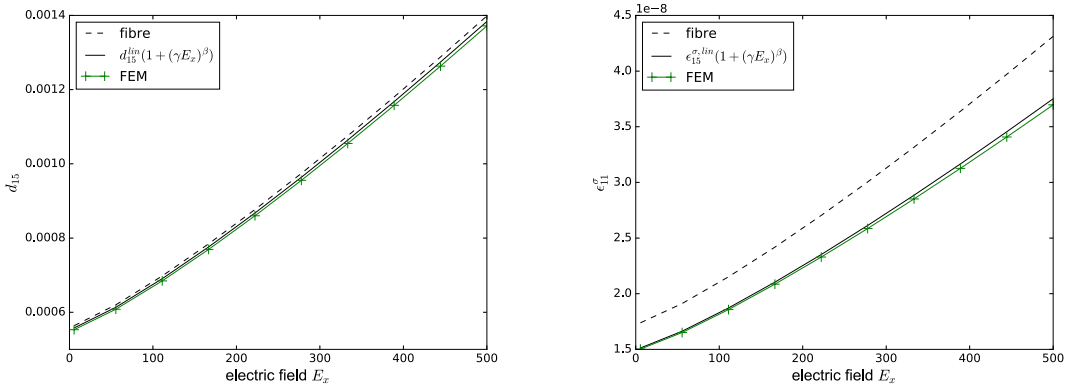

Figure 6: Nonlinear coefficient d_{15} and ϵ_{11}^{σ} as function of the input electric field $E_x = \Delta\phi/h_p$.

6 ACKNOWLEDGEMENTS

This work has been supported by the Linz Center of Mechatronics (LCM) in the framework of the Austrian COMET-K2 program.

REFERENCES

[1] Henno Allik and Thomas J. R. Hughes. Finite element method for piezoelectric vibration. *International Journal for Numerical Methods in Engineering*, 2(2):151–157, 1970.

[2] E. Carrera and M. Boscolo. Classical and mixed finite elements for static and dynamic analysis of piezoelectric plates. *Int. J. Numer. Methods Engrg.*, 70(10):1135–1181, 2007.

[3] E. Carrera and P. Nali. Mixed piezoelectric plate elements with direct evaluation of transverse electric displacement. *Int. J. Numer. Methods Engrg.*, 80(4):403–424, 2009.

[4] S. Klinkel and W. Wagner. A geometrically non-linear piezoelectric solid shell element based on a mixed multi-field variational formulation. *International Journal for Numerical Methods in Engineering*, 65(3):349–382, 2006.

[5] R. Lerch. Finite element analysis of piezoelectric transducers. In *Ultrasonics Symposium, 1988. Proceedings., IEEE 1988*, pages 643–654 vol.2, Oct 1988.

[6] R. Lerch. Simulation of piezoelectric devices by two- and three-dimensional finite elements. *IEEE Transactions on Ultrasonics, Ferroelectrics, and Frequency Control*, 37(3):233–247, May 1990.

[7] V. Mueller and Q.M. Zhang. Nonlinearity and scaling behavior in donor-doped lead zirconate titanate piezoceramic. *Applied physics letters*, 72(21):2692–2694, 1998.

[8] J. C. Nédélec. Mixed finite elements in $\mathbb{R}^3$. *Numerische Mathematik*, 35:315–341, 1980.

[9] J. C. Nédélec. A new family of mixed finite elements in $\mathbb{R}^3$. *Numerische Mathematik*, 50:57–81, 1986.

[10] Rogelio Ortigosa and Antonio J. Gil. A new framework for large strain electromechanics based on convex multi-variable strain energies: Finite element discretisation and computational implementation. *CMAME*, 302:329–360, 2016.

[11] A. Pechstein and J. Schöberl. Tangential-displacement and normal-normal-stress continuous mixed finite elements for elasticity. *Math. Models Methods Appl. Sci.*, 21(8):1761–1782, 2011.

[12] A. Pechstein and J. Schöberl. Anisotropic mixed finite elements for elasticity. *International Journal for Numerical Methods in Engineering*, 90(2):196–217, 2012.

[13] A.S. Pechstein and J. Schöberl. An analysis of the TDNNS method using natural norms. *ArXiv e-prints*, June 2016.

[14] K.Y. Sze and L.Q. Yao. Modelling smart structures with segmented piezoelectric sensors and actuators. *Journal of Sound and Vibration*, 235(3):495–520, 2000.

[15] M.A. Trindade and A. Benjeddou. Finite element characterization and parametric analysis of the nonlinear behaviour of an actual d_{15} shear mfc. *Acta Mechanica*, 224(11):2489–2503, 2013.

[16] Chih-Ping Wu and Hong-Ru Lin. Three-dimensional dynamic responses of carbon nanotube-reinforced composite plates with surface-bonded piezoelectric layers using Reissners mixed variational theorem-based finite layer methods. *Journal of Intelligent Material Systems and Structures*, 2014.

VIII ECCOMAS Thematic Conference on Smart Structures and Materials
SMART 2017
A. Güemes, A. Benjeddou, J. Rodellar and J. Leng (Eds)

NON-LINEAR ANALYSIS OF A PRE-STRESSED PIEZOELECTRIC MULTI-LAYER PLATE

FLORIAN TOTH*, MANUEL DORFMEISTER†, MICHAEL SCHNEIDER†, ULRICH SCHMID† AND MANFRED KALTENBACHER*

*Institute of Mechanics and Mechatronics
TU Wien
Getreidemarkt 9, 1060 Vienna, Austria
e-mail: florian.toth@tuwien.ac.at, web page: http://www.mec.tuwien.ac.at/

† Institute of Sensor and Actuator Systems
TU Wien
Gusshausstrasse 27-27, 1040 Vienna, Austria
web page: http://www.isas.tuwien.ac.at/

Key words: MEMS, Piezo, Pre-Stress, Circular Plate

Abstract. A geometrically non-linear mechanical model for a MEMS actuator is developed based on von Karman plate theory. Piezoelectric and thermally stressed layers are incorporated within the framework of classical lamination theory. The formulation is completely general with respect to the possible configuration of layers. It is then employed to treat circular plates under the assumption of axially-symmetric deformations. Finally, some results for a selected piezo-actuator are presented.

1 INTRODUCTION

Loss of stability through buckling or snap-through is usually undesired in engineering structures. However, buckling phenomena can also be exploited e.g. to determine material parameters through indirect experiments [1], or in actuator applications [2]. While the determination of critical loads (i.e. the load at which a bifurcation occurs) is often sufficient for the prevention against the loss of stability in standard applications, the exploitation of buckling phenomena in actuator applications requires precise knowledge about the post-critical behaviour of the investigated system.

This makes geometrically non-linear formulation necessary. The simplest of such formulations is based on von Karman plate theory, resulting in a set of equations which is difficult to solve [3, 4, 5]. For the case of circular, isotropic plates it is possible to prove the existence of a solution to the von Karman plate equations [6]. Considerable simplification is possible by employing Berger's approximation [5, 7]. Originally developed for isotropic plates, it can also be applied to composite plates without coupling stiffness matrix [8]. The challenging nature of the von Karman equations has inspired the development of many numerical methods [9, 10, 11, 12,

13]. The incorporation of piezoelectric layers into classical lamination theory can be done in a straightforward manner [14, 15].

The investigated microelectromechanical system (MEMS) consists of a circular, multilayer plate with the intended use as an actuator for digital sound reconstruction (DSR). The multilayer structure is pre-stressed due to the production process leading to buckling of the plate structure. The piezo layer is actuated to switch from one to the other stable equilibrium. The advantage of such an actuator exploiting the post-buckling behaviour is a significantly larger stroke level.

2 MECHANICAL MODEL

One of the key points of the mechanical modelling of the actuator system is the correct description of the electromechanical coupling including pre-stress. In order to accurately describe the post-buckling behaviour we require a large-displacement framework. However, the model must be simple enough to enable a mathematical analysis of the non-linear behaviour of the structure to be suitable for the tailored design of actuators. In order to obtain a computationally efficient model the multi-layer structure will be treated as a thin plate.

2.1 Plate Kinematic

Adopting the Kirchhoff hypothesis we can describe the strain state in the plate by

$$\bar{\boldsymbol{\epsilon}} = \boldsymbol{\epsilon} + z\boldsymbol{\kappa}, \tag{1}$$

where the in-plane strain tensor $\boldsymbol{\epsilon}$ and the curvature tensor $\boldsymbol{\kappa}$ describe the deformation of the reference surface of the plate, and z is transverse coordinate measured from the reference surface. We choose to use the von Karman assumptions to derive the simplest possible geometrically non-linear plate formulation. Thus, we write the deformation tensors of the reference surface as

$$\boldsymbol{\epsilon} = \frac{1}{2}\left(\boldsymbol{\nabla}\boldsymbol{u} + (\boldsymbol{\nabla}\boldsymbol{u})^T + \boldsymbol{\nabla}u_3\boldsymbol{\nabla}u_3\right), \tag{2}$$

$$\boldsymbol{\kappa} = -\boldsymbol{\nabla}\boldsymbol{\nabla}u_3, \tag{3}$$

with the displacement vector $\boldsymbol{u} = [u_1, u_2, u_3]$. The above formulation allows the coupling of transverse displacements, i.e. u_3, and in-plane strains.

2.2 Constitutive Model

As we are dealing with a thin plate we assume a plane stress state with a vanishing normal stress in thickness direction. All materials are modelled as transversally isotropic with the axis of the vanishing normal stress perpendicular to the isotropic plane. Employing Voigts linearised theory of piezoelectricity and additionally considering thermal strains we can write the linearised constitutive relation as

$$\underbrace{\begin{bmatrix}\sigma_{11}\\ \sigma_{22}\\ \sigma_{12}\end{bmatrix}}_{\bar{\boldsymbol{\sigma}}} = \underbrace{\begin{bmatrix}Q_{11} & Q_{12} & 0\\ Q_{12} & Q_{11} & 0\\ 0 & 0 & Q_{66}\end{bmatrix}}_{\bar{\boldsymbol{C}}}\underbrace{\begin{bmatrix}\epsilon_{11}\\ \epsilon_{22}\\ 2\epsilon_{12}\end{bmatrix}}_{\bar{\boldsymbol{\epsilon}}} - \bar{\boldsymbol{C}}\underbrace{\begin{bmatrix}\alpha_1\\ \alpha_1\\ 0\end{bmatrix}}_{\bar{\boldsymbol{\alpha}}}\Delta T - \underbrace{\begin{bmatrix}\bar{e}\\ \bar{e}\\ 0\end{bmatrix}}_{\bar{\boldsymbol{e}}^T}E_3, \tag{4}$$

$$D_3 = \bar{\boldsymbol{e}}\bar{\boldsymbol{\epsilon}} - \bar{\boldsymbol{e}}\bar{\boldsymbol{\alpha}}\Delta T + \bar{\eta}E_3, \tag{5}$$

where $\bar{\boldsymbol{\sigma}}$ is the plane stress tensor (in Voigt notation), ΔT is the temperature change with respect to a reference temperature, E_3 is the electric field strength in thickness direction and D_3 is the dielectric displacement in thickness direction. The components Q_{ij} of the effective plane-stress stiffness tensor $\bar{\boldsymbol{C}}$ can be computed from the components C_{ij} of the transversally isotropic stiffness tensor by

$$Q_{11} = C_{11} - \frac{C_{13}^2}{C_{33}}, \qquad Q_{12} = C_{12} - \frac{C_{13}^2}{C_{33}}, \qquad Q_{66} = \frac{C_{11} - C_{12}}{2}, \tag{6}$$

and the components of the effective plane-stress piezoelectric coupling tensor $\bar{\boldsymbol{e}}$ as well as the effective plane-stress permittivity $\bar{\eta}$ are given by

$$\bar{e} = e_{31} - \frac{C_{13}}{C_{33}} e_{33}, \qquad \bar{\eta} = \eta_{33} + \frac{e_{33}^2}{C_{33}}, \tag{7}$$

where e_{ij} and η_{ij} denote the entries of the transversally isotropic piezoelectric coupling and electric permittivity tensors, respectively.

We have already neglected any electric field components in in-plane direction. Therefore, Gauss' law simplifies to $\partial D_3/\partial z = 0$, stating that the dielectric displacement is constant in each layer. We can now insert the kinematic assumption (1) into (5) and integrate over the layer thickness Δz to obtain

$$D_3 = \frac{1}{\Delta z} \int D_3 \, \mathrm{d}z = \bar{\boldsymbol{e}}\boldsymbol{\epsilon} + \bar{z}\bar{\boldsymbol{e}}\boldsymbol{\kappa} - \bar{\boldsymbol{e}}\bar{\boldsymbol{\alpha}}\Delta T + \bar{\eta}\frac{\Delta V}{\Delta z}, \tag{8}$$

where $\bar{z}$ denotes the vertical coordinate of the middle of the layer and ΔV the voltage difference applied to the electrodes at the top and bottom of the layer [8, 15]. Reinserting back into (5) yields

$$E_3 = \frac{\bar{z} - z}{\bar{\eta}} \bar{\boldsymbol{e}}\boldsymbol{\kappa} + \frac{\Delta V}{\Delta z}, \tag{9}$$

which is finally inserted into (4). Thus, the constitutive relation for each layer reads

$$\bar{\boldsymbol{\sigma}} = \bar{\boldsymbol{C}}\boldsymbol{\epsilon} + z\left(\bar{\boldsymbol{C}} - (\bar{z} - z)\bar{\boldsymbol{E}}\right)\boldsymbol{\kappa} - \boldsymbol{\tau}, \tag{10}$$

where the tensor

$$\bar{\boldsymbol{E}} = \frac{\bar{\boldsymbol{e}}^T\bar{\boldsymbol{e}}}{\bar{\eta}}, \tag{11}$$

accounts for stiffening due to the equipotential conditions on the electrodes of the piezo. For non-piezoelectric layers the coupling tensor is zero and thus there is no stiffening. The stress components due to piezo actuation or temperature change are included via

$$\boldsymbol{\tau} = \bar{\boldsymbol{C}}\bar{\boldsymbol{\alpha}}\Delta T + \bar{\boldsymbol{e}}^T\frac{\Delta V}{\Delta z}. \tag{12}$$

It is interesting to note that both effects can be treated with the same forcing term in the constitutive equation.

As a last step we integrate (10) over the thickness of the plate to obtain the constitutive relation on the plate level

$$\begin{bmatrix} \boldsymbol{n} \\ \boldsymbol{m} \end{bmatrix} = \begin{bmatrix} \boldsymbol{A} & \boldsymbol{B} \\ \boldsymbol{B} & \boldsymbol{D} \end{bmatrix} \begin{bmatrix} \boldsymbol{\epsilon} \\ \boldsymbol{\kappa} \end{bmatrix} - \begin{bmatrix} \tilde{\boldsymbol{n}} \\ \tilde{\boldsymbol{m}} \end{bmatrix}, \tag{13}$$

which relates the section forces and moments $\boldsymbol{n}$ and $\boldsymbol{m}$ defined as

$$\boldsymbol{n} = \sum_l \int \bar{\boldsymbol{\sigma}}_l \, \mathrm{d}z, \qquad \boldsymbol{m} = \sum_l \int z \bar{\boldsymbol{\sigma}}_l \, \mathrm{d}z, \tag{14}$$

to the deformation of the reference surface via the in-plane stiffens matrix $\boldsymbol{A}$, the coupling stiffness matrix $\boldsymbol{B}$, and the bending stiffness matrix $\boldsymbol{D}$, well known from classical lamination theory. The section forces and moments due to the combined effect of piezo actuation and thermal stress are included via $\bar{\boldsymbol{n}}$ and $\bar{\boldsymbol{m}}$, respectively. They are computed equivalently to (14) by replacing $\bar{\boldsymbol{\sigma}}$ with $\boldsymbol{\tau}$. The laminate stiffness matrices are

$$\boldsymbol{A} = \sum_l \int \bar{\boldsymbol{C}} \, \mathrm{d}z = \sum_l \Delta z_l \bar{\boldsymbol{C}}_l, \tag{15}$$

$$\boldsymbol{B} = \sum_l \int z \left(\bar{\boldsymbol{C}} - (\bar{z} - z) \bar{\boldsymbol{E}} \right) \mathrm{d}z = \sum_l \bar{z}_l \Delta z_l \bar{\boldsymbol{C}}_l, \tag{16}$$

$$\boldsymbol{D} = \sum_l \int \left(z^2 (\bar{\boldsymbol{C}}_l + \bar{\boldsymbol{E}}_l) - z \bar{z}_l \bar{\boldsymbol{E}}_l \right) \mathrm{d}z = \sum_l \frac{\Delta z_l^3}{12} \left(\bar{\boldsymbol{C}}_l + \bar{\boldsymbol{E}}_l \right) - \bar{z}^2 \Delta z \left(\bar{\boldsymbol{C}}_l + 2 \bar{\boldsymbol{E}}_l \right), \tag{17}$$

with the abbreviations

$$\Delta z_l = z_{l+1} - z_l, \qquad \bar{z}_l = \frac{z_{l+1} + z_l}{2}, \tag{18}$$

for the layer thickness and center coordinate.

2.3 Equilibrium Equations

We neglect any in-plane forces other than the ones introduced by piezo actuation or temperature change. Furthermore, we only consider the static equilibrium. The equilibrium equations can then be written as

$$\boldsymbol{\nabla} \cdot \boldsymbol{n} = 0, \tag{19}$$

$$\boldsymbol{\nabla} \cdot \boldsymbol{\nabla} \cdot \boldsymbol{m} + \boldsymbol{\nabla} \cdot (\boldsymbol{n} \cdot \boldsymbol{\nabla} u_3) - p_3 = 0, \tag{20}$$

where p_3 denotes a pressure acting transverse to the plate [8].

We now introduce a cylindrical coordinate system with its origin in the center of the plate. Restricting ourselves to rotationally symmetric loading, and thus deformations and section forces and moments, above partial differential equations are reduced to a set of coupled ordinary differential equations with respect to the radial coordinate r. Applying the divergence and gradient operators in cylindrical coordinates in (19) and (20) one obtains

$$n_r' + \frac{n_r - n_\phi}{r} = 0, \tag{21}$$

$$\left(r m_r' + m_r - m_\phi \right)' + \left(r m_r u_z' \right)' + p_z r = 0, \tag{22}$$

for the non-trivial components, where the indices r, ϕ and z indicate the radial and circumferential and axial direction and $()'$ denotes the derivative with respect to r. The above moment equation can be easily integrated once [16, 17] to obtain

$$2\left(rm_r' + m_r - m_\phi + rm_r u_z'\right) + p_z r^2 \quad = \quad 0. \tag{23}$$

Inserting the deformation measures (2) and (3) for axially symmetric deformations of the reference surface in cylindrical coordinates into (13) on obtains the following expressions for section forces and moments

$$n_r = \frac{A_{r\phi}u_r}{r} + A_{rr}u_r' - \frac{B_{r\phi}u_z'}{r} + \frac{A_{rr}u_z'^2}{2} - B_{rr}u_z'' - \bar{n}, \tag{24}$$

$$n_\phi = \frac{A_{rr}u_r}{r} + A_{r\phi}u_r' - \frac{B_{rr}u_z'}{r} + \frac{A_{r\phi}u_z'^2}{2} - B_{r\phi}u_z'' - \bar{n}, \tag{25}$$

$$m_r = \frac{B_{r\phi}u_r}{r} + B_{rr}u_r' - \frac{D_{r\phi}u_z'}{r} + \frac{B_{rr}u_z'^2}{2} - D_{rr}u_z'' - \bar{m}, \tag{26}$$

$$m_\phi = \frac{B_{rr}u_r}{r} + B_{r\phi}u_r' - \frac{D_{rr}u_z'}{r} + \frac{B_{r\phi}u_z'^2}{2} - D_{r\phi}u_z'' - \bar{m}. \tag{27}$$

These can now be inserted into (21) and (23) to obtain two non-linearly coupled ordinary differential equations (ODEs) of third order in $u_z(r)$ and second-order in $u_r(r)$.

As boundary conditions at the center, i.e. $r = 0$ and the outer radius $r = R$ we require

$$u_r(0) = 0, \quad u_z'(0) = 0, \quad u_z(R) = 0, \quad n_r(R) = -k_n u_r(R), \quad m_r(R) = k_m u_z'(R), \tag{28}$$

where we have introduced the boundary stiffness factors k_n and k_m. These can be used to transit between simply supported and freely movable in radial direction, i.e. $k_m \to 0$ and $k_n \to 0$, to clamped, i.e. $k_m \to \infty$ and $k_n \to \infty$, behaviour. The clamped behaviour can of course also be enforced by requiring

$$u_z'(R) = 0, \quad \text{and} \quad u_r(R) = 0. \tag{29}$$

The latter is mathematically exact, the former can be seen as a penalty formulation.

The coupled second and third order ODEs can be cast into a system of first order ODEs by introducing axillary variables for the derivatives. The resulting system of 5 non-linearly coupled first order ODEs, $\boldsymbol{y}'(r) = \boldsymbol{f}(\boldsymbol{y}, r)$ with $\boldsymbol{y} = [u_z'', u_z', u_z, u_r', u_r]^T$ and boundary conditions $\boldsymbol{g}(\boldsymbol{y}(0), \boldsymbol{y}(R)) = \boldsymbol{0}$, can then be solved numerically. This is for example possible by the shooting method [18]. In the current work we employ a collocation based boundary value problem solver [19]. For the numerical solution one has to consider that the equations have a singularity at $r \to 0$. However, knowing that the physical solution must be bounded, we can form the limits $\lim_{r\to 0} \boldsymbol{f}$ and $\lim_{r\to 0} \boldsymbol{g}$ by the application of L'Hôpital's rule.

3 ACTUATOR CONFIGURATION

As an example we consider an circular actuator with a diameter of 800 µm as shown in Fig. 1. The plate consists of a 2 µm thick Silicon (Si) substrate, including a 200 nm thick a-SiC:H 'stress-layer' which is used to adapt the pre-stress of the system in the production process. The electrodes surrounding the 400 nm Aluminium-Nitride (AlN) piezo layer consist of 50 nm

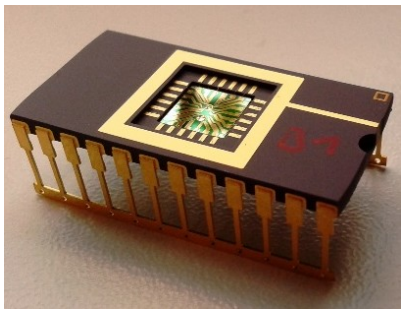



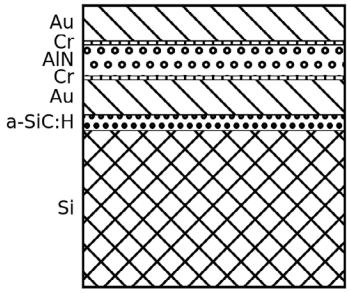

Figure 1: Chip with MEMS actuator (left); Top view of the actuator showing the electrode configuration (center); Material layers assumed in the analysis (right).

Table 1: Assumed values for the material parameters.

	Q_{11}/Pa	Q_{12}/Pa	$\bar{e}$/Cm^{-2}	$\bar{\eta}$/Fm^{-1}	α/K^{-1}
Si	1.93e+11	5.02e+10			
a-SiC:H	1.93e+11	5.02e+10			2.60e-06
Au	9.40e+10	3.76e+10			
Cr	3.07e+11	9.20e+10			
AlN	3.55e+11	1.00e+11	-2.75e+00	1.26e-10	

Chromium (Cr) and 450 nm Gold (Au). Thus, we have a total thickness of $h = 3.6\,\mu$m. The assumed material properties are given in Tab. 1.

To take into account the electrode configuration of the actuator (as can be seen in Fig. 1) one needs to consider the possibility of radially varying actuation voltages. The center electrode might have a different actuation voltage as the outer ring shaped-electrode. In order to avoid numerical difficulties we assume smooth transitions between actuation voltages by combining tanh-functions.

4 RESULTS

In a first step we investigate the impact of different actuation schemes on the resulting deformation of the composite plate. Three different actuations are considered: First only the center electrode is actuated. In the second configuration the center electrode and the ring electrode are actuated in different directions, i.e. with a negative and positive voltage, respectively. In the third configuration we assume that the ring electrode ends before the outer radius of the plate, thus the actuation voltage is zero at this location. The shape of the total actuation voltage and the resulting deformation of the actuator are depicted in Fig. 2. For the case of free rotation at the outer edge (simply supported) the bending moment introduced by the piezo actuation leads to curvature of the plate. The negative voltage at the center electrode leads to a positive curvature and thus to a displacement in negative z-direction. If the positive voltage of the ring electrode is added the resulting negative curvature leads to an overall positive vertical displacement. The behaviour is dominated by the larger ring electrode. If the ring electrode

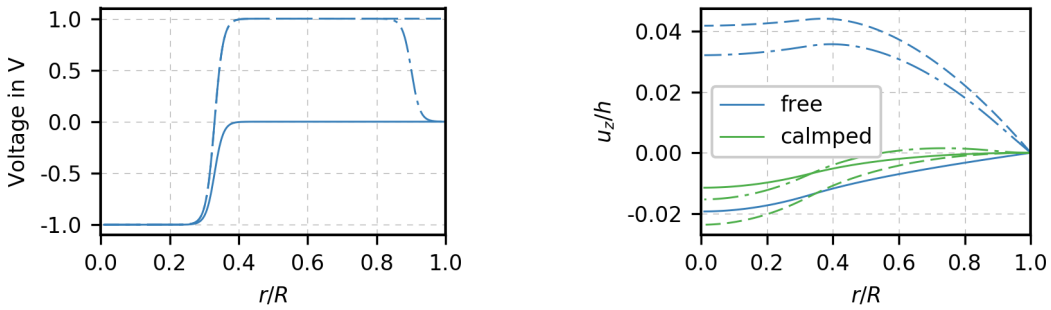

Figure 2: Impact of the electrode configuration on the deformation shape: Level of the actuation voltage (left); and resulting deformation shape for different boundary conditions (right).

ends before the outer edge of the plate the total displacement is slightly smaller. For a clamped outer edge the behaviour is different: The boundary condition does not allow for any deformation due to constant piezo actuation (provided it is below the buckling load). However, the change of actuation gradient of the actuation voltage between center electrode and ring electrode causes a deformation of the actuator. The internal forcing introduced by the actuation is similar to an external moment at the transition between the electrodes. The overall displacement is significantly smaller in the case of a clamped outer edge.

Finally, we explore the effect of compressible residual stress introduced in the stress-layer. In the current case this is modelled as thermal expansion. The temperature is therefore regarded as a loading parameter, which could be different for different effects introducing the residual stress. On the level of the plate the residual stresses in the layers lead to residual section forces and moments. Once the critical section force is reached the plate can buckle. As the configuration is un-symmetric, i.e. we have a non-zero $\boldsymbol{B}$-matrix, there exists a preferred buckling direction. As can be seen from the bifurcation diagram in Fig. 3 this is the upper side for the investigated configuration. The diagram shows the typical pitchfork bifurcation as expected for a plate. Observing the sharpness of the bifurcation one can conclude that the imperfection due to the unsymmetrical stacking of layers is small. Once the critical load is exceeded, several equilibrium positions may exist. Further increasing the load up to the second buckling load one can recognise additional buckling mode shapes. It should be noted that, transitions between the different branches due to snap-buckling [8] cannot be treated within the assumption of an axially-symmetric deformation.

5 CONCLUSIONS

A formulation for piezoelectric plate actuators has been presented. The mathematically equivalent effects of thermal stress and piezo actuation are included into the formulation by a modified constitutive law, which can be incorporated into classical lamination theory in a straight forward manner. The equilibrium equations based on the von Karman plate theory for circular plates with axially-symmetric deformation shape were derived for general un-symmetric laminates. The resulting non-linear, coupled ODEs were then solved numerically to obtain the deformed actuator configuration for different electrode actuations. Comparison of the impact

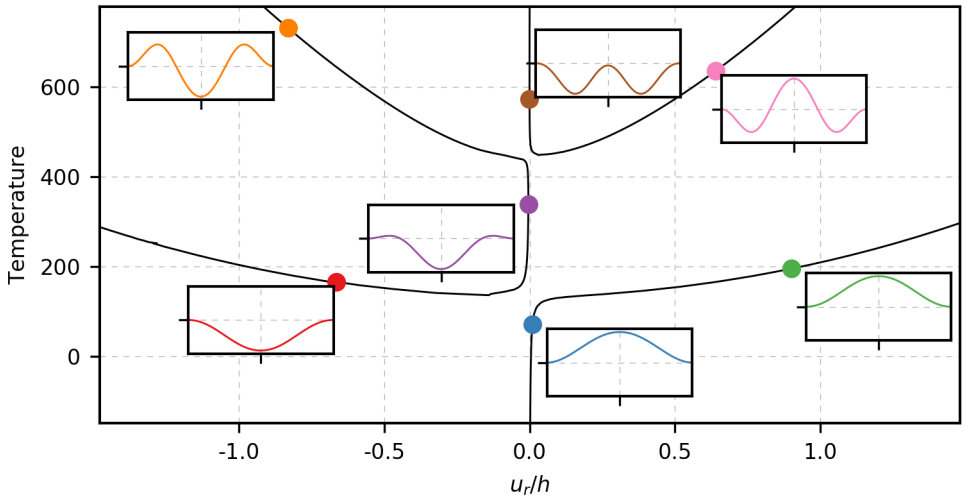

Figure 3: Bifurcation diagram of center displacement versus temperature in the stress-layer as loading parameter. The shape of the actuator for selected equilibrium points is shown as inserts.

of the boundary condition at the outer edge demonstrated the importance of correct modelling assumptions in therms of an equivalent boundary stiffness. Finally, a bifurcation plot for the investigated actuator was created using the temperature in a 'stress-layer' as the loading parameter.

The proposed modelling strategy is computationally inexpensive. It can be naturally applied to arbitrary layered configurations. It offers great flexibility in the incorporation of actuation patters and the treatment of boundary conditions at the edge of the plate. Therefore, it shows potential for the tailored design of actuators.

References

[1] Wilder, E.A., Guo, S., Lin-Gibson, S., Fasolka, M.J., and Stafford, C.M., Measuring the modulus of soft polymer networks via a buckling-based metrology, *Macromolecules* (2006) **39**(12):4138–4143.

[2] Yang, D., Mosadegh, B., Ainla, A., Lee, B., Khashai, F., Suo, Z., Bertoldi, K., and Whitesides, G.M., Buckling of elastomeric beams enables actuation of soft machines, *Advanced Materials* (2015) **27**(41):6323–6327.

[3] Coman, C.D., On the compatibility relation for the Föppl–von Kármán plate equations, *Applied Mathematics Letters* (2012) **25**(12):2407–2410.

[4] Chia, C.Y., Geometrically nonlinear behavior of composite plates: A review, *Applied Mechanics Reviews* (1988) **41**(12):439.

[5] Villaggio, P., *Mathematical Models for Elastic Structures*. Cambridge University Press (CUP) (1997).

[6] Dickey, R.W., Nonlinear bending of circular plates, *SIAM Journal on Applied Mathematics* (1976) **30**(1):1–9.

[7] Berger, H.M., *A new approach to the analysis of large deflections of plates*. PhD thesis, California Institute of Technology, (1954).

[8] Krommer, M., Vetyukov, Y., and Staudigl, E., Nonlinear modelling and analysis of thin piezoelectric plates: Buckling and post-buckling behaviour, *Smart Structures and Systems* (2016) **18**(1):155–181.

[9] Dai, H.H., Paik, J.K., and Atluri, S.N., The global nonlinear galerkin method for the analysis of elastic large deflections of plates under combined loads: A scalar homotopy method for the direct solution of nonlinear algebraic equations, *Computers, Materials & Continua* (2011) **23**(1):69–100.

[10] Kirby, R. and Yosibash, Z., Solution of von-kármán dynamic non-linear plate equations using a pseudo-spectral method, *Computer Methods in Applied Mechanics and Engineering* (2004) **193**(6-8):575–599.

[11] Wang, X., Liu, X., Wang, J., and Zhou, Y., A wavelet method for bending of circular plate with large deflection, *Acta Mechanica Solida Sinica* (2015) **28**(1):83–90.

[12] Azrar, L., Boutyour, E.H., and Potier-Ferry, M., Non-linear forced vibrations of plates by an asymptotic-numerical method, *Journal of Sound and Vibration* (2002) **252**(4):657–674.

[13] Kamiya, N., Sawaki, Y., Nakamura, Y., and Fukui, A., An approximate finite deflection analysis of a heated elastic plate by the boundary element method, *Applied Mathematical Modelling* (1982) **6**(1):23–27.

[14] Krommer, M., The significance of non-local constitutive relations for composite thin plates including piezoelastic layers with prescribed electric charge, *Smart Materials and Structures* (2003) **12**(3):318–330.

[15] Reddy, J.N., *Mechanics of Laminated Composite Plates and Shells: Theory and Analysis, Second Edition*. CRC Press (2003).

[16] Sheploak, M. and Dugundji, J., Large deflections of clamped circular plates under initial tension and transitions to membrane behavior, *Journal of Applied Mechanics* (1998) **65**(1): 107.

[17] Faris, W.F., *Nonlinear Dynamics of Annular and Circular Plates under Thermal and Electrical Loadings*. PhD thesis, Virginia Polytechnic Institute and State University, (2003).

[18] Wang, Y.G., Shi, J.L., and Wang, X.Z., Large amplitude vibration of heated corrugated circular plates with shallow sinusoidal corrugations, *Applied Mathematical Modelling* (2009) **33**(9):3523–3532.

[19] Jones, E., Oliphant, T., and Peterson, e., Pearu, SciPy: Open source scientific tools for Python, (2001–).

VIII ECCOMAS Thematic Conference on Smart Structures and Materials
SMART 2017
A. Güemes, A. Benjeddou, J. Rodellar and J. Leng (Eds)

NONLINEAR ELECTRO-ELASTICITY FOR PIEZOELECTRIC MATERIALS AND STRUCTURES USING A MULTIPLICATIVE DECOMPOSITION OF THE DEFORMATION GRADIENT

ALEXANDER HUMER*, ELISABETH STAUDIGL† AND MICHAEL KROMMER†

*Institute of Technical Mechanics
Johannes Kepler University Linz
Altenbergerstraße 69, 4040 Linz, Austria
e-mail: alexander.humer@jku.at, http://www.jku.at/tmech/

† Research Group Mechanics of Solids, Institute of Mechanics and Mechatronics, TU Wien
Getreidemarkt 9, 1060 Vienna, Austria
e-mails: elisabeth.staudigl@tuwien.ac.at, michael.krommer@tuwien.ac.at,
http://www.mec.tuwien.ac.at/research/mechanics of solids/EN/

Key words: Nonlinear electro-elasticity, constitutive modeling, multiplicative decomposition, smart materials

Abstract. Nonlinear modeling of the inelastic behavior of materials by a multiplicative decomposition of the deformation gradient tensor is commonly used in geometrically nonlinear problems. Among the various scope of problems, the decomposition has proven applicable in thermoelasticity, elastoplasticity, as well as for the description of residual stresses arising in growth processes of biological tissues. In the context of smart materials, electro-elastic elastomers, shape-memory alloys and piezoelectric materials have been considered. The present paper reviews the nonlinear field equations of electro-elasticity and provides a general representation of the constitutive equations adopting the multiplicative decomposition of the deformation gradient. In extension to previous contributions, the electrostatic body forces and couples are consistently accounted for within the framework of thermodynamics. Exemplarily, the general relations are particularized for a simple choice of free energy functions.

1 INTRODUCTION

As opposed to diverse well-established theories within the range of small deformation problems, large deformation or even finite strains occurring in materials that show both an elastic and an inelastic response are more difficult to handle. One reason for the complexity is that the intuitive splitting of strains into an elastic part and an inelastic part does not carry over to nonlinear strain measures in large deformation problems in view of the limited physical meaning of

such decomposition, see, e.g., [1, 2]. To circumvent this problem, the concept of a multiplicative decomposition of the deformation gradient has proven to be a successful approach that has been adopted in thermoelasticity, elastoplasticity and for the modeling of residual stresses in growing materials, see [3] for a review. In the context of smart materials, the multiplicative decomposition was employed in the modeling of shape-memory alloys [4] and electro-active polymers [5]. A first approach regarding the electro-mechanical coupling in piezoelectric materials was presented in [6], where electrostatic body forces and couples, however, remained disregarded.

The main aim of the present paper is to provide a complete, thermodynamically consistent representation of the constitutive equations in problems of nonlinear electro-elasticity, where the multiplicative decomposition of the deformation gradient serves as key concept. For this purpose, we first discuss the balance equations of non-linear electro-elasticy in the familiar spatial representation. From the balance of energy, we can subsequently identify the general structure of the constitutive equations. Having transferred our theoretical basis into the material representations, we introduce the fundamental concept of a multiplicative decomposition of the deformation gradient into an electric part and a mechanical part. The decomposition involves the notion of an intermediate configuration that is introduced into the deformation path. Once the constitutive equations are given, we consider a particular type of a material response as an example.

2 THREE-DIMENSIONAL BALANCE EQUATIONS

To begin with, we recall the balance relations that govern the electro-elastic behavior of dielectric bodies subjected to an electric field. The electric field equations are typically given in a spatial (or Eulerian) representation, in which a given (current) configuration of the material bodies involved is referred to. On the contrary, the material (or Lagrangian) representation, in which physical quantities refer to a reference state, is typically preferred in solid mechanics problems. As the material representation of the electric field quantities is less intuitive, we begin with giving the balance laws in their spatial (or Eulerian) representation following the reasoning of Eringen and Maugin [7] and Yang [8].

Let Ω denote the volume occupied by a material body in the current configuration. In dielectric bodies, for which the free charge density vanishes, i.e., $\rho_e = 0$, Gauss' law of conservation of charge reads

$$\int_{\partial\Omega} \boldsymbol{d} \cdot \boldsymbol{n} \, \mathrm{d}a = \int_{\Omega} \operatorname{div} \boldsymbol{d} \, \mathrm{d}v = 0, \tag{1}$$

where $\boldsymbol{d}$ denotes the dielectric displacement and $\boldsymbol{n}$ is the outer unit normal to a surface element $\mathrm{d}a$. Requiring the balance equations to hold not only for the entire body but also for every sub-volume, we obtain the local representation by requiring the integrand of the volume integral to vanish,

$$\operatorname{div} \boldsymbol{d} = 0. \tag{2}$$

Faraday's law in quasistatic form,

$$\int_{\partial\Omega} \operatorname{curl} \boldsymbol{e} \, \mathrm{d}a = \boldsymbol{0}, \tag{3}$$

which again must hold for an arbitrary surface, implies that the electric field $\boldsymbol{e}$ can be represented

by the spatial gradient a the electric potential ϕ, i.e.,

$$\operatorname{curl} \boldsymbol{e} = \boldsymbol{0} \quad \Leftrightarrow \quad \boldsymbol{e} = -\operatorname{grad} \phi. \tag{4}$$

Proceeding with the balance laws of mechanics, we first assume that the mass m of a body remains conserved over time, which is why its material time derivative vanishes:

$$\dot{m} = \frac{\mathrm{d}}{\mathrm{d}t} \int_\Omega \rho \, \mathrm{d}v = \int_\Omega (\rho \, \mathrm{d}v)^{\cdot} = \int_\Omega \dot{\rho} + \rho \operatorname{div} \boldsymbol{v} \, \mathrm{d}v = 0, \tag{5}$$

where the $\boldsymbol{v} = \dot{\boldsymbol{x}}$ is the velocity field of the body's material points. The local form of the balance of mass consequently follows as

$$(\rho \, \mathrm{d}v)^{\cdot} = \dot{\rho} + \rho \operatorname{div} \boldsymbol{v} = 0. \tag{6}$$

The balance of linear momentum reflects the electromechanical coupling in dielectric media by means of the presence of electrostatic body forces

$$\boldsymbol{f}^E = (\operatorname{grad} \boldsymbol{e}) \cdot \boldsymbol{p}, \tag{7}$$

where $\boldsymbol{p}$ denotes the (macroscopic) polarization vector and $\boldsymbol{e}$ is the electric field. The change in linear momentum is balanced by body forces $\rho \, \boldsymbol{f} + \boldsymbol{f}^E$ as well as the surface traction $\boldsymbol{t}$ acting on a surface element with the outer normal $\boldsymbol{n}$,

$$\frac{\mathrm{d}}{\mathrm{d}t} \int_\Omega \rho \, \dot{\boldsymbol{v}} \, \mathrm{d}v = \int_\Omega \rho \, \boldsymbol{f} + \boldsymbol{f}^E \, \mathrm{d}v + \int_{\partial\Omega} \boldsymbol{t} \, \mathrm{d}a. \tag{8}$$

Using Gauss' theorem, the local form of the balance law is obtained as

$$\rho \, \dot{\boldsymbol{v}} = \operatorname{div} \boldsymbol{\sigma} + \rho \, \boldsymbol{f} + \boldsymbol{f}^E = \operatorname{div} \left(\boldsymbol{\sigma} + \boldsymbol{\sigma}^E \right) + \rho \, \boldsymbol{f}, \qquad \boldsymbol{f}^E = \operatorname{div} \boldsymbol{\sigma}^E, \qquad \boldsymbol{t} = \boldsymbol{\sigma} \cdot \boldsymbol{n}, \tag{9}$$

where the electrostatic body forces are represented by the divergence of the electrostatic stress tensor $\boldsymbol{\sigma}^E$. The sum of the Cauchy stress and the electrostatic stress tensor is referred to as total stress tensor

$$\boldsymbol{\sigma}^{\mathrm{tot}} = \boldsymbol{\sigma} + \boldsymbol{\sigma}^E, \qquad \boldsymbol{\sigma}^E = \boldsymbol{e}\boldsymbol{d} - \frac{1}{2} \epsilon_0 \, (\boldsymbol{e} \cdot \boldsymbol{e}) \, \mathbf{I}. \tag{10}$$

The electric couple $\boldsymbol{c}^E$ enters the balance of angular momentum

$$\frac{\mathrm{d}}{\mathrm{d}t} \int_\Omega \boldsymbol{x} \times \rho \, \boldsymbol{v} \, \mathrm{d}v = \int_\Omega \boldsymbol{x} \times \left(\rho \, \boldsymbol{f} + \boldsymbol{f}^E \right) + \boldsymbol{c}^E \mathrm{d}v + \int_{\partial\Omega} \boldsymbol{x} \times \boldsymbol{t} \, \mathrm{d}a, \qquad \boldsymbol{c}^E = \boldsymbol{p} \times \boldsymbol{e}, \tag{11}$$

whose local form yields the symmetry relation

$$\boldsymbol{\sigma}^S = \left(\boldsymbol{\sigma}^S \right)^T, \qquad \boldsymbol{\sigma}^S = \boldsymbol{\sigma} + \boldsymbol{\sigma}^P, \qquad \boldsymbol{\sigma}^P = \boldsymbol{e}\boldsymbol{p}. \tag{12}$$

In the above equation, the polarization stress tensor $\boldsymbol{\sigma}^P$ has been introduced. The polarization stress represents the distributed couples that occur in a dielectric material in presence of an

electric field. Substituting the polarization stress in the definition of the total stress tensor (10), we find

$$\boldsymbol{\sigma}^{\mathrm{tot}} = \boldsymbol{\sigma}^S - \boldsymbol{\sigma}^P + \boldsymbol{\sigma}^E = \boldsymbol{\sigma}^S + \boldsymbol{\sigma}^M, \qquad \boldsymbol{\sigma}^M = \boldsymbol{\sigma}^E - \boldsymbol{\sigma}^P = \epsilon_0 \boldsymbol{e}\boldsymbol{e} - \frac{1}{2}\epsilon_0 (\boldsymbol{e}\cdot\boldsymbol{e})\,\mathbf{I}, \tag{13}$$

where the Maxwell stress tensor $\boldsymbol{\sigma}^M$ has been introduced.

Consistency with thermodynamical principles is a crucial aspect in constitutive modeling. For this reason, the balance of energy plays a central role in our considerations. The global form of the balance of energy reads

$$\int_\Omega \rho \left(\frac{1}{2}\boldsymbol{v}\cdot\boldsymbol{v} + e\right) \mathrm{d}v = \int_\Omega \left(\rho\,\boldsymbol{f} + \boldsymbol{f}^E\right)\cdot\boldsymbol{v} + \ell^E \,\mathrm{d}v + \int_{\partial\Omega} \boldsymbol{t}\cdot\boldsymbol{v}\,\mathrm{d}a, \qquad \ell^E = \rho\,\boldsymbol{e}\cdot\frac{\mathrm{d}}{\mathrm{d}t}\left(\frac{\boldsymbol{p}}{\rho}\right), \tag{14}$$

where e is the internal energy density and the electric power ℓ^E has been introduced. The corresponding local form is obtained as

$$\rho\,\dot{e} = \boldsymbol{\sigma} : \operatorname{grad}\boldsymbol{v} + \ell^E = \boldsymbol{\sigma} : \operatorname{grad}\boldsymbol{v} + \rho\,\boldsymbol{e}\cdot\frac{\mathrm{d}}{\mathrm{d}t}\left(\frac{\boldsymbol{p}}{\rho}\right). \tag{15}$$

By means of a Legendre transformation, $\psi = e - \boldsymbol{e}\cdot\boldsymbol{p}/\rho$, we change the independent variables and obtain the balance of free energy as

$$\rho\,\dot{\psi} = \rho\,\dot{e} - \rho\,\dot{\boldsymbol{e}}\cdot\frac{\boldsymbol{p}}{\rho} - \rho\,\boldsymbol{e}\cdot\frac{\mathrm{d}}{\mathrm{d}t}\left(\frac{\boldsymbol{p}}{\rho}\right) = \boldsymbol{\sigma} : \dot{\mathbf{F}}\cdot\mathbf{F}^{-1} - \boldsymbol{p}\cdot\dot{\boldsymbol{e}}, \tag{16}$$

where the spatial velocity gradient has been expressed in terms of the deformation gradient, i.e., $\operatorname{grad}\boldsymbol{v} = \dot{\mathbf{F}}\cdot\mathbf{F}^{-1}$.

3 CONSTITUTIVE RELATIONS

To determine the constitutive equations, we compute the rate of the free energy $\psi = \psi(\boldsymbol{e}, \mathbf{F})$,

$$\dot{\psi} = \frac{\partial\psi}{\partial\mathbf{F}} : \dot{\mathbf{F}} + \frac{\partial\psi}{\partial\boldsymbol{e}}\cdot\dot{\boldsymbol{e}}. \tag{17}$$

Comparing the local balance of free energy with the above expression for its rate, we can identify the general relations for Cauchy's stress tensor and the polarization vector as

$$\boldsymbol{\sigma} = \rho\frac{\partial\psi}{\partial\mathbf{F}}\cdot\mathbf{F}^T, \qquad \boldsymbol{p} = -\rho\frac{\partial\psi}{\partial\boldsymbol{e}}. \tag{18}$$

In order to find a compact expression for the total stress tensor $\boldsymbol{\sigma}^{\mathrm{tot}}$, we augment the free energy by the vacuum contribution ψ^{aug},

$$\Omega = \psi - \psi^{\mathrm{aug}}, \qquad \dot{\Omega} = \frac{\partial\Omega}{\partial\mathbf{F}} : \dot{\mathbf{F}} + \frac{\partial\Omega}{\partial\boldsymbol{e}}\cdot\dot{\boldsymbol{e}}, \qquad \rho\,\psi^{\mathrm{aug}} = \frac{1}{2}\epsilon_0\,(\boldsymbol{e}\cdot\boldsymbol{e})\,. \tag{19}$$

The rate of the augmented free energy Ω then reads

$$\rho\,\dot{\Omega} = \rho\,\dot{\psi} - \rho\,\dot{\psi}^{\mathrm{aug}} = \boldsymbol{\sigma} : \dot{\mathbf{F}}\cdot\mathbf{F}^{-1} - \boldsymbol{p}\cdot\dot{\boldsymbol{e}} - \epsilon_0\left\{\boldsymbol{e}\cdot\dot{\boldsymbol{e}} + \frac{1}{2}(\boldsymbol{e}\cdot\boldsymbol{e})\,\mathbf{F}^{-T} :\ \dot{\mathbf{F}}\right\}, \tag{20}$$

where the material time derivative of the determinant of the deformation gradient,

$$\dot{J} = (\det \mathbf{F})^{\cdot} = \frac{\partial \det \mathbf{F}}{\partial \mathbf{F}} : \dot{\mathbf{F}} = J\mathbf{F}^{-T} : \dot{\mathbf{F}}, \tag{21}$$

has been regarded. Recalling the definition of the total stress (13) along with the fundamental relation among the electric field quantities,

$$\boldsymbol{d} = \epsilon_0 \boldsymbol{e} + \boldsymbol{p}, \tag{22}$$

we obtain

$$\rho \dot{\Omega} = \left\{ \boldsymbol{\sigma} - \frac{1}{2}\epsilon_0 (\boldsymbol{e} \cdot \boldsymbol{e}) \mathbf{I} \right\} : \dot{\mathbf{F}} \cdot \mathbf{F}^{-1} - \boldsymbol{d} \cdot \dot{\boldsymbol{e}} = \left(\boldsymbol{\sigma}^{\mathrm{tot}} - \boldsymbol{e}\boldsymbol{d} \right) : \dot{\mathbf{F}} \cdot \mathbf{F}^{-1} - \boldsymbol{d} \cdot \dot{\boldsymbol{e}}. \tag{23}$$

The comparison with the general rate expression

$$\dot{\Omega} = \frac{\partial \Omega}{\partial \mathbf{F}} : \dot{\mathbf{F}} + \frac{\partial \Omega}{\partial \boldsymbol{e}} \cdot \boldsymbol{e}, \tag{24}$$

allows us to determine the constitutive equations for the total stress and the dielectric displacement as

$$\boldsymbol{\sigma}^{\mathrm{tot}} = \rho \frac{\partial \Omega}{\partial \mathbf{F}} \cdot \mathbf{F}^T + \boldsymbol{e}\boldsymbol{d}, \qquad \boldsymbol{d} = -\rho \frac{\partial \Omega}{\partial \boldsymbol{e}}. \tag{25}$$

4 MATERIAL FORMULATION OF GOVERNING EQUATIONS

From a solid mechanics point of view, we prefer to formulate the governing equations in terms of material quantities that refer to the reference configuration of the considered body. The physical fields are functions of the position vector $\boldsymbol{X}$ of the material points in the reference configuration rather than their current position $\boldsymbol{x}$, which is not known in advance. For this purpose, we transform the integrals in the global form of the balance equations into integrals over the domain in the reference configuration. Using Nanson's formula, $\boldsymbol{n}\,\mathrm{d}a = J\,\mathbf{F}^{-T} \cdot \boldsymbol{N}\,\mathrm{d}A$, Gauss' law (1) can be rewritten as

$$\int_{\partial\Omega_0} \boldsymbol{\mathcal{D}} \cdot \boldsymbol{N}\,\mathrm{d}A = 0, \qquad \mathrm{Div}\,\boldsymbol{\mathcal{D}} = 0, \tag{26}$$

where "Div" denotes the material divergence, i.e., derivatives with respect to material coordinates. The material counterpart to the dielectric displacement $\boldsymbol{d}$ has been introduced as

$$\boldsymbol{\mathcal{D}} = J\,\boldsymbol{d} \cdot \mathbf{F}^{-T}, \qquad \boldsymbol{d} = J^{-1}\boldsymbol{\mathcal{D}} \cdot \mathbf{F}^T \tag{27}$$

If we replace the spatial gradient of the electric potential in (4) by the material gradient, we obtain a natural definition of the material electric field as

$$\boldsymbol{\mathcal{E}} = -\,\mathrm{Grad}\,\phi = \boldsymbol{e} \cdot \mathbf{F}, \qquad \boldsymbol{e} = \boldsymbol{\mathcal{E}} \cdot \mathbf{F}^{-1}. \tag{28}$$

Regarding the balance of linear momentum, we recover the well-known relations of nonlinear continuum mechanics,

$$\rho_0 \dot{\boldsymbol{v}} = \mathrm{Div}\left(\mathbf{S} + \mathbf{S}^E\right) + \rho_0 \boldsymbol{f}, \tag{29}$$

where the second Piola-Kirchhoff stress tensor $\mathbf{S}$ and Cauchy's stress tensor $\boldsymbol{\sigma}$—along with the other stress tensors introduced above—are related through

$$\mathbf{S} = J\,\mathbf{F}^{-1}\cdot\boldsymbol{\sigma}\cdot\mathbf{F}^{-T}, \qquad \boldsymbol{t}_0 = \mathbf{F}\cdot\mathbf{S}\cdot\boldsymbol{N}. \tag{30}$$

The Lagrangian stress vector is denoted by $\boldsymbol{t}_0$ and $\rho_0 = \rho\,J$ is the mass density per unit volume in the reference configuration. Substituting the material electric field quantities, we obtain the second Piola-Kirchhoff electrostatic stresses as

$$\mathbf{S}^E = \mathbf{C}^{-1}\cdot\boldsymbol{\mathcal{E}}\boldsymbol{\mathcal{D}} - \frac{1}{2}\epsilon_0 J\left(\boldsymbol{\mathcal{E}}\cdot\mathbf{C}^{-1}\cdot\boldsymbol{\mathcal{E}}\right)\mathbf{C}^{-1}. \tag{31}$$

The balance of angular momentum yields the symmetry of the tensor $\mathbf{S}^S$,

$$\mathbf{S}^S = J\,\mathbf{F}^{-1}\cdot\boldsymbol{\sigma}^S\cdot\mathbf{F}^{-T} = \mathbf{S} + \mathbf{S}^P, \qquad \mathbf{S}^P = J\,\mathbf{F}^{-1}\cdot\boldsymbol{ep}\cdot\mathbf{F}^{-T} = \mathbf{C}^{-1}\cdot\boldsymbol{\mathcal{E}}\boldsymbol{\mathcal{P}}. \tag{32}$$

In the above relation for the polarization stress, the definition of the material polarization vector has been introduced. Hence, the polarization transforms in the same way as the dielectric displacement, i.e.,

$$\boldsymbol{\mathcal{P}} = J\,\boldsymbol{p}\cdot\mathbf{F}^{-T}, \qquad \boldsymbol{p} = J^{-1}\boldsymbol{\mathcal{P}}\cdot\mathbf{F}^{T}. \tag{33}$$

In material representation, relation (22) therefore becomes

$$\boldsymbol{\mathcal{D}} = \epsilon_0 J\boldsymbol{\mathcal{E}}\cdot\mathbf{C}^{-1} + \boldsymbol{\mathcal{P}}. \tag{34}$$

Partitioning the surface of the body $\partial\Omega_0$ into S_u and S_t, where the deformation $\boldsymbol{x}$ and the traction $\boldsymbol{t}$ is prescribed, we can formulate the mechanical boundary conditions as

$$\boldsymbol{X}\in S_u: \quad \boldsymbol{x} = \boldsymbol{\xi}, \qquad \boldsymbol{X}\in S_t: \quad \boldsymbol{t}_0 = \boldsymbol{\tau}_0. \tag{35}$$

Similarly, let S_ϕ denote the surface where the electric potential is prescribed, whereas the free surface charge s_e density is given on S_d, the electric boundary conditions are

$$\boldsymbol{X}\in S_\phi: \quad \phi = \varphi, \qquad \boldsymbol{X}\in S_d: \quad \boldsymbol{\mathcal{D}}\cdot\boldsymbol{N} = -\sigma_e, \tag{36}$$

To directly determine the constitutive equations of the material stress and polarization, we express the free energy as a function of the material electric field.

$$\psi(\boldsymbol{e},\mathbf{F}) = \psi(\boldsymbol{e}(\boldsymbol{\mathcal{E}},\mathbf{F}),\mathbf{F}) = \bar{\psi}(\boldsymbol{\mathcal{E}},\mathbf{F}) \tag{37}$$

The change in the independent variables has been emphasized by an overbar in order to avoid ambiguities. When taking the derivative of $\bar{\psi}$ with respect to the deformation gradient for a fixed material electric field ($\boldsymbol{\mathcal{E}} = \text{const}$), the dependence of the physical electric field $\boldsymbol{e} = \boldsymbol{e}(\boldsymbol{\mathcal{E}},\mathbf{F})$ on the deformation gradient needs to be regarded,

$$\frac{\partial\bar{\psi}}{\partial\mathbf{F}} = \frac{\partial\psi}{\partial\mathbf{F}} + \frac{\partial\psi}{\partial\boldsymbol{e}}\cdot\frac{\partial\boldsymbol{e}}{\partial\mathbf{F}}, \qquad \frac{\partial\psi}{\partial\mathbf{F}} = \frac{\partial\bar{\psi}}{\partial\mathbf{E}} : \frac{\partial\mathbf{E}}{\partial\mathbf{F}} + \frac{\boldsymbol{p}}{\rho}\cdot\frac{\partial\boldsymbol{e}}{\partial\mathbf{F}}. \tag{38}$$

Introducing Green's strain tensor $\mathbf{E} = (\mathbf{F}^T \cdot \mathbf{F} - \mathbf{I})/2$ and substituting the relation for the polarization (18),

$$\frac{\partial \bar{\psi}}{\partial \mathbf{E}} : \frac{\partial \mathbf{E}}{\partial \mathbf{F}} = \mathbf{F} \cdot \frac{\partial \bar{\psi}}{\partial \mathbf{E}}, \qquad \boldsymbol{p} \cdot \frac{\partial \boldsymbol{e}}{\partial \mathbf{F}} = -\boldsymbol{e}\boldsymbol{p} \cdot \mathbf{F}^{-T}, \tag{39}$$

gives the constitutive equations for the Piola-Kirchhoff stress tensors $\mathbf{S}$ and $\mathbf{S}^S$, respectively,

$$\mathbf{S} = \rho_0 \frac{\partial \bar{\psi}}{\partial \mathbf{E}} - J\mathbf{F}^{-1} \cdot \boldsymbol{e}\boldsymbol{p} \cdot \mathbf{F}^{-T} = \rho_0 \frac{\partial \bar{\psi}}{\partial \mathbf{E}} - \mathbf{S}^P, \qquad \mathbf{S}^S = \rho_0 \frac{\partial \bar{\psi}}{\partial \mathbf{E}} \tag{40}$$

The material polarization vector follows as

$$\boldsymbol{\mathcal{P}} = -\rho_0 \mathbf{F}^{-1} \cdot \frac{\partial \psi}{\partial \boldsymbol{e}} = -\rho_0 \mathbf{F}^{-1} \cdot \frac{\partial \bar{\psi}}{\partial \boldsymbol{\mathcal{E}}} \cdot \frac{\partial \boldsymbol{\mathcal{E}}}{\partial \boldsymbol{e}} = -\rho_0 \frac{\partial \bar{\psi}}{\partial \boldsymbol{\mathcal{E}}}. \tag{41}$$

To conclude material representation of the governing equations, we consider the relations for the total stress tensor and the dielectric displacement. The total stress tensor follows as the sum of the symmetric stress tensor $\mathbf{S}^S$ and the Maxwell stresses $\mathbf{S}^M$,

$$\mathbf{S}^{\text{tot}} = \rho_0 \frac{\partial \bar{\psi}}{\partial \mathbf{E}} + \mathbf{S}^M, \qquad \mathbf{S}^M = \epsilon_0 J \left\{ \mathbf{C}^{-1} \cdot \boldsymbol{\mathcal{E}}\boldsymbol{\mathcal{E}} \cdot \mathbf{C}^{-1} - \frac{1}{2} \left(\boldsymbol{\mathcal{E}} \cdot \mathbf{C}^{-1} \cdot \boldsymbol{\mathcal{E}} \right) \mathbf{C}^{-1} \right\}. \tag{42}$$

Rewriting the augmentation term $\psi^{\text{aug}}(\mathbf{e}, \mathbf{F})$ as a function $\bar{\psi}^{\text{aug}}(\boldsymbol{\mathcal{E}}, \mathbf{F})$, we find the relation

$$\mathbf{F} \cdot \frac{\partial \bar{\psi}^{\text{aug}}}{\partial \mathbf{E}} = \frac{\partial \psi^{\text{aug}}}{\partial \mathbf{F}} + \frac{\partial \psi^{\text{aug}}}{\partial \boldsymbol{e}} \cdot \frac{\partial \boldsymbol{e}}{\partial \mathbf{F}} = \frac{\epsilon_0 J}{\rho_0} \left\{ \frac{1}{2} \mathbf{F}^{-T} \left(\boldsymbol{\mathcal{E}} \cdot \mathbf{C}^{-1} \cdot \boldsymbol{\mathcal{E}} \right) - \mathbf{F}^{-T} \cdot \boldsymbol{\mathcal{E}}\boldsymbol{\mathcal{E}} \cdot \mathbf{C}^{-1} \right\}. \tag{43}$$

among the derivatives, which allows us to formulate the total stresses in terms of $\bar{\Omega}(\boldsymbol{\mathcal{E}}, \mathbf{F})$

$$\mathbf{S}^{\text{tot}} = \rho_0 \frac{\partial \bar{\Omega}}{\partial \mathbf{E}}, \qquad \bar{\Omega} = \bar{\psi} + \bar{\psi}^{\text{aug}}. \tag{44}$$

Proceeding in the same way for the derivatives with respect to the material electric field,

$$\frac{\partial \bar{\psi}^{\text{aug}}}{\partial \boldsymbol{\mathcal{E}}} = \frac{\partial \psi^{\text{aug}}}{\partial \boldsymbol{e}} \cdot \frac{\partial \boldsymbol{e}}{\partial \boldsymbol{\mathcal{E}}} = \frac{\epsilon_0 J}{\rho_0} \boldsymbol{\mathcal{E}} \cdot \mathbf{C}^{-1}, \tag{45}$$

we obtain the constitutive equation for the material electric displacement vector:

$$\boldsymbol{\mathcal{D}} = \epsilon_0 J \boldsymbol{\mathcal{E}} \cdot \mathbf{C}^{-1} + \boldsymbol{\mathcal{P}} = \rho_0 \frac{\partial \bar{\psi}^{\text{aug}}}{\partial \boldsymbol{\mathcal{E}}} - \rho_0 \frac{\partial \bar{\psi}}{\partial \boldsymbol{\mathcal{E}}} = -\frac{\partial \bar{\Omega}}{\partial \boldsymbol{\mathcal{E}}}. \tag{46}$$

5 MULTIPLICATIVE DECOMPOSITION

Before we can specify the constitutive equations in more detail, we need to introduce the multiplicative decomposition of the deformation gradient, which has proven to be an intuitive approach in the modeling of the material response involving inelastic processes [3]. Accordingly, the deformation gradient is split into an electric and a mechanical part,

$$\mathbf{F} = \mathbf{F}_m \cdot \mathbf{F}_e. \tag{47}$$

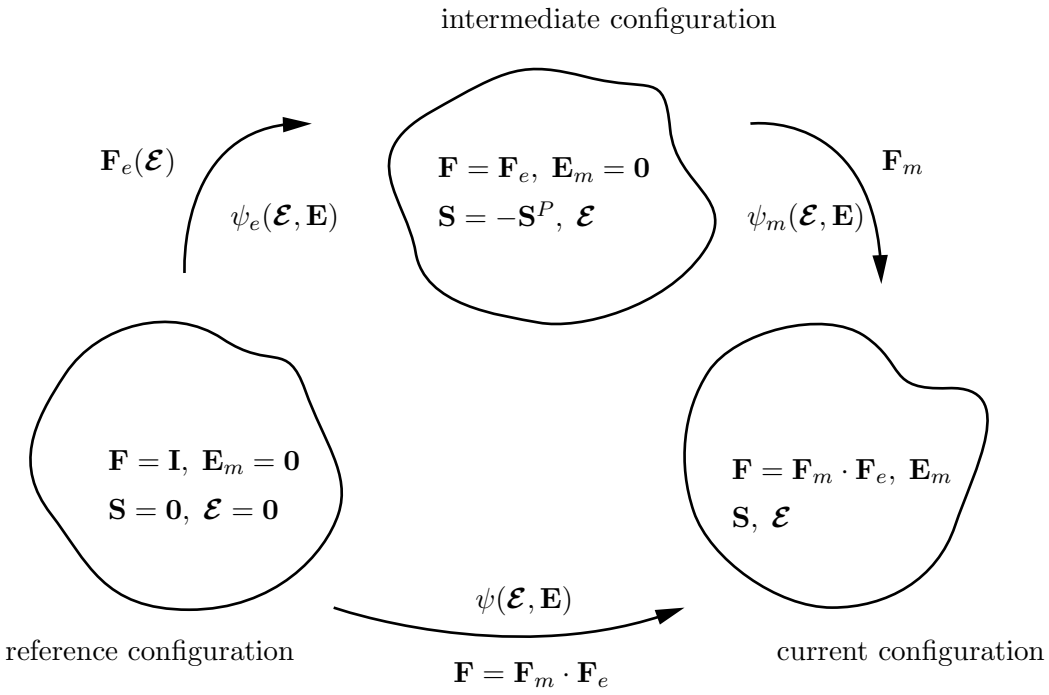

Figure 1: Concept of the multiplicative decomposition of the deformation gradient: a (fictitious) intermediate configuration is introduced into the deformation path.

The concept of a multiplicative decomposition introduces an additional configuration into the deformation path, see Fig. 1. By requiring the electric part of the deformation gradient to solely depend on the (material) electric field, i.e., $\mathbf{F}_e = \mathbf{F}_e(\boldsymbol{\mathcal{E}})$, this intermediate configuration can be regarded as a configuration that evolves from the reference configuration in presence of an electric field. As opposed to conventional approaches, in which strain measures associated with either the reference configuration or the current configuration are additively split into mechanical and inelastic parts, the present approach leads to a more natural notion of strain. With both operating on the intermediate configuration, we sum up an Almansi-type strain related to the deformation path governed by $\mathbf{F}_e$ and a Green-type strain related to the mechanical part $\mathbf{F}_m$,

$$\mathbf{e}_e = \frac{1}{2}\left(\mathbf{I} - \mathbf{F}_e^{-T} \cdot \mathbf{F}_e^{-1}\right), \qquad \mathbf{E}_m = \frac{1}{2}\left(\mathbf{F}_m^T \cdot \mathbf{F}_m - \mathbf{I}\right), \tag{48}$$

from which Green's (total) strain follows upon a pull-back to the reference configuration

$$\mathbf{E} = \mathbf{F}_e^T \cdot (\mathbf{e}_e + \mathbf{E}_m) \cdot \mathbf{F}_e. \tag{49}$$

The above considerations suggest the free energy to be split into two parts that are associated with the respective paths in the deformation,

$$\bar{\psi} = \psi_m(\mathbf{E}_m) + \psi_e(\boldsymbol{\mathcal{E}}, \mathbf{E}), \tag{50}$$

where the mechanical part depends on $\mathbf{E}_m = \mathbf{F}_e^{-T} \cdot \mathbf{E} \cdot \mathbf{F}_e^{-1} - \mathbf{e}_e$ only. The constitutive equation for the (symmetric) Piola-Kirchhoff stress $\mathbf{S}^S$ then becomes

$$\mathbf{S}^S = \rho_0 \frac{\partial \psi_m}{\partial \mathbf{E}_m} : \frac{\partial \mathbf{E}_m}{\partial \mathbf{E}} + \rho_0 \frac{\partial \psi_e}{\partial \mathbf{E}} = \rho_0 \mathbf{F}_e^{-1} \cdot \frac{\partial \psi_m}{\partial \mathbf{E}_m} \cdot \mathbf{F}_e^{-T} + \rho_0 \frac{\partial \psi_e}{\partial \mathbf{E}}. \tag{51}$$

For the (material) polarization, we obtain the relation

$$\boldsymbol{\mathcal{P}} = -\rho_0 \frac{\partial \psi_m}{\partial \mathbf{F}_e} : \frac{\partial \mathbf{F}_e}{\partial \boldsymbol{\mathcal{E}}} - \rho_0 \frac{\partial \psi_e}{\partial \boldsymbol{\mathcal{E}}} \tag{52}$$

6 EXEMPLARY CONSTITUTIVE RELATIONS

In what follows, we want to particularize the relations for the material response by choosing simple examples for ψ_m and ψ_e. To begin with, we assume the electric part as a quadratic function in the (material) electric field

$$\rho_0 \psi_e = -\frac{1}{2} \boldsymbol{\mathcal{E}} \cdot \boldsymbol{\chi} \cdot \boldsymbol{\mathcal{E}}, \tag{53}$$

where $\boldsymbol{\chi}$ denotes the second-order susceptibility tensor. With this choice, the (symmetric) Piola-Kirchhoff stress $\mathbf{S}^S$ simplifies to

$$\mathbf{S}^S = \rho_0 \mathbf{F}_e^{-1} \cdot \frac{\partial \psi_m}{\partial \mathbf{E}_m} \cdot \mathbf{F}_e^{-T}, \tag{54}$$

since $\partial \psi_e / \partial \mathbf{E} = \mathbf{0}$, and the polarization vector reads

$$\boldsymbol{\mathcal{P}} = -\rho_0 \frac{\partial \psi_m}{\partial \mathbf{E}_m} : \frac{\partial \mathbf{E}_m}{\partial \boldsymbol{\mathcal{E}}} + \boldsymbol{\mathcal{E}} \cdot \boldsymbol{\chi}. \tag{55}$$

For the mechanical part in the deformation path, we exemplarily consider a stress response similar to the St. Venant-Kirchhoff material, which can be regarded as a generalization of Hooke's law to large deformation problems,

$$\rho_i \psi_m = \frac{1}{2} \mathbf{E}_m : {}^4\mathbf{D} : \mathbf{E}_m, \tag{56}$$

where ${}^4\mathbf{D}$ denotes the fourth-order tensor of elastic moduli. As compared to the conventional St. Venant-Kirchhoff relations, Green's (total) strain is replaced by $\mathbf{E}_m$ in the above relation and the density is the mass density per unit volume in the intermediate configuration $\rho_i = J_e^{-1} \rho_0$ (with $J_e = \det \mathbf{F}_e$). With J_e depending on the electric field only, the constitutive equation for the (symmetric) Piola-Kirchhoff stress $\mathbf{S}^S$ becomes

$$\mathbf{S}^S = J_e \mathbf{F}_e^{-1} \cdot \left({}^4\mathbf{D} : \mathbf{E}_m \right) \cdot \mathbf{F}_e^{-T}. \tag{57}$$

Taking the derivative of ψ_m with respect to the the material electric field $\boldsymbol{\mathcal{E}}$, we obtain the material polarization vectors as

$$\boldsymbol{\mathcal{P}} = -\left\{ \rho_0 \psi_m \mathbf{I} - (\mathbf{I} + 2\mathbf{E}_m) \cdot \left({}^4\mathbf{D} : \mathbf{E}_m \right) \right\} \cdot \mathbf{F}_e^{-T} : \frac{\partial \mathbf{F}_e}{\partial \boldsymbol{\mathcal{E}}} + \boldsymbol{\mathcal{E}} \cdot \boldsymbol{\chi}. \tag{58}$$

To determine the total stress tensor, we first introduce the material counterpart of the Maxwell stresses

$$\mathbf{S}^M = \epsilon_0 J \mathbf{C}^{-1} \cdot \boldsymbol{\mathcal{E}}\boldsymbol{\mathcal{E}} \cdot \mathbf{C}^{-1} - \frac{1}{2}\epsilon_0 J \left(\boldsymbol{\mathcal{E}} \cdot \mathbf{C}^{-1} \cdot \boldsymbol{\mathcal{E}}\right) \mathbf{C}^{-1}. \tag{59}$$

The total stresses therefore read

$$\mathbf{S}^{\text{tot}} = J_e \mathbf{F}_e^{-1} \cdot \left({}^4\mathbf{D} : \mathbf{E}_m\right) \cdot \mathbf{F}_e^{-T} + \epsilon_0 J \mathbf{C}^{-1} \cdot \boldsymbol{\mathcal{E}}\boldsymbol{\mathcal{E}} \cdot \mathbf{C}^{-1} - \frac{1}{2}\epsilon_0 J \left(\boldsymbol{\mathcal{E}} \cdot \mathbf{C}^{-1} \cdot \boldsymbol{\mathcal{E}}\right) \mathbf{C}^{-1}. \tag{60}$$

Using the relation that holds among the electric field, the polarization and the dielectric displacement, the latter is obtained as

$$\boldsymbol{\mathcal{D}} = \epsilon_0 J \boldsymbol{\mathcal{E}} \cdot \mathbf{C}^{-1} - \left\{\rho_0 \psi_m \mathbf{I} - (\mathbf{I} + 2\mathbf{E}_m) \cdot \left({}^4\mathbf{D} : \mathbf{E}_m\right)\right\} \cdot \mathbf{F}_e^{-T} : \frac{\partial \mathbf{F}_e}{\partial \boldsymbol{\mathcal{E}}} + \boldsymbol{\mathcal{E}} \cdot \boldsymbol{\chi}. \tag{61}$$

Having determined the relations for $\mathbf{S}^S$ and $\boldsymbol{\mathcal{P}}$, the electric part of the deformation gradient $\mathbf{F}_e$ remains to be specified to close the governing equations. We can, for instance, assume a series expansion in the form

$$\mathbf{F}_e = \mathbf{I} + \boldsymbol{\mathcal{E}} \cdot {}^3\mathbf{e} + \boldsymbol{\mathcal{E}}\boldsymbol{\mathcal{E}} : {}^4\mathbf{b} + \dots, \tag{62}$$

where ${}^3\mathbf{e}$ represents the third-order tensor of piezoelectric coefficients and ${}^4\mathbf{b}$ is the fourth-order material tensor related to electro-striction.

The concept of an intermediate configuration, which is intrinsically linked to the multiplicative decomposition of the deformation gradient, suggests the idea of *"de-stressing"* that is familiar from other fields of constitutive theories. In the context of nonlinear thermomechanics, the notion of *"isothermal de-stressing"* is introduced for the conceptual removal of stresses from the current configuration while keeping the temperature constant, i.e., preserving the inelastic (thermal) strains. In elastoplasticity, the idea of *"elastic de-stressing"* describes the process of removing stresses from the current configuration such that the intermediate configuration differs from the reference configuration by the plastic deformation. In nonlinear electro-elasticity, we have already encountered several notions of stresses in our derivations, which raises the question of which stresses are to be removed from the current configuration in order to recover the intermediate configuration. To identify the proper concept of de-stressing, we start from the requirement that no mechanical deformation is present in the intermediate configuration, i.e., $\mathbf{F}_m = \mathbf{I}$, $\mathbf{E}_m = \mathbf{0}$, since its evolution from the reference configuration due to the presence of an electric field is solely described by $\mathbf{F}_e$. Irrespective of the particular structure of the mechanical part of the free energy ψ_m, we presume that it is of quadratic order in $\mathbf{E}_m$ at least. If the electric part follows Eq. (53), the symmetric second Piola-Kirchhoff stress tensor vanishes identically, i.e., $\mathbf{S}^S = \mathbf{0}$. The (mechanical) stresses in the intermediate configuration therefore equal the negative of the polarization stresses,

$$\mathbf{S} = \mathbf{S}^S - \mathbf{S}^P = -\mathbf{S}^P = -\mathbf{C}_e^{-1} \cdot \boldsymbol{\mathcal{E}}\boldsymbol{\mathcal{P}}, \qquad \mathbf{C}_e^{-1} = \mathbf{F}_e^{-1} \cdot \mathbf{F}_e^{-T}. \tag{63}$$

The total stress tensor in the intermediate configuration is therefore identical to the Maxwell stresses (42),

$$\mathbf{S}^{\text{tot}} = \mathbf{S}^S + \mathbf{S}^M = \mathbf{S}^M = J_e \mathbf{C}_e^{-1} \cdot \boldsymbol{\mathcal{E}}\boldsymbol{\mathcal{E}} \cdot \mathbf{C}_e^{-1} - \frac{1}{2}\epsilon_0 J_e \left(\boldsymbol{\mathcal{E}} \cdot \mathbf{C}_e^{-1} \cdot \boldsymbol{\mathcal{E}}\right) \mathbf{C}_e^{-1}. \tag{64}$$

Eventually, the (material) polarization vector follows from the electric free energy (53) as

$$\boldsymbol{\mathcal{P}} = \boldsymbol{\mathcal{E}} \cdot \boldsymbol{\chi}. \tag{65}$$

From the above relations, we can summarize the following observations:

- The symmetric stress tensor $\mathbf{S}^S$ is zero in the intermediate configuration. De-stressing therefore implies removing $\mathbf{S}^S$ in the current configuration.
- The mechanical stress tensor $\mathbf{S}$ does not vanish in the intermediate configuration but equals the negative of the (non-symmetric) polarization stress. We can interpret this result in terms of body forces that are present in the intermediate configuration. As opposed to the total electrostatic body forces, which are represented by the divergence of $\mathbf{S}^E$, however, only the non-symmetric part related to the susceptibility (i.e., polarizability),

  $$\mathbf{S} = -\mathbf{S}^P = -(\mathbf{S}^E - \mathbf{S}^M), \tag{66}$$

  contributes to the mechanical stresses $\mathbf{S}$. The contribution from the symmetric Maxwell tensor $\mathbf{S}^M$ vanishes in the intermediate configuration.
- The material polarization vector $\boldsymbol{\mathcal{P}}$ only contains the electric part; no mechanical coupling exists in the intermediate configuration.
- In general, the intermediate configuration need not be compatible, i.e., the material volume elements do no longer fit together upon the de-stressing from the configuration. The incompatibility of the intermediate configuration causes additional stresses acting on the body in the current configuration.

7 CONCLUSIONS

In the present paper, we have discussed the general structure of the constitutive equations in the framework of nonlinear electro-elasticity. The modeling of the material response is based on thermodynamic principles and allows for various kinds of electro-mechanical coupling. The multiplicative decomposition of the deformation gradient into an electric and a mechanical part plays a key role in the present approach. The electric part describes the evolution of an intermediate configuration from the reference configuration due to the presence of an electric field, whereas the mechanical part plays a crucial role in the stress response associated with the mechanical part in the deformation path. Due to the presence of electrostatic body forces and couples, the concept of de-stressing from the current configuration has been adapted to the diverse notions of stresses in the present problem of electro-elasticity. The main advantage of the present approach for the constitutive modeling lies in the fact that we can immediately resort to classical energy functions of nonlinear elasticity and electrostatics for the parts of the free energy associated with the electric and the mechanical deformation path, respectively. The electro-mechanical coupling due to, e.g., piezoelectricity or electrostriction, is reflected in the structure of the electric part of the deformation gradient.

ACKNOWLEDGEMENTS

Support by the Austrian COMET-K2 program of the Linz Center of Mechatronics (LCM), funded by the Austrian Federal Government and the Federal State of Upper Austria, is gratefully acknowledged.

REFERENCES

[1] Haupt, P. *Continuum Mechanics and Theory of Materials*. Springer, 2nd edition, 2002.

[2] Bonet, J. and Wood, R.D. *Nonlinear Continuum Mechanics for Finite Element Analysis*. Cambridge University Press, second edition, 2008.

[3] Lubarda, V.A. Constitutive theories based on the multiplicative decomposition of deformation gradient: Thermoelasticity, elastoplasticity, and biomechanics. *Applied Mechanics Reviews*, 57(4):95–108, 2004.

[4] Arghavani, J, Auricchio, F, Naghdabadi, R, Reali, A, and Sohrabpour, S. A 3d finite strain phenomenological constitutive model for shape memory alloys considering martensite reorientation. *Continuum Mechanics and Thermodynamics*, 22(5):345–362, 2010.

[5] Skatulla, S., Sansour, C., and Arockiarajan, A. A multiplicative approach for nonlinear electro-elasticity. *Computer Methods in Applied Mechanics and Engineering*, 245–246:243–255, 2012.

[6] Humer, A. and Krommer, M. Modeling of piezoelectric materials by means of a multiplicative decomposition of the deformation gradient. *Mechanics of Advanced Materials and Structures*, 22(1-2):125–135, 2015.

[7] Eringen, A.C. and Maugin, G.A. *Electrodynamics of continua. Vol. 1: Foundations and solid media*. Springer-Verlag, New York, 1990.

[8] Yang, J. *An Introduction to the Theory of Piezoelectricity*. Springer, 2005.

VIII ECCOMAS Thematic Conference on Smart Structures and Materials
SMART 2017
A. Güemes, A. Benjeddou, J. Rodellar and J. Leng (Eds)

NONLINEAR MODELLING OF DIELECTRIC ELASTOMER SINGLE LAYER PLATES USING A MULTIPLICATIVE DECOMPOSITION OF THE DEFORMATION GRADIENT TO ACCOUNT FOR ELECTROSTRICTION

ELISABETH STAUDIGL, MICHAEL KROMMER AND YURY VETYUKOV

Research group - Mechanics of Solids
Institute for Mechanics and Mechatronics, TU Wien
Getreidemarkt 9, A-1060 Vienna, Austria
e-mails: {elisabeth.staudigl,michael.krommer,yury.vetyukov}@tuwien.ac.at
web page: http://www.mec.tuwien.ac.at/research/mechanics_of_solids/EN/

Key words: Nonlinear electro-elasticity, incompressible dielectric elastomers, electrostriction, multiplicative decomposition, thin single layer plates, electro-mechanical stability

Abstract. In this paper we study dielectric elastomers accounting for constitutive coupling by means of electrostriction using a multiplicative decomposition of the deformation gradient tensor. The resulting constitutive relations are reduced to the special case of thin single layer plates made of incompressible dielectric elastomers. As an example problem we study the electro-mechanically coupled behavior of such a single layer plate in the absence of mechanical forces with special emphasis on the effect of electrostriction on the breakdown instability.

1 Three-dimensional constitutive relations

This section discusses relations involving certain physical entities, which are the non-symmetric Cauchy stress tensor $\boldsymbol{\sigma}$ and the spatial polarization vector $\mathbf{p}$, as well as their material counterparts, the second Piola-Kirchhoff stress tensor $\mathbf{S} = J\mathbf{F}^{-1} \cdot \boldsymbol{\sigma} \cdot \mathbf{F}^{-T}$ and the material electric polarization vector $\boldsymbol{\mathcal{P}} = J\mathbf{F}^{-1} \cdot \mathbf{p}$. $\mathbf{F}$ is the deformation gradient tensor, $J = \det\mathbf{F}$ its determinant and $\mathbf{C} = \mathbf{F}^T \cdot \mathbf{F}$ is the symmetric right Cauchy-Green tensor. Moreover, we have the spatial electric field vector $\mathbf{e}$ and the material one $\boldsymbol{\mathcal{E}} = \mathbf{e} \cdot \mathbf{F}$. With the free energy per unit mass $\Psi = \Psi(\mathbf{C}, \boldsymbol{\mathcal{E}})$ and the mass density ρ_0 in the reference

configuration we write the thermodynamic relation

$$\rho_0\dot{\Psi} = \left(\mathbf{S} + \boldsymbol{\mathcal{P}}\boldsymbol{\mathcal{E}}\cdot\mathbf{C}^{-1}\right)\cdot\cdot\,\frac{1}{2}\dot{\mathbf{C}} - \boldsymbol{\mathcal{P}}\cdot\dot{\boldsymbol{\mathcal{E}}}, \tag{1}$$

in which $\mathbf{S}^{pol} = \boldsymbol{\mathcal{P}}\boldsymbol{\mathcal{E}}\cdot\mathbf{C}^{-1}$ is the so-called second Piola-Kirchhoff polarization stress tensor. We also note that the skewsymmetric part of the bracketed term must vanish due to the local balance of moment of momentum, which reads

$$\operatorname{skew}\left(\mathbf{S} + \boldsymbol{\mathcal{P}}\boldsymbol{\mathcal{E}}\cdot\mathbf{C}^{-1}\right) = \mathbf{0}; \tag{2}$$

$\mathbf{S}^S = \mathbf{S} + \boldsymbol{\mathcal{P}}\boldsymbol{\mathcal{E}}\cdot\mathbf{C}^{-1}$ is denoted as the symmetric stress tensor in the following. The above thermodynamic relation is a well known form of the time derivative of the free energy as it has been frequently reported in the literature, see e.g. [1], [2].

1.1 Multiplicative decomposition

Following the approach proposed in [3] we introduce a multiplicative decomposition of the deformation gradient tensor as

$$\mathbf{F} = \mathbf{F}_{me}\cdot\mathbf{F}_{el}, \tag{3}$$

with a mechanical part $\mathbf{F}_{me}$ and an electrical part $\mathbf{F}_{el} = \mathbf{F}_{el}(\boldsymbol{\mathcal{E}})$, such that the right Cauchy-Green tensor is $\mathbf{C} = \mathbf{F}_{el}^T\cdot\mathbf{C}_{me}\cdot\mathbf{F}_{el}$ with the mechanical part $\mathbf{C}_{me} = \mathbf{F}_{me}^T\cdot\mathbf{F}_{me}$. Now, the free energy is assumed as the sum of a purely mechanical part depending only on $\mathbf{C}_{me}$ and an electrical part; hence, we write

$$\Psi = \Psi_{me}(\mathbf{C}_{me}) + \Psi_{el}(\mathbf{C}, \boldsymbol{\mathcal{E}}), \tag{4}$$

and compute the time derivative to

$$\dot{\Psi} = \frac{\partial\Psi_{me}}{\partial\mathbf{C}_{me}}\cdot\cdot\,\dot{\mathbf{C}}_{me} + \frac{\partial\Psi_{el}}{\partial\mathbf{C}}\cdot\cdot\,\dot{\mathbf{C}} + \frac{\partial\Psi_{el}}{\partial\boldsymbol{\mathcal{E}}}\cdot\dot{\boldsymbol{\mathcal{E}}}. \tag{5}$$

All second rank tensors in this relation are symmetric. It remains to compute the time derivative $\dot{\mathbf{C}}_{me}$. Using $\mathbf{C}_{me} = \mathbf{F}_{el}^{-T}\cdot\mathbf{C}\cdot\mathbf{F}_{el}^{-1}$ we find

$$\dot{\mathbf{C}}_{me} = \mathbf{F}_{el}^{-T}\cdot\dot{\mathbf{C}}\cdot\mathbf{F}_{el}^{-1} - 2\operatorname{sym}\left(\mathbf{C}_{me}\cdot\dot{\mathbf{F}}_{el}\cdot\mathbf{F}_{el}^{-1}\right). \tag{6}$$

With the symmetry of $\partial\Psi_{me}/\partial\mathbf{C}_{me}$ and $\mathbf{F}_{el} = \mathbf{F}_{el}(\boldsymbol{\mathcal{E}})$ the first term in the above relation for $\dot{\Psi}$ becomes

$$\frac{\partial\Psi_{me}}{\partial\mathbf{C}_{me}}\cdot\cdot\,\dot{\mathbf{C}}_{me} = \mathbf{F}_{el}^{-1}\cdot\frac{\partial\Psi_{me}}{\partial\mathbf{C}_{me}}\cdot\mathbf{F}_{el}^{-T}\cdot\cdot\,\dot{\mathbf{C}} - \left(2\mathbf{F}_{el}^{-1}\cdot\frac{\partial\Psi_{me}}{\partial\mathbf{C}_{me}}\cdot\mathbf{C}_{me}\cdot\cdot\,\frac{\partial\mathbf{F}_{el}}{\partial\boldsymbol{\mathcal{E}}}\right)\cdot\dot{\boldsymbol{\mathcal{E}}}, \tag{7}$$

and eventually we find

$$\dot{\Psi} = \left(\mathbf{F}_{el}^{-1} \cdot \frac{\partial \Psi_{me}}{\partial \mathbf{C}_{me}} \cdot \mathbf{F}_{el}^{-T} + \frac{\partial \Psi_{el}}{\partial \mathbf{C}} \right) \cdot\cdot \dot{\mathbf{C}} - \left(2\mathbf{F}_{el}^{-1} \cdot \frac{\partial \Psi_{me}}{\partial \mathbf{C}_{me}} \cdot \mathbf{C}_{me} \cdot\cdot \frac{\partial \mathbf{F}_{el}}{\partial \boldsymbol{\mathcal{E}}} - \frac{\partial \Psi_{el}}{\partial \boldsymbol{\mathcal{E}}} \right) \cdot \dot{\boldsymbol{\mathcal{E}}}. \quad (8)$$

Comparing the two relations for $\dot{\Psi}$ renders two constitutive relations, one for the symmetric second Piola-Kirchhoff stress tensor and one for the material polarization vector,

$$\begin{aligned} \mathbf{S}^S = \mathbf{S} + \boldsymbol{\mathcal{P}} \boldsymbol{\mathcal{E}} \cdot \mathbf{C}^{-1} &= 2\rho_0 \mathbf{F}_{el}^{-1} \cdot \frac{\partial \Psi_{me}}{\partial \mathbf{C}_{me}} \cdot \mathbf{F}_{el}^{-T} + 2\rho_0 \frac{\partial \Psi_{el}}{\partial \mathbf{C}}, \\ \boldsymbol{\mathcal{P}} &= 2\rho_0 \mathbf{F}_{el}^{-1} \cdot \frac{\partial \Psi_{me}}{\partial \mathbf{C}_{me}} \cdot \mathbf{C}_{me} \cdot\cdot \frac{\partial \mathbf{F}_{el}}{\partial \boldsymbol{\mathcal{E}}} - \rho_0 \frac{\partial \Psi_{el}}{\partial \boldsymbol{\mathcal{E}}}. \end{aligned} \quad (9)$$

Here, the material polarization is composed of two parts, an electrical one $\boldsymbol{\mathcal{P}}_{el}$ and $\boldsymbol{\mathcal{P}}_{coup}$ that accounts for the constitutive coupling; these two are

$$\boldsymbol{\mathcal{P}}_{el} = -\rho_0 \frac{\partial \Psi_{el}}{\partial \boldsymbol{\mathcal{E}}} \quad \text{and} \quad \boldsymbol{\mathcal{P}}_{coup} = 2\rho_0 \mathbf{F}_{el}^{-1} \cdot \frac{\partial \Psi_{me}}{\partial \mathbf{C}_{me}} \cdot \mathbf{C}_{me} \cdot\cdot \frac{\partial \mathbf{F}_{el}}{\partial \boldsymbol{\mathcal{E}}}. \quad (10)$$

Hence, the polarization stress tensor can as well be decomposed into two parts, $\mathbf{S}^{pol} = \mathbf{S}^{pol,el} + \mathbf{S}^{pol,coup}$, with

$$\begin{aligned} \mathbf{S}^{pol,el} &= \boldsymbol{\mathcal{P}}_{el} \boldsymbol{\mathcal{E}} \cdot \mathbf{C}^{-1} = -\rho_0 \left(\frac{\partial \Psi_{el}}{\partial \boldsymbol{\mathcal{E}}} \right) \boldsymbol{\mathcal{E}} \cdot \mathbf{C}^{-1}, \\ \mathbf{S}^{pol,coup} &= \boldsymbol{\mathcal{P}}_{coup} \boldsymbol{\mathcal{E}} \cdot \mathbf{C}^{-1} = \rho_0 \left(2\mathbf{F}_{el}^{-1} \cdot \frac{\partial \Psi_{me}}{\partial \mathbf{C}_{me}} \cdot \mathbf{C}_{me} \cdot\cdot \frac{\partial \mathbf{F}_{el}}{\partial \boldsymbol{\mathcal{E}}} \right) \boldsymbol{\mathcal{E}} \cdot \mathbf{C}^{-1}. \end{aligned} \quad (11)$$

In particular, we consider $\Psi_{el}(\mathbf{C}, \boldsymbol{\mathcal{E}})$ as

$$\rho_0 \Psi_{el} = -\frac{1}{2} \chi \varepsilon_0 \boldsymbol{\mathcal{E}} \cdot \left(\mathbf{C}^{-1} \cdot \boldsymbol{\mathcal{E}} \right), \quad (12)$$

with the permittivity in vacuum ε_0 and the constant susceptibility χ. This specific form of Ψ_{el} differs from the one used in [3] as it does not involve J. The derivatives with respect to $\boldsymbol{\mathcal{E}}$ and $\mathbf{C}$ are easily computed and result into

$$\begin{aligned} -\rho_0 \frac{\partial \Psi_{el}}{\partial \boldsymbol{\mathcal{E}}} \boldsymbol{\mathcal{E}} \cdot \mathbf{C}^{-1} = \chi \varepsilon_0 \left(\mathbf{C}^{-1} \cdot \boldsymbol{\mathcal{E}} \right) \left(\boldsymbol{\mathcal{E}} \cdot \mathbf{C}^{-1} \right) &= \chi \varepsilon_0 \mathbf{C}^{-1} \cdot (\boldsymbol{\mathcal{E}} \boldsymbol{\mathcal{E}}) \cdot \mathbf{C}^{-1}, \\ 2\rho_0 \frac{\partial \Psi_{el}}{\partial \mathbf{C}} &= \chi \varepsilon_0 \mathbf{C}^{-1} \cdot (\boldsymbol{\mathcal{E}} \boldsymbol{\mathcal{E}}) \cdot \mathbf{C}^{-1}, \end{aligned} \quad (13)$$

such that

$$\mathbf{S}^{pol,el} = -\rho_0 \frac{\partial \Psi_{el}}{\partial \boldsymbol{\mathcal{E}}} \boldsymbol{\mathcal{E}} \cdot \mathbf{C}^{-1} = 2\rho_0 \frac{\partial \Psi_{el}}{\partial \mathbf{C}} \quad (14)$$

holds. Therefore, the constitutive relation for the sum of the stress tensor and the polarization stress tensor due to the coupling polarization $\boldsymbol{\mathcal{P}}_{coup}$, the so-called symmetric electro-mechanical stress tensor $\mathbf{S}^{em} = \mathbf{S} + \boldsymbol{\mathcal{P}}_{coup}\boldsymbol{\mathcal{E}} \cdot \mathbf{C}^{-1}$ can be written as

$$\mathbf{S}^{em} = 2\rho_0 \mathbf{F}_{el}^{-1} \cdot \frac{\partial \Psi_{me}}{\partial \mathbf{C}_{me}} \cdot \mathbf{F}_{el}^{-T}. \tag{15}$$

Moreover, with $\mathbf{C}_{me} = \mathbf{F}_{el}^{-T} \cdot \mathbf{C} \cdot \mathbf{F}_{el}^{-1}$, the coupling polarization vector can be written as

$$\boldsymbol{\mathcal{P}}_{coup} = \mathbf{S}^{em} \cdot \mathbf{C} \cdot \mathbf{F}_{el}^{-1} \cdot\cdot \frac{\partial \mathbf{F}_{el}}{\partial \boldsymbol{\mathcal{E}}}. \tag{16}$$

This completes the constitutive modelling, which we summarize as follows:

$$\mathbf{S}^{S} = \mathbf{S} + \boldsymbol{\mathcal{P}}\boldsymbol{\mathcal{E}} \cdot \mathbf{C}^{-1} = \mathbf{S}^{em} + \mathbf{S}^{pol,el} \quad \text{and} \quad \boldsymbol{\mathcal{P}} = \boldsymbol{\mathcal{P}}_{el} + \boldsymbol{\mathcal{P}}_{coup}, \tag{17}$$

with

$$\begin{aligned} \mathbf{S}^{em} &= 2\rho_0 \mathbf{F}_{el}^{-1} \cdot \frac{\partial \Psi_{me}}{\partial \mathbf{C}_{me}} \cdot \mathbf{F}_{el}^{-T} \quad \text{and} \quad \mathbf{S}^{pol,el} = 2\rho_0 \frac{\partial \Psi_{el}}{\partial \mathbf{C}}, \\ \boldsymbol{\mathcal{P}}_{el} &= -\rho_0 \frac{\partial \Psi_{el}}{\partial \boldsymbol{\mathcal{E}}} \quad \text{and} \quad \boldsymbol{\mathcal{P}}_{coup} = \mathbf{S}^{em} \cdot \mathbf{C} \cdot \mathbf{F}_{el}^{-1} \cdot\cdot \frac{\partial \mathbf{F}_{el}}{\partial \boldsymbol{\mathcal{E}}}. \end{aligned} \tag{18}$$

With the aid of these constitutive relation the thermodynamic relation can also be written as

$$\rho_0 \dot{\Psi} = \underbrace{\mathbf{F}_{el} \cdot \mathbf{S}^{em} \cdot \mathbf{F}_{el}^{T} \cdot\cdot \frac{1}{2}\dot{\mathbf{C}}_{me}}_{=\rho_0 \dot{\Psi}_{me}(\mathbf{C}_{me})} + \underbrace{\mathbf{S}^{pol,el} \cdot\cdot \frac{1}{2}\dot{\mathbf{C}} - \boldsymbol{\mathcal{P}}_{el} \cdot \dot{\boldsymbol{\mathcal{E}}}}_{=\rho_0 \dot{\Psi}_{el}}. \tag{19}$$

In this sub-section the multiplicative decomposition was introduced as proposed by [3]; in addition the constitutive relations resulting from this decomposition have been discussed in detail and an alternative form for the electrical part of the free energy was proposed.

1.2 Total stress formulation

In this sub-section we introduce the notion of the the Maxwell stress tensor and of the total stress tensor, which are common in the field of nonlinear electro-elasticity to account for pondomotive forces. We begin by augmenting the free energy by a term accounting for the polarization in vacuum,

$$\rho_0 \Omega = \rho_0 \Psi - \frac{1}{2}\varepsilon_0 J \boldsymbol{\mathcal{E}} \cdot \left(\mathbf{C}^{-1} \cdot \boldsymbol{\mathcal{E}}\right) = \rho_0 \Psi + \rho_0 \Psi_{aug}. \tag{20}$$

Now we compute $\rho_0 \dot{\Omega}$; with $\Psi_{aug} = \Psi_{aug}(\mathbf{C}, \boldsymbol{\mathcal{E}})$ this results into

$$\rho_0 \dot{\Omega} = \rho_0 \dot{\Psi} + \rho_0 \frac{\partial \Psi_{aug}}{\partial \mathbf{C}} \cdot\cdot \dot{\mathbf{C}} + \rho_0 \frac{\partial \Psi_{aug}}{\partial \boldsymbol{\mathcal{E}}} \cdot \dot{\boldsymbol{\mathcal{E}}}, \tag{21}$$

which immediately finds

$$\rho_0\dot{\Omega} = \left(\mathbf{S} + \boldsymbol{\mathcal{P}}\boldsymbol{\mathcal{E}}\cdot\mathbf{C}^{-1} + 2\rho_0\frac{\partial\Psi_{aug}}{\partial\mathbf{C}}\right)\cdot\cdot\,\frac{1}{2}\dot{\mathbf{C}} - \left(\boldsymbol{\mathcal{P}} - \rho_0\frac{\partial\Psi_{aug}}{\partial\boldsymbol{\mathcal{E}}}\right)\cdot\dot{\boldsymbol{\mathcal{E}}}. \tag{22}$$

With the derivative of the augmentation term in the free energy with respect to $\boldsymbol{\mathcal{E}}$, which is

$$\rho_0\frac{\partial\Psi_{aug}}{\partial\boldsymbol{\mathcal{E}}} = -\varepsilon_0 J\mathbf{C}^{-1}\cdot\boldsymbol{\mathcal{E}} \tag{23}$$

and the derivative with respect to $\mathbf{C}$,

$$\rho_0\frac{\partial\Psi_{aug}}{\partial\mathbf{C}} = \frac{1}{2}\varepsilon_0 J\left[\mathbf{C}^{-1}\cdot\boldsymbol{\mathcal{E}}\boldsymbol{\mathcal{E}} - \frac{1}{2}\mathbf{I}\left(\boldsymbol{\mathcal{E}}\boldsymbol{\mathcal{E}}\cdot\cdot\,\mathbf{C}^{-1}\right)\right]\cdot\mathbf{C}^{-1} = \frac{1}{2}\mathbf{S}^{Max} \tag{24}$$

we have

$$\rho_0\dot{\Omega} = \left(\mathbf{S} + \boldsymbol{\mathcal{D}}\boldsymbol{\mathcal{E}}\cdot\mathbf{C}^{-1} - \frac{1}{2}\varepsilon_0 J\mathbf{C}^{-1}\left(\boldsymbol{\mathcal{E}}\boldsymbol{\mathcal{E}}\cdot\cdot\,\mathbf{C}^{-1}\right)\right)\cdot\cdot\,\frac{1}{2}\dot{\mathbf{C}} - \boldsymbol{\mathcal{D}}\cdot\dot{\boldsymbol{\mathcal{E}}}, \tag{25}$$

in which $\boldsymbol{\mathcal{D}} = \boldsymbol{\mathcal{P}} + \varepsilon_0 J\mathbf{C}^{-1}\cdot\boldsymbol{\mathcal{E}}$ is the material electric displacement vector. The bracketed term is the total second Piola-Kirchhoff stress tensor $\mathbf{S}^{tot}$, which is the sum of the mechanical stress $\mathbf{S}$, the polarisation stress $\mathbf{S}^{pol}$ and the Maxwell stress $\mathbf{S}^{Max}$. Therefore,

$$\rho_0\dot{\Omega} = \mathbf{S}^{tot}\cdot\cdot\,\frac{1}{2}\dot{\mathbf{C}} - \boldsymbol{\mathcal{D}}\cdot\dot{\boldsymbol{\mathcal{E}}} \tag{26}$$

holds. Finally, without presenting a derivation, we note that the material electric displacement vector can be written in the well known form

$$\boldsymbol{\mathcal{D}} = -\rho_0\frac{\partial\Psi_{me}}{\partial\boldsymbol{\mathcal{E}}} - \rho_0\frac{\partial\Psi_{el}}{\partial\boldsymbol{\mathcal{E}}} - \rho_0\frac{\partial\Psi_{aug}}{\partial\boldsymbol{\mathcal{E}}} = -\rho_0\frac{\partial\Omega}{\partial\boldsymbol{\mathcal{E}}} \tag{27}$$

as the derivative of the augmented free energy with respect to the material electric field, and the total second Piola-Kirchhoff stress tensor follows from

$$\mathbf{S}^{tot} = 2\rho_0\frac{\partial\Psi_{me}}{\partial\mathbf{C}} + 2\rho_0\frac{\partial\Psi_{el}}{\partial\mathbf{C}} + 2\rho_0\frac{\partial\Psi_{aug}}{\partial\mathbf{C}} = 2\frac{\partial\Omega}{\partial\mathbf{C}} \tag{28}$$

as twice the derivative of the augmented free energy with respect to the right Cauchy-Green tensor. Both, the total stress tensor as well as the material displacement vector are involved in the balance / equilibrium conditions as well as the continuity conditions. We introduce the total first Piola-Kirchhoff stress tensor as $\mathbf{P}^{tot} = \mathbf{F}\cdot\mathbf{S}^{tot}$ and note the relations

$$\nabla_0\cdot\mathbf{P}^{tot} = \mathbf{b}_{me}\,, \quad \mathbf{n}\cdot[\![\mathbf{P}^{tot}]\!] = \mathbf{0} \quad \text{and} \quad \nabla_0\cdot\boldsymbol{\mathcal{D}} = 0\,, \quad \mathbf{n}\cdot[\![\boldsymbol{\mathcal{D}}]\!] = 0, \tag{29}$$

which can be found for instance in [4],[5]. $\mathbf{b}_{me}$ are mechanical body forces and ∇_0 is the invariant differential operator of the reference configuration.

1.3 The concept of a fictitous intermediate "*stress-free*" configuration

The symmetric electro-mechanical stress tensor

$$\mathbf{S}^{em} = \mathbf{S} + \boldsymbol{\mathcal{P}}_{coup}\boldsymbol{\mathcal{E}} \cdot \mathbf{C}^{-1} = 2\rho_0 \mathbf{F}_{el}^{-1} \cdot \frac{\partial \Psi_{me}}{\partial \mathbf{C}_{me}} \cdot \mathbf{F}_{el}^{-T} \tag{30}$$

vanishes, if $\mathbf{C}_{me} = \mathbf{I}$ as long as the specific form of the mechanical part of the free energy $\Psi_{me}(\mathbf{C}_{me})$ ensures this condition. In the absence of a rigid-body rotation this also results into $\mathbf{F}_{me} = \mathbf{I}$, and hence, $\mathbf{F} = \mathbf{F}_{el}$, which constitutes an intermediate configuration. The deformation from this configuration to the actual configuration by means of $\mathbf{F}_{me}$ results into a stress $\mathbf{S}^{em}$, which can be computed from a purely elastic constitutive relation. A

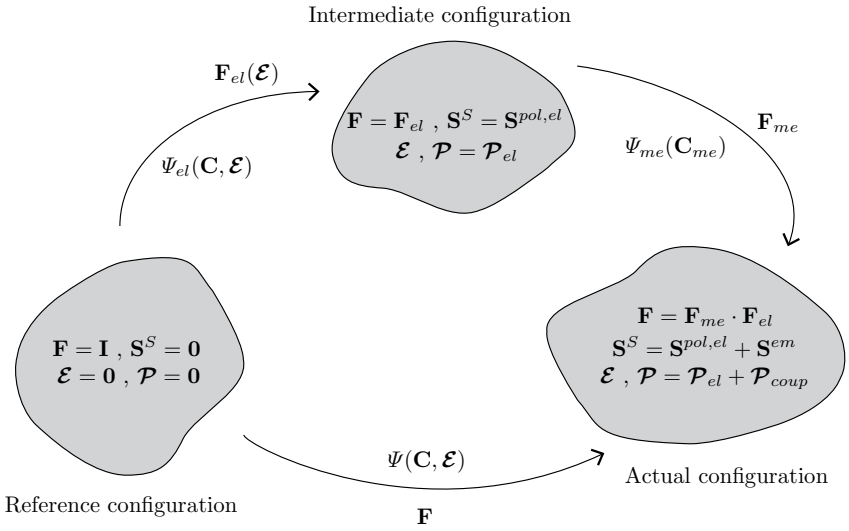

Figure 1: Schematic overview of involved configurations for constitutive modelling within the multiplicative decomposition

schematic overview of the three configurations is shown in Figure 1.

- In the reference configuration the electric field vector and the electric polarization vector vanish, $\boldsymbol{\mathcal{E}} = \mathbf{0}$ and $\boldsymbol{\mathcal{P}} = \mathbf{0}$, and the deformation gradient tensor equals the identity tensor, $\mathbf{F} = \mathbf{I}$. Hence, the symmetric stress tensor is trivial as well, $\mathbf{S}^S = \mathbf{0}$.
- In the intermediate configuration, which emerges due to to the electric field $\boldsymbol{\mathcal{E}}$ by means of the electrical deformation gradient tensor $\mathbf{F}_{el} = \mathbf{F}_{el}(\boldsymbol{\mathcal{E}})$, the polarization vector is equal to its electrical part, $\boldsymbol{\mathcal{P}} = \boldsymbol{\mathcal{P}}_{el}$, and the symmetric stress tensor equals the electrical part of the polarization stress tensor, $\mathbf{S}^S = \mathbf{S}^{pol,el}$. To a certain degree the constitutive process, which corresponds to the deformation from the reference configuration to the intermediate configuration, is characterized by the electrical part of the free energy $\Psi_{el}(\mathbf{C}, \boldsymbol{\mathcal{E}})$.

- The actual configuration, which is a result of any type of sources, emerges by means of the mechanical deformation gradient tensor $\mathbf{F}_{me}$; hence, it is charcterized by $\mathbf{F} = \mathbf{F}_{me} \cdot \mathbf{F}_{el}$. The symmtric electro-mechanical stress tensor $\mathbf{S}^{em}$ is assigned to this deformation, and the symmetric stress tensor is $\mathbf{S}^{S} = \mathbf{S}^{pol,el} + \mathbf{S}^{em}$. The electric field vector $\boldsymbol{\mathcal{E}}$ is kept constant, but the polarization vector contains the coupling polarization as well, $\boldsymbol{\mathcal{P}} = \boldsymbol{\mathcal{P}}_{el} + \boldsymbol{\mathcal{P}}_{coup}$. This constitutive process is characterized by the mechanical part of the free energy $\Psi_{me}(\mathbf{C}_{me})$.

Allthough this concept of an intermediate "*stress-free*" configuration in terms of the symmetric electro-mechanical stress tensor is quite appealing for the constitutive modelling, this intermediate configuration does not exist in the real problem, even if $\mathbf{F}_{el}$ is compatible and no mechanical forces act on the body. This can be explained with the presence of the Maxwell stress tensor as soon as an electrical deformation gradient $\mathbf{F}_{el} = \mathbf{F}_{el}(\boldsymbol{\mathcal{E}})$, and therefore an electric field is applied. The Maxwell stress tensor represents additional source terms - in terms of a body force as well as a surface traction - preventing this "*stress-free*" intermediate configuration to exist. It is however possible that a "*stress-free*" configuration with $\mathbf{F} \neq \mathbf{F}_{el}$ exists, in which the total stress tensor vanishes, rather than the electro-mechanical stress tensor.

1.4 Specific constitutive relations

We introduce the electrical part of the deformation gradient tensor $\mathbf{F}_{el}$ as

$$\mathbf{F}_{el} = \exp\mathbf{D}, \tag{31}$$

in which $\mathbf{D}$ is a second rank symmetric tensor; this specific law was proposed in [3]. Then, we may as well write $\mathbf{D} = \ln\mathbf{F}_{el}$ and by a proper choice of $\mathbf{D}$ we ensure that the electrical part of the deformation gradient tensor is actually an electrical right stretch tensor, $\mathbf{F}_{el} = \mathbf{R}_{el} \cdot \mathbf{U}_{el} \equiv \mathbf{U}_{el}$. Therefore, $\mathbf{D}$ is identical to an electrical logarthmic strain tensor $\mathbf{D} = \ln\mathbf{U}_{el}$. We introduce a unit vector in the direction of the material electric field vector $\boldsymbol{\mathcal{E}}$, which we denote as $\mathbf{m}$. Then, we choose

$$\mathbf{D} = c_1 \left(\boldsymbol{\mathcal{E}} \cdot \boldsymbol{\mathcal{E}}\right) \mathbf{m}\mathbf{m} + c_2 \left(\boldsymbol{\mathcal{E}} \cdot \boldsymbol{\mathcal{E}}\right) \left(\mathbf{I} - \mathbf{m}\mathbf{m}\right), \tag{32}$$

in order to account for electrostriction, which we consider to be quadratic in $\boldsymbol{\mathcal{E}}$. c_1 and c_2 are electrostrictive material parameters. Moreover, we can write $\mathbf{F}_{el} = \lambda_{el,3}\mathbf{m}\mathbf{m} + \lambda_{el}\left(\mathbf{I} - \mathbf{m}\mathbf{m}\right)$, in which

$$\lambda_{el,3} = \exp\left(c_1 \boldsymbol{\mathcal{E}} \cdot \boldsymbol{\mathcal{E}}\right) \quad \text{and} \quad \lambda_{el} = \exp\left(c_2 \boldsymbol{\mathcal{E}} \cdot \boldsymbol{\mathcal{E}}\right). \tag{33}$$

It remains to specify the specific form of the mechanical part $\Psi_{me}(\mathbf{C}_{me})$ of the free energy $\Psi = \Psi_{me}(\mathbf{C}_{me}) + \Psi_{el}(\mathbf{C}, \boldsymbol{\mathcal{E}})$. In the present paper we will be using a neo-Hookean hyperelastic strain energy function,

$$\rho_0 \Psi_{me}(\mathbf{C}_{me}) = \Psi_{me}\left(I_{\mathbf{C}_{me}}, II_{\mathbf{C}_{me}}, III_{\mathbf{C}_{me}}\right) = \frac{\mu}{2}\left(I_{\mathbf{C}_{me}} - 3 - 2\ln J\right) + K(\ln J)^2, \tag{34}$$

with the Lame parameter μ and the bulk modulus K. The purely electrical part $\rho_0\Psi_{el}(\mathbf{C},\boldsymbol{\mathcal{E}})$ and the augmentation term $\rho_0\Psi_{aug}(\mathbf{C},\boldsymbol{\mathcal{E}})$ have already been defined.

2 Thin dielectric elastomer single layer plates

We consider thin single layer plates made of a dielectric elastomer with a constitutive relation as introduced above. The dielectric elastomer layer is equipped with electrodes at its horizontal surfaces; hence, it is near at hand to approximate the material electric field vector $\boldsymbol{\mathcal{E}}$ as $\boldsymbol{\mathcal{E}} = \mathcal{E}\mathbf{m}$, in which $\mathbf{m}$ is the unit vector in thickness direction in the reference configuration. Moreover, we assume the right-Cauchy Green tensor as $\mathbf{C} = \mathbf{C}_2 + C_{33}\mathbf{mm}$, in which $\mathbf{C}_2$ refers to the plane part of $\mathbf{C}$. Likewise, $\mathbf{C}_{me} = \mathbf{C}_{2,me} + C_{33,me}\mathbf{mm}$ holds due to the specific form of $\mathbf{F}_{el}$. With these assumptions, we specify the augmented free energy Ω as

$$\rho_0\Omega = \rho_0\Psi_{me}\left(I_{\mathbf{C}_{me}}, II_{\mathbf{C}_{me}}, III_{\mathbf{C}_{me}}\right) - \frac{1}{2}\varepsilon_0\left(\chi + J\right)\frac{\mathcal{E}^2}{C_{33}}, \tag{35}$$

in which $I_{\mathbf{C}_{me}} = \mathrm{tr}\mathbf{C}_{me}$, $II_{\mathbf{C}_{me}} = \mathbf{C}_{me}\cdot\cdot\,\mathbf{C}_{me}$ and $III_{\mathbf{C}_{me}} = \mathrm{det}\mathbf{C}_{me}$ are the three invariants of $\mathbf{C}_{me}$. With $\mathbf{C}_{me} = \mathbf{F}_{el}^{-T}\cdot\mathbf{C}\cdot\mathbf{F}_{el}^{-1}$, we can write these invariants as

$$I_{\mathbf{C}_{me}} = \lambda_{el}^{-2}I_{\mathbf{C}_2} + \lambda_{el,3}^{-2}C_{33}\,,\; II_{\mathbf{C}_{me}} = \lambda_{el,3}^{-4}C_{33}^2 + \lambda_{el}^{-4}II_{\mathbf{C}_2}\,,\; III_{\mathbf{C}_{me}} = \lambda_{el}^{-4}\lambda_{el,3}^{-2}C_{33}III_{\mathbf{C}_2}. \tag{36}$$

We study only incompressible materials and we apply the incompressibility condition to both, $\mathbf{F}_{el}$ and $\mathbf{F}$. Concerning $\mathbf{F}_{el}$ this results into $\mathrm{det}\mathbf{F}_{el} = 1$; hence, we have

$$\mathrm{det}\mathbf{F}_{el} = \lambda_{el,3}\lambda_{el}^2 = \exp\left((c_1 + 2c_2)\mathcal{E}^2\right) = 1 \quad\rightarrow\quad c_1 = -2c_2, \tag{37}$$

such that $\lambda_{el}^{-2} = \lambda_{el,3} = \exp\left(c_1\mathcal{E}^2\right) \equiv \lambda_e^{-2}$. Moreover, $\mathrm{det}\mathbf{C} = 1$ results into $C_{33} = \mathrm{det}\mathbf{C}_2^{-1} = III_{\mathbf{C}_2}^{-1}$. Then, the invariants of $\mathbf{C}_{me}$ are

$$I_{\mathbf{C}_{me}} = \lambda_e^{-2}I_{\mathbf{C}_2} + \lambda_e^4III_{\mathbf{C}_2}^{-1}\,,\quad II_{\mathbf{C}_{me}} = \lambda_e^8III_{\mathbf{C}_2}^{-2} + \lambda_e^{-4}II_{\mathbf{C}_2}\,,\quad III_{\mathbf{C}_{me}} = 1. \tag{38}$$

For the incompressible neo-Hookean material we write the augmented free energy as

$$\rho_0\Omega = \frac{\mu}{2}\left(\lambda_e^{-2}\mathrm{tr}\mathbf{C}_2 + \lambda_e^4III_{\mathbf{C}_2}^{-1} - 3\right) - \frac{1}{2}\varepsilon III_{\mathbf{C}_2}\mathcal{E}^2 \equiv \rho_0\Omega_2, \tag{39}$$

with the permittivity $\varepsilon = \varepsilon_0(\chi + 1) = \varepsilon_r\varepsilon_0$, with the relative permittivity $\varepsilon_r = \chi + 1$ and the electrical stretch $\lambda_e = \exp\left(c_2\mathcal{E}^2\right) = \exp\left((-c_1/2)\mathcal{E}^2\right)$. The plane part $\mathbf{S}_2^{tot}$ of the total stress tensor and the thickness component $\mathcal{D}_3$ of the material electric displacement vector, which are the only non-zero parts of the total stress tensor and of the electric displacement vector, are

$$\mathbf{S}_2^{tot} = 2\rho_0\frac{\partial\Omega_2}{\partial\mathbf{C}_2} \quad\text{and}\quad \mathcal{D}_3 = -\rho_0\frac{\partial\Omega_2}{\partial\mathcal{E}} = \varepsilon III_{\mathbf{C}_2}\mathcal{E} - \rho_0\frac{\partial\Omega_2}{\partial\lambda_{el}}\frac{\partial\lambda_{el}}{\partial\mathcal{E}}. \tag{40}$$

3 Electromechanical stability

As a preliminary study we consider a plate, for which the deformation is not constrained and no mechanical forces are applied. We denote the thickness with h and we apply a voltage V between the two electrodes; hence, $\mathcal{E}_3 = V/h \equiv \mathcal{E}$ holds. In such a problem the resulting in-plane deformation is homogenous and characterized by a constant spherical plane right Cauchy-Green tensor. Therefore, $\mathbf{C}_2 = C\mathbf{I}_2$ with $C = \lambda^2$ applies; here, λ is the principal stretch in both in-plane directions, $\lambda_1 = \lambda_2 = \lambda$, and $\mathbf{I}_2 = \mathbf{I} - \mathbf{mm}$ is the plane part of $\mathbf{I}$. Moreover, the two invariants of $\mathbf{C}_2$ are

$$I_{\mathbf{C}_2} = 2C = 2\lambda^2\,, \quad III_{\mathbf{C}_2} = C^2 = \lambda^4. \tag{41}$$

Under these conditions, the augmented free energy for the incompressible neo-Hookean material is written in terms of the principal stretch λ as

$$\rho_0\Omega_2 = \frac{\mu}{2}\left(2\lambda_e^{-2}\lambda^2 + \lambda_e^4\lambda^{-4} - 3\right) - \frac{1}{2}\varepsilon\lambda^4\mathcal{E}^2. \tag{42}$$

The plane part of the total second Piola-Kirchhoff stress tensor follows from

$$\mathbf{S}_2^{tot} = 2\rho_0\frac{\partial\Omega_2}{\partial\mathbf{C}_2} = 2\rho_0\frac{\partial\Omega_2}{\partial\lambda}\frac{\partial\lambda}{\partial\mathbf{C}_2} = \rho_0\frac{1}{\lambda}\frac{\partial\Omega_2}{\partial\lambda}\mathbf{I}_2; \tag{43}$$

here, we have used the relation $\partial\mathbf{C}_2/\partial\lambda = 2\lambda\mathbf{I}_2$. We assume the contribution to the surface tractions at the vertical edges, which results from the Maxwell stress in the surrounding medium to be negligible, such that the plane part of the total second Piola-Kirchhoff stress tensor vanishes in this specific problem. With the augmented free energy $\rho_0\Omega_2$ for the conservative problem at hand, the equilibrium condition can be stated in the form of the Principle of Gibbs,

$$\rho_0\frac{\partial\Omega_2}{\partial\lambda} = \left(\lambda_e^{-2}\lambda - \lambda_e^4\lambda^{-5}\right) - \lambda^3\frac{\varepsilon}{\mu}\mathcal{E}^2 = 0, \tag{44}$$

from which equilibrium stretches λ are obtained. It remains to specify the material parameters μ, ε_r and c_1. We use a polyurethane elastomer, for which material parameters were reported in [6] as $\varepsilon_r = 8.8$, $Y = 3\mu$ with $Y = 3.6$MPa. In order to proceed with identifying the electrostrictive parameter c_1, we write the equilibrium conditions using the thickness stretch λ_3, which follows from the incompressibilty condition as $\lambda^2 = \lambda_3^{-1}$. Therefore, we have

$$\left(\lambda_e^{-2}\lambda_3^{-1} - \lambda_e^4\lambda_3^2\right) - \lambda_3^{-2}\frac{\varepsilon}{\mu}\mathcal{E}^2 = F(\lambda_3, \mathcal{E}^2) = 0. \tag{45}$$

The nonlinear function $F(\lambda_3, \mathcal{E}^2)$ is approximated in the vicinity of $\lambda_3 \approx 1$ and $\mathcal{E}^2 \approx 0$, which results into the linear relation

$$\varepsilon_3 = -\left(\frac{\varepsilon}{3\mu} - c_1\right)\mathcal{E}^2 = -M\mathcal{E}^2, \tag{46}$$

with the Biot strain $\varepsilon_3 = \lambda_3 - 1$ and an apperant electrostrictive coefficient M. Two particular effects contribute to the strain: the electrostrictive effect, which in our approach is accounted for by the parameter c_1 and the Maxwell effect which is mainly due to Coulomb interaction and charcterized by the first term in this linear relation. The experimentally identified value taken from [6] is $M = 7.07 \times 10^{-16}\mathrm{m}^2\mathrm{V}^{-2}$, which results into $c_1 = -6.86 \times 10^{-16}\mathrm{m}^2\mathrm{V}^{-2}$. Figure 2 shows the equilibrium Biot strain as a function of the square of the

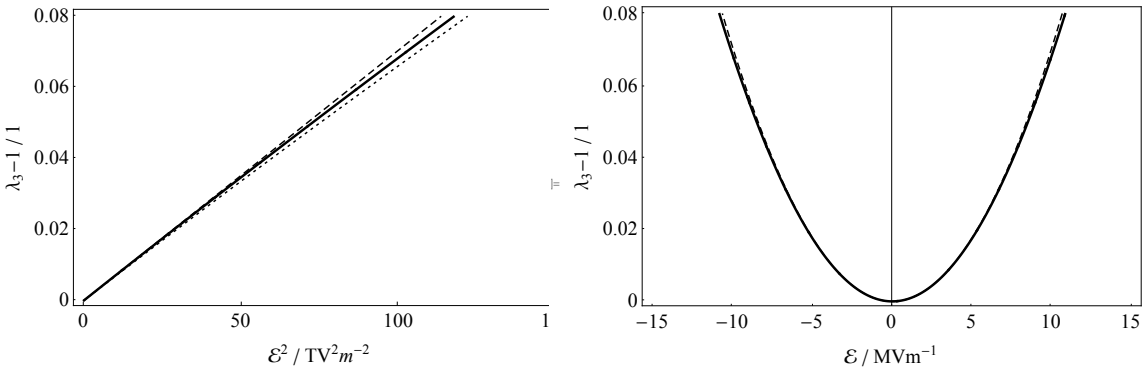

Figure 2: Equilibrium Biot strains in the small signal and deformation regime

electric field (left) and as a function of the electric field (right) for relatively small electric fields and strains. The presented results are very close to the experimental ones provided in [6]. The solid line corresponds to a solution using the multiplicative decomposition as proposed in this paper, the dashed line is the linearized response from eq. (46), and the dotted line in the left plot shows the electrical Biot strain $\varepsilon_{el,3} = \lambda_{el,3} - 1$ with the electrical part of the thickness stretch $\lambda_{el,3} = \lambda_e^{-2} = \exp(c_1\mathcal{E}^2)$. Within the small signal

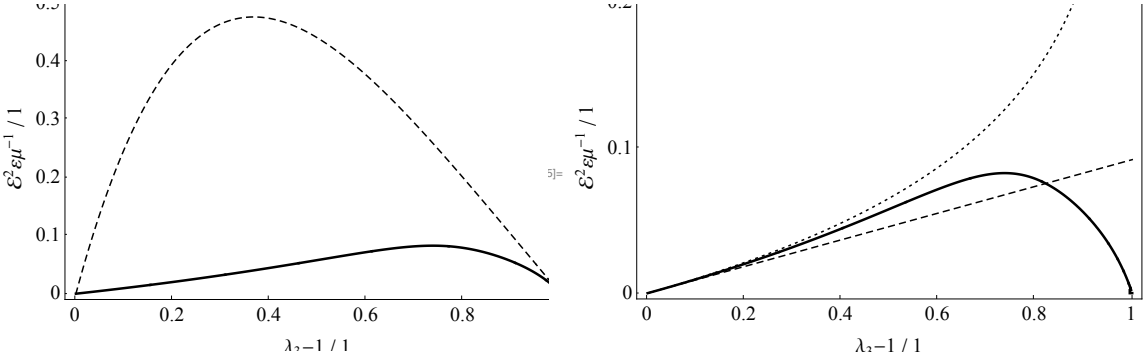

Figure 3: Equilibrium Biot strains in the large deformation regime

and deformation regime the deviation between the different curves and solutions is quite

small; this changes, if we increase the electric field, as shown in Figure 3. In the left plot we compare the present solution (solid line) accounting for electrostriction with a solution, for which electrostriction is neglected, $c_1 = 0$, see e.g. [7]. One can see the extremely high importance of electrostriction, which was also pointed out in [6]. Electrostriction also significantly reduces the critical electric field and increases the corresponding critical Biot strain, at which the so-called electromechanical breakdown occurs. Beyond this point (horizontal tangent in the plot) no more stable equilibrium solutions exist. In the right plot of Figure 3 we compare our solution (solid line), the linearized response (dashed line) and the electrical part of the Biot strain (dotted line). As long as the Biot strain and the electric field are relatively small the three curves coincide quite well, a behavior that is fully lost for large strains. The deviation of the actual Biot strain from the electrical part of the Biot strain characterizes the deviation of the actual configuration from the intermediate one, and hence, the evolution of the symmetric electro-mechanical stress tensor. Finally,

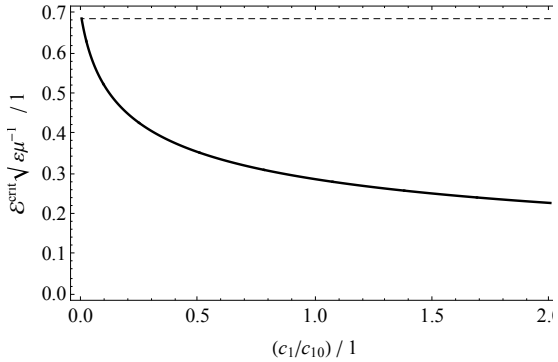

Figure 4: Critical electric field $\mathcal{E}_{crit}$ vs. electrostrictive coefficient c_1

we discuss the effect of electrostriction on the electromechanical breakdown in some more detail. For that sake, we compute the second derivative of the augmented free energy with respect to the stretch λ to

$$\rho_0 \frac{\partial^2 \Omega_2}{\partial \lambda^2} = \left(\lambda_e^{-2} + 5\lambda_e^4 \lambda^{-6}\right) - 3\lambda^2 \frac{\varepsilon}{\mu} \mathcal{E}^2. \tag{47}$$

Stability of an equilibrium point requires this second derivative to be positive. From the equilibrium condition and the stability margin $\rho_0 \frac{\partial^2 \Omega_2}{\partial \lambda^2} = 0$ we find

$$\left(\frac{\lambda_{crit}}{\lambda_{e,crit}}\right)^{-6} = \frac{1}{4} \quad \text{and} \quad \sqrt{\frac{\varepsilon}{\mu}} \left(\exp\left(-c_1 \mathcal{E}_{crit}^2\right) \mathcal{E}_{crit}\right) = \frac{\sqrt{3}}{4^{\frac{2}{3}}} = 0.687, \tag{48}$$

from which we can compute the critical value $\mathcal{E}_{crit}$, $\lambda_{e,crit}$ and furthermore λ_{crit}. For $\lambda_e = 1$, which means $c_1 = 0$, this result is well-known from the literature, see [8]. In Figure 4 we present the dependance of the breakdown electric field $\mathcal{E}_{crit}$ on the electrostrictive coefficient c_1, which is scaled with respect to the value c_{10} we have used in the above results.

4 Concusion & Outlook

The present paper was focussed on the discussion of a multiplicative decomposition of the deformation gradient tensor in dielectric elastomers to account for electrostriction. Only single layered plates were studied. In the future the approach will be extended to geometrically nonlinear shells with layers made of such dielectric elastomers. Moreover, the specific constitutive law for the electrical part of the deformation gradient will be revisited.

Acknowledgement

This work has been partially carried out at LCM GmbH as part of a K2 project. K2 projects are financed using funding from the Austrian COMET-K2 programme. The COMET K2 projects at LCM are supported by the Austrian federal government, the federal state of Upper Austria, the Johannes Kepler University and all of the scientific partners which form part of the K2-COMET Consortium.

REFERENCES

[1] Klinkel S, Zwecker S and Mueller R (2013) A Solid Shell Finite Element Formulation for Dielectric Elastomers. *Journal of Applied Mechanics* **80**, 021026-1–021026-11.

[2] Mehnert M, Hossain M and Steinmann P (2016) On nonlinear thermo-electro-elasticity, *Proceedings of the Royal Society A* **472**, 20160170.

[3] Skatulla S, Sansour C and Arockiarajan A (2012) A multiplicative approach for nonlinear electro-elasticity. *Computer Methods in Applied Mechanics and Engineering* **245-246**, 243–255.

[4] Dorfmann A and Ogden RW (2005) Nonlinear electroelasticity. *Acta Mechanica* **174**, 167–183.

[5] Vu DK, Steinmann P and Possart G (2007) Numerical modelling of non-linear electroelasticity, *International Journal for Numerical Methods in Engineering* **70**, 685–704.

[6] Diaconu I and Dorohoi DO (2005) Properties of polyurethane thin films, *Journal of Optoelectronics and Advanced Materials* **7**(2),921–924.

[7] Staudigl E, Krommer M and Vetyukov Yu (2017) Finite deformations of thin plates made of dielectric elastomers: Modeling, Numerics and Stability, *Journal of Intelligent Materials Systems and Structures*, submitted.

[8] Xu B-X, Mueller R, Klassen M and Gross D (2010) On electromechanical stability analysis of dielectric elastomer actuators. *Applied Physics Letters* **97**, 162908.

ECCOMAS SMART 2017
VIII ECCOMAS Thematic Conference on Smart Structures and Materials
Madrid, Spain, 5–8 June 2017

NON-LINEAR SWITCHING KINETICS OF FERROELECTRIC MONO-DOMAIN SINGLE CRYSTALS

Vishal Boddu[1], **Florian Endres**[1], **and Paul Steinmann**[1]

[1]Chair of Applied Mechanics
University of Erlangen-Nuremberg
Egerlandstrae 5, 91052 Erlangen, Germany
e-mail: vishal.boddu@fau.de

Keywords: Switching Kinetics, Polarization Switching, Ferroelectric, Domain Switching.

Abstract. *Understanding the electric polarization switching kinetics in ferroelectric materials is critical to many applications such as fast high-density non-volatile random access memory devices. Experimental studies of the domain switching process in bulk and thin film ferroelectrics under an external electric loading have explained the switching kinetics using the Kolmogorov-Avrami-Ishibashi (KAI) model. The KAI model is based on the classical approach of nucleation and subsequent growth of reversed domains. It describes the time-dependent normalized change in polarization as a Lorentzian function.*

We perform molecular dynamics simulations to investigate the electric polarization switching kinetics of mono-domain ferroelectric $BaTiO_3$ single crystals under external electric loading at room temperature using the core-shell model. In the core-shell model every ion is represented in terms of a charged core and a charged electron shell which introduces electronic polarizability in the ions. We study the polarization switching process with atomistic detail and discuss the applicability of the KAI model in explaining the non-linear polarization switching kinetics of mono-domain ferroelectric perfect single crystals.

1 Introduction

The electric polarization of a dielectric material is an intensive vector quantity that intuitively carries the meaning of the electric dipole moment per unit volume. The presence of a spontaneous and switchable polarization is the defining property of a ferroelectric material. Such materials are indispensable in a countless number of industrial and scientific applications. In the ferroelectric phase, ferroelectric materials form domains in which the electric polarization is aligned in the same direction. The electric polarization alignment in the ferroelectric domains can develop in two or more specific directions depending on the crystal symmetry of the material. When an external electric field is applied, the ferroelectric domains undergo a change in the electric polarization direction. Understanding the kinetics of such ferroelectric domain switching processes is crucial for technological applications of ferroelectric materials.

Polarization switching kinetics in ferroelectric materials under external electric fields have been extensively investigated both experimentally and theoretically for the past few decades [2, 17, 15, **?**]. Earlier experimental studies of the kinetics of polarization switching in ferroelectric crystals have shown that the switching is almost invariably an *extrinsic* process involving inhomogeneous nucleations of small domains of reversed polarization and subsequent growth of these domains to fill the crystal [10, 5].

Within a ferroelectric domain, alternative studies have shown that the polarization switching does not occur by a spontaneous reorientation of the overall polarization in the domain at once. According to mean field theory [9], the polarization state of a ferroelectric crystal can switch homogeneously, without emergence of nucleated domains, but it must be subject to an electric field large enough to overcome the very large energy barrier associated with the long-range correlation of the polarization [8, 12]. This continuous switching mechanism as opposed to the nucleation mechanism is called *intrinsic* switching mechanism.

The intrinsic switching polarization behavior was first observed in ferroelectric polymers [20]. However, ferroelectric switching experiments with $BaTiO_3$ and $PbTiO_3$ films demonstrated that this behavior is not unique to ferroelectric polymers, and therefore may be a general property of ferroelectric materials [6, 7]. Nano-scale studies of ferroelectric thin films reveal that the nature of polarization switching changes from extrinsic for thicker films, to intrinsic for thinner films.

The commonly accepted approach to explain the polarization switching kinetics is the Kolmogorov-Avrami-Ishibashi (KAI) model, based on the classical theory of Kolmogorov and Avrami [2, 17]. The general idea of this model is that the emerged independent nucleated domains grow unrestrictedly under the influence of an applied electric field. This approach, which enables a correct description of the macroscopic switching kinetics in ferroelectric bulk materials, has been also applied to a description of switching in ferroelectric thin films. For a uniformly polarized ferroelectric material under an external electric field E, the KAI model offers a general mathematical description of the time t-dependent change in the polarization $\Delta P\,(t)$ as

$$\Delta P\,(t) = 2\,P_s\,[1 - \exp\,(-\,(t/t_o)^n)]\,, \tag{1}$$

where n and t_o are the effective dimensionality and characteristic switching time, respectively, and P_s is the spontaneous polarization.

For the past 50 years theory and, more recently, computer-based simulation and computational methods have played a crucial role in developing a deeper understanding of ferroelectric behavior. In particular, atomistic simulations are indispensable for a fundamental understanding of such materials on the atomistic length scale. In this regard, the atomistic models of

ferroelectric materials, such as the core-shell model and the bond-valence models, have been developed by researchers for the purpose of studying ferroelectric behavior from the atomistic point of view. These models are the current state-of-the-art and have shown to be suitable to study ferroelectric behavior. In the atomistic simulation of ionic materials, the ions are treated as particles and the interaction between them is modeled via a sum of long-ranged Coulomb and short-ranged interactions. At the atomistic length scale the electric dipole of a single unit cell divided by its volume gives the electric polarization of the unit cell. Therefore, using atomistic simulations the mono-domain switching process can be studied with atomistic detail by computing the polarization of each unit cell in the simulation system at any instant of time.

We perform molecular dynamics simulations of domain switching processes in ferroelectric, tetragonal $BaTiO_3$ single crystals using the core-shell model potential. In particular we investigate the switching kinetics and processes in mono-domains under a range of electric fields.

2 CORE-SHELL MODEL

The core-shell model has been used in molecular dynamics simulations to gain insights into the properties of ferroelectric materials [4, 13, 3]. In the core-shell model every ion is represented in terms of a charged (atom) core and a charged (electron) shell, linked by a non-linear spring. In the conventional core-shell model the shells are assumed to be massless. Because the shells have no mass, they respond instantaneously to the motion of the cores i.e., at any instant during molecular dynamics simulation the shells are repositioned so as to be in the minimum potential energy configuration with respect to the current cores' configuration. In this work we adopt an alternative approach by assigning a small mass to the shells and treating their motion dynamically similar to that of the cores since this approach has been shown to be computationally more efficient [11]. We therefore treat cores and shells as point mass particles interacting through potentials.

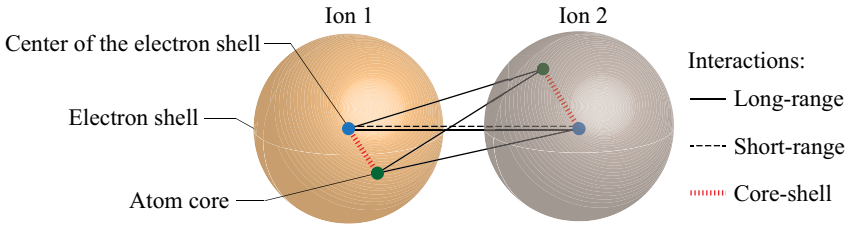

Figure 1: Schematic representation of the interactions in the core-shell model. Each atom is treated as having two components: a charged shell and a charged core connected by a nonlinear spring.

The interaction between cores and shells is described by three different interaction potentials. The interaction between the core and the shell of an atom is treated exclusively by an isotropic, non-linear spring with the potential parameters k_2 and k_4,

$$\phi^S\left(|\mathbf{r}_{ij}|\right) = \frac{1}{2}k_2|\mathbf{r}_{ij}|^2 + \frac{1}{24}k_4|\mathbf{r}_{ij}|^4. \tag{2}$$

The position vectors of particles i and j are given by $\mathbf{r}_i$ and $\mathbf{r}_j$, respectively. The norm of the distance vector between two interacting particles i and j is given by $|\mathbf{r}_{ij}| = |\mathbf{r}_j - \mathbf{r}_i|$.

The interactions between shells of different atoms, which describe the electron cloud repulsion and the Van der Waals attraction, are modelled using the Buckingham potential,

$$\phi^B\left(|\mathbf{r}_{ij}|\right) = A\ \exp\left(-\frac{|\mathbf{r}_{ij}|}{\rho}\right) - \frac{c}{|\mathbf{r}_{ij}|^6}. \tag{3}$$

The variables A, ρ, and c denote potential parameters.

Finally, the electrostatic interactions among the charged particles are considered through a Coulomb potential,

$$\phi_i^C = \frac{1}{4\pi\epsilon_0} \sum_{j \neq i}^{N} \frac{q_i q_j}{|\mathbf{r}_{ij}|}. \tag{4}$$

The particle i's charge is given by q_i, ϵ_0 is the electric permittivity of free space and the total number of particles is denoted by N. Note that there is no electrostatic interactions between an atom's core and its respective shell in the core-shell model. Figure 1 schematically illustrates the interaction between two atoms using the core-shell model.

3 COMPUTATION OF POLARIZATION

The electric polarization is the most essential concept in any theoretical description of ferroelectric materials [18]. It is an intensive vector quantity that intuitively carries the meaning of the electric dipole moment per unit volume. In the early 1990s it was realized that, even at a theoretical level, polarization differences are conceptually more fundamental than the *absolute* polarization. Experimentally, the quantity measured in a polarization-reversal process is the difference in polarization between the two enantiomorphous structures; making use of symmetry, one can then equate this difference to twice the spontaneous polarization [14]. Theoretically, the electric polarization can be calculated based on the charges and the positions of the ions within a unit cell. A centrosymetric structure that is exactly in between the two enantiomorphous structures can be thought of as a reference structure with zero absolute polarization. In the case of ferroelectric tetragonal $BaTiO_3$, this would be the cubic phase. Therefore, the cubic phase structure of $BaTiO_3$ is taken to be the reference configuration in the atomistic simulations. Any evolution from the (initial) reference configuration will result in a non-zero polarization.

The ions' nominal charges cannot be used due to quantum mechanical effects [16]. For the accurate computation of polarization either the so-called Born effective charges or the core-shell charges should be used. In this study, we compute the polarization of each unit cells using the core-shell charges. The change in the polarization $\mathbf{P}$ from the reference configuration of a single unit cell is given by

$$\delta\mathbf{P} = \frac{1}{V} \sum_{m=1} z_m \cdot \delta\mathbf{r}_m, \tag{5}$$

where $\delta\mathbf{r}_m$ is the change of the position vector of the m-th charged particle, z_m is the corresponding charge and V is the volume of the unit cell in the reference configuration. However, if one uses the Born effective charges, the change in polarization of a unit cell is given by

$$\delta\mathbf{P} = \frac{e}{V} \sum_{m=1} \mathbf{Z}_m \cdot \delta\mathbf{r}_m, \tag{6}$$

where $\mathbf{Z}_m$ is the corresponding Born effective charge tensor of the m-th basis atom and e represents the elementary charge since Born effective charges have no dimensional unit.

4 RESULTS AND DISCUSSION

We perform isothermal-isobaric (NPT) molecular dynamics simulations to study the ferroelectric switching process in tetragonal, mono-domain $BaTiO_3$ single crystals at atmospheric pressure and a temperature of 310 K. We use the isotropic, an-harmonic core-shell model potential for $BaTiO_3$ that has been fitted to results of first-principles density functional theory

calculations with generalized gradient approximation [19]. All the simulations are performed with systems of size $40 \times 20 \times 20$ unit cells under periodic boundary conditions. The thermostat and barostat relaxation times are both set to 0.1 ps. All shells are assigned a mass of 2 a.u. and their respective cores are assigned the remaining atomic mass [1]. The times step used is 0.4 fs.

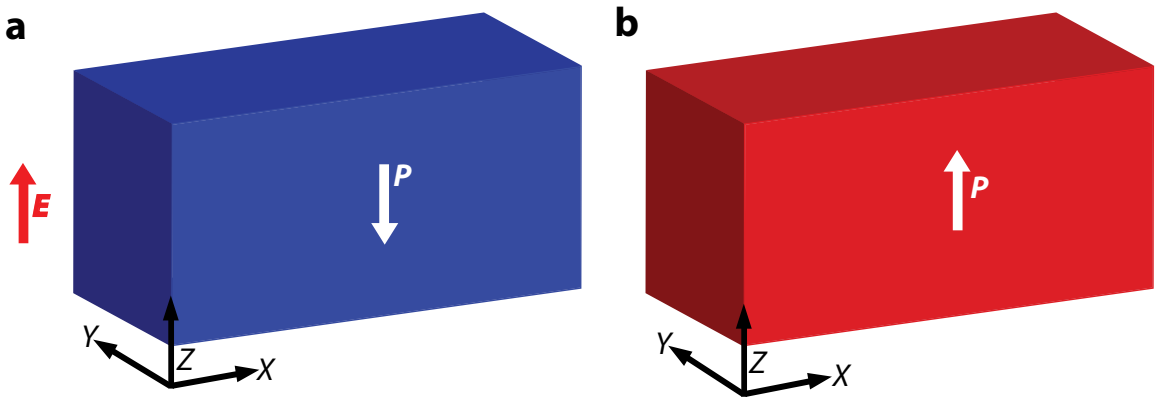

Figure 2: **a**, Schematic representation of the mono-domains with its polarization along the negative Z direction. After the mono-domain is prepared, an electric field along the positive Z direction is applied. In the presence of a sufficiently large field, the mono-domain undergoes a ferroelectric switching. **b**, Schematic representation of the mono-domain after ferroelectric switching with its polarization along the positive Z direction.

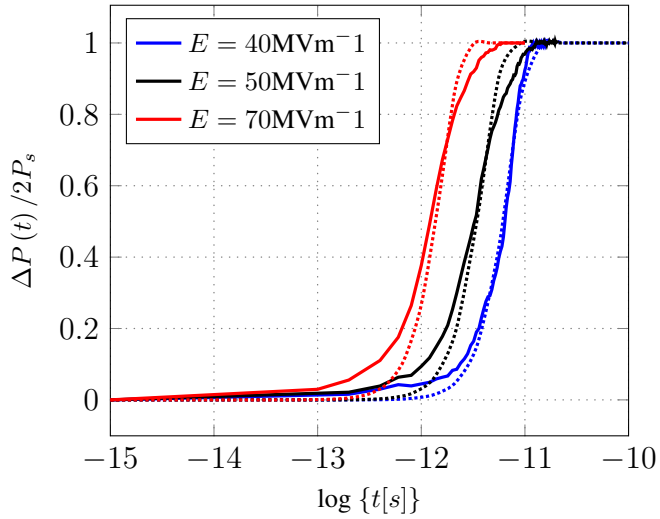

Figure 3: Normalized change in electric polarization of the $40 \times 20 \times 20$ supercell mono-domain under various electric fields. The dotted lines represent the predictions of the KAI model.

The mono-domain system is generated through a two step process. The unit cells in the system are first poled using an external electric field for 4 ps. The system is initially poled in the $-Z$ direction see figure 2 **a**. The external field is then removed and the system is equilibrated for another 4 ps. Now, if the system is kept under no external bias, the mono-domain maintains a constant average polarization. After the mono-domain is prepared, the time t is set to zero and an external electric field is applied in the $+Z$ direction. We then follow the switching process by computing the polarization of each lattice unit cell in the system.

Figure 3 shows the time-dependent normalized change in overall polarization during the switching process as computed using the atomistic simulations. The polarization switching kinetics as predicted by the KAI model is represented using dotted lines. We observe that the switching times under weaker electric fields are relatively longer. The time-dependent normalized change in polarization can be described using a Lorentzian function as predicted by the KAI model.

5 CONCLUSIONS

The electric polarization switching process in mono-domain ferroelectric $BaTiO_3$ single crystals under various electric fields are investigated using atomistic simulations. The time-dependent normalized change in overall polarization during the switching processes indicate a non-linear switching kinetic behavior. We find that the non-linear polarization switching kinetics as computed using the atomistic simulations are in good agreement with the switching kinetics predicted by the KAI model.

Acknowledgements

The authors would like to thank the German Research Foundation (DFG) for the financial support under the research group project FOR 1509 Ferroic Functional Materials.

REFERENCES

[1] A Asthagiri, Z Wu, N Choudhury, and Ronald E Cohen. Advances in first-principles studies of transducer materials. *Ferroelectrics*, 333(1):69–78, 2006.

[2] Melvin Avrami. Kinetics of phase change. ii transformation-time relations for random distribution of nuclei. *The Journal of Chemical Physics*, 8(2):212–224, 1940.

[3] Vishal Boddu, Florian Endres, and Paul Steinmann. Molecular dynamics study of ferroelectric domain nucleation and domain switching dynamics. *Scientific Reports*, 7(1):806, 2017.

[4] Florian Endres and Paul Steinmann. Size effects of 109 domain walls in rhombohedral barium titanate single crystals - a molecular statics analysis. *Journal of Applied Physics*, 119(2), 2016.

[5] Ennio Fatuzzo and Walter J Merz. Switching mechanism in triglycine sulfate and other ferroelectrics. *Physical Review*, 116(1):61, 1959.

[6] R. Gaynutdinov, M. Minnekaev, S. Mitko, A. Tolstikhina, A. Zenkevich, S. Ducharme, and V. Fridkin. Polarization switching kinetics in ultrathin ferroelectric barium titanate film. *Physica B: Condensed Matter*, 424:8 – 12, 2013.

[7] Matthew J Highland, Timothy T Fister, Marie-Ingrid Richard, Dillon D Fong, Paul H Fuoss, Carol Thompson, Jeffrey A Eastman, Stephen K Streiffer, and G Brian Stephenson. Polarization switching without domain formation at the intrinsic coercive field in ultrathin ferroelectric $PbTiO_3$. *Physical review letters*, 105(16):167601, 2010.

[8] Yoshihiro Ishibashi. Theory of polarization reversals in ferroelectrics based on landau-type free energy. *Japanese Journal of Applied Physics*, 31(9R):2822, 1992.

[9] Rolf Landauer. Electrostatic considerations in $BaTiO_3$ domain formation during polarization reversal. *Journal of Applied Physics*, 28(2):227–234, 1957.

[10] Walter J Merz. Domain formation and domain wall motions in ferroelectric $BaTiO_3$ single crystals. *Physical Review*, 95(3):690, 1954.

[11] PJ Mitchell and David Fincham. Shell model simulations by adiabatic dynamics. *Journal of Physics: Condensed Matter*, 5(8):1031, 1993.

[12] N. A. Pertsev, J. Rodrguez Contreras, V. G. Kukhar, B. Hermanns, H. Kohlstedt, and R. Waser. Coercive field of ultrathin $Pb(Zr_{0.52}Ti_{0.48})O_3$ epitaxial films. *Applied Physics Letters*, 83(16):3356–3358, 2003.

[13] Simon R Phillpot, Susan B Sinnott, and Aravind Asthagiri. Atomic-level simulation of ferroelectricity in oxides: Current status and opportunities. *Annu. Rev. Mater. Res.*, 37:239–270, 2007.

[14] Raffaele Resta and David Vanderbilt. Theory of polarization: a modern approach. In *Physics of Ferroelectrics*, pages 31–68. Springer, 2007.

[15] V Ya Shur and EL Rumyantsev. Kinetics of ferroelectric domain structure: retardation effects. *Ferroelectrics*, 191(1):319–333, 1997.

[16] Nicola A Spaldin. A beginner's guide to the modern theory of polarization. *Journal of Solid State Chemistry*, 195:2–10, 2012.

[17] Alexander K Tagantsev, Igor Stolichnov, Nava Setter, Jeffrey S Cross, and Mineharu Tsukada. Non-kolmogorov-avrami switching kinetics in ferroelectric thin films. *Physical Review B*, 66(21):214109, 2002.

[18] In L.D. Landau and E.M. Lifshitz, editors, *Electrodynamics of Continuous Media*, volume 8 of *Course of Theoretical Physics*, pages 455 – 460. Pergamon, Amsterdam, second edition revised and enlarged edition, 1984.

[19] Jason M Vielma and Guenter Schneider. Shell model of $BaTiO_3$ derived from ab-initio total energy calculations. *Journal of Applied Physics*, 114(17):174108, 2013.

[20] G Vizdrik, Stephen Ducharme, VM Fridkin, and SG Yudin. Kinetics of ferroelectric switching in ultrathin films. *Physical Review B*, 68(9):094113, 2003.

VIII ECCOMAS Thematic Conference on Smart Structures and Materials
SMART 2017
A. Güemes, A. Benjeddou, J. Rodellar and J. Leng (Eds)

NUMERICAL STUDY OF INTERACTION OF NONLINEAR GUIDED WAVES WITH BREATHING DAMAGE IN ISOTROPIC MATERIAL

SANDRA GSCHOßMANN[*] and MARTIN SCHAGERL[*,†]

[*] Institute of Constructional Lightweight Design
Johannes Kepler University
Altenberger Strasse 69, 4040 Linz, Austria
e-mail: sandra.gschossmann@jku.at, web page: http://www.ikl.jku.at/

[†] Christian Doppler Laboratory for Structural Strength Control of Lightweight Constructions
Johannes Kepler University
Altenberger Strasse 69, 4040 Linz, Austria
e-mail: martin.schagerl@jku.at, web page: http://www.ikl.jku.at/cd

Key words: Guided waves, Nonlinear, Breathing damage, Finite Element Method, Structural Health Monitoring

Abstract. The research field on Structural Health Monitoring attracts more and more scientists due to the increasing use of lightweight structures. During operation structures are affected by loads. When the loads exceed a certain limit it may cause damages which reduce the carrying capacity of structures. The application of Structural Health Monitoring methods permits the detection and localization of damages in structures. Moreover, to assess the structural remaining service life during operation one may want to quantify and qualify damages in structures. Therefore the nonlinear guided wave technique is a promising approach to monitor lightweight structures. This numerical study is focused on the interaction of nonlinear guided waves with breathing damage in isotropic material and its potential to quantify and qualify different damages. Due to contact acoustic nonlinearity a guided wave packet which passes through a breathing crack is distorted. This fundamental changes are observable in form of higher harmonics. The results show that the proposed numerical approach can predict the interaction of guided waves with breathing cracks in isotropic plates. It is shown that different type of damages with varying size, orientation and position influence the nonlinear guided wave differently. Moreover, the results show that the nonlinear guided waves possess high capabilities for damage detection, localization quantification and qualification of breathing cracks in isotropic plates.

1 INTRODUCTION

Over the past few years, there has been a substantial increase in using lightweight structures in different fields due to their attracting properties such as high stiffness and light weight. Structural Health Monitoring (SHM) has been investigated as a promising approach for monitoring

the structural behavior of lightweight structures during their service life. The application of SHM usually involves several levels. However, A. Rytter classified them into four levels [1]. These levels are damage detection, damage localization, damage quantification and damage qualification. Examples for methods with high potential for Structural Health Monitoring are Inkjet-printed carbon nanotube strain distribution sensors [2], the Electromechanical Impedance Method [3] or the zero-strain trajectory evaluation [4]. Among all SHM techniques, the guided waves technique has attracted many researchers due to its potential for global applications, its easy way of installation and its possibility to detect damages insight thin-walled structures. In case of a thin-walled plate, a network of sensors can be used to fulfill the first three levels of Structural Health Monitoring according to A. Rytter. The basic principle of guided waves applied as a SHM method is based on sending out wave packets that travels through the plate and receive them at several positions within an area of interest. If there exists a damage, the propagating wave packets interact with it and the received sensor signals change, i.e. the damage is detectable. This is of course only true for damages large enough according to the wavelength λ of the guided waves. But not only detection of damages is possible also the localization of damages can be assessed by guided waves. Therefore a system of at least one actuator and three sensor elements is necessary to determine the position of a damage [5]. A further question to asses the structural reliability is, what is the type of the damage? At this point recent studies show the nonlinear guided wave technique as a promising approach for Structural Health Monitoring [6, 7, 8, 9, 10, 11]. However, the numerical modeling of the interaction of guided waves with damages is very challenging. When a packet of guided waves passes through a breathing damage, it undergoes fundamental changes which can be observed in form of distortions. These changes are observable in form of higher harmonics in frequency domain of the sensor signal. In addition to the existence of the damage, these fundamental changes can provide important information about the location, the type or the size of the damage. This study is focused on investigations of the effects of different parameters such as damage size and damage orientation on propagation of nonlinear guided waves in structures with breathing damages. A numerical Finite Element Method (FEM) approach is used for prediction of propagation of nonlinear guided waves in isotropic plates with three different breathing damages.

2 THEORY

The nonlinear guided wave estimation is generally based on two different approaches [10, 7]. On the one hand there is the mesoscopic nonlinearity or material nonlinearity [12, 13, 14]. Due to defects like, inclusions, grain boundaries, gas holes, etc. the material itself induces nonlinear effects which can be detected. On the other hand there is the contact acoustic nonlinearity (CAN) due to the interaction of propagating acoustic waves with breathing cracks [15]. Compared to CAN the material nonlinearity for the considered isotropic plate is negligible and is not considered in this study. The contact acoustic nonlinearity is caused by opening and closing of contact interfaces when elastic waves like guided waves pass these interfaces. Cracks or delaminations possess such contact interfaces. Due to the asymmetrically stress-strain characteristic of isotropic material in compression and tension, the incident guided wave with a frequency f is distorted in case of CAN, i.e. it is highly nonlinear and consequently the signals show higher harmonics. The distortion of the incident guided wave occurs due to a local stiffness change in

the damaged area, when the wave passes the crack. The tension part of the wave opens the crack whereby the local stiffness decreases. However, the compression part of the wave closes the crack and increases the local stiffness [6, 10]. Beside the effects of stiffness change due to compression and tension also nonlinear effects due to the friction between the breathing crack surfaces and the occurrence of Hertzian pressure exist and generate higher harmonics [9, 10]. Effects of friction and Hertzian pressure are not considered in this work.

3 NUMERICAL INVESTIGATION

In a numerical parametric study the influence of different cracks on propagating guided waves are investigated by a simple plate. Particularly the occurrence of higher harmonics or nonlinear guided waves due to CAN will be discussed. This study is focused on the first higher harmonic, i.e. wave packets with double frequency of the incident wave frequency f.

To save computational time and memory space a simplified 2D-model of the thin walled structure is used to investigate the wave propagation and the effects of the considered cracks. The 2D-model is implemented in the finite element software Abaqus® version 6.14-2, illustrated in Fig. 1. By applying a boundary condition $u_y(t)$ on the top and the bottom surface within a

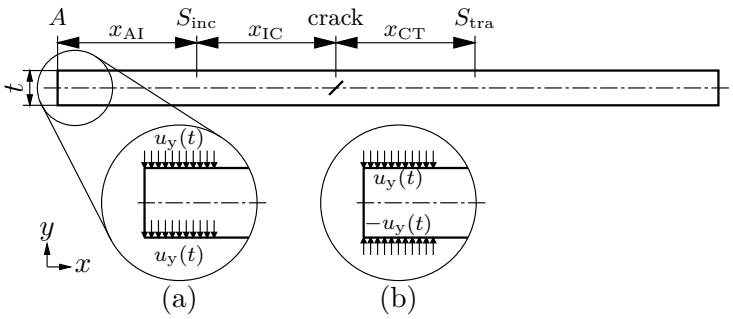

Figure 1: 2D-Finite element model for (a) asymmetric mode and (b) symmetric mode excitation

defined area of 10 mm on the left hand side of the model, guided wave packets are excited. The function $u_y(t)$ has the form of a von Hann windowed sine function with five peaks, a maximum amplitude of $\hat{u}_y = 2\,\mu$m and a frequency $f = 260$ kHz. At this frequency f the tuning function using a piezoelectric element of the size $10 \times 10 \times 0.25$ mm shows its first maximum for the symmetric S0 mode, see Fig. 2 (a). Also the asymmetric A0 mode has a significant amplitude at this frequency. Consequently the first higher harmonic has a frequency $f = 520$ kHz. However, for a better understanding the asymmetric mode A0 and the symmetric mode S0 are analyzed separately in two different models. A single A0 wave packet is excited by applying a out-of-plane displacement $u_y(t)$ at the top and bottom surface in the same direction as shown in Fig. 1 (a). To excite only a S0 wave packet the surfaces move in opposite direction as can be seen in Fig. 1 (b). The considered plate has a thickness $t = 2$ mm and the material is isotropic. The material parameters for aluminum EN-AW 5005 H14 are considered for the numerical investigations. The wave signals, especially the displacement $u_x(t)$ and $u_y(t)$ are evaluated on the positions S_{inc} and S_{tra}. Both positions have the same distance $x_{IC} = x_{CT} = 125$ mm to the crack. According to the group velocity c_g, the excited wave packets have, the total length of the plate is chosen that no

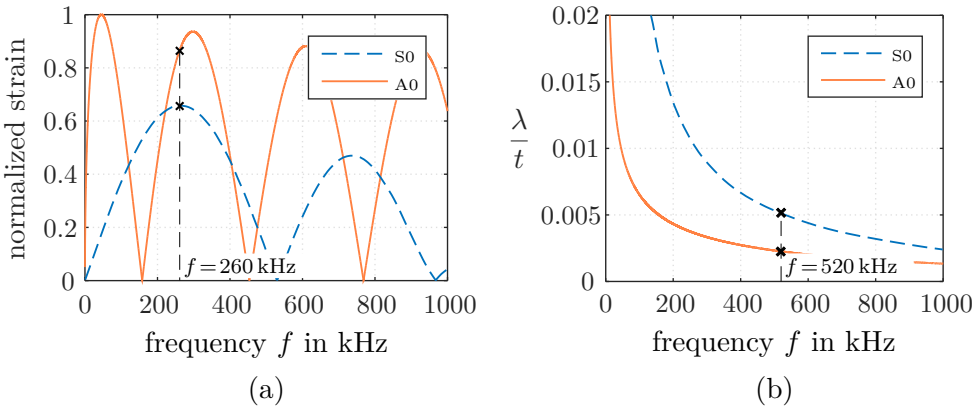

Figure 2: (a) Lamb wave tuning functions for a aluminum plate with a thickness $t = 2$ mm and a piezoelectric element with the dimension of 10×0.25 mm and (b) ratio of wavelength λ to plate thickness t for the S0 and A0 mode

reflections from the boundaries influence the signals at the positions S_{inc} and S_{tra}.

This study investigates the effects of three different types of cracks on guided waves. Figure 3 presents the considered models for the crack types and parameters as implemented in FEM. The first crack type, a surface crack, is located on the top surface, see Fig. 3 (a), whereby the length l varies from 0.125 mm to 0.5 mm and the angle α varies from 0 ° to 75 °. The second crack type (Fig. 3 (b)) contains a volume crack within the plate. In this case the cracklength l varies from 0.25 mm to 1 mm and the angle α varies from 0 ° to 165 °. With the third crack type (Fig. 3 (c)) a delamination like subsurface crack is realized. The vertical crack position p varies in five steps of $t/6$ through the plate and the cracklength l varies from 1 mm to 3 mm. All three crack types

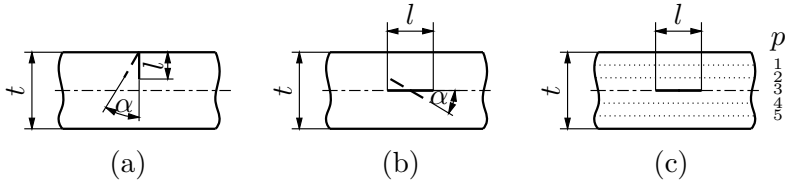

Figure 3: Crack type models: a) surface crack, b) volume crack and c) subsurface crack

are modeled with the special Abaqus crack interaction module *seam*. With this seam function the surfaces of the cracks are separated with no distance in between. To prevent penetration of the crack surfaces a kinematic contact assignment without friction is implemented. Relating to the mesh, the maximum length of the mainly quadratic shaped elements l_{max} is defined as [16]

$$l_{\text{max}} = \frac{\lambda_{\text{min}}}{20}. \tag{1}$$

Since the wavelength λ decreases with increasing frequency f and the wavelength λ for the asymmetric mode A0 is smaller than for the symmetric mode S0 the minimum wavelength λ_{min} is the wavelength λ of the asymmetric mode A0 of a frequency $f = 520$ kHz. This relation can

also be seen in Fig. 2 (b). In this case the minimum wavelength $\lambda_{\min}$ is approximately 4.5 mm and the maximum element size $l_{\max}$ is approximately 0.225 mm. In the area of the cracks, the size of the elements decreases down to 0.01 mm side length. To ensure a stable solution [16], the minimum time increment $\Delta t_{\min}$ for the explicit solver should be

$$\Delta t_{\min} = \frac{1}{20 \cdot f_{\max}}. \tag{2}$$

With a maximum frequency $f_{\max} = 520\,\text{kHz}$ the minimum time increment $\Delta t_{\min}$ is 96 ns. Depending on the group velocity c_g of the excited wave packets the simulation time is chosen such that for every model the distorted wave packets due to the interaction with the crack are entirely included at position S_{inc} and S_{tra}.

4 RESULTS

This chapter gives an overview of all the major results of the numerical Finite Element (FE) study. The displacement $u(t)$ in in-plane ($u_x(t)$) as well as in out-of-plane ($u_y(t)$) direction are evaluated for the S0 and for the A0 wave. The signals over the whole time domain are considered for both the incident sensor position S_{inc} and the transmitted sensor position S_{tra}. By the Fast-Four-Transformation (FFT) function of Matlab® release R215b the time domain signals are transformed into frequency domain signals. For example, in Fig. 4, the time domain

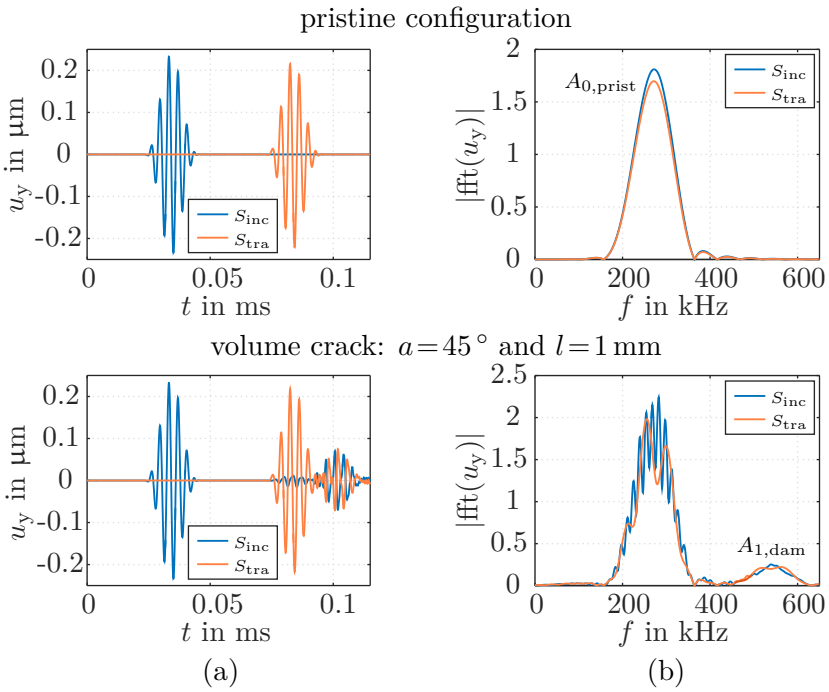

Figure 4: Comparison of the S0 wave results for the pristine configuration (top) and a volume crack with an angle of $\alpha = 45\,°$ and a length $l = 1\,\text{mm}$ (bottom): (a) time domain signals and (b) amplitude of the FFT for the incident and the transmitted $u_y(t)$ signals

as well as the frequency domain results for a S0 wave excitation in pristine configuration and

a volume crack are compared. The results for the volume crack show distortions of the wave signals in time domain compared to the pristine signals. According to the frequency domain signals higher harmonics with an amplitude $A_{1,\mathrm{dam}}$ occur in the damaged configuration due to CAN. For the mentioned crack types and their parameters mainly the ratio of the first higher harmonic amplitude $A_{1,\mathrm{dam}}$ to the first harmonic amplitude of the pristine configuration $A_{0,\mathrm{prist}}$ is investigated. The results for each crack type are presented below.

4.1 Surface crack

The evaluation of the numerical FE simulations of the surface crack model are illustrated in Fig. 5 and Fig. 6. On the one hand the results are divided into different sensor positions (incident and transmitted) on the other hand they are divided into in-plane displacement and out-of-plane

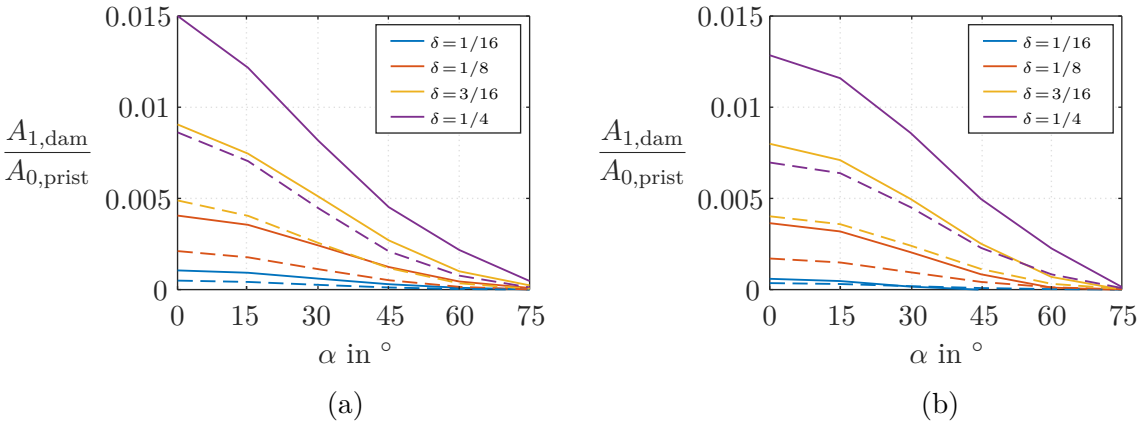

Figure 5: $A_{1,\mathrm{dam}}/A_{0,\mathrm{prist}}$ ratio for in-plane A0 (solid lines) and S0 (dashed lines) FE displacement results for surface cracks with different ratio of $\delta = l/t$ at (a) S_{inc} position and (b) S_{tra} position

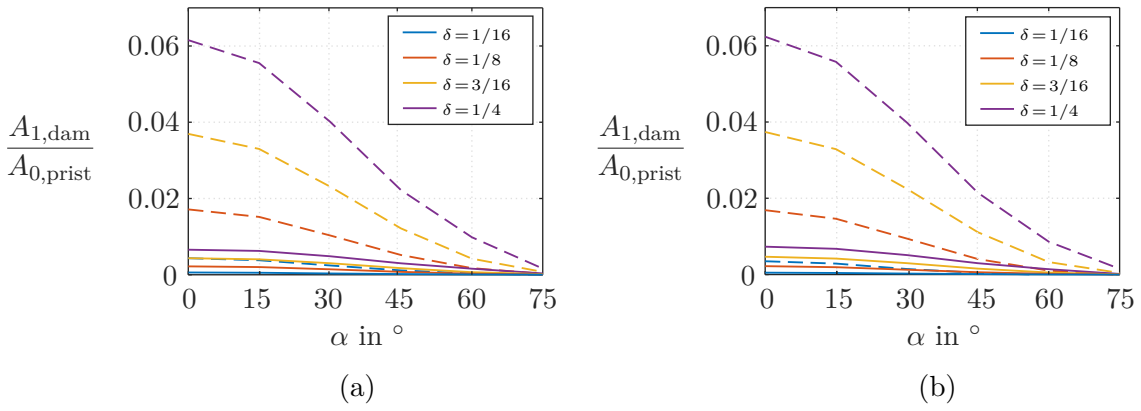

Figure 6: $A_{1,\mathrm{dam}}/A_{0,\mathrm{prist}}$ ratio for out-of-plane A0 (solid lines) and S0 (dashed lines) FE displacement results for surface cracks with different ratio of $\delta = l/t$ at (a) S_{inc} position and (b) S_{tra} position

displacement results. All presented results show the ratio of $A_{1,\mathrm{dam}}$ to $A_{0,\mathrm{prist}}$ over the angle α for different ratio δ of cracklength l to plate thickness t. As in all further results, the amplitude of the first higher harmonic $A_{1,\mathrm{dam}}$ rises with increasing ratio of δ. Both sensor positions show a nearly five times larger signal amplitude for the S0 wave in out-of-plane direction compared to the A0 wave. In in-plane direction the A0 wave signal amplitude is slightly higher than the S0 wave signal. However, compared to the out-of-plane signals, the in-plane signals are quite smaller. Consequently, out-of-plane measurement systems for the detection of nonlinear guided waves are more sensitive against surface cracks when a S0 wave is considered. Furthermore, all the results ($A_{1,\mathrm{dam}}/A_{0,\mathrm{prist}}$) show a cosine dependency from angle α and a power to a dependency of the ratio $\delta = l/t$. This leads to the general equation for $A_{1,\mathrm{dam}}$

$$A_{1,\mathrm{dam}} = A_{0,\mathrm{prist}} \left(\frac{l}{t}\right)^a b\,(\cos(c\,\alpha) + 1) \tag{3}$$

that approximately fits the first higher harmonic amplitude in case of surface cracks very well. The function $\cos(\alpha)$ indicates that the amplitude of the first higher harmonics $A_{1,\mathrm{dam}}$ depend on the vertical projection of the crack length l. For every considered sensor position (incident and transmitted), wave form (A0 and S0) and displacement (in-plane or out-of-plane) the constants a, b and c that fit the FE results best can be found. However, Table 1 lists the best fit constants evaluated with the nonlinear least square method in Matlab® release R215b with the corresponding coefficient of determination (R^2) value.

Table 1: Values for the constants a, b, c and R^2 in case of the different wave forms, sensor positions and displacements for the surface crack

wave form	sensor pos.	disp.	a	b	c	R^2
A0	incident	u_x	1.857	0.094	0.041	0.993
A0	transmitted	u_x	1.929	0.094	0.040	0.993
A0	incident	u_y	1.697	0.035	0.037	0.995
A0	transmitted	u_y	1.831	0.047	0.039	0.995
S0	incident	u_x	2.043	0.069	0.044	0.994
S0	transmitted	u_x	2.084	0.063	0.042	0.997
S0	incident	u_y	1.884	0.417	0.041	0.997
S0	transmitted	u_y	1.958	0.445	0.041	0.993

4.2 Volume crack

In case of the volume crack, the numerical FE results for the ratio of $A_{1,\mathrm{dam}}$ to $A_{0,\mathrm{prist}}$ over the angle α for different ratios $\delta = l/t$ are shown in Fig. 7 and Fig. 8. The results show a distribution with one or two superimposed Gaussian functions and the first higher harmonic amplitude $A_{1,\mathrm{dam}}$ can be approximated by

$$A_{1,\mathrm{dam}} = A_{0,\mathrm{prist}} \left(\frac{l}{t}\right)^a (b_1\,\mathrm{e}^{-(\frac{\alpha-c_1}{d_1})^2} + b_2\,\mathrm{e}^{-(\frac{\alpha-c_2}{d_2})^2}). \tag{4}$$

Looking at the in-plane results (Fig. 7) one can see that on the one hand the A0 wave is more

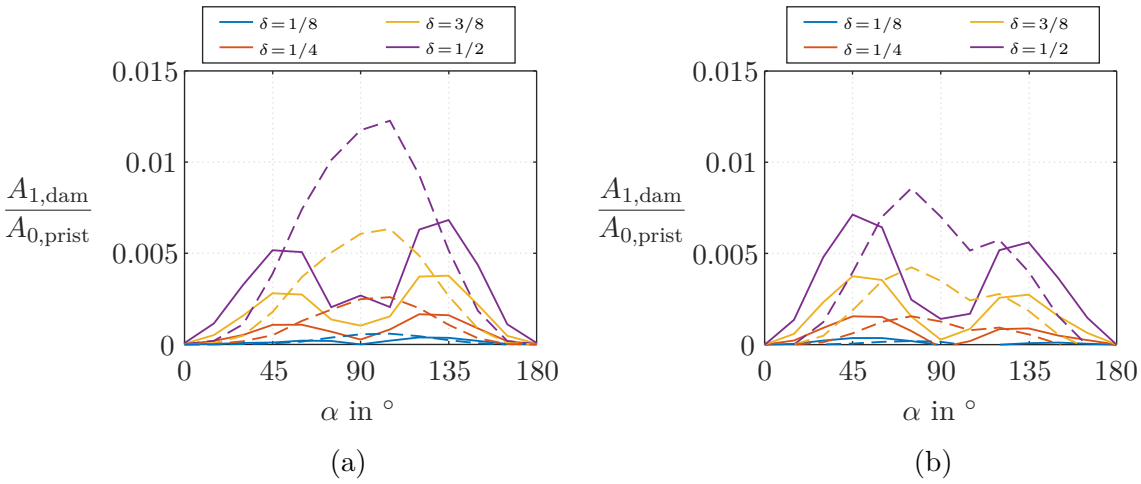

Figure 7: $A_{1,\mathrm{dam}}/A_{0,\mathrm{prist}}$ ratio for in-plane A0 (solid lines) and S0 (dashed lines) FE displacement results for volume cracks with different ratio of $\delta = l/t$ at (a) S_{inc} position and (b) S_{tra} position

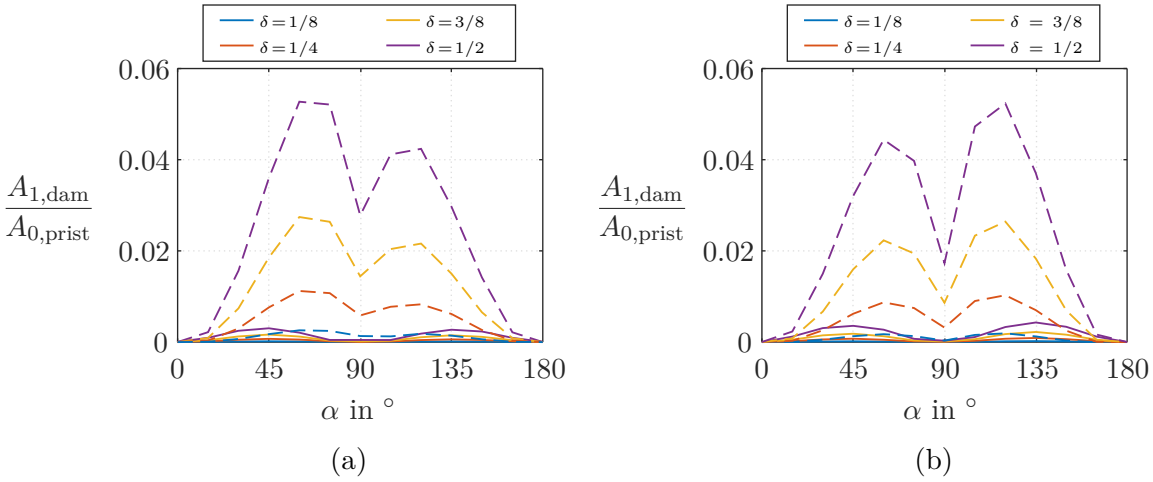

Figure 8: $A_{1,\mathrm{dam}}/A_{0,\mathrm{prist}}$ ratio for out-of-plane A0 (solid lines) and S0 (dashed lines) FE displacement results for volume cracks with different ratio of $\delta = l/t$ at (a) S_{inc} position and (b) S_{tra} position

sensitive to volume cracks for angles $\alpha < 50\,^\circ$ and $\alpha < 130\,^\circ$ than the S0 wave. On the other hand for angles $50\,^\circ < \alpha < 130\,^\circ$ the S0 wave is more sensitive than the A0 wave. This counts for both sensor positions. Furthermore, for the out-of-plane results, see Fig. 8, the first higher harmonic amplitude for the S0 wave is four times larger than the in-plane results. However, the higher harmonic amplitude for the A0 wave in out-of-plane direction is negligible small compared to the S0 wave amplitude.

By fitting the FE-results for the volume crack with the nonlinear least square method the constants $a, b_1, c_1, d_1, b_2, c_2$ and d_2 for Eq. 4 are found. The best fit values are listed in Table 2 with the corresponding coefficient of determination (R^2) value.

Table 2: Values for the constants $a, b_1, c_1, d_1, b_2, c_2, d_2$ and R^2 in case of the different wave forms, sensor positions and displacement for the volume crack

wave	sensor pos.	disp.	a	b_1	c_1	d_1	b_2	c_2	d_2	R^2
A0	incident	u_x	2.100	0.0228	51.11	29.06	0.0310	130.40	25.71	0.977
A0	transmitted	u_x	2.284	0.0369	48.87	25.88	0.0282	130.60	25.74	0.987
A0	incident	u_y	2.151	0.0140	43.30	25.09	0.0120	137.30	26.39	0.990
A0	transmitted	u_y	2.340	0.0190	43.20	25.81	0.0230	134.90	25.61	0.992
S0	incident	u_x	2.335	0.0635	93.90	43.11	–	–	–	0.993
S0	transmitted	u_x	2.562	0.0507	73.29	31.12	0.0286	124.40	21.59	0.994
S0	incident	u_y	2.310	0.2720	62.56	27.32	0.2110	119.40	26.95	0.990
S0	transmitted	u_y	2.409	0.2430	59.55	25.53	0.2900	119.50	25.23	0.980

4.3 Subsurface crack

The FE results for the ratio of $A_{1,\text{dam}}$ to $A_{0,\text{prist}}$ over the angle α with different ratio $\delta = l/t$ of a delamination like subsurface crack are shown in Fig. 9 and Fig. 10. One can see, that for in-plane results only the A0 wave provides higher harmonics. The out-of-plane results, show higher harmonics with a similar amplitude for both, the A0 mode and S0 mode. Generally the amplitude of the higher harmonics increase for subsurface crack positions closer to the plate surface. Hence, if the subsurface crack lies in the mid-plane of the plate the higher harmonics estimation is not useful because of the non existing higher harmonics.

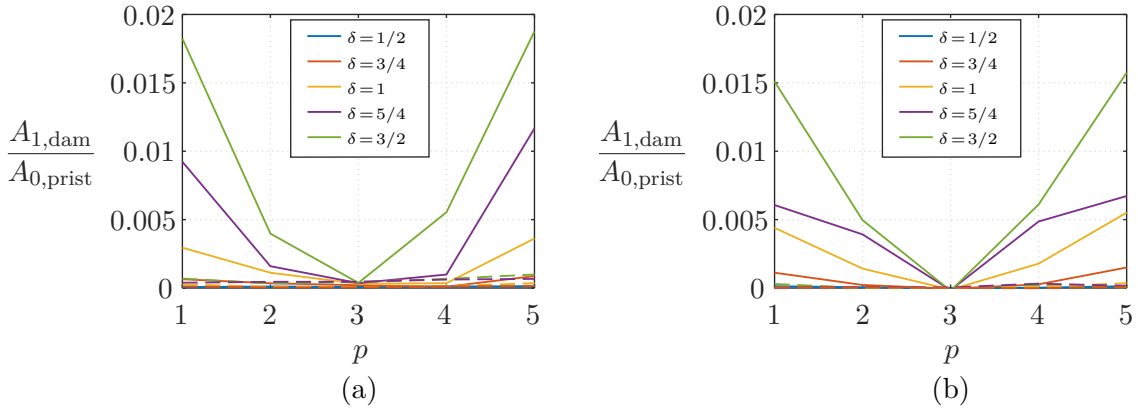

Figure 9: $A_{1,\text{dam}}/A_{0,\text{prist}}$ ratio for in-plane A0 (solid lines) and S0 (dashed lines) FE displacement results for subsurface cracks with different ratio of $\delta = l/t$ at (a) S_{inc} position and (b) S_{tra} position

5 CONCLUSIONS

The presented results clearly show a dependency of the amplitude for the first higher harmonic $A_{1,\text{dam}}$ from the type of the damage, its orientation and size. Higher harmonics appear at waves which are reflected from the cracks as well as at transmitted waves. For some crack types the A0

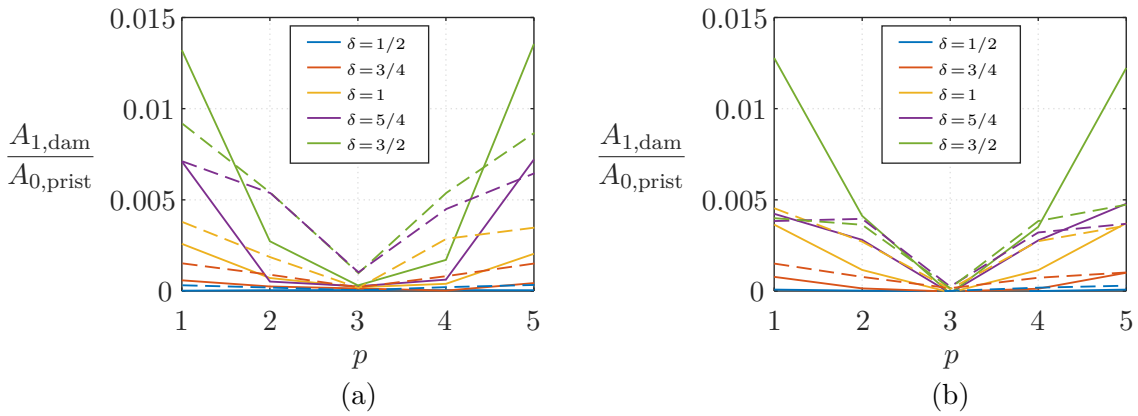

Figure 10: $A_{1,\mathrm{dam}}/A_{0,\mathrm{prist}}$ ratio for out-of-plane A0 (solid lines) and S0 (dashed lines) FE displacement results for subsurface cracks with different ratio of $\delta = l/t$ at (a) S_{inc} position and (b) S_{tra} position

mode is more sensitive to the damage parameters, for others it is the S0 mode. On the one hand, if one uses for instance an in-plane measurement system, like a piezoelectric element, to detect nonlinear guided waves and gets only higher harmonics for the A0 mode it provides an evidence for a subsurface crack. When the in-plane measurement results for the S0 mode are much higher than for the A0 mode a volume crack may be more vertical oriented. Or, if the higher harmonic of the A0 mode is a bit larger than the amplitude for the S0 mode the damage might be a surface crack or a slightly oriented volume crack. On the other hand, if one uses a out-of-plane measurement system, like a laser interferometer and gets only higher harmonics for the S0 wave, this could be an indication for a surface or a volume crack. Further investigations, especially with different excitation frequencies f, may change the curves for the higher harmonic amplitude because of the dispersive characteristic of guided waves. It is expected that the combination of several measurements with different excitation frequencies f makes it clearer to quantify and qualify damages.

REFERENCES

[1] Rytter, A. *Vibrational Based Inspection of Civil Engineering Structures*. Aalborg: Dept. of Building Technology and Structural Engineering. Aalbor University, Phd thesis, (1993)

[2] Zhao, Y.; Schagerl, M.; Gschoßmann, S. and Beisteiner, C. *An Inkjet-Printed Carbon Nanotube Strain Distribution Sensor for Quasi Real-Time Strain Monitoring of Lightweight Design Materials*, Advances in Science and Technology, (2017) **101**:3–8

[3] Kralovec, C. and Schagerl, M. *Electro-mechanical impedance measurements as a possible SHM method for sandwich debonding detection*. Materials Science Forum. Trans Tech Publications, to appear 2017.

[4] Schagerl, M.; Viechtbauer, C. and Schaberger, M. *Optimal Placement of Fiber Optical Sensors along Zero-strain Trajectories to Detect Damages in Thin-walled Structures with Highest Sensitivity*. Structural Health Monitoring 2015 - System Reliability for Verification and Implementation, (2015) **1**:1096–1103

[5] Tua, P.S.; Quek, S.T. and Wang, Q. *Detection of cracks in plates using piezo-actuated Lamb waves.* Smart Materials and Structures, (2004) **13**:643–660

[6] Shen, Y. and Giurgiutiu, V. *Predictive simulation of nonlinear ultrasonics.* Proc. SPIE 8348, Health Monitoring of Structural and Biological Systems (2012), **8348**:83482E–83482E-11

[7] Shen, Y. and Giurgiutiu, V. *Predictive modeling of nonlinear wave propagation for structural health monitoring with piezoelectric wafer active sensors.* Journal of Intelligent Material Systems and Structures, (2014) **25**:506–520

[8] Soleimanpour, R.; Ng, C.T. and Wang, C.H. *Higher harmonic generation of guided waves at delaminations in laminated composite beams.* Structural Health Monitoring an International Journal, online first, (2016) 1–18

[9] Solodov, I.Y. *Ultrasonics of non-linear contacts: propagation, reflection and NDE-applications.* Ultrasonics, (1998) **36**:383-390

[10] Solodov, I.Y. *Nonlinear acoustic NDT: approaches, methods, and applications.* Proc. NDT in Progress, 5th International Workshop of NDT Experts. Prague, (2009)

[11] Wan, X.; Zhang, Q.; Xu, G. and Tse, P.W. *Numerical Simulation of Nonlinear Lamb Waves Used in a Thin Plate for Detecting Buried Micro-Cracks.* Sensors (Basel, Switzerland), (2014) **14**:8528–8546

[12] Breazeale, M. A. and Ford, J. *Ultrasonic Studies of the Nonlinear Behavior of Solids.* Journal of Applied Physics, (1965) **36**:3486–3490

[13] Deng, M. A. *Analysis of second-harmonic generation of Lamb modes using a modal analysis approach.* Journal of Applied Physics, (2003) **94**:4152–4159

[14] Bermes, C.; Kim, J.Y.; Qu, J. and Jacobs, L.J. *Experimental characterization of material nonlinearity using Lamb waves.* Applied Physics Letters, (2007) **90**:021901

[15] Wu, W.Q.; Ni, Y.F.; Qiu, G. and Zhang, D. *Investigation of contact acoustic nonlinearity at solid interface.* Proc. IEEE Ultrasonics Symposium, (1998) **2**:1175–1178

[16] Moser, F.; Jacobs, L.J. and Qu, J. *Modeling elastic wave propagation in waveguides with the finite element method.* NTD & E International, (1999) **32**:225–234

Stress-Free Actuation Response Field Dependent Nonlinearity Handling for Piezoelectric Smart Structures: A Critical Review

Ayech Benjeddou*†

* Sorbonne Université, Université de Technologie de Compiègne, CNRS, UMR 7337 ROBERVAL. Centre de Recherche Royallieu, CS 60319, 60203 Compiègne CEDEX, France. E-mail: ayech.benjeddou@utc.fr, web page: http://www.utc.fr

† Institut Supérieur de Mécanique de Paris (SUPMECA), 3 Rue Fernand Hainaut, 93407 Saint Ouen, CEDEX, France. Email: benjeddou@supmeca.fr - Web page: http://www.supmeca.fr

ABSTRACT

From the beginning of the smart structures era, more than three decades ago, early smart structures experimentations have proved that the piezo-electrically induced strain–electric field relation is nonlinear. This was handled in experiments simulation by considering either strain or field dependent piezoelectric coefficient [1] but the strain dependence, implemented iteratively using linear constitutive equations, was preferred to the field one as it correlated better. Nevertheless, the former was not satisfactory for a glass fibre composite host [2]. Later, a good correlation of the previous configuration was obtained through thermodynamically motivated rotationally invariant nonlinear constitutive equations having an additional electrostrictive parameter [3]. A similar theory has been used for the nonlinear response modelling of longitudinal mode Macro Fiber Composite (MFC) actuators [4]. Late in the previous decade, a simple phenomological model of vibrating domain wall has been implemented successfully using linear constitutive equations in order to consider the contribution of domain wall motion to the electromechanical properties of piezoceramic bimorph actuators [5]. However, the performance of other phenomenological approaches that use geometrical and Preisach material nonlinearities is under expectation [6].

Above literature review shows that neither of the proposed approaches is currently fully satisfactory for handling the stress free actuation response field dependent nonlinearity in piezoelectric smart structures. Nevertheless, the shear MFC piezoelectric constant nonlinear field dependence has been recently implemented using linear constitutive equations and a power law which parameters have been fitted from test data [7]. The obtained test-model correlation was very encouraging; it is here presented as an alternative way to simulate realistically the inherent field dependence nonlinearity.

REFERENCES

[1] E.F. Crawley and J. De Luis, "Piezoelectric actuators for intelligent structures", *AIAA J.*, Vol. **25**, pp. 1376–1383, (1987).

[2] E.F. Crawley and E.H. Anderson, "Detailed models of piezoceramic actuation of beams", *J. Intell. Mater. Syst. Struct.*, Vol. **1**, 4–25, 1990.

[3] H.F. Tiersten, "Electroelastic equations for electroded thin plates subject to large driving voltages", *J. Appl. Phys.*, Vol. **74**, pp. 3389–3393, 1993.

[4] R.B. Williams, D.J. Inman and W.K. Wilkie, "Nonlinear response of the Macro Fiber Composite actuator to monotonically increasing excitation voltage", *J. Intell. Mater. Syst. Struct.*, Vol. **17**, 601–608, 2006.

[5] Y. Shindo, F. Narita and J. Nakagawa, "Dynamic electromechanical response and self-sensing of functionally graded piezoelectric cantilever transducers", *J. Intell. Mater. Syst. Struct.*, Vol. **20**, 119–126, 2009.

[6] K. Schulz, S. Klinkel and W. Wagner, "A finite element formulation for piezoelectric shell structures considering geometrical and material non-linearities", *Int. J. Numer. Meth. Engng.*, Vol., pp., 2011.

[7] A. Benjeddou, "Voltage dependent non-linear response shear macro-fibre composite actuators", In *2nd Int. Workshop on Advanced Dynamics & Model-based Control of Structures & Machines*, Vienna (Austria), Sept. 20-24, 2015.

VIII ECCOMAS Thematic Conference on Smart Structures and Materials
SMART 2017
A. Güemes, A. Benjeddou, J. Rodellar and J. Leng (Eds)

DAMAGE IDENTIFICATION METHOD FOR THREE-DIMENSIONAL TRUSS STRUCTURES BASED ON SUBSTRUCTURING APPROACH AND VARX MODELLING

U. UGALDE[*], J. ANDUAGA[*], O. SALGADO[*] AND A. ITURROSPE[†]

[*] IK4-Ikerlan Technology Research Centre, Control and Monitoring Area
Mondragon, Spain
e-mail: uugalde@ikerlan.es, www.ikerlan.es

[†] Mondragon Goi Eskola Politeknikoa, Dpt Electronics and Computer Sciences
Mondragon, Spain

Key words: Substructuring, Structural Health Monitoring, Damage Identification, VARX Modelling, Three-Dimensional Truss Structure.

Abstract. *A novel SHM method is proposed for damage localisation and quantification combining the substructuring approach and Vector Auto-Regressive with Exogenous input (VARX) models. The substructuring approach aims to divide the monitored structure into several isolated substructures. Each individual substructure is modelled as a VARX model, and the health of each substructure is determined analysing the variation of the VARX model's coefficients. The method allows determining whether the isolated substructure is damaged, and besides allows locating and quantifying the damage within the substructure. It is not necessary to have a physics-based model of the structure and only vibration data of the substructures are required to estimate their VARX models. The proposed method is validated by simulations in a three-dimensional truss structure.*

1 INTRODUCTION

Structural Health Monitoring (SHM) is a technological area which develops a damage detection and characterization strategies for engineering structures [1]. SHM is regarded as a very important engineering field in order to secure structural and operational safety; issuing early warnings on damage or deterioration, avoiding costly repairs or even catastrophic failures [2].

Most of the existing vibration based SHM methods can be classified into two different approaches: global approaches and local approaches [3]. In the global approaches, the goal is to monitor the health of the entire structure. These global methods have been tested and implemented in different types of structures during the last 30-40 years [4]. However, for many large systems, global monitoring is not viable due to the lack of sensitivity of global features to local damages, inaccuracies of developed models etc [5]. On the other hand, local SHM methods are focused on evaluating the condition of smaller parts within the entire structures by means of substructuring approach. This approach aims to overcome global method's

limitations, dividing the whole structure into substructures and analysing each one individually.

Several papers have been published proposing substructuring methods for large scale structures. Koh et al [6] presented a "divide and conquer" strategy to monitor large structures based on the division of the whole structure into isolated substructures. For each substructure, structural parameters are identified using the extended Kalman filter (EKF). However, the EKF usually requires a physics-based model, which is not always available [7]. Most recently, Xing et al [8] and Lei et al [9] proposed another substructural damage detection method using Auto-Regressive Moving Average with eXogenous input (ARMAX) models. The substructures are represented by an ARMAX model and the natural frequency of each substructure is extracted from the mentioned model for its posterior analysis. Nonetheless it is preferably applicable to small and simple structures.

The authors of this article proposed in [10][11][12] a damage localisation and quantification method based on substructuring approach and Vector Auto-Regressive with eXogenous input (VARX) models. The proposed method was able to monitor multi-DOF substructures analysing the variation of the VARX models. Only vibration data was measured from the substructures and it was not necessary to have a physics-based model of the structure. This new article incorporates some improvements over the initial method and a validation by simulations in a three-dimensional truss structure.

The rest of the paper is organised as follows. In section 2, the proposed method is presented. In section 3, the method is evaluated by series of simulations. Finally the concluding remarks are presented in section 4.

2 THE PROPOSED METHOD

The dynamics of the structure is described by a lumped parameter model. It is assumed that the structure consists of bars and the forces can only be transmitted along the axial direction of these bars. Besides, the structure is subjected to arbitrary external loading that is assumed to be known and could act on any node.

The structure is divided into different isolated substructures. The substructures have *n* internal (*i*) and *m* interface (*j*) nodes. The interface nodes are located in the border between the selected substructure and the remaining structure. The internal nodes are located within the substructure and they are not connected to the nodes of the remaining structure.

The dynamic equation for an internal node *l* is formulated as follows:

$$\mathrm{M}_{il}\ddot{\mathbf{z}}_{\mathbf{il}} = \sum_{p=1}^{N}(\mathbf{f}_{\mathbf{p}}(\mathbf{z}_{\mathbf{i}},\dot{\mathbf{z}}_{\mathbf{i}},\mathbf{z}_{\mathbf{j}},\dot{\mathbf{z}}_{\mathbf{j}})) + \mathbf{f}_{\mathbf{il}} \tag{1}$$

where M_{il} is the lumped mass matrix of the internal node *l* and $\ddot{\mathbf{z}}_{\mathbf{il}}$ is a vector that contains the accelerations of the internal node *l* in x, y and z axes respectively ($\ddot{z}_{ilx}$, $\ddot{z}_{ily}$ and $\ddot{z}_{ilz}$). $\boldsymbol{f_p}$ is a

vector with linear or non-linear functions used to calculate the total force applied in the internal node *l* by the *N* nodes connected to him. $\mathbf{z_i}$,$\dot{\mathbf{z}}_\mathbf{i}$, $\mathbf{z_j}$ and $\dot{\mathbf{z}}_\mathbf{j}$ are the displacement and velocity vectors of the internal and interface nodes that are connected to the internal node *l* in x, y and z axes. Furthermore, $\mathbf{f_{il}}$ contains the external force applied in the internal node *l* in x, y and z axes (f_{ilx}, f_{ily}, f_{ilz}).

Expanding $\boldsymbol{f_p}$ function as Taylor series [13] and selecting only the first term, the dynamic equations for an internal node *l* are stated as:

$$m_{ilx}\ddot{z}_{ilx}=\sum_{p=1}^{N}(k_{ilx\text{-}px}(z_{ilx}-z_{px})+k_{ilx\text{-}py}(z_{ily}-z_{py})+k_{ilx\text{-}pz}(z_{ilz}-z_{pz})+c_{ilx\text{-}px}(\dot{z}_{ilx}-\dot{z}_{px})+c_{ilx\text{-}py}(\dot{z}_{ily}-\dot{z}_{py})+c_{ilx\text{-}pz}(\dot{z}_{ilz}-\dot{z}_{pz}))+f_{ilx} \quad (2)$$

$$m_{ily}\ddot{z}_{ily}=\sum_{p=1}^{N}(k_{ily\text{-}px}(z_{ilx}-z_{px})+k_{ily\text{-}py}(z_{ily}-z_{py})+k_{ily\text{-}pz}(z_{ilz}-z_{pz})+c_{ily\text{-}px}(\dot{z}_{ilx}-\dot{z}_{px})+c_{ily\text{-}py}(\dot{z}_{ily}-\dot{z}_{py})+c_{ily\text{-}pz}(\dot{z}_{ilz}-\dot{z}_{pz}))+f_{ily}$$

$$m_{ilz}\ddot{z}_{ilz}=\sum_{p=1}^{N}(k_{ilz\text{-}px}(z_{ilx}-z_{px})+k_{ilz\text{-}py}(z_{ily}-z_{py})+k_{ilz\text{-}pz}(z_{ilz}-z_{pz})+c_{ilz\text{-}px}(\dot{z}_{ilx}-\dot{z}_{px})+c_{ilz\text{-}py}(\dot{z}_{ily}-\dot{z}_{py})+c_{ilz\text{-}pz}(\dot{z}_{ilz}-\dot{z}_{pz}))+f_{ilz}$$

where z_{ilx}, z_{ily}, z_{ilz} and $\dot{z}_{ilx}$, $\dot{z}_{ily}$, $\dot{z}_{ilz}$ are the displacements and velocities of the internal node *l* and z_{px}, z_{py}, z_{pz} and $\dot{z}_{px}$, $\dot{z}_{py}$, $\dot{z}_{pz}$ are the displacements and velocities of the *N* (internal or interface) nodes that are connected to the internal node *l*. Furthermore, *k* and *c* are coefficients related to the stiffness and damping values of the *N* bars that are connected to the internal node *l*.

The *n* internal nodes of the substructure are represented as in equation 1-2 in order to obtain the substructural dynamic equation. The finite central difference method [14] is used to obtain an approximation of the displacements from the velocity and acceleration data. The substructural dynamic equation in matrix form and in terms of displacements is represented as follows:

$$\begin{bmatrix} z_{i1x}(n) \\ z_{i1y}(n) \\ z_{i1z}(n) \\ \dots \\ z_{inx}(n) \\ z_{iny}(n) \\ z_{inz}(n) \end{bmatrix} = -A_1 \begin{bmatrix} z_{i1x}(n-1) \\ z_{i1y}(n-1) \\ z_{i1z}(n-1) \\ \dots \\ z_{inx}(n-1) \\ z_{iny}(n-1) \\ z_{inz}(n-1) \end{bmatrix} - A_2 \begin{bmatrix} z_{i1x}(n-2) \\ z_{i1y}(n-2) \\ z_{i1z}(n-2) \\ \dots \\ z_{inx}(n-2) \\ z_{iny}(n-2) \\ z_{inz}(n-2) \end{bmatrix} \quad (3)$$

$$+B_{10}\begin{bmatrix} z_{j1x}(n) \\ z_{j1y}(n) \\ z_{j1z}(n) \\ \dots \\ z_{jmx}(n) \\ z_{jmy}(n) \\ z_{jmz}(n) \end{bmatrix} + B_{11}\begin{bmatrix} z_{j1x}(n-1) \\ z_{j1y}(n-1) \\ z_{j1z}(n-1) \\ \dots \\ z_{jmx}(n-1) \\ z_{jmy}(n-1) \\ z_{jmz}(n-1) \end{bmatrix} + B_{12}\begin{bmatrix} z_{j1x}(n-2) \\ z_{j1y}(n-2) \\ z_{j1z}(n-2) \\ \dots \\ z_{jmx}(n-2) \\ z_{jmy}(n-2) \\ z_{jmz}(n-2) \end{bmatrix} + B_{21}\begin{bmatrix} F_{i1x}(n-1) \\ F_{i1y}(n-1) \\ F_{i1z}(n-1) \\ \dots \\ F_{inx}(n-1) \\ F_{iny}(n-1) \\ F_{inz}(n-1) \end{bmatrix}$$

where z_{i1x}, ... , z_{inz} are the displacements of the n internal nodes and z_{j1x}, ... , z_{jmz} are the displacements of the m interface nodes.

Equation 3 could be regarded as a VARX model [15], where z_{i1x}, ... , z_{inz} correspond to the endogenous variables and z_{j1x}, ... , z_{jmz} and F_{i1x}, ... , F_{imz} correspond to the exogenous variables. A_1 and A_2 are the endogenous coefficient matrices and B_{10}, B_{11}, B_{12}, and B_{21} are the exogenous coefficient matrices. The elements of the mentioned matrices are related to the physical properties of the substructure.

In the proposed method, the displacements in the internal and interface nodes of the substructure are measured and the corresponding VARX model is estimated. It is assumed that the substructure is healthy in the initial phase, so the VARX model estimated with the initial data is taken as a reference. Displacement data is measured again in the evaluation phase and the corresponding VARX model is estimated. In the proposed method, endogenous and exogenous coefficient matrices of these new VARX models are compared to the same matrices of the reference model and as a result the condition of the substructure is evaluated.

3 EVALUATION BY SIMULATIONS

Structure's finite element model has been developed in ANSYS. The model is formed by 14 steel balls joined by 31 aluminium tubes, forming the geometry shown in figure 1. Each ball weights 0.235 kg and each tube is 707 mm long, with an external diameter of 22 mm and an internal diameter of 20 mm. The tubes are modelled using truss elements and the balls are introduced as point masses. The structure is fixed in its four edges.

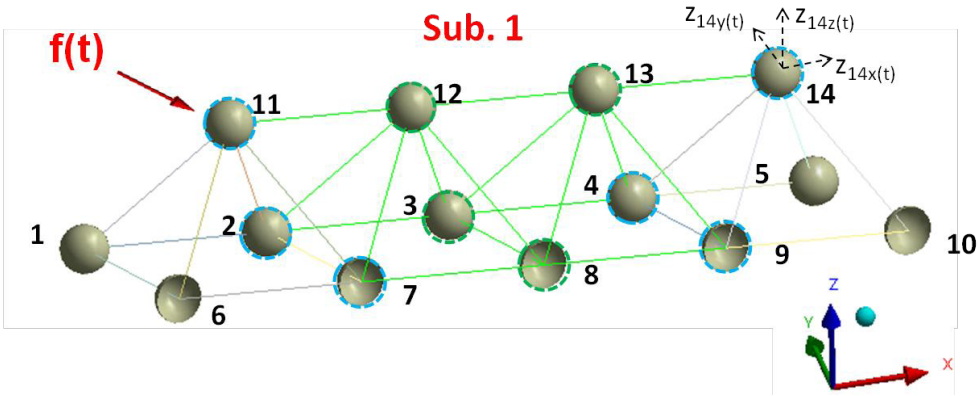

Figure 1: Structure's finite element model

The first five natural frequencies of the model are 109.95 Hz, 165.01 Hz, 265.80 Hz, 315.11 Hz and 379.49 Hz, and the corresponding mode shapes are shown in figure 2.

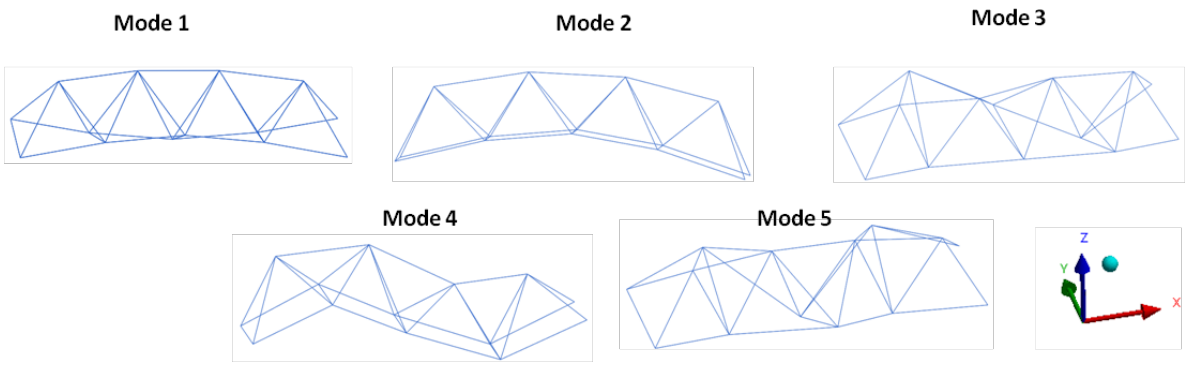

Figure 2: Finite element model's mode shapes

As it is shown in figure 1, a substructure formed by sixteen tubes is selected for its monitoring. The structure is excited applying a Gaussian white noise force out of the substructure. The dynamic equations for the isolated substructure could be formulated as:

$$M'\begin{bmatrix}\ddot{\mathbf{z}}_3(t)\\ \ddot{\mathbf{z}}_8(t)\\ \ddot{\mathbf{z}}_{12}(t)\\ \ddot{\mathbf{z}}_{13}(t)\end{bmatrix} + K'\begin{bmatrix}\mathbf{z}_3(t)\\ \mathbf{z}_8(t)\\ \mathbf{z}_{12}(t)\\ \mathbf{z}_{13}(t)\end{bmatrix} + K''\begin{bmatrix}\mathbf{z}_2(t)\\ \mathbf{z}_4(t)\\ \mathbf{z}_7(t)\\ \mathbf{z}_9(t)\\ \mathbf{z}_{11}(t)\\ \mathbf{z}_{14}(t)\end{bmatrix} = 0 \tag{4}$$

Accelerations $\ddot{\mathbf{z}}_3$, $\ddot{\mathbf{z}}_8$, $\ddot{\mathbf{z}}_{12}$, $\ddot{\mathbf{z}}_{13}$ and displacements $\mathbf{z}_3$, $\mathbf{z}_8$, $\mathbf{z}_{12}$, $\mathbf{z}_{13}$ correspond to internal DOFs, whereas displacements $\mathbf{z}_2$, $\mathbf{z}_4$, $\mathbf{z}_7$, $\mathbf{z}_9$, $\mathbf{z}_{11}$, $\mathbf{z}_{14}$ correspond to interface DOFs, all of them in x, y and z axes. *M'* represents the mass of the substructure, *K'* represents the stiffness of the tubes located between internal nodes and *K''* represents the stiffness of the tubes located between internal and interface nodes.

Following the procedure described in section 2, the dynamical behaviour of the substructure can be described by a VARX model stated in equation 5. The endogenous variables are the displacements in nodes 3, 8, 12 and 13 ($\mathbf{z}_3$, $\mathbf{z}_8$, $\mathbf{z}_{12}$ and $\mathbf{z}_{13}$), whereas the exogenous variables are the displacements in nodes 2, 4, 7, 9, 11 and 14 ($\mathbf{z}_2$, $\mathbf{z}_4$, $\mathbf{z}_7$, $\mathbf{z}_9$, $\mathbf{z}_{11}$ and $\mathbf{z}_{14}$).

$$\begin{bmatrix}\mathbf{z}_3(n)\\ \mathbf{z}_8(n)\\ \mathbf{z}_{12}(n)\\ \mathbf{z}_{13}(n)\end{bmatrix} = A_1\begin{bmatrix}\mathbf{z}_3(n\text{-}1)\\ \mathbf{z}_8(n\text{-}1)\\ \mathbf{z}_{12}(n\text{-}1)\\ \mathbf{z}_{13}(n\text{-}1)\end{bmatrix} + A_2\begin{bmatrix}\mathbf{z}_3(n\text{-}2)\\ \mathbf{z}_8(n\text{-}2)\\ \mathbf{z}_{12}(n\text{-}2)\\ \mathbf{z}_{13}(n\text{-}2)\end{bmatrix} + B_1\begin{bmatrix}\mathbf{z}_2(n\text{-}1)\\ \mathbf{z}_4(n\text{-}1)\\ \mathbf{z}_7(n\text{-}1)\\ \mathbf{z}_9(n\text{-}1)\\ \mathbf{z}_{11}(n\text{-}1)\\ \mathbf{z}_{14}(n\text{-}1)\end{bmatrix} \tag{5}$$

Matrices A_1, A_2 and B_1 shown in equation 5 are formulated as follows:

$$A_1 = \left(T_s^2 M'^{-1}\right)\left(\frac{2}{T_s^2}M' - K'\right) \tag{6}$$

$$A_2 = \left(T_s^2 M'^{-1}\right)\left(\frac{1}{T_s^2}M'\right)$$

$$B_1 = \left(T_s^2 M'^{-1}\right)(K'')$$

Equation 6 shows that A_1 depends on the mass and stiffness of the tubes located between internal nodes, whereas B_1 depends on the mass of the mentioned tubes and the stiffness of the tubes located between internal and interface nodes. Matrices A_1, A_2 and B_1 depend also on the sampling period (T_s).

Figure 3 shows which submatrices within A_1 and B_1 contain useful information for the monitoring of the substructure. There are two analysable submatrices within A_1 for the monitoring of the tubes located between internal nodes, whereas only one analysable submatrix within B_1 for the monitoring of the tubes located between internal and interface nodes. Only the diagonal terms of these submatrices should be analysed, and among the three possible terms, we should analyse a particular one depending on the orientation of the tube. So if the tube is orientated in the x axis, we should analyse only the first term of the diagonal, whereas if the tube is orientated in y or z axes, we should analyse only the second or the third term respectively. Consequently, if the tube is orientated in x, y and z axes, we should analyse the entire diagonal.

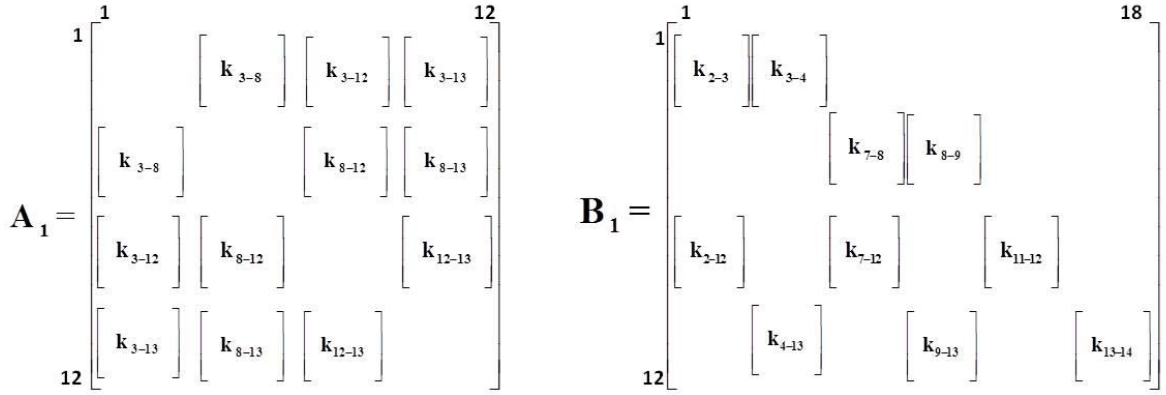

Figure 3: Structure of matrices A_1 and B_1

Table 1 shows the terms that are analysed within matrices A_1 and B_1 in order to locate damages in the sixteen tubes of the substructure. We assume the damages consist in a reduction of the tube's stiffness.

Table 1: Analysed terms within matrices A_1 and B_1

Tube	Orientation	Analysed terms
k_{3-8}	*y*	$A_{1;2,5}$, $A_{1;5,2}$
k_{3-12}	*x*, *y*, *z*	Entire diagonal of both submatrices (A_1)
k_{3-13}	*x*, *y*, *z*	Entire diagonal of both submatrices (A_1)
k_{8-12}	*x*, *y*, *z*	Entire diagonal of both submatrices (A_1)
k_{8-13}	*x*, *y*, *z*	Entire diagonal of both submatrices (A_1)
k_{12-13}	*x*	$A_{1;7,10}$, $A_{1;10,7}$
k_{2-3}	*x*	$B_{1;1,1}$
k_{2-12}	*x*, *y*, *z*	Entire diagonal of the submatrix (B_1)
k_{3-4}	*x*	$B_{1;1,4}$
k_{4-13}	*x*, *y*, *z*	Entire diagonal of the submatrix (B_1)
k_{7-8}	*x*	$B_{1;4,7}$
k_{7-12}	*x*, *y*, *z*	Entire diagonal of the submatrix (B_1)
k_{8-9}	*x*	$B_{1;4,10}$
k_{9-13}	*x*, *y*, *z*	Entire diagonal of the submatrix (B_1)
k_{11-12}	*x*	$B_{1;7,13}$
k_{13-14}	*x*	$B_{1;10,16}$

As it is explained in section 2, the condition of the substructure is evaluated analysing deviations between the new A_1 and B_1 matrices (evaluation phase) and the initial ones (initial phase). A particular damage indicator (DI) is calculated for each substructural tube analysing changes in the terms shown in table 1. For example, the damage indicator for the tube located between the internal nodes 3 and 8 (k_{3-8}) will be obtained as follows:

$$DI\,(k_{3-8}) = \left(\left| \frac{|A^{e}_{1;2,5}| - |A^{i}_{1;2,5}|}{|A^{i}_{1;2,5}|} \right| + \left| \frac{|A^{e}_{1;5,2}| - |A^{i}_{1;5,2}|}{|A^{i}_{1;5,2}|} \right| \right) x \frac{100}{2} \qquad (7)$$

where $A^{i}_{1;2,5}$ and $A^{i}_{1;5,2}$ are the terms estimated in the initial phase and $A^{e}_{1;2,5}$ and $A^{e}_{1;5,2}$ are the terms estimated in the evaluation phase. The proposed damage indicator estimates the stiffness reduction induced in the tube.

The model is excited in node 11 and in x, y and z axes by a Gaussian white noise force (see figure 1). The displacements in the fourteen nodes are simulated with a data sampling frequency of 5 kHz. 10,000 samples of the simulated data are used to estimate the VARX models described in equation 5. The mentioned VARX models are estimated using the Econometric Toolbox of Matlab and the *Multivariate Least Square* (MLS) estimator [16].

Twelve different damaged scenarios are evaluated. In nine of them the damages are located within the substructure (k_{8-13}, k_{12-13} and k_{9-13}). In the other three scenarios the damages are located out of the substructure (k_{9-14}). Only one tube is damaged in each scenario and three severity levels are analysed, stiffness reductions of 12.5%, 25% and 50%.

Table 2 presents the obtained results in the assessed scenarios. In those scenarios which contain damage within the substructure, we show the damage indicator obtained for the

damaged tube and also the highest damage indicator obtained for the other substructural tubes. In those scenarios in which the damaged tube is located out of the substructure, we only show the highest damage indicator obtained for the substructural tubes.

Table 2: Results in the assessed scenarios

Scenario		Damage Indicator (%)	
		Damaged tube	**Healthy tube (max)**
$\mathbf{k_{9\text{-}14}}$ **(%)**	**12.5**	--	0.96
	25	--	1.58
	50	--	1.89
$\mathbf{k_{8\text{-}13}}$ **(%)**	**12.5**	12.38	0.78
	25	25.49	0.98
	50	49.21	1.28
$\mathbf{k_{12\text{-}13}}$ **(%)**	**12.5**	12.59	0.54
	25	24.59	0.69
	50	49.11	0.93
$\mathbf{k_{9\text{-}13}}$ **(%)**	**12.5**	12.73	0.88
	25	25.88	1.13
	50	50.99	1.29

The results show that the damage is located properly in the assessed twelve scenarios. In those scenarios in which the damage is located out of the substructure, the highest damage indicator is 1.89%. In the rest of the scenarios, the highest damage indicator corresponds to the damaged tube, with a maximum quantification error of 0.99% for these damaged tubes. Besides, the highest damage indicator among the tubes that have not been damaged is 1.29%. Therefore, the proposed method allows damage localisation and quantification within the substructures.

4 CONCLUSIONS

This paper proposes a novel SHM method to detect, locate and quantify damages in structures. A substructure of interest is isolated by a substructuring method. Substructure's VARX model is estimated with the healthy data and it is taken as a reference. Substructural vibration data is measured again when the substructure should be evaluated and the corresponding VARX models are estimated. These new VARX models are compared to the reference in order to evaluate the condition of the substructure. Only vibration data is required to estimate the VARX models and it is not necessary to have a physics-based model.

The proposed method is validated by simulations in a three-dimensional truss structure. The results show that the method allows detecting, locating and quantifying damage within the substructure with a maximum stiffness estimation error of 1.89%.

Our research group is already building a laboratory structure in order to carry out an experimental validation. The results will be published soon.

5 ACKNOWLEDGEMENT

This study is partially funded by the Ministry of Economy and Competitiveness of the Spanish Government (WINTURCON project, DPI2014-58427-C2-2-R). The authors wish to express also their acknowledgement to the Basque Government for their financial support of this research through the MECOFFbi (File number:KK-2016/00027) project, as part of the ELKARTEK Strategic Program. Any opinions, findings and conclusions expressed in this article are those of the authors and do not necessarily reflect the views of the funding agency.

REFERENCES

[1]J. Ko and Y. Ni, "Technology developments in structural health monitoring of large-scale bridges," *Engineering structures,* vol. 27, pp. 1715-1725, 2005.

[2]A. Mita, "Structural dynamics for health monitoring," Sankeisha Co., Ltd, Nagoya, vol. 114, 2003.

[3]L. Jankowski, Lukasz and I. P. P. o. Techniki, Dynamic load identification for structural health monitoring: Institute of Fundamental Technological Research Polish Academy of Sciences, 2013.

[4]S. W. Doebling, C. R. Farrar, M. B. Prime, and others, "A summary review of vibration-based damage identification methods," Shock and vibration digest, vol. 30, pp. 91-105, 1998.

[5]J. Hou, L. Jankowski, Lukasz, and J. Ou, "Structural damage identification by adding virtual masses," Structural and Multidisciplinary Optimization, vol. 48, pp. 59-72, 2013.

[6]C. G. Koh, L. M. See, and T. Balendra, "Estimation of structural parameters in time domain: a substructure approach," Earthquake Engineering \& Structural Dynamics, vol. 20, pp. 787-801, 1991.

[7]A. W. Oreta and T.a. Tanabe, "Element identification of member properties of framed structures," Journal of Structural Engineering, vol. 120, pp. 1961-1976, 1994.

[8]Z. Xing and A. Mita, "A substructure approach to local damage detection of shear structure," Structural Control and Health Monitoring, vol. 19, pp. 309-318, 2012.

[9]L. Mei, A. Mita, and Z. H. Xing, "Substructure damage detection method for shear structure using sub-time series and ARMAX," in *Key Engineering Materials*, 2013, pp. 149-159.

[10]U. Ugalde, J. Anduaga, F. Martínez and A. Iturrospe, "SHM method for damage localization based on substructuring and VARX models," in arXiv preprint:1501.01905, 2015.

[11]U. Ugalde, J. Anduaga, F. Martínez and A. Iturrospe, "Novel SHM method to locate damages in substructures based on VARX models," in Journal of Physics: Conference Series, 2015, p. 012013.

[12]U. Ugalde, J. Anduaga, F. Martínez and A. Iturrospe, "A SHM method for identifying damage based on VARX modelling and substructuring approach," in Proceeding of the 8th European Workshop on Structural Health Monitoring, Bilbao, Spain July 5-8, 2016.

[13]L. B. Zhao, J. Y. Zhang, and Y. X. Zhao, "Taylor Series Numerical Method in Structural Dynamics," Advanced Materials Research, vol. 33, pp. 1213-1220, 2008.
[14] P. J. Olver, “Introduction to partial differential equations”, Springer, 2014.
[15]H. Lutkepohl, "New introduction to multiple time series analysis,” Springer, 2007.
[16]Y. M. Bishop, S. E. Fienberg, P. W. Holland, R. J. Light, and F. Mosteller, "Book Review: Discrete Multivariate Analysis: Theory and Practice," Applied Psychological Measurement, vol. 1, pp. 297-306, 1977.

VIII ECCOMAS Thematic Conference on Smart Structures and Materials
SMART 2017
A. Güemes, A. Benjeddou , J. Rodellar and Jinsong Leng (Eds)

IC DEBONDING FAILURE DETECTION IN RC BEAMS STRENGTHENED WITH FRP USING IMPEDANCE SENSORS AND A HIERARCHICAL CLUSTERING METHODOLOGY

RICARDO PERERA[*], ENRIQUE SEVILLANO[*], ANTONIO RUIZ[†] AND LLUIS TORRES[&]

[*] Department of Mechanical Engineering, ETSII
Universidad Politécnica de Madrid
José Gutiérrez Abascal 2, 28006 Madrid, Spain
e-mail: ricardo.perera@upm.es

[†] Department of Geological Engineering
Universidad Politécnica de Madrid
Ríos Rosas 21, 28003 Madrid, Spain

[&] Analysis and Advanced Materials for Structural Design (AMADE),
Polytechnic School, University of Girona
Campus Montilivi s/n, 17071 Girona, Spain

Key words: FRP, RC beams, Debonding, Hierarchical clustering, Impedance sensors.

Abstract. One of the common failure modes of reinforced concrete (RC) beams strengthened in flexure with a bonded fiber-reinforced polymer (FRP) is intermediate crack (IC) debonding, which is originated at a critical section in the vicinity of flexural cracks and propagates to a plate end. This premature debonding brittle failure is, without a doubt, an important disadvantage of this technique

For that reason, developing reliable Structural Health Monitoring (SHM) technologies has become a very attractive area and an important challenge for these kinds of structures. Methodologies able to monitor the long-term efficiency of bonding and successfully identify the initiation of FRP debonding constitute a challenge to be met.

One very promising active non-destructive evaluation method for this particular application is impedance-based structural health monitoring (SHM) using piezoelectric ceramic (PZT) sensor-actuators. The electrical impedance of the PZT can be directly related to the mechanical impedance of the host structural component where the PZT transducers are attached and, furthermore, it is measured at high frequencies with which this methodology appears to be very sensitive to incipient damage in structural systems as desired for our application. However, the large amount of information captured by PZT sensors during the continuous monitoring makes a comprehensive analysis of the entire repertoire of data difficult. Hierarchical clustering analysis has been used in this work in order to develop a two-dimensional classification of the information obtained from the impedance measurements. Clustering analysis will organize the experimental impedance measurements obtained over

time for different PZT sensors according to the similarity or dissimilarity of their profiles, placing the cases with similar patterns in neighbouring rows and columns of a clustergram. In this way, the damage identification can be done qualitatively and quantitatively in an intuitive manner.

1 INTRODUCTION

Although a lot of research has been put into the use of FRP composites for repairing and strengthening structures in service, few efforts have been made so far in order to efficiently predict the failure of these complex structural systems, usually by some form of debonding in the interface between the FRP and the concrete. A typical dominant failure mode such as intermediate crack (IC) debonding, initiated at a major flexural crack and then propagated towards a plate end, is an example of this. Although many works have been published in the last years about experimental study and computational modelling of the debonding phenomenon, little work has been developed up to date on bond health monitoring and the initiation of debonding at a very early stage, in spite of its importance. Therefore, methodologies able to monitor the long-term efficiency of bonding and successfully identify the initiation of FRP debonding constitute a challenge to be met.

Many different SHM methods have been proposed in the literature for all kinds of structures, based on either a global or a local monitoring of structures [1]. One very promising active non-destructive evaluation method for this particular application is impedance-based structural health monitoring (SHM) using piezoelectric ceramic (PZT) sensor-actuators [2]. The electrical impedance of the PZT can be directly related to the mechanical impedance of the host structural component where the PZT transducers are attached. Since the structural mechanical impedance will be affected by the presence of structural damage, comparisons of admittance (inverse of impedance) spectra at various times during the service period of the structure can be used as damage indicator. Any change in the spectra might be an indication of a change in the structural integrity.

The electrical impedance is measured at high frequencies with which this methodology appears to be very sensitive to incipient damage in structural systems as desired for our application. Furthermore, due to their size and lightness PZT sensors are non-intrusively attached and do not affect the dynamic response of the structure.

Up to now, the impedance method has been used in numerous applications to detect damage [3-7]. To the author's knowledge, only a few works are focused on the prediction of damage detection in FRP strengthened RC beams using EMI [8-12]. One of the advantages of the EMI method is that it can be implemented for continuous and on-line monitoring. The presence of damage can be known by evaluating the impedance measured over time. However, the large amount of information captured by PZT sensors during the continuous monitoring makes a comprehensive analysis of the entire repertoire of data difficult. Reliable data analysis and rational data interpretation are challenging problems for engineers. The availability of an approach able to analyze and focus the main features of the entire set of observations would be desirable in order to implement a robust and reliable procedure of damage identification based on a series of experimental measurements. Clustering methods allow grouping data based on some kind of similarity. For any series of measurements, the application of sensible measures of similarity among them would make it possible to group or

cluster those data with similar patterns and, therefore, detect and locate the appearance of damage. Hierarchical clustering analysis has been explored in this work as a tool for debonding detection in RC beams externally flexural strengthened with FRP composites using the EMI technique.

2 ELECTRO-MECHANICAL IMPEDANCE METHOD

In the EMI method, PZT transducers are bonded through surface by means of high strength epoxy adhesive to the structure to be monitored. The principle behind this technique is to apply high-frequency structural excitations through PZT transducers, and measure the impedance of structures. The electromechanical admittance (inverse of the impedance) signatures of the PZT acquired at different times are used to evaluate the damage since these are related to the mechanical impedance of the host beam. Hence, the measurement of impedance can reflect the changes of material properties which might be due to damages.

The conventional EMI method assesses the integrity of a mechanical structure by observing some of the changes in the electromechanical impedance of the PZT between two different stages. For this, different scalar damage metrics are defined which allow for a quantitative measurement of the damage severity. In this sense, the root mean square deviation (RMSD) is the most commonly used indicator for the impedance method [2]. It is computed from the difference in the impedance value at each frequency as follows

$$RMSD(\%) = \sqrt{\frac{\sum_{i=1}^{n}[\mathrm{Re}(Z_0(\omega_i)) - \mathrm{Re}(Z_1(\omega_i))]^2}{\sum_{i=1}^{n}\mathrm{Re}(Z_0(\omega_i))^2}} \cdot 100 \quad (1)$$

where $Z_0(\omega_i)$ is the impedance of the PZT measured at a previous stage, which might agree with the healthy condition of the structure, $Z_1(\omega_i)$ is the corresponding value at a subsequent stage, which might agree with a post-damage stage, at the ith frequency point; n is the number of frequency points. Considering that the real part of impedance is more sensitive to the changes in impedance signature, Eq. (1) is also usually defined in terms of the conductance (real part of the admittance). For the RMSD index, the larger the difference between the baseline reading and the subsequent reading, the greater the value of the index denoting changes of structural dynamic properties which can be due to damage.

3 HIERARCHICAL CLUSTERING METHOD

The application of indicators such as RMSD (Eq.1) to impedance measurements allows summarizing the information contained in the impedance spectrum into a single value, which can be useful as damage indicator. A well designed hierarchical clustering will provide concise, meaningful and fast summarizations of the large amount of data supplied by the PZT sensors showing even hidden aspects difficult to capture with another methodology. Furthermore, clustering methods can be combined with a graphical representation of the data making their exploration easier.

Basically, a hierarchical clustering algorithm will allow us to group or cluster unlabeled or non-classified data such as impedance measurements over time, into spatially compact and connected clusters so that data locations belonging to the same cluster are more similar than

those in different clusters [13]. Furthermore, if, as in this case, previously labelled training data are not available, which might be used as pattern, an unsupervised clustering should be implemented. One practical example might be to try to separate into two groups the data of vectors containing the impedance measurements from two different sensors, or from two different damage states.

The proposed clustering approach starts by specifying a dissimilarity measure between two locations by measuring the distance between objects. The most commonly used are the Euclidean distance (Eq.2), the Minkowski distance (Eq.3), the Cityblock distance (Eq.4) and the Chebychev distance (Eq.5):

$$d_{st}^2 = (\tilde{x}_s - \tilde{x}_t)(\tilde{x}_s - \tilde{x}_t)' \tag{2}$$

$$d_{st} = \sqrt[p]{\sum_{j=1}^{n} \left|\tilde{x}_{sj} - \tilde{x}_{tj}\right|^p} \tag{3}$$

$$d_{st} = \sum_{j=1}^{n} \left|\tilde{x}_{sj} - \tilde{x}_{tj}\right| \tag{4}$$

$$d_{st} = \max_j \left\{\left|\tilde{x}_{sj} - \tilde{x}_{tj}\right|\right\} \tag{5}$$

where $\tilde{x}_s$ and $\tilde{x}_t$ are vectors containing different data sets, p is the order of the Minkowski space and n is the dimension of each data set.

Then, an agglomerative hierarchical clustering algorithm can operate directly on this dissimilarity matrix to find clusters of sample locations. The clusters generated previously are linked again by pairs under the same criterion, forming a new hierarchical tree. The procedure is continuously repeated until all the dependencies are established. The criterion used in this work is based on grouping objects using the Unweighted Pair Group Method with the Arithmetic mean (UPGMA), attributed to Sokal and Michener [14], which is also known as the unweighted average distance (Eq. 6).

$$d_{st} = \frac{|\tilde{x}_s|}{|\tilde{x}_s| + |\tilde{x}_t|} \tag{6}$$

With this metric, the distance between any two clusters is taken as the mean distance between the elements of each cluster. Subsequently, the clusters previously constituted are linked to each other and to other objects, creating new and bigger clusters until all the objects in the original data set are linked together in the pursued hierarchical tree.

4 APPLICATION TO RC BEAMS EXTERNALLY STRENGTHENED WITH FRP

The proposed approach has been checked as a tool to detect intermediate crack debonding in a FRP strengthened RC beam. This failure mode, due to the debonding of the FRP reinforcement originating from an intermediate flexural crack, is critical for this kind of structures because it is occurs in a sudden and brittle way [15, 16]. Because of that, its identification in its initial stage is essential to prevent a future failure, which might be catastrophic.

The assessment of the method has been carried out on the beam shown in Figure 1. In the test programme performed, the strengthened beam was subjected to a series of four-point increasing static load tests with the purpose of gradually introduce the cracks into the specimen. After each static test, the impedance was measured by using eleven identical P-876

DuraAct Patch Transducers [17] of 0.5 mm thickness which were externally bonded with an epoxy adhesive along the FRP strip with a constant spacing of 12 cm (Figure 1). Impedance tests were performed by sweeping a wide frequency band of 10–100 kHz. Five independent impedance measurements were taken and used as raw data (D01 to D015) before loading the beam. After that, four different loading stages were considered by applying the static loads of 26 (stage D1), 40 (stage D2), 65 (stage D3) and 100 kN (stage D4). Before measuring the impedances, the beam was previously unloaded after each loading stage. The experimental set-up is shown in Figure 2.

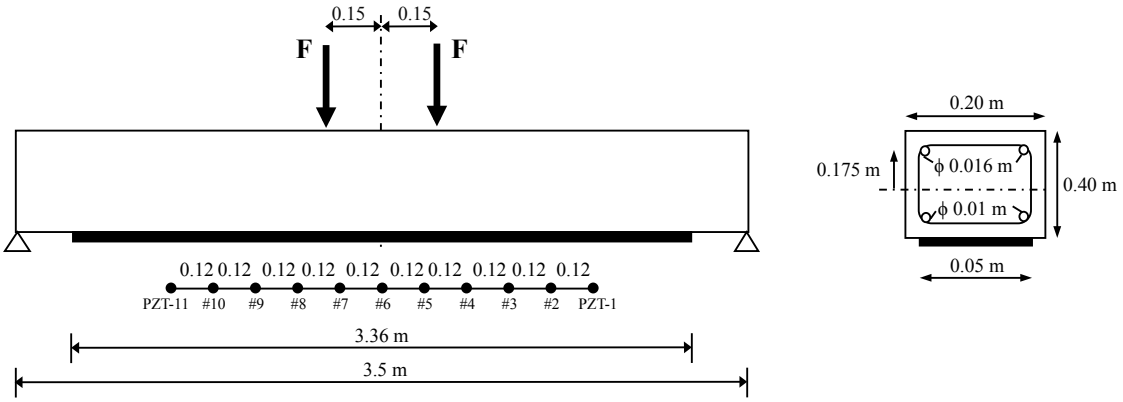

Figure 1: Sensor location map for the FRP strengthened RC beam

The assessment of the method has been carried out on the beam shown in Figure 1. In the test programme performed, the strengthened beam was subjected to a series of four-point increasing static load tests with the purpose of gradually introduce the cracks into the specimen. After each static test, the impedance was measured by using eleven identical P-876 DuraAct Patch Transducers [17] of 0.5 mm thickness which were externally bonded with an epoxy adhesive along the FRP strip with a constant spacing of 12 cm (Figure 1). Impedance tests were performed by sweeping a wide frequency band of 10–100 kHz. Five independent impedance measurements were taken and used as raw data (D01 to D015) before loading the beam. After that, four different loading stages were considered by applying the static loads of 26 (stage D1), 40 (stage D2), 65 (stage D3) and 100 kN (stage D4). Before measuring the impedances, the beam was previously unloaded after each loading stage. The experimental set-up is shown in Figure 2.

A preliminary analysis was carried out with the purpose of demonstrating if different impedance signatures from different sensors can be clustered into different damage groups. Figure 3 shows the hierarchical trees obtained with this analysis. From this figure, it is clear that all D0 and D1 cases are clustered together in all sensors which, in a first analysis, agrees with the experimental reality since, after the first loading stage, visible cracks were not detected in the beam, at least apparently. For the following loading stages, three groups of sensors might be obtained according to identification of the different damage stages. A first group corresponds to the sensors more distant to the loading points (sensors 1, 9 and 10). All the sensors belonging to this group are able to distinguish the stages D2, D3 and D4. In a second group, sensors 2, 7 and 8 would be included. These sensors are closer to the loading points than those belonging to the first group. For this group, damages D3 and D4 are linked

together, which means they are identified with a similar severity. However, differences are remarkable with respect to damage D2. In a last group (sensors 3, 4 and 6), D2 and D3 are clustered together and distinguished from D4. Several significant cracks were caused after damage D4 in the surroundings of sensors 3 and 4 and, additionally, cracks already present in the vicinity of sensors 3, 4 and 6 (specially the last one) became noticeably thicker. This is the main reason for distinguishing between D4 and the remaining damages in this region



Figure 2: Experimental setup

This first analysis has allowed making a first classification of the most important sensing regions in the beam and the damage severity according to these regions without doing any special statistical analysis.

A clustergram in which sensors are clustered in columns and the different frequency sub-ranges and loading cases are clustered in rows is shown in Figure 4. In this clustergram, two main groups of sensors can be distinguished according to the level of detection. In the first group (sensors 1, 4, 8, 9 and 10) some isolated damage indications in different levels, frequency sub-intervals and loading stages appear, which agrees with the multiple damage scenario observed in the experimental tests. Sensors belonging to the second group (sensors 2, 3, 6 and 7) show a higher value of deviation in RMSD. To detect the future initiation of interfacial debonding, focus should be addressed on the sensors of this group since contiguous cells with a high deviation may be indicative of a higher number of cracks.

For instance, sensors 6 and 7 show damage indications which grow and spread along the four loading stages. This may be a symptom, especially after the fourth loading stage, that the damage found between sensors 6 and 7 might be the origin of the future debonding, as was effectively checked when the beam was loaded until failure after the last loading stage. Furthermore, for sensor 7, damage indications of certain importance appear at high sub-frequency intervals (60 kHz to 90 kHz), which means that the damages would be closer to this sensor. This actually happened to be correct after the last load step until failure.

5 CONCLUSIONS

A new approach has been proposed to detect midspan debonding in FRP-strengthened RC

beams. The approach is based on unsupervised hierarchical clustering and allows the processing of massive information as that obtained from a continuous structural monitoring by using PZT sensors. With this method, it has been possible to track in a fast a visual way the evolution of the damage in a complex structure such as the FRP-strengthened RC beam, obtaining thus a premature conclusion about debonding appearance from the concentration of other kind of damages, which are the flexural cracks scattered along the beam and due to the loading program followed.

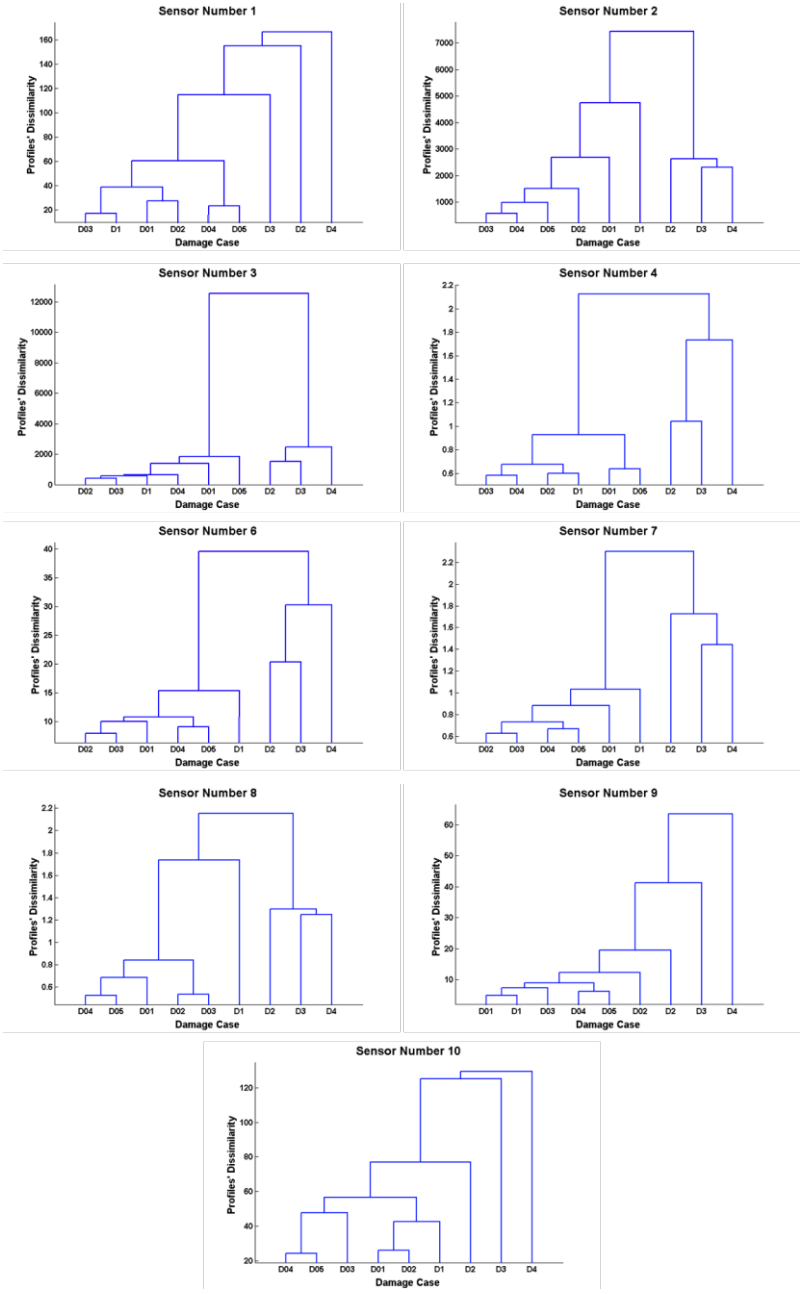

Figure 3: Hierarchical trees

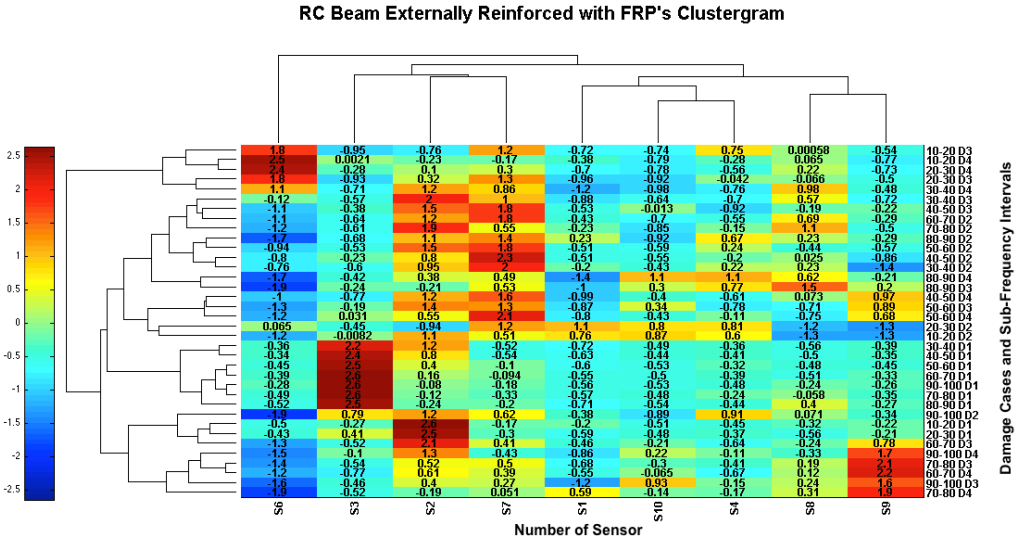

Figure 4: Clustergram

ACKNOWLEDGEMENTS

The writers acknowledge the support for the work reported in this paper from the Spanish Ministry of Science and Innovation (project BIA2013-46944-C2-1-P).

REFERENCES

[1] Bhalla S, Soh CK. High frequency piezoelectric signatures for diagnosis of seismic/blast induced structural damages. NDT & E Inter. 2004, 37, 23-33.

[2] Park G, Inman DJ. Structural health monitoring using piezoelectric impedance measurements. Phil. Trans. R. Soc. A 2007; 365: 373–392.

[3] Min J, Park S, Yun CB, Lee CG, Lee C. Impedance-based structural health monitoring incorporating neural network technique for identification of damage type and severity. Eng Struct 2012; 39:210-220.

[4] Giurgiutiu V, Reynolds A, Rogers CA. Experimental investigation of E/M impedance health monitoring of spot-welded structure joints. J Intel Mater System Struct 1999;10:802-11.

[5] Giurgiutiu V, Zagrai AN, Bao JJ. Piezoelectric wafer embedded active sensors foraging aircraft structural health monitoring. Struct Health Monit 2002;1:41-61.

[6] Park S, Kim JW, Lee C, Park SK. Impedance-based wireless debonding condition monitoring of CFRP laminated concrete structures. NDT&E Int 2011; 44:232-238.

[7] Xu DY, Cheng X, Huang SF, Jiang MH. Identifying technology for structural damage based on the impedance analysis of piezoelectric sensor. Constr Build Mater 2010; 24:2522-2527.

[8] Saafi M, Sayyah T. Health monitoring of concrete structures strengthened with advanced composite materials using piezoelectric transducers. Compos Part B-Eng 2001; 32: 333-342.

[9] Giurgiutiu V, Harries K, Petrou M, Bost J, Quattlebaum JB. Disbond detection with piezoelectric wafer active sensors in RC structures strengthened with FRP composite

overlays. Earthq Eng Eng Vib 2003; 2: 213-223.
[10] Koh YL, Chiu WK. Numerical study of detection of disbond growth under a composite repair patch. Smart Mater Struct 2003; 12: 633–641
[11] Perera R, Sevillano E, Arteaga A, De Diego A. Identification of intermediate debonding damage in FRP-plated RC beams based on multi-objective particle swarm optimization without updated baseline model. Composites: Part B, 2014, 62, 205-217.
[12] Sun R, Sevillano E, Perera R. Debonding detection of FRP strengthened concrete beams by using impedance measurements and an ensemble PSO adaptive spectral model. Composites Structures, 2015, 125, 374-387.
[13] Cai R, Zhang Z, Tung KH, Dai C, Hao Z. A general framework of hierarchical clustering and its applications. Information Sciences, 2014, 272, 29-48.
[14] Sokal RR, Michener CD. A Statistical Method for Evaluating Systematic Relationships. The University of Kansas Science Bulletin, 1958, 38, 1409-1438.
[15] Ascione L, Feo L. Modeling of composite/concrete interface of RC beams strengthened with composite laminates. Compos. Part B-Eng. 2000, 31(6-7), 535-540.
[16] Sun R, Sevillano E, Perera R. A discrete spectral model for intermediate crack debonding in FRP-strengthened RC beams. Composites: Part B, 2015, 69, 562-575.
[17] PI Piezo Technology, P-876 DuraAct Patch Transducer Whitepaper. 2014. Internet: http://piceramic.com/product-detail-page/p-876-101790.html.

VIII ECCOMAS Thematic Conference on Smart Structures and Materials
SMART 2017
A. Güemes, A. Benjeddou, J. Rodellar and Jinsong Leng (Eds)

MONITORING OF AN EXTERNAL PRESTRESSING USED AS A STRENGTHENING TECHNIQUE IN A HISTORICAL MASONRY STEEPLE

M. LLORENS[*], R. SEÑÍS[†], B. MORENO[**] AND S. PAVÓN[†]

[*] Department of Mechanical Engineering and Industrial Constructions (EMCI)
Universitat Politècnica de Girona
17071 Girona, Spain
e-mail: miquel.llorens@udg.edu

[†] Department of Architectural Technology (TA)
Polytechnic University of Catalonia (UPC - BarcelonaTech)
08034 Barcelona, Spain
e-mail: roger.senis@upc.edu; susana.pavon@upc.edu

[**] Smart Structural Sensing Technologies, S.L. (3STECH)
Joan Alsina, 5
17003 Girona, Spain
e-mail: bmoreno@3stech.eu

Key words: Vistabella church, Historical masonry, Strengthening technique, External prestressing, Control monitoring.

Abstract. The Sacred Heart Church of Vistabella (La Secuita, Spain) was designed by Josep Maria Jujol and built in the early twenties of the XX century. The slenderness of its steeple makes it extremely exposed to wind action, to the extent that its stability has been threatened since the construction started. At the end of 1934, the upper spire crumbled away, being rebuilt and reinforced with steel passive bars.

After some numerical approaches, it became clear that the lightness of such a masonry construction along with the feebleness of the connections between the structural members were at the basis of the problem.

In order to provide additional vertical load without substantively modifying the structural scheme, a solution based on external prestressed bars, was implemented. The bars replace the existing passive bars, which have proven to be totally useless. The active system proposed allows to eliminate the masonry's tensile stresses under the action of the wind. The additional loading to be applied varies depending on the level (three levels in total), according to the gradual post-tensioning system proposed as a strengthening technique of the steeple.

Therefore, it has been necessary to design a procedure able to introduce independent tensions at the different levels throughout the same tie and the corresponding monitoring system to control the tensioning process during the implementation.

The procedure, the theory that supports it, and the results of the follow-up are described in detail, these being the objective of the paper.

1 INTRODUCTION

The Sacred Heart Church of Vistabella (La Secuita, Spain), which dates from 1923, was designed by the architect Josep Maria Jujol (1879-1949), one of the masters of Catalan Modernism, as documented in the Master Plan [1]. It was commissioned and constructed (1917-1923) by the neighbors of the same town so that Vistabella could have its own parochial church. In plan, the church is organized around a square of 13m and is characterized by two-parabolic brick arches that are the structural base of the building (Figure 1).

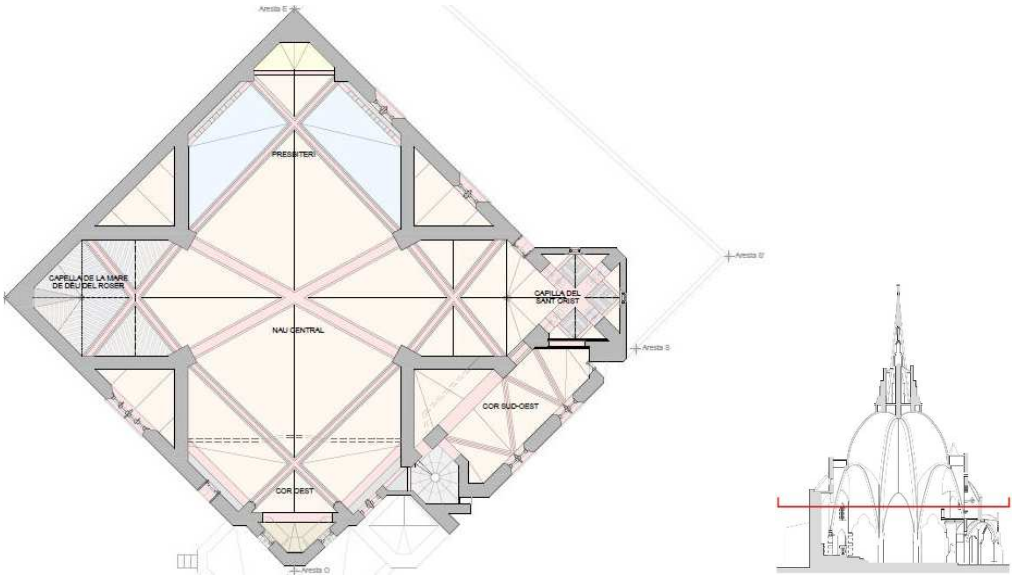

Figure 1: Disposition in plan of the two-parabolic brick arches in relationship with the nave. (Image of the Master Plan [1]).

In fact, the same extension of the central parabolic arcs become the resistant elements (brick masonry ribs) of the structural system of the bell tower (Figure 2), which at its crown reaches almost 28 m in height, forming a unique architectural element where the structure is the project purpose (bell tower). This unequivocal conjunction of architectural design and resistant design according to the resistant function of the form, endows the architectural concept with greater integrity through the existence of a single compositional-structural order (architecture vs. structure) [2-4].

The structure of the steeple consists of four inclined T-shaped masonry ribs, crowned by a cross. Two intermediate levels sustained in short and shallow masonry arches, act as a bracing systems (Figure 2).

Given the exposed geometric characteristics and mechanical properties of the elements that make up the church, it presents general pathologies documented in the Master Plan [1], defining the magnitude and relevance of the pathologies and structural fissures. These affect in a more pronounced and decisive way to the bell tower because it is the most slender and exposed element, especially to the horizontal action of the wind.

At the time of carrying out the structural strengthening of a unique architectural construction with a certain formal complexity, such as an ancient masonry building, the first step is to have the geometric and mechanical characteristics of the resistant elements that

conform it. This initial task, in architectural heritage structures, can be usually quite complicated, both by its nature and by its history, being necessary to act with rigor and thorough knowledge of the problem to be evaluated, becoming a necessary multidisciplinary task (historical search, on-site assessment, modelling and structural analysis) [5-8].

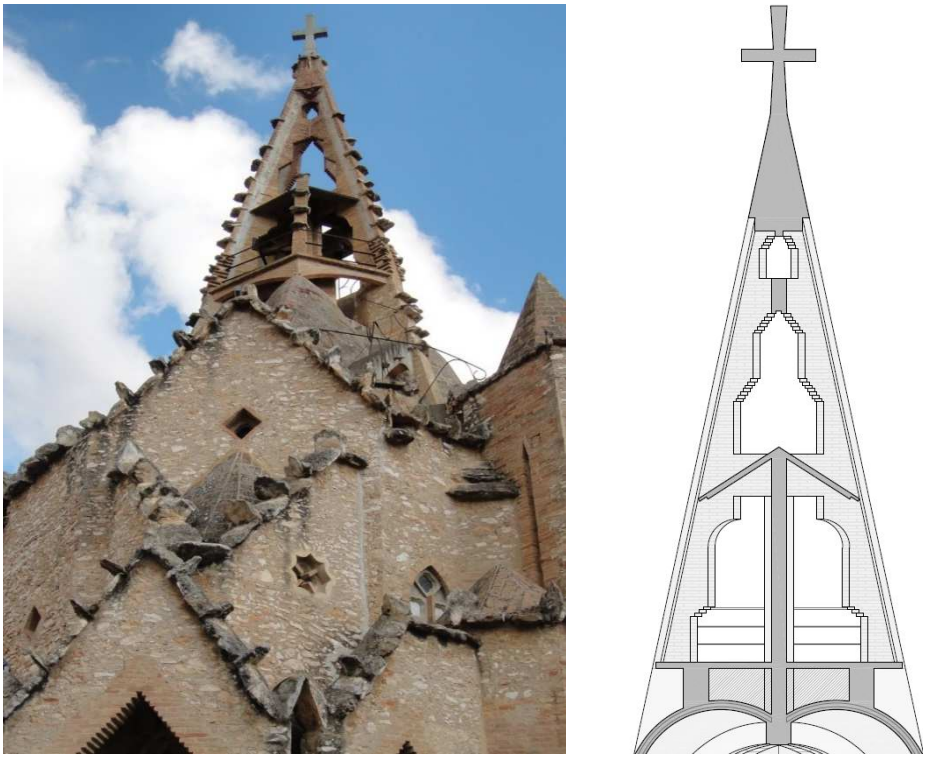

Figure 2: View and elevation of the Vistabella's steeple

This information is presented in previous papers [4,9], based on the relevant references [7,8,10,11]. At the end of 1934, the upper spire crumbled away, being rebuilt and reinforced with a pair of steel passive bars per rib (eight bars in total).

Given the current state of the steeple, as well as the different structural elements that make it up, it requires an intervention with which it is sought to definitively fix the different pathologies that can affect resistance and/or stability, partial or total, of the bell tower. In this case by means of an external prestressing system used as a strengthening technique.

2 DESCRIPTION OF THE EXTERNAL TENSIONING SYSTEM

The external tensioning system consists of the installation of eight vertical active bars threaded at its ends and hooked up to eight pre-existing bars situated in the base of the cross that crowns the steeple. Due to historical reasons, the active bars have been situated at the same position where previously the passive reinforcement designed by Jujol was. Therefore, a bar was placed on each side of the four T-shaped cross-sections that formed the main support of the structure (Figure 3).

These new bars are tensioned -after crossing the intermediate levels- from the lowest point, located in the area near the base of the element. By prestressing them, a permanent vertical

loading will be introduced in the structure, improving its structural behaviour in front of the horizontal loads (wind action). Moreover, the prestressing process had to balance two different requirements: on one hand, the need to add load to the structure, and on the other - due to the slenderness of the masonry ribs- do not exceed the allowable compression of the material.

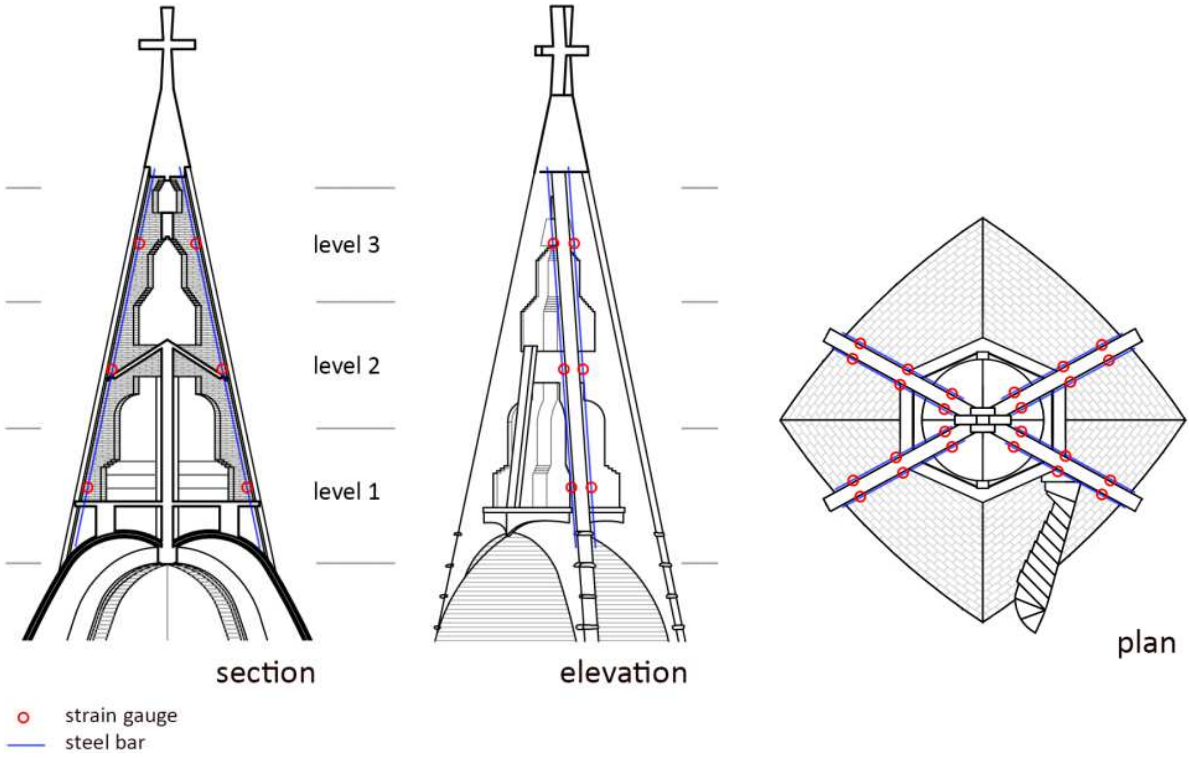

Figure 3: Position of the steel bars and strain gauges

This intervention is conceptually assimilated, in part, to the proposal by the architect Dr. Robert Brufau in an industrial chimney in Roda de Ter (project not executed). A structural approach that Brufau himself states: "The intervention would be to do some vertical post-tensioning of the whole masonry, introducing axial compressions through a prestressed tie [...]. This operation wanted to minimize the risk that no undesired tension stresses were ever present at the brick masonry" [12].

3 THE PROCEDURE PROPOSED

The vertical post-tensioning of the structure was designed according to a stepwise gradual process, divided in three stages in correspondence with the existing floors (levels). In turn, the load corresponding to each stage was divided into two increases/sequences (S) to apply stress increments to the masonry elements as slowly as possible. Likewise, the bars were loaded alternately so as not to unbalance the steeple supporting structure.

The low force necessary to reach the required level of stress in the threaded bars, together with the lack of space and accessibility difficulties, justified the use of a simple torque wrench instead of a stressing jack.

The parameters of the gradual post-tensioning proposed are summarized in Table 1, according to the lengths of the bars for each level, based on the follow equations (1,2):

$$\Delta L = \frac{N \cdot L}{A \cdot E} \tag{1}$$

$$\varepsilon = \frac{N/A}{E} \tag{2}$$

Table 1. Values of the gradual post-tensioning (T) proposed

Level	Bar length (mm)	Final ΔL (mm) (1)	Relative ΔL (mm)	Gradual T (kN)	Gradual ΔL (mm)	ε (μm/m) gradual (2)	ε (μm/m) final (2)	S
Level 3	2300	0,59	0,59	5,00	0,30	129	258	1-2
Level 2	2500	1,29	0,64	5,00	0,32	129	516	3-4
Level 1	4150	3,21	1,07	5,00	0,53	129	773	5-6

These proposed values (Table 1) are the result of a numerical simulation used as a pre-test technique, and thus allowed calculating the level of the compression stresses in the supporting walls before performing the post-tensioning procedure.

These values were cross-checked through an experimental technique -the hole drilling test [4]- carried out in a previous campaign in the walls sustaining the steeple. After combining the different efforts of compression -self-weight, dead/live loads and post-tension-, it was verified that they didn't exceed the allowed stress of the masonry.

All this allows to establish the gradual post-tensioning process in three stages. After completing the first loading stage, the bars will be attached to the underside of the top floor (level 3), welding them to a steel plate specially placed therefor. A presstress tension added that way to the upper level would remain constant, allowing applying a second stage that -depending on the stiffness of the floor- would increase the stress in the lower levels without affecting the upper one. After fixing the bars to the top of the second level, the same will done to complete the third stage, according to the process proposed.

To carry out the process described, for the vertical post-tensioning, the setting and the control implementation (monitoring) is necessary. In table 2, the implementation control parameters of the gradual process are presented (3 stages; 6 sequences).

Table 2. Implementation control parameters of the gradual post-tensioning (T) for each stage (1-3)

	STAGE 1: Sequences (S) 1 and 2							
Level	Value T (kN) final STAGE	%	Control ε (μm/m) final STAGE	S	Gradual T (kN)	Accumulated T (kN)	%	Control ε (μm/m) (2)
Level 3	9,0	90,0%	232	1	4,5	4,5	45,0%	116
				2	4,5	9,0	90,0%	232
Level 2	9,0	45,0%	232	1	4,5	4,5	22,5%	116
				2	4,5	9,0	45,0%	232
Level 1	9,0	30,0%	232	1	4,5	4,5	15,0%	116
				2	4,5	9,0	30,0%	232

	STAGE 2: Sequences (S) 3 and 4							
Level	Value T (kN) final STAGE	%	Control ε (μm/m) final STAGE	S	Gradual T (kN)	Accumulated T (kN)	%	Control ε (μm/m) (2)
Level 3	9,8	98,0%	253	3	0,4	9,4	94,0%	242
				4	0,4	9,8	98,0%	253
Level 2	18,6	93,0%	479	3	4,8	13,8	69,0%	356
				4	4,8	18,6	93,0%	479
Level 1	18,6	62,0%	479	3	4,8	13,8	46,0%	479
				4	4,8	18,6	62,0%	479

	STAGE 3: Sequences (S) 5 and 6							
Level	Value T (kN) final STAGE	%	Control ε (μm/m) final STAGE	S	Gradual T (kN)	Accumulated T (KN)	%	Control ε (μm/m) (2)
Level 3	10,0	100,0%	258	5	0,1	9,9	99,0%	255
				6	0,1	10,0	100,0%	258
Level 2	20,0	100,0%	516	5	0,7	19,3	96,5%	498
				6	0,7	20,0	100,0%	516
Level 1	30,0	100,0%	773	5	5,7	24,3	81,0%	626
				6	5,7	30,0	100,0%	773

For this reason, twenty-four strain gauges (eight per level) have been placed along the steel bars, to individually control the stresses at any bar and level, by means of monitoring these, based on the relevant references [13-16]. The ties have been prestressed from their lower end. Whenever all bars of a certain level reached the design value, they were attached to the bracing system situated underneath. The monitoring stetting is explained below.

3.1 The monitoring setup

The entire system was monitored by placing twenty-four strain gauges of ferritic steel ($\alpha = 10{,}8 \cdot 10^{-6} \cdot K^{-1}$). The eight threaded steel bars were controlled at three different points (Figure 3), what allowed verifying the loading staggered process at each of its stages.

The repercussion in terms of increased tension of any of the levels in the previous ones was registered too; therefore, the stiffness of the different floors depending on their ability to prevent the transmission of efforts from a section to another of the bar was set in an approximate way. The whole process was recorded at a sampling ratio of 1 Hz. The data acquisition system (DAQ) used during the test was a SOMAT MX 1650 BR, manufactured by the company HBM.

3.2 The test

The post-tensioning process of the stages lasted more than six hours.

In the first stage, due to the geometric adjustment of the active structure within the existing walls and horizontal diaphragms, abrupt changes in the measurements were noticed. Its origin was the sudden release of stresses due to the breaking of surfaces partially detached or weakened while drilling the masonry elements and due to isolated episodes of friction

between the active bars and the masonry. After this brief adjustment period of the system, in which the contact surfaces between the steel bars and the existing structure were regularized and smoothed, -the bars passed through the existing horizontal structure, through holes made therein-, the sampling process took place without interruption or particular disturbances.

While doing the second load stage, a noticeable increase in tension was measured in the upper section, what indicated that the hypothesis according to which the floors had enough stiffness to prevent such a circumstance, no longer could be considered. The stress in the active structure was released until the upper level recovered the predicted values. This meant a loss of tension in the second level -the value decreased until values close to those measured in the upper one- that should be recovered while tensioning the level below.

In Figures 4-6, it can be seen, the response of the increases/sequences 1-3 of every one of the strain gauges situated in three different levels along one of the active bars.

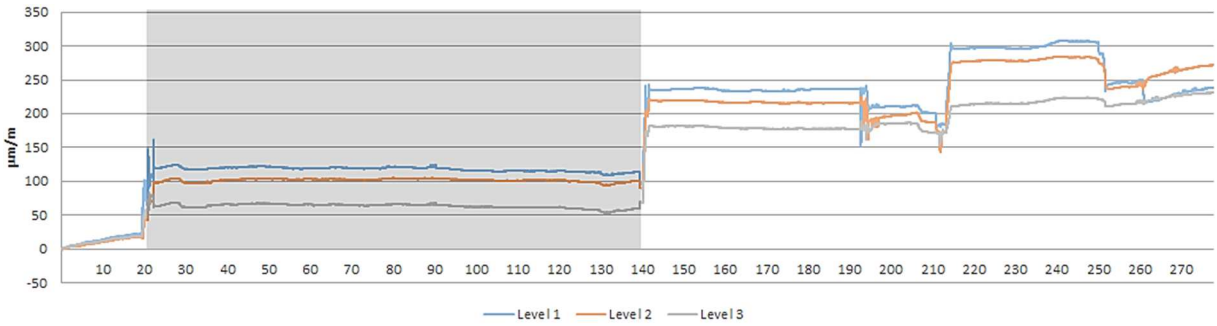

Figure 4: First increase (First stage)

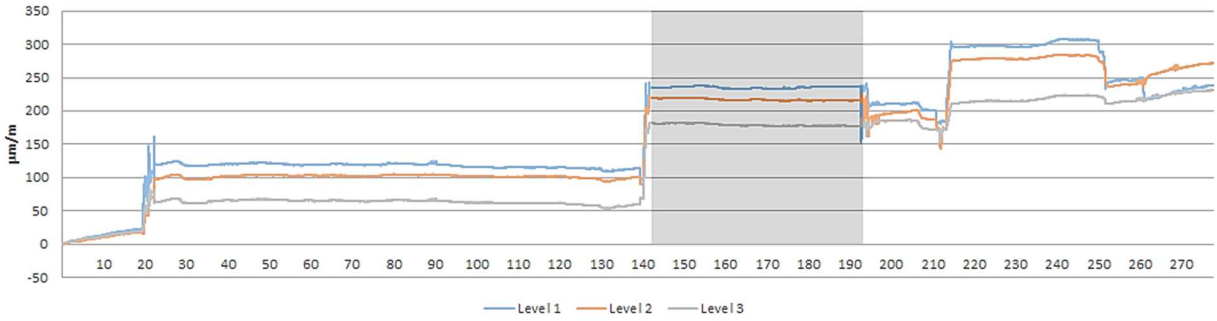

Figure 5: Second increase (First stage)

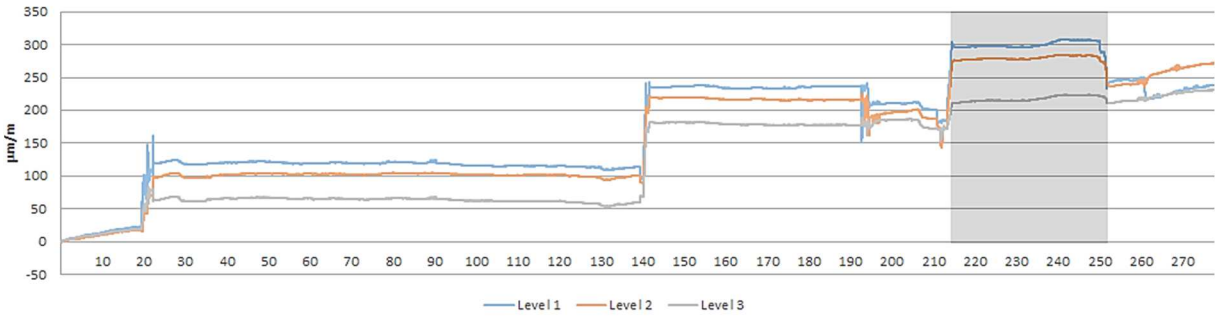

Figure 6: Third increase (Second stage)

According to the results of the third increase -first increase of the second stage- (Figure 6), it was necessary to adjust the system since the stiffness of the bracing system wasn't enough to prevent the transmission of load above those points that were considered already stabilized. After adjusting the procedure to take into account such a situation, the structure was artificially loaded until reaching the design values.

This implied establishing a new procedure for the last stage, correcting the excessive increase of the load at the top (level 3). This meant to realize a total of five increases (Stage 1: Increases 1 and 2; Stage 2: Increase 3; Stage 3: Increases 4 and 5) instead of the six proposed (two for stage) and for a total tensioning load lower than the projected, according to the results that are presented.

4 THE NEW PROCEDURE (THIRD STAGE)

A new procedure was proposed to achieve the initial objective: the load relative to the second stage was reduced to an intermediate value, until the values corresponding to the first stage approached the values originally planned during the design of the loading test. To control the third stage of the post-tensioning, the system was set to zero, keeping the former set of values as a reference. The value of the readings was then set to zero in order to clearly appreciate the effect of the third level of load on the two previous sections, in which the active bar had already been fixed to the structure (level 2).

Since the stiffness of the two floors was similar -cross arches with thin double-curved shells filling the remaining void spaces and a flat top layer of tiles covering the whole of the ensemble- it was assumed that after the post-tensioning of the third stage, a similar increase to the one observed when tensing the second would happen. No influence of the post-tensioning of the third stage in the first stage was expected.

Finally, it was decided to maintain a similar stress in the bars corresponding to the first and second stages, while those applied to the third stage were raised above double.

Since the steeple behaves as a cantilevered structure in front of the action of the wind, the distribution of the tensile stresses grows parabolically as they move away from the top, what makes reasonable such distribution of forces/stresses.

The measures of the third stage (increases 4 and 5) of loading can be observed in the following charts (Figures 7 and 8). Only the effect of such stage is represented. Therefore to have a general overview of the whole procedure, the previous charts must be considered (Figures 4-6).

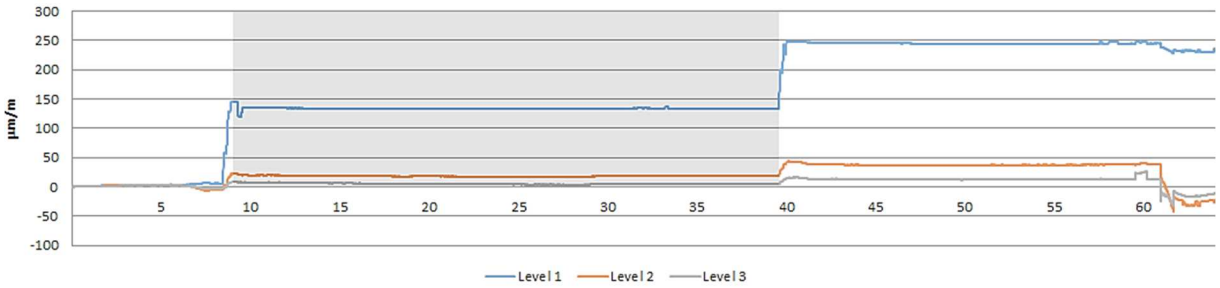

Figure 7: Fourth increase (Third stage)

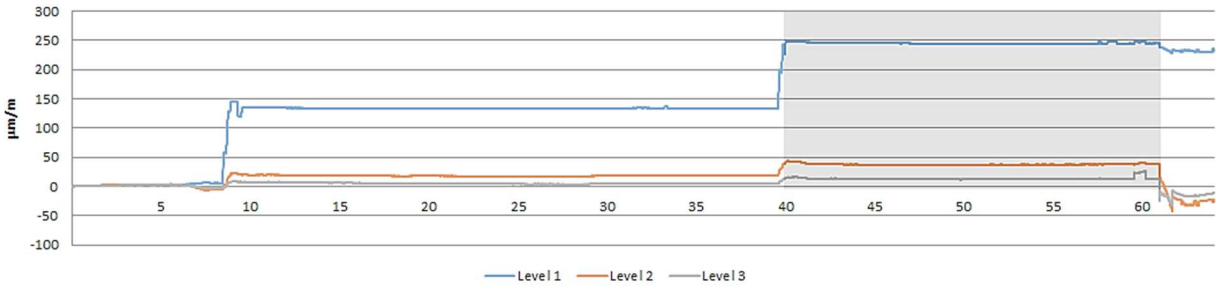

Figure 8: Fifth increase (Third stage)

5 THE RESULTS

As was assumed, the influence of the third loading step on the upper sections of the previously fixed active bars was almost negligible, especially in the uppermost section. The reason probably being that the two horizontal diaphragms acted in unison, offering a greater stiffness against the vertical force induced by the active system. After carrying out the test, the final averaged results were:

- First stage (level 3) : ≈ 200 µs
- Second stage (level 2) : ≈ 240 µs
- Third stage (level 1) : ≈ 500 µs

The range of measured deformations is far from both the maximum values assumed by the strain gauges ($\delta \geq 5000$ µs) and those compatible with the yield limit of the bars ($\delta \geq 1375$ µs). Therefore, Hooke's law can be applied to the conversion of the measured data into stress, to subsequently convert such output into a force:

- First stage (level 3) : ≈ 8.44 kN per unit steel bar.
- Second stage (level 2) : ≈ 10.13 kN per unit steel bar.
- Third stage (level 1) : ≈ 21.10 kN per unit steel bar.

The results obtained in the test and the control monitoring are similar to the values proposed (Table 1), according to the numerical simulation previously realized.

6 CONCLUSIONS

According the results obtained, the following conclusions are presented:

- A procedure to post-tensioning a masonry steeple has been defined, developed and installed on site.
- The level of tension required to counteract the adverse effect of the wind on the structure is low enough to allow the use of relatively simple tools.
- Monitoring the structure has allowed to know at all times the real situation, to quantify the applied efforts and, consequently, to make the most adequate decision in each moment.
- The combination of the numerical simulation and the experimental procedure is possible with satisfactory results.

REFERENCES

[1] Llinàs, J. and Miralles, R. Pla Director per obres de reparació i restauració de l'església del Sagrat Cor de Vistabella. Direcció General del Patrimoni Cultural, Barcelona (2008).

[2] Señís, R. Optimización de mallas estructurales de acero envolventes de edificios en altura. Análisis de las direcciones principales identificadas por sus líneas isostáticas. PhD Thesis. Barcelona (2014): Polytechnic University of Catalonia.

[3] Señís, R. Design criteria and structural analysis of the Center for Attention and Management of Emergency Calls 112 Catalunya in Reus. *Informes de la Construcción* (2016) 68(541): e139.

[4] Señís, R. and Llorens, M. Structural assessment of the Vistabella Church's Tower (Spain): Material characterization by the Hole-Drilling technique and continuum FEM. *Construction and Building Materials* (2017). [In revision]

[5] ICOMOS/ISCARSAH Committee. ICOMOS charter - principles for the analysis, conservation and structural restoration of architectural heritage (2003).

[6] ISO/TC98. ISO/FDIS 13822 bases for design of structures - assessment of existing structures. Genève (2010): ISO.

[7] Pérez-Gálvez, F., Rodríguez-Liñán, C. and Rubio, P. Determinación de las características mecánicas de los muros de fábrica de ladrillo en la arquitectura doméstica sevillana de los siglos XVIII y XIX. *Informes de la Construcción* (2009) 61(514):19-28.

[8] Roca, P., Cervera, M., Pelà, L., Clemente, R. and Chiumenti, M. Continuum FE models for the analysis of Mallorca Cathedral. *Engineering Structures* (2013) 46:653-670.

[9] Señís, R. Anàlisi del comportament estructural i avaluació del dany del campanar de l'església de Vistabella (La Secuita) per al seu reforç. In: *Proceedings of the Congrés d'Arquitectura*. Barcelona (2016):1-7.

[10] Lombillo, I. Investigación teórico - experimental sobre ensayos ligeramente destructivos (MDT) utilizados para la caracterización mecánica in situ de estructures de fábrica del patrimonio construido. PhD Thesis. Santander (2010): University of Cantabria.

[11] Lombillo, I., Thomas, C., Villegas, L., Fernández-Álvarez, J.P. and Norambuena-Contreras, J. Mechanical characterization of rubble stone masonry walls using non and minor destructive tests. *Construction and Building Materials* (2013) 43:266-277.

[12] Brufau, R. Construint fum. *Quaderns d'arquitectura i urbanisme* (2007) 253:74-77.

[13] Augenti N., Nanni A. and Parisi F. Construction Failures and Innovative Retrofitting. *Buildings* (2013) 3:100-121.

[14] Mircam S. and Molins C. *Inventory of Repair and Strengthening Methods with Iron and Steel*. MSc Dissertation. Barcelona (2009): Polytechnic University of Catalonia.

[15] Leftheris B.P, Stavroulaki M.E, Sapounaki A.C. and Stavroulakis G.E. *Computational mechanics for heritage structures*. WIT Press (2006). ISBN 1-84564-034-9.

[16] Van Balen K. and Verstrynge E. *Structural analysis of historical constructions: Anamnesis, diagnosis, therapy, controls*. CR Press (2006). ISBN 978-1-315-61699-1.

Seismic Monitoring of the Civic Tower in Rieti equipped with a Non-Conventional TMD

E.M. Tronci *, D. Pietrosanti, G. Cordisco, M. De Angelis†

* Department of Structural and Geotechnical Engineering
Sapienza University of Rome
Via Eudossiana 18, 00184 Rome, Italy
e-mail: eleonoram.tronci@uniroma1.it

† Department of Structural and Geotechnical Engineering
Sapienza University of Rome
Via Eudossiana 18, Rome, Italy
e-mail: eleonoram.tronci@uniroma1.it

ABSTRACT

The Vibration Control [3] and the Structural Health Monitoring [2] have become by now two of the most important topics. Researches have strongly focused on these themes, in several countries and especially in Italy, in front of the latest earthquakes and seismic event occurred all over the world. Consequently the need of analysing the integrity of the structure as accurately as possible emerged, especially in the experimental cases in which the structure has been equipped with specific vibration control systems to protect it from extreme excitations.

One of the key points in a seismic monitoring campaign is the correct choice of system identification techniques to efficiently analyse the dynamic behaviour of the structure. There are methods defined in the frequency domain or in the time domain, the second ones have recently taken a prominent place in the field of structural health monitoring of civil structures. These techniques classically lead to system characterization starting from the input and output measurements. However it is extremely uncommon to measure the excitation affecting the system in the case of civil structures, particularly when the input is an earthquake, while the seismic response is easily available. Then some algorithms have been adapted and modified for the Output Only case, as OKID [6] and SSI [5].

Among the passive vibration control techniques the Tuned Mass Damper, TMD, has become always more interesting and used thanks to advantages it supplies, such an extreme simplicity in the installation and maintenance and cost benefits. In the Conventional TMD a new auxiliary tuned mass is connected to the structure with the purpose of dissipating vibration energy, while in the Non-Conventional TMD the *tuned* mass is obtained by reconverting the structural function of other masses already present in the structure [1,4].

The aim of the paper is to study the dynamic behaviour and to check the structural integrity of the Civic Tower of Rieti equipped with a Non-Conventional TMD, adopting output only system identification techniques. Despite the fact that OKID and SSI have been defined for stationary inputs, in this paper they will be used and tested also with non stationary excitations such as earthquakes. A long-term seismic monitoring system has been settled in using a combination of eight accelerometers disposed in different positions. This allowed to monitor the tower with respect to the recent seismic swarm that run over the area around Rieti for the last four months. The dynamic behavior and the structural integrity of the Tower is analysed windowing the output recording in three intervals: before, during and after seismic event. Structural integrity is investigated comparing frequencies and damping ratios identified by using pre and post event recordings, while the dynamic behaviour is investigated also during the seismic event.

Keywords: Seismic Monitoring, Non-Conventional TMD, Output Only Identification, OKID and SSI algotithms, Damage Identification

REFERENCES

[1] De Angelis M, Perno S, Reggio A. Dynamic response and optimal design of structure with large mass ratio TMD. *Earthquake Engineering and Structural Dynamics* 2012; 41(1):41–60.

[2] Farrar C.R. and Worden K. Structural health monitoring: A machine learning perspective. John Wiley and Sons, 2013.

[3] Housner, G. W., et al. Structural control: Past, present, and future. *Journal of Engineering Mechanics* 1997; 123 (9), 897-971.

[4] Reggio A, De Angelis M. Optimization of a non-conventional TMD implemented via inter-storey isolation, *Proceedings of Eurodyn 2014 - IX International Conference on Structural Dynamics*: Porto, Portugal, 2014; 1713–1720.

[5] Van Overschee P, De Moor B. *Subspace Identification for Linear Systems: Theory, Implementation, Applications*. Kluwer Academic Publishers: Dordrecht, The Netherlands, 1996.

[6] Vicario F, Phan MQ, Betti R, Longman RW. Output-only observer/Kalman filter identification (O 3 KID). *Structural Control and Health Monitoring* 2015; 22:847–872.

VIII ECCOMAS Thematic Conference on Smart Structures and Materials
SMART 2017
A. Güemes, A. Benjeddou , J. Rodellar and Jinsong Leng (Eds)

SIGNAL-BASED BENDING STRESS MONITORING USING GUIDED WAVES IN HOLLOW CYLINDERS

JABID. QUIROGA[*†], LUIS MUJICA[†] RODOLFO VILLAMIZAR[*], MAGDA RUIZ[†] AND JHONATHAN. CAMACHO[†*]

[*] Mechanical and Electric and Electronics Schools
Universidad Industrial de Santander
Cra 27 Calle 9, Ciudad Universitaria, Bucaramanga, Colombia
e-mail: jabib@uis.edu.co

[†] Universitat Politécnica de Catalunya (UPC) BARCELONATECH, Department of Mathematics, Escola d'Enginyeria de Barcelona Est. (EEBE), Campus Diagonal Besòs, Edifici A, C. Eduard Maristany, 10-14, 08019, Barcelona, Barcelona, Spain

Key words: SHM, Stress Monitoring, Acoustoelasticity, Subtraction.

Abstract. This work provides a time domain approach to detect stress changes in hollow cylinders using low frequency ultrasound guided waves; the proposed scheme makes uses of the subtract method for stress level estimation. Residuals are generated by signal subtraction of the reference signal, at nominal condition, from the current signal. The stress condition is detected when the RMS of the residual goes above certain threshold. A simple supported hollow cylinder is utilized in this research and the different levels of stress, bending moment, are obtained using a vertical variable force applied in the middle of the specimen; the induced stresses are in the elastic region of the stress-strain diagram. The guided waves are generated via a couple of piezoelectric transducers operating in a pitch-catch configuration to excite and detect longitudinal and flexural waves. A Matlab® script is utilized to perform ultrasonic signal generation, signal acquisition and processing. Results of each stress scenario demonstrates the feasibility and potential of using this formulation in the evaluation of the bending stress in hollow cylinders. The studied monitoring scheme can be used on-line and it is a cost-effective approach.

1 INTRODUCTION

Stress monitoring is an imperative task and plays an important role to increase the reliability and safety of structures and pipelines. The presence of high stress values can compromise the system integrity and turn in an unsafe condition. A reliable prognosis of the stress condition in a structure is an important basis for an effective service life management.

Guided waves based stress monitoring schemes has not been extensively studied, most of the research is based on tracking the slight velocity changes of the guided wave propagating under stress, as a result of the acoustoelasticity effect. Many technical problems associated to difficulties in the velocity change measurement and the high dependency of the material internal structure in the acoustoelastic effect have motivated few interest in using the guided waves for stress monitoring purposes.

Some suitable researches are presented next; The role of the guided wave excitation frequency as an attempt to maximize the sensitivity of acoustoelastic stress measurements in steel bars is examined in [1]. Experimental results showed the disperse behaviour of the ultrasonic waves propagating in the bars causes the frequency-dependence of the acoustoelasticity sensitivity to stress. The largest sensitivity are found for low values of the frequency *x* diameter product and for wave structures with the predominance of axial displacement over radial displacement. Therefore, the use of certain frequencies can certainly be highly advantageous for stress monitoring in bars. One of the structural element most studied in terms of monitoring levels of stress is the wire strands, so relevant researches have be accomplished to this purpose. In [2] a guided wave based stress monitoring method in seven-wire strands is proposed. In the experimentation magnetostrictive transducers are utilized to excite and detect axi-symmetric guided waves. Group-velocity measurements on single straight wires under low values of stress show differences with the theoretical estimates, although the discrepancy is substantially reduced above 48% of UTS. Additionally, if the effect of strand elongation is added to the acoustoelastic effect by allowing the magnetostrictive sensors to follow the deforming specimen, a substantial increase in stress measurement sensitivity can be attained. It should be noted that the measurement of absolute stress levels requires reference data taken in the unloaded case. Results from acoustoelastic measurements on single wires and on strands are presented, exhibiting the feasibility of the method for stress measurement. Following with the strand wires, [3] investigates the use of ultrasonic nonlinearity as a means to determine the level of load applied to the strands. Since an axial load on a multi-wire strand produces proportional contact stresses between adjacent wires, ultrasonic nonlinearity from the inter-wire contact must be related to the level of axial load.

In the case of stress or loads applied to plates, a method to estimate arbitrary biaxial loads using the phase velocity changes of lamb waves, measured along multiple directions of propagation, is developed and verified via simulations in [4]. In this paper is described how numerical solutions of the acoustoelastic wave equation, for an isotropic plate, allow to decouple the effects of a homogeneous biaxial stress into its two principal components. Thus, the acoustoelastic response of a specific mode and frequency is described by only two constants, which can be determined from a uniaxial loading experiment. Although effective, this proposed scheme needs an array of actuator a sensor and a prior-knowledge base to estimate the load.

On the other hand, the stress monitoring has been also studied from a signal processing perspective. The time-reversal technique is applied in [5] to detect variations in the external applied traction in a strip of aluminium plate. Two different parameters of the time-reversed signal are used for monitoring the strain state, the peak amplitude and the focusing time. It is also used the changes in the group delay to determine the strain level quantitatively. Experimental validation is performed for low stress levels and acoustoelasticity effect is neglected. Another signal processing approach, signal subtraction, have been used in systems with permanently attached or embedded sensors to detect any change of the condition of the system. It becomes possible to make highly accurate measurements throughout the life of the structure by using reference (or baseline) signal subtraction [6]. The evaluation of the structure condition is governed permanently by the residual signal left after subtraction.

In this work, longitudinal and flexural guided wave modes are generated by non-

axisymmetric surface loading on a hollow cylinder using PZTs. Although, the multimodal propagation of the ultrasonic signal is more complex, the implementation cost can be drastically be reduced by employing only one actuator and one sensor. Changes in the levels of bending stress are detected by comparing the propagated wave in the current state with the nominal condition using a simple subtraction algorithm to produce residuals to evaluate changes in the stress.

2 ACOUSTOELASTICITY EFFECT

Acoustoelasticity defines the dependence of ultrasonic bulk wave velocities on stress. This effect is based on the theory of finite deformation of the propagation of bulk elastic waves in isotropic solids subjected to a stress [7]. In this sense, the acoustoelasticity establishes five elastic constants to describe the relation between stress and bulk wave velocity for isotropic materials subject to uniaxial stress; two second order elastic constant, Lamé constants (e.g. λ and μ), and three, third order elastic constants, Murnaghan´s constants (m, n, l). Thus, once the Murnaghan´s constants of a particular specimen are determined, any experimental measurement of one of the bulk velocities reveals the stress at which the specimen is subject to.

For a homogeneous and isotropic infinite solid subjected to a uniaxial stress, the bulk velocities of longitudinal and transverse plane waves, propagating in the same direction as the applied stress, can be written in the first-order approximation, respectively, as Eqs (1-2) [7].

$$C_1^\sigma = \sqrt{\frac{\lambda+2\mu}{\rho}}\left\{1+\frac{\sigma}{2(\lambda+2\mu)(3\lambda+2\mu)}\left(\frac{\lambda+\mu}{\mu}(4\lambda+10\mu+4m)+\lambda+2l\right)\right\} \tag{1}$$

$$C_2^\sigma = \sqrt{\frac{\lambda}{\rho}}\left\{1+\frac{\sigma}{2\mu(3\lambda+2\mu)}\left(4\lambda+4\mu+m+\frac{\lambda n}{4\mu}\right)\right\} \tag{2}$$

Where C_1^σ and C_2^σ are the longitudinal and shear acoustoelastic bulk velocities respectively, ρ is the mass density, σ is the tensile stress, and m, n and l are the Murnaghan´s constants. Expression inside curly brackets represents the stress response of the bulk wave under investigation. These velocities are the basis of the phase and group velocities calculation and they are synthesized in the dispersion curves. Because of dispersion, signals with different spectral components can propagate at different phase speeds as they travel along the waveguide. Now, analytical studies of the guided waves propagation in cylindrical waveguides are complex and result in an estimation (stress-free, isotropic and hollow) of the actual behavior of the waves. The analytic approach aimed at calculating of the dispersion curves in cylindrical waveguides is based on two uncoupled wave equations (3-4), where C_1 and C_2 are the longitudinal and shear bulk velocities respectively and ϕ and H are the dilatation scalar potential and the vector potential respectively. Equations (3-4) are the foundation of the wavenumber(ξ)-frequency(w) relation and consequent of the phase velocity $v_{ph}(w(\xi))$ and group velocities $v_g(w(\xi))$ for the stress-free case. A more detailed description of these relations can be found in [8][9]

$$C_1\nabla^2\phi = \partial^2\phi/\partial t^2 \tag{3}$$

$$C_2 \nabla^2 H = \partial^2 H / \partial t^2 \quad (4)$$

For wave propagation in stressed specimens, C_1 and C_2 in equations (3-4) can be replaced by the acoustoelastic bulk velocities $C_1^\sigma(\sigma)$ and $C_2^\sigma(\sigma)$. As it can be inferred, the presence of stress in the propagation path yields v_{ph} ($w(\xi)$, σ), $v_g w(\xi)$, σ). Some recent experimental works have shown this conclusion, i.e. variations of the guided wave velocities in stress presence [7][10], where the longitudinal mode $L(0,1)$ is used to track the variations of the phase velocity in a waveguide rod-like exposes to stress.

3 SUBTRACTION APPROACH

In SHM, a symptom represents a specific characteristic resulting from a certain condition in the system. Symptoms of abnormal conditions are manifested as deviations of a nominal value evaluated by subtracting the current state to the baseline obtained in the structure nominal condition. The subtraction approach relies on the hypothesis that the recorded signal is stable if damage or abnormal condition is not present [6]. If it were possible to achieve perfect subtraction between the current signal and the baseline signal, the presence of an abnormal condition could be deduced from the observation of changes in the residual of the subtraction. In a real inspection problem, where perfect subtraction is not achievable, the occurrence of a new condition can be detected only when the residual of the new condition is sufficiently higher than the residual after subtraction in the nominal condition. Besides abnormal conditions, many other factors, i.e. changes in temperature, loading conditions; instrumentation drift; boundary conditions; structural changes and other environmental conditions [11] may also exert influence on residuals. These influences are undesirable because they may result in a misjudgment of the condition of the system (false alarm).

On the other hand, guided waves propagating in a stressed material exhibit a relative time shift due to the combined effects of acoustoelasticity and material elongation, which can be observable in the residuals via subtraction.

In order to achieve stress tracking it is crucial to minimize the residual in the subtraction between the normal current signal obtained in service and the nominal reference signal. In this work, the Optimal Baseline is considered in order to select the best matching baseline among the available reference signals of the nominal condition. The optimal baseline is the reference signal for which the subtraction from the normal current signal (stress-free) yields the residual with the minimum Root Mean Square (RMS).

4 EXPERIMENTAL SETUP

The proposed approach is examined in a dedicated test bench; the experimental setup is a 1” schedule 40, ASTM A106, steel pipe of L=6 m-length, supported at the two ends by fixed supports as shown in Figure 1. The different bending stress conditions are produced by changing the magnitude of an elastic band, located in the middle part of the pipe ($L/2$). The different simulated maximum stress scenarios are named by the subindex of σ, which is the vertical cylinder deflection in cm of the ($L/2$) position, positive for concave upwards and negative for concave downwards i.e. σ_1=9.33 MPa, σ_2=17.95 MPa, σ_3=26.8 MPa, σ_4=34.2 MPa, σ_{-2}=36.6 MPa and $\sigma_{-3.5}$=53.23 MPa. This latter value correspond to the 25% of the yield strength. A couple (actuator and sensor) of PZT is attached in upper part of the pipe in a

pitch-catch configuration. The actuator is excited with a Gaussian pulse signal of five cycles (narrow bandwidth). Because of limited surface loading, the acoustic fields generated by a partial-loading source includes axisymmetric longitudinal modes as well as non-axisymmetric flexural modes. Therefore, the dispersed wave propagates in the hollow cylinder as a combination of longitudinal and flexural modes activated for the excitation frequency content. In addition, due to a high ratio of wall thickness respect to internal radius in the studied waveguide, the cylinder contour dominates at very low frequency (wall thickness is far less than the wavelength) yielding also the superposition of several guided waves, as shown in Figure 3. The dispersion curves are obtained using the freeware GUIGUW [12].

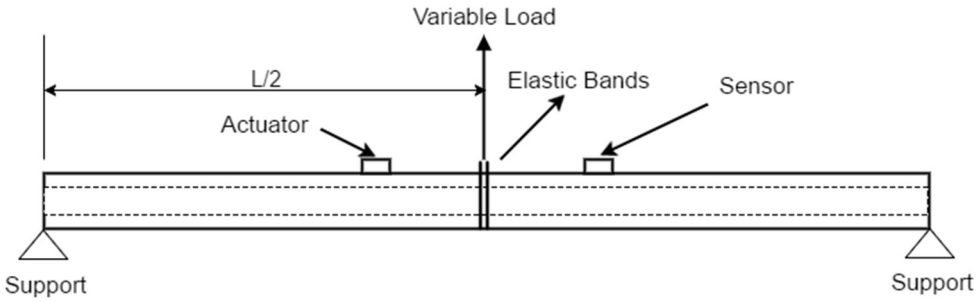

Figure 1: Schematic representation of the hollow cylinder test bench.

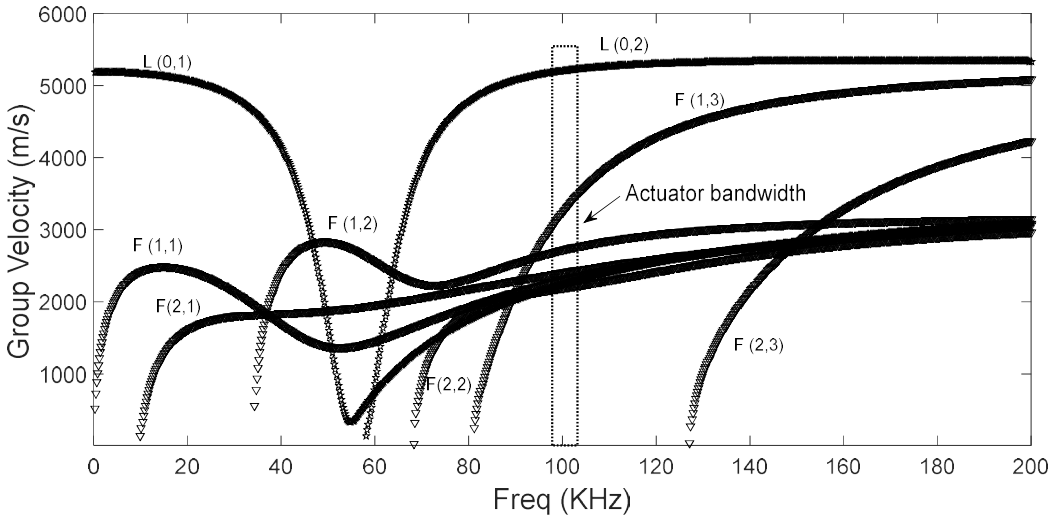

Figure 2: Group velocity dispersion curve for a 1" A-106 hollow pipe

5 TIME DOMAIN STRESS MONITORING APPROACH

This section presents the proposed stress monitoring scheme based on a subtraction approach. The guided wave propagation in a specimen under stress compared with the wave in the nominal condition experiences a time shift because of acoustoelasticity effect and the material elongation. An initial reference time trace, $S_0(t)$, containing guided wave signals is captured from the hollow cylinder. For the purposes of this analysis, it is assumed that this time trace contains just one signal resulting from the nominal condition. In the reference time trace, the signal from the structural feature corresponds to wave propagation over a distance *d*

at velocity v in the time window (Δt). Later, the presence of stress in the structure has changed and another time trace, $S_1(t)$, is recorded at the same (Δt) with a different acoustoelastic velocity $v(\sigma)$ and an elongated distance $d_e(\sigma)$. The purpose of this analysis is to estimate the residual signal from this normal structural feature when $S_0(t)$ is subtracted from $S_1(t)$. In this work, to improve the residual sensibility a normalized cross correlation r_{xy} between the current sensed signal $S_1(t)$ and the nominal sensed signals $S_0(t)$ is obtained by the discretized equation (8).

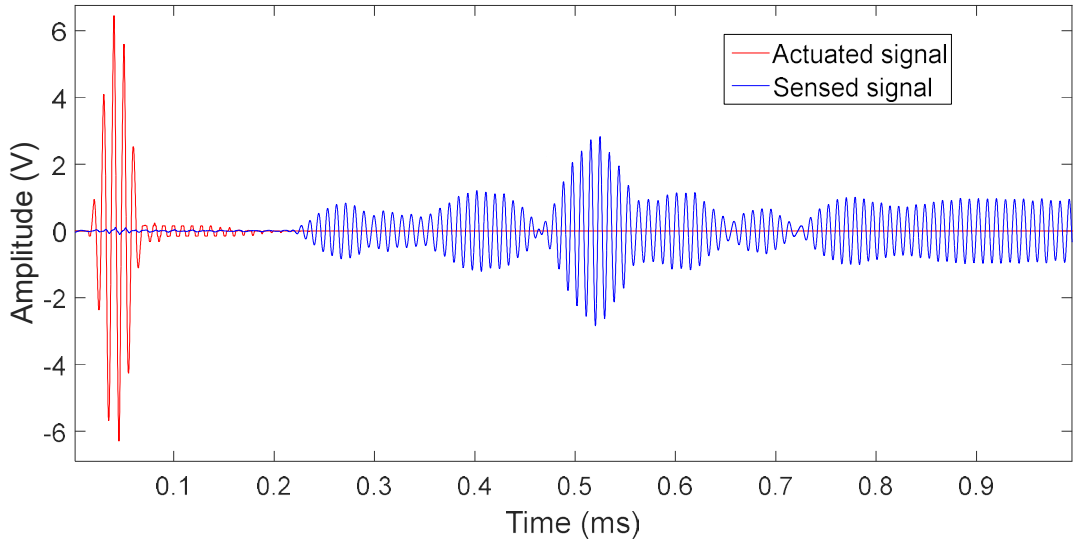

Figure 3: Actuated and sensed signal in the hollow cylinder

$$r_{xy}(n) = \frac{1}{N}\sum_{n=0}^{N} S_0(n)S_i(n-t) \tag{8}$$

where $r_{xy}(n)$ is the cross correlation between $S_0(n)$ and S_i and N is the number of signal samples, t is defined in the interval $(-N * T_s\,, (N-1) * T_s)$. Then, residuals R_i, are the difference between the nominal auto correlation, Ec (9), and the different stressed cross correlation scenarios, Ec (8).

$$r_{xx}(n) = \frac{1}{N}\sum_{n=0}^{N} S_0(n)S_0(n-t) \tag{9}$$

$$R_i(n) = r_{xx}(n) - r_{xy}(n) \tag{10}$$

Where i denotes the stressed scenarios. Based on the residual signal two features for stress monitoring are defined, the RMS value of R_i, Ec. (11), and the current position of the peak value with respect to the nominal position, named Reference Time (RT), Ec. (13). The latter feature allow to discriminate between concave upwards and concave downwards cylinder deflection.

$$V_{RMS} = \sqrt{\frac{1}{2N-1}\sum_{t=-N}^{N-1}|R_i(t)|^2} \tag{11}$$

$$(A_i\,,\,p_i) = max[R_i(t)] \tag{12}$$

$$RT = p_i - p_0 \tag{13}$$

Where A_i is the maximum residual value of signal R_i and p_i is the time position of this value. The p_0 occurs in the peak of the auto-correlation R_0. The average correlation for each studied scenarios are calculated using 100 experiments. Figure 4 presents the studied scenarios in the plane *RMS*-*Rt*.

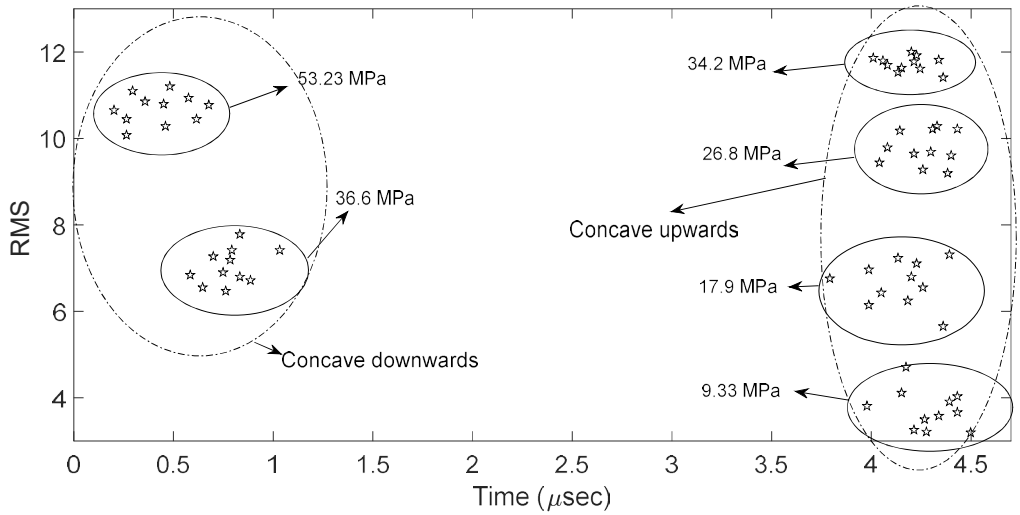

Figure 4: Residual *RMS* and *RT* for the stressed scenarios

6 CONCLUSIONS

Experimental results for the studied hollow cylinder show that the proposed method of estimating applied bending stresses from a couple of PZT in a pitch-catch configuration can provide decent results. While the stress estimation and its resolution is not as good as the acquired using, e.g. dedicated strain gauges, the method has the benefit of not requiring extra sensors if guided wave transducers are already in place as part of a structural health monitoring system. Therefore, this method is of particular interest for estimating bending stresses by using the same instrumentation and captured signals that are utilized for in situ imaging of damage.

The monitoring stage is carrying out using the *RMS* and the *RT* of the residuals obtained by signal subtraction. As shown in Figure 4, the couple *RMS*-*RT* is able to discriminate not only the different stresses but also the hollow cylinder bending shape. The *RMS* value tends to growth with the increase of the absolute stress magnitude for bending concave upwards and concave downwards, but the *RMS* value rise is in different proportion for each bending shape.

It should be noted that the measurement of absolute stress levels requires reference data taken in the unloaded case before implementing this approach in the field. On the other hand, the *Rt* value is close to zero for the bending concave downwards. Thus, not a meaningful time shifting is expected of the correlated signal for this type of bending.

One limitation of this approach is the assumption that there are no other contributions to time shifts other than stress variations. Though this assumption may be reasonable in the laboratory, it may not hold in a realistic operating environment where temperature changes can be expected simultaneously with stress variations. Therefore, it is recommended that future work include performing experiments incorporating temperature changes, which would serve to both validate the proposed approach and to quantify the temperature effect.

ACKNOLEDGEMENTS

This work has been partially funded by the Spanish Ministry of Economy and Competitiveness through the research projects DPI2014-58427-C2-1-R

REFERENCES

[1] Rizzo P and Lanza di Scalea F. Effect of Frequency on the Acoustoelastic Response of Steel Bars *Exp. Tech.* (2003) **27** 40–3

[2] di Scalea F L and Rizzo P. Stress measurement and defect detection in steel strands by guided stress waves *J. Mater. Civ. Eng.* (2003)**15** 219

[3] Nucera C and Scalea F L d. Monitoring load levels in multi-wire strands by nonlinear ultrasonic waves *Struct. Heal. Monit.* (2011)**10** 617–29

[4] Shi F, Michaels J E and Lee S J. In situ estimation of applied biaxial loads with Lamb waves *J. Acoust. Soc. Am.* (2013)**133** 677–87

[5] Kubrusly A C, Pérez N, Adamowski J C and Von Der Weid J P. Strain sensitivity model for guided waves in plates using the time-reversal technique *IEEE Trans. Ultrason. Ferroelectr. Freq. Control* (2013)**60** 2566–74

[6] Croxford A J, Wilcox P D, Drinkwater B W and Konstantinidis G. Strategies for guided-wave structural health monitoring *Proc. R. Soc. A Math. Phys. Eng. Sci.* (2007)**463** 2961–81

[7] Chaki S and Bourse G. Guided ultrasonic waves for non-destructive monitoring of the stress levels in prestressed steel strands *Ultrasonics* (2009)**49** 162–71

[8] Rose J L. *Ultrasonic Waves in Solid Media,* Cambridge University Press (2014)

[9] Seco F and Jiménez A R. Modelling the Generation and Propagation of Ultrasonic Signals in Cylindrical Waveguides. *Ultrason. waves, Intech Open Access Publ.* (2012)1–28

[10] Chaki S and Bourse G. Stress level measurement in prestressed steel strands using acoustoelastic effect *Exp. Mech.* (2009)**49** 673–81

[11] Tindaro C. *Signal Processing for Guided Wave SHM*, PhD Thesis, Imperial College (2009)

[12] Bocchini P, Asce M, Marzani A and Viola E. Graphical User Interface for Guided Acoustic Waves *J. Comput. Civ. Eng.* (2011)**25** 202–10

Synthesis and characterization of bismaleimide based thermosetting polymeric system with two-way reversible shape memory behavior

Qiwei Zhang*, Yanju Liu†, and Jinsong Leng††

* Centre for Composite Materials and Structures
Harbin Institute of Technology (HIT)
No. 2 YiKuang Street, 150080, Harbin, China
Email: qwzhang@hit.edu.cn

† Department of Astronautical Science and Mechanics
Harbin Institute of Technology (HIT)
No. 92 West Dazhi Street 150001, Harbin, China
Email: yj_liu@hit.edu.cn

†† Centre for Composite Materials and Structures
Harbin Institute of Technology (HIT)
No. 2 YiKuang Street, 150080, Harbin, China
Email: lengjs@hit.edu.cn

ABSTRACT

Shape memory polymers (SMPs) as a type of smart materials have achieved remarkable advances in recent years. Thermosetting SMPs with potential applications in aerospace, textiles and household products have attracted great interests of researchers for its unique properties. In order to further enhance and broaden the applications of SMPs, more unprecedented functions are necessary for the applications above, especially for aerospace [1,2].

In this paper, the synthesis and characterization of bismaleimide based SMPs, which are capable of realizing reversible shape change under constant load conditions, are reported. Seeking to synthesize thermoset polymers with intrinsic two-way reversible shape memory behaviour, we introduce here a biphenyl block that exploit a crystallization induced elongation (CIE). We show that all synthetic products exhibited crystallizable switching domains needed for two-way reversible shape memory behaviour. The glass transition temperature and shape memory properties are varied by using diglycidyl ether of 4, 4′-dihydroxybiphenol to creating crosslinking structure between the linear chains. Given the simplicity of fabrication, we envision application as multi-shape coatings, adhesives, and films.

REFERENCES

[1] J. Leng, X. Lan, Y. Liu, S. Du. Shape-memory polymers and their composites: Stimulus methods and applications. *Progress in Materials Science.* Vol. **56**, pp. 1077-1135 (2011).

[2] Y. Liu, H. Du, L. Liu, J. Leng. Shape memory polymers and their composites in aerospace applications: a review. *Smart Materials and Structures*. Vol. **23**, 023001. (2014).

VIII ECCOMAS Thematic Conference on Smart Structures and Materials
SMART 2017
A. Güemes, A. Benjeddou , J. Rodellar and Jinsong Leng (Eds)

THERMAL AND MECHANICAL PROPERTIES OF SELF-HEALING EPOXY/GRAPHENE NANOCOMPOSITES

I. AGUIRRE DE CÁRCER *, M.G. PROLONGO*, C. SALOM*, J. PARRADO*, R. MORICHE AND S.G. PROLONGO†

* Dpt. Materiales y Producción Aeroespacial, Universidad Politécnica de Madrid, Spain.
e-mail: mg.prolongo@upm.es, catalina.salom@upm.es
†Dpt. Ciencia e Ingeniería de Materiales, Universidad Rey Juan Carlos, Madrid, Spain
e-mail: silvia.gonzalez@urjc.es

Key words: self-healing epoxy, graphene, thermal-mechanical-electrical properties.

Abstract. The goal of the present work is to analyze the influence of the type of graphene and graphene content on the thermo-mechanical properties of an epoxy nanocomposite formed by an epoxy resin base on diglycidyl ether of bisphenol A (DGEBA) and 4-aminophenyl disulphide (AFD) as curing agent. This is a "dynamic" epoxy matrix (vitrimer), which has reversible crosslinks based on aromatic disulphide bonds. The idea is to take the advantage of the high thermal conductivity of graphene nanocomposites to promote the self-healing. The study of the epoxy-graphene systems was carried out using two types of un-functionalized graphene with different nanoplatelet dimensions. Dispersions of GNPs in the DGEBA were studied by Differential Scanning Calorimetry (DSC) in order to investigate the curing reaction. Dynamic Mechanical Thermal Analysis (DMTA) and tensile stress-strain measurements were performed to compare the glass transition temperature, the storage modulus in the glassy and rubber states, the Young modulus, deformation at break, mechanical strength and toughness. Electrical conductivity and combined tensile stress-electrical resistance experiments are reported for these nanocomposites.

1 INTRODUCTION

Recently it has been presented a new epoxy vitrimer [1] formed through the reaction of diglycidyl ether of bisphenol A (DGEBA) with 4-aminophenyl disulphide (AFD). This is a "dynamic" epoxy matrix, which has reversible crosslinks based on aromatic disulphide bonds. Vitrimers are new polymer networks that can be healable/repairable and recyclable. They can flow when reaching a given temperature, since the exchange reaction is initiated with temperature however they retain a fixed crosslinking density throughout the thermal processing, with covalent bonds in a constant exchange [2]. The new epoxy network DGEBA/AFD presents good mechanical properties, while showing reprocessability, reparability and recyclability [1]. Moreover it has exceptional characteristics compared to other vitrimers: 1) ease of synthesis from readily available materials, 2) fast stress relaxation at high temperature (vitrimer behaviour) without the need of a catalyst and 3) easy applicability for the manufacture of (re) processable, repairable and recyclable FRPCs [1]. Recently we have studied the self-heating by the Joule effect in composites reinforced with CNTs and GNPs [3]. We confirm that Graphitic nanofillers induce an increase of the thermal

conductivity of the epoxy resin, proportional to the nanofiller content and that the electrical conductivity has a clear percolation threshold. Electrical conductivity is needed to create the Joule Effect. In this work, we study the curing, thermo-mechanical and electrical properties of a self-heating epoxy (DGEBA-AFD) and their graphene nanocomposites. The idea is to take the advantage of the high thermal conductivity of grapheme nanocompoposites to promote the self-healing.

2 EXPERIMENTAL

2.1 Materials

An aeronautical grade epoxy prepolymer based on a basic DGEBA, Araldite LY556 (LY), was purchased from Huntsman. The curing agent: 4-aminophenyl disulfide (AFD) was purchased from TCI Europe. AFD was mixed at stoichiometric concentration with respect to oxirane rings. Moreover samples containing an excess of AFD (11% by weight) have been prepared.

The epoxy-graphene nanocomposites were prepared using two types of graphene with different nanoplatelet dimensions: GNPn was purchased from Cheap-Tubes (GNPS grade 4) and GNP_{M25} was purchased from XGScience. GNPn graphene nanoplatelets have average thickness < 4 nm and an average lateral size of 1-2μm, and GNP_{M25} graphene nanoplatelets have average thickness of 6-8 nm and an average lateral size of 25 μm. Frekote from Loctite was employed as mold release product.

2.2 Preparation of the dispersions and nanocomposites

Dispersions of graphene nanoplatelets in the epoxy prepolymer were obtained through sonication during 60 min using a horn and a sonicator UP400S Hielscher: 0.5 s cycles with a power of 400 W and amplitude of 50%. The temperature did not exceed 80°C. Dispersions were prepared with 1wt%, 4wt% and 6wt% of GNPs. Once the dispersions were obtained, the curing agent (AFD) was added at 80-85 °C and mixed during 5 min, these samples were studied by differential scanning calorimetry (DSC) in order to investigate the curing reaction.

Moreover specimens for dynamic mechanical thermal analysis (DMTA) and for tensile tests were prepared. For this purpose after adding the AFD to the dispersions they were degased under vacuum (15 min, 50 mmHg) and poured in aluminum molds of suitable dimensions and cured in an oven following the protocol: 8h at 140 ºC under atmospheric pressure. The molds were coated with a release product.

AFD /LY ratio was stoichiometric (molar ratio amino hydrogen / epoxy group = 1.00). There have been also prepared samples having (11wt% excess of AFD) in order to compere results of the neat system with the previously reported [1]

2.3 Techniques

Differential Scanning Calorimetry (DSC): a Mettler Toledo mod.822e differential scanning calorimeter was used. The instrument was calibrated with indium and zinc. Measurements were performed under a nitrogen atmosphere Samples of 10-20 mg were weighted in aluminum pans. The reaction enthalpy (ΔH) and the exothermic peak temperature (T_p) were obtained from the first scans (-50ºC to 270ºC) of the reactive mixtures and dispersions. For

each composition several first scans were done at different heating rates from 3 to 10 °C·min^{-1} in order to calculate the apparent activation energy of the curing reaction (E_a). To obtain the T_g of the nanocomposites samples were scanned from 25 ºC to 250 ºC at 10ºCmin$^{-1.}$ The T_g*s* were taken at the midpoint of the heat capacity change.

Dynamic Mechanical Thermal Analysis (DMTA): a DMTA V Rheometric Scientific instrument was used. Measurements of cured samples were performed in dual cantilever bending mode at 1, 2, 5, 10 and 50 Hz, with temperature increasing from 30 °C to 220 °C at a heating rate of 2 °C·min^{-1}. Specimens dimensions were: 35×10×1.8 mm^3. The elastic or storage modulus (E'), the loss modulus (E'') and loss tangent ($tan\delta$) were recorded for each frequency as a function of temperature. The maxima in $tan\delta$-temperature curves were determined to identify the α-relaxations associated to the glass transitions.

Tensile tests: a MTS machine model QTest 2L with a load cell of 2 kN, using an MTS extensometer model 63411F-54 was used to study tensile mechanical properties of the nanocomposites. Experiments were performed at room temperature (22 ºC) at constant speed of 1 mm· min^{-1} until fracture. The specimen dimensions were 140 x10 x 1.8 mm^3. The stress-strain curves were recorded for six samples of each composition. The average values of mechanical properties: tensile modulus, tensile strength, strain to failure were calculated for each composition. Mechanical tests with the simultaneous measurement of the electrical resistance were performed using a Zwick Roell 100 kN machine with a coupled load cell of 5 kN and a meter instrument Agilent 34410A.

DC volume electrical conductivity was measured according to ASTM D257 using a Source Meter Unit instrument (Keithley 2410). The electrical resistance was determined from the slope of the current-voltage curve, and the electrical conductivity taking into account the geometry of specimens (10 x 10 x 1 mm^3). Six samples of 6%GNPn nanocomposite were measured in the range of 0-15 V.

3 RESULTS AND DISCUSSION

3.1 Curing of GNP/epoxy dispersions by DSC

The thermograms of neat epoxy (LY-AFD) and 4wt% GNP_n/epoxy dispersion are shown in Figure 1.The exothermic peak corresponds to the epoxy-amine curing reaction. Table 1 shows the DSC results for neat LY-AFD mixtures having stoichiometric ratio and 11wt% excess of AFD, together with the results for the corresponding GNP_n and GNP_{M25} dispersions in LY-AFD, at different heating rates (v). As it was expected T_{peak} increases with increasing heating rate, this is because faster heating rates offer less time for reaction, and to compensate for the reduced time the curves shift to a higher temperatures. -ΔH for each composition slightly decreases as the heating rate increases, but the variation is almost within the experimental error. Moreover there are not significant changes of -ΔH adding excess of AFD neither in the presence of 1% and 4% of GNP, indicating that all the epoxy groups in the LY-AFD mixture have reacted.

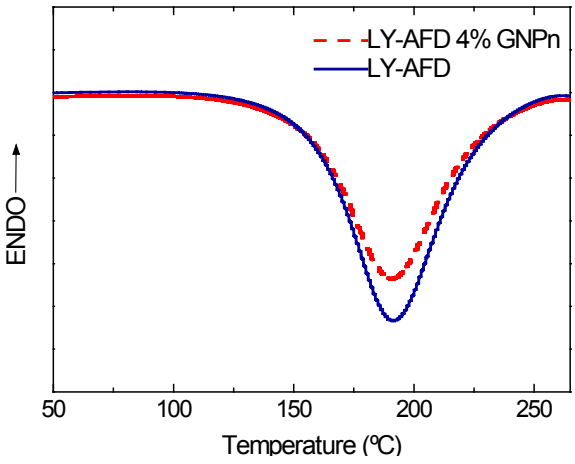

Figure 1: DSC thermograms (10ºC/min) of epoxy (LY-AFD) and 4wt% GNP_n/epoxy

Table 1: DSC results of curing epoxy (LY-AFD) and GNP/epoxy dispersions

	v (ºC/min)	***-ΔH*** (J/gLY)*	T_{peak} (ºC) †	T_g (ºC) ††	***Ea*** (kJ/mol)
LY-AFD	3	583	162	122	64±1
	4	574	169	128	
	5	564	175	131	
	8	550	187	136	
	10	524	193	136	
LY-AFD +1%GNP_n	3	578	160	124	62±1
	4	544	167	129	
	5	528	173	130	
	8	529	186	136	
	10	514	193	136	
LY-AFD + 4%GNP_n	10	530	192	137	-
LY-AFD + 4%GNP_{M25}	10	556	192	138	-
LY-AFD (11% excess)	3	568	159	113	62±0.5
	4	559	166	118	
	5	574	172	120	
	8	555	185	124	
	10	551	191	129	
LY-AFD (11% excess) + 4% GNP_n	10	558	191	130	-

Estimated error: * ±20 J/g, † ±0.5ºC, †† ±0.5ºC.

T_{peak} of samples containing 4% of GNP_n and 4% of GNP_{M25} is slightly lower than T_{peak} of LY-AFD (see Table 1) this reflects a small catalytic effect of GNP. However, no catalytic effect was noticed for samples containing lower GNP content, a previous work with another epoxy resin having 1% of GNP_{M25} showed similar behaviour [4]. The values of T_{peak} of LY-AFD (11% excess) are lower than the corresponding to LY-AFD which is due to the faster reaction of primary amine with respect to secondary amine. From the slope of the plots ln v vs. T_{peak}^{-1}, according to Arrhenius equation, the apparent activation energy of the curing reaction (E_a) was obtained and the results are given in Table1. A decrease of E_a is clearly detected of LY-AFD (11% excess) confirming that with amine excess the reaction goes faster.

The T_g values of samples cured during the first DSC scan are given in Table 1. The networks having excess of AFD have lower T_g than the stoichiometric LY-AFD samples. The preferential reaction of primary amine leads to networks with higher molecular weight between crosslinks, which corresponds with lower degree of crosslinking, and lower T_g. Regarding the effect of graphene on T_g the presence of GNPs has little influence on the T_g of the epoxy network for samples dynamically cured in the DSC.

3.2 Thermo-mechanical properties of DMTA of GNP/epoxy nanocomposites

DMTA curves (E'-temperature and tanδ-temperature for neat LY-AFD thermoset and for LY-AFD-GNPs nanocomposites at 1 Hz are given in Figures 2a and 2b.

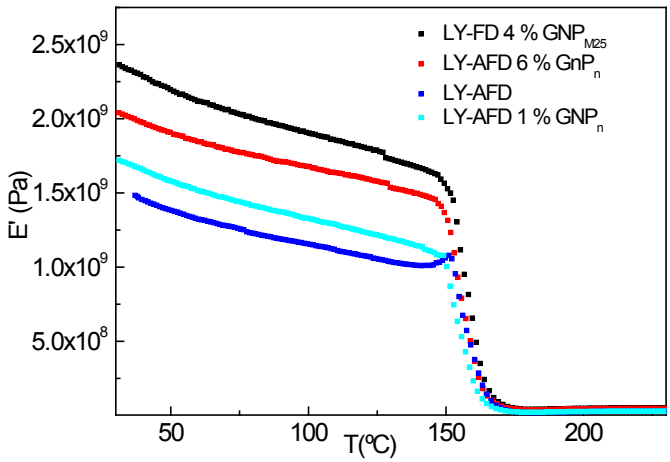

Figure 2a: E'-temperature of epoxy (LY-AFD) and epoxy/graphene nanocomposites

It can be see (Figure 2a) that in the glassy state ($T < T_g$) the nanocomposites have higher E' than the neat epoxy thermoset. Table 2 collect E' values for all the nanocomposites in the glassy and rubbery state ($T < T_g$). As it can be observed the addition of GNP increases the storage modulus in the glassy ($T < T_g$) and rubbery ($T > T_g$) states with regard to neat epoxy thermoset. The increment is proportional to the graphene content and is more important in the rubbery state. Moreover GNP_{M25} is a more effective reinforcement than the GNP_n as a consequence of its bigger size. The sample having AFD excess presents E' *rubbery* lower than the stoichiometric (LY-AFD) which is due to its lower degree of crosslinking. The

opposite behavior is observed in the glassy state, because the stoichiometric network has all amine-epoxi bonds formed but is a less packed and more open network.

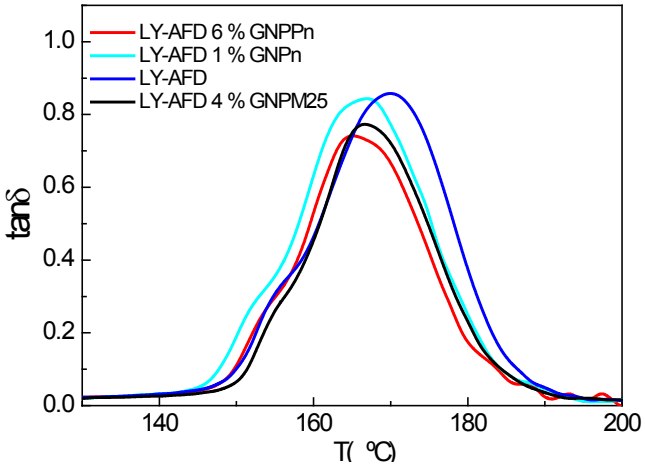

Figure 2b: *E´*-temperature of epoxy (LY-AFD) and epoxy/graphene nanocomposites

Table 2: *E´* modulus, temperature of $tan\delta_{max}$, of epoxy thermoset and GNP nanocomposites.

Sample	***E´glassy*** (80ºC) GPa	***E´rubbery*** (220ºC) MPa	***Ttan*δ_{max}** (ºC)
LY-AFD	1.23	28	170
LY-AFD (1% GNP_n)	1.41	29	167
LY-AFD (6% GNP_n)	1.75	47	165
LY-AFD (4% GNP_{M25})	2.00	50	166
LY-AFD(11% excess)*	1.35	27	168
LY-AFD(11% excess) + 4% GNP_n	1.54	33	162

*Curing: 2,5h -120ºC+ 2h-150ºC

It is noteworthy that the tanδ - temperature curves (Figure2b) show a main peak around 162ºC-170ºC and a shoulder at 12-15ºC below. This reflects that the epoxy matrix behaves mechanically as no homogeneous, that is, there are regions with high mobility that relax at lower temperatures and rigid regions that relax at higher temperature. This behaviour is minimized in networks cured with excess of AFD, where the tanδ - temperature curves show a single peak.

The temperature of $\tan\delta_{max}$ at 1 Hz (α-relaxation associated to the glass transition) for the neat epoxy thermoset and for the nanocomposites are included in Table 2. The T_g is taken as temperatura at which $\tan\delta(1\text{Hz})$ reaches a máximum and usually $T_g s$ from $\tan\delta_{max}(1\text{Hz})$ are higher than the $T_g s$ from DSC.The nanocomposites (see Table 2) have lower temperature of $\tan\delta_{max}$ than neat epoxy thermoset, i.e., a less perfect epoxy networks are formed in presence of GNPs.

3.3 Tensile properties of DMTA of GNP/epoxy nanocomposites

The tensile properties of nanocomposites were determined by tensile stress–strain measurements. Figure 3 shows the more representative stress–strain curves for epoxy thermosets and GNP nanocomposites. From the curves the values of tensile modulus *E*, tensile strength (stress at break), strain at break and area under stress-strain curves which is a measure of the toughness were calculated. Tensile test results are given in Table 3. The tensile modulus of the nanocomposites is higher than that of the epoxy thermoset evidencing the reinforcing action of the GNPs. The tensile strength, deformation at break and toughness values hardly changes with low GNP content (1%). However tensile strength, deformation at break and toughness decrease for 4% and 6% of GNP nanocomposites. This suggests the presence of defects in these nanocomposites.

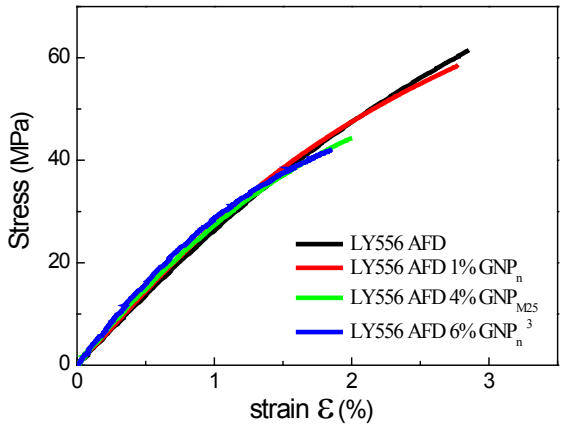

Figure 3: Stress–strain curves for epoxy (LY-AFD) and epoxy/graphene nanocomposites

Table 3: Stress-strain results for epoxy thermosets and GNP nanocomposites

Sample	**Young Modulus** (GPa)	**Tensile strength** (MPa)	**Deformacion at break** (%)	**Toughness** (MJ/m^3)
LY-AFD	2.76 ± 0.09	60± 4	2,8 ± 0.3	0.97
LY-AFD 1%GNP_n	2.83 ± 0.07	56 ± 3	2.7 ± 0.2	0.93
LY-AFD 6%GNP_n	3.32 ± 0.19	42 ± 2	1.8 ± 0.3	0.46
LY-AFD 4%GNP_{M25}	3.21 ± 033	46 ± 4	2.1 ± 0.4	0.51

3.4 Combined tensile tests-electrical conductivity GNP/epoxy nanocomposites

It is known that in nanocomposites the electrical conductivity shows a percolation threshold, this means that at GNP contents lower than the percolation threshold, the composites are insulator but their electrical conductivity increases abruptly at higher contents. The electrical percolation depends on the connectivity between nanoplatelets. Previous works [3] have shown that for GNP_{M25}-epoxy nanocomposites the percolation threshold is close to 3%. As GNP_n has smaller dimensions, it is expected that its electrical percolation would be reached at higher GNP_n content. In order to select a suitable composition to carry out the combined tensile stress-electrical conductivity tests, we have determined the conductivity of nanocomposites. Figure 4 shows the Intensity-Voltage dependence for six samples of LY-AFD-6%GNP_n. From the slopes of Intensity-Voltage lines and considering the sample geometry, a value of $10.4 \cdot 10^{-5}$ $S \cdot m^{-1}$ was found, which is suitable for the combined tests.

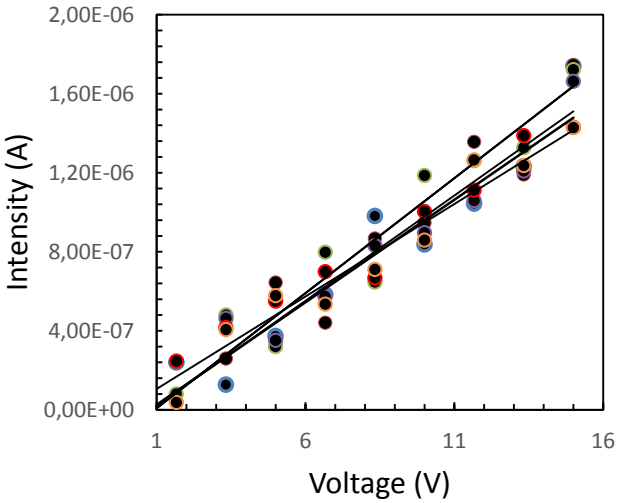

Figure 4: Intensity vs.-voltage for LY-AFD-6%GNP_n nanocomposites

In order to perform the combined tensile stress-electrical conductivity test of LY-XB-6%GNP_n nanocomposite, the specimens prepared for the tensile stress–strain test were painted around the perimeter with conductive silver paint at set intervals. Copper wire was then attached to the painting and covered with an adhesive thermoplastic, so efficient electrical contacts between the silver and the copper were produced. This set up creates five channels which allow the measurement of the electrical properties of the material at differentiated locations as can be seen in Figure 5 a. The tensile force-time curve of this set up was assayed at 5 mm/min while measuring simultaneously the two point electrical resistance at the different channels. The combined tensile force-electrical conductivity test for the LY-AFD-6%GNP_n specimen is shown in Figure 5 b. It can be seen the tensile force-time curve together the normalized resistance-time curves for the five different channels.
As the strain builds up in the specimen the electrical resistance through the different channels increases as seen by the rise in normalized resistance of all the channels. When the stress

disappears, in this case due to the specimen breaking, the conductivity of the channels returns to basal values, but the channel where the break occurs (chanel 11 in Figure 5) shows no conductivity after the break. This experiment would indicate that addition of 6% of graphene is not adequate as electrical sensor in the experimental conditions (high strain rate). Nevertheless this result suggest that reducing strain rate and/or GNP_n content, GNP_n could be used as electrical sensor.

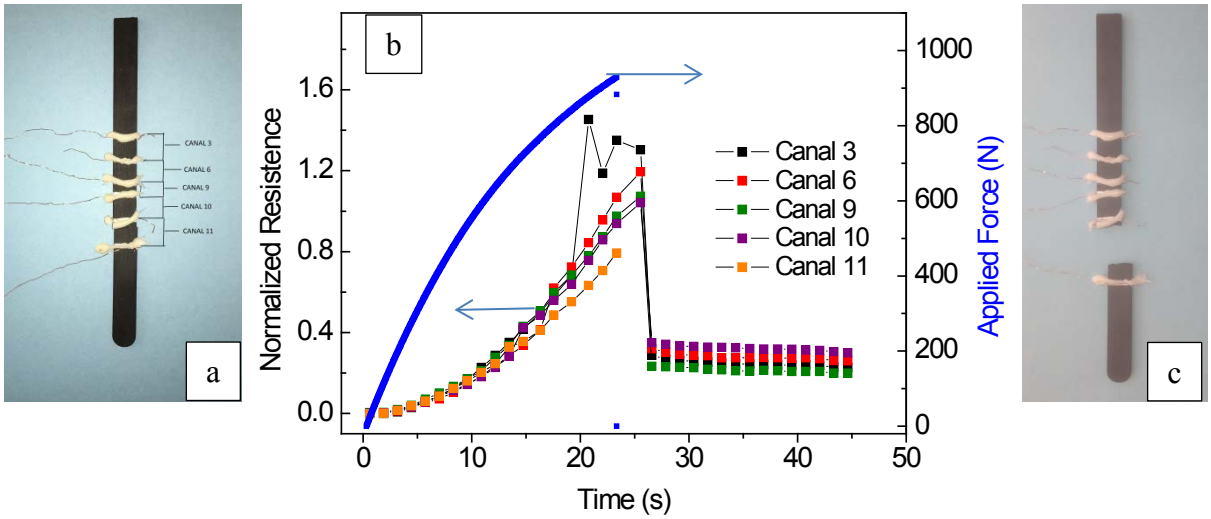

Figure 5: Combined tensile tests-electrical conductivity for LY-AFD-6%GNP_n nanocomposite: a)Specimen set up with five conductive channels before test, b) Force- time curve (—) together with resistance-time curves (□) measured in five channels, c) specimen after break.

4 CONCLUSIONS

- Incorporation of GNP up to 6% does not significantly modify the curing reaction of LY-AFD, nor in the presence of an excess of 11% of AFD.
- A small catalytic effect of GNP on curing LY-AFD was detected and the curing rate in excees of AFD (11%) is faster than in the stoichiometric LY-XB mixture.
- The networks having excess of AFD have lower T_g than the stoichiometric LY-AFD samples due to their higher molecular weight between crosslinks.
- The nanocomposites present increased glassy and rubbery moduli with regard to neat epoxy thermoset. The increment is proportional to the graphene content and is more important in the rubbery state.
- GNP_{M25} is a more effective reinforcement than the GNP_n as a consequence of its bigger size.

- The sample having AFD excess presents *E´ rubbery* lower than the stoichiometric (LY-AFD) due to its lower degree of crosslinking. The opposite behavior is observed in the glassy state, because is a more packed network.
- Increasing GNP content increases the tensile modulus at room temperature. Tensile strength, strain at break and toughness decrease with the increase of GNP content suggesting the presence of defects.
- The measured conductivity of LY-AFD-6%GNP_n is $10.4 \cdot 10^{-5}$ $S \cdot m^{-1}$ been suitable to carry out the combined tensile stress-electrical conductivity tests.
- The combined tensile force-electrical conductivity test for the LY-AFD-6%GNP_n specimen suggests that reducing strain rate and/or GNP_n content, GNP_n could be used as electrical sensor.

Acknoledgements

The authors acknowledge the financial support by Ministerio de Economía y Competitividad of Spain Government (Projects: MAT2013-46695-C3 y MAT2016-78825-C2)

REFERENCES

[1] Ruiz de Luzuriaga A., Martín R., N. Markaide, Rekondo A., Cabañero G., Rodríguez J. and Odriozola I. Epoxy resin with exchangeable disulfide crosslinksto obtain reprocessable, repairable and recyclable fiber-reinforced thermoset composites. *Mater. Horiz*. (2016) **3**:241-247.

[2] Azcune I. and Odriozola I. Aromatic disulfide crosslinks in polymer systems : selt-healing, reprocesability, recyclability and more.*Eur. Polym. J.* (2016) **84**:147-160.

[3] Prolongo S.G, Moriche R. Del Rosario G., Jiménez-Suárez A. Prolongo M.G. and Ureña A. Joule effect self-heating of epoxy composites reinforced with graphitic nanofillers. *J Polym Res* (2016) **23**:189 1-7

[4] Prolongo M.G., Salom C., Arribas C., Sánchez-Cabezudo M., Masegosa R.M., Prolongo S.G. Influence of graphene nanoplatelets on curing and mechanical properties of graphene/epoxy nanocomposites. *J Thermal Anal Calorim* (2016)**125**:629-636.

VIII ECCOMAS Thematic Conference on Smart Structures and Materials
SMART 2017
A. Gemes, A. Benjeddou , J. Rodellar and Jinsong Leng (Eds)

COMPUTATIONAL AND EXPERIMENTAL ANALYSIS OF SURFACE ACOUSTIC WAVE PROPAGATION ON PIEZOELECTRIC GaAs LAYER

CLAUDIO MARUCCIO[1], MARCO SCIGLIUZZO[2], SILVIA RIZZATO[2], GIUSEPPE QUARANTA[3], GIUSEPPE MARUCCIO[2]

[1] Department of Innovation Engineering, University of Salento, Via Monteroni, Lecce, Italy. E-mail: claudio.maruccio@unisalento.it

[2] Department of Mathematics and Physics "E. De Giorgi", University of Salento, via Monteroni, Lecce, Italy.

[3] Department of Structural and Geotechnical Engineering, Sapienza University of Rome, via Eudossiana 18, Rome, Italy.

Key words: Multiphysics modeling, surface acoustic waves, phononic crystals.

Abstract

A computational study of the electromechanical response of nano-structure engineered two port surface acoustic wave (SAW) delay lines on GaAs is presented. The influence on the results of geometrical, material and mesh parameters is also discussed. Furthermore, preliminary experimental results are provided to validate the numerical study. The device consists in two interdigital transducers (IDTs) composed of 80 couples of electrodes, with a pitch p_{idt}=8μm and distant d_{idt}=1502μm. Fully coupled multiphysics finite element (FE) analyses are developed to capture the SAWs propagation on GaAs along the [110] crystallography direction. In particular, a microwave burst of SAWs propagating on GaAs is fully characterized including multiple transit effects. These results are of major interest for understanding the dynamical behavior of complex systems such as SAW based sensors or energy harvesting devices at the nano and microscale.

1 INTRODUCTION

Propagation of acoustic/elastic waves in structures is a fundamental problem with applications in numerous fields: biology and medicine (cancer chips) [2], mechanics (strain sensors) [18], communications (filters) [3], phononic crystals (PCs) [12] and SAW sensors and resonators [1]. Many groups are also studying these devices in their quantum limits [30]. Elastic metamaterials with inertial locally resonant structures are proposed in [24] while applications for piezoelectric microstructures and energy harvesting are investigated by [6]. Within this framework, the determination of the acoustic band structure of periodic elastic composites is of primary interest [20]. Wave band gaps in two dimensional piezoelectric PCs have been determined recently, see for example [21] and [22]. Moreover, the presence of interfaces may also affect the final band structure of materials [24]. In the last years, several numerical techniques have been developed to analyze the response of PCs (see [19] for a review) but only recently researchers started to focus on surface acoustic waves propagation in phononic materials. Both experimental [5], [13] and numerical [11] studies are today available.

The computational modeling is approached through finite difference, FE or plane wave expansion (PWE) methods, see [10],[4] and [14]. FE analysis and experimental study of SAW propagation through two-dimensional pillar-based surface PC is reported for example in [7] and [9], while the P-Matrix method is used in [8].

In general, modeling of SAW devices can be accomplished via the impulse response, transmission matrix or FE method [15]. Because of the small wavelength compared with the dimensions of the whole SAW equipment, the FE discretization requires a huge number of elements, thus resulting in a large system which is time consuming for real case studies. Modal analysis is often used to determine eigenmodes and eigenfrequencies of the periodic SAW system during the design stage [5]. These data are sufficient for devices working in stationary conditions. Unfortunately, dynamics plays a crucial role in the global response of many apparatus, such as for microfluidic SAW applications [29]. Few studies are available where wave propagation on the surface of a piezoelectric layer is fully characterized. Moreover, the majority of these works take into account devices on Lithium Niobate (LiNbO) where even few finger pairs are enough to generate a strong signal. Xu et al. 2001 [16] provided results in the time and frequency domains for a Y-Z LiNbO SAW filter where the apparatus consists in a couple of transducers with 11 electrodes and a separation of 24 λ (where λ is the wavelength). Mohibul et al. 2016 [17] simulated a SAW delay lines on X-Y LiNbO substrate with 2 or 4 finger pairs and a distance of 2.4 λ. Therefore, reliable numerical predictions of the time domain response for applications that require weaker piezoelectric substrate (like quartz or GaAs) is of fundamental interest. For example, the pulse echo method [25] is a well known technique to determine the wave velocities from pulse transit time measurements. Since the plane wave velocities are related to the fundamental material constants, the procedure allows also the estimation of elastic and piezoelectric coefficients with a good accuracy. It is clear that when new composite multiphysic materials are developed in the laboratory, numerical simulations may support a correct characterization of their response.

The final aim of this research is to propose an improved multi-functional device for applications such as wave sensors, filters and resonators with higher accuracy [26] or for energy harvesting vibrations in the MHz or GHz regime. In this paper, we present a preliminary computational study of the electromechanical response of two port SAW delay lines on GaAs. The numerical model is also founded on preliminary experimental work [1] and the device consists in two IDTs composed of 80 couples of electrodes, with a pitch p_{idt}=8μm and distant 1502 μm. Fully coupled multiphysics FE analyses are developed to simulate a microwave burst of SAWs propagating on GaAs along the [110] crystallography direction where the multiple transit effects are predicted with a good accuracy. Moreover, in order to clarify a possible role in this experiment of a PC structure, numerical analyses are performed to extract design parameters with the aim to achieve a final band structure in the frequency range of interest. These results can led us towards a future study of interaction between SAW and periodic structures such us the system in Figure 1. According to [26], we consider in this work PCs in place of conventional metallic reflective gratings, mainly with the aim to reduce the final size of the chips. Moreover, computational modeling of the PC structure presents several advantages for future work concerning fabrication of improved lens for energy-transmission devices [31] or waveguides [32].

2 PIEZOELECTRIC SOLID AND FE EQUATIONS

According to [25], the fundamental equations that describe elastic waves propagation in a piezoelectric linear elastic solid are:

$$T_{ij,j}(\mathbf{r},t) = \rho(\mathbf{r})\frac{\partial^2 u_i(\mathbf{r},t)}{\partial \mathrm{t}^2}; \qquad D_{i,i} = 0; \qquad i = 1..3; \tag{1}$$

where ρ is the density and u_i, T_{ij}, D_i are the three displacements, stress tensor and electric displacement components, respectively. Moreover, the constitutive equations read:

$$T_{\mathrm{ij}}(\mathbf{r},t) = c^E_{\mathrm{ijkl}}(\mathbf{r})u_{k,l}(\mathbf{r},t) + e_{\mathrm{kij}}(\mathbf{r})\phi_{,k}(\mathbf{r},t); \qquad D_i(\mathbf{r},t) = e_{\mathrm{ikl}}(\mathbf{r})u_{k,l}(\mathbf{r},t) - \epsilon^S_{\mathrm{ik}}(\mathbf{r})\phi_{,k}(\mathbf{r},t); \tag{2}$$

where c^E_{ijkl}, e_{kij}, ϵ^S_{ij} are the rank 4 elastic tensor, the rank 3 piezoelectric tensor and the rank 2 dielectric tensor, respectively. Moreover, ϕ is the electric potential and $\mathbf{r} = (x_1, x_2, x_3)$ is the spatial vector. Maxwell equations and strain-displacement relations lead to:

$$S_{\mathrm{ij}} = \frac{1}{2}\left(\frac{\partial \mathrm{u}_i}{\partial \mathrm{x}_j} + \frac{\partial \mathrm{u}_j}{\partial \mathrm{x}_i}\right); \qquad E_i = -\frac{\partial \phi}{\partial x_i}; \tag{3}$$

where S_{ij} and E_i are the strain and electric field components, respectively. Substituting equations (2) into (1) gives a system of four coupled wave equations for the three components of the displacement and the electric potential:

$$-\rho\frac{\partial^2 u_i}{\partial \mathrm{t}^2} + c^E_{\mathrm{ijkl}}\frac{\partial^2 u_k}{\partial \mathrm{x}_j \partial \mathrm{x}_l} + e_{\mathrm{kij}}\frac{\partial^2 \phi}{\partial \mathrm{x}_k \partial \mathrm{x}_j} = 0; \qquad e_{\mathrm{ikl}}\frac{\partial^2 u_k}{\partial \mathrm{x}_i \partial \mathrm{x}_l} - \epsilon^S_{\mathrm{ik}}\frac{\partial^2 \phi}{\partial \mathrm{x}_i \partial\, \mathrm{x}_k} = 0; \tag{4}$$

According to [15], the standard nodal FE discretization can be employed:

$$u_i \approx u_i^h = \sum_{p=1}^{n_n} N^p u_i^p, \tag{5}$$

$$\phi \approx \phi^h = \sum_{p=1}^{n_n} N^p \phi^p, \tag{6}$$

where N^p indicates the shape functions and n_n denotes the number of nodes for each FE. Moreover, u_i^p and ϕ^p are nodal values. By applying the Galerkin method, the resulting discretized coupled FE equations of motion for a given domain discretization are:

$$\begin{bmatrix} \mathbf{M}_{uu} & \mathbf{0} \\ \mathbf{0} & \mathbf{0} \end{bmatrix} \begin{pmatrix} \ddot{\mathbf{u}}_d \\ \ddot{\boldsymbol{\phi}} \end{pmatrix} + \begin{bmatrix} \mathbf{K}_{uu} & \mathbf{K}_{\mathrm{u}\phi} \\ \mathbf{K}_{\phi\mathrm{u}} & -\mathbf{K}_{\phi\phi} \end{bmatrix} \begin{pmatrix} \mathbf{u}_d \\ \boldsymbol{\phi} \end{pmatrix} = \begin{pmatrix} \mathbf{f}_u \\ \mathbf{f}_\phi \end{pmatrix} \tag{7}$$

where $\mathbf{u}_d$ and $\boldsymbol{\phi}$ are the nodal displacement vector and the electric potential vector, respectively. The upper dots indicate the time-derivative. The matrices $\mathbf{M}_{uu}$, $\mathbf{K}_{uu}$ are the structural mass and the stiffness matrices, respectively. The matrices $\mathbf{K}_{\mathrm{u}\phi}$ and $\mathbf{K}_{\phi\mathrm{u}}$ are the stiffness matrices due to piezoelectric mechanical coupling. The matrix $\mathbf{K}_{\phi\phi}$ is the stiffness matrix resulting from electrical fields. The vectors $\mathbf{f}_u$ and $\mathbf{f}_\phi$ are the force vectors due to mechanical and electrical contributions.

2.1 MODELING PHONONIC CRYSTAL BAND STRUCTURE

According to [14] and [19], due to the spatial periodicity of the PC, see Figure 2, it results:

$$\rho(\mathbf{r}) = \rho(\mathbf{r}+\mathbf{a}); \qquad c^E_{\mathrm{ijkl}}(\mathbf{r}) = c^E_{\mathrm{ijkl}}(\mathbf{r}+\mathbf{a}); \qquad e_{\mathrm{kij}}(\mathbf{r}) = e_{\mathrm{kij}}(\mathbf{r}+\mathbf{a}) \tag{8}$$

where $\mathbf{a}$ is a vector indicating the spatial repetition of the basic cell. Consequently, the elastic and electric quantities relative to an eigenmode have the form:

$$u_i(\mathbf{r},t) = \bar{u}_i(\mathbf{r})e^{\iota(\omega \mathrm{t} - \mathbf{k}\cdot\mathbf{r})}; \qquad \phi_i(\mathbf{r},t) = \bar{\phi}_i(\mathbf{r})e^{\iota(\omega \mathrm{t} - \mathbf{k}\cdot\mathbf{r})}; \tag{9}$$

where ω is an angular frequency, $\mathbf{k}$ is the Bloch-Floquet wave vector and $\bar{\phi}_i(\mathbf{r})$, $\bar{u}_i(\mathbf{r})$ are periodic functions. Moreover, ι is the imaginary unit. According to the Bloch-Floquet theorem, all fields present a periodicity and consequently the full band structure of a phononic structure is obtained solving the following eigenfrequency problem for just a unit cell:

$$\begin{pmatrix} \mathbf{K}_{\mathrm{uu}} - \omega^2 \mathbf{M}_{\mathrm{uu}} & \mathbf{K}_{\mathrm{u}\phi} \\ \mathbf{K}_{\phi\mathrm{u}} & -\mathbf{K}_{\phi\phi} \end{pmatrix} \begin{pmatrix} \mathbf{u}_d \\ \boldsymbol{\phi} \end{pmatrix} = \begin{pmatrix} 0 \\ 0 \end{pmatrix}. \tag{10}$$

In particular the problem is limited to the first Brillouin zone being the angular frequency a periodical function of the wave vector. In practise all the degrees of freedom on two opposite boundaries, namely A and B of the unit cell, are linked with the following equation:

$$\begin{pmatrix} u_{iB} \\ \phi_B \end{pmatrix} = \begin{pmatrix} u_{iA} \\ \phi_A \end{pmatrix} e^{-\iota(k_{x_r} L)}; \qquad r = 1...2 \tag{11}$$

with k_{x_1} and k_{x_2} components of the Bloch wave vector in the x_1 and x_2 directions and L the unit cell side dimension. Finally, k_{x_r} varies in the range between 0 to π/L.

2.2 MODELING SAW RESPONSE

Material, mechanical and electrical friction effects generate a damping in the propagating wave. These phenomena are mathematically modeled by adding a velocity–proportional damping term that, within the FE approximation, results in a damping matrix $\mathbf{C}_{uu}$. According to the classical Rayleigh damping approach, it is considered:

$$\mathbf{C}_{uu} = \alpha \mathbf{M}_{uu} + \beta \mathbf{K}_{uu} \tag{12}$$

where α and β are constant multipliers for the mass and stiffness matrix respectively. They are determined by assuming a constant damping ratio ξ. The class of Newmark schemes is used for the time discretization [32]. Depending on the choice of the integration parameters β_h and γ_h, explicit or implicit algorithms are possible. An implicit approach is used in this study. In particular, according to [16], if τ is the time-step counter and a linear interpolation between time steps τ and $\tau + 1$ [28] is considered for, both, displacement and velocity, then:

$$\underline{\mathbf{u}}_{\tau+1} = \underline{\mathbf{u}}_\tau + \Delta t \underline{\dot{\mathbf{u}}}_\tau + \frac{\Delta t^2}{2} \left((1 - 2\beta_h) \underline{\ddot{\mathbf{u}}}_\tau + 2\beta_h \underline{\ddot{\mathbf{u}}}_{\tau+1} \right), \tag{13a}$$

$$\underline{\dot{\mathbf{u}}}_{\tau+1} = \underline{\dot{\mathbf{u}}}_\tau + \Delta t \left((1 - \gamma_h) \underline{\ddot{\mathbf{u}}}_\tau + \gamma_h \underline{\ddot{\mathbf{u}}}_{\tau\ +1} \right), \tag{13b}$$

where Δt is the time-step. Substituting Equations 13 in Equation 7 at time $\tau + 1$, after including the damping contribution, the following recurrence relations are obtained:

$$\begin{aligned} &(\mathbf{M}_{uu} + \gamma_h \Delta t \mathbf{C}_{uu} + \beta_h \Delta t^2 \mathbf{K}_{uu}) \underline{\ddot{\mathbf{u}}}_{\tau+1} = \mathbf{f}_{u,\tau+1}, \\ &- \mathbf{K}_{u\phi} \underline{\boldsymbol{\phi}}_{\tau+1} - \mathbf{C}_{uu} (\underline{\dot{\mathbf{u}}}_\tau + (1 - \gamma_h) \Delta t \underline{\ddot{\mathbf{u}}}_\tau), \\ &- \mathbf{K}_{uu} (\underline{\mathbf{u}}_\tau + \Delta t \underline{\dot{\mathbf{u}}}_\tau + \Delta t^2/2 (1 - 2\beta_h) \underline{\ddot{\mathbf{u}}}_\tau), \end{aligned} \tag{14}$$

and

$$-\mathbf{K}_{\phi\phi} \underline{\boldsymbol{\phi}}_{\tau+1} = \underline{\mathbf{f}}_{\phi,\tau+1} - \mathbf{K}_{\phi\mathrm{u}} \underline{\mathbf{u}}_{\tau+1}. \tag{15}$$

In the previous equations, the subscript d of the nodal displacement vector is omitted for synthesis of notation.

2.2.1 COURANT-FRIEDRICHS-LEWY CONDITION AND MESHING

The spatial extension of the elements and the time step are closely connected by the Courant-Friedrichs-Lewy (CFL) condition [27]. In a two dimensional time–dependent FE algorithm with a time step Δt and minimum element dimensions Δx_1 and Δx_2, it is possible to introduce a numeric velocity $\mathbf{v}$

$$v_{x_1} = \frac{\Delta x_1}{\Delta t}; \qquad v_{x_2} = \frac{\Delta x_2}{\Delta t}. \tag{16}$$

The CFL condition states that for a wave propagating in a discrete lattice at a velocity $\mathbf{c}$, the following condition must be fullfilled:

$$C = \frac{c_{x_1}}{v_{x_1}} + \frac{c_{x_2}}{v_{x_2}} < 1, \tag{17}$$

where C is called CFL number. In order to grasp the detailed dynamics of the SAWs propagation, the dimension of the mesh is fixed to a small fraction of the wavelength λ. Using a square mesh, with $\Delta x_1 = \Delta x_2 = \frac{\lambda}{N}$ where N is the number of IDTs, the time step is determined as:

$$\Delta t = \frac{C}{N} \frac{\lambda}{c_{x_1} + c_{x_2}} \tag{18}$$

Since the simulation concerns SAWs propagation, we take $c_{x_2} = 0$, so that

$$\Delta t = \frac{C}{N} \frac{1}{f_0} \tag{19}$$

where f_0 is the first eigenfrequency of the SAW unit cell. In particular, since the IDTs are periodic, f_0 is obtained performing a modal analysis of a small portion of the SAW device with a length corresponding to the wavelength λ and forcing suitable periodic boundary conditions and deformations in the FE model.

3 EXPERIMENTAL WORK

SAWs are generated in the piezoelectric GaAs layer using IDTs where each finger is connected to an electric terminal. Width and spacing of the fingers are determined to achieve a center eigenfrequency of IDTs equal to 360 MHz. Each finger is 2μm wide and 500μm long. The devices are fabricated by optical lithography. The substrate is a 2 inches GaAs wafer with 350μm thickness. The crystallographic direction is [110]. Once the fabrication is completed, the devices are connected to a printed circuit board (PCB) for radio frequency measurements. The sample is electrically bonded to the PCB with 25μm aluminum wires. The experimental setup is illustrated in Figure 3 and consists in a laptop connected to a signal generator and a spectrum analyzer, a PCB, the program Labview that spans the frequency range of interest and an oscilloscope.

4 RESULTS

4.1 BAND GAP

The first step of the analysis is the design of a PC with an optimized band gap around 360MHz. This frequency corresponds at the center value of the experimental device bandwidth. This result is achieved considering two different periodic structures obtained combining a soft matrix with a stiff inclusion. The first case consists in square periodic structures where the unit cell presents an

inner silicon core immersed in an epoxy matrix. The second case instead assumes that the PC is obtained using the same GaAs wafer employed to fabricate the SAW devices. Now GaAs represents the stiff inclusion while the matrix is substituted by the voids. However, the effect of the holes is modeled assuming a very soft matrix. Material properties are provided in Table 1. Combining

Table 1: Material properties of the unit cell.

Material	Elastic Modulus (GPa)	Poisson ratio	Density (kg/m3)
Silicon	160	0.27	2331
Epoxy	12	0.3	1180
GaAs	85.5	0.31	5320
Soft Matrix	2	0.3	1000

Comsol Software capabilities with a Matlab script, it is possible to solve Equation 10 spanning the full Brillouin zone, see Figure 2. The resulting final band structures of the PC are provided in Figure 4. For a silicon or GaAs based unit cell, L is equal respectively to 5.5μm and 2.0μm. Two different values of the filling factor η are considered for each configuration. It is clear that the desired values for the bandgap amplitude can be achieved by increasing the unit cell filling factor. Moreover it is noticed that the resulting geometrical configurations for the PCs are compatible with electron beam lithography manufacturing constraints.

4.2 SAW BURST

The SAW delay lines are made of a piezoelectric GaAs layer. There are two interdigital transducers on the opposite sides of the device: the first is the transmitter and the second is the receiver. A scheme of the position and shape of IDTs is provided in Figure 1. According to the experimental setup, the number N of IDT pairs used is 80. The distance d_{idt} between the input and output transducer is fix and equal to 1502μm. The distance between each pair of IDTs is half of the wavelength λ. Two possible situations are analyzed in detail. In the first case, we included wave absorbers in the model to simulate the spatial extension of the SAW delay lines in the longitudinal direction. This case study corresponds to the experimental one. In the second configuration, we assume that the propagating waves are fully confined in a cavity which length equals 351 λ, i.e. we inserted in the model reflective surfaces that simulate the existence of a barrier such as in presence of a PCs slab. In practise, there is no dispersion of the energy that is localized in a very small area where for example energy harvesters could be located. Dissipation is due to only very small mechanical and electrical damping factors. Material properties used in the analysis are provided in the Appendix where the constitutive tensor employed in the FE simulations is obtained performing the Rayleigh product between the fourth order constitutive tensor in the original coordinate system and the rotation tensor. This reference system change is necessary to solve the wave propagation problem only with a 2D model where the FE equations are solved referring to the crystallography direction [110]. It is noticed here that a fine mesh is used and simulation of a single burst for a time of 4000 ns requires around 1 week on a personal computer. The final goal of the transient dynamic simulation presented is to investigate wave propagation on the surface of a SAW delay line as well as to predict the output voltage measured by the terminal IDTs. First of all, we characterize the effect of damping on the signal amplitude. Figure 5 shows the results for ξ_1 equal to 0.1% and ξ_2 equal to 0.001%. Finally, in Figure 6, a comparison between the experimental output voltage curve (for a device with 80 IDTs) and the numerical prediction is provided. It is evident that the FE model predicts correctly the wave speed propagation in the piezoelectric layer and capture qualitatively the multiple transit effects due to partial reflections of the waves with the IDTs. However, it is

noticed a delay in the post peak response between the experimental and numerical curve, which is probably due to three dimensional effects that the 2D simulation can not reproduce. The effects of SAWs propagation in a cavity are depicted in Figure 7, which clarifies the possible confinement of the energy within phononic crystal barriers (in fact, the voltage is less than 3 mV in Figure 6 after $5 * 10^{-6}$ seconds while in Figure 7 we obtain values around 2–3 times higher after $7 * 10^{-6}$ seconds).

5 CONCLUSIONS

Simulation with high accuracy of wave propagation on piezoelectric materials and in presence of PCs is a challenging problem with several engineering, medical and physical applications. In this paper we assessed the electromechanical response of SAWs propagating on a GaAs piezoelectric film using a simple IDTs configuration. The problem has been approached numerically and experimentally. Preliminary results have demonstrated that wave speeds and multiple transit effects are catched with high fidelity. This result combined with pulse echo techniques is fundamental to gain insight into physical properties of new engineered multi-functional composite materials. An important application of this study is the possibility to simulate and develop a new class of high sensitive SAW sensors. Future work will concern the characterization of the power capacity of nanowires or nanowalls structures grown directly on the piezoelectric layer where MHz or GHz vibrations can be scavenged. In fact, based on our numerical simulations, a relevant increase of energy confinement is assessed for a traveling SAW in a cavity.

6 APPENDIX

Since GaAs presents a cubic lattice, the elastic, piezoelectric and dielectric tensors according to Voigt notation read:

$$c_{ij} = \begin{pmatrix} c_{11} & c_{12} & c_{12} & 0 & 0 & 0 \\ c_{12} & c_{11} & c_{12} & 0 & 0 & 0 \\ c_{12} & c_{12} & c_{11} & 0 & 0 & 0 \\ 0 & 0 & 0 & c_{44} & 0 & 0 \\ 0 & 0 & 0 & 0 & c_{44} & 0 \\ 0 & 0 & 0 & 0 & 0 & c_{44} \end{pmatrix}, \tag{20}$$

$$e_{ij} = \begin{pmatrix} 0 & 0 & 0 & e_{14} & 0 & 0 \\ 0 & 0 & 0 & 0 & e_{14} & 0 \\ 0 & 0 & 0 & 0 & 0 & e_{14} \end{pmatrix}, \qquad \epsilon_{ij} = \begin{pmatrix} \epsilon_{11} & 0 & 0 \\ 0 & \epsilon_{11} & 0 \\ 0 & 0 & \epsilon_{11} \end{pmatrix}. \tag{21}$$

In order to study the dynamics on the surface perpendicular to (0,0,1), a new frame of reference with origin O' is introduced such that:

$$\mathbf{x} = \begin{pmatrix} x \\ y \\ z \end{pmatrix} = \begin{pmatrix} \frac{\sqrt{2}}{2} & -\frac{\sqrt{2}}{2} & 0 \\ \frac{\sqrt{2}}{2} & \frac{\sqrt{2}}{2} & 0 \\ 0 & 0 & 1 \end{pmatrix} \begin{pmatrix} x' \\ y' \\ z' \end{pmatrix} = \mathbf{R}\mathbf{x}' \tag{22}$$

Consequently, the new form of the material tensors in this frame of reference are:

$$c'_{ijkl} = R^{-1}_{im} R^{-1}_{nj} c_{mnpq} R_{pk} R_{ql}; \qquad e'_{kij} = R^{-1}_{im} R^{-1}_{nj} e_{lmn} R_{lk} \tag{23}$$

or in explicit form:

$$c'_{ij} = \begin{pmatrix} \frac{1}{2}(c_{11}+c_{12}+2c_{44}) & \frac{1}{2}(c_{11}+c_{12}-2c_{44}) & c_{12} & 0 & 0 & 0 \\ \frac{1}{2}(c_{11}+c_{12}-2c_{44}) & \frac{1}{2}(c_{11}+c_{12}+2c_{44}) & c_{12} & 0 & 0 & 0 \\ c_{12} & c_{12} & c_{11} & 0 & 0 & 0 \\ 0 & 0 & 0 & c_{44} & 0 & 0 \\ 0 & 0 & 0 & 0 & c_{44} & 0 \\ 0 & 0 & 0 & 0 & 0 & \frac{1}{2}(c_{11}-c_{12}) \end{pmatrix}, \tag{24}$$

$$e'_{ij} = \begin{pmatrix} 0 & 0 & 0 & 0 & e_{14} & 0 \\ 0 & 0 & 0 & -e_{14} & 0 & 0 \\ e_{14} & -e_{14} & 0 & 0 & 0 & 0 \end{pmatrix}, \tag{25}$$

$$\epsilon'_{ij} = \begin{pmatrix} \epsilon_{11} & 0 & 0 \\ 0 & \epsilon_{11} & 0 \\ 0 & 0 & \epsilon_{11} \end{pmatrix}. \tag{26}$$

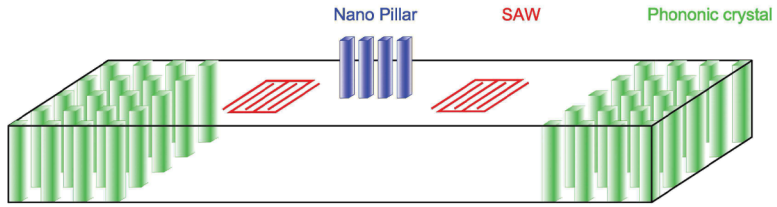

(a) Nanopillar

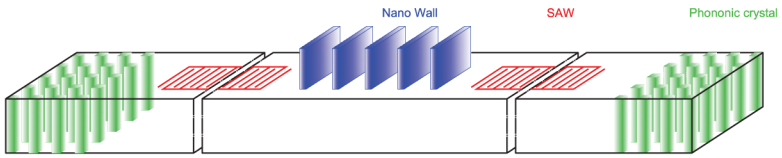

(b) Nanowalls

Figure 1: Multi-functional device structure.

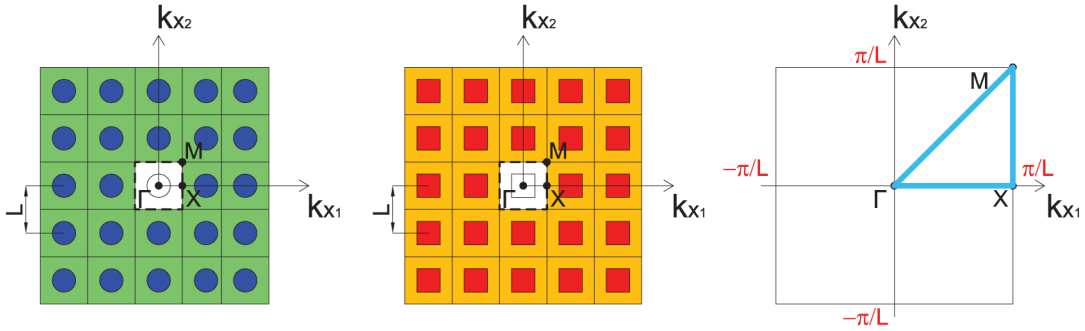

Figure 2: Irriducible Brillouin zone.

ACKNOWLEDGEMENTS

Claudio Maruccio acknowledges the support from the Italian MIUR through the project FIRB Futuro in Ricerca 2010 *Structural mechanics models for renewable energy applications* (RBFR107AKG).

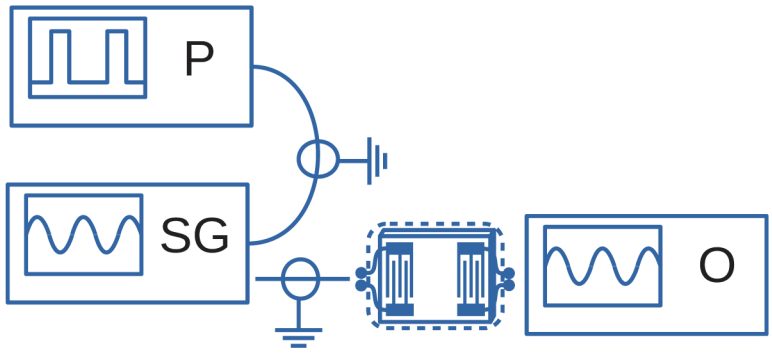

Figure 3: Layout of the SAW device measurement setup: the software Labview installed on a laptop controls the signal generator in input (SG) and the spectrum analyzer in output (SA).

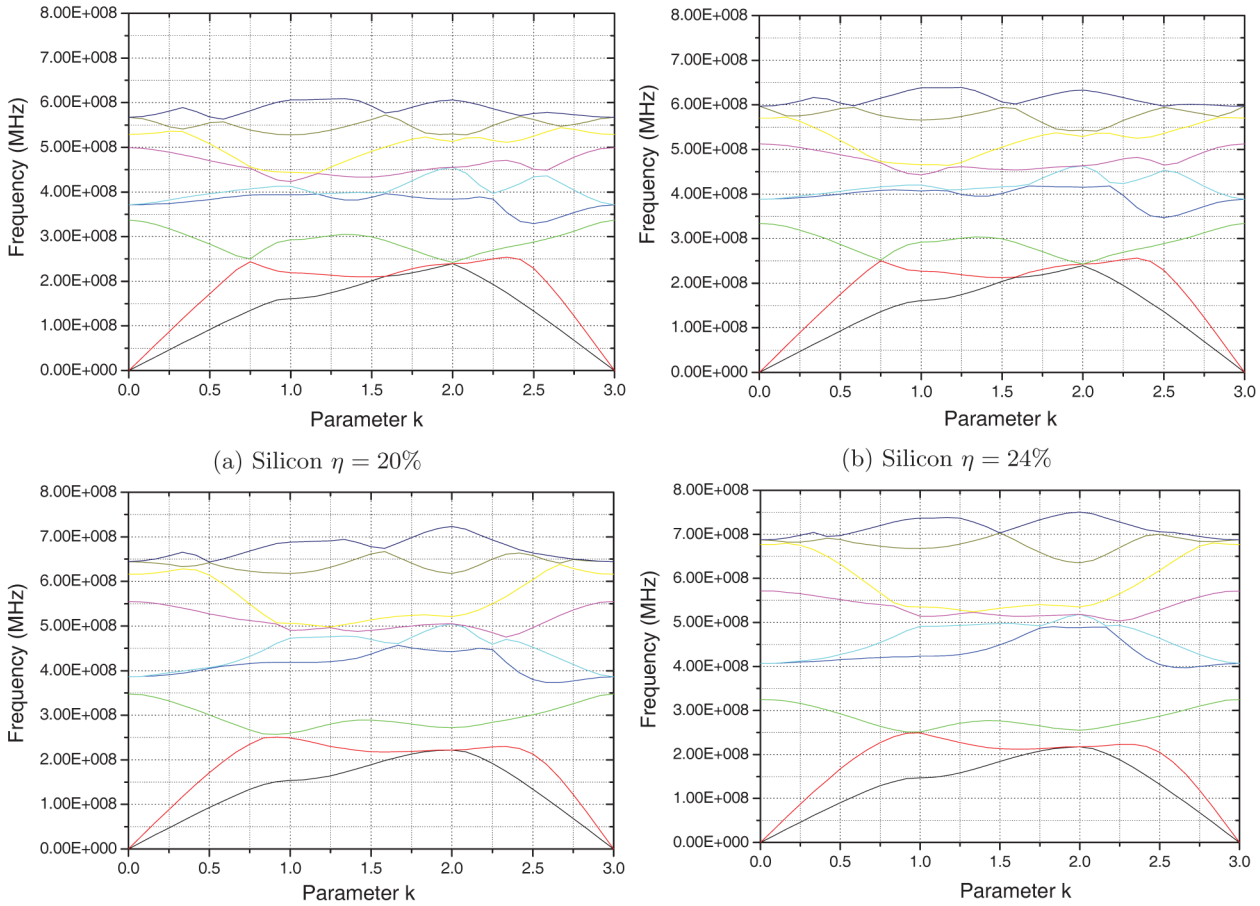

(a) Silicon $\eta = 20\%$

(b) Silicon $\eta = 24\%$

(c) GaAs $\eta = 15\%$

(d) GaAs $\eta = 20\%$

Figure 4: Resulting phononic crystal band structures

References

[1] Rizzato S., Scigliuzzo M., Chiriaco M.S., Scarlino P., Monteduro A.G., Maruccio C., Tasco V. and Maruccio G., 2017, Achieving GHz regime on GaAs with harmonic SAW devices by optical lithography, submitted.

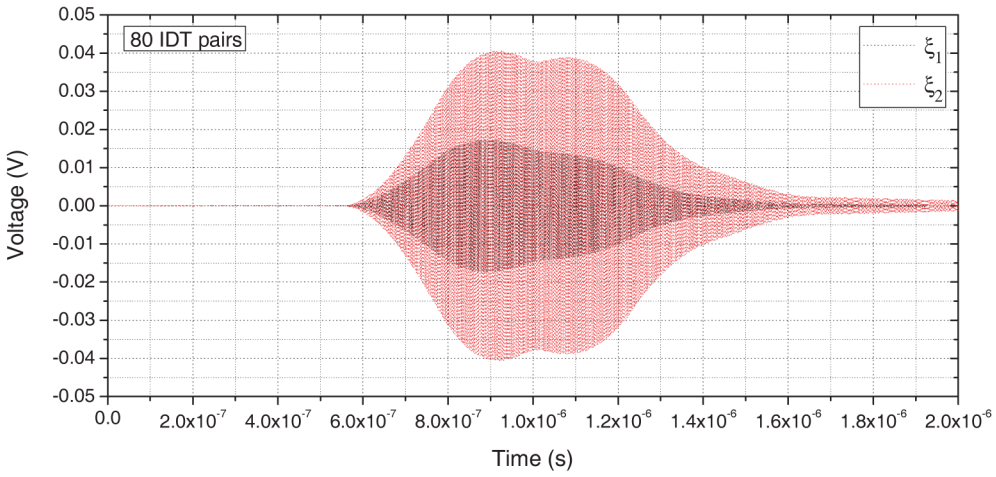

Figure 5: Influence of damping on the SAW response (80 IDTs case)

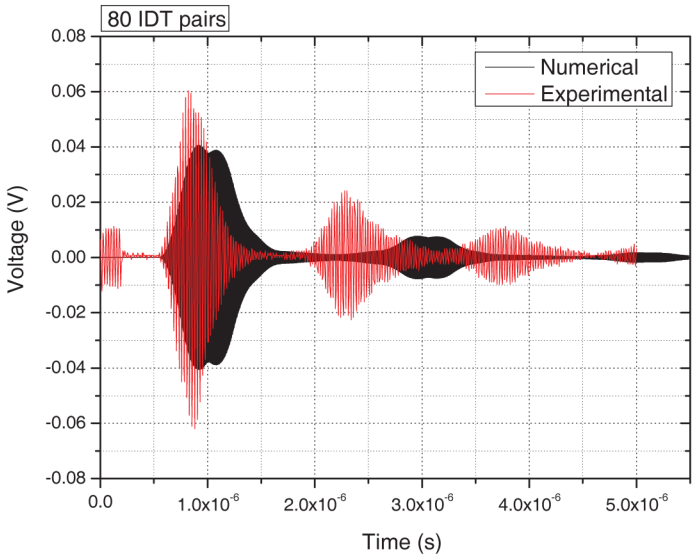

Figure 6: Comparison numerical vs experimental results.

[2] Broeker P., Luecke K., Perpeet M. and Gronewold T.M.A., 2012, A nanostructured saw chip based biosensor detecting cancer cells, Sensors and Actuators B: Chemical 165: pp. 1-6.

[3] Lin C. M., Wu T., Chen Y. and Chou T., 2015, Improved frequency responses of saw filters with interdigital transducers on zno/diamond/si layered structure, Journal of Mechanics, 23: pp. 253-259.

[4] Khelif A., Achaoui Y. and Aoubiza B., 2012, Surface acoustic waves in pillars-based two-dimensional phononic structures with different lattice symmetries, J. Appl. Phys., 112(033511): pp. 1-4.

[5] Malfanti I., Taschin. A., Bartolini P., Bonello B. and Torre R., 2011, Propagation of acoustic surface waves on a phononic surface investigated by transient reflecting grating spectroscopy, Journal of the Mechanics and Physics of Solids, 59, pp. 2370-2381.

[6] Gonella S., To A., Liu W.K., 2009, Interplay between phononic bandgaps and piezoelectric microstructures for energy harvesting, Journal of the Mechanics and Physics of Solids, Vol. 57,

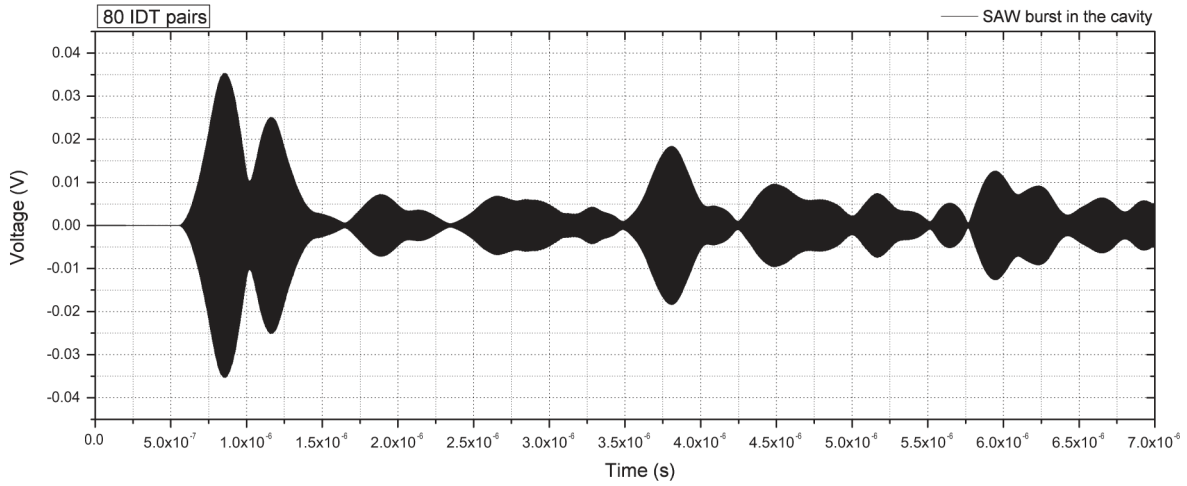

Figure 7: Simulation of SAW burst propagation in a cavity.

Iss. 3, pp. 621-633, ISSN 0022-5096.

[7] Yankin S., Talbi A., Du Y., Gerbedoen J.C., Preobrazhensky V., Pernod P. and Matar O.B., 2014, Finite element analysis and experimental study of surface acoustic wave propagation through two-dimensional pillar-based surface phononic crystal, Journal of Applied Physics, 115, 244508, doi: http://dx.doi.org/10.1063/1.4885460.

[8] Tian Y., Li Y., Ke Y., Yuan C. and He S., 2016, P-Matrix Analysis of Surface Acoustic Waves in Piezoelectric Phononic Crystals, IEEE Transactions on Ultrasonics, Ferroelectrics and Frequency Control, 63:5, pp. 757-763.

[9] Guo Y., Schubert M. and Dekorsy T., 2016, Finite element analysis of surface modes in phononic crystal waveguides, Journal of Applied Physics, 119:12.

[10] Assouar M.B. and Oudich M., 2011, Dispersion curves of surface acoustic waves in two-dimensional phononic crystal, Appl. Phys. Lett. 99, 123505, doi: http://dx.doi.org/10.1063/1.3626853.

[11] Li Y., Hou Z., Oudich M. and Assouar M.B., 2012, Analysis of surface acoustic wave propagation in a two-dimensional phononic crystal, Journal of Applied Physics 112, 023524, doi: http://dx.doi.org/10.1063/1.4740050.

[12] Hussein M., Leamy M.J. and Ruzzene M., 2014, Dynamics of Phononic Materials and Structures: Historical Origins - Recent Progress and Future Outlook, Appl. Mech. Rev., 66(4), 040802.

[13] Yankin S., Talbi A., Du Y., Gerbedoen J.C., Preobrazhensky V., 2014, Finite element analysis and experimental study of surface acoustic wave propagation through two dimensional pillar based surface phononic crystal, Journal of Applied Physics 115, 244508.

[14] Wu T.T., Hsu J.C., Sun J.H. and Benchabane S., 2016, Surface Acoustic Waves in Phononic Crystals, Chapter 6, Book: Phononic Crystals, pp. 145-189, Springer.

[15] Subramanian K.R.S. Sankaranarayanan, Venkat R. Bhethanabotla and Babu Joseph, 2010, Modeling of Surface Acoustic Wave Sensor Response, Chapter 4, Book: Sensors for Chemical and Biological Applications, CRC Press, pp. 97-134, ISBN: 978-0-8493-3366-8.

[16] Xu G. and Jiang Q., 2001, A Finite Element Analysis of Second Order Effects on the Frequency Response of a SAW Device, Journal of Intelligent Material Systems and Structures, Vol. 12, Iss. 2, pp. 69-77.
[17] Kabir K.M.M., Matthews G.I., Sabri Y.M., Russo S.P., Ippolito S.J. and Bhargava S.K., 2016, Development and experimental verification of a finite element method for accurate analysis of a surface acoustic wave device, Smart Materials and Structures, 25(3), 035040.
[18] Fu C., Lee K., Lee K., Yang S.S., Wang W., 2014, A stable and highly sensitive strain sensor based on a surface acoustic wave oscillator, Sensors and Actuators A: Physical, Vol. 218, pp. 80-87, ISSN 0924-4247.
[19] Laude V. and Khelif A., 2016, Computational Problems and Numerical Techniques for the Analysis of Phononic Crystals, Chapter 4, Book: Phononic Crystals, pp. 85-107, Springer.
[20] Kushwaha M.S., Halevi P., Dobrzynski L. and Djafari-Rouhani B., 1993, Acoustic band structure of periodic elastic composites, Phys. Rev. Lett., 71(13), pp. 2022-2025.
[21] Qian Z.H., Jin F., Li F.M. and Kishimoto K., 2008, Complete band gaps in two-dimensional piezoelectric phononic crystals with 1-3 connectivity family, Int. J. of Solids and Structures, Vol. 45, Iss. 17, pp. 4748-4755, ISSN 0020-7683.
[22] Wang Y.Z., Li F.M, Huang W.H., Jiang X., Wang Y.S. and Kishimoto K., 2008, Wave band gaps in two-dimensional piezoelectric/piezomagnetic phononic crystals, Int. J. of Solids and Structures, Vol. 45, Iss. 14-15, pp. 4203-4210, ISSN 0020-7683.
[23] Bigoni D., Guenneau S., Movchan A.B. and Brun M., 2013, Elastic metamaterials with inertial locally resonant structures: Application to lensing and localization, Phys. Rev. B, 87, 174303.
[24] Bigoni D. and Movchan A.B., 2002, Statics and dynamics of structural interfaces in elasticity, Int. J. of Solids and Structures, Vol. 39, Iss. 19, pp. 4843-4865, ISSN 0020-7683.
[25] IEEE Standard on Piezoelectricity, 1987. Vol. 176, ANSI/IEEE Std.
[26] Wu T., Wang W., Sun J.H., Hsu J.C. and Chen Y.Y., 2009, Utilization of phononic-crystal reflective gratings in a layered surface acoustic wave device, Appl. Phys. Lett. 94, 101913.
[27] Courant R., Friedrichs K., Lewy H., 1928, Über die partiellen Differenzengleichungen der mathematischen Physik, Mathematische Annalen, Vol. 100, n. 1, pp. 32-74.
[28] Smith I.M., Griffiths D.V., 1998, Programming the finite element method, John Wiley and Sons, New York.
[29] Zeng Q., Guo F., Yao L., Zhu H.W., Zheng L., Guo Z.X., Liu W., Chen Y., Guo S.S. and Zhao X.Z., 2011, Milliseconds mixing in microfluidic channel using focused surface acoustic wave, Sensors and Actuators B, 160, pp. 1552-1556.
[30] Gustafsson M.V., Aref T., Kockum A.F., Estrom M.K., Johansson G. and Delsing P., 2014, Propagating phonons coupled to an artificial atom, Science, Vol. 346, Issue 6206, pp. 207-211.
[31] Kanno Y., Tsuruta K., Fujimori K., Fukano H. and Nogi S., 2014, Phononic-Crystal Acoustic Lens by Design for Energy-Transmission Devices, Electronics and Communications in Japan, Vol. 97, No. 1.
[32] Sun J.H. and Wu T., 2006, Propagation of surface acoustic waves through sharply bent two-dimensional phononic crystal waveguides using a finite-difference time-domain method, Physical Review B, 74, 174305.
[33] Bathe K.J., 1982, Finite Element Procedures in Engineering Analysis, Prentice-Hall.

VIII ECCOMAS Thematic Conference on Smart Structures and Materials
SMART 2017
A. Güemes, A. Benjeddou, J. Rodellar and J. Leng (Eds)

FINITE ELEMENT SIMULATION OF LITHIUM NIOBATE BASED SURFACE ACOUSTIC WAVE DELAY LINES FOR PRESSURE AND TEMPERATURE SENSING.

H. CHAMBON*, P. NICOLAY*, G. BRUCKNER* AND A. BENJEDDOU†+

*Carinthian Tech Research, CTR AG
Europastraße 12, 9524 Villach, Austria
e-mail: hugo.chambon@ctr.at

† Sorbonne Universités, Université de Technologie de Compiègne,
CNRS, UMR 7337 ROBERVAL
Centre de Recherche Royallieu, CS 60319, 60203 Compiègne CEDEX, France

+ SUPMECA, 3 rue Fernand Hainaut, 93407 Saint Ouen CEDEX, France

Key words: Surface acoustic wave, sensors, finite element simulation, sensitivity.

Abstract. This paper focuses on the contribution of the Finite Element Method (FEM) to the design of a complete Surface Acoustic Wave (SAW) sensor. In SAW sensor design, FEM is especially used to compute the effect of the quantity we would like to measure (called measurand) on the SAW velocity.

As the wave propagation time is much lower than the typical time constant of the phenomenon we would like to observe, it is possible to conduct this simulation in three steps.

In a first step, a FEM study of the whole sensor (including the housing) is carried out in order to compute the temperature, stress and strain fields generated in the sensor's sensitive area by the measurand.

In a second step, a dynamic electro-mechanical study of the device including the InterDigital Transducer (IDT) used to generate and pick up the waves, is performed. This simulation takes into account the precomputed stress, strain and temperature fields. It is therefore possible to compute the sensor's sensitivity to the measurand. This model takes advantage of the periodicity of the IDT structure to compute phenomenological parameters, namely Coupling Of Mode (COM) parameters, which can later on be used to calculate the electrical response of the sensor (step 3).

The two first steps of this process are illustrated using a sensor based on a 2.45 GHz Lithium Niobate ($LiNbO_3$) delay line developed at CTR.

1 INTRODUCTION

Surface acoustic wave (SAW) devices use interdigital transducers (IDT, comb shaped electrodes) to generate waves at the surface of a piezoelectric substrate. The velocity of the generated

waves changes with the surface state (stress and strain, mass deposition or temperature), which makes it possible to use these devices as sensors by arranging the IDTs in delay lines or resonator structures. Due to their simplicity, it is possible to build robust SAW sensors. In addition, their passiveness and capability to be interrogated wirelessly make them good candidates for harsh environment sensing applications. They are therefore of potential interest for structural health monitoring [1].

An accurate finite element simulation of such devices is of interest when it comes to reducing their development time and improving their sensitivity. However, due to the high aspect ratio of the device (the whole sensor is usually in the millimeter range while a single finger of an IDT is in the micrometer range), the simulation of a whole device using the finite element method (FEM) would be too time consuming. That is why the simulation of a whole SAW sensor should be carried out in three steps which is made possible because the effect to measure is slow compared to the wave propagation phenomenon. In a first step, the effect of the measurand (in terms of temperature, strain and stress fields) is computed along the propagative path of the sensor. It is possible here to take the influence of the sensor housing into account. In a second step, the so-called coupling of mode (COM) parameters are extracted from the simulation of a simplified infinite grating of electrodes [2, 3]. These phenomenological parameters are computed for all the surface states present in the acoustic path (i.e. IDT, reflector gratings, free surface...). They can already be used to compute the sensitivity of the sensor with respect to temperature, strain and stress. Finally, in a third step, the frequency response of the whole device can be computed using the obtained sets of COM parameters and the device geometry (position and number of electrodes, aperture...). A complete description of this method can be found in [1].

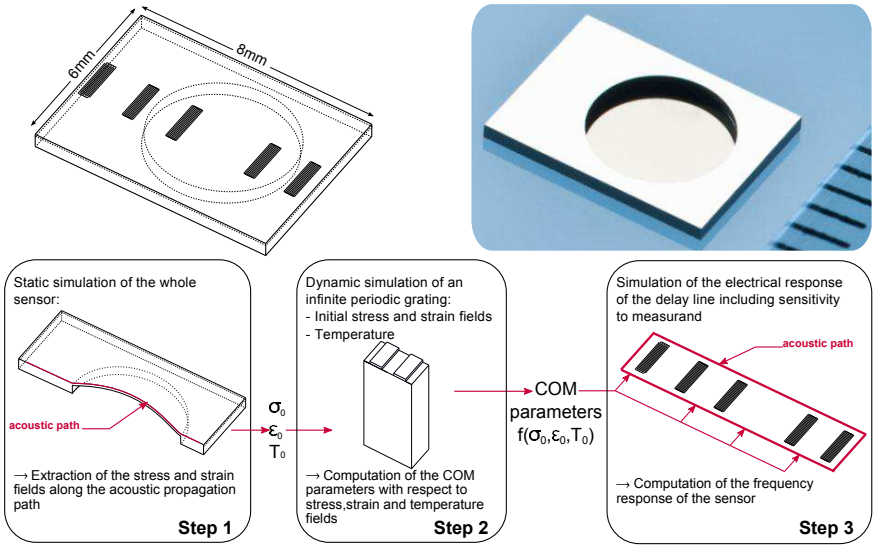

Figure 1: Illustration of the simulation process applied to a CTR pressure sensor

This paper focuses on the two first steps since they are sufficient to compute the sensor's sensitivity. They are illustrated in this paper using a CTR sensor as an example. This sensor is aimed at detecting changes in intra-cranial pressure. It is made of a thin membrane which

is deformed under pressure. This deformation generates stress and strain fields that affect the wave velocity. The sensitivity of the sensor to pressure and temperature has been computed. It is compared to experimental results, at the end of section 4. In our case, the computation of the "free surface" wave velocity is sufficient to calculate the sensor's sensitivity. However, the whole set of COM parameters have been computed to illustrate the general computation procedure, as described above.

2 COUPLING OF MODE THEORY (A SUMMARY)

The COM model makes it possible to simulate SAW devices in an efficient way. Nevertheless, the accuracy of the model depends on its parameters (the so-called COM parameters). COM parameters can be determined experimentally. It is, however, a tedious procedure. For this reason, it is advantageous to extract them from a numerical model.

The determination of the COM parameters results from an analysis of the behavior of waves propagating in an infinite grating. The main parameters of such a grating are illustrated in figure 2 (p is the pitch, W is the aperture, h and a are respectively the electrode thickness and width).

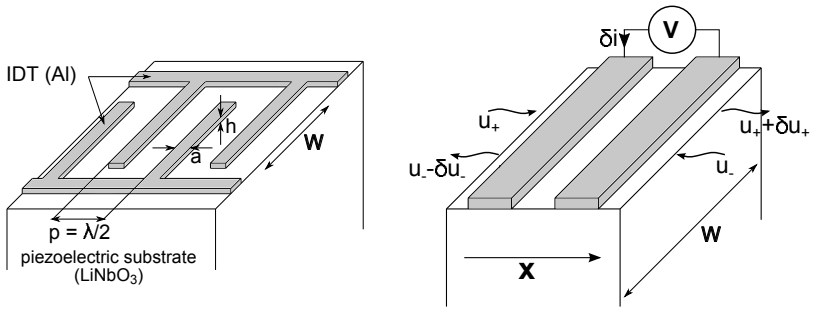

Figure 2: Schematic of an IDT (left) and model used to extract COM parameters (right).

The COM theory considers two mechanical waves u_+ and u_- propagating respectively in the positive and negative directions. When traveling through the grating, these waves can reflect and contribute to the propagation in the opposite directions. The COM model considers only the reflection of the first harmonic. It also assumes that the amplitudes may decrease due to attenuation and that there is a linear transduction coefficient due to piezoelectricity. This leads to the following equations [2, 3]:

$$\frac{du(x)_+}{dx} = -j(\frac{\omega}{v_{SAW}} - j\gamma)u_+(x) - j\kappa_{12}u_-(x)e^{-j2\pi x/p} + j\zeta V e^{-j\pi x/p} \quad (1)$$

$$\frac{du(x)_-}{dx} = j\bar{\kappa_{12}}u_+(x)e^{j2\pi x/p} + j(\frac{\omega}{v_{SAW}} - j\gamma)u_-(x) - j\bar{\zeta}Ve^{j\pi x/p} \quad (2)$$

$$\frac{dI(x)}{dx} = -2j\bar{\zeta}u_+(x)e^{j\pi x/p} - 2j\zeta u_-(x)e^{-j\pi x/p} + j\omega CV \quad (3)$$

Where v_{SAW} (m/s) is the SAW velocity , $\gamma(m^{-1})$ is the attenuation , κ_{12} $(\%/m)$ is the reflection coefficient, ζ $(\Omega^{-1/2})$ is the transduction coefficient and C $(F/period)$ is the capacitance.

Assuming that the waves are $2p$-periodic:

$$u_+(x) = R(x)e^{-j\pi x/p} \tag{4}$$

$$u_-(x) = S(x)e^{j\pi x/p} \tag{5}$$

This yields, after substitution in equations (1-3), the COM equation :

$$\begin{Bmatrix} \frac{dR(x)}{dx} \\ \frac{dS(x)}{dx} \\ \frac{dI(x)}{dx} \end{Bmatrix} = \begin{bmatrix} -j\theta_u & -j\kappa_{12} & j\zeta \\ j\bar{\kappa_{12}} & j\theta_u & -j\bar{\zeta} \\ -2j\bar{\zeta} & -2j\zeta & j\omega C \end{bmatrix} \begin{Bmatrix} R(x) \\ S(x) \\ V(x) \end{Bmatrix} \tag{6}$$

In this matrix, $\theta_u = \frac{\omega}{v_{SAW}} - \frac{\pi}{p} - j\gamma$ (rad/m) is the detuning factor. The behavior of the system can be fully described using the five COM parameters (v_{SAW}, κ_{12}, ζ, C, γ). These parameters are determined from the simulation of an infinite periodic grating, using different electrical boundary conditions, as described in details in [2, 3].

2.1 Short circuit behavior

When considering no attenuation ($\gamma = 0$), the equations system (6) under short-circuit (SC) conditions (i.e. $V = 0$) corresponds to an homogeneous system. The grating behaves like if there are no electric field and transduction ($\zeta = 0$) :

$$\begin{Bmatrix} \frac{dR(x)}{dx} \\ \frac{dS(x)}{dx} \end{Bmatrix} = \begin{bmatrix} -j\theta_u & -j\kappa_{12} \\ j\bar{\kappa_{12}} & j\theta_u \end{bmatrix} \begin{Bmatrix} R(x) \\ S(x) \end{Bmatrix} \tag{7}$$

We look for solutions of the form:

$$\begin{Bmatrix} R(x) \\ S(x) \end{Bmatrix} = \begin{Bmatrix} R_0 \\ S_0 \end{Bmatrix} e^{jqx} \tag{8}$$

Substituting the solution in (7), we get this system :

$$\begin{bmatrix} -j\theta_u - jq & -j\kappa_{12} \\ j\bar{\kappa_{12}} & j\theta_u - jq \end{bmatrix} \begin{Bmatrix} R_0 \\ S_0 \end{Bmatrix} = \{0\} \tag{9}$$

Which has non-zero solutions only if the matrix determinant is zero:

$$\theta_u{}^2 - q^2 - |\kappa_{12}|^2 = 0 \tag{10}$$

The general solutions are:

$$\begin{Bmatrix} R^{SC}(x) \\ S^{SC}(x) \end{Bmatrix} = A \begin{Bmatrix} 1 \\ \frac{jq-\theta_u}{\kappa_{12}} \end{Bmatrix} e^{-jqx} + B \begin{Bmatrix} \frac{jq-\theta_u}{\bar{\kappa_{12}}} \\ 1 \end{Bmatrix} e^{jqx} \tag{11}$$

Where A and B are constants determined by the boundary conditions and q is the wave number of the existing mode, given by:

$$q = \begin{cases} \pm\sqrt{\theta_u{}^2 - |\kappa_{12}|^2} & \text{if } \theta_u{}^2 > |\kappa_{12}|^2 \\ \pm j\sqrt{|\kappa_{12}|^2 - \theta_u{}^2} & \text{if } \theta_u{}^2 < |\kappa_{12}|^2 \end{cases} \tag{12}$$

Substituting the detuning factor (θ_u) in the dispersion relation (12) we find a quadratic polynomial equation in terms of frequency. The two solutions of this polynom are the two frequencies that define the stop band edges of the dispersion relation for the short circuit condition:

$$f_{SC}^{\pm} = \frac{v_{SAW}}{\lambda}(1 \pm \frac{\lambda|\kappa_{12}|}{2\pi}) \tag{13}$$

The average of these two frequencies and their difference give the SAW velocity and the reflection coefficient:

$$v_{SAW} = \lambda\frac{f_{SC}^{+} + f_{SC}^{-}}{2} \text{ and } |\kappa_{12}| = \frac{\pi}{v_{SAW}}(f_{SC}^{+} - f_{SC}^{-}) \tag{14}$$

2.2 Open grating behavior

In open grating (OG) condition, the current is zero. Thus, the third line in (6) gives an expression of the voltage [2, 3]:

$$V = \frac{2}{C\omega}(\bar{\zeta}R(x) + \zeta S(x)) \tag{15}$$

Substituting this in the first two lines of equation (6) yields:

$$\begin{Bmatrix} \frac{dR(x)}{dx} \\ \frac{dS(x)}{dx} \end{Bmatrix} = \begin{bmatrix} -j(\theta_u - \frac{2|\zeta|^2}{C\omega}) & -j(\kappa_{12} - \frac{2\zeta^2}{C\omega}) \\ j(\bar{\kappa_{12}} - \frac{2\bar{\zeta}^2}{C\omega}) & j(\theta_u - \frac{2|\zeta|^2}{C\omega}) \end{bmatrix} \begin{Bmatrix} R(x) \\ S(x) \end{Bmatrix} \tag{16}$$

A non-trivial solution exists if the matrix determinant is zero:

$$(\frac{2\pi f}{v_{SAW}} - \frac{\pi}{p} - \frac{2|\zeta|^2}{C\omega})^2 - |\kappa_{12} - \frac{2\zeta}{C\omega}|^2 = 0 \tag{17}$$

This gives the two following solutions :

$$f_{OG}^{\pm} = \frac{v_{SAW}}{2\pi}(\frac{\pi}{p} + \frac{2|\zeta|^2}{C\omega} \pm |\kappa_{12} - \frac{2\zeta^2}{C\omega}|) \tag{18}$$

These two frequencies define the stop band edges in open grating condition. In addition, we can assume that the coupling and transduction coefficients are real [2]. Then, subtracting the two stop band frequencies for the open grating condition yields:

$$f_{OG}^{+} + f_{OG}^{-} = \frac{v_{SAW}}{\pi}(\frac{\pi}{p} + \frac{2|\zeta|^2}{C\omega}) \tag{19}$$

Therefore, from the latter and the first of (14), we get the relation between ζ and C:

$$\frac{2|\zeta|^2}{\pi C\omega} = \frac{(f_{OG}^{+} + f_{OG}^{-}) - (f_{SC}^{+} + f_{SC}^{-})}{v_{SAW}} \tag{20}$$

We need another relation between ζ and C to determine them. This can be obtained from the harmonic admittance of the IDT.

2.3 Harmonic admittance

To determine the harmonic admittance in the case of no attenuation ($\gamma = 0$), we apply a harmonic driving voltage [2, 3]. Since the potential on the electrode fingers does not depend on the position x, a particular solution of the mechanical equations (first two lines) in (6) has the form:

$$\begin{Bmatrix} \tilde{R}(x) \\ \tilde{S}(x) \end{Bmatrix} = \begin{Bmatrix} A_+ \\ A_- \end{Bmatrix} V \tag{21}$$

Substituting this in the first two lines of (6) provides:

$$\frac{dA_+V}{dx} = -j\theta_u A_+ V - j\kappa_{12} A_- V + j\zeta V \tag{22}$$

$$\frac{dA_-V}{dx} = j\bar{\kappa_{12}} A_+ V + j\theta_u A_- V - j\bar{\zeta} V \tag{23}$$

Since $\frac{dV}{dx} = 0$ and after simplification by V we get:

$$\begin{bmatrix} -j\theta_u & -j\kappa_{12} \\ j\bar{\kappa_{12}} & j\theta_u \end{bmatrix} \begin{Bmatrix} A_+ \\ A_- \end{Bmatrix} = \begin{Bmatrix} -j\zeta \\ j\bar{\zeta} \end{Bmatrix} \tag{24}$$

Inverting this system, yields $\begin{Bmatrix} A_+ & A_- \end{Bmatrix}$. Thus, the solutions (21) become:

$$\begin{Bmatrix} \tilde{R}(x) \\ \tilde{S}(x) \end{Bmatrix} = \frac{1}{{\theta_u}^2 - |\kappa_{12}|^2} \begin{Bmatrix} \theta_u\zeta - \kappa_{12}\bar{\zeta} \\ \theta_u\bar{\zeta} - \bar{\kappa_{12}}\zeta \end{Bmatrix} V \tag{25}$$

Substituting further this solution in the third line of (6) yields the harmonic admittance:

$$Y(f) = \frac{dI/dx}{V} = -2j\frac{2\theta_u|\zeta|^2 - 2\mathrm{Re}(\bar{\kappa_{12}}\zeta^2)}{\theta_u^2 - |\kappa_{12}|^2} + j2\pi fC \tag{26}$$

This harmonic admittance shows a resonance and an anti-resonance at two different frequencies. After substituting the already known COM parameters (v_{SAW}, κ_{12}, $\zeta(C)$), it becomes possible to extract the capacitance (C) by fitting the simulated harmonic admittance using equation (26).

3 FEM SIMULATION OF AN INFINITE PERIODIC GRATING ON $LiNbO_3$

Simulation of the infinite periodic grating can be done using COMSOL Multiphysics® [4]. The model is implemented in 3D. From this model, COM parameters can be extracted using specific boundary conditions reproducing the three configurations (short circuit, open grating, harmonic admittance), described in the previous section.

3.1 Geometry

It is possible to reduce the model geometry to a pair of fingers, using periodic boundary conditions on potential and displacement. In addition, as the aperture of the device is considered infinite, it can be (in the model) reduced to a fraction of the wavelength by using periodic boundary conditions. The substrate thickness is also reduced to a few wavelengths, using a perfectly

matched layer (PML) placed at the bottom of the substrate [5]. This PML avoids reflections of acoustics modes at the bottom of the substrate. An air layer is also taken into account above the substrate. Nevertheless, $LiNbO_3$ has a high permittivity. Thus, air is expected to have a relatively weak influence on the results. The resulting model is often called "unit cell model". It is shown in figure 3.

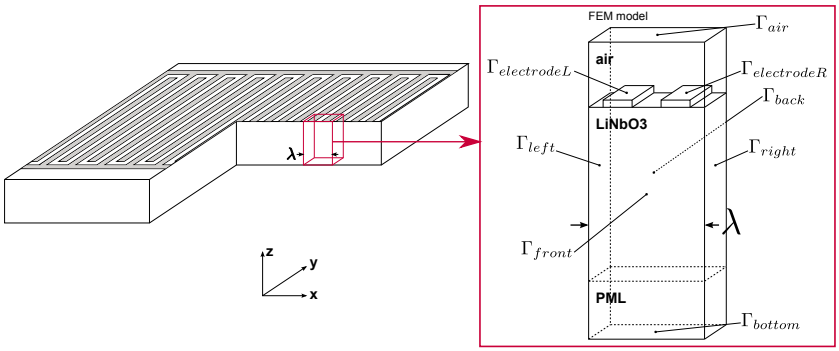

Figure 3: Comsol FEM model of an infinite periodic grating

3.2 Physics and boundary conditions

As the electrodes have a high conductivity compared to the piezoelectric substrate or air layer, their conductivity is assumed to be infinite. Consequently, electrodes are not simulated from an electrostatic point of view. Also, the air layer is supposed to have no stiffness or mass. As a result, the mechanical equation is not solved in the air layer. The electromechanical behavior of the piezoelectric material is described by the following equations that couple the stress σ and the strain S to the electrical field E and to the electric displacement field D:

$$\begin{aligned} \sigma_{ij} &= c^E_{ijkl} S_{kl} - e_{kij} E_k \quad i,j,k,l = 1,2,3 \\ D_i &= e_{ikl} S_{kl} + \epsilon^S_{ik} E_k \end{aligned} \tag{27}$$

Where c^E is the short circuit stiffness matrix, e is the stress piezoelectric matrix, and ϵ is the blocked permittivity matrix. The constants used in this study are presented in [6]. In addition, assuming small displacements, the strains are $S_{kl} = \frac{1}{2}(u_{k,l} + u_{l,k})$, and $E_k = -V_{,k}$. Thus the mechanical and electrostatic equations are (in absence of body and surface charges and body force):

$$\rho \ddot{u}_j = \sigma_{ij,i} \qquad \text{or} \quad \rho \ddot{u}_j = c^E_{ijkl} u_{k,li} + e_{kij} V_{,ki} \tag{28}$$

$$0 = D_{i,i} \qquad 0 = e_{ikl} u_{k,li} - \epsilon^S_{ik} V_{,ki} \tag{29}$$

The boundary conditions used for the electrostatic and mechanical equations are detailed in Table 1.

The model is also able to compute the COM parameters for an initially pre-stressed structure. Under the assumption that the displacement causing the waves is small compared to the initial displacement responsible for the pre-stress field (σ^0), the mechanical equation becomes [7]:

$$\rho \ddot{u}_j = c^E_{ijkl} u_{k,li} + e_{kij} V_{,ki} + \sigma^0_{ik} u_{j,ki} \quad j = 1,2,3 \tag{30}$$

Table 1: Electrostatic and Mechanical boundary conditions

	Electrostatic			
Boundary	Short circuit	Open grating	Harmonic admittance	Mechanical
Γ_{left},Γ_{right}		$V_{\Gamma_{left}} = V_{\Gamma_{right}}$		$u_{i\Gamma_{left}} = u_{i\Gamma_{right}}$
Γ_{front},Γ_{back}		$V_{\Gamma_{front}} = V_{\Gamma_{back}}$		$u_{i\Gamma_{front}} = u_{i\Gamma_{back}}$
Γ_{air}		free		N.A.
Γ_{bottom}		$V = 0$		$u_i = 0$
$\Gamma_{electrodeR}$	$V = 0$	$\int D_i.n_i \, \mathrm{d}S = 0$	$V = cos(\omega t)$	$\sigma_{ij}.n_i = 0$
$\Gamma_{electrodeL}$	$V = 0$	$\int D_i.n_i \, \mathrm{d}S = 0$	$V = 0$	$\sigma_{ij}.n_i = 0$

In addition, to consider the effect of the initial strain on the material stiffness and density, the stiffness tensor and the density must be modified according to their respective sensitivity to the applied strain [8].

3.3 Material data

The effect of initial strain on the stiffness constants is described as follows (linear dependency):

$$\tilde{c}^E_{pq} = c^E_{pq} + c_{pqr} S_r \quad i, p, q, r = 1, ..., 6 \tag{31}$$

The constants c_{ijk} are called third-order stiffness coefficients. They are determined experimentally [9]. They are generally presented in a $6 \times 6 \times 6$ matrix. However, due to crystal symmetries, only a few coefficients are needed to depict the entire matrix. In the case of $LiNbO_3$, 14 coefficients are sufficient. Besides, the strain field affects the density. The change in density is directly proportional to the change in volume:

$$\Delta\rho = \frac{\rho_- \rho_0}{\rho_0} = -\frac{V - V_0}{V} \approx -(S_{xx} + S_{yy} + S_{zz}) \tag{32}$$

The effect of temperature is easier to consider since it only affects material parameters. Assuming that the material properties are linearly dependent on the temperature variation (ΔT), we get:

$$[\tilde{c}^E_{pq}] = c^E_{pq}(1 + TC(c^E_{pq}) \times \Delta T) \tag{33}$$

$$[\tilde{e}_{ip}] = e_{ip}(1 + TC(e_{ip}) \times \Delta T) \tag{34}$$

$$[\tilde{\epsilon}^S_{ij}] = \epsilon^S_{ij}(1 + TC(\epsilon^S_{ij}) \times \Delta T) \tag{35}$$

The temperature dependent coefficients (TC) are determined experimentally and are well known for $LiNbO_3$ [10].

3.4 Mesh

The structure is meshed using prismatic elements with a quadratic interpolation. The mesh has been refined close to the electrode edges to better consider the singularity in charge that

occurs there. In addition, the elements become coarser along the depth of the substrate to follow the attenuation of the Rayleigh wave. An example of the mesh used for this study can be seen in figure 4. This particular mesh has 2095 elements and 34602 nodes. The mesh has been refined iteratively, thus increasing the number of degrees of freedom (nDOF) to ensure a proper convergence of the solution. The convergence is monitored taking the COM parameters as figures of merit (see figure 4).

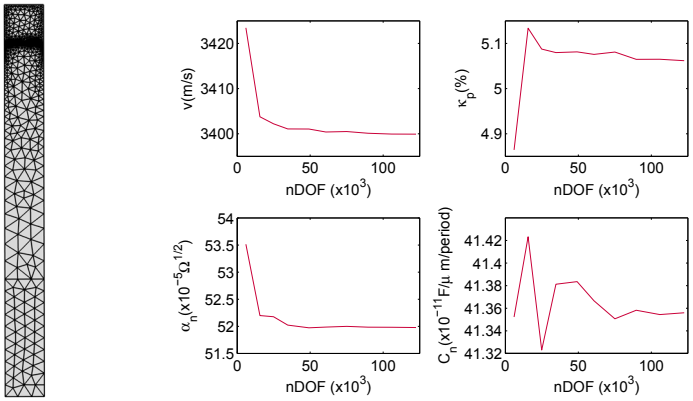

Figure 4: Example of mesh with 2095 elements and 34602 DOF (left), variation of the COM parameters according to the nDOF (right).

4 RESULTS

The methodology described above has been tested on a sensor that is currently in development at CTR (see figure 1). This implantable device can detect very low pressure variation in the liquid surrounding the brain. It can also sense temperature. It is made of a thin $LiNbO_3$ circular membrane deposited on a silicon substrate. The acoustic track (the path where the acoustic waves travel) is oriented along the crystallographic Z axis. The sensitivity of the sensor to pressure and temperature can be computed and compared to the experimental results.

4.1 Simulation of the sensor's sensitivity to pressure

To determine the sensor's sensitivity to pressure only, the simulation is carried out at the reference temperature T_0 (in our case, $T_0 = 20°C$). When the membrane is deformed under pressure, the generated strain and stress fields affect the wave propagation. As a first step, the whole sensor is simulated in static state, without considering the acoustic phenomena. Taking advantage of symmetries in material, geometry and load, only one forth of the sensor is modeled. The boundary conditions are illustrated in figure 5.

From this simulation, the stress and strain fields are extracted along the acoustic path. The acoustic path is divided into two sections designed to optimize the sensor sensitivity (see figure 5). Since we consider only a linear effect of the perturbation field on the material properties, only the average values over the section lengths of the fields are taken as inputs for the computation of the COM parameters. We summarize in Table 2 the obtained COM parameters, for the two

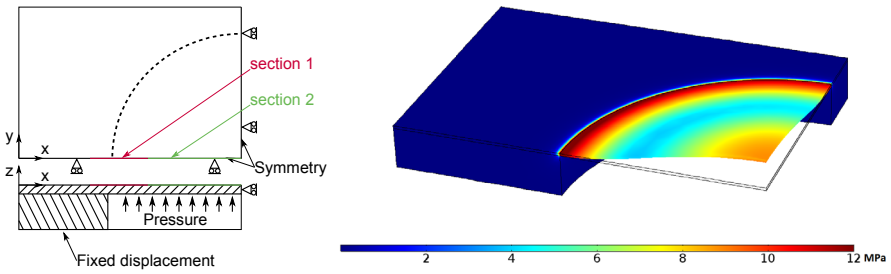

Figure 5: Model for the static simulation of the entire sensor (left). Representation of the Von Mises stress (MPa) over the structure for a $3000Pa$ applied pressure (right).

sections, when a $3000Pa$ pressure is applied on the membrane. For comparison purposes, we also computed the initial state, where no pressure is applied.

Table 2: COM parameters in initial state and under $3000Pa$ load. The initial state values are identical for section 1 and 2.

Normalized parameter	Initial state unloaded	Section 1 loaded	Section 2 loaded	Unit
v_{SAW}	3432.907	3432.435	3432.230	m/s
$\kappa_p(=\lambda\kappa_{12})$	3.271	3.227	3.226	%
$\zeta_n(=\zeta\lambda^{3/2}/W^{1/2})$	53.713	53.625	53.528	$10^{-5}\times\Omega^{-1/2}$
$C_n(=C\lambda/W)$	40.959	41.031	41.109	$10^{-11}\times F/\mu m/period$

As mentioned in introduction, the sensitivity (the change in phase due to the load) is computed from the velocity by using the equation:

$$\phi_{load} = \phi_0(1 + S - \frac{v - v_0}{v_0}) \tag{36}$$

Where ϕ_0 and v_0 are the initial phase and SAW velocity in the section (when no load is applied), S and v are respectively the deformation in the propagation direction and velocity in the loaded section. The sensitivity is compared to the experimental results (see figure 6, left).

4.2 Simulation of sensor's sensitivity to temperature only

The sensitivity to temperature is computed without any pressure applied. As the sensor is made of two different materials, strain and stress fields are generated when the sensor is heated up (bimorph effect). This affects the wave propagation conditions, in addition to the pure temperature effect itself. A static thermomechanical study can be carried out to determine the initial stress and strain fields due to the bimorph effect, using the same model as previously. The resulting fields are significant. They have the same magnitude as the one computed when applying pressure only (see figure 7).

Then the acoustic behavior can be computed using the unit cell model. The COM parameters were extracted for a temperature $T_1 = 30°C$. The parameters are given in Table 3 and compared to the COM parameters of a reference pure $LiNbO_3$ at the same temperature (T_1).

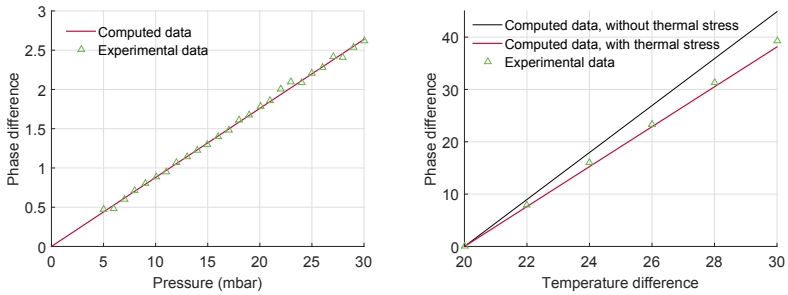

Figure 6: Comparison of the experimental and simulated sensitivities to pressure (left) and temperature (right)

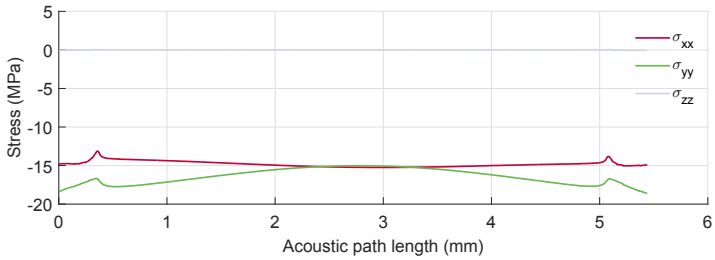

Figure 7: Stress in the principal directions over the acoustic path generated by a $10°C$ increase en temperature ($\sigma_{zz} = 0$).

Table 3: COM parameters for a $10°C$ increase in temperature.

Normalized parameter	Initial state at T_0	Section 1 at T_1	Section 2 at T_1	Pure $LiNbO_3$ at T_1	Unit
v_{SAW}	3432.907	3429.736	3429.765	3429.467	m/s
$\kappa_p (= \lambda\kappa_{12})$	3.271	3.2189	3.2189	3.218	%
$\zeta_n (= \zeta\lambda^{3/2}/W^{1/2})$	53.713	53.762	53.767	53.638	$10^{-5} \times \Omega^{-1/2}$
$C_n (= C\lambda/W)$	40.959	41.196	41.191	41.294	$10^{-11} \times F/\mu m/period$

These parameters (Tables 2 and 3) enable to compute the sensor's sensitivity to pressure and temperature taking the bimorph effect (thermal stress) into account. First of all, we can see that the pressure sensitivity is in almost perfect agreement with the experimental data. Concerning the temperature, the results demonstrate that taking the thermal stress into account improves the accuracy of the simulation. However, there is still a small discrepancy between computed and experimental data which could be explained by the unknown pre-stressed state of the membrane due to manufacturing process or to the inaccuracy of the third order material coefficients. It would also be interesting to study the effect of the certainly occurring buckling of the membrane when the temperature increases.

5 CONCLUSION

This paper reports on an efficient and accurate method to model SAW sensors using a finite element software. The method is demonstrated on a sensor sensitive to both pressure and temperature. The results obtained are compared to experimental measurements. They are accurate enough to enable further improvement of the sensor's design.

ACKNOWLEDGMENTS

This project has been partly supported by the COMET K1 centre ASSIC Austrian Smart Systems Integration Research Center. The COMET Competence Centers for Excellent Technologies program is supported by BMVIT, BMWFW and the federal provinces of Carinthia and Styria.

REFERENCES

[1] P. Nicolay, H. Chambon, and G. Brukner, Simulation of the properties and behavior of an implantable passive and wireless surface acoustic wave RFID tag, for structural health monitoring applications, *Proc. VIII ECCOMAS Thematic Conference on Smart Structures and Materials* SMART 2017.

[2] K. Hashimoto, Surface acoustic wave devices in telecommunications, *Springer*, 2000.

[3] V.P. Plessky and J. Koskela, Coupling-of-Modes Analysis of SAW Devices, *Int. J. Hi. Spe. Ele. Syst.* 10, 867 (2000).

[4] COMSOL Multiphysics, COMSOL AB, Stockholm, Sweden.

[5] K. Shaposhnikov, M. Kaltenbacher, and P. Nicolay, Fast Full-FEM Computation of COM Parameters. Application to Multilayered SAW Structures, *Proc. IEEE Ultrasonics Symp.* (2014)

[6] G. Kovacs, M. Anhorn, H. E. Engan, G. Visintini, and C.C.W. Ruppel, Improved material constants for $LiNbO_3$ and $LiTaO_3$, *Proc. IEEE Ultrasonics Symp.* (1990)

[7] V. V. Bolotin, Nonconservative problems of the theory of elastic stability. *Macmillan* (1963)

[8] A.L. Nalamwar and M. Epstein, Surface acoustic waves in strained media, *J. Appl. Phys.* 47(1), 43-48 (1976).

[9] Y. Cho and K. Yamanouchi, Nonlinear, elastic, piezoelectric, electrostrictive, and dielectric constants of lithium niobate, *J. Appl. Phys.* 61(3), 875-887 (1987).

[10] R.T. Smith and F.S. Welsh, Temperature dependence of the elastic, piezoelectric, and dielectric constants of lithium tantalate and lithium niobate, *J. Appl. Phys.* 42(6), 2219-2230 (1971).

VIII ECCOMAS Thematic Conference on Smart Structures and Materials
SMART 2017
A. Güemes, A. Benjeddou , J. Rodellar and Jinsong Leng (Eds)

SAW DELAY LINES AS WIRELESS SENSORS FOR INDUSTRIAL APPLICATIONS

GUDRUN BRUCKNER*, JOCHEN BARDONG*, ALFRED BINDER*, PASCAL NICOLAY*

* Carinthian Tech Research, CTR AG
Europastraße 12, High Tech Campus Villach
9524 Villach, Austria
e-mail: gudrun.bruckner@ctr.at ,web page: http://www.ctr.at

Key words: SAW, Implantable, Passive Wireless Sensors, Structural Health Monitoring.

Abstract. The paper gives a review on SAW (Surface Acoustic Wave) sensing applications and on the underlying sensing principles with the focus on reflective delay lines. SAW devices are used to detect physical quantities like temperature, pressure and strain and applied as RFID-tags (Radio Frequency IDentification), especially in harsh environments. We describe various wireless temperature sensors with and without ID functionality designed for different applications in steel industry like CMC (continuous mould casting), refractory slide gates and tagging of slag vessels as well as for the long range temperature reading of power lines. We also give an example for pressure measurements based on a membrane sensor design.

1 INTRODUCTION

SAW devices are for long known for their sensing capability [1]. The devices are made of piezoelectric substrates that allow surface acoustic waves to propagate along the surface. As described in [2], [3] the devices are connected to an antenna and interrogated by a reader system which works on a radar like principle. The devices are completely passive, they derive their required energy from the electromagnetic request signal and hence no power supply or batteries are needed for the operation on the sensor side. As the lifetime of the sensors is long and no maintenance is required they can be implanted into various materials provided the antenna is not shorted or shielded by metallic surroundings.

While the SAW devices themselves are multipurpose devices that can measure several physical quantities like temperature, pressure, strain and be used as ID-tags, each application has its own boundary conditions and must be considered independently. Some important factors that influence the performance of the system are the operation temperature, the reading range and the close surroundings of the sensor, which can affect the performance of the antenna or shield the RF-link.

Any application requires the selection of crystals applied as SAW substrate as well as the

choice of metal for the electrodes and the selection of the package. Further, the decision on the sensing principle must be made: both resonators and delay lines have their advantages and disadvantages depending on factors like measured value, sensor size, reading distance and sampling rate, operating temperature range, required accuracy and costs. The radio link, the allowed size of the antenna, the desired multi sensor reading and moving parts also have a strong impact on the device and system design. Examples in this paper are based on reflective delay lines as they provide high flexibility for multi sensor designs.

2 TEMPERATURE SENSING

When a SAW device is exposed to temperature, the propagation velocity of the wave is changed and hence the operation frequency of the IDT (Inter Digital Transducer) and the length of the propagation path. The related change of the delay time is used as a measure for the temperature. The sensitivity to temperature is for delay lines described by the TCD (Temperature Coefficient of Delay) which depends strongly on the chosen substrate material and orientation and the type of propagating wave but is generally in the order of 10-100 ppm/°C. The temperature behavior is generally assessed as a quadratic or cubic function and shows often a turnover point within the operation range. For temperature sensing application, substrates with practically linear temperature dependency have to be identified.

2.1 Temperature sensor for power lines

As SAW devices don't need power connections, they can be installed in electrically critical environment like power switches, transformers and power lines. In the example given here the SAW devices are installed on overhead transmission lines surveilling the temperature of the cable and hence the amount of current flowing. This allows tuning the current to its maximum, with respect to the actual environmental conditions. For good thermal contact the sensors are installed directly on the power cables. The sensor antenna is on the same potential as the power line and electrically fully isolated from ground. The sensors are read out at a distance up to 15 m, using transmitting and receiving antennas mounted on the tower. The reader is powered by solar panels and is fully remotely configurable from the database server [4].

Measurement Range	up to 15 m
T accuracy	0.3 K
T resolution	0.02 K
T range	-40°C -150°C
Sampling Frequency	1 min

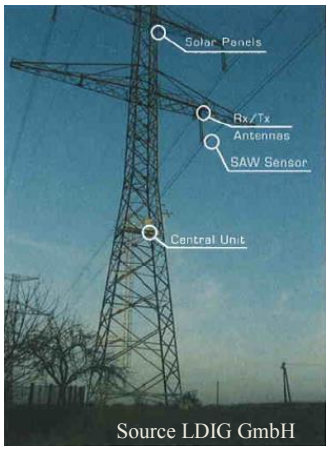


SAW device and antenna

Figure 1: Temperature monitoring of power transmission lines: main parameters and system configuration.

The environmental temperatures do not impose harsh conditions on the SAW substrate. In the desired temperature range of -40°C to 150°C practically any commercially available SAW substrate can be applied. We were hence free to choose a substrate with high coupling coefficient and - as we want to get a high sensitivity to temperature - high TCD (~92 ppm/°C), namely Lithium Niobate (LN).

Applying this substrate and Al-based electrodes, we were able to reach an operating frequency of 2.45 GHz. This requires some effort, as the desired resolution of the metallic structures is about 300 nm and hence close to the process limit of optical lithography. The 2.45 GHz operation is essential as the application requires wireless long-range-reading, and therefore the restrictions of the ISM bands have to be observed. Due to legal restrictions a wide band design of 80 MHz can only be realized within the 2.45 GHz ISM-band. This wide band is essential to achieve high resolution in time domain. With the current design employing phase analysis a resolution of 0.02 K was reached [4].

3.2 Condition monitoring in high-speed high-voltage drives

The utilization of SAW temperature sensors is not limited to the temperature range and sampling frequency shown in the previous example. For measurements up to 250°C in high-speed high-voltage large drives a SAW temperature reading system was specifically developed. The designated type of electrical drive was an induction motor with a solid squirrel cage rotor with a power rating of 4 MW at 15000 rpm up to 16 MW at 6000 rpm. Passive wireless SAW devices are the ideal sensors in these conditions where other contact free systems like optics or inductive coupling reach their limits because of the desired readout frequency and reading distance ~0.5 m.

The main challenge in this application is the high rotation frequency and a clever integration of the antennas. The SAW sensor including antenna is mounted on the rotor. The size of the sensor and reading antennas is limited, as the design of the machine should be changed as little as possible. The high rotation speed together with the small antenna dimensions result in an overlap timeframe of the antennas of only 100 µs. Such a fast reading can only be achieved by the FMCW (Frequency Modulated Continuous Wave) reading principle together with a trigger. The corresponding reader architecture is described in [5].

A delay line design on LN at 2.45 GHz was used for the SAW sensor. Fig. 2 shows the impulse response of a device with 3 peaks and how the peak-time and peak-amplitude change with temperature. The TCD of LN has only a small quadratic component and shows no turn over point within the operation range (-200°C to 400°C). Hence the delay time is always shifted to higher values with temperature as demonstrated in Fig. 2. The nearly linear response to temperature allows a unique conversion between delay time and temperature which is rarely the case for other SAW substrates.

The sensing resolution of such a system depends strongly on the signal to noise ratio (SNR) of the received radio signal. In the current configuration the SNR could be increased by averaging the signals obtained from 10 rotations, see Fig. 3. At several 1000 rpm the change of the rotor temperature is small within the averaging time for 10 or even 100 samples and therefore the averaging is well justified. Fig. 3 shows the antenna design and how it is integrated in the balancing groove of the rotor. In this configuration a resolution of 0.2°C could be achieved at a reading range of 0.5 m.

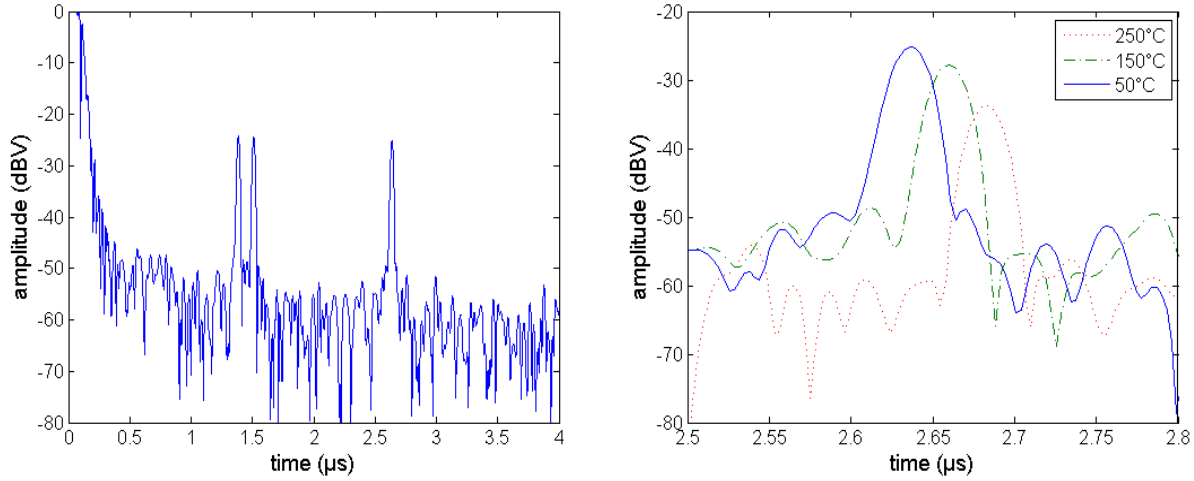

Figure 2: Left: Time response of the SAW delay line sensor. Right: Temperature effect on the last peak.

3 TAGGING

SAW delay lines can also be used as RFID-tags, especially in harsh environment like in automotive, oil and steel industry.

Different codes are realized by pulse position encoding (PP-encoding) in time domain. This means, that the positions of the n reflectors are changed to accomplish a unique pattern for each tag [2, 6]. The achievable data range depends on the temperature range of operation but is bigger than 10^{10} for a wide range operation up to 300°C [7]. For room temperature the data capacity can be increased by phase encoding [8].

For delay lines the width of the peaks and hence the number of codes that can be generated within a certain length of the tag is determined by the bandwidth of the system. Wide band applications can only be achieved for substrates with high coupling, as the relative obtainable bandwidth is proportional to k^2 (k=coupling coefficient), and for an appropriate ISM band. 2.45 GHz devices on LN fulfill both requirements.

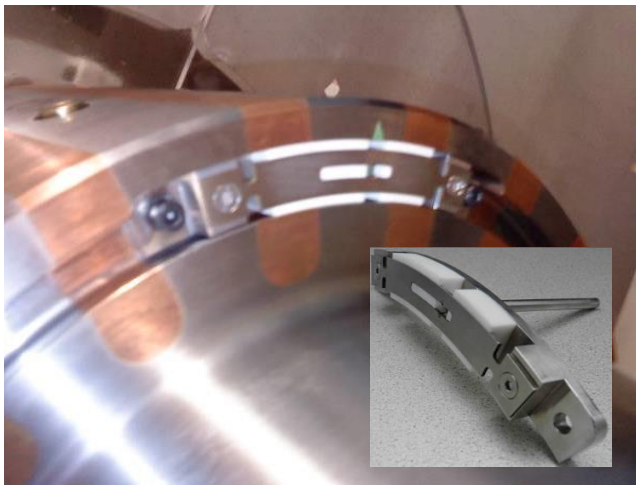

	SNR [dB]	Signal amplitude [dB]
Rotor angle 0 deg	26.5	59.5
Rotor angle +60 deg	21.0	53.5
Rotor angle -60 deg	18.0	51.5
15500 rpm, no averaging	26.0	58.5
15500 rpm, 10x averaging	35.0	57.0

Figure 3: Left: Antenna design installed in rotor. Right: SNR and amplitude for different configurations.

Processing of SAW based ID-tags is done by the combination of several mask images and can only be performed with dedicated equipment. PP-encoding with 8 reflectors on a basis of ten allows the realization of 10^6-10^8 codes, depending on the number of reflectors that are used to compensate for temperature effects and for redundancy, and requires nine masks - one for each reflector plus one for the IDT- for the production.

The maximum operation temperature of these devices depends, apart from the used substrate, on the metal chosen for the electrodes and the packaging. Al-electrodes can be applied up to about 250°C. Above that, Al based multi-layer structures must be used [9]. At temperatures above 400°C, Lithium-Niobate and Lithium-Tantalate (LT) are no longer applicable.

In the high temperature region the design of SAW based ID-tags becomes extremely difficult. One reason is that high temperature stable electrodes must be used and these metals (e.g. Au, Pt, Ir) tend to downshift the operating frequency for a given design. The effect can be compensated by using smaller structures but this requires an even higher resolution in the lithography process. This is extremely critical for Langasite (LGS) and CTGS, two materials known for their high temperature sustainability, as these materials have low propagation velocities. The structure width for a 2.45 GHz device is therefore exceedingly small. Thus e-beam technology or nanoimprinting must be used for the fabrication. Moreover these substrates have a much lower coupling coefficient and higher propagation losses, which make them less suited for ID-Tags applications.

AlN-based devices could be one option for high temperature ID-tags. While the coupling is smaller, the propagation velocity is about twice as high as for LN and LT. This provides some additional margin to deal with the frequency shift induced by heavy electrodes as the structures do not need to be as small as with LN, for example.

3.4 Identification in harsh environment

We have designed RFID-tags for the identification of drill pipes in oil industry. These tags must withstand temperatures up to 250°C together with a pressure of abrasive liquids of 1300 bar. Tag and sensor antenna must be integrated into the tool joint (Fig. 4). Hence the dimensions of the antenna must be smaller than 3 cm in diameter with a thickness of less than 5 mm. The reading is done with a hand held reader and therefore requires a relatively small reading distance of 0.5-1m. For SAW ID-tags the signal strength and thus the reading range is inversely proportional to the number of reflectors and the length of the propagation path. As a consequence the reading range decreases with the number of codes. Within the current boundary conditions we could successfully realize an ID-tag with 10^6 codes.

We have constructed a high pressure stable metallic housing with about the same dimensions as a T039 housing that was tested up to 1300 bar. While the package itself could be welded to ensure tightness in the high pressure range, the design of the glass feed through was the most critical issue. A picture of the housing is shown in Fig. 4.

Generally speaking, the size of an antenna for a given frequency and allowed power is related to the reading distance. In the current application the antenna must be small and installed in direct contact to metal. The diameter of the tool joint where the device is inserted becomes smaller with lifetime, because of significant abrasion. Hence the tag must be recessed for protection, which makes the establishment of a wireless link really tricky.

Fig. 4 shows a solution where the tag and antenna are embedded into a high temperature thermoplastic by injection molding. This process is applicable as the SAW sensors can withstand high process temperatures, and would not be possible for Silicon based devices. The antenna is completely surrounded by the dielectric and hence sufficiently decoupled from the surrounding metal to allow wireless interrogation for a limited reading distance.

High pressure housing



Tag installed in tool joint



SAW tag plus antenna



Figure 4: High pressure SAW tag with integrated antenna, installed in tool joint of oil drilling pipes.

Another example of tagging in harsh environment is the identification of slag vessels. In steel production different types of slag must be dumped on different heaps. The transport is performed within vessels that are filled with hot slag and transported by cranes. The identification of the slag vessels allows directing the cranes automatically to the right location. The system requires a larger reading range than for the tagging of the oil drilling pipes but allows also the operation of bigger antennas. To provide an extremely robust ID- tag the antenna is made of ~ 5mm thick metal applying a slot design (Fig. 5). The SAW devices are integrated into a metallic housing hence allowing welding between antenna and sensor. A high temperature stable duroplast is used for electrical isolation. The tag is mounted outside the slag vessels and must sustain temperatures of ~200°C and mechanical shock. We could proof a long term stable operation of several years. Fig. 5 shows a picture of the tag with antenna before operation and a tag covered with slag that is still operational.

Vessels on the slag heap



Heavy duty tag before operation



Tag covered by slag but still working



Figure 5: Heavy duty SAW tag used for the identification of slag vessels.

Depending on customer requirement such an RFID-tag can be enhanced for temperature reading. The combination of a wireless temperature sensor with an ID-tag was applied for the surveillance of slide gates. Slide gates, as shown in Fig. 6, are large valves in the steel casting

process, which are used to regulate the flow of liquid steel. Two refractory plates are used to control the flow via the overlap of the holes, one in each of the two slide gates. During casting these ceramic plates are exposed to high temperatures of approximately 1540°C, high mechanical loads of several tons of liquid steel, and chemical attack by alloys. Depending on the steel grade, the throttling parameters and the casting time the plates have to be replaced after a certain operating time before a critical degree of wear is reached. The continuous temperature monitoring, together with the ID capability allows optimizing the casting process itself and the individual slide gate usage by simplifying the logistics. Thus costs and unscheduled interruptions of the casting are minimized. The SAW transponder is exposed to temperatures up to 300°C, a temperature range that cannot be addressed by semiconductor based electronics. A dedicated antenna was designed for the high temperatures and geometrical boundary conditions. It could be integrated in the rim of the slide gate and was fixed with mortar. Because of the high operation temperature Macor and SiO_2 were used as dielectric material [10]. A picture of a slide gate with integrated antenna is shown in Fig. 6.

4 MULTI SENSOR READING

In steel industry, temperature monitoring is even more crucial for continuous casting moulds (CCM), which are used for casting molten metal into slabs without interruption. Real time temperature reading allows optimizing the process control and extension of the wear-time. For optimal process control several temperature sensors must be installed within the moulds. Wired sensors are quite impractical as they must be disassembled at any exchange of the mould. Wireless SAW sensors can overcome this obstacle. They simplify the maintenance of the casting mould significantly as they allow the removal and reassembly of the inner parts without effort of wiring. In order to limit the number of antennas within the system several SAW sensors must be connected to one antenna link.

Whenever more than one SAW device must be read by one antenna, a dedicated SAW design is required [11]. As SAW sensors are completely passive, all devices within an antenna cone are answering at once whenever interrogated by the reader and mere software protocols are not sufficient to separate the information from different devices. The SAW devices themselves must be processed in a way that allows their distinction. Practically, this can be done either in frequency domain FDMA (Frequency Domain Multiple Access) or in time domain TDMA (Time Domain Multiple Access) and both methods are generally limited to a small number of sensors.



Slide gate with integrated SAW sensor

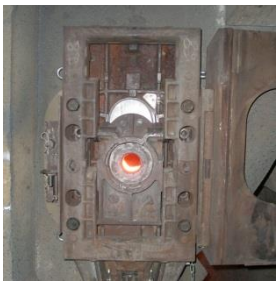

Slide gate plate at the ladle maintenance station



Moulds for continous melt casting

Figure 6: Temperature monitoring of slide gates, left and middle, and in continuous mould casting.

FDMA requires the SAW devices to operate at different frequencies and is done by the design of different IDTs [12]. This means that the bandwidth of the used ISM band must be broken down for the different sensors. Applying some safety margins, this means that for a total bandwidth of 80 MHz only about 15 MHz are available for a five sensor system. These 15 MHz limit the addressable temperature range. For a 2.4 GHz application and a substrate with high TCD (~ 100ppm/°C), the frequency shift is ~2.4 MHz per degree. This implies that less than 70 degrees can be measured before the responses start to overlap. For a wide temperature operation in FDMA like 300°C, it is hence necessary to use materials with lower temperature coefficients. Such materials can be found but they may not have the same performance in terms of k^2 and velocity. In addition, the reading system must provide a much higher accuracy to compensate for the smaller sensitivity.

TDMA is not subjected to these restrictions. The whole bandwidth can be used for all sensors and therefore also the same IDT can be applied. In TDMA design, the total allowed delay time is the limiting factor but this value can be as large as 4 µs. For a large bandwidth design the peak-width that is inversely proportional to the bandwidth is in the order of 20 ns while the time shift of the peaks can be as big as 120 ns for 300°C. A multi sensor design for several sensors is thus feasible in time domain. Such a system was tested for CCM casting and a patent was filed [13].

5 STRAIN & PRESSURE MEASUREMENT

SAW devices react to stress and strain by the change of the propagation velocity and the length of the propagation path. Hence the changes in frequency f and delay time t can be used to detect strain ε, pressure or applied force wirelessly. In the simplest mechanical configuration the SAW devices are used like strain gauges. The sensitivity to strain S can be expressed by $\varepsilon \cdot S = \Delta f/f$ or $\varepsilon \cdot S = \Delta t/t$. As frequency and time measurements are complementary, both effects are identical. The distinctions of both measurements arise from different designs and reading methods.

For both frequency and time reading, different geometries can be applied. Membranes are generally used for pressure measurement, while force or high pressure can be detected in cantilever geometry [14]. An example for torque measurement based on resonators can be found in these proceedings [15]. The sensitivity to strain S is in the order of 1 ppm/µS [16, 17]. The measurement with sub-percent accuracy requires either high precision frequency analysis [18] or phase analysis in time domain. Both methods have already proven their suitability [14-15, 21].

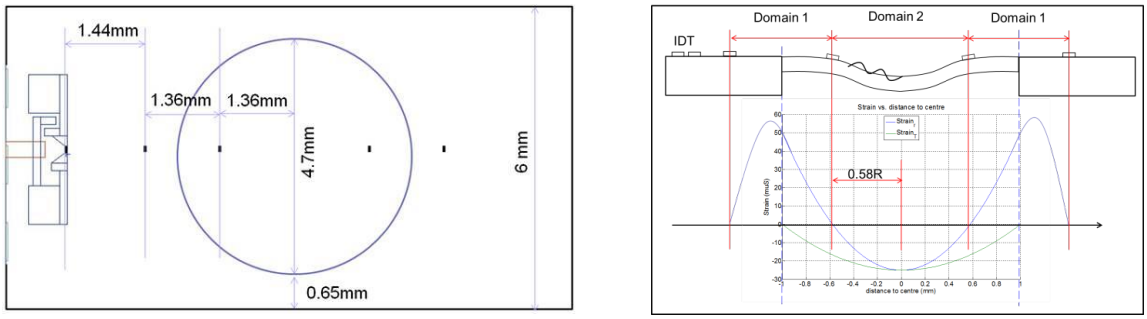

Figure 7: Design of a membrane based pressure sensor.

3.5 Low pressure design

Low pressure (<100 mbar) SAW sensors require the fabrication of thin membranes (30µm) with large diameters (3-5 mm) and precise compensation of phase shifts caused by the RF link or temperature effects. Fig. 7 gives the example of a reflective delay line design for a wireless implantable brain pressure sensor [19, 20]. The results presented here are obtained from an enhanced version of the sensor design presented in [21]. Extensive studies have been performed to compare the experimental results with simulated data [22].

In reflective delay lines each reflector can be considered as an individual sensor. Hence using two reflectors is equivalent to differential measurement. In the current design four reflectors are placed on defined positions to maximize the sensor effect and compensate temperature as well as delay line shifts.

The sensor is fabricated on LN and operates at 2.45 GHz. As it is meant for medical application, the pressure range was set to 60 mbar and the operation temperature is limited to < 50°C. Fig. 8 shows the sensor response after correction of temperature effects. The system measures the phase of all reflectors and combines the results to obtain pressure and temperature information. The sensor response is linear and gives a sensitivity of 8.8 rad/100 mbar, which corresponds to a phase shift of ~ 2π for the desired operation range. The restriction to 2π facilitates the phase analysis as the phase reading stays unique. The variance of the measurement is 0.03 rad which results in a resolution of 0.5% FS.

First results have been obtained for the wireless reading of the devices applying a 2.45 GHz patch antenna with a diameter of ~ 33 mm and a thickness of 1.6 mm. The antenna is designed to be implantable under the scalp of the patient. For the experiments saline solution was used as a mockup for body tissue and blood. Despite the high damping of these materials, it was possible to measure the devices at a distance of 10 mm, which is sufficient for the readout of the brain pressure sensor.

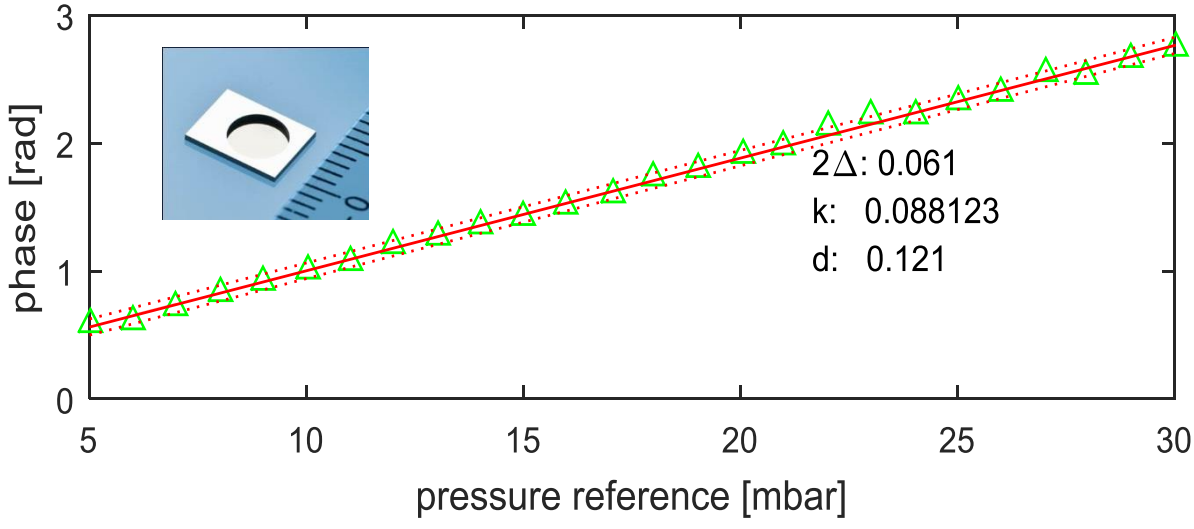

Figure 8: Sensitivity to pressure for a membrane based wireless SAW sensor.

5 CONCLUSION

We have presented several examples for the application of SAW sensors for industrial and medical usage. SAW sensors can cover a wide band of sensing tasks like wireless temperature, strain and pressure sensing or be used as RFID-tags. The applications demonstrate that SAW devices can work in difficult conditions like inside human body and close to metallic surfaces or on moving parts. Provided a thorough design and appropriate reading conditions, many sensing tasks can be addressed by these types of sensors including structural health monitoring.

4 ACKNOWLEDGEMENTS

This project is partly supported within the COMET – Competence Centers for Excellent Technologies - Program by BMVIT, BMWFJ and the Province of Carinthia.

REFERENCES

[1] L. Reindl, G. Scholl, T. Ostertag, H. Scherr, U. Wolff and F. Schmidt, Theory and Application of Passive SAW Radio Transponders as Sensors, *IEEE Trans. Ultrason. Ferroelectr. Freq. Control* 45 (5), pp.1281-1292 (1998).

[2] S. Härmä and V. P. Plessky , Surface Acoustic Wave RFID Tags, Development and Implementation of RFID Technology, Cristina Turcu (Ed.), InTech, (2009); doi: 10.5772/6522.

[3] P. Nicolay, H. Chambon, G. Bruckner, Simulation of the properties and behaviour of an implantable passive and wireless surface acoustic wave RFID tag, for structural health monitoring applications, *Proc. VIII ECCOMAS Thematic Conference on Smart Structures and Materials, SMART 2017* (2017).

[4] C. Bernauer et. al., Temperature Measurement On Overhead Transmission Lines (OHTL) Utilizing Surface Acoustic Wave (SAW) Sensors, *19th International Conference on Electricity Distribution* (2007).

[5] A. Binder, R. Fachberger, Wireless SAW Temperature Sensor System for High-Speed High-Voltage Motors*, IEEE Sensors Journal* (2010).

[6] V. P. Plessky, L. M. Reindl, Review on SAW RFID Tags, IEEE Trans. Ultrason. Ferroelectr. Freq. Control 75 (3), 654 (2010).

[7] G. Bruckner and R. Fachberger, SAW ID tag for industrial application with large data capacity and anticollision capability, *Proc. IEEE International Ultrasonics Symposium (IUS)*, Beijing, pp. 300-303 (2008); doi: 10.1109/ULTSYM.2008.0074

[8] C. S. Hartmann, "A global SAW ID tag with large data capacity," *Proc. IEEE International Ultrasonics Symposium (IUS)*, vol.1, pp. 65-69 (2002); doi: 10.1109/ULTSYM.2002.1193354

[9] A. Binder, G. Bruckner, J. Bardong, Passive SAW Based RFID Systems Finding their Way to Harsh Environment Applications, *Proceedings SensorCOMM* (2013); ISBN: 978-1-61208-296-7

[10] R. Fachberger, A. Binder and A. Erlacher, SAW-RFID and temperature monitoring of slide gate plates, *IEEE Sensors*, Christchurch, pp. 1514-1517 (2009); doi: 10.1109/ICSENS.2009.5398467
[11] C. Hartmann, P. Hartmann, P. Brown, J. Bellamy, L. Claiborne and W. Bonner, Anti-collision methods for global SAW RFID tag systems, *Proc. IEEE International Ultrasonics Symposium(IUS)*, pp. 805-808 vol.2. (2004) ; doi: 10.1109/ULTSYM.2004.1417859
[12] D.C. Malocha et al., A Passive Wireless Multi-Sensor SAW Technology Device and System Perspectives, Sensors 2013, 13(5), pp. 5897-5922 (2013); doi: 10.3390/s130505897
[13] L.Cestari et al., Arrangement for measuring physical parameters in continuous casting moulds, *US2013/0333473*, A1 Dec.12 2013 (2013)
[14] A. Binder, G. Bruckner, N. Schobernig and D. Schmitt, "Wireless Surface Acoustic Wave Pressure and Temperature Sensor with Unique Identification Based on LiNbO3,in *IEEE Sensors Journal*, vol. 13, no. 5, pp. 1801-1805, (2013); doi: 10.1109/JSEN.2013.2241052
[15] V. Kalinin, Wireless Passive Resonant SAW Sensors for Monitoring Temperature, Strain, Torque and Pressure, *Proc. VIII ECCOMAS Thematic Conference on Smart Structures and Materials, SMART 2017* (2017) .
[16] G. Bruckner, G. Stampf, G. Franz, R. Fachberger and R. Hauser, SAW strain sensitivity of selected Rayleigh wave crystal cuts, *Proc. IEEE International Ultrasonics Symposium (IUS)*, Rome, pp. 823-826 (2009); doi: 10.1109/ULTSYM.2009.5442070
[17] G. Bruckner, J. Schicker and P. Schlumpf, Stress sensitivity of SAW Rayleigh waves on Lithiumniobate and its application in pressure sensor design, *Proc. IEEE International Ultrasonics Symposium (IUS)*, Prague, pp. 2140-2143 (2013); doi: 10.1109/ULTSYM.2013.0547
[18] V. Kalinin, "Comparison of frequency estimators for interrogation of wireless resonant SAW sensors*," 2015 Joint Conference of the IEEE International Frequency Control Symposium & the European Frequency and Time Forum*, Denver, CO, pp. 498-503 (2015); doi: 10.1109/FCS.2015.7138893
[19] David J. Price, Digitised ICP over Three Decades, Intracranial Pressure and Brain Monitoring XIV, *Acta Neurochirurgica* Supplement vol.114, Springer-Verlag/Wien (2012); doi 10.1007/978-3-7091-0956-4_1
[20] Christopher McLeod, Problems and solutions for implanted SAW sensors, *SAW Sensor Symposium* , Dresden (2016)
[21] G. Bruckner, J. Schicker, N. Schobernig, V. Stojanov, P. Schlumpf , Design Study of a Wireless Pressure Sensor for Medical Application, *AMA Conferences 2013 - SENSOR 2013, OPTO 2013, IRS 2 2013*; doi: 10.5162/sensor2013/B1.3
[22] H. Chambon, P. Nicolay, G. Bruckner, and A. Benjeddou, Finite Element Simulation of Lithium Niobate Based Surface Acoustic Wave Delay Lines for Pressure and Temperature Sensing, *Proc. VIII ECCOMAS Thematic Conference on Smart Structures and Materials, SMART 2017* (2017) .

VIII ECCOMAS Thematic Conference on Smart Structures and Materials
SMART 2017
A. Güemes, A. Benjeddou , J. Rodellar and Jinsong Leng (Eds)

SIMULATION OF THE PROPERTIES AND BEHAVIOUR OF AN IMPLANTABLE PASSIVE AND WIRELESS SURFACE ACOUSTIC WAVE RFID TAG, FOR STRUCTURAL HEALTH MONITORING APPLICATIONS.

P. NICOLAY*, H. CHAMBON*, G. BRUCKNER*

* Carinthian Tech Research, CTR AG
Europastraße 12, 9524 Villach, Austria
e-mail: pascal.nicolay@ctr.at, web page: http://www.ctr.at

Key words: Structural Health Monitoring, Implantable Sensor, Passive and Wireless Sensor, SAW sensor, Simulations.

Abstract. Surface Acoustic Wave (SAW) passive and wireless sensors are a promising solution for condition and structural health monitoring applications (SHM). In the introductory part of the paper, we briefly present the SAW technology as well as its main embodiments and known applications. Trends in the field of implanted SAW sensors for SHM are presented in the second section of the paper, including newly obtained experimental results. As the evaluation of the feasibility of a SAW-based monitoring solution is of great importance for scientists and engineers in the SHM field, the third part of the paper is dedicated to the computation of the basic properties of a SAW sensor, of the Reflective Delay Line (R-DL) kind.

1 INTRODUCTION

Surface Acoustic Wave (SAW) sensors are passive and wireless devices that can be interrogated using standard radar techniques [1]. A radio-frequency (RF) interrogation signal is sent to the sensor, where it is picked up by an antenna and converted into elastic waves, which propagate along the surface of the sensor's constitutive material. The conversion is made by a so-called Inter Digital Transducer (IDT), thanks to the piezoelectric properties of the material. The IDT is made of very thin metal fingers (50-100nm in thickness) patterned using standard photolithography techniques. The distance p between two adjacent fingers goes from 0.5 to several micrometres, depending on the chosen operating frequency. Indeed, the operating frequency is given by the simple formula $f=V/\lambda$, where V is the SAW velocity and λ is the wavelength ($\lambda=2p$). For instance, a 2.45GHz SAW Device made of Aluminium IDTs deposited on Y-Z Lithium Niobate has a wavelength λ close to 1.4µm.

The SAWs can then propagate until they reach another IDT, where they will be converted back to RF and reemitted towards the SAW reader. They can also be trapped inside an acoustic resonant cavity, made by reflector gratings positioned on each side of the emitting IDT. In this case, the looked-after information will be coded in its resonant frequency. This frequency can be extracted either from the ringing of the resonator once the driven excitation at a frequency closed to the resonant one is stopped [2], or directly from a frequency sweep and a direct identification of the resonant frequency [3]. In a third configuration, a fraction of the acoustic energy is reflected back by thin metal fingers deposited along the propagation path [1]. The backwards propagating SAW are converted back in an electromagnetic signal by the emitting IDT itself, thus creating echoes in the RF response of the sensor. The three configurations are schematically presented in Fig. 1. The first configuration is a standard SAW Delay Line (DL). The second one is a SAW Resonator. The third one is a reflective Delay Line (R-DL). The resonator-based solution presents advantages over the two other solutions [4]. Especially, it is much smaller than the R-DL solution. However, the R-DL solution presents the unique advantage of a direct identification (ID) of the interrogated sensor. Indeed, the ID of the sensor can be coded in the series of echoes that is equivalent to a bar-code. This confers the SAW R-DL an RFID capability. For this reason, they are often called SAW RFID Tags. Both solutions have their pros and cons, which have to be evaluated prior to selecting the best solution for a given application.

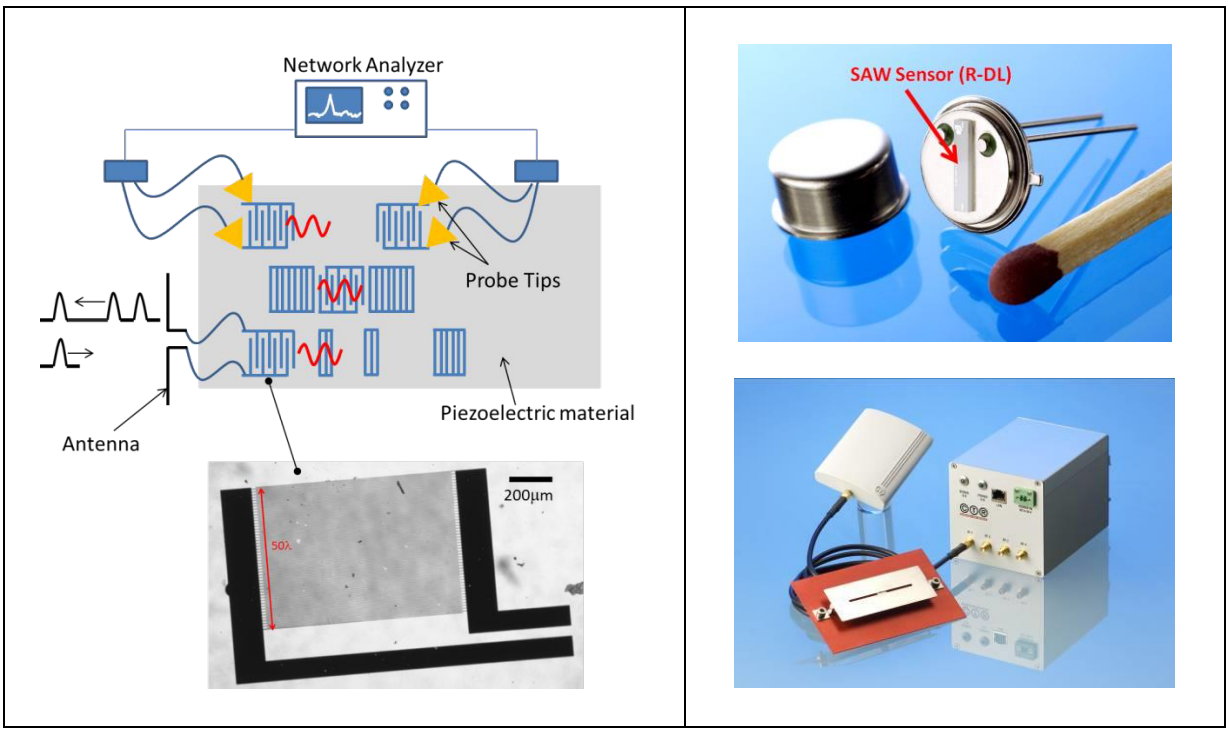

Figure 1: The three main SAW Sensor configurations: SAW Delay Line, SAW Resonator, SAW Reflective Delay Line (top left), a zoom on an IDT (bottom left), in-packaged SAW R-DL (top right), a whole SAW Sensor system (CTR AG): reader + antenna, sensor + slit antenna.

The sensitivity of a SAW sensor to environmental conditions comes essentially from the sensitivity of the SAW velocity upon the temperature and strain fields present in the SAW propagation medium [5-6]. For instance, in the case of the R-DL, a temperature increase will (usually) soften the material which will result in a decrease of the SAW velocity. This will shift the echoes to the right, in the time domain, and it will be possible to infer the temperature and/or strain state of the sensor from the position of the echoes.

Wireless SAW Sensors can usually be interrogated up to a distance of a few tens of centimetres, depending on the temperature (the distance rapidly decreases when the temperature increases). As they are made only of a piece of crystal material on which metal fingers are deposited, they are intrinsically very robust. This feature, combined with a small size (a few squared millimetres) and the capability for passive operation (no embedded electronics) and wireless interrogation makes them a candidate of choice for various applications, where standard Silicon-based electronics cannot be used. SAW devices are notably a very good solution to sense temperature and strain in harsh environment, under high pressure, at high (>300°C) or cryogenic temperature, in corrosive or radiative environment etc.… Numerous applications can be found in the steel, air and space, and automotive industries [7-9].

2 SAW SENSORS FOR SHM APPLICATIONS, DISCUSSION

Most of SHM applications would require the SAW sensors to be implanted in a structure, possibly made of concrete (tunnels, bridges…), polymer or composite materials. The first difficulty would arise from the necessity to interrogate the embedded sensors through the matrix material. First of all, SAW sensors are completely passive devices that re-emit only a fraction of the emitted signal. In addition, as SAW wireless sensors operate most often in the 433MHz ISM Band for the resonators or in the 2.45GHz ISM Band for the R-DLs, the emitted and received signals can easily be blocked by any conductive material present on the path of the RF signals. This is made worse by legal regulations that limit the maximum radiated energy in the ISM bands to a few mW only. It is therefore not possible to compensate for the attenuation due to (even poorly) conductive material present in the path of the signals, by strongly amplifying the interrogation signal itself. Among the applications that cannot be addressed by (embedded) SAW Sensors is for instance, the monitoring of carbon fibers-based structural elements. Indeed, the carbon fibers are conductive enough to extinguish any RF signal sent to and back from a SAW sensor. On the contrary, Fiberglass-based structural elements constitute a possible application niche for SAW devices.

A second difficulty would arise from the necessity to interrogate many sensors at the same time. Indeed, if many sensors are present in a small region of a given structural element, they will all answer the interrogation signal together, which will generate overlaps in the different responses. Solutions exist to simultaneously interrogate several SAW sensors together. For instance, CTR engineers developed the so-called anti-collision technique that makes it possible to simultaneously interrogate up to 4-6 sensors [10]. But this number is still very small, in comparison to what is often needed for SHM applications. There is no known solution yet, to interrogate more than a few SAW sensors simultaneously.

A third difficulty has to do with the necessity to protect the SAW surface. A SAW chip is very sensitive to any material deposited on its surface. Liquids for instance, can easily extinguish the SAWs. Moreover, the IDTs are quite fragile and can be easily scratched. It is therefore necessary to encapsulate the SAW chips in an adequate protective housing. To design the right housing able to protect the SAW and at the same time, to ensure a good coupling between the quantity to measure and the SAW chip (e.g. external pressure) is each time a technical challenge [7]. That's why several groups in the world are engaged in the development of so-called package-less solutions. One promising way is to use guided waves that are located inside the SAW chip and do not "see" its surface. Researchers are notably using multi-layered substrates, where a thin layer of a given material is sandwiched between two other layers presenting very different acoustic impedances. The "interface" waves generated in the thin layer are then guided by the two other layers, and are insensitive to surface states [11]. Another interesting possibility would be to use special modes that are by nature propagating below and parallel to the surface, at a depth where they cannot "sense" the surface anymore. Recent investigations performed at CTR using a Delay Line deposited on the Y-X orientation of Langasite (a well-known piezoelectric material, suited for very high temperature applications) showed the existence of a mode that might fit this description. As can be seen in the spectrogram of the impulse response of the Delay Line, presented in Fig. 2, several modes are present. These modes can all be identified, using a technique specifically developed to analyse this kind of SAW response [12-13]. The SAW mode is found at 160MHz. More interestingly, the analysis shows that one of the main signals, at 260 MHz and 0.65 µs is probably a specific Guided Bulk Acoustic Wave mode (G-BAW), which arises from the interaction between two counter-propagating BAW modes, reflected by the substrate top and bottom surfaces (Fig. 2, red arrow). The sensitivity of the mode to the surface state was tested experimentally, in two ways. First, the surface roughness was strongly altered using sand-blasting. Second, droplets of Nail polish were deposited on the propagation path. In both cases, the SAW signal was completely suppressed, whereas the so-called G-BAW signal stayed strong. Further analysis is required to fully understand the origin of this mode. However, it is a promising mode for a whole range of possible applications.

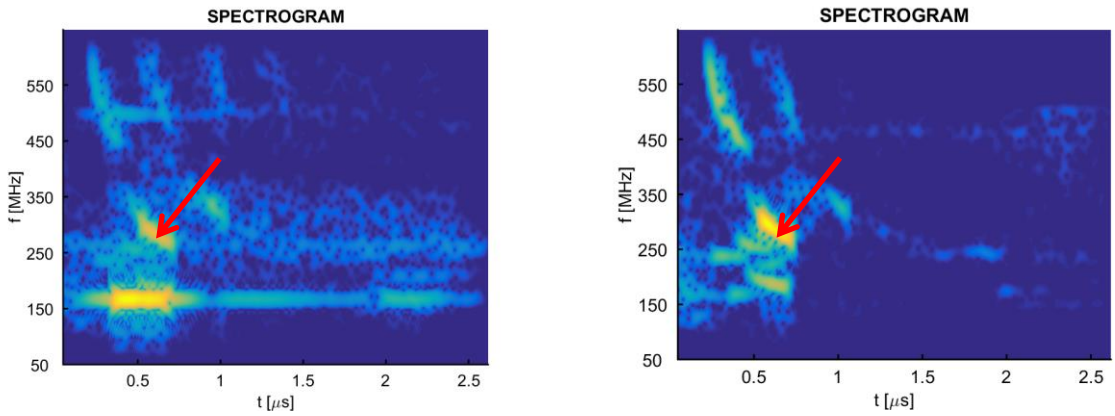

Figure 2: Spectrogram of the RF signature of a LGS Y-X SAW Delay Line, before (links) and after (right) deposition of Nail polish droplets on the propagation path.

The fourth difficulty arises from the antenna itself. If there is a possibility to interrogate the sensor in near field, clever designs can be found to avoid using an antenna [14]. If the sensors must be interrogated at a distance of at least several centimetres, it becomes necessary to use a specifically designed antenna, whose dimension is proportional to the wavelength. It is therefore inversely proportional to the frequency. At 2.45GHz, a quarter-wave antenna has its biggest dimension close to 3cm. The size can be reduced in some extent using high-permittivity materials in the fabric of the antenna, but the length of the antenna will stay in the centimetres range. There is however, some flexibility in the choice of the antenna geometry. It can be a patch antenna as well as a thin dipole or monopole antenna (i.e. a wire). Its shape can also be adapted, depending on the application requirements [7].

The last main limitation has to do with the reading frequency of a SAW sensor. As SAW sensors are passive elements, their signal-to-noise ratio is quite low. It is therefore necessary to average over a vast number of measurement points, to reach the required accuracy. The maximum reading frequency that is reachable with the CTR FMCW reader is close to 100Hz. However, for most applications, this frequency is down to 5-10Hz. This is especially the case for applications where the temperature accuracy has to be better than ±0.5°C.

In summary, SAW Sensors/RFID Tags are always a promising solution where wireless interrogation is required and where standard, silicon-based solutions cannot work. If the sensor also have to be small (<1cm), and if none of the five limitations described above are critical to the application, the SAW technology is an option to be considered. Especially, if the RFID functionality is required, SAW R-DL might end up being, if not the only possible solution, one of the best remaining options. To assess further the feasibility of the envisioned SAW-based concept, it might be useful to start with basic simulations. It is the purpose of section 3 to explain how to perform basic simulations of the properties of a given SAW R-DL, based on Lithium Niobate.

3 SIMULATION OF THE PROPERTIES OF A SAW R-DL

As described above, SAW sensors are essentially made of a sensitive element (SAW chip), a housing or functional packaging, and an antenna. All these parts interact together and influence the RF signature of a SAW sensor. It is therefore necessary to simulate them all, to compute the final RF behaviour of the sensor.

The transfer function and/or the impulse response of the SAW chip are the most difficult to simulate. The SAW chip is usually modelled using a combination of FEM and semi-analytical methods based on the Coupling-of-Modes theory (COM) and some kind of transfer matrix method. The idea is to use FEM to simulate the behaviour of the SAWs propagating in an IDT-like periodic grating, then to use an inverse method to extract (from the obtained FEM results) the parameters of a phenomenological model (the COM model) that describes in a simplified but still very accurate way, the behaviour of the SAWs in the grating. The COM model relies on five parameters: the velocity v, the coupling coefficient κ, the transduction coefficient α, the attenuation γ, and the normalized capacitance C_n. It was shown that the electrical properties of an actual IDT (i.e. its admittance $Y(f)$ and therefore its impulse response in time domain) can in most cases, be subsequently computed using these five COM

parameters only. The COM parameters and transfer matrix techniques are first used to compute the 3-port admittance matrix of the IDTs and reflectors separately. These are then combined (using the same transfer matrix techniques) to obtain the final admittance characteristics of the whole device. This method is described in details in [15-16]. Once the admittance is known, it becomes easy to use the SAW chip as a SnP-file, inside a circuit simulator. As the electrical characteristics of the other elements (antenna, housing, PCB…) can be independently simulated using adequate software and "reduced" to their own SnP-file, it becomes possible to connect them together (electrically) in the circuit simulator and to compute the RF response of the whole sensor. The whole procedure is described in [17], for a CTR R-DL based on Lithium Niobate (LN). In [17], only free softwares were used to perform the computations. However, the COM parameters were given for one IDT relative thickness only. In Table 1, we present the evolution of the COM parameters in a wider relative thickness range. These computations were performed using proprietary software, described in [18].

Table 1: COM Parameters for Aluminum electrodes on Y-Z LN with η=0.5 and different h/λ values

Parameter	Value						Unit
h/λ	0.7	1.1	1.5	1.9	2.3	2.7	%
V	3430.9	3429.0	3426.8	3424.3	3421.6	3418.5	m/s
κ	3.44	3.58	3.76	3.94	4.15	4.36	%
α	52.9	52.8	52.6	52.6	52.3	52.0	$\times 10^{-5}\ \Omega^{-1/2}$
C_n	39.5	39.5	39.5	39.5	39.5	39.5	$\times 10^{-5}$ pF/µm/period
γ	~0	~0	~0	~0	~0	~0	dB/λ

The sensor's sensitivities to strain and temperature variations can also be obtained, through simulation. The basic idea is to compute first the strain and/or temperature fields to which the SAW chip is subjected. This step takes into account the whole structure of the sensor including the housing or functional packaging. It also takes into account the environmental conditions. These simulations can advantageously be performed using well-known standard FEM tools, like COMSOL or ANSYS. Then, it becomes necessary to compute the reaction of the SAW chip to these strain and temperature fields. Basically, these fields essentially translate into pre-stressing, modification of the material stiffness constants and geometrical compression or extension of the propagation path. The modification of the material constants under temperature or strain bias is described by second and third order coefficients that can be found in the literature for several of the most used SAW crystals [19-20]. Up-to-date FEM tools offer the possibility to solve this kind of problem, by taking into account pre-stressing and modification of the material constants, in the computation of the acoustic properties of a given propagation medium. It is therefore possible to use existing FEM tools to compute the strain and/or temperature sensitivity of a whole SAW sensor/RFID Tag. This procedure is described in more details in [21].

As an example, we present the result of a computation performed to analyse the effect of long bond wires on the electrical characteristics of a SAW R-DL, based on the Y-Z orientation of Lithium Niobate. These bond wires were used to connect a SAW chip to its PCB, through an implantable ceramic housing. First, we computed the RF response of the SAW chip alone, following the procedure detailed in [17]. The impulse response of the sensor is shown in Fig. 3(a). The SnP File describing the electrical behaviour of the sensor was then connected to two bond wires, in a circuit simulator. It was then easy to check the effect of a change in the length of the two wires (see Fig. 3(b)). This corresponds well to what was previously observed, experimentally. These results have been used to optimize the length of the bond wires (~2.3mm), in order to match the sensor to 50Ω and strongly improve the sensor's signal-to-noise ratio. This simple example shows that the method presented here can not only be used to evaluate the RF characteristics of a SAW R-DL beforehand, but can also be used for design and optimization proposes.

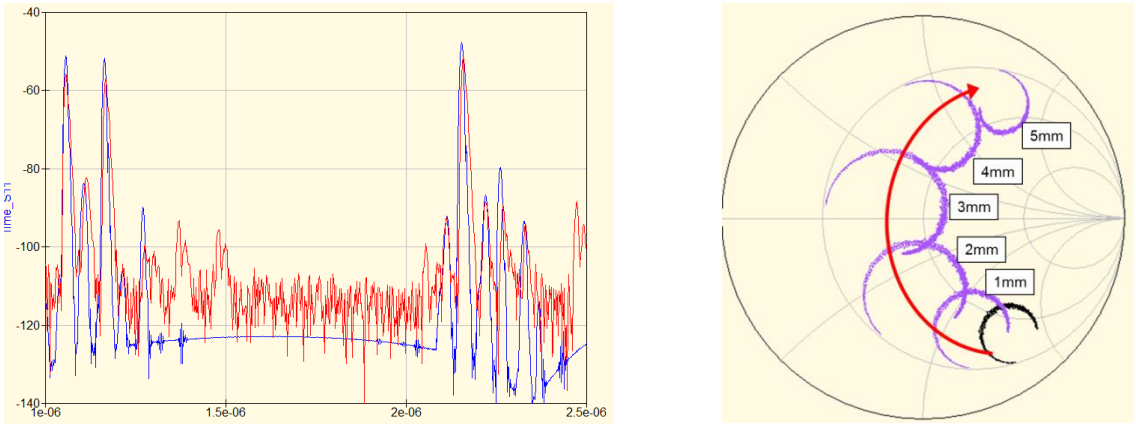

(a) (b)

Figure 3: (a) Impulse response of a SAW R-DL built on Y-Z LN. Time (x-axis) is represented in seconds. Losses (y-axis) are represented in dBm. Measured data and simulated data are represented respectively in red and blue; (b) Effect (on the electrical characteristics of the whole sensor) of the length of the bond wires connecting the IDT bus bars to the sensor's PCB. Smith Chart representation.

4 CONCLUSION

In this paper, we discuss the suitability of SAW sensors and SAW RFID Tags for Structural Health Monitoring applications. We also describe a simulation procedure, to compute the whole RF characteristics of such a device, taking into account the housing and other surrounding elements. It is the purpose of future work to develop further this co-simulation method, notably to optimize the design of SAW sensors for very high temperature applications.

ACKNOWLEDGMENTS

This project has been partly supported by the COMET K1 centre ASSIC Austrian Smart Systems Integration Research Center. The COMET – Competence Centers for Excellent Technologies – program is supported by BMVIT, BMWFW and the federal provinces of Carinthia and Styria.

REFERENCES

[1] L. Reindl, G. Scholl, T. Ostertag, H. Scherr, U. Wolff, and F. Schmidt, Theory and Application of Passive SAW Radio Transponders as Sensors, *IEEE Trans. Ultrason. Ferroelectr. Freq. Control* **45** (5), 1281-1292 (1998).

[2] V. Kalinin, G. Bown, J. Beckley, and R. Lohr, Pulsed Interrogation of the SAW Torque Sensor for Electrical Power Assisted Steering, *Proc. IEEE Ultrasonics Symp.*, 1577-1580 (2004).

[3] J.-M Friedt, C. Droit, G. Martin, and S. Ballandras, A Wireless Interrogation System Exploiting Narrowband Acoustic Resonator for Remote Physical Quantity Measurement, *Rev. Sci. Instrum.*, 81(1):014701 (2010).

[4] J. Beckley, V. Kalinin, M. Lee, and K. Voliansky, Non-contact Torque Sensors Based on SAW Resonators, *Proc. IEEE International Frequency Control Symp.*, 202-213 (2002).

[5] B.K. Sinha and H.F. Tiersten, On the Influence of Uniaxial Biasing Stresses on the Velocity of Piezoelectric Surface Waves, *Proc. IEEE Ultrasonics Symp.*, 475-479 (1976).

[6] B.K. Sinha and H.F. Tiersten, On the Temperature Dependence of the Velocity of Surface Waves in Quartz, *J. Appl. Phys.* 51(9), 4659-4665 (1980).

[7] G. Bruckner, J. Bardong, A. Binder, P. Nicolay, SAW Delay Lines as Wireless Sensors for Industrial Applications, *Proc. VIII ECCOMAS Thematic Conference on Smart Structures and Materials, SMART 2017* (2017).

[8] V. Kalinin, Wireless Passive Resonant SAW Sensors for Monitoring Temperature, Strain, Torque and Pressure, *Proc. VIII ECCOMAS Thematic Conference on Smart Structures and Materials, SMART 2017* (2017).

[9] A. Maskay and M. Pereira da Cunha, High Temperature Static Strain Microwave Acoustic Sensor, *Proc. IEEE Ultrasonics Symp.* (2016).

[10] G. Bruckner and R. Fachberger, SAW ID Tag for Industrial Application with Large Data Capacity and Anticollision Capability, *Proc. IEEE Ultrasonics Symp.*, 300-303 (2008).

[11] S. Zhgoon, A. Shvetsov, and K. Bhattacharjee, Modal Properties of Isolated Layer Longitudinal Leaky Acoustic Wave, *Proc. IEEE Ultrasonics Symp.*, 1681-1684 (2010).

[12] N. Naumenko, P. Nicolay, and J. Bardong, Theoretical and Experimental Investigation of Spurious Modes in a SAW Delay Line Based on Langasite, *Proc. IEEE Ultrasonics Symp.* (2015)

[13] N. Naumenko, P. Nicolay, and O. Elmazria, Towards an Optimal Architecture of High Temperature LGS-Based SAW Sensors, *Proc. IEEE Ultrasonics Symp.* (2016).

[14] V. Kalinin, Wireless Physical SAW Sensors for Automotive Applications, *Proc. IEEE Ultrasonics Symp.*, 212-221 (2011).
[15] J. Koskela, V.P. Plessky, SAW/LSAW COM Parameter Extraction from Computer Experiments with Harmonic Admittance of a Periodic Array of Electrodes, *IEEE Trans. Ultrason. Ferroelectr. Freq. Control* 46 (4), 806-816 (1999).
[16] V.P. Plessky, J. Koskela, Coupling-of-Modes Analysis of SAW Devices, *Int. J. Hi. Spe. Ele. Syst.* 10, 867 (2000).
[17] P. Nicolay, Co-simulation of a SAW Sensor, *IJCER* **5** (5), 38-51 (2016).
[18] K. Shaposhnikov, M. Kaltenbacher, and P. Nicolay, Fast Full-FEM Computation of COM Parameters. Application to Multilayered SAW Structures, *Proc. IEEE Ultrasonics Symp*. (2014)
[19] Y. Nakagawa, K. Yamanouchi, and K. Shibayama, Third-order Elastic Constants of Lithium Niobate, *J. Appl. Phys.*, 44 (9), 3969-3974 (1973).
[20] K.K. Wong, Properties of Lithium Niobate, INSPEC (2002).
[21] H. Chambon, P. Nicolay, G. Bruckner, and A. Benjeddou, Finite Element Simulation of Lithium Niobate Based Surface Acoustic Wave Delay Lines for Pressure and Temperature Sensing, *Proc. VIII ECCOMAS Thematic Conference on Smart Structures and Materials, SMART 2017* (2017).

WIRELESS PASSIVE RESONANT SAW SENSORS FOR MONITORING TEMPERATURE, STRAIN, TORQUE, AND PRESSURE

VICTOR A. KALININ

Transense Technologies plc
1 Landscape Close, Weston-on-the-Green
Bicester, OX25 3SX, UK
e-mail: victor.kalinin @transense.co.uk

Key words: Passive Wireless Sensor, SAW Sensor, SAW Resonator, Temperature Measurement, Strain Measurement, Torque Measurement, Pressure Measurement.

Abstract. The paper overviews principles of operation of passive wireless SAW resonant sensing systems for temperature, strain, torque, and pressure measurements. Advantages and disadvantages of SAW resonators as wireless sensing elements are discussed in conjunction with the current EMC regulations. Design of differential resonant sensing elements and their sensitivity to strain and temperature are presented. Influence of antennas on sensor characteristics is discussed. Methods of interrogation of passive wireless resonant sensors are reviewed and design of some readers developed at Transense Technologies plc is presented. A trade-off between the sensor bandwidth, the read range and the sensor resolution is discussed. Applications of wireless passive SAW resonant sensors are presented for monitoring pressure and temperature in automotive tyres, for measuring torque in electrical power assisted steering, at the output of engines and at the input of automotive gearboxes, as well as for monitoring torque in wind turbine and marine applications.

1 INTRODUCTION

To our knowledge, the first suggestion to use surface acoustic wave (SAW) resonators as non-contact passive strain and torque sensing elements is dated by 1990 [1] although the idea of using SAW devices as wired physical sensors emerged and was actively developed much earlier, in the 70s [2-3]. The SAW technology was booming that time after invention of the interdigital transducer (IDT) for efficient excitation of SAW at radio frequencies (RF). An attractiveness of SAW devices as sensors is in their ability to be excited and send back their response wirelessly through a simple and compact RF antenna connected to their terminals. Completely passive operation of the sensing elements without a need in a local dc power source is important for applications where providing dc power is either inconvenient or expensive, for instance, on moving parts or in a harsh environment.

The 20 years' gap between emergence of SAW electronic components such as filters, resonators, delay lines and the first passive wireless SAW sensors is partly explained by a complexity of interrogators (readers) required for such sensors. A progress in CMOS RFICs and microprocessors made the wireless SAW sensors economically viable only by the end of the 80s. Since then, passive wireless sensors based on SAW resonators were a focus of

intensive research for a number of groups, especially in Germany and Austria [4-6] and, by 2010, such sensors were developed for pressure, temperature and torque sensing, in particular, for automotive applications [7]. Nowadays, development of wireless SAW resonant sensors continues for various sectors of industry, e.g. for control and condition monitoring of engines, gearboxes, switchboards, furnaces, hydraulic couplings, etc.

Wireless sensing has become a general trend in industry in the last two decades due to a progress in miniaturization of RF and microwave transmitters and receivers, reduction of their power consumption, advances in MEMS and system-on-chip technology. Apart from passive sensors a wide range of active wireless sensors and sensor networks has been developed [8,9]. They either use batteries or rely on energy harvesting or rectification of RF interrogation signals like RF-ID tags. Clearly, different types of sensors have quite different read range, bandwidth and require different levels of interrogation power. Since there is no universal solution that suits all possible applications it is important to select the right technology for the right purpose.

The aim of this paper is to give an overview of the principles of operation of wireless SAW resonant sensing systems, discuss their capabilities and limitations, and present solutions for automotive and industrial applications that have been developed at Transense Technologies plc up to the present moment. This information could be helpful for deciding on whether the SAW resonant sensors are suitable or not for a particular application.

2 PRINCIPLES OF OPERATION

A passive sensing system in its simplest configuration consists of a sensing element connected to an antenna and a remote interrogator (reader) with its own antenna. The reader launches a RF interrogation signal at the frequency f_i such that its spectrum overlaps with the frequency response of the sensing element. If the sensing element contains resonators, then the resonant frequency f_r should be not too far away from f_i. In this case, the interrogation signal can excite the sensing element thus modifying the signal scattered from the sensor antenna back to the reader antenna. The reader's receiver picks up the scattered signal, analyses it and extracts information on the measured physical quantity influencing the frequency response of the sensing element.

Wireless SAW sensing elements are based either on resonators or reflective delay lines.

2.1 SAW resonator as a sensing element

A one-port SAW resonator is a device fabricated on a polished piezoelectric substrate by means of photolithography with an IDT surrounded by Bragg reflecting gratings (Fig. 1a) both made of Al film with the thickness of the order of 100 nm. The IDT converts the RF electrical signal applied to its terminals into a SAW propagating towards the gratings. The latter consist of hundreds of stripes so that the reflection coefficient for the SAW is close to unity at the Bragg frequency. Thus, a resonant cavity formed by the two gratings has a very high Q factor that is difficult to achieve using other technologies. The resonant frequency is

$$f_r \approx V_R/\Lambda \qquad (1)$$

where V_R is the phase velocity of the Rayleigh SAW and the doubled grating pitch Λ is close to the SAW wavelength λ. Resonators can be fabricated on substrates made of both weak

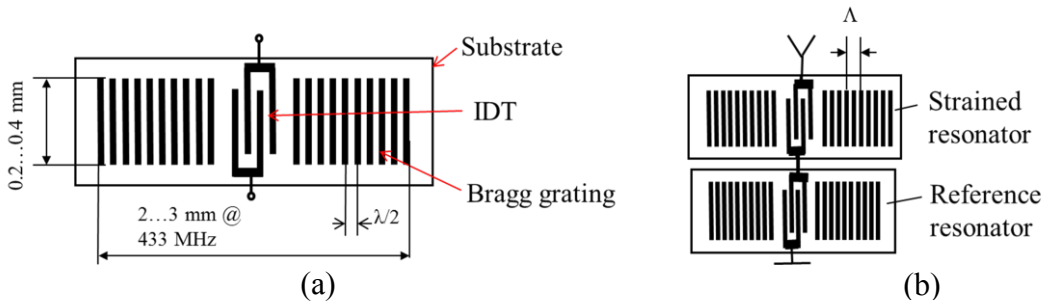

Figure 1: SAW resonator layout (a) and a differential wreless sensor based on resonators (b).

(quartz) and strong ($LiNbO_3$) piezoelectric materials. It makes sense to use license-free ISM (Industrial, Scientific, Medical) frequency bands that are centered around 433.92 MHz, 868 MHz, 915 MHz, 2.45 GHz and 5.8 GHz. If the frequency is below 1 GHz, the SAW propagation loss is low and unloaded Q can be as high as 10000-20000 so a long impulse response and hence a good accuracy of measurements can be achieved. SAW resonators are quite compact devices even if they work at 433 MHz (λ = 7.3 μm for quartz), the lowest UHF ISM band (see Fig. 1a).

What allows the resonators to be used as physical sensors is dependence of the resonant frequency on temperature T and strain s due to variation of both V_R and Λ with T and s. All components of the strain tensor influence f_r to some extent but it is most sensitive to s_{xx} where x is the SAW propagation direction normal to the IDT fingers and grating stripes. Sensitivity to strain allows measurements of force, acceleration, pressure, torque and other physical quantities that can be related to the strain on the surface of the SAW substrate.

An alternative to the resonators, reflective delay lines [5], have the same advantages as other SAW devices: small dimensions, operation at UHF, good sensitivity of the phase delay to temperature and strain, capability of working in harsh environment, insensitivity to stray magnetic fields. On top of them they can implement time division and code division multiplexing (TDMA and CDMA) as well as OFDM that are very useful for building a system with multiple sensors working within one antenna field of a wireless reader [10,11]. However, delay lines are broadband devices so, unlike resonators, it is problematic to use them in relatively narrow 433 MHz and 868-915 MHz ISM bands. Besides, for the same size as the resonators, they have a shorter impulse response (≤5 μs) and a larger insertion loss (typically 30-50 dB) both affecting the measurement accuracy. Their interrogation usually takes longer, around 10-50 ms, when using frequency modulated CW signal (FMCW).

Selection of the type of the SAW sensing element depends on the application. The best choice for a multi-sensor system that must comply with EMC regulations is a delay line sensor working within the international 2.45 GHz ISM band. If one sensor within one reader antenna field is sufficient then a multi-resonator sensor working at 433 MHz or 868-915 MHz is preferable, especially when fast interrogation is required. If sensing is performed in a shielded area or the EMC regulation compliance is not essential, multiple multi-resonator sensors implementing frequency division multiplexing can be used outside the ISM bands.

2.2 SAW resonator as a passive back-scatterer

To turn the one-port SAW resonator into a wireless sensing element, one just needs to connect an antenna to its terminals. If the sensor is supposed to work in free space within a far field of the reader antenna then the sensor antenna usually has a simple dipole, monopole, loop, patch or slot design with dimensions far less than the wavelength λ_{EM} and the gain of -10…2 dBi. The reader antenna can be more directional or with low directivity as well depending on the application and the available space. If the sensor and the reader antennas are supposed to work in the near field of each other, they may have more specialized designs. An example is non-contact sensors for measuring torque on rotating shafts and plates discussed below. They employ microstrip rotary couplers as a sensor-reader antenna system [13].

Independently of the design, the input impedance of the sensor antenna varies with its position relative to the reader antenna and surrounding objects. This variation causes a variable pulling effect on the frequency of natural oscillations of the SAW resonator/antenna system. As shown in [12,13], this parasitic effect often comparable with a useful effect caused by a measurand can be reduced by proper selection of the sensor antenna impedance and/or matching components. Usually, the aim is to achieve a compromise between the amount of pulling effect, the length of the SAW response on one hand and the amplitude of the SAW response on the other hand. The overall influence of the antenna impedance on the theoretical resolution of a SAW resonant sensor is analyzed in [14].

In practice, the antenna pulling effect can never be fully eliminated by matching. To suppress it further, a differential sensor design is usually used when the measurement of the difference between the resonant frequencies is performed for two resonators working at slightly different frequencies [15]. In case of strain measurements, one of the resonators can be unstrained and used as a reference or it can be strained differently (Fig. 1b).

The SAW resonator can also perform just a function of a passive transponder while the sensing function is performed by an external capacitive or inductive sensor connected to it together with the antenna [16]. However, the frequency variation with the measurand is often very non-linear and instable in this case so we prefer to rely on the SAW resonator itself as a sensing element.

2.3 Wireless interrogation

The aim of the reader is to measure the resonant frequency wirelessly or in a non-contact way that can be done by a number of different methods. One method relies on excitation of the resonator by a frequency modulated CW signal (CWFM) and tracking of the minimum of the reflection coefficient S_{11} seen at the reader antenna input. The block diagram of such reader capable of simultaneous tracking of two SAW resonators through an RF rotary coupler is shown in Fig. 2 [17]. Such a reader provides a small rms value of the frequency error of ≈60 Hz at 200 MHz but is suitable only for short range/near field interrogation.

Pulsed readers are more suitable both for long range/far field and short range interrogation. An RF interrogation pulse is launched at the frequency f_i close but not necessary equal to f_r with the spectral width comparable or larger than the resonator bandwidth. It excites natural oscillation of the resonator in the sensor. After the end of the pulse, the oscillation continues for the time

$$\tau_n = 2.3Q_L/(\pi f_r) \qquad (2)$$

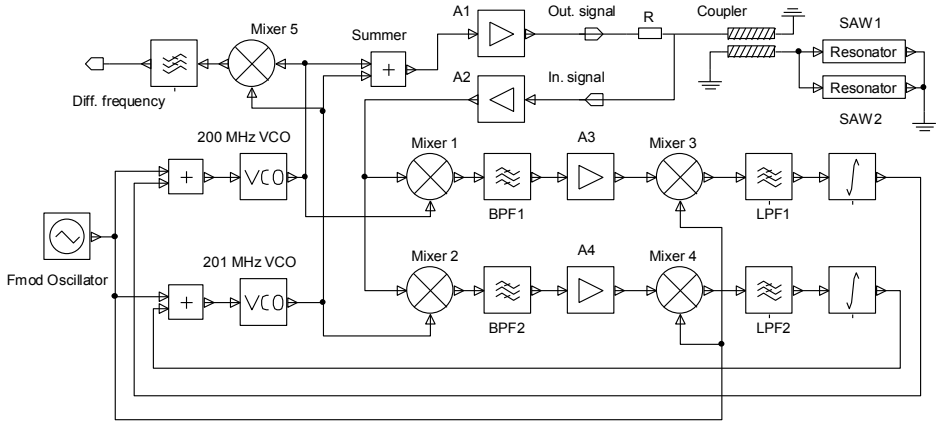

Figure 2: Block diagram of the reader for simultaneous CWFM interrogation of two resonators.

until it decays exponentially by a factor of 10 (Q_L is the Q factor of the resonator loaded by the antenna). It is re-radiated by the sensor antenna and picked up by the reader's receiver. Since the interrogation signal is over, the SAW response can be easily distinguished from it and from the environmental echo that is much shorter than $\tau_n \approx$ 10-20 μs at 433 MHz.

The task of the reader is to estimate f_r either directly from a single sampled SAW response or based on the amplitudes of several SAW responses measured at a number of interrogation frequencies. The second approach is simpler from the computational point of view [18] but it takes longer or, if just two or three frequencies are used, suffers from a limited tracking bandwidth of the sensor. Besides, amplitude measurements are more subject to random errors than frequency estimation algorithms. For these reasons, the first approach is more attractive [16,19]. Various algorithms can be used for the frequency estimation [20] but we prefer DFT based estimator giving random frequency errors not far away from the theoretical limit for practical SNR > 15 dB and at the same time computationally not as complex as methods based on singular value decomposition.

The block diagram of the pulsed reader and its implementation in the form of a single-sided PCB based on the RF ASIC transceiver MLX11006 and TMS320F2808 DSP is shown in Fig. 3. The reader is capable of sequential interrogation of several SAW resonators working within 420-440 MHz range with the sensitivity ≈-86 dBm at SNR = 17 dB. Measurement of a single resonant frequency takes $126 + 24N_c$ μs for short range and $126 + 37.2N_c$ μs for long range applications where N_c is a number of coherently accumulated SAW responses. The rms value of random frequency errors is around $(300…560)/N_c^{1/2}$ Hz for the peak input power P_{in} of the SAW responses from 0 to -35 dBm typical for short range applications. For long range applications, P_{in} can be as low as ≈-85 dBm giving random errors up to $7/N_c^{1/2}$ kHz.

Sequential interrogation increases the measurement update period and hence reduces the bandwidth B for the differential sensor containing more than one resonator. To broaden the bandwidth, it is desirable to interrogate two resonators in parallel by means of their simultaneous narrowband excitation. This strategy is implemented in a more complex and expensive high-speed reader [21] shown in Fig. 4. It takes only 62 μs for the reader to measure two resonant frequencies without coherent accumulation of SAW responses. This

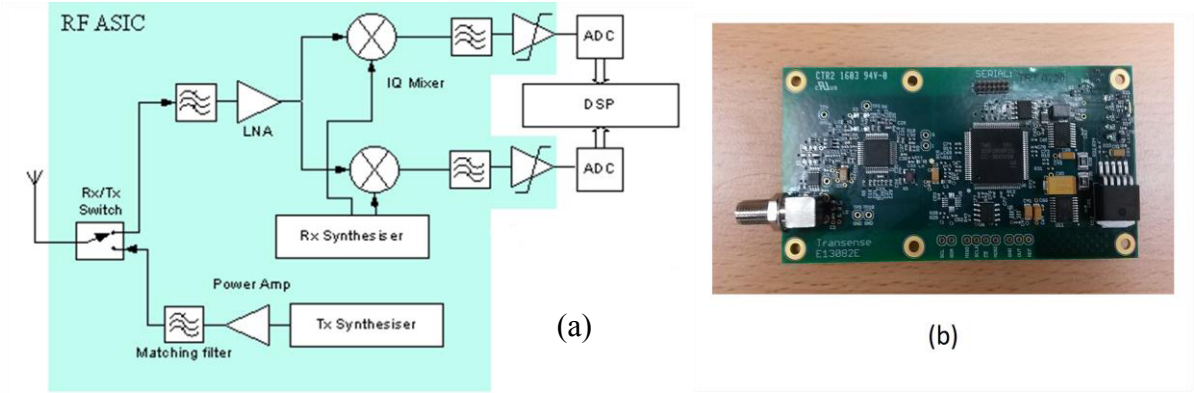

Figure 3: Block diagram of the pulsed reader (a) and its implementation (b)



Figure 4: High-speed reader for simultaneous interrogation of two resonators

increases the sensor bandwidth almost by a factor of five compared to the standard reader shown in Fig. 3, which is useful for monitoring fast process such as vibrations and torque at the output of IC engines.

3 SAW PRESSURE AND TEMPERATURE SENSOR

This sensor was developed by 2006 for automotive tire pressure monitoring system (TPMS) [7,22]. It uses a 4x8x0.35 mm SAW sensing element made of quartz (Fig. 5a) with three resonators two of which parallel to each other form a differential pressure sensor. The quartz die is installed on two ledges of the metal base of the package; the central resonator is deformed by a dimple of the metal lid working as a diaphragm while the left one is used as a reference. The pressure sensitivity of their difference frequency varies from 2.5 kHz/psi (for 10 Bar sensors) to 5.8 kHz/psi (for 3 Bar sensors) depending on the thickness of the lid. The inclined resonator on the left and the rightmost resonator form a differential temperature sensor with the sensitivity of about 1.7 kHz/°C.

Resonant frequencies of the three resonators are selected in such a way that they stay within the European 433 MHz ISM band (1.74 MHz wide) at all pressures and within the required temperature range from -40°C to +100°C. All three resonators are connected in parallel to a single shortened whip antenna and the reader is connected to four small dipole antennas installed under wheel arches by twisted pair cables through an RF switch. The interrogation power is selected to be ≈0.5 mW to comply both with EU requirements and

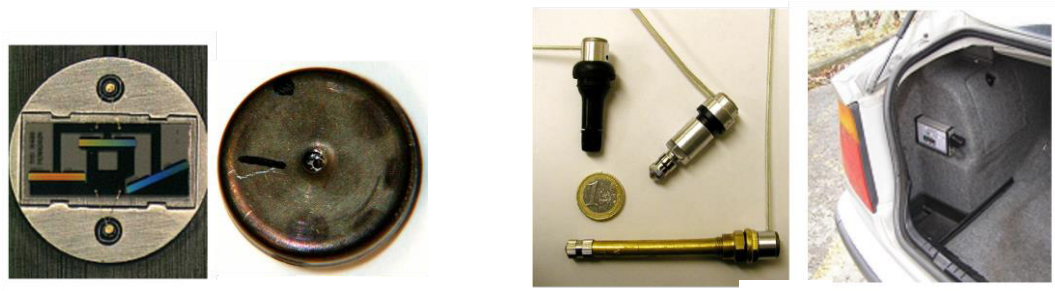

(a) (b)

Figure 5: SAW pressure & temperature sensor (a), its installation in the tire valve and the TPMS reader in the car boot (b)

FCC regulations in the US where 433 MHz band is not an ISM band. $N_c \leq 30$ SAW responses are coherently accumulated for each resonator to reduce random errors. In addition, frequency measurements are averaged over N_a = 40 interrogation attempts. As a result, the rms difference frequency errors are σ_F < 350 Hz resulting in the rms errors of measured temperature σ_T < 0.2°C and pressure σ_P < 0.14 psi for the 10 Bar sensor. The achieved overall accuracy of the system is better than 1 psi and 2 °C.

The developed pressure and temperature wireless sensor can be used not only for TPMS and not only at the distance of about 1 m between the reader and sensor antennas. Due to FCC (Part 15) regulations, the pressure and temperature readings cannot be updated faster than every T_{up} = 10 s with the reader transmission time limited by 330 ms. The update rate could be faster without this limitation but there is always a trade-off between the required sensor resolution defined by σ_F, the sensor bandwidth $B \sim 1/(2T_{up})$, and the read range L for a given interrogation power P_{int}. For a far field, free space communication [14,23],

$$\sigma_F = \sqrt{2\left(\sigma_a^2 + \sigma_f^2\right)/(N_c N_a)} \tag{3}$$

where

$$\sigma_a = \frac{12\pi^2 C f_r}{Q_L G_s G_r T_R}\left[\frac{4k_B T F B_r T_s}{K_{Rx} P_{int}(1-|\Gamma|^2)\tau_n}\right]^{1/2}\left(\frac{L}{\lambda_{EM}}\right)^2 \tag{4}$$

is the receiver's additive noise contribution into the rms value of the measured frequency without coherent accumulation, $C \approx 2.5$ is the increase factor due to the DFT based frequency estimator being worse that the theoretical limit defined by Cramer-Rao lower bound. $G_{s,r}$ are antenna gains for the sensor and the reader, T_R is the voltage gain for the resonator + antenna depending on the antenna mismatch, k_B is Boltzmann's constant, F is the ASIC's noise factor, B_r is the receiver's noise bandwidth, T_s is the sampling period for the SAW response within τ_n, Γ is the reflection coefficient for the reader antenna, σ_f is the contribution of the phase noise of the receiver's local oscillator and K_{Rx} is the power loss coefficient in the receiver's front-end circuit and due to a delay between the end of the interrogation pulse and the first sample. On the other hand, for a sequential interrogation of three SAW resonators,

$$T_{up} = 3N_a(126 + 37.2N_c)\ \mu s. \tag{5}$$

Based on (3)-(5) one can estimate an achievable sensor bandwidth for a given read range and

required resolution σ_F using the graph in Fig. 6. It is plotted for P_{int} = 0.5 dBm, $G_{s,r}$ = 0 dBi, F = 9 dB, Γ = 0.17, B_r = 1.5 MHz, T_s = 0.24 μs, σ_f = 560 Hz, K_{Rx} = 0.37. A reasonable value of $T_R \approx 0.24$ is obtained for the typical resonator parameters: Q = 10000, series resonant impedance 50 Ω, static capacitance C_0 = 4.4 pF, and the antenna impedance R_{as}+jX_{as} = 70 + j200 Ω ensuring a small variation of f_r with the antenna reactance according to

$$T_R \cong B_0 R_{as}\sqrt{\left(7.5\tau_n^{\,2}\left(f_p - f_r\right)^2 + \left(1-\tau_n/\tau_0\right)^2\right)Z^{-1}}, \quad Z = \left(1 - B_0 X_{as}\right)^2 + \left(B_0 R_{as}\right)^2, \tag{6}$$
$$f_r = f_p\left[1 + \left(0.5\,C/C_0\right)\left(B_0 X_{as} - 1\right)Z^{-1}\right], \quad \tau_n = \tau_0\left[1 + R_{as}\tau_0/\left(4.6LZ\right)\right]^{-1}, \; B_0 = 2\pi f_p C_0,$$

where f_p is the antiresonance frequency of the unloaded resonator and C is its motional capacitance.

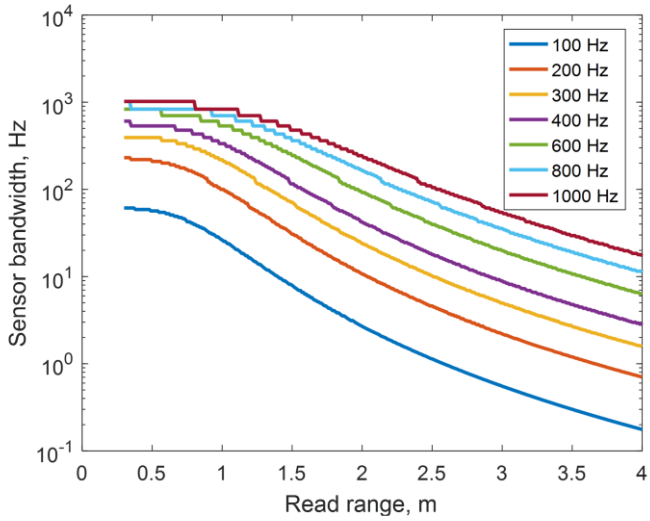

Figure 6: Sensor bandwidth achievable for a given standard deviation σ_F of the measured difference frequency at P_{int} = 0.5 mW against the read range in free space.

One can see that the achievable sensor bandwidth decreases with the read range quite rapidly because of a need in a larger number of coherent accumulations N_c and averages N_a to achieve the required frequency resolution. One should bear in mind that the maximum achievable read range is limited by a threshold signal-to-noise value SNR_{min} below which the frequency estimator is unreliable so (4) is only valid for

$$L \le 8.9\lambda\sqrt[4]{N_c(1-|\Gamma|^2)K_{Rx}P_{int}(G_sG_rT_R)^2/(SNR_{min}k_BTB_rF)} \tag{7}$$

that is around 9 m for SNR_{min} = 15 dB. One should also bear in mind that conditions for the signal propagation can be much worse in reality than in free space due to reflections and absorption of electromagnetic waves as it is in the case of TPMS.

A realistic upper temperature limit for the resonant sensors based on quartz is around 250°C. A different material for the SAW substrate should be used at higher temperatures such as, langasite [24] or AlN/sapphire that can work at least up to 850°C although the Q factor drops noticeably with temperature.

4 TEMPERATURE COMPENSATED STRAIN AND TORQUE SENSOR

Differential SAW resonant sensing elements on quartz substrates for measuring shear strain are shown in Fig. 7a [7]. The resonators M1SAW-M4SAW work at f_1 = 437 MHz, f_2 =435 MHz, f_4 = 431 MHz and f_5 = 429 MHz that are located beyond the 433 MHz ISM band so they should be interrogated either through near field antennas/couplers or in a shielded environment to comply with EMC regulations. The difference frequencies $F_{m1} = f_1 - f_2$ and $F_{m2} = f_4 - f_5$ depend linearly on strain as shown in Fig. 7b with the sensitivity 2.6-3 kHz/με for the resonator axes coinciding with principal components of shear strain. The sensitivity as well as the offset of the characteristics change slightly with temperature since the temperature characteristic of a SAW resonator depends on strain [17]. A temperature compensation of the sensing elements is required for an accuracy better than 1%. It is achieved by adding one more resonator, TSAW, to one of them. Its frequency is f_3 = 433 MHz and $F_t = f_2 - f_3$ is used

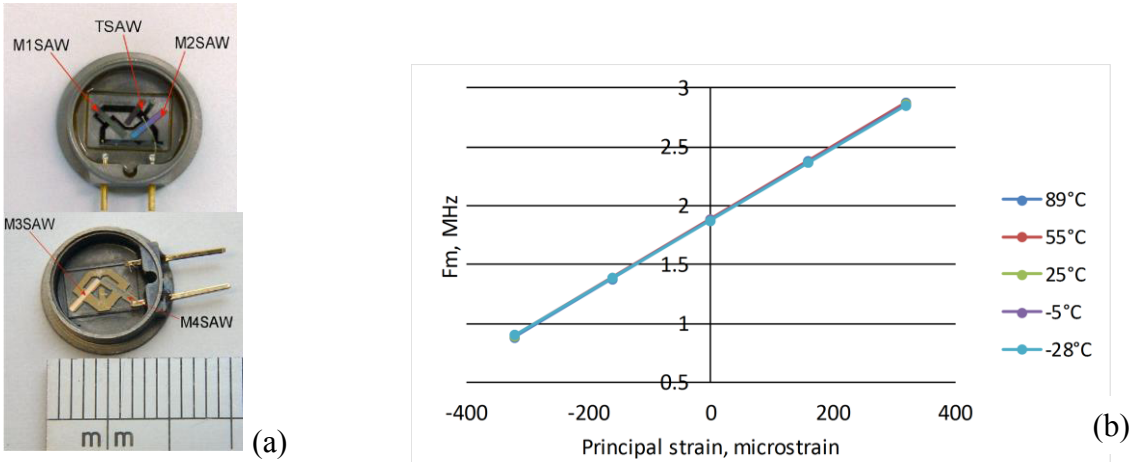

Figure 7: SAW strain sensing elements (a) and their characteristics (b).

for an independent temperature measurement and compensation as described in [25].

The same sensing elements can also be used for measuring uniaxial strain. In this case, M1SAW and M3SAW are positioned along the strain axis and the sensitivity of $F_{m1,2}$ is 1.8-2.4 kHz/με. The sensing elements shown in Fig. 7a are packaged in metal packages and sealed by laser welded lids. However, all-quartz packages assembled by a wafer-level process more suitable for high-volume manufacturing are also available. The maximum survivable strain limit for both types of quartz sensing elements is around 1500 με.

Since the sensing elements can measure shear strain they are also capable of measuring torque when bonded to a flat area on the surface of a shaft or a disc where the torque is applied. Several non-contact SAW torque sensors were developed for automotive industry [7]. Fig. 8a shows a shaft used in electrical power assisted steering (EPAS) with two bonded sensing elements. They are connected to the rotor of an RF coupler and the stator connected to the standard reader. The sensor range is ±36 Nm, the resolution is ≈0.06 Nm, the total error is below 1% FS within -40…+85°C and the torque update period T_{up} = 0.5 ms for N_c = 5.

Another automotive torque sensor installed on the input gearbox shaft for IndyCar is shown in Fig. 8b. It also contains two SAW sensing elements for bending compensation

that are connected to a coaxial RF rotor couple. The range of the sensor is ±1 kNm, the resolution is better than 2 Nm, the error is below 1% FS and T_{up} = 0.3 ms for N_c = 1.

Fig. 8c shows a flexplate connecting an engine to a torque converter with a single sensing element installed. One can also see a rotor microstrip couple for non-contact near-field communication. The sensor range is ±400 Nm, the resolution is ≈1.1 Nm, the total error is around 1% FS within -40…+125°C and the torque update period T_{up} = 0.15 ms if a standard reader is used. If a high-speed reader is used, T_{up} = 62 μs allowing to see fine details of firing pulses in the torque signal at the IC engine output.

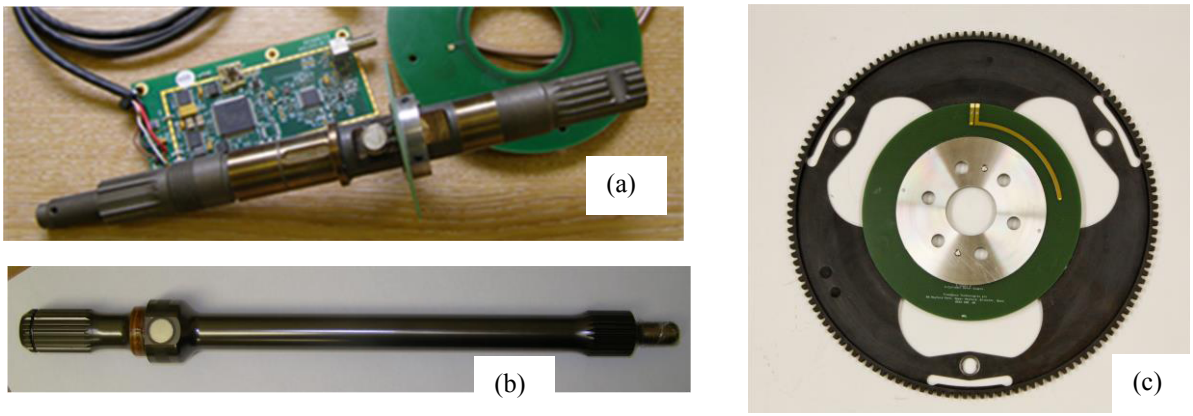

Figure 8: Non-contact torque sensor installed on a steering shaft (a), input gearbox shaft (b) and flexplate (c).

Apart from automotive sector, several non-contact torque sensors were developed for other industrial applications, for instance, monitoring conditions of wind turbine gearboxes. To simplify an aftermarket installation, the sensing elements were installed on plate transducers (Fig. 9a) that could be calibrated separately from a 120-mm high speed shaft and easily installed on it using flexible clamps (Fig. 9b). The sensor range is 5 kNm, the error after calibration is less than 0.7% FS and T_{up} = 0.73 ms for N_c = 10. A similar design was used for a sensor installed on a 180-mm propeller shaft of a Norwegian passenger ship. The sensor was tested by Kongsberg Maritime during one year without degradation of performance although it showed some creep (Fig. 10) that should be reduced by optimizing the clamp design.

5 CONCLUSIONS

- Resonant SAW sensors have several advantages over other types of wireless SAW sensors, in particular, low insertion loss and short interrogation time. However, they are less suitable for multi-sensor systems since they cannot employ TDMA and CDMA within license-free frequency bands.
- Resonant differential sensors can be used for wireless measurement of temperature, pressure, strain, and torque but one should bear in mind a trade-off between the sensor bandwidth, the read range, and the sensor resolution. Fast update rate of several kilohertz with high resolution can only be achieved within a short range, preferably using near field antennas.
- Several wireless resonant SAW sensors have been developed for automotive and

industrial sectors. New prospects for high volume applications will emerge with further reduction of SAW packaging cost, development of high-Q sensing elements for a wider 2.45 GHz ISM band as well as more sensitive, faster, and cheaper readers.

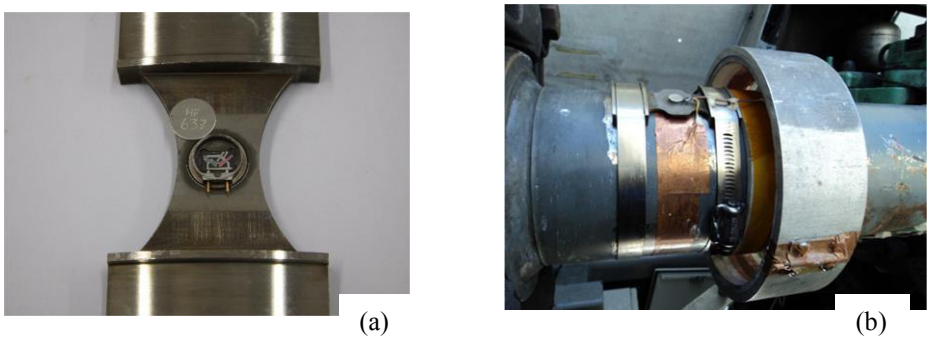

(a) (b)

Figure 9: Plate torque transducer (a) and installation of the SAW torque transducers on the wind turbine high speed gearbox shaft (b).

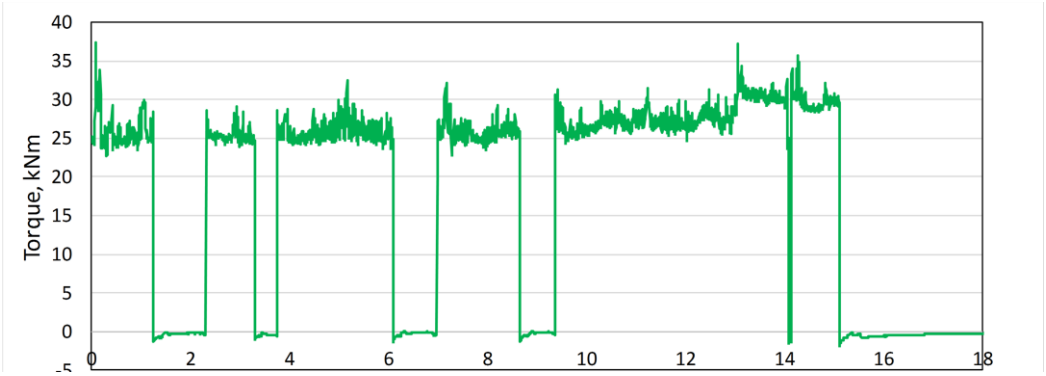

Figure 10: Torque data logged from the marine SAW torque sensor during 24 hours

REFERENCES

[1] A. Lonsdale and B. Lonsdale, Method and apparatus for measuring strain. Int. patent public. No. WO 91/13832, 19 Sept. 1991, Int. Applic. No. PCT/GB91/00328, Int. filing date: 4 March 1991, Priority: 9004822.4, 3 March 1990, GB.

[2] T. M. Reeder, D. E. Cullen and M. Gilden, SAW oscillator pressure sensors. *Proc. 1975 IEEE Int. Ultrason. Symp.*, pp. 264-268, (1975).

[3] D. Hauden, S. Rouseau, J. J. Gagnepain, Sensitivities of SAW oscillators to temperature, forces and pressure: application to sensors. *Proc. 34th Ann. Freq. Contorl Symp.*, pp. 312-319, (1980).

[4] L. Reindl, G. Scholl, T. Ostertag, H. Scherr, U. Wolff, and F. Schmidt, Theory and application of passive SAW radio transponders as sensors. *IEEE Trans. Ultrason., Ferroelectrics and Freq. Control,* (1998) **45**:1281–1292,

[5] F. Schmidt and G. Scholl, Wireless SAW identification and sensor systems, in a book: *Advances in surface acoustic wave technology, systems and applications (Vol. 2)*, Ed.: C. C. W. Ruppel, T. A. Fieldly, World Scientific, (2001).

[6] W. Buff, S. Klett, M. Rusko, J. Ehrenpfordt, and M. Goroll, Passive remote sensing for temperature and pressure using SAW resonator devices. *IEEE Trans. Ultrason., Ferroelectrics, and Frequency Control*, (1998) **45**:1388–1392.
[7] V. Kalinin. Wireless physical SAW sensors for automotive applications. *Proc. 2011 IEEE Int. Ultrason. Symp.*, pp. 212–221, (2011).
[8] R. Frank, *Understanding smart sensors, 2nd ed.*, Artech House, (2000).
[9] N. Bulusu, S. Jha, *Wireless sensor networks*, Artech House, (2005).
[10] J. H. Kuypers, *et al.*, Passive 2.45 GHz TDMA based multi-sensor wireless temperature monitoring system: results and design considerations. *Proc. 2006 Int. IEEE Ultrason. Symp.,* pp. 1453-1458, (2006).
[11] N. Y. Kozlovski, D. C. Malocha, and A. R. Weeks, A 915 MHz SAW sensor correlator system. *IEEE Sensors Journ.,* (2011) **11**:3426-3432.
[12] V. Kalinin, Modelling of a wireless SAW system for multiple parameter measurement. *Proc. IEEE Int. Ultrason. Symp.*, pp. 1790-1793, (2001).
[13] V. Kalinin, RF rotary couplers for contactless torque sensors based on SAW resonators. *Proc. Europ. Freq. and Time Forum*, Toulouse, France, (2008).
[14] V. Kalinin, Passive wireless strain and temperature sensors based on SAW devices. *Proc. IEEE Radio and Wireless Conf.,* pp. 187-190, (2004).
[15] W. Buff, M. Rusko, M. Goroll, J. Ehrenprofdt, T. Vandahl, Universal pressure and temperature SAW sensor for wireless applications. *Proc. IEEE Int. Ultrason. Symp*., pp. 359-362, (1997).
[16] W. Buff, SAW sensors for direct and remote measurement. *Proc. 2002 Int. IEEE Ultrason. Symp.,* pp. 420-428, (2002).
[17] J. Beckley, V. Kalinin, M. Lee, K. Voliansky, Non-contact torque sensors based on SAW resonators. *Proc. 2002 IEEE Freq. Control Symp.*, pp. 202-213, (2002).
[18] J.-M Friedt, C. Droit, G. Martin, and S. Ballandras, A wireless interrogation system exploiting narrowband acoustic resonator for remote physical quantity measurement. *Rev. Sci. Instrum.,* (2010) **81**:014701.
[19] V. Kalinin, G. Bown, J. Beckley and R. Lohr, Pulsed interrogation of the SAW torque sensor for electrical power assisted steering. *Proc. IEEE Int. Ultrason., Ferroelectrics, and Freq. Control Joint 50th Anniversary Conf.,* pp. 1577-1580, (2004).
[20] V. Kalinin, Comparison of frequency estimators for interrogation of wireless resonant SAW sensors. *Proc. Int. 2015 IEEE Freq. Control Symp.,* pp. 498-503, (2015).
[21] V. Kalinin, J. Beckley, I. Makeev, High-speed reader for wireless resonant SAW sensors. *Proc. Europ. Freq. and Time Forum,* pp. 428-435, (2012).
[22] B. Dixon, V. Kalinin, J. Beckley, and R. Lohr, A second generation in-car tire pressure monitoring system based on wireless passive SAW sensors. *Proc. IEEE Freq. Control Symp.,* pp. 374–380, (2006).
[23] V. Kalinin, "Influence of receiver noise properties on resolution of passive wireless resonant SAW sensors", *Proc. 2015 Int. IEEE Ultrason. Symp.*, pp. 1452-1455, (2005).
[24] A. Canabal, P. M. Davulis, G. M. Harris and M. Pereira do Cunha, High-temperature battery-free wireless microwave acoustic resonator sensor system. *Electron. Lett.,* (2010) **46**:471-472.
[25] V. Kalinin, G. Bown, A. Leigh. Contactless torque and temperature sensor based on SAW resonators. *Proc. 2006 Int. IEEE Ultrason. Symp.*, pp. 1490-1493, (2006).

VIII ECCOMAS Thematic Conference on Smart Structures and Materials
SMART 2017
A. Güemes, A. Benjeddou, J. Rodellar and J. Leng (Eds)

A FINITE STRAIN CONSTITUTIVE MODEL CONSIDERING TRANSFORMATION INDUCED PLASTICITY FOR SHAPE MEMORY ALLOYS UNDER CYCLIC LOADING

LEI XU*, THEOCHARIS BAXEVANIS† AND DIMITRIS LAGOUDAS*‡

*Department of Aerospace Engineering, Texas A&M University
College Station, TX 77840, USA

† Department of Mechanical Engineering, University of Houston
Houston, TX 77204, USA

‡ Department of Material Science and Engineering, Texas A&M University
College Station, TX 77840, USA

Key words: Shape Memory Alloys, Constitutive Model, Finite Strain, Transformation-Induced Plasticity, Cyclic Loading

Abstract. Many engineering applications of Shape Memory Alloys (SMAs) involve passing back and forth through phase transformation many times. Repeated phase transformation develops permanent deformations originating from the significant distortion that phase transformation induces at the austenite–martensite interfaces and grain boundaries. This distortion drives dislocation activity resulting in an observable macroscopic Transformation-Induced Plastic (TRIP) deformation, which occurs at effective stress levels much lower than the plastic yield limit of the material. TRIP strains may accumulate up to 20% during the lifetime of an SMA component and thus a finite strain constitutive model is required for simulating their response. In this work, a 3-D finite strain model is developed based on logarithmic strain which is the only strain measure whose rate is equal to the stretching, that describes phase transformation and TRIP deformation in a thermodynamically consistent setting. The model is implemented in Abaqus finite element software through a user defined material subroutine (UMAT). Boundary value problems such as strip and a torque tube under both pseudoelastic and actuation cyclic loadings are performed to test the capabilities of the newly proposed model.

1 INTRODUCTION

SMAs have the ability to recover a pre-defined shape when subjected to appropriate thermo-mechanical loading. Since the discovery of the shape memory effect, SMAs has been extensively investigated to be used as sensors, controllers and actuators etc. towards building smart system integrated with adaptive and intelligent functions.

Over the several past decades, a substantial number of SMA constitutive models at the continuum level have been proposed, most of them being based on the infinitesimal strain assumption within the small deformation regime. A review of such models can be found in Boyd and Lagoudas [3], Birman and November [1], Raniecki and Lexcellent [18, 19], Patoor et al. [15, 16], Hackl and Heinen [7], Levitas and Preston [11, 12]. The majority of above mentioned models are dealing with stable material response that exhibits no evolutionary features. However, many engineering applications of SMAs involve passing back and forth through phase transformation many times. Repeated phase transformation develops permanent deformations originating from the significant distortion that phase transformation induces at the austenite martensite interfaces and grain boundaries especially for the initial cyclic loadings. This distortion drives dislocation activity resulting in an observable macroscopic transformation-induced plastic deformation, which occurs at effective stress levels much lower than the plastic yield limit of the material. From experiment results, TRIP strains may accumulate up to 20% during the lifetime of an SMA component, and thus a finite strain constitutive model accounting large strains and rotations is required for give better predications.

A three-dimensional constitutive model at finite strain regime for SMAs incorporating TRIP is proposed in this work. The adopted logarithmic strain measure and rate [20, 21, 22] enables the model to effectively capture the material response under finite strains with rotations, and attribute modeling advantages in the presence of large accumulated plastic strain under cyclic thermo-mechanical loading for SMAs. The martensitic volume fraction, transformation strain, and TRIP strain are used to characterize material nonlinear behavior while back stress tensor and a drag stress term are used to introduce the effects of the kinematic and isotropic hardening in the model.

To this end, the paper is organized as follows. In Section 2, we represent some preliminaries on kinematics in continuum mechanics. Section 2.4 will concentrate on the thermodynamic framework to formulate the constitutive model by using logarithmic strain and logarithmic rate. Boundary value problems will be addressed to test the capability of proposed model in Section 3. At the end, we summarize this paper with conclusion in Section 4.

2 PRELIMINARY

2.1 Kinematics

Let $\mathbf{X}$ and $\mathbf{x} = \chi(\mathbf{X}, t)$ denote the position vector of the material points of a body $\mathcal{B}$ in the reference (undeformed) configuration at initial time t_0 and at the current (deformed) configuration at time t, respectively. The deformation process from the initial configuration to current configuration can be characterized by the deformation gradient,

$$\mathbf{F}(\mathbf{x}, t) = \frac{\partial \mathbf{x}}{\partial \mathbf{X}} \tag{1}$$

Then, the velocity gradient $\mathbf{L}$ is defined through as follows:

$$\mathbf{L} = \dot{\mathbf{F}}\mathbf{F}^{-1} \tag{2}$$

The velocity gradient $\mathbf{L}$ can be additively decomposed into a symmetric part called the rate of deformation tensor, i.e. $\mathbf{D}$, plus an anti-symmetric part called the spin tensor, i.e. $\mathbf{W}$,

$$\mathbf{L} = \mathbf{D} + \mathbf{W}; \quad \begin{cases} \mathbf{D} = \frac{1}{2}(\mathbf{L} + \mathbf{L^T}), \\ \mathbf{W} = \frac{1}{2}(\mathbf{L} - \mathbf{L^T}), \end{cases} \tag{3}$$

The following polar decomposition formula is well known, in which $\mathbf{R}$ is the rotation tensor and $\mathbf{V}$ is the left stretch.

$$\mathbf{F} = \mathbf{VR} \tag{4}$$

The left Cauchy-Green tensor $\mathbf{B}$ is defined by

$$\mathbf{B} = \mathbf{F}\mathbf{F}^T = \mathbf{V}^2 \tag{5}$$

The logarithmic strain of Eulerian type $\mathbf{h}$ is given through,

$$\mathbf{h} = \frac{1}{2}\ln \mathbf{B} = \ln \mathbf{V} \tag{6}$$

The Kirchhoff stress tensor is defined as equation 7, where J is the determinant of the deformation gradient $\mathbf{F}$.

$$\boldsymbol{\tau} = J\boldsymbol{\sigma} \tag{7}$$

2.2 Logarithmic rate and Logarithmic spin

In finite deformation analysis, the rate of the deformation tensor $\mathbf{D}$ can be additively decomposed into an elastic part $\mathbf{D}^e$ and a dissipative part $\mathbf{D}^{dis}$. One of the main tasks is to adopt an appropriate objective rates to achieve the principle of objectivity in its rate form constitutive equations. Many objective rates, such as the Jaumann, Green–Naghdi, and Truesdell rates, have been proposed by different researchers. However, none of them was able to set up a direct relation between the rate of deformation tensor $\mathbf{D}$ and an objective rate of strain measure, thus many spurious phenomena, such as shear stress oscillation, dissipative energy or residual stress accumulated in elastic deformation, are observed when these rates are being used. Until recently the so-called logarithmic rate proposed by Xiao et al. [20, 21, 22], Bruhns et al. [4, 5, 6], Meyers et al. [13, 14] successfully resolved such self-inconsistent issues. It was shown that the logarithmic rate of the logarithmic strain $\mathbf{h}$ of Eulerian type is identical with the rate of deformation tensor $\mathbf{D}$, which is expressed as:

$$\mathring{\mathbf{h}}^{log} = \dot{\mathbf{h}} + \mathbf{h}\boldsymbol{\Omega}^{log} - \boldsymbol{\Omega}^{log}\mathbf{h} = \mathbf{D} \tag{8}$$

Where $\mathring{\mathbf{h}}^{log}$ means the logarithmic rate of logarithmic strain and $\dot{\mathbf{h}}$ is the conventional time rate of logarithmic strain. $\boldsymbol{\Omega}^{log}$ is called logarithmic spin introduced by Xiao and Bruhns [20] with its explicit expression as:

$$\boldsymbol{\Omega}^{log} = \mathbf{W} + \sum_{i \neq j}^{n} \left(\frac{1 + (\lambda_i/\lambda_j)}{1 - (\lambda_i/\lambda_j)} + \frac{2}{\ln(\lambda_i/\lambda_j)}\right)\mathbf{B}_i\mathbf{D}\mathbf{B}_j \tag{9}$$

Where $\mathbf{W}$ is the spin tensor; $\lambda_{i,j}(i, j = 1, 2, 3...)$ are the eigenvalues of left Cauchy-Green tensors $\mathbf{B}$; $\mathbf{B}_{i,j}$ are the corresponding subordinate eigenprojections of $\mathbf{B}$.

2.3 Additive decomposition of logarithmic strain

Starting from the additive decomposition of the rate of deformation tensor $\mathbf{D}$,

$$\mathbf{D} = \mathbf{D}^e + \mathbf{D}^{tr} + \mathbf{D}^p \tag{10}$$

The total stress power supplied from outside working on body $\mathcal{B}$ per unit volume can be calculated and additively decomposed into,

$$P_{stress_power} = \boldsymbol{\tau} : \mathbf{D} = \boldsymbol{\tau} : \mathbf{D}^e + \boldsymbol{\tau} : \mathbf{D}^{tr} + \boldsymbol{\tau} : \mathbf{D}^p \tag{11}$$

From energy point of view, additive decomposition of kinematics in finite deformation analysis can be interpreted as total stress power being split into a recoverable part of $\boldsymbol{\tau} : \mathbf{D}^e$, an irrecoverable dissipation part $\boldsymbol{\tau} : \mathbf{D}^{tr}$ for transformation process and a plastic dissipation part $\boldsymbol{\tau} : \mathbf{D}^p$ associated with plasticity deformation.

By virtue of equation 8, elastic part $\mathbf{D}^e$, transformation part $\mathbf{D}^{tr}$ and plastic part $\mathbf{D}^p$ in equation 10 can be rewritten as the logarithmic rate of elastic logarithmic strain $\mathbf{h}^e$, logarithmic rate of transformation logarithmic strain $\mathbf{h}^t$ and logarithmic rate of plastic logarithmic strain $\mathbf{h}^p$ respectively,

$$\mathring{\mathbf{h}}^{e_log} = \mathbf{D}^e; \quad \mathring{\mathbf{h}}^{t_log} = \mathbf{D}^{tr}; \quad \mathring{\mathbf{h}}^{p_log} = \mathbf{D}^p \tag{12}$$

Combine equation 10 and equation 12, the following equation can be obtained.

$$\mathring{\mathbf{h}}^{log} = \mathring{\mathbf{h}}^{e_log} + \mathring{\mathbf{h}}^{t_log} + \mathring{\mathbf{h}}^{p_log} \tag{13}$$

Apply logarithmic corotational integration[8] in equation 13 on both sides, the following additive decomposition of total logarithmic strain can be received. Namely, the total logarithmic strain can be additively split into an elastic part, a transformation part and a plasticity part.

$$\mathbf{h} = \mathbf{h}^e + \mathbf{h}^t + \mathbf{h}^p \tag{14}$$

2.4 FINITE STAIN SMA MODEL WITH TRIP

2.4.1 Thermodynamic potential of constitutive model

A Gibbs free energy expression is proposed [2, 10]

$$\begin{aligned} G = -\frac{1}{2\rho_0}\boldsymbol{\tau} : \boldsymbol{S}\boldsymbol{\tau} - \frac{1}{\rho_0}\boldsymbol{\tau} : [\ \boldsymbol{\alpha}(T - T_0) + \mathbf{h}^t + \mathbf{h}^p] - \frac{1}{\rho_0}\int_0^\xi (\boldsymbol{\beta} : \frac{\partial \mathbf{h}^t}{\partial \xi} + \eta) d\xi \\ + c\Big[(T - T_0) - T\ln(\frac{T}{T_0})\Big] - s_0(T - T_0) + u_0 \end{aligned} \tag{15}$$

where $\boldsymbol{\tau}$ is the Kirchhoff stress tensor, T is the temperature and $\boldsymbol{\Upsilon} = \{\mathbf{h}^t, \mathbf{h}^p, \boldsymbol{\beta}, \eta, \xi\}$ is the set of internal state variables, with $\boldsymbol{\beta}$, η, ξ denoting a back-stress tensor, a drag-stress scalar, and the martensite volume fraction, respectively. $\boldsymbol{\beta}$ and η describe hardening effects. Moreover, $\boldsymbol{S}(\xi)$ is the fourth-order compliance tensor by using rule of mixtures, $\boldsymbol{\alpha}$ is the second order thermoelastic expansion tensor, c is effective specific heat, s_0, u_0 are effective specific entropy at reference state and effective specific internal energy at reference state, respectively, and T_0 is the reference temperature.

Following the standard Coleman-Noll procedure in dissipation inequality, the following constitutive relations can be obtained

$$\mathbf{h} = -\rho_0 \frac{\partial G}{\partial \boldsymbol{\tau}} = \boldsymbol{S}\boldsymbol{\tau} + \boldsymbol{\alpha} : (T - T_0) + \mathbf{h}^t + \mathbf{h}^p \tag{16}$$

$$s = -\rho_0 \frac{\partial G}{\partial T} = \frac{1}{\rho_0}\boldsymbol{\tau} : \boldsymbol{\alpha} + c\ln(\frac{T}{T_0}) - s_0 \tag{17}$$

where s denotes the entropy. Apart from the constitutive relation obtained, the following strict form of the dissipation inequality can also be derived

$$-\rho_0 \frac{\partial G}{\partial \mathbf{h}^t} : \overset{\circ}{\mathbf{h}}{}^t - \rho_0 \frac{\partial G}{\partial \mathbf{h}^p} : \overset{\circ}{\mathbf{h}}{}^p - \rho_0 \frac{\partial G}{\partial \xi}\dot{\xi} \geqslant 0 \tag{18}$$

The following section will concentrate on setting up the evolution equations between different internal state variables.

2.4.2 Evolution equation for transformation strain

One key assumption of the classical SMAs model postulated by Boyd and lagoudas [3] is that any change in the current microstructural state of the material is strictly a result of a change in the martensitic volume fraction. We thus propose the following evolution relationship between ξ and $\mathbf{h}^t$.

$$\overset{\circ}{\boldsymbol{h}}{}^t = \boldsymbol{\Lambda}\dot{\xi}, \quad \boldsymbol{\Lambda} = \begin{cases} \boldsymbol{\Lambda}_{fwd}, \ \dot{\xi} > 0, \\ \boldsymbol{\Lambda}_{rev}, \ \dot{\xi} < 0, \end{cases} \tag{19}$$

where, $\boldsymbol{\Lambda}_{fwd}$ is the transformation direction tensor during forward transformation process, while $\boldsymbol{\Lambda}_{rev}$ is the transformation direction tensor during reverse transformation process, they are defined respectively in equation 20. It is worth to point out that the rate in equation 19 is logarithmic rate for finite deformation analysis defined in Section 2.2

$$\boldsymbol{\Lambda}_{fwd} = \frac{3}{2} H^{cur} \frac{\boldsymbol{\tau}^{\text{eff}'}}{\bar{\tau}^{\text{eff}}}; \qquad \boldsymbol{\Lambda}_{rev} = H^{cur} \frac{\mathbf{h}^t}{\bar{\mathbf{h}}^t}. \tag{20}$$

$\boldsymbol{\tau}^{\text{eff}}$ is the effective stress tensor, which is defined as equation 21, the back stress tensor $\boldsymbol{\beta}$ will be introduced shortly.

$$\boldsymbol{\tau}^{\text{eff}} = \boldsymbol{\tau} + \boldsymbol{\beta} \tag{21}$$

$\boldsymbol{\tau}^{'}$ is the deviatoric stress tensor part defined by $\boldsymbol{\tau}^{'} = \boldsymbol{\tau} - \frac{1}{3}\text{tr}(\boldsymbol{\tau})\mathbf{I}$, in which $\mathbf{I}$ is the second order identity tensor. The von mises equivalent stress is given by

$$\bar{\tau} = \sqrt{\frac{3}{2}\boldsymbol{\tau}^{'} : \boldsymbol{\tau}^{'}} \tag{22}$$

H^{cur} denotes the current maximum transformation strain for current stress state. From experiment observation, the maximum transformation strain H^{cur} is not a constant value throughout all stress state, it is a exponential function depending on current stress state as defined through an curve fitting in equation 23, in which H^{max} is the maximum saturated transformation strain and k_t is a curve fitting material parameter.

$$H^{cur}(\boldsymbol{\tau}) = H^{max}(1 - e^{-\text{k}_t \bar{\boldsymbol{\tau}}^{\text{eff}}}) \tag{23}$$

2.4.3 Evolution equation for plastic strain

In order to model the large irrecoverable transformation induced plastic strain, a evolution equation for the plastic strain is also proposed here. It has a similar structure as the evolution equation proposed by Lagoudas and Entchev [10]. Instead of using the Cauchy stress, infinitesimal strain tensor and the conventional time rate for the rate form evolution equation, we used the Kirchhoff stress, logarithmic strain tensor and the logarithmic rate to reformulate the evolution relation in equation 24.

$$\mathring{\boldsymbol{h}}^p = \boldsymbol{\Lambda}^p \dot{\xi}, \quad \boldsymbol{\Lambda}^p = \begin{cases} \boldsymbol{\Lambda}^p_{fwd}, \ \dot{\xi} > 0, \\ \boldsymbol{\Lambda}^p_{rev}, \ \dot{\xi} < 0, \end{cases} \tag{24}$$

In the above rate form evolution equation, $\boldsymbol{\Lambda}^p_{fwd}$ is the forward TRIP direction tensor while $\boldsymbol{\Lambda}^p_{rev}$ is the reverse TRIP direction tensor. They have the explicit expression in equation 25 respectively. The rate here is logarithmic rate.

$$\boldsymbol{\Lambda}^p_{fwd} = \frac{3}{2} C_1^p \frac{H^{cur}(\boldsymbol{\tau})}{H^{max}} \frac{\boldsymbol{\tau}^{\text{eff}'}}{\bar{\boldsymbol{\tau}}^{\text{eff}}} e^{-\frac{\zeta^d}{C_2^p}}; \quad \boldsymbol{\Lambda}^p_{rev} = -C_1^p \frac{H^{cur}(\boldsymbol{\tau})}{H^{max}} \frac{\mathbf{h}^{t-r}}{\bar{\mathbf{h}}^{t-r}} e^{-\frac{\zeta^d}{C_2^p}}. \tag{25}$$

In the above defined TRIP direction tensor, the accumulated detwinned martensitic volume fraction ζ^d is introduced through the following equation, the way it was introduced here is based on the assumption that self-accommodating martensitic phase transformation plays no role on the development of the plastic strains [10].

$$\zeta^d = \int_0^t |\dot{\xi}^d(t)| dt \tag{26}$$

The detwinned martensitic volume fraction ξ^d is introduced as equation 27

$$\xi^d = \frac{H^{cur}(\boldsymbol{\tau})}{H^{max}} \xi \tag{27}$$

2.4.4 Drag stress and back stress

In this model, a second order back stress tensor and a scalar drag stress term are introduced to accounting for the kinematic and isotropic hardening features during the transformation process. They are essentially representing microstructure effects such as grain boundaries, misfit between austenite-martensite interface, micro voids and cracks etc. The back stress tensor is defined in a similar way by Lagoudas and Entchev [10], which has the tensorial equation 28. The difference is here we used logarithmic strain measure instead of infinitesimal strain measure.

$$\boldsymbol{\beta} = -\frac{\boldsymbol{h}^t}{\bar{\boldsymbol{h}}^t} \big[D_1^b (H^{cur}\xi) + D_2^b (H^{cur}\xi)^2 + D_3^b (H^{cur}\xi)^3 + D_4^b (H^{cur}\xi)^4 + D_5^b (H^{cur}\xi)^5 \big] \tag{28}$$

The scalar drag stress term is the same as it was in paper Lagoudas and Entchev [10]. It is revisited here in equation 29 for clarity .

$$\eta = -D_1^d \big[-\ln(1-\xi) \big]^{\frac{1}{m_1}} + D_2^d \xi \tag{29}$$

2.4.5 Transformation function

In this section, a criterion for the occurrence of both the forward and reverse transformation will be defined to make the model completed. After the introduction of evolution equation for internal state variables, we substitute the evolution equation 19 and 24 into the strict form dissipation inequality 18, the following inequality can be derived:

$$(\boldsymbol{\tau} : \boldsymbol{\Lambda} - \rho_0 \frac{\partial G}{\partial \xi})\dot{\xi} = \pi \dot{\xi} \geqslant 0 \tag{30}$$

In the above equation, the quantity π is called the general thermodynamic driving force conjugated to ξ. Substitute Gibbs free energy expression equation 15 into equation 30, the explicit expression of general thermodynamic driving force π is obtained:

$$\begin{aligned} \pi = \frac{1}{2}\boldsymbol{\tau} : \Delta \boldsymbol{S}\boldsymbol{\tau} + \boldsymbol{\tau}^{\text{eff}} : \boldsymbol{\Lambda} + \boldsymbol{\tau} : \boldsymbol{\Lambda}^p + \boldsymbol{\tau} : \Delta\alpha(T - T_0) + \eta \\ -\rho_0 \Delta c\big[T - T_0 - T\ln(\frac{T}{T_0})\big] + \rho_0 \Delta s_0 (T - M^{0s}) + Y \end{aligned} \tag{31}$$

Where $\Delta \boldsymbol{S}, \Delta\alpha, \Delta c, \Delta s_0, \Delta u_0$ represent the difference of these material parameters between austenitic and martensitic phase by virtue of the rule of mixture. M^{0s} is introduced as a combination of other parameter such that

$$M^{0s} = T_0 + \frac{1}{\rho_0 \Delta s_0}(Y + \rho_0 \Delta u_0) \tag{32}$$

Consistent with the framework by Qidwai and Lagoudas [17], we are assuming that whenever the thermodynamic driving force reaches a critical value Y or $(-Y)$, the forward (reverse) phase transformation will take place. Thus transformation function Φ is introduced here to working as a criterion as defined by equation (33).

$$\Phi = \begin{cases} \pi - Y, \ \dot{\xi} > 0, \\ -\pi - Y, \ \dot{\xi} < 0, \end{cases} \tag{33}$$

To satisfy the second law of thermodynamics and the principle of maximum dissipation for the internal state variables, some certain constraints have to apply on the model, this constraint can be expressed in terms of so-called Kuhn-Tucker conditions:

$$\begin{aligned} &\dot{\xi} \geqslant 0; \quad \Phi(\boldsymbol{\tau}, T, \xi) = \ \ \pi - Y \leqslant 0; \quad \Phi\dot{\xi} = 0; \quad (\mathbf{A} \Rightarrow \mathbf{M}) \\ &\dot{\xi} \leqslant 0; \quad \Phi(\boldsymbol{\tau}, T, \xi) = -\pi - Y \leqslant 0; \quad \Phi\dot{\xi} = 0; \quad (\mathbf{M} \Rightarrow \mathbf{A}) \end{aligned} \tag{34}$$

3 NUMERICAL RESULTS

In order to demonstrate the capabilities of proposed model, two types of problems are presented here in this section. The first problem analyzed is a strip under unaxial tension loading while the other problem is a torque tube under torsion loading. For both problems, isothermal stress-induced transformation case and isobaric thermal-induced transformation case are performed respectively. The results are obtained through using the commercial finite element software Abaqus combined with user defined material subroutine (UMAT). Material parameters used in all the cases are presented in Table 1 from the book by Lagouas et al. [9].

Table 1: Material parameters for SMA used for the numerical results [9]

Parameter	Value	Parameter	Value
E_A	70 [GPa]	D_b^1	3.40 $\times$ 10 ^{3} [MPa]
E_M	50 [GPa]	D_b^2	-2.23 $\times$ 10 ^{5} [MPa]
$\nu_A = \nu_M$	0.33	D_b^3	8.32 $\times$ 10 ^{6} [MPa]
$\alpha_A = \alpha_M$	2.2 $\times 10^{-5}$ [K^{-1}]	D_b^4	-1.50 $\times$ 10 ^{8} [MPa]
H^{max}	0.05	D_b^5	1.03 $\times$ 10 ^{9} [MPa]
k_t	0.0052 [MPa^{-1}]	D_d^1	8.0 [MPa]
ρc^A	2.12 [MJ/(m^{3}K)]	D_d^2	1.7 [MPa]
ρc^M	2.12 [MJ/(m^{3}K)]	m_1	3.5
$\rho \Delta s_0$	-0.422 [MJ/(m^{3}K)]	C_1^P	3.6 $\times$ 10 $^{-3}$
M^{0s}	311.0 [K]	C_2^P	18.0
		Y	6.0 [MJ/m^3]

3.1 Uniaxial isothermal loading case

This boundary value problem describes a SMA strip sample under cyclic isothermal uniaxial tensile load up to a maximum value of 800 MPa. During the loading step, the load is linearly increased from initial value 0 MPa to its maximum value 800 MPa, which activates the forward stress-induced transformation. After the load reach the peak value, it begins unloading from 800 MPa to 0 MPa, which results in a reverse transformation. The temperature is keeping a constant value of 360 K throughout this whole process. Loading cycle is repeated 50 times. The material stress versus strain response curve for this case is depicted in Figure 1. In order to have a clean picture, only several loading cycles are chosen to show in the figure. It can been seen that there is a substantial amount of irrecoverable plastic strain accumulated during this cyclic loading process. The TRIP strain in the only first cycle is about 0.7% and saturated with a value close to 6% after 30 cycles. The material response is stabilized and the plastic strain accumulated in the 50th is almost zero.

3.2 Uniaxial isobaric loading case

This boundary value problem is simulating a SMA strip under cyclic actuation loading. The SMA strip is first subjected to a constant uniaxial tensile load of 200 MPa, then it undergoes multiple coolings and heatings by changing the temperature from 360 K to 260 K back and forth. The strain versus temperature curve is plotted in Figure 2, again only several typical curves are chosen to show to have a clean result. As is shown in Figure 2, there is a large amount of irrecoverable plastic strain accumulated during the cyclic actuation loadings. The TRIP strain starts with value around 0.6% and end up with almost a zero value after 30 cycles, the actuation response is also stabilized and the accumulated TRIP strain saturated with a value around 4.8% after 50 cycles.

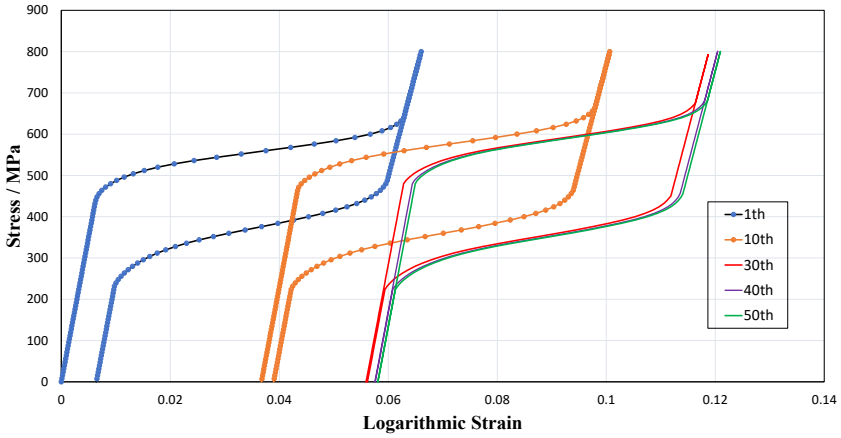

Figure 1: Pseudoelastic response of strip from 1st to 50th cycle

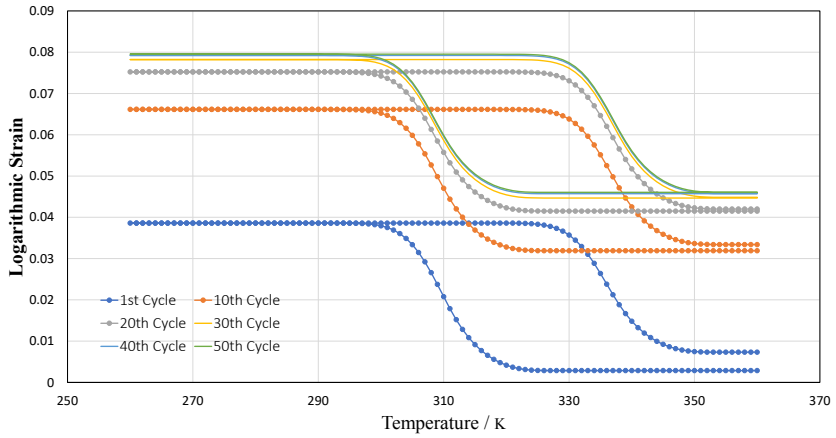

Figure 2: Actuation response of strip from 1st to 50th cycle

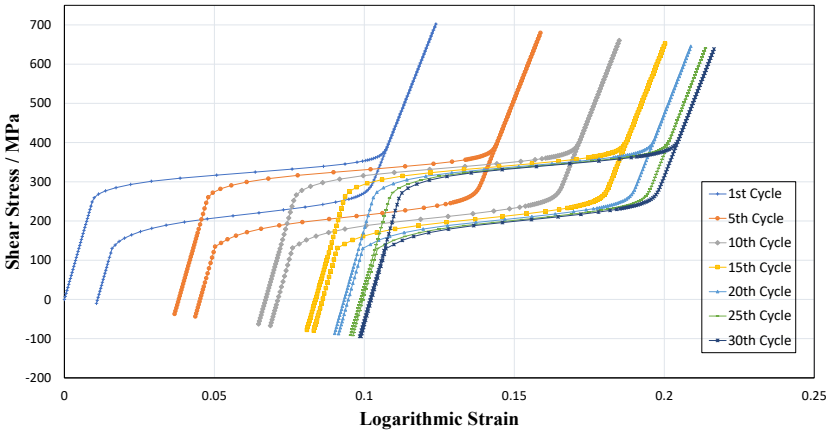

Figure 3: Actuation response of torque tube from 1st to 30th cycle

3.3 Torsion isothermal loading case

In this section, a torque tube problem is used to demonstrate the capability of proposed model for loading case with rotations. The tube is subjected to a torque linearly changing from its initial 0 value to a maximum value during loading, and linearly decreasing from its maximum value to 0 value for unloading. The temperature is kept as a constant value of 360 °C throughout the cyclic loading process.The material pseudoelastic stress versus strain curve is plotted in Figure 3. The plotting information comes from a point at the torque tube inner surface. From the figure, it is interesting to see the difference between these results and those obtained from unaxial case in 3.1. Apart from the saturated TRIP strain and stabilized material response, the pseudoelastic curve of torque tube shifted down compared to it was in uniaxial case. This can be explained by the internal stress introduced through the training process. Since the shear stress is not uniform along the radial direction, thus the plastic strain accumulated due to phase transformation is also not uniform along radial direction, the outer surface will have larger TRIP strain as a result of the larger shear stress it experienced while the inner part will have a smaller one. A nonuniform shear stress distribution make the response of tube shifted compared to its counterparts in the uniaxial case.

3.4 Torsion isobaric loading case

The last problem analyzed is the torque tube under cyclic actuation loading. Similar to the loading case in section 3.1, the SMA tube is first subjected to a constant torque, then it will experience the cooling and heatings by changing the temperature from 360 K to 290 K back and forth. The actuation response of torque tube is shown in Figure 4, similar as what observed in Figure 2, there is also a large amount of irrecoverable plastic strain accumulated. The TRIP strain saturates with a value around 9% in the end, and the actuation response is also stabilized after 30 cycles.

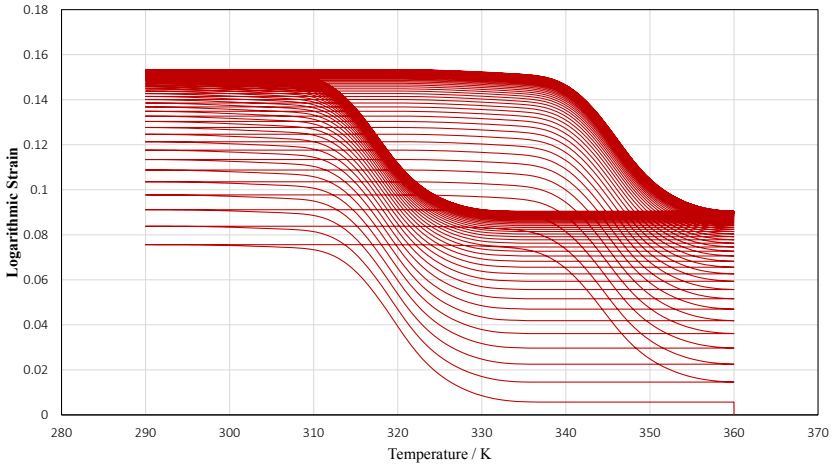

Figure 4: Actuation response of torque tube from 1st to 30th cycle

4 CONCLUSIONS

In the paper, a three-dimensional constitutive model at finite strain regime for phase transformation materials with large accumulating transformation induced irrecoverable plastic strain is proposed in this work. Boundary value problems such as a strip and a torque tube under both pseudoelastic and actuation loadings are performed to demonstrate the capabilities of the proposed model. Numerical results of strip problem demonstrated that the proposed model can characterize the material nonlinear evolution features, such as TRIP strain accumulation and its saturation, stabilized material response after certain loading cycles in a good manner. The torque tube problem also showed that the model can predict the internal stress introduced through the material training process. In the future, the presented model will be calibrated through and compared to the experiment results.

REFERENCES

[1] Birman, V., 1997. Review of mechanics of shape memory alloy structures. Applied Mechanics Reviews 50 (11), 629–645.

[2] Bo, Z., Lagoudas, D. C., 1999. Thermomechanical modeling of polycrystalline smas under cyclic loading, part iii: Evolution of plastic strains and two-way shape memory effect. International Journal of Engineering Science 37 (9), 1175–1203.

[3] Boyd, J. G., Lagoudas, D. C., 1996. A thermodynamical constitutive model for shape memory materials. part i. the monolithic shape memory alloy. International Journal of Plasticity 12 (6), 805–842.

[4] Bruhns, O., Xiao, H., Meyers, A., 1999. Self-consistent eulerian rate type elasto-plasticity models based upon the logarithmic stress rate. International Journal of Plasticity 15 (5), 479–520.

[5] Bruhns, O., Xiao, H., Meyers, A., 2001. Large simple shear and torsion problems in kinematic hardening elasto-plasticity with logarithmic rate. International journal of solids and structures 38 (48), 8701–8722.

[6] Bruhns, O., Xiao, H., Meyers, A., 2001. A self-consistent eulerian rate type model for finite deformation elastoplasticity with isotropic damage. International Journal of Solids and Structures 38 (4), 657–683.

[7] Hackl, K., Heinen, R., 2008. A micromechanical model for pretextured polycrystalline shape-memory alloys including elastic anisotropy. Continuum Mechanics and Thermodynamics 19 (8), 499–510.

[8] Khan, A. S., Huang, S., 1995. Continuum theory of plasticity. John Wiley & Sons.

[9] Lagoudas, D. C., 2008. Shape memory alloys. Science and Business Media, LLC.

[10] Lagoudas, D. C., Entchev, P. B., 2004. Modeling of transformation-induced plasticity and its effect on the behavior of porous shape memory alloys. part i: constitutive model for fully dense smas. Mechanics of Materials 36 (9), 865–892.

[11] Levitas, V. I., 1998. Thermomechanical theory of martensitic phase transformations in inelastic materials. International Journal of Solids and Structures 35 (9), 889–940.

[12] Levitas, V. I., Preston, D. L., 2002. Three-dimensional landau theory for multivariant stress-induced martensitic phase transformations. i. austenite martensite. Physical review B 66 (13), 134206.

[13] Meyers, A., Xiao, H., Bruhns, O., 2003. Elastic stress ratcheting and corotational stress rates. Tech. Mech 23, 92–102.

[14] Meyers, A., Xiao, H., Bruhns, O., 2006. Choice of objective rate in single parameter hypoelastic deformation cycles. Computers & structures 84 (17), 1134–1140.

[15] Patoor, E., Eberhardt, A., Berveiller, M., 1996. Micromechanical modelling of superelasticity in shape memory alloys. Le Journal de Physique IV 6 (C1), C1–277.

[16] Patoor, E., Lagoudas, D. C., Entchev, P. B., Brinson, L. C., Gao, X., 2006. Shape memory alloys, part i: General properties and modeling of single crystals. Mechanics of materials 38 (5), 391–429.

[17] Qidwai, M., Lagoudas, D., 2000. On thermomechanics and transformation surfaces of polycrystalline niti shape memory alloy material. International Journal of Plasticity 16 (10), 1309–1343.

[18] Raniecki, B., Lexcellent, C., 1998. Thermodynamics of isotropic pseudoelasticity in shape memory alloys. European Journal of Mechanics-A/Solids 17 (2), 185–205.

[19] Raniecki, B., Lexcellent, C., Tanaka, K., 1992. Thermodynamic models of pseudoelastic behaviour of shape memory alloys. Archiv of Mechanics, Archiwum Mechaniki Stosowanej 44, 261–284.

[20] Xiao, H., Bruhns, I. O., Meyers, I. A., 1997. Logarithmic strain, logarithmic spin and logarithmic rate. Acta Mechanica 124 (1-4), 89–105.

[21] Xiao, H., Bruhns, O., Meyers, A., 1997. Hypo-elasticity model based upon the logarithmic stress rate. Journal of Elasticity 47 (1), 51–68.

[22] Xiao, H., Bruhns, O., Meyers, A., 2006. Elastoplasticity beyond small deformations. Acta Mechanica 182 (1-2), 31–111.

VIII ECCOMAS Thematic Conference on Smart Structures and Materials
SMART 2017
A. Güemes, A. Benjeddou , J. Rodellar and Jinsong Leng (Eds)

DOMAIN INTERFACES AND FATIGUE FAILURE OF NITI POLYCRYSTALLINE STRIPS

Shaobin ZHANG and Yongjun HE*

IMSIA, UMR 8193 CNRS-EDF-CEA-ENSTA, Université Paris Saclay
828 Boulevard des Maréchaux, 91762 Palaiseau Cedex, France
e-mail: yhe@ensta.fr

Key words: Shape Memory Alloy, Fatigue, Lüders-like Band Front, Branching Interfaces, Domain Pattern.

Abstract. Lüders-like band is an important deformation feature in a stretched pseudoelastic NiTi polycrystalline strip and its formation/evolution can influence the fatigue life of the NiTi strips significantly. For "elastic" fatigue tests on the specimens with unchanged domain/band patterns (immobile domain interfaces), it is normally expected that the fatigue failure would occur at the band front (the interface separating the Martensite and the Austenite domains); however, it was revealed recently that the fatigue failure can happen inside the Martensite domain. To further understand this phenomenon, the "elastic" fatigue tests and in-situ high-resolution recording of the interface morphology were conducted on NiTi strips of different thicknesses. It is found that the strip's thickness can influence the morphology of the domain interface so as to affect the strip's fatigue life. Moreover, the fatigue failure can occur at the domain interfacial zone or inside Martensite domain, depending on the morphology of the domain interface which depends on the strip's thickness. It is implied that the domain interface could be a key feature governing the fatigue failure of NiTi strips.

1 INTRODUCTION

NiTi polycrystalline Shape Memory Alloy (SMA) with superelasticity and shape memory effects have extensive applications in biomedical, civil, aeronautic and micro-electro-mechanical engineering [1–5], most of which are under cyclic loading and thus the fatigue performance is important (including functional fatigue [6–8] and structural fatigue [7,9]). Particularly, the structural fatigue (with significant microstructure damage leading to device/structure failure) has to be well understood before promoting large-scale engineering applications. Most of the existing fatigue study on NiTi SMA was focused on the fatigue criteria [10–15] in terms of the nominal stress-strain responses (nominal stress/strain amplitude, mean stress/strain, energy dissipation, etc.), ignoring an important deformation feature — Lüders-like bands (macroscopic localized deformation domain) which could be formed in the SMA structures such as wires/tubes [16–23] and plates/strips [17,24–32] due to the material's

mechanical softening property. Recently, it was revealed that the macroscopic domain formation/evolution can influence the fatigue life of the NiTi strips significantly [33–35]. Interestingly (out of general expectation[36–39]), the Lüders-band front (the domain wall/interface separating the high-strain Martensite domain and the low-strain Austenite domain) is not always a fatigue failure zone: for the NiTi strip with the domains (A domains, M domains and the domain interfaces) under only "elastic" cyclic tensile loading (i.e., no interface propagation), the fatigue fracture failure occurs in a M domain rather than at a domain interface [34]. To understand this phenomenon, we conducted the fatigue tests on NiTi strips of different thicknesses. It is found that the strip's thickness can influence the morphology of the domain interface and the associated interfacial energy (as the theoretical prediction in [40]) so as to affect the strip's fatigue life. Therefore, this paper reports the study on how the strip's thickness influences the domain interface morphology and the associated fatigue failure. In the following, the material properties and experimental procedures are described in Section 2, the experimental results and discussion are presented in Section 3. Finally, a brief summary and conclusions are given in Section 4.

2 MATERIAL PROPERTIES AND EXPERIMENTAL SETUP

Dog-bone strips used in the tests have the same width of 2.5 mm and gauge length of 25.0 mm, but different thicknesses t: 0.2 mm, 0.5 mm and 1.0 mm. All the specimens were electro-discharge machined from pseudoelastic polycrystalline NiTi sheets from Johnson Matthey Inc. USA (Austenite finish temperature $A_f \approx 10$ °C) and the specimen surfaces were "pickled" as received from the supplier. While the slim specimens were cut from the sheet (t = 0.2 mm, composition 55.7 wt.% Ni) with the gauge length directions perpendicular to the rolling direction (RD), the medium and thick specimens were cut from the sheets (t = 0.5 mm and 1 mm respectively, composition 56.0 wt.% Ni) along RD. The cyclic fatigue tests on the strips were performed on an Instron machine (ElectroPuls E3000) by controlling the nominal mean strain $\varepsilon_{mean} = (\varepsilon_{max}+\varepsilon_{min})/2$ (ε_{max} is the applied maximum strain and ε_{min} the minimum) and the nominal strain amplitude $\varepsilon_{ampl} = (\varepsilon_{max}-\varepsilon_{min})/2$. A small nominal strain amplitude ε_{ampl} = 0.25% was applied on all the strips to make sure the specimens taking "elastic" cyclic deformation — the band pattern (and the domain interface) doesn't change with the cyclic loading. In the fatigue test, the strip was first stretched to ε_{max} with a slow strain rate (10^{-4} s^{-1}), then the fatigue test was conducted between ε_{max} and ε_{min} cyclically until the fatigue failure occurs. To keep the specimen's temperature close to the ambient temperature (around 21 °C), a fan was used to accelerate airflow to increase heat convection and all the tests were performed with a low strain rate (10^{-3} s^{-1}). During the tests, two CMOS cameras of 2048×1088 pixels (Basler acA2000-340 km) with Nikkor lens were used to record the specimen's surface morphology with a maximum recording rate of 50 frames/s. One camera was fixed at the distance of 35 cm from the specimen to record the morphology of the whole specimen surface (so-called "global view"). In addition, to observe closely the detailed morphologies of the propagating and branching interfaces

(domain walls), another camera was installed close to the specimen (about 1 cm distance, so-called "local view") to obtain high-resolution images of the regions near interfaces. The optical images of both global and local view were processed by Digital Image Correlation (DIC) software Vic-2D (Correlated Solutions) to obtain the local strain fields.

3 EXPERIMENTAL RESULTS AND DISCUSSION

This section includes two parts. The first part reports the typical stress-strain response of the specimens and the associated interface propagation when a specimen was first loaded from nominal strain $\varepsilon = 0$ to the maximum nominal strain ε_{max} to create the band (domain) pattern. particularly with the camera focusing on the interfacial zone ("local view"), the high-resolution morphology of domain interfaces and its branching were observed during the domain propagation. The domain interface is first controlled (by nominal mean strain) to stop at a certain position of the specimens, and then the specimen is submitted to the "elastic" cyclic fatigue test until the fatigue failure (the amplitude of the cyclic nominal strain amplitude ε_{ampl} = 0.25% was so small that the interface didn't move any more in the tests). Also the fatigue life is independent of the applied ε_{mean} (i.e. independent of the position of the band fronts in the gauge section (see [34])) The cyclic stress-strain response and the fatigue failure are discussed in the second part.

3.1 Morphology and propagation of the domain interfaces

Before each fatigue test, a slow strain-controlled tensile loading-unloading cycle (2000 s for the whole cycle with the maximum nominal strain ε_{max} of 7% for t = 0.2 mm specimens (cut perpendicularly to RD) and c = 8% for t = 0.5 mm and 1.0 mm specimens (cut along RD)) was performed on the NiTi dog-bone specimen which can be approximately viewed as an isothermal case. Usually, under the low strain rate, the specimen's temperature varies slightly so that only one band is nucleated and grows with the band-front propagation during the martensitic phase transformation [24–26,41–43].

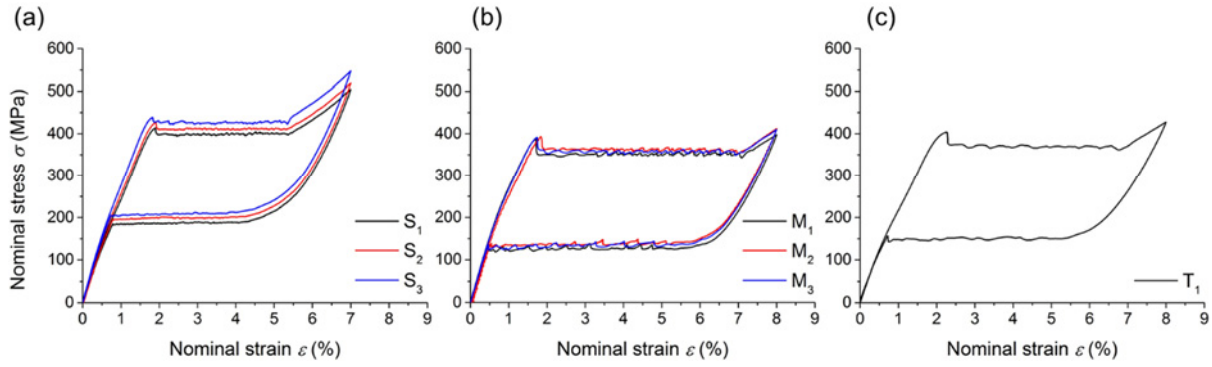

Figure 1: Isothermal stress-strain curves of the strain-controlled test at room temperature $T_0 \approx 21°C$ for (a) slim (S_1-S_3), (b) medium (M_1-M_3) and (c) thick specimens (T_1).

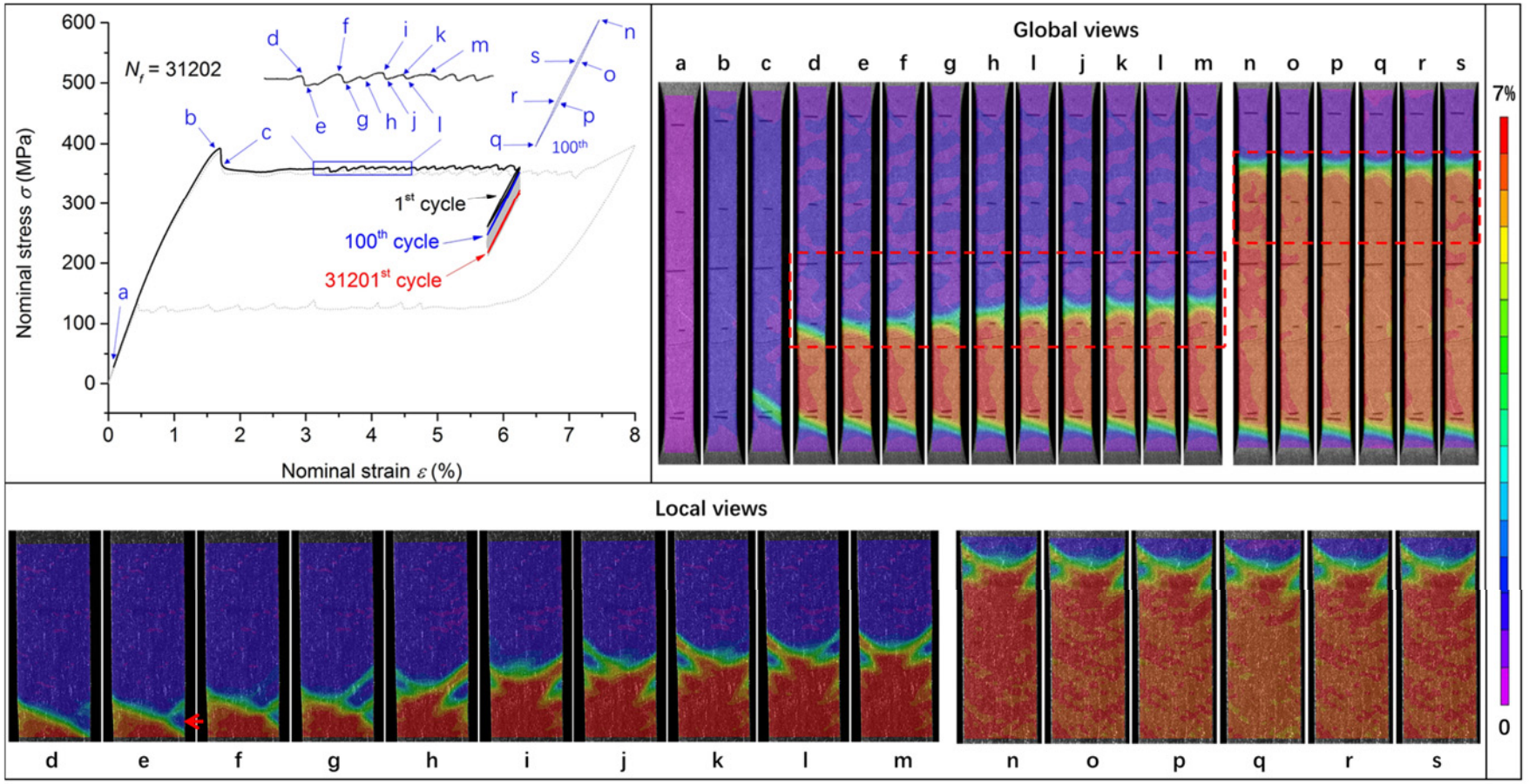

Figure 2: Nominal stress-strain response curve with global and local morphologies and strain fields demonstrating the Lüders band evolution in a NiTi strip (medium specimen M_1) in a strain-controlled tensile fatigue test. Point 'd' to 's' are marked at the magnified stress-strain curves and the local view images correspond to the parts inside the red dashed frames on the global view. The typical small region/island (low-strain A domain) which is surrounded/isolated by the old and new band interfaces is marked with red arrow in local view 'e'.

As shown in Fig. 1, the specimens of different thicknesses (t = 0.2mm, 0.5 mm and 1.0 mm) used in the fatigue tests have similar isothermal stress-strain responses except for the difference in the Austenite-Martensite phase transformation plateau stress (around 415 MPa for t = 0.2 mm specimens and 375 MPa for t = 0.5 mm and 1.0 mm specimens) and the plateau strain (around 3.6% for t = 0.2 mm specimens and 5.0% for t = 0.5 mm and 1.0 mm specimens), which might be due to differences of the composition and cutting between the slim specimens (t = 0.2 mm) and the medium/thick specimens (the same composition and cutting for t = 0.5 mm and 1.0 mm).

To illustrate the whole process of the fatigue tests, a full stress-strain curve and the associated band front propagation of a medium specimen (t = 0.5 mm) are shown as an example in Fig. 2. It is seen in the DIC strain patterns (global views) that the specimen deforms "elastically" and homogeneously (without Lüders-like bands from the start point 'a' to 'b' before stress drop. When the applied nominal strain ε reaches 1.7%, a macro-band (Lüders-like band) appears (see the global view 'c' in Fig. 2). With increasing nominal strain (from "c" to "d"), the band grows smoothly with two inclined interfaces (domain walls) dividing the specimen into two types of global domains (so-called "Marteniste (M) domain" with high local strain $\varepsilon_M \approx 6.7\%$ and "Austenite (A) domain" with $\varepsilon_A \approx 0.8\%$). The angle between the interface normal and the loading axis (gauge-length direction) is around 35° for the compatibility or energy minimization of the mismatch between the M domain and A domain [19,25,40,41].

However, when the applied nominal strain further increases, as shown in the global views from "e" to "m", the M domain grows with the propagation of the interfaces which become almost perpendicular to the loading axis, in order to reduce the bending moments on the specimen (Note: the asymmetry patterns with global inclined interfaces causes bending moments, see [19]). But, with the high-resolution local views ("e", "f", "g" and "h") on the global "perpendicular" interfaces (global domain walls), we can see many small-scale interfaces (so-called "local interfaces" or "local domain walls"). These local interfaces keep the compatible orientation (around 35°); and their nucleation causes small stress drops as shown in the magnified stress-strain plateau. For example, a new local interface (or a very narrow local M band) is nucleated at point "e" with a small stress drop. Then a small triangle region/island (low-strain A domain, pointed by the red arrow in the local view 'e') is surrounded/isolated by the old and new interfaces; when the applied nominal strain continues to increase, the island merges into the existed M domain (see local views "f" and "g"). At the same time, another new band nucleates (local view "g"). Similar process of the band nucleation and merging (band front branching) repeats when the global M domain grows (see local views from 'h' to 'm') until the nominal strain reaches the maximum value for starting the cyclic fatigue test. Therefore, the process of band front propagation (interface propagation) is not always smooth but includes small-scale bands nucleation and merging which leads to stress fluctuations in the stress-strain curves. Particularly, this unsmooth/branching propagation of the band front leaves behind certain small-scale islands causing residual local strain variation inside the global M domain, even though the islands have merged into the M domain (see the

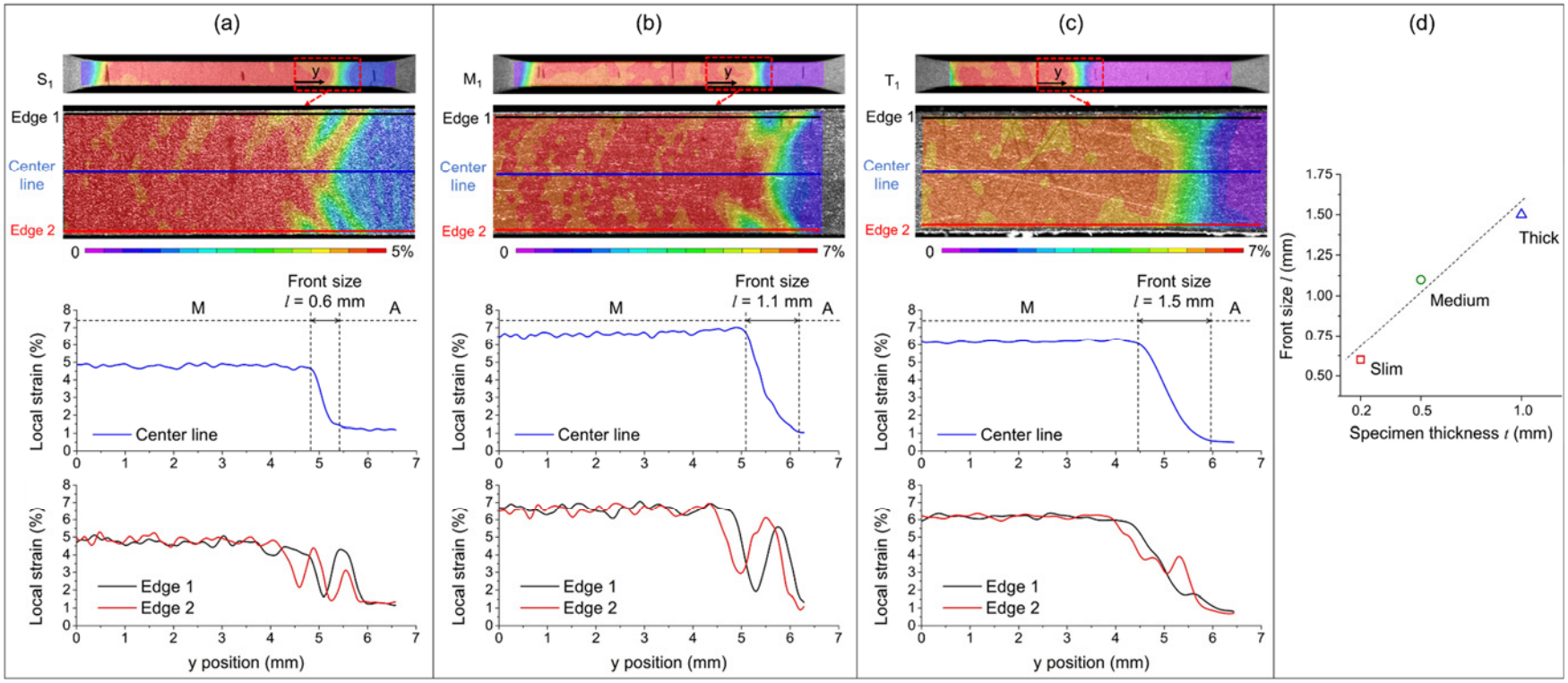

Figure 3: Typical morphologies, strain fields and strain variation (near the band front) along the centerlines and two edges of the specimens of different thickness at the beginning of the fatigue tests: (a) t = 0.2 mm (specimen S_1), (b) 0.5 mm (specimen M_1) and (c) 1.0 mm (specimen T_1). Here, 'y' is the loading direction paralleled to the gauge length. (d) Dependence of the front size l (interface/band-front thickness) on the specimen's thickness (the black dashed line just guides the eyes).

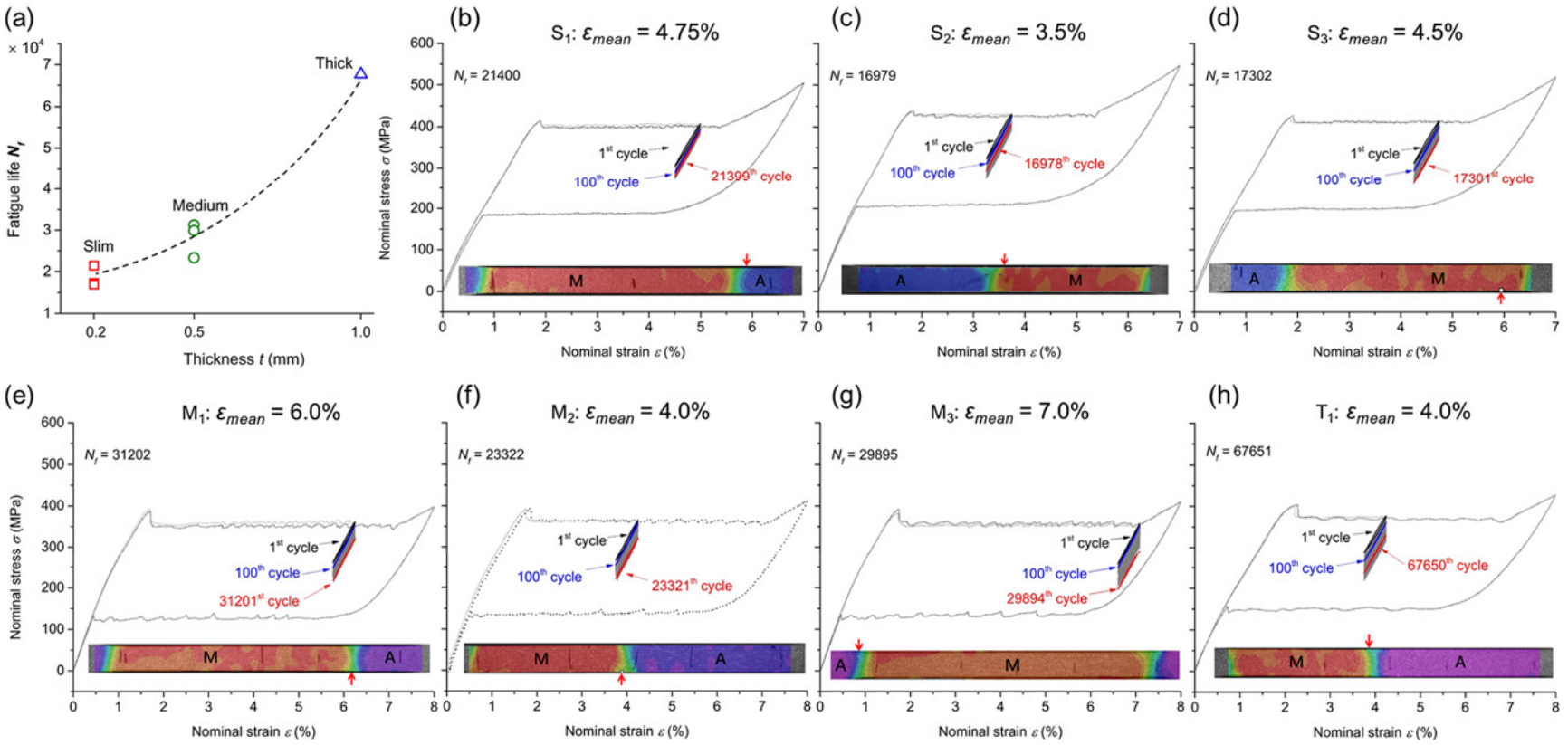

Figure 4: (a) Thickness-dependent fatigue life of NiTi strips (the black dashed line just guides the eyes). (b) - (h) Nominal stress-strain curves of fatigue cycles of the slim (S_1 - S_3), medium (M_1 - M_3) and thick specimens (T_1) under nominal strain amplitudes 0.25% in comparison with their isothermal curves (dashed lines). The black, blue and red lines represent respectively the 1st, the 100th, and the final cycle before failure. The corresponding strain maps at the loading end of 100th cycle are shown under the stress-strain curves; the final fatigue-failure crack nucleation positions are marked by the red arrows.

strain variation along two edges and the center line of the specimens in Fig. 3).

Figure 3 shows the high-resolution DIC strain patterns (local views) around the global domain interfaces at the beginning of the fatigue tests on the specimens of different thicknesses: t = 0.2 mm, 0.5 mm and 1.0 mm. It is seen that the morphologies of the band fronts depend on the specimen's thickness significantly. For the slim specimen (t = 0.2 mm) as shown in Fig. 3(a), the global domain interface in fact includes several sharp crossing branches (with compatible orientation around 35°), forming a 'V' shape macroscopically. So, the center line of the specimen has different strain profiles from that of specimen's edges, as shown in Fig. 3(a) where the strain profiles along the two edges have much more variations than that along the center line. The reason is that the islands left behind the propagating branching interfaces have residual effects on the specimen's two edges (although most parts of the islands would finally merge into the M domain). However, when the specimen's thickness increases, the interface branching becomes weaker. For example, in Fig. 3(c), the global domain interface of the thick specimen (t = 1.0 mm) has little branching, and its strain profiles along the two edges are much smooth than that of the slim specimen (Fig. 3(a)). Besides, with the comparison of the strain profiles along the center lines of the three different specimens (Fig. 3(a)-(c)), we can see that the interface thickness l (the size of the transition zone from A domain to M domain) increases almost linearly with the specimen thickness t as shown in Fig. 3(d), which agrees with the recently theoretical prediction in [40]. The thicker the strip's thickness, the larger the transition zone (higher interfacial energy density) is. That is why branching (formation of more interfaces) is not easy (not energy-preferred or energy-minimization) in thick specimens.

3.2 "Elastic" tensile fatigue tests

The specimens under cyclic fatigue loading with nominal strain amplitude ε_{ampl} = 0.25% deform like "elasticity" with very small hysteresis of stress-strain loops and keeping the domain patterns unchanged. For example, in Fig. 2, the cyclic stress decreases with increasing cycle number, but the stress-strain hysteresis is always small. During the cycles, the domain pattern doesn't change (see the global and local views from 'n' to 's' during the 100th cycle in Fig. 2. For such "elastic" fatigue tests on the specimens with unchanged domain patterns (immobile domain walls)), it is normally expected [36–39] that the fatigue failure would occur at the domain wall; but some previous study such as [34] shows that the fatigue failure can happen inside the M domain rather than at the domain walls. The results of current tests on all the specimens of different thicknesses are summarized in Fig. 4; the positions of the fatigue failure are marked by the red arrows in Fig. 4(b) to (h). For the slim specimens (S_1-S_3 of t = 0.2 mm shown in Fig. 4(b)-(d)), the fatigue failure can occur at (close to) the global domain wall (for the specimens S_1 and S_2) or inside M domain, far from the domain wall (for S_3). By contrast, for the medium and thick specimens, the fatigue failures always occur at (near) the global domain walls as shown in Fig. 4(e)-(h). The reason for the possibility of the fatigue failure inside M domain (far from the global domain walls) might be the residual effects of the islands

left (inside the M domain) behind the propagating domain walls when creating the domain patterns before starting the "elastic" fatigue cyclic tests. The residual-island effect causes the strain variation at the specimen's edges (as shown in strain profiles in Fig. 3(a)) which might lead to local stress concentration improving the possibility of the fatigue crack nucleation there.

The fatigue life N_f for all the specimens are summarized in Fig. 4(a), where N_f increases with the specimen thickness t significantly from around 2×10^4 cycles for $t = 0.2$ mm to around 7×10^4 cycles for $t = 1.0$ mm. There might be several factors influence the specimen's fatigue life, such as the material properties (composition, texture, etc.) and the specimen's geometry (such as thickness t). In current study, although the slim specimens have slight different properties from the other specimens (comparing Fig. 1(a) with (b) and (c)), the medium specimens and thick specimens were purchased from one batch (of the same composition) from the suppler. And both the types of specimens were cut from the sheets along the rolling direction so that they have almost the same pseudoelasticity as shown in Fig. 1(b) and (c) where they have almost the same plateau-stress level and plateau strain (A-M transformation strain). So, it is the specimen thickness, rather than material properties, that mainly governs the variation in the fatigue life of the different specimens in Fig. 4. With the observation on the thickness-dependent interface branching and interfacial transition zone in Fig. 3, we propose that the reason for the thickness-dependent "elastic" fatigue life might be the abrupt strain change across the interface; the thicker the specimen is, the larger the interfacial zone is (the less strain gradient is) and the "elastic" fatigue life N_f is longer. More systematic experiments with both macro- and micro-observations are needed to further clarify the physical mechanism of the thickness-dependent fatigue life.

4 CONCLUSIONS

The paper reports the cyclic "elastic" fatigue tests on the NiTi polycrystalline strips of different thicknesses. During the "elastic" tensile cyclic test, the interfaces between the A domains and M domains didn't move. Besides a "global" camera monitoring the whole specimen's surface, another "local" camera focusing on the interface zone to obtain high-resolution branching interface morphology helps reveal the difference of the detailed interface branching between the specimens of different thicknesses. That provides hints for understanding the dependences of the specimen's fatigue failure on the specimen's thickness. Some preliminary conclusions can be drawn from the tests:

- Domain interface branching is observed in slim and medium specimens; the propagating branching interface leaves behind some islands which induces to a local strain variation inside the global Martensite domain. With increasing the specimen's thickness, the interface branching becomes weaker, almost no branching in the thick specimens ($t = 1.0$ mm). The reason is that the size (thickness) and energy density of the domain interface increases with the specimen's thickness (based on the experiments in Fig. 3(d) and theoretical prediction in [40]). The higher the interfacial energy, the more difficult the

interface formation is. Therefore, there is less interface branching (less interfaces nucleation) in the thick specimens.

- For slim specimens with lots of interface branching, fatigue crack nucleation is not always at the global domain interfaces because islands left inside the Martensite domain behind the propagating front might be the crack nucleation sites; by contrast, for the medium and thick specimens with less interface branching, fatigue failure always occur at global domain interfaces. It is implied that domain interface could be an important feature governing the fatigue life of NiTi strips.
- The "elastic" cyclic fatigue life of NiTi strips increases with the specimen's thickness. The reason might be the smaller strain gradient across the domain walls/interfaces in thicker specimens.

REFERENCES

[1] J. Mohd Jani, M. Leary, A. Subic, M. a. Gibson, A review of shape memory alloy research, applications and opportunities, Mater. Des. 56 (2014) 1078–1113.

[2] S. Barbarino, E.I. Saavedra Flores, R.M. Ajaj, I. Dayyani, M.I. Friswell, A review on shape memory alloys with applications to morphing aircraft, Smart Mater. Struct. 23 (2014) 63001.

[3] A. Nespoli, S. Besseghini, S. Pittaccio, E. Villa, S. Viscuso, The high potential of shape memory alloys in developing miniature mechanical devices: A review on shape memory alloy mini-actuators, Sensors Actuators, A Phys. 158 (2010) 149–160.

[4] L. Petrini, F. Migliavacca, Biomedical Applications of Shape Memory Alloys, J. Metall. 2011 (2011) 1–15.

[5] Dimitris C. Lagoudas, Shape Memory Alloys: Modeling and Engineering Applications, 2008.

[6] G. Scirè Mammano, E. Dragoni, Functional fatigue of Ni-Ti shape memory wires under various loading conditions, Int. J. Fatigue. 69 (2014) 71–83.

[7] G. Eggeler, E. Hornbogen, A. Yawny, A. Heckmann, M. Wagner, Structural and functional fatigue of NiTi shape memory alloys, Mater. Sci. Eng. A. 378 (2004) 24–33.

[8] X. Zhang, D. Huang, X. Yan, X. Zhou, Modeling functional fatigue of SMA using a more accurate subdivision of martensite volume fractions, Mech. Mater. 96 (2016) 12–29.

[9] G. Kang, D. Song, Review on structural fatigue of NiTi shape memory alloys: Pure mechanical and thermo-mechanical ones, Theor. Appl. Mech. Lett. 5 (2015) 245–254.

[10] D. Song, G. Kang, Q. Kan, C. Yu, C. Zhang, Non-proportional multiaxial whole-life transformation ratchetting and fatigue failure of super-elastic NiTi shape memory alloy micro-tubes, Int. J. Fatigue. 80 (2015) 372–380.

[11] D. Song, Observations on the Residual Martensite Phase of NiTi Shape Memory Alloy Micro-Tubes under Uniaxial and Multiaxial Fatigue-loading, in: Proc. ASME 2016 Int.

Mech. Eng. Congr. Expo., 2016.
[12] D. Song, G. Kang, Q. Kan, C. Yu, C. Zhang, Non-proportional multiaxial transformation ratchetting of super-elastic NiTi shape memory alloy: Experimental observations, Mech. Mater. 70 (2014) 94–105.
[13] D. Song, G. Kang, Q. Kan, C. Yu, C. Zhang, Effects of peak stress and stress amplitude on multiaxial transformation ratchetting and fatigue life of superelastic NiTi SMA micro-tubes: Experiments and life-prediction model, Int. J. Fatigue. (2016).
[14] Y. Zhang, J. Zhu, Z. Moumni, A. Van Herpen, W. Zhang, Energy-based fatigue model for shape memory alloys including thermomechanical coupling, Smart Mater. Struct. 25 (2016) 35042.
[15] Z. Moumni, A. Van Herpen, P. Riberty, Fatigue analysis of shape memory alloys: energy approach, Smart Mater. Struct. 14 (2005) S287–S292.
[16] P. Sedmák, J. Pilch, L. Heller, J. Wright, M. Frost, P. Šittner, Grain-resolved analysis of localized deformation in nickel-titanium wire under tensile load, Science (80-.). (2016).
[17] L.C. Brinson, I. Schmidt, R. Lammering, Stress-induced transformation behavior of a polycrystalline NiTi shape memory alloy: Micro and macromechanical investigations via in situ optical microscopy, J. Mech. Phys. Solids. 52 (2004) 1549–1571.
[18] N.J. Bechle, S. Kyriakides, Localization in NiTi tubes under bending, Int. J. Solids Struct. 51 (2014) 967–980.
[19] Y.J. He, Q.P. Sun, Effects of structural and material length scales on stress-induced martensite macro-domain patterns in tube configurations, Int. J. Solids Struct. 46 (2009) 3045–3060.
[20] Y.J. He, Q.P. Sun, Scaling relationship on macroscopic helical domains in NiTi tubes, Int. J. Solids Struct. 46 (2009) 4242–4251.
[21] Q.P. Sun, Z.Q. Li, Phase transformation in superelastic NiTi polycrystalline micro-tubes under tension and torsion - From localization to homogeneous deformation, Int. J. Solids Struct. 39 (2002) 3797–3809.
[22] Z.Q. Li, Q.P. Sun, The initiation and growth of macroscopic martensite band in nano-grained NiTi microtube under tension, Int. J. Plast. 18 (2002) 1481–1498.
[23] G. Tan, Y. Liu, P. Sittner, M. Saunders, Luders-like deformation associated with stress-induced martensitic transformation in NiTi, Scr. Mater. 50 (2004) 193–198.
[24] J.A. Shaw, S. Kyriakides, Thermomechanical aspects of NiTi, J. Mech. Phys. Solids. 43 (1995) 1243–1281.
[25] J.A. Shaw, S. Kyriakides, On the nucleation and propagation of phase transformation fronts in a NiTi alloy, Acta Mater. 45 (1997) 683–700.
[26] X. Zhang, P. Feng, Y. He, T. Yu, Q. Sun, Experimental study on rate dependence of macroscopic domain and stress hysteresis in NiTi shape memory alloy strips, Int. J. Mech. Sci. 52 (2010) 1660–1670.
[27] S. Daly, G. Ravichandran, K. Bhattacharya, Stress-induced martensitic phase transformation in thin sheets of Nitinol, Acta Mater. 55 (2007) 3593–3600.

[28] H. Petryk, S. Stupkiewicz, Interfacial energy and dissipation in martensitic phase transformations. Part I: Theory, J. Mech. Phys. Solids. 58 (2010) 390–408.
[29] P. Sittner, Y. Liu, V. Novak, On the origin of L??ders-like deformation of NiTi shape memory alloys, J. Mech. Phys. Solids. 53 (2005) 1719–1746.
[30] Y.J. He, Q.P. Sun, Rate-dependent domain spacing in a stretched NiTi strip, Int. J. Solids Struct. 47 (2010) 2775–2783.
[31] J.F. Hallai, S. Kyriakides, Underlying material response for Luders-like instabilities, Int. J. Plast. 47 (2013) 1–12.
[32] G. Murasawa, K. Kitamura, S. Yoneyama, S. Miyazaki, K. Miyata, A. Nishioka, T. Koda, Macroscopic stress–strain curve, local strain band behavior and the texture of NiTi thin sheets, Smart Mater. Struct. 18 (2009) 55003.
[33] L. Zheng, Y. He, Z. Moumni, Effects of Lüders-like bands on NiTi fatigue behaviors, Int. J. Solids Struct. 83 (2016) 28–44.
[34] L. Zheng, Y. He, Z. Moumni, Lüders-like band front motion and fatigue life of pseudoelastic polycrystalline NiTi shape memory alloy, Scr. Mater. 123 (2016) 46–50.
[35] L. Zheng, Y. He, Z. Moumni, Investigation on fatigue behaviors of NiTi polycrystalline strips under stress-controlled tension via in-situ macro-band observation, Int. J. Plast. (2016).
[36] N. Nayan, V. Buravalla, U. Ramamurty, Effect of mechanical cycling on the stress-strain response of a martensitic Nitinol shape memory alloy, Mater. Sci. Eng. A. 525 (2009) 60–67.
[37] A.R. Pelton, Nitinol fatigue: A review of microstructures and mechanisms, J. Mater. Eng. Perform. 20 (2011) 613–617.
[38] D. Roy, V. Buravalla, P.D. Mangalgiri, S. Allegavi, U. Ramamurty, Mechanical characterization of NiTi SMA wires using a dynamic mechanical analyzer, Mater. Sci. Eng. A. 494 (2008) 429–435.
[39] R.. Tabanli, N.. Simha, B.. Berg, Mean stress effects on fatigue of NiTi, Mater. Sci. Eng. A. 273–275 (1999) 644–648.
[40] L. Dong, R.H. Zhou, X.L. Wang, G.K. Hu, Q.P. Sun, On interfacial energy of macroscopic domains in polycrystalline NiTi shape memory alloys, Int. J. Solids Struct. 80 (2016) 445–455.
[41] J.A. Shaw, S. Kyriakides, Initiation and propagation of localized deformation in elasto-plastic strips under uniaxial tension, Int. J. Plast. 13 (1997) 837–871.
[42] Y.J. He, Q.P. Sun, Macroscopic equilibrium domain structure and geometric compatibility in elastic phase transition of thin plates, Int. J. Mech. Sci. 52 (2010) 198–211.
[43] K. Kim, S. Daly, The effect of texture on stress-induced martensite formation in nickel–titanium, Smart Mater. Struct. 22 (2013) 75012.

Effect of Loading Rate on Mechanical Behavior of NiTiNOL Plate - An Experimental and Computational Study

Fatma Mutlu, Gulcan Ozerim and Gunay Anlas

Mechanical Engineering Department
Bogazici University
Bebek, Istanbul, 34342 Turkey
fatma.mutlu@boun.edu.tr; gulcan.ozerim@boun.edu.tr; anlas@boun.edu.tr

ABSTRACT

In this study, the effect of loading rate on the mechanical behavior of NiTiNOL plate is investigated. Displacement controlled tension tests are performed on dogbone test specimens under different loading rates in quasi-static range. From stress vs. strain diagrams of the tests, Elastic Moduli of austenite and martensite, transformation start and finish stresses, and Upper - Lower Plateau Stresses (UPS – LPS) are obtained. During the tests, Digital Image Correlation (DIC) is used and the temperature is recorded via a thermal camera. The displacement field is obtained from the DIC images to calculate the strain distribution. Full martensite and transformation regions are estimated using the strain field. With increasing loading rate, the forward transformation stresses increase and, the reverse transformation stresses decrease, with an expansion in the hysteresis area. Elastic Moduli of austenite and martensite are found to be unaffected. In addition, the temperature of the specimens increase with increasing loading rate. The tests are simulated using the ZM thermo-mechanically coupled model in ABAQUS. The experimental results are compared with the computational ones. It is concluded that increasing loading rate affects the mechanical behavior of NiTiNOL due to thermo-mechanical coupling.

REFERENCES

[1] ASTM, “Standard test method for tension testing of nickel-titanium Superelastic materials”, *ASTM Standard*, Vol. **5**, pp. 1-4, (2014).

[2] C. Maletta, and F. Furgiuele, “1D Phenomenological Modeling of Shape Memory and Pseudoelasticity in NiTi Alloys”, INTECH Open Access Publisher, (2012).

[3] W. Zaki, and Z. Moumni, “A three-dimensional model of the thermomechanical behavior of shape memory alloys”, *Journal of the Mechanics and Physics of Solids*, Vol. **55**, No. 11, pp. 2455-2490, (2007).

VIII ECCOMAS Thematic Conference on Smart Structures and Materials
SMART 2017
A. Güemes, A. Benjeddou, J. Rodellar and J. Leng (Eds)

EVOLUTION OF MARTENSITIC TRANSFORMATION IN LOADED NITI COMPONENTS: COMPARISON OF SYNCHROTRON XRD TOMOGRAPHY DATA WITH FEM SIMULATIONS

P. SEDLÁK*, M. FROST*, L. HELLER†, L. KADEŘÁVEK† AND P. ŠITTNER†

*Institute of Thermomechanics of the Czech Academy of Sciences
Dolejškova 5, 18200 Prague, Czech Republic
e-mail: mfrost@it.cas.cz
web page: http://www.it.cas.cz/d5

† Institute of Physics of the Czech Academy of Sciences
Na Slovance 2, 18221 Prague, Czech Republic
web page: http://ofm.fzu.cz

Keywords: NiTi Shape Memory Alloys, Martensite, X-ray Diffraction Tomography, Numerical Simulations

Summary: We have studied spatial distribution of martensite phase in a segment of a stretched snake spring, which was shape set from a polycrystalline NiTi shape memory alloy. Synchrotron X-ray diffraction was performed and obtained data were processed via a simple fitting procedure. A finite element simulation of the stretching was conducted utilizing a NiTi-tailored constitutive model with an internal scalar variable representing the volume fraction of martensite. Predicted distribution of the variable was compared with experimental data and a quantitative correspondence was found. Substantial effect of the tension-compression asymmetry of the material response was observed since the material is loaded in bending. This case study demonstrates that the constitutive model and its implementation allow for plausible quantitative predictions of the mechanical behavior of NiTi polycrystalline samples.

1 INTRODUCTION

Mechanical response of shape memory alloys (SMA) at temperatures close to the transition interval is rather complex since several deformation mechanisms are often active simultaneously and they even mutually interact. The dominant phenomenon, responsible for so-called superelasticity, is a reversible solid-to-solid phase transformation between a parent phase, austenite, and a product phase, martensite. Martensite forms in various hierarchically ordered microstructures whose particular arrangement is sensitive to presence/absence and type of applied mechanical load and manifests itself as macroscopic deformation, so-called transformation strain. Transition

between different types of such microstructures is often termed as reorientation of martensite and gives rise to so-called pseudoplasticity [1]. As shown by dedicated studies [2, 3], elastic properties of the polycrystalline shape memory alloys strongly evolve at temperatures close to phase transition and polycrystalline martensite exhibits significant deformation-dependent elastic anisotropy due to the reorientation.

Mutual coupling of dissipative (transformation, reorientation) and non-dissipative (elasticity) deformation mechanisms was exemplified in many studies [4] and attracts permanent attention of computational modeling community [5–9]. An optimal continuum mechanics-based constitutive model should also capture some other experimental features of macroscopic SMA behaviors rooted in complex microstructural phenomena, e.g. intermediate transformations [10], tendency to transform in a localized manner in some specific situations [11, 12] or coupling of transformation, reorientation and plasticity [13], since they often co-determine mechanical response in general loading scenarios of SMA polycrystals. Despite a substantial progress achieved in modeling [14, 15], such a "general" model still provides a real challenge.

Validation of current continuum mechanics-based models usually builds on comparison of simulated macroscopic global mechanical response – expressed, e.g., in terms of stress (force) and strain (deformation) – with experimental counterparts evaluated in simple geometries and loading modes. However, such models can often provide more detailed data: i) local distributions of variables due to suitable representation of complex geometry, e.g. via finite element approach, ii) additional information on local-averaged microstructural state since the macroscopic models of SMA usually comprise some mathematical objects capturing information from a more fine-grained scale (phase fraction, mean transformation strain, etc.). Up-to-date experimental techniques provide valuable data for comparison both in the former (digital image correlation [16, 17], thermovision [18] or their combination [19]) and in the latter (synchrotron X-ray diffraction [20]) cases. Clearly, such an additional cross-check can be useful for theoretical [21] as well as practical reasons [22].

In this short communication, we compare spatial distribution of phase fraction in a mechanically loaded NiTi polycrystalline sample determined by synchrotron X-ray diffraction (XRD) tomography with a finite element simulation utilizing our own developed constitutive model. The specimen is a wire shaped into the form of a flat snake spring which is a perspective geome-

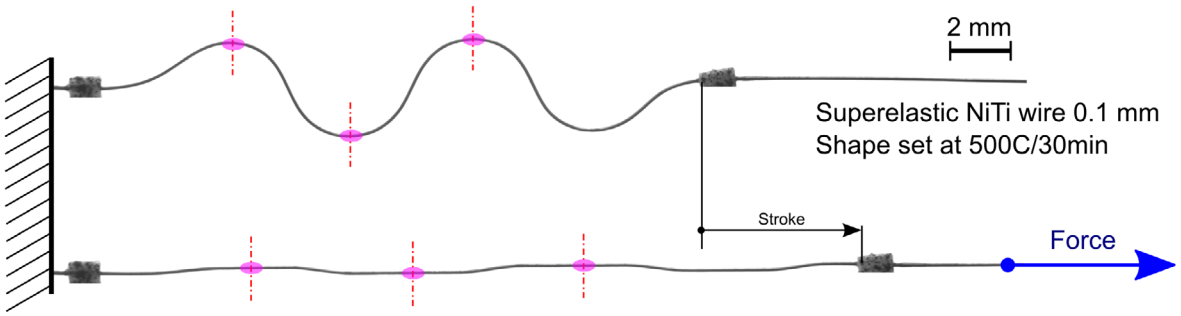

Figure 1: A scheme of the stretching test of the flat snake spring. The upper part shows a snapshot of the unloaded snake spring after fixing in the testing device, the lower part shows a snapshot of its shape after 4.8 mm stroke.

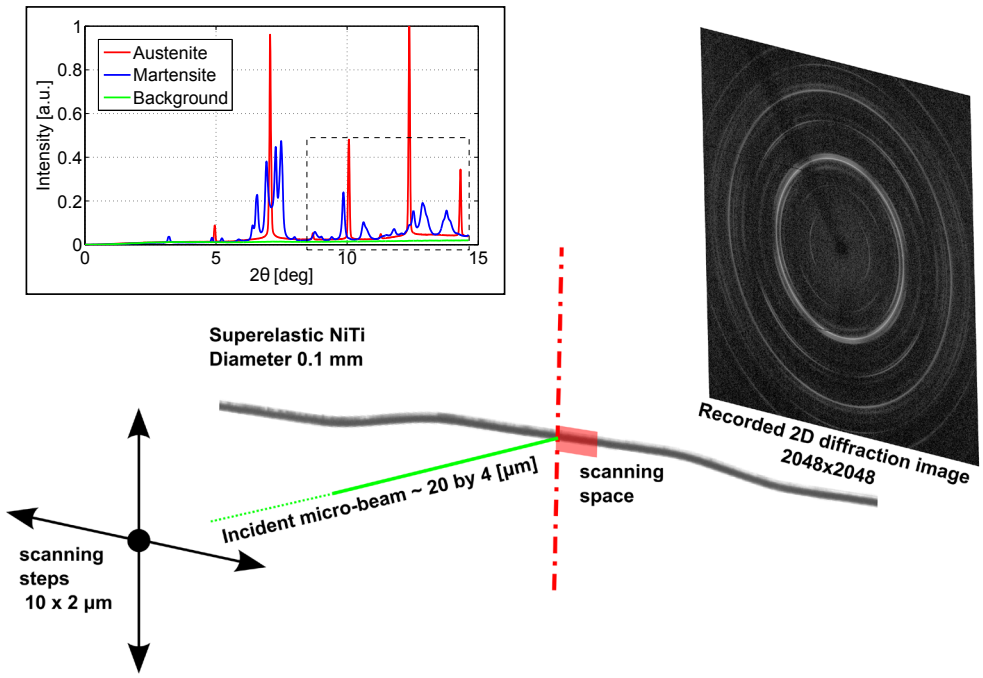

Figure 2: A scheme of the XRD measurement setup. An incident high-energy micro-beam is focused into a spot (20 by 4 μm) where the sample is located and the resulting 2D diffraction pattern is recorded. A scanning area of 120×270 μm containing a short element of the wire was probed by changing horizontal and vertical position of the beam. The inset shows three reference spectra obtained from 2D diffraction patterns, see text for details.

try for applications [23–25]. Stretching of the spring induces tensile and compressive stresses at opposite sides of the wire cross-section so that inhomogenous distribution of phases is induced within. The aim here is to access capabilities of the model to capture the mechanical response with a particular emphasis on the spatial distribution of the phase fraction of martensite.

2 EXPERIMENTAL

A flat snake spring was shape set from a 100 μm thin cold drawn NiTi wire (FWM NiTi#1-CW [26]) using an in-house designed and built stainless steel fixtures in an air furnace at 500 °C for 30 min. For dimensions see Fig. 1. The spring was first stretched at in-house assembled testing device with a linear actuator (maximum speed 100 mm/s) and a sensitive load cell (maximum load 10 N). The maximum stroke was 4.8 mm so that no irreversible strains were induced in the specimen (the initial shape recovered after unloading). The ambient temperature was 25 °C and to ensure isothermal conditions, experiment was conducted at a very slow loading rate (1.5 mm/min). Force and stroke data were recorded continuously.

In-situ observation of material microstructure was performed with synchrotron radiation diffraction at ESRF, Grenoble (beamline 15A). A schematic sketch of the experimental setup is in Fig. 2. The snake spring was clamped into a stress rig in such a way that the plane of the spring was perpendicular to the incident X-ray beam. Then it was stretched applying a force

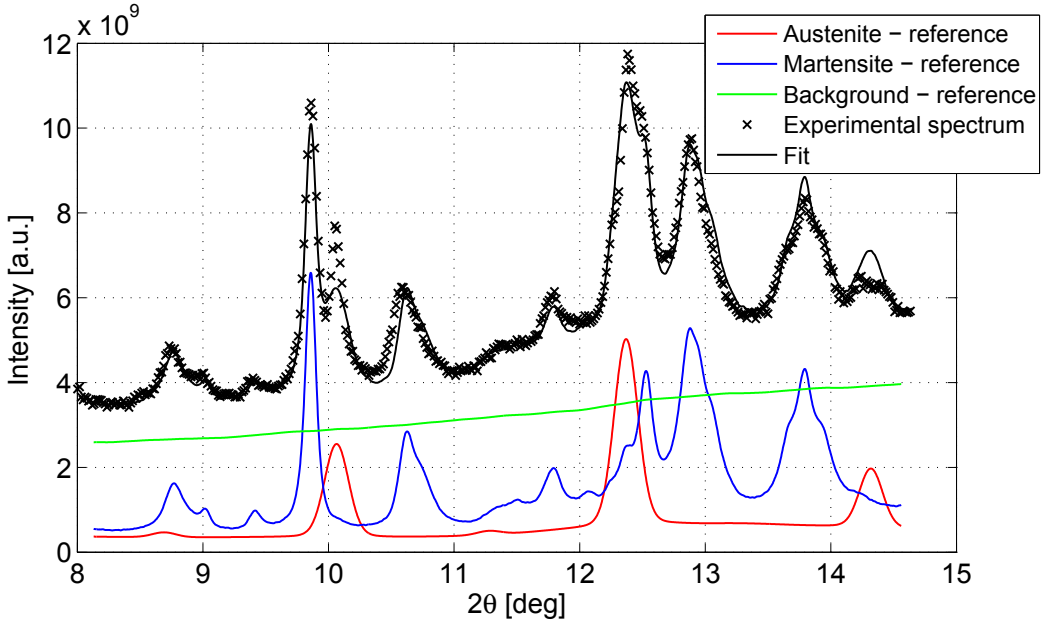

Figure 3: An example of the fitting procedure used in the data analysis. Five parameters were used to fit the obtained diffraction profile (black crosses) with three reference spectra (red, green and blue lines).

of 0.7 N (corresponds to the situation in Fig. 1). The high energy X-ray radiation of 0.268 nm wavelength was used in order to limit intensity losses by absorption. The sample was scanned by a micro-focused beam (cross-section of the spot 4 μm by 20 μm) in a regular grid of 60 (vertical direction) by 27 (horizontal direction) points. The vertical scan step through the cross-section of the wire was 2 μm, the horizontal step along the wire axis was 10 μm.

A Perkin Elmer a-Si detector (coupled with a CsI(Tl) screen) with the pixel size of 200 μm $\times$ 200 μm and the total size of 2048×2048 pixels placed at the distance of 770 mm from the sample allowed to record all diffracted intensities up to diffraction angle, denoted 2θ, equal to 15 °. The acquisition time for each of 2D diffraction patterns was set to 1 s. Additionally, three reference diffraction patterns were acquired: the first one by irradiating the material of the wire at room temperature and no stress, i.e. in austenitic state with possible presence of some R-phase, the second one after it was cooled down to full (temperature-induced) martensite by liquid nitrogen (other experimental conditions fixed). Finally, the background noise was recorded. The inset in Fig. 2 shows relation between diffraction intensity and diffraction angle for the three reference spectra.

Processing of diffraction patterns obtained from a strained NiTi wire is hindered by several factors: i) the strong texture of stress-induced martensite, ii) original wire texture of austenite, iii) fine-grained wire microstructure with broad diffraction lines, iv) broadening of lines because of applied stresses or the overlap of dominant diffraction lines of austenite, R-phase and martensite. All these factors make traditional full-profile fitting procedures, which reconstruct the measured data by fitting structural parameters and calculating integral intensities, extremely difficult to handle since the number of fitted parameters becomes enormous (crystallographic parameters, phase fraction parameters, parameters describing texture and diffraction profiles) and

their inverse determination is an ill-posed problem. Finally, quite a simple approach was found as the most effective: each diffraction profile was fitted utilizing the reference spectra and five fitting parameters (volume of austenite/R-phase, Lorentzian broadening of austenitic lines, volume of martensite, Lorentzian broadening of martensitic lines and intensity of the background). Difficulties related to a strong texture were eliminated with a suitable integration of 2D diffraction patterns based on the assumption that the texture of both austenite and stress-induced martensite is symmetric with respect to the axis of the wire; let us note that the dominant stress component in the deformed spring was tension or compression oriented in the direction tangential to the wire axis. The part of the spectra with minimal overlapping of austenite and martensite lines (2θ between 8 and 14.6 °) was chosen for the phase analysis. Figure 3 shows an example of experimental and fitted spectra. We can see a fairly accurate fit especially of martensitic peaks showing that the spectrum of a strongly-textured stress-induced martensite can be fitted with the spectrum of a temperature-induced (hence untextured) martensite if a suitable spatial integration of diffracted intensities is applied. Discrepancies observed in the case of austenitic/R-phase peaks are probably because of the continuous structural evolution of R-phase with applied stress, i.e. reorientation of R-phase (cf. [2]), which leads to variation of structural factors and, consequently, to changes in diffracted intensities.

From the fitting coefficients, we have determined the relative phase fraction of martensite within a small volume of the material given by the intersection of incident beam with the snake spring geometry. By interpolation of the values obtained for each beam position, we got the spatial distribution presented later in Fig. 6. Hence, the 2D plot encompass (averaged) information from the 3D segment of the spring.[1]

3 MODELING

For finite element analysis, we use an extended version of the continuum mechanics-based rate-independent constitutive model introduced in [27,28] and further refined in [29]. The model is tailored for simulations of mechanical response of NiTi-based SMA components in complex loading modes at prescribed temperature (which, however, can vary both spatially and temporally). Four internal variables – volume fraction of martensite, volume fraction of R-phase, transformation strain tensor of martensite and transformation strain tensor of R-phase – are introduced to capture a possible two-stage transformation sequence common in commercially available NiTi wires. The core of the model are two particular functions: the energy function (thermodynamic potential) consisting of elastic, chemical and internal parts, and the dissipation function, in which both transformation and reorientation contributions are concerned. The constitutive response in a material point is determined via so-called principle of minimum dissipation potential. Since hysteresis (hence dissipation) of the transformation between austenite and R-phase is very small compared to the transformation to martensite, see e.g. [10,18], macroscopic changes of a material response related to R-phase can be effectively modeled through a hyperelastic (non-dissipative) approximation. Namely, the inelastic strain of R-phase appears in the elastic part of the free energy (additive decomposition of the total strain) and it does not

[1] However, the averaging poses no serious limitation since the phase distribution in the direction of the beam is relatively homogeneous thanks to bending-dominated loading mode; this was also verified by the numerical simulation, see Section 4.

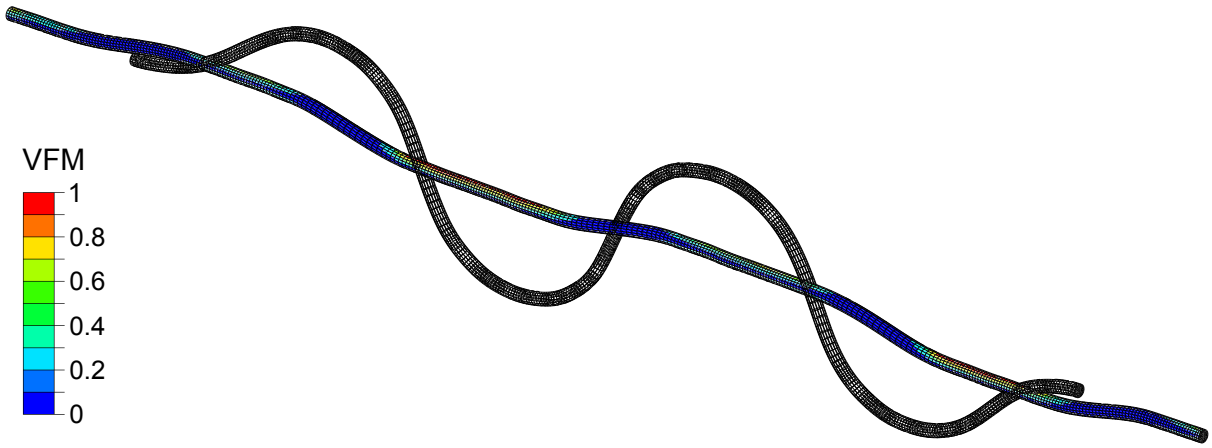

Figure 4: Finite element mesh of the snake spring: free-standing in grey, stretched in colors corresponding to the computed volume fraction of martensite (see the colorbar).

appear in the dissipation function. The chemical part contains a term depending on the volume fraction of R-phase as proposed in [27]. A constraint on the transformation strain tensors based on its invariants is imposed through a specific material function so that volume preserving property, tension-compression asymmetry and (texture-induced) transformation strain anisotropy observed in experiments are respected by the model. Furthermore, a particular form of phase- and transformation strain-dependent tensor of elastic constants allows to capture substantially different elastic properties of austenite, temperature-induced martensite and (generally anisotropic) stress-induced martensite, see [3] and [29] for experimental and modeling details, respectively. A numerical implementation of the model into Abaqus finite element software was performed through the User MATerial subroutine (UMAT) and the alternative minimization technique is employed for solving a general quasi-static boundary condition problems as thoroughly described in [28]. Let us note that irreversible strains due to dislocation slip are neglected in the present model.

Finite element analysis was performed with Abaqus FEA software. A complete geometrical model of the flat snake spring consists of a fine, structured mesh of 8-node linear brick elements with centroid integration (C3D8R). Each cross-section perpendicular to the wire axis consists of 64 symmetrically arranged elements (four lines of symmetry), see details in Fig. 6c). Along the wire axis, which lies in the xy plane, the whole snake spring is uniformly divided into 370 rows of elements. Stretching of the snake spring in the fixture was simulated by a gradual, symmetrical change of prescribed displacement of all nodes at both the first and the last cross-sections in x axis, while the central nodes at these cross-sections were fixed in y and z directions and all other nodes were left free to move. Because of assumed transverse isotropy along the axis of the wire (follows from the texture of the wire), material orientation was set in each element via *ORIENTATION functionality of Abaqus FEA. Figure 4 shows both initial and stretched configuration of the mesh. Material parameters were obtained by adjusting the values fitted to the particular type of the wire in [27] and adapting the recent results on martensite elasticity published in [3] for the martensite elasticity model introduced in [29].

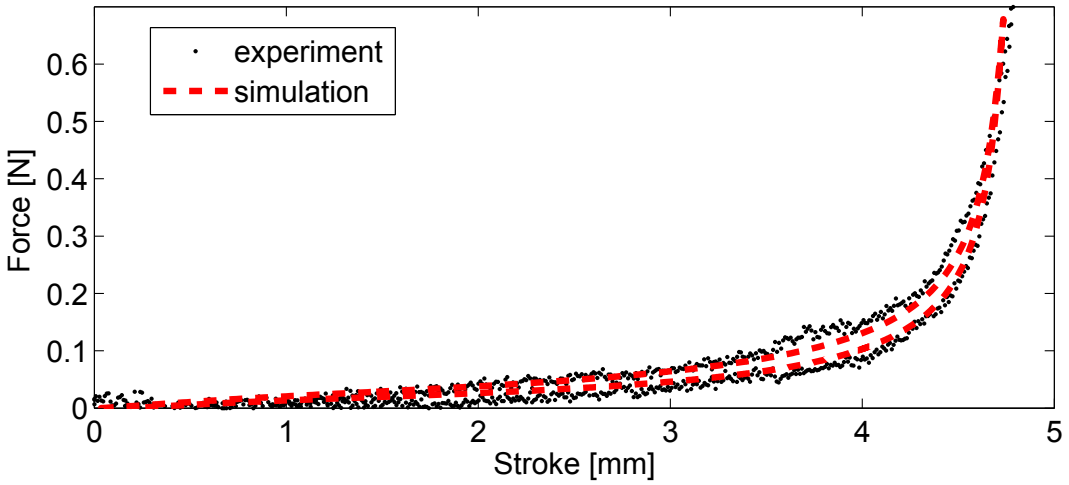

Figure 5: Measured (black dots) and simulated (red dashed line) dependence of total force on stroke. Scatter of experimental data caused by sensitivity of the load cell.

4 RESULTS

Figure 5 shows the relation between the total stroke of the snake spring and the corresponding total force (cf. Fig. 1) for quasistatic stretching; experimental data (black dots) are compared with the simulation (red dashed line). A very good correspondence is observed, although the total hysteresis related to energy dissipation is slightly higher in the experiment. This could be attributed to internal frictions of the experimental device and to some experimental scatter related to sensitivity of the load cell (see values close to the unloaded state). A gentle rise of the force up to the half of the maximum stroke corresponds to predominantly elastic deformation of curved parts of the spring and extensive in-plane rotations of straighter segments. At higher values of stroke, martensite occurs first in the spots on the wire surface with the highest curvature and propagates on the surface (cf. Fig. 4, where the color scale corresponds to the computed distribution of the internal variable representing volume fraction of martensite). The steep increase of force for highest strokes is related to propagation of the transformation "deeper into the wire", i.e. towards the central axis of the wire.

Figure 6 reveals the spatial distribution of volume fraction of martensite determined by XRD tomography, a), and the spatial distribution of the internal scalar variable volume fraction of martensite in the corresponding part of the computational model, b). Subfigure c) shows distribution of the variable within the leftmost cross-section of the investigated area; it demonstrates a relative homogeneity of the variable in z direction (i.e. perpendicular to plane of the snake spring) related to the bending-dominated loading mode.[2] Minimal discrepancy between a) and b) suggests that the internal variable in the model represents well the volume fraction

[2]However, the spatial distribution presented in subfigure b) was obtained by weighted integration of the variable along the horizontal directions within each cross-section. In other words, each point in b) represents the average value from a material segment of the wire perpendicular to the plane of the wire axis, which is a direct equivalent to the experimental picture in a).

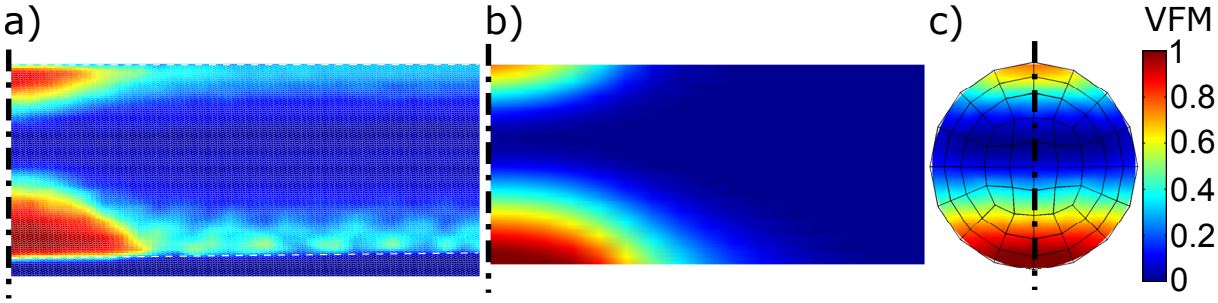

Figure 6: Spatial distribution of XRD-determined volume fraction of martensitic phase within the scanning area probed in the experiment a); black dash-dot line corresponds to red dash-dot lines in Figs. 1 and 2, white dashed line marks boundary of the material as computed from experimental data. Spatial distribution of the internal scalar variable volume fraction of martensite as determined by the finite element computation in the corresponding part of the mesh b) and within its leftmost cross-section c); note also the arrangement of elements within the cross-section. The same color scale used for the three plots.

of martensitic phase from the physical point of view. In all subfigures, the red upper and lower areas correspond to the martensite induced by compressive and tensile loading, respectively (see orientation of the snake in the XRD experiment in Fig. 2). Hence, the tension-compression asymmetry[3] is well demonstrated by the different extent of transformed material.

The experimental data also exhibit a non-negligible fraction of martensite (up to 40%) in several spots close to the wire surface. A possible explanation could be either presence of some inhomogeneities of the material or its structure or localization of the phase transformation. Although localization of martensitic transformation has been well documented in tensile loading of straight NiTi wires [20] or in bending of NiTi tubes [16], the authors are not aware of any experimental observation in the case of bent NiTi wires. Let us finally note that white dashed lines in subfigure a) mark boundary of the material as computed from experimental data, hence they demonstrate very good spatial resolution of applied methods.

5 CONCLUSIONS

We have investigated the spatial distribution of volume fraction of martensite in a segment of a stretched flat snake spring from a polycrystalline NiTi SMA by experimental and theoretical tools. First, we have recorded synchrotron X-ray diffraction patterns of a sample manufactured from a NiTi wire and processed the data utilizing three reference patterns and a simple fitting procedure. As a counterpart, we have conducted a finite element simulation with an enhanced constitutive model tailored for such a material and evaluated distribution of the corresponding internal variable so that a direct comparison of both distributions by the naked eye is possible. Our results show that i) the developed procedure of quantitative phase analysis can provide a viable alternative to conventional full-profile fitting methods in particular situations, ii) the constitutive model and its implementation allow for plausible quantitative predictions of phase distributions in mechanically loaded polycrystalline NiTi specimens, iii) examination of phase distributions can provide new findings on physical processes occurring in SMA and their inter-

[3] i.e. a lower level of stress needed for initiation of phase transformation in tension than in compression

actions; further examples of application of the proposed methodology for such an examination in the case of NiTi SMA are to be published soon.

Acknowledgements: We acknowledge ESRF synchrotron facility in Grenoble, France for provision of experimental beam time at beamline ID 15A within experiment no. MA2114 and the local contact Agnieszka Poulain for assisting authors throughout the experiment at ESRF. We kindly acknowledge the financial support of this work provided by the Czech Science Foundation by projects No. 16-20264S – in the framework of which scripts for automatic processing of 2D diffractograms were developed – and No. 14-36566G (AdMat).

REFERENCES

[1] K Otsuka and X Ren. Physical metallurgy of Ti-Ni-based shape memory alloys. *Prog. Mater. Sci.*, 50:511–678, 2005.

[2] P Šittner, M Landa, P Lukáš, and V Novák. R-phase transformation phenomena in thermomechanically loaded NiTi polycrystals. *Mech. Mater.*, 38:475–492, 2006.

[3] M Thomasová, H Seiner, P Sedlák, M Frost, M Ševčík, I Szurman, R Kocich, J Drahokoupil, P Šittner, and M Landa. Evolution of macroscopic elastic moduli of martensitic polycrystalline NiTi and NiTiCu shape memory alloys with pseudoplastic straining. *Acta Mater.*, 123:146–156, 2017.

[4] P Šittner, L Heller, J Pilch, P Sedlák, M Frost, Y Chemisky, A Duval, B Piotrowski, T Ben Zineb, E Patoor, F Auricchio, S Morganti, A Reali, G Rio, D Favier, Y Liu, E Gibeau, C Lexcellent, L Boubakar, D J Hartl, S Oehler, D C Lagoudas, and J Van Humbeeck. Roundrobin SMA modeling. In P Šittner, L Heller, and V Paidar, editors, *ESOMAT 2009 - The 8th European Symposium on Martensitic Transformations*, page 08001. EDP Sciences, 2009.

[5] J Arghavani, F Auricchio, R Naghdabadi, A Reali, and S Sohrabpour. A 3-D phenomenological constitutive model for shape memory alloys under multiaxial loadings. *Int. J. Plast.*, 26:976–991, 2010.

[6] Y Chemisky, A Duval, E Patoor, and T Ben Zineb. Constitutive model for shape memory alloys including phase transformation, martensitic reorientation and twins accommodation. *Mech. Mater.*, 43:361–376, 2011.

[7] A F Saleeb, S A Padula, and A Kumar. A multi-axial, multimechanism based constitutive model for the comprehensive representation of the evolutionary response of SMAs under general thermomechanical loading conditions. *Int. J. Plast.*, 27:655–687, 2011.

[8] D C Lagoudas, D J Hartl, Y Chemisky, L G Machado, and P Popov. Constitutive model for the numerical analysis of phase transformation in polycrystalline shape memory alloys. *Int. J. Plast.*, 32–33:155–183, 2012.

[9] X Gu, W Zaki, C Morin, Z Moumni, and W Zhang. Time integration and assessment of a model for shape memory alloys considering multiaxial nonproportional loading cases. *Int. J. Solids Struct*, 54:28–99, 2015.

[10] G Helbert, S Saint-Sulpice, Land Arbab Chirani, L Dieng, T Lecompte, S Calloch, and P Pilvin. Experimental characterisation of three-phase NiTi wires under tension. *Mech. Mater.*, 79:85–101, 2014.

[11] JA Shaw and S Kyriakides. On the nucleation and propagation of phase transformation fronts in a niti alloy. *Acta Mater.*, 45(2):683–700, 1997.

[12] Q P Sun and Z Q Li. Phase transformation in superelastic NiTi polycrystalline micro-tubes under tension and torsion – from localization to homogeneous deformation. *Int. J. Solids Struct.*, 39:3797–3809, 2002.

[13] XM Wang, YF Wang, ZZ Lu, CH Deng, and ZF Yue. An experimental study of the superelastic behavior in NiTi shape memory alloys under biaxial proportional and non-proportional cyclic loadings. *Mech. Mater.*, 42:365–373, 2010.

[14] C Cisse, W Zaki, and T Ben Zineb. A review of constitutive models and modeling techniques for shape memory alloys. *Int. J. Plast.*, 76:244–284, 2016.

[15] C Cisse, W Zaki, and T Ben Zineb. A review of modeling techniques for advanced effects in shape memory alloy behavior. *Smart Mater. Struct.*, 25(10):103001, 2016.

[16] B Reedlunn, CB Churchill, EE Nelson, JA Shaw, and SH Daly. Tension, compression, and bending of superelastic shape memory alloy tubes. *J. Mech. Phys. Solids*, 63:506–537, 2014.

[17] C Bewerse, KR Gall, GJ McFarland, P Zhu, and LC Brinson. Local and global strains and strain ratios in shape memory alloys using digital imagecorrelation. *Mat. Sci. Eng. A*, 568:134–142, 2013.

[18] Y Xiao, P Zeng, and L Lei. Experimental observations on mechanical response of three-phase NiTi shape memory alloy under uniaxial tension. *Mater. Res. Express*, 3:105701, 2016.

[19] NJ Bechle and S Kyriakides. Evolution of phase transformation fronts and associated thermal effects in a NiTi tube under a biaxial stress state. *Extrem Mech. Letters*, 8:55–63, 2016.

[20] P Sedmák, J Pilch, L Heller, J Kopeček, J Wright, P Sedlák, M Frost, and P Šittner. Grain-resolved analysis of localized deformation in nickel-titanium wire under tensile load. *Science*, 353(6299):559–562, 2016.

[21] D Jiang, S Kyriakides, CM Landis, and K Kazinakis. Modeling of propagation of phase transformation fronts in NiTi under uniaxial tension. *Eur. J. Mech. A*, 64:131–142, 2017.

[22] E Alarcon, L Heller, SA Chirani, P Šittner, J Kopeček, L Saint-Sulpice, and S Calloch. Fatigue performance of superelastic NiTi near stress-induced martensitic transformation. *Int. J. Fatigue*, 95:76–89, 2017.

[23] Y Chemisky, A Duval, B Piotrowski, T Ben Zineb, V Tahiri, and E Patoor. Numerical tool for SMA material simulation: application to composite structure design. *Smart Mater. Struct.*, 18:104012, 2009.

[24] E Villa, S Arnaboldi, A Tuissi, M Giacomelli, and E Turco. Mechanical analysis of hybrid textile composites with NiTi wires. *J. Mater. Eng.*, 18:517–521, 2009.

[25] A Nespoli, E Villa, and S Besseghini. Thermo-mechanical properties of snake-like NiTi wires and their use in miniature devices. *J. Therm. Anal. Calorim.*, 109:39–47, 2012.

[26] http://fwmetals.com/services/resource-library/nitinol-1/.

[27] P Sedlák, M Frost, B. Benešová, P Šittner, and T Ben Zineb. Thermomechanical model for NiTi-based shape memory alloys including R-phase and material anisotropy under multi-axial loadings. *Int. J. Plast.*, 39:132–151, 2012.

[28] M Frost, B Benešová, and P Sedlák. A microscopically motivated constitutive model for shape memory alloys: formulation, analysis and computations. *Mat. Mech. Solids*, 21:358–382, 2016.

[29] M Frost, P Sedlák, L Kadeřávek, L Heller, and P Šittner. Modeling of mechanical response of NiTi shape memory alloy subjected to combined thermal and non-proportional mechanical loading: a case study on helical spring actuator. *J. Intel. Mat. Syst. Str.*, 27:1927–1938, 2016.

VIII ECCOMAS Thematic Conference on Smart Structures and Materials
SMART 2017
A. Güemes, A. Benjeddou , J. Rodellar and Jinsong Leng (Eds)

FINITE-ELEMENT ANALYSIS OF HYDROGEN EFFECT ON DEFLECTED ORTHODONTIC NITI WIRE

W. ELKHAL LETAIEF[*, †], A. FATHALLAH[*], T. HASSINE[*] AND F. GAMAOUN[*]

[*] Laboratory of Mechanics of Sousse (LMS)
National Engineering School of Sousse (ENISo)
University of Sousse
Hammam Maarouf, Sousse 4054 Tunisia

[†] e-mail: wissem.khal@gmail.com

Key words: Shape Memory Alloys, Constitutive Modeling, Finite Element, Hydrogen Diffusion, Bending Test.

Abstract. Thanks to its greater flexibility and biocompatibility with human tissue, the superelastic NiTi alloys have taken an important part of orthodontic wires' market. However, wire fractures are notified after a few months from fixing in the teeth. This behavior is due to the hydrogen presence in the oral cavity, which brittles the NiTi arch wire. In this paper, finite-element analyses of NiTi alloys are established while considering the hydrogen influences on the superelasticity effect. Moreover, a diffusion-mechanical coupled model is developed on the base of our previous experimental results. The model is integrated in ABAQUS finite-element software via a UMAT subroutine. Additionally, a finite-element model of deflected NiTi wire within three brackets is simulated in the presence of hydrogen. The numerical results demonstrate that the force applied to the tooth drops linearly with respect to the increase in the hydrogen amount. This behavior is attributed to the expansion of the NiTi structure after absorbing hydrogen. In addition, it shows that hydrogen obstructs certain martensite variants to transform back to their parent phase, which explains the loss of superelasticity.

1 INTRODUCTION

The superelastic NiTi alloys have been considered among the best materials applied to the orthodontic wires during the first stage of treatment [1]. Their important flexibility has offered to the orthodontists the opportunity to overcome the most complicated dental postures. In addition, they provide a constant force for a large range of tooth displacement thanks to their martensite-austenite transformations. In fact, experimental studies have been established to characterize the mechanical behavior of orthodontic NiTi wires. For instance, the bending tests have been carried out at different thermal and mechanical boundary conditions in order to simulate the real case of wires fixed in teeth [2] [3]. Nevertheless, these bending studies disregard the fact that NiTi absorbs the hydrogen impurities that are localized in the oral cavity.

Actually, hydrogen has shown important impacts on the mechanical behavior of the NiTi alloys during tensile tests, such as embrittlement and sudden fracture [4] [5]. In addition, a heightening in stress transformation and a shortening in plateau size have been noticed since

the hydrogen obstructs some austenitic NiTi lattices to transform to the martensite phase [6] [7]. Furthermore, Runciman et al. [8] indicated that even the transformation temperatures would decrease linearly with respect to the hydrogen concentration until achieving its saturation. Besides, we demonstrated in previous work that hydrogen would induce the expansion of the NiTi structure. This result was obtained through in situ stress relaxation tests where the NiTi wires were charged with hydrogen during imposing strain [9].

As far as the modeling of the hydrogen effect on mechanical behavior is concerned, different approaches have been developed for various alloys [10] [11]. However, we distinguish the coupled diffusion-mechanical models which have been derived thermodynamically by appending the chemical potential into the balance laws [12]. Nevertheless, the modeling of hydrogen effects on the mechanical Shape Memory Alloys (SMA) behavior has not been well considered by researchers. Yet, a recent model has been established which regards the shortening of the plateau size and the increase in the transformation stresses; whereas, it disregards the hydrogen-induced expansion [13]. On the other hand, all the interest of the SMA modelers has focused on including the different mechanisms of martensite-austenite transformation to highlight the pseudoelasticity and shape memory effect at numerous combined mechanical and thermal loadings [14] [15] [16].

In this paper, we put forward an SMA model accounting the hydrogen effects (e.g. the increase in transformation stress, the loss of superelasticity and the hydrogen-induced expansion). In addition, we simulate these effects on a deflected wire so as to reproduce the real case of orthodontic NiTi wires during their fixing in the oral cavity. Accordingly, the plan of this paper is structured into four principal sections, including the introduction. Section 2 shows the development of the diffusion-mechanical coupled model. In section 3, we simulate the response of the derived model for different loading types. Finally, we resume the aim of the paper in the conclusion section.

2 MODELLING SMA BEHAVIOR WITH HYDROGEN EFFECTS

2.1 Fick's law

To compute the balance law for the diffusion of hydrogen concentration C, we use the second Fick's law.

$$\dot{C} = div(D\nabla C) \tag{1}$$

where D denotes the hydrogen diffusivity.

2.2 Constitutive SMA model

$$G(\sigma, T, C, \varepsilon^t, \xi) = -\frac{1}{2\rho}\sigma{:}S{:}\sigma - \frac{1}{\rho}\sigma{:}[\alpha(T-T_0)+\beta(C-C_0)+\varepsilon^t] + c\left[(T-T_0) - T\ln\left(\frac{T}{T_0}\right)\right] - s_0T + u_0 + \frac{1}{\rho}g^t(\xi) + \frac{C}{\rho}g^h(\xi) \tag{2}$$

Following the work of Lagoudas et al. [14], we use the free energy of Gibbs as a thermodynamic potential to characterize the thermodynamic material state (2). We employ the Cauchy stress σ, the temperature T and the hydrogen concentration C as external state variables. Concerning the internal state variables, we work with the transformation strain ε^t and the

martensite volume fraction ξ to describe the evolution of the austenite-martensite transformation.

The parameters $\rho, S, \alpha, \beta, c, s_0$, and u_0 are respectively the density, the compliance tensor, the thermal expansion coefficient tensor, the chemical expansion coefficient tensor, the specific heat, the specific entropy and the specific internal energy. The function $g^t(\xi)$ is the transformation hardening energy, which defines the energy evolution during transformation. Concerning the function $g^h(\xi)$, it is the diffusion hardening energy, which defines the variation of transformation stresses and temperatures with respect to the hydrogen concentration C.

In this model, we consider that S, s_0 and u_0 differ from phase to phase where we consider a linear function of ξ.

$$S(\xi) = S^A + \xi(S^M - S^A) = S^A + \xi\Delta S \qquad s_0(\xi) = {s_0}^A + \xi\Delta s_0 \qquad u_0(\xi) = {u_0}^A + \xi\Delta u_0 \tag{3}$$

Proceeding with the theory of Gurtin et al. [12] and the Coleman-Noll procedure, we identify the expression of the total strain ε, the specific entropy s and the chemical potential μ as follows:

$$\varepsilon = -\rho\frac{\partial G}{\partial \sigma} = S{:}\,\sigma + \alpha(T - T_0) + \beta(C - C_0) + \varepsilon^t \tag{4}$$

$$s = -\frac{\partial G}{\partial T} = \frac{1}{\rho}\sigma{:}\,\alpha + c\,ln\left(\frac{T}{T_0}\right) + s_0 \tag{5}$$

$$\mu = \rho\frac{\partial G}{\partial C} = -\sigma{:}\,\beta + g^h(\xi) \tag{6}$$

We assume that the transformation strain rate and the martensite volume fraction rate are linearly dependent where the parameter H denotes the maximum transformation strain [14].

$$\dot{\varepsilon^t} = \dot{\xi}\begin{cases}\frac{3}{2}H\frac{\sigma'}{\bar{\sigma}'}\ ;\ \dot{\xi} > 0\\ \frac{\varepsilon^{t-r}}{\xi^{t-r}}\ ;\ \dot{\xi} < 0\end{cases} = \Lambda\dot{\xi} \tag{7}$$

After the identification of Coleman-Noll, we obtain the following dissipative equation.

$$-\left(\rho\frac{\partial G}{\partial \varepsilon^t}{:}\,\varepsilon^t + \rho\frac{\partial G}{\partial \xi}\dot{\xi}\right) = -\left(\rho\frac{\partial G}{\partial \varepsilon^t}{:}\,\Lambda + \rho\frac{\partial G}{\partial \xi}\right)\dot{\xi} = \pi_\xi\dot{\xi} \geq 0 \tag{8}$$

where π_ξ is the thermodynamic force.

$$\pi_\xi = \sigma{:}\,\Lambda + \frac{1}{2}\sigma{:}\,\Delta S{:}\,\sigma + \rho\Delta s_0 T - \rho\Delta u_0 - \frac{\partial g^t}{\partial \xi} - \frac{\partial g^h}{\partial \xi}C \tag{9}$$

This force needs the evaluation of energies $g^t(\xi)$ and $g^h(\xi)$ as below:

$$g^t(\xi) = \begin{cases}\rho b^M(\xi + ne^{-\left(\frac{\xi}{n}\right)} - n) + (\mu_1 + \mu_2)\xi;\ \dot{\xi} > 0\\ \rho b^A(ne^{-\left(\frac{1-\xi}{n}\right)} - ne^{-\left(\frac{1}{n}\right)}) + (\mu_1 - \mu_2)\xi;\ \dot{\xi} < 0\end{cases} \tag{10}$$

$$g^h(\xi) = f^h\xi \tag{11}$$

The parameters of the transformation hardening energy $g^t(\xi)$ and the diffusion hardening energy $g^h(\xi)$ are determined by establishing the Kuhn-Tucker conditions at the limits of forward and reverse transformations.

$$\begin{cases} \Phi^+ = \ \pi_\xi - Y - y^h C \le 0 \ ; \ \Phi^+ \dot{\xi} = 0 \ ; \ \dot{\xi} \ge 0 \\ \Phi^- = -\pi_\xi - Y - y^h C \le 0 \ ; \ \Phi^- \dot{\xi} = 0 \ ; \ \dot{\xi} \le 0 \end{cases} \tag{11}$$

As far as the martensite volume fraction is concerned, it is generally bounded between 0 and 1. It is 0, whenever the structure is fully austenitic, and 1 whenever the structure is fully martensitic. In previous experimental results [6], it was proved that hydrogen would block the austenite-martensite transformation as much as the concentration was important. Accordingly, we propose that the lower ξ_A and upper bounds ξ_M of the martensite volume fraction vary exponentially with respect to the hydrogen concentration.

$$\begin{cases} \xi_A = (1 - e^{-\frac{C}{C_{\xi A}}})\xi \\ \xi_M = \left(1 - e^{-\frac{C}{C_{\xi M}}}\right)\xi + e^{-\frac{C}{C_{\xi M}}} \end{cases} \tag{12}$$

3 THREE-DIMENSIONAL STRUCTURAL ANALYSIS

3.1 Method

In this part, we simulate the constitutive model for different mechanical tests. The simulation is carried out through the finite-element analysis software ABAQUS while utilizing essentially the user material UMAT subroutine. This latter is used to define a non-ordinary thermo-mechanical or diffusion-mechanical coupled model while relying on the analogy between thermal and diffusional equilibriums.

The simulation is performed three-dimensionally on wire with a rectangular section of 0.4×0.55 mm². Table 1 presents all the values of material parameters needed to simulate the numerical response of the developed model. Moreover, we consider that temperature is constant and uniform over the tests ($T = 299\ K$). Concerning the hydrogen charging, we apply a uniform hydrogen concentration throughout the volume of wire.

The step chosen is the "coupled temp-displacement (transient)" where the mechanical and diffusional equilibriums are considered. This step type needs the "coupled temperature-displacement elements" where we choose "an 8-node thermally coupled brick, trilinear displacement and temperature C3D8T".

Table 1. Material properties and diffusion properties

Parameters	Values	Units	Parameters	Values	Units
Thermo-diffusion elastic properties			$\vartheta^A = \vartheta^M$	0.33	
$\boldsymbol{E^A}$	50	GPa	α	$2.2\ 10^{-5}$	K^{-1}
$\boldsymbol{E^M}$	26	GPa	β	$1.2\ 10^{-7}$	$m^3/mole$
Transformation properties			M_s	220	K
$\rho\Delta s$	-0.318	MPa/K	M_f	215	K
H	0.06		A_s	250	K
n	0.01		A_f	255	K
Diffusion hardening			D	$3.6\ 10^{-15}$	m^2/s
f^h	$1.5\ 10^{-4}$	$MPa\ m^3/mole$	$C_{\xi A}$	2000	$mole/m^3$
y^h	$1.5\ 10^{-4}$	$MPa\ m^3/mole$	$C_{\xi M}$	120000	$mole/m^3$

3.2 Results and comparison

- **Tensile test**

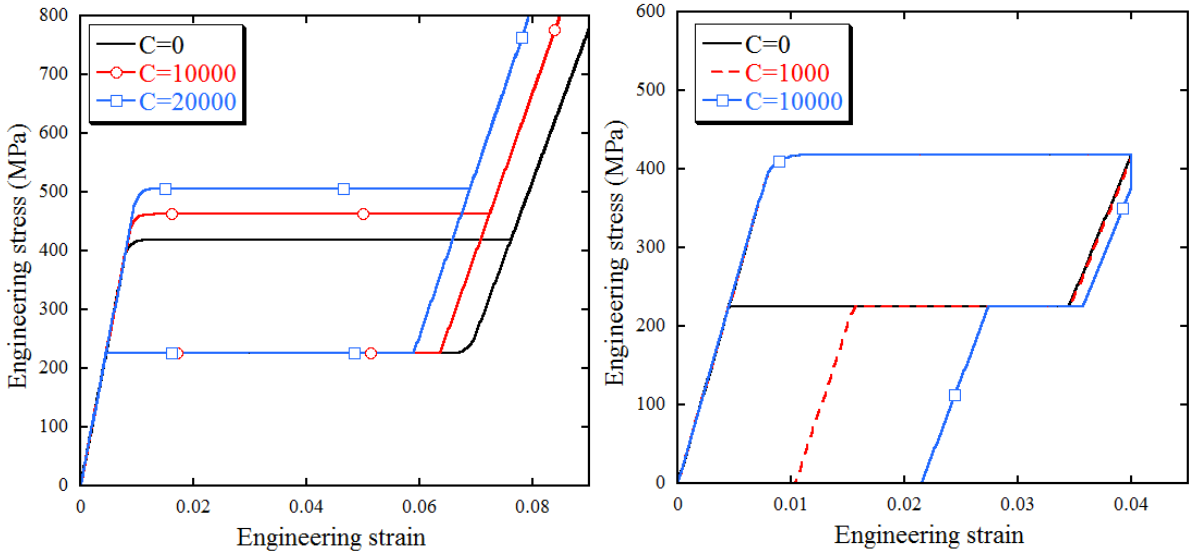

Figure 1: (a) Numerical tensile results of uncharged and charged NiTi with hydrogen concentration of 10,000 and 20,000 $mole/m^3$ **(b)** Numerical tensile results of one cycle load of uncharged and charged NiTi with hydrogen concentration of 1,000 and 10,000 $mole/m^3$ at 4% of imposed strain.

Figure 1 illustrates the numerical tensile results of uncharged and charged NiTi alloys with different hydrogen concentration. It is indicated that the curve of an uncharged alloy is composed of three deformation stages: austenite deformation, plateau transformation, and martensite deformation. We remark, that during transformation, the stress becomes constant until the end of the plateau. This result is controlled by the transformation hardening energy $g^t(\xi)$. For the hydrogenated alloy, we simulate the tensile tests after applying hydrogen concentration over the volume at a zero stress. The results indicate that the model predicts the increase in the transformation stress of the upper plateau. This increase is accounted for by the diffusion hardening energy $g^h(\xi)$. Concerning the shortening of the plateau's size, it is subjected to the variation of the upper bound of the martensite volume fraction ξ_M, which is regarded in equation (12).

Figure 2 depicts the numerical results of one-cycle load of uncharged and charged NiTi with different hydrogen concentration at 4% imposed strain. It is indicated that the curve of the uncharged NiTi presents no residual strain after one-cycle load. Concerning the curves of the charged NiTi, they are obtained in three steps. Firstly, we load the wire until obtaining 4% of strain. Secondly, at this point, we impose the strain and we apply the hydrogen concentration over the volume. It is observed that stress decreases during uptaking hydrogen, especially for $10{,}000 mole/m^3$ of concentration. This fact is caused by the use of the chemical expansion coefficient tensor β. Concerning the last step, we unload the part until obtaining a zero stress. Unlike the uncharged curve, we remark that the residual strain is shown. Moreover, this strain rises as much as the hydrogen concentration goes up. Indeed, this residual strain is performed

by means of varying the lower bound of the martensite volume fraction ξ_A. This parameter presents the volume fraction of martensite blocked by the presence of hydrogen.

- **Bending test**

The orthodontic NiTi wires mainly undergo bending load when they are fixed in the teeth. Simultaneously, they absorb hydrogen impurities localized in the oral cavity. Accordingly, it is necessary to identify the hydrogen effects on bent NiTi wires. However, using the developed diffusion-mechanical coupled model, we simulate the hydrogen effects on deflected NiTi wire. In this respect, we take the experimental result of Razali et al. [17] where the bending test of uncharged NiTi within three brackets was established. We reproduce the same test numerically utilizing the ABAQUS software. Then, we apply the hydrogen concentration during imposing deformation in order to reveal the hydrogen effects introduced in the present constitutive model.

In the simulation part, the used brackets are the conventional type with a slot of 0.45 and 0.7mm, respectively in height and width (Figure3). Like the experiment, we set a 7.5mm distance between the middle of the brackets. Regarding the interaction between the wire and the brackets, we use a "surface-to-surface" contact while introducing a friction coefficient of 0.2. In addition, we let the NiTi wire free on its extremities as set up in the experimental test. This type of simulation needs the activation of the "NLGEOM" option that includes the non-linear geometric effects. This option considers the large displacement whereby the slip between the arch wire and brackets are performed. Besides, the bending test induces a large rotation of several elements. Subsequently, a convergence problem will be faced due to the non-isotropy of material during transformation. Yet, it is necessary to use an "assign material orientation" option to rotate all the tensor including that of the tangent stiffness.

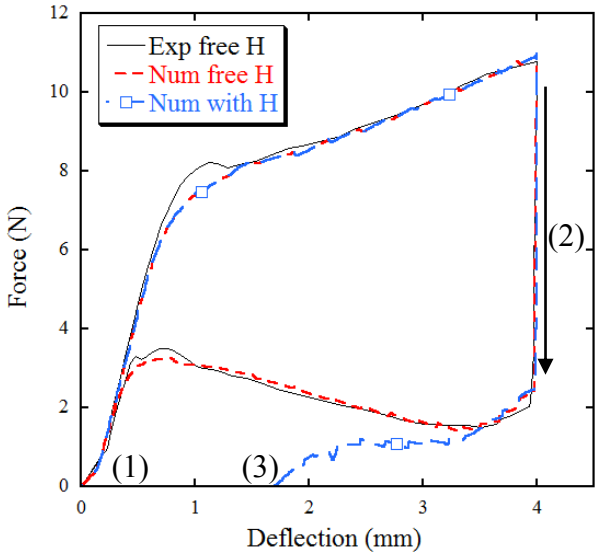

Figure 2: Load-deflection curve of experimental and numerical tests of uncharged and charged NiTi wire with hydrogen during bending in three brackets.

Figure 2 represents the deflection curves during the loading-unloading tests of NiTi wires bent until 4mm with a deflection rate of 1mm/min. The force demonstrated in the curve shows

the reaction force of the wire applied to the median brackets. It is noted that the numerical curve of the developed constitutive model reproduces well the experimental deflection curve of the uncharged NiTi. In fact, these curves are composed of different parts. Firstly, it is indicated that the force grows linearly with respect to the deflection. At practically 8N of force, we remark that a change in the slope is established. This change is caused by the forward transformation, which is activated mainly in the contact zones between the arch wire and brackets. During the unloading part, we observe a fall in force by about 9N owing to a slip of the arch wire. Afterwards, a lower plateau is performed wherein the activation of reverse transformation is provoked. During this plateau, we noticed that the force rises as much as the deflection declines. This behavior is the result of the friction between the wire and the brackets, which induces a supplementary reaction force.

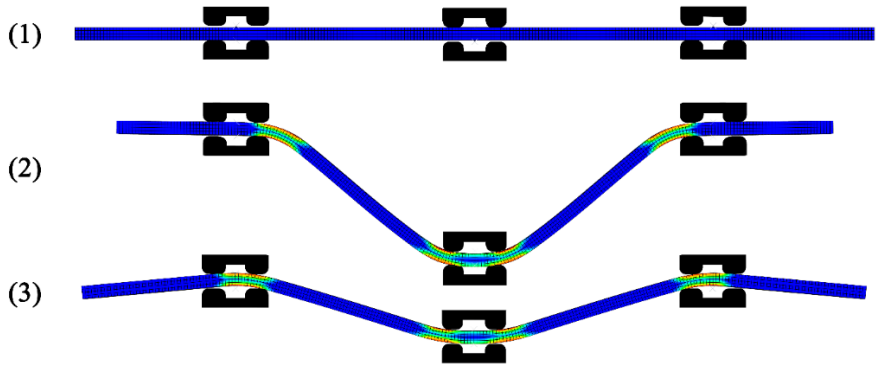

Figure 3: Numerical result of NiTi before and after being bent within three bracket and being charged with hydrogen simultaneously.

Figure 3 demonstrates the simulation of the hydrogen effects on a deflected wire within three brackets, as it is the case for the orthodontic NiTi wire. The color contour indicates the martensite volume fraction in each element. However, the austenite is presented by the blue color; whereas, the martensite is presented by the red color. Indeed, we indicate the deformation of the wire at three different deflection stages, where the first one is the initial state without applying effort. In stage 2, the wire is kept bent at 4mm of deflection while absorbing hydrogen. It is noted that the activation of the martensite transformation occurs only in contact zones between the brackets and the wire. In the third stage, we provide the shape of the wire after unloading to a zero force. Although they are both unloaded, the new shape is different from that of the initial stage; hence, a loss of superelasticity is provoked. Similarly, as it is noticed in figure 2, the numerical curve of the NiTi charged with hydrogen shows a residual deflection by about 1.7 mm. This fact is due to the canceling of reverse transformation since the hydrogen blocks such a martensite structure to transform back into the parent phase. This result is attributed to the variation of the bounds of the martensite volume fraction with regards to the hydrogen concentration (12). Moreover, it demonstrates that the force drops linearly in relation to the increase in the hydrogen amount during an imposing deflection. This behavior is caused by the slip induced by the expansion of the NiTi structure.

4. CONCLUSION

The aim of this paper is to develop a constitutive SMA model accounting the hydrogen effects on the mechanical behavior of NiTi alloys. The model has been derived thermodynamically on the base of our previous experimental results and previous work of Lagoudas et al. (2008) and Gurtin et al. (2010). However, the constitutive model includes the variation of the transformation stresses and temperatures with respect to the hydrogen concentration. Moreover, it predicts the loss of superelasticity since the hydrogen obstructs some NiTi structures for transforming to the martensite phase or for transforming back to the austenite phase. In addition, the hydrogen-induced expansion of the NiTi structure is considered in the expression of the total strain. Besides, we have implemented the obtained constitutive model in ABAQUS finite-element software through a UMAT subroutine. Afterwards, we have established a bending test within three brackets while absorbing hydrogen in order to simulate the real case of orthodontic wires fixed in the teeth. The numerical results have shown that the loss of superelasticity has been remarked owing to the blocked martensite variants by hydrogen diffusion. The confirmation of bending simulation will be treated experimentally in our future work.

REFERENCES

[1] Lombardo, L., Marafioti, M., Stefanoni, F., Mollica, F. and Siciliani, G. Load deflection characteristics and force level of nickel titanium initial archwires. *The Angle Orthodontist* (2012) **83**:507-521.

[2] Wilkinson, P. D., Dysart, P. S., Hood, J. A. and Herbison, G. P. Load-deflection characteristics of superelastic nickel-titanium orthodontic wires. *American journal of orthodontics and dentofacial orthopedics* (2002) **121**:483-495.

[3] Francisconi, M. F., Janson, G., Henriques, J. F. C. and Freitas, K. M. S. D. Evaluation of the force generated by gradual deflection of orthodontic wires in conventional metallic, esthetic, and self-ligating brackets. *Journal of Applied Oral Science* (2016) **24**:496-502.

[4] Gamaoun, F., Ltaief, M., Bouraoui, T. and Ben Zineb, T. Effect of hydrogen on the tensile strength of aged Ni–Ti superelastic alloy. *Journal of Intelligent Material Systems and Structures* (2011) **22**:2053-2059.

[5] Yokoyama, K. I., Hirata, Y., Inaba, T., Mutoh, K. and Sakai, J. I. Strong interactions between hydrogen in solid solution and stress-induced martensite transformation of Ni–Ti superelastic alloy. *Philosophical Magazine Letters* (2017) **97**:11-18.

[6] Gamaoun, F. and Hassine, T. Ageing effect and rate dependency of a NiTi shape memory alloy after hydrogen charging. *Journal of Alloys and Compounds* (2014) **615**:S680-S683.

[7] Elkhal Letaief, W. E., Hassine, T. and Gamaoun, F. Effect of Hydrogen on the Stress Relaxation of Aged NiTi Shape Memory Alloys. *Acta Physica Polonica A* (2016) **129**:714-716.

[8] Runciman, A., Chen, K. C., Pelton, A. R. and Trépanier, C. Effects of hydrogen on the phases and transition temperatures of NiTi. In *Proceedings of the International Conference on Shape Memory and Superelastic Technologies* (2006) (pp. 185-196).

[9] Elkhal Letaief, W., Hassine, T. and Gamaoun, F. In situ stress relaxation mechanism of a superelastic NiTi shape memory alloy under hydrogen charging. *Philosophical Magazine Letters* (2017) **97**:50-57.

[10] Chester, S. A., and Anand, L. A coupled theory of fluid permeation and large deformations for elastomeric materials. *Journal of the Mechanics and Physics of Solids* (2010) **58**:1879-1906.

[11] Anand, L. A thermo-mechanically-coupled theory accounting for hydrogen diffusion and large elastic–viscoplastic deformations of metals. *International journal of solids and structures* (2011) **48**:962-971.

[12] Gurtin, M.E., E. Fried and L. Anand. *The Mechanics and Thermodynamics of Continua*. Cambridge: Cambridge University Press, (2010).

[13] Lachiguer, A., Bouby, C., Gamaoun, F., Bouraoui, T. and Zineb, T. B. Modeling of hydrogen effect on the superelastic behavior of Ni-Ti shape memory alloy wires. *Smart Materials and Structures* (2016) **25**:115047.

[14] Lagoudas, D., Hartl, D., Chemisky, Y., Machado, L. and Popov, P. Constitutive model for the numerical analysis of phase transformation in polycrystalline shape memory alloys. *International Journal of Plasticity* (2012) **32**:155-183.

[15] Auricchio, F., Fugazza, D., and Desroches, R. Rate-dependent thermo-mechanical modelling of superelastic shape-memory alloys for seismic applications. *Journal of Intelligent Material Systems and Structures* (2008) **19**:47-61.

[16] Hartl, D. J., and Lagoudas, D. C. Constitutive modeling and structural analysis considering simultaneous phase transformation and plastic yield in shape memory alloys. *Smart Materials and Structures* (2009) **18**:104017.

[17] Razali, M. F., Mahmud, A. S., Mokhtar, N. and Abdullah, J. (2016, February). Finite-element analysis of NiTi wire deflection during orthodontic levelling treatment. In *IOP Conference Series: Materials Science and Engineering* (Vol. 114, No. 1, p. 012040). IOP Publishing.

VIII ECCOMAS Thematic Conference on Smart Structures and Materials
SMART 2017
A. Güemes, A. Benjeddou, J. Rodellar and J. Leng (Eds)

HYBRID SHAPE-MEMORY-ALLOY-TEXTILE ACTUATOR INTEGRATED COMPRESSION GARMENT

JAMIE L. KENNEDY*, NESTOR CASTANEDA†, ANTONIOS KONTSOS†, AND ADAM K. FONTECCHIO*

*Materials for Electrical Smart Systems (MESS)
College of Engineering, Drexel University
3101 Market Street, Philadelphia, PA, USA
e-mail: jlk1121@gmail.com, Web page : http://www.drexelnanophotonics.com/

† Theoretical and Applied Mechanics Group (TAMG)
College of Engineering, Drexel University
3401 Chestnut Street, Philadelphia, PA, USA
e-mail: nest.castaneda@gmail.com, Web page : http://tamg.mem.drexel.edu

Key words: SMA, Shape Memory Alloy, Textile Analysis, Compression Garment, Actuator

Abstract. In a world of two extremes for blood-clot prevention, a medium ground of hospital-level care in a transportable system with higher comfort can be achieved through smart-fabric technology. This paper demonstrates the ability of a textile-based robotic compression garment capable of the employment of blood-clot prevention. Shape memory alloys, SMAs, are utilized as a smart material inside of a woven-textile actuator and integrated into current static compression garments. Proof-of-concept experimentation and prototype testing were completed for this design. To determine the potential limitations to the design, tensile testing was completed on current static compression garments, ranging from 5 mmHg to 35 mmHg, to test the effect the actuator would have on the knitted material. This paper displays how the gauge length and displacement rate have a relationship to the required force to achieve a particular displacement in the knitted fabric. The outcomes of this work are the design and execution of a textile-based robotic compression garment. Experimental evidence is delivered based on lone actuator testing, integration of actuator testing, and compression fabric tensile testing.

1 INTRODUCTION

In 2008, a Surgeon General's Call to Action was published on how to prevent Deep Vein Thrombosis, DVT, and Pulmonary Embolism, PE. These two diseases are responsible for high death counts due to the formation and travel of blood clots [1, 2]. To help prevent these diseases compression garments can be worn with varying levels of pressure applied on the body, typically on the arms and legs. With the main devices being two extremes, a static compression garment and an intermittent-pneumatic compression, IPC, boot with a non-movable air pump, hospital-level care is not available in a transportable, comfortable and cost-effective system. This paper

demonstrates the ability of a textile-based robotic compression garment to prevent blood-clots, among other cardiovascular applications. A medium ground is accomplished where a patient can obtain hospital-level quality care anywhere with higher comfort. To achieve this goal, the implementation of smart materials into knitted and woven fabrics was accomplished to produce textile-based robotic systems [3]. This paper utilizes shape memory alloys, SMAs, as a smart material inside of a woven textile, a hybrid woven-SMA actutator.

Shape memory alloys are a unique material that can transform into a trained or "memorized" shape when a thermal condition is met. This ability is brought about by the shape memory effect, SME, which is a one-way thermal and mechanical transformation of the material from a low to a high temperature phase. The thermal transformation temperature is determined through material and mechanical properties of the SMA, as well as the heat treatment process. The SMA is set in the desired annealed position at a heat-treatment temperature. Then once the SMA cools to a low temperature phase, it is flexible and can be bent and moved to any desired position, as variants form in the material structure. Finally, when heat is reapplied to the SMA and it reaches its high transistion temperature, the SMA will return to the original annealing position it was set to at the heat treatment temperature [4, 5].

The design of this textile-based robotic compression garment is to integrates these hybrid SMA-woven texile actuators into current static compression garments. This paper demonstrates proof-of-concept experimentation of this design. To determine the potential limitations to the design, tensile testing was completed on current static compression garments varying in pressure. These experiments revealed the effect a hybrid SMA actuator would have on the knitted compression material. The relationships between the required force to achieve a particular displacement in the knitted fabrics were studied. Stress and relaxation testing was also completed to further the analysis of the effect of the hybrid actuators. Design and execution of a textile-based robotic compression garment through experimental evidence is delivered based on lone actuator testing, integration of actuator testing, and compression fabric tensile testing. Force and displacement are measured and compared for each experiment through a numerical analysis to confirm accuracy in each step of integration.

2 BACKGROUND

With the unique characteristics and scalable actuation structures, SMAs are a good fit for medical applications, devices and prosthetics. Through biocompatibility and actuation SMAs are used across the board for medical purposes ranging from catheter devices to full muscle tendons [6, 7]. Within the narrow scope of the medical field there is the application of massaging fabrics for DVT and PE patients where an intermittent pressure needs to be employed on bed-ridden patients to improve circulation to prevent blood clots from forming. Current prevention techniques for these medical conditions include compression devices and garments. Studies have shown that blood flow is improved from compression socks, but graduated compression is necessary [8]. Meaning that instead of the compression being constant throughout the garment it is gradually fitting the body part it is meant for. For example, if it is meant for the calf portion of the body, the ankle area up to the calf section of the leg would have less compression than the actual area of the calf creating a gradient of low to high pressure. Static compression can restrict blood flow at rest [8]. In further studies, it has been shown that circumference change

of the compression garment directly affects the positive outcome of prevention because there is a difference from when muscles are in use and when a person is at rest [9]. Various studies have been completed on compression garments and the relationships between the peripheral forces in the knitted fabric and the pressure on the body part due to the circumference [10, 11, 12, 13, 14, 15, 16]. There are also modeling studies using the finite element method, FEM, to predict garment pressure due to the geometric body structures [17, 18].

As stated previously, the two main devices that are currently employed for the task of preventing PE and DVT are the IPC boot and thrombi-embolic deterrent, TED, hose. The current hospital device for prevention of blood clots is the IPC boot, which is a large and bulky device with air pumps and missing comfort. The simple task of getting out bed to go to the bathroom requires assistance to take off the equipment and reapply when getting back into bed, which can be very exhausting for a patient. In contrast, the TED hose is a simplistic stocking or sleeve that is worn as an everyday sock. However, the garment only applies a static compression, which doesn't prevent all medical conditions related to PE and DVT. Graduated static compression garments are starting to be used during running and exercise for recovery and prevention of varicose veins. The IPC's intermittent, or sequential, pressure frequencies range depending on the type of device used for prevention, but typical have three modes, which are rated high, medium, and low. The high is considered 6 to 12 compressions per minute, CPM, medium is 1 to 6 CPM and the low is less than 1 CPM (2.0 Hz, 1.0 Hz, and 0.5 Hz, respectively). The TED device, which is a static compression sock does not allow for any intermittent pressure but sustains pressure constantly.

Experimental and analytical studies have been conducted regarding the mechanical properties of a compression garment and the output of pressure [12, 13, 14, 19]. Pressure is calculated from the circumference of the body part, C_b, the bandwidth the the compression garment, s, and the tangential force of the fabric, F_t, Figure 1(a). In Ilksa *et al*, equation (1) is utilized to calculate the force of the fabric from a given pressure, P [12]. From this equation, the range of F_t per a given fabric can be calculated, which is used to test the actuators while integrated into static current compression garments. The following analytical comprehension of pressure from a compression garment due to circumference and force of a garment is adapted from [12, 14].

$$F_t = \frac{PC_b s}{2\pi} \tag{1}$$

Knowing the pressure produced by a compression garment can allow the user to calculate the tangential force of a particular fabric because pressure is also defined by the tension in the fabric, T, over the radius of the garment, r, equation (2).

$$P = \frac{T}{r} \tag{2}$$

Tension is defined as the F_t in a fabric and the circumference of the garment, C_g, equation (3), while force can be defined by the Young's Modulus of the material, E, area, A_o, and strain, ε, equation (4).

$$T = \frac{F}{C_g(1+\varepsilon)} \tag{3}$$

$$F = EA_o\varepsilon \tag{4}$$

By combining equations (1), (2), (3), and (4), the change in pressure of a compression garment can be defined by equation (5). Otherwise, by knowing the F_t of the fabric through experimentation the pressure can be calculated by equation (6). The division by 133.32 is to convert the pressure value of hPa to mmHg, millimeter of mercury, which is the conventional way to display a pressure value in compression garments.

$$P = \frac{2\pi EA_o\varepsilon}{133.32C_bC_g(1+\varepsilon)} \tag{5}$$

$$P = \frac{2\pi F}{133.32C_bC_g(1+\varepsilon)} \tag{6}$$

These equations utilize the circumference of the body part, C_b, with the circumference of the garment, C_g, to determine the pressure on the body part. By using equation (6), the initial pressure on the body without actuation can be found followed by the calculation of the new pressure on the body from actuation and expanding that circumference value. This method is used to determine the effects the integrated actuators have on the pressure of the commercial compression garment. The hybrid actuators lower the pressure on the body part. The change in pressure is due to the circumference change of the compression garment. Theoretically, this is due to the distance that the compression sock is lifted off of the skin, H, which can be calculated from basic geometry in equations (7)-(11) assuming that the original inner circumference of the garment is equal to the circumference of the body, C_b, and the height that the garment is above the skin is zero initally, $H_o = 0$.

$$C_b = 2\pi R_b \tag{7}$$

$$C_g = 2\pi(R_b + H) \tag{8}$$

$$H = \frac{C_g}{2\pi} - R_b \tag{9}$$

$$H = \frac{C_g}{2\pi} - \frac{C_b}{2\pi} \tag{10}$$

$$H = \frac{x}{2\pi} \tag{11}$$

In conjunction, R_b is the radius of the body and x is the added length in the garment circumference, which is equal to $C_g - C_b$. While H is equal to $R_g - R_b$. Similar to Holschuh *et al*'s approach, the SMAs are integrated into the compression garment to elongate the circumference of the overall sleeve. The previous theory utilized nitinol, a common form of SMA, in a spring form factor as a linear actuator, however the SMA is not integrated into the textile as the springs are attached on each side to the fabric to form sleeve [20]. The advantage to the design presented in this paper is that the SMAs are a part of the textile structure. This allows for high recovery

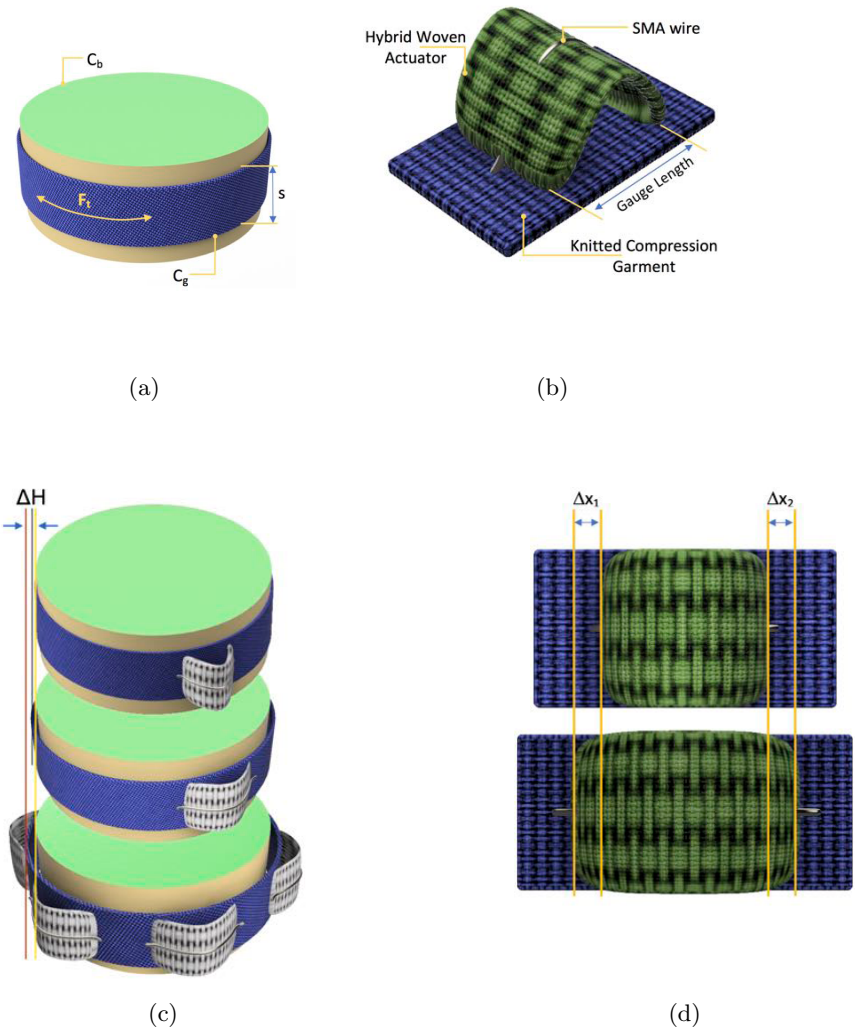

Figure 1: (a) A depiction of a static-compression garment with a tangential force, F_t, bandwidth, s, body circumference, C_b, and garment circumference, C_g. (b) Hybrid SMA actuator integrated onto the knitted garment displaying gauge length. (c) The design with one hybrid actator (top: off, middle: on) and 6 hybrid actuators integrated into the static compression garment displaying the change of in diameter, ΔH. (d) The actuator off (top) and on (bottom) with a change in length, Δx, for the knitted fabric.

and control from the elastic displacement in the garment, as well as the garment's temperature understanding and safety levels.

3 EXPERIMENTAL SETUP AND METHODS

As discussed, the primary application of this work is to develop a blood-clot prevention device through the employment of hybrid woven textile-SMA actuators integrated into a static-compression garment to form a textile-based robotic intermittent-compression garment. This research was completed by two seperate tasks: 1) performing low force and displacement tensile testing on current static-compression fabric specimens and 2) testing the effect of a single hybrid SMA-textile actuator on three different current static-compression socks. The hybrid actuators used in this particular research set utilized Ni-Ti-Cu SMA wires annealed in a straight, 180°, position at 500°C for exactly 1 hour, which were 60 mm in length and 0.5 mm in diameter. Previous work has displayed that this can allow the actuator to present a linear force of 0.038 N as a lone SMA wire and a linear force of 0.42 N integrated into a hybrid woven textile-SMA actuator from a torque of 0.001 Nm and 0.012 Nm, respectively [3]. Before constructing and analyzing the intermittent-compression garment directly, tensile testing was completed on the current static-compression socks to understand the mechanical conditions in which the actuators would be operating.

Four types of static-compression socks utilized in this work with pressure ranges of 1-5 mmHg, 8-15 mmHg, 20-30 mmHg, and 30-35 mmHg, which are considered very light, light, medium, and firm compression, respectively. From equation (1), the tangential force range for each tested-sock fabric was calculated, Table 1. The static-compression garments used in this study were standard products obtained from a pharmaceutical store. The pressure values seen in Table 1 were determined from labels on the packaging of each product.

The tensile tests were performed in a Mark-10 ESM301 load frame equipped with a 50N load cell (0.1N resolution) Figure 2(a). Specimens from the different static compression socks were cut out with the following dimensions: 80 mm in the circumferential, course, direction with a 25 mm bandwidth. Coupons were further prepared with 15 mm tape tabs at both gripping ends to ensure proper gripping, resulting in a 50 mm specimen gauge length, the distance between the gripping ends or the distance between the ends of the textile actuator, Figure 2(b) and Figure 1(b), respectively. This size was determined as the area of the compression fabric which would be effected by the hybrid SMA-textile actuator. The tensile testing was ran on compression garment samples 2 through 4: light, medium, and firm at a 25 mm/min displacement rate. These are knitted fabrics and therefore possess the ability to significantly stretch with recovery. How much and how easily each can stretch is due to the tangential force, Table 1 and Figure 1(b). The independent variables studied in this research were the gauge length, the rate of displacement, and an applied current. The dependant variables in the system are the force, displacement, and pressure outcomes. A displacement controlled tensile test was ran to understand the force needed obtain a particular displacement in the fabric. Furthermore, by changing the loading condition such that coupons from specimens 2 to 4 were loaded up to 30mm displacement at same settings as above, the climbing pressure values for each static compression sock was confirmed with holding a consistant displacement of 30 mm. The results showed an increasing level of force needed to reach the displacement, 1.5, 2.0, and 2.5 N, respectively.

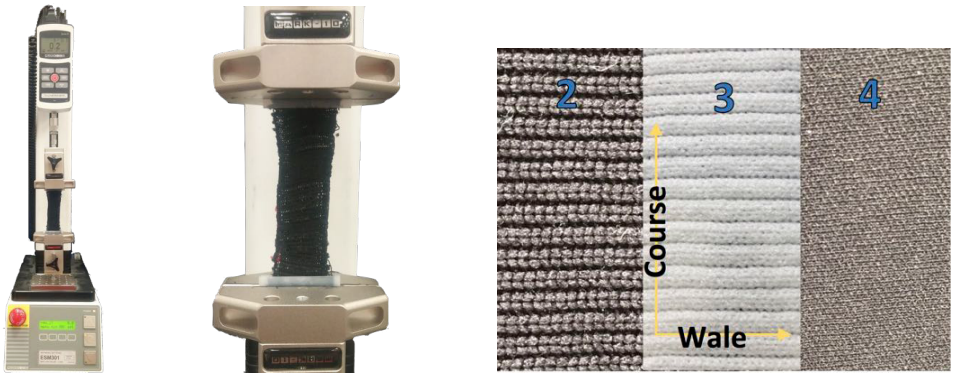

(a) (b) (c)

Figure 2: (a) Mark-10 50N force gauge, model M5-500, attached to a Mark-10 motorized test stand, model ESM301. (b) Fabric coupon inside the tensile testing rig. (c) Static compression socks: Samples 2, 3, and 4.

For a more detailed look at the displacement and recovery of the fabric due to a force, tests were conducted with the light pressure compression garment, 8-15 mmHg. Figure 3(a) is the loading and unloading at a speed of 25 mm/min with a maximum displacement of 1.5 mm; there is a distinct pattern of ossilatory behavior. This is due to the structure of the knit, Figure 2(c), which is a rib stitch. Since displacement over time is linear with no ossilatory pattern, the pattern is due to force change from the strucure of the material, specifically the yarns sliding and the redistribution of load with regards the ribbed knit.

The goal of testing the static-compression socks was to determine potential design limitations the fabric could impose when integrating the actuator with the garment, such as the gauge lenght, g_L. This is the distance between the two ends of the integrated actuator, Figure 1(b) and during tensile testing, it is the distance between the grips of the testing apparatus, Figure 2(b). Even though the coupon is 80 mm in length, when placed in the tensile tester the gauge length, may be adjusted to a shorter length. This test provides information regarding the starting bent angle of the hybrid textile actuator, as the starting angle the larger the gauge length. The tested gauge lengths were: 20 mm, 30 mm, 50 mm, and 60 mm.

To continue testing, a hybrid SMA-textile actuator was attached to each of the three types of fabrics; two of which are show in Figure 2(c), light and firm, respectively, to form prototypes of an intermittent textile-based compression garment. The actuators were comprised of a plain weave from the acrylic-polyester braid yarn. To hold the SMA wire and the magnetic-wire leads in place during actuation a cotton "cap" is sewn onto each end of the actuator. The actuators were attached to the knitted fabric using a cotton thread with a diameter size of 1 mm, Figure 4(a). The sock was placed around a foam cylinder with a circumference of 387 mm, which is the national average of the upper calf for adults 20 years of age and older [21]. A current of 2A is applied at a frequency of 0.05 Hz with a heating to cooling rate of 5 and 15 seconds, respectively, was applied to the actuator. This is considered the low setting of the IPC device, at less than

Sample	Knit Type	Compression	Pressure (mmHg)	Tangential Force (N)
1	1x1 Rib	Very Light	1 - 5	3.97 - 19.9
2	1x1 Rib	Light	8 - 15	31.8 - 59.5
3	2x1 Rib	Medium	20 - 30	79.3 - 119
4	Jersey	Firm	30 - 35	119 - 132.3

Table 1: Four static compression garments with varying levels of pressure, determined by a tangential force in the fabric, as well as the structure of the knit.

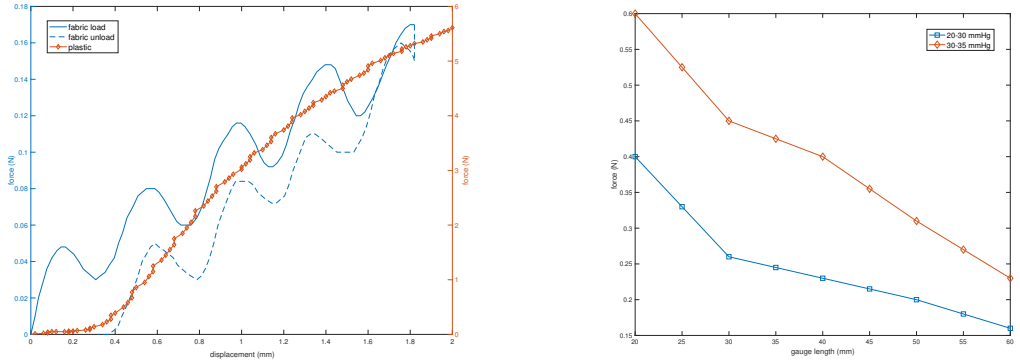

(a) (b)

Figure 3: (a) Tensile testing of static-compression garment Sample 3, 20-30 mmHg, at a rate of 25 mm/min with a 50 mm gauge length and 25 mm sample width. (b) Force per gauge length from the measurements of 20 mm to 60 mm for the 20-30 mmHg and 30-35 mmHg compression garment over a displacement of 1 mm at a displacement rate of 25 mm/min.

1CPM. This experiment was recorded and analyzed using the Tracker software, a visual tracking physics-based software, to obtain the circumference change or stretch of the fabric due to the actuation period of the hybrid textile actuator, Figure 4(b). Using tracking dots applied to the fabric, along with Tracker, Δx was observed from a change in the x-direction, $Lx2 - Lx_1$, and a change in the y-drection, $Ly2 - Ly_1$. During heating, the actuator stretches the knitted textile in the wale direction and shrinks in the course direction. Using the values obtained from the Tracker software, the new pressure on the body can be calculated using equation (5). During the actuator testing, a thermocouple was utilized to obtain the temperature of the woven actuator and the temperature of the compression garment. This is to determine the effects of the SMA wire's heat dissipation. Through joule heating, where a current is applied across the SMA, the hybrid actuator's surface temperature rizes depending on the textile type, but at this low of a frequency of 0.5 Hz, the surface temperature levels off at around the 10th actuation period for most textiles tested [3].

Table 2: Sample 2 Displacement Rate Results

Displacement Rate	Final Load	Tension
10 mm/min	0.1267 N	0.0569 N/mm
15 mm/min	0.1333 N	0.0615 N/mm
20 mm/min	0.1533 N	0.0604 N/mm
25 mm/min	0.1367 N	0.0614 N/mm
30 mm/min	0.1333 N	0.0596 N/mm
35 mm/min	0.1267 N	0.0531 N/mm

4 RESULTS AND DISCUSSION

The two tasks of this research produced design criteria for the SMA driven textile-based intermitted-compression garment. This included force to displacement understanding for static-compression fabrics with different pressure values, gauge length influence, and displacement rate of the fabric. Starting with the low force vs displacement tensile testing, the knitted fabric revealed an ossilatory pattern with a irreverable recovery range of 0.4 mm, Figure 3(a). This is important because it defines the starting point for the next actuation period. The tensile testing also revealed what displacement is expected from a known force of the actuator. It confirms that the force seen by the actuator is able to displace the fabric allowing for a change in the garment circumference. In all three fabrics, there is a distinct change in force over displacement due to gauge length, Figure 3(b). According to previous work, Kennedy *et al*, the larger the starting the angle, and therefore gauge length, the smaller torque outcome. However, assuming all dimensions stay the same, this study revealed that a more obtuse starting angle requires a lower force from the textile actuator to produce an outcome of the same displacement for a more acute starting angle. The authors account this terms of amount of fabric to stretch.

There is also a relation to the rate at which the static-compression knit is displaced and the displacement load, Table 2. This envolves the structure of the knit with load distribution as the yarns slide during change in length. The displacement seen in this testing is in the course direction, which seperates the vertical rows of the rib stitch. Table 2 displays the load needed to displace Sample 2, 8-15 mmHg, 2 mm in length for displacement rates 10, 15, 20, 25, 30, and 35 mm/min. The table also displays the rate of force needed for 1 mm of displacement. This value is also known as tension, N/m, in the fabric. It is valuable to understand this relationship between the rate of force per displacement and the displacement rate for integration of the textile actuator. This dataset has a curve fitting for a quadratic expression of 0.91.

Table 3 shows the results for the integration of the textile-based actuator. So for sample 2, there was a displacement rate of 6.6 mm/min. This produced a change in circumference of the material by 0.53 mm. By expanding the force rate per displacement dataset and forcasting the lower displacement rate, a calculated value of 0.054 N/mm force rate is found. At this force rate and a displacement in the fabric of 0.530 mm, the textile-based actuator produced a force of 0.028 N. This aligns with the amount of force the actuator has produced in testing.

By using equation (6), the initial pressure on the body without actuation can be found followed by the calculation of the new pressure on the body from actuation, which is through expanding the garment circumference value. This shows a lowered pressure on the body part in

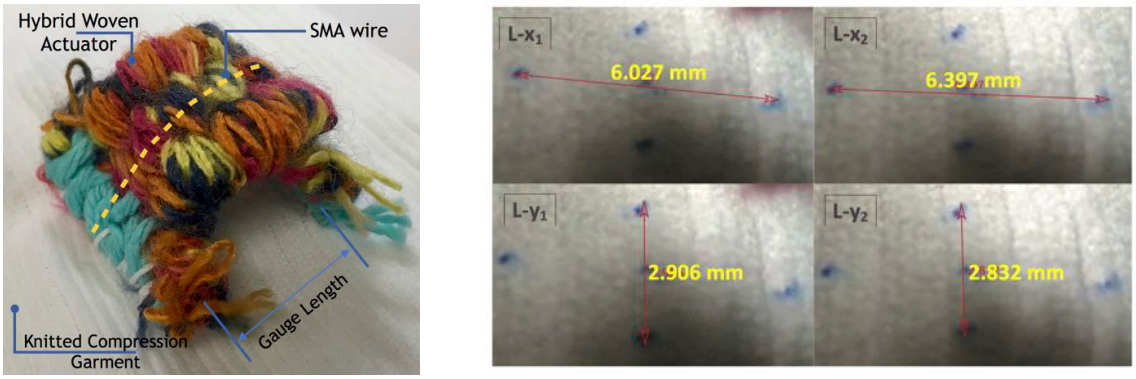

(a) (b)

Figure 4: (a) A hybrid SMA-textile actuator attached to the 20-30 mmHg compression sock. (b) The circumference change of the 20-30 mmHg garment during actuation, Δx.

Sample Number	**Circumference Change 1 Actuator (mm)**	**Pressure Change 1 Actuator (mmHg)**	**Pressure Change 6 Actuators (mmHg)**	**Displacement Rate (mm/min)**
1	1.2	-0.0474	-0.284	14.4
2	0.53	-0.149	-0.891	6.60
3	0.29	-0.297	-1.78	3.60

Table 3: The measured garment circumference and pressure change, as well as the displacement rate, from a single actuator at a gauge length of 30 mm. Through calculations the change in pressure for 6 actuators is found.

mmHg. The resulting change in circumference, Δx, on average, for each type of textile are shown in Table 3. Expanding, this change in circumference for 6 actuators leads to a diameter change of 0.277 - 1.16 mm, equation (11), depending on the initial static-compression garment. This is the distance that the compression sock would be lifted off of the skin. Again, assuming that the original inner circumference of the garment is equal to the circumference of the body, C_b, the change in diameter or height that the garment is above the skin, H, is zero. When actuated, the circumference of the garment, C_g, is increased by the amount stretched by the actuator, x, which

makes H increase and relieve pressure on the body part. With the six-actuator geometry, Figure 1(c), the change in diameter values witnessed in these experiments would produce a pressure change of 0.284, 0.891, and 1.78 mmHg, Table 3, respectively. In terms of temperature, the body threshold for longterm exposure is about 40°C. The through dissipation of the actuator's woven structure, the design allows for surface temperature of the textile-based actuator to be kept under 36°C and the surface temperature of the compression garment, which would be in contact with the skin, under 26°C. These values are in relation to a 22°C room temperature. Therefore, that is a relative change of 14°C for the surface temperture of the actuator and 4°C change in the compression garment. This design keeps the heat away from the body part and therefore, lowers or eliminates the risk of high temperatures on the skin.

5 CONCLUSIONS

This paper provides insight into the ability of hybrid woven SMA-textile actuators to produce the desired outcomes for textile-based robotic and compression garment applications. The proof-of-concept research done for the compression garment shows that the intermittent relief of pressure is possible through the integration of the hybrid actuators in current static-compression garments. Tensile testing revealed the design limitations that the static-compression garment fabric has on the possible design considerations such as gauge length of the actuator and pressure value of the chosen initial compression garment.

The experimental results for the hybrid actuators showed that there was less of a displacement with the higher pressure compression garments, but a higher relief of pressure is achieved on the body. This is another design parameter to account for when fabricating future prototypes. For a Ni-Ti-Cu-Acrylic-Polyester six-actuator geometry, a pressure difference is seen from 0.3 mmHg to 1.8 mmHg depending on the existing compression garments starting pressure. The actuator is a design parameter of its own with past work showing different force, displacement, and temperature outcomes for different material, mechanical, and annealing properties [3].

This is not a final solution, but rather a step in the right direction for smart-fabric integration into the field of medical compression garments for blood-clot prevention. Overall, this research was successful in revealing the impact that the hybrid actuators could have in the textile-based robotic and compression garment industry, as well as, the integration of hybrid SMA-textile actuator into a bio-inspired design, which could produce a functioning, perhaps autonomous, robots. The small SMA wire inside of the attached woven actuator allows for a great enough force to produce a change in pressure. The SMA has a small footprint in this design with a large impact. The low ratio of the SMA to the textile and low frequency actuation period allows for more control of the wire during actuation and less heat build up around the wire. In future testing and prototypes, this information will be useful to determine placement and outcomes of the actuator's presence in the textile system. Furthermore, modeling the compression garment's knitted fabric patterns will be important to understand how the actuator's presence influences the static-compression garment. These tests are a beginning stage to this modeling process.

REFERENCES

[1] Rathbun S., The surgeon generals call to action to prevent deep vein thrombosis and pulmonary embolism, Circulation, 119(15):e480-2, 2009.

[2] Kesieme, E., Kesieme, C., Jebbin, N., Irekpita, E. and Dongo, A., Deep vein thrombosis: a clinical review. J Blood Med, 2(2), pp.59-69, 2011.

[3] Kennedy, J., A Study of Shape Memory Alloys as Actuators for Textile Robotics and Compression Garment Applications, Ph.D. Thesis, Drexel University, (2016).

[4] Bhattacharyya, A., Sweeney, L. and Faulkner, M.G., Experimental characterization of free convection during thermal phase transformations in shape memory alloy wires. Smart materials and Structures, 11(3), p.411, 2002.

[5] Sayyaadi, H., Zakerzadeh, M.R. and Salehi, H., A comparative analysis of some one-dimensional shape memory alloy constitutive models based on experimental tests. Scientia Iranica, 19(2), pp.249-257, 2012.

[6] Shabalovskaya, S., Anderegg, J. and Van Humbeeck, J., Critical overview of Nitinol surfaces and their modifications for medical applications. Acta Biomaterialia, 4(3), pp.447-467, 2008.

[7] Morgan, N.B., Medical shape memory alloy applicationsthe market and its products. Materials Science and Engineering: A, 378(1), pp.16-23, 2004.

[8] Byrne, B., Deep vein thrombosis prophylaxis: the effectiveness and implications of using below-knee or thigh-length graduated compression stockings, Heart & Lung: The Journal of Acute and Critical Care, 30:4, 277–284, 2001.

[9] Mosti, G.B., and Mattaliano, V., Simultaneous changes of leg circumference and interface pressure under different compression bandages, European journal of vascular and endovascular surgery, 33:4, 476–482, 2007.

[10] Du, Z., and Hu, H., A study of spherical compression properties of knitted spacer fabrics Part I: Theoretical analysis, Textile Research Journal, 2012.

[11] Hong, L., Dongsheng, C., Qufu, W., and Ruru, P., A study of the relationship between clothing pressure and garment bust strain, and Young's modulus of fabric, based on a finite element model, Textile Research Journal, 81:13, 1307–1319, 2011.

[12] Ilska, A., Kowalski, K., Kłonowska, M., and Kowalski, T., Influence of Stress and Relaxation Characteristics of Knitted Fabrics on the Unit Pressure of Compression Garments Supporting External Treatment, Fibres & Textiles in Eastern Europe, 2014.

[13] Kowalski, K., Mielicka, E., and Kowalski, T., Modelling and Designing Compression Garments with Unit Pressure Assumed for Body Circumferences of a Variable Curvature Radius, Fibres & Textiles in Eastern Europe, 2012.

[14] Leung, W., Yuen, D., Ng, S.,i and Shi, S., Pressure prediction model for compression garment design, Journal of Burn Care & Research, 31:5, 716–727, 2010.

[15] Sang, J., Lee, M., abd Park, M., Structural effect of polyester SCY knitted fabric on fabric size, stretch properties, and clothing pressure, Fashion and Textiles, 2:1, 1–9, 2015.

[16] Wang, L., Felder, M., and Cai, J., Study of properties of medical compression fabrics, Journal of Fiber Bioengineering & Informatics, 4:1, 15–22, 2011.

[17] Dan, R., Fan, X., Chen, D., and Wang, Q., Numerical simulation of the relationship between pressure and displacement for the top part of men's socks, Textile Research Journal, 2010.

[18] Zhang, M., Dong, H., Fan, X., and Dan, R., Finite element simulation on clothing pressure and body deformation of the top part of men's socks using curve fitting equations, International Journal of Clothing Science and Technology, 27:2, 207–220, 2015.

[19] Mirjalili, S., Rafeeyan, M., and Soltanzadeh, Z., The analytical study of garment pressure on the human body using finite elements, Fibres & Textiles in Eastern Europe, 3 (68), 69–73, 2008.

[20] Holschuh, B., and Newman, D., Two-spring model for active compression textiles with integrated NiTi coil actuators, Smart Materials and Structures, 24:3, 2015.

[21] McDowell, M., Fryar, C., Ogden, C., and Flegal, K., Anthropometric reference data for children and adults: United States, 20032006. National health statistics reports; no 10. Hyattsville, MD: National Center for Health Statistics, 2008.

VIII ECCOMAS Thematic Conference on Smart Structures and Materials
SMART 2017
A. Güemes, A. Benjeddou, J. Rodellar and J. Leng (Eds)

INDUCTION HEATING OF SHAPE MEMORY ALLOY COMPONENTS USING LIQUID METAL ENERGY CIRCUITS FOR HIGH BANDWIDTH DISTRIBUTED ACTUATION

BRENT R. BIELEFELDT*, JACOB L. MINGEAR* AND DARREN J. HARTL*

*Department of Aerospace Engineering
Texas A&M University
College Station, TX, United States of America
e-mail: darren.hartl@tamu.edu, web page: http://www.maestrolab.tamu.edu

Key words: Shape Memory Alloys, Liquid Metal, Induction Heating, Adaptive Structures, COMSOL Multiphysics

Abstract. Shape memory alloy (SMA) components are an important innovation to the design of various aerospace applications due to their high actuation work density and relative simplicity, making them ideal candidates for structurally embedded actuators. However, these thermally driven materials are unable to provide a rapid cyclic response compared to traditional actuators due to the difficulty of adding heat to and especially removing heat from large metallic bodies. Induction heating is widely used in metals production and processing to quickly increase temperature in a controlled manner, and can be integrated with SMA components to expedite the actuation process. One potential option for increased cyclic frequency in SMA actuators involves the use of integrated liquid metal energy circuits, whereby applying an alternating electric current to the liquid metal circuits results in the generation of eddy currents in the surrounding SMA material, delivering a large amount of thermal energy distributed throughout an SMA body via localized Joule heating. This work presents a multiphysical finite element model of a beam containing a liquid metal circuit and heated via localized induction heating. The results are compared to preliminary experimental results, which represent the first known demonstrations of an SMA component actuated via liquid metal energy circuits. The ability of the liquid metal circuits to act as an active cooling mechanism is also computationally demonstrated. The results of this work will be used to develop a parameterized optimization framework to discover actuator/circuit configurations that best improve cyclic response.

1 INTRODUCTION

Shape memory alloys (SMAs) are active materials that can undergo considerable mechanical deformation before recovering their original shape via a temperature- and/or stress-induced response. A solid-to-solid transformation between the high-temperature/low-stress *austenite*

phase and low-temperature/high-stress *martensite* phase results in inelastic recoverable strains known as *transformation strains*, which can be recovered during transformation back into the parent state [1]. One of the most common SMAs, equiatomic nickel-titanium (NiTi or Nitinol), can exhibit fully recoverable transformation strains of around 7% and actuation stresses exceeding 300 MPa [2].

Typical aerospace applications for SMAs are in the area of actuation, where their high actuation work density, compactness, and reliability make them ideal candidates for structurally embedded actuators. Such applications have considered SMA actuators in the form of torsional actuators [3, 4, 5], bending beams [6, 7, 8, 9], and wires [10, 11, 12]. However, the use of SMA actuators is limited by their inability to maintain a rapid cyclic response compared to traditional actuators due to the time necessary to add or remove heat from the component. Joule (or resistive) heating is the most direct method for introducing thermal energy, but such a method is amperage-limited to small components. Conduction heating is also limited by part size as well as the low thermal conductivity of SMAs (approximately 5% that of aluminum [13]). Induction heating is widely used in metals production and processing to rapidly increase heat in a controlled manner, and has thus become an attractive option for heating large SMA components [14]. Techniques for cooling SMA components include forced air convection, water immersion, and heat sinking, with the latter two methods yielding the most promising results [15, 16]. However, these methods rely on additional and possibly heavy sub-systems and lead to more complex actuator designs.

One potential option for increasing the cyclic frequency of SMA actuators involves the use of integrated liquid metal energy circuits. Orienting electrically conductive channels of liquid metal into resistive heater traces or coils on or inside the actuator enables localized electrothermal heating. An alternating current applied to a liquid metal coil induces a time-harmonic magnetic field, which in turn can generate an induced internal current in the SMA actuator. These currents, known as *eddy currents*, result in the localized Joule heating of the actuator. This heating method has been preliminarily demonstrated for SMA wires embedded in a polymer matrix as well as monolithic SMA components (Figure 1) [17]. These liquid metal channels could also be used to remove heat from the actuator, as cooled liquid metal flowing through the actuator could replace the heated liquid metal as well as draw heat energy away from the SMA component. A similar method using convective liquids has been demonstrated by Coppola et al. [18], where water and polyalphaolen oil were flowed through vascular channels in an SMA actuator system to rapidly cool the component via forced convection. Non-toxic, room-temeprature liquid metals with higher thermal conductivities than water and oil, such as gallium-indium eutectic (GaIn, 75.5/24.5 wt.%) or gallium-indium-tin eutectic (GaInSn, 68.5/21.5/10.0 wt.%), could be used to further expedite the cooling process [19, 20], thus creating a multifunctional mechanism to improve rapid cyclic (heating and cooling) responses in SMA actuators.

This work seeks to demonstrate the viability of an integrated SMA-liquid metal actuator in a mostly computational framework. The heating response of such an actuator is compared to that of more traditional induction methods (i.e. a copper induction coil placed on the surface of the actuator). It will be shown that this novel heating method is not only feasible, but that it significantly outperforms traditional induction methods. This paper discusses the modeling of these actuator systems and also explores the ability of liquid metal channels to aid in the cooling of SMA actuators.



(a) Additively manufactured SMA beam actuator.

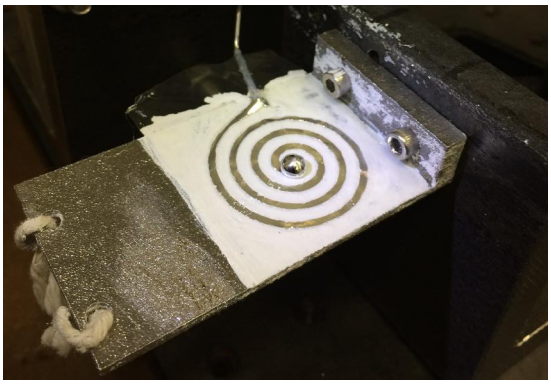

(b) SMA beam mounted as a cantilever, with white latex paint electrically insulating a stationary liquid metal energy circuit.

Figure 1: Experimental work on integrating liquid metal energy circuits in monolithic SMA components [17].

2 PREVIOUS WORK

As mentioned in Seciton 1, previous work on integrated SMA-liquid metal actuators has focused primarily on experimental demonstrations [17]. One potential actuator system features SMA wires embedded in a polymer matrix with liquid metal-filled vascular channels beneath the SMA components. Currently this system relies solely upon Joule heating of the SMA wires via current applied to the liquid metal channels. A 150×7×4 mm composite actuator with a single Smartflex NiTi wire from SAES Getters with of radius r=0.5 mm was fabricated, and a current of 8.7 A was applied to a liquid metal channel. As the SMA wires were heated and contracted, the 150 mm long composite actuator deflected downwards a total of 35 mm after 80 s. Room-temperature liquid metal was then used to flush the heated liquid metal out of the channel, removing heat from the actuator and causing the SMA wires to recover their original shape.

A second potential actuator system uses selective laser melting (SLM), an additive-manufacturing process, to produce complex, monolithic SMA components with vascular channels inside the components themselves. A simple SMA beam with a planar spiraling channel exposed on its top surface was manufactured using a Nanoval selective laser melter (Figure 1a). A latex-based paint was applied to the open-faced channel to electrically insulate the liquid metal coil from the SMA beam (Figure 1b). After applying a load of 1.5 kg to the tip of the beam (corresponding to a 3 mm tip deflection), a Roy 1500 induction heater was used to apply an alternating current to the liquid metal coil. Induction heating lead to a temperature increase of 70 °C in approximately 3 minutes at the center of the coil. The actuator tip recovered its deflection upwards a total of 0.5 mm, or a recovery of 16.7%. This experiment has prompted computational studies to further explore the capabilities of SMA induction heating using liquid metal energy circuits as well as investigate novel cooling mechanisms using liquid metal.

3 MULTIPHYSICAL MODELS

To demonstrate the feasibility of an integrated SMA-liquid metal actuator, one-way coupled models are created using the COMSOL Multiphysics® software package [21]. The following sections detail these models and the various physical mechanisms considered during analysis.

3.1 TRADITIONAL EXTERNAL INDUCTION COIL

To form a baseline measurement based on traditional induction techniques, a 2-D axisymmetric model of a copper induction coil placed on the surface of an SMA domain is created using COMSOL (Figure 2). The model consists of an SMA disk with radius $r_{SMA} = 15\,\text{mm}$ and thickness $t_{SMA} = 4.5\,\text{mm}$, with five wires of radius $r_{wire} = 1\,\text{mm}$ spaced 0.65 mm apart corresponding to concentric coils and approximating a spiral induction coil with $N = 5\,\text{turns}$ resting on the positive-z surface of the SMA component. These components are surrounded by an air domain with radius $r_{air} = 160\,\text{mm}$ and thickness $t_{air} = 100\,\text{mm}$. An axisymmetric boundary condition is placed on the r=0 edge of the model. The finite element mesh consists of 8,557 quadratic elements, with greater mesh density in the area surrounding the actuator (Figure 3).

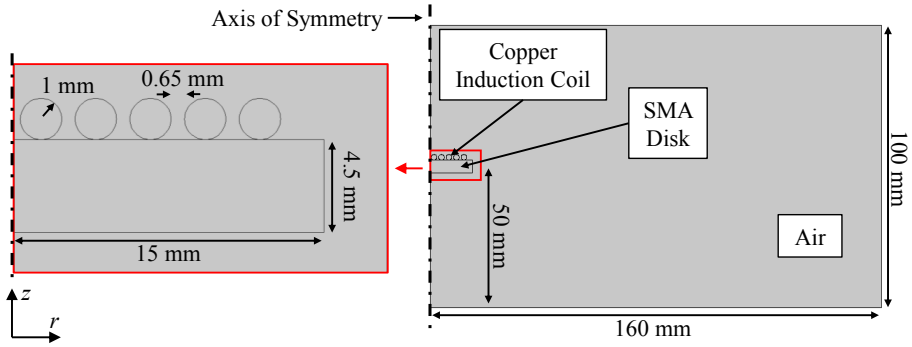

Figure 2: 2-D model of an external induction coil resting on an SMA disk. The dotted line denotes the axis of symmetry.

The finite element model couples COMSOL's Magnetic Fields and Heat Transfer in Solids modules, solving the electromagnetic and heat transfer equations simultaneously. Magnetic insulation boundary conditions and an ambient temperature $T_{amb} = 293.15\,\text{K}$ are applied to the edges of the air domain. The initial temperature of the component is also set to T_{amb}. A constant current I is applied to each copper wire, simulating a single oscillating current running through the entire coil. Relevant material properties can be fount in Table 1. It is important to note that the phase transformation behavior of SMAs is not modeled in this proof-of-concept work; only the electrical, thermal, and magnetic properties are considered.

3.2 EMBEDDED LIQUID METAL ENERGY CIRCUIT FOR HEATING

A 2-D axisymmetric model of a liquid metal energy circuit embedded in an SMA component constructed in COMSOL is shown in Figure 4. The dimensions of the SMA component and

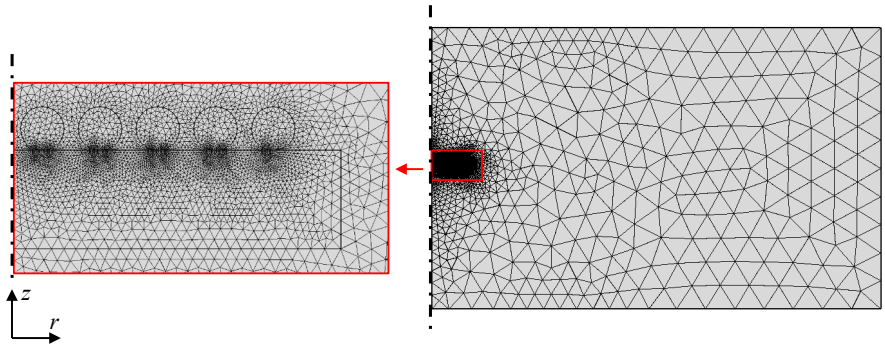

Figure 3: Mesh of the 2-D external induction coil model.

Table 1: Relevant material properties for the external induction coil model. Air and copper properties taken from [21]; SMA properties taken from [14].

Property	**Value**
Air	
Relative permeability, μ_r	1
Relative permittivity, ε_r	1
Electrical conductivity, σ	$0\,\mathrm{S/m}$
SMA	
Relative permeability, μ_r	1
Relative permittivity, ε_r	1
Electrical conductivity, σ	$1.25 \times 10^6\,\mathrm{S/m}$
Thermal conductivity, k	$18\,\mathrm{W/m{\cdot}K}$
Heat capacity, C_p	$400\,\mathrm{J/kg{\cdot}K}$
Density, ρ	$6{,}440\,\mathrm{kg/m^3}$
Copper	
Relative permeability, μ_r	1
Relative permittivity, ε_r	1
Electrical conductivity, σ	$6.0 \times 10^7\,\mathrm{S/m}$
Thermal conductivity, k	$400\,\mathrm{W/m{\cdot}K}$
Heat capacity, C_p	$385\,\mathrm{J/kg{\cdot}K}$
Density, ρ	$8{,}700\,\mathrm{kg/m^3}$

domain are equal to those discussed in Section 3.1. A liquid metal energy circuit with $N = 5$ turns embedded in the SMA component is represented using five channels having a semi-circular cross section with a radius of $r_{channel} = 1\,\mathrm{mm}$ spaced $0.65\,\mathrm{mm}$ apart. An asymmetric boundary condition is again placed on the r=0 edge of the model. The model consists of 4,720 triangular elements in a manner consistent with Section 3.1 (Figure 5).

As in Section 3.1, the model couples the Magnetic Fields and Heat Transfer in Solids COMSOL modules. Identical boundary conditions are placed on the air domain, and a constant

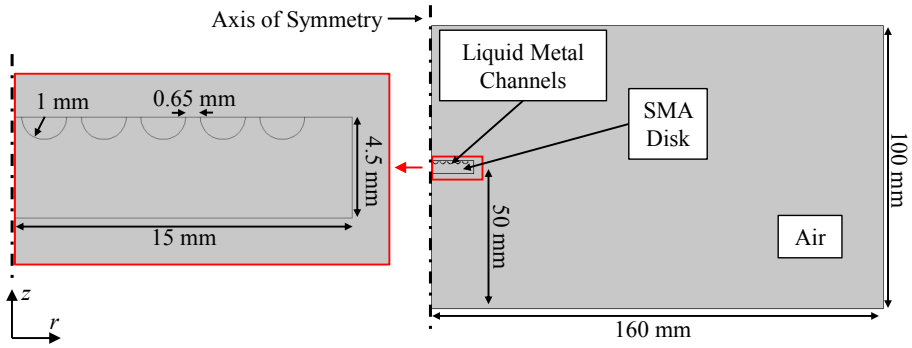

Figure 4: 2-D model of a liquid metal energy circuit embedded in an SMA disk. The dotted line denotes the axis of symmetry.

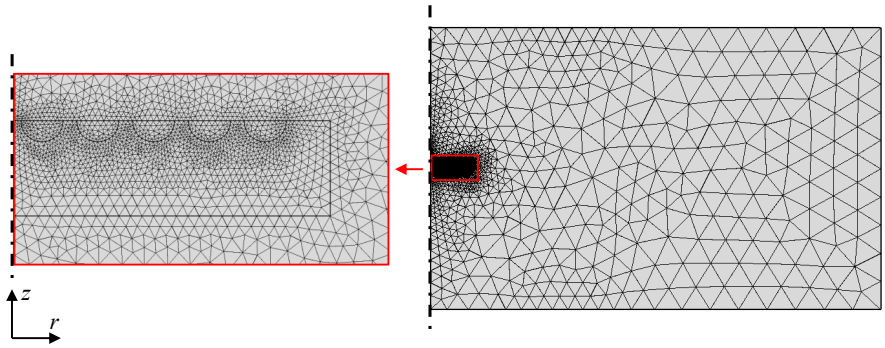

Figure 5: Mesh of the 2-D embedded induction coil model.

current I is applied to each of the liquid metal channels. Here we assume that the liquid metal is electrically isolated from the SMA (i.e., the applied current can only flow through the liquid metal coil and not the SMA). The material properties of the air and SMA domains are consistent with those in Table 1, while relevant liquid metal properties can be found in Table 2.

Table 2: Relevant material properties for the embedded liquid metal energy coil model [22].

Property	**Value**
Liquid Metal	
Relative permeability, μ_r	1
Relative permittivity, ε_r	1
Electrical conductivity, σ	3.8×10^6 S/m
Thermal conductivity, k	16.5 W/m·K
Heat capacity, C_p	300 J/kg·K
Density, ρ	6,440 kg/m^3

3.3 EMBEDDED LIQUID METAL ENERGY CIRCUIT FOR COOLING

To examine the ability of liquid metal energy circuits to aid in the cooling of SMA actuators, a 3-D model of the component discussed in Section 3.2 is created in COMSOL (Figure 6a). The SMA disk has a radius $r_{SMA} = 15\,\text{mm}$ and thickness $t_{SMA} = 4.5\,\text{mm}$ (cf. Section 3.1). The 2-D representation of the liquid metal energy circuit is replaced by a 3-D coil with an inner radius $r_{coil,i}$=1 mm, outer radius $r_{coil,o}$=13 mm, and N=5 turns. The cross-section of the coil is again a semicircle with a radius $r_{channel}$=1 mm. The model consists of 91,933 tetrahedral elements and 2,673 edge elements, with increased mesh density in the areas surrounding the coil (Figure 6b).

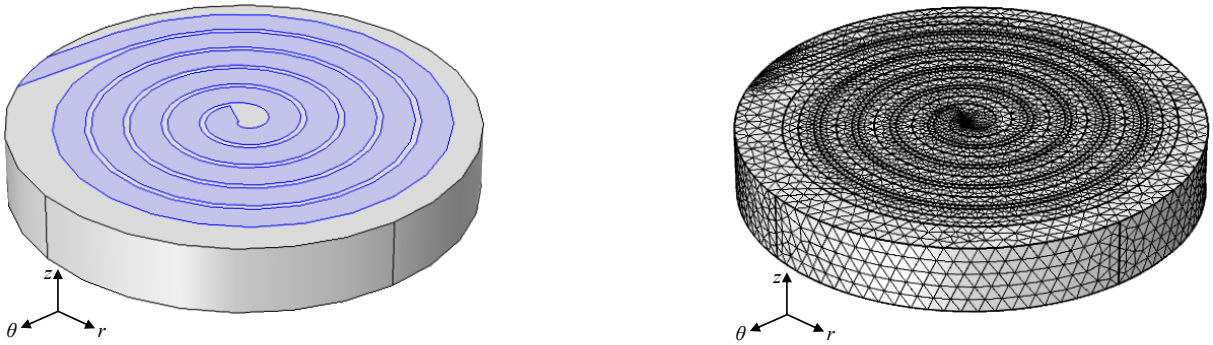

(a) Geometry of the 3-D actuator model. The liquid metal energy circuit is denoted by the shaded region.

(b) Mesh of the 3-D actuator model.

Figure 6: 3-D model of an integrated SMA-liquid metal component.

The initial temperature of the component is determined by mapping the final temperature of the embedded liquid metal energy circuit model discussed in Section 3.3 (cf. Section 4.1). To demonstrate the effectiveness of liquid metal cooling, two cases are examined. The first case considers cooling via forced convection, with air flowing over the component at a speed of v_{air}=1 m/s. The second case considers liquid metal flowing through the coil, removing heat from the component. The former is achieved using the Heat Transfer in Solids module, while the latter utilizes the Heat Transfer in Pipes module in COMSOL. The walls of the coil are assumed to have a surface roughness of 0.05 mm, which comes from preliminary characterization of SLM 3-D printed NiTi SMA. The initial temperature of the liquid metal inside the coil is equal to the surrounding SMA (i.e., as informed from the heat mapping). Liquid metal with a dynamic viscosity $\nu = 2.4 \times 10^{-3}\,\text{Pa·s}$ flows through the coil with a velocity of v_{lm}=0.1 m/s (based on observations in preliminary experiments [17]) with an inlet temperature of 300 K.

4 RESULTS

4.1 INDUCTION HEATING

Induction heating analyses of the models discussed in Sections 3.1-3.2 consider a frequency of f=150 kHz and currents applied to the respective coils for 60 seconds. Figure 7 shows a

comparison of the temperature at the center of the revolved component for both the external induction coil and embedded liquid metal energy circuit with applied currents of 12 A and 20 A. In each plot, the dotted line represents a study in which the liquid metal domain is considered only electromagnetically (i.e., for heat generation) but is not considered when solving the heat transfer equations. This represents a conservative case in which the heating of the SMA component is caused by localized heating from induced eddy currents and not from temperature increase of the resistive liquid metal itself. The solid red line corresponds to results that consider also the direct resistive heaing of the coil itself, which increases total heat generation. For an applied current of 12 A, using an external induction coil corresponds to a predicted temperature increase of approximately 15 K in 60 s. However when using an embedded liquid metal energy circuit (and ignoring Joule heating of the liquid metal circuit itself), temperatures increase by nearly 20 K in the same amount of time. Performance is further increased when considering Joule heating from the liquid metal; with a predicted final temperature of 332 K, the liquid metal energy circuit nearly triples the temperature increase predicted when using an external induction coil. Similar trends are observed for an applied current of 20 A. Analysis predicts a final temperature of 402 K after a temperature increase of nearly 110 K in 60 s, when using an embedded liquid metal energy circuit.

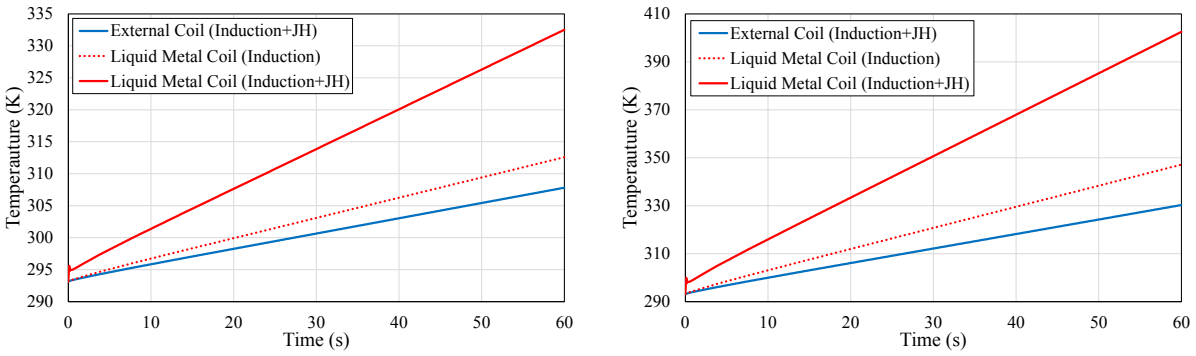

(a) 12 A applied current.

(b) 20 A applied current.

Figure 7: Comparison of heating capability for the external induction coil and embedded liquid metal energy circuit (150 kHz); "JH" indicates Joule heating of the coil itself is considered.

Contour plots of the induced current (or eddy currents) generated by both induction coils considered for an applied current of 20 A are shown in Figure 8. It is noticeable that not only does the embedded liquid metal energy circuit induce eddy currents of greater magnitude, but also that the eddy currents penetrate deeper into the component than those generated by the external induction coil. This is one advantage of the induction coil being embedded in the component rather than on its surface. One would expect eddy currents of greater magnitude to generate higher temperatures, and eddy currents penetrating deeper into the component to further facilitate heating. Figure 9 shows temperature profiles for the three induction heating cases considered. As expected, the temperature contours shown in Figure 9a and Figure 9b closely match those of the eddy current contours in Figure 8a and 8b, respectively. Figure 9 also

highlights a second advantage of the induction coil being embedded in the component. Note that while the coils in Figure 9a are increasing in temperature, the seem to have little/no effect on the temperature of the component. Meanwhile, the heat generated by applying current to the liquid metal embedded in the component (Figure 9c) further facilitates heating due to the increased contact area with the SMA component. This, combined with the generation of stronger and farther-reaching eddy currents, could alloy for more rapid cyclic actuation in SMA components.

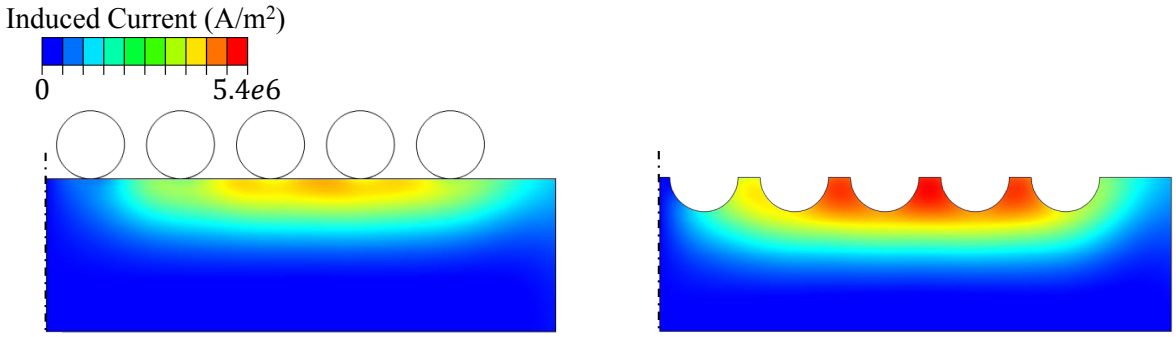

(a) External induction coil.

(b) Embedded liquid metal energy circuit.

Figure 8: Comparison of induced current contours for the both induction coils considered for an applied current of 20 A. The dashed lines represent an axis of symmetry.

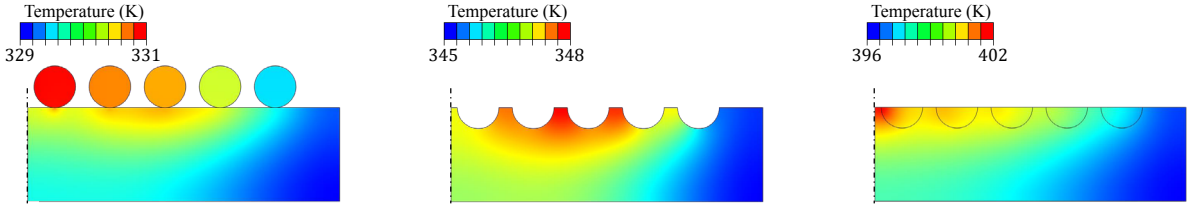

(a) External induction coil.

(b) Embedded liquid metal energy circuit (disregarding Joule heating of the coil).

(c) Embedded liquid metal energy circuit (considering Joule heating of the coil).

Figure 9: Comparison of temperature profiles for the three induction heating cases considered for an applied current of 20 A. The dashed lines represent an axis of symmetry. Individual temperature scales are used for comparison with Figure 8.

4.2 COOLING

As discussed in Section 3.3, the initial temperature for the 3-D thermal model is set by mapping the final temperature field found using the 2-D embedded induction coil model (cf. Figure 9c). Two methods of cooling are then considered: 1) forced convection via air flow over the component and 2) liquid metal flowing through the coil to remove heat from the component. Figure 10 shows the temperature at the center of the coil on the $+z$ face during cooling for these

two methods. Forced convection cools the component to 371 K, or a reduction of approximately 28% of the temperature change upon heating. Liquid metal flowing through the component is able to reduce its temperature to 312 K, or a recovery of nearly 84% of its temperature change.

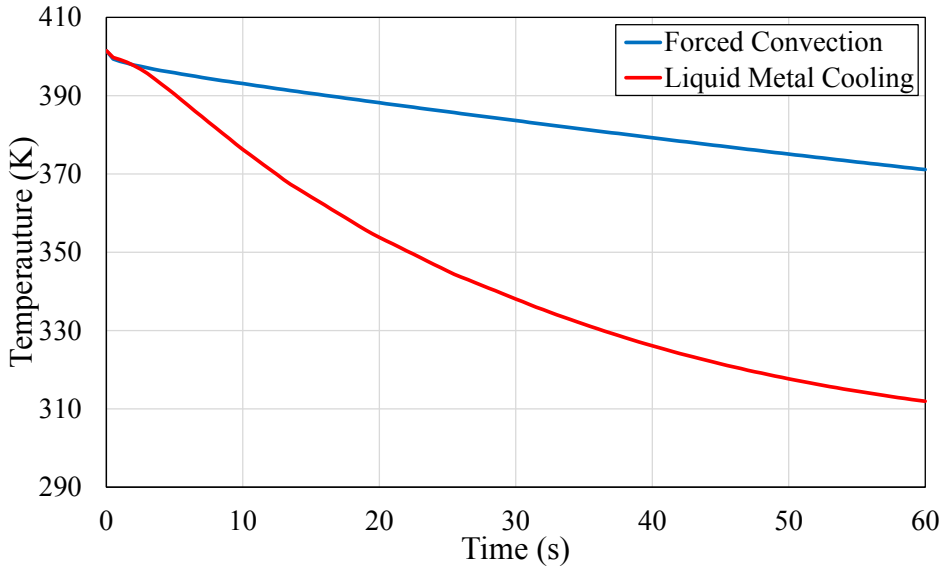

Figure 10: Comparison of forced convective cooling and liquid metal cooling for an SMA component.

Figure 11 shows temperature contours of the component at various times during the liquid metal cooling process. As room temperature liquid metal flows through the inlet and into the component, its high thermal conductivity allows it to rapidly remove heat from the SMA component. This process would continue until the component reaches a desired temperature (e.g. past its transformation temperature), at which point a current could be applied to the liquid metal, beginning the actuation process again.

5 CONCLUSIONS

The high specific energy density of shape memory alloys make them ideal actuators, but their inability to provide a rapid cyclic actuation response hinders their more widespread use in the aerospace industry. This work has investigated a novel method to increase SMA actuation frequency by using embedded liquid metal energy circuits to inductively heat SMA components. Computational analysis has shown that applying 20 A of current to a liquid metal coil at a frequency of 150 kHz can lead to a temperature increase of nearly 110 K in 60 s. These liquid metal energy circuits can also be used to rapidly cool SMA components. Room temperature liquid metal flowed through a heated SMA component is predicted to recover nearly 84% of the component's original temperature change upon heating in 60 s. Combining these processes could increase the actuation frequency of SMA components (Figure 12). For example, when considering the transformation temperatures of an SLM 3-D printed SMA component [23], utilizing liquid metal energy circuits results in an actuation cycle of 116 s, nearly times higher than when

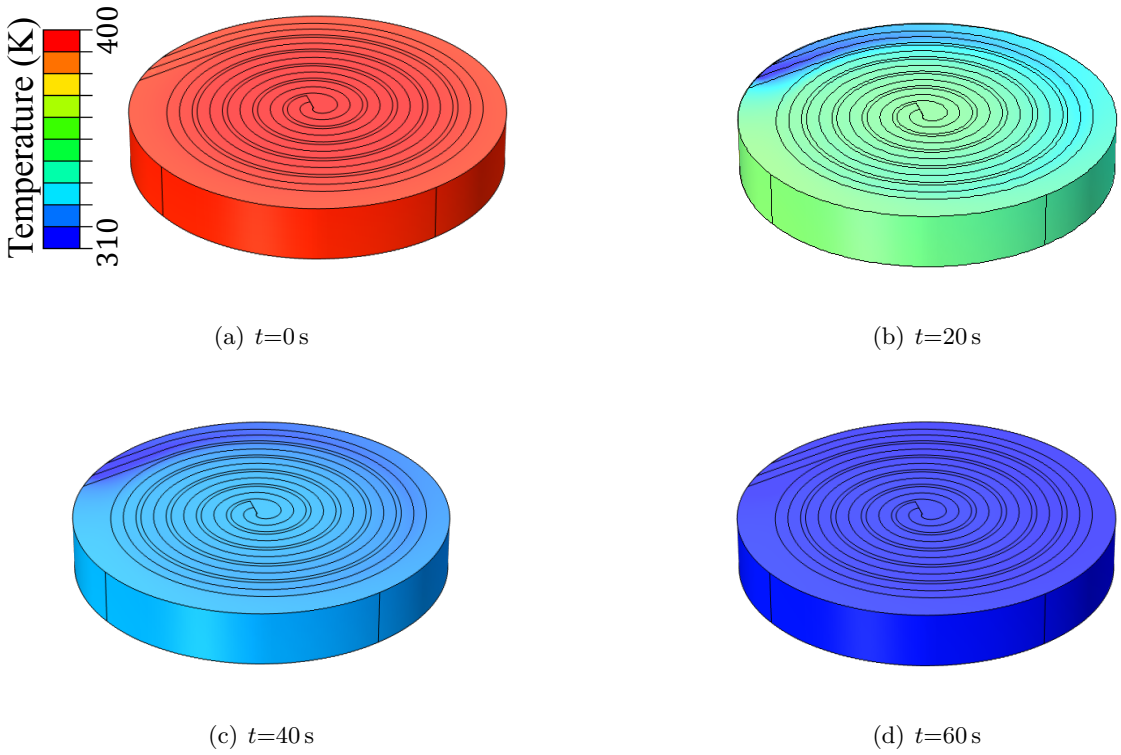

(a) t=0 s (b) t=20 s

(c) t=40 s (d) t=60 s

Figure 11: Temperature contours at various times during liquid metal cooling as computed using a 3-D thermal model and pipe flow.

using traditional induction coils and forced convective cooling (576 s).

Future work will focus on modeling induction heating using liquid metal energy circuits in 3-D (i.e., non-axisymmetric) components, as well conducting experiments to validate computational results. These findings will be used to develop a parameterized optimization framework to develop liquid metal energy circuit configurations that maximize SMA actuation frequency.

6 ACKNOWLEDGMENTS

This work is supported in part by the US Air Force Office of Scientific Research under a grant number FA9550-16-1-0087, titled Avian-Inspired Multifunctional Morphing Vehicles monitored by Dr BL Lee. Computational analysis performed using a research license granted by COMSOL Multiphysics®.

REFERENCES

[1] Kazuhiro Otsuka and Clarence Marvin Wayman. *Shape memory materials*. Cambridge university press, 1999.

[2] Dimitris C Lagoudas. Shape memory alloys. *Science and Business Media, LLC*, 2008.

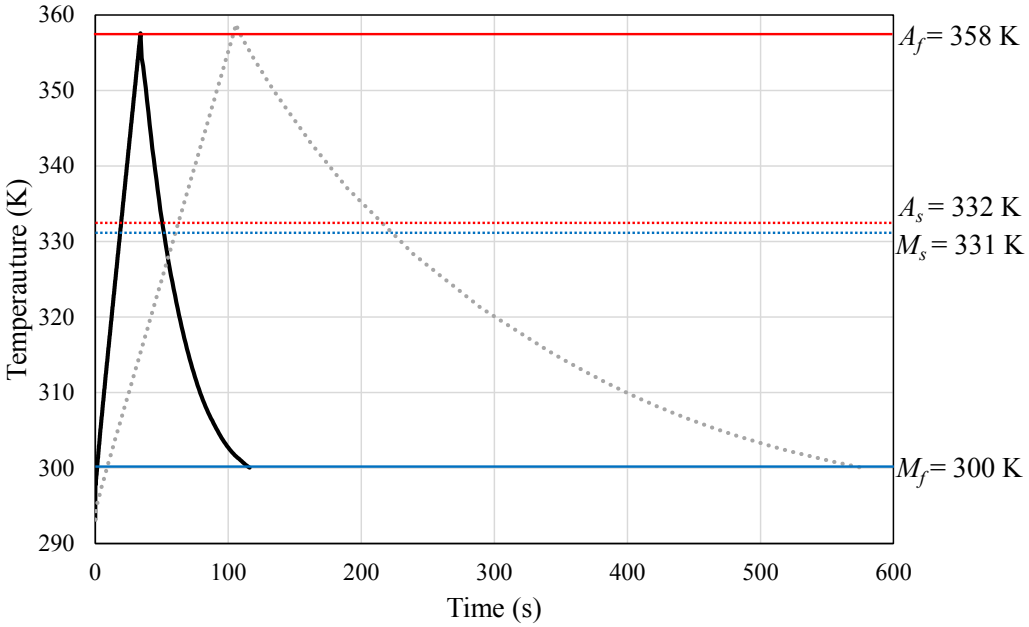

Figure 12: Comparison of actuation frequency for an integrated SMA-liquid metal component (solid line) and traditional induction/cooling methods (dotted line). SMA transformation temperatures taken from SLM 3-D printed SMA components [23].

[3] Ugo Icardi and Laura Ferrero. SMA actuated mechanism for an adaptive wing. *Journal of Aerospace Engineering*, 24(1):140–143, 2010.

[4] Robert Saunders, Darren Hartl, Joshua Herrington, Logan Hodge, and James Mabe. Optimization of a composite morphing wing with shape memory alloy torsional actuators. In *ASME 2014 Conference on Smart Materials, Adaptive Structures and Intelligent Systems*, pages V002T02A014–V002T02A014. American Society of Mechanical Engineers, 2014.

[5] J Herrington, L Hodge, C Stein, Y Babbar, RN Saunders, DJ Hartl, and JH Mabe. Development of a twisting wing powered by a shape memory alloy actuator. *AIAA SciTech*, 2015.

[6] Bernie Carpenter and John Lyons. EO-1 technology validation report: lightweight flexible solar array experiment. *NASA/GSFC. Last updated: August*, 8, 2001.

[7] Jin-Ho Roh, Jae-Hung Han, and In Lee. Finite element analysis of adaptive inflatable structures with SMA strip actuator. In *Smart structures and materials*, pages 460–471. International Society for Optics and Photonics, 2005.

[8] DJ Hartl, DC Lagoudas, FT Calkins, and JH Mabe. Use of a Ni60Ti shape memory alloy for active jet engine chevron application: I. thermomechanical characterization. *Smart Materials and Structures*, 19(1):015020, 2009.

[9] DJ Hartl, JT Mooney, DC Lagoudas, FT Calkins, and JH Mabe. Use of a Ni60Ti shape memory alloy for active jet engine chevron application: II. experimentally validated numerical analysis. *Smart Materials and Structures*, 19(1):015021, 2009.

[10] Jeanette J Epps and Inderjit Chopra. In-flight tracking of helicopter rotor blades using shape memory alloy actuators. *Smart Materials and Structures*, 10(1):104, 2001.

[11] Christopher L Bertagne, Darren J Hartl, and Thomas J Cognata. Analysis of highly coupled thermal-structural responses in morphing radiative bodies. In *23rd AIAA/AHS Adaptive Structures Conference*, page 1510, 2015.

[12] Christopher L Bertagne, Jorge Chong, Darren J Hartl, John D Whitcomb, Lisa R Erickson, and Rubik Sheth. Experimental characterization of a shape memory alloy-based morphing radiator. In *24th AIAA/AHS Adaptive Structures Conference*, page 1568, 2016.

[13] JP Holman. Heat transfer, 1986. *Mc Gran–Hill Book Company, Soythern Methodist University*, 1986.

[14] Robert N Saunders, James G Boyd, Darren J Hartl, Jonathan K Brown, Frederick T Calkins, and Dimitris C Lagoudas. A validated model for induction heating of shape memory alloy actuators. *Smart Materials and Structures*, 25(4):045022, 2016.

[15] Minoru Hashimoto, Masanori Takeda, Hirofumi Sagawa, Ichiro Chiba, and Kimiko Sato. Application of shape memory alloy to robotic actuators. *Journal of robotic systems*, 2(1):3–25, 1985.

[16] R Andrew Russell and Robert B Gorbet. Improving the response of SMA actuators. In *Robotics and Automation, 1995. Proceedings., 1995 IEEE International Conference on*, volume 3, pages 2299–2304. IEEE, 1995.

[17] Jacob Mingear, Aaron Greer, Brent Bielefeldt, and Darren J Hartl. Liquid metal integration for expedited heating and cooling of monolithic and composite SMA actuators. In *25th AIAA/AHS Adaptive Structures Conference*, page 1443, 2017.

[18] Anthony M Coppola, Liangfa Hu, Piyush R Thakre, Miladin Radovic, Ibrahim Karaman, Nancy R Sottos, and Scott R White. Active cooling of a microvascular shape memory alloy-polymer matrix composite hybrid material. *Advanced Engineering Materials*, 18(7):1145–1153, 2016.

[19] Michael D Dickey, Ryan C Chiechi, Ryan J Larsen, Emily A Weiss, David A Weitz, and George M Whitesides. Eutectic gallium-indium (EGaIn): a liquid metal alloy for the formation of stable structures in microchannels at room temperature. *Advanced Functional Materials*, 18(7):1097–1104, 2008.

[20] Tingyi Liu, Prosenjit Sen, and Chang-Jin Kim. Characterization of nontoxic liquid-metal alloy galinstan for applications in microdevices. *Journal of Microelectromechanical Systems*, 21(2):443–450, 2012.

[21] COMSOL AB. Comsol multiphysics® v. 5.2a. 2017.

[22] DJ Hartl, GJ Frank, GH Huff, and JW Baur. A liquid metal-based structurally embedded vascular antenna: I. concept and multiphysical modeling. *Smart Materials and Structures*, 26(2):025001, 2016.

[23] Mohsen Taheri Andani, Soheil Saedi, Ali Sadi Turabi, MR Karamooz, Christoph Haberland, Haluk Ersin Karaca, and Mohammad Elahinia. Mechanical and shape memory properties of porous ni 50.1 ti 49.9 alloys manufactured by selective laser melting. *Journal of the Mechanical Behavior of Biomedical Materials*, 68:224–231, 2017.

VIII ECCOMAS Thematic Conference on Smart Structures and Materials
SMART 2017
A. Güemes, A. Benjeddou, J. Rodellar and J. Leng (Eds)

IN-SITU LASER-ULTRASONIC CHARACTERIZATION OF AUSTENITE-MARTENSITE TRANSFORMATION

PETR SEDLÁK*, HANUŠ SEINER*, MARTINA THOMASOVÁ†, MICHAELA JANOVSKÁ*, PAVLA STOKLASOVÁ*, TOMÁŠ GRABEC†, KRISTÝNA ZOUBKOVÁ†, MARTIN ŠEVČÍK*, JAN ZÍDEK* AND MICHAL LANDA*

*Institute of Thermomechanics
Czech Academy of Sciences
Dolejskova 5, 182 00 Prague, Czech Republic
e-mail: ML@it.cas.cz, web page: http://www.it.cas.cz

† Faculty of Nuclear Sciences and Physical Engineering
Czech Technical University in Prague
Trojanova 13, Prague 120 00, Czech Republic

Key words: Elasticity, NiTi, phase transformations, laser-ultrasonic characterization

Abstract. A novel method for in-situ characterization of structural processes in NiTi wires is proposed. This method is based on contactless generation and detection of longitudinal ultrasonic waves in a wire subjected to mechanical loadings; focused laser pulses are used for generation of the waves, a laser vibrometer is then used for their detection. The contact-less arrangement enables application of this method for a broad range of temperatures and loading modes. The method is utilized for characterization of stress-induced phases in a superelastic medical grade NiTi wire of the diameter 100 μm. The results show that the elastic moduli of the stress-induced martensite phase significantly depend on the temperature, exhibiting a more than 50 % decrease at elevated temperatures and at stress levels close to the plateau stress for the reverse transition. This indicates a structural instability on NiTi martensite under these conditions.

1 INTRODUCTION

Shape memory alloy (SMA) polycrystalline materials can be reversibly strained up to several percents, which is utilized in many useful applications. Such relatively large strains are accommodated by the material due to structural changes caused by reversible martensitic phase transformations. The general thermo-mechanical response of SMA is rather complex because several mutually interdependent deformation mechanisms are often active.

Monitoring the evolution of the elastic parameters of the SMAs in-situ during the loading/unloading processes is a very helpful tool for analyzing such complex structural changes.

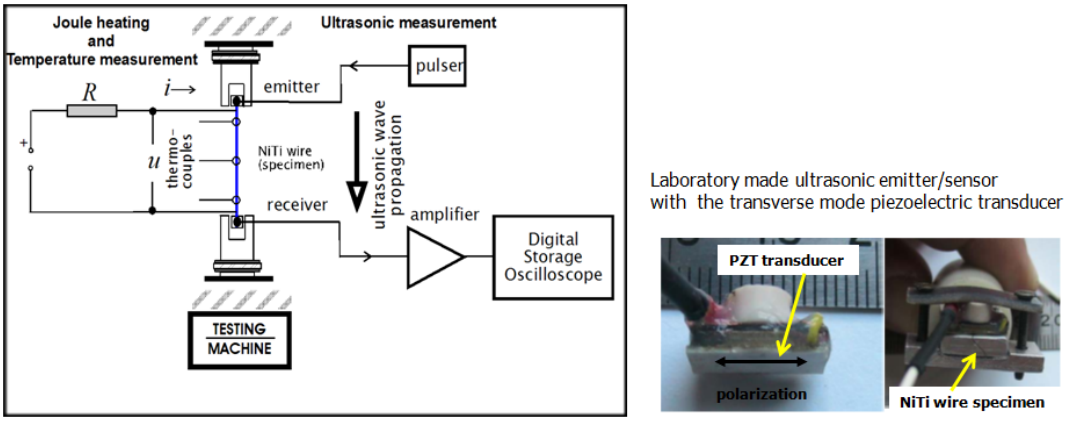

Figure 1: Experimental arrangement of the contact-based ultrasonic technique (USERIST system).

The elastic constants provide an averaged (effective) information on the material at the macro-scale, and thus, unlike local characterization methods, is suitable for capturing the progress of the structural changes in SMAs during the thermomechanical treatment. Similar information can be also obtained by in-situ resistivity measurements, while both methods are complementary and the most detailed results can be obtained by their combination.

Such an approach was explored in the previous decade by Šittner at al. [1, 2, 3] who suggested an original method for investigation deformation processes in SMAs called USERIST. This method used simultaneously the acoustic waves and the electric current as probing signals for NiTi wires exposed to stress and temperature loadings (Fig.1). The technique was successively used for detection of the start and the finish of the transformation processes during thermal cycling and cyclic mechanical loadings, especially with the focus laid on B2→R transformation [2, 3]. In the USERIST set-up, special contact PZT transducers with transverse polarization were designed for generation and detection of ultrasound in wire specimens (Fig.1). A typical ultrasonic signal (100 kHz – 1 MHz) detected during acoustic wave propagation in a NiTi wire (200 μm in diameter) at the distance 190 mm from the emitter (a pulse generation of acoustic waves) by the USERIST apparatus is shown in Fig.2. It can be seen that both L as well as T-waves (corresponding to long-wavelength limits of longitudinal and torsional modes, see the section 2.1) were detectable and both Young's and shear moduli were evaluable during thermo-mechanical load cycling.

Nevertheless, the contact USERIST system had also several disadvantages, in particular:

- There were additional unpredictable loadings of the tested wire due to the transducer clips;
- the method was technically difficult for wire diameter less than 100 μm;
- the application of complex loadings was technically restricted, e.g. a measurement with torsion loading of the wire was impossible;
- to obtain results under other temperatures than the ambient temperature, the whole set-up had to be immersed in a heat-conducting medium.

In this paper, we present a fully noncontact all-optical alternative to the USERIST experimental arrangement, in particular a laser-based ultrasonic technique for characterization thin wires exposed to complex loadings. Compared with the contact method, the laser-based technique is much less restrictive with respect to the diameter of the wire, the range of applicable frequencies, as well as the mechanical loading modes. Hence, a more systematic study of the processes in NiTi wires is possible.

2 METHODS AND EXPERIMENTS

2.1 Principles of ultrasonic in-situ characterization of NiTi thin wires

In an isotropic cylindrical waveguide (as a NiTi wire), the axisymmetric vibrational modes may be divided into two decoupled branch groups [4] : Torsional $T(0, m)$, with azimuthal displacement only, and longitudinal $L(0, m)$ with both axial and radial displacements. All other modes break the axial symmetry; these modes are flexural, $F(n, m)$ for $n > 0$ and exhibit coupled three-dimensional displacements. The geometrical dispersion of harmonic waves propagation along an infinite cylinder is performed by the dependence of phase velocity $c_\varphi = \omega/k$, where $\omega = 2\pi f$ is an angular frequency and k is a wave number. It can be seen that the wave packet (pulse) propagates in the dispersion media by group velocity given by $c_g = (\mathrm{d}\omega/\mathrm{d}k)$.

The dispersion curves of all three types of modes (torsional, longitudinal, and flexural) calculated by the procedure described in [5] for specific material properties of NiTi ($E = 65\,\mathrm{GPa}$, $\nu = 0.432$, $\rho = 6.46\,\mathrm{g/cm^3}$), are shown in Fig. 3. The dispersion branches $L(0, 1)$ and $T(0, 1)$ may be used for determination of elastic properties E, G from velocity measurements : The velocity of the longitudinal mode $L(0, 1)$ is $c_\varphi = c_g = (E/\rho)^{1/2}$ for limit $f \to 0$, and the mode $T(0, 1)$ is not dispersive and the related propagation velocity is $c_\varphi = c_g = (G/\rho)^{1/2}$. For thin NiTi wires ($\sim 100\,\mu$m in diameter), the long-wavelength approximation can be used for frequency range up to tens of MHz.

2.2 Experimental details

The generation of the ultrasonic waves was provided by short infrared pulses from a Nd:YAG laser (nominal pulse width 8 ns/25 mJ, 1064nm wavelength). An optical fiber coupling adapter enables safe and easy manipulation and precise beam adjustment. The power optical fiber was ended by an optical focuser (focus spot size better then $400\,\mu$m). The pulse energy was attenuated to the minimal value $\approx 1\,$mJ and repetition frequency of pulses was set to $5\,$Hz. This arrangement enabled a repeatable thermoelastic excitation of the thin wire without any observable damage. The wave arrivals (out-of-plane displacement) from the source were detected by a laser interferometer implemented in an optical microscope. This detection system was a part of a Polytec MSA-500 dynamical analyzer for microsystems. The frequency bandwidth of the interferometer decoder was 24 MHz (-3dB). The system enables scanning by the probe beam along points of a predefined mesh. In this case, the objective M Plan Apo (5×, Infinity corrected, N.A. 0.14) with the field of view (FOV) 1.8 × 1.34 mm / $1.3\,\mu$m pixel resolution in the MSA system was used. Within the FOV, three positions (G/R/B) on the tested wire were defined for detection (Fig.4) by the laser interferometer. In each selected point, signals triggered by a flash of the excitation IR laser were recorded by the MSA-500 internal acquisition system (100 MS/s,12 bits) in the time-domain regime. Resulting signal was obtained by averaging from

150 singleshots. Complete experimental system in the prototype version is described in the Fig.5. Joule heating of the wire and natural cooling regimes were applied. The instantaneous temperature was monitored by a miniature thermocouple (size 0.2 mm, type T) directly connected on the wire near the grip on the loaded side (left-side). A PMMA tube with holes for pump beam and detection was used for outside environmental shielding. In this prototype version, the tensile loading was provided manually by a micrometric screw. The full final version of the apparatus (Fig.5) then used a motorized stage and also an optional device for torsion loading.

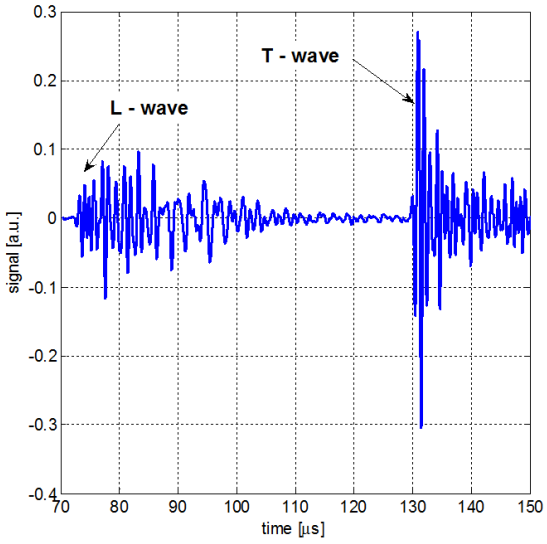

Figure 2: A typical ultrasonic signal generated and detected by the shear-polarized transducers (USE-RIST system).

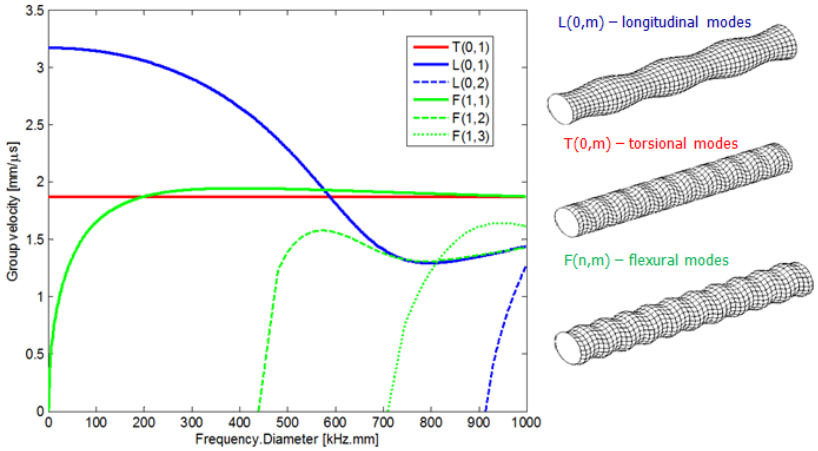

Figure 3: Calculated dispersion branches for acoustic wave propagation in a thin NiTi wire.

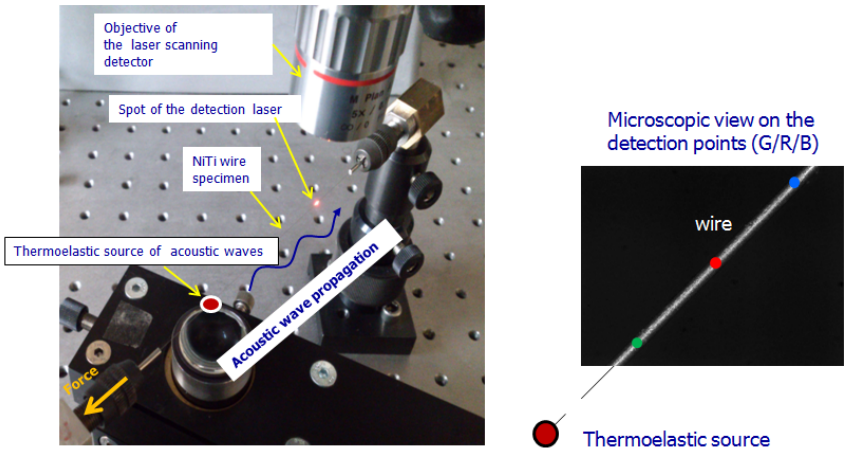

Figure 4: The laser-ultrasonic system for characterization of thin wires. The photograph (on the left) shows the tested wire, the adjusted focuser of the pump beam and the objective of the detection system. The snapshot from the microscope screen (on the right) shows the measurement points marked as G-R-B (a sequence with the increasing distance from the source). The nominal distance between neighboring detection points is 800 μm.

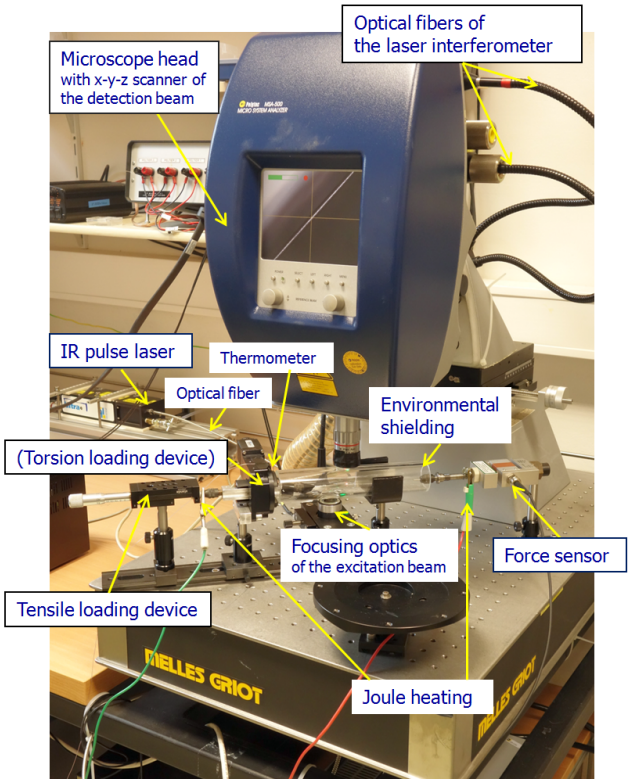

Figure 5: The complete experimental arrangement, including the LU measurement system, the loading systems, the devices for force and temperature measurements, and the wiring for the Joule heating system.

A precise force sensor for maximal loading up to 20N was implemented for force monitoring.

The superelastic medical grade NiTi wire (FWM-Fort Wayne Metals) of the diameter 100 μm [6] was used for experiments. A typical signal obtained on this wire (at room temperature and stress-free conditions) is plotted in figure 6. In this case of the ultrasonic excitation, the strong dispersive flexural mode $F(1,1)$ was dominant. Nevertheless the first arrival of small broadband wavelet corresponding to the L-wave was fairly detectable. Only this part of the detected signals was used for analysis,after proper normalization of the amplitudes. Let us note that the phase of the ultrasonic signal changes by the austenite-martensite transformation. Local thermal shock in austenite state causes propagation of the volume expansion along the wire, whereas the thermo-elastic excitation in the fully martensite state initiates propagation of an instantaneous shrinkage. The distances among G/R/B position remained fixed during the test; the L-wave speeds were then evaluated from the mutual delays of the signal between these three position.

3 RESULTS AND DISCUSSION

The examined NiTi wire at room temperature showed a typical superelastic behavior (Fig.7): After elastic loading of austenite connected also with partial or full transformation to R-phase, the material transformed at almost constant stress level of 450 MPa to martensite. This transformation proceeded heterogeneously via propagation of martensitic bands. When the full volume of the wire was transformed to martensite, almost reversible straining of martensite succeeded with apparent modulus of approximately 30 GPa. During unloading, the reverse transformation proceeded also heterogeneously at almost constant stress of 200 MPa. The measured elasticity of austenite at room temperature was slightly above 70 GPa. During martensitic transformation it monotonically decreased to value of 47 GPa. The exact evolution of elasticity in this part as a function of total strain was affected by heterogeneous nature of the transformation as the measurement of elasticity was done only on a part of the wire. Interestingly, during the straining of martensite, the elasticity is not remain constant but markedly increased with the increasing stress, reaching at high stress levels almost the elasticity of the parent austenitic phase. This evolution of martensitic elasticity was fully reversible following the same curve during loading and unloading. Considering very low stress amplitudes of propagating elastic wave and also low observed attenuation, we could conclude that stress dependence of martensite elasticity was not related to moving of internal boundaries (phase boundaries or twins) but must be an intrinsic property of martensite related to its instability above austenite-start temperature. We focused in more details to this striking behavior of martensite and measured its elastic properties up to 1000 MPa also for two additional temperatures 40 and 60 °C (Fig.8 a), measurements at temperatures higher than 60 °C started to be affected by irreversible plastic deformation. In Fig.8 a, the lower-limit of measured stress interval corresponds to stress level of reverse martensitic transformation, which increases with increasing temperature. We can see further pronounced softening of martensite elasticity with increasing temperature and similar stress hardening of elasticity as for the measurement at room temperature. The results in Fig.8 b document the behavior of highly unstable martensite. The temperature dependence of elastic softening and strong stress dependence of its elasticity reveals strong deformation of the energy potential. By extrapolating this tendency to higher temperatures (not experimentally reachable in our sample due to plastic deformation), the NiTi material could gain so called over-critical

behavior where all inner boundaries between austenite and martensite disappear and material would have a rubber-like behavior. A similar limit was reached in other SMAs like FePd [7] or highly amorphous NiTi [8].

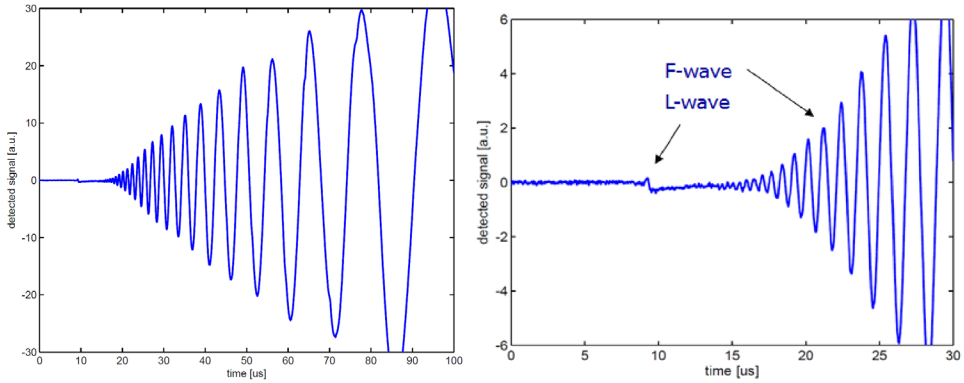

Figure 6: Detected ultrasonic signal on the FWM 100 μm wire generated by thermoelastic source; detail of the same signal for the first 30 μm (right side).

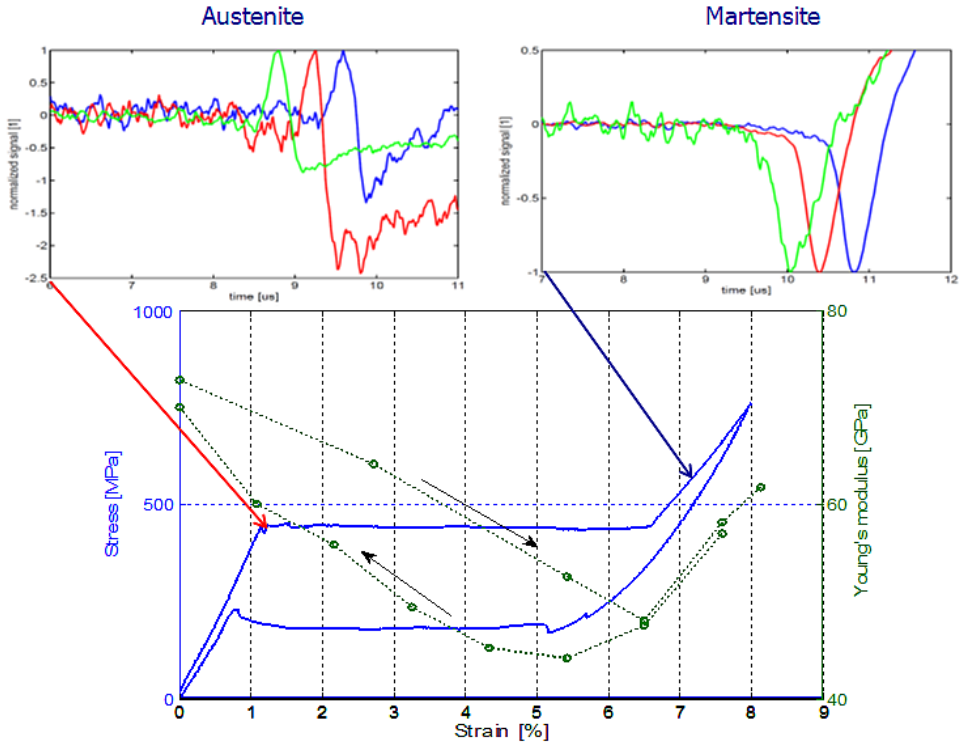

Figure 7: Tensile test of the superelastic NiTi wire at RT; the triplet of amplitude-normalized signals at positions G/R/B is compared for the austenite and martensite states; the evolution of effective elasticity of the wire during loading cycle.

4 CONCLUSION

A contact-less laser based method for in-situ material characterization of thin functional wires was presented and applied for analysis of NiTi wires by propagation of thermoelastically

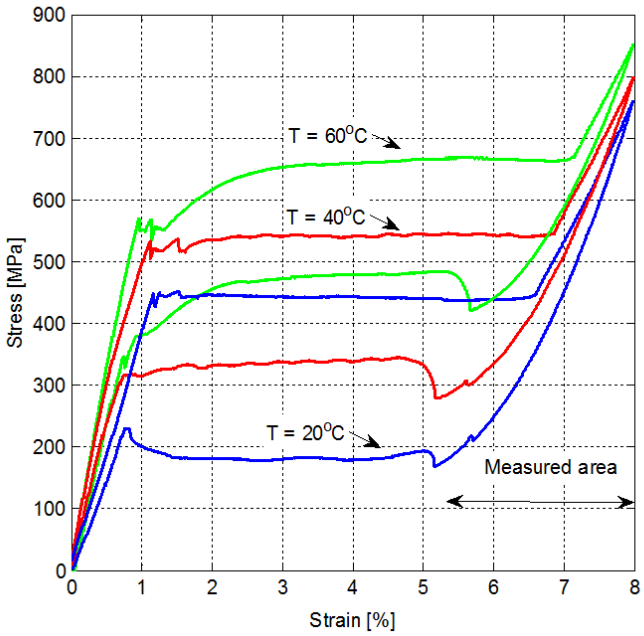

a)

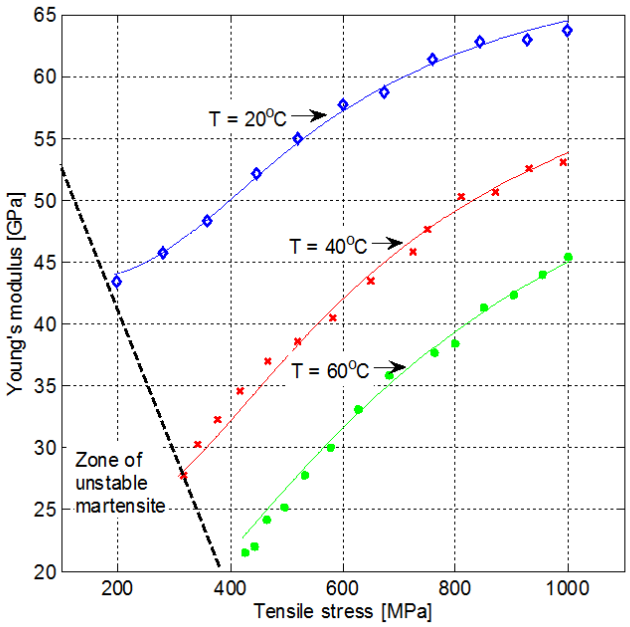

b)

Figure 8: a) Stress-strain curve of superelastic NiTi wire at three different temperatures, b) evolution of Young's modulus of stress-induced martensite with applied stress.

excited acoustic waves. The evolution of elastic moduli of the wire with tensional straining was obtained for various temperatures. The preliminary results reveal unexpected behavior of fully transformed martensite of superelastic NiTi: with increasing temperature, the elasticity of the wire significantly softens, reaching as low values as 21 GPa (a more than 50 % decrease compared with the room temperature behavior). This indicates a loss of stability of the stress-induced martensite phase at elevated temperatures; its evolution upon further heating cannot be, however, analyzed due to massive plastic slip in the material. Nevertheless, the newly developed contactless approach was shown to be a suitable tool for analyzing the NiTi behavior in the vicinity of this stability limit.

Acknowledgements

This work has been financially supported by the AdMat project of the Czech Science Foundation (14-36566G).

REFERENCES

[1] Šittner, P., Novák, V., Landa, M.,Lukáš, P. Formation processes in functional materials studied by in situ neutron diffraction and ultrasonic techniques, *Materials Science and Engineering A* (2007) **462**: 1222

[2] Šittner, P., Novák, V., Lukáš, P., Landa, M. Stress-Strain-Temperature Behaviors Due to B2-R-B19 Transformation in NiTi Polycrystals, *Journal of Mechanical Engineering* (2006) **128**: 268-278.

[3] Šittner, P., Sedlák, P., Landa, M., Novák, V., Lukáš, P. In-situ experimental evidence on R-phase related deformation processes in activated NiTi wires, *Materials Science and Engineering A* (2006) **438-40**: 579-584.

[4] Rose,J.L. *Ultrasonics Waves in Solid Media*, Cambridge Univ Press, NY (1999)

[5] Seco, F. and Jimenez,A.R. Modelling the generation and propagation of ultrasonic signals in cylindrical waveguides, in *Ultrasonic waves*, Intech Open Access Publisher (2012), chapter 1, 1-28

[6] Šittner,P., et al Roundrobin SMA modeling, *ESOMAT 2009*, 08001, `http://ofm.fzu.cz/roundrobin-sma-modelling`

[7] Seiner, H. Stoklasová, P., Sedlák, P., Ševčík, M., Janovská, M., Landa, M., Fukuda, T. Yamaguchi, T. Kakeshita, T. Evolution of soft-phonon modes in Fe-Pd shape memory alloy under large elastic-like strains, *Acta Materialia* (2016) **105**: 182-188

[8] Ren, X. Strain glass and ferroic glass - Unusual properties from glassy nano-domains *Phys. Status Solidi* (2014) **B 251**: 1991

Long storage effects on Ni-Ti specimens: a laboratory testing campaign

Casciati S.*, Casciati F.† and Faravelli L.†

* DICAR, University of Catania
Piazza Federico di Svevia
96100 Siracusa, Italy
e-mail: sacasci@unict.it

† DICAr, University of Pavia
Via Ferrata 3
27100 Pavia, Italy
e-mail: fabio@dipmec.unipv.it & lucia@dipmec.unipv.it

ABSTRACT

Shape Memory Alloys (SMA) are smart materials with potential exploitations as dampers for civil engineering. Indeed, the experimental analysis of SMA shows a hysteretic behavior both in stress-strain or strain-temperature representations [1]. The exposition to different environment temperatures, in winter versus summer, suggests avoiding the adoption of thin wires due to their flat hysteretic response. Attention is addressed to wires of diameter 2.46 mm, whose hysteresis shows S-shape cycles [2].

The time scale of civil engineering construction spans over several months, if not years when judgmental conflicts arise. This could cause long time storage of the acquired material before their assemblage according to the structural design. Several authors in the literature [3-5] mentioned the effects of a storage at room temperature, i.e., its ability to change the properties of the alloys.

The results of an experimental campaigns on specimens that underwent a long storage at room temperature is reported in this contributions. The effects are clearly detected but their extent is quite unpredictable.

REFERENCES

[1] S. Casciati, L. Faravelli and M. Vece (2017) Investigation on the fatigue performance of Ni-Ti thin wires, Structural Control & Health Monitoring, Vol. 24 (1), Article Number: UNSP e1855
[2] V. Torra, S. Casciati, and M. Vece (2016). Shape Memory Alloys Wires: From Small to Medium Diameter. Proceedings of CIMTEC 2016, 5th International Conference on Smart and Multifunctional Materials, Structures and Systems, Perugia, Italy.
[3] S. Kustov, J. Pons, E. Cesari, and M. Morin (2002). Two-stage reverse transformation in hyperstabilized β_1' martensite. Scripta Materialia., 46, 817-22.
[4] S. Kustov, J. Pons, E. Cesari, J. Van Humbeeck, and M. Morin (2004). Stabilization and hyperstabilization of Cu–Al–Be β_1' martensite by thermal treatment and plastic deformation. Materials Science and Engineering: A, 378, 283-288
[5] K. Sapozhnikov, S. Golyandin, S. Kustov, and E. Cesari (2008). Defect assisted diffusion and kinetic stabilization in Cu–Al–Be β_1' martensite. Materials Science and Engineering: A, 481-482, 532–537.

VIII ECCOMAS Thematic Conference on Smart Structures and Materials
SMART 2017
A. Güemes, A. Benjeddou, J. Rodellar and J. Leng (Eds)

EXPERIMENTALLY MOTIVATED NUMERICAL RECONSTRUCTION OF MACROSCOPIC MARTENSITIC TRANSFORMATION FRONT IN NITI SUPERELASTIC WIRES

M. FROST*, P. SEDLÁK*, P. SEDMÁK♯,† AND P. ŠITTNER†

*Institute of Thermomechanics of the Czech Academy of Sciences
Dolejškova 5, 18200 Prague, Czech Republic
e-mail: mfrost@it.cas.cz
web page: http://www.it.cas.cz/d5

♯ European Synchrotron Radiation Facility
71 Avenue des Martyrs, 38043 Grenoble, France
web page: http://www.esrf.eu/

† Institute of Physics of the Czech Academy of Sciences
Na Slovance 2, 18221 Prague, Czech Republic
web page: http://ofm.fzu.cz/localized-deformation-of-niti-in-tension

Keywords: NiTi Shape Memory Alloys, Localized Deformation, 3D X-ray Diffraction, Numerical Simulations

Summary: In particular geometries and loading modes, martensitic phase transformation in NiTi shape memory alloys (SMA) develops inhomogenously via formation and propagation of macroscopic transformation bands resembling Lüders bands well-known from deformation of certain steels. In this work, we analyze morphology and mechanics of a macroscopic transformation front separating regions of austenite and martensite phases in NiTi superelastic wires under tension.

Recently, three-dimensional X-ray diffraction method was employed to determine complete strain and stress states of a huge set of polycrystalline grains close to the transformation front. Taking into account the experimental findings, we have adapted our macroscopic constitutive model of NiTi SMA by modifying the free energy function – so that it can capture the strain-softening type of response – and including non-local (gradient-like) effects. The finite element implementation of the model was performed in *Abaqus FEA* software and allowed for a successful numerical reconstruction of the transformation front in a loaded wire as well as its stable propagation at a constant external force. Thanks to material parameters adjusted with respect to experimental measurements, the simulation qualitatively reproduced a significantly inhomogeneous stress state within the parent phase and predicted non-uniform stress distribution within the product phase even far from the front.

1 INTRODUCTION

Shape memory alloy (SMA) polycrystals are metallic materials that can be repeatedly reversibly strained up to several percents, far beyond the elastic deformation limit. This surprising effect is called superelasticity and it is already utilized in many engineering applications. The material is able to accommodate such relatively high strains due to a reversible structural change of the crystal lattice, so called martensitic phase transformation. In NiTi-based SMA, transformation between the parent phase, austenite, and the product phase, martensite, often proceed in a spatially inhomogeneous manner; localized martensitic bands form and propagate along the sample leaving a material with modified dimensions and microstructure (phase) behind. The macroscopic picture is very similar to the localization of plastic deformation observed in certain steels and alloys [1]. However, there are specific features of localization in NiTi alloys: a) the attainable inelastic strains due to martensitic transformation are loading mode-dependent and limited due to their crystallographic nature, b) elastic properties of stress induced martensite are strongly anisotropic and change pronouncedly close to the phase transformation, c) the microstructural aspects, e.g. interaction of phases and their compatibility at interfaces, are complex and not fully understood yet, even though the phenomenon (sometimes also called *Lüders-like* deformation) has been thoroughly experimentally investigated in the last two decades, e.g. [2–6]. It is interesting to note that localization occurs only in NiTi SMA with a suitable texture and only in particular loading modes (e.g. tension) and deformation rates [7]. However, if it appears, localization is a critical issue for fatigue as it is connected with relatively high phase and strain gradients at the phase interface. Naturally, this motivates investigation of the phenomenon in NiTi wires, which are employed in many typical commercial applications of SMA, e.g. in braided stents, light-weight actuators or functional textiles [8–10], and, whose fatigue performance is thus of primary importance.

Recently, a detailed experimental analysis of martensite band front (MBF) in a stretched superelastic NiTi wire was performed on the grain-by-grain scale [11]. Subsequent reconstruction of macroscopic phase and stress fields stimulated our attempt to develop an enhanced constitutive model which could be employed in a complementary finite element (FE) analysis of the MBF. Numerical simulations of localization in NiTi SMA are quite rare in the literature. As justified in [12], localization in NiTi is not merely a geometric effect, hence, strain softening is very likely involved. In the pioneering works, e.g. [2, 13], authors used a simple J_2-elastoplasticity model with strain softening to study localization in NiTi samples deformed in pure tension. They were able to capture some basic features of forming localization bands and to study influence of latent heat via incorporation of thermal coupling. Based on experiments on laminates, Hallai and Kyriakides [14] refined the original constitutive law to obtain a smooth uniaxial stress-strain response. These models adhered to isotropic plasticity-based constitutive laws disregarding specifics of SMA materials. Theoretical research on the influence of dimensional scaling on localization patterns for particular simple geometries was conducted in [15]. Duval with coworkers [16] utilized nonlocal gradient approach to incorporate localization into a two-dimensional superelastic reduction of a rather advanced SMA constitutive model. This work was further refined by Armattoe et al. [17] to allow for any thermomechanical loading. Recently, two other conventional constitutive SMA models have been also modified for strain softening and employed together with gradient [18] or integral [19] regularization methods.

In this work, we extend an earlier developed, fully three-dimensional NiTi SMA constitutive model [20] to capture localization effects. The model features an elaborated form of dissipation function (directly related to "yield functions") and takes into account some phenomena specific to textured NiTi SMA which makes it particularly suitable for simulations of experimental observations of localization in this alloy. We modify the constitutive law to capture the strain softening and employ so-called nonlocal integral averaging technique to regularize the ensuing mathematical model, which allows for a correct (mesh-independent) implementation the model into finite element analysis software. Thanks to experimental data, we can adjust material parameters in the model so that the simulation mimicking tensile loading of a NiTi wire is realistic and in quantitative agreement with corresponding results of experimental analysis.

2 EXPERIMENTAL BACKGROUND

Here we briefly introduce the unique experimental investigation of morphology of martensite band front in a stretched SMA filament by three-dimensional X-ray diffraction technique and summarize the findings relevant for modeling. The experiment was performed at the European Synchrotron Research Facility (Materials science beamline ID11, Grenoble, France) on a superelastic NiTi wire (Ti-50.8 at.%Ni manufactured by Fort Wayne Metals) with diameter 0.1 mm, which was heat treated by a short electric current pulse to reach desired microstructure with eliminated R-phase. The sample was mounted on a load frame, stretched to create a MBF and its length was then fixed. The load frame was rotated around the axis parallel to the wire axis (ω-rotation) and the diffraction pattern for each ω-angle (which contains reflections within the whole cross-section of the wire) were recorded on a 2D detector (see Fig. 1A). By moving the sample position with 4 μm steps in the vertical direction and repeating the ω-rotation, 50 "layers" were scanned within the probed length of the wire of 200 μm so that complete "austenitic neighborhood" of MBF was scanned. Each spot bears partial information on the position, structure, orientation and elastic deformation of the crystal lattice within one of the grains. The already transformed martensite grains were not analyzed for grain resolved information since diffraction from martensite phase was not as spotty as required for the three-dimensional XRD method; hence, the final experimental dataset contained $15,000$ austenitic grains (Fig. 1C). The volume of each grain was evaluated from the integrated intensity of the X-ray reflections. More details on the data acquisition and analysis as well as results of complementary measurements can be found in [11].

Components of elastic strain tensor and stress tensor for each grain were calculated based on refined unit cell parameters and tensor of elastic constants of the austenite lattice. In addition, grain resolved stress components weighted by the grain size were averaged over equivolumetric cells (radial symmetry exploited) and interpolated to reconstruct the macroscopic internal stress field. Stress resolution of 20 MPa and spatial resolution of about 1 μm were reached. This allowed to quantify strong internal stress gradients and elevated shear stresses developing at the edge of the nose-cone shaped macroscopic phase interface (Fig. 1B) which forms the core of the propagating MBF [11]. Surprisingly, whereas the macroscopic nominal tensile stress needed for propagation of the MBF ("plateau stress") was about 420 MPa, the averaged mean equivalent stress at and close to the phase interface reached almost 600 MPa. This contradicts the widely accepted assumption that the martensitic transformation in NiTi wire takes place under stresses

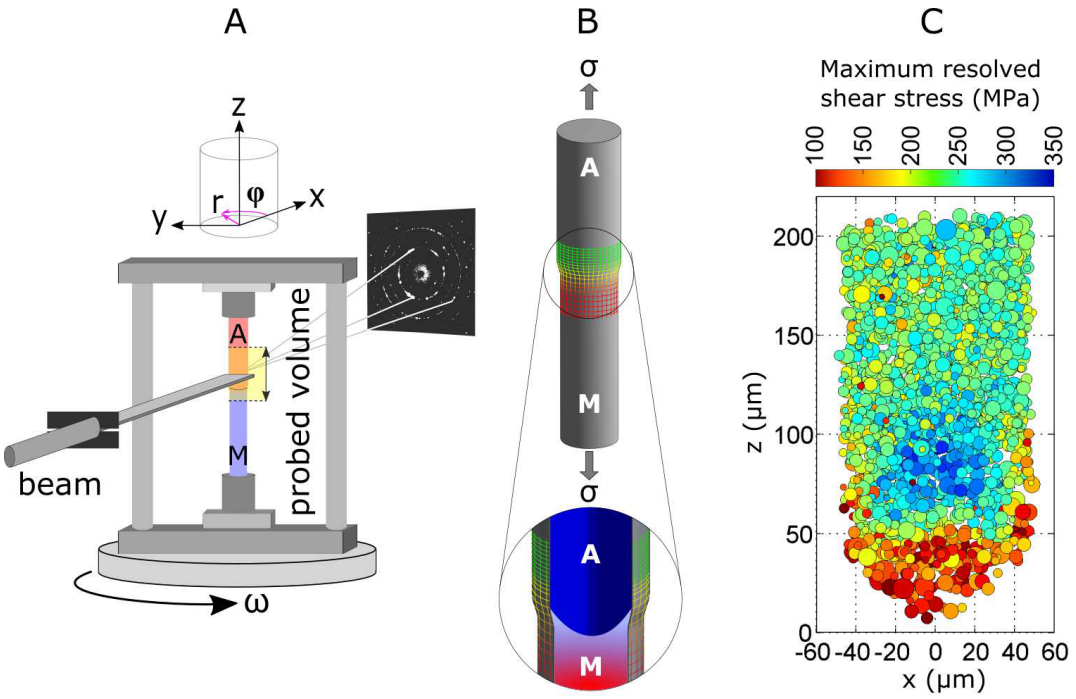

Figure 1: In the 3D XRD experiment, a superelastic NiTi wire was stretched until the middle of the transformation plateau and the wire segment containing the martensite band front (B) was probed by a monochromatic beam (A) of highly energetic photons. Grain microstructure (C) was reconstructed from 2D diffraction patterns obtained from the wire rotated about its axis and scanned with respect to the synchrotron beam and grain-resolved strain and stress tensors were calculated. See [11] for further details.

close to nominal tensile stress and motivated the particular adjustment of parameters related to the strain softening in the constitutive model.

3 MODELING

3.1 Constitutive Model and Its Regularization

The original (local, rate-independent) constitutive model has been formulated within continuum mechanics framework in [20] and the FE implementation has been validated in [9, 21]. Internal variables – volume fraction of martensite, ξ, mean transformation strain, $\varepsilon^{\mathrm{tr}}$, – allow to capture microstructural effects on the macroscopic level of description via a dissipation function whose enhanced form was derived from experiments in a systematic way [22]. A parameterized constraint on the latter variable assures that the volume preserving property, tension-compression asymmetry and (texture-induced) transformation strain anisotropy are captured. A particular form of the free energy couples the influence of strain and temperature on the phase transformation. Let us note that the elastic part of the energy depends on the internal variables, whereas plastic deformation due to dislocation slip is neglected. In analogy to similar approaches in the literature [17, 18], a substantial material softening (i.e. stress needed to further promotion of the transformation decreases with increasing strain) is incorporated; the

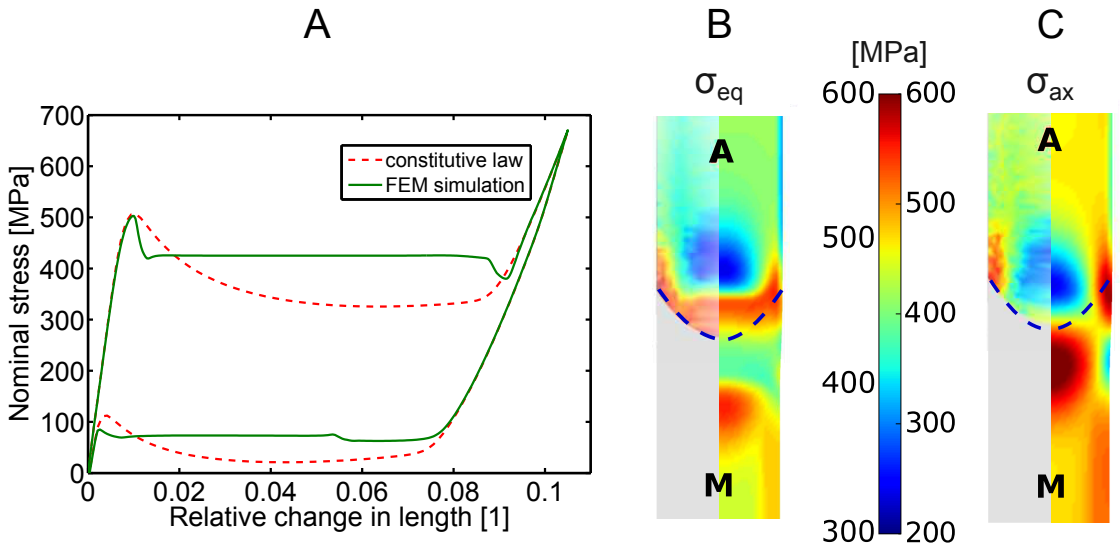

Figure 2: Continuum-based constitutive model for SMA adapted to allow for pronounced strain softening in a uniaxial tensile test (A, dash line) exhibits both nucleation overpeaks and propagation plateaux. Excellent quantitative agreement between computed (left half) distributions of von Mises equivalent stress (B, color range 300 – 600 MPa) and axial stress (C, color range 200 – 600 MPa) and their macroscopic-averaged experimental counterparts (right half) was reached.

regularizing-hardening term of the free energy r^{hard} is now modified as follows

$$r^{\text{hard}}(\xi, \varepsilon^{\text{tr}}) = k\xi \left(\frac{\langle \varepsilon^{\text{tr}} \rangle}{1 - \langle \varepsilon^{\text{tr}} \rangle} \right)^2 (E_0^{\text{int}} + E_1^{\text{int}} \mathrm{e}^{-\beta\xi}) \tag{1}$$

Here, $\langle \varepsilon^{\text{tr}} \rangle$ denotes a particular convex function of transformation strain defined in [20], k denotes the maximum transformation strain in pure tension, E_0^{int} is a hardening coefficient, whereas E_1^{int} and β are material parameters adjusting the extent of softening during phase transformation.

Figure 2A illustrates the proposed constitutive law on superelasticity. The nominal stress-strain relation in uniaxial loading (of a single material point) exemplifies the reversible phase transformation with pronounced hysteresis, strain softening and different elasticity of phases. The energy term (1) makes the material mechanically instable during the phase transformation. Unfortunately, loss of material stability implies (in statics) loss of ellipticity of governing equations, which has severe negative consequences: the ensuing mathematical formulation (boundary value problem) becomes ill-posed, thus, numerical simulations (e.g. FE analysis) exhibit sensitivity on the size of finite elements and on the mesh structure. To recover regularity of constitutive models, various generalized continuum formulations have been proposed in the literature [23]. An effective regularization can be reached by introducing an additional nonlocal counterpart to the internal dissipative variable(s) [24, 25], then one of two closely related methods are most often employed [26]. In the nonlocal gradient approach, the local and corresponding nonlocal variables are linked via an additional partial equation, in the nonlocal integral approach, these variables are linked via an integral relation and the nonlocal variable in a material point is defined as a weighted spatial integral average of the local one with the weight function usually

concentrated into a close neighborhood of the point. In the present formulation, we apply the integral approach and introduce a nonlocal counterpart to the volume fraction of martensite, denoted $\bar{\xi}$, which substitutes the local variable ξ in the exponential term on the right hand side of Eq. (1); hence, r^{hard} depends both on local and nonlocal volume fractions of martensite). The integral relation takes the form

$$\bar{\xi}(x) := \int_{\mathbb{R}^3} \xi(y)\omega_d(x,y)\,\mathrm{d}y \quad \forall\, x \in \Omega, \tag{2}$$

where the integration kernel $\omega_d(x,y)$ is chosen as the normalized Gaussian radial function with center in x and standard deviation d, and Ω denotes the set of material points constituting the sample. Combined experimental and theoretical research by Ball et al. [27] suggests that when emerging from a mechanically stabilized martensitic single crystal, austenite tends to nucleate predominantly close to specific locations on the surface of the sample determined by its geometry. Inspired by that work, we complete the definition (2) by formal assignment $\forall\, y \in \mathbb{R}^3 \setminus \Omega : \xi(y) := 1 - \xi(x)$, independently for each material point x in question.

3.2 Finite Element Analysis

The complete constitutive model was implemented into FE software *Abaqus FEA*. Exploiting the advantage of its UMAT subroutine, alternative minimization has been employed as thoroughly described in [22]. The original code has been complemented by subroutines UEXTERNALDB and USDFLD in order to regularly update values of the nonlocal variable in material points. The numerical implementation of this nonlocal extension has been tested in [28].

The experimental setup in Section 2 was modeled as a simple mechanical problem: axial tension of a straight homogenous NiTi SMA wire segment at a constant temperature. We assumed that radial symmetry is preserved in the situation at hand and employed Abaqus axisymmetry setting and generated a uniform structured mesh of $4,000$ quadrilateral (square) 4-node elements with centroid integration (CAX4R): 20 elements per radius $r = 50\,\mu$m and 200 per length $l_0 = 500\,\mu$m arranged in a rectangular domain. Both the radial displacement of nodes on the symmetry axis and the axial displacement of nodes at the lower end of the computation domain were fixed. At the upper end of the domain, axial displacement was uniformly and gradually increased up to 8% of the total length of the wire and then decreased back to no strain condition. The locus, where nonlocal events (e.g. cracks, shearband) start in regular bodies, is usually set by an intentionally imposed stress concentrator, e.g. by element(s) with flawed material properties or by reduction of cross-section of computation domain [2, 13, 17, 18]. Here, we have employed temperature dependence of critical (transformation-triggering) stress in SMA. Hence, the otherwise spatially constant temperature field of 20 °C was decreased by 5 °C in all nodes at the fixed end so that forward phase transformation initiated there and propagated along the wire segment towards the other end; similarly, temperature at the other end was increased by 5 °C for controlled initialization of the reverse transformation. Let us note that the whole domain was in pure austenite initially. Values and brief explanation of material parameters used in the simulation are summarized in Table 1. They reflect the particular behavior of the wire and its heat treatment, and are comparable to values in [20, 29]. Let us note that parameters related to the extended regularization term, E_0^{int}, E_1^{int} and β were adjusted so that simulated stress gradients quantitatively reflect the experimental observations in Section 2; presence of R-phase

Table 1: The set of material parameters used in the simulation.

Parameter	Value	Unit	Brief description
$E^{\mathrm{A}}, E^{\mathrm{M}}$	$71, 41$	[GPa]	Young moduli of austenite and martensite.
$G^{\mathrm{A}}, G^{\mathrm{M}}$	$25, 22$	[GPa]	Shear moduli of austenite and martensite.
k	0.095	[1]	Maximum transformation strain in tension.
a	0.8	[1]	Tension-compression asymmetry parameter.
$A, B, \varphi, \ldots$	$0.75, 1, 0$	[1]	Parameters of anisotropic transform. strain surface
$\ldots, L, M, N$	$0.9, 0.9, 0.9$	[1]	if the wire axis aligned with the x-direction, see [20].
$A_{\mathrm{s}}, A_{\mathrm{f}}$	$-10, 0$	[°C]	Temperature parameters related to the direct phase
$M_{\mathrm{s}}, M_{\mathrm{f}}$	$-30, -40$	[°C]	transformation between austenite and martensite,
T_0	-20	[°C]	see [20] for details.
σ_0^{reo}	120	[MPa]	Martensite reorientation stress at T_0.
Σ^{reo}	-0.9	[MPa/°C]	Change of reorientation stress with temperature.
Δs^{AM}	0.364	[MPa/°C]	Difference between specific entropies of martensite and austenite.
c^{reg}	0.01	[MPa]	Parameter of regularization function r, see [20].
$E_0^{\mathrm{int}}, E_1^{\mathrm{int}}$	$1, 70$	[MPa]	Parameters of r^{hard} in Eq. (1).
β	5	[1]	Parameter of r^{hard} in Eq. (1).
d	2.5	[μm]	Standard deviation of the Gaussian kernel in Eq. (2).

was suppressed. To reduce computation costs, in each time increment, the nonlocal volume fraction is computed based on values of internal variables obtained in the previous converged increment and ξ is set equal to one outside the computation domain for the whole computation.

The simulated relation between nominal stress (force per reference cross-section) and relative elongation of the wire is also shown in Figure 2A. The incipient nucleation event manifested as a stress peak is followed by a flat stress plateau corresponding to propagation of the martensitic band within the wire. The stress drop at the end of the plateau is connected with annihilation of the band front on the upper end of the computational domain. A similar behavior is observed during the unloading. Figures 2B and 2C present distributions of von Mises equivalent stress and axial stress close to MBF, respectively. For easier comparison, the left half of each figure presents experimental results whereas the right one the simulation with the same color scale used. The dashed line denotes the conical MBF as determined from last distinguishable austenitic grains in the experiment (grains below the line were already at least partially in martensitic state, hence they could not be resolved by the present technique). Simulation counterparts show the distributions also in the martensitic region. Presented figures correspond to a particular snapshot when the relative elongation of the wire reaches about 5% in loading; but the whole simulation shows identical distributions around MBF for any state on the loading plateau as the stable MBF simply propagates along the wire.

In both distributions, stress state in austenite far from the MBF is homogenous whereas distinct and severe stress gradients develop close to MBF and, according to simulation, also far in martensite (see 2B and C). In austenite, simulation results – both spatial distributions and

scales of values – perfectly match the experimental data: the equivalent stress reaches maximum on and close to the whole MBF cone and minimum in the central region just above, whereas the axial stress is maximized on the wire surface close to MBF and minimized in the central region on the conical MBF. As discussed in [11], the raised equivalent stress on the MBF cone is a crucial feature for triggering the phase transformation within the bulk wire. The redistribution of stress close to MBF is a direct consequence of the strain softening, though it is also influenced by the isochoric nature of martensitic transformation leading to reduced wire diameter of martensitic band below MBF.

Natural consequence of mechanical balance of MBF structure is also an enhanced tensile radial component of stress in the wire center and a suppressed compressive hoop stress on the wire surface in the martensitic region just behind MBF (not presented, see [11]). Moreover, owing to different stress conditions material is exposed to during the transformation process in the middle and on the periphery of cross-section of the wire, different transformation strains develop in the respective regions when the MBF passes through. This conversely results into increased values of both axial and equivalent stresses on and close to the surface of the wire in the martensitic region behind the MBF as seen in the simulation. Let us note that same basic features of the equivalent stress distribution have been obtained in numerical results by Iadacola and Shaw in [13] and they could contribute to better understanding of cross-section strain heterogeneity observed in [30] recently.

4 CONCLUSIONS

Our earlier developed constitutive model for NiTi SMA polycrystals has been extended to capture strain-softening response and regularized by a nonlocal integral type of approach. Implementation of the model into *Abaqus FEA* software and adjusting material functions with respect to experimental measurements allowed for FE simulations successfully reproducing the crucial features of the localized phase transformation in a NiTi wire loaded in tension as local tapering or significant stress redistribution. General conclusions can be summarized as follows: a) advanced experimental techniques (e.g. 3D XRD) provide qualitatively new data which could be used for better understanding and successful modeling of localization phenomena, b) complex heterogeneous stress fields are induced in the vicinity of a martensite band front in NiTi wire even for such a simple loading modes as uniaxial tension, c) localization phenomena must be incorporated into existing SMA models if correct and reliable predictions of NiTi mechanical response is required.

Acknowledgements: This work has been financially supported by the AdMat Project (14-36566G) of the Czech Science Foundation.

REFERENCES

[1] W Sylwestrowicz and E O Hall. The deformation and ageing of mild steel. *Proc. Phys. Soc. London, Sect. B*, 64:495–502, 1951.

[2] J A Shaw and S Kyriakides. Initiation and propagation of localized deformation in elasto-plastic strips under uniaxial tension. *Int. J. Plast.*, 13:837–871, 1997.

[3] Q P Sun and Z Q Li. Phase transformation in superelastic NiTi polycrystalline micro-tubes under tension and torsion – from localization to homogeneous deformation. *Int. J. Solids Struct.*, 39:3797–3809, 2002.

[4] B Reedlunn, C B Churchill, E E Nelson, J A Shaw, and S H Daly. Tension, compression, and bending of superelastic shape memory alloy tubes. *J. Mech. Phys. Solids*, 63:506–537, 2014.

[5] C Elibol and MF-X Wagner. Investigation of the stress-induced martensitic transformation in pseudoelastic NiTi under uniaxial tension, compression and compressionshear. *Mater. Sci. Eng. A*, 621:76–81, 2015.

[6] EA Pieczyska, H Tobushi, and K Kulasinski. Development of transformation bands in TiNi SMA for various stress and strain rates studied by a fast and sensitive infrared camera. *Smart Mater. Struct.*, 22:035007, 2013.

[7] P Šittner, Y Liu, and V Novák. On the origin of lüders-like deformation of NiTi shape memory alloys. *J. Mech. Phys. Solids*, 53:1719–46, 2005.

[8] J M Jani, M Leary, A Subic, and M A Gibson. A review of shape memory alloy research, applications and opportunities. *Materials and Design*, 56:10781113, 2014.

[9] M Frost, P Sedlák, A Kruisová, and M Landa. Simulations of self-expanding braided stent using macroscopic model of NiTi shape memory alloys covering R-phase. *J. Mater. Eng. Perform.*, 23:2584–2590, 2014.

[10] L Heller, K Janouchová, P Šittner, and D Vokoun. Functional textiles driven by transforming NiTi wires. In *MATEC Web of Conference*, volume 33. EDP Sciences, 2015.

[11] P Sedmák, J Pilch, L Heller, J Kopeček, J Wright, P Sedlák, M Frost, and P Šittner. Grain-resolved analysis of localized deformation in nickel-titanium wire under tensile load. *Science*, 353:559–562, 2016.

[12] B C Chang, J A Shaw, and M A Iadicola. Thermodynamics of shape memory alloy wire: Modeling, experiments, and application. *Contin. Mech. Thermodyn.*, 18:83–118, 2006.

[13] M A Iadicola and J A Shaw. Rate and thermal sensitivities of unstable transformation behavior in a shape memory alloy. *Int. J. Plast.*, 20:577–605, 2004.

[14] J F Hallai and S Kyriakides. Underlying material response for lüders-like instabilities. *Int. J. Plast.*, 47:1–12, 2013.

[15] YJ He and QP Sun. Scaling relationship on macroscopic helical domains in NiTi tubes. *Int. J. Solids Struct.*, 46:4242–4251, 2009.

[16] A Duval, M Haboussi, and T Ben Zineb. Modelling of localization and propagation of phase transformation in superelastic SMA by a gradient nonlocal approach. *Int. J. Solids Struct*, 48:1879–1893, 2011.

[17] KM Armattoe, M Haboussi, and T Ben Zineb. A 2D finite element based on a nonlocal constitutive model describing localization and propagation of phase transformation in shape memory alloy thin structures. *Int. J. Solids Struct*, 51:12081220, 2014.

[18] H Badnava, M Kadkhodaei, and M Mashayekhi. A non-local implicit gradient-enhanced model for unstable behaviors of pseudoelastic shape memory alloys in tensile loading. *Int. J. Solids Struct*, 51:40154025, 2014.

[19] H Ahmadian, S H Ardakani, and S Mohammadi. Strain-rate sensitivity of unstable localized phase transformation phenomenon in shape memory alloys using a non-local model. *Int. J. Solids Struct*, 63:167–183, 2015.

[20] P Sedlák, M Frost, B. Benešová, P Šittner, and T Ben Zineb. Thermomechanical model for NiTi-based shape memory alloys including R-phase and material anisotropy under multi-axial loadings. *Int. J. Plast.*, 39:132–151, 2012.

[21] M Frost, A Kruisová, V Sháněl, P Sedlák, P Haušild, M Kabla, D Shilo, and M Landa. Characterization of superelastic NiTi alloys by nanoindentation: Experiments and simulations. *Acta Phys. Pol., A*, 128:664–669, 2015.

[22] M Frost, B Benešová, and P Sedlák. A microscopically motivated constitutive model for shape memory alloys: formulation, analysis and computations. *Mat. Mech. Solids*, 21:358–382, 2016.

[23] Z P Bažant and M Jirásek. Nonlocal integral formulations of plasticity and damage: Survey of progress. *J. Eng. Mech.*, 128:1119–1149, 2002.

[24] M Jirásek and S Rolshoven. Comparison of integral-type nonlocal plasticity models for strain softening materials. *Int. J. Eng. Sci.*, 41:1553–1602, 2003.

[25] E Lorentz and S Andrieux. Analysis of non-local models through energetic formulations. *Int. J. Solids Struct*, 40:2905–2936, 2003.

[26] RHJ Peerlings, MGD Geers, R De Borst, and WAM Brekelmans. A critical comparison of nonlocal and gradient-enhanced softening continua. *Int. J. Solids Struct*, 38:7723–7746, 2001.

[27] JM Ball, K Koumatos, and H Seiner. Nucleation of austenite in mechanically stabilized martensite by localized heating. *J. Alloy. Compd.*, 577:S37–S42, 2011.

[28] M Frost, P Sedlák, and P Šittner. Numerical study on localization of phase transformation in NiTi shape memory wires. *Solid State Phenomena*, 258:141–144, 2017.

[29] M Frost, P Sedlák, L Kadeřávek, L Heller, and P Šittner. Mechanical response of NiTi shape memory alloy subject to combined thermal and non-proportional mechanical loading: a case study on helical spring actuator. *J. Intel. Mat. Syst. Str.*, 27:1927–1938, 2016.

[30] H M Paranjape, P P Paul, H Sharma, P Kenesei, J-S Park, T W Duerig, L C Brinson, and A P Stebner. Influences of granular constraints and surface effects on the heterogeneity of elastic, superelastic, and plastic responses of polycrystalline shape memory alloys. *J. Mech. Phys. Solids*, 102:46–66, 2017.

Morphing Wing I - Finite Element Modelling of a NiTi SMA Wire

W L H Wan A Hamid*, L Iannucci† and P Robinson†

* Department of Aeronautics
Imperial College London
South Kensington Campus, SW7 2AZ London, United Kingdom
E-mail: w.wan-a-hamid@imperial.ac.uk

† Department of Aeronautics
Imperial College London
South Kensington Campus, SW7 2AZ London, United Kingdom
Email: lo.iannucci@imperial.ac.uk - Web page: http://www.imperial.ac.uk/people/lo.iannucci
Email: p.robinson@imperial.ac.uk - Web page: http://www.imperial.ac.uk/people/p.robinson

ABSTRACT

This paper presents the development of a Finite Element Model of a NiTi shape memory alloy (SMA) wire using a commercial explicit finite element software, Ls-Dyna. A user-defined material model (UMAT) has been developed by implementing one of the earliest SMA constitutive models, the Tanaka model [1], into Ls-Dyna through a FORTRAN code. The aim is to use this model to study SMA-actuated morphing wing configurations. Morphing has attracted considerable attention among researchers for the past few decades due to the potential of providing optimum flight conditions at various flight missions. A combination of the morphing wing with smart materials such as SMAs offers further advantages such as a significant reduction in weight and system complexity, compared to an actuation achieved by mechanical motors or hydraulic systems.

A structure consisting of a spring and a SMA wire in series is presented as the simplest example of an actuated structure. The SMA wire was modelled as a beam element with one integration point, which is equivalent to a truss element, whereas the linear spring was modelled as a discrete element. One complete heating-cooling cycle was applied on the SMA wire. Upon heating, a reverse transformation (martensite-to-austenite) occurred, caused the wire to shorten and consequently extended the spring. Hence the stress in the wire increased while the SMA strain decreased until the end of the transformation. Upon cooling, a forward martensitic transformation (austenite-to-martensite) took place and reduced the stiffness of the wire. As a result, the spring contracted and the wire extended, and so the stress decreased while the SMA strain increased until the end of the transformation.

This finite element prediction of the thermomechanical behaviour was compared to an analytical solution for small displacement, and a close agreement was achieved. The model was also tested for a fully constrained recovery case, and the results matched analytical solutions where the spring stiffness was set to infinity. The model was then tested for mesh sensitivity, by increasing the number of elements along the length of the SMA wire from one element to 2, 5, 10, and 100 elements, and all solutions showed excellent agreement.

A parameter analysis was then carried out to analyze the dependence of the thermomechanical behaviour on several parameters such as the length and cross-sectional area of the SMA wire, as well as the spring stiffness (stiffness of the actuated structure). As expected, the FE model showed that the recovery stress (maximum stress at the end of heating cycle) increased whereas the recovery strain (maximum strain at the end of heating cycle) decreased with increase in the SMA length and spring stiffness, and with decrease in the SMA cross-sectional area.

The user-defined model was finally applied as a design tool to study the SMA actuation of a composite morphing wing concept, and the deflection of the trailing edge was evaluated. In conclusion, this work provides a foundation for future exploration of SMA-actuated morphing wings using Ls-Dyna, and will permit an optimization of the internal structure using LS-OPT and fluid-structure interaction (FSI) simulations to include the effect of incoming air flow on the movement of the wings.

REFERENCES

[1] K. Tanaka, S. Kobayashi and Y. Sato, "Thermomechanics of Transformation Pseudoelasticity and Shape Memory Effect in Alloys", *International Journal of Plasticity*, Vol. **2**, pp. 59-72, (1986).

[2] I. Chopra and J. Sirohi, *Smart Structures Theory*, Cambridge University Press, 2014.

Non-uniform transformation behaviour of NiTi in a discrete condition due to the functionally graded design

Bashir S. Shariat*, Reza Bakhtiari

Laboratory for Functional Materials
School of Mechanical and Chemical Engineering
The University of Western Australia
35 Stirling Highway, Crawley, WA 6009, Australia
Email: bashir.samsamshariat@uwa.edu.au

ABSTRACT

NiTi shape memory alloys exhibit unique thermomechanical properties, most notably pseudoelasticity and shape memory effect [1]. Based on these features, they can be used in a wide range of applications, including sensors, actuators and medical devices [2,3]. To utilize and control the response of the alloy to the external stimuli, functionally graded NiTi has been proposed. This article presents a design of discrete pseudoelastic NiTi wires that are geometrically graded perpendicular to the external loading axis. This design configuration allows a flexible global response of NiTi which can be adopted for different engineering requirements. Finite element analysis (FEA) has been performed to reveal the local stress-strain distribution inside the wires. Also, the global stress-strain behaviour from FEA has been validated by the experiments. The modelling results demonstrate the propagation direction and martensite fraction of the wires during loading cycle.

REFERENCES

[1] Y. Liu, S.P. Galvin, Criteria for pseudoelasticity in near-equiatomic NiTi shape memory alloys, Acta Mater. 45(11) (1997) 4431-4439.

[2] J. Van Humbeeck, Non-medical applications of shape memory alloys, Mater. Sci. Eng. A 273-275 (1999) 134-148.

[3] N.B. Morgan, Medical shape memory alloy applications—the market and its products, Mater. Sci. Eng. A 378(1–2) (2004) 16-23.

VIII ECCOMAS Thematic Conference on Smart Structures and Materials
SMART 2017
A. Güemes, A. Benjeddou, J. Rodellar and J. Leng (Eds)

NUMERICAL SIMULATION OF THE BEHAVIOR OF STEEL T-STUBS CONNECTED BY FE-SMA BOLTS

Cheikh Cissé*, Wael Zaki† and Tarak Ben Zineb††

*† Khalifa University of Science, Technology, and Research,
P.O. Box 127788, Abu Dhabi, UAE
e-mail*: cheikh.cisse@kustar.ac.ae
e-mail†: wael.zaki@kusar.ac.ae

†† Université de Lorraine, LEMTA, UMR 7563,
Vandoeuvre-lès-Nancy F-54500, France
e-mail: tarak.ben-zineb@univ-lorraine.fr

Key words: T-stub, shape memory alloys, shape memory effect, plastic deformation, FEM.

Abstract. The paper focuses on the numerical investigation of the thermomechanical behavior of steel T-stubs connected by bolts that are made of iron-based shape memory alloys (Fe-SMAs). The 3D macroscopic model used in this work was previously developed by the authors considering different thermomechanical properties between austenite and martensite, and coupling between phase transformation and plasticity. The model is implemented in a UMAT code using a time-discrete integration that follows a "multi-surface plasticity"-like approach. The numerical results show that the shape memory effect (SME) can be used to preload the bolt if the initial length of its shank is less than the total thickness the flanges. For an initial shank length of 21.38 mm and a total flange thickness of 21.4 mm, the SME produced average contact forces of 101 N between the bolt head and the flange, and 37 N between the two flanges. The resulting average contact pressures were 210 MPa and 25 MPa, respectively. The average bolt force after preload was approximately 22.6 kN. Subsequent application of 0.2 mm normal displacements at the top and bottom faces of the upper and lower webs induced local plastic deformation around the flange holes and phase transformation in the bolt. The reversibility of martensitic transformation and the confinement of the plastic deformation in a limited zone around the holes allowed nearly complete shape recovery by heating. The obtained results highlight the importance of using low-cost Fe-SMAs as alternatives to steel bolts for connecting T-stubs.

1 INTRODUCTION

Many engineering applications require joints between the different elements of the structure. This implies the use of connections that maintain the structure integrity. For the specific case of metal frames, bolted connections are among the most widely used joining techniques. The design steps of bolted steel beam-to-column joints have been established in modern codes such as Eurocode3 [1] wherein three failure modes have been identified in the tension region of the

structure. In mode I, failure occurs by plastic yielding of the flanges; in mode II, failure occurs by yielding of the flanges followed by bolts fracture; and in mode III, failure occurs only by fracture of the bolts. Failure of the structure can, however, be avoided by using materials that can recover their inelastic strain. An example of such smart materials are shape memory alloys (SMAs) that can retrieve their initial shape by pseudoelasticity or shape memory effect (SME). Compared to other SMAs, iron-based shape memory alloys (Fe-SMAs) present good compromises due to their low production cost and relatively good shape recovery (up to 4%). Experimental investigations confirm the high suitability of Fe-Mn-Si SMAs for large engineering structures such as smart composites [2], reinforced concrete beams [3, 4, 5, 6], pipe joints [7], crane rail fishplates [8], seismic dampers [9], etc. If these alloys have drawn strong attention in the last decade, development in modeling and simulation is still required to help expedite the design cycle for Fe-Mn-Si devices. Contrary to NiTi and Cu-based SMAs that have been intensively investigated numerically [10, 11], very few constitutive models are available for Fe-SMAs, with most still limited to uniaxial formulations and/or simulations [12, 13, 14, 15]. Existing 3D models for Fe-based SMAs either consider linear hardening during inelastic deformations [16] or loose their accuracy in presence of plastic deformation despite the nonlinear hardening approach [17]. Rare are the nonlinear 3D models that capture the thermomechanical response of Fe-SMAs, with high fidelity, in presence of phase transformation, plastic deformation, and a combination of both [18, 19]. The purpose of this work is to assess numerically the thermomechanical response of an assembly composed of steel T-stubs connected by Fe-SMA bolts, using the model developed in [18].
The paper is organized as follows: Section 2 gives the constitutive equations of the model and section 3 is dedicated to the finite element analysis of the structure using ABAQUS.

2 MATHEMATICAL MODELING

The complete set of state variables used to derive the model consists of the total strain tensor $\boldsymbol{\varepsilon}$, temperature T, local strain tensors $\boldsymbol{\varepsilon}_{\mathrm{a}}$ for austenite and $\boldsymbol{\varepsilon}_{\mathrm{m}}$ for martensite, local transformation strain tensor $\bar{\boldsymbol{\varepsilon}}_{\mathrm{tr}}$, local average plastic strain tensor of austenite $\bar{\boldsymbol{\varepsilon}}_{\mathrm{pl}}$, volume fraction of martensite ξ, magnitude of cumulated plastic strain p, macroscopic transformation strain tensor $\boldsymbol{\varepsilon}^{\mathrm{tr}}$, and macroscopic plastic strain tensor $\boldsymbol{\varepsilon}^{\mathrm{pl}}$. The potential of the model is given by a Lagrangian $\mathcal{L}$ corresponding to the Voigt mixture of the elastic energy of austenite Φ_{a} and the elasto-chemical energy of martensite Φ_{m}, incremented with the interaction energy between martensite variants $\mathcal{I}_{\mathrm{tr}}$, the interaction energy between plastic slip systems $\mathcal{I}_{\mathrm{pl}}$, the interaction energy describing the coupling between transformation and plasticity $\mathcal{I}_{\mathrm{cp}}$, and the constraints energy Φ_{KT} expressing the Kuhn-Tucker slackness conditions on ξ and on $\boldsymbol{\varepsilon}_{\mathrm{a}}$, $\boldsymbol{\varepsilon}_{\mathrm{m}}$ and $\boldsymbol{\varepsilon}$:

$$\mathcal{L} = (1-\xi)\Phi_{\mathrm{a}} + \xi\Phi_{\mathrm{m}} + \mathcal{I}_{\mathrm{tr}} + \mathcal{I}_{\mathrm{pl}} + \mathcal{I}_{\mathrm{cp}} + \Phi_{\mathrm{KT}}. \tag{1}$$

From considerations of thermodynamic consistency, the driving forces for phase transformation $\mathcal{A}_{\mathrm{tr}}$ and plasticity $\mathcal{A}_{\mathrm{pl}}$ are taken as the partial derivatives of the Lagrangian with respect to the

associated dissipative state variables

$$\mathcal{A}_{\rm tr} = -\frac{\partial \mathcal{L}}{\partial \xi}, \tag{2}$$

$$\mathcal{A}_{\rm pl} = -\frac{\partial \mathcal{L}}{\partial p}. \tag{3}$$

Within the framework of generalized standard materials, the thermodynamic forces of the dissipative processes are also taken as sub-gradients of a real-valued convex pseudo-potential of dissipation $\mathcal{D}$ that is positive, lower semi-continuous, and positively homogeneous of degree one with respect to the rate variables $\dot{\xi}$ and $\dot{p}$. This helps defining the following loading functions

$$\mathcal{F}_{\rm m}^{\rm tr} = \mathcal{A}_{\rm tr} - \mathcal{D}_{\rm m}^{\rm tr}, \text{ for forward phase transformation,} \tag{4}$$

$$\mathcal{F}_{\rm a}^{\rm tr} = -\mathcal{A}_{\rm tr} - \mathcal{D}_{\rm a}^{\rm tr}, \text{ for reverse phase transformation,} \tag{5}$$

$$\mathcal{F}_{\rm a}^{\rm pl} = \mathcal{A}_{\rm pl} - \mathcal{D}_{\rm a}^{\rm pl}, \text{ for plastic deformation.} \tag{6}$$

The model is completed by the following Kuhn-Tucker conditions associated to the dissipative variables:

- $\mathcal{F}_{\rm m}^{\rm tr} \leq 0$, $\dot{\xi} \geq 0$ and $\dot{\xi}\mathcal{F}_{\rm m}^{\rm tr} = 0$, for forward transformation,
- $\mathcal{F}_{\rm a}^{\rm tr} \leq 0$, $-\dot{\xi} \geq 0$ and $(-\dot{\xi})\mathcal{F}_{\rm a}^{\rm tr} = 0$, for reverse transformation,
- $\mathcal{F}_{\rm a}^{\rm pl} \leq 0$, $\dot{p} \geq 0$ and $\dot{p}\dot{\mathcal{F}}_{\rm a}^{\rm pl} = 0$, for plastic deformation.

Using the Lagrangian and pseudo-potential of dissipation defined in [18], the explicit expressions of the loading functions and the stress-strain relation are given by

$$\begin{aligned}\mathcal{F}_{\rm m}^{\rm tr} = {} & \frac{G_{\rm ma}}{6}\sigma_{\rm eq}^2 + \frac{\kappa_{\rm ma}}{2}\sigma_{\rm h}^2 + \boldsymbol{\sigma} : (\bar{\boldsymbol{\varepsilon}}_{\rm tr} - \bar{\boldsymbol{\varepsilon}}_{\rm pl}) - \zeta_{\rm m}(T - M_{\rm s}^0) - H_{\rm v}(\bar{\boldsymbol{\varepsilon}}_{\rm tr} : \boldsymbol{\varepsilon}^{\rm tr})(\boldsymbol{\varepsilon}^{\rm tr} : \boldsymbol{\varepsilon}^{\rm tr})^{\frac{n_{\rm v}-1}{2}} \\ & - H_{\rm pv}\delta_{\rm pv}(\bar{\boldsymbol{\varepsilon}}_{\rm tr} : \boldsymbol{\varepsilon}^{\rm pl})\Big[(\boldsymbol{\varepsilon}^{\rm tr} : \boldsymbol{\varepsilon}^{\rm pl})\delta_{\rm pv}\Big]^{n_{\rm pv}} - \sigma_{\rm m}^{\rm tr}\varepsilon_{\rm L} - H_{\rm s}p^2 + (\lambda_1 - \lambda_2),\end{aligned} \tag{7}$$

$$\begin{aligned}\mathcal{F}_{\rm a}^{\rm tr} = {} & -\frac{G_{\rm ma}}{6}\sigma_{\rm eq}^2 - \frac{\kappa_{\rm ma}}{2}\sigma_{\rm h}^2 - \boldsymbol{\sigma} : (\bar{\boldsymbol{\varepsilon}}_{\rm tr} - \bar{\boldsymbol{\varepsilon}}_{\rm pl}) + \zeta_{\rm a}(T - A_{\rm s}^0) + H_{\rm v}(\bar{\boldsymbol{\varepsilon}}_{\rm tr} : \boldsymbol{\varepsilon}^{\rm tr})(\boldsymbol{\varepsilon}^{\rm tr} : \boldsymbol{\varepsilon}^{\rm tr})^{\frac{n_{\rm v}-1}{2}} \\ & + H_{\rm pv}\delta_{\rm pv}(\bar{\boldsymbol{\varepsilon}}_{\rm tr} : \boldsymbol{\varepsilon}^{\rm pl})\Big[(\boldsymbol{\varepsilon}^{\rm tr} : \boldsymbol{\varepsilon}^{\rm pl})\delta_{\rm pv}\Big]^{n_{\rm pv}} - \sigma_{\rm a}^{\rm tr}\varepsilon_{\rm L} + H_{\rm x}\xi - (\lambda_1 - \lambda_2),\end{aligned} \tag{8}$$

$$\mathcal{F}_{\rm a}^{\rm pl} = (1-\xi)\left[\boldsymbol{\sigma} - H_{\rm p}(\boldsymbol{\varepsilon}^{\rm pl} : \boldsymbol{\varepsilon}^{\rm pl})^{\frac{n_{\rm p}-1}{2}}\boldsymbol{\varepsilon}^{\rm pl} - H_{\rm pv}\delta_{\rm pv}\Big[(\boldsymbol{\varepsilon}^{\rm tr} : \boldsymbol{\varepsilon}^{\rm pl})\delta_{\rm pv}\Big]^{n_{\rm pv}}\boldsymbol{\varepsilon}^{\rm tr}\right] : \boldsymbol{N}^{\rm pl} - < \sigma_{\rm a}^{\rm pl} - \beta T > . \tag{9}$$

$$\boldsymbol{\sigma} = \left[(1-\xi)\boldsymbol{K}_{\rm a}^{-1} + \xi\boldsymbol{K}_{\rm m}^{-1}\right]^{-1} : (\boldsymbol{\varepsilon} - \boldsymbol{\varepsilon}^{\rm tr} - \boldsymbol{\varepsilon}^{\rm pl}), \tag{10}$$

where $G_{\rm ma} = \frac{1}{G_{\rm m}} - \frac{1}{G_{\rm a}}$ and $\kappa_{\rm ma} = \frac{1}{\kappa_{\rm m}} - \frac{1}{\kappa_{\rm a}}$ are the differences in inverse shear and inverse bulk moduli of the two phases, $\boldsymbol{K}_{\rm a}$ and $\boldsymbol{K}_{\rm m}$ are the elastic stiffness tensors of austenite and martensite, $H_{\rm v}$, $n_{\rm v}$, $H_{\rm p}$, $n_{\rm p}$, $H_{\rm pv}$ and $n_{\rm pv}$ are hardening parameters, $\delta_{\rm pv} = {\rm sgn}(\boldsymbol{\varepsilon}^{\rm tr} : \boldsymbol{\varepsilon}^{\rm pl})$, T_0 is the equilibrium temperature of the alloy, $\sigma_{\rm m}^{\rm tr}$ and $\sigma_{\rm a}^{\rm tr}$ are the critical stresses for forward and reverse phase transformations, respectively, $\sigma_{\rm a}^{\rm pl}$ is the plastic yield strength of austenite, $\zeta_{\rm a}$ and $\zeta_{\rm m}$ are constants proportional to the slopes of $A_{\rm s}$ and $M_{\rm s}$ lines, β is the slope of the yield line,

the term "$H_{\mathrm{s}}p^2$" describes the curbing effect of plasticity on transformation, the term "$H_{\mathrm{tr}}\xi$" reflects the shift of the A_{s} line towards the lower temperature side when the amount of preformed martensite increases, and λ_1, λ_2 and $\boldsymbol{\lambda}$ are positive Lagrange multipliers. The transformation and plastic flow rules are obtained from the generalized normality rule, as follows:

$$\dot{\boldsymbol{\varepsilon}}^{\mathrm{tr}} = \dot{\xi}\varepsilon_{\mathrm{L}}\boldsymbol{N}^{\mathrm{tr}}, \text{ with } \boldsymbol{N}^{\mathrm{tr}} = \begin{cases} \frac{3}{2}\frac{\boldsymbol{V}_{\mathrm{tr}}^{\mathrm{dev}}}{V_{\mathrm{tr}}^{\mathrm{eq}}}, \text{ if } \dot{\xi} > 0, \\ \frac{\boldsymbol{\varepsilon}^{\mathrm{tr}}}{\xi}, \text{ if } \dot{\xi} < 0, \end{cases} \tag{11}$$

$$\dot{\boldsymbol{\varepsilon}}^{\mathrm{pl}} = \dot{\xi}\boldsymbol{N}^{\mathrm{pl}}, \text{ with } \boldsymbol{N}^{\mathrm{pl}} = \begin{cases} \frac{3}{2}\frac{\boldsymbol{V}_{\mathrm{pl}}^{\mathrm{dev}}}{V_{\mathrm{pl}}^{\mathrm{eq}}}, \text{ if } \sigma_{\mathrm{eq}} \neq 0, \\ \frac{\boldsymbol{\varepsilon}^{\mathrm{pl}}}{\varepsilon_{\mathrm{pl}}^{\mathrm{eq}}}, \text{ otherwise.} \end{cases} \tag{12}$$

In the above two equations, $\boldsymbol{V}_{\alpha}^{\mathrm{dev}}$ and V_{α}^{eq} are, respectively, the deviatoric part and von Mises norm of the first order tensors $\boldsymbol{V}^{\alpha}$, with $\alpha = \{\mathrm{tr}, \mathrm{pl}\}$,

$$\boldsymbol{V}^{\mathrm{tr}} = \left[\boldsymbol{\sigma} - H_{\mathrm{v}}(\boldsymbol{\varepsilon}^{\mathrm{tr}} : \boldsymbol{\varepsilon}^{\mathrm{tr}})^{\frac{n_{\mathrm{v}}-1}{2}}\boldsymbol{\varepsilon}^{\mathrm{tr}} - H_{\mathrm{pv}}\delta_{\mathrm{pv}}\left[(\boldsymbol{\varepsilon}^{\mathrm{tr}} : \boldsymbol{\varepsilon}^{\mathrm{pl}})\delta_{\mathrm{pv}}\right]^{n_{\mathrm{pv}}}\boldsymbol{\varepsilon}^{\mathrm{pl}}\right], \tag{13}$$

$$\boldsymbol{V}^{\mathrm{pl}} = \left[\boldsymbol{\sigma} - H_{\mathrm{p}}(\boldsymbol{\varepsilon}^{\mathrm{pl}} : \boldsymbol{\varepsilon}^{\mathrm{pl}})^{\frac{n_{\mathrm{p}}-1}{2}}\boldsymbol{\varepsilon}^{\mathrm{pl}} - H_{\mathrm{pv}}\delta_{\mathrm{pv}}\left[(\boldsymbol{\varepsilon}^{\mathrm{tr}} : \boldsymbol{\varepsilon}^{\mathrm{pl}})\delta_{\mathrm{pv}}\right]^{n_{\mathrm{pv}}}\boldsymbol{\varepsilon}^{\mathrm{tr}}\right]. \tag{14}$$

3 FINITE ELEMENTS ANALYSIS

Since both phase transformation and plastic deformation are inelastic mechanisms, the implicit time-discrete integration of the model was accomplished similarly to "multi-surface plasticity". The model was implemented in a user defined material subroutine (UMAT) using the "convex cutting plane" approach of the well-known return mapping algorithm and appended to ABAQUS. This software allows to account for the contact between elements with frictional sliding and flange separation under large displacements. The finite element analysis of the structure was carried out using the material parameter given in Table 1 for the bolts made of Fe-31.6Mn-6.45Si-0.018C (wt%). The T-stubs were assumed to be made of A992 steel with the a yield stress of 450 MPa, an elastic modulus of 205 GPa and poisson ration of 0.29.

Table 1: Material parameters for Fe-31.6Mn-6.45Si-0.018C (wt%).

Parameter	Value	Parameter	Value	Parameter	Value
E_{a}	130 GPa	E_{m}	260 GPa	ν	0.3
$\sigma_{\mathrm{a}}^{\mathrm{tr}}$	130 MPa	$\sigma_{\mathrm{m}}^{\mathrm{tr}}$	72 MPa	$\sigma_{\mathrm{a}}^{\mathrm{pl}}$	260 MPa
ζ_{a}	0.086 MPa/°C	ζ_{m}	0.043 MPa/°C	β	0.5 MPa/°C
M_{s}^0	0 °C	A_{s}^0	100 °C	A_{f}^0	130 °C
H_{v}	1165.7 MPa	H_{p}	497.8 MPa	H_{pv}	19567 MPa
n_{v}	0.52	n_{p}	0.45	n_{pv}	0.48
ε_{L}	0.04	H_{x}	13.2 MPa	H_{s}	5000 MPa

3.1 Modeling of the geometry

The T-stubs specimen were assumed to be obtained from W14 steel beam and connected by M10 Fe-SMA bolts as shown in Figure 1. The structure was modeled in ABAQUS by

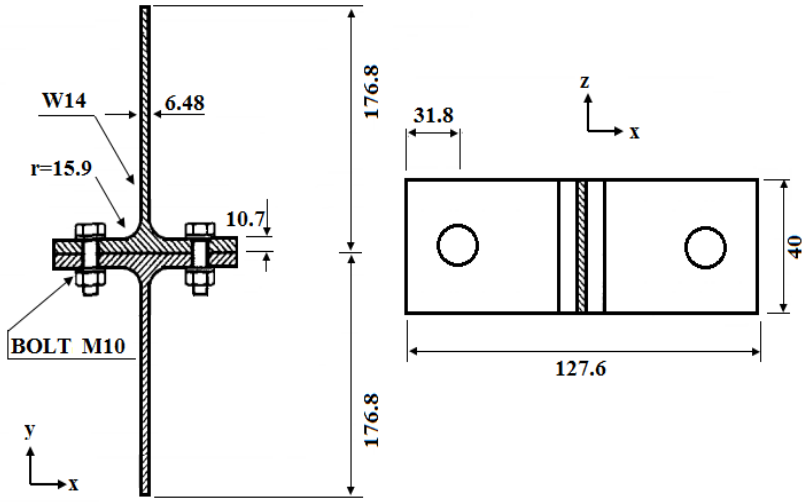

Figure 1: Geometry of the specimen.

taking advantage of the symmetry with respect to YZ plane. Therefore only half the structure was considered as shown in Figure 2(a). The bolt and stub parts were created separately and surface-to-surface contacts were modeled using the "interaction" module of ABAQUS. The parts were meshed using eight-node brick elements (C3D8), with a total number of 1828 elements in each T-stub and 3825 elements in the bolt (see Figure 2(b)).

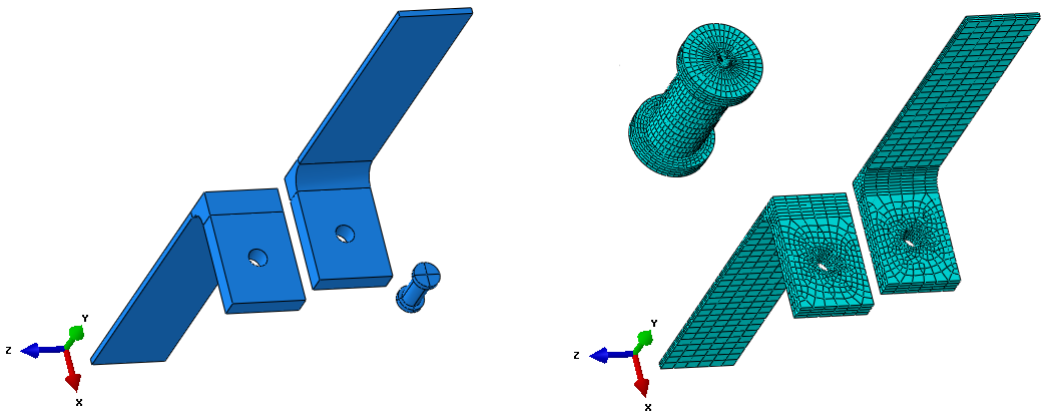

(a) partitioned geometry. (b) meshed parts.

Figure 2: Partitioned and meshed parts.

3.2 Numerical results for the bolt preload

Bolt preload is important in fastened structure. In fact, a tightened bolt that carries only portion of the structure load can survive in an application where loose or untightened bolt that carries entirely the load would fail. In contrast to steel bolts, preloading of Fe-SMA bolts through SME requires the initial length of the shank to be less than the total thickness of the structure. In this work, the total thickness of the two webs was 21.4 mm. The shank of initial length 21.38 mm was pre-strained by applying a normal displacement of 0.3 mm to the inner part of the bolt head at room temperature, while keeping the nut fixed. Figure 3 highlights an average von Mises stress of 292 MPa and an average volume fraction of martensite of 0.25 at the end of the pre-straining stage. Due to inelastic transformation strain, a gap is obtained between the bolt and T-stub after unloading. After heating, the bolt partially retrieves its

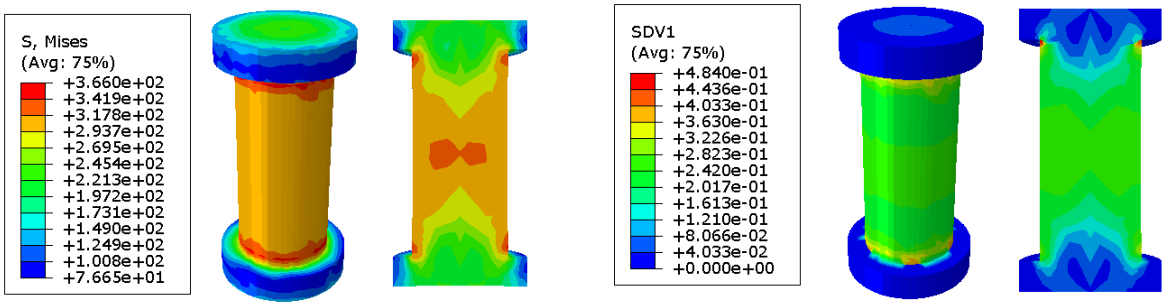

(a) stress distribution after loading.

(b) martensite distribution after loading.

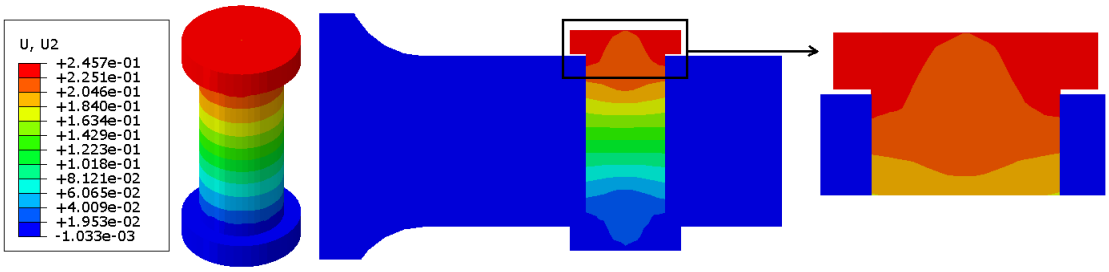

(c) gap between bolt and stub after unloading.

Figure 3: Results after pre-straining and unloading.

initial shape. The corresponding distribution of stress and residual displacement, as well as the complete reverse phase transformation and vanished plastic deformation are illustrated in Figure 4. The obstruction of the reverse deformation of the bolt by the flanges brought the different parts into contact, as shown in Figure 5. The contact force was maximum between the flange and bolt head/nut (168.9 N) and reached 62.9 N between the two flanges, corresponding to contact pressures of 285.5 MPa and 24.9 MPa, respectively. For the average von Mises stress of 72 MPa in the shank, the corresponding bolt force was 22.6 kN. The evolution of the contact forces and contact pressures during the the heating stage are shown in Figure 6. The results point out a contact temperature of 121 °C at which 90% of the initial length of the shank was

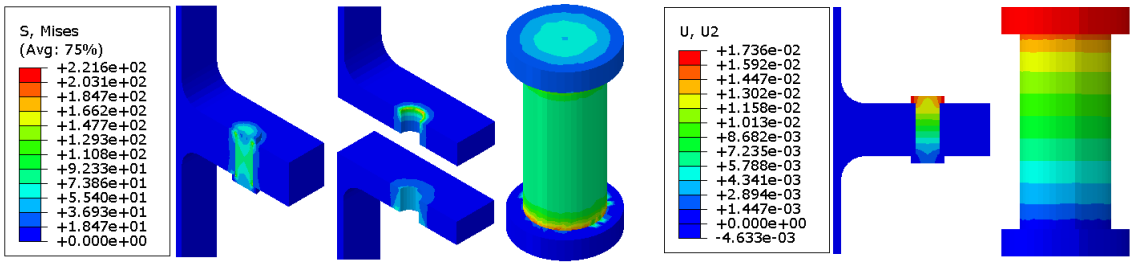

(a) stress distribution after heating. (b) displacement after heating.

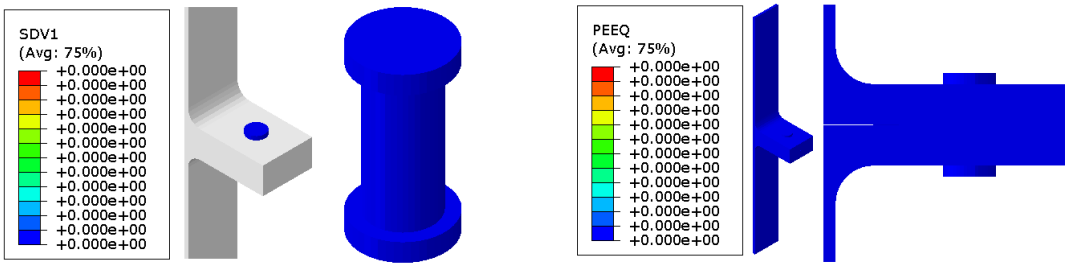

(c) martensite distribution after heating. (d) plastic strain after heating.

Figure 4: Results after pre-straining, unloading and heating.

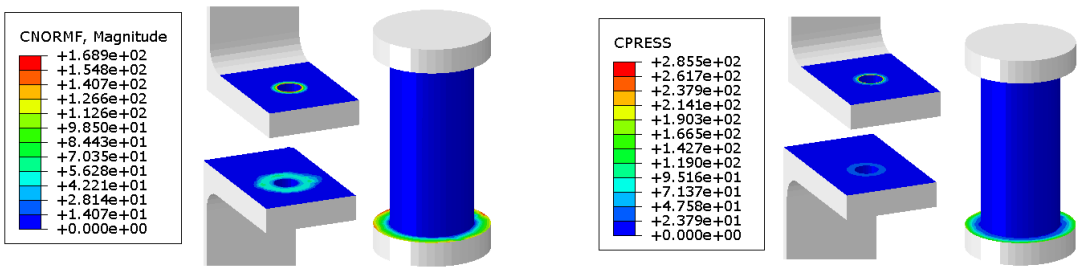

(a) normal contact force. (b) contact pressure.

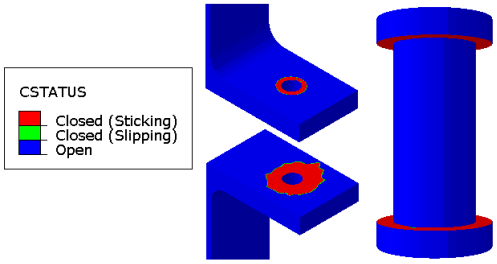

(c) contact status.

Figure 5: Contact behavior after pre-straining, unloading and heating.

recovered. Subsequent cooling to room temperature had no effect on the values of the contact force and pressure.

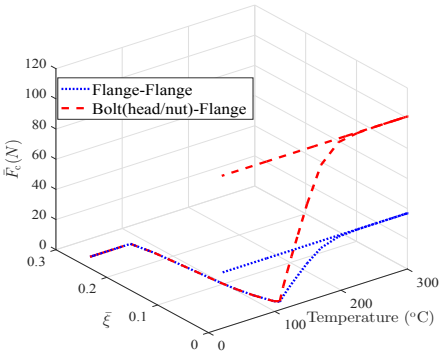

(a) evolution of the contact force (3D).

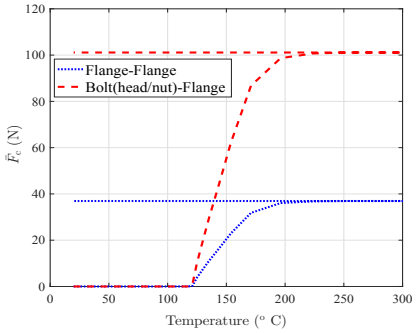

(b) evolution of the contact force (2D).

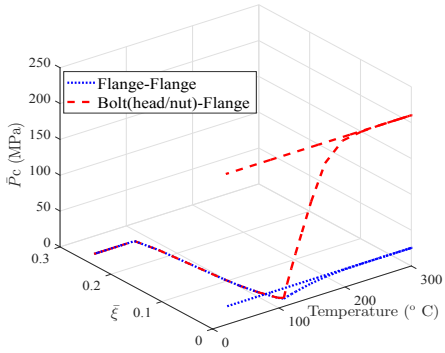

(c) evolution of the contact pressure (3D).

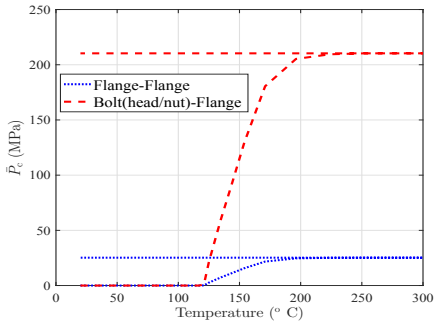

(d) evolution of the contact pressure (2D).

Figure 6: Evolution of the contact force and pressure during the heating stage.

3.3 Numerical results of the T-stub deformation

After preloading the structure, the T-stubs were deformed by applying normal displacements of 0.2 mm at the top and bottom surfaces of the upper and lower webs. The results in Figure 7 highlight a non symmetric distribution of the von Mises stress in the bolt due to the flange opening. This was reflected also in the distribution of martensite. The yield strength of the perfectly plastic flange having been reached, plastic deformation occurred locally at the edges of the hole surfaces. It is worth noticing that the contact zones at the end of the stubs deformation were different from those reported after preloading. The contact area between the bolt head and nut with the upper and lower flanges were reduced to two points, while the two flanges were in contact over a small area toward the ends. These observations suggest a Mode II failure of the structure for higher displacement of the webs. The evolutions of the average contact force and pressure between the two flanges are given in Figure 8. It is worth noting, in the present case, that the contact force between the two flanges corresponds to the "prying force". Contrary to the bolt preloading stage, the contact resulted from mechanical loading with an average pressure of 140 MPa and an average force of 170 N. Unloading reduces the contact pressure to 14 MPa and the contact force to 17 N. Subsequent heating then generates partial reverse transformation

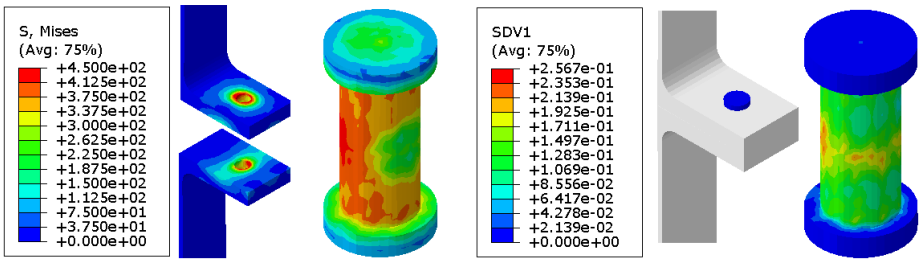

(a) stress distribution after loading. (b) martensite distribution after loading.

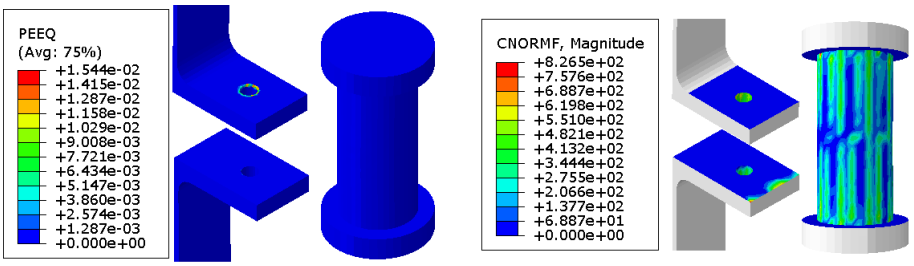

(c) plastic strain after loading. (d) contact force.

Figure 7: Results after loading of the T-stubs.

in the bolt. Nevertheless, due to plastic deformation at the flange hole surfaces, the contact pressure and force were much lower, compared to the those obtained initially after preloading, but was enough to switch the locations of the contact areas.

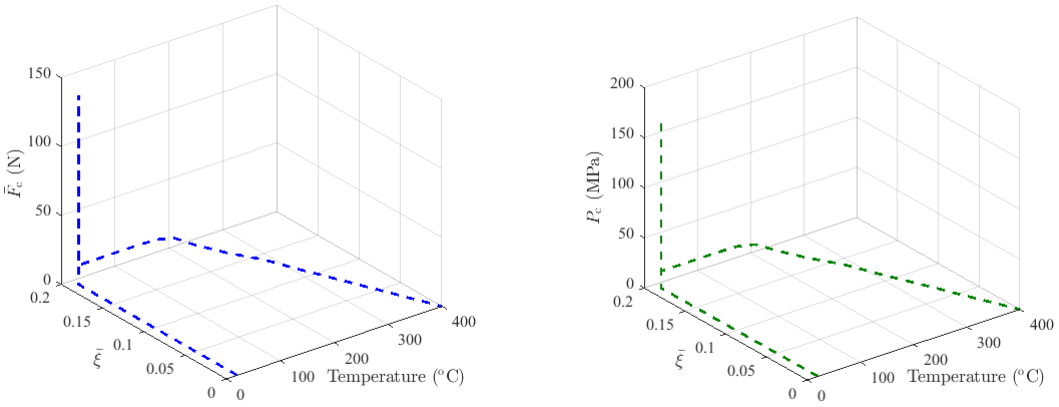

(a) evolution of the prying force. (b) evolution of the contact pressure.

Figure 8: Contact behavior after deformation of the T-stub and heating.

4 CONCLUSIONS

This work focused on the thermomechanical response of steel T-stubs connected by Fe-SMA bolts, using a nonlinear 3D model that was previously developed by the authors. The integration of the time-discrete equations was accomplished using an implicit algorithm following the multisurface plasticity approach. The simulation results indicate out that the SME of the Fe-SMA bolt can be used to preload the structure, provided that the initial length of the shank is less than the total thickness of the flanges. Applying a normal displacement on the top and bottom surfaces of the upper and lower webs induced plastic deformation at the hole surfaces of the stubs and phase transformation in the bolts. After unloading and heating, the initial shape of the structure was recovered nearly completely, due to the confinement of the plastic deformation near the bolt-to-stub contact zone.. The obtained results demonstrate the advantage of using Fe-SMA bolts as fasteners of T-stubs instead of steels.

REFERENCES

[1] C. EN, "Eurocode 3: Design of steel structures-part 1-1: General rules and rules for buildings," *European Committee for Standardization*, 2005.

[2] Y. Watanabe, T. Wakatsuki, H. Sato, and T. Maruyama, "Bending strength of Fe–Mn–Si–Cr shape memory alloy machining chips reinforced smart composite," in *ICCM Int Conf Compos Mater*, 2007.

[3] T. Sawaguchi, T. Kikuchi, K. Ogawa, S. Kajiwara, Y. Ikeo, M. Kojima, and T. Ogawa, "Development of prestressed concrete using Fe–Mn–Si-based shape memory alloys containing NbC," *Materials transactions*, vol. 47, no. 3, pp. 580–583, 2006.

[4] C. Czaderski, M. Shahverdi, R. Brönnimann, C. Leinenbach, and M. Motavalli, "Feasibility of iron-based shape memory alloy strips for prestressed strengthening of concrete structures," *Construction and Building Materials*, vol. 56, pp. 94–105, 2014.

[5] M. Shahverdi, C. Czaderski, and M. Motavalli, "Iron-based shape memory alloys for prestressed near-surface mounted strengthening of reinforced concrete beams," *Construction and Building Materials*, vol. 112, pp. 28–38, 2016.

[6] M. Shahverdi, C. Czaderski, P. Annen, and M. Motavalli, "Strengthening of RC beams by iron-based shape memory alloy bars embedded in a shotcrete layer," *Engineering Structures*, vol. 117, pp. 263–273, 2016.

[7] H. Tanahashi, T. Maruyama, and H. Kubo, "Applications of Fe-Mn-Si alloy for pipe joints," *Trans. Mat. Res. Soc. Jpn*, vol. 18, p. 1149, 1994.

[8] T. Maruyama, T. Kurita, S. Kozaki, K. Andou, S. Farjami, and H. Kubo, "Innovation in producing crane rail fishplate using Fe–Mn–Si–Cr based shape memory alloy," *Materials Science and Technology*, vol. 24, no. 8, pp. 908–912, 2008.

[9] T. Sawaguchi, T. Maruyama, H. Otsuka, A. Kushibe, Y. Inoue, and K. Tsuzaki, "Design Concept and Applications of Fe–Mn–Si-Based Alloys from Shape Memory to Seismic Response Control," *Materials Tansactions*, vol. 57, no. 3, pp. 283–293, 2016.

[10] C. Cissé, W. Zaki, and T. Ben Zineb, "A review of constitutive models and modeling techniques for shape memory alloys," *International Journal of Plasticity*, vol. 76, pp. 244 – 284, 2016.

[11] C. Cissé, W. Zaki, and T. B. Zineb, "A review of modeling techniques for advanced effects in shape memory alloy behavior," *Smart Materials and Structures*, vol. 25, no. 10, p. 103001, 2016.

[12] I. Goliboroda, K. Rusinko, and K. Tanaka, "Description of an Fe-based shape memory alloy thermomechanical behavior in terms of the synthetic model," *Computational materials science*, vol. 13, no. 4, pp. 218–226, 1999.

[13] F. Nishimura, U. Liedl, and E. Werner, "Simulation of martensitic transformations in TRIP-steel and Fe-based shape memory alloy," *Computational Materials Science*, vol. 26, pp. 189–196, 2003.

[14] T. Lazghab and K. Wu, "One-dimensional shape memory alloy model with plastic deformation effects," *ICOMAT14–17th June*, 2005.

[15] C. Cissé, W. Zaki, and T. B. Zineb, "A model for iron-based shape memory alloys considering variable elastic stiffness and coupling between plasticity and phase transformation," in *ASME 2015 Conference on Smart Materials, Adaptive Structures and Intelligent Systems*. American Society of Mechanical Engineers, 2015, pp. V001T03A012–V001T03A012.

[16] F. Jemal, T. Bouraoui, T. Ben Zineb, E. Patoor, and C. Bradaï, "Modelling of martensitic transformation and plastic slip effects on the thermo-mechanical behaviour of Fe-based shape memory alloys," *Mechanics of Materials*, vol. 41, no. 7, pp. 849–856, 2009.

[17] W. Khalil, A. Mikolajczak, C. Bouby, and T. Ben Zineb, "A constitutive model for Fe-based shape memory alloy considering martensitic transformation and plastic sliding coupling: Application to a finite element structural analysis," *Journal of Intelligent Material Systems and Structures*, vol. 23, pp. 1143–1160, 2012.

[18] C. Cissé, W. Zaki, X. Gu, and T. B. Zineb, "A nonlinear 3D model for iron-based shape memory alloys considering different thermomechanical properties for austenite and martensite and coupling between transformation and plasticity," *Mechanics of Materials*, vol. 107, pp. 1–21, 2017.

[19] C. Cissé, W. Zaki, and T. B. Zineb, "Finite element analysis of a 3D Fe-based SMA cellular beam with highly heterogeneous stress and strain distributions," in *SPIE 2017 Conference on Smart Structures and Materials, Nondestructive Evaluation and Health Monitoring*, vol. 10165. SPIE, 2017, pp. 101 650E–101 650E–8.

VIIIECCOMAS Thematic Conference on Smart Structures and Materials
SMART 2017
A. Güemes, A. Benjeddou , J. Rodellar and JinsongLeng (Eds)

NITI ALLOYS: FATIGUE AND SELF-HEATING METHOD AFTER HYDROGEN EMBRITTLEMENT

M. ROKBANI[*], L. SAINT-SULPICE[†], S. ARBAB CHIRANI[†] & T. BOURAOUI[*]

[*]ENIM, LGM, Université de Monastir, TUNISIE
Email: rokbani_maha@hotmail.fr
[†] ENIB, LBMS, Université de BREST, FRANCE
Email: sulpice@enib.fr
[†] ENIB, LBMS, Université de BREST, FRANCE
Email: arbab@enib.fr
[*]ENIM, LGM, Université de Monastir, TUNISIE
Email: tarak.bouraoui@gmail.com

Key words: Ni-Ti; Fatigue; Hydrogen embrittlement; Self- heating method.

Abstract. Due to their biocompatibility and superelastic effect, NiTi wires are successfully used in orthodontic clinics. These devices are subjected to work under cyclic or repetitive loadings and may be in contact with corrosive environments leading to unexpectable failures where the hydrogen embrittlement is a relatively common case.
The aim of the present work is to investigate the fatigue behavior of superelastic NiTi with a particular emphasis to the effect of hydrogen on fatigue properties. Fatigue tests were analyzed using self-heating measurements which consist on observing thermal effects during cyclic loadings.
The results obtained with this approach showed a trend of a decrease in the fatigue life of NiTi alloys after hydrogen embrittlement and the fatigue limit extrapolated will be compared with the results obtained with the classical S-N curves method. To evaluate the reability and safety of these instruments in dental applications, rotational bending tests were also carried out.

1 INTRODUCTION

NiTi wires exhibit good corrosion resistance and biocompatibility owing to thin protective film on their surface. They have also shown excellent ductility and fatigue life. However, it is known that some wires may break in the oral cavity. The interaction fatigue-hydrogen absorption can be the main cause of these failures.

Yokoyama et al **[1]** found that when the amount of hydrogen exceeds 50-200 mass ppm, a pronounced degradation of the mechanical properties of the NiTi alloys occurs. Fatigue life decreases significantly by the increasing of the hydrogen content **[2]**. However, the field of study the effect of hydrogen embrittlement on NiTi fatigue properties remains little explored. Fatigue properties are generally determined through a series of cyclic tests which are long and require a large number of specimens. To reduce time and cost consuming of fatigue characterization, over the last few years many research teams have been working on

alternative and faster methods based on self-heating measurements under mechanical cyclic loadings **[3]**.

This technique has been validated successfully for steels and a good correlation is obtained between the fatigue limit and the stress level beyond which an increase of the temperature is observed. This method has been rarely applied on NiTi alloys **[4]**.

In this paper we propose an extension of this self-heating based approach to determine fatigue properties of NiTi wires before and after hydrogen charging in 0.9 % NaCl solution.

2 MATERIALS AND EXPERIMENTLA METHODS

A commercially NiTi superelastic orthodontic wire with a dimension of 0, 64*0, 46 mm^2 and with a nominal chemical composition (50.8 wt % and 48.2 wt %) has been considered in this study. Specimens were cut to 30 mm length.

To study the effect of hydrogen on fatigue properties of NiTi alloys, platinum and the specimen alloy were based in 0.9 % NaCl solution as the anode and cathode respectively. These alloys were charged with hydrogen at room temperature for 2, 4 and 8 hours. Gaseous hydrogen generated on the surface of the specimen was controlled by the current density at 10 A/ m^2.

A differential scanning calorimeter (DSC) has been used to determine the phase transformation temperatures as presented in **Figure (1)**. The austenitic finish temperature (A_f) was identified at 20 °C. This alloy is in the austenitic phase because all tests are run in a room temperature (25 °C).

For the evaluation of degradation on superelastic performance after hydrogen charging, tensile tests of the uncharged and charged alloys were carried out at room temperature on an Instron-type machine at a strain of 10^{-4} s^{-1} within a few minutes after removal from the electrolytic bath. The gauge length of the specimen is 10 mm.

Self-heating tests were conducted using a servo-hydraulic fatigue device. This method consists in applying on the same specimen successive blocks of 3000 cycles for different increasing levels of applied stress from 50 to 450 MPa with 20 MPa increment, loading ratio R of 0.1 and a frequency of 30 Hz. For each block of loading the temperature evolution of the specimen is measured with an infrared camera.

The more appropriate approach used for fatigue analyses of Ni-Ti medical devices is rotating bending fatigue tests (BRF). These tests are also performed at room temperature with a rotational speed of 400 rpm. The rotational bending test controlled in deformation show the influence of this parameter on the lifetime of the uncharged and charged wires with hydrogen subjected to cyclic stress.

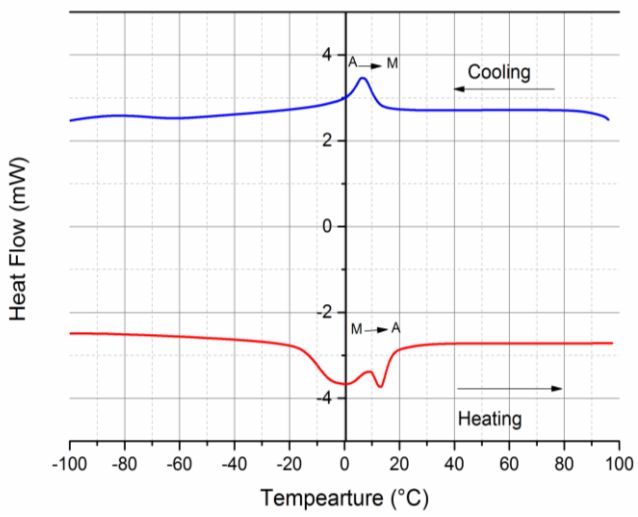

Figure 1. DSC curve of NiTi wire

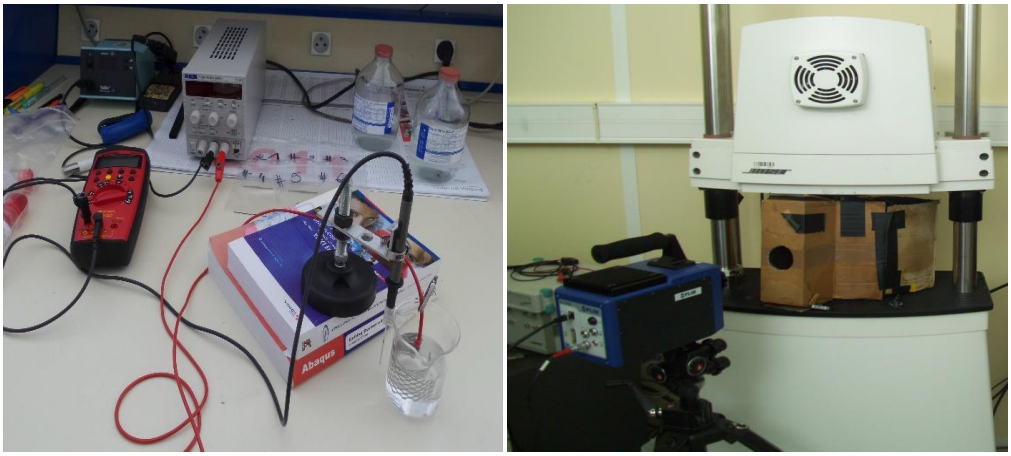

Figure 2. a) Equipment for hydrogen charging in 0.9 % NaCl. **b)** Fatigue equipment for self-heating test.

3 RESULTS AND DISCUSSIONS

3.1 Effect of hydrogen on mechanical properties

Figure (4.a) shows a typical stress-strain curve for a tensile loading-unloading for NiTi superelastic alloy. The plateau of A-M phase transformation has a 7.4 % strain size with a phase transformation yield of 390 MPa. After hydrogen charging, the critical stress of martensitic transformation was increased with increasing hydrogen charging **(Figure 4.b)**. The increase in the martensite stress plateau suggests that with the presence of hydrogen, more energy is required for the austenite to martensite transition. These results are in good agreement with previous works **[5]**.

Tensile strength of NiTi alloys charged with hydrogen was clearly affected as shown in **Figure (5)**. The value of the tensile strength decreased with the increasing immersion time in 0.9 % NaCl. It was observed that after hydrogen charging the specimen presents an increase in the yield stress value corresponding to the activation of martensitic transformation.

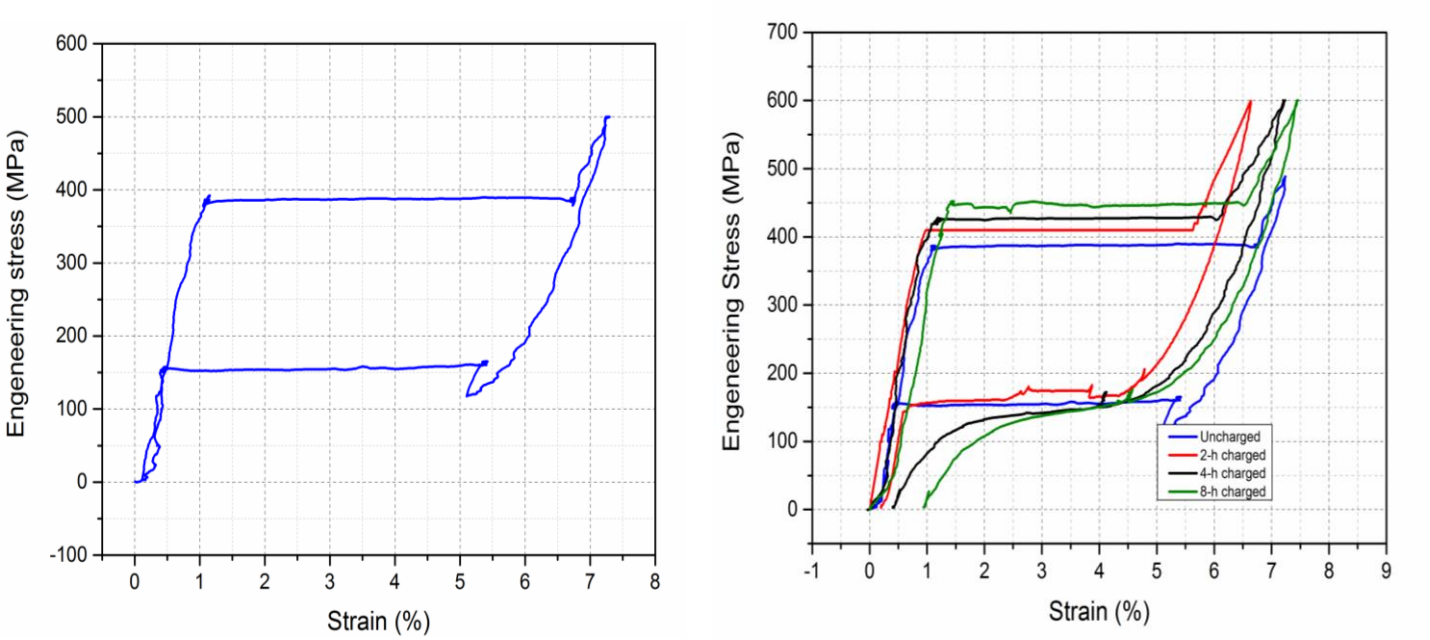

Figure 4. Stress-Strain curve for. a) Virgin specimen. b) After hydrogen charging in 0.9 % NaCl.

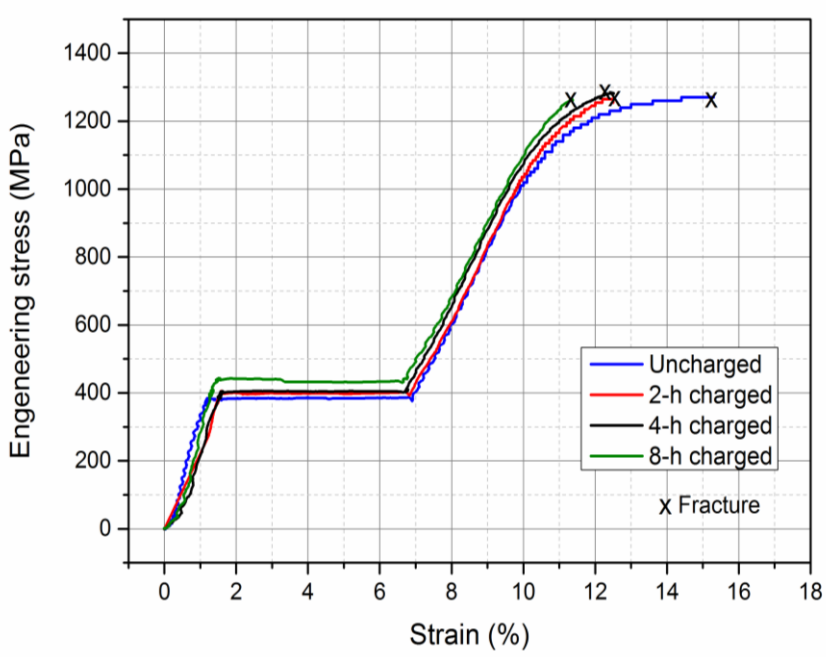

Figure 5. Typical tensile curve of virgin Ni-Ti superelastic alloy and charged for 2, 4 and 8 hours in 0.9 % NaCl.

3.2 Fatigue testing

3.2.1. Self-heating test

To evaluate the fatigue properties of the studied material, a self heating test under uniaxial stress loading is performed and analyzed. The change in temperature variation is measured by the infrared camera. During cycling, the temperature difference between the specimens and the jaws varies during the life of the specimen as presented in **Figure (6)**. In the present study, the temperature rise on the surface of the wire was defined as the difference between the saturation and the initial temperature.

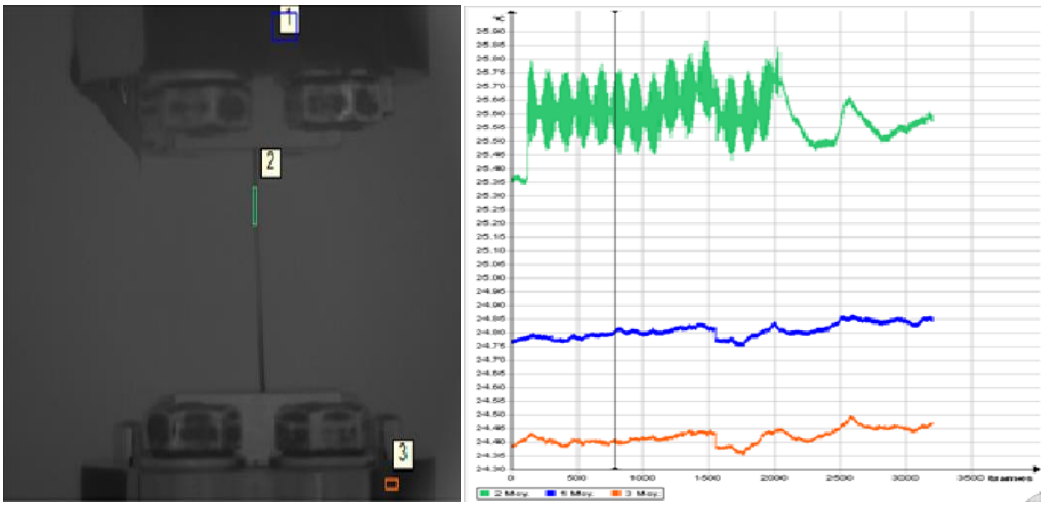

Figure 6. The mean temperature measured by the infrared camera

For each loading level applied, we have determined the evolution of the stabilized mean temperature of the specimen to obtain the self-heating curve for the virgin specimen presented in **Figure (7**). It appeared that below a certain level of loading, the temperature rise is not observed. However, beyond 170 MPa a first regime with low temperatures rises is observed followed by a second regime where the increase of temperature is much marked. An empirical method is applied to predict the endurance limit of virgin specimen. This method is illustrated by the **Figure (7)**: A linear regression is performed on the last points of self-heating curve and the intersection between this line and x axis is evaluated at about 360 MPa.

During the block with the maximal level stress (450 MPa) the NiTi presents a very high temperature increase which is about 8.3 °C. The sudden rise in temperature can be explained by the fact that the fatigue limit of the material has been exceeded giving rise to dissipative mechanisms. These mechanisms correspond to microplasticity in the case of classical metals **[3]**, for Ni-Ti alloys we assume that an additional mechanism occurs which it is associated with the phase transformation.

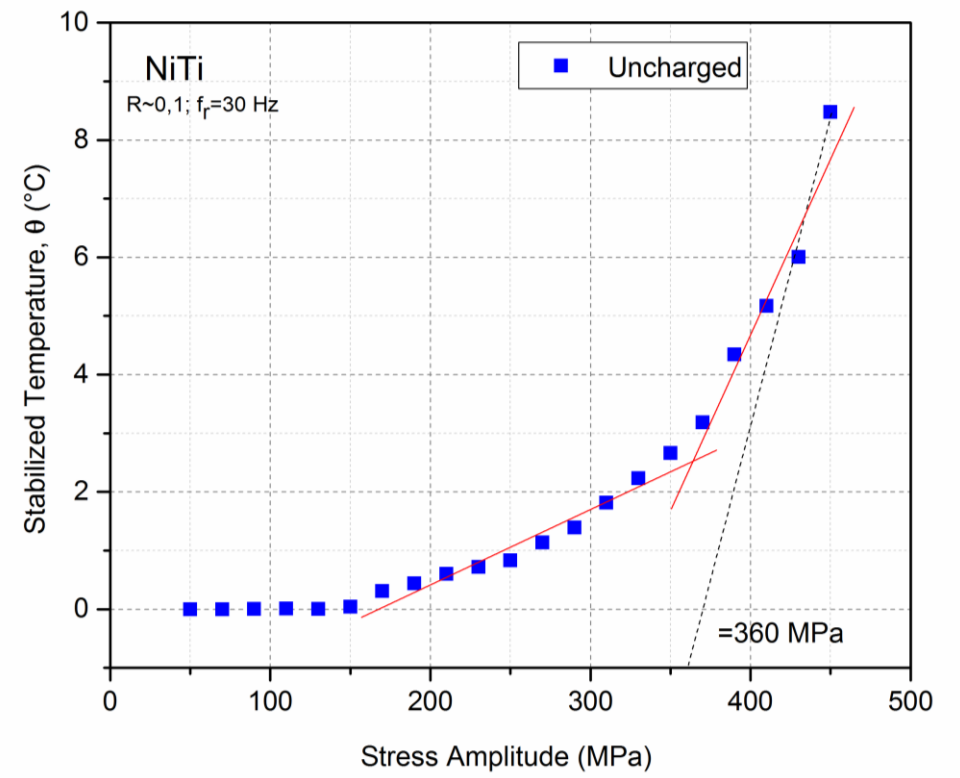

Figure 7. Self-heating curve for virgin specimen and determining the endurance limit

The last point presented on self heating curve **(Figure 7)** is corresponding to the last point before failure. For the virgin specimen, the fracture occurs at a maximum stress applied exceeding 450 MPa. However, for specimens charged with hydrogen the failure occurs earlier with a more pronounced rise of temperature as presented in **Figure (8)**.

After hydrogen charging, the results of self-heating tests show that the increasing time of hydrogen charging is connected with the increasing in the temperature of the specimen and a decreasing in it fatigue life. The same empirical approach has been applied to determine fatigue endurance for charged specimens and the values are summarized in **Table 2**. In the case of uncharged specimen with hydrogen, the endurance limit is about 360 MPa and after 8 hours of charging in is evaluated at about 170 MPa. The difference of fatigue resistance can decrease by 190 MPa.

For the same applied stress, the increase of the temperature in the specimen is a consequence of dissipative process associated with cyclic loadings and the presence of hydrogen. From these observations, we can conclude that the presence of hydrogen amplifies this dissipation and reduces the endurance limit

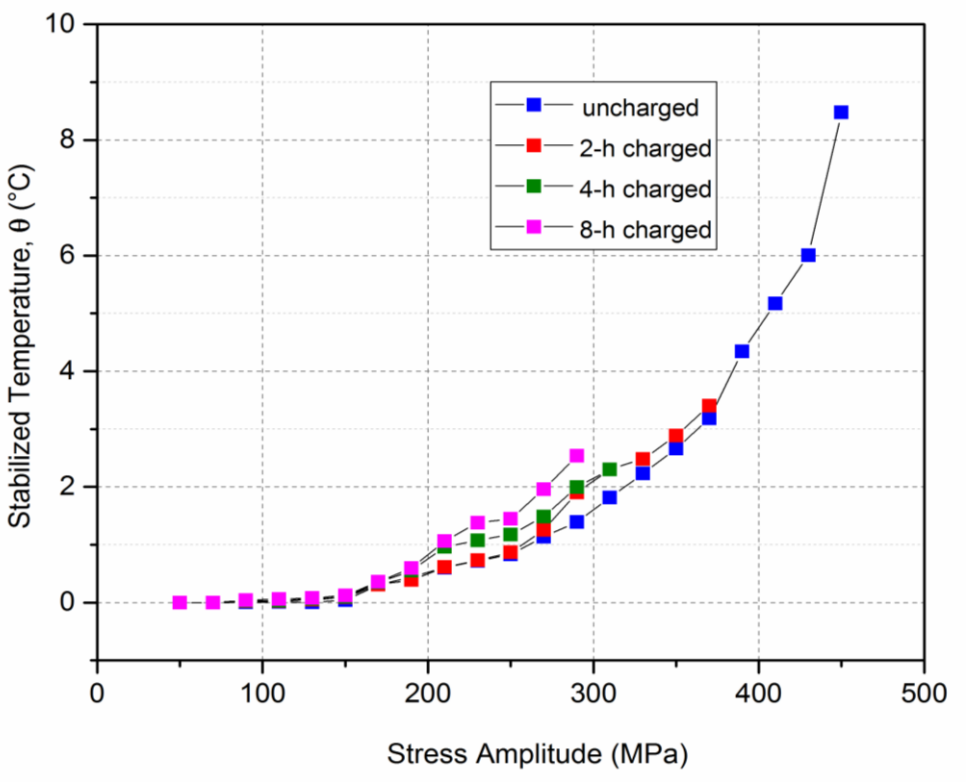

Figure 8. Self-heating curve for charged specimens

Table 2. Prediction of the endurance limit of uncharged and charged NiTi wires

Immersion-time in 0.9 % NaCl	Endurance limit (MPa)
Uncharged	360
2-h charged	220
4-h charged	190
8-h charged	170

Classic fatigue tests will be performed on NiTi wires in the same previous conditions of self-heating test. The experimental classic tests will serve to validate the self-heating approach because one proposal of our study is to make comparison between data obtained with the two different techniques.

3.2.2. Rotating-Bending fatigue tests

The rotational bending test is carried out at ambient temperature. For each wire uncharged or charged with hydrogen, the number of fracture cycles obtained by (BRF) test was recorded as shown in **Figure (9).** In this study, it was proved that for virgin specimens when the deformation applied correspond to the martensitic transformation, the fracture didn't occur. For charged specimens we noticed a decrease of number of cycles with the increasing of immersion time so we can notice that fatigue life decreased and it depends on the absorbed quantity of hydrogen which is relative to the time charging in 0.9 % NaCl. These observations are comparable and have the same trend with some previous works **[5]** dealing with rotational bending fatigue tests of NiTi.

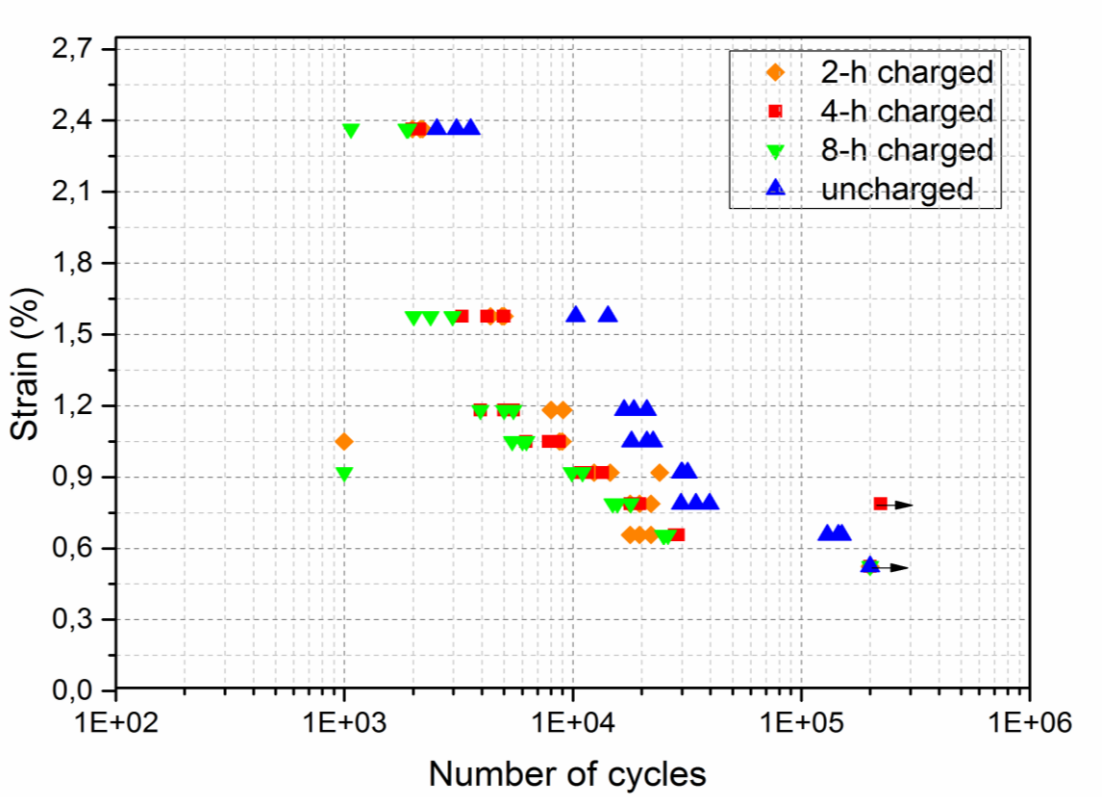

Figure 9. (Strain-N) curve for uncharged and charged specimens in 0.9 % NaCl solution for 2, 4 and 8 hours.

4 CONCLUSION

Self-heating tests under cyclic loadings carried out on NiTi wires allowed a prediction of the endurance limit of virgin and hydrogen charged specimens. This new technique rarely applied to NiTi alloys showed that the fatigue strength decreases significantly with increasing hydrogen content. The rise of temperature observed can be explained by the fact that the

fatigue life of the material exceeded giving dissipative mechanisms which are more important with the presence of hydrogen. A validation of the fatigue parameters obtained by this new technique is necessary with performing conventional fatigue tests to obtain S-N curves.

REFERENCES

[1] K. YOKOYAMA, T. OGAWA, K. ASAOKA, J. SAKAI and M. NAGUMO, Degradation of tensile strength of Ni-Ti superelastic alloy due to hydrogen absorption in methanol solution containing hydrochloric acid. Materials Science and Engineering A 360 (2003): 153-159.

[2] A. SHERIFF, R. PELTON and L. A. PRUITT, Proceeding of ASM Materials & processes for Medical Devices, Conference M (2005):38-43.

[3] C. DOUDAR, S. CALLOCH, F. HILD, P. CUGY and A. GALTIER, A Probabilistic Two-Scale Model for high Cycle Fatigue Life Predictions, Fatigue & Fracture of Engineering Materials & Structures 3 (2005): 279-289

[4] V. LEGRAND, L. SAINT-SULPICE, L. PINO, S. ARBAB CHIRANI, and S. CALLOCH. Fatigue et auto-échauffement sous sollicitation cyclique des alliages à mémoire de forme. Mémoire (2015)

[5] F. GAMAOUN, M. LTAIEF, T. BOURAOUI, and T. BEN ZINEB, Effect of hydrogen on the tensile strength of aged Ni–Ti superelastic alloy. Journal of Intelligent Material. Systems and Structures 22 (2011): 2053–2059.

Shape memory alloy foams: 3D topology reconstitution and numerical analysis of superelastic behaviour

Shijie Zhu [a,*], Céline Bouby [b, c], Abel Cherouat [a], Tarak Ben Zineb [b, c]

[a] ICD/GAMMA3, University of Technology of Troyes, 12 rue Marie-Curie, Troyes 10010, France

[b] LEMTA, UMR 7563, Université de Lorraine, Vandœuvre-lès-Nancy, France
[c] LEMTA, UMR 7563, CNRS, Vandœuvre-lès-Nancy, France

*E-mail addresses: shijie.zhu@utt.fr (S. Zhu), celine.bouby@univ-lorraine.fr (C. Bouby), abel.cherouat@utt.fr (A. Cherouat), tarak.ben-zineb@univ-lorraine.fr (T. Ben Zineb).

ABSTRACT

In this paper, a 3D foam CAD Representative Volume Element (RVE) of porous Ni-Ti shape memory alloy (SMA) is reconstituted using ellipsoid cell units in order to simulate its superelastic behaviour.

The 3D reconstitution process is accomplished by using the “taking” and “placing” algorithm based on uniform distribution and normal distribution ([1]). In the RVE, dimensions, positions and orientations of the ellipsoid cell units are randomly selected.

A constitutive model for shape memory alloy including phase transformation, martensitic reorientation and twins accommodation ([2]) is adopted to simulate the superelastic behaviour of the SMA foam. Numerical simulations are presented to validate the proposed model for foam structures. The obtained results show that the force-displacement or stress-strain responses of the RVE are highly dependent on the foam porosity. The effects of porosity, size, orientation, and ratio of long axis and short axis of cell unit on the superelastic behaviour of SMA foam are studied numerically.

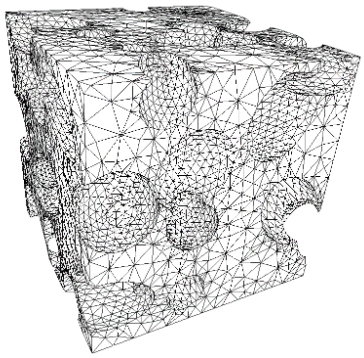

(a) Foam CAD (porosity 50%)

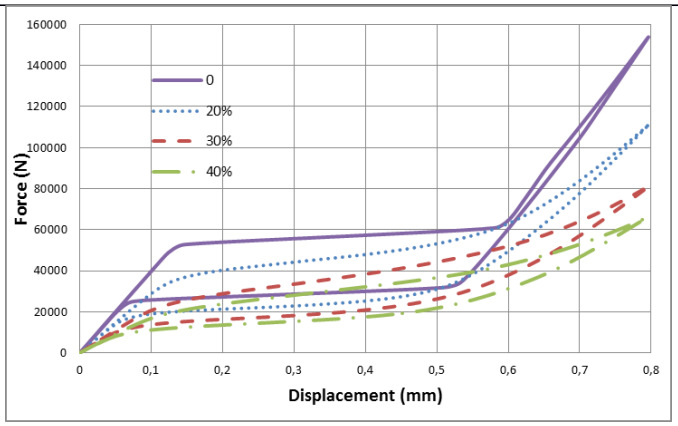

(b) Force-displacement responses for different porosity values

REFERENCES

[1] M. De Giorgi, A. Carofalo, V. Dattoma, R. Nobile, F. Palano, "Aluminium foams structural modelling", *Computers & Structures*, Vol. **88**, pp. 25-35, (2010).

[2] Y. Chemisky, A. Duval, E. Patoor, T. B. Zineb, "Constitutive model for shape memory alloys including phase transformation, martensitic reorientation and twins accommodation", *Mechanics of Materials*, Vol. **43**, pp. 361-376, (2011).

VIIIECCOMAS Thematic Conference on Smart Structures and Materials
SMART 2017
A. Güemes, A. Benjeddou , J. Rodellar and JinsongLeng (Eds)

SIZE EFFECTS IN A SHAPE MEMORY ALLOY ROD CAUSED BY INHOMOGENEITY OF TEMPERATURE AND STRESS FIELDS STUDIED THROUGH SOLVING OF A 1D CONNECTED THERMAL AND MECHANICAL PROBLEM

ALEKSANDR E. VOLKOV[*], ANNA S. KUKHAREVA[†], NATALIA A. VOLKOVA[††], AND YULIYA V. MALKOVA[††]

[*] Saint-Petersburg State University (SPbSU)
Universitetskiy pr.,28, 198504 Saint-Petersburg, Russia
e-mail: a.volkov@spbu.ru

[†]Emperor Alexander I St.-Petersburg State Transport University
Moskovsky pr., 9, 190031 Saint-Petersburg, Russia
e-mail: kukhareva_as@mail.ru

[††] Saint-Petersburg State University (SPbSU)
Universitetskiy pr.,28, 198504 Saint-Petersburg, Russia
e-mail: navolkova@list.ru, y.malkova@spbu.ru

Key words: Shape memory alloy, Transformation plasticity, Boundary-value problem, Finite difference method, Size effect.

Abstract. This work presents the results of numerical solutions of a one-dimensional connected thermal and mechanical boundary-value problem for an infinite shape memory alloy (SMA) cylinder loaded by an axial force heated or cooled from the surface. At present there exist rather few works devoted to solving a boundary-value problem for SMA in a completely connected formulation. This work continues the theoretical study of the transformation plasticity effect at an inhomogeneous temperature field.The constitutive equations of SMA are realized by a microstructural model accounting for the deformations due to elasticity, thermal expansion and phase transformation. The formulation of the boundary-value problem includes the equations for mechanical equilibrium and heat diffusion. The mechanical stress field is caused by the applied force and inhomogeneous unelastic strain fields. The connectivity of the mechanical and thermal problems results from the influence of the stress on the phase transformation and from the release or absorption of the transformation latent heat. It is noted that calculated radial temperature distributions are monotone, while different stress components distributions are non-monotone due to non-simultaneous progress of the phase transformation in near-surface and inner layers of the SMA cylinder. Stress in the local region can two times overtop the mean value. The elongation of a thick SMA rod on cooling due to the transformation plasticity effect is smaller than that of a thin one (the size effect). The elongation also decreases when the cooling rate is increased.

1 INTRODUCTION

Shape memory alloys (SMA) are capable to accumulate on cooling and recover on heating considerable inelastic (phase) deformations and, thanks to such deformation behavior, they find application in various branches of technology and medicine [1-5]. Experiments show that in many prominent SMA, such as TiNi, Ti(NiX) (X = Cu, Fe, Cr, Nb, Pd, Au, Pt), (TiX)Ni (X=Zr, Hf), CuAlNi, CuAlBe, CuAlMn thermoelastic martensitic transformations governing their functional-mechanical properties are controlled uniquely by the temperature and the stress and do not depend directly on time. Since variations of the temperature field in an SMA specimen develop due the heat diffusion, the temperature in general is not homogeneous. The inhomogeneity of the temperature causes the inhomogeneities of the martensitic phase concentration and the inelastic phase deformation, which in turn cause the inhomogeneity of the stress. The phase transformation itself also influences the temperature field due to the release of the latent heat. Thus, the evolution of the phase strain becomes dependent on the ambient temperature rate. The effect of the temperature and stress inhomogeneity grows with the characteristic dimension of the SMA specimen resulting in the so-called size effect. This effect is the reason of the reduction of the transformation plasticity strain accumulated by a specimen on cooling under a stress and, correspondingly, of the strain recovery on heating.

In any case, whena specimen is heated or cooled from the surface and its dimensions are such that the temperature inhomogeneity cannot be neglected, the calculation of the strain demands solving of two boundary-value problems: of the mechanical equilibrium and heat diffusion.The constitutive equations must be able describing the evolution of the phase transformation and the phase strain at arbitrary regimes of variations of stress and temperature including those when stress increase or decrease occurs during monotonic variation of temperature. Macroscopic phenomenological models are most simple and their usein boundary-value problems reduce the computation time allowing to take more nodes in finite difference or finite elements methods. On the other hand such models better describe the SMA behaviour when the stress during cooling or heating remains constant or varies monotonically, which in general is not so. Still, in works [6,7] it was shown that the use of a phenomenological model for constitutive equations and some simplifying assumptions allows obtaining qualitatively correct description of the strain accumulation on cooling and its recovery on heating.

The boundary-value problem can be simplified by neglecting the effect of the latent heat release on the temperature field or/and by neglecting the effect of the stress on the transformation. Without these assumptions the heat diffusion equation and the mechanical equilibrium equations are connected. Available examples concern 1-D problems for an infinite plate, tube or cylinder. In the work [8] there was solved the problem for an SMA sleeve first cooled from the surface to the martensitic state, secondly, expanded an applying of an inner pressure and then heated after having been set on the elastic tube. Thus, the simulation imitated an actual procedure of the preparation and assembling of a thermomechanical coupling. The evolution of the contact pressure was calculated. In the previous work of the authors [9] an attempt was made to simulate the deformation of a cylinder on cooling from the surface. It was shown that it was possible to use a computation time demanding microstructural model describing the functional-mechanical behavior of SMA.

2 BOUNDARY-VALUE PROBLEM

2.1 Formulation of the boundary-value problem

The body under consideration is a circular cylinder of infinite length with radius *b* loaded by an axial force *F* and cooled from the surface. For convenience cylindrical coordinates *r*, θ, *z* are used. Stresses in the cylinder are caused by the external force F_z, inhomogeneous temperature and phase unelasticstrain. For convenience cylindrical coordinates *r*, θ, *z* are used, the axis of the cylinder coinciding with the axis *z*. Because of the axial symmetry of the problem the strain and stress tensors depend only on the radius *r*. Among the components of the displacement vector *u*, nonzero are only $u_r(r)$ and $u_z(z)$, the dependence $u_z(z)$ being linear. With these assumptions nonzero are only the diagonal components $\varepsilon_r(r) = \frac{du_r}{dr}$, $\varepsilon_\theta(r) = \frac{u_r}{r}$, $\varepsilon_z =$ const of the small strain tensor and the diagonal components $\sigma_r(r)$, $\sigma_\theta(r)$, $\sigma_z(r)$ of the Cauchy stress tensor σ (for compactness we write ε_r, ε_θ, ε_z, σ_r, σ_θ, σ_z instead of ε_{rr}, $\varepsilon_{\theta\theta}$, ε_{zz}, σ_{rr}, $\sigma_{\theta\theta}$, σ_{zz}).Further, we assume that the total strain ε can be split into the sum of the elastic ε^e and unelastic *e* strains. Unelastic strain *e* in turn consists of the thermal expansion strain e^{Te} and the phase strain e^{Φ}:

$$\varepsilon = \varepsilon^e + e, \quad e = e^{Te} + e^{\Phi}. \tag{1}$$

For the elastic and thermal expansion strains we use the common Hook's (Duhamel-Neumann) law. Thus, we write:

$$\begin{aligned} \sigma_r &= E_1(\varepsilon_r^e + \nu_1(\varepsilon_\theta^e + \varepsilon_z^e)), \\ \sigma_\theta &= E_1(\varepsilon_\theta^e + \nu_1(\varepsilon_r^e + \varepsilon_z^e)), \\ \sigma_z &= E_1(\varepsilon_z^e + \nu_1(\varepsilon_\theta^e + \varepsilon_r^e)), \\ E_1 &= \frac{E(1-\nu)}{(1+\nu)(1-2\nu)}, \nu_1 = \frac{\nu}{(1-\nu)} \end{aligned} \tag{2}$$

$$e_r^{Te} = e_\theta^{Te} = e_z^{Te} = \alpha(T - T_0) \tag{3}$$

where *E* and ν are the Young's modulus and the Poisson's ratio, α is the heat expansion coefficient and T_0 is the initial temperature. With the assumptions on the symmetry of the problem and on the way of loading the only not reducing to identity mechanical equilibrium equation and the boundary conditions are the following.

$$\frac{d\sigma_r}{dr} + \frac{1}{r}(\sigma_\theta - \sigma_r) = 0 \tag{4}$$

$$\sigma_r|_{r=b} = 0, \quad 2\pi \int_0^b r\sigma_z(r)dr = F_z \tag{5}$$

We assume that the Newton's condition of heat exchange with environment holds. We also take into account the transformation latent heat release. Since the temperature *T* is the function of the radius *r* and time *t*, we have the equation:

$$c\rho \frac{\partial T}{\partial t} = \lambda\left(\frac{\partial^2 T}{\partial r^2} + \frac{1}{r}\frac{\partial T}{\partial r}\right) + W, \tag{6}$$

The initial and boundary conditions are:

$$T(r)|_{t=0} = T_0, \quad -\lambda \frac{\partial T}{\partial r}\Big|_{r=b} = H(T|_{r=b} - T_{\text{amb}}), \quad \frac{\partial T}{\partial r}\Big|_{r=0} = 0 \tag{7}$$

In formulae (5) and (6) c is the specific heat capacity, ρ is the density, T_0 is the initial temperature, λ is the heat conductivity, T_{amb} is the ambient temperature and W is the volume power of the heat sources, which describe the latent heat release. If the specific (per unit of mass) latent heat of the transformation is q_0, then we can state that

$$W = \rho q_0 \dot{\Phi}_M, \tag{8}$$

whereΦ_M is the volume fraction of martensite and a dot above the symbol denotes the time derivative. The last block of equations consists of the constitutive equations describing the evolution of the volume fraction of martensite and of the phase deformation. These equations are taken from the microstructural model described in [10] and they can be schematically written as:

$$\dot{e} = F_1(T, \dot{T}, \sigma, \dot{\sigma}, X), \tag{9}$$

$$\dot{X} = F_2(T, \dot{T}, \sigma, \dot{\sigma}, X) \tag{10}$$

$$X = \left(\Phi_1(1), \dots, \Phi_N(1), \dots, \Phi_1(N_{gr}), \dots, \Phi_N(N_{gr})\right), \tag{11}$$

$$\Phi_M = \frac{1}{N_{gr}} \sum_{\omega=1}^{N_{gr}} \frac{1}{N} \sum_{i=1}^{N} \Phi_i(\omega) \tag{12}$$

where X denotes the set of internal variables, which are the volume fractions $\Phi_i(\omega)$ (i=1,…N), of Bain's martensite variants in each of 1,…,ω,…,N_{gr} grains, comprising the representative volume of the two-phase body. Note that the presence of variable Φ_M in formulae (12) and (8), as well as of e in (9) and (2) makes all the equations connected.

2.2 Algorithm of numerical simulation

From equations (1), (2) and (4) one obtains the Lame's equation for the displacement:

$$\frac{d^2u}{dr^2} + \nu_1 \frac{1}{r}\frac{du}{dr} - \nu_1 \frac{u}{r} = \frac{d}{dr}\left(e_r + \nu_1(e_\theta + e_z)\right) + (1 - \nu_1)\frac{e_\theta - e_r}{r}, \tag{13}$$

where u stands for the radial displacement u_r. If the functions $e_r(r)$, $e_\theta(r)$ and $e_z(r)$ are known, from equation (13) one can find $u(r)$ in the form:

$$u = \left(A_1 + C_1(r)\right)r + \frac{A_2 + C_2(r)}{r},$$

where functions $C_1(r)$ and $C_2(r)$ should be found by the method of variation of constants. Constants A_1, A_2 and ε_z are to be found from the boundary conditions (5) and the condition $A_2 + C_2(r) = 0$, having the meaning that $u(r)$ is bounded at $r = 0$. Knowing $u(r)$ from (1) and (2) one obtains the functions $\sigma_r(r)$, $\sigma_\theta(r)$, $\sigma_z(r)$. Thus, we have an operator $\sigma(r) = M(F, e(r))$, which can be rewritten in the differential form

$$\Delta\sigma(r) = M(\Delta F, \Delta e(r)), \tag{14}$$

where Δ denotes a small increment. Formula (14) allows finding the stress increment $\Delta\sigma(r)$, provided the increments of unelastic strain $\Delta e(r)$ and of the axial force ΔF are known. Note that for the problem under consideration this operator contains only algebraic functions and quadratures, which makes simple its numerical realization.

From equation (6) and conditions (7) we can find the increment of temperature $\Delta T(r)$ corresponding to the time increment Δt, when the function $W(r)$ and the increment of the ambient temperature T_{amb} are known. Numerically this can be done, for example, by finite difference grid method. Thus we have the operator:

$$\Delta T(r) = H(\Delta t, \Delta T_{\text{amb}}, W(r)). \tag{15}$$

The constitutive equations (9) – (12) realize the operator, which we also write in the differential form

$$\Delta \text{e} = F_1(T, \Delta \text{T}, \sigma, \Delta\sigma, X), \tag{16}$$

From (16) we can find the increments of the unelastic strain components.

To solve the nonlinear problem described above we used an iteration procedure which can be illustrated by the following scheme

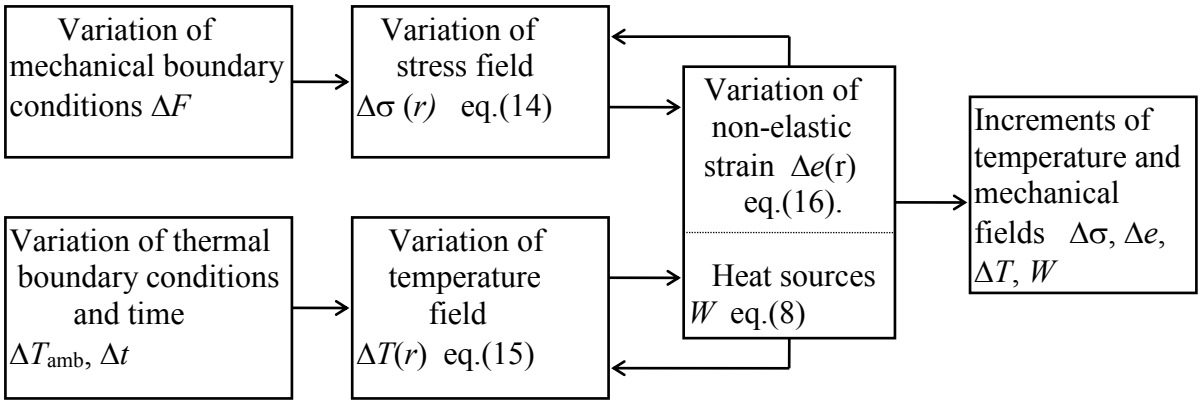

We note that both $\Delta\sigma(r)$ and $\Delta T(r)$ influence the fields of Δe(r) and W so the problem is completely connected. We used an iteration procedure of a relaxation type. Its convergence strongly depended on the choice of the iteration parameters.

3 SIMULATION RESULTS

The simulation was carried out for TiNi SMA with the following characteristics: The transformation temperatures A_f= 365K, A_s = 350K, M_s = 315K, M_f= 300K; Young's modulus E=78GPa; Poisson's ratio ν=0.33; heat conductivity λ=10W·(m·K)$^{-1}$; specific heat c=4.7·10^{2}J·kg^{-1}·K^{-1}; density ρ=6.5·10^{3}kg·m^{-3}; specific latent heat q_0= –23J·g^{-1}; heat expansion coefficients for martensite and austenite α_A=14·10^{-6}K^{-1}, α_M=6·10^{-6}K^{-1}; heat exchange coeffitient with the environment H=10^{4}W·m^{-2}·K^{-1}. Strain increment was calculated with the accuracy ε_e=10^{-8}, and heat release – ε_W=10^{3}J·m^{-3}s^{-1}.

To study the influence of the ambient temperature rate on the effect of the transformation plasticity we chose cylinders with radii 10 mm and 100 mm. Then we simulated cooling

through an interval of the direct martensitic transformation under a constant force corresponding to initial stress of 100 MPa. Four values of the ambient temperature rate were taken: 0.01, 1.0, 10 and 100 $K \cdot s^{-1}$. The ambient temperature was varied from 350 K to 290 K after which followed a time exposure at 290K until the temperature became homogeneous.

Results of calculations have shown that even at a small ambient temperature rate a non-uniform distribution of temperatures over the radius (figure 1a) is observed that leads to non-uniform distribution of a volume fraction of martensite and stress (figures 1b, c, 2).

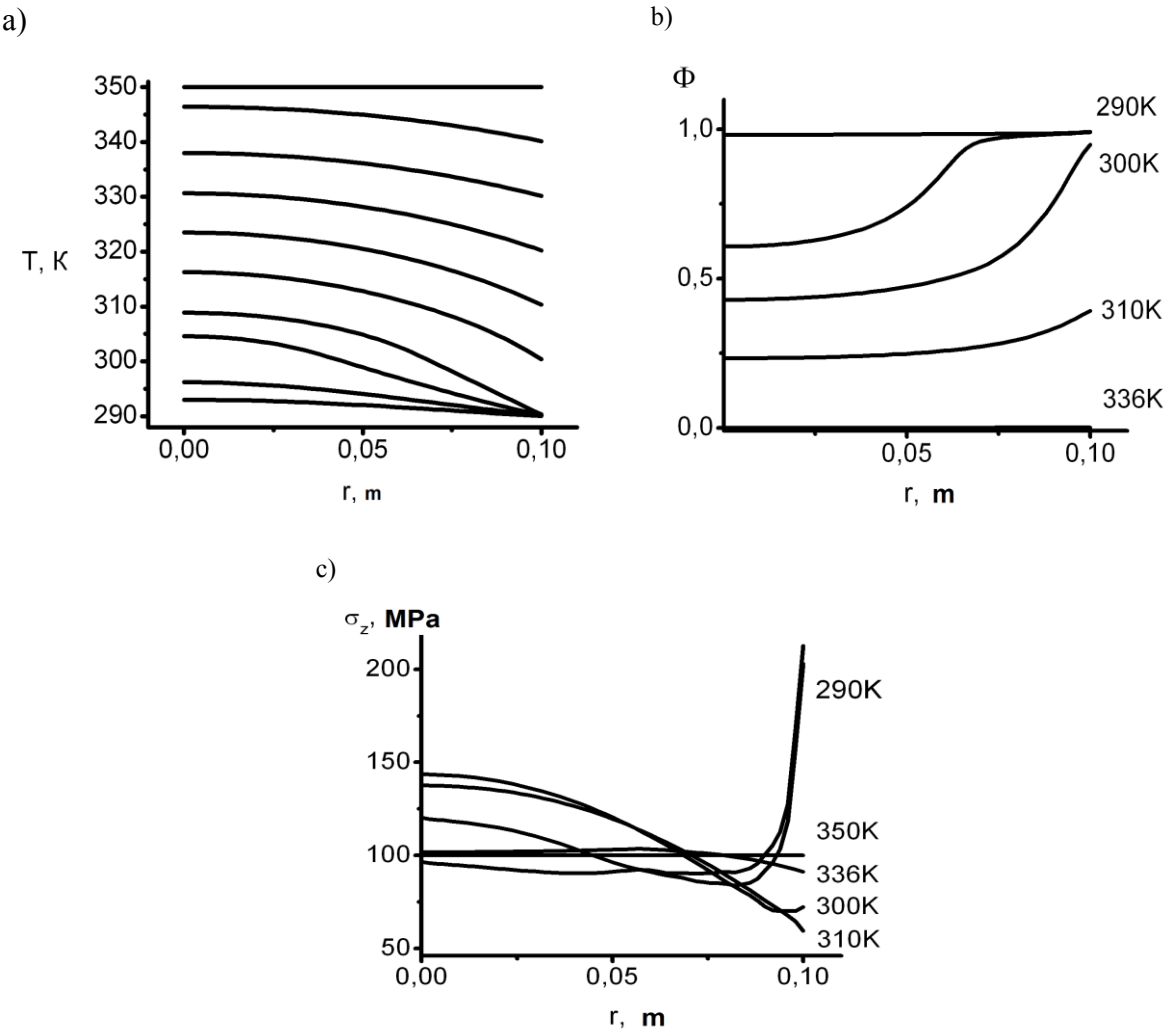

Figure 1: Radial distribution of temperature (a), volume fraction of martensite (b) and normal axial stress (c) in a cylinder with radius 100 mm on variation of the ambient temperature from 350 K to 290 K at a temperature rate 0.01 K/s and a time exposure until homogenization of temperature. Graphs correspond to some consequent time moments. Numbers near the curves indicate at the values of the ambient temperature.

Note that the stress in the outer layers of the cylinder can overtop more than twice the mean value of the stress.

Because of the stress and temperature in homogeneity, the size of the transformation

plasticity effect decreases with an increase of the speed of cooling (figure 3).

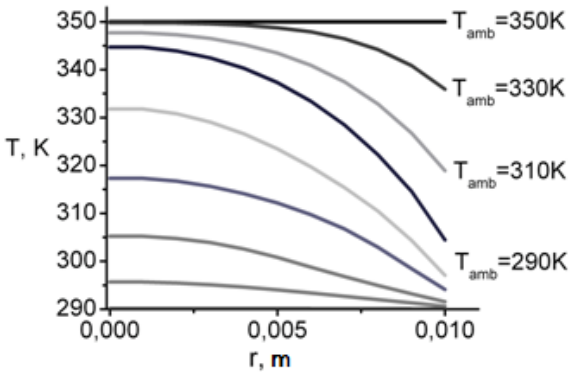

Figure 2: Radial temperature distribution in a cylinder with radius 10 mm on its cooling with the ambient temperature rate -10 K/s. Numbers near curves indicate at the ambient temperature.

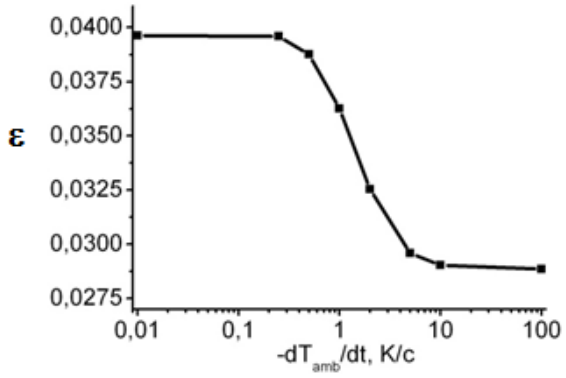

Figure 3: Dependence of the strain accumulated on cooling (transformation plasticity effect) on the ambient temperature rate.

4 CONCLUSIONS

- It is possible to solve a boundary-value problem for an SMA body, with the constitutive equations set by the microstructural model.
- In the conditions of the Newtonian convective heat exchange even at a small ambient temperature rate the radial distribution of temperatures are non-uniform causing non-homogeneous distributions of the volume fraction of martensite and stress. This results in the appearance of the size effect of the transformation plasticity strain, which decreases with an increase in the sizes of a body.
- During the realization of the transformation plasticity effect and upon its termination the spatial heterogeneity of temperature and phase structure leads to formation of areas in which the level of the stress can more than twice exceed its average value.

5 ACKNOWLEDGEMENTS

This work was carried out with the support of the grant by the Russian Foundation of Basic Research (RFBR) 15-01-07657.

REFERENCES

[1] Engineering aspects of shape memory alloys. Ed. by T.W.Duerig, K.N.Melton, D.Stockel and C.M.Wayman, N-Y. 1990. 499p.

[2] Razov A., Cherniavsky A. Application of SMAs in modern spacecraft and devices. *J. de Physique IV* (2003) **112**, N 10, 1173-1176.

[3] RazovA. I. Application of Titanium Nickelide-Based Alloys in Engineering (2004) *The Physics of Metals and Metallography* (ISSN 0031-918X) **97**, Suppl.1. 97-126.

[4] Benafan O., Brown J., Calkins F.T., Kumar P., Stebner A.P., Turner T.L., Vaidyanathan R., Webster, J., Young M.L. Shape memory alloy actuator design: CASMART

collaborative best practices and case studies. *International Journal of Mechanics and Materials in Design*. (2014) **10**, Issue 1, 1- 42.

[5] Jaronie Mohd Jani, Martin Leary, Aleksandar Subic, Mark A. Gibson. A review of shape memory alloy research, applications and opportunities, *Materials&Design*. (2014) **56**, N 4. 1078-1113.

[6] Movchan A.A., Kazarina S. A., Mashikhin A. E., Mishustin I. V., Saganov E. B., Safronov P. A. Boundary value problems of mechanics for shape memory alloys. *Uchenye Zapiski Kazanskogo Universiteta. Seriya Fiziko-Matematicheskie Nauki* (2015) **157**, Book 3, 97–110.

[7] Orlov B.C., TyutyunnikovN.P. Numerical simulation of the forward and reverse reactions in the rods and plates made of a shape memory alloy",*Mekhanika kompozitsionnykh materialov i konstruktsii*(2007)**13**: N 1, 131-140.

[8] V.A. Likhachev, A.I. Razov, A.E. Volkov. "Finite difference simulation of a thermomechanical coupling "*Proc. of the Second Int. Conf. on SMST.*(1997) 335 –340.

[9] A.S. Kukhareva, A.E. Volkov. "Calculation of the stress-strain state of an infinite shape memory alloy cylinder subjected to cooling or heating with different temperature rate",*Mekhanika kompozitsionnykh materialov i konstruktsii* (2009) **15**: N 1, 128–136.

[10] Belyaev F., Evard M., Volkov A., Volkova N. A microstructural model of SMA with microplastic deformation and defects accumulation: Application to thermocyclic loading. *Materials Today: Proceedings 2S* (2015) S583 – S587.

Dexterous in-hand micromanipulation: from trajectories planning to experimental validation

Jean-Antoine SEON, Redwan DAHMOUCHE, Michaël GAUTHIER

***Abstract*— Micro-manipulation and micro-assembly techniques play today a key role in the development of new integrated smart systems that can find applications in strategic fields such as transport, telecommunication, health and defense. However, the existing micro-handling solutions lack of speed, flexibility and autonomy which represents an obstacle to the development of these technologies. Our approach consist in developing local micro-manipulation techniques using dexterous micro-hands. This paper focuses on the trajectory generation of a dexterous micro-hand to achieve automated repositioning and shows major differences between macro-hand and micro-hand. The first simulation results show that original trajectories, able to perform dexterous micro-manipulation in presence of adhesion forces, can be generated in about a second.**

I. INTRODUCTION

Robots manipulators at the macro-scale have different designs depending on the location of the actuated joints: i) a robotic arm with a sufficient number of Degrees of Freedom (DOF) and a basic gripper; ii) a basic arm with a dexterous hand or; iii) a redundant arm and a dexterous hand. At this scale, the most common industrial architecture is the first one. Using dexterous hands usually aims at improving the versatility and the accuracy of the robot [1] and tries to approach the human dexterity [2] [3].

Contrary to the macro-scale, micro-manipulations are usually limited to simple pick and place operations [4] [5]. Accurate multi-axes rotational positioning of micro-objects is particularly difficult to obtain which limits the possible micro-assembly operations [6] [7] [8]. Since it is not trivial to obtain multi-DOF arms able to perform rotations at the micro-scale, we are proposing to use a basic arm (translation micro-stages for instance) and a dexterous hand composed of translating fingers [9] [10].

Another characteristic related to manipulation at the micro-scale is the presence of surface forces which predominate gravitational and inertial forces. These sticky forces, caused by Van der Waals, electrostatic and capillarity forces, have been considered by the micro-robotics community for more than a decade as perturbation forces and tried to get rid of them. Indeed, the manipulated micro-objects stick to substrate during the grasping (a high pull-off force has to be applied) and stick to the gripper during the release [11]. As these forces make the automation difficult, micro-manipulation operations are often done manually [12]. This solution is usually not satisfactory as the number of micro-system units to produce is usually huge.

Contrary to various approaches that try to minimize this effect in order to fallback to dexterous manipulation at the macro-scale [13] [14], we propose in this paper to exploit these adhesion forces that can contribute to the stability of the object during the manipulation. Indeed, previous experiments have shown that a single finger can be sufficient to have a stable grasp (Fig.1).

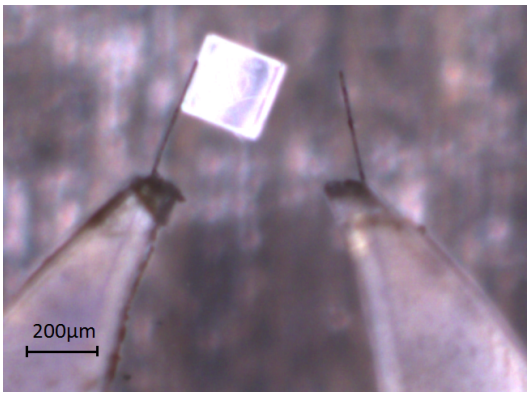

Fig. 1: Illustration of the adhesion effect: only one finger is required to have a stable grasp

As the dominant forces and the application of dexterous robotic manipulation are different at the micro-scale compared to the macro-scale, these differences have to be taken into account to develop feasible and successful dexterous micro-manipulation. The main contribution of this paper is the study of the impact of adhesion forces on grasping micro-objects and the development of a trajectory planner for in-hand dexterous micro-manipulation where original fingers trajectories are proposed.

The next Section gives an overview of the in-hand micro-manipulation problem while Section III gives a general formalization of this problem. Section IV details our methodology to compute stable grasps and generate trajectories. Finally, Section V presents some trajectories for three fingers manipulation with and without adhesion in the case of planar objects.

II. PROBLEM DEFINITION

In-hand manipulation refers to the ability to manipulate an object, in translation or in rotation, with multiple fingers. At the macro-scale in-hand manipulations can be achieved in different ways: by rolling [15], sliding [16] or finger gaiting

The authors are with FEMTO-ST Institute, AS2M department, Université de Franche-Comté/CNRS/ENSMM/UTBM, 24 rue Savary, 25000 Besançon, France.

Corresponding author: ja.seon@femto-st.fr

[17]. Conversely, in-hand micro-manipulation are way more difficult to realize. For instance, controlled slip at micro-scale may be very complicated because of the importance of tactile sensing for such manipulations. Thus, we choose to restrict in-hand micro-manipulation in this paper to rotations performed using rolling without sliding and finger gaiting.

Furthermore, macro-manipulation is largely focused on designing anthropomorphic hands and on the grasping problematic. Thus, macro-hands must be very versatile in order to grasp quickly unknown objects contrary to the micro-hands which can be designed to manipulate well known rigid objects. Indeed, we assume that, in micro-assembly, components are fully characterized and the objective is to correctly orientate and position the different rigid parts to successfully realize the assembly. Thus, we choose to generate trajectories for well known rigid micro-objects.

Moreover, as the inertial forces are negligible compared to the adhesion forces at micro-scale, it is possible to consider the micro-manipulation process under a quasi-static assumption. Thus, the manipulation process is a succession of stable states.

Finally, physics of the micro-scale induce two problematic for the manipulation process. The first one is that adhesion forces can be viewed as a stabilizing effect on the grasping part. The second one concerns the finger gaiting problem as, to perform high amplitude rotations, finger reconfigurations may occurs. However, at micro-scale, removing a finger requires to apply a pull-off force which may disturb the grasp.

III. Modeling and Background

As this article emphasis on the differences between macro and micro-manipulation, firstly we are going to show how the formalization of manipulation is impacted when considering adhesion forces.

A. Grasping Forces

Let us consider the general case of six DOF manipulation using N fingers. In order to manipulate the object, fingers must exert a grasping force on the object surface. The most common modeling of the contact forces at the macro-scale is the *Coulomb law*. This means that, as far as the contact force lies in a three dimensions cone there is no slippage:

$$\sqrt{f_{t_1}^2 + f_{t_2}^2} \leq \mu f_n \tag{1}$$

where f_{t_1} and f_{t_2} are tangential component of the force, f_n is the normal component parameter andμ is the friction coefficient.

Furthermore, in the case of micro-manipulation, this contact law is slightly modified. Indeed, adhesion is a stabilization factor and has an impact on the friction cone. Let us consider that the adhesion force between a finger and the object is f_{po}. Then, the Coulomb law can be rewritten as follows:

$$\sqrt{f_{t_1}^2 + f_{t_2}^2} \leq \mu(f_n + f_{po}) \tag{2}$$

The adhesion force moves the friction cone as depicted in Fig.2. Thus, contrary to the macro-scale, where only positive grasping forces can be applied (push the object), at micro-scale, it is possible to apply negatives grasping forces (pull the object) as long as the force lies in the modified friction cone.

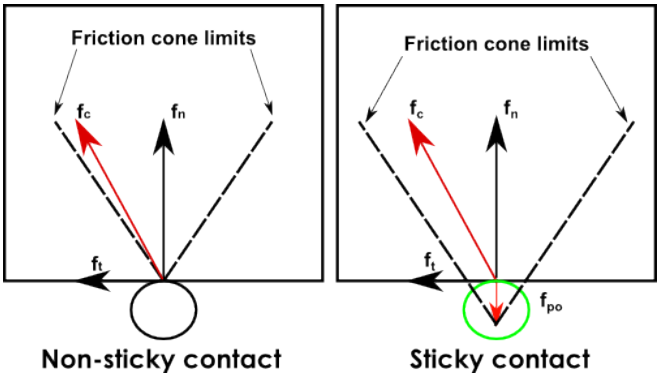

Fig. 2: Side view illustrating the impact of adhesion on the friction cone.

B. Equilibrium

When N fingers grasp an object, all the contact forces must be balanced in order to put the object at equilibrium. Thus, the following equation must be satisfied:

$$-w_{ext} = G.f_c = \sum_{i=1}^{N} w_{c_i} \tag{3}$$

where w_{ext} is the external wrench (force and moment) applied on the object (for example the weight), the matrix $G \in \Re^{6\times 3N}$ is called the grasp matrix [18] which depends on the contact position, $f_c \in \Re^{3N}$ is the vector containing the N grasping forces and $w_{c_i} \in \Re^6$ is the ith grasping wrench.

The equilibrium problem is then equivalent to finding a set of forces f_c verifying Eq.3 with the non-slippage constraint defined by Eq.2. These constraints can be used to rewrite the equilibrium problem considering the limits of the friction cones. Indeed, in the case of six DOF manipulation, the resulting wrench applied on the ith contact is a linear combination of j wrenches that approximate the three dimensions cone:

$$\begin{cases} w_{c_i} = \sum_j \alpha_{i,j}.w_{l_{i,j}} + \beta_i.w_{po_i} \\ \alpha_{i,j} \geq 0 \\ \beta_i \geq 0 \end{cases} \tag{4}$$

where $w_{l_{i,j}}$ is one wrench that approximate the ith friction cone, w_{po_i} the wrench induce by adhesion forces, and $\alpha_{i,j}$ and β_i coefficients which must be positives to stay inside the friction cone. In the case particular case of macro-manipulation, w_{po_i} is equal to zero. Then, the equilibrium problem for N fingers can be rewritten as a function of the N friction cones:

$$-w_{ext} = \sum_{i=1}^{N} w_{c_i} = \sum_{i=1}^{N} \left(\sum_j \alpha_{i,j}.w_{l_{i,j}} + \beta_i.w_{po_i} \right) \tag{5}$$

Thus, the equilibrium problem is equivalent to find a set of $(\alpha_{i,j}, \beta_i)$ positive (not all of them null) verifying the previous equation.

Since inertial forces are negligible, the sufficient condition to perform stable micro-manipulation is that the manipulated object must be at the equilibrium at each step of the manipulation sequence.

Moreover, the reconfiguration problem is similar to the equilibrium problem. Indeed, to remove a finger the remaining contact must resist the external pull-off force f_{po} applied on the removing contact. This means that reconfiguration problem is equivalent to finding f_c such that

$$-w_{ext} - w_{po} = G.f_c \tag{6}$$

where w_{po} is the wrench induced by the release of one of the contacts. Obviously in this case the matrix G is in $\Re^{6\times 3(N-1)}$ and f_c in $\Re^{3(N-1)}$ and this problem can also be expressed as function of the friction cones.

IV. Dexterous Manipulation with Adhesion Forces

As stated in the previous section, we assume that the manipulated objects are well known, and the computing of all the contact configurations which verify equilibrium is thus possible. Consequently, equilibrium positions are going to be the starting point of our trajectory planning which consist in navigating between stable configurations from an initial position to a final position. Then, the trajectory planner defines the finger trajectories required to rotate along a defined angle, starting from the initial configuration.

A. Equilibrium and Reconfiguration Maps

In the case of neglected external perturbation ($w_{ext} = 0$), one way to verify if a configuration of N contacts can verify equilibrium, is to test if the convex hull formed by the friction cones wrenches ($w_{l_{i,j}}$) contains the origin of the wrench space [19]. Thus, when external perturbations are considered the existence of a solution is equivalent to testing if the convex hull contains the external wrench.

Then, it is possible to create several sets (maps) which depict all the equilibrium configuration with regards to the number of contacts:

$$M_k = \Big\{ (c_1,..,c_k) \in \Re^{(3\times k)} \mid -w_{ext} \in Convhull\left(w_{l_{1,1}},...,w_{l_{k,j}}\right) \Big\} \tag{7}$$

where k is the number of contacts, c_k is a vector containing the contact coordinates on the object surface and $Convhull(w_{l_{1,1}},...,w_{l_{k,j}})$ represent the convex hull.

Figure 3 gives a representation of one of the M_k sets in the case of a planar circle without external perturbations. Contact position are sorted using curvilinear abscissa. The depicted areas represent the equilibrium configurations in the case of a two fingers grasp without any adhesion forces at the contact. Obviously such type of sets are symmetric.

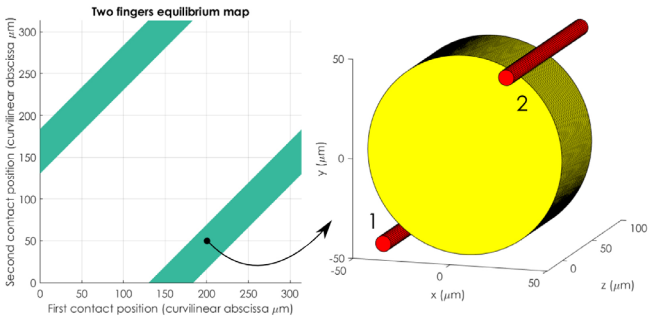

Fig. 3: Representation of the set M_2 (equilibrium map) for a circle, without considering adhesion forces (non-sticky behavior, $\forall i, w_{po_i} = 0$)

Furthermore, when finger gaiting is required another map is needed: the reconfiguration map. This set is directly related to the ability to remove a finger from the object. Consider a N fingers grasp on which the last finger must be removed and note w_{po} the resulting wrench induced by the adhesion forces. This configuration is said reconfigurable when w_{po} is included in the convex hull formed by the friction cones' wrenches of the $N-1$ remaining contacts. This can be formalized as follows:

$$D_k = \Big\{ (c_1,..,c_k) \in \Re^{(3\times k)} \mid (c_1,..,c_{k-1}) \in M_{k-1}, -w_{po,k} \in Convhull\left(w_{l_{1,1}},...,w_{l_{k-1,j}}\right) \Big\} \tag{8}$$

For each M_k ($k > 1$), it is possible to define a corresponding D_k. Figure 4 (left) shows all the reconfiguration positions for a defined third contact location in the case of a three fingers grasp. A non-reconfigurable position is also represented in Fig.4 (right). In this particular case, the stability cannot be ensure so this configuration cannot be used for manipulation.

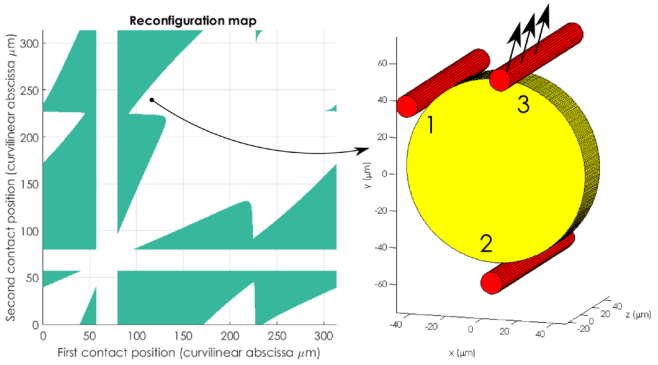

Fig. 4: Representation of the set D_3 (reconfiguration map) for an assigned location of the third contact considering adhesion (sticky behavior, $\forall i, w_{po_i} \neq 0$).

B. Trajectory Generation

1) Representation: All the M_k and D_k maps can be seen as graph where every equilibrium position is a node. The goal is to move in and between the different maps to realize

the desired movement. More particularly, navigating through a M_k map is considered as a direct manipulation of the object whereas navigating between two sets M_i and M_j is considered as finger gaiting. In this case, the reconfiguration map D_k are also part of the graph. Each node in D_k is specifically used to link two adjacent sets (M_k and M_{k-1}) when a finger is removed. Moreover, as adhesion does not perturb the grasp when adding a finger, the link between M_k and M_{k+1} is direct.

Thus, the initial configuration is represented as a specific node in one of the maps. Moreover, as only rolling is considered, the in-hand manipulation can be seen as the required rolling distance to perform the desired rotation. Hence, the goal node is not unique and we need to define the optimal trajectory.

2) Navigation: In order to plan our trajectory we must define the way to navigate in the different maps. In the case of manipulation through rolling, a node in M_k is not connected to all the neighboring nodes (also in M_k). Indeed, in order to manipulate an object with N contacts using rolling without sliding, it is required that all fingers roll of the same amount and in the same direction on the object surface. Consequently, the rolling constraint induces a unique available path in a M_k map (depending on the radius of the fingers). Thus, each node in M_k has only two neighbors in the same map.

Then, when navigating between maps two cases can occur: adding a finger or removing a finger. When adding a finger, which is equivalent to switching from M_k to M_{k+1}, the current node is connected to all the configurations with an extra contact included in M_{k+1}. When removing a finger, the current node, using k fingers, is connected to all the configurations composed with $k-1$ fingers and with the current node included in D_k.

3) Algorithm: One popular way to search through a graph is the A^* algorithm. This heuristic graph search algorithm provides complete and optimal path between the initial and the goal node. A^* has been used in micro-manipulation [20] and also in micro-assembly [21] but based on our knowledge it has not been used for planning in hand manipulations. We chose to implement an A^* algorithm for our trajectory planner in order to obtain optimal solutions.

An important part of the graph search is the cost function used to connect two nodes. Considering the way we can navigate through the graph, we define three cost functions corresponding to the three possible actions: rolling, adding a finger and removing a finger.

For the first case (rolling), the cost function is defined as the rolling distance needed to go from the current node to the next one. This distance is the arc length between two positions on the object surface and is noted $L_r(Node(i), Node(f))$.

When adding a finger, the cost function can take two values: (i) if the finger has not been used previously, then the cost function will be a non zero constant C_a. This value allows to estimate the traveled distance from the previous position to the new one. (ii) if the finger has been used previously, then the cost function will be an estimation of the distance between the last contact position and the new one ($L_r(Node(prev), Node(new))$ plus C_{a_r} a non zero constant).

Moreover, A^* algorithm requires defining an admissible heuristic. As the in hand manipulation is a rotation it is possible to define the heuristic as the remaining rotation from the current node. Moreover, as rolling is used to rotate the object it is also possible to define the heuristic as a distance. Indeed, consider that the finger used for the manipulation has a radius r_d and that rot is the rotation amplitude in radians. Then, at the initial node, the heuristic will be $d_{rot} = r_d \times rot$. Obviously this heuristic never overestimates the distance to the goal so it is an admissible heuristic.

V. Results

The methodology presented in the previous section has been implemented and tested to generate trajectories for planar objects. Moreover, in micro-assembly most of the objects made in micro-fabrication are planar objects so the results presented here are still interesting in the application framework.

A. Impact of Adhesion on Equilibrium and Reconfiguration Maps

First of all, we are going to show the effect of the adhesion forces on the maps (M_k and D_k) used for the trajectory generation. As an example, we consider the M_2 map described in Fig.5 to show the impact of adhesion on the equilibrium configurations. Note that this map correspond to the object depicted in Fig.7

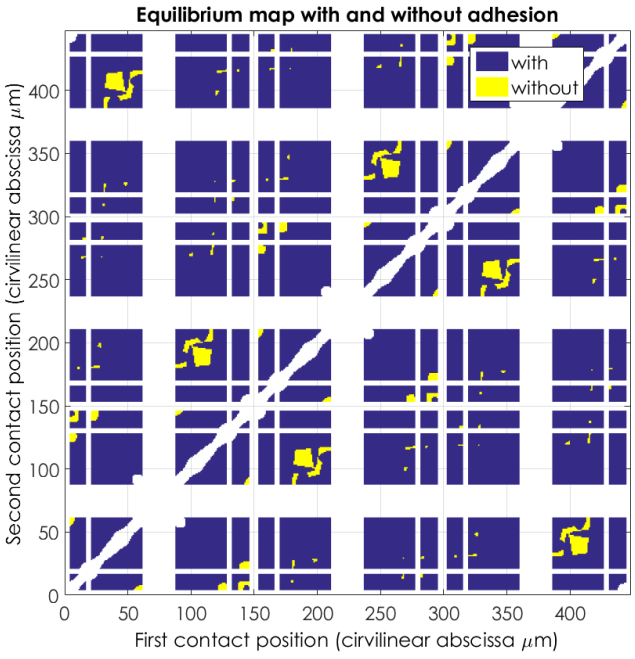

Fig. 5: Representation of the set M_2 (equilibrium map) with and without adhesion for an arbitrary shaped object depicted in Fig.7.

Figures 5 shows the stabilizing effect of the adhesion on an arbitrary shaped object. For this example, we used uniform friction value on the surface ($\mu = 0.3$), an adhesion force of 1 μN, a neglected external wrench and fingers with a radius of 3.5 μm. The yellow areas correspond to the contact configurations where it is possible to obtain equilibrium without adhesion. As predicted, the area is significantly bigger when adhesion is considered. This means that there is more possibility to manipulate the object when adhesion is used.

Moreover, Fig.6 shows the reconfiguration nodes for a defined removed finger. It can be seen that, without adhesion, all the stable configurations with two fingers are also admissible reconfiguration nodes. In contrast, with adhesion, there is fewer reconfigurations positions compared to the stable configurations. Thus, with adhesion, more trajectories are available in a defined M_k map (Fig.5) but reconfiguration are a limiting factor.

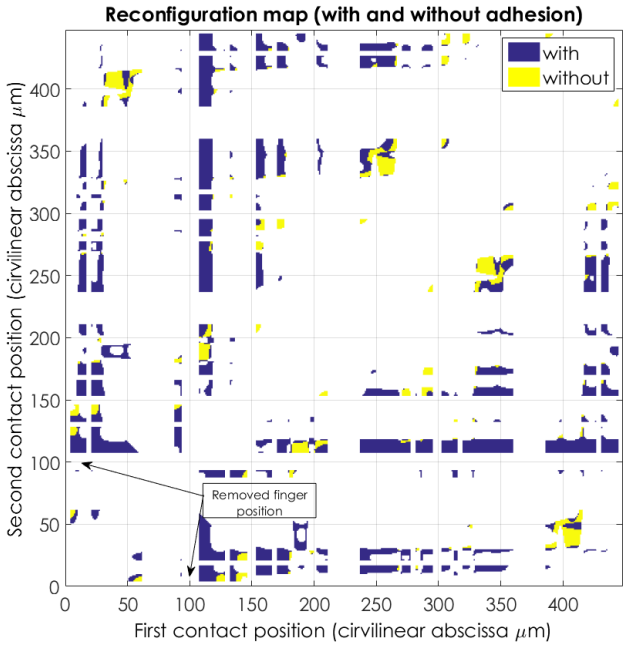

Fig. 6: Representation of the set D_3 (reconfiguration map) with and without adhesion on a an arbitrary shaped object depicted in Fig.7.

B. Impact of Adhesion on Trajectory Generation

We consider the case of an in hand manipulation with a maximum of three fingers. This means that the nodes are represented by M_1, M_2, M_3 for manipulation and D_2 and D_3 for reconfiguration. All the following results have been generated using the same parameters presented in the previous section.

Figure 7 illustrates the computed trajectory for a 130° rotation with adhesion. As shown by Fig.7a, the initial configuration is a grasp with only two fingers. From this configuration, the optimal path to realize the rotation is a two fingers manipulation.

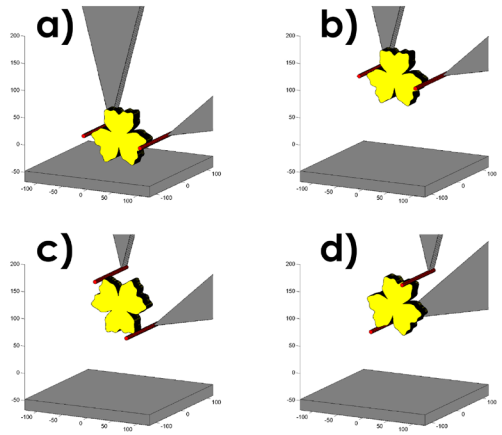

Fig. 7: Images sequence describing the clockwise trajectory generated by the planner for a 130° rotation considering adhesion phenomena.

Figure 8 shows a trajectory for the same rotation but without considering the adhesion phenomena. It can be seen that for the same rotation amplitude the manipulation sequence is more complex in this case. Indeed, three fingers are required and finger gaiting step occurs because of the friction limits.

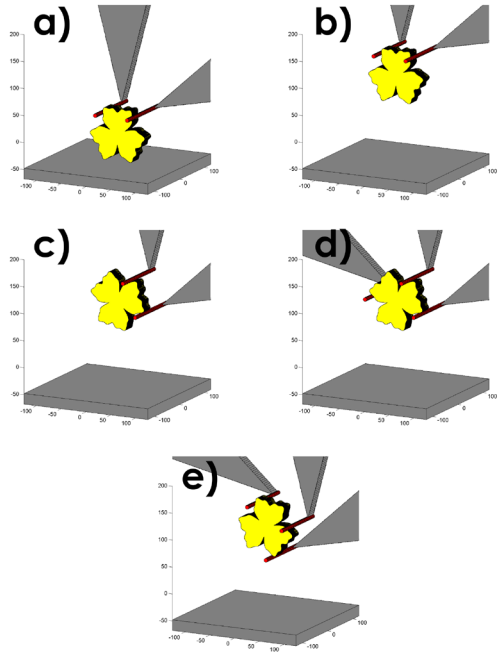

Fig. 8: Images sequence describing the clockwise trajectory generated by the planner for a 130° rotation without considering adhesion phenomena.

The previous trajectories seem to show that with adhesion the manipulation process is faster. A statistical analysis has been performed to confirm this impression. For each case (with and without adhesion) 250 trajectories were generated

and the cost of each trajectory were computed. This cost, based on the cost function and on the heuristic described in the previous section, estimate the traveled distance by the finger during the manipulation.

Figure 9 shows this statistical results for the arbitrary shaped object. For each rotation amplitude it can be seen that the manipulation process is always faster when considering adhesion phenomena. Thus, taking advantage of adhesion effects have a positive impact on the manipulation process.

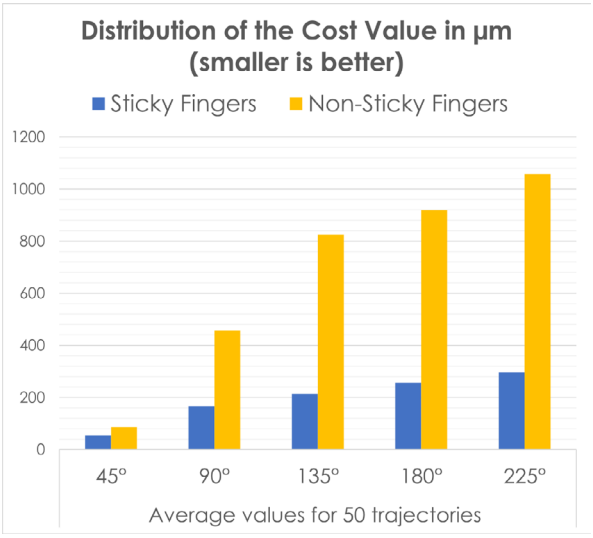

Fig. 9: Chart representing the distribution of the trajectory cost value for various rotation amplitudes and condition of use. For each rotation amplitude and each case fifty rotations were generated.

VI. Conclusion

In this paper, a trajectory planner for dexterous micro-manipulation taking into account adhesion forces was presented. This planner is based on a A^* algorithm in order to generate optimal trajectories (relative to cost functions) and take into account the specificity of the micro-scale: the adhesion phenomena.

Our planner was validated in simulation considering different conditions of use. The results show that in-hand micro-manipulation is significantly different than macro-manipulation. Thus, original trajectories were generated. Adhesion phenomena cannot be neglected and we showed that it can be useful in the manipulation process. Moreover, even if the adhesion is not fully predictable this planner can be used to generate trajectory in the worst cases (*i.e* considering grasping without adhesion and considering reconfiguration with adhesion).

The next step of this work will involve optimization of the contact forces on the generated trajectory and implementation of these new trajectories on an experimental micro-manipulation setup developed in our laboratory [22]. In addition, as the problem was formalized for three dimensions in-hand micro-manipulation, the current planner will be extended to non-planar objects and manipulations.

Acknowledgment

This work was supported by ACTION, the French ANR Labex no. "ANR-11-LABX-01-01" (`http://www.labex-action.fr`), by the Equipex ROBOTEX project (contract "ANR-10-EQPX-44-01") and by the Conseil Régional de Franche-Comté.

References

[1] R. R. Ma and A. M. Dollar, "On dexterity and dexterous manipulation," in *15th International Conference on Advanced Robotics (ICAR)*. IEEE, 2011, pp. 1–7.

[2] K. Koganezawa and A. Ito, "Artificial hand with stiffness adjuster," in *International Conference on Intelligent Robots and Systems (IROS)*. IEEE, 2014, pp. 21–27.

[3] J.-P. Saut, "Planification de mouvement pour la manipulation dextre d'objets rigides," Ph.D. dissertation, Université Pierre et Marie Curie-Paris VI, 2007.

[4] H. Xie and S. Régnier, "Three-dimensional automated micromanipulation using a nanotip gripper with multi-feedback," *Journal of Micromechanics and Microengineering*, vol. 19, no. 7, p. 075009, 2009.

[5] H. K. Chu, J. K. Mills, and W. L. Cleghorn, "Dual-arm micromanipulation and handling of objects through visual images," in *International Conference on Mechatronics and Automation (ICMA)*. IEEE, 2012, pp. 813–818.

[6] K. Rabenorosoa, C. Clevy, P. Lutz, A. N. Das, R. Murthy, and D. Popa, "Precise motion control of a piezoelectric microgripper for microspectrometer assembly," in *International Design Engineering Technical Conferences and Computers and Information in Engineering Conference*. American Society of Mechanical Engineers, 2009, pp. 769–776.

[7] M. Gauthier and S. Régnier, *Robotic micro-assembly*. John Wiley & Sons, 2011.

[8] J. T. Feddema, P. Xavier, and R. Brown, "Micro-assembly planning with van der waals force," *Journal of Micromechatronics*, vol. 1, no. 2, pp. 139–153, 2001.

[9] Q. Zhou, P. Korhonen, J. Laitinen, and S. Sjövall, "Automatic dextrous microhandling based on a 6-dof microgripper," *Journal of Micromechatronics*, vol. 3, no. 3, pp. 359–387, 2006.

[10] K. Inoue, T. Tanikawa, and T. Arai, "Micro hand with two rotational fingers and manipulation of small objects by teleoperation," in *International Symposium on Micro-NanoMechatronics and Human Science*. IEEE, 2008, pp. 97–102.

[11] N. Chaillet and S. Régnier, *Microrobotics for micromanipulation*. John Wiley & Sons, 2010.

[12] A. G. Banerjee and S. K. Gupta, "Research in automated planning and control for micromanipulation," *Transactions on Automation Science and Engineering*, vol. 10, no. 3, pp. 485–495, 2013.

[13] M. Savia and H. N. Koivo, "Contact micromanipulationsurvey of strategies," *Transactions on Mechatronics*, vol. 14, no. 4, pp. 504–514, 2009.

[14] J. Dejeu, M. Bechelany, P. Rougeot, L. Philippe, and M. Gauthier, "Adhesion control for micro-and nanomanipulation," *ACS nano*, vol. 5, no. 6, pp. 4648–4657, 2011.

[15] A. Bicchi and R. Sorrentino, "Dexterous manipulation through rolling," in *International Conference on Robotics and Automation*, vol. 1. IEEE, 1995, pp. 452–457.

[16] D. L. Brock, "Enhancing the dexterity of a robot hand using controlled slip," in *International Conference on Robotics and Automation*. IEEE, 1988, pp. 249–251.

[17] S. R. Leveroni, "Grasp gaits for planar object manipulation," Ph.D. dissertation, Massachusetts Institute of Technology, 1997.

[18] A. Bicchi, "On the closure properties of robotic grasping," *The International Journal of Robotics Research*, vol. 14, no. 4, pp. 319–334, 1995.

[19] J. Ponce and B. Faverjon, "On computing three-finger force-closure grasps of polygonal objects," *Transactions on Robotics and Automation*, vol. 11, no. 6, pp. 868–881, 1995.

[20] Y. Wu, D. Sun, and W. Huang, "Force and motion analysis for automated cell transportation with optical tweezers," in *9th World Congress on Intelligent Control and Automation (WCICA)*. IEEE, 2011, pp. 839–843.

[21] D. J. Cappelleri, M. Fatovic, and U. Shah, "Caging micromanipulation for automated microassembly," in *International Conference on Robotics and Automation (ICRA)*. IEEE, 2011, pp. 3145–3150.

[22] B. Brazey, R. Dahmouche, J.-A. Seon, and M. Gauthier, "Experimental validation of in-hand planar orientation and translation at microscale," *Intelligent Service Robotics, Special Issue on Multi-scale Manipulation Toward Robotic Manufacturing Technologies*, 2015.

Hybrid force-position control of the robotic hand prosthesis ProMain-I

Astrid Rubiano *, Jose L. Ramirez † and Laurent Gallimard‡

* Facultad de Ingeniería
Universidad Militar Nueva Granada
Cr 11 No 101 – 80 Bogotá D.C., Colombia
Email: astrid.rubiano@unimilitar.edu.co, web page: http://www.umng.edu.co

† Facultad de Ingeniería
Universidad Cooperativa de Colombia
Avenida Caracas No. 37 – 63 Bogotá D.C., Colombia
E-mail: jose.ramirez@campusucc.edu.co, web page: http://www.ucc.edu.co

‡ LEME Laboratory
Université Paris Nanterre
50, rue de Sèvres 92410 Ville d'Avray, France
Email: laurent.gallimard@u-paris10.fr, web page: https://leme.u-paris10.fr/

ABSTRACT

The bio-inspired robotic hand prosthesis ProMain-I [1] has been developed, tested and manufactured completely at the LEME laboratory. The hand has three fingers, which are disposed to perform precision grasping, each finger has three joints: MetacarpoPhalangeal (MP), Proximal Interphalangeal (PIP) and Distal Interphalangeal (DIP). All joints have one Degree of Freedom (DoF) to perform flexion and extension.

The hand controller is addressed in three main stages: (i) the identification of the finger transfer function; (ii) the position control of the finger; (iii) the formulation of a hybrid force-position control system. The identification of the finger takes into account the parametric model of the ProMain actuator, i.e. the XL-320 Dynamixel™ servo-motor, coupled with the finger mechanism. The position is identified directly using experimental data obtained from the actuator, and the fingertip force transfer function is obtained from a complete measure of the kinematic and fingertip force. The controller and transfer function parameters are estimated using an optimization approach. We also present the ProMain-I hand characteristics, and the new smart force sensor [2], which has been designed and manufactured (in the LEME laboratory) to implemented the feedback force loop.

As a result, we present the robotic finger parametric model to characterize the finger in force and position. Finally, we introduce a force-position hybrid controller, which has let to achieve grasping gestures, setting the force reference to hold objects in steady way.

REFERENCES

[1] J.L. Ramírez, A. Rubiano, N. Jouandeau, L. Gallimard, and O. Polit. *Smart structures and materials*, chapter Artificial muscles design methodology applied to robotic fingers, pages 1–17. Springer, 2015.

[2] A. Rubiano, J. L. Ramírez, L. Gallimard, O. Polit, and N. Jouandeau. Capteur tactile capable de retranscrire le toucher, FR1655991, Jun. 2016..

VIII ECCOMAS Thematic Conference on Smart Structures and Materials
SMART 2017
A. Güemes, A. Benjeddou , J. Rodellar and Jinsong Leng (Eds)

REMOTE OPTICAL POWERING USING FIBER OPTICS IN MICRO-MECHATRONIC SYSTEMS

J.D. López-Cardona[1]✉, C. Vázquez[1], D.S. Montero[1], P.J. Pinzón[1], A. Tapetado[1] and P. Contreras[1]

[1]Grupo de Displays y Aplicaciones Fotónicas (GDAF).
Universidad Carlos III de Madrid,
Electronics Technology Dpt, Avda. de la Universidad 30, 28911, Leganés (Madrid), Spain
✉Corresponding author e-mail: julopezc@ing.uc3m.es

Key words: Power over fiber (PoF), smart structures, mechatronics, Microelectromechanical systems (MEMS), multimode optical fibers.

ABSTRACT

New advances in micro-mechatronic systems and related sensors and actuators (i.e. a MEMS) along with their usually low power requirements make them good candidates to take advantage of Power over Fiber (PoF) technology. This PoF technology uses light for electrically powering different systems. Remotely located micro-mechatronic systems using optical fibers can integrate PoF, as in endoscopic optical coherence tomography based on microelectromechanical system mirrors. Other potential applications can be found in critical systems that require redundant power supply, in scenarios avoiding electromagnetic interference, or in systems demanding different power requirements in multiple nodes. This paper proposes the implementations of the power over fiber technology together with MEMS in different scenarios and show some experiments performed with different types of optical fiber, multimode silica and plastic fiber.

1. INTRODUCTION

Optical fiber is a widely used transmission medium due to its potential as a high capacity communication channel of light signals. An emerging technology is currently under development where the optical fiber is used to transmit power to a remote station in the form of light energy which is then used to feed an electronic device. This technology is called in English "Power over Fiber", abbreviated PoF or PWoF.

The idea of the use of optical fiber for the transmission of energy in the form of light has its origins in the 70's, in the field of telephony. The first works were presented in 1978 and 1979, called "Sound Alert Acted on an Optical Fiber" and "Optically Operated Voice Communication through a Fiber Lightguide", respectively, which showed the feasibility of the technology to supply energy to an acoustic sensor [1] and the use of it in a data link [2]. At the same time, the first patent was presented for by J. Lemelson [3].

PoF systems usually consist of a high-power laser diode (HPLD), a transmission line (optical fiber), and a converter (i.e. a photovoltaic, PV, cell or optical isolator, OPI). The evolution of the PoF systems from their beginnings to the present has been oriented to improve the performance of both their stand alone elements and the system as a whole. Some

important advances are: enhancement of the photovoltaic cell conversion efficiencies and transmitted power levels, the use of optical fiber transmission techniques [4] for the integration of power and data through the same channel and improvements in the energy distribution.

On the other hand, the use of this technology has diversified into multiple fields of application such as remote sensor feeding [5] [6], communications antennas [7] [8], vision systems [9] 10], etc. In this range of applications, microelectromechanical systems (MEMS) have also played an important role as a sensor element and as a key technology for the development of some functionalities of optical devices. The first development of an Optical-MEMS device (MOEMS) dates from 1970 with the use of an array of micro-mirrors to create a bitmap image [11]. In the specific case of PoF systems, the use MEM-based systems have been proposed for the development of the optical switching logic of a Quasi-Passive (QPAR) node in an evolution of current passive optical access networks (PON), [12]. One of the advantages of this application is to be able to remotely power the node, giving a greater versatility to the network. From the above it is clear that the potential of integrating both PoF and MEM-based systems is huge. However, a deeper analysis of the capabilities of remote power feeding via PoF is required to fully benefit from both technologies. It is worth mentioning that the use of PoF technology may lead to additional benefits, such as the capacity of galvanic isolation between the transmitter and the receiver, its immunity to electromagnetic interference (EMI) and its intrinsically safe nature. The latter advantage is of interest in applications such as the sensing of flammable gases.

In this work, a first approach is made by combining power over fiber technology and MEMS, in the automotive and biomedicine sectors. Experimental results over a self-developed power over fiber system are also shown.

The document is divided into 4 sections. The next section discusses different scenarios for the integration of both MEMS and PoF technology. In section 3, the developed system and some experimental results are presented. Finally, section 4 addresses the main conclusions.

2. SCENARIOS FOR THE USE OF POF TECHNOLOGY IN MICRO-MECHATRONIC SYSTEMS

Currently due to technological advances, there are examples of micromechanical systems (MMS) with high levels of integration such as MEMS. The integration of microsensors, microactuators, microelectronics and microstructures in the same device allows them to be used in a large number of applications such as temperature sensing, pressure, inertial forces, chemical compounds, magnetic fields, radiation, etc. There are leading manufacturers in the field of MEMS such as: STMicroelectronics, Robert Bosch and Texas Instruments [13], which have solutions that can be integrated with PoF technology. Their devices require low power consumption and may be used in a wide range of applications. PoF technology enables the development of reliable, scalable remote sensing systems due its aforementioned advantages and the extended use of optical fiber nowadays. As an example, Table 1 shows some MEMS manufacturers and some MEMS power consumption.

There are multiple sectors for the MEMS-based application market including automotive, consumer electronics, and industrial [13]. On the other hand, the optical fiber is widely used

as a high bandwidth transmission medium; consequently there are multiple applications in which both technologies can coexist, as represented in Figure 1.

Table 1: Examples of power consumption of some MEMS

MEMS	CONSUMPTION	MANUFACTURERS	APPLICATION
AIS1120SX	26mW	STMicroelectronics	Accelerometer (automotive)
LIS331HH	36uW	STMicroelectronics	Accelerometer
DLP3000	200 mW	Texas Instruments	Chemical Analyzers, Machine Vision
VQ548MP	297mW (at Power on)	SGXsensortech	Flammable gas detectors

One sector that can benefit from the advantages of MEM systems, together with other emerging technologies, is the automotive sector. Plastic optical fiber is a transmission medium used in cars that use the standard MOST150 (Media Oriented Systems Transport) among others. In this scenario, where there is already a previous synergy between both MEMS and the optical fiber; the PoF technology may provide an added value to the system.

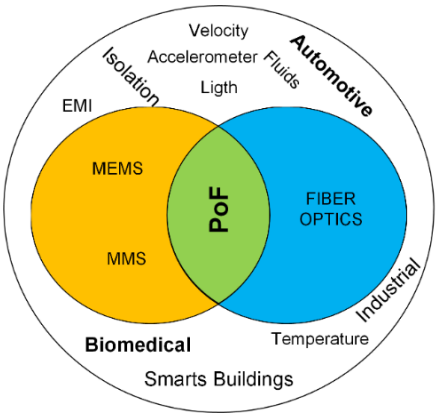

Figure 1: Examples of scenarios where fiber optic technology and MEMS coexist

According to Forbes' official website, technologies such as Autonomous Vehicle, Driver Override Systems and Biometric Vehicle Access, will be technologies present in 2020 [14]. All of them suppose a growth and diversification issue for the sensing community that is present within the automobile. Moreover they will also require a greater bandwidth boosted by the development of Advanced Driver Assistance Systems (ADAS), in the framework of creating more reliable and autonomous vehicles. The ADAS systems, based on MEMS, provide support for intelligent automotive technologies, such as LIDAR, and LEDDAR, which in combination with power over fiber technology can make the system more robust. Both the LIDAR system, and its later improvement LEDDAR, allow cutting-edge functionalities such in-car obstacle detection, collision warning and avoidance, etc. In these technologies the use of MEMS based on micro-mirrors plays a major role. In [15], a technique using MEMS based on micro-mirrors is described to amplify the range of 2D sweeps. In [16]

a system is presented that allows to increase the visual field of the technologies, without compromising the power consumption.

PoF technology in a car could be used for many reasons. The need of redundant power for critical systems in case of main source failure, the weight reduction as well as the immunity to electromagnetic interference (noise) are highlighted as main benefits provided by PoF technology.

In relation to weight reduction, new generations of cars need more copper wire for their operation. Specifically, today an electric car has about 165lbs in copper wires for different purposes [17]. The Tesla S model uses three times more copper wiring than an internal combustion engine vehicle [18]. In this sense the use of plastic optical fiber instead of copper to transmit power could lead to a remarkable decrease in weight, as optical fiber is lighter than copper. A specific case of study, using the PoF instead of PoE (Power over Ethernet) is following analyzed. PoE technology basically consists of transmitting power to a remote device using the physical medium supported by the Ethernet local area network standard. The cable currently used for this purpose, standardized in IEEE802.3af and IEEE802.3, is the Cat5e type [19], whose weight is 31g/m [20]. In contrast, a 1mm core diameter plastic optical fiber has a weight less than 5g/m [21], which means approximately a sixfold weight reduction.

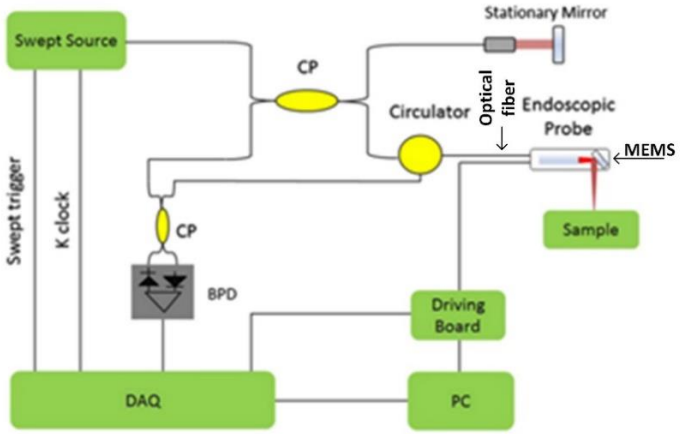

Figure 2: MEMS-based endoscopic swept-source optical coherence tomography system [22]

The power over fiber technology can also be applied in the biomedicine sector where different MEMS could coexist with PoF technology, as in the case of the Optical Coherent Tomography (OCT) technique. This technique was first presented in 1991 as a non-invasive technique for biomedical applications however its integration with MEMS appeared later [22]. This technique has evolved over the years by combining the latest technological advances in order to improve its sensitivity [23]. In [22] by the use of both Microelectromechanical System (MEMS) and the OCT technique, a MEMS-based OCT solution was presented. It describes an optoelectronic system that employs optical elements (passive and active) but also MEMS, being a key element in the design, see Figure 2. The MEMS mirrors are active elements with a maximum required power of 103mW (4.5V, 23mA) [22], which alternatively could be supplied via a power over fiber system.

In this way, we propose an improvement in the system described in [22] by the integration in the same optical fiber lead of: a) the power required for the MEMS operation, and b) the light reflected back by the micro-mirrors that performs the OCT technique. In this way everything is done in the optical domain.

3. IMPLEMENTATION OF A POWER OVER FIBER SYSTEM

Basic aspects

A block diagram of a generic PoF system is illustrated in Figure 3. It shows the high power laser diode (HLPD), the optical fiber and the photovoltaic cell (PV). The converter stage remotely transforms the received optical power into power electricity, P_{elec}^{PV} thus driving an electronic circuit directly. These PV converters are the most suitable devices for this optical power conversion process due to their efficiency performance and no requirement for any kind of biasing.

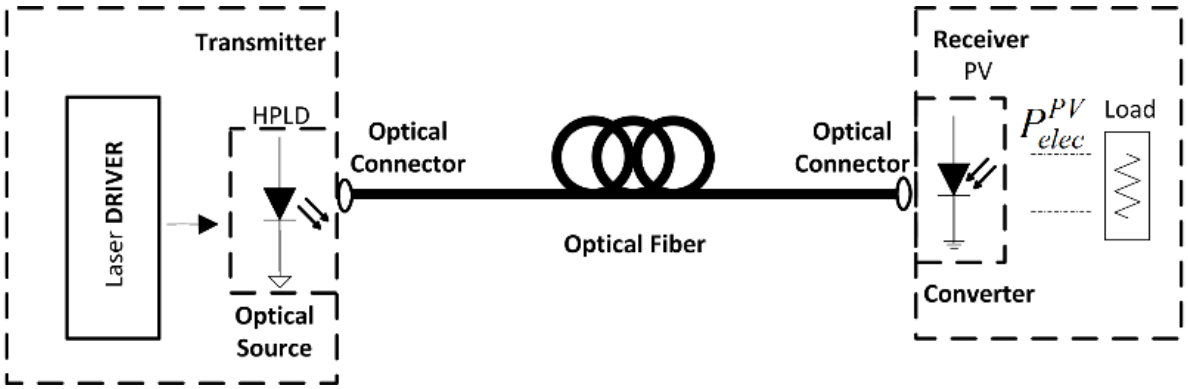

Figure 3: A block diagram of a generic PoF system

In a power over fiber system different aspects must be considered for the design:

- proper match between the HPLD wavelength, the PV converter efficiency, and the optical fiber attenuation.
- the type of multiplexing topology to be used: spatial (SDM) or wavelength (WDM).
- control of the power dissipation in both the cell and the receiving element.
- appropriate level of injected optical power to avoid the phenomenon of fiber fuse and / or irreversible damages to the optical elements including the connectors and the optical fiber itself.

Some applications require relatively high efficiencies and miniaturization, especially if endoscopic applications are proposed. In this sense, it is important to select the correct cell in terms of sizing and efficiency for the operating wavelength. There are cells of only 1 mm^2 × 0.4 mm effective area and height, respectively, without heatsink. The presence or not of the heatsink depends on the power dissipating in the cell. Figure 4 (a) shows the PV cell mounted within a FC-type connector (which also acts as a heatsink) as well as an uncovered counterpart, see Figure 4 (b).



(a) (b)

Figure 4: Photovoltaic cells, (a) cell with FC connector (b) uncovered cell [10]

The cell efficiencies depend on both the materials and the operation wavelength. Table 2 summarizes the current main three operating windows used by power over fiber systems.

Table 2: Materials, operating windows and efficiencies of PoF systems [24][25].

Materials	Wavelength [nm]	Efficiency (%)
GaAs	790 to 850	52
In-GaAs	915 to 980	34
InP	1400 to 1550	26

Developed system

We have developed specific prototypes providing optical remote powering of hundreds of mW in DC and pulse mode for different types of multimode silica and polymer optical fibers[26][27].

The system includes a high power laser diode (HPLD) of 1.5W@2.2A with a central wavelength of 805nm and with a FC connector. At reception, a power converter (PV) is located. A picture of the system is shown in Figure 5, where the HPLD and the PV are connected via a silica optical fiber with a 200µm core diameter.

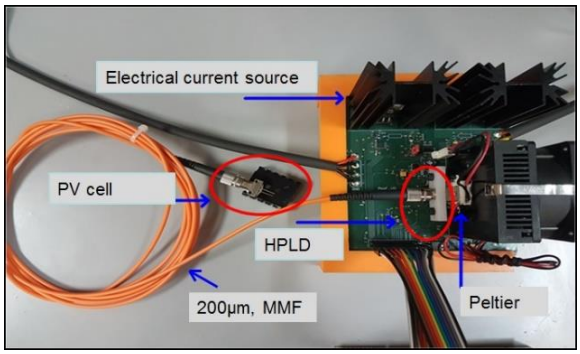

Figure 5: Prototype of the developed system, with a 200 µm diameter silica optical fiber

The designed laser driver provides a slow start and a current limit to protect the laser. The slow start is controlled by the charging of a capacitor (not shown in Figure 6) for avoiding rapid changes in the current and temperature of the laser diode. Additionally it performs a temperature and a current control loop system to stabilize the output optical power. A simplified scheme is shown in Figure 6 (a), where a variable current source controlled by the Rvar resistor is depicted. Figure 6 (b) shows the simulation of the laser diode current when

the laser is on without a slow start, where an increase of 70mA above the nominal current is observed. In contrast, Figure 6 (c) shows a gradual increase up to the operating current, without transient current peaks.

A key design factor is the temperature of the laser diode, as the optical emission power strongly depends on temperature. This parameter also greatly affects the laser lifetime. The laser diode, as a non-ideal element, dissipates energy in the form of heat depending on the point of operation and this causes an increase in temperature. According to the laboratory experiments we have developed, our laser diode, at an ambient temperature of 25˚C and 2.2A of operating current, increases its temperature by more than 15˚C. This variation is controlled with a Peltier element that stabilizes the temperature of the laser diode at 25˚C ± 0.01%.

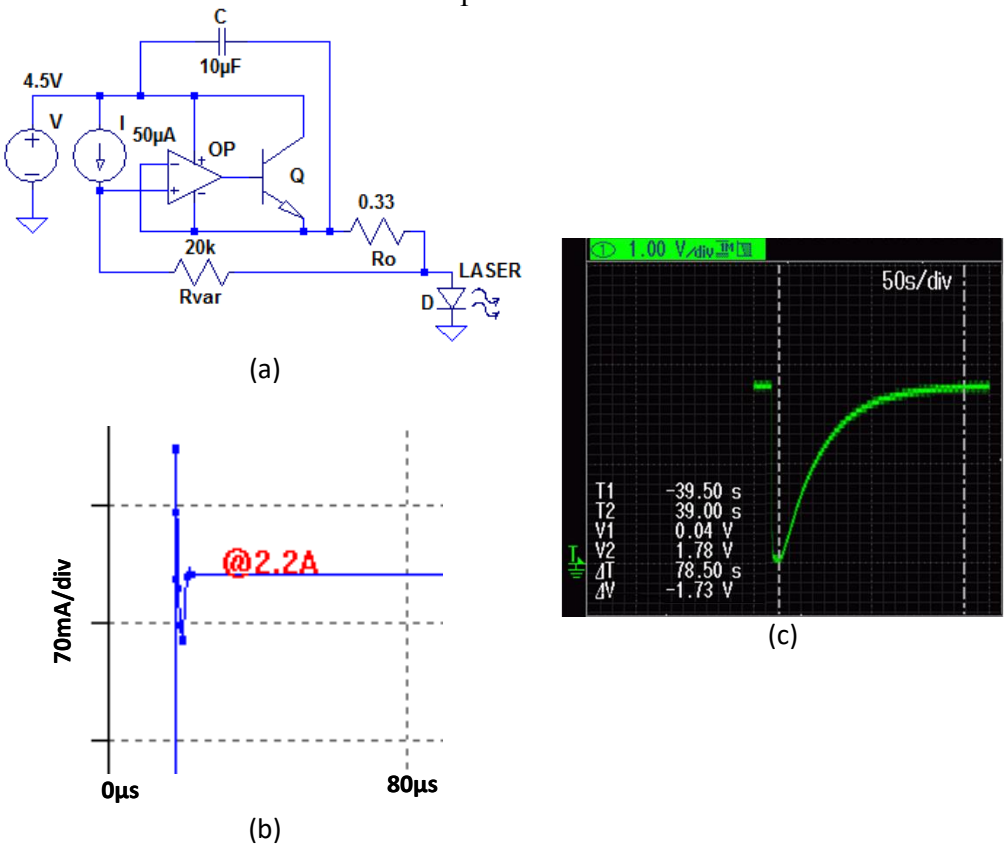

Figure 6: (a) Simplified electrical diagram. (b) Simulation without implementing the slow start of the laser diode. (c) Experimental test with slow start implementation

The current is controlled via software in the digital domain with a precision of 3mA, representing a variation in optical power of 2mW taking into account the transfer function of the laser diode.

As transmission media, multimode fibers of different lengths and core diameter sizes have been tested. The highest transmission power density has been achieved with 200µm core diameter multimode silica optical fibers obtaining a maximum coupling efficiency of light injected into the fiber from the laser's output. The PV cell is optimized for maximum power conversion efficiency at 805nm wavelength corresponding to the emission wavelength of the laser diode.

Experiments

As previously stated, some tests with different types of fibers: silica multimode fibers and step index (SI) polymer optical fibers (POF) are carried out. The remote powering devices, mainly sensors within a sensor network, may be fed with low and medium powers (P), (P<100mW) at distances of hundreds of meters for silica fibers and few meters for SI-POF fibers.

A previous work was reported in [26] where the power transmission was evaluated using a 120μm core diameter graded-index plastic optical fiber, GI-POF. The achievable electrical power delivered(P_{elec}^{PV}), was 49.5mW for an intermediate fiber length of 50m. Table 3 summarizes the set of experimental trials carried out in this work with other fiber types.

Table 3: Measurements of electrical power fed at the remote system with different types of optical fibers and with an optical power laser of 1.5W

Fibers types [Core diameter]	Fiber link lengths[m]	Electrical power, P_{elec}^{PV} [mW]
Silica [62.5μm] OM1	1	240
Silica [200 μm]	1	409
Silica [200 μm]	300	360
SI-Plastic [1 mm]	2.1	197

Discussion

In some power over fiber applications it may be of interest to know the energy radiated in the form of heat by the optical fiber. Depending on the application this parameter can be critical as it may affect the surrounding environment to the optical fiber. Figure 7 shows a preliminary study of the thermal behavior of a coated plastic optical fiber. In this measurement we have coupled 1.5W of optical power into 10 meters of (SI-POF) (Optical fiber # 1).

In the case of the use of the OCT together with the PoF technology using invasive techniques, such as the vision of internal organs [28], is important to know the radiation profile of the fiber because it could lead to some incompatibility issues. In this case the optimization of the system or the use of special coatings may be necessary. Another element that influences the temperature increase of the surrounding environment is the OPI (PV cell) that in this technique would be located inside the element "Endoscopic Probe" (see Figure 2). An unnecessary dissipation of the OPI would imply an increase of the temperature of the element "Endoscopic Probe".

In the case of the OCT technique it is possible to use spatial multiplexing techniques in case there is a not desirable overlap between the OCT spectrum and the PoF system. Spatial multiplexing consists in separating the spectra for power transmission and OCT operation on different physical media.

Finally, an important parameter in a power over fiber system is the power that is needed in the remote device (i.e., MEM system or MEM sensor). Typically power requirements are low (P <100mW), although in some applications there may be a higher demand. Today it is possible to transmit tens of watts in a length of 300 meters [29] [30], by the same optical fiber with double-clad fiber [31].

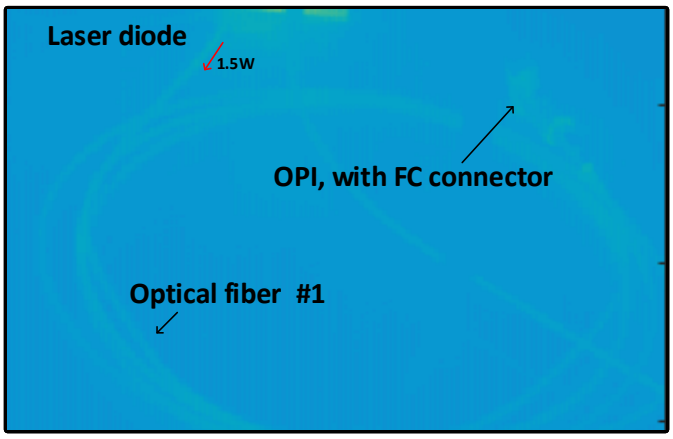

Figure 7: Thermal radiation profile of a SI-POF fiber, 1mm (diameter). The ambient temperature is 22 ℃

4. CONCLUSIONS

Power over fiber systems are an emerging technology like MEMS, whose integration in some environments may be interesting to consider. On the one hand, the miniaturization of systems provided by MEM technology and, on the other hand, the robustness to electromagnetic interference provided by PoF systems. A prototype of power over fiber has been developed that allows the transmission of hundreds of milliwatts of optical power over distances of hundreds of meters with silica fiber and several meters with plastic fibers. It has been analyzed the interest for its use in biomedical applications and in the automotive sector in conjunction with MEM devices.

ACKNOWLEDGEMENT

This work is sponsored by Spanish Ministerio de Economía, Industria y Competitividad project TEC2015-63826-C3-2-R, FEDER and Comunidad de Madrid under grant S2013/MIT-2790-SINFOTON-CM and FSE.

REFERENCES

[1] R. C. Miller and R. B. Lawry, "Optically Powered Speech Communication Over a Fiber Lightguide," *Bell Syst. Tech. J.*, vol. 58, no. 7, pp. 1735–1741, Sep. 1979.

[2] B. C. DeLoach, R. C. Miller, and S. Kaufman, "Sound Alerter Powered Over an Optical Fiber," *Bell Syst. Tech. J.*, vol. 57, no. 9, pp. 3309–3316, Nov. 1978.

[3] J. H. Lemelson, "Communication system and method," U.S. Patent 4434510, 1978.

[4] D. Wake, N. J. Gomes, C. Lethien, C. Sion, and J. P. Vilcot, "An optically powered radio over fiber remote unit using wavelength division multiplexing," *2008 IEEE Int. Meet. Microw. Photonics jointly held with 2008 Asia-Pacific Microw. Photonics Conf. MWP2008/APMP2008*, pp. 197–200, 2008.

[5] J. Yan, J. Wang, Y. Lu, J. Jiang, and H. Wan, "Novel Wireless Sensor System Based on Power-over-Fiber Technique," no. 9, pp. 14–16, 2015.

[6] J. B. Rosolem *et al.*, "A fiber optic powered sensor designed for partial discharges monitoring on high voltage bushings," *SBMO/IEEE MTT-S Int. Microw. Optoelectron. Conf. Proc.*, vol. 2015–Decem, 2015.

[7] D. Wake, A. Nkansah, N. J. Gomes, C. Lethien, C. Sion, and J. P. Vilcot, "Optically powered remote units for radio-over-fiber systems," *J. Light. Technol.*, vol. 26, no. 15, pp. 2484–2491, 2008.

[8] F. Perini, S. Rusticelli, M. Murgia, and J. Monari, "Power over fiber systems for the italian SKA-LOW demonstrators," pp. 2–5.

[9] M. Dreschmann *et al.*, "Reconfigurable hardware for power-over-fiber applications," *Proc. - 2010 Int. Conf. F. Program. Log. Appl. FPL 2010*, pp. 525–531, 2010.

[10] G. Bottger *et al.*, "An Optically Powered Video Camera Link," *IEEE Photonics Technol. Lett.*, vol. 20, no. 1, pp. 39–41, 2008.

[11] H. Toshiyoshi, "MEMS for micro optics: from fiber optic communication to display (Invited Paper)," 2005, p. 605007.

[12] Y. Bi, J. Jin, A. R. Dhaini, and L. G. Kazovsky, "QPAR: A Quasi-Passive Reconfigurable Green Node for Dynamic Resource Management in Optical Access Networks," *J. Light. Technol.*, vol. 32, no. 6, pp. 1104–1115, Mar. 2014.

[13] "Global Global Micro Electromechanical Systems(MEMS) Market Professional Survey Report 2016." [Online]. Available: http://marketersmedia.com/micro-electromechanical-systems-mems-global-market-professional-survey-report-2016/146254. [Accessed: 01-Jan-2017].

[14] "Top 10 Advanced Car Technologies by 2020," 2015. [Online]. Available: https://www.forbes.com/sites/kbrauer/2015/01/19/top-10-advanced-car-technologies-by-2020/#460ad7306705. [Accessed: 01-Jan-2017].

[15] L. Ye, G. Zhang, Z. You, and C. Zhang, "A 2D resonant MEMS scanner with an ultra-compact wedge-like multiplied angle amplification for miniature LIDAR application," in *2016 IEEE SENSORS*, 2016, pp. 1–3.

[16] Y. Wang and M. C. Wu, "Micromirror based optical phased array for wide-angle beamsteering," in *2017 IEEE 30th International Conference on Micro Electro Mechanical Systems (MEMS)*, 2017, pp. 897–900.

[17] "$8 Trillion Alternative Energy Boom Is a Win for Copper," 2015. [Online]. Available: http://www.usfunds.com/investor-library/frank-talk/8-trillion-alternative-energy-boom-is-a-win-for-copper/#.WL8bTIWcHmI. [Accessed: 01-Jan-2017].

[18] "This commodity is going to be a huge beneficiary of the shift to electric cars," 2016. [Online]. Available: http://www.businessinsider.com/copper-to-benefit-from-electric-cars-2016-4. [Accessed: 01-Jan-2017].

[19] "Next-Generation PoE: IEEE 802.3bt," 2016. [Online]. Available: www.microsemi.com. [Accessed: 24-Mar-2017].

[20] "Cat5e Cable." [Online]. Available: http://www.farnell.com/datasheets/1311844.pdf. [Accessed: 24-Mar-2017].

[21] "2014-Plastic Optical Fiber (POF) technology for Automotive, Home network systems." [Online]. Available: http://www.ieee802.org/3/GEPOFSG/public/May_2014/Tsukamoto_GEPOF_01_0514.pdf. [Accessed: 24-Mar-2017].

[22] D. Wang *et al.*, "Endoscopic swept-source optical coherence tomography based on a two-axis microelectromechanical system mirror," *J. Biomed. Opt.*, vol. 18, no. 8, p. 86005, Aug. 2013.

[23] A. Al-Mujaini, U. K. Wali, and S. Azeem, "Optical coherence tomography: clinical applications in medical practice.," *Oman Med. J.*, vol. 28, no. 2, pp. 86–91, Mar. 2013.

[24] M. Dumke, G. Heiserich, S. Franke, L. Schulz, and L. Overmeyer, "Power Transmission by Optical Fibers for Component Inherent Communication," *J. Syst. Cybern. Informatics*, vol. 8, no. 1, pp. 55–60, 2010.

[25] Xing Xu, Sigang Yang, Chi Zhang, T. I. Yuk, and K. K. Y. Wong, "Optically Powered Communication System With Distributed Amplifiers," *J. Light. Technol.*, Nov. 2010.

[26] J. D. López-Cardona, D. S. Montero, P. J. Pinzón, and C. Vázquez, "GIPOF-based Power Delivery Systems," in *25th Internacional Conference on Plastic Optical Fibres*, 2016.

[27] C. Vázquez, D. S. Montero, P. J. Pinzón, J. D. López-Cardona, P. Contreras, and A. Tapetado, "Integration of power over fiber on RoF systems in different scenarios," *Proc. SPIE*, vol. 10128. p. 101280E–101280E–7, 2017.

[28] G. J. Tearney *et al.*, "In vivo endoscopic optical biopsy with optical coherence tomography.," *Science*, vol. 276, no. 5321, pp. 2037–9, Jun. 1997.

[29] Y. Minamoto and M. Matsuura, "Optically Controlled Beam Steering System With 60-W Power-Over-Fiber Feed for Remote Antenna Units," *Opt. Fiber Commun. Conf.*, pp. 1–3, 2016.

[30] J. Sato, H. Furugori, and M. Matsuura, "40-Watt Power-Over-Fiber Using a Double-Clad Fiber for Optically Powered Radio-Over-Fiber Systems," in *Optical Fiber Communication Conference*, 2015, pp. 1–3.

[31] M. Matsuura and J. Sato, "Power-over-fiber using double-clad fibers for radio-over-fiber systems," *2014 19th Eur. Conf. Networks Opt. Commun. NOC 2014*, pp. 126–131, 2014.

Shape Memory Alloy (SMA) based actuation mechanism for a soft robotic hand prosthesis

Jose L. Ramirez*, Astrid Rubiano† and Olivier Polit‡

* Facultad de Ingeniería
Universidad Cooperativa de Colombia
Avenida Caracas No. 37 – 63 Bogotá D.C., Colombia
E-mail: jose.ramirez@campusucc.edu.co, web page: http://www.ucc.edu.co

† Facultad de Ingeniería
Universidad Militar Nueva Granada
Cr 11 No 101 – 80 Bogotá D.C., Colombia
Email: astrid.rubiano@unimilitar.edu.co, web page: http://www.umng.edu.co

‡ LEME Laboratory
Université Paris Nanterre
50, rue de Sèvres 92410 Ville d'Avray, France
Email: olivier.polit@u-paris10.fr, web page: https://leme.u-paris10.fr/

ABSTRACT

This contribution presents a constitutive model that uses thermo-mechanical formulation to describe shape memory alloys (SMA) behavior. The formulation is suitable to characterize the material and also to complement the dynamic modeling of a SMA based rotary actuator. Furthermore, a one dimension particularization is introduced that is used to approximate the behavior of the SMA wires in the context of the rotary actuator. Moreover, the SMA constitutive model is merged with two governing equations that describe the dynamic of rotation and the dynamics of the temperature applied to the SMA wire using an electrical current as input.

Three experiments are presented in order to: i) Identify the Young's modulus of SMA in martensite and austenite phases; ii) Identify thermic SMA characteristics; iii) Kinematic evaluation of a SMA based rotary actuator. The final identification of the SMA parameters is carry out using optimization techniques that allows to fit the model to the real material behavior.

Concerning the application of SMAs in robotic hands, the obtained results show that the SMA fulfill the precision grasping requirements [1]. We use the obtained results using SMA to propose an evolution of the hand prosthesis ProMain-I [2], which is an under actuated robotic hand prosthesis endowed with three fingers, each one driven by a soft epicyclic mechanism, as a result we present a new prototype called ProMain-II. This hand prototype is equipped with the new version of the soft epicyclic mechanism using an SMA wire in parallel to the flexible tendon for the ProMain-II soft robotic prosthesis hand. This actuation system allows controlling the stiffness of the actuated joints controlling the damping effect evidenced during the experiments performed with the ProMain-I finger.

REFERENCES

[1] J.L. Ramírez, A. Rubiano, N. Jouandeau, L. Gallimard, and O. Polit. *Smart structures and materials*, chapter Artificial muscles design methodology applied to robotic fingers, pages 1–17. Springer, 2015.

[2] A. Rubiano, J. L. Ramirez, L. Gallimard, O. Polit, and N. Jouandeau. Châıne articulée comprenant un unique actionneur et ensemble de châınes articulées associées FR1656914, Jul. 2016.

VIII ECCOMAS Thematic Conference on Smart Structures and Materials
SMART 2017
A. Güemes, A. Benjeddou, J. Rodellar and J. Leng (Eds)

SHAPE MEMORY ALLOY ELEMENT DESIGN AND CHARACTERIZATION FOR AN OPTICALLY DRIVEN QUADRISTABLE ACTUATOR

HANI AL-HAJJAR*, SANTIAGO V. BAYONA, SIDDHANT P. CHANDGADKAR, XINGXING LIU, EMMANUEL DORÉ* AND FRÉDÉRIC LAMARQUE*

*CNRS, UMR 7337 Roberval,
Sorbonne Universités, Université de Technologie de Compiègne
CS 60 319 — 60 203 Compiègne cedex, France
e-mail: hani.al-hajjar@utc.fr, web page: http://www.utc.fr/

Key words: Shape Memory Alloy, Quadristable Micro-Actuator, Micro-Fabrication, Optical Wireless Actuation

Abstract. An optical wireless quadristable micro-actuator based on antagonistic pre-shaped beams for two rows (inner, outer) is presented in this article. The actuator was developed using the Timoshenko-based mathematical model and analyzed for output force and energy values. The actuator was fabricated by the deep reactive ion etching (DRIE) technique, using bonded silicon on insulator (SOI) wafer. The quadristable frame possessed bistable beams with a thickness of 25 μm and theoretical stroke values of 300 μm and 200 μm for the inner and outer rows, respectively. The actuation of the system was performed by Nitinol shape memory alloy (SMA) elements, laser heated to switch the positions of stability for the inner bistable beams and outer quadristable beams. An 8 μm layer of SiO_2 was deposited upon one side of each SMA element ($0.1 \times 1 \times 3$ mm), to provide a biasing force during actuation, eliminating the load effect of SMA elements and introducing a two-way shape memory effect. The stroke of the SMA element was analytically modeled, for force measurements and the effect of phase transitions between austenite and martensite.

1 INTRODUCTION

Long range remote control and availability of micro-actuators is one of the major bottlenecks to implementing autonomous micro-robots in a workspace. A method of transferring energy over a long range to a micro-actuator is to use radiofrequency or optical signals. For RF signals, the transmitting antenna is generally characterized by a high gain, narrow beam width and extremely low side and back lobes. In this application, the receiving antenna (rectenna) refers to an antenna with the ability to receive and rectify microwaves in the receiving part of a wireless power transmission system [1]. This system suffers from the problem of electromagnetic interference between electronics within a robot. Ali et al applied the RF control to shape memory

alloys (SMA) with the use of spiral coils to transform the magnetic field into current [2, 3]. However, this approach required additional components, when applied to a micro-actuator.

Optical remote supply can serve to wirelessly transfer energy to micro-actuators over a distance of a few meters, without any load imposed upon their structures. In [4], a photo-thermal mechanical contactless long-range actuation method was proposed. In this study, a laser was employed as the long range contactless energy source. The laser beam heated a bimorph cantilever (active part of the micro-actuator) and deformed due to focused light, via a micro-machined lens array placed at the top of the micro-actuator. This bimorph component was part of the illuminated leg consisting of two layers with different thermal expansion ratios.

More recently, Mori et al demonstrated a remote actuation method applied to a MEMS capacitive actuator [5]. Optical means can also be applied to micro-manipulation of meso-objects. In [6], an opto-fluidic effect based on the long-range contactless actuator approach was demonstrated. When the laser beam was focused onto a certain position on a petri dish with a thin layer of liquid, the increased temperature created a flow, which was used to manipulate the small glass beads in the liquid. However, these studies do not propose solutions when several actuators must be manipulated at the same time.

This article presents remote operation of shape memory alloys (SMAs), with deposited optical thin-film filters, to make possible the selective response to incoming laser radiation [7, 8, 9]. This work followed previous suggestions on optically-driven actuator systems [4, 10] that needed complicated lens systems to focus the laser beam on a specific SMA element.

This article explains the work on optically, remote-controlled bistable actuators in which 'one-way' SMAs were actuated with the help of SiO_2 layers, initiating 'two-way' SMA behaviour. Thanks to this strategy, the micro-actuator was stable in each of its positions, because the contact between the beams and the SMAs was avoided [11]. A proposition is made to extend the use of such SMAs to more complex micro-actuators, having four stable positions. The integration steps that were necessary to provide a remote controlled micro-actuator are also described.

2 SMA ELEMENT STROKE MODELLING

2.1 Working principles of SMA element actuation

The initial concept for the wireless actuation was performed by laser heating annealed Nitinol (55% Ni – 45% Ti) SMA elements. However, the actuation of this initial system could be only performed in one direction, since such SMA elements memorize their shape after being optically heated. Consequently, once all the SMA elements were in a strictly perpendicular position with respect to the frame, re-heating the SMA elements for another cycle proved to be ineffectual. The SMA elements would not displace the same distance as what was viewed initially, resulting in a decreased quadristable stroke. Therefore, a solution was proposed to implement a two-way memory approach to the actuation of the SMA elements. The quadristable structure would be able to displace the same distance after multiple heating cycles, whilst the SMA elements would return to their original positions (before heating), after cooling [11]. This required implementing a biasing force on the SMA elements, shown in Figure 1.

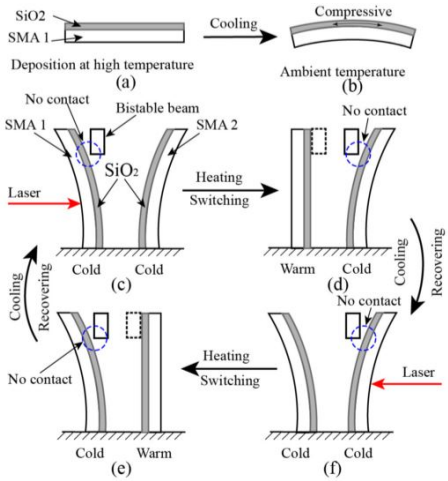

Figure 1: Compressive SiO_2 layer used as biasing spring for two-way memory actuation of SMA [11]

In Figure 1 (a) and (b), an SiO_2 layer is shown to be deposited upon SMA 1, labelled to be at a high temperature (to achieve a flat structure). Since the thermal expansion ratio of Nitinol SMA elements is larger than that of SiO_2, it was noticed that the SMA element contracted more than the SiO_2 layer, when cooled from the deposition temperature to room temperature [12]. Consequently, compressive stresses within the SiO_2 layer would force the SMA element to subdue to the same compression [12]. With these observations, the bistable beams within the quadristable structure could actuate without load effect (Figure 1 (c)-(f)). Walking through the two-way memory principle, the curved SMA element in Figure 1 (c) is currently at a position where there is no contact with the bistable silicone beam [12]. Once the SMA element is optically heated to the austenitic final temperature, the martensite phase in the initial SMA element converts to austenite phase, holding a greater elastic modulus. Since this process can occur after multiple cycles, it is known that the shape memory effect allows an SMA element to recover its original form (which in this case was the flat, perpendicular form). Due to this recovery action based off the memorized shape, a conversion from optical energy to mechanical energy could be performed, switching the bistable beam from a left stable position to a right stable position. Once the laser light moves away from the initial SMA element, it can cool and re-transform to martensite. As well, when the cooling occurs, the SiO_2 can regain its compressive strength and force the SMA to bend into its original cold state shape. Furthermore, this process could be repeated multiple times to achieve the same displacement results, since the SMA elements would be forced to curve backwards the same distance due to the presence of a thin-film SiO_2 layer [12].

2.2 Mathematical modelling of the SMA element deformation

With the knowledge of the physical characteristics of the SMA elements during actuation, a mathematical model was constructed to determine their theoretical stroke. However, due to changes in the physical properties of the SMA elements when heated, the calculations became more involved. The first step in conducting the calculations was to determine the effects of

phase transformations on the SMA elements.

Considering that there are four critical temperatures within an SMA element, the two main phases of austenite and martensite were investigated. When an SMA element was heated, the austenite start temperature (A_s) and the austenite final temperature (A_f) were observed. During the cooling process, as shown in Figure 1, the return to the martensite phase was identified through the martensite start temperature (M_s) and the martensite final temperature (M_f). These transitions of the SMA element would initiate the shape memory effect. When the SMA element was cooled from a temperature above A_f to a temperature below M_f (thermoelastic martensite phase), twinning behaviour was recorded within the grains of the SMA element structure [12]. This is shown in Figure 2 (a). Next, when a stress of a certain critical value was applied to the SMA element, detwinning of the atoms would occur, where the bonded atoms would rotate with respect to each other [12]. This process would require minimal force. As shown in the stress-strain chart in Figure 2 (b), the curve for the detwinning process is very shallow, demonstrating a low Young's modulus. Proceeding towards the zone of plastic deformation, if the SMA element was heated up to a temperature greater than that of A_s, the austenite phase would propagate through the detwinned crystalline structure, resulting in a greater elastic modulus and a stable crystalline structure. Since twinned martensite and austenite possess the same shape, deformation would recover, demonstrating the shape memory effect [12].

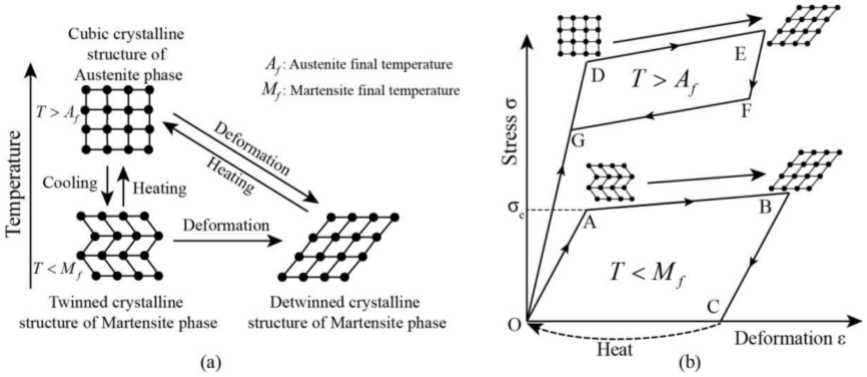

Figure 2: (a) Phase transformation of SMA element; (b) Stress-strain curve of shape memory effect at $T < M_f$ and at $T > A_f$ [12]

Referring to Figure 2 (b), with the inclusion of the SiO_2 layer, when the SMA element was cooled to martensite phase and bent by the biasing force, the material would be operating along the OAB curve. After heating the element to austenite phase, the stress of super elasticity start point (D) was assumed to be higher than any other stress point within the cycle. Thus, the cycle was operating along the OD curve. Due to this assumption, the SMA element could hold a constant elastic modulus of E_{SMA_A}, during the austenite phase.

On the other hand, a constant elastic modulus could not be assumed for the entirety of the martensite phase. Firstly, when the stress was below the critical stress (σ_c), the SMA element crystalline structure was twinned [12]. The elastic modulus for this zone was denoted to be E_{SMA_T}. During plastic deformation, the elastic modulus decreased to $E_{SMA_{DT}}$.

After labelling the main physical properties during phase transformation, the next step required the usage of the superposition method. This assumed that the SMA element was flat upon deposition of the SiO_2 layer, and initially there was no stress within the element. Since Nitinol has a greater thermal expansion ratio than SiO_2, compressive stresses would be present within the thin-film layer upon deposition. This stress could be calculated as shown below [12]:

$$S = E_{\mathrm{SiO_2}} \Delta\alpha_{SMA_\mathrm{SiO_2}} \Delta T \tag{1}$$

Where the elastic modulus of the SiO_2 ($E_{\mathrm{SiO_2}}$), the thermal expansion ratio difference between Nitinol and SiO_2 ($\alpha_{SMA_\mathrm{SiO_2}}$), and the change in temperature between deposition temperature and ambient temperature (ΔT) were multiplied together.

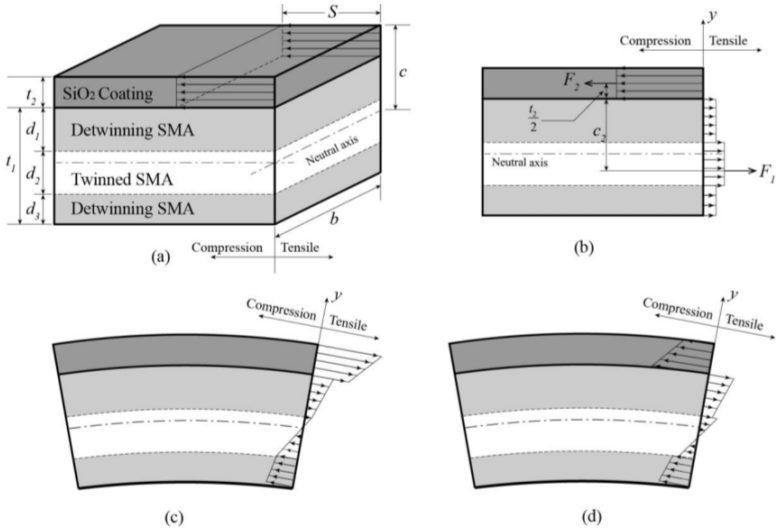

Figure 3: (a) Stress during constraint of elongation and bending; (b) Stress during elongation; (c) Stress during bending; (d) Stress during bending and elongation [12]

If the constraint of the stress within the element was removed, as shown in Figure 3 (b), the stress within the structure would allow the SMA element to lengthen. Since the thin-film deposition layer and the SMA element would elongate, tensile forces would be present within the structure, reducing the effect of compressive stresses provided by the SiO_2 [11]. During this process, it was assumed elongation and deformation would occur in the same plane. Thus, the deformation of the SMA element at this point was found to be represented by equation (2) [12]:

$$\epsilon = \Big(\frac{S}{E_{\mathrm{SiO_2}}}\Big) \frac{E_{\mathrm{SiO_2}} t_2}{E_{SMA_{DT}}(d_1 + d_3) + E_{SMA_T} d_2 + E_{\mathrm{SiO_2}} t_2} \tag{2}$$

Noting the important terms of the equation, d_1, d_2 and d_3 represented the thicknesses of the one twinned and two detwinned segments of the SMA element. As well, t_2 represented the thickness of the SiO_2 layer. Considering the tensile forces to be two 'point applied' forces, F_1 and F_2, the following expression was derived (where b was the width of the SMA element) [12]:

$$F_2 = F_1 = \epsilon b\big(E_{SMA_{DT}}(d_1 + d_3) + E_{SMA_T} d_2\big) \tag{3}$$

Since there were two equivalent action forces, a moment could be created, equivalent to [12]:

$$M = F_1\Big(c_2 + \frac{t_2}{2}\Big) \tag{4}$$

c_2, the distance between the applied force F_1 and the intersection between the thin-film layer and the SMA element (Figure 3 (b)), was calculated using the weighted method expression [12]:

$$c_2 = \frac{E_{SMA_{DT}} d_1\Big(\frac{d_1}{2}\Big) + E_{SMA_T} d_2\Big(d_1 + \frac{d_2}{2}\Big) + E_{SMA_{DT}} d_3\Big(d_1 + d_2 + \frac{d_3}{2}\Big)}{E_{SMA_{DT}} d_1 + E_{SMA_T} d_2 + E_{SMA_{DT}} d_3} \tag{5}$$

If the element was completely released, stress due to bending deformation (Figure 3 (c)) would be introduced. The bending would introduce a moment, M_b, in the opposite direction of the initial moment, M. A schematic of this stress distribution can be viewed in Figure 3 (d). Equivalent moments would result in equilibrium within the structure. Choosing the y-axis for the bending moment, as shown in Figure 3 (c), the bending moment would be [12]:

$$\begin{aligned} M_b = &\int_{-(t_1+t_2-c)}^{-(t_1+t_2-c)+d_3} by\Big(-\sigma_c - \epsilon_1 E_{SMA_T} + \kappa E_{SMA_{DT}}\big(y + (t_1+t_2-c) - d_3\big)\Big)dy \\ &+ \int_{-(t_1+t_2-c)+d_2+d_3}^{-(t_1+t_2-c)+t_1} by\Big(\sigma_c - \epsilon_1 E_{SMA_T} + \kappa E_{SMA_{DT}}\big(y + (t_1+t_2-c) - d_2 - d_3\big)\Big)dy \\ &+ \int_{-(t_1+t_2-c)+d_3}^{-(t_1+t_2-c)+d_2+d_3} E_{SMA_T}\kappa b \cdot y^2 dy + \int_{c}^{c-t_2} E_{\mathrm{SiO_2}}\kappa b \cdot y^2 dy \end{aligned} \tag{6}$$

Denoting the major terms of the equation, κ represented the curvature of the overall element. σ_c represented the critical stress before detwinning of the crystalline structure, and c (distance between the neutral axis and the exterior surface of the thin-film layer) could be calculated using a weighted method expression similar to that of equation (5).

The combination of equations (4) and (6) could solve for the curvature of the SMA element. Referring to Figure 2 (b), where the austenite elastic modulus was deemed to be constant, the curvature of the SMA element once heated to martensite phase (κ_A) was found to be [12]:

$$\kappa_A = \frac{6St_2\Big(t_1 + \frac{E_{\mathrm{SiO_2}}}{E_{SMA_A}}t_2\Big)(t_1+t_2)}{E_{SMA_A}\left(\frac{E_{\mathrm{SiO_2}}}{E_{SMA_A}}(t_1+t_2)^2 + t_1^4\Big(1 - \frac{E_{\mathrm{SiO_2}}}{E_{SMA_A}}\Big)\right)} \tag{7}$$

Thus, the stroke between the heated and ambient temperature state was expressed [12]:

$$S_{SMA_\mathrm{SiO_2}} = \delta_{LowTemp} - \delta_{HighTemp} \tag{8}$$

$$S_{SMA_\mathrm{SiO_2}} = \frac{1}{\kappa}\big(1 - cos(l_{SMA}\kappa)\big) - \frac{1}{\kappa_A}\big(1 - cos(l_{SMA}\kappa_A)\big) \tag{9}$$

The length of the SMA element, l_{SMA}, and the deflection of the SMA element at low/ambient ($\delta_{LowTemp}$) and high temperatures ($\delta_{HighTemp}$) (with respect to a flat line with zero curvature) were terms required for the derivation of the expression. The effect of these temperatures on the SMA element can be seen in Figure 4.

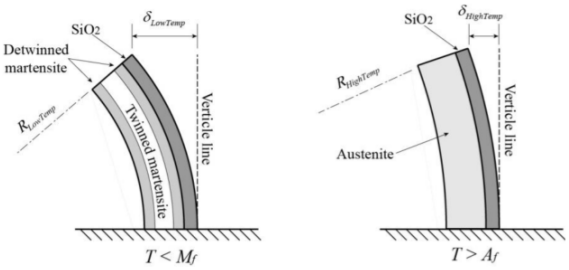

Figure 4: Deformation of SiO_2 and SMA element at low (T < M_f) and high temperatures (T > A_f)

3 SMA ELEMENT FORCE MEASUREMENTS

To measure the performance of the SMA element stroke used in this actuation procedure, a setup was assembled. A sensor output a voltage signal, with a sensitivity of 2.4 mV/mN, over a measurement range of 0 - 1000 mN. The sensor was positioned on two linear stages, set in an orthogonal configuration. The procedure of the measurement experiment firstly required the adjustment of the force centering ball to be in line with the top edge of the SMA element. This reflected the force to be imposed by the inner ring or the inner frame of the quadristable system, on the SMA elements. The SMA elements were to be positioned so that approximately 0.4 mm of the length of the SMA elements were above the surface of the quadristable frame. Thus, using the top edge of the SMA element for the force measurement proved to be useful data in approximating the stroke measurements within the quadristable system [11].

Once the centering ball was positioned, the ball was slowly moved towards the SMA element, until a change in the force sensor's output voltage was recorded. At this point, it was acknowledged that the ball was in contact with the SMA element. Next, a red laser of wavelength 660 nm and power 100 mW was switched on, to heat the SMA element [11]. Due to optical heating, the SMA element proceeded through a phase transformation to austenite. The SMA element became flat and perpendicular with respect to the support on which it was vertically positioned. Consequently, the recovery action of the SMA element exerted a force upon the centering ball. The laser continued to stay on, while the force sensor moved away from the SMA element, until no output voltage was recorded. From this experiment, the total movement of the force sensor could be considered as the SMA element stroke, as seen through the relationship in Figure 5.

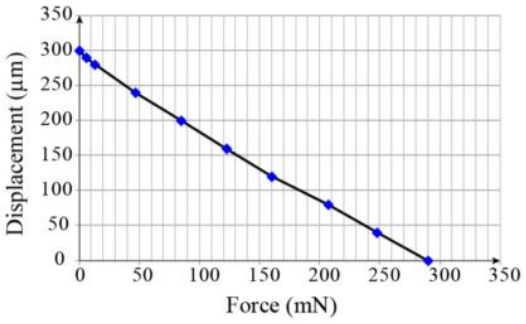

Figure 5: SMA element force vs. displacement results [11]

As it can be concluded from the results of an SMA element with an 8 μm thick SiO_2 layer, from an initial output force of 290 mN, there was a force present until the sensor was 300 μm away from the sensor. Thus, this value could be considered as the stroke of the SMA elements to be used in the quadristable system.

4 INTEGRATION OF SMA ELEMENTS INTO QUADRISTABLE STRUCTURE

4.1 Design and micro-fabrication of quadristable micro-actuator

The main goals when designing the actuator were to obtain a structure that could easily perform the action of micro-conveyance with the help of SMA elements, and to demonstrate the ability to wirelessly activate these SMA elements. Thus, the constraints of the design were to have a lightweight, flat frame that could hold multiple stable positions. The outcome was a silicone quadristable system as shown in Figure 6 (a) - (b), connected via silicone beams.

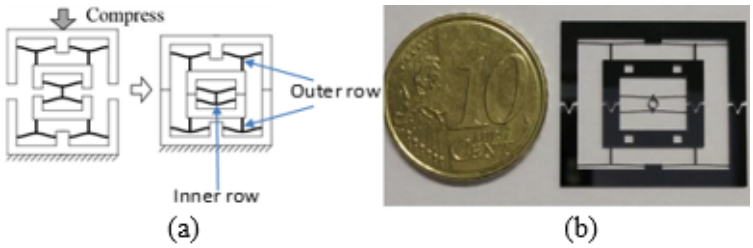

Figure 6: (a) Pre-load of quadristable mechanism based on antagonistic pre-shaped double beams; (b) Fabricated quadristable actuator on silicon wafer before pre-load

When the outer and inner frames of the quadristable actuator were permanently fixed together, using cyanoacrylate glue, the pre-load of the quadristable mechanism was conducted. This was based on the antagonistic properties of the pre-shaped double beams. The outer row would always display the same side of stability, whereas the actuation of the inner frame could be conducted regardless the stability of the outer frame. However, the output force of the actuation would be different, depending upon the stability of the quadristable system. This force provided by the pre-load allowed the SMA elements to perform the system's actuation.

Fabricating the quadristable micro-actuator required great precision and accuracy. Obtaining bistable beams of the correct thickness was of great importance, since thin beams would hamper the stroke range of the actuator. As well, to obtain the symmetrical output force of antagonistic pre-shaped double beams, the beams within the entire frame needed to possess the exact same shape. Thus, the deep reactive ion etching (DRIE) technique was used to fabricate the quadristable frame and bistable beams, with the silicon-on-insulator (SOI) wafer [11].

Once the micro-fabrication was complete, six bistable beams of length 8 mm and thickness 25 μm, respectively, were created. A central ring of diameter 1 mm provided a link between the inner bistable beams, allowing for the bistable properties between the two antagonistic inner beams to be exposed. The four outer beams were connected by thin silicone rods, to the inner bistable frame. This would ensure that stability on the outer beams would reflect the bistable and antagonistic properties of the inner frame, as shown in Figure 6 (b).

4.2 Integration of SMA elements

Once the thin-film processing of Nitinol SMA elements was conducted, they were ready to be integrated within the quadristable system. A support made from PMMA plastic was glued to the bottom of the quadristable frame, and positioned in a manner to impose the necessary forces required for actuation of the silicone beams.

Before inserting SMA elements into their respective positions, they were laser cut to the dimensions of $0.1 \times 1 \times 3$ mm. The heat-affected zone during laser cutting was found to be less than 10 μm, which was deemed insignificant as compared to the size of the SMA element. Therefore, there was no issue with regards to the laser cutting process impeding the performance of the shape memory effect. Once the laser cutting was completed, the SMA element was pickled in hydrofluoric acid to improve the surface conditions for thin film deposition. Next, the SiO_2 was deposited on the SMA elements, using the technique of magnetron sputtering of a silica target with an argon plasma. This process was conducted at a pressure of 1 Pa, an RF power of 300 W, and a growth speed of approximately 2 μm per hour [11]. Once completed, a deposited thickness of 8 μm was achieved, allowing for strong compressive stresses to perform the role of a biasing spring throughout the cooling scenarios of the optically-based actuation.

Referring to the experimental force measurements of the SMA elements, it was found that the stroke value of 300 μm would only apply to the SMA elements within the inner bistable frame. This is because the bistable beams were found to have a total stroke of 300 μm. On the other hand, the entire bistable frame (quadristable beams) was found to have a total stroke of 200 μm. Thus, to avoid a load effect and exaggerated actuation causing the beams to break, the unheated SMA elements were kept at a distance of 20 μm from both the bistable beams and the inner bistable frame. As well, considering the Timoshenko-based mathematical model for the design of the quadristable actuator, an output force of approximately 15 mN was required for the actuation of each row. This force was easily met by the force vs. displacement results of the SMA elements. In conclusion, the stroke of the SMA elements was strong enough to switch the stability of the quadristable frame from one position to another, in the setup constructed for the integration of the SMA elements.

5 EXPERIMENTAL TEST AND RESULTS

The final step in the completion of the article was the analysis of data collected through experimentation. The quadristable structure was wirelessly actuated to determine the strokes of the inner bistable beams and the bistable frame. Using a laser with the same characteristics as the one used for the theoretical stroke measurements of the SMA elements (P = 100 mW, λ = 660 nm), the beam was firstly positioned upon an optical beam steering micro-mirror / MEMS mirror with a diameter of 2 mm (S1492, Mirrorcle Technology) [11]. As shown in Figure 7, the MEMS mirror could rotate within a range of 5°, in a computer-controlled environment. The laser beam also passed through three different lenses of different focal lengths, in order for the diameter of the laser beam to be correctly focused upon the SMA element. It was predicted that the laser beam would exhibit elliptical characteristics, when focused upon the SMA elements.

In terms of optically heating each respective SMA element, the MEMS mirror was angled in order to focus upon each SMA element in a timed cycle. As shown in Figure 7, the SMA elements were positioned under the quadristable structure using a fixed PMMA support.

Finally, measuring the stroke of the SMA elements was performed using a fibre-optic sensor. A small prism with reflective properties was positioned upon the inner ring of the quadristable system. Then, a fibre-optic sensor was positioned in front of the mirror. This sensor would output a voltage, which was converted to a displacement value using a mathematical relationship determined during calibration exercises of the sensor.

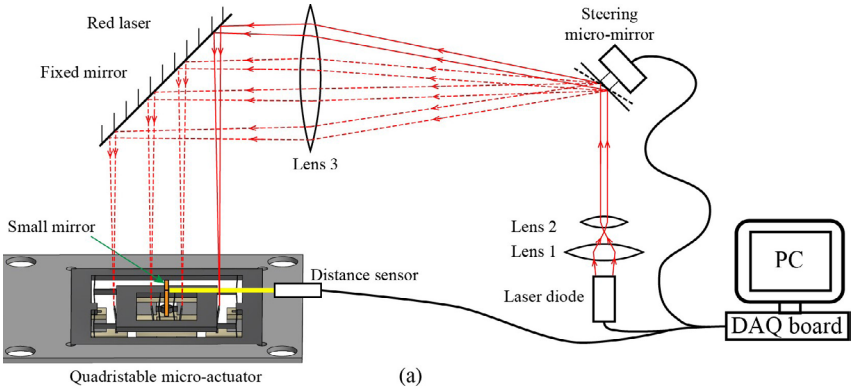

Figure 7: Experimental setup for wireless actuation of quadristable micro-actuator [12]

In terms of other control variables for the experiment, the heating and cooling durations of the SMA elements were timed at four seconds for the inner bistable row, and eight seconds for the outer row. This ensured that the SMA elements and the bistable beams / frame would be able to stabilize before another switch in stability. Even though the snap duration was timed to be less than 20 ms, these heating and cooling duration cycles provided enough time to observe the properties and for the distance sensor to register the change in the voltage values, after a slight vibration in the quadristable system.

After 4000 heating-cooling cycles, the inner stroke was found to be (267 $\pm$ 3) μm, while the outer row stroke was found to be (187 $\pm$ 2) μm. Also, the SMA elements and quadristable structure were found to be in a satisfactory physical condition. The thin-film deposition on the SMA element did not appear to be severely cracked, since the actuation of the system over several cycles did not skew the results (the uncertainty includes the difference between several averaged actuation exercises). A comparison between the theoretical stroke of the SMA elements and the experimental stroke can be found in Table 1.

Table 1: SMA elements' stroke measurement results

	Theoretical Stroke (μm)	Experimental Stroke (μm)
Inner Row	300	267 $\pm$ 3
Outer Row	200	187 $\pm$ 2

Analyzing the differences between the experimental and theoretical stroke values, the gluing process between the inner and outer frames of the system may have affected the overall rigidity

of the system and susceptibility to movement/actuation. As well, the weight of the reflective mirror on the inner ring may have also required a greater force to be exerted by the SMA elements, on the inner bistable beams, for actuation. Finally, miniscule cracks within the thin-film SiO_2 deposition layer may have reduced the effect of pre-load by the SMA elements upon the system. Therefore, over time, the biasing spring characteristics of the deposition layer may have worn off, resulting in a smaller experimental stroke for the inner row. A representation of the actuation of the quadristable micro-actuator can be seen in Figure 8.

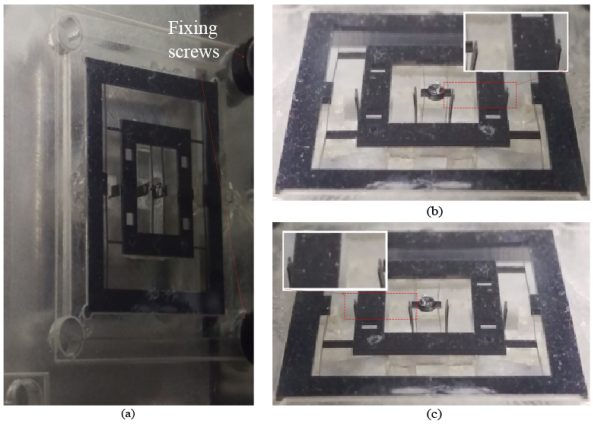

Figure 8: (a) Top angle view of quadristable frame and SMA mount; (b) Side view when inner and outer rows in right stable position; (c) Side view when inner and outer rows in left stable position

6 CONCLUSION

The purpose of this article was to identify the design, characterization and implementation of shape memory alloy elements' theory within an optical wireless quadristable actuator. Fabricated using the DRIE technique on SOI wafer, the micro-actuator was formed by connections between bistable and quadristable beams. These beams switched between stable positions with the assistance of SMA elements, laser heated to actuate the system. The SMA elements possessed an SiO_2 layer, which acted as a biasing force in a two-way memory effect property of the SMA elements. Three lenses, a MEMS mirror and a laser diode provided the correct setting to actuate the quadristable system. Errors found within experimentation included gluing properties and fatigue/stress of the beams and SMA elements. Further research will be conducted to minimize the errors during actuation. Suggestions include reducing the weight of the reflective mirror on the ring, diminishing the usage of cyanoacrylate glue in the system, and limiting the surface area of the thin-film SiO_2 layer to improve the speed of the shape memory effect within the system.

7 ACKNOWLEDGEMENTS

The authors would like to thank the National Agency for Research (ANR) for funding this READMI project (Reference ANR-13-BS03-0003-01). This work was also carried out in the framework of Labex MS2T, funded by the French government, in accordance with the *Investment for the Future* program. This program is managed by ANR (Reference ANR-11-IDEX-0004-02).

REFERENCES

[1] J. Li, "Wireless power transmission: State-of-the-arts in technologies and potential applications (invited paper)", in *Asia-Pacific Microwave Conference*, Melbourne, 2011, pp. 86-89.

[2] M. Mohamed Ali and K. Takahata, "Frequency-controlled wireless shape-memory-alloy microactuators integrated using an electroplating bonding process", *Sensors and Actuators A: Physical*, vol. 163, no. 1, pp. 363-372, 2010.

[3] M. Mohamed Ali, B. Bycraft, A. Bsoul and K. Takahata, "Radio-Controlled Microactuator Based on Shape-Memory-Alloy Spiral-Coil Inductor", *Journal of Microelectromechanical Systems*, vol. 22, no. 2, pp. 331-338, 2013.

[4] S. Baglio, S. Castorina, L. Fortuna and N. Savalli, "Modeling and design of novel photo-thermo-mechanical microactuators", *Sensors and Actuators A: Physical*, vol. 101, no. 1-2, pp. 185-193, 2002.

[5] I. Mori, M. Kubota, E. Lebrasseur and Y. Mita, "Remote power feed and control of MEMS with 58 V silicon photovoltaic cell made by a CMOS post-process dry release and device isolation method", in *Symposium on Design, Test, Integration and Packaging of MEMS/MOEMS (DTIP)*, Cannes, 2014, pp. 79-82.

[6] E. Vela, M. Hafez and S. Rgnier, "Contactless automated manipulation of mesoscale objects using opto-fluidic actuation and visual servoing", *Review of Scientific Instruments*, vol. 85, no. 5, p. 055107, 2014.

[7] S. Zaidi, F. Lamarque, J. Favergeon, O. Carton, C. Prelle, M. Lejeune and A. Zeinert, "Wavelength Dependent Remote Power Supply for Shape Memory Alloy", *Journal of Intelligent Material Systems and Structures*, vol. 21, no. 2, pp. 175-184, 2010.

[8] S. Zaidi, F. Lamarque, C. Prelle, O. Carton and A. Zeinert, "Contactless and selective energy transfer to a bistable micro-actuator using laser heated shape memory alloy", *Smart Materials and Structures*, vol. 21, no. 11, p. 115027, 2012.

[9] O. Carton, M. Lejeune, F. Lamarque, S. Zaidi and A. Zeinert, "Thermo-mechanical characterization of optical thin films filters deposited onto shape memory alloy micro-actuators", *Smart Materials and Structures*, vol. 23, no. 12, p. 125035, 2014.

[10] L. Han and S. Chen, "Wireless bimorph micro-actuators by pulsed laser heating", *Sensors and Actuators A: Physical*, vol. 121, no. 1, pp. 35-43, 2005.

[11] X. Liu, H. Al-Hajjar, F. Lamarque, E. Doré, O. Carton, A. Zeinert and S. Charvet, "An Optical Wireless Bistable Micro-actuator", in *Mechatronics and Automation (ICMA)*, Beijing, 2015.

[12] X. Liu, "Contribution to optical wireless multi-stable micro-actuation", Ph.D, Université de Technologie de Compiègne, 2015.

VIII ECCOMAS Thematic Conference on Smart Structures and Materials
SMART 2017
A. Güemes, A. Benjeddou , J. Rodellar and Jinsong Leng (Eds)

STRUCTURING AND DESCRIBING REQUIREMENTS IN A FLEXIBLE MESH FOR DEVELOPMENT OF SMART INTERDISCIPLINARY SYSTEMS

IRIS GRAESSLER*, JULIAN HENTZE*

* Heinz Nixdorf Institute (HNI)
Paderborn University
Fürstenallee 11, 33102 Paderborn, Germany
e-mail: julian.hentze@hni.upb.de, web page: https://www.hni.uni-paderborn.de/en/pe/

Key words: Requirements Engineering, System Development, Flexible Meshes

Abstract. This paper proposes an approach, which transfers requirements list into a flexible mesh. The flexible mesh contains of requirements and relations as objects. The mesh is able to analyze a huge number of requirements and its relations. In comparison to requirement lists, the usage of the mesh is more flexible: There are possibilities to categorize, to implement changes and to identify critical and high-connected objects for deeper analysis. The mesh, through reuse and learning capability, can be an attractive support for requirements management, especially for small and medium-sized companies, that do not want to or cannot use extensive established software for their requirements engineering.

1 INTRODUCTION

Today the development effort of high-tech systems like smart mechatronic products and Cyber Physical Systems (CPS) is increased by technical and organisational complexity [1, 2]. Different development approaches try to handle the complexity as well as the interdisciplinary and internationally disturbed development process. Examples for development approaches are Systems Engineering [3, 4, 5, 6] or the mechatronic V-model, described in the guideline VDI2206:2004 [7]. Both approaches aim to unite the languages and methodologies of different disciplines. Target of the development approaches is System Integrity, which means that technical, schedule and financial aspects are in balance during the whole project and especially at decision gates at the end of the different milestone phases [6].

At the beginning of each development process, not important which development approach is followed, requirements are focussed [6, 7]. Requirements Engineering means the elicitation, management and documentation of all requirements, which are necessary to develop the target product [8]. Requirements should include all information from every relevant stakeholder about the expected product. They are basis for verification and validation, which means to examine whether the system is built right (verification) and whether the right system is built (validation) [6]. A verified and validated system fulfils all the requirements.

The Standish Group 2011 study [9] shows the importance of Requirements Engineering for the development of smart technical systems. Insufficient knowledge in the area of requirements and insufficient clarification are two of the main reasons for the non-fulfilment of project

objectives [9, 10]. The study shows the need for increased frontloading to enhance Requirements Engineering.

Intention of this paper is to describe the idea and the ongoing development of a flexible mesh as a basis for structuring and handling requirements for the development of smart technical systems. The aim of the tool is to create opportunities especially but not only for Small and Medium-sized Enterprises (SME) to analyse the requirements of an individual project. The advantage of the flexible mesh tool is in the depiction of the relations between the different requirements. In addition to attributes, which are described in requirements lists as well [11], the analysis of relations provide further information about the importance and criticality of requirements. This overall analysis of relations between requirements, accomplishes the realization of the idea of Systems Thinking [6, 12]. Especially in large projects with high uncertainties, this early investigation and identification of critical requirements can be useful to prioritize the Work Breakdown Structure (WBS) for the project and to overcome the critical aspects. This can mean both negative risks and positive opportunities [6].

2 STATE OF THE ART

2.1 Requirements Engineering

Requirements Engineering (RE) already is an important topic in industry [2]. RE defines the needs of the customer and any additional stakeholder for the system which should be developed and translate the needs and wishes in technical and formal written requirements [6]. Most of the costs of a development project are defined in the early requirement stage of the development process [6]. Therefore requirements are collected in structured lists, which are clustered in different categories [13]. These categories should support the user in identification by associations as well as in structuring. The different key activities of Requirements Engineering are illustrated in Figure 1.

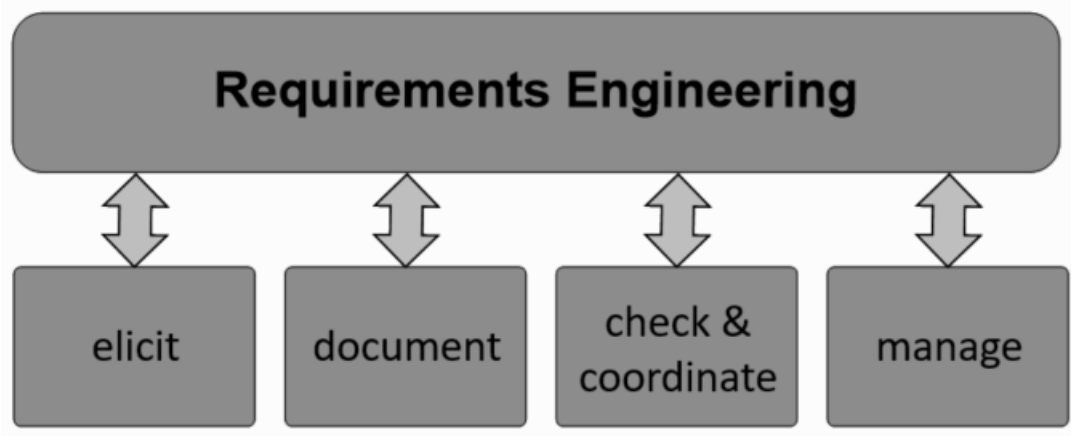

Figure 1: Key activities of Requirements Engineering [8]

Companies elicit and document requirements with different methods in diverse software tools. Examples are IBM - Rational Doors, Magic Draw, ReqSuite or Omnitracker. Because of high costs for the software tools and high complexity in the application, SME ordinarily use standard office tools like Microsoft Word or Microsoft Excel to work with their requirements,

although the number of requirements is frequently high [14]. This handling in unspecific tools leads to a light-minded dealing with the topic of requirements engineering. The structure of Pahl/ Beitz feature list [13] is usual to categorize and to classify the requirements especially for mechanical products. Instead of handle requirements for the development, many companies just use the Requirements Engineering for documentation.

2.2 Dependencies between requirements

The main quantity of all requirements is not independent. The requirements for the overall system cannot be fulfilled by individual satisfaction of all the individual requirements. Requirements are connected in different ways and have influences on each other in direct or indirect relations. These influences are often not intended and partially not identified by the stakeholder, that formulates requirements. Dependencies of requirements influence the whole development process for smart interdisciplinary systems. Especially topics as change management, reuse of components or functions, design and implementation can depend in a high level on the relations of requirements [15]. As described in [16], Requirements Engineering and thus also the use of requirements management tools like the flexible mesh, should be considered in an extended part of the development process. In [16] this is explained for the mechatronic V-model of VDI 2206:2004. Requirements Engineering should follow the whole V-model with a parallel process to the development progress [7].

2.3 SysML Requirements diagram

The SysML requirements diagram is specified in Systems modelling Language (SysML) 1.3: SysML provides modelling constructs to represent text-based requirements and relate them to other modelling elements [17, 18]. The requirements diagram can depict the requirements in graphical, tabular or tree structure format. A requirement can also appear on other diagrams to show its relations to other modelled elements. The requirements modelling constructs are intended to provide a bridge between traditional requirements management tools and the further SysML models [19]. Most important is the connection to the block definition diagram (bdd), which assigns the requirements to systems, subsystems or elements that fulfil or is in an important interconnection with the requirement [17]. By defining the architectural structure of a system, the requirements were allocated to elements and subsystems. SysML requirements diagram (req) in different system levels and in divers granularities help to understand interfaces and definitions of different parts of the system.

3 DEVELOPMENT OF THE FLEXIBLE MESH

The flexible mesh is built in a simple structure as a java-based tool: The object-orientated implementation bases on three main classes: First and most important is the requirements class, which describes the requirement and its attributes. Additionally the relations class extends the flexible mesh by the description of different kinds of relations. The classes are described in details in section 3.1 and section 3.2. A third class, not necessary for the content but for the realization and application of the mesh, includes the code for visualization of the user interface and the controlling of the whole program. All generated objects no matter whether requirement or relations are numbered by an individual and unique integer for identification. The objects are placed and saved in an array or a list (depends on implementation).

The structure of the mesh is shown in Figure 2. The UML class diagram describes the different attributes and methods of the first version. The visualization class is also responsible for controlling and starting the mesh and exists only once. All methods are allocated at this class. The number of object created by the requirements class is theoretically unlimited. Every relation object that exists has to be connected with two requirements objects. The number of relation objects for a requirement object is also unlimited.

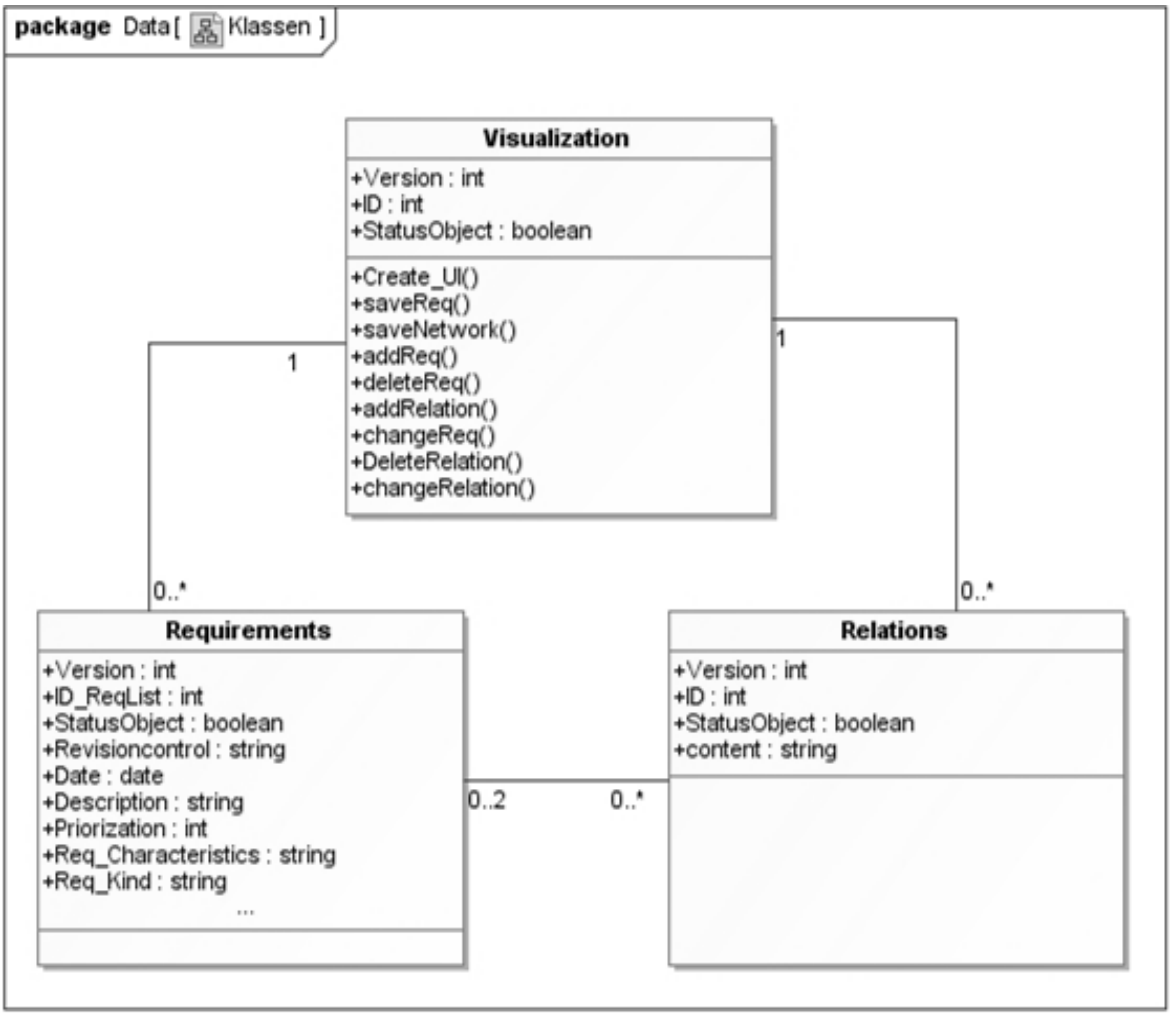

Figure 2: Exemplary UML-class diagram of the basic structure of the flexible mesh tool in an early version

3.1 Description of requirement class

Different categories, which are used to structure the classic requirements list, can be transferred to the flexible mesh to filter the whole requirements portfolio and enhance the possibility to have different views at the flexible requirements mesh [12]. For the first version of development of the flexible mesh, requirements class will base on attributes of Pahl/ Beitz [13]. That means all the descriptive attributes from the four categories content, identification, retracing and organization, which are illustrated and described in more details in Figure 3.

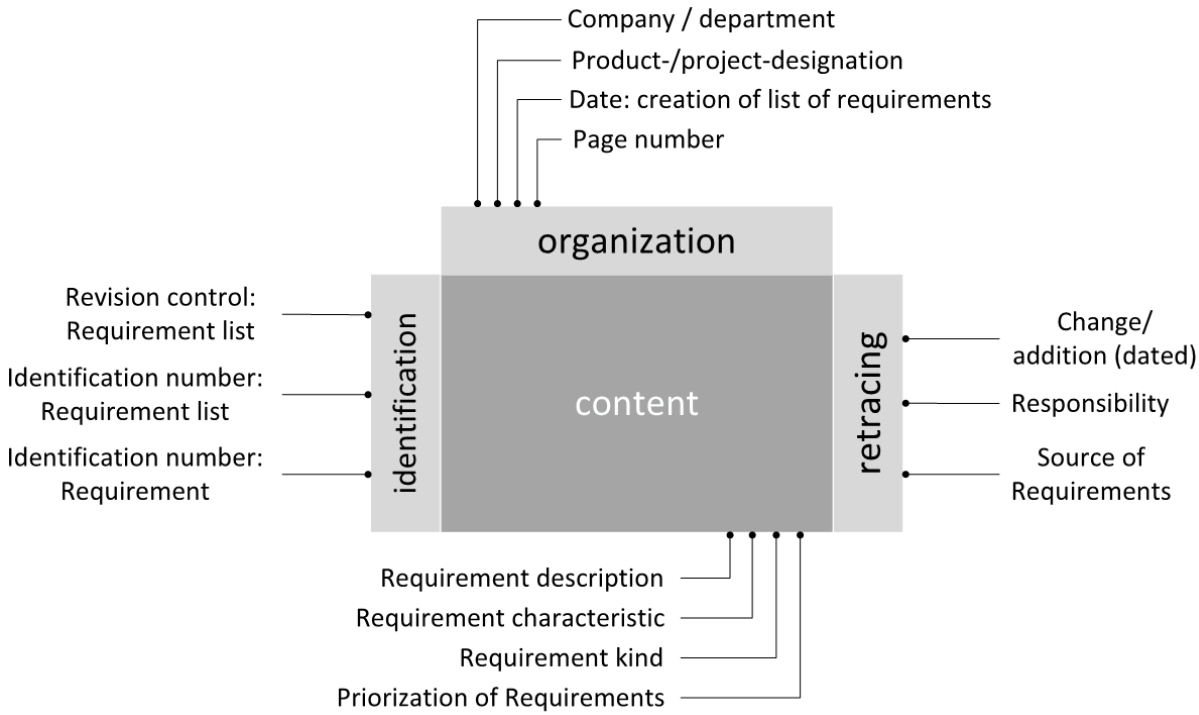

Figure 3: Structure of a requirements list [13]

In addition to the categorization of the relations, these get descriptions of force and direction. This feature is not implemented at the first version, because the possibility rating the different relations in an individual comparison has to be checked first. This implementation would enlarge the users input to an unacceptable level.

3.2 Description of relations class

The description of the relations class is based on references from Pohl [20] und Dahlstedt [21]. They analysed different ways of interconnections between requirements and classified the possible relations in categories. It is important to understand, that all this requirements are focussing interdependencies between each other. Relations to other formalised objects e.g. parts of the system or functions are not included in the analysis. That means there is a differentiation to SysML requirements diagram. It is rather IBM rational doors, which inspire the flexible mesh. The structure of Pohl [20] is shown in Figure 4.

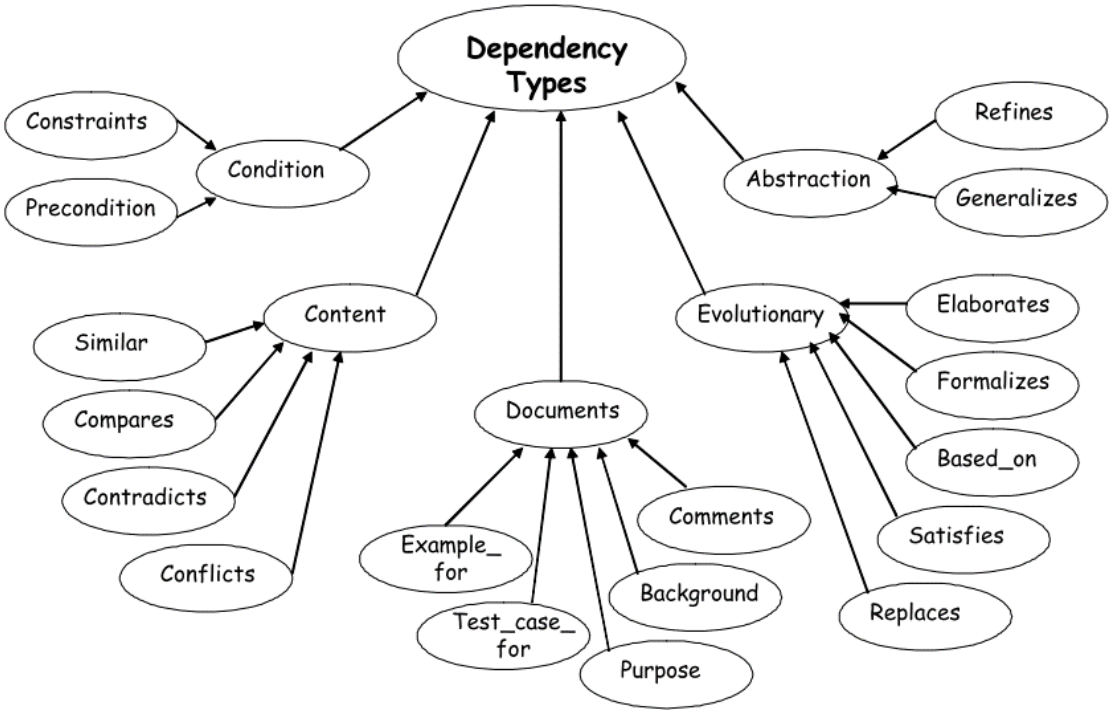

Figure 4:Categorisation of dependency type by Pohl 1996 [20]

To identify a differentiated, tailored and updated categorization, a graph with all possible and established relations is built in the first step [15]. A comparison with the requirements for the design of the flexible mesh is made to reduce the number of possible relations. The number of different relations should not be that high as at Pohl's categorisation, because the implementation of the relations between the requirements is not automated in the first versions of implementation of the flexible mesh. The effort for building a holistically matrix is very high. The user has to check the square of the total number of requirements.

An important addition to the all the dependency types in literature, the type unknown is added for the flexible mesh. This is important to implement relations for example at the beginning of the project, where are no more detailed information at that status of development. The final categorisation for the first version of the flexible mesh is shown in Figure 5. In this case, no relation can assume more than one characteristic. It is possible to have two different types of relations between two requirements. These cannot be low-level characteristics. For example, an "and-" with an "or-relation" cannot exist between the same two objects in parallel, because this would be contradictory.

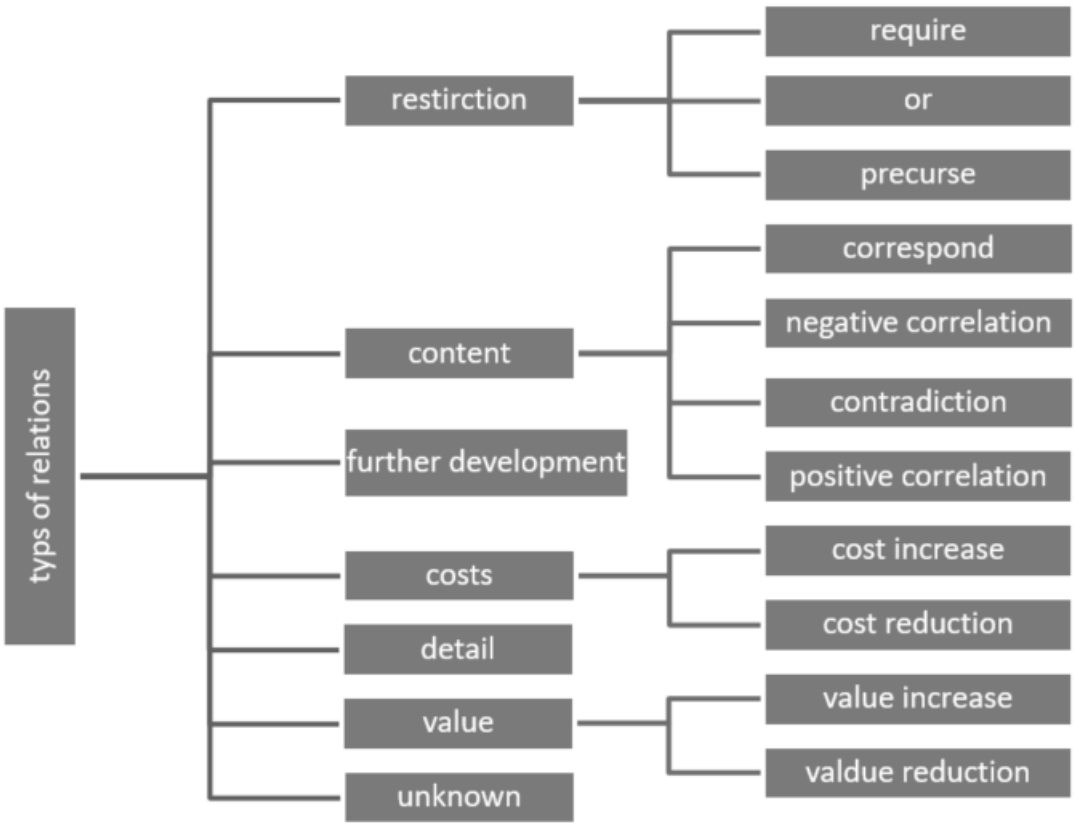

Figure 5: Types of relations between requirements in the flexible mesh

4 APPLICATION OF THE FLEXIBLE MESH FOR DEVELOPMENT OF SMART INTERDISCIPLINARY SYSTEMS

For the use of the flexible mesh, some conditions have to be fulfilled. The mesh does not support in the elicitation of requirements. The technical formalised requirements are the first input for the mesh. The transfer from different MS excel columns to attributes is easy to realize. The identification of relations in a matrix between the requirements needs intensive work by interdisciplinary product experts. This matrix is named “Requirements structure Matrix” (RSM). The different types of connections are entered here with letters.

4.1 Integrate Requirements

Important for effective use of the flexible mesh is the possibility of reuse requirements and relations from a database. This applies both to the description of requirements, and to the reconciliation of relations between the requirements. The user interface of the software should support the user with drop-down suggestions to use the same description as in a former project. The individual description by details is still necessary, but much easier as without information.

4.2 Structure Requirements

The structure of requirements is a basic property of the mesh. The mesh have to be able to document all the requirements in the same way as a requirements list. Therefore the categories, explain in the sections before, are implemented as an attribute for every object. Simple algorithms are able to sort the requirements by those categories, independent or dependent from relations or other attributes. This structuring could help to improve the development in different disciplines and to identify interfaces during the project.

4.3 Analyse Requirements

Analysing the flexible mesh means to identify numerical data. For example, the number of relations connected to one requirement is a hint for complex fulfilment of the requirement or for the importance. Requirements with no relations should be investigated: This could be a sign for extremely high or low importance of the requirement.

4.4 Maintain Requirements

An important goal of the flexible mesh is to have the possibility to implement changes during the development process. The addition or deletion of a requirement can influence other requirements. This analysis is an advantage of the flexible mesh. Changing the attributes and relations of a requirement is default and easy to handle.

5 CONCLUSION AND OUTLOOK

The most important benefit of the mesh is not a flexible structure, but flexibility in using the mesh for individual and clear structured Requirements Engineering. Aim of the flexible mesh of requirements is a tool to structure, analyse and maintain requirements in a development project. It should be able to extract critical requirements and identify the core requirements, which have the strongest interconnection to each other. Later on in the development process, there should be the possibility to illustrate which requirements are verified and connect them with a testing procedure and the following individual testing-results to use the mesh as a kind of checklist. The proposed flexible mesh is used as an instrument for testing and validating research work, which concerns elicitation, the structure and the implementation of changes during product engineering process. The mesh provides a flexible tool to handle requirements for interdisciplinary systems. In future work the approach should be validated and expanded for a higher number of requirements in complex systems.

Three key advantages are listed hereafter:

- Open source software for application in teaching and industry, especially for SME instead of using MS-Office tools
- Consideration of relations between requirements and first indications to learn more about influences of requirements
- Identification and possibility of analysis of requirements with high number of relations

Four key challenges and main research topics are listed below:

- High effort in implementing requirements and relations
- Reuse of requirements and relations from a connected database have to be tested and

validated
- Development of useful algorithms for structuring and analysis of different effects of dependencies
- Willingness for structured handling of requirements during the development process in companies

Whether the network has a real benefit for the economy must show itself in the application. In principle, it is to be developed and implemented for SME. However, first it is the basis for scientific investigations with regard to the relationship between requirements.

The development and implementation of the mesh is in progress, what means that many of the ideas in this paper are not realized or validated at this time. This work is still in progress: It will enrich understanding and knowledge about Requirements Engineering and the usage of requirement tools and methods for the development of smart interdisciplinary systems.

REFERENCES

[1] M. Abramovici and O. Herzog, Eds., Engineering im Umfeld von Industrie 4.0: Einschätzungen und Handlungsbedarf, München: acatech; Herbert Utz Verlag GmbH, 2016.
[2] J. Gausemeier and R. Dumitrescu, "Systems Engineering in der industriellen Praxis", Studie, Fraunhofer IEM, 2015.
[3] U.S. Department of Transportation, "Systems Engineering Guidebook for Intelligent Transportation Systems: Version 3.0," 2009.
[4] U.S. Department of Defense, "Systems Engineering Fundamentals," 2001.
[5] National Aeronautics and Space Administration, "Systems Engineering Handbook," Rev1, Washington D.C., 2007.
[6] D. D. Walden, "INCOSE Systems Engineering Handbook: A Guide for System Life Cycle Processes and Activities,"
[7] VDI 2206 - Design methodology for mechatronic systems, VDI 2206, 2004.
[8] K. Pohl and C. Rupp, Requirements engineering fundamentals, 2nd ed. Santa Barbara, CA: Rocky Nook, 2015.
[9] Standish Group, "Chaos Manifesto 2011," West Yarmouth, USA, 2011.
[10] C. Ebert, Systematisches Requirements Engineering: Anforderungen ermitteln, spezifizieren, analysieren und verwalten, 4th ed. Heidelberg: dpunkt-Verl., 2012.
[11] VDI 2221 Methodik zum Entwickeln und Konstruieren technischer Systeme und Produkte, VDI 2221, 1993.
[12] R. Haberfellner, Systems Engineering: Grundlagen und Anwendung, 12th ed. Zürich: Orell Füssli, 2012.
[13] J. Feldhusen and K.-H. Grote, Pahl/Beitz Konstruktionslehre: Methoden und Anwendung erfolgreicher Produktentwicklung: Springer, 2012.
[14] C. Oleff, "Vergleich und Analyse von Systems Engineering- Methodiken und Identifikation von Anwendungs- potentialen für ein Kleinunternehmen," Bachelorarbeit, HNI, Universität Paderborn, Paderborn, 2015.
[15] Christian Oleff, "Erarbeitung eines Referenzmodells für die Identifikation und Klassifizierung von Zusammenhängen zwischen Anforderungen," Studienarbeit im

Rahmen des Wirtschaftsingenieur Studiums, Heinz Nixdorf Institut, Universität Paderborn, Paderborn, 2017.
[16]I. Gräßler, J. Hentze, and X. Yang, "Eleven Potentials for Mechatronic V-Model," in Production Engineering and Management: 6th International Conference, 2016, pp. 257–268.
[17]T. Weilkiens, Systems Engineering mit SysML/UML: Modellierung, Analyse, Design, 3rd ed. Heidelberg, Neckar: dpunkt, 2014.
[18]O. Alt, Modell-basierte Systementwicklung mit SysML: In der Praxis. München: Hanser, Carl, 2012.
[19]OMG Systems Modeling Language (OMG SysML™), 2012.
[20]K. Pohl, Process-centered requirements engineering. Taunton: Research Studies Press, 1996.
[21]Å. G. Dahlstedt and A. Persson, "Requirements Interdependencies: State of the Art and Future Challenges," in Engineering and Managing Software Requirements, A. Aurum and C. Wohlin, Eds., Berlin, Heidelberg: Springer-Verlag Berlin Heidelberg, 2005, pp. 95–116.

VIII ECCOMAS Thematic Conference on Smart Structures and Materials
SMART 2017
A. Güemes, A. Benjeddou, J. Rodellar and J. Leng (Eds)

AN OPTIMAL METHOD FOR PERIODIC STRUCTURES DESIGN

G. CAZZULANI*, E. BELLONI*, E. RIVA*, J. MARCONI*, F. BRAGHIN*

*Politecnico di Milano
Via La Masa 1, 20156 Milano, Italy
e-mail: gabriele.cazzulani@polimi.it, web page: http://www.polimi.it/

Key words: Smart Structures, Optimal, Band-Gap, Attenuation, Periodic Beam

Abstract. Periodic structures act as mechanical filters for elastic wave propagation, therefore they can be used to attenuate vibrations within precise frequency bands, that are known as band-gaps. Nowadays, the design of such structures is faced using dispersion band-maps: varying the system parameters, one can figure out how position and width of the attenuation regions move. However, this approach is not satisfactory, being the solution based on the designer experience. Furthermore, it is impossible to make considerations about its optimality. In this paper, a new method is proposed, providing an optimal solution in the sense that the designed structure exhibits the maximum attenuation at the desired frequency, under certain physical and geometrical constraints. Starting from waves reflection and transmission coefficients, a purely analytical model for rods and beams design has been developed. The design of band-gap position has been decoupled from its magnitude of attenuation by means of a corrective factor depending on how a wave is bounced at cells interfaces. Plus, the same model has been used to predict the position of the neighboring band-gaps. As a result, dispersion band-maps are needed just for optimality check, but not for design purposes. In order to validate the model, a passive periodic structure has been manufactured, and experimental response is compared to the analytical one.

1 INTRODUCTION

Periodic structures are the repetition in space of a fundamental block of matter, called unit cell, characterized by internal variations of geometrical and/or elastic material properties. The mechanical mismatch affects the wave propagation: every time a discontinuity is present, part of the incoming wave is reflected while only the remaining part is transmitted. The global behavior along the structure shows wide frequency ranges were waves are canceled by destructive superposition [1]: these are the generally called band-gaps. Nowadays, the choice of the geometrical parameters is a trial-and-error procedure: non-dimensional parameters allow to decrease the number of variables to be handled [2]. Moreover, such parameters are varied in order to show how the attenuation regions move in the frequency domain. The correspondent diagrams are known as band-maps [3]. In this way, one can easily choose a set of geometrical properties in order to attenuate a target frequency band, but nothing can be said about its optimality.

The maximization of band-gap width and magnitude of attenuation in 1D-2D and 3D periodic structures is a well known challenge and object of research [4]. An optimal way in order to reach this target onto 1D structures (rod and beam cases) is provided in this paper. An analytical formulation is used, based on how the waves are reflected in presence of a mechanical impedance mismatch.
At first, the mathematical tools needed for the structural optimization are presented. In particular, the transfer matrix method allow to study the attenuation properties of a unit cell, while reflection and transmission matrices are used to modify the design procedure. Subsequently, an algorithm for tuning the band-gaps position at the desired frequency, and at the maximum attenuation point, is presented for the rod and beam cases. Finally, the frequency response of a periodic beam has been measured in order to validate the design process.

2 TRANSFER MATRIX METHOD

The transfer matrix method is a mathematical tool that allows to study the wave propagation behavior of a periodic structure just referring to its unit cell. The transfer matrix $[T]$ links the left and right state vectors $\underline{u}$, which contain displacements and forces at boundaries [5]-[6]. For the sake of simplicity, here only the formulation for a rod is presented, but a similar procedure exists for beams (and even more complicated case-studies such as multi-dimensional structures). The standing wave solution for longitudinal wave propagation along a rod is expressed by the following relationship:

$$u(x) = a_1 e^{-j\kappa x} + a_2 e^{j\kappa x} \tag{1}$$

where κ is the wavenumber and a_1,a_2 are the wave amplitudes. Left and right displacements u can be written in matrix form:

$$\underline{d} = \begin{pmatrix} u(0) \\ u(L) \end{pmatrix} = \begin{bmatrix} 1 & 1 \\ e^{-j\kappa L} & e^{j\kappa L} \end{bmatrix} \begin{pmatrix} a_1 \\ a_2 \end{pmatrix} = H_d \underline{c} \tag{2}$$

Furthermore, using the elastic constitutive laws for a rod, forces at boundaries are:

$$\underline{f} = \begin{pmatrix} -EA\dfrac{\partial u(0)}{\partial x} \\ EA\dfrac{\partial u(L)}{\partial x} \end{pmatrix} = \begin{bmatrix} j\kappa & -j\kappa \\ -j\kappa e^{-j\kappa L} & j\kappa e^{j\kappa L} \end{bmatrix} \begin{pmatrix} a_1 \\ a_2 \end{pmatrix} = H_f \underline{c} \tag{3}$$

where L is the length of the rod element, E is the Young's modulus and A is the cross-section area. Inverting Equation 2 and substituting into Equation 3, one gets a closed form of the dynamic stiffness matrix for a rod:

$$H_f H_d^{-1} \underline{d} = \underline{f} \quad D = H_f H_d^{-1} \quad \rightarrow \quad D = \frac{EA\kappa}{\sin \kappa L} \begin{bmatrix} \cos \kappa L & -1 \\ -1 & \cos \kappa L \end{bmatrix} = \begin{bmatrix} D_{LL} & D_{LR} \\ D_{RL} & D_{RR} \end{bmatrix} \tag{4}$$

Enforcing continuity of displacements and force equilibrium gives the transfer matrix $[T]$:

$$\begin{cases} u_{R,i} = u_{L,i-1} \\ F_{R,i} = -F_{L,i-1} \end{cases} \quad \rightarrow \quad T = \begin{bmatrix} -D_{LR}^{-1} D_{LL} & D_{LR}^{-1} \\ -D_{RL} + D_{RR} D_{LR}^{-1} D_{LL} & -D_{RR} D_{LR}^{-1} \end{bmatrix} \tag{5}$$

where:

$$\begin{pmatrix} u_{L,i+1} \\ F_{L,i+1} \end{pmatrix} = [T] \begin{pmatrix} u_{L,i} \\ F_{L,i} \end{pmatrix} \tag{6}$$

The coupling of two different rod elements introduces a mechanical impedance mismatch within the unit cell. The global transfer matrix is therefore:

$$[T] = [T_1][T_2] \tag{7}$$

Equation 6 describes how a perturbation is transmitted from the left to the right side of a cell. Thus, it contains information regarding attenuation and propagation properties of the system. Floquet-Bloch theorem links the eigenvalues of the transfer matrix to the wave propagation properties [7]:

$$\begin{cases} \underline{u}_{i+1} = T_i \underline{u}_i \\ \underline{u}_{i+1} = \lambda_i \underline{y}_i \end{cases} \tag{8}$$

where $\lambda_i = e^{j\mu} = e^{j(\alpha+j\beta)L}$ is one eigenvalue[1] and $\mu = \kappa L$ is the propagation constant that in general is complex: the real part is the phase of the wave within L while the imaginary part provides the wave decay between left and right boundaries. The relation between μ and ω is represented by the dispersion diagram, separating real part (propagation) and imaginary part (attenuation). ζ, Ω and Λ are the non-dimensional parameters that are chosen in order to decrease the number of variables involved [2]-[3]. For the rod case:

$$\zeta = \frac{A_2\sqrt{E_2\rho_2}}{A_1\sqrt{E_1\rho_1}} \qquad \Omega = \kappa_1 L_1 \qquad \Lambda = \frac{\kappa_2 L_2}{\kappa_1 L_1} \tag{9}$$

ζ is the mechanical impedance mismatch, Ω is the non-dimensional frequency, Λ is the non-dimensional length ratio. Different parameters are chosen for beams:

$$\zeta = \sqrt[3]{\frac{J_2}{J_1}} \qquad \Omega = \kappa_1 L_1 \qquad \Lambda = \frac{L_2}{L_1} \tag{10}$$

3 REFLECTION AND TRANSMISSION

Wave reflection and transmission at interfaces plays an important role in periodic structures: wave superposition is responsible of the filtering effect, i.e. the higher the portion of wave that is reflected, the stronger the attenuation within a band-gap. Also the phase of reflected waves affects this superposition phenomenon. Rod and beam reflection coefficients are evaluated considering an infinitely long structure.

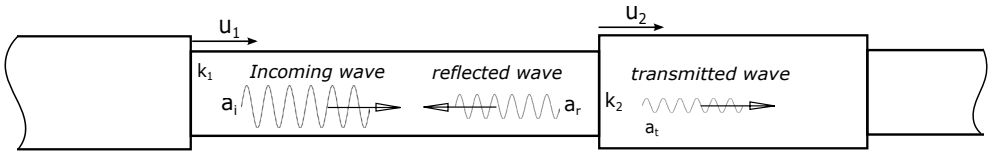

Figure 1: Waves involved in reflection and transmission mechanisms.

[1]This is a mono-coupled system then only a couple of eigenvalue exists. Furthermore, thanks to the symplectic nature of the transfer matrix, such eigenvalues are in reciprocal couple [8]-[3].

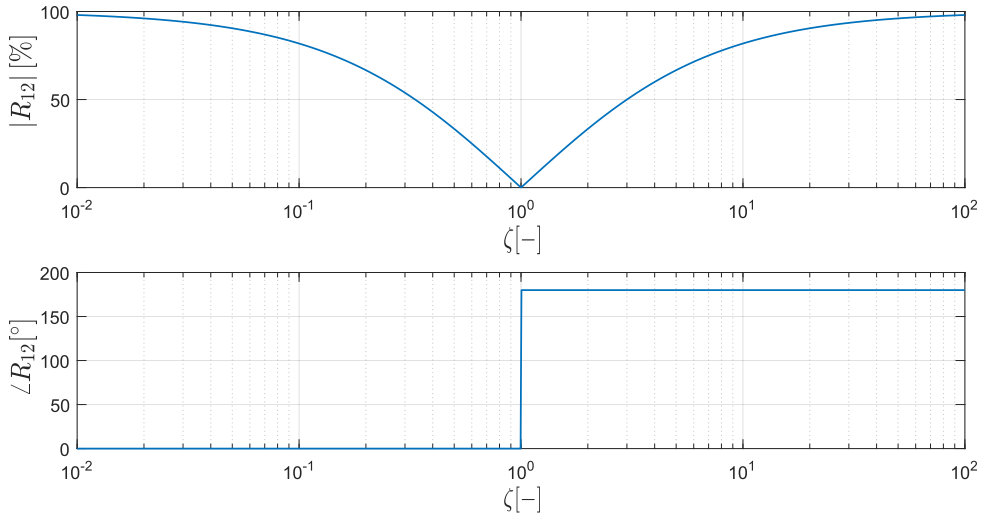

Figure 2: Rod reflection coefficient, varying ζ. Magnitude on the top, phase on the bottom.

3.1 Rod

Referring to Figure 1, the wave solution for the left part (u_1) is made of an incoming term plus the reflected one. For the second trunk a rightwards propagating term (u_2) is assumed.

$$\begin{cases} u_1 = a_i e^{-j\kappa_1 x} + a_r e^{j\kappa_1 x} \\ u_2 = a_t e^{-j\kappa_2 x} \end{cases} \tag{11}$$

Imposing continuity of displacements and forces equilibrium, one can find the transmission and reflection coefficients:

$$\begin{aligned} R_{12} &= \frac{a_r}{a_i} = \frac{1 - \dfrac{A_2 E_2 \kappa_2}{A_1 E_1 \kappa_1}}{1 + \dfrac{A_2 E_2 \kappa_2}{A_1 E_1 \kappa_1}} = \frac{1-\zeta}{1+\zeta} \\ T_{12} &= \frac{a_t}{a_i} = \frac{2}{1 + \dfrac{A_2 E_2 \kappa_2}{A_1 E_1 \kappa_1}} = \frac{2}{1+\zeta} \end{aligned} \tag{12}$$

Looking at Figure 2, one can notice that a_r/a_i and a_t/a_i are purely real and independent from the excitation frequency, and the phase shift is always 0 or $-\pi$ for a wave at the interface. At increasing mechanical impedance mismatch, the amplitude of the reflected wave approaches to 100% of the amplitude of the incoming one.

3.2 Beams

A similar procedure for the reflection and transmission coefficients is used for beams [1]:

$$\begin{aligned} w_1(x,t) = a^+ e^{-j\kappa_1 x} + a^- e^{j\kappa_1 x} + a_N^+ e^{-\kappa_1 x} + a_N^- e^{\kappa_1 x} \\ w_2(x,t) = b^+ e^{-j\kappa_2 x} + b_N^+ e^{-\kappa_2 x} \end{aligned} \tag{13}$$

where a and b are wave amplitudes. Superscripts $+$ and $-$ denote left and right propagating

waves, while subscript N denotes a naturally damped wave[2]. Displacements w, rotations θ, bending moments M and shears T are written in a compact way:

$$\begin{aligned} \begin{pmatrix} w_1(0) \\ \theta_1(0) \end{pmatrix} = \begin{bmatrix} 1 & 1 \\ -jk_1 & -k_1 \end{bmatrix} \cdot \underline{a}^+ + \begin{bmatrix} 1 & 1 \\ jk_1 & k_1 \end{bmatrix} \cdot \underline{a}^- = [A]\,\underline{a}^+ + [B]\,\underline{a}^- \\ \begin{pmatrix} w_2(0) \\ \theta_2(0) \end{pmatrix} = \begin{bmatrix} 1 & 1 \\ -jk_2 & -1k_2 \end{bmatrix} \cdot \underline{b}^+ = [C]\,\underline{b}^+ \end{aligned} \tag{14}$$

$$\begin{aligned} \begin{pmatrix} M_1(0) \\ T_1(0) \end{pmatrix} = E_1 J_1 k_1^2 \left(\begin{bmatrix} -1 & 1 \\ -jk_1 & k_1 \end{bmatrix} \cdot \underline{a}^+ + \begin{bmatrix} -1 & 1 \\ jk_1 & -k_1 \end{bmatrix} \cdot \underline{a}^- \right) = [D]\,\underline{a}^+ + [E]\,\underline{a}^- \\ \begin{pmatrix} M_2(0) \\ T_2(0) \end{pmatrix} = E_2 J_2 k_2^2 \left(\begin{bmatrix} -1 & 1 \\ -jk_2 & k_2 \end{bmatrix} \cdot \underline{b}^+ \right) = [F]\,\underline{b}^+ \end{aligned} \tag{15}$$

where J is the cross section inertia modulus. The amplitude vectors are:

$$\underline{v}^- = \begin{pmatrix} v^- \\ v_N^- \end{pmatrix} \qquad \underline{v}^+ = \begin{pmatrix} v^+ \\ v_N^+ \end{pmatrix} \tag{16}$$

Displacement and rotation continuity, bending moment and shear equilibrium at interfaces allow to solve for $\underline{a}^-$ and $\underline{b}^+$:

$$\begin{cases} [A]\,\underline{a}^+ + [B]\,\underline{a}^- = [C]\,\underline{b}^+ \\ [D]\,\underline{a}^+ + [E]\,\underline{a}^- = [F]\,\underline{b}^+ \end{cases} \tag{17}$$

$$\begin{cases} \underline{a}^- = \left([E] - [F]\,[C]^{-1}\,[B] \right)^{-1} \left([F]\left[C^{-1}\right][A] - [D] \right) \underline{a}^+ = [R]\,\underline{a}^+ \\ \underline{b}^+ = \left[C^{-1}\right][A] + \left[C^{-1}\right][B]\,[R]\,\underline{a}^+ \end{cases} \tag{18}$$

A compact formulation of Equation 19 gives the reflection matrix $[R]$ and the transmission matrix $[T]$:

$$\begin{aligned} \begin{pmatrix} a^- \\ a_N^- \end{pmatrix} = \begin{bmatrix} R_{pp} & R_{pa} \\ R_{ap} & R_{aa} \end{bmatrix} \begin{pmatrix} a^+ \\ a_N^+ \end{pmatrix} = [R] \begin{pmatrix} a^+ \\ a_N^+ \end{pmatrix} \\ \begin{pmatrix} b^+ \\ b_N^+ \end{pmatrix} = \begin{bmatrix} T_{pp} & T_{pa} \\ T_{ap} & T_{pp} \end{bmatrix} \begin{pmatrix} a^+ \\ a_N^+ \end{pmatrix} = [T] \begin{pmatrix} a^+ \\ a_N^+ \end{pmatrix} \end{aligned} \tag{19}$$

Naturally damped waves (denoted by subscript N) and propagating waves are generated both in left and right direction in correspondence of an impedance mismatch. Subscript p, a denotes a propagating wave generated by a damped one. Figure 3 shows that the phase shift for beams is varying with the geometrical and elastic impedance mismatch. This fact influences the amount of attenuation and band-gaps width, introducing a further degree of complexity in the design problem.

[2]An Euler Bernoulli beam is a bi-coupled system, thus there are two pairs of counter propagating waves. It is possible to notice that a pair of waves is always attenuating at all the frequencies [5].

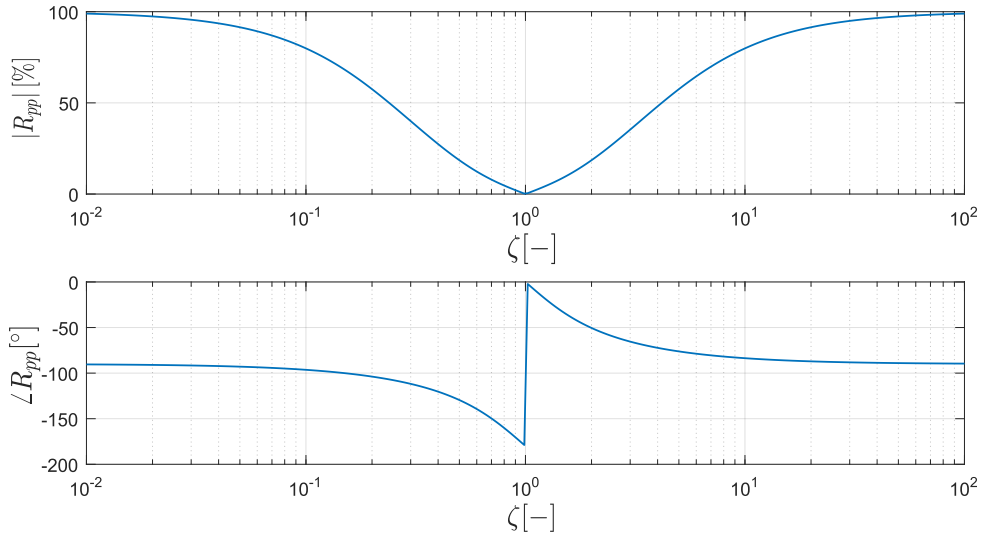

Figure 3: Reflection coefficient R_{pp}, varying ζ.

4 DESIGN

It is possible to tune band-gaps central frequency position using the following relation:

$$\pi + k\pi = \alpha L = \frac{2\pi}{\lambda(\omega)} L \quad \rightarrow \quad \begin{cases} L_1 = \frac{(1+k)}{4}\lambda_1(\omega) \\ L_2 = \frac{(1+k)}{4}\lambda_2(\omega) \end{cases} \tag{20}$$

where λ is the wavelength. Attenuation is achieved when the real part of the propagation constant ($\mu = \alpha + j\beta$) is π and its multiples. Equation 20 means that the phase of the wave lies half within the first part of cell and the remaining half within the second one. The total phase within the cell is therefore π and multiples. Evaluating L_1 and L_2 with this method, the position of the kth band-gap is centered around the desired tuning frequency. The inversion of Equation 20 gives the frequencies at which the other k^{th} band-gaps are centered, having L_1, L_2 fixed. Band-maps for rods and beams are evaluated considering the imaginary part of the propagation constant given by the Transfer matrix method.

4.1 Rod

Non-dimensional parameters variation demonstrates the optimality of the solution. The band-gap central attenuation is maximized using odd values of k, while using even ones it vanishes: the first vertical dashed line in Figure 4 correspond to the tuning frequency, using $k = 1$. The others are evaluated inverting Equation 20, imposing L_1 and L_2 and solving for ω. This show the periodic nature of the optimal point. Furthermore, the higher the L_2 value, the lower the canceled frequency, because a lower wavelength matches L_2. Figure 4 shows that more band-gaps appear in the same frequency range in this case, but the provided attenuation is not maximum, until $\frac{L_2}{L_1} = 3, 5, 7$[3]. In general, the higher the number of cells, the higher the attenuation throughout the structure. Thus, it is better to keep as low as possible the unit cell length. In Figure 4(b) L_1 and L_2 are recomputed every time the mechanical impedance

[3]I.e. when the dashed lines are crossing at each others.

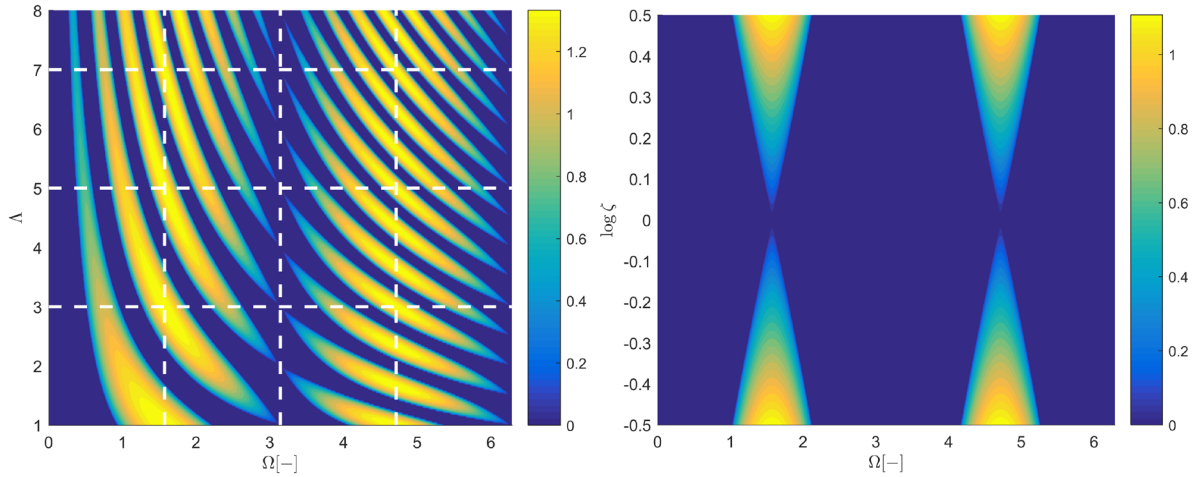

(a) (b)

Figure 4: Non dimensional band-maps for rods. Figure 4(a) Λ-Ω with $\zeta = 4$, Figure 4(b) ζ-Ω.

mismatch is changed. As a result, the tuning process is decoupled from the choice of ζ that has to be maximized in order to get the highest and widest possible attenuation[4].

4.2 Beam

The same approach presented for rods is exploited, using even values of k[5]. The resulting tuning

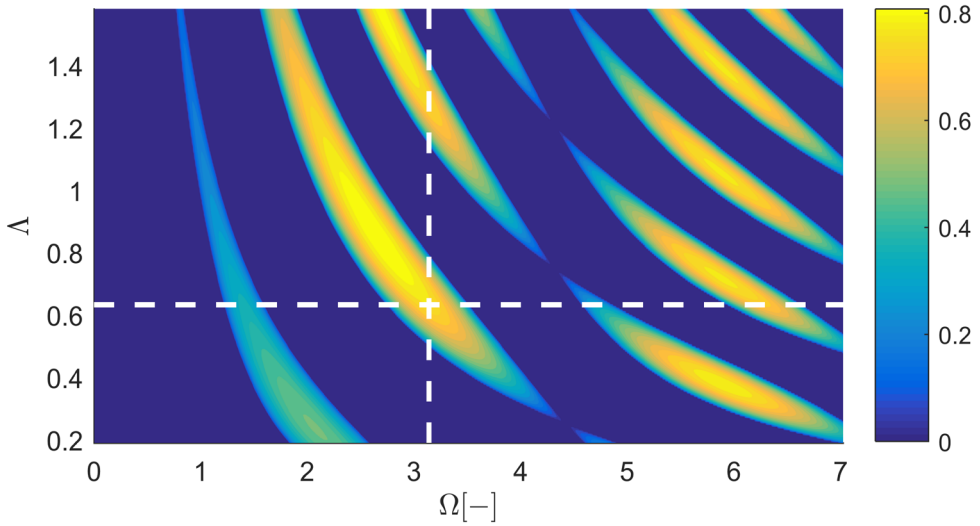

Figure 5: Non-optimal tuning.

process is described by the dashed line in Figure 5. In this case, the proposed algorithm is not able to give the optimality point. For this reason, a corrective factor that depends on the

[4]I.e. the amplitude of the reflection coefficient has to be maximized enhancing wave cancellation by superposition

[5]For the beam, odd values of k provide a narrow band, while even ones give wide and strong attenuation.

reflection coefficient R_{pp} has been introduced:

$$\pi + k\pi = \frac{2\pi}{\lambda} L + \Delta\phi \quad \rightarrow \quad \begin{cases} L_1 = \frac{\lambda_1(1+k)}{2} - \frac{\Delta\phi_1}{2\pi} \\ L_2 = \frac{\lambda_2(1+k)}{2} - \frac{\Delta\phi_2}{2\pi} \end{cases} \tag{21}$$

Where $\Delta\phi_1$ and $\Delta\phi_2$ are expressed as follows:

$$\Delta\phi_1 = -\frac{\pi}{2} - \angle R_{pp,1to2} \qquad \Delta\phi_2 = -\frac{\pi}{2} - \angle R_{pp,2to1} \tag{22}$$

where subscript $1to2$ denotes the transition from the left beam element to the right one and vice-versa, for subscript $2to1$. The correction allows to improve waves destructive interference, canceling the effect of the variable phase shift onto the tuning process. In Figure 6(a) the optimal attenuation point is restored at the desired frequency. Figure 6(b) shows that the

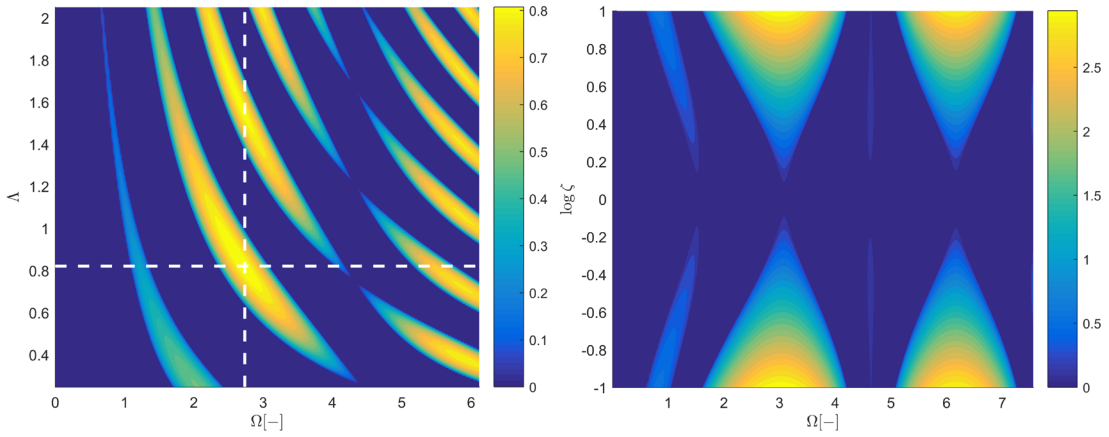

(a) (b)

Figure 6: Non dimensional band-maps for beams. Figure 6(a) Λ-Ω having $\zeta = 4$, Figure 6(b) ζ-Ω.

width and magnitude of attenuation is decoupled from the choice of band-gap central frequency, recomputing L_1 and L_2 when ζ is varied. The first attenuation zone is an exception. This is attributed to the presence of naturally damped waves generated in the reflection process, for which the decay is not enough along the first beam element. In fact, when the wave hits the neighboring interface, it generates a further set of waves that modify the filtering behavior of the periodic structure.

5 EXPERIMENTAL VALIDATION

In order to validate the design process, a periodic beam made of aluminum is manufactured. Maximum and minimum allowable height have been set based on physical constrains such as maximum transversal dimension, static resistance (minimum section) and total available length. L_1 and L_2 values are computed according to the following analytical steps:

- Selection of the desired band-gap position (6600 Hz, $k = 1$).

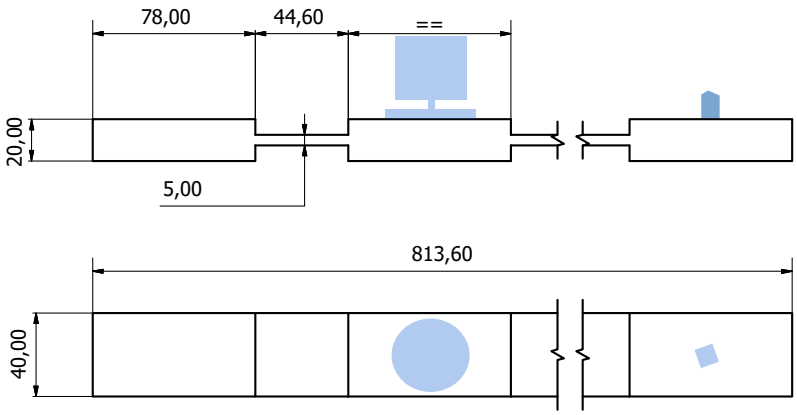

Figure 7: Experimental setup, force at the second cell, measurement at the last one.

- Evaluation of the reflection coefficients and phase shift extrapolation.
- Correction of L_1 and L_2 according to Equation 21.

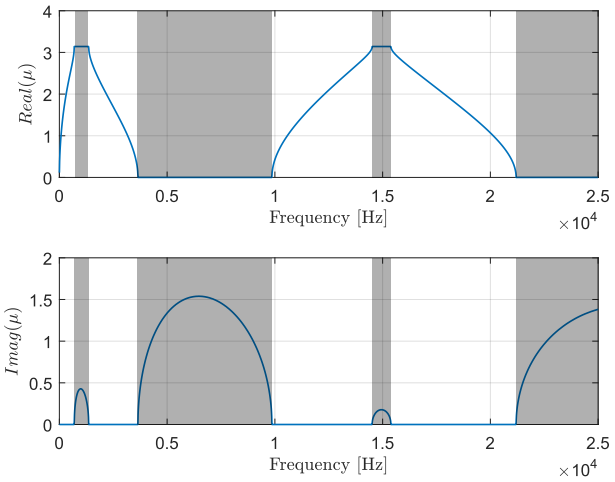

Figure 8: Real and imaginary part of the propagation constant μ for the manufactured system.

l_1	$0.078m$
h_1	$0.02m$
l_2	$0.0446m$
h_2	$0.005m$
E	$70000Mpa$
rho	$2700kg/m^2$
N	6

Table 1: Optimal beam dimensions.

The results of the analytic procedure are listed in Table 1, while the wave propagation properties given by the transfer matrix method are shown in Figure 8. An inertial shaker is used as excitation system while an accelerometer, PCB 352C33, measure vibrations in the middle of the last cell, according to the arrangement in Figure 7. The system is put onto a soundproofing material in order to insulate the structure and in order to preserve free-free conditions. For the acquisition, an NI 9234 module, with internal signal conditioning is used. The response of the beam is obtained forcing the system with a white noise. The correspondence between the analytic, numeric and experimental frequency response can be seen in Figure 9. Good matching has been achieved even at high frequencies. The numeric model is found to be more precise with respect to the analytic one, since it consider out of plane motions and boundary effects. In particular, torsional and axial modes lead to unexpected peaks within the attenuation regions.

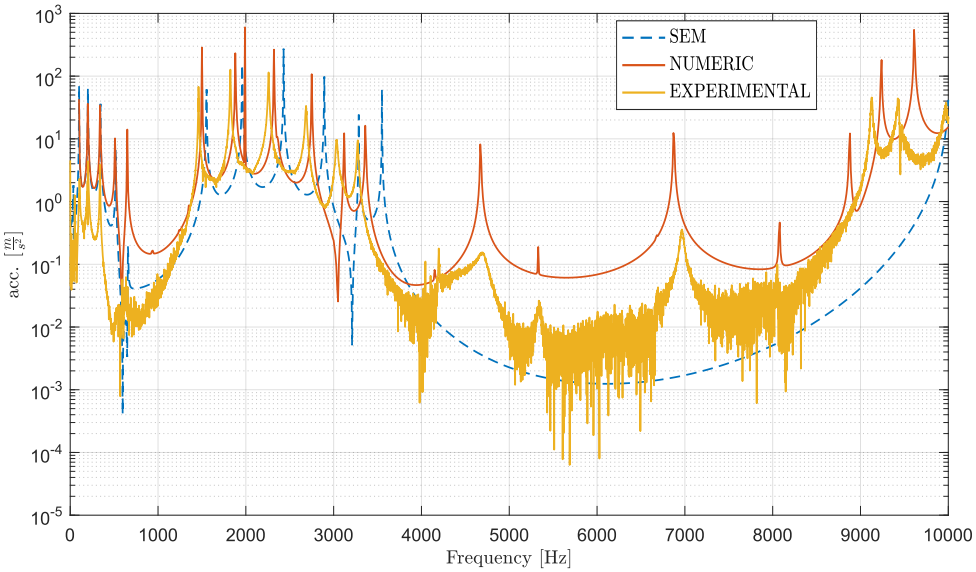

Figure 9: Frequency response, H1 estimator.

6 CONCLUSIONS

The paper proposed a method allowing to find the geometrical properties of a periodic structure such that the attenuation is maximized, given the material properties and the minimum/maximum height (that is chosen maximizing the mechanical impedance mismatch). As a result, one can design a periodic beam or rod without dealing with band-maps and non-dimensional parameters. Optimal solution is provided to maximize the attenuation at one frequency. A periodic beam has been manufactured, so that the analytic procedure has been validated experimentally by measuring its frequency response.

REFERENCES

[1] BR Mace. *Wave reflection and transmission in beams*. Journal of Sound and Vibration, 97(2):237246, 1984..

[2] Carta, Giorgio and Brun, Michele *Bloch–Floquet waves in flexural systems with continuous and discrete elements*, Mechanics of Materials, 87 11–26, 2015.

[3] Romeo, Francesco and Luongo, Angelo *Invariant representation of propagation properties for bi-coupled periodic structures*, Journal of sound and vibration, pages 257(5) 869–886, 2002.

[4] L. DAlessandro, E. Belloni, R. Ardito, A. Corigliano, and F. Braghin., *Modeling and experimental verification of an ultra-wide bandgap in 3D phononic crystal*, Applied Physics Letters, 109(22),2016 AIP Publishing

[5] Mead, DJ, *Wave propagation and natural modes in periodic systems: II. Multi-coupled systems, with and without damping*, Elsevier, 40(1) 19–39, 1975.

[6] Mead, DJ, *Wave propagation and natural modes in periodic systems: I. Mono-coupled systems*, Journal of Sound and Vibration, Elsevier, 40(1) 1-18, 1975.

[7] Felix Bloch *ber die quantenmechanik der elektronen in kristallgittern.* Zeitschrift fr Physik, 52(7):555600, 1929

[8] Belloni, Edoardo and Braghin, Francesco and Cazzulani, Gabriele and Cenedese Mattia *Invariant representation of wave propagation properties for a mono-coupled electromechanical periodic structure* Proceedings of the ASME 2016 Conference on Smart Materials, Adaptive Structures and Intelligent Systems SMASIS 2016 September 28-30, 2016, Stowe, VT, USA, 2016.

[9] James F. Doyle. *Wave propagation in structures : an FFT-based spectral analysis methodology.* Springer-Verlag, New York, 1989.

[10] M.I. Hussein, M.J. Leamy, and M. Ruzzene. *Dynamics of phononic materials and structures: Historical origins, recent progress, and future outlook.* Applied Mechanics Reviews, 66:04080204080238, 2014.

[11] L. Brillouin. *Wave Propagation in Periodic Structures: Electric Filters and Crystal Lattices.* Chemische Reihe. Lehrbucher und Monographien aus dem Gebiete der exakten Wissenschaften. Dover Publications, 1953.

VIII ECCOMAS Thematic Conference on Smart Structures and Materials
SMART 2017
A. Güemes, A. Benjeddou, J. Rodellar and J. Leng (Eds)

DESIGN OF A SMART PERIODIC BEAM WITH COUPLING BETWEEN LOCAL RESONANCES AND BRAGG BAND-GAPS

E. BELLONI*, G. CAZZULANI*†, M. CENEDESE* AND F. BRAGHIN*

*Department of Mechanical Engineering
Politecnico di Milano
Via La Masa, 1, 20156, Milano, Italy
†e-mail: gabriele.cazzulani@polimi.it

Key words: Periodic Structures, Design Maps, Piezoelectric Materials, band-gap, shunt resonators, coupling

Abstract. The success of periodic structures is linked to their peculiar behaviour regarding wave propagation: they have frequency ranges, the so called band-gaps, in which an incoming wave is attenuated. Band-gaps can be generated with two mechanisms: Bragg scattering, directly related to the wavelength of the incoming wave, or local resonances, useful for sub-wavelength applications. In this paper we show that gluing a set of piezoelectric patches on a beam with a periodic disposition, it is possible to obtain both the effect, and possibly couple them. While Bragg band-gaps are ensured due to the periodic arrangements, local resonances are obtained connecting each piezoelectric patch to an RL shunt circuit. Non-dimensional design maps are generated to see both the effects and their interaction. Furthermore, it is shown that two subsequent Bragg band-gaps can be linked thanks to the contribution of the lumped resonators. Results obtained analytically with the Spectral Element method have been corroborated both with FE simulations and experimental tests, and the effects of the resistors on band gap linking are widely discussed.

1 INTRODUCTION

Even though the first examples of periodic structures date back in time [1, 2], the real advantages of such structures have been appreciated thanks to solid state physics [3] and then analyzed with a more engineering point of view [4]. Such structures, composed by the periodic repetition of a fundamental block of matter named unit cell, are endowed with the so-called band-gaps, i.e. they show wide attenuation zones along their frequency response, created with different mechanisms [5, 6]. In particular, if the wavelength is comparable with unit cell size, a band-gap is generated thanks to Bragg scattering phenomenon. This idea is used to create photonic [7] and phononic [8, 9] crystals: more specifically, these last are designed to interact with acoustic and elastic waves along a wide range of frequencies [10, 11, 12, 13, 14]. A different way to generate a band-gap, in this case not dependent on wavelength, is to use a set of resonator

distributed along the structure: a band-gap now appears in the vicinity of resonators' tuning frequency, thus such structures are generally named locally resonant metamaterials [15, 16]. Due to the freedom on band-gap position tuning [17] and the evidence of exotic elastic properties [18, 19], also in this case there are numerous applications in literature, covering a vast range in frequency [20, 21, 22, 23]. The use of piezoelectric inserts [24] in periodic structures is widely discussed in literature [25], creating electromechanical metamaterials when coupled with resonant circuits [26, 27, 28, 29, 30].
Starting from the case-study of a homogeneous beam with a periodic array of piezoelectric patches [31, 32, 33], this paper proposes a design approach based on non-dimensional maps [34, 35, 30]. In this way, the influence of mechanical and electrical parameters on band-gaps' position and width is clearly visible. Furthermore, it is possible to have a visual representation of the coexistence of band-gaps generated both with Bragg scattering phenomenon (a periodic gluing of piezoelectric patches) and local resonators (a resonating RL shunt circuit is wired to each patch [36]). The choice of tuning the circuit in between two band-gaps is investigated: a wider attenuation zone, here named electromechanical band-gap, is obtained thanks to the mutual influence of both phenomena. Analytical results are then corroborated with experimental tests. The method here proposed provides a fast and robust procedure to make a proper choice of mechanical and electrical parameters at the same time, suggesting a procedure to create a wider attenuation zone in frequency through the mutual influence of two different physical phenomena.

2 Piezoelectric patches

As already discussed, the piezoelectric patches will be used to create an impedance mismatch along the homogeneous Aluminum beam, thus inducing some Bragg band-gaps. Then, a resonant circuit is connected to each patch (see Figure 1 for an equivalent lumped parameter model) and tuned in between two existing band-gaps in order to create a wider region of attenuation.

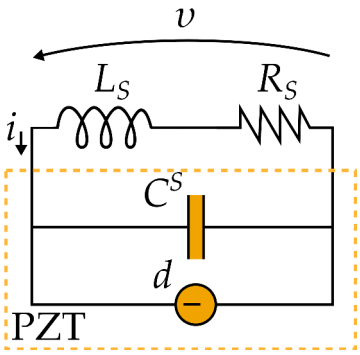

Figure 1: Equivalent electrical representation of the piezoelectric element, coupled with a resonant RL circuit.

The first step is to create a model of the piezoelectric patch, thus the subscript of constitutive model constants is 31 (electric field in direction 3, deformation in direction 1, see Figure 3b).

The piezoelectric constitutive equations are [37, 30, 38]:

$$\begin{cases} S_1 = \dfrac{1}{Y_{11}^E} T_1 + d_{31} E_3 \\ D_3 = d_{31} T_1 + \epsilon_{33}^T E_3 \end{cases} \tag{1}$$

with S_1 strain, T_1 applied stress, E_3 electric field, D_3 elastic displacement, Y_{11}^E Young's modulus in short circuit ($E = 0$), d_{31} piezoelectric strain coefficient and ϵ_{33}^T electric permittivity in stress free conditions ($T = 0$). From now on, the subscripts will be omitted to improve readability. Considering now the electrical charge q, the area of piezoelectric patch A_p, the patch's height h_p and the voltage v imposed among the two electrodes, the following equations stand:

$$D = \frac{q}{A_p} \quad ; \quad A_p = b_p l_p \quad ; \quad E = \frac{v}{h_p} \tag{2}$$

Thus, doing some substitutions, one can write:

$$\begin{cases} T = Y^E \left(S - \dfrac{d}{h_p} v \right) \\ q = d A_p Y^E S + C_p^S v \end{cases} \tag{3}$$

where $C_p^S = \epsilon^S A_p / h_p$ is the piezoelectric capacity at zero strain ($S = 0$). It is also possible to write $C_p^S = C_p^T (1 - k^2)$, where $k^2 = d^2 Y^E / \epsilon^T$ is the so-called piezoelectric coupling coefficient. Now, one can consider the circuit as in Figure 3 and solve in frequency domain (symbol ˆ is used):

$$\hat{I} = j\omega d A_p Y^E \hat{S} + j\omega C_p^S \hat{V} \tag{4}$$

and considering the impedance Z_s, the relation $\hat{V} = -Z_s \hat{I}$ stands. Then, the relation between strain and voltage is:

$$\hat{V} = -\frac{d Y^E A}{C_p^S} \frac{j\omega C_p^S Z_s}{1 + j\omega C_p^S Z_s} \hat{S} \tag{5}$$

In the final stress-strain relation in frequency domain, the elastic modulus of the piezoelectric patch is no more constant:

$$\hat{T} = Y^E \left(1 + \frac{k^2}{1 - k^2} \frac{j\omega C_p^S Z_s}{1 + j\omega C_p^S Z_s} \right) \hat{S} = Y^D \left(1 - \frac{k^2}{1 + j\omega C_p^S Z_s} \right) \hat{S} = Y^E \bar{Y}(\omega) \hat{S} = Y(\omega) \hat{S} \tag{6}$$

and in particular:

$$\bar{Y}(\omega) = 1 + \frac{k^2}{1 - k^2} \frac{j2 \dfrac{\omega}{\omega_{LC,S}} \xi - \dfrac{\omega^2}{\omega_{LC,S}^2}}{1 - \dfrac{\omega^2}{\omega_{LC,S}^2} + j2 \dfrac{\omega}{\omega_{LC,S}} \xi} \tag{7}$$

where $\omega_{LC,S}^2 = (C_p^S \, L_S)^{-1}$ is the locked frequency, $\omega_{LC,T}^2 = (C_p^T \, L_S)^{-1} = \omega_{LC,S}^2 (1 - k^2)$ is the free stress frequency and $\xi = 0.5 C_p^S \, R_S \omega_{LC,S}$ is a parameter that quantifies the electrical damping (i.e., the resistor effect). Three main frequency regions can be distinguished for $\bar{Y}(\omega)$:

- $\omega << \omega_{LC,T}$: short circuit zone, no influence of electrical elements and $Y(\omega) \sim Y^E$;
- $\omega >> \omega_{LC,S}$: open circuit zone, where the coupling is relevant and $Y(\omega) \sim Y^E/(1-k^2) = Y^D$;
- $\omega_{LC,T} < \omega < \omega_{LC,S}$: resonant zone.

In the resonant zone, $\bar{Y}(\omega)$ presents a resonance at $\omega = \omega_{LC,S}$ and an antiresonance at $\omega = \omega_{LC,T}$, as shown in Figure 2. Considering an ideally undamped shunting circuit, this means that at these frequency the bar is respectively fully rigid ($\bar{Y} \to \infty$) and completely compliant ($\bar{Y} = 0$) respectively. Furthermore, in the range between them (modulated by the value of k), the elastic

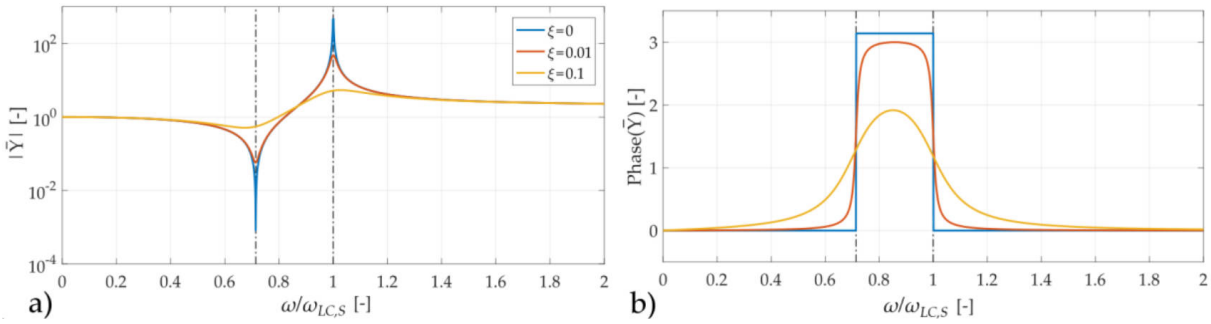

Figure 2: Properties of a piezoelectric patch with resonant shunt expressed with non-dimensional parameters. Absolute value (a) and phase (b) of the normalized elastic modulus for three values of the damping ratio. Dashed lines are the boundaries of resonant zone.

modulus is negative: this phenomenon, as already discussed, is peculiar of locally resonant metamaterials and has a strong influence on wave propagation behavior. Note that, in real systems, the value of k in 31 configuration generally does not exceed 0.4, thus the authority of piezoelectric patches is lower with respect to longitudinal (33) inserts described in [39, 30].

3 Periodic Beam with Shunted Piezoelectric Patches

The unit cell of the periodic system is the one shown in Figure 3a: on a homogeneous Aluminum beam a couple of piezoelectric patches are glued, one on top and the other on the bottom part. Each patch is then connect to a resonating circuit, composed by a resistor and an inductor (see also Figure 1). The patch actually consists in a layer of material: assuming perfect adhesion with the substrate, it changes the wave propagation behavior by a local modification of mass, axial and bending stiffness. So, the application of periodic patches implies impedance discontinuity that generates Bragg band-gaps. Furthermore, the application of patches in couples keeps the bending and axial waves decoupled (see [27] for a non-symmetric example, with coupling between bending moment and axial force). Each patch has two electrodes, that are connected to a resonant RL circuit: the electrode in contact with the Aluminum substrate is considered the ground of the circuit. Using the classic ABD theory for laminates [40], it is possible to estimate the influence of the piezoelectric layer in section 2 of the unit cell (refer to Figure 3a). Assuming

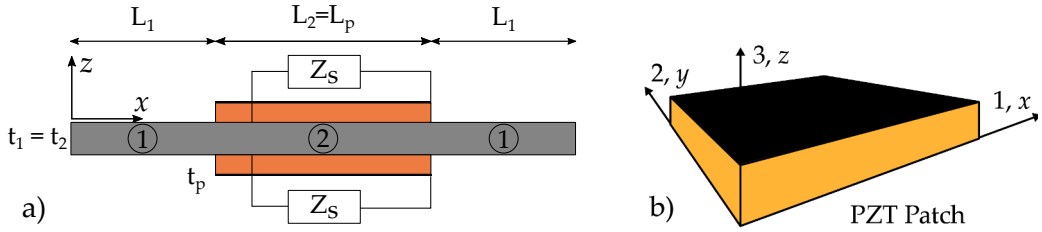

Figure 3: a) Representation of the unit cell, composed by a homogeneous Aluminum beam and a couple of piezoelectric patches, each connected to a lumped circuit with a generic impedance Z_s. b) Main directions of the piezoelectric patch.

$b_1 = b_p = b$ thickness in y-direction, the bending stiffness is:

$$\begin{aligned} D_2(\omega) &= E_1 \frac{bt_1^3}{12} + E_p(\omega)\frac{b}{6}[(t_1+2t_p)^3 - t_1^3] = \\ &= E_1 \frac{bt_1^3}{12}\left(1 + \frac{E_p(\omega)}{E_1}\left[\left(1+2\frac{t_p}{t_1}\right)^3 - 1\right]\right) = D_1^{\text{stat}}\bar{D}_p(\omega) \end{aligned} \tag{8}$$

Regarding the linear mass variation due to piezoelectric patches, this relations stands:

$$m_2 = \rho_1 b_1 t_1 + 2\rho_p b_p h_p = \rho_1 A_1 \left(1 + 2\frac{\rho_p t_p}{\rho_1 t_1}\right) = m_1^{\text{stat}}\bar{m}_p \tag{9}$$

Now, one has all the elements to solve a wave propagation problem along the structure. In this paper the transfer matrix method is used. Considering a state vector $\mathbf{z} = \begin{Bmatrix} w & \theta & T & M \end{Bmatrix}^T = \begin{Bmatrix} \mathbf{d} & \mathbf{f} \end{Bmatrix}^T$, for a beam element, the transfer matrix which link left and right state vectors is [41, 30]:

$$[T] = \frac{1}{2}\begin{bmatrix} c+C & (s+S)/\kappa & -(s-S)/(\kappa^3 D) & (c-C)/(\kappa^2 D) \\ (-s+S)\kappa & c+C & -(c-C)/(\kappa^2 D) & -(s+S)/(\kappa D) \\ (s+S)\kappa^3 D & -(c-C)\kappa^2 D & c+C & (s-S)\kappa \\ (c-C)\kappa^2 D & (s-S)\kappa D & -(s+S)/\kappa & c+C \end{bmatrix} \tag{10}$$

where $c = \cos(\kappa l)$, $s = \sin(\kappa l)$, $C = \cosh(\kappa l)$, $S = \sinh(\kappa l)$ and $\kappa = \sqrt[4]{m\omega^2/D}$ is the wavenumber. The transfer matrix for the unit cell in Figure 3a is then $[T] = [T_2][T_1][T_2]$. Using the Floquet-Bloch boundary conditions and solving the problem, one ends up with two propagation constants $\mu_i = \kappa_i L$: the real part of such quantities is representative of attenuation, i.e. band-gaps, while the imaginary part means that a wave can propagate without attenuation [42, 43, 44]. In particular, in the case of an Euler-Bernoulli beam here analyzed, a propagation constant is always attenuating, then the second one (μ_2) defines the wave propagation behavior along the structure. Figure 4 clearly shows the trend of band-gaps in frequency. Considering the case of short circuit (blue solid line), only Bragg band-gaps arise in frequency when the real part of μ_2 is equal to 0. When the local resonators are introduced, it is clearly visible that a

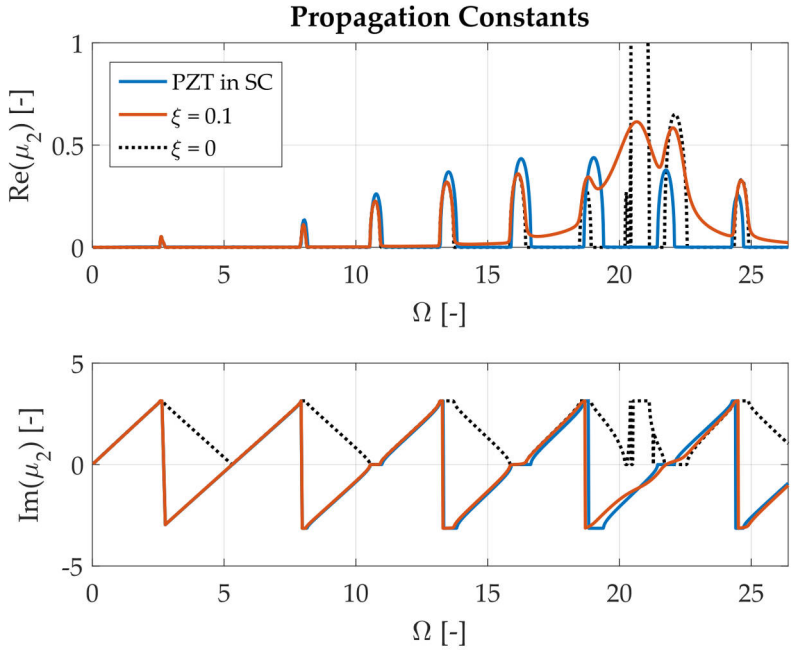

Figure 4: Real and imaginary parts of μ_2 as function of the non-dimensional frequency Ω in different configurations of the electrical circuit: short circuit, undamped and strongly damped. The sudden phase change from $+\pi$ to $-\pi$ is only due to the inversion of hyperbolic cosine.

new band-gap is present. In particular introducing damping, it is remarkable to notice how the lumped resonator allows to link two subsequent band-gaps: this phenomenon is here referred to as electromechanical band-gap.

4 Design maps

It is possible to write the dispersion behavior of periodic system as function of a number of non-dimensional parameters [34, 41, 30, 38]: this approach is useful to create a set of design maps, a quick way to represent the mutual influence of all the parameters on wave propagation. In this case, one can identify a large number of possible non-dimensional parameters, thus some hypotheses are now made to simplify the problem.
First of all, it is assumed that the beam and the piezoelectric patches have all the same width ($b_1 = b_2 = b_p$). Then, by choosing the materials (in this case Aluminum and PZT-5H), the ratios between Young's moduli ($\Sigma_Y = Y_p^E/Y_2$) and densities ($\Sigma_\rho = \rho_p/\rho_2$) are defined. Also the ratio between piezoelectric patch's height and beam's one ($\tau = h_p/h_1$) is considered as known (basically, the one used for the experimental tests). Now it is convenient to define:

$$\Omega = \kappa_1 L_1 \;\; ; \;\; \Lambda = \frac{L_2}{L_1} \;\; ; \;\; \zeta = \sqrt[3]{\frac{D_2}{D_1}} \;\; ; \;\; \eta = \sqrt[4]{\frac{m_2 D_1}{m_1 D_2}} \;\; ; \;\; \Omega_{LC,S} = \frac{\omega_{LC,S} L_1}{c_1} \;\; ; \;\; \xi = \frac{C_p^S R_S}{2} \omega_{LC,S} \tag{11}$$

With some analytical steps, it is possible to write:

$$\zeta^3 = 1 + \bar{Y}_p(\omega)\Sigma_Y[(1+2\tau)^3 - 1] = \zeta^3(\Omega, \tau, \Omega_{LC,S}, \xi) \tag{12}$$

and thus:

$$\eta^4 = \frac{1}{\zeta^3}(1 + \Sigma_p \tau) = \eta^4(\zeta, \tau) \tag{13}$$

In the end, the propagation constants of this beam depend on:

$$\mu_i = \mu_i(\Omega, \zeta, \Lambda, \Omega_{LC,S}, \xi) \;\text{ for }\; i = 1, 2 \tag{14}$$

Figure 5 represents band-gaps trend in frequency for different design parameters. In this case

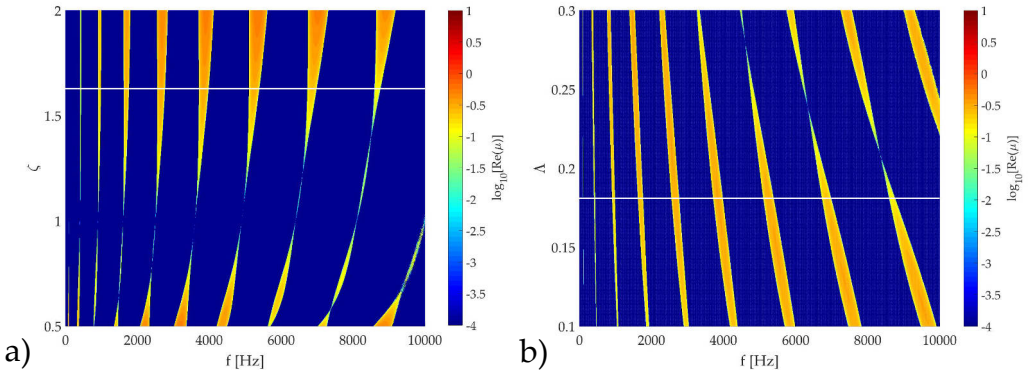

Figure 5: Maps with non dimensional design parameters. The x axis contains frequencies in Hz to improve readability. The two white lines indicate the ratios that are used for the experimental prototype. Color scale is an estimation of the attenuation level based on logarithm of the real part of the propagation constant. a) $f - \zeta$ map with $\Lambda = 0.18$ and $\eta = 0.9$; b) $f - \Lambda$ map with $\zeta = 1.6$ and $\eta = 0.9$.

the open circuit condition is considered, thus the band-gaps now present are only due to Bragg scattering. The horizontal white lines are the configurations chosen for the experimental tests. Figure 6 shows the effect of resonating circuit's tuning frequency on wave propagation behavior.

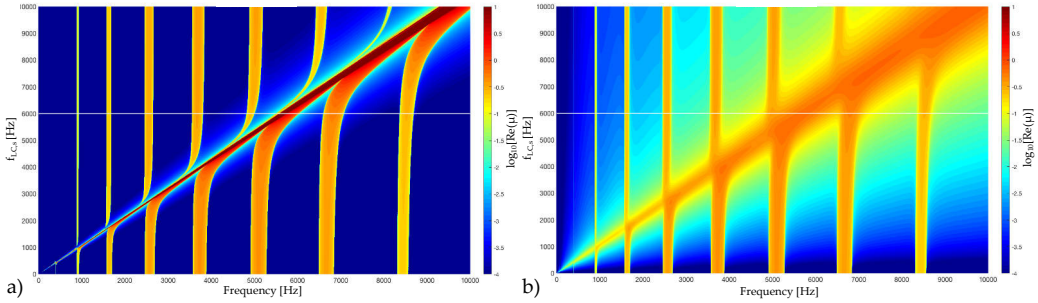

Figure 6: Maps for the design of an homogeneous beam with piezoelectric patches connected to shunt circuits. The effect of tuning frequency $f_{LC,s}$ of the piezoelectric patch has been plotted with a low ($\xi = 0.01$, a) and high ($\xi = 5$, b) level of electric damping. The white lines refer to the configuration chosen for the experimental tests.

Bragg band-gaps still exist, but the contribution of lumped resonators is clearly visible, having a mutual influence on band-gap width and shape. Again, one can notice how the lumped resonator

is able to link two subsequent band-gaps, in particular when some damping is introduced (like in Figure 6b): the damping smooths out the deep attenuation peak of the resonator, but allows to spread its contribution on a wider range of frequencies. Furthermore, it is clearly visible how the higher the tuning frequency, the wider the resonator contribution: this is linked to the resonant zone of the piezoelectric patch shown in Figure 2.

5 Experimental tests

For the experimental setup, it was chosen a uniform Aluminum Anticorodal beam with height $t = 0.004$ m, thickness $b = 0.04$ m and length $L = 1.60$ m. The beam is divided in 5 unit cells, with a couple of piezoelectric patches per cell as already discussed. The patches used for this applications are the PPA-1013, produced by Midé: they are single piezoelectric layer extensional devices with height 0.00149 m and length 0.046 m (see [45] for further details). In order to obtain

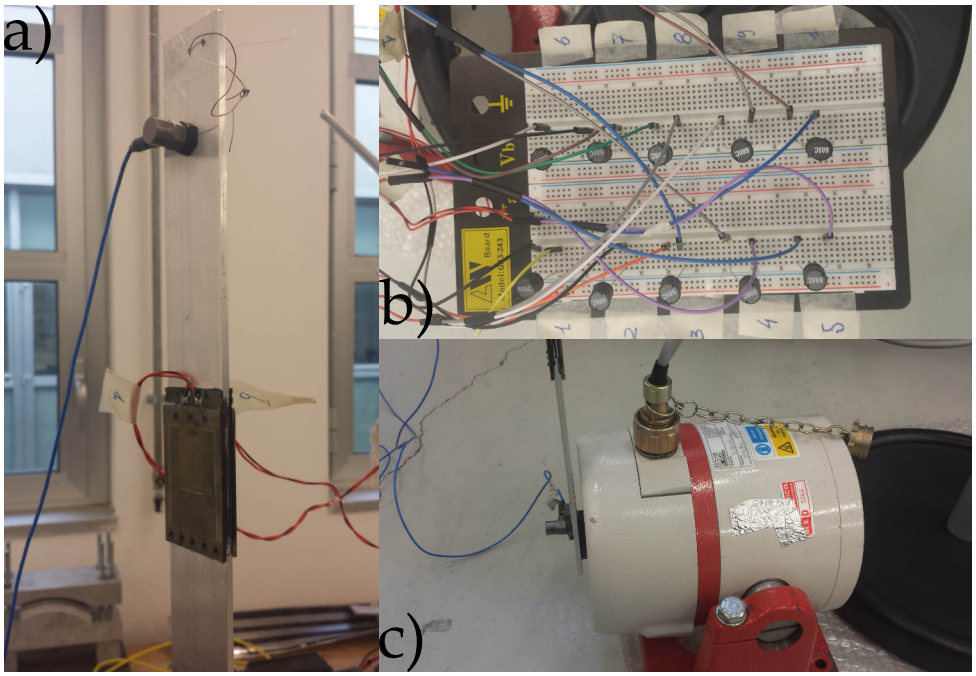

Figure 7: a) Tip of the beam, placed in vertical position. A couple of piezoelectric patches, with their wires, and an accelerometer are visible. b) A simple shunt system composed by only inductors of 35 mH. c) The shaker used at the bottom of the beam to impose a white noise excitation.

a configuration which is closer to free-free boundary conditions (the clamp-clamp one has some test issues, especially for high frequencies), the idea was to place the beam in vertical position, connecting it to a an inertial shaker, LDS-V406, with a passband of 9 kHz in its bottom end, see Figure 7. The circuit shown in Figure 7b is composed by only an inductor, but one has to consider that it has an internal non-negligible resistance which will smooth out the theoretical narrow attenuation peak. Two PCB 352C33 accelerometers were used, one at the bottom end and one at the tip of the beam. Signals are conditioned and acquired with an NI 9234 module, and then post-processed with Matlab. Together with the experimental results, also a Spectral

Element (SE) model is created and used to simulate this case study [46]. Figure 8 shows the

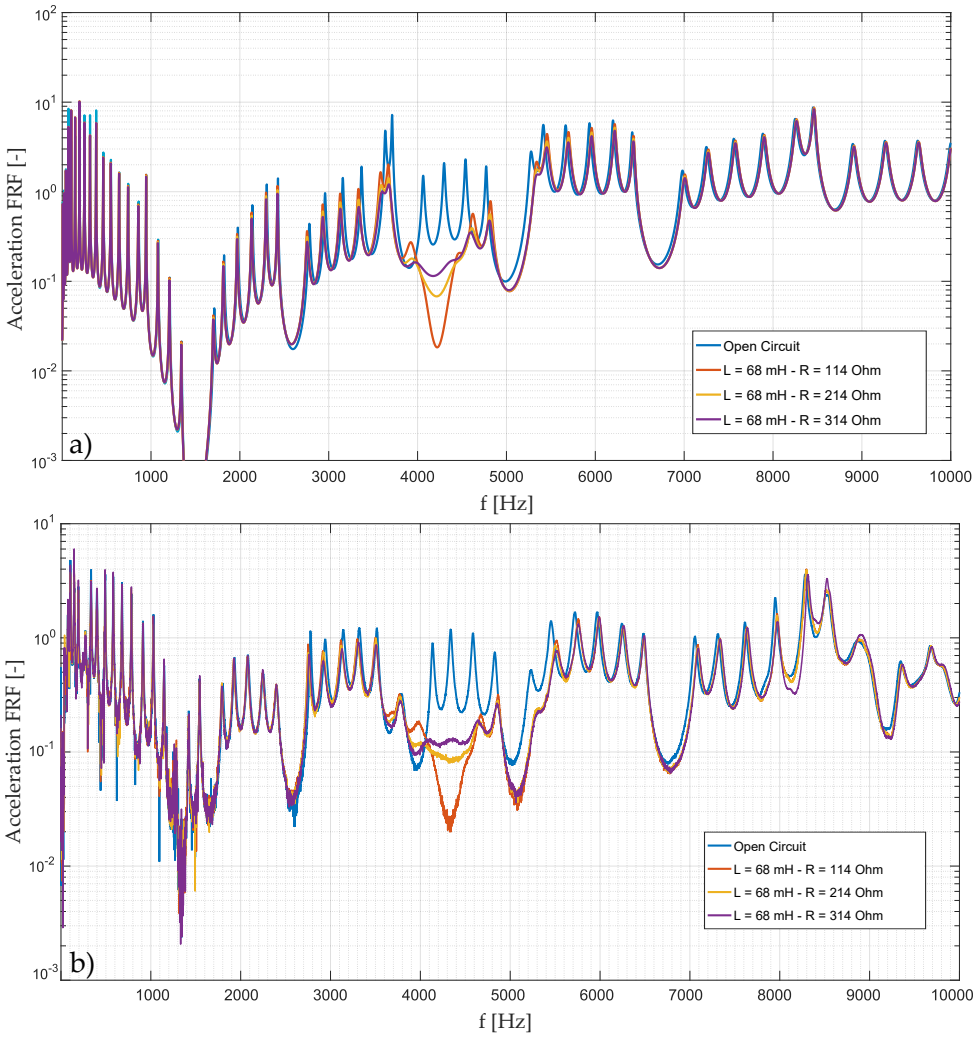

Figure 8: Analytical frequency response function obtained with a SEM (a) compared with the experimental results (b). In legend the values used for the resistors. Tuning frequency: 4300 Hz.

results of shunt tuning around 4300 Hz in between two band-gaps, with a comparison between analytical SE results (a) and experimental ones (b). Results are in good accordance with the model. It is clearly visible the effect of increasing resistors on the attenuation peak: its depth is smoothen out, but its influence is more distributed in frequency, creating a wider flattening zone, i.e. an electro-mechanical band-gap. The trend of peaks and band-gaps is well matched in frequency, apart from some small differences ascribable to material damping and torsional motions of the beam, that are not considered by the SE model.

6 Conclusions

The paper describes a periodic structure composed by a homogeneous Aluminum beam with a periodic set of piezoelectric patches in shunt configuration. The system has been analytically modeled and it has been demonstrated that band-gaps are generated with two different mechanism: Bragg scattering and local resonators. Using non-dimensional maps for the design of the system, it has been shown how the phenomena can interact, creating a wider attenuation zone, here called electro-mechanical band-gap. Using the design criteria developed, a experimental test-bench has been manufactured and tested. Results are in good accordance with both the design maps indications and the analytical SE model.

REFERENCES

[1] I. Newton. *Philosophiae Naturalis Principia Mathematica - Book II.* Imprimatur S. Pepys, Reg. Soc. Praeses, London, 1686.

[2] J.W.S. Rayleigh. *The theory of sound.* MacMillan and Co., LTD., London, 1896.

[3] C. Kittel. *Introduction to Solid State Physics, 8th Ed.* Wiley, 2004.

[4] L. Brillouin. *Wave Propagation in Periodic Structures: Electric Filters and Crystal Lattices.* Dover Publications, Inc., New York, 1946.

[5] C. Croënne, E.J.S. Lee, H. Hu, and J.H. Page. Band gaps in phononic crystals: Generation mechanisms and interaction effects. *AIP Advances*, 1(4):041401, 2011.

[6] X. Yan-Long, C. Chang-Qing, and T. Xiao-Geng. The existence of simultaneous bragg and locally resonant band gaps in composite phononic crystal. *Chinese Physics Letters*, 30(4):044301, 2013.

[7] J.D. Joannopoulos, S.G. Johnson, J.N. Winn, and R.D. Meade. *Photonic Crystals: Molding the Flow of Light, 2nd Ed.* Princeton University Press, 2011.

[8] M.I. Hussein, M.J. Leamy, and M. Ruzzene. Dynamics of phononic materials and structures: Historical origins, recent progress, and future outlook. *Applied Mechanics Reviews*, 66:040802–040802–38, 2014.

[9] V. Laude. *Phononic Crystals: Artificial Crystals for Sonic, Acoustic, and Elastic Waves.* De Gruyter Studies in Mathematical Physics. De Gruyter, 2015.

[10] M. Maldovan. Sound and heat revolutions in phononics. *Nature*, 503:209–217, 2013.

[11] X.-F. Li, X. Ni, L. Feng, M.-H. Lu, C. He, and Y.-F. Chen. Tunable unidirectional sound propagation through a sonic-crystal-based acoustic diode. *Physics Review Letters*, 106:084301, 2011.

[12] N. Li, J. Ren, L. Wang, G. Zhang, P. Hänggi, and B. Li. *Colloquium*: Phononics: Manipulating heat flow with electronic analogs and beyond. *Reviews of Modern Physics*, 84:1045–1066, 2012.

[13] P. Sheng. A step towards a seismic cloak. *Physics*, 7, 2014.

[14] L. D'Alessandro, E. Belloni, R. Ardito, A. Corigliano, and F. Braghin. Modeling and experimental verification of an ultra-wide bandgap in 3d phononic crystal. *Applied Physics Letters*, 109, 2016.

[15] Z.Y. Liu, X.X. Zhang, Y.W. Mao, Y.Y. Zhu, Z.Y. Yang, C.T. Chan, and P. Sheng. Locally resonant sonic materials. *Science*, 289:1734–1736, 2000.

[16] G. Ma and P. Sheng. Acoustic metamaterials: From local resonances to broad horizons. *Science Advances*, 2(2), 2016.

[17] X. Zhou, X. Liu, and G. Hu. Elastic metamaterials with local resonances: an overview. *Theoretical and Applied Mechanics Letters*, 2(4):041001, 2012.

[18] N. Fang, D. Xi, J. Xu, M. Ambati, W. Srituravanich, C. Sun, and X. Zhang. Ultrasonic metamaterials with negative modulus. *Nature Materials*, 5:452–456, 2006.

[19] Z. Yang, J. Mei, M. Yang, N.H. Chan, and P. Sheng. Membrane-type acoustic metamaterial with negative dynamic mass. *Physical Review Letters*, 101:204301, 2008.

[20] S. Krödel, N. Thomé, and C. Daraio. Wide band-gap seismic metastructures. *Extreme Mechal Letters*, 4:111–117, 2015.

[21] A. Climente, D. Torrent, and J. Sánchez-Dehesa. Omnidirectional broadband acoustic absorber based on metamaterials. *Applied Physics Letters*, 100(14), 2012.

[22] J.M. Restrepo-Flórez and M. Maldovan. Mass separation by metamaterials. *Scientific Reports*, 6:21971, 2016.

[23] A.M. Baz. An active acoustic metamaterial with tunable effective density. *Journal of Vibration and Acoustics*, 132:041011, 2010.

[24] Q.A. Qin. *Advanced Mechanics of Piezoelectricity*. 2013.

[25] L. Airoldi, M. Senesi, and M. Ruzzene. *Piezoelectric Superlattices and Shunted Periodic Arrays as Tunable Periodic Structures and Metamaterials*, pages 33–108. Springer Vienna, Vienna, 2012.

[26] T. Delpero. *Design of Adaptive Structures with Piezoelectric Materials*. PhD thesis, ETH Zurich, 2014.

[27] E.A.F. Parra, A. Bergamini, E. Belloni, T. Delpero, and P. Ermanni. Design optimization of generalized coupling coeffcient for vibration attenuation in metamaterials with local piezoelectric shunts. *ICAST2015: 26th International Conference on Adaptive Structures and Technologies, October 14-16th, 2015, Kobe, Japan*, 2015.

[28] F Tateo, M Collet, M Ouisse, and KA Cunefare. Design variables for optimizing adaptive metacomposite made of shunted piezoelectric patches distribution. *Journal of Vibration and Control*, 22(7):1838–1854, 2016.

[29] L. Junyi and D.S. Balint. Optimal shunt parameters for maximising wave attenuation with periodic piezoelectric patches. *Journal of Intelligent Material Systems and Structures*, 2016.

[30] E. Belloni, F. Braghin, G. Cazzulani, and M. Cenedese. Invariant representation of wave propagation properties for a mono-coupled electro-mechanical periodic structure. *Proceedings of the ASME 2016 Conference on Smart Materials, Adaptive Structures and Intelligent Systems SMASIS 2016 September 28-30, 2016, Stowe, VT, USA*, 2016.

[31] B.S. Beck, K.A. Cunefare, M. Collet, and M. Ruzzene. Periodic piezoelectric sensor-actuator array for vibration suppression on a beam. *Proc. SPIE*, 7643:76430P–76430P–9, 2010.

[32] L. Airoldi and M. Ruzzene. Design of tunable acoustic metamaterials through periodic arrays of resonant shunted piezos. *New Journal of Physics*, 13, 2011.

[33] B. Lossouarn, J.F. Deü, and M. Aucejo. Multimodal vibration damping of a beam with a periodic array of piezoelectric patches connected to a passive electrical network. *Smart Materials and Structures*, 24(11):115037, 2015.

[34] F. Romeo and A. Luongo. Invariant representation of propagation properties for bi-coupled periodic structures. *Journal of Sound and Vibration*, 257:869–886, 2002.

[35] F. Romeo. *Map-based approaches for periodic structures*, pages 161–256. Springer Vienna, Vienna, 2012.

[36] N.W. Hagood and A. von Flotow. Damping of structural vibrations with piezoelectric materials and passive electrical networks. *Journal of Sound and Vibration*, 146:243–268, 1991.

[37] D. J. Leo. *Engineering Analysis of Smart Material Systems*. John Wiley & Sons, 2007.

[38] E. Belloni. *On the design and control of periodic structures*. PhD thesis, Politecnico di Milano, 2017.

[39] O. Thorp, M. Ruzzene, and A. Baz. Attenuation and localization of wave propagation in rods with periodic shunted piezoelectric patches. *Smart Materials and Structures*, 10(5):979, 2001.

[40] A.T. Nettles. Basic mechanics of laminated composite plates. Technical report, NASA - Marshall Space Flight Center, 1994.

[41] G. Carta and M. Brun. Bloch-Floquet waves in flexural systems with continuous and discrete elements. *Mechanics of Materials*, 87:11–26, 2015.

[42] D.J. Mead. Wave propagation and natural modes in periodic systems: I. mono-coupled systems. *Journal of Sound and Vibration*, 40:1–18, 1975.

[43] D.J. Mead. Wave propagation and natural modes in periodic systems: Ii. multi-coupled systems, with and without damping. *Journal of Sound and Vibration*, 40:19–39, 1975.

[44] M.G. Faulkner and D.P. Hong. Free vibrations of a mono-coupled periodic system. *Journal of Sound and Vibration*, 99:29–42, 1985.

[45] *PPA PRODUCTS - Datasheet and User Manual, Midé, 2016.*

[46] U. Lee. *Spectral Element Method in Structural Dynamics.* Wiley, 2009.

Energy Flow Characteristics of Periodically Distributed Piezoelectric Shunting Circuits

Y. Fan*†, O. Bareille†, M. Ichchou†, L. Li* and J.-P. Laine†

* School of Energy and Power Engineering (SEPE)
Beihang University
100191 Beijing, China
e-mail: fanyu04@buaa.edu.cn

† Laboratoire de Tribologie et Dynamique des Systeme (LTDS)
Ecole Centrale de Lyon
69130 Ecully, France
Email: olivier.bareille@ec-lyon.fr

ABSTRACT

An electromechanical waveguide can be constructed by periodically distributing piezoelectric materials on to the host structure and shunting identical electric circuits to each parts. The design of electric impedances endows the waveguide with the desired dynamic features for vibration control or wave filtering. In this paper we investigate the energy flow characteristics of the electromechanical waveguide when it is assembled into an existing structural system and working as a substructure. A rapid multi-scale numerical strategy is employed to analyze the forced response and energy flow of such built-up structures. The influence of number of piezoelectric patches and the excitation are discussed, showing the necessity of evaluating the waveguide performance in the proposed context. Results also indicate the essential difference between waveguides with finite and infinite unit cells. Bragg band gap and damping mechanisms are compared, clarifying the their intrinsic differences in terms of energy flow. Finally the electric impedance formed by negative capacitance and resistor is optimized when the unit cell's geometric configuration is fixed. Different criteria are used as objective functions, leading to different mechanisms of preventing the energy injection.

REFERENCES

[1] Y. Fan, M. Collet, M. Ichchou, L. Li, O. Bareille, Z. Dimitrijevic, A wave-based design of semi-active piezoelectric com-posites for broadband vibration control, Smart Mater. Struct. 25 (2016) 55032.

[2] Y. Fan, M. Collet, M. Ichchou, L. Li, O. Bareille, Z. Dimitrijevic, Energy flow prediction in built-up structures through a hybrid finite element/wave and finite element approach, Mech. Syst. Signal Process. 66–67 (2016) 137–158.

[3] Y. Fan, M. Collet, M. Ichchou, L. Li, O. Bareille, Z. Dimitrijevic, Enhanced wave and finite element method for wave propagation and forced response prediction in periodic piezoelectric structures, Chinese J. Aeronaut. in press (2017).

VIII ECCOMAS Thematic Conference on Smart Structures and Materials
SMART 2017
A. Güemes, A. Benjeddou, J. Rodellar and J. Leng (Eds)

INERTIA AMPLIFICATION IN PHONONIC CRYSTALS FOR LOW FREQUENCY BANDGAPS

T. Delpero[†], G. Hannema[††], B. Van Damme[††], S. Schoenwald[††], A. Zemp[††], A. Bergamini[†*]

Empa, Materials Science and Technology
Überlandstrasse 129
CH-8600 Dübendorf, Switzerland
*email: andrea.bergamini@empa.ch
[†] Laboratory for Mechanical Integrity of Energy Systems
[††] Laboratory for Acoustics/Noise Control

Key words: Periodic Structures, Phononic Crystal, Inertia Amplification

Abstract. The formation of bandgaps in phononic crystals (PC) is object of extensive investigation by a lively scientific community. While achieving low frequency values for the position of the first bandgap is in general terms not an unsurmountable challenge, the combination of material properties such as high stiffness, low density and reduced size of the unit cell, with low (in absolute terms) frequency bandgaps may well require some careful consideration. In previous work, we have found that the relation between the mentioned material properties and the position of the first bandgap for a given PC geometry can be well described by the relation $\omega* = f_{BG} \cdot L \cdot (\rho_{UC}/C_{UC})^{0.5}$, where f_{BG} is the start frequency of the first bandgap, L, C_{UC}, ρ_{UC} are a characteristic length, the stiffness and the density of the unit cell, respectively. $\omega*$ appears to be a property related to the geometry of the unit cell. In an effort to design PCs with low $\omega*$ values, we have devised a novel implementation of inertia amplification based on coupling of the energy of longitudinal waves into the rotational oscillation of inertia elements within the unit cell. In this contribution, we present examples of PCs based on this approach and discuss the interaction of acoustic waves with the discussed lattices.

1 INTRODUCTION

In recent years, the interest for the use of periodically structured materials has experienced intense activity, due to their potential to achieve unusual macroscopic properties, both in the quasi-static and dynamic regime. Among these, ultra-light materials [11], pentamode materials [2], auxetic materials [8] or double negative materials [6] have been reported. In the dynamic domain, the ability to affect the propagation of mechanical waves, by creating partial or complete band gaps exploiting local resonance phenomena in the mechanical [10] or electrical [3] domain, inertial amplification [16] or the formation of Bragg-type band gaps [15] has been object of interest.

From a structural engineering point of view, the ability to modify the way mechanical waves propagate through a structure and thus to deal with structural vibrations at a very fundamental level, is certainly an exciting prospect that explains the intense activity in this field. However, the application of periodically arranged materials for structural purposes is subject to a number of requirements that transcend the simple ability to affect the propagation of mechanical waves in certain frequency ranges. These are related to their utilization in *load carrying structures* subject dynamic loads that can lead to excessive vibration amplitudes. Typical requirements for structural materials used for aerospace or automotive applications include high stiffness and strength, low mass density, and small size of the unit cell, among others. As will be shown later, the realization of all these properties in the same material with low frequency band gaps is a challenge.

A quick inspection of the equation describing the position and width of the band gap in a diatomic spring-mass chain [5]:

$$\omega_A = \sqrt{\frac{2C}{M_1}} \tag{1}$$

$$\omega_{OB} = \sqrt{\frac{2C}{M_2}} \tag{2}$$

informs us on the basic relationship between the characteristic properties of the unit cell (mass of the atoms and spring constant of the elastic link between them) and the position of the start frequency of the band gap of a diatomic chain with masses $M_1 > M_2$ and elastic links with the constant C, as shown in figure 1:

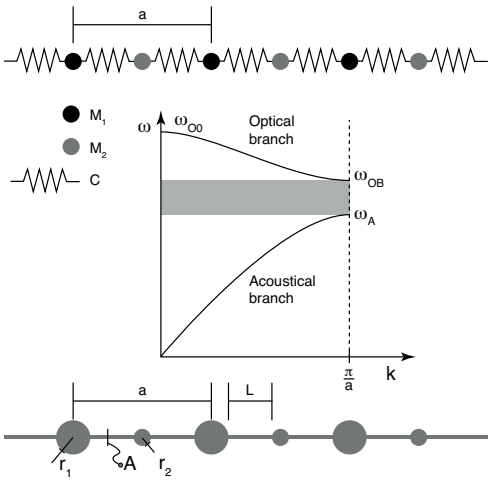

Figure 1: A diatomic, one dimensional spring-mass chain (top), the associated dispersion curves (e.g. for longitudinal waves) and a corresponding real-life implementation based on spherical mass elements and rod-like links (bottom).

2 PHONONIC CRYSTALS

In a phononic crystal (PC), as it could be realized by additive manufacturing (AM) techniques in a single material process, the ideal elastic links and point masses considered in the discussion of a spring-mass chain, have finite dimensions. The elastic links can be, for example, simple rods of length L with a cross-sectional area $A = \pi r_b^2$ for a rod radius r_b. The mass elements can be realized as spherical elements with the radii $r_1 > r_2$, as shown in the bottom of figure 1. The unit cell size of the chain is a. For such a system, the spring constant $\tilde{C}$ and the masses M_1 and M_2 of the *atoms* are given by:

$$\tilde{C} = \frac{E_M A}{L} \tag{3}$$

$$M_1 = \frac{4\pi r_1^3}{3}\rho_M \tag{4}$$

$$M_2 = \frac{4\pi r_2^3}{3}\rho_M \tag{5}$$

Whereas E_M and ρ_M are the Young's modulus and the mass density of the material, respectively and L, r_1 and r_2 are shown in figure 1. If we consider a system in which the relative dimensions of the mass and stiffness elements are kept constant, then we are able to formulate a simple scaling law to relate a characteristic length within the crystal and the material properties to the position of the bottom frequency of the band gap ω_A. To obtain this relation, we can rewrite ω_A as shown in (6):

$$\omega_A = \sqrt{\frac{3AE_M}{2\pi r_1^3 L \rho_M}} = \tilde{s}\frac{1}{L}\sqrt{\frac{E_M}{\rho_M}} \tag{6}$$

By appropriately combining all geometrical quantities into $\tilde{s}$, we obtain the compact form on the right hand side of (6), where L serves as a linear scaling parameter, for a given geometry of the unit cell. $\tilde{s}$ is then a property of the geometry, while E_M and ρ_M are material properties.

$$\tilde{s} = \sqrt{\frac{3AL}{4\pi r_1^3}} \tag{7}$$

By extension, it is reasonable to expect that the same approach can be taken to characterize the effect of the geometry of a phononic crystal (PC) on wave propagation of other modes, such as transversal waves. For vibrations associated with bending deformations of the spring elements, the spring constant $\hat{C}$ is given by

$$\hat{C} = \frac{3E_M I}{L^3} \tag{8}$$

Whereas I is the second moment of area of the cross-section of the elastic element $I = \frac{\pi r^4}{4}$. Also in this case, obviously, the spring constant $\hat{C}$ scales linearly with L, if we assume that all dimensions of the systems are scaled uniformly. So, with the due changes accounting for the different modes of deformation (longitudinal vs. bending), also in this case, we can state that

the value of ω_A scales with L, E_M, and ρ_M according to the right hand side of (6), whereas the parameters flowing into a scaling parameter for bending deformations $\hat{s}$, will be the ones related to the spring constant $\hat{C}$:

$$\hat{s} = \sqrt{\frac{9r_b^4}{8r_1^3 L}} \tag{9}$$

In previous work [4], we have reported on the design, preparation and testing of a lattice material with the goal to obtain low frequency band gaps while maintaining as small as possible a unit cell size, low effective density and high stiffness. The 3D PC presented in that work was based on a diatomic Zincblende geometry (tetrahedrally coordinated A and B atoms). It was realized by connecting mass elements (alternatingly made of hollow polymer and solid bronze elements) using thin-walled poly-imide struts, for more detail refer to cited reference.

The resulting 3D phononic crystal, with a cubic unit cell of 50 mm, was demonstrated to have a first complete band gap starting at approximately f_{BG} ≈2 kHz, a mass density ρ_{eff} =62 kg/m^3 and stiffness values (expressed as the elements of the homogenized symmetric matrix) as follows: $\mathbb{C}_{11} = \mathbb{C}_{22} = \mathbb{C}_{33}$ =1.24 MPa, $\mathbb{C}_{12} = \mathbb{C}_{13} = \mathbb{C}_{23}$ =1.05 MPa, $\mathbb{C}_{44} = \mathbb{C}_{55} = \mathbb{C}_{66}$ =0.33 MPa. While a statement about the relevance of these material properties is only significant relative to a specific application, it is true that in structural applications, high stiffness values and high stiffness/density ratios are of paramount importance.

In this context, a logical approach to improving the performance (defined as the ability to provide high stiffness, low density and low frequency bandgaps in a small unit cell) of the designed phononic crystals is to explore other potentially interesting crystal symmetries found in nature. Here, a vast selection of system parameters, such as crystal symmetry, unit cell size, density and modulus of the constituting materials, makes for an almost unlimited freedom in the design of the unit cell. In order to effectively compare the influence of geometry on the position of the first band gap, parametric studies as the ones presented in [7] and [4], where the position of the band gap is related to the unit cell size and the wave velocity in the elastic elements of the lattice are useful. However, this type of normalization does not give immediate insight in engineering properties of the unit cell. For purpose of comparison of PCs with very different geometry and size, we thus introduce following non-dimensional parameter that is function of the geometry of the unit cell of the PC:

$$\omega^* = f_{BG} L \sqrt{\frac{\rho_{UC}}{C_{UC}}} \tag{10}$$

Here, f_{BG} $[Hz]$ represents the bottom frequency of the of the first band gap, L $[m]$ is a characteristic length of the unit cell, ρ_{UC} $[kg/m^3]$ is the density of the unit cell (i.e. the mass of the unit cell divided by the volume of the unit cell) and C_{UC} $[MPa]$ is a stiffness constant of the unit cell, as opposed to the material properties used in (6). The value of ω^* obtained for the PC at hand was approximately 0.35. For a diatomic chain, the theoretical limit for ω^* for $M_1/M_2 \to \infty$ is $1/\pi$. This can be easily verified, by calculating the limit of (10) for $M_1/M_2 \to \infty$, while considering also the limit case for ρ_{UC}.

Our previous work presented a numerical exploration and parametric study of nature-inspired crystal symmetries that essentially fit the model of point masses connected by springs elements

in a 3D symmetry. Together wit the knowledge about the relationship between density and stiffness in bending dominated and stretching dominated lattice structures [1], this lead to the conclusion that the performance of such lattice structures, in the terms described by 10, is bounded.

3 INERTIAL AMPLIFICATION IN 3D PHONONIC CRYSTALS

The intrinsic link between mass density or stiffness and start frequency of the first band gap in phononic crystals in which the mass elements are considered as point masses, without any special consideration for their geometric properties, can be eased by introducing concepts such as inertia amplification [16, 14]. Here the design of macroscopic phononic crystals clearly departs from the abstraction of a periodic distribution in space of mass elements connected by springs (typically representing an electrostatic interaction between ions or atoms) and considers the degrees of freedom offered in the design of these structures. Specifically, in the periodic structures described in [16], next to the mass elements in the spring-mass lattice, additional mass elements were introduced whose motion is governed by a simple mechanism connecting them to the 'primary masses', as illustrated in figure 2:

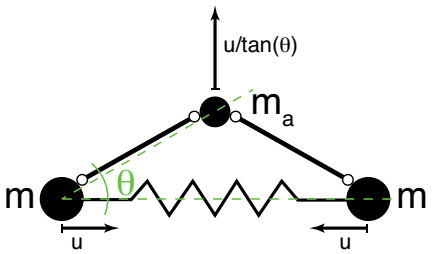

Figure 2: The inertia amplification mechanism presented in [16] exploits the kinematics of the mechanism connecting the masses in the system leading to an amplification of the displacement of m_a by a factor $1/\tan\theta$ relative to the displacement of m.

In the system shown in the figure, m_a moves along the center line between the two main masses m. The equivalent mass of the system is given by (11):

$$\tilde{M}_{eq} = (2m + \frac{m_a}{\tan(\theta)^2}) \tag{11}$$

Assuming sufficiently small values of θ, large equivalent mass values for the vibrating system can be achieved, thus, substituting $\tilde{M}_{eq}$ for M_1 in (1) results in lower values for the bottom frequency of the first band gap than a mechanism free system would allow for.

However, also in the case briefly outlined above, the mass elements can be assumed to be ideal point masses. Here, we report on a PC in which the geometry of the mass elements is exploited to further improve the ratio between position of the starting frequency of the first bandgap and effective density of the unit cell. If we consider the masses of a spring-mass chain to have a geometric extension, we can exploit geometrical properties of the element such as its moment of inertia. Figure 3 shows a sketch of the unit cell of the proposed PC.

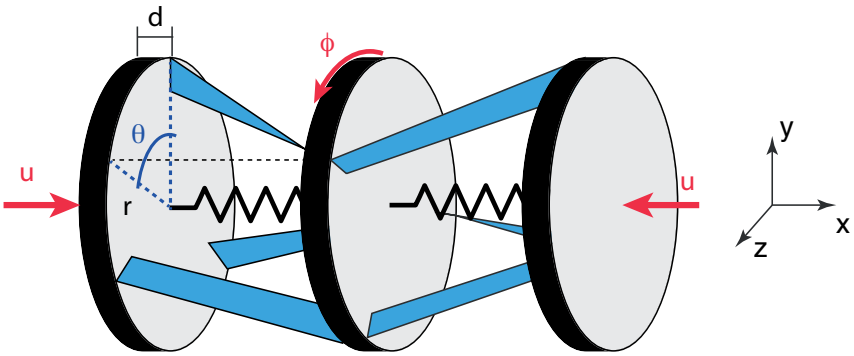

Figure 3: Unit cell of a phononic crystal with inertial amplification mechanism and coupling of longitudinal and torsional displacement. In this system, next to the mass of the moving masses, their rotational inertia contributes to the creation of low frequency resonances.

In the structure presented in figure 3, the blue connectors between the disks are construed as very stiff beams hinged to the disks at their connection. Between the disks, a spring element provides the elastic response of the system. In the underformed state, the blue connectors intersect the disks at an angle, such that a relative motion of the disks in the x-direction couples a relative rotary motion u of the disks (indicated by the red arrow 'ϕ', in figure) about the x-axis. Through this rotational motion, the moment of inertia of the disks makes a contribution to the overall inertia terms of the system.

For the unit cell at hand, the effective mass of the resonator is found to be [9]:

$$M_{eq} = m + \frac{\Theta}{\tan^2(\theta) r^2} \tag{12}$$

Where m is the mass of a disk, r is the radius of the disks, θ is the twist angle between the disks, i.e. the angle between the contact points of the connectors with the disks, as indicated in the figure, and Θ is the moment of inertia of the disk ($\Theta = \frac{1}{2}mr^2 = \rho\frac{1}{2}d\pi r^4$).

4 NUMERICAL AND EXPERIMENTAL RESULTS

In the following we report on an implementation of a PC with longitudinal-torsional coupling and inertia amplification, as shown in figure 4. The PC was made of glass fiber reinforced poly-amide, by AM (selective laser sintering). Here, in contrast to the PC presented in previous work, the structure could be realized in a single material.

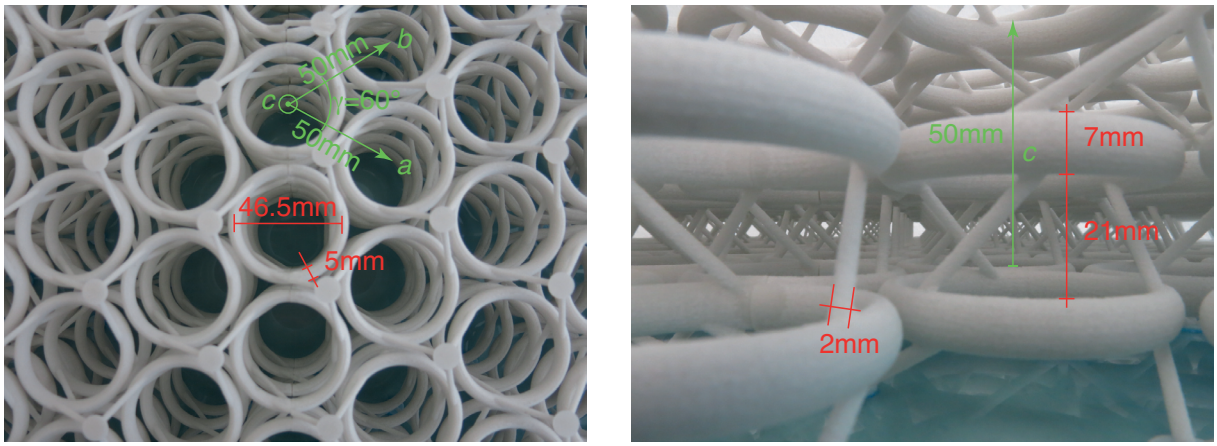

Figure 4: Implementation of a PC with longitudinal-torsional coupling and inertia amplification, made by AM (selective laser sintering) using fiber reinforced PA12. The main dimensions of the PC components are shown in red. The lattice parameters $a = b = c = 50\,\text{mm}$, $\gamma = 60°$ are highlighted in green

The structure presented here, was designed to demonstrate the effect of longitudinal-torsional coupling of lattice vibrations and inertial amplification mechanisms on the discussed non-dimensional parameter ω^*. The transmission of sound waves along the $c-$axis was of special interest, as the PC was tested for its transmission properties as core material in a sandwich structure, as discussed later.

The overall dimensions of the PC unit cell are given in figure 4. The dispersion properties of the PC consisting of a hexagonally densely packed arrangement of the unit cell was calculated by solving for the eigenfrequencies of the unit cell while imposing Floquet boundary conditions along the three crystallographic directions, so as to consider the edges of the first Brillouin Zone, as usual when investigating the dispersion properties of crystalline solids. The dispersion curves are shown in figure 5:

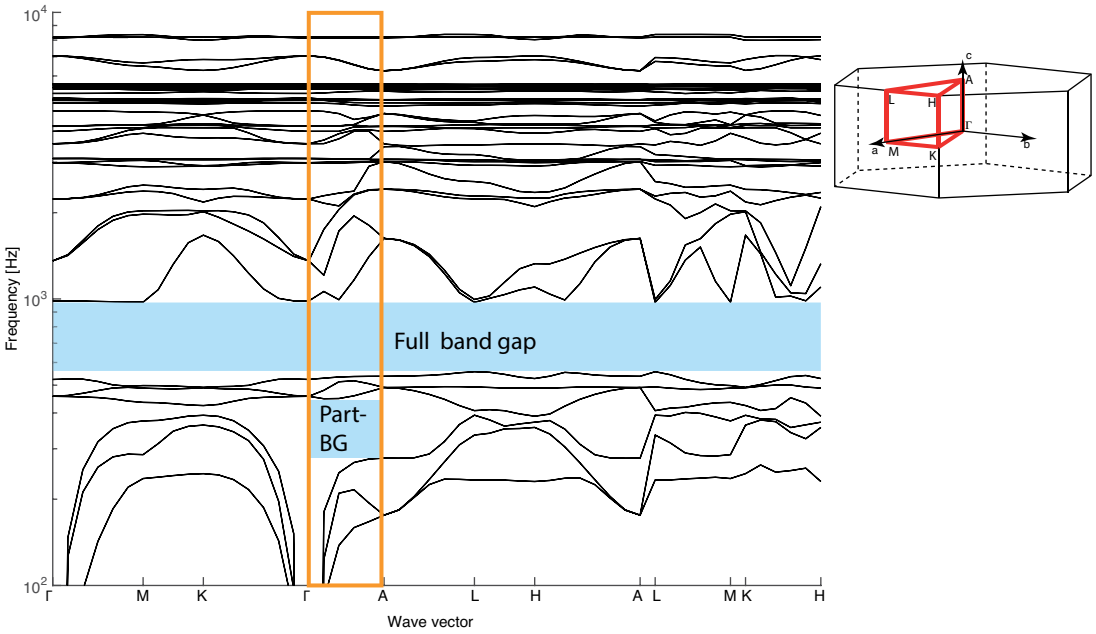

Figure 5: Dispersion relation for the PC shown in figure 4, plotted against the reduced wave vector. The portion of the reduced wave vector (ΓA) highlighted in orange, corresponds to the through-thickness direction (parallel to c) of the structure of the sample shown in the photograph. On the top right: irreducible Brillouin Zone of the lattice at hand, drawn after [12].

The calculated dispersion curves indicate that in the frequency interval between approximately 550 Hz and 1000 Hz a full band gap can be expected, whereas in the direction parallel to the $c-$axis, the propagation of waves is characterized by a partial band gap between approximately 260 Hz and 400 Hz.

While a direct verification of the calculated dispersion properties of the PC at hand exceeded the scope of our study, we carried out experiments to investigate the transmission of mechanical waves through a sandwich panel consisting of a core made of a finite sample of the PC and two PMMA plates serving as sandwich faces. The transmission properties were investigated both, by exciting the structure with an electrodynamic shaker and by applying sound pressure on one side of the panel and measuring the output pressure in a test room on the other side.

For the shaker measurements, the sample was excited on one side using a B&K electrodynamic shaker while measuring the velocity field on the two faces (in consecutive identical experiments) using a Polytec PSV 400 scanning laser vibrometer. The velocities were averaged over the two surfaces, respectively, to calculate the velocity level difference shown in figure 6. The test with airborne excitation was conducted placing the sandwich structure in the opening between the coupled rooms of a test facility typically used for sound insulation measurements. The velocity field was measured on both the faces, as in the structure borne test.

Figure 6 shows the ΓA portion of the dispersion curve (left) and the transmission spectra (as calculated using FEM, measured by exciting the sample with a shaker or with uniform sound) of a PC with the approximate dimensions 500 mm x 500 mm x 100 mm sandwiched between two

4 mm thick PMMA plates (right).

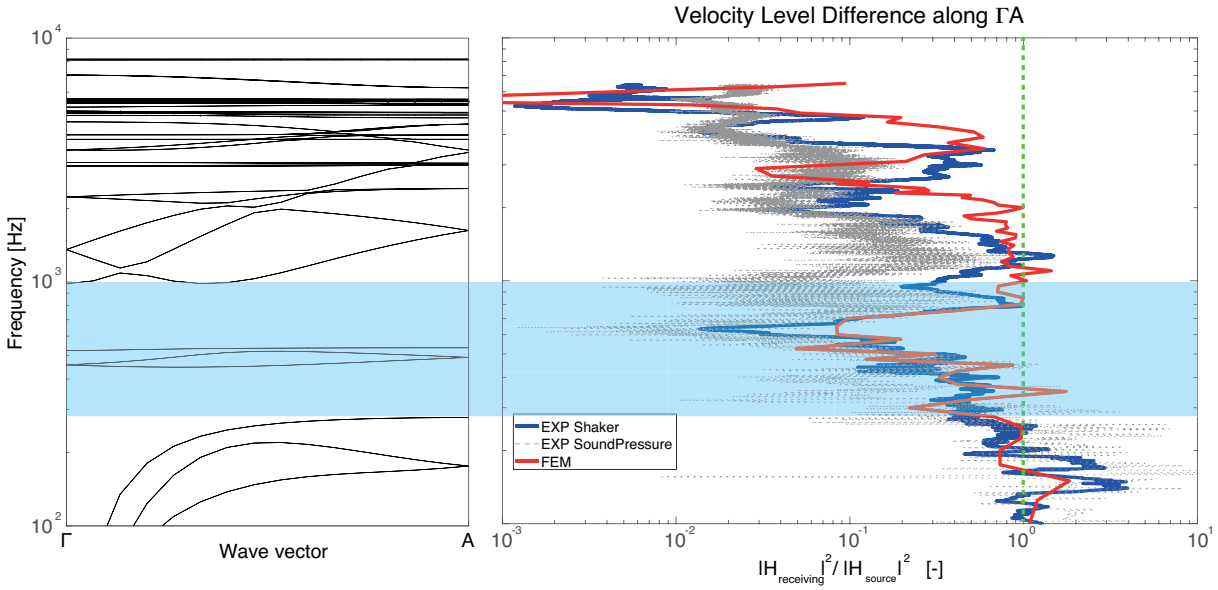

Figure 6: Dispersion curves along the $c-$direction of PC(left) and transmission spectra of a sandwich structure consisting of the PC with 4 mm thick PMMA plates as faces (right). The modes still present within the range marked as band gap have mostly local character, as indicated by their flat slope and do not contribute to the transmission of mechanical power, as indicated also by the transmission plot. The green dotted line in the transmission spectrum indicates a transmittance of 100%. Values to the left of it, indicate attenuation of the waves.

On the right hand side of figure 6, a very good agreement of FEM calculation (as calculated assuming a point excitation as in the shaker experiment) of the transmission spectrum of the structure with the spectra determined experimentally, both in the shaker and in the acoustic transmission experiment. The same model of the unit cell as used for the calculation of the transmission properties shown in the figure was used, assuming Floquet boundary conditions, to calculate the dispersion curves shown in figures 5 and 6. The blue band across the two parts of the figure indicates the position of the calculated band gap relative to the reduction in transmissibility of the mechanical waves across the structure. All finite element calculations were carried out, without assuming material damping. We could observe a good correlation between the position of the partial band gap in the $c-$direction and the reduced transmission of waves in that frequency range and the good correlation between transmission properties as calculated numerically and determined experimentally. This can be considered to be a strong indication that the observed attenuation of the waves across the sample is likely due to the presence of the calculated partial band gap.

Based on the same numerical models, as used for the dispersion and transmission calculations, other relevant properties of the PC were estimated: The effective density of the PC unit cell resulted to be 103 kg/m^3 and the stiffness constant in $c-$direction was calculated as 1.2 MPa.

By inserting these values in (10) we can obtain the ω^* value for the presented PC, relative to the propagation of waves along the $c-$axis of the PC:

$$\omega_c^* = 260Hz0.05m\sqrt{\frac{103kg/m^3}{1.2MPa}} = 0.12 \tag{13}$$

5 CONCLUSIONS and OUTLOOK

The introduction of a non-dimensional figure of merit to show the effect of geometry on the relation between stiffness, size, density and position of the first band gap is a useful approach to the comparison between PCs with substantially different unit cell geometries, so as to avoid drawing inaccurate conclusions about the performance of unit cell designs. Based on the proposed figure of merit, Bragg type band gaps in PCs based on point masses are associated with a limit for ω^* of $1/\pi$.

The PC design presented in this contribution offers a significant advantage as compared to PCs with point mass elements. It can be stated, that for the same stiffness, size and effective density the position of the first band gap can be approximately three times lower than in a PC with 'conventional point masses'. This is achieved thanks to the introduction of inertia amplification and of longitudinal-torsional coupling mechanisms, which allow for the exploitation of additional design degrees of freedom for the geometry of the unit cell of PCs. The identification of a specific application also allows to consider partial band gaps in the development of a phononic material with suitable properties. In the case presented here, the attenuation in the region of the partial band gap is fairly modest, if compared to the attenuation in the full band gap region.

While the calculation of the dispersion properties of periodic structures makes it possible to easily identify the effect of design parameters on their wave propagation properties, and to compare different designs based on easily derived figures of merit, the information provided by these tools is not complete. Indeed, the knowledge of the position of the bottom edge of a band gap does not provide information about the attenuation level that a finite number of unit cells in a structure will provide for mechanical waves. Also, the proposed figure of merit does not provide information on the width of the frequency range in which the propagation of mechanical waves is affected.

While information on the width of the forbidden frequency range can be fairly easily derived based on similar considerations as described by (7) and (10), the estimation of the depth of band gaps of finite structures is, already for geometrically simple systems, a less trivial matter, as shown for example in the case of locally resonant metamaterials, in [13].

The investigation of the effectiveness with which designed unit cells attenuate mechanical waves in terms of the number of unit cells required to achieve a given level of attenuation within the frequency range of the band gap is a matter of great interest and shall be object of further investigation. Furthermore, establishing design guidelines, based on simple analytical models relating the geometry and material properties with the position of band gaps in the frequency domain will be of great practical value.

The PC sample investigated in this work was prepared by AM, as the geometrically complex structures needed to realize the proposed approach was best suited for this method of preparation. To date, the manufacturing costs associated with this process are such that it is typically only considered for manufacturing prototype volumes, however the expectation is that future

developments and of the technology and increase in volume will make it possible to exploit the flexibility in manufacturing offered by AM and the benefits of engineered phononic materials for specific applications.

REFERENCES

[1] M. F. Ashby. The properties of foams and lattices. *Philosophical transactions. Series A, Mathematical, physical, and engineering sciences*, 364(1838):15–30, 2006.

[2] T. Bückmann, M. Thiel, M. Kadic, R. Schittny, and M. Wegener. An elasto-mechanical unfeelability cloak made of pentamode metamaterials. *Nature communications*, 5(May):4130, 2014.

[3] F. Casadei, T. Delpero, A. Bergamini, P. Ermanni, and M. Ruzzene. Piezoelectric resonator arrays for tunable acoustic waveguides and metamaterials. *Journal of Applied Physics*, 112:064902, 2012.

[4] T. Delpero, S. Schoenwald, A. Zemp, and A. Bergamini. Structural engineering of three-dimensional phononic crystals. *Journal of Sound and Vibration*, 363:156–165, 2015.

[5] G. Grosso and G. Pastori Parravicini. *Solid State Physics*. Academic Press, 2000.

[6] T. A. M. Hewage, K. L. Alderson, A. Alderson, and F. Scarpa. Double-Negative Mechanical Metamaterials Displaying Simultaneous Negative Stiffness and Negative Poisson's Ratio Properties. *Advanced Materials*, pages 10323–10332, 2016.

[7] S. Kroedel, T. Delpero, A. Bergamini, P. Ermanni, and D. M. Kochmann. 3D Auxetic Microlattices with Independently Controllable Acoustic Band Gaps and Quasi-Static Elastic Moduli. *Advanced Engineering Materials*, 16(4):357–363, 2014.

[8] R. S. Lakes. Advances in negative Poisson's ratio materials. *Advanced Materials*, 5(4):293–296, 1993.

[9] I. Leibacher. Personal communication. October 2016.

[10] Z. Liu, X. Zhang, Y. Mao, Y. Zhu, Z. Yang, C. Chan, and P. Sheng. Locally Resonant Sonic Materials. *Science*, 289(5485):1734–1736, sep 2000.

[11] T. A. Schaedler, A. J. Jacobsen, A. Torrents, A. E. Sorensen, J. Lian, J. R. Greer, L. Valdevit, and W. B. Carter. Ultralight Metallic Microlattices. *Science*, 334(6058):962–965, 2011.

[12] W. Setyawan and S. Curtarolo. High-throughput electronic band structure calculations: Challenges and tools. *Computational Materials Science*, 49(2):299–312, 2010.

[13] C. Sugino, S. Leadenham, M. Ruzzene, and A. Erturk. An investigation of electroelastic bandgap formation in locally resonant piezoelectric metastructures. *Smart Materials and Structures*, 26(5):055029, 2017.

[14] S. Taniker and C. Yilmaz. Phononic gaps induced by inertial amplification in BCC and FCC lattices. *Physics Letters, Section A: General, Atomic and Solid State Physics*, 377(31-33):1930–1936, 2013.

[15] T.-T. Wu, Z.-G. Huang, T.-C. Tsai, and T.-C. Wu. Evidence of complete band gap and resonances in a plate with periodic stubbed surface. *Applied Physics Letters*, 93(11):111902, 2008.

[16] C. Yilmaz, G. M. Hulbert, and N. Kikuchi. Phononic band gaps induced by inertial amplification in periodic media. *Physical Review B - Condensed Matter and Materials Physics*, 76(5), 2007.

VIII ECCOMAS Thematic Conference on Smart Structures and Materials
SMART 2017
C. Sugino, M. Ruzzene, and A. Erturk

MERGING MECHANICAL AND ELECTROMECHANICAL LOCALLY RESONANT BANDGAPS IN METAMATERIALS

CHRISTOPHER SUGINO*, MASSIMO RUZZENE*† AND ALPER ERTURK*

*G.W. Woodruff School of Mechanical Engineering
Georgia Institute of Technology
Atlanta, GA, 30332, USA

† D. Guggenheim School of Aerospace Engineering
Georgia Institute of Technology
Atlanta, GA, 30332, USA

Key words: Metamaterial, locally resonant, mechanical, electromechanical, bandgap

Abstract. It is well known that locally resonant (LR) metamaterials exhibit bandgaps at wavelengths much larger than the lattice size, which can be exploited in various applications such as low-frequency vibration attenuation. In this work, we explore the combination of mechanical and electromechanical LR bandgaps in the same single metastructure for bandwidth enhancement by focusing on a cantilevered composite Euler-Bernoulli beam under transverse vibrations. The nature of bandgap formation in mechanical/elastic and electromechanical/electroelastic (more specifically piezoelectric) LR metamaterials is fundamentally different. LR bandgap in mechanical metamaterials made from a continuous structure with array of spring-mass attachments tuned to a certain frequency is associated with a frequency-dependent modal mass term. However, LR bandgap in electromechanical metamaterials made from an array of resonant piezoelectric shunt circuits (again, tuned to a certain frequency) is associated with a frequency-dependent modal stiffness term. As an important consequence, the mechanical LR bandgap forms above the target frequency of tuned resonators, and its size depends on the resonator to host structure mass ratio; while the electromechanical LR bandgap forms below the target frequency, and its size depends on the overall system-level electromechanical coupling coefficient. We show that targeting the same resonant frequency in spring-mass and inductive-capacitive circuits in the same single structure results in an enhanced bandgap. Modal analysis of the finite composite metastructure is presented and closed form expressions are obtained to analytically estimate the hybrid mechanical-electromechanical bandgap.

1 INTRODUCTION

Locally resonant metamaterials are capable of exhibiting bandgaps at wavelengths much larger than the lattice size of the structure, enabling low-frequency vibration attenuation in

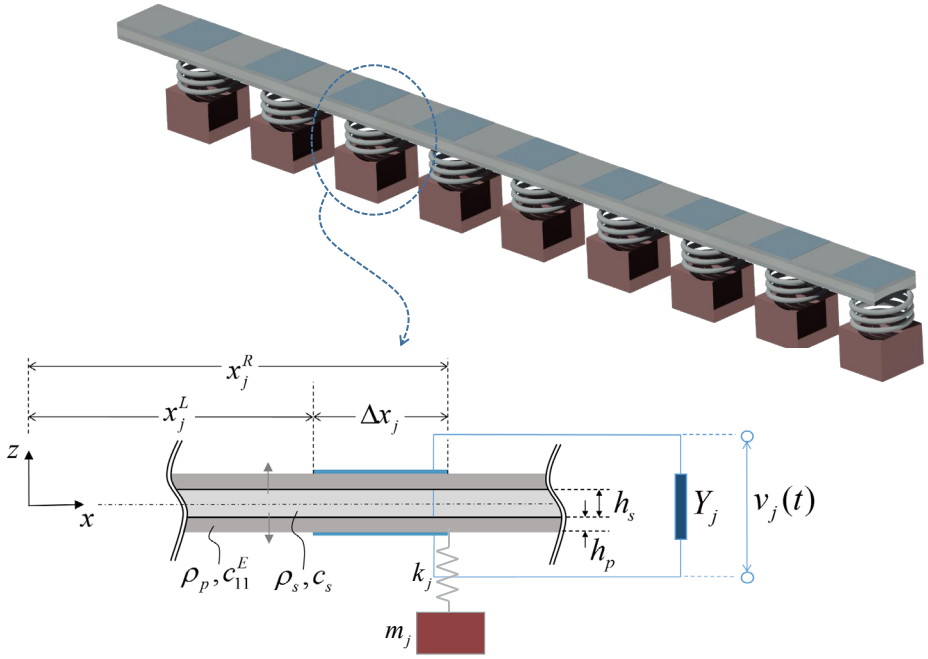

Figure 1: Schematic of the combined mechanical-electromechanical metastructure. The piezoelectric bimorph beam has segmented electrodes, with a resonator placed at the right end of each electrode.

small structures. Liu et al. [1] showed first demonstrated this behavior using hard metal spheres embedded in a soft rubber as mechanical resonators. More recently, the use of piezoelectric elements has enabled the use of resonant shunt circuits, which has the benefit of significantly lower mass requirements. Previously, we have examined the dynamics of both purely mechanical [2] and purely electromechanical metastructures [3], obtaining closed-form expressions for the locally resonant bandgap edge frequencies in each case. Here we combine the two systems to show that the two bandgaps can be combined into a single, larger bandgap for increased bandwidth.

2 COMBINED MECHANICAL AND ELECTROMECHANICAL METASTRUCTURE

Consider a piezoelectric bimorph beam with rectangular cross section made from two continuous piezoelectric layers sandwiching a central shim, with the piezoelectric layers poled in opposite transverse directions (i.e. series connection). The outer surface electrodes are segmented as pairs and connected to a total of S shunt circuits, which span a region $x_j^L < x < x_j^R$, where $j = 1 \ldots S$ is an index numbering the shunt circuits, and x_j^L and x_j^R are the left and right ends of the jth pair of electrodes, respectively. This system was considered by Sugino et al. [3], here we introduce mechanical metastructure performance by adding S mechanical resonators to the structure at the right end of each electrode, i.e. at $x = x_j^R$. A schematic of the system is shown in Fig. 1.

The governing equations for the bimorph, resonators, and shunt circuits can be obtained as

$$EI\frac{\partial^4 w}{\partial x^4} + m\frac{\partial^2 w}{\partial t^2} - \sum_{j=1}^{S} k_j u_j(t)\delta(x - x_j^R) - \vartheta \sum_{j=1}^{S} v_j(t)\frac{\partial^2}{\partial x^2}\left[H(x - x_j^L) - H(x - x_j^R)\right] = f(x,t) \tag{1}$$

$$m_j\ddot{u}_j + k_j u_j(t) + m_j\ddot{w}(x_j^R, t) = 0 \tag{2}$$

$$C_{p,j}\dot{v}_j(t) + \mathscr{Y}_j\left[v_j(t)\right] + \vartheta\int_{x_j^L}^{x_j^R}\frac{\partial^3 w}{\partial x^2 \partial t}dx = 0 \tag{3}$$

where $w(x,t)$ is the transverse displacement of the beam, k_j is the stiffness of the jth resonator, $u_j(t)$ is the displacement of the jth resonator, $v_j(t)$ is the voltage across the jth pair of electrodes, $\mathscr{Y}_j$ is a linear operator corresponding to the admittance of the shunt circuit, $H(x)$ is the Heaviside function, and $f(x,t)$ is some external forcing. The effective properties of the bimorph are

$$EI = \frac{2b}{3}\left(c_s\frac{h_s^3}{8} + \bar{c}_{11}^E\left[\left(h_p + \frac{h_s}{2}\right)^3 - \frac{h_s^3}{8}\right]\right) \tag{4}$$

$$m = b(\rho_s h_s + 2\rho_p h_p) \tag{5}$$

$$\vartheta = \frac{\bar{e}_{31} b_e}{2h_p}\left[\left(h_p + \frac{h_s}{2}\right)^2 - \frac{h_s^2}{4}\right] \tag{6}$$

$$C_{p,j} = \bar{\varepsilon}_{33}^S b_e\frac{(x_j^R - x_j^L)}{2h_p} \tag{7}$$

The parameters c_s, ρ_s, and h_s are the central substrate layer's elastic modulus, mass density, and thickness, respectively, while b is the width of the beam. The piezoelectric layers have mass density ρ_p, thickness h_p, width b, elastic modulus at constant electric field $\bar{c}_{11}^E$, effective piezoelectric stress constant $\bar{e}_{31}$, and permittivity component at constant strain $\bar{\varepsilon}_{33}^S$. To discretize the partial differential equation for the beam displacement, we assume a modal analysis type expansion for $w(x,t)$, i.e.

$$w(x,t) = \sum_{r=1}^{N}\phi_r(x)\eta_r(t) \tag{8}$$

where $\phi_r(x)$ are the mass-normalized mode shapes of the structure without resonators (the plain structure) at short circuit, $\eta_r(t)$ are the modal coordinates to be determined, and N is number of modes used in the expansion. Substituting Eq. (8) into Eq. (1), multiplying by another mode shape, and applying orthogonality gives

$$\ddot{\eta}_r(t) + \omega_r^2\eta_r(t) + \sum_{j=1}^{S} m_j\phi_r(x_j^R)\sum_{k=1}^{N}\ddot{\eta}_k(t)\phi_k(x_j^R) + \sum_{j=1}^{S} m_j\ddot{u}_j(t)\phi_r(x_j^R) - \vartheta\sum_{j=1}^{S} v_j(t)\Delta\phi'_{r,j} = q_r(t) \tag{9}$$

where ω_r^2 is the rth natural frequency of the plain structure at short circuit, $\Delta\phi'_{r,j}$ is a slope difference defined as

$$\Delta\phi'_{r,j} = \left(\frac{d\phi_r}{dx}\right)_{x_j^L}^{x_j^R} = \frac{d\phi_r}{dx}(x_j^R) - \frac{d\phi_r}{dx}(x_j^L) \tag{10}$$

and

$$q_r(t) = \int_0^L f(x,t)\phi_r(x)dx \tag{11}$$

is the modal excitation. Substituting Eq. (8) into Eqs. (2) and (3) yields

$$m_j\ddot{u}_j(t) + k_j u_j(t) + m_j \sum_{k=1}^{N} \ddot{\eta}_k(t)\phi_k(x_j^R) = 0 \tag{12}$$

$$C_{p,j}\dot{v}_j(t) + \mathscr{Y}_j\left[v_j(t)\right] + \vartheta \sum_{r=1}^{N} \ddot{\eta}_r(t)\Delta\phi'_{r,j} = 0 \tag{13}$$

For a finite number of modes and shunt circuits/resonators, Eqs. (9), (12), and (13) can be solved for the approximate mode shapes and resonant frequencies of the system, as well as the system response, using techniques such as matrix inversion or modal decomposition. For more analytical insight, we take the Laplace transforms of Eqs. (9), (12), and (13), substituting the resonator equation and voltage equation into the modal governing equation to obtain

$$(s^2+\omega_r^2)H_r(s) + \mu\frac{s^2\omega_t^2}{s^2+\omega_t^2}\sum_{k=1}^{N} H_k(s)\sum_{j=1}^{S} m\phi_k(x_j^R)\phi_r(x_j^R)\Delta x_j + \frac{\alpha s}{s+h(s)}\sum_{k=1}^{N} H_k(s)\sum_{j=1}^{S} EI\frac{\Delta\phi'_{r,j}}{\Delta x_j}\frac{\Delta\phi'_{k,j}}{\Delta x_j}\Delta x_j = Q_r(s) \tag{14}$$

where $H_r(s)$ and $Q_r(s)$ are the Laplace transforms of $\eta_r(t)$ and $q_r(t)$ respectively, s is the Laplace domain complex variable, $\omega_t^2 = k_j/m_j$ is the squared resonant frequency of every mechanical or electromechanical resonator, α is a dimensionless parameter related to electromechanical coupling, given by

$$\alpha = \frac{2\theta^2 h_p}{EI\varepsilon_{33}^S b_e} \tag{15}$$

and $h(s) = Y_j(s)/C_{p,j}$ is a normalized admittance, assumed to be the same for each pair of electrodes, where $Y_j(s)$ is the Laplace transform of $\mathscr{Y}_j$. Additionally, it has been assumed that $m_j = \mu m\Delta x_j$, where μ is the added mass ratio, a dimensionless parameter equal to the ratio of the total resonator mass to the total mass of the original structure.

Equation (14) is a system of $N+2S$ linear equations that can be solved numerically for the response at some excitation frequency ω by substituting $s = j\omega$ and using Gaussian elimination or matrix inversion. However, we observe that as the number of electrodes becomes large, and as the electrodes become very small,

$$\sum_{j=1}^{S} m\phi_k(x_j^R)\phi_r(x_j^R)\Delta x_j \approx \int_0^L m\phi_r(x)\phi_k(x)dx = \delta_{rk} \tag{16}$$

$$\sum_{j=1}^{S} EI\frac{\Delta\phi'_{r,j}}{\Delta x_j}\frac{\Delta\phi'_{k,j}}{\Delta x_j}\Delta x_j \approx \int_0^L EI\frac{d^2\phi_r}{dx^2}\frac{d^2\phi_k}{dx^2}dx = \omega_r^2\delta_{rk} \tag{17}$$

where δ_{rk} is the Kronecker delta, since the two integrals are the orthogonality conditions of the mode shapes of the plain beam at short circuit. These approximations are exact as the shunt circuits become infinitesimally long and as the number of shunt circuits approaches infinity. Both approximations are effectively Riemann sum approximations of integrals, and as such they will not converge at the same rate, since the function being integrated is different in each approximation.

Under the assumptions of Eqs. (16) and (17), the system of equations in Eq. (14) becomes decoupled, allowing us to solve explicitly for $H_r(s)$ as

$$H_r(s) = \frac{Q_r(s)}{s^2\left(1 + \dfrac{\mu\omega_t^2}{s^2+\omega_t^2}\right) + \omega_r^2\left(1 + \dfrac{\alpha s}{s + h(s)}\right)} \tag{18}$$

From this analysis it is clear that the presence of infinitely many resonators on the structure gives rise to frequency-dependent modal mass, and that the presence of infinitely many shunt circuits gives rise to frequency-dependent modal stiffness. Furthermore, the frequency-dependence is the same for every mode shape of the plain structure.

3 COMBINED MECHANICAL-ELECTROMECHANICAL LOCALLY RESONANT BANDGAP

Since the focus of this work is the combined locally resonant bandgap, we consider purely inductive shunt circuits, such that $h(s) = \omega_t^2/s$, where the shunt inductance L_s is selected such that

$$\omega_t^2 = \frac{1}{L_s C_{p,j}} \tag{19}$$

i.e., such that the resonant frequency of the electrical circuits is the same as the resonant frequency of the mechanical resonators. The response is then

$$H_r(s) = \frac{Q_r(s)}{s^2\left(1 + \dfrac{\mu\omega_t^2}{s^2+\omega_t^2}\right) + \omega_r^2\left(1 + \dfrac{\alpha s^2}{s^2+\omega_t^2}\right)} \tag{20}$$

To find the new resonant frequencies of each mode, we can substitute $s = j\omega$ and solve for the roots of the polynomial in the denominator. This yields the two positive, real solutions

$$\hat{\omega}^+ = \sqrt{\frac{1+\mu+\Omega_r^2(1+\alpha)}{2}\left(1 + \sqrt{1 - \frac{4\Omega_r^2}{(1+\mu+\Omega_r^2(1+\alpha))^2}}\right)} \tag{21}$$

$$\hat{\omega}^- = \sqrt{\frac{1+\mu+\Omega_r^2(1+\alpha)}{2}\left(1 - \sqrt{1 - \frac{4\Omega_r^2}{(1+\mu+\Omega_r^2(1+\alpha))^2}}\right)} \tag{22}$$

where $\hat{\omega} = \omega/\omega_t$, and $\Omega_r = \omega_r/\omega_t$ are normalized frequencies. These expressions give the two resonances corresponding to the mode with original short circuit natural frequency ω_r. It can

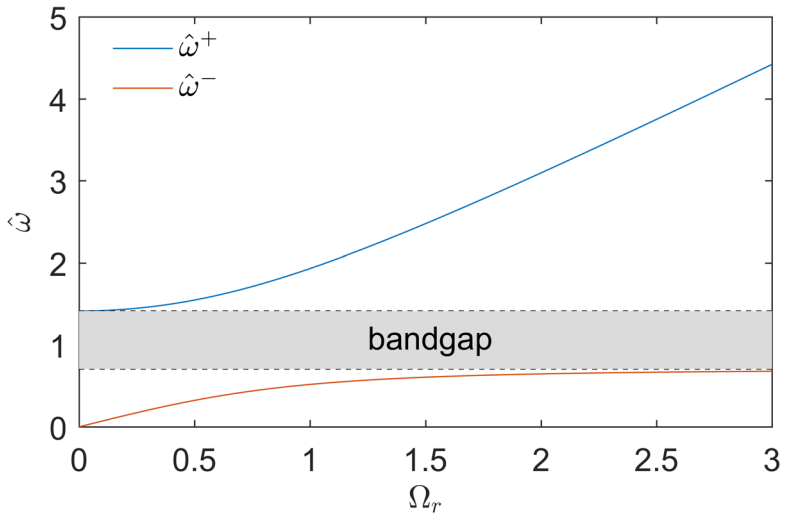

Figure 2: Normalized resonant frequencies $\hat{\omega}$ vs. normalized original resonant frequency Ω_r for mass ratio $\mu = 1$ and dimensionless coupling term $\alpha = 1$. The bandgap edge frequencies as predicted by Eq. (23) are shown with dashed lines, and the shaded region gives the frequency range of the bandgap.

be shown that there can never be any resonances in the frequency range

$$\frac{\omega_t}{\sqrt{1+\alpha}} < \omega < \omega_t\sqrt{1+\mu} \tag{23}$$

which corresponds to the frequency range of the combined mechanical-electromechanical locally resonant bandgap. The two resonances are plotted against Ω_r in Fig. 2.

4 FINITE NUMBER OF MECHANICAL AND ELECTROMECHANICAL RESONATORS

Clearly the approximations of Eqs. (16) and (17) require additional validation for systems with a finite number of segmented electrodes and resonators. For concreteness, we assume that the resonators are placed evenly on the beam, such that $x_j^L = (j-1)L/S$ and $x_j^R = jL/S$. For some particular set of values for ω_t, α, and μ, the approximate response of the beam to base excitation can be obtained using matrix inversion at each value of S, and the response can be plotted as a surface (or map) against S and the excitation frequency ω. This is shown in Fig. 3 for a cantilever beam excited by base motion with $\mu = 1$, $\alpha = 0.44$, $\omega_t = 300\omega_1$.

Interestingly, the mechanical bandgap first appears near $S = 10$, whereas the electromechanical bandgap appears near $S = 20$. The difference in the minimum required number of resonators is due to the two separate approximations in Eqs. (16) and (17), where it is clear that Eq. (16) converges more quickly than Eq. (17). It can be expected that the difference in minimum required resonators will decrease for lower target frequencies ω_t, and increase with higher target frequencies. Additionally, it is clear that the two bandgaps never truly merge, as there are always resonances present between the electromechanical and mechanical bandgaps. For very large S, the frequency range of these intermediate resonances collapses to effectively

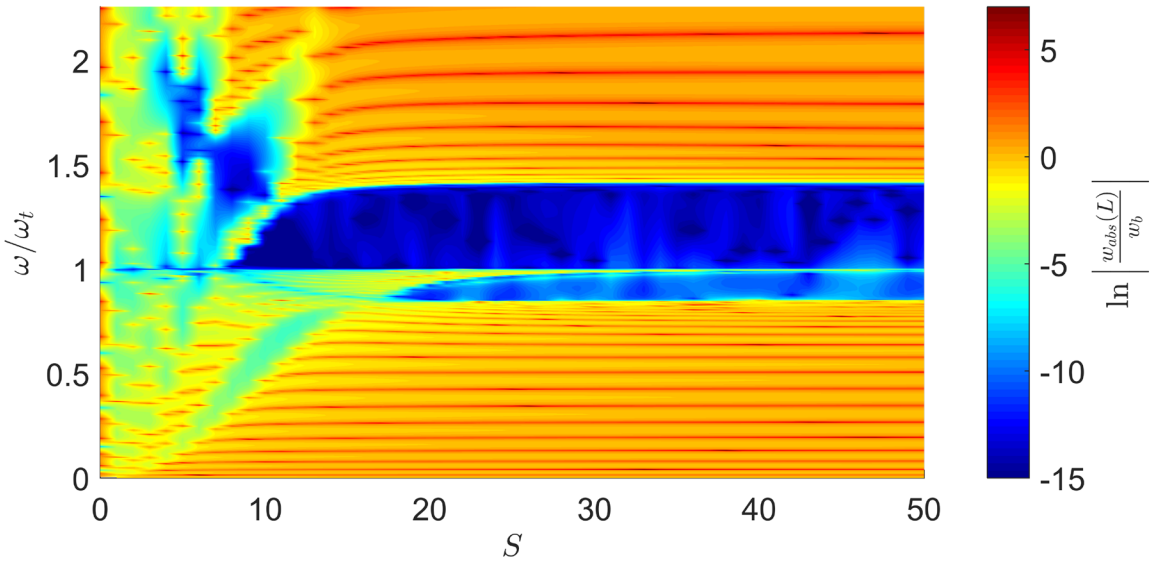

Figure 3: Beam transmissibility at the tip vs. number of shunt circuits/resonators S and normalized excitation frequency ω with $\mu = 1$, $\alpha = 0.4$, $\omega_t = 300\omega_1$. The two bandgaps are clearly visible as the regions of sharp vibration attenuation.

a single frequency value ω_t, giving rise to some degenerate behavior as multiple modes exhibit nearly the same resonant frequency.

5 CONCLUSIONS

A combined mechanical-electromechanical metastructure has been studied for the creation of increased-bandwidth locally resonant bandgaps. The improved locally resonant bandgap is obtained by tuning both the mechanical resonators and resonant shunt circuits to the same frequency, which allows the mechanical and electromechanical locally resonant bandgaps to be combined into a single, wider bandgap. For a sufficient number of mechanical and electromechanical resonators, the edge frequencies of the combined bandgap are derived in closed form, depending only on the target frequency, added mass ratio, and a dimensionless electromechanical coupling term. Numerical case studies show that the mechanical bandgap requires less resonators to appear than the electromechanical bandgap, but for a sufficiently large number of resonators both bandgaps appear. A small frequency range is always present in between the two bandgaps with numerous resonances, which is reduced as the number of resonators becomes large. It is expected that this transition frequency range would be significantly reduced by any damping present in the system.

REFERENCES

[1] Liu, Z., Zhang, X., Mao, Y., Zhu, Y.Y., Yang, Z., Chan, C.T., and Sheng, P. Locally resonant sonic materials. *Science*. (2000) **289**:1734–1736.

[2] Sugino, C., Leadenham, S., Ruzzene, M., and Erturk, A. On the mechanism of bandgap formation in locally resonant finite elastic metamaterials. *Journal of Applied Physics*. (2016) **120**:134501.

[3] Sugino, C., Leadenham, S., Ruzzene, M., and Erturk, A. An investigation of electroelastic bandgap formation in locally resonant piezoelectric metastructures. *Smart Materials and Structures*. (2017) to appear.

VIII ECCOMAS Thematic Conference on Smart Structures and Materials
SMART 2017
A. Güemes, A. Benjeddou, J. Rodellar and J. Leng (Eds)

NON-RECIPROCAL ELASTIC WAVE PROPAGATION IN TIME-SPACE PERIODIC STRUCTURES

Kaijun Yi*, Manuel Collet* and Sami Karkar*

*LTDS UMR5513 Ecole Centrale de Lyon, 36 Avenue Guy de Collongue, 69130 Ecully, France
e-mail: kaijun.yi@doctorant.ec-lyon.fr (Kaijun Yi)
manuel.collet@ec-lyon.fr (Manuel Collet)
sami.karkar@ec-lyon.fr (Sami Karkar)

Key words: time-space modulation, non-reciprocity, frequency conversion

Abstract. Time-space periodic structures (or dynamic structures) possess properties modulated both in time and space. They have been extensively studied in diverse areas. This paper theoretically studies the unusual wave propagation phenomena induced by elastic waves incident on time-space periodic beams. The scattering matrix is developed to predict the characteristics of the reflected and transmitted waves. It is shown that the scattering matrix directly indicates the non-reciprocal wave transmission and frequency splitting phenomena caused by the dynamic beam, it also reveals a frequency conversion phenomenon, which is rarely noticed by researchers but has very significant influence on the application of dynamic structures.

1 INTRODUCTION

Media with varying properties both in time and space have been studied for decades. Typically, there are two types of such media, namely activated and kinetic media [1]. Activated media are obtained by instantaneous or gradual change of the media's properties without any transport. In contrary, kinetic media are realized through transport of components of the media. In practice, activated media could be driven by electric field [2] or smart materials [3, 4, 5], therefore they can also be called time-space modulated media or dynamic media, the concerned structures in this paper belong to them.

Time-space modulated media were firstly exploited in implementations of electromagnetism. A. Cullen [6] proposed a transmission line with distributed time-space varying inductances to obtain parametric amplification. Later, J. C. Simon [7] studied the influence of the time-space periodic modulation on the electromagnetic waves by using perturbation method. J. C. Simon's study by only retaining the fundamental and first orders harmonics were questioned by A. Hessel and A. Oliner [8], the latter developed a rigorous solution for propagation of waves in time-space periodic media by expressing the wave in a Floquet form and taking into account all of the harmonics. Using this rigorous method, E. Cassedy and A. Oliner [9, 10] studied the interactions of electromagnetic waves with the time-space modulation, and discussed the stability of the time-space varying system.

Time-space modulated media were also intensively studied in vibrations and acoustics. Ordinary (static) materials, like metals and traditional composites, are all passive and possess conventional properties, which are difficult to meet the requirements for designing advanced structures. To overcome these limitations, A. Lurie [1] proposed to vary the properties of materials in a suitable spatio-temporal pattern, to make the materials be able to respond adequately at each time to the demand required by the environment. These smart materials are termed "dynamic materials" by A. Lurie, as well as his collaborators and his followers. In [11], A. Lurie designed an array composed of cells with two segments, the properties of these segments are changing in time and space, like the whole array is moving with a constant velocity. He obtained the effective material parameters of the dynamic array and predicted that by appropriately designing the activated array, a screening effect which can protect some parts of the structure from an incident disturbance can be obtained. S. Weekes [12] validated A. Lurie's homogenization results by performing direct numerical simulations. In recent years, more and more researchers from vibrations and acoustics are attracted by time-space modulated structures [13, 14, 15, 16]. A significant contribution was made by G. Trainiti et al. [14], who obtained the dispersion relations of time-space periodic beams by using a rigorous theoretical method similar to that proposed in [9]. They also numerically demonstrated strong non-reciprocal elastic wave propagation at specific frequencies.

In summary, after being extensively studied in diverse areas, many unusual phenomena induced by time-space modulated media have been observed: screening effect [11, 12], non-reciprocal wave propagation [13, 14, 15, 16, 17], frequency splitting [18, 16]. However, all these phenomena were demonstrated by numerical simulations, like Finite Element (FE) method, Finite Difference Time Domain (FDTD) method, to name a few. Although some efforts [11, 14, 17] have been done to predict behaviors of time-space modulated media, there is still lack of an efficient tool to accomplish such purpose. Besides, numerical results can well demonstrate particular phenomena, but can't provide sufficient insights into them.

In this paper, reflection and transmission of longitudinal elastic waves incident on time-space periodic beams are theoretically studied. In section 2, the dispersion relations of longitudinal waves in time-space periodic beams are obtained using the Plane Wave Expansion (PWE) method, a way to describe the dispersion spectrum of the longitudinal Bloch modes is also provided. The scattering matrix is developed (section 3). It shows to be a very handy tool to describe the characteristics of the reflected and transmitted waves (section 4). The scattering matrix directly indicates the non-reciprocal wave transmission and frequency splitting phenomena caused by the dynamic beam, it also reveals a frequency conversion phenomenon, which is rarely noticed by researchers but has very significant influence on the application of dynamic structures. Discussions on the practical applications of dynamic structures are made in section 5 and remarkable conclusions of the presented work are summarized in section 6.

2 DISPERSION RELATIONS

The beam lying along the x direction in figure 1(a) is studied. The density of the beam is a constant value ρ_0, the Young's modulus is modulated according to a cosine wave function:

$$E(x,t) = E_0 + E_m cos(\omega_m t - k_m x) \tag{1}$$

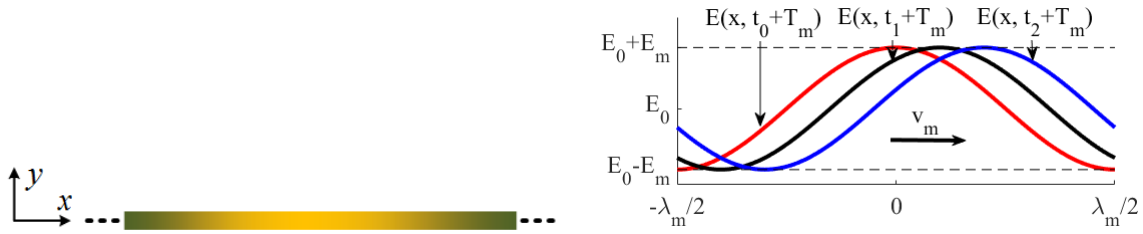

(a) (b)

Figure 1: (a) A slender time-space periodic beam lying along the x direction. (b) The wave-like time-space modulation of the Young's modulus defined by $E(x,t) = E_0 + E_m cos(\omega_m t - k_m x)$. The time period $T_m = 2\pi/\omega_m$, the wavelength (space period) $\lambda_m = 2\pi/k_m$ and the wave speed $v_m = \omega_m/k_m$.

in which, E_0 is the Young's modulus when there is no modulation, E_m is the modulation amplitude, ω_m and k_m are respectively the angular frequency and wavenumber of the modulation wave, whose wavelength is $\lambda_m = 2\pi/k_m$. The modulation wave propagates along the beam with the speed $v_m = \omega_m/k_m$, as illustrated in figure 1(b). In the following discussion, the modulation expressed in equation (1) is described by two dimensionless parameters, namely the dimensionless modulation amplitude $\alpha_m = E_m/E_0$ and dimensionless modulation speed $\beta_m = v_m/c_0$, here $c_0 = \sqrt{E_o/\rho_0}$ is the phase velocity of the longitudinal wave in an uniform beam. The modulation wave could propagate in both direction, $\beta_m > 0$ indicates the wave propagates in the positive direction and $\beta_m < 0$ means the opposite. Note that the time-space periodicity can also be obtained by modulating the density or the Young's modulus and density simultaneously. The modulation wave is not limited to harmonics, it can also be square or triangular waves.

The longitudinal motion $u(x,t)$ in the time-space periodic beam under the long-wavelength limit is governed by:

$$\frac{\partial}{\partial x}[E(x,t)\frac{\partial u(x,t)}{\partial x}] - \rho_0 \frac{\partial^2 u(x,t)}{\partial t^2} = 0 \tag{2}$$

Studies in this paper are restricted to the cases satisfying following condition [9]:

$$|\beta_m| < \frac{1}{\sqrt{1+\alpha_m}} \tag{3}$$

under which, the time-space system is stable and the solution of equation (2) can be expressed in the generalized Bloch wave form:

$$u(x,t) = \sum_{q=-\infty}^{+\infty} U_q e^{i[(\omega+q\omega_m)t-(k+qk_m)x]} \tag{4}$$

Following the PWE method [14] to obtain the dispersion relations, the Young's modulus function in equation (1) is expanded by using Fourier series:

$$E(x,t) = \sum_{p=-\infty}^{+\infty} \hat{E}_p e^{ip(\omega_m t-k_m x)} \tag{5}$$

in which, $\hat{E}_p$ are the Fourier coefficients of corresponding bases.

Truncating the terms in equation (4) to a finite number $2N+1$, then substituting equations (4) and (5) into (2) and forming the complex inner product with $e^{in(\omega_m t-k_m x)}$ yields a well-posed Quadratic Eigenvalue Problem (QEP) with a set of $2N+1$ equations. The QEP is solved in terms of k by fixing ω, which results in a vector $\boldsymbol{k}$ with $4N+2$ eigenvalues and a $(2N+1)$-by-$(4N+2)$ matrix $\boldsymbol{U}$. Each eigenvalue in $\boldsymbol{k}$ together with the corresponding column in $\boldsymbol{U}$ in the form of equation (4) represent a Bloch mode that could exist in the structure. Therefore, there are $4N+2$ longitudinal Bloch modes solved from the QEP. The dispersion relations of these Bloch modes are obtained by sampling ω in a range of interest.

To well describe the longitudinal Bloch modes in time-space periodic beams, they are classified into positive-going and negative-going groups according to their group velocities, which are calculated by $c_g = \partial\omega/\partial k$. Bloch modes in each group are organized according to their wavenumber in an ascending fashion. The nth Bloch modes in the positive-going and negative-going groups are respectively represented by P_n and N_n, with $n = -N, ..., 0, ..., +N$. According to equation (4), they are expressed as:

$$\begin{aligned} P_n(x,t,k_n^+,\omega) &= \sum_{q=-N}^{+N} P_{(n,q)} e^{i[(\omega+q\omega_m)t-(k_n^+ +qk_m)x]} \\ N_n(x,t,k_n^-,\omega) &= \sum_{q=-N}^{+N} N_{(n,q)} e^{i[(\omega+q\omega_m)t-(k_n^- +qk_m)x]} \end{aligned} \tag{6}$$

in which, $k_n^{\pm}$ are eigenvalues obtained from the QEP, $\{P_{(n,-N)}, ..., P_{(n,0)}, ..., P_{(n,+N)}\}^T$ and $\{N_{(n,-N)}, ..., N_{(n,0)}, ..., N_{(n,+N)}\}^T$ are the corresponding eigenvectors. As an example, figure 2 shows the band diagram of the beam with $\alpha_m = 0.4$, $\beta_m = 0.2$. In the figure, the dimensionless frequency $\Omega = \lambda_m f/c_0$ and dimensionless wavenumber $\mu = \lambda_m k$ are used. It is noticeable that the band diagram is asymmetric with respect to the $\mu = 0$ line. The dispersion curves of positive-going and negative-going modes repeat along an oblique line, whose slope is $2\pi/\beta_m$. For example, when the dispersion curve of P_{-1} mode is horizontally shifted by Ω_m (which is the dimensionless modulation frequency, $\Omega_m = \frac{\lambda_m \omega_m}{2\pi c_0} = \beta_m$), then vertically shifted by μ_m (which is the dimensionless wavenumber, $\mu_m = \lambda_m k_m = 2\pi$), it totally overlaps the dispersion curve of P_0 mode. In the figure, the frequency ranges where the real part of μ is changeless with

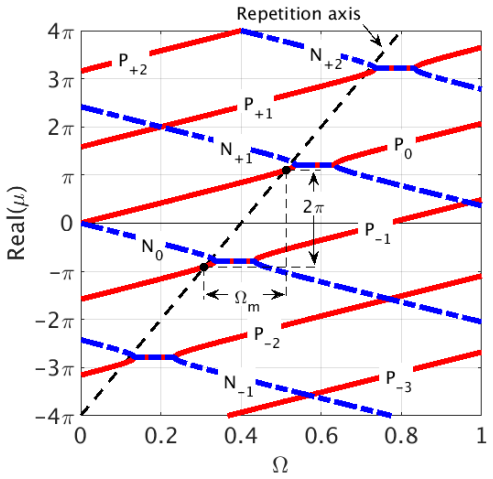

Figure 2: Band diagram of the beam with $\alpha_m = 0.4$, $\beta_m = 0.2$. Ω_m is the dimensionless modulation frequency, P_n and N_n respectively indicate the nth positive-going and negative-going longitudinal Bloch modes, the frequency ranges where the real part of μ is changeless with the frequency are stop bands of corresponding Bloch modes.

the frequency are stop bands of corresponding Bloch modes. It can be seen that stop bands of different orders Bloch modes are separated. In some published papers [14, 15], the two stop bands of P_0/N_{+1} and N_0/P_{-1} modes in figure 2 are termed directional band gaps, i.e., within these stop bands only positive-going or negative-going waves can propagate. It is remarked here that these descriptions are not appropriate. Because, for example, at frequencies within the stop bands of N_0/P_{-1} modes, even though these two modes can't propagate in the beam, but the other orders positive and negative-going Bloch modes could.

3 THE SCATTERING MATRIX

In this section, reflection and transmission of elastic waves incident on a time-space periodic beam are theoretically studied, a scattering matrix to describe this problem is proposed. The time-space periodic beam in figure 3 occupying the region $x_1 < x < x_2$ is considered, the left and right ends of it are respectively connected to a semi-infinite uniform beam. The Young's modulus and density of the dynamic beam are the same as in section 2, those of the uniform beams are E_0 and ρ_0.

Assume that two longitudinal harmonics with frequency ω are respectively incident on the dynamic beam from left and right, they are:

$$\begin{aligned} P_{i_1}(x,t) &= A_0 e^{i\omega(t-\frac{x}{c_0})} \\ N_{i_2}(x,t) &= G_0 e^{i\omega(t+\frac{x}{c_0})} \end{aligned} \tag{7}$$

here, A_0 and G_0 are corresponding amplitudes.

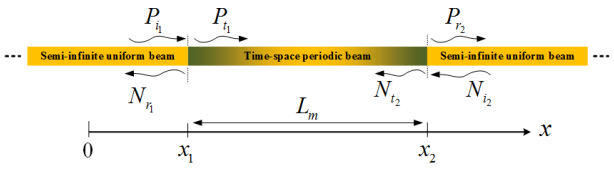

Figure 3: Reflection and transmission of elastic waves incident on a time-space periodic beam.

These incident harmonics will induce positive-going and negative-going waves inside the dynamic beam. Mathematically these induced waves can be represented as superposition of the Bloch modes supported by the beam. When $2R+1$ Bloch modes are used, according to equations (6), these waves are represented as:

$$\begin{aligned} P_{t_1}(x,t) &= \sum_{n=-R}^{+R} C_n P_n = \sum_{n=-R}^{+R} \sum_{q=-R}^{+R} C_n P_{(n,q)} e^{i[(\omega+q\omega_m)t-(k_n^+ +qk_m)x]} \\ N_{t_2}(x,t) &= \sum_{n=-R}^{+R} D_n N_n = \sum_{n=-R}^{+R} \sum_{q=-R}^{+R} D_n N_{(n,q)} e^{i[(\omega+q\omega_m)t-(k_n^- +qk_m)x]} \end{aligned} \tag{8}$$

in which, C_n and D_n are contribution coefficients of corresponding Bloch modes. Note that, the number of Bloch modes used in equations (8) must be smaller than the number of Bloch modes obtained from the QEP, details about this will be discussed later.

It can be seen from equations (8) that the induced waves inside the dynamic beam have harmonic components with frequencies $\omega + q\omega_m$, $q = -R, ..., 0, ..., R$. Therefore, the reflected waves at both ends of the dynamic beam must be superposition of harmonics with all possible frequencies $\omega + q\omega_m$:

$$
\begin{aligned}
N_{r_1}(x,t) &= \sum_{q=-R}^{+R} B_q e^{i(\omega+q\omega_m)(t+\frac{x}{c_0})} \\
P_{r_2}(x,t) &= \sum_{q=-R}^{+R} F_q e^{i(\omega+q\omega_m)(t-\frac{x}{c_0})}
\end{aligned}
\tag{9}
$$

B_q and F_q are amplitudes of corresponding harmonics.

For the convenience of the following formulations, equations (7) are rewritten to be coincident with the expressions in (8) and (9):

$$
\begin{aligned}
P_{i_1}(x,t) &= \sum_{q=-R}^{+R} A_q e^{i(\omega+q\omega_m)(t-\frac{x}{c_0})},\ A_{q\neq 0} = 0 \\
N_{i_2}(x,t) &= \sum_{q=-R}^{+R} G_q e^{i(\omega+q\omega_m)(t+\frac{x}{c_0})},\ G_{q\neq 0} = 0
\end{aligned}
\tag{10}
$$

The scattering matrix relating the incident waves (P_{i_1}, N_{i_2}) and reflected waves (N_{r_1}, P_{r_2}) are obtained by exploiting the continuous conditions which must be satisfied at interfaces $x = x_1,\ x_2$. These conditions are:

$$
\begin{aligned}
P_{i_1}(x_1,t) + N_{r_1}(x_1,t) &= P_{t_1}(x_1,t) + N_{t_2}(x_1,t) \\
E_0 \frac{\partial[P_{i_1}(x,t) + N_{r_1}(x,t)]}{\partial x}|_{x=x_1} &= E(x_1,t) \frac{\partial[P_{t_1}(x,t) + N_{t_2}(x,t)]}{\partial x}|_{x=x_1} \\
P_{t_1}(x_2,t) + N_{t_2}(x_2,t) &= P_{r_2}(x_2,t) + N_{i_2}(x_2,t) \\
E(x_2,t) \frac{\partial[P_{t_1}(x,t) + N_{t_2}(x,t)]}{\partial x}|_{x=x_2} &= E_0 \frac{\partial[P_{r_2}(x,t) + N_{i_2}(x,t)]}{\partial x}|_{x=x_2}
\end{aligned}
\tag{11}
$$

Substituting the expressions of waves (equations (8) to (10)) and the Fourier expansion of the Young's modulus of the dynamic beam (equation (5)) into the continuous conditions, and exploiting the orthogonality of harmonic functions $e^{i(\omega+q\omega_m)t}$ yields:

$$
\begin{aligned}
\mathbf{M}_{A_1}\boldsymbol{A} + \mathbf{M}_{B_1}\boldsymbol{B} - \mathbf{M}_{C_1}\boldsymbol{C} - \mathbf{M}_{D_1}\boldsymbol{D} &= 0 \\
\mathbf{M}_{A_2}\boldsymbol{A} - \mathbf{M}_{B_2}\boldsymbol{B} - \mathbf{M}_{C_2}\boldsymbol{C} - \mathbf{M}_{D_2}\boldsymbol{D} &= 0 \\
\mathbf{M}_{C_3}\boldsymbol{C} + \mathbf{M}_{D_3}\boldsymbol{D} - \mathbf{M}_{F_3}\boldsymbol{F} - \mathbf{M}_{G_3}\boldsymbol{G} &= 0 \\
\mathbf{M}_{C_4}\boldsymbol{C} + \mathbf{M}_{D_4}\boldsymbol{D} - \mathbf{M}_{F_4}\boldsymbol{F} + \mathbf{M}_{G_4}\boldsymbol{G} &= 0
\end{aligned}
\tag{12}
$$

here, $\boldsymbol{A}$, $\boldsymbol{B}$, $\boldsymbol{C}$, $\boldsymbol{D}$, $\boldsymbol{F}$ and $\boldsymbol{G}$ are column vectors respectively containing coefficients A_q, B_q, C_n, D_n, F_q and G_q as elements, $n, q = -R, ..., 0, ...R$. Dimensions of matrices before these vectors are all $(2R+1)$-by-$(2R+1)$. Details of these matrices are not shown here.

According to equations (12), the relation between incident and reflected waves are obtained:

$$\begin{Bmatrix} \boldsymbol{B} \\ \boldsymbol{F} \end{Bmatrix} = \mathbf{S} \begin{Bmatrix} \boldsymbol{A} \\ \boldsymbol{G} \end{Bmatrix} \tag{13}$$

in which, $\mathbf{S}$ is the scattering matrix. However, this matrix characterizes the scattering properties when multiple harmonics with frequencies $\omega + q\omega_m$ $(q = -R, ..., 0, ..., R)$ are incident. The scattering matrix for incident harmonics with only frequency ω (see equations (7) or (10)) is obtained through a further linear transformation:

$$\mathbf{S}_0(\omega) = \mathbf{T}\mathbf{S}(\omega) \tag{14}$$

here, the transformation matrix $\mathbf{T}$ is a $(4R+2)$-by-$(4R+2)$ matrix, except $\mathbf{T}(R+1, R+1) = \mathbf{T}(3R+2, 3R+2) = 1$, other elements are zero.

4 UNUSUAL PHENOMENA INDICATED BY THE SCATTERING MATRIX

In this section, abilities of the scattering matrix in equation (14) are demonstrated. The scattering matrix is divided into four blocks:

$$\mathbf{S}_0 = \begin{bmatrix} \mathbf{R}_L & \mathbf{T}_R \\ \mathbf{T}_L & \mathbf{R}_R \end{bmatrix} \tag{15}$$

Elements in blocks $\mathbf{R}_L$ and $\mathbf{T}_L$ are respectively Reflection and Transmission coefficients when a harmonic is incident from the Left side. Elements in blocks $\mathbf{T}_R$ and $\mathbf{R}_R$ are respectively Transmission and Reflection coefficients when a harmonic is incident from the Right side.

To show the results, modulation parameters of the dynamic beam are chosen as $\alpha_m = 0.4$, $\beta_m = 0.2$. Corresponding dispersion diagram of the beam is shown in figure 2. From that figure, it can be seen that the stop band of P_0 mode is $0.536 \leq \Omega \leq 0.634$, and that of N_0 mode is $0.335 \leq \Omega \leq 0.433$. Within these stop bands, strong non-reciprocal wave propagation and transmission are numerically demonstrated in [14, 15], and frequency splitting of the transmitted wave is numerically proved in [16]. These unusual phenomena are all directly described by the scattering matrices as shown in figure 4. In the simulations, the length of the dynamic beam is $L_m = 20\lambda_m$, and the truncation order of equations (8) is $R = 4$. The length can have significant influences on the scattering properties of the dynamic beam, it is simply remarked here that $20\lambda_m$ is long enough to eliminate those influences. Also it can be seen from figure 4 that the truncation $R = 4$ is enough to take into account all the noticeable scattered harmonics.

In figure 4, the represented scattering matrices are divided according to equation (15). Pixels represent the absolute values of elements in the scattering matrix. Only the elements corresponding to the incident harmonic with frequency ω are retained during the filter process in equation (14), thus just the central columns of the four blocks have nonzero elements. Each pixel of these central columns is associated with a harmonic component of the reflected and transmitted waves distinguished by the index q (see equations (9)). The numbers at left of the two figures indicate the corresponding q values. For example, the brightest spot in the top-left block in figure 4(a) represents the reflection coefficient into the harmonic with $q = -1$: $e^{i(\omega-\omega_m)(t+\frac{x}{c_0})}$.

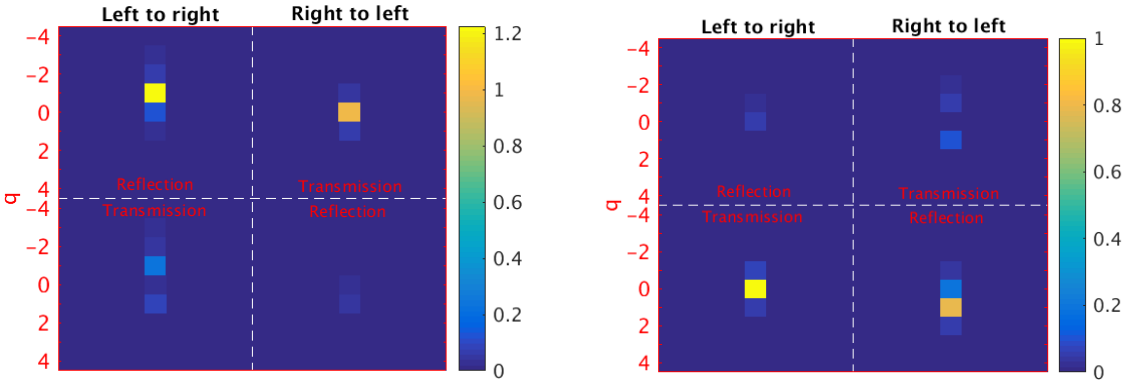

(a) $\Omega = 0.585$ (b) $\Omega = 0.384$

Figure 4: Absolute values of elements in the scattering matrix $\mathbf{S}_0$ at frequencies (a) inside the stop band of P_0 mode and (b) inside the stop band of N_0 mode. The modulation parameters are $\alpha_m = 0.4$, $\beta_m = 0.2$. The length of the dynamic beam is $L_m = 20\lambda_m$.

At frequencies inside the stop band of P_0 mode (figure 4(a)), it can be observed that when a harmonic with frequency ω is incident from the left, most of it will be reflected (see the top-left block), also there will be waves transmitted through the dynamic beam (see the bottom-left block). The reflected and transmitted waves all contain multiple harmonics with frequencies $\omega + q\omega_m$, $q = -3, -2, -1, 0, 1$. Particularly, the reflected waves are dominated by the harmonic with frequency $\omega - \omega_m$, which means that the main frequency component is down-converted. This phenomenon is rarely noticed by researches, but it has very significant influences on the applications of dynamic media. In contrary, when a harmonic is incident from the right side, the transmission is much more significant than the reflection. (see the right two blocks). Frequency splitting is also observed in this case.

Similar phenomena can be observed at frequencies inside the stop band of N_0 mode from figure 4(b). In these situations, more waves will be reflected when the harmonic is incident from the right side, and the main frequency is up-converted to $\omega + \omega_m$.

5 DISCUSSIONS

The strong non-reciprocity of dynamic structures within the stop bands of the two fundamental Bloch modes is very attractive to realized (approximate) one-way wave propagation. In an open system (finite systems can be treated as infinite in specific situations [19, 20]), as in figure 3, the dynamic beam may be used to build unidirectional vibration insulators. However, the frequency conversion phenomena must be taken into account when the scattered harmonics by the dynamic structure are considerably reflected back.

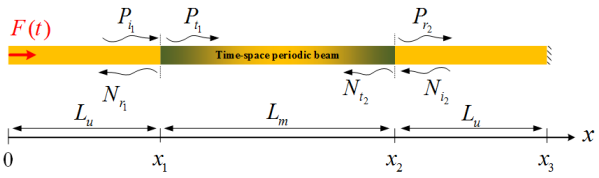

Figure 5: The finite sandwich beam with a dynamic part in the center.

For example, in a sandwich beam composed of three parts shown in figure 5, when a harmonic is incident on the dynamic beam from the left side at a frequency ω within the stop band of P_0 mode, most of the harmonic will be reflected back into a harmonic with a down-converted frequency $\omega - \omega_m$. This harmonic then reflected back by the left end of the whole beam. If the frequency $\omega - \omega_m$ is outside the stop band of P_0 mode, most of it will be transmitted through the dynamic beam. Even though the frequency $\omega - \omega_m$ is still inside the stop band after the first scattering (this can happen when the modulation speed is small), the above described process will repeat until the frequency is outside the stop band. Similar phenomena happen inside the stop band of N_0 mode. Therefore, one-way vibration insulators are impossible in these situations.

6 CONCLUSIONS

- An approach to describe the Bloch modes in time-space periodic structures are provided. Caused by the extra time periodicity, dynamic structures posses no full band gap as observed in space-only periodic media. Stop bands of different orders Bloch modes could be well separated. At any frequency, multiple Bloch modes may be stimulated and make considerable contribution to the forced wave propagation.

- The scattering matrix is developed to characterize the reflected and transmitted waves by time-space periodic structures. It is shown that the scattering matrix directly indicates the non-reciprocal wave transmission and frequency splitting phenomena caused by the dynamic beam, it also reveals a frequency conversion phenomenon, which is rarely noticed by researchers but has very significant influence on the application of dynamic structures.

References

[1] Konstantin A Lurie. *An introduction to the mathematical theory of dynamic materials*, volume 15. Springer Science & Business Media, 2007.

[2] Hugo Lira, Zongfu Yu, Shanhui Fan, and Michal Lipson. Electrically driven nonreciprocity induced by interband photonic transition on a silicon chip. *Physical review letters*, 109(3):033901, 2012.

[3] YY Chen, R Zhu, MV Barnhart, and GL Huang. Enhanced flexural wave sensing by adaptive gradient-index metamaterials. *Scientific reports*, 6, 2016.

[4] Yu Fan, Manuel Collet, Mohamed Ichchou, Lin Li, Olivier Bareille, and Zoran Dimitrijevic. A wave-based design of semi-active piezoelectric composites for broadband vibration control. *Smart Materials and Structures*, 25(5):055032, 2016.

[5] Kaijun Yi, Manuel Collet, Mohamed Ichchou, and Lin Li. Flexural waves focusing through shunted piezoelectric patches. *Smart Materials and Structures*, 25(7):075007, 2016.

[6] AL Cullen. A travelling-wave parametric amplifier. *Nature*, 181(4605):332–332, 1958.

[7] J-C Simon. Action of a progressive disturbance on a guided electromagnetic wave. *IRE Transactions on Microwave Theory and Techniques*, 8(1):18–29, 1960.

[8] AA Oliner and A Hessel. Wave propagation in a medium with a progressive sinusoidal disturbance. *IRE Transactions on Microwave Theory and Techniques*, 9(4):337–343, 1961.

[9] ES Cassedy and AA Oliner. Dispersion relations in time-space periodic media: Part i—stable interactions. *Proceedings of the IEEE*, 51(10):1342–1359, 1963.

[10] ES Cassedy. Dispersion relations in time-space periodic media part ii—unstable interactions. *Proceedings of the IEEE*, 55(7):1154–1168, 1967.

[11] Konstantin A Lurie. Effective properties of smart elastic laminates and the screening phenomenon. *International Journal of Solids and Structures*, 34(13):1633–1643, 1997.

[12] Suzanne L Weekes. Numerical computation of wave propagation in dynamic materials. *Applied numerical mathematics*, 37(4):417–440, 2001.

[13] N Swinteck, S Matsuo, K Runge, JO Vasseur, Pierre Lucas, and Pierre A Deymier. Bulk elastic waves with unidirectional backscattering-immune topological states in a time-dependent superlattice. *Journal of Applied Physics*, 118(6):063103, 2015.

[14] Giuseppe Trainiti and Massimo Ruzzene. Non-reciprocal elastic wave propagation in spatiotemporal periodic structures. *New Journal of Physics*, 18(8):083047, 2016.

[15] H Nassar, XC Xu, AN Norris, and GL Huang. Modulated phononic crystals: Non-reciprocal wave propagation and willis materials. *Journal of the Mechanics and Physics of Solids*, 101:10–29, 2017.

[16] C Croënne, JO Vasseur, O Bou Matar, M-F Ponge, PA Deymier, A-C Hladky-Hennion, and B Dubus. Brillouin scattering-like effect and non-reciprocal propagation of elastic waves due to spatio-temporal modulation of electrical boundary conditions in piezoelectric media. *Applied Physics Letters*, 110(6):061901, 2017.

[17] Lang-Quan Shui, Zhu-Feng Yue, Yong-Shou Liu, Qing-Chang Liu, Jiao-Jiao Guo, and Xin-Dang He. Novel composites with asymmetrical elastic wave properties. *Composites Science and Technology*, 113:19–30, 2015.

[18] Jakob S Jensen. Space–time topology optimization for one-dimensional wave propagation. *Computer Methods in Applied Mechanics and Engineering*, 198(5):705–715, 2009.

[19] HGD Goyder and RG White. Vibrational power flow from machines into built-up structures, part i: introduction and approximate analyses of beam and plate-like foundations. *Journal of sound and vibration*, 68(1):59–75, 1980.

[20] Yu Fan, Manuel Collet, Mohamed Ichchou, Lin Li, Olivier Bareille, and Zoran Dimitrijevic. Energy flow prediction in built-up structures through a hybrid finite element/wave and finite element approach. *Mechanical Systems and Signal Processing*, 66:137–158, 2016.

VIII ECCOMAS Thematic Conference on Smart Structures and Materials
SMART 2017
A. Güemes, A. Benjeddou, J. Rodellar and Jinsong Leng (Eds)

SMART PANEL WITH SWITCHING AND SWEEPING PIEZOELECTRIC PATCH VIBRATION ABSORBERS

L. DAL BO*, D. CASAGRANDE, P. GARDONIO

Università degli Studi di Udine, DPIA,
Via delle Scienze,208-33100 Udine, Italy
e-mail: dalbo.loris@spes.uniud.it

Key Words: piezoelectric shunt, vibration absorber, smart panel, vibration control

Abstract. This paper describes the design and development of a smart panel equipped with five piezoelectric patches, which are connected to time-varying resistive-inductive shunts. The shunted piezoelectric patches form an array of vibration absorbers, which, usually, would be tuned to reduce the flexural vibration response of the hosting panel at given resonance frequencies. Instead, in this study, the resistive and inductive components of the shunts are either periodically commuted among given values or continuously varied within given ranges. In this way, the operation frequency of the piezoelectric patch vibration absorbers are respectively switched over given resonance frequencies or uniformly swept in a given frequency range to produce a broad band control of the resonant flexural response of the hosting panel. The study describes the design and laboratory implementation of the reference fixed tuning and of the proposed switching and sweeping tuning operation modes. In addition, it presents preliminary experimental measurements on the flexural response of the panel when the piezoelectric patches are connected to the classical fixed tuned shunts and to the proposed switching and sweeping shunts.

1 INTRODUCTION

This paper is focused on the practical implementation of time–varying shunted piezoelectric patches, which can be bonded on thin structures to control the resonant response of multiple low order flexural modes. The idea of using shunted piezoelectric patches that produce an electromechanical vibration absorber effect to reduce the resonant response of structures dates back to the work proposed by Forward in 1979 [1]. Since then, many studies were dedicated both to the understanding of the basic working principles and to the conception of innovative solutions for the implementation of shunted piezoelectric patch vibration absorbers on flexible structures. In particular, Hagood and von Flotow [2] and Wu [3], proposed the idea of connecting to piezoelectric transducers shunt circuits formed by resistive-inductive (RL) components arranged respectively in series and in parallel. The combination of the RL-elements with the inherent capacitive effect of the piezoelectric patch produces an electrical resonating circuit, which is coupled to the structure via the piezoelectric transduction. Thus, the RL-shunted piezoelectric patch forms an electro-mechanical vibration absorber [4], which can be

effectively used to control the harmonic response of structures subject to tonal excitations or the resonant response of structures subject to broad band excitations [5]. These early works were followed by many studies, which, for example, were dedicated to the improvement of the electromechanical vibration absorption by reducing the inherent capacitive effect of the piezoelectric patches with active shunt circuits [6-13] or by implementing multi-resonant shunts that allowed the control of multiple resonant modes of the hosting structure [14-21]. In parallel, there have been quite a few theoretical works on simple analytical formulations based on a single structural mode model for the derivation of the optimal RL parameters that should be implemented in the shunt to minimise the resonant response of the hosting structure [22-24]. However, as shown in ref. [25], when piezoelectric patches are bonded on thin two dimensional flexible structures, the tuning of the RL components of the shunt is somewhat more complex since the coupling between the structure and the piezoelectric patch occurs via multiple structural modes. Indeed the most critical aspect for the design and implementation of a shunted piezoelectric patch vibration absorber is the tuning of the RL components. As normally done with classical vibration absorbers, the inductive component should be chosen in such a way that the resonance of the RLC circuit is closely tuned to the resonance of the structural mode to be controlled. Also, the resistive component should be tuned in such a way to minimise the overall response of the targeted mode, which, normally is expressed in terms of H_2 or H_∞ norms. This short introduction reports only a part of the many works published on shunted piezoelectric patch vibration absorbers. The reader is referred to the following articles and book for a comprehensive overview of the works and ideas presented on this topic over the years [26-29].

This paper presents experimental work on the implementation of two new types of time-varying shunts, which were introduced in refs. [30,31]. In the first type, the resistive and inductive components of the shunt are periodically commuted among given values such that the resonance frequency and the inherent damping of the piezoelectric patch absorber are continuously switched among optimal values to control the resonant response of the targeted modes of the hosting structure. In the second type, the resistive and inductive components of the shunt are continuously varied within given ranges such that the resonance frequency and the inherent damping of the of the piezoelectric patch absorber are respectively uniformly swept in a given frequency range and continuously adapted to control the resonant responses of all modes of the hosting structure that resonate in the target frequency band.

The paper is structured in five sections. Section two describes the panel used as a test case, which is equipped with five shunted piezoelectric patch transducers. Section three presents a comprehensive overview on the fixed tuning of the shunt RL components in order to control the resonant response of a target flexural mode of the hosting panel. The section is enriched with an instructive analogy study that visualises the effects of the shunt components in terms of mechanical lumped parameter elements that can be assembled into the modal mass-spring-damper scheme normally used to derive the response of the flexural mode of the structure to be controlled. Section four presents preliminary experimental results on the vibration control produced by the five shunted piezoelectric patches when three types of shunts are implemented: first, classical fixed shunts, each tuned to control a specific resonant flexural mode of panel; second, switching shunts, each tuned to iteratively control the five resonant flexural modes of the panel considered with the fixed shunts; third, sweeping shunts, each continuously adapted to work in a frequency band that encompass the five resonant flexural modes of the panel considered with the fixed shunts. Finally, section five presents the conclusion of this study.

2 SMART PANEL

Figure 1a shows the laboratory setup used in this study with the rectangular panel clamped on a box structure. As summarised in Table 1, the panel considered in this study is made of aluminium and has thickness of 1 mm and a length and width of 414 mm and 314 mm respectively. Five piezoelectric patches are bonded on the bottom side of the panel. The dimensions, positions and physical properties of the patches are summarised in Table 2. The panel is excited at position $x_p = 85$ mm and $y_p = 110$ mm by a shaker located in the box. Finally the flexural response of the panel is monitored at a single point with an accelerometer fixed on the top side of the panel at position $x_m = 147$ mm and $y_m = 97$ mm. The physical and geometrical parameters of the test ring are summarized in Tables 1 and 2.

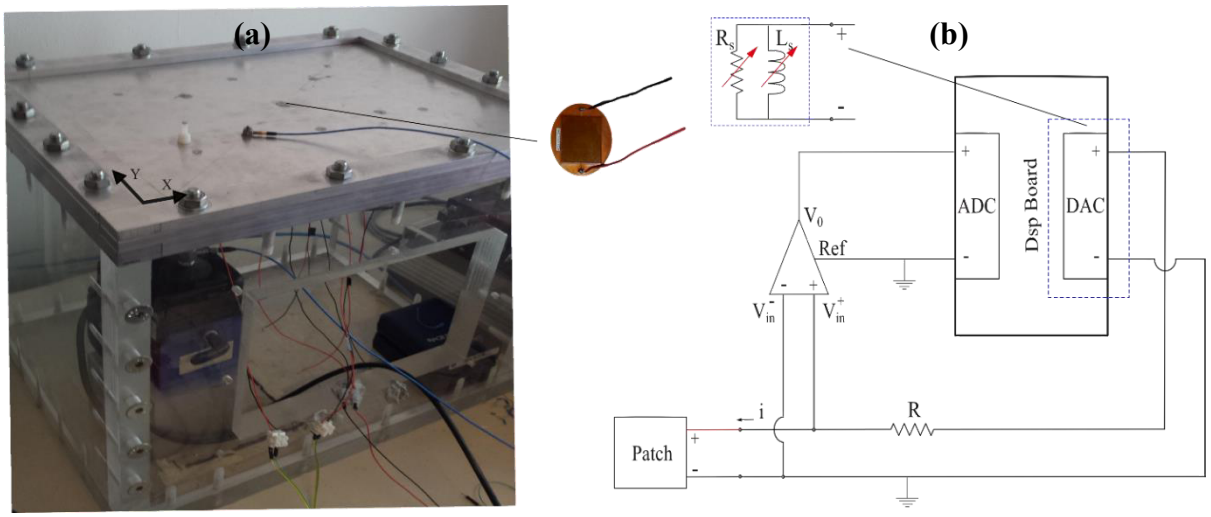

Figure 1: Laboratory setup: (a) picture, (b) control tuning scheme

Table 1: Dimension and physical parameters of the panel

Parameter	Value
Dimension	$l_x \times l_y = 414 \times 314$ mm
Thickness	$h_p = 1$ mm
Density	$\rho_p = 2700$ Kg/m^3
Young's modulus	$Y_p = 7 \times 10^{10}$ N/m^2
Modal damping ratio	$\zeta_p = 0.02$

Table 2: Dimension and physical parameters of the piezoelectric tranucers

Parameter	Value
Dimension	$a_{pex} \times a_{pey} = 80 \times 80$ mm
Thickness	$h_{pe} = 1$ mm
Centre Position j=2,3,4,5	$x_{c1}, y_{c1} = l_{xp}/2, l_{yp}/2$ $x_{cj}, y_{cj} = l_{xp}/2 \pm 60, l_{yp}/2 \pm 60$
Density	$\rho_{pe} = 7600$ Kg/m^3
Young's modulus	$Y_{pe}^E = 5 \times 10^{10}$ N/m^2
Piezo const.	$d_{31} = d_{32} = -190 \times 10^{-12}$ m/V
Capacitance	$C_{pi} = 268 \times 10^{-9}$ F

The magnified picture in figure 1a shows one of the five piezoelectric patches bounded on the bottom surface of the plate, while the scheme in figure 1b shows the electronic circuit used to synthesise the shunt. The electric terminals of each patch are connected to the input channel of a dSPACE controller via an instrumental amplifiers (INA). The input voltage to the controller is thus proportional to the voltage at the terminals of the piezoelectric patch. The dSPACE controller implements in real time the response of the shunt circuit; thus the output voltage, which is actually the voltage at the terminals of the piezoelectric patch, is equivalent to the voltage drop produced by the shunt.

3 PIEZOELECTRIC PATCH VIBRATION ABSORBER

3.1 Mechanical analogues of electrical shunts connected to an idealised piezoelectric transducer

Before entering into the details of the implementation of the switching and sweeping shunts, this section provides a comprehensive overview of the mechanical analogues of simple electrical shunt components and of parallel and series RLC shunt circuits connected to an idealised piezoelectric transducer, which does not include the inertia and stiffness effects of the piezoelectric material. Thus, the mechanical analogue of a shunted piezoelectric patch is studied with the simplified lumped parameter model shown in figure 2, which considers an idealised transducer blocked at the base that converts voltage into a modal force excitation and, vice versa, converts a modal velocity into current.

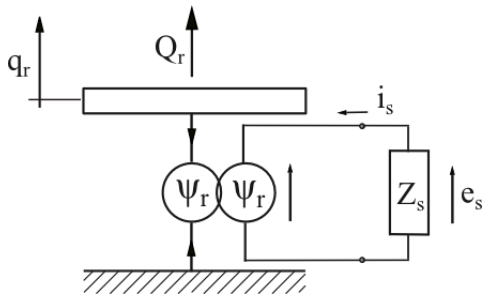

Figure 2: Model of an idealised modal piezoelectric transducer with an electrical shunt.

Considering the following transduction relations:

$$Q_r = \psi_r e_s \ , \tag{1}$$

$$i_s = -\psi_r \dot{q}_r \ , \tag{2}$$

and recalling that, for the notation shown in figure 2b,

$$e_s = -Z_s i_s \ , \tag{3}$$

the following equivalent mechanical impedance expression can be derived for the shunted idealised piezoelectric transducer:

$$Z_{\mathrm{mr}} = \frac{Q_r}{\dot{q}_r} = \psi_r^2 Z_s \ . \tag{4}$$

Table 3. Impedances of electrical element and circuits.

Shunt	Electro–mechanical scheme	Electrical impedance Z_e	Equivalent mechanical impedance Z_{mr}	Equivalent mechanical system
R	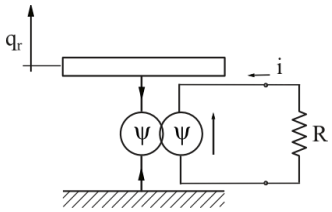	R	$\psi^2 R$	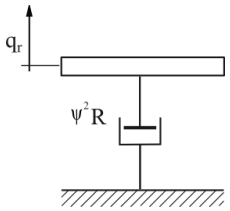
C	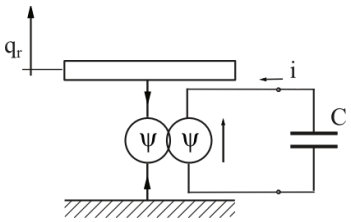	$\frac{1}{j\omega C}$	$\frac{\psi^2}{j\omega C}$	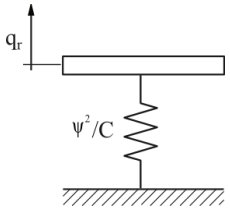
L	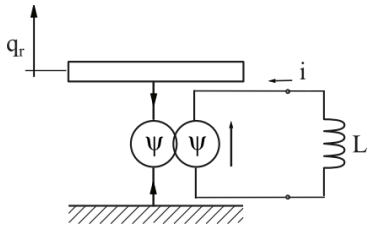	$j\omega L$	$\psi^2 j\omega L$	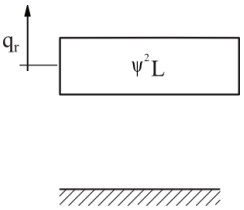
RCL (P)	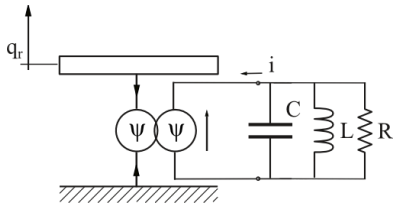	$\frac{1}{\frac{1}{R}+j\omega C+\frac{1}{j\omega L}}$	$\frac{\psi^2}{\frac{1}{R}+j\omega C+\frac{1}{j\omega L}}$	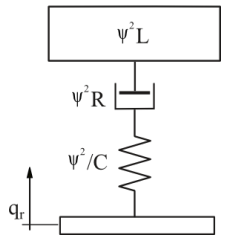
RLC (S)	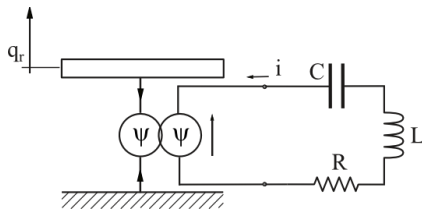	$R+j\omega L+\frac{1}{j\omega C}$	$\psi^2\left(R+\frac{1}{j\omega C}+j\omega L\right)$	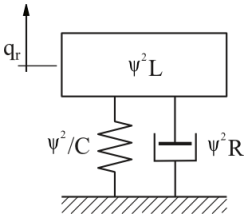

Equation (4) is used in Table 3 to derive the equivalent mechanical impedance effects produced by different types of electric loads connected to the idealised piezoelectric transducer. Considering first the equivalent mechanical impedances for the elementary elements, it is noted that the resistor produces a mechanical dissipative effect proportional to $\psi^2 R$. Thus, to obtain

a large damping effect, the resistance should be large. The capacitance produces a mechanical elastic effect proportional to ψ^2/C and thus to obtain a large stiffness effect the electric capacitance should be small compared to ψ^2. Finally, the inductance produces a mechanical inertia effect proportional to $\psi^2 L$. Hence, in this case, to obtain large inertia effect, the inductance should also be large. Considering now electric passive networks formed by RLC components connected either in series or in parallel, it is found that the parallel RLC produces stiffness, damping and mass effects in series and the series RLC generates mass damping and stiffness effects in parallel. Both configurations give rise to resonant responses. Thus the idealised piezoelectric patch transducer connected to a RLC shunt could be used to synthesise a mechanical vibration absorber [4].

3.2 Mechanical analogues of electrical shunts connected to a realistic piezoelectric transducer

This section considers the mechanical analogue of a realistic piezoelectric transducer connected to various types of electrical shunts. As shown in figure 3, in this case the transducer is modelled with the idealised transducer considered in the previous section with in parallel a block mass, a damper and a spring that represent the inertia, damping and stiffness effects of the piezoelectric material. Also the transducer is connected in parallel with a capacitor, which represents the inherent capacitive effect of the piezoelectric element and with the shunt circuit.

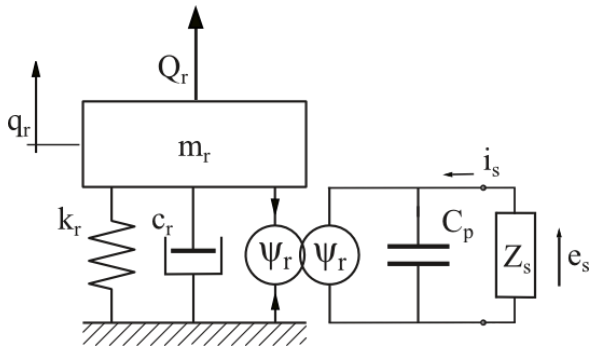

Figure 3: Model of an idealised modal piezoelectric transducer with an electrical shunt.

The results derived in Table 3 can be straightforwardly applied to the electromechanical systems considered in Table 4. The first system considers a short-circuit piezoelectric transducer, which, as shown in the centre scheme, corresponds to the mass-damper-spring system for the piezoelectric material. In fact, the short circuit annihilates the transduction and the inherent capacitive effects of the piezoelectric element. Thus, the impedance FRF of this system is characterised by a resonant behaviour, where the resonance frequency and the peak amplitude depend only on the mechanical properties of the piezoelectric material. The second system considers a piezoelectric transducer connected to an inductor. In this case, as shown in the centre scheme, the combined effect of the inherent capacitance of the piezoelectric element and of the inductance of the shunt produces a series spring-mass system connected on top of the spring-damper-mass system for the mechanical part of the transducer. In this case, as shown in the right hand side graph, the single resonance impedance FRF (black line) is changed into

Table 4. Mechanical equivalent impedance when the piezoelectric transducer is short-circuited and connected to either a RL or a RLC shunt.

Electro–mechanical scheme	Equivalent mechanical scheme	Mechanical admittance (FRF) $Y_{mr} \triangleq Z_{mr}^{-1} = \dot{q}_r / Q_r$
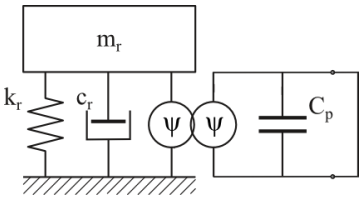	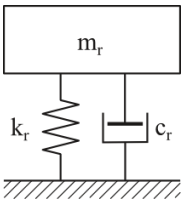	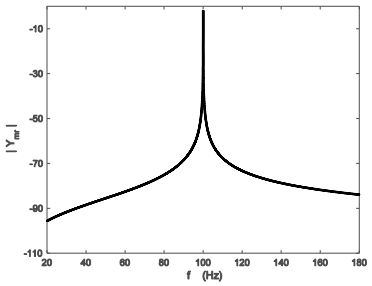
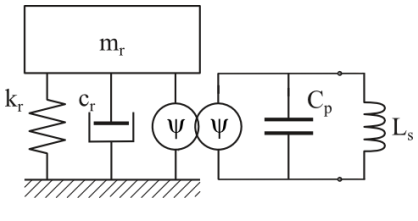	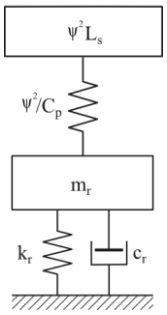	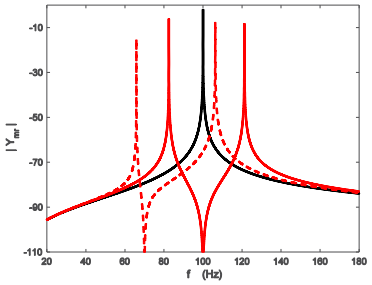
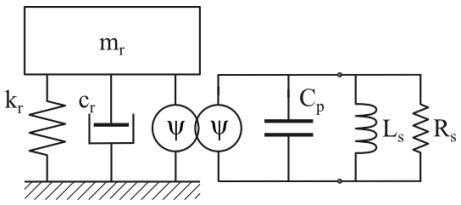	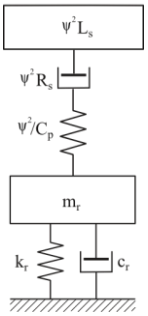	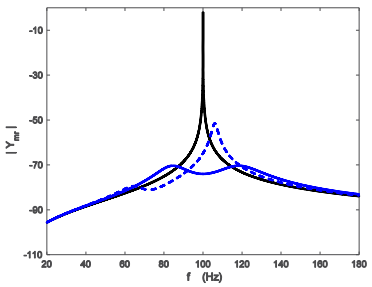

a double resonance impedance FRF, and the pair of peaks can be shifted in frequency by varying the inductance. Also, the aperture between the two peaks can be increases by reducing the inherent capacitance of the transducer. The third system considers a piezoelectric transducer connected to an inductor and a resistor in parallel. In this case, as shown in the centre scheme, the combined effect of the inherent capacitance of the piezoelectric element and of the shunt parallel inductance and resistance produces a series spring-damper-mass system connected on top of the spring-damper-mass system for the mechanical part of the transducer. As shown in the right hand side graph, the single resonance impedance FRF (black line) is changed into a double damped resonance impedance FRF. The extent of the damping effect can be straightforwardly varied by changing the resistance in the shunt. Thus the parallel RL shunt combined in parallel with the inherent capacitive effect of the piezoelectric transducer can be

effectively used to produce an equivalent vibration absorber mechanical system, which can be used to reduce the resonant response of a mechanical system.

3.3 Simplified model of the plate with the RL shunted piezoelectric patch

As discussed in ref. [31], normally the response of a structure with embedded a shunted piezoelectric patch is studied considering a simplified model that considers the response of target mode of the structure only. Thus, for the smart panel shown in figure 4a, the simplified model model shown in figure 4b is considered.

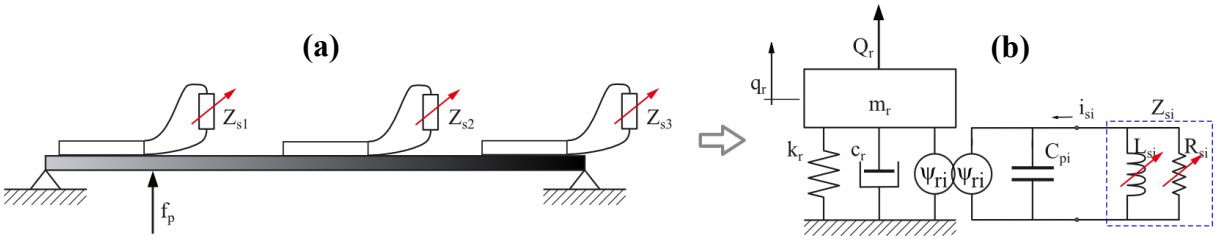

Figure 4: Plate with time-varying shunted piezoelectric patch absorbers: (a) scheme and (b) lumped parameter model considering the *i*-th patch and the *r*-th natural mode

In this case, as discussed in ref. [31], the complex response of the *r*-th flexural mode per unit modal excitation of the *r*-th mode is given by the following expression:

$$Y_r(\omega) = \frac{\dot{q}_r(\omega)}{Q_r(\omega)} = \frac{j\omega}{-\omega^2 m_r + j\omega\left(c_r + Z_{spi}\psi_{ri}^2\right) + k_r} \quad . \tag{5}$$

Here, $\dot{q}_r$ and Q_r are the *r*-th complex modal velocity and modal excitation, whereas e_{si}, i_{si} are the tension and current at the *i*-th shunt. Also, m_r, c_r k_r are the *r*-th modal mass, damping, stifness for the panel and piezoelectric patch materials, while ψ_{ri} is the *r*-th transduction coefficient of the *i*-th patch. Finally,

$$Z_{spi} \triangleq \frac{Z_{Cpi} Z_{si}}{Z_{si} + Z_{Cpi}} \quad , \tag{6}$$

where Z_{Cpi} is the capacitive impedance of the *i*-th piezoelectric patch and Z_{si} is the impedance of the *i*-th RL shunt. Thus, as shown in ref. [31], minimising the H_2 norm of $Y_r(\omega)$ the optimal inductance and resistance in the shunt are given by:

$$L_{si} = \frac{m_r}{k_r C_{pi}} = \frac{1}{\omega_r^2 C_{pi}} \quad \text{and} \quad R_{si} = \sqrt{\frac{m_r}{\psi_{ri}^2 C_{pi}}} \quad , \tag{7,8}$$

where ω_r is the natural frequency of the *r*-th flexural mode. Eqs. (7) and (8) are the starting trial values used to tune the shunts in the experiments presented in this paper.

4 SWITCHING AND SWEEPING OPERATION MODES

This section discusses the vibration control effects produced when the shunts of the five piezoelectric patch vibration absorbers implement either classical fixed tunings or the proposed switching and sweeping operation modes. The target modes to be controlled have been chosen with resonance frequencies comprised between 50 and 320 Hz. As summarised in table 5, the fixed shunts are tuned to control the first five flexural modes of the plate. Also the switching shunts are set to iteratively control the resonant response of the plate first five flexural modes while the sweeping shunts are uniformly varied in such a way as to control all flexural modes that resonates in the frequency range comprised between 50 and 320 Hz. Both switching and sweeping modes are implemented asynchronously.

Table 5: Operational frequency control for each absorber and for each operational control method

Type	Absorber 1 [Hz]	Absorber 2 [Hz]	Absorber 3 [Hz]	Absorber 4 [Hz]	Absorber 5 [Hz]
Fixed	52	96	128	222	311
Switching	52,96,128,222,311	96,128,222,311,52	128,222,311,52,96	222,311,52,96,128	310,52,96,128,222
Sweeping	50-320	50-320	50-320	50-320	50-320

4.1 Fixed tuning Shunt

The optimal resistive and inductive components of the five fixed tuning shunts have been derived with a trial and error procedure, starting from the values derived with Eqs. (7) and (8) considering the resonances of the modes to be controlled, which are listed in the first row of table 5. Figure 5 shows the spectrum of the velocity measured with the accelerometer per unit force exerted by the shaker when the panel is equipped with five piezoelectric patches either in short circuit (solid red line) or connected with fixed tuning shunts (solid black line). The graphs shows that the shunted piezoelectric patch absorbers produce between 2 and 8 dB reductions of the resonance peaks of the targeted modes.

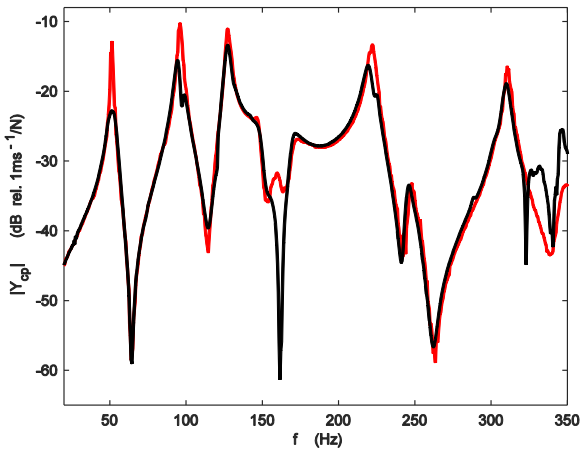

Figure 5: spectrum of the velocity measured with the accelerometer per unit force exerted by the shaker when the panel is equipped with five piezoelectric patches in short circuit (solid red line) and connected with fixed tuning shunts (solid black line).

4.2 Switching operation mode

For the switching operation mode, the shunts were equipped with a control algorithm that switches sequentially the shunt RL elements between the tuning values listed in third row table (5). As proposed in ref. [31] , the duration of each switching iteration is set to be equal to the time constant of the shunt circuit $\tau_s = 1/(\xi_s \omega_s)$, where $\xi_s = \sqrt{L_s/(4R_s^2 C_{pi})}$ and ω_s are respectively the damping factor (equal to $0{,}3$) and the natural frequency of the RLC circuit formed by the capacitor C_{pi} and the RL shunt components set to control the *r*-th flexural mode of the panel. Figure 6 shows the spectrum of the velocity measured with the accelerometer per unit force exerted by the shaker when the panel is equipped with five piezoelectric patches in short circuit (solid red line) and connected with the switching shunts (solid black line). The switching shunts produce very similar control effects than the fixed shunts, with reductions of the resonance peaks of the targeted flexural modes comprised between 3 and 8 dB.

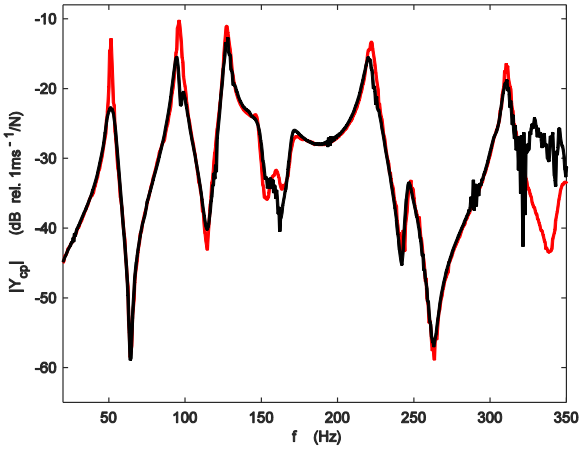

Figure 6: spectrum of the velocity measured with the accelerometer per unit force exerted by the shaker when the panel is equipped with five piezoelectric patches in short circuit (solid red line) and connected with switching shunts (solid black line).

4.3 Sweeping operation mode

For the sweeping operation mode, no specific tuning of the RL shunt is implemented. In this case the natural frequency of the shunts electrical circuit is swept between the lower and upper limits of the frequency control range according to the following law

$$\omega_{sw} = \omega_i + (\omega_f - \omega_i)\sin(2\pi f_s t)^2 \ . \tag{9}$$

Here, ω_i and ω_f are the lower and upper values of the control frequency range shown in the second raw of table 5 and f_s is the sweeping frequency, which has been set to 6 Hz as proposed in ref. [31]. As discussed in ref. [31], the inductance is sweep following the law $L_s(t) = 1/(\omega_{sw}^2 C_p)$, where ω_{sw} is given in Eq. (9). Also the resistance is swept in such a way as to keep the damping ratio in the shunt circuit equal to $\xi_s = 6\%$, in which case

$R_s(t) = \sqrt{L_s(t) \big/ \left(4\xi_s^2 C_{pi}\right)}$ [31]. The five absorbers act on the whole control frequency band $\omega_f - \omega_i$ asynchronously with the phase shift of $\pi/5$ between each other.

Figure 7 shows the spectrum of the velocity measured with the accelerometer per unit force exerted by the shaker when the panel is equipped with five piezoelectric patches in short circuit (solid red line) and connected with the sweeping shunts (solid black line). The sweeping shunts produce very similar control effects than the fixed shunts and switching shunts, with reductions of the resonance peaks of the flexural modes that resonates in the target frequency band comprised between 2 and 8 dB.

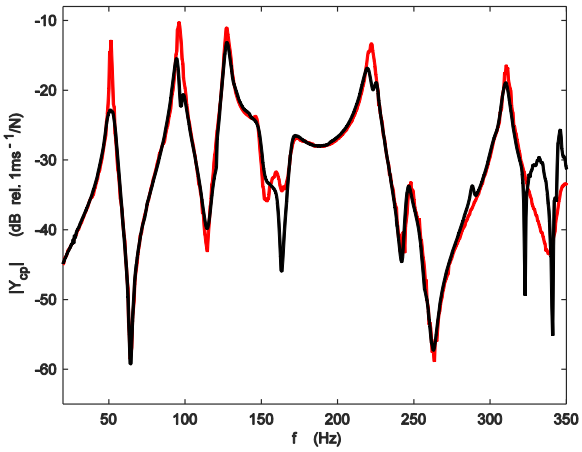

Figure 7: spectrum of the velocity measured with the accelerometer per unit force exerted by the shaker when the panel is equipped with five piezoelectric patches in short circuit (solid red line) and connected with sweeping shunts (solid black line).

5 CONCLUSIONS

This paper has presented the design and development of a smart panel equipped with an array of five piezoelectric patches, which are connected to time-varying resistive-inductive shunts. First of all, a comprehensive analysis of the mechanical equivalent effects produced by shunts connected idealised and real piezoelectric transducers have been analyse to provide the key concepts behind the implementation of shunted piezoelectric patch vibration absorbers. The experimental implementation of fix tuned, switching and sweeping shunts on five piezoelectric patches bonded on a thin panel has then been assessed. As shown in table 6 below, the initial experimental results presented in this study have shown that the proposed switching and sweeping operation modes produce about the same vibration reductions at the target resonance frequencies than the fixed tuning shunts. This is a rather interesting results for the sweeping operation mode, which is operated blindly within a given frequency band. Thus it works without need of tuning, that is without the need of system identification of the dynamic response of the structure. Moreover, this characteristic makes the system robust to changes of operation condition, particularly of the hosting structure, which could be affected by tensioning or temperature change effects.

The experimental results presented in this paper should be considered merely as initial results of on going experimental work. The low reductions obtained at this stage can be improved by implementing RL shunts, with and active negative capacitance component that would reduce the inherent capacitive effect of the piezoelectric patch and thus increase the vibration absorption effect.

Table 6: Peak reductions at the monitor position produced by the fixed, switching and sweeping shunts

[Hz]	52	96	128	222	311
Fixed	9.9	5.3	2.4	3	2.5
Sweeping	9.8	5.2	1.6	2.2	2.4
Switching	10.0	4.4	2	3.5	2.6

REFERENCES

[1] Forward R L 1979 Electronic damping of vibrations in optical structures *Applied Optics* **18** (5) 690-697.

[2] N.W. Hagood, A. von Flotow, Damping of structural vibrations with piezoelectric materials and passive electrical networks, *Journal of Sound and Vibration* 146 (1991) 243-268.

[3] S. Y. Wu, Piezoelectric shunts with parallel RL circuits for structural damping and vibration control, *Proceedings of the SPIE* 2720 (1996) 259-269.

[4] J.P. Den Hartog, *Mechanical Vibrations*, McGraw-Hill, New York, 1956.

[5] Gardonio P and Zilletti M 2013 Integrated tuneable vibration absorbers: a theoretical study *Journal of the Acoustical Society of America* **134** (5) 3631-3644.

[6] R.L. Forward, Electromechanical transducer-coupled mechanical structure with negative capacitance compensation circuit, *United States patent* 4,158,787, 1979.

[7] M.S. Tsai, K.W. Wang, On the structural damping characteristics of active piezoelectric actuators with passive shunt, *Journal of Sound and Vibration* 221 (1999) 1-22.

[8] J. Tang, K.W. Wang, Active-passive hybrid piezoelectric networks for vibration control: comparison and improvement, *Smart Materials and Structures* 10 (2001) 794-806.

[9] M.S. Tsai, K.W. Wang, A coupled robust control/optimization approach for active-passive hybrid piezoelectric networks, *Smart Materials and Structures* 11 (2002) 389-395.

[10] R.A. Morgan, K.W. Wang, An active-passive piezoelectric absorber for structural vibration control under harmonic excitations with time-varying frequency, part 2: algorithm development and analysis, *Transactions of the ASME Journal of Vibration and Acoustic* 124 (2002) 77-83.

[11] E. Fukada, M. Date, K. Kimura, T. Okubo, H. Kodama, P. Mokry, Y. Yamamoto, Sound isolation by piezoelectric polymer films connected to negative capacitance circuits, *IEEE transactions on dielectrics and electrical insulation* 11 (2004) 328-333.

[12] C.H. Park, A. Baz, Vibration control of beams with negative capacitive shunting of interdigited electrode piezoceramics, *Journal of Vibration and Control* 11 (2005) 331-346.

[13] M. Neubauer, R. Oleskiewicz, K. Popp, T. Krzyzynski, Optimization of damping and absorbing performance of shunted piezo elements utilizing negative capacitance, Journal of Sound and Vibration 298 (2006) 84-107

[14] Hollkamp J J 1994 Multimodal passive vibration suppression with piezoelectric materials and resonant shunts *Journal of Intelligent Material Systems and Structures* **5** (1) 49-56.

[15] Wu S-Y 1998 Method for multiple mode piezoelectric shunting with single PZT transducer for vibration control *Journal of Intelligent Material Systems and Structures* **9** 991-998.

[16] Moheimani S O R Fleming A J and Behrens S 2001 Highly resonant controller for multimode piezoelectric shunt damping *Electronics Letters* **37** 1505-1506.
[17] Fleming A J Behrens S and Moheimani S O R 2002 Optimization and implementation of multimode piezoelectric shunt damping systems *IEEE/ASME Transactions on Mechatronics* **7** 87-94.
[18] Kim J and Lee J-K 2002 Broadband transmission noise reduction of smart panels featuring piezoelectric shunt circuits and sound-absorbing material *Journal of the Acoustical Society of America* **112** 990-998.
[19] Behrens S Moheimani S O R and Fleming A J 2003 Multiple mode current flowing passive piezoelectric shunt controller *Journal of Sound and Vibration* **266** (5) 929-942.
[20] Moheimani S O R and Behrens S 2004 Multimode Piezoelectric Shunt Damping With a Highly Resonant Impedance *IEEE Transactions on Control Systems Technology* **12** 484-491.
[21] Lossouarn B, Deü J-F, Aucejo M and Cunefare K A Multimodal vibration damping of a plate by piezoelectric coupling to its analogous electrical network Smart Mater. Struct. 25 (2016)
[22] K. Yamada, H. Matsuhisa, H. Utsuno, K. Sawada, Optimum tuning of series and parallel LR circuits for passive vibration suppression using piezoelectric elements, *Journal of Sound and Vibration* 329 (2010) 5036-5057.
[23] J. Hogsberg, S. Krenk, Balanced calibration of resonant shunt circuits for piezoelectric vibration control, *Journal of Intelligent Materials Systems and Structures,* 23 (2012) 1937-1948.
[24] P. Soltani, G. Kerschen, G. Tondreau, A. Deraemaeker, Piezoelectric vibration damping using resonant shunt circuits:an exact solution *Smart Materials and Structures* 23 (2014) 125014.
[25] P. Gardonio and D. Casagrande, Shunted piezoelectric patch vibration absorber on two-dimensional thin structures: Tuning considerations, Journal of Sound and Vibration 395 (2017) 26-47
[26] Lesieutre G A 1998 Vibration Damping and Control using shunted piezoelectric materials *The shock and Vibration Digest* **30** (3).
[27] Ahmadian M and De Guilio P 2001 Recent advances in the use of piezoceramics for vibration suppression *The shock and Vibration Digest* **33** (1).
[28] Moheimani S O R 2003 A survey of recent innovations in vibration damping and control using shunted piezoelectric transducers *IEEE Transactions on Control Systems Technology* **11** (1) 482-494.
[29] Moheimani S O R and Fleming A J 2006 *Piezoelectric transducers for vibration control and damping* (London: Springer-Verlag).
[30] D. Casagrande, P. Gardonio, M. Zilletti. *Sweeping piezoelectric patch vibration absorbers.* MoViC–RASD Thirtheen International Conference on Motion and Vibration Control and Twelveth International Conference on Recent Advances in Structural Dynamics, Southampton, UK, 3-6 July 2016. pp 1–12.
[31] D. Casagrande P. Gardonio, M. Zilletti, *Smart panel with time-varying shunted piezoelectric patch absorbers for broadband vibration control*, Submitted to Journal of Sound and Vibration (2017)

VIII ECCOMAS Thematic Conference on Smart Structures and Materials
SMART 2017
A. Güemes, A. Benjeddou, J. Rodellar and J. Leng (Eds)

ULTRASONIC WAVE PROPAGATION IN PERIODIC CERAMIC MICRO-SCAFFOLDS FABRICATED BY ROBOCASTING

H. SEINER*, P. SEDLÁK*, M. ŠEVČÍK*, A. KRUISOVÁ*, M. LANDA*, B. ROMÁN-MANSO†, P. MIRANZO‡ AND M. BELMONTE‡

*Institute of Thermomechanics
Czech Academy of Sciences
Dolejškova 5, 18200 Prague, Czech Republic
e-mail: hseiner@it.cas.cz, web page: http://lum.it.cas.cz/

† School of Engineering and Applied Sciences
Harvard University,
52 Oxford St, 02318 Cambridge MA, USA
e-mail: romanmanso@seas.harvard.edu, web page: http://lewisgroup.seas.harvard.edu

‡ Institute of Ceramics and Glass (ICV-CSIC)
Campus de Cantoblanco, Kelsen 5, 28049 Madrid, Spain
e-mail: mbelmonte@icv.csic.es, web page: http://www.icv.csic.es

Key words: Additive manufacturing, Ceramics, Phononic crystals, Acoustic bandgaps.

Abstract. Longitudinal elastic wave propagation in ultrasonic frequency range (2 − 12 MHz) through periodic ceramic micro-architectures was studied by a though-transmission method. Silicon carbide micro-scaffolds fabricated by an additive manufacturing method called Robocasting were used for the experiments; micro-architectures with tetragonal, hexagonal and orthorhombic spatial arrangements were employed. The results prove that these micro-scaffolds exhibit well-detectable frequency band gaps, resulting from internal resonances of the periodic structure, especially when direction of the wave propagation is parallel to one of the symmetry directions of the micro-architecture.

1 INTRODUCTION

Robocasting [1, 2, 3] is a free-form fabrication method for preparation of geometrically complex ceramic structures and scaffolds. This method belongs among the so-called additive manufacturing techniques, in which the materials are built up in a layer-by-layer manner with perfectly controlled internal architecture and finely tunable properties. In the case of Robocasting, the individual, subsequently added layers consist of thin rods of a special ceramic ink printed into an oil bath through a nozzle. As the nozzle is controlled by a computer-driven positioning system, the resulting patterns of rods may have any desired spatial arrangement. This arrangement

persists also after the drying and sintering processes, during which the individual rods forming the structure adopt mechanical properties of fully dense sintered ceramics, such as a high elastic modulus or superior thermal and environmental resistance.

The robocast structures have many potential applications, ranging from their use as high-quality filters [4] to exploiting their spatial periodicity for materials acting as band gap structures for electromagnetic field [5]. Most importantly, these structures are nowadays considered as optimal candidates for applications in bone tissue engineering [6, 7]. For many of these application, and for the biomedical applications in particular, the knowledge of mechanical properties of the robocast structures is essential. There have been several attempts to improve the understanding of the mechanics of the robocast materials by finite elements method (FEM) modeling reported in the literature. Genet et al. [8] have used such models to analyze the failure mechanism of calcium phosphate scaffolds; similar analysis, supported by experimental observations, was carried out by Miranda et al. [9] for hydroxyapatite. These works, however, were mainly focused on the fracture toughness of the scaffolds and the underlying micro-mechanical mechanisms of failure, while the macroscopic acoustic properties of the scaffolds was not discussed in any details. In this paper, on the contrary, we focus on the elastic wave propagation phenomena in the robocast scaffolds. The periodic spatial arrangement of the ceramic rods in these materials makes them apparently similar to the so-called acoustic metamaterials [10, 11, 12], or phononic crystals [13, 14, 15], i.e. artificially created materials in which the elastic wave propagation exhibits several unique features, such as the negative refraction index, strong focusing of the energy fluxes carried by the propagating waves, or acoustic frequency band gaps. The aim of this paper is to bring experimental evidence that these phenomena take place in the robocast scaffolds, especially that there are well-identifiable band gaps for longitudinal ultrasonic wave propagation in these materials. The phononic crystal-like properties of robocast scaffolds have been predicted by the the current authors by means of FEM calculations [16, 17]; the same calculations were then used for interpretation of the experimental results, as reported in [18].

2 EXPERIMENT

2.1 Materials

Silicon carbide (SiC) robocast scaffolds with six different micro-architectures were used for the study. The details on the manufacturing process (including chemical compositions of the ceramic inks, etc.) are given elsewhere [18]. The used scaffolds were rectangular prisms of approximately $10 \times 10 \times 5$ mm^3 in dimensions; the central parts of these prisms contained the regular periodic architectures. Optical micrographs of the periodic arrangements are shown in Fig.1; these where:

(a) a tetragonal scaffold with inter-rod spacing (i.e. distance between centers of neighboring rods) of 650 μm, denoted hereafter as LS-sample

(b) a tetragonal scaffold with inter-rod spacing of 310 μm, denoted hereafter as SS-sample

(c) a hexagonal scaffold with inter-rod spacing of 580 μm, denoted hereafter as LH-sample

(d) a hexagonal scaffold with inter-rod spacing of 420 μm, denoted hereafter as SH-sample

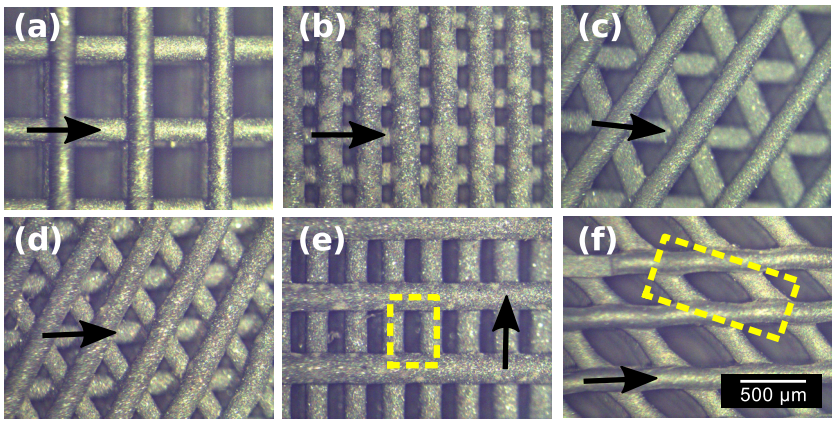

Figure 1: Optical micrographs of the used robocast micro-scaffolds (see the text for the denotations and detailed descriptions of the individual micro-architectures). For the OR-sample (e) and MO-sample (f), the othorhombic unit cells are outlined by dashed lines. The black arrows indicate the direction in which the ultrasonic wave propagation was measured.

(e) an orthorhombic scaffold with inter-rod spacings of 590 μm and 310 μm and with the orthorhombic axes lying parallel to the rods, denoted hereafter as OR-sample

(f) an orthorhombic scaffold with inter-rod spacing of 460 μm and with the orthorhombic axes inclined by approximately $\pi/8$ from the rods, denoted hereafter as MO-sample (due to the monoclinicity of the structure)

As seen in Fig.1, the architectures were regular but the diameters of the rods were significantly varying along their lengths. The rods were obviously narrower in their fee-standing segments (most clearly seen for SH- and MO-samples) than close to the crossing points; this probably resulted from differing tension/compression conditions along the axis of the rod during the sintering process. In average, the diameter of the rods varied between 190 and 240 μm for all samples.

2.2 Ultrasonic measurements

The ultrasonic wave propagation through the samples was studied using a through-transmission method (see Fig.2 for an outline). Each sample was contacted by a CrystalBond wax onto two 0.5 mm thin glass plates to ensure flat co-planar faces for contacting of ultrasonic probes.

Then, narrow-band longitudinal ultrasonic pulses were sent through the sample, each consisting of ten harmonic periods at given frequency inside of an amplitude-envelope ('input signal' curve in Fig.2). Glass plates were always glued onto two lateral faces of the sample and oriented such that they enabled measurements of waves propagating along one of the orientations of the rods. For the OR sample (Fig.1(e)), the propagation direction was along the longer spacing between the rods. For all other samples, the propagation direction was along the horizontal direction in Fig.1.

For the generation of the input signals and the acquisition of the transmitted signals, a NI-PXI card system (National Instruments, US) was used, including a functional generation

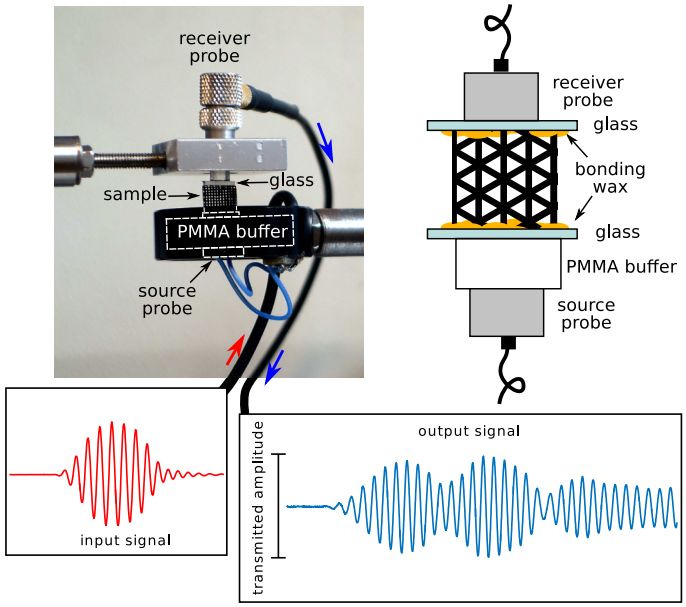

Figure 2: Outline of the experimental set-up: the input signal (red curve) was sent into a $LiNbO_3$ crystal (source probe) which transformed it into a mechanical pulse. The pulse was transmitted though a PMMA buffer and through the sample (along the orientation of the rods) into a receiver probe.

card 5422 (16 bits/40 MHz) employed for burst signal generation, and an acquisition card 5122 (14 bits/100 MHz) for signal recording. A high power ultrasonic system Ritec RAM 5000 was employed for generating and recording the signals. This system was equipped by a gated amplifier (nominal frequency range 50 kHz - 22 MHz, output RMS power 5 kW at 50 ohms/2.5 MHz) and a broadband receiver (frequency band 40 kHz - 80 MHz / 72dB gain).

As a source probe, a $LiNbO_3$ single crystal (central frequency 20 MHz) glued on a 10 mm Homosil substrate was used; the receiver probe was a commercial delayed ultrasonic probe Panametric V206 (0.12", 20 MHz). Input burst pulses with nominal frequencies (f_{in}) between 2 MHz and 12 MHz were used; this frequency range was scanned with a 0.1 MHz resolution.

From each transmitted signal, a central harmonic part was selected, covering ± 3 full periods about the maximal transmitted amplitude for each input frequency, (i.e covering the time interval $[t_0 - 3/f_{\text{input}}; t_0 + 3/f_{\text{input}}]$, where t_0 corresponds to the time-of-arrival of the maximum of the transmitted amplitude). To visualize the transmission of the acoustic energy through each scaffold, the signals were then plotted in these intervals with respect to dimensionless quantity tf_{input}. This approach enabled a direct assessment of the band-gap structures for all samples, regardless of the time delays due to variations of velocity of sound propagations.

3 RESULTS

The results for all studied micro-architectures are shown in Fig.3(b-g). In the first row (Fig.3(a)), the result of a preliminary test for the experimental set-up is shown. In this case, the input pulse was send through a bulk (plexiglass) sample of the same dimensions as the robocast samples. It is clearly seen that for the bulk sample the energy was continuously transmitted

through the whole frequency range.

For all robocast samples, the energy is transmitted only in certain frequency intervals. Moreover, there are observed slight deviations of the real temporal periodicity of the transmitted signal from the input frequency (seen as diverging patterns), which also means that some of the input frequencies were not transmitted though the structures.

For the SS-sample, clear band-gaps (BGs) are seen approximately between 4 and 5 MHz and between 7 and 8 MHz. Between these two gaps, some energy is transmitted, but these signals are of much lower amplitude than below 4 MHz or above 8 MHz. Similarly clear BG structure is seen also for the LH-sample, where, however, the second BG appears to reach the upper limit of the frequency range. The locations of the BGs for the LS- and LH- can be shown to correspond well to band-gaps calculated for idealized scaffolds with prescribed geometries by the finite elements method (FEM), using the Bloch wave approach introduced in [17]. The details of these calculations fall beyond the scope of this paper and will be given elsewhere [18]. Here we mention only the fact that the frequency ranges in which the energy is transmitted corresponds to dispersion curves of acoustic longitudinal modes for both structures. For the SS- and SH-samples the FEM calculation predicts that the first longitudinal acoustic branch ends up at approximately 10 MHz for SS sample and at approximately 7 MHz for the SH sample, and that there are no upper longitudinal modes expectable for the higher frequencies within the measured range, and thus, the experimental results are again easily interpretable. Both these samples exhibit sharp cut-off frequencies. A sharp BG is seen also for the OR-sample, lying approximately between 6 and 10 MHz. However, the transmitted amplitude above this BG is very low, and so the real frequency-filtering properties of this structure are somehow in question.

For the MO-sample, the situation is even less clear. Although the transmitted amplitude is obviously attenuated between 6 MHz and 10 MHz, there are some signals appearing nearly randomly in this interval. A real BG can be identified only in a narrow range between 8 and 9 MHz. Then, the transmitted signal again disappears at approximately 9.5 MHz (denoted by a question mark in Fig.3), but this effect is probably too local to be identified as another BG. In summary, it can be concluded that for this sample the transmitted amplitude significantly varies with the frequency, but no clear band structure can be observed. This is probably due to the fact that for this scaffold the chosen propagation direction is not the symmetry direction of the architecture, and so some energy may be also transmitted from the source probe to the receiver probe along the rods inclined by $\pi/4$ from the propagation direction. As shown for tetragonal scaffolds in [16], there is a strong energy focusing along the rods in the robocast architectures; in principle, the acoustic energy can be carried only along the the individual rods, which leads to extremely strong elastic anisotropy and other unusual wave propagation phenomena. It is plausible that similar energy focusing appears also in the MO sample. In this case, however, the energy is driven out from the principal directions, as they are inclined by $\pi/8$ (or $3\pi/8$, alternatively) from the principal directions.

4 CONCLUSIONS

We have shown experimentally that ceramic scaffolds fabricated by Robocasting exhibit a band structure for longitudinal wave propagation, and that this structure depends on the symmetry class and other geometric parameters of the micro-architecture. Taking into account

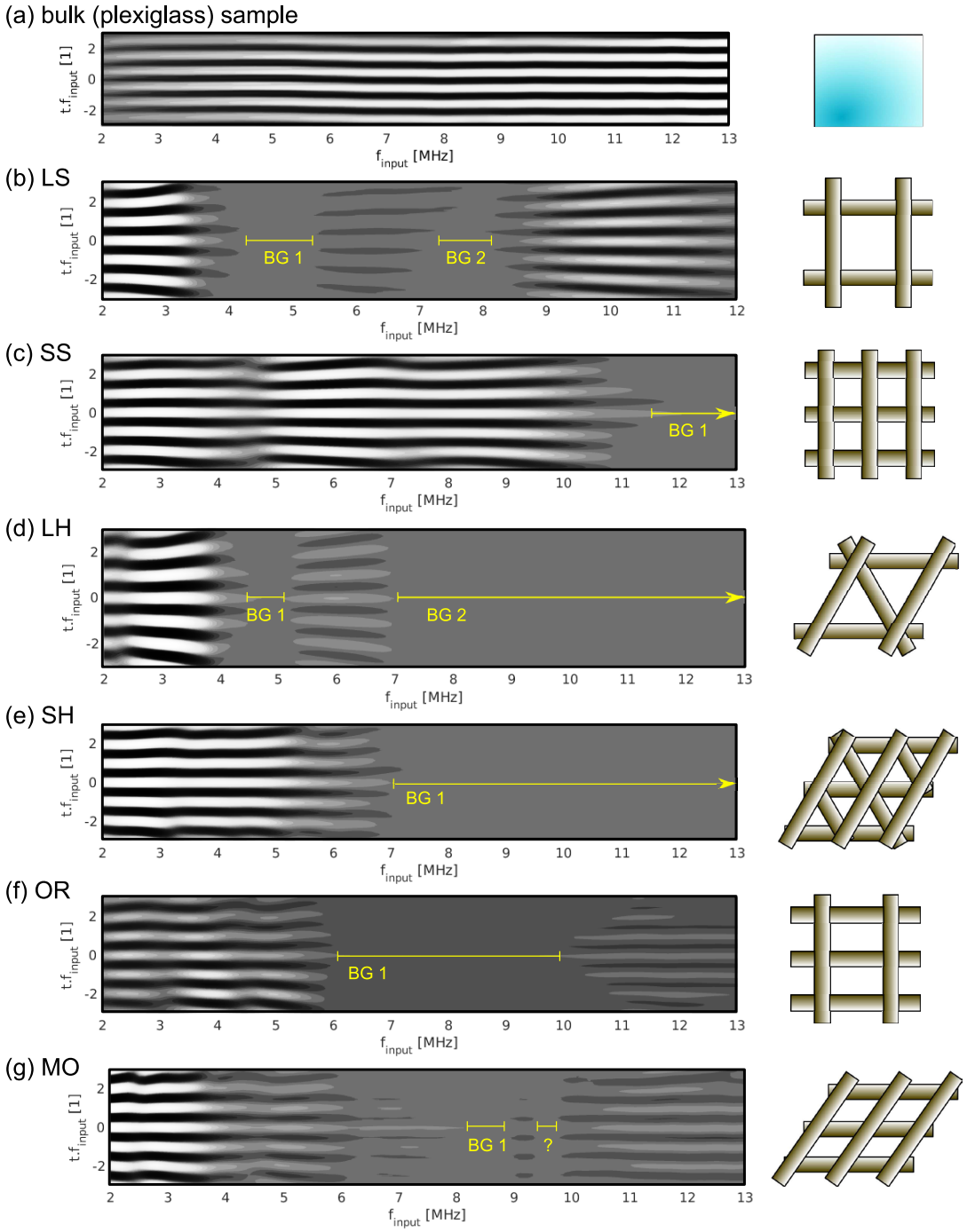

Figure 3: Signals transmitted through a bulk plexiglass sample (a) and various robocast micro-scaffolds (b-g). The gray-scale represents the signal amplitude. For each frequency, six periods from the highest-amplitude parts of the signal are shown. The yellow markers denote the possible locations of the band-gaps. All signal maps are normalized with respect to the highest amplitude over all frequencies.

the high versatility and variability of the robocasting process, we have also shown the potential of this additive manufacturing method for fabrication of phononic crystals with prescribed frequency-filtering properties.

The most obvious band-gap structure was observed for samples with the highest symmetry class (tetragonal and hexagonal) and with the largest inter-rod spacings. For these samples, the wavelengths for the given frequency range were comparable with the spatial periodicity of the scaffold, and so several internal resonant modes were initiated. For more dense architectures (SS, SH and RO), only one cut-off frequency was observed, i.e. these architectures were shown to act as low-pass filters. For the MO architecture, on the other hand, no real BGs were observed, which can be ascribed to energy leaking along rods inclined from the propagation direction.

Acknowledgement

This work was supported by Czech Science Foundation, project No. 17-01618S, and by the Spanish Government, project MAT2015-67437-R (MINECO, FEDER, UE).

REFERENCES

[1] Smay, J.E., Gratson G., Shepherd, R., Cesarano, J. and Lewis, J.A. Directed Colloidal Assembly of 3D Periodic Structures, *Adv. Mater.* (2002) **14**:1279–1283.

[2] Smay, J.E. and Lewis, J.A. Solid Free-Form Fabrication of 3-D Ceramic Structures, in: N.P. Bansal, A.R. Boccaccini (Eds.), *Ceramics and Composites Processing Methods*. John Wiley and Sons (2012) 459–484.

[3] Cai, K., Román-Manso, B., Smay, J.E., Zhou, J., Osendi, M.I. Belmonte, M. and Miranzo, P. Geometrically Complex Silicon Carbide Structures Fabricated by Robocasting, *J. Am. Ceram. Soc.* (2012) **95**: 2660–2666.

[4] Stuecker, J.N., Cesarano J. and Smay, J.E., Robocasting Periodic Lattices For Advanced Filtration, in: *Solid Freeform Fabrication Proceedings.* 12th Solid freeform fabrication symposium, University of Texas at Austin (2001) 561–566.

[5] Smay, J.E., Cesarano J., Lin, S.Y., Stuecker, J.N. and Lewis, J.A., Robocasting of Photonic Band Gap Structures. in: *Solid Freeform Fabrication Proceedings.* 12th Solid freeform fabrication symposium, University of Texas at Austin (2001) 1053-2153.

[6] Miranda, P., Saiz, E., Gryn, K. and Tomsia, A.P. Sintering and robocasting of β-tricalcium phosphate scaffolds for orthopaedic applications. *Acta Biomater.* (2006) **2**:457–466.

[7] Cohen, D.L., Lipton, J.I., Bonassar, L.J. and Lipson, H., Additive manufacturing for in situ repair of osteochondral defects. *Biofabrication* (2010) **2**:035004.

[8] Genet, M., Houmard, M., Eslava, S., Saiz, E. and Tomsia, A.P. A two-scale Weibull approach to the failure of porous ceramic structures made by robocasting: Possibilities and limits *J. Eur. Ceram. Soc.* (2013) **33**:679–688.

[9] Miranda, P., Pajares, A., Saiz, E., Tomsia, A.P. and Guiberteau, F. Fracture modes under uniaxial compression in hydroxyapatite scaffolds fabricated by robocasting. *J. Biomed. Mater. Res. A.* (2007) **83**:646–655.

[10] Craster, R.V. and Guenneau S. (Eds.) *Acoustic Metamaterials: Negative Refraction, Imaging, Lensing and Cloaking (Springer Series in Materials Science Vol. 166).* Springer, London (2013).

[11] Guenneau, S., Movchan, A., Petursson, G. and Ramakrishna, S.A. Acoustic metamaterials for sound focusing and confinement. *New J. Phys.* (2007) **9**:399.

[12] Lee, J.-H., Koh, C.Y., Singer, J.P., Jeon, S.-J., Maldovan, M., Stein, O. and Thomas, E.L., 25th Anniversary Article: Ordered Polymer Structures for the Engineering of Photons and Phonons, *Adv. Mater.* (2014) **26**:532–569.

[13] Yang, S., Page, J.H., Liu, Z., Cowan, M.L., Chan, C.T. and Sheng, P. Focusing of Sound in a 3D Phononic Crystal, *Phys. Rev. Lett.* (2004) **93**:024301.

[14] Zhang, X. and Liu, Z. Negative refraction of acoustic waves in two-dimensional phononic crystals. *Appl. Phys. Lett.* (2004) **85**:341–343.

[15] Zhao, H., Liu, Y., Yu, D., Wang, G., Wen, J. and Wen, X. Absorptive properties of three-dimensional phononic crystal. *J. Sound Vib.* (2007) **303**:185–194.

[16] Kruisová, A., Seiner, H., Sedlák, P., Landa, M., Román-Manso, B., Miranzo, P. and Belmonte, M. Metamaterial behavior of three-dimensional periodic architectures assembled by robocasting. *Appl. Phys. Letters* (2014) **105**:211904.

[17] Kruisová, A., Seiner, H., Sedlák, P., Landa, M., Román-Manso, B., Miranzo, P. and Belmonte, M., Finite elements modeling of mechanical and acoustic properties of a ceramic metamaterial assembled by robocasting. *Appl. Mech. Mater.* (2016) **821**:364–371.

[18] Kruisová, A., Ševčík, M., Seiner, H., Sedlák, P., Landa, M., Román-Manso, B., Miranzo, P. and Belmonte, M. Ultrasonic bandgaps in 3D-printed periodic ceramic microlattices, submitted to Ultrasonics (2017).

VIII ECCOMAS Thematic Conference on Smart Structures and Materials
SMART 2017
A. Güemes, A. Benjeddou, J. Rodellar and J. Leng (Eds)

VIBRATION DAMPING IN PERIODIC 1D-STRUCTURES BY R-SHUNTED PIEZOELECTRIC ELEMENTS

JAN HØGSBERG

Department of Mechanical Engineering, Technical University of Denmark
Nils Koppels Allé, Building 404, DK-2800 Kgs. Lyngby, Denmark
e-mail: jhg@mek.dtu.dk

Key words: Vibration damping, Periodic Structures, Piezoelectric shunt

Abstract. In periodic structures the wave propagation can be attenuated by introducing damping at a targeted frequency or wavenumber. Piezoelectric elements are included in a 1D structure and shunted with an electrical resistance. An accurate expression for the complex-valued natural frequency of the propagating wave in a representative unit cell is obtained by introducing an augmented modal representation of the wave motion, taking into account the modal interaction introduced by the presence of the supplemental shunt. This solution strategy leads to a very compact and accurate frequency solution, which gives an explicit calibration formulae for the resistive shunts. The results are investigated by a simple numerical example, which verifies the accuracy of the frequency solution and calibration procedure.

1 INTRODUCTION

The introduction of periodic inclusions or imperfections is an effective strategy for reducing, canceling and even controlling wave propagation in dynamic systems. A thorough review can be found in [1, 2]. During the last couple of decades the introduction of smart inclusions has received considerable attention, because the temporal characteristics of the inclusions can easily be altered, introducing for example band gaps by mechanical or electrically induced resonators [3, 4, 5].

The present paper considers the application of shunted piezoelectric inclusions in a 1D periodic structure with the purpose of introducing damping to the band structure at a targeted wavenumber. Thus, the aim is not specifically to introduce band gaps, where the propagation of waves is entirely prohibited, but instead to maximize damping, and thereby the attenuation, of the waves in the structure. The approach is therefore similar to vibration damping of structures, where the motion is directly associated with the temporal harmonic component instead of the wavenumber dependency.

The piezoelectric inclusions in the periodic structure are shunted with a pure resistive network [6], where vanishing and infinite resistance are directly governed by the short- and open-circuit electrode configurations, respectively. A modal analysis framework is applied, where the short- and open-circuit eigenvalue problems provide the two limiting natural frequencies for a given

wavenumber. Based on the vibration damping approach considered in for example [7, 8], the modal displacement is augmented by an additional term, representing the influence from the wave forms not targeted by the shunts. The magnitude of this additional term is then calibrated so that the open-circuit natural frequency is exactly captured. The derived frequency solution is compact and simple and allows explicit determination of the optimal shunt resistance with respect to maximum damping of the targeted wave form. Finally, the accuracy of the calibration and the derived frequency solution is illustrated by a simple numerical example.

2 THE PERIODIC 1D STRUCTURE

The structure is a unidirectional elastic rod or bar of infinite length that is periodic with a repetitive unit cell. Each homogeneous part of the unit cell is linear elastic with mass density ρ, elastic modulus E, cross section area A and length ℓ.

2.1 The structural equations

The equilibrium equation of the periodic bar is determined by vanishing virtual work in a finite element formulation with two nodal displacements contained in the element displacement vector $\mathbf{u}_e(t) = [u_1, u_2]_e^T$. The element virtual work can then be expressed as

$$\delta W_e(t) = \delta \mathbf{u}_e(t)^T \Big(\mathbf{m}_e \ddot{\mathbf{u}}_e(t) + \mathbf{k}_e \mathbf{u}_e(t) + \mathbf{b}_e f_e(t) - \mathbf{f}_e(t) \Big) \tag{1}$$

with element mass matrix, stiffness matrix and participation vector:

$$\mathbf{m}_e = \frac{(\rho A)_e \ell_e}{6} \begin{bmatrix} 2 & -1 \\ -1 & 2 \end{bmatrix}, \quad \mathbf{k}_e = \frac{(EA)_e}{\ell_e} \begin{bmatrix} 1 & -1 \\ -1 & 1 \end{bmatrix}, \quad \mathbf{b}_e = \begin{bmatrix} -1 \\ 1 \end{bmatrix} \tag{2}$$

Wave propagation is investigated for an infinite periodic bar without external loading ($\mathbf{f}_e(t) = \mathbf{0}$). The wave propagation in the rod is obtained by assuming a complex exponential solution for the discretized virtual work equation (1). In the discretized structure the spatial dependence of the wave is determined by the wavenumber to element length relation ($\gamma \ell_e$). Thus, it is computationally convenient to enforce this wavenumber dependence at the element level and the element displacement is therefore represented in the factorized form

$$\mathbf{u}_e(t) = \exp(i\omega t) \mathbf{E}(\gamma \ell_e) \mathbf{A}_e \mathbf{u} \tag{3}$$

where $\mathbf{u}$ contains the nodal amplitudes of the wave motion in the global numerical model, $\mathbf{A}_e$ is the allocation array of element e, ω is the angular frequency of the assumed harmonic motion, while the wavenumber dependent exponential matrix

$$\mathbf{E}(\gamma \ell_e) = \begin{bmatrix} \exp(-i\gamma \ell_e) & 0 \\ 0 & \exp(-2i\gamma \ell_e) \end{bmatrix} \tag{4}$$

represents the spatial advancement of the wave propagation through the element.

The global equations of motion are determined by a summation of the element virtual work in (1). When substituting the wave propagation solution (3), the total virtual work is given as

$$\delta W = \sum_e^{N_e} \delta W_e = \delta \mathbf{u}^T \Big((-\omega^2 \mathbf{M} + \mathbf{K}) \mathbf{u} - \mathbf{W} \mathbf{f} \Big) = 0 \tag{5}$$

introducing the global mass and stiffness matrices

$$\mathbf{M} = \sum_e^{N_e} (\mathbf{E}\mathbf{A}_e)^T \mathbf{m}_e (\mathbf{E}\mathbf{A}_e) \quad , \quad \mathbf{K} = \sum_e^{N_e} (\mathbf{E}\mathbf{A}_e)^T \mathbf{k}_e (\mathbf{E}\mathbf{A}_e) \tag{6}$$

As $\mathbf{E}\mathbf{A}_e$ is complex-valued, its transpose is of hermitian type with an implied complex conjugation. In (5) the electromechanical force term is represented by the compact notation

$$\mathbf{W}\mathbf{f} = \sum_p^{N_p} (\mathbf{E}\mathbf{A}_p)^T \mathbf{b}_p f_p = \sum_p^{N_p} \mathbf{w}_p f_p \,, \quad \mathbf{w}_p = (\mathbf{E}\mathbf{A}_p)^T \mathbf{b}_p \tag{7}$$

where the subscript $p = 1 \ldots N_p$ denotes the reduced number of elements N_p with electromechanical properties. The participation vectors $\mathbf{w}_p$ for these elements are collected as columns in the associated participation array

$$\mathbf{W} = \left[\mathbf{w}_1, \mathbf{w}_2, \ldots, \mathbf{w}_{N_p}\right], \quad \mathbf{f} = [f_1, f_2, \ldots, f_{N_p}]^T \tag{8}$$

with the corresponding electromechanical forces contained in the force vector $\mathbf{f}$. The equilibrium equation follows from (5) and can be written in homogeneous form as

$$(-\omega^2 \mathbf{M} + \mathbf{K})\mathbf{u} + \mathbf{W}\mathbf{f} = \mathbf{0} \tag{9}$$

The electromechanical force vector $\mathbf{f}$ is governed by the individual R-shunts connected to the piezoelectric elements and the properties of an R-shunt are therefore summarized in the next section. Because the temporal characteristics of the shunt is described in terms of the angular frequency ω, the present analysis is based on an inverse approach, where the wavenumber $\gamma\ell_e$ in (4) is prescribed, while the complex-valued angular frequency ω is determined by the associated eigenvalue problem. This and alternative solution strategies are thoroughly reviewed in [2].

The modeling of the unit cell is illustrated in Fig. 1, where the gray areas in (a) identify the piezoelectric inclusions. The periodicity of the bar then identifies the unit cell, in (b) discretized by five elements. The periodicity is enforced by equating displacement and force at the two boundary nodes, which in practice can be realized by connecting the first and fifth node by the element stiffness, as shwon in Fig. 1(c) where the shunt is furthermore represented by a supplemental element between the third and fourth node.

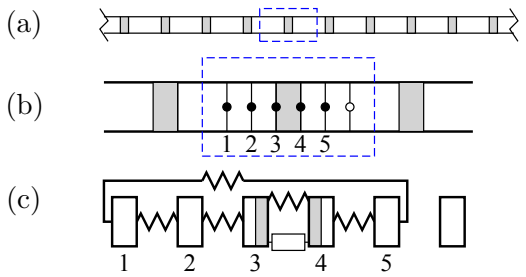

Figure 1: (a) Periodic bar with (b) unit cell and (c) representative spring-mass system.

2.2 The R-shunt

In (8) the vector $\mathbf{f}$ may contain electromechanical forces from several piezoelectric elements within the unit cell. These are individually shunted to resistances R, which may not necessarily be the same for each element. In (8b) the supplemental electromechanical force is defined as

$$f_p(t) = \theta V(t) \qquad , \qquad p = 1, 2, \ldots N_p. \tag{10}$$

where $V(t)$ is the voltage across the element nodes, while θ represents the electromechanical coupling coefficient. The piezoelectric coupling is governed by the electrical balance equation,

$$Q(t) = -\theta \mathbf{b}_p^T \mathbf{u}_p(t) + CV(t) \tag{11}$$

where $Q(t)$ is the charge in the element, while C is the capacitance of the piezoelectric element associated with blocked strain conditions. A pure resistive shunt R is considered, whereby $V(t) = -R\dot{Q}(t)$. Thus, elimination of $Q(t)$ in (11) followed by multiplication with θ gives the differential equation,

$$RC\dot{f}_p(t) + f_p(t) = R\theta^2 \mathbf{b}_p^T \dot{\mathbf{u}}_p(t) \tag{12}$$

which represents a Maxwell element with dashpot $R\theta^2$ and spring θ^2/C in series. For vanishing shunt resistance (short-circuit) the element force $f_p(t) = 0$, while for infinite resistance (open-circuit) it becomes $f_p(t) = (\theta^2/C)\mathbf{b}_p^T \dot{\mathbf{u}}_p(t)$, associated with an increase in stiffness and hence natural frequency. In the intermediate range the R-shunt introduces damping and the aim of the present paper is to determine an expression for the optimal calibration of R, associated with maximum attainable damping in the unit cell and thus the entire periodic structure.

The Maxwell-type filter equation (12) is conveniently analyzed in the frequency domain, assuming a harmonic force of the form

$$f_p(t) = f_p \exp(i\omega t) \tag{13}$$

By substitution of (3) and (13), the filter equation (12) for element p can be expressed as

$$i\omega\tau f_p + f_p = i\omega\tau \Delta k \mathbf{w}_p^T \mathbf{u}_p \tag{14}$$

where the time scale and stiffness change are defined as

$$\tau = RC \quad , \quad \Delta k = \frac{\theta^2}{C} \tag{15}$$

The filter equation (14) is conveniently expressed in transfer function format as

$$f_p = G(\omega)\Delta k \mathbf{w}_p^T \mathbf{u}_p \quad , \quad G(\omega) = \frac{i\omega\tau}{1 + i\omega\tau} \tag{16}$$

with real and imaginary parts shown in Fig. 2. It is seen that the corner frequency $1/\tau$ determines the transition from zero to the upper unit limit. The corner frequency also locates the maximum imaginary part $\mathrm{Im}[G(1/\tau)] = \frac{1}{2}$ where the slope of the real part is largest.

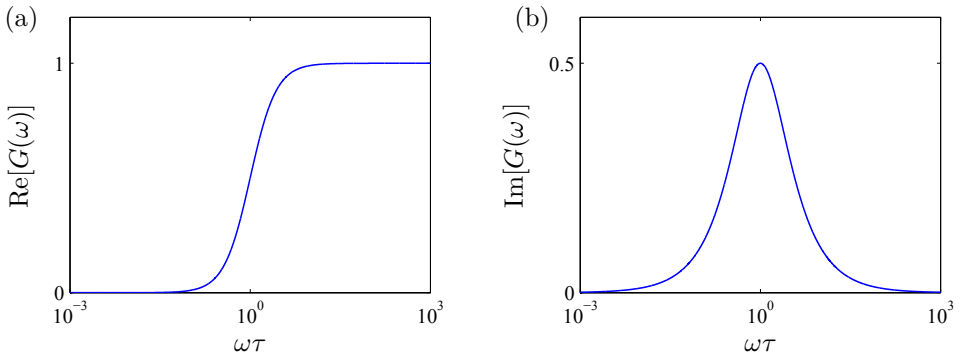

Figure 2: (a) Real and (b) imaginary part of frequency dependent function $G(\omega)$.

In (8) the electromechanical forces f_p are collected in the vector $\mathbf{f}$, whereby the filter equations (14) can be expressed in vector format as

$$i\omega\mathbf{f} + \mathbf{D}\mathbf{f} = i\omega\Delta\mathbf{k}\mathbf{v} \tag{17}$$

where the vector

$$\mathbf{v} = \mathbf{W}^T\mathbf{u} \tag{18}$$

contains the wave amplitudes specifically for the N_p piezoelectric elements. The matrix $\mathbf{D}$ is assumed diagonal with $D_{pp} = 1/\tau$, while the diagonal elements of $\Delta\mathbf{k}$ are $\Delta k_{pp} = \theta^2/C$.

The combined set of equations in (9) and (17) govern the complex valued natural frequency ω associated with the wave form solution implied by (3). It is determined as the eigenvalue to

$$i\omega \begin{bmatrix} \mathbf{u} \\ i\omega\mathbf{u} \\ \mathbf{f} \end{bmatrix} = \begin{bmatrix} \mathbf{0} & \mathbf{I} & \mathbf{0} \\ -\mathbf{M}^{-1}\mathbf{K} & \mathbf{0} & -\mathbf{M}^{-1}\mathbf{W} \\ \mathbf{0} & \Delta\mathbf{k}\mathbf{W}^T & -\mathbf{D} \end{bmatrix} \begin{bmatrix} \mathbf{u} \\ i\omega\mathbf{u} \\ \mathbf{f} \end{bmatrix} \tag{19}$$

where the damping is evaluated by the imaginary part of ω.

3 Modal analysis

The proper choice of shunt resistance and the corresponding attainable damping level depends on the modal properties of the periodic structure, represented by its unit cell. In the present case an augmented modal representation of the targeted wave form is therefore introduced to obtain accurate estimates of the complex frequency solution for the shunted structure.

3.1 The two limiting cases

The natural frequencies and mode shape vectors are now determined in the two limits associated with short- and open-circuit conditions, corresponding to $R \to 0$ and ∞, respectively. For shorted electrodes ($R = 0$) the corresponding force amplitudes $\mathbf{f}_p = \mathbf{0}$ and the frequency equation in (9) retains the generalized eigenvalue problem

$$\Big(\mathbf{K} - \omega_j^2\mathbf{M}\Big)\mathbf{u}_j = \mathbf{0} \tag{20}$$

where ω_j is the real-valued natural frequency and $\mathbf{u}_j$ is the eigenvector of wave form j.

In the open-circuit case with infinite shunt resistance ($R \to \infty$) the time scales $\tau \to \infty$, whereby $\mathbf{D} = \mathbf{0}$. It then follows from (17) that $\mathbf{f} = \Delta\mathbf{k}\mathbf{W}^T\mathbf{u}$, whereby (9) is rewritten into the corresponding open-circuit eigenvalue problem,

$$\Big(\mathbf{K} + \Delta\mathbf{K} - (\omega_j^2 + \Delta\omega_j^2)\mathbf{M}\Big)(\mathbf{u}_j + \Delta\mathbf{u}_j) = \mathbf{0} \tag{21}$$

where the increment in the global stiffness matrix is defined as

$$\Delta\mathbf{K} = \mathbf{W}\Delta\mathbf{k}\mathbf{W}^T \tag{22}$$

In (21) the increase in the eigenvalue $\Delta\omega_j^2$ implies a corresponding increase in natural frequency, while $\Delta\mathbf{u}_j$ represents the associated modification in the wave form of mode j.

In the following the structural wave amplitude vector is represented in terms of the wave forms associated with short-circuit electrode conditions governed by (20),

$$\mathbf{u} = \sum_j^N \mathbf{u}_j q_j \quad \Rightarrow \quad \mathbf{v} = \mathbf{W}^T\mathbf{u} = \sum_j^N \mathbf{W}^T\mathbf{u}_j q_j = \sum_j^N \mathbf{v}_j q_j \tag{23}$$

where q_j is the modal coordinate associated with wave form $\mathbf{u}_j$, while $\mathbf{v}_j = \mathbf{W}^T\mathbf{u}_j$ represents the specific contribution from the piezoelectric elements. Substitution of (23a) into (9), followed by pre-multiplication with the transposed mode shape $\mathbf{u}_j^T$, gives the scalar modal equation

$$(-\omega^2 m_j + k_j)q_j + \mathbf{v}_j^T\mathbf{f} = 0 \tag{24}$$

where $m_j = \mathbf{u}_j^T\mathbf{M}\mathbf{u}_j$ and $k_j = \mathbf{u}_j^T\mathbf{K}\mathbf{u}_j$ are modal mass and stiffness, respectively.

3.2 The augmented modal representation

Assume that a particular wave form $j = r$ is targeted by the R-shunts. A simple representation is based on the single mode assumption $\mathbf{u} = \mathbf{u}_r q_r$, which corresponds to $\mathbf{v} = \mathbf{v}_r q_r$. However, because the shunts act locally at the position of the piezoelectric element in the unit cell, they inherently activate higher wave forms, which are therefore needed in the presentation to capture the detailed propagation. This spill-over from residual forms is in the present case represented explicitly by the augmented modal representation [7, 8],

$$\mathbf{v} = \mathbf{v}_r q_r - \frac{1}{k_r'}(\mathbf{v}_r\mathbf{v}_r^T)\mathbf{f} \tag{25}$$

where the modal flexibility $1/k_r'$ depends on the magnitude of the modal interaction. The formulation follows [8], concerning viscoelastic constrained layer damping of structures. First, (25) is substituted into the filter equation (17), which is then pre-multiplied with $\mathbf{v}_r^T$. Hereby, the shunt force vector can be isolated as

$$\mathbf{v}_r^T\mathbf{f} = \frac{\dfrac{\Delta k_r}{k_r}G_r(\omega)}{1 + \kappa_r'\dfrac{\Delta k_r}{k_r}G_r(\omega)}k_r q_r \tag{26}$$

where the modal frequency dependent transfer function is defined as

$$G_r(\omega) = \frac{1}{\Delta k_r} \mathbf{v}_r^T \mathbf{G}(\omega) \Delta \mathbf{k} \mathbf{v}_r \tag{27}$$

with the modal stiffness increment

$$\Delta k_r = \mathbf{v}_r^T \Delta \mathbf{k} \mathbf{v}_r = \mathbf{u}_r^T \Delta \mathbf{K} \mathbf{u}_r \tag{28}$$

It should be noted that for identical R-shunts, the matrix $\mathbf{G}(\omega) = G(\omega)\mathbf{I}$, whereby $G_r(\omega) = G(\omega)$. In (26) the residual mode correction is contained in the non-dimensional flexibility

$$\kappa_r' = \frac{k_r}{k_r'} \tag{29}$$

which vanishes when the R-shunts do not introduce any notable modal coupling.

The expression (26) is now substituted into the modal equation of motion (24), whereby the natural frequency ω may be isolated. It is convenient to introduce the increment

$$\Delta\omega^2 = \omega^2 - \omega_r^2 \tag{30}$$

relative to the short-circuit solution ω_r^2. In the open-circuit limit, the increment $\Delta\omega^2 = \Delta\omega_r^2$ is obtained from the eigenvalue problem (21). The frequency solution can now be written as

$$\frac{\Delta\omega^2}{\omega_r^2} = \frac{\dfrac{\Delta k_r}{k_r} G_r(\omega)}{1 + \kappa_r' \dfrac{\Delta k_r}{k_r} G_r(\omega)} \tag{31}$$

In the short circuit case, with vanishing resistance, the modal transfer function $G_r = 0$ and the solution (31) captures the real-valued short-circuit solution $\Delta\omega^2 = 0$, which corresponds to $\omega^2 = \omega_r^2$, determined by (20). However, for a finite value of $G_r(\omega)$ the solution (31) is implicit with respect to ω, requiring iterations to exactly solve for the complex frequency.

3.3 Residual mode coefficient

In the frequency solution (31) a positive residual mode coefficient κ_r' reduces the natural frequency and thus the attainable damping introduced by the piezoelectric R-shunts. The residual mode coefficient κ_r' is now calibrated so that the frequency solution (31) captures the correct natural frequency ($\Delta\omega^2 = \Delta\omega_r^2$) in the open-circuit limit, obtained by (21) and associated with $\tau \to \infty$. In the open-circuit limit the transfer matrix $\mathbf{G}(\omega) = \mathbf{I}$, whereby the modal transfer function $G_r(\omega) \to 1$ in (27). Substitution of $\Delta\omega^2 = \Delta\omega_r^2$ and $G_r = 1$ into the frequency solution (31) then gives

$$\kappa_r' = \frac{\omega_r^2}{\Delta\omega_r^2} - \frac{k_r}{\Delta k_r} = \frac{k_r}{\Delta k_r}\Big(\frac{1}{\Delta\mu_r} - 1\Big) \tag{32}$$

introducing the an apparent modal mass ratio

$$\Delta\mu_r = \frac{\Delta m_r}{m_r} = \frac{\Delta k_r}{\Delta\omega_r^2}\frac{\omega_r^2}{k_r} \tag{33}$$

where Δm_r represents the change in modal mass from short- to open-circuit condition with respect to the short-circuit mode shape vector. By elimination of κ_r' in (31) the resulting frequency solution can then be written as

$$\frac{\Delta\omega^2}{\Delta\omega_r^2} = \frac{i\omega\tau_r\Delta\mu_r}{1+i\omega\tau_r\Delta\mu_r} \tag{34}$$

in which the modal time scale τ_r is defined by the relations

$$i\omega\tau_r = \frac{G_r(\omega)}{1-G_r(\omega)} \quad \text{or} \quad G_r(\omega) = \frac{i\omega\tau_r}{1+i\omega\tau_r} \tag{35}$$

The solution in (34) is seen to recover $\Delta\omega^2 = 0$ and $\Delta\omega_r^2$ in the short- and open-circuit limits.

3.4 Shunt calibration

The shunt resistance, represented by the time scale $\tau = RC$, is now calibrated to give the largest attainable imaginary part of the natural frequency, which corresponds to maximum attenuation of the targeted wave form. It is assumed that $\omega\tau_r \simeq \omega_r\tau_r$, whereby the frequency solution (34) becomes explicit and the imaginary part can be derived as

$$\mathrm{Im}\left[\frac{\Delta\omega^2}{\Delta\omega_r^2}\right] = \frac{\omega_r\tau_r\Delta\mu_r}{1+(\omega_r\tau_r\Delta\mu_r)^2} \tag{36}$$

The maximum imaginary part is obtained when $\omega_r\tau_r\Delta\mu_r = 1$, which corresponds to

$$\tau_r^{opt} = \frac{1}{\omega_r\Delta\mu_r} \quad \Rightarrow \quad \omega_r C R_{opt} = \frac{1}{\Delta\mu_r} \tag{37}$$

Thus, the optimal resistance is inversely proportional to the relative modal mass increment (33). The applied shunt resistances should therefore be optimized according to the condition in (37). Substitution of (37) into (36) gives $\mathrm{Im}[\Delta\omega^2] = \frac{1}{2}\Delta\omega_r^2$, which can be approximated as

$$\frac{\mathrm{Im}[\Delta\omega]}{\omega_r} \simeq \frac{\Delta\omega_r^2}{4\omega_r^2} = \frac{1}{4\Delta\mu_r}\frac{\Delta k_r}{k_r} = \frac{\Delta k_r}{4k_r}\omega_r C R_{opt} \tag{38}$$

This relation shows that the attainable damping is directly determined by the change in frequency between short- and open-circuit electrodes. The accuracy of (37) is now demonstrated.

4 NUMERICAL EXAMPLE

The piezoelectric element (PZT) is characterized by an axial elastic stiffness $EA_p = \frac{5}{7}EA$, where EA is the stiffness of the host aluminum (Al) structure. The corresponding relation for the mass per unit length is $\rho A_p = \frac{14}{5}\rho A$. The element length ℓ_e corresponds to the thickness of a typical disc-type actuator with cross-section diameter $d = 5\ell_e$. The electromechanical coupling coefficient θ and capacitance C are effectively represented by the electrical stiffness $\theta^2/C = \frac{1}{2}(EA/\ell_e)$, here expressed in terms of the mechanical element stiffness EA/ℓ_e. The unit cell is shown in Figure 3(a), with nine elements of identical length discretizing a symmetric Al-PZT-Al configuration.

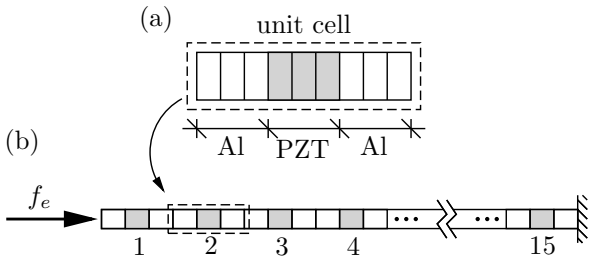

Figure 3: Bar with 15 Al-PZT-Al unit cells, discretized by nine elements.

In the unit cell each of the three piezoelectric elements are shunted with an individual resistance R, which is calibrated to provide maximum attenuation in the acoustical branch at the non-dimensional wavenumber $\gamma\ell_e N_e/\pi = 0.5$. At this wavenumber the eigenvalue problems (20) and (21) provide ω_r^2 and $\Delta\omega_r^2$, respectively. For the present unit cell the relative increment is $\Delta\omega_r^2/\omega_r^2 = 0.15$, while the associated modal mass increment $\Delta\mu_r = 1.33$ follows from (33). Thus, the optimal time scale $\tau_r^{opt}\omega_r = 0.75$ is obtained by (37).

In Fig. 4(a) the red curve represents the dispersion curve associated with the complex-valued

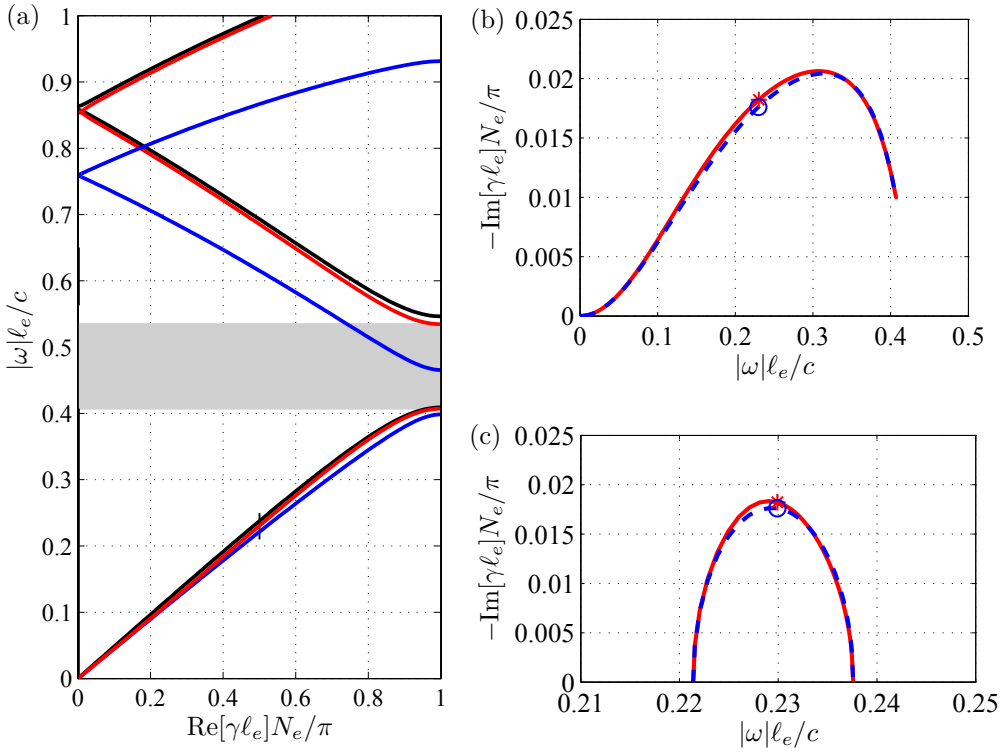

Figure 4: (a) Dispersion curve (red) with short- (blue) and open-circuit (black) limits. (b) Imaginary part of complex-wavenumber (red) and explicit solution (blue dashed). (c) Root-locus curve with τ as gain parameter and markers representing optimal calibration τ^{opt} determined by (37).

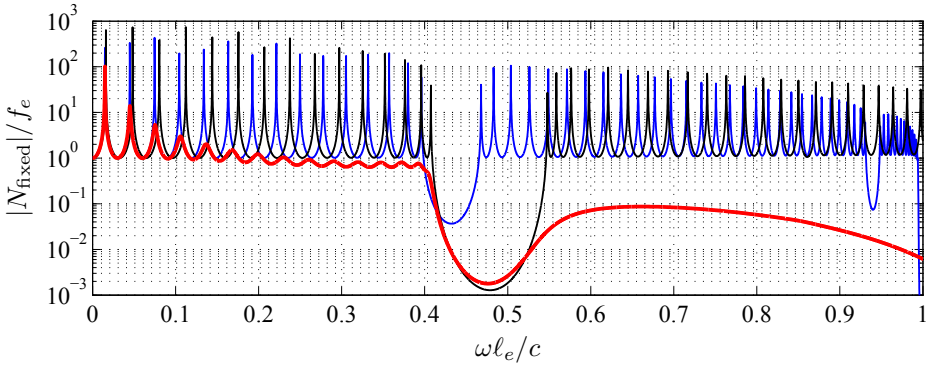

Figure 5: Transmitted normal force N_{fixed} at right end: $\tau = \tau^{opt}$ (red), 0 (blue) and ∞ (black).

natural frequency ω obtained by (19). The frequency is represented by its absolute value $|\omega|$ and normalized by the wave speed $c = \sqrt{E/\rho}$ of the host material. Hereby, the wavenumber γ becomes complex-valued with oscillations governed by the positive real part and attenuation represented by the negative imaginary part. In Fig. 4(a) the blue and black curves represent the two limiting cases with short- and open-circuit conditions, respectively. At the targeted wavenumber (depicted by the short vertical black line) the red curve is centered between the blue and black curves. Furthermore, R-shunting opens the band gap indicated by the gray area at $|\omega|\ell_e/c \simeq 0.5$.

For the particular calibration of the R-shunt, Fig. 4(b) shows the imaginary part of the wavenumber, where the blue dashed curve represents the solution obtained by the explicit expression in (36). The red asterisk and blue circle represent the complex root obtained for τ^{opt}. Fig. 4(c) shows a corresponding root locus at the targeted wavenumber with time scale τ as gain parameter. It can be seen from Figs. 4(b,c) that the derived frequency solution (34) accurately recovers the exact complex root and almost exactly estimates the optimal time scale associated with maximum imaginary part of the complex frequency or wavenumber. Thus, the optimal wave attenuation can be estimated and designed without solving a full complex eigenvalue problem for the unit cell.

As indicated in Fig. 3(b) a harmonic external force with amplitude f_e is now applied at the free end of a free-fixed bar with 15 unit cells. Figure 5 shows the amplitude of the normal force N_{fixed} at the right fixed end. The blue and black curves represent the solutions for short- and open-circuit conditions, while the red curve is obtained for R-shunted piezoelectric elements with $\tau = \tau_r^{opt}$. It is seen that the vibration amplitudes are significantly reduced at the targeted frequency $\omega\ell_e/c = 0.23$, the band gap around $\omega\ell_e/c = 0.5$ is widened and waves in the optical branch at $\omega\ell_e/c > 0.5$ are practically eliminated. A small amount of Rayleigh damping ($\zeta = 0.0001$ at $\omega\ell_e/c = 0.23$) is introduced to avoid singularities in the short- and open circuit limits.

5 CONCLUSIONS

The accuracy of the derived frequency solution is illustrated by the final example. It should even be mentioned, that on the right hand side of (34), it is assumed that $\omega \simeq \omega_r$, whereby iterations are avoided. But because the format in (34) is derived so that the two real-valued

short- and open-circuit frequencies are exactly recovered, the solution is inherently accurate as long as the level of attainable damping is moderate. The present approach is based on the simple inverse analysis, as discussed in [2], where the wavenumber is assumed given and the complex frequency is obtained by an eigenvalue problem for the unit cell, similar to that in vibrational problems. This type of analysis has its limitations and the proposed method should therefore be extended to direct methods, based on a transfer matrix between unit cells. Furthermore, the accurate representation of the modal interaction can also be applied in the calibration of resonant shunts, as demonstrated for vibrations in [7]. This will improve the calibration of shunt resonators [9], where the tuning of the inductance can be very sensitive with respect to the changes in mode shapes, due to the presence of the shunt. Thus, the present paper is merely a first illustration of how to control the full modal analysis and capture important spill-over effects without having to deal with the entire modal dimension and future results with implications on wave attenuation and vibration damping in periodic structure could be obtained by a strategy similar to that outlined here.

REFERENCES

[1] Mead, D.J. Wave propagation in continuous periodic structures: Research contributions from Southampton, 1964-1995, *Journal of Sound and Vibration* (1996) 190:495-524.

[2] Hussein, M.I., Leamy, M.J. and Ruzzene, M. Dynamics of phononic materials and structures: Historical origins, recent progress, and future outlook, *Applied Mechanics Reviews* (2014) 66:125014 (11pp).

[3] Jensen, J.S. Phononic band gaps and vibrations in one- and two-dimensional mass-spring structures, *Journal of Sound and Vibration* (2001) 266:1053-1078.

[4] Thorp, O., Ruzzene, M. and Baz, A. Attenuation and localization of wave propagation in rods with periodic shunted piezoelectric patches, *Smart Materials and Structures* (2001) 10:979-989.

[5] Chen, S.B., Wang, G. and Song, Y. Low-frequency vibration isolation in sandwich plates by piezoelectric shunting arrays, *Smart Materials and Structures* (2016) 25:125024 (8pp).

[6] Preumont, A. *Vibration Control of Active Structures. An Introduction*, 3rd edition, Springer, Heidelberg, (2011).

[7] Høgsberg, J. and Krenk, S. Balanced calibration of resonant piezoelectric RL shunts with quasi-static background flexibility correction, *Journal of Sound and Vibration* (2015) 341:16-30.

[8] Høgsberg, J. Explicit solution for the natural frequency of structures with partial viscoelastic treatment, *Mechanics of Advanced Materials and Structures* (2016) 23:784-790.

[9] Hagood, N.W. and von Flotow, A. Damping of structural vibrations with piezoelectric materials and passive electrical networks, *Journal of Sound and Vibration* (1991) 146:243-268.

VIII ECCOMAS Thematic Conference on Smart Structures and Materials
SMART 2017
A. Güemes, A. Benjeddou, J. Rodellar and J. Leng (Eds)

WAVE FINITE ELEMENT METHOD APPLIED TO AN ELECTROMECHANICAL WAVEGUIDE

B. LOSSOUARN*, M. AUCEJO*, J.-F. DEÜ*

*Structural Mechanics and Coupled Systems Laboratory,
Conservatoire national des arts et métiers
2 rue Conté, Paris, France
e-mail: boris.lossouarn@cnam.fr

Key words: Wave Propagation, Transfer Matrix, Piezoelectric Coupling, Electrical Network.

Abstract. A novel Finite Element formulation is proposed for cases involving the coupling of mechanical and electrical waveguides. This allows using the Transfer Matrix formalism proposed in the Wave Finite Element method. Electrical variables are added to the state vectors in order to compute propagation constants for electromechanical waves. Frequency response fonctions of coupled structures can also be obtained for various mechanical and electrical boundary conditions.

1 INTRODUCTION

A Finite Element method for structures covered with piezoelectric elements was proposed by Thomas et al. [1] who focused on thin piezoelectric patches shunted with independent electrical circuits. The model is based on a condensation of the electrical degrees of freedom in order to recast the system into a standard mechanical formulation. However, this method is not applicable when considering interconnections of several patches through an electrical network. In this case, an electromechanical waveguide is created and a wave can propagate simultaneously in the mechanical and electrical domains. Because there are electrical nodes that interconnect successive elements, the electrical degrees of freedom cannot be condensed in the mechanical problem. For example, this arises when considering a structure coupled to its electrical analogue for a multimodal vibration damping purpose [2, 3]. Based on a periodic distribution, a Transfer Matrix Method can be implemented but it requires the use of external electrical degrees of freedom. A novel Wave Finite Element method dedicated to electromechanical periodic waveguides is then required.

In this study, electric charge displacement and voltage vectors are defined by analogy with displacement and force vectors. The equivalent of a dynamic stiffness matrix is obtained from the constitutive equations of the electromechanical problem. The main difference with a purely mechanical formulation [4, 5, 6, 7] or a problem involving independent piezoelectric shunts [8, 9] is that the state vectors include both mechanical and electrical variables [10]. The global "dynamic stiffness matrix" is then rearranged to bring together the left and right variables.

With this partitioning, the Wave Finite Element method can be applied and a Transfer Matrix is defined after condensation of the internal mechanical degrees of freedoms. This method offers a convenient numerical model for the analysis of wave propagation in periodic structures involving an interconnected array of piezoelectric patches. Finally, we show the example of a rod coupled to a line of inductors. The propagation constants are extracted from the Transfer Matrix and we point out the different waves propagating through the electromechanical waveguide as well as the band-gap effects.

2 FINITE ELEMENT MODEL

2.1 Piezoelectric coupling

In this paper, we consider an electromechanical waveguide such as the one in Fig. 1. An electrical network is coupled to a mechanical structure through an array of piezoelectric elements. Each unit cell involves a pair of piezoelectric patches connected in parallel. Other geometries or electrical connections could be considered but we restrain the analysis to a single piezoelectric degree of freedom per unit cell. The variables V_I and $\dot{q}_\mathrm{I}$ represent the voltage across the pair of piezoelectric patches and the electrical current flowing through it. A convenient finite element model was proposed by Thomas et al. [1] for problems involving thin piezoelectric patches and independent shunts. If $\boldsymbol{q_m}$ represents the mechanical displacements and $\boldsymbol{F_m}$ corresponds to the external forces, the coupled problem is given as

$$\begin{bmatrix} \boldsymbol{M_m} & \boldsymbol{0} \\ \boldsymbol{0} & 0 \end{bmatrix} \begin{bmatrix} \ddot{\boldsymbol{q}}_{\boldsymbol{m}} \\ \ddot{V}_\mathrm{I} \end{bmatrix} + \begin{bmatrix} \boldsymbol{K_m} & \boldsymbol{K_c} \\ -\boldsymbol{K_c}^{\boldsymbol{T}} & C^\varepsilon \end{bmatrix} \begin{bmatrix} \boldsymbol{q_m} \\ V_\mathrm{I} \end{bmatrix} = \begin{bmatrix} \boldsymbol{F_m} \\ q_\mathrm{I} \end{bmatrix}, \tag{1}$$

where $\boldsymbol{M_m}$, $\boldsymbol{K_m}$ and $\boldsymbol{K_c}$ are respectively the mass, stiffness and coupling matrices. The constant C^ε is the piezoelectric capacitance when no motion is allowed, i.e. $\boldsymbol{q_m} = \boldsymbol{0}$. Considering a shunt made of an impedance Z in parallel with the piezoelectric elements at angular frequency ω, the relation $V_\mathrm{I} = -\mathrm{j}\omega Z q_\mathrm{I}$ allows condensing the electrical degrees of freedom. Indeed, from Eq. (1) we obtain

$$\boldsymbol{M_m}\ddot{\boldsymbol{q}}_{\boldsymbol{m}} + \left[\boldsymbol{K_m} + \frac{1}{C^\varepsilon + \dfrac{1}{\mathrm{j}\omega Z}} \boldsymbol{K_c}\boldsymbol{K_c}^{\boldsymbol{T}} \right] \boldsymbol{q_m} = \boldsymbol{F_m}, \tag{2}$$

which represents a standard mechanical problem with an added-stiffness term due to piezoelectric coupling [1, 11].

However, this method is not applicable when considering interconnections of successive unit cells with an electrical network. There are electrical charges that are flowing in and out of the unit cell. This means that there is no direct relation between the internal variables V_I and q_I. In the end, the electrical variables cannot be condensed in the mechanical problem. A novel formulation that is able to take into account external electrical degrees of freedom is thus required.

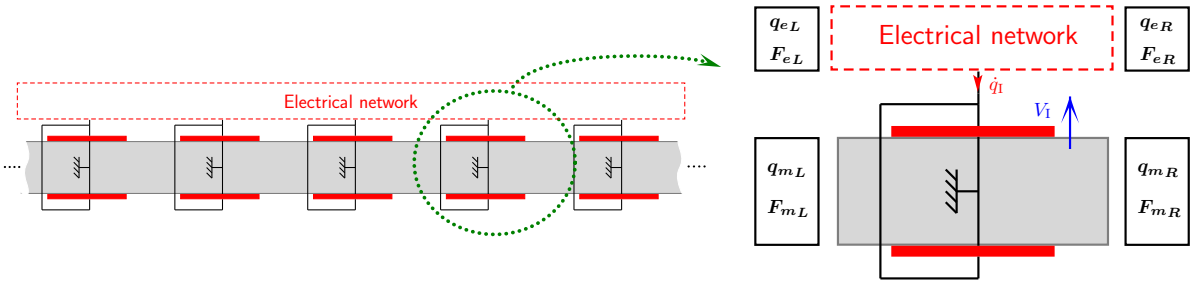

Figure 1: Interconnected array of piezoelectric patches and corresponding electromechanical unit cell highlighting left and right degrees of freedom.

2.2 Electrical degrees of freedom

From the topology of the electrical network, the electric charge q_I flowing through the pair of piezoelectric patches can be defined relatively to a charge vector $\boldsymbol{q_e}$ as

$$q_\mathrm{I} = \boldsymbol{S^T q_e}. \tag{3}$$

If we focus on a one-dimensional unit cell, the vector $\boldsymbol{q_e} = \left[\begin{array}{cc} \boldsymbol{q_{eL}} & \boldsymbol{q_{eR}} \end{array} \right]^T$ refer to the electrical charges that are exchanged with the neighboring left and right unit cells. The matrix $\boldsymbol{S}$ depends on the internal connections of the considered portion of electrical network. By analogy with the force vector $\boldsymbol{F_m}$, we define $\boldsymbol{F_e} = \left[\begin{array}{cc} \boldsymbol{F_{eL}} & \boldsymbol{F_{eR}} \end{array} \right]^T$ that contains the voltage contributions on both sides of the electrical part of the unit cell. In the following, we consider that the total energy of the purely electrical problem (when $\boldsymbol{q_m} = \boldsymbol{0}$) can be written under the form

$$E_e = \frac{1}{2}\boldsymbol{q_e^T K_e q_e} + \frac{1}{2}\boldsymbol{\dot{q}_e^T M_e \dot{q}_e}, \tag{4}$$

where $\boldsymbol{K_e}$ and $\boldsymbol{M_e}$ are symmetric matrices that are the analogues of the mechanical stiffness and mass matrices. Then, the energy in the electrical network excluding the piezoelectric capacitor is $E_e - \dfrac{q_\mathrm{I}^2}{2C^\varepsilon}$. Furthermore, the electrical power flowing into the electrical network in Fig. 1 is equal to

$$P_e = \boldsymbol{F_e^T \dot{q}_e} - V_\mathrm{I}\dot{q}_\mathrm{I} \tag{5}$$

If the electrical network is a conservative system, a power balance induces that the input power is equal to the time derivative of the energy as

$$P_e = \frac{d\left(E_e - \dfrac{q_\mathrm{I}^2}{2C^\varepsilon}\right)}{dt}. \tag{6}$$

The symmetry property of both matrices $\boldsymbol{K_e}$ and $\boldsymbol{M_e}$ thus gives

$$\boldsymbol{F_e^T \dot{q}_e} - V_\mathrm{I}\dot{q}_\mathrm{I} = \boldsymbol{q_e^T K_e \dot{q}_e} + \boldsymbol{\dot{q}_e^T M_e \ddot{q}_e} - \frac{q_\mathrm{I}}{C^\varepsilon}\dot{q}_\mathrm{I}, \tag{7}$$

which is equivalent to

$$\boldsymbol{\dot{q}_e^T}\left(\boldsymbol{F_e} - \boldsymbol{S}V_\mathrm{I} - \boldsymbol{K_e q_e} - \boldsymbol{M_e \ddot{q}_e} + \frac{1}{C^\varepsilon}\boldsymbol{S S^T q_e}\right) = 0 \tag{8}$$

This true for any electric current vector $\dot{\boldsymbol{q}}_{\boldsymbol{e}}$ so

$$\boldsymbol{F_e} = \boldsymbol{K_e q_e} + \boldsymbol{M_e}\ddot{\boldsymbol{q}}_{\boldsymbol{e}} + \boldsymbol{S}V_{\mathrm{I}} - \frac{1}{C^{\varepsilon}}\boldsymbol{S}\boldsymbol{S}^{\boldsymbol{T}}\boldsymbol{q_e}. \tag{9}$$

In the end, as we also know from Eq. (1) that

$$V_{\mathrm{I}} = \frac{1}{C^{\varepsilon}}\left(\boldsymbol{S}^{\boldsymbol{T}}\boldsymbol{q_e} + \boldsymbol{K_c}^{\boldsymbol{T}}\boldsymbol{q_m}\right), \tag{10}$$

we get a relation between the voltage vector $\boldsymbol{F_e}$ and the displacement vectors:

$$\boldsymbol{F_e} = \boldsymbol{K_e q_e} + \boldsymbol{M_e}\ddot{\boldsymbol{q}}_{\boldsymbol{e}} + \frac{1}{C^{\varepsilon}}\boldsymbol{S}\boldsymbol{K_c}^{\boldsymbol{T}}\boldsymbol{q_m}. \tag{11}$$

Note that a principle of superposition applies because $\boldsymbol{F_e}$ is a sum of two contributions. The first one corresponds to the voltage vector when $\boldsymbol{q_m} = \boldsymbol{0}$, i.e. when no mechanical displacement is allowed. This is a purely electrical contribution that only depends on the electrical network and the piezoelectric capacitance. On the other hand, the second contribution, observed when $\boldsymbol{q_e} = \boldsymbol{0}$, is directly related to piezoelectric coupling.

2.3 Electromechanical formulation

Now that all the mechanical and electrical vectors have been defined for both displacements and forcing terms, they can be organized into a single matrix formulation. Under harmonic excitation at angular frequency ω, Eqs. (1) and (10) lead to a force vector

$$\boldsymbol{F_m} = \left[\boldsymbol{K_m} + \frac{1}{C^{\varepsilon}}\boldsymbol{K_c}\boldsymbol{K_c}^{\boldsymbol{T}} - \omega^2\boldsymbol{M_m}\right]\boldsymbol{q_m} + \frac{1}{C^{\varepsilon}}\boldsymbol{K_c}\boldsymbol{S}^{\boldsymbol{T}}\boldsymbol{q_e}. \tag{12}$$

Similarly, Eq. (11) gives a voltage vector

$$\boldsymbol{F_e} = \left[\boldsymbol{K_e} - \omega^2\boldsymbol{M_e}\right]\boldsymbol{q_e} + \frac{1}{C^{\varepsilon}}\boldsymbol{S}\boldsymbol{K_c}^{\boldsymbol{T}}\boldsymbol{q_m} \tag{13}$$

This leads to the following dynamic stiffness matrix formulation involving a combination of mechanical and electrical degrees of freedom:

$$\left[\begin{bmatrix} \boldsymbol{K_m} + \frac{1}{C^{\varepsilon}}\boldsymbol{K_c}\boldsymbol{K_c}^{\boldsymbol{T}} & \frac{1}{C^{\varepsilon}}\boldsymbol{K_c}\boldsymbol{S}^{\boldsymbol{T}} \\ \frac{1}{C^{\varepsilon}}\boldsymbol{S}\boldsymbol{K_c}^{\boldsymbol{T}} & \boldsymbol{K_e} \end{bmatrix} - \omega^2\begin{bmatrix} \boldsymbol{M_m} & \boldsymbol{0} \\ \boldsymbol{0} & \boldsymbol{M_e} \end{bmatrix}\right]\begin{bmatrix} \boldsymbol{q_m} \\ \boldsymbol{q_e} \end{bmatrix} = \begin{bmatrix} \boldsymbol{F_m} \\ \boldsymbol{F_e} \end{bmatrix}. \tag{14}$$

The coupled problem is thus organized like any purely mechanical problem involving mass and stiffness matrices. The only difference is that the global displacement and force vectors contain both mechanical and electrical contributions. With such an electromechanical formulation, classical methods such as the assembly of element matrices or Transfer Matrix methods can be applied.

3 WAVE FINITE ELEMENT METHOD

3.1 Transfer matrix

The dynamic stiffness matrix given in Eq. (14) is rearranged to bring together the mechanical and electrical left and right degrees of freedom [10], as

$$\begin{bmatrix} \tilde{\boldsymbol{D}}_{\mathrm{LL}} & \tilde{\boldsymbol{D}}_{\mathrm{LI}} & \tilde{\boldsymbol{D}}_{\mathrm{LR}} \\ \tilde{\boldsymbol{D}}_{\mathrm{IL}} & \tilde{\boldsymbol{D}}_{\mathrm{II}} & \tilde{\boldsymbol{D}}_{\mathrm{IR}} \\ \tilde{\boldsymbol{D}}_{\mathrm{RL}} & \tilde{\boldsymbol{D}}_{\mathrm{RI}} & \tilde{\boldsymbol{D}}_{\mathrm{RR}} \end{bmatrix} \begin{bmatrix} \boldsymbol{q}_{\mathrm{L}} \\ \boldsymbol{q}_{\boldsymbol{m}\mathrm{I}} \\ \boldsymbol{q}_{\mathrm{R}} \end{bmatrix} = \begin{bmatrix} \boldsymbol{F}_{\mathrm{L}} \\ \boldsymbol{0} \\ \boldsymbol{F}_{\mathrm{R}} \end{bmatrix} \tag{15}$$

where $\boldsymbol{q}_{\mathrm{L}} = \begin{bmatrix} \boldsymbol{q}_{\boldsymbol{m}\mathrm{L}} & \boldsymbol{q}_{\boldsymbol{e}\mathrm{L}} \end{bmatrix}^T$, $\boldsymbol{q}_{\mathrm{R}} = \begin{bmatrix} \boldsymbol{q}_{\boldsymbol{m}\mathrm{R}} & \boldsymbol{q}_{\boldsymbol{e}\mathrm{R}} \end{bmatrix}^T$, $\boldsymbol{F}_{\mathrm{L}} = \begin{bmatrix} \boldsymbol{F}_{\boldsymbol{m}\mathrm{L}} & \boldsymbol{F}_{\boldsymbol{e}\mathrm{L}} \end{bmatrix}^T$ and $\boldsymbol{F}_{\mathrm{R}} = \begin{bmatrix} \boldsymbol{F}_{\boldsymbol{m}\mathrm{R}} & \boldsymbol{F}_{\boldsymbol{e}\mathrm{R}} \end{bmatrix}^T$. This expression is based on the decomposition of the mechanical vectors $\boldsymbol{F}_{\boldsymbol{m}} = \begin{bmatrix} \boldsymbol{F}_{\boldsymbol{m}\mathrm{L}} & \boldsymbol{0} & \boldsymbol{F}_{\boldsymbol{m}\mathrm{R}} \end{bmatrix}^T$ and $\boldsymbol{q}_{\boldsymbol{m}} = \begin{bmatrix} \boldsymbol{q}_{\boldsymbol{m}\mathrm{L}} & \boldsymbol{q}_{\boldsymbol{m}\mathrm{I}} & \boldsymbol{q}_{\boldsymbol{m}\mathrm{R}} \end{bmatrix}^T$ where $\boldsymbol{q}_{\boldsymbol{m}\mathrm{I}}$ is the mechanical displacement vector of the internal nodes of the unit cell. With this partitioning, the procedures of the Wave Finite Element method [4, 5, 6, 7, **?**, 9, 11] can be implemented. This starts with an elimination of the internal degrees of freedoms through

$$\begin{bmatrix} \boldsymbol{D}_{\mathrm{LL}} & \boldsymbol{D}_{\mathrm{LR}} \\ \boldsymbol{D}_{\mathrm{RL}} & \boldsymbol{D}_{\mathrm{RR}} \end{bmatrix} \begin{bmatrix} \boldsymbol{q}_{\mathrm{L}} \\ \boldsymbol{q}_{\mathrm{R}} \end{bmatrix} = \begin{bmatrix} \boldsymbol{F}_{\mathrm{L}} \\ \boldsymbol{F}_{\mathrm{R}} \end{bmatrix}, \quad \text{where} \quad \begin{array}{l} \boldsymbol{D}_{\mathrm{LL}} = \tilde{\boldsymbol{D}}_{\mathrm{LL}} - \tilde{\boldsymbol{D}}_{\mathrm{LI}} \tilde{\boldsymbol{D}}_{\mathrm{II}}^{-1} \tilde{\boldsymbol{D}}_{\mathrm{IL}} \\ \boldsymbol{D}_{\mathrm{LR}} = \tilde{\boldsymbol{D}}_{\mathrm{LR}} - \tilde{\boldsymbol{D}}_{\mathrm{LI}} \tilde{\boldsymbol{D}}_{\mathrm{II}}^{-1} \tilde{\boldsymbol{D}}_{\mathrm{IR}} \\ \boldsymbol{D}_{\mathrm{RL}} = \tilde{\boldsymbol{D}}_{\mathrm{RL}} - \tilde{\boldsymbol{D}}_{\mathrm{RI}} \tilde{\boldsymbol{D}}_{\mathrm{II}}^{-1} \tilde{\boldsymbol{D}}_{\mathrm{IL}} \\ \boldsymbol{D}_{\mathrm{RR}} = \tilde{\boldsymbol{D}}_{\mathrm{RR}} - \tilde{\boldsymbol{D}}_{\mathrm{RI}} \tilde{\boldsymbol{D}}_{\mathrm{II}}^{-1} \tilde{\boldsymbol{D}}_{\mathrm{IR}} \end{array}, \tag{16}$$

and the condensed dynamic stiffness matrix is then transformed into a transfer matrix:

$$\begin{bmatrix} \boldsymbol{q}_{\mathrm{R}} \\ \boldsymbol{F}_{\mathrm{R}} \end{bmatrix} = \begin{bmatrix} -\boldsymbol{D}_{\mathrm{LR}}^{-1} \boldsymbol{D}_{\mathrm{LL}} & -\boldsymbol{D}_{\mathrm{LR}}^{-1} \\ \boldsymbol{D}_{\mathrm{RL}} - \boldsymbol{D}_{\boldsymbol{RR}} \boldsymbol{D}_{\mathrm{LR}}^{-1} \boldsymbol{D}_{\mathrm{LL}} & -\boldsymbol{D}_{\mathrm{RR}} \boldsymbol{D}_{\mathrm{LR}}^{-1} \end{bmatrix} \begin{bmatrix} \boldsymbol{q}_{\mathrm{L}} \\ -\boldsymbol{F}_{\mathrm{L}} \end{bmatrix}. \tag{17}$$

As both force vectors $\boldsymbol{F}_{\mathrm{L}}$ and $\boldsymbol{F}_{\mathrm{R}}$ corresponds to external forcing, the use of $-\boldsymbol{F}_{\mathrm{L}}$ is required in order to ensure the continuity of the state vector [4, 5].

3.2 Propagation constants

A one-dimensional periodic structure can be defined as a series of identical unit cells. As in Eq. (17), the relation between the mechanical states at the right and left ends of a unit cell is described by a transfer matrix $\boldsymbol{T}$ through

$$\begin{bmatrix} \boldsymbol{q}_{\mathrm{R}} \\ \boldsymbol{F}_{\mathrm{R}} \end{bmatrix} = \boldsymbol{T} \begin{bmatrix} \boldsymbol{q}_{\mathrm{L}} \\ -\boldsymbol{F}_{\mathrm{L}} \end{bmatrix}. \tag{18}$$

The Floquet-Bloch theory induces that, for a wave propagating in the one-dimensional medium, the state on the right of a unit cell is equal to $e^{\pm\mu}$ times the state on the left [7, 12], the sign depending on the direction of the wave. Here, μ is the propagation constant, which is usually defined as $\mu = \delta + \mathrm{j}\theta$, where δ is the attenuation constant, j is the imaginary unit and θ is the phase constant [8]. Alternatively, the propagation constant can be written $\mu = \alpha a + \mathrm{j}ka$, where α is the attenuation rate, k is the wavenumber and a is the length of the unit cell. From Eq. (18), if $\begin{bmatrix} \boldsymbol{q}_{\mathrm{L}} & -\boldsymbol{F}_{\mathrm{L}} \end{bmatrix}^T$ is an eigenvector of the transfer matrix $\boldsymbol{T}$,

$$\begin{bmatrix} \boldsymbol{q}_{\mathrm{R}} \\ \boldsymbol{F}_{\mathrm{R}} \end{bmatrix} = e^{\pm\mu} \begin{bmatrix} \boldsymbol{q}_{\mathrm{L}} \\ -\boldsymbol{F}_{\mathrm{L}} \end{bmatrix}. \tag{19}$$

Consequently, $\mu = \ln(\lambda)$, where λ represents an eigenvalue of the transfer matrix $\boldsymbol{T}$. Considering state vectors including both mechanical and electrical variables, we obtain phase and attenuation constants related to the propagation in an electromechanical waveguide. Generally speaking, we can not distinguish mechanical waves from electrical waves because of the coupling between both physical domains.

3.3 Frequency response functions

Apart from propagation constants, a transfer matrix model also allows to compute frequency response functions [5, 6]. According to the definition of a periodic structure, each unit cell is described by an identical transfer matrix $\boldsymbol{T}$. Consequently, a basic solution to obtain the mechanical state on the right of the nth unit cell consists in raising the corresponding transfer matrix to the power of n,

$$\begin{bmatrix} \boldsymbol{q_n} \\ \boldsymbol{F_n} \end{bmatrix} = \boldsymbol{T}^{\boldsymbol{n}} \begin{bmatrix} \boldsymbol{q_0} \\ -\boldsymbol{F_0} \end{bmatrix} = \begin{bmatrix} \boldsymbol{T_n^{qq}} & \boldsymbol{T_n^{qF}} \\ \boldsymbol{T_n^{Fq}} & \boldsymbol{T_n^{FF}} \end{bmatrix} \begin{bmatrix} \boldsymbol{q_0} \\ -\boldsymbol{F_0} \end{bmatrix}, \tag{20}$$

where the subscript 0 refers to the left end of the first unit cell and the forcing vectors corresponds to forces or voltages applied to the considered electromechanical structure. Then, when considering a finite number of n unit cells, the boundary conditions need to be introduced. For example, with a prescribed force vector $\boldsymbol{F_0}$ applied to the left end of a free-free periodic structure, as $\boldsymbol{F_n} = \boldsymbol{0}$, the displacement $\boldsymbol{q_n}$ at the right end is defined from Eq. (20) as

$$\boldsymbol{q_n} = (\boldsymbol{T_n^{qq}} \boldsymbol{T_n^{Fq}}^{-1} \boldsymbol{T_n^{FF}} - \boldsymbol{T_n^{qF}}) \boldsymbol{F_0}. \tag{21}$$

Similar methods can be used for other boundary conditions such as free or blocked for the mechanical part and short-cicuited or open-circuited for the electrical part. In any case, it becomes possible to define frequency response functions between any variables at both ends of the electromechanical structure.

3.4 Application to longitudinal propagation

The case of a rod subjected to longitudinal propagation is considered. As show in Fig. 2, the rod is covered with an array of periodic patches which are interconnected through a line of inductors. This build an electrical network that is the discrete analogue of a rod [2, 13]. For a

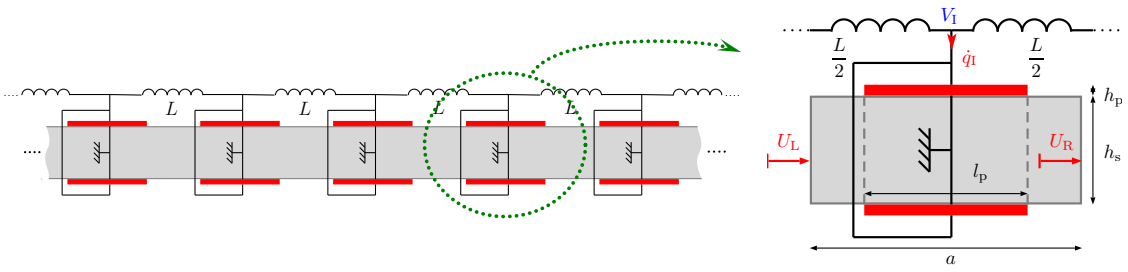

Figure 2: Rod covered with an array of interconnected piezoelectric patches.

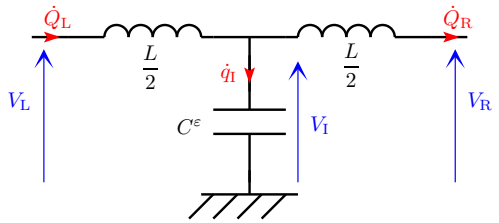

Figure 3: Electrical unit cell without piezoelectric coupling.

rod, the element stiffness matrix, mass matrix and coupling matrix can be defined as

$$\boldsymbol{K}_{\boldsymbol{m}}^{\mathrm{e}} = \frac{YS}{a_e}\begin{bmatrix} 1 & -1 \\ -1 & 1 \end{bmatrix} \quad , \quad \boldsymbol{M}_{\boldsymbol{m}}^{\mathrm{e}} = \frac{\rho S a_e}{6}\begin{bmatrix} 2 & 1 \\ 1 & 2 \end{bmatrix} \quad \text{and} \quad \boldsymbol{K}_{\boldsymbol{c}}^{\mathrm{e}} = e\begin{bmatrix} -1 \\ 1 \end{bmatrix}, \tag{22}$$

where Y is the equivalent Young's modulus of the considered element, ρ is its density, a_e is its length, S is its cross-sectional area and e is the piezoelectric coupling coefficient [1, 2]. The global matrices $\boldsymbol{K_m}$, $\boldsymbol{M_m}$ and $\boldsymbol{K_c}$ for the unit cell are then obtained from an assembly of the element matrices. The corresponding displacement and force vectors are

$$\boldsymbol{q_m} = \begin{bmatrix} U_\mathrm{L} \\ \boldsymbol{U}_\mathrm{I} \\ U_\mathrm{R} \end{bmatrix} \quad \text{and} \quad \boldsymbol{F_m} = \begin{bmatrix} -N_\mathrm{L} \\ \boldsymbol{0} \\ N_\mathrm{R} \end{bmatrix}, \tag{23}$$

where the state variable U is related to longitudinal displacement, N corresponds to the normal force and $\boldsymbol{U}_\mathrm{I} = \boldsymbol{q}_{\boldsymbol{m}\mathrm{I}}$ is the mechanical displacement vector of the internal nodes of the unit cell. Considering the electrical part of the unit cell represented in Fig. 3, the line of inductors gives a single degree of freedom on each side of the unit cell which leads to

$$\boldsymbol{q_e} = \begin{bmatrix} Q_\mathrm{L} \\ Q_\mathrm{R} \end{bmatrix} \quad \text{and} \quad \boldsymbol{F_e} = \begin{bmatrix} V_\mathrm{L} \\ -V_\mathrm{R} \end{bmatrix}, \tag{24}$$

where Q corresponds to electrical charge displacements and V is used for voltage variables. From the topology of the unit cell in Fig. 3 and the inductive and capacitive contributions to the total electrical energy, we get

$$q_\mathrm{I} = Q_\mathrm{L} - Q_\mathrm{R} \quad \text{and} \quad E_e = \frac{(Q_\mathrm{L} - Q_\mathrm{R})^2}{2C^\varepsilon} + \frac{L}{4}\dot{Q}_\mathrm{L} + \frac{L}{4}\dot{Q}_\mathrm{R}. \tag{25}$$

Then, Eqs. (3) and (4) give

$$\boldsymbol{S} = \begin{bmatrix} 1 \\ -1 \end{bmatrix} \quad , \quad \boldsymbol{K_e} = \frac{1}{C^\varepsilon}\begin{bmatrix} 1 & -1 \\ -1 & 1 \end{bmatrix} \quad \text{and} \quad \boldsymbol{M_e} = \frac{L}{2}\begin{bmatrix} 1 & 0 \\ 0 & 1 \end{bmatrix}. \tag{26}$$

In the end, the global dynamic stiffness matrix in Eq. (14) is computed and reorganized into a transfer matrix $\boldsymbol{T}$ by considering left and right state vectors

$$\boldsymbol{q}_\mathrm{L} = \begin{bmatrix} U_\mathrm{L} \\ Q_\mathrm{L} \end{bmatrix} \quad , \quad \boldsymbol{q}_\mathrm{R} = \begin{bmatrix} U_\mathrm{R} \\ Q_\mathrm{R} \end{bmatrix} \quad , \quad \boldsymbol{F}_\mathrm{L} = \begin{bmatrix} -N_\mathrm{L} \\ V_\mathrm{L} \end{bmatrix} \quad \text{and} \quad \boldsymbol{F}_\mathrm{R} = \begin{bmatrix} N_\mathrm{R} \\ -V_\mathrm{R} \end{bmatrix}. \tag{27}$$

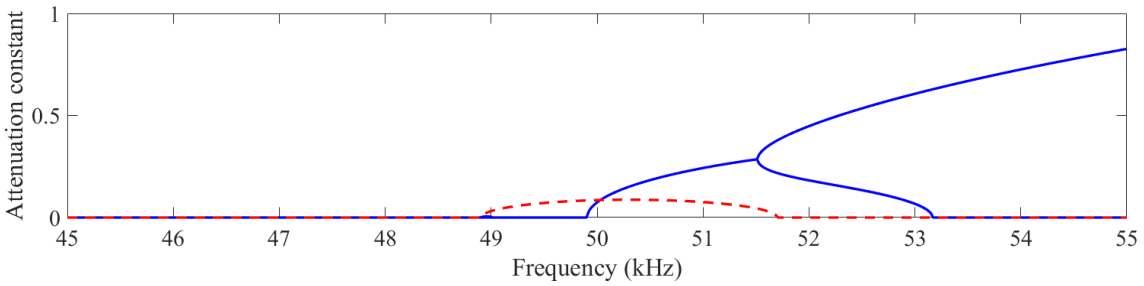

Figure 4: Attenuation constants - (−−) without network, (—) with $L = 1.2$ mH.

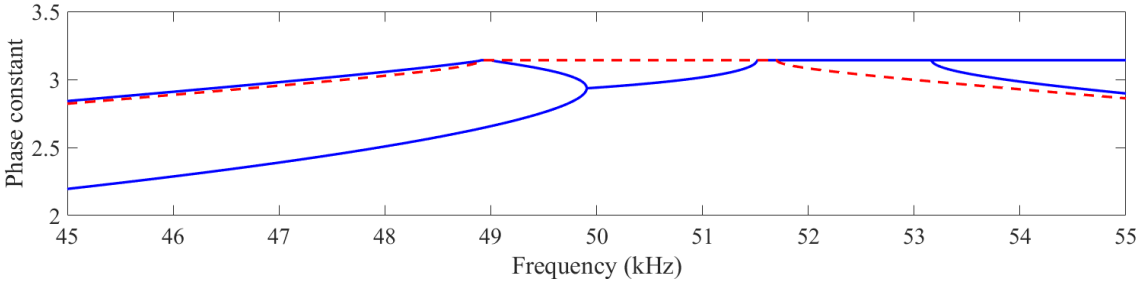

Figure 5: Phase constants - (−−) without network, (—) with $L = 1.2$ mH.

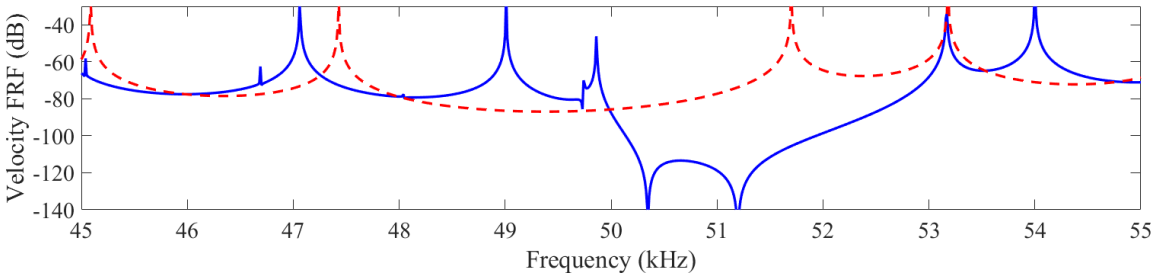

Figure 6: Frequency response function - (−−) without network, (—) with $L = 1.2$ mH.

This gives a relation between two state vectors including both mechanical and electrical variables:

$$\begin{bmatrix} U_{\mathrm{R}} \\ Q_{\mathrm{R}} \\ N_{\mathrm{R}} \\ -V_{\mathrm{R}} \end{bmatrix} = \boldsymbol{T} \begin{bmatrix} U_{\mathrm{L}} \\ Q_{\mathrm{L}} \\ N_{\mathrm{L}} \\ -V_{\mathrm{L}} \end{bmatrix}. \tag{28}$$

Once the Transfer Matrix is obtained, its eigenvalues lead to the attenuation and phase constants. The following numerical calculations are based on the same geometry and material constants as in Ref. [2]. The objective is to show that propagation constants and frequency response functions can be computed for an electromechanical waveguide. The results are given in Figs. 4, 5 and 6. It is observed that the coupling to an electrical line strongly modify

the propagation constants. For this specific example, the original purely mechanical band-gap [8, 10] is replaced by an electromechanical band-gap corresponding to a larger attenuation constant. The effect on the frequency response function of a free-free rod made of 20 unit cells is illustrated in Fig. 6 where we see a strong reduction of vibration amplitude between 50 and 53 kHz. All of this shows that the proposed numerical model can be used for analyzing the coupling between mechanical and electrical band-gaps when considering propagation in electromechanical waveguides [14]. The proposed example is based on a simple geometry but there is no restriction regarding the complexity of the mechanical structure and the number of degrees of freedom as long as the stiffness, mass and coupling matrices have been defined.

4 CONCLUSIONS

- Considering electromechanical waveguides, energy considerations lead to the definition of a charge displacement vector and voltage vector that can be related to each other from the topology of the electrical network.
- The introduction of electrical degrees of freedom allows the use of a formulation based on the equivalent of a dynamic stiffness matrix that represents the whole electromechanical problem for a macro element which is the unit cell in the present paper.
- The Wave Finite Element method can be directly applied by considering electromechanical state vectors instead of purely mechanical ones.
- This gives us a way to analyze the coupling between mechanical and electrical waveguides from the computation of propagation constants and frequency response functions.
- It is shown that couplings between mechanical and electrical band-gaps occur, which can be of interest for the control of wave propagation in periodic structures.

REFERENCES

[1] O. Thomas, J.-F. Deü, J. Ducarne, Vibrations of an elastic structure with shunted piezoelectric patches: efficient finite element formulation and electromechanical coupling coefficients. *International Journal for Numerical Methods in Engineering*, **80**, 235–268, 2009.

[2] B. Lossouarn, M. Aucejo, J.-F. Deü, Multimodal coupling of periodic lattices and application to rod vibration damping with a piezoelectric network. *Smart Materials and Structures*, **24**, 045018, 2015.

[3] B. Lossouarn, J.-F. Deü, M. Aucejo, Multimodal vibration damping of a beam with a periodic array of piezoelectric patches connected to a passive electrical network. *Smart Materials and Structures*, **24**, 115037, 2015.

[4] B.R. Mace, D. Duhamel, M.J. Brennan, L. Hinke, Finite element prediction of wave motion in structural waveguides. *The Journal of the Acoustical Society of America*, **117**, 2835–2843, 2005.

[5] J. M. Mencik, D. Duhamel, A wave-based model reduction technique for the description of the dynamic behavior of periodic structures involving arbitrary-shaped substructures and large-sized finite element models. *Finite Elements in Analysis and Design*, **101**, 1–14, 2015

[6] P. B. Silva, J. M. Mencik, J. R. Franca Arruda, Wave finite elementbased superelements for forced response analysis of coupled systems via dynamic substructuring. *International Journal for Numerical Methods in Engineering*, 2015.

[7] P. G. Domadiya, E. Manconi, M. Vanali, L. V. Andersen, A. Ricci, Numerical and experimental investigation of stop-bands in finite and infinite periodic one-dimensional structures. *Journal of Vibration and Control*, **22**, 920–931, 2016.

[8] L. Airoldi, M. Ruzzene, Wave Propagation Control in Beams Through Periodic Multi-Branch Shunts. *Journal of Intelligent Material Systems and Structures*, **22**, 1567–1579, 2011.

[9] Y. Fan, M. Collet, M. Ichchou, L. Li, O. Bareille and Z. Dimitrijevic, A wave-based design of semi-active piezoelectric composites for broadband vibration control. *Smart Materials and Structures*. **25**, 055032, 2016.

[10] Y. Lu, J. Tang, Electromechanical tailoring of structure with periodic piezoelectric circuitry. *Journal of Sound and Vibration*, **331**, 3371–3385, 2012.

[11] T. L. Huang and M. N. Ichchou and O. A. Bareille and M. Collet and M. Ouisse, Traveling wave control in thin-walled structures through shunted piezoelectric patches. *Mechanical Systems and Signal Processing*, **39**, 59–79, 2013.

[12] D.M. Mead, Wave propagation in continuous periodic structures: research contribution from Southampton. *Journal of Sound and Vibration*, **190**, 495–524, 1996.

[13] L. Brillouin, *Wave propagation in periodic structures*. McGraw-Hill, 1946.

[14] A. E. Bergamini, M. Zündel, E. A. Flores Parra, T. Delpero, M. Ruzzene, P. Ermanni, Hybrid dispersive media with controllable wave propagation: A new take on smart materials. *Journal of Applied Physics*, **118**, 154310, 2015.

VIII ECCOMAS Thematic Conference on Smart Structures and Materials
SMART 2017
A. Güemes, A. Benjeddou, J. Rodellar and J. Leng (Eds)

WAVE PROPAGATION CONTROL IN 1D HYBRID PHONONIC CRYSTAL USING MINIATURIZED PROGRAMMABLE FLOATING VIRTUAL INDUCTANCES

Edgar A. Flores Parra*, Andrea Bergamini† , Lars Kamm††, Paul Zbinden†† AND Paolo Ermanni*

*ETH Zürich, Composite Materials and Adaptive Structures Laboratory
Leonhardstrasse 21,CH-8092 Zürich Switzerland
e-mail: edgarf@ethz.ch, www.structures.ethz.ch

† Empa, Materials Science and Technology, Laboratory for Mechanical Integrity of Energy Systems
Überlandstrasse 129, CH-8600, Dübendorf, Switzerland
www.empa.ch

†† Hochschule für Technik, Institut für Mikroelectronik und Embedded Systems
Oberseestrasse 10, CH-8640, Rapperswil, Switzerland
www.hsr.ch

Key words: Phononic, hybrid, inductance, programmable, dispersion, mode veering

Abstract. This work reports on the integration and implementation of a programmable hybrid phononic crystal (hPC) for transverse wave propagation control. The innovative hPC is built on a newly developed and tested array of miniaturized programmable floating virtual inductances. The hybrid characteristic results from the coupling between the mechanical waveguide in the form of an elastic beam, and the discrete electrical transmission line formed by the array of miniturized inductances. The medium features attenuation of transverse mechanical wave motion engendered by energy transfer to the electrical domain over a frequency range where the dispersion curves of the hPC are characterized by eigenvalue mode veering. An analytical model based on the transfer matrix method is presented to expeditiously calculate the dispersion curves of the hPC. Moreover, this work provides numerical, and experimental results which validate both the efficiency and tunability of the programmable electrical transmission line. The novelty of this contribution is an analytical model for calculating the dispersion curves of the 1D hPC, and a miniaturized programmable virtual inductance which gives way to a smart material.

1 INTRODUCTION

Increased interest has emerged in attenuation of mechanical vibrations by controlling elastic waves with periodic arrangements of piezoelectric shunts. Most of the past studies with passive

shunts have focused on reduction of structural vibrations with arrays of locally shunted piezoelectric elements [1, 2, 3]. To a lesser extent, schemes with interconnected piezoelectric shunts have been also investigated [4, 5, 6]. The effect of interconnected piezoelectric elements on the dynamic behavior of a structure has been namely explored by dell'Isola et al. [7, 8, 6, 5] to control multi-modal vibration damping. While the different reported configurations of passive shunts achieve their objective of producing frequency regions of high attenuation or reducing the amplitude of specific modes, the electrical components which enabled such shunts have remained relatively rudimentary, i.e: difficult to tune, too large to integrate as part of the structure[9]. This paper reports on the design, fabrication and testing of an integrated 1D hybrid phononic crystal with a unit cell comprised of a miniaturized programmable floating virtual inductance (PFVI) for wave propagation control. The hybrid term results from coupling between a mechanical waveguide in the form of an elastic beam, and the electrical transmission line formed by interconnecting multiple PFVI.

Bandgaps in phononic crystals (PC) emerge from periodic modulations of mass density and/or elastic constants [10, 11] of the material resulting from the basis of the crystal (e.g. diatomic materials [12]). Such band gaps exist for wavelengths on the order of the unit cell size. Conversely, in metamaterials (MM), the inclusion of suitably designed locally resonating units allow for the sub-wavelength modification of the dispersive properties of a medium, as reported by Liu, amongst others, in the mechanical domain [13]. In both PCs and MMs, waves propagate through a mechanical medium and interact with "inclusions" that either scatter them to generate destructive interference at certain wavenumbers, or that absorb and dissipate energy through local resonances. In many of the reported materials, the nature of the inclusions is purely mechanical [13, 14, 15]. In other cases, adaptive materials are exploited to modify the unit cell geometry [16], and tune the properties of the locally resonating units [17, 18, 19] or modify the connectivity of a PC [20]. In the latter cases, the electrical domain of the unit cell is self-contained, exchanging energy only with the mechanical domain of the unit cell, thus acting as an inclusion in the mechanical medium. As a result, the mechanical domain of the unit cell is the only pathway for the exchange of energy between cells. The work of Bergamini et al.[4] showed that weak coupling interaction between modes of mechanical and electrical waveguides can lead to wave attenuation, as a result of an energy exchange between them. These mode interactions can be classified into veering, crossing and lock-in as discussed by Mace et al. [21].

Albeit, the results of this work build on an already documented physical phenomenon for the control of elastic waves, this work presents a technological bridge between theory and practical implementation. The interconnected virtual inductances used in the work by Bergamini et al.[4] proved the physical phenomenon for controlling waves with a 1D hPC. However, in this contribution the developed PFVI, is capable of achieving inductance values an order of magnitude greater than in the previously mentioned work while ensuring a stable transmission line formed by a daisy chain of PFVI circuits. Moreover, each PFVI on the transmission line is programmable by interfacing with a computer. To the authors' knowledge, this is the first time a programmable transmission line has been implemented to control the propagation of mechanical waves. Lastly, an analytical model to calculate the dispersion curves the 1D hPC is presented. The model is based on the transfer matrix method, and is similar to the one presented by Ruzzene [22].

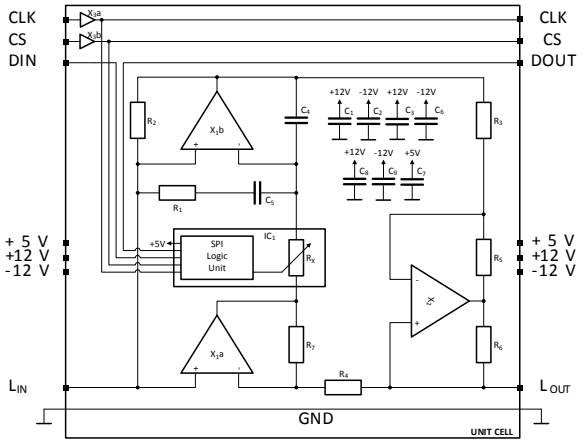

Figure 1: Analog circuit of PFVI.

Quantity	Name	Value	Packaging
5	C_1, C_2, C_3, C_6, C_7	100 nF	0402 SMD
1	C_4	10 nF	0402 SMD
1	C_5	1 nF	0402 SMD
2	C_8, C_9	10 μF/25 V	0603 SMD
1	IC1	AD5290	MSOP-10
3	R_1, R_5, R_6	100 Ω	0402 SMD
3	R_2, R_3, R_4	3.9 kΩ	0402 SMD
1	R_7	360 Ω	0402 SMD
1	X_1	AD8034	SOT-23/8
1	X_2	AD8033	SC70-5
1	X_3	NC7WZ16P6	SC70-6

Table 1: List of components of PFVI.

2 DESIGN OF PROGRAMMABLE FLOATING VIRTUAL INDUCTANCE (PFVI)

For the development of the miniaturized PFVI we chose the circuit designed by von Grunigen[23] based on its high quality factor and good stability. The circuit design was implemented in Surface Mount Technology (SMT), to fit a unit cell size 10 mm by 15 mm that was deemed appropriate based on previous work. The electrical characteristics of the PFVI are given in Table 2.

Since the a virtual inductance is also comprised of active components, it requires a power source to provide the voltages and current given in Table 2 for operation. The circuit was powered using an Agilent E3631A 80W triple output power supply.

With the hardware in place, the next step was to implement the programmable capabilities. To this end the line was design to interface with a computer using a National Instruments NI USB-8451 as seen in Fig. 5. The use of a serial peripheral interface (SPI) allowed for programming of all the circuits connected in a daisy chain. The SPI bus is a synchronous serial

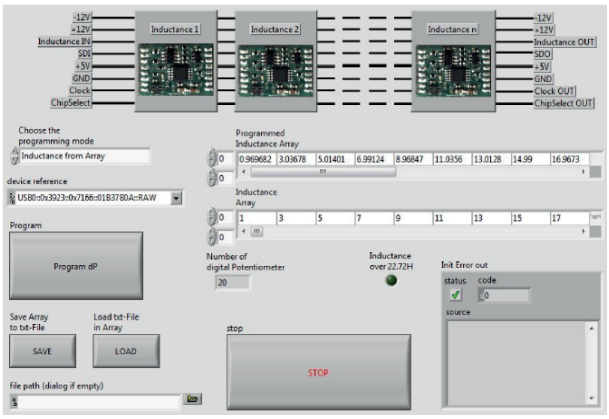

Figure 2: Illustration of interconnected circuits with corresponding input and output connections, as well as LabVIEW graphical user interface (GUI) for programming of the inductances.

Parameter	Condition	Value
Analog supply voltage		$\pm$ 12 V
Digital supply voltage		5 V
Analog supply current	MAX	$\pm$ 15 mA
Digital supply current	MAX	1 mA
Power	MAX	365 mW
Input voltage	MAX	$\pm$ 10 V
Input current	MAX	$\pm$ 2 mA
Output voltage		$\pm$ 10 V
Output current		$\pm$ 2 mA
Bandwidth	$R_L > 10\,\Omega$	10 kHz
Quality	Forward	> 50
	Backward	< 50
Tolerance	L$\leq$ 2 H	$\pm$ 150 mH
	L$>$ 2 H	$\pm$ 70 mH

Table 2: Electrical characteristics of PFVI.

communication interface used for communicating over short distances. Using the SPI interface called for four connections linking the computer to the programmable circuits. The interface starts communication by setting the chip select (CS) line logic to zero. The data is clocked through the serial shift registers in the daisy chain configuration. The transfer is complete when all data values are shifted and the CS line logic is set to one. The inductance of all, or each individual PFVI can be set to any value between 1- 22 H with the resolution given in Table 2.

The quality in the production of the transmission line comprised of 21 interconnected PFVI circuits, in particular due to the difficulty of soldering of the SMT components, the fabrication process was ensured by outsourcing to a commercial supplier. The 4 layer PFVI circuits were printed on a 0.9 mm PCB FR4 board.

3 NUMERICAL TRANSMITTANCE

For the numerical transmittance and dispersion studies, presented in the following sections, the host structure was made of aluminium with Youngs Modulus E_s=69 GPa, density ρ_s= 2700 kg/m^3, Poisson's ratio ν = 0.33 and thickness t_s=1 mm. The material of the piezoelectric element was PIC151 with the open circuit Youngs Modulus E_p^D =77.4 GPa, density ρ_p =7760 kg/m^3, compliance constant $S_{E_{11}}$=1.5x10^{-11} m^2/N, permittivity in the polarization direction $\epsilon_{33}^T/\epsilon_0$=2400, coupling coefficient k_{31} = 0.37.

The numerical transmittance calculation was carried out with COMSOL Multiphysics. As seen in Fig. 3 we considered an aluminum beam with a thickness t_s= 1 mm, width b= 10 mm and a total length of L_T= 480 mm. In the center portion of the structure, an hPC with unit cell size, a=15 mm, was added, consisting of 20 unit cells positioned between 90 mm and 395 mm from the origin, each had piezoelectric elements with radius r=5 mm and thicknesses t_p= 0.5 mm. The superscript, s, refers to the substrate which serves as the host structure, while the subscript, p, refers to the piezoelectric element. Lastly, the inductive elements were modeled using the electric circuits physics of COMSOL. The inductances values were the same as those used in the calculation of the dispersion curves, in order to establish a direct correlation between the dispersion curves and the transmittance of the hPC. The system was excited mechanically by a discrete force F applied 7.5 mm from the origin, Fig. 3. The steady state response of the system was calculated over the frequency range of interest.

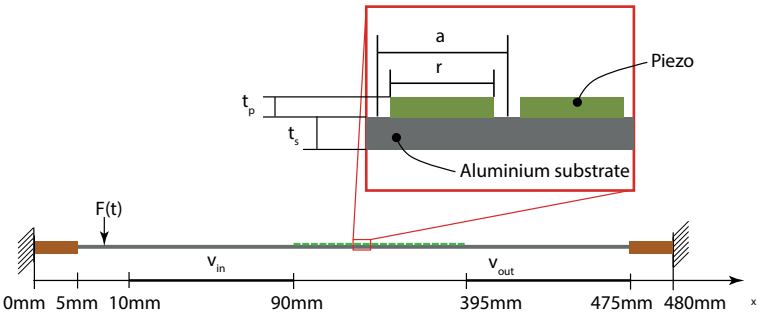

Figure 3: Overview and dimensions of the investigated finite hPC. The dimensions a, t_p , t_s are detailed in the text.

4 TRANSFER MATRIX INVERSE DISPERSION

The dispersion curves of the hPC were calculated using the transfer matrix method[22]. The unit cell is divided into the two continuous subregions illustrated in Fig 4. The first subregion, with length βa, consists of the aluminum substrate and the piezoelectric element. The second subregion, with length (1-β)a, is characterized by part of the substrate and the electrical impedance.The transfer matrices were computed separately for each subregion. This dispersion model is two dimensional, thus, for a piezoelectric element with radius r=5 mm, a unit cell of length a=15 mm, and an out-of-plane width b=10 mm the coefficient β=0.5236 is obtained.

4.1 Modeling subregion 1

The system of equations for the first subregion, assuming harmonic oscillation, is given below:

$$EI = E_s I_s + E_p I_p \tag{1}$$
$$= b\left(E_s\left(\frac{bt_s^3}{12} + t_s(t_s - z_c)^2\right) + E_p\left(\frac{bt_p^3}{12} + t_p(t_p + z_c)^2\right)\right)$$

$$m = b(t_s\rho_s + t_p\rho_p) \tag{2}$$
$$z_c = \frac{E_s\frac{t_s^2}{2} - E_p\frac{t_p^2}{2}}{t_p + t_s} \tag{3}$$
$$\alpha = bd_{31}/S_{E_{11}} \tag{4}$$
$$C_p' = (b/t_p)\epsilon_{33}^T - d_{31}^2/S_{E_{11}} \tag{5}$$

The coupled system of equations can be written in matrix form, Eq. 6, where $\mathbf{A_i}$ and $\mathbf{B_i}$ are

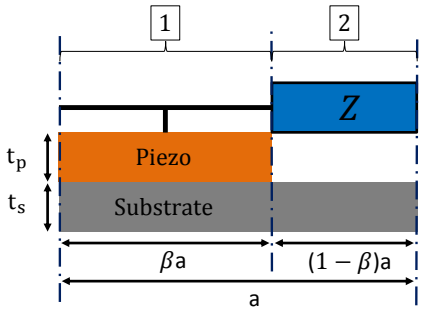

Figure 4: Unit cell illustration showing the aluminum substrate, the piezoelectric element and electrical impedance separated into two continuous subregions (1 and 2).

the coefficient matrices for the two subregions of the unit cell.

$$\mathbf{A_i}\frac{d\mathbf{z}(x)}{dx} = \mathbf{B_i}\mathbf{z}(x) \tag{6}$$

$$\mathbf{z(x)} = \begin{bmatrix} \omega \\ \omega^{'} \\ Q \\ M_b \\ V \\ I \end{bmatrix} \quad \mathbf{A_1} = \begin{bmatrix} 1 & 0 & 0 & 0 & 0 & 0 \\ 0 & EI & 0 & 0 & 0 & 0 \\ 0 & 0 & 1 & 0 & 0 & 0 \\ 0 & 0 & 0 & 1 & 0 & 0 \\ 0 & 0 & 0 & 0 & 1 & 0 \\ 0 & 0 & 0 & 0 & 0 & 1 \end{bmatrix}$$

$$\mathbf{B_1} = \begin{bmatrix} 0 & 1 & 0 & 0 & 0 & 0 \\ 0 & 0 & 0 & 1 & \alpha\left(\frac{t_p}{2}+z_c\right) & 0 \\ -m\omega^2 & 0 & 0 & 0 & 0 & 0 \\ 0 & 0 & -1 & 0 & 0 & 0 \\ 0 & 0 & 0 & 0 & 0 & 0 \\ 0 & \frac{-\mathrm{i}\omega\alpha}{D}\left(\frac{t_p}{2}+z_c\right) & 0 & 0 & -\mathrm{i}\omega\left(C_p^{'}+\frac{\alpha^2}{D}\left(\frac{t_p}{2}+z_c\right)^2\right) & 0 \end{bmatrix}$$

4.2 Modeling subregion 2

Even though the second subregion has no electromechanical coupling, energy can travel along the electrical and mechanical waveguides. The electrical waveguide is characterized by the distributed impedance $Z^{'}$

$$Z^{'} = \frac{Z}{(1-\beta)\mathrm{a}} = \frac{\mathrm{i}\omega L + R}{(1-\beta)\mathrm{a}} \tag{7}$$

The current flowing into the infinitesimal element is the same as the current flowing out leading to a null spatial derivative of the current.

$$\frac{dI}{dx} = 0 \tag{8}$$

Conversely, the distributed impedance will influence the spatial derivative of the voltage.

$$\frac{dV}{dx} = -Z^{'}I = \frac{\mathrm{i}\omega L + R}{(1-\beta)\mathrm{a}}I \tag{9}$$

The equations describing the mechanical behavior of the second subregion can be deduced from the ones of the first subregion, by setting the piezoelectric element thickness to zero ($\mathrm{t_p} = 0$), Eq. 10.

$$\begin{aligned} \frac{d\omega}{dx} &= \omega_x \\ EI\frac{d\omega_x}{dx} &= M_b \\ \frac{dQ}{dx} &= m\ddot{\omega} \\ \frac{dM_b}{dx} &= -Q \end{aligned} \tag{10}$$

Without the piezoelectric element the bending stiffness and mass simplify to Eq. 11 and 12.

$$EI = E_s I_s = E_s b \frac{t_s^3}{12} \tag{11}$$

$$m = b t_s \rho_s \tag{12}$$

$$\mathbf{z}(\mathbf{x}) = \begin{bmatrix} \omega \\ \omega^{'} \\ Q \\ M_b \\ V \\ I \end{bmatrix} \quad \mathbf{A_2} = \begin{bmatrix} 1 & 0 & 0 & 0 & 0 & 0 \\ 0 & EI & 0 & 0 & 0 & 0 \\ 0 & 0 & 1 & 0 & 0 & 0 \\ 0 & 0 & 0 & 1 & 0 & 0 \\ 0 & 0 & 0 & 0 & 1 & 0 \\ 0 & 0 & 0 & 0 & 0 & 1 \end{bmatrix}$$

$$\mathbf{B_2} = \begin{bmatrix} 0 & 1 & 0 & 0 & 0 & 0 \\ 0 & 0 & 0 & 1 & 0 & 0 \\ -m\omega^2 & 0 & 0 & 0 & 0 & 0 \\ 0 & 0 & -1 & 0 & 0 & 0 \\ 0 & 0 & 0 & 0 & 0 & \frac{\mathrm{i}\omega L + R}{(1-\beta)\mathrm{a}} \\ 0 & 0 & 0 & 0 & 0 & 1 \end{bmatrix}$$

By inverting $\mathbf{A_1}$ and $\mathbf{A_2}$ the final form of the system of equations is given, Eq. 13.

$$\mathbf{C_1} = \mathbf{A_1^{-1}} \mathbf{B_1} \qquad \mathbf{C_2} = \mathbf{A_2^{-1}} \mathbf{B_2} \tag{13}$$

Using the matrix exponential, Eq. 14 is obtained

$$\mathbf{T_1} = e^{\mathrm{a}(\beta)\mathbf{C_1}} \qquad \mathbf{T_2} = e^{\mathrm{a}(1-\beta)\mathbf{C_2}} \tag{14}$$

The unit cell transfer matrix is then defined by Eq. 15.

$$\mathbf{T} = \mathbf{T_2} \mathbf{T_1} \tag{15}$$

The transfer matrix describes the relation between the status vector $\mathbf{z}(x)$ at the beginning and at the end of the cell $\mathbf{z}(x + \mathrm{a})$.

$$\mathbf{z}(x + \mathrm{a}) = \mathbf{T}\mathbf{z}(x) \tag{16}$$

The Floquet-Bloch theorem is used to compute the frequency dependent wavenumber k . This theorem relates $\mathbf{z}(x + a)$ and $\mathbf{z}(x)$ through a periodic boundary condition which depends on the wavenumber.

$$\mathbf{z}(x + \mathrm{a}) = \mathbf{z}(x) e^{-\mathrm{i}\mathrm{a}k} \tag{17}$$

$$\mathbf{T}(\omega)\mathbf{z}(x) = \mathbf{z}(x) e^{-\mathrm{i}\mathrm{a}k} \tag{18}$$

Analogously, we can relate both ends to the unit cell using the transfer matrix method, Eq. (16).

$$\left(\mathbf{T}(\omega) - e^{-\mathrm{i}\mathrm{a}k}\mathbf{I}\right)\mathbf{z}(x) = 0 \tag{19}$$

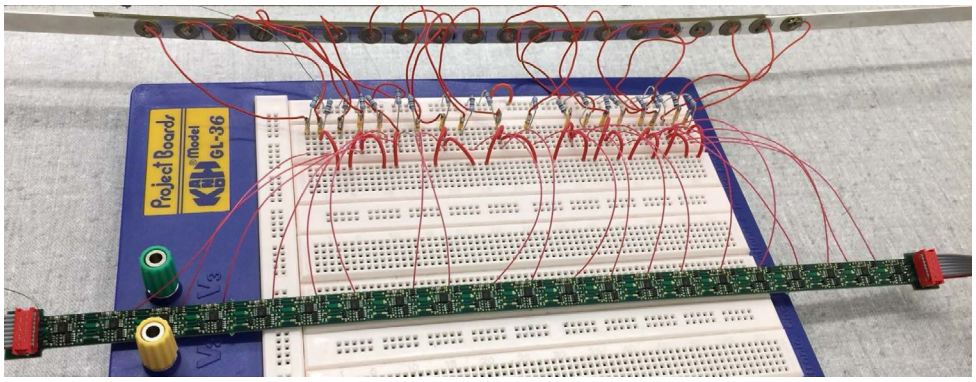

Figure 5: Experimental array of PFVI connected to finite sample of 1D hPC

Combining Eq. 16 and Eq. 19 leads to Eq. 20 which is a standard eigenvalue problem. Eq. 21 is obtained from the solution to the eigenvalue problem yielding the frequency dependent wavenumber. The real part of k portrays information on the propagation of the wave while the imaginary part describes the attenuation. From Eq. 21 the dispersion curves for the hPC are plotted over the chosen frequency range.

$$\mathbf{T}(\omega) - \lambda \mathbf{I} = 0 \quad \text{with} \quad \lambda(k) = e^{-\mathrm{i}ak} \tag{20}$$

$$k(\omega) = \frac{\ln(\lambda)}{-\mathrm{i}a} \tag{21}$$

5 EXPERIMENTAL SETUP

The PFVI was designed with a conductive metal pad to interface with the electrode of the piezoelectric element to form an electromechanical entity. Since, this first array of interconnected PFVI was intended as a test bench it was printed on a standard rigid FR4 PCB substrate. Although, the printed array of PFVI only had a thickness of 0.9 mm, it was still sufficiently rigid to act as an additional mechanical waveguide if directly interfaced with the piezoelectric elements. Hence, the array of interconnected PFVI was connected to each piezoelectric element with electrical wires as seen in Fig. 5.

We excited the structure using an additional piezoelectric element attached approximately in the same position where the discrete force was applied in the numerical model. The piezoelectric element was excited with a sine sweep spanning from from 100 Hz to 20 kHz, and an applied voltage amplitude of 10 VPP using a high voltage power amplifier. The out-of-plane velocity on the surface of sample was measured using a Polytec PSV 400 scanning laser vibrometer. The transmission properties of the hPC were calculated based on velocity amplitude averaged over regions extending 100 mm on either side of the hPC. We carried out a Fast Fourier transform of the time-domain data for the out of plane velocity along the length of the sample to obtain the frequency response. The numerical investigation was carried out conceptually in the same way, except for the fact that the behavior of the system was investigated in a frequency response analysis, thus the frequency data was directly available from the solution.

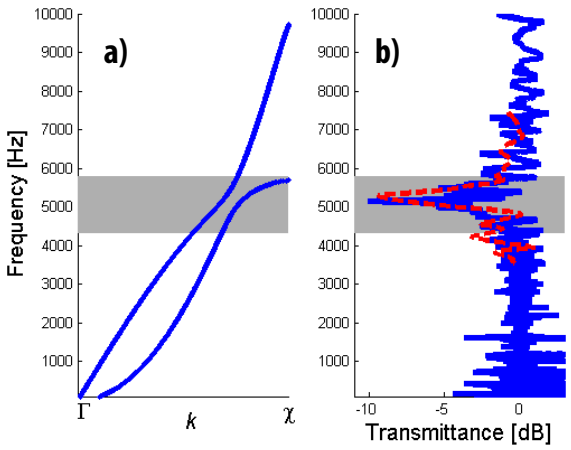

Figure 6: a) Dispersion monoatomic unit cell L=1 H b) Experimental transmittance (solid line), and numerical transmittance (dotted line) for finite hPC with monoatomic configuration L=1 H.

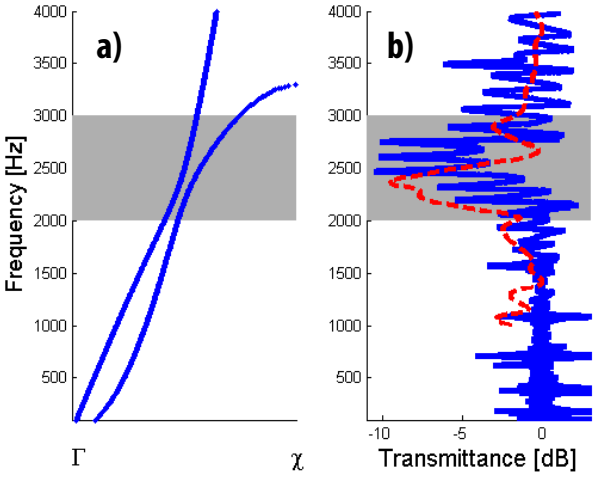

Figure 7: a) Dispersion monoatomic unit cell L=3 H b) Experimental transmittance (solid line), and numerical transmittance (dotted line) for finite hPC with monoatomic configuration L=3 H.

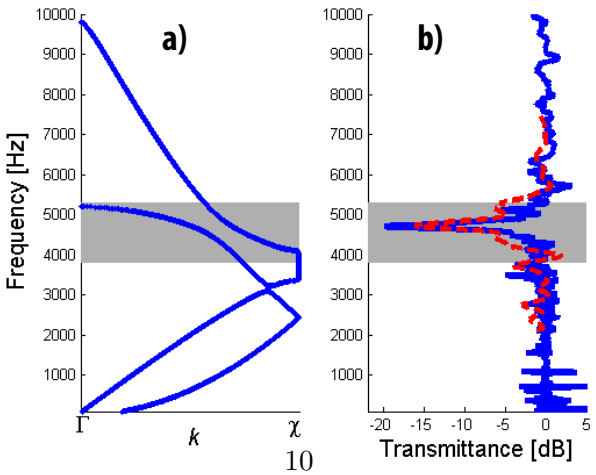

Figure 8: a) Dispersion diatomic unit cell L_1=1 H and L_2=1.5 H b) Experimental transmittance (solid line), and numerical transmittance (dotted line) for finite hPC with diatomic configuration L_1=1 H and L_2=1.5 H.

6 RESULTS AND DISCUSSION

Fig. 6 and 7 show the dispersion and transmittance curves of the monoatomic (single inducance value accross all cells) unit cell configuration, for two different inductance values. In Fig. 6a) and 7a) we can see that eigenvalue coupling occurs in the form of mode veering. As expected, the veering is centered at a lower frequency for a higher inductance value. Moreover, in agreement with the work of Bergamini et al. [4], Fig. 6b) and 7b) show that the regions of low transmittance take place around the mode veering frequency. Moreover, the experimental transmittance curves (solid blue) are in good agreement with the numerical transmittance results obtained from COMSOL (solid red line) in both the frequency range of attenuation as well as the amplitude.

To further exploit the control of elastic waves, utilizing the capability to program the individual inductances of the hPC, a diatomic (alternating inductance values) unit cell configuration L_1=1 H and L_2=1.5 H was investigated as seen in Fig. 8. Just as for the monoatomic configuration, the analytical dispersion curves show the presence of mode veering over the same frequency range as the low transmittance in the numerical and experimental curves.

Based on these results, we can conclude that varying the parameters of the electrical domain has a paramount effect on the mechanical properties of the hPC. Furthermore, the potential to instantaneously and accurately tune the electrical parameters, thus reconfigure the hPC, gives way to a versatile lightweight "smart" material for wave attenuation.

7 CONCLUSION

In this work, we have demonstrated a high level of integration between the electrical and mechanical domains of a hPC to create an artificial "smart" material. Useful and unusual material properties are achieved by focusing "material development" efforts on the design and implementation of a suitable analog circuit. This approach may represent a new paradigm in the development of materials with novel programmable properties similar to the introduction of electronic components into a number of devices and machines that in the last century were traditionally "purely mechanical", such as car engines, and typewriters. The inclusion of a digital interface (digital potentiometer) in an otherwise analog circuit, opens the doors to distributed computing power. Building blocks for the implementation of such distributed intelligence are presented, for example in the work by Shen et al.[24].

Moreover, work is currently being carried out to redesign and fabricate the electrical domain of the hPC on a flexible substrate to achieve a greater and seemless level of integration. Beyond the demonstration of facile tunability of the dispersion properties of a hybrid phononic crystal, we believe that the contribution of the present paper is a first paramount step towards a true integration of electrical and mechanical design of advanced materials.

REFERENCES

[1] J. J. Hollkamp, "Multimodal passive vibration suppression with piezoelectric materials and resonant shunts," *Journal of Intelligent Material Systems and Structures* **5**, pp. 49–57, 1994.

[2] B. S. Beck, K. A. Cunefare, M. Ruzzene, and M. Collet, "Experimental analysis of a cantilever beam with a shunted piezoelectric periodic array," *Journal of Intelligent Material*

Systems and Structures .

[3] A. Spadoni, M. Ruzzene, and K. Cunefare, "Vibration and wave propagation control of plates with periodic arrays of shunted piezoelectric patches," *Journal of Intelligent Material Systems and Structures* **20**, pp. 979–990, 2009.

[4] A. E. Bergamini, M. Zündel, E. A. F. Parra, T. Delpero, M. Ruzzene, and P. Ermanni, "Hybrid dispersive media with controllable wave propagation: A new take on smart materials," *Journal of Applied Physics* **118**(15), p. 154310, 2015.

[5] B. Lossouarn, J. Deü, and M. Aucejo, "Multimodal vibration damping of a beam with a periodic array of piezoelectric patches connected to a passive electrical network," *Smart Materials and Structures* **24**(11), p. 115037, 2015.

[6] F. Dell'Isola, C. Maurini, and M. Porfiri, "Passive damping of beam vibrations through distributed electric networks and piezoelectric transducers: prototype design and experimental validation," *Smart Materials and Structures* **13**(2), p. 299, 2004.

[7] R. C. Batra, F. DellIsola, S. Vidoli, and D. Vigilante, "Multimode vibration suppression with passive two-terminal distributed network incorporating piezoceramic transducers," *International Journal of Solids and Structures* **42**(11), pp. 3115–3132, 2005.

[8] C. Maurini, F. Dell'Isola, and D. Del Vescovo, "Comparison of piezoelectronic networks acting as distributed vibration absorbers," *Mechanical Systems and Signal Processing* **18**(5), pp. 1243–1271, 2004.

[9] A. J. Fleming and S. R. Moheimani, "Adaptive piezoelectric shunt damping," *Smart Materials and Structures* **12**(1), p. 36, 2003.

[10] L. Brillouin, *Wave propagation in periodic structures: electric filters and crystal lattices*, Courier Corporation, 1946.

[11] P. A. Deymier, *Acoustic metamaterials and phononic crystals*, vol. 173, Springer Science & Business Media, 2013.

[12] S. Krödel, T. Delpero, A. Bergamini, P. Ermanni, and D. M. Kochmann, "3d auxetic microlattices with independently controllable acoustic band gaps and quasi-static elastic moduli," *Advanced Engineering Materials* **16**(4), pp. 357–363, 2014.

[13] Z. Liu, X. Zhang, Y. Mao, Y. Zhu, Z. Yang, C. Chan, and P. Sheng, "Locally resonant sonic materials," *Science* **289**(5485), pp. 1734–1736, 2000.

[14] T.-T. Wu, Z.-G. Huang, T.-C. Tsai, and T.-C. Wu, "Evidence of complete band gap and resonances in a plate with periodic stubbed surface," *Applied Physics Letters* **93**(11), p. 111902, 2008.

[15] J.-H. Lee, J. P. Singer, and E. L. Thomas, "Micro-nanostructured mechanical metamaterials," *Advanced materials* **24**(36), pp. 4782–4810, 2012.

[16] J.-F. Robillard, O. B. Matar, J. Vasseur, P. A. Deymier, M. Stippinger, A.-C. Hladky-Hennion, Y. Pennec, and B. Djafari-Rouhani, "Tunable magnetoelastic phononic crystals," *Applied Physics Letters* **95**(12), p. 124104, 2009.

[17] L. Airoldi and M. Ruzzene, "Wave propagation control in beams through periodic multi-branch shunts," *Journal of Intelligent Material Systems and Structures* , p. 1045389X11408372, 2011.

[18] F. Casadei, T. Delpero, A. Bergamini, P. Ermanni, and M. Ruzzene, "Piezoelectric resonator arrays for tunable acoustic waveguides and metamaterials," *Journal of Applied Physics* **112**(6), p. 064902, 2012.

[19] M. Collet, K. A. Cunefare, and M. N. Ichchou, "Wave motion optimization in periodically distributed shunted piezocomposite beam structures," *Journal of Intelligent Material Systems and Structures* , 2008.

[20] A. Bergamini, T. Delpero, L. D. Simoni, L. D. Lillo, M. Ruzzene, and P. Ermanni, "Phononic crystal with adaptive connectivity," *Advanced Materials* **26**(9), pp. 1343–1347, 2014.

[21] B. R. Mace and E. Manconi, "Wave motion and dispersion phenomena: Veering, locking and strong coupling effects," *The Journal of the Acoustical Society of America* **131**(2), pp. 1015–1028, 2012.

[22] L. Airoldi, M. Senesi, and M. Ruzzene, "Piezoelectric superlattices and shunted periodic arrays as tunable periodic structures and metamaterials," in *Wave Propagation in Linear and Nonlinear Periodic Media*, pp. 33–108, Springer, 2012.

[23] D. C. von Grunigen, D. Ramseier, and G. Moschytz, "Simulation of floating impedances for low-frequency active filter design," *Proceedings of the IEEE* **74**(2), pp. 366–368, 1986.

[24] Y. Shang, Z. Shen, and S. Xiao, "On the design of single-layer circuit analog absorber using double-square-loop array," *IEEE Transactions on Antennas and Propagation* **61**(12), pp. 6022–6029, 2013.

[25] N. P. Salowitz, Z. Guo, S.-J. Kim, Y.-H. Li, G. Lanzara, and F.-K. Chang, "Microfabricated expandable sensor networks for intelligent sensing materials," *IEEE Sensors Journal* **14**(7), pp. 2138–2144, 2014.

Deformation mechanics of carbon-fiber reinforced shape-memory-polymer composites

Xin Lan[1]*, Liwu Liu[2], Yanju Liu[2] and Jinsong Leng[1]

[1] Centre for Composite Materials and Structures, Science Park of Harbin Institute of Technology (HIT), P.O. Box 3011, No. 2 YiKuang Street, Harbin 150080, China

(* E-mail: lanxin@hit.edu.cn)

[2] Department of Astronautical Science and Mechanics, Harbin Institute of Technology (HIT), P.O. Box 301, No. 92 West Dazhi Street, Harbin 150001, China

Keywords : shape- memory-polymers, lateral deformations, microbuckling mechanics, space deployable structures

The space deployable structures based on carbon fiber reinforced shape memory polymer composites (SMPCs) show great prospects. Considering the problems that SMPCs are difficult to meet the practical applications in space deployable structures in the recent ten years, this paper aims to research the mechanics of deformation, actuation and failure of SMPCs. In the overall view of the shape memory polymer material's nonlinearity (nonlinearity and stress softening in the process of pre-deformation and recovery, relaxation in storage process, irreversible deformation), by the multiple verifications among theory, finite element and experiments, one obtains the deformation and actuation mechanism for the process of "pre-deformation, energy storage and actuation" and its non-fracture constraint domain. Then, the parameters of SMPCs will be optimized. Theoretical analysis is realized by the strain energy function, additionally considering the interaction strain energy between the fiber and the matrix. For the common resin-based or soft-material-based composites under pure bending deformation, we expect to uniformly explain the whole process of buckling occurrence, evolution and finally failure, especially for the early evolution characteristics of fiber microbuckling inside the microstructures. The research results are meaningful for the practical applications for SMPC deployable structures in space.

Considering the deformation mechanisms of SMPCs, the local post-microbuckling is required for the unidirectional fiber reinforced composite materials, at the conditions of its large geometrical deflection. The cross section of SMPC is divided into three areas: non-buckling stretching area, non-buckling compressive area, and buckling compressive area. Three variables are considered: critical buckling position, and neutral plane, the fiber buckling half-wavelength. Considering the condition of the small strain and large displacement, the strain energy expression of the SMP/fiber system was derived, which contains two types, e.g., strain energy of SMP and fiber. According to the minimum energy principle, the expression for all key parameters were derived, including the critical buckling curvature, neutral plane position, the buckling half-wavelength, fiber buckling amplitude, and strain.

Active deformable composite structures: Opportunities and Challenges

Jinsong Leng*, Yanju Liu†

* Centre for Composite Materials and Structures
Harbin Institute of Technology (HIT)
No. 2 YiKuang Street, 150080, Harbin, China
Email: lengjs@hit.edu.cn

† Department of Astronautical Science and Mechanics
Harbin Institute of Technology (HIT)
No. 92 West Dazhi Street 150001, Harbin, China
Email: yj_liu@hit.edu.cn

ABSTRACT

Soft active polymers are capable of changing shapes or sizes when subjected to external stimuli, including heat, electric and magnetic field, solution and light, etc. [1]. This special feature makes them the promising materials for active deformable composite structures, which have broad application potentials in the future [2]. As typical soft active materials, shape memory polymers (SMPs) and their composites (SMPCs) have many advantages, including fast response, long lifetime, high resilience, light weights, stretchable, low cost and easy processing. In particular, their stiffness can change significantly in large scale when triggered by temperature or other stimuli. Moreover, they can also deliver active properties and autonomic responding. Multiple shape memory effect, multistage stimulus, reversible and programmable selective actuation are also systematically investigated, indicating that this kind of materials not only remember more than two shapes but also respond diverse stimuli.

In recent years, the applications of SMPs and SMPCs in active deformable structures are developed, including smart sensors, tactile displays, self-healing systems, smart textiles, biomedical devices etc. The high-performance, loadbearing substructures of aircraft, satellites and robots are designed for structural efficiency. Folded SMPC structures could deploy steadily without impact and have the feasibility to be used as the active parts of large-scale deployable space structures like hinge, truss, and antenna. Their stiffness variability would enable morphing wing structures to change shapes under different flight conditions, thus improve the manoeuvrability of future aircraft. Besides, smart mandrels structures based on SMPs, which are dimensionally accurate, rapidly removable, and reusable, have been developed for fabrication of complex-curved composite structures. 4D printing has also been generated through adding another dimension, the time-dependent shape change, to 3D printing. With the help of 4D printing, it is achievable to fabricate relatively micro active deformable composite structures, which would be used in flexible or stretchable electronic devices, minimally invasive surgeries and drug delivery. Most widely recognized potential is for fabricating flexible display, artificial blood vessels, anti-counterfeiting brands, and information carriers.

The development of novel active deformable composite structures that have excellent performances, including shape changing and memory, variable stiffness, self-assembly, would have enormous impacts on a vast number of fields and could provide new research perspectives. It would not be an exaggeration to say that the appearance of active deformable composite structures, like shape memory composite structures, could lead to revolutionary developments in several areas.

REFERENCES

[1] J. Leng, X. Lan, Y. Liu, S. Du. Shape-memory polymers and their composites: Stimulus methods and applications. *Progress in Materials Science.* Vol. **56**, pp. 1077-1135 (2011).

[2] Y. Liu, H. Du, L. Liu, J. Leng. Shape memory polymers and their composites in aerospace applications: a review. *Smart Materials and Structures*. Vol. **23**, 023001. (2014).

Mechanoluminescence-based active sensing for structural health monitoring and failure prevention

Yang He*, Yanju Liu † and Jinsong Leng††

* Centre for Composite Materials and Structures
Harbin Institute of Technology (HIT)
No. 2 YiKuang Street, 150080, Harbin, China
Email: he2007yang@163.com

† Department of Astronautical Science and Mechanics
Harbin Institute of Technology (HIT)
No. 92 West Dazhi Street 150001, Harbin, China
Email: yj_liu@hit.edu.cn

†† Centre for Composite Materials and Structures
Harbin Institute of Technology (HIT)
No. 2 YiKuang Street, 150080, Harbin, China
Email: lengjs@hit.edu.cn

ABSTRACT

Mechanoluminescent (ML) material exhibits brilliant light emission during deformation and fracture processes, and the intensity is directly related to loading rate and magnitude [1, 2]. It provides a viable route to in-situ and distributed structural health monitoring by attaching to the surface of composites, or embedding within composites. Such mechanoluminescence based sensor is useful for detection of mechanical changes including stress redistribution, crack formation, fracture type, and fragment stability. The coupling of the mechanoluminescent light into polymeric and silica fibres can detect even internal cracks when little indication of damage appears on the surface.

This work aims to characterize the light-emissions properties of mechanoluminescent concentrated polymers and evaluate their application as sensor of damage and crack propagation. Two types of Eu-doped ML phosphors were embedded into epoxy resin to fabricate ML polymers. The luminescence of ML polymers under quasi-static uniaxial loading were captured by digital camera and the recorded images were processed to quantify the relationship between light emission and structure damage. The direct conversion from mechanical motion to photonic energy has been validated and the mechanoluminescent polymers have been proved effective in structural health monitoring and failure prevention.

REFERENCES

[1] C.N. Xu, T. Watanabe, M. Akiyama, X.G. Zheng. Direct view of stress distribution in solid by mechanoluminescence. *Applied Physics Letters,* Vol. **74**, pp: 2414-2416, (1999).

[2] I. Sage, G. Bourhill. Triboluminescent materials for structural damage monitoring. *Journal of Materials Chemistry*. Vol.**11**, pp: 231-245, (2001).

Numerical and experimental studies on Broadband Piezoelectric Energy Harvester Induced by Magnets

Qingqing Lu*, Yanju Liu † and Jinsong Leng††

* Department of Astronautical Science and Mechanics
Harbin Institute of Technology (HIT)
No. 92 West Dazhi Street 150001, Harbin, China
Email: lu102022@163.com

† Department of Astronautical Science and Mechanics
Harbin Institute of Technology (HIT)
No. 92 West Dazhi Street 150001, Harbin, China
Email: yj_liu@hit.edu.cn

†† Centre for Composite Materials and Structures
Harbin Institute of Technology (HIT)
No. 2 YiKuang Street, 150080, Harbin, China
Email: lengjs@hit.edu.cn

ABSTRACT

During the research of traditional resonant vibration energy harvester, the issue of narrow operational frequency bandwidth limits energy conversion efficiency[1]. To overcome these challenges, a broadband E-shape piezoelectric energy harvester induced by magnets is designed, manufactured and tested. A nonlinear electromechanical model based on Hamilton variation principle is developed, and the effect of nonlinear magnetic restoring force at different spacing distances is simulated. Through the simulation of nonlinear magnetic restoring force at different spacing distances, the distances between two different magnets are chosen to enable the system with nonlinear property. The output voltage response of the system is simulated under different excitation conditions, and the effect of space distance is discussed. The performance of E-shape energy harvester is experimentally investigated, and the E-shape energy harvester with different spacing distances are tested under several excitation accelerations. The output voltage in frequency domain of the system is shown excellent performance and the frequency bandwidth of the system acquired significantly improved.

REFERENCES

[1] Heung Soo Kim, Joo-Hyong Kim and Jaehwan Kim. A Review of Piezoelectric Energy Harvesting Based on Vibration. *International Journal of Precision Engineering and Manufacturing*. Vol. **12**, pp. 1129-1141, (2011).

Softening of particle filled dielectric elastomer under the actions of force and voltage

Yanju Liu*, Liwu Liu† and Jinsong Leng††

* Department of Astronautical Science and Mechanics
Harbin Institute of Technology (HIT)
No. 92 West Dazhi Street 150001, Harbin, China
Email: yj_liu@hit.edu.cn

† Department of Astronautical Science and Mechanics
Harbin Institute of Technology (HIT)
No. 92 West Dazhi Street 150001, Harbin, China
Email: liuliwu_006@163.com

†† Centre for Composite Materials and Structures
Harbin Institute of Technology (HIT)
No. 2 YiKuang Street, 150080, Harbin, China
Email: lengjs@hit.edu.cn

ABSTRACT

Dielectric elastomer (DE) is a material with low modulus and high permittivity, so it can be actuated by voltage [1]. Duo to this working principle, it can be designed to sensors, actuators and generators. These applications can be widely used in smart robotics, energy harvesting, medical devices, and area of aeronautics and astronautics [1]. Rubbers can be used as DE material, but they are usually restricted by their electromechanical coupling performance. One solution is to enhance their dielectric property by filling functional particles [2]. However, stress softening is a typical trait of filled rubbers, which it is widely known as Mullins effect [3].

In this paper, we studied the softening behaviour of dielectric elastomer composite (DEC) under electromechanical coupling field. The carbon nanotube filled silicon elastomer was used as DEC. Based on the cyclic loading test, we modelled the stress softening using pseudo-elastic theory, and the theory and experiment agree well. Then we combined the thermodynamics of dielectric elastomer and extended the softening behaviour to the electromechanical coupling situation. With an initial force, softening causes "residual strain" and may avoid instability during reloading. With an initial voltage, the unloading stress evolves from positive to negative, which looks like a "stress hardening". We further introduced the viscoelastic model to theoretically investigate the influence of loading conditions on softening behaviours. As a result, hysteresis and residual strain appear, and we find that the characteristic length determines the softening behaviour. If considering the creep of preload, the stress or voltage will decrease, especially with large characteristic length.

This work may lead to a better understanding of softening behaviour in dielectric elastomer composite.

REFERENCES

[1] R. Pelrine, R. Kornbluh, Q. Pei, J. Joseph. High-speed electrically actuated elastomers with strain greater than 100%. *Science*. Vol. **287**, pp: 836-839, (2000).

[2] P. Brochu and Q. Pei. Advances in dielectric elastomers for actuators and artificial muscles. *Macromolecular Rapid Communications*. Vol. **31**, pp. 10-36, (2010).

[3] L. Mullins. Effect of stretching on the properties of rubber. *Journal of Rubber Research*. Vol. 16, pp. 275-289, (1947).

Thermodynamics and instability of dielectric elastomer

Liwu Liu*, Yanju Liu † and Jinsong Leng††

* Department of Astronautical Science and Mechanics
Harbin Institute of Technology (HIT)
No. 92 West Dazhi Street 150001, Harbin, China
Email: liuliwu_006@163.com

† Department of Astronautical Science and Mechanics
Harbin Institute of Technology (HIT)
No. 92 West Dazhi Street 150001, Harbin, China
Email: yj_liu@hit.edu.cn

†† Centre for Composite Materials and Structures
Harbin Institute of Technology (HIT)
No. 2 YiKuang Street, 150080, Harbin, China
Email: lengjs@hit.edu.cn

ABSTRACT

Dielectric elastomer is a kind of typical soft active material. It can deform obviously when subjected to an external voltage [1, 2]. When a dielectric elastomer with randomly oriented dipoles is subject to an electric field, the dipoles will rotate to and align with the electric field. The polarization of the dielectric elastomer may be saturated when the voltage is high enough. When subjected to a mechanical force, the end-to-end distance of each polymer chain, which has a finite contour length, will approach the finite value, reaching a limiting stretch. On approaching the limiting stretch, the elastomer stiffens steeply.

Here, we develop a thermodynamic constitutive model of dielectric elastomers undergoing polarization saturation and strain-stiffening, and then investigate the stability (electromechanical stability, snap-through stability) and voltage induced deformation of dielectric elastomers. Analytical solution has been obtained and it reveals the marked influence of the extension limit and polarization saturation limit on its instability. The developed thermodynamic constitutive model and simulation results would be helpful in future to the research of dielectric elastomer based high-performance transducers.

REFERENCES

[1] R. Pelrine, R. Kornbluh, Q. Pei, J. Joseph. High-speed electrically actuated elastomers with strain greater than 100%. *Science*. Vol. **287**, pp: 836-839, (2000).

[2] P. Brochu and Q. Pei. Advances in dielectric elastomers for actuators and artificial muscles. *Macromolecular Rapid Communications*. Vol. **31**, pp. 10-36, (2010).

VIII ECCOMAS Thematic Conference on Smart Structures and Materials
SMART 2017
A. Güemes, A. Benjeddou, J. Rodellar and J. Leng (Eds)

DEFECT DETECTION COMBINING MULTIFREQUENCY ULTRASONIC GUIDED WAVES AND TOPOLOGICAL DERIVATIVE

A. MARTÍNEZ*, J.A. GÜEMES†, J.M. PERALES‡ AND J.M. VEGA*

* Departamento de Matemática Aplicada a la Ingeniería Aeroespacial
Escuela Técnica Superior de Ingeniería Aeronáutica y del Espacio
Cardenal Cisneros 3, 28040 Madrid, España
e-mail: anjo.mdominguez@alumnos.upm.es

† Center of Composites Materials and Smart Structures
Escuela Técnica Superior de Ingeniería Aeronáutica y del Espacio
Cardenal Cisneros 3, 28040 Madrid, España

‡ Departamento de Aeronaves y Vehículos Espaciales
Escuela Técnica Superior de Ingeniería Aeronáutica y del Espacio
Cardenal Cisneros 3, 28040 Madrid, España

Key words: Non-destructive testing, Defect detection, Elastic waves, Multi-frequency, Topological derivative, Inverse Problems.

Abstract. Ultrasonic guided waves are an attractive alternative to conventional methods. By analyzing these waves, the presence of flaws may be detected. Mathematically, this is an inverse problem. A large variety of mathematical methods to solve inverse problems consist in minimizing an instrumental objective function, which gives the difference between the measured and calculated signals. Among these, the topological derivative describes the sensitivity of the objective function to infinitesimal inclusions on the material. In this work we investigate the reconstruction of an obstacle buried in an aluminium plate by a non-iterative method based on the computation of topological derivatives. This is done by extending to the present context some ideas by Funes et al. (2016) that gave very good results in the context of the two-dimensional wave equation. The main purpose is to suitably combine multi-frequency data obtained via piezoelectric emitters and receivers. In the first part of the work, the method to detect defects is described. In the second part, as a proof of the concept, some reconstruction examples are shown.

1 INTRODUCTION

Defect detection via elastic waves [1] in a material medium exhibiting known physical properties is a problem that has attracted a lot of attention in recent years. There are many fields

where this kind of problem may be useful to be solved such as non-destructive testing of structures [2], medical diagnosis [14], natural resources exploration or even location of anti-personnel landmines [16].

Mathematically, processing data from elastic waves in a material media to identify defects and inclusions (which affect material parameters such as Young's modulus, E, Poisson's ratio, ν, and density) is an *inverse problem* [10]. By solving this inverse problem, we can obtain the response of the system to material properties variations. Likewise, the *direct problem* would be calculating the system response when we know its physical properties.

Trying to solve an inverse problem has been an issue of interest for many years. This problem may be solved as an optimization problem, which aims at looking for defects immersed in a region that minimize a convenient functional. Iterative methods were the first used [11]. However, these techniques require a prior knowledge of the number of defects or a high number of iterations is needed unless we have a good initial approximation. Among the recent methods, there is a promising one based on the computation of the so-called *topological derivative* [18, 12, 5], which gives the *sensitivity* of the difference between the experimental and calculated responses of the system to infinitesimal inclusions on the material. The idea is that localized defects at expected at those points where the topological derivative exhibits its largest negative values. The topological derivative will be computed by means of solving an adjoint problem, which is an effective way to obtain the gradient of a scalar function.

A very effective method was developed in [6] that appropriately combines the topological derivatives for monochromatic excitations, using a fairly large number of frequencies. The number of emitters/receivers combinations, instead, is small and, moreover, they are close to each other, which favors compact designs of the inspection device. These ideas where tested in the two-dimensional wave equation, which is a somewhat academic context. The main object of the present paper is to extend these ideas to a more realistic elastic problem. At the same time, the concepts developed in [8, 4, 9, 17] are used for the computation of the topological derivative in an elastic media. To that end, the mathematical formulation of the topological derivative and the involved direct, inverse and adjoint problems are detailed in sections 2 and 3. Then, in section 4, some reconstruction examples are shown. Finally, some concluding remarks are exposed in section 5.

2 FORMULATION: THE ELASTIC PROBLEM

This work is about detecting a set of small defects Ω in an aluminium plate D, whose dimensions are 1x1x0.004 m^3. In order to excite the structure, we place some source points x_i along its face which may act as emitters or receivers. A possible way to simulate a piezoelectric device [7] can be modeling the source term by means of a Dirac delta function δ_{x_i} at each excitation point, acting in the in-plane directions. As the thickness of the plate is much smaller than the in-plane dimensions, the elastodynamic state can be approximated by a plane stress assumption, as long as the excitation wavelength is much greater than the plate thickness [13]. Hence, we have $D = (-0.5, 0.5) \times (-0.5, 0.5)$. Neumann boundary conditions are imposed to model the defects

since it is a useful way to reproduce the air inside them (the so-called *sound-hard* defect). Alike, more general transmission conditions could also be specified. Homogeneous Dirichlet conditions are applied at the bottom corners so as to avoid singularities in the stiffness matrix. Harmonic problems are considered, thus, the governing equation and boundary conditions are

$$\nabla\cdot\bar{\bar{\sigma}}+\rho\omega^2\vec{u}=-\vec{f}\quad\text{in}\quad D\setminus\Omega, \tag{1}$$

$$\bar{\bar{\sigma}}\cdot\vec{n}=0\quad\text{at}\quad\partial\Omega, \tag{2}$$

$$\begin{gathered}\bar{\bar{\sigma}}\cdot\vec{n}=0\quad\text{at}\quad\partial D\setminus P,\quad\text{with}\\ P=\{(x,y)\in\mathbb{R}^2\mid x=-0.5,y=-0.5\}\cup\{(x,y)\in\mathbb{R}^2\mid x=0.5,y=-0.5\},\end{gathered} \tag{3}$$

$$\vec{u}=0\quad\text{at}\quad P, \tag{4}$$

where ρ is the *density*, ω is the *angular frequency*, and $\vec{n}$ is the *outward unit normal*. Note that the elastic parameters appear in the equation through the *stress tensor* $\bar{\bar{\sigma}}=\bar{\bar{\sigma}}(\lambda,\mu,\vec{u})$, where λ and μ are the *Lame parameters* and $\vec{u}$ is the *displacement vector*. As anticipated, the source term $\vec{f}$ will be a set of point forces reproducing a piezoelectric excitation. This *direct problem* (solution is computed knowing the coefficients appearing in the formulation) will be used below to generate synthetic measured data.

The aim of the *inverse problem* is to establishing the position of the defects Ω that produce a given displacement at each receiver (measured experimentally). However, unlike the direct problem, this is an ill-posed problem, namely, it could have many solutions or even no solution. In adition, small errors in the measured data can provide very dissimilar solutions. Therefore, in order to regularize the problem, we can pose it in a less demanding way: finding the defects Ω that minimize the following objective functional,

$$\mathcal{F}(D\setminus\Omega)=\frac{1}{2}\sum_{i=1}^{nrec}\|\vec{u}(x_i)-\vec{u}_{meas}(x_i)\|^2, \tag{5}$$

where x_i is the location of the measurements. Considering different emitters/receivers and more than one frequency, we have

$$\mathcal{F}(D\setminus\Omega)=\frac{1}{2}\sum_{k=1}^{nfreq}\sum_{j=1}^{nemi}\sum_{\substack{i=1\\ i\neq j}}^{nrec}\alpha_{kj}\|\vec{u}^j_{w_k}(x_i)-\vec{u}^j_{meas,w_k}(x_i)\|^2, \tag{6}$$

where α_{kj} are constants that weight the individual contribution of each emitter and frequency.

3 TOPOLOGICAL DERIVATIVE

The topological derivative of a functional $\mathcal{F}$ defined in a region $\Re$, can be seen as the sensitivity of $\mathcal{F}$ with respect the creation of a small cavity at each point $\mathbf{x} \in \Re$. More precisely, we can define it as this limit

$$T(\mathbf{x}) = \lim_{\varepsilon \to 0} \frac{\mathcal{F}(\Re \setminus \mathcal{B}_\varepsilon(\mathbf{x})) - \mathcal{F}(\Re)}{h(\varepsilon)}, \qquad \mathbf{x} \in \Re, \tag{7}$$

where $B_\varepsilon(\mathbf{x})$ is a ball with radius ε centered at $\mathbf{x}$ and $h(\varepsilon) > 0$ is a monotone decreasing function that tends to zero and selected such that the limit (7) exists and is non-zero. For general three-dimensional transmission problems or sound-hard obstacles we can take $h(\varepsilon) = \frac{4}{3}\pi r^3$.
Let rewrite the limit (7) as

$$\mathcal{F}(\Re \setminus \mathcal{B}_\varepsilon(\mathbf{x})) = \mathcal{F}(\Re) + h(\varepsilon) T(\mathbf{x}) + o(h(\varepsilon)), \qquad \text{as } \varepsilon \to 0, \tag{8}$$

which gives the fundamental idea to the detection method: agglutinating points where the topological derivative is large and negative, since in such points $\mathcal{F}(\Re \setminus \mathcal{B}_\varepsilon(\mathbf{x})) < \mathcal{F}(\Re)$.
Trying to calculate the topological derivative using the above limit definition it is not practical. A large number of computations would have to be done. However, it is possible to obtain simpler expressions in terms of the solution of a direct problem and an adjoint problem. In our case, the topological derivative of the single-frequency functional defined in (5) at a point x is given by

$$T_{w,j}(x) = \bar{\bar{\sigma}}_{adj} : A : \bar{\bar{\sigma}}_{dir} - \rho\omega^2 \vec{u}_{adj} \cdot \vec{u}_{dir}, \tag{9}$$

where A is the following fourth order tensor [3]

$$A = \frac{1}{\mu(1+\nu)} \left[2I_4 - \frac{1 - \nu + 2\nu^2}{2(1-\nu^2)} I_2 \otimes I_2 \right]. \tag{10}$$

Note that $\bar{\bar{\sigma}}_{adj}$, $\bar{\bar{\sigma}}_{dir}$, $\vec{u}_{adj}$ and $\vec{u}_{dir}$ are the stress tensors and displacement fields of the following direct and adjoint problems,

• Direct problem:

$$\nabla \cdot \bar{\bar{\sigma}}_{dir} + \rho\omega^2 \vec{u}_{dir} = -\vec{f} \quad \text{in} \quad D, \tag{11}$$

$$\bar{\bar{\sigma}}_{dir} \cdot \vec{n} = 0 \quad \text{at} \quad \partial D \setminus P, \tag{12}$$

$$\vec{u}_{dir} = 0 \quad \text{at} \quad P, \tag{13}$$

• Adjoint problem:

$$\nabla\cdot\bar{\bar{\sigma}}_{adj}+\rho\omega^2\vec{u}_{adj}=-\sum_{i=1}^{nrec}\left(\vec{u}_{dir}-\vec{u}_{meas}\right)\delta_{x_i}\quad\text{in}\quad D, \tag{14}$$

$$\bar{\bar{\sigma}}_{adj}\cdot\vec{n}=0\quad\text{at}\quad\partial D\setminus P, \tag{15}$$

$$\vec{u}_{adj}=0\quad\text{at}\quad P. \tag{16}$$

For a more precise reconstruction of the defects, combining excitations for different frequencies tends to be a powerful tool, as very clearly shown in [6]. Hence, by linearity, the topological derivative of the corresponding overall objective functional is just the linear combination of each independent derivative. Therefore, the topological derivative of the functional (6) is just

$$T\left(x\right)=\sum_{k=1}^{nfreq}\sum_{j=1}^{nemi}\alpha_{kj}T_{w_k,j}. \tag{17}$$

To take account of the contribution of each emitter and each frequency, we must weight every single derivative since they may have different orders of magnitude. An important detail that concerns while weighting the derivatives is that we can not take the whole domain. We must avoid the nearby regions of the emitters so as to they induce high peaks in the derivatives not to be considered. Hereinafter, we will call this region S. Thus, the values of α_{kj} can be computed as

$$\alpha_{kj}=\frac{1}{|min_{D\setminus S}T_{wk,j}|}. \tag{18}$$

This expression for the weights was shown in [6] to give very good results in the context of the wave equation.

4 COMPUTATIONS

In this section, we briefly comment some aspects related with the numerical solution of the experiment, direct and adjoint problems. Three different kind of defects have been designed to make some reconstructions. The first one is a circular defect,

$$\Omega_1=\left\{(x,y)\in\mathbb{R}^2\mid(x+0.10)^2+(y-0.2)^2\leq 0.045^2\right\}, \tag{19}$$

the second is an elliptical defect,

$$\Omega_2=\left\{(x,y)\in\mathbb{R}^2\mid(x+0.15)^2/0.09^2+(y+0.2)^2/0.025^2\leq 1\right\}, \tag{20}$$

and the third case, $\Omega_3=\Omega_1\cup\Omega_2$, is a plate where both are embedded. A FEM model [15] has been used to integrate the equations. Simulations have been computed over a 157790 second-order quad element mesh for the circular defect, 158048 for the elliptical one and 157084 for the both defects situation. For the direct and adjoint problem, it was used a 158266 second-order

quad element mesh. These spatial discretizations were selected keeping always a ratio between the wavelength and element size greater than 12. The strategy is to choose the highest excitation frequency (which consistently has the smallest wavelength) and force the mesh to satisfy the previous condition. All simulations have been performed using ANSYS Mechanical inside the Harmonic Response module. Below, reconstruction examples are shown. As anticipated, the topological derivative calculated after equation (17), $T(x)$, is a scalar function, defined in the whole plate and is such that the holes are most likely located at those regions where $T(x)$ exhibits its largest negative values. The plots of $T(x)$ along the plate for the three considered cases are given in Figs. 1, 2 and 3.

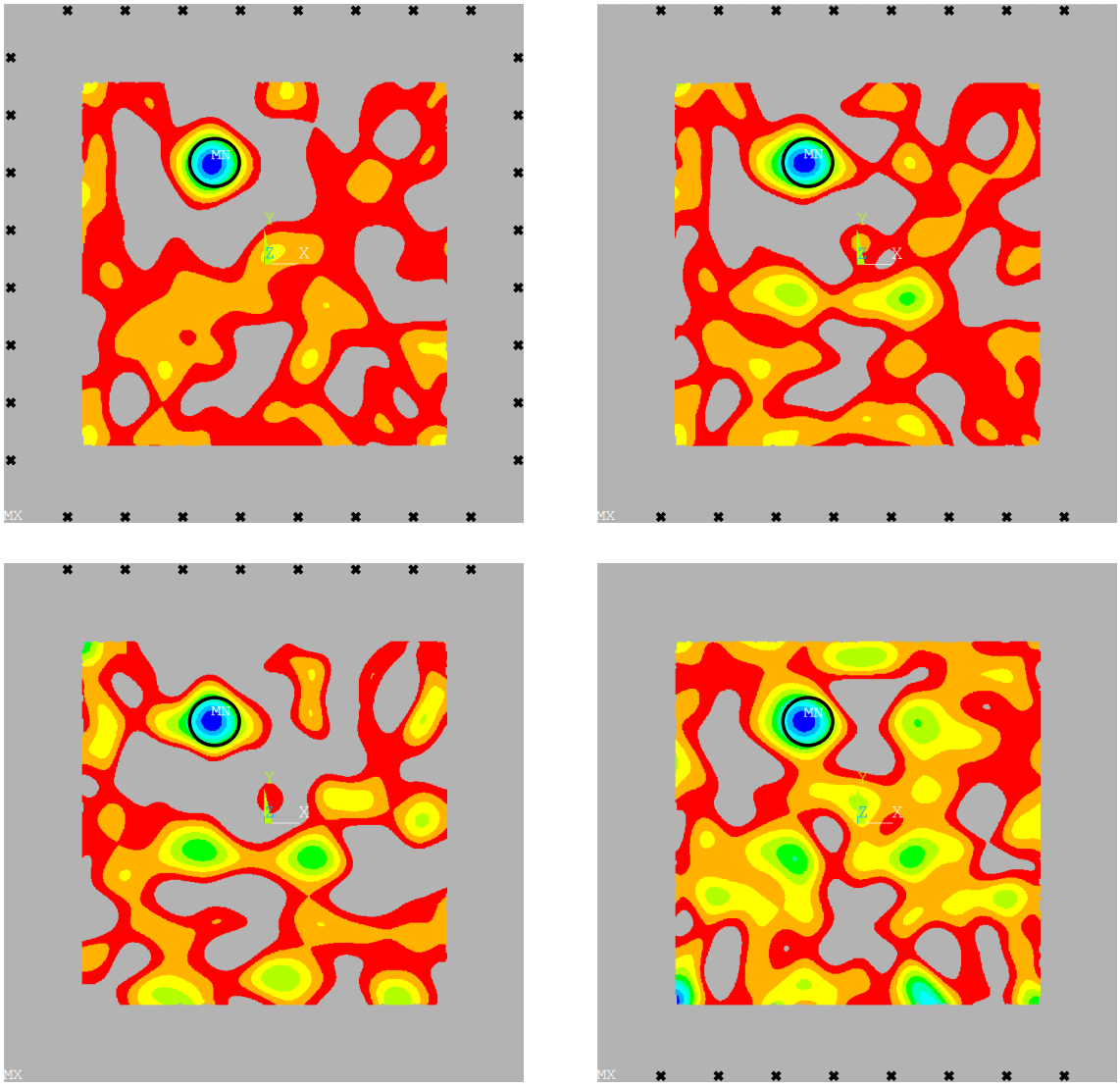

Figure 1: Topological derivatives varying the number and location of the emitters/receivers for a circular defect.

The blue regions in those plots indicate the guess for the positions of the defects. Note that the emitters/receivers are located along the four edges of the plate indicated by black crosses in the figures. The nearby region S has been eliminated, namely,

$$S = [-0.5, 0.5] \times [-0.5, 0.5] - (-0.35, 0.35) \times (-0.35, 0.35)\,. \tag{21}$$

Also, a black line has been drawn in order to indicate the position of the defects. We begin the reconstructions with a favorable situation of having 32 emitters/receivers and then we try to get results with a less number of them. For the case of the circular and elliptical defects, 5 frequencies are combined from 7750Hz to 15690Hz.

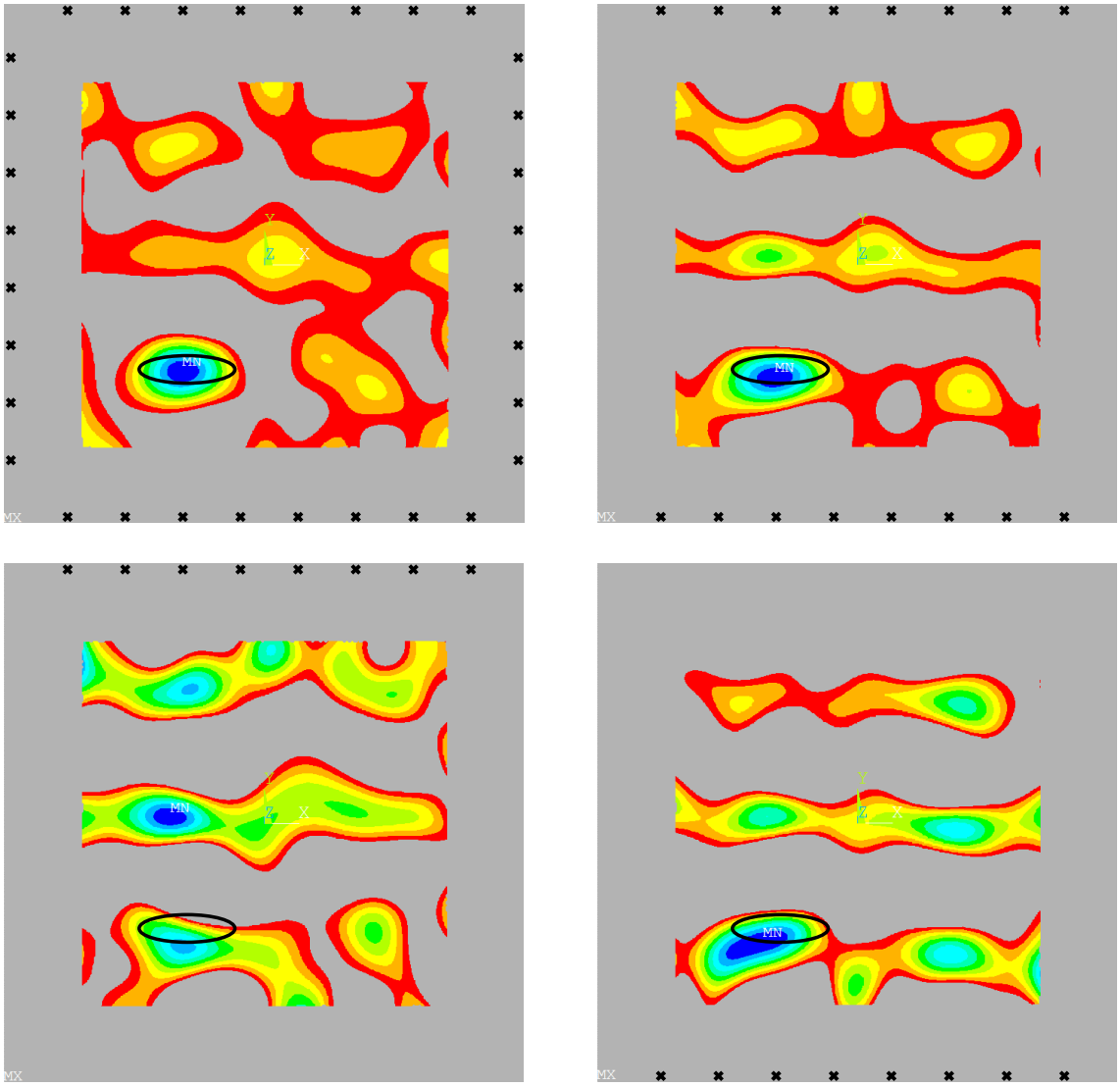

Figure 2: Topological derivatives varying the number and location of the emitters/receivers for an elliptical defect.

Finally, a 32 emitters/receivers reconstruction is shown combining 3 frequencies for the both defects case. It is noticed that the topological derivative still gives good approximations of the defects even when the number of emitter/receivers is reduced. Alike, the circular defect provides a better reconstruction with limited data than the elliptical one. In addition, when both defects are embedded, the method can make a proper distinction between them although the shape identification is still not clear.

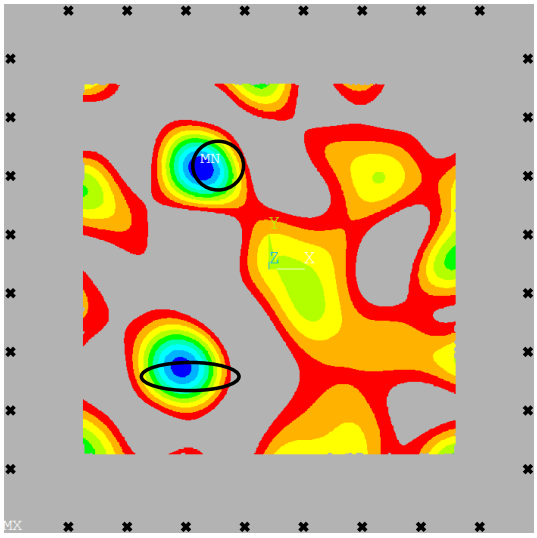

Figure 3: Topological derivative when both defects are embedded in the plate. In this case, the measure set consists in 32emitters/receivers combining 3 frequencies.

5 CONCLUSIONS

A method based on the multi-frequency topological derivative has been described intending to use for NDT. In contrast with more generic techniques, known as *radar methods*, here the physics of the problem is fundamental to be accounted. As is apparent, the higher number of measurements the better results we obtain. However, as we can se (specially in the circular case), with a low number or emitter/receivers reasonable results are achieved. These reconstructions with a low data number could be the first approximation in order to implement an iterative method which may enhance the initial guess. Also, in some cases, the position of the emitters/receivers seems to affect the quality of the derivatives: optimizing their place may be a future work. For the sake of simplicity, piezoelectric devices has been modeled as point forces in this work, nonetheless, a full 3D electroelastic coupled model has been developed. Implement the topological derivative in the abovementioned 3D model is a considerable challenge as the computational cost increases significantly. This computational cost can be highly reduced using a reduced order model for the direct and adjoint problems. However, this improvement is well beyond of the scope of this paper. Finally, as a main conclusion, we can say that the method described in this work could be a competitor among the NDT techniques utilized at present, however, it still needs extensive improvements.

REFERENCES

[1] R. J. Atkin and N. Fox. *An Introduction to the Theory of Elasticity*. Courier Corporation, 2005.

[2] D. Balageas, C.-P. Fritzen, and A. Güemes. *Structural Health Monitoring*, volume 90. John Wiley & Sons, 2010.

[3] C. Bellis and M. Bonnet. A fem-based topological sensitivity approach for fast qualitative identification of buried cavities from elastodynamic overdetermined boundary data. *Int. J. Solids Struct.*, 47(9):1221–1242, 2010.

[4] M. Bonnet and B. B. Guzina. Sounding of finite solid bodies by way of topological derivative. *Int. J. Numer. Meth. Eng.*, 61(13):2344–2373, 2004.

[5] G. R. Feijoo. A new method in inverse scattering based on the topological derivative. *Inverse Probl.*, 20(6):1819, 2004.

[6] J. F. Funes, J. M. Perales, M.-L. Rapún, and J. M. Vega. Defect detection from multi-frequency limited data via topological sensitivity. *J. Math. Imaging. Vis.*, 55(1):19–35, 2016.

[7] V. Giurgiutiu. *Structural Health Monitoring: With Piezoelectric Wafer Active Sensors*. Academic Press, 2007.

[8] B. B. Guzina and M. Bonnet. Topological derivative for the inverse scattering of elastic waves. *Quart. J. Mech. Appl. Math.*, 57:161–179, 2004.

[9] B. B. Guzina and I. Chikichev. From imaging to material identification: a generalized concept of topological sensitivity. *J. Mech. Phys. Solids.*, 55(2):245–279, 2007.

[10] P. C. Hansen. *Discrete Inverse Problems: Insight and Algorithms*. Society for Industrial and Applied Mathematics, 2010.

[11] F. Hettlich and W. Rundell. Iterative methods for the reconstruction of an inverse potential problem. *Inverse Probl.*, 12(3):251, 1996.

[12] M. Higuera, J. M. Perales, M.-L. Rapún, and J. M. Vega. Combining active thermographics and topological derivative. In *Proceedings of the 8th European Workshop On Structural Health Monitoring*, 2016.

[13] H. Lamb. On waves in an elastic plate. *Proc. R. Soc. A*, 93(648):114–128, 1917.

[14] I. Larrabide, A. A. Novotny, R. A. Feijóo, and E. Taroco. A medical image enhancement algorithm based on topological derivative and anisotropic diffusion. In *Proceedings of the XXVI Iberian Latin-American Congress on Computational Methods in Engineering-CILAMCE*, pages 1–14, 2005.

[15] J. N. Reddy. *An Introduction to The Finite Element Method*, volume 2. McGraw-Hill New York, 1993.

[16] W. R. Scott, C. T. Schroeder, J. S. Martin, and G. D. Larson. Use of elastic waves for the detection of buried land mines. In *Geoscience and Remote Sensing Symposium, 2001. IGARSS'01. IEEE 2001 International*, volume 3, pages 1116–1118. IEEE, 2001.

[17] R. Serrano. Detección de grietas en placas con técnicas multifrecuencia. Master's thesis, Universidad Politécnica de Madrid, Spain, 2014.

[18] J. Sokolowski and J.-P. Zolesio. *Introduction to Shape Optimization*. Springer, 1992.

DELAMINATION MONITORING IN ELECTRICALLY CONDUCTIVE COMPOSITES

M. QUARESIMIN*, S.K. NOTHDURFTER†, M. ZAPPALORTO*, F. PANOZZO*, A. RULLO†

* Department of Management and Engineering (DTG)
University of Padova
Stradella San Nicola, 3, 36100 Vicenza, Italy
e-mail: michele.zappalorto@unipd.it

† Automobili Lamborghini S.p.A. – Advanced Composites Research Center (ACRC)
Via Modena, 12, 40019 Sant'Agata Bolognese (Bo), Italy

Key words: Structural Health Monitoring; Modelling; Conductive Matrix

Abstract. Composite parts are usually subjected to high load levels and impacts during their in-service life, leading to damages such as matrix cracks and delamination between the plies. It is proven in the literature that the electrical resistance change of electrically conductive laminates can be used as a quantitative parameter to monitor the presence of damage, and its extension. In the present paper, an analytical model to calculate the electric potential distribution of a symmetric composite laminate, in the presence of a delamination, is presented. The laminate is modelled as composed by electrically orthotropic plies, with a delamination in the middle plane. The case of a Mode I interlaminar fracture toughness test is later considered, and a procedure to predict the electric resistance of the specimen, and its variation as a function of the delamination length, is presented. The analytical predictions are compared with a bulk of finite element analyses, showing in all cases a satisfactory agreement.

1 INTRODUCTION

In the last decades, structural health monitoring of composite parts has arisen an increasing interest from the industrial and the scientific community. Several efforts have been devoted to develop techniques to reliably monitor the presence of damage in composite structures, providing real-time information on the health status of the part. In fact, due to the outstanding strength and stiffness of composite materials, in combination with their low density, their use is becoming wider especially for structural applications where lightweight is needed. Especially in the wind turbine, aeronautic and automotive fields, the use of composite materials can reduce significantly the weight of the structure.
Structural parts made of composite materials can be subjected to impacts during their in-service life, leading to the formation of matrix cracks and delamination between the plies [1 – 3]. Such damages do not necessarily lead to the failure of the part, however they reduce the load bearing capability and its stiffness. Therefore, being able to monitor the presence of

damage would be extremely important for engineering applications, increasing the overall safeness of the structure, and enabling the switch from a time-based to a condition-based maintenance, with a significant reduction of the inspection costs.
The variation of the electric potential distribution in conductive composites has proven to be a reliable parameter to monitor the presence of damage [4 – 5]. However most of the works presented in the literature are mainly experimental, highlighting the lack of theoretical models capable of seizing the fundamental aspects that underlie the phenomenon.
In the present work, an analytical model is presented to calculate the electric potential distribution of a conductive composite plate in the presence of a delamination between the central plies. A fully analytical procedure is given to calculate the electric resistance of the laminate, and its variation as a function of the delamination length. The model is validated by comparison with finite element analyses on plates with different geometries and electrical properties, showing an excellent agreement.

2 ANALYTICAL MODELLING

Consider a composite panel made of electrically conductive plies, where a duty current I is injected through the lateral surfaces, as schematically represented in Figure 1. The plate is composed of an electrically orthotropic material, with longitudinal resistivity η_x, and through-the-thickness resistivity η_z (Figure 1). The laminate presents a delamination between the central plies, such that:

- the delamination has the same width of the laminate;
- no current can flow between the two delaminated faces.

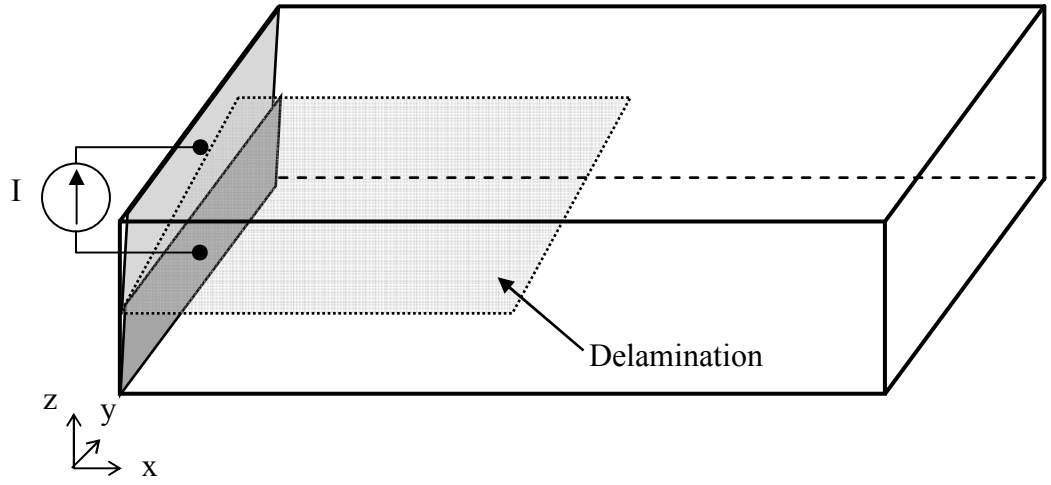

Figure 1: Schematic representation of the delaminated composite plate

According to these hypotheses, the problem can be treated as plane, and, with reference to Figure 2, the laminate can be subdivided into two different zones:

1) A delaminated zone (number 1 and 3 in Figure 2)
2) A non-delaminated zone (number 2 in Figure 2)

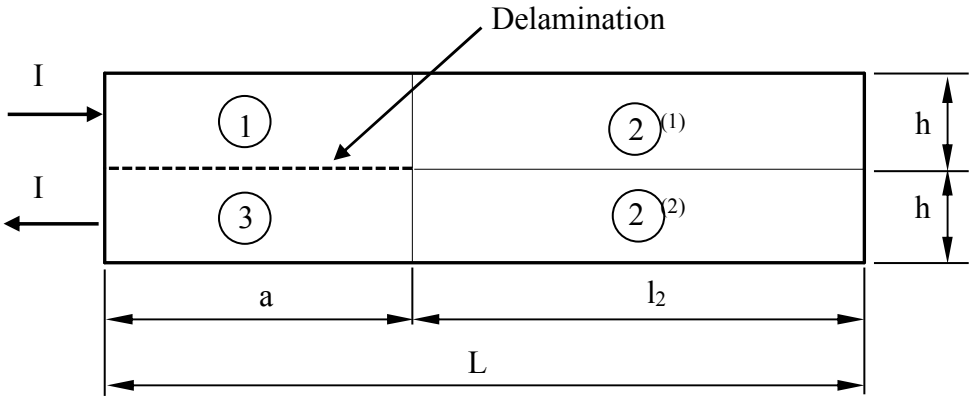

Figure 2: Plane representation of the laminate

According to the schematic of Figure 2, and assuming an unitary width, the zones denoted with the number 1 and 3 can be treated as ohmic resistors. The electrical resistance of these zones is given by:

$$\Delta V_1 = \Delta V_3 = \eta_x \, I \frac{l_1}{h} \tag{1}$$

The presence of a delamination is such that, in the non-delaminated zone, electric potential depends on the z-coordinate. As proposed in Ref [6], the through-the-thickness electric potential difference can be expressed as:

$$\Delta V_2 = \frac{2}{\sqrt{3}} \sqrt{\eta_x \cdot \eta_z} \; I \coth\left[\frac{1}{h}\sqrt{3\frac{\eta_x}{\eta_z}}(L-a)\right] \tag{2}$$

Eqs. (1-2) can be combined to calculate the electrical resistance of the composite:

$$R = \frac{\Delta V_1 + \Delta V_2 + \Delta V_3}{I} = 2\eta_x\left[\frac{a}{h} + \frac{1}{\sqrt{3}}\sqrt{\frac{\eta_z}{\eta_x}} \coth\left[\frac{1}{h}\sqrt{3\frac{\eta_x}{\eta_z}}(L-a)\right]\right] \tag{3}$$

Eventually, considering an initial delamination length a_0, the ratio between the increase of electrical resistance, and its initial value reads as:

$$\frac{\Delta R}{R_0} = \frac{R(a) - R(a_0)}{R(a_0)} = \frac{a - a_0}{a_0 + \frac{h}{\sqrt{3}}\sqrt{\frac{\eta_z}{\eta_x}}} \tag{4}$$

3 MODEL VALIDATION

To validate the analytical expression, a number of finite element analysis were carried out with the commercial code Ansys 14.5. The geometry of a typical DCB specimen was modelled using 8-nodes plane elements (Plane 230). As schematically shown in Figure 3, the

nodes of the lateral surfaces of the specimen were loaded with a uniform current density such that the total current flowing in the specimen equates I = 1 A. In addition, the electric potential of the node indicated with letter B in Figure 3 is constrained to 0 Volt. The potential difference between points A and B is was calculated for different delamination length, then calculating the resulting electrical resistance.

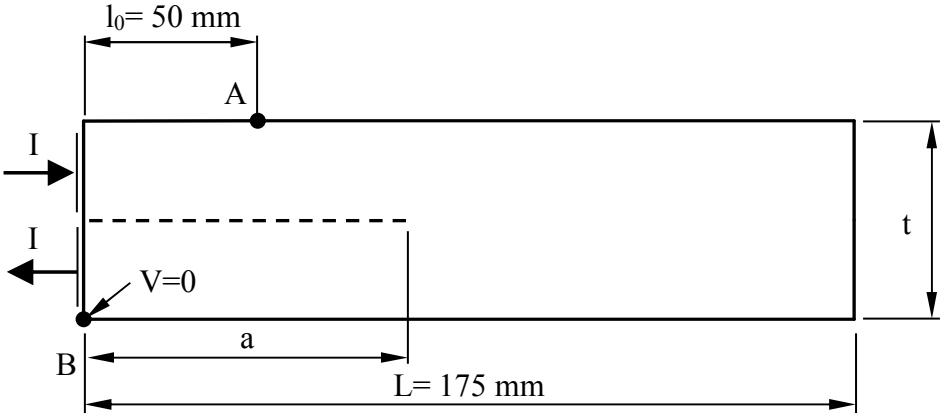

Figure 3: Geometry used for the finite element analyses

A first comparison between theoretical predictions and numerical results is shown in Figure 4, where the influence of the thickness of the plate has been investigated. In particular, for a given resistivity ratio η_z/η_x=100, the electrical response of plates with thickness equal to 2, 4 and 6 mm was studied. As expected, electrical resistance increases significantly with the increase of the delamination length, confirming the capability of electric potential-based methods to sense the presence of damage. In addition, the theoretical results suggest that a higher response can be obtained with laminates with lower thicknesses.

The influence of the ratio between the longitudinal and the through-the-thickness resistivities on the electrical response of the delaminated plate is shown in Figure 5, where, once again, a very good agreement can be noticed between the analytical estimations and the results of the numerical simulations. Figure 5 shows that, for a given value of the delamination length, the electrical response is higher for laminates with a lower electrical anisotropy ratio (i.e., the ratio η_z/η_x). This result indicates that the use of matrix filled with conductive particles (such as carbon nanotubes) increases the damage sensitivity of the material in terms of electrical resistance change.

4 CONCLUSION

An analytical model for the prediction of the electrical resistance of a composite plate in the presence of a delamination was presented. The validity of the analytical expression is verified through comparison with the results of numerical simulations. The thickness of the laminate and the ratio between the resistivities of the plies were found to influence the electrical response of the part. In particular, the highest sensitivity to the presence of a delamination can be obtained with laminates with low thickness and a low ratio between the out-of-plane and the longitudinal resistivity.

In all cases, a sound agreement was found between the analytical predictions and the numerical results.

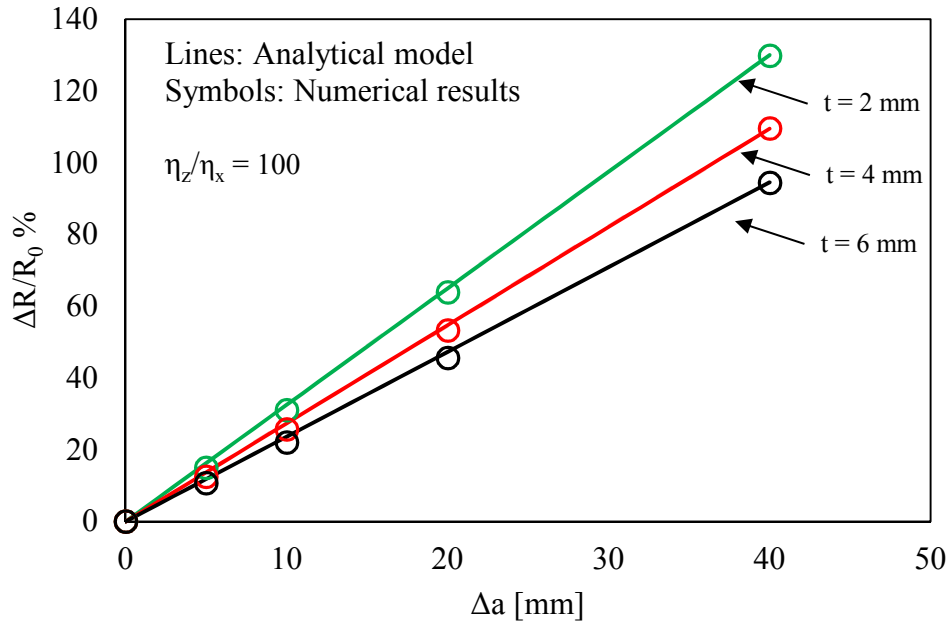

Figure 4: Comparison between theoretical predictions and numerical results for specimen with different thickness

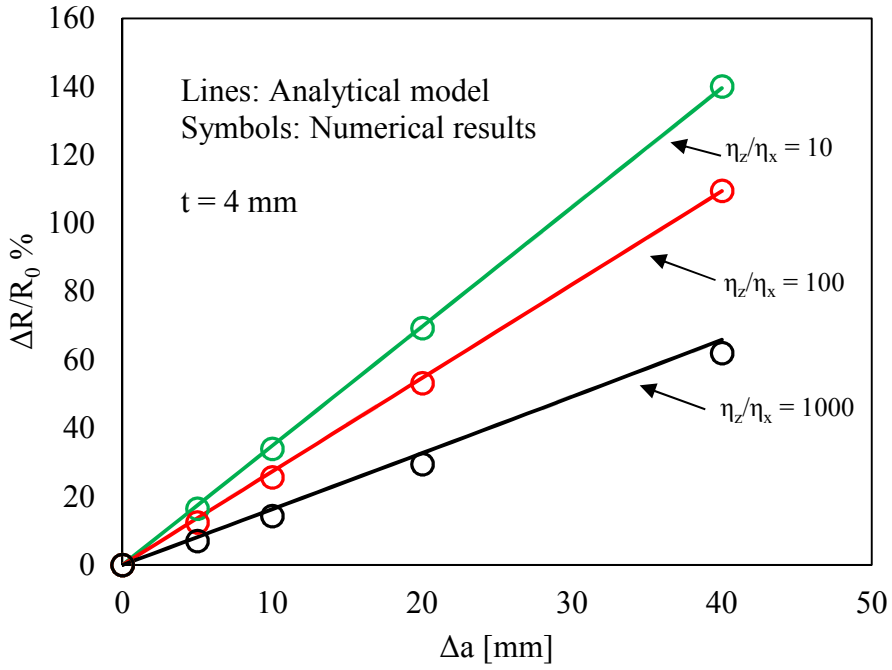

Figure 5: Influence of the resistivity ratio on the electrical response of the composite plate

REFERENCES

[1] Lopes, C. S., Seresta, O., Coquet, Y., Gürdal, Z., Camanho, P. P. and Thuis, B. *Low-velocity impact damage on dispersed stacking sequence laminates. Part I: Experiments*. Composites Science and Technology (2009) **69**:926-936.

[2] Aymerich, F., and Maili, S. *Ultrasonic evaluation of matrix damage in impacted composite laminates*. Composites Part B: Engineering (2000) **31**:1-6.

[3] Hou, J.P., Petrinic, N., Ruiz, C. and Hallett, S.R. *Prediction of impacr damage in composite plates*. Composites Science and Technology (2000) **60**:273-281.

[4] Swait, T.J., Jones, F.R., Hayes, S.A. *A practical structural health monitoring system for carbon fibre reinforced composite based on electrical resistance*. Composites Science and Technology (2012) **72**:1515-1523.

[5] Wang, S., Chung, D.D.L., Chung, J.H. *Impact damage of carbon fiber polymer-matrix composites, studied by electrical resistance measurement*. Composites: Part A (2005) **36**:1707-1715.

[6] Zappalorto, M., Panozzo, F., Carraro, P.A., Quaresimin, M. *Electrical response of a laminate with a delamination: modelling and experiments*. Composites Science and Technology (2017) **143**: 31-45.

VIII ECCOMAS Thematic Conference on Smart Structures and Materials
SMART 2017
A. Güemes, A. Benjeddou , J. Rodellar and Jinsong Leng (Eds)

NUMERICAL EVALUATION OF ECONOMIC RISK USING BAYESIAN THEOREM FROM CONDITION MONITORING DATA

ATSUSHI IWASAKI *

* Division of Mechanical Science and Technology, Gunma University
1-5-1 Tenjin-cho, Kiryu, 376-8515, Gunma, Japan
e-mail: aiwasaki@gunma-u.ac.jp

Key words: Statistical Analysis, Structural Reliability, Probability of Failure, Risk Analysis, Risk Based Maintenance, Bayesian Theorem

Summary. In this paper, we propose a method for numerically evaluating the probability of failure from the diagnostic results of condition monitoring using the Bayesian theorem. When performing maintenance using real-time monitoring results, a diagnostic result without any inspection error is ideal. However, failure is not caused even if the monitoring method sufficiently overestimates any small damage that can cause failure. Moreover, failure is not caused even if the method slightly underestimates large damage. In other words, for reducing the probability of failure, improving the accuracy of estimating specific damage levels is necessary. In this study, a method for reducing the risk by improving the diagnostic accuracy of specific damage levels by means of controlling the sampling ratio of the training data employed for learning the use of a weight function is proposed. The consequences of overestimation and underestimation of damage differ. The risk caused by underestimation is called failure risk and that caused by overestimation is called economic risk. In this paper, the effect of weighted regression on risk reduction is discussed. The proposed method is validated by employing it to identify delamination in a CFRP beam via the electric potential change method.

1 INTRODUCTION

This study is regarding a method for numerical evaluation of probability of failure (PoF) by using Bayesian theorem from the diagnostic result of real-time condition monitoring. Engineering risk is defined by the combination of PoF and the consequences of failure as follows.

$$\text{Risk} = \text{PoF} \times \text{Consequences of Failure.} \quad (1)$$

The method of making decisions about maintenance plans using engineering risk is called risk-based maintenance (RBM). RBM is used in the petrochemical industry. API581 (USA)[1] and Z107 (Japan)[2] are major examples of the RBM standard. By making use of RBM, inspection plans and additional maintenance programs are decided in which the associated risks are used as an index. The risk index is plotted on the risk matrix (Fig.1). The upper right

area is the high-risk area, and the lower-left area is the low-risk area. With RBM, by decreasing the equipment in a low- or high-risk area, maintenance programs are optimized. Therefore, making decisions pertaining to maintenance programs, each of which combines various inspections, by calculating PoF from each inspection becomes possible because the consequence of failure depends on the equipment. This study is focused on a method for evaluating risk from the diagnostic result of real-time condition monitoring.

When performing maintenance based on the results of real-time condition monitoring, it is ideal to obtain diagnostic results that do not contain any inspection error. However, failure does not occur if the monitoring method sufficiently overestimates small damage. Indeed, failure does not occur even if there is a slight underestimation of a large damage. In other words, for reducing the PoF, improving the accuracy of estimating specific damage levels is necessary. In this study, we propose a method for reducing risk by improving the diagnostic accuracy of specific damage levels by means of controlling the sampling ratio of the training data employed to learn the use of a weight function.

Regarding the damage identification method, an inverse problem for damage or fault identification is an optimization problem for minimizing estimation error. To identify the relation between sensor measurement and damage properties, several statistical analysis methods such as multiple regression, response surface, generalized regression model, discriminant analysis, and spatial statistics[2-7] or optimization methods such as neural network, and genetic algorithm are used[8-11]. The magnitude of the estimated error is reduced when the method is advanced. However, to evaluate the risk of a structure using diagnostic results, it is important to accurately evaluate the probability of underestimation of severe damage, which causes structural failure. Hence, evaluating the probability distribution of the occurrence of true damage size for any estimated result is necessary. Therefore, this paper proposes a method for estimating the occurrence probability of true damage versus any estimated result using the occurrence probability estimates of the cause events via Bayesian theorem. Using this method, the residual strength distribution of the acquired distribution and the PoF are estimated. The proposed method is validated by applying it to the problem of identifying delamination of CFRP beams using the electric potential method[3].

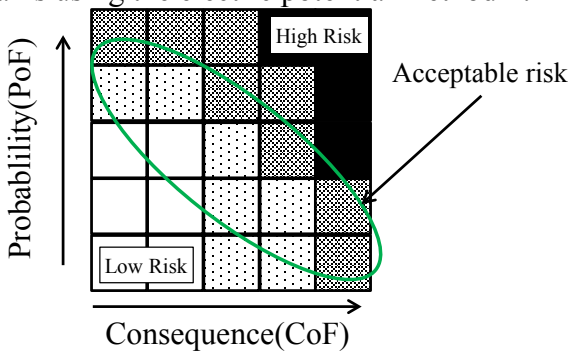

Figure 1: Risk matrix for RBM

2 ELECTRIC POTENTIAL CHANGE METHOD

2.1 Summary of method

The proposed method for evaluating PoF is applied for identifying delamination of a CFRP

beam using the electric potential method[3, 21-23] in conjunction with regression analysis.

As the carbon fiber in a composite material has conductivity, if we use the electric potential method, the damage present in a large area of a structure can be diagnosed by passing electricity through a structure made of the composite material. The electric potential method does not cause strength reduction and can be applied to existing structures at a low cost. In this study, we attempt to identify delamination cracks in CFRP laminates. In recent years, several studies have described an electric resistance change method to identify internal damage to CFRP laminates[3, 4]. The electric resistance change method does not require expensive instruments. As this method adopts reinforced carbon fiber itself as a sensor for damage detection, it does not reduce the static strength or fatigue strength of the structure under test and it is applicable to existing structures. The effectiveness of the electric potential method has been demonstrated in our previous reports[5, 6]. In these studies, a delamination crack in a composite beam was identified based on the change in electric potential between electrodes attached to the composite beam surface. The relation between delamination cracks and changes in electric potential was identified by solving an inverse problem.

The specimen configuration used herein is shown in Figure 2. The specimen is a CFRP beam with a thickness of 2 mm and a stacking sequence of $[0_2/90_2]$s. To measure the change in electric potential caused by a delamination crack, seven electrodes (each measuring 10 mm in length) are mounted on one side of the specimen. FEM analysis is performed using a commercially available FEM tool (ANSYS). Four-node-rectangular elements (each measuring 0.125 mm × 0.125 mm in size) are adopted for the analysis. A delamination crack is modeled by releasing a nodal point of an element. The electric conductance ratio is experimentally obtained from a CFRP laminate with a volume fraction of 62%, as follows:

$\sigma_{90}/\sigma_0 = 3.7 \times 10^{-2}$

$\sigma_t/\sigma_0 = 3.8 \times 10^{-2}$

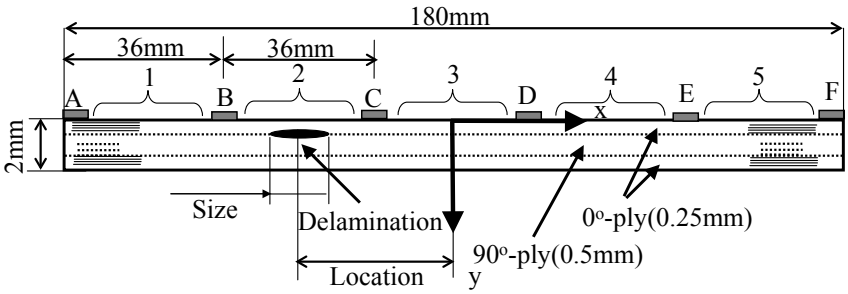

Figure2: Model of specimen

2.2 Identification of delamination crack

Delamination cracks are identified by analyzing the change in electric potential induced by them. The electric potential change in each region is defined as v_i (i = 1–5). For diagnosis, a vector length Z and standardized potential changes V_i are used as the parameters.

$$Z = \sqrt{\sum_{i=1}^{5} v_i^{\,2}}, \quad V_i = v_i / Z \ (i = 1 \cdots 5) \tag{2}$$

The size of delamination is identified using the following linear polynomial:

$$y = \beta_0 + \sum_1^5 \beta_i V_i + \beta_6 Z \tag{3}$$

where y is the predictor variable (in this case, damage size) and β_i represents the regression coefficients. The number of datasets used in the regression is 74.

3. NUMERICAL EVALUATION OF ECONOMIC RISK USING BAYESIAN THEOREM

In general, for damage identification, the maximum or the average estimation error is mainly discussed when evaluating each method. Hence, the distribution of the estimated value versus each true value is discussed. However, when evaluating the reliability of a structure or of the PoF from diagnostic results, it is important to consider the distribution of true value versus each estimated damage value. The distribution of true value versus each estimated value approximates that of estimated value versus each true value when (a) each damage size correlates to a uniform probability distribution of occurrence and (b) the distributions of the regression error for each damage size are equivalent. However, for damage identification, the occurrence probability of the large damage is smaller than that of the small damage because a large damage is caused by the accumulation of small damages or growth of small damages. Thus, the above assumption fails. Moreover, the range in which damage evaluation necessitates greater accuracy is the range where failure to detect the occurrence of damage is critical. In contrast, accurately estimating small damage is unimportant and the identification accuracy need not be uniform over the size range of damage. In summary, we describe the use of Bayesian theorem to estimate the probability distribution of true damage size in comparison with that of damage size estimated from the regression error.

3.1 Estimation of distribution of occurrence probability of true damage size vs. each diagnostic result obtained using Bayesian theorem

Bayesian theorem [12-15] is a simple mathematical theorem used for calculating conditional probabilities. In engineering, it is used mainly for structural reliability assessment from small sample [16-20] (e.g., RBM). In this study, the theorem is used to estimate the occurrence probability of true damage according to an estimated damage size. Bayesian theorem is generally expressed as

$$P(E_i \mid F) = \frac{P(E_i)P(F \mid E_i)}{\sum_j P(E_j)P(F \mid E_j)} \text{ (i, j = 1, 2, …)}, \tag{4}$$

where $P(E_i)$ is the probability of occurrence of event E_i, $P(F \mid E_i)$ is the conditional probability that event F is caused by event E_i, and $P(E_i \mid F)$ is the "posterior probability" or the conditional probability that event E_i is caused by event F. From the viewpoint of identifying damage sizes, damage occurrence is the event that generates the arbitrarily estimated results, and $P(a_i)$ is the occurrence probability of the true damage size a_i. $P(EstA_k \mid a_i)$ is the probability that the occurrence of damage a_i leads to the estimated results $EstA_k$. In this case,

Eq. (4) can be modified as follows.

$$P(a_i \mid EstA_k) = \frac{P(a_i)P(EstA_k \mid a_i)}{\sum_j P(a_j)P(EstA_k \mid a_j)} \quad , \tag{5}$$

where the left side is the posterior probability. Hence, $P(a_i|EstA_k)$ is the occurrence probability of $EstA_k$ because of the true damage size a_i. By estimating the occurrence probability of all a_i values, the occurrence probability distribution of the true damage parameter and the estimated value can be determined.

3.2 Procedure for estimating PoF for each estimated result

PoF is estimated with the following formula by using the limit state function method:

$$PoF = P[g(R-S) < 0] \tag{6}$$

where R is the strength, S is the applied force, and g is the limit state function. Figure 3 shows the procedure for estimating the probability distribution of failure and the estimated result. First, the occurrence probability distribution of true damage size versus each estimated size is deduced by the procedure given in 3.1. Residual strength is a function of damage properties. In this paper, buckling failure caused by delamination cracking is assumed and the distribution of residual buckling strength is calculated using the proposed method.

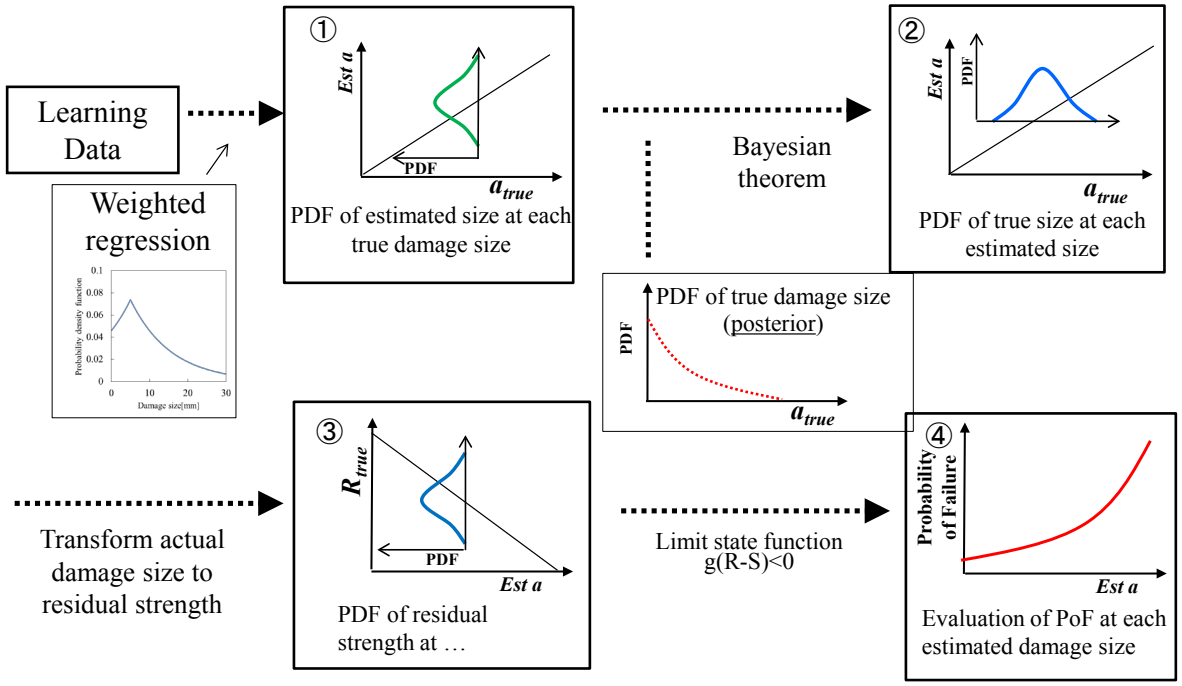

Figure 3: Procedure for estimating PoF

3.3 Evaluation of accidental and economic risks

Figure 4 shows the accidental and economic risks evaluated using the proposed method. Accidental risk is defined as the risk of failure caused by underestimation of damage size, while economic risk is defined as the risk of unnecessary maintenance costs arising from overestimation of damage size. The adjusted PoF (PDF of PoF versus PDF of occurrence of estimated damage size: PoO) is plotted on the vertical axis, and the estimated size is plotted on the horizontal axis. The accidental risk is evaluated as the area surrounded by the adjusted PoF and the threshold for maintenance operation. The threshold is set as the accidental risk and exhibits a constant value (0.03). The economic risk is evaluated as the area surrounded by the adjusted PoF, PoO, and threshold. As the acceptable level of accidental risk is limited, this study aims to reduce economic risk when accidental risk is constant.

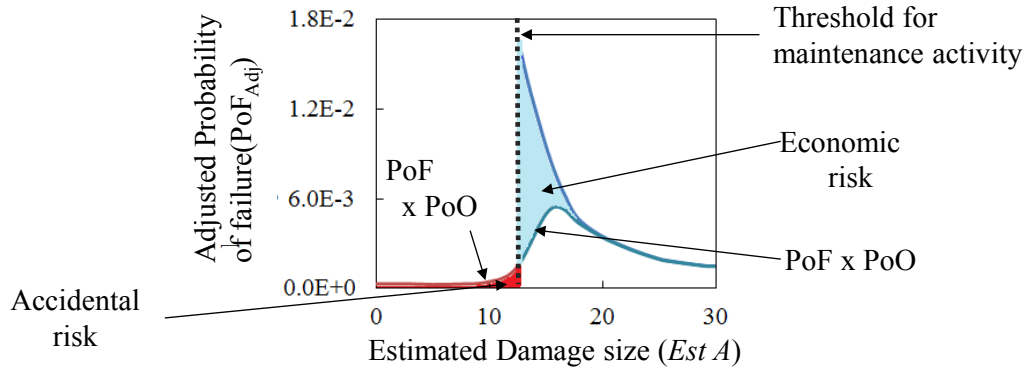

Figure 4: Accidental and economic risks from evaluated PoF

4. APPLICATION OF METHOD TO DAMAGE IDENTIFICATION USING ELECTRIC POTENTIAL CHANGE METHOD

As mentioned above, the proposed method for estimating PoF is applied for identifying delamination in a CFRP beam using the electric potential method via regression analysis.

4.1 Estimation of distribution of true damage size vs. each estimated result using Bayesian theorem

Assuming the prior occurrence distribution of the true damage size, we estimate the true damage size versus each estimated result using Bayesian theorem. Exponential distribution is used as the prior distribution. Owing to the prior distribution, the mean of true damage length is lower than the estimated damage length.

4.2 Estimation of distribution of buckling strength

A delamination crack deteriorates compressive strength. In this study, we consider buckling failure of the surface layer due to delamination. Buckling strength is calculated as follows:

$$p_w = \frac{4\pi^2 EI}{a^2} \quad , \tag{7}$$

where p_w is the buckling strength, E is the stiffness, and I is the moment of inertia of areas.

4.3 Estimation of PoF

Any external force applied to the structure is assumed to be normally distributed, which causes buckling failure when the average length of delamination is 15 mm. Figure 6 shows the PoF for each estimated damage length. The abscissa shows the estimated size, and the ordinate shows PoF. Failure occurs at 15 mm or less because the external force is not constant. As shown in the figure, the PoF starts rising when the damage is smaller than 15 mm (Area A in the figure) and is saturated when the damage is approximately 17 mm (Area B in the figure). From the results, it is possible to evaluate the PoF for each estimated result using the proposed method. Figure 6 shows a plot of true damage length versus damage length estimated using a diagnostic method. Area A is the result of underestimation, and it causes accidental risk. Area B is the result of overestimation, and it causes economic risk (i.e., unnecessary maintenance). To reduce the total risk, both accidental and economic risks must be reduced; however, the effects of the two risks are not the same. Thus, reducing the size of Area A is more important.

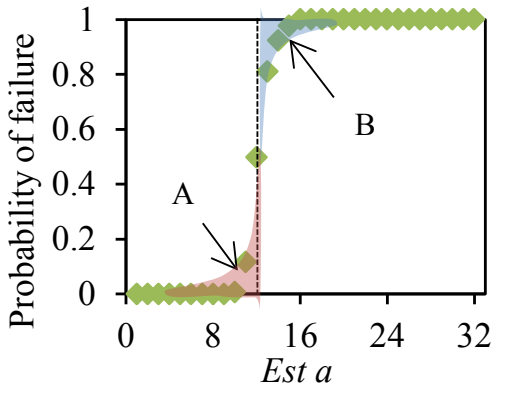

Figure 5: Estimated PoF versus each estimated size

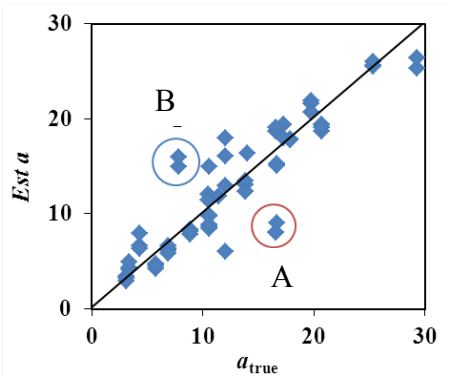

Figure 6: True damage length versus damage length estimated by diagnostic method

4.4 Risk reduction using weighted regression

To reduce economic risk, weighted regression is applied. In this case, weighted regression around the delamination lengths of 3–8 mm is conducted. Figure 7 shows the accidental and economic risks obtained using non-weighted and weighted regression. As shown in the figure, adjusted PoF is reduced in the weighted area. As the accidental risk is constant, the threshold for maintenance is shifted to the right and economic risk is reduced. As the probability of occurrence of small damages is high, improving the accuracy of small damage estimation using weighted regression can reduce total economic risk.

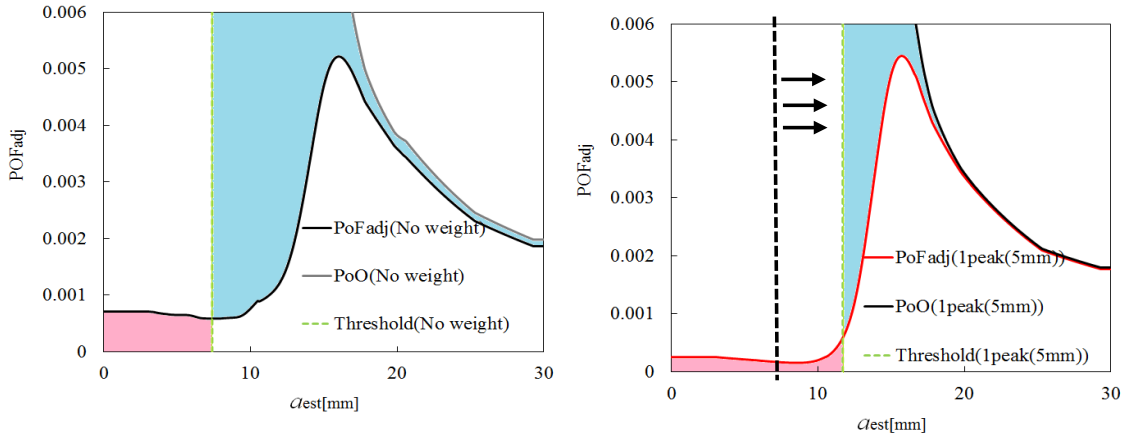

(a) Without weight (b) With weight

Figure 7: Accidental and economic risks estimated (a) with and (b) without weighted regression

4. CONCLUSION

In this research, a method for numerical evaluation of the PoF using Bayesian theorem for each diagnostic result of real-time condition monitoring is proposed.

For evaluation, the occurrence probability distribution of true damage size for each estimated damage size is calculated using Bayesian theorem and the residual strength of the damaged structure is estimated from the calculated distribution. PoF is determined using the limit state function method. As a result, PoF starts rising for damages smaller than the critical level and it is saturated for damages higher the critical level. In conclusion, we confirmed that the proposed method evaluates the PoF for each estimated result.

- Using the proposed method, it is possible to evaluate the PoF for each estimated result or evaluate PoF directly from the monitoring data. Moreover, threshold damage size, which carries lower risk than acceptable risk, can be defined by the method.
- To reduce total risk, both accidental and economic risks must be reduced. However, the effects of the two risks are not the same. Thus, reducing the probability of accidental risk is more important.
- By improving the accuracy of estimating small damage by weighted regression, total economic risk can be reduced.

REFERENCES

[1] A.Iwasaki, A.Todoroki, Improvement of the Inverse Problem for the Damage Identification using Generalized Linear Mixed Model, Transactions of the JSME, A76(768), 1040-1047, 2010

[2] A.Iwasaki, Delamination identification of CFRP structure using discriminant analysis via the support vector machine, Transactions of the JSME, 80(810), smm0020, 2014

[3] A.Iwasaki, A.Todoroki, Statistical Evaluation of modified Electrical Resistance Change Method for Delamination Monitoring of CFRP Plate, Structural health monitoring, An International journal, 4, 2, 119-136, 2005

[4] A.Iwasaki, A.Todoroki, S.Izumi, S.Sakai, Diagnostic Method for Delamination Monitoring of CFRP Plate using Kriging Interpolation Method, Key Engineering Materials, 353-358, 1422-1426, 2007
[5] K.Takahashi, A.Todoroki, Y.Shimamura, A.Iwasaki, Statistical Damage Detection of Laminated CFRP Beam Using Electrical Resistance Change Method, Key Engineering Materials, 353-358, 1330-1333, 2007
[6] S.Yashiro, M.Nishikawa, T.Okabe, N.Takeda, Damage assessment of CFRP laminate with embedded FBG sensor using response surface methodology, Proc of JSME M&M division, 1017-1018, 2003
[7] M.L.Friswell, Damage identification using inverse methods, Philosophical Transaction, The Royal Society A, 365, 393-410, 2007
[8] C.R.Farrar, K.Worden, An introduction to structural health monitoring, Philosophical Transaction, The Royal Society A, 365, 303-315, 2007
[9] G.Ben, T.Yamaguchi, Y.Fukuda, Y.Aoki, K.C.Park, Damage Detection of CFRP Laminates by Using Localized Flexibilities, Transactions of the JSME, A66(644), 721-726, 2000
[10] H. Martz, R. Waller, "Bayesian reliability analysis", Krieger, 0894643959(1991)
[11] T.Nakazuma, "Bayesian Statistics", Asakura, 4254295405(2007)
[12] N.O.Siu, D.L. Kelly, Bayesian parameter estimation in probabilistic risk assessment, Reliability Engineering and System Safety, 62, pp. 89-116(1998)
[13] J.Quigley, T.Bedford, L.Walls, Estimating rate of occurrence of rare events with empirical bayes: A railway application, Reliability Engineering and System Safety, 92, 619-627(2007)
[14] S.Sakai, S.Okajima, S.Izumi, A.Iwasaki, Bayesian Inference of Fatigue Life Estimated by Inspection Data, J of the The Society of Materials Science Japan, 54-3, 308-313, 2005
[15] S.Okajima, S.Sakai, S.Izumi, A.Iwasaki, Bayesian Estimation of Fatigue damage rate based on small sample, proc of 20th JSMS Symposium on Reliability Engineering and International Workshop, 60-65, 2004
[16] S.Okajima, S.Izumi, S.Sakai, Extended Bayesian Inference Method for Evaluating Pipe Failure Probability in Corrosion Rate Fluctuation Model, J of the The Society of Materials Science Japan, 57-4, 401-407, 2008
[17] S.Okajima, S.Izumi, S.Sakai, Introduction of Hierarchical Bayes Model for the Evaluation of Pipe Failure Rate Using Cross-Industry Database of Pipe Failure, Transactions of the JSME, A74(741), 741-748, 2008
[18] K.Hirohata, T.Kawakami, M.Mukai, N.Kawamura, Q.Y, M.Shiratori, Proposal for structural reliablity design method based on response surface methodology and bayes theory, Transactions of the JSME, A67(660), 35-41, 2001
[19] "API RP 581 Risk-Based Inspection Technology", API standards, American Petroleum Institute, 2016
[20] "HPIS Z 107 Risk Based Maintenance Handbook", HPI Standard, High Pressure Institute of Japan, 2016
[21] Y.Tanaka, A.Todoroki, Y.Shimamura, Smart Structure for Delamination Detection of CFRP Using Response Surface of Electric Resistance Change of Multiple Electrodes, Transactions of the JSME, A65(640), 2432-2438, 1999
[22] M. Ueda, A.Todoroki, Delamination monitoring of quasi-isotropic CFRP laminate using electric potential change method, Modern Physics letters B, 22, 11, 869-874, 2011
[23] A.Todoroki, K.Omagari, Detection of matrix crack density of CFRP using electrical potential change method with multiple probes, Journal of Solid Mechanics and Materials Engineering, 2, 6, 718-729, 2008

VIII ECCOMAS Thematic Conference on Smart Structures and Materials
SMART 2017
A. Güemes, A. Benjeddou, J. Rodellar and J. Leng (Eds)

GUIDED WAVE TIME-REVERSAL IMAGING OF MACRO-FEATURES IN ANISOTROPIC COMPOSITES WITH SPARSE DISTRIBUTED MEASUREMENT LOCATIONS

ARTEM EREMIN*, EVGENY GLUSHKOV*, NATALIA GLUSHKOVA* AND ROLF LAMMERING†

*Institute for Mathematics, Mechanics and Informatics (IMMI)
Kuban State University
Stavropolskaya st. 149, 350040 Kranodar, Russia
e-mail: eremin_a_87@mail.ru, web page: http://immi.kubsu.ru

† Institute of Mechanics
Helmut-Schmidt-UniversityUniversity of the Federal Armed Forces Hamburg
Holstenhofweg 85, 22043 Hamburg, Germany
e-mail: rolf.lammering@hsu-hh.de, web page: http://www.hsu-hh.de/mechanik

Key words: Elastic Guided Waves, Time-reversal Approach, Asymptotic Representations, Damage Imaging

Abstract. A computational time-reversal technique for the estimation of damage and/or actuator location and extent is proposed and implemented. It relies on the analytically based numerical simulation of the re-emitted guided wave signals measured with laser Doppler vibrometry at a sparse set of points on the specimen surface. The approach performance has been experimentally tested on composite plates showing reliable and adequate results for both active (piezoactuators) and passive (artificial defects) source characterization.

1 INTRODUCTION

Reliable estimation of damage parameters is of great importance for integrity assurance of safety-critical thin-walled engineering constructions fabricated from modern composite materials. Active structural health monitoring (SHM) systems, employing a distributed network of integrated actuators and sensors to interrogate the structure with diagnostic ultrasonic guided wave (GW) signals, have become a recognized solution for defect characterization [1]. While the approaches for imperfection occurrence detection and localization are well-established, the methods for defect extent and severity reconstruction are in the scope of current research efforts.

Being a recognized solution for damage imaging, tomography-based techniques require a dense set of active transducers, which presents a practical burden for their implementation on large-scale structures due to power supply and weight-cost issues. Modern passive sensors, e.g. fiber-optic [2] or nanocomposite ones [3], provide competitive sensitivity to propagating GW and require

fewer cable connections. Therefore, the joint employment of active and passive elements might be a promising solution for in situ imaging systems if a reliable level of imaging quality could be achieved.

The use of the computational time reversal (TR) technique in SHM systems offers a promising option to perform damage characterization with only a few actuators [4, 5]. According to the TR concept [6], GWs generated by a source, transmitted through the structure and recorded by a sensor network, refocus approximately on the source being time reversed and re-emitted from measurement locations, providing an opportunity to estimate its initial location and size. The source may be either active (actuator) or passive (reflective obstacles, structure boundaries, etc.). The practical realization of TR based damage imaging requires wave propagation transfer function (Green's matrix) of the structure. It may be obtained experimentally, collecting the data of wavefields mechanically excited at multiple points within the target structure and measuring the response functions at a set of sensors, or using various theoretic models based on the finite element, finite difference or semi-analytical solutions.

In the current paper, the application of a semi-analytical time-reversal approach for the damage locating and sizing in thin-walled anisotropic composite structures using elastic GWs is presented and discussed. Time-reversed out-of-plane velocities, acquired with a contactless laser vibrometer at a sparse set of measurement points on the specimen surface for pristine and damaged states, serve as input data for the developed algorithm. The theoretical modelling of the re-emitted guided wave propagation is performed in the context of general linear elastodynamics for three-dimensional laminate anisotropic media. It is based on the efficient explicit analytical representations for quasi-cylindrical guided waves in terms of the Green's matrix of the layered structure considered [7]. The results of the practical implementation of the developed method are illustrated by examples of the location and size estimation of artificial damages in laminate carbon fiber-reinforced plastic specimens. The influence of actuator/sensor number used for TR process, mutual sensor network-damage location, and excitation signal type on the algorithm performance is investigated.

2 MATHEMATICAL MODEL

Transient oscillations $\mathbf{u}(\mathbf{x},t) = \{u_x, u_y, u_z\}$, $\mathbf{x} = (x,y,z)$ of a free laminate waveguide of thickness H: $W = \{\mathbf{x} : |x|, |y| < \infty, -H < z < 0\}$, fabricated from M identical transversely-isotropic prepregs ideally-bonded with each other, are considered. Mechanical properties of each lamina are characterized by the density ρ, and five independent engineering constants, namely, two Young's moduli E_x, E_z, two shear moduli G_{yz}, G_{xy} and one Poisson coefficient ν_{xy}. The direction of the axis Ox coincides with the fiber orientation in the upper layer. The waveguide is excited by a load $\mathbf{q}(x,y,0,t)$, which originates from a surface-bonded piezoelectric wafer active sensor (PWAS) occupying the area A_1 (Fig. 1, a). Any kind of macroscopic inhomogeneity, if being presented in the structure, is characterized by the area S on the surface $z = 0$, which exact shape and location are initially unknown (Fig. 1, b).

In order to simulate a sparse spatially distributed array of passive sensors with the non-contact laser-vibrometry, it is assumed that the measurement data, acquired in a form of a scalar function, namely, out-of-plane velocities $v_z(t) = \dot{u}_z(t)$, are available only at a limited number of surface points P_j, $j = 1, 2, ..., N$ (Fig. 1), yielding a set of signals $v_{z,j}(t) = v_z(P_j, t)$,

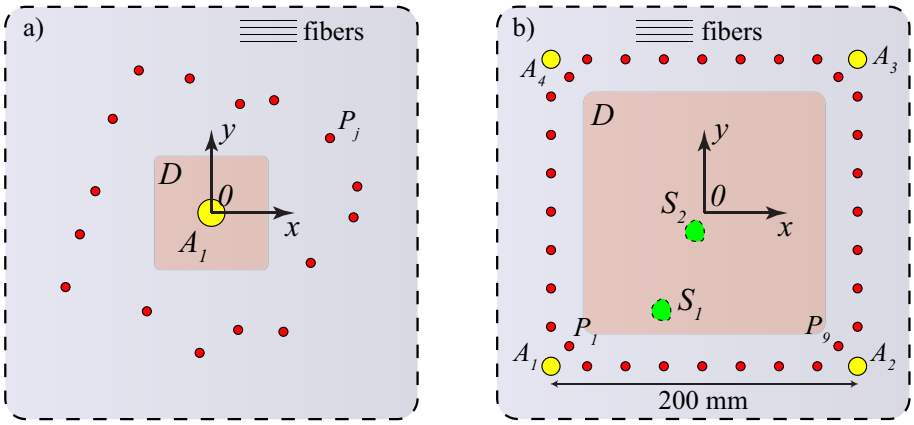

Figure 1: Sketch of the problem geometry: a) primary source (actuator A_1) localization, b) areas of artificial damage S_1 or S_2

$t \in [0, T]$; T is a truncation time limit. The recorded signals are further converted into the frequency domain, where the TR operation is equivalent to the complex conjugation of the signal spectrum: $v_{z,j}(t) \to v_{z,j}(\omega) \overset{TR}{\to} v^*_{z,j}(\omega)$. Here $\omega = 2\pi f c_s/h$ is dimensionless angular frequency, $c_s = 1000$ m/s is a unit of velocity, $h = 0.001$ m is a unit of length, f is the dimensional frequency in Hz, and superscript $*$ indicates the complex conjugate.

Serving as an input for the computational time-reversal procedure, each of the signals $v^*_{z,j}(\omega)$ gives rise to the wavefields $\hat{\mathbf{u}}_j(x, \omega)$ excited from the locations P_j, $j = 1, ..., N$. Their sum forms the spectrum of the total time-reversed field $\hat{\mathbf{u}}(\mathbf{x}, \omega) = \sum\limits_{j=1}^{N} \hat{\mathbf{u}}_j(\mathbf{x}, \omega)$. In terms of the semi-analytical integral approach, time-harmonic oscillations $\hat{\mathbf{u}}_j$ are expressed via the convolution of the Green's matrix $k(\mathbf{x}, \omega)$ for the three-dimensional laminate anisotropic media and the surface load vector-function $\mathbf{q}_j(\mathbf{x}, \omega)$ [8]. This representation is further reduced to the numerically efficient far-field GW asymptotics [7]

$$\hat{\mathbf{u}}_j(\mathbf{x}, \omega) \sim \sum_{n=1}^{N_p} \sum_{m=1}^{M_n} b_{nm}(\varphi, z) \mathbf{q}_j e^{i s_{nmj} r_j} / \sqrt{\zeta_n r_j} \tag{1}$$

Here $b_{nm}(\varphi, z)$ is a GW shape matrix-function originating from the Fourier symbol K of the Green's matrix through the residue theory and stationary phase method, N_p is the number of real poles ζ_n of K, M_n is the number of stationary points of n-th mode, s_{nmj} are wavenumbers of quasi-cylindrical GWs, propagating in the direction φ from the source point P_j, r_j is the distance from this location to the observation point $\mathbf{x}$. The representation (1) keeps the information about the source $\mathbf{q}_j$ and gives an opportunity for a quantitative analysis of the source-generated GWs.

Stresses $\mathbf{q}_j$, which are required in the Eq. (1), are generally unknown. Therefore, since out-of-plane velocities $v_{j,z}(t)$ are acquired at the measurement points P_j, it is further assumed that the vector-function $\mathbf{q}_j(\omega)$ describes a vertical point load, which amplitude is assigned to be proportional to the measured out-of-plane displacements: $\mathbf{q}_j = \{0, 0, q_{3,j}\}\delta(\mathbf{x} - P_j)$, $q_{3,j}(\omega) = \mathbf{u}^*_z(P_j, \omega) = v^*_{z,j}(\omega)/\omega$. If obstacles (damage) are present in the considered waveguide, a prior knowledge of the baseline signal $\mathbf{u}_0(P_j, \omega)$ for a pristine (undamaged) structure is additionally

supposed, and the difference between the actual displacements and "pristine" ones serves as an input for the computational model: $q_{3,j}(\omega) = \mathbf{u}_z^*(P_j,\omega) - \mathbf{u}_0^*(P_j,\omega)$. In the frequency range of interest, which is below the first cut-off frequency for the laminated waveguided, the motion of fundamental antisymmetric mode $A0$ is predominant in the oscillations excited by a point vertical load. Therefore, without the loss of generality, only the third term in the first sum of Eq. 1 relating to the $A0$ GW is further considered.

The spatial focusing of TR GWs is quantified through the directivity pattern of the out-of-plane displacement field, which should increase in the vicinity the original input source location. It is expressed via the function $\Delta(\mathbf{x}) = \Delta_0(\mathbf{x})/\Delta_1$, $\mathbf{x} \in D$, where $\Delta_0(x) = \max\limits_{t\in[-T,\,0]} |\mathcal{F}^{-1}[\hat{\mathbf{u}}_z(\mathbf{x},\omega)]|$, $\Delta_1 = \max\limits_{x\in D}\Delta_0(\mathbf{x},\omega)$, $\mathcal{F}^{-1}$ stands for an inverse Fourier transform from frequency to time domain; $\hat{\mathbf{u}}_z$ is the time-harmonic out-of-plane displacement field computed with the Eq. (1), and D is a domain of interest on the specimen surface [9]. The point $\hat{\mathbf{x}}_c$, where the value Δ_1 is achieved, is considered as the central point of the area $\hat{\Omega}$, occupied by the reconstructed obstacle. In order to quantify the size of $\hat{\Omega}$, the diameter d of the main lobe in the vicinity of $\hat{\mathbf{x}}_c$ corresponding to a half of the maximum peak value ($\Delta(\mathbf{x}) \geq 0.5$) (-6 dB level) is taken as an extent approximation [10].

3 EXPERIMENTAL SETUP

In the experiments, a cross-ply carbon-fiber-reinforced polymer (CFRP) plate with the dimensions $1000 \times 1000 \times 2.25$ mm^3 made from unidirectional prepregs (lay-up $[0^o, 90^o]_s$) is used. The prepregs's material constants are $E_x = 120.5$ GPa, $E_y = 7.82$ GPa, $G_{yz} = 2.61$ GPa, $G_{xy} = 5.01$ GPa, $\nu_{xy} = 0.24$; $\rho = 1522$ kg/m^3. Four vertically polarized adhesively bonded thin PWASs of circular shape (thickness $h = 0.25$ mm, radius $a = 3$ mm), located at the vertices of a square with a 200 mm side, are utilized for GW excitation (denoted as A_i, $i = 1, ..., 4$ in Fig. 1, b). PWASs are driven by a Tektronix AFG 3022B arbitrary signal generator. The generated signal is preamplified to the range ±75 V-pp by NF HSA4014 external high-frequency power amplifier before it is applied to the piezoactuator. The out-of-plane velocity field $v_z(\mathbf{x}, t)$ of propagating waves is measured on the plate surface with a Polytec PSV-500 scanning laser Doppler vibrometer.

Two sets of experiments have been performed. At first, a pristine structure is considered, and the location and extent of the PWAS A_1 is to be estimated with the developed TR procedure using up to $N = 16$ measurement points P_j randomly distributed around it (Fig. 1, a) with the nearest and farthest points located 82 mm and 127 mm away from the actuator. Within the second set of experiments, three small aluminium cylinders of various radii R (namely, $R = 5$, 6 and 10 mm), permanently attached to the plate surface with water utilized as a couplant and additional mass of 100 grams placed on their top to ensure the better contact, are considered as artificial obstacles. Points P_j, $j = 1, ..., 32$ are now located along the sides of the square formed by the PWASs. In this case, preliminarily an undamaged plate is considered and each of the actuators A_i, $i = 1, ..., 4$ is excited turn by turn to collect a set of baseline signals. After that one of the cylinders is placed either in the position S_1 or S_2 (Fig 1, b) and the excitation is performed once again, gaining the signals $v_{z,j}(t)$ from the previous subsection.

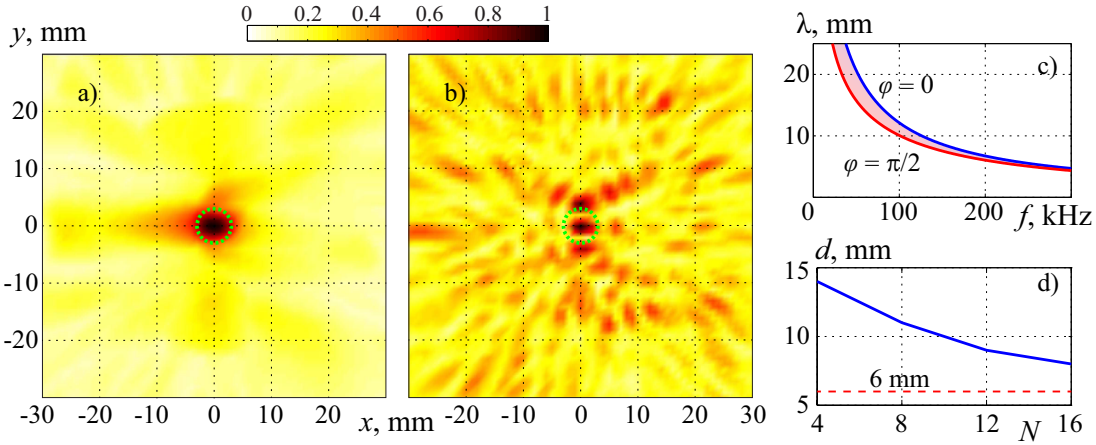

Figure 2: Characterization of the primary source: a,b - directivity patterns $\Delta(\mathbf{x})$; c - dispersion diagrams of $A0$ mode wavelengths; d - estimated diameter of the PWAS A_1

4 RESULTS AND DISCUSSION

As a preliminary study, a principal possibility of the source localization and its size quantification with the developed approach is estimated and the influence of the excitation signal type and the amount of measurement points N on the directivity pattern $\Delta(x)$ is investigated. For this purpose, PWAS A_1 is excited by a broad-band rectangular pulse of width $t_p = 3$ μs or by a narrow-band Hann-windowed 5-cycle sine toneburst with central frequency $f_c = 200$ kHz.

The evaluated surfaces of $\Delta(\mathbf{x})$ in the domain $D = \{(x, y) : |x|, |y| < 30\}$ for $N = 16$ are shown in Fig. 2, a,b respectively. In both of these subplots, the value Δ_1 is achieved at the same point $\hat{\mathbf{x}}_c = (0, 0)$ mm serving as an estimation for the source center location, which is equal to the actual actuator position within the chosen coordinate system. However, it is clear that the actuator size cannot be reliably reconstructed from the narrow-band toneburst excitation data, though the wavelength of the fundamental antisymmetric mode $A0$, being predominant for the frequencies considered, is ranged from ≈ 6 mm for $\varphi = \pi/2$ to ≈ 6.7 mm for $\varphi = 0$ (Fig. 2, c) at $f_c = 200$ kHz, which is almost equal to the PWAS diameter. At the same time, a pulse-type excitation signal provides more precise size estimation, which is illustrated in Fig. 2, d, where the dependency of the diameter d of reconstructed actuator area $\hat{\Omega}$ from the amount of measurement points N is shown. Such a behavior might be explained by the strong presence of low-frequency components in the measured response $v_{z,j}(\omega)$ for the rectangular pulse excitation. At the same time, for the second signal type the spectrum $v_{z,j}(\omega)$ is concentrated near f_c and low-frequency components are almost absent. The overestimation of the actuator size, visible in Fig. 2, d, could is conditioned by the low amplitudes of $v_{z,j}(\omega)$ for $f > 180$ kHz in the case of the pulse excitation.

At the next step, the developed approach is applied for the imaging of artificial obstacles. Each of the actuators A_i, $i = 1, ..., 4$ is excited with the above mentioned rectangular pulse signal, yielding after the numerical re-emission from the points P_j its own directivity pattern $\Delta^{(i)}(\mathbf{x})$. The final imaging function is constructed as an average of $\Delta^{(i)}$: $\Delta_s(\mathbf{x}) = \frac{1}{4}\sum_{i=1}^{4} \Delta^{(i)}(\mathbf{x})$.

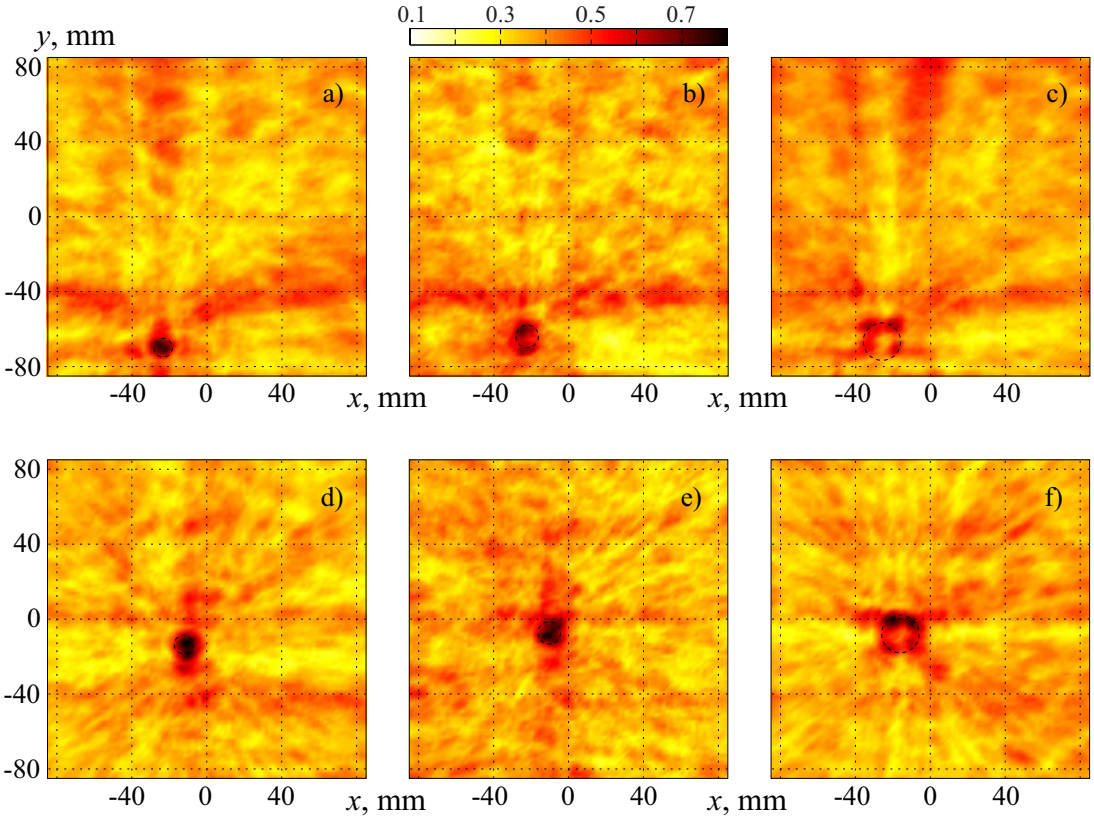

Figure 3: Localization of artificial surface obstacles: a,d - $R = 5$ mm; b,e - $R = 6$ mm; c,f - $R = 10$ mm. Upper plots correspond to the test location S_1, bottom ones stand for position S_2. Dashed circles indicate the true location and size of defects

An example of its surfaces evaluated in the domain $D = \{(x, y) : |x|, |y| < 85\}$ for all the three types of artificial defects (left, middle and right columns) and both possible locations S_1 and S_2 (upper and lower subplots, respectively) utilizing $N = 16$ measurement points (each odd point is taken, starting from P_1 and going counterclockwise, Fig. 1, b) is shown in Fig. 3. In each subplot the actual position and size of the obstacle are indicated by a dashed circle. It should be noted that the vertical scale differs from the one in Fig. 2, a,b. Though each of the functions $\Delta^{(i)}(\mathbf{x})$ reaches its maximum value equal to 1 elsewhere in the domain D by definition, their combination $\Delta_s(\mathbf{x})$ does not necessarily possesses this property, which is visible in Fig. 3. The reason for such behaviour is that the maxima $D_1^{(i)}$ are not achieved at the same point for all the actuators A_i, but rather indicate the obstacle part closest to the current surface load [11]. Nevertheless, the point $\hat{\mathbf{x}}_{c,s}$, where the local maxima of $\Delta_s(\mathbf{x})$ is achieved, seems to be a rather precise estimate of the obstacle location. For example, for the smallest of obstacles ($R = 5$ mm) evaluated values of $\hat{\mathbf{x}}_{c,s}$ are $(-23, -69)$ mm and $(-11, -14)$ mm for the positions S_1 and S_2, respectively, while the true locations are $(-23, -70)$ mm and $(-12, -14)$ mm. Similarly, for the second defect ($R = 6$ mm) the following values are obtained: $(-25, -66)$ mm and $(-10, -10)$ mm versus $(-23, -67)$ mm and $(-10, -8)$ mm. Considering the third obstacle ($R = 10$ mm), local maxima of $\Delta_s(\mathbf{x})$ is

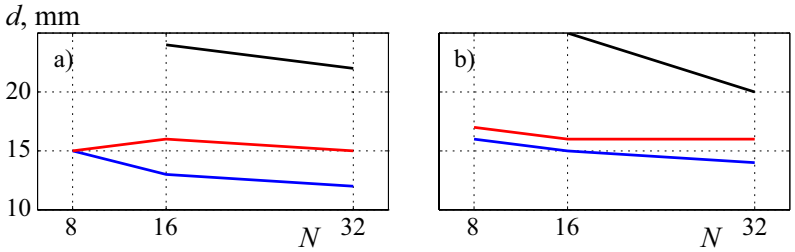

Figure 4: Estimated diameter d of the area $\hat{\Omega}$, which approximates the obstacle extent

achieved at the obstacle border (Fig. 3, c,f), rather than at its center. It might be conditioned either by the small amount of active PWASs utilized in the experiment or by the presence of a small groove in the middle of that cylinder surface, which used to be in contact with the plate (preliminary measurements with the high-precision digital optical microscope confirm this suggestion).

Utilizing the aforementioned "-6 dB" criteria applied to the function $\Delta_s(\mathbf{x})$ allows for the approximate obstacle size evaluation. The results are summarized in Fig. 4 for $N = 8$, 16 and 32 measurement points. The overestimation of the damage size is explained by the poor presence of higher frequency components in the spectrum of the input signals, e.g., the amplitudes $v_{z,j}(\omega)$ acquired even at the points P_j closest to the obstacle location are nearly zero for $f > 150$ kHz. However, an important result is that the first and second obstacles being of close size are clearly distinguishable.

5 CONCLUSIONS

Theoretical and practical aspects of the time reversal method application for damage and/or source localization in thin-walled composite constructions by the means of active GW SHM are presented. Re-emission of time-reversed signals is achieved through the computer model, which is based on the semi-analytical integral approach and efficient asymptotic representations for quasi-cylindrical GWs. Experimental verification of the proposed technique is performed for CFRP plate-like samples with artificial damages of varying extent, excited by piezoelectric wafer active sensors. The obtained results confirm the possibility of a reliable estimation of the inhomogeneity position and size with just a few measurement locations.

The authors are grateful to the Alexander von Humboldt Foundation for the Fellowship for Postdoctoral Researchers of the first author providing the possibility to carry out the joint research. This work is partly funded by the Ministry of Education and Science of the Russian Federation (Project No. 9.1022.2017/ПЧ) and Russian Foundation for Basic Research jointly with Krasnodar Regional Administration (Project No. 16-41-230744).

REFERENCES

[1] Giurgiutiu, V. *Structural Health Monitoring with piezoelectric wafer active sensors*. Academic Press, 2nd Edition, (1989).

[2] Wee, J., Wells, B., Hackney, D., Bradford, P. and Peters, K. Increasing signal amplitude

in fiber Bragg grating detection of Lamb waves using remote bonding *Appl. Opt.* (2016) **55**:5564–5569.

[3] Liu, M., Zeng, Z., Xu, H., Liao, Y., Zhou, L., Zhang, Z. and Su, Z. Applications of a nanocomposite-inspired in-situ broadband ultrasonic sensor to acousto-ultrasonics-based passive and active structural health monitoring *Ultrasonics* (2017) **78**:166–174.

[4] Wang, C.H., Rose, J.T. and Chang, F.K. A synthetic time-reversal imaging method for structural health monitoring *Smart Mater. Struct.* (2004) **13**:415–423.

[5] Wang, C.H. and Rose, L.R.F. Imaging damage using mixed passive and active sensors *Key Eng. Mater.* (2013) **558**:244–251.

[6] Fink, M., Cassereau D., Derode, A., Prada, C., Roux, P., Tanter, M., Thomas, J.-L. and Wu, F. Time-reversed acoustics *Rep. Prog. Phys.* (2000) **63**:1933–1995.

[7] Glushkov, E., Glushkova, N. and Eremin, A. Forced wave propagation and energy distribution in anisotropic laminate composites *J. Acoust. Soc. Am.* (2011) **129**:2923–2934.

[8] Glushkov, E., Glushkova, N., Lammering, R., Eremin, A. and Neumann, M.-N. Lamb wave excitation and propagation in elastic plates with surface obstacles: proper choice of central frequencies *Smart Mater. Struct.* (2011) **20**:015020.

[9] Park, H.W. Numerical simulation and investigation of the spatial focusing of time reversal A0 Lamb wave mode using circular piezoelectric transducers collocated on a rectangular plate *J. Sound. Vib.* (2013) **332**:2672–2687.

[10] Derode, A., Tourin, A. and Fink, M. Time reversal versus phase conjugation in a multiple scattering environment *Ultrasonics* (2002) **40**:275–280.

[11] Eremin, A.A., Glushkov, E.V., Glushkova, N.V. and Lammering, R. Time reversal approach for the inhomogeneity localization in an elastic plate *Acoust. Phys.* (2017) **63**:10 pp (to appear).

VIII ECCOMAS Thematic Conference on Smart Structures and Materials
SMART 2017
A. Güemes, A. Benjeddou , J. Rodellar and Jinsong Leng (Eds)

HEALTH AND USAGE MONITORING OF INTA UNMANNED AIRCRAFTS FOR SURVEILLANCE AND FLYING TARGETS

MALTE FRÖVEL, RICARDO ATIENZA AND FELIX TERROBA

Instituto Nacional de Técnica Aeroespacial "Esteban Terradas", INTA
Crta de Ajalvir pk4, 28850 Torrejón de Ardoz, Spain
e-mail: frovelm@inta.es, terrobarf@inta.es, www.inta.es

Key words: Smart Structures, Fiber optics, Unmanned Air Vehicles, SHM, HUMS

Abstract. The structural health and usage monitoring of remotely piloted air systems (RPAS) or Unmanned Air Vehicles (UAV) is of increasing interest for the evaluation of flight load, the use of data in order to estimate the remaining lifetime of the structure and also for a fast and reliable assessment of structural impacts due to unexpected events that can produce significant loads on the structure, such as hard landings and gusts. This is especially important with composite material structures where damage is quite often barely visible. In-flight load and usage monitoring enables fast turnaround times and increases the availability of the UAV.

The Spanish National Institute for Aerospace Technology (INTA) is developing for over two decades now UAVs for surveillance, reconnaissance and aerial targets. At the moment, a health and usage monitoring system (HUMS) for the INTA's medium altitude and long endurance (MALE) UAV called MILANO and for the flying target DIANA is in development. Both systems are based on fiber Bragg grating sensors (FBGSs) that measure strain and temperature. The use of optical sensors instead of electrical has the advantages of lower weight penalty, longer durability and total immunity to electromagnetic interferences.

The HUMS of MILANO and DIANA is based on the experience gained during flight test activities of SIVA, an all- composite material tactical UAV developed and assembled by INTA. Structural deformations have been measured during flight of SIVA and have been used to calculate structural flight loads. Temperature induced thermal strains have been compensated.

This paper explains the results and data evaluation of the performed flight tests, describes the equipment used and the sensor applications and presents the health and usage monitoring of INTA UAVs.

1 INTRODUCTION

Unmanned Air Vehicles (UAV, also called Remotely Piloted Aircraft Systems or RPAS) are of increasing interest to the military and civilian aviation. Many different designs are already on the market for surveillance and reconnaissance, flying targets and combat. Most of the times the vehicles structures are made of carbon fiber reinforced plastics (CFRP) in order to obtain higher structural efficiency by making use of its very high specific strength and stiffness.

Structural load monitoring of UAVs is of high relevance not only for the evaluation of flight loads and the use of this data in order to estimate the remaining lifetime of the structure, but also for a fast and reliable assessment of structural impacts due to unexpected events that can produce significant loads on the structure, such as hard landings and gusts. This is especially important with CFRP structures where damage is quite often barely visible and conventional nondestructive inspection techniques are time consuming and require highly trained operators. In-flight monitoring enables fast turnaround times and increases the availability of the UAVs.

There appear to be very few cases in which flight load and usage monitoring has been performed with UAVs. The known cases apart from INTA activities with SIVA [1], [2] and MILANO [3] are the structural loads monitoring of the NISHANT UAV by an Israeli- Indian group [4], the HERON UAV from IAI company [5] and NASA activities on IKAHARNA (Predator B) UAV for load monitoring and also 3D shape control of its very flexible wings [6]. In all cases mentioned, fiber Bragg grating sensors (FBGSs) have been used for measuring both strain and temperature. FBGSs are very attractive for the use in UAVs due to their very low weight, minimal volume, multiplexibility, reliability and immunity to electromagnetic influences. Many sensors can be routed in a single optical fiber and they do not interfere or are not interfered by communication and observation antenna systems on board.

Recent developments are the high strength FBGS manufactured in the so called “draw tower process”, DTG, with polyimide or Ormocer coating [7], [8] that are very robust sensors, suitable to stand the harsh aeronautic environment of flight. Test campaigns have been performed at the Spanish National Institute for Aerospace Technology (INTA) that proved the reliability of these FBGSs in a wide temperature range from -150 to 200ºC [9], [10], in cryogenic condition [11], in dry and wet condition, under fatigue loading [12] and in embedded and surface bonded condition in both composite material and metal [13].

Currently there is no flight certified interrogator for FBGSs on the market, although developments from Smart Fibers Company [14], Insensys/ Epsilon Optics Company [15], 4DSP Company [16] and Technobis Company [17] are adequate systems for airborne applications.

The following paper describes the activities of INTA using a HUMS based on robust DTG of three of their UAVs, the tactical SIVA, the MALE MILANO and the fast flying target DIANA.

2 INTA UAVS WITH INTEGRATED MONITORIZATION

A lot of experiences have been gained in the last 20 years at INTA in the design, manufacturing and application of internally developed UAVs for surveillance, reconnaissance and fast flying targets. One of the UAVs developed and assembled by INTA is SIVA, an all-

composite material, tactical UAV with a 6 m wing span, 40 kg of payload, 4000 m of service ceiling and six hours of endurance.

A SIVA is instrumented with fifteen FBGSs that measure both strain and temperature in different structural points of interest, such as the outer wing, the metallic wing attachment, the front and rear fuselage, a stabilizer and the landing gear, see figure 1. Structural deformations of the SIVA have been measured during several flights and structural flight loads have been calculated. Temperature induced thermal strains have been compensated for. The SIVA UAV has been equipped with an autonomous fiber optic load monitoring system consisting of a time domain interrogator from INSENSYS (now EPSILON OPTICS) that collects information from an optical fiber harness and strain and temperature sensors.



Figure 1. INTA UAVs with integrated monitoring systems. Up: MILANO. Down left: DIANA and Down right: SIVA showing the sensor position and fiber routing

MILANO UAV was developed out of a research and development project for MALE operations of INTA. The all CFRP structure has a wing span of 12.5 m, service of ceiling of 9000 m and more than 20 h of endurance, see figure 1. The first flight of this MALE UAV is expected in year 2017. MILANO has been equipped with about 70 FBGSs in the central and external wings, central and aft fuselage. The main objectives of the installed sensor systems are flight loads monitoring, special event monitoring, design data verification and data collection for certification. The temperature compensation of the data will be made with the installed temperature sensors and previously performed calibrations. The data will be extracted and analyzed on ground after each flight or group of flights in order to estimate the residual life of the structure.

DIANA I-A is an INTA development for a fast flying aerial target. It is designed to perform real air threat simulations of current and future weapon systems. It is a system intended to train operators of weapons systems, as well as the evaluation and calibration of such systems. The DIANA I-A target drone is launched by pneumatic catapult and recovered at sea by parachute

deployment. Its objectives are high speed straight path flights, high maneuverability simulating escape and low-altitude maneuvers, low cost in manufacturing, service and maintenance, the integration of tow targets and the capability of real threat emulation. The HUMS of DIANA´s highly loaded front fuselage measures the strain distribution in the four front stringers. A reference strain distribution of each instrumented UAV has been taken of the pristine structure before the flight by loading the structure with calibrated weights. Any significant change in the strain distribution indicates a stiffness change of at least one of the measured structural components and is an indicator of a possible structural damage.

1. FLIGHT TESTS OF SIVA

Several flight tests have been carried out with SIVA proving a good performance of the monitoring system. The flight tests had the aim to demonstrate the performance reliability of the monitoring equipment, the sensors, their harness and the subsequent data evaluation under real in service conditions. Figure 2 shows the flight test data from twelve strain sensors and three temperature sensors during a short 20-minute flight. Taxying, take off, cruise and maneuvers, landing and new taxying can be seen on the graph. A detail of the landing, where the highest loads have been detected in the wing attachment and in the landing gear, can be seen in figure 3. The flight tests demonstrated the reliability of the monitoring system and its components and identified the structural loads during maneuvers, starts and landings. Special events such as hard landings and gust loads can be recognized and flagged automatically when passing a predefined threshold. All these data can help the maintenance crew after each flight in their decision to perform a detailed inspection or to go for the next sortie. Analysis of the fatigue state of SIVA can be performed by the determination of load spectrums of the obtained data, the use of cycle counting techniques and the comparison of the results with fatigue measurements performed on specimen and component level. The obtained results of the SIVA flight tests series encouraged to take a step forward and start the development of a HUMS for INTA's MALE UAV MILANO.

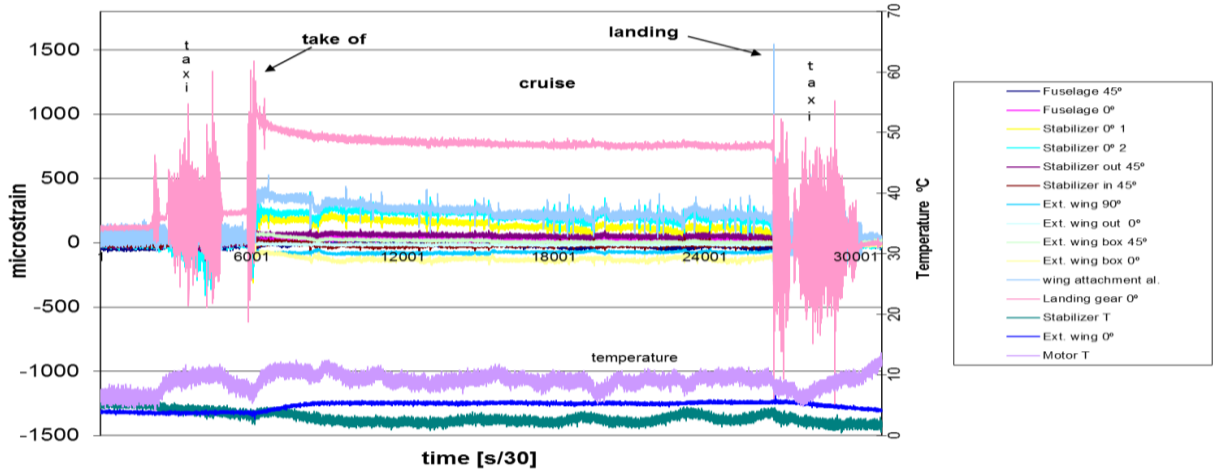

Figure 2. Flight test data of SIVA showing strain measured by twelve strain and three temperature FBGSs

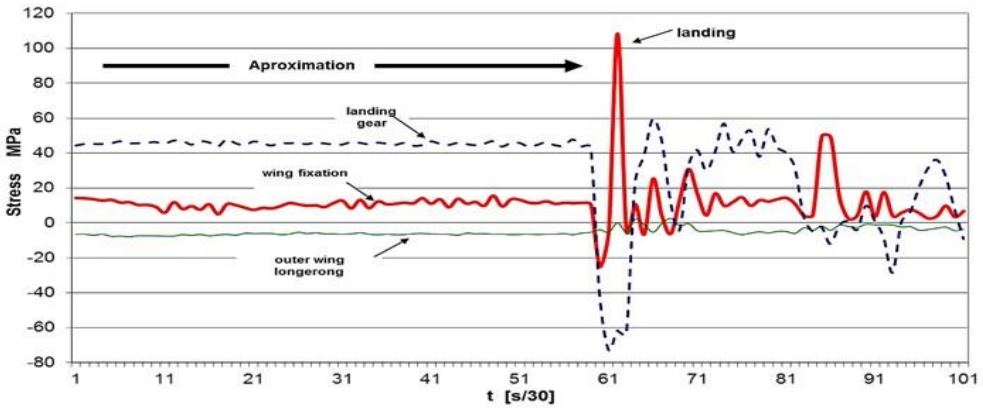

Figure 3. Detail of three seconds duration during landing showing the stresses in the landing gear, aluminum wing attachment and outer wing spar.

2. GROUND TEST EVALUATION OF MILANO WING

The MILANO has been fully instrumented but no flight tests have been performed yet. The performance of the monitoring system has been tested in ground tests on its structure. The wing has been loaded with the corresponding flight loads demanded for the flight certification. The strain distribution in the wing box has been measured with 9 FBGSs that are surface bonded on the leading and trailing edge wing spars as it can be seen in the sketch of figure 5. During the ground tests bearing failures occurred in two rivets on the leading edge side and in one rivet on the trailing edge side of the connection of the composite skin to the metal external wing attachment, figure 4.

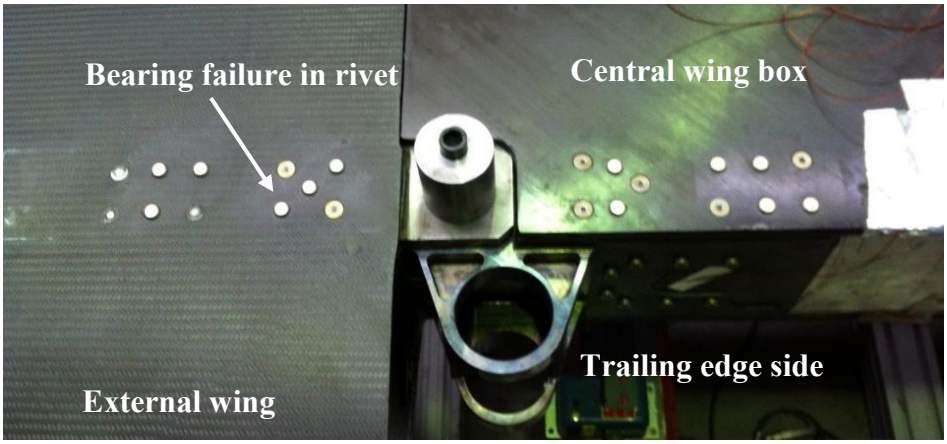

Figure 4. Image of the joint between central and external wing on the trailing edge side showing the location of the bearing failure of one rivet.

After the damage, the global wing deflection under load had almost no notable change, but the strain distribution changed in the central wing box and that was clearly detected by the installed FBGSs, figure 5. A significant change of the strain distribution can be seen in the trailing and leading edge sensors Nº 1 and Nº 2 and in the transversal wing spar sensor of the leading edge side Nº 7, where a sudden variation of more than 100 microstrain could be detected when the damage occurred. This sudden change of the strain value is already for itself an indicator, but the presence of a damage is even more visible, when calculating the difference of the measured strains at the different sensor locations. Another indicator of damage is the strain offset at zero load after the test which is clearly visible in sensor 7 for the individual measurement, but is even better visible, when calculating the differences of the sensor pairs 2 and 1 (or 8 and 9). When statistical techniques such as the principal component analysis (PCA) are applied [18], changes from the normal strain distribution become automatically detectable and possible damage can be flagged. In this case it is not possible to know the exact location of the damage or its size, but the fact that damage has occurred in a component and that inspection is required can be identified.

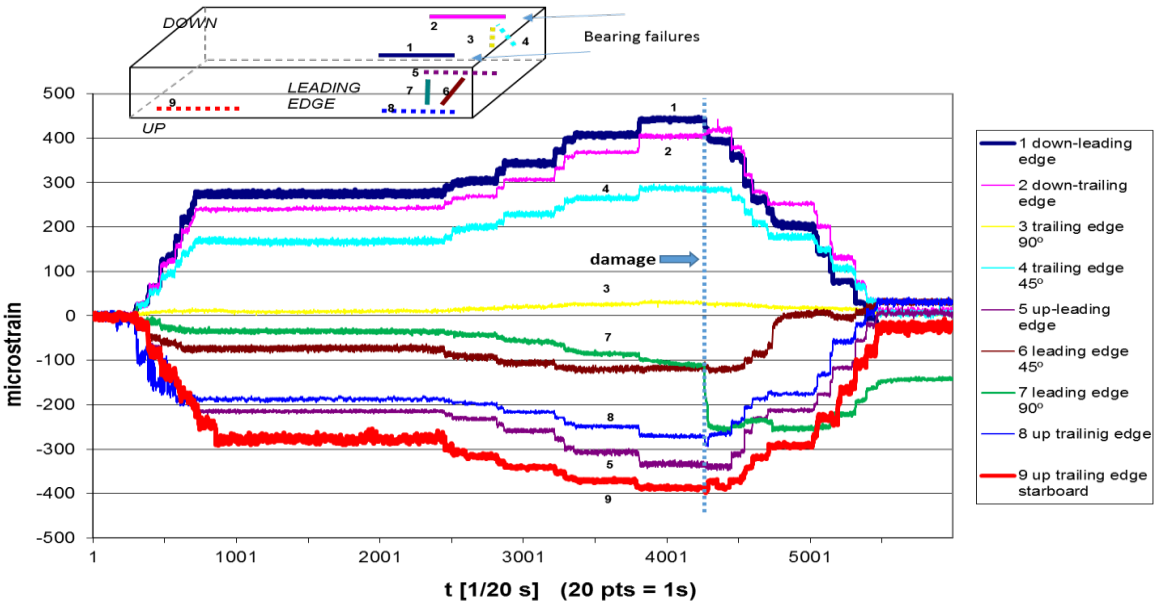

Figure 5. Strain distribution in the wing box during loading tests when the bearing failure occurred. The dotted vertical line indicates the occurrence of the damage. The sketch shows the central wing box and the sensor positions

3. INSTRUMENTATION OF TWO DIANAS FOR FLIGHT TESTS

Calibrations and tests have been performed on a DIANA test fuselage, were real damages have been introduced and the response of the monitoring system has been calibrated. After this, two in-service DIANAS have been instrument with a monitoring system based on FBGSs attached in the frontal part of each of the four stringers.

Robust FBGS type OS3200 from MICRON OPTICS Company were surface bonded using X120 two component epoxy adhesive from HBM Company. The two target drones have been calibrated before flight with the 100N weight applying it in the front bulkhead, see **Figure** . After the calibration, the optical cables with their connectors have been stored inside the equipment bay of each respective drone and both drones have been sent to perform a flight test campaign.



Figure 8: Calibration of the two in-service DIANAS with 100N weight.

4. CONCLUSIONS

The viability for airborne applications of FBGS optical fiber sensors, their optical fiber harness and the corresponding interrogator have been demonstrated during flight tests of SIVA tactical UAV. The experience gained on SIVA UAV has been used to design an in-flight Health and Usage Monitoring System (HUMS) for the MALE UAV MILANO. FBGSs have been used both for load monitorization and for fatigue life estimation, special event recording, design verification and optimization. The ground tests on the MILANO wing demonstrated the potential to detect structural damages during flight by the change of the load path and strain distributions.

The HUMS tested in the front fuselage of DIANA I-A target drone has been demonstrated to be a fast and reliable technique for the detection of small and barely visible. It is a useful tool for the maintenance personal to allow fast turnaround times of the drone where no ultrasonic tests can be performed due to the materials and surface protection layers used in its structure. The system will be extensively tested in flight with two target drones.

5. REFERENCES

[1] M. Frövel, G. Carrión, J. M. Pintado, “Structural Loads Monitoring of an Unmanned Air Vehicle”, 5th European Workshop on Structural Health Monitoring, EWSHM-10, ISBN 978-1-60595-024-2, Sorento, Italia, 2010

[2] Malte Frövel, Monografías del SOPT, “Mantenimiento predictive y monitorización structural en plataformas militares”, Ministerio de Defensa, Subdirección General de Publicaciones y Patrimonio Cultural, 2016,

http://www.tecnologiaeinnovacion.defensa.gob.es/es-es/Contenido/Paginas/detallepublicacion.aspx?publicacionID=211

[3] M. Frövel, G. Carrión, J. M. Pintado, J. Cabezas, F. Cabrerizo; "Health and Usage Monitoring of INTA unmanned Vehicles", Structural Health Monitoring Journal, DOI: 10.1177/1475921716676992, 2016 http://shm.sagepub.com/cgi/reprint/1475921716676992v1.pdf?ijkey=ui2YWMd3i0ae34h&keytype=finite

[4] Kressel, A. Handelman, Y. Botsev, J. Balter, P. Guedj, N. Gorbatov, M. Tur, Acr Pillai, M. H. Prasad, N. Gupta, A. M. Joseph and R. Sundaram, "Evaluation of flight data from an airworthy structural health monitoring system integrally embedded in an unmanned air vehicle", 6th European Workshop on Structural Health Monitoring, EWSHM-12, Dresden, Germany, ISBN_978-3-940283-41-2,pp: 1004-1007, 2012

[5] I. Kressel, J. Balter, N. Mashiach, I. Sovran, O. Shapira, N.Y. Shemesh, B. Glam, A. Dvorjetski, T. Yehoshua, M. Tur, "High speed in-flight structural health monitoring system for medium altitude long endurance unmanned air vehicle", 7th European Workshop on Structural Health Monitoring, pp. 274-280, Nantes, France, July 8-11, 2014.

[6] NASA information, http://www.nasa.gov/centers/dryden/history/pastprojects/WSFM/index.html, http://www.spacedaily.com/reports/NASA_evaluates_new_wing_sensor_999.html,

[7] Chojetzki C., Rothhardt M., Ommer J., Unger S., Schuster K., Müller H.R., "High-reflective Draw-tower fiber Bragg gratings-arrays and single gratings of type II"; Optical Engineering, Vol 44 (6), June 2005.

[8] Rothhardt M., Chojetzky C., Müller H.R.: "High mechanical strength single pulse draw tower gratings", Proc. SPIE Vol. 5579, Part A, pp. 127-135, 2004

[9] M. Frövel, E. del Olmo, J. M. Pintad; "Optical fiber Bragg grating sensors embedded in CFRP composites for structural health monitoring of aerospace structures"; Proceedings of the Adaptronic Congress 08, Berlin

[10] M. Frövel, G. Carrión, C. Gutiérrez, C. Moravec, J. M. Pintado. "Temperature and humidity dependent performance of FBG- strain sensors embedded in carbon/epoxy composites", Proceedings of SPIE Smart Structures/NDE, 16th annual international symposium, San Diego, USA, 2009

[11] M. Frövel , A. Güemes , J.M. Pintado , E. Olmo, A. Obst; "Multiplexable Fiber Bragg grating temperature sensors embedded in CFRP structures for cryogenic applications", 3rd European Workshop on Structural Health Monitoring, Conference Centre Granada, Spain, 2006

[12] M. Frövel, E. del Olmo, G. Carrión, J. M. Pintado, "Influence of Fatigue Loads and Temperature on the Response of FBGS embedded in Composite Material for Aerospace

Applications", 5th European Workshop on Structural Health Monitoring, EWSHM-10, ISBN 978-1-60595-024-2,Sorento, Italia, 2010

[13] Malte Frovel, Javier Sanmillán, Gabriel Carrión, José María Pintado, Fernando Cabrerizo, Felix Terroba, Arnd Reutlinger, Thorbjoern Buck, "Robust integration of optical fiber sensors for aerospace applications in composite material structures", Proceedings of the EWSHM, Bilbao, Spain, 2016, http://www.ndt.net/search/docs.php3?showForm=off&id=19870

[14] Smart fibers product information, http://www.smartfibres.com/Attachments/SFref298.pdf, http://www.smartfibres.com/docs/SFRef269.pdf, http://www.smartfibres.com/Attachments/SFref298.pdf,

[15] Insensys, Epsilon Optics product information, http://www.epsilonoptics.com/interrogators.html,

[16] 4DSP product information, http://www.4fos.com/RTS150.php,

[17] Technobis product information, http://www.technobis-fibre-technologies.nl/index.php/2012-06-29-19-32-23,

[18] J. Sierra, M, Frövel, E. Del Olmo, A. Güemes, J.M. Pintado; "A robust procedure for damage identification in a lattice spacecraft structural element by mean of strain field pattern recognition techniques", European conference on Composite materials, ECCM, Sevilla, Spain, June 2014

VIII ECCOMAS Thematic Conference on Smart Structures and Materials
SMART 2017
A. Güemes, A. Benjeddou, J. Rodellar and J. Leng (Eds)

IMPACT DETECTION AND IDENTIFICATION IN SENSORIZED STRUCTURES BY NEURAL NETWORK PROCESSING OF DYNAMIC TRANSIENT HISTORIES

VÍCTOR RAMÍREZ† AND DIEGO GARIJO*

†Safran Engineering Services (Safran Group)
Calle Arnaldo de Vilanova, 5, 28906 Getafe (Madrid), Spain
e-mail: victor.ramirez-gonzalez@safrangroup.com

* IMDEA Materials Institute
Calle Eric Kandel, 2, 28906 Getafe (Madrid), Spain
e-mail: diego.garijo@imdea.org

Key words: Impact, Sensorized Structures, Artificial Neural Networks, Structural Health Monitoring, White Noise

Abstract. The detection of impact events has become a major challenge for the Structural Health Monitoring (SHM) community due to the severe damages that external menaces can induce in structures, e.g. airframe components exposed to impact of birds, runway debris, ice, failed engine fragments or tool drop. Notable efforts are being devoted to the effective monitoring of dynamic transient responses in experimental tests with sensorized aeronautical specimens subjected to ballistic impacts. This work prospects the use of Artificial Neural Networks (ANN) with supervised learning procedure to identify the severity of an impact event from the processing of dynamic transient histories retrieved at discrete points within the structure. Such dynamic response is built with Abaqus / Explicit Finite Element (FE) simulations of spherical projectiles shot against metallic plates. A Bernstein collocation technique is used for the reduction of the sampled data histories down to a selectable number of coefficients. The investigation focuses on the accuracy of the predictions provided by the ANN-FEA scheme and on the sensitivity and robustness of the algorithm versus unavoidable perturbing noise present in the in–service operative conditions of the detection system.

1 INTRODUCTION

The installation of sensor devices into modern structural designs constitutes today a necessary practice for the effective Structural Health Monitoring (SHM) in the aerospace, automotive and civil industries [1]. In addition to the detection of damage and the structural diagnosis and prognosis, sensors measurements can be employed for the assessment of complex constitutive responses of materials such as composites (Figure 1a) or for the identification of perturbations in the nominal operative conditions of structural systems. In particular, the analysis of dynamic

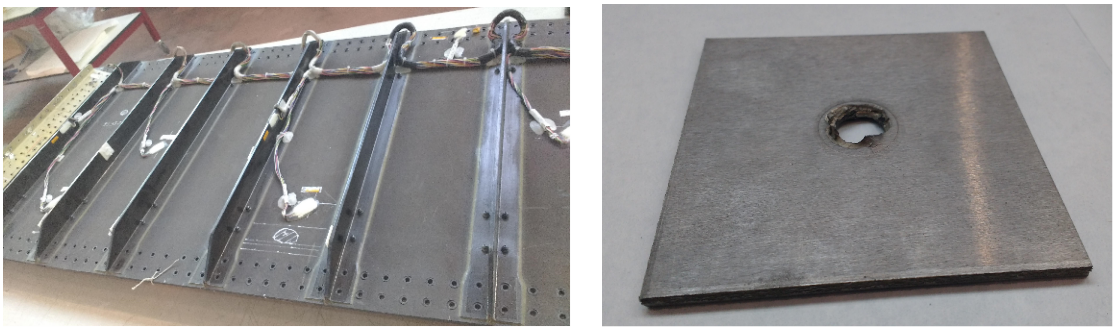

(a) (b)

Figure 1: Sensorized CFRP structure (a) and metallic plate perforated due to ballistic impact (b), IMDEA Materials Institute facilities.

transient histories retrieved from experimental tests with sensorized specimens subjected to ballistic impact (Figure 1b) is of major interest for material engineers and designers of protective shields for aerospace applications, e.g. Seidt *et al.* [2] (2012), Yaghoubi and Liaw [3] (2012), Pereira *et al.* [4] (2013). Moreover, taking advantage of the increased capacity of computational resources available today, the Virtual Testing (VT) framework [5][6], based on advanced simulation techniques, is being used to progressively replace the expensive and time–consuming experimental campaigns by high–fidelity Finite Element Analyses (FEA) of structures subjected to ballistic impacts [7].

As a continuation of the vibration–based SHM investigation presented by Ramírez *et al.* [8] in 2016, focused on the detection and identification of embedded damage in structural components from the shifts produced in their eigenfrequencies by means of the combined use of Artificial Neural Networks (ANN) and FEA, the present work proposes the application of an ANN–FEA scheme to identify the severity of an impact event (in terms of projectile velocity and angle of incidence) from dynamic transient histories gauged at discrete points within a structure. The training set required for the supervised learning procedure is generated numerically with Abaqus / Explicit [9] FE simulations of spherical projectiles launched against metallic plates characterized with Johnson–Cook plasticity and damage models. The design of this system aimed at the in–service recognition of critical impacts on damageable areas of vehicles is conditioned by the unavoidable presence of random noise in the sensor measurements during such in–service operation. Thus, emphasis is placed on the capability of the ANN to manage the non-uniqueness nature of the solution of the inverse problem, taking as input data from sensors sampled temporal series affected by white noise generated with MATLAB [10] technology.

2 INVERSE PROBLEM IN HIGH VELOCITY IMPACT EVENTS

The structural response $\mathbf{Y}_d(t)$ of a system subjected to an external dynamic perturbation $\mathbf{p}_d(\boldsymbol{\theta})$ can be expressed, in a general form [8][11]:

$$\mathbf{Y}_d(t) = \mathbf{F}\left(\mathbf{K}\left(\mathbf{p}_d(\boldsymbol{\theta}), \sigma_s, t\right), \mathbf{C}\left(\mathbf{p}_d(\boldsymbol{\theta}), \sigma_s, t\right), \mathbf{M}\left(\mathbf{p}_d(\boldsymbol{\theta}), \sigma_s, t\right)\right) \tag{1}$$

wherein t stands for time, and $\mathbf{K}$, $\mathbf{C}$ and $\mathbf{M}$ are, respectively, the stiffness, damping and mass matrices of the system, which are altered by the structural damage induced by $\mathbf{p}_d(\boldsymbol{\theta})$, and

additionally affected by stochastic environmental and in–service factors that are assumed to be arranged following a random distribution σ_s. Generally, in complex structures, the function $\mathbf{Y}_d(t)$ can only be retrieved at discrete locations at which sensors are installed and provide sampled data in time, $\mathbf{Y}_i$. The distribution σ_s typically results in an overlapped random noise signal in the sampled series: $\mathbf{Y}_i^\sigma$. With the measurements $\mathbf{Y}_i^\sigma$, the estimation of the values $\boldsymbol{\theta}$ that characterize the perturbation $\mathbf{p}_d$ constitutes the so–called *inverse problem* of SHM:

$$\boldsymbol{\theta}^* = \mathbf{F}^{-1}(\mathbf{Y}_i^\sigma) \tag{2}$$

Investigations show that problem (2) suffers from non-uniqueness and instability of its solutions [8][11]. Since the mechanical behaviour of the system can be highly complex, the *direct function* $\mathbf{F}$ in (1) has to be, in many cases, inferred from physical tests or simulated numerically. Thus, explicit closed forms for its *inverse function* $\mathbf{F}^{-1}$ in (2) are not achievable. As described in section 2.3, a machine learning procedure is suitable for tackling these issues associated to the inverse problem (2).

For the case of high velocity impacts (HVI), e.g. airframes exposed to threats such as collision of small metallic fragments, the dynamic perturbation $\mathbf{p}_d$ can be fully defined in terms of the kinetic energy of the projectile and its velocity vector at impact. Thus, for the analyses presented in this work, $\boldsymbol{\theta} = [v_i \quad \alpha]^T$, v_i being the magnitude of the velocity and α the angle of incidence of the impactor. A predictor system for the in–service assessment of v_i and α can provide valuable information regarding the severity of the detected impact, and help to determine the subsequent actions to be taken after the detection, including the need of immediate repair, interruption or cancellation of the operation, or, on the contrary, to discard critical damage in the structure.

2.1 Finite Element modelling of ballistic impact

The simulations used to generate the training set for the ANN are carried out by means of the explicit Abaqus solver [9]. FEMs of rectangular plates impacted by spherical projectiles are built using solid C3D8R elements in the discretization. In the case of the targets, a two–level strategy with a coarse mesh in the outer region and a refined structured mesh at the central region of interest is adopted. Selectable mesh density at impact area and selectable number of elements in the through–the–thickness direction are employed. For both, targets (aluminum plates) and impactors (steel spheres), the Johnson–Cook material and damage model [12] is selected. This model is widely accepted for high strain metals such as aluminum. It takes into account strain rate and thermal effects, and various investigations exist in the literature which provide the full sets of material parameters needed to implement computationally this model (Kay [13], 2003; Buyuk *et al.* [14], 2009). The range of velocities and angles of incidence selected to generate the training set for the ANN are $0 \leq v_i \leq 300$ m/s and $0° \leq \alpha \leq 45°$. Further details and results of the developed numerical models are provided in Figure 2.

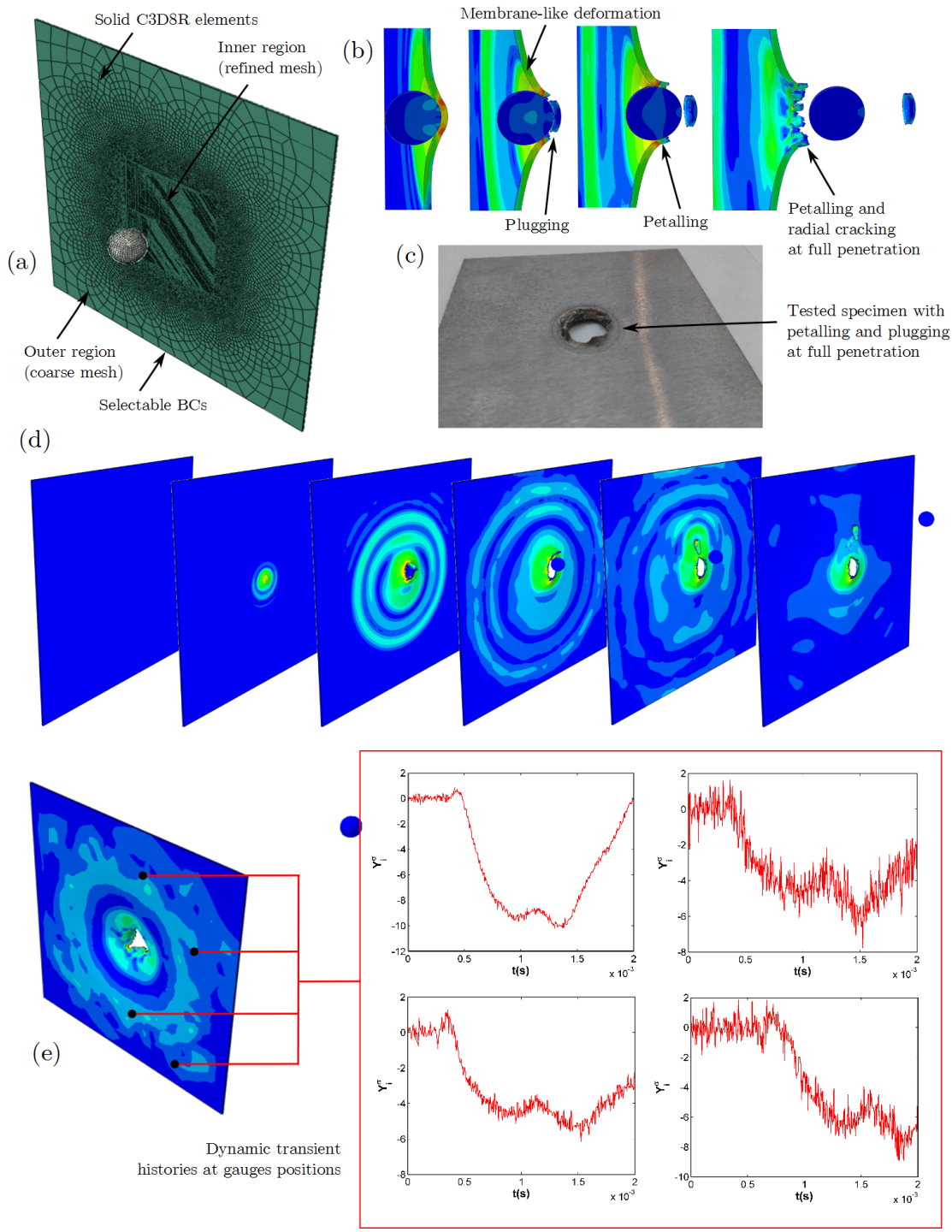

Figure 2: (a) FEM description; (b) damage and failure mechanisms in metallic plates under ballistic impact; (c) tested specimen with full perforation; (d) stress field in sequence of oblique impact; (e) dynamic transient histories of different shot scenarios at different gauge positions and with different signal–to–noise ratios.

Four sensorized positions around the expected impact location in the plate are chosen for the sampling of the dynamic transient histories $\mathbf{Y}_i^\sigma$ (Figure 2e). Out–of–plane displacements are selected as representative gauged magnitudes for the study, but others may also be suitable once the high–fidelity VTs are properly correlated versus physical experiments. Examples of alternative monitored magnitudes in previous numerical–experimental investigations are impactor reaction force histories (Lopes *et al.* [15], 2009) or dynamic transient strain histories (Yaghoubi and Liaw [3], 2012). The overlapped random noise signal is incorporated into the histories by means of MATLAB function **awgn** as white noise with selectable signal–to–noise ratio.

2.2 Collocation method for the reduction of sampled transient histories

Depending on the sensors' data acquisition rate, the computational storage may become critical when working with signals sampled in time. For the time window considered in this study (2 ms), the dynamic transient histories are discretized in a total of 401 points. A reduction of the dimension of the problem must be pursued in order to enable the training of the ANN with a finite number of elements in the training set. Here, a Bernstein collocation technique [16] is proposed for the reduction of the sampled data histories down to a finite number of coefficients. The Bernstein collocation yields a smooth and continuous approximation $\mathcal{B}$ of selectable polynomial order $N-1$ of any bounded function. In particular, for the sampled series $\mathbf{Y}_i^\sigma$ (Figure 3):

$$\mathbf{B}_i^\sigma = \mathcal{B}\left(\mathbf{Y}_i^\sigma\right) = \sum_{k=1}^{N} B_{k-1}^{N-1}\left(t\right) a_{ki}^\sigma = \mathbf{B}^T \mathbf{a}_i^\sigma \tag{3}$$

where the kth element of the array $\mathbf{B}^T$ is given by the expression:

$$B_{k-1}^{N-1}\left(t\right) = \binom{N-1}{k-1} t^{k-1} \left(1-t\right)^{N-k} \tag{4}$$

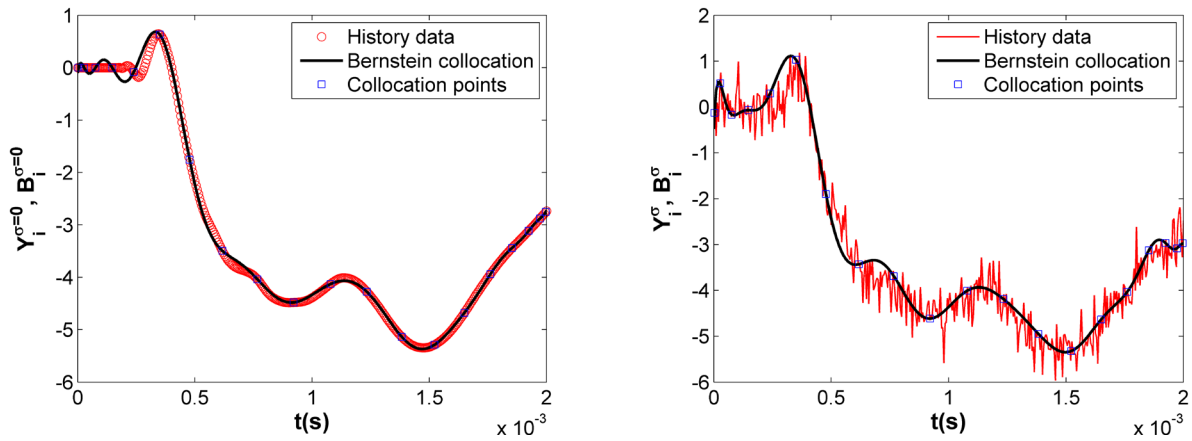

(a) (b)

Figure 3: Dynamic transient history sampled after HVI and associated Bernstein approximation, (a) no overlapped white noise ($\sigma = 0$); (b) overlapped white noise ($\sigma \neq 0$) with signal–to–noise ratio $\rho_{SN} = 10$.

The array of Bernstein coefficients $\mathbf{a}_i^\sigma$ is obtained from the collocation at the Chebyshev nodes (instants) τ_j, $j = 1, \dots N$ in the sampled interval of time: $\mathbf{a}_i^\sigma = \mathbf{H}^{-1}\mathbf{\Lambda}_i^\sigma$, wherein $[\mathbf{\Lambda}_i^\sigma]_j = \mathbf{Y}_i^\sigma(\tau_j)$ and $[\mathbf{H}]_{jk} = B_{k-1}^{N-1}(\tau_j)$. Therefore, the coefficients $\mathbf{a}_i^\sigma$, which already contain a random component associated to the white noise in the original signal, are directly used as inputs of the ANN, without need of further filter of the signal by conventional techniques (e.g. FFT). The numerical experiments presented in section 3 illustrate the performance of this method working with $N = 20$ coefficients, what implies a reduction x(1/20) of the problem dimension.

2.3 Neural Network prediction

Multiple impact scenarios $\boldsymbol{\theta}^t = \begin{bmatrix} v_i^t & \alpha^t \end{bmatrix}^T$ in the ranges of velocity and angle of incidence previously specified are generated for training the ANN by means of Python scripting for Abaqus [9] explicit FEA. Once the dynamic transient histories are post–processed as described in section 2.2, from the set of M training data $\mathbf{L}_t^T = \begin{bmatrix} \mathbf{a}_{1,t}^\sigma & \mathbf{a}_{2,t}^\sigma & \dots & \mathbf{a}_{M,t}^\sigma \end{bmatrix}$, the ANN prediction $\mathbf{\Theta}^*$ is computed as a weighted sum of the contributions of the H neurons that compose the hidden layer of the network [8]:

$$\mathbf{\Theta}_k^*(\mathbf{a}_m^\sigma, \mathbf{p}^*) = \sum_{i=1}^{H} \nu_{ki}^* S\left(\sum_{j=1}^{N} w_{ij}^* a_{j,m}^\sigma + u_{ki}^*\right) \tag{5}$$

$\mathbf{a}_m^\sigma$ being the N *measured* Bernstein coefficients associated to the unknown impact scenario $\boldsymbol{\theta}^*$ to be determined (this is, the predicted solution of the *inverse problem*). In equation (5), S is the activation (sigmoidal) function of the ANN and $\mathbf{p}^*$ is the array of the ANN parameters ($\mathbf{p}^T = [u_{ki} \;\; v_{ki} \;\; w_{ki}]$, $i = 1, \dots, H$; $j = 1, \dots, N$; $k = 1, \dots, K = \operatorname{len}(\boldsymbol{\theta})$) that results from the minimization of the quadratic norm of error $J(\mathbf{p})$, $\mathbf{p}^* = \arg\min_{\mathbf{p}}(J(\mathbf{p}))$:

$$J(\mathbf{p}) = \frac{1}{2} \sum_{\mathbf{a}_{i,t}^\sigma \in \mathbf{L}_t^T} \left[\mathbf{\Theta}\left(\mathbf{a}_{i,t}^\sigma, \mathbf{p}\right) - \boldsymbol{\theta}^t\right]^T \left[\mathbf{\Theta}\left(\mathbf{a}_{i,t}^\sigma, \mathbf{p}\right) - \boldsymbol{\theta}^t\right] \tag{6}$$

In order to calculate $\mathbf{p}^*$, MATLAB uses by default the Levenberg–Marquardt algorithm (LMA). Other coded procedures such as the standard and the limited–memory Broyden–Fletcher–Goldfarb–Shanno (BFGS & L–BFGS) algorithms have also demonstrated excellent performances in multivariable optimization problems.

Following the strategy proposed in Ramírez *et al.* [8], an extended training set $\mathbf{EL}_t^T$ is proposed in order to improve the predictions of the ANN when it is fed with dynamic histories with perturbing noise. The set $\mathbf{EL}_t^T$ is built with multiple copies of the training impact scenarios affected by different random training noises σ_t:

$$\mathbf{EL}_t^T = \left[\mathbf{a}_{1,t}^{\sigma_t} \;\; \mathbf{a}_{2,t}^{\sigma_t} \;\; \dots \;\; \mathbf{a}_{M,t}^{\sigma_t} \underbrace{\dots \;\; \mathbf{a}_{1,t}^{\sigma_t} \;\; \mathbf{a}_{2,t}^{\sigma_t} \;\; \dots \;\; \mathbf{a}_{M,t}^{\sigma_t} \;\; \dots}_{M_E \text{ additional training sets}}\right] \tag{7}$$

The numerical experimentation presented in section 3 addresses if a better predicting performance is retrieved from an ANN when it is trained with an extended set $\mathbf{EL}_t^T$.

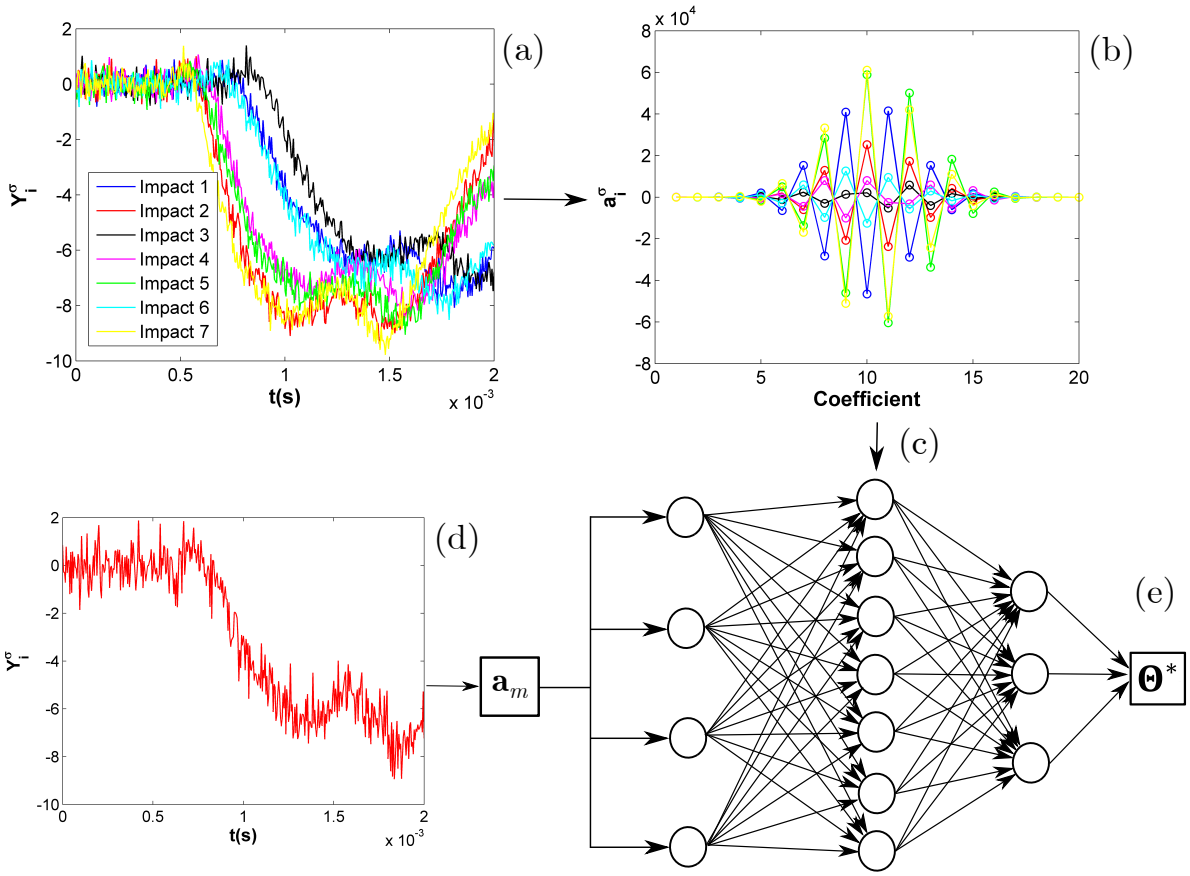

Figure 4: General workflow for impact identification: (a) generation of training set; (b) post–processing of transient histories; (c) training of the ANN; (d) impact detection and data acquisition; (e) severity prediction.

3 NUMERICAL EXPERIMENTATION

MATLAB Neural Network Toolbox technology is employed to predict the velocity and the angle of incidence of the impactor, $\mathbf{\Theta}^* = [v_i^* \quad \alpha^*]^T$, with a single–layer–perceptron with $H = 40$ neurons in the hidden layer. The extension $\mathbf{EL}_t^T$ is generated with $M_E = 50$ copies of the primary training set, which contains $M = 176$ temporal samplings. The dynamic transient histories are reduced to a Bernstein basis of $N = 20$ polynomials. Regularized Bernstein coefficients are considered to balance their weight in the algorithm. The random white noise introduced by means of the function **awgn** is swept in the range $\rho_{SN} = 5 - 30$.

The ANN–FEA scheme is tested with multiple impact scenarios $\left[v_{ij}^* \quad \alpha_j^*\right]^T$ contained in the ranges of interest and affected by random noise σ_s. Figure 5a illustrates a global norm of error $E \in [0, 1]$ (prediction accuracy increasing with E) in the velocity predictions for several $\rho_{SN}(\sigma_s)$ & $\rho_{SN}(\sigma_t)$ combinations. Note that lower ρ_{SN} values correspond to signals noticeably distorted due to noise (Figure 5b). When the in–service noise σ_s is barely perceptible, Figure 5a shows that the ANN predictions are satisfactory for also small training noises σ_t. The

accuracy of the predictions decreases if over–training ($\rho_{SN}(\sigma_t) < \rho_{SN}(\sigma_s)$) is applied (Figure 6a vs 6b), as it was detected in Ramírez *et al.* [8]. In any case, for $\rho_{SN}(\sigma_s) \geq 15$, the velocity predictions are moderately accurate in spite of the over–training (Figure 6a) and highly accurate for $\rho_{SN}(\sigma_t) = \rho_{SN}(\sigma_s)$ (Figure 6b). The trend changes for signals noticeably distorted ($\rho_{SN}(\sigma_s) < 15$), for which the optimum performance is achieved with ANN trained with the same noise than the foreseen one (Figure 6c vs 6d). Over– and under– training, especially the latter one, yield worse predictions (Figure 5a).

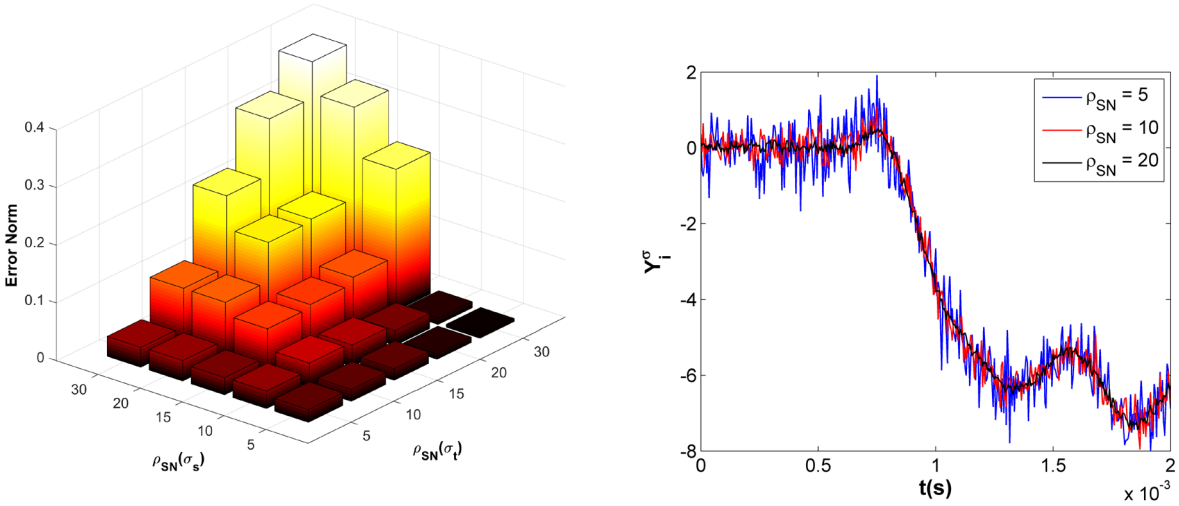

(a) (b)

Figure 5: (a) Global norm of error in impact velocity for several combinations $\rho_{SN}(\sigma_s)$ & $\rho_{SN}(\sigma_t)$; (b) dynamic transient history affected by noises of different intensities.

In the case of the angle of incidence, the predictions for highly distorted histories lack the accuracy presented for the velocity, but remarkable corrections can be attained if the ANN is trained with the proper noise (Figure 7a vs 7b), and over– and under– trainings are avoided.

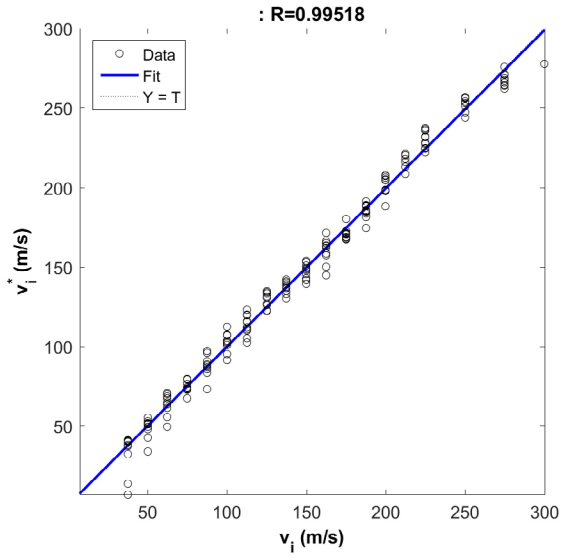

(a) $\rho_{SN}(\sigma_s) = 15$, $\rho_{SN}(\sigma_t) = 5$

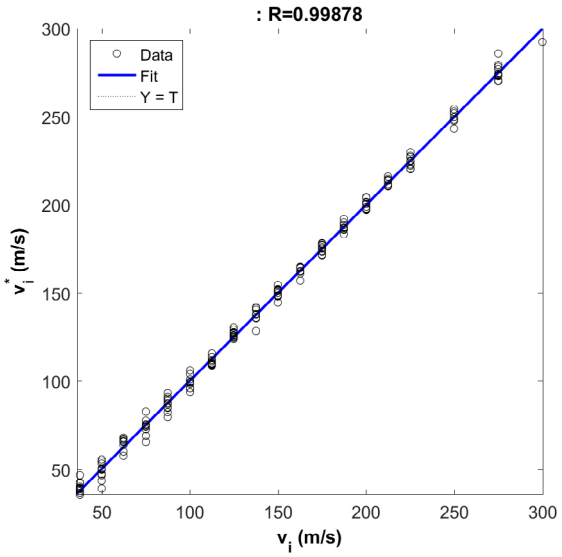

(b) $\rho_{SN}(\sigma_s) = 15$, $\rho_{SN}(\sigma_t) = 15$

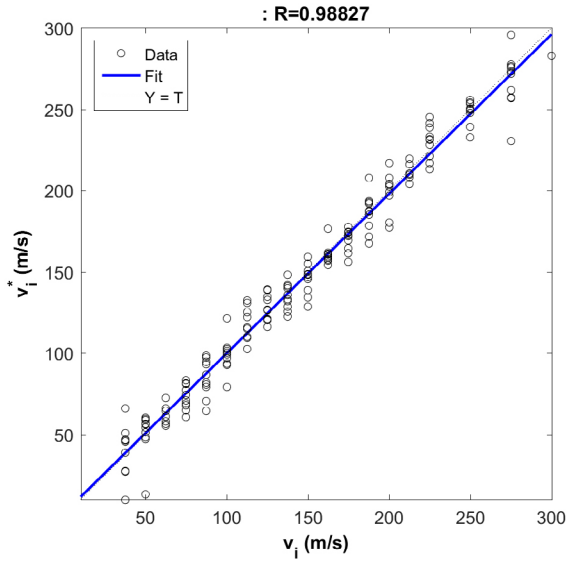

(c) $\rho_{SN}(\sigma_s) = 5$, $\rho_{SN}(\sigma_t) = 5$

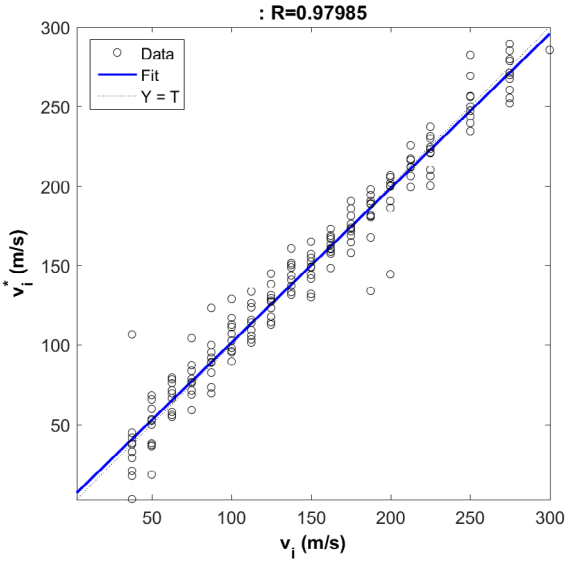

(d) $\rho_{SN}(\sigma_s) = 5$, $\rho_{SN}(\sigma_t) = 15$

Figure 6: Actual and predicted values of impact velocity, (a) $\rho_{SN}(\sigma_s) = 15$, $\rho_{SN}(\sigma_t) = 5$; (b) $\rho_{SN}(\sigma_s) = 15$, $\rho_{SN}(\sigma_t) = 15$; (c) $\rho_{SN}(\sigma_s) = 5$, $\rho_{SN}(\sigma_t) = 5$; (d) $\rho_{SN}(\sigma_s) = 5$, $\rho_{SN}(\sigma_t) = 15$.

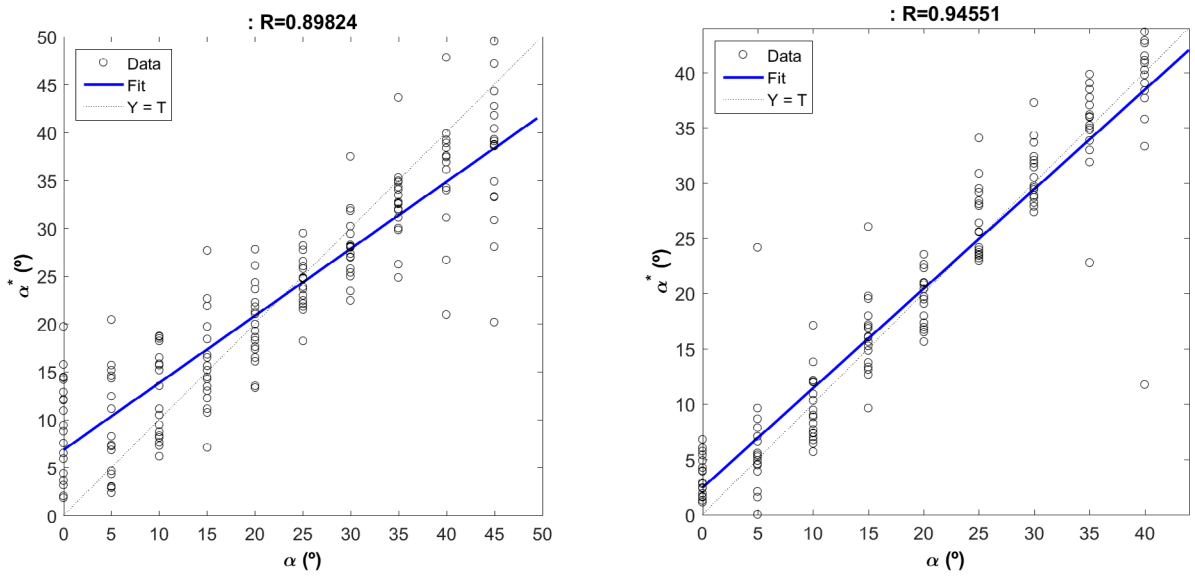

(a) (b)

Figure 7: Actual and predicted values of angle of incidence, (a) $\rho_{SN}(\sigma_s) = 15$, $\rho_{SN}(\sigma_t) = 5$; (b) $\rho_{SN}(\sigma_s) = 15$, $\rho_{SN}(\sigma_t) = 15$.

4 CONCLUSIONS

This work assesses the capability of an ANN–FEA system to predict, from sampled data at sensorized positions, the severity of the collision of an external menace against a representative panel of a vehicle structure. The analysis employs gauged transient dynamic histories associated to impact events, mainly in the HVI regime.

The algorithm achieves satisfactory predictions, in particular in the case of the magnitude of the velocity of impact. Depending on the level of perturbing noise introduced in the signal, the ANN–FEA requires a different preconditioning based on a particular training noise to yield an optimum performance. For time histories with remarkable overlapped noise, over– and under–training should be avoided in order to optimize the accuracy.

Regarding the actions that can be explored for further improvement of the ANN–FEA performance, future works may be focused on the investigation and application to this case of the alternatives identified in the literature, e.g. to enlarge the number of elements of the training set, to design ANN of complex architectures (note that the presented analyses are performed with a single–layer–perceptron) or the consideration of deep learning algorithms.

ACKNOWLEDGEMENTS

The authors wish to acknowledge Safran Group and IMDEA Materials Institute for their support and collaboration.

REFERENCES

[1] Balageas, D., Fritzen, C.-P. and Güemes, A. (Eds.) *Structural Health Monitoring.* ISTE Ltd, London, UK (2006).

[2] Seidt, J.D., Pereira, J.M., Hammer, J.T., Gilat, A. and Ruggeri, C.R. Dynamic load measurement of ballistic gelatine impact using an instrumented tube. NASA Report NASA/TM2012-217661, *XII International Congress and Exposition on Experimental and Applied Mechanics*, Costa Mesa, California, June 11-14 (2012).

[3] Yaghoubi, A.S. and Liaw, B. Thickness influence on ballistic impact behaviors of GLARE 5 fiber-metal laminated beams: experimental and numerical studies. *Compos. Struct.* (2012) **94**(8):2585-2598.

[4] Pereira, J.M., Revilock, D.M., Lerch, B.A. and Ruggeri, C.R. Impact testing of aluminum 2024 and titanium 6Al-4V for material model development. NASA Report NASA/TM2013-217869. Glenn Research Center, Cleveland, Ohio (2013).

[5] LLorca, J., González, C., Molina–Aldareguía, J.M. and Lopes, C.S. Multiscale modeling of composites: toward virtual testing... and beyond. *JOM* (2013) **65**(2):215-225.

[6] Lopes, C.S., González, C., Falcó, O., Naya, F., LLorca, J. and Tijs, B. Multiscale virtual testing: the roadmap to efficient design of composites for damage resistance and tolerance. *CEAS Aeronautical Journal* (2016) **7**(4):607-619.

[7] Garijo, D., Martínez, F., Lopes, C.S., LLorca, J., González, C., López–Puente, J., Loya, J.A., Toral–Vázquez, J., Votsios, V. and Martino, E. Multiscale FE modelling and design of composite laminates under impact. In: Zweben, C. and Beaumont, P.W.R. (Eds.) *Comprehensive Composite Materials II* Vol. 8. Accepted for Publication October 2016.

[8] Ramírez, V., Hermida, J., Huertos, D., Sánchez, B. and Garijo, D. An assessment of the effect of random noise in the frequency measurements of a vibration-based SHM system with Artificial Neural Network damage predictor. *8th European Workshop On Structural Health Monitoring* (EWSHM 2016), 5–8 July 2016, Bilbao, Spain.

[9] ABAQUS, 2013. v6.13 online documentation, Analysis user's manual 37.1.10. SIMULIA Inc., Dassault Systémes.

[10] MATLAB, 2011. Online documentation, MathWorks, https://es.mathworks.com/.

[11] Fritzen, C.–P. Vibration–based structural health monitoring – concepts and applications. *Key Eng. Mater.* (2005) **293**–**294**:3–20.

[12] Johnson, G.R. and Cook, W.H. Fracture characteristics of three metals subjected to various strains, strain rates, temperatures and pressures. *Eng. Fract. Mech.* (1985) **21**(1):31-45.

[13] Kay, G. Failure modeling of titanium 6Al–4V and aluminum 2024–T3 with the Johnson–Cook material model. DOT/FAA/AR–03/57, Office of Aviation Research, Washington, D.C. 20591 Technical Report (2003).

[14] Buyuk, M., Kan, S. and Loikkanen, M. Explicit finite-element analysis of 2024–T3/T351 aluminum material under impact loading for airplane engine containment and fragment shielding. *ASCE J. Aerosp. Eng.* (2009) **22**(3):287-295.

[15] Lopes, C.S., Gürdal, Z., Camanho, P.P., Maimí, P. and González, E.V. Simulation of low–velocity impact damage on composite laminates. *50th AIAA/ASME/ASCE/AHS/ASC Structures, Structural Dynamics, and Materials Conference*, 4–7 May 2009, Palm Springs, California.

[16] Garijo, D. Free vibration analysis of non–uniform Euler-Bernoulli beams by means of Bernstein pseudospectral collocation. *Eng. Comput.* (2015) **31**(4):813-823.

VIII ECCOMAS Thematic Conference on Smart Structures and Materials
SMART 2017
A. Güemes, A. Benjeddou, J. Rodellar and J. Leng (Eds)

INVESTIGATION OF THE ELECTROMECHANICAL IMPEDANCE CHANGES RELATED TO THE STATE OF THE INVESTIGATED STRUCTURES

Piotr Fiborek*, Pawel H. Malinowski*, Pawel Kudela*, Tomasz Wandowski* and Wieslaw M. Ostachowicz*,†

*Institute of Fluid–Flow Machinery, Polish Academy of Sciences,
14 Fiszera Street, 80–231, Gdansk, Poland
e-mail: pfiborek@imp.gda.pl, web page: http://www.imp.gda.pl

† Warsaw University of Technology,
Faculty of Automotive and Construction Machinery,
Warsaw, Poland
e-mail: wieslaw@imp.gda.pl

Key words: Electromechanical Impedance Method, Time–domain Spectral Element Method, CFRP.

Abstract. The research focuses on the electromechanical impedance (EMI) method. The EMI method can be treated as non-destructive testing (NDT) or SHM (structural health monitoring) approach. It is important to have a reliable tool that allows to verify the integrity of the investigated objects. The EMI method was applied here to assess the carbon fibre reinforced polymer (CFRP) samples. The single and adhesively bonded samples were investigated. In the reported research the EMI spectra up to 5 MHz were considered. The investigation comprised of modelling by using spectral element method and experimental measurements. Numerical and experimental spectra were analysed. Differences in spectra were observed caused by differences in considered samples.

1 INTRODUCTION

Electromechanical impedance (EMI) spectroscopy is effective and powerful technique in structural health monitoring (SHM) for real–time structural damage assessment [1, 2]. The basis of this method is the influence of mechanical impedance of the inspected host structure on the electrical impedance of piezoelectric sensor attached to the structure. Assuming that the mechanical property of the sensor remains unchanged over the monitoring period any changes in measurements of the electrical impedance can be considered as a difference in the stiffness of the structure, which in turn can indicate that defect has occurred.

Fundamentals of EMI method were introduced by Liang *et al.* [3]. An analytical model of PZT actuator bonded to one end of a single degree–of–freedom mass–spring–damper system was

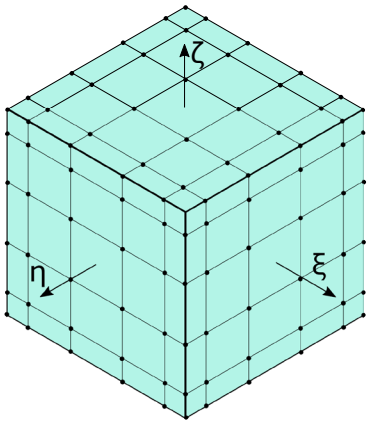

Figure 1: 3D Spectral element

presented in this pioneer work. Zhou *et al.* [4] extended this approach and developed model of PZT attached to two–dimensional structure like thin plates, shells and beams. In the early papers the authors adopted quasi–static sensor approximation until Giurgiutiu and Zagrai [5] derived an expression where the dynamics of a sensor was incorporated. The dynamics of single PZT with various boundary condition (free, clamped and elastically constrained) and sensor attached to a beam were considered. Further investigation with the sensor bonded to other structures were conducted by Zagrai and Giurgiutiu [6].

All the analytical models developed over the two decades give the accurate prediction for sensor–structure interaction. However, number of geometries and boundary conditions are limited. Therefore, many numerical models have been proposed to overcome these drawbacks. The possibility of finite element method (FEM) application to simulate EMI technique was investigated by Liu *et al.* [7]. FEM model of a free PZT and bonded to one–dimensional beam element was compared with analytical results and experimental measurements. Gresil *et al.* [8] analysed FEM model for PZT attached to glass fibre reinforced composite structures.

This article presents calculation of impedance spectra for PZT attached to carbon fibre reinforced polymer (CFRP) plate. The problem is solved by the time–domain spectral element method (SEM). The method combines flexibility of FEM and fast convergence of spectral methods in frequency domain. Thus, it has found application in SHM as a powerful tool for modelling the phenomena of propagation of elastic waves in structures [9]. SEM had been also used in EMI analysis for PZT bonded to one–dimensional aluminium plate and restricted to low-frequency range [10].

2 TIME–DOMAIN SPECTRAL ELEMENT METHOD FOR ELECTROMECHANICAL IMPEDANCE SIMULATION

2.1 Spectral element formulation

Idea of SEM is very similar to FEM with the difference in element nodes distribution and approximation function describing changes of displacements. The elements nodes are non-uniformly distributed as show in the Fig. 1 and are obtained as a roots of following equations

[11].

$$(1-\xi^2)P'_{p-1}(\xi)=0, \quad (1-\eta^2)P'_{q-1}(\eta)=0, \quad (1-\zeta^2)P'_{r-1}(\zeta)=0 \tag{1}$$

where $\xi,\eta,\zeta \in [-1,1]$, P_{p-1}, P_{q-1} and P_{r-1} are Legendre polynomials of degree $(p-1)$, $(q-1)$ and $(r-1)$, respectively and symbol $'$ denotes first derivative. Three–dimensional shape function is constructed as a tensor product of the one–dimensional shape functions $N_m(\xi)$, $N_n(\eta)$, $N_l(\zeta)$ (the Lagrange polynomials of $p-1$, $q-1$ and $r-1$ degree, respectively):

$$N_u(\xi,\eta,\zeta)=N_m(\xi)N_n(\eta)N_l(\zeta) \quad for \quad m=1\dots p, n=1\dots q, l=1\dots r \tag{2}$$

The element matrices are computed by Gauss–Lobatto–Legendre (GLL) integration scheme where the integration points (GLL points) coincide with the element nodes. The GLL quadratures is also tensor product of the one–dimensional quadratures with the associated weights w_m,w_n and w_l equal to the following equations:

$$w_m=\frac{2}{p(p-1)(P_{p-1}(\xi_m))^2}, \quad w_n=\frac{2}{q(q-1)(P_{q-1}(\eta_n))^2}, \quad w_l=\frac{2}{r(r-1)(P_{r-1}(\zeta_l))^2} \tag{3}$$

As a consequence of orthogonality of shape functions as well as application of GLL quadrature the mass matrix is always diagonal in the formulation.

2.2 Elementary governing equations of motion

Piezoelectric effect is described by the material law according to [13]:

$$\begin{bmatrix} \sigma \\ \mathbf{D} \end{bmatrix} = \begin{bmatrix} \mathbf{c}^E & -\mathbf{e}^T \\ \mathbf{e} & \epsilon^S \end{bmatrix} \begin{bmatrix} \mathbf{E} \\ \mathbf{S} \end{bmatrix} \tag{4}$$

where c^E, e and ϵ^S are tensor of elastic, piezoelectric modulus and dielectric constants, respectively, E and D are the electric field and electric displacement, σ and S are stress and strain. The superscripts E and S indicate that quantities are measured at zero electric field and zero strain, respectively and the subscript T denotes transpose matrix. The elementary governing equations of motion can be written in the matrix form:

$$\begin{bmatrix} \mathbf{M}^e_{uu} & \mathbf{0} \\ \mathbf{0} & \mathbf{0} \end{bmatrix} \begin{Bmatrix} \ddot{u}^e \\ \ddot{\Phi}^e \end{Bmatrix} + \begin{bmatrix} \mathbf{C}^e_{uu} & \mathbf{0} \\ \mathbf{0} & \mathbf{0} \end{bmatrix} \begin{Bmatrix} \dot{u}^e \\ \dot{\Phi}^e \end{Bmatrix} + \\ + \begin{bmatrix} \mathbf{K}^e_{uu} & \mathbf{K}^e_{u\Phi} \\ \mathbf{K}^{eT}_{u\Phi} & \mathbf{K}^e_{\Phi\Phi} \end{bmatrix} \begin{Bmatrix} u^e \\ \Phi^e \end{Bmatrix} = \begin{Bmatrix} F^e \\ Q^e \end{Bmatrix} \tag{5}$$

where $\mathbf{M}^e_{uu}$, $\mathbf{C}^e_{uu}$, $\mathbf{K}^e_{uu}$ are structural mass, damping and stiffness matrices, respectively; $\mathbf{K}^e_{u\Phi}$ piezoelectric coupling matrix, $\mathbf{K}_{\Phi\Phi}$ is the dielectric permittivity matrix; u^e is the nodal displacement and Φ^e is the electric potential, respectively; F^e is the force vector; Q^e is the nodal vector; $\dot{()}=\frac{\partial()}{\partial t}$. The formulae of element matrices are:

$$\begin{aligned}
\mathbf{M}^e_{uu} &= \sum_{i=1} \int_{V_e} \rho \mathbf{N}_u^T \mathbf{N}_u \mathrm{d}V_e \\
\mathbf{K}^e_{uu} &= \sum_{i=1} \int_{V_e} \mathbf{B}_u^T \mathbf{c} \mathbf{B}_u \mathrm{d}V_e \\
\mathbf{K}^e_{u\Phi} &= \sum_{i=1} \int_{V_e} \mathbf{B}_u^T \mathbf{e}^T \mathbf{B}_\Phi \mathrm{d}V_e \\
\mathbf{K}^e_{\Phi\Phi} &= -\sum_{i=1} \int_{V_e} \mathbf{B}_\Phi^T \epsilon^{S^T} \mathbf{B}_\Phi \mathrm{d}V_e
\end{aligned} \tag{6}$$

(7)

with

$$\begin{aligned}
\mathbf{B}_u &= \begin{pmatrix} \frac{\partial N_u}{\partial x} & 0 & 0 & 0 & \frac{\partial N_u}{\partial z} & \frac{\partial N_u}{\partial y} \\ 0 & \frac{\partial N_u}{\partial y} & 0 & \frac{\partial N_u}{\partial z} & 0 & \frac{\partial N_u}{\partial x} \\ 0 & 0 & \frac{\partial N_u}{\partial z} & \frac{\partial N_u}{\partial y} & \frac{\partial N_u}{\partial x} & 0 \end{pmatrix}^T \\
\mathbf{B}_\Phi &= \begin{pmatrix} \frac{\partial N_u}{\partial x} & \frac{\partial N_u}{\partial y} & \frac{\partial N_u}{\partial z} \end{pmatrix}^T
\end{aligned} \tag{8}$$

where, ρ is the mass density, $\int_{V_e} \mathrm{d}V_e$ is a volume integral.

Structural damping C^e_{uu} is defined according to Rayleigh damping model:

$$\mathbf{C}^e_{uu} = \alpha_M \mathbf{M}^e_{uu} + \beta_K \mathbf{K}^e_{uu} \tag{9}$$

where α_M and β_K is the mass– and stiffness–proportionality coefficients. However, β_K is assumed to be zero. In this way very efficient central difference scheme can be applied for solving equation of motion 7 which leads to reduced computation time.

2.3 Electrical impedance and admittance calculation

Electrical impedance, as an inverse of admittance, is the ratio of the voltage to the current in an alternating circuit:

$$\overline{Z}(\omega) = \frac{1}{\overline{Y}(\omega)} = \frac{\overline{V}(\omega)}{\overline{I}(\omega)} = \frac{\overline{V}(\omega)}{j\omega\overline{Q}(\omega)} \tag{10}$$

where $j = \sqrt{-1}$, ω is the angular frequency, $\overline{V}$, $\overline{I}$ and $\overline{Q}$ are the electric voltage, the current and the charge signals in the frequency domain, respectively [12]. The voltage signal is a signal of electric voltage applied to loaded electrode of the PZT during simulation. Characteristic of this signal is chosen to be a non–zero at the interesting frequency range. While the charge signal is a sum of charges induced on the loaded electrode $q(t) = \sum Q^e_\Gamma(t)$.

Impedance $\overline{Z}$ and admittance $\overline{Y}$ are complex quantities, thus they can be written as:

$$\begin{aligned}
\overline{Z}(\omega) &= R + jX \\
\overline{Y}(\omega) &= G + jB
\end{aligned} \tag{11}$$

where R, X, G and B are resistance, reactance, conductance and susceptance, respectively.

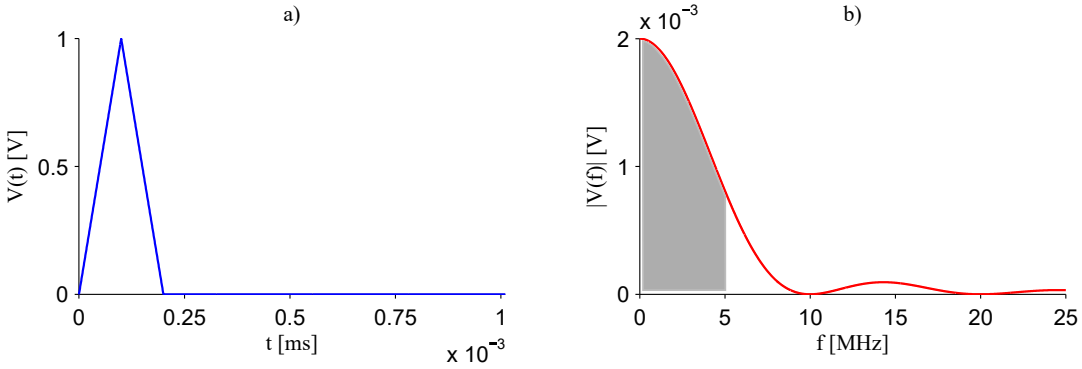

Figure 2: Excitation signal of PZT in a) time domain, b) frequency domain

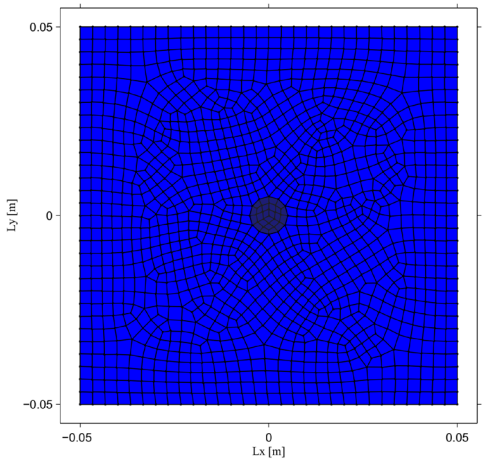

Figure 3: In–plane mesh of CFRP plates

3 NUMERICAL CALCULATION AND EXPERIMENTAL VALIDATION

3.1 Experimental investigation

The impedance spectrum of the piezoelectric transducer was obtained experimentally using HIOKI IM3570 Impedance Analyzer in range of frequency from 1kHz to 5MHz. The round transducer (CeramTec, Sonox P502) of 10 mm diameter and 0.5 mm thickness was attached at the centre of the square composite plate. Two types specimens were investigated. First one was composed of six–layers of unidirectional CFRP laminate (HEXCEL M21/35%/268/T700GC-12K300) of 100 mm length, 100 mm width and 1.572 mm thickness with stacking sequence of $[0^o/0^o/90^o/90^o/0^o/0^o]$. Next, two above plates were bonded together by the adhesive film (Cytec, FM300K.05).

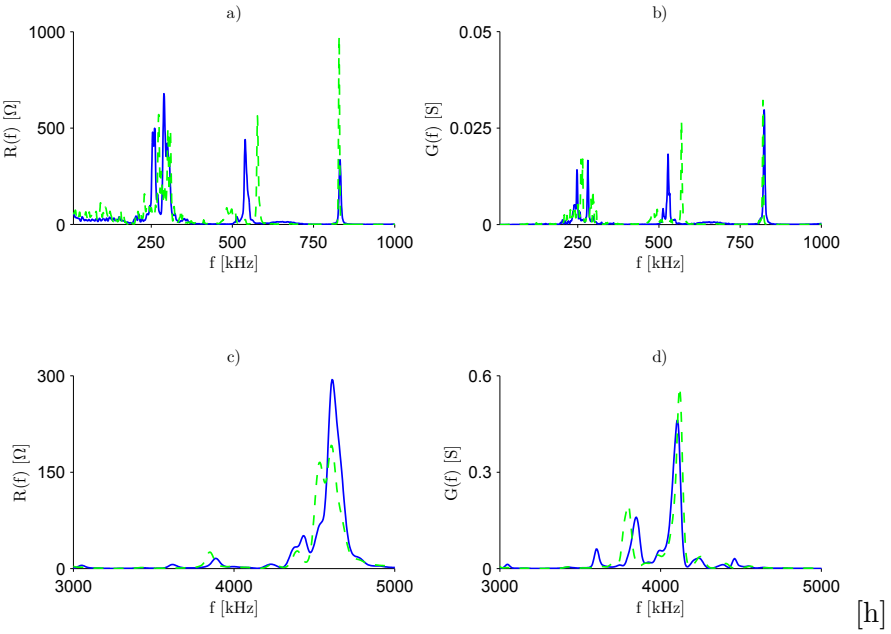

[h]

Figure 4: Resistance a), c) and conductance b), d) for PZT attached to single plate (dashed line) and adhesive bonded plates (solid line)

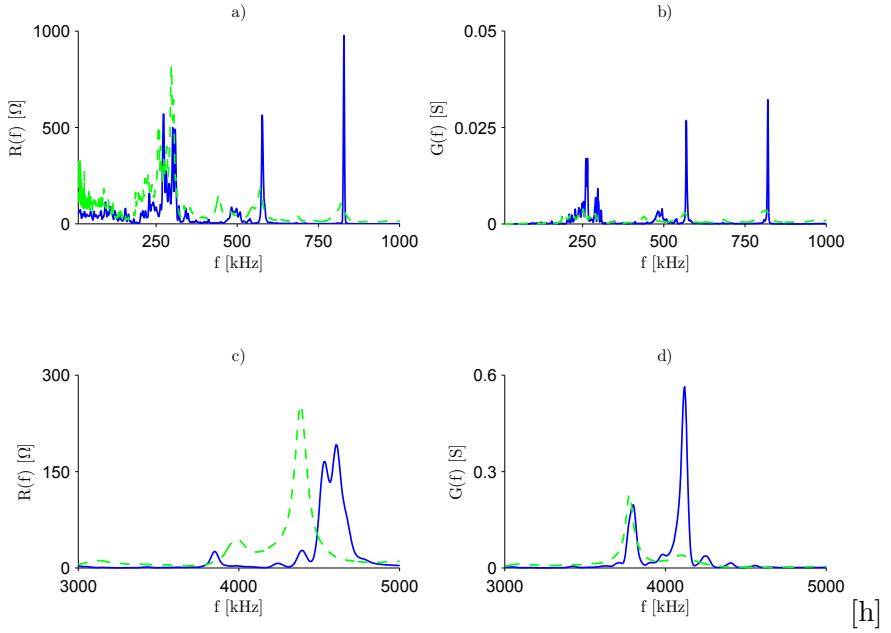

[h]

Figure 5: Measured (dashed line) and simulated (solid line) resistance a), c) and conductance b), d) for PZT attached to one plate.

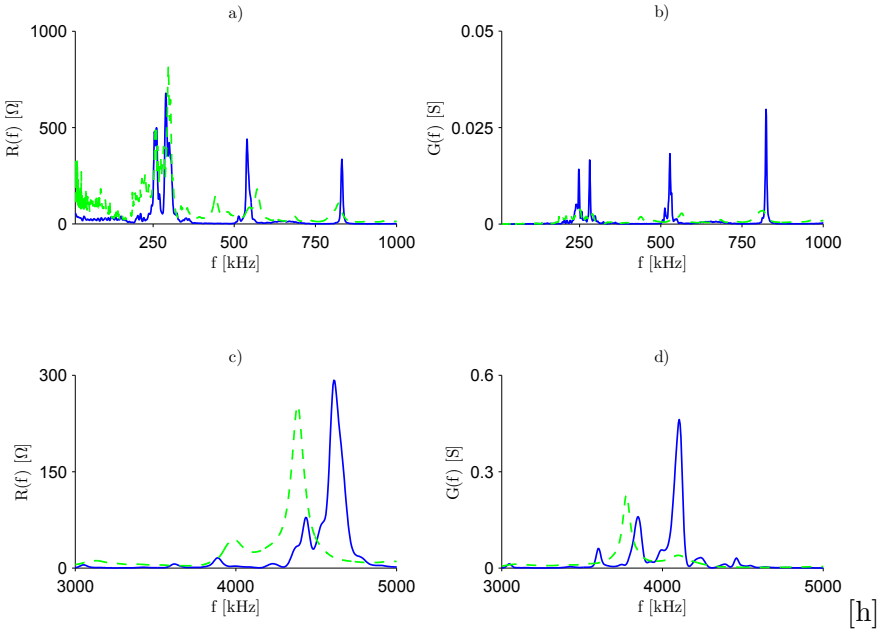

[h]

Figure 6: Measured (dashed line) and simulated (solid line) resistance a), c) and conductance b), d) for PZT attached to adhesively bonded CFRP plates.

3.2 Model of PZT attached to CRFP plate

All components used in the simulation (*i.e.* plates, adhesive film between plates, PZT transducer and glue between plate and PZT) are modelled by the three–dimensional (3D) spectral elements. Number of nodes per element depends on considered range of frequency. For frequency below 1 MHz each element has 324 nodes (6x6x9 nodes along each edge of element) and 576 nodes (8x8x9) for frequency 1 MHz–5 MHz. Each node has three displacement degrees of freedom (DOF) and one additional electric voltage DOF in case of PZT. Plates and adhesive film are composed of 1254 elements distributed in plane as it is shown in the Fig. 3. While the PZT and glue layer are composed of 24 elements which coincide with the plate elements distinguished in the Fig. 3 by a dark blue colour. CFRP laminate is considered as a homogeneous orthotropic material.

The upper surface of the PZT represents the electrode where excitation voltage is applied and bottom surface of PZT represents grounded electrode. Excitation signal has a form of a triangular pulse. Range of frequency considered in the simulation covers a grey area in the Fig. 2(b).

Resistance and conductance characteristics for two cases in the frequency range: 1 kHz–1000 kHz and 3 MHz–5 MHz are shown in the Fig. 4. According to the principles of EMI method the shifts of resonant frequency and changes of values between both structures are observed. Comparison of measured and simulated values of R and G is shown in the Figs. 5 and 6.

4 CONCLUSIONS

In this paper model of electromechanical impedance spectra of piezoelectric transducer attached to two types of composite plates is presented. Simulation and experimental validation was conducted for high frequency range up to 5 MHz. The simulated resistance and conductance are in good agreement with measurement data. However, some resonance peaks show differences in magnitude and frequency shift. These discrepancies may be caused by: asymmetric electrodes, thickness of the adhesive layer, lack of the stiffness–proportional coefficient in the structural damping model, influence of wires and solder and temperature impact.

In the next step proposed model will be utilized to simulate damage detection in the structures.

5 ACKNOWLEDGEMENT

The research leading to these results has been supported by project funded by National Science Centre, Poland under the decision no. DEC–2013/11/D/ST8/03355.

REFERENCES

[1] Malinowski, P., Wandowski, T. and Ostachowicz W., The use of electromechanical impedance conductance signatures for detection of weak adhesive bonds of carbon fibre–reinforced polymer, *Struct. Health Monit.*, (2015)**14**:332–344

[2] Park, G., Sohn, H., Farrar, C.R and Inman, D.J, Overview of piezoelectric impedance–based health monitoring and path forward. *Shock Vib. Dig.* (2003) **35**:451–463

[3] Liang, C. Sun F.P. and Rogers, C.A., Coupled electro–mechanical analysis of adaptive material systems – determination of the actuator power consumption and system energy transfer. *J. Intell. Mater. Syst. Struct.* (1994) **5**:12–20.

[4] Zhou, S. Liang C. and Rogers, C.A., An impedance–based system modelling approach for induced strain actuator–driven structures. *J. Vib. Acoust.* (1996) **5**:12–20.

[5] Giurgiutiu, V. and Zagrai, A.N., Characterization of piezoelectric wafer active sensors. *J. Intell. Mater. Syst. Struct.* (2000) **11**:959–975.

[6] Zagrai, A.N. and Giurgiutiu, V., Electro–mechanical impedance method for crack detection in thin plates. *J. Intell. Mater. Syst. Struct.* (2001) **12**:709–718.

[7] Liu, W. and Giurgiutiu, V., Finite element simulation of piezoelectric wafer active sensors for structural health monitoring with coupled field elements. *In: 6th International Workshop on Structural Health Monitoring*, Stanford, 2007.

[8] Gresil, M., Yu, L., Giurgiutiu, V. and Sutto, M. Predictive modeling of electromechanical impedance spectroscopy for composite materials. *Struct. Health Monit.* (2012) **11**:671–683.

[9] Kudela, P. and Ostachowicz, W., 3D time-domain spectral elements for stress waves modelling. *J. Phys. Conf. Ser.* (2009) **181**:89–104.

[10] Fritzen, C.P. and Schulte, R.T., Modelling of wave propagation and impedance spectra with the spectral element method. *Proceedings of the 7th international workshop on structural health monitoring*, vol. 2, Stanford University, Stanford, (2009): 2282-2289.

[11] Kudela, P., Żak, A., Krawczuk, M. and Ostachowicz, W., Modelling of wave propagation in composite plates using the time domain spectral element method. *J. Sound Vibration* (2007) **302**:728–745

[12] Kaltenbacher M., *Numerical simulation of mechatronic sensors and actuators*. Springer, Second Edition, (2007)

[13] Giurgiutiu, V. and Lyshevski, S.E., *Micromechatronics. Modeling, analysis and design with Matlab*. CRC Press, Second Edition, (2009)

MODELLING THE CORRELATION BETWEEN THE DAMAGE STATE AND THE ELECTRICAL RESISTANCE CHANGE IN SYMMETRIC LAMINATES

M. ZAPPALORTO, M. QUARESIMIN, F. PANOZZO, P.A. CARRARO AND N. DE ROSSI

Department of Management and Engineering (DTG)
University of Padova
Stradella San Nicola, 3, 36100 Vicenza, Italy
e-mail: michele.zappalorto@unipd.it

Key words: Health monitoring, Modelling, Conductive matrix

Abstract. The nano-modification with carbon nanotubes (CNT) of the insulating matrix of conventional composites leads to innovative multifunctional materials, with enhanced physical properties. For instance, electrical conductivity can be provided to composites made of non-conductive fibers by the addition of very limited amounts of CTNs. The onset of matrix cracks leads to the interruption of conductive paths of CNTs within the nano-modified matrix, resulting to an irreversible increase of the electrical resistance. In the present work, a closed form solution is presented to accurately predict the variation of the electrical resistance of conductive laminates caused by the presence of off-axis cracks in the transverse layers. The analytical predictions, compared to a bulk of finite element analyses, show a very good agreement.

1 INTRODUCTION

The damage evolution of multidirectional laminates made of unidirectional plies, subjected to static [1 – 2] or fatigue [3 – 5] loads is a complex phenomenon that involves an initial onset of transverse matrix cracks, with a continuous increase of the crack density (i.e., the number of cracks per unitary length). The propagation of matrix cracks does not necessarily lead to a failure of the part, however it can reduce the stiffness of the material, compromising the overall functionality of the structure.

Within this frame, it is evident that methods to monitor the damage state of composite structures are crucial to improve the in-service safeness and reliability. As a further beneficial effect, health monitoring of FRP-structures can significantly reduce the inspection costs, allowing to switch from a time-based to a condition-based maintenance. Structural health monitoring is conventionally done through a dense network of sensors mounted on the surface or embedded within the material, for instance using piezoelectric sensors and actuators [6], or FBG sensors [7].

Advances in nanotechnology have made it possible, in the very recent years, to manufacture multifunctional materials with exceptional properties. The addition of a very

limited amount of Carbon nanotubes (CNT) to conventional polymers can increase the electrical conductivity of several orders of magnitude, changing their electrical behavior from insulator to semiconductive. In addition, due to the nanometric scale of this nanoreinforcement, CNTs can penetrate between conventional fibrous reinforcements, creating a percolated conductive network. As reported in the literature, the onset of transverse cracks within the material causes an interruption of the conductive network, with an irreversible increase of the electrical resistance [8]. Böger [9] performed dynamic tensile tests on glass fibre specimen with carbon black and CNT-modified matrix, observing that a relation between the dynamic modulus and the variation of the electrical resistance does exist. Gao et al. [10] reported that an irreversible increase of the electrical resistance was measured as a consequence of the crack density increase for cross-ply specimens made of glass fibres and CNT-modified matrix. Similar results were found also by Thostenson and Chou [11], however the authors did not investigate on the mechanisms that underlie the relationship between the change in the electric properties and the damage state of the material.

After this brief review, it is clear that the chance of monitoring damage through electrical measurements is very attractive and promising. However, at present, most of the works are mainly experimental, and only limited efforts have been done to provide analytical tools to correlate the resistance increase to the state of damage in multidirectional laminates.

In the present work, a theoretical study is presented to partially fill the gap described above:

- Initially, a closed form solution is developed to predict the electrical resistance change of electrically conductive laminates with a $[(\theta_1)_m/ (\theta_2)_n]_S$ layup, as a function of the crack density in one layer;
- Then, an analytical model is presented to calculate the longitudinal elastic modulus degradation for $[(\theta_1)_m/ (\theta_2)_n]_S$ laminates as a function of the crack density;
- Eventually, the models are combined, obtaining a closed form expression to predict the elastic modulus degradation as a function of the electrical resistance increase of the cracked laminate.

Theoretical predictions are compared with multiphysical finite element analyses, showing a sound agreement.

2 A MODEL TO CALCULATE THE STIFFNESS DROP AS A FUNCTION OF THE ELECTRICAL RESISTANCE CHANGE

Consider a symmetric laminate made of unidirectional plies, with a layup $[(\theta_1)_m/(\theta_2)_n]_S$, where θ_1 and θ_2 are two generic angles. Each ply has an orthotropic behavior in terms of electrical resistivity, in particular, the in-plane resistivities along and perpendicular to the fibres are denoted with η_1 and η_2, whereas the out-of-plane resistivity is referred to as η_3. The total thickness of the layers with orientation θ_1 and θ_2 is h_1 and h_2, respectively.

A potential drop is applied on the faces of the laminate, so that a total current I_x flows within the part. As shown in Figure 1, where only the upper half of the laminate has been represented due to the symmetry of the problem, the plies with orientation angle θ_2 are interested by the presence of cracks. The following simplifying assumptions are made:

- off-axis cracks in the θ_2 layers are parallel to the fibre direction;
- the width of the cracks is equal to the entire width of the laminate;
- cracks are regularly spaced with distance L.

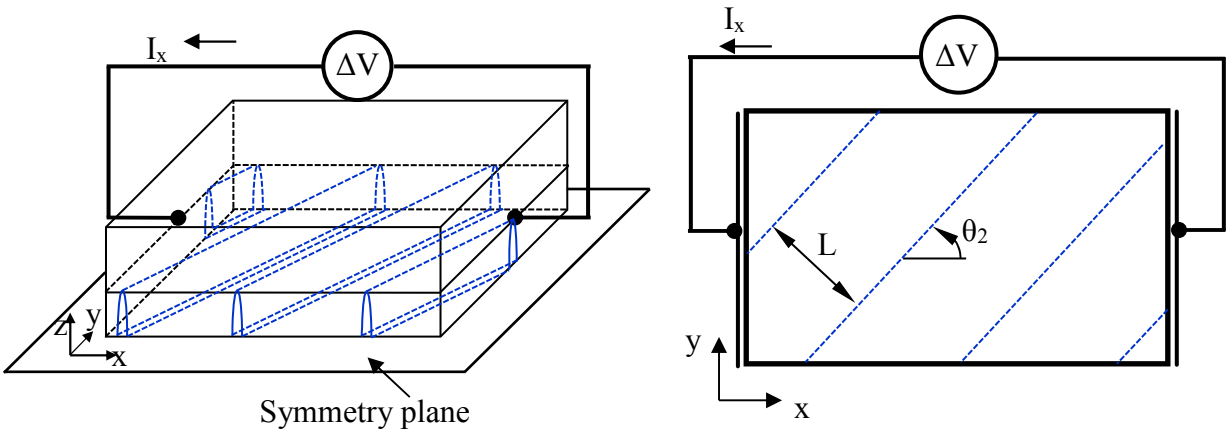

(a) (b)

Figure 1 : (a) Schematic of the cracked laminate. (b) top view of the laminate

Under these hypotheses, the phenomenon can be considered periodic, thus allowing to restrict the study to a representative volume comprised between two adjacent cracks, as schematically represented in Figure 2.

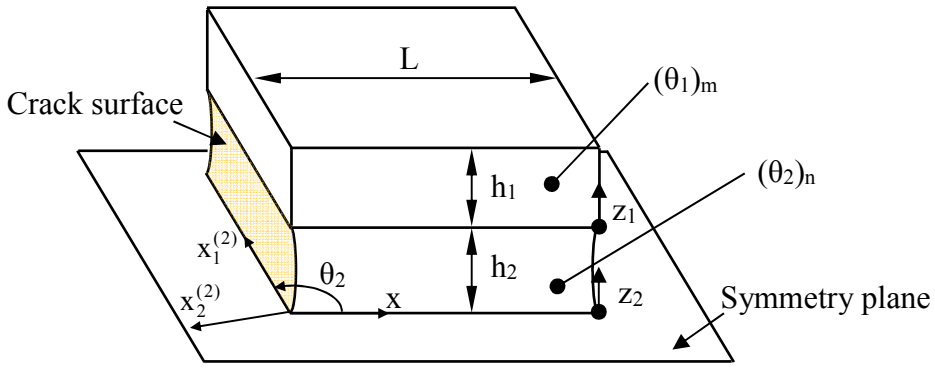

Figure 2 : Representative volume element of the upper half of the laminate

The presence of cracks causes an interruption of the conductive pathways, and a perturbation of the current density along the $x_1^{(2)}$ direction (see Figure 1), resulting in the irreversible increase of the electrical resistance of the laminate. According to the formulation reported in Ref. [12], the crack density ρ (i.e., 1/L) of the laminate can be expressed as a function of its electrical resistance change:

$$\rho = \frac{\frac{\alpha}{2}\left(\frac{R}{R_0}-1\right)}{\left[(1-\varphi)^{\frac{5}{2}}\,\omega^{\frac{5}{2}} - \left(\frac{R}{R_0}-1\right)^{\frac{5}{2}}\right]^{\frac{2}{5}}} \tag{1}$$

where:

$$\omega = -\frac{\beta\, h_2\,(\delta+\chi)}{h_2\,\delta\beta - \lambda\alpha^2 + \chi\left(h_2\,\beta + \alpha^2\sin\theta_2\right) + 2\delta\alpha^2\sin\theta_2} \tag{2}$$

For more details about the formulation of the parameter ω, the reader should refer to Ref [12]. The elastic modulus of the cracked laminate can be expressed as a function of the crack density by means of the following expression [12]:

$$E_x(\rho) = \left[\left(\bar{S}_{16}^{(1)}\gamma_{12} + \bar{S}_{11}^{(1)}\gamma_{11} + \bar{S}_{12}^{(1)}\gamma_{22}\right)\cos^2\theta_2 - \left(\bar{S}_{66}^{(1)}\gamma_{12} + \bar{S}_{16}^{(1)}\gamma_{11} + \bar{S}_{16}^{(1)}\gamma_{22}\right)\cos\theta_2\sin\theta_2 + \left(\bar{S}_{26}^{(1)}\gamma_{12} + \bar{S}_{21}^{(1)}\gamma_{11} + \bar{S}_{22}^{(1)}\gamma_{22}\right)\sin^2\theta_2\right]^{-1} \tag{3}$$

where the terms $\bar{S}_{ij}^{(1)}$ are the components of the compliance matrix of the plies with orientation θ_1 expressed in the coordinate system $x_1^{(2)}$ $x_2^{(2)}$ shown in Figure 2, whereas the terms γ_{ij} are functions of the crack density, and are calculated according to Ref [12].
By substitution of Eq. (1) within Eq. (3), a direct correlation between the electrical resistance increase and the elastic modulus degradation can be obtained.

3 MODEL VALIDATION

To validate the analytical model, finite element analyses were carried out with the code Ansys 14.5. To this end, an APDL script was written to automatically build RVEs with periodic boundary conditions according to Ref. [13]. Electrical and elastic properties used both for the analytical calculations and the numerical models are listed in Table 1. In particular, typical elastic properties of a glass/epoxy unidirectional lamina were taken into account, whereas electrical conductivity of a glass fibre lamina with carbon black-modified epoxy matrix is used [14]. In all the calculations, a ply thickness of 0.3 mm was used.

Table 1 : Electrical and elastic properties of the unidirectional lamina

η_1=61450 Ω mm	η_2=132170 Ω mm	η_3=70810 Ω mm
E_1= 48830 MPa	E_2= E_3= 14070 MPa	ν_{12}= ν_{13}= 0.31
ν_{23}= 0.40	G_{12}= G_{13}= 5200 MPa	G_{23}= 5000 MPa

A first comparison between the predictions obtained through Eq. (3), and the numerical results is shown in Figure 3, where the influence of the orientation angle of the non-cracked layers (θ_1) is investigated for laminates with a layup $[\theta_1/90_2]_S$. In all the cases, the decrease of the longitudinal modulus is associated with an irreversible increase of the electrical resistance, confirming the capability of electrical methods to sense the presence of damage. As it can be seen, for a fixed value of the elastic modulus decrease, the maximum increase in the electrical resistance is reached for cross-ply laminates, whereas a lower sensitivity was found for laminates with different θ_1 angles.

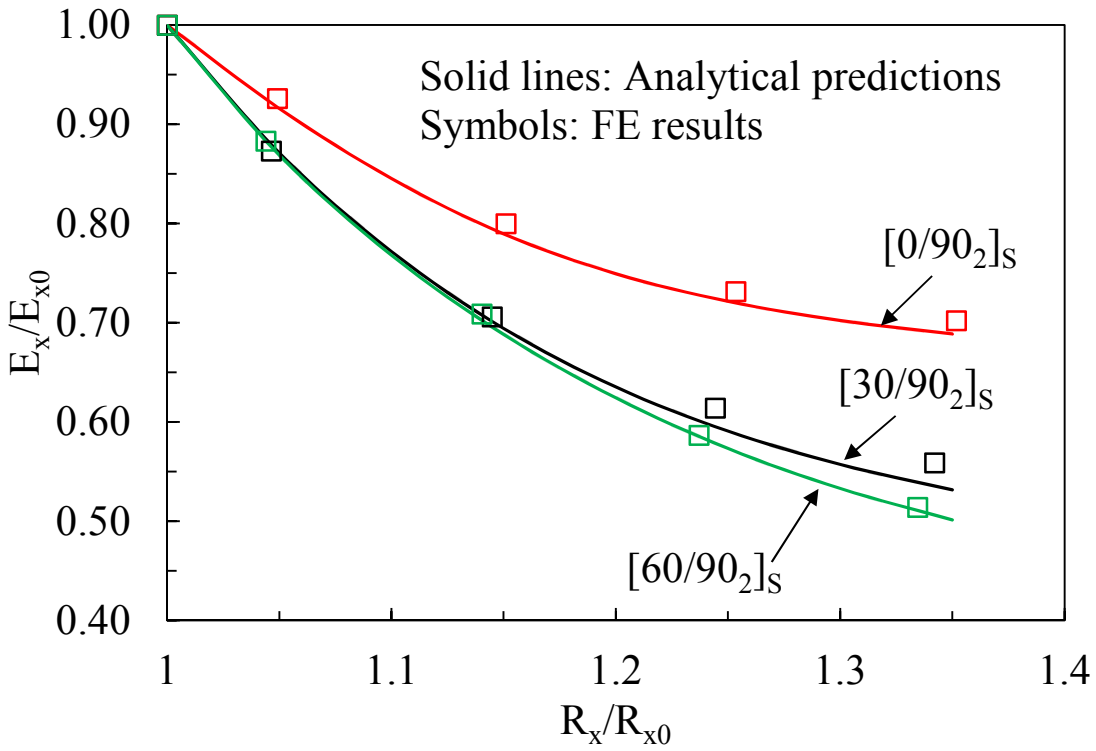

Figure 3: Influence of the orientation angle θ_1 on the electrical/mechanical response of the cracked laminate

In Figure 4 the influence of the orientation angle θ_2 on the electrical/elastic response of the laminate is studied for a fixed angle $\theta_1 = 0°$. In this case, among the configuration analyzed, the layup that presents the highest sensitivity in terms of electrical resistance change is the one with $\theta_2 = 60°$.
A very satisfactory agreement between analytical predictions and numerical results is evident from figures 3 and 4.

4 CONCLUSION

In this work, an analytical solution was presented to predict the longitudinal stiffness decrease as a function of the electrical resistance change in conductive $[(\theta_1)_m/ (\theta_2)_n]_S$ laminates with cracks in the middle layers. In order to verify the accuracy of the model, the theoretical results have been compared with finite element analyses, showing a very

satisfactory agreement. The influence of the layup of the laminate, in terms of orientation of the cracked and non-cracked plies has been investigated.

As a major conclusion, it can be stated that multidirectional laminates manufactured with electrically conductive polymer are provided with remarkable damage sensing capabilities, which also depends on the layup of the laminates. A decrease of the elastic modulus of the laminate due to the presence of cracks is always associated with an irreversible increase of the electrical resistance, thus confirming the potentials of electric-based technique to sense the health status of composites.

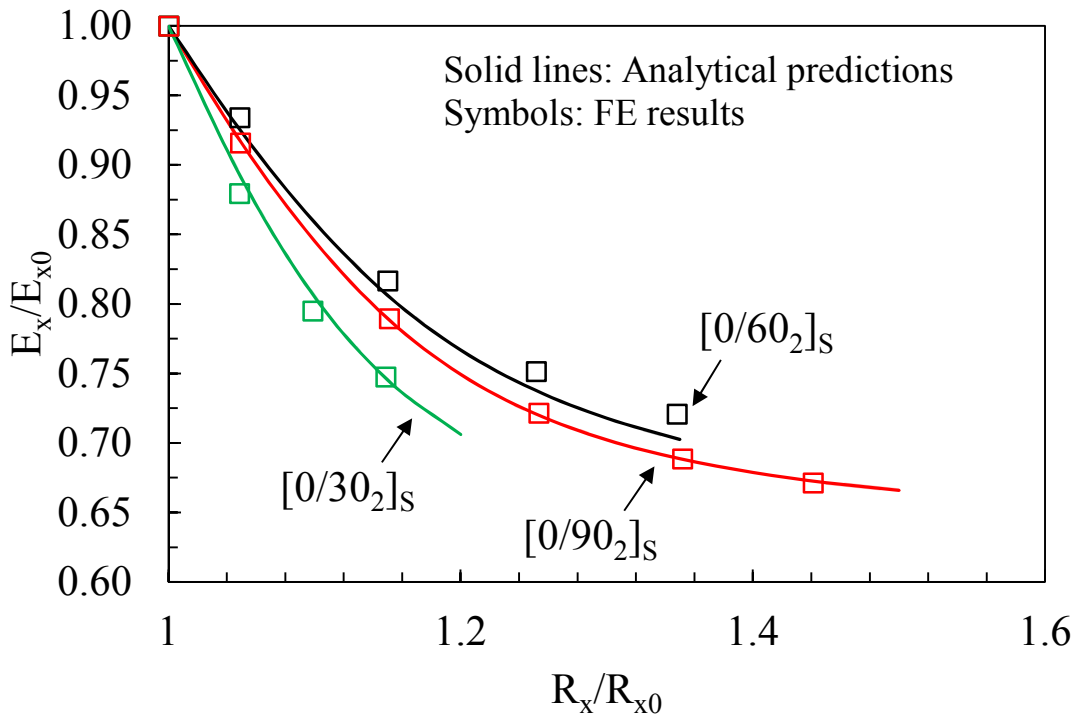

Figure 4: Influence of the orientation angle θ_2 on the electrical/mechanical response of the cracked laminate.

REFERENCES

[1] Varna, J., Joffe, R., Akshantala, N.V. and Talreja, R. *Damage in composite laminates with off-axis plies*. Composites Science and Technology (1999) **59**: 2139-2147.

[2] Singh, C.V. and Talreja, R. *Evolution of ply cracks in multidirectional composite laminates*. International Journal of Solid and Structures (2010) **47**: 1338-1349.

[3] Tong, J. *Three stages of fatigue crack growth in GFRP composite laminates*. Journal of Engineering Materials and Technology (2001) **123**: 139-143.

[4] Wharmby, A.W. and Ellyin, F. *Damage growth in constrained angle-ply laminates under*

cycling loading. Composites Science and Technology (2002) **62**:1239-1247.

[5] Sun, Z., Daniel, I.M. and Luo, J.J. *Modeling of fatigue damage in a polymer matrix composite*. Material Science and Engineering (2003) **A361**:302-311.

[6] Kessler, S.S., Spearing, S.M. and Soutis, C. *Damage detection in composite materials using Lamb wave methods*. Smart Materials and Structures (2002) **11**: 269-278.

[7] Okabe, Y., Yashiro, S., Kosaka, T. and Takeda, N. *Detection of transverse cracks in CFRP composites using embedded fiber Bragg grating sensors*. Smart Material and Structures (2000) **9**: 832-838.

[8] Baltopoulos, A., Plydorides, N., Pambaguian, L., Vavouliotis, A. and Kostopoulos, V. *Exploiting carbon nanotube networks for damage assessment of fiber reinforced composites*. Composites Part B (2015) **76**: 149-158.

[9] Böger, L., Wichmann, M.H.G., Meyer, L.O. and Schulte, K. *Load and health monitoring in glass fibre reinforced composites with an electrically conductive nanocomposite epoxy matrix*. Composites Science and Technology (2008) **68**: 1886-1894.

[10] Gao, L., Thostenson, E.T., Zhang, Z. and Chou, T.-W. *Sensing of Damage Mechanisms in Fiber-Reinforced Composites under Cyclic Loading using Carbon Nanotubes*. Advanced Functional Materials (2009) **19**:123-130.

[11] Thostenson, E.T. and Chou, T.-W. *Carbon nanotube networks sensing of distributed strain and damage for life prediction and self healing*. Advanced Materials (2006) **18**:2937-2841.

[12] Panozzo, F., Zappalorto, M., Carraro, P.A. and Quaresimin, M. *A closed form solution to correlate the electrical resistance change and the damage state in* $[(\theta_1)_m/(\theta_2)_n]_S$ *laminates.* Submitted for publication.

[13] Li, S., Singh, C.V. and Talreja, R. *A representative volume element based on translational symmetries for FE analysis of cracked laminates with two arrays of cracks*. International Journal of Solid and Structures (2009) **46**:1793-1804.

[14] Markov, A., Fiedler, B. and Schulte, K. *Electrical conductivity of carbon black/fibres filled glass-fibre-reinforced thermoplastic composites*. Composites: Part A (2006) **37**:1390-1395.

Multi-Level Damage Detection Strategy for Composite Structures

Z. Sharif Khodaei*,[1] and M.H. Aliabadi†,[1]

[1]Department of Aeronautics, Imperial College London,
*Email: z.sharif-khodaei@imperial.ac.uk; †m.h.aliabadi@imperial.ac.uk.

ABSTRACT

Structural health monitoring (SHM) has emerged as a new concept for conditions based maintenance (CBM). The first step in designing any SHM system is to define what the intended function of the proposed diagnostic system is. The intended function of any SHM system can be a selection or a combination of the following elementary functions: existence of damage, damage location, damage size and damage severity. Each intended function will require different number and location of transducers. In this work, a multi-level decision fusion strategy is proposed based on ultrasonic guided wave (UGW) [1, 2] and Electro-mechanical impedance (EMI) based methods [3]. In this work a three level damage detection is proposed: Level 1 diagnosis results in damage existence with minimum sensors covering a large area by finding the maximum energy difference for the guided waves propagating in pristine structure and the post-impact state; Level 2 diagnosis provides damage detection and approximate localization using an approach based on Electro-Mechanical Impedance (EMI) measures, while Level 3 characterizes damage (exact location and size) in addition to its detection by utilising a Weighted Energy Arrival Method (WEAM). The proposed multi-level strategy is verified and validated experimentally by detection of Barely Visible Impact Damage (BVID) on a curved composite fuselage panel.

REFERENCES

1. Sharif-Khodaei, Z. and M. Aliabadi, *Assessment of delay-and-sum algorithms for damage detection in aluminium and composite plates.* Smart materials and structures, 2014. **23**(7): p. 075007.
2. Michaels, J.E., A.J. Croxford, and P.D. Wilcox. *Imaging algorithms for locating damage via in situ ultrasonic sensors*. in *Sensors Applications Symposium, 2008. SAS 2008. IEEE*. 2008. IET.
3. Sharif-Khodaei, Z., M. Ghajari, and M. Aliabadi, *Impact Damage Detection in Composite Plates using a Self-diagnostic Electro-Mechanical Impedance-based Structural Health Monitoring System.* Journal of Multiscale Modelling, 2015. **6**(04): p. 1550013.

VIII ECCOMAS Thematic Conference on Smart Structures and Materials
SMART 2017
A. Güemes, A. Benjeddou , J. Rodellar and Jinsong Leng (Eds)

NON-DESTRUCTIVE EVALUATION OF DELAMINATION IN COMPOSITE MATERIAL BASED ON VIBRATIONAL APPROACH

GRIGORII S. SEROVAEV*, ALEKSEY P. SHESTAKOV AND DMITRII A. OSHMARIN

* Institute of Continuous Media Mechanics
Academika Koroleva st, 1, 614013 Perm, Russia
e-mail: serovaev@icmm.ru

Key words: composite materials, delamination, damage detection, vibrational methods

Abstract. In this paper a numerical study of the possibility of creating a monitoring system of structures, made of polymer composite materials on the basis of vibration approaches, is provided. The study of modes of vibration, occurring at the appearance of delamination in a structure, has been performed. In the numerical model of the plate, the study of the possibility of vibration excitation in the zone of delamination has been carried out, allowing to detect the presence and location of the defect. The estimation of the parameters, affecting the effectiveness of the application of this approach, has been also discussed.

1 INTRODUCTION

Layered composite materials are widely used in the manufacture of all sorts of structural objects in different fields of industrial production: from civilian vehicles to aerospace structures [1]. Due to its layered nature such materials are prone to delamination type defects which may occur from low energy impacts or loss of adhesion between layers and represent a major threat to the safety of composite structures [2]. The problem of detection of delamination in composite materials in the early stage of development is of particular importance in maintaining structural integrity.

A variety of methods intended for damage control of structures exist nowadays in different stages of development and implementation. Among these methods two main classes can be distinguished: destructive and non-destructive control. Methods of destructive inspection can provide appropriate manufacturing quality control in the construction of various buildings and roads, mainly made of classical materials such as concrete and metals, however, such an approach requires the intervention in the composition of the final product, thus changing its mechanical characteristics that is not acceptable for most constructions used in aviation and other industries. On the other hand, non-destructive testing methods should provide an assessment of structural integrity without changing its composition [3], which, in addition to the possibility of on-line monitoring, makes this class of methods most suitable for the organization of structural health monitoring system. Various visual techniques belong to non-destructive evaluation approach. The inability to detect damage beyond visual inspection zone

significantly reduces application area of such techniques [4]. Moreover, the effectiveness of these techniques greatly depends on the skills of the specialist conducting the inspection.

One of the major subtypes of non-destructive evaluation methods are approaches that employ vibration processes for damage detection [5]. Vibrational methods, in turn, can be divided into several subgroups: 1) The class of methods that uses modal parameters (natural frequencies, mode shapes, the curvature of the mode shapes, etc.) to assess the mechanical state of investigated object [6-7]; 2) Methods based on wave propagation analysis in the studied object [8].

The process of non-destructive evaluation consists of several sub steps:
1) The identification of a defect or damage in the studied object
2) Determination of the defect location
3) Evaluation of the defect size
4) Determination of the residual resource of the structure

As a constantly developing research field a lot of scientific studies are dedicated to vibration control methods, which allows to highlight their main advantages and drawbacks [9-12].

This study is devoted to the application of vibrational damage detection method in order to identify the presence and location of delamination in composite structure by analyzing special frequencies and their mode shapes which are specific for delamination type defects. The unique feature of such frequencies is that the amplitude of vibrations in the area of delamination is significantly bigger compared to the rest of the structure. To activate this vibration shapes an external driving force must be applied to the structure which can be executed by the system of piezoelectric devices attached to the investigated structure. This approach is implemented on the numerical finite element model of the composite plate with internal delamination. Also internal damping properties of the material which are crucial for reliable numerical modeling of vibration processes and frequencies that are needed to activate these mode shapes are discussed in the framework of the research.

The main advantage of using vibration frequencies of defects is their strong dependence on the size of delamination but weak dependence on its location which gives the opportunity to tune the damage detection system to the defect of the specific size. The study has shown the applicability of proposed method in order to detect delamination in composite structure.

2 VIBRATIONAL DAMAGE DETECTION APPROACH

A square plate 300x300 mm, made of a laminated composite material, is considered as the object of research. The presence of n = 15 layers along the thickness of the plate is supposed with the thickness of one layer h_{1c} = 0.26 mm, hence the entire plate thickness is h_{1c}*n = 3.9 mm. The composite material is modeled as a homogeneous anisotropic elastic body, with the following effective mechanical characteristics: E_x = 58 GPa, E_y = 58 GPa, E_z = 10 GPa, G_{xy} = 4.5 GPa, G_{yz} = 3 GPa, G_{xz} = 3 GPa, ν_{xy} = 0.05, ν_{yz} = 0.18, ν_{xz} = 0.3, density ρ = 1800 kg / m^3.

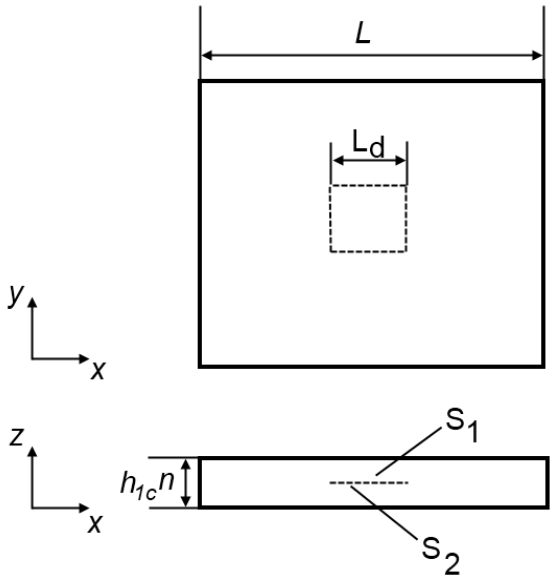

Figure 1: The scheme of the research object

Delamination type defect with the size of L_d, geometrically located between the 6 and 7th layers of the composite material (Fig. 1), was introduced into the plate under consideration. The adjacent surfaces of delamination (S_1, S_2) are considered to be free from stress.

This study was carried out numerically using the finite element method conducted in ANSYS. Finite elements with quadratic approximation were used in numerical simulations. Mesh nodes in the zone of delamination, belonging to the S_1 and S_2 surfaces, geometrically coincide but are not connected with each other. Fig. 2 shows a cross section of the plate model with delamination during flexural vibrations.

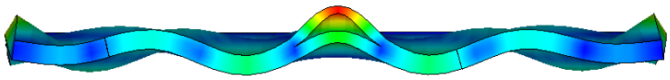

Figure 2: The cross-section of the plate model with delamination during flexural vibrations

The finite-element formulation in matrix form can be written as follows

$$[M]\{\ddot{u}\} + [C]\{\dot{u}\} + [K]\{u\} = \{F\} \quad (1)$$

Where $[M]$ - mass matrix of the system, $[C]$ – structural damping matrix, $[K]$ - stiffness matrix of the system, $\{F\}$ - load function, $\{u\}$ - the vector of nodal displacements, $\{\dot{u}\}$ – nodal velocity vector, $\{\ddot{u}\}$ - the vector of nodal accelerations.

In the absence of external influences and structural damping, the problem is reduced to the typical problem of finding eigenvalues and eigenvectors

$$u_i(\bar{x}, t) = e^{i\omega t}\xi_i(\bar{x}) \quad (2)$$

Where ω - natural frequency, ξ_i - eigenvector or mode shape. The finite element formulation of the problem has the following form

$$([K] - \omega^2[M])\{u_0\} = \{0\} \quad (3)$$

Where $\{u_0\}$ - the vector of nodal values of natural vibration modes.

In case of harmonic analysis structural damping is taken into account and force vector can be specified as:

$$\{F\} = F_{max} e^{i(\omega t+\varphi)} \quad (4)$$

Where F_{max} – force amplitude, φ – force phase shift.

2.1 Natural vibration frequencies and modes corresponding to delamination

The change in natural vibration frequencies only signals the occurrence of a defect, but does not give an answer to the question about its location, in other words, the approach, based on the registration of changes in eigenfrequencies, is effective to solve the first sub step of the general problem of damage detection [13]. An equally important question is to detect the location of the defect in the structure. Together with natural frequencies, natural vibration modes change as well, the study of which is of great importance for the localization of the defect. The study of the vibration modes has helped to determine that for delamination, which is the most common type of defects, typical for composite structures, special natural frequencies and corresponding mode shapes appear. The main distinctive feature of these modes is a significant increase in the amplitude of the vibrations in the delamination zone (Fig. 3).

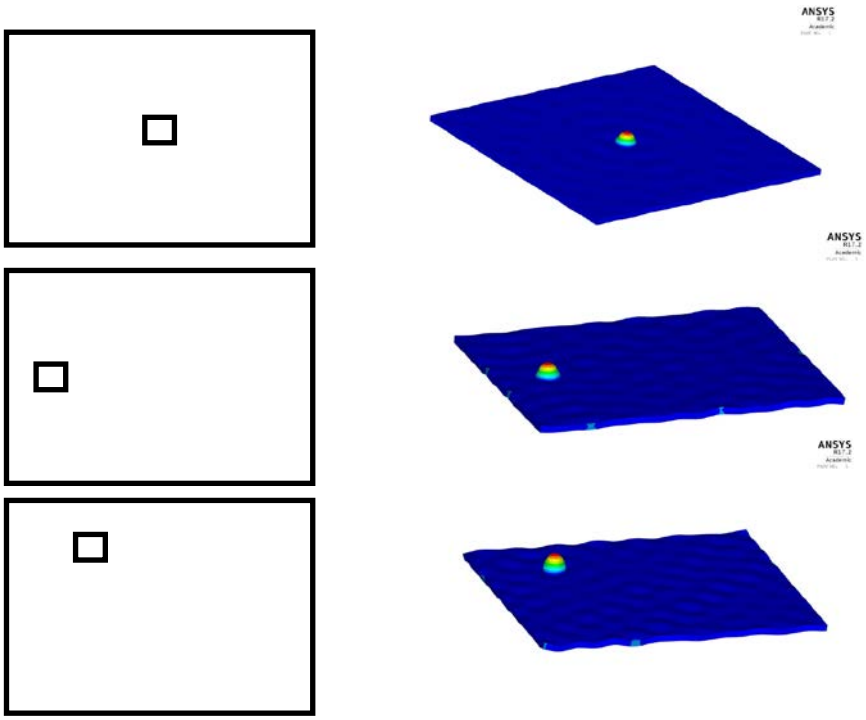

Figure 3:Vibration modes of a defect for different locations of delamination on the plate

The emergence of these forms of vibrations is caused by the fall of stiffness in the defect area. As a result, a layered structure appears to be locally divided into two or more parts, weakly interacting with each other. The defect region in this case, can be represented as a plate rigidly fixed along its contour. The frequency, corresponding to these forms of

vibrations, is determined by the size of the defect, total thickness of delaminated layers and the mechanical characteristics of the material.

For real structures, the detection of the defect at an early stage of its development is desirable, when the defect size is still small and do not pose any threat to the exploited object. The vibration frequency of the defect is inversely proportional to its size, so to detect delaminations of small sizes, an examination of structural vibrations at high frequencies of several tens of kHz is required. A modulus of elasticity in the direction perpendicular to the plane of the plate (for the presented model - E_z) has a determining influence on the magnitude of vibration frequencies corresponding to delamination. For composite materials with pronounced anisotropic properties, a modulus of elasticity in this direction may be significantly lower than the other moduli, which will greatly reduce the vibration frequency of the defect. For instance, for the given model of the plate in the isotropic approximation with a modulus of elasticity of E = 58 GPa, the vibration frequency of the defect with the size of 10x10 mm equals to 107 kHz. When accounting for anisotropic properties of the material listed above, a modulus of elasticity E_z = 10 GPa, together with an elastic modulus the calculated vibration frequency significantly decreases as well and possesses the value 52 kHz.

The analysis of the vibration modes at the described frequencies has identified their several distinctive features: such frequencies are weakly dependent on the location of the defect in the structure, the vibration frequency corresponding to the defect, is practically unchanged for the considered object in the form of a plate with the size of 300x300 mm, regardless of the location of delamination, with free boundary conditions of the plate. There is also a weak dependence of these frequencies observed on the size of the structure. These peculiarities are evident, due to the fact that the structure outside defect area acts as a rigid clamping to the zone of delamination. Stability of these frequencies makes them attractive for implementation of vibration damage detection approaches.

In real structures an external load must be applied to excite vibrations of a certain kind. In order to excite vibrations in the defect zone, the frequency of external periodic influence should be equal to the natural frequency of the defect, calculated from the modal analysis. Steady state vibration analysis gives an opportunity to study the possibility of vibration excitation in the defect zone and the parameters, affecting the efficiency of the given defect detection method.

2.2 Structural damping of a composite plate

One of the fundamental parameters, which is necessary for reliable simulation of steady state vibrations of the structure, is internal damping. Proper identification and accounting of the parameters in numerical modeling, describing internal dissipation mechanisms of the object under study, make it possible to take into account such features of structural behavior as attenuation of vibrations for different distance between the location of external periodic load application and the defect zone.

The determination of dissipative characteristics of the composite was based on the experimental analysis of attenuation of free vibrations of the composite plate suspended on rubber filaments [14]. On the basis of the performed experiment a dynamic complex modulus, used for numerical simulation of forced steady state vibrations, was calculated.

2.3 Vibration excitation in the zone of delamination

The study of natural frequencies and modes of vibration has shown that there are special frequencies and corresponding modes of vibration existing for a delamination type defect. To investigate the possibility of excitation of these modes of vibration and damage detection, the problem of forced steady state vibrations at the frequency of the driving force, obtained from the analysis of natural vibration frequencies, is considered. In structural health monitoring system attached piezoelectric devices can act as a source of external periodic load. At this stage of research, instead of direct piezoelectric modeling a force with the amplitude of 10 kN has been applied to the nodes of the finite element mesh with certain coordinates, thus the results are qualitative rather than quantitative. Different points of the application of an external periodic influence at different distances from the location of the defect (points P1 ... P4 in Fig. 4) are considered in the study. Each calculation compared the distribution along the line, indicated by a dotted line in Fig. 4, of u_z displacement component for the original plate without any defect and for the plate, containing a centrally located delamination of 10x10 mm.

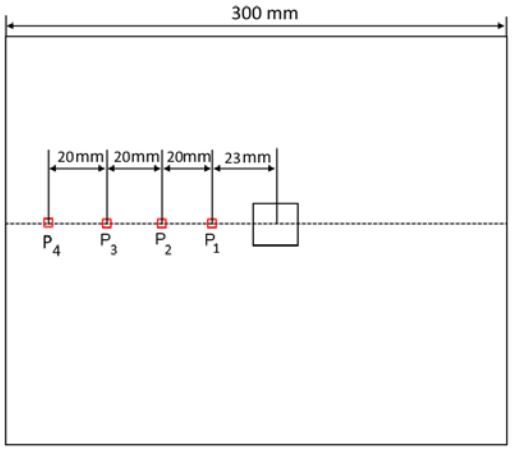

Figure 4: Different points of the application of an external periodic influence

Fig. 5, shows a field of u_z displacement of the considered plate, containing delamination, while solving the problem of forced steady state vibrations. Due to internal dissipation mechanisms, not instantaneous excitation propagation takes place from the location of an external load, which coming to the defect region, causes large amplitude vibrations of delamination. The displacement distribution along the line, shown in Fig. 5 demonstrates a substantial increase of the vibration amplitude in the zone of delamination as compared to the structure without any defects. A significant factor in this case is the frequency of external excitation, which leads to the formation of waves, the length of which should be comparable with the size of the defect. Otherwise, at wavelengths greater than the size of the defect, excitation of large vibrations in the defect region is impossible, and therefore its identification is not possible either. This situation is shown in Fig 6. In this case, the elastic modulus of the material was lowered, as a result natural frequency of the defect, decreased as well (from 107 kHz to 52 kHz). By applying an external load at the obtained frequency and performing a

numerical calculation of forced steady state vibrations, excitation of vibrations of high amplitude in the defect region does not take place, as the wavelength at this frequency of vibrations exceeds the size of the defect, and delamination remains unnoticed.

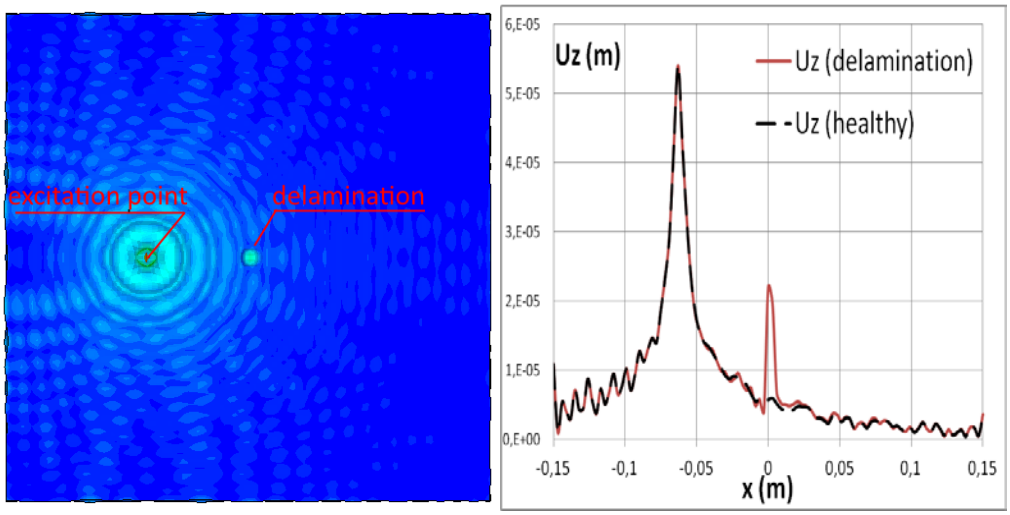

Figure 5: (left) u_z displacement field in the plate with delamination under forced steady state vibrations (107 kHz); (right) distribution of u_z displacement along the line, passing through the center of delamination.

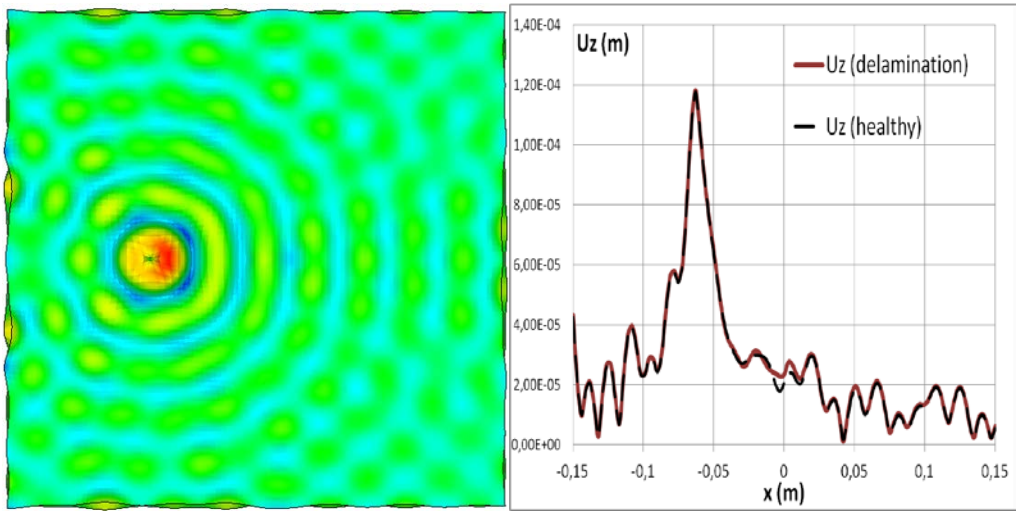

Figure 6: (left) u_z displacement field in the plate with delamination under forced vibrations (52 kHz) in case when wavelenth is bigger than defect size; (right) distribution of u_z displacement along the line, passing through the center of delamination.

Distributions of u_z displacement similar to the graph in Fig. 5 for different locations of the application of an external periodic influence (Fig. 7) are shown below.

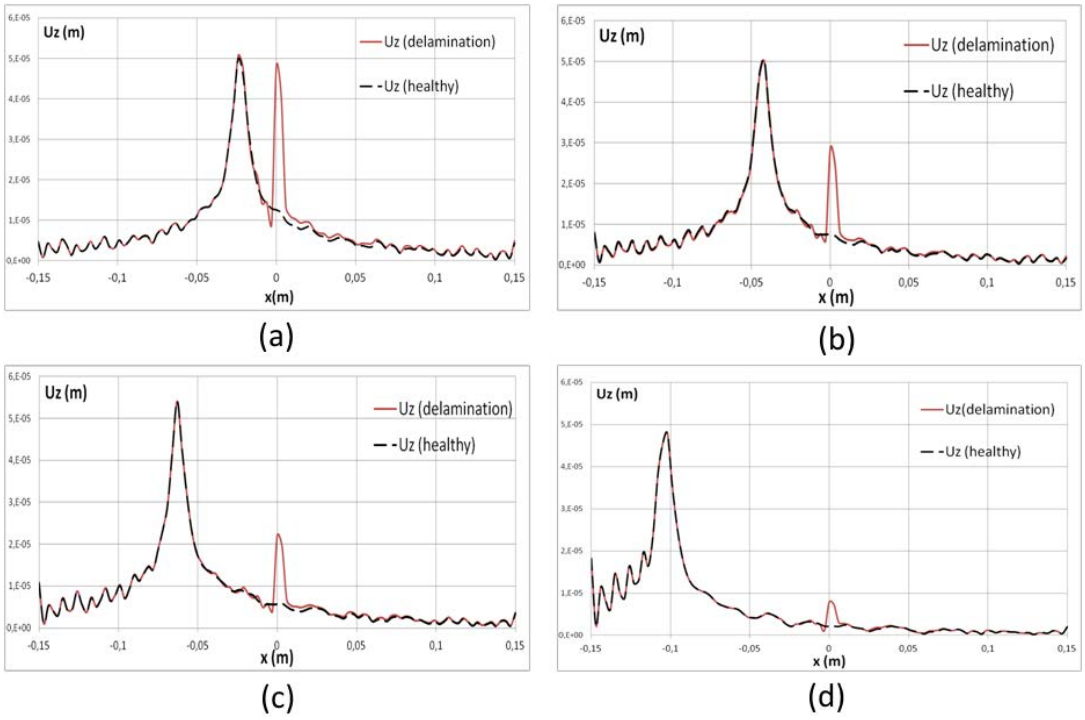

Figure 7: Distribution of u_z along the line, passing through the center of delamination for different distance between external harmonic force location and delamination (a) 23 mm b) 43 mm c) 63 mm d) 103 mm from the geometric center of the plate)

Analyzing the obtained distributions for the delaminated and healthy plates, it is seen that the amplitude of the measured parameter in the zone of delamination is significantly greater than the amplitude for the defect-free structure in the same area. The consideration of the difference and the ratio of the obtained distributions, shown in Fig. 8 and 9 for displacement and the application of an external influence at a distance of 63 mm from the defect region, clearly demonstrates the change of the signal in the zone of delamination. The delamination area is dashed in the figures.

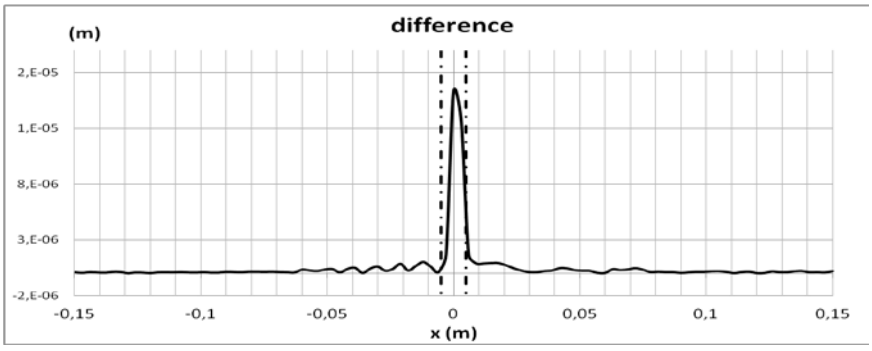

Figure 8: The difference between the u_z displacement component of the delaminated plate with respect to the healthy plate

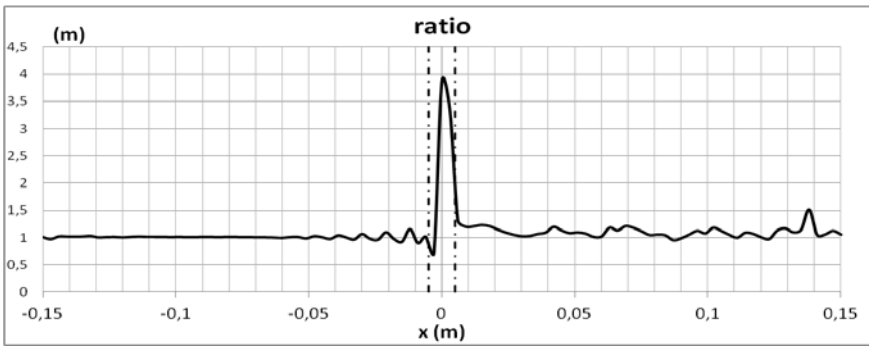

Figure 9: The ratio of the u_z displacement component of the delaminated plate with respect to the healthy plate

Outside the delamination region the changes of the measured parameters with respect to the defect-free structure are practically absent, which makes it possible to estimate, apart from the location, the size of the defect. At the same time the difference between the signals of delaminated and healthy plate in defect area decreases with increasing distance between external force location and delamination.

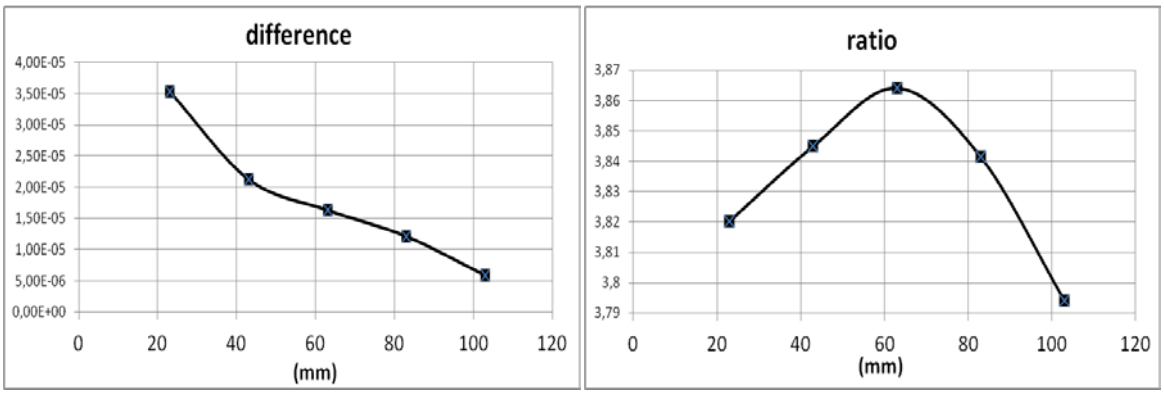

Figure 10: Change of the difference and ratio of the u_z displacement of the delaminated and defect-free plates, for different distance between the location of the application of an external periodic influence and the defect zone

The analysis of the amplitude differences of the healthy and defective plates has shown that the ratio of the amplitudes is maintained (in the zone of delamination the amplitude of the measured value increases about 3.8 times in relation to the non-defected plate) and the difference decreases as the load is removed from the defect zone. This result is displayed in Fig. 10 for the distribution of displacement u_z. Horizontal axes of the graphs correspond to the distance between the center of delamination and location of external force application.

3 CONCLUSIONS

In the framework of the study natural frequencies and mode shapes corresponding to the delamination type defect were studied. A significant increase in the amplitude of the vibrations in the defect region for such frequencies, as well as a weak dependence of their

value on the location of the defect, makes them convenient for implementation of vibration-based damage detection approaches based on the excitation of resonance vibrations of the delamination with the frequency of the exciting periodic external force obtained from the modal analysis. Numerical research has shown the effectiveness of this approach for localization of the defect's location and its size.

The reported study was supported by RFBR, research project No 16-31-00305.

REFERENCES

[1] Staab, G.H. *Laminar Composites*, Butterworth Heinemann, Boston, 1999. 314 p.

[2] Adams, D.E. *Health Monitoring of Structural Materials and Components*, John Wiley & Sons Ltd, Chichester, 2007. 460 p.

[3] Stepinski, T., Uhl, T., Staszewski, W. *Advanced Structural Damage Detection: From Theory to Engineering Applications*. JohnWiley&Sons, 2013. 352 p.

[4] Verma, S.K., Bhadauria, S.S., Akhtar, S. Review of nondestructive testing methods for condition monitoring of concrete structures. *Journal of Construction Engineering* (2013) **4**.

[5] Fan, W., Qiao, P. Vibration-Based Damage Identification Methods: a Review and Comparative Study. *Structural Health Monitoring* (2011) Vol. 10 **1**:83–111.

[6] Asnaashari, E., Sinha, J.K. Crack detection in structures using deviation from normal distribution of measured vibration responses. *Journal of Sound and vibration* (2014) **333:**4139-4151.

[7] Quaranta, G., Carbonu, B., Lacarbonara, W. Damage detection by modal curvatures: numerical issues. *Journal of Vibration and Control* (2014) 1-15.

[8] Raghavan, A., Cesnik, C.E.S. Review of Guided-wave Structural Health Monitoring. *The Shock and Vibration Digest* (2007) V. 39 **2**:91–114.

[9] Morassi, A., Vestroni, F. *Dynamic Methods for Damage Detection in Structures*. Springer, 2008. 221 p.

[10] Qiao, P., Lestari, W., Shah, M.G., Wang, J. Dynamics-based Damage Detection of Composite Laminated Beams using Contact and Noncontact Measurement Systems. *Journal of Composite Materials* (2007) V. 41 **10**:1217-1236.

[11] Michaels, J.E. Detection, localization and characterization of damage in plates with in situ array of spatially distributed ultrasonic sensors. *Smart Mater. Struct* (2008) **17:**1-15.

[12] Zhang, Z., Shankar, K., Ray, T., Morozov, E.V., Tahtali, M. Vibration-based inverse algorithms for detection of delamination in composites. *Composite Structures* (2013) **102**:226-236.

[13] Serovaev, G.S., Matveenko, V. P. Numerical study of the response of dynamic parameters to defects in composite structures, *Frattura ed Integrità Strutturale* (2016) **38**:392-398.

[14] Oshmarin, D.A., Serovaev,G.S., Shestakov,A.P. Evaluation of the applicability of vibrational methods for monitoring the mechanical state of composite structures. *AIP Conference Proceedings* (2016) **1785**

VIII ECCOMAS Thematic Conference on Smart Structures and Materials
SMART 2017
A. Güemes, A. Benjeddou, J. Rodellar and J. Leng (Eds)

ON THE DETERMINATION OF MATERIAL DEGRADATION IN COMPOSITES BY USE OF NON-LINEAR WAVE PROPAGATION ANALYSIS

Nguyen Vu Ngoc*, Natalie Rauter† and Rolf Lammering*

*Institute of Mechanics
Helmut-Schmidt-University/ University of the Federal Armed Forces Hamburg
Holstenhofweg 85, 22043 Hamburg, Germany
e-mail: n.vn@hsu-hh.de, web page: www.hsu-hh.de/mechanik/

†Nordex Energy GmbH, Langenhorner Chaussee 600, 22419 Hamburg, Germany

Key words: *Structural Health Monitoring,* Lamb*-waves, higher-harmonic generation, transversely isotropic material, hyperelastic material*

Abstract. Fiber-reinforced plastics (FRP) are increasingly used in lightweight constructions. Due to improved but also more complex mechanical properties compared to conventional materials, there is a need to develop further advanced inspection methods for structures made of FRP. Microstructural damage in the matrix material as well as in the fiber matrix interface in the FRP component is difficult to detect by known non-destructive testing methods. Recent investigations show that guided waves are capable of detecting microstructural initial damage in FRP structures and are applicable for structural health monitoring (SHM), especially when non-linear wave propagation and so-called higher-harmonic wave modes are used. The method makes use of the fact that damaged structures behave in a non-linear way. This inspection approach has been applied numerically and experimentally successfully for the detection of microstructural damages in isotropic materials [7]. Their applicability is currently expanded to fiber reinforced plastics [15]. In this article, the numerical aspect of the investigation of the non-linear wave propagation is considered.

1 Introduction

In metallic structures, the damage mechanisms and the fatigue behavior are fairly well researched. Accordingly, there are a lot of suitable assessment and testing procedures for such structures, e.g. X-ray, ultrasonic or visual inspection. In layered fiber composite structures, on the other hand, there is a more complicated damage pattern. Namely, in layered composites, microstructural damage is produced even at hundreds of load cycles, which is not the case in

metallic materials such as aluminum. These damages are less critical in the initial phase, since only a slight reduction in the stiffness is determined. However, they can lead to a sudden structural failure by their accumulation [9]. For this reason, an early detection of the intial damage as well as possibility of monitoring their development is very desirable. In addition, composite structures are often thin-walled and cover a large area. As a result, conventional inspection procedures can only be used with great cost and amount of time. It has been shown over time that guided waves or LAMB waves are suitable tools for the mentioned application purpose. Damaged structures cause a non-linear behavior of the wave propagation in the structure. This results in so-called higher-harmonic wave modes. In order to develop inspection methods for SHM systems by means of non-linear wave propagation, a particularly good understanding of the wave propagation behavior is needed.

Beside the experimental investigation, the theoretical and numerical examination plays a very important role. In order to map the non-linear material behavior and thus the non-linear propagation behavior of the waves numerically, a suitable non-linear material model is required. Previous numerical studies for isotropic and transversely isotropic materials are based on non-linear potential formulations, more in the section 2.2. It could be shown, that thus it is possible to generate the so-called cumulatively higher-harmonic modes. In this article we present a new hyperelastic material law for FRP, which provides the capacity of investigating non-linear in transversely isotropic materials. It is shown that the use of non-linear wave propagation in the generation of cumulatively higher-harmonic modes is an appropriate tool to detect microstructural damages also in FRP components, e.g. due to fatigue phenomena [15]. Ongoing work is concerned with the extension of this methodology to other layered structures, e.g. symmeric cross-ply laminates and structures with more complex lay-ups.

2 Theoretical Foundations

In this section, the linear and non-linear propagation of guided waves (LAMB waves) in thin-walled structures will be under investigation. Subsequently, the hyperelasticity considering the material non-linear effect in wave propagation is discussed.

2.1 Guided wave propagation

LAMB waves are guided waves propagating between two stress-free surfaces of a thin-walled structure. They arise through reflections and interference of longitudinal waves (pressure waves) and transverse waves (shear waves) at the surfaces. Based on the symmetry of the plate motion with respect to the plate central plane, a distinction is made between symmetric and antisymmetric LAMB wave modes. LAMB waves are dispersive waves since the propagation velocity depends on the frequency. This fact can be summarized in so-called dispersion curves, see figure 1.

The starting point for the description of LAMB wave propagation is the homogeneous momentum

balance without the volume forces as well as the boundary conditions

$$\mathrm{Div}\left(\mathbf{P}\left(\mathbf{H}\right)\right) - \rho\ddot{\mathbf{u}} = \mathbf{0}, \tag{1}$$

$$\mathbf{P}\left(\mathbf{H}\right) \cdot \mathbf{N} = \mathbf{0}, \tag{2}$$

here, $\mathbf{H} = \mathrm{Grad}\left(\mathbf{u}\right)$, $\mathbf{P}$ is the first PIOLA-KIRCHHOFF stress tensor, $\mathbf{u}$ ist the displacement vector, ρ is the density and $\mathbf{N}$ ist the normal vector of the stress-free surfaces.

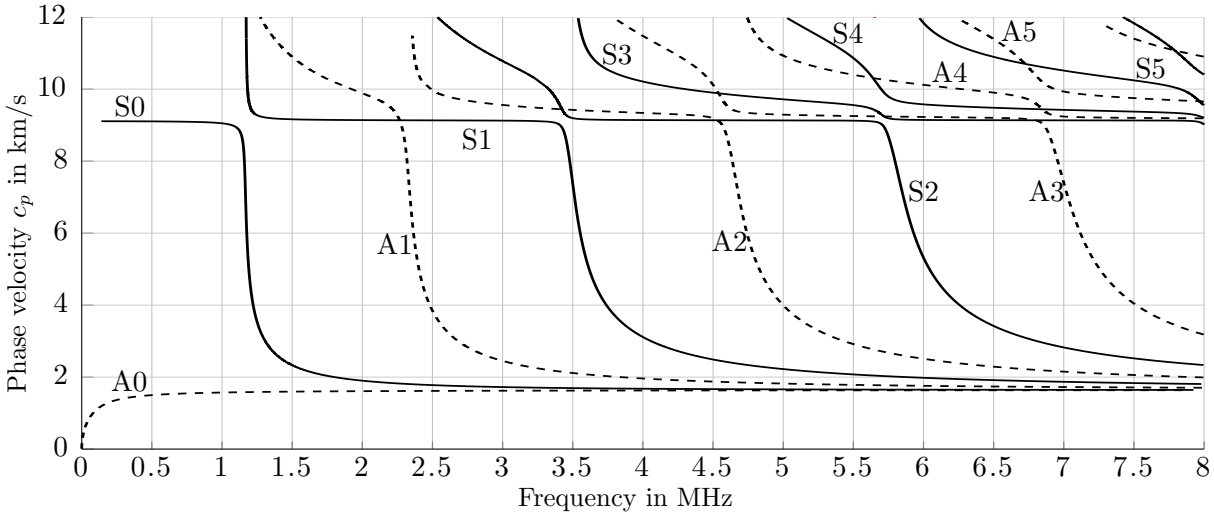

Figure 1: Dispersion curves for a unidirectional FRP in the fiber direction, Sj stands for the symmetric LAMB wave mode Sj, Aj - antisymmetric LAMB wave mode Aj

In the case of a non-linear material law, corresponding second order differential equations in space and time of the displacements are obtained. In the literature, it is usually assumed that the total displacement field is composed of the primary and secondary wavefields $\mathbf{u}_1$ (linear part) and $\mathbf{u}_2$ (non-linear part),

$$\mathbf{u} = \mathbf{u}_1 + \mathbf{u}_2, \text{ with } \left\|\mathbf{u}_1\right\| \gg \left\|\mathbf{u}_2\right\|. \tag{3}$$

This leads to a homogeneous differential equation of $\mathbf{u}_1$ and an inhomogeneous differential equation $\mathbf{u}_2$ of this form:

$$f(\mathbf{u}_1'', \ddot{\mathbf{u}}_1) = \mathbf{0}, \tag{4}$$

$$f(\mathbf{u}_2'', \ddot{\mathbf{u}}_2) = \mathbf{F}(\mathbf{u}_1). \tag{5}$$

Solving the differential equation (4) asuming the linear Green's strain tensor provides the solution for the primary displacement field as well as the above-mentioned dispersion curves. A solution approach for the amplitude of the secondary wave field was presented in [2] or in [19], for example.

The formation of the secondary waves is due to the non-linearity of the medium used. This non-linear propagation behavior of the waves is demonstrated using the following sketch (fig. 2):

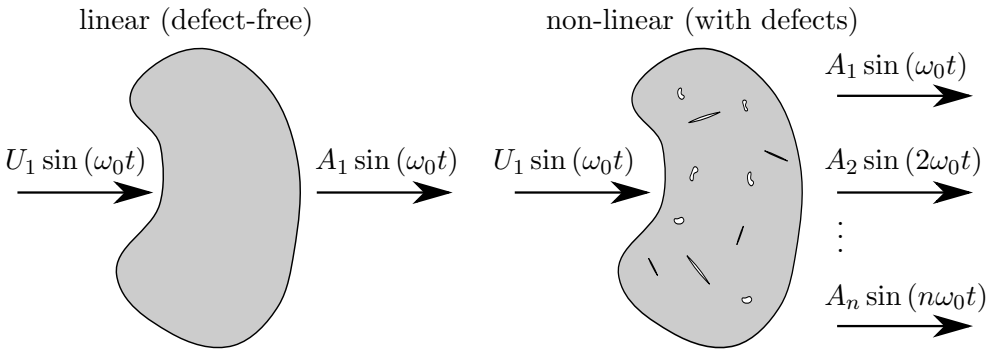

Figure 2: Linear and non-linear wave propagation in solid bodies

In a linear medium, a monofrequential excitation leads to a monofrequent signal response. If a non-linear medium is present, the secondary wave field is obtained, which consists of frequency components as multiples of the fundamentally excited frequency. That non-linear behavior of the structure appears when a non-linear geometry, a non-linear material behavior or interacting surfaces, e.g. cracks in the structure exist.

As a measure of the non-linear effect of wave propagation, the so-called non-linear acoustical parameter β is often used. A detailed derivation of this parameter for longitudinal waves in the 1-dimensional case can be found in [14], for example,

$$\beta = \frac{8}{k^2 X} \frac{A_2}{A_1^2}. \tag{6}$$

The amplitudes of the second wave field are usually very small compared to those of the primary wave field, i.e. $A_2 \ll A_1$. In order to enable to dectect these amplitudes and thus to determine the non-linearity of the structure, it is necessary to generate the so-called cumulative higher-harmonic wave modes, of which amplitudes grow linearly with increasing propagation distance.

2.2 Hyperelastic material model

In the following, we will focus on the material non-linearity behavior only. Hyperelastic material models are used to model linear and non-linear elastic material behavior. Firstly, an overview of the hyperelastic material models is provided. Finally, we present the new hyperelastic material model for transversely isotropic material - an improved material model compared to the known models and its validation.

2.2.1 Discription of hyperelasticity

Hyperelastic material models are characterized by the existence of an elastic strain energy function ψ as the potential of the stresses

$$\psi = \int \mathbf{S} \, \mathrm{d}\mathbf{E}, \tag{7}$$

where $\mathbf{S}$ is the second PIOLA-KIRCHHOFF stress tensor and $\mathbf{E}$ is the GREEN-LAGRANGE strain tensor.

Thus, in a hyperelastic material model, the stress-strain relationship can be derived from the strain energy function. Based on this potential formulation, the stress tensor $\mathbf{S}$ and the stiffness tensor $\mathbb{C}$ can be calculated as follows

$$\mathbf{S} = 2\frac{\partial \psi\left(\mathbf{C}\right)}{\partial \mathbf{C}} = \frac{\partial \psi\left(\mathbf{E}\right)}{\partial \mathbf{E}}, \tag{8}$$

$$\mathbb{C} = 4\frac{\partial^2 \psi\left(\mathbf{C}\right)}{\partial \mathbf{C}^2} = \frac{\partial^2 \psi\left(\mathbf{E}\right)}{\partial \mathbf{E}^2}, \tag{9}$$

here $\mathbf{C} = \mathbf{F}^T \cdot \mathbf{F}$ is the right CAUCHY-GREEN deformation tensor, $\mathbf{F}$ is the deformation gradient.

2.2.2 Hyperelasticity in tranverely isotropic composites

Linear models

In the case of a linear elastic, transversely isotropic material, the strain energy function ψ can be formulated by use of 5 invariants I_1, I_2, I_3, I_4, I_5 of the CAUCHY-GREEN tensor $\mathbf{C}$ [10]:

$$\psi^{lin} = \psi\left(I_1,\, I_2,\, I_3,\, I_4,\, I_5\right), \tag{10}$$

with $I_1 = \operatorname{tr}\mathbf{C}$, $I_2 = \frac{1}{2}\left(\left(\operatorname{tr}\mathbf{C}\right)^2 + \operatorname{tr}\mathbf{C}^2\right)$, $I_3 = \det\mathbf{C}$, $I_4 = \mathbf{a}_0 \cdot \mathbf{C}\mathbf{a}_0$ and $I_5 = \mathbf{a}_0 \cdot \mathbf{E}^2\mathbf{a}_0$. The unit vector $\mathbf{a}_0$ denotes the material principal direction.

In [16] the following material model was presented on the basis of experimental investigations

$$\begin{aligned}\psi_C^{lin} =& c_1(I_1-3)^2 + c_2\left(I_2 - 3 - 2\left(I_1-3\right)\right) + c_3(I_4-1)^2 \\ &+ c_4\left(I_5 - 1 - 2\left(I_4-1\right)\right) + c_5\left(I_4-1\right)\left(I_1-3\right).\end{aligned} \tag{11}$$

With respect to the GREEN-LAGRANGE strain tensor $\mathbf{E} = (\mathbf{C} - \mathbf{I})/2$, the strain energy function ψ is given by [8]

$$\psi_E^{lin} = \frac{\lambda}{2}(\operatorname{tr}\mathbf{E})^2 + \mu_T \operatorname{tr}\mathbf{E}^2 + \alpha\left(\mathbf{a}\cdot\mathbf{E}\mathbf{a}\right)\operatorname{tr}\mathbf{E} + 2\left(\mu_L - \mu_T\right)\left(\mathbf{a}\cdot\mathbf{E}^2\mathbf{a}\right) + \frac{\beta}{2}(\mathbf{a}\cdot\mathbf{E}\mathbf{a})^2. \tag{12}$$

c_1, c_2, c_3, c_4, c_5 in equation (11) or λ, α, β, μ_L, μ_T in equation (12) are five independent material constants, which are necessary to describe unidirectional material behavior.

These two linear models as well as other known hyperelastic, transversely isotropic material models are based on the assumption of incompressibility. This is not always given. In particular because the matrix material possesses a compressible behavior and it transfers this behavior to the entire structure because of its high content [15].

Non-linear models

In order to be able to investigate non-linear wave propagation, a non-linear material model is required. Two model approaches for non-linear transversal isotropic materials are now presented.

An approach from biomechanics can be found in [11, 10]. In this concept it is assumed that the entire potential consists of an isotropic and an anisotropic part.

$$\bar{\psi}_{HG}\left(\bar{\mathbf{C}}, \mathbf{a}_0\right) = \bar{\psi}_{iso}\left(\bar{\mathbf{C}}\right) + \bar{\psi}_{aniso}\left(\bar{\mathbf{C}}, \mathbf{a}_0\right), \tag{13}$$

$\bar{\mathbf{C}}$ denotes the modified right CAUCHY-GREEN deformation tensor which is calculated as follows

$$\bar{\mathbf{C}} = \bar{\mathbf{F}}^T \cdot \bar{\mathbf{F}},\ \bar{\mathbf{F}} = J^{-\frac{1}{3}}\mathbf{F},\ J = \det \mathbf{F}. \tag{14}$$

For $\bar{\psi}_{iso}$ we refer to the known potential formulations for isotropic materials of NEO-HOOKE and MOONEY-RIVLIN. Detailed discriptions of these can be taken from [4] and [3]. The anisotropic part is formulated by using an exponential functional approach of the 4th invariant [10].

In this approach, only three material parameters are required to describe the transversal isotropic material behavior. However, this assumes incompressibility.

Another non-linear approach comes from the so-called five-constant theory of MURNAGHAN. In his original model for isotropic material, a TAYLOR series expansion up to the third order of the potential function with respect to the invariants I_1, I_2, I_3 is taken into account [13].

An extension of this concept for transversely isotropic materials can be found in [19]. The potential function ψ is composed of a linear and a non-linear part ψ_E^{lin} and ψ_E^{nlin}

$$\psi = \psi_E^{lin} + \psi_E^{nlin}, \tag{15}$$

with $\psi_E^{nlin} = \psi_E^{nlin}\left(\beta_1, \beta_2, ..., \beta_9, \mathcal{O}\left(\mathbf{E}^3\right), \mathbf{a}_0\right)$.

Incompressibility is not a prerequisite for the development of this model. In this case, however, a total of 14 material constants (5 - linear λ, α, β, μ_L, μ_T and 9 - non-linear $\beta_1, \beta_2, ..., \beta_9$) must still be determined.

On the one hand, the non-linear model according to MURNAGHAN has not yet been implemented in commercial FE-software. On the other hand, this model requires a large number of parameters for the modeling of complex materials such as FRP. These facts complicate numerical investigations.

The new non-linear model

A new constitutive model is now being developed which involves some improvements compared to the non-linear models presented above. As a result, the strain energy density ψ_{ti} is as follows

$$\psi_{ti} = \psi_C^{lin} + \psi_C^{Simo}. \tag{16}$$

In this concept, the linear, incompressible formulation ψ_C^{lin} from (11) and the non-linear, compressible formulation ψ_C^{Simo} of SIMO [18] are used

$$\psi_C^{Simo} = \frac{K}{4}\left(J^2 - 2\ln J - 1\right), \tag{17}$$

where K can be interpreted as the bulk modulus. Thus, in this model, only 6 independent material parameters $(c_1, c_2, ..., c_5, K)$ are required, which are much less than 14 in the MURNAGHAN's

formulation. By using this mixed formulation, the compressible behavior of the fiber-reinforced plastic can now be considered. This behavior is controlled by varying the parameter K.

In the transversely isotropic case, the fibers extend into an axis direction of the selected coordinate system (X_1, X_2, X_3). Without loss of generality, it can be assumed that X_1-axis corresponds to the fiber direction, i.E. $\mathbf{a}_0 = \mathbf{e}_1$.

From the chosen potential formulation, the stresses and the stiffnesses result according to (8) und (9) [15]

$$\begin{aligned}\mathbf{S}_{ti} =& 4c_1\left(I_1-3\right)\mathbf{I} + 2c_2\left(I_1\mathbf{I}-\mathbf{C}\right) - 4c_2\mathbf{I} + 4c_3\left(I_1-1\right)\mathbf{e}_1\otimes\mathbf{e}_1 \\ &+ 2c_4\left(\mathbf{e}_1\cdot\mathbf{C}\otimes\mathbf{e}_1 + \mathbf{e}_1\otimes\mathbf{C}\cdot\mathbf{e}_1 - 2\mathbf{e}_1\otimes\mathbf{e}_1\right) \\ &+ 2c_5\left(\left(I_4-1\right)\mathbf{I} + \left(I_1-3\right)\mathbf{e}_1\otimes\mathbf{e}_1\right) + \frac{K}{2}\left(J^2-1\right)\mathbf{C}^{-1}, \qquad (18)\\ \mathbb{C}_{ti} =& 8c_1\mathbf{I}\otimes\mathbf{I} + 4c_2\left(\mathbf{I}\otimes\mathbf{I} - \mathbb{I}^s\right) + 4c_3\mathbf{e}_1\otimes\mathbf{e}_1\otimes\mathbf{e}_1\otimes\mathbf{e}_1 \\ &+ 4c_4\left(\mathbf{e}_1\cdot\mathbb{I}^s\otimes\mathbf{e}_1 + \mathbf{e}_1\otimes\mathbb{I}^s\cdot\mathbf{e}_1\right) + 4c_5\left(\mathbf{I}\otimes\mathbf{e}_1\otimes\mathbf{e}_1 + \mathbf{e}_1\otimes\mathbf{e}_1\otimes\mathbf{I}\right) \\ &+ K\left(J\mathbf{C}^{-1}\otimes\mathbf{C}^{-1} + \left(J^2-1\right)\frac{\partial\mathbf{C}^{-1}}{\partial\mathbf{C}}\right). \qquad (19)\end{aligned}$$

$\mathbf{I}$ is the second order unit tensor. The fourth order tensor $\mathbb{I}^s$ is obtained by the partial derivative of an arbitrary second order tensor with respect to itself

$$\mathbb{I}^s = \frac{\partial\mathbf{C}}{\partial\mathbf{C}} = \frac{\partial\mathbf{E}}{\partial\mathbf{E}} = \frac{1}{2}\left(\delta_{ik}\delta_{lj} + \delta_{il}\delta_{jk}\right)\mathbf{e}_i\otimes\mathbf{e}_j\otimes\mathbf{e}_k\otimes\mathbf{e}_l. \qquad (20)$$

It is in (19) obviously a non-linear formulation, since the stiffness tensor is not independent of the deformation gradient $\mathbf{F}$.

2.3 Cumulative higher-harmonic generation

In order to ensure the generation of cumulative higher-harmonic or second-harmonic modes, certain criteria must be fulfilled. This is discussed in detail e.g. in [2] for isotropic and in [19] for transversely isotropic materials. The so-called reciprocity relation and the normal mode expansion technique are adopted [1, 2, 17] .

The reciprocity relation describes the interaction between stress characterizing by stress field $\mathbf{P}$ and particle motion characterizing by velocity field $\mathbf{v}$ of the primary and secondary wave fields.

$$\mathrm{Div}\left(\mathbf{v}_2^*\cdot\bar{\mathbf{P}}_1 + \mathbf{v}_1\cdot\bar{\mathbf{P}}_2^*\right) = 0. \qquad (21)$$

By using the normal mode expansion technique, the variables of the secondary wave fields in the reciprocity relation are respresented by Fourier-series. These approaches together with (5) lead to a differential equation for the determination of the amplitudes of the higher-harmonic modes $A_m\left(X_1\right)$. A detailed representation can be found in [6, 15], for example.

When examined the modal amplitudes $A_m(X_1)$, the following can be established in [5, 6] and in [19]. The cumulative second-harmonic modes can be generated if primary waves and secondary waves have the same phase velocity and a power flow exists between these two wave modes.

It could be shown that in non-linear isotropic and transversely isotropic material models, the power flow can be present only between symmetric wave modes. In isotropic materials, the non-linear hyperelastic models according to Landau–Lifshitz and to Murnaghan [5, 6] are used. The non-linear hyperelastic model used in [19] is derived from the five-constant theory of Murnaghan [13]. The power flow condition for the newly introduced material model is also analyzed analytically in [15]. It is hereby confirmed that the power flow for a symmetrical secondary wave field is not equal to zero.

If the request for identical phase velocities of the mode pair is not given, the amplitude of the higher-harmonic mode shows oscillating behavior, which is described by the dispersion length L

$$L = \left| \frac{\pi c_p^{2f} c_p^f}{f\left(c_p^{2f} - c_p^f\right)} \right|. \tag{22}$$

3 The finite element model

The goal for the development of the new non-linear model is not only to consider compressible behavior and to reduce the number of material parameters required. Instead, the new model is supposed to correctly represent the non-linear mechanical behavior and is therefore supposed to be suitable for the investigation of non-linear wave propagation.

3.1 Parameter determination

By making use of the symmetry properties of the tensor $\mathbb{C}_{ti}$ based on the potential formulation, we obtain the symmetric material matrix $\tilde{\mathbb{C}}$ as a reduced form of $\mathbb{C}_{ti}$

$$\tilde{\mathbb{C}} = \begin{bmatrix} \tilde{\mathbb{C}}_{11} & \mathbf{0} \\ \text{sym.} & \tilde{\mathbb{C}}_{22} \end{bmatrix}, \tag{23}$$

with

$$\tilde{\mathbb{C}}_{11} = \begin{bmatrix} 8\left(c_1 + c_3 + c_4 + c_5\right) + K & 4\left(2c_1 + c_2 + c_5\right) + K & 4\left(2c_1 + c_2 + c_5\right) + K \\ & 8c_1 + K & 8c_1 + 4c_2 + K \\ \text{sym.} & & 8c_1 + K \end{bmatrix}, \tag{24}$$

$$\tilde{\mathbb{C}}_{22} = \begin{bmatrix} -2c_2 & 0 & 0 \\ & -2c_2 + 2c_4 & 0 \\ \text{sym.} & & -2c_2 + 2c_4 \end{bmatrix}. \tag{25}$$

The generalized transversely isotropic behavior according to Hooke is described by 5 material constants $C_{11}, C_{12}, C_{22}, C_{23}, C_{44}$ (table 1), which are obtained by a conversion of the engineering

constants $E_{\parallel}, E_{\perp}, \nu, G_{\parallel}, G_{\perp}$ from experimental investigations, see [12], for example. In this new non-linear potential formulation, the bulk modulus of the matrix material is used for K, since the compressible behavior of the composite is determined by the matrix material. Thus, the 5 material constants $c_1, c_2, ..., c_5$ can be calculated by a coefficient comparison (table 2).

Table 1: Material properties for the linear, transversally isotropic material model (HOOKE), [15]

C_{11}	C_{12}	C_{22}	C_{23}	C_{44}	Unit
122.3	8.08	2.38	5.82	3.75	GPa

Table 2: Material properties for the newly developed material model (eq. 16), [15]

c_1	c_2	c_3	c_4	c_5	K	Unit
0.527	-1.875	13.66	1.25	0.568	3.89	GPa

3.2 Modeling using the new material law

The newly constitutive law is now to be subjected to s static and a dynamic validation with regard to its mechanical behavior. The implimentation is carried out in the FE-software FEAP. For sake of brevity, the validation is not given at this point. The next section will briefly discuss its results only.

Finally, the numerical analysis in terms of generating cumulative higher-harmonics is carried out with a model shown in figure 3. On the basis of the power flow condition already discussed above, the plate is now intentionally symmetrically excited. The excitation is undertaken in a low-frequency range (100 kHz to 500 kHz) to investigate the possible formation of the so-called quasi cumulative second-harmonic modes. Here, a windowed excitation signal with 10 periods in the burst is selected.

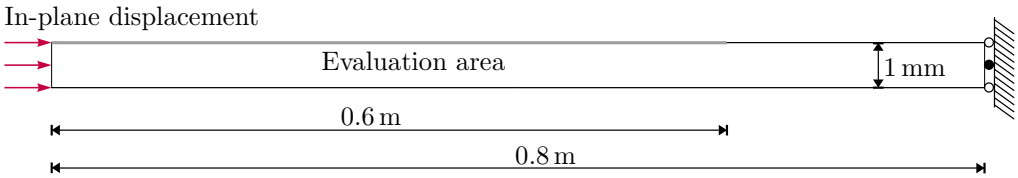

Figure 3: Schematic of the wave guide model for the analysis of the non-linear effect due to non-linear hyperelastic material, [15].

4 Numerical results

The static and dynamic validation shows that the implimentation of the new non-linear material model has been carried out correctly. The new material model leads to physically meaningful results in both cases. While in the dynamic simulation no difference between linear and non-linear calculation in the time domain can be detected, the existence of second-harmonic modes in the frequency domain can be observed. Furthermore, it is also apparent that the use of the

dispersion curves from the linear calculation is still permitted for the analysis of the non-linear wave propagation. Thus, it can be confirmed that the developed model can be used for the simulation of the non-linear wave propagation concerning the generation of cumulative second-harmonic modes.

The result of the frequency analysis and that of the amplitude behavior investigation of the next numerical simulation are shown representatively for the excitation frequency $f = 500\,\mathrm{kHz}$ in figure 4. First, it becomes clear that the secondary wave field is generated at approximately twice the frequency ($2f$). When looking back at the dispersion curves 1, we find that both the fundamental mode and the second-harmonic mode must be mode S0. However, this mode pair S0-S0 does not possess exactly the same phase velocity, so that the amplitude of the second-harmonic mode must have an oscillating behavior with a certain dispersion length according to the theory. The corresponding values for different excitation frequencies are listed in the table 3.

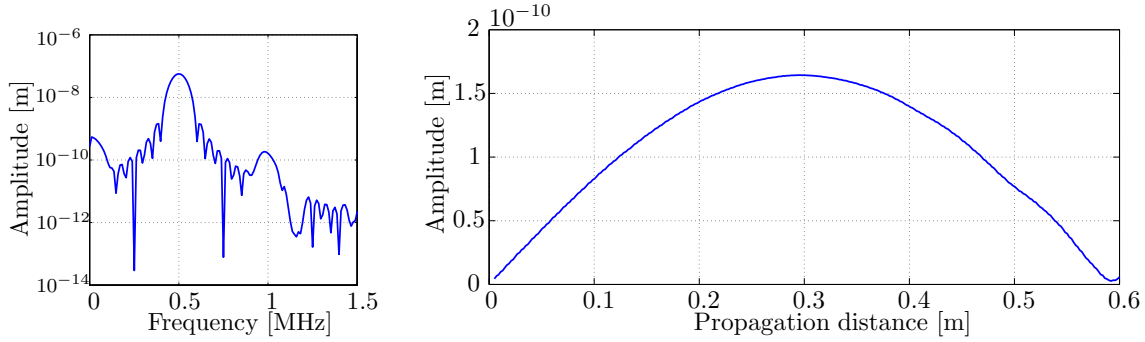

(a) Frequency components of the in-plane time signal.

(b) Behavior of the second-harmonic amplitude with the propagation distance

Figure 4: Analysis of the non-linear wave propagation and the behavior of the second-harmonic mode amplitude based on the in-plane motion of the S_0–S_0 mode pair at 500 kHz, [15].

At the excitation frequency 500 kHz, the difference in the phase velocity of the wave mode pair S0-S0 takes the largest value. In that case, the numerical calculation also provides the smallest dispersion length ($\frac{1}{2}L_{500}^{numr.} = 0.591\,\mathrm{m}$). This corresponds to the theoretical expectation. Thus, the numerical value deviates only slightly from the theoretical value (1.5 %). If the excitation frequency decreases further, the dispersion length grows (see table 3).

Table 3: Phase velocity mismatch and dispersion length for the S_0–S_0 mode pair, [15].

f	c_p^f [m s^{-1}]	c_p^{2f} [m s^{-1}]	$L^{theor.}$ [m]
500	9111	9034	1.07
400	9114	9091	4.50
300	9116	9107	15.6
200	9117	9114	65.5
100	9118	9117	589

Thus, it can be stated that in the low-frequency range the mode pair S0-S0 is very well suited

for the generation of quasi cumulative second-harmonic mode.

In addition, an analysis of the non-linear wave propagation in the constitutive law is carried out by varying the bulk modulus K. Based on this analysis, it can be stated that the parameter K can be used to control the degree of non-linear behavior in the wave propagation as well as that of the material compressibility.

By modeling non-linear wave propagation using the new material law, quasi cumulative second-harmonic modes can be generated with a suitable excitation. From this, according to (6) the non-linearity and thus the numerical material degradation can be calculated. The numerical investigation thus shows that the degradation of the material due to microstructural damage in transversally isotropic structures may be reproduced by the model presented. An inverse calculation using the generation of quasi cumulative second-harmonic modes has already been carried out successfully.

5 Conclusion and outlook

The non-linear material behavior and thus the non-linear wave propagation can be represented by a non-linear hyperelastic material model. There are approaches for the non-linear modeling of transversally isotropic materials, which, however, have certain limitations on the ability to be implemented and on the consideration of the compressible material behavior, especially in layered composites. The presented model requires only 6 parameters for the material description, one of which (K) has to be specified in advance, instead of 14 by using the non-linear model according to Murnaghan. This parameter affects the compressible behavior and the non-linear degree of the model simultaneously. A static as well as dynamic validation was carried out successfully and proved that the newly developed model is suitable for the investigation of non-linear wave propagation in transversely isotropic materials, at least in a 2-dimensional case. Furthermore, it was shown in the framework of the numerical study that linearly calculated dispersion curves can still be used for the investigation of non-linear wave propagation. In the low-frequency range, the mode pair S0-S0 can be used to generate quasi cumulative second-harmonic mode. In conclusion, it can be confirmed that the newly introduced model presents itself as a good alternative to the existing non-linear material models for cumulative higher-harmonic generation.

Subsequent to the present work, the generation of cumulative second-harmonic modes can be dealt with for the mode pairs S1-S1, S2-S2 or S1-S2, for example. An extension of the developed concept to layered FRP would also be relevant for future research purposes in this area.

Acknowledgements: The financial support of the Deutsche Forschungsgemeinschaft (DFG) ist gratefully acknowledged.

REFERENCES

[1] B. A. Auld. *Acoustic fields and waves in solids*, volume 1. Wiley, New York, 1973.

[2] B. A. Auld. *Acoustic fields and waves in solids*, volume 2. R.E. Krieger, Malabar, Fla., 2nd edition, 1990.

[3] K.-J. Bathe and P. Zimmermann. *Finite-Elemente-Methoden*. Springer, Berlin, 2nd, revised and extended edition, 2002.

[4] T. Belytschko, W. K. Liu, B. Moran, and K. I. Elkhodary. *Nonlinear finite elements for continua and structures*. CourseSmart. John Wiley & Sons Inc, Hoboken, New Jersey, 2nd edition, 2014.

[5] V. K. Chillara and C. J. Lissenden. Review of nonlinear ultrasonic guided wave nondestructive evaluation: Theory, numerics, and experiments. *Optical Engineering*, 55(1):011002, 2016.

[6] W. de Lima and M. F. Hamilton. Finite-amplitude waves in isotropic elastic plates. *Journal of Sound and Vibration*, 265(4):819–839, 2003.

[7] M. Deng and J. Pei. Assessment of accumulated fatigue damage in solid plates using nonlinear lamb wave approach. *Applied Physics Letters*, 90(12):121902, 2007.

[8] M. Fiolka. *Theorie und Numerik volumetrischer Schalenelemente zur Delaminationsanalyse von Faserverbundlaminaten: Zugl.: Kassel, Univ., Diss., 2007*, volume 2008,2 of *Berichte des Instituts für Mechanik*. Kassel Univ. Press, Kassel, 2008.

[9] B. Harris. *Fatigue in composites: Science and technology of the fatigue response of fibre-reinforced plastics*, volume Number 16 of *Woodhead Publishing Series in Composites Science and Engineering*. Woodhead Publishing Limited, Cambridge, England, 2003.

[10] G. A. Holzapfel. *Nonlinear solid mechanics: A continuum approach for engineering*. Wiley, Chichester u.a., 2000.

[11] G. A. Holzapfel, T. C. Gasser, and R. W. Ogden. A new constitutive framework for arterial wall mechanics and a comparative study of material models. *Journal of Elasticity*, 61(1/3):1–48, 2000.

[12] C. Mittelstedt and W. Becker. *Strukturmechanik ebener Laminate*. Technische Universität Darmstadt FB Mechanik, Bibliothek, Darmstadt, 1st edition, 2017.

[13] F. D. Murnaghan. *Finite deformation of an elastic solid*. Wiley & Sons, New York, 1951.

[14] C. Pruell. *Generation and detection of lamb waves for the characterization of plastic deformation*. PhD thesis, Georgia Institute of Technology, 2007.

[15] N. Rauter. *Analyse des Einflusses der Werkstoffdegradation auf die nichtlineare Wellenausbreitung in unidirektionalen Compositen: Experimentelle Untersuchung mit numerischer Analyse und Modellbildung*. PhD Thesis, Helmut-Schmidt-Universität, Hamburg, 2017.

[16] S. Reese, T. Raible, and P. Wriggers. Finite element modelling of orthotropic material behaviour in pneumatic membranes. *International Journal of Solids and Structures*, 38(52):9525–9544, 2001.

[17] J. L. Rose. *Ultrasonic waves in solid media*. Cambridge Univ. Pr, Cambridge, 1st paperback edition, 2004.

[18] J. C. Simo and C. Miehe. Associative coupled thermoplasticity at finite strains: Formulation, numerical analysis and implementation. *Computer Methods in Applied Mechanics and Engineering*, 98(1):41–104, 1992.

[19] J. Zhao, V. K. Chillara, B. Ren, H. Cho, J. Qiu, and C. J. Lissenden. Second harmonic generation in composites: Theoretical and numerical analyses. *Journal of Applied Physics*, 119(6):064902, 2016.

VIII ECCOMAS Thematic Conference on Smart Structures and Materials
SMART 2017
A. Güemes, A. Benjeddou, J. Rodellar and J. Leng (Eds)

SCATTERING ANALYSIS OF LAMB WAVES AT SUBSURFACE CRACKS IN ISOTROPIC PLATES

Christoph Humer[†], Christoph Kralovec[†] and Martin Schagerl[†,‡]

[†]Christian Doppler Laboratory for Structural Strength Control of Lightweight Constructions
Johannes Kepler University Linz
Altenbergerstr. 69, 4040 Linz, Austria
e-mail: christoph.humer@jku.at, christoph.kralovec@jku.at, web page:
http://www.ikl.jku.at/cd

[‡] Institute of Constructional Lightweight Design
Johannes Kepler University Linz
Altenbergerstr. 69, 4040 Linz, Austria
e-mail: martin.schagerl@jku.at - Web page: http://www.ikl.jku.at

Key words: Lamb wave, Non-reflective boundary (NRB), Wave damage interaction coefficient (WDIC), Structural health monitoring (SHM)

Abstract. The present work investigates the scattering behavior of a circular subsurface crack in isotropic material for an incident asymmetric A0 Lamb wave by a finite element (FE) model. This local FE model is designed according to the combined analytical finite element approach (CAFA) and uses a steady-state analysis in combination with non-reflective boundaries (NRB). The basic idea of CAFA is presented and the used FE model is explained in detail. The crack parameters size and depth are varied and the dependency of the scattered wave field on these parameters is analyzed by comparing the wave damage interaction coefficients (WDICs). The comparison of the WDICs show dependencies on the crack parameters for particular directions and observed trends are reported. Furthermore, conclusions on the future applications of found results are given.

1 INTRODUCTION

In recent years, the detection of damages (e.g. cracks, corrosion or delamination) is of increasing interest in the areas of non-destructive testing (NDT) and structural health monitoring (SHM). Numerous methods like, e.g., the electro-mechanical impedance method [7], conductive surface layers [14] and others use a variety of physical effects to detect structural damage. Hence, these methodes are entering more and more fields of engineering. However, particularly for lightweight structures Lamb waves are very suitable due to their simple and robust implementation and sensitivity for small structural changes. Furthermore, in thin-walled structures these waves can travel over long distances and propagate even in curved shapes. A drawback of the method is its multi-modal nature and dispersive behavior that makes applications quite

challenging. The basic concept of damage detection by Lamb waves is that these interrogating wave packages interact with damages and lead to a scattering of the wave field. This scattering indicates damage, and furthermore contains information about the damage. The wave-damage interaction is generally complicated and an analytical solution is currently only available for simple damage shapes such as circular holes [4, 5]. In contrast to that, the propagation of Lamb waves in pristine structures is well-studied and first described analytically by Horace Lamb in 1916 [8]. Therefore different semi-analytical models have been developed, e.g., the combined analytical finite element model approach (CAFA) [13] or the semi-analytical finite element (SAFE) method [1], to combine the advantages of the analytical and numerical approaches. The CAFA uses a combination of the steady-state analysis with non-reflective boundaries (NRB) [12] to enable a versatile and time efficient FE simulation of Lamb wave scattering at damages.

In the present work a local FE model is used to simulate the scattering behavior of a circular subsurface crack in an isotropic plate such that the numerical results can be integrated into the CAFA framework. The present work analyzes the subsurface crack parameters size and location over thickness (depth). The influence of these parameters is reported for an incident A0 Lamb wave mode.

2 SEMI-ANALYTICAL METHODOLOGY

The general idea of the semi-analytical method CAFA is to describe the global Lamb wave propagation analytically and the local wave-damage interaction numerically by a FE model [13]. In Fig. 1 a sketch of the global and local model is depicted. In the global structure the wave propagation from the point of actuation to the sensor point and the damage is described by an analytical transfer function. The damage disturbs the interrogating wave packets and scatters the incoming waves in different directions with varying intensity. This scattering of the wave field is highly dependent on the geometry of the damage as well as on the material of the structure and the incoming Lamb wave. The analytical formulation of the scattering behavior is mathematically challenging and at the moment only available for simple shapes like circular holes [4, 5]. Hence in the CAFA a local FE model is used to simulate the wave-damage interaction, providing the so-called wave damage interaction coefficients (WDIC) [13]. These WDICs represent the scattering behavior of a damage in the analytical framework. By knowing the WDICs of a damage its influence on the Lamb wave packets can be calculated analytically. This is implemented in the so-called WaveFormRevealer 2-D [11], which shows the time signals at a desired sensor position for a given wave-damage interaction of a damage. For detailed information about CAFA see [13, 2].

The WDIC is a complex number and its absolute value is defined as a function of frequency f and sensing angle ϕ for a given structure and radius of the sensing circle r_{Sen} [13], to

$$C_{\mathrm{AB}}(f,\phi) = \left| \frac{u^{\mathrm{B}}_{\mathrm{SC}}}{u^{\mathrm{A}}_{\mathrm{IN}}} \frac{1}{H^{(1)}_1(\xi^{\mathrm{B}} r_{\mathrm{Sen}})} \right|. \tag{1}$$

The indices A and B indicate the wave mode of the incident and the scattered wave field. For instance, C_{SA} describes the scattering behavior of an incoming symmetric S0 to a scattered asymmetric A0 Lamb wave mode. In Eq. (1) the displacement amplitude $u^{\mathrm{B}}_{\mathrm{SC}}$ (at the sensing circle) of the scattered wave field with mode B is normalized by the displacement amplitude $u^{\mathrm{A}}_{\mathrm{IN}}$

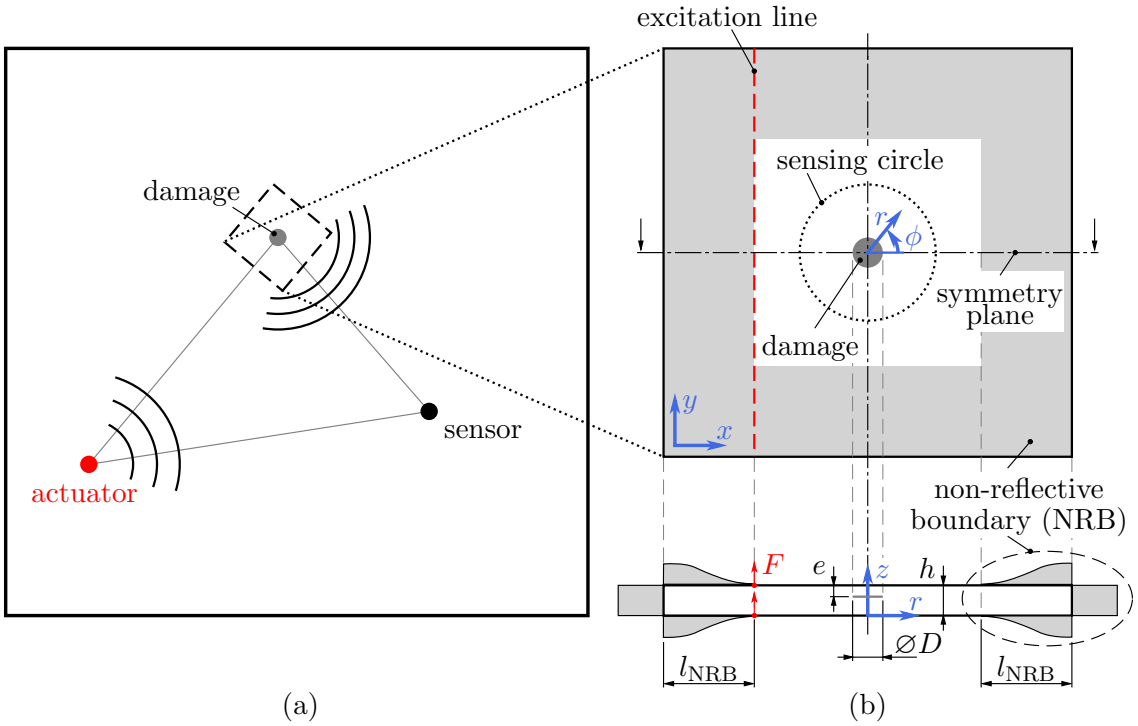

Figure 1: Semi-analytical methodology: (a) global model of the structure with actuators and sensors (b) sketch of the local FE model for wave-damage interaction simulation

(at the center point of the damage in the pristine model) of the incident wave with mode A. This ratio is multiplied by the reciprocal value of the first kind Hankel function $H_1^{(1)}(\xi^{\mathrm{B}} r_{\mathrm{Sen}})$ of order one, depending on the wavenumber ξ^{B} and the radius of the sensing circle r_{Sen}. This function considers the radial wave propagation of the scattered wave field around the damage. Generally C_{AB} depends on the direction of the incident wave as well, but for a symmetrical damage in isotropic material – as considered in this work – the result has to be symmetric about the initial wave propagation direction. However, this is also the case for the phase shift φ_{AB} of the WDICs, which is not presented in this paper. Generally the damage scatters the incident wave into all directions and therefore a cylindrical coordinate system at the center of the damage (see Fig. 1 (b)) is useful to describe the scattered wave field. Considering cylindrical coordinates the scattered wave field can be split up into the symmetrical and the asymmetrical displacement by [13]

$$u_{\mathrm{SC}}^{\mathrm{S0}} = \frac{u_{\mathrm{r}}^{\mathrm{T}} + u_{\mathrm{r}}^{\mathrm{B}}}{2} \qquad \text{and} \qquad u_{\mathrm{SC}}^{\mathrm{A0}} = \frac{u_{\mathrm{r}}^{\mathrm{T}} - u_{\mathrm{r}}^{\mathrm{B}}}{2}, \tag{2}$$

where $u_{\mathrm{r}}^{\mathrm{T}}$ is the displacement at the top surface and $u_{\mathrm{r}}^{\mathrm{B}}$ at the bottom surface for a given sensing direction ϕ (see Fig. 2). Besides the distinction between symmetric and asymmetric mode the scattered wave field needs to be separated from the total wave field. The displacement of the total wave $u_{\mathrm{r}}^{\mathrm{TOT}}$ is the superposition of the incident wave displacement $u_{\mathrm{r}}^{\mathrm{IN}}$ and the displacement

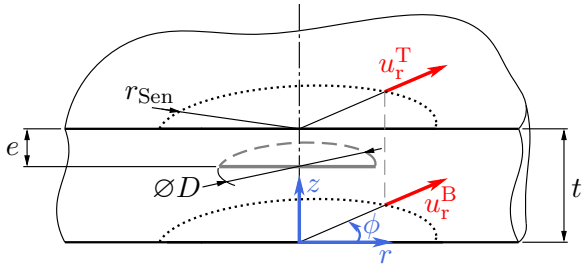

Figure 2: Sketch of the damaged region

of the scattered wave field u_r^{SC}. Hence the scattered wave displacement is calculated by

$$u_r^{SC} = u_r^{TOT} - u_r^{IN}, \tag{3}$$

which is known as baseline subtraction [9]. The displacement of the incident wave u_r^{IN} is evaluated for the pristine structure at the center position of the damage.

Usually a transient numerical analysis is used to calculate the wave-damage interaction. This type of dynamic simulation needs a small time increment and is computationally expensive. Besides that, the transient simulation results are assigned to the considered excitation signal. In contrast, the CAFA utilizes a steady-state analysis with harmonic excitation for a range of excitation frequencies to simulate the wave-damage interaction. This simulation yields the complex-valued displacements of the steady state for the considered excitation frequencies. No time history is calculated. The steady-state results need further processing to be comparable to a transient analysis or to an experimental measurement. A typical excitation signal is shown in Fig. 3 (a). This signal is a windowed sine function (Von-Hann window) for a frequency $f = 200\,\text{kHz}$ and five periods. By using the fast Fourier transform (FFT) the frequency spectrum of the excitation signal is calculated, as it is visualized in Fig. 3 (b). The basic idea of the WDIC calculation in CAFA is to use the spectrum of the excitation signal as weighting function for the results of the steady-state analysis and sum up the weighted results. This weighting and summation process reconstructs the results of the wave-damage interaction in the frequency domain and leads to a good approximation of the scattering in the time domain. Due to the windowing process in the time domain the bandwidth of the excitation signal is infinite in the frequency domain. However, the values decrease rapidly besides the main lobe (see Fig. 3 (b)). Hence the main lobe and the first side lobes of the frequency spectrum describe the excitation signal very well. In the further work only these, more precise, the indicated values in Fig. 3 (b) are used for the weighting process. I.e., the displacement amplitude results from the steady-state analysis are multiplied by the corresponding amplitudes of the frequency spectrum and summed up. Thus, every possible excitation signal can be reconstructed by adapting the frequency spectrum after the steady-state simulations, which makes this approach very versatile.

3 FE MODEL FOR NUMERICAL WDIC CALCULATION

The numerical model presented in Fig. 1 (b) is designed according to the semi-analytical method CAFA and uses the commercial software ABAQUS 6.14 to calculate the local wave-

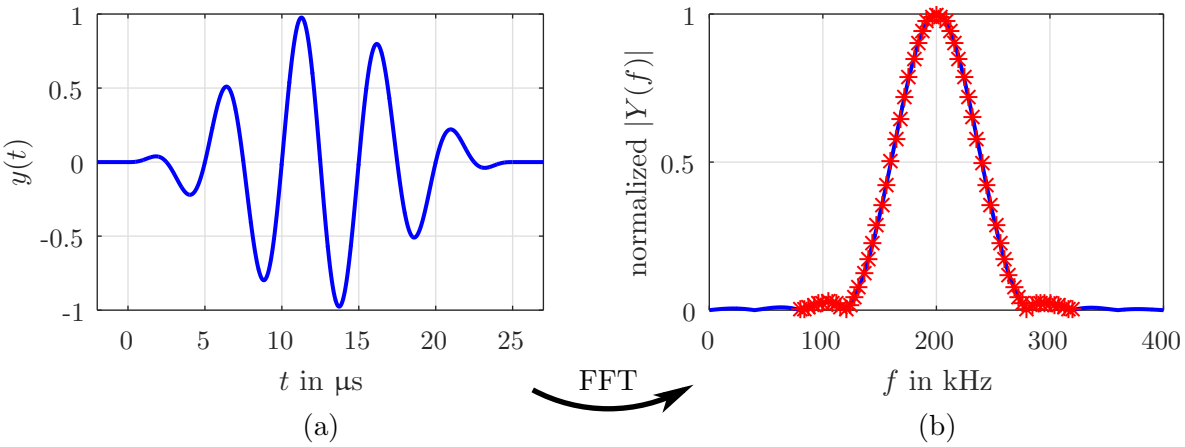

Figure 3: (a) Excitation signal for $f = 200\,\text{kHz}$ and 5 periods (Von-Hann window) (b) normalized frequency spectrum (solid line) and weighting coefficients (asterisks)

damage interaction. In a global structure the actuator is typically far away from the damage. Hence the curvature of the circular-crested wave front becomes neglectable. Due to this assumption the wave-damage interaction is analyzed for incident straight-crested Lamb waves. For the simulation of a straight-crested wave front the model is excited over the whole width along an excitation line as it is depicted in Fig. 1 (b). In Fig. 1 (b) the whole model is shown, whereby only half of it is simulated by the use of symmetry conditions at the symmetry plane. This model reduction has been verified by comparing the results of the whole and the symmetric model. Hence, the total size of the symmetric numerical model is $100 \times 50 \times 1.6\,\text{mm}$. The plate is meshed with linear solid elements (C3D8). For the discretization in thickness direction a minimum number of four elements is used to resolve the stress distribution of each Lamb wave mode. The maximum element size for the in-plane direction of the model is determined by the excitation wavelength. It is recommended to use at least ten elements per shortest wavelength [3]. The maximum considered frequency $f = 320\,\text{kHz}$ yields $\lambda_{\text{A0}} = 5.9\,\text{mm}$ as shortest wavelength for the asymmetric A0 mode. Hence the used in-plane element size of maximum 0.5 mm is adequate. The wave-damage interaction may result in high stress gradients and therefore a finer mesh is generated around the damage. Hence a continuous mesh refinement in the center region is realized as depicted in Fig. 4. The sensing points are equally distributed at every 9° along the sensing circle with a radius $r_{\text{Sen}} = 12.5\,\text{mm}$. The investigated damage is a circular subsurface crack that is located parallel to the surface (see Fig. 2) in an isotropic plate of thickness $t = 1.6\,\text{mm}$. The material of the plate is considered to be aluminum. The used material properties are listed in Tab. 1. During the numerical study the damage diameter D and the damage depth e are varied. In the FE model the crack has no opening and is generated by a node separation without any contact conditions. It should be mentioned that the steady-state analysis only works for linear problems and therefore no contact conditions can be included in this method. However, for damage detection with Lamb waves it is important to check if a particular wave mode is sensitive to the investigated damage type. Therefore, a closer look

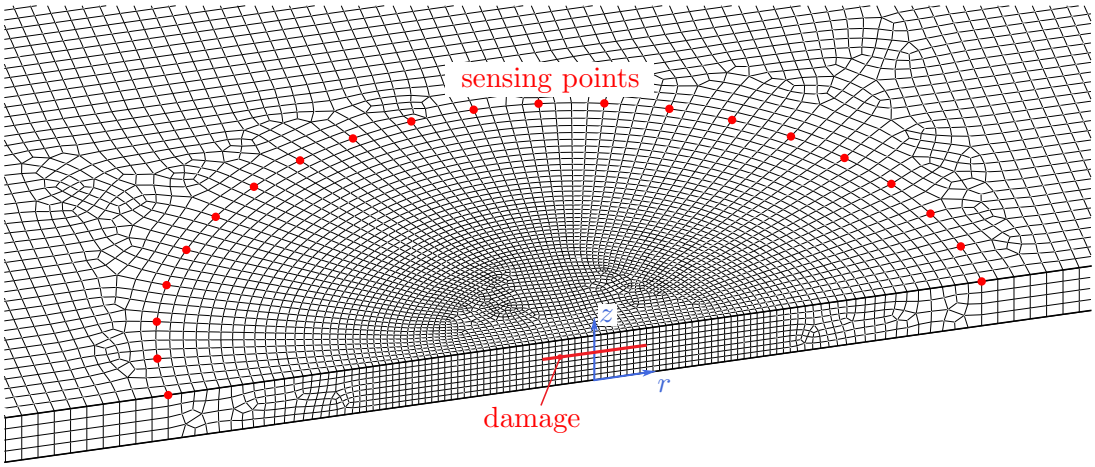

Figure 4: Mesh of the FE model in the center region and sensing points

Table 1: Material properties of aluminum

Material parameter	Symbol	Quantity
Young's modulus	E	70 GPa
Poisson's ratio	ν	0.33
mass density	ρ	2700 kg/m^3

to the different mode shapes may help selecting the Lamb wave mode. As reported in [9] the asymmetric mode A0 interacts with composite delaminations, which are very similar to subsurface cracks within the thickness of the structure. Furthermore, for a given frequency the A0 mode is generally more sensitive to smaller damages due to its smaller wavelength compared to the symmetric mode S0. The fundamental asymmetric mode A0 is excited by forces along the excitation line on the top and the bottom surface of the plate acting in the same direction as it is sketched in Fig. 1 (b). The steady-state analysis is simulated in a frequency range from 80 kHz to 320 kHz in steps of 2 kHz to cover the main frequencies of the excitation signal as shown in Fig. 3 (b). Furthermore, this frequency range enables an effective coupling between the structure and the piezoelectric actuator for future experiments [6].

For a finite element model the propagating waves interact with both, the damage and the models boundaries. To analyze only the effect of the damage on the incident wave no other reflections should disturb the area of interest. For transient analysis the model size can be enlarged until the reflections do not influence the investigated time span. This is not possible for the steady-state analysis. Hence so-called non-reflective boundaries [12] are added to the circumference of the model to eliminate the boundary reflections. As shown in Fig. 1 (b) velocity dependent damping elements are added according to [12] with the half Hanning function and a damping ratio of $\delta = 0.3$. Furthermore, the NRB width l_{NRB} should at least be twice the considered wavelength [12]. For the investigated frequency range a NRB width $l_{\mathrm{NRB}} = 30\,\mathrm{mm}$ has been implemented and found to be sufficient.

4 INFLUENCE OF SUBSURFACE CRACK GEOMETRY

The wave-damage interaction is highly dependent on the geometry of the damage. This parameter study investigates a circular subsurface crack (parallel to the surface) in isotropic material. Different crack sizes D and depths e are analyzed. The plate thickness is $t = 1.6\,\text{mm}$. The used material properties for the typical lightweight material aluminum are listed in Tab. 1. Furthermore, all simulations are evaluated for an incident asymmetric A0 Lamb wave mode with the same excitation signal, which is a windowed sine function (Von-Hann window) of five periods and a frequency $f = 200\,\text{kHz}$ (see Fig. 3). The used steady-state analysis yields complex-valued WDICs, which describe the scattering behavior for the analytical framework of the CAFA. The WDICs absolute values C_{AB} are calculated according to Eq. (1).

4.1 Subsurface crack size to wavelength ratio

Generally the detectable damage size is dependent on the wavelength [9, 10]. Therefore, the dimensionless crack size to wavelength ratio $\Lambda = \frac{D}{\lambda}$ is introduced to investigate the influence of the crack size D on the scattering behavior. Furthermore, the subsurface crack position e is characterized by the dimensionless crack depth to plate thickness ratio $\varepsilon = \frac{e}{t}$. As already mentioned the considered excitation frequency is $f = 200\,\text{kHz}$, which yields $\lambda_{\text{A0}} = 7.9\,\text{mm}$ for the wavelength of the asymmetric mode in this structure. The damage size is varied from $\Lambda = 0.25$ to $\Lambda = 1.27$ ($D = 2\,\text{mm}$ to $D = 10\,\text{mm}$) for the crack depth to plate thickness ratio $\varepsilon = \frac{1}{4}$ respectively $\varepsilon = \frac{3}{8}$. Figure 5 shows the WDICs absolute value C_{AA} plotted over the sensing angle ϕ. The incident wave direction is marked by a small arrow. For isotropic material and a symmetric damage the results are symmetric about this direction. As one can see in Fig. 5 (a) and (b) a crack size to wavelength ratio of $\Lambda = 0.25$ might not be detectable experimentally (for $\varepsilon = \frac{1}{4}$ and $\varepsilon = \frac{3}{8}$). A damage size to wavelength ratio $\Lambda = 0.5$ is found to yield a scattered wave field that can be measured in real life applications. However, comparing the WDICs for the sensing direction $\phi = 0°$ (forward scattering) a dependency on the crack size to wavelength ratio Λ exists, showing a monotonous increase of the absolute value C_{AA} with the increasing crack size for both values of ε. For the opposite direction $\phi = 180°$ (backward scattering) this is only true for $\varepsilon = \frac{3}{8}$ (see Fig. 5 (b)). In Fig. 5 (a) the WDICs amplitude for $\Lambda = 1.27$ yields a smaller value than for $\Lambda = 1.01$ in the backward scattering direction $\phi = 180°$. For the perpendicular direction ($\phi = 90°$) the scattered wave amplitudes for $\Lambda = 0.5$ and $\Lambda = 0.76$ are approximately equal. If a sensor would be located in this direction one could not distinguish between these damage sizes. However, besides these particular directions no monotonous dependency of the scattered wave field on the damage size to wavelength ratio Λ is found. The amplitude of the scattered wave field does not necessarily increase for an increasing crack size D.

4.2 Subsurface crack depth to plate thickness ratio

The investigated circular subsurface crack is parallel to the surface of the plate and located at a certain depth e (see Fig. 2). Hence as second parameter the depth e of the subsurface crack is varied throughout the plate thickness. The influence of the crack depth e is investigated by the crack depth to plate thickness ratio $\varepsilon = \frac{e}{t}$. The damage size to wavelength ratio $\Lambda = 1.01$ ($D = 8\,\text{mm}$) is kept constant for all values of ε. In Fig. 6 (a) the WDICs absolute values C_{AA} are plotted as a function of the sensing direction ϕ and crack depth to plate thickness ratio ε.

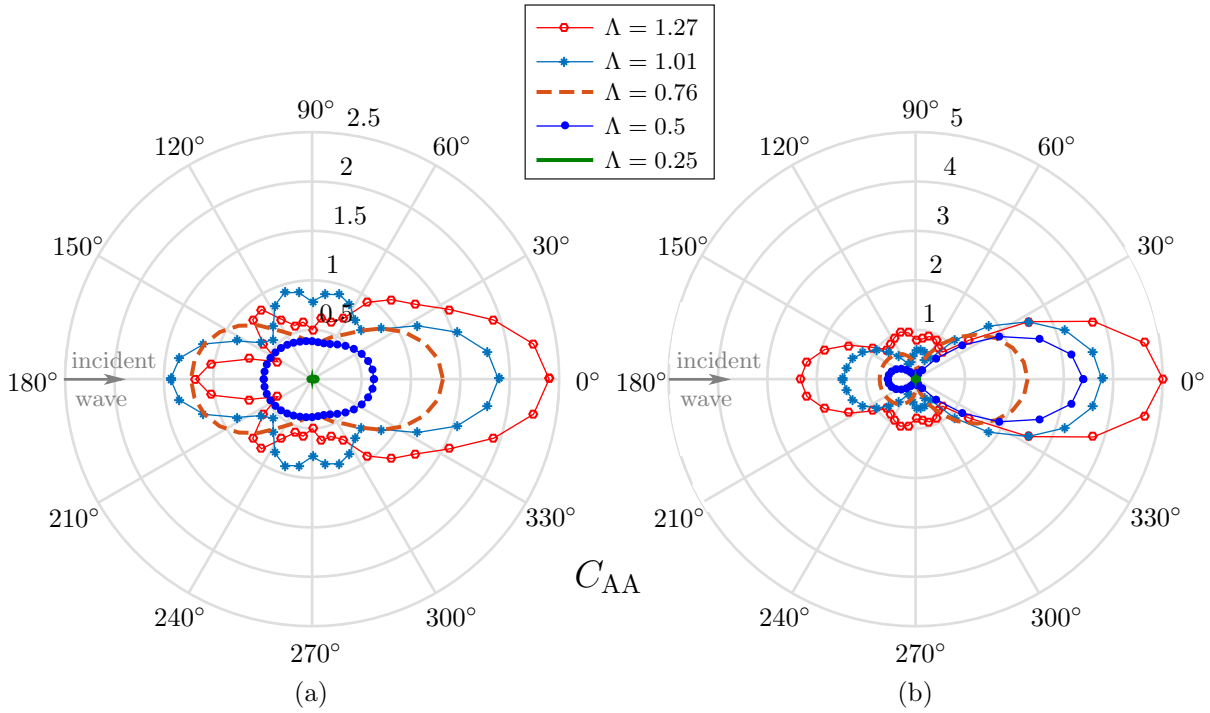

Figure 5: Comparison of absolute WDICs values for different crack size to wavelength ratios $\Lambda = \frac{D}{\lambda}$ for (a) $\varepsilon = \frac{1}{4}$ and (b) $\varepsilon = \frac{3}{8}$

By this representation, the scattering behavior can be observed easily for a varying ε at a certain sensing direction ϕ, e.g., the forward scattering direction $\phi = 0°$ (triangles), or the backward scattering direction $\phi = 180°$ (asterisks). These particular directions are also highlighted in Fig. 6 (b), which illustrates the WDICs in layers for the different values of the crack depth to thickness ratios ε. In Fig. 6 (a) a constant value for ε show the dependency of the WDICs on the sensing direction ϕ, which is the scattering pattern, e.g., the circular markers indicate the scattering pattern for $\varepsilon = \frac{1}{4}$ in Fig. 6 (a) and (b). As expected, the scattering pattern is symmetric about the incidence direction due to the in-plane symmetry of the damage (tested by the full model). Moreover, the results for different ε are symmetric about the mid-surface ($\varepsilon = \frac{1}{2}$) of the plate (see Fig. 6 (b)), i.e., the results for the damage depth to plate thickness ratio $\varepsilon = \frac{1}{4}$ and $\varepsilon = \frac{3}{4}$ are identical. However, in Fig. 6 (a) and (b) one can see the sensitivity of different sensing directions ϕ with respect to crack depth to plate thickness ratio ε. Generally the sensing directions $0° \leq |\phi| \leq 45°$ yield the highest values for all crack positions ε throughout the plate. The WDICs do not show a general dependency on the subsurface crack depth to plate thickness ratio ε. However, for $\phi = 0°$ (forward scattering) the scattering amplitude is increasing monotonously with the increase of the depth e until $\varepsilon = \frac{1}{2}$. Furthermore, for the opposite direction $\phi = 180°$ (backward scattering) the scattered amplitude shows a local minimum for $\varepsilon = \frac{1}{2}$ besides the global minima ($C_{\mathrm{AA}} \to 0$ for $\varepsilon \to 0$ and $\varepsilon \to 1$).

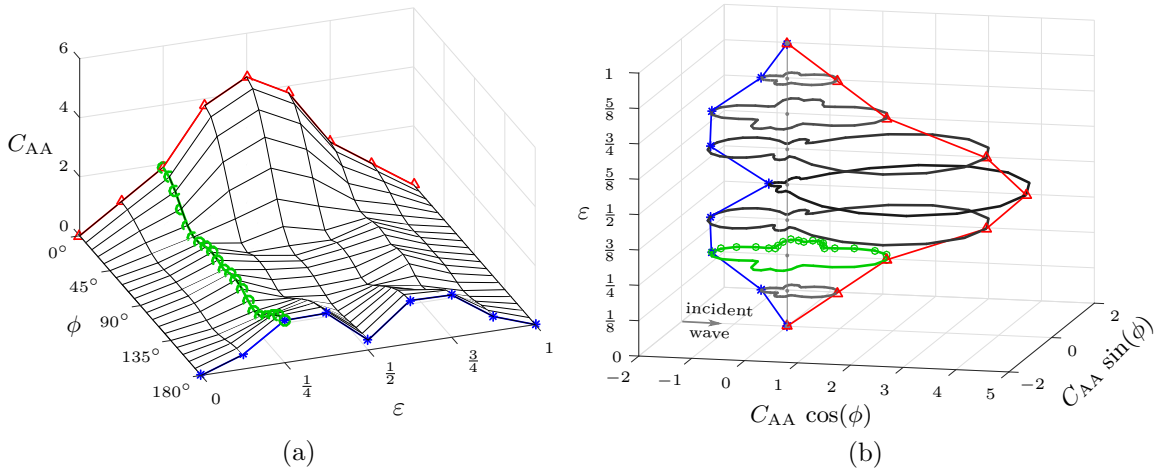

Figure 6: Scattering behavior for different crack depth to plate thickness ratios $\varepsilon = \frac{e}{t}$ ($\Lambda = 1.01$)

5 CONCLUSIONS AND OUTLOOK

In this paper the scattering behavior of a circular subsurface crack in isotropic material is investigated by a local FE model, which is designed according to the semi-analytical method CAFA. The subsurface crack parameters size D and depth e are characterized by the dimensionless crack size to wavelength ratio $\Lambda = \frac{D}{\lambda}$ and the crack depth to plate thickness ratio $\varepsilon = \frac{e}{t}$. These determining parameters Λ and ε are varied and their influence on the scattering behavior is analyzed for an incident asymmetric A0 Lamb wave. Generally the scattering pattern is symmetric about the direction of the incident wave due to the in-plane symmetry of the damage and the isotropic material behavior. Furthermore, the WDICs are symmetric about the mid-surface of the plate, e.g., the scattering patterns for $\varepsilon = \frac{1}{4}$ and $\varepsilon = \frac{3}{4}$ are identical. The amplitudes of the scattering wave field do not show a general dependency on the dimensionless parameters Λ and ε. However, for particular sensing directions ϕ some trends can be observed. For the forward scattering direction $\phi = 0°$ the WDICs show monotonously increasing values for an increase of the crack size to wavelength ratio Λ within the tested range. Furthermore, in this sensing direction a monotonous dependency of the scattering wave amplitudes on the crack depth to plate thickness ratio ε exist. The WDIC values are increasing for increasing ε till the maximum in the mid-surface of the plate ($\varepsilon = \frac{1}{2}$) is reached. In contrast, the scattering wave amplitudes for the backward scattering direction $\phi = 180°$ are minimal for a damage in the mid-surface of the plate ($\varepsilon = \frac{1}{2}$) for all investigated values of Λ. However, the large variety of the scattering patterns presented in this work offer a promising source for the identification of subsurface cracks and conclusions on their parameters. For a real application this could be utilized by using several sensors in different directions. Furthermore, lightweight constructions do typically have specific areas or damage modes of interest, which could be monitored optimally by considering scattering patterns – as the presented – in the sensor placement.

For further investigations experiments are planned to validate the presented results. Moreover, it is planned to investigate different damage types by local FE models as presented in this paper. The long term objective is to provide a catalog of WDICs for various damage types

enabling their identification and the conclusion on their location and size within the CAFA framework. Besides that, it is planned to adapt the numerical model for the investigation of delamination damages in laminated composite material, as it is frequently used for lightweight constructions.

REFERENCES

[1] Ahmad, Z., and Gabbert, U. Simulation of Lamb wave reflections at plate edges using the semi-analytical finite element method. *Ultrasonics 52*, 7 (2012), pp. 815–820.

[2] Bhuiyan, Y., Shen, Y., and Giurgiutiu, V. Ultrasonic inspection of multiple-rivet-hole lap joint cracks using global analysis with local finite element approach. In *SPIE Smart Structures and Materials+Nondestructive Evaluation and Health Monitoring* (2016), International Society for Optics and Photonics, pp. 98051Z–98051Z.

[3] Cawley, P., and Alleyne, D. The use of Lamb waves for the long range inspection of large structures. *Ultrasonics 34*, 2-5 (1996), pp. 287–290.

[4] Diligent, O., Grahn, T., Bostrm, A., Cawley, P., and Lowe, M. J. S. The low-frequency reflection and scattering of the S0 Lamb mode from a circular through-thickness hole in a plate: Finite element, analytical and experimental studies. *Journal of the Acoustical Society of America 112* (2002), pp. 2589–2601.

[5] Grahn, T. Lamb wave scattering from a circular partly through-thickness hole in a plate. *Wave Motion 37*, 1 (2003), pp. 63–80.

[6] Gschossmann, S., Humer, C., and Schagerl, M. Lamb wave excitation and detection with piezoelectric elements: Essential aspects for a reliable numerical simulation. *8th European Workshop On Structural Health Monitoring (EWSHM 2016)* (2016).

[7] Kralovec, C., and Schagerl, M. Electro-mechanical impedance measurements as a possible SHM method for sandwich debonding detection. *Materials Science Forum*, Trans Tech Publications, to appear 2017.

[8] Lamb, H. On waves in an Elastic Plate. *Proceedings of the Royal Society of London Vol. 93* (1916), pp. 114–128.

[9] Ng, C.-T., and Veidt, M. Scattering of the fundamental anti-symmetric Lamb wave at delaminations in composite laminates. *The Journal of the Acoustical Society of America 129*, 3 (2011), pp. 1288–1296.

[10] Nithurshan Nadarajah, Benjamin Steven Vien, Wing Kong Chiu, and L. R. Francis Rose. Computational Study of the A0 Scattered Field Due to an Edge Delamination. *Journal of Mechanics Engineering and Automation 5*, 4 (2015).

[11] Shen, Y., and Giurgiutiu, V. WFR-2d: An analytical model for PWAS-generated 2D ultrasonic guided wave propagation. In *SPIE Smart Structures and Materials+ Nondestructive Evaluation and Health Monitoring* (2014), International Society for Optics and Photonics, pp. 906411–906411.

[12] Shen, Y., and Giurgiutiu, V. Effective non-reflective boundary for Lamb waves: Theory, finite element implementation, and applications. *Wave Motion 58* (2015), pp. 22–41.

[13] Shen, Y., and Giurgiutiu, V. Combined analytical FEM approach for efficient simulation of Lamb wave damage detection. *Ultrasonics 69* (July 2016), pp. 116–128.

[14] Zhao, Y., Schagerl, M., Gschomann, S., and Beisteiner, C. An inkjet-printed carbon nanotube strain distribution sensor for quasi real-time strain monitoring of lightweight design materials. *Advances in Science and Technology 101* (2017), pp. 3–8.

SENSOR INTEGRATION AND DATA EXPLOTATION OF STRUCTURAL HEALTH MONITORING NETWORK INTEGRATED ON A UNMANANNED AERIAL VEHICLE (UAV)

A. Fernandez-Lopez*, M. Frovel†, A. Lozano-Martín*, P. Fernandez-Diaz-Maroto*, I. Gonzalez-Requena*, J. M. Pintado†, M. A. Torre†, F. Terroba††and A. Güemes*

* Laboratory of Composite Materials and Smart Structures, Department of Aeronautics,
Universidad Politécnica de Madrid
Plaza del Cardenal Cisneros, 3, 28040 Madrid, Spain
e-mail: antonio.fernandez.lopez@upm.es

Instituto Nacional de Técnica Aeroespacial (INTA)
† Composite Materials Department
††Aeronautic Programs Department
Crta de Ajalvir pk4, 28850 Torrejón, Spain
e-mail: frovelm@inta.es

ABSTRACT

Unmanned Aerial Vehicles (UAVs) are flying robots that require little or no human control while flying. The number of UAV has growth exponentially due to rise in applications such as video taking, surveillance and delivering cargo to customers. Despite the promise of the technology, UAV are not very reliable currently, either civil or military. They lack of sensing mechanisms to detect issues in operation, such impacts, hard landings and overload, together with the difficulties to detect structural problems during the UAV operation could compromise not only the safety of the UAV, also all along the entire flying area.

This paper presents the design, development implementation, and validation of a Structural Health Monitoring (SHM) system applied to the rear fuselage of the UAV developed by INTA for R&D activities (MILANO). The rear fuselage, a 2.5 meters carbon/epoxy structure with frames and stringers, was instrumented with fiber optic sensors and PZT. Two different types of fiber optic sensors were considered: Fiber Bragg Gratings and distributed fiber sensing based on Rayleigh backscatter. The objective of the fiber optic sensor network is to detect the changes induced on the strain field due to damage appearance. This information will be employed to train a neural network which provides the self-diagnosis of the structural integrity. Additionally, the PZT network will be used as active system for structure interrogation through elastic waves.

Initially, on ground test campaign will be used to validate theoretical models and completion of the neural network training and also to compare and evaluate capabilities of the three selected sensing systems. Later, another structure will be integrated into the UAV for real flight operations. Real operative capabilities of the SHM systems will be investigated, evaluating also system interferences with real operations and evaluating the exploitation methodologies for decrease operative costs and the detection of damage in service operations.

REFERENCES

[1] W.J. Staszewski, C. Boller, and G.R. Tomlinson. “Health Monitoring of Aerospace Structures”. John Wiley & Sons, Ltd, Chichester, 2004.

[2] Y. K. Yap “Structural Health Monitoring For Unmanned Aerial Systems” Technical Report No. UCB/EECS-2014-70, 2014

VIII ECCOMAS Thematic Conference on Smart Structures and Materials
SMART 2017
A. Güemes, A. Benjeddou, J. Rodellar and J. Leng (Eds)

SENSOR OPTIMIZATION FOR IMPACT DETECTION: A BAYESIAN APPROACH

V. Mallardo*, Z. Sharif Khodaei† and M.H. Aliabadi†

* Department of Architecture, University of Ferrara
Via Quartieri 8, 44121 Ferrara, Italy
e-mail: mlv@unife.it,

† Department of Aeronautics, Imperial College London,
SW7 2AZ, London, UK
e-mail: z.sharif-khodaei@imperial.ac.uk; m.h.aliabadi@imperial.ac.uk

Key words: Impact detection, Passive sensing, Optimization, Bayesian approach

Abstract. A Bayesian optimization strategy resulting in optimal sensor locations for impact localization under operational conditions is developed and presented. The impact detection methodology is based on developing meta-models utilizing artificial neural network (ANN) through the recorded sensor signals generated by various impact events. The novelty of the proposed method is to include the probability of one or more sensors failing under operation as well as non-uniform probability of impact occurrence in the structure. Finally, the proposed optimization algorithm is applied to a composite stiffened panel.

1 INTRODUCTION

Structural Health Monitoring (SHM) techniques have attracted a lot of attention with the recent advances in sensor technologies which enables integration of sensors onto the structure with minimum interference. There are various SHM systems based on different sensor technologies such as Piezoelectric (PZT) transducers, Fibre Optic (FO) sensors and more recently Carbon or Graphene based sensors (CNT and GNP). Each type of sensor has advantages and disadvantages. SHM systems can be designed to have different outcomes: Impact detection, Damage detection, damage location, damage size and severity and structural prognosis. The SHM system can be use in passive or active way. Passive sensing only records the response of the structure to an external event such as impact and consequent damage while in active sensing, the response of the structure to an actively emitted signal is recorded and assessed. PZT transducers can be used in both passive and active sensing due to their electrical and mechanical coupling. The structural diagnosis via SHM leads towards condition based maintenance (CBM) and away from scheduled maintenance (SM) which is expensive and time consuming. By accurately detecting [1] and characterizing [2] an impact event, the subsequent damage can be detected through active sensing of the area under impact [3, 4, 5, 6, 7, 8], rather than monitoring the whole structure.

There are many different methods developed for impact identification, both numerically and experimentally [9, 10, 11, 12, 13]. The simplest impact localization strategy is based on Time of Fight (ToF) of the impact induced ultrasonic waves by triangulation. This approach is strongly limited by the assumption that wave velocity must be known and uniform in all directions which limits its application to simple isotropic structures. Moreover, the flexural wave velocity is not constant and is a function of the signal frequency and depends on the impact mass and velocity which is not known a priori. For anisotropic material, it is possible to obtain velocity characteristics as function of the angle of the wave propagation to estimate the location of the impact combined with triangulation technique provided that an optimal sensor configuration is set up [10], which is difficult to be achieved in built up structures with complex geometry. Another set of techniques is model based algorithms which involve modelling the dynamic response of the structure subjected to a known impact [14, 15]. However, their application to complex structure of non-linear response is questionable. The last grop of techniques is machine learning algorithms which require modelling complex relationship (non-linear meta-model development) between input and output data. Artificial Neural Network (ANN) is a machine learning algorithm which has been used for impact detection and identification [16, 1, 17]. In addition the success of the detection algorithm is directly related to the number and location of the sensors [18].

All of the impact detection and identification techniques mentioned so far, are based on the sensor data recorded during an impact event. Most of the established methods have been validated and tested in laboratory under controlled environment. However, for the SHM system to be applicable to real structure their performance must be assessed under real operational conditions. Therefore the aim of this paper is to present an optimization strategy for impact detection which takes into account the uncertainties in the recorded data as well as probability of one or more sensors failing under operational conditions. In addition, it considers non-uniform probability of impact occurrence which is representative of different parts of an aircraft prone to different impact scenarios, see Figure 1. Bayesian optimization strategy is used to account for uncertainties in the optimal sensor positioning which increases the reliability of the decision making SHM system. The very first application of Bayes theory to the optimal sensor placement is given in [19] for active sensing. In this work the application of the Bayes theory to sensor optimization for passive sensing is reported, more details of the methodology can be found in [20]. The passive sensing procedure used in this work is based on the meta-model technique developed from a large library of impact scenarios on a composite stiffened panel [21].

2 Sensor Optimization: A Bayesian approach

In this section a Bayesian optimization strategy is presented which for a given sensor number, finds their optimal positioning by maximizing the probability of impact detection in presence of uncertainties in the sensor data, including probability of one or more sensor failure and non-uniform probability of impact occurrence in the part. The uncertainties in the recorded sensor data can be result of noise in the software and hardware set-up, bonding quality, temperature change, structural load if measure experimentally. If the data is simulated numerically, the uncertainties result from mesh size and uniformity, material parameters, bonding and geometrical tolerances in positioning of the transducers. In addition, failure of one or more sensors (sen-

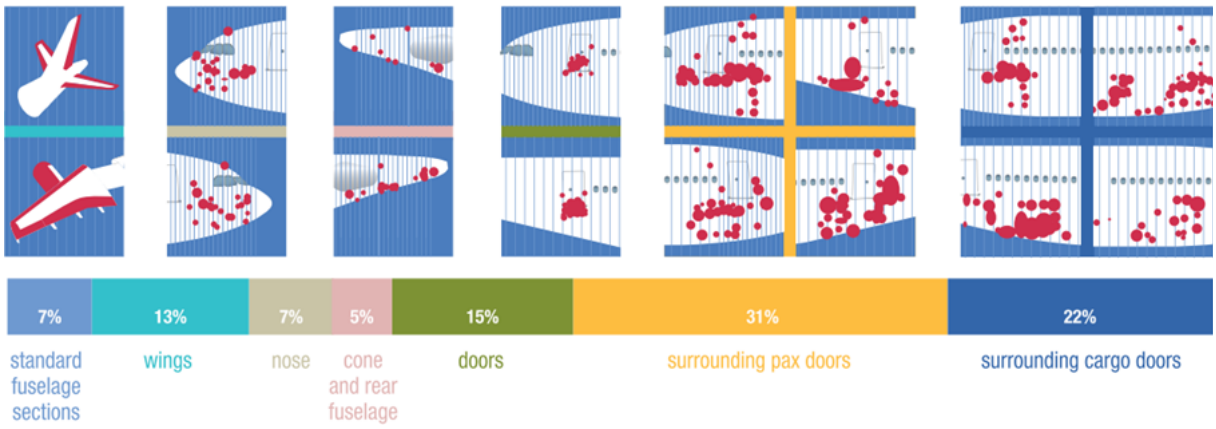

Figure 1: Global percentages of impacts by zones of the aircraft [22]

sor breakage, debonding, detachment of wires) can result in erroneous signals which results in false alarm or miss-detection. Therefore, it is important that this probability is built into the optimization strategy.

In the proposed approach, the ToF of impact generated waves recorded by a sensor network is used to estimate the location of the impact event through developed meta-models using ANN. In order to compute the optimal sensor combination, a minimization problem is solved by the application of the Genetic Algorithm (GA) as developed in [21]. The fitness function which is minimized in each optimization step is derived from the performance of the impact detection methodology, i.e. maximizing the probability of detection (PoD) function. First the development of the meta-model for impact detection and the corresponding fitness function which is input to the optimization step is explained. This is then followed by the optimization strategy detailed in section 2.2.

2.1 Impact detection algorithm

The methodology used in this work to detect impact events from recorded PZT sensor data is ANN. ANN is a machine learning algorithm which uses a set of training data to build a non-linear function relating the input (feature extraction from sensor data) to the output (location of the impact). Each input neuron is connected to an output neuron through hidden layers. Each connection is weighted which gets adapted during the learning phase. For the meta-model to reach a regularization, it needs to be trained with a wide range of impact scenarios representing all probable impacts on the structure which is a fuselage stiffened panel. It is very expensive (time and cost) to have to develop this library of impact scenarios experimentally due to the wide range of variation of impactor mass, height and velocity. Therefore, a numerical model was developed and validated to generate the recorded sensor signals due to a wide range of impact simulation. The impacts consisted of a range of mass (small mass such as debris impact and large mass such as tool drop), velocity and impact locations (from inside and outside the panel, at the foot of the stringer, under/over the stiffener, in the bay). The details of the numerical simulations can be found in [1]. Once the ANN is trained, the performance of the network is evaluated through a new set of data called the test set. The parameter which has been used to

represent each network's performance is the PoD function. The evaluation of the PoD follows [21] by defining the error function as the Euclidean distance between the predicted location (x_p, y_p) and the actual location (x_a, y_a) of each impact i belonging to the test set:

$$e_i = \sqrt{e_{ix}^2 + e_{iy}^2} \tag{1}$$

where e_{ix} is the error in $x-$direction while e_{iy} is the error in $y-$direction. The PoD function follows a Gaussian distribution and is generated by Monte Carlo approach including the uncertainties in the ToF of the simulated sensor data. The uncertainties in the ToF of the signals can be represented by two different noise distributions: δ_1 and δ_2, respectively which are two independent Gaussian variables with zero mean and standard deviation σ_1 and σ_2. The former is defined as the noise related to the error introduced by variation in material properties and geometrical tolerances (either numerical or experimental), while the latter is related to the noise introduced by the instrumentation (cross-talk, background noise) and/or environmental conditions (temperature, humidity). The probabilistic description of the measured ToF in the ith sensor can be expressed as:

$$t_{m_k} = t_{c_k} + \delta_1 + \delta_2 \tag{2}$$

where t_{m_k} and t_{c_k} are the measured and computed ToF in the kth sensor, respectively. The computed ToF is obtained from the signals simulated by the FE analysis.

2.2 Optimization formulation: Bayes' theory

To find the optimal sensor positioning, different techniques can be applied. When the size of the optimization problem is large, exhaustive search is not a realistic option. In this work GA is applied to deal with the dimensionality of the problem. GA is a global probabilistic search algorithm inspired by natural selection principle. GA starts with an initial population (i.e. sensor networks) and for each iteration, it calculates the performance of each sensor network. For the next iteration, the new population of N individuals is generated from the previous number of individuals by retrieving n_e 'elite' individuals, by 'mutation' with probability p_m and 'cross-over' p_c percentage of parents. In this work, at every iteration of the GA optimization, to calculate the performance of each individual sensor network, individual ANNs are developed and evaluated. The input to each ANN is the ToF of the recorded sensor signal. Uncertainty in the measured ToF, t_{m_k} is included for $k = 1, \ldots, N_s$ (N_s being the total number of sensors). The likelihood function for ToF of any k sensor can be expressed as:

$$p(t_{m_k} \mid \mathbf{x}, \mu_k, \sigma^2) = \frac{1}{\sqrt{2\pi\sigma^2}} \exp\left[-\frac{1}{2\sigma^2}(t_{m_k} - t_{c_k})^2\right] \tag{3}$$

where $\mathbf{x}$ gives the position of the impact, μ the mean of the distribution and $\sigma^2 = \sigma_1^2 + \sigma_2^2$ the total variance. The mean value can be assumed to be equal to the computed ToF. Using Bayes' theorem, the likelihood function can be related to the posterior probability distribution function (PDF) and the prior distribution via the following relation:

$$p(\mathbf{x}_i \mid t_{m_k}) = \frac{p(t_{m_k} \mid \mathbf{x}_i)\, p(\mathbf{x}_i)}{p(t_{m_k})} \tag{4}$$

The optimal sensor configuration can then be formulated as a minimization problem by solving the following problem:

$$\min_{\mathbf{s}\in\mathbf{S}} p\left[\bigcup_{i\in I}(\mathbf{x}_i \mid e_i > e_{i_T})\right] \tag{5}$$

where $\mathbf{s}$ is a vector of all sensor readings, I is the number of impacts each located at $\mathbf{x}_i$, with e_i, representing the error between the actual and the predicted impact location. The vector $\mathbf{e}_T$ represents a threshold value representing the acceptable performance of the SHM system to detect the impact which can be given in terms of distance. The minimization given in Eq. 5 means that the optimal sensor configuration is reached by minimizing the probability of not detecting an impact occurring at location $\mathbf{x}_i$. As the impact events are independent, the above problem can be stated as:

$$\frac{1}{I}\min_{\mathbf{s}\in\mathbf{S}}\sum_{i\in I} p\left[(\mathbf{x}_i \mid e_i > e_T)\right] \tag{6}$$

By applying the Bayes' theorem we obtain:

$$\min_{\mathbf{s}\in\mathbf{S}}\sum_{i\in I}\left[1-p\left(e_i \le e_T \mid \mathbf{x}_i\right)\right]p(\mathbf{x}_i) = \min_{\mathbf{s}\in\mathbf{S}}\sum_{i\in I}\left[1-PoD_i\right]p(\mathbf{x}_i) = \min_{\mathbf{s}\in\mathbf{S}} J(e_T) \tag{7}$$

where $PoD_i = p\left(e_i \le e_T \mid \mathbf{x}_i\right)$ is the probability that the impact occurring in $\mathbf{x}_i$ is predicted with an error $e_i \le e_T$. If the ToA measurements are assumed to obey Eq. 3, then $p\left(e_i \le e_T \mid \mathbf{x}_i\right)$ is the conditioned marginal probability of $p\left(e_i \le e_T, \mathbf{x}_i, \sigma^2\right)$, i.e.:

$$\begin{aligned} p\left(e_i \le e_T \mid \mathbf{x}_i\right) &= \frac{p\left(e_i \le e_T, \mathbf{x}_i\right)}{p(\mathbf{x}_i)} = \frac{\int_{-\infty}^{\infty} p\left(e_i \le e_T, \mathbf{x}_i, \sigma^2\right) d\sigma^2}{p(\mathbf{x}_i)} \\ &= \int_{-\infty}^{\infty} p\left(e_i \le e_T \mid \mathbf{x}_i, \sigma^2\right) p(\sigma^2) d\sigma^2 \end{aligned} \tag{8}$$

The prior probabilities $p(\mathbf{x}_i)$ and $p(\sigma^2)$ are the probabilities of impact occurrence on the certain type of the structure and its variation. For example for part of an aircraft, this information can be obtained from the fleet. The integral in Equation (8) can be computed numerically by imposing σ^2 to vary in a fixed pre-defined interval. The PoD_i term can be computed following a Monte Carlo approach and by assuming the Gaussian variation of the ToF in each sensor.

If the probability of faulty sensors is defined by $p(M_s)$, with M_s being the pre-defined number of faulty sensors, then the optimal sensor combination can be searched by minimizing the probability of not detecting an impact an impact located at $\mathbf{x}_i$ (i.e., $e_i > e_T$):

$$\min_{\mathbf{s}\in S} p\left(\mathbf{x}_i \mid M_s, e_i > e_T\right) \tag{9}$$

where $\mathbf{s}$ is a vector identifying the chosen sensor network from the set $\mathbf{S}$ containing all of the possible combinations of N_s. The optimal sensor combination can be searched among a chosen set I of impacts:

$$\min_{\mathbf{s}\in\mathbf{S}}\ p\left[\bigcup_{i\in I}(\mathbf{x}_i \mid M_s, e_i > e_T)\right] \tag{10}$$

As the impact events are independent:

$$\frac{1}{I}\min_{\mathbf{s}\in\mathbf{S}}\sum_{i\in I} p\left(\mathbf{x}_i \mid M_s, e_i > e_T\right) \tag{11}$$

By applying Bayes' theorem and assuming that the impact and the sensor failure are independent events, we have:

$$\min_{\mathbf{s}\in\mathbf{S}}\sum_{i\in I} p\left(e_i > e_T \mid \mathbf{x}_i, M_s\right) p(\mathbf{x}_i)p(M_s) \tag{12}$$

and therefore:

$$\min_{\mathbf{s}\in\mathbf{S}}\sum_{i\in I} \left[1 - p\left(e_i \leq e_T \mid \mathbf{x}_i, M_s\right)\right] p(\mathbf{x}_i)p(M_s) \tag{13}$$

Analogously to what has been proposed in the previously, the marginal probability in Equation (13) can be expressed as:

$$p\left(e_i \leq e_T \mid \mathbf{x}_i, M_s\right) = \int_{-\infty}^{\infty} p\left(e_i \leq e_T \mid \mathbf{x}_i, \sigma^2, M_s\right) p(\sigma^2) d\sigma^2 \tag{14}$$

If $PoD_{i,M_s}(\mathbf{x})$ indicates the probability to detect an impact at $\mathbf{x}_i$ for a given number of possible failed sensors M_s and a given probability distribution of the ToF measurements, then the minimization process assumes the following expression:

$$\min_{\mathbf{s}\in\mathbf{S}}\sum_{i\in I} \left[1 - \mathrm{PoD}_{i,M_s}(\mathbf{x}_i)\right] p(\mathbf{x}_i)p(M_s) = \min_{\mathbf{s}\in\mathbf{S}} J(e_T, M_s) \tag{15}$$

The terms $p(\mathbf{x}_i), p(M_s)$ and $p(\sigma^2)$ represent the prior probabilities of having an impact at location $\mathbf{x}_i$, having M_s number of possible failed sensors and having a certain variance in the ToF distribution, respectively. In the next section, the proposed Bayesian optimisation is applied to a composite stiffened panel.

3 Application to Composite Stiffened Panel

The proposed Bayesian optimisation has been applied to a composite stiffened panel made of unidirectional and woven carbon/epoxy to find the optimal sensor positions. The geometry of the panel (2045 mm by 1070 mm) is shown in Figure 2. The response of the panel under impact events has been modelled numerically. A non-linear FE model of the panel was developed in ABAQUS and used to simulate impacts at various locations. A total of 300 PZT sensors were modelled to record the impact generated signals at 50 mm intervals, shown by small rectangles in Figure 2. The plate was meshed using 2 mm general purpose shell elements. More details on the numerical modelling of the impact events can be found in [2].

A total of 1265 impacts of different masses (a large mass and a small mass simulating a tool drop and a hail impact), velocity and various locations were carried out to develop a library of all possible impact scenarios on the stiffened panel. To reduce the dimensionality of the problem, in the optimization analysis, 45 possible sensor locations have been considered (as depicted in Figure 3), and the search is carried out to find the best 4 sensor location with and without the probability of sensor failure included. First, the optimization was carried out to find the best four sensor network. The parameters used for the GA are the following:

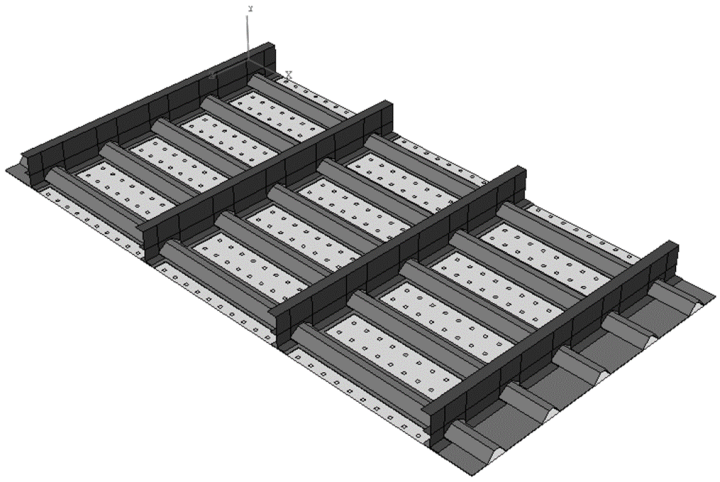

Figure 2: Composite stiffened panel with all possible sensor locations

(a) $N_{cy} = 500$ the number of cycles to generate the best ANN;

(b) $P_{sd} = 3\sigma$ the width of the Gaussian distribution;

(c) $\epsilon_t = 10^{-10}$ the strain threshold at which the ToA is computed;

(d) $N_{MC} = 1000$ the number of samples generated in the Monte Carlo approach;

(e) $e_T = 50$ mm provides the measure of the error in the impact localization prediction above which the impact is considered as "not detected".

An initial population of $N = 200$ individuals is set. At each iteration of the GA, a new population of N individuals is generated from the previous one by retrieving $n_c = 4$ elite individuals, mutating with 20% probability and by cross-over of 80% of the parents. A special cross-over operation, as described in [20], was developed to avoid repeated sensors in the child. Furthermore $p(\mathbf{x_i})$ and $p(M_s)$ are assumed to have uniform distributions. The optimal 4-sensor network as a result of the optimization and its performance are listed in Table 3. It can be seen that the best performance is achieved when the sensors are placed at the corners of the plate [1-4-41-45], maximizing the coverage area as expected. To validate that the chosen sensor combination is indeed the optimal one, its performance has been compared to similar sensor combinations with similar coverage areas. The results in Table 3 show that the performances of the sensor networks are very similar, but the optimal one is slightly higher. Furthermore, as expected, their performance deteriorates quickly with increasing the probability of failed sensors. The minimum number of sensors required to triangulate the location of the impact is three, therefore it is reasonable to see that the performance of the ANN drops significantly when the number of failed sensors is increased from $M_s = 1$ to 2 which means only two sensors are active. The way the sensor failure is included in the evaluation of the performance of the trained ANN is that once a faulty is detected (for example by measuring the Electro-Mechanical Impedance response [23]) then, the faulty sensor is removed from the network and the remaining

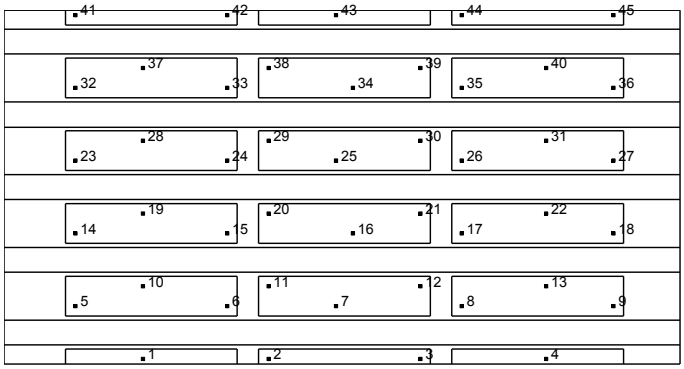

Figure 3: Stiffened panel with forty-five possible sensor locations.

sensors are used to detect the location of the impact. The next validation example was to give part of the stiffened panel higher probability of impact occurrence to evaluate its effect on the optimal sensor distribution.

Table 1: Performance of the sensor networks with and without probability of sensor failure

Sensor Combination	**Performance (%), $M_s = 0$**	**Performance (%), $M_s = 1$**	**Performance (%), $M_s = 2$**
[1-4-41-45] (optimal)	83.1	74.1	9.6
[1-9-41-45]	82.8	73.8	10.2
[4-5-41-45]	82.8	73.8	9.3

The non-uniform probability is defined by assuming that it is more likely to have impacts near the top-left corner zone (in an area equal to the half of the entire panel), as presented in Figure 4. The optimal solutions are depicted in Figure 5.

For the uniform distribution of $p(\mathbf{x})$, the optimization process locates the sensors close to the corners (see Figure 5a). On the contrary, the optimal solution with the non-uniform prior probability has one sensor closer to the area with higher probability of impact (see Figure 5b). The other three sensors remain in the corner position as the lower probability is set equal to 0.2. Decreasing such a probability would move the three corner sensors towards the top-left area. The performances of the two (uniform and non-uniform) optimal combinations provided in Figure 5(for $P_{sd} = 10\%\mu$, $\epsilon_t = 10^{-10}$, $e_T = 45$ mm) are:

- Network [1-4-41-51]: It's performance=70% with uniform probability and 65% with non-uniform probability of impact occurrence;

- Network [1-25-41-45]: It's performance=62% with uniform probability and 72% with non-uniform probability of impact occurrence;

The results validates that the optimal sensor network resulting from including non-uniform prior probability of impact occurrence in the optimization algorithm does indeed have a better performance compared to the performance of the optimal network assuming uniform probability.

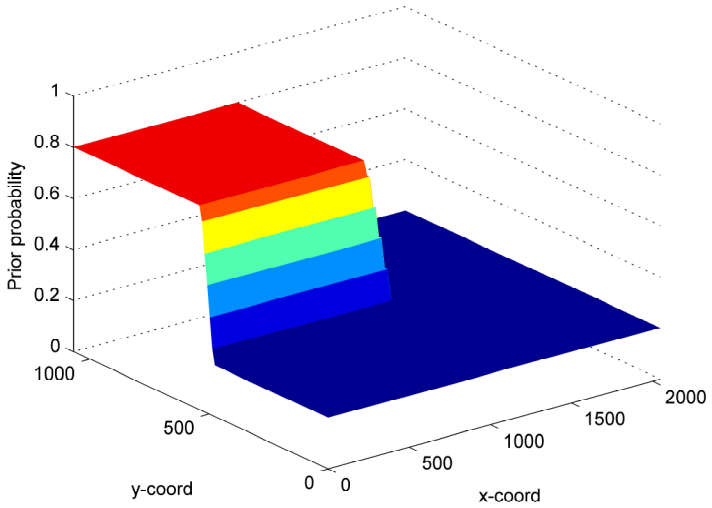

Figure 4: Non-uniform prior probability $p(\mathbf{x})$ considered in the example depicted in Figure 5(b). $x-$ and $y-$ coordinates in millimetre.

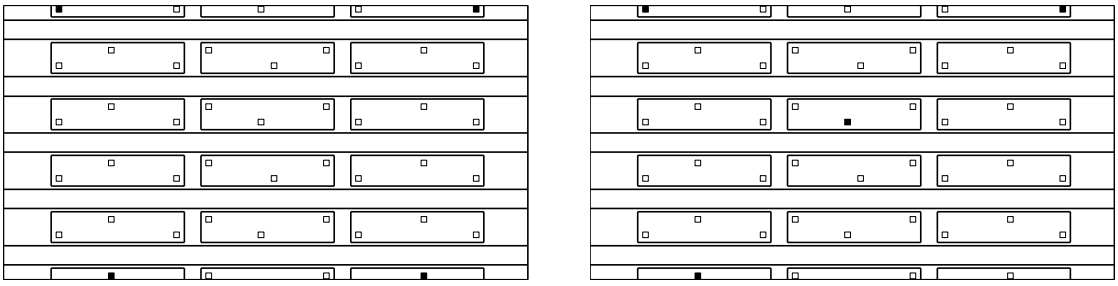

(a) (b)

Figure 5: Best four-sensor combination. Uniform probability (**a**); non-uniform probability (**b**).

4 Conclusion

In this work, a Bayesian probabilistic approach has been proposed for optimal sensor positioning for impact detection using PZT transducer surface mounted onto the structure. The focus of the work has been application to real structure under operational conditions. Therefore, the novelty of the proposed algorithm is to include: (*i*) uncertainty in the recorded sensors data (which are used as inputs to the detection algorithm), (*ii*) probability of one or more sensors failing during operation and (*iii*) non-uniform probability of impact occurrence.

The impact detection methodology adopted in this work is the meta-models based on ANN whose performance is the fitness function input to the optimization. The developed strategy was then tested on a composite stiffened panel, modelled numerically to simulate a large database of impact scenarios. The optimization was then applied to the stiffened panel with and without sensor failure probabilities and with uniform and non-uniform probability of impact distributions. The results clearly indicated that including sensor malfunctioning in the optimisation procedure

(to increase the reliability of the SHM system) results in a different optimal sensor location. In addition, the number of malfunctioning sensors influences their optimal placement. Therefore, it is very important that the designers of the SHM system define the rate and the probability of sensor malfunctioning a priori and include them in the optimisation algorithm. Lastly, that the optimal sensor location changes when different probabilities of impact occurrence are defined for the same structure, and it increases the overall probability of impact detection when considered in the optimisation strategy.

REFERENCES

[1] Z. Sharif Khodaei, M. Ghajari, and M.H. Aliabadi. Determination of impact location on composite stiffened panels. *Smart Materials and Structures*, 21(10):105026, 2012.

[2] M. Ghajari, Z. Sharif-Khodaei, M.H. Aliabadi, and A. Apicella. Identification of impact force for smart composite stiffened panels. *Smart Materials and Structures*, 22(8):085014, 2013.

[3] CH. Zhong, A.J. Croxford, and P.D. Wilcox. Remote inspection system for impact damage in large composite structure. 471(2173):20140631, 2015.

[4] E.B. Flynn, M.D. Todd, P.D Wilcox, B.W. Drinkwater, and A.J. Croxford. Maximum-likelihood estimation of damage location in guided-wave structural health monitoring. page rspa20110095, 2011.

[5] A. Raghavan and C. Cesnik. Review of guided-wave structural health monitoring. *Shock and Vibration Digest*, 39(2):91–116, 2007.

[6] Z. Sharif-Khodaei and M.H. Aliabadi. Assessment of delay-and-sum algorithms for damage detection in aluminium and composite plates. *Smart Materials and Structures*, 23(7):075007, 2014.

[7] M.S. Salmanpour, Z. Sharif Khodaei, and M.H. Aliabadi. Guided wave temperature correction methods in structural health monitoring. *Journal of Intelligent Material Systems and Structures*, page 1045389X16651155, 2016.

[8] J.E. Michaels. Detection, localization and characterization of damage in plates with an in situ array of spatially distributed ultrasonic sensors. *Smart Materials and Structures*, 17(3):035035, 2008.

[9] F. Ciampa and M. Meo. Impact detection in anisotropic materials using a time reversal approach. *Structural Health Monitoring*, 11(1):43–49, 2012.

[10] F. Ciampa, M. Meo, and E. Barbieri. Impact localization in composite structures of arbitrary cross section. *Structural Health Monitoring*, 11(6):643–655, 2012.

[11] T.S. Plagianakos, K.L. Lika, and E.G. Papadopoulos. Low-velocity impact response of smart sandwich composite plates with piezoelectric transducers: Modeling and experiments. *Journal of Intelligent Material Systems and Structures*, doi:10.1177/1045389X15580662, 2015.

[12] Z. Senderos, B. Niell, and E. Niell. High-speed impact location detection on anisotropic composite panels using embedded piezoelectric sensors. *Journal of Intelligent Material Systems and Structures*, 25(15):1921–1936, 2014.

[13] C. Zhang, J. Qiu, H. Ji, and S. Shan. An imaging method for impact localization using metal-core piezoelectric fiber rosettes. *Journal of Intelligent Material Systems and Structures*, 26(16):2205–2215, 2015.

[14] R. Seydel and Fu-Kuo Chang. Impact identification of stiffened composite panels: I. system development. *Smart Materials and Structures*, 10(2):354, 2001.

[15] R. Seydel and Fu-Kuo Chang. Impact identification of stiffened composite panels: Ii. implementation studies. *Smart materials and structures*, 10(2):370, 2001.

[16] W.J. Staszewski, K. Worden, R. Wardle, and G.R. Tomlinson. Fail-safe sensor distributions for impact detection in composite materials. *Smart Materials and Structures*, 9(3):298, 2000.

[17] JR LeClerc, Keith Worden, Wieslaw J Staszewski, and Jonathan Haywood. Impact detection in an aircraft composite panela neural-network approach. *Journal of Sound and Vibration*, 299(3):672–682, 2007.

[18] V. Mallardo and M.H. Aliabadi. Optimal sensor placement for structural, damage and impact identification: A review. *SDHM: Structural Durability & Health Monitoring*, 9(4):287–323, 2013.

[19] Eric B. Flynn and Michael D. Todd. A bayesian approach to optimal sensor placement for structural health monitoring with application to active sensing. *Mechanical Systems and Signal Processing*, 24(4):891 – 903, 2010.

[20] V. Mallardo, Z. Sharif Khodaei, and M.H. Aliabadi. A bayesian approach for sensor optimisation in impact identification. *Materials*, 9(11):946, 2016.

[21] V. Mallardo, M.H. Aliabadi, and Z. Sharif Khodaei. Optimal sensor positioning for impact localization in smart composite panels. *Journal of Intelligent Material Systems and Structures*, 24(5):579–573, 2012.

[22] V. Faivre and E. Morteau. Damage tolerant composite fuselage sizing. *FAST-Flight Airworthiness Support Technology Magazine, Airbus Technical Magazine*, (48):13, 2016.

[23] Z. Sharif-Khodaei, M. Ghajari, and M.H. Aliabadi. Impact damage detection in composite plates using a self-diagnostic electro-mechanical impedance-based structural health monitoring system. *Journal of Multiscale Modelling*, page 1550013, 2015.

VIII ECCOMAS Thematic Conference on Smart Structures and Materials
SMART 2017
A. Güemes, A. Benjeddou, J. Rodellar and J. Leng (Eds)

SPARSITY CONSTRAINED EXTENDED KALMAN FILTER CONCEPT FOR DAMAGE LOCALIZATION AND IDENTIFICATION IN MECHANICAL STRUCTURES

Daniel Ginsberg*, Claus-Peter Fritzen† and Otmar Loffeld‡

*Department of Mechanical Engineering
University of Siegen
Paul-Bonatz-Strasse 9 -11, 57076 Siegen, Germany
e-mail: daniel.ginsberg@uni-siegen.de

†Department of Mechanical Engineering and Center of Sensor Systems (ZESS)
University of Siegen
Paul-Bonatz-Strasse 9 -11, 57076 Siegen, Germany
e-mail: claus-peter.fritzen@uni-siegen.de

‡Center of Sensor Systems (ZESS)
University of Siegen
Paul-Bonatz-Strasse 9 -11, 57076 Siegen, Germany
e-mail: loffeld@zess.uni-siegen.de

Key words: L_1-Minimization, Sparse Reconstruction, Extended Kalman Filter, Damage Identification

Abstract. Structural health monitoring (SHM) systems are necessary to achieve smart predictive maintenance and repair planning as well as they lead to a safe operation of mechanical structures. In the context of vibration based SHM the measured structural responses are employed to draw conclusions about the structural integrity.

This usually leads to a mathematically inverse problem which needs regularization. The restriction of the solution set of this inverse problem by using prior information about the damage properties is advisable to obtain meaningful solutions. Compared to the undamaged state usually only a few local stiffness change occur while the other areas remain unchanged. This change can be described by a sparse damage parameter vector. Such a sparse vector can be identified by employing L_1-regularization techniques.

This paper presents a novel framework for damage parameter identification by combining sparse solution techniques with an extended Kalman filter. In order to ensure sparsity of the damage parameter vector the measurement equation is expanded by an additional nonlinear L_1-minimizing observation. This fictive measurement equation accomplishes stability of the extended Kalman filter and leads to a sparse estimation.

For verification, a proof-of-concept example on a quadratic aluminum plate is presented.

1 INTRODUCTION

Structural health monitoring (SHM) is developed in order to ensure a safe operation of mechanical structures and to reduce life cycle cost by replacing schedule-driven inspections by Condition-Based Maintenance (CBM). One major task of SHM systems is the detection and identification of damage in an early state of structural damage evolution. For vibration-based SHM an integrated sensor network is required to measure the structural vibration excited either by an artificial or a natural source, e.g. wind and traffic loads. By means of the integrated sensor system the effect of the damage on the structural vibration response can be measured. Now, SHM systems need smart data processing algorithms in order to draw back conclusions about the exact cause for the measured effect. Thus, vibration based damage identification can be seen as the inversion of the principle of cause and effect. This leads in praxis to a mathematical inverse problem. If there are many causes which will lead to the same measurable effect, the inverse problem is additionally ill-posed. Ill-posedness means that that either the existence, the uniqueness or the stability of the solution is violated.

In the last decades many methods have been developed and a considerable amount of literature has been published on the inverse problem of structural damage identification, an overview on this topic can be found for example in [1, 2]. Damage identification techniques can be classified as frequency or time domain or time-frequency domain methods. Classical frequency domain approaches consider the changes of the natural frequencies, modal damping and mode shapes due to damage. As these quantities provide information on a global level, they are often insensitive to small local structural damage. Especially if only lower structural modes are used. In the medium or higher frequency range problems may occur to identify these modes since this requires a very dense sensor network. Therefore, time domain approaches seem to be comfortable for structural damage identification.

Several time domain approaches have already been proposed, such as least-squares estimation methods [3, 4] or methods using particular filters [5, 6]. For the latter the extended Kalman filter (EKF) is the most well-known system parameter estimation method [7, 8]. EKF-based system parameter identification belongs to the class of model-based approaches. Here, an undamaged reference model is tested against the actual system in each filter step. In the filter process the state vector of the Kalman filter equations is typically augmented [8] or sometimes even replaced [9] by the system parameter to be estimated. By making use of the input-output signal an estimation of the system parameters is obtained in each filter step. Even so the original Kalman filter is known as optimal linear filter, EKF-based damage identification is still facing some challenges, e.g. high computational effort for complex structures and intrinsic ill-posedness of the inverse problem [10]. To overcome ill-posedness usually the damage parameter space is reduced by considering only damage hot spots or by a drastic increase of the sensor number. In order to perform damage monitoring on the whole structure and to keep the required number of sensors low, a sparsity constrained extended Kalman filter concept is proposed in this contribution.

Therefore, a priori information about the damage properties is used to solve the inverse problem and to obtain meaningful solutions. For example, cracks can be interpreted as spatial singularities, which cause only a very local structural stiffness reduction. Thus, a system parameter vector which describes the change in structural stiffness has only a few non-zeros

elements corresponding to the actual damage location. Such a vector is called sparse. In many fields of applied mathematics L_1-regularizing techniques have been proven to promote such kind of sparse solutions (e.g. Compressive Sensing [11, 12]). The proposed damage identification method links the concept of L_1-regularization with extended Kalman filter by expanding the measurement equation by an additional nonlinear L_1-minimizing observation.

The paper is structured as follows: Section 2 describes the L_1-minimizing sparse solution strategy for inverse problems. The problem of damage parameter estimation using a non-linear state-space description is formulated in section 3. In section 4 the concept of sparse solution is incorporated in the extended Kalman filter concept. A proof-of-concept simulation study is carried out in section 5. Here the functionality of the proposed identification method is demonstrated by analyzing different damaged scenarios on a quadratic aluminum plate structure. Finally, concluding remarks are presented in section 6.

2 SPARSE SOLUTION OF INVERSE PROBLEM

Most ill-posed inverse problems can be formulated by a linear algebraic equation system of the form:

$$\mathbf{y} = \mathbf{H} \cdot \mathbf{A} \tag{1}$$

or can be transformed into such a system. In Eq. (1) $\mathbf{y} \in \mathbb{R}^M$ is a vector which contains all measurable output information and $\mathbf{A} \in \mathbb{R}^N$ all possible causes. The transition matrix $\mathbf{H} \in \mathbb{R}^{M \times N}$ describes the linear effect-causes relationship. If the dimension of $\mathbf{y}$ is smaller than the dimension of $\mathbf{A}$ ($M < N$) the linear system of equation is called underdetermined. In this case Eq. (1) has an infinite number of possible solutions, which means an infinite number of different causes will result in the same effect. The challenge of solving such an equation system is the determination of the right one.

In order to close the gap of information and to obtain a solution additional constraints $\Omega(\mathbf{A})$ need to be formulated, which regularize the problem. The most common regularization is the *Tikhonov-Regularization* [13],

$$\hat{\mathbf{A}}_2 = \underset{\mathbf{A} \in \mathbb{R}^N}{\arg\min} \left\{ \|\mathbf{y} - \mathbf{H} \cdot \mathbf{A}\|_2^2 + \lambda \|\mathbf{A}\|_2^2 \right\} . \tag{2}$$

with the constraint $\Omega(\mathbf{A})$:

$$\Omega(\mathbf{A}) = \|\mathbf{A}\|_2^2 \quad \text{and} \quad \|\mathbf{A}\|_2 = \sqrt{\sum_i A_i^2} \tag{3}$$

Here, the solution of Eq. (1) is generated via an optimization problem. The constraint can be interpreted as additional information which regularize the inverse problem and forces the L_2-norm of the solution vector $\hat{\mathbf{A}}_2$ to be minimal. Furthermore, for Tikhonov-Regularization $\mathbf{y}$ is not necessarily equal $\mathbf{H} \cdot \mathbf{A}$ so that the solution is stabilized if $\mathbf{y}$ is polluted by noise. However, for most applications the choice of L_2-minimization as constraint is not suitable to close the gap of information and to obtain meaningful results.

In recent years, new reconstruction strategies for solving underdetermined linear systems of equations have been proposed, pushed forward by the developments in the field of Compressive

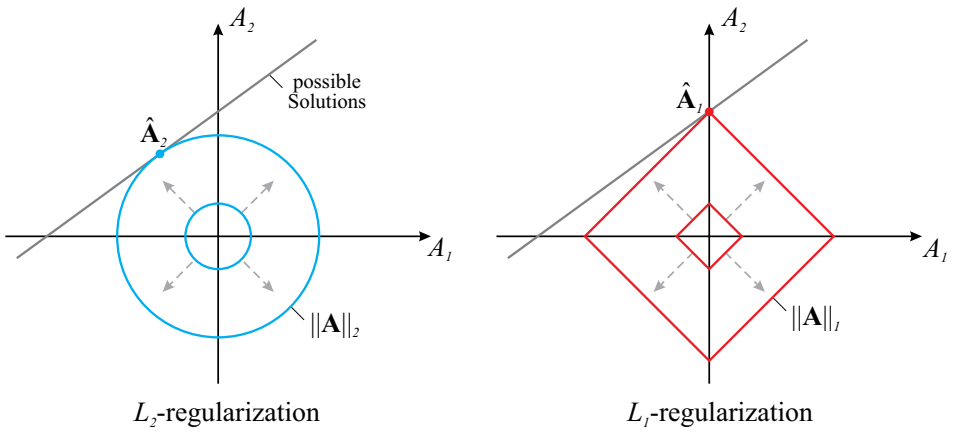

Figure 1: Comparison of L_2- and L_1-regularization of underdetermined equation systems

Sensing (CS) [11, 12]. For these reconstruction methods it is assumed that the solution vector has just a few nonzero elements or can be transformed to such a sparse vector by using some other coordinate spaces. This assumption holds for most vectors which describe some real world phenomena (e.g. images, sounds, forces); the elements inside such vectors are not completely arbitrary and have some kind of internal structure. Such a structure is always used for compressing data, e.g. wavelet transformation of images or Fourier transformation of sounds. So the information carried by these vectors is mostly a lot smaller than the dimension of the vectors itself suggests. However, it is not known in advance known which elements are nonzero, but the information that the solution vector is sparse can be included as additional information in the reconstruction strategy [14].

The number of nonzero elements s inside the vector $\mathbf{A}$ can be expressed by means of the L_0-norm

$$s = \|\mathbf{A}\|_0 = |\mathrm{supp}\,(\mathbf{A})| \ , \tag{4}$$

where $\mathrm{supp}\,(\mathbf{A}) := \{i : A_i \neq 0\}$ denotes the support set of the vector $\mathbf{A}$ and $|\circ|$ the cardinality of this set. If the dimension N of the vector $\mathbf{A}$ is much bigger than the number of nonzero elements s ($N \gg s$), then $\mathbf{A}$ is a sparse vector.

The sparsest solution which agrees with our measurements could be obtained by minimizing the following expression:

$$\hat{\mathbf{A}}_0 = \underset{\mathbf{A}\in\mathbb{R}^N}{\arg\min} \|\mathbf{A}\|_0 \quad \text{subject to} \quad \mathbf{y} = \mathbf{H}\cdot\mathbf{A} \tag{5}$$

Unfortunately, solving Eq. (5) requires a combinatorial search, which makes it nearly impossible to solve computationally. Under the assumption of a sparse solution, e.g. in [12] is shown shown that by replacing the L_0-norm with the L_1-norm almost the same solution can be obtained as solving Eq. (5):

$$\hat{\mathbf{A}}_1 = \underset{\mathbf{A}\in\mathbb{R}^N}{\arg\min} \|\mathbf{A}\|_1 \quad \text{subject to} \quad \mathbf{y} = \mathbf{H}\cdot\mathbf{A} \tag{6}$$

The L_1-norm is the sum of all absolute values of the vector entries A_j,

$$\|\mathbf{A}\|_1 = \sum_j |A_j| \ . \tag{7}$$

Eq. (6) is now a convex optimization Problem which can by solved be some linear programming techniques. The reason why L_1-regularization also delivers sparse solutions, is illustrated in Fig. 1. It can be seen that L_2-regularization leads to a solution closest to the origin while L_1-regularization finds a solution on the coordinate axes, with just a few nonzero elements.

3 PROBLEM STATEMENT

In general, the dynamics of a nonlinear, time-varying structure can be described similar to [2] as:

$$\begin{aligned} \mathbf{M}\left(\boldsymbol{\Theta}_k, \mathbf{x}_k, k\right) \ddot{\mathbf{x}}_k + \mathbf{g}\left(\boldsymbol{\Theta}_k, \mathbf{x}_k, \dot{\mathbf{x}}_k, k\right) &= \mathbf{u}_k \\ \boldsymbol{\Theta}_{k+1} &= \boldsymbol{\Gamma}\left(\boldsymbol{\Theta}_k, \mathbf{x}_k, \dot{\mathbf{x}}_k, k\right) \\ \mathbf{y}_k &= \mathbf{h}^*\left(\boldsymbol{\Theta}_k, \mathbf{x}_k, \dot{\mathbf{x}}_k, k\right) \end{aligned} \tag{8}$$

The first line of Eq. (8) is the nonlinear equation of motion in discrete time domain $t_k = k\Delta t,\ k \in \mathbb{N}$. $\mathbf{M}(\cdot) \in \mathbb{R}^{m\times m}$ is the mass matrix and $\mathbf{g}(\cdot) \in \mathbb{R}^m$ the force vector of elastic and damping forces. These can depend on the nodal displacement $\mathbf{x} \in \mathbb{R}^m$, the nodal velocity $\dot{\mathbf{x}} \in \mathbb{R}^m$ and the time step k. The damage parameter $\boldsymbol{\Theta} \in \mathbb{R}^p$ describes the change of structural integrity (loss of stiffness, loss of mass, etc.) by location and damage extent. For Structural Health Monitoring this is the parameter which needs to be reconstructed. Moreover, the damage parameter $\boldsymbol{\Theta}$ usually has also influence on the equation of motion. $\mathbf{u} \in \mathbb{R}^m$ is the vector of the external acting loads on the structure. The number of degrees of freedom (DOF) is m. The nonlinear function $\boldsymbol{\Gamma}(\cdot) \in \mathbb{R}^p$ describes the evolution of the damage parameter in the second line of Eq. (8). The third line of Eq. (8) is the measurement equation which links the model quantities (displacement, velocities and system parameters) with the output $\mathbf{y} \in \mathbb{R}^n$ of the measurement device by means of the function $\mathbf{h}^*(\cdot) \in \mathbb{R}^n$. The number of measurements equals n.

Mostly the evolution of the damage parameter $\boldsymbol{\Theta}$ and the structural dynamic vibrations occur on two different time scales. Compared to the structural vibrations, the evolution of damage is a rather slow process. Thus, the damage parameter $\boldsymbol{\Theta}$ seems to remain constant during a short time span of data acquisition [2].

Now, a state space model can be defined, in which the unknown damage parameter vector is the state vector. The evolution of it is modeled by a Gaussian Markov process, also called as random walk process [9]

$$\begin{aligned} \boldsymbol{\Theta}_{k+1} &= \boldsymbol{\Theta}_k + \mathbf{w}_k \\ \mathbf{y}_k &= \mathbf{h}\left(\boldsymbol{\Theta}_k, [\mathbf{U}]_k, \mathbf{x}_0, \dot{\mathbf{x}}_0, k\right) + \mathbf{v}_k \ , \end{aligned} \tag{9}$$

where $\mathbf{w}_k \in \mathbb{R}^p$ is zero-mean white process noise with covariance $\mathbf{Q}_k$, $\mathbf{w}_k \sim N(\mathbf{0}, \mathbf{Q}_k)$. Here, the measurement equation in the second line is defined slightly different as above. Unlike Eq. (8), the output measurement data are obtained depending on the initial nodal displacement and velocity $\mathbf{x}_0$ and $\dot{\mathbf{x}}_0$ and vector $[\mathbf{U}]_k = [\mathbf{u}_1, \mathbf{u}_2, \ldots, \mathbf{u}_k]^T$, which describes the external load input from

the time step $k = 1$ to the current time step k. So the equation of motion is implicitly included in the nonlinear measurement equation $\mathbf{h}(\cdot) \in \mathbb{R}^n$. $\mathbf{v}_k \in \mathbb{R}^n$ represents the measurement noise with covariance $\mathbf{R}_k$, $\mathbf{v}_k \sim N(\mathbf{0}, \mathbf{R}_k)$. For reasons of clarity and without loss of generality, in the remainder of this paper it is assumed that $\mathbf{x}_0 = \mathbf{0}$ and $\dot{\mathbf{x}}_0 = \mathbf{0}$.

4 EXTENDED L_1-MINIMIZING KALMAN FILTER

In the following, the concept of L_1-minimizing sparse reconstruction is incorporated into an extended Kalman filter framework. Loffeld et al. were the first to propose an L_1-minimizing Kalman filter approach for solving underdetermined sparse problems [15]. Here, this idea is adopted to stabilize the extended Kalman filter parameter estimation process for a large damage parameter space p and a low number of sensors n.

Structural damages due to e.g. cracks can often be interpreted as spatial singularities, as they lead to a stiffness reduction in a very local area of the system rather than a global stiffness reduction. Thus, it can be assumed that the unknown damage parameter vector $\mathbf{\Theta}$ is sparse. The sparsity will be considered as a constraint, which will be part of the state space model as an additional, nonlinear observation. It is promoted by the L_1-norm of the state vector:

$$\hat{\mathbf{y}}_k = \gamma_k = \|\mathbf{\Theta}_k\|_1 = \sum_{j=1}^{p} |\Theta_{j,k}| \tag{10}$$

Starting from $\gamma_0 = \|\mathbf{\Theta}_0\|_1$ the fictive measurement γ_k can now successively be decreased in each time step k by a scaling factor $\alpha < 1$,

$$\gamma_{k+1} = \alpha \|\mathbf{\Theta}_k\|_1 \tag{11}$$

The scalar Eq. (10) pushes down the L_1-norm of the state vector and thus leads to a sparse estimation of $\mathbf{\Theta}$. The now obtained augmented observation vector $\tilde{\mathbf{y}}_k$ reads as follows:

$$\tilde{\mathbf{y}}_k = \begin{bmatrix} \mathbf{y}_k \\ \gamma_k \end{bmatrix} = \begin{bmatrix} \mathbf{h}(\mathbf{\Theta}_k, [\mathbf{U}]_k, k) \\ \|\mathbf{\Theta}_k\|_1 \end{bmatrix} + \begin{bmatrix} \mathbf{v}_k \\ \nu_k \end{bmatrix} \tag{12}$$

$\nu_k \in \mathbb{R}$ reflects the uncertainty of the additional L_1-minimizing observation equation.

For estimating the states of the now obtained nonlinear state space model an extended Kalman filter (EKF) is used. The EKF linearizes the nonlinear model in each time step around the *a posteriori* estimated state vector, using a first-order Taylor series approximation. After linearization the traditional prediction-correction algorithm of the Kalman filter can be applied.

Starting from the initial conditions $\hat{\mathbf{\Theta}}_{0|0}$ and $\mathbf{P}_{0|0}$, a forecast of the state is made in the prediction step:

$$\begin{aligned} \hat{\mathbf{\Theta}}_{k|k-1} &= \hat{\mathbf{\Theta}}_{k-1|k-1} \\ \mathbf{P}_{k|k-1} &= \mathbf{P}_{k-1|k-1} + \mathbf{Q}_k \end{aligned} \tag{13}$$

In the corrector step the actual measurements $\mathbf{y}_k$ and the fictive measurements $\tilde{\mathbf{y}}_k$ are considered and compared with the prediction. The residual $\Delta\tilde{\mathbf{y}}_k$ is weighted by the Kalman gain matrix $\mathbf{K}_k$ and added to the prediction $\hat{\mathbf{\Theta}}_{k|k-1}$:

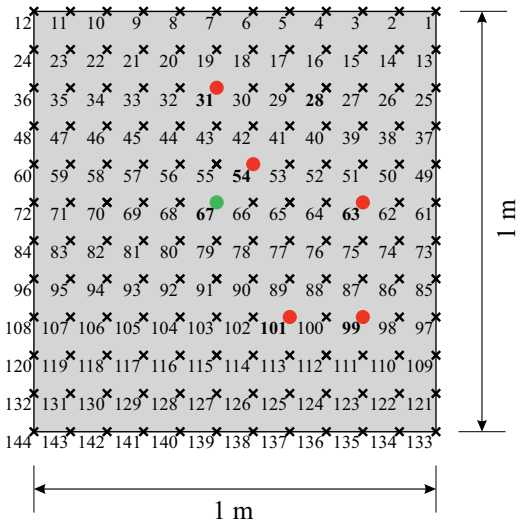

Figure 2: Node numbering of the finite element plate model; node 31, 54, 63, 99 and 101 are acceleration measurement positions; node 67 is the structure excitation position

$$\begin{aligned} \Delta\tilde{\mathbf{y}}_k &= \tilde{\mathbf{y}}_k - \mathbf{h}\left(\boldsymbol{\Theta}_{k|k-1}, [\mathbf{U}]_k, k\right) \\ \mathbf{K}_k &= \mathbf{P}_{k|k-1}\mathbf{H}_k^T\left(\mathbf{H}_k\mathbf{P}_{k|k-1}\mathbf{H}_k^T + \tilde{\mathbf{R}}_k\right)^{-1} \\ \hat{\boldsymbol{\Theta}}_{k|k} &= \hat{\boldsymbol{\Theta}}_{k|k-1} + \mathbf{K}_k\Delta\tilde{\mathbf{y}}_k \\ \mathbf{P}_{k|k} &= \left(\mathbf{I} - \mathbf{K}_k\mathbf{H}\right)\mathbf{P}_{k|k-1} \end{aligned} \tag{14}$$

For the proposed damage parameter estimation strategy only the measurement equation is nonlinear and needs to be linearized:

$$\mathbf{H}_k = \begin{bmatrix} \left.\frac{\partial \mathbf{h}\left(\boldsymbol{\Theta}_k, [\mathbf{U}]_k, k\right)}{\partial \boldsymbol{\Theta}}\right|_{\boldsymbol{\Theta}=\hat{\boldsymbol{\Theta}}_{k|k-1}} \\ \left.\frac{\partial \|\boldsymbol{\Theta}_k\|_1}{\partial \boldsymbol{\Theta}}\right|_{\boldsymbol{\Theta}=\hat{\boldsymbol{\Theta}}_{k|k-1}} \end{bmatrix} \tag{15}$$

The derivative of $\mathbf{h}(\cdot)$ with respect to $\boldsymbol{\Theta}$ is approximated by the finite difference method. The Jacobi matrix of the L_1-minimizing constraint

$$\frac{\partial \|\boldsymbol{\Theta}\|_1}{\partial \boldsymbol{\Theta}} = \begin{bmatrix} \frac{\partial \|\boldsymbol{\Theta}\|_1}{\partial \Theta_1} & \frac{\partial \|\boldsymbol{\Theta}\|_1}{\partial \Theta_2} & \cdots & \frac{\partial \|\boldsymbol{\Theta}\|_1}{\partial \Theta_p} \end{bmatrix}, \tag{16}$$

can be obtained by:

$$\frac{\partial \|\boldsymbol{\Theta}\|_1}{\partial \Theta_j} = \frac{\Theta_j}{|\Theta_j|} \tag{17}$$

The determination of the partial derivative in each time step k is computationally very expensive. In order to save computing time, this can be performed just in every second or third step. This also helps to stabilize the filter process in the beginning.

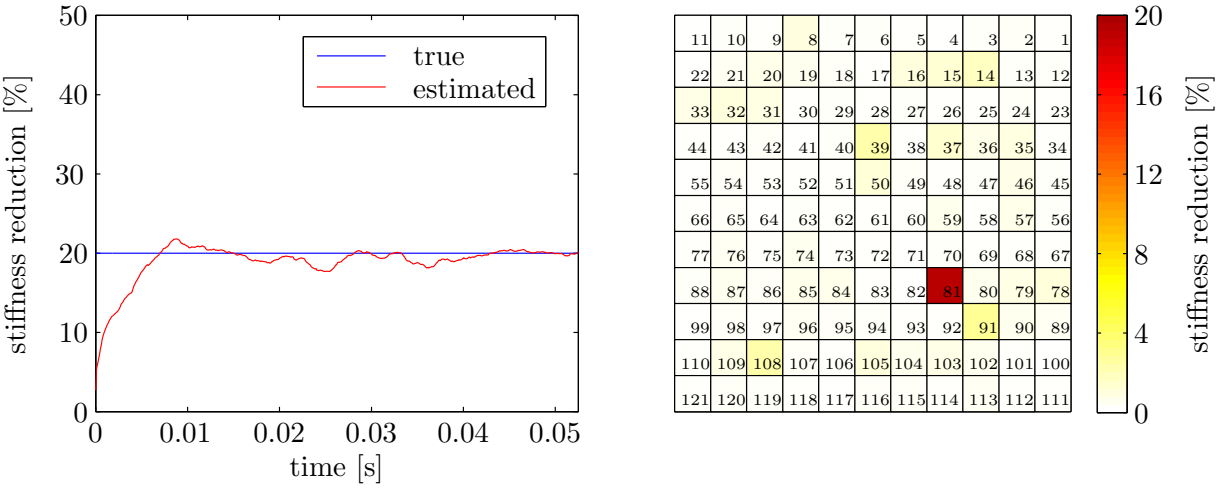

Figure 3: Damage identification result; left: evolution of damage parameter no. 81; right: estimated stiffness reduction for all elements at the end of simulation time

As usually structural damage has no direct impact on the measurements at the same specific time step k, it is advisable to extend the physical measurement $\mathbf{y}_k$ and to process a bloc of l physical measurements in each Kalman filter step:

$$\begin{bmatrix} \mathbf{y}_k \\ \mathbf{y}_{k+1} \\ \mathbf{y}_{k+2} \\ \vdots \\ \mathbf{y}_{k+l} \end{bmatrix} = \mathbf{h}^l \left(\mathbf{\Theta}_k, [\mathbf{U}]_k, k, l \right) + \mathbf{v}_k^l \tag{18}$$

By this *en bloc* processing, the filter is no longer operating in real time but with a time lag $t_l = l\Delta t$ in the past.

5 PROOF OF CONCEPT

In order to demonstrate the functionality of the proposed damage identification strategy a proof of concept simulation study is performed. The observed mechanical structure is a simple square aluminum plate of 1 m × 1 m edge length and 2 mm thickness. The structural dynamics of the plate due to external forces are described by a finite element model. The plate is modeled by 121 quadratic shell elements and 144 nodes (each with 6 degrees of freedom), see Fig. 2. The employed structural responses are simulated acceleration measurements perpendicular to the plate plane. The obtained simulated measurement signals are low-pass filtered by a cut-off frequency of 200 Hz. Thus, for damage detection only the low frequency content of the time signals is employed. White Gaussian noise, with a standard deviation of three percent of the maximum measurement value, is added to the simulated outputs to imitate real acceleration measurement data. Throughout all investigations shown in this paper, only five accelerometers are used.

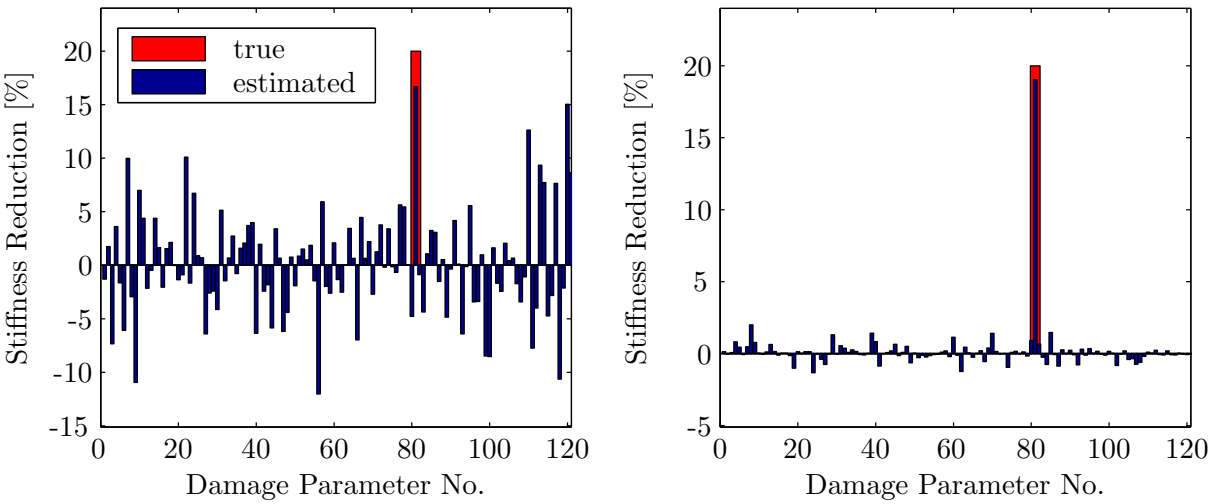

Figure 4: Comparison of damage parameter estimation; left: Kalman filter estimation without additional L_1-observation; right: Estimation result with L_1-minimizing observation

A widely used approach to introduce structural damage on a substructure or element level which represents the changes of the structural stiffness $\Delta\mathbf{K}$ compared to a reference model $\mathbf{K}_0$ is:

$$\Delta\mathbf{K} = \sum_j \mathbf{K}_j \Theta_j \ , \tag{19}$$

where $\mathbf{K}_j$ is the jth substructure or element stiffness matrix, respectively. By determination of the unknown correction parameters $\boldsymbol{\Theta} = [\Theta_1,\ \Theta_2,\ \ldots,\ \Theta_p]$ the damage can be localized and quantified.

In a first simulation study the stiffness of element no. 81 has been decreased by 20 %. The plate structural vibration is excited by an impulse force load perpendicular to the plate surface at node no. 67 of known time history. The obtained simulated acceleration time data are now used for structural damage identification. Fig. 3 shows the identification result. On the left hand side the evolution of the damage parameter corresponding to element no. 81 is plotted over time. It can be seen that starting from initial conditions (all damage parameters zero) the parameter of the damage element tends to the true value of stiffness reduction. The plot on the right hand side shows that for all the other elements the corresponding damage parameters are close to zero. So the damage is localized and quantified.

Fig. 4 compares the damage parameter estimation results for the proposed extended Kalman filter method with and without additional L_1-minimizing observation. It is obvious that no clear damage estimation result can be achieved without L_1-minimizing observation. Even though the reconstructed damage parameter error for the damage element no. 81 is not too big, many more element stiffness changes (reduction and increase) are identified. On the other hand it can be clearly distinguished between damaged and undamaged elements if the additional observation is employed, as L_1-minimization promotes this sparse solution.

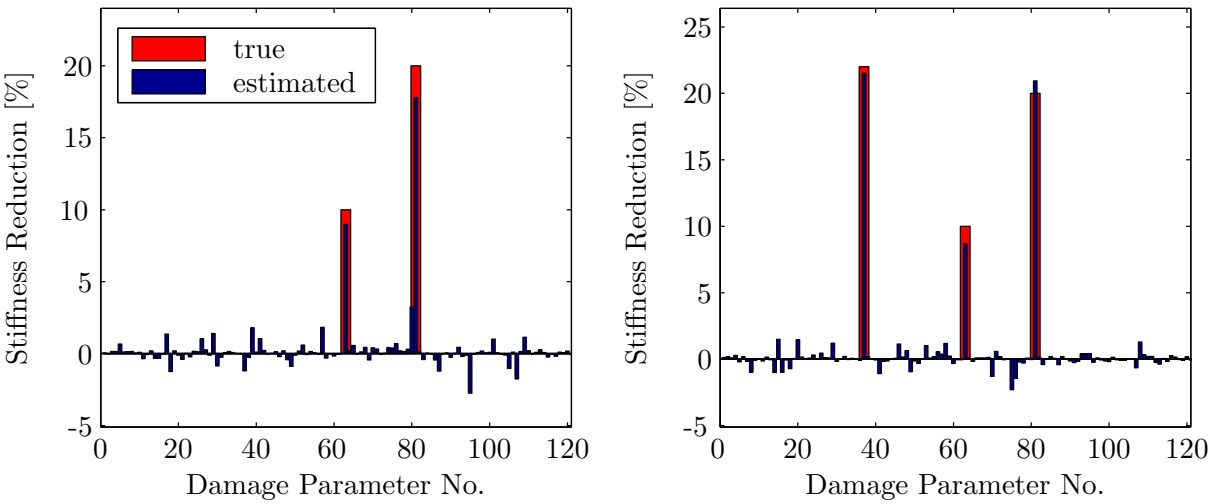

Figure 5: Multiple Damage Scenarios both identified with additional L_1-observation: two damaged elements no. 63 and no. 81; right: three damaged elements no. 37, no. 63 and no. 81

In a next step a multiple damage scenario is investigated. Here the plate structural damage is modelled by a stiffness reduction of various elements with different amount. Which means the damage parameter vector needs to be slightly denser than in the case of a single element stiffness change.

Fig. 5 shows the damage identification results at the end of simulation time for two and three damaged elements. In both cases a similar clear damage identification as before is obtained. In Fig. 6 a damage scenario is simulated and reconstructed in which a bigger area is damaged by means of an element stiffness reduction. In the left part of the figure the true damage pattern is shown. The identified damage pattern on the right hand side agrees with the true one. Beside the actual damage elements, only a few other elements show a negligible stiffness change.

6 CONCLUSION

In this contribution a new time domain method for damage detection has been proposed. The properties of damage are employed in order to use sparse reconstruction strategies for the upcoming ill-posed inverse problem. Sparsity of the estimated damage parameter state vector is ensured within the extended Kalman filter by adding a fictive non-linear L_1-minimizing observation.

It has been shown that the proposed reconstruction method is able to determine the damage location and the damage extent simultaneously. In contrast to the extended Kalman filter process without additional L_1-observation a clear damage pattern is obtained. This was shown for single damage scenarios as well as for multiple damage events. Considering the damage parameter space of size 121 in the demonstrated study, the number of sensors using only five accelerometers is significantly lower than the parameter space.

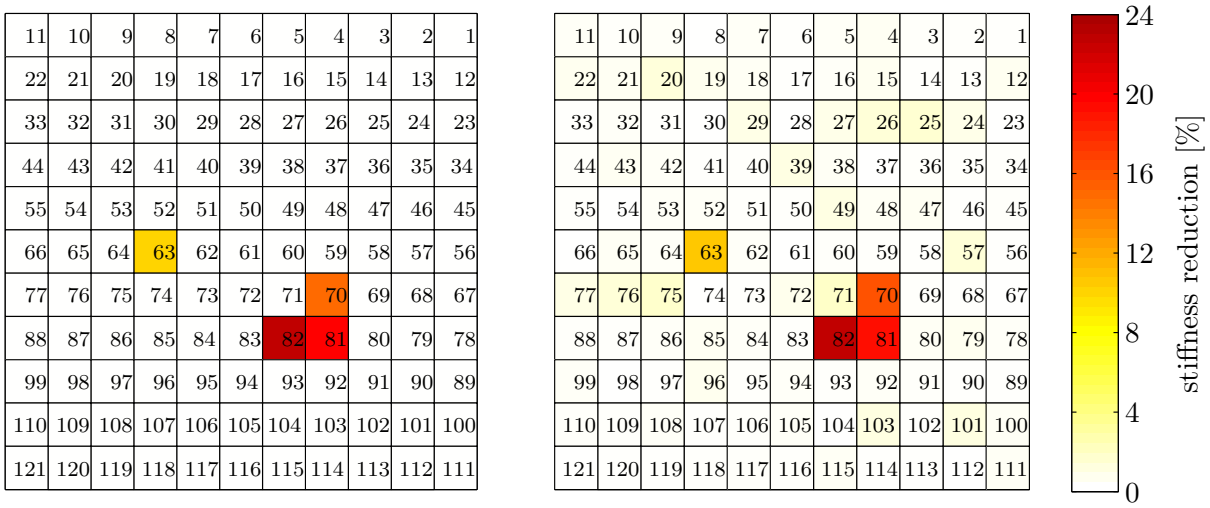

Figure 6: Damage identification result for bigger damaged areas; left: true damage pattern; right: estimated damage pattern

REFERENCES

[1] Sohn, H., Farrar, C. R., Hemez, F. M., Shunk, D. D., Stinemates, D. W., Nadler, B. R. and Czarnecki, J. J. *A review of structural health monitoring literature: 1996-2001*, Los Alamos National Laboratory, (2003)

[2] Balageas, D. and Fritzen, C.P. and Güemes, A. *Structural Health Monitoring*, Hermes Science Publishing, (2006)

[3] Smyth, A. W., Masri, S. F., Chassiakos A. G. and Caughey, T. K. *On-Line Parametric Identification of MDOF Nonlinear Hysteretic Systems*, ASCE Journal of Engineering Mechanics. (1999) **125**(2):133-142.

[4] Yang, J. N. and Lin, S. *Identification of Parametric Variations of Structures Based on Least Squares Estimation and Adaptive Tracking Technique*, ASCE Journal of Engineering Mechanics. (2005) **131**(3):290-298.

[5] Ching, J., Beck, J. L. and Porter, K. A. *Bayesian state and parameter estimation of uncertain dynamical systems*, Probabilistic Engineering Mechanics. (2006) **21**(1):81-96.

[6] Sato, T., Qi, K. *Adaptive H_∞ filter: its application to structural identification*, ASCE Journal of Engineering Mechanics. (1998) **141**(11):1233-1240.

[7] Corigliano, A. and Mariani, S. *Parameter identification in explicit structural dynamics: performance of the extended Kalman filter*, Computer Methods in Applied Mechanics and Engineering. (2004) **193**(36-38):3807-3835.

[8] Liu, X., Escamilla-Ambrosio, P.J. and Lieven, N.A.J. *Extended Kalman filtering for the detection of damage in linear mechanical structures*, Journal of Sound and Vibration. (2009) **325**(4-5):1023-1046.

[9] Ebrahimian, H., Astroza, R. and Conte, J. P. *Extended Kalman filter for material parameter estimation in nonlinear structural finite element models using direct differentiation method*, Earthquake Engineering & Structural Dynamics. (2015) **44**(10):1495-1522.

[10] Zhang, C., Huang, J.-Z., Song, G.-Q., Dai L. and Li, H.-K. *Detection of structural damage via free vibration responses by extended Kalman filter with Tikhonov regularization scheme*, Structural Monitoring and Maintenance. (2016) **3**(2):115-127.

[11] Candès, E.J., and Wakin, E.J. *An introduction to compressive sampling*, IEEE Signal Processing Magazine. (2008) **25**(2):21-30.

[12] Donoho, D.L. and Huo, X. *Uncertainty Principles and Ideal Atomic Decomposition*, IEEE Trans. Inf. Theor.. (2006) **47**(7):2845-2862.

[13] Tikhonov, A.N. and Arsenin, V.I.A. *Solutions of ill-posed problems*, Scripta series in mathematics. (1977).

[14] Fritzen, C.-P. and Ginsberg, D. *Sparse Solution Techniques in Load and Damage Monitoring Systems*, Advances in Science and Technology, 7th Forum on New Materials - Part E. (2017) **101**:35-44.

[15] Loffeld, O., Seel, A., Conde, M. H. and Wang, L. *A Nullspace Based L1 Minimizing Kalman Filter Approach to Sparse CS Reconstruction*, Advances in Science and Technology, 11th European Conference on Synthetic Aperture Radar (EUSAR 2016). (2016).

VIII ECCOMAS Thematic Conference on Smart Structures and Materials
SMART 2017
A. Güemes, A. Benjeddou, J. Rodellar and J. Leng (Eds)

STRUCTURAL DAMAGE LOCALIZATION THROUGH AN INNOVATIVE HYBRID ENSEMBLE APPROACH

GUSTAVO MORENO*, RODOLFO VILLAMIZAR *, JHONATAN CAMACHO†, MAGDA L. RUIZ† AND LUIS E. MUJICA†

*Universidad Industrial de Santander
Escuela de Ingenierías Eléctrica, Eléctrca, Electrónica y de Telecomunicaciones
CEMOS Research Group
Cra 27 Calle 9 C. Universitaria, Bucaramanga, Colombia
e-mail: gustavo.moreno2@correo.uis.edu.co, rovillam@uis.edu.co, web page: http://www.uis.edu.co/

† Universitat Politécnica de Catalunya (UPC) BARCELONATECH
Department of Mathematics, Escola d'Enginyeria de Barcelona Est. (EEBE)
Campus Diagonal Besòs, Edifici A, C.
Eduard Maristany, 10-14, 08019, Barcelona, Spain
e-mail: jhonatan.camacho@estudiant.upc.edu, magda.ruiz@upc.edu, luis.eduardo.mujica@upc.edu - Web page: http://www.upc.edu

Key words: Damage localization, Ensemble learning, Principal Component Analysis, Supervised methods

Abstract. Damage localization in structures can be achieved by using an appropriate data interpretation algorithm based on the expected structural response. According to the several algorithms reported in literature, a different degree of accuracy is obtained according to complexity requirements. This paper presents a hybrid algorithm approach as alternative to combine some of the reported methods by employing an ensemble architecture. Thus, this damage assessment algorithm integrates advantage of individual techniques in order to increase the performance of the whole expert system. The proposed architecture employs a network of piezoelectric devices to produce guided waves along the structure. The traveling of guided waves is affected by damage producing scattering, reflection and mode conversion, which can be characterized with statistical processing and pattern recognition methods. In this paper, supervised learning by means on ensemble learning, cross-correlation features, and PCA statistical indices are combined for locating damages. An experimental validation is conducted on an aircraft turbine blade structure instrumented with an array of piezoelectric devices (PZT), where it is demonstrated the potential of the methodology to significantly enhance localization tasks

1 INTRODUCTION

Laminate metallic structures can be found at different application areas as aeronautical, naval and civil industries. For example wings in aircraft, ship hulls, domes, turbine blades, which are exposed to different kinds of damages as corrosion, cracking, and impacts. Thus in recent years different Structural Health Monitoring(SHM) tecniques using guided waves and activated and sensed by means of piezoelectric devices has been proposed to assess the current structural state. Under this principle different methodologies have obtained a high performance for detecting damages [1, 2, 3], but also different works have demonstrated progress on damages localization, for example in [4], a PZT sensors network was used for estimating the damage location, [5] used the signal envelope for estimating wave group velocity through time of flight (TOF) and with that location a different damages as crack, hole, clamp, while in [6] the Total Focusing Method is used to locate damages by using the TOF of a guided wave generated by means of PZTs on a aluminium square plate. On other hand, ensemble learning is a computational technique whose main property is its capacity to combine adequately different models, classifiers or types of features ([7, 8]). Different variations of ensemble learning have reported, where different taxonomies are used. For example [9, 10, 11] use multiple models, while [12] combines classifiers, [13] proposes committee of experts and [14] classifier fusion. This is because philosophy of ensemble learning is not only the combination of classifiers but also of different models, types of features, methods or any other combination that allow to improve the estimation [15, 16, 17]. Thus, ensemble learning could be an adequate technique for locating damages on laminate structures by combining different baseline models obtained when an array of several piezoelectric devices are attached to laminate structures, which is the purpose of this paper.

2 CONCEPTUAL FRAMEWORK

The structural damage assessment methodology proposed in this paper is based on three main methods: Piezo-diagnostics, Principal Component Analysis (PCA) and Ensemble Learning (EL). This section contains the theoretical concepts related to PCA feature extraction involved in the piezo-diagnostics technique which is used as approach for characterization of guide wave travelling along the structure. Also, the procedure to obtain reliable regression models for locating damages by means of Ensemble Learning and PCA features is described.

2.1 Piezodiagnostics

Piezodiagnostics technique can be considered as a structural health monitoring approach, where damage assessment is achieved by analyzing structural response from guided waves obtained by means of PZT transducers [**?**]. Several works reported in literature are based on guided wave analysis by using PZT devices, which have been demonstrated to be useful for damage detection and location with different precision degrees and sensitivity. In this work, a piezoelectric active system is implemented to obtain measurements, where Principal Component Analysis is used as statistical method to characterize the their signatures.

2.2 Principal Component Analysis (PCA)

Previous works have demonstrated the effectiveness of using features computed by applying Principal Component Analysis to piezoelectric measurements in order to characterize the structure signature [3, **?**, 18]. Thus, statistical damage indices are computed from PCA features, which allows the detection of damages. The application of PCA comprises baseline model building and damage indices estimation. The baseline model is built by applying PCA to a baseline matrix X formed by m rows of repeated experiments of the undamaged state and n columns of signals time samples. Thus, undamaged measurements are represented in the reduced space of principal components according to equation 1.

$$X = TP' + E = model + noise \tag{1}$$

The model in 1 belongs to a new reduced space of coordinates with minimal redundancy, based on the variance / covariance of PZT measurements from pristine condition. T is the projection to the reduced space, P is a linear transformation matrix that relates the data matrix X in the new coordinates and denotes the principal components (eigenvectors). The noise $E-$matrix is the part of X that is not explained by the model and describes the residual variance neglected by the statistical model. The singular values λ obtained from PCA decomposition are the respective variances of the reduced-space. Damage detection is achieved by means of statistical indexes with high sensitivity to model deviations. In this case, two widely used indexes (T^2 and $Q-$statistic) are computed. T^2 statistic is a variation measurement of each experiment within the statistical PCA model (undamaged model) and $Q-$index is the squared 2-norm that measures deviations of the experiment respect to the lower-dimensional PCA representation. Reader is refered to [3] to see details about PCA framework and its calculation. These statistical indices are used both to detect the damage and as feature inputs for the supervised location algorithms based on EL.

2.3 Ensemble Learning

Ensemble Learning (EL) is a computational technique that potentiates the advantages and minimizes the limitations of different learning algorithms by combining several procedures [7],[8]. In EL a robust model is obtained by exploiting features diversity and multiple model generalization in order to obtain a better response than individual algorithms. In this work, an ensemble learning scheme is evaluated with the purpose of obtaining a precise damage location system by combining different algorithms. Figure 1 shows the concept of EL, where the feature inputs are processed and manipulated by multiple learning algorithms organized in a cascading scheme.

According to Figure 1, the selected topology and taxonomy of the EL corresponds to a boosting method. It constructs models in an iterative manner, where new models learn to fix the prediction errors of a prior model in the chain. Thus, boosting ensemble algorithms creates a sequence of models that attempt to correct the mistakes of the models before them in the sequence. The LSBoost boosting algorithm which stands for least squares boosting, is used to fit regression ensembles by minimizing mean-squared error [19]. Also, in Figure 1 it is remarked that EL requires to define a combination strategy (fuser) in order to obtain the final diagnostic decision. In this sense, the final output prediction is produced on the concept of weighted average according to the performance of ensemble models across the predictions of all of the sub-models.

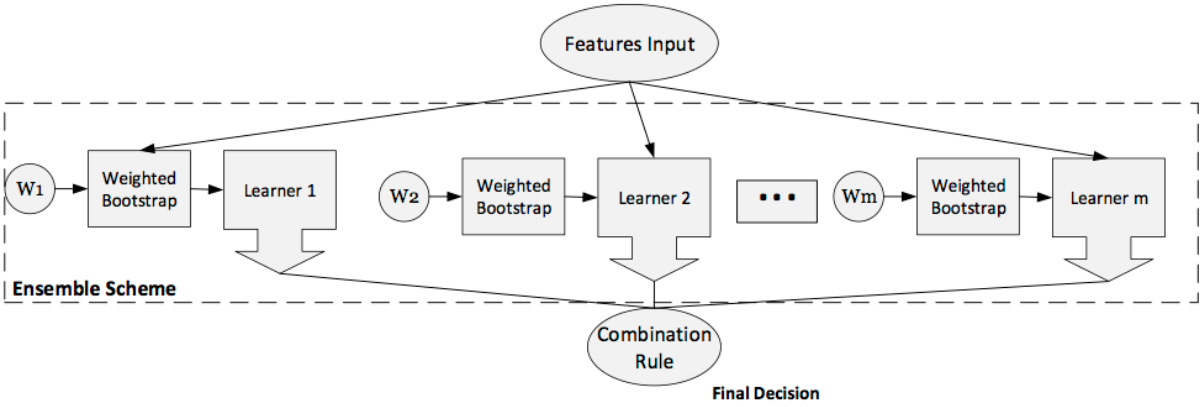

Figure 1: Ensemble Learning Approach

3 Damage localization based on Ensemble Learning

The proposed methodology consists of detecting and localizing damages in laminar structures by using statistical indices obtained from Principal Component Analysis (T^2 and Q) and regression models obtained by means of ensemble learning. The guided wave principle is applied by using an array of PZTs devices attached around the monitored area.

3.1 Damage detection

Damages detection stage is based on the computation of T^2 vs Q statistical indices of current guided waves generated along the structure by means of a PZT active system. To achieve the goal, the following steps are carried out (see figure 2).

Guided wave generation and sensing	Data preprocesing	PCA modellin/analysis	Graphical interpretation
PZA array	Acting/sensing signal cross correlation	PCA baseline model	Scatter plot T^2 vs Q
Signal acquisition system	Data normalization and organization	Computation of statistical indices	Decision based on

Figure 2: Damage detection stage

3.1.1 Guided wave generation and sensing

An array of PZTs is attached to the laminar structure such that the monitoring interest area want to be covered. The instrumentation is configured to excite every PZT by means of a high frequency k-pulse burst tone and to sense in the others ones (each PZT activation is denominated actuation phase). Thus, wave guided are recorded at each PZT when everyone of the other PZTs act in a separate way.

3.1.2 Data preprocessing

This step consists of conditioning data by using: i) De-trending analysis, ii) Cross correlation analysis between every sensed signal and actuation signal, and iii) Group Scaling (GS).

i Initially, linear trends are removed from piezo-electrical measurements due to artefacts noise and low frequency disturbance.

ii Then, cross correlation analysis is applied to exclude common external noise signals and to obtain a better separation boundaries for damage conditions. Thus, actuation and sensing signals are previously correlated to apply principal component analysis (PCA). The cross-correlation function between two signals $x(t)$ and $y(t)$ is defined as follows:

$$R_{xy}(t, t+\tau) = \lim_{N\to\infty} \frac{1}{N} \sum_{k=1}^{N} x_k(t) y_k(t+\tau), \tag{2}$$

where N is the number of signal samples and τ is the lag time interval used to compute the cross-correlation function. Finally a data matrix X for every actuation phase is built and organized from the cross-correlated functions obtained for each actuator/sensor pair and by considering initially only measurements of several repetitions from pristine condition (baseline) and also repetitions at the same condition (damage) as shown in Figure 3.

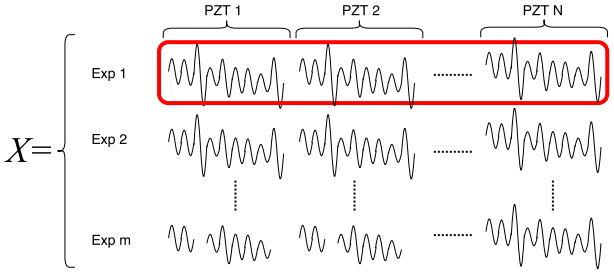

Figure 3: Graphical representation of the undamaged baseline matrix X

iii Each baseline matrix is normalized by applying Group Scaling procedure for avoiding scaling and bias issues. Normalization reduces the influence of different source of variability due to changes in environmental and operational conditions. In Group Scaling each datapoint of the undamaged baseline matrix is scaled by considering changes between sensors [18]. The standarization is computed by using the mean of each time sample for every experiment and the standard deviation of each sensor sample vector.

3.1.3 PCA modelling and analysis

PCA is used in this approach for two situations: Obtaining a statistical baseline model (modeling) and computing T^2 and Q statistical indices for current signals by means of baseline model (validation). According to [3] PCA follows the next general procedure:

i Organize the data set of the pristine structure (cross correlated signals in this case) as an $m \times n$ matrix, where n is the number of variables (correlated signal samples $\times$ number of sensors) and m is the number of trials.

ii Normalize the data by means of standard deviations of the sensor and mean of the trial.

iii Calculate the projection matrix (P) using any of the ways described in the literature and keep it as a statistical model.

iv When the structure is to be assessed, the same experiments should be conducted, the resulting data is correlated, organized and normalized and finally projected in the new space as $T = XP$, where X is the current data and P the projection matrix calculated using the healthy structure.

v Calculation of the T^2 and Q indices as follows:

$$Q_i = x_i \left(I - PP^T\right) x_i^T, \tag{3}$$

$$T_i^2 = x_i \left(P\Lambda^{-1}P^T\right) x_i^T \tag{4}$$

where x_i denotes the vector of $i^{th}-$ experimental trial and Λ is a diagonal matrix that contain the eigenvalues or variance of the selected components.

3.1.4 Graphical Interpretation

In this step the scatter plots of T^2 vs Q are obtained for current measurement of each actuation phase, by using the respective baseline model. By a simple visual comparison of the current points regarding to undamaged cases, damage detection can be inferred.

3.2 Damage Localization

Once a damage is detected, the next stage is to locate it. For this purpose, regression models are obtained by using T^2 and Q statistical indices as input variables and the x and y location of damage as output variables. Ensemble learning is applied to obtain the mentioned regression models, where a set of experiments of undamaged and damage cases must be used to obtain the regression model and a different one to validate them (see Figure 4). Two types of regression models are obtained: i) One for each actuation phase and each damage and, ii) only one model using all the actuation phases for each damage (coordinate x and y).

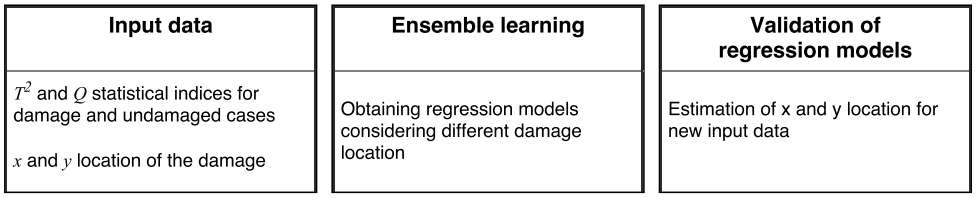

Figure 4: Damage localization stage

4 EXPERIMENT AND VALIDATION RESULTS

4.1 Experimental setup

An aircraft turbine blade hosted at Universidad Politécnica de Madrid was used to validate the proposed methodology. This was manufactured by a homogenous material with a similar density than titanium (3.57 g/mL), dimension 262mm x 86mm and with one stringer in each of the both faces. An array of 11 PZTs were attached on one face of the blade surface, but for this case 7 of them are used to build each actuation phase. The transducers dimensions are 27 mm diameter and 0.4mm thickness, which are excited by a 7-pulse, 80 kHZ burst signal generated by means of a Arbitrary Wave Generation (AWG) function of the of a PicoScope^{TM} 2208A and amplified by means of the power amplifier Krohn-Hite Model7602M.

Three damages were recreated on the structure by attaching coins at three different locations as follows (see figure 5):
(D1) a 2€ coin attached to blade at the blue region
(D2) a 12€ coin attached to blade at the red region
(D3) a 0.52€ coin attached to blade at the magenta region
An individual experiment consists of generating a guide wave at one PZT and to sense this guided wave at the others six (6) PZTs during 0.50025ms at a sample time of 0.056μs (a total of 53598 samples by experiment). Then, for each actuation phase a total of 150 individual experiments by each damage and 150 experiments for the undamage case (UND) were conducted.

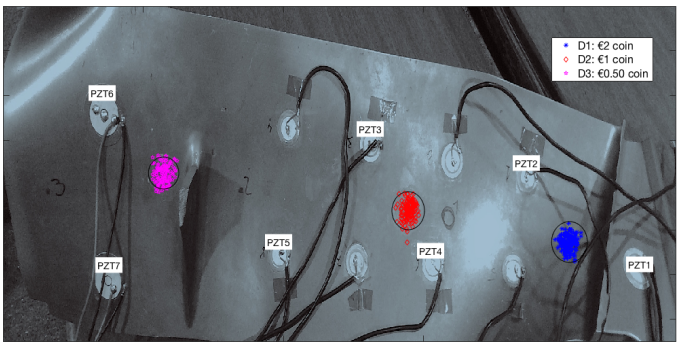

Figure 5: Experimental structure: Instrumented aircraft turbine blade

4.2 Damage detection

The seven (one by each activation phase) statistical (PCA) baseline models are obtained by using 120 of the 150 experiments conducted for the undamaged (UND) case. Figure 6 presents the retained variance for the activation phase 5 (acting at PZT 5 and sensing at the other ones) when 35 PC's are selected. Figure 7 presents the scatter plot of T^2 vs Q when PZT signals are not cross correlated, while figure 8 corresponds to the same scatter plot when PZT signals are cross correlated. It is observed that a better clustering and differentiation between cases can be obtained by applying cross correlation. Similar performance was obtained for the other actuation phases, thus by using these plots, damages can be clearly detected in a graphical representation.

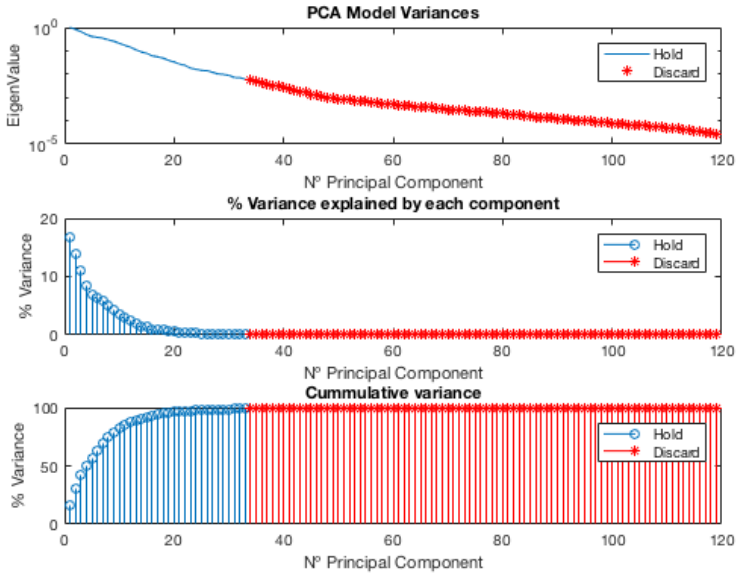

Figure 6: PCA baseline model for actuation phase 5 explained by variances per component a) Variance b) % variance c) cumulated % of variance

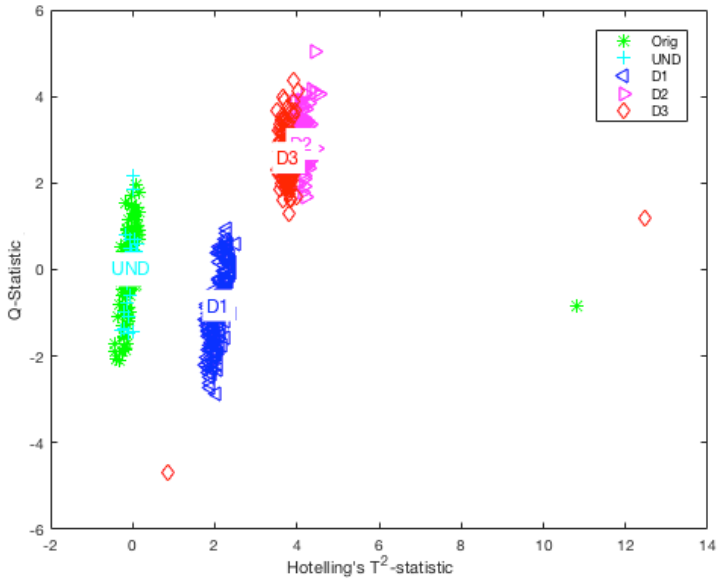

Figure 7: T^2 vs Q plot for actuation phase 5 for the data with no correlation

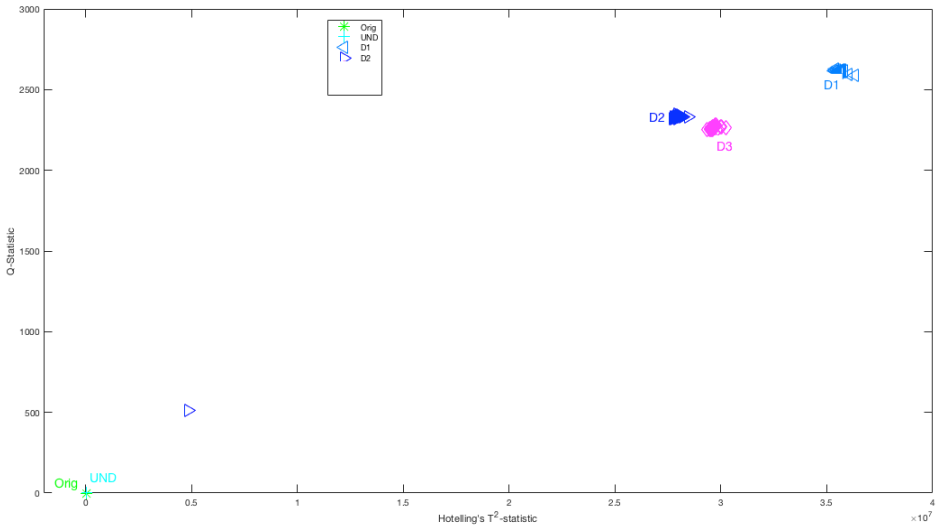

Figure 8: T^2 vs Q plot for actuation phase 5 for the cross correlated signals

4.3 Damage location

To predict or estimate the location of the damages, 80 observations or experimental trials (20 per damage case and 20 for each undamaged case) are used to train the individual learners. As weak learners, decision trees are selected. The ensemble regression model is obtained by using the method LSBoost, which is the gradient descent method for boosting regression or regression tree models. Finally, 20 iterations are selected for boosting, however it can be seen from Figure 9, that the resubstitution error is near to zero from eighth iteration.

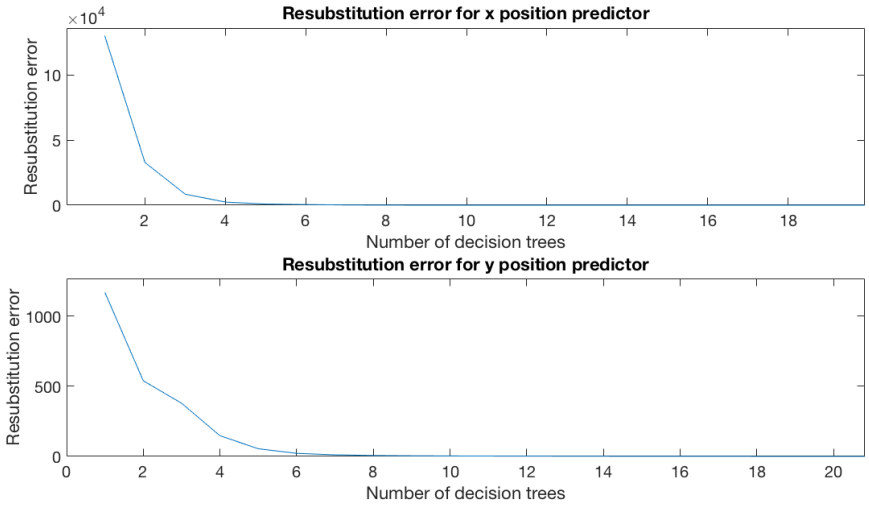

Figure 9: Error by each iteration of the ensemble learning

Once the model is trained, the approach is validated by using the remaining conducted experiments (120 per each damage). The input of the regression model is the pair of indices by each experiment (T^2 and Q statistic) and the output is the pair of coordinates for the position of the damage (x and y location). Figures 10, 11 and 12 present the estimated damage positions, and estimation errors by using the regression model of the actuation phase 5. It is observed that an adequate estimation of damage position is achieved by using only one actuation phase. Similar results are found for the other actuation phases.

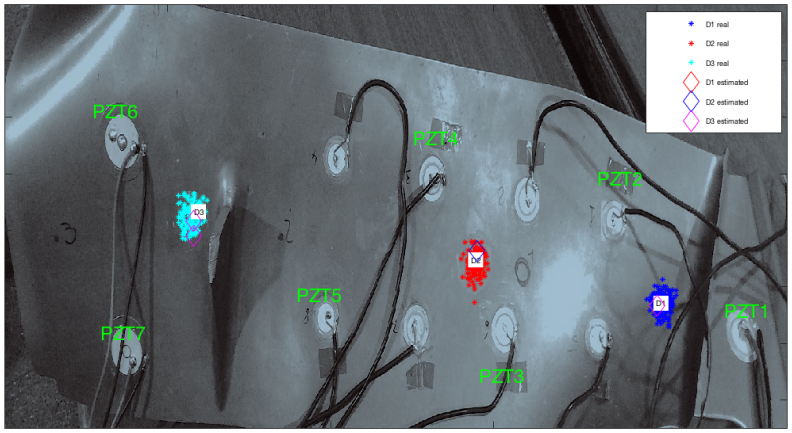

Figure 10: Real vs estimated position for an ensemble regression model using the actuation phase 5

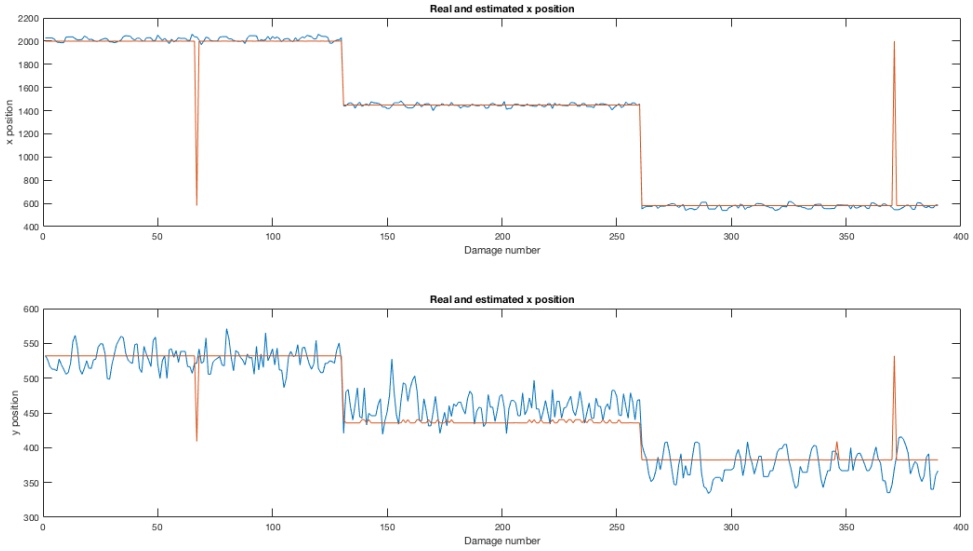

Figure 11: Real vs estimated x and y coordinates by each damage for an ensemble regression model using the actuation phase 5

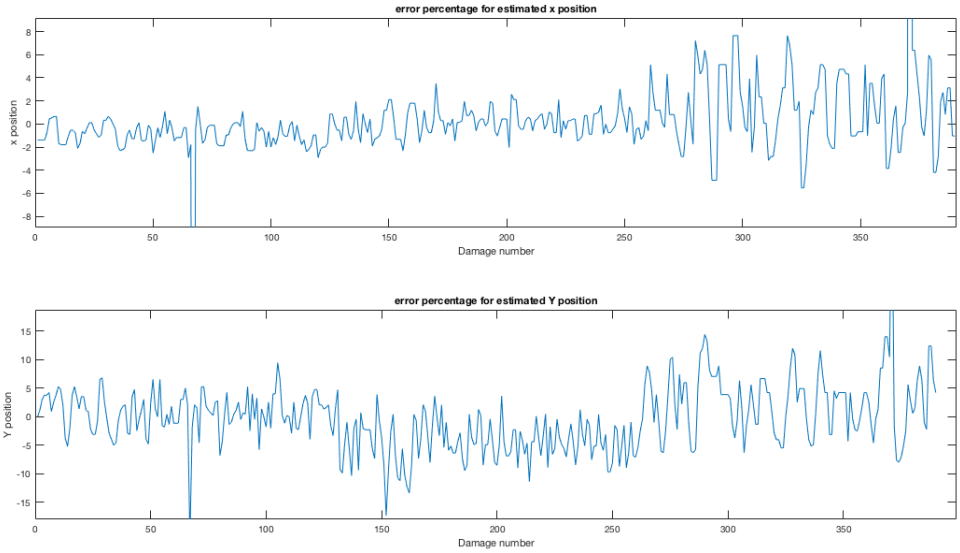

Figure 12: x and y estimation error an ensemble regression model using the actuation phase 5

5 CONCLUSIONS

A damage detection an localization approach for laminar structures was presented in this paper by combining PCA analysis, cross correlation analysis and ensemble learning. It was demonstrated that cross correlation analysis between actuated and sensed guide wave improve the clustering and differentiation of statistical indices between damages.On other hand, by using only T^2 and Q statistical indices detection of type mass adding can be clearly detected by a simple graphical analysis.

Damages recreated in an aircraft turbine blade were located with a good approximation by using regression models obtained through ensemble learning with only 8 learning cycles and a weak learner (Tree). It was taken advantage of PCA statistical indices to create compact and separated cluster between damages and ensemble learning for obtaining a good regression model. However, a disadvantage of using supervised learning is that previous knowledge of type of damages to be detected is necessary to train the expert system.

REFERENCES

[1] Goswami, S. and Bhattacharya, P. *Pattern Recognition for damage detection in aerospace vehicle structures*, Proc. of 3rd Int. Conf. Emerg. Appl. Inf. Technol.(2012), **178—182**.

[2] Kudela, P., Ostachowicz, W. and Zak, A. *Damage detection in composite plates with embedded PZT transducers*, Mech. Syst. Signal Process. vol. 22, Iss. 6, (2008), **1327—1335**.

[3] Mujica, L. E., Rodellar, J., Fernandez, A. and Guemes, A. *Q-statistic and T2-statistic PCA-based measures for damage assessment in structures*, Struct. Heal. Monit. (2010), Vol 10, Iss. 5, **539–553**.

[4] Mujica L.E, Tibaduiza D. and Rodellar J. *Data-driven multiactuator piezoelectric system for structural damage localization*, Proc. Fifth World Conf. on Struc. Cont. and Mon. (5WC-SCM), Tokyo, Japan, (2010) **1–13**.

[5] Salmanpour, M., Sharif Z. and Aliabadi, M. *Guided wave temperature correction methods in structural health monitoring*, J. Intel. Mater. Syst. Struct., (2016), **1-–15**.

[6] Muller, A., Robertson-Welsh, B., Gaydecki, P., Gresil, M. and Soutis, C., *Structural Health Monitoring Using Lamb Wave Reflections and Total Focusing Method for Image Reconstruction*, App. Comp. Mat., Vol. 24, N.2,(2017), **553–573**.

[7] Drucker, H., Cortes, C., Jackel, L. D., LeCun, Y. and Vapnik, V. *Boosting and other ensemble methods*, Neural Comput., vol. 6, Iss.6, (1994), **1289–1301**.

[8] Yan, W. and Goebel, K.F. *Designing classifier ensembles with constrained performance requirements*, Defense and Security, (2004), **59–68**.

[9] Jacobs, R.A. *Methods for combining experts' probability assessments*, Neural Comput. vol. 7, Iss.5, (1995), **867—888**.

[10] Maclin, R., Shavlik, J. W. and others, *Combining the predictions of multiple classifiers: Using competitive learning to initialize neural networks*, IJCAI, (1995), **524-–531**.

[11] Smyth, P. *Bounds on the mean classification error rate of multiple experts*, Pattern Recognit. Lett., vol. 17, iss. 12, (1996), **1253—1257**.

[12] Kittler, J., Hatef, M. Duin, R.P.W. and Matas, J. *On combining classifiers*, IEEE Trans. Pattern Anal. Mach. Intel., vol. 20, Iss.3, (1998), **226—239**.

[13] Tsymbal, A., Pechenizkiy, M., Puuronen, S. and Patterson, D.W. *Dynamic integration of classifiers in the space of principal components*, Proc. of East Eur. Conf. on Adv. in Datab. and Inf. Sys., (2003), **278-–292**.

[14] Cho, S.B. and Kim, J.H. *Combining multiple neural networks by fuzzy integral for robust classification*, IEEE Trans. Syst. Man. Cybern., vol. 25, Iss. 2, (1995), **380—384**.

[15] Opitz, D. and Maclin, R. *Popular ensemble methods: An empirical study*, J. Artif. Intel. Res., vol. 11, (1999), **169-–198**.

[16] Rokach, L. *Ensemble-based classifiers*, Artif. Intell. Rev., vol. 33, iss. 1–2, (2010), **1—39**.

[17] Polikar, R. *Ensemble based systems in decision making*, IEEE Circ. Syst. Mag., vol. 6, Iss. 3, (2006) **21-–45**.

[18] Mujica, L.E., Vehi, J., Ruiz, M., Verleysen, M., Staszewski, W., and Worden, K. *Multivariate statistics process control for dimensionality reduction in structural assessment.* Mechanical Systems and Signal Processing, Vol. 22, N.1, (2008) **155-171**.

[19] Nigel, D., Helmbold, D. *Boosting Methods for Regression.* Machine Learning, Vol. 47, N.2, (2002) **153-200**.

VIII ECCOMAS Thematic Conference on Smart Structures and Materials
SMART 2017
A. Güemes, A. Benjeddou , J. Rodellar and Jinsong Leng (Eds)

STRUCTURAL HEALTH MONITORING (SHM) OF STRUCTURES BY ELECTROMECHANICAL IMPEDANCE (EMI) TECHNIQUE USING NON-LINEAR MATERIAL MODEL OF PIEZOELECTRIC MEDIUM

NILANJAN MALLIK*, SANJEEV SINGH†

* Assistant Professor, Department of Mechanical Engineering
Indian Institute of Technology (BHU)
Varanasi 221005, Uttar Pradesh, India
e-mail: nmallik.mec@iitbhu.ac.in, web page: http://www.iitbhu.ac.in

† Research Scholar, Mechanical Engineering
Indian Institute of Technology (BHU)
Varanasi 221005, Uttar Pradesh, India

Key words: Structural health monitoring, Smart Structures, Electromechanical impedance, Piezoelectric materials, Material non-linearity, Conductance signature.

Abstract. Piezoelectric materials because of direct and converse effects are used both as sensors and actuators. The electromechanical impedance characteristics of the piezoelectric materials are utilized for diagnosing health of the structures. The electromechanical impedance (EMI) technique is employed in the frequency range of 30 to 400 kHz. In the EMI technique, a piezoelectric patch is bonded to the surface of the monitored structure using a high strength epoxy adhesive and electrically excited via an impedance analyzer. The response of the structure is captured through another piezoelectric patch bonded on the structure and acting as sensor. In such situation, the piezoelectric patch can be modelled as undergoing axial vibration and interacting with the host structure. The one-dimensional vibration of piezoelectric patch is governed by one-dimensional wave equation derived based on dynamic equilibrium of piezoelectric patch. A first principle based modelling of non-linear constitutive relation of piezoelectric medium is presented. Non-linear material property is implemented in the wave equation to obtain non-linear wave equation. Material non-linearity gives rise to an internal source term in the non-linear wave equation. This non-homogeneous wave equation is solved by Green's function approach. This modelling is further implemented for evaluation of its response in structural health monitoring application. Equilibrium condition of the piezoelectric patch is established by considering inertia and stiffness effects. Expression for current in piezoelectric patch is obtained from electric displacement equation. Henceforth electromechanical impedance expression is derived. Electromechanical admittance is the inverse of the electromechanical impedance. The real part of the admittance is the conductance and the imaginary part of admittance is the susceptance. The variation of conductance and susceptance with respect to frequency is plotted.

1 INTRODUCTION

Strong electromechanical effect and instantaneous response to applied electric field are the reasons for increased use of piezoelectric materials for advanced sensor and actuator applications in intelligent/smart systems. Piezoelectric materials are extensively being used as sensor for structural health monitoring (SHM) applications. Piezoelectric transducers are bonded on the structures to assess its condition i. e. to evaluate, identify, classify and estimate structural conditions by means of electric signals provided by electromechanical coupling. Damage detection techniques are based on either passive or active methods. Former method uses set of sensors which detects dynamic states of the structure and in the mean-time should be non-invasive. On the other hand, the active methods may change the structural state with the aim to obtain information and modify structural dynamics. Among several active methods electromechanical impedance (EMI) technique presents a great capacity for capturing structural changes. The effective electromechanical behaviour of piezoelectric materials depend on the applied electric field strength and stress intensity. In general, the linear behaviour of piezoelectric materials is confined to relatively low levels of applied electric field and stress and are described well by the standard linear piezoelectric constitutive equations. Non-linear behaviours are observed above certain "threshold" values of electric field and stress [1]. In the unpoled state, the orientation of the spontaneous polarisation is distributed randomly, and piezoelectric material has no macroscopic polarization. Under the application of strong electric field/mechanical stresses, the orientation of the spontaneous polarization can be switched. This may cause a nonlinear polarization-electric field ($P-E$) relationship, a non-linear strain-electric field ($\in -E$) response and a non-linear strain–stress ($\in -\sigma$) relationship. Eventually, strong non-linear or hysteresis loops become evident above the coercive field/stress when reversing the applied electric field or switching polarization. This makes prediction of the response of a piezoelectric actuator to an applied electric field or input voltage extremely difficult. In order to assess the reliability of piezoelectric material, it is important to understand the non-linear behaviour of piezoelectric material. The non-linear loops of piezoelectric materials have been investigated by employing analytical approaches and finite element analysis (FEA) methods. Tan and Tong [2] developed a one-dimensional analytical model for predicting the non-linear behaviour of piezoelectric materials and piezoelectric fiber reinforced composite (PFRC) materials. They also conducted a numerical study to investigate the non-linear loops for piezoelectric materials and PFRC materials. Tan and Tong also developed two micromechanics models to investigate non-linear piezoelectric behaviour and presented effective properties for nonlinear elastic, piezoelectric and dielectric constants. Non-linear elastic wave propagation was studied theoretically by McCall [4]. He used linear and non-linear elastic constants to develop non-linear wave equation and applied Green's function technique to solve the non-linear wave equation. McCall and Guyer [5] extended the study on non-linear elastic wave propagation to include hysteresis effect. Tinoco et. al. [6] presents a electromechanical impedance technique based on decoupled measurements to detect damage in plates. Damage detection study based on EMI technique considering non-linear behaviour of piezoelectric transducers is scarce in literature.

Thus present study deals with a theoretical analysis of damage detection of structures using electromechanical impedance technique considering non-linear material model of piezoelectric transducers. A rectangular shaped piezoelectric transducer and sensor are

bonded on the top surface of the beam structure. The structure is excited with a predetermined frequency signal given to the transducer. And signal from sensor is recorded for damage assessment. First a non-linear wave equation is constructed considering material non-linearity effect. This equation is solved to obtain displacement of the sensor. Finally, constitutive equation is used to calculate the current output from the sensor. Expressions for both real and imaginary components of the current are obtained and plotted.

2 NON-LINEAR CONSTITUTIVE RELATIONS

The non-linear constitutive relations of purely piezoelectric materials with homogeneous and orthotropic properties are represented by following equations

$$\begin{Bmatrix}\sigma_1\\ \sigma_2\\ \sigma_3\\ \sigma_4\\ \sigma_5\\ \sigma_6\end{Bmatrix} = \begin{bmatrix} C_{11}^E & C_{12}^E & C_{13}^E & 0 & 0 & 0\\ C_{12}^E & C_{22}^E & C_{23}^E & 0 & 0 & 0\\ C_{13}^E & C_{23}^E & C_{33}^E & 0 & 0 & 0\\ 0 & 0 & 0 & C_{44}^E & 0 & 0\\ 0 & 0 & 0 & 0 & C_{55}^E & 0\\ 0 & 0 & 0 & 0 & 0 & C_{66}^E \end{bmatrix} \begin{Bmatrix}\epsilon_1\\ \epsilon_2\\ \epsilon_3\\ \epsilon_4\\ \epsilon_5\\ \epsilon_6\end{Bmatrix} - \begin{bmatrix} 0 & 0 & e_{31}\\ 0 & 0 & e_{32}\\ 0 & 0 & e_{33}\\ 0 & e_{24} & 0\\ e_{15} & 0 & 0\\ 0 & 0 & 0 \end{bmatrix} \begin{Bmatrix}E_1\\ E_2\\ E_3\end{Bmatrix} \tag{1}$$

$$+\frac{1}{2}\begin{bmatrix} C_{111}^E & C_{122}^E & C_{133}^E & 0 & 0 & 0 & C_{123}^E & C_{113}^E & C_{112}^E\\ C_{122}^E & C_{222}^E & C_{233}^E & 0 & 0 & 0 & C_{113}^E & C_{213}^E & C_{212}^E\\ C_{133}^E & C_{233}^E & C_{333}^E & 0 & 0 & 0 & C_{112}^E & C_{212}^E & C_{312}^E\\ 0 & 0 & 0 & C_{444}^E & 0 & 0 & C_{423}^E & 0 & 0\\ 0 & 0 & 0 & 0 & C_{555}^E & 0 & 0 & C_{513}^E & 0\\ 0 & 0 & 0 & 0 & 0 & C_{666}^E & 0 & 0 & C_{612}^E \end{bmatrix} \begin{Bmatrix} \epsilon_1^2\\ \epsilon_2^2\\ \epsilon_3^2\\ \epsilon_4^2\\ \epsilon_5^2\\ \epsilon_6^2\\ \epsilon_2\epsilon_3\\ \epsilon_1\epsilon_3\\ \epsilon_1\epsilon_2 \end{Bmatrix}$$

$$-\frac{1}{2}\begin{bmatrix} e_{111} & e_{122} & e_{133} & 0 & 0 & 0\\ e_{122} & e_{222} & e_{233} & 0 & 0 & 0\\ e_{133} & e_{233} & e_{333} & 0 & 0 & 0\\ 0 & 0 & 0 & e_{423} & 0 & 0\\ 0 & 0 & 0 & 0 & e_{513} & 0\\ 0 & 0 & 0 & 0 & 0 & e_{612} \end{bmatrix} \begin{Bmatrix} E_1^2\\ E_2^2\\ E_3^2\\ E_2E_3\\ E_1E_3\\ E_1E_2 \end{Bmatrix}$$

$$-\begin{bmatrix} l_{111} l_{121} l_{131} & 0 & 0 & 0 l_{112} l_{122} l_{132} & 0 & 0 & 0 l_{113} l_{123} l_{133} & 0 & 0 & 0 \\ l_{211} l_{221} l_{231} & 0 & 0 & 0 l_{212} l_{222} l_{232} & 0 & 0 & 0 l_{213} l_{223} l_{233} & 0 & 0 & 0 \\ l_{311} l_{321} l_{331} & 0 & 0 & 0 l_{312} l_{322} l_{332} & 0 & 0 & 0 l_{313} l_{323} l_{333} & 0 & 0 & 0 \\ 0 & 0 & 0 & l_{441} 0 & 0 & 0 & 0 & 0 & 0 & 0 & 0 & 0 & l_{443} & 0 & 0 \\ 0 & 0 & 0 & 0 & 0 & 0 & 0 & 0 & l_{552} & 0 & 0 & 0 & 0 & l_{553} & 0 \\ 0 & 0 & 0 & 0 & 0 & 0 & 0 & 0 & 0 & 0 & 0 & 0 & 0 & 0 & l_{663} \end{bmatrix} \begin{Bmatrix} \epsilon_1 E_1 \\ \epsilon_2 E_1 \\ \epsilon_3 E_1 \\ \epsilon_4 E_1 \\ \epsilon_5 E_1 \\ \epsilon_6 E_1 \\ \epsilon_1 E_2 \\ \epsilon_2 E_2 \\ \epsilon_3 E_2 \\ \epsilon_4 E_2 \\ \epsilon_5 E_2 \\ \epsilon_6 E_2 \\ \epsilon_1 E_3 \\ \epsilon_2 E_3 \\ \epsilon_3 E_3 \\ \epsilon_4 E_3 \\ \epsilon_5 E_3 \\ \epsilon_6 E_3 \end{Bmatrix}$$

$$\begin{Bmatrix} D_1 \\ D_2 \\ D_3 \end{Bmatrix} = \begin{bmatrix} 0 & 0 & 0 & 0 & e_{15} 0 \\ 0 & 0 & 0 & e_{24} & 0 & 0 \\ e_{31} e_{32} e_{33} & 0 & 0 & 0 \end{bmatrix} \begin{Bmatrix} \epsilon_1 \\ \epsilon_2 \\ \epsilon_3 \\ \epsilon_4 \\ \epsilon_5 \\ \epsilon_6 \end{Bmatrix} + \begin{bmatrix} \varepsilon_{11}^{\epsilon} & 0 & 0 \\ 0 & \varepsilon_{22}^{\epsilon} & 0 \\ 0 & 0 & \varepsilon_{33}^{\epsilon} \end{bmatrix} \begin{Bmatrix} E_1 \\ E_2 \\ E_3 \end{Bmatrix} \tag{2}$$

$$+\frac{1}{2}\begin{bmatrix} e_{111} e_{122} e_{133} e_{144} & 0 & 0 & e_{123} e_{113} e_{112} \\ e_{211} e_{222} e_{233} & 0 & e_{255} & 0 & e_{223} e_{213} e_{212} \\ e_{311} e_{322} e_{333} e_{344} e_{355} e_{366} e_{323} e_{313} e_{312} \end{bmatrix} \begin{Bmatrix} \epsilon_1^2 \\ \epsilon_2^2 \\ \epsilon_3^2 \\ \epsilon_4^2 \\ \epsilon_5^2 \\ \epsilon_6^2 \\ \epsilon_2 \epsilon_3 \\ \epsilon_1 \epsilon_3 \\ \epsilon_1 \epsilon_2 \end{Bmatrix} + \frac{1}{2}\begin{bmatrix} \varepsilon_{111}^{\epsilon} & 0 & 0 & \varepsilon_{123}^{\epsilon} \varepsilon_{113}^{\epsilon} \varepsilon_{112}^{\epsilon} \\ 0 & \varepsilon_{222}^{\epsilon} & 0 & \varepsilon_{223}^{\epsilon} \varepsilon_{213}^{\epsilon} \varepsilon_{212}^{\epsilon} \\ 0 & 0 & \varepsilon_{333}^{\epsilon} \varepsilon_{323}^{\epsilon} \varepsilon_{313}^{\epsilon} \varepsilon_{312}^{\epsilon} \end{bmatrix} \begin{Bmatrix} E_1^2 \\ E_2^2 \\ E_3^2 \\ E_2 E_3 \\ E_1 E_3 \\ E_1 E_2 \end{Bmatrix}$$

$$+\begin{bmatrix} l_{111} & 0 & 0 & l_{121} & 0 & 0 & l_{131}l_{132} & 0 & 0 & 0 & l_{143} & 0 & 0 & l_{153} & 0 & l_{162} & 0 \\ 0 & l_{212} & 0 & 0 & l_{222} & 0 & l_{231}l_{232} & 0 & 0 & 0 & l_{243} & 0 & 0 & l_{253}l_{261} & 0 & 0 \\ 0 & 0 & l_{313} & 0 & 0 & l_{323} & 0 & 0 & l_{333}l_{341}l_{342} & 0 & l_{351}l_{352} & 0 & 0 & 0 & l_{363} \end{bmatrix} \begin{Bmatrix} \epsilon_1 E_1 \\ \epsilon_1 E_2 \\ \epsilon_1 E_3 \\ \epsilon_2 E_1 \\ \epsilon_2 E_2 \\ \epsilon_2 E_3 \\ \epsilon_3 E_1 \\ \epsilon_3 E_2 \\ \epsilon_3 E_3 \\ \epsilon_4 E_1 \\ \epsilon_4 E_2 \\ \epsilon_4 E_3 \\ \epsilon_5 E_1 \\ \epsilon_5 E_2 \\ \epsilon_5 E_3 \\ \epsilon_6 E_1 \\ \epsilon_6 E_2 \\ \epsilon_6 E_3 \end{Bmatrix}$$

For the present analysis an extensional mode piezoelectric patch is chosen and analysis is confined to one dimensional one. The nonlinear constitutive equation for one dimensional case can be obtained from Eqs. (1) and (2) as

$$\sigma_1 = C_{11}^E \epsilon_1 + \frac{1}{2} C_{111} \epsilon_1^2 - e_{31} E_3 - \frac{1}{2} e_{331} E_3^2 - l_{113} \epsilon_1 E_3 \tag{3}$$

$$D_3 = e_{31} \epsilon_1 + \frac{1}{2} e_{311} \epsilon_1^2 - \varepsilon_{33}^{\epsilon} E_3 - \frac{1}{2} \varepsilon_{333}^{\epsilon} E_3^2 - l_{113} \epsilon_1 E_3 \tag{4}$$

3 ANALYSIS OF EMI RESPONSE OF PIEZOELECTRIC PATCH

The equation of motion of elastic wave propagation inside elastic medium is given by

$$\rho \frac{\partial^2 u(x,t)}{\partial t^2} = \frac{\partial \sigma_1}{\partial x} \tag{5}$$

Where, ρ is the density of the medium before deformation, $u(x,t)$ is the displacement along longitudinal (x) direction and is dependent on both space and time, σ_1 is the component of the stress tensor along 1-material coordinate direction which is parallel to x-direction. The strain displacement relationship is given by

$$\epsilon_1 = \frac{\partial u(x,t)}{\partial x} + \frac{1}{2}\left(\frac{\partial u(x,t)}{\partial x}\right)^2 \tag{6}$$

When piezoelectric patch is used as sensor using Eq. (3) into Eq. (5) and using Eq. (6) and discarding the stresses due to electric field the wave equation can be rewritten as

$$\rho \frac{\partial^2 u(x,t)}{\partial t^2} = C_{11} \frac{\partial^2 u(x,t)}{\partial x^2} + \frac{1}{2} C_{111} \frac{\partial}{\partial x}\left[\left\{\frac{\partial u(x,t)}{\partial x}\right\}^2\right] \tag{7}$$

The wave equation given in Eq. (7) can be represented in frequency domain as given below

using Fourier transform

$$\left[\frac{\partial^2}{\partial x^2}+k^2\right]u(x,\omega)=-\frac{1}{2}C_{11r}\frac{\partial}{\partial x}\left[\int\frac{1}{2\pi}\frac{\partial u(x,\omega')}{\partial x}\frac{\partial u(x,\varphi)}{\partial x}d\omega'\right] \tag{8}$$

Where, $k^2=\frac{\omega^2\rho}{C_{11}}$, $\varphi=\omega-\omega'$ and $C_{11r}=\frac{C_{111}}{C_{11}}$. Equation (8) is a non-homogeneous Helmholtz equation having no external source. The right hand side of Eq. (8) represents internal source due to material non-linearity and represented as $f(x,\omega)$. The solution of this equation can be represented as a series given below

$$u(x,\omega)=u^{(0)}(x,\omega)+\eta u^{(1)}(x,\omega)+\eta^2u^{(2)}(x,\omega)+\cdots \tag{9}$$

Similarly, the internal source term can also be represented as same type of series

$$f(x,\omega)=f^{(0)}(x,\omega)+\eta f^{(1)}(x,\omega)+\eta^2f^{(2)}(x,\omega)+\cdots \tag{10}$$

In Eqs. (9) and (10), η is a parameter which represents power of internal source, numbers in parenthesis of the superscript denote order of the differentiation and $u_h(x,\omega)=u^{(0)}(x,\omega)$ is the solution of displacement for homogeneous Helmholtz equation when there is no internal source present i. e. when material non-linearity is not considered and is used in the first step of the iteration process of solution. The homogeneous Helmholtz equation is given as

$$\left[\frac{\partial^2}{\partial x^2}+k^2\right]u(x,\omega)=0 \tag{11}$$

The solution of Eq. (11) is given as

$$u_h(x,\omega)=Ae^{j(kx-\omega t)} \tag{12}$$

It should be noted that each successive order of displacement is obtainable with the knowledge of previous order of the displacement. From right hand side of the Eq. (8) successive order of internal source can be obtained. The first two orders of the internal source used in the present analysis are given as

$$f^{(0)}(x,\omega)=f_r^{(0)}(x,\omega)+jf_i^{(0)}(x,\omega) \tag{13}$$

$$f^{(1)}(x,\omega)=f_r^{(1)}(x,\omega)+jf_i^{(1)}(x,\omega) \tag{14}$$

Where,

$$f_r^{(0)}(x,\omega)=\frac{C_{11r}k^3A^2}{4\pi\omega}[\cos(2kx)-\pi\omega\delta(\omega)\sin(2kx)] \tag{15}$$

$$f_i^{(0)}(x,\omega)=\frac{C_{11r}k^3A^2}{4\pi\omega}[\sin(2kx)+\pi\omega\delta(\omega)\cos(2kx)] \tag{16}$$

$$f_r^{(1)}(x,\omega)=\frac{C_{11r}k^4A^3}{2\pi\omega}[\sin(2kx)+\pi\omega\delta(\omega)\cos(2kx)] \tag{17}$$

$$f_i^{(1)}(x,\omega)=\frac{C_{11r}k^4A^3}{2\pi\omega}[\pi\omega\delta(\omega)\sin(2kx)-\cos(2kx)] \tag{18}$$

After substituting Eqs. (9) and (10) into Eq. (8) and equating like powers of η from both sides following relation is obtained

$$\left[\frac{\partial^2}{\partial x^2} + k^2\right] u^{(n)}(x,\omega) = -f^{(n)}(x,\omega) \quad ; \; n = 1,2,\cdots \tag{19}$$

Equations (19) can be solved analytically using Green's function that satisfies

$$\left[\frac{\partial^2}{\partial x^2} + k^2\right] G(x,x',\omega) = -\delta(x-x') \tag{20}$$

The non-homogeneous Helmholtz equations along with homogeneous Dirichlet boundary condition is solved using Green's function [7]. The solution is given by

$$u^{(n)}(x,\omega) = \int G(x,x',\omega) f^{(n)}(x',\omega)\, dx \tag{21}$$

The solution of the first order of displacement used for the present analysis is given below

$$u^{(0)}(x,\omega) = u_r^{(0)}(x,\omega) + j u_i^{(0)}(x,\omega) \tag{22}$$

Where,

$$u_r^{(0)}(x,\omega) = \frac{C_{111} k^2 A^2}{8\pi\omega}\left\{-\frac{\cos kx}{k} - \pi\omega\delta(\omega)\frac{\sin 3kx}{3k}\right\} \tag{23}$$

$$u_i^{(0)}(x,\omega) = \frac{C_{111} k^2 A^2}{8\pi\omega}\left\{\frac{(\cos 3kx - \sin 3kx)}{6k} + \frac{(\cos kx + \sin kx)}{2k} - \pi\omega\delta(\omega)\frac{\cos kx}{k}\right\} \tag{24}$$

The successive orders of the displacements are calculated using MATLAB programming. The expressions are not given here. The total displacement is then calculated using Eq. (9) and letting $\eta \to 1$. It should be noted here that the total displacement is a complex quantity and can be represented as

$$u(x,\omega) = u_r(x,\omega) + j u_i(x,\omega) \tag{25}$$

Next applying the force balance equation along longitudinal axis at the boundary at $x = L$, where L is the half-length of the piezoelectric sensor and equating real and imaginary parts from both sides of the resulting equation one will get a polynomial equation of A of order depending on number of orders considered in displacement solution. This polynomial can be solved numerically to get unknown constant A. Now from Eq. (4) using strain displacement relation given by Eq. (6) and the solution of displacement given by Eq. (25) expression of admittance can be obtained as

$$Y = G + jB \tag{26}$$

Where G is the conductance and B is the susceptance. The expressions for G and B are not given here they are directly calculated using MATLAB programming.

4 NUMERICAL RESULTS

The piezoelectric sensor used for present analysis is made of Lithium Niobate, $LiNbO_3$. The linear and non-linear material properties of $LiNbO_3$ are taken from Tan and Tong [3] and are given in Tables 1 and 2, respectively.

Table 1: Linear material properties of $LiNbO_3$

C_{11}^E (GPa)	e_{31} C/m^2	$\varepsilon_{33}^{\epsilon}$ 10^{-9}F/m
203	0.2	0.257

Table 2: Non-linear material properties of $LiNbO_3$

C_{111}^E (GPa)	e_{133} C/m^2	$\varepsilon_{33}^{\epsilon}$ 10^{-19}F/V	l_{133} 10^{-9}F/m
-2120	-10	2.91	2.32

Figures 1 and 2 illustrates typical conductance and susceptance responses of the sensor. The plots clearly show resonance and anti-resonance frequencies. The current analysis considers a homogeneous medium. A more realistic analysis can be performed using a medium with presence of crack and expressing the behavior of such medium in terms of respective Green's function. This will allow to make a comparative study of responses between a uncracked and cracked structures, which is out of scope of the present study.

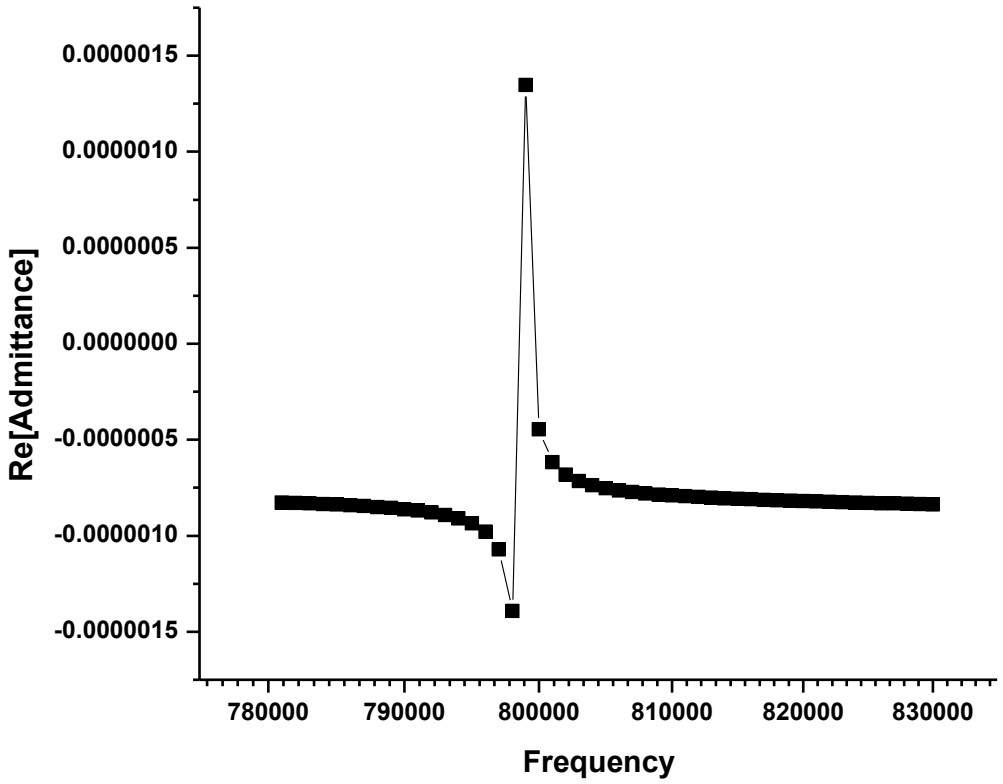

Figure 1: Conductance response of piezoelectric sensor

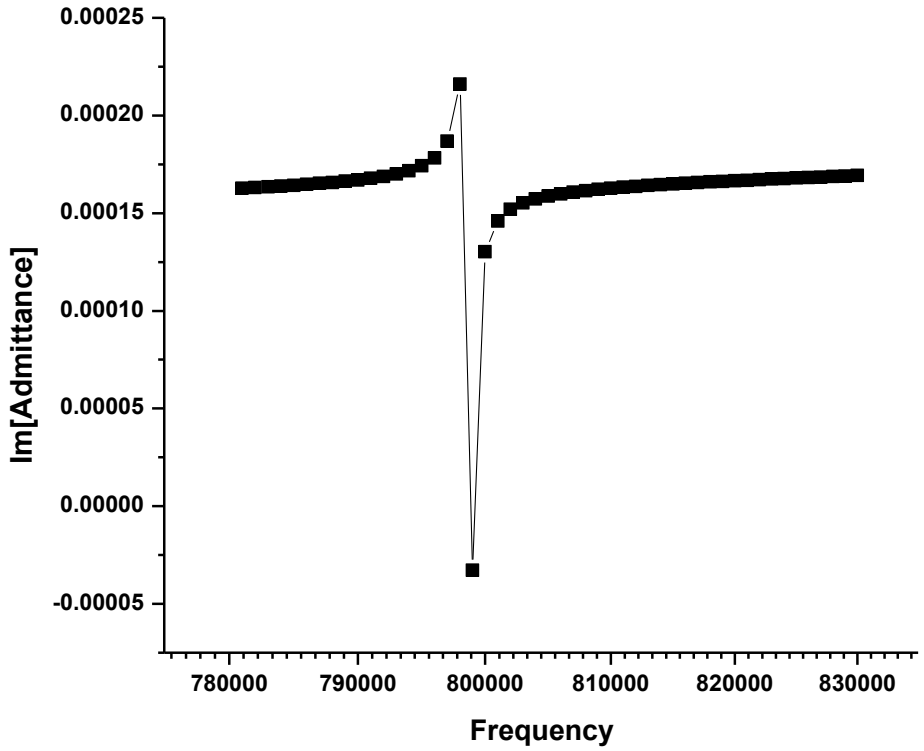

Figure 2: Conductance response of piezoelectric sensor

5 CONCLUSIONS

The present analysis deals with a theoretical analysis of damage detection of structures using electromechanical impedance technique considering non-linear material model of piezoelectric transducers. A rectangular shaped piezoelectric transducer and sensor are bonded on the top surface of the structure. The structure is excited with a predetermined frequency signal given to the transducer. And signal from sensor is recorded for damage assessment. First a non-linear wave equation is constructed considering material non-linearity effect. The material non-linearity adds to internal source term in the wave equation. This non-homogeneous equation is solved by Green's function approach to obtain displacement of the sensor. Finally, constitutive equation is used to calculate the current output from the sensor. Expressions for both real and imaginary components of the admittance are obtained and plotted. The present method gives a robust method to handle SHM problem considering material non-linearity. This method can be extended to include the effect of presence of crack by considering suitable Green function in the solution. Thus comparative study between pristine and cracked structures cane be made through this study. Experimental verification of the present study is out of scope.

REFERENCES

[1] Hall, D.A. Review nonlinearity in piezoelectric ceramics. *Journal of Materials Science*

(2001) **36**:4575–601.
[2] Tan, P. and Tong, L. A one dimensional model for non-linear behavior of piezoelectric composite materials. *Composite Structures* (2002) **58**:551-561.
[3] Tan, P. and Tong, L. Micromechanics models for non-linear behavior of piezoelectric fiber reinforced composite materials. *Intl. Jl. of Solids and Structures* (2001) **38**:8999-9032.
[4] McCall, K.R. Theoretical study of non-linear elastic wave propagation. *Jl. of Geophysical Research* (1994) **99(B2):**2591-2600.
[5] McCall, K.R. and Guyer, R.A. Equation of state and wave propagation in hysteretic non-linear elastic materials. *Jl. of Geophysical Research* (1994) **99(B12):**23887-23897.
[6] Tinoco, H.A., Callegas, L.R., Marulanda, D.J. and Serpa, A.L. Damage detection in plates using the electromechanical impedance technique based on decoupled measurements of piezoelectric transducers. *Jl. of Sound and Vibration* (2016) **384:**146-162.
[7] Duffy, D.G. *Advanced Engineering Mathematics with MATLAB* CRC press (2011).

VIII ECCOMAS Thematic Conference on Smart Structures and Materials
SMART 2017
A. Güemes, A. Benjeddou, J. Rodellar and J. Leng (Eds)

STRUCTURAL HEALTH MONITORING BY COMBINING MACHINE LEARNING AND DATA ASSIMILATION TECHNIQUES

E. LOPEZ, G. QUARANTA, E. ABISSET-CHAVANNE AND F. CHINESTA

ESI Chair
ICI Institute @ Ecole Centrale Nantes
1 rue de la Noe, BP 92101, F-44321 Nantes cedex 3, France
e-mail: elena.lopez-tomas@ec-nantes.fr

Key words: Structural Health Monitoring, Dammage Identification, Machine Learning, Data Assimilation

Abstract. The damage detection and quantification in structures is one of the most challenging application of Smart Structures concepts. A great number of permanently attached sensors are needed inside the structure in order to capture and quantify the damage evolution. In spite of the very recent developments achieved by model order reduction techniques, real-time decision-making is still difficult to perform from modeling-based simulations. Manifold learning techniques allow taking real-time decisions in order to control processes, but it is necessary to exctract information and knowledge from real or synthetic data in order to build the solution manifold and to extract the non-correlated parameters defining the manifold dimensionality. Then, as soon as new data is available, it can be checked in real time if it belongs or not to the solution manifold; if yes, the solution can be interpolated from the neighboring data without requiring further calculation/simulation, allowing real-time decision-making. Furthermore, in order to reduce the number of sensors in the structure, data assimilation can be applied in the initial data in order to extend everywhere the information collected at some points (minimum number and optimally placed), reducing considerably the computation cost. The present work focuses in structural damage identification and location in the context of Health Monitoring, using manifold learning techniques. Data assimilation is used on the original time series (synthetic data) to be able to speed-up even more the procedure.

1 INTRODUCTION

In the context of the Structural Health Monitoring, in which one of the objectives is the non-destructive testing, the goal of this work is the real-time identification and location of damage in a structure. However and in spite of the very recent developments achieved by model order reduction techniques, real-time decision-making is still difficult to perform from modeling-based simulations.

Manifold learning techniques allow to take real-time decisions in order to control processes, but it is necessary to exctract information and knowledge from real or synthetic data in order to build the solution manifold and to extract the non-correlated parameters defining the manifold dimensionality. Then, as soon as new data is available, it can be checked in real time if it belongs or not to the solution manifold; if yes, the solution can be interpolated from the neighboring data without requiring further calculation/simulation, allowing real-time decision making. In this work we have built an elastodynamic model, in order to generate synthetic data to be able to obtain the manifold.

Let's consider the problem depicted in Figure 1. The geometrical and mechanical properties of the square domain $\Omega = [0, L] \times [0, L]$ are defined in Table 1:

Table 1: Characteristics of the square domain.

L: Length (m)	1
E: Young modulus (N/m^2)	$2 \cdot 10^{11}$
ν: Poisson coefficient	0.25

A linear elastic behavior is supposed, so that the relation between the stress $\boldsymbol{\sigma}$ and the strain $\boldsymbol{\varepsilon}$ is

$$\boldsymbol{\sigma} = \mathbb{C}\boldsymbol{\varepsilon} \tag{1}$$

where $\mathbb{C}$ is the Hooke's fourth order tensor, and the relation between the strain and the displacement $\mathbf{u}$ is

$$\boldsymbol{\varepsilon} = \nabla_s \mathbf{u} \tag{2}$$

where ∇_s is the symmetric gradient operator. On the right hand side it is imposed a force $F(t) = A\sin(\omega t)$, where $A = 10^6$ and $\omega = 2\pi$. Considering an isotropic material, plane stress conditions and using the Voigt notation, the Hooke's tensor can be written as

$$\mathbf{D} = \frac{E}{1-\nu^2}\begin{bmatrix} 1 & \nu & 0 \\ \nu & 1 & 0 \\ 0 & 0 & (1-\nu)/2 \end{bmatrix} \tag{3}$$

and the relation (1) as

$$\begin{bmatrix} \sigma_{xx} \\ \sigma_{yy} \\ \sigma_{xy} \end{bmatrix} = \frac{E}{1-\nu^2}\begin{bmatrix} 1 & \nu & 0 \\ \nu & 1 & 0 \\ 0 & 0 & (1-\nu)/2 \end{bmatrix}\begin{bmatrix} \varepsilon_{xx} \\ \varepsilon_{yy} \\ \gamma_{xy} \end{bmatrix} \tag{4}$$

The material is supposed to be homogeneous with a damaged area inside where the Young modulus is defined as $E_f = E/10$.

The displacement field evoultion $\mathbf{u}(\mathbf{x}, t)$ for $\mathbf{x} \in \Omega$ and $t \in I = [0, T]$ is described by the linear momentum balance equation

$$\rho \ddot{\mathbf{u}}(\mathbf{x}, t) = div\, \boldsymbol{\sigma} \tag{5}$$

where ρ is the density (kg/m^3). The boundary $\partial\Omega$ is partitioned into Dirichlet, Γ_D, and Neumann, Γ_N, frontiers and the boundary conditions depicted in Figure 1 and initial conditions $\mathbf{u}(\mathbf{x}, t = 0) = 0$, $\dot{\mathbf{u}}(\mathbf{x}, t = 0) = 0$ are associated to the equation.
The variational problem equivalent to (5) is: find $\mathbf{u} \in \mathcal{S}$, with $\dot{\mathbf{u}} \in \mathcal{S}$ and $\ddot{\mathbf{u}} \in \mathcal{W}$ such that

$$\rho \int_\Omega \ddot{\mathbf{u}}\mathbf{v}\, d\mathbf{x} + \int_\Omega \boldsymbol{\varepsilon}(\mathbf{u}) : \mathbb{C} : \boldsymbol{\varepsilon}(\mathbf{v})\, d\mathbf{x} = \int_{\Gamma_N} F(t)\mathbf{v}\, d\mathbf{x} \tag{6}$$

$\forall \mathbf{v} \in \mathcal{V}$, with the appropriate spaces introducing the required regularity in space and time

$$\begin{aligned}
\mathcal{S} &= \big\{\mathbf{v} : \mathbf{v}(\cdot, t) \in \mathcal{H}^1(\Omega),\ \mathbf{v}(\mathbf{x}, \cdot) \in \mathcal{L}^2(I),\ \mathbf{v}(\mathbf{x}, 0) = 0\big\},\\
\mathcal{W} &= \big\{\mathbf{v} : \mathbf{v}(\cdot, t) \in \mathcal{H}^{-1}(\Omega),\ \mathbf{v}(\mathbf{x}, \cdot) \in \mathcal{L}^2(I)\big\},\\
\mathcal{V} &= \big\{\mathbf{v} : \mathbf{v}(\mathbf{x}) \in \mathcal{H}^1(\Omega),\ \mathbf{v} = 0 \text{ on } \Gamma_D \times I\big\}.
\end{aligned}$$

We introduce a FEM space discretization with linear element over a uniform triangular mesh composed of 51×51 nodes such that the damaged area contains 128 elements. Using (2), (4) and (6), we obtain [6] the following system

$$\mathbf{M}\ddot{\mathbf{u}}(t) + \mathbf{K}\mathbf{u}(t) = \mathbf{f}(t), \tag{7}$$

where $\mathbf{M}$ is the mass matrix, $\mathbf{K}$ the stiffness matrix and $\mathbf{f}(t)$ the force vector. The displacement field $\mathbf{u}$ is then computed using a standard time-marching Newmark method, with parameters $\beta = 1/4$ and $\gamma = 1/2$, in a time interval of $T = 2\,s$ and a time step of $\Delta t = 0.001\,s$.

Once the displacement field $\mathbf{u}$ is obtained, it is easy to obtain the strain field $\boldsymbol{\varepsilon}$. Thus, in order to separate the fractured from the non-fractured domain, we are going to apply the k-PCA on the strain field $\boldsymbol{\varepsilon}$.

Let's first explain the origin of the kPCA. Principal Components Analysis (PCA) can be viewed as an information extractor from a data set that attempts to find a linear subspace of lower dimensionality than the original space. If the data has more complicated structures which can not be well represented in a linear subspace, standard PCA will not be very helpful. Fortunately, kernel-PCA (kPCA) allows us to generalize standard PCA to nonlinear dimensionality reduction [1, 2, 3]. The rationale of kPCA consists of linearly separate the data if it is previously projected to a higher dimensional space than the original one. In this technique there is no need to explicitly determine the analytical expression of the mapping, which is one of its main advantages.

Furthermore, data assimilation can be applied in the initial data in order to extend everywhere the information collected at some points (minimum number and optimally placed), reducing considerably the computation cost.

The following work is focused in the damage identification and location of a structure in the context of Health Monitoring, using manifold learning techniques. Data assimilation is used on the original time series (synthetic data) to be able to speed-up even more the process.

2 FRACTURE LOCATION WITH ALL DATA

In this section we are going to identify and locate the damaged region using all the points in the domain, applying k-PCA on the data coming from the elastodynamic model desscribed in the previous section.

2.1 Location via Machine Learning techniques

Our main objective in this work is to achieve a perfect separation between the damaged and the undamaged domains presented in Figure 1.

In order to offer a vision of the methodology used, the kPCA, PCA will first be arranged to explain in detail and based on it, we will detail the modifications required by the kPCA on the PCA. Let us consider D observed variables defining the vector $\mathbf{X} \in \mathbb{R}^D$. These are commonly referred to in the Model Order Reduction (MOR) literature as snapshots. We assume that these variables are therefore not uncorrelated and, notably, that there exists a linear transformation $\mathbf{W}$ defining the vector $\mathbf{Y} \in \mathbb{R}^d$, where $d < D$ represents the unknown so-called latent variables, according to

$$\mathbf{X} = \mathbf{W}\mathbf{Y}. \tag{8}$$

The transformation $\mathbf{W}, D \times d$, is assumed to verify the orthogonality condition $\mathbf{W}^T\mathbf{W} = \mathbf{I}_d$, where $\mathbf{I}_d$ represents the $d \times d$-identity matrix ($\mathbf{W}\mathbf{W}^T$ is not necessarily $\mathbf{I}_D$). The existence of such a transformation is precisely at the origin of PCA methods.

We assume the existence of M different snapshots $\mathbf{X}_1, ..., \mathbf{X}_M$, that can be stored in the columns of the $D \times M$ matrix $\mathbb{X}$. The associated $d \times M$ reduced matrix $\mathbb{Y}$ contains the associated vectors $\mathbf{Y}_i, i = 1, ..., M$.

PCA is able to calculate both d (the necessary number of members in the basis of the reduced-order subspace) and the transformation matrix $\mathbf{W}$. PCA proceeds by guaranteeing maximal preserved variance and decorrelation in the latent variable set. From a statistical point of view, therefore, it can be assumed that the latent variables are uncorrelated (no linear dependencies among them) or mutually orthogonal, thus constituting a basis. In practice, this means that the covariance matrix of $\mathbb{Y}$, defined as

$$\mathbf{C}_{yy} = E\{\mathbb{Y}\mathbb{Y}^T\}, \tag{9}$$

is diagonal. Thus, we consider

$$\mathbf{C}_{xx} = E\{\mathbb{X}\mathbb{X}^T\} = E\{\mathbf{W}\mathbb{Y}\mathbb{Y}^T\mathbf{W}^T\} = \mathbf{W}E\{\mathbb{Y}\mathbb{Y}^T\}\mathbf{W}^T = \mathbf{W}\mathbf{C}_{yy}\mathbf{W}^T, \tag{10}$$

that by pre-multiplying and post-multiplying by $\mathbf{W}^T$ and $\mathbf{W}$ respectively, and taking into account that $\mathbf{W}^T\mathbf{W} = \mathbf{I}$, leads to

$$\mathbf{C}_{yy} = \mathbf{W}^T\mathbf{C}_{xx}\mathbf{W}. \tag{11}$$

The covariance matrix $\mathbf{C}_{xx}$ can then be factorized by applying the singular value decomposition,

$$\mathbf{C}_{xx} = \mathbf{V}\mathbf{\Lambda}\mathbf{V}^T, \tag{12}$$

with $\mathbf{V}$ containing the orthonormal eigenvectors and $\mathbf{\Lambda}$ the diagonal matrix containing the eigenvalues (non-negative real numbers), assumed in descending order.

Substituting the factorized expression of the covariance matrix (12) into Eq. (11) it results

$$\mathbf{C}_{yy} = \mathbf{W}^T\mathbf{V}\mathbf{\Lambda}\mathbf{V}^T\mathbf{W}. \tag{13}$$

This equality holds only when the d columns of $\mathbf{W}$ are taken collinear with d columns of $\mathbf{V}$.

From a geometrical point of view, the columns of $\mathbf{V}$ indicate the directions in $\mathbb{R}^2$ that span the subspace of the latent variables. PCA find an alternative coordinate system given by $\mathbf{V}$ in which all these points are described from a single coordinate.

Nonlinear methods are often more powerful than linear ones, because the connection between the latent variables and the observed ones may be much richer than a simple matrix multiplication. Thus, the extraction of the manifold is compulsory and PCA is unable to accomplish the job. These limitations justify the use of nonlinear dimensionality reduction techniques, as the kernel-PCA (kPCA).

PCA works with the sample covariance matrix, $\mathbb{X}\mathbb{X}^T$. On the contrary, kPCA works with the matrix of pairwise scalar products that defines the Gram matrix $\mathbf{S} = \mathbb{X}^T\mathbb{X}$. It proceeds from

$$\mathbf{S} = \mathbb{X}^T\mathbb{X} = \mathbb{Y}^T\mathbf{W}^T\mathbf{W}\mathbb{Y} = \mathbb{Y}^T\mathbb{Y}, \tag{14}$$

whose eigenvalue decomposition results

$$\mathbf{S} = \mathbf{U}\mathbf{\Lambda}\mathbf{U}^T = \left(\mathbf{U}\mathbf{\Lambda}_{1/2}\right)\left(\mathbf{\Lambda}_{1/2}\mathbf{U}^T\right) = \left(\mathbf{\Lambda}_{1/2}\mathbf{U}^T\right)^T\left(\mathbf{\Lambda}_{1/2}\mathbf{U}^T\right), \tag{15}$$

from which it results

$$\mathbb{Y} = \mathbf{I}_{d\times M}\mathbf{\Lambda}_{1/2}\mathbf{U}^T. \tag{16}$$

The idea behind kernel-PCA methods is simple: data not linearly separable in D dimensions, could be linearly separated if previously projected to a space in $Q > D$ dimensions. Thus, surprisingly, kPCA begins by projecting the data to an even higher dimensional space. One the biggest advantages of this technique is that there is no need to explicitly determine the analytical expression of the mapping.

The symmetric matrix related to the mapped snapshots $\mathbb{Z}^T\mathbb{Z}$ has to be decomposed in eigenvalues and eigenvectors, after performing to the vectors involved in $\mathbb{Z}$ the double centering.

Now, the eigenvalue-eigenvector decomposition can be performed according to

$$\mathbb{Z}^T\mathbb{Z} = \mathbf{U}\mathbf{\Lambda}\mathbf{U}^T, \tag{17}$$

from which it results

$$\mathbb{Y} = \mathbf{I}_{d\times M}\mathbf{\Lambda}_{1/2}\mathbf{U}^T. \tag{18}$$

It is worth noting that the previous procedure only needs scalar products in the intermediate space $\mathbb{R}^Q$. The Mercers theorem allows computing such scalar products in the original space

$\mathbb{R}^D$, by using the so-called kernel-trick. There are many possible choices [4] and then the model calibration becomes its principal advantage and at the same time its main drawback.

Moreover, PCA-based transformations preserve distances, where other nonlinear dimensionality reduction strategies fail to accomplish it.

Here our M different snapshots are the components in the x direction of the strain tensor computed in Section 1, $\boldsymbol{\varepsilon}_{xx,i}$, $i = 1, ..., M$, that can be stored in the columns of the DxM matrix $\mathbb{X}$, being $D = 2001$ the initial high dimensionality corresponding to the different time steps for each element of the domain, and $M = 5000$ is the number of elements of the mesh in our discretization, according to the details shown in Section 1. The associated dxM reduced matrix $\mathbb{Y}$ contains the corresponding reduced vectors $\boldsymbol{\varepsilon}_{xx,red,i}$, $i = 1, ..., M$.

Figure 2 reflects the result of applying the kPCA on the previously defined data matrix $\mathbb{X}$, and we can appreciate a very accurated separation between the fractured (in red) and the non-fractured (in blue) elements of the plate. There are some non-fractured points that are overlapping the fractured ones; that is because the kPCA detects the non-fractured elements which are just around the contour of the fractured zone.

3 DATA MINING VIA DATA ASSIMILATION

The objective here is the same as in the previous section, but now the goal is to reduce as much as possible the number of nodal values because in practical applications, we do not have the possibility to place a number of sensors as large as the number of finite elements in the FE mesh. Thus, we want to find the minimum number of sensors needed to detect the damage.

Thus, here we consider data acquisition in few locations (properly chosen), and then to assimilate the fields from this reduced amount of data. The data assimilation is thus done using an appropriate reduced base. In order to choose the best assimilation technique, the 1D problem depicted in Figure 3 is firstly taken into consideration. The geometrical and mechanical properties of the domain $\Omega = [0, L]$ are defined in Table 2.

Table 2: Characteristics of the domain.

L: Length (m)	5
E: Young modulus (N/m^2)	$2 \cdot 10^{11}$

As before an isotropic homogeneous material with linear elastic behavior is considered, which has a damaged area where the Young modulus is defined as $E_f = E/10$. On the right side a force $F(t) = A\cos(\omega t)$, where $A = 10^6$ and $\omega = 2\pi$, is imposed. The displacement field evoultion $u(x, t)$ for $x \in \Omega$ and $t \in I = [0, T]$ is thus described by the linear momentum balance equation and its boundary and initial conditions

$$\begin{cases} \rho\ddot{u}(x,t) = \dfrac{\partial \sigma}{\partial x} & \text{in} \quad \Omega \times I \\ u = 0 & \text{on} \quad \{0\} \times I \\ \sigma = A\sin(\omega t) & \text{on} \quad \{L\} \times I \\ u = 0 & \text{on} \quad \Omega \times \{0\} \\ \dot{u} = 0 & \text{on} \quad \Omega \times \{0\} \end{cases} \tag{19}$$

where ρ is the density (kg/m^3). The problem (19) is solved using a FEM space discretization with linear element over a uniform mesh composed of 100 nodes and a standard time-marching Newmark method (for the system (7)) , with parameters $\beta = 1/4$ and $\gamma = 1/2$, in a time interval of $T = 5\,s$ and a time step of $\Delta t = 0.001\,s$. The found vector of the solution's nodal values $\mathbf{u}$ will be called from now $\mathbf{u_{FEM}}$.

3.1 Basis choice: Modal Analysis versus Finite Element Basis

The goal is now to find an appropriate reduced base of dimension much lower than $N = 99$ (the dimension of the complete FEM basis).
A possible choice consists in using the modal base obtained computing the eigenproblem associated to the system (7), but this choice do not allow to obtain acceptable approximations of the different fields with a low number of measurement point.

Thus it is necessary to find another possible reduced base. A possible choice is to select a reduced FEM base, that is, the shape functions associated to a coarser discretization of the domain. This coarser discretization is obtained selecting appropriate nodes of the previous finer discretization. In this work the points has been chosen approximately uniformly distribuited into the domain and, as previously said, linear shape functions have been used. The results related to this choice of the reduced base are presented in Figures 4 and 5.

The choice of this reduced base for the data assimilation appears pretty much better.

The results of the 1D case suggest to use the reduced FEM base in order to perform the data assimilation on the 2D case of Figure 1. As in the 1D case, the shape functions associated to a coarser discretization of the domain are chosen. This coarser discretization is obtained selecting appropriate nodes of the previous finer discretization (51×51 nodes). In this work the points (in which, as already noted, the solution is imposed to be the synthetic value computed with the complete FEM model) has been chosen approximately uniformly distribuited into the domain and linear shape functions have been used. The strain, that is expected being discontinuous across the damaged area boundary, appears to be particularly appropriate to be used by a classifier. In particular the ε_{xx} component of the strain tensor seems to be the most characteristic quantity regarding the configuration of the system and the force imposed. In Figure 6 the ε_{xx} field assimilated using different sizes of the reduced base, as well as the complete synthetic field obtained with the complete FEM model, at a specific timestep, can be observed.

It can be noted how, with a grid of only 5×5 it is already possible to visually detect the location of the damaged zone.

3.2 Location via Machine Learning techniques

Following the same rationale than in Section 2.1, k-PCA technique is now applied on $\tilde{\mathbb{X}}$, matrix that stores the components in the x direction of the assimilated strain tensor coming from the data assimilation analysis computed in Section 3.1, $\tilde{\varepsilon}_{xx,i}$, $i = 1, ..., M$.

Results are sketched in Figure 7. We can observe a perfect separation between the fractured (in red) and the non-fractured (in blue) elements of the plate performing data assimilation in 10 points in each direction of the domain Figure 7 (right). But more attractive is the solution considering only 5 points in each direction (left), in which we are able to separate quite good the fractured and the non-fractured elements.

4 CONCLUSIONS

- We have shown that the use of manifold learning techniques, the k-PCA in this paper, allows us to separate the fractured region from the non-fractured one, perfectly locating the damaged region.

- In order to reduce the number of sensors (nodal values) in the structure, data assimilation can be applied in the on the original time series in order to extend everywhere the information collected at some points (minimum number and optimally placed), speeding-up even more the procedure, performing real-time decision making in the context of Health Monitoring.

REFERENCES

[1] B. Scholkopf, A. Smola, K.R. Muller. Nonlinear component analysis as a kernel eigenvalue problem. *Neural Computation*, (1998),**10/5**, 1299-1319.

[2] B. Scholkopf, A. Smola, K.R. Muller. Kernel principal component analysis. In Advances in Kernel Methods – Support Vector Learning, (1999) MIT Press, 327-352.

[3] Q. Wang. *Kernel Principal Component Analysis and its Applications in Face Recognition and Active Shape Models*. arXiv:1207.3538.

[4] J.A. Lee, M. Verleysen. *Nonlinear dimensionality reduction*. Springer, Berlin, (2007).

[5] Barrault M, Nguyen N. C, Maday Y, Patera A. T. An "empirical interpolation method": Application to efficient reduced-basis discretization of partial differential equations. *C. R. Acad. Sci. Paris, Sries I.*, (2004), **339**, 667-672.

[6] Fish J, Belytscho T. *A First Course in Finite Elements*. John Wiley & Sons Ltd, Chichester, (2007).

[7] Chaturantabut S, Sorensen D. C. Nonlinear Model Reduction via discrete empirical interpolation. *SIAM J. SCI. COMPUT.*, (2010),**32(5)**, 2737-2764.

[8] Germoso C, Fraile A, Alarcon E, Aguado J V, Chinesta F. From standard to fractional structural visco-elastodynamics: Application to seismic site response. *Physics and Chemistry of the Earth*, (2016), *http://dx.doi.org/10.1016/j.pce.2016.01.005*.

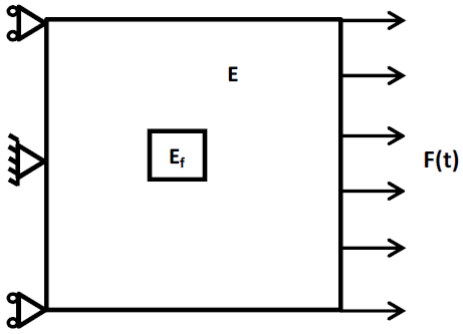

Figure 1: The 2D model object of our study.

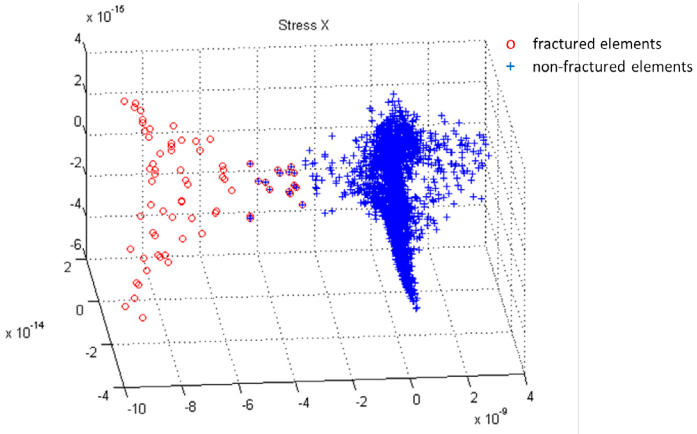

Figure 2: kPCA result considering all the points.

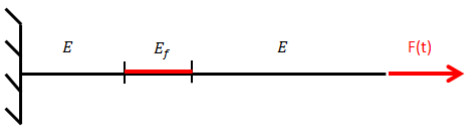

Figure 3: The 1D model object of our study.

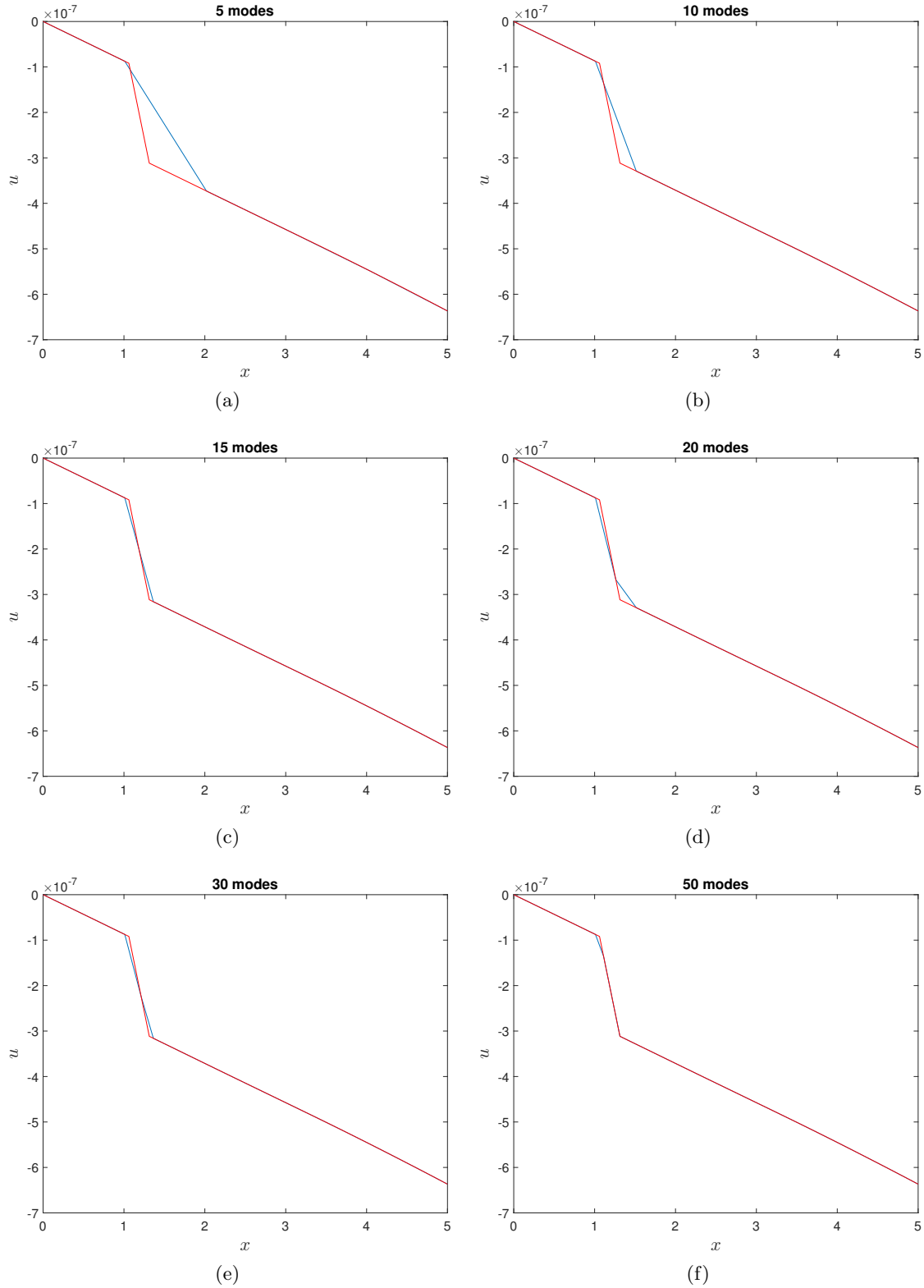

Figure 4: Displacement field assimilated with the **reduced FEM base** (in blue) vs. complete displacement field, the complete FEM solution, (in red), for different dimensions of the reduced base, at a fixed timestep.

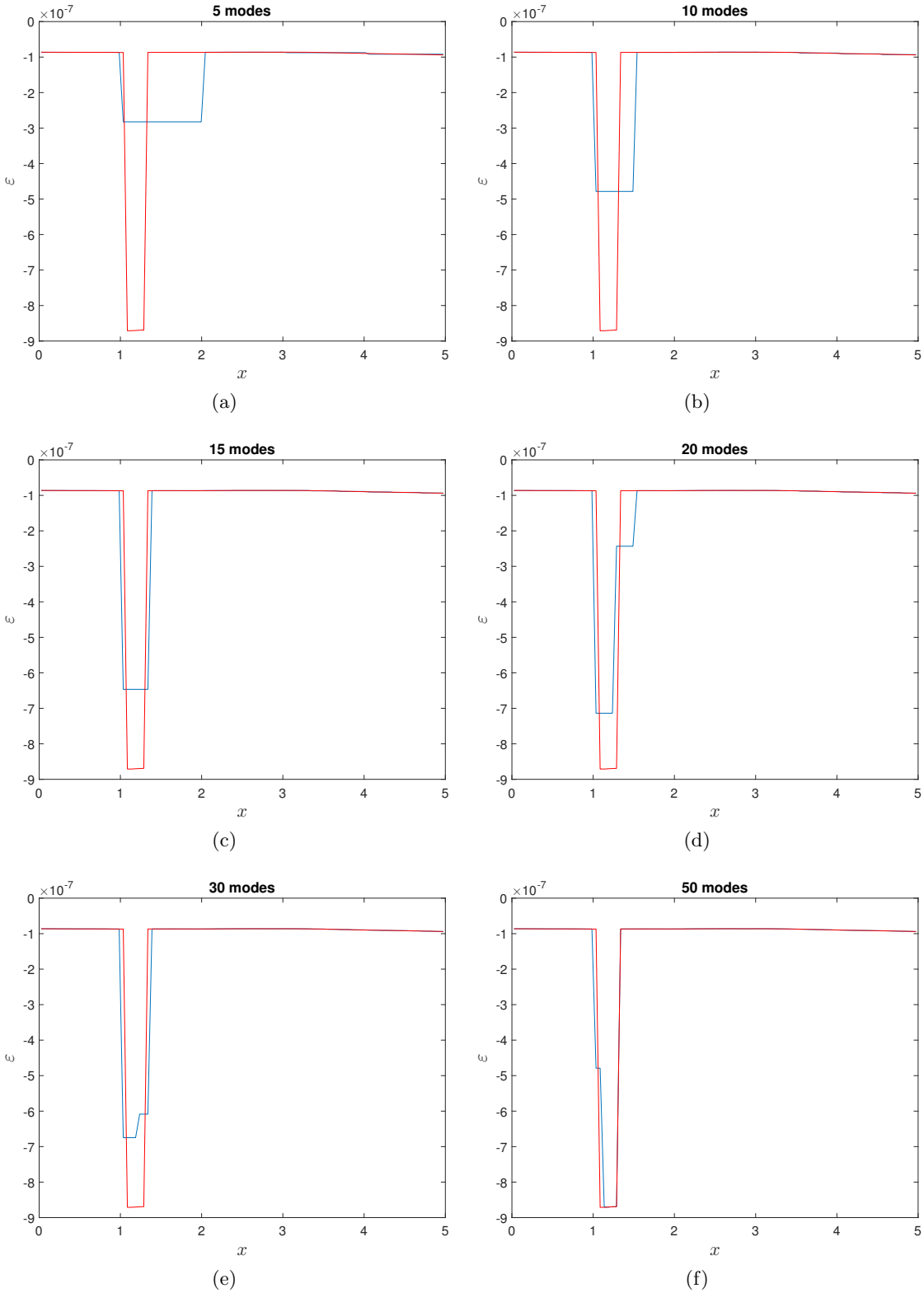

Figure 5: Strain field assimilated with the **reduced FEM base** (in blue) vs. complete displacement field, the complete FEM solution, (in red) for different dimensions of the reduced base, at a fixed timestep.

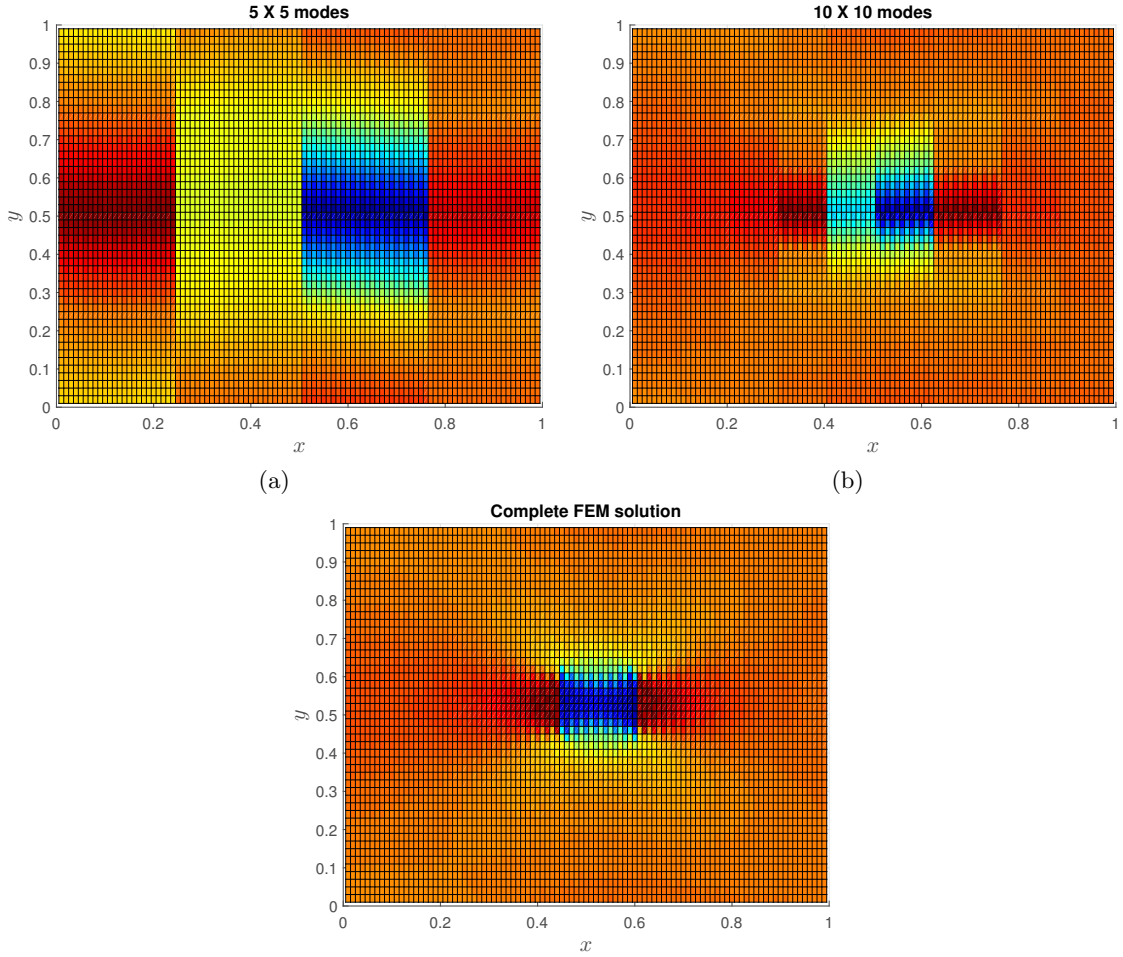

(a) (b)

(c)

Figure 6: ε_{xx} field assimilated with the **reduced FEM base** for different dimensions of the reduced base (a,b) and complete sinthetic ε_{xx} (c), at a fixed timestep.

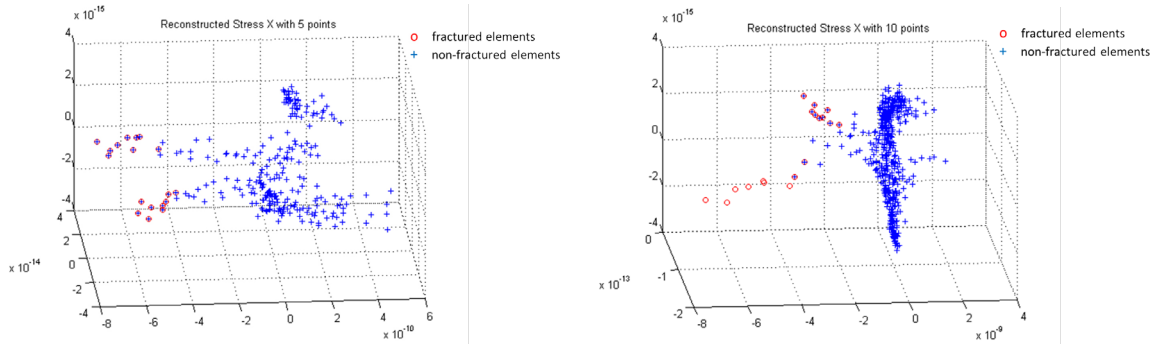

Figure 7: Reconstructed kPCA solution with 5 (left) and 10 (right) points coming from data assimilation.

VIII ECCOMAS Thematic Conference on Smart Structures and Materials
SMART 2017
A. Güemes, A. Benjeddou , J. Rodellar and Jinsong Leng (Eds)

WAVE BASED CHARACTERIZATION OF LOW-VELOCITY IMPACTS ON COMPOSITE PLATE STRUCTURES.

THEODOSIS C. THEODOSIOU, CHRISTOFOROS S. REKATSINAS AND DIMITRIS A. SARAVANOS

Dept. of Mechanical Engineering & Aeronautics
University of Patras, 26500 Rion-Patras, Greece
e-mail: saravanos@mech.upatras.gr, saam.mech.upatras.gr

Key words: Impact, Composite Materials, Piezoelectric Sensors, Event Characterization

Abstract. This paper proposes a methodology for impact event reconstruction by exploiting the dynamic characteristics of impact-induced stress waves, captured by a limited number of sensors. Initially, the impact location is determined using a geometrical optimization algorithm, which the pursued impact location with wave frequencies and respective propagation velocities. Then, impactor mass and velocity are determined by investigating the dynamic characteristics of waves in dimensionless space. As soon as the impact location and impactor characteristics are known, a simulation may be conducted using Time-Domain Spectral Finite Elements in order to replicate the impact event and reproduce impact force and response of the impacted structure.

1 INTRODUCTION

The detection and characterization of foreign object impacts on composite structures is a problem of great interest for the development of structural health management systems in aerospace community. Numerous approaches may be found in the literature for the detection of impact events, including wavelet-based time-frequency analysis [1], nonlinear triangulation, impact force reconstruction methods [2] [3], time reversal methods [4], etc., however, most are limited in scope and efficiency. The present paper addresses the development of a mechanics based computationally efficient approach for: (1) identification of impact site, (2) estimation of impactor mass and velocity, and (3) reconstruction of the impact force of low velocity local impact events.

A series of numerical tools have been developed, based on physical models and laws. The relationships between impact parameters and Lamb wave characteristics are thoroughly analyzed using an innovative Time-Domain Spectral Finite Element [5]–[7], while wave characteristics are correlated to elastic and laminate properties using semi-analytical wave dispersion models [8]. The previous analytical and numerical tools address the complex effect of anisotropy on Lamb wave propagation in composite structures and embrace the various impact mechanics regimes mandated by impactor and target structure interaction.

Building on them, new methodologies are presented leading to the localization and characterization of impact events. A network of sensors is attached at optimal sites to capture impact-induced waves. Localization is performed by identification of propagating

antisymmetric waves and geometric compatibility optimization using their group velocities. Furthermore, the variation of wave amplitude in time is analyzed and correlated to impactor mass and velocity. Due to the ambiguity involved in impactor characterization, the methodology is based on dimensional analysis. This further enables direct connection with other well-established impact characterization methodologies [9], [10].

A series of impact simulation results are presented which reveal the governing impact parameters and quantify their relation to wave velocity, frequency and amplitude. Simulation results are also exploited for inverse model training and demonstration of the impact detection and characterization capability.

2 THEORETICAL BACKGROUND

2.1 Simulation of impact using Time Domain Spectral Finite Elements

The proposed methodology is based on a developed multi node Time Domain Spectral Finite Element for plates (TDSFE) with C_0 Lagrange shape functions [11]. Exploitation of high order Lagrangian polynomial shape functions ensures the efficient spatial discretization in the plane of the plate. The nodes of the proposed element are located at Gauss-Lobatto-Legendre (GLL) integration points provided as solutions of the equation $(1-\xi_i^2)\cdot P_{p,\xi}(\xi_i)=0$, where $\xi \in [-1,1]$ is the local coordinate of the element. Figure 1. Outline of the developed 81-node plate TDSFE.shows an 81-node plate TDSFE.

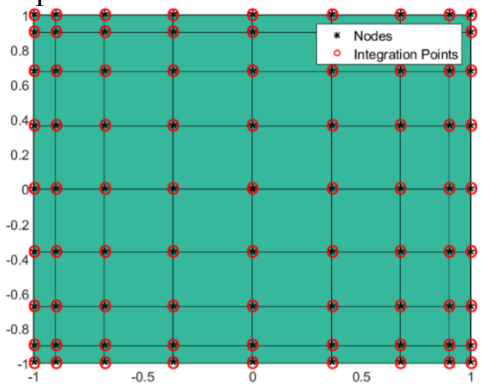

Figure 1. Outline of the developed 81-node plate TDSFE.

The generalized displacement degrees of freedom in the element, are approximated as,

$$\mathbf{U}_L(x,y,t)=\sum_{i=1}^{Nr\ Nodes}\mathbf{N}^i(x,y)\cdot\hat{\mathbf{U}}^i(t) \tag{1}$$

where $\widehat{\boldsymbol{U}}^i$ indicates nodal variables of the ith not, and $\mathbf{N^i}$ contains the in-plane shape function matrix. The element stiffness and mass matrices, $\mathbf{K_e^{ij}}$ and $\mathbf{M_e^{ij}}$, can be calculated as in classical FEA:

$$\mathbf{K_e^{ij}}=\int_{-1}^{1}\int_{-1}^{1}\mathbf{R^i}^{\,T}\cdot\mathbf{K_L}\cdot\mathbf{R^j}|J|d\xi d\eta \tag{2}$$

$$\mathbf{M_e^{ij}}=\int_{-1}^{1}\int_{-1}^{1}\mathbf{N^i}^{\,T}\cdot\boldsymbol{\rho}_\mathbf{L}\cdot\mathbf{N^j}|J|d\xi d\eta \tag{3}$$

In the previous relations $\mathbf{R^i}$, $\mathbf{N^i}$ denote the strain and displacement shape functions of the respective nodes; $|J|$ the determinant of the Jacobian of the element, which is calculated at each integration point of GLL quadrature. It should be rather obvious in Eq. (3) that the collocation of nodes with the GLL integration points leads to a consistent diagonal or nearly diagonal element mass matrix, which boosts the speed of an explicit time integration schemes without degrading the quality of the approximation.

2.2 Impact Localization

Assume a composite plate of length L, width $W$and thickness t. A set of N sensors are attached on arbitrary locations $\boldsymbol{S_i}(x_i, y_i), i = 1 \dots N$. All sensors are connected to a proper data acquisition system (DAQ) that captures their response in time. The actual response of sensors is typically voltage, but it can be translated to equivalent strains or displacements using the manufacturer's datasheet; therefore, sensor response is generically denoted as transverse displacement $w = w(t)$ throughout this paper. The plate is impacted by spherical impactor of mass m_{imp} and velocity v_{imp} at location $\boldsymbol{P}(x_0, y_0)$ at time t_0; both the impact location and impact time are unknown. Upon contact, elastic waves are generated sourcing from the impact location and propagating along all directions. Waves travel with group velocity c_g, which depends on wave frequency and propagation direction due the anisotropic nature of the composite plate. i.e. $c_g = c_g(\theta, f)$. Waves eventually arrive at each sensor at time $t_i, i = 1 \dots N$, which can be determined from the DAQ system. The system under investigation is conceptually depicted in Figure 2.

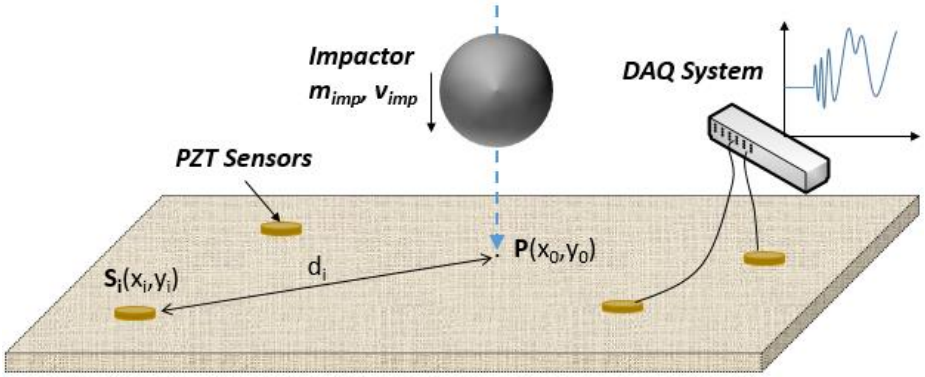

Figure 2. Conceptual system configuration for impact investigations. A set of sensors are attached at locations $S_i(x_i, y_i)$. Impact takes place at an arbitrary location $P(x_0, y_0)$. A DAQ system continuously monitors sensors' output.

The distance of the generalized i[th] sensor from the impact site is

$$d_i = \sqrt{\left(x_0 - x_i\right)^2 + \left(y_0 - y_i\right)^2}, \quad i = 1 \dots N \ . \tag{4}$$

The time need for a wave to travel from the impact site to the ith sensor is

$$\delta t_i = t_i - t_0 = c_g\left(\theta_i, f_i\right) \cdot d_i, \quad i = 1 \dots N \ . \tag{5}$$

This formulation implies that the signal acquired from each sensor needs to be processed in order to calculate the frequency and the arrival time. Then, Eqs. (4), (5) can be seen as a

nonlinear system of N equations for the unknown impact site (x_0, y_0). The directionality effects for group velocity, i.e. the relation $c_g = c_g(\theta, f)$ can be calculated as described in [8].

2.3 Impactor Characterization

The characterization of the impactor has two aspects: (1) Estimation of impactor mass, and (2) Estimation of impactor velocity. No simple set of equations can be derived as in the case of localization, thus, a different approach needs to be followed. Dimensional analysis is employed to this cause. First, the key parameters affecting the impact investigation are identified. Assuming that modeling is tailored for a specific composite system, these can be reduced to the following parameter set: impactor mass (m_{imp}), impactor velocity (v_{imp}), modal mass of the structure (m_s), modal stiffness (k_s), contact stiffness (k_y), and wave amplitude (A). Impactor mass and velocity are pursued, while the others can be determined numerically or experimentally. Alternative quantities could have been selected, leading to equivalent results. However, the proposed parameters enable direct incorporation of other successful theories [12]–[14].

Numerical simulations have revealed a dependence of dimensionless wave characteristics on dimensionless mass and impactor velocity; namely, both the wave amplitude and its variation in time can be correlated to impactor mass and velocity in dimensionless space. Although dimensional analysis reveals the correlations among the various parameters, it does not provide any information on the formulation. The exact formulation depends on the system under investigation and implies the requirement for a training step. The exact procedure will be demonstrated in Section 3.

3 NUMERICAL IMPLEMENTATION

In order to demonstrate the proposed methodology, a 400x400x4mm^3 has been considered made of 16 Glass/Epoxy composites plies with $[(0/90)_2]_{2S}$ stacking sequence. The ply properties are summarized in Table 1.

Table 1. Elastic ply properties considered for the plate under investigation.

E_{11}	23.126	GPa	ν_{23}	0.271	-
E_{22}	20.780	GPa	G_{12}	3.218	GPa
E_{33}	12.431	GPa	G_{13}	2.279	GPa
ν_{12}	0.116	-	G_{23}	2.779	GPa
ν_{13}	0.271	-	ρ	1792	kg.m^{-3}

The plate is monitored using four sensors located at $\boldsymbol{S_1}(0.078,0.218)$, $\boldsymbol{S_2}(0.198, 0.098)$, $\boldsymbol{S_3}(0.318, 0.218)$, $\boldsymbol{S_4}(0.198, 0.338)$. A rigid spherical impactor hits the plate at an arbitrary location $\boldsymbol{P}(x_0, y_0)$ at an unknown time $t \geq 0$. The goal is to identify the impact location and the impactor mass and velocity, by means of analysis of impact-induced wave characteristics. The assembly resembles the conceptual schematic of Figure 2.

3.1 Estimation of impact location

After the impact event, each sensor captures a signal due to the impact-induced propagating stress waves. In Figure 3a, it is clear that the signal of Sensor 4 is overwhelmed and no wave

can be identified. This may be happening due to multiple reasons, e.g. impact took place near that sensor, a reflection arrived together with a wave etc. Such signals are of little value with respect to the wave-based methodology and, therefore, not further considered in calculations. The remaining signals are post-processed in order to extract their wave dominated response, i.e. before reflections occur. This is depicted in Figure 3b, where only a small portion of the signal has been preserved to be included in calculations.

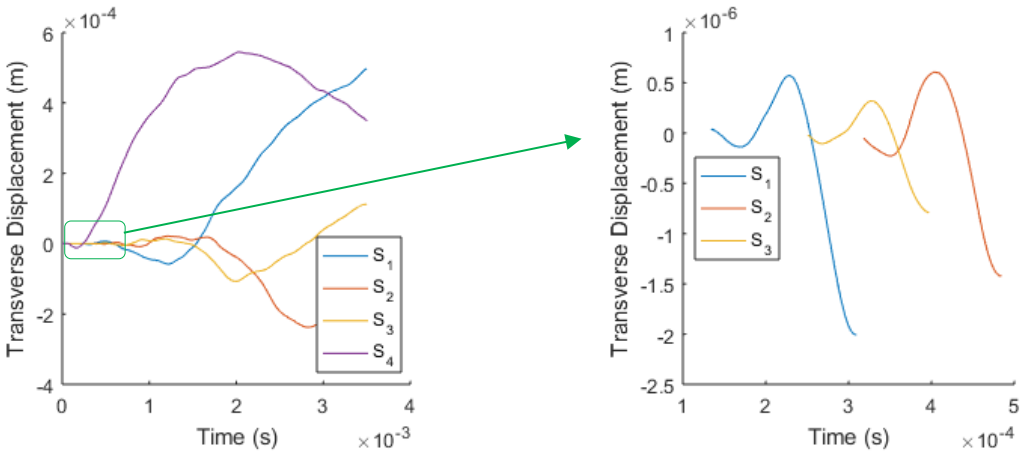

Figure 3. Captured signals. (a) Raw data converted to displacements. (b) Only the wave-dominated region of each signal has been preserved.

Using the time interval between two successive peaks as a semi period, the frequency content of each wave can be identified, as well as its arrival time at the respective sensor (Table 2).

Table 2. Frequency content and arrival time at each sensor.

Sensor ID	Frequency (kHz)	Arrival Time (ms)
1	8.55	0.169
	6.11	0.228
2	9.01	0.350
	6.35	0.405
3	8.57	0.269
	7.13	0.327

In this specific example, each sensor captures two different frequencies. Depending on the impact location and the geometry of the plate, more or less frequencies may be identified; at least one per sensor is necessary to perform localization. Each row of Table 2 corresponds to an equation for the system in Eq. (5); this system is solved numerically and the impact location $\boldsymbol{P}(x_0, y_0)$ is estimated. The selection of a suitable numerical solver and its proper setup is of great importance, but not pursued in this paper. Solution of the system using the fore mentioned data yields the prediction shown in Figure 4; the actual impact location is depicted by the x-mark, while the prediction is shown by the open circle. Clearly, the prediction is very close the actual impact site. The fact that the impact site is close to Sensor 4, also justifies the fact that the respective signal was overwhelmed and, therefore, discarded.

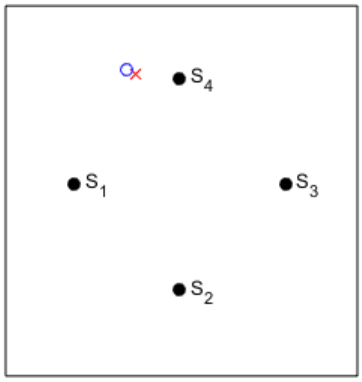

Figure 4. Estimation of impact location. Filled circles denote the sensor locations; the x-mark represents the actual impact site; and the open circle show the predicted impact site.

The efficiency of the proposed methodology has been assessed by a series of impact simulations at random locations using the TDSFE modeling presented in Section 2.1. Impactor mass varies between 80g and 150g, while velocity varies between 0.5m/s and 3m/s. This range has been selected in order to keep impact events at a low-energy regime, and preserve the local nature of impact. Results are summarized in Table 3. The vast majority of predictions is very close to the respective actual impact sites. However, there may exist cases where signals are not clear, as in the case shown in Figure 5. The signal of Sensor 1 is not a pure wave, most likely due to reflections interference. Such a signal would lead to false frequency calculations, and increase the error in predictions (e.g. case 4 in Table 3). It is, therefore, suggested to treat such cases with extreme caution and if possible to review/update calculations manually. This will be subject to further improvement of the algorithm.

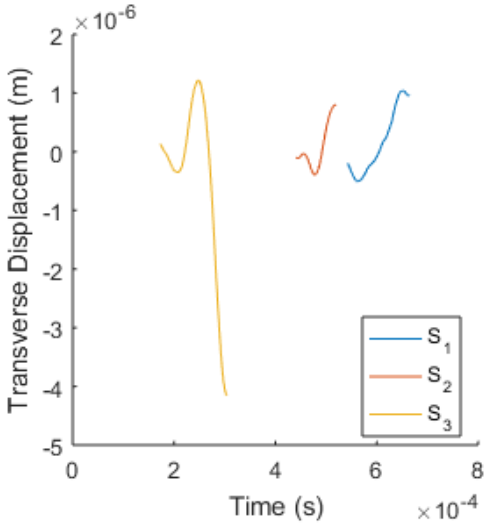

Figure 5. Example of wave signals that may lead to misleading results. The signal of Sensor 81 is not a clear wave, and calculations may be compromised.

Table 3. Comparison between actual and predicted impact site.

Case ID	Actual Impact Site	Predicted Impact Site	Distance (m)
1	(0.147,0.342)	(0.130,0.350)	0.019
2	(0.246,0.218)	(0.242,0.218)	0.005
3	(0.067,0.346)	(0.057,0.342)	0.012
4	(0.013,0.393)	(0.236,0.315)	0.236
5	(0.120,0.393)	(0.031,0.384)	0.090
6	(0.002,0.273)	(0.002,0.302)	0.029
7	(0.220,0.142)	(0.231,0.166)	0.027
8	(0.118,0.378)	(0.098,0.400)	0.030
9	(0.333,0.026)	(0.348,0.000)	0.030
10	(0.074,0.400)	(0.019,0.400)	0.054
11	(0.107,0.106)	(0.109,0.060)	0.046
12	(0.220,0.300)	(0.222,0.265)	0.035
13	(0.260,0.066)	(0.267,0.106)	0.040
14	(0.046,0.327)	(0.000,0.333)	0.047
15	(0.238,0.142)	(0.253,0.185)	0.046
16	(0.140,0.266)	(0.141,0.261)	0.006
17	(0.280,0.273)	(0.207,0.300)	0.078
18	(0.060,0.313)	(0.058,0.362)	0.050
19	(0.002,0.340)	(0.000,0.400)	0.060
20	(0.362,0.386)	(0.351,0.395)	0.014

3.2 Estimation of impactor mass

Estimation of impactor mass is a two-step process. First, a phenomenological model has to be trained, i.e. derive expressions for correlating the impactor mass to wave characteristics in dimensionless space. Then, trained model can be employed to back-calculate the impactor mass. The proposed approach can be accommodated even by only one sensor.

3.2.1 Training for Impactor Mass

A series of impact cases need to be investigated in order to correlate impactor mass to the variation of stress waves. For each impact case, the dimensionless mass is calculated as

$$\mu = \frac{m_{imp}}{m_s} \tag{6}$$

where m_{imp} is the actual impactor mass and m_s is the modal mass of the impacted plate, as defined in [10]. Wave peaks are identified, and their amplitude (a_i) is recorded along with the respective arrival time (t_i). These are normalized on the amplitude of the first peak (a_0) of the captured signal. The variation of the normalized peaks in time can be adequately approximated by a quadratic formula:

$$\overline{a}_i = \frac{a_i(t_i)}{a_0} \simeq At^2 + Bt + C \tag{7}$$

The dominant term is the quadratic one. Its coefficient, namely A in Eq. (7), can be cast into dimensionless space by multiplication with a quantity of "time^{-2}" units:

$$\overline{A} = A \cdot \frac{m_{imp}}{k_y} = A \cdot \frac{\mu \cdot m_s}{k_y} \tag{8}$$

where k_y is the contact stiffness and can be derived by simulations or experimentally. As shown in Figure 6, the variation of $\bar{A}$ is well approximated by a polynomial relation. For the case under investigation, contact stiffness has been found 200MPa and the polynomial expression for $\bar{A}$ is

$$\overline{A} = \sum_{i=0}^{3} p_i \cdot \mu^i, \quad p_0\text{=-0.1175}, p_1\text{=1.234}, p_2\text{=0.9952}, p_3\text{=-0.2262} \tag{9}$$

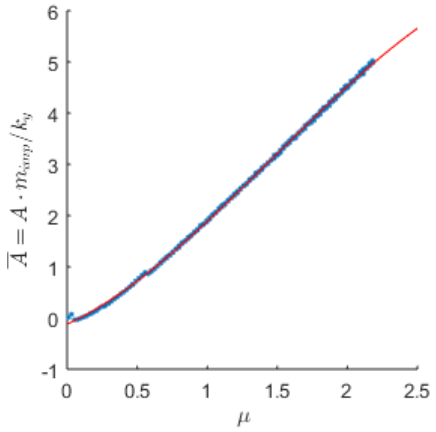

Figure 6. Dependence of wave amplitude variation on mass, in dimensionless space.

3.2.2 Estimation of Impactor Mass

After training has been performed and the polynomial coefficients of Eq. (9) have been calculated, the model can be employed in actual impact cases. Impactor mass prediction is demonstrated using again the same composite plate considered throughout this section. Impact waves are captured and wave peaks are identified (Figure 7). These are normalized and approximated be a quadratic equation.

$$\overline{a} = 2.966 \cdot 10^9 \cdot t^2 + 3.92 \cdot 10^5 \cdot t + 1 \tag{10}$$

The coefficient of the highest power term is $A = 2.966 \cdot 10^9$, in this example. Note that only the first three peaks have been considered, as the last part of the signal seems to contain reflections. Without loss of generality, Eq. (10) and the curve of Figure 7b have been shifted to $t = 0$, in order to simplify the equation.

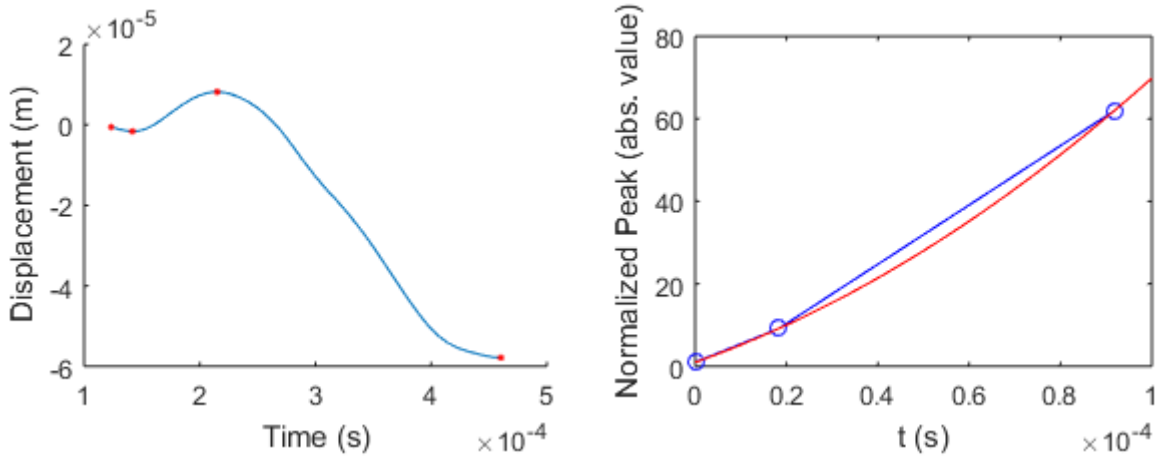

(a) (b)

Figure 7. Extraction of wave characteristics for estimation of impactor mass. (a) Identification of wave peaks. (b) Polynomial fitting of the normalized absolute peak amplitude.

If the impactor mass were known, the coefficient of the dominant term of Eq. (10) would be normalized using Eq. (8). On the other hand, training of the model has yielded Eq. (9). Then, the following objective function can be formulated:

$$F(\mu) = \left| A \cdot \frac{\mu \cdot m_s}{k_y} - \sum_{i=0}^{3} p_i \cdot \mu^i \right| \tag{11}$$

Solving for $F(\mu) = 0$ yields the values of μ that satisfy both Eq. (8) and (9); in a general case, minimization the objective function should be adequate. Then, impactor mass can be derived from Eq. (6). This is depicted in Figure 8, where μ has already been converted to impactor mass. Clearly, the prediction is excellent; predicted impactor mass: 86.6g, actual impactor mass: 85g.

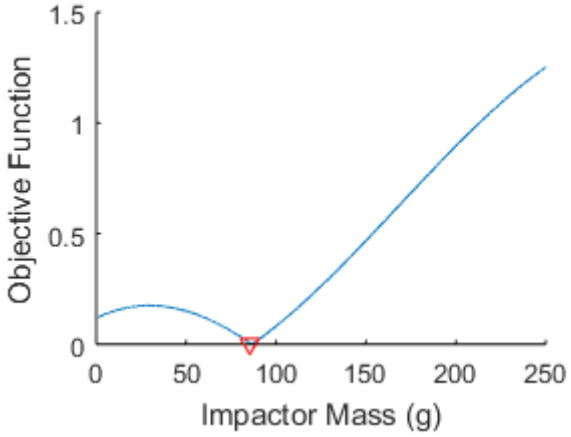

Figure 8. Roots of the objective function designate candidate values for the impactor mass. The marker shows the actual impactor mass, which practically coincides with the root of the objective function.

As in localization, a number of cases have been further analyzed to assess the quality of predictions. These cases are different than the ones considered in training, but within range.

Comparisons demonstrate excellent agreement between actual and predicted mass (Figure 9). In cases referring to the same mass, different impactor velocity has been considered.

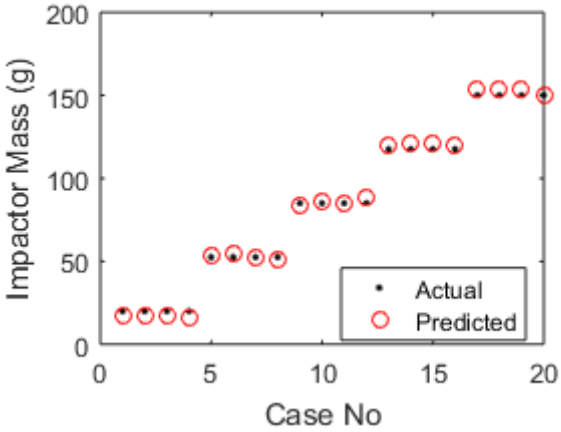

Figure 9. Excellent agreement between actual and predicted masses. Cases with same mass, consider different velocity.

Exact comparisons are listed in Table 4, where excellent agreement is observed. The sole exception is the mass range up to 20g. This deviation was actually expected since the fitting curve in Figure 6 fails to interpolate very small values. However, even if the percentage error is high for these cases, the actual deviation of up to 5g is quite reasonable.

Table 4. Excellent agreement between actual and predicted impactor mass.

Case No	Predicted mass (g)	Actual mass (g)	Error (%)	Case No	Predicted mass (g)	Actual mass (g)	Error (%)
1	16.89	20.00	15.55	11	84.48	85.00	0.61
2	17.14	20.00	14.31	12	88.67	85.00	4.31
3	16.69	20.00	16.55	13	120.00	117.50	2.12
4	16.64	20.00	16.80	14	120.44	117.50	2.51
5	53.30	52.50	1.52	15	120.89	117.50	2.89
6	54.35	52.50	3.52	16	120.20	117.50	2.29
7	52.01	52.50	0.94	17	153.52	150.00	2.35
8	51.21	52.50	2.46	18	153.82	150.00	2.54
9	84.13	85.00	1.02	19	153.67	150.00	2.45
10	86.57	85.00	1.85	20	149.93	150.00	0.05

3.3 Estimation of impactor velocity

For the estimation of impactor velocity, a similar approach is followed, employing a training and a prediction phase. Contrary to mass prediction that is based on the variation of amplitude, velocity predictions consider only the amplitude of the first arriving peak, but assumes that mass has already been predicted in the previous step.

3.3.1 Training for Impactor Velocity

Again, a series of impact cases need to be investigated in order to correlate impactor velocity with the first peak amplitude of the stress waves. The same training data as for mass training may be used, since various velocities have been considered. After the arriving wave peak (a) has been measured, it is normalized by multiplication with a quantity of units "$\frac{1}{length}$":

$$a = \frac{a}{v_{imp}} \cdot \sqrt{\frac{k_y}{m_{imp}}} = \frac{a}{v_{imp}} \cdot \sqrt{\frac{k_y}{\mu \cdot m_s}} \tag{12}$$

where v_{imp} is the impactor velocity. The normalized peak ($\tilde{a}$) exhibits an exponential decay with respect to dimensionless mass (Figure 10). For the demonstration case considered, the exact formulation is

$$a = 0.046 \cdot \mathrm{e}^{-4.53\mu} + 0.031 \cdot e^{-0.34\mu} \tag{13}$$

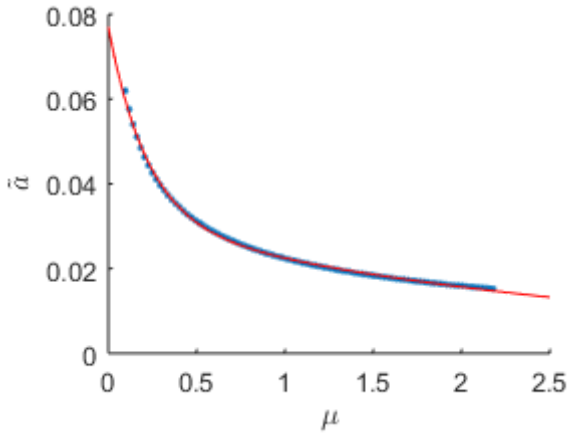

Figure 10. Exponential fitting of the normalized absolute arriving wave peak amplitude.

3.3.2 Estimation of Impactor Velocity

After training has been performed and Eq. (13) has been formulated, the model can be employed in actual impact cases. Impact waves are captured and the first wave peak is identified. Impactor mass has already been calculated. If impactor velocity were known, then the wave peak would be normalized using Eq. (12). However, training of the model has yielded Eq. (13). Then, then following objective function can be formulated:

$$G(\mu) = \left| \frac{a}{v_{imp}} \cdot \sqrt{\frac{k_y}{\mu \cdot m_s}} - \left(0.046 \cdot \mathrm{e}^{-4.53\mu} + 0.031 \cdot e^{-0.34\mu}\right) \right| \tag{14}$$

Since the dimensionless mass μ is already known from mass estimation, setting $G(\mu) = 0$ yields the impactor velocity. For the case under investigation, the predicted velocity 0.98m/s is

very close to the actual one (1m/s). A number of cases have been further analyzed to assess the quality of predictions. Again, the validation cases are different than the ones considered in training. Comparisons demonstrate excellent agreement between actual and predicted mass (Figure 11). In cases referring to the same velocity, different impactor mass has been considered.

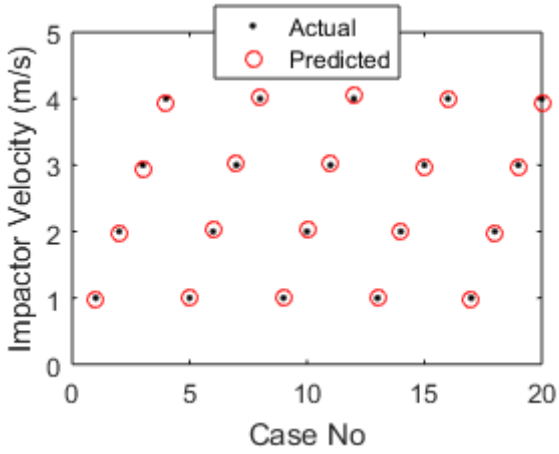

Figure 11. Excellent agreement between actual and predicted velocities. Cases with same velocity, consider different mass.

Exact comparisons are listed in Table 4, where excellent agreement is observed.

Table 5. Excellent agreement between actual and predicted impactor mass.

Case No	Predicted velocity (m/s)	Actual velocity (m/s)	Error (%)	Case No	Predicted velocity (m/s)	Actual velocity (m/s)	Error (%)
1	0.98	1.00	1.84	11	3.04	3.00	1.21
2	1.96	2.00	2.08	12	4.04	4.00	0.94
3	2.95	3.00	1.74	13	0.99	1.00	0.53
4	3.92	4.00	1.99	14	1.99	2.00	0.65
5	1.01	1.00	0.84	15	2.98	3.00	0.65
6	2.02	2.00	0.88	16	3.98	4.00	0.58
7	3.02	3.00	0.82	17	0.98	1.00	1.57
8	4.03	4.00	0.73	18	1.97	2.00	1.52
9	1.01	1.00	1.23	19	2.95	3.00	1.62
10	2.02	2.00	1.06	20	3.95	4.00	1.36

3.4 Force reconstruction

After the impact event has been characterized, an equivalent TDSFE model can be assembled and simulated in order to replicate the impact event and reconstruct impact force. Figure 12 shows comparisons for the impact force for two different events. The exact impact parameters are shown in the respective insets. One of the selected events has been well-predicted, and force reconstruction is perfect. The other one, has been poorly predicted (15.55%

error in mass prediction), yet, force reconstruction is again excellent.

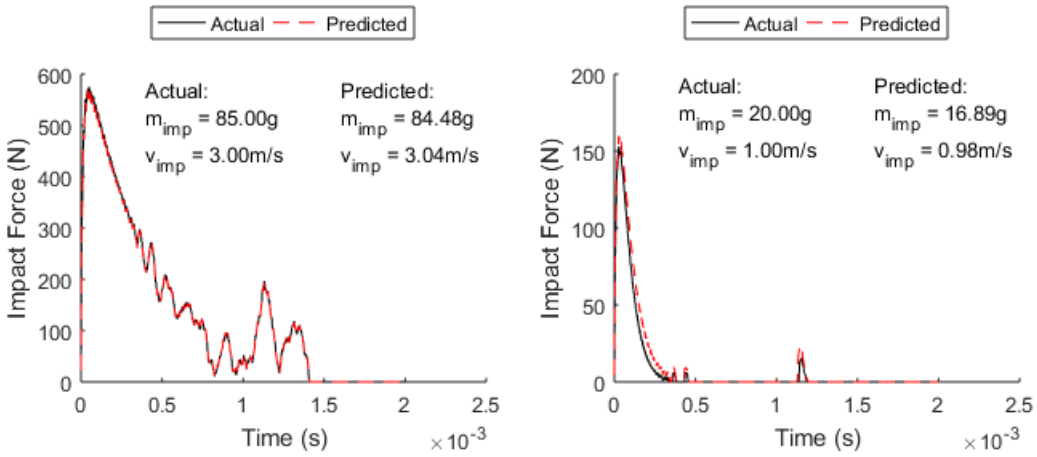

Figure 12. Comparisons between actual and reconstructed impact force. (a) Comparisons for a well-characterized case. (b) Comparisons for a poorly-characterized cases (15% error in mass prediction). In both cases, force reconstruction is perfect.

Finally, considered impact cases have been mapped to the Impact Characterization Diagram [10]. All of them lay at the local regime (Figure 13), following the assumptions for the selection of impactor mass and velocity range.

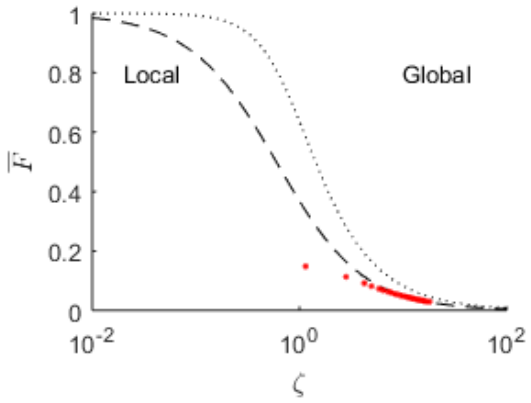

Figure 13. Mapping of impact cases to the Impact Characterization Diagram supports the assumption for local impact events.

4 CONCLUSIONS

A methodology for impact event characterization and impact force reconstruction has been presented. The frequency content, which determines the propagation velocity of the elastic waves, has been exploited into a geometrical compatibility algorithm, in order to identify the vicinity of impact. The variation of wave amplitude in time has been correlated to impactor mass and velocity. A series of training cases have been analysed to determine the various modeling parameters. The trained models have been applied to actual impact data, in order to perform both localization and impactor characterization. Subsequently, a TDSFE model has

been assembled to reconstruct the impact force time history. Comparisons between actual and predicted results demonstrate that impact force reconstruction is excellent.

5 REFERENCES

[1] H. Jeong and Y.-S. Jang, "Wavelet analysis of plate wave propagation in composite laminates," *Compos. Struct.*, vol. 49, no. 4, pp. 443–450, 2000.

[2] L. Gaul and S. Hurlebaus, "Determination of the impact force on a plate by piezoelectric film sensors," *Arch. Appl. Mech. (Ingenieur Arch.*, vol. 69, no. 9–10, pp. 691–701, 1999.

[3] P. Sedlak, Y. Hirose, M. Enoki, and J. Sikula, "Arrival Time Detection in Thin Multilayer Plates on the Basis of Akaike Information Criterion," *J. Acoust. Emiss.*, vol. 26, pp. 182–188, 2008.

[4] C. Chen, Y. Li, and F.-G. Yuan, "Development of Time-Reversal Method for Impact Source Identification on Plate Structures," *Shock Vib.*, vol. 20, no. 3, pp. 561–573, 2013.

[5] T. C. Theodosiou, C. S. Rekatsinas, and D. A. Saravanos, "An Explicit Time Domain Spectral Finite Element for Guided Wave SHM in Composite Plate Strips with Physically Modelled Active Piezoelectric Sensors," in *International Workshop on Structural Health Monitoring*, 2015.

[6] C. S. Rekatsinas, C. V. Nastos, T. C. Theodosiou, and D. A. Saravanos, "A time-domain high-order spectral finite element for the simulation of symmetric and anti-symmetric guided waves in laminated composite strips," *Wave Motion*, vol. 53, pp. 1–19, 2015.

[7] C. S. Rekatsinas and D. A. Saravanos, "A Time Domain Spectral Layerwise Finite Element for Wave SHM in Composite Strips with Physically Modelled Active Piezoelectric Actuators and Sensors," *J. Intell. Mater. Syst. Struct.*, 2016.

[8] A. Barouni and D. A. Saravanos, "A layerwise semi-analytical method for modeling guided wave propagation in laminated and sandwich composite strips with induced surface excitation," *Aerosp. Sci. Technol.*, vol. 51, pp. 118–141, 2016.

[9] A. S. Yigit and A. P. Christoforou, "On the impact of a spherical indenter and an elastic-plastic transversely isotropic half space," *Compos. Eng.*, vol. 4, no. 11, pp. 1143–1152, 1994.

[10] A. S. Yigit and A. P. Christoforou, "Limits of asymptotic solutions in low-velocity impact of composite plates," *Compos. Struct.*, vol. 81, no. 4, pp. 568–574, 2007.

[11] C. Rekatsinas and D. Saravanos, "A Hermite Spline Layerwise Time Domain Spectral Finite Element for Guided Wave Prediction in Laminated Composite and Sandwich Plates," *J. Vib. Acoust.*, 2017.

[12] M. A. Majeed, A. S. Yigit, and A. P. Christoforou, "Elastoplastic contact/impact of rigidly supported composites," *Compos. Part B Eng.*, vol. 43, no. 3, pp. 1244–1251, 2012.

[13] A. P. Christoforou and A. S. Yigit, "Characterization of impact in composite plates," *Compos. Struct.*, vol. 43, no. 1, pp. 15–24, 1998.

[14] A. P. Christoforou, A. S. Yigit, and M. Majeed, "Characterization and Scaling of Low Velocity Impact Response of Structures With Local Plastic Deformation: Implications for Design," in *Volume 6: 1st Biennial International Conference on Dynamics for Design; 14th International Conference on Advanced Vehicle Technologies*, 2012, p. 125.

Wind Turbine Fault Detection Through Singular Spectrum Analysis

Francesc Pozo*, Yolanda Vidal* and Leonardo Acho*

* Control, Dynamics and Applications (CoDAlab)
Escola d'Enginyeria de Barcelona Est (EEBE)
Universitat Politècnica de Catalunya (UPC)
Campus Diagonal-Besòs UPC, 08930 St. Adrià de Besòs, Barcelona, Spain
e-mail : francesc.pozo@upc.edu, yolanda.vidal@upc.edu, leonardo.acho@upc.edu,
web page : http://codalab.upc.edu

ABSTRACT

Nowadays, wind energy is one of the most important renewable sources. However, its future as a highly efficient and low cost energy passes through the use of larger and more flexible wind turbines (WT). Hence, requiring efficient *on-line* fault detection methods to increase their feasibility and reduce its operation and maintenance costs. In this sense, this work addresses the problem of online fault detection of a wind turbine, as given in [1], under pitch and torque actuators faults, as well as pitch angle measurements sensor faults.

Among the data-driven existent fault detection methods, there has been a great effort in the ones based on principal component analysis (PCA) [2]. For instance, with the combination of uni- and multi-variate hypothesis testing [3,4,5]. Usually, these methods use time-dependent measurements. In this work, we propose to use these measurements transformed into the frequency domain to determine whether the WT presents some faults or it is healthy. The proposed fault detection scheme starts by computing the baseline singular spectrum analysis (SSA) model from the healthy WT. Subsequently, when the WT is inspected or supervised, new measurements are obtained, transformed and projected into the baseline SSA model to diagnose the WT condition.

The effectiveness of the proposed method is evaluated by numerical simulation on a well-known wind turbine benchmark [6] in the presence of wind turbulence and on realistic faulty scenarios. According to the numerical results, our proposal demonstrates to be efficient in detecting on-line the status condition of the WT.

REFERENCES

[1] J. Jonkman, S. Butterfield, W. Musial and G. Scott, Definition of a 5-MW reference wind turbine for offshore system development. *National Renewable Energy Laboratory, Golden, CO, Technical Report No. NREL/TP-500-38060*, (2009).

[2] L.E. Mujica, A. Fernández, A. Güemes and J. Rodellar. Q-statistic and T2-statistic PCA based measures for damage assessment in structures, *Structural Health Monitoring,* Vol. 10(5), pp. 539-553, 2011.

[3] L. Mujica, M. Ruiz, F. Pozo, J. Rodellar, A. Güemes, "A structural damage detection indicator based on principal component analysis and statistical hypothesis testing", *Smart Materials and Structures*, Vol. 23, (2014).

[4] F. Pozo and Y. Vidal, "Wind turbine fault detection through principal component analysis and statistical hypothesis testing", *Energies*, Vol. **9**(3), (2016).

[5] F. Pozo, Y. Vidal and L. Acho, "Wind turbine fault detection through principal component analysis and multivariate statistical inference", 8th European Workshop on Structural Health Monitoring (EWSHM 2016), Bilbao (Spain), July 2016.

[6] P. F. Odgaard, and E. J. Kathryn, "Wind turbine fault detection and fault tolerant control - An enhanced benchmark challenge", American Control Conference, Washington (USA), 2013.

AUTHORS INDEX

Abed-Meraim, F. 188
Abisset-Chavanne, E. 1900
Acho, L. 290, 1926
Agís, R. 852
Aguirre de Cárcer, I. 1399
Ahlquist, S. 943
Ai, Q. 931
Al Hajjar, H. 1610
Alaluf, D. 1064
Alén, C. 839
Alexander, P. 943
Aliabadi, M.H. 1820, 1855
Alonso-Alarcón, J. F. 400
Aminbaghai, M. 1285
Anaya, M. 698
Anduaga, J. 1359
Anlas, G. 1490
Anoshkin, A. 571
Araujo, A. 1160
Araujo, A.L. 1042
Arbab Chirani, S. 1572
Arras, M. 957
Arrieta, A.F. 969
Atek, S. 538
Atienza, R. 1783
Aucejo, M. 1721
Avakian, A. 336
Baginski, P. 157
Bai, J. 893, 1183, 1202, 1284
Bai, X. X. 129, 892
Bakhtiari, R. 1560
Balduzzi, G. 1285
Banerjee, S. 618
Barbero, E. J. 327
Barcala-Montejano, M. A. 400, 413, 993
Bardera-Mora, R. 400, 413, 993
Bardong, J. 1433
Bareille, O. 1656
Barkanov, E. 490
Barlas, T. 267
Baxevanis, Th. 1465
Bedoui, F. 1202
Behrooz, M. 860
Belinha, J. 1160
Belloni, E. 1632, 1643
Belly, C. 77
Belmonte, M. 1702
Ben Zineb, T. 1561, 1581
Benjeddou, A. 1101, 1148, 1358, 1421
Bergamini, A. 1657, 1731
Bernasconi, A. 1184
Bielefeldt, B. 1524
Biglar, M. 302
Binder, A. 1433
Bishara, D. 1255
Bluhm, J. 1276
Boddu, V. 1340
Bouby, C. 1581
Bouraoui, T. 1572
Bowen, C.R. 630
Braghin, F. 1632, 1643
Brazey, B. 1590
Brei, D. 943
Brewick, P. 1265
Bruckner, G. 1421, 1433, 1444
Butaud, P. 77
Cabboi, A. 731
Cacho-Perez, M. 809
Caetano, E. 732
Cai, F. L. 892
Camacho, J. 1390
Camacho-Navarro, J. 1878
Carboni, B. 1265
Carlsson, R. 550
Carraro, P. A. 1813
Carreón-González, E. 852
Carrera, E. 176, 200, 207
Casagrande, D. 1689
Casciati, F. 1547
Casciati, S. 1547
Castaneda, N. 1511
Castillo Acero, M.A. 51
Castro, G. 577
Castro, M. 1192, 1224
Cazzulani, G. 1632, 1643
Cenedese, M. 1643
Chambers, J. 904
Chambon, H. 1421, 1444
Chandgadkar, S. 1610
Chen, H.P. 424
Chen, M. 1284
Chen, X. 594
Cheng, H. 905
Cherouat, A. 1581
Chevallier, G. 77
Chinesta, F. 1900
Choi, Y. 851, 871
Chong, K.P. 32
Cinefra, M. 207
Cisse, Ch. 1561
Collet, M. 1677
Constantin, N. 278
Contreras, P. 1598
Cordisco, G. 1388
Crespo-Moreno, J. 400
Cunha, A. 732
Dahmouche, R. 1590
Dal Bo, L. 686, 1689

Dauskardt, R. 1215
Daya, E.L. 188
De Angelis, M. 1388
De Keyser, R. 104
De Luca, J. 1224
de Nova-Trigueros, J. 413, 993
De Rossi, N. 1760, 1813
de Vicente, J. 852, 883
Dekemele, K. 104
Delpero, T. 1657
Deü, J.-F. 1721
Díaz, I. M. 764, 839, 850
Dilena, M. 754
Dore, E. 1610
Dorfmeister, M. 1307
Dozio, L. 1089
Drossel, W. 348
Drossel, W.-G. 359, 493
Du, X. 115
D'Ottavio, M. 1089
Elkhal Letaief, W. 1502
Elmquist, L. 550
Endres, F. 1340
Eremin, A. 1775
Ermanni, P. 969, 1731
Erturk, A. 1669
Erturk, C. 1669
Eugeni, M. 538
Eydam, A. 349
Eßlinger, S. 349
Fan, B. 1183, 1202
Fan, Y. 1656
Fang, D.N. 33
Faraj, R. 86, 138
Faravelli, L. 1547
Fathallah, A. 1502
Fedele Dell'Oste, M. 754
Feller, J. F. 1192, 1224
Fernandez, J. 809
Fernandez-Diaz-Maroto, P. 1854
Fernandez-Lopez, A. 1854
Ferreira, A. 1160
Fiborek, P. 1804
Flores Parra, E. 1731
Fontecchio, A. 1511
Foo, C.C. 480
Fraga, S. 577
Friswell, M. 1018
Friswell, M.I. 630
Fritzen, C.- P. 1866
Frost, M. 1491, 1548
Frouk Benallel, B. 537
Frovel, M. 1783, 1854
Fu, J. 115, 893
Füssl, J. 1285
Gallimard, L. 1597
Galván, U. 776
Gamaoun, F. 1502
García-Nieto, C. 66
García-Palacios, J. H. 764, 839, 850
García-Ramírez, J. 413, 993
Garcia-Teran, J.M. 809
Gardonio, P. 642, 686, 1689
Garijo, D. 1792
Gaudenzi, P. 538
Gauthier, M. 1590
Gebhardt, S. 349, 370
Geier, S. 619, 654, 1203
Gentile, C. 731, 796
Gerlach, G. 349
Ginsberg, D. 1866
Glushkov, E. 1775
Glushkova, N. 1775
Gonzalez-Requena, I. 1854
Gordaninejad, F. 860
Grabec, T. 1538
Graczykowski, C. 86
Graessler, I. 1622
Grandal, T. 577
Gromada, M. 302
Gschossmann, S. 1347
Gude, M. 349, 371
Guemes, A. 1854
Guignabert, A. 77
Güemes, A. 583, 1184
Güemes, J.A. 1750
Han, F. 1244
Han, T. H. 237
HannemaBa, G. 1657
Hartl, D. 971, 1524
Hartzell, Ch. 851
Hassine, T. 1502
He, D. 1183, 1202
He, Y. 1746
He, Y.J. 1478
Heller, L. 1491
Hemmatian, M. 906
Hensel, S. 359
Hentze, J. 1622
Himmler, D. 348
Hinc, K. 86
Hoffmeyer, D. 1030
Hohlfeld, K. 349
Holnicki-Szulc, J. 86, 138, 145, 166
Humer, A. 1295, 1316
Humer, C. 1843
Huxdorf, O. 255
Høgsberg, J. 1030, 1148, 1710
Iannucci, L. 1559
Ibrahimbegovic, A. 315
Ichchou, M. 1656
Ihnatowicz, E. 674
Inman, D. J. 984
Iturrospe, A. 1359

Iurlov, M. 1054, 1125
Iurlov, M.A. 1113
Iurlova, N. 1054, 1125
Iurlova, N.A. 1113
Iwasaki, A. 1766
Jabareen, M. 1255
Jankowski, Ł. 94, 138, 525
Janovská, M. 1538
Jara, J. 745, 776, 797
Jeong, W. M. 291
Jiménez-Alonso, Javier F. 831
Johansson, C. 550
Kaczmarczyk, T. Z. 674
Kaderavek, L. 1491
Kalinin, V. 1453
Kaltenbacher, M. 1307
Kamm, L. 1731
Karakalas, A. 1005
Karkar, S. 1677
Kennedy, J. 1511
Khajehsaeid, H. 536
Khodaparast, H. 1018
Khodaparast, H.H. 630
Kim, C. W. 785
Kim, W. 237, 247, 291
Kimme, S. 348
Knap, L. 86, 166
Kontogiannis, A. 1005
Kontsos, A. 1511
Koriath, H-J. 359
Kosheleva, N 571
Kosheleva, N.A. 606
Kovalov, A. 490
Kpeky, F. 188
Kralovec, C. 1843
Kras, A. 642
Krenk, S. 1148
Krommer, M. 1316, 1328
Kruisova, A. 1702
Kudela, P. 1804
Kuider, B. 537
Kukhareva, A.S. 1582
Kulikov, G. M. 176, 200, 231
Kumar, A. 821
Körner, C. 348, 370
Lacarbonara, W. 1265
Lachat, R. 594
Lagoudas, D. 1465
Lai, J. 893
Laine, J.-P. 1656
Lamarque, F. 1610
Lammering, R. 1775, 1831
Lan, X. 1744
Landa, M. 1538, 1702
Leal, P. 971
Lemartinel, A. 1224
Leng, J..... 1398, 1744, 1745, 1746, 1747, 1748, 1749
León-Calero, M. 413, 993
Li, G. 207
Li, L. 1656
Li, W. 916, 1183
Li, Y. 916
Liao, G. 619, 654, 893
Liao, Y 1172
Lin, J. 984
Lin, Y.-H. 267
Liu, Ch. 905
Liu, J. 480
Liu, L. 1744, 1748, 1749
Liu, M 1172
Liu, X. 1610
Liu, Y.... 1398, 1744, 1745, 1746, 1747, 1748, 1749
LLorens, M. 1378
Lobanov, D. 571
Loccufier, M. 104
Loffeld, O. 1866
Lopes, T. 1233
Lopez, E. 1900
López-Cardona, J.D. 1598
Lorenzana, A. 809
Lorsch, P. 255
Lossouarn, B. 1721
Lozano-Martin, A. 1854
Lu, Q. 1747
Lubieniecki, M. 674
Lubineau, G. 1244
Luna Vera, O. S. 785
Luntz, J. 943
Machairas, T. 1005
Madinei, H. 630
Madsen, H. 267
Magalhães, F. 732
Magdaleno, A. 809
Mahrholz, T. 619, 654, 1203
Majewska, K. 445, 561
Majrouhi Sardroud, J. 721
Malakooti, M. H. 984
Malinowski, P. 35, 1804
Malkova, Y.V. 1582
Mallardo, V. 1855
Mallik, N. 1890
Mamontov, A.A. 200
Mamontov, S.A. 200
Marconi, J. 1632
Marinas, G. 764
Marques, H. 424
Martínez, A, ... 1750
Martínez, G. 745, 776, 797
Martinez-Ayuso, G. 630
Maruccio, C. 1409
Maruccio, G. 1409
Masri, S. 1265
Matten, G. 77
Matveenko, V. 571, 1054, 1125

Matveenko, V.P. 606, 1113
Mechbal, N. 436
Mejía, L. 797
Melnik, R. 666
Meyer, Y. 594
Michaelis, A. 349, 370
Mieloszyk, M. 445, 561
Mikułowski, G. 94, 166
Mingear, J. 1524
Miranzo, P. 1702
Modler, N. 349, 383
Mohammed, N. 537
Mokrani, B. 1064
Moleiro, F. 1042
Molinari, G. 969
Monner, H.P. 917
Montero, D.S. 1598
Moosavian, A. 984
Morassi, A. 754
Moreno, B. 1378
Moreno-Beltrán, G. 1878
Moreno-Navarro, P. 219, 315
Morillas, J. 883
Mota Soares, C. 1160
Mota Soares, C.A. 1042
Mota Soares, C.M. 1042
Moutinho, C. 732
Mróz, A. 94, 145
Muchenik, T. I. 327
Mujica, L. 1390, 1878
Mulakkal, M. 511
Mutlu, F. 1490
Müller, B. 359
Mäder, T. 493
Nasedkin, A. 1137
Nestler, M. 493
Neumeister, P. 349
Nicolay, P. 1421, 1433, 1444
Nisi Gaterol, G. 538
Nitzsche, F. 957
Niu, X. 424
Nothdurfter, S.K. 1760
Olmos, B. 745, 776, 797
Onat, C. 453
Oshima, Y. 785
Oshmarin, D. 1054, 1113, 1125, 1821
Ostachowicz, W. 35, 445, 561, 1804
Ouisse, M. 594
Ozerim, G. 1490
Palacios-Quiñonero, F. 709
Palanisamy, R. P. 291
Pallav, K. 821
Palma, R. 219
Panozzo, F. 1760, 1813
Park, J.S. 247
Pavon, S. 1378
Pechstein, A. 1295
Pekcan, G. 860
Peng, Y. 115
Perales, J.M. 1750
Pereira, E. 764, 839, 850
Perera, R. 1369
Pérez-Aparicio, J.L. 219, 315
Peter, S. 359
Peyret, N. 77
Pierer, A. 359
Pietrosanti, D. 1388
Pintado, J.M. 1854
Pinzón, P.J. 1598
Plotnikova, S.V. 200
Pohle, C. 348
Polit, O. 1089, 1609
Ponton, A. 1233
Popławski, B. 94, 138
Pozo, F. 698, 1926
Preumont, A. 1064
Printz, A. 1215
Prolongo, M.G. 1399
Prolongo, S.G. 1215, 1399
Putz, M. 359
Qian, L. J. 129
Quaranta, G. 1409, 1900
Quaresimin, M. 1760, 1813
Quiroga, J. 1390
Radestock, M. 255
Ramirez, J.L. 1597, 1609
Ramírez, V. 1792
Rams, J. 66
Rauter, N. 1831
Rebillat, M. 436
Reddy, J.N. 1042
Rekatsinas, C. S. 1912
Ren, X. 502
Rhein, S. 370
Ricoeur, A. 314, 328, 336
Riemenschneider, J. 255, 490
Riquer, R. 77
Riva, E. 1632
Riziotis, V. 1005
Rizzato, S. 1409
Robinson, P. 1559
Rodellar, J. 290, 709
Rodriguez-Lence, F. 583
Rodríguez-Sevillano, A. A. 400, 413, 993
Roemer, J. 674
Rokbani, M. 1572
Rolston, N. 1215
Roman-Manso, B. 1702
Romero-García, A. 400
Roscow, J.I. 630
Rossell, J.M. 709
Roy, S. 618
Rubiano, A. 1609
Rubiano Fonseca, A. 1597

Rubió-Massegú, J. 709
Ruccolo, A. 796
Ruiz, A. 1369
Ruiz, M. 1390, 1878
Rullo, A. 1760
Runkel, F. 969
Rupitsch, S. 383
Ruzzene, M. 34, 1669
Saenz-Castillo, D. 583
Sáez, Andrés 831
Sahin, M. 453
Saint-Sulpice, L. 1572
Saisi, A. 731
Salgado, O. 1359
Salom, C. 1399
Sánchez, M. 66, 1184
Sánchez-Romate, X.F. 66, 1184
Saravanos, D. 1005
Saravanos, D. A. 1912
Sbarufatti, C. 1184
Scaccabarozzi, D. 1184
Schagerl, M. 1347, 1843
Schlosser, A. 314
Schmid, U. 1307
Schmidt, M. 359, 370, 371
Schneider, M. 1307
Schoenwald, S. 1657
Schröder, J. 1276
Schubert, A. 359
Schwankl, M. 348
Schönecker, A. 349
Schönherr, J. 493
Scigliuzzo, M. 1409
Seńko, J. 86
Sedaghati, R. 872, 906
Seddon, A. 511
Sedlák, P. 1491, 1538, 1548, 1702
Sedmák, P. 1548
Seiner, H. 1538, 1702
Sekuła, K. 145
Senis, R. 1378
Seon, J.A. 1590
Serovaev, G. 1821
Ševčík, M. 1538
Sevillano, E. 1369
Sevodina, N. 1054, 1125
Sevodina, N.V. 1113
Shahrivar, K. 852
Shamieh, H. 872
Shardakov, I 571
Shardakov, I.N. 606
Shariat, B.S. 1560
Sharif Khodaei, Z. 1820, 1855
Shaw, A. 1018
Shaw, A.D. 630
Shen, J. 502
Shen, S. 892
Sherman, S. 904
Shestakov, A. 1821
Shipunov, G. 571
Shportenko, D. 400
Shu, H. 905
Sim, S.-H. 291
Sinapius, M. 1203
Singh, S. 1890
Šittner, P. 1491, 1548
Sodano, H. A. 984
Soleymani, R. 536
Solomou, A. 1005
Soria, J. M. 764, 850
Sorohan, S. 278
Spaskova, E 571
Specht, S. 1276
Stachowicz, F. 302
Staudigl, E. 1316, 1328
Stein, S. 370, 371
Steinmann, P. 1340
Stoklasová, P. 1538
Stroud, H. 971
Su, Z 1172
Suchaneck, G. 349
Suwała, G. 138, 166
Szklarski, J. 525
Tamura, M. 464
Tapetado, A. 1598
Tedesco, A. 1233
Telford, R. 929
Terroba, F. 1783, 1854
Theodosiou, T. C. 1912
Thumrongvut, J. 471
Tian, H. 502
Tibaduiza, Diego A. 698
Toftekær, J. 1148
Torre, M.A. 1854
Torres, L. 1369
Toth, F. 1307
Trask, R. 511
Trindade, M.A. 1077, 1101
Tronci, E.M. 1388
Trzepieciński, T. 302
Tutivén, C. 290
Ugalde, U. 1359
Ureña, A. 66, 1184
Valvano, S. 176
Van Damme, B. 1657
Vasista, S. 917
Vázquez, C. 1598
Vazquez, E. 577
Vazquez, J. A. 577
Vega, J.M. 1750
Velasquez, J.Q. 1077
Venegas Bayona, S. 1610
Vescovini, R. 1089
Vetyukov, Yu. 1328

Vidal, Y. 290, 1926
Villamizar, R. 1390, 1878
Vitola, J. 698
Volkov, A.E. 1582
Volkova, N.A. 1582
Voronkov, A 571
Voronkov, A.A. 606
Vu Ngoc, N. 1831
Wan A Hamid, W.L.H. 1559
Wandowski, T. 35, 1804
Wang, C. 1018
Wang, D. 666
Wang, K. 1064
Wang, L. 666
Wang, M. 905
Wang, X. 850
Watson, B. 1215
Weaver, P. 931
Weaver, P.M. 929
Weber, T. 349, 371
Wedler, J. 370
Wen, M. 904
Wereley, N. 851, 871, 904
Wereley, N.M. 50, 905
Wiedemann, M. 619, 654
Wierach, P. 490, 619, 654, 1203
Wingen, M. 328
Winkler, A. 349, 371, 383
Wittstock, V. 359
Wu, SJ. 412
Wüst, M. 383
Xidong, W. 839
Xie, X.. 412
Xie, Y.M. 502
Xin, Y. 1244
Xu, H 1172
Xu, L. 1465
Xu, S. X. 129
Xu, X. 115, 1244
Yaman, Y. 453
Yang, S. 892
Yarra, S. 860
Yi, J.-H. 237, 247, 291
Yi, K. 1677
Yim, S. 237
Yu, H. 1244
Yu, M. 115, 893, 904
Zaki, W. 1561
Zappalorto, M. 1760, 1813
Zappino, E. 207
Zawidzki, M. 525
Zbinden, P. 1731
Zemp, A. 1657
Zhang, Q. 1398
Zhang, S 1478
Zhang, S.Q. 1284
Zhang, S.Y. 1284
Zhang, Y. 630
Zhang, Z.Q. 480
Zhou, J. 1244
Zhou, L.M. 1172
Zhu, S. 1581
Zhuang, L. 943
Zídek, J. 1538
Zornoza, A. 577
Zoubková, K. 1538
Zuaoui, S. 537
Zuiko, V. 571
Żywica, G. 157, 674


ECCOMAS


CTR
CARINTHIAN TECH RESEARCH

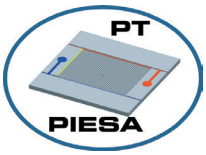
PT
PIESA


supméca


utc Recherche
Roberval
SORBONNE UNIVERSITES


FIDAMC


cnrs


CIMNE
International Center
for Numerical Methods in Engineering